

AD A106987

LEVEL

①

DTIC
ELECTE
OCT 29 1981
E

DTIC FILE COPY

This document has been approved
for public release and sale; its
distribution is unlimited.

UNCLASSIFIED

SECURITY CLASSIFICATION OF THIS PAGE (When Data Entered)

(10) Tokyo / Inui

REPORT DOCUMENTATION PAGE		READ INSTRUCTIONS BEFORE COMPLETING FORM
1. REPORT NUMBER	2. GOVT ACCESSION NO.	3. RECIPIENT'S CATALOG NUMBER
	AD-A106987	
4. TITLE (and Subtitle)		5. TYPE OF REPORT & PERIOD COVERED
(6) Proceedings of the Thirteenth Symposium on Naval Hydrodynamics (October 6-10, 1980) Held at Tokyo (Japan)		Proceedings
7. AUTHOR(s)	8. CONTRACT OR GRANT NUMBER(s)	6. PERFORMING ORG. REPORT NUMBER
or 2-106-614 1980 Takao Inui, editor		
9. PERFORMING ORGANIZATION NAME AND ADDRESS		10. PROGRAM ELEMENT, PROJECT, TASK AREA & WORK UNIT NUMBERS
The Shipbuilding Research Association of Japan, Tokyo The Senpakv - Shinko Building 1-15-16 Toranomon, Minato-Kv Tokyo 105, Japan		
11. CONTROLLING OFFICE NAME AND ADDRESS		12. REPORT DATE
Office of Naval Research Code 432 Arlington, Virginia 22217		1981
14. AND		13. NUMBER OF PAGES
Naval Studies Board National Academy of Sciences - National Research Council Washington, D.C. 20418		905
		15. SECURITY CLASS. (of this report)
		unclassified
		15a. DECLASSIFICATION/DOWNGRADING SCHEDULE
16. DISTRIBUTION STATEMENT (of this Report)		
Approved for Public Release; Distribution Unlimited		
17. DISTRIBUTION STATEMENT (of the abstract entered in Block 20, if different from Report)		
(12) 882		
18. SUPPLEMENTARY NOTES		
19. KEY WORDS (Continue on reverse side if necessary and identify by block number)		
hull form wave energy design practice viscous flow oscillation hydrodynamics propulsion boundary layer cavitation hydrofoils		
20. ABSTRACT (Continue on reverse side if necessary and identify by block number)		
The technical program for the Symposium was constructed around one core theme of "the impact of hydrodynamics theory upon design practice with emphasis on high performance and/or energy saving ships," and consisted of three sessions on Hull Form, two on Viscous Flow and one each on Propulsion, Cavitation and Wave Energy. The authors of the forty-five papers which were presented were drawn from the international community of ship hydrodynamics research scientists with fourteen nationalities represented on the technical program.		

81 10 23

EDITION OF NOV 65 IS OBSOLETE
S/N 0101-1 F50-4-6601

UNCLASSIFIED

412 627

SECURITY CLASSIFICATION OF THIS PAGE (When Data Entered)

THIRTEENTH SYMPOSIUM ON NAVAL HYDRODYNAMICS

Impact of hydrodynamics theory upon design practice, with
emphasis on high performance and/or energy saving ships

OCTOBER 6-10, 1980

SASAKAWA HALL, TOKYO

PROCEEDINGS

Edited by
Takao Inui

Sponsored jointly by
The Office of Naval Research
The Naval Studies Board of
the National Academy of Sciences
— National Research Council
Washington, D.C.
The Shipbuilding Research Association of Japan
Tokyo

Accession For	
NTIS GRA&I	<input checked="checked" type="checkbox"/>
DTIC TAB	<input type="checkbox"/>
Unannounced	<input type="checkbox"/>
Justification	
By	
Distribution/	
Availability Codes	
Dist	Avail and/or Special
A	

Published by

THE SHIPBUILDING RESEARCH ASSOCIATION OF JAPAN
1981

Support for the publication of the Proceedings was jointly provided by the Office of Naval Research of the U.S. Department of the Navy and by the National Academy of Sciences. The content does not necessarily reflect the position or the policy of the Navy, the U.S. Government, or the National Academy of Sciences and no endorsement should be inferred.

Partial financial support for the preparations for the Symposium was provided by the Japan Shipbuilding Industry Foundation.

We express here our sincerest gratitude to them.

The Proceedings are available from:

The Shipbuilding Research Association of Japan
Address: The Senpaku-Shinko Bldg.
1-15-16 Toranomon, Minato-ku
Tokyo 105, Japan

Tel: (03) 502-2059

PROGRAM COMMITTEE

Emeritus Prof. Takao Inui (Chairman)	The University of Tokyo
Prof. George F. Carrier	Harvard University
Mr. Ralph D. Cooper	Office of Naval Research
Mr. Lee M. Hunt	National Academy of Sciences
Dr. Yasufumi Yamanouchi	Mitsui Engineering & Shipbuilding Co., Ltd.
Dr. Koichi Yokoo	Shipbuilding Research Centre of Japan

JAPAN ORGANIZING COMMITTEE

Mr. Shigeichi Koga (Chairman)	President, the Shipbuilding Research Association of Japan
Mr. Muneharu Saeki	Director-General, the Ship Research Institute
Mr. Eiichi Tasaka	Director-General, the Japan Shipbuilding Industry Foundation
Prof. Seizo Motora	Vice-President, the Society of Naval Architects of Japan
Dr. Yoshio Akita	Vice-President, Nippon Kaiji Kyokai
Mr. Takashi Nakaso	Executive Manager, the Shipbuilders' Association of Japan
Mr. Ryo Sanada	Executive Director, the Japanese Ship Owners' Association
Dr. Koichi Yokoo	Executive Director, the Shipbuilding Research Centre of Japan
Mr. Toshimasa Mitsui	Executive Vice-President, Mitsubishi Heavy Industries, Ltd.
Mr. Kotaro Nemoto	Managing Director, Ishikawajima-Harima Heavy Industries Co., Ltd.
Dr. Kazuo Hamano	Executive Senior Managing Director, Mitsui Engineering & Shipbuilding Co., Ltd.
Mr. Toshikazu Yuguchi	Vice-President, Hitachi Shipbuilding & Engineering Co., Ltd.
Mr. Akira Takeuchi	Senior Director, Nippon Kokan K.K.
Mr. Kenzo Nihei	Executive Vice-President, Kawasaki Heavy Industries, Ltd.
Dr. Yoshitomo Ohkawa	Executive Managing Director & General Manager, Sumitomo Heavy Industries, Ltd.
Emeritus Prof. Takao Inui	Chairman of Program Committee
Dr. Noritaka Ando	Managing Director, the Shipbuilding Research Association of Japan

Preface

The Office of Naval Research, the National Academy of Sciences and the Shipbuilding Research Association of Japan jointly sponsored the Thirteenth Symposium on Naval Hydrodynamics which was held in Tokyo, Japan during the period 6-10 October 1980. The Symposium was the culmination of several years of intense and careful preparation and organization, and its success from the technical and scientific point of view as well as from the cultural and social point of view is a reflection of these factors.

The technical program for the Symposium was constructed around the core theme of "the impact of hydrodynamics theory upon design practice with emphasis on high performance and/or energy saving ships," and consisted of three sessions on Hull Form, two on Viscous Flow and one each on Propulsion, Cavitation and Wave Energy. The authors of the forty-five papers which were presented were drawn from the international community of ship hydrodynamics research scientists with fourteen nationalities represented on the technical program.

As always in the case of a symposium of such magnitude, many people contributed in many ways to the success of the Thirteenth Symposium on Naval Hydrodynamics. First and foremost among these, however, is Professor Takao Inui of the University of Tokyo who served as chairman of the Program Committee and was the focal point in Japan for all activities involved in the organization and management of the Symposium. He was ably assisted by Dr. Yasufumi Yamanouchi of the Mitsui Engineering and Shipbuilding Co., Ltd. and Dr. Koichi Yokoo of the Shipbuilding Research Centre of Japan, who served on the Program Committee, and by Professor Seizo Motora of the University of Tokyo and members of the Working Group of the Symposium, who assisted in the planning and execution of the many details associated with the technical program. Many thanks are also due to Mr. Shigeichi Koga, President of the Shipbuilding Research Association of Japan, for the invaluable assistance and support rendered by his organization and for his gracious words of welcome during the opening ceremonies of the Symposium. A similar expression of appreciation is extended to Dr. Saunders Mac Lane, Vice-President of the National Academy of Sciences, and Dr. Rudolph J. Marcus, Scientific Director of the Office of Naval Research Scientific Liaison Group in Tokyo, who also gave introductory addresses in behalf of their respective organizations during the opening ceremonies. The National Academy of Sciences was further represented by Mr. Lee M. Hunt, Executive Director of the Academy's Naval Studies Board, and by Professor George F. Carrier of Harvard University and the Naval Studies Board, who participated on the Program Committee and provided valuable counsel and assistance throughout the entire planning period for the Symposium.

Ralph D. Cooper
Program Director
Fluid Dynamics Program
Office of Naval Research

CONTENTS

PROGRAM COMMITTEE	iii
JAPAN ORGANIZING COMMITTEE	iii
PREFACE	v
INTRODUCTORY ADDRESSES	
Address by Mr. Shigeichi Koga	1
Address by Dr. Saunders Mac Lane	2
Address by Dr. Rudolph J. Marcus	3
SPEECHES AT BUFFET PARTY	
Opening Speech	
by Emeritus Prof. Takao Inui	5
Congratulatory Speeches	
by Mr. Marshall P. Tulin	6
by General Max Aucher	7
Kagami-Biraki Ceremony	
by Prof. John V. Wehausen	7
Information about the 14th Symposium	
by Prof. T. Francis Ogilvie	8
Closing Speech	
by Prof. Seizo Motora	8

Session I: Propulsion

On Application of the Lifting Surface Theory to Marine Propellers Koichi Koyama	13
Prediction of the Transient Cavitation on Marine Propellers by Numerical Lifting-Surface Theory Chang-Sup Lee	41
Practical Applications of the Discrete Vortex Element Method for Calculation of Propeller Induced Excitation Forces Hajime Yuasa, Norio Ishii, Bror Persson, Oddvar Frydenlund and Kjell Holden	65
Prediction of Propeller-Induced Fluctuating Pressures and Correlation with Full-Scale Data Noritane Chiba, Takao Sasajima and Tetsuji Hoshino	89

Session II: Cavitation

New Applications of Cavity Flow Theory Marshall P. Tulin and Chun Che Hsu	107
Off-Design Performance Prediction Method for Supercavitating Propellers Okitsugu Furuya	133
Cavitation on High Speed Propellers in Oblique Flow — Influence of Propeller Design and Interaction with Ship Hull Olle Rutgersson	159
Recent Research Results on Cavity Flows about Hydrofoils Alain R. Rowe and Jean-Louis Kueny	181
Boundary Layer and Cavitation Studies of NACA 16-012 and NACA 4412 Hydrofoils Jan H.J. van der Meulen	195
The Influence of Hydrofoil Oscillation on Boundary Layer Transition and Cavitation Noise Young T. Shen and Frank B. Peterson	221

Session III: Hull Form 1 Wave Making Problems

Mathematical Notes on the Two-Dimensional Kelvin-Neumann Problem Fritz Ursell	245
Numerical Solution of Transient and Steady Free-Surface Flows about a Ship of General Hull Shape Robert K.-C. Chan and Frank W.-K. Chan	257
On the Time Dependent Potential and Its Application to Wave Problems Hiroyuki Adachi and Shigeo Ohmatsu	281
Second-Order Theory of Oscillating Cylinders in a Regular Steep Wave Apostolos Papanikolaou and Horst Nowacki	303
Characteristics of Nonlinear Waves in the Near-Field of Ships and Their Effects on Resistance Hideaki Miyata	335
Flow Past Oscillating Bodies at Resonant Frequency Gedeon Dagan and Touvia Miloh	355

Session IV: Hull Form 2 Problems in Waves

The Unified Theory of Ship Motions J. Nicholas Newman and Paul Sclavounos	373
Diffraction Problems of a Slender Ship with a Blunt Bow Advancing in Head Seas Shoichi Nakamura, Matao Takagi and Ryusuke Hosoda	399
Added Resistance in Waves in the Light of Unsteady Wave Pattern Analysis Makoto Ohkusu	413
Rolling and Steering Performance of High Speed Ships — Simulation Studies of Yaw-Roll-Rudder Coupled Instability Haruzo Eda	427

Session V: Hull Form 3 Problems in Design

Vertical Impact of a Disk on Compressible Fluid Surface Chiu-Si Chen	443
Seakeeping and Resistance Trade-Offs in Frigate Hull Form Design R.T. Schmitke and D.C. Murdey	455
Optimizing the Seakeeping Performance of Destroyer-Type Hulls Nathan K. Bales	479
Prediction of Resistance and Propulsion of a Ship in a Seaway Odd M. Faltinsen, Knut Minsaas, Nicolas Liapis and Svein O. Skjærdal	505
The Seakeeping Characteristics of a Small Waterplane Area, Twin-Hull (SWATH) Ship James A. Fein, Margaret D. Ochi and Kathryn K. McCreight	531
Hull Form Design of the Semi-Submerged Catamaran Vessel Yuzo Kusaka, Hiroshi Nakamura and Yoshikuni Kunitake	555
Theoretical and Experimental Investigations of Non-Equilibrium Jet of Air Cushion Vehicles Tao Ma, Wei-Lin Zhou and Xiong Gu	569

Session VI: Viscous Flow 1 Boundary Layer

Calculation of Viscous-Inviscid Interaction in the Flow Past a Ship Afterbody Martin Hoekstra and Hoyte C. Raven	585
Calculation of Thick Boundary Layer and Wake of Ships by a Partially Parabolic Method Kenji Muraoka	601
Influence of Wall Curvature on Boundary Layer Development on Ship Hulls Jürgen Kux	617
Prediction of Viscous Flow around a Fully Submerged Appended Body Nicholas-Christos G. Markatos and Colin Brian Willis	631

Effective Wake: Theory and Experiment Thomas T. Huang and Nancy C. Groves	651
Experiments on the Reduction of Bilge Vortex Formation by Discharging Air into Boundary Layer Valter Kostilainen	675

Session VII: Viscous Flow 2 Interactions and Scale Effect

Viscous Effect on Waves of Thin Ship Takeshi Kinoshita	693
Numerical Viscous and Wave Resistance Calculations Including Interaction Lars Larsson and Ming-Shun Chang	707
Calculation of Near Wake Flow and Resistance of Elliptic-Waterplane Ships Kazuhiro Mori	729
GEMAK—A Method for Calculating the Flow around Aft-End of Ships A. Yücel Odabasi and Öner Saylan	747
An Investigation of Certain Scale Effects in Maneuvering Tests with Ship Models Peter Oltmann, Som D. Sharma and Karsten Wolff	779
On the Nature of Scale Effect in Manoeuvring Tests with Full-Bodied Ship Models Evgeny Nikolaev and Marina Lebedeva	803

Session VIII: Wave Energy

Wave Power, The Primary Interface Brian M. Count and Edward R. Jefferys	817
Extraction of Energy from Wind and Ocean Current Theodore Y. Wu	829
Characteristics of New Wave-Energy Conversion Devices Masatoshi Bessho, Osamu Yamamoto, Norihisa Korian and Mikio Uematsu	841

Theoretical and Experimental Study on Wave Power Absorption Hisaaki Maeda, Hirohisa Tanaka and Takeshi Kinoshita	857
Rafts for Absorbing Wave Power Pierre Haren and Chiang C. Mei	877
The Sea Trials and Discussions on the Wave Power Generator Ship "KAIMEI" Yoshio Masuda, Gentaro Kai, Takeaki Miyazaki and Yoshiyuki Inoue	887
LIST OF PARTICIPANTS	899
PREVIOUS BOOKS IN THE NAVAL HYDRODYNAMICS SERIES	905

Introductory Addresses

Address by Mr. Shigeichi Koga

President of the Shipbuilding Research Association of Japan

Ladies and Gentlemen,

It is a great pleasure for me, on behalf of the Shipbuilding Research Association of Japan, to express my cordial welcome to all the participants at the Thirteenth Symposium on Naval Hydrodynamics.

Taking this opportunity, I would like to express my sincere appreciation to the co-sponsors, the Office of Naval Research and the National Academy of Sciences, for providing us with great assistance. Without their kind co-operation, we could not have organized the meeting here today. I would also like to thank the Program Committee for their utmost efforts toward the realization of this Symposium in 1980. It was the Committee that decided to hold the Thirteenth Symposium in Tokyo this fall.

We will never forget many others for their kind support to the symposium. I have to express my warm appreciation to the Japan Organizing Committee, its Working Groups, the Shipbuilders' Association of Japan, Japan Shipbuilding Industry Foundation, and Dr. Noritake Ando, and other staff members for their contributions.

Since the first meeting in Washington, D.C. in 1956, the symposium has been held continuously every other year. After the third meeting held in Scheveningen, the Netherlands in 1960, it has become customary that the even-numbered symposiums would be held in the United States and the odd-numbered ones be held outside the United States. Our Scheveningen symposium was followed by ones held in Bergen, Rome, Paris, and London.

This is the symposium held in Asia for the first time.

The core theme at each symposium has always reflected the most important issues in the field of naval hydrodynamics at the respective time. At the first symposium to be held in the 1980s, we have selected the subjects on the High Performance Ships and the Energy Saving Ships as the core theme because they have the greatest concerns since the outbreak of the world oil crisis. Forty-five reports will be presented in the symposium by famous authorities from fourteen different countries on the theme of the "Impact of Hydrodynamic Theory upon Design Practice with Emphasis on High Performance and/or Energy Saving Ships." I am confident that the symposium will no doubt achieve excellent results through your active discussions.

To our happy surprise, more than three hundreds have participated today, while at first we expected only more or less two hundreds.

Participants are from twenty-one countries, that is, Brasil, Bulgaria, Canada, China, Denmark, Egypt, Finland, France, Federal Republic of Germany, Israel, Italy, Korea, the Netherlands, Norway, the Soviet Union, Spain, Sweden, the United Kingdom, the United States, Yugoslavia and Japan.

We are especially delighted to welcome so many beautiful ladies here in Tokyo from abroad. October is one of the most beautiful months in Tokyo and I hope the climate will be very comfortable to you. I wish all of you will enjoy the autumn of

Japan.

In closing my speech, I sincerely wish that the symposium will be very successful, and that all of

you will bring our most important ship, "Friendship", to your home.

Thank you.

Address by Dr. Saunders Mac Lane

Vice-President of the National Academy of Sciences

It is my particular pleasure and privilege to welcome you to this symposium on behalf of one of the sponsors, the National Academy of Sciences of the United States of America.

The National Academy in my country covers a great variety of science, running from the social sciences through the medical sciences, the biological sciences, physical sciences and mathematics, to engineering. Moreover, the National Academy of Sciences maintains and guides our National Research Council. This Council carries out studies on many varieties of science as they are applied to or needed for problems of national and international interest.

It so happens that this National Research Council has had a long and effective connection with the Symposium on Naval Hydrodynamics. I believe that the first symposium of this series was held in 1956. One of the sponsors at that time was a committee of the National Research Council, namely, the then-active Committee on Undersea Warfare. Therefore, right at the beginning, the National Academy was involved in this symposium. This was also the case in the second symposium in 1958, when the same NRC committee was engaged in planning for the second symposium.

There was then, as far as I can discover, a considerable hiatus. The biannual symposia continued, but the National Research Council, for one reason or another, was not directly connected, although our Office of Naval Research was active in

organizing these symposia. Happily, at the time of the Twelfth Symposium in 1978, the National Research Council again appeared as one of the sponsors, this time in terms of a new committee, the Naval Studies Board of our National Research Council. That particular symposium, as I know directly, was an exceedingly successful one. Many of us, George Carrier, I, and others profited from our participation. Now I am pleased that the same Naval Studies Board of the National Research Council is active in sponsoring this Thirteenth Symposium.

So far, I have spoken to the continuity and tradition of this symposium.

Happily, there are also new and exciting additions to the content of the symposium. First, it is held in Japan. This we can especially welcome, because this ensures an active participation by our many scientific colleagues from Japan, with their wide-ranging and penetrating knowledge. It is right and proper that Japanese scientists should be interested in matters of naval hydrodynamics. Clearly an island country such as Japan must be vitally interested in connections with the sea, and indeed Japan has long been so interested. We are especially pleased, therefore, that this symposium is held here, in the lively city of Tokyo, with the sponsorship of the Shipbuilding Research Association of Japan.

This time, also, the international composition of this symposium is especially impressive, as

indeed it should be, because of the wide international interest in the problems with which we are dealing. At this Thirteenth Symposium there are, according to my count, papers presented by scientists from fourteen different nations. These nations are: Brasil, Bulgaria, Canada, China, Denmark, Egypt, Finland, France, Federal Republic of Germany, Israel, Italy, Japan, Korea, The Netherlands, Norway, Spain, Sweden, the United Kingdom, the United States of America, the Union of Soviet Socialist Republics and Yugoslavia. We are especially happy that this symposium is able to include such a wide range of international experts and interests, because we do know that scientific questions such as those that we meet in naval hydrodynamics are questions which have profited directly from the international exchange of ideas and the stimulation of contacts across national boundaries. The United States is pleased to be a part in this activity.

The special topics of this symposium are also particularly welcome. It deals both with high-performance ships and with the very timely consideration of ships that so can be propelled as to save energy. For my own part, I am especially interested in this, being from a long time ago a sailor, and I think with pleasure of the great privilege of sailing where the only propulsion is that of the wind. I realize that this symposium will hardly get down to the consideration of wind-propelled vessels, but I submit that for such vessels we have the longest tradition of connection with

hydrodynamics and also with aerodynamics, during the many centuries over which Man has gone adventuring out to sea, propelled only by sails driven by the wind, either on old-type vessels or on the most modern Catamarans or 12-meters as raced in the races today.

Finally, this symposium has the great attraction of dealing with a number of fundamental subjects about naval hydrodynamics. You can easily imagine that this is of particular interest to a person of my own background, since I have worked myself in mathematics and I am especially proud of the way basic mathematical ideas have come from, and have been fed into, the topics which we deal with here in this symposium, topics such as cavitation, wave-making, boundary layer problems, and wave energy questions. Not only because of the international and other interests, but also because of the highly fascinating technical problems, I will be interested, as all of us will be, in the ideas to be developed in this symposium.

On these traditional grounds, a long-continuing symposium, and on these specially new grounds, the particular features to be examined in the present symposium, I am happy to be able to act here as Vice-President of the National Academy of Sciences, one of the sponsors of this symposium, in welcoming you to participation in the five exciting days that we have before us.

Thank you.

Address by Dr. Rudolph J. Marcus
*Scientific Director of the Office of Naval
Research Scientific Liaison Group in Tokyo*

It is a pleasure for me to bring you the good wishes of the Office of Naval Research and of the American Embassy for a productive meeting.

I know that I speak for Dr. Jerome Smith, who unfortunately could not be here today, when I express our appreciation to the two sponsoring organizations and their representatives here, Mr. Koga, President of the Shipbuilding Research Association of Japan, and Dr. Saunders Mac Lane, Vice-President of the U.S. National Academy of Sciences. I am sure that all of us also appreciate the excellent work done by Professor Inui of the University of Tokyo, and his many able and dedicated co-workers, in organizing this meeting.

This is the thirteenth meeting in a series, each with scholarly participants of many different countries. After each meeting a proceedings has been published. Collectively these are widely used reference volumes. Since my organization, the Office of Naval Research, strongly believes in wide dissemination and further use of research results, I feel that your activities at this and past meetings are very useful and constructive.

Let me tell you a little bit about the Office of Naval Research. The Office of Naval Research (ONR) was the first, and from 1946-52 the most important, federal government agency which funded a broad range of basic and applied research in university and industrial laboratories in the United States. When the National Science Foundation (NSF) began operations, its initial personnel was recruited largely from ONR; NSF's

first Director, Dr. Alan Waterman, had previously been Chief Scientist of ONR. ONR continues to be a major sponsor of fundamental research in the physical and social sciences in academic and industrial institutions in the United States and elsewhere. All ONR-sponsored work in universities in unclassified and ONR policy is to encourage publication of research results in the open technical literature. The breadth of ONR's interest is indicated by the names of its divisions: physical sciences, mathematical and information sciences, biological sciences, psychological sciences, arctic and earth sciences, material sciences, and ocean science and technology.

Visits by ONR staff scientists are made to numerous scientists, no matter who sponsors their work, in the United States, Europe, and the Far East. These visits have as their purpose to foster information exchange and to encourage cooperative research. The Office of Naval Research Scientific Liaison Group in Tokyo was established in 1975 to facilitate such visits in this part of the world. ONR staff scientists based in Tokyo visit laboratories and other facilities and discuss matters of common scientific interest with their academic and industrial colleagues in the Far East. The Group's liaison activities as well as its reports are wholly unclassified.

Speaking for the Office of Naval Research and for the American Embassy, where our office is located, it is my honor to wish your good luck and success in your work.

Thank you.

Speeches at Buffet Party

Opening Speech

By Emeritus Prof. Takao Inui

Univ. of Tokyo

Ladies and Gentlemen,

It is a great privilege for me this evening to be able to greet you as Chairman of the Program Committee.

The Symposium on Naval Hydrodynamics has been blessed with great achievements during its twenty-four year history which began in 1956. And I have realized that we, the Japanese researchers, have benefited greatly by attending these Symposia.

We had long been studying the possibilities of holding a symposium in Japan, in the hopes that we could repay all the good will which has been shown to us. Unfortunately, it was difficult for the Society of Naval Architects of Japan to host this symposium due to the special circumstances of our country after the war.

In February 1976, the International Seminar on Wave Resistance was held in Tokyo and Osaka. On that occasion, the first preliminary meeting for feasibility study of the symposium in Japan was assembled. In addition to five Japanese members, Mr. Cooper, who was one of the Seminar Session Chairmen, Dr. Bertin and Prof. Kovaznay from the Tokyo Branch of the Office of Naval Research were present at the meeting.

Either the Shipbuilding Research Association of Japan or Shipbuilding Research Center of Japan

was considered as a possible Japanese host organization. The year 1980 was selected as the first possible date. Otherwise we must wait till 1992 or 2004, i.e. twelve year interval. The symposia outside the United States are to be held at four-year intervals and in Japan we have three-year interval, i.e., off-season of ITTC and ISSC. This multiplied interval resulted in twelve years.

Later, the Shipbuilding Research Association of Japan kindly accepted to be the host for the symposium in 1980, and the official announcement was made at the Twelfth Symposium held in June 1978 at Washington, D.C.

It is unfortunate, however, that we had to face a serious depression in the shipbuilding industry after that due to the second oil crisis. In fact, we had even the third "crisis" or "Koga" crisis in January 1979. I was shocked when we were advised by President Koga to reconsider the plans for the Tokyo Symposium.

Tonight, I am very pleased to see that the symposium was finally realized.

I would like to take this opportunity to thank all of you for your participation which contributed a great deal to the symposium. At the same time, I would like to express our special thanks to the Office of Naval Research, the National Academy of Science, the Shipbuilding Research Association of Japan, the Shipbuilders' Association of Japan, and the Japan Shipbuilding Industry Foundation, for

extending to us their kind offices throughout the preparation stages.

I am afraid that all of you are quite tired by now after going through the tight schedule since last Monday. You are also requested to attend the

session tomorrow, which, in Japan, is a national holiday, "Sports Day". I sincerely hope that you will have a fruitful and happy day. Have a good time here tonight.

Thank you very much.

Congratulatory Speech
By Mr. Marshall P. Tulin
Hydronautics, Inc.

Thank you Mr. Master of Ceremonies, Professor Inui, our Japanese host, and all of our Japanese friends. I think there are, by official count, a hundred and thirty-one of us who have traveled to this wonderful country from abroad to participate in this Symposium, and I don't think any of us would like to leave without expressing certain thoughts. I am honored to have the role to try to do that in my own words. I would like to address myself first to our Japanese host, Professor Inui, and all of our Japanese friends. You know it's not possible for us to visit this beautiful and fascinating country without being almost overwhelmed by your personal kindness and your graciousness. In addition, we experience every day at the Symposium your extraordinary efficiency and organization. This is of course a most appropriate locale for the Thirteenth Symposium because in addition to these attributes you're carrying out here throughout the country intensive and high-quality research in our field which is making its impact and has made its impact for many years throughout the world. And so, I think you are something like the New York Yankees of the Naval Hydrodynamics Symposium with all of these assets going for you. And in addition you have, of course, a secret weapon, the beautiful and charming Japanese women who have made their presence known to us in subtle ways; I think the twenty-five foreign

women who are here would like especially to thank these Japanese women for their great kindness in showing them Tokyo, acquainting them with Japanese ways, and in otherwise charming us.

I think, too, some note should be made on this occasion—mention should be made of Professor Inui's particular role, as of course he is responsible for the Symposium being located here in Tokyo, and we have to thank him for that. It happens to be a time when he has just retired from Tokyo University, and I think we would want to show our regard and appreciation for his contributions which have taken place over a period of at least thirty years. He is, of course, known to us as a man who eliminates waves, referring to development of his bulbous bow which made such an impact in ship design. But I also think of him as a wave maker, and I think that his effect on Japanese naval architecture both in its practice and in research will be propagated far into the future through his own research, through his own students working in industry, and through his students who are now teaching. I think there are some ten of his past students who are teaching in Japanese universities, and only when I came to Japan four years ago was I able really to appreciate in detail the important role Professor Inui has played throughout Japan.

This is as close as we are going to come to the twenty-fifth anniversary of this Symposium because it was founded in 1956 and next year is its twenty-fifth anniversary; but the next time we meet will be twenty-six years; therefore on this twenty-fourth year perhaps some note should be made of this anniversary. I think it is especially fitting that in that time we've reached halfway around the world, and our numbers are growing. I make special note of the presence here of representatives from the People's Republic of China for the first time at this Symposium. And finally, I think most of you must know that the man who has been primarily

responsible for keeping this Symposium in progress since 1960—it was founded in '56—is Mr. Ralph Cooper of the Office of Naval Research, who has been responsible for its organization. This is his last year, as most of you know he is retiring, and I think note should be made, and appreciation should be paid to his very important and vital role.

I hope—if I have left anything out, that you will please express it personally to our hosts.

I thank you very much.

Congratulatory Speech
By General Max Aucher
Bassin d'Essais des Carenes

Ladies and Gentlemen. Dr. Inui and Dr. Takahashi, on behalf of the ONR Organizing Committee, asked myself to make a short speech as a representative of the European participants at the Symposium.

Dr. Takahashi justified his choice saying that the French language was the most harmonious of the world, and so my speech could be understood by Japanese ears perfectly. I do not know if the French is more harmonious than German, Swedish, or Dutch, but what I know is that my French is the baddest of my European colleagues. You can't appreciate it.

For us, European peoples, Japan is a marvelous and exotic country, and everybody had dreamed in his youth or later of doing touristic cavort in Japan. For many European people who are present, the Eleventh ITTC Conference and the success in Tokyo some fourteen years ago had been such an occasion. Since our Symposia concerning hydrodynamics or naval science took place in Tokyo, I am sure that all the participants have got a good remembrance of the city. Nevertheless, for us,

European people this staying in Tokyo should be more pleasant if we could understand the Japanese language. How much it would be beneficial if we were able to appreciate your pretty city, to understand the information on signs in town, to know the name of the street and to be understood easily by the taxi driver.

Many ITTC Technical Committees are profited by the occasion of ONR Symposium to be added to their own meeting in Tokyo. So, we have to thank for their hospitalities and their kindness, Dr. Sugai from the Ship Research Institute, Dr. Murakami from Meguro Basin, Dr. Yamanouchi from Mitsui Basin, Dr. Tamura from Mitsubishi Basin at Nagasaki, and Dr. Kato from Tokyo University.

Now, to conclude, I also add to express our grateful thanks to the member of the ONR Organizing Committee for the manner they are allotted the program doing a pleasant cocktail for us to ease this section and gastronomy such as this buffet party.

Thank you very much.

Kagami-Biraki Ceremony
By Prof. John V. Wehausen
Univ. of California

The toast I would like to propose is to all the young ship hydrodynamicists of Japan. I have the same feelings now as I had four years ago at the International Seminar on Wave Resistance, that

this is a very impressive group of young people, intelligent, well-educated and enthusiastic. It speaks well for their teachers and for the future of Japan. I propose a toast to them.

Information about the 14th Symposium
By Prof. T. Francis Ogilvie
Univ. of Michigan

I understand the reason that Ralph Cooper is not here is rather a typical reason, namely that he is out working trying to arrange transportation for a lot of people. He is always on the job.

I have two announcements to make about the next meeting—one I make with some trepidation, and the other with complete pleasure. The first one I make with trepidation is that we have offered to

be host at the University of Michigan for the next ONR Symposium. Obviously, this is going to be a difficult act to follow in every way. The second thing is, and I'm sorry Ralph Cooper is not here, but after talking to many many people about this, we have decided to dedicate the next ONR meeting, the Fourteenth Symposium to Ralph Cooper in thanks for his many many years of organizing these meetings as well as a lot of other things.

Closing Speech
By Prof. Seizo Matora
Univ. of Tokyo

I am greatly honoured to have been asked to say a few words in closing this party, on behalf of the Society of Naval Architects of Japan.

Let me first express my appreciation to all of you, especially to those of the Office of Naval Research, and the National Academy of Science,

for your generous efforts in making this ONR Symposium such a great success. I am very happy that we were able to hold the Symposium in Japan this time, and firmly believe that the sessions have proved to be very fruitful.

I would like to thank you very much for giving

young researchers in Japan this great opportunity to meet and speak with you all. I am sure that these young people will contribute greatly to the field of Naval Hydrodynamics in the future.

It is also my hope that the Buffet Party this evening has helped to further mutual understanding, both academically and socially, between all participants. I was particularly surprised to learn that we had so many musicians and other talented performers among us. The abbreviation "ONR" this evening could have stood for "Office of Nice Recreation."

Let me take advantage of this opportunity to inform you of future international symposia now

being planned by the Society of Naval Architects of Japan.

One is the 2nd International Conference on Stability of Ships to be held in the autumn of 1982; the other is a Symposium on Practical Design in Shipbuilding (known as PRADS) scheduled for the autumn of 1983. We hope that many of you will be able to participate in these meetings.

This time of the year is considered the best season in Japan. I hope that you will be able to take back good memories of Japan, and that our country may be attractive enough for you to come back soon.

Thank you very much, and good night.

Session I

PROPULSION

Chairman

George F. Carrier
Harvard University
Cambridge, Massachusetts
U.S.A.

On Application of the Lifting Surface Theory to Marine Propellers

Koichi Koyama
Ship Research Institute
Tokyo, Japan

ABSTRACT

Three methods of propeller lifting surface theory proposed by Hanaoka and their numerical investigations performed by the author are shown and discussed. Method 1 is devised to be able to calculate the unsteady propeller lifting surface with a rather small digital computer. Method 2 employs the doublet-lattice method from the view point of wide applications. Method 3 deals successfully with the difficulty in the singularity at the blade tip. The quantitative evaluation of the numerical lifting surface theory is performed by comparing the results of calculations and experiments. The investigation into numerical results reveals the advantages and disadvantages of the three methods from the practical point of view. It is shown numerically and experimentally that Method 3 yields the accurate solution near the tip of blade.

NOMENCLATURE

Propeller

x, r, θ cylindrical coordinates
 r, σ, μ helical coordinates of control point
 r', σ', μ' helical coordinates of loading point
 $r = \theta + x/h, c = \theta - x/h, \mu = r/h$
 $2\pi h$ pitch of helicoid
 ρ mass density of fluid
 V advance velocity of propeller
 ω angular velocity of propeller
 ν angular frequency of oscillation
 $\Pi = \Pi_0 e^{i\nu t}$ lift density, or pressure jump
 $\gamma^* = \gamma_0^* e^{i\nu t}$ circulation density of

bound vortex

$\Pi_0 = \rho W^* \gamma_0^*$
 γ circulation density
 $\Gamma_0^* = c \int_{-1}^1 \gamma_0^* d\xi$
 $\Gamma = c \int_{-1}^1 \gamma d\xi$ circulation of blade section
 $w = w_0 e^{i\nu t}$ upwash on lifting surface
 $\phi = \phi_0 e^{i\nu t}$ acceleration potential
 $p = v/\Omega$ order of harmonic of inflow field
 $p^* = v/\Omega^*$
 $\partial/\partial n, \partial/\partial n'$ normal derivative on the helical surface at the control and loading points
 w_I induced velocity at a blade by steady free vortex
 $w_a = -w_I \cos \epsilon_I$
 $w_t = w_I \sin \epsilon_I$
 $\sin \epsilon_I = 1/\sqrt{1+\mu^2}, \cos \epsilon_I = \mu/\sqrt{1+\mu^2}$
 \bar{w}_a radial mean value of w_a
 \bar{w}_t/r radial mean value of w_t/r
 $V^* = V + \bar{w}_a, \Omega^* = \Omega + \bar{w}_t/r, W^* = V^*/\sqrt{1+\mu^2}, h = V^*/\Omega^*$
 r_0 propeller radius
 r_b boss radius
 l number of blades
 $u_0 = r_0/h, \mu_b = r_b/h$
 s distance measured along the helicoid
 s_1, r_1 position of leading edge
 s_2, r_2 position of trailing edge
 $\eta = (\mu - \bar{\mu})/\mu^*, \eta' = (\mu' - \bar{\mu}')/\mu'^*$

$$\mu^* = (\mu_0 - \mu_b)/2, \quad \bar{\mu} = (\mu_0 + \mu_b)/2$$

$$\xi = (\tau - \tau_0)/\bar{\tau}, \quad \xi' = (\tau' - \tau'_0)/\bar{\tau}', \quad \xi^* = (\tau - \tau'_0)/\bar{\tau}$$

$$\bar{\tau}' = (\tau'_2 - \tau'_1)/2, \quad \tau'_0 = (\tau'_1 + \tau'_2)/2$$

$$c' = h\sqrt{1+\mu^{*2}} \bar{\tau}'/2 \quad \text{half chord length}$$

$$c = h\sqrt{1+\mu^2} \bar{\tau}/2 \quad \text{half chord length}$$

$$\bar{c} = 2c'/(r_0 - r_b) = \sqrt{1+\mu^{*2}} \bar{\tau}'/(2\mu^*)$$

Wing

x, y, z Cartesian coordinates of control point
 x', y', z' Cartesian coordinates of loading point
 V velocity of wing
 w upwash on lifting surface
 γ circulation density
 b half span
 l_1, l_2 positions of leading and trailing edges of the blade element including the control point
 l'_1, l'_2 positions of leading and trailing edges of the blade element including the loading point
 $c = (l_2 - l_1)/2, c' = (l'_2 - l'_1)/2$ half chord length
 $x_0 = (l_1 + l_2)/2, x'_0 = (l'_1 + l'_2)/2$
 $\bar{c} = c'/b, \lambda = b/c'$
 $\eta = y/b, \eta' = y'/b$
 $\xi = (x - x_0)/c, \xi' = (x' - x'_0)/c', \xi^* = (x - x'_0)/c'$

$$T(\xi', \eta') = \xi' \frac{dc'}{dy'} + \frac{dx'_0}{dy'}$$

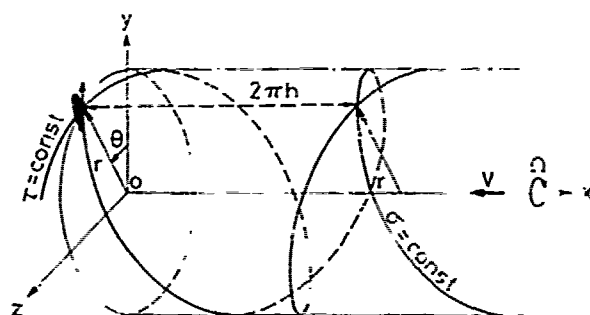


Fig.1.1 Helical Coordinates

1. INTRODUCTION

1.1 Main Theme and Background

It goes without saying that the lifting surface theory plays an important role in the hydrodynamic analysis of marine propellers. The theory has been developed for a long time in the field of aeronautics. While almost all of the applications of the theory are to wings of airplanes, there is an old application to screw propellers by Kondo[1]. We can see Sparenberg's[2] and Hanaoka's[3] contributions as pioneers in application of the theory to marine pro-

pellers. At present we are going to confirm numerically the quantitative relation between upwash distribution and loading distribution on blades of propellers by the theory. High speed computers make it possible to achieve such a complex calculation. There are many studies in development of such calculations[4]~[8].

It is significant that the form of vortex sheet is refined to adapt the actual phenomenon or that the reasonable viscous coefficient is introduced. In analysis of lifting surface however much depends upon numerical calculation. For the discrepancy between theory and experiment, it is difficult to decide which is more dominant cause: analytical inaccuracies in the numerical method, or physical differences between the idealized model and the actual phenomenon. So it is an important subject that numerical results for hydrodynamic characteristics by the lifting surface theory are estimated with confidence. The methods are not satisfactory if their results show some differences with each other even for the existing simple propeller lifting surface model. Comparative calculations on pressure distributions on the propeller blade performed at 15th ITTC show that the results obtained by many methods are apart from each other[9]. Although there is a great variety of the methods, the disagreement between the methods raises a problem from the practical point of view. How is the degree of agreement of the results of the numerical lifting surface theories?

On the other hand the lifting surface theory can be applied to various aspects such as prediction of performance, vibratory forces, cavitation, etc., so it is convenient that there exists suitable method for each aspect.

In this paper, three methods, named here Method 1, Method 2, and Method 3, of propeller lifting surface theory proposed by Hanaoka and their numerical investigations performed by the author, are shown and discussed. Method 1 was developed in an early stage of the study of lifting surface theory [10]~[13]. Numerical procedure in the method is devised to be able to calculate the unsteady propeller lifting surface with a rather small digital computer. With the current of popularization of larger capacitated digital computers, Method 2 was developed with doublet-lattice method from the view point of wide applications[14], [15]. These two methods don't give converged solution near the tip of blade, which becomes an obstacle to the calculation of cavitation. Method 3 deals successfully with the difficulty[15]~[18].

In chapter 2, the degree of agreement between them is revealed, which is considered to show the situation of accuracy of the present lifting surface theory. And further, calculated results are compared with experiments. Although doublet-lattice method employed by Method 2 is easy to deform the wake vortex sheet or to combine duct system, the method is employed from the view point

of study of numerical accuracy in this paper. In chapter 3, the discrepancy between the three methods is discussed, which shows the advantages and disadvantages for each method. The disadvantage of Method 3 is to require long computation time, and the advantage appears in the solution in the region near the tip of blade. So a planar wing is used for the numerical and experimental verification of Method 3. In chapter 4, the possibility of application of the three methods is discussed.

1.2 Integral Equation for Propeller Lifting Surface

The theoretical model for the propeller lifting surface used in this paper should be described at first. The propeller with its 2 -identical and symmetrically spaced blades is considered to operate in the fluid which is inviscid, incompressible, free of cavitation and infinite in extent. The blades of the propeller are assumed to be so thin that they can be replaced with bound vortex sheets. The disturbed velocity induced by the boss is assumed to be neglected. The bound vortices and the free vortices following them are distributed on the right helical surface, which may be called "a datum plane." The boundary condition of the flow on the blade is considered approximately on the projected blade surface on the datum plane. The pitch of the datum plane which is called hydrodynamic pitch $2\pi h$, is iteratively determined by considering the operating condition and induced velocity. The hydrodynamic pitch does not agree with the pitch of the helical surface made by the locus of traveling blade. In the case of unsteady propeller the flow field is assumed to oscillate harmonically with circular frequency ω . Although the model mentioned above is constructed by simplifying the actual phenomena, it contains the essential nature.

Our problem is to know the hydrodynamic characteristics of the propeller blade with given geometry, operating condition and inflow velocity. The problem comes to the mathematical problem of solving the singular integral equation.

In the vortex theory, velocity potential for the flow field mentioned above is expressed by doublet distribution of velocity field on the helical surface. In the case of linear theory, the velocity potential is equal to the expression obtained by the acceleration potential theory, which is demonstrated by Hanaoka[3]. In the case of the nonlinear propeller theory based on the assumption of constant hydrodynamic pitch such as the model dealt with in this paper, it is possible that the expression of the velocity potential by the vortex theory is converted to the form similar to the expression by the acceleration potential theory[11].

The normal differentiation of the velocity potential yields the upwash on the blade. If $w = w_0 \exp(i\omega t)$ denotes upwash on the blade, and $\Gamma = \Gamma_0 \exp(i\omega t)$ denotes lift

density of the blade in the fluid motion oscillating with circular frequency ω , the expression

$$w_0 = \frac{1}{8\pi\omega} \sum_{m=0}^{2-1} e^{-i2\pi m\tau/\lambda} \frac{\partial}{\partial n} \int_{-\infty}^{\tau} e^{-ip^*(\tau-T)/2} dT$$

$$\times \left(\iint_S \Gamma_0 \frac{\partial}{\partial n} \left(\frac{1}{R} \right) \Big|_{C=C_0} ds' dr' \right) \quad (1.1)$$

is obtained[14]. This is the integral equation for propeller lifting surface usually used. w_0 is the known function given by the boundary condition for the propeller geometry, operating condition, and inflow velocity. Complex amplitude of lift density Γ_0 or complex amplitude of circulation density of the bound vortex γ^* is unknown function yielding the hydrodynamic characteristics, where the relation

$$\Gamma_0 = \omega h \gamma^* \quad (1.2)$$

is kept[3]. After the normal differentiation, expression (1.1) becomes[3],[17],

$$w_0 = \frac{\sqrt{1+u^2}}{8\pi} \int_{u_b}^{u_0} du' \int_{-1}^1 \frac{1}{v^* \sqrt{1+u'^2}} \tau' d\zeta' \sum_{m=0}^{2-1} e^{-i2\pi m\tau/\lambda}$$

$$\times \int_{-\infty}^v e^{-ip^*(v-s)} \left\{ \frac{3(1+u'^2)s \sin(s_m)}{R^2} \right.$$

$$\left. + \frac{1}{1+u'^2} \frac{\partial}{\partial s} \frac{u u' s + \sin(s_m)}{R^3} \right\} ds \quad (1.3)$$

where

$$v = (\tau - \tau')/2$$

$$R = \sqrt{s^2 + u^2 + u'^2 - 2uu' \cos(s_m)}$$

$$s_m = s - 2\pi m/\lambda$$

For the case of the linear theory, hydrodynamic pitch agrees with the pitch of the helical surface made by the locus of traveling blade. For this case, $p^* = p$. Further the expression (1.1) or (1.3) with the condition $p^* = p = 0$, yields the expression for the steady propeller lifting surface, when $w = w_0$, $\Gamma = \Gamma_0$, and $\gamma = \gamma_0$.

Hanaoka shows theoretically that the singularity at the circular tip of blade is inherent in the kernel function of the integral equation of the existing lifting surface theory such as (1.1), (1.3), which causes the non-convergence of the numerical solution near the circular tip of blade. And he proposes the treatment of the singularity by spanwise integrating by parts and introducing the tip condition[16],[17]. Integrating by parts with respect to u' in (1.3), and introducing the tip condition

$$\Gamma \Big|_{\mu=\mu_0, \mu_b} = 0 \quad (1.4)$$

the expression

$$\begin{aligned} w_0 = & - \frac{\mu^*}{4\pi\sqrt{1+\mu^2}} \int_{\mu_b}^{\mu_0} d\mu' \int_1^{\infty} d\xi' \frac{\partial}{\partial \mu'} (\bar{c}_Y \bar{c}^* e^{-ip^*v}) \\ & \times \sum_{m=0}^{i-1} e^{-i2pm\pi/\lambda} \int_{-\infty}^v e^{ip^*s} Z(s, \mu, \mu') ds \\ & + \frac{\mu^*}{4\pi\sqrt{1+\mu^2}} \int_{\mu_b}^{\mu_0} d\mu' \int_{-1}^1 \frac{1}{c_Y \bar{c}^*} \sum_{m=0}^{i-1} e^{-i2pm\pi/\lambda} \\ & \times Z(v, \mu, \mu') T(\xi') d\xi' \quad (1.5) \end{aligned}$$

is obtained, where

$$\begin{aligned} Z(s, \mu, \mu') &= (1+\mu^2) s \cdot \sin(S_m) X(s, \mu, \mu') \\ &+ \partial(Y(s, \mu, \mu'))/\partial s, \\ 3(1+\mu^2)/R^5 &= \partial(X(s, \mu, \mu'))/\partial \mu', \\ (\mu \mu' s \sin(S_m))/R^3 &= \partial(Y(s, \mu, \mu'))/\partial \mu', \\ T(\xi') &= -dv/d\mu' = (\xi' d\bar{c}'/\partial \mu' + \partial \bar{c}'/\partial \mu')/2. \quad (1.6) \end{aligned}$$

1.3 Three Numerical Methods

Three numerical methods for the propeller lifting surface are described in this section. The three methods are called Method 1, Method 2, and Method 3 respectively in this paper. Method 1 and Method 2 deal with the existing integral equation (1.3), and Method 3 deals with the new integral equation (1.5).

Numerical methods for solving the integral equation for lifting surface are divided into two groups, namely, mode function method and discrete function method.

In the mode function method, the solution, or circulation density over the lifting surface is expressed by series of continuous functions.

$$\gamma^*(\xi, \eta) = \sum_{N=0}^R B^{(N)}(\eta) \lambda_N(\xi) \quad (1.7)$$

where ξ, η denote chordwise variable and spanwise (radial) variable respectively. The functions $\lambda_N(\xi)$ are preselected chordwise functions such as Birnbaum series, Glauert series etc. The functions $B^{(N)}(\eta)$ are unknown spanwise functions. One of the difficulties of the method is the treatment of the logarithmic singularity. There are collocation method[19], kernel function procedure[20], Flax's method[21], etc., in the group.

On the other hand, in the discrete

function method, the lifting surface is divided into small elements or replaced with many line segments, so that the solution is expressed by discrete values at finite points distributed over the surface. It seems that number of elements must be large enough in the method. There are vortex-lattice method[22], doublet-lattice method[23], box method[24], finite panel method[25], etc., in the group.

Method 1 and Method 3 in this paper belong to mode function method group, and Method 2 belongs to discrete function method group.

Method 1 may be called series expansion method. Two-dimensional integral equation for lifting surface (1.3) is converted into simultaneous one-dimensional integral equations, in expanding the two-variable integral equation in power series of one-variable by Taylor's theorem and equating the coefficient functions of successive powers to zero [10], [13]. Expression (1.7) is used for the form of solution. The method is equivalent to Flax's method on condition that the mode function is the orthogonal series. The method, however, is distinguished by easy calculation of coefficients of simultaneous equations in comparison with Flax's method. The method can deal with the simple mean camber line accurately without many chordwise control points in contrast to the collocation method. The method reduces the labour for numerical integration along the helical surface to the minimum. Especially for the case of unsteady calculation, the machine running time for the calculation is not so long. The detail of the method is shown in Ref.[26] and the example of the calculation is shown in Ref.[27], in which comparison is made with other methods. In Method 1, it is assumed that $p^*=p$, although the pitch of datum plane does not agree with the pitch of the helical surface made by the locus of travelling blade.

In Method 2, existing integral equation (1.1) is solved by the doublet-lattice method. The blade is divided into many blade elements by cylindrical surfaces, and each blade element is divided into many boxes. Surface distribution of doublet in the pressure field is replaced by line doublets with constant strength and direction in every box as shown in Appendix 1[14], [15]. The chordwise arrangement is determined by Lan's method[28], which is devised so as to give the accurate solution near the leading edge. In the method surface integral over the blade in equation (1.1) is replaced by the summation of boxes and the line integral in each box. The line doublet with constant strength and with radial direction causes analytical radial integration in each box. Numerical integration is only helical line integral corresponding to the free vortex. Method 2 is distinguished by the analytical radial integration.

In Method 3 new integral equation (1.5) which treats the singularity at blade tip, is solved by a collocation method. Accurate solution near the tip of blade characterizes

Method 3[15]~[18]. The numerical solutions of the existing lifting surface theories standing on the integral equation (1.3) do not converge at the circular wing tip on account of the singularity. The restriction in the existing theories can be removed by using the integral equation (1.5). Employing the integral equation (1.5), the range of validity of propeller lifting surface theory is extended to include the tip of blade. As shown in Appendix 2, integral equation (1.5) is transformed into the form suitable for numerical calculation, and it is further converted into linear algebraic equations by using the mode function (1.7). The location of upwash points where the boundary condition of the lifting surface is satisfied are determined by Multhopp's collocation method[19]. New integral equation (1.5) is more difficult to calculate generally than integral equation (1.3). The former however includes weaker logarithmic singularity, while the logarithmic singularity in the latter becomes strong near the edges of the blade.

2. QUANTITATIVE EVALUATION OF NUMERICAL LIFTING SURFACE THEORY

How is the degree of agreement of the results of the numerical lifting surface theories? There is a comparative calculation on planar lifting surface[29]. The results show that it is necessary to be careful in the evaluation and the applica-

tion of the numerical method.

In this chapter the numerical results of the three methods for the steady and unsteady propeller lifting surface are presented and the comparison and evaluation of them are made. The methods are verified experimentally by the measurement of pressure distribution on the propeller blade.

2.1 Numerical Calculation

Numerical calculations are performed for the propeller C, which is ITTC Comparative Test propeller Troost B4-475[27], by the three methods mentioned in previous section. Particulars and the figure of the propeller are shown in Table 2.1 and Fig. 2.1.

The local velocity variation in hull wake about the propeller shaft at any radius can be thought of as a sum of harmonic functions of blade position angle. For each harmonic function, the integral equation is set and solved. The nominal axial and tangential wake field for a Series 60 $C_b=0.60$ is used for the calculation in the same way as ITTC Comparative Calculation. The harmonic coefficients are shown in Table 2.2. The value in the table is defined by the ratio of inflow velocity to propeller advance velocity. The asymmetrical components included in the measurement of wake field are also considered in the calculation, although the components are omitted in the table because of smallness.

The number of spanwise control points N_R ,

Table 2.1 Particulars of Propeller C

BOSS RATIO	0.167
PITCH RATIO	1.025 at blade tip (increase)
EXP. AREA RATIO	0.475
BLADE THICKNESS R.	0.045
NUMBER OF BLADES	4
BLADE SECTION	Troost Type B

Table 2.3 Number of Control Points

	N_R	N_C
Method 1	7	4
Method 2	7	5
Method 2	15	10
Method 3	7	4

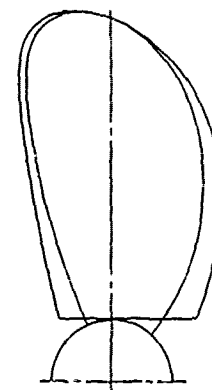
Table 2.2 Components of Wake Harmonics

axial component

$r/r_o =$	0.199	0.289	0.424	0.584	0.743	0.878	0.968
p=0	-0.567	-0.420	-0.203	0.021	0.101	0.123	0.134
1	-0.238	-0.263	-0.307	-0.331	-0.280	-0.253	-0.248
2	0.052	-0.004	-0.082	-0.148	-0.156	-0.143	-0.146
3	0.045	0.031	0.010	-0.029	-0.070	-0.076	-0.077
4	0.022	0.041	0.037	-0.004	-0.027	-0.031	-0.035
5	-0.062	-0.049	-0.039	-0.020	-0.015	-0.020	-0.022

tangential component

$r/r_o =$	0.199	0.289	0.424	0.584	0.743	0.878	0.968
p=0	0.	0.	0.	0.	0.	0.	0.
1	0.010	-0.033	-0.100	-0.163	-0.174	-0.170	-0.164
2	0.008	0.014	0.009	-0.018	-0.050	-0.060	-0.064
3	0.016	0.018	0.016	0.008	-0.009	-0.017	-0.022
4	0.041	0.023	0.007	0.004	-0.000	-0.006	-0.008
5	0.003	-0.004	-0.005	0.001	-0.002	-0.004	-0.005



propeller C

Fig.2.1 Outlines of the Blade

and the number of chordwise control points or the number of terms of mode function N_C ($=R+1$) in the numerical calculation are shown in Table 2.3. The advance coefficient for steady calculation is determined by the mean advance velocity of the propeller, $J=0.645$. The hydrodynamic pitch in the three methods are kept equal for the base of comparison. It is determined by the iterative calculation by Method 1, $h=0.298r_v$.

Results of the steady calculations for the propeller in uniform flow are exhibited in Figs.2.2,2.3. Fig.2.2 shows the radial distribution of circulation of blade section Γ . Fig.2.3 shows the chordwise distribution of circulation density γ . Hydrodynamic characteristics of the propeller in the hull wake are obtained by calculating all wake harmonics. Results for the case of low frequency fluid oscillation $p=1$ are shown in Figs.2.4,2.5. Results for high frequency $p=5$ are shown in Figs.2.6,2.7. Fig.2.4 and Fig.2.6 show the radial distribution of the complex amplitude of circulation of bound vortex of blade section Γ^* . Fig.2.5 and Fig.2.7 show the chordwise distribution of the complex amplitude of circulation density of bound vortex γ^* .

In the first place it is clear from the figures for both steady and unsteady calculations that satisfactory agreement between the three methods in circulation density as well as the circulation of blade section is

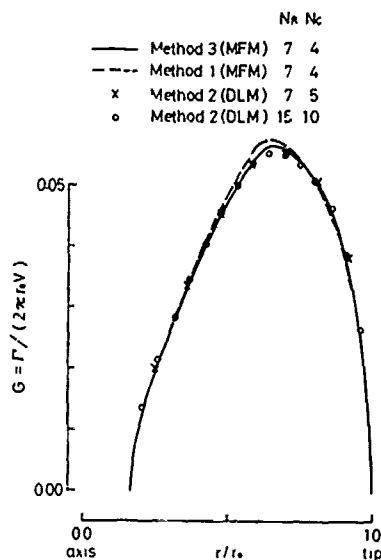


Fig.2.2 Radial Distribution of Circulation of Blade Section ($p=0$)

obtained with a few exceptions. We can evaluate the three numerical lifting surface theories by the reliability shown in the results.

Logarithmic singularity appears in the spanwise integral in the mode function method, and it becomes strong in the existing method when the control point is located near the edge or tip of the blade in order to increase the control points. In this case calculations are apt to be inaccurate. So the proper treatment of the singularity is necessary. The treatment is performed in Method 1 though the problem in the method is not so severe because the control point is at midchord. The logarithmic singularity in the kernel function of the integral equation (1.5) in Method 3 is weaker than that of existing integral equation (1.3) as shown in Appendix 2. So in Method 3 the logarithmic correction is not treated. In Method 2 it

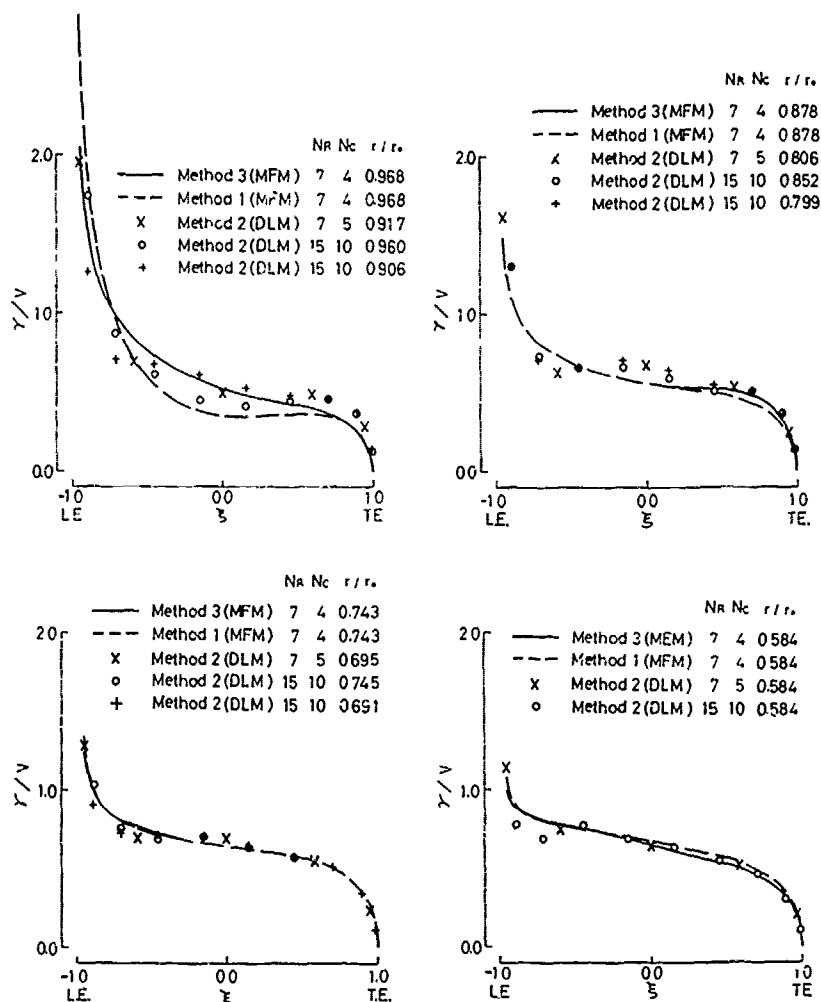


Fig.2.3 Chordwise Distribution of Circulation Density ($p=0$)

is not necessary to treat the singularity, and it is said that increase of the control points tends to convergence. In this case, the location of the control points and loading points is important. In this paper, calculations for two arrangements of lattice $N_R \times N_C = 7 \times 5$ and 15×10

in Method 2 are performed in order to confirm the convergence of the solution. Agreement of the circulation of blade section or circulation density between two arrangements is good for both steady and unsteady calculations as shown in the figures, which shows the good convergence of the method.

Next let us observe the notable discrepancies between the methods in detail.

For the case of large p (Figs.2.6,2.7) the results by Method 1 show obvious difference from those by Method 2 or Method 3. The discrepancy in amplitude and phase of circulation density in aft part of the chord appears clearly. It causes the discrepancy in circu-

lation of blade section. The cause of the discrepancy is the different hydrodynamic models, that is, $p^* = p$ is assumed in Method 1 and $p^* \neq p$ in the other methods[18]

Results of the circulation of blade section by Method 2 agree with those by

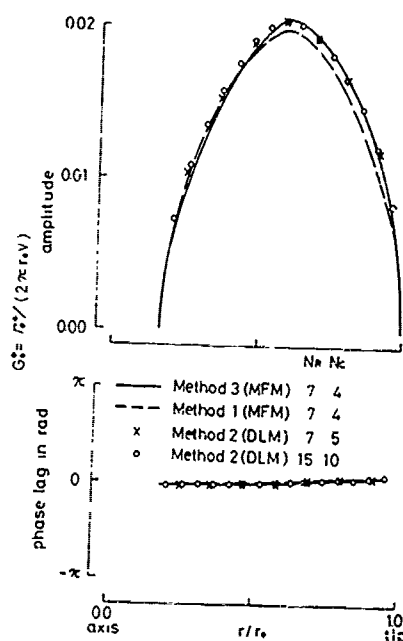


Fig.2.4 Radial Distribution of Circulation of Bound Vortex of Blade Section ($p=1$)

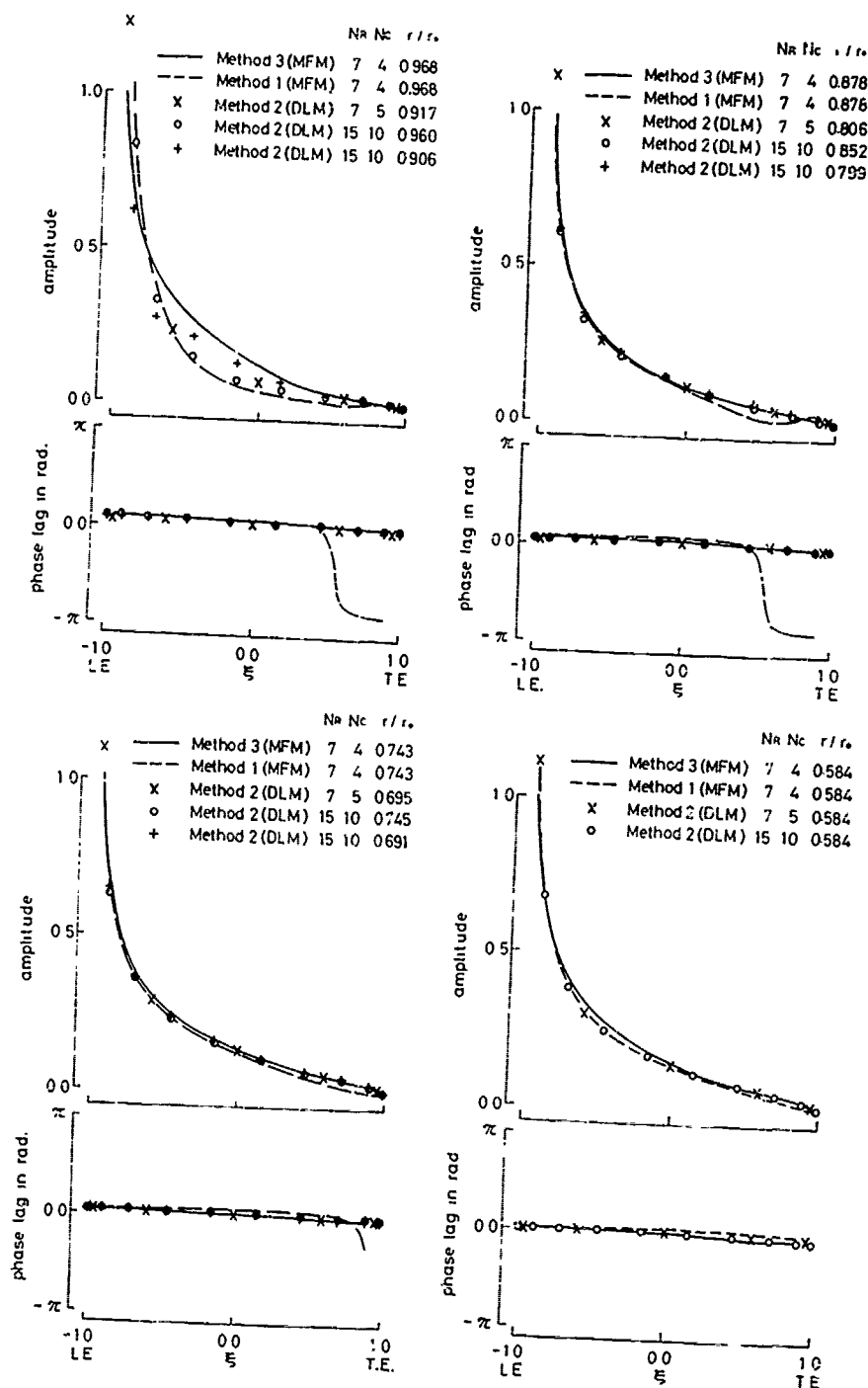


Fig.2.5 Chordwise Distribution of Circulation Density of Bound Vortex γ_0^*/V ($p=1$)

Method 3 for both steady and unsteady calculations (Figs. 2.2, 2.4, 2.6). However the agreement of the circulation density between Method 2 and Method 3 is unsatisfactory for the steady calculation, although it is satisfactory for the unsteady calculation (Figs. 2.3, 2.5, 2.7). This will be discussed in the following chapter.

Circulation density near the tip of blade ($r/r_0 \approx 0.968$) by Method 1

or Method 2, does not agree with that by Method 3 for both steady and unsteady calculations (Figs. 2.3, 2.5, 2.7). The discrepancy is caused by the different integral equations (1.3) and (1.5). The circulation density near the

tip of blade by Method 3 is considered to be accurate by reason that Method 3 uses the integral equation (1.5) treating the singularity at the tip of blade. The reason will be discussed in the following chapter.

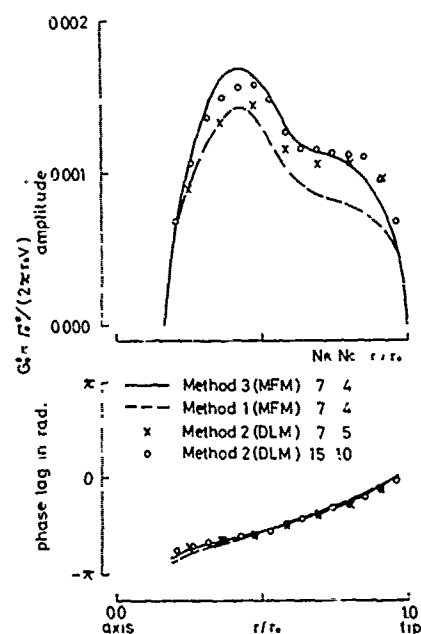


Fig. 2.6 Radial Distribution of Circulation of Bound Vortex of Blade Section ($p=5$)

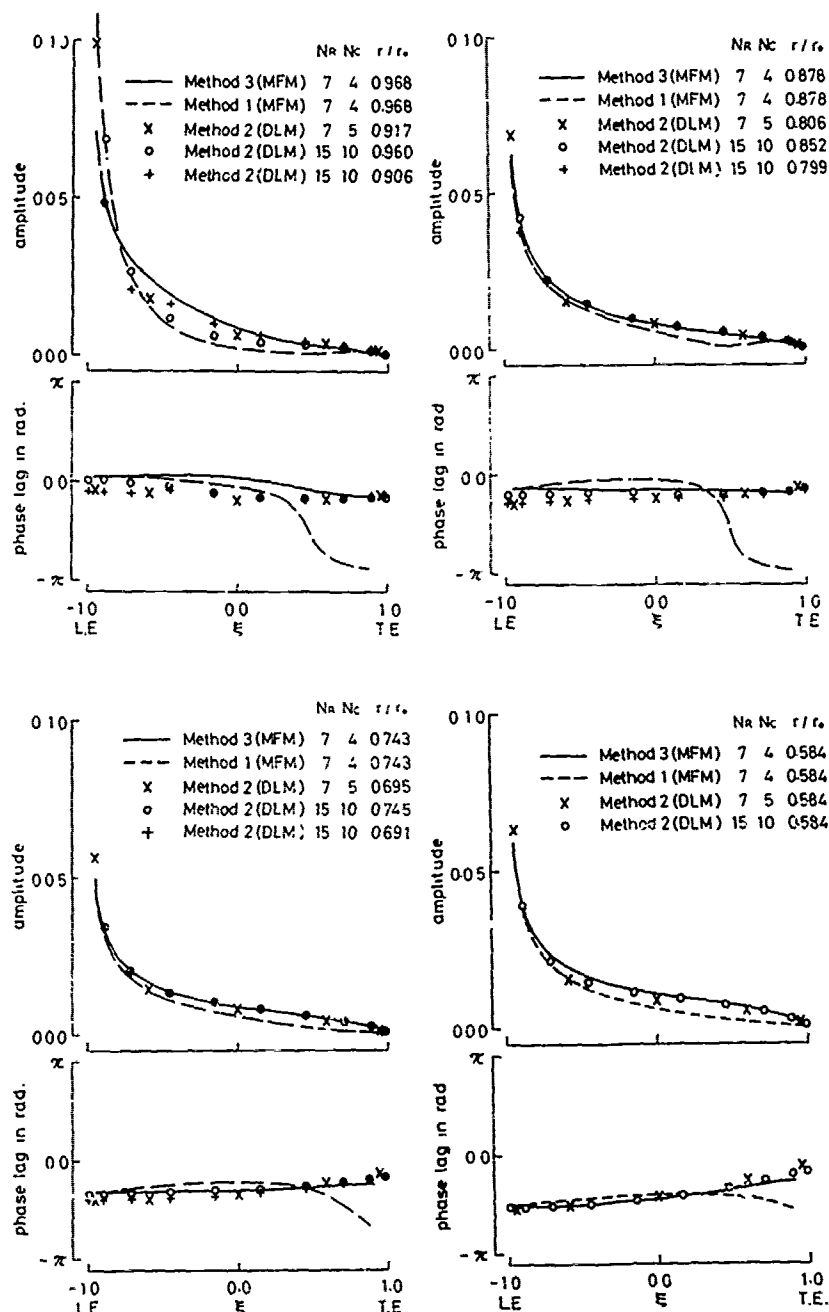


Fig. 2.7 Chordwise Distribution of Circulation Density of Bound Vortex γ^* / V ($p=5$)

2.2 Comparison with Experiment

As there are some papers showing the correlation of the macroscopic hydrodynamic forces such as thrust and torque between numerical lifting surface theory and experiment [4],[5],[7],[8], in this paper microscopic value such as pressure or lift density on the blade of a model propeller is used for the comparison between theory and experiment. Particulars of the model propeller used for the measurement are shown in Table 2.4. The measurements of pressure distributions over the blade was carried out using very small pressure gauges made of semi-conductor. Characteristics of the gauges are shown in Table 2.5. Five pressure gauges are mounted at $0.77r_0$ on the blade. Chordwise positions

of the gauges are every 20% of the chord on the back and 40% on the face. The experiment was performed in the cavitation tunnel. The detail of the model propeller and the measuring system is shown in Ref.[30].

The results of the measurement of pressure distribution on the propeller operating in uniform flow are shown in Fig.2.8. The theoretical value is obtained by thick-airfoil theory for the equivalent airfoil section whose mean camber line is deformed so that the loading distribution corresponds to that obtained by propeller lifting surface[4]. Method 1 is used for the calculation of the lifting surface. The reduction factor ($\kappa=0.882$) of the circulation which corresponds to that of lift curve slope, is taken into account for the calculation. The fluctuation of lift density, that is, pressure jump, at 40% chord position of the propeller operating in non-uniform flow is shown in Fig.2.9. In this case, mesh screen was used to reproduce the wake distribution.

Fig.2.8 and Fig.2.9 show that the agreement between theory and experiment is satisfactory.

In order to refine further the correla-

tion between theory and experiment, it is considered to be necessary to improve the theoretical method such as wake model or more reasonable viscous correction as well as the measuring technique.

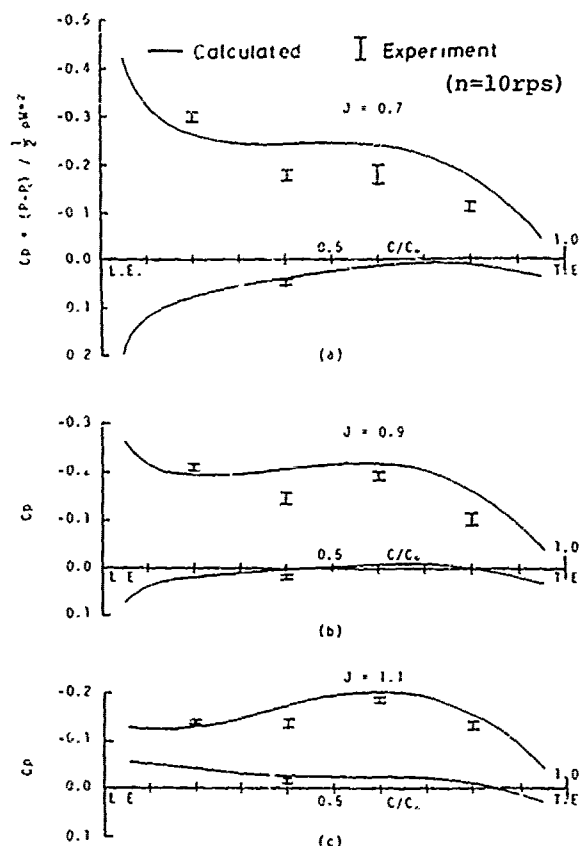


Fig.2.8 Pressure Distribution over the Blade ($r/r_0=0.77$)

Table 2.4 Particulars of the Test Propeller

DIAMETER	(m)	0.250
BOSS RATIO		0.180
PITCH RATIO		1.264 at $0.7r_0$
EXP. AREA RATIO		0.800
BLADE THICKNESS RATIO		0.050
ANGLE OF RAKE		7.5°
NUMBER OF BLADES		6
BLADE SECTION		SRI-a

Table 2.5 Characteristics of Pressure Gauge

Range	kg/cm ²	1
Sensitivity	mV/Vf.s.	33
Non-linearity	%f.s.	0.8
Hysteresis	%f.s.	0.8
Zero-shift	%f.s./ 1°C	0.1
Sensitivity shift	%f.s./ 1°C	-0.3
Impedance	k Ω	1
Natural frequency	kHz	100
Allowable temperature	$^\circ\text{C}$	0 - 40

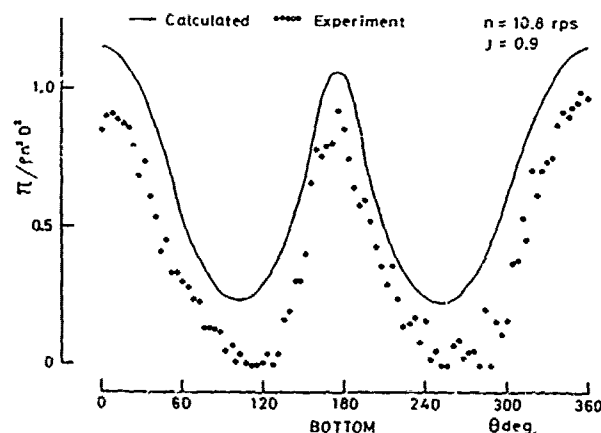


Fig.2.9 Fluctuation of Lift Density ($r/r_0=0.77$, $\xi=-0.2$)

3. INVESTIGATION INTO NUMERICAL LIFTING SURFACE THEORY

In the preceding chapter the numerical lifting surface theories were evaluated quantitatively by numerical calculations and experiments. Although circulation density obtained is considered to be accurate over the almost whole of the blade, discrepancy in the value between three methods appears in some chordwise distribution or in the region near the tip of blade. Further investigation is necessary to judge the discrepancy, which is discussed in this chapter.

3.1 Chordwise Distribution of Circulation Density Especially near the Leading Edge

Although the agreement of circulation density between three methods is almost good for the unsteady calculations, the circulation density obtained by Method 2 has a tendency to be a little small around 20% chord position comparing to other methods (Figs.2.5,2.7). In steady calculation there are some regions where circulation density by Method 2 does not show good agreement with the other methods (Fig.2.3). This is because the upwash in steady propellers is determined by interpolating the dimensions of blade section given in the table. As the locations of upwash points are different in the three methods, the distributions of upwash in the three methods

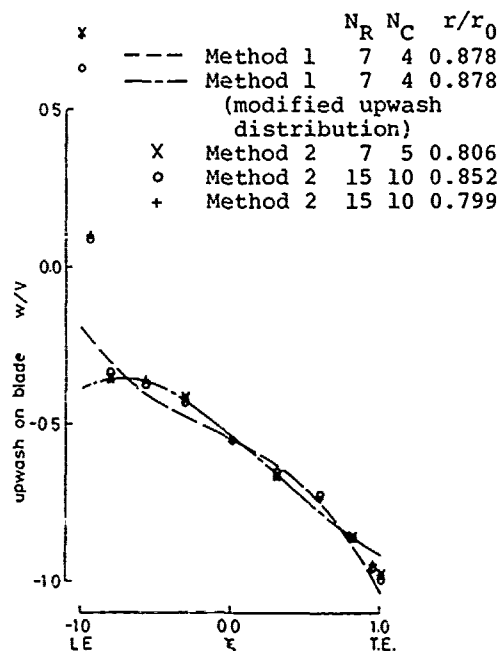


Fig.3.1 Upwash Distribution over the Blade of Propeller C in Steady Condition

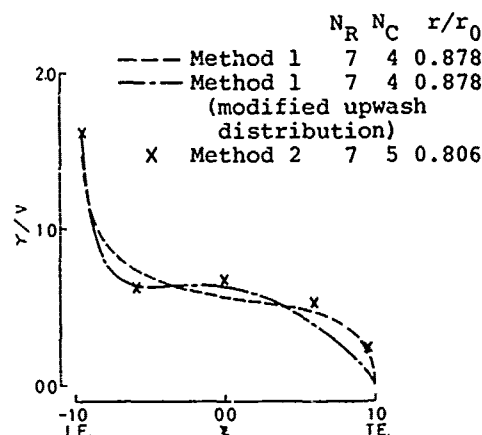


Fig.3.2 Chordwise Distribution of Circulation Density for Propeller C in Steady Condition ($p=0$)

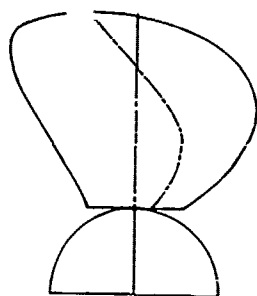
are slightly different with or.. another.

Upwash distributions used in the steady calculation in section 2.1 and new upwash distribution "Method 1 (modified upwash distribution)" are shown in Fig.3.1. The new upwash distribution indicated by the dot-dash-line fits on the distribution used for Method 2 in fore half of the chord. Fig. 3.2 shows the results of calculation for the new upwash distribution. Agreement of the new comparison between "Method 1 (modified upwash distribution)" and Method 2 becomes good in fore and middle parts of the chord and becomes bad in aft, in contrast to the previous comparison between Method 1 and Method 2. The upwash distribution closely following the geometry is sometimes uneven which causes the uneven chordwise distribution of circulation density such as the results obtained by Method 2. This means that four terms of mode functions are not always sufficient.

3.2 Circulation Density near the Tip

Discrepancy of circulation density near the tip of blade $r/r_0 \neq 0.968$ between Method 3 using the new integral equation(1.5) and Methods 1,2 using the existing integral equation(1.3) can be seen for both steady calculation (Fig.2.3) and unsteady calculation (Figs.2.5,2.7). Another example including the shortcoming of the existing integral equation is shown in the following.

Propeller B has blades with low aspect ratio as shown in Table 3.1 and Fig.3.3 . For such a propeller the problem in the singularity at the blade tip becomes severe and it affects the solution in slightly inner region. This is shown in Fig.3.4, in which three results by Method 1, Method 3, and Sugai's method[4] are compared. Sugai's



propeller B

Fig.3.3 Expanded Outline of the Blade

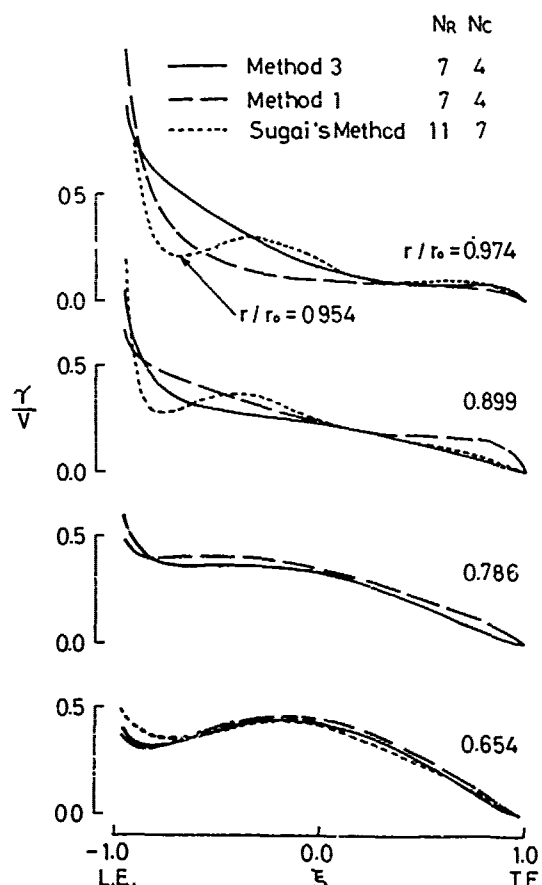


Fig.3.4 Chordwise Distribution of Circulation Density for Propeller B in Steady Condition ($p=0$, $J=0.819$)

Table 3.1 Particulars of Propeller B

BOSS RATIO	0.307
PITCH RATIO	1.201 at $0.7r_0$ (increase)
EXP. AREA RATIO	0.598
ANGLE OF RAKE	0°
NUMBER OF BLADES	4

method employs the existing integral equation(1.3) and Multhopp's collocation method [19]. Number of control points is $N_R^*N_C = 11 \times 7$. Fig.3.4 exhibits that the solution by Method 1 or Sugai's method does not agree with that by Method 3 even at $r/r_0=0.899$.

In proposing Method 3, Hanaoka demonstrates theoretically that the accurate numerical solution near the circular tip of blade is not yielded by the existing integral equation(1.3) but by the new integral equation(1.5) [16],[17]. This is shown numerically and experimentally in the following sections, in which the planar wing is used instead of the propeller blade for convenience.

3.3 Numerical Calculation of the Circular Planar Wing

Propeller lifting surface is not different essentially with planar lifting surface. In this section it is shown for the case of steady circular planar wing without camber that the new integral equation which is the same kind as that used in Method 3, yields the converged numerical solution near the wing tip, and that the agreement between the numerical solution and the analytical solution is good.

The existing integral equation for steady planar lifting surface is expressed as

$$w = \frac{1}{4\pi b} H \int_{-1}^1 d\eta' \int_{-1}^1 \frac{c' \gamma}{(\eta - \eta')^2} \times \left\{ 1 + \frac{\xi^* - \xi'}{\sqrt{(\xi^* - \xi')^2 + \lambda^2 (\eta - \eta')^2}} \right\} d\xi' \quad (3.1)$$

The expression corresponds to the integral equation(1.3) for propellers. Hanaoka treats the singularity at the wing tip in the integral equation(3.1), and presents the new integral equation expressed as[16],

$$w = -\frac{1}{4\pi} \oint_{-1}^1 d\eta' \oint_{-1}^1 \frac{\partial(\bar{c}\gamma)/\partial\eta'}{\eta - \eta'} \times \left\{ 1 + \frac{\sqrt{(\xi^* - \xi')^2 + \lambda^2 (\eta - \eta')^2}}{\xi^* - \xi'} \right\} d\xi'$$

$$-\frac{1}{4\pi} H \int_{-1}^1 d\eta' \int_{-1}^1 \frac{\gamma \cdot \lambda \cdot (\eta - \eta') \cdot T(\xi', \eta')}{\bar{c}(\xi - \xi')^2 \sqrt{(\xi - \xi')^2 + \lambda^2 (\eta - \eta')^2}} d\xi' \quad (3.2)$$

The expression corresponds to the integral equation (1.5) used in Method 3 for propellers.

Results of the numerical calculation for a circular planar wing at unit angle of attack ($\alpha=1$ rad.) are exhibited in Fig. 3.5 [31]. $A_B^{(N)}(\eta)$ denotes the coefficient of mode function defined by

$$\frac{\gamma}{V} = \sum_{N=0}^R A_B^{(N)}(\eta) \cdot \lambda_N(\xi) \quad (3.3)$$

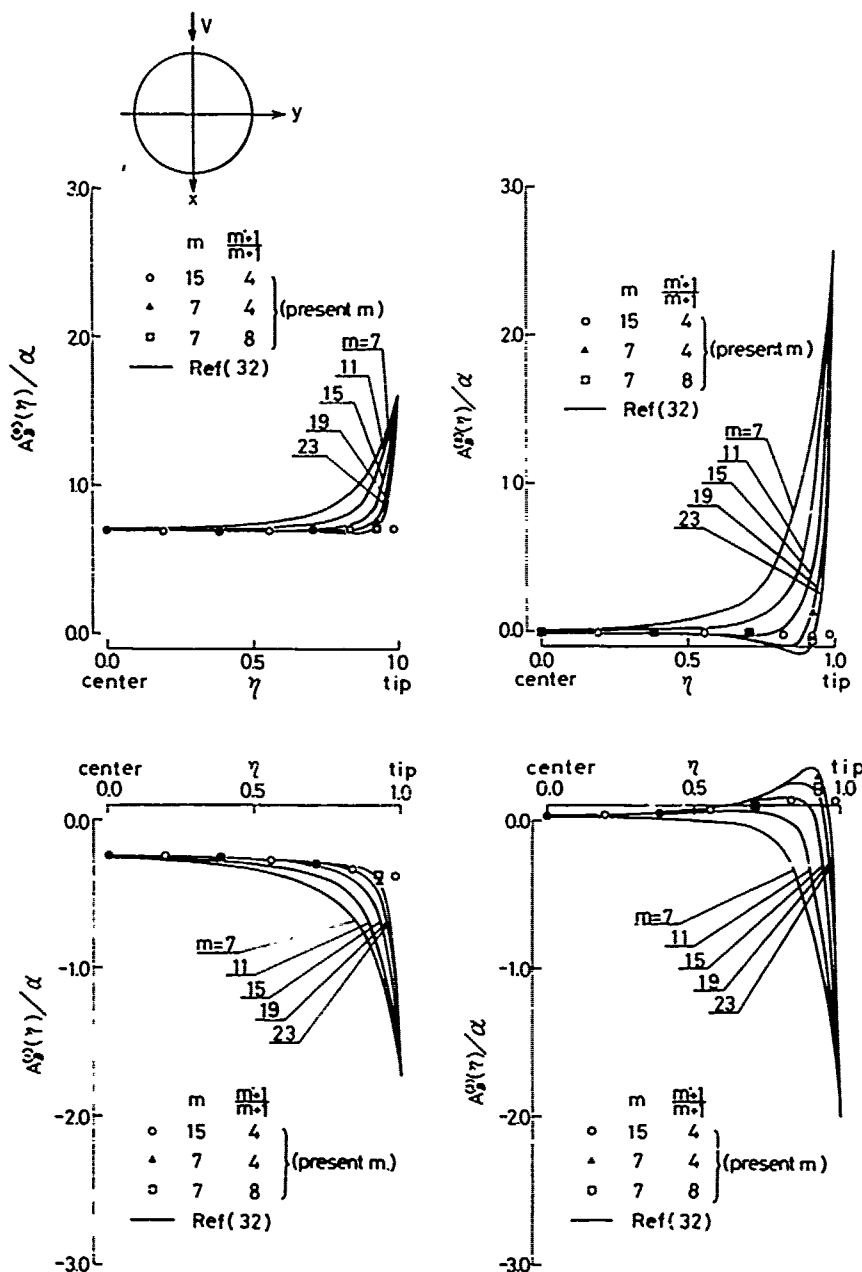


Fig.3.5 Coefficients of Birnbaum Series (Circular Planar Wing)

where V is velocity of wing and $\lambda_N(\xi)$ is Birnbaum series. m and m' denote the number of spanwise control points and integral points respectively. In Fig. 3.5, two kinds of calculation methods are shown, that is, the present method and the existing method [32]. The present method deals with the new integral equation (3.2), and the existing method deals with the integral equation (3.1). The latter method is a little different from Multhopp's collocation method, but its numerical results are almost the same as that by Multhopp's method [32]. Fig. 3.5 exhibits that the former (new integral equation) shows good convergence with increasing number of spanwise control points, and that the latter (existing integral equation) does not show the convergence near the tip of blade. Calculation for the circular planar wing by Method 1 also shows the similar tendency as the latter results in Fig. 3.5 [33].

Figs. 3.6, 3.7 show the comparison with the analytical results. Fig. 3.6 exhibits the spanwise distribution of lift coefficient, which shows that results of both the present method using equation (3.2) and Multhopp's method using equation (3.1) agree with analytical value [34]. Fig. 3.7 shows the comparison of chordwise distribu-

tion of lift density between the present method using integral equation(3.2) and Jordan's analytical calculation [35] standing on Kinner's theory[36]. It should be said that the difference is small. Judging from these figures, chordwise distribution of lift density obtained by the existing integral equation includes remarkable error near the blade tip, and the present method using integral equation(3.2) yields satisfactory distribution of lift density.

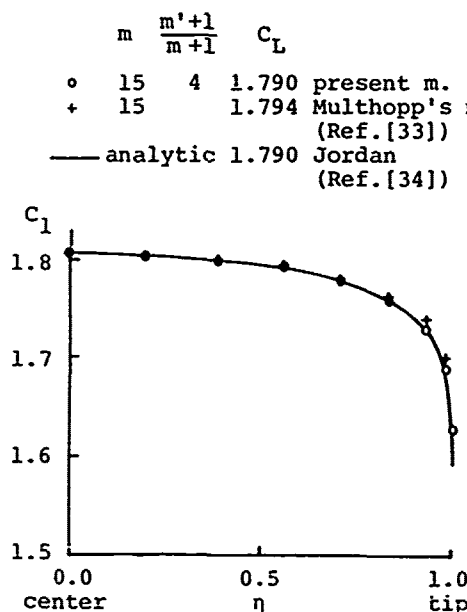


Fig.3.6 Local Lift Coefficient over Span (Circular Planar Wing)

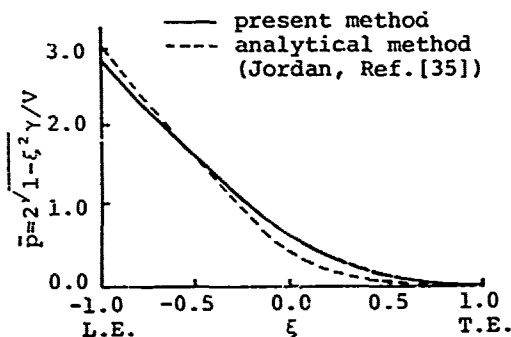


Fig.3.7 Chordwise Pressure Distribution Function near Wing Tip ($\eta=0.980$)

3.4 Wind Tunnel Experiment of the Circular Planar Wing

In this section it is shown by the wind tunnel experiment of circular planar wings that the circulation density near the wing tip obtained by using the new integral equation(3.2) corresponding to Method 3 is superior in accuracy than that using the existing integral equation(3.1).

Pressure distribution on the circular planar wing was measured in the Göttingen-type wind tunnel, and it was compared with theoretical results. Three wings (Wing No. 1, Wing No.2, and Wing No.3) used in the experiment are shown in Fig.3.8. Every wing is circular plane form with 25 cm radius and without camber. Only the thickness distribution is different with each other. The apparatus for setting the wing is shown in Fig.3.9. It is semi-closed tunnel type in order that effects of the boundary is minimized. Wind velocity was set at $V=30$ m/s .

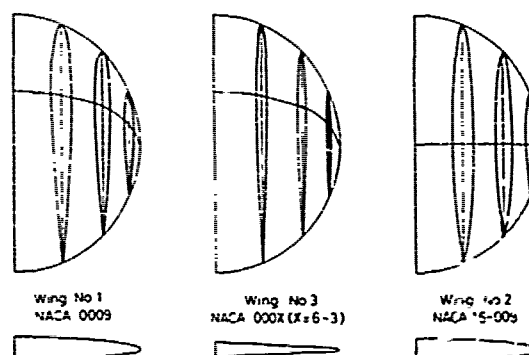


Fig.3.8 Circular Planar Wing Models

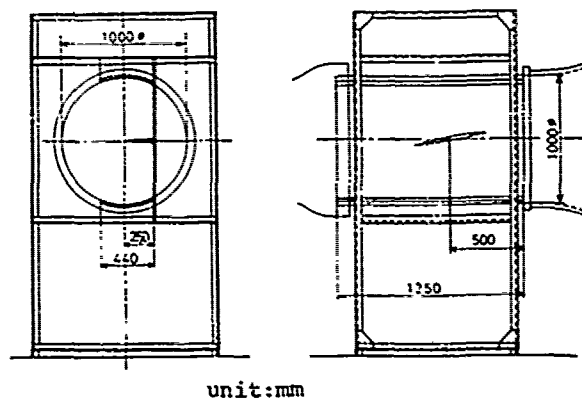


Fig.3.9 Arrangement for the Wind Tunnel Testing

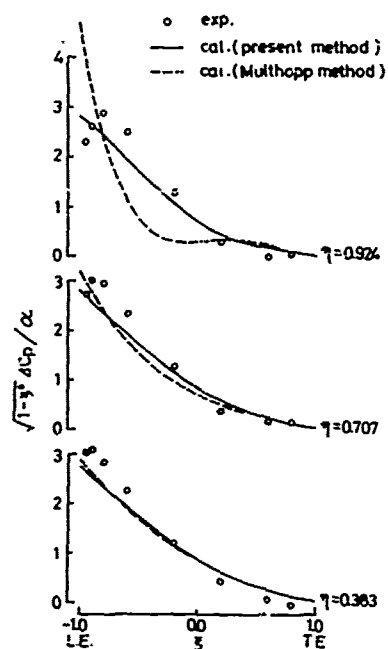


Fig.3.10 Pressure Jump Distribution over Wing No.1 ($\alpha=5^\circ$)

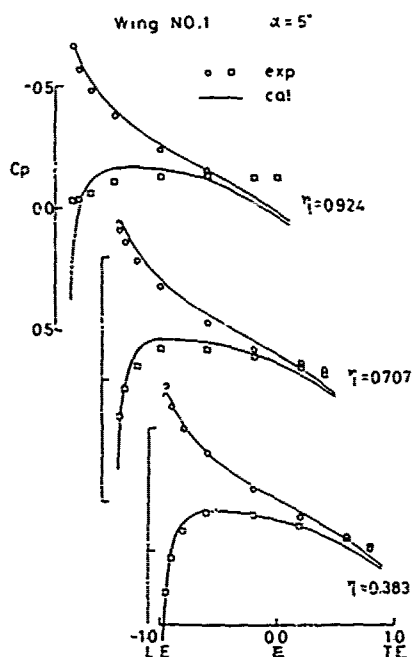


Fig.3.11 Pressure Distribution over Wing No.1 ($\alpha=5^\circ$)

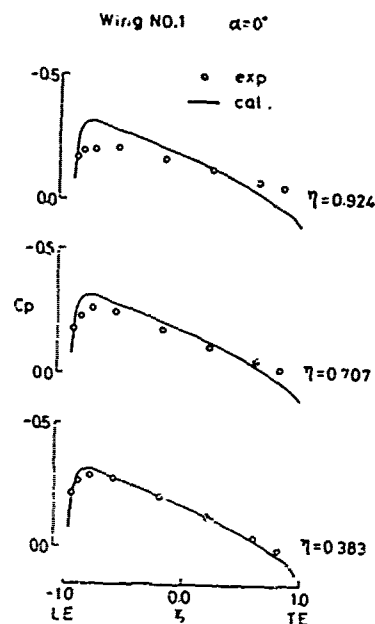


Fig.3.12 Pressure Distribution over Wing No.1 ($\alpha=0^\circ$)

An example of the comparison of lift density between theory and experiment is shown in Fig.3.10. The values by experiment are obtained from the pressure distribution on Wing No.1 at 5° angle of attack. Theoretical result by Multhopp's method using the integral equation (3.1) does not show good agreement with experiment near the tip of wing unlike near the center of wing. On the other hand the theoretical result by the present method using the new integral equation (3.2) shows good agreement with experiment even near the tip of wing. The same tendency of the lift density is obtained for the other wings. The results of the experiment reveals that results by the method using the new integral equation (3.2) are accurate even near the wing tip in contrast to the methods using the existing integral equation (3.1).

Pressure distribution on Wing No.1 at $\alpha=5^\circ$ angle of attack is shown in Fig. 3.11. Theoretical result is obtained by using the new integral equation (3.2) and the equivalent wing section as mentioned in section 2.2. Agreement between theory and experiment is not good near the tip. Fig. 3.12 shows the pressure distribution on Wing No.1 at $\alpha=0^\circ$ angle of attack. The agreement between theory and experiment is good near the center of wing and is not good near the tip, which shows that three dimensional effect by thickness distribution is large near the tip of blade. The three dimensional effect can explain the disagreement of pressure distribution near

the tip in Fig.3.11. The effect is variable according to the thickness distribution such as Wing No.1,2,3 unlike lift density. Result of the experiment show that the effect is smaller for the thin wing such as Wing No.3 or for the wing whose spanwise distribution of maximum thickness is not swept such as Wing No.2.

4. APPLICATION

The application of the propeller lifting surface theory is divided into three steps, namely, theory, numerical calculation, and propeller design. It is considered that main subject in the present situation is to establish the accurate calculation program with reliable numerical procedure. It is necessary to know sufficiently the accuracy and limitations of the calculation procedure, when it is used. From this point of view, discussions in preceding sections were developed. As the results, advantages and disadvantages of the three methods became clear, which show the direction of their applications.

Method 1 yields valid circulation density in wide range except near the tip and yields valid circulation of blade section in all range for the usual broad bladed propeller. The method is useful for the calculation of propeller forces. However the effect of p^*p should not be neglected in the calculation of unsteady propeller forces. Method 2 gives the converged chordwise distribution of circulation density. It is supposed to give the accurate solution near the leading edge and to be useful for the calculation of cavitation. Method 3 yields the accurate solutions for the circulation density near the blade tip as well, even though the blades are highly broad. The method is considered to be useful for the calculation of cavitation.

There are many possibilities of application of the propeller lifting surface theory to the propeller design. The following are some examples of the application method to be employed in the design procedure. The blade outline is adjusted according to the inflow variation of hull wake from the view point of vibratory propeller forces, when Method 1 is useful. If blade outline is given, the relation between upwash and loading is controlled by the lifting surface theory. If the pitch of the helical surface is assumed to fix, single calculation of the matrix of coefficients corresponding to the integral equation, makes it possible to obtain upwash distribution by the loading distribution and to obtain loading distribution by the upwash distribution with ease. In this case, Method 2 or Method 3 can control accurately the pitch correction or camber correction in the design method, from the cavitation point of view.

5. CONCLUSIONS

By comparing the three numerical meth-

ods, the lifting surface theory was discussed from the view point of application to marine propellers. The conclusions are as follows.

- (1) Results of numerical calculations by the three methods for the same hydrodynamic model show good agreement with each other except some regions. The agreement between numerical result and experiment is satisfactory. As the results the evaluation of the theory becomes clear.
- (2) The advantage and disadvantage of the three methods become clear by the investigation into the numerical results by the methods. Method 1, Method 2, and Method 3 are useful for the calculation of propeller forces, detailed chordwise distribution of circulation density, and circulation density near the tip of blade respectively.
- (3) It is verified numerically and experimentally for the case of a planar wing, that Method 3 yields the accurate solution near the tip of wing.
- (4) The possibility of application of the three methods to some aspects is shown.

ACKNOWLEDGMENT

The author wishes to acknowledge his indebtedness to Prof. T. Hanaoka for his valuable advice and kind encouragement, which initiated the present study.

REFERENCES

1. Kondo, K., "The Potential-theoretical Fundamentals of Aerodynamics concerning the Screw Propeller", the Memo. of Faculty of Eng. Kyushu Imp. Univ., Vol.9, No.3, 1942.
2. Sparenberg, J.A., "Application of Lifting Surface Theory to Ship Screws", International Shipbuilding Progress, Vol.7, No.67, 1960.
3. Hanaoka, T., "Hydrodynamics of an Oscillating Screw Propeller", 4th Symposium on Naval Hydrodynamics, Washington, Aug., 1962.
4. Sugai, K., "A Method for Calculating the Hydrodynamic Characteristics of Marine Propellers", J. of the Soc. of Naval Arch. of Japan, Vol.128, Dec.1970.
5. van Gent, W., "Unsteady Lifting-Surface Theory for Ship Screws: Derivation and Numerical Treatment of Integral Equation", J. of Ship Research, Vol.19, No.4, Dec.1975.
6. Klingsporn, H., "Numerische Untersuchung der Integral-gleichung der Propellertragflächentheorie", Schiffstechnik, Vol.20, No.99, 1973.
7. Tsakonas, S., Jacobs, W.R., and Ali, M.R., "Propeller Blade Pressure Distribution Due to Loading and Thickness Effects", J. of Ship Research, Vol.23, No.2, June, 1979.
8. Kerwin, J.E., and Lee, C.S., "Prediction of Steady and Unsteady Marine Propeller Performance by Numerical Lifting-Surface Theory", SNAME Trans., Vol.86, 1978.
9. Report of the Propeller Committee, Proceedings, 15th ITTC, The Hague, 1978, pp. 266-271.

10. Hanaoka, T., "A New Method for Calculating the Hydrodynamic Load Distributions on a Lifting Surface", Rep. of Ship Research Institute, Vol. 6, No. 1, Jan. 1969.

11. Hanaoka, T., "Numerical Lifting-Surface Theory of a Screw Propeller in Non-Uniform Flow (Part 1 Fundamental Theory)", Rep. of Ship Research Institute, Vol. 6, No. 5, Sept. 1969.

12. Koyama, K., "A Numerical Analysis for the Lifting Surface Theory of a Marine Propeller", J. of the Soc. of Naval Arch. of Japan, Vol. 132, Dec. 1972.

13. Koyama, K., "A Numerical Method for Propeller Lifting Surface in Non-Uniform Flow and Its Application", J. of the Soc. of Naval Arch. of Japan, Vol. 137, June 1975.

14. Hanaoka, T., "Fundamental Theory of a Screw Propeller - III (Two Numerical Methods for Solving Propeller Lifting-Surface Problems by the Use of Discrete Loading Functions)", Rep. of Ship Research Institute, Vol. 14, No. 6, Nov. 1977.

15. Koyama, K., "A Method for Treating the Singularity at the Blade Tip of Marine Propellers", J. of the Soc. of Naval Arch. of Japan, Vol. 145, June 1979.

16. Hanaoka, T., "Tip Condition and Numerical Method Concerning Lifting-Surface Theory (4-Integration by Parts in the Integral Equation)", Rep. of Ship Research Institute, Vol. 15, No. 4, July 1978.

17. Hanaoka, T., "Tip Condition and Numerical Method Concerning Lifting-Surface Theory (5-Lifting-Surface Theory of Oscillating Wing and Screw Propeller)", Rep. of Ship Research Institute, Vol. 15, No. 6, Nov. 1978.

18. Koyama, K., "A Method for Treating the Singularity at the Blade Tip of Marine Propellers (2nd Report)", J. of the Soc. of Naval Arch. of Japan, Vol. 146, Dec. 1979.

19. Multhopp, H., "Methods for Calculating the Lift Distribution of Wings (Subsonic Lifting Surface Theory)", R&M, No. 2884, 1950.

20. Watkins, C.E., Woolston, D.S., and Cunningham, H.J., "A Systematic Kernel Function Procedure for Determining Aerodynamic Forces on Oscillating or Steady Finite Wings at Subsonic Speeds", NACA TR R-48, 1959.

21. Flax, A.H., "General Reverse Flow and Variational Theorems in Lifting-Surface Theory", J. Aero. Sci., Vol. 19, No. 6, 1952.

22. Falkner, V.M., "The Calculation of Aerodynamic Loading on Surfaces of any Shape", R&M, No. 1910, 1943.

23. Albano, E., and Rodden, W.P., "A Doublet-Lattice Method for Calculating Lift Distributions on Oscillating Surface in Subsonic Flows", AIAA Journal, Vol. 7, No. 2, 1969.

24. Hsu, P.T., "Some Recent Developments in the Flutter Analysis of Low-Aspect-Ratio Wings", Proc. National Specialists Meeting on Dynamics and Aeroelasticity, Inst. of Aero. Sci., 1958.

25. Shen, C.C., Lopez, M.L., and Wasson, N.F., "A Jet-Wing Lifting-Surface Theory Using Elementary Vortex Distributions", AIAA Paper, No. 73-652, 1973.

26. Ito, T., Takahashi, H., and Koyama, K., "Calculation on Unsteady Propeller Forces by Lifting Surface Theory", Symposium on Hydrodynamics of Ship and Offshore Propulsion Systems, Oslo, March 1977.

27. Schwanecke, H., "Comparative Calculation on Unsteady Propeller Blade Forces", 14th ITTC, Rep. of Propeller Committee, App. 4, 1975.

28. Lan, C.E., "A Quasi-Vortex-Lattice Method in Thin Wing Theory", J. Aircraft, Vol. 11, No. 5, 1974.

29. Langan, T.J., and Wang, H.T., "Evaluation of Lifting-Surface Programs for Computing the Pressure Distribution on Planar Foils in Steady Motion", NSRDC Rep. 4021, 1973.

30. Takei, Y., Koyama, K., and Kurobe, Y., "Measurement of Pressures on a Blade of a Propeller Model", Papers of Ship Research Institute, No. 55, March 1979.

31. Hanaoka, T., and Koyama, K., "Calculation of the Pressure Loading for a Circular Wing by New Method", 10th Fluid Mechanic Symposium, Japan Society for Aeronautical and Space Science, Kyoto, Oct., 1978.

32. Koyama, K., and Haraguchi, T., "A Study of Numerical Solution of Lifting-Surface Problem", the Proc. of 1977's Autumn Meeting of Ship Research Institute, 1977.

33. Koyama, K., "Numerical Investigation into the Lifting Surface Theory for Planar Wings", Rep. of Ship Research Institute, Vol. 13, No. 1, Jan. 1976.

34. Jordan, P.F., "Remarks on Applied Subsonic Lifting Surface Theory", WGLR-DGRR Annual Meeting, Karlsruhe, Oct. 1967.

35. Jordan, P.F., "The Parabolic Wing Tip in Subsonic Flow", AIAA Paper, No. 71-10, Jan. 1971.

36. Kinner, W., "Die kreisförmige Tragfläche auf potentialtheoretischer Grundlage", Ing. Archiv 8, 1937.

37. Hough, G.R., "Remarks on Vortex-Lattice Methods", J. Aircraft, Vol. 10, No. 5, 1973.

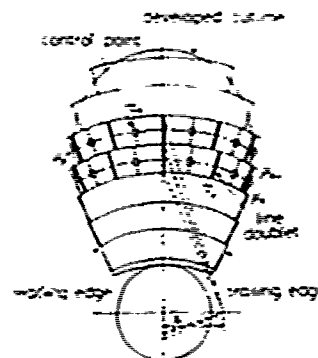


Fig. A1 Arrangement of Lattice

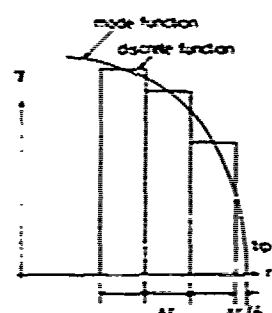


Fig. A2 Radial Location of Blade Elements

APPENDIX 1 Outline of Method 2 (Doublet-Lattice Method)

Integral equation (1.1) in the main body can be expressed as

$$w_0 = \frac{1}{2\pi} \int_{-\infty}^{\tau} e^{-ip^*(\tau-T)/2} \frac{\partial \phi_0}{\partial n} \Big|_{\sigma=\sigma'} dT \quad (A1.1)$$

$$\phi_0 = \frac{1}{4\pi\rho h} \sum_{m=0}^{l-1} e^{-i2pm\tau/l} \iint_S \bar{u}_0 \frac{\partial}{\partial n} \left(\frac{1}{R} \right) ds' dr' \quad (A1.2)$$

where the variable τ in the operator $\partial/\partial n$ in (1.1) is replaced by the variable T in the operator $\partial/\partial n$ in (A1.1).

Lifting surface expressed by the surface distribution of doublet in pressure field as shown in (A1.2) is replaced by the discrete distribution of line doublet on lattice. The blade is divided into N_R blade elements by cylindrical surfaces. The blade element is further divided into N_C boxes by radius vectors from the center of curvature of the helix. Line doublet with constant moment in pressure field is set on a radius vector in the box, and the control point for upwash is set on the center of boundary line between boxes as shown in Fig.A1. Arrangement of the blade elements and boxes is determined agreeably to Hough's[37] and Lan's[28] proposal which is shown in Figs. A2 and A3. Kutta's condition is satisfied owing to the boundary condition at the trailing edge control points.

As the relation between moment of the doublet and circulation density of bound vortex is given by equation(1.2), surface distribution of γ^* in a box can be replaced by the equivalent vortex line $\tilde{\gamma}$ as

$$\bar{u}_0 ds' = c\omega^* \tilde{\gamma}, \quad \tilde{\gamma} = \gamma^* a ds' \quad (A1.3)$$

Then acceleration $\tilde{u}(\tau, u) = \partial \phi_0 / \partial n \Big|_{\sigma=\sigma'}$ is expressed as

$$\tilde{u}(\tau, u) = \sum_{k=1}^{N_R} \sum_{j=1}^{N_C} \tilde{\gamma}_{jk} \tilde{u}_k(\tau - \tau_j, u) \quad (A1.4)$$

$$\tilde{u}_k(\tau - \tau_j, u) = \frac{v^*}{4\pi} \sum_{m=0}^{l-1} e^{-i2pm\tau/l} \int_{u_k}^{u_{k+1}} \frac{1}{\sqrt{1+u'^2}} \times \frac{\partial^2}{\partial n \partial n'} \left(\frac{1}{R} \right) \Big|_{\sigma=\sigma'} du' \quad (A1.5)$$

In this case, integration with respect to u' in (A1.5) can be performed analytically, which is the principal advantage of Method 2. After the integration (A1.5) becomes

$$\tilde{u}_k(\tau - \tau_j, u) = \frac{v^*}{4\pi h^2} \sum_{m=0}^{l-1} e^{-i2pm\tau/l} \left[\frac{1}{\sqrt{1+u'^2}} v \cdot \sin(v_m) \right.$$

$$\left. \times (X_{k+1}(v, u) - X_k(v, u)) \right.$$

$$\left. + \frac{1}{\sqrt{1+u'^2}} \frac{\partial}{\partial v} (Y_{k+1}(v, u) - Y_k(v, u)) \right], \quad (A1.6)$$

$$X_k(v, u) = X(v, u, u_k), \quad Y_k(v, u) = Y(v, u, u_k), \quad (A1.7)$$

where $X(v, u, u')$ and $Y(v, u, u')$ are defined in (1.6).

Finally the integral equation is transformed to the linear algebraic equations written as

$$\tilde{w}_{\alpha\beta} = \sum_{k=1}^{N_R} \sum_{j=1}^{N_C} \tilde{\gamma}_{jk} \tilde{z}_{jk}^{\alpha\beta} \quad (A1.8)$$

$$\tilde{z}_{jk}^{\alpha\beta} = \frac{1}{4\pi h} \sum_{m=0}^{l-1} e^{-i2pm\tau/l} \left[\frac{1}{\sqrt{1+u'^2}} \int_{-\infty}^v e^{-ip^*(v-s)} \right.$$

$$\left. \times s \cdot \sin(s_m) (X_{k+1}^{\beta}(s) - X_k^{\beta}(s)) ds \right.$$

$$\left. - \frac{ip^*}{\sqrt{1+u'^2}} \int_{-\infty}^v e^{-ip^*(v-s)} (Y_{k+1}^{\beta}(s) - Y_k^{\beta}(s)) ds \right.$$

$$\left. + \frac{1}{\sqrt{1+u'^2}} (Y_{k+1}^{\beta}(v) - Y_k^{\beta}(v)) \right] \quad (A1.9)$$

$$X_k^{\beta}(s) = X(s, u_{\beta}, u_k), \quad Y_k^{\beta}(s) = Y(s, u_{\beta}, u_k) \quad (A1.10)$$

When $u_k < u_{\beta} < u_{k+1}$ and $v > 0$, the integrand of (A1.9) shows higher order singularity, which is treated in the sense of Hadamard's finite part of an infinite integral[14].

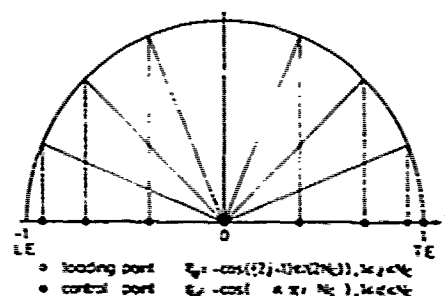


Fig.A3 Chordwise Location of Boxes

APPENDIX 2 Outline of Method 3 (Tip Singularity Treated Method)

The function $Z(s, \mu, \mu')$ in the integral equation (1.5) in the main body has a singular behavior for $s \rightarrow 0$ as

$$Z(s, \mu, \mu') = \frac{\text{sgn}(\mu' - \mu)}{s^2} - \frac{\text{sgn}(\mu' - \mu)}{2} \left\{ \frac{1 + \mu\mu'}{(\mu' - \mu)^2} + \frac{\mu}{\mu' - \mu} - \frac{3 - \mu^2}{3(1 + \mu^2)} \right\} + \dots, \text{ for } m=0,$$

$$Z(s, \mu, \mu') = -\frac{1}{s^2} \left\{ \frac{1 - \mu\mu'}{(\mu' + \mu)^2} - \frac{\mu}{\mu' + \mu} - \frac{3 - \mu^2}{3(1 + \mu^2)} \right\} + \dots, \text{ for } m=l/2. \quad (\text{A2.1})$$

Equation (1.5) is transformed with separating the singularity shown above. After the definition of the expression

$$w_0 e^{ip^* \tau / 2} = \bar{w}_0, \quad \gamma e^{ip^* \tau' / 2} = \bar{\gamma}_0, \quad (\text{A2.2})$$

equation (1.5) becomes

$$\bar{w}_0 = \bar{w}_0 + \bar{w}_1 + \bar{w}_2,$$

$$\bar{w}_1 = \frac{\mu^*}{2\pi\sqrt{1+\mu^2}} \int_{-1}^1 \frac{1}{\bar{c}\bar{\gamma}_0} d\xi' \int_{-\infty}^v \frac{e^{ip^* s}}{s^2} ds + \bar{w}_I,$$

$$\bar{w}_I = -\frac{\mu^*}{4\pi\sqrt{1+\mu^2}} \int_{\mu_b}^{\mu_0} d\mu' \int_{-1}^1 d\xi' \frac{\partial(\bar{c}\bar{\gamma}_0)}{\partial\mu'} \int_{-\infty}^0 e^{ip^* s} \left\{ \sum_{n=0}^{l-1} e^{-i2p\pi n/l} Z(s, \mu, \mu') - \frac{\text{sgn}(\mu' - \mu) - I(\frac{l}{2}) e^{-ip\pi}}{s^2} \right\} ds,$$

$$\bar{w}_1 = -\frac{\mu^*}{4\pi\sqrt{1+\mu^2}} \int_{\mu_b}^{\mu_0} d\mu' \int_{-1}^1 d\xi' \frac{\partial(\bar{c}\bar{\gamma}_0)}{\partial\mu'} \int_0^v e^{ip^* s} \left\{ \sum_{n=0}^{l-1} e^{-i2p\pi n/l} Z(s, \mu, \mu') - \frac{\text{sgn}(\mu' - \mu) - I(\frac{l}{2}) e^{-ip\pi}}{s^2} \right\} ds,$$

$$\bar{w}_2 = \frac{\mu^*}{4\pi\sqrt{1+\mu^2}} \int_{\mu_b}^{\mu_0} d\mu' \int_{-1}^1 \frac{1}{\bar{c}\bar{\gamma}_0} T(\xi') e^{ip^* v} \left\{ \sum_{n=0}^{l-1} e^{-i2p\pi n/l} Z(v, \mu, \mu') - \frac{\text{sgn}(\mu' - \mu) - I(\frac{l}{2}) e^{-ip\pi}}{v^2} \right\} d\xi', \quad (\text{A2.3})$$

where notation $I(a)$ denotes 1 if a is integer and denotes 0 if a is not integer.

$\bar{w}_0 - \bar{w}_I$ involves the upwash of the two dimen-

sional airfoil, \bar{w}_I involves the upwash by free vortices following lifting lines, and $\bar{w}_1 + \bar{w}_2$ involves the lifting surface correction.

Unknown function $\bar{\gamma}_0$ is approximated by

$$\bar{\gamma}_0(\xi, \eta) = \sum_{N=0}^R \bar{\gamma}_N(\eta) \lambda_N(\xi) \quad (\text{A2.4})$$

with the known elementary chordwise distribution $\lambda_N(\xi)$.

Influence functions

$$\bar{\gamma}_N(\eta, \eta') = \frac{\mu - \mu'}{2\sqrt{1+\mu^2}} k_N \left\{ \sum_{m=1}^{l-1} e^{-i2p\pi m/l} Y(0, \mu, \mu') + \int_{-\infty}^0 e^{ip^* s} \left\{ \sum_{m=0}^{l-1} e^{-i2p\pi m/l} (1+\mu^2) s \sin(s_m) \times X(s, \mu, \mu') - 2 \frac{\text{sgn}(\mu' - \mu) - I(\frac{l}{2}) e^{-ip\pi}}{s^2} \right. \right.$$

$$\left. - ip^* \left\{ \sum_{m=0}^{l-1} e^{-i2p\pi m/l} (Y(s, \mu, \mu') - \mu) - \frac{\text{sgn}(\mu' - \mu) - I(\frac{l}{2}) e^{-ip\pi}}{s} \right\} ds \right\},$$

$$\bar{\gamma}_N(\xi^*, \eta, \eta') = \frac{\mu - \mu'}{2\sqrt{1+\mu^2}} \int_{-1}^1 \lambda_N(\xi') d\xi' \int_{\eta'}^v e^{ip^* s} \left\{ \sum_{n=0}^{l-1} e^{-i2p\pi n/l} Z(s, \mu, \mu') - \frac{\text{sgn}(\mu' - \mu) - I(\frac{l}{2}) e^{-ip\pi}}{s^2} \right\} ds,$$

$$\bar{\gamma}_N(\xi^*, \eta, \eta') = -\frac{\mu^* \bar{c}(\mu - \mu')}{2\sqrt{1+\mu^2}} \int_{-1}^1 \lambda_N(\xi') T(\xi') e^{ip^* v} \times \left\{ \sum_{n=0}^{l-1} e^{-i2p\pi n/l} Z(v, \mu, \mu') - \frac{\text{sgn}(\mu' - \mu) - I(\frac{l}{2}) e^{-ip\pi}}{v^2} \right\} d\xi', \quad (\text{A2.5})$$

are defined, where $\sum_{n=1}^{l-1}$ denotes summation except $n=l/2$. The functions show the nature for $\eta \rightarrow \eta'$,

$$\bar{\gamma}_N(\eta, \eta') = \frac{1}{2} k_N + \frac{\mu^* \nu k_N}{4(1+\mu^2)} (\eta - \eta') \ln |\eta - \eta'| + \dots,$$

$$\bar{\gamma}_N(\xi^*, \eta, \eta') = g_{1,N}(\xi, 0) + \frac{\lambda_N^{(1)}(\xi)}{2C^2} (\eta - \eta')^2 \ln |\eta - \eta'|$$

$$\begin{aligned}
& + \frac{\mu^* \mu}{2(1+\mu^2)} g_{1,N}(\xi, 0) (\eta - \eta') \ln |\eta - \eta'| + \dots, \\
\gamma_N(\xi^*, \eta, \eta') &= -\sqrt{1+\mu^2} \Lambda_N(\xi) - \frac{\sqrt{1+\mu^2}}{2} \frac{\Lambda_N^{(2)}(\xi)}{c^2} \\
& \times (\eta - \eta')^2 \ln |\eta - \eta'| - \frac{\mu^* \mu}{2\sqrt{1+\mu^2}} \Lambda_N(\xi) (\eta - \eta') \ln |\eta - \eta'| \\
& + \dots,
\end{aligned} \tag{A2.6}$$

where

$$\begin{aligned}
k_N &= \int_{-1}^1 \lambda_N(\xi') d\xi', \\
g_{1,N}(\xi, 0) &= \frac{1}{2} \int_{-1}^1 \operatorname{sgn}(\xi - \xi') \lambda_N(\xi') d\xi', \\
\Lambda_N(\xi) &= \mathcal{T}(\xi) \lambda_N(\xi), \quad \lambda_N^{(1)}(\xi) = \frac{d}{d\xi} \lambda_N(\xi), \\
\Lambda_N^{(2)}(\xi) &= \frac{d^2}{d\xi^2} \lambda_N(\xi).
\end{aligned} \tag{A2.7}$$

Using the influence functions (A2.5), \tilde{w}_I , \tilde{w}_1 , \tilde{w}_2 in (A2.3) can now be written as

$$\begin{aligned}
\tilde{w}_I &= -\frac{1}{2\pi} \sum_{N=0}^R \int_{-1}^1 \frac{1}{d(\tilde{c}B^{(N)})} \frac{\gamma_N(\eta, \eta')}{\eta - \eta'} d\eta', \\
\tilde{w}_1 &= -\frac{1}{2\pi} \sum_{N=0}^R \int_{-1}^1 \frac{1}{d(\tilde{c}B^{(N)})} \frac{\gamma_N(\xi^*, \eta, \eta')}{\eta - \eta'} d\eta', \\
\tilde{w}_2 &= -\frac{1}{2\pi} \sum_{N=0}^R \int_{-1}^1 \frac{1}{B^{(N)}} \frac{\gamma_N(\xi^*, \eta, \eta')}{\eta - \eta'} d\eta'.
\end{aligned} \tag{A2.8}$$

Numerical calculation of the influence function $\gamma_N(\eta, \eta')$, $\gamma_N(\xi^*, \eta, \eta')$, and $\gamma_N(\xi^*, \eta, \eta')$ in (A2.5) is easy because singularities are not included in the integrands. It is necessary to devise the integration with respect to η' in (A2.8). Regular part including the unknown coefficient $B^{(N)}(\eta')$ in the integrand is approximated by interpolation formula, and singular integration is performed analytically [15].

Discussion

A.Y. Odabaşı (BSRA)

Mr. Koyama has presented us with a very interesting and enlightening paper. Within the limits imposed by the choice of the methods there is very little to add to the statements in the paper except that:-

(1) The use of Tikhonov's regularisation method 1), 2) might have avoided the problems arising from the logarithmic singularity near the edge or the tip of the blade.

(2) It might be beneficial to use Lighthill's leading edge correction 3) or its extended version to resolve the singular behaviour at the leading edge which, after inspecting the computed results, might also improve the results of the Method 3.

(3) Examination of Figure 3.5 and some other related publications of Mr. Koyama indicates that the convergence of the mode function approach with the selected number of modes is suspect and a study on their convergence properties may prove useful.

The main points I would like to raise are:-

(i) What is the role of the trailing vortex deformation and roll-up on the loading and pressure distribution near the tip, and

(ii) How realistic is the boundary condition (1.4) in accounting for the blade tip effect.

The answer to the first question is quite difficult since, to the knowledge of the present contributor, all the lifting surface computer programs for marine propellers employ an assumed wake geometry, whether deformed or not. It is however known from wing and rotor applications that these deformations can produce pronounced changes near the blade tip. Amongst the methods considered only the Method 2 can accommodate these kind of changes and hence this should be taken as an advantage of this method.

The condition (1.4) imposed for the tip is unnecessarily restrictive, since it does not indicate how Γ should tend to zero, and may not be fulfilled in the actual flow conditions. A more realistic condition would be the finiteness of the velocities as used by Belotserkovskii 4), 5). In this case the free vortex sheet would leave the blade tip from the leading edge depending on the radial and normal velocities. It is certain however that implementation of Belotserkovskii's incremental time step method for marine propellers would be quite costly due to the necessarily large storage and computation time requirements and a compromise may be adopted provided that other than the upwash changes on the blades the behaviour of the free vortex sheet is not of our concern.

In such a compromise the edge conditions of semi-infinite wings 6) may be adopted which demands that:-

$$\begin{aligned} \gamma & \rightarrow \sqrt{1/\delta} & \text{as } (s, \tau) \rightarrow (s_1, \tau_1) \\ \gamma & \rightarrow \sqrt{\delta} & \text{as } (s, \tau) \rightarrow (s_2, \tau_2) \\ \gamma & \rightarrow \sqrt{y} & \text{as } y \rightarrow 0 \\ \gamma & \rightarrow \gamma_\infty & \text{as } y \rightarrow \infty \end{aligned}$$

where δ is the distance to the edge of the blade and y is measured from the tip of the blade (positive towards the root). Following the directions given in Ref. 6) one may then devise a loading correction due to the tip effect as:-

$$\gamma_T = \gamma_\infty - \gamma \quad (1)$$

where γ_T is the loading correction due to the tip effect and γ_∞ is the uncorrected loading. The use of the relationship (1) produces an integral equation relating γ_T to γ_∞ which can be solved iteratively.

The advantage to be gained by the use of this compromise approach is that the effect of the trailing vortex deformation, including roll-up, can be accounted for by modifying γ_T and consequently these effects can be included within a mode function method.

Before closing this contribution, I would like to express my appreciation to Mr. Koyama for his fine paper and I look forward with interest to his views in relation to the comments I have made.

REFERENCES

- 1) Tikhonov, A.N., "The Solution of Incorrectly Formulated Problems and the Regularisation Method", Dokl. Akad. Nauk. SSSR, Vol. 151, p. 501 (1963)
- 2) Tikhonov, A.N. and Glasco, V.B., "Use of the Regularisation Method in Non-Linear Problems", Zh. Vychisl. Mat. i Mat. Fiz., Vol. 5, p. 463 (1965)
- 3) Lighthill, M.J., "A New Approach to Thin Aerofoil Theory", The Aeronautical Quart., Vol. 3, p. 193 (1951)
- 4) Belotserkovskii, S.M. and Nisht, M.I., "Non-Stationary Non-Linear Theory of a Thin Wing of Arbitrary Planform", Fluid Dynamics, Vol. 9, p. 583 (1976)
- 5) Belotserkovskii, S.M., Vasin, V.A. and Loktev, B.E., "Non-Linear Mathematical Simulation of Unsteady Flow Past a Helicopter Rotor", Sov. Phys. Dokl., Vol. 23, p. 393 (1978)
- 6) Hall, G.F., Shamroth, S.J., McDonald, H. and Briley, W.R., "The Inviscid Pressure Field on the Tip of a Semi-Infinite Wing and Its Application to the Formation of a Tip Vortex", NASA CR-2748 (1976)

First of all I would like to express my appreciation to Mr. Koyama for his work, as lifting surface methods showed to be the right tools to be used in order to get answers to the demands concerning the work of the propeller in unsteady water. By application of the computer program, worked out in the Netherlands Model Basin at Wageningen on base of the Sparenberg's lifting surface theory, on the work of an optimum designed subcavitating propeller family of a single screwed tank ship, I tried myself to get some of such answers.

The problem was concerning the variations of blade and propeller dynamic forces outcoming from the velocity field inhomogeneity. The questions were:

- Which is the difference in the results if using lifting line or lifting surface calculation methods?
- Which would be the influence of blade frequency variation on the variation of the dynamic forces maximal amplitudes in the case of optimum designed propellers?

Here are some figures representing the then gotten results. The numbering of the figures is not continuous as it relates to the paper of the more complete work issued by Schiffstechnik Bd.27 - 1980.

The ship was a tanker of 225000 tdw, which was designed to reach 16.5 knots at trials with 40000 dhp at 90 rpm.

Figs.1 and 2 show the plan of the first designed propellers: a W.B. 5-60 propeller and a five bladed wake adapted propeller designed by lifting line method.

Figs.6 and 7 show the resulting distributions along the blade span of the circumferential mean wake components and their variation during one revolution.

Figs.8 and 9 show two - dimensional intake water velocities representations for central and side ship propeller locations. Fig.10 shows the resulting pulsating mean disk intake velocity angles for a given diameter calculated by open water propeller data at constant J values. Fig. 11 shows how the inclusion of tangential water velocities change the resulting intake angles.

Figs.18 and 19 show the resulting fluctuations of blade thrust and torque calculated by mine and Vedeler's open water data methods, by the lifting line method of Burrill and the lifting surface method of NSP, Wageningen. Figs.20 a,b and c relate to the results gotten by the same methods for the propeller dynamic force components.

The last eight figures relate to the analysis of blade frequency influence on dynamic forces values worked out by lifting surface method and evaluated in form of coefficients, which are proportions to steady or mean values.

At harmonics 0 and 1 resulted additional steady values as represented on Fig.21 for each blade and on Fig.22 for

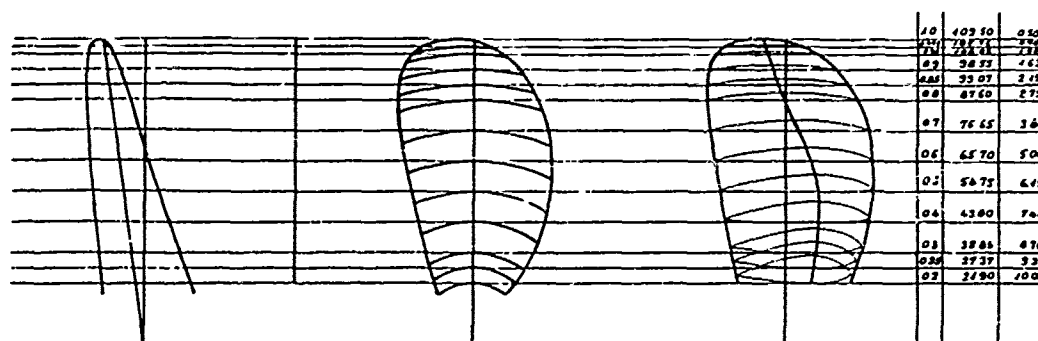
the propeller. Further on are presented variations resulting for one blade in maximum amplitudes of thrust, Fig.23, of torque, Fig.24, and of bending moment, Fig.25. Propeller maximum amplitudes for thrust and shaft torque are given on Fig. 26, as for vertical and horizontal transverse forces on Fig.27 and for transversal moments on Fig.28.

The blade frequency values were evaluated once by number of blade variation (Z) and secondly by number of revolutions variation (N). It was concluded that the growing of number of revolutions meant always lower coefficients of maximum amplitudes at constant blade number while the variation of blade number at constant revolutions can get into resonance with the wake field and therefore give periodicity to the functions of force amplitudes at blade frequency variations.

REFERENCES

- 1) Vučinić, A., "Theoretical Fundamental Researches on Dynamical and Propeller Loadings Caused by Unsteady Inflow", University of Rijeka, (1975)
- 2) Vedeler, B., "On Marine Propeller Forces in Calm Water and Waves and the Strength of Propeller Shaft Systems in Single Screw Ships", Det Norske Veritas Report 68-12-M, (1968)
- 3) Burrill, L.C., "Calculation of Marine Propeller Performance Characteristics", Trans. of the North East Coast Institution of Engineers and Shipbuilders, Vol.60, (1944)
- 4) Ritger, P.D. and Breslin, J.P., "A Theory of the Quasisteady and Unsteady Thrust and Torque of a Propeller in a Ship Wake", David Taylor Report 686, SIT, (1958)
- 5) Tsakonas, S. and Jacobs, W.R., "Theoretical Calculations of Vibratory Thrust and Torque and Comparisons with Experimental Measurements", Stevens Institute of Technology, Davidson Laboratory Report No.827, Feb., (1961)
- 6) Sparenberg, J.A., "Application of Lifting Surface Theory to Ship Screws", International Shipbuilding Progress, No.67, 1.7, March (1960)
- 7) Shiori, J. and Tsakonas, S., "Three-Dimensional Approach to the Gust Problem for a Screw Propeller", Davidson Laboratory Report 940, SIT, (1963), Journal of Ship Research, Vol.7, No.4, April (1964)
- 8) Hanaoka, T., "Introduction to the Nonuniform Hydrodynamics Concerning a Screw Propeller", Journal of the Society of Naval Architects of Japan, No.109 and "On the Integral Equation Concerning an Oscillating Screw Propeller by Lifting Line Theory", ibid, No.110
- 9) Verbrugh, P., "Unsteady Lifting Surface Theory for Ship Screws", Report No. 68-036-AH of the Netherlands Ship Model Basin, April (1968)
- 10) Sjøntvedt, T., "Propeller Induced Excitation Forces", Det Norske Veritas, Publication No.74, January (1971)

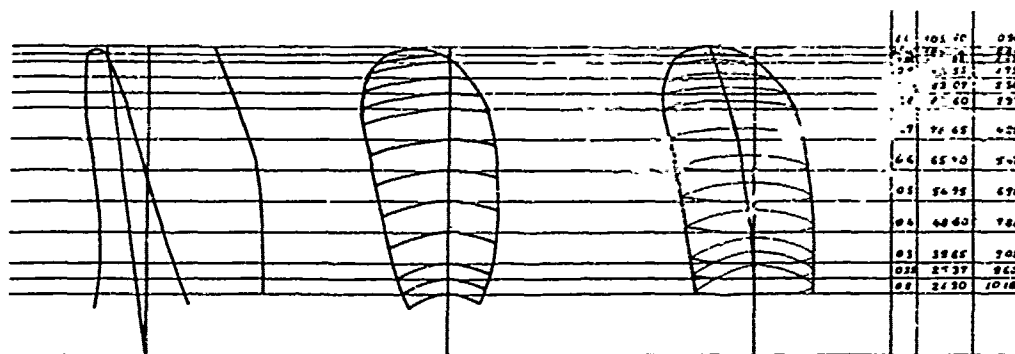
W.B-Series Propeller Prop. Model No.11



Diameter $D = 8760$ mm
 Pitch at root 6800 mm
 at 0.7R 6800 mm
 at blade tip 6800 mm
 Disc area 60.270 m^2
 Exp. blade area 36.162 m^2
 Number of blade 5
 Scale ratio of model propeller 1 : 40

Fig.1

Standard Propeller Prop. Model No.C20?



Diameter $D = 8760$ mm
 Pitch at root 6370 mm
 at 0.7R 6601 mm
 at blade tip 7110 mm
 Disc area 60.270 m^2
 Exp. blade area 31.260 m^2
 Number of blade 5
 Scale ratio of model propeller 1 : 40

Fig.2

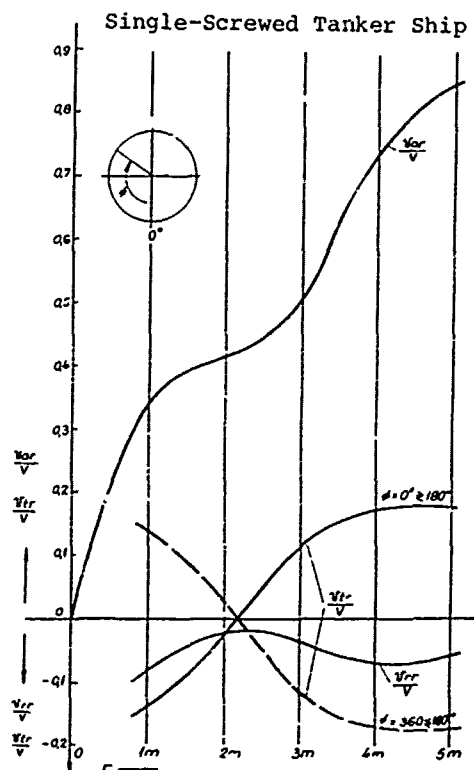


Fig. 6 Mean Wake Velocity at Each Radius in the Axial Tangential and Radial Direction

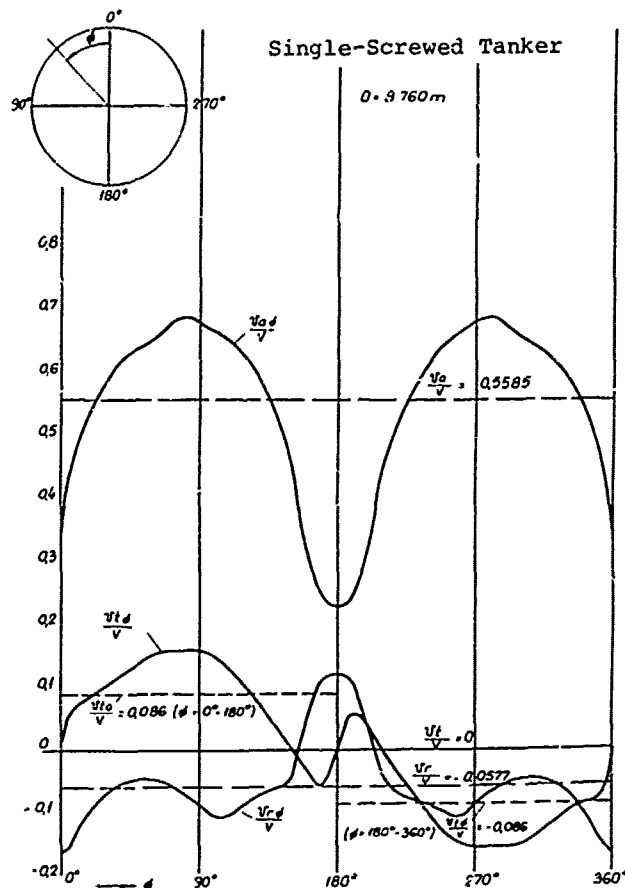


Fig. 7 Circumferential Pulsation of Nominal Wake in the Axial Tangential and Radial Direction

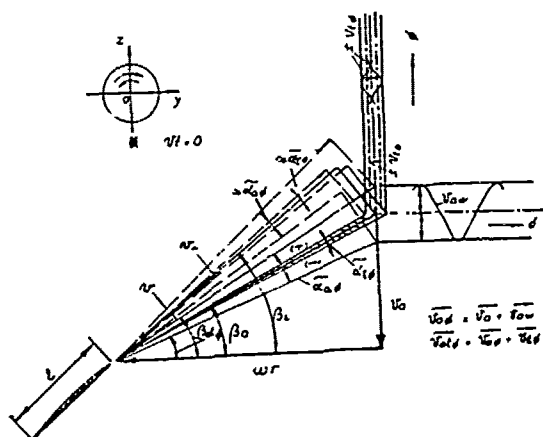


Fig. 8 Axial and Tangential Pulsation of Intake Water Velocities Due to Wake Inhomogeneity for Single-Screwed Ship

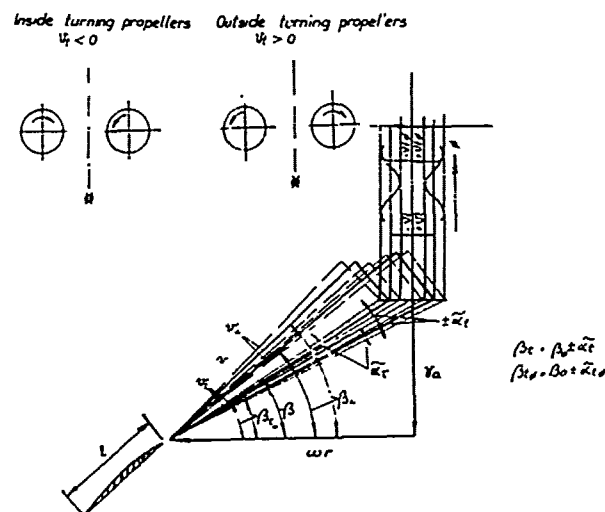


Fig. 9 Tangential Pulsation of Intake Water Velocities Due to Wake Inhomogeneity for Side Screwed Ship

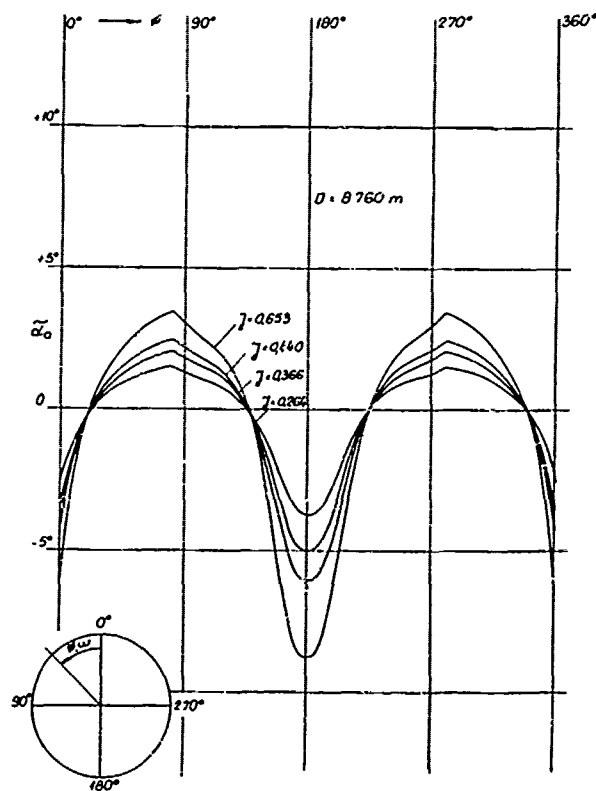


Fig. 10 Single-Screw Tanker Wake Field Pulsation of Screw Mean Intake Velocity Angle Due to Axial Wake

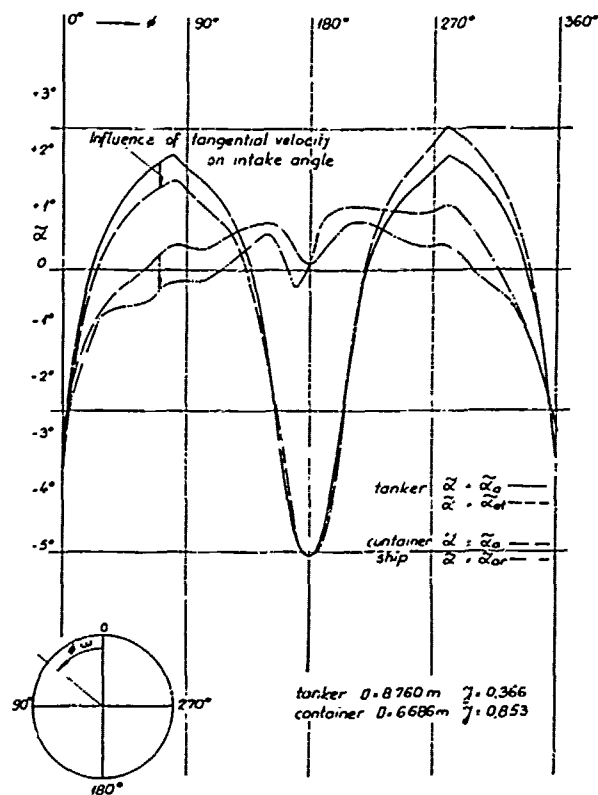


Fig. 11 Pulsation of Screw Mean Intake Velocity Angle Due to Axial and Axial-Tangential Wake Variation

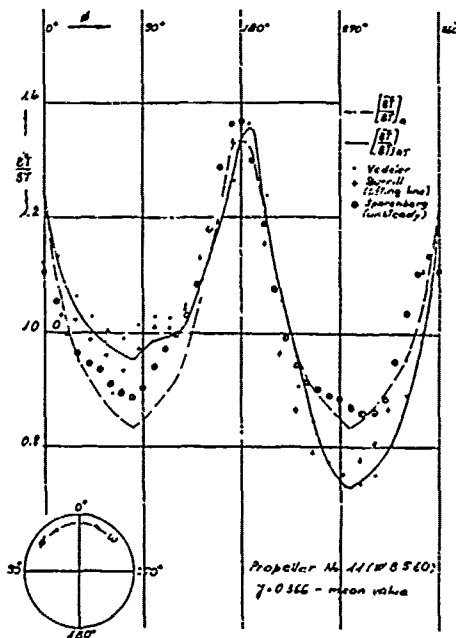


Fig. 18 Fluctuation of Blade Thrust from Open Water Test Data and Theoretical Methods

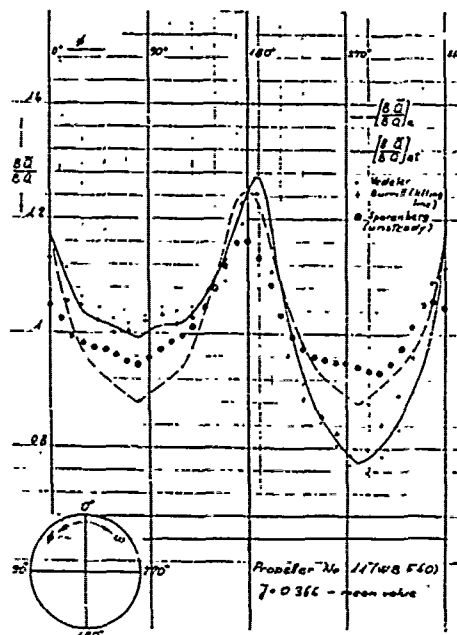


Fig. 19 Fluctuation of Blade Shaft Torque from Open Water Test Data and Theoretical Methods

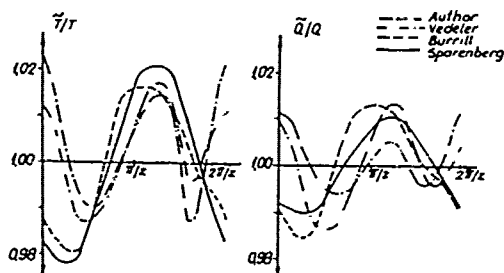


Fig. 20 a

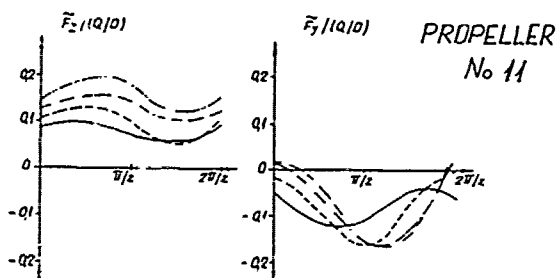


Fig. 20 b

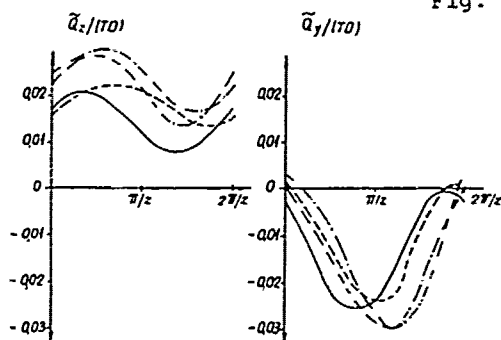
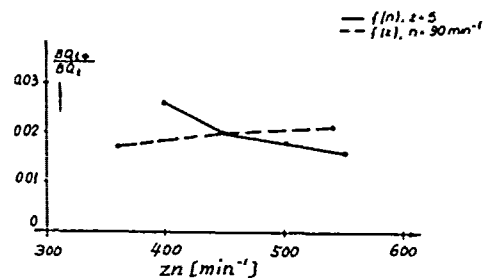
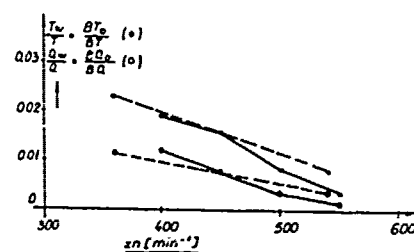


Fig. 20 c



Coefficients of Blade Additional Steady Bending Moments, Harmonic 0



Coefficients of Propeller and Blade Additional Steady Thrust and Turning Moments, Harmonic 0

Fig. 21

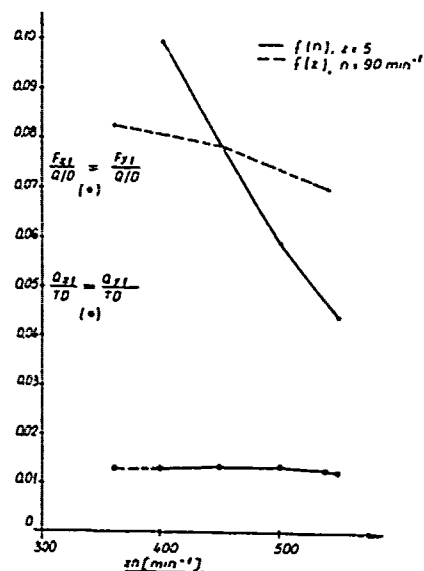


Fig. 22 Coefficients of Propeller Steady Transverse Force and Moments, Harmonic 1

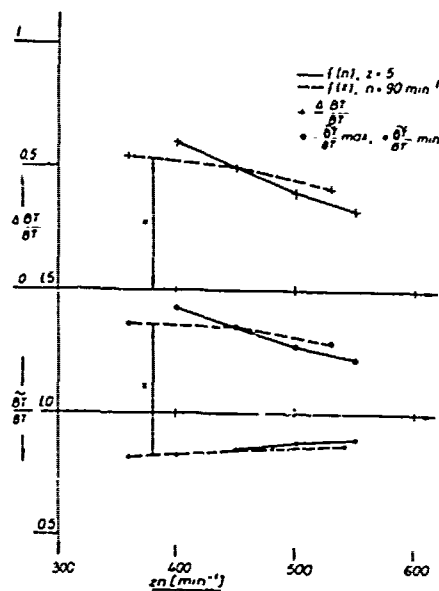


Fig. 23 Maximum Amplitudes of Blade Thrust Coefficients (till $\mu = z + 1$)

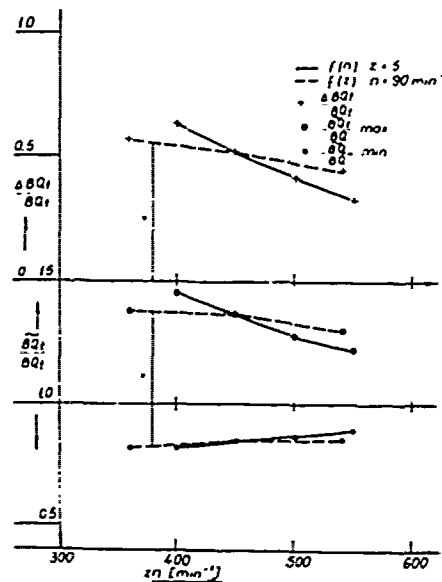


Fig. 25 Maximum Amplitudes of Blade Bending Moment Coefficients (till $\mu = z + 1$)

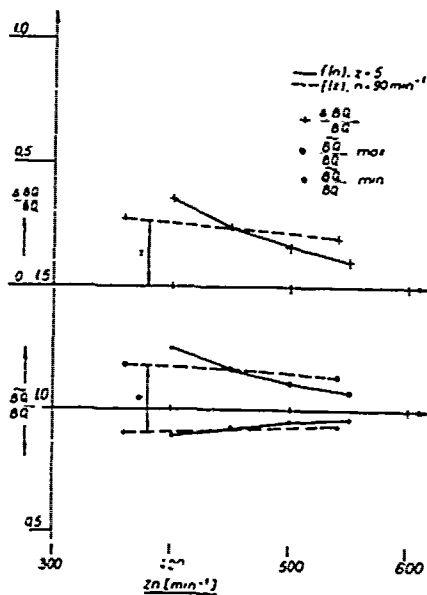


Fig. 24 Maximum Amplitudes of Blade Moment Coefficients (till $\mu = z + 1$)

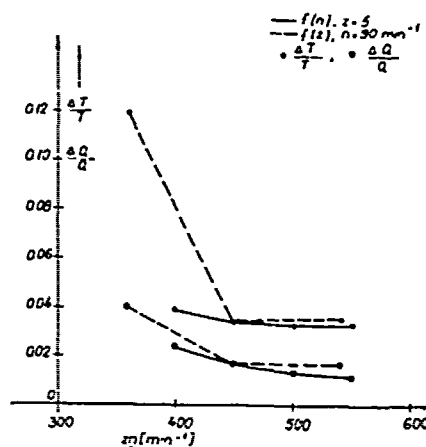


Fig. 26 Propeller Thrust and Shaft Torque Amplitudes Coefficients at $\mu = z$

Author's Reply

K. Koyama (SP/)

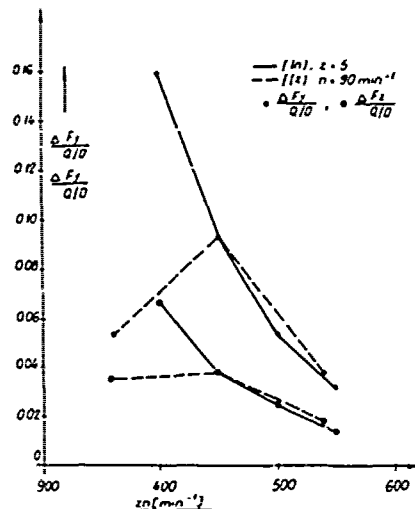


Fig. 27 Propeller Transverse Forces Amplitudes Coefficients (till $\mu = z + 1$)

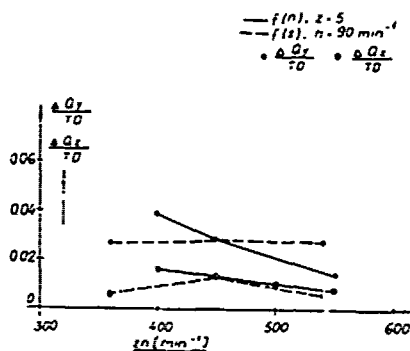


Fig. 28 Propeller Transverse Moments Amplitudes Coefficients (till $\mu = z + 1$)

I would like to express thanks to Dr. Odabaşı and Prof. Vučinić for their interest and valuable discussions. In response to the discussion made by Dr. Odabaşı, I would like to express my opinion in the following.

I think the simple lifting surface model used in the present paper is useful from the practical point of view. The problem dealt in Method 3 is the difficulty, which appears in the numerical solution for the simple lifting surface such as a steady circular planar wing. The solid lines in Fig. 3.5 show that the difficulty in the existing methods is serious. The point of Method 3 is that expression (3.1) and expression (3.2) are entirely different. The expression (3.2) stands on the base of the tip condition $\Gamma=0$. The condition is considered to be reasonable.

Dr. Odabaşı's two proposals concerning the trailing vortex deformation and the realistic tip condition are very interesting and valuable from the view point of making more realistic model. I hope such kind of calculation will be carried out in future.

As far as the convergence of the function approach is concerned, I differ from Dr. Odabaşı in opinion. In early stage of my study, the solid lines in Fig. 3.5 seemed to show the insufficiency of the terms of mode function near the tip of wing. But the results of new calculation indicated by circle symbols, triangle symbols, and square symbols in the figure show the sufficiency of the terms. I think that the discrepancy between the present result and the analytical result shown in Fig. 3.7 is tolerable from the practical point of view.

Prediction of the Transient Cavitation on Marine Propellers by Numerical Lifting-Surface Theory

Chang-Sup Lee

Korea Research Institute of Ships

Daejeon, Korea

ABSTRACT

A theoretical tool to predict the transient behavior of cavities on marine propellers has been in need, especially, to reduce the ship hull vibration. But complicated nature of the cavitating flow prohibited so far the development of exact theories in this area, allowing only a few empirical theories to exist. In this paper the unsteady partial- and/or super-cavitating propeller problem is solved in a rational way, treating the unsteady terms exactly, by using the lifting-surface theory based on method of vortex/source distribution.

The boundary value problem is formulated with mixed boundary conditions, i.e., the flow tangency condition on the wetted portion of the blades and the dynamic condition on the cavitating part of the blades. A cavity closure condition is used to provide an additional relation for the determination of the cavity extent. The problem is then solved directly in the time domain in a stepwise manner, and an efficient iteration scheme is devised to calculate the cavity extent. This theory, initiated originally for unsteady subcavitating propeller problem, gives comparison between performances with and without cavity, as well as temporal variation of cavity extent and cavity volume.

The cavitating patterns predicted by the present theory are compared with direct observations of the cavities at the water tunnel with a model propeller both in uniform flow and in screen generated non-uniform flow. Comparisons are considered to be good. A test computation is made for a full-scale propeller in a wake measured behind a model ship, and compared with the full-scale observation. Although the

comparison is not satisfactory, an estimate on the boundary layer thickness of ship indicates that the prediction might be improved if correct scaling effects are considered when obtaining the wake behind a full-scale ship.

NOMENCLATURE

a_{pq}	= coefficient matrix, defined in Eq. (60)
c	= blade section chord length
d_{ij}	= defined in Eq. (32)
D	= propeller diameter
e_{ij}	= defined in Eq. (57)
f_o	= maximum blade section camber at a given radius
F	= defined in Eq. (45)
Fr	= propeller Froude number based on propeller rotational speed, $Fr = n^2 D / g$
h	= cavity thickness function
H_{ijnm}	= induced velocity at (i,j) th control point due to (n,m) th unit strength cavity source
I	= total number of unknowns, $I = N + 1 + N_Q$
i, j	= chordwise and spanwise indices of the control point, respectively
J_A	= advance coefficient, $J_A = V_A / nD$
K	= number of blades
K_{ijnm}	= induced velocity at (i,j) th control point due to (n,m) th unit strength vortex
K_T	= mean thrust coefficient, $K_T = T / \rho n^2 D^4$
l	= cavity length
M	= number of chordwise panels over radius
n	= propeller rotational speed, revolutions per second
\underline{n}	= vector normal to blade camber surface

N = number of spanwise vortices within a chordwise strip
 N_Q = number of cavitating elements at each radial interval
 N_w = number of discrete time steps since beginning of motion
 n, m = chordwise and spanwise indices of the singularity, respectively
 p = pressure
 p_v = vapor pressure
 p_∞ = pressure at depth of the shaft center at upstream infinity
 p = propeller pitch
 q = strength of continuous sources per unit area
 Q_{nm} = strength of (n, m) th concentrated line source per unit length
 r = radial coordinate
 r_H = hub radius
 R = propeller radius
 Re = Reynolds number
 R_n = defined in Eq. (4)
 s = fraction of chord from leading edge
 t_0 = maximum blade section thickness at a given radius
 T = thrust
 u, v, w = perturbation velocities in the (ξ, η, ζ) directions
 U_r = helical inflow velocity, defined in Eq. (36)
 v = resultant velocity
 $\bar{V}_A(r, \theta_0)$ = inflow velocity at coordinate (r, θ_0) in propeller plane
 w_g = gust velocity normal to camber surface
 x_m = rake
 x, y, z = cartesian coordinate system fixed on propeller: x positive downstream, y positive radially outward, and z being determined to complete the right hand system
 x_0, y_0, z_0 = cartesian coordinate system fixed on ship: x_0 identical to x , positive downstream, y_0 measured positive upward from the shaft center, and z_0 positive when pointing port
 Γ_{nm} = strength of (n, m) th discrete vortex element
 ϵ = angle of spanwise vortex line relative to η coordinate
 θ_0 = angular coordinate of key blade relative to y_0 coordinate fixed on ship
 θ_m = skew angle
 ξ, η, ζ = coordinate system defined on the camber surface: ξ intersection of the camber surface and a cylindrical surface concentric with x axis, positive when pointing downstream, ζ normal to the camber surface, positive when pointing upstream, and η being determined to complete the right hand system on the camber surface
 σ_n = cavitation number based on the propeller rotational speed, $\sigma_n = (p_\infty - p_v) / \frac{1}{2} \rho n^2 D^2$
 ϕ_{ijnm} = velocity potential at (i, j) th control point due to (n, m) th unit

strength source element
 ϕ = perturbation velocity potential
 \square = closed vortex; see Eq. (33)
 \square_w = shed vortex quadrilateral; see Eq. (33)

1. INTRODUCTION

As the loading on the blades increases, the propeller begins suffering from a hydrodynamic phenomenon called cavitation. It is well known that the vibratory pressure force on ship hull due to the cavity constitutes the major portion of the total unsteady hull surface forces. With an increasing demand for ships with less vibration, it has been being paid much attention in recent years. The presence of the cavity becomes even more important when the cavity undergoes a sudden collapse on the blade. This imparts a high pressure impact leading to serious damage of the propeller blades, and at the same time radiates undesirable noise.

There are numerous lifting-surface theories for solutions to the subcavitating propeller problems, which may be considered to be of sufficient practical value for the design purpose. Yet the theories for the cavitating propeller are far from being practical. The difficulties in the cavity flow problem arise mainly due to the presence of the cavity itself, whose extent is not known a priori.

Original contributors to this problem developed non-linear (two-dimensional) free-streamline theories. It is rather recent that the linearized problem has been formulated and solved for the thin or slender body cavity flows; see Tulin(Ref.1) and Geurst(Ref.2) for details.

While most of the previous work involved solutions in the mapped plane using analytic function theory, a solution method in the physical plane by using the singularity distribution method was developed at M.I.T. Golden(Ref.3) in his pioneering work introduced the discrete singularity method for the solution of the cavitating, lifting problem for steady two-dimensional hydrofoil. This method was improved by Jiang(Ref.4) for the solution of the unsteady super-cavitating hydrofoil problem of finite aspect ratio, and further improved by Van Houten(Ref.5) to solve the two-dimensional partially cavitating unsteady flow problem.

The cavity flow around a marine propeller is so complicated that little progress has been made in treating this awful problem. Most of the existing theories are developed in a quasi-steady manner and use steady two-dimensional solution extensively to determine the cavity extent; see for example those of Van Oossanen(Ref.6) and Huse(Ref.7).

It is obvious from the experimental observation that the cavity behavior is neither quasi-steady nor two-dimensional. Primitive strip-theory fails because the interactions of the cavities along the adjacent chordwise strips are so strong that

the cavity length can not be determined solely from two-dimensional consideration. The behavior of the cavity extent is non-linear in time, i.e., the cavity grows gradually as the blade enters high wake region, but collapses rather rapidly when the blade advances against the adverse pressure gradient. In this regard pure harmonic representation of cavity behavior sees shortcomings at the outset. Thus a truly unsteady three-dimensional cavity theory is desired to explain the important hydrodynamics of the unsteady cavitating propeller problem. From the present state of our knowledge in this field the numerical cavitating propeller theory is presumably the best way to the solution with the great aid of the modern computer.

Many descriptions on the propeller geometry and unsteady propeller theory, previously presented as a paper by Kerwin and the present author (Ref. 8), are included here with minor changes to complete the development of the propeller lifting-surface theory.

2. FORMULATION OF THE PROBLEM

2.1. Fundamental Assumptions

The propeller blades are considered to be a set of symmetrically arranged thin blades of arbitrary form, rotating with a constant angular velocity about a common axis in an unbounded, incompressible fluid. The presence of extraneous boundaries such as the propeller hub, the rudder, and the ship hull, is neglected, except that the last is recognized as a body generating the non-uniform flow field.

The blades are assumed to operate at a small angle of attack, and the spatial variation of the ship wake is assumed small accordingly. The blade boundary layer and shed vortex wake thickness is assumed to be thin so that the fluid rotation due to the propeller is confined in a thin layer.

It is assumed that the formation and decay of the cavity occurs instantaneously depending only upon whether the pressure exceeds the prescribed cavity pressure or vapor pressure, which is assumed to be constant. The thickness of the cavity is also assumed to be small so that linearization in thickness is possible. Some important phenomena such as cavity inception and surface tension are not considered. It is assumed that the cavity starts at the leading edge of the blade, and that only the suction side of the blade is cavitating in the present work.

The cavitation number, σ_n , is defined based on the propeller rotational speed as

$$\sigma_n = (p_m - p_v) / \frac{1}{2} \rho n^2 D^2, \quad (1)$$

where p_m is the pressure at shaft center, p_v the vapor pressure, ρ the density of the water, n the number of revolutions per second, and D the diameter of the propeller. The Froude number, Fr , is also defined

based on the propeller rotational speed as

$$Fr = n^2 D / g, \quad (2)$$

where g is the gravitational acceleration. The inverse of the Froude number serves as a direct measurement of the hydrostatic pressure (or local cavitation number) variation from the shaft center to the top of the propeller plane. The cavitating flow field will be uniquely characterized by the above two non-dimensional parameters.

The propeller is considered to be operating in a known inflow field representing the wake field of the ship. The components of the wake field are customarily specified only in the plane of the propeller, and it is assumed that their variation over the axial extent of the propeller can be ignored.

2.2. Boundary Value Problem

Let us consider a propeller operating in an unbounded, incompressible fluid. The propeller may be in either a non-cavitating or cavitating condition. The principle of conservation of mass is the governing equation in the fluid region encompassing the blades, the shed wake, and the cavity, i.e.,

$$\nabla \cdot \mathbf{V} = 0, \text{ throughout the fluid} \quad (3)$$

where \mathbf{V} is the total fluid velocity. The problem is uniquely defined by imposing the boundary conditions as follows:

(i) Quiescence condition at infinity: At infinite upstream, the perturbation velocity due to the presence of the propeller and cavity should vanish.

(ii) Tangency condition on the wetted surface: The kinematic boundary condition on the wetted portion of the blade surface is the impermeability to the fluid, and is best described in a blade-fixed coordinate system rotating with the propeller,

$$\mathbf{n} \cdot \mathbf{V} = 0, \text{ on the wetted surface} \quad (4)$$

where \mathbf{n} is the vector normal to the camber surface, defined positive when pointing upstream.

(iii) Kutta condition at the trailing edge: The flow should leave the trailing edge in a tangential direction.

(iv) Kelvin's theorem for the conservation of circulation

(v) Kinematic and dynamic conditions in the wake: The velocity jump must be purely tangential to shed vortex wake sheet, and the pressure must be continuous across this vortex wake sheet.

The above five boundary conditions are sufficient to define the fully-wetted,

subcavitating unsteady propeller problem. For the cavitating propeller, additional conditions are necessary due to the presence of the cavity. The interface of the cavity and the surrounding fluid is termed the cavity surface, $F(\underline{x}, t) = 0$.

(vi) Kinematic condition on the cavity surface: Since the interface is moving with the fluid particles, the substantial derivative of the quantity $F(\underline{x}, t)$ should vanish,

$$DF/Dt = 0, \text{ on the cavity surface} \quad (5)$$

(vii) Cavity closure condition: It is assumed that the cavity thickness be zero along the boundary of the cavity surface,

$$h(\underline{x}, t) = 0, \text{ along the cavity boundary} \quad (6)$$

(viii) Dynamic condition on the cavity surface: The pressure on the cavity surface is considered to be the same as the prescribed vapor pressure inside the cavity, p_v , i.e.,

$$p = p_v, \text{ on the cavity surface} \quad (7)$$

2.3. Singularity Distribution Method

The method of singularity distribution is one of the most powerful techniques for the solution of the fluid flow problem. This method has become very popular in recent years with the development of the high-speed computer, for the integral equations formed by applying the boundary conditions around the fluid boundary are easily adaptable to numerical computation.

Under the smallness assumptions made in the earlier section, the propeller blades, cavity, and loading can be represented by the distribution of sources and vortices lying on the mean camber surface of each blade and shed wake. This representation is shown in Fig. 1.

The source distribution is employed to represent the jump of the normal velocity at the camber surface. There are two distinct sets of source sheets; the first is to represent the thickness of the blades, and the second is to represent the cavity thickness. We will assume at the outset, however, that the source distribution for the blade thickness is independent of time, and that its spatial distribution may be derived from a stripwise application of thin-wing theory at each radius. The source strength for the cavity thickness will be determined by solving the boundary value problem. It should also be noted that the extent of the cavity is not known in advance and should be determined as a part of the solution.

The vortex distribution is employed to represent the jump of the tangential velocity both at the camber surface and in the trailing wake sheet. The vortex strength is a vector lying in the surface

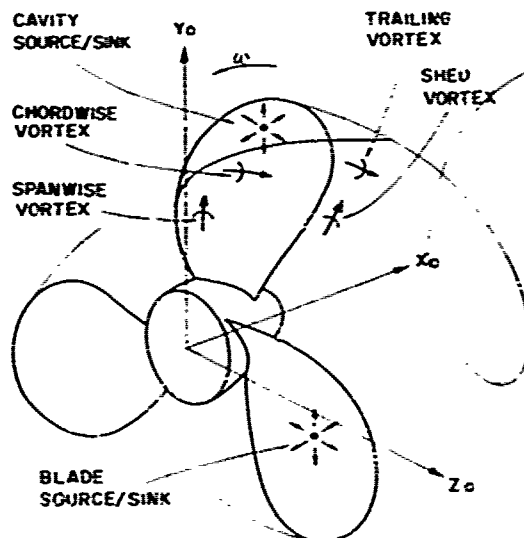


Figure 1. Pictorial of propeller to illustrate basic singularities

and may be resolved into components along two arbitrarily assigned directions on the surface. The vortex distribution on the blade will be resolved into "spanwise" and "chordwise" components while the corresponding components in the wake will be termed "shed" vorticity and "trailing" vorticity. The vortex strength will also be determined as a part of the solution to the boundary value problem.

When the method of singularity distribution is employed, the principle of conservation of mass is satisfied in the fluid region away from the singular sheet. The quiescence condition at upstream infinity is also satisfied by the nature of the singularity, since the induced velocity is at most inversely proportional to the distance from the singular point. The application of the remaining boundary conditions will lead to coupled integral equations. An approach to the solution of the integral equation is to discretize the continuous distribution of singularities into discrete singularities of unknown strengths, and to form a set of simultaneous equations for the determination of these strengths by satisfying the boundary conditions on the selected collocation points or control points.

3. MATHEMATICAL MODELING OF PROPELLER-CAVITY SYSTEM

3.1. Blade Geometry

We begin by defining a cartesian coordinate system fixed on the propeller, with the x axis defined as positive downstream and the y axis located at any desired angular orientation relative to the key blade. The z coordinate completes the right handed system. Cylindrical coordi-

nates are defined in the usual way, with the angle θ measured clockwise from the y axis when viewed in the direction of positive x, and the radial coordinate, r, given by

$$r = \sqrt{y^2 + z^2} \quad (8)$$

The skew angle, $\theta_m(r)$, is by definition the angular coordinate of the mid-chord line as measured from the y axis at radius r. The x coordinate of the mid-chord line, as illustrated in Fig. 2 is defined as the rake, $x_m(r)$, and the space curve defined parametrically by $\theta_m(r)$ and $x_m(r)$ provides the skeleton upon which the blade camber surface is constructed.

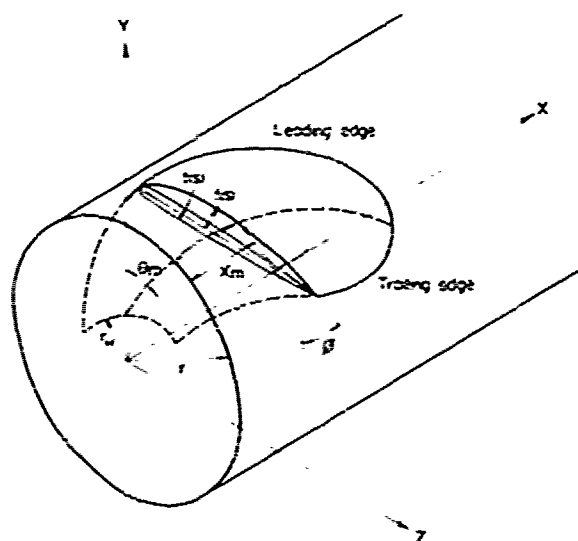


Figure 2. Illustration of propeller blade construction

The leading and trailing edge of the blades may now be constructed by passing a helix of pitch angle $\phi(r)$ through the mid-chord line. If the blade section expanded chord length at this radius is $c(r)$, the leading and trailing edge coordinates are

$$\begin{aligned} x_{l,t} &= x_m \pm \frac{c}{2} \sin \phi \\ \theta_{l,t} &= \theta_m \pm \frac{c}{2r} \cos \phi \\ y_{l,t} &= r \cos \theta_{l,t} \\ z_{l,t} &= r \sin \theta_{l,t} \end{aligned} \quad (9)$$

where the subscripts l and t denote the leading and trailing edges, respectively.

It is now convenient to define a non-dimensional chordwise coordinate, s, which is zero at the leading edge and unity at the trailing edge. Its value at the mid-chord line, by definition, will then be $\frac{1}{2}$. The blade section camber and thickness is defined by the functions $f(s)$ and $t(s)$, respectively. As shown in Fig. 2, these

are measured in a cylindrical surface of radius r in a direction normal to the helical coordinate. The cartesian and cylindrical coordinates of a point on the blade camber surface with radial coordinate r, and chordwise coordinate s may therefore be expressed in terms of skew, rake, chord, and camber.

In order to generalize the results to blades other than the key blade, we define a blade indexing angle

$$\phi_k = \frac{2\pi(k-1)}{K}, \quad k=1,2,\dots,K \quad (10)$$

where K is the number of blades and k is identifying index of any blades. The key blade, by definition, is identified by the index $k=1$. With this addition, the coordinates of a point on the camber surface of the k'th blade may be written as

$$\begin{aligned} x &= x_m + c(s-k) \sin \phi - f \cos \phi \\ \theta &= \theta_m + c(s-k) \frac{\cos \phi}{r} + f \frac{\sin \phi}{r} + \phi_k \\ y &= r \cos \theta \\ z &= r \sin \theta \end{aligned} \quad (11)$$

3.2. Geometry of the Trailing Wake

The geometry of the trailing vortex wake has an important influence on the accuracy of the calculation of induced velocities on the blade. The usual approach is to approximate the trailing wake sheet by a pure helical surface with a prescribed pitch angle obtained either from the undisturbed inflow $\beta(r)$ or the hydrodynamic pitch angle $\beta_i(r)$ calculated from lifting line theory. Although the present program was originally developed with the non-linear roll-up wake model (Ref. 8), undeformed wake model with pitch angle β_w is selected to keep the linearity of the problem for the purpose of comparison with other theories.

3.3. Discretization of Singularity Distribution

The continuous distribution of vortices and sources are replaced by a lattice of concentrated straight line elements of constant strength for the purpose of digital computation.

The discretization scheme in the chordwise direction should in principle be determined so as to satisfy the Kutta condition. For the steady two-dimensional non-cavitating flow, James (Ref. 9) showed that the Kutta condition can be satisfied implicitly by suitable arrangements of vortices and control points. For the two-dimensional cavitating hydrofoil, Van Houten (Ref. 5) used a unique spacing, which gives good agreement with Geurst's (Ref. 2) steady solution. This arrangement is selected for use for the chordwise discretization of the propeller blade, together with uniform spacing in the radial direction.

The radial interval from the hub, r_H , to the tip, R, is divided into M equal

intervals with the end points of the discrete spanwise vortices located at radii

$$\rho_m = r_H + \frac{(R-r_H)(4m-3)}{4M+2}, m=1,2,\dots,M+1 \quad (12)$$

The chord from the leading to the trailing edge at radius ρ_m is divided into N intervals, with functions to define the boundaries of each element as

$$\tilde{s}_n = 1 - \cos(n\pi/2N), n=0,1,2,\dots,N \quad (13)$$

where \tilde{s}_0 denotes the leading edge.

Equations (12) and (13) are sufficient to define the vertices of $M \times N$ four sided elements on the camber surface. The spanwise vortices will be placed on the quarter chord of each element with their ends at points

$$s_n^I = \tilde{s}_{n-1} + \delta\tilde{s}_n/4, n=1,2,\dots,N \quad (14)$$

where

$$\delta\tilde{s}_n = \tilde{s}_n - \tilde{s}_{n-1} \quad (15)$$

The line sources will be placed on the mid-chord of the chord segments defined by s_n^I . Thus the nondimensional chordwise coordinates of the line sources will be

$$\begin{aligned} s_n^Q &= (s_n^I + s_{n+1}^I)/2, n=1,2,\dots,N-1 \\ s_N^Q &= (s_N^I + 1.0)/2 \end{aligned} \quad (16)$$

The control points for the tangency boundary condition will be placed on the mid-span of the line segment connecting the two points (s_i^I, ρ_m) and (s_{i+1}^I, ρ_{m+1}) .

The normal vector is calculated as a cross-product of the vectors tangent to the spanwise and chordwise curves passing through the tangency boundary condition control points. It should be noted that the control points for the tangency boundary condition lie in the center of the quadrilateral elements formed by the vortex lattice.

The control points for the dynamic boundary condition on the cavity surface are placed on the mid-span of the spanwise vortex lines defined by Eq.(14). But Jiang (Ref.4) found that the positions of the line sources and control points for the dynamic boundary condition nearest the leading edge should be interchanged to simulate the proper singular behavior of the source strength at the leading edge; i.e., there must not be a dynamic boundary condition control point ahead of the leading line source. The vortex arrangement and control points for the tangency boundary condition are illustrated in Fig. 3.

The trailing vortices in the wake region are extensions of the chordwise vortices on the blade to infinite downstream with wake pitch angle β_w . The discretized representation of the vortex sheet then consists of $M+1$ concentrated

trailing vortex lines whose trailing edge coordinates match the corresponding values on the blade.

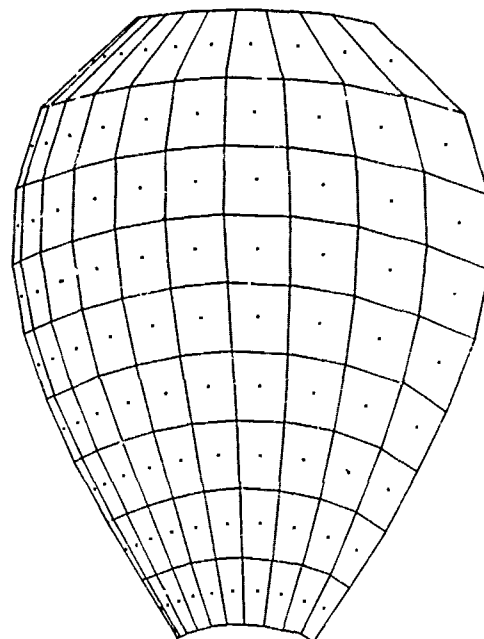


Figure 3. Illustration of discrete vortex elements and tangency control points on key blade

In order to facilitate computation of the convection of the shed vorticity in unsteady flow the angular increment, $\delta\theta$, and the time increment, δt , are related by the equation:

$$\delta\theta = \omega\delta t, \quad (17)$$

in this way, if the influence of the tangential induced velocity on convection speed is ignored, the strength of the n 'th shed vortex at the current time step will be equal to the $(n-1)$ st shed vortex at the preceding time step.

In order to extend Eq.(14) to the range of trailing wake, Eq.(15) is modified as

$$\delta\tilde{s}_n = \rho\delta\theta, \text{ for } n > N \quad (18)$$

where the angular increment, $\delta\theta$, is defined in Eq.(17). The application of Eqs.(14) and (15), extended to allow $n > N$, and Eq.(16) will determine the position of the singularities and control points in the wake. For a given blade geometry, the discretized system is uniquely determined by the two parameters M and N . In the present work $\delta\theta$ is set to 6 degrees for all computations.

3.4. Representation of Other Blades and Wake

While the discrete singularity arrangement used to represent the key blade and its

wake can be reproduced exactly on each of the other blades, such an approach would obviously be inefficient. Due to the relatively large distance between the control points on the key blade and the singularities on the other blades, a coarse spacing may be used on the latter with no significant change in results. In addition, induced velocities need not be computed at all control points, but only at a sufficient number to enable the values at the remaining control points to be obtained by interpolation.

As described in Section 4.2, the strengths of the singularities on the other blades are known in terms of the corresponding values on the key blade at a previous time step.

Figure 4 shows a projected view of all five blades of a propeller illustrating this reduction in the number of elements on the other blades.

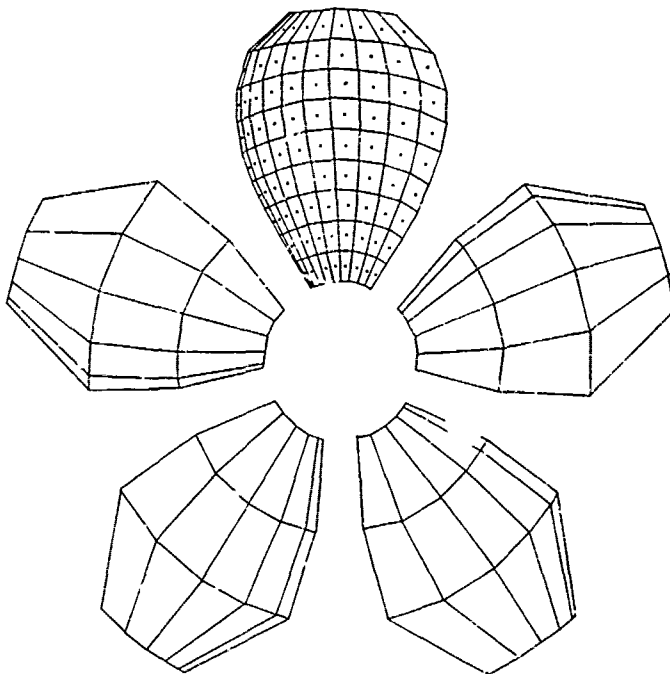


Figure 4. Illustration of discrete singularity elements on key blade and other blades

4. METHODS OF SOLUTION

4.1. Calculation of Induced Velocities

Once the propeller-cavity-wake systems are discretized, the induced velocities at any point in space by these line source or vortex elements can be very easily computed; see for example Kerwin and Lee (Ref. 8).

From the law of Biot-Savart, the induced velocity at any point x due to a vortex element of strength Γ situated on the curve C may be expressed as

$$\underline{v}^{\Gamma}(\underline{x}) = \frac{\Gamma}{4\pi} \int \frac{d\underline{\xi} \times \underline{D}}{|\underline{D}|^3} \quad (19)$$

$C(\underline{\xi})$

where \underline{D} is a vector extending from each point $\underline{\xi}$ on the vortex curve C to the field point \underline{x} .

For sources, the induced velocity at any point \underline{x} due to a source element of strength Q may be expressed in a similar manner:

$$\underline{v}^Q(\underline{x}) = -\frac{Q}{4\pi} \int \nabla \left(\frac{1}{D} \right) d\xi \quad (20)$$

$C(\underline{\xi})$

Applying Eqs. (19) and (20), the induced velocities at the control point \underline{x}_{ij} due to a set of discrete vortices or sources may now be expressed as

$$\begin{aligned} \underline{v}_{ij}^{\Gamma} &= \sum_{n,m} K_{ijnm} \Gamma_{nm} \\ \underline{v}_{ij}^Q &= \sum_{n,m} H_{ijnm} Q_{nm} \end{aligned} \quad (21)$$

where

$$K_{ijnm} = \frac{1}{4\pi} \int \frac{d\underline{\xi} \times \underline{D}}{|\underline{D}|^3} \quad C(\underline{\xi}_{nm})$$

$$H_{ijnm} = -\frac{1}{4\pi} \int \nabla \left(\frac{1}{D} \right) d\xi \quad C(\underline{\xi}_{nm})$$

$$\underline{D} = \underline{x}_{ij} - \underline{\xi}_{nm}$$

The equations for boundary conditions, stated in earlier chapter, can be formulated in terms of strengths of vortices and sources by applying Eq. (21) to the control points for kinematic and dynamic boundary conditions. The derivation of these equations is in principle straightforward and are given in detail in Appendices 1 through 4. Then in Appendix 5 we obtain a set of simultaneous equations by combining the equations for boundary conditions. These equations, which would otherwise be a coupled integral equation with continuous distributions of sources and vortices, are simple in structure and can be solved in a various way.

4.2. Stepwise Solution in Time Domain

The discretized boundary value problem is established in Appendix 5, where the unknown variables are the strengths of the vortices and sources on the key blade and a pressure inside the cavity.

The stepwise solution method is employed for the solution of the boundary value problem in the time domain, in which the results from the key blade are used to

update the strengths of singularities on the remaining blades, while trailing and shed vortices are being convected downstream to account for propeller advance.

The solution process for the cavitating propeller is significantly more expensive than for the fully wetted propeller. Therefore, the initial startup procedure is carried out for the fully wetted propeller only. Then the solution for the cavitating propeller is started from the solution to the associated unsteady wetted flow problem, by introducing the cavity source terms. Since the cavity closure condition equation contains the cavity shape of the previous time step in the right hand side, a bad approximation for it may slow the convergence. It is, therefore, recommended to "turn on" the process for the cavity solution just before the key blade enters the high ship wake region, at which the blade will start cavitating. The process may be considered to have converged when two successive propeller revolutions produce results which are identical to within the desired accuracy.

4.3. Iterations for Cavity Extent

To determine the cavity extent and source distribution, two spatial iteration processes are to be employed in addition to the updating procedure illustrated in the preceding section.

Unknown cavity length and source distribution will always be confined to one chordwise (or streamwise) strip by assuming that the cavity extent and source and vortex distributions on the other streamwise strips be known either by an initial approximation or by the most recent solutions on those strips. The iteration starting from the hub strip (or from the tip strip) to the tip strip (or to the hub strip) and then back to the other end of the propeller blade is found to be very efficient, showing a very fast and stable convergence character. For most cases tested, two or three radial (outward or inward) iterations were sufficient to get the converged values.

To determine the cavity length and source strength for a particular strip, we begin by guessing the cavity length (again from the adjacent strip or from the previous iteration) corresponding to the discretized element boundaries. Pressure (or the cavitation number) corresponding to the assumed cavity length will be determined by solving Eq. (60). If the computed cavity pressure is lower than the vapor pressure, a longer cavity length will be tried until the computed pressure becomes higher than the vapor pressure. If the initial computed pressure is higher than vapor pressure, a shorter cavity length is used until the computed pressure becomes too low.

A linear interpolation formula can be used to determine the cavity length corresponding to the vapor pressure using the

results of the two final trials. The strength of the cavity sources as well as that of the vortices on that strip can also be interpolated in a similar manner as is done to get the cavity length, since the dynamic boundary condition equation (56) on the cavity surface is linear. It is assumed that the linear interpolation is appropriate for the present computer program.

Although we can solve the simultaneous equations (60) directly, an alternative approach can be deduced by closely examining the elements of the coefficient matrix, a_{pq} . As is the case in the fully-wetted problem, the coefficients of the vortex strength in the tangency condition equation (58) are invariant in time for given chordwise panel, and hence this portion can be inverted once in the beginning and used to solve the simultaneous equations (60). This procedure, called the partitioning method in algebra, is found to be particularly useful for the solution of the simultaneous equation with a large invertible submatrix.

4.4. Determination of Blade Forces

The force and moment acting on the propeller blade can be obtained by integrating the pressure jump over the blade camber surface,

$$\begin{aligned} \underline{F} &= \int \Delta p \underline{n} \, dA, \\ \underline{M} &= \int \Delta p (\underline{r} \times \underline{n}) \, dA, \end{aligned} \quad (22)$$

where Δp is the pressure jump across the camber surface, \underline{n} the normal vector on the camber surface defined positive when pointing upstream, and \underline{r} the position vector from the origin to the point of integration.

5. CAVITY PREDICTION AND COMPARISON WITH EXPERIMENTS

5.1. Comparison with Experiment, DTNSRDC Propeller 4381 in Uniform Flow

A sample calculation with DTNSRDC Propeller 4381 (Ref. 10) is made to check the cavity extent in uniform flow. In order to simulate the steady cavity flow, the variation in the hydrostatic pressure is suppressed and the cavity patterns of all of the blades are assumed identical.

The arrangement of vortices and control points for the tangency boundary condition for this propeller appear in Fig. 3 for the key blade, and those for all of the five blades are shown in Fig. 4. This propeller shows the symmetrical blade outline, without any skew or warp, and the design advance coefficient, J_A , is 0.889.

Sample condition is chosen as $\sigma_n = 1.92$ at $J_A = 0.7$ to produce a reasonable amount of partial cavitation. Figure 5 shows the theoretical prediction of cavity extent and cavity thickness distribution and the cavity extent observed at the Water Tunnel. During the experiment, the strobolight was set to trigger once-per-revolution, so that the cavity extent of each blade could be observed.

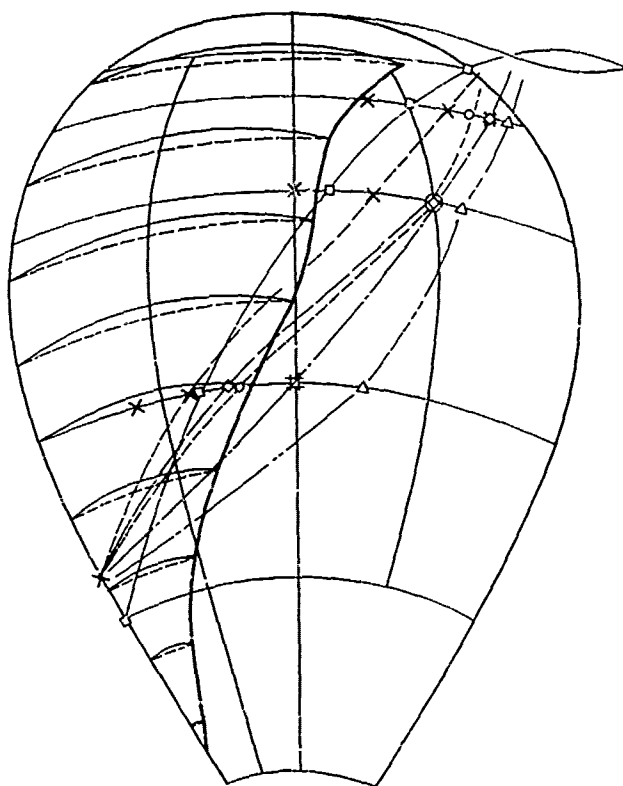
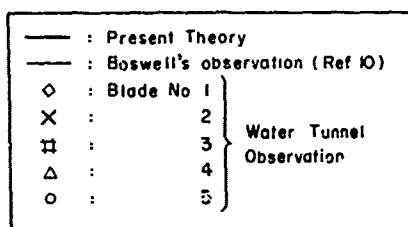


Figure 5. Comparison of cavity extent between prediction and observations for DTNSRDC Propeller 4381 at $J_A=0.7$ with $\sigma_n=1.92$

Each blade was observed in the 12 o'clock (top center) position to eliminate blade to blade variation in hydrostatic pressure and inflow velocity. It should be noted that the extent of the observed cavity varies from blade to blade to a considerable degree. This scatter is thought to be caused either by the manufacturing irregularities or by slight damage to the leading edge of each blade. To show the effect of hydrostatic pressure, the cavity extent of the number 2 blade at the six o'clock position is added. The light solid line is taken from the experiment of Boswell (Ref.10) at DTNSRDC. The agreement between the experiment and the theory is good compared with the blade to blade variation in the extent of the measured cavity. It is not easy to obtain the thickness of the cavity from observation without using sophisticated methods such as the stereo-

photographic measurement. Although there is no direct measurement of cavity thickness, the predicted thickness is considered reasonable. The force calculation obtained by integration of the pressure distribution reveals 2.5% thrust increase over the one obtained for the fully-wetted case, which might be an additional camber effect due to the cavity.

5.2. Comparison with Experiment, DTNSRDC Propeller 4381 behind Screen Generated Wake

The first unsteady cavity computation is performed simulating DTNSRDC Propeller 4381 in a screen generated wake simulating a high speed single screw commercial vessel. The velocity field, measured by the laser doppler velocimeter at the Water Tunnel, is shown in Fig. 6. The wake field is nearly symmetric about the centerplane of the ship, with a sharp peak located near top center. A sequence of photographs showing the model propeller operating in the screen generated wake taken at uniform four degree intervals is reported by Kerwin, et al (Ref.11), and is reproduced in Fig. 7 for the purpose of direct comparison. The cavitation number, σ_n , was selected as 3.53, and the propeller Froude number, $Fr=n^2D/g$, as 10.45.

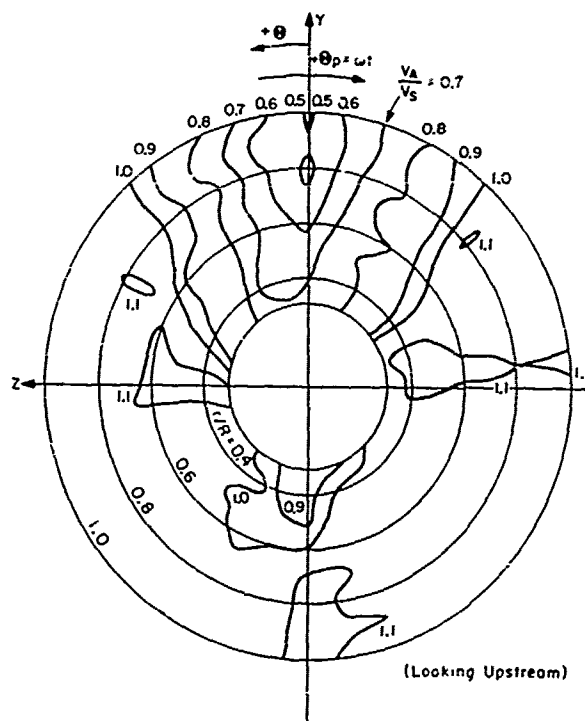


Figure 6. Velocity field measured behind screen

The cavity extent and thickness distribution computed with the discrete time steps of six degree interval are presented in Fig. 8. Excellent agreement was obtained between the experiment and theory.

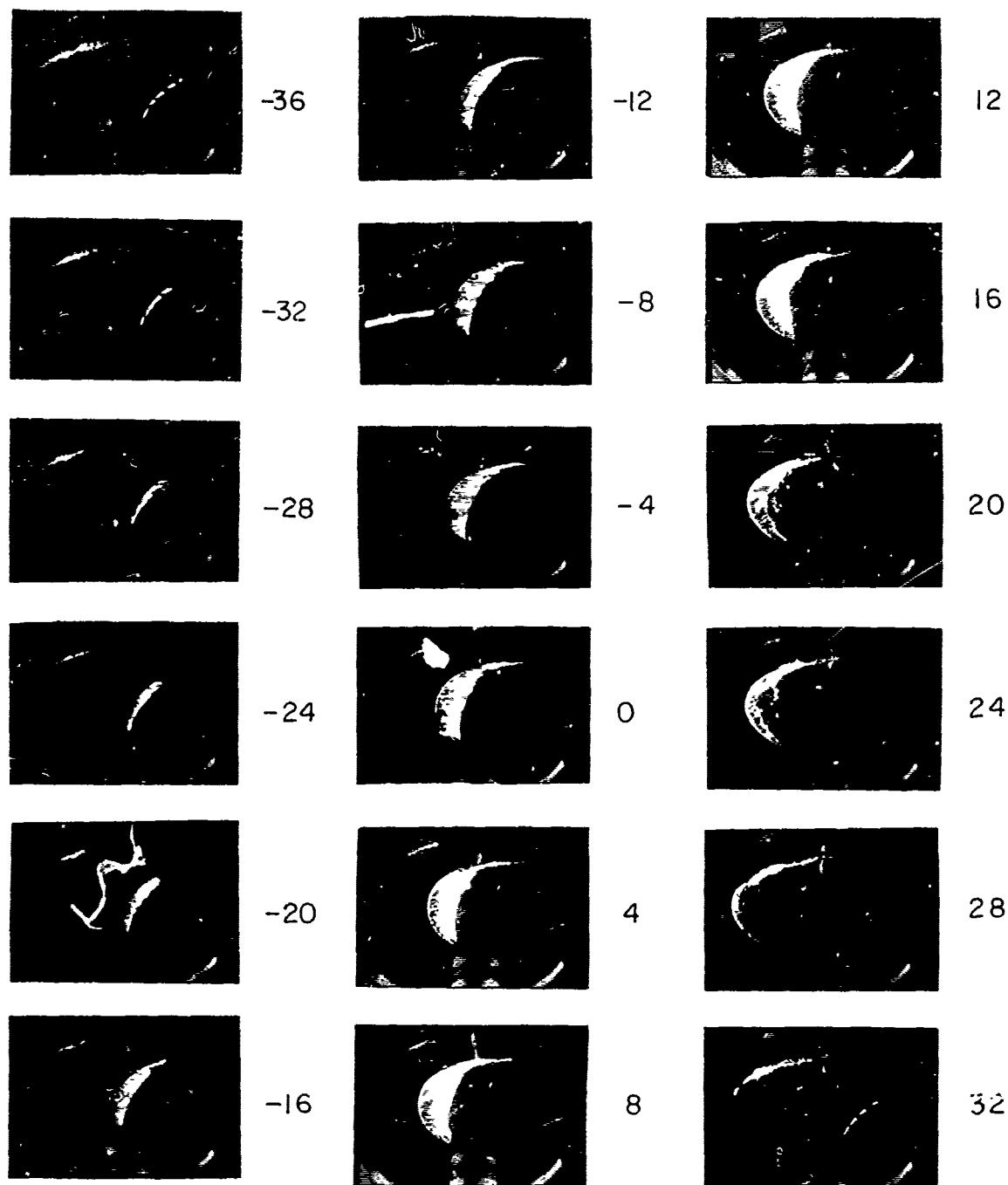


Figure 7. DTNSRDC Propeller 4381 pictured at intervals of 4° at $J_A=0.889$ with $\sigma_n=3.53$

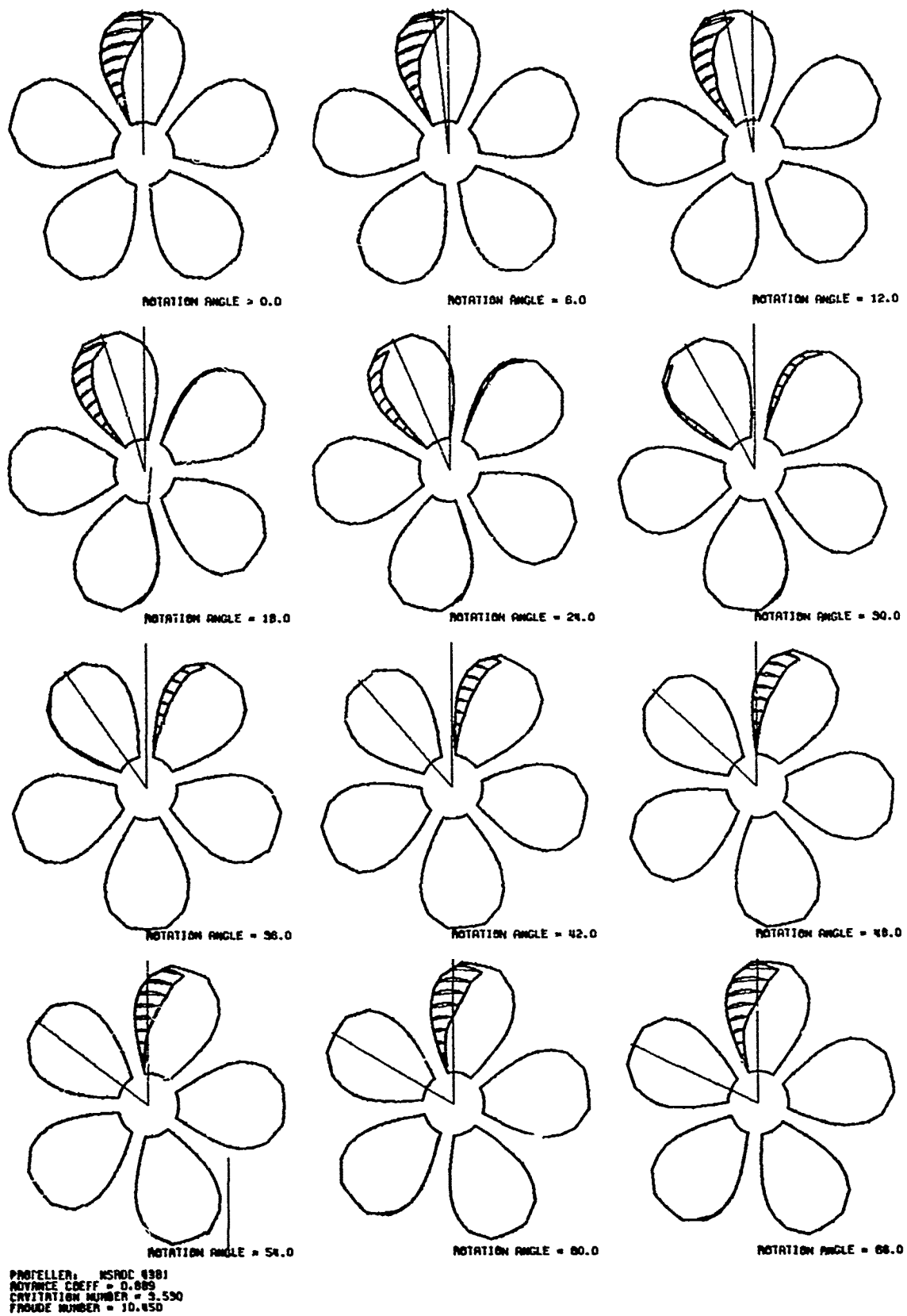


Figure 8. Predicted cavity extent and thickness distribution

The fact that the theory works so well for this high speed model propeller indicates that the same degree of accuracy might be obtained for the full-scale propeller, if scaling effects are carefully considered.

Figure 9 shows the time history of the cavity volume variation and the cavity length at a particular radius, $r/R=0.77$. To show the convergence rate, computed results for the first three revolutions of the cavitating propeller are plotted in a single figure. Note that the results of the first cavity revolution are very close to the final converged values. This is because we start solving the cavity problem after achieving the converged solution to the non-cavitating flow problem, and also because, in this particular case, only one blade is cavitating at a time, hence there is no interaction between cavities on different blades.

Figure 9 also shows that the cavity volume is a maximum where the cavity center (not the blade center) passes through the maximum wake. Also the cavity volume is symmetric in time while the cavity length versus volume is only slightly greater for the collapsing cavity than for the growing cavity. For the partially cavitating propeller, the cavity is fattened rearwards slightly as the blade rotates. Also, the cavity falls off relatively smoothly, showing that the cavity collapses toward the leading edge. Substantially different behavior will be observed for the low speed fully cavitating propeller in the next section.

By integrating the pressure distributions on the blade surface at each time step, the total forces and moments can be obtained, and the thrust components with and without cavitation are plotted in Fig. 10 versus the angular position of the key blade. It is clear from this figure that the thrust variation is insensitive to the presence of the cavity. Harmonic analysis of this force component reveals that the mean thrust of the cavitating propeller increases by 2.6% above the non-cavitating mean value.

5.3. Comparison with Full-scale Observation

The ultimate goal of any theoretical or experimental study is to design a full-scale propeller to meet performance specifications. It is, therefore, essential to compare the theoretical predictions with full-scale observations in order to truly verify the theory. Full-scale experiments are very difficult and expensive and hence are rarely made. It is fortunate, however, that a report by Holden and Øfsti (Ref.12) containing stereo-photographic observation of the propeller of the M/S Berge Vanga was made available for comparison with the present work. The principal particulars of the Oil/Ore carrier and her propellers are given in Ref.13, with the wake data measured behind the model ship.

Figure 11 shows the discrete vortex

arrangement with the control points for the tangency boundary condition for all of the blades. The blade is skewed back 15 degrees with a pitch ratio, $P/D=0.7$ at a fractional radius, $r/R=0.8$. Figure 12 is reproduced from Holden, et al (Ref.13), and shows the typical wake velocity field of a twin screw ship. Unlike the wake of a high speed single screw vessel with a fine after-body, the velocity field of the model oil/ore carrier has a very wide wake extending from the hull to the shaft. The calculated mean effective wake fraction, W_{eff} is 0.418. The volumetric advance coefficient, J_A , is therefore 0.39. The cavitation number, $\sigma_n = \rho g H / \frac{1}{2} \rho n^2 D^2$ was obtained as 2.02 based on the estimated shaft submergence, $H=15.3m$, and the propeller Froude number, $Fr = n^2 D / g$, is 2.28.

Before proceeding with comparison with full scale data, there are a number of observations to be made about the general behavior of the results. The computed cavity extent and thickness distribution at six degree intervals are given in Fig. 13. These figures demonstrate that supercavitating flow can be predicted by the present scheme. It is noticeable that the blades are cavitating mostly near the tip region, whereas for the DTNSRDC Propeller 4381 the cavity extends from the hub to the tip more or less uniformly. Figure 13 is typical of low speed merchant vessels and tankers.

Another interesting feature may be observed when the cavity is about to collapse. From the first six plots in Fig. 13, it may be seen that as the blade approaches 90 degrees after top dead center, the cavity has maximum thickness near the trailing edge and almost zero thickness near the leading edge. Since the present mathematical cavity model assumes that the cavity always begins at the leading edge, the thin cavity at the leading edge may be interpreted as a cavity "pull-back" phenomenon, which is observed in experiments where the cavity extends nearly to or beyond the trailing edge of the blade.

A typical cavity length at $r/R=0.75$ and the cavity volume variations with respect to time are given in Fig. 14 from which a couple of important phenomena can be observed.

The first is the convergence behavior. The computer program was run for five propeller revolutions after achieving the converged fully-wetted solution. It can be clearly seen that the cavities on the other blades have a significant blockage effect on the cavity volume variation on the key blade. This effect, which was not noticed for the case of DTNSRDC Propeller 4381, shows the convergence rate, including an oscillatory response for each propeller revolution. Hence more propeller rotations are required to achieve convergence.

The second phenomenon is the cavity "pull-back" which is already noted from Fig. 13. From Fig. 14, one can easily see that the cavity length continues to increase, even after the volume reaches its maximum near 70° after top center. The cavity

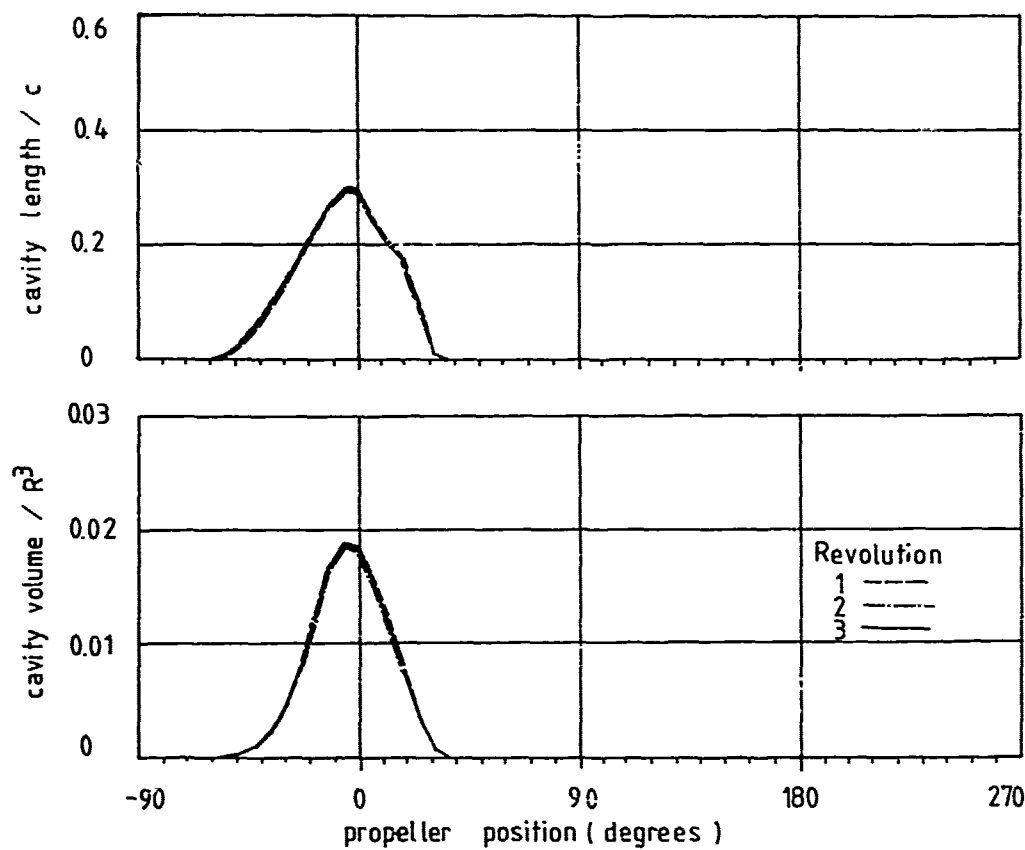


Figure 9. Cavity length (at $r/R=0.77$) and cavity volume variations with angular position

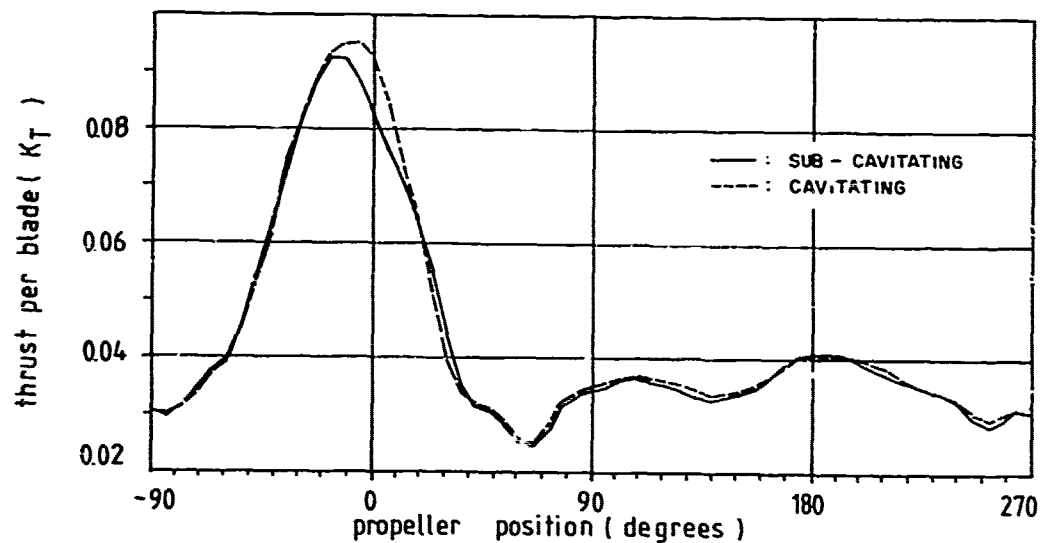


Figure 10. Thrust per blade with angular position for sub-cavitating and cavitating conditions

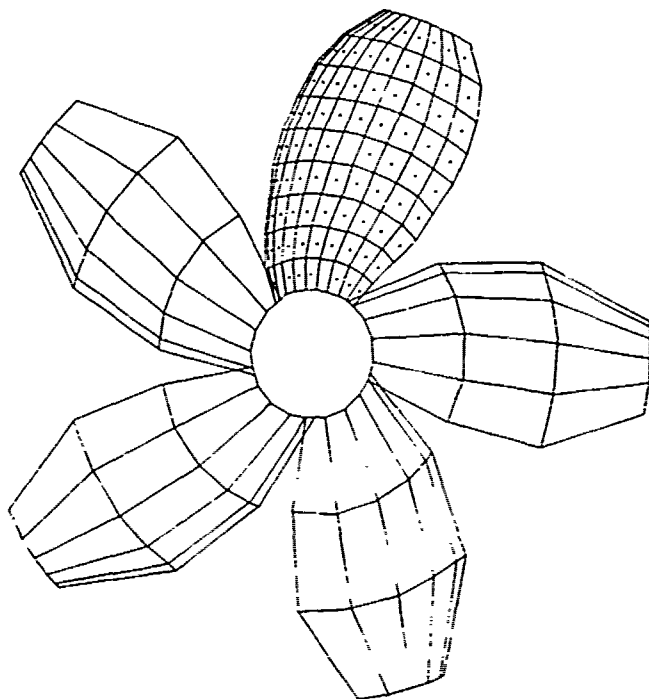


Figure 11. Arrangement of discrete vortex elements and tangency control points

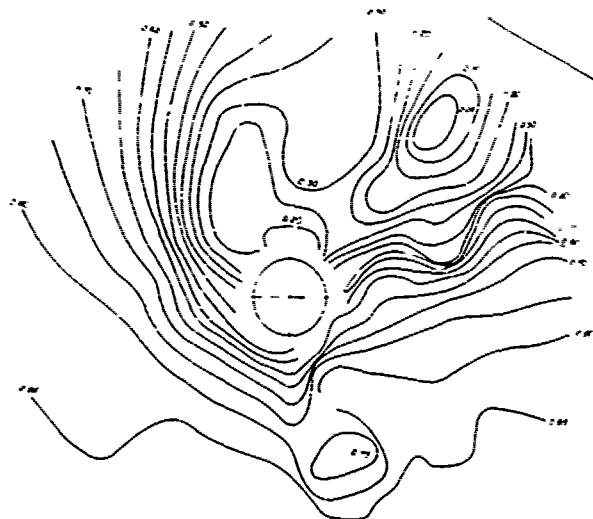


Figure 12. Wake field measured behind the 1/39.5 scale model ship (Reproduced from Ref.13)

length variation with time shows a sudden collapse of the cavity, whereas the cavity length on the DTNSRDC Propeller 4381 fell off smoothly. The abrupt collapse of cavity length in conjunction with the cavity shape shown in Fig. 13 indicates that instead of collapsing toward the leading edge, the cavity collapses in the pulled back position.

The thrust acting on the key blade versus time is shown in Figure 15. It can be seen that there is a general trend of increase of thrust, resulting in 19% increase in the steady thrust over the non-cavitating mean value. The figure also shows a curious kink at 102 degrees, which is related to the sudden disappearance of the cavity at that moment. Although this effect may be exaggerated by the coarse time step and by the assumption that the cavity starts at the leading edge, it arises from the unsteady pressure term, $-\rho \partial \phi / \partial t$, due to the collapsing cavity source.

Let us now return to the comparison of the predictions with the full-scale observations. First of all, the predicted cavity thickness is reasonably close to, but slightly larger than, that of the full-scale experiments; the maximum predicted thickness is 24cm when the key blade is at 72 degrees past the top center, whereas the maximum thickness obtained by stereo-photographic observation by Holden and Øfsti (Ref.12) ranges from 10 to 20cm. However, the cavity extent predicted by the present theory is much larger than that obtained aboard the ship. Thus, the theoretical prediction of the maximum cavity volume, 240 liters, is 12 times larger than the one reported by Holden and Øfsti.

Recalling the good correlation with model data in the case of DTNSRDC Propeller 4381, similar agreement had been expected for this propeller, too. But it turns out that the correlation between the prediction and full-scale observation is rather unsatisfactory. The poor results are considered to be caused mostly by bad wake input to the computer program. The wake measurement was made on a 1/39.5 scale model at a towing tank following conventional practice, and hence a correction should have been made to account for the effect of different Reynolds number when extrapolating from the model wake to the full scale wake.

Without resorting to the complex ship boundary layer theory, an estimate is made of the order of magnitude difference of the boundary layer thickness between the model and ship. Assuming 1/7-th power velocity distribution, the boundary layer thickness, δ , is inversely proportional to the 1/5-th power of Reynolds number; see Schlichting (Ref.14), i.e.,

$$\frac{\delta}{L} \sim \frac{1}{Re^{1/5}}, \quad (23)$$

where L is the length of the ship, and Re the Reynolds number. If we assume Froude scaling for the model test, we find that

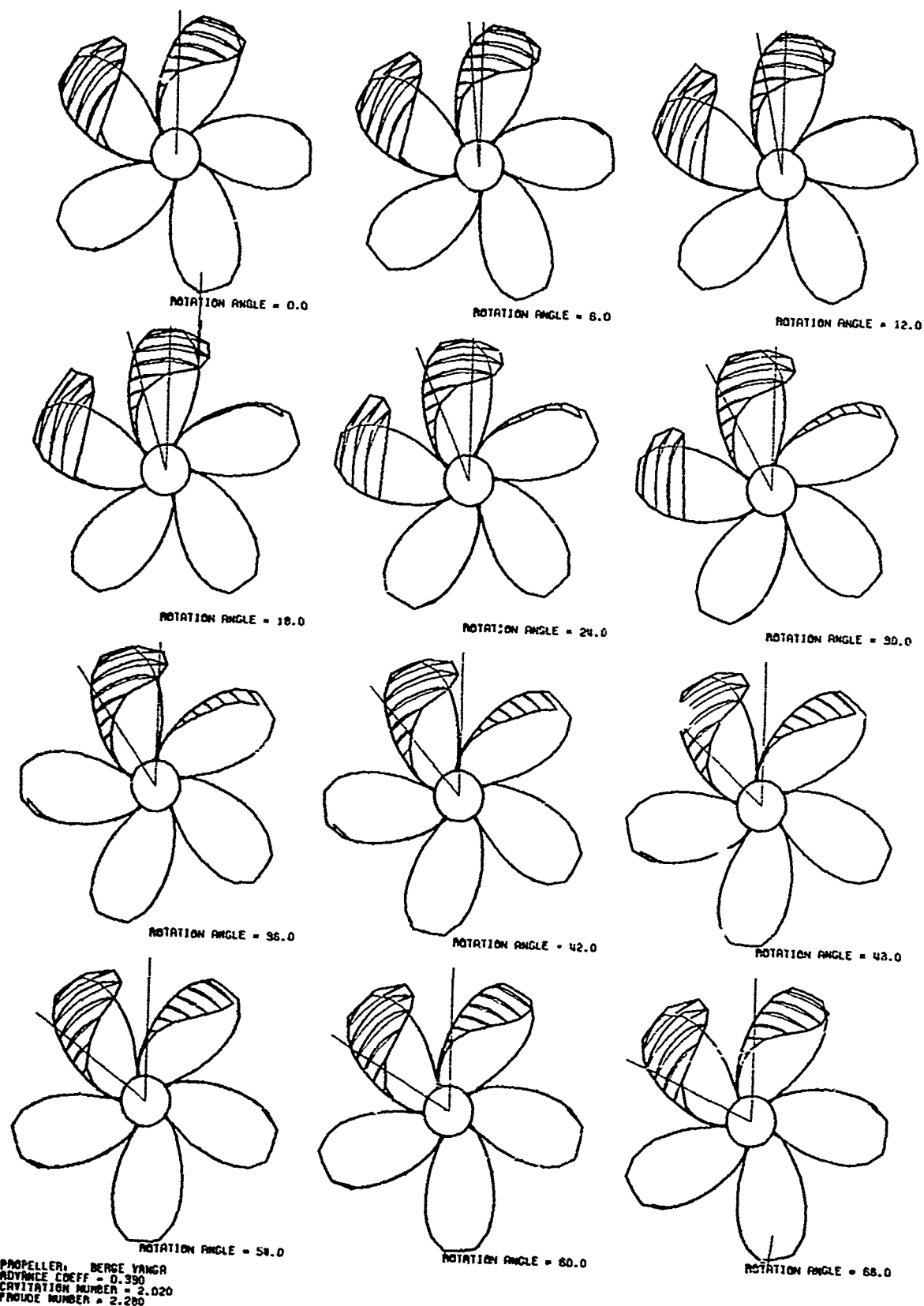


Figure 13. Predicted cavity extent and thickness distribution

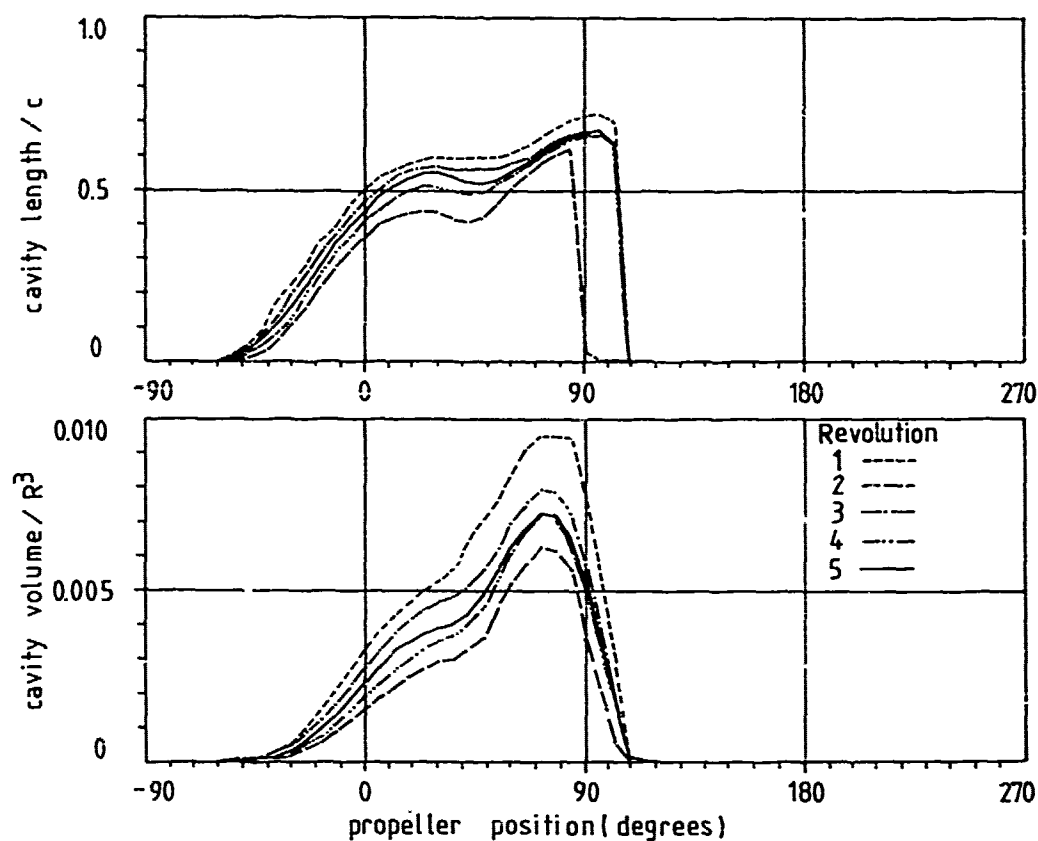


Figure 14. Cavity length (at $r/R=0.75$) and cavity volume variations with angular position

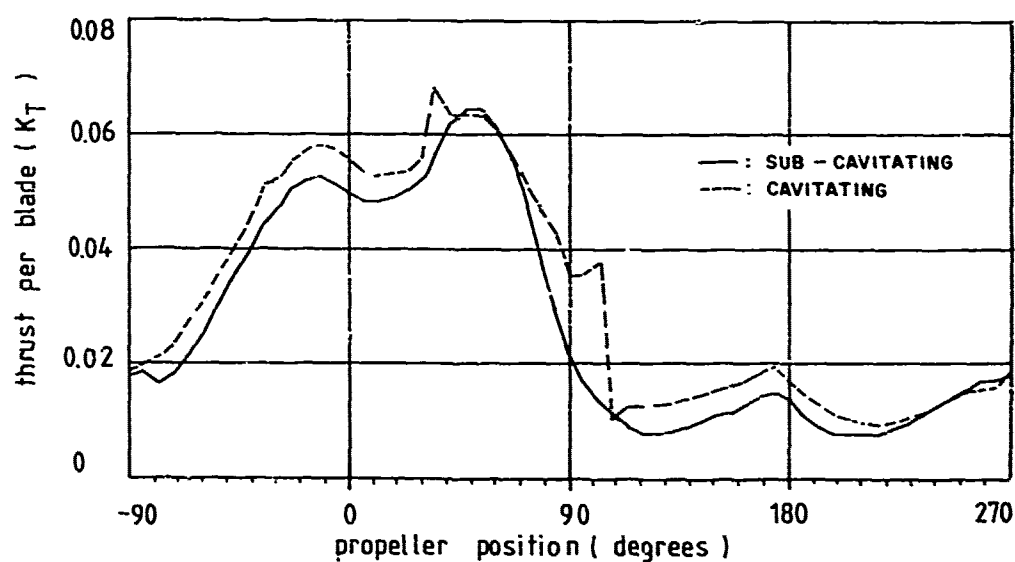


Figure 15. Thrust per blade with angular position for sub-cavitating and cavitating conditions

$$Re \sim L^{1.5} \quad (24)$$

Substituting Eq. (24) into Eq. (23), we obtain

$$\frac{\left(\frac{\delta}{L}\right)_m}{\left(\frac{\delta}{L}\right)_s} = \left(\frac{L_s}{L_m}\right)^{0.3} \quad (25)$$

where the subscripts m and s denote the model and ship, respectively.

The ratio (25) is 3 for the model scale ratio, $L_s/L_m=39.5$. If this ratio is introduced to Fig. 12, the high wake region will be moved toward the ship hull surface, and hence the correlation between the experiments and the prediction with a modified wake might be improved.

Ship boundary layer theory is certainly an important field in hydrodynamics, which needs to be explored. Should a method to overcome the Reynolds number scaling effect in a rational way be developed, the theoretical full scale prediction might be possible for the practical design purpose in the near future.

6. CONCLUSION

A numerical lifting-surface procedure is developed for the prediction of the transient cavity extent and volume variations with time of the cavitating propellers.

It is an exact theory proposed for the prediction of cavity behavior in a rational way, where the unsteady pressure term, $-\rho \partial \phi / \partial t$, in the Bernoulli's equation is treated without simplification in the discretized time domain, and the cavity extent is determined by an iteration procedure in a three-dimensional manner.

The comparison of the cavity extent between the experimental observation and the theoretical prediction for a model propeller both in the uniform flow and in the screen generated non-uniform flow is considered satisfactory. But the prediction of the cavity extent for a full-scale propeller is not satisfactory, indicating that the extrapolation from the wake measured behind the model ship to the full-scale wake is important for the prediction of the cavity.

ACKNOWLEDGEMENT

Most of the work contained in this paper was done at M.I.T. I am grateful to Professors Justin E. Kerwin, Patrick Leehey, and Robert J. Van Houten for their guidance throughout the work. I would like to thank S. Dean Lewis and Sukeyuki Kobayashi for experimental works at the M.I.T. water tunnel. Final computations were performed by using IBM 370/148 in Daejeon, Korea. Thanks are extended to members of Propeller Group, Korea Research Institute of Ships, for the assistance in preparing the manuscript. This work was initially

sponsored by Maritime Administration of the U.S. Department of Commerce, and funded by Korean Government for the work at KRIS. The cooperation of Det norske Veritas, who provided us with a valuable full-scale data, is greatly acknowledged.

REFERENCES

1. Tulin, M.P., "Supercavitating Flows-Small Perturbation Theory," *Journal of Ship Research*, Vol. 7, No. 3, Jan. 1964.
2. Geurst, J.A., "Linearized Theory of Two-Dimensional Cavity Flows," Thesis, Delft Technical Institute, The Netherlands, 1961.
3. Golden, D.W., "A Numerical Method for Two-Dimensional, Cavitating, Lifting Flow," MIT, Department of Ocean Engineering, 1975.
4. Jiang, C.W., "Experimental and Theoretical Investigation of Unsteady Supercavitating Hydrofoils of Finite Span," Ph.D. Thesis, MIT, Department of Ocean Engineering, 1977.
5. Van Houten, R.J., Unpublished, 1978.
6. Van Oossanen, P., "Theoretical Prediction of Cavitation of Propellers," *Marine Technology*, Vol. 14, No. 4, 1977.
7. Huse, E., "Effect of Cavitation on Propeller-Induced Vibratory Forces," Report of Propeller Committee, Fourteenth International Towing Tank Conference, 1975.
8. Kerwin, J.E. and Lee, C.S., "Prediction of Steady and Unsteady Marine Propeller Performance by Numerical Lifting-Surface Theory," *Trans. SNAME*, Vol. 86, 1978.
9. James, R.M., "On the Remarkable Accuracy of the Vortex Lattice Method," *Computer Methods in Applied Mechanics and Engineering*, Vol. 1, 1972.
10. Boswell, R.J., "Design, Cavitation Performance, and Open-water Performance of a Series of Research Skewed Propellers," DTNSRDC Report 3339, March 1971.
11. Kerwin, J.E., Lewis, S.D., and Kobayashi, S., "Systematic Experiments to Determine the Influence of Skew and Warp on Hull Vibratory Excitation due to Transient Cavitation," *Ship Vibration Symposium*, Arlington, Virginia, Oct. 1978.
12. Holden, K. and Øfsti, O., "Investigations on Propeller Cavitation Thickness Distribution," Det norske Veritas Report 74-259-C, 1975.
13. Holden, K., Sjøntvedt, T., and Øfsti, O., "On Stability and Volume of Marine Propeller Cavitation and Corresponding Spectral Distribution in Hull Pressure Fields," *Symposium on High Powered Propulsion of Large Ships*, Wageningen, The Netherlands, Dec. 1974.
14. Schlichting, H., *Boundary Layer Theory*, 6th ed., McGraw-Hill, 1968.

Appendix 1. Tangency Condition on Wetted Surface

The kinematic boundary condition on the wetted parts of the blade surface is that the resultant normal velocity in the body-fixed surface coordinate system should vanish; see Equation (4). The total fluid velocity may be written as a summation of the individual contributions as follows:

$$\underline{0} = \underline{n} \cdot \underline{V} = \underline{n} \cdot (\underline{V}^I + \underline{V}^C + \underline{V}^I + \underline{V}^B + \underline{V}^O), \quad (26)$$

on the camber surface

The superscripts I and O denote the velocities induced by the vortices and cavity sources lying on the key blade and its wake, the superscript O denotes the velocity induced by the singularities lying on the other blades and wakes, the superscript B denotes the velocity induced by the sources representing blade thickness, and the superscript I denotes inflow velocity including the ship wake and propeller rotational velocity. Applying Eq. (21), the induced velocity can be written as a summation of the contributions of each discrete singularity element representing the propeller and its wake, and hence Eq. (26) may be rewritten for the (i,j)th control point

$$\begin{aligned} 0 = & \sum_{m=1}^M \left[\sum_{n=1}^N K_{ijnm}^S \Gamma_{nm}^S + \sum_{n=1}^{N_w} K_{ijnm}^W \Gamma_{nm}^W \right] \\ & + \sum_{m=1}^{M+1} \left[\sum_{n=1}^N K_{ijnm}^C \Gamma_{nm}^C + \sum_{n=1}^{N_w-1} K_{ijnm}^t \Gamma_{nm}^t \right] \\ & + \sum_{m=1}^M \sum_{n=1}^{N_Q} H_{ijnm} Q_{nm} \\ & + \underline{n}_{ij} \cdot \left(\underline{V}_{ij}^I + \underline{V}_{ij}^B + \underline{V}_{ij}^O \right), \end{aligned} \quad (27)$$

where Γ_{nm} is the strength of discrete vortex element located at the n-th chordwise and m-th spanwise element, and the superscripts s, c, w, and t stand for spanwise, chordwise, shed wake, and trailing vortices, respectively. The symbol Q_{nm} denotes the strength of line source element per unit length located at the (n,m)th element, and N_Q denotes the number of cavitating elements at each radial interval, which will be determined as a part of a solution to the boundary value problem. The strength of the chordwise vortices is expressed by satisfying the principle of vortex conservation at each vortex lattice intersection. Thus, for the (n,m)th intersection

$$\begin{aligned} \Gamma_{nm}^C &= \Gamma_{n,m-1}^S - \Gamma_{nm}^S + \Gamma_{n-1,m}^C \\ &= \sum_{l=1}^n \{ \Gamma_{l,m-1}^S - \Gamma_{l,m}^S \} \end{aligned} \quad (28)$$

Kelvin's theorem is applied to each chordwise panel of the blade and wake to determine the strength of the first shed vortex; the chordwise panel being the area between two adjacent chordwise vortex lines and their associated trailing vortices. The total circulation around the blade section and its shed wake must be zero; thus

$$\Gamma_{lm}^W = - \left\{ \sum_{n=1}^N \Gamma_{nm}^S + \sum_{n=2}^{N_w} \Gamma_{nm}^W \right\} \quad (29)$$

Substituting Eqs. (28) and (29) into Eq. (27), and rearranging the summations for the shed vortices, one obtains

$$\begin{aligned} & \sum_{m=1}^M \sum_{n=1}^N \{ K_{ijnm}^S + \sum_{i=n}^N (K_{ijl(m-1)}^C - K_{ijlm}^C) \\ & - K_{ijlm}^W \} \Gamma_{nm}^S + \sum_{n=2}^{N_w} \{ K_{ijn(n-1)}^W + K_{ijn(n-1)(m+1)}^t \\ & - K_{ijn(n-1)m}^W - K_{ijnm} \} \Gamma_{nm}^{(t-n+1)} \\ & + \sum_{m=1}^M \sum_{n=1}^{N_Q} H_{ijnm} Q_{nm} = d_{ij}, \end{aligned} \quad (30)$$

where $\Gamma_m(t)$ is the total circulation around the m-th blade section at time t

$$\Gamma_m(t) = \left\{ \sum_{n=1}^N \Gamma_{nm}^S \right\}(t), \quad (31)$$

where t is the time index for the present time step, and d_{ij} is the following combination of known quantities

$$d_{ij} = - \underline{n}_{ij} \cdot (\underline{V}_{ij}^I + \underline{V}_{ij}^B + \underline{V}_{ij}^O) \quad (32)$$

Focusing on one chordwise panel, it can be seen that the coefficient of Γ_{nm}^S represents the induced velocity by a closed vortex, which is composed of the (n,m)th spanwise vortex on the blade, the first shed vortex in the wake, and two chordwise vortices connecting the ends of the spanwise vortex and first shed vortex as shown schematically in Fig. 15. The coefficient of $\Gamma_m^{(t-n+1)}$ represents the velocity induced by shed vortex quadrilaterals at time (t-n+1). It should be noticed that Kelvin's conservation of vorticity theorem is satisfied automatically by the closed vortex structures. It seems natural to introduce another notation for closed vortices, and hence Eq. (30) can be rewritten

$$\begin{aligned} & \sum_{m=1}^M \sum_{n=1}^N w_{K_{ijnm}} \Gamma_{nm}^S + \sum_{m=1}^M \sum_{n=1}^{N_Q} w_{H_{ijnm}} Q_{nm} \\ & = d_{ij} - \sum_{m=1}^M \sum_{n=2}^{N_w} w_{K_{ijnm}} \Gamma_m^{(t-n+1)}, \end{aligned} \quad (33)$$

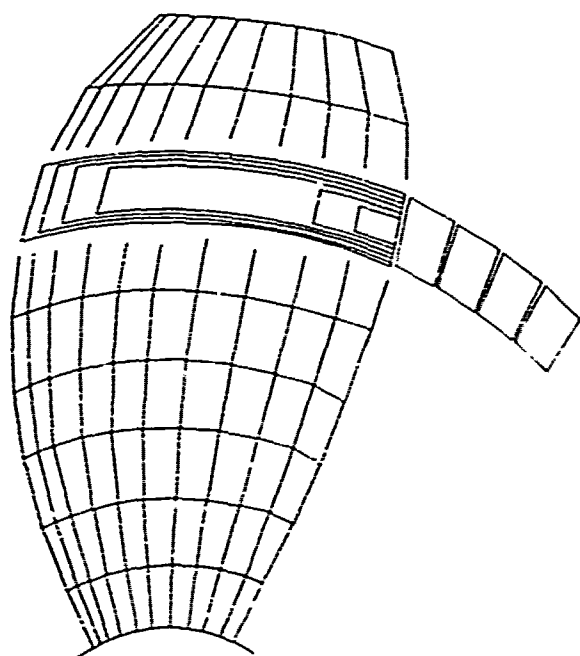


Figure 16. Illustration of closed vortices on blade and in wake

where the left superscript w is introduced to distinguish the normal component of induced velocities from tangential component that will be defined later.

Appendix 2. Kinematic Condition on Cavity Surface

In order to derive the equation for the kinematic boundary condition (5) on the cavity surface, we will define a system of curvilinear coordinates (ξ, η, ζ) which is useful in dealing with quantities on or near the camber surface. We define that the ξ coordinate be the intersection of the camber surface and a cylindrical surface concentric with the x axis, and positive when pointing downstream. The ζ coordinate is defined to be normal to the camber surface, and positive when pointing upstream. The η coordinate is defined on the camber surface to complete the orthogonality of the coordinate system, therefore it is positive when pointing towards the tip of the blade of a right handed propeller.

Since the singularities will be distributed on the camber surface, $\zeta=0$, this coordinate system is particularly convenient to represent the local singularity effects; the tangential velocity jump due to vorticity is on the ξ - η plane, and the normal velocity jump due to the source is in the ζ direction.

Let us define the ζ coordinate of the cavity surface by $g(\xi, \eta, t)$. The exact kinematic boundary condition can be derived by requiring that the substantial derivative of the quantity $F(\xi, \eta, \zeta, t) = \zeta - g$

(ξ, η, t) vanish on the cavity surface; i.e.,

$$DF/Dt = (\partial/\partial t + \underline{V} \cdot \nabla)(\zeta - g) = 0 \quad (34)$$

After differentiating, we obtain the exact equation for kinematic boundary condition,

$$U_3 + w = \partial g / \partial t + (U_1 + u) \partial g / \partial \xi + (U_2 + v) \partial g / \partial \eta, \quad (35)$$

on $\zeta = g(\xi, \eta, t)$,

where (U_1, U_2, U_3) and (u, v, w) are the inflow and induced velocities, respectively, in the (ξ, η, ζ) -directions.

We define the helical inflow velocity, U_r , as

$$U_r = \sqrt{\bar{V}_A^2(r) + (-r)^2}, \quad (36)$$

where $\bar{V}_A(r)$ is the longitudinal inflow velocity averaged over one propeller revolution and $-r$ is the radian rotational velocity of the propeller. Under the assumptions, the geometric quantities such as angle of attack of the section, camber ratio, and thickness ratio are small. Chordwise fluctuations in the incoming flow will be assumed to be small compared to U_r , and spanwise velocities will be neglected. Gusts, or perturbations normal to the camber surface, will be taken into account. Hence we may write

$$U_1 = U_r, \quad U_2 = 0, \quad U_3 = w_g, \quad (37)$$

where w_g denotes the gust. The perturbation velocities are assumed to be small accordingly, and hence higher order terms in Eq. (35) can be neglected to result in a linearized kinematic boundary condition equation

$$w_g + w = \partial g / \partial t + U_r \partial g / \partial \xi, \quad \text{on } \zeta = 0 \quad (38)$$

The assumption of small thickness allows the boundary condition to be applied on the camber surface, $\zeta=0$, consistent with the linearization.

Equation (38) implies that the kinematic boundary condition is effectively reduced to the two-dimensional chordwise strip, since the η -coordinate does not appear explicitly. This would allow the pure two-dimensional stripwise application of the kinematic boundary condition possible.

Let us define the cavity thickness, $h(\xi, \eta, t)$, in terms of cavity surface and camber surface, $f(\xi, \eta)$,

$$h(\xi, \eta, t) = g(\xi, \eta, t) - f(\xi, \eta) \quad (39)$$

If we apply Eq. (38) to the upper and lower surface of the cavity, and if we introduce the source density $q(\xi, \eta, t)$ as the velocity jump across the cavity thickness, then we will obtain an expression for the cavity thickness

$$q(\xi, \eta, t) = 2h / \partial t + U_r \partial h / \partial \xi \quad \text{on } \zeta = 0 \quad (40)$$

It should be noted that Eq.(40) can be equally applied to the blade thickness problem.

Appendix 3. Cavity Closure Condition

The closure condition(6) for the cavity states that the cavity thickness be zero along the leading and trailing edges of the cavity, and also along the inner (hub) and outer (tip) extreme boundaries of the cavity surface. This condition can be stated in the discretized space that

$$h_0=0, \quad h_L=0 \quad (41)$$

where the subscripts 0 and L are indices for the leading and trailing edges of cavity, respectively.

In order to derive an expression for cavity closure condition, it is first necessary to recast Eq.(40) into a discretized form; i.e., for the (n,j)th element, omitting the radial index j for simplicity, unless otherwise required for clarity,

$$q_n = \frac{\bar{h}_n - \bar{h}_n^{(t-1)}}{\Delta t} + U_r \frac{h_n - h_{n-1}}{\Delta \xi_n}, \quad (42)$$

$$\bar{h}_n = \frac{h_n + h_{n-1}}{2}$$

where h_n is the cavity thickness at the panel boundary as shown in Fig. 17, $\Delta \xi_n$ is the chord length of the element, and the superscript (t-1) denotes the previous time step. The quantities at the present time will be described without the superscript.

To simplify the manipulation, we introduce notations

$$R_n = \Delta \xi_n / 2U_r \Delta t \quad (43)$$

$$Q_n = q_n \Delta \xi_n \cos \epsilon$$

where Q_n is the strength of line source element, consistent with the definition used in the main text, and ϵ is the tilted angle of line source relative to η coordinate. Equation (42) is now rearranged to result in the recurrence formula for the cavity thickness

$$h_n = \frac{1-R_n}{1+R_n} h_{n-1} + \frac{1}{1+R_n} \frac{Q_n}{U_r} \sec \epsilon + \frac{F R_n}{1+R_n} (h_n + h_{n-1})^{(t-1)}, \quad (44)$$

where a factor F is introduced to account for the relative position of the cavity trailing end at the previous time step with respect to the spanwise boundaries of the element. This factor is defined as follows; refer to fig. 18,

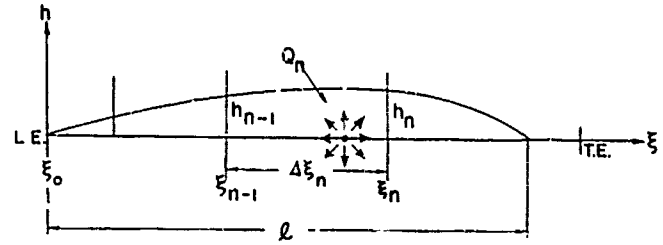


Figure 17. Illustration of cavity thickness form

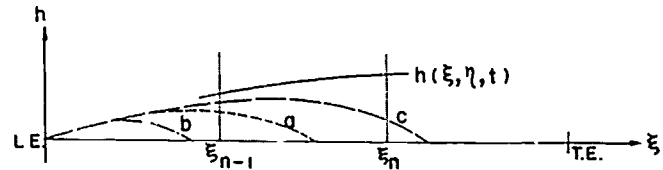


Figure 18. Sketch for definition of F

$$F = \begin{cases} \frac{\ell^{(t-1)} - \xi_{n-1}}{\Delta \xi_n}, & \text{for (a)} \\ 0 & \text{for (b)} \\ 1 & \text{for (c)} \end{cases} \quad (45)$$

where $\ell^{(t-1)}$ is the cavity length at the previous time step.

Recursive use of the thickness formula (4), together with the closure condition relations (41), after tedious algebraic work, will result in a numerical closure condition equation in discretized form

$$\begin{aligned} & \sum_{n=1}^{L-1} \left(\frac{L}{\pi} \frac{1-R_k}{1+R_k} \right) \cdot \frac{1}{1+R_n} \cdot \frac{Q_n}{U_r} \sec \epsilon \\ & + \frac{1}{1+R_L} \cdot \frac{Q_L}{U_r} \sec \epsilon \\ & = \left[- \sum_{n=1}^{L-1} \left(\frac{L}{\pi} \frac{1-R_k}{1+R_k} \right) \cdot \frac{R_n}{1+R_n} (h_n + h_{n-1})^{(t-1)} \right. \\ & \quad \left. - F \cdot \frac{R_L}{1+R_L} \cdot h_{L-1}^{(t-1)} \right], \\ & \text{where } F = \frac{\ell^{(t-1)} - \xi_{L-1}}{\Delta \xi_L}, \\ & \text{for } L^{(t-1)} = L \\ & - \sum_{n=1}^{L-1} \left(\frac{L}{\pi} \frac{1-R_k}{1+R_k} \right) \cdot \frac{F \cdot R_n}{1+R_n} (h_n + h_{n-1})^{(t-1)} \end{aligned}$$

$$\begin{aligned}
\text{where } F = & \begin{cases} 1, & \text{for } n < L^{(t-1)} \\ \frac{\xi_L^{(t-1)} - \xi_{L-1}^{(t-1)}}{\Delta \xi_L^{(t-1)}}, & \text{for } n = L^{(t-1)} \end{cases} \\
& \text{for } L^{(t-1)} < L \\
& - \sum_{n=1}^{L-1} \left(\frac{L}{\pi} \frac{1-R_k}{1+R_k} \right) \cdot \frac{R_n}{1+R_n} (h_n + h_{n-1})^{(t-1)} \\
& - \frac{R_L}{1+R_L} (h_L + h_{L-1})^{(t-1)}, \text{ for } L^{(t-1)} > L
\end{aligned} \quad (46)$$

where $L^{(t-1)}$ is the number of the cavitating elements at the previous time step along the chordwise strip of interest.

To facilitate further manipulation, it may be found convenient to rewrite Eq. (46) in the form

$$\sum_{n=1}^L \lambda_n Q_n = \lambda_R' \quad (47)$$

where λ_R is the abbreviated notation of the right hand side of Eq. (46), and

$$\lambda_n = \begin{cases} \left(\frac{L}{\pi} \frac{1-R_k}{1+R_k} \right) \frac{1}{1+R_n} \cdot \frac{\sec \epsilon}{U_r}, & \text{for } n \leq L-1 \\ \frac{1}{1+R_L} \cdot \frac{\sec \epsilon}{U_r}, & \text{for } n=L \end{cases} \quad (48)$$

It should be noted that this closure condition is applied to each chordwise strip.

Appendix 4. Dynamic Condition on Cavity Surface

The linearized form of Bernoulli's equation, applicable to each chordwise strip, can be written as

$$p - p_\infty = \rho \frac{\partial \phi}{\partial t} - \rho u U_r - \rho g y_0. \quad (49)$$

where ϕ is the perturbation potential, y_0 is the vertical coordinate fixed on ship measured positive upward from the shaft center, and p_∞ is the pressure at infinite upstream at the depth of the shaft center.

We will use a backward difference formula for the time rate of change of the velocity potential, i.e.,

$$\frac{\partial \phi}{\partial t} \approx \frac{1}{\Delta t} (\phi - \phi^{(t-1)}) \quad (50)$$

Equation (49) may then be written in a form

$$\begin{aligned}
-\frac{\rho}{\Delta t} \phi - \rho u U_r - (p - p_\infty) \\
= -\frac{\rho}{\Delta t} \phi^{(t-1)} + \rho g y_0.
\end{aligned} \quad (51)$$

The streamwise component of induced velocity, u , in the left hand side of Eq. (51) is expressed as linear functions of the strengths of vortices and sources, in a manner similar to what was done for the normal component in Eq. (27). Therefore, the expression for the streamwise component of induced velocity at the (i, j) th control point is written as

$$\begin{aligned}
u_{ij} = & \sum_{n,m} u_{K_{ijnm}} \Gamma_{nm}^s \\
& + \sum_{n,m} u_{H_{ijnm}} Q_{nm} + u_{ij}^0,
\end{aligned} \quad (52)$$

where the coefficients of Γ_{nm}^s and Q_{nm} are defined as in Eq. (33) with the left superscript, u , denoting the streamwise component of induced velocity, and u_{ij}^0 is the streamwise component of induced velocity due to singularities other than those on the key blades.

The potential at the (i, j) th control point along the suction side of the blade may be written as

$$\phi_{ij} = \phi_{ij}^\Gamma + \phi_{ij}^Q + \phi_{ij}^0. \quad (53)$$

ϕ_{ij}^Γ is the odd part of the velocity potential across the camber surface, which is approximated by

$$\phi_{ij}^\Gamma \approx \frac{1}{2} \sum_{n=1}^i \Gamma_{nj}^s. \quad (54)$$

ϕ_{ij}^Q is the cavity-induced potential and may be written as

$$\phi_{ij}^Q = \sum_{n,m} \phi_{ijnm} Q_{nm} \quad (55)$$

where ϕ_{ijnm} the potential due to a unit source element; ϕ_{ij}^0 is the potential due to the cavity sources on the other blades and is computed much the same way as ϕ_{ij}^Q .

Substitution of Eqs. (52) through (55) into Eq. (51) leads to the following result, for the (i, j) th control point,

$$\begin{aligned}
-\frac{\rho}{\Delta t} \left\{ \frac{1}{2} \sum_{n=1}^i \Gamma_{nj}^s + \sum_{m=1}^M \sum_{n=1}^{N_Q} \phi_{ijnm} Q_{nm} \right\} \\
- \rho U_r \left\{ \sum_{m=1}^M \sum_{n=1}^N u_{K_{ijnm}} \Gamma_{nm}^s \right. \\
\left. + \sum_{m=1}^M \sum_{n=1}^{N_Q} u_{H_{ijnm}} Q_{nm} \right\} \\
- (p - p_\infty) = e_{ij}.
\end{aligned} \quad (56)$$

The right hand side containing all the known terms will be defined as

$$e_{ij} = -\frac{\rho}{\Delta t}(\Gamma_{ij}^{(t-1)} + \phi_{ij}^{Q(t-1)}) + \frac{\rho}{\Delta t}(\phi_{ij}^O - \phi_{ij}^{O(t-1)}) + \rho g y_O + \rho u_{ij}^O U_r \quad (57)$$

Appendix 5. Formation of the Simultaneous Equations

Equations (33), (47) and (56), derived from the boundary conditions, must be solved simultaneously with a suitable choice of control points. However, Equation (56), the dynamic boundary condition equation for the cavity, should be applied only to the cavitating region, whose extent is not known a priori. Hence iterative techniques must be used to determine the cavity extent. Since we assumed that the cavity starts at the leading edge, the task is now to determine the spanwise and chordwise extent of the cavity. The iterative procedures to find the cavity extent are very long and time-consuming. It is found to be efficient to consider the unknowns in one chordwise strip at a time. This procedure reduces the size of the matrix. The cavity length is determined for the chordwise strip being considered. Then spanwise strip-by-strip iteration becomes necessary to update the interactions of the adjacent strips. These two steps are described in detail in Section 4.3.

Let us assume that we are solving the problems for the j -th chordwise strip with assumed N_Q cavitating elements, and that the values on the other strips are known from previous calculations. Then Equation (33) may be rewritten for the j -th strip

$$\sum_{n=1}^N w_{K_{ijnj}} \Gamma_{nj}^S + \sum_{n=1}^{N_Q} w_{H_{ijnj}} Q_{nj} = \tilde{d}_{ij}, \text{ for } i=1,2,\dots,N \quad (58)$$

where \tilde{d}_{ij} is the combination of known contributions, especially including the influence from adjacent strips. Equation (56) may also be rewritten, for the j -th strip, with a slight rearrangement

$$\begin{aligned} & -\frac{\rho}{2\Delta t} \sum_{n=1}^i \Gamma_{nj}^S - \rho U_r \sum_{n=1}^N u_{K_{ijnj}} \Gamma_{nj}^S \\ & - (p-p_\infty) \\ & - \sum_{n=1}^{N_Q} \left(\frac{\rho}{\Delta t} \phi_{ijnj} + \rho U_r u_{H_{ijnj}} \right) Q_{nj} = \tilde{e}_{ij}, \\ & \text{for } i=1,2,\dots,N_Q \end{aligned} \quad (59)$$

where \tilde{e}_{ij} is again defined for convenience as in \tilde{d}_{ij} . Equations (58), (47) and (59) are sufficient to determine $I=N+1+N_Q$ unknowns, which are composed of N unknown strengths of vortices, N_Q unknown strengths of sources and a pressure inside the cavity. A set of simultaneous equations may take the familiar form

$$\sum_{q=1}^I a_{pq} x_q = b_p, \text{ for } p=1,2,\dots,I, \quad (60)$$

where a_{pq} is the coefficient matrix obtained by suitably arranging the coefficients of Γ_{nj}^S , $(p-p_\infty)$, and Q_{nj} from Eqs. (58), (47), and (59), x_q is the q -th unknown of a vector

$$\underline{x} = \{\Gamma_{1j}^S, \Gamma_{2j}^S, \dots, \Gamma_{Nj}^S, (p-p_\infty), Q_{1j}, Q_{2j}, \dots, Q_{N_Q j}\}^T, \quad (61)$$

and b_p is the p -th element of a vector composed of the right hand sides of Eqs. (58), (47), and (59), respectively. The solution to this matrix equation is straightforward, at least conceptually.

Discussion

T. Hoshino (MHI)

The author is to be congratulated for his significant contribution to the numerical method in lifting-surface theory of marine propellers.

I would like to ask the author the following questions.

(1) Fig.9 indicates that the cavity volume calculated by the present theory for NSRDC Propeller 4381 reaches a maximum before the generating line of the blade passes the wake peak. According to my experiments, however, the cavity volume reaches a maximum after the generating line of the blade has passed the wake peak as shown in Fig.A. I would like to ask author's comments on this discrepancy in phase between calculation and experiment.

(2) I think that the stepwise approach for the unsteady problem requires time consuming computations. How much computation time does it take for one propeller and one wake distribution by your IBM 370/148 ?

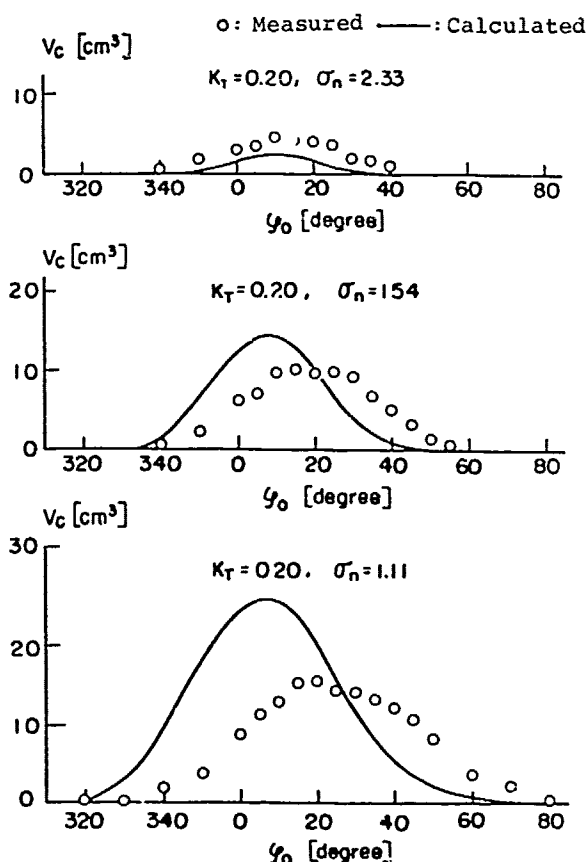


Fig. A Comparison between measured and calculated cavity volume

B. Yim (DTN SRDC)

Congratulations to Dr. Lee for a fine paper. The author has solved a very difficult problem with satisfactory results. Even the linear solution for the partially cavitating propeller seems to be predicted quite well. I presume Dr. Lee has made substantial numerical experiments to test the convergence with respect to mesh sizes, time steps, etc. When I solved the design problem for a supercavitating propeller, I thought the convergence was pretty good for design quantities. However, to incorporate the hub effect, radial velocities were computed without considering the hub boundary condition, and it was found that the values of the radial component of induced velocities were quite unstable, although other results were reasonably stable. After the hub boundary condition was considered, such phenomena disappeared. I wonder whether such a thing might occur here since the hub effect has not been considered.

In such a complicated problem as numerical evaluation, the measure of computer time is always crucial. It is mentioned in the text that the solution process for the cavitating propeller is significantly more expensive than for the fully wetted propeller. It might also depend upon how wide the cavity planform is. It would be desirable for the author to show us some measures of computer time for various cases.

H. Isshiki (Hitachi S & E)

One object of this paper is, if I'm not wrong, to make clear the unsteady effect on the cavitation of a marine propeller running behind a ship. But the author's calculation includes other effects such as the interaction effect between blades and three dimensional effect. Then, I would like to ask if the author could distinguish the unsteady effect from other ones in your numerical results, and what the author's opinion is on "the quasi-steady assumption" in the conventional theories.

W. van Gent (NSMB)

This paper and also the foregoing one give a good picture of recent developments in the application of lifting surface theory to ship propellers. The first paper gives a comparison of the various basic methods, which had not yet been given before. This paper gives an attempt to include cavitation into the lifting surface model.

Both papers consider the propeller in irrotational flow, however, and this may limit the validity of the application in ship wakes. The author concludes that the poor correlation for full scale is due to lack of knowledge of the scaling procedure

from model wake. I am of the opinion that treatment of the propeller in rotational flow can improve this situation. What is the opinion of the author ?

It has to be noted, that in a ship wake we have large shear. This situation differs from turbomachinery cases, where usually small shear is assumed.

Author's Reply

C.S. Lee (KRIIS)

Mr. Hoshino raised a question on the discrepancy of the phases between theory and experiment. I agree with him that there should be some phase lag. Unfortunately, the wake generated by the screen is not exactly symmetric, and hence about six degree difference for this short cavity case

is not sufficient to draw any conclusion. But in the Fig.10, some phase lag can at least be observed.

Dr. Yim asked whether I had any convergence problems near the hub region. As far as I remember, I had no such convergence problem with my modeling. It is possible that I did not have such problem just because the chordwise strip nearest the hub never had large cavities in the sample calculation.

It is quite natural that everybody was concerned on the computing time required for the numerical procedure. It is, however, inherently dependent on the machine used and also on the size of cavities. The CPU time for one revolution of propeller for the case of NSRDC Propeller 4381 was about one hour on IBM 370/148 computer. But it took about twenty minutes on Honeywell 6180 computer which is still slower by an order of magnitude than the modern IBM or CDC machine.

Finally I would like to express my appreciations to Mr. Hoshino, Dr. Yim and all the other oral discussers for their interests in my paper.

Practical Applications of the Discrete Vortex Element Method for Calculation of Propeller Induced Excitation Forces

Hajime Yuasa, Norio Ishii
Mitsui Engineering & Shipbuilding Co., Ltd
Japan

Bror Persson, Oddvar Frydenlund and Kjell Holden
Det norske Veritas
Norway

ABSTRACT

Application of discrete vortex elements for numerical calculations of propeller loading and blade cavitation is presented. The various advantages of such methods are discussed with respect to flexibility and correct modelling of the real physical phenomena.

In this paper, we have concentrated on the following items:

- Steady and unsteady propeller loading
- Steady propeller/duct loading
- Blade tip flow and leading edge separating vortex
- Two dimensional cavitation
- Three dimensional cavitation
- Propeller cavitation
- Hull surface pressure

The availabilities of the numerical model have been confirmed in comparison with the model and full scale experiments.

1. INTRODUCTION

Due to an increasing interest about propeller/duct systems as propulsion units on merchant ships and for dynamic positioning a joint research project between Mitsui Engineering & Shipbuilding Co., Ltd. and Det norske Veritas was started in 1976. The goal of the project was to develop a method for prediction of blade loading, amount of blade cavitation and induced pressure fluctuations transferred through the water. Application of the method on thrusters required that operation at bollard conditions was subject to detailed studies.

Existing methods for prediction of blade loading and detailed blade pressure distributions are based on either lifting line or lifting surface theories, which often show unsatisfactory results when pro-

peller units are operating at a very low inflow velocity. Furthermore, there was also a need for a more advanced method to directly predict shapes and volumes of blade cavities on a three dimensional wing.

During the project the following items have been studied in detail and theoretical methods have been developed:

- a) Two dimensional airfoil theory - application of vortex elements to predict pressure distribution and loading in steady and unsteady flow.
- b) Propeller performance in uniform flow - thrust/torque characteristics.
- c) Propeller/duct performance in uniform flow - thrust/torque characteristics.
- d) Two dimensional theories for prediction of cavity shape and volume.
- e) Tip flow studies on three dimensional wings and propeller blades operating with leading edge separation.
- f) Propeller blade loading in non-uniform flow.
- g) Propeller blade cavitation in uniform and non-uniform flow by combining the various items.
- h) Pressure fluctuations transferred through water induced by propeller blades and fluctuating blade cavity volumes.

2. MODELLING OF PROPELLER/DUCT SYSTEMS BY A DISCRETE VORTEX ELEMENT METHOD

A general numerical method is formulated for the calculation of unsteady propeller forces. The method is based on a discrete element approach, which in this connection appears to offer a number of advantages, i.e.:

- a) Accurate prediction of mean loading can

be obtained both at design and off-design conditions (J -values approaching zero).

- b) Arbitrary blade geometry may be handled
- c) Radial as well as tangential wake may easily be included.
- d) Modifications to include cavitation are straightforward, since no loading mode functions are employed. Cavitation is modelled by a source/sink distribution in the same way as thickness effects of the blade are accounted for.
- e) A discrete element method lends itself naturally to a step-by-step solution in the time domain, which is also essential for the calculation of unsteady cavitation.

2.1 Basic Equations

The propeller is assumed to operate in an inviscid, incompressible fluid. A mathematical function describing the motion must therefore satisfy Laplace's equation (1) with prescribed function values or gradients at the boundary (in this case the propeller camber surface).

$$\nabla^2 \phi = 0 \quad (1)$$

Fundamental solutions that satisfy equation (1) are e.g. given by:

$$\bar{v}_{ind}(x,y,z) = -\frac{1}{4\pi} \int \frac{\bar{R} \times \bar{y}}{|\bar{R}|^3} dv \quad (2)$$

$$\bar{v}_{ind}(x,y,z) = \frac{1}{4\pi} \int \frac{\bar{R} \cdot \bar{q}}{|\bar{R}|^3} dv \quad (3)$$

expressing the induced velocities at a field point (x,y,z) caused by arbitrary distributions of vortices $\gamma(\xi,\eta,\zeta)$ and sources $q(\xi,\eta,\zeta)$ located at the source point (ξ,η,ζ) . The distance between the source point and the field point is denoted by R .

The restriction to be imposed on the flow at the camber surface is that there should be no flow through this surface. This condition of no flow may be put into mathematical form as:

$$\bar{v}_{TOT} \cdot \bar{n} = 0 \quad (4)$$

where \bar{n} is the normal vector of the camber surface.

\bar{v}_{TOT} is the total velocity vector, which is composed of:

- a) Induced velocities from the vortices on the reference blade and in the slip stream, as well as induced velocities from other blades and their slip streams.
- b) Inflow velocity to the propeller consisting of an axial velocity and a tangential velocity.

In the case of a cavitating propeller an additional boundary condition is needed on the cavitating part of the camber surface. This condition may in linearized form

be stated:

$$\bar{v}_{TOT} \cdot \bar{e}_t = \text{const.} \quad (5)$$

where \bar{e}_t denotes the unit vector in tangential direction. Equation (5) expresses the assumption that the pressure within the cavity is constant.

Due to the fact that there is a radial (spanwise) direction of circulation on blade, $\Gamma = \Gamma(r)$, trailing vortices will exist in the propeller slip stream. The amount of vorticity in the wake, γ_w , is related to the bound circulation according to:

$$\gamma_w = -\frac{d\Gamma(r)}{dr} = -\frac{d}{dr} \int_0^c \gamma(r,\xi) d\xi \quad (6)$$

where c is the chord length at section r .

When the motion is time dependent, the shedding of "radial" (bound) vorticity into the slip stream, must be taken into account.

2.2 Propeller

2.2.1 Numerical Approach

The first step in making a numerical description of the problem is to locate discrete vortex elements on the propeller camber surface (the non-cavitating case will be described at first).

6 spanwise sections are applied and each of the spanwise chordlines are divided into 13 equally spaced elements.

From each of the 6 radial subdivision lines, a free vortex (trailing vortex) is extended from the leading edge across the trailing edge of the propeller to the "roll-up point". An extensive description of the rollup process is given in Ref.[1]. A bound vortex and its corresponding trailing elements (Fig.1) constitutes a "horse shoe" vortex. Using horse shoe vortices assures that the Kelvin's theorem is satisfied at each vortex grid point on the blade. All horse shoe vortices are closed except for those at "mid-span". Since these vortices

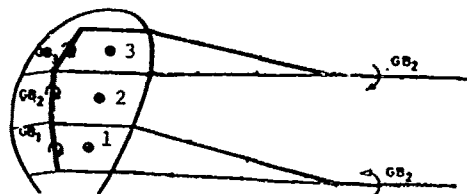


Fig. 1 Arrangement of Horse Shoe Vortex

are open, they generate the tip and hub vortex respectively. The location of this "mid-span" section is in fact an unknown entity and should be determined by iteration. However, for practical purposes it may be prescribed. The location of the vortex points and control points on the chord has been done in accordance with James' method

(Ref. 2).

A schematic view of this method in two dimensions is seen in Fig. 2. The source/sink elements representing either thickness or cavitation (or both) are also indicated. Fixing the propeller in a Cartesian reference system, it is now possible to calculate induced velocities at a control point on the camber surface by applying equations (2) and (3) in discretized form. The grid points of the vortex element system are defined by the coordinates $x(I,J)$, $y(I,J)$, $z(I,J)$, I -chordwise index, J -spanwise index. Location of control points are obtained by calculating the geometrical mean value of the four vortex grid points. The normal vector to be applied in equation (4) is obtained by forming the cross product of the diagonal vectors formed by the grid points.

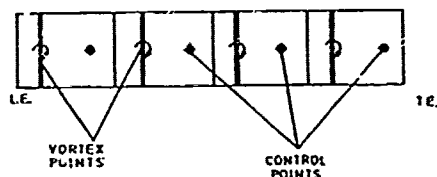


Fig. 2 Location of Vortex and Control Points in Two Dimensions

Fig. 1 shows a simplified vortex system on a propeller. In this case only one element is used along the chord. For each control point 1, 2, 3, equation (4) should be satisfied. This set-up therefore gives a system of 3 equations for the 3 unknowns GB_1 , GB_2 , GB_3 . At control point 1, the following equation is a discrete form of (4):

$$\begin{aligned} & n_{x1} (GB_1 \cdot K_{11}^x + GB_2 \cdot K_{21}^x + GB_3 \cdot K_{31}^x) \\ & + n_{r1} (GB_1 \cdot K_{11}^r + GB_2 \cdot K_{21}^r + GB_3 \cdot K_{31}^r) \\ & + n_{t1} (GB_1 \cdot K_{11}^t + GB_2 \cdot K_{21}^t + GB_3 \cdot K_{31}^t) \\ & = v^{x1} \cdot n_{x1} + v^{r1} \cdot n_{r1} + v^{t1} \cdot n_{t1} \quad (7) \end{aligned}$$

At control point 2 and 3 similar equations may be formulated. n_{x1} , n_{r1} , n_{t1} are the components of the normal vector at control point 1. GB_1 , GB_2 , GB_3 are the strength of the bound vortices. $K_{ij}^{x,r,t}$ $i = 1, 3$; $j = 1, 3$ are the induced velocities at control point j due to a unit vortex at location i in axial, radial and tangential direction respectively. From Fig. 1, it is seen that the trailing vortices from the horse shoe vortex 1 and 3 cancel at the rollup point. The only vortex which contributes to the tip and hub vortices is horse shoe GB_2 . v^{x1} , v^{r1} , v^{t1} are the contribution to the normal velocity from the axial and rota-

tional motion at control point 1. In addition, $v^{x,r,t}$ contain contributions from the source/sink distribution generated by the thickness form. It should also be noted that the coefficients $K_{ij}^{x,r,t}$ contain contributions from the other ij blades. In the steady loading case the set of equations may be solved directly for the unknowns GB_1 , GB_2 , GB_3 . Ref. 1 gives the numerical approach for calculating the forces once the GB-distribution is known.

The coefficients $K_{ij}^{x,r,t}$ are implicit functions of the vortex ij geometry in the propeller slip stream. This means that the $K_{ij}^{x,r,t}$ should continuously be changing when time dependent motion is considered. The consequence of this is that the coefficients in the equations will change and the complete solution of a set of simultaneous equations would have to be solved at every angular position. The computing time for this system would be too large for the method to be of any practical interest. It has therefore been necessary to introduce modifications in the method of solution and in the treatment of the coefficients $K_{ij}^{x,r,t}$. $K_{ij}^{x,r,t}$ may be split up in a sum of contributions from the reference blade and the other blades.

$$K_{ij}^{x,r,t} = K_{ij}^{x,r,t}(\phi_1)_i + \sum_{n=2}^{NBLADE} K_{ij}^{x,r,t}(\phi_n) \quad (8)$$

where

$K_{ij}^{x,r,t}(\phi_1)$ refers to the reference blade, and

$K_{ij}^{x,r,t}(\phi_n)$, $n = 2, \dots, NBLADE$ to the contributions from other blades.

In the general case the blade loading is different on the various blades due to variations in the incoming wake.

Denoting the vortex distribution on the blades by $GB(\phi)_{ij}$, the equation (7) may be written:

$$\begin{aligned} & n_{x1} [GB_1(\phi_1) \cdot K_{11}^x(\phi_1) + \\ & \sum_{n=2}^{NBLADE} GB_1(\phi_n) \cdot K_{11}^x(\phi_n) + \\ & GB_2(\phi_1) \cdot K_{21}^x(\phi_1) + \\ & \sum_{n=2}^{NBLADE} GB_2(\phi_n) \cdot K_{21}^x(\phi_n) + \\ & GB_3(\phi_1) \cdot K_{31}^x(\phi_1) + \sum_{n=2}^{NBLADE} GB_3(\phi_n) \cdot K_{31}^x(\phi_n)] \\ & + n_{r1} [GB_1(\phi_1) \cdot K_{11}^r(\phi_1) + \sum \dots] \\ & + n_{t1} [GB_1(\phi_1) \cdot K_{11}^t(\phi_1) + \sum \dots] \\ & = v^{x1} \cdot n_{x1} + v^{r1} \cdot n_{r1} + v^{t1} \cdot n_{t1} \quad (9) \end{aligned}$$

It is assumed that if the loading on other blades: ($N=2, NBLADE$) are known, the contribution from these blades to the boundary condition can be taken into the right-hand side of the equation. The only unknown part of the equations will then be the vortex distribution on the reference blade.

To avoid solving a set of simultaneous equations at each timestep, a procedure has been chosen which involves just one inversion of the coefficient matrix in the simultaneous equations. This procedure can be applied if:

a) The coefficients for the unknown on the reference blade do not change during one revolution.

b) The contributions from other blades are known.

Requirement a) can be satisfied by letting the pitch of the trailing wake system be constant at each angular position. This constant value can be obtained by calculating a mean loading from an average wake.

When the calculations on the reference blade are done, the resultant circulation distribution is stored at that particular angular position. As the first following blade enters this angular position, it picks up the loading previously obtained for the reference blade.

The other blades, which have not reached an angular position previously occupied by the reference blade, will retain the mean loading. By always letting the following blades take on the loading calculated for the reference blade, requirement b) can be satisfied.

In open water propeller cavitation, the equation (4) is still valid on the wetted part of the camber surface. The expression for \bar{V}_{TOT} may be modified to include the velocity jump due to source/sink distribution representing the cavity. Since this velocity jump is normal to the camber surface, it may be written:

$$\bar{V}_{TOT} + \frac{1}{2} q\bar{n}$$

and combined with equation (4):

$$\frac{1}{2} q_j + (\bar{V}_{TOT} \cdot \bar{n})_j = 0 \quad (10)$$

at each control point j for the vortex distribution γ . Similarly, equation (5) may be put in the form:

$$\frac{1}{2} \gamma_i + (\bar{V}_{TOT} \cdot \bar{e}_t)_i = \text{const.} \quad (11)$$

at each control point for the source/sink distribution q . The constant in equation (11) contains the unknown cavitation number σ . To obtain a complete set of linear equations, an additional condition is needed. This last condition may in the steady state case be put in the discrete form:

$$\sum q_i = 0 \quad (12)$$

which indicates that the cavity is closed. The summation in (12) is to be carried out over all cavitating elements along the chord. The control points for the source/sink distribution are located at the midpoint of the bound vortex elements and vice versa.

By combining the equations (7), (10), (11) and (12) a numerical representation for propeller cavitation may be obtained.

2.2.2 Calculated Results for Non-Cavitating Propeller

2.2.2.1 Uniform Flow

To obtain the open water characteristics, three J -values have been analyzed, $J=0.1$, $PD/2$ and PD ; PD being the pitch/diameter ratio. The results are displayed in Figs. 3-5. The agreement between measured and calculated K_T is poorer for the higher J -values ($K_T \rightarrow 0$). At very high blade loading, vortex separation may occur at the propeller leading edge (see Appendix).

The pressure distribution along the chord has been computed for one propeller where the experimental distribution is available (Ref. 3). The results from open water calculations are given in Fig. 6.

2.2.2.2 Non-Uniform Flow

Although some unsteady effects have been neglected, calculations in wake have been modified compared to the quasi-steady method. This has been accomplished by letting each of the blades have different loading according to their angular position. The unsteady effect which has been neglected is the radially shed vortices in the wake. These vortices are the "memory" of the motion and will be included in the further development together with calculations of "added mass" effects. Calculations in wake have been performed for a 10 deg. and 90 deg. net wake screen and show satisfactorily agreement (Figs. 7&8, quoted from Ref. 4).

2.2.2.3 Inclined Shaft

The calculations in non-uniform flow were done with the prescribed trailing vortex system of the propeller related to the mean loading on the blades. On the inclined shaft case, the periodic change in the slip stream geometry is thought to have a greater influence on the loading. The procedure from unsteady motion in a ship wake may probably not be applicable in inclined shaft calculations. Results from sample calculations are given in Fig. 9.

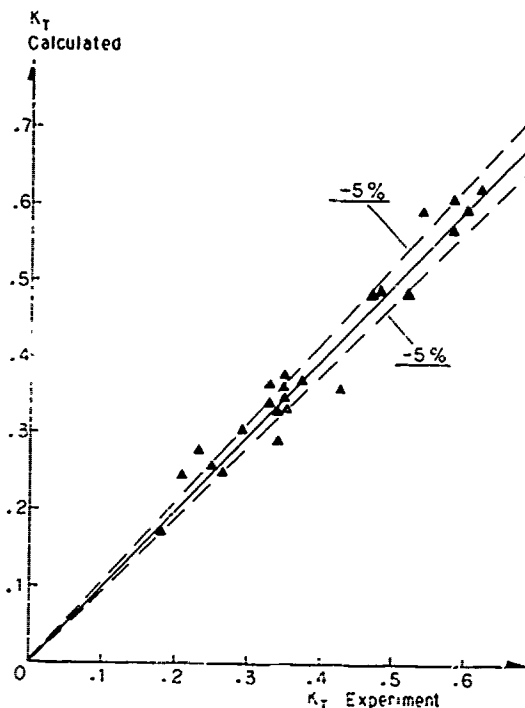


Fig. 3 Correlation between Calculated and Measured K_T (Thrust Coefficient) at $J=0.1$ for the Various Model Propellers

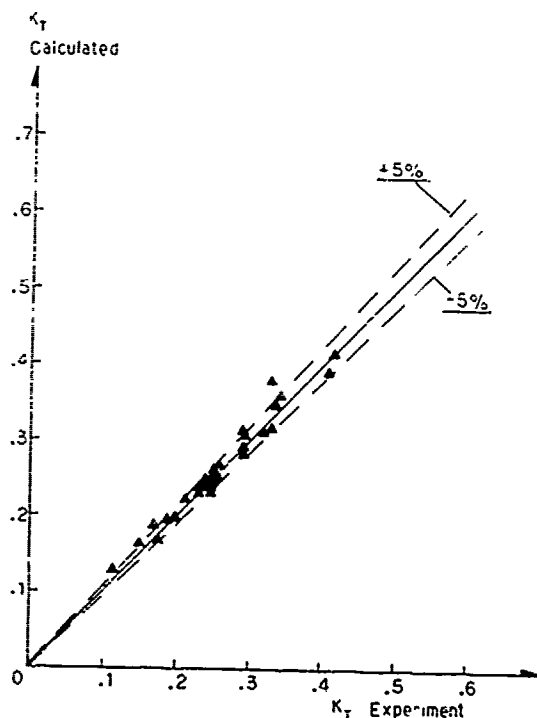


Fig. 4 Correlation between Calculated and Measured K_T at $J=PD/2$ for the Various Model Propellers

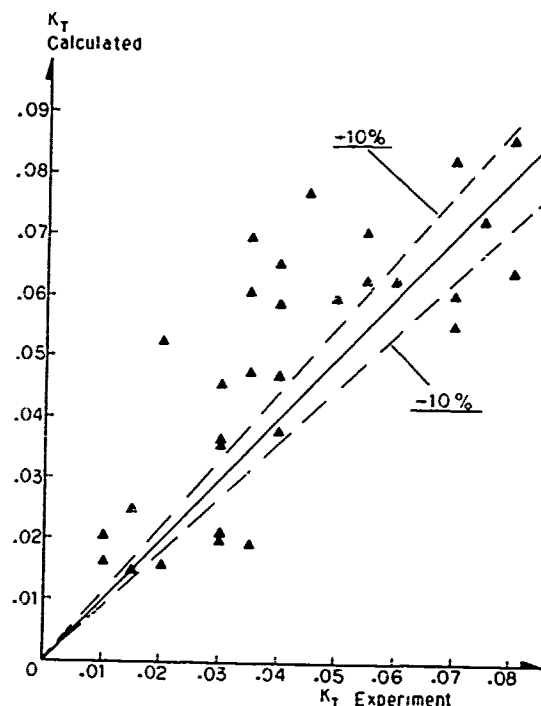


Fig. 5 Correlation between Calculated and Measured K_T at $J=PD$ for the Various Model Propellers

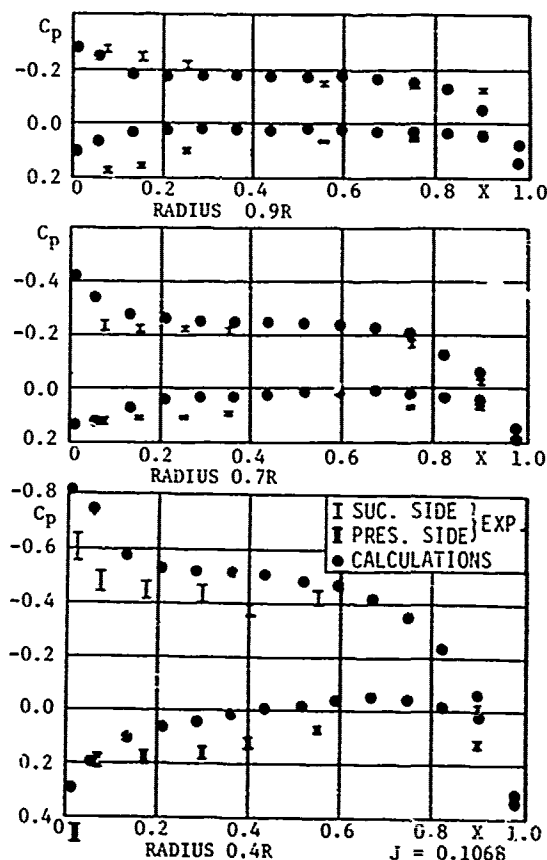


Fig. 6 Pressure Distribution along Chord for a Propeller Blade

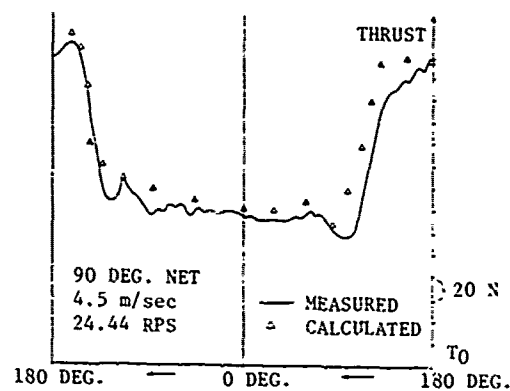


Fig. 7 Thrust Fluctuation in Wake during a Revolution

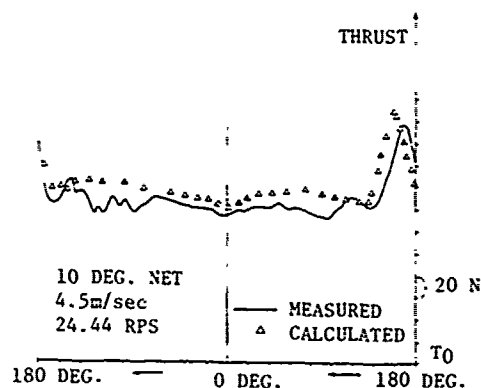


Fig. 8 Thrust Fluctuation in Wake during a Revolution

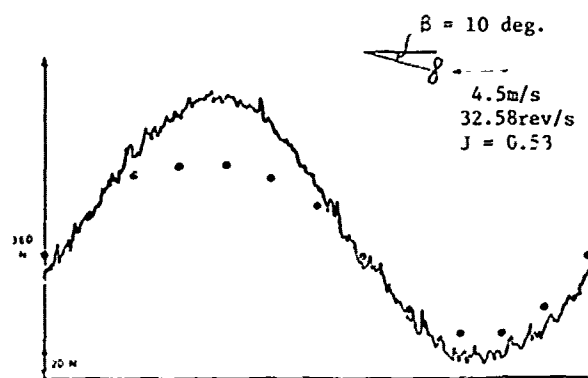


Fig. 9 Thrust Fluctuation by Inclined Shaft during a Revolution

2.3 Propeller/Duct System in Uniform Flow

2.3.1 Fundamental Assumption

Propeller blades and duct are regarded as thin foil surfaces with arbitrary shape. A vortex arrangement placed on the camber surfaces of propeller blades and duct is adopted as the hydrodynamic model of propeller/duct system.

Concerning the thickness of blades and duct, the strength of source distributions is obtained from the chordwise gradient of the thickness applying thin foil theory.

Fig. 10 shows the horse-shoe vortex arrangements by the discrete vortex elements with the Cartesian coordinate system. In this figure, Γ means the circulation strength for the unit length of a vortex element joining two grid points with a straight line.

The subscripts D, P, S and C refer to the initials of Duct, Propeller, Spanwise and Chordwise.

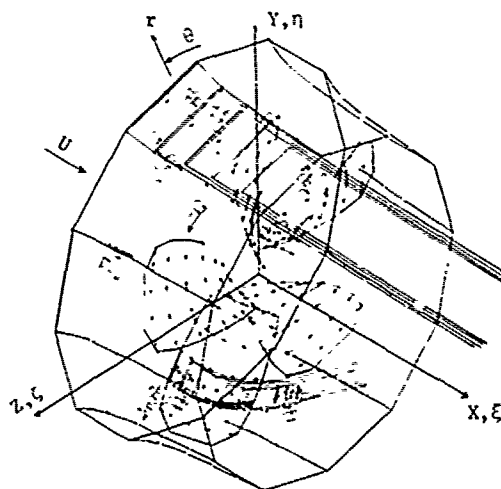


Fig. 10 Coordinate System and Horse Shoe Vortex Arrangement for Propeller/Duct System

Defining the discretized vortex strength $\Gamma_{n,m}^S$ and $\Gamma_{n+1,m}^S$ for the spanwise elements before and behind point i on the camber surface, the circulation distribution density γ_i of the vortex continuously distributed is as follows:

$$\gamma_i = (\Gamma_{n,m}^S + \Gamma_{n+1,m}^S) / (2 \cdot \Delta k_{n,m}^S) \quad (13)$$

Hence, $\Delta k_{n,m}^S$ is the mean distance between $\Gamma_{n,m}^S$ and $\Gamma_{n+1,m}^S$. In the same manner, the source strength q_i continuously distributed can also be expressed,

$$q_i = (Q_{n,m} + Q_{n+1,m}) / (2 \cdot \Delta k_{n,m}^S) \quad (14)$$

by using the discretized line source strength $Q_{n,m}$ and $Q_{n+1,m}$ per unit length.

The boundary conditions are set up at points $i, i+1, \dots$ namely, control points which are obtained by calculating the geometrical mean values of the four vortex grid points.

Concerning the propeller lifting surface, the numerical approaches are principally based on Section 2.2.

2.3.2 Numerical Analysis

The integral equation which has the unknown strength of vortices distributed on each camber surface of propeller blades and duct, for example at point (x, y, z) can be expressed as on the duct camber surface:

$$\begin{aligned} -w_D(x, y, z) = & \iint_{S_D} \gamma_D \cdot K_{DD} dS_D + \iint_{W_D} f(\gamma_D) \\ & \cdot K_{DD} dW_D + \iint_{S_P} \gamma_P \cdot K_{PD} dS_P + \iint_{W_P} f(\gamma_P) \\ & \cdot K_{PD} dW_P \end{aligned} \quad (15)$$

where,

1st term - normal component velocities induced by the bound vortices on duct camber surface,

2nd term - normal component velocities induced by the free vortices in duct wake,

3rd term - normal component velocities induced by the bound vortices on whole propeller blade camber surfaces,

4th term - normal component velocities induced by the free vortices in propeller wake,

$w_D(x, y, z)$ - boundary value i.e. the normal component composed of inflow and source induced velocities.

For point (x, y, z) on propeller blade the similar equation can be introduced as:

$$\begin{aligned} -w_P(x, y, z) = & \iint_{S_P} \gamma_P \cdot K_{PP} dS_P + \iint_{W_P} f(\gamma_P) \\ & \cdot K_{PP} dW_P + \iint_{S_D} \gamma_D \cdot K_{DP} dS_D + \iint_{W_D} f(\gamma_D) \\ & \cdot K_{DP} dW_D \end{aligned} \quad (16)$$

Thus, the simultaneous integral equations are formed from the equation (15) and (16).

Applying the discrete vortex elements instead of the continuous vortex distributions in the equations (15) and (16), the following discretized expressions can be obtained:

$$\begin{aligned} -\bar{n}_i \cdot (\bar{v}_i^I + \bar{v}_i^Q) = & \sum_{m=1}^{M_D} \left\{ \sum_{n=1}^{N_D} u_{inm}^{DS} \Gamma_{nm}^{DS} + \right. \\ & \sum_{n=1}^{N_{DW}} u_{inm}^{DW} \Gamma_{nm}^{DW} \left. + \sum_{m=1}^{M_D+1} \left\{ \sum_{n=1}^{N_D} u_{inm}^{DC} \Gamma_{nm}^{DC} + \right. \right. \\ & \sum_{n=1}^{N_{DW}-1} u_{inm}^{DT} \Gamma_{nm}^{DT} \left. + \sum_{m=1}^{M_P} \left\{ \sum_{n=1}^{N_P} u_{inm}^{PS} \Gamma_{nm}^{PS} + \right. \right. \\ & \sum_{n=1}^{N_{PW}} u_{inm}^{PW} \Gamma_{nm}^{PW} \left. + \sum_{m=1}^{M_P+1} \left\{ \sum_{n=1}^{N_P} u_{inm}^{PC} \Gamma_{nm}^{PC} + \right. \right. \\ & \left. \left. \sum_{n=1}^{N_{PW}-1} u_{inm}^{PT} \Gamma_{nm}^{PT} \right\} \right\} \end{aligned} \quad (17)$$

where,

\bar{v}_i^I - inflow velocity vector at control point i as in Fig. 10

\bar{v}_i^Q - source induced velocity vector at point i

Γ_{nm} - unknown circulation of the vortex element (n, m)

$n = 1, 2, \dots, N_x$ - index of chordwise direction

$m = 1, 2, \dots, M_x$ - index of spanwise direction

$$u_{inm} = \bar{n}_i \cdot \bar{u}_{inm} \quad (18)$$

u_{inm} is corresponding to the kernel function of the integral equations (15) & (16) and also the induced velocity at point i from an unknown vortex element Γ_{nm} supposed to have unit strength which is placed at the address (n, m) . The three-dimensional vector \bar{u}_{inm} is calculated by Biot-Savart's law, and \bar{n}_i is the unit vector in normal direction at point i .

The left hand side of the equation (17) is the known values consisting of both inflow velocities and source induced velocities at point i .

Equation (17) is the general expression of the formula for a propeller/duct lifting surface. As limiting the application of this equation on the steady motion problem,

the shed wake vortices Γ_{nm}^{DW} and Γ_{nm}^{PW} can be neglected, because the trailing vortices keep constant strength downstream to infinity. Thus,

$$\Gamma_{nm}^{DW} = \Gamma_{nm}^{DT} - \Gamma_{n+1m}^{DT} = 0 \quad (19)$$

$$\Gamma_{nm}^{TW} = \Gamma_{nm}^{PT} - \Gamma_{n+1m}^{PT} = 0$$

The circulations of a chordwise vortex and a trailing vortex can be expressed by that of spanwise (bound) vortices as follows:

$$\begin{aligned} \Gamma_{nm}^{DT} &= \Gamma_{nm}^{DC} \\ \Gamma_{nm}^{DC} &= \Gamma_{nm-1}^{DS} - \Gamma_{nm}^{DS} + \Gamma_{n-1,m}^{DC} \\ &= \sum_{i=1}^n (\Gamma_{i,m-1}^{DS} - \Gamma_{i,m}^{DS}) \end{aligned} \quad (20)$$

As described above, unknown vortex elements Γ_{nm}^{DS} only remain on the duct camber surface and also Γ_{nm}^{PS} on the propeller blade camber surface in the same manner.

In the present DP program, the following ways of grid panel division are applied as shown in Fig. 10.

Propeller blade camber surface:

spanwise 6 x chordwise 12 = 72

Duct camber surface:

spanwise 12 x chordwise 10 = 120

Duct trailing vortices are regarded as a set of straight lines parallel to the uniform flow.

From the experiences in our flow observations, propeller slip stream inside a duct and also in the downstream can be considered as the axial component being predominant. Therefore, it is assumed that the trailing vortices shed from the T.E. of each blade form a helicoidal vortex sheet having constant pitch.

The wake pitch at the design point of Prop./Duct (advance coefficient $J \approx 0.5PD$ PD: prop. pitch ratio) can be assumed to be the same as the geometrical pitch of each blade section, and approximately be applied over the relatively wide range of J-values.

The forces arising on a propeller blade and a duct are calculated by summing up the following components:

- a) The force acting on a source element with the strength Q_{nm} per unit length which is obtained from Lagally's theorem

$$\bar{F}_{nm}^Q = -\rho \Delta l_{nm}^S \cdot \bar{V}_{nm} \cdot Q_{nm} \quad (21)$$

Hence, ρ is fluid density, Δl_{nm}^S the length of spanwise element of the

singularity, and \bar{V}_{nm} the total velocity calculated at the midpoint of the element.

- b) The force acting on a vortex element with the strength Γ_{nm} per unit length which is computed from Kutta-Joukowski's theorem

$$\bar{F}_{nm}^G = \rho \Delta l_{nm}^S \bar{V}_{nm} \times \Gamma_{nm} \quad (22)$$

This calculation is made for all spanwise and chordwise elements of blades and a duct.

- c) The viscous drag force of a duct which is represented by the formula (Ref. 5) as follows:

$$\begin{aligned} \bar{F}^F &= -\frac{\rho}{2} \sum_{m=1}^{M_D} l_m^C \cdot \Delta l_m^S \bar{V}_m |\bar{V}_m| C_d \\ C_d &= 2 \cdot C_f \{1 + 2 \cdot (t_{m \max} / l_m^C)^2\} \\ C_f &= 0.455 / (\log_{10} R_n)^{2.58} \end{aligned} \quad (23)$$

where, l_m^C is the m-th chord length in the spanwise direction, Δl_m^S the mean length of spanwise element, \bar{V}_m the mean resultant velocity in the chordwise direction, $t_{m \max}$ the maximum thickness, and R_n Reynolds number. The viscous drag force of a propeller is based on Ref. 6.

- d) The pressure distributions can be obtained by the theorem of Bernoulli at a point on blades or a duct surface:

For instance, at control point i

$$C_{PU} = 1 - (\bar{V}_i^U / U)^2 \quad (24)$$

$$C_{PL} = 1 - (\bar{V}_i^L / U)^2$$

$$\bar{V}_i^U = \bar{V}_i + (\Gamma_{nm}^S + \Gamma_{n+1m}^S) / 4 \Delta l_{nm}^C$$

$$\bar{V}_i^L = \bar{V}_i - (\Gamma_{nm}^S + \Gamma_{n+1m}^S) / 4 \Delta l_{nm}^C$$

where Γ_{nm}^S and Γ_{n+1m}^S are the spanwise (bound) vortex element on both sides of control point i.

2.3.3 Calculation Results

To obtain prop./duct open water characteristics, the described numerical model has been applied over a wide range of J-values for the sample conv. ducted prop. with 19A Duct (L/D=0.5) series models. The results are displayed in Figs. 11~14.

In this calculations, the correction factor has been used for the duct thrust at low J-values smaller than PD/3, i.e. high duct loading where the effect of viscous

separation may arise as described in Ref. 7.

The pressure distribution along the propeller blade chordlines has been obtained for one conventional ducted propeller where the experimental distribution is

available (Ref. 8) as shown in Fig. 15. Further investigations on propeller/duct performance, duct circulation and pressure distribution are reported in Ref. 9.

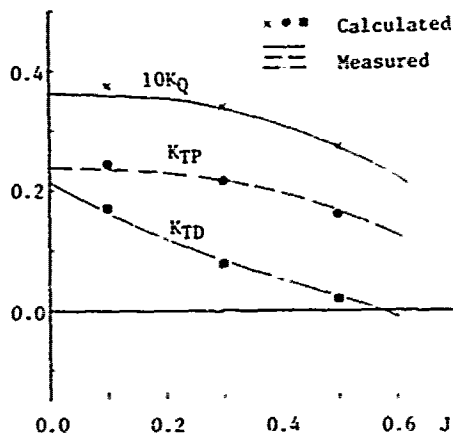


Fig. 11 Performance of the Sample Prop./Duct with 5 Blades (Conv. Ducted prop. with 19A Duct, $L/D=0.5$)

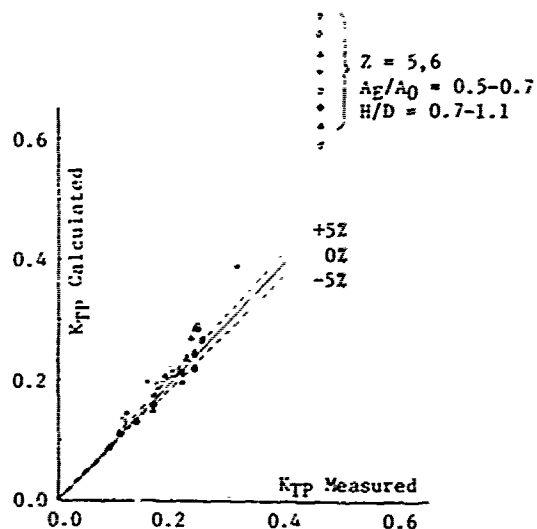


Fig. 13 Correlation between Calculated and Measured K_{TP} (Propeller Thrust Coeff.) at Various J -Values for the Sample Prop./Duct Series

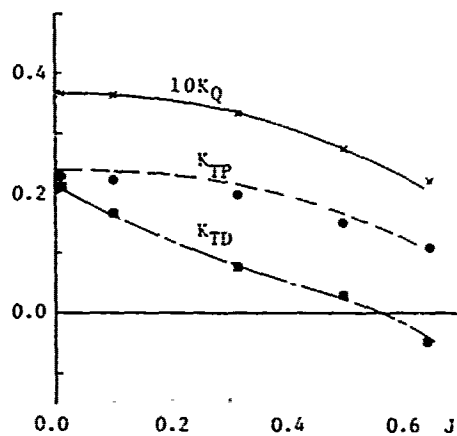


Fig. 12 Performance of the Sample Prop./Duct with 6 Blades

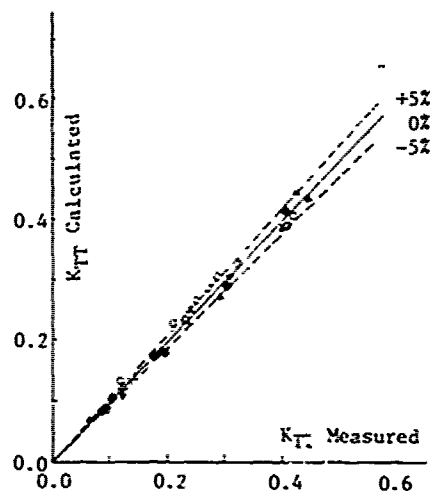


Fig. 14 Correlation between Calculated and Measured K_{TT} (Total Thrust Coeff.) at Various J -Values for the Sample Prop./Duct Series

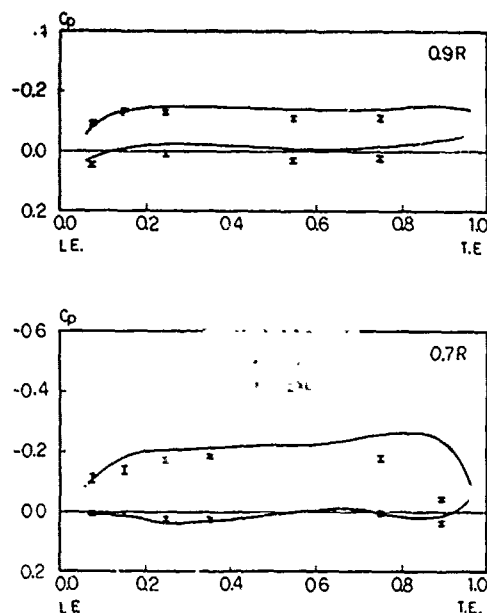


Fig. 15 Pressure Distribution along Blade Chordlines for a Prop./Duct

3. PROPELLER CAVITATION

There are basically two different approaches which point themselves out in a natural way when trying to formulate the problem with a cavitating propeller mathematically.

The first one is to use the angle of attack concept combined with a purely two-dimensional cavitation theory. This is the method used traditionally, and several attempts to determine the gross volume variation of the cavity have been reported, see e.g. Johnsson [10 & 11] and van Oossanen [12]. A new version based on this approach will be described in Section 3.1. The angle of attack and the local cavitation number including the three dimensional effects are well defined for each blade section at every angular position by the unsteady lifting surface theory with non-linear wake pitch. However, the influence of cavity flow is not taken into consideration for the boundary conditions of the lifting surface theory.

The second natural approach is an attempt to carry out a direct solution of the basic three-dimensional equations, describing cavitation on a propeller blade. Such a method will be briefly described in

Section 3.2. The method is three-dimensional in the sense that the calculations are based on the complete three-dimensional equations, a certain degree of two-dimensionality is introduced due to the fact that the equations are solved stripwise on the propeller. The reason for this is the difficulty of formulating a global closure condition for the cavity.

3.1 Two-dimensional Cavitation Theory

3.1.1 Basic Equations

Cavitation on two-dimensional hydrofoil has been studied by several authors e.g. Geurst [13], Meijer [14], Hanaoka [15] and Izumida et al [16].

In this chapter, linearized two-dimensional cavitation theory will be applied sectionally on a propeller blade. Numerical solutions are obtained by means of a vortex/source lattice method as described by Jiang & Leehey [17].

The cavity is assumed to commence at the leading edge and to terminate on the surface of the foil (closed type cavitation). The hydrofoil is assumed to be placed in a parallel flow with velocity U_∞ and with an angle of attack α with respect to the free stream as shown in Fig. 16. The suction side of the profile is denoted by $f(x)$, the pressure side by $g(x)$, the cavity shape by $\delta(x)$ and the cavity length by l . The thickness of the hydrofoil and the cavity is represented by a source distribution $q(x)$, and the discontinuity of the perturbed velocity in the x -direction is represented by a vortex distribution $\gamma(x)$.

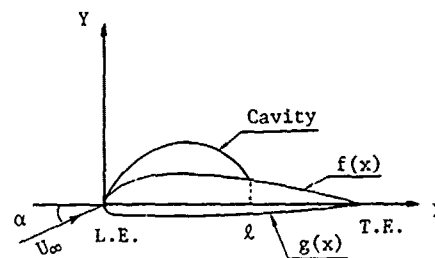


Fig. 16 Schematic Representation of Hydrofoil with Partial Cavity

In linearized form, the cavitation problem can then be formulated as a set of coupled, singular integral equations, see e.g. [17] and [18].

$$\frac{1}{2}\gamma(x) + \frac{1}{2\pi} \int_0^1 \frac{q(\xi)}{x-\xi} d\xi - U_\infty \cdot \frac{\alpha}{2} = 0 \quad (25)$$

$$(0 \leq x \leq l, y=+0)$$

$$\frac{1}{2\pi} \int_0^1 \frac{\gamma(\xi)}{x-\xi} d\xi - \frac{1}{2}q(x) = U_\infty \cdot \alpha - U_\infty \frac{df(x)}{dx} \quad (26)$$

$$(l \leq x \leq 1, y=+0)$$

$$\frac{1}{2\pi} \int_0^1 \frac{\gamma(\xi)}{x-\xi} d\xi + \frac{1}{2}q(x) = U_\infty \cdot \alpha - U_\infty \frac{dg(x)}{dx} \quad (27)$$

$$(0 \leq x \leq 1, y=-0)$$

$$\int_0^1 q(x) dx = 0 \quad (28)$$

Cavity shape can be calculated by integrating the following equation:

$$\frac{d\delta(x)}{dx} = \frac{U_\infty \cdot \alpha + v_\gamma + v_q}{U_\infty + u_\gamma + u_q} \quad (y = +0) \quad (29)$$

where v_γ and v_q denote the induced velocities due to the vortex and the source distribution, respectively.

3.1.2 Results of Computation

The calculated results have been compared with measured ones for two kinds of MAU-typed wing sections and a 4% thickness Plano-Convex hydrofoil. The tests were carried out in the high speed cavitation tunnel at Tokyo Univ..

Figs. 17~19 show the relationship between cavity extent and α/σ . As the theory is based on the closed type cavitation model, the calculations are limited to cavity extents less than 75% at the chord length. In Figs. 17~19, the results for the three types of foils show that the agreement between the experiments and the numerical results is satisfactory in case of the thin foils i.e. for the Plano-Convex hydrofoil and the MAU 0.9R wing section.

Max. cavity thickness as a function of cavity length for the three types of foils is shown in Figs. 20~22. Fig. 23 shows the calculated results of cavity profiles in comparison with the observed ones. Again the agreement is found to be better for thin foil sections.

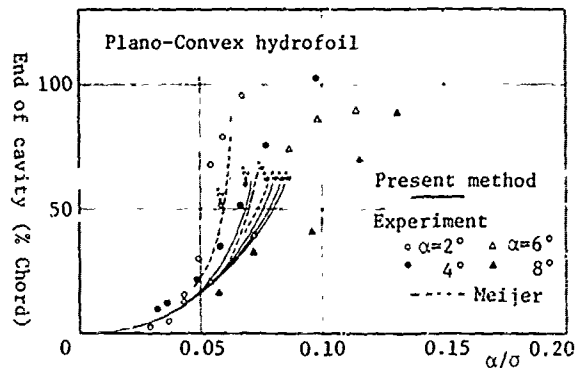


Fig. 17 Cavity Length as a Function of α/σ for Plano-Convex Hydrofoil

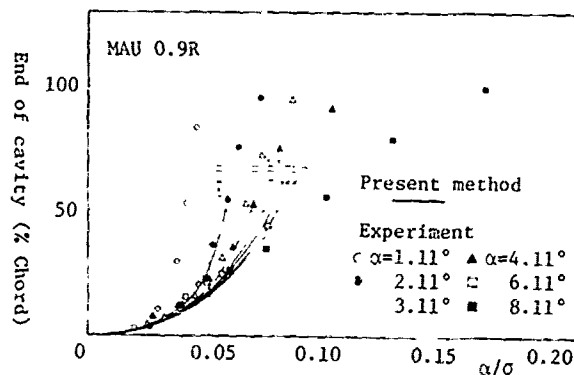


Fig. 18 Cavity Length as a Function of α/σ for MAU 0.9R Wing Section

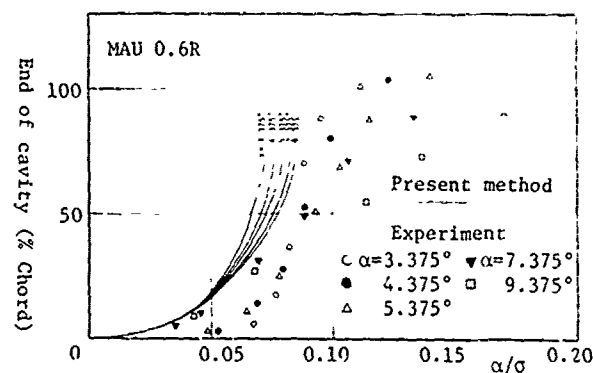


Fig. 19 Cavity Length as a Function of α/σ for MAU 0.6R Wing Section

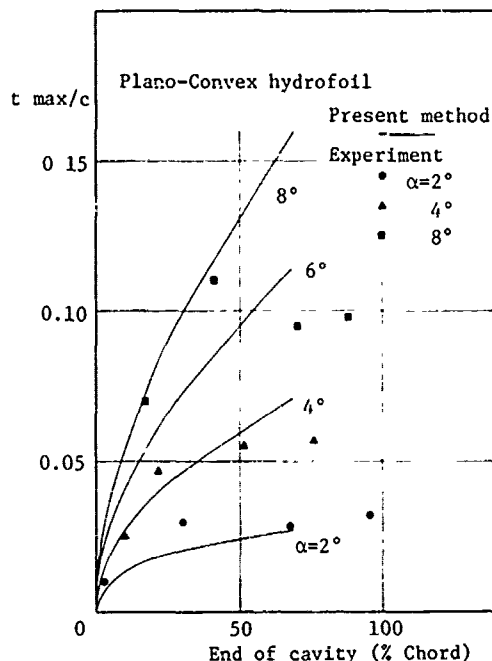


Fig. 20 Max. Cavity Thickness as a Function of Cavity Length for Plano-Convex Hydrofoil

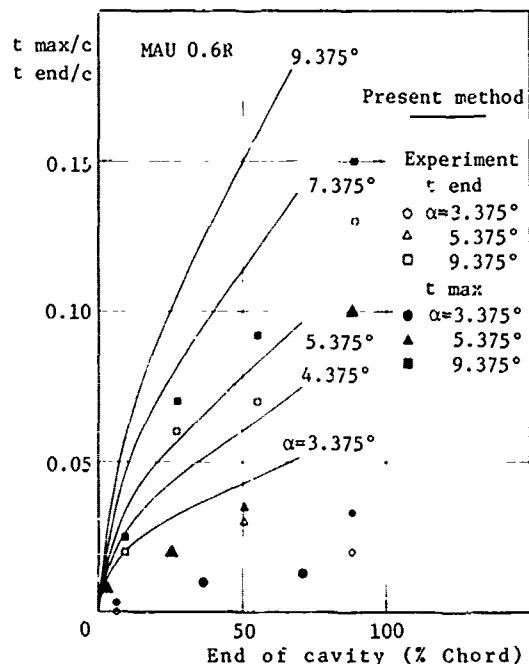


Fig. 22 Max. Cavity Thickness as a Function of Cavity Length for MAU 0.6R Wing Section

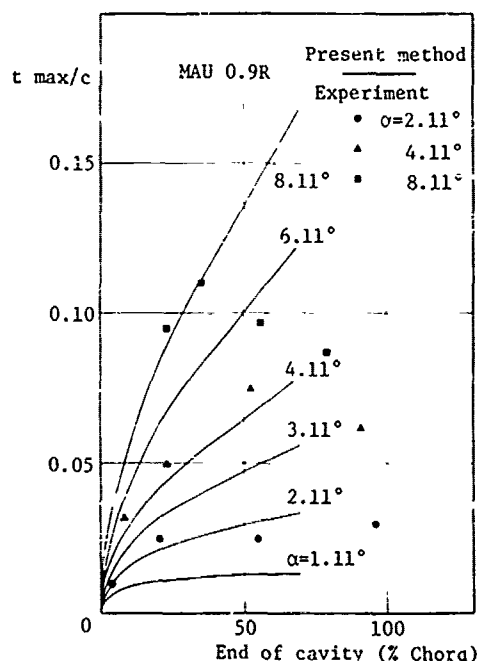


Fig. 21 Max. Cavity Thickness as a Function of Cavity Length for MAU 0.9R Wing Section

3.2 Three-dimensional Cavitation Theory

The set of equations describing the flow field on a cavitating propeller is given in discrete form by eqs. (10), (11) and (12). The theory behind this formulation is briefly sketched in chapter 2, for details the reader is referred to Frydenlund & Persson [19] or Jiang & Leehey [17].

The basis of this formulation is the assumption that the propeller camber surface is covered by a distribution of vortices and sources/sinks. The boundary conditions satisfied are that the flow is tangent to the camber surface on the wetted portion of the blade and that the pressure is constantly equal to the vapour pressure on the cavitating portion of the blade. These boundary conditions in linearized form lead to eqs. (10), (11). Eqs. (10), (11) are solved stripwise on the propeller, together with the auxiliary condition that the cavity should be closed at each radial section. The influence of adjacent sections, of the slip stream behind the blade, and of other blades, is taken into account. It is found that this solution produces a single-valued connection between the cavity length and the cavitation number, contrary to what happens in the two-dimensional case. The complete solution is carried out as an iterative procedure, the cavitation number at

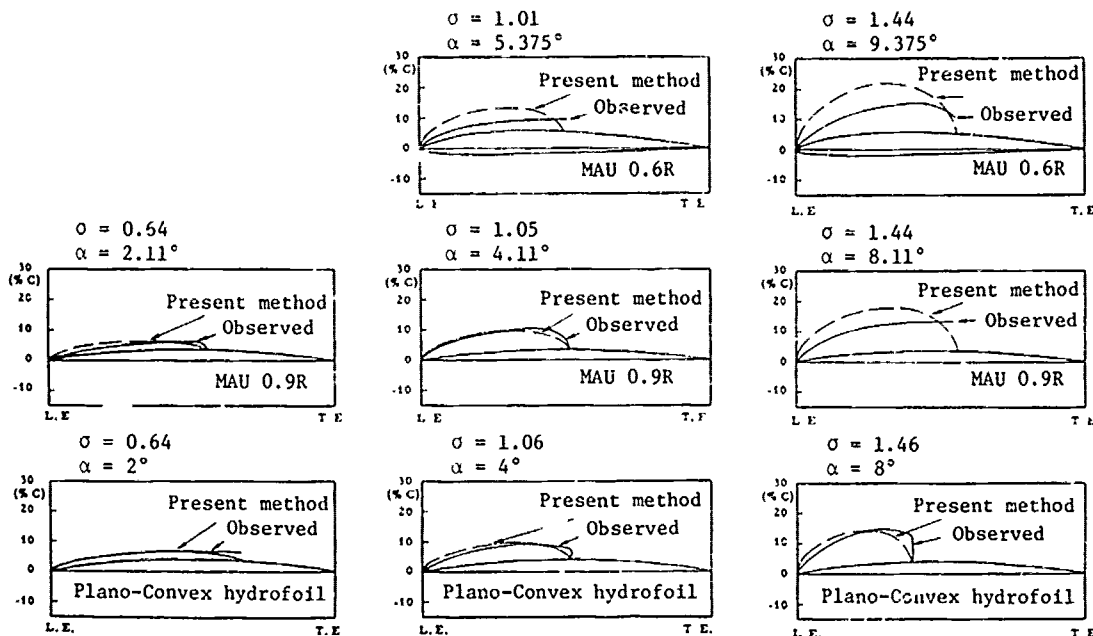


Fig. 23 Comparison of Cavity Shape between Observations and Calculations

each radial section is prescribed, the cavity length is relaxed until the computed cavitation number agrees with the prescribed value. A typical result from an open water calculation is displayed in Fig. 24.

A continued effort is being made to include unsteady effects in the cavitation model.

3.3 Propeller Cavitation

3.3.1 Prediction Method

The linearized two-dim. cavitation theory as described in 3.1.1 will now be applied to predict propeller cavitation. The following steps have been adopted to calculate propeller blade cavitation at each blade angular position in non-uniform wake flow.

Step 1 The unsteady lifting surface theory due to Hanaoka-Koyama [20] is used to give the variation of circulation distribution on a blade surface during one revolution which gives the equivalent two-dim. wings with the induced cambers on each r/R section at every angular blade position. Applying the Imai's two-dim. wing theory [21] on these wings, the radial distributions of angle of attack α and cavitation number σ are locally obtained.

Step 2 To save computing time, the data tables of cavity extent versus α/σ are given by the two-dim. cavitation theory on each r/R section of a blade. In this case the angle of attack is to have an interval of 1° ranging up to maximum value obtained in Step 1. As shown in Fig. 1/19, there is some disagreement between the measured and the calculated cavity length. In order to improve the calculation of cavitation, the following corrections have been derived from the measured values. Using the calculated value $(\alpha/\sigma)_C$, the following expression is to be adopted in the range between ϵ_1 and ϵ_2 in Fig. 25 where the linearized theory gives reasonable solutions:

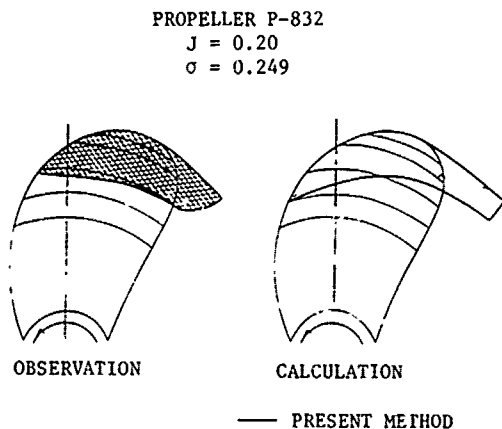


Fig. 24 Propeller Cavitation Patterns in Uniform Flow (Observed and Calculated)

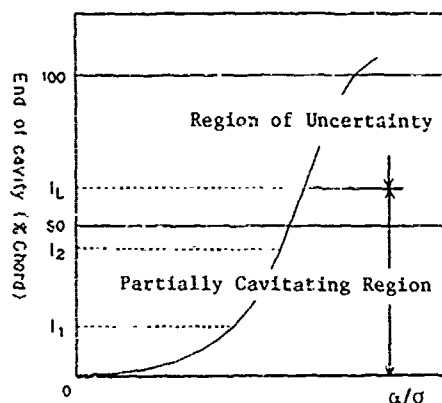


Fig. 25 Empirical Model of Cavity Length Versus α/σ

$$\alpha/\sigma = (\alpha/\sigma)_c \cdot (10.8t/c + 0.53) \cdot \{1.0 + 2.2 \cdot (3 - \bar{\alpha}) \cdot (t/c - 0.053)\} \quad (30)$$

here, t/c is blade thickness ratio. In this range the cavity length is approximated as follows:

$$l = k \cdot (\alpha/\sigma)^n \quad (31)$$

The upper limit of cavity length obtainable from the linearized theory is assumed to be l_L :

$$l_L = 0.82 - 3.1(t/c) \quad (32)$$

which yields the value of $(\alpha/\sigma)_L$

In case the cavity length exceeds l_L :

$$l = k(\alpha/c)^n + 3.0\{(\alpha/\sigma) - (\alpha/\sigma)_L\} \quad (33)$$

approximately, which can be used into the supercavitating region. Fig. 25 shows the empirical model of cavity length versus α/σ .

Step 3 Giving the angles of attack and cavitation numbers obtained in Step 1, cavity lengths are calculated by interpolating the data tables for each propeller blade r/R section. Thus, the cavitation length of a propeller is finally obtained at every angular blade position.

Step 4 Concerning the cavity thickness, the similar way as described above has been adopted. However, approaching to the tip of a propeller blade, the three dimensional effect on the cavity thickness becomes an important phenomena. Accordingly, the thickness of propeller cavitation is predicted by means of multiplying the calculated values by a correction factor in that region of a blade. The correction factor has been obtained from investigations of the measured cavity thickness in a few full-scale stereophoto measurements (Ref. 22 & 23).

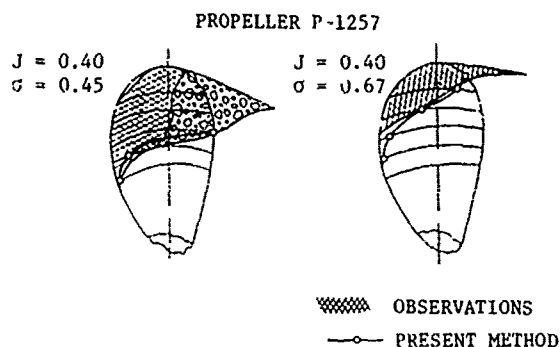


Fig. 26 Propeller Cavitation Patterns in Uniform Flow (Observed and Calculated)

3.3.2 Results of Computation

3.3.2.1 Model Propellers in Uniform Flow

The present method has been applied to a model propeller operating in uniform flow and compared with the result of model test. The test conditions are as follows:

Fig. 26 Model Propeller P1257 [23]

$$J = 0.4, \sigma = 0.45$$

$$J = 0.4, \sigma = 0.67$$

The principal data of the model propellers are shown in Table 1.

Table 1 Principal Particulars of Model Propellers

Model Propeller	P1257
Dia. (M)	0.250
Pitch Ratio	1.02
Exp. Area Ratio	0.53
Number of Blades	4

Table 2 Principal Particulars of Full Scale Propellers

Ship	Ship A	Ship B
Dia. (M)	7.70	6.65
Pitch Ratio	0.66	0.70
Exp. Area Ratio	0.71	0.61
Number of Blades	5	5

Fig. 26 shows comparisons between the observed and the calculated cavitation extents.

3.3.2.2 Full Scale Propellers

The present method has been applied to propellers operating in a non-uniform wake field and compared with full scale observations. The model wake fields are corrected to the corresponding full scale wake fields by Sasajima-Tanaka's method.

Table 2 denotes the principal particulars of two full scale propellers which are used for the simulations of unsteady cavitation, and also hull surface pressure impulses in the next chapter.

The operating condition is shown as follows:

Fig. 27 Ship A

$$J = 0.37,$$

$$\sigma = 1.61$$

Fig. 28 Ship B

$$J = 0.37,$$

$$\sigma = 3.21$$

where the values of σ described above are the representation at the shaft center of each propeller.

The cavitation patterns are predicted at each angular blade position with an interval of 10° from the top position i.e. twelve o'clock to the turning direction. Fig. 27 displays the cavitation patterns of ballast condition of Ship A. Full scale propeller cavitation was observed in the region from the top position to 60° . Fig. 28 displays the same for Ship B with the sketches of the full scale observations from 18° to 55° .

4. HULL SURFACE PRESSURE FLUCTUATIONS

4.1 Basic Theory

The basic theory for calculation of pressure fluctuations caused by a cavitating propeller, when the variation of the cavity volume is assumed known, has been reported by several authors, see e.g. Noordzij [24]. This theory will be briefly reviewed here, just in order to point out a minor modification in the calculation

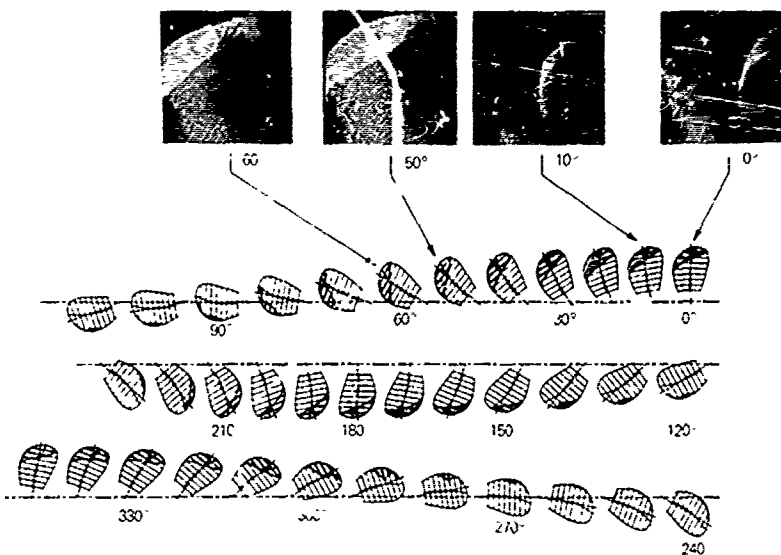


Fig. 27 Observed and Calculated Cavitation Patterns of Ship A ($J = 0.37$, $\sigma = 1.61$)

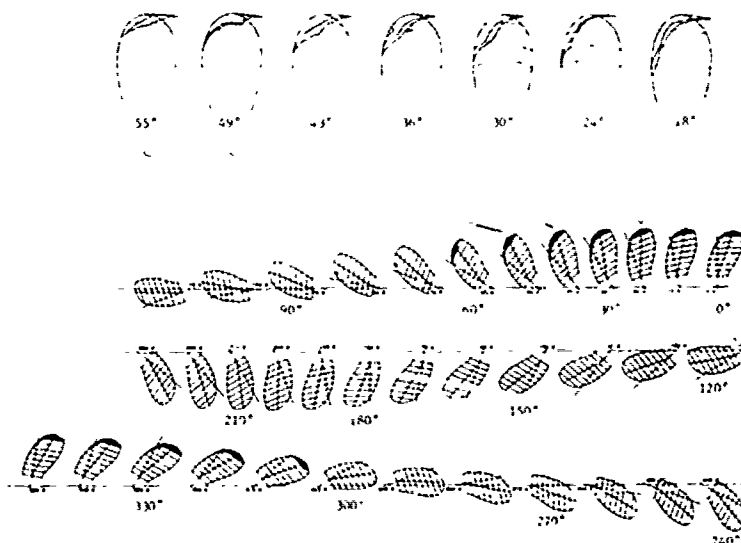


Fig. 28 Observed and Calculated Cavitation Patterns of Ship B ($J = 0.37$, $\sigma = 3.21$)

procedure which has proven to be efficient. Only the contribution due to the cavity will be discussed.

The velocity potential ϕ due to a moving, pulsating cavity can be expressed [24]:

$$\phi = -\frac{1}{4\pi} \int_{r_i(t)}^{r_T} \int_{\theta_L(r)}^{\theta_C(r,t)} \left[\frac{\partial \tau}{\partial t} + \frac{U \cos \beta \cos \mu}{r} \cdot \frac{\partial \tau}{\partial \theta} \right] \frac{r dr d\theta}{R \cos \beta \cos \mu} \quad (34)$$

Here polar coordinates have been used in accordance with Figs. 29, 30. Furthermore, U denotes the inflow velocity at section r ; β is the pitch angle; μ is the rake angle, and τ is the cavity shape. The cavity is assumed to extend radially from an inner radius $r_i(t)$ to the tip radius r_T . A strip of width dr of this cavity, at radial position r , is considered. The cavity extends from the leading edge, with angular coordinate $\theta_L(r)$, to the cavity closure point denoted by $\theta_C(r, t)$. Note that r_i and θ_C depend on the time t . The distance R between the source point (γ, r, θ) and the field point is given by Fig. 29.

$$R(x, y, z, \gamma, r, \theta) = \{ [x - r \cos(\gamma - \theta)]^2 + [y + r \sin(\gamma - \theta)]^2 + [z + \frac{p\theta}{2\pi} - r t g \mu]^2 \}^{1/2} \quad (35)$$

By application of Bernoulli's equation, the pressure at the field point, which is stationary in the coordinate system (x, y, z) , can be written:

$$P(x, y, z, t) = -\rho \left(\frac{\partial \phi}{\partial t} + V \frac{\partial \phi}{\partial z} \right) \quad (36)$$

where ϕ is defined by eq. (34). In deriving eq. (36), higher order derivatives of the perturbation potential ϕ have been neglected.

It is now appropriate to transform the time variable t into angular position γ of the blade, i.e. by introducing

$$\gamma = 2\pi n t \quad (37)$$

where n denotes the number of revolutions per sec. Furthermore, it is convenient to move the operator $\partial/\partial t$ in eq. (34) outside the integral sign and to perform a partial integration of the second term containing $\partial\tau/\partial\theta$, thus giving:

$$P(x, y, z, t) = -\rho \frac{\partial^2}{\partial \gamma^2} \int_{r_i(\gamma)}^{r_T} \int_{\theta_L(\gamma)}^{\theta_C(r, \gamma)} \tau G_1 r dr d\theta + \rho \frac{\partial}{\partial \gamma} \int_{r_i(\gamma)}^{r_T} \int_{\theta_L(\gamma)}^{\theta_C(r, \gamma)} \tau G_2 r dr d\theta$$

$$+ \rho \int_{r_i(\gamma)}^{r_T} \int_{\theta_L(r)}^{\theta_C(r, \gamma)} \tau G_3 r dr d\theta \quad (38)$$

after inserting eq. (34) into eq. (36). Here the functions G_1, G_2, G_3 are given by:

$$G_1 = \frac{\pi n^2}{R \cos \beta \cos \mu}$$

$$G_2 = \left[\frac{\pi n^2}{\cos \beta \cos \mu} \cdot \frac{\partial R}{\partial \gamma} + \frac{nU}{2r} \cdot \frac{\partial R}{\partial \theta} - \frac{nV}{2 \cos \beta \cos \mu} \cdot \frac{\partial R}{\partial z} \right] / R^2$$

$$G_3 = \left[\frac{UV}{4\pi r} \cdot \frac{\partial}{\partial z} \left(\frac{1}{R^2} \cdot \frac{\partial R}{\partial \theta} \right) + \frac{nV}{2 \cos \beta \cos \mu} \cdot \frac{\partial}{\partial z} \left(\frac{1}{R^2} \cdot \frac{\partial R}{\partial \gamma} \right) \right]$$

In obtaining eq. (38), use has been made of the fact that by definition $\theta_C = \theta_L$ at $r = r_i$, i.e. that the closure point coincides with the leading edge at the section where the cavitation begins. By expressing p in the form shown in eq. (38), the problem of calculating values of $\partial^2 \tau / \partial t^2$ and $\partial \tau / \partial t$ locally on the blade has been avoided. Here the integrals of τ are evaluated before the differentiation is carried out.

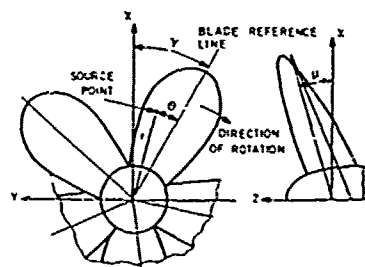
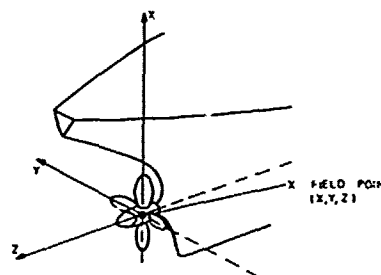


Fig. 29 Coordinate System and Notations, Propeller

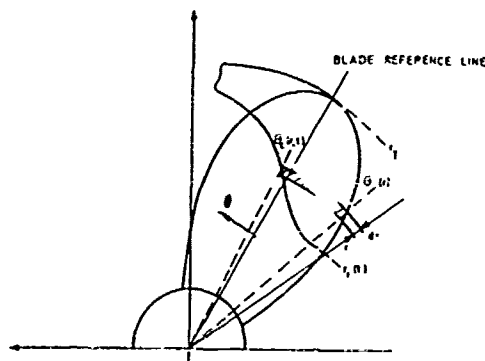


Fig. 30 Coordinate System and Notations, Cavity

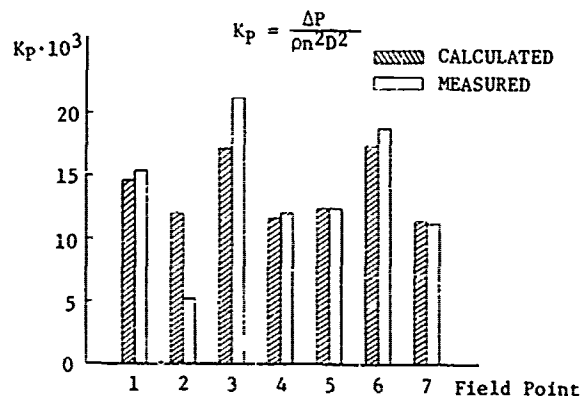


Fig. 31 Propeller-induced Pressure Amplitudes on the Hull for the First Harmonic (Comparison between Experiments and Calculations)

This has proven to be an efficient and accurate way to determine the pressure field. It is to be noted that the same equations outlined here, can be used to calculate the contribution from the propeller blade thickness.

To test the calculation procedure, values of the cavity shape variation taken from full-scale stereophoto measurements have been used as input to eq. (38). The results are for a 350,000 TDW tanker. Fig. 31 displays a comparison between the theoretically calculated and the measured pressure fluctuations at certain field points.

4.2 Numerical Analysis of Hull Surface Pressure

Knowing the geometry of the cavities as a function of time, the corresponding periodic source distributions can be determined. The numerical calculations have been carried out by means of Huse's method [25], i.e. the geometry of cavities on a

blade is replaced to a set of simplified cavity sections representing the cavity thickness and extension at each radius of the blade. The pressure fluctuations induced on a hull surface are to be obtained from the calculated results multiplied by the solid boundary factor of 2.0. The velocity potential includes the following effects:

- (a) blade thickness
- (b) blade loading
- (c) motion and volume variation of cavities
- (d) tip vortex cavities

4.3 Calculation Results of Hull Surface Pressure

For Ship A and B, the calculations on hull surface pressure have been carried out. The volume variation of cavitation for Ship A is presented in Fig. 32. The figure shows the max. cavity thickness for various radial sections as a function of angular blade positions. In Fig. 33 the pressure amplitudes on the hull surface for the first harmonic of blade rate frequency are displayed in comparison with the experiments for Ship A and B.

5. CONCLUDING REMARKS

Development of numerical methods based on discrete vortex elements has been carried out for calculations of hydrodynamic forces, pressure distributions, amount of blade cavitation and hull surface pressure fluctuations for propeller/duct systems:

- The advantages of such methods and experiences may be summarized as follows:
- a) Relatively small numbers of discretized panels - vortex and source elements - are needed to describe the lifting surfaces to obtain satisfactory results for practical use.
 - b) Propeller as well as propeller/duct performance in uniform flow can be calculated with sufficient accuracy

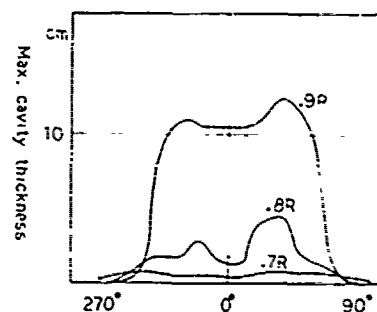
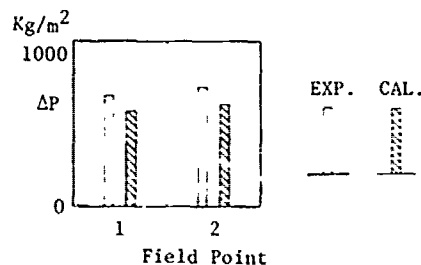


Fig. 32 Max. Cavity Thickness for Various Radial Positions as a Function of Angular Positions of Blade

SHIP A

	X/D	Y/D	Z/D
1	1.08	0.32	0.0
2	1.08	-0.32	0.0



SHIP B

	X/D	Y/D	Z/D
1	0.391	-0.647	-0.135
2	0.466	-0.534	-0.135
3	0.481	-0.466	-0.316

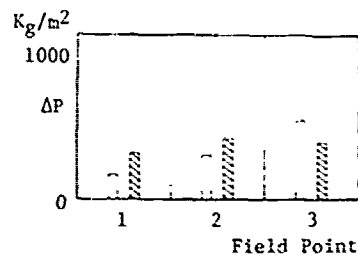


Fig. 33 Propeller-included Pressure Amplitudes on the Hull for the First Harmonic (Comparison between Experiments and Calculations)

for a wide range of propeller designs and advance ratios including bollard condition.

- c) For propeller blade loading in non-uniform flow - wake field and inclined shaft - the calculated blade thrust fluctuations compared with experiments show good agreement.
- d) Tip flow studies on three-dimensional wings and propeller blades by means of flow visualization tests and pressure measurements illustrate that leading edge separation occurs on highly skewed propeller and swept blades. This strong vortex core influences significantly the pressure distribution on the blades and should be included in further development of the methods described.
- e) To calculate the extent of cavitation on a propeller two different approaches have been tested:
 - (i) A two-dimensional theory has been applied in a stripwise manner making use of a three-dimensional angle

of attack found by using a non-cavitating lifting surface model.

This method shows reasonable good agreement compared to experiments.

- (ii) A three-dimensional method has been used to calculate the cavitation in an open water case. This method produces a single-valued connection between the cavity length and the cavitation number contrary to what happens in the two-dimensional case. This approach seems to have very promising features.

- f) Pressure fluctuations on the hull have been calculated by using the results of predicted propeller cavitation for two full scale ships. From the comparison between the calculated and the measured values it may be concluded that the theory gives results of acceptable accuracy for practical use.

ACKNOWLEDGEMENT

The research project "Excitation Forces for Duct/Tunnel Propeller Systems" was started in 1976 as a joint project between Mitsui Engineering and Shipbuilding Co., Ltd. and Det norske Veritas.

The goal of the project was to develop a computer program for determination of propeller blade loading, extent of blade cavitation and induced pressure fluctuations transferred through water. The developed methods should serve as a basis for dimensioning of thruster-systems operating at low advance ratios, including bollard conditions.

The project work has been carried out by a team:

H. Yuasa	Mitsui Eng. & Shipb.
N. Ishii	Mitsui Eng. & Shipb.
O. Frydenlund	DnV
B. Persson	DnV
K. Holden	DnV.

Members of the Steering Group:

Dr. Yamanouchi	Mitsui Eng. & Shipb.
T. Sjøntvedt	DnV.

During the project period 01.05.77 - 01.05.79 regular meeting and discussions have been arranged with Prof. J. Kerwin, Prof. P. Leehay and their staff at Massachusetts Institute of Technology, Department of Ocean Engineering, and with Dr. Hanaoka at Ship Research Institute in Tokyo and Prof. Kaio at Tokyo University. The project team would like to express their sincere thanks and gratitude for their contribution to the successful completion of the project.

REFERENCES

1. Frydenlund, O.. "Propeller Analysis by Application of a Lifting Surface Method. Open Water Characteristics for Marine Propellers", Det Norske Veritas, Report No. 78-130.
2. James, R. M., "On the Remarkable Accuracy of the Vortex Lattice Method", Computer Methods in Applied Mechanics and Engineering.

neering, Vol.1, 1972.

3. Høiby O., "Three-Dimensional Effects in Propeller Theory", Norwegian Ship Model Experimental Tank, Publ. No.105, 1970.

4. Report PR-548, AB Karlstads Mekaniska Werkstad, Marine Laboratory, Kristinehamn, Sweden, 1973.

5. Oosterveld, M. W. C., "Wake Adopted Ducted Propeller", Publication No.345, NSMB, Netherlands.

6. Kerwin, J. E., Lee, C., "Prediction of Steady and Unsteady Marine Propeller Performance by Numerical Lifting-surface Theory", SNAME New York, Nov. 16~18, 1978.

7. Caracostas, N., "Off-Design Performance Analysis of Ducted Propellers" SNAME Propeller '78 Symposium, May 24~25, 1978.

8. Minsaas, K., "Design of Propellers in Ducts of Given Shapes-Part 1", Norwegian Ship Model Experiment Tank Publication, No. 115, Jan. 1972.

9. Yuasa, H., "Application of Numerical Lifting-Surface Theory on Steady Performance of Propeller/Duct System", Journal of the Society of Naval Architects of Japan, Vol. 147, June 1980.

10. Johnsson, C.-A., "On Theoretical Predictions of Characteristics and Cavitation Properties of Propellers", SSPA Publication No.64, 1968.

11. Johnsson, C.-A., "Correlation of Predictions and Full Scale Observations of Propeller Cavitation", Int. Shipb. Progress, Vol.20, No.226, 1973, pp.75-91.

12. Oossanen, P. van, "Calculation of Performance and Cavitation Characteristics of Propellers Including Non-Uniform Flow and Viscosity", Doctor's Thesis, Delft Technical University, 1974, NSMB Publ. No. 457.

13. Geurst, J. A., "Linearized Theory for Partially Cavitated Hydrofoils", Int. Shipb. Progress, Vol.6, No.60, 1959.

14. Meijer, M. C., "Some Experiments on Partly Cavitating Hydrofoils", Int. Shipb. Progress, Vol.6, No.60, 1959.

15. Hanaoka, T., "Linearized Theory of Cavity Flow Past a Hydrofoil of Arbitrary Shape", Papers of Ship Research Institute, Tokyo, Japan, Paper No.21, 1967.

16. Izumida, Y., Tamiya, S., Kato, H. & Yamaguchi, H., "The Cavitation Characteristics of Two-Dimensional Hydrofoils", Journal of the Society of Naval Architects of Japan, Vol.146, Dec. 1979.

17. Jiang, C.-W. and Leehey, P., "Experimental and Theoretical Investigation of Unsteady Supercavitating Hydrofoils of Finite Span", Massachusetts Institute of Technology, Dept. of Ocean Engineering, Report No.83481-4, 1977.

18. Yuasa, H., Ishii, N., "Practical Calculations for Prediction of Propeller Cavitation and Propeller Induced Hull Surface Pressure", Journal of the Society of Naval Architects of Japan, Vol.147, June 1980.

19. Prydenlund, O., Persson, B., "Application of a Discrete Vortex, Source Distribution Model to Propeller Cavitation", Det Norske Veritas, Report No.79-007, 1979.

20. Koyama, K., "A Numerical Method for Propeller Lifting Surface in Non-Uniform Flow and Its Application", Journal of the Society of Naval Architects of Japan, Vol. 137, June 1975.

21. Imai, I., "Fluid Dynamics, Vol.1", 2nd Edition, Syokabo Tokyo, P216~P229.

22. Holden, K., Søntvedt, T., Øfsti, O., "On Stability and Volume of Marine Propeller Cavitation and Corresponding Spectral Distribution in Hull Pressure Fields", Symp. on High Powered Propulsion of Large Ships, Wageningen 1974.

23. Høiland, A., Holden, K., Søntvedt, T., "Propeller Cavitation as a Source of Vibration", Jahrbuch der Schiffbautechnischen Gesellschaft, 67. Band, 1973.

24. Noordzij, L., "Considerations on the Hull Excitation Force Induced by a Cavitating Propeller", Int. Shipbuilding Progress, Vol.25, No.288, 1978, pp.199-211.

25. Huse, E., "Pressure Fluctuations on the Hull Induced by Cavitating Propellers", Norwegian Ship Model Experimental Tank, Report No.111, 1972.

26. Omura, M. and Takaoka, T., "Prediction of Vortex-Lift Characteristics by an Extended Vortex-Lattice Method", Journal of the Japan Society for Aeronautical and Space Sciences, Vol.20, No.226, Feb. 1972.

APPENDIX

LEADING-EDGE SEPARATING VORTEX AND PRESSURE DISTRIBUTIONS ON PROPELLER BLADES

The leading-edge separation forms a sharp vortex core from the mid-span to the tip along the leading-edge of a swept wing or a propeller blade making the flow stable on the suction side preventing stall at large angles of attack.

Flow visualization tests have been carried out on two kinds of planar wing models by means of air bubble method, and on two propeller models with the similar shapes of the wings by means of oil film method. These flow patterns are compared with measured pressure distributions on the planar wings, and the influences of LSV on the characteristics of the blade are discussed.

A lifting surface theory is applied to simulate the flow pattern and the pressure distributions, and non-linear calculation is tried to investigate the influence of such phenomena on the calculated results.

Experiment

The flow visualization tests have been carried out in the Circulating Water Channel of Akishima Laboratory.

The two planar wing models have 500mm span, same chord length and section shape with flat pressure side respectively, but the outline (skewness) of the wings follows each of the two propeller models. The propeller models are of a conventional propeller and a skewed one (CP & SP respectively) with the particulars shown in Table 1. Photos.A1 and A2 show the results of flow visualization on the two kinds of planar wing i.e. with conventional typed blade shape (CW) and with the skewed (SW). The angle of attack (α) is 15 degrees at the velocity (V) = 1 m/sec., and air bubbles are shedding from a small hole on the leading-edge of both wings. At such a large angles of attack, the extreme difference of the flow patterns between CW and SW is found, namely a largely developed LSV occurs on the suction side of SW and seems to make the flow stable, while nearly stalled and unstable flow on CW.

Figs.A1-A4 show the flow patterns and the pressure distributions on CW and SW at $\alpha = 10$ degrees and $V = 1$ m/sec. Figs.A1 and A2 are drawn from the several photos which were taken at slow shutter speed when air bubbles shedding from a hole after another. The holes are placed on the leading-edge at the several radial

sections of each wing. Air bubbles are supplied from a mini-compressor through thin nylon tubes installed inside the models.

	SKewed TYPE	CONV. TYPE
NO. OF BLADES	5	5
DIAMETER	0.175m	0.180m
PITCH RATIO	0.970	1.000
EXP. AREA RATIO	0.890	0.650
RAKE	0°	10°
SKEW	abt. 27°	abt. 7°

Table 1 Principal Particulars of Propeller Models

Figs.A3 and A4 show the pressure distributions measured at the same condition as Figs.A1 and A2 on the suction side of CW and SW respectively. At 0.6 R section the pressure distributions of CW and SW are very similar, while at 0.9 R section the region of the chordwise extent of flat and large negative pressure value of SW is approximately twice of CW. This flat region of SW fully extends toward the tail end more than CW at the 0.95 R section. Referring to Figs.A1 and A2 these regions appear on the belts covered by LSV. Accordingly, it is easily supposed that the sharper and stronger LSV in case of SW induces increasingly flat and large negative pressure distributions. Photos.3-6 show the results of the tests by means of oil film

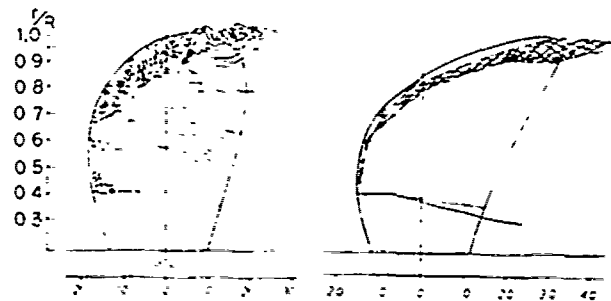


Fig.A1 CW
($\alpha=10^\circ$, $V=1$ m/sec)

Fig.A2 SW
($\alpha=10^\circ$, $V=1$ m/sec)

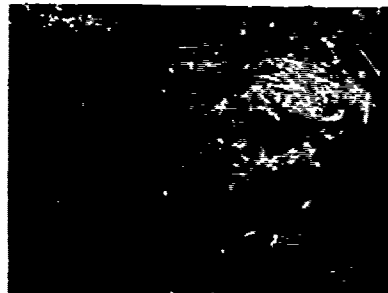


Photo.A1 Flow around CW
($\alpha=15^\circ$, $V=1$ m/sec)



Photo.A2 Flow around SW
($\alpha=15^\circ$, $V=1$ m/sec)

method for the two kinds of propeller models. The test conditions are at Reynolds number = $4.3 \sim 5.7 \times 10^5$ and advance coefficient (J) = 0.0 and 0.3 in uniform flow. From these pictures the regions of oil film stripped off are just located on the same regions of LSV which are observed on the planar wings. It was confirmed that Reynolds number around the range mentioned above did not affect the features of LSV on the propeller models mostly.

Applying discrete vortex elements [6], [26], the lifting surface problems on the wings are solved. The flow pattern of free vortices shedding from the edge of the wings is simulated by iterative calculations as shown in Fig.A5 for CW at the same condition as in Fig.A1. In comparison with the phenomena visualized, the simulation seems to be realistic on the tip flow rolling up but not enough on LSV. The calculated pressure distributions are shown in Figs.A6 and A7 in comparison with the measured values for CW and SW, respectively. The good agreements between them are obtained for 0.6 R section but not enough for 0.95 R section on each wing.

- (1) The LSV occurs on both blade shapes of skewed and conventional type, and the former has sharper and stronger vortex core to make the flow more stable than the latter.
- (2) In the region of the blade surface covered by LSV and tip vortex, flat and large negative pressure distributions are obtained.
- (3) The computational simulation shows realistic flow pattern around the wing on the whole, and good agreements with the measured pressure distributions in case of 0.6 R section of the wings.



Photo.A3 CP J=0.0



Photo.A4 CP J=0.3

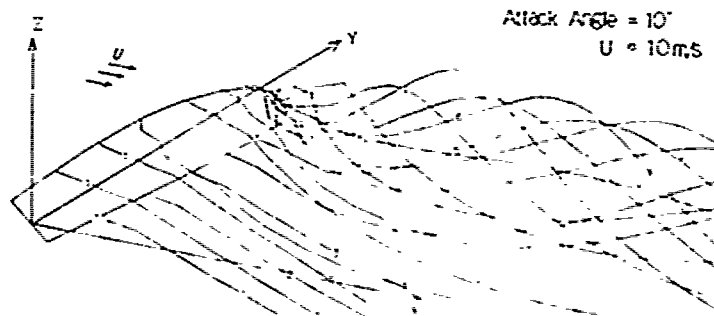


Fig.A5 Simulated Flow Pattern Around CW

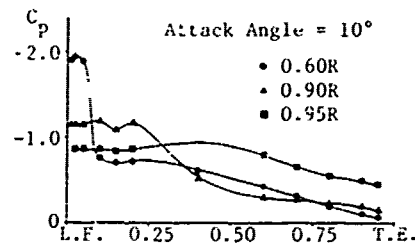


Fig.A3 Measured Pressure Distributions on CW ($\alpha=10^\circ$, $V=1\text{m/sec}$)

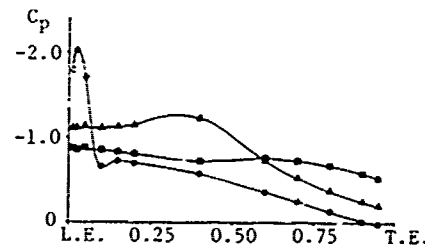


Fig.A4 Measured Pressure Distributions on SW ($\alpha=10^\circ$, $V=1\text{m/sec}$)



Photo.A5 SP J=0.0 Photo.A6 SP J=0.3

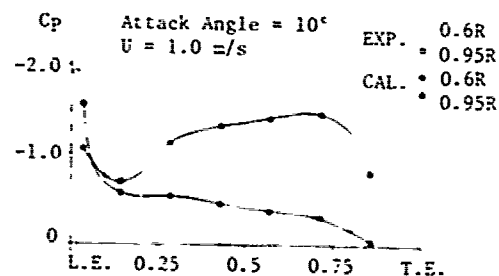


Fig.A6 Pressure Distributions on CW

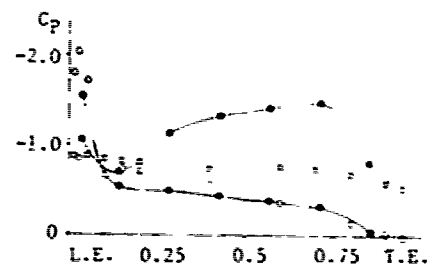


Fig.A7 Pressure Distributions on SW

Discussion

E.A. Weitendorf and K.Y. Chao (HSVA)

First of all we would like to congratulate the authors for the good calculation results. Concerning the paper we have the following questions:

1. Results of calculated cavity length

The results of Figs. 17, 18, 19 seem to be very similar to results which can be obtained by conformal mapping and a closed cavity model. With a closed cavity model, however, there is a singularity at the end of the cavity sheet. How can such a singularity be treated? And in this context: How does the calculated pressure distribution for the cavitating condition look like?

2. Boundary conditions

Regarding the boundary conditions, given for instance in Eqs. (25), (26), (27) of the paper it would be interesting to know how those boundary conditions could be solved when using an open cavity model.

3. Correction factor for the cavity thickness

The references No. 22 and 23 of paper contain full scale results. In reference No. 22 full scale stereophoto results of the sheet cavitation are presented. In this context we would like to ask how these full scale results are utilized for the calculations? Is it possible to show the correction factors derived from full scale investigations in a kind of diagram?

In reference 23 different results are given. On page 52 of reference 23, for instance, was mentioned that the maximum cavitation thickness will be equal to the tip vortex diameter. Are the results of reference 23 used in this connection with the tip vortex or in another manner?

T. Hoshino (MHI)

The authors are to be congratulated on this interesting paper, but frankly speaking the discussor felt a little bit hard to follow the contents of the paper, since so many items have been presented piece by piece in the paper.

So, I want to focus my discussion on the following two points and ask the authors comments.

(1) The vortex lattice method (VLM) has been accepted as a very useful tool to attack the various problems concerning propellers.

The present paper adopted the conventional VLM, in which the chord is divided

into N uniform elements with a vortex at a quarter chord point and a control point at three-quarter chord point of each element.¹⁾ For the steady two-dimensional wing, James¹⁾ showed that the total lift is determined exactly for a flat plate or parabolic camber line by this conventional VLM but it always gives the vortex strength $\gamma(x)$ about 11% lower than the exact solution at the first element. This difference on the vortex strength near the leading edge will result in the significant error in estimating the pressure distribution and the cavity shape on blades. On the other hand, Lan²⁾ showed that the quasi-VLM with cosine spacing arrangements of both vortex and control points gives the exact vortex distribution for the steady two-dimensional wing. Therefore, the quasi-VLM is superior to the conventional VLM for estimating the pressure distribution and the cavity shape on blades.

(2) In the present paper, the unsteady cavitation patterns of the propeller operating in non-uniform flow was calculated by quasi-steady method. It is well known that there is phase difference between the observed and the calculated cavitation patterns. This phase difference may come from the fact that quasi-steady method neglects the dynamic effect of a cavity. In Fig. A quoted from Ref. 3), the cavitation patterns calculated with and without phase correction are compared with those observed in cavitation tunnel. This shows clearly the usefulness of introducing phase correction in quasi-steady method. The comparison between the measured and the calculated pressure fluctuations is shown in Fig. B. The results show that agreement is better when the phase angle is corrected as in the case of cavitation patterns.

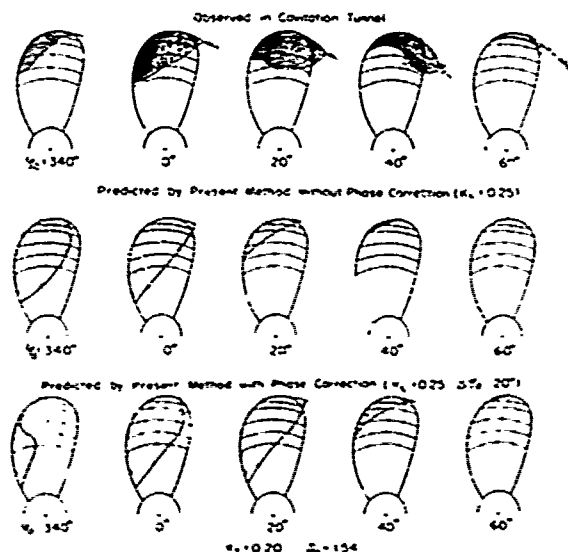


Fig. A Comparison of cavitation patterns with and without phase correction

REFERENCES

- 1) James, R.M., "On the Remarkable Accuracy of the Vortex Lattice Method", Computer Method in Applied Mechanics and Engineering, Vol.1, 1972
- 2) Lan, C.E., "A Quasi-Vortex-Lattice Method in Thin Wing Theory", J. Aircraft, Vol.11, No.9, 1974
- 3) Hoshino, T., "Estimation of Unsteady Cavitation on Propeller Blades as a Base for Predicting Propeller-Induced Pressure Fluctuations", Journal of the Society of Naval Architect of Japan, Vol. 148, 1980 (to be presented)

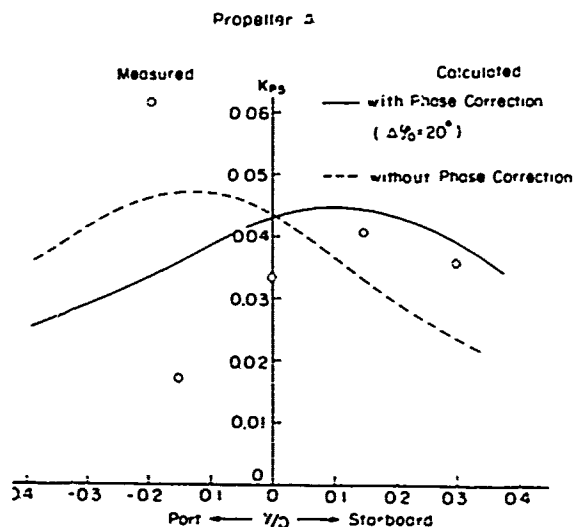


Fig. B Transverse distribution of blade frequency amplitudes of pressure fluctuations ($K_T=0.2$, $c_n=1.54$)

G. Dyne (SSPA)

The authors have in their calculations used the discrete vortex element method developed at MIT. The free helical vortex sheets behind the propeller blades are in this method assumed to roll up into discrete tip and hub vortices. This assumption has the advantage that it simplifies the calculations, but the question is: Is it true? Do the vortex sheets really roll up in discrete vortices in a similar way to the vortex sheet behind a wing of finite span?

One consequence of the assumption is that the vorticity is concentrated to the edge and the centerline of the slipstream. The flow inside the slipstream is then the same as for a propeller with constant circulation along the radius. Also the propeller induced mean axial velocities must then be independent of the radius. Pitot tube measurements in the slipstream of propellers in open water show, however, that the axial velocity varies considerably in the radial direction, which must mean that there is vorticity at almost all radii of the slipstream.

My questions to the authors are :

1. Are you convinced that the vortex sheets of a propeller roll up into discrete vortices?
2. Do you know of any laser-doppler measurements which confirm the correctness of this vortex model?

Author's Reply

H. Yuasa

To Waitendorf and Chao

1. Results of calculated cavity length

The singularities do not present any problem in the numerical calculations since the discrete vortices and sources are located away from the singular points. Thus, for a finite number of elements the vortex and source elements are always finite. As the same basic equations are solved, the results are of course similar to the results obtained with conformal mapping theory. The pressure distribution shows a singular behaviour, the same as for the conformal mapping solution.

2. Boundary conditions

In linearized form, the cavitation problem can be formulated as a set of coupled, singular integral equations (25) to (28) for a closed cavity model. In the case of an open cavity model, the closure condition instead takes the form

$$\int_0^t \phi(\xi) d\xi = \delta(t)$$

where $\delta(t)$ is a prescribed value. The solution can then be obtained in the same way as for the closed cavity case.

3. Correlation factor for the cavity thickness

The full scale stereophoto results are utilized for the determination of the correction factor. From the comparison between the full scale results and the calculated values, the correction factor is chosen as 5.0 in the region of the propeller tip decreasing to 1.0 at 0.8R of the propeller blade.

In this paper, the variation of the tip vortex diameter is not considered independently, but it is considered to be contained in the variation of the sheet cavitation.

To Hoshino

In the two dimensional cavitation calculations, several spacing arrangements have been tried. The equal spacing as we use has been found to produce sufficiently accurate results for our purpose.

In the first step of the calculation of propeller cavitation in non-uniform wake, we apply the unsteady lifting surface theory by Hanaoka - Koyama for the non-cavitating case. The unsteady cavitation pattern is then calculated by using this unsteady solution to generate angles of attack etc. Therefore, the phase shift caused by the unsteady loading is to same extent taken into account in the present method.

To Dyne

We think one should consider the wake model for what it is, just a mathematical model which seems to work well in practice. We know of measurements carried out at MIT which confirms the contraction process but not necessarily the details of the roll up. However, we think that it has been clearly demonstrated by Prof. Kerwin and others at MIT that this wake model produces good results.

Prediction of Propeller-Induced Fluctuating Pressures and Correlation with Full-Scale Data

Noritane Chiba, Takao Sasajima and Tetsuji Hoshino

Nagasaki Experimental Tank

Mitsubishi Heavy Industries, Ltd

Japan

ABSTRACT

A method is presented to predict the propeller-induced fluctuating pressure. The method consists of calculation of pressure distribution with unsteady propeller theory, estimation of cavity shape and prediction of fluctuating pressure. The cavity shape and fluctuating pressure are compared with the carefully conducted experiments and some empirical corrections were introduced.

The method was applied to measurements in model experiments and full scale data. And it was found that the present method gives good correlation with measurements for the blade frequency components, but further refinement of the method is necessary for higher frequency components.

NOMENCLATURE

C_p : Non-dimensional pressure on propeller blade
 D : Diameter of propeller
 e : Vapour pressure
 $2\pi h$: Pitch of helical vortex sheet
 K_L : Correction factor for cavity length
 K_{pi} : Non-dimensional pressure fluctuation

$$= \frac{\Delta p_i}{\rho n^2 D^2}$$

 N : Number of blades of propeller
 n : Distance normal to the propeller blade, and number of revolution of propeller

p : Total pressure fluctuation
 Δp_i : i -th blade frequency component of pressure fluctuation
 p_ℓ : Pressure fluctuation induced by blade loading
 p_t : Pressure fluctuation induced by blade thickness
 p_c : Pressure fluctuation induced by cavity
 R : Distance from singularity element to field point
 r_o : Radius of propeller
 r_b : Radius of propeller boss
 s : Distance along the chord of the blade
 S_c : Sectional area of two-dimensional cavity
 t : Time
 V_a : Axial velocity to propeller
 \bar{v}_a : Average axial induced velocity
 v_t : Average tangential induced velocity
 v^* : Axial velocity, including induced velocity = $V_a + \bar{v}_a$
 w^* : Resultant velocity including induced velocity
 x, r, ϕ : Cylindrical coordinates shown in Fig.1.

η_E	: Thickness of rear end of cavity
η_t	: Thickness distribution of blade
θ	: Angular position with respect to generating line
θ_c	: Angular position of center of cavity
θ_L	: Leading edge of blade
θ_T	: Trailing edge of blade
θ_1	: Leading edge of cavity
θ_3	: Trailing edge of cavity
ξ_1	: Leading edge of cavity on two-dimensional wing
ξ_3	: Trailing edge of cavity on two-dimensional wing
ρ	: Mass density of water
σ_L	: Local cavitation number
ϕ	: Velocity potential due to cavitating propeller
ϕ_b	: Velocity potential due to blade loading
ϕ_t	: Velocity potential due to blade thickness
ϕ_c	: Velocity potential due to cavity
θ_0	: Angular position of generating line of a blade
ω	: Angular velocity of the propeller
u_{*r}	: Tangential velocity including induced velocity

1. INTRODUCTION

The need for a method to design ships with less vibration has been growing in the recent years with increasing requirements for betterment in habitability and for avoiding structural damages. The vibration is induced by many sources, among which a propeller plays in many cases major part of it. Propeller-induced vibratory forces consist of so-called "propeller shaft forces" and "surface forces". Propeller shaft forces come from the time dependent change of blade forces transmitted to hull structure through the propeller shaft. Propeller shaft forces can be predicted with fairly good accuracy by existing methods (Ref.1).

Surface forces come from the time dependent change of pressure around the propeller transmitted to the hull surface through water. The surface force is obtained by integrating the pressure over the hull surface. This pressure fluctuation is remarkably increased by unsteady cavity

which occurs on the blades of a propeller operating in non-uniform flow field behind a ship. The pressure fluctuation thus increased by the unsteady cavity can cause serious vibration problems. Since ship vibration is a combined result of excitation force and response of ship structure, efforts should be directed not only to reduce excitation force, but also to decrease response amplitude of ship structure at the blade frequency and its multiplies.

Usually, propeller-induced hull pressure in cavitating condition is predicted from the model experiments in cavitation tunnels or in the depressurized towing tank. But model experiments need much time and cost to be performed. Especially, in the design stage of propeller, quick and cost-saving methods are demanded. Therefore, theoretical prediction methods are studied by many researchers (Refs.2,3,4,5,6,7).

The most difficult point in the theoretical methods is how to formulate the behavior of unsteady cavity on the propeller blade. This is an unsteady and three-dimensional mixed boundary value problem, therefore some approximations have to be introduced to obtain a practical solutions. The three-dimensional cavity is assumed to be composed of two-dimensional cavity at each radius and further the dynamic behavior of the two-dimensional cavities is treated with quasi-steady approach.

For estimation of the shape of two-dimensional cavity, steady two-dimensional cavity theories, such as Guerst's (Ref.8), Hanaoka's (Ref.9) and Nishiyama's (Ref.10) are used as a base. A simpler method, which determines the length of cavity from the curve of pressure distribution and the cavitation number, is also used (Refs.2,11). The quasi-steady approach means that a two-dimensional cavity on the blade element is determined only by the instantaneous flow conditions to the blade element (obtained by unsteady theory of non-cavitating propellers) such as pressure distribution along the chord, incident angle and cavitation number, and the dynamic behavior of the cavity is not considered.

The method of prediction presented in this paper employs also such two-dimensional and quasi-steady approximation, but is characterized by that the correction factors are introduced from the comparisons with carefully conducted model experiments such as measurements of cavity thickness, measurements of cavity extents and pressure fluctuations.

The method was applied to the model experiments and further to the full scale data. The predicted pressure fluctuations are well correlated with the measured ones, as far as the first blade frequency components are concerned.

2. THEORETICAL CALCULATION

The coordinate system and the velocity diagram of the propeller are shown in Figs. 1 and 2. The pressure fluctuation induced

by a cavitating propeller is usually expressed by the following linearized equation.

$$p(t) = -\rho \left(\frac{\partial \phi}{\partial t} + V \frac{\partial \phi}{\partial x} \right) \quad (1)$$

$$\phi = \phi_i + \phi_t + \phi_c \quad (2)$$

where ϕ is the velocity potential due to the three components, ϕ_i , ϕ_t and ϕ_c .

ϕ_i : Velocity potential due to loading on the propeller blades.

ϕ_t : Velocity potential due to blade thickness of the propeller.

ϕ_c : Velocity potential due to cavity on the blade.

The velocity potential due to blade loading is expressed with the vortex distribution, as follows.

$$\phi_i(x, r, \theta, t) = \frac{1}{4\pi} \sum_{k=0}^{N-1} \int_{r_b}^{r_o} \frac{r_o}{\sqrt{h^2 + r'^2}} dr' \int_{-\pi}^{\pi} \gamma(r', \theta', t) \frac{\partial}{\partial n} \left(\frac{1}{R_f} \right) \cdot W^* d\theta' \quad (3)$$

where,

$$R_f^2 = [x - h(\theta' + \Omega^* t)]^2 + r^2 + r'^2 - 2rr' \cos(\theta - \theta' + \Omega^* t - \frac{2\pi k}{N})$$

The vortex distribution is expanded into Fourier series as

$$\gamma(r', \theta', t) = \sum_{\lambda=0}^{\infty} \gamma_{\lambda}(r', \theta') e^{i\lambda \Omega^* t} \quad (4)$$

From eqs. (3) and (4), the pressure fluctuation due to blade loading is expressed as follows.

$$p_i(x, r, \theta, t) = -\frac{\rho}{4\pi} \sum_{k=0}^{N-1} \int_{r_b}^{r_o} dr' \int_{-\pi}^{\pi} \gamma_{\lambda}(r', \theta') e^{i\lambda(\Omega^* t - \frac{2\pi k}{N})} \cdot \frac{r'(x - h\theta') - rr' \sin(\theta - \theta' + \Omega^* t - \frac{2\pi k}{N})}{R_{fo}^3} \cdot W^* d\theta' \quad (5)$$

where,

$$R_{fo}^2 = (x - h\theta')^2 + r^2 + r'^2 - 2rr' \cos(\theta - \theta' + \Omega^* t - \frac{2\pi k}{N})$$

In the present method, the vortex distribution in eq. (5) is obtained as a result of the calculation by Hanaoka-Koyama's unsteady lifting surface theory (Refs. 12, 13).

The blade thickness can be replaced by the source distribution along the chord. The strength of the source is approximately related to blade thickness as follows.

$$\sigma_t(r, \theta) = W^* \frac{\partial \eta_t}{\partial s} = \frac{W^*}{\sqrt{h^2 + r^2}} \frac{\partial \eta_t(r, \theta)}{\partial r} \quad (6)$$

The velocity potential due to the source is

$$\phi_t(x, r, \theta, t) = -\frac{1}{4\pi} \sum_{k=0}^{N-1} \int_{r_b}^{r_o} \frac{r_o}{\sqrt{h^2 + r'^2}} dr' \int_{-\pi}^{\pi} \sigma_t(r', \theta', t) \frac{1}{R_b} \cdot d\theta' \quad (7)$$

where,

$$R_b^2 = (x - h\theta')^2 + r^2 + r'^2 - 2rr' \cos(\theta - \theta' + \Omega^* t - \frac{2\pi k}{N})$$

The pressure fluctuation due to the source is as follows.

$$p_t(x, r, \theta, t) = -\frac{\rho}{4\pi} \sum_{k=0}^{N-1} \int_{r_b}^{r_o} dr' \int_{-\pi}^{\pi} \sigma_t(r', \theta', t) \frac{W^*}{R_b} \cdot \frac{r'(x - h\theta') + rr' \sin(\theta - \theta' + \Omega^* t - \frac{2\pi k}{N})}{R_b^3} \cdot d\theta' \quad (8)$$

The sum of $p_i(x, r, \theta, t)$ and $p_t(x, r, \theta, t)$ is the pressure fluctuation induced by the non-cavitating propeller. Strictly speaking, $p_i(x, r, \theta, t)$ is affected by the occurrence of unsteady cavity on the blade, but is assumed to be unchanged.

The pressure fluctuation induced by the unsteady cavity is obtained by expressing the cavity as the time dependent source. The strength of the source of cavity is related to the shape of cavity as follows.

$$\sigma_c(r, \theta, t) = \left(\frac{\partial}{\partial u} + \frac{W^*}{\sqrt{h^2 + r^2}} \frac{\partial}{\partial r} \right) \eta_c(r, \theta, t) \quad (9)$$

The pressure fluctuation induced by this source is

$$p_c(x, r, \theta, t) = -\frac{\rho}{4\pi} \sum_{k=0}^{N-1} \int_{r_b}^{r_o} \frac{r_o}{\sqrt{h^2 + r'^2}} dr' \int_{-\pi}^{\pi} \frac{\partial \sigma_c(r', \theta', t - \frac{2\pi k}{\Omega^* N})}{\partial t} \cdot \frac{1}{R_b} \cdot d\theta'$$

$$-\frac{\rho}{4\pi} \sum_{k=0}^{N-1} \int_{r_b}^{r_o} \sqrt{h^2 + r'^2} dr' \int_{\theta_1}^{\theta_3} \sigma_c(x', \theta', t - \frac{2\pi k}{N}) \cdot \frac{v^*(x - h\theta') + rr'\Omega^* \sin(\phi - \theta' + \Omega^*t - 2\pi k/N)}{R_b^3} d\theta' \quad (10)$$

In the present method, the shape of cavity on each blade element is estimated as follows. From the instantaneous blade loading calculated before and the blade thickness, the pressure distribution curve on the blade is obtained as shown in Fig.3. With the pressure distribution and the local cavitation number which is based on the immersion of the blade element at that instance, the length of cavity is determined as $(\xi_3 - \xi_1) \cdot C$ in Fig.3, where ξ_3 satisfies the following equation.

$$K_L = \frac{\int_{\xi_2}^{\xi_3} (\sigma_L + C_p) d\xi}{\int_{\xi_1}^{\xi_2} (\sigma_L + C_p) d\xi} \quad (11)$$

In eq.(11), C_p is assumed to be zero when the cavity extends downstream of the trailing edge. The value $K_L = 0.25$ is determined through comparisons with model experiments, one of which is shown in Fig.4.

Another method to estimate the length of cavity was proposed in the previous studies (Refs.2,7). That is based on Knapp's theory on dynamic similarity for a spherical bubble (Ref.14) as

$$R = Kt \sqrt{\frac{\Delta P}{\rho}} \quad (12)$$

R : Bubble radius

t : Time for growth or decay of a bubble

ΔP : Pressure difference between inside and outside of the bubble

ρ : Mass density of liquid

The point ξ_3 in Fig.3 is determined as the location where the bubble, which has grown in the range from ξ_1 to ξ_2 , decays to the initial radius. Namely, this is expressed as follows.

$$\int_{\xi_1}^{\xi_2} t \sqrt{-(\sigma + C_p)} d\xi = K' \int_{\xi_2}^{\xi_3} t \sqrt{\sigma + C_p} d\xi \quad (13)$$

where K' is an empirical factor. However, the concept of replacing the length of sheet cavity with the travelling path of a bubble is not yet fully understood. Therefore, this concept is not adopted in the present method.

The thickness of cavity is determined assuming an open model of partial cavity,

and expressed after Isay (Ref.15) as follows,

$$\eta_c(x) = \eta_E \cdot [(\xi - \xi_1)/(\xi_3 - \xi_1)]^{1/m} \quad (15)$$

where it is assumed that $m=2$.

The maximum thickness appears at the end of cavity. η_E was determined by simplifying Nishiyama's formula (Ref.10) as follows.

$$\eta_E = 2 \cdot \alpha_0 (\xi_3 - \xi_1) \cdot C \quad (16)$$

α_0 is the incident angle for the equivalent two-dimensional section which has the same vortex distribution $\gamma(r, \theta)$ as given by eq. (3).

To examine the above simple expressions, the shape of cavity on model propellers were measured with the small streamline shaped pins set normal to the blade. The photographs of the pins and measurement of cavity thickness are shown in Fig.5. Although the pins also cavitated, the shape of cavity upstream of the pins did not seem to be affected by the cavitating pins. By comparing the results from the measurement with the calculation, eqs.(15) and (16) are found to give a good approximation, as shown in Fig.6, for the cavity shape if the cavity starts from the leading edge of the propeller blade. In case the cavity is not attached to the leading edge, i.e. collapsing stage of the cavity, approximation is not so good, but eqs.(15) and (16) are applied in the present calculation.

The pressure fluctuation induced by thus obtained cavity shape is approximated with the assumption that the distance to the field point is large compared with cavity dimension. Thus the pressure fluctuation is expressed by the sectional area and trailing edge thickness of cavity.

$$p_c(x, r, \theta, t) = \frac{N-1}{4\pi} \left[\int_{r_b}^{r_o} \left(\frac{\partial^2 S_c}{\partial t^2} + W^* \frac{\partial \eta_E}{\partial t} \right) \cdot \frac{1}{R_{bo}} \cdot dr' - \int_{r_b}^{r_o} \left(\frac{\partial S_c}{\partial t} + W^* \eta_E \right) \right]$$

$$\frac{v^*(x - x_c) + rr'\Omega^* \sin(\phi - \theta_c + \Omega^*t - 2\pi k/N)}{R_{bo}^3} \cdot dr'] \quad (17)$$

where,

$$S_c(r', t) = \sqrt{h^2 + r'^2} \int_{\theta_1}^{\theta_3} \eta_c(r', \theta', t) \cdot d\theta'$$

$$\eta_E(r', t) = \int_{\theta_1}^{\theta_3} \frac{\partial \eta_c}{\partial \theta'} \cdot d\theta'$$

$$R_{bo}^2 = (x - r\theta_c)^2 + r^2 + r'^2 - 2rr' \cos(\phi - \theta_c + \Omega^*t - \frac{2\pi k}{N})$$

From the above, the total pressure fluctuation is obtained as a sum of p_i , p_t and p_c in free space. On the hull surface, the solid boundary factor 2 is multiplied with the sum (Ref.16).

Several trials of calculation revealed that the phase of the change of cavity extent on the blade in calculation is about 20 degrees in advance compared with the experiments (Ref.17). Therefore, the calculated phase of cavity is delayed by 20 degrees as an empirical correction. Fig.7 shows the comparison of cavity extent thus calculated and those observed in tunnel.

When the pressure fluctuations were calculated based on the cavitation patterns predicted above, the results from calculation were found to be about four times as large as those derived from experiments as shown in Fig.8. Then the pressure fluctuation induced by the unsteady cavity is corrected by factor 0.25.

Hence the final form of total pressure fluctuation is as follows.

$$p(x, r, z, t) = 2 \cdot [p_i(x, r, z, t) + p_t(x, r, z, t) + \frac{1}{4} p_c(x, r, z, t - \Delta t)] \quad (18)$$

where Δt is time lag corresponding to phase difference of 20 degrees.

The reasons why such differences in phase of cavity extent and pressure amplitude occur are not fully understood, but the effect of hysteresis of cavity will be one of them. The present method, as in the case with all the other published methods, treats the dynamic behavior of cavity in a quasi-steady sense. But in reality, the shape of cavity is governed by dynamics theory.

As shown in Appendix, a simple consideration on this phenomenon made by replacing the cavity by a spherical bubble suggests that the solution of dynamic equation will result in the delay of cavity decay. Therefore, the corrections for the calculated results in terms of the phase of cavity extent may be interpreted as effect of dynamic behavior of cavity.

3. MODEL EXPERIMENTS

Model experiments supply data for individual requirement, but experimental data are subject to errors coming from many sources such as test conditions, size of model, etc. In case of validating a prediction method or determining empirical correction factors therein, extreme care should be taken to choose reliable data.

In this section, is described how the experiments are made in Nagasaki Experimental Tank to obtain reliable data to check and correct the calculation method in the preceding section.

3.1 Measuring System of Pressure Fluctuation

The measuring section of cavitation tunnel is 500 mm square and the flow field is simulated with wire mesh screen and dummy stern. Pressure fluctuation is measured, in most cases, with the pressure transducers set flush with the flat plate above the propeller. The scheme is shown in Fig.9. The flat plate is supported by the four struts, which penetrate the upper window of the tunnel and are connected to the flexures. The flexibility of the flexures was so selected that the resonant frequency of the system is far below the blade frequency of usual tests. The frequency characteristics were also examined by changing the propeller revolutions at the same advance ratio and cavitation number. The non-dimensional pressure coefficients K_p 's, plotted over the propeller revolutions are almost flat as shown in Fig.10. That is, there is not a resonant frequency within the range of usual operations.

3.2 Effect of Air Content

It is known that dissolved air or free air bubbles in water affect the measured value of pressure fluctuation (Refs.18,19, 20). The effect of air content was also examined in our tunnel. Fig.11 shows the pressure signals and its harmonic components obtained for the air content ratios α/α_s of 10% and 36%. The pressure signals are regular with higher air content, corresponding to more stable cavitation pattern on the blades. The decrease of blade rate components and the increase of other components might come from the instability of the cavity. As a practice, therefore air content is kept above 30% of saturation in measurements of pressure fluctuation. This tendency is in accordance with the results of SSPA (Ref.20).

3.3 Wall Effect

To check the degree of wall effect due to the reflection of pressure from the wall, two geometrically similar propellers were tested in the flow field made similar to the propellers. The measurements were carried out in the same advance ratio, cavitation number and tip clearance ratio. The measured pressure signals and the Fourier coefficients of pressure fluctuations K_p 's are compared in Fig.12. This figure shows relatively good similarity between the results from the two propellers. Therefore, the wall effect on the pressure fluctuation is thought to be relatively small and no correction is made as a practice.

4. COMPARISONS WITH MEASUREMENTS

In order to examine the applicability of the present method to predict pressure fluctuation, comparisons were made between calculations and measurements. The measurements include model experiments and full scale measurements.

For correction with model experiments,

those data were chosen which are competent for the assumption of the calculation, especially with stable cavity appearing when a blade passes wake peak. The correlation was examined, therefore, for the cases of relatively high wake peak, not too large blade area ratio and the tests carried out with air content $1/15$ over 30%. Model propellers for several kinds of ships were included viz., full ships such as tankers and high speed container ships. Fig.13 shows the measured pressure fluctuations plotted over the calculated ones. The calculated values of the first blade frequency components are in good correlation with those of measurements. But as for the twice blade frequency components, correlation is not so good.

In full scale measurements, the pressure fluctuations were measured with the pressure transducers mounted flush with the hull plate. In predicting the full scale pressure fluctuations by the present method, both axial and tangential components of wake were taken into account. The axial component in full scale was estimated by shifting inward the wake contour curves, so as to make the mean wake to be the same as that of full scale. The tangential component was retained as measured on model ship in the towing tank. The local cavitation number changed with the change of immersion of the blade due to rotation. Fig.14 shows the comparisons of pressure fluctuations. The ships were discriminated by the marks, \bigcirc , Δ , \square etc. The blade frequency components show relatively good correlation between prediction and measurement. But the twice blade frequency components do not.

From the above, it can be said that the present method can predict the first blade frequency component of pressure fluctuation, but further studies are necessary to improve the accuracy in higher order frequency components.

5. CONCLUSION

A method of predicting the propeller-induced pressure fluctuation is presented. This method consists of calculation of unsteady pressure distribution on the blade, estimation of shape of cavity with quasi-steady approach and calculation of pressure from the above. For practical purposes, a relatively simple theoretical consideration is adopted together with empirical correction factors. The corrections were made for the phase of variation in cavity extent and for the pressure fluctuations by comparing with the carefully conducted experiments.

The pressure fluctuations calculated by the present method were compared with the model experiments and further compared with full scale measurements. It is shown that the present method can predict well the blade frequency components, but correlation for the twice blade frequency components is not good. It is suggested that the dynamic behavior of cavity needs to be

investigated in the future studies to increase the accuracy of this method. Improvement of theory will be expected by further measurements of cavity shape.

ACKNOWLEDGEMENT

The authors express their deep gratitude to Mr. Tanibayashi for his encouragement to prepare the paper. They also thank all the members in Nagasaki Experimental Tank for carrying out the experiments.

REFERENCES

1. Sasajima, T., "Usefulness of Quasi-Steady Approach for Estimation of Propeller Bearing Forces," SNAME Propeller '78 Symposium, 1978.
2. Johnsson, C. A. and Sondtvedt, T., "Propeller Cavitation and Response of 230,000 DWT Tankers, 9th Symposium on Naval Hydrodynamics, Sept., 1972.
3. Noordzij, L., "Pressure Field Induced by a Cavitating Propeller," International Shipbuilding Progress, Vol.23, No.260, Apr., 1976.
4. Takahashi, H., "Estimation of Surface Force Induced by Propeller," Journal of SNAJ, Vol.140, 1976.
5. Fitzsimmons, P. A., "Cavitation Induced Hull Pressures: A Comparison of Analytical Results, Ship and Model Measurements," RINA Symposium on Propeller Induced Ship Vibration, London, 1979.
6. Szantyr, J., "A Computer Program for Calculation of Cavitation Extent and Excitation Forces for a Propeller Operating in Non-uniform Velocity Field," International Shipbuilding Progress, Vol.26, No.296, Apr. 1979.
7. Yuasa, H. and Ishii, N., "Practical Calculation for Prediction of Propeller Cavitation and Propeller Induced Hull Pressure (in Japanese)," Journal of SNAJ, Vol.147, 1980.
8. Guerst, J. A., "Linearized Theory for Partially Cavitating Hydrofoils," International Shipbuilding Progress, Vol.6, No.60, 1959.
9. Hanaoka, T., "Linearized Theory of Cavity Flow Past a Hydrofoil of Arbitrary Shape," Paper of Ship Research Institute, No.21, 1967.
10. Nishiyama, T. and Ito, J., "Calculation of Partially Cavitating Flow by a Singularity Method (1st Report) (in Japanese)," Trans. of Japan Society of Mech. Eng., Vol.43, No.370, 1977.
11. Oossanen, P. van, "Theoretical Prediction of Cavitation on Propellers," Marine Technology, Vol.14, No.4, Oct. 1977.
12. Hanaoka, T., "Numerical Lifting-Surface Theory of a Screw Propeller in Non-uniform Flow (Part 1, Fundamental Theory) (in Japanese)," Paper of Ship Research Institute, Vol.6, No.5, 1969.
13. Koyama, K., "A Numerical Method for Propeller Lifting Surface in Non-uniform Flow and Its Application (in Japanese)," Journal of SNAJ, Vol.137, 1975.

14. Knapp, R. T. et al., "Cavitation," McGraw-Hill Book Co., 1970

15. Isay, W. H., "Kavitation," Vorlesungsmanuscript Nr.9C, Institute für Schiffbau der Universität Hamburg, 1978.

16. Hoshino, T., "Pressure Fluctuation Induced by a Spherical Bubble Moving with Varying Radius," Trans. of the West-Japan Society of Naval Architects, No.58, 1979.

17. Hoshino, T., "Estimation of Unsteady Cavitation on Propeller Blades as a Base for Predicting Propeller-Induced Pressure Fluctuations," Journal of SNAJ, Vol. 148, 1980. (to be presented)

18. Keller, A. P. and Weitendorf, E. A., "Influence of Undissolved Air Content on Cavitation Phenomena at the Propeller Blades and on Induced Hull Pressure Amplitudes," IAHR Symposium on Two Phase Flow and Cavitation in Power Generation Systems, Grenoble, 1976.

19. Noordzij, L., "Some Experiments on Cavitation Inception with Propellers in the NSMB-Depressurized Towing Tank," International Shipbuilding Progress, Vol.23, No.265, 1976.

20. Johnsson, C. A., Rutgersson, O., Olsson, S. and Björheden, O., "Vibration Excitation Forces from a Cavitating Propeller. Model and Full Scale Tests on a High Speed Container Ship," 11th Symposium on Naval Hydrodynamics, 1976.

APPENDIX

The cavity extent calculated by eq. (11) is well correspondent to the observed one when the shift of blade position is introduced by about 20 degrees. The reason of the shift may be explained by the following consideration.

The calculated volume of the cavity changes as shown in Fig.A. As explained in Section 2, the cavity is treated in a quasi-steady manner. But in reality, the cavity changes its volume according to the pressure difference between inside and outside of the cavity. If the cavity is assumed to be a spherical bubble with the same volume as the cavity, its radius R changes as follows.

$$RR + \frac{3}{2}(R)^2 = \frac{p-e}{\sigma} \quad (A-1)$$

where p is the pressure outside of the bubble, e is the pressure inside of the bubble, and surface tension is neglected. The change of volume of the cavity shown in Fig.A was calculated according to eq. (A-1). The pressure outside of the bubble was assumed to be equal to that at the point, 70% chord from leading edge at $0.9R$. The volume change of cavity calculated with (A-1) is also shown in Fig. A. The volume decreases more slowly than that calculated by the quasi-steady method. This will cause the delay of phase of cavity.

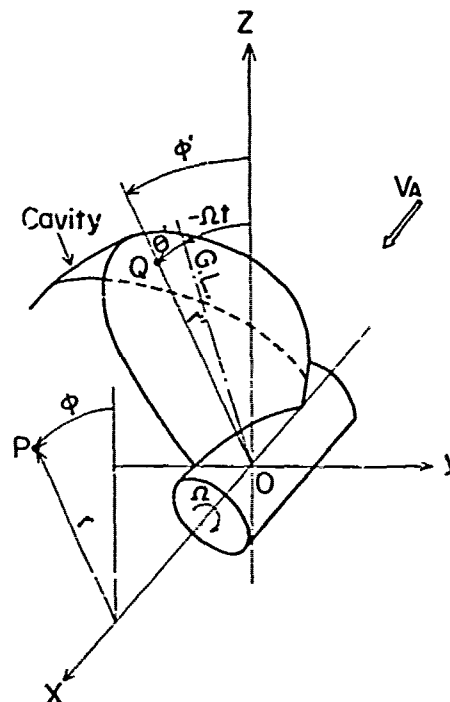


Fig. 1 Coordinate System of Propeller

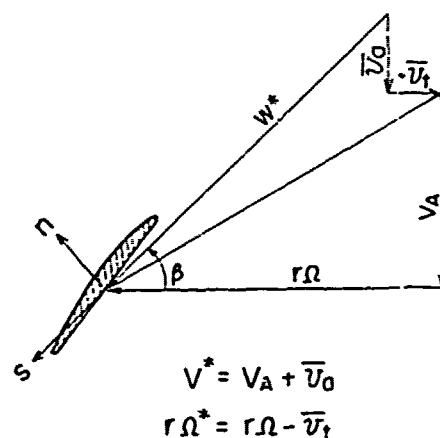


Fig. 2 Velocity Diagram for a Blade Element of Propeller

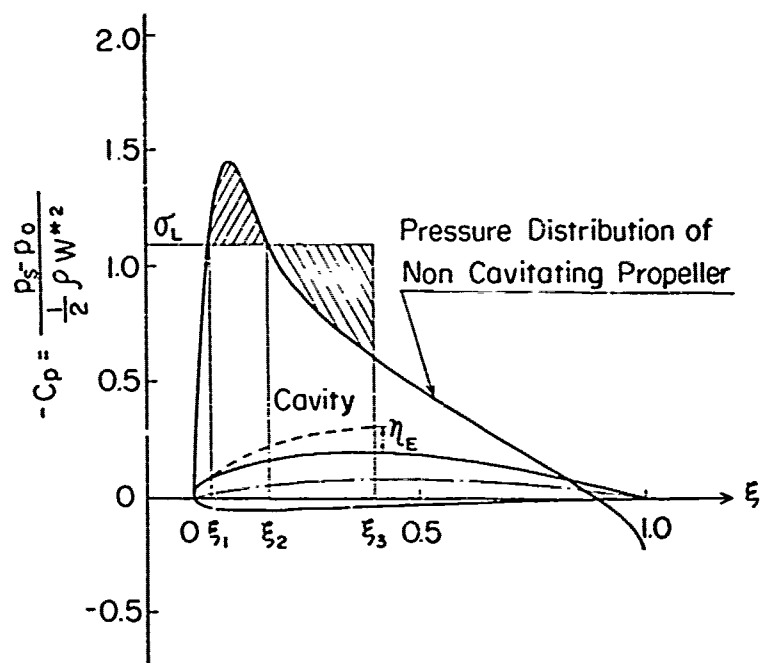


Fig. 3 Explanation of Cavity Extent

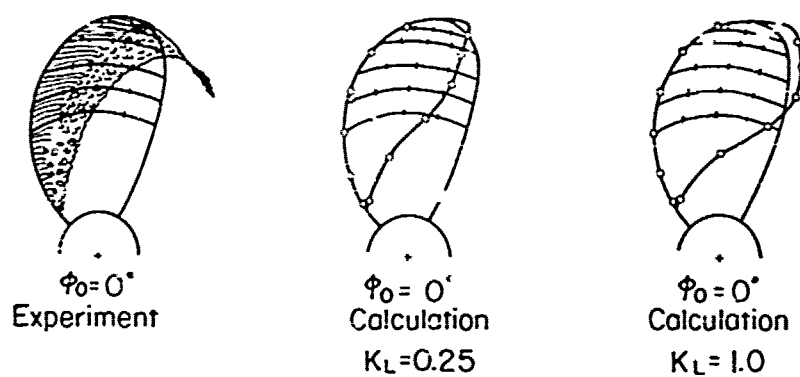
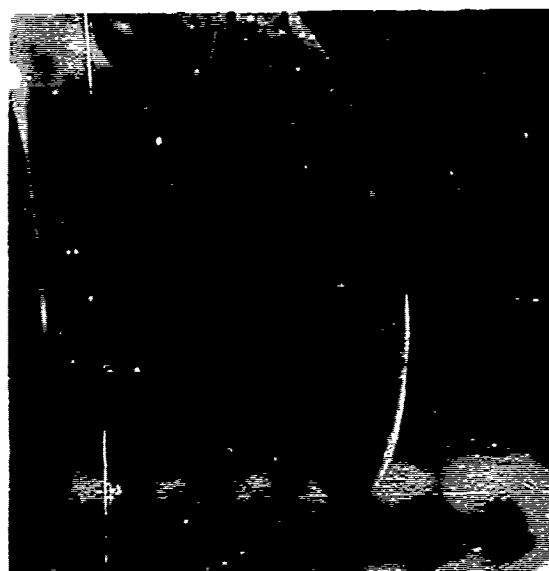


Fig. 4 Comparison of Cavity Extent
($\phi_0 = 0^\circ$)



Cavitating Propeller with Pins



Close-up of Pins

Fig. 5 Measurement of Cavity Thickness by Pins

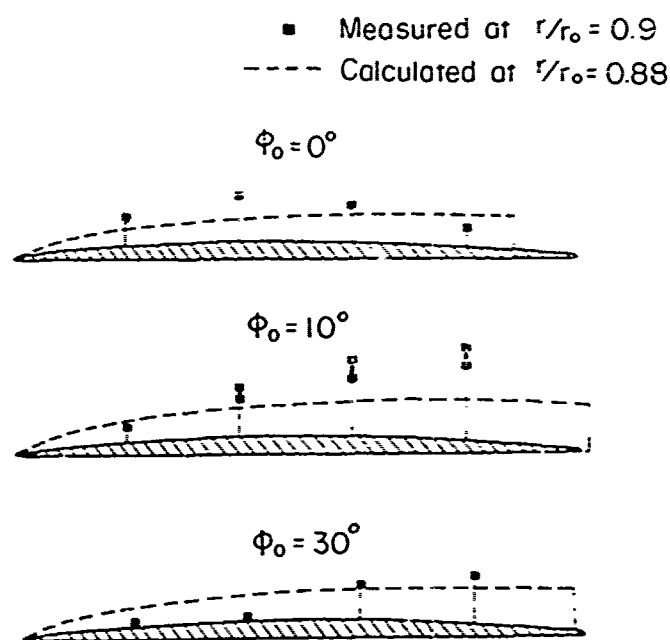


Fig. 6 Comparison of Calculated and Measured Cavity Thickness

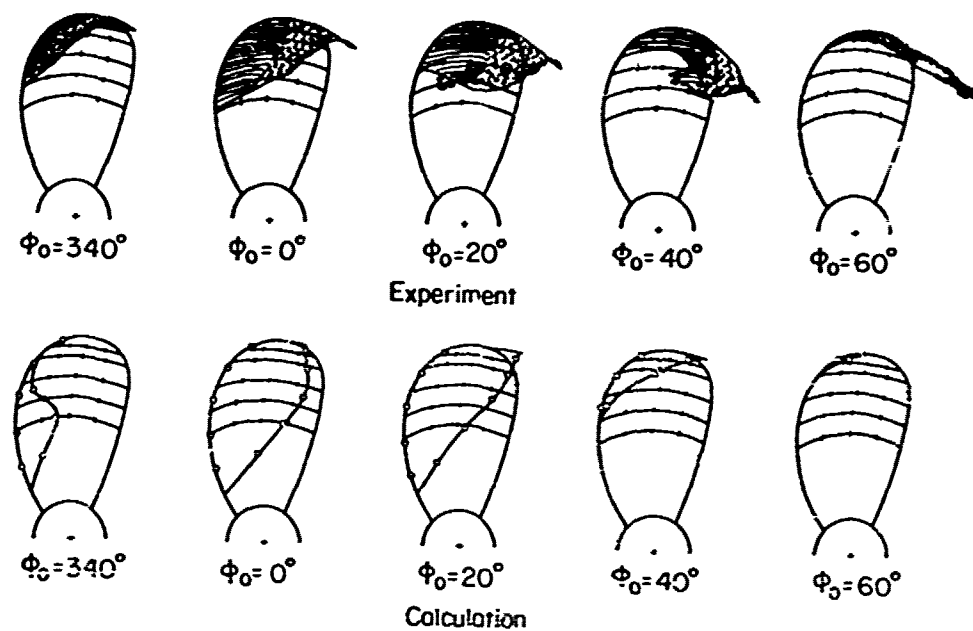


Fig. 7 Comparison of Cavity Extent ($\phi_0 = 0^\circ$)

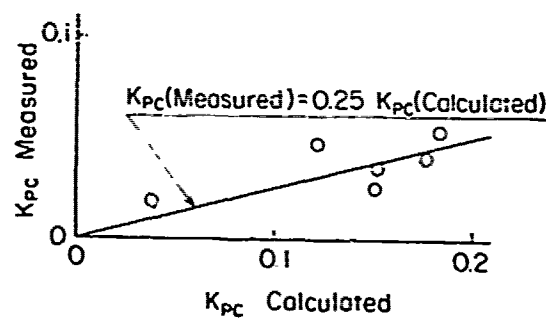


Fig. 8 Comparison of Pressure Fluctuation Induced by Unsteady Cavity

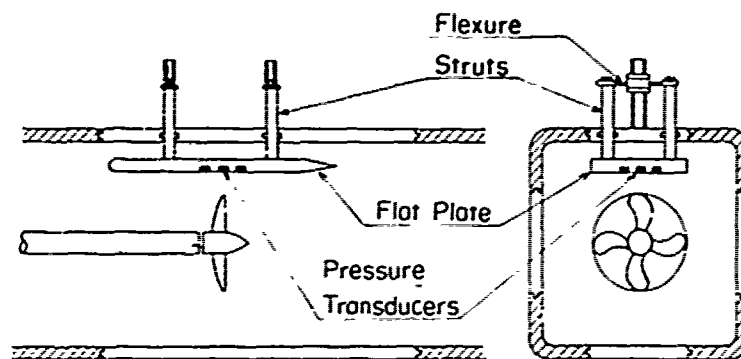


Fig. 9 Arrangement for Measuring Pressure Fluctuation

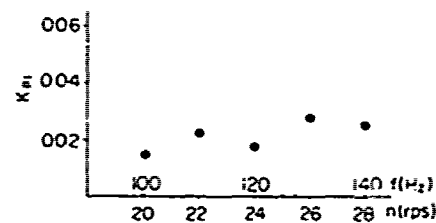


Fig. 10 Variation of K_{p1} on Propeller Revolutions

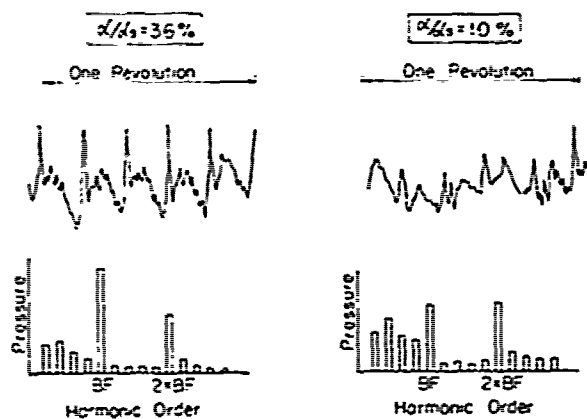


Fig. 11 Effect of Air Content Ratio on Pressure Fluctuation

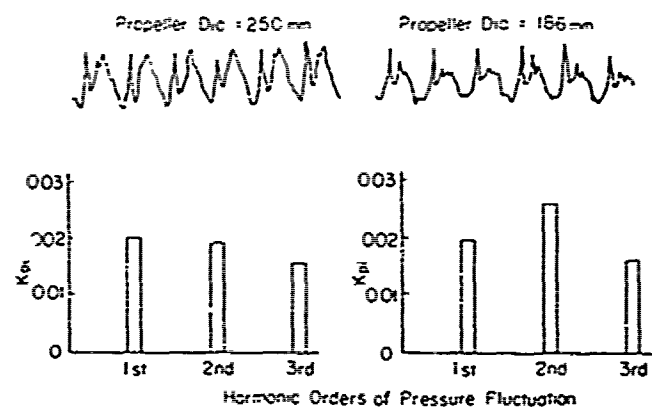


Fig. 12 Comparison of Pressure Fluctuation for Geometrically Similar Propeller

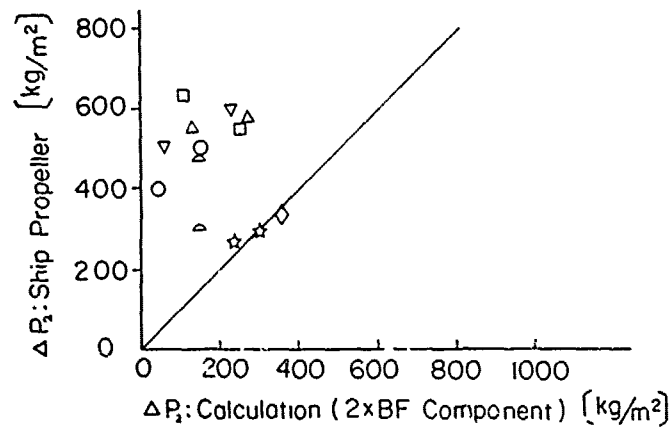
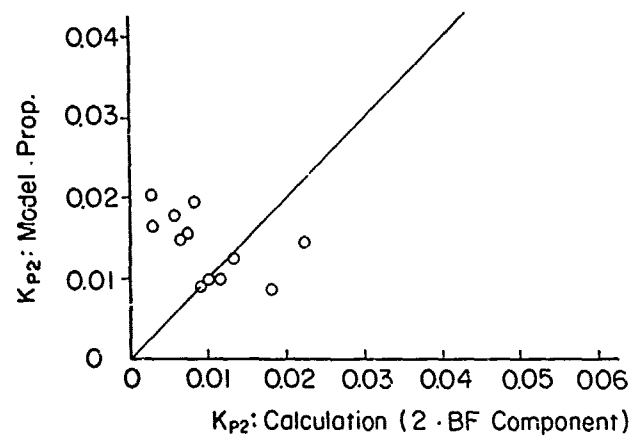
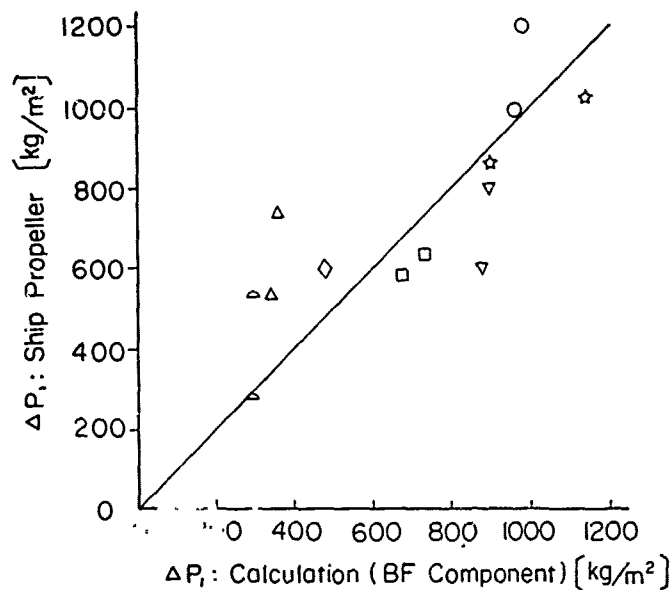
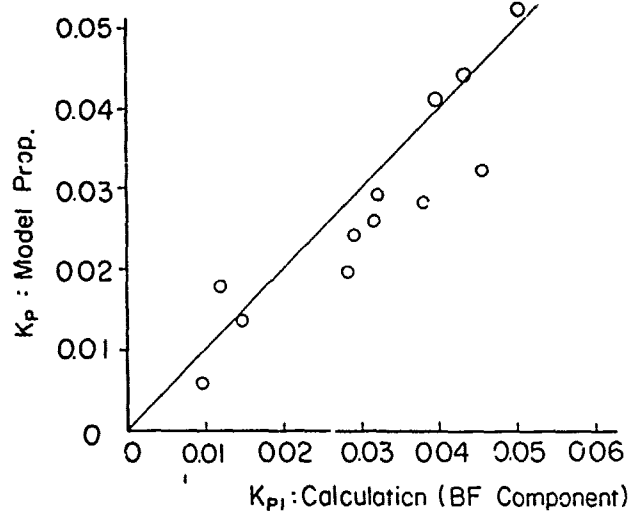


Fig. 13 Comparison of Calculated and Measured Pressure Fluctuation (Model)

Fig. 14 Comparison of Calculated and Measured Pressure Fluctuation (Full Scale)

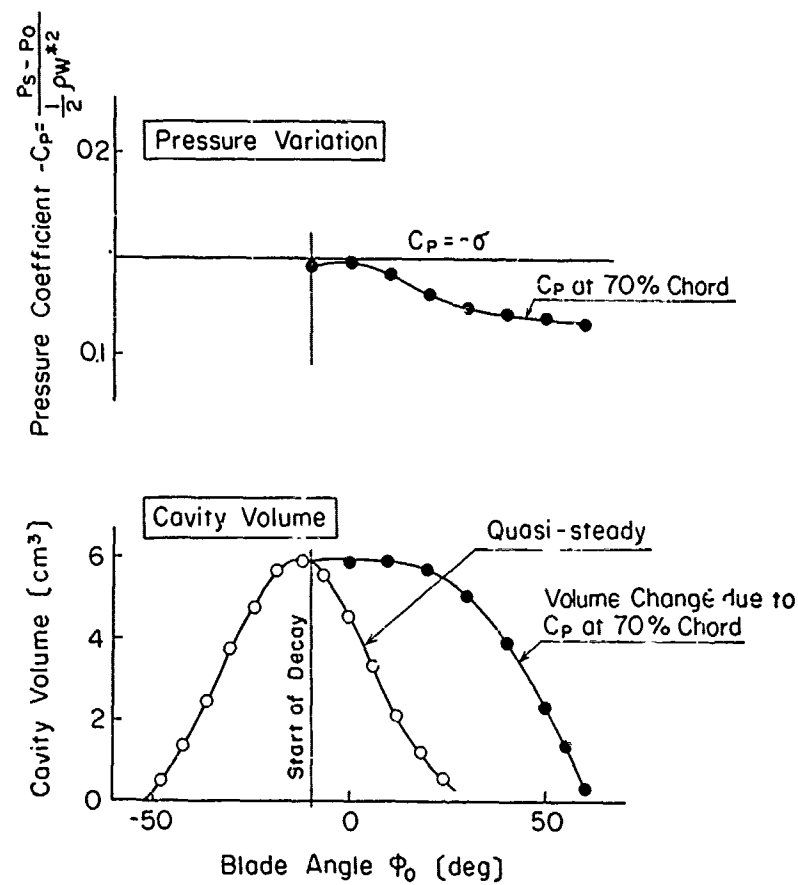


Fig. A Variation of Cavity Volume

Discussion

C.S Lee (KRIIS)

An ability to predict the transient cavity on a propeller working in a highly non-uniform ship wake is needed for the resolution of ship hull vibration and noise problems. The authors should be praised for their contributions to this not-that-easy problem.

The authors seem to me to suffer from the overprediction of cavity extent and the phase difference. I suppose that a more refined calculation of vorticity distribution, through an iteration process if necessary, may be necessary for the correct prediction of cavity extent. In this connection Fourier series representation of vorticity distribution, Eq.(4), may not be suitable. If the time-derivative term in Eq.(1) is considered at the same time, the phase lead may also be resolved.

I'd like to hear author's opinion on this comment.

H. Isshiki (Hitachi S & E)

The authors introduce several empirical corrections: 0.25 for K_L in Eq.(11), 20 degrees for the phase delay angle of the cavity extent and 1/4 as the correction factor for P_c in Eq.(18). Are these values applicable to the wide range of ship and propeller combinations.

The authors use Rayleigh's eq. of motion of a (free) bubble to explain the differences in the phase delay of the cavity extent and pressure amplitude between the theory and the experiment. I wonder, then, if "the effect of hysteresis of cavity" means the virtual inertia effect of the cavity bubble due to the surrounding water.

According to the Eq.(A-1) of a free bubble motion, the free bubble increases or decreases its size unboundedly under a constant pressure outside the bubble, because there is no restoring force. On the otherhand, the bubble on the foil has an equilibrium, and this equilibrium may be stable under proper conditions. Therefore, the dynamic similarity between the free bubble and the cavity bubble on the foil should be a limited one, and should be used with a proper limitation.

E.A. Weitendorf (HSVA)

(1) Calculated results of pressure fluctuations due to cavitation (as the authors did) may be sufficient from an engineering standpoint by applying a correcting factor of 0.25 (Fig.8) in order to get good agreement between measurement and calculation; but from a scientific point of view one should try to find the real reasons of the

difference between calculated and measured results.

(2) Fig.10 of the paper shows accord to my opinion the influence of bubble dynamics and Reynolds effect on the pressure impulses and it is not clear (as the authors said) that there is no resonance effect in the measured results. Using propellers of 186mm and 150mm is insufficient in spite of my personal hope that there is no influence of the wall effect to investigate this influence and the wall effect.

Fig.1 Tank Overh.

Fig.2 Mediumsized HSVA Tunnel 570mm

Fig.3 Large HSVA Tunnel 750mm

From the pressure impulses including their harmonics depend of the cavity volume development and not on its shape in respect to time in the ships wake field in contest with bubble dynamics. Reference on this can be given;

Zimmermann, B.: "Calculation of the Unstationary Pressure on a Plate, Caused by Cavitation Areas on Propeller Blades (in German)". Report 362, Institut für Schiffbau der Univ. Hamburg, 1977

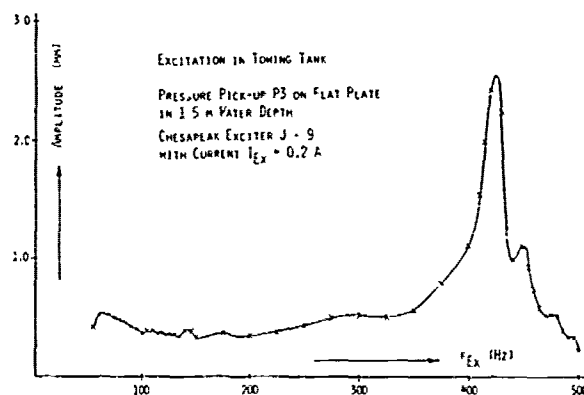


Fig. 1

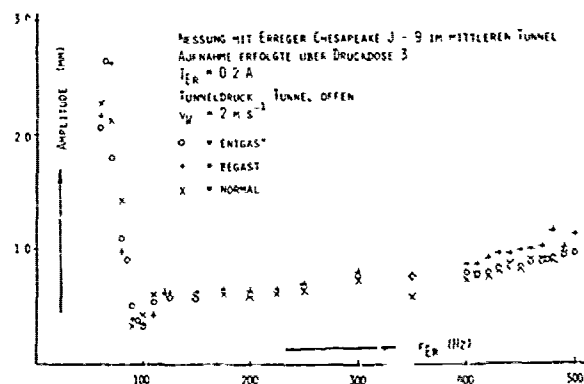


Fig. 2

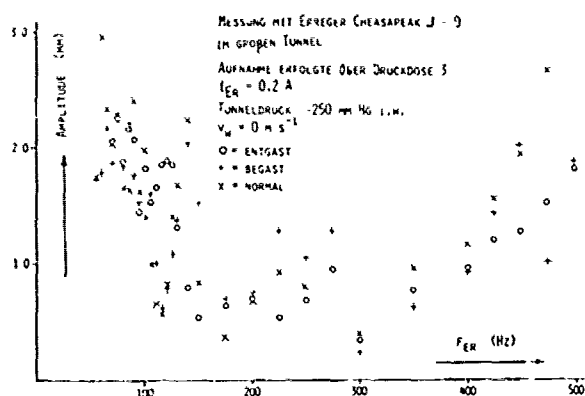


Fig. 3

N. Chiba (MHI)

We wish to thank all the discussers for their valuable contributions.

Dr. Chang-Sup Lee's comments are concerned with the calculation method of vortex distribution. In this paper, pressure on the blade in non-cavitating condition is used as the base to calculate the cavity extent. Therefore, the iteration process is not necessary to get the cavity extent. And in this sense, Fourier series expression of vorticity is one of the suitable method to express non-cavitating condition. But as we do not think that the present method is not the final goal of this study, the methods such as proposed by Dr. Lee in this symposium will be discussed in our

future studies to improve the accuracy of prediction method.

Dr. Isshiki asked first the applicability of the correction factors. The extensive calculation was made by one of the authors on propellers including those with high skew or with varying pitch distributions. The result showed fairly good correlation with experiments. The results will be presented at the meeting of the Society of Naval Architects of Japan in the coming autumn.

As for the second discussion of Dr. Isshiki, Eq.A-1 had been used in the previous study of one of the authors on the behavior of cavity bubbles on an oscillating hydrofoil and well explained the tendency of phenomena. Then Eq.A-1 was used here to try to explain the difference of phase of 20° .

The authors agree with the first comment of Dr. Weitendorf. Of course, we are going to study further theoretically and experimentally. Especially in experimental studies, it will be necessary to measure cavity shapes on much more propellers in many cavitation tunnels and in full scale and correlate them to pressure fluctuations. The second discussion of Dr. Weitendorf is concerned with wall effect. From our experience, the measured pressure amplitude with resonance became two or three times as large as those without resonance. In Fig. 10, there is no such pressure amplitudes. So it is recognized that there is no such resonance in the measuring system. Although it may be insufficient to conclude from Fig. 12 that there is no wall effect at all in physical meaning, this figure can tell us the wall effect is so small that the correction for the measured pressure will not be necessary in practical sense. To confirm this, further studies are going to be planned in Nagasaki Experimental Tank on wall effect in such a way as Dr. Huse or Dr. Weitendorf indicated.

Session II

CAVITATION

Chairman

Kaare M. Gisvold

Norwegian Hydrodynamic Laboratories

Trondheim, Norway

New Applications of Cavity Flow Theory

Marshall P. Tulin and Chun Che Hsu

Hydronautics Inc

Laurel Maryland U S A

ABSTRACT

Some new applications are made of "free streamline" or cavity flow theory to both non-cavitating flows involving wakes and separation bubbles, and to cavitating flows.

A method for the prediction of turbulent separated wake or separation bubble pressures is developed resulting in a simple relation between forebody drag coefficient, cavity length, wake pressure, and two viscous parameters: the boundary layer shape parameter H_2 at the rear of the separation bubble, and the friction coefficient acting on the dividing streamline between the external flow and the separated region. The problem is closed using relationships between cavity drag, cavity length, and wake pressure coefficient, based on cavity flow (inviscid) theory. The utility of the results is demonstrated in application to the wake flow past a vertical flat plate and a thin double wedge airfoil at incidence.

A new physical model of the flow past cavitating bodies is suggested allowing for a post-cavity separation and deceleration zone in which the forebody drag is realized in momentum loss in the external flow. This loss is brought about by friction on the dividing streamline behind the cavity, which separates the external flow and a closed separated region containing recirculating eddies.

A recent theory for the prediction of flows with attached leading edge cavities is reviewed and comparisons of results are made with measurements. The theory is based on a perturbation on a fully wetted flow which is applied to both planar and three-dimensional flow past lifting foils.

New results relating to unsteady sheet cavitation are given, based on a recent theory which is applicable to typical foil

sections operating in wakes. It is shown that growing cavities are reduced in length relative to steady cavities and collapsing cavities increased in length, leading to a hysteresis-like behavior as observed in practice. The theory is also used to explain why only the shorter of the two cavities predicted in steady theory is observed (the longer is unstable).

NOMENCLATURE

AR	Aspect ratio of wings. $(\text{Span})^2/\text{area}$
a	Parameter related to cavity length
a_L	Parameter related to laminar flow characteristics of bodies
B	Parameter related to the wing span
c	Chord length of foils or bodies
C_D	Drag coefficient of foils or bodies
C_D^*	Drag coefficient of the pseudo-body
C_f^*	Frictional coefficient of the pseudo-body
C_L	Total lift coefficient of foils or wings
C_{L_o}	Lift coefficient of foils or wings due to fully-wetted flow
C_{L_1}	Additional lift coefficient of foils or wings due to leading edge cavitation
C_p	Pressure coefficient
C_s	Shear stress coefficient

C_{r_n}	Thrust force coefficient of foils due to finite nose radius	$q_{o,\alpha}$	Component of q_o due to incidence
E_j	Jones' correction factor, wing semi-perimeter/span	$q_{o,\tau}$	Component of q_o due to foil thickness
F	Form factor related to viscous flow characteristics	R_c	Reynolds number based on chord length
f	Thickness of wake behind cavity	R_ℓ	Reynolds number based on cavity (or wake) length
H	Boundary-layer shape parameter, $\delta^*/\bar{\theta}$	R_l	Denotes rear part of
h	Semi-width of normal plates	r_n	Leading edge (nose) radius of foils
Im	Denotes imaginary part of	s	Direction along the sheet cavity
k	Parameter related to cavity length and drag	S_c	Cavity surface
k_τ	Parameter related to drag and suction force	S_f	Foil wetted surface
λ	Cavity (or wake) length	S_f^*	Foil surface lying under the cavity
λ_c	Time rate change of cavity length, $\frac{d\lambda}{dt}$	t	Time
M, N	Constants in formula for complex potential	u, v	Velocity component in x, y coordinates
$M_\infty(t)$	Time-dependent source strength	u_c	Velocity on cavity
p_c	Cavity (or wake) pressure	u_s	Velocity component along s direction
p_∞	Free stream pressure	v_η	Velocity component along η direction
q_c	Cavity (or wake) speed	\bar{V}	Cavity volume
q_s	Cavity speed along s	$\frac{d\bar{V}}{dt}$	Time rate of change of cavity volume, $\frac{d\bar{V}}{dt}$
q_o	Local flow speed due to fully wetted flow	x, y	Horizontal and vertical ordinates in physical plane
q_1	Local flow speed due to leading edge cavitation	z	Complex variable, $x + iy$
q_∞	Free stream speed		

α	Incidence of foils or wings
δ_c	Maximum cavity thickness
δ^*	Boundary layer displacement thickness
ζ	Complex variable, $\xi + i\eta$
η', ξ	Vertical and horizontal ordinates in transformed ξ -plane
n	Direction normal to sheet cavity
θ_0	Local fully-wetted flow angle
θ_1	Local flow angle due to leading edge cavitation
δ	Boundary layer momentum thickness
ρ	Fluid density
σ	Cavitation number
τ	Acceleration number
τ_c	Shear stress
ϕ	Scalar potential
ϕ_0	Scalar potential due to fully wetted flow
ϕ_1	Scalar potential due to leading edge cavitation
ψ	Complex potential, $\phi + i\psi$
ψ	Stream function
ψ'	Complex velocity, $d\psi/dz$
ψ_0'	Complex velocity due to fully wetted flow
ψ_1'	Complex velocity due to leading edge cavitation
w	Hodograph variable, $zn\psi'$
w_0	Hodograph variable, $zn\psi_0'$, due to fully wetted flow
w_1	Hodograph variable, $zn\psi_1'$, due to leading edge cavitation
ω	Frequency of oscillation

Subscripts:

2D	Denotes two dimensional flow
3D	Denotes three dimensional flow

ACKNOWLEDGEMENT

A substantial portion of this research has been carried out under Office of Naval Research Contract N00014-78-0144, a part of the General Hydromechanics Research Program of the David Taylor Naval Ship Research Development Center, U.S. Navy, whose support is gratefully acknowledged.

INTRODUCTION

Free streamline, or cavity flow theory in its classical form deals with flows past objects which are bounded in part by separated regions (whether we call them cavities or wakes) throughout which the pressure is constant or almost so at any particular instant. We may distinguish three main types of these separated regions:

Type A): "Wakes" and "Separation Bubbles," filled with the same fluid (in the same phase) as in the external flow, but wherein the motion of the contained fluid is too slow to support substantial pressure gradients. In this case the external and internal flows are separated by a viscous shear layer within which important shear stresses are generated.

Type B): "Cavities," filled for the most part with the vapor or gas phase of the fluid in the external flow, and within which the gas density is negligible except in the extreme case of certain cryogenic fluids.

Type C): "Ventilated Cavities," filled with a non-condensable gas which is essentially foreign to the fluid in the external flow.

Examples of these three types (A, B, and C) of separated regions abound in engineering practice, both in the marine and other fields. They include:

A.) Stabilized wakes behind blunt bodies and essentially planar foils at sufficiently high (stalled) incidence, both isolated and

comprising elements in cascade.

Leading edge separation bubbles on planar foils and highly swept wings, such as deltas.

B.) Long cavities (supercavitation) behind propeller, hydrofoil, and pump elements operating at sufficiently high speeds.

Short cavities (partial or leading edge) on propellers, impellers and foils.

C.) Long cavities (supercavitation) behind propellers either partially submerged or ventilated, and hydrofoil elements ventilated to the atmosphere

Long cavities behind objects entering the water at high speeds.

These flows involve a rich variety of physical phenomena, of both viscous and inviscid nature. Fortunately, the viscous effects can often be modeled or dealt with in such a way that the external flow can be treated as essentially inviscid and potential flow mathematics can be invoked. Indeed, the subject has benefitted enormously from the application of a variety of powerful mathematical techniques involving analytical functions and mappings, singular integral equations, and small perturbation expansions. All these developments were given birth over a hundred years ago with the invention of the hodograph mapping technique by Helmholtz and Kirchhoff in an attempt to model Type A flows with resistance.

Application of free streamline theory to Type B and C flows, particularly in the marine field, received very strong stimulation about twenty-five years ago with the development of linearized theory, its application to efficient foil design, and the use of those foils in actual supercavitating propellers. In the two decades following these events, a wide variety of problems of Type B and C have been taken up and solved, and particularly those in the supercavitating regime.

Although problems yet remain unsolved in this regime, and especially of a three-dimensional nature, activity has abated. However, significant developments have and still are taking place on both problems (Type B) involving short and unsteady cavities produced by cavitation, and on problems (Type A) involving wakes and separation bubbles. These are problems which arise in extremely important practical contexts in engineering.

In the present paper we shall:

I.) Discuss briefly the physics and physical modeling of cavity flows. Present a simple new theory by the present authors correcting the viscous and inviscid aspects of Type A flows, and thereby allowing calculation of the wake or bubble pressure coefficient. Apply this theory to turbulent leading edge separation on a sharp nosed double wedge airfoil, and to a vertical flat plate with stabilized trailing wake, for comparison with experiments.

II.) Describe briefly new theory and results obtained by the present authors within the last few years on the subject of steady leading edge cavities, Type B, as are

normally experienced by the blades of ship propellers operating in wakes.

III.) Present the results of a new analysis of unsteady sheet cavitation, particularly as it pertains to leading edge cavities.

I. THE PHYSICS AND MODELING OF CAVITY FLOWS

The length of a cavity is determined by many factors, notably: the forebody drag, the pressure coefficient in the cavity ($-c_3$); gravity; interference with other bodies and bounding surfaces; unsteady effects; see Tulin [1]. The cavity length is, however, generally finite; exceptions are brought about by strong blockage caused by operation between walls or in cascades, or grid arrangements.

A cavity results in or is associated with a resistance on the body to which it attaches, except in certain pathological cases of Type C flows. These have been discussed by Tulin [2], from which Figure 1 is taken.

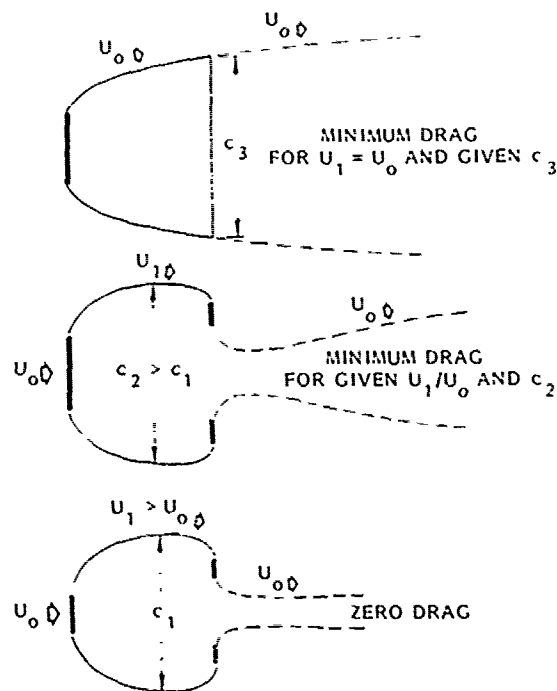


FIGURE 1 - MINIMUM DRAG BODIES, $U_0 = q_\infty$,
 $U_1 = q_c$
FROM: TULIN [2]

Far downstream of a cavity, a trailing momentum wake must exist, in which the magnitude of momentum loss must reflect the cavity resistance of the body (as well as other sources of resistance, should they be present). Thus the modeling of a flow involving a cavity must be accompanied by a modeling of the wake, too. This was pointed out by Tulin [1], see Figure 2, from whom we quote below:

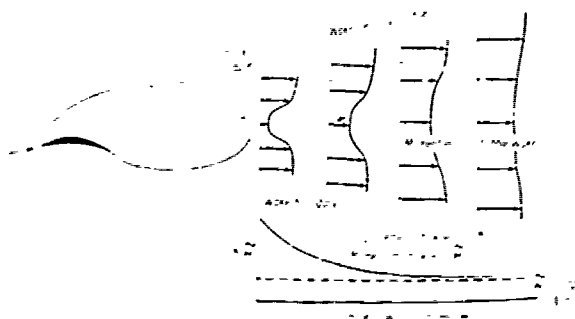


FIGURE 2 - A CAVITY FLOW WITH WAKE
(SCHEMATIC), $U_0 = q_\infty$
FROM: TULIN [1]

"A viscous wake, trailing to infinity downstream, must exist behind a real finite cavity in nature. Momentum considerations require that the forebody drag experienced by a real supercavitating body be manifested by a momentum defect in the far wake behind the body and its cavity. Cavity drag must therefore manifest itself in much the same way as friction and form drag do in the flow past a body without a cavity. In this latter case, it is a matter of experience that the displacement thickness of the wake generally decreases continuously from the region right behind the body, toward an asymptotic value equal to the momentum thickness; this behaviour is due to the continual downstream smoothing of the blunt wake profile found close to the body itself. We should expect precisely the same behaviour of the cavity-wake displacement thickness since the wake profile must be most blunt in the turbulent region just behind cavity collapse - the region where the momentum losses are actually experienced by the fluid. The effect of the wake on the outer potential flow may be determined by replacing it with a body whose thickness is taken equal to the wake displacement thickness. The asymptotic thickness is thus $f(\infty)/c = C_D/2$.

For blunt bodies, whose drag coefficient is $O(1)$, the wake thickness is about the same size as the body itself, and should not therefore be neglected in any proper model of the flow. At the same time, the wake thickness is seen to be somewhat thinner than the body width for $C_D < 2$, as is always the case for small and moderate values of σ ($\sigma < 1$); therefore, a proper model must neither ignore the wake nor involve too wide a trailing wake.

For slender bodies, whose drag coefficient is of the order of the body thickness or inclination squared, the wake thickness need only arise in connection with second-order terms; that is, a linearized or first order theory may properly neglect the wake.

All well-known wake models may be divided into two categories. They either involve no trailing wakes at all: Riabouchinsky [3]; Efros [4]; Kreisel [5], Gilbarg [6]; and Tulin [7]; or they involve thick wakes whose thickness is generally greater than that of the frontal projection of the body: Joukowski [8], Roshko [9], Eppler [10], and Wu [11], Fabula [12]. The former of these groups is clearly more suitable for the treatment of slender bodies, and the latter for blunt bodies. Note, however, that even in the case of blunt bodies, the latter group of models will generally very much exaggerate the wake thickness. In any case, none of the models mentioned is suitable for the proper representation of supercavitating flow past both blunt and slender bodies."

For the realistic and versatile modeling of a cavity and its wake, too, Tulin [1] proposed two spiral vortex models, allowing termination of the cavity itself in a trailing wake whose asymptotic downstream thickness corresponds precisely to the displacement thickness of the viscous wake associated with the forebody resistance, Figure 3. In

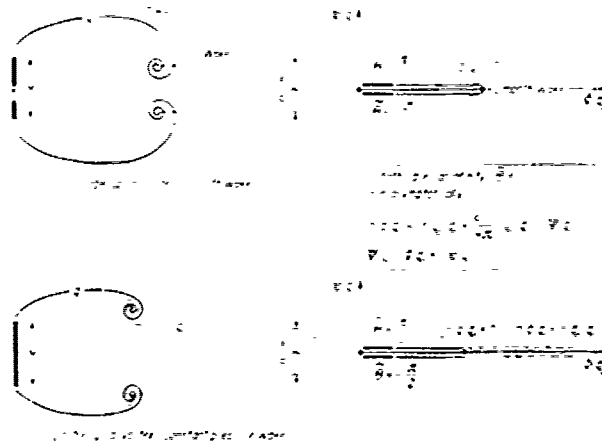


FIGURE 3 - SPIRAL VORTEX, TRAILING WAKE
MODELS OF REAL CAVITY FLOWS
FROM: TULIN [1]

one of these models (single spiral) the pressure on the wake boundary decays from stagnation to free stream, while in the other (double spiral) the pressure on the wake boundary is everywhere free stream. Variations on these models, allowing for a tailored decay in the pressure aft of the vortex to its asymptotic value could and have, Michel [13], since been proposed. The exact way this should be done, depends in detail upon the viscous processes which give actual rise to the momentum loss in the external flow, and which varies from cases to case. In any event, the evidence is that the two spiral models of Tulin seem to bracket flows in reality.

How do these viscous processes work on cavities? Too little has been said in the

past on this important question, partly because for supercavitating flows of Type B and C it has usually been of relatively little importance from a practical point of view whether cavity lengths and wakes have been properly modeled, since the forces on the forebody in these cases vary hardly at all with cavity length differences arising from the use of different cavity models. However, in the case of partial cavities on propellers, Type B, it is precisely the length and volume of the cavity which it is necessary to know, because of the pressures radiated by the changes in cavity volume. Then, in the case of Type A cavities, the length plays a vital role in the determination of the cavity pressure, which has been a central unsolved problem for flows of this type; we shall elaborate this point later, below.

We visualize the general situation in Figures 4 and 5. We have taken into account

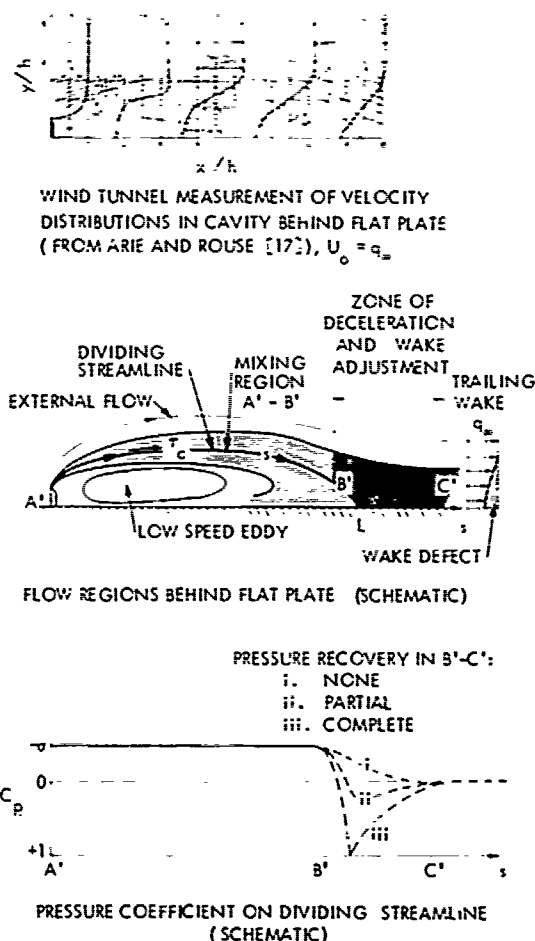


FIGURE 4 - CAVITY-WAKE (TYPE A), SCHEMATIC

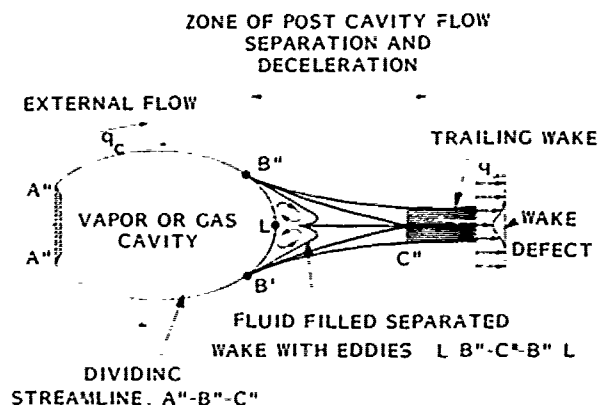


FIGURE 5 - CAVITY (TYPES B AND C) WITH POST-CAVITY SEPARATED WAKE (SCHEMATIC)

(Figure 4; Type A) that the external flow can experience both a retarding friction on the cavity wall due to mixing between external and internal flows, zone A'-B', and deceleration losses at the rear of the body in zone B'-C'. These latter losses correspond to form drag in the case of solid bodies. Following C' the wake is established and further momentum losses do not occur. In the case of flow Types B and C (Figure 5), we visualize a separated region in the external flow immediately to the rear of the cavity. Along the streamline B''-C'' bounding the separation, the external flow experiences retarding friction and deceleration losses. These losses realize the forebody pressure drag, which obviously cannot be recovered in any part as thrust on the rear of the cavity. Of course, in actuality the separated flow immediately behind a cavity is unsteady, but we suggest Figure 5 as a model for the mean, time-averaged, flow there.

The magnitude of the pressure recovery in the region B'-C', Type A flows, depends essentially on the thickness of the frictional layer at B' in comparison with the scale of the cavity there. When this layer is sufficiently thick, then stagnation and separation of the external flow is avoided and at the same time a gradual transition in pressure coefficient from $-\sigma$ to 0 becomes possible, as envisioned in Figure 4. This is, of course, also the case on most bodies normally used in practice, including ship hulls and foils. Then the momentum losses can be estimated using the classical momentum equation, assuming the boundary layer not too thick and the body reasonably slender (we restrict ourselves now to planar flows, for the sake of simplicity). Goldstein [14]:

$$\frac{d\bar{\theta}}{ds} + \frac{(11 + 2)}{q_c} \frac{dq_c}{ds} \cdot \bar{\theta} = C_s \quad (1)$$

where

$$C_s = \tau_c / \rho q_c^2$$

We may also estimate the losses in the region B''-C'', Figure 5, in the case of flows of Type

B and C by application of (1).

This completes the viscous modeling, except for estimates of the boundary layer shape factor H and C_s in (1). We shall see later that the boundary layer in the external flow in the region B'-C' seems close to separation, suggesting a value $H \approx 3.0$; Schaubauer and Klebanoff [15] found $H = 2.8$ at turbulent separation, in their planar experiment. The value of the friction coefficient, C_s , can be estimated in the usual case of turbulent flow from experiment or from mixing layer type semi-empirical theory; we suppose it to be constant along the mixing region A'-B' in turbulent flows. In the case of laminar flows, however, theory shows $C_s = \alpha_1 R^{-1/2}$, decreasing with distance s along the cavity we estimate $\alpha_1 \approx 10^{-1}$ from the laminar mixing theory).

Based on this modeling, a quantitative connection is made between the external flow in its inviscid realization and the viscous flow details. In the case of flows of Types B and C, the cavity pressure is, of course, prescribed, so that the effect of viscous flow is mainly of interest in connection with the choice of flow model: in order to estimate the length of the region B'-C' and therefore the nature of the transition from cavity to wake, it would be necessary to know the effective value of C_s behind the cavity, yet unknown. In the case of Type A flows, we shall show that the present modeling does allow an estimation of the cavity pressure a priori, and therefore provides the necessary closure of the problem. We shall utilize it to estimate cavity pressures in the case of turbulent separated regions for comparison with experiment, and in the case of laminar regions for comparison with earlier theories.

The Estimation of Cavity Pressures in Near Wakes Behind Planar Bluff Bodies: Type A Flows.

Principle and Fundamental Theory

The principle behind the calculation of the cavity (near wake) pressure lies in the simple necessity for the pressure drag on the forebody alone (C_D) to balance exactly the total drag acting on the closed pseudo-body, C_D^* , comprising the forebody and the near wake: the pseudobody is defined by the closed streamline between 0 and L in Figure 6, i.e. $C_D = C_D^*$. The equality of C_D and C_D^* is obvious, since either gives rise to the same momentum loss in the far wake (at C'):

$$C_D \equiv C_D^* = 2 \frac{\tilde{q}(C')}{h} \quad (2)$$

$$C_D = \left[\int_{\text{forebody}} p \cdot n_x ds \right] / \frac{1}{2} \rho q_\infty^2 h \quad (3)$$

$$C_D^* = \left[\int_{\text{pseudobody}} p \cdot n_x ds + \int C_s \cdot q_c^2 \cdot n_y ds \right] / \frac{1}{2} \rho q_\infty^2 h \quad (4)$$

and

$$\tilde{q}(s) = 2 \left[q_c(s) \right]^{-(H+2)} \cdot \int_0^s C_s \left[q_c(s') \right]^{H+2} ds' \quad (5)$$

The relations, (3) and (4), follow from definitions, and (5) is the solution of the differential Equation (1), as is easily verified (the factor 2 in (5) arises from the two side of the cavity).

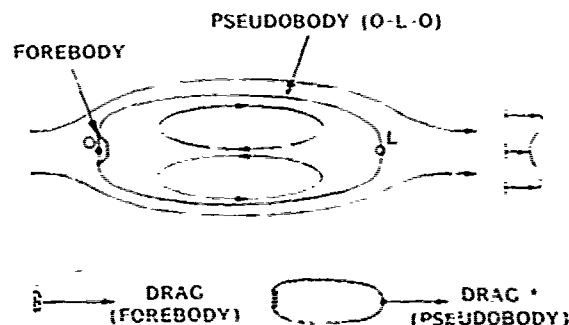


FIGURE 6 - EQUIVALENCE OF FOREBODY AND PSEUDO-BODY DRAGS

The forebody drag, depending for a given body on the cavity pressure coefficient, $C_p = -\alpha$, can be calculated on the basis of inviscid theory (free streamline theory).

It is convenient to express C_D^* as:

$$C_D^* = C_f^* (1 + F) \quad (6)$$

where the friction drag:

$$C_f^* = \left[\int_{\text{pseudobody}} C_s \cdot q_c^2 \cdot n_y ds \right] / \frac{1}{2} \rho q_\infty^2 h \quad (7)$$

and where the form drag factor, F , is:

$$F = \frac{\int p \cdot n_x ds}{\int C_s \cdot q_c^2 \cdot n_y ds} \quad (8)$$

where both integrals are taken around the pseudobody.

In view of (1) and (6), the form drag may be calculated from (5):

$$1 + F = \frac{\tilde{q}(C') \cdot q_\infty^2 / 2}{\int_0^{s(i)} C_s \cdot q_c^2 \cdot n_y ds} \quad (9)$$

In the case of a slender cavity at high Reynolds numbers, where to a good approximation $C_s = \text{const.}$ and $q_s = q_c$ for $0 < s < i$; $C_s = 0$ for $i < s$; $n_y \approx 1$; and in the decelerating zone we set $H = H_i$, constant; and recalling that $(q_c/q_\infty)^2 = 1 + \sigma$; then,

$$\tilde{q}(C') = 2(q_c/q_\infty)^{H_i+2} \int_0^{s(i)} C_s ds$$

$$\text{and, } 1 + F = (q_c/q_\infty)^{H_i} = (1 + \sigma)^{H_i/2} \quad (10)$$

This is, in itself, a valuable result, relating form factor to the body pressure coefficient (which depends in turn on its thickness), and on the shape parameter H_i at the stern.

Now, from the definition (7) it follows that $C_{i'}^* = 4 C_s (i/h) (q_c/q_\infty)^2$ and combining this with (10) in (6)

$$\frac{C_D}{4 C_s} = (i/h) (1 + \sigma)^{H_i/2} \quad (11)$$

This fundamental result is sufficient for the calculation of σ as a function of C_s for a given forebody, since C_D and i/h are functions of cavity pressure (σ) which can be calculated using inviscid theory.

This result may be further refined using cavity theory results. In the case of sufficiently long cavities, it has been found, Tulin [1], that,

$$i/h = k \frac{C_D}{\sigma^2} \quad (12)$$

where k depends on the cavity flow model:

a.) $k = 8/\pi$ (Closed cavity, Tulin [16])

b.) $k = \frac{8}{\pi} \left(\frac{1 + \sqrt{1 - \sigma/2}}{2} \right)^2$
Single Spiral Vortex with
Trailing Wake, (Tulin [1]).

c.) $k = \frac{\pi}{2}$ (Double Spiral
Vortex, Tulin [1])

For values of σ up to unity, the value of k given by b.) is less than a.) and greater than c.), while $k(c) = 0.6k(a)$. It is worth noting that relationship (12) can be extremely sensitive to the presence of bounding surfaces such as tunnel walls, but we will not discuss this complication here.

Combining (12) and (11) leads to the very simple result:

$$\frac{\sigma^2}{(H_i + 2)/2} = k C_s \quad (14)$$

This is plotted as Figure 7 using a value of $H_i = 3$.

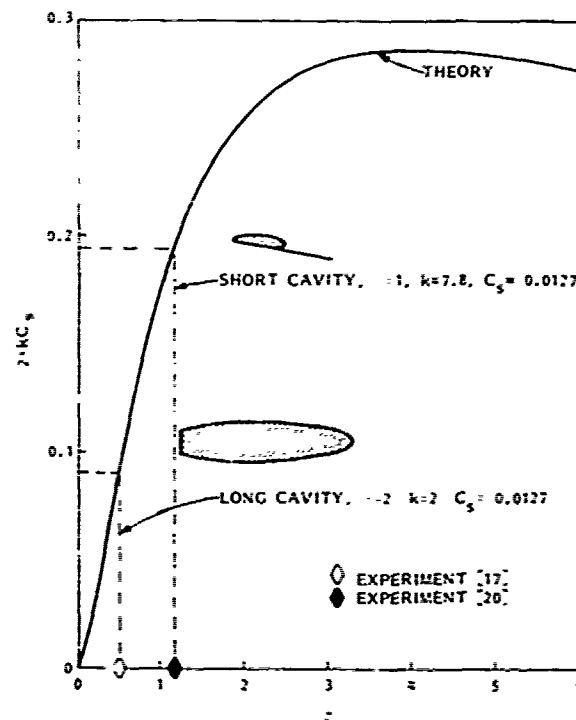


FIGURE 7 - $2kC_s$ AS FUNCTION OF σ

Experimental Comparison

There exists, Arie and Rouse [17], an excellent detailed experimental study of a stabilized cavity-wake behind a flat plate (some of the results are shown as Figure 4). In their wind tunnel simulation of the wake flow past a vertical plate (wall effects were corrected for by modifying the shape of the tunnel walls) they found: $\sigma = 0.57$; $C_D = 1.38$; $C_s^{**} = 1.27 \times 10^{-2}$; $(i/c) = 8.4$. In addition the boundary layer profile at the end of the cavity is approximately linear (i.e., $u(y)/u(\delta) \approx y/\delta$), corresponding to $H_i = 3.0$.

The calculation of length based on (11), and using the aforementioned experimental

* We have corrected Eq. (7) of Tulin [1] which contained a numerical error.

** The value of C_s is determined from Arie and Rouse, Figure 5c, but correcting a mistake in their nomenclature ($u'v'/q_\infty$ should be $u'v'/q_\infty^2$).

values of $C_{D,0}$, h_L , and C_s , yields $(l/c)_{\text{theo.}} = 8.8$, which is in reasonable agreement (5%) with the measured value (8.4).

The calculation of k from (12), using again the measured values of (l/h) , $C_{D,0}$, and C_s , yields a value of $k = 2$, which is in reasonable agreement with the value $k = 2.16$, given by (13b).

These favorable comparisons confirm the usefulness of (11) and (12) when applied to stabilized turbulent wakes behind bluff bodies.

In the case of laminar wakes (which are not practically important in ship hydrodynamics, but for which some past analyses exist), the analysis can be repeated, leading to:

$$\frac{C_D}{(l/c)^2 (1 + \epsilon)} (H_L + 2)^2 = 8 \epsilon_L \cdot R_c^{-1/2} \quad (15)$$

and combining with (12) leads to the following asymptotic results ($R_c \rightarrow \infty$):

$$\epsilon = \left(\frac{k}{R_c C_D} \right)^2 \cdot 8 \epsilon_L \quad (16)$$

and

$$l/c = \frac{R_c C_D^2}{(8 \epsilon_L)^2} \quad (17)$$

The latter asymptotic result, in its dependence on R_c and C_D , corresponds to the earlier results of others, obtained by other means, starting with Imai [15]. Recently F.T. Smith [19] has analyzed the viscous aspects of this problem, obtained similar results, and concluded that for bodies without fixed separation, the free streamline (inviscid solution) should have continuous curvature at separation, i.e., smooth separation; in this case, C_D can be calculated by application of cavity theory using the latter condition, even in the case of a smooth bluff body, as a circular cylinder.

Note that upon the assumption of laminar flow, the cavity-wake length increases with the Reynolds number without bound. The turbulent asymptotic behaviour ($R_c \rightarrow \infty$) of bluff body wakes is seen to depend on two questions: does the model of flow assumed here (negligible eddy velocity) remain valid as $R_c \rightarrow \infty$?; and, if so, what is the behaviour of C_s as $R_c \rightarrow \infty$. If the answer to the first of these questions is affirmative, then the asymptotic cavity length will be finite provided the asymptotic value of C_s is also finite.

Further application of the present ideas can readily be made, to the question of tunnel wall effect on wake pressure for example.

The Prediction of Turbulent Separation Bubbles at the Leading Edge of Thin Airfoils

Turbulent separation bubbles (so called

thin airfoil stall) exist at sufficiently high Reynolds number on thin foils with both sharp and rounded leading edges, for foil thicknesses less than about 9 percent, as shown experimentally by McCullough and Gault [20]. The ideas of the previous section can readily be combined with short cavity inviscid theory (which is discussed subsequently in this paper), to predict the pressure coefficient at separation, and to approximate the bubble length. McCullough and Gault have given detailed measurements of the separated flow over a sharp nosed, double-wedge foil of 4.23 percent thickness, see Figure 8, where one of the measurements are shown. For present purposes we shall assume this close enough to a sharp flat plate.

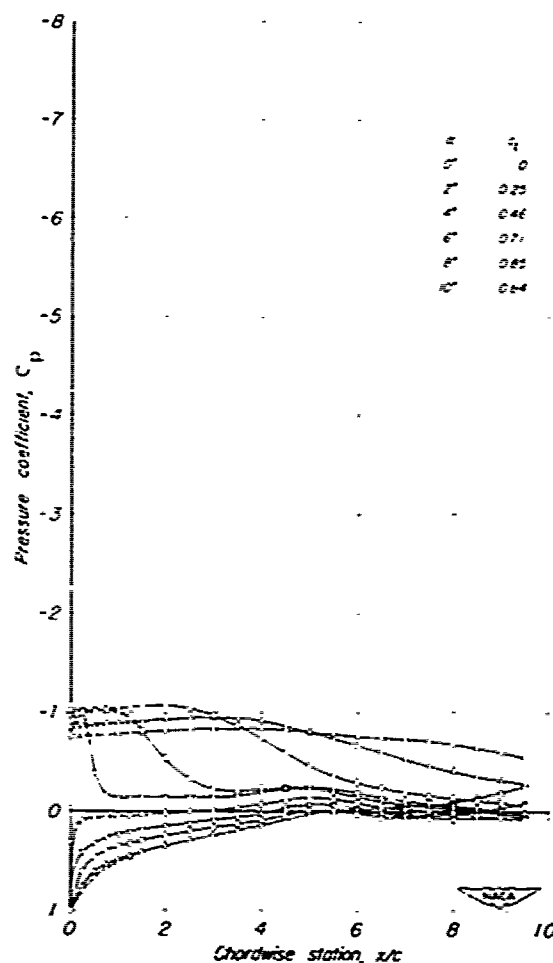


FIGURE 8 - PRESSURE DISTRIBUTION OVER THE 4.23-PERCENT-THICK DOUBLE-WEDGE AIRFOIL SECTION

FROM: McCULLOUGH AND GAULT [20]

The relation corresponding to (11) is, in view of the fact that the cavity is single sided:

$$\frac{C_D}{(\ell/c)[1 + \sigma]} (H_\ell + 2)/2 = 2 C_S \quad (i.)$$

The comparison of ℓ/c computed on the basis of (18) with experimental values is shown in the table below; the values of C_D were determined experimentally by integration of the pressures on the foil surface; the values of σ were determined from measurement of pressures at the boundary of the separation bubble and are slightly higher than measured on the foil surface; C_S is taken again as 1.27×10^{-2} as measured by Arie and Rouse and discussed earlier; $H_\ell = 3$; the experimental values of ℓ/c are determined from the measured pressure distributions on the foil surface and have been defined (somewhat arbitrarily) as the point where the magnitude of the pressure coefficient has dropped to 80 percent of the average pressure under the main part of the bubble, Figure 8.

TABLE 1 - COMPARISON OF MEASUREMENTS AND THEORY: LEADING EDGE BUBBLE

$\alpha(^{\circ})$	Double Wedge Measurements					Theory (Eq. (15))
	C_L	C_D	σ	$(\ell/c)\sigma^2/C_D$	$\ell/c(C_p = 0.8\bar{C}_p)$	ℓ/c
2	0.24	0.007	1.2	7.8	0.038	0.037
4	0.47	0.028	1.2	7.7	0.15	0.149
6	0.72	0.066	1.2	7.9	0.36	0.36

For this particular definition of $(\ell/c)_{\text{expt}}$ it is seen that the agreement is excellent over the entire range of incidence up to 6° . In addition we note that the following formulation is consistent with the measurements:

$$\ell/c = 7.8 \frac{C_D}{\sigma^2} \quad (19)$$

which compares with:

$$\ell/c = \frac{32}{\pi} \frac{C_D}{\sigma^2} \quad (20)$$

based on linearized theory, for a sharp edged plate. As we discuss later in this paper, cavity theory which takes into account the wake behind the cavity predicts reduced values of cavity length, improving the comparison between (19) and (20). We note that for foils with finite leading edge radius, theory predicts smaller C_D but larger and non-constant values of k than for the sharp nosed foil, with the difference disappearing at higher incidence (longer cavities).

As a result of the agreement shown between the prediction of the present

cavity-wake theory and experiments in the case of both trailing turbulent wakes (Arie and Rouse), and turbulent separation bubbles (McCullough and Gault), we conclude that this theory very well explains quantitatively important basic features of these separate flows, and deserves further study and application, especially to the problem of both steady and unsteady separation on lifting foils and wings. This new theory therefore gives additional meaning and importance to past and current cavity flow developments.

II. THE CHARACTERISTICS OF PARTIAL, LEADING EDGE, CAVITIES.

We consider first the case of steady flow about lifting foils, including the effects of foil thickness and of finite span. Afterwards, Section III, we consider non-steady effects, such as occur during operation of foils in gust or propeller blades in wakes.

Past Theory and Measurements; 1955-77.

Alan Acosta [21] first presented a

theoretical prediction of steady, leading edge, sheet cavities as a function of the cavitation parameter α/σ , Figure 9, where α is the incidence of the foil and σ the

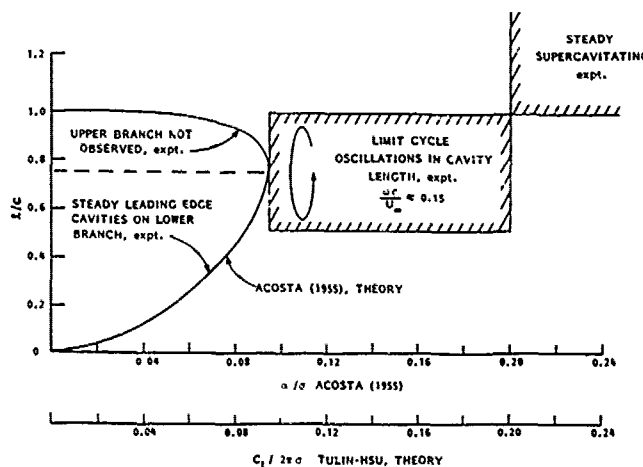


FIGURE 9 - BEHAVIOUR OF SHEET CAVITIES ON FIXED FLAT PLATE FOIL

cavitation number. Acosta's result referred specifically to a flat plate in steady motion and was obtained utilizing linear (slender body) theory. According to his prediction, two distinct steady leading edge cavities exist for all values of $\alpha/\sigma < 0.0962$ and none for larger values. Experiments on two-dimensional foils, Wade and Acosta [22], confirmed the existence of a rather stable short cavity for $\alpha/\sigma < 0.10$ and showed this to be the shorter of the two cavities predicted in theory. For values of $0.10 < \alpha/\sigma < 0.20$ these experiments found a strong tendency to a low frequency, $\omega c/U_\infty = 0.10 \rightarrow 0.20$, cavity oscillation with an amplitude of about a half chord. For larger values of α/σ a rather steady supercavitating flow ensued.

Acosta's results were found independently by Geurst and Timman [23] utilizing the same theoretical model. At about the same time, Meijer [24] reported on the results of experiments on several thin (4%) foils: one a double circular arc and the other a circular arc on the top and flat on the bottom (plano-convex). The experimental results for the cavity lengths on the double circular arc, together with those for a thin wedge tested by Parkin [25], showed good agreement with the theory of Acosta and Geurst-Timman. The results for the asymmetrical foil differed systematically, however, approaching the flat plate theory only at high angles of attack.

About ten years were to pass before the slender body theory of partial cavitation was extended to the case of a two-dimensional hydrofoil of arbitrary shape by Hanaoka [26]. In the meantime Geurst [27] gave theoretical results for thin cambered foils without thickness, and Wade [28] gave results for thin plano-convex foils and made comparisons with the experiments of Balhan [29], Meijer [24], and Wade-Acosta [22]. The first of these concerned foils 4% thick at angles between 2-6 degrees. The latter concerned a foil of 7% thickness at angles from 2-10 degrees. The correspondence between predicted and measured cavity lengths was not very good, and worsened at larger angles and for the thicker foil.

Hanaoka's theory is also based on conventional linearizing assumptions, but he relaxed the condition of cavity closure and introduced an arbitrary cavity thickness at termination. In this way he was able to obtain a theory bridging the gap between partial and supercavitating flow. Hanaoka found empirically that his theory when applied to the flat plate gave good agreement with thin symmetrical foils for short cavities when he assumed cavity closure. In that case his results correspond to Acosta, Geurst-Timman and his conclusions to those of Wade [28]. Again, assuming cavity closure, Hanaoka compared Meijer's data for the asymmetrical foil with theory and found rough agreement; that is, trends were reproduced but actual values of cavity length tended to be longer than predicted.

In addition to linearized theories, there exist several non-linear treatments of partially cavitating flows on flat plates: Wu [30], Kutznetsov and Terentev [31], and Terentev [32]. The first of these utilizes a wake model in which the wake is as thick as the cavity at its maximum. The second utilizes the re-entrant jet model, and the last a vertical flat plate termination of the cavity. The last two might be expected not to differ much and to give the closest agreement for cavity lengths with reality. A comparison is made later herein between results of the re-entrant jet model and the present theory. A further non-linear theory utilizing the re-entrant jet model dealt with the flow about a cavitating wedge at incidence, but was not utilized for the prediction of cavity length, Cox and Clayden [33].

Finally it should be mentioned that partial cavitation on cascade of foils becomes important in connection with cavitating inducer pumps, and the conventional linearized theory has been applied to the case of partially cavitating cascades by Wade [34] for flat plates and by Hsu [35] for cambered plates.

The Theory of Tulin-Hsu [36]; Perturbation on the Fully Wetted Flow.

The status described above seemed to leave room for further theoretical developments, since experimental comparisons were not really satisfying except for a flat plate, and since finite span effects had not been adequately studied, despite some beginnings by Hanaoka [37] and Ukon, Tamiya, and Kato [38]. Further, there seemed reason to believe that the predictions of conventional linearized theory can be wrong and misleading with regard to the effect of foil thickness in the case of foils with finite leading edge radii. The reason for this is that the effect of the leading edge radius in reducing the peak pressures at the nose have an important influence on cavity length, but are not taken into account in slender body theory.

The theory of Tulin and Hsu [36] is based on a perturbation on the fully wetted flow which assumes that the cavity is short in extent compared with the chord and span of the foil, so that the cavity causes only a small perturbation to the non-cavitating flow about the given foil (or propeller blade). Starting as it does with the fully wetted flow assumed known, this theory differs markedly from the usual linearized (slender body) theory which perturbs on the uniform free stream flow, and would seem to offer the following advantages: i) it can be applied to thick as well as slender bodies; ii) it deals accurately with the effect of leading edge radius where slender body theory does not; iii) in a further approximation, it can be applied as a two-dimensional perturbation to a known three-dimensional flow. The latter possibility

arises because the span of the cavity is likely to be much larger than the cavity length, even though the foil may not itself possess a high aspect ratio. Given means to calculate fully wetted flows on finite aspect ratio lifting surfaces, the present theory allows predictions to be made about the properties of their leading edge cavities; the method can also be applied to propellers. In consequence of the T-H theory, the result of Acosta, Figure 9, can immediately be interpreted to apply to foils where the circulation is reduced over two-dimensional values on account of three dimensional (finite span) effects; this is accomplished simply for flat plate foils by replacing α in Figure 9 by $C_L/2\pi$, see the lower scale.

The method of T-H depends on the definition of the complex velocity ($\Psi' = u - iv$) as the product of two analytic functions:

$$\Psi' = \Psi_0' \cdot \Psi_1' \quad (21)$$

where $\Psi_0' = q_0 e^{-i\theta_0}$ is by definition the complex velocity of the flow about the body in the absence of cavitation, and $\Psi_1' = q_1 e^{-i\theta_1}$ represents the effect of cavitation. In the case of a short cavity, $\Psi_1' = O(1 + \epsilon)$ where ϵ increases with the cavity volume. The theory assumes $\epsilon \ll 1$; it is asymptotic to the limit of short cavities. The flows in the physical and complex potential plane ($\Psi = \phi + i\psi$) are shown in Figure 10. The problem as posed, utilizes Tulin's single spiral vortex model for cavity termination.

For the solution, it is useful to define the function $\omega = \ln \Psi' = \ln q - i\theta$. It follows from (21) that:

$$\omega = \omega_0 + \omega_1 = \ln(q_0 q_1) - i(\theta_0 + \theta_1) \quad (22)$$

We may assume that the fully wetted flow has been found, so that ω_0 is given. The problem is then reduced to that of finding ω_1 with the boundary conditions:

$$\text{Re}(\omega_1) = \ln q_1 = \ln q_c / q_0 \quad \phi_B < \phi < \phi_D \quad (23)$$

where $q_c = (1 + \sigma)^{1/2}$. Except in the vicinity of points of small radius of curvature on the body, it may also readily be shown that:

$$\theta(\Psi) = \theta(\Psi_0) + O(\epsilon) \quad (24)$$

or, to first order:

$$\text{Im}(\omega_1) = \theta_1 = 0 \quad \begin{cases} \phi_A < \phi < \phi_B; \psi = 0^+ \\ \phi_D < \phi < \phi_E; \psi = 0^+ \\ \phi_A < \phi < \phi_E; \psi = 0^- \end{cases} \quad (25)$$

The conditions at infinity are:

$$\begin{aligned} \text{Re}(\omega_1) &= 0 \\ \text{Im}(\omega_1) &= 0 \end{aligned} \quad (26)$$

The cavity closure condition is:

$$\begin{aligned} \text{Im} \oint \omega_1 d\Psi &= f \\ f &= \frac{\text{Cavity Drag}}{\rho q_\infty^2} \end{aligned} \quad (27)$$

where we shall subsequently show in Section III that in unsteady flow the same closure condition applies except that f becomes modified to account for the rate of change in cavity volume.

We are particularly interested in applying the theory to the calculation of short cavities on thin bodies like foils. In such cases, the theory may be simplified by taking advantage of appropriate approximations, which must be carefully applied.

The leading edge on foils used in practice, even though rounded, are of such sharp curvature that a leading edge cavity may be assumed to start immediately at the edge. At the same time, when leading edge cavitation does occur, the distance between the edge and the stagnation point is zero to second order in the angle of attack. Tulin [39], so that we take the points A and B as coincident to second order, i.e., $b \equiv 0$. In addition, we may then show that (24) applies in the vicinity of the leading edge stagnation point, too.

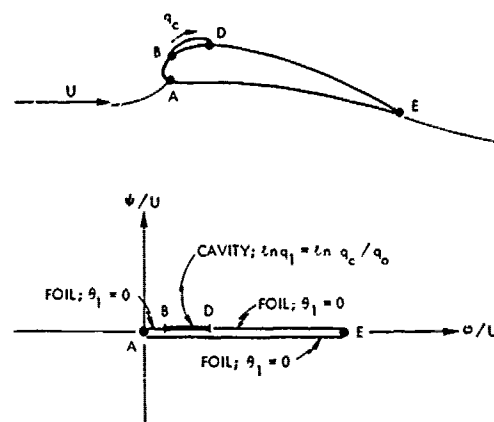


FIGURE 10 - SCHEMATICS OF SHORT CAVITY FLOW AND BOUNDARY VALUE PROBLEMS

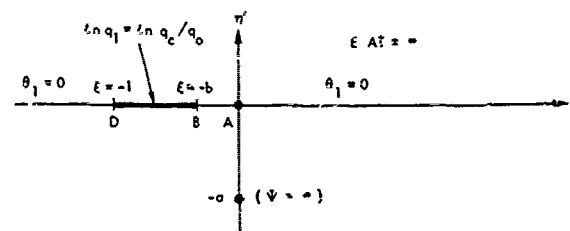


FIGURE 11 - BOUNDARY VALUE PROBLEMS IN TRANSFORMED ζ -PLAN

Then the appropriate solution of the mixed boundary value problem in the transformed half plane, Figure 11:

$$\zeta = -i\alpha \sqrt{\frac{\psi/\phi_E}{\psi/\phi_E - 1}} = \xi + i\eta' \quad (28)$$

is given by:

$$\omega_1(\zeta) = -\frac{1}{\pi\sqrt{\zeta(1+\zeta)}} \left[\int_{-1}^0 \frac{[\frac{1}{2}\ln(1+\sigma) - \ln q_0(t)]}{(T-\zeta)} \sqrt{T(1-T)} dT - i\pi(M\zeta+N) \right] \quad (29)$$

where the constants M , N and σ are determined from the two conditions at infinity, (26), and the closure condition, (27). Note that ϕ_E is assumed specified, which is equivalent in fact to specifying the cavity length.

Appropriate relations for the lift, drag, cavity ordinates, and cavity volume may also be derived, but are not given here.

Note that in (29), the constant being determined, that the solution has been reduced to an integral which depends only upon the fully wetted velocity distribution $q_0(t)$ (i.e., the velocity in the absence of cavitation), over the region where the cavity exists and not otherwise upon the shape of the foil. We have therefore reduced the problem of determining the cavity flow to the problem of determining the velocity distribution on the body in the absence of cavitation! Of course, very powerful tested methods exist for the solution of the latter problem in both the two and three-dimensional case. This is a very different situation than that which arises in the conventional linearized (slender body) formulation, when a mixed boundary value problem arises and must be solved, involving both velocity conditions on the cavity, and shape conditions on the body.

Finally we note that the T-H theory contains within itself the conventional linearized theory, and it can be shown that the results of Acosta [21] for short cavities on a flat plate at incidence are recovered exactly from the theory by setting $q_0(t) = 1$.

Applications of the T-H Theory.

Flat Plate. We shall first show, using the flat plate as an example, that there are three non-linear effects which cause the cavity to be different than predicted by Acosta. These are effects additional to that caused by a different choice of the cavity model (for example, double spiral rather than single spiral). Recall that Acosta's theory is based upon Tulin's 1955 closure condition, which is

equivalent to the single spiral vortex with zero trailing wake thickness

These three non-linear effects are:

a.) purely geometrical, increasing with increasing incidence; b.) due to finite leading edge radius (plate thickness); c.) due to the trailing wake thickness, increasing with increasing drag. We shall show that a.) tends to increase the cavity length while b.) and c.) tend to shorten it.

The appropriate representation of $q_0(t)$ in the case of a flat plate of zero thickness is the exact theory result:

$$q_0(\phi) = 1 + \alpha \sqrt{\frac{1 - \phi/\phi_E}{\phi/\phi_E}} \quad (30)$$

Calculations have been made based on this representation of q_0 and are shown to be in good agreement with the "exact" non-linear calculations of Kutznetsov and Terentev [31] based on the re-entrant jet model, Figure 12, as well as with the results of Acosta for incidence less than about 2° . Note that the effect of the non-

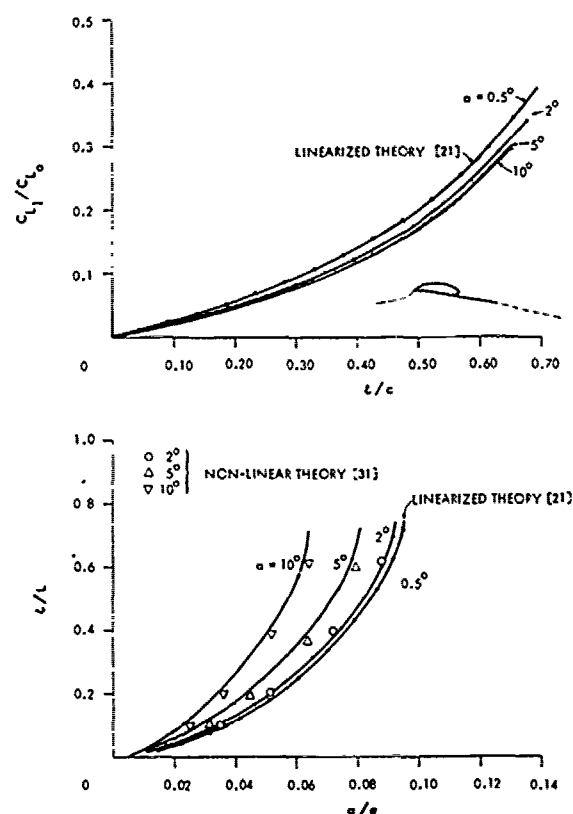


FIGURE 12 - FLAT PLATE FOIL CHARACTERISTICS WITH SHORT CAVITY $\tau/c = 0$; $AR = \infty$; $\alpha = 0.5 - 10.0^\circ$

linearity, a.) above, is to increase the cavity length. We also comment that this non-linearity may be approximately accounted

for by replacing α/σ with $\frac{\alpha}{\sigma}(1 + \pi\alpha)$ as the independent variable in the Acosta (slender body theory) result.

In order simply to represent the effect of leading edge radius, r_n/c , we consider a flat plate with thickness, $2r_n$, with a semi-circular leading edge of radius r_n . In order to represent the interaction between thickness and incidence we correct the velocity distribution using the rule of Lighthill [40]. Then:

$$q_o(\phi) = 1 + \alpha \sqrt{\frac{1 - \phi/\phi_E}{\phi/\phi_E + r_n/2c}} \quad (31)$$

The effect of leading edge radius due to plate thickness has been calculated using this representation of $q_o(\phi)$. The results, Figure 13, show that leading edge

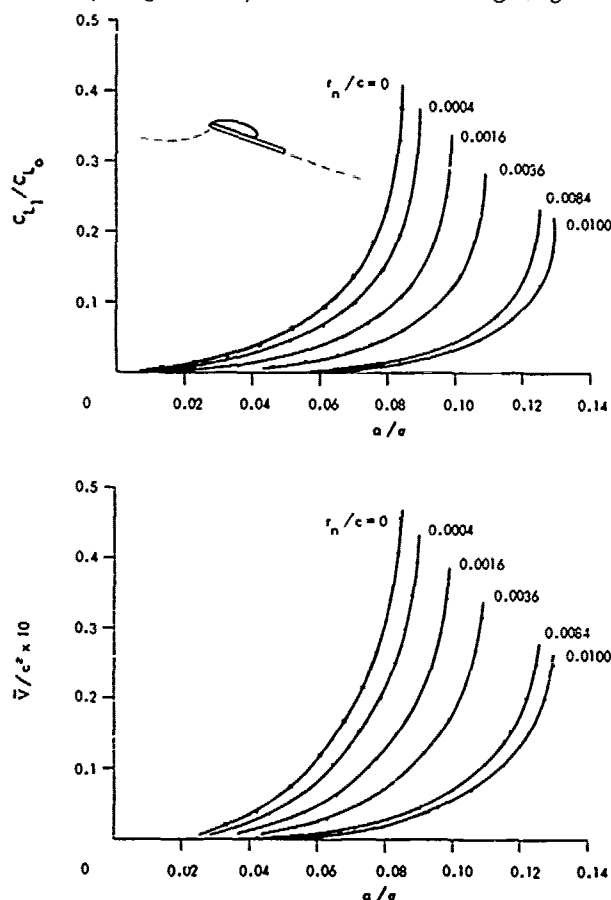


FIGURE 13 - FLAT PLATE WITH CONSTANT THICKNESS AND ROUNDED LEADING EDGE, CHARACTERISTICS WITH SHORT CAVITY $AR = \infty$; $r_n/c = 0 - 1\%$; $\alpha = 4^\circ$

radius very much ameliorates the effect of incidence, and is very important to take into account. It is, however, of opposite effect than the geometrical non-linearity a.), and the two effects can have a tendency to cancel each other.

In order to evaluate the non-linearity c.) above, we have calculated the drag coefficient, C_D , due to the leading edge cavity, Figure 14, the thickness of the trailing wake, $f/c = C_D/2$, and the subsequent effect

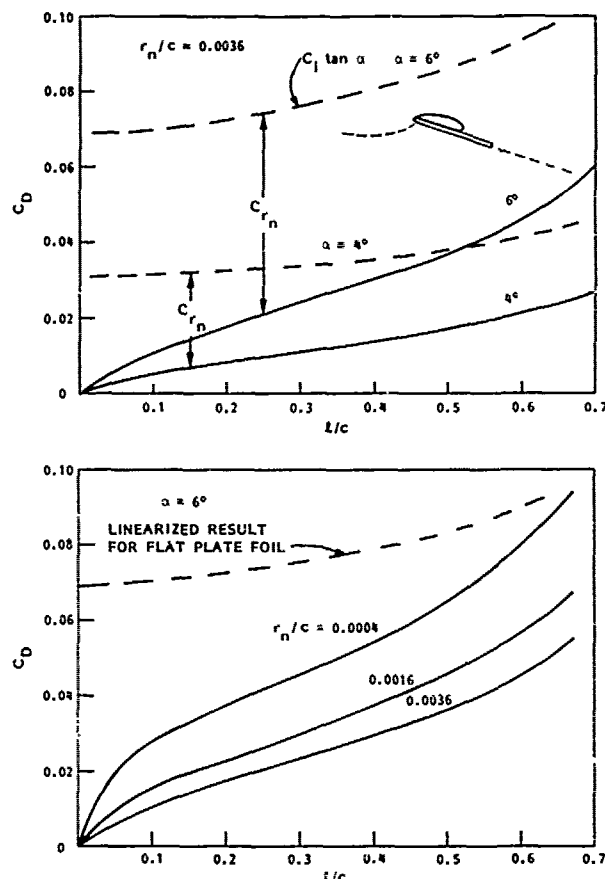


FIGURE 14 - CAVITY DRAG AS FUNCTION OF CAVITY LENGTH

on the cavity length, Figure 15.

For $r_n/c = 0$, and with cavity separation at the leading edge, it is necessary for the force on the plate to be normal to it, so that $C_D = C_L \tan \alpha$. In the case of finite leading edge radius, however, a finite thrust force, C_{r_n} will, however, exist at the leading edge (partial recovery of leading edge thrust) so that $C_D = C_L \tan \alpha - C_{r_n}$, or,

$$C_D = k_T \cdot C_L \tan \alpha \quad (32)$$

where $k_T = k_T(r_n/l; l/c) < 1$. The results of calculation, Figure 14, show how effectively the leading edge radius reduces the cavity drag, for cavities of equal length, the effect being more pronounced, the shorter the cavity.

The major cause of the cavity shortening due to increasing nose radius (as

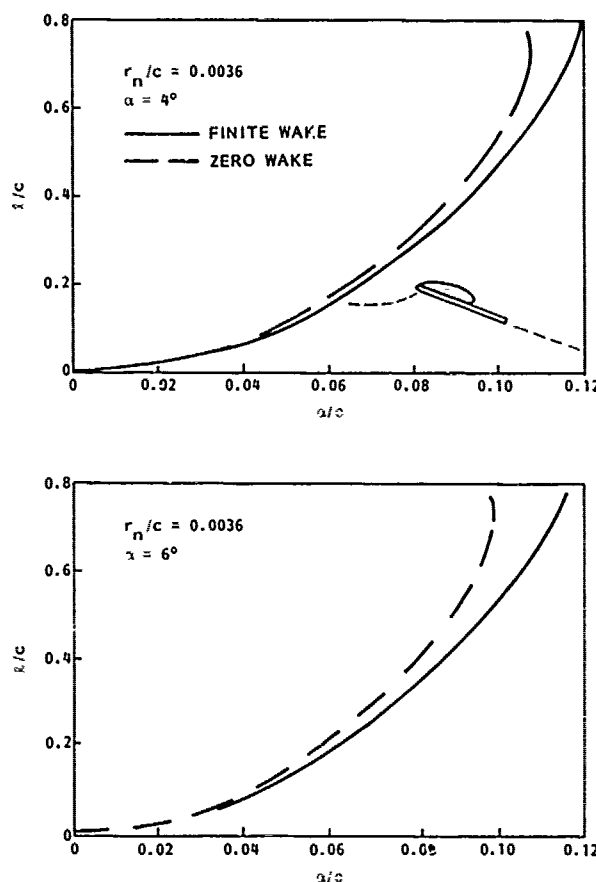


FIGURE 15 - EFFECT OF FINITE WAKE ON CAVITY LENGTH

already shown in Figure 13) is the drag reducing effect of nose radius. This can be understood from plots of l/c vs C_D/σ^2 , Figure 16, which show that k , i.e., $(l/c) \frac{\sigma^2}{C_D}$ is larger in the case of the flat plate with nose radius than in the sharp edge case, actually increasing with decrease in (l/c) . Incidentally, this Figure implies that in the case of thin airfoil stall treated in the preceding section, that the bubble pressure coefficient attains a larger negative value for shorter bubbles, approaching the sharp edged value as the bubble length approaches mid-chord. This effect was observed experimentally by McCullough and Gault [20] in the case of the NACA 64 A 006 airfoil.

Comparison of Two-Dimensional Applications with Experiment.

Does the single spiral vortex model applied to short cavities using the T-H

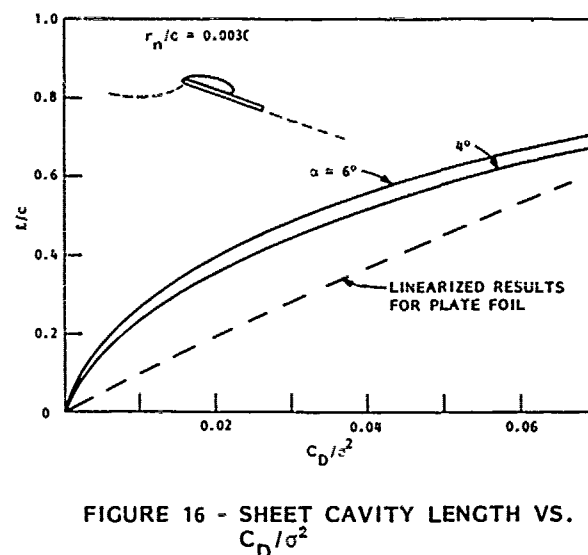


FIGURE 16 - SHEET CAVITY LENGTH VS. C_D/σ^2

theory yield good agreement with experiment? In Figures 17-20 we make some comparisons. The calculations are based on exact (inviscid) theory for $q_0(\phi)$ but with the circulation adjusted (reduced) in accord with the measured values of lift (no cavitation); the effect of trailing wake was taken into account and was important. The foils for which systematic experimental observations were available are: a 4 percent biconvex [Meijer, 24]; plano-convex of thickness 4 percent [Meijer, 24]; 6 percent [Uhlman and Jiang, 41]; 7 percent [Wade and Acosta, 22]. The agreement is in general very good up to angles of $4-6^\circ$, with an increasing tendency for theory to overpredict cavity length as the incidence increases. Notice that as the thickness of the biconvex foil increases, the cavity length both measured and predicted is reduced.

The theoretical overprediction at the higher incidences is likely due to viscous stall effects on the foil, as in the case of Wade and Acosta the lift curve slope decreases when the comparison begins to fail. In fact, it must be recognized that if a separation bubble can exist at $\sigma(\text{sep}) < \sigma(\text{cavitation})$, then cavitation will be inhibited. We have seen that for sharp nosed thin foils $\sigma(\text{sep}) \approx 1.0$. The incidence corresponding to cavitation inhibition will therefore be in

this case approximately equal to $\frac{\alpha}{\sigma}$. Therefore for $\frac{\alpha}{\sigma} > 0.10$, cavitation will be inhibited for angles above about 6° and be replaced by thin airfoil stall, giving rise to more complex flow patterns than dealt with by this theory.

For the future it would be desirable to understand the high incidence behaviour better as well as to make comparisons with experimental data on foils with rounded leading edges.

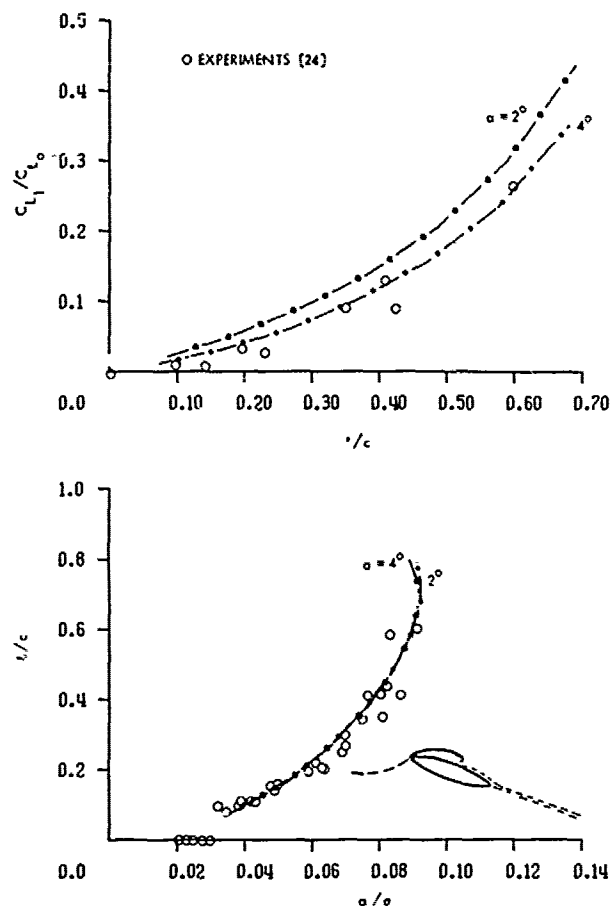


FIGURE 17 - COMPARISON WITH EXPERIMENTAL DATA OF MEIJER FOR 4% BICONVEX FOIL

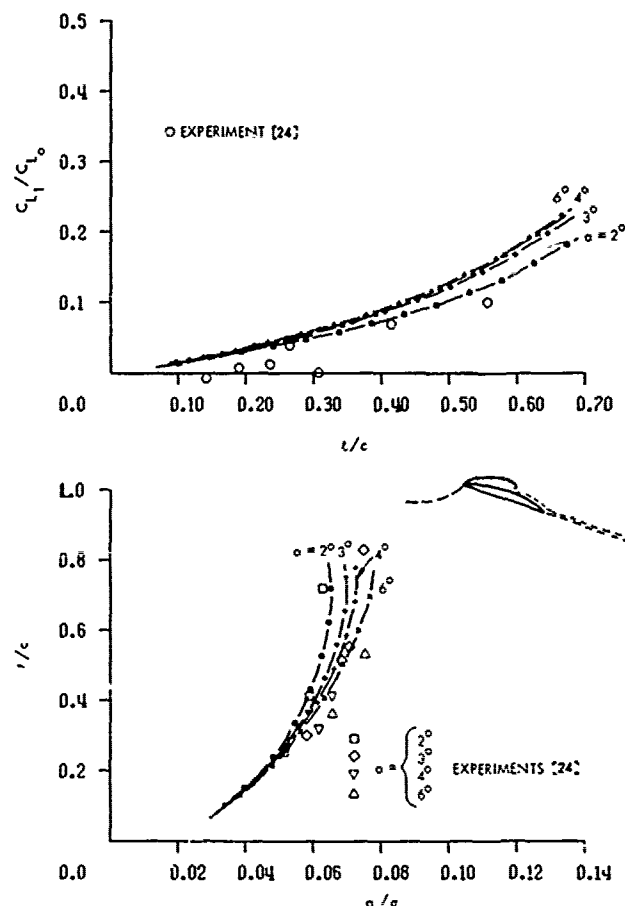


FIGURE 18 - COMPARISON WITH EXPERIMENTAL DATA OF MEIJER FOR 4% PLANO-CONVEX FOIL

Three Dimensional Effects.

This is the case of prime practical interest. Unfortunately, however, the calculation of cavities on three-dimensional lifting surfaces such as foils and propellers is considerably more difficult than in the planar case, because of the influence of the entire surface on the local cavity shape and length. Indeed, the rigorous application of conventional linearized (slender body) theory to the three-dimensional case has not yet been successfully demonstrated, to our knowledge.

Here we take the point of view that the problem may be solved approximately by calculation of the fully wetted three-dimensional flow as rigorously as possible, $\phi_{o,3D}$.

(x,y,z) and adding to it at each spanwise section a two dimensional perturbation, $\phi_1(x,y,z)$ representing the effect of 2D cavitation. In calculating $\phi_{1,2D}$ we utilize (29) with $q_o(t) = q_{o,3D}(t)$. Two factors must

conspire to validate this approximation:

i.) that the cavity is short in comparison to its own span, and

ii.) that the fully wetted flow does not vary too rapidly in the span-wise direction. We would, therefore, not expect this approximation to apply in the tip region of the foil or blade.

We have tested this approximation by calculating the cavity lengths at the center of rectangular wings of aspect ratio 2 and 4 (6° wedge profile) and comparing with measurements of Kermee [42]. We did not calculate $q_{o,3D}$ by lifting surface methods,

but instead used the aspect ratio correction of R.T. Jones [43] in order to estimate $q_{o,3D}$ from $q_{o,2D}$, which was calculated from exact inviscid theory. The Jones correction for the surface velocity due to incidence yields:

$$q_{o,3D} = 1 + \frac{1}{E_j} q_{o,\tau,2D} + \frac{AR}{E_j AR+2} q_{o,\alpha,2D} \quad (33)$$

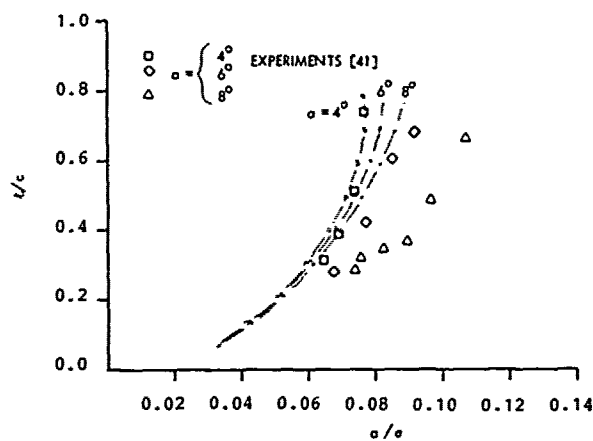
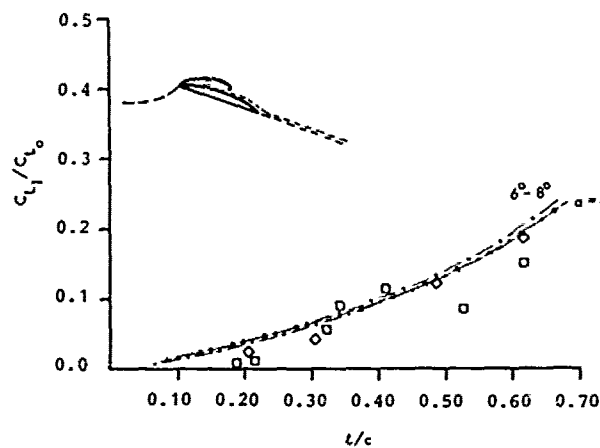


FIGURE 19 - COMPARISON WITH EXPERIMENTAL DATA OF UHLMAN AND JIANG FOR 6% PLANO-CONVEX FOIL

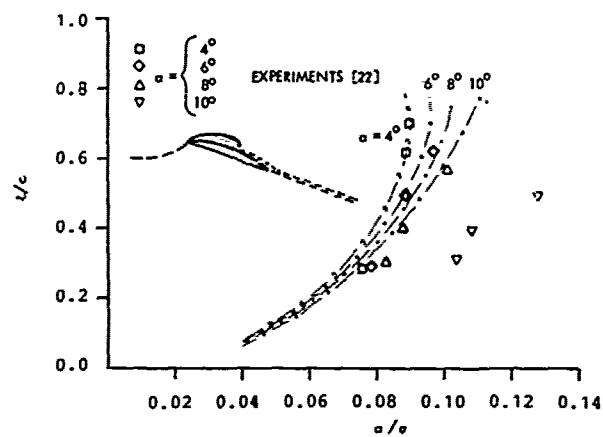
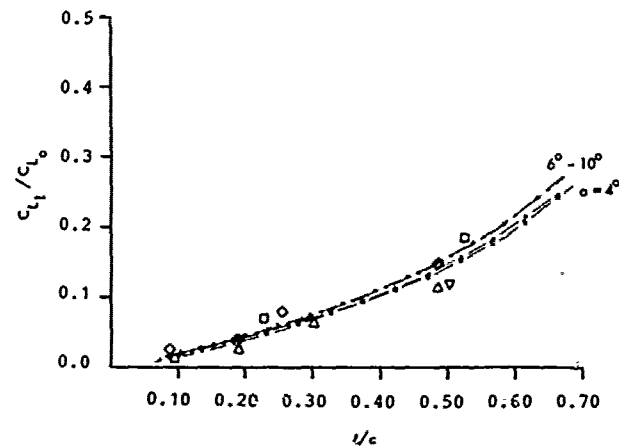


FIGURE 20 - COMPARISON WITH EXPERIMENTAL DATA OF ACOSTA AND WADE FOR 7% PLANO-CONVEX FOIL

The effect of trailing wake was taken into account.

The comparison between the theoretical predictions and experiments are shown in Figure 21, and is, in general, reasonably good, even though the angles of attack are quite large and the aspect ratios quite small (the data show considerable scatter). This comparison gives reason to believe that the present theory can be applied to three-dimensional flows of practical interest, including propeller blades.

III. UNSTEADY SHEET CAVITATION

In engineering practice cavities of all Types (A, B, and C) exist in an unsteady state, often cyclic in nature. Examples are: leading edge cavitation (Type B) on propellers operating in wakes or on inclined shafts, semi-submerged (Type C); supercavitating propellers, intermittent thin airfoil stall (Type A) on helicopter and turbine blades.

The problem of intermittent cavitation on marine propellers operating in ship wakes is especially severe, as it often results in severe noise and vibration, and occasionally in structural failure of nearby plating.

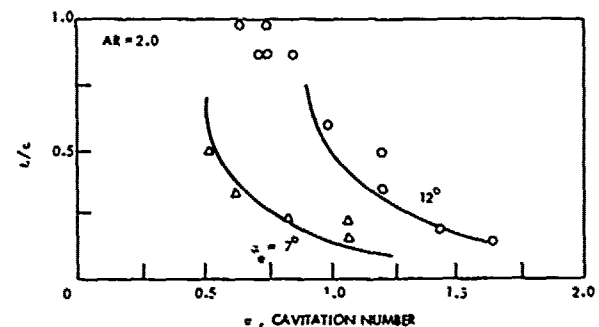
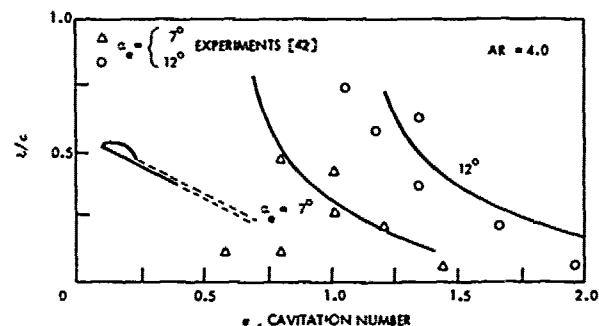


FIGURE 21 - COMPARISON WITH EXPERIMENTAL DATA OF KERMEEN FOR RECTANGULAR FLAT PLATE WINGS

The behaviour of non-steady cavities on foils is complex: several different types of cavitation have been observed to exist in both steady and unsteady flows over foils, including propeller sections. The present work is devoted to further understanding of non-steady sheet cavities, and especially cavities on thin foils with leading edge detachment.

The Formulation of the Unsteady Problem (Sheet Cavitation)

Here we review a more detailed derivation presented by Tulin [44], ATTC. Euler's equation, which applies at each point in the flow, can readily be written in the form:

$$\nabla \left(\frac{\partial \phi}{\partial t} + q^2/2 + p/\rho \right) = 0 \quad (34)$$

In its linearized form, on the cavity (which lies in the x-z plane):

$$(q_\infty \frac{\partial}{\partial x} + \frac{\partial}{\partial t}) \phi_x = 0 \quad (35)$$

so that ϕ_x is preserved by particles flowing on the cavity. In fact, Tulin [44] has derived an exact expression for the change in particle velocity tangential to the cavity, u_s . He found:

$$\frac{Du_s}{Ds} = -V_\eta \cdot \frac{d\theta}{ds} \quad (36)$$

where $ds/d\theta$ is the radius of curvature of the cavity at any point, and V_η its velocity normal to itself (for a steady cavity, $V_\eta \equiv 0$). The change in the speed, u_s/q_∞ of a particle travelling on the cavity is thus $O(\frac{\omega \delta}{q_\infty})$, which is of small order. Tulin [44]

thus concluded that the tangential particle speed on the cavity is equal to its value at the leading edge, except in the immediate vicinity of the trailing edge (this region is eventually ignored in the boundary value problem).

At the leading edge:

$$\frac{q^2(o,t)}{u_\infty^2} = \frac{u_s^2(o,t) + V_\eta^2(o,t)}{q_\infty^2} = 1 + \sigma - \tau \quad (37)$$

$$\text{where } \sigma(t) = \frac{p_\infty - p_c(t)}{\rho q_\infty^2/2} \quad (38)$$

$$\tau(t) = \frac{\phi_t(o,t) - \phi_t(\infty,t)}{q_\infty^2/2} \quad (39)$$

We have allowed for the pressure on the cavity to vary with time, as it might in the case of Types A and C, although in the case of a vapor filled cavity, $p_c = p_v$ (const). We call $\tau(t)$ the acceleration

number.

We assume, as usual, that at the point of cavity detachment the separation of the cavity is smooth. Then (37) can be written:

$$\frac{u_s(o,t)}{q_\infty} = \left[1 + \sigma - \tau - \left(\frac{V_\eta(o)}{q_\infty} \right)^2 \right]^{\frac{1}{2}} \quad (40)$$

The difficulty in evaluating (40) lies in the determination of τ , which Tulin undertakes from Green's formula applied to the entire surface on which the cavity lies. We omit the details but Tulin [44] finally finds that in the case of thin wings:

$$\tau(o,t) = \frac{\phi_t(o,t)}{q_\infty^2/2} = 0 \left[\left(\frac{\delta_c'}{l} \right) \left(\frac{\omega l}{q_\infty} \right) \right] 1 + \left(\frac{\omega c}{q_\infty} \right) \left(\frac{l}{c} \right) \left[\ln(l/c) + \ln(c/B) \right] \quad (41)$$

As a result,

$\tau(o,t) \ll 1$ if $(\frac{\omega c}{q_\infty}) \ln(B/c) = O(1)$ and $(\frac{\omega \delta_c'}{q_\infty}) \ll 1$ which includes cases of marine interest.

The subsequent discussion reproduces Tulin [44].

The Streak Diagram.

The trajectory of a particle travelling on a cavity can be displayed in a diagram representing s , the distance traveled by the particle since leaving a specific point on the leading edge vs. the time, t_0 . Note that in Figure 22a the streak diagram refers to only one particular origin on the leading edge; for the sake of generality we have shown a case where the cavity detachment point moves relative to the leading edge. In the case of a thin foil and where the flow may be assumed planar, the streak diagram takes the form shown as Figure 22b.

The slope of the streak line is given

$$\text{by: } \frac{ds}{dt} = u_s.$$

On the cavity, the variation in the slope is given by (36). The initial slope is given by (40) and a value of $\tau(o,t)$ determined from (41). As a result:

$$u_s = u_c = q_\infty \sqrt{1 + \sigma} \quad (42)$$

excluding terms of $O[(\frac{\omega l}{q_\infty})(\frac{\delta_c'}{l})]$; it has been assumed that,

$$\left(\frac{\omega c}{q_\infty} \right) \ln(B/c) = O(1) \quad (43)$$

as is usually the case for ship propellers

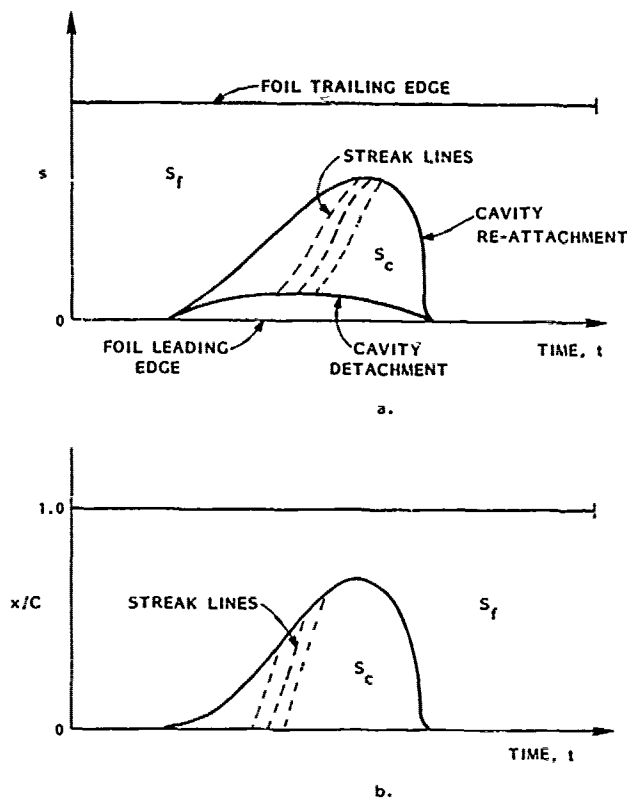


FIGURE 22 - STREAK LINE DIAGRAM
a. GENERAL
b. PLANAR, THIN FOIL

operating in wakes.

This very important result, (42), provides the basis for an essentially simple unsteady theory asymptotic to the frequency limits:

$$\frac{\tilde{\omega} \delta_c}{q_\infty} \ll 1 \quad ; \quad \frac{\tilde{\omega} c}{q_\infty} = 0(1) \quad (44)$$

In fact, the second of these conditions (moderate reduced frequency) implies the former in the usual case of thin cavities.

In the usual case of cavitating flows, $\sigma = \text{const.}$, and (42) implies everywhere parallel streak lines, as shown in Figure 23, and a boundary value problem, excluding the closure condition, identical to the steady flow case where (42) also applies. As we shall see in the subsequent section, the closure condition will be effected by the unsteadiness to the order of our approximation.

The streak diagram immediately allows the prediction of two pathological phenomena in the flow: 1.) cavity "ploughing," and 2.) cavity "breaking" or shocks." The former of these can arise during the expansion of a sheet cavity when the expansion rate is excessive ($\ell_t > u_c$), as in the region between b and c in Figure 23a. There, the cavity is overcoming fluid which has pre-

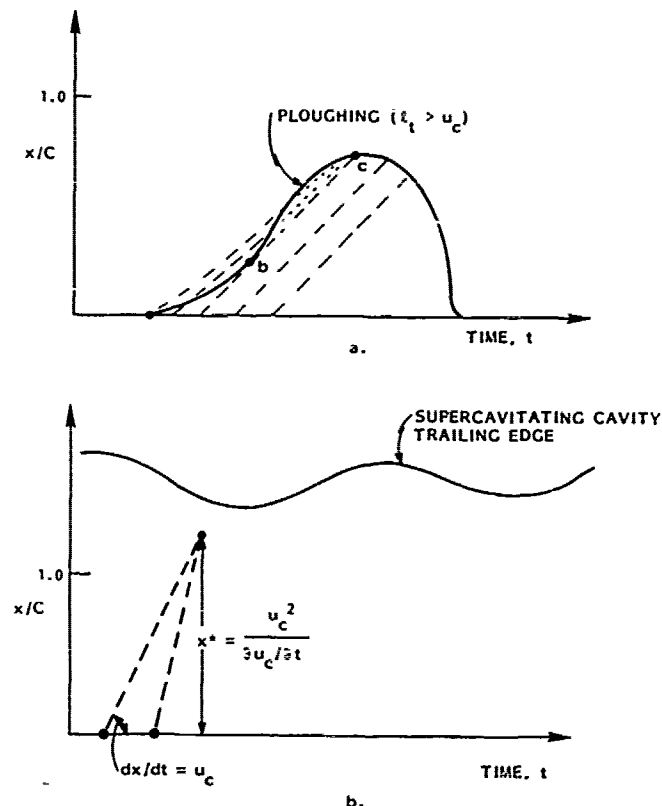


FIGURE 23 - PATHOLOGICAL CAVITY CONDITIONS
a. "PLOUGHING"
b. "BREAKING"

viously flowed over the foil, a condition likely to be very disruptive of the cavity.

Cavity "breaking" can occur only when the slope of the streak lines varies from line to line, as would occur when $\sigma = \sigma(t)$, as in a ventilated flow undergoing pulsations. In this case the streak lines have the possibility to intersect. The condition for this intersection can be shown to be, see Figure 23b:

$$x^* = \frac{u_s^2(o, t)}{\partial u_s / \partial t(o, t)} \quad (45)$$

The intersection of streak lines implies very sharp gradients in u_s or, according to (36), growing kinks in the flow, somehow reminiscent of wave breaking.

Cavity Growth and the Closure Condition.

The rate of change of cavity volume is (the body shape is assumed not to change):

$$\frac{\partial \bar{V}}{\partial t} = \iint \frac{\partial \phi}{\partial \eta} d(S_c - S_f) \quad (46)$$

Using the definition of ϕ and since the body itself is closed, i.e.,

$$\iint \frac{\partial \phi_0}{\partial \eta} d(S_f + S_f^*) = 0 \quad \text{and} \quad \frac{\partial \phi}{\partial \eta} \Big|_{f,f} = 0.$$

$$\frac{\partial \bar{v}}{\partial t} = \iint \frac{\partial \phi_1}{\partial \eta} d(S_c) = M_\infty(t) \quad (47)$$

Since the flow exterior to the body is divergence free, the integral in (47) may be taken around any contour and represents the source strength at infinity, $M_\infty(t)$.

This result, (47), represents the closure condition in nonsteady flow.

The cavity shape itself can be calculated from the relationship:

$$(y_c - y_f) \Big|_{s,t} = \int_{t_0}^{t(s)} \frac{d(y_c - y_f)}{dt} dt \quad (48)$$

where the integrand follows the particle (which is located at s at time t) starting from detachment (t_0). This integration in retarded time is not easy to carry out analytically except in the case of slow changes in cavity shape. We shall not consider such expansions here. Rather we shall consider qualitatively the effect of the cavity dynamics on its shape.

During growth, the forebody thickness of the cavity is determined by sources created at an earlier (retarded) time, when the cavity length was reduced; therefore, a growing cavity can be expected to be thinner and have smaller volume than its steady state counterpart (same length). On the other hand, for a collapsing cavity, the opposite is true. Furthermore the maximum thickness of a collapsing cavity can be expected to occur further to its rear than for its steady counterpart. These effects are illustrated schematically in Figure 24.

The Flat Plate Solution and Implication

$$\left(\frac{\omega c}{q_\infty} = 0(1) \right).$$

In this case, the usual boundary value problem ($u_c = q_\infty \sqrt{1 + \sigma}$ on the cavity) is supplemented by the non-steady closure condition (47). The steady solution given by Acosta (1955) is readily extended to the non-steady case, leading to the following implicit expression for the cavity length; see Figure 25:

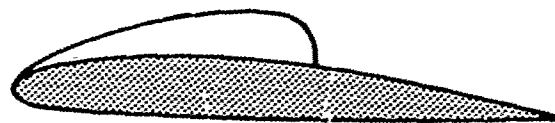
$$\frac{C_L}{2\pi\sigma} = \left(\frac{1}{\sqrt{L/c} (1 + \sqrt{1 - L/c})} \right) \times \left[\frac{\sqrt{1 - L/c} (1 - \sqrt{1 - L/c})}{2} + \frac{\dot{\bar{v}}}{\pi q_\infty c \sigma} \right] \quad (49)$$



GROWING, $\dot{\bar{v}} > 0$



STEADY



COLLAPSING, $\dot{\bar{v}} < 0$

FIGURE 24 - SHEET CAVITIES FOR SAME C_L/σ . (SCHEMATIC)

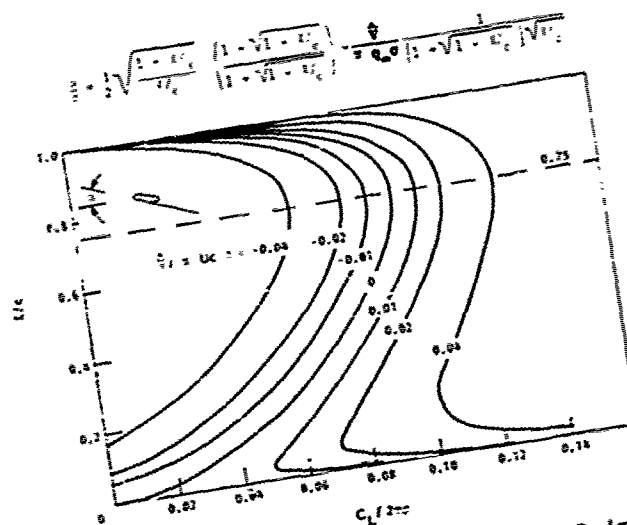


FIGURE 25 - SHEET CAVITY LENGTHS VS. C_L/σ : DYNAMIC CONDITION

For all collapsing cavities ($\dot{V} < 0$) there are, as in the steady case, two solutions for each value of $C_L/2\pi\sigma$ less than a critical value (one long and one short cavity) and no solutions for larger values.

In the case of growing cavities ($\dot{V} > 0$) there are either none, one (long), three (two short and one long), or one (short) solution. The situation is illustrated in Figure 26. During cyclic motion, solutions must generally be found in the regions ③ and ⑥ in the Figure 26.

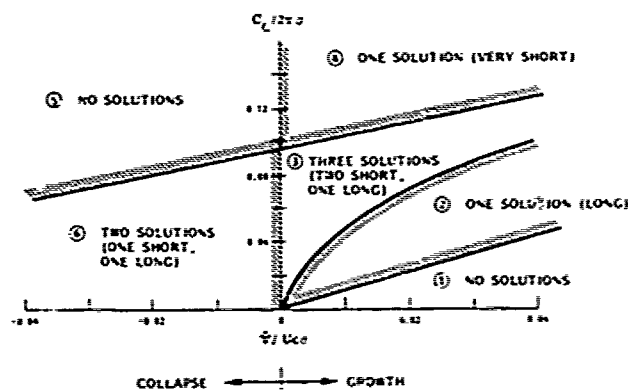


FIGURE 26 - THE SIX REGIONS FOR DYNAMIC CAVITIES

Stability of Acosta's Solution.

We note that any point on the upper branch (b-c) of the zero growth curve ($\dot{V} = 0$) will, if slightly disturbed, diverge; a point just above the curve will diverge to increasing values of l and a point just below will diverge to the lower branch (short cavities). These facts explain why only the short cavity branch of Acosta's solution are observed.

Limit Cycles at Large C_L .

For steady values of $C_L/2\pi\sigma$ larger than the critical value (0.0962), any length will diverge with changing growth rates. In practice, the growing cavity eventually tears off at the rear, and the shortened cavity resumes its growth in a limit cycle behaviour, see Wade and Acosta [22].

Hysteresis.

During cavity motions forced by cyclic changes in C_L , as occur when a propeller enters and leaves a wake peak or when a foil is oscillated as in Bark and Berlekorn [45] or Shen and Peterson [46], the cavity length will follow a similar trajectory in Figure 25. At extremely low frequencies, so that $\dot{V}/\pi q c \ll 0.01$ everywhere, the trajectory will lie very close to the steady state curve (l vs C_L). As the frequency of motion

increases, the hysteresis loop will become evident, see Figure 27. It arises since growing cavities must be shorter than a stable cavity, while collapsing cavities must be longer.

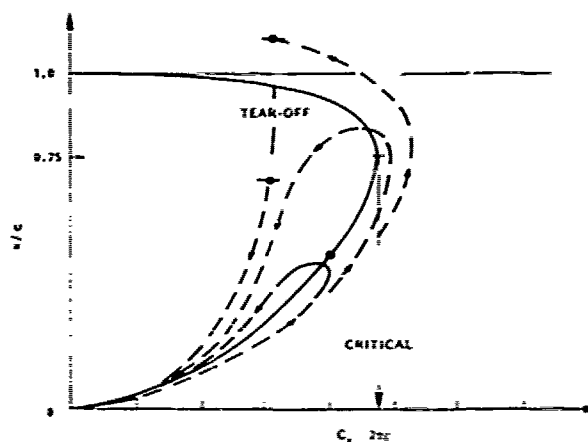


FIGURE 27 - CAVITY MOTIONS, HYSTERESIS (SCHEMATIC)

Note the following effects which accompany hysteresis: 1.) the maximum cavity length is reached after C_L has reached its maximum and begun to decline; note that collapse cannot occur until after $C_L/2\pi\sigma$ declines to a value < 0.0962 ; 2.) the maximum length would seem to be reduced with increasing frequency; 3.) the collapse rates seem inevitably higher than growth rates, and especially when values of C_L are reached beyond critical; 4.) when C_L exceeds its critical value, the possibility of divergence also exists as in the steady case, so that the cyclic motion can include a tearing off of the rear of the cavity followed by collapse of the remaining short piece.

The first of these effects is difficult to observe without knowledge of C_L . The remainder of these effects have been observed. For example, Figure 28 taken from Bark and Berlekorn [45] (illustrates 3. above), which is an especially important effect in view of the high pressures generated during rapid collapse.

Unsteady hydrodynamic effects on a fully wetted foil undergoing oscillations lead both to a lag between the lift generated and the angle of attack, and a reduction in the maximum C_L generated. The latter effect should generally result in shorter cavities with increasing frequency, a similar tendency as occurs due to cavity dynamic effects.

The accurate calculation of a trajectory curve in l vs C_L would require a continuous calculation of the cavity volume including unsteady effects for a given cyclic motion.

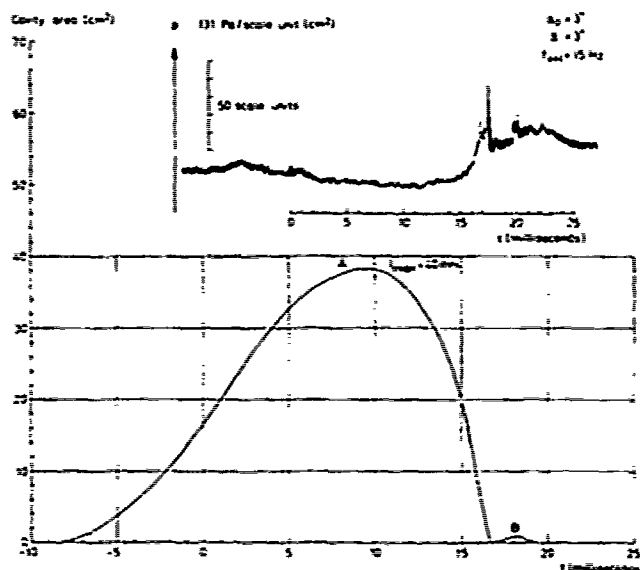


FIGURE 28 - CAVITY AREA AND GENERATED PRESSURE AS FUNCTIONS OF TIME OSCILLATION PERIOD 14 FROM: BARK AND BERLEKON [45]

Extension of the Theory.

To the unsteady approximation used in the calculation of the flat plate non-steady curve, the theory of Tulin and Hsu [36] can readily be applied to the calculation of dynamic cavities for foils in general unsteady motion.

The steps involved are. 1.) the calculation of the fully wetted velocity distribution including finite span and unsteady (including wake) effects: this can often be done utilizing lifting surface theory; 2.) the use of the T-H theory utilizing (42) and (44), in addition; 3.) the continuous calculation of the cavity shape and volume using retarded time. Note that there are three distinct unsteady effects which must, in theory, be taken into account here: a.) the effect of unsteadiness on the fully wetted velocity distribution; b.) the effect of the cavity closure condition, $\dot{V}_c(t) = \partial \bar{V} / \partial t$, on the solution of the T-H problem; and c.) the effect of retarded time on the cavity volume, for use in calculating $\dot{V}_c(t)$. We are

currently pursuing these kinds of calculations starting with the first of these effects a.) and b.) in the case of marine propellers operating on an inclined shaft, utilizing the non-steady fully wetted solutions provided by Kerwin [47].

SUMMARY

1. We have shown how cavity flow theory may be applied to wakes and separation bubbles (Type A cavities) as well as gas filled cavities (Types B and C). In particular we have applied the principle of

forebody-pseudobody drag equivalence, see Figure 6, and derived relatively simple relations between the wake pressure (c) and two parameters characterizing the viscous aspects of the flow, see Figure 7. These parameters are H_L , the boundary layer shape factor ($\delta^*/\bar{\delta}$) at the rear of the wake and, in the case of turbulent flow, the constant friction coefficient on the dividing streamline, C_s .

2. Comparison is made between measurements and theory in the case of a trailing wake behind a vertical flat plate and the leading edge separation bubble on a thin double-wedge airfoil, resulting in good agreement.

3. As part of the wake theory, a result is obtained which relates the form drag on a closed planar body with the pressure coefficient along its surface (and indirectly with the body thickness ratio), Eq. (10).

4. A physical model is proposed for the flow past gas filled cavities allowing for a post-cavity separation and deceleration zone, in which the forebody drag is realized in momentum loss in the external flow. This loss is brought about by friction on the dividing streamline behind the cavity, which separates the external flow and a closed separated region containing recirculating eddies, see Figure 5.

5. A recent new theory of Tulin and Hsu for the prediction of flows with attached leading edge cavities is reviewed. This theory is based on a perturbation on the fully wetted flow (without cavitation) and allows for account of leading edge roundness, which has an important influence on cavity length and volume.

6. Comparison is made between cavity length measurements and theory for planar biconvex and plano-convex foils with good agreement for angles of incidence up to 4-6°, beyond which viscous separation likely initiates.

The theory is extended to three-dimensional foils by considering the effect of leading edge cavitation and a two-dimensional perturbation to a three-dimensional flow. The three-dimensional effects are very important. A comparison is made between cavity length measurements and theory for rectangular wings of aspect ratio 2 and 4 with good agreement.

7. A very recent theory of Tulin is reviewed for unsteady sheet cavitation. The results show that typical unsteady leading edge cavities may be treated as steady when proper account is taken of the rate of change of cavity volume.

8. The notion of streak diagrams is introduced and used to predict the possibility of pathological cavity behaviours, including "ploughing" and cavity "breathing."

9. Tulin's unsteady theory is applied to the case of flat plate sections and predictions are made of cavity length depending on a cavity volume rate of change parameter. It is shown that growing cavities are reduced in length relative to steady cavities and collapsing cavities increased in length. This gives rise to a hysteresis-like behaviour of dynamic cavities, as observed in practice. The results of the theory also explain why only the shorter of the two cavities predicted in steady theory is observed (the larger is unstable).

REFERENCES

1. Tulin, M.P., "The Shape of Cavities in Supercavitating Flows," Proc. 11th Intern. Congress of Appl. Mech., 1964, pp. 1145-1155.
2. Tulin, M.P., "Supercavitating Flows and Practical Applications," Cavit. Real Fluids, Elsevier Publ. Co. (1964).
3. Riabouchinsky, D., "On Steady Fluid Motion With Free Surface," Proc. London Math. Society, Vol. 19, Ser. 2, 1920, pp. 206-215.
4. Efron, D., "Hydrodynamical Theory of Two-Dimensional Flow With Cavitation," Dokl. Akad. Nauk USSR, Vol. 51, 1946, pp. 267-270.
5. Kreisel, G., "Cavitation With Finite Cavitation Numbers," Gi. Brit. Admiralty Research Lab., Report No. P 1/H/36, 1946.
6. Gilbarg, D., and Rock, D., "On Two Theories of Plane Potential Flows With Finite Cavities," Naval Ord. Lab. Memo. 8718, 1946.
7. Tulin, M.P., "Steady Two-Dimensional Cavity Flows About Slender Bodies," DTNB Report No. 843, 1953.
8. Joukowski, N., "A Modification of Kirchhoff's Method of Determining Two-Dimensional Motions of a Fluid Given Constant Velocity Along an Unknown Streamline," Coll. Works 2, No. 3; Also Rec. Math. 25, 1896.
9. Koshko, A., "On the Wake and Drag of Bluff Bodies," Journal of Aero. Science, Vol. 22, No. 2, 1955, p. 124.
10. Eppler, R., "Beitrage zu Theorie und Anwendung der Unstetigen Stromungen," Journal Nat. Mech. Anal., Vol. 3, 1954, pp. 591-644.
11. Wu, T.Y., "A Wake Model for Free-Streamline Theory," Journal Fluid Mechanics, Vol. 13, Part 2, 1962.
12. Fabula, A., "Thin Airfoil Theory Applied to Hydrofoils with Single Cavity and Arbitrary Free Streamline Detachment," Fluid Mechanics, Vol. 12, Part 2, 1962.
13. Michel, J.M., "Wake of Developed Cavities," J. Ship Research, Vol. 21, No. 4, 1967, pp. 225-238.
14. Goldstein, S., Modern Development in Fluid Dynamics, Dover Publications, Inc., 1965.
15. Schubauer, G.B. and Klebanoff, P.S., "Investigation of Separation of Turbulent Boundary Layer," NACA TN 2133, 1950.
16. Tulin, M.P., "Supercavitating Flow Past Foils and Struts," Proc. NPL Symp.
17. Arie, M. and Rouse, H., "Experiments on Two-Dimensional Flow Over a Normal Wall," J. Fluid Mechanics, Vol. 1, Part 2, 1956.
18. Imai, I., "Discontinuous Potential Flow as the Limiting Form of the Viscous Flow for Vanishing Viscosity," Journal Phys. Soc., Japan, Vol. 8, 1953, p. 399.
19. Smith, F.T., "Laminar Flow of an Incompressible Past a Bluff Body: The Separation Reattachment, Eddy Properties and Drag," J. Fluid Mechanics, Vol. 92, Part 1, 1979.
20. McCullough, G.B., and Gault, D.E., "Examples of Three Representative Types of Airfoil-Section Stall at Low Speed," NACA TN 2502, 1951.
21. Acosta, A.J., "A Note on Partial Cavitation of Flat Plate Hydrofoils," Calif. Inst. Tech. Hydrodynamics Lab. Report No. E-19.9, 1955.
22. Wade, R.B. and Acosta, A.J., "Experimental Observation on the Flow Past a Plano-Convex Hydrofoil," Trans. ASME, J. Basic Engineering, Vol. 88, No. 1, 1966, pp. 273-283.
23. Geurst, J.A., and Timman, R., "Linearized Theory of Two-Dimensional Cavitation Flow Around a Wing Section," IX Inter. Congress of Applied Mechanics, 1956.
24. Weijer, M.C., "Some Experiments on Partially Cavitating Hydrofoils," Inter. Shipbuilding Progress, Vol. 6, No. 60, 1959.
25. Parkin, D.R., "Experiments on Circular Arc and Flat Plate Hydrofoils," J. Ship Research, Vol. 1, No. 4, 1958.
26. Hanaoka, T., "Linearized Theory of Cavity Flow Past a Hydrofoil of Arbitrary Shape," Ship Research Institute, Japan, 1967.
27. Geurst, J.A., "Linearized Theory for Partially Cavitating Hydrofoils," Inter. Shipbuilding Progress, Vol. 6, No. 60, 1959.
28. Wade, R.B., "Linearized Theory of a Partially Cavitating Plano-Convex Hydrofoil Including the Effects of Camber and Thickness," J. Ship Res., Vol. 11, No. 1, 1967, pp. 20-27.
29. Balhan, J., "Wetingsen aan Enige bi, Schaepechroener Gebruikelijke Profielen in Vloekke Stroming met en Zonder Cavitie," Ned. Scheepsbouwkundig Proefstation te Wageningen, 1951.
30. Wu, T.Y., "A Wake Model for Free-Streamline Flow Theory, Part 1, Fully and Partially Developed Wake Flows and Cavity Flows Past an Oblique Flat Plate," J. Fluid Mechanics, Vol. 13, Part 2, 1962, pp. 161-181.
31. Kutznetsov, A.V., and Terentev, A.C., "On Analysis of Partially Cavitating Flow Around Flat Plate," Izvestia Vysshikh Uchebnykh Zavedenii Matematika No. 11 (6C), 1967.
32. Terentev, A.C., "Partially Cavitating Flow Around Plate," Izvestia Vysshikh Uchebnykh Zavedenii Matematika No. 6.
33. Cox, A.D., and Clayden, W.A., "Cavitating Flow About A Wedge at Incidence," J. Fluid Mechanics, Vol. 3, Part 6, 1958.

34. Wade, R.B., "Flow Past a Partially Cavitating Cascade of Flat Plate Hydrofoils," Calif. Inst. Tech. Engineering Report No. E-79-4, 1963.

35. Hsu, C.C., "Flow Past a Cascade of Partially Cavitating Cambered Blade," HYDRO-NAUTICS, Incorporated Technical Report 703-G, 1969.

36. Tulin, M.P. and Hsu, C.C., "The Theory of Leading Edge Cavitation on Lifting Surfaces With Thickness," Proc. of Symp. Hydrodynamics of Ship and Offshore Propulsion Systems, 1977.

37. Hanaoka, T., "Three-Dimensional Theory of Partially Cavitating Hydrofoil," No. 123 J. Soc. Naval Arch. of Japan, 1969, pp. 22-30 in Japanese.

38. Ukon, Y., Tamiya, S. and Kato, H., "Pressure Distribution and Cavity Model on a Partially Cavitating Hydrofoil of Finite Span," Proc. 14th Intern. Towing Tank Conference, 1975.

39. Tulin, M.P., "Supercavitating Flows - Small Perturbation Theory," J. Ship Research, Vol. 3, No. 3, 1964.

40. Lighthill, M.J., "A New Approach to Thin Aerofoil Theory," Aero. Quart., Vol. 3, 1951, pp. 193-210.

41. Uhlman, J.S., Jr., and Jiang, C-W., "Experiments on a Partially Cavitating Plano-Convex Hydrofoil with Comparison to Theory," Dept. of Ocean Engr., Mass. Inst. Tech. Report No. 83481-2, 1977.

42. Kermeen, R.W., "Experimental Investigations of Three-Dimensional Effects on Cavitating Hydrofoils," Calif. Inst. Tech. Engineering Report No. 47-14, 1960.

43. Jones, R.T., "Correction of the Lifting Line Theory for the Effect of Chord," NACA TN 817, 1941.

44. Tulin, M.P. "An Analysis of Unsteady Sheet Cavitation," Proc. 19th American Towing Tank Conference, 1980.

45. Bark, G. and Van Berlekom, W.B., "Experimental Investigations of Cavitation Noise," 12th Symposium on Naval Hydrodynamics, 1979, pp. 470-493.

46. Shen, Y.T., and Peterson, F.B., "Unsteady Cavitation on an Oscillating Hydrofoil," 12th Symposium on Naval Hydrodynamics, 1979.

47. Kerwin, J.E. and C.S. Lee, "Prediction of Steady and Unsteady Marine Propeller Performance by Numerical Lifting Surface Theory," SNAME, Vol. 86, 1978, pp. 218-253.

Discussion

A.J. Acosta (7)

It's always a pleasure to read the original and far-sighted work of Messrs. Tulin and Hsu. I was particularly intrigued by the easy way in which unsteady cavity motions of low frequency are handled in their present paper. These unsteady cavity motions have been literally the despair of theoreticians in the field and the new "quasi-steady" approximations presented herein are a most welcome alternative to the blizzard of analysis required in formal theories.

The use of the developments leading to Eq.(49) and its subsequent use to explain the stability of the "short" cavity partial cavitation solution was most interesting to me. This writer had always assumed the "long" cavity branch to be unstable for a different reason however, namely, that at constant σ , $C_{L\alpha}$ is negative for quasi steady behavior which then leads to the notion of a diverging cavity oscillation because of the shed vortex wake downwash. This mechanism still appears to be a possible one for the dynamic cavities of Fig.25. Perhaps the authors could comment on the possible effect of this vortex wake on their flows as Ref.44 is not generally available.

The effect of growing and collapsing cavities on cavity length and lift coefficient is also most interesting and provides a likely mechanism for the hysteresis often observed for cycle partial cavitation. It is interesting to note that a consistent closed cavity (Tulin) model for low frequency unsteady flows* shows that the dynamic cavity length fluctuation lags the quasi-steady one by an amount proportional to the frequency in agreement with the arguments presented in the paper. These kinds of conclusions may however be modified by the mathematical model chosen for cavity closure in dynamic flows. Would the authors care to discuss this point further as it has been such a troublesome one in the past?

* Acosta, A.J., Furuya, O., "A Brief Note on Linearized, Unsteady Supercavitating Flows", J. Ship Res. 23, No.2, 1979, p.85-88

A.Y. Odabaşı (BSRA)

Since the publication of the present authors' perturbation method [36] we at B.S.R.A. converted and applied it to the prediction of propeller cavitation and cavitation induced pressures. Our experience showed that the presence of a finite cavity end thickness has a strong influence on both the cavity geometry and the pressures emanating from a cavitating propeller. With the increasing cavity end thickness

cavity length and area first decrease and after exceeding a critical value they start to increase again. Therefore the choice of the drag coefficient becomes crucial and the linear theory predictions are inadequate for this purpose. I would therefore like to hear the advice and views of the authors.

Author's Reply

M.P. Tulin (Hydroautics)

We are grateful to Prof. Acosta for his comments and kind remarks.

With regard to his alternative explanation for the instability of the upper branch of k/c vs α/σ , we cannot comment now as we have not sufficiently studied his mechanism.

In regard to the effect of the wake, the result, Figure 25 of our paper, should be interpreted to apply at low frequencies. In this case when the value of C_L is interpreted to include the unsteady effect of vortex shedding in the wake, our theory is adequate.

We agree with Prof. Acosta's earlier use of the (essentially) closed cavity model in dynamic flows. It is certainly appropriate (with slight modification for the trailing momentum wake due to drag) when applied to steady flows as we have shown in our paper, and we see no reason to abandon it in the case of unsteady flows as are met in practice. We are gratified that the earlier analysis of Acosta and Furuya in the case of supercavitating flows showed a lag in cavity length of the same type as revealed by our analysis for short cavities.

We thank Dr. Odabaşı for his interest in our work, and are glad to note its earlier application by him in the case of ship propellers.

We too find the cavity thickness at termination of some importance in determining cavity lengths. This thickness, f , is proportional to cavity drag (Eq. 27 of our text) and in our own calculations we use the theory to predict cavity drag for $f=0$ and then re-calculated using f based on that drag. In our experience, the effect of f in practice was always to reduce the cavity length. Dr. Odabaşı states that linear theory is inadequate for the calculation of cavity drag, but in this we would not agree, as the cavity drag, although of second order in lift, is already expressed in the linear theory.

Off-Design Performance Prediction Method for Supercavitating Propellers

Okitsugu Furuya

Tetra Tech, Inc

Pasadena California, U S A

ABSTRACT

In order to account for the effect of the flow blockage due to the existence of cavity on the supercavitating propeller performance, a two-dimensional cascade theory was used for the basis of the sectional blade loading data. Three-dimensional propeller corrections were then made for these data by applying a typical propeller lifting-line method. Unlike the design method, the present performance prediction theory (often called the "off-design" method) should satisfy the boundary condition at each radial position of the propeller blade, namely the velocity diagram. This led to a set of nonlinear functional equations to be solved for determining the functional distribution of the vortex strength. Newton's iterative method was applied for determining the unique solution. Numerical results compared favorably with existing experimental data for highly choking conditions or long cavity cases, but not quite satisfactorily for short cavity cases.

NOMENCLATURE

a, b, c = ξ -coordinates in two-dimensional cascade problem
 a_o = two-dimensional lift coefficient
 \bar{A} = scale factor of cascade mapping function
 c = chord length of blade
 C_p = power coefficient ($=P/k_p V_a^3 \pi R^2$)
 C_T = thrust coefficient ($=T/k_p V_a^2 \pi R^2$)
 d = spacing between two blades
 D = propeller diameter ($=2R$)
 g = number of blades
 G = normalized circulation ($=\Gamma/2\pi R V_a$)
 i_a, i_t = induction factors for the axial and tangential induced velocities w_a and w_t

J = speed coefficient ($V_a/nD = \pi \lambda$)
 m = source strength
 n = propeller rotational speed
 p_1, p_c = static pressures at upstream uniform flow and inside the cavity
 P = power
 Q = torque
 r = radial position from the propeller axis
 r_h = propeller hub radius
 R = propeller radius
 s = half of the span length, also used as arc length on the blade measured from the cavity separation point
 sol = solidity ($=c/d$)
 S = total wetted arc length of the blade
 T = thrust
 U_1 = velocity at upstream infinity without downwash correction nor cavity source-term correction
 U_2 = velocity at downstream infinity
 U_∞ = geometric mean velocity
 V = relative velocity to the blade
 $(= ((wr)^2 + V_a^2)^{1/2})$
 V_a = advance speed^a (axial flow speed)
 V_c = induced velocity due to the cavity thickness effect
 V_e = effective velocity including induced velocities
 $(= \{(wr - w_t)^2 + (w_a + V_a)^2\}^{1/2})$
 w_a, w_t = induced velocities in the axial and tangential directions, respectively
 x = normalized radial position ($=r/R$)
 α_2 = deflected flow angle referred to the nose-tail line
 α_i = induced flow angle
 α_e = effective incidence angle
 α_g = geometric incidence angle
 α_m = geometric mean flow angle
 β = pitch angle
 $(= \tan^{-1} V_a/wr = \tan^{-1} J/\pi x)$

β_i = pitch angle including downwash effect
 $(= \tan^{-1}(w_a + V_a)/(\omega r - w_t))$
 $\bar{\beta}$ = local slope of blade
 γ = geometric stagger angle
 Γ = circulation
 δ = stagger angle in potential plane
 $(= \alpha_e + \gamma)$
 ζ = transform potential plane
 η = propeller efficiency $(= C_T/C_P)$
 λ = advance coefficient $(= V_a/\omega r)$
 ξ = real axis of the ζ -plane
 ρ = density of fluid
 σ_e = local cavitation number $(= (p_1 - p_c)/\frac{1}{2}\rho V_e^2)$
 ω = angular velocity of propeller

1. HISTORY

Various investigations on supercavitating (s/c) propellers have been conducted to date and these can be divided into three major categories, i.e., those of (1) design methods, (2) off-design methods, and (3) experiments. The pioneer work in the first category was conducted by Posdunine [1~4] during the 1940's but the first systematic work was presented by Tachmindji and Morgan, et. al. [5, 6]. They provided a design method of s/c propellers based on a conventional propeller design method combined with s/c hydrofoil theories. Their works were followed by the papers of Caster [7] who generated a design chart for 2-, 3-, and 4-bladed s/c propeller series. The works by English [8], Davis and English [9], Tulin [10], Barr [11], Scherer and Bohn [12], and Bohn and Altmann [13] covered various problems in s/c propeller design procedure. Cox [14] established a rather complete formula by applying the singularity-distribution method for s/c propeller flow. The DWTNSRDC of the U.S. Navy has been the center of activity in this field in recent years and the most sophisticated approach has been developed there. Unlike the other works mentioned above, Yim combined the propeller lifting-surface theory with a two-dimensional supercavitating cascade flow theory, leading to various publications [15-17]. Baker [18] also developed an engineering design method by using a modified lifting surface theory. The only other work which applied the lifting surface theory is that of Luu and Sulmont [18], but in a much simpler way.

Regarding the off-design method, however, very few works have been done so far. Nishiyama [19] applied a lifting-line theory in combination with linearized two-dimensional finite cavity theories, whereas Luu and Sulmont [20] used the force data at the choking condition obtained with linearized s/c cascade theory. Neither of them seemed to successfully predict the s/c propeller performance over a wide range of advance speed J with high accuracy.

The propellers designed with the method developed at NWTNSRDC were tested and the results were presented by Hecker and Peck [21], Venning and Haberman [22], Voorde and Esveldt [23], Peck and McDonald [24], and

Peck [25]. In addition, Bohn [26] recently presented experimental results for a Hydro-nautics-designed s/c propeller.

The state of art for the supercavitating propeller theories may be well described by the latest comparison in [25]. Two supercavitating propellers were independently designed by Hydro-nautics [13] and DWTNSRDC [18] for use on a hydrofoil ship the size of which was rather small to achieve the ship speed higher than 50 knots. Model tests were conducted for these propellers, the results of which are summarized in Table 1 (from [25]). It is clearly seen from Table 1 that the design of Hydro-nautics overestimated the thrust coefficient K_T and η by more than 10%, whereas that of DWTNSRDC underestimated K_T and η by 6% and 20%, respectively. The design methods of Hydro-nautics [13] and DWTNSRDC [18] are rather of an engineering type but inclusive of various important aspects such as the lifting surface correction, cascade effect, and flow retardation correction, despite the fact that the approaches taken by them were rather different.

We must say that although the latest design methods have become more sophisticated and complicated, a large discrepancy between the design data and model data still exists. The discrepancy is almost of the same amount as that found in the earlier works (see Table 1 in [22], for example). To the author the major problem seems to stem from lack of an accurate prediction of the state of cavitation. This argument may be supported by the difference in the speed coefficients between the design and model tests as shown in Table 1. For the Hydro-nautics propeller it was found that the J_{test} was much smaller than J_{design} , whereas for the DWTNSRDC propeller the situation was entirely opposite. It means that the former propeller reached the supercavitating condition much earlier than designed so that a good efficiency was not achieved. The latter propeller could extend the condition to much larger J , resulting in having a higher performance than that of design. It all amounts to the fact that due to only one additional factor, i.e., existence of cavitation, it makes both design and prediction methods for s/c propellers extremely difficult. Finally, in order to prove the accuracy of Yim's design method [15-17] we should still await the results of model tests which will become available in the near future.

2. APPROACH

Unlike the conventional propellers, the development of a prediction method for supercavitating (s/c) propeller performance at off-design conditions involves an additional complexity due to the existence of the cavity as mentioned above. Such propellers as used at high speeds are expected to have cavities on blades which will cause blocking or choking on the flow passages as the extent of cavity becomes large both in length and thickness. Some propeller designers

have already pointed out the importance of the cascade effect in s/c propeller design in their earlier papers such as [6].

A similar effect was also found important even for subcavitating propellers: the paper by Kerwin and Leopold [27] showed that large incidence angle corrections are necessary due to blade thickness effect even if the blade thickness is small. The correction became particularly significant as the thickness ratio to the blade spacing became high, e.g., near the hub. This blade thickness effect is considered to be exactly the same effect on the propeller performance as that of the blocked cavity flow. It is for this reason that cascade data are to be incorporated into the performance prediction of s/c propellers.

For pump and turbine designers, it is conventional to use cascade theories because the blade spacing is quite small and also the blades are totally enclosed with shrouds. There exist very little radial flow components so that the flow can be considered to be almost two-dimensional in a cascade flow configuration. A question now arises whether the loading data obtained with a cascade theory can be applied even to the propeller configuration in which the blade solidity is not as high as that of pumps and turbines. Particularly, the solidity near the propeller blade tip area is quite small. The major objective of the present work is, therefore, to determine the validity and limitations of using a cascade theory in a performance prediction method for supercavitating propellers.

The method of solving the present problem is a combination of a two-dimensional (2-D) s/c cascade theory with a lifting line theory. The procedure to be used is stated as follows. Specifying all physical and geometric conditions of the s/c propeller, 2-D loadings at several radial or spanwise locations of blades will be calculated. A difficult question exists, however, as to what effective flow incidence angles, α_e , must be used for the 2-D analysis. The induced flow effects in propeller configurations are usually strong so that the geometric flow incidence angles, α_g (see Figure 1 for definition of α_g) are quite different from the effective incidence angles, α_e .

The present propeller problem is similar to that of a single foil having a large aspect ratio; an integral equation which relates the lifting force to the effective incidence angle must be solved for determining the distribution of circulation $\Gamma(z)$ over the span, i.e.,

$$\Gamma(z)/k_a \bar{c} U = \alpha_g - \frac{1}{4\pi} \int_{-S}^S \frac{\partial \Gamma(z')}{\partial z'} \frac{dz'}{z-z'} \quad (1)$$

For the present propeller problem, the induced velocities are represented by two components, i.e., the axial and tangential velocities, W_a and W_t . Assuming the aspect ratio of the propeller blade is large, we can apply a lifting line theory for the evaluation of the propeller induced

velocities. The formula for the propeller case is, of course, somewhat more complicated than that for the single foil case. The free vortex sheets for the propeller flow are of semi-infinite helical spiral shape instead of plane shape for the single foil flow. The effective angle of flow incidence, α_e , is then obtained by subtracting the angle induced by W_a and W_t from α_g (see Figure 1 for the flow diagram). Applying this α_e to the lift curves calculated by the 2-D s/c theory, we can determine the two-dimensional circulation distribution with help of Joukowski's theorem. In order to determine the distribution function for the three-dimensional circulation Γ , the induced velocities should satisfy the boundary condition which is essentially the velocity triangle shown in Figure 1, similar to (1) in its form. A set of nonlinear integral equations will then be solved by using Newton's iterative method, the details of which will be described later.

An inherent problem exists when one tries to apply the two-dimensional s/c cascade theory to three-dimensional flow analysis. In the 2-D s/c cascade theory, there exists a choking flow condition. With a certain combination of incidence angle and cavitation number for a specified cascade geometry, the cavity extends to downstream infinity, which is called "choking" condition. The flow passage is now blocked or choked totally so that it becomes impossible for the total mass flow to increase or for the incidence angle beyond this point to increase. In actual propeller operations, however, there are no limitations on shaft rotation speed, ship speed, and submergence depth to be changed. This means that the local flow incidence angle to the propeller blade and/or local cavitation number can change over a complete range of such values, sometimes beyond those at which the 2-D choking condition occurs. A question now arises as to what loading function is to be used if a combination of the input parameters, i.e., cavitation number and incidence angle for the two-dimensional cascade flow, is beyond the boundary of the choking condition and thus no force data exist.

In order to correct this difficulty, two simple modifications on the cavitation number are tried presently. The first method is the evaluation of the flow retardation effect due to the existence of blade cavities. (A different type of approach was discussed by Tulin [28]). As a first approximation the cavity is represented by a row of line sources in cascade geometry and the retarded flow velocities are superimposed on the incoming flow velocity. The complex potential of such flow is given by

$$W = U_1 z e^{-i(\gamma + \alpha_e)} + m \ln \left\{ \sinh \left(\frac{\pi z}{d} \right) \right\},$$

where U_1 , m and γ designate the undisturbed upstream velocity, source strength and stagger angle, respectively (see Figure 2

for definition). The velocity potential is thus obtained:

$$\frac{dW}{dz} = U_1 e^{-i(\gamma+\alpha_e)} + \frac{m\pi}{d} \tanh(\pi z/d).$$

As $x \rightarrow \pm \infty$, the x - component of the velocity changes by $\pm m\pi/d$, respectively. If we know the thickness of the cavity, i.e., $d \cdot e$, the strength of source, m , is calculated by using the continuity equation

$$\left\{ U_1 \cos(\gamma+\alpha_e) - \frac{m\pi}{d} \right\} d = \left\{ U_2 \cos(\gamma+\alpha_2) + \frac{m\pi}{d} \right\} (d - de)$$

or

$$\frac{m\pi}{d} = \frac{U_1 \cos(\gamma+\alpha_e) - U_2 \cos(\gamma+\alpha_2)(1-e)}{2-e}. \quad (2)$$

It means that although the mass flow, $U_1 \cos(\gamma+\alpha_e) \cdot d$ per blade from the upstream infinity, comes into the cascade, the amount of $m\pi$ is rejected for going through the blade passage due to the existence of cavity. The rejected mass flow, $m\pi$, can be converted into the velocity V_c

$$V_c = \frac{m\pi}{d} \frac{1}{\cos(\gamma+\alpha_e)}. \quad (3)$$

The effective upstream flow velocity to be used in the 2-D analysis is then corrected by subtracting this flow component. The corrected cavitation number then becomes larger than that calculated on the basis of the flow velocity at upstream infinity, thus delaying the encounter with the choking condition.

As a result of the retarding flow correction mentioned above, the calculated propeller performance checks better with experimental data for some range of smaller J 's than those without corrections. Yet, the discrepancy remains large as J becomes further smaller, indicating the limitation of such correction method for fully choked propeller flow analysis. The second method is thus devised to further improve the accuracy of the present prediction method. For very small J 's, the local angle made with blade section becomes extremely large and far beyond the choking condition. Once the flow locally chokes, any excessive mass of flow cannot go through the blade passages, thus must go around the propeller blade tips. For fully choked conditions, therefore, no matter how much excessive flow comes into a propeller, the local flow pattern around the blade remains the same. This means that the forces on the blade should stay on the choking line in the force vs. cavitation number curve once the incoming flow condition reaches that for the choking condition. Figure 3 shows a typical force coefficient angle in which the choking condition boundary is indicated.

In order to implement the above idea into the present theory, the following

is proposed and used. For any combination of incidence angle α_e and cavitation number α_e with which the loading data are available, or equivalently the cavity length is finite, those data are directly used as sectional loadings. On the other hand, if no data are found for α_e and α_e specified, i.e., crossing the boundary lines of the choking condition, the force data at the choking condition will be selected only as a function of incidence angle with neglecting cavitation number. Luu and Sulmont [20] applied a similar method to the supercavitating propeller problem; a difference existed in that the force data of the choking condition were used over a complete range of J . The results of Luu and Sulmont [20] showed a good agreement with experiments for small advance coefficients J . Obviously, for larger J 's the cavity length at each blade becomes finite so that their assumption of using the infinite cavity data becomes irrelevant. As a result, the agreement between the theory and experiment showed discrepancy for larger J 's.

As for two-dimensional supercavitating cascade theories, only linearized theories were available until just recently; a nonlinear two-dimensional supercavitating cascade theory has been made available by Furuya [29], facilitating a calculation tool with nonlinear effects fully incorporated. This theory will be employed for determining the two-dimensional sectional loadings for propeller blades throughout the present investigation.

Finally, it must be mentioned that for determining the induced velocities the source effect (which was shown in Cox [14]), was purposely neglected in the present lifting-line theory. The present concept of using the cascade data as sectional loadings stems from the fact that the blockage effect due to the blade cavities must somehow be incorporated into the s/c propeller analysis. If the single-foil data were used, it would be reasonable to include the source distribution for representing the thickness of cavity in the lifting line expression and then to calculate the induced velocities due to the source. However, in the present method the cavity blockage effect is included in the counterpart, i.e., in the two-dimensional sectional loading calculation so that the double count must be avoided. The argument mentioned herein is rather intuitive and thus the final judgment for the validity of the present discussion must be made in comparison with experimental data. Another way for the theory justification will be the formal matching procedure of the inner solution with the outer solution, in this case, the two-dimensional solutions with the three-dimensional solution. If such a method can be developed, the result will clarify the effect of the cavity thickness at each radial position on the supercavitating propeller performance.

3. MATHEMATICAL FORMULATIONS

A two-dimensional supercavitating

cascade problem has recently been solved by using hodograph variables and satisfying exact boundary conditions everywhere [29]. In this method the cascade geometry, upstream flow conditions and cavitation number are specified. Then the hydrodynamic characteristics of the cascade are determined. A system of five nonlinear functional equations must be solved for five unknown solution parameters as well as a functional relationship between the geometric and transform planes. A combination of a functional iterative method with Newton's method can conveniently solve the above equations with fast convergence. More details of the theory and numerical method are described in [29].

As has been discussed in the previous section, the 2-D s/c cascade data need the three-dimensional propeller geometric correction. The simplest correction may be that of a lifting-line theory under the assumption that the propeller blade has a relatively large aspect ratio. In this approach the induced velocities evaluated at the lifting line represent the effect of the three-dimensional propeller flow, or the free vortices left behind the blades in the helical spiral shape. These induced velocities contain all the information of propeller geometry and its wakes necessary for the 2-D s/c cascade data correction. Now the effective flow incidence angle α_e to be used for the 2-D analysis can be readily constructed with the induced velocities as has already been shown in Figure 1.

With the propeller geometry, rotational speed ω and the flow incoming velocity V_a specified, the two-dimensional s/c cascade problem can be solved by assuming that the flow induced angle α_i is known at each radial position r , or equivalently $x = r/R$, i.e.,

$$\alpha_e(x) = \alpha_g(x) - \alpha_i(x) \quad (4)$$

$$\beta_i(x) = \beta_g(x) + \alpha_i(x) \quad (5)$$

$$\sigma_e(x) = \frac{p_1 - p_c}{\frac{1}{2} \rho V_e^2(x)} \quad (6)$$

The previously mentioned five equations are written in the following symbolic form

$$f_1 \equiv R_e \{ \omega(\zeta_1) \} - \alpha_e = 0 \quad (7)$$

$$f_2 \equiv I_m \{ \omega(\zeta_1) \} + \ln U_2 = 0 \quad (8)$$

$$f_3 \equiv g_3 - \alpha_2 = 0 \quad (9)$$

$$f_4 \equiv s(-1) - S = 0 \quad (10)$$

$$f_5 \equiv g_5 - d \{ \sin(\alpha_e + \gamma) - U_2 \sin(\alpha_2 + \gamma) \} = 0 \quad (11)$$

where no unknown input data exist since α_i has already been assumed to be known. The explicit expressions for $R_e \{ \omega(\zeta_1) \}$,

$I_m \{ \omega(\zeta_1) \}$, g_3 , g_5 and $s(-1)$ are given in Appendix A (also see [29] for more details). Applying Newton's iteration method, one can determine the solution parameters including the flow angle at downstream infinity, α_2 . The strength of circulation at this radial location will then be obtained by considering the momentum balance around a blade in cascade configuration;

$$\Gamma(x) = d v_e \frac{\sin(\alpha_e - \alpha_2)}{\cos(\delta_2 - \gamma)} \quad (12)$$

where all quantities here are a function of x or normalized radial location $x = r/R$. This strength of circulation is now incorporated in the propeller lifting line theory.

By normalizing $\Gamma(x)$ and expressing it by $G(x)$, we can determine the induced velocities in the axial and tangential directions

$$\frac{W_a(x)}{V_a} = \frac{1}{2} \int_{x_h}^1 \frac{dG(x')}{dx'} \frac{1}{x-x'} i_a(z_i) dx' \quad (13)$$

$$\frac{W_t(x)}{V_a} = \frac{1}{2} \int_{x_h}^1 \frac{dG(x')}{dx'} \frac{1}{x-x'} i_t(z_i) dx' \quad (14)$$

where

$$G(x) = \Gamma(x)/2\rho V_a \quad (15)$$

$$x_h = r_h/R$$

$$\tan \beta_i = (1 - W_a(x)/V_a) / (-x/J - W_t(x)/V_a) \quad (16)$$

and i_a and i_t are the induction factors of Lerb [29], the detailed descriptions of which are given in Appendix B. In the present analysis the location of the vortex sheets is adjusted through using β_i as given in Equation (15). Lerb [30] proved in his paper from the discussion of energy balance that the location of the vortex sheet should be on the helical spiral surface of angle β_i instead of β_g . As will be seen later, the present solution method requires an iterative procedure. Taking advantage of this situation, we can incorporate newly calculated W_a/V_a and W_t/V_a into β_i in (5), which is used for determining the induction factors for the subsequent iteration. The downwash angle α_i is now calculated by the following relationship

$$\alpha_i(x) = \tan^{-1} \left\{ \frac{1}{V_e} (W_a(x) \cos \beta_i + W_t(x) \sin \beta_i) \right\} \quad (17)$$

Equations (4-17) form fully nonlinear integral equations for $\Gamma(x)$ and these equations must be solved for determining the performance characteristic of the supercavitating propeller.

4. NUMERICAL PROCEDURE

Two numerical methods for solving the above nonlinear integral equations were tested for their convergence. The first method was what is called a substitutional iterative method and the second one was Newton's iterative method.

4.1 Substitutional Iterative Method

First, assuming the effective incidence angles $\alpha_e^{(n)}(x)$, $n=0$, at various spanwise locations, one can then determine the downwash angles $\alpha_j^{(n)}(x)$ and a cavitation number $\sigma(x)$ from equations (4) and (6). With these data used the two-dimensional s/c cascade data will be calculated, including α_2 , the deflected flow angle at downstream infinity.

The sectional circulation distribution $\Gamma(x)$ is then obtained by Equation (12) with which we can calculate w_a , w_t and $\alpha_i^{(n+1)}(x)$ with Equations (13-16) and (4). The values of $\alpha_i^{(0)}(x)$ are now checked if they were correctly assumed. If not, with a new $\alpha_i^{(n+1)}(x)$ and $\sigma_i^{(n+1)}$, we proceed to the next iteration until a convergent solution is obtained. In each iteration, $\hat{\sigma}_i^{(n)}$, starting with an assumed value ($\hat{\sigma}_i^{(0)} = \hat{\sigma} + \alpha_i^{(0)}$), must be calculated and a new value of $\hat{\sigma}_i^{(n)}$ must be used in calculations of w_a and w_t as mentioned before. It must also be noted that the cavitation number σ based on V is used for the first iteration but σ_e based on V_e is used from the second iteration on. If the test for the convergence of solution parameters, for example, α_i , is passed, we proceed to calculate the propeller characteristics such as thrust, power coefficients and efficiency. This method was applied to a representative case and it was found that converged solutions were obtained only if the starting values of $\alpha_e^{(0)}$ were correctly assumed, i.e., close to the actual solutions.

4.2 Newton's Iterative Method

In the second method we incorporate Newton's method into the nonlinear integral equations for improving the convergence of iteration. This requires a new arrangement of the problem in order to identify the solution parameters.

From Equations (16), (B-16) and (E-17),

$$\begin{aligned} \underline{f} \equiv & \left[\tan(\hat{\sigma}_g(x) - \alpha_e(x)) \right] \left(\frac{\pi x}{J} \right) \\ & - \frac{1}{1-x_h} \sum_{m=1}^k G_m h_m^2(\phi(x)) \\ & - \left\{ 1 + \frac{1}{1-x_h} \sum_{m=1}^k G_m h_m^t(\phi(x)) \right\} = 0 \end{aligned} \quad (18)$$

and from Equations (15) and (B-11)

$$g \equiv \sum_{m=1}^k G_m \sin m \phi(x) - \frac{\Gamma(x, \alpha_e(x), \sigma_e)}{2\pi R V_a} = 0. \quad (19)$$

Choosing k -discrete control points in the radial direction of the blade, we have k -independent equations in (18). Also the same number of G_k 's are chosen for the solution parameters in addition to k unknown $\alpha_{ek} = \alpha_e(x)$. We now have $2k$ -solution parameters for a system of nonlinear integral equations (18) and (19) having an order of $2k$.

Rewriting these equations and parameters symbolically by

$$\underline{f} = (\underline{f}, \underline{g})$$

$$\underline{x} = (G_k, \alpha_{ek}),$$

we can describe the above set of equations as follows:

$$\underline{f}(\underline{x}) = 0$$

thus Newton's iterative loop is established by

$$\underline{J}(\underline{x}^{(n)}) \cdot (\underline{x}^{(n+1)} - \underline{x}^{(n)}) = -\underline{f}(\underline{x}^{(n)})$$

where \underline{J} is a Jacobian matrix whose component is given by

$$\underline{J} = \partial F_i / \partial x_j.$$

In the present case each component of \underline{J} is either analytically or numerically calculated;

$$\begin{aligned} \frac{\partial F_i}{\partial x_j} = & \begin{cases} \frac{\partial f_i}{\partial G_j} = \tan(\hat{\sigma}_g(x_i) - \alpha_{ei}) \\ \quad \left\{ -jh_j^a(\phi(x_i)) / (1-x_k) \right. \\ \quad \left. -jh_j^t(\phi(x_i)) / (1-x_h) \right\}; i, j = 1-k, \\ \frac{\partial f_i}{\partial \alpha_{ek}} = -\Lambda(x_i) \delta_{ik} / \cos^2(\hat{\sigma}_g(x_i) - \alpha_{ek}); \\ \quad i = 1-k, j = k+1-2k, \ell = j-k \end{cases} \end{aligned}$$

$$\begin{aligned} \frac{\partial F_i}{\partial x_j} = & \begin{cases} \frac{\partial g_i}{\partial G_j} = \sin\{j\phi(x_i)\}; \\ \quad i = k+1-2k, j = 1-k, \ell = i-k \\ \frac{\partial g_m}{\partial \alpha_{e\ell}} = -\frac{\delta_{m\ell}}{2\pi R V_a} \cdot \frac{\partial}{\partial \alpha_{e\ell}} \Gamma(x_m, \alpha_{em}, \sigma_e); \\ \quad j = k+1-2k, m = i-k, \\ \quad \ell = j-k \end{cases} \end{aligned}$$

where all partial derivatives are analytically calculated except for Γ for which a finite difference method is used. Our experience in using the present Newton's method indicated rather slow but steady convergence for almost all cases. It has also been found that the method is much less sensitive to the initial starting values for solution parameters.

5. CALCULATIONS OF THRUST, TORQUE COEFFICIENTS AND EFFICIENCY

In the cascade flow the force acting on the blades is known to be normal to a geometric mean angle α_∞

$$\alpha_\infty = \cos^{-1} \left\{ \frac{1}{2U_\infty} (V_e \cos \alpha_e + U_2 \cos \alpha_2) \right\} \quad (20)$$

where

$$U_\infty = \frac{1}{2} \left\{ V_e^2 + U_2^2 + 2V_e U_2 \cos(\alpha_e - \alpha_2) \right\}^{1/2} \quad (21)$$

and V_e is taken to be unity in the 2-D calculations.

Thus, a sectional thrust is obtained

$$dT = g \rho U_\infty \Gamma \cos(\beta_i + \alpha_e - \alpha_\infty) dr$$

and integration of dT over the span yields

$$\begin{aligned} T &= g \rho \int_{r_h}^R U_\infty \Gamma \cos(\beta_i + \alpha_e - \alpha_\infty) dr' \\ &= g 2\pi R^2 \rho V_a \int_{x_h}^1 U_\infty(x') G(x') \cos(\beta_i \\ &\quad + \alpha_e - \alpha_\infty) dx'. \end{aligned} \quad (22)$$

The thrust coefficient C_T is obtained by normalization

$$\begin{aligned} G &= \frac{T}{\frac{1}{2} \rho V_a^2 \pi R^2} = 4g \int_{x_h}^1 \frac{U_\infty(x')}{V_a} G(x') \cos(\beta_i \\ &\quad + \alpha_e - \alpha_\infty) dx'. \end{aligned} \quad (23)$$

Similarly the power coefficient C_P is calculated

$$\begin{aligned} dP &= r \omega dQ dr \\ &= r \omega g \rho U_\infty \Gamma \sin(\beta_i + \alpha_e - \alpha_\infty) dr \end{aligned}$$

or

$$\begin{aligned} P &= g 2\pi \omega R^3 \rho V_a \int_{x_h}^1 x' U_\infty(x') G(x') \sin(\beta_i \\ &\quad + \alpha_e - \alpha_\infty) dx' \end{aligned} \quad (24)$$

and

$$C_P = \frac{P}{\frac{1}{2} \rho V_a^3 \pi R^2} = \frac{4g}{\lambda} \int_{x_h}^1 x' \frac{U_\infty(x')}{V_a} \sin(\beta_i + \alpha_e - \alpha_\infty) dx'$$

$$G(x') \sin(\beta_i + \alpha_e - \alpha_\infty) dx' \quad (25)$$

where

$$\lambda = \frac{V_a}{\omega R}.$$

More conventional definitions for thrust and torque coefficients are given by K_T and K_Q

$$K_T = T / \rho n^2 D^4 \quad (26)$$

$$K_Q = Q / \rho n^2 D^5 \quad (27)$$

The relationships between these parameters and C_T , C_P are readily obtained

$$K_T = \frac{\pi J^2}{8} C_T \quad (28)$$

$$K_Q = \frac{J^3}{16} C_P \quad (29)$$

thus

$$\eta = \frac{K_T}{K_Q} \frac{J}{2\pi} \quad (30)$$

6. NUMERICAL RESULTS

Two theoretical methods for overcoming the difficult situation which arose from the choking condition have presently been proposed; the use of a row of source distributions for the first approach and that of choking conditions data for the second approach. Numerical computations were made for each method and the results will be presented in comparison with experimental data. For the former method supercavitating propeller of TMB Model 3770 was chosen and for the latter method that of Hydronautics 7607.02 was used.

6.1 Method No. 1 (Use of Source Singularities)

The s/c propeller Model 3770 was designed based on the method of Tachmindji and Morgan [4, 5] and its design characteristics are shown in Tables 2 and 3. The propeller blade profile is that of a Tulin-Burkart two-term camber with an additional camber factor to account for a lifting surface effect [31]. In order to establish the data basis for propeller calculation the lift and drag forces were calculated for various radial blade locations, i.e., at $x = 0.4$ to 0.9 by 0.1 increment and are shown in Figures 3 and 4.

In these figures we see that a significant cascade effect occurs in cavity flows. In Figure 3(a), for example, where the solidity is small, 0.244, near the tip (at $x = 0.9$) with a stagger angle of 74 degrees, it is seen that the lift coefficient C_L increases as the incidence angle increases. This phenomenon is quite similar to that observed in single lifting foil cases. It means that the solidity of 0.244 at this location with $\gamma = 74^\circ$ is yet too small to see much of a cascade effect and thus the flow is similar to that of a single foil

except that the choking phenomenon appears. However, at $x = 0.8$ where the solidity becomes slightly larger, i.e., 0.365, with a stagger angle of 72.4 degrees, the lift coefficient C_L at $\alpha_e = 6^\circ$ decreases rapidly as σ becomes small (see Figure 3(b)), until finally its value becomes even smaller than that obtained at $\alpha_e = 4^\circ, 3^\circ$ and 2° . The reason why this occurs at smaller σ 's is obvious: the smaller the cavitation number, the longer and thicker is the cavity so that the cavity boundary with a low cavity pressure is close to the pressure side of the neighboring blade, causing a loss in lift. It is also seen that the cavitation number σ_e at which this change in C_L occurs in Figures 3(a)-(f) checks quite well with the value of σ_e at which the length of cavity starts extending to infinity (choking conditions). One can also observe a similar behavior in C_L for $\alpha_e = 4^\circ$, occurring here at a smaller σ_e than for the $\alpha_e = 6^\circ$ case. This trend becomes even stronger (see Figures 3(c) through 3(f) since the solidity becomes larger, increasing from 0.479 to 0.912. In Figure 3(f) where $x = 0.4$ and the largest solidity occurs, the relation between the lift and incidence angle completely flips over for a range of σ_e 's, i.e., the lift is higher at lower incidence angles.

This peculiar behavior for cavitating cascade flow observed above never happens in the cases of single lifting foils. Physically it can be understood and explained as follows. When the solidity becomes large and thus the blades are more closely packed in the cascade configuration, the adjacent blades are strongly affected by the existence of cavity thus causing significant hydrodynamic effects. This effect becomes stronger as the cavity becomes thicker and longer or as the flow incidence angles become larger and the cavitation number becomes smaller as has been seen above.

It is interesting to compare the lift coefficients obtained in the present nonlinear cascade theory and those of supercavitating single foils. The latter values at $\sigma_e = 0$ are easily computed from the design lift coefficients, correction factors listed in Table 2 and angles of attack:

$$C_{LS0} = C_{Ld} \cdot K + \pi/2 \quad (31)$$

where the subscripts S and 0 in (31) designate "single foil" and "zero cavitation number", respectively. C_{LS0} calculated based on Equation (31) are plotted in each Figure 3(a) through 3(f). It is seen that a well known approximation for finite cavity length by a correction factor $(1 + \sigma)$, commonly used for a single foil flow, cannot be applied to the s/c flow in the cascade configuration whatsoever. It is also noted that C_{LS0} 's are much larger than those values extrapolated from the linear portions of C_L curves, again showing a remarkable supercavitating cascade effect on lifting forces.

It is also seen that the choking con-

ditions marked in Figures 3(a) through 3(f) vary to a great degree depending on the solidity. With small solidity and a small incidence angle, the choking flow does not occur until σ_e becomes fairly small, say 0.007 (see Figure 3(a)), while a σ_e of 0.041 is enough to cause the same condition for a large solidity and a large angle of attack (see Figure 3(f)). This behavior is also attributable to the increasing cascade blockage effects with increase in solidity and incidence angle.

Figures 4(a) through (f) show drag coefficients parallel to the upstream flow direction, each corresponding to Figure 3(a) through (f), respectively. It is seen that these drag forces also exhibit a trend similar to that of the lift coefficient.

It must be pointed out that the numerical computations presently carried out with the two-dimensional supercavitating cascade programs are a most time-consuming and difficult part during the present analysis. In particular, such flow configurations that have large solidity with large stagger angles and large incidence angles often cause numerical instabilities in the functional iterative procedure. Careful choice of initial guess for the iterative method is necessary.

Using these two-dimensional cascade data for the s/c propeller analysis with the first method of using a row of source singularities, K_T , K_Q and η was calculated at the design point. This is shown in Table 4 in comparison with the design data and experimental data. It is seen that the present method predicts them better than the design method itself. It is quite interesting to see the differences in local flow characteristics between the design method [22] and the present off-design method.

Four different parameters including local cavitation number, effective flow incidence angle, downwash angle and lift coefficients are shown in Table 4. The local cavitation numbers of the present method shown in the table are those corrected on the basis of the cavity thickness data from the 2-D cascade calculations, whereas those of the design method are simply based on $v = ((\omega r)^2 + v_a^2)^{1/2}$. The discrepancies shown in Table 4 are quite substantial and particularly those for the downwash angle α_i and thus effective flow angle α_e . It is considered that these discrepancies are attributable to the differences in the force coefficients used by the two different methods.

In Figure 5 we compare the present results with experimental data for $\sigma_{va} = .500$, i.e., at an off-design condition over some range of J . It is seen that the correlation for K_T , K_Q and η at J ranging from 0.44 to .5 is good but that the discrepancy starts growing as J goes beyond this range. Particularly for the smaller J range the data obtained with the prediction method depart rapidly from the experimental data. This indicates that the method has some limitation for predicting the off-design characteristics; the prediction accuracy deteriorates

at highly choking conditions. It seems that the discrepancy for larger J 's stems from the use of inappropriate 2-D cascade data. In this range, the experimental evidence indicated that the partially cavitating condition occurred.

6.2 Method No. 2 (Use of Choking Condition Data)

One of the latest s/c propellers designed and tested was that of Hydronautics' Model 7607.02 [13]. In order to test the second method for the s/c propeller performance prediction we used this propeller. Similar lift and drag charts to those in Figures 3 and 4 were generated with the 2-D s/c cascade theory. Only the lift data are shown here in Figure 6, showing a similar trend in C_L vs. σ to that seen before. With these 2-D cascade data used, the s/c propeller characteristics were obtained with the second method proposed previously. Figure 7 shows η , K_Q and σ for a wide range of J , at design cavitation number, $\sigma_{va} = .343$ whereas Figure 8 shows the same quantities at off-design cavitation number, i.e., $\sigma_{va} = 3.0$ which was assumed to be that for the ship taking-off condition. It is clearly seen that the presently predicted data compare well with experimental data over a much wider range of J except for the partially cavitating range of J . It is indicative that the second method is superior to the first one, particularly for the highly choked s/c propellers, as was expected from the results of Luu and Sulmont [18].

The computing time required for determining the supercavitating propeller characteristics was the range of only one hundred dollars, but the preliminary two-dimensional s/c cascade calculations cost us a few thousand to several thousand dollars even with use of the CDC-7600 at the Lawrence Berkeley Laboratory Computer Center. With this single fact only, the possibility of using the lifting surface theory for the performance prediction method will be eliminated.

7. CONCLUSION

Two slightly different methods have been proposed for the performance prediction of supercavitating propellers at off-design conditions. The basic concept of these two methods is, however, essentially the same, i.e., a combination of two-dimensional supercavitating cascade theory and propeller lifting line theory. The only difference between these methods exists in a methodology of avoiding to encounter the two-dimensional choking condition beyond which no 2-D data are available for use in propeller calculations. For the first method the flow retardation effect was represented by distributing a row of line sources, the strength of which was determined proportionally to the thickness of cavity. Any induced velocity due to this was incorporated into the effective

flow velocity. By applying this retarded flow effect, the cavitation number to be used becomes larger than that without any correction, thus alleviating the chance of encountering choking condition. In the second method, as soon as the choking condition was reached by changing α_e and σ_e , the force data at such condition was used as only a function of α_e but neglecting σ_e .

The representative computations showed a better prediction capability with the latter method than the first one over a wide range of J and σ_{va} . Discrepancies, however, still exist for both extremely small J 's and large J 's. In order to further improve the present theory, the following aspects are recommended to be investigated.

1) A question existed in the second method as to the validity of using the cascade data even for the short and thin cavity flow regime. More specifically, where is the boundary of using single-foil data and cascade data? In order to clarify this point a more rigorous theoretical approach such as the singular perturbation method may be necessary. For the subcavitating propeller flow this type of method already exists, e.g., that of Brockett [32]. When such a method is applied to the s/c propeller flows, the correction, due to the cavity flow effect, for the local sectional flow, similar to the cascade effect will naturally evolve.

2) A more immediate improvement may be made by choosing the geometric mean flow angle as a reference flow angle for the cascade data selection. Instead, during the present study we considered the effective flow velocity V_e as an incoming flow angle for the 2-D cascade flow configuration. A difference in the calculations of final propeller characteristics may be small for small J 's where the incidence-angles are already of large number but will be substantial for larger J 's. This may improve the prediction accuracy of the present method for larger J 's at which an appreciable discrepancy presently exists.

3) In addition to the above correction for larger J range, the data of partially cavitating cascade flow are necessary. There exists no such theory to date which can generate accurate data and thus the development of a nonlinear partially cavitating cascade theory is in order.

8. ACKNOWLEDGMENT

The present work was supported by the David W. Taylor Naval Research and Development Center under Contract Nos. N00600-76-C-0790, N00600-77-C-1381, and N00167-78-C-0050. Many helpful discussions were held with Drs. W. Morgan and B. Yim and Messrs. G. Dobay and E. Caster, and these are gratefully acknowledged.

REFERENCES

1. Posdunine, V.L., "On the Working of Supercavitating Screw Propellers", (in English), *Doklady AN SSSR*, Vol. 39, No. 8,

1943; also, Transactions of the Institution of Naval Architects, Vol. 86, 1944.

2. Posdunine, V.L., "The Construction and Performance of Supercavitating Propellers", Izv. OTN AN SSSR, Nos. 1-2, 1945.

3. Posdunine, V.L., "Basic Theory of the Construction and Performance of Supercavitating Propellers", Izv. OTN AN SSSR, Nos. 1-11, 1945.

4. Posdunine, V.L., "The Effectiveness of Supercavitating Propellers", Izv. OTN AN SSSR, No. 10, 1947.

5. Tachmindji, A.J., Morgan, W.B., Miller, M.L., and Hecker, R., "The Design and Performance of Supercavitating Propellers", DTMB Report, C-807, February 1957.

6. Tachmindji, A.J., and Morgan, W.B., "The Design and Estimated Performance of a Series of Supercavitating Propellers", Proceedings of the Second ONR Symposium on Naval Hydrodynamics, Government Printing Office, Washington, D.C., 1958.

7. Caster, E.B., "TMB 2-, 3-, and 4-Bladed Supercavitating Propeller Series", David Taylor Model Basin Report 1637, January 1963.

8. English, J.W., "An Approach to the Design of Fully Cavitating Propellers", ASME Symposium on Cavitation in Fluid Machinery, November 1965.

9. Davis, B.V., and English, J.W., "The Evolution of a Fully Cavitating Propeller for a High-Speed Hydrofoil Ship", Proceedings of the Seventh ONR Symposium on Naval Hydrodynamics, pp. 961-1017, 1968.

10. Tulin, M.P., "Supercavitating Propellers--History, Operating Characteristics, Mechanism of Operation", Proceedings of the Fourth (1962) ONR Symposium on Naval Hydrodynamics, Government Printing Office, Washington, D.C., 1964.

11. Barr, R.A., "Supercavitating and Superventilated Propellers", Transactions Society of Naval Architects and Marine Engineers, Vol. 78, pp. 417-450 (1970).

12. Scherer, J.O., and Bohn, J., "The Design of Supercavitating Propellers", Hydrodynamics Technical Report 7307-6, August, 1976.

13. Bohn, J. and Altman, R., "Two Supercavitating Propeller Designs for Hydrofoil Ships", Hydrodynamics Technical Report 7607.01-1.

14. Cox, G.G., "Supercavitating Propeller Theory - The Derivation of Induced Velocity", Seventh Symposium, Naval Hydrodynamics, August 25-30, 1968, Rome, Italy, Sponsored by the Office of Naval Research, Department of the Navy, pp. 929-949.

15. Yim, B., "Optimum Propellers with Cavity and Friction Effects", Journal of Ship Research, Vol. 20, No. 20, June 1976, pp. 118-123.

16. Yim, B., "Blade Sections and Optimum Pitch Distribution of Supercavitating Propellers", David W. Taylor Naval Ship Research and Development Center Report 4642, December 1975.

17. Yim, B., "Lifting-Surface Theory of Supercavitating Propellers", presented at the International Association for

Hydraulic Research Joint Symposium, June 1978.

18. Luu, T.S., and Sulmont, P., "Design of Supercavitating Propellers on the Basis of Lifting Surface Theory", International Shipbuilding Progress, Vol. 16, No. 176, pp. 116-124, April 1969.

19. Nishiyama, T., "Lifting-Line Theory of Supercavitating Propellers at Non-Zero Cavitation Numbers", ZAMM 51, pp. 577-586, 1971.

20. Luu, T.S., and Sulmont, P., "Calculation of the Performance of a Supercavitating Propeller ($\sigma = 0.4$) for Different Advance Coefficients (J) - Confrontation, Theory, Experiment", CREA Final Report Contract No. F61052-68-C-0074.

21. Hecker, R., and Peck, J.G., "Experimental Performance of TMB Supercavitating Propellers 3767, 3768, 3769, 3770, 3785 and 3820", TMB Report 1553, August 1961.

22. Venning, E., Jr., and Haberman, W.L., "Supercavitating Propeller Performance", Transactions Society of Naval Architects and Marine Engineers, Vol. 70, pp. 354-417, 1962.

23. Van de Voorde, C.B., and Esveldt, J., "Tunnel Tests on Supercavitating Propellers", Proceedings of the Fourth ONR Symposium on Naval Hydrodynamics, pp. 28-317, 1962.

24. Hecker, R., Peck, J.G., and McDonald, N.A., "Experimental Performance of TMB Supercavitating Propellers", TMB Report 1432, 1964.

25. Peck, J.G., "Cavitation Performance Characteristics of Supercavitating Propellers 4898 and 4999", DTNSRDC Ship Performance Department, Department Report SPD-680-02, December 1977.

26. Bohn, J.C., "Model Tests of a Supercavitating Propeller Designed for a Hydrofoil Ship", Hydrodynamics Report 7607.59, August 1977.

27. Kerwin, J.E., and Leopold, R., "Propeller-Incidence Correction Due to Blade Thickness", Journal of Ship Research, Vol. 7, No. 2, October 1963, pp. 1-6.

28. Tulin, M.P., "Supercavitating Propellers - Momentum Theory", Journal of Ship Research, pp. 153-169, December 1965.

29. Furuya, O., "Exact Supercavitating Cascade Theory", Journal of Fluid Eng., Vol. 97, ASME, December 1975.

30. Lerbs, H.W., "Moderately Loaded Propellers with a Finite Number of Blades and an Arbitrary Distribution of Circulation", Trans. SNAME, Vol. 60, 1952.

31. Morgan, W.B., et. al., "Propeller Lifting Surface Corrections", Trans. SNAME, Vol. 76, pp. 309-347, 1968.

32. Brockett, T., "Propeller Perturbation Problems", NSRDC Report 3880, October 1972.

TABLE 1
LATEST COMPARISON DATA BETWEEN THE THEORY AND EXPERIMENT (after [25])

DESIGN CONDITIONS	Power (Max., Cont.)	16000 HP for 2 Propellers			
	1 - t	.925			
	1 - w_t	.870			
	Shaft Centerline at Design Speed	6.84 ft.			
	Max. Diameter	5.0 ft.			
	Number of Blades	4			

COMPARISON	PROPELLER MODEL NUMBER	4698		4699	
	DESIGNER	JOHN & ALTMAN [13] (Hydroautics)		Baker [18] (DWTNSRDC)	
		Design	Model Data	Design	Model Data
	ϵ	.34		.34	
	J	1.01	.96	1.04	1.13
	X_T	.0900	.0795	.0943	.101
	η	.62	.52	.64	.77

TABLE 2
DESIGN CHARACTERISTICS OF NSRDC MODEL 3770
SUPERCAVITATING PROPELLER (from Reference [22])

Blade Number (g)	3
Pitch/Diameter	.786
EAR	.508
Chord/Diameter at $x = 0.7$.351
Design α_e at $x = 0.7$	2°
Design C_L at $x = 0.7$.147
Section	TMB Modif.
J	.440
σ_{Va} at $x = 0.7$.617

TABLE 3
COMPARISON OF K_T , K_Q AND η BETWEEN THE PRESENT RESULT,
DESIGN DATA AND EXPERIMENTAL DATA FOR 3770
SUPERCAVITATING PROPELLER AT DESIGN POINT,
 $\sigma_{Va} = .617$ AND $J = .440$

	Design Data (Ref. [22])	Experimental Data (Ref. [22])	Present Results
K_T	.1004	.085	.0819
K_Q	.0130	.0115	.0106
$\eta(\%)$	54.1	52.0	54.0

TABLE 4
COMPARISON OF THE DETAILED FLOW CHARACTERISTICS OF 3770
BETWEEN THE DESIGN METHOD [22] AND PRESENT METHOD
AT DESIGN POINT, $\sigma_{Va} = .617$ AND $J = .440$

Nondimensional Radius x	Local Cavitation Number σ		Effective Incidence Angle α_e		Downwash Angle α_i		Lift Coefficient C_L	
	Design Method Ref. [22]	Present Method	Design Method Ref. [22]	Present Method	Design Method Ref. [22]	Present Method	Design Method Ref. [22]	Present Method
0.4	.0656	.0798	2.06°	6.80°	9.87°	5.13°	.198	.281
0.6	.0302	.0398	1.99°	5.97°	7.23°	3.23°	.153	.168
0.7	.0223	.0290	1.91°	5.15°	6.45°	3.19°	.139	.141
0.8	.0170	.0227	1.91°	5.00°	5.76°	2.65°	.131	.118
0.9	.0134	.0173	1.91°	4.60°	5.21°	2.51°	.125	.094

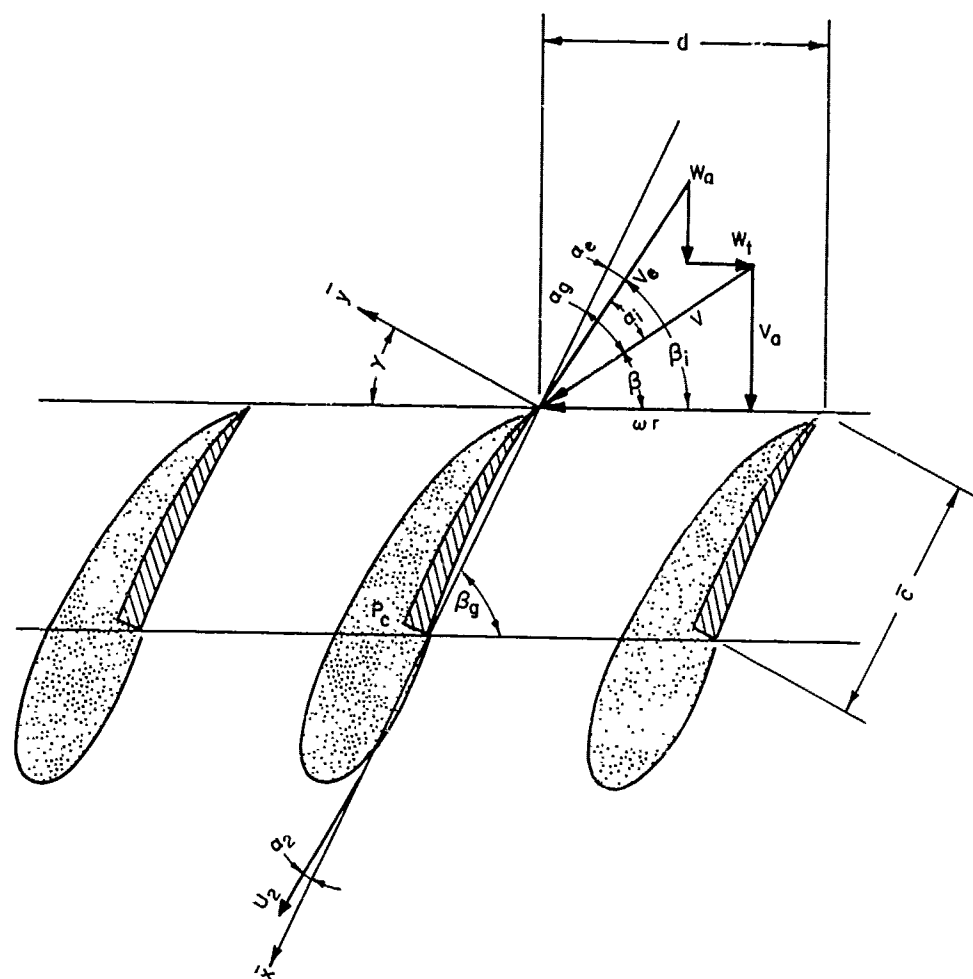


Figure 1 Flow Configuration in Cascade Geometry of Propeller at a Constant Radius r with Velocity Diagram

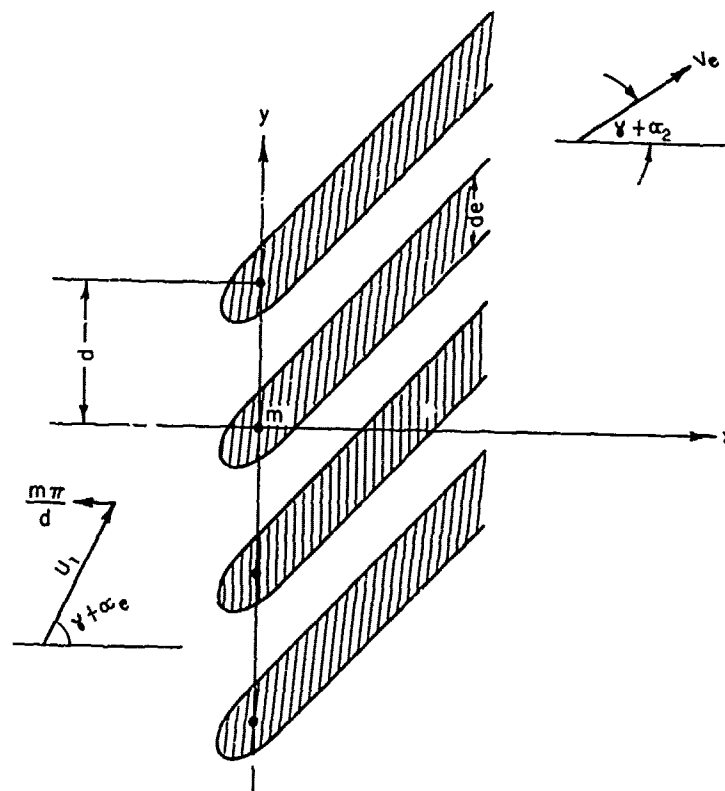
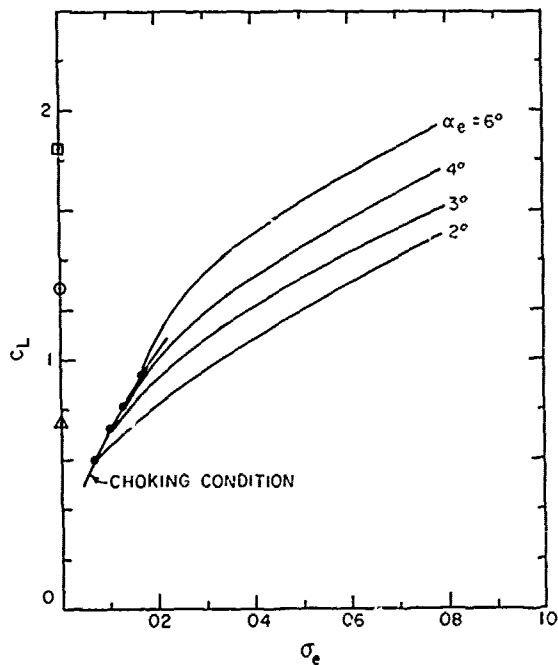
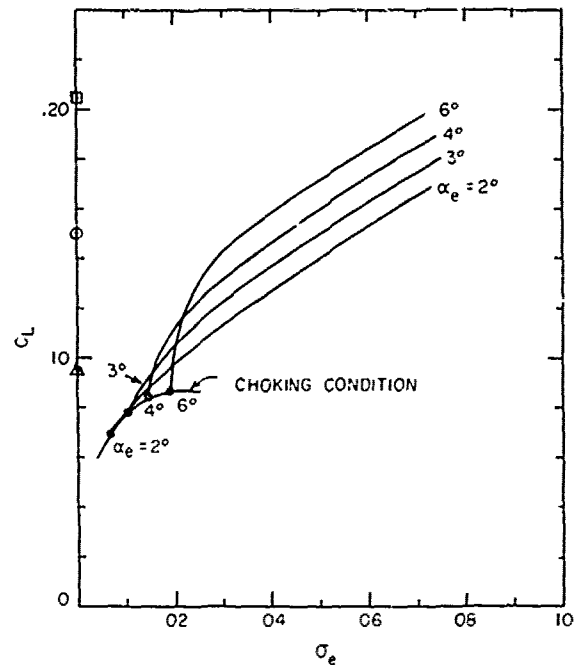


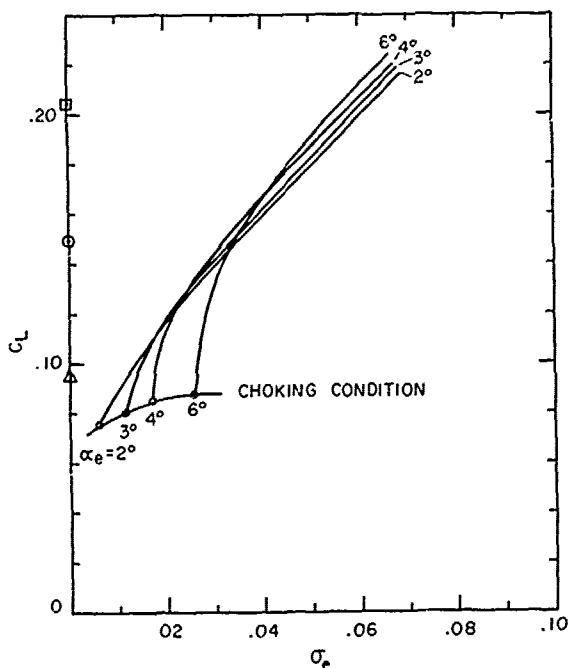
Figure 2 Representation of Cavity Thickness by Distribution of Source Singularities in a Cascade Row



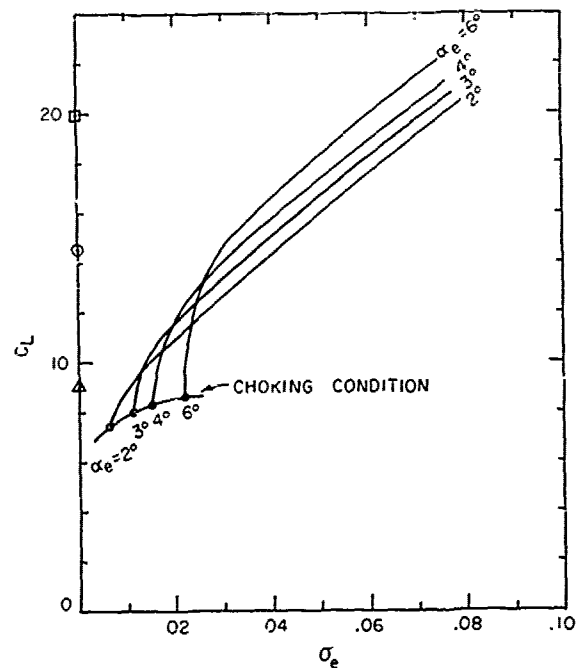
(a) Blade Spanwise Location $x = .9$
where $\gamma = 74.03^\circ$ and $\text{sol} = .244$



(b) $x = .8$, $\gamma = 72.4^\circ$
 $\text{sol} = .365$

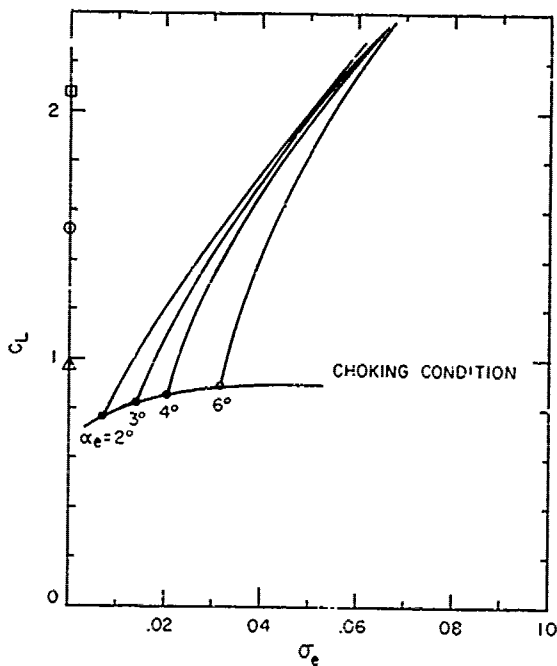


(c) $x = .7$, $\gamma = 70.33^\circ$
 $\text{sol} = .479$

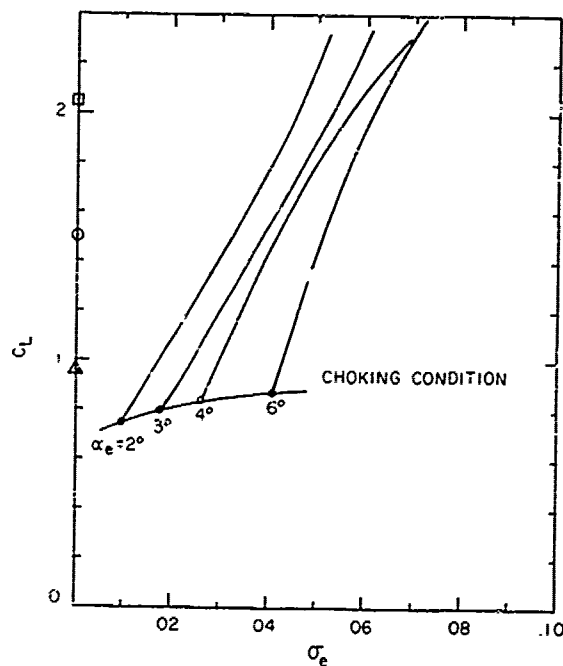


(d) $x = .6$, $\gamma = 67.61^\circ$
 $\text{sol} = .594$

Figure 3 Lift Coefficient C_L , Normal to the Upstream Velocity vs. Cavitation Number σ_e for Incidence Angles $\alpha_e = 2^\circ, 3^\circ, 4^\circ$ and 6° . Δ \circ \square are C_L Values of $\alpha_e = 2^\circ, 4^\circ, 6^\circ$ Respectively Calculated from a Linearized Theory for a Single Foil (Equation 31).

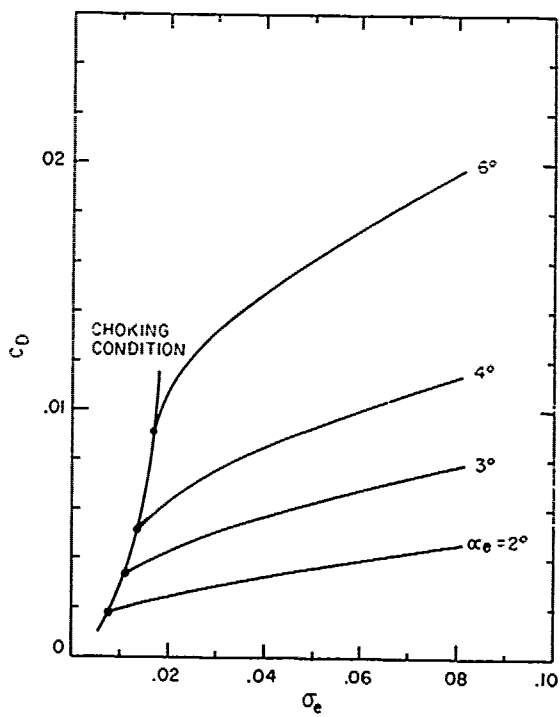


(e) $x = .5$, $\gamma = 63.94^\circ$
sol = .728

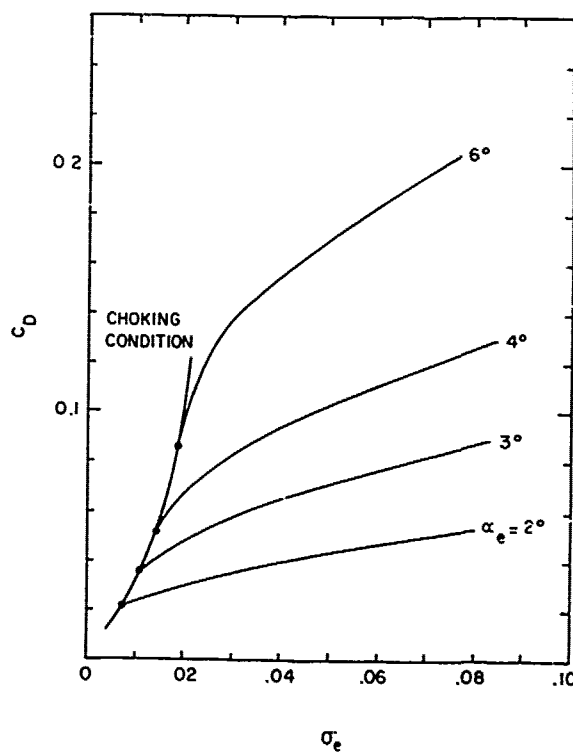


(f) $x = .4$, $\gamma = 58.77^\circ$
sol = .912

Figure 3 (Cont'd)

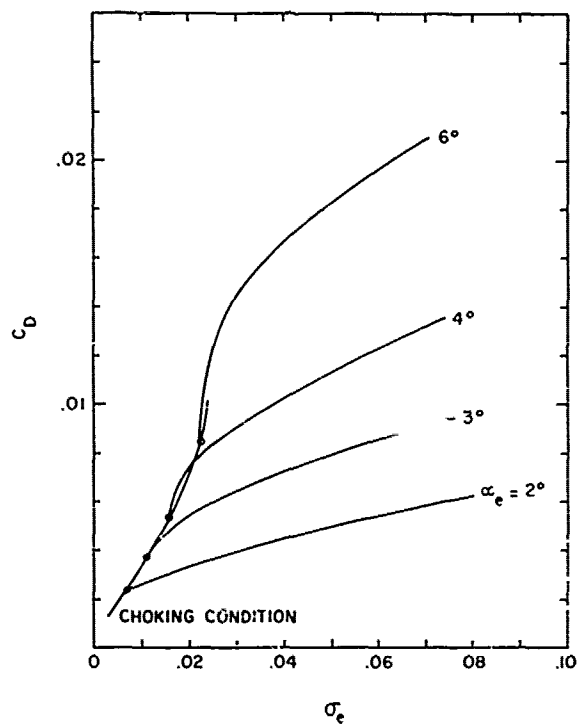


(a) $x = .9$

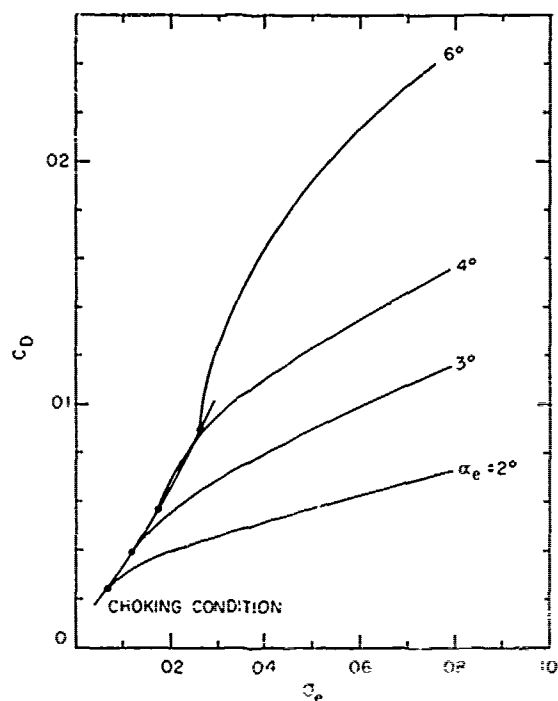


(b) $x = .8$

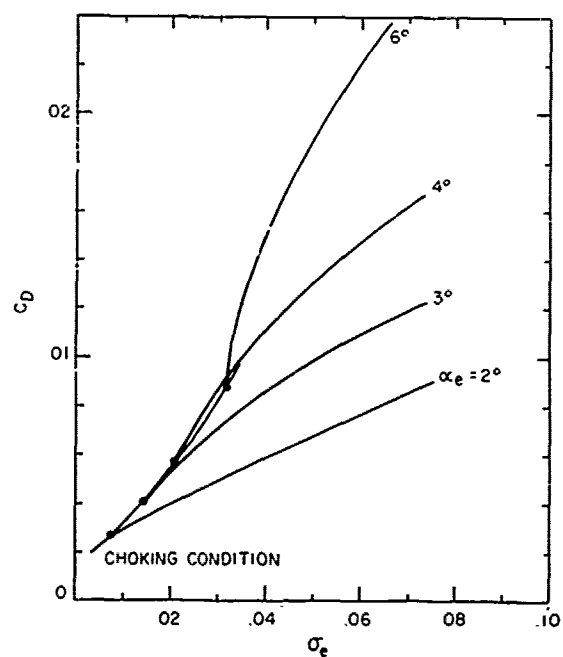
Figure 4 Drag Coefficient C_D Corresponding to Figure 3



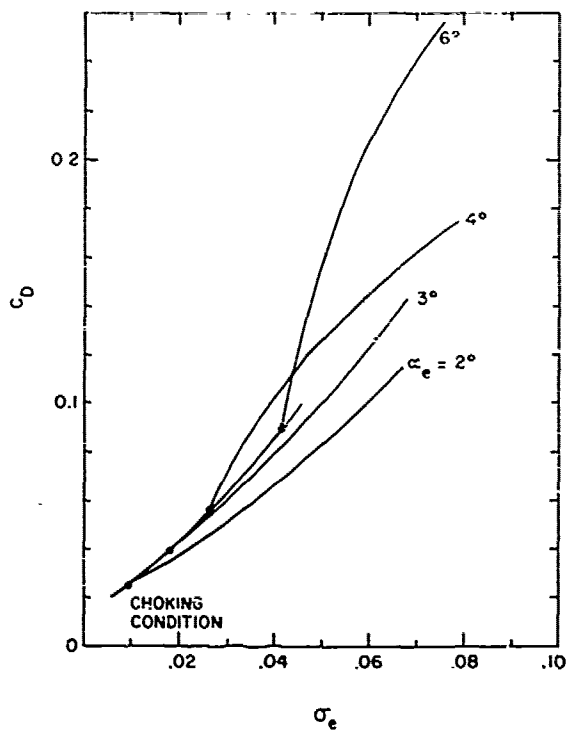
(c) $x = .7$



(d) $x = .6$



(e) $x = .5$



(f) $x = .4$

Figure 4 (Cont'd)

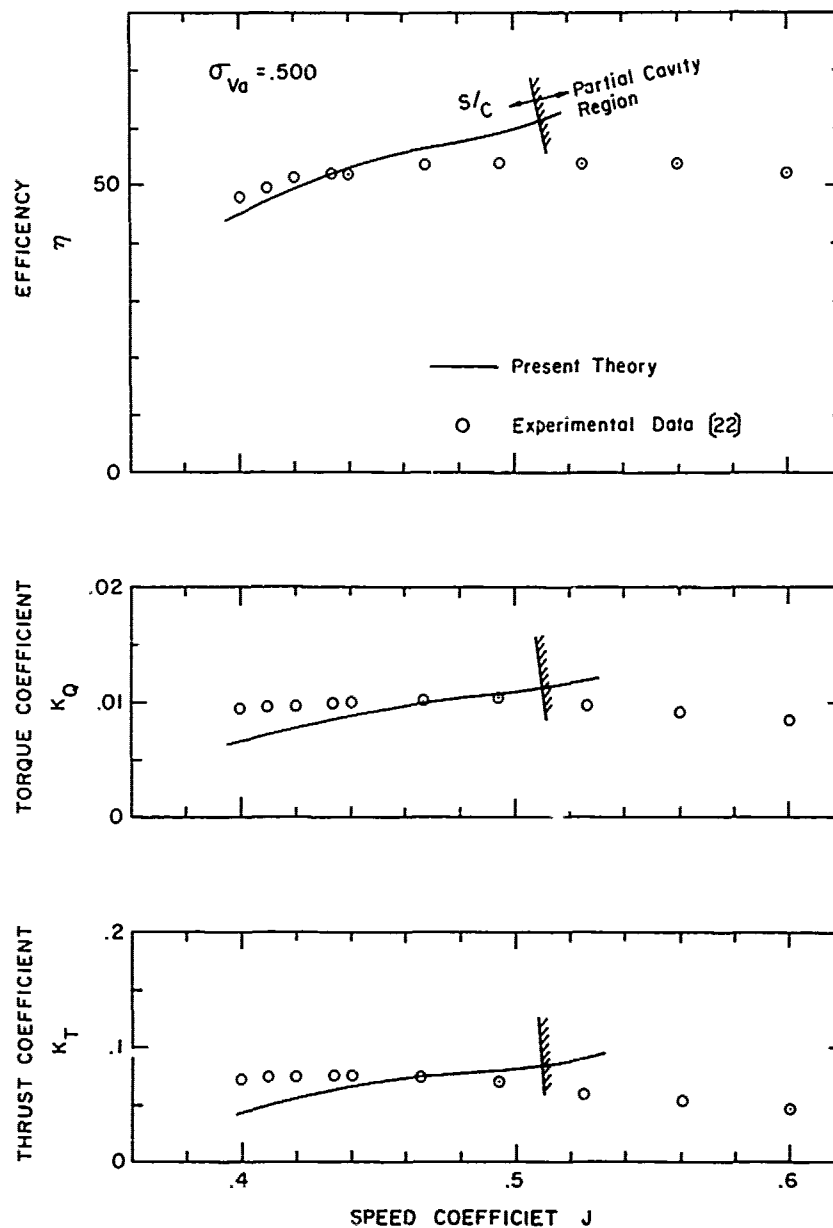
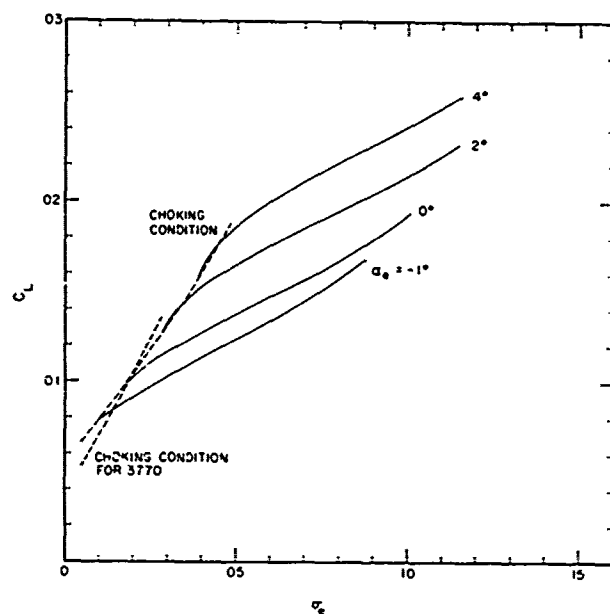
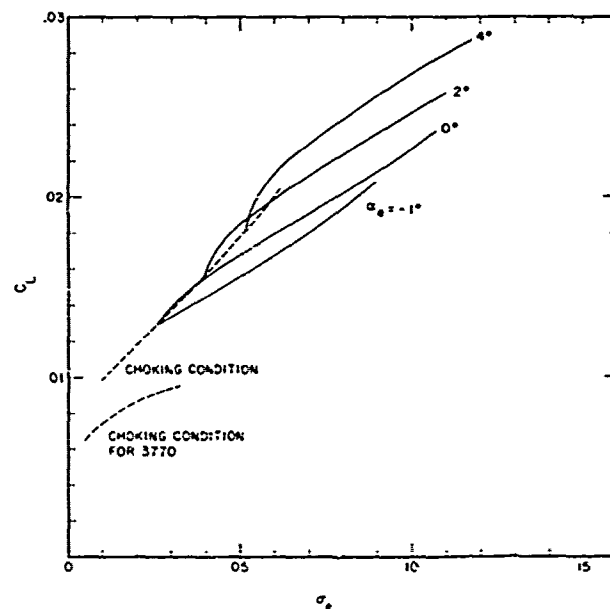


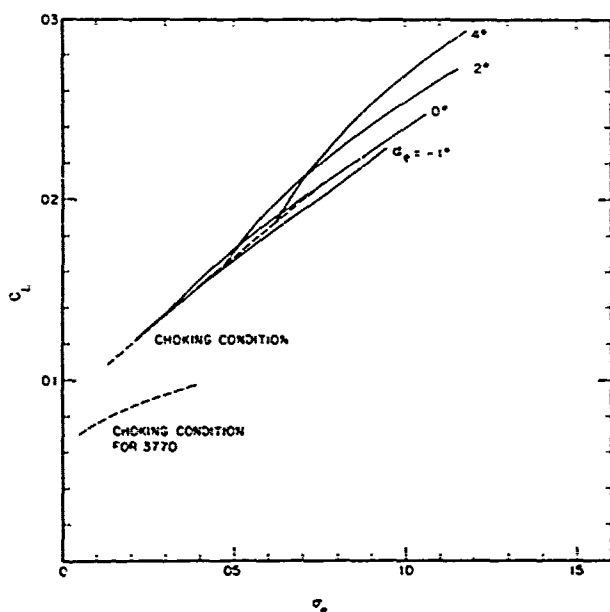
Figure 5 Comparison of 3770 Performance between the Theory and Experimental Data [22] at $\sigma_{Va} = .500$



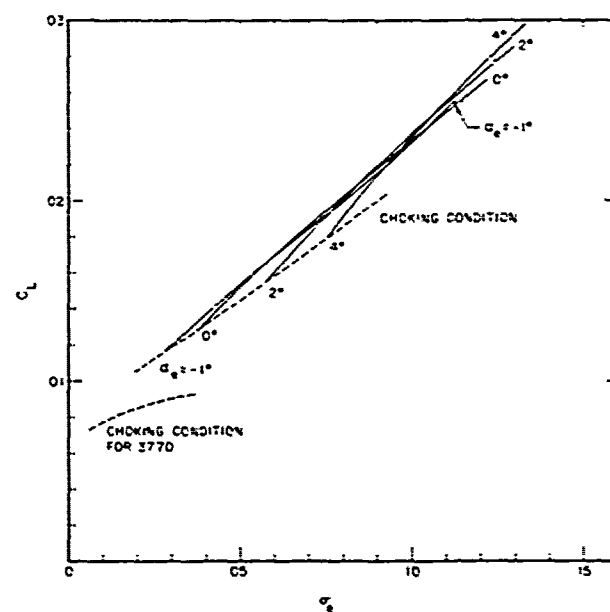
(a) $x = .9, \gamma = 64.61^\circ$
sol = .192



(b) $x = .8, \gamma = 61.02^\circ$
sol = .294

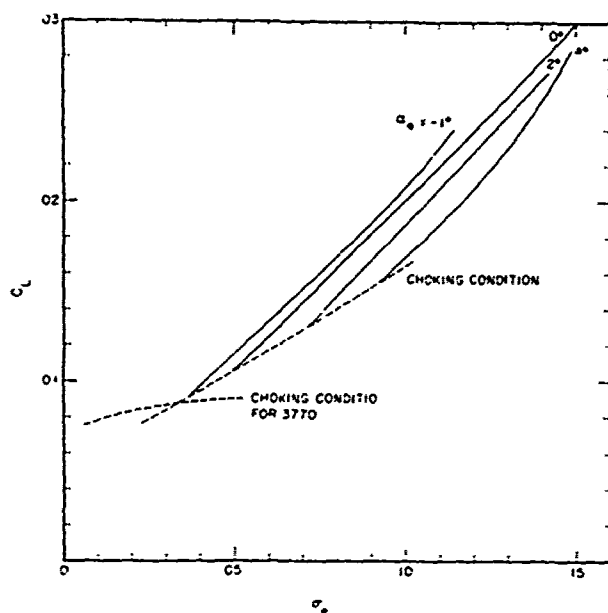


(c) $x = .7, \gamma = 57.53^\circ$
sol = .389

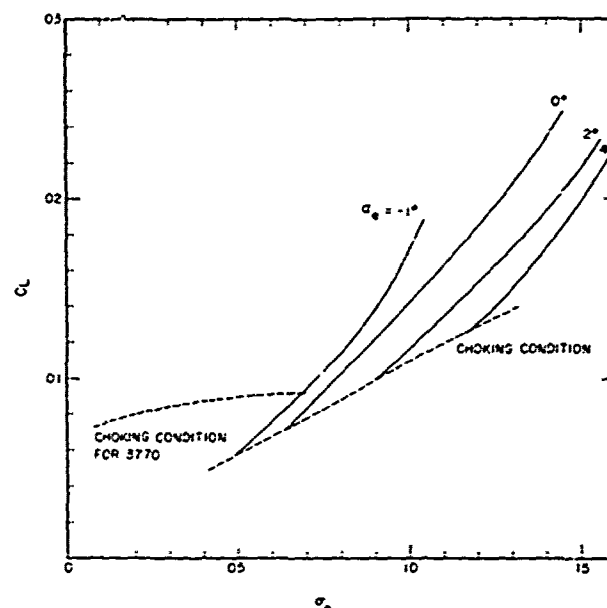


(d) $x = .6, \gamma = 53.63^\circ$
sol = .485

Figure 6 Lift Coefficient C_L Normal to the Upstream Velocity vs. Cavitation Number σ_e as a Function of Incidence Angle α_e for 7607.02 Propeller Section Profile. (The choking condition for TMB 3770 is also shown.)



(e) $x = .5$, $\gamma = 48.88^\circ$
sol = .585



(f) $x = .4$, $\gamma = 43.13^\circ$
sol = .684

Figure 6 (Cont'd)

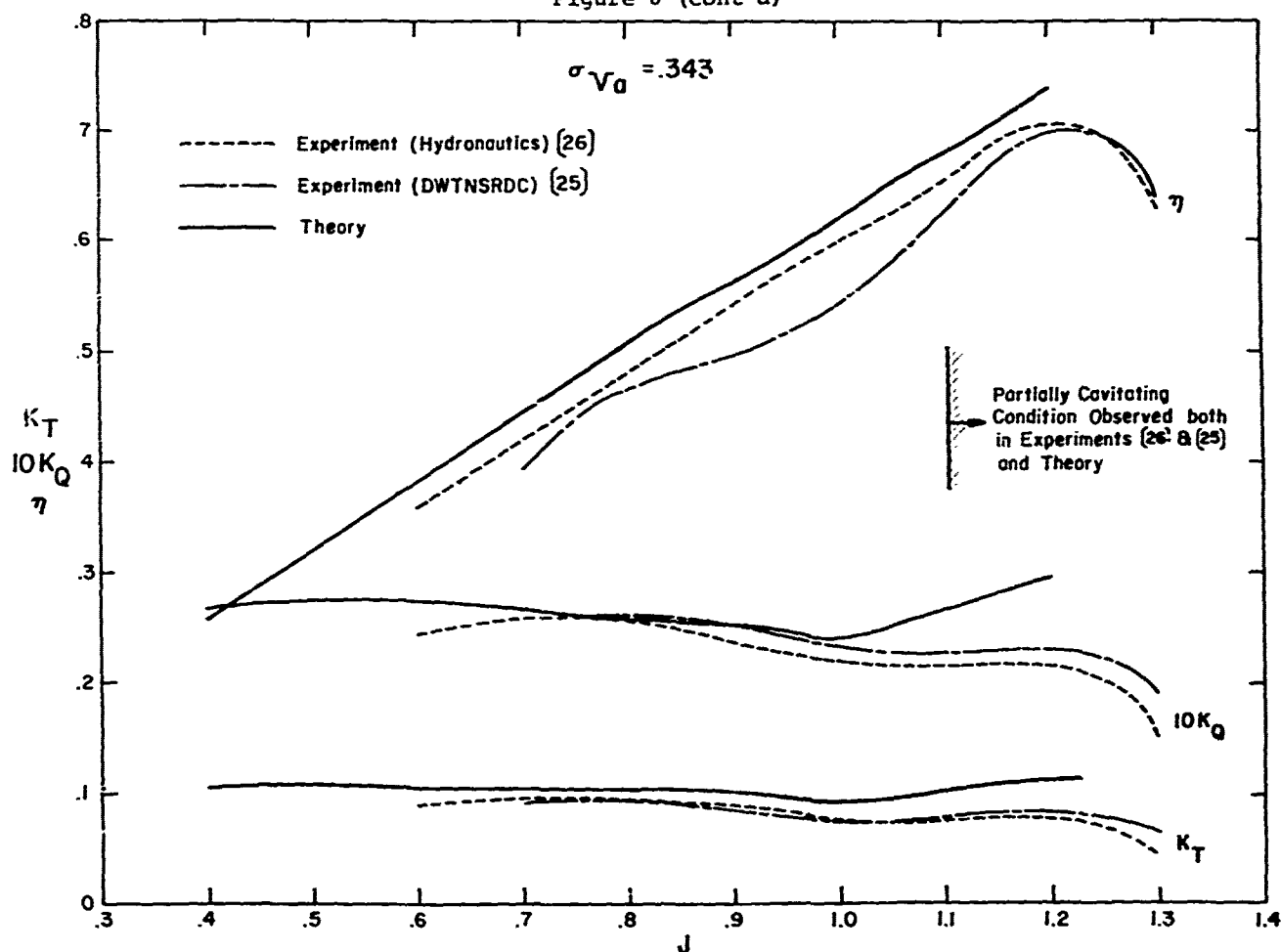


Figure 7 Comparison between Experiments and Theory for the Off-Design Performance of s/c Propeller 7607.02 at $\sigma_{va} = .343$

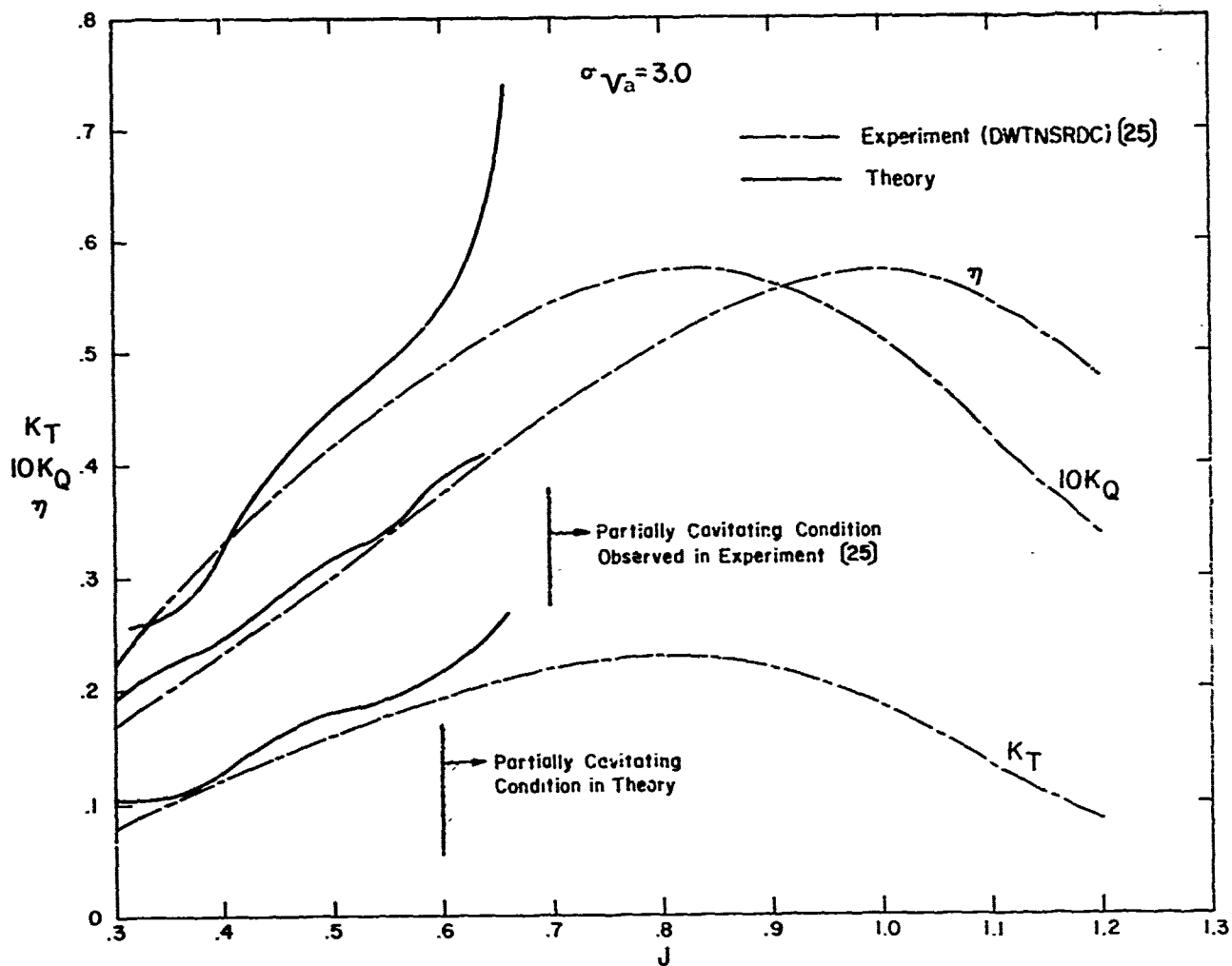


Figure 8 The Same as Figure 7 except for $\sigma_{Va} = 3.0$

APPENDIX A

TWO-DIMENSIONAL NONLINEAR SUPERCAVITATING CASCADE THEORY (Ref. [29])

The detailed mathematical formulation is described in [29]. However, some important features which will provide a better understanding of the present propeller theory are presented herein. In particular, $\text{Re}\{\omega(\zeta_1)\}$, $\text{Im}\{\omega(\zeta_1)\}$, g_3 , $s(-1)$ and g_5 in Equations (7) to (11) in the text are given as follows.

$$\begin{aligned}\omega(\zeta_1) &= \text{Re}\{\omega(\zeta_1)\} + i \text{Im}\{\omega(\zeta_1)\} \\ &= \sqrt{(\zeta_1 + 1)(\zeta_1 - b)} \left\{ \frac{1}{2-i} \right. \\ &\quad \int_a^{-1} \frac{-i2 \ln(\sqrt{1+\sigma}/U_2)}{\sqrt{(\xi'+1)(\xi'-b)}} \frac{d\xi'}{\xi'-\zeta_1} \\ &\quad + \frac{1}{2-i} \int_{-1}^b \frac{2\bar{B}(\xi')}{i\sqrt{(1+\xi')(b-\xi')}} \frac{d\xi'}{\xi'-\zeta_1} \\ &\quad + \frac{1}{2-i} \int_0^b \frac{2\pi}{\sqrt{(1+\xi')(b-\xi')}} \frac{d\xi'}{\xi'-\zeta_1} \\ &\quad \left. + \frac{1}{2-i} \int_b^c \frac{i2 \ln(\sqrt{1+\sigma}/U_2)}{\sqrt{(\xi'+1)(\xi'-b)}} \frac{d\xi'}{\xi'-\zeta_1} \right\} \\ &\quad (A-1)\end{aligned}$$

where

$$\zeta_1 = \tilde{A} \exp \{i(\pi/2 - \gamma)\},$$

$$g_3 = \frac{1}{\pi} \ln(\sqrt{1+\sigma}/U_2).$$

$$\begin{aligned}&\left\{ \ln \frac{-(b+1)}{2\sqrt{(a+1)(a-b)} + (a+1) + (a-b)} \right. \\ &\quad \left. + \ln \frac{(b+1)}{2\sqrt{(c+1)(c-b)} + (c+1) + (c-b)} \right\} \\ &\quad + \left(\frac{\pi}{2} - \sin^{-1} \frac{1-b}{1+b} \right) \\ &\quad + \frac{1}{\pi} \int_{-1}^b \frac{\bar{B}(\xi') d\xi'}{\sqrt{(1+\xi')(b-\xi')}} , \quad (A-2)\end{aligned}$$

$$\begin{aligned}s(-1) &= - \int_{\xi}^{-1} h(\xi', a, b, c, U_2(a_2)) \\ &\quad \cdot k(\xi', A) d\xi' \quad (A-3)\end{aligned}$$

where

$$\begin{aligned}h(\xi, a, b, c, U_2(a_2)) &= \left[\exp \left\{ - \frac{\ln(\sqrt{1+\sigma}/U_2)}{\pi} \right. \right. \\ &\quad \left(\pi + \sin^{-1} \frac{(1+\xi)(a-b) + (\xi-b)(1+a)}{(\xi-a)(1+b)} \right. \\ &\quad \left. \left. + \sin^{-1} \frac{(1+\xi)(c-b) + (\xi-b)(1+c)}{(c-\xi)(1+b)} \right) \right. \\ &\quad \left. + \frac{\sqrt{(1+\xi)(b-\xi)}}{\pi} \int_{-1}^b \frac{\bar{B}(\xi')}{\sqrt{(1+\xi')(b-\xi')}} \right. \\ &\quad \left. \frac{d\xi'}{\xi'-\xi} \right\} \\ &\quad \times \frac{2\sqrt{b}\sqrt{(1+\xi)(c-\xi)} + \xi(b-1) + 2b}{\{-\xi(1+b)\}} \cdot \frac{1}{U_2}\end{aligned}$$

(A-4)

$$k(\xi, \tilde{A}) = \frac{d}{d\xi} \frac{\xi \cos \delta}{(\xi - \tilde{A} \sin \delta)^2 + (\tilde{A} \cos \delta)^2} \quad (A-5)$$

and

$$\delta = \alpha_e + \gamma, \quad (A-6)$$

$$\frac{d}{d\xi} \left\{ e^{-i\delta} \ln \frac{\xi_1 - c}{\xi_1 - a} + e^{i\delta} \ln \frac{\xi_1 - c}{\xi_1 - a} \right\}$$

In these equations a, b, c are ξ -coordinates in the mapped plane (see Figure A-2), \tilde{A} is a parameter associated with the cascade mapping function and U is the velocity at downstream infinity where the continuity equation provides

$$U_2 = \frac{\cos(\alpha_e + \gamma)}{\cos(\alpha_2 + \gamma)}.$$

All these parameters are unknown solution parameters to be determined by solving Equations (7) to (11) in the text. The potential plane W , transform plane ξ and physical plane z are shown in Figures A1 to A3.

CALCULATIONS OF INDUCED VELOCITIES W_a and W_t BY A LIFTING LINE THEORY

$$\frac{w_a}{v_a} = \frac{1}{2} \int_{x_h}^1 \frac{dG(x')}{dx'} \frac{1}{x-x'} i_a(\beta_i) dx' \quad (B-1)$$

$$\frac{w_t}{v_a} = \frac{1}{2} \int_{x_b}^1 \frac{dG(x')}{dx'} \frac{1}{x-x'} i_t(z_i) dx' \quad (B-2)$$

$$G(x) = \frac{\dot{\gamma}(x)}{2\pi R V_3} \quad (B-3)$$

$$i_a(z_i) = \begin{cases} g \frac{x}{x' \tan \beta_i} \left(\frac{x'}{x} - 1 \right) (1 + B_2), & x < x' \\ -g \frac{x}{x' \tan \beta_i} \left(\frac{x'}{x} - 1 \right) B_1, & x > x' \end{cases} \quad (B-4)$$

$$i_t(r_i) = \begin{cases} g\left(\frac{x'}{x} - 1\right)B_2, & x \cdot x' \\ -g\left(\frac{x'}{x} - 1\right)(1 + B_1), & x \cdot x' \end{cases} \quad (B-5)$$

$$B_{1,2} = \left(\frac{1+y^2}{1+y'^2} \right)^{\frac{1}{2}} \left[\frac{1}{e^{gA_{1,2}}} \mp \frac{1}{2g} \frac{y'^2}{(1+y'^2)^{1.5}} \right. \\ \left. \cdot n \left(1 + \frac{1}{e^{gA_{1,2-1}}} \right) \right] \quad (B-6)$$

$$A_{1,2} = \pm \left(\sqrt{1+y^2} - \frac{1}{\sqrt{1+y^2}} \right)^{\pm} \ln \frac{\pm \frac{1}{2} \ln \frac{(\sqrt{1+y^2}-1)(\sqrt{1+y^2}+1)}{(\sqrt{1+y^2}+1)(\sqrt{1+y^2}-1)}}{(B-7)}$$

$$y' = \frac{1}{\tan \theta_i} \quad (B-8)$$

$$y = \frac{x}{x' \tan \beta_1} \quad (8-9)$$

By introducing ϕ for a change of variables

$$x = \frac{1}{2} (1 + x_h) - \frac{1}{2} (1 - x_h) \cos \phi, \quad (\text{B-10})$$

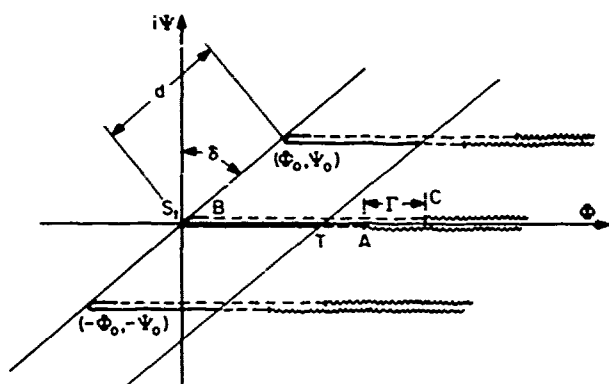


Figure A1 Potential Plane $W = \xi + i\eta$

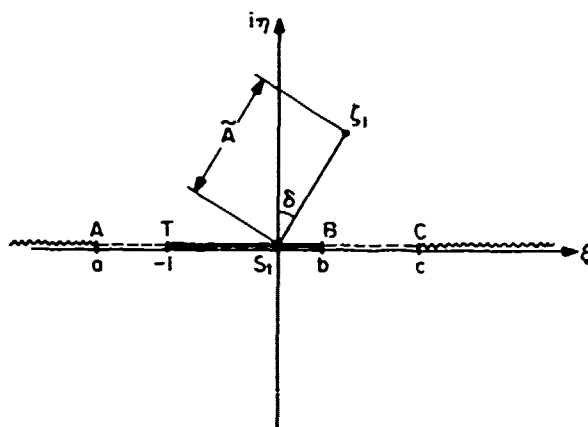
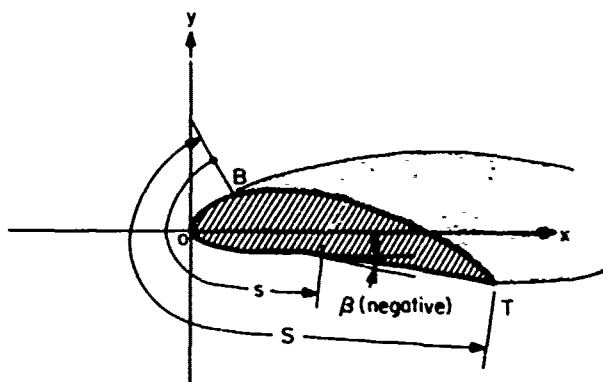
Figure A2 Transform Plane $z = r + in$ 

Figure A3 **Definition of the Arc Length
and the Body Inclination for
the Wetted Portion of the Foil**

we can write $G(x)$ and i_a and i_t in Fourier sine and cosine series, respectively

$$G(\phi') = \sum_{m=1}^{\infty} G_m \sin m\phi' \quad (B-11)$$

$$i(\phi, \phi') = \frac{i_0(\phi)}{2} + \sum_{n=1}^{\infty} I_n(\phi) \cos n\phi'. \quad (B-12)$$

The coefficients G_m and $I_n(\phi)$ in (B-11) and (B-12) are readily obtained as follows

$$G_m = \frac{2}{\pi} \int_0^{\pi} G(\phi') \sin m\phi' d\phi' \quad (B-13)$$

$$I_n^a(\phi) = \frac{2}{\pi} \int_0^{\pi} i_a(\phi, \phi') \cos n\phi' d\phi' \quad (B-14)$$

$$I_n^t(\phi) = \frac{2}{\pi} \int_0^{\pi} i_t(\phi, \phi') \cos n\phi' d\phi' \quad (B-15)$$

where x and x' have been replaced by ϕ and ϕ' .

Now W_a and W_t are written in the following forms

$$\frac{W_a(\phi)}{V_t} = \frac{1}{1-x_h} \sum_{m=1}^{\infty} m G_m h_m^a(\phi) \quad (B-16)$$

$$\frac{W_t(\phi)}{V_t} = \frac{1}{1-x_h} \sum_{m=1}^{\infty} m G_m h_m^t(\phi) \quad (B-17)$$

where

$$h_m^{a,t}(\phi) = \frac{\pi}{\sin \phi} \left[\sin m\phi \sum_{n=0}^{\infty} I_n^{a,t}(\phi) \cos n\phi \right. \\ \left. + \cos m\phi \sum_{n=m+1}^{\infty} I_n^{a,t}(\phi) \sin n\phi \right]. \quad (B-18)$$

It must be noted that, at $\phi = 0$ and $\phi = \pi$

$$h_m^{a,t}(0) = \pi \left[m \sum_{n=0}^{\infty} I_n^{a,t}(0) + \sum_{n=m+1}^{\infty} n I_n^{a,t}(0) \right] \quad (B-19)$$

$$h_m^{a,t}(\pi) = -\pi \cos m\pi \left[m \sum_{n=0}^{\infty} I_n^{a,t}(\pi) \cos n\pi \right. \\ \left. + \sum_{n=m+1}^{\infty} n I_n^{a,t}(\pi) \cos n\pi \right] \quad (B-20)$$

where L'Hospital rule has been used.

Discussion

B. Yin (DTNSRDC)

The prediction of propeller performance is hard to do, even for a subcavitating propeller. The performance results obtained by Dr. Furuya for supercavitating propellers are very impressive. Several comments are as follows:

1) Numerical results for nonlinear supercavitating cascades seem a little strange near the choking cavitation number. We all understand that the cavity length changes rapidly near the choking cavitation number; however, I do not know that the lift or drag coefficient changes as rapidly as is shown in Figures 3 and 4. If the change is this rapid it would be due to the nonlinear effect. It may be interesting to compare with the following Figure (Reference 1) which was obtained by using linear theory. It seems that it needs to be verified by experiments or otherwise, since from existing experiments for supercavitating propellers it is very hard to guess the similar phenomenon.

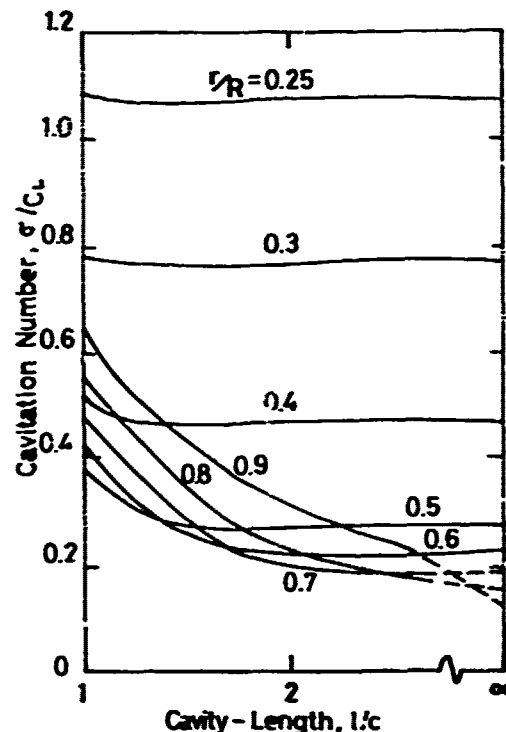
2) The method of calculating the flow retardation effect by a two-dimensional source seems to require more explanation. In two-dimensional supercavitating cascade theory, the speed at upstream infinity is a given quantity, and the original solution should already include this blockage effect in the relation between inlet and exit flows. In fact, the flow retardation effect in supercavitating propellers is the three-dimensional effect, acting quite differently from the cascade effect or the influence of neighboring cavities. The axial velocity component of oncoming flow near the blade decreases due to the former effect and increases due to the latter (Reference 17) partially cancelling each other. Because of this, early consideration of an isolated supercavitating foil instead of cascades sometimes worked very well. If we consider the radial component of oncoming velocity, it is not certain whether the total oncoming speed changes enough to affect the cavitating phenomena of the near field cascade. However, according to Reference 17 in the design problem, the flow field of three-dimensional lifting surface and cavity sources decreased the pitch distribution, which was calculated by lifting-line and linear-cascade theories. This would mean that in the prediction theory, the effect of three-dimensional lifting surface and cavity sources would increase the calculated angle of attack. Therefore, the flow retardation effect would make the cavity thicker and longer in the analysis for a given supercavitating propeller, quite contrary to the indication in the present paper.

3) Since it was mentioned about the

research in supercavitating propellers at the David W. Taylor Naval Ship R&D Center, it may be appropriate here to touch upon the experimental results. We designed four- and six-bladed propellers by the method given in Reference 17, manufactured the models, and tested them in the DTNSRDC 36-inch cavitation tunnel both for cavity height and performance. The experiment on cavity height indicated that the theory predicted well for blade sections at radii larger than half of the propeller radius for both propellers. It also showed that the leading-edge shape of the model needed to be manufactured more carefully. The experiment on performance showed that the efficiency at the design point was predicted within 4 percent for the four-bladed and 3 percent for the six-bladed propellers and the thrust coefficient was over predicted within 10 percent for the four-bladed and 5 percent for the six-bladed propellers. The incorporation of the nonlinear effect on the lift and drag coefficient of the cavitating foil brought the prediction at the design point within 3 percent of the experimental values.

REFERENCES

- 1) Yin, B., "Supercavitating Foil of An Arbitrary Shape Beneath or Above a Free Surface or in a Cascade," Proceedings on the Second International Conference on Numerical Ship Hydrodynamics, Univ. of Calif., Berkeley (1977)



Relation between cavitation number and cavity-length of supercavitating cascade in blade sections of supercavitating propeller model 3770

A.R. Rowe (LM Grenoble)

Firstly, is it important to know very well the position of the detachment point at the leading edge. In the theory presented, however, this position is fixed for the two-dimensional problem. What it happens when the inner problem is matched with the outer.

Secondly, to my knowledge no numerical calculation has been developed in the framework of the surface lifting theory, using discrete singularities for supercavitating propellers. I would like to know if that's true, and if it's yes, what are the main difficulties.

Author's Reply

O. Furuya (Tetra Tech)

The author thanks Dr. Yin for his valuable comments and would like to respond to them one by one.

1) Professor Hutton and his student of University of Southampton recently used a linearized cascade theory for calculating the force coefficients of flat plate and circular foil cascades and compared with the results of the nonlinear theory. It was found that although the absolute values were different, both results showed quite a similar trend for $dC_L/d\alpha$. It is

believed that the rapid change of C_L near the choking condition is inherent in supercavitating cascade flow.

2) The purpose of having used the cascade flow for the supercavitating propeller analysis is that it will account for the adjacent blade effect and thus for the blade loading function. However, it was believed that the effective flow velocity should be corrected due to the cavity blockage effect.

3) I would like to congratulate Dr. Yin for his effort on developing a design method for s/c propellers and having success in designing better propellers. We all look forward to seeing the comparative results of theory and experiment in the near future.

To A.R. Rowe

The blade profile shape commonly used for this type of propeller is of so-called supercavitating type having a sharp leading edge. There is no difficulty in determining the cavity separation point.

The lifting surface theory which has never been used for the off-design analysis will provide an inherent difficulty in any cavity flow analysis.

The extent of cavitation is not known a priori so that an iteration procedure should be employed to solve the problem. Furthermore, unlike the design method, the off-design theory requires the boundary condition on the blade to be satisfied, which already offers an enough complication.

Cavitation on High Speed Propellers in Oblique Flow—Influence of Propeller Design and Interaction with Ship Hull

Olle Rutgersson

Swedish Maritime Research Centre (SSPA)

Göteborg, Sweden

ABSTRACT

The working conditions of propellers working behind high speed displacement ships are discussed.

Results from cavitation tests of six different propellers working behind a twin-screw ship model are given. The results are discussed in regard to influence of propeller geometry on erosion, thrust breakdown, relative rotative efficiency and pressure fluctuations.

Finally comparison is made between tests of propeller-hull interaction with a simple plate model and a complete ship model. Some results of the propeller-propeller interaction for a triple screw ship are also given.

NOMENCLATURE

a	vertical clearance between propeller and hull (m)
A_D	developed blade area (m^2)
A_0	$\pi D^2/4$ (m^2)
C	pressure fluctuation, single amplitude (Pa)
C_p, C_{pT}	$\Delta p/\rho/2V^2$ = pressure coefficient
D	propeller diameter (m)
f	maximum camber of propeller blade section (m)
F_N	V_S/\sqrt{gL} = Froude number
H_0	draught of propeller centre at zero speed (m)
J	V_A/nD = advance ratio of propeller
J_B	advance ratio at behind condition

J_0	advance ratio at free running condition
K_p	$2C/\rho n^2 D^2$ = amplitude coefficient, pressure fluctuations
K_{pnc}	amplitude coefficient at cavitation free conditions
K_Q	$Q/\rho n^2 D^5$ = propeller torque coefficient
K_T	$T/\rho n^2 D^4$ = propeller thrust coefficient
K_{TB}	thrust coefficient at behind condition
K_{T0}	thrust coefficient at free running condition
l	profile length (m)
L	ship length between perpendiculars (m)
n	number of revs (r/s)
P_{atm}	atmospheric pressure (Pa)
P_0	cyclic pressure at propeller centre a)
P_v	vapour pressure (Pa)
Δp	pressure difference between undisturbed flow and propeller centre (Pa)
P	pitch (m)
P_p	power (Mw)
Q	propeller torque (Nm)
r	radius of propeller blade section (m)
R	$D/2$ (m)
T	propeller thrust (N)

ΔT_A	sinkage of ship stern (m)
V_A	advance speed of propeller (m/s)
V_S	ship speed (m/s)
$V_{0.7R}$	$V_A \sqrt{1 + (0.7\pi/J)^2}$ = inflow velocity for blade section at 0.7R
w	wake fraction
x	r/R
y_{\max}	maximum face camber of propeller blade section
η_R	η_R/η_0 = relative rotative efficiency
η_B	propeller efficiency at behind condition
η_0	propeller efficiency at free running condition
ρ	density of water (kg/m ³)
σ_{VA}	$(p_0 - p_v)/0.5\rho V_A^2$ = cavitation number
σ_0	$(p_0 - p_v)/0.5\rho V_{0.7R}^2$ = cavitation number
σ_T	$\sigma_{VA} - \frac{C_{pT}}{(1-w)^2}$ = cavitation number in tunnel
τ_c	propeller loading coefficient
ϕ	pitch angle (degrees)

1. INTRODUCTION

When using water propellers for the propulsion of high speed vessels inclined propeller shafts are necessary in most cases. The cavitation patterns for propellers working under such conditions are characterized by fairly pronounced variation of the extension for the inner radii, the extension near the tip being more independent of blade position. This is in contrast to the conditions for single screw merchant ship propellers, for which the largest variations of cavitation extension normally occur near the blade tips, the inner radii being free from cavitation.

In the present paper the cavitation properties of propellers working in oblique flow behind trimmed high speed displacement ships are studied.

2. WORKING CONDITIONS

The environmental conditions influencing the work of the propellers can be discussed under the following subheadings:

- o wake field
- o cavitation number
- o propeller loading

2.1 Wake Field

The relation between the water speed at the propeller disk and the ship speed is defined by the wake fraction in the following way:

$$V_A/V_S = 1 - w \quad (1)$$

When analysing the influence on propeller performance it is convenient to split up the wake field into:

- o circumferential variations of axial wake
- o mean value of axial wake
- o mean inflow angle relative to propeller shaft

The viscosity has a dominant influence on the wake field of full ship forms. On these ships the propeller works partly inside the boundary layer, which causes two characteristic effects:

- o large variations in the circumferential wake field
- o water speed always considerably lower than ship speed

On high speed vessels the propeller normally works outside the hull boundary layer [1]. Disturbances from inclined propeller shafts and struts will, however, create narrow peaks in the circumferential wake distribution [1, 2]. The mean wake is usually low on high speed ships ($1 - w \approx 1$). The variations with ship speed and trim can, however, be considerable [2, 3]. In Fig 1 results from measurements with Prandtl tubes in the towing basin are shown. The ship model represents the 3-propeller project shown in Chapter 4 of this paper

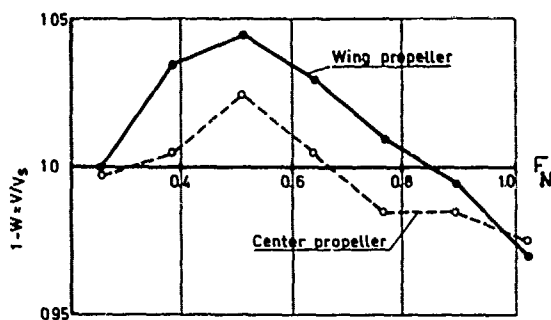


Fig 1 Influence of ship speed on axial wake for a triple-screw ship

In Fig 1 an example is given of the variations of the wake at the propeller plane with ship speed. The values given are mean values of $\pm 90^\circ$ blade position and are therefore approximately valid for the propeller centre. The variations with ship speed are characteristic for this type of ship. $1 - w$ shows a rapid increase at speeds just below $F_N = 0.5$, a maximum at $F_N = 0.5$ and then a decrease with increased speed so that $1 - w \approx 1$ at $F_N = 1$. The magnitude of these variations depends on the hull form and can be considerably higher than shown in Fig 1. The variations with ship speed are shown to be more pronounced for the wing propellers. The reason for this is probably the location of the wing propellers being closer to the wave perturbations than that of the centre propeller.

The wake of a high speed craft is sensitive not only to variations in speed but also to trim changes, as shown in Fig 2.

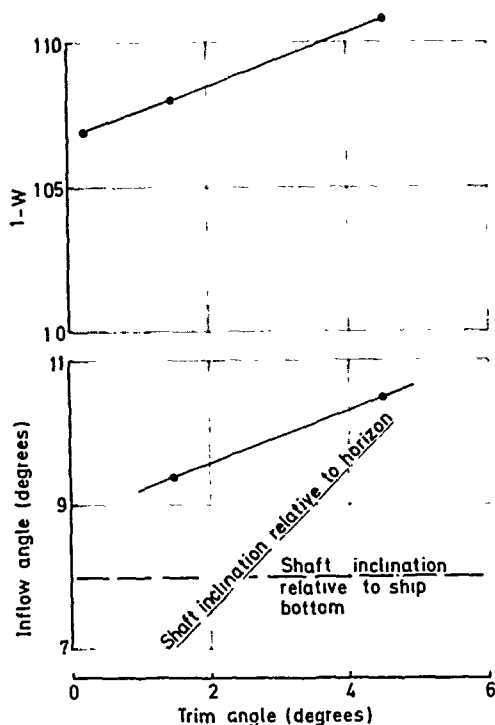


Fig 2 Influence of trim on axial wake and inflow angle on a twin-screw ship

The wake shown in Fig 2 was measured at $F_N = 0.55$ in the towing basin on the twin-screw ship model described in Chapter 3. A larger trim by the stern gives higher speeds at the propeller disk and also a larger inflow angle relative to the propeller shaft. The inflow angle measured by a 5-hole Pitot tube is shown to be larger than eight degrees, which is the angle between ship bottom and propeller shaft. When the ship is trimmed by the stern the inflow angle increases by about one third of the rate of the increase in trim angle.

The characteristic features of the wake field of a high speed craft seem to be:

- o the mean wake is often negative ($1 - w > 1$)
- o the mean wake is sensitive to speed and trim variations
- o the flow is oblique relative to the propeller shaft

As the wake changes with trim variations at constant speed one could assume the wake to be rather much influenced by the potential flow. The total wake is then the sum of the effect of viscosity, w_v , potential flow (without wave making), w_p , and wave making, w_w .

$$w = w_v + w_p + w_w \quad (2)$$

In order to obtain the magnitude of the different parts in Eq 2 some theoretical calculations have been carried out by the Hess & Smith method [4] and compared with measurements. This method does not include the influence of the free surface.

In the towing basin the local wake at the propeller centre was measured to $w = -0.076$. Measurements behind the same model mounted in the cavitation tunnel with the same trim as in the basin but with wooden plates representing the water surface gave $w = -0.035$. Theoretical calculations gave -0.074 for the tunnel configuration and -0.033 without the tunnel (still flat plates as the water surface). These results lead to the conclusion:

Viscosity wake	$w_v = +0.039$
Potential wake	$w_p = -0.033$
Wave making wake	$w_w = -0.083$
Blockage in the tunnel	$w_B = -0.041$

Thus the wave making part dominates in this case and useful results from theoretical calculations cannot be obtained unless the free surface is taken into account.

2.2 Cavitation Number

The performance of the propulsion system of a high speed craft is highly dependent of the development of cavitation on the propeller. The basis of a good correlation between model and prototype must therefore be a realistic estimation of the cavitation number:

$$\sigma_{VA} = \frac{P_0 - P_v}{\rho/2 V_A^2} \quad (3)$$

The static pressure at the propeller centre, p_0 , is usually calculated as the sum of the atmospheric pressure and the pressure of the water column from the propeller centre up to the free surface. The wave pattern in the case of a high speed craft, however, makes the estimation of the static pressure more complex. In the first place it is not obvious which surface should be used for the calculations. Secondly, the potential flow induces pressures, which in some cases cause important changes of the cavitation number. Figs 3 and 4 show some results from measurements of the static pressure at the propeller centre on the triple-screw model mentioned earlier. Fig 3 shows the pressure difference between a Pitot tube ahead of the model and a Pitot tube at the propeller disk.

The absolute static pressure at the propeller centre is obtained by adding Δp of Fig 3 to the atmospheric pressure and the pressure of the water column from the propeller centre to the undisturbed water surface.

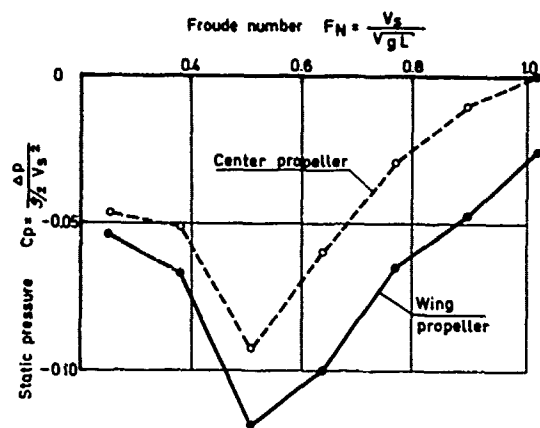


Fig 3 Influence of ship speed on the static pressure measured on a triple-screw model

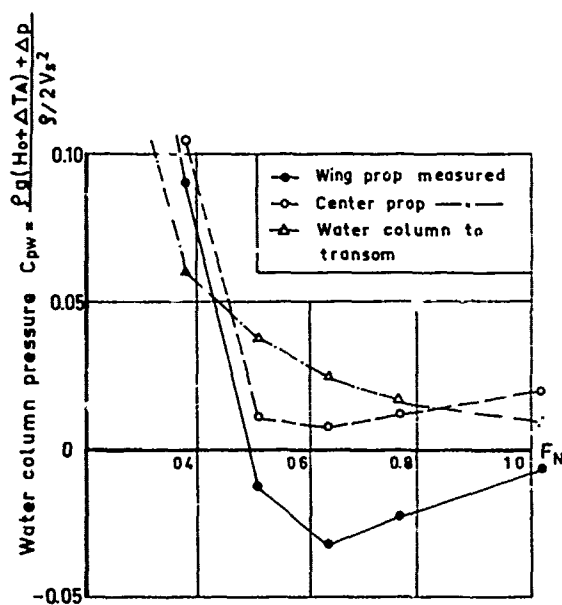


Fig 4 Comparison of measured and calculated water column pressure for triple-screw model

- Measured pressures
- Calculated pressures
- Filled points: towing tank
- Open points: cavitation tunnel

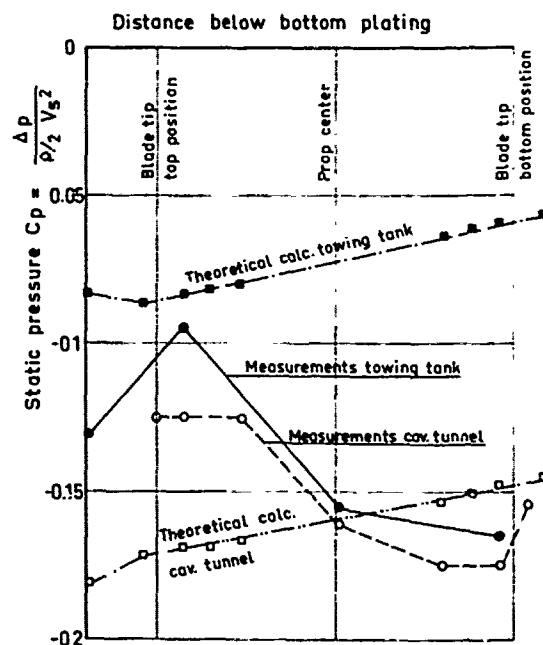
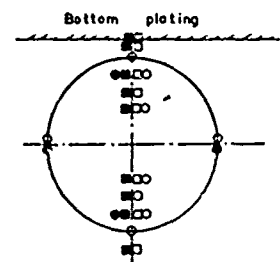


Fig 5 Comparison of measured and calculated static pressures for a twin-screw model at $F_N = 0.55$

$$\sigma_{VA} = \frac{P_{atm} - P_v + \rho g(H_0 + \Delta T_A)}{\rho/2 V_S^2 (1 - w)^2} + \frac{C_p}{(1 - w)^2} \quad (4)$$

In Fig 4 this method is compared with the method of using the water column up to the transom as an approximate value of the static pressure.

At high speeds, $F_N \approx 1.0$, the agreement between the methods is shown to be good. At lower speeds where the trim and sinkage at the stern are large the calculated static pressure is too high. For the wing propellers this difference is not negligible.

The theoretical calculations described in 2.1 also included static pressure. The values obtained have in Fig 5 also been compared with measured static pressures.

The measurements in the towing basin and in the cavitation tunnel happened to give almost identical results for the propeller centre. This is not usually the case and correction for this difference is made when calculating the cavitation number for the cavitation tunnel.

$$\sigma_T = \sigma_{VA} - \frac{C_{pT}}{(1 - w)^2} \quad (5)$$

In Fig 5 the theoretical calculations also agree very well with the measurements at the propeller centre in the tunnel. The differences for locations closer to the hull are probably due to disturbances from shaft and struts, which were not included in the calculations. The calculations for the towing basin show also here that useful results cannot be obtained unless the free surface is taken into account.

2.3 Propeller Loading

The propeller loading is also a fundamental parameter for the cavitation test. The estimation of the propeller loading includes all the traditional towing tank problems:

- o towing tests for measurements of resistance of hull and appendages [5]
- o self propulsion tests for determination of the thrust deduction factor and wake fraction [3, 5]
- o calculation of propeller loadings by the use of scale factors and correlation factors, empirically estimated on the basis of earlier experience

$$K_T/J^2 = \frac{T}{\rho D^2 V_A^2} \quad (6)$$

For most merchant ships the cavitation does not develop so far as to influence the propeller characteristics. The self propulsion tests in the towing tank can therefore form the basis of the prediction of power

and number of revolutions at different speeds. The purpose of the cavitation tests is for most merchant ships to check the erosion properties of the propeller and to measure the vibration excitation forces and the noise generated by the propeller.

The characteristics of a high speed propeller are, however, very much influenced by cavitation. Further, this influence is different in constant flow and when the propeller is working behind the hull (as shown later on). Thus both propulsion tests and cavitation tests are necessary for a reliable power prediction. In the latter case the tests have to be carried out in behind condition.

The purposes of the different tests are:

- o open water tests in towing tank give the relation between thrust and advance coefficients and form the basis of calculation of effective wake fraction
- o propulsion tests in towing tank give propeller thrust and wake for different ship speeds
- o cavitation tests in behind condition give the relation between thrust, torque, efficiency and number of revs at cavitating conditions. Input parameters are the cavitation number according to Eq (5) and the propeller loading according to Eq (6)

3. SYSTEMATIC PROPELLER TESTS

A number of systematic propeller series for propellers specially designed for high speed ships have been presented in the literature, for example [6, 7, 8, 9]. These propellers have, however, usually been tested in uniform flow. Very little is known of the influence of propeller geometry on for example erosion, interaction with hull and pressure fluctuations when the propellers are working behind a hull. It is the purpose of the present investigation to improve the knowledge in this field somewhat.

3.1 Propeller Geometry

Six 3-bladed high speed propeller models with the diameter 250 mm were chosen for the investigation. The main propeller parameters are shown in Table 1.

The three first propellers (Conv 1.05, Conv 0.75 and Conv 0.50) represent a blade area variation of propellers of rather conventional design, with symmetrical blade shape and NACA sections.

Propeller Warp 0.75 is a blade shape (warp 120°) variation of the conventional propeller with blade area ratio 0.75.

The two last propellers have two different supercavitating sections. Propeller S.C. 0.50 has a face shape according to the 3-term distribution and a modified 2-term thickness distribution [9]. The last propeller model was designed to have improved cavitation properties in the partially

Table 1 Main propeller parameters

Propeller No	Design point J	K_T	σ	A_D/Λ_0	Profiles	Pitch distr	Blade shape	Designation	Notation in figures
P1391	1.16	0.19	∞	1.05	NACA 16	unload	sym	Conv 1.05	—○—
P1477	1.16	0.19	∞	0.75	NACA 16	unload	sym	Conv 0.75	—□—
P1514	1.16	0.19	∞	0.50	NACA 16	unload	sym	Conv 0.50	—△—
P1714	1.16	0.19	∞	0.75	NACA 16	unload	120° warp	Warp 0.75	—●—
P1439	1.15	0.146	0.58	0.50	wedge	opt	sym	SC 0.50	—■—
P1790	1.15	0.146	0.58	0.50	spec	opt	sym	PC 0.50	—▲—

cavitating (PC) region. The profile is a combination of 5-term face shape and an empirically derived back shape.

Further information about the propellers, such as blade shape, pitch distribution, camber distribution and design method is given in the Appendix.

3.2 Ship Model

The ship model used for the investigation is a twin-screw patrol craft in scale 1:5.0 with a propeller arrangement according to Fig 6.

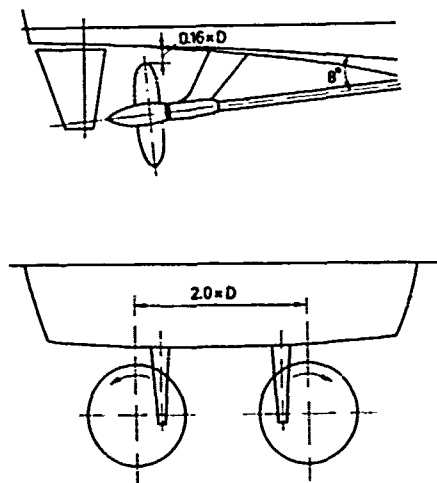


Fig 6 Propeller arrangement on ship model

The main interest in this investigation is devoted to the speed range 30-35 knots. In order to have a typical low speed point 20 knots was, however, also included in the test program. The propeller loadings used for this study were chosen to suit the pitch and diameter of the propellers.

The full scale ship correlating to these loadings could be a twin-screw patrol craft with a displacement of about 100 m³ operating at speeds of about 30 knots with propellers with a diameter of

1.25 m absorbing about 1.5 Mw at about 700 r/m.

Table 2 Propeller loadings and cavitation numbers tested

V_S (knots)	K_T/J^2	$1 - w$	σ_T
20	0.248	1.05	2.07
30	0.156	1.02	0.941
35	0.134	1.0	0.70

3.3 Test Facilities

The cavitation tests were carried out in SSPA large cavitation tunnel. The tunnel is fitted with two interchangeable test sections, i e:

- o one circular, high-speed test section
- o one rectangular, low speed test section, large enough for tests with combinations of propellers and complete ship models

A sketch of the tunnel with the large test section in place is given in Fig 7. The most important data of the test sections are given in Table 3.

Table 3 Main data of test sections of cavitation tunnel 2

	High speed section	Low speed section	
		original	with insert
Length (m)	2.5	9.6	9.6
Area B x H (m ²)	diam 1 m	2.6 x 1.5	2.6 x 1.15
Max speed (m/s)	23	6.9	8.8
Min cav number	0.06*	1.45	0.50

*Empty tunnel. At propeller tests cavitation on right-angle gear dynamometer sets $\sigma = 0.15$ as the lower limit.

The low speed test section is covered by a recess, in which the ship model was placed. The model was the one used for tests in the towing basin and was at this investigation made of fibre-glass. The model was placed in the tunnel with the correct draught at the stem and with the same trim

Pro-
peller

$V_s = 20$ knots

$V_s = 30$ knots

$V_s = 35$ knots

Conv.
1.05



Conv.
0.75



Conv.
0.50



Fig 8 Cavitation patterns at tests with a complete ship model

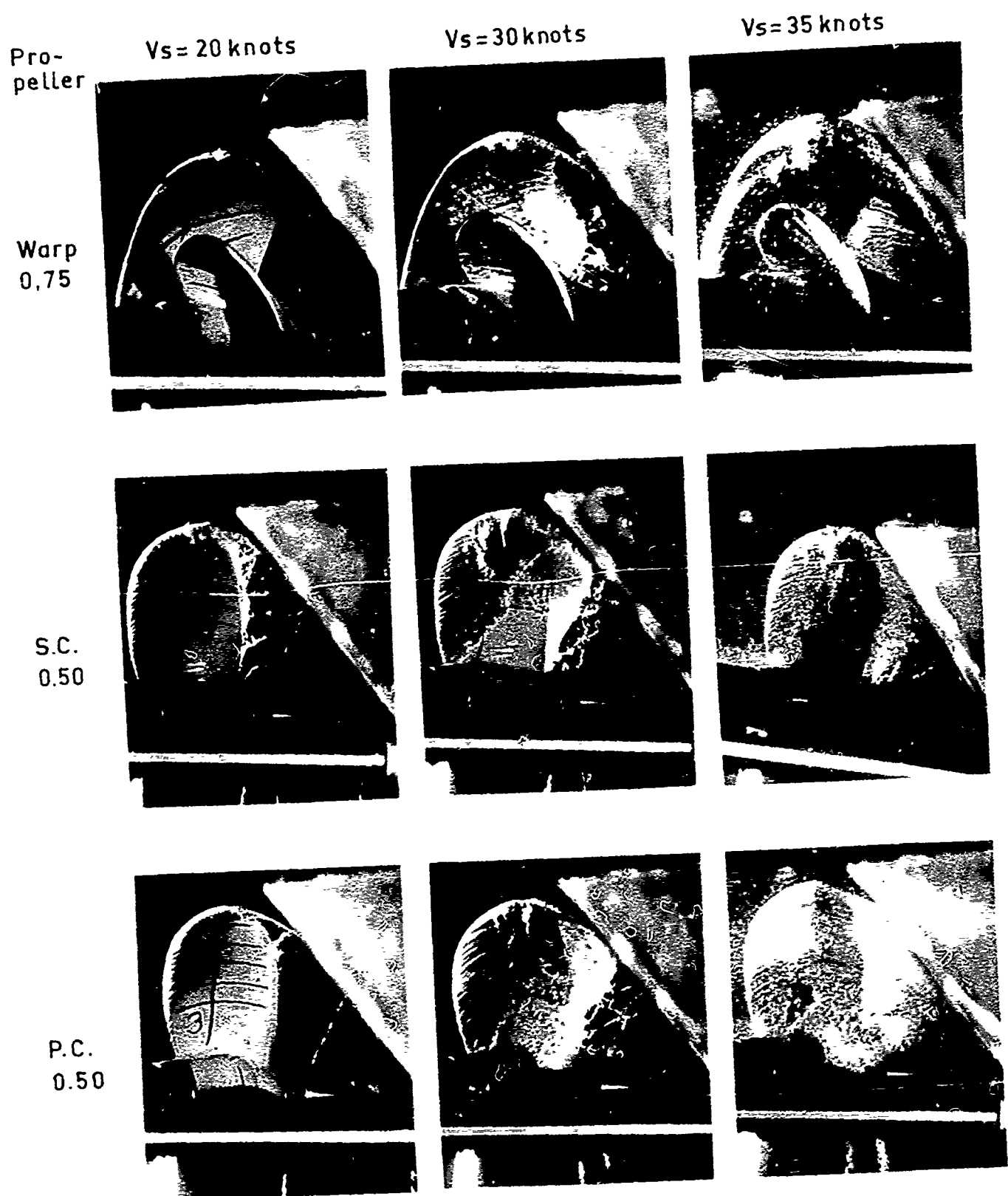


Fig 9 Cavitation patterns at tests with a complete ship model

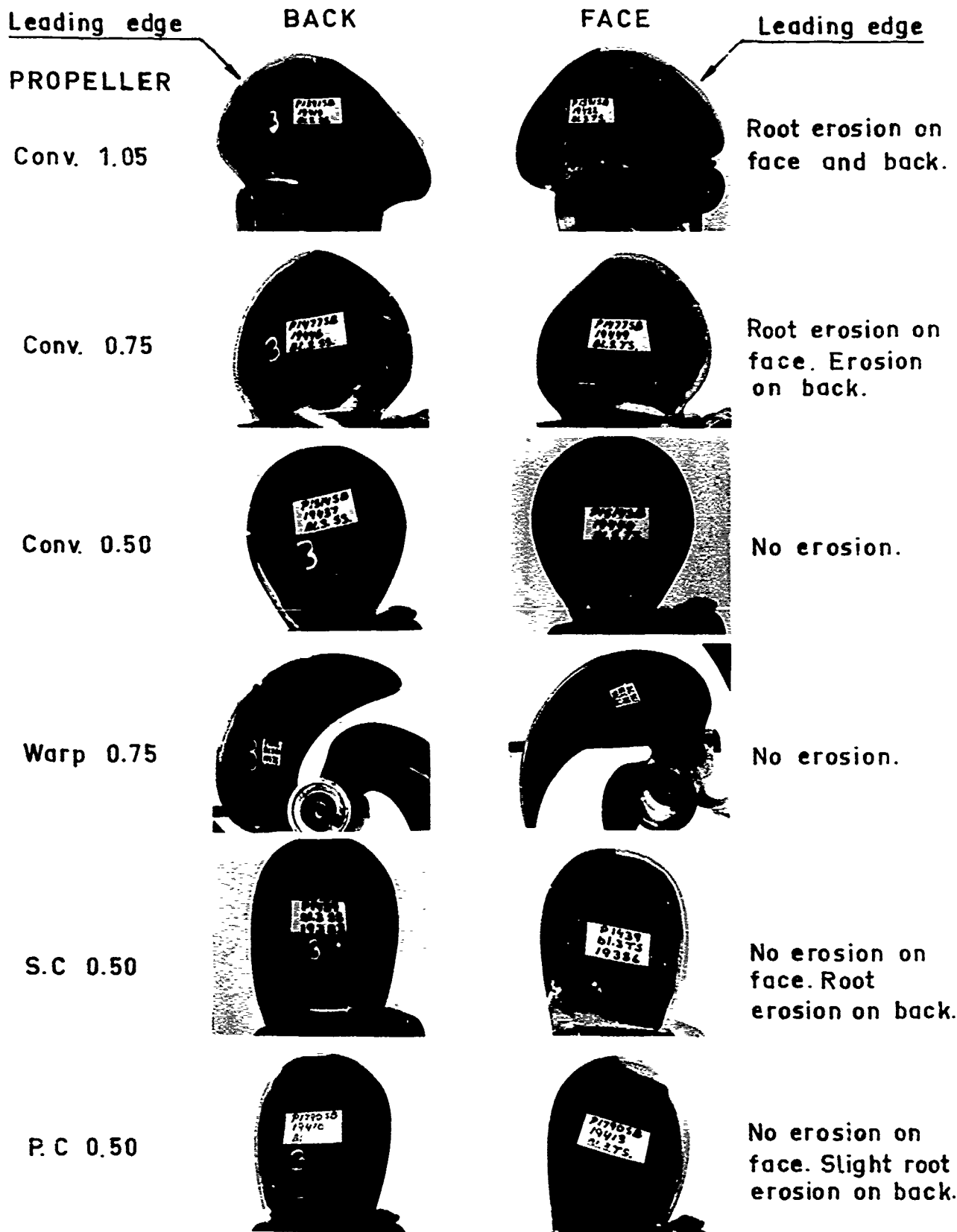


Fig 10 Cavitation erosion obtained with the paint test technique after 30 minutes test at propeller loading corresponding to 30 knots

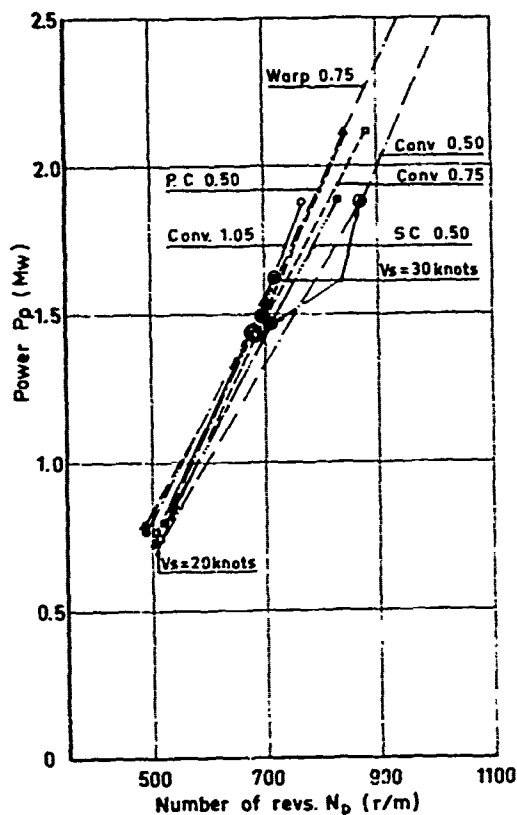


Fig 11 Power and number of revs for the prototype predicted from cavitation tunnel tests

were completely free from erosion, depending on almost fully cavitating conditions at this propeller loading.

When running the tests the number of revs is adjusted so that the propeller loading according to Eq 6 is obtained. At this loading the torque coefficient and advance ratio are then measured, forming the basis for calculations of power demand and number of revs for the prototype.

The power demands for the different propellers shown in Fig 11 are fairly close to each other at 20 and 30 knots (except for propellers Conv 0.50 and Warp 0.75 at 30 knots). Note especially that the propellers of the supercavitating type have only slightly higher power demands than the conventional propellers with blade area ratios 1.05 and 0.75. At 35 knots the differences between the propellers are, however, considerable.

The pressure fluctuations induced on the hull are important results from the cavitation tests, as excited vibrations and noise emanate from them. Fig 12 shows the pressure fluctuations measured on the hull just above the propellers. The values given are the mean blade frequency amplitudes analysed by the digital method described

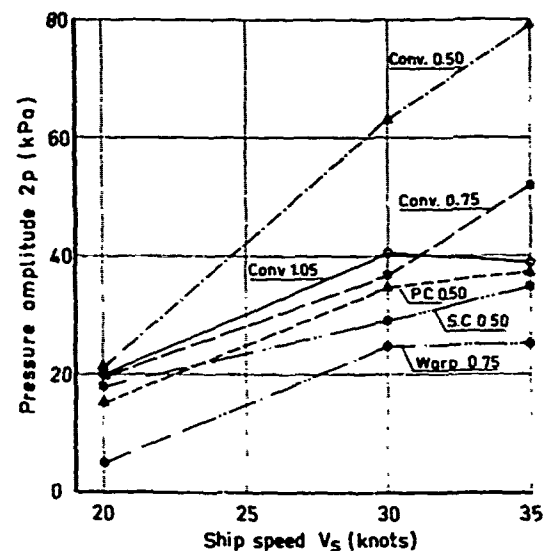


Fig 12 Comparison of blade frequency amplitudes induced on the hull of the prototype

in [12].

When comparing the propellers in Fig 12 three things are noticeable:

- o propeller Conv 0.50 induces very large amplitudes
- o propeller Warp 0.75 induces rather low amplitudes
- o the propellers of the supercavitating type do not induce larger amplitudes than the conventional propellers.

3.5 Influence of Cavitation on Pressure Amplitudes

The pressure amplitudes in Fig 12 have also been plotted in Fig 13 as the dimensionless amplitude coefficient K_p used for the scaling of pressure fluctuations. Using this coefficient the levels are shown to be fairly constant at decreasing cavitation numbers in spite of the fact that the cavitation extensions are increasing. A probable explanation of this, also proposed in [13], could be that the pressure amplitudes are increased at lower cavitation numbers due to the cavitation, but at the same time decreased because of reduced propeller loading.

In [2] it was shown that K_p for a non-cavitating propeller divided by the thrust coefficient K_T is almost independent of the advance ratio. Using this parameter the influence of clearance ratio on the pressure amplitudes for 3-bladed propellers is shown in Fig 14, reproduced from [2]. The theoretical curve was calculated by a method outlined in [14] and the experimental values emanate from different investigations in the SSPA large cavitation tunnel. The points with flags are the propellers in the present investigation.

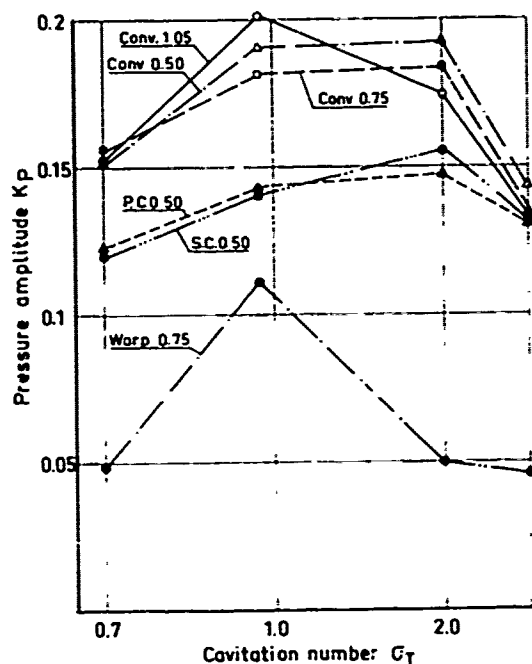


Fig 13 Influence of cavitation number on the dimensionless pressure amplitudes

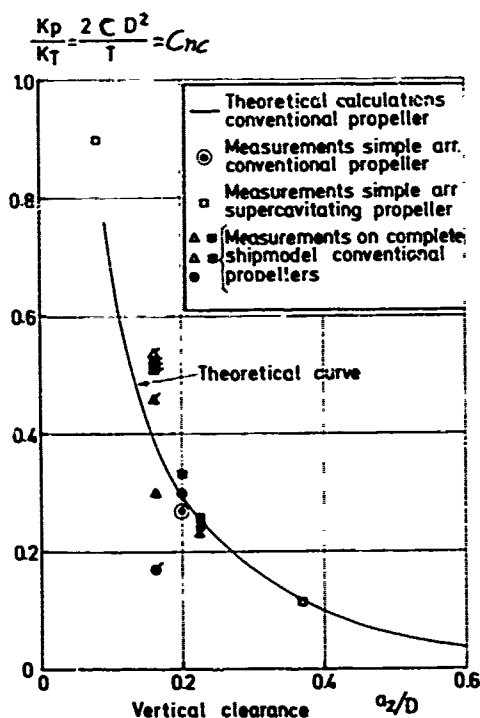


Fig 14 Influence of clearance on the blade frequency pressure amplitudes of a non-cavitating propeller

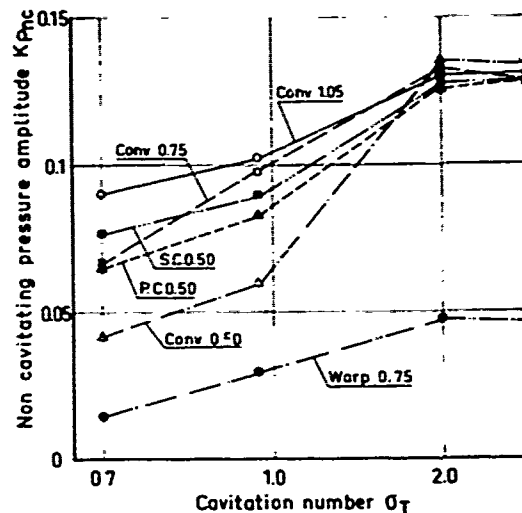


Fig 15 Variation of the non-cavitating contribution to the pressure amplitudes

By assuming that also for a cavitating propeller the non-cavitating contribution is proportional to the thrust coefficient the following expression is obtained:

$$K_{Pnc} = C_{nc} \cdot K_T \quad (7)$$

where C_{nc} is given by Fig 14.

The non-cavitating pressure amplitudes thus reflecting the thrust coefficient are given in Fig 15.

The relation between the values in Figs 13 and 15 gives the cavitation amplification of the pressure amplitudes in Fig 16. The amplification factors given in Fig 16 show magnitudes which seem to be well correlated to the cavitation pictures given in Figs 8 and 9. The photographs with the most extensive cavitation correspond to the largest values of the amplification factor. Two levels of this factor are also shown in Fig 16. The majority of the propellers end up at values around 2.0 at $\sigma = 0.7$. For the propellers with complete thrust breakdown, however, the amplifications are about 3.5.

3.6 Influence of Hull on Propeller Characteristics

In [2, 9] the influence of hull on the characteristics of a cavitating propeller was reported to be a kind of wall effect reducing thrust and torque up to 10%. In Fig 17 the hull influence obtained in this investigation is given as the influence on thrust and efficiency. The thrust coefficients and efficiencies in behind condition (K_{TP} , η_P) were measured at cavitation tests with the complete ship model according to Fig 6 with the cavitation number σ_T

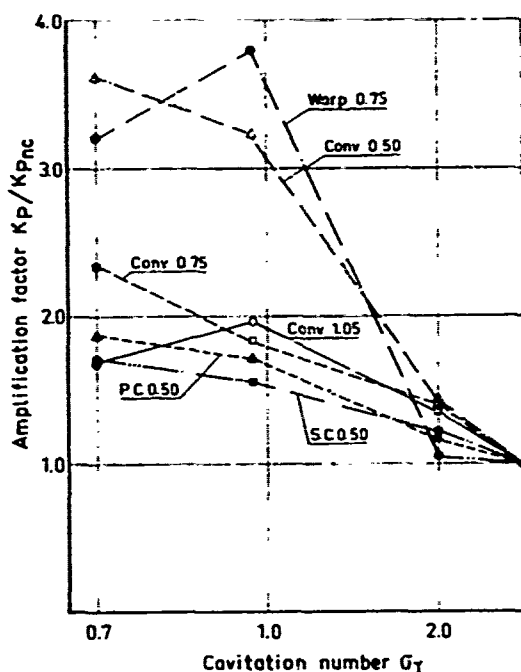


Fig 16 Variation of the cavitation amplification with cavitation number

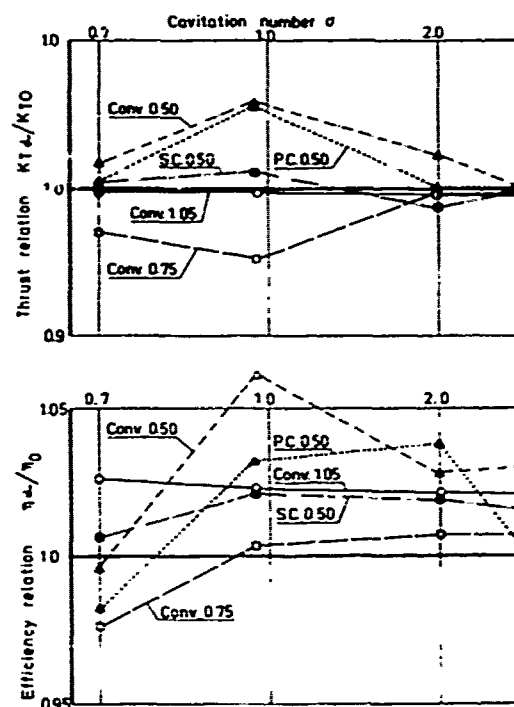


Fig 15 Influence of shaft inclination 8 degrees on the characteristics measured in the high speed test section

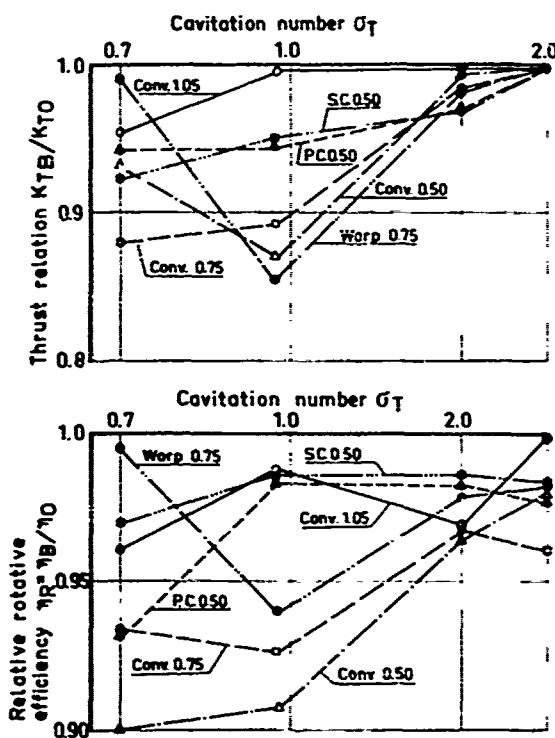


Fig 17 Hull influence on thrust and efficiency

in the tunnel. These values have been compared with thrust coefficients and efficiencies (K_{T0} , η_0) measured with the same propeller model working in homogeneous flow at zero shaft inclination in the high speed test section of the cavitation tunnel. In order to compare identical cavitation numbers K_{T0} and η_0 were measured at the cavitation number $\sigma_{VA} = \sigma_T - 0.16$, which is the cavitation number at the propeller centre when the ship model is mounted in the tunnel.

The influence shown in Fig 17 thus includes not only the influence of the hull but also the influence of rudders and the shaft inclination. The influence of rudders covering only half the propeller diameter has been shown to be very small [15]. The influence of the shaft inclination 8 degrees on the tested propellers except propeller Warp 0.75 is given in Fig 16. This influence is shown to be very different from the influence of the hull shown in Fig 17. The thrust coefficients and efficiencies are generally increased a few per cent when inclining the shaft, while the influence given in Fig 17 is a reduction of these coefficients. Thus if the obliqueness of the flow had been excluded the tendencies given in Fig 17 would probably have been even further emphasized.

When studying the influence of cavi-

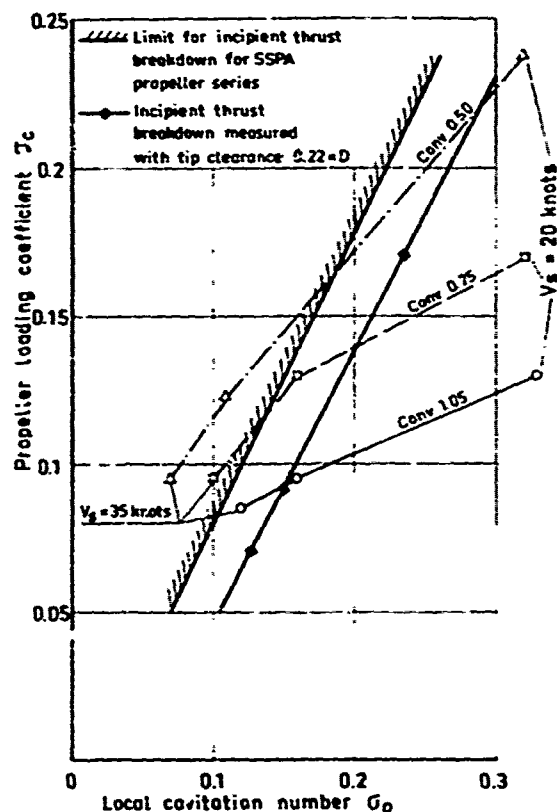


Fig 19 Influence of hull on the limit for incipient thrust breakdown

$$J_c = \frac{T/\cos\phi_{0.7}}{\frac{\pi D^2}{4} \cdot A_D/A_0 \cdot 1/2 \rho V_{0.7}^2}$$

$$\sigma_0 = \frac{P_0 - P_v}{1/2 \rho V_{0.7}^2}$$

tion number on the curves for propellers Conv 0.75, Conv 0.50 and Warp 0.75 in Fig 17 it is somewhat surprising to see the relations between cavitation numbers 0.94 and 0.7. The hull influence seems to be larger at moderate cavitation extensions ($\sigma = 0.94$) than at the extreme cavitation conditions at $\sigma = 0.7$. This means that the limits for thrust breakdown should be very much influenced by the hull. In Fig 19 the loading conditions for propellers Conv 1.05, Conv 0.75 and Conv 0.50 have been plotted in a graph showing the limit for thrust breakdown for these propellers when tested in the high speed test section [16]. According to this limit the loadings 30 knots for Conv 0.75 and 35 knots for Conv 1.05 should not have thrust breakdown. However, when working behind the ship model they did have

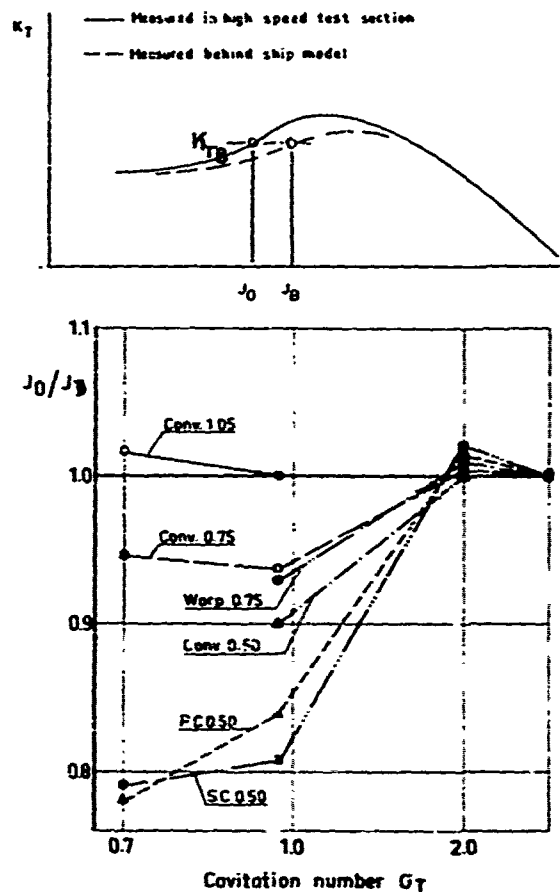


Fig 20 Hull influence treated as an influence on the advance ratio

thrust breakdown, as shown in Fig 17. In Fig 19 some experimental values obtained in the high speed test section with a propeller similar to Conv 1.05 are also given. At these latter tests also a plate with clearance ratio 0.22 was mounted in the tunnel. The agreement between these plate tests and the tests with the complete ship model seems to be very good. The limits for thrust breakdown obtained in unbounded flow apparently give too small blade area ratios. This is also in accordance with the full scale experience given in [17].

The very small hull influence shown in Fig 17 at the extreme cavitation conditions ($\sigma = 0.7$ Warp 0.75, Conv 0.50) is in agreement with studies of wall effects in [18] and [19]. When discussing wall effects on supercavitating and ventilated propellers Morgan in the summary report [20] states that according to the theories of Tulin [18] there should be no influence of wall effects. Results of measurements on geosim propellers in a cavitation tunnel given in [19] lead to the same conclusion. However, if the influence of the hull is considered to be a blockage effect then correction of the advance ratios (which means correction of the wake) should be more appropriate than correction of the thrust coefficient. In Fig 20 this treatment has been used on

the results of Fig 17.

The hull influence given in Fig 20 is shown to increase continuously with decreasing cavitation number. The points for $\sigma = 0.7$ and propellers Conv 0.50 and Warp 0.75 have, however, been left out of Fig 20. The reason for this is that they are situated in the supercavitating region of the characteristics where the thrust coefficients are almost independent of the advance ratio. The ratio J_0/J_B could therefore be anything from 1.0 to 0.8. Treated in this way it is therefore very difficult to tell whether there is a large influence of wall effects in supercavitating conditions due to the fact that the thrust coefficient is almost independent of advance ratio or a negligible influence of wall effects.

4. INTERACTION ON A TRIPLE-SCREW SHIP

In this chapter some results from cavitation tests of a triple-screw ship according to Fig 21 will be given. First the hull influence at single-screw operation will be discussed and finally the propeller-propeller influence is shown.

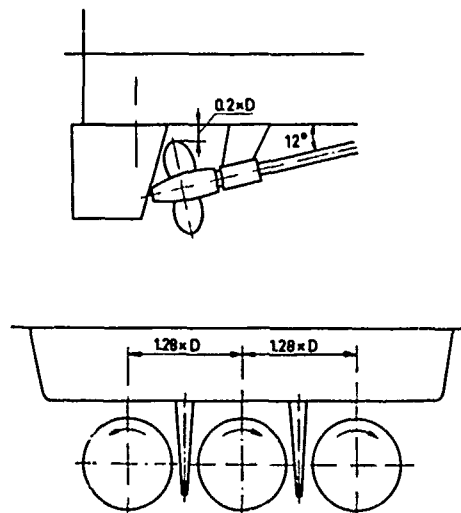


Fig 21 Propeller arrangement on triple-screw model

4.1 Influence of Propeller-Hull Clearance

The influence of clearance on the propeller characteristics has been investigated at tests in the high speed test section with a plate located above the propeller [2, 9]. Results from these tests are shown in Fig 22. One notable observation at these tests was the very slow decrease of the hull influence for the super-

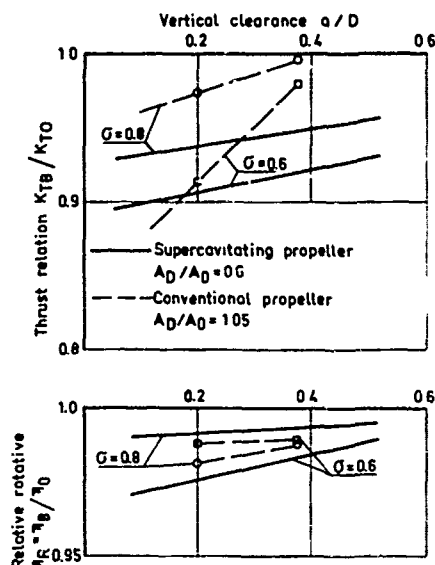


Fig 22 Influence of clearance on propeller thrust and efficiency obtained by tests with a plate arrangement

cavitating propeller at increasing clearances. These results have, however, now been confirmed at the clearance ratio 0.2 by tests with a complete ship model. At the tests with the triple-screw ship also single-screw operation was tested as a comparison with the earlier tested plate arrangement. These results are given in Fig 23. The agreement between the test arrangements is shown to be very good at small and moderate advance ratios. At $J = 1.1$ the tests with the complete ship model, however, give lower thrust and torque than the tests with the plate arrangement. The results from measurements on the prototype, also given in Fig 23, are shown to give the same tendency as the tests with the complete ship model.

In order to confirm the results of Fig 22 also at large propeller-hull clearances some further tests with complete ship models are needed.

4.2 Propeller-Propeller Interaction

At tests with the ship model shown in Fig 21 identical wake fractions at atmospheric tests were measured at triple-screw operation and with each of the propellers alone on the ship model. With the same number of revs on all three propellers there was obviously no interaction between the propellers at non-cavitating conditions.

For the cavitating propellers the interaction shown in Fig 24 was, however, measured. These results were obtained by

- Model tests
- Plate arrangement with rudders
 - o-- Complete ship model with rudders
 - o-- only center propeller
- Fullscale tests
- ▲ Measurements on centerpropeller $\sigma = 0.65$

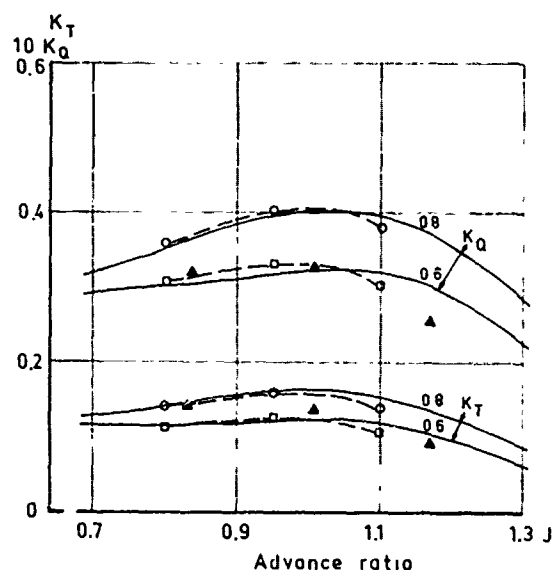


Fig 23 Comparison of propeller characteristics obtained at tests with plate arrangement and at tests with a complete ship model

comparing thrust and efficiency in triple-screw operation (K_{TB3} , η_{B3}) with the thrust and efficiency measured when each of the propellers was working alone on the ship model (K_{TB} , η_B). The propeller-propeller interaction in Fig 24 is shown to imply a further reduction of thrust and efficiency. The influence is larger for the wing propellers than for the centre propeller. It is also very much dependent of the advance ratio. In fact the advance ratio seems to be a more important parameter than the cavitation number. $J = 0.8$ with almost supercavitating conditions gives less influence than $J = 0.95$. This is a similar tendency to that shown concerning propeller-hull influence in Fig 17, where the heavily cavitating propellers were less influenced by the hull than the partly cavitating propellers.

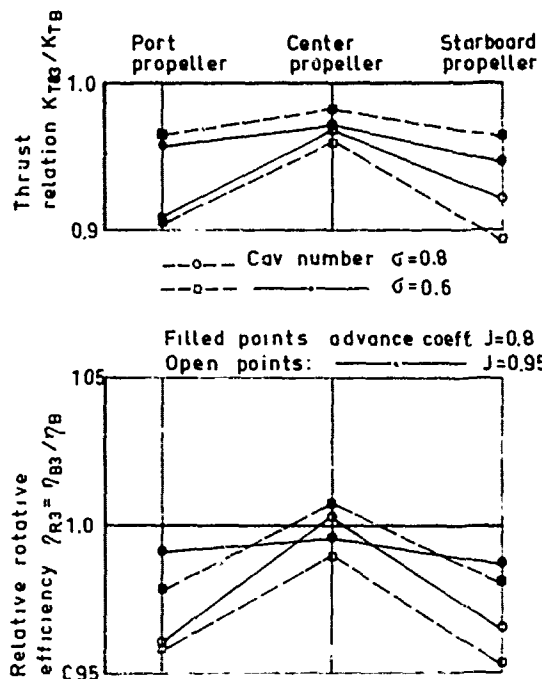


Fig 24 Interaction between propellers on a triple-screw ship

5. CONCLUSIONS

From the results presented in the present paper the following conclusions may be drawn:

5.1 Working Conditions

- o Wake and static pressure at the propeller plane are sensitive to ship speed and trim. Accurate loading conditions should be based on measurements of these.
- o Useful results of theoretical calculations of wake and static pressure cannot be obtained unless the free surface is taken into account.

5.2 Systematic Propeller Tests

- o Propellers of the supercavitating type give less risk of erosion, do not induce larger pressure amplitudes on the hull and demand only slightly more power than propellers of the conventional type.
- o Propellers with highly warped blade shape induce considerably lower pressure amplitudes on the hull than propellers with symmetrical blade shape.
- o The cavitation amplification of the pressure amplitudes induced on the hull was about 2 for "moderate" cavitation

conditions and about 3.5 when complete thrust breakdown occurred.

- o The hull influence on thrust and efficiency implies a reduction of up to 15% of the thrust coefficient and a reduction of up to 10% of the efficiency.
- o The hull influence on the limit for thrust breakdown implies that too small blade area ratios are chosen when using limits obtained in unbounded flow.
- o The hull influence on the propeller characteristics may be a blockage effect. The influence at supercavitating conditions can then be considerably larger than it appears to be when thrust correction is used.

5.3 Interaction on a Triple-Screw Ship

- o The hull influence on propeller characteristics seems to be remarkably constant at increasing clearances.
- o Good agreement between measurements of thrust and torque with plate arrangement and with complete ship model.
- o Propeller-propeller interaction implies further reduction of thrust and efficiency.
- o Propeller-propeller influence is larger on wing propellers than on centre propeller and is larger at "moderate" advance ratios than at small advance ratios.

ACKNOWLEDGEMENTS

The author wishes to express his gratitude to the Naval Material Department of the Defence Material Administration of Sweden for sponsoring parts of the present investigation and to Dr Hans Edstrand, Director General of SSPA, for the opportunity to carry out the study. Thanks are also due to those members of the staff of SSPA who took part in the investigation. Without their urgent work this paper would not have been possible.

REFERENCES

1. Reed, A, Day, W, "Wake Scale Effects on a Twin-Screw Displacement Ship", Proceedings of the 12th ONR Symposium on Naval Hydrodynamics, 1978
2. Rutgersson, O, "On the Importance of Rudder and Hull Influence at Cavitation Tests of High Speed Propellers", Proceedings of the High-Speed Surface Craft Conference, Brighton, UK, 1980
3. Taniguchi, K, Chiba, N, "Investigation into the Propeller Cavitation in Oblique Flow", Experimental Tank Laboratory, Mitsubishi Shipbuilding & Engineering Co Ltd, Report No 1800, 1964
4. Hess, J L, Smith, A M O, "Calculation of Non-Lifting Potential Flow about Arbitrary Three-Dimensional Bodies", Douglas Aircraft Company Report No E.S.40622, 1962

5. Blount, D L, Fox, D L, "Small Craft Power Prediction", Marine Technology, Vol 13, No 1, Jan 1976

6. Gawn, R W L, Burril, L C, "The Effect of Cavitation on the Performance of a Series of 16-Inch Model Propellers", Trans INA, Vol 99, 1957

7. Newton, R N, Rader, H P, "Performance Data of Propellers for High-Speed Craft", Trans RINA, Vol 103, 1961

8. Venning, E, Haberman, W, "Supercavitating Propeller Performance", Trans SNAME, 1962

9. Rutgersson, O, "Supercavitating Propeller Performance. Influence of Propeller Geometry and Interaction between Propeller, Rudder and Hull", Proceedings of the Joint Symposium on Design and Operation of Fluid Machinery, Fort Collins, USA, 1978. See also SSPA Publ No 82, 1979

10. Johnsson, C-A, "Some Experiences from Excitation Tests in the SSPA Large Cavitation Tunnel", Trans RINA, 1979

11. Lindgren, H, Bjärne, E, "Studies of Propeller Cavitation Erosion", Proceedings of Conference on Cavitation, I Mech E, Edinburgh, 1974

12. Johnsson, C-A, Rutgersson, O, et al, "Vibration Excitation Forces from a Cavitating Propeller. Model and Full Scale Tests on a High Speed Container Ship", Proceedings of the 11th ONR Symposium on Naval Hydrodynamics, London, 1976. See also SSPA Publ No 78, 1976

13. Weitendorf, E-A, "Kavitationseinflüsse auf die vom Propeller induzierten Druckschwankungen", Institut für Schiffbau der Universität Hamburg, Bericht Nr 338, 1976

14. Johnsson, C-A, "Pressure Fluctuations around a Marine Propeller. Results of Calculations and Comparison with Experiment", SSPA Publ No 69, 1971

15. Suhrbier, K, "An Experimental Investigation on the Propulsive Effect of a Rudder in the Propeller Slipstream", International Shipbuilding Progress, Feb, 1974

16. Rutgersson, O, "Propellers SSPA-FMV Series K131. Summary of Cavitation Properties for Propellers 3.105, 3.075 and 3.050", SSPA Report K131-24, 1974 (in Swedish)

17. Blount, D L, Fox, D L, "Design Considerations for Propellers in a Cavitating Environment", Marine Technology, Vol 15, No 2, Apr 1978

18. Tulin, M P, "Supercavitating Propeller Momentum Theory", Hydro-nautics Technical Report 121-4, 1964

19. van de Voorde, C B, Esvelde, J, Tunnel Tests on Supercavitating Propellers", Proceedings of the 4th ONR Symposium on Naval Hydrodynamics", 1962

20. Morgan, W B, "The Testing of Hydrofoils and Propellers for Fully-Cavitating or Ventilated Operation", Proceedings of the 11th International Towing Tank Conference, Tokyo, 1966

21. Johnsson, C-A, "Comparison of Propeller Design Techniques", Proceedings of the 4th ONR Symposium on Naval Hydrodynamics, 1962. See also SSPA Publ No 52, 1963

22. Pien, P C, "The Calculations of Marine Propellers Based on Lifting-Surface Theory", Journal of Ship Research, Vol 5, 1961.

23. Nelka, J, "Experimental Evaluation of a Series of Skewed Propellers with Forward Rake", NSRDC report 4113

APPENDIX

Geometry of Tested Propellers

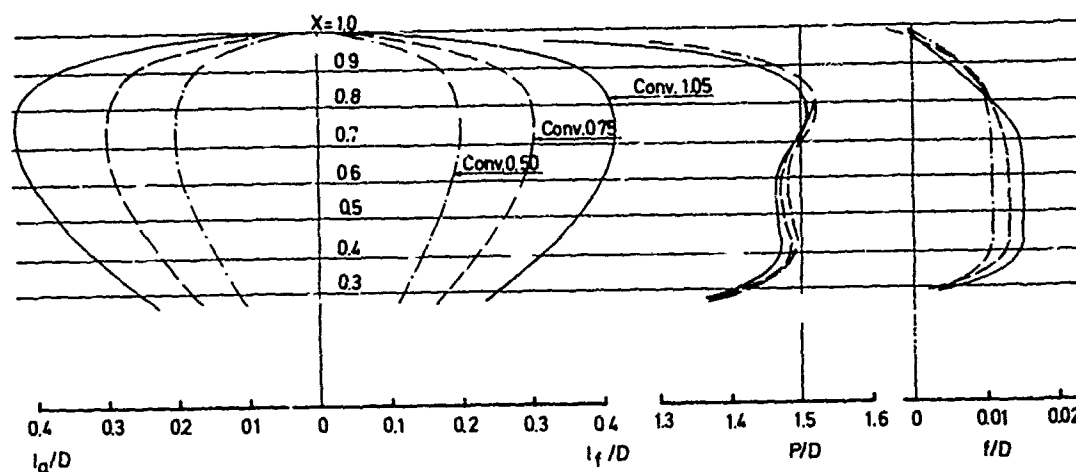


Fig 25 Blade shape and distributions of pitch and camber for propellers Conv 1.05, Conv 0.75 and Conv 0.50

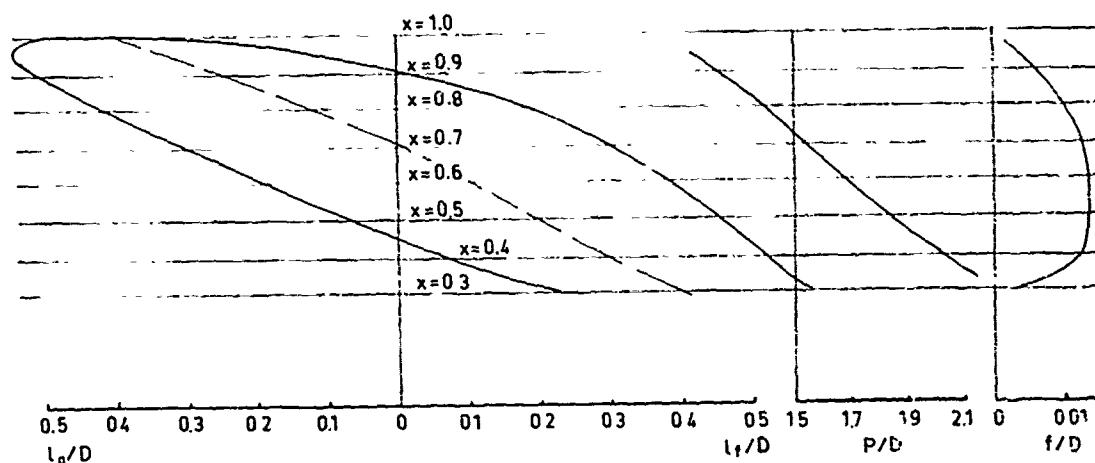


Fig 26 Blade shape and distributions of pitch and camber for propeller Warp 0.75

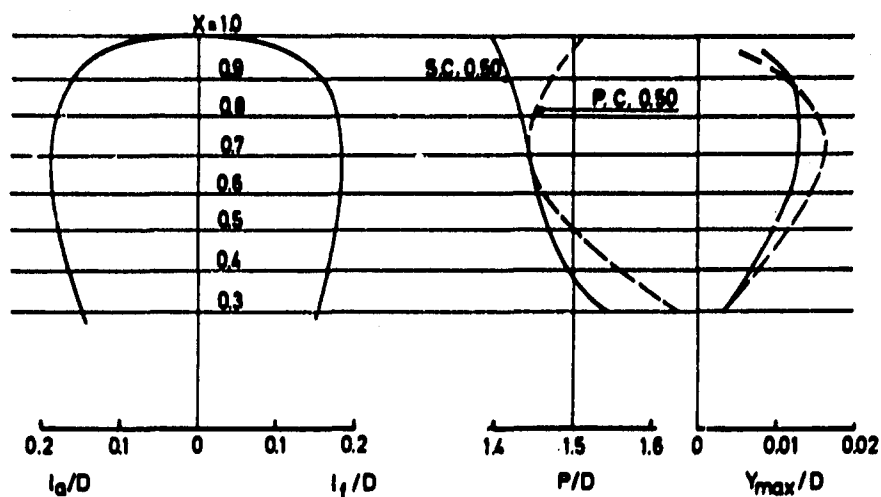


Fig 27 Blade shape and distributions of pitch and face camber for propellers S.C. 0.50 and P.C. 0.50

The propellers with NACA 16 profile shape have all been designed by the same procedure and with the same rather unloaded circulation distribution. The lifting line calculations were carried out according to a modified procedure for calculation of induction factors described in [21]. The lifting surface corrections were then calculated according to Pien's method [22] programmed at SSPA. For propellers with symmetrical blades and no rake this design procedure gives very good estimates of pitch and camber.

The propeller Warp 0.75 has the same chord lengths and circulation distribution as propeller Conv 0.75, the blades, however, being skewed 120 degrees. Further the skew-induced rake has been compensated by raking the blades forward about 60 degrees. In this way the clearance curve for propellers Conv 0.75 and Warp 0.75 are almost identical. When propeller Warp 0.75 was designed, however, very little was known about the effect of extreme forward rake on the propeller characteristics. The design was therefore carried out by the same procedure as for unraked propellers. Later it has been shown that the effect of rake is to increase thrust and torque [23], which is not predicted by the design method. The propeller Warp 0.75 is consequently considerably overpitched at the inner radii.

The propellers S.C. 0.50 and P.C. 0.50 have been designed according to the procedure given in [8] with empirically derived pitch corrections according to [9]. The radial circulation distribution is optimum. Propeller S.C. 0.50 has wedge-shaped sections according to [9] with a 3-term face combined with a 2-term modified thickness distribution. Propeller P.C. 0.50 represents a first attempt to improve the performance of the supercavitating sections

at partially cavitating conditions. In this case a 5-term face is combined with an empirically derived shape of the back.

In Fig 28 the free stream propeller characteristics are plotted in the following way.

Propeller thrust and efficiency at cavitating conditions at the advance ratio J_B used in the behind condition have been related to thrust and efficiency at non-cavitating conditions at the same advance ratio.

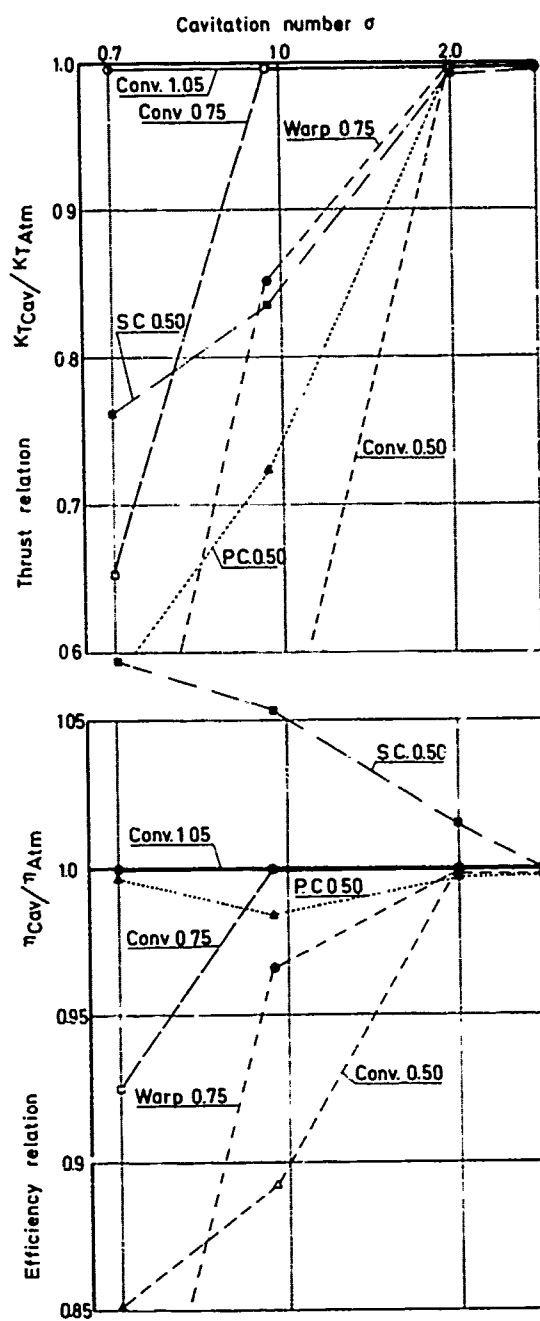


Fig 28 Effect of cavitation on the free stream propeller characteristics

Discussion

K R Suhrbier (*Vosper Thornycroft*)

I thank the author for his stimulating paper. Regarding Fig.17 I would like to say that comparisons of conventionally defined relative rotative efficiencies η_R can be misleading for inclined shaft arrangements if extended to cavitating conditions. The η_R changes shown should not be regarded as an 'exact' measure of propulsive efficiency changes, simply because the 'behind' thrust used is not the effective or net thrust; the effect of cavitation on the propeller normal force (due to oblique inflow) is not considered. If it were included in a more complete analysis it would either show up, as a somewhat compensating effect, in the hull efficiency η_H or in a different η_R or K_T ratio, depending on the approach used. The data on the influence of shaft inclination (Fig. 18) is affected in a similar way.

I have some difficulty with the author's findings on the propeller-hull or clearance influence. The effects shown in Fig.22 and in the author's earlier papers do not seem to agree with our experimental data. So far, we did not find (in several similar tests for different purposes) effects of this kind or magnitude. Further experiments will be carried out by us in the near future and they might help to clear up this discrepancy. A 20% reduction in efficiency, as mentioned in the paper, is not in line with our experience with high-speed craft.

With reference to Fig. 12 I would like to add that it is not sufficient in our (and others') experience to compare just the pressure amplitudes of the tip position, because the peak pressures may be further downstream depending on the extent of cavitation.

E.A. Weitendorf (*HSVA*)

In Fig.14 of the paper the influence of the tip clearance of the blade frequency pressures in the non-cavitating condition is given. By the way, these values can easily be calculated.

In Fig.16 of the paper an amplification factor for cavitation is displayed.

The first pressure impulse measurements in 1967 by Denny published and our measurements published in 1973 showed a decrease of the blade frequency pressures due to the thrust breakdown was found by using five pressure pick-ups in longitudinal direction parallel to the propeller shaft — a point already mentioned by the fore-going discussor. It is well known that there are mainly at least two physical phenomena: An increase of blade frequency pressures due to the displacement effect of the cavity as

found in the wake of merchant ships and secondly a decrease of the blade frequency pressures due to the thrust break down caused by the cavity. But in Fig.16 of the paper no value of less than 1.0 can be detected, at least for the conventional propellers.

Can the author give an explanation for the cavitation amplification factor of this type? Thank you.

Author's Reply

O. Rutgersson (*SSPA*)

I thank Mr. Suhrbier and Dr. Weitendorf for their attention to the paper.

I agree with the discussors that it is generally insufficient to compare pressure fluctuations measured in only one transducer. In this investigation actually 8 transducers were used. However since all transducers showed the same relation between the propellers the results from only the tip transducer were shown in the paper.

Dr. Weitendorf seems to have misunderstood the purpose of Fig.14-16. The reason for extracting the amplification factor in Fig.16 is to give the magnitude of the effect the discussor is mentioning. The decrease in amplitude due to thrust reduction is shown in Fig.15 and the increase due to cavitation is shown in Fig.16.

Mr. Suhrbier is correctly saying that the definition of η_R given in the paper only takes account for the forces in the shaft direction. An "exact" definition however means that forces must be measured both in struts and rudders and have not yet been considered.

Finally I am very sorry that Mr. Suhrbier has not been able to find the propeller-hull influence in his investigations because I am quite convinced it should be there. The magnitude mentioned in the conclusions of the paper is perhaps somewhat provocative (15% reduction of thrust and 10% * reduction of efficiency). A closer look at Fig.17 will however show that these figures are valid for a 50% blade area propeller of conventional design on a 30 knots vessel. This is of course not a realistic propeller for this speed and I doubt if such a case exists in the discussors investigations. More realistic propellers of 100% blade area of conventional design on supercavitating propellers give a reduction of 0-8% in thrust and a reduction of 2-4% in efficiency. This effect is thus rather small but very significant and important according to the results of a number of projects tested at SSPA. A well defined test technique and a very good dynamometer is however necessary in order to measure this effect.

* In the preprints it was misleadingly stated 20% reduction of efficiency.

Recent Research Results on Cavity Flows about Hydrofoils

Alain Rowe

Centre National de la Recherche Scientifique
Institut de Mécanique de Grenoble

Jean-Louis Kueny

Université Scientifique et Médicale de Grenoble
Institut de Mécanique de Grenoble

France

ABSTRACT

The behaviour of a base-vented hydrofoil in a free surface channel is studied. The flow is simulated by a displacement surface outside which eddy effects, the influence of viscosity and air compressibility are neglected. The model used to characterize the displacement surface is derived from Michel's model and takes gravity effects into account. The theory is developed according to a perturbation method which uses two small parameters: ϵ to which foil thickness and incidence are proportional, and β the reciprocal of the square of Froude number. Unknown variables are expressed in the form of asymptotic expansions

$$\chi = \chi_0 + \epsilon (\chi_1^0 + \beta \chi_1^1) + \sigma(\epsilon)$$

where coefficients such as χ_1^1 depend on the shape of the free boundaries. The classical resolution method consists in transforming the field of flow into a half plane, but consideration of the bottom and free surface leads to considerable distortions which render numerical calculations delicate and requires a powerful computer (C.D.C. 6600, double precision). The contribution of the free surface is evaluated after studying its asymptotic behaviour at infinity. The wake contribution which is significant in the 0th-order problem with respect to β , vanishes in the 1st-order problem. The simplifying hypothesis consisting of replacing the wake by a displacement surface is thus justified. Comparison of theoretical with experimental results shows fairly good agreement with regard to:

- the effect of the ventilation number K on forces and on cavity length l
- the variation in free boundary geometry with respect to angle of at-

- tack
- the speed effects.

NOMENCLATURE

- C = length of chord measured on lower side ($C=1$)
- F = function characterizing the shape of the foil
- Fr = Froude number = U_∞ / \sqrt{gC}
- \bar{g} = gravitational acceleration constant
- h_1 = submergence depth
- h = nominal water depth in the test section
- h^2 = $h - h_1$
- K^2 = ventilation number = $(P_\infty - P_c) / \frac{1}{2} \rho U_\infty^2$
- k = α / ϵ
- l = cavity length
- P_0 = pressure on the free surface
- P_∞ = $P_0 + \rho \bar{g} h_1$
- P_c = pressure cavity
- U_∞ = free stream velocity
- U, V = components of the speed
- u_1, v_1 = components of the perturbation speed at the first order
- b, c, d, f, g = abscissae of the points B, C, D, F, G in the auxiliary t plane
- y_l = ordinate of the free surface
- y_c = ordinate of the cavity
- y_s = ordinate of the wake displacement surface
- α = attack angle
- β = $1/Fr^2$
- ϵ = small parameter characterising the thickness of the foil
- ρ = density of water.

INTRODUCTION

While a great deal of research has been carried out over the past years on supercavitating hydrofoils with unwetted upper side, the same cannot be said for

base vented hydrofoils which have received fairly little attention. This lack of interest would seem to stem from the fact that the first test made with these foils [1] to [3] indicated problems of flow stability and cavitation around the leading edge. In fact, these tests, which were carried out under unsatisfactory conditions, are not very significant and can hardly be used as a basis for understanding how a base-vented foil operates under real-life conditions. More recent tests, the results of which were published in 1979 [5] and 1980 [6], have shown that by choosing a suitable pressure distribution, and on condition that a wall-mounted support system is used, thereby avoiding the presence of a vertical strut which disturbs the flow above the foil, a stability domain at high speed is obtained, always including the cavitation-free area. It is the development of cavitation on the upper or lower side of the foil that causes stalling. Thus, by using a wall-mounted foil of aspect ratio 2, Rowe obtained a stability domain of about 5 degrees for a cavitation number σ equal to 0.16. As far as the cavitation-free area is concerned, its extent is not negligible since, for a cavitation number of 0.19, an angular deviation of the order of 1.7° is possible under two-dimensional flow conditions. This value is slightly greater than the theoretical values calculated ($\sim 1.3^\circ$ - See ref. [4], [6] and [7]). Moreover, in view of the fact that the middle of the non-cavitating range coincides almost exactly with the ideal angle of attack, and that at this angle of incidence the lift of the foil remains approximately constant regardless of the operation conditions (variation in ventilation number, proximity of a free surface, wall effect), it is to be expected that base-vented hydrofoils could in practice be used in certain cases.

The detailed study of operation of such a foil is not therefore without interest. However, this study raises a certain number of specific problems which are not encountered in the study of supercavitating hydrofoils with unwetted upper side. For example, in the case of tests conducted in a tunnel, the correct measurement of the cavitation-free area requires special precautions in order to be sure of constant air content in the upstream flow. Moreover, the fact that the foil is held by a strut promotes separation of the boundary layer over the foil by causing the air in the cavity to rise, thereby modifying the value of the pressure coefficient. With a supercavitating hydrofoil, this defect is no longer apparent since the lower part of the strut that penetrates the cavity, and the upper side of the foil, are at a pressure known in advance. Other difficulties are encountered from the theoretical standpoint: the calculation must be non-linear, at least in the region of the leading edge. Now the non-linear theory proposed by FURUYA [8] for supercavitating hydrofoils with unwetted upper side falls into the case of base

vented hydrofoils. The model must be capable of restoring a geometry which is as close as possible to reality in order to take into account as accurately as possible the effect of the boundaries which limit the field of flow. This condition is particularly crucial when the foil is placed in a liquid with free surface since, in such a case the deformation of this surface, directly related to the cavity deformation, may induce a considerable angle of attack. With a supercavitating hydrofoil, the limitation is not as severe since the pressure acting on the upper side of the foil is known and, in addition, the slope $dc_l/d\alpha$ is half that of a base vented hydrofoil. Thus, the same error made on the value of induced angle of incidence $\Delta\alpha$ halves the error in lift in the case of a supercavitating foil.

In the following paragraphs, the behaviour of a base vented foil placed in a free-surface canal is examined in detail. From the practical point of view, this is perhaps the most interesting case since it allows consideration to be given to both tests in a towing tank and tests in a free-surface water tunnel. Three points are examined:

- the effect of ventilation number on forces and on the shape of free boundaries
- the effect of a change in the angle of attack
- the effect of speed.

This study is based on the use of Michel's model [9], previously presented by Rowe and Kueny [6], and modified to make allowance to gravity effects. A number of details on the calculation method are given below, then the theoretical results are compared with the experimental results published in [5] and [6].

1. CALCULATION METHOD

The foil, with lower chord equal to unity, is placed in a channel at an immersion depth h_1 (Figure 1). The depth of water in the channel at infinity upstream is

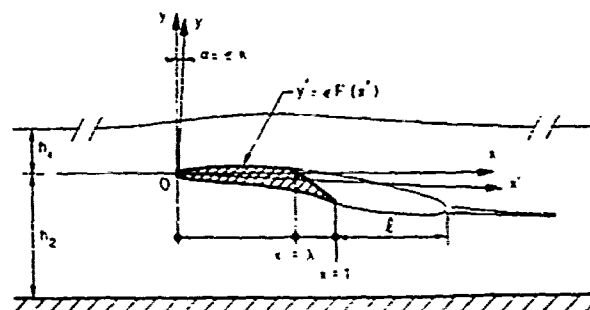


FIGURE 1 Configuration of the flow

$h_1 + h_2$. The foil is followed by a cavity whose length measured from the rear of the lower side of the foil has a value of l , and a wake assumed to extend to infinity. The shape of the foil, previously described

by Rowe [5] is defined with regard to the axis Ox' , Oy' by the relationship $y' = \epsilon F(x')$ where ϵ is a small parameter characterising the thickness of the foil and F a function of order unity, except near the leading edge, which characterizes the shape of the foil. The angle of attack is characterized by number k such that $\alpha = (Ox', Oy') = \epsilon k$. β is taken to be the reciprocal of the square of the Froude number, defined by choosing as characteristic length the length of the lower chord of the foil :

$$\beta = g / U_{\infty}^2 \quad (1)$$

\bar{g} is the acceleration due to gravity, and U_{∞} the flow speed at upstream infinity. The ventilation number is designated by K :

$$K = (P_{\infty} - P_c) / \frac{1}{2} \rho U_{\infty}^2 \quad (2)$$

On the cut representing the limit position of the cavity, when $\epsilon \rightarrow 0$, the cavity length ℓ being maintained constant whatever the value of small parameter ϵ , the condition : limit $P_c = P_{\infty}$ imposes :

$$\lim_{\ell \text{ fixed}} K = 0 \quad (\epsilon \rightarrow 0) \quad (3)$$

When ϵ is not zero, for the assumed constant cavity length considered, ventilation number K is a function of ϵ . The flow is then disturbed by the presence of the foil followed by its cavity and wake. For a previously imposed geometry, i.e., for fixed values of h_1 , h_2 , ℓ and K , and a given function F , the other values characterizing the flow are expressed in terms of the parameter ϵ . It can easily be verified that these values allow the following asymptotic expansions :

$$U/U_{\infty} = 1 + \epsilon u_1 + \sigma(\epsilon)$$

$$V/U_{\infty} = \epsilon v_1 + \sigma(\epsilon)$$

$$y_{\ell} = h_1 + \epsilon y_{\ell 1} + \sigma(\epsilon) \quad (4)$$

$$y_c = \epsilon y_{c1} + \sigma(\epsilon)$$

$$K = \epsilon K_1 + \sigma(\epsilon)$$

the problem can be considered as solved if coefficients u_1 , v_1 , $y_{\ell 1}$, y_{c1} , K_1 can be calculated. The first order solution of the problem in ϵ is obtained by applying the first-order boundary conditions to the flow boundaries corresponding to zero order (Figure 2a). The conditions of steady flow, incompressibility, irrotationality and inviscidity are not satisfied in the wake. As the perturbation produced by this wake cannot be neglected, the difficulty is overcome by assuming that there are two completely distinct areas behind the cavity, marked by a line representing a surface close to infinity, outside which the preceding conditions are satisfied. This surface is identified with the displacement surface of the wake whose unknown shape is

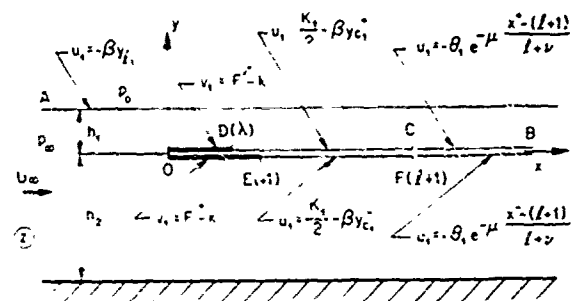


FIGURE 2a Geometry corresponding to the zero order in ϵ

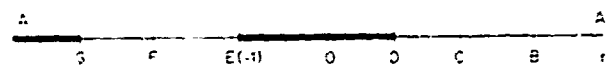


FIGURE 2b Auxiliary plane of calculation

expressed in the form of the expansion

$$y_s = \epsilon y_{s1} + \sigma(\epsilon) \quad (5)$$

the displacement surface is defined by adopting the behaviour law :

$$C_p = 2\epsilon \left[\theta_1 e^{-\mu \frac{x - (l+1)}{l+nu}} - \beta y_{s1} \right] \quad (6)$$

where μ and ν are two free parameters, and θ_1 is a parameter which is calculated in view of the conditions adopted to close the problem :

- zero perturbation at infinity upstream
- integrable singularity at the leading edge
- pressure continuity at the trailing edges of the foil
- zero perturbation at infinity downstream
- zero thickness of the displacement surface at infinity downstream.

Outside the surface corresponding to the foil, its cavity and wake, perturbation speed $w_1 = u_1 - iv_1$ is a harmonic function because it satisfies the hypothesis of irrotationality and incompressibility of a perfect fluid. It also satisfies the boundary conditions represented on figure 2a. These conditions bring into play the Froude number and the shape of the cavity and the free surface. Since $y_{\ell 1}$ and y_{c1} are unknown, the variables are calculated first of all by assuming $u_1 = 0$ on the free surface, and $u_1 = K_1/2$ on the cavity, then the perturbation due to gravity is calculated by assuming that the previously calculated variables $y_{\ell 1}$ and y_{c1} are correct values. Thus successive solutions have to be found to two mixed boundary condition Hilbert pro-

blems which are dealt with by the classical method. In the following, b, c, d, f, g designate the abscissae of the points B, C, D, F, G in the auxiliary plane $t=r+i$ (Figure 2b). Since bottom and free surface effects are taken into account, considerable distortions are introduced into the calculation plane t (for example, length of the upper wake image CB in the calculation plane = 10^{-14} for $h_1 = 1, h_2 = 4, \ell = 10$) which makes the numerical calculation both long and difficult, thereby requiring the use of a high-capacity computer (CDC 6600 in double precision). It is for this reason that no attempt was made to determine the exact shape of the free boundaries taking gravity into account. The contribution of the wake, a significant factor in the gravity free problem, does not appear in the second problem. The simplifying hypothesis whereby the wake boundary is represented by a displacement surface is thus justified. The calculation method, which consists in calculating the gravity effect on the basis of a gravity free solution, is justified by the fact that, for this problem, the behaviour of the free surface is realistic for the hypothetical case of supercritical flow. Thus, the free surface is calculated as a jet line and cannot oscillate downstream of the obstacle. The value of the depth of water at downstream infinity is taken equal to $h_1 + h_2$, which is justifiable in view of the above-mentioned restriction. The effect of the free surface is calculated by making an analytical study of its asymptotic behaviour at infinity. This study is important as the convergence of the integrals in the second problem depends on the manner in which $y\ell_1 \rightarrow 0$. The expansion of $y\ell_1$ to infinity depends on the position of the foil in the channel. The calculations were made for the case of $p = h_1/\ell < 1$. The shape of the free surface is obtained for the entire domain by matching the numerical solution calculated at finite distance, and the asymptotic solution in a suitably chosen auxiliary plane. The asymptotic solution at infinity is of the following form:

- at upstream infinity $y\ell_1 \approx Ae^{\pi x/2(h_1+h_2)}$
- at downstream infinity $y\ell_1 \approx B e^{-x/\ell}$ (7)

where coefficients A and B depend on the wake boundary behaviour law [6].

Of course, a singularity appears at the leading edge since the tangent to the foil at this point has infinite slope. The solution is then regularised according to the previously described technique [7]. Taking into account the conventional symbols as defined in the appendix as well as in [6], the uniformly valid solution of the problem with gravity is:

$$\frac{a^*}{U_\infty} = \left[\frac{x^2 + \epsilon^2 (\pm t_1 \sqrt{x} + 2t_1^2 x)}{x + \epsilon^2 (\pm t_1 \sqrt{x} + 2t_1^2 x + \frac{1}{4})} \right]^{\frac{1}{2}} \left[1 \pm \frac{\frac{\epsilon}{\pi} \sqrt{\frac{d(h_1+h_2)}{2\pi b}} [A_0 - k B_0]}{[x + \epsilon^2 (\pm t_1 \sqrt{x} + 2t_1^2 x)]^{\frac{1}{2}}} \right] \quad (8)$$

$$+ \epsilon [(U_1)_0 + k (U_1)_\alpha] = \frac{\epsilon}{\pi} \sqrt{\frac{d(h_1+h_2)}{2\pi b}} \frac{A_0 - k B_0}{\sqrt{x}}$$

with

$$A_0 = (\theta_1)_0 \left[\int_0^1 \frac{S^-}{T} dr' - \int_0^1 \frac{S^+}{T} dr' \right] - \frac{1}{2} (K_1)_0 \left[\int_0^1 \frac{dr'}{T} - \int_0^1 \frac{dr'}{T} \right] - \int_0^1 \frac{r'}{R} dr'$$

$$+ \beta \left[\int_0^1 \frac{(y_{c1})_0}{T} dr' - \int_0^1 \frac{(y_{c1})_\alpha}{T} dr' - \int_0^1 \frac{(y_{f1})_0}{T} dr' \right]$$

$$B_0 = (\theta_1)_\alpha \left[\int_0^1 \frac{S^-}{T} dr' - \int_0^1 \frac{S^+}{T} dr' \right] + \frac{1}{2} (K_1)_\alpha \left[\int_0^1 \frac{dr'}{T} - \int_0^1 \frac{dr'}{T} \right] - \int_0^1 \frac{r'}{R} dr'$$

$$- \beta \left[\int_0^1 \frac{(y_{c1})_\alpha}{T} dr' - \int_0^1 \frac{(y_{c1})_0}{T} dr' - \int_0^1 \frac{(y_{f1})_\alpha}{T} dr' \right]$$

and

$$\begin{aligned} (K_1)_0 &= (K_1)_\alpha = \frac{2\beta}{D} \left[12 \quad p3 \quad - \quad 11 \quad 15 \right] \\ (K_1)_\alpha &= (K_1)_0 = \frac{2\beta}{D} \left[12 \quad p4 \quad - \quad 11 \quad 16 \right] \\ (\theta_1)_0 &= (\theta_1)_\alpha = \frac{\beta}{D} \left[12 \quad p3 \quad - \quad 11 \quad 15 \right] \\ (\theta_1)_\alpha &= (\theta_1)_0 = \frac{\beta}{D} \left[12 \quad p4 \quad - \quad 11 \quad 16 \right] \end{aligned} \quad (10)$$

where coefficients $(K_1)_0, (K_1)_\alpha, (\theta_1)_0, (\theta_1)_\alpha$ correspond to the problem without gravity.

$$(U_1)_0 = \frac{1}{\pi} \frac{R}{T} \left[\frac{1}{2} (K_1)_0 110 \quad - \quad (\theta_1)_0 120 \quad - \quad 140 \quad 11 \right]$$

$$- \beta \left(\int_0^1 \frac{(y_{c1})_0}{T} \frac{dr'}{r'} - \int_0^1 \frac{(y_{c1})_\alpha}{T} \frac{dr'}{r'} - \int_0^1 \frac{(y_{f1})_0}{T} \frac{dr'}{r'} \right)$$

$$(U_1)_\alpha = \frac{1}{\pi} \frac{R}{T} \left[\frac{1}{2} (K_1)_\alpha 110 \quad - \quad (\theta_1)_\alpha 120 \quad - \quad 130 \quad 11 \right]$$

$$- \beta \left(\int_0^1 \frac{(y_{c1})_\alpha}{T} \frac{dr'}{r'} - \int_0^1 \frac{(y_{c1})_0}{T} \frac{dr'}{r'} - \int_0^1 \frac{(y_{f1})_\alpha}{T} \frac{dr'}{r'} \right)$$

$$\theta_1 = (\theta_1)_0 + k(\theta_1)_\alpha \quad \left| \begin{array}{l} y\ell_1 = (y\ell_1)_0 - k(y\ell_1)_\alpha \\ y_{c1} = (y_{c1})_0 - k(y_{c1})_\alpha \end{array} \right. \quad (12)$$

Quantities $D, R, R', T^-, S^+, (11), (12), (S1), (T1)$ have been defined in [6]. Quantities $(P3), (P4), (15), (16)$ are defined in appendix.

2. EFFECT OF THE VENTILATION NUMBER

Altmann and Elata [10] showed for the first time in 1967 that the lift of a base-vented hydrofoil placed near a free surface depends on the ventilation number. These authors showed that when $K \rightarrow 0$, lift increases. An explanation of this argument was given by Rewe ([4] and [7]) who also found that, before increasing, lift starts by

decreasing. The reasons for this initial decrease are still not very clear since, when the length of the wetted part of the upper side of the foil is equal to the length of the lower side, the theory no longer agrees with experimental results. In this case, the effect of pressure acting on the rear part of the foil becomes difficult to analyse, and the loss in lift that is observed [4] is not a trivial result.

The theoretical results presented in the present paragraph have been obtained with gravity effects neglected. The results obtained in high speed experiments ($Fr = 11.19$) are compared with these theoretical results. The curves marked S_0 correspond to the double spiral vortex model proposed by Tulin. S_1 corresponds to the model presented here, in which the following values were given to μ and ν :

$$(S_1) \rightarrow \mu = 1 ; \nu = 0 \quad (13)$$

From figure 3, it is clear that this model gives a value of the lift coefficient much closer to reality than that obtained with S_0 . However, in the case of

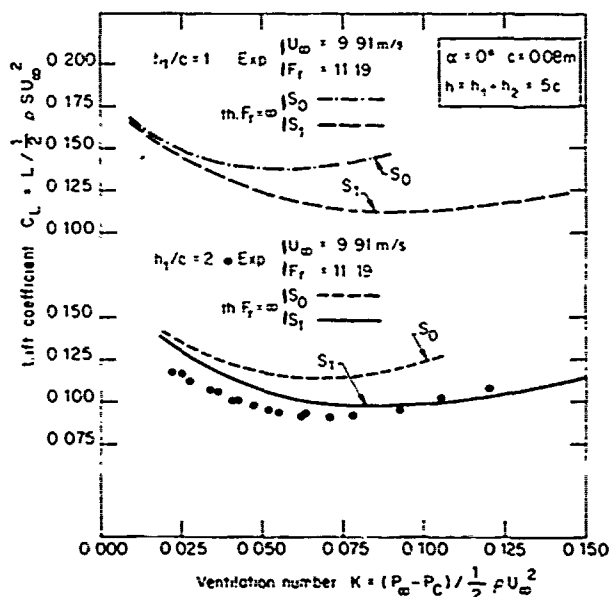


FIGURE 3. Lift coefficient versus ventilation number for two submergence depths

small values of K , the lift coefficient is overvalued. As will be seen below, and despite the fact that the Froude number is high, the difference can be partly explained by a gravity effect. Figure 4 shows a very good agreement between experimental and theoretical results for the drag. The reason is that near the ideal angle of attack, the drag varies very little. Therefore, it is not sensible to the incidence effect induced by the free surface and the model's deficiencies are not

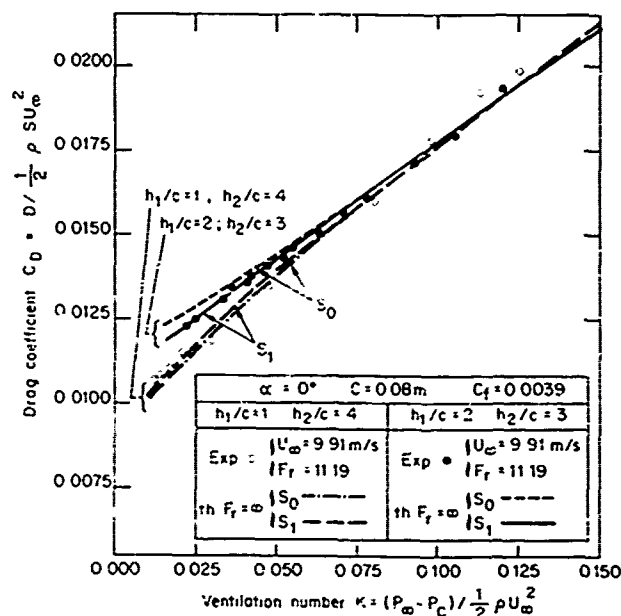


FIGURE 4. Drag coefficient versus ventilation number for two submergence depths

obvious. Figure 5 shows that the cavity length foreseen by the model S_1 is slightly too short in the case of small values of K . Figures 6 and 7 represent the free boundaries that are obtained with this model. Figure 6 also shows that when cavity length increases, its thickness increases to the rear in a seemingly exaggerated manner. By changing the values of μ and ν , very different downstream behaviour is obtained (Figure 8). The corresponding model is designated by S_2 :

$$(S_2) \rightarrow \mu = 7 ; \nu = 6 \quad (14)$$

By calculating foil lift with S_2 , a value nearly identical with that corresponding to the S_1 model is obtained (See Figure 13, $\beta = 1$). This is because the slope of the foil surface in the proximity of the foil is practically the same in both models (K fixed).

3. EFFECT OF A CHANGE IN ANGLE OF ATTACK

The behaviour of the foil and the cavity when the angle of incidence increases is studied. By reason of the procedure used to inject air into the cavity (See Ref [4] and [6]), this behaviour can be studied with a fixed air flow rate. When the cavity is long and the angle of attack not too large, a small variation in this angle has practically no effect on the pressure in the cavity. The cavity shortens and the same result as that shown on Figures 9 and 10 is found. When the cavity is short, the pressure within varies more rapidly, and it is difficult to keep it constant by

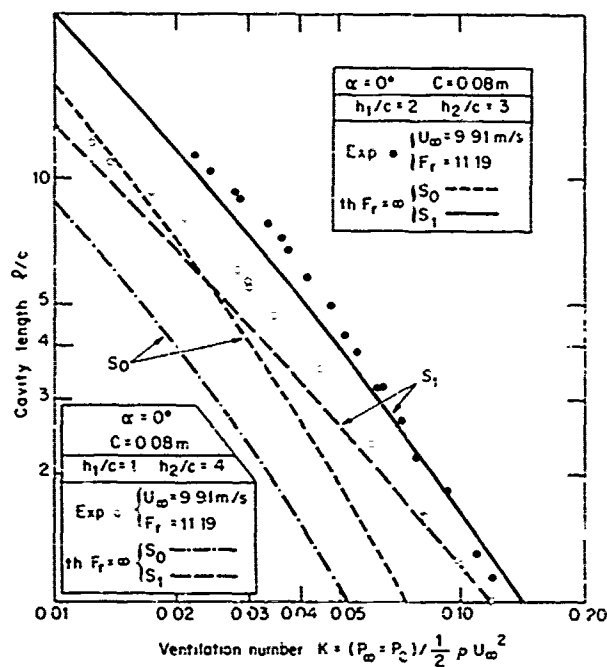


FIGURE 5. Cavity length versus ventilation number for two submergence depths

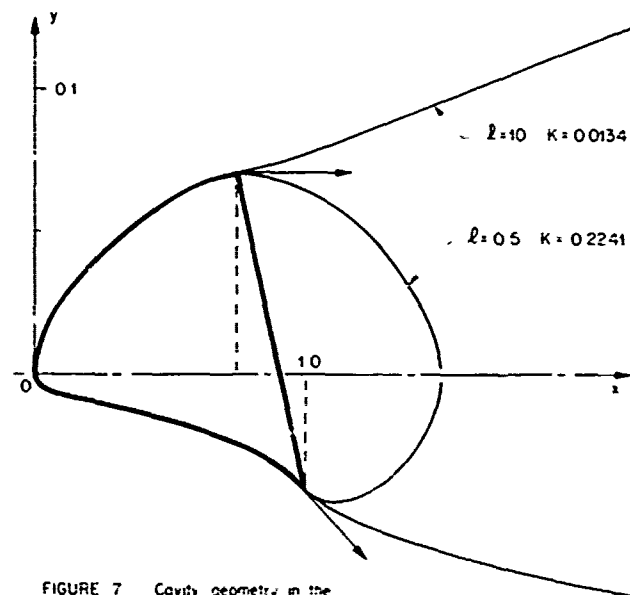


FIGURE 7. Cavity geometry in the neighbourhood of the foil ($h_1 = 1, h_2 = 4$)

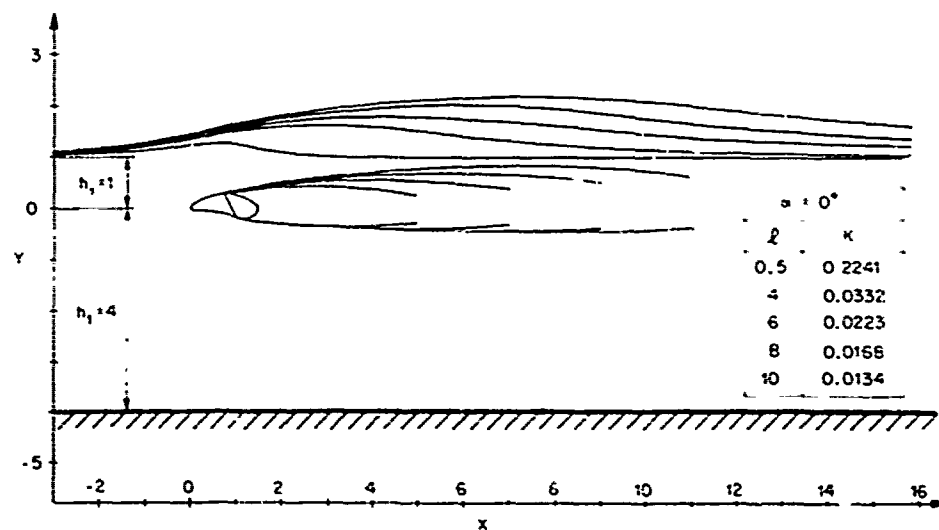


FIGURE 6. Influence of the ventilation number on the geometry

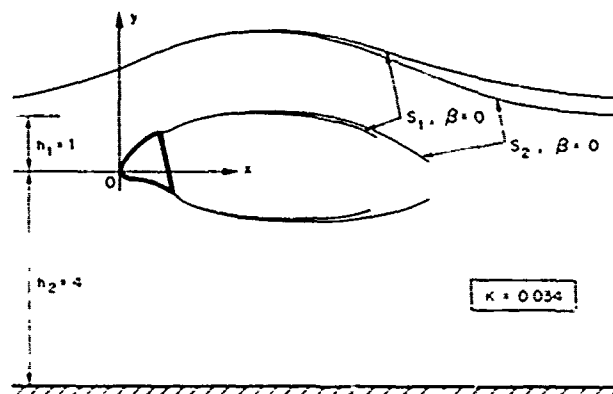


FIGURE 8. Influence of the wake model on the geometry

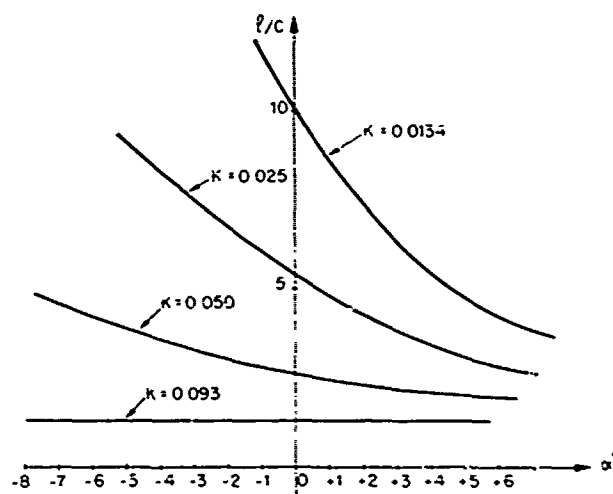


FIGURE 9. Influence of the angle of attack on the cavity length (K fixed)

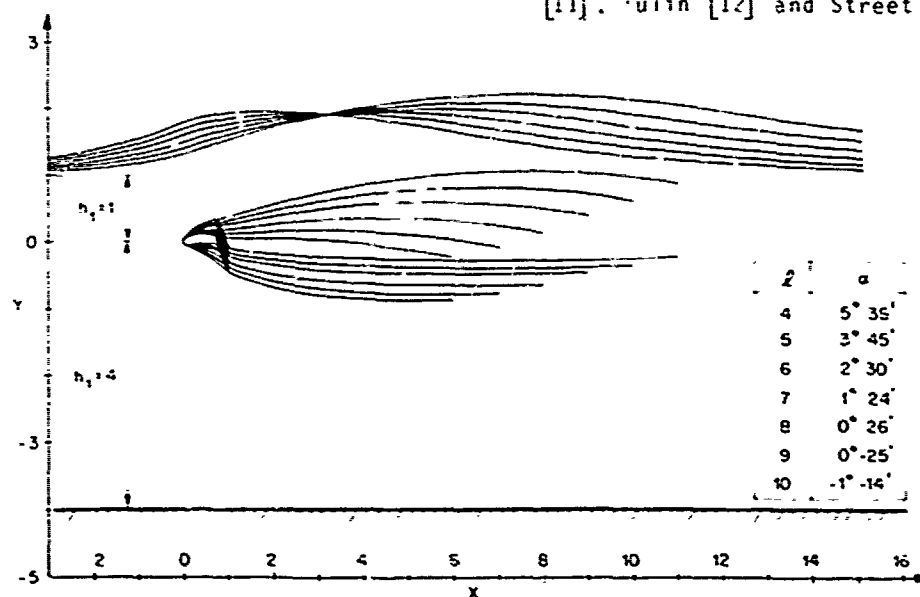


FIGURE 10. Influence of the angle of attack on the geometry for ventilation number $K = 0.0158$

varying the airflow because of the pulsing effect of the cavity. Any comparison with theory then becomes illusory. A valid assessment of the ventilation problem would necessitate a special study, and this goes beyond the limits of this study. From the tests carried out, some general ideas can be given :

- the variation in the cavity length affected by modification in angle of attack is largely due to the change in the kinetic conditions of the flow. This is confirmed by the calculations although the conditions are not exactly the same.
- this variation is also due to the fact that the change in angle of attack modifies the conditions in which the air is evacuated with the flow. Thus, for a fixed air flow, if the angle of attack becomes large, the air in the cavity evacuates much more easily ; in this way, the pressure in the cavity decreases and so does its length. It seems that a rapid decrease in the cavity pressure is always observed when cavitation appears at leading edge. At the same time, a sudden shortening of the cavity is observed. This is explained by the fact that, after the onset of cavitation at the leading edge, the interface of the cavity becomes very turbulent and permeable, which consequently favours air entrainment.

According to figure 10, a point would seem to exist on the free surface such that its position is independent of the angle of incidence. The result observed numerically has not been demonstrated analytically. It may perhaps be explained by linearisation of the problem.

4. EFFECT OF SPEED

It has generally been assumed that this effect was due to gravity effects. Parkin [11], Tulin [12] and Street [13] have

indeed shown that gravity can introduce significant variations in forces, while at the same time modifying the shape of the free boundaries. From the theoretical point of view, however, up till now no study has been carried out taking into account both the free surface and the gravity effects. In the experimental field, Altmann and Eläta have made a number of systematic tests with a supercavitating wedge section, and they have obtained significant force variations. Previous tests made with base-vented sections do not allow any concrete conclusions to be drawn.

Figure 11 shows the variation in cavity length plotted against ventilation number for different values of the Froude number. It can be seen that for the tests corresponding to $\beta = 0.008$, excellent agreement with the S_2 model is obtained and this cannot be considered as pure luck since the coefficients μ and ν were adjusted to this effect. Even more interesting is the change in results when β increases. For example, when $\beta = 0.05$, there is no longer agreement with experimental results. On the other hand, at this speed, if the S_1 model is used to calculate the effect of gravity, excellent agreement between theoretical and experimental results is once more obtained. On the basis of these results, it can be assumed

that speed has an effect on the flow, not only through direct gravity effects, but also through a wake effect which is itself influenced by gravity as well as by unidentified dimensionless parameters dependent upon speed. In order to harmonise the results obtained at $\beta = 0.008$ and at $\beta = 0.05$, the value of coefficients μ and ν can be varied in relation to β according to the following relations :

$$(S^*) \quad \mu = 0.04/\beta \quad \nu = 0.04/\beta - 1 \quad (15)$$

thus giving the model S^* :

$$C_p = 2\epsilon \left[\theta_1 e^{\frac{l+1-x}{1+25\beta(l-1)}} - \beta y_{s1} \right] \quad (16)$$

From a practical point of view, the necessity of using a type (16) law, dependent on speed, to start off the calculation of free lines, means that the slower the speed, the more the model must give a thick cavity at infinite Froude number. This is quite coherent with the fact that the effect of gravity is to close the cavity.

Figure 12 shows what is obtained with $\beta = 0.089$ using this new model. It can be seen that the results are in very good agreement with experimental results. Thus, the model S^* provides a good description of the flow for a Froude number range of

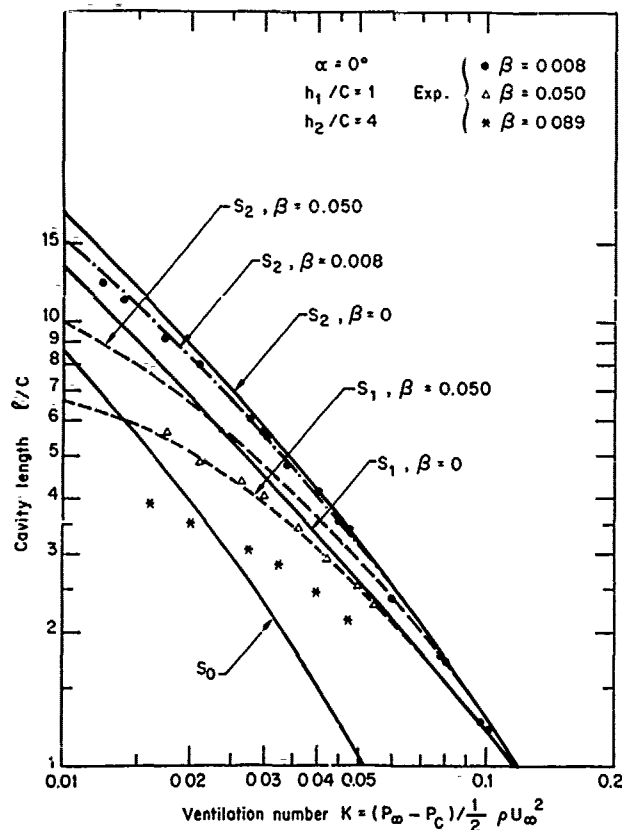


FIGURE 11. Influence of the speed on the cavity length.

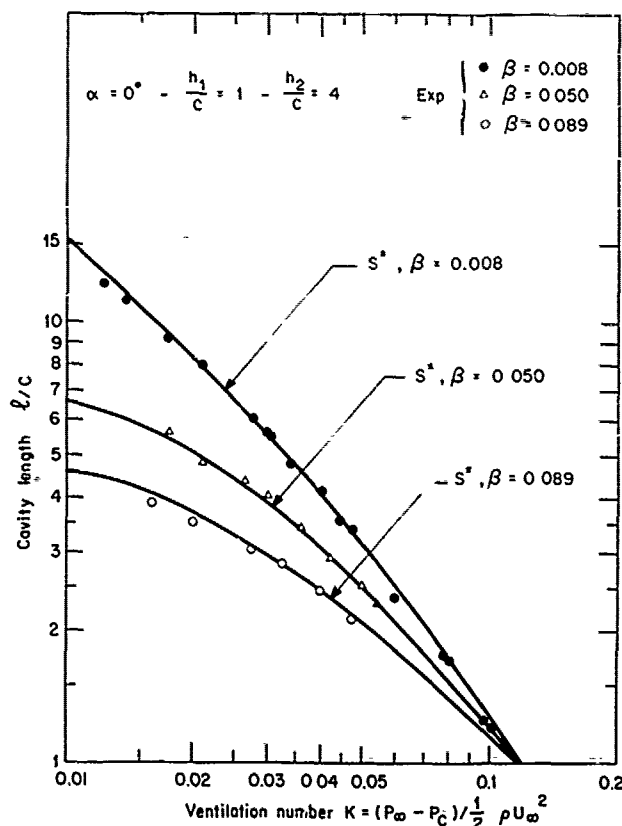


FIGURE 12. Influence of the speed on the cavity length.

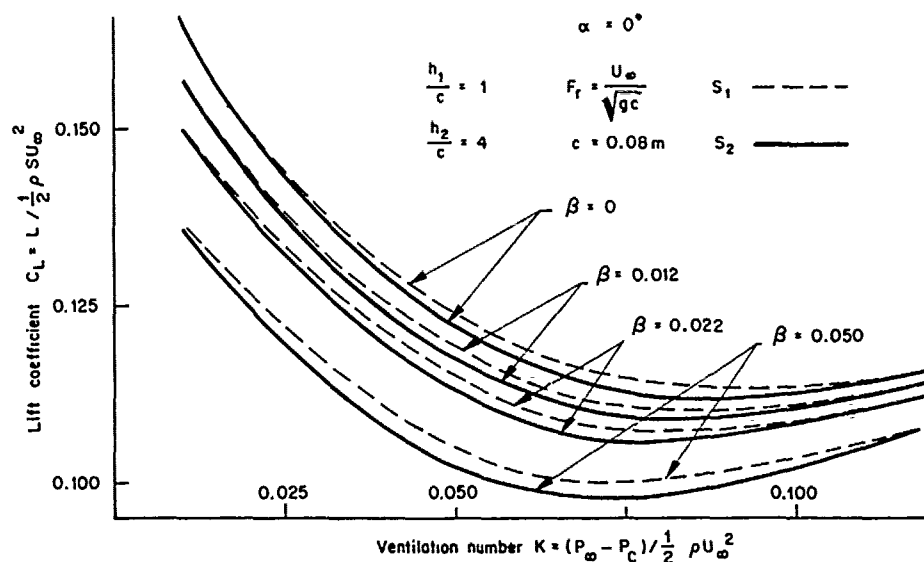


FIG 13 . Effect of transverse gravity field on relation between lift coefficient and ventilation number
Comparison of the laws S_1 and S_2

three to infinity. It would be tempting to use this model now to study the effect of gravity on forces. However, such a study may seem a little artificial as the model S^* is derived from a parametric adjustment. If the gravity effects on the lift that are obtained with the two models S_1 and S_2 are then compared (see figure 13), it is found that these models give almost the same results. This is mainly because of the fact that the contribution of that part of the free surface downstream of the cavity is almost negligible compared with the contribution of that part located above the foil and cavity. Thus, despite the fact that for the two models S_1 and S_2 the contribution of the downstream part of the free surface is very different, in neither case does this contribution count for very much. To calculate the effect of gravity on lift, only the model S_2 was used, in the knowledge that the model S^* would give very similar results. Figure 14 shows that the calculated reduction in lift due to gravity effects is very close to the reduction in lift observed experimentally, at least for small ventilation numbers. When the ventilation number is high, the theoretical and experimental results do not agree, but it has already been indicated that when the cavity is small, the theory seems to have a number of failings. In addition, it seems that, in this case, the upper boundary of the cavity tends to wet the rear part of the foil. After having taken into account the gravity effect, there is still a very slight difference between theoretical and experimental results, even for low values of ventilation number. This difference, expressed as an angle of attack, represents

an angular shift of less than six minutes. This shift can be explained by experimental error. For example, the three-dimensional effects caused by the side walls may induce an angle of attack.

CONCLUSIONS

In order to be able to make a correct forecast of the forces acting on a base-vented hydrofoil, the following experimental and theoretical conditions are needed :

- From the experimental standpoint, use a wall-mounting system for the foil to avoid the presence of a support strut which disturbs flow around the foil.
- The theory must take into account the free surface, the bottom of the test section, the cavity and the cavity wake. For long cavities, it is also necessary to make allowance for the gravity effect, even at high speed.

Independently of the gravity effect, the flow rate would seem to have an effect on law $\mathcal{L}(K)$. This effect is probably linked to mechanisms which do not come within the scope of the present study.

ACKNOWLEDGMENTS

This research was supported by the Direction des Recherches, Etudes et Techniques, Group VI, division Hydrodynamique, under contracts n° 77/352 and 78/490.

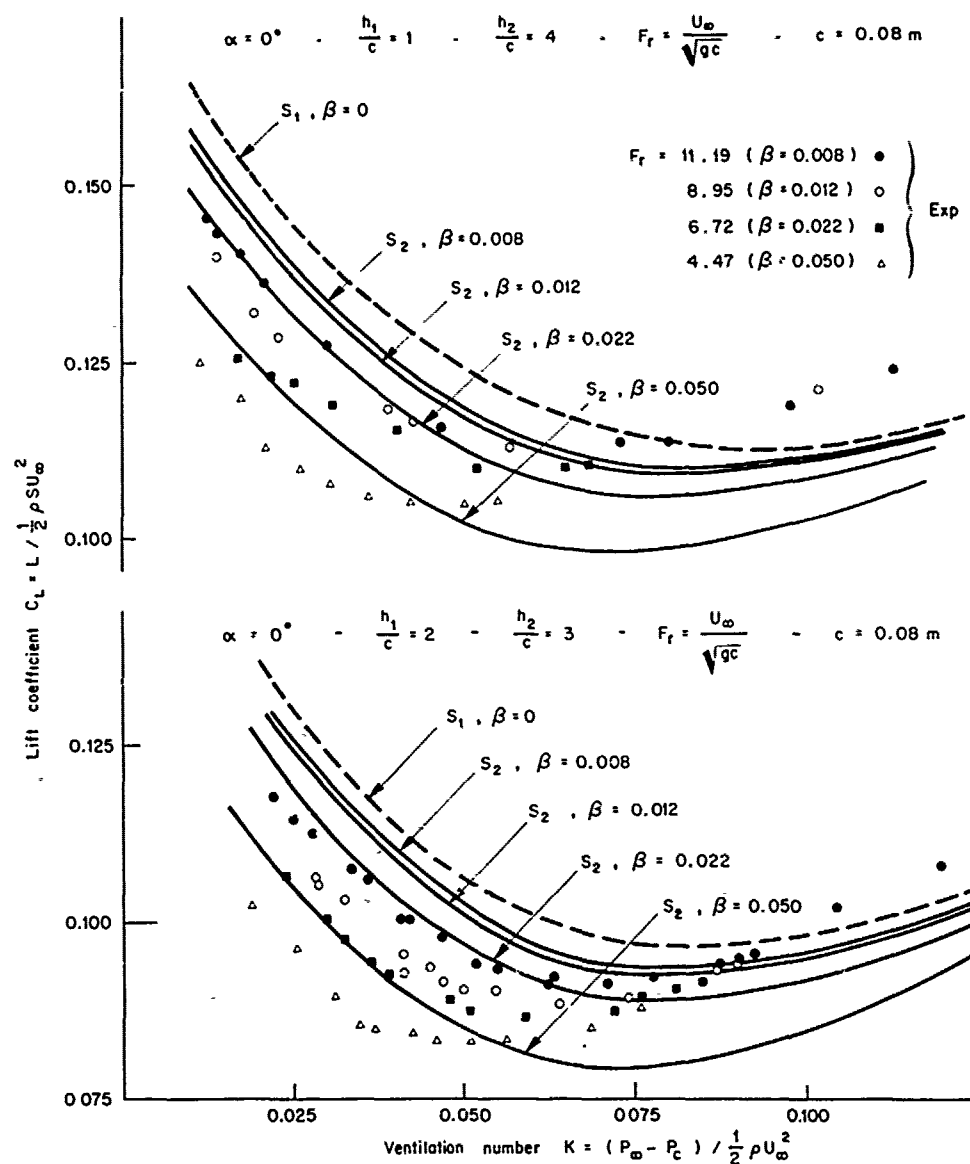


FIG 14 . Effect of transverse gravity field on relation between lift coefficient and ventilation number .
Comparison of theoretical and experimental results

REFERENCES

[1] Christoffer, K.W., 1961, "Experimental investigation of a high speed hydrofoil with parabolic thickness distribution and an aspect ratio", Langley Research Center, NASA Tech. Note D728.

[2] Johnson, V.E. and RASNICK, T.A., 1959, "Investigation of a high speed hydrofoil with parabolic thickness distribution" Langley Research Center, NASA Tech. Note D 119.

[3] Lang, T.G. and DAYBELL, D.A., 1962, "Free surface water-tunnel tests of an uncambered base vented parabolic hydrofoil of aspect ratio one" China Lake, California Narweps Report 7920.

[4] Rowe, A.R., 1973, "Profils hydrodynamiques bidimensionnels à base ventilée en présence d'une surface libre", Thèse doct. ing. 2° Partie. Institut de Mécanique de Grenoble.

[5] Rowe, A.R., 1979, "Evaluation study of a three-speed hydrofoil with wetted upper-sides", Journal of Ship Research, Vol.23, N°1, pp.55-65.

[6] Rowe, A.R. and Kueny, J.L., 1980, "Supercavitating hydrofoils with wetted upper sides", Journal de Mécanique, vol.19 n°2, Juin 1980.

[7] Rowe, A.R. and Michel, J.M., "Two dimensional base-vented hydrofoils near a free surface : influence of the ventilation number", Journal of Fluids Engineering, Special section on cavity flows, Dec.1975, pp.465-474.

[8] Furuya, O., 1975, "Non-linear calculation of arbitrarily shaped supercavitating hydrofoils near a free surface". J. Fluid Mech. 68, pp.21-40.

[9] Michel, J.M., 1977, "Wakes of developed cavities", Journal of Ship Research, vol.21, n°4, pp.225-238.

[10] Altmann and Elata, 1967, "Effects of ambient conditions, the gravity field and struts, on flow over ventilated hydrofoils" Hydronautics, Tech. Rept. 605-1, Laurel Hd.

[11] Parkin B.R., 1957, "A note on the cavity flow past a hydrofoil in a liquid with gravity", C.I.T. Pasadena California Report N°47-9.

[12] Tulin, M.P., 1965, "The shape of cavities in supercavitating flows" Hydronautics, Tech. Rept. 121-5.

[13] Street, R.L., 1965, "A note on gravity effects in supercavitating flow", J. Ship Research, March, pp.39-45.

APPENDIX

$$S_{21} = \int_0^{0.5} C \left[\int_f^{-1} \frac{(y_{c1})_0^-}{T'} \frac{r' dr'}{b - rr'} \right] \frac{dr}{1-r}$$

$$S_{22} = \int_0^{0.5} C \left[\int_d^c \frac{(y_{c1})_0^+}{T'} \frac{r' dr'}{b - rr'} \right] \frac{dr}{1-r}$$

$$S_{31} = \int_0^{0.5} C \left[\int_f^{-1} \frac{(y_{c1})_\alpha^-}{T'} \frac{r' dr'}{b - rr'} \right] \frac{dr}{1-r}$$

$$S_{32} = \int_0^{0.5} C \left[\int_d^c \frac{(y_{c1})_\alpha^+}{T'} \frac{r' dr'}{b - rr'} \right] \frac{dr}{1-r}$$

$$L_{21} = \int_0^{0.5} C \left[\int_b^{+\infty} \frac{(y_{l1})_0^-}{T'} \frac{r' dr'}{b - rr'} \right] \frac{dr}{1-r}$$

$$L_{31} = \int_0^{0.5} C \left[\int_b^{+\infty} \frac{(y_{l1})_\alpha^-}{T'} \frac{r' dr'}{b - rr'} \right] \frac{dr}{1-r}$$

$$S_{23} = \int_{0.5}^1 C \left[\int_f^{-1} \frac{(y_{c1})_0^-}{T'} \frac{r'^2 dr'}{(b - rr')(b - r')} \right] dr$$

$$S_{24} = \int_{0.5}^1 C \left[\int_d^c \frac{(y_{c1})_0^+}{T'} \frac{r'^2 dr'}{(b - rr')(b - r')} \right] dr$$

$$S_{33} = \int_{0.5}^1 C \left[\int_f^{-1} \frac{(y_{c1})_\alpha^-}{T'} \frac{r'^2 dr'}{(b - rr')(b - r')} \right] dr$$

$$S_{34} = \int_{0.5}^1 C \left[\int_d^c \frac{(y_{c1})_\alpha^+}{T'} \frac{r'^2 dr'}{(b - rr')(b - r')} \right] dr$$

$$L_{23} = \int_{0.5}^1 C \left[\int_b^{+\infty} \frac{(y_{l1})_0^-}{T'} \frac{r'^2 dr'}{(b - rr')(b - r')} \right] dr$$

$$L_{33} = \int_{0.5}^1 C \left[\int_b^{+\infty} \frac{(y_{l1})_\alpha^-}{T'} \frac{r'^2 dr'}{(b - rr')(b - r')} \right] dr$$

$$P3 = (S21 - S23) - (S22 - S24) - (L21 - L23)$$

$$P4 = (S31 - S33) - (S32 - S34) - (L31 - L33)$$

$$I5 = \int_f^{-1} \frac{(y_{c1})_0^-}{T'} \frac{r' dr'}{b-r'} - \int_d^c \frac{(y_{c1})_0^+}{T'} \frac{r' dr'}{b-r'} - \int_b^{+\infty} \frac{(y_{l1})_0}{T'} \frac{r' dr'}{b-r'}$$

$$I6 = \int_f^{-1} \frac{(y_{c1})_\alpha^-}{T'} \frac{r' dr'}{b-r'} - \int_d^c \frac{(y_{c1})_\alpha^+}{T'} \frac{r' dr'}{b-r'} - \int_b^{+\infty} \frac{(y_{l1})_0}{T'} \frac{r' dr'}{b-r'}$$

Discussion

O. Furuya (Tetra Tech.)

According to the lift data obtained from the experiment shown in Fig.3, the lift-to-drag (L/D) ratio of the base-ventilated hydrofoil is only in a range of 6 to 10. On the other hand, this value can easily reach 20 for the supercavitating hydrofoil having the sharp leading edge and 10 even for that with leading edge radius of 0.5% chord l). It is understood that many hydrodynamic and structural limitations exist for the former type of foil in order to keep the upper foil portion wetted, whereas for the latter no such limitations are designers' concern. I would like to know, therefore, if the authors have tested such a foil that will provide a higher L/D value and can still maintain the upper portion of the foil fully wetted. If this is not possible, what is the reason for using such a lifting device which is more vulnerable to the flow environment than supercavitating foils?

The second question goes to the comparison of lift data between the experiment and theory. When the authors used the double-spiral vortex model, the apparent discrepancy existed over a complete range of cavitation number (see Fig.3). The authors modified the flow model by introducing a continuously changing pressure distribution from the cavity end point to the downstream infinity. The amplitude and slope of pressure change were arbitrarily determined by two free parameters μ and ν . They demonstrated in Fig. 3 that, with $\mu = 1$ and $\nu = 0$ chosen, a better agreement between the theory and experiment was obtained for large ventilation numbers K but not for smaller K 's.

This fact is quite easily understood if one pays attention to the cavity length. By changing the velocity distribution on the wake, it is possible to influence the flow around the foil if the cavity length is short (or for larger ventilation numbers) but such effect diminishes as the cavity length becomes longer (or for smaller K 's). A question now arises as to the current theory's inability in accurately predicting the lift force for the smaller K 's cases. It is a well-known fact that the analytical result for the cavitating flow is insensitive to the selection of type of wake model if the cavity length is large (or smaller K 's). If there is a theory which is unable to predict the force coefficient accurately for smaller K 's, one should realize that such a theory must have an inherent deficiency in its force prediction capability. It seems to me that the modification of the wake velocity with arbitrary amplitude and decay factors is just an ad-hoc remedy but not an essential one.

It is found in our computations 2) and the nonlinear theory with double-

spiral vortex model predicted accurate force coefficients for supercavitating hydrofoils under a free surface over a wide range of cavitation parameters. It is my suspicion that there might exist a limitation of the linearized theory for this type of base-ventilated flow near a free surface. I would like to ask the authors if they intend to apply the nonlinear theory to the present title problem in the near future.

REFERENCES

- 1) Furuya, O., 1975, "Nonlinear calculation of arbitrarily shaped supercavitating hydrofoils near a free surface", *Journal of Fluid Mech.*, Vol. 68, Part I, pp.21-40.
- 2) Furuya, O., 1975, "Numerical procedures for the solution of two-dimensional supercavitating flows near a free surface", *Proceedings, First International Conference on Numerical Ship Hydrodynamics*, October, at the National Bureau of Standards, Md.
- 3) Furuya, O., and Acosta, A.J., 1976, "Experimental Study of superventilated finite aspect ratio hydrofoils near a free surface", 11th Symposium of Naval Hydrodynamics, sponsored by the Office of Naval Research, London, March.

Author's Reply

A.R. Rowe (M. Grenoble)

The first question of Dr. Furuya has three reply elements.

First element : When we have begun to study base vented foils with wetted upper-sides, many studies had been developed concerning supercavitating foils with unwetted upper-sides. On the other hand, only few information was existing concerning base vented foils. It looked interesting to have more information.

Second element : If a flap is added on the rear part of a base-vented foil, it is easy to obtain a good subcavitating foil. With a true supercavitating foil this is more difficult.

Third element : The results presented on Fig.3 correspond to an angle of attack of zero degree. In those conditions, the flow is not well adopted. At the ideal angle of attack, the lift coefficient reaches the 0.19 value and the lift to drag ratio is of the order of 17 for the ventilation number 0.025 (see Ref. [6]).

The second question is very interesting; in fact, it is the reason why we have developed this study. As at low ventilation number theoretical model gives all the same results, we have thought that the gravity effects could explain the gap observed. This point of view seemed justified because when the ventilation number is low,

the characteristic length to take into account to calculate the Froude number is the chord plus the cavity length. So at 10 m/s, for $K = 0.025$, the cavity length is 7 and the characteristic Froude number is only 3.9. In fact, the calculation shows that the gap observed becomes $\Delta C_L = 0.008$ when we take into account the gravity effect. This $\Delta C_L = 0.008$ corresponds to $\Delta\alpha \approx 5'$, which is very small. I think that this $\Delta\alpha \approx 5'$ is not due to the linearized theory. In fact, this theory is well adapted to base vented foils which always are used with very little angle of attack. On the contrary, it is quite possible that the experimental conditions give a discrepancy of

this order : influence of the side walls giving three-dimensional effects is not negligible as well as influence of the level of turbulence of the tunnel, measurement of the true geometrical angle of attack. It is much easier to test true supercavitating hydrofoils : as the flow is very perturbed the causes of error are minimized. Moreover for the same $\Delta\alpha$, the ΔC_L is twice more little with a true supercavitating hydrofoil. Concerning the last point, a numerical non linear method has been developed, the method is very efficient, but it is difficult to compare because the closure conditions are not the same. We will try in the next future.

Boundary Layer and Cavitation Studies of NACA 16-012 and NACA 4412 Hydrofoils

Jan H.J. van der Meulen
Netherlands Ship Model Basin
Wageningen, The Netherlands

ABSTRACT

Boundary layer and cavitation phenomena on two hydrofoils are studied in a high speed water tunnel provided with a rectangular test section. The boundary layer is visualized with a tracer, using an in-line holographic technique. Depending on the Reynolds number and angle of attack, typical boundary layer phenomena are observed, such as laminar separation at the leading edge or downstream, transition to turbulence of the separated shear layer with or without reattachment, and transition to turbulence of the laminar boundary layer. Cavitation phenomena are studied visually, photographically and by means of in-line holography. It is found that the appearance of cavitation on both hydrofoils, such as sheet, bubble and cloud cavitation, is related to the viscous flow behaviour.

NOMENCLATURE

C_p	Pressure coefficient
$C_{p_{min}}$	Minimum pressure coefficient
C_{p_T}	Pressure coefficient at transition
P	Static pressure
P_0	Undisturbed static pressure in test section
P_{min}	Minimum static pressure
P_v	Vapour pressure
Re	Reynolds number
V_0	Undisturbed free stream velocity in test section
c	Chord length of hydrofoil
x	Distance along chord
x_C	Position of leading edge of cavity
x_S	Position of laminar separation
x_T	Position of transition

α	Angle of attack
α_0	Zero lift angle of attack
ν	Kinematic viscosity
ρ	Liquid density
σ	Cavitation number
σ_i	Incipient cavitation number
σ_d	Desinent cavitation number

1. INTRODUCTION

During the past decade, several studies have been devoted to the relationship between the boundary layer flow about axisymmetric bodies and cavitation. Using the Schlieren method for boundary layer flow visualization, Arakeri and Acosta [1] were able to relate cavitation inception on a hemispherical nose with the occurrence of a laminar separation bubble. Further studies by Van der Meulen [2, 3], Gates [4] and Gates and Acosta [5] revealed the influence of polymer additives on laminar flow separation, and hence on cavitation. Arakeri and Acosta [6] classified axisymmetric bodies into four groups, depending on the viscous flow behaviour. In each group characteristic types of cavitation are found. The authors indicated similarities with practical flow situations. Most applications, however, refer to the flow about foil sections. It may be inferred that the viscous flow about foil sections is related with the section shape, the angle of attack and the Reynolds number. It seems questionable whether all viscous flow regimes found on hydrofoils are found also on axisymmetric bodies. Therefore, a classification into groups can better be based on hydrofoils.

The aerodynamics of wing sections has been studied at great length. Studies of the boundary layer flow are mainly concerned with the influence on lift and drag forces.

In general, these studies do not provide adequate data that can be readily used for corresponding cavitation studies. This implies that the relationship between viscous effects and cavitation on hydrofoils can only be assessed by performing both flow visualization and cavitation experiments. A first and important example of this approach is due to Casey [7]. He measured the position of a laminar separation bubble on a NACA 0015 hydrofoil in a wide range of angles of attack by means of an oil-film technique. This position was compared with the position of the leading edge of attached cavities at inception and an excellent agreement was found. Similar experiments were made by Blake, Wolpert and Geib [8] with a Liebeck N112 hydrofoil. For the untripped hydrofoil the position of (attached) bubble cavitation was found to coincide with the position of a laminar separation bubble, whereas for the tripped hydrofoil travelling bubble cavitation occurred. Van der Meulen [9] related the appearance of cavitation on a NACA 16-012 hydrofoil at angles of attack of 7° and 10° with the boundary layer flow. A holographic technique was used to visualize the boundary layer. The present study is an extension of this work and is aimed at classifying types of cavitation on hydrofoils and relating them with the viscous flow behaviour.

2. EXPERIMENTAL METHODS AND PROCEDURE

2.1 Test Facility And Hydrofoils

The experiments were made in the high speed water tunnel of the Netherlands Ship Model Basin. A detailed description of this tunnel with its air content control system is given in [10]. For the present study a new test section was used. It has a 40 mm x 80 mm rectangular cross section and the maximum water speed is 40 m/s. Two hydrofoils were tested. The first one is the NACA 16-012 hydrofoil, which has a symmetrical profile shape and a leading edge radius of 0.703% of the chord length. The second one is the NACA 4412 hydrofoil, which has a 4% camber and a leading edge radius of 1.58% of the chord length. Both hydrofoils had a chord length of 70 mm and a span of 40 mm. They were both made of brass.

One of the reasons for selecting the NACA 16-012 hydrofoil is that the same section is used in a comparative cavitation test program initiated by the International Towing Tank Conference Cavitation Committee. The NACA 4412 hydrofoil was selected because this hydrofoil had been subjected to an extensive cavitation test program at the California Institute of Technology, as reported by Kermeen [11].

2.2 Holographic Method

To obtain detailed information on the cavity type and the boundary layer flow on

the hydrofoils, in-line holography has been used. Visualization of the boundary layer was effected by injecting a sodium chloride solution from a small hole (dia. 0.21 mm) located at the leading edge of the hydrofoil. This boundary layer flow visualization technique, in which a liquid is injected with an index of refraction slightly different from the surrounding liquid, and in which the three-dimensional flow pattern of the injected fluid is recorded in a hologram, has been used earlier by Van der Meulen [2, 3] to visualize the boundary layer flow on axisymmetric bodies. However, in the case of axisymmetric bodies, the image of the body on the hologram is a single line giving the contour of the body as illuminated by the laser beam, whereas in the case of two-dimensional hydrofoils, the image of the hydrofoil on the hologram is a single line representing the whole surface of the hydrofoil as touched by the laser beam. Hence, small deviations in the direction of the laser beam relative to the surface of the hydrofoil will mask the surface and thus mask the boundary layer flow. Such deviations are difficult to eliminate. This problem was overcome by slightly curving backward the nose line of the hydrofoils and slightly decreasing the section thickness further downstream toward the side walls. Thus the chord length at the side walls was only 68 mm. In this way a center section was obtained with a chord length of 70 mm suitable for flow visualization. Initially, the sodium chloride concentration was 2%, but in subsequent testing a concentration of 5% was used. The ratio of the injection to test section velocity was usually around 0.1. Injection was made by a plunger moving with an adjustable speed in a cylinder.

A schematic diagram of the in-line holographic set-up is shown in Figure 1. A ruby laser ($\lambda = 694$ nm) with a 30 mJ single mode pulse duration of 10 ns was used as a light source, serving a plane parallel beam of 60 mm diameter with the aid of a telescopic system. Agfa-Gevaert 8E75 Holotest plates (5000 lines/mm) were used as a recording medium. Reconstruction from the holograms was made with a 2 mW HeNe laser ($\lambda = 633$ nm). The reconstructed image was studied with a microscope; the applied magnification was usually 40 x. Further details on the holographic procedure and resolution are given by Van Renesse and Van der Meulen [12].

2.3 Procedure

The tests performed in the high speed tunnel comprised holographic recordings of the boundary layer flow and of cavitation, cavitation inception measurements and photographs of cavitation. These photographs were made with a camera mounted vertically above the hydrofoil so that its field of view through a plexiglass window in the top of the test section covered a length in chordwise direction of 40 mm and a width in spanwise direction of 27 mm. Prior to each

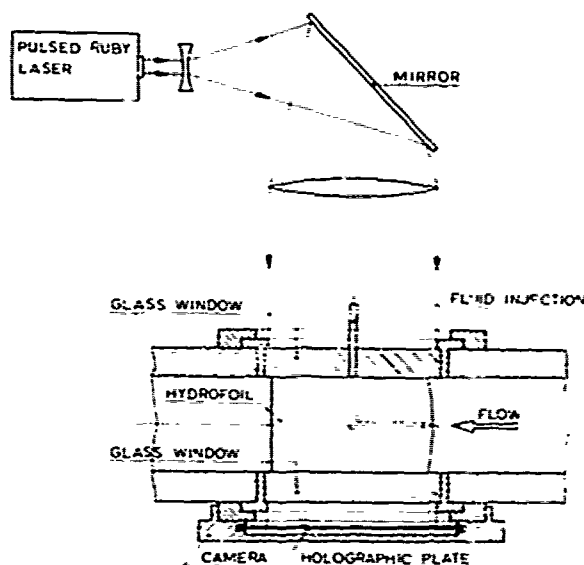


Fig. 1 Schematic diagram of in-line holographic system for making holograms of cavitation and flow phenomena on hydrofoils.

series of tests (at a certain angle of attack), the hydrofoil was cleaned and the tunnel refilled. To adjust the air content, the water was passed through the deaeration circuit for a period of 1.5 h at a constant pressure in the deaeration tank. All tests were made at a constant air content of about $4.6 \text{ cm}^3/\text{l}$ (1 cm^3 of air per liter of water at STP corresponds to 1.325 ppm by weight). The water temperature was usually around 20°C . However, to extend the Reynolds number range for the inception measurements, at the highest test speed the temperature was allowed to rise to a maximum value of about 35°C .

A survey of all angles of attack at which tests were made is given in Table 1 and 2. The angle of attack in these tables

Table 1 Test angles of attack for NACA 16-012 hydrofoil.

Inception meas. and photographs	Holographic recordings
2°	2°
3°	3°
4°	
5°	5°
6°	
7°	7°
10°	10°
12°	12°
16°	

Table 2 Test angles of attack for NACA 4412 hydrofoil.

Inception meas. and photographs	Holographic recordings
0°	
2°	2°
4°	4°
6°	6°
8°	8°
10°	10°
12°	
16°	16°

refers to the geometric angle of attack. The effective angle of attack and the pressure distribution about the hydrofoils are affected by the restricted height of the test section. No attempt is made to make any corrections. The geometric conditions for the flow visualization and cavitation tests were the same, and thus those results can be compared without any restriction.

3. BOUNDARY LAYER STUDIES

3.1 NACA 16-012 Hydrofoil

The boundary layer flow on the suction side of the NACA 16-012 hydrofoil has been studied for the following angles of attack: 2° , 3° , 5° , 7° , 10° and 12° . Since $\alpha = 3^\circ$ appeared to be a critical angle, some additional observations were made for $\alpha = 2.9^\circ$.

For $\alpha = 2^\circ$, observations were made in the range $V_\infty = 1 - 20 \text{ m/s}$, where V_∞ is the undisturbed free stream velocity in the test section. At low speeds, a laminar bound-



Fig. 2 Laminar separation on NACA 16-012 hydrofoil for $\alpha = 2^\circ$ and $Re = 9.72 \times 10^5$ ($V_\infty = 1.0 \text{ m/s}$). The flow is from left to right. $x_S/c = 0.70$.

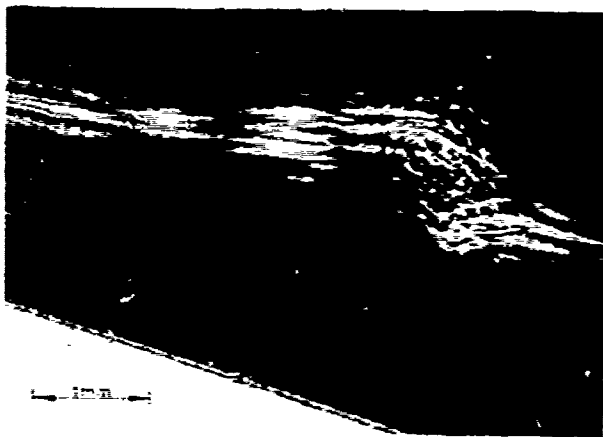


Fig. 3 Transition to turbulence of laminar separated shear layer on NACA 16-012 hydrofoil for $\alpha=2^\circ$ and $Re=0.72 \times 10^5$ ($V_0=1.0$ m/s). $x_T/c=0.96$.

any layer is found with laminar separation for downstream followed by transition to turbulence of the separated shear layer. A photograph of the reconstructed image showing laminar separation is presented in Figure 2. The flow direction in this and all following photographs is from left to right. The Reynolds number is 0.72×10^5 ($V_0=1.0$ m/s). The Reynolds number Re is given by $Re = \frac{V_0 c}{\nu}$.

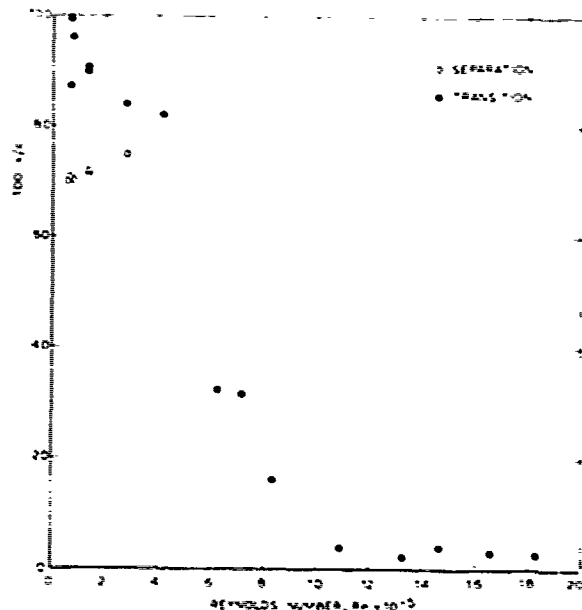


Fig. 4 Positions of separation and transition versus Reynolds number for NACA 16-012 hydrofoil at $\alpha=2^\circ$.

where c is the chord length of the hydrofoil ($c = 70$ mm), and ν the kinematic viscosity. Laminar separation occurs at $x_S/c = 0.70$, where x is the distance along the chord. Further downstream, transition to turbulence occurs, as shown in Figure 3. The position of transition is at $x_T/c = 0.96$. The positions of separation of transition for all holograms taken at $\alpha = 2^\circ$ are plotted in Figure 4. Below $Re = 2 \times 10^5$, the mean value of the position of separation is $(x_S/c)_S = 0.706$. Up till $Re = 4 \times 10^5$ laminar separation is still present, but above $Re = 5 \times 10^5$ a laminar boundary layer is observed with normal transition to turbulence. In this and all subsequent figures, the position of transition to turbulence refers to the position of the first eddy and should thus be distinguished from the position of instability which refers to the position of the first wave.

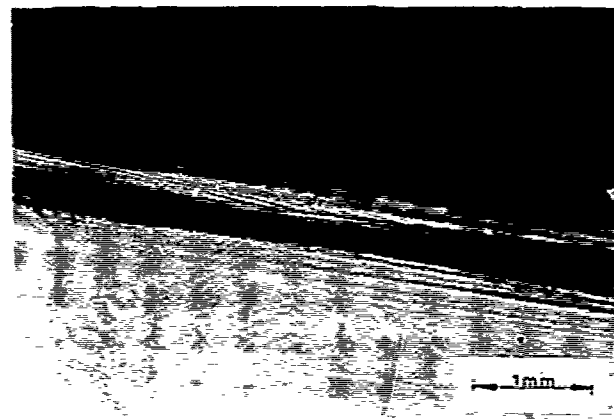


Fig. 5 Laminar separation on NACA 16-012 hydrofoil for $\alpha=3^\circ$ and $Re=0.8 \times 10^5$ ($V_0=1.15$ m/s). $x_S/c=0.697$.

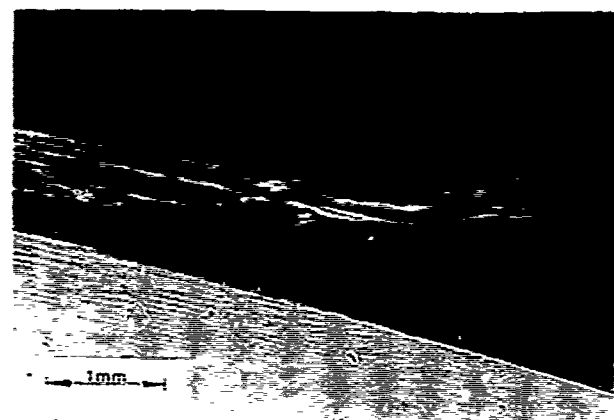


Fig. 6 Transition to turbulence of laminar separated shear layer on NACA 16-012 hydrofoil for $\alpha=3^\circ$ and $Re=0.8 \times 10^5$ ($V_0=1.15$ m/s). $x_T/c=0.843$.

For $\alpha = 3^\circ$, a laminar boundary layer is found at $Re = 0.8 \times 10^5$ ($V_0 = 1.15$ m/s), followed by laminar separation and transition to turbulence far downstream. Photographs of laminar separation and transition are shown in Figures 5 and 6, with $x_s/c = 0.697$ and $x_T/c = 0.843$. Observations made at $Re = 1.47 \times 10^5$ ($V_0 = 2.0$ m/s) showed the presence of a short laminar separation bubble, as shown in Figure 7. Data

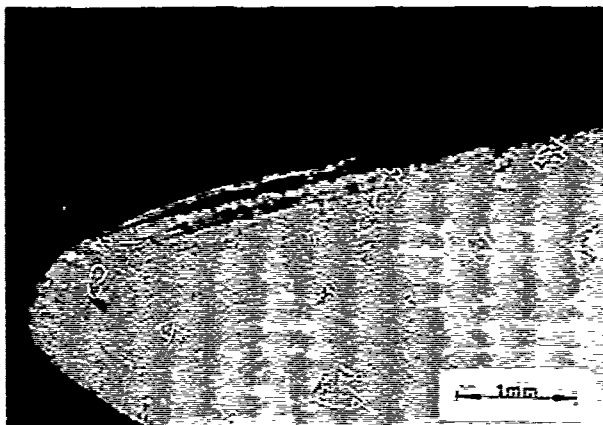


Fig. 7 Laminar separation bubble on NACA 16-012 hydrofoil for $\alpha = 3^\circ$ and $Re = 1.47 \times 10^5$ ($V_0 = 2.0$ m/s).

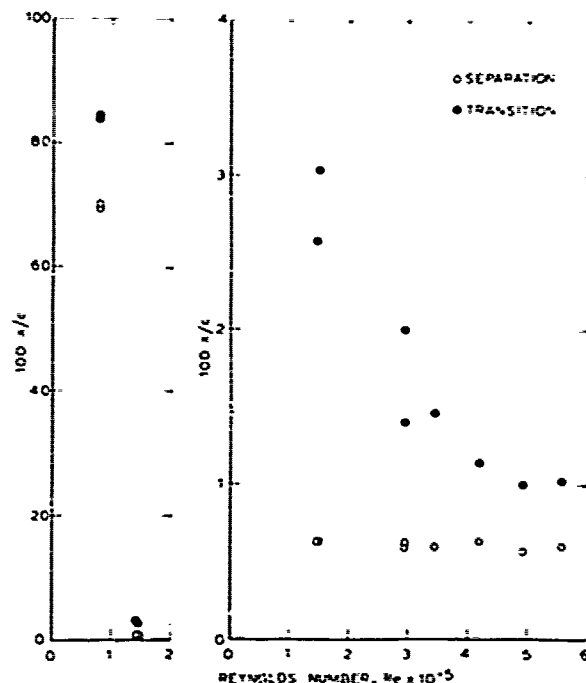


Fig. 8 Positions of separation and transition versus Reynolds number for NACA 16-012 hydrofoil at $\alpha = 3^\circ$.

on the positions of separation and transition are plotted in Figure 8. The mean value of the position of laminar separation for the short bubble is $(\bar{x}_s/c)_B = 0.0061$.

Some observations of the boundary layer flow were made at $\alpha = 2.9^\circ$. The quality of the holograms in this series was rather poor and accurate data were hard to obtain. However, the main features of the boundary layer could still be distinguished and it was found that above $V_0 = 4$ m/s a laminar boundary layer existed with normal transition to turbulence. The absence of leading edge separation (short bubble) appeared to have a large influence on cavitation, as will be discussed later.

For $\alpha = 5^\circ$, a laminar separation bubble is found up till $Re = 5 \times 10^5$. An example at $Re = 0.73 \times 10^5$ ($V_0 = 1.0$ m/s) is shown in Figure 9. Above $Re = 5 \times 10^5$ laminar separation was no longer present, since turbulence began earlier. An example at $Re = 7.6 \times 10^5$ ($V_0 = 12.0$ m/s) is shown in Figure 10. Data on the positions of separation and transition are plotted in Figure 11.

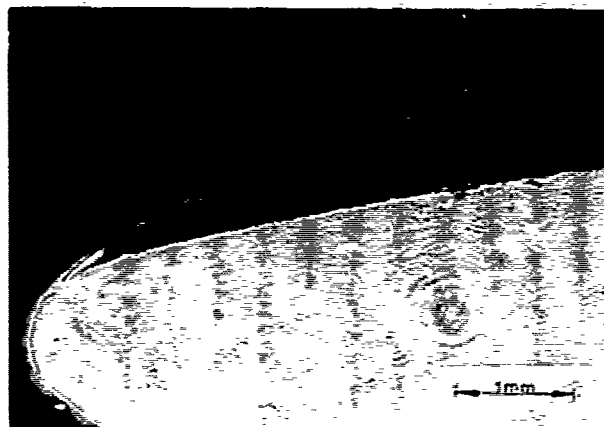


Fig. 9 Laminar separation bubble on NACA 16-012 hydrofoil for $\alpha = 5^\circ$ and $Re = 0.73 \times 10^5$ ($V_0 = 1.0$ m/s).

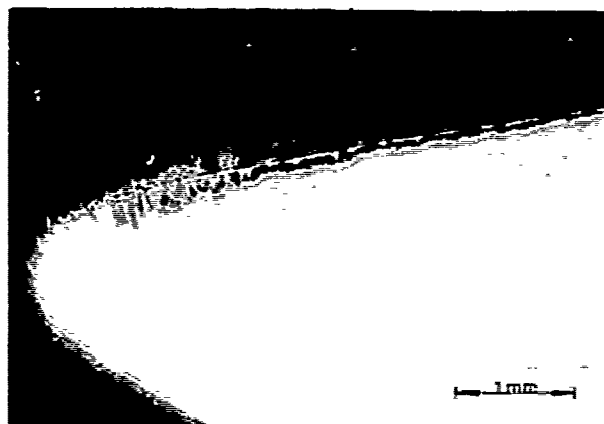


Fig. 10 Transition to turbulence of laminar boundary layer on NACA 16-012 hydrofoil for $\alpha = 5^\circ$ and $Re = 7.6 \times 10^5$ ($V_0 = 12.0$ m/s).

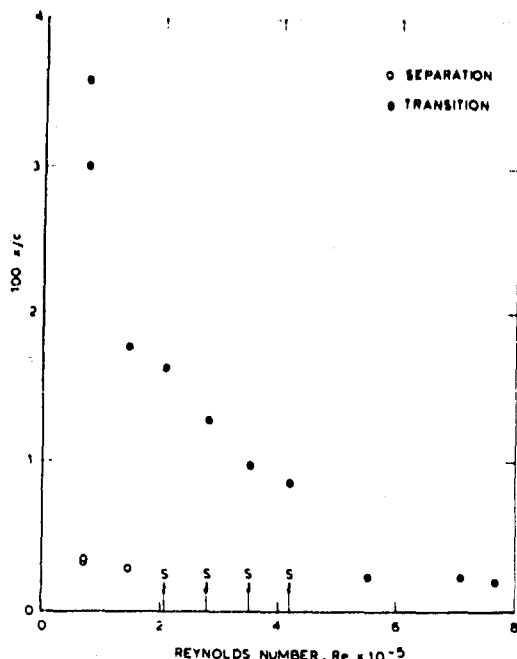


Fig. 11 Positions of separation and transition versus Reynolds number for NACA 16-012 hydrofoil at $\alpha=5^\circ$.

In some holograms the precise position of separation was difficult to establish, but separation did occur. These cases are marked with "S".

For $\alpha = 7^\circ$, laminar separation occurs at the leading edge, followed by transition to turbulence of the separated shear layer and, although hardly visible and apparently being a limiting case, reattachment. An example at $Re = 0.76 \times 10^5$ ($V_0 = 1.15$ m/s) is shown in Figures 12A and 12B. These photographs were made from the same hologram and have an overlap. Data on the posi-



Fig. 12A Laminar separation and transition to turbulence on NACA 16-012 hydrofoil for $\alpha=7^\circ$ and $Re=0.76 \times 10^5$ ($V_0=1.15$ m/s).

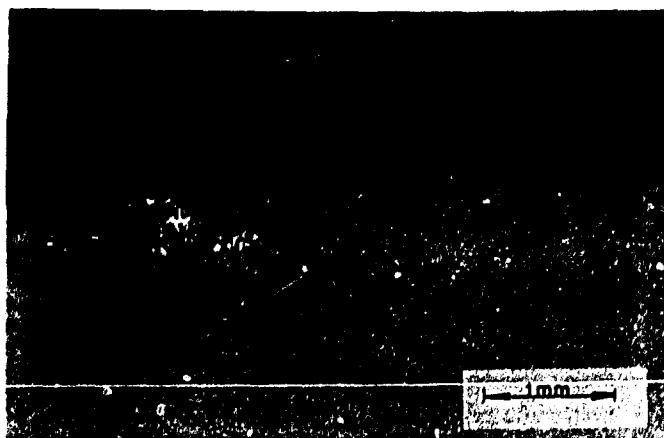


Fig. 12B Continued from Fig. 12A. Photographs show overlap.

tions of separation and transition are plotted in Figure 13. The mean value of the position of laminar separation is $(\bar{x}_S/c)_{10} = 0.0035$, which is very close to the value mentioned in [9].

For $\alpha = 10^\circ$, laminar separation occurs at the leading edge, followed by transition to turbulence of the separated shear layer without reattachment. Data on the positions of separation and transition are plotted in Figure 14. At the highest speed tested ($V_0 = 8.0$ m/s; $Re = 5.73 \times 10^5$) transition to turbulence occurred on the nose of the hydrofoil, prior to the position of separation. The mean value of the position of laminar separation is $(\bar{x}_S/c)_{19} = 0.0030$, which is close to the value mentioned in [9].

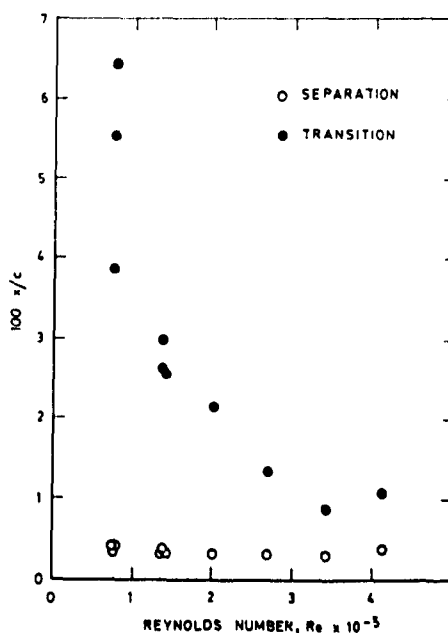


Fig. 13 Positions of separation and transition versus Reynolds number for NACA 16-012 hydrofoil at $\alpha=7^\circ$.

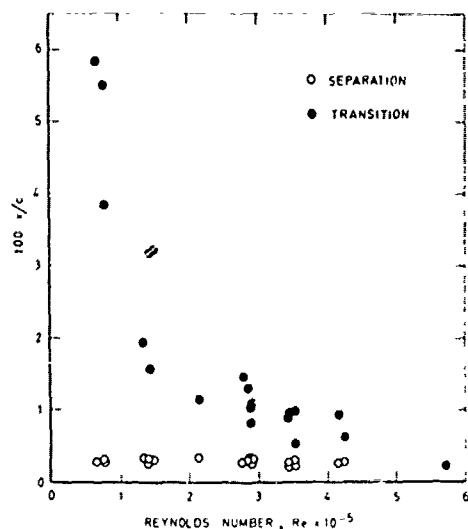


Fig. 14 Positions of separation and transition versus Reynolds number for NACA 16-012 hydrofoil at $\alpha=10^\circ$

The behaviour of the boundary layer for $\alpha = 12^\circ$ is very similar to that for $\alpha = 10^\circ$. Laminar separation is observed, followed by an unattached free shear layer. A clear example of this phenomenon is shown in Figures 15A and 15B ($V_\infty = 0.73$ m/s; $Re = 0.50 \times 10^5$). These photographs were made from the same hologram and have an overlap. Data on the positions of separation and transition are plotted in Figure 16. The mean value of the position of laminar separation is $(\bar{x}_S/c)_{12} = 0.0030$.

3.2 NACA 4412 Hydrofoil

The boundary layer flow on the suction



Fig. 15A Laminar separation and unattached free shear layer on NACA 16-012 hydrofoil for $\alpha=12^\circ$ and $Re=0.50 \times 10^5$ ($V_\infty=0.73$ m/s).



Fig. 15B Continued from Fig. 15A. Photographs show overlap.

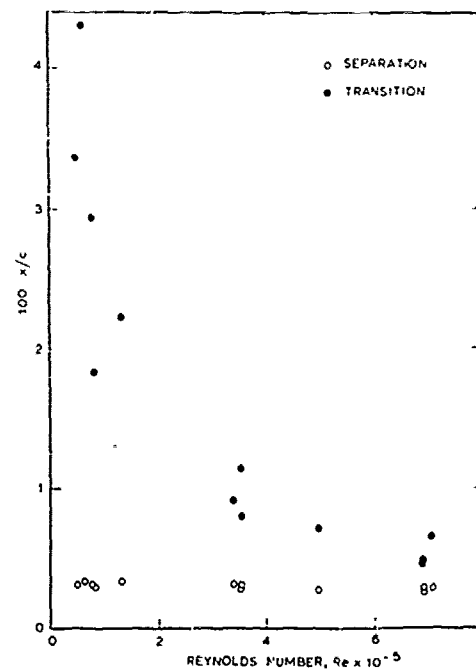


Fig. 16 Positions of separation and transition versus Reynolds number for NACA 16-012 hydrofoil at $\alpha=12^\circ$.

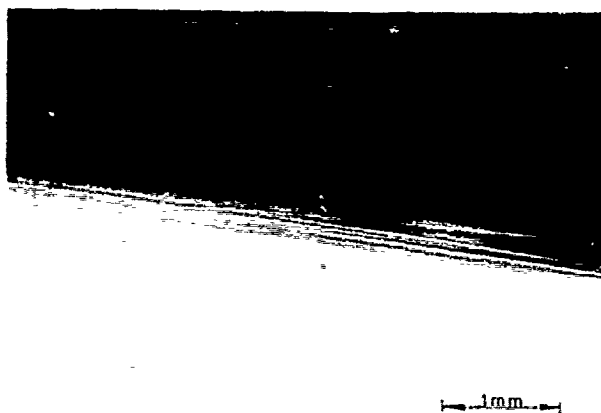


Fig. 17 Laminar separation on NACA 4412 hydrofoil for $\alpha=2^\circ$ and $Re=0.72 \times 10^5$ ($V_o=1.0$ m/s). $x_s/c=0.506$.

side of the NACA 4412 hydrofoil has been studied for the following angles of attack α : 2° , 4° , 6° , 8° , 10° and 16° .

For $\alpha = 2^\circ$, observations were made in the range $V_o = 1 - 20$ m/s. Up till $V_o = 4$ m/s, a laminar boundary layer is found with laminar separation far downstream followed by transition. An example of laminar separation at $Re = 0.72 \times 10^5$ ($V_o = 1.0$ m/s) is shown in Figure 17. The position of separation is at $x_s/c = 0.506$. At higher speeds, a laminar boundary layer is observed with normal transition to turbulence. An example of transition at $Re = 14.1 \times 10^5$ ($V_o = 19.9$ m/s) is shown in Figure 18. The position of transition is at $x_t/c = 0.457$. Data on the positions of separation and transition are plotted in Figure 19. Below $Re = 2 \times 10^5$, the mean value of the position of laminar separation is $(\bar{x}_s/c)_4 = 0.509$.

The behaviour of the boundary layer



Fig. 18 Transition to turbulence of laminar boundary layer on NACA 4412 hydrofoil for $\alpha=2^\circ$ and $Re=14.1 \times 10^5$ ($V_o=19.9$ m/s). $x_t/c=0.457$.

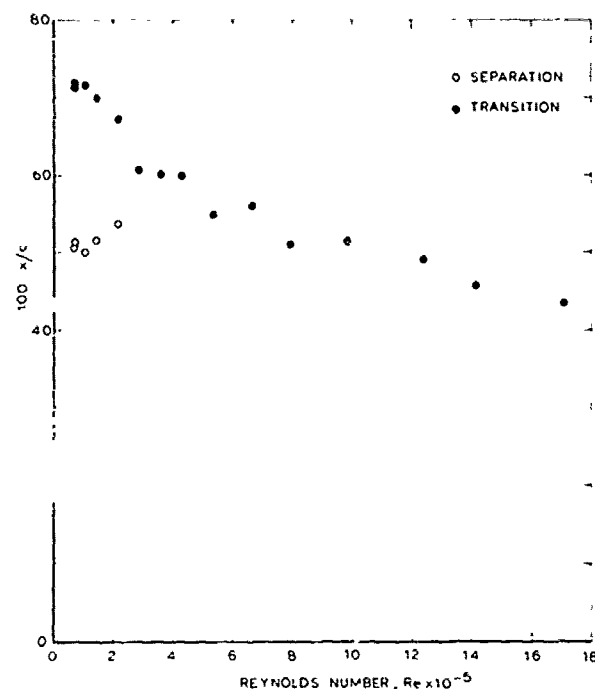


Fig. 19 Positions of separation and transition versus Reynolds number for NACA 4412 hydrofoil at $\alpha=2^\circ$.

for $\alpha = 4^\circ$ is very similar to that for $\alpha = 2^\circ$. An example of laminar separation at $Re = 0.63 \times 10^5$ ($V_o = 0.89$ m/s) is shown in Figure 20. The position of separation is at $x_s/c = 0.427$. An example of transition to turbulence of the laminar boundary layer at $Re = 4.25 \times 10^5$ ($V_o = 6.0$ m/s) is shown in Figure 21. The position of transition is at $x_t/c = 0.480$. Data on the positions of separation and transition are plotted in Figure 22. Below $Re = 2 \times 10^5$, the mean value of

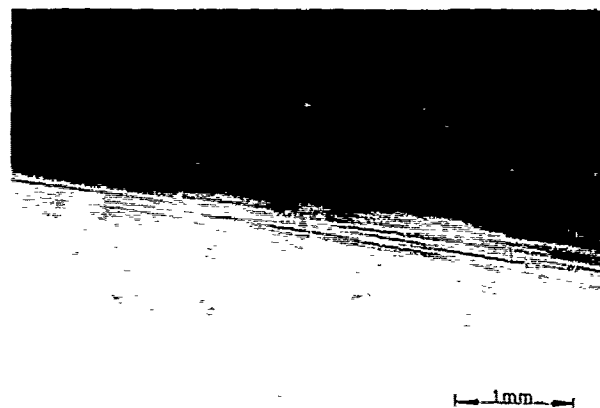


Fig. 20 Laminar separation on NACA 4412 hydrofoil for $\alpha=4^\circ$ and $Re=0.63 \times 10^5$ ($V_o=0.89$ m/s). $x_s/c=0.427$.

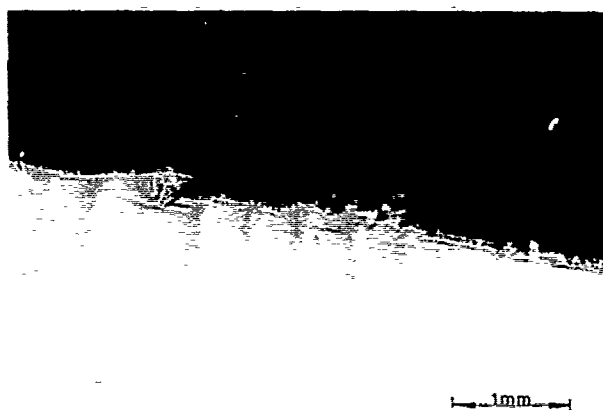


Fig. 21 Transition to turbulence of laminar boundary layer on NACA 4412 hydrofoil for $\alpha=4^\circ$ and $Re=4.25 \times 10^5$ ($V_o=6.0$ m/s). $x_T/c=0.480$.

the position of laminar separation is $(\bar{x}_S/c)_4 = 0.426$.

The behaviour of the boundary layer for $\alpha = 6^\circ$ is also very similar to that for $\alpha = 2^\circ$. An example of laminar separation at $Re = 0.79 \times 10^5$ ($V_o = 1.0$ m/s) is shown in Figure 23. The position of separation is at $x_S/c = 0.375$. The photograph in Figure 24 was taken from the same hologram and shows transition to turbulence of the laminar free

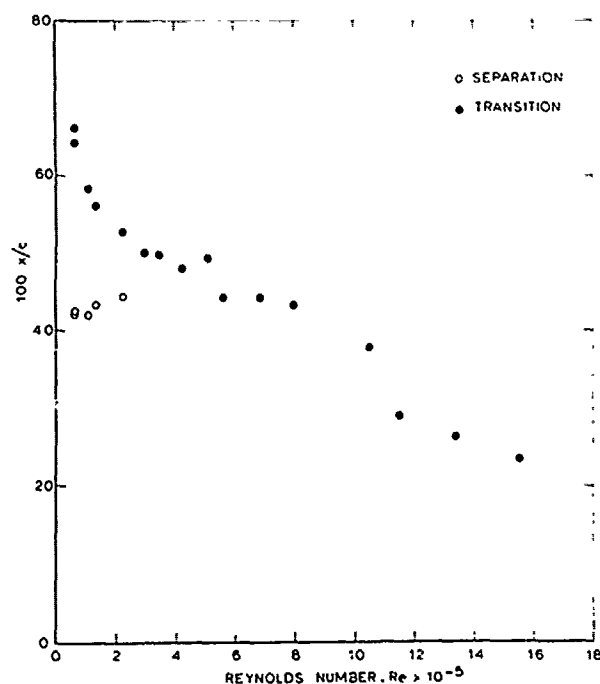


Fig. 22 Positions of separation and transition versus Reynolds number for NACA 4412 hydrofoil at $\alpha=4^\circ$

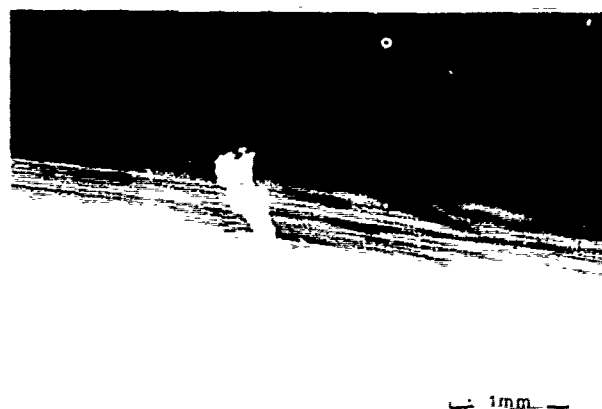


Fig. 23 Laminar separation on NACA 4412 hydrofoil for $\alpha=6^\circ$ and $Re=0.79 \times 10^5$ ($V_o=1.0$ m/s). $x_S/c=0.375$.

shear layer. The position of transition is at $x_T/c = 0.558$. Data on the positions of separation and transition are plotted in Figure 25. Below $Re = 1.75 \times 10^5$, the mean value of the position of laminar separation is $(x_S/c)_4 = 0.386$.

For $\alpha = 8^\circ$, observations were made in the range $V_o = 1 - 9$ m/s. Up till $V_o = 2$ m/s, a laminar boundary layer is found with laminar separation downstream, followed by transition. An example of laminar separation at $Re = 0.63 \times 10^5$ ($V_o = 0.89$ m/s) is shown in Figure 26. The position of separation is at $x_S/c = 0.333$. The photograph in Figure 27 was taken from the same hologram and shows transition to turbulence of the laminar free shear layer. The position of transition is at $x_T/c = 0.523$. At $V_o = 2$ m/s, the position of laminar separation has moved to the leading edge, whereas transition to turbulence is still located far downstream. Hence, in this case a long separation bubble



Fig. 24 Transition to turbulence of laminar separated shear layer on NACA 4412 hydrofoil for $\alpha=6^\circ$ and $Re=0.79 \times 10^5$ ($V_o=1.0$ m/s). $x_T/c=0.558$.

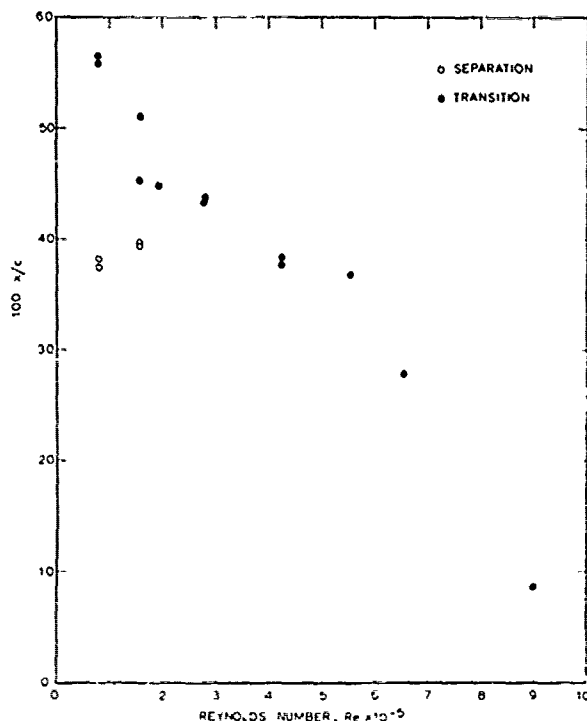


Fig. 25 Positions of separation and transition versus Reynolds number for NACA 4412 hydrofoil at $\alpha=6^\circ$.

is found. In the hologram, the position of separation was difficult to locate since the bubble was very thin. At increasing speed, the position of transition moves further upstream, so that at the highest speed tested ($V_0 = 8.8$ m/s) a short bubble is found. Data on the positions of separation and transition are plotted in Figure



Fig. 26 Laminar separation on NACA 4412 hydrofoil for $\alpha=8^\circ$ and $Re=0.63 \times 10^5$ ($V_0=0.89$ m/s). $x_S/c=0.333$.

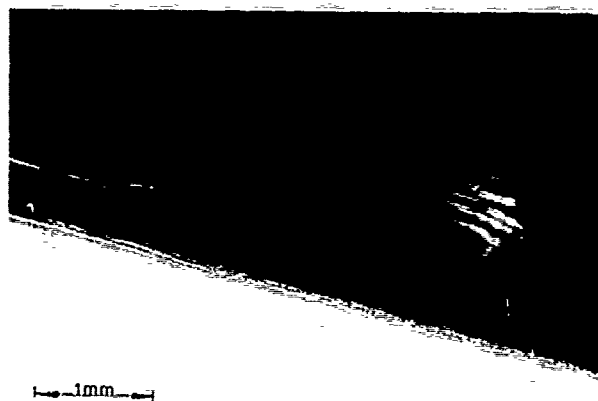


Fig. 27 Transition to turbulence of laminar separated shear layer on NACA 4412 hydrofoil for $\alpha=8^\circ$ and $Re=0.63 \times 10^5$ ($V_0=0.89$ m/s). $x_T/c=0.523$.

28. The mean value of the position of the leading edge separation is $(\bar{x}_S/c)_8 = 0.0233$.

For $\alpha = 10^\circ$, a long bubble is found at low speeds. An example of transition to turbulence of the laminar free shear layer at $Re = 0.64 \times 10^5$ ($V_0 = 0.89$ m/s) is shown in Figure 29. The position of transition is at $x_T/c = 0.405$. When the speed is in-

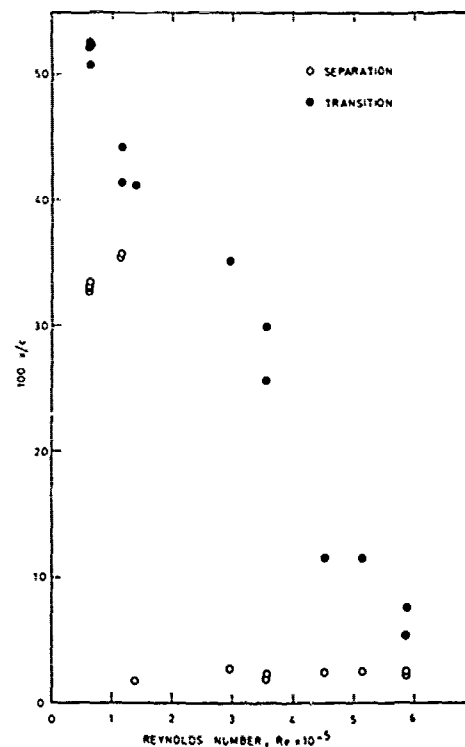


Fig. 28 Positions of separation and transition versus Reynolds number for NACA 4412 hydrofoil at $\alpha=8^\circ$.

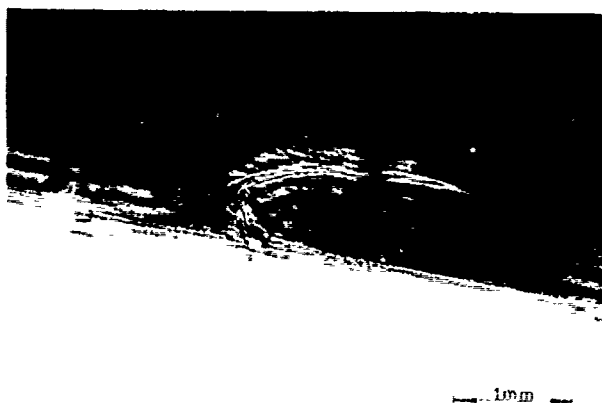


Fig. 29 Transition to turbulence of laminar separated shear layer for long bubble on NACA 4412 hydrofoil for $\alpha=10^\circ$ and $Re=0.64 \times 10^5$ ($V_0=0.89$ m/s). $x_T/c=0.405$.

creased, the position of transition moves suddenly upstream, close to the leading edge, thus creating a short bubble. An example at $Re = 2.0 \times 10^5$ ($V_0 = 3.0$ m/s) is shown in Figure 30. The positions of separation and transition are at $x_S/c = 0.0169$ and $x_T/c = 0.047$. Data on the positions of separation and transition are plotted in Figure 31. The mean value of the position of the leading edge separation is $(\bar{x}_S/c)_{14} = 0.0164$.

For $\alpha = 16^\circ$, laminar separation is found at the leading edge, followed by transition to turbulence of the laminar free shear layer, and reattachment. Apparently, this angle is a limiting case since reattachment could not be distinguished in some of the holograms. An example of laminar separation at $Re = 0.62 \times 10^5$ ($V_0 = 0.89$ m/s) is shown in Figure 32. Another example at $Re = 3.47 \times 10^5$ ($V_0 = 4.9$ m/s) showing the whole bubble is presented in Figure 33.

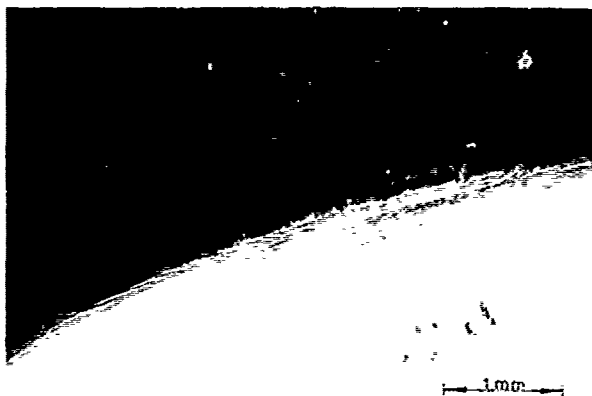


Fig. 30 Laminar separation bubble on NACA 4412 hydrofoil for $\alpha=10^\circ$ and $Re=2.0 \times 10^5$ ($V_0=3.0$ m/s).

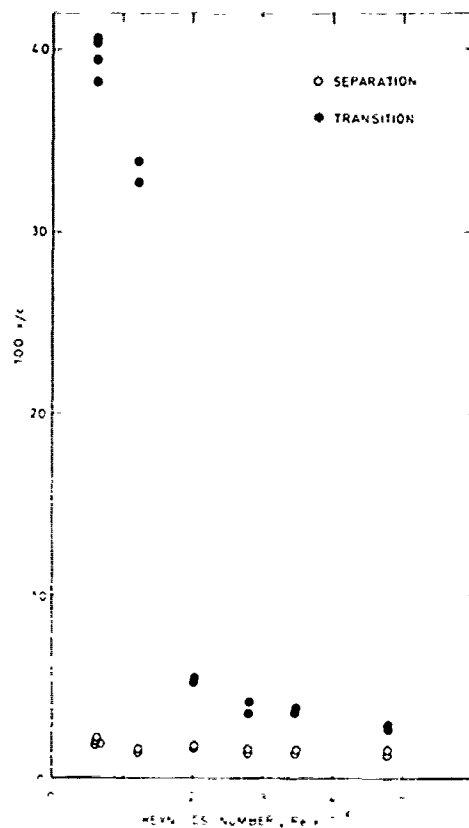


Fig. 31 Positions of separation and transition versus Reynolds number for NACA 4412 hydrofoil at $\alpha=10^\circ$.

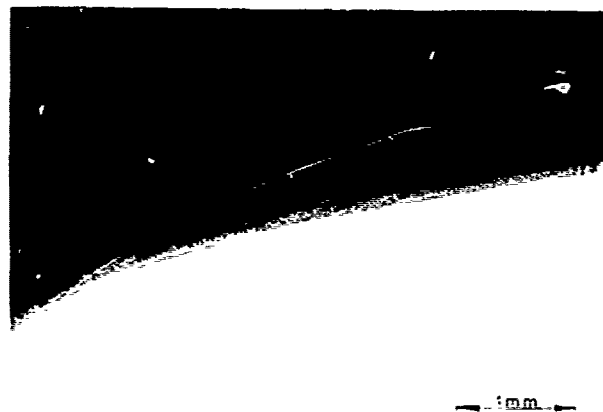


Fig. 32 Laminar separation on NACA 4412 hydrofoil for $\alpha=16^\circ$ and $Re=0.62 \times 10^5$ ($V_0=0.89$ m/s).

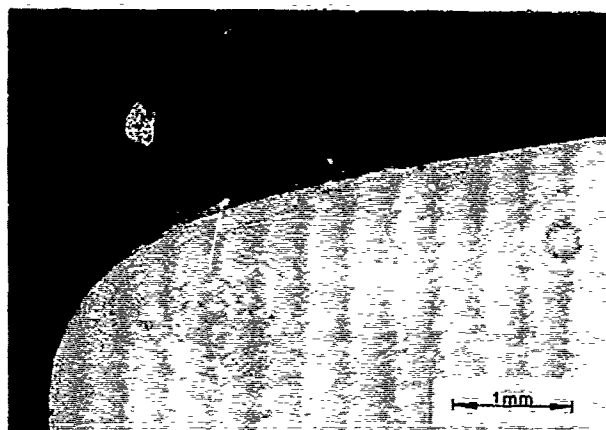


Fig. 33 Laminar separation bubble on NACA 4412 hydrofoil for $\alpha=16^\circ$ and $Re=3.47 \times 10^5$ ($V_o=4.9$ m/s).

Data on the positions of separation and transition are plotted in Figure 34. The mean value of the position of separation is $(x_s/c)_{14} = 0.0060$.

3.3 Analysis

In analyzing the results of the boundary layer flow visualization experiments for both hydrofoils, some typical similarities are found. When the boundary layer flow phenomena at very low Reynolds numbers are disregarded, the boundary layer flow behaviour may be classified into four groups. Descriptions of the observed behaviour, with

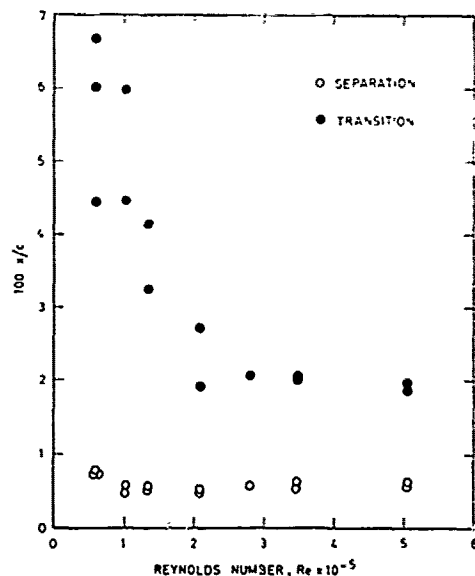


Fig. 34 Positions of separation and transition versus Reynolds number for NACA 4412 hydrofoil at $\alpha=16^\circ$.

reference to the relevant hydrofoils and angles of attack, are listed below.

- A. Laminar boundary layer with, far downstream, transition to turbulence.
NACA 16-012 hydrofoil, $\alpha = 2^\circ$
NACA 4412 hydrofoil, $\alpha = 2^\circ, 4^\circ$ and 6° .
3. Laminar separation at leading edge with subsequent transition to turbulence and reattachment (separation bubble).
NACA 16-012 hydrofoil, $\alpha = 3^\circ$ and 5°
NACA 4412 hydrofoil, $\alpha = 8^\circ$ and 10° .
- C. Laminar separation at leading edge with subsequent transition to turbulence with or without reattachment (transitional case)
NACA 16-012 hydrofoil, $\alpha = 7^\circ$
NACA 4412 hydrofoil, $\alpha = 16^\circ$.
- D. Laminar separation at leading edge with subsequent transition to turbulence without reattachment (unattached free shear layer)
NACA 16-012 hydrofoil, $\alpha = 10^\circ$ and 12° .

The zero lift angle of attack α_o for the NACA 16-012 hydrofoil is 0° , whereas for the cambered NACA 4412 hydrofoil it is -4° . Hence, a comparison based on $\alpha - \alpha_o$ instead of α would have shown more distinctly that the behaviour of the boundary layer for the NACA 16-012 hydrofoil is much more sensitive to an angle of attack change than for the NACA 4412 hydrofoil. This is mainly caused by the large difference in leading edge thickness.

The distinction between the observed long and short laminar separation bubbles is based on the general description given by Gaster [13]. Long bubbles were only observed for the NACA 4412 hydrofoil at $\alpha = 8^\circ$ and 10° . The free shear layer of the long bubbles was located at a very short distance from the body surface.

4. CAVITATION STUDIES

4.1 Cavitation Appearance

The appearance of cavitation on the hydrofoils has been derived from different sources. First, visual observations were made under stroboscopic lighting during the cavitation inception measurements. Secondly, each series of cavitation inception measurements was followed by a series of tests during which photographs were made of limited, moderately developed and developed cavitation, taken at specific test section speeds. Thirdly, holograms were made for specific conditions. These holograms provided detailed information on the cavity shape (bubble, sheet) and cavity location (attached, unattached). In many cases, however, the small gaps between the ends of the hydrofoil and the glass windows in the test section walls caused premature cavitation in the corners. In those cases, cavitation on the centre section of the hydrofoil was

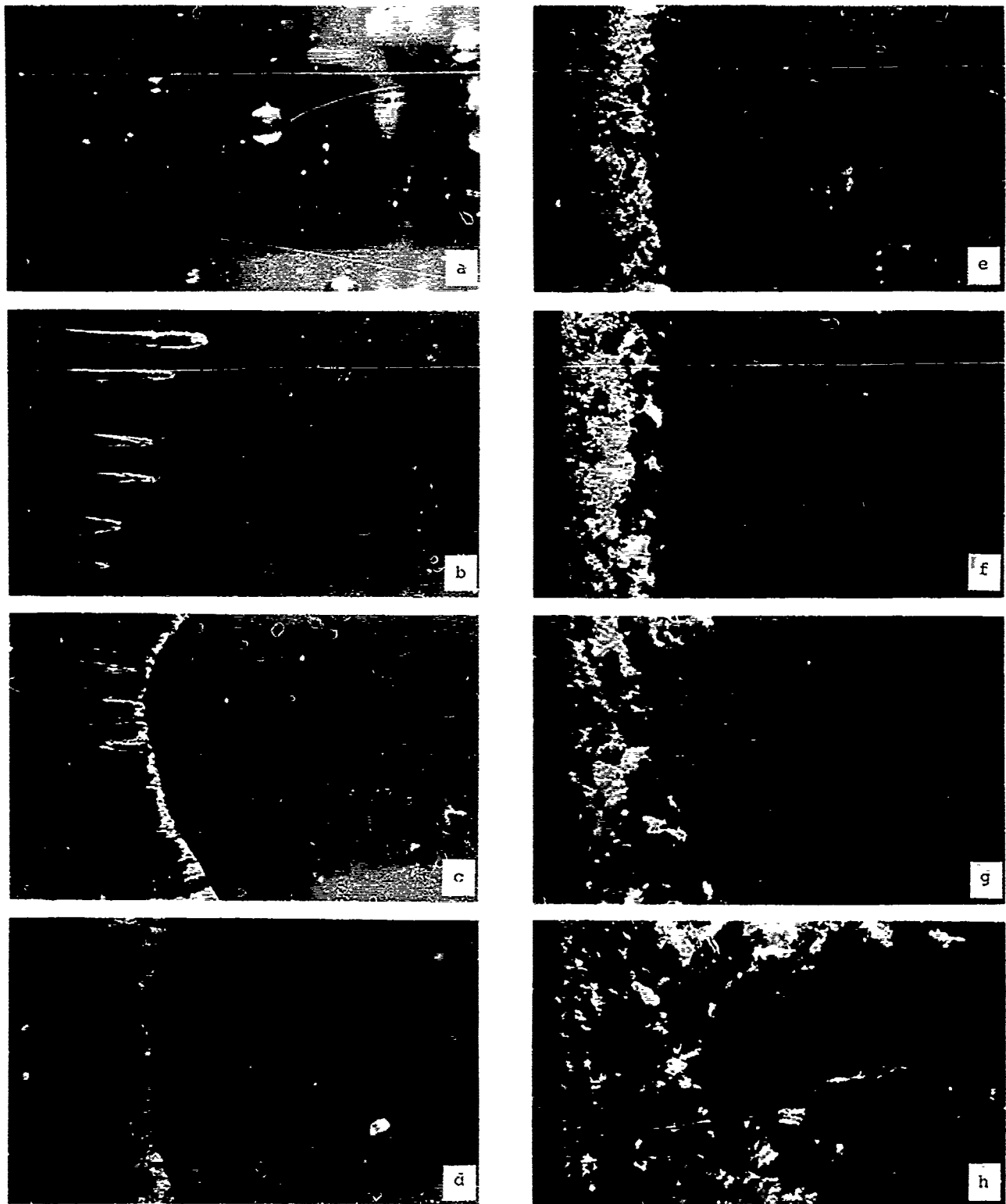


Fig. 35 Photographs showing appearance of cavitation on NACA 16-012 hydrofoil at $V=10$ m/s, and for angles of attack of (a) 2° , (b) 3° , (c) 4° , (d) 5° , (e) 6° , (f) 7° , (g) 10° and (h) 12° . The flow direction is from left to right.

masked, except for the leading edge.

4.1.1 NACA 16-012 hydrofoil

A photographic record of the cavitation appearance on the NACA 16-012 hydrofoil for $\alpha = 2^\circ, 3^\circ, 4^\circ, 5^\circ, 6^\circ, 7^\circ, 10^\circ$ and 12° is shown in Figure 35. These photographs of moderately developed cavitation were all taken at $V_o = 10$ m/s. The flow direction on these (and all following) photographs is from left to right. The photographs cover about 50% of the length of the hydrofoils starting from the leading edge ($x/c = 0 - 0.5$).

The type of cavitation occurring at $\alpha = 2^\circ$ is typically bubble cavitation (Figure 35a). Most of the bubbles are attached to the surface and travel with the main flow. This type of cavitation is also called travelling bubble cavitation. The bubbles appear in a wide area ($x/c = 0.2 - 0.8$); the largest ones are observed at $x/c = 0.6$. At higher speeds (up to 30 m/s) some streak cavitation was observed. The streak cavities were caused by small particles, trapped on the hydrofoil nose.

The appearance of cavitation at $\alpha = 3^\circ$, is very much dependent on the precise angle of attack. Initial observations at $\alpha = 2.99^\circ (\pm 0.1^\circ)$ and an air content of $8.4 \text{ cm}^3/\text{l}$ showed bubble cavitation at low speeds ($V_o = 10 - 15$ m/s) and streak cavitation at high speeds. Subsequent observations at $\alpha = 3.09^\circ (\pm 0.1^\circ)$ and an air content of $5.2 \text{ cm}^3/\text{l}$ showed streak cavitation at low speeds (Figure 35b) and sheet cavitation (with some streaks) at high speeds. An example, taken at $V_o = 20$ m/s, is shown in Figure 36. Bubble cavitation did not occur. Initially, it was assumed that this was caused by the lower air content. Therefore, additional tests were made at $\alpha = 3.09^\circ$, during which the air content was gradually increased to $13.7 \text{ cm}^3/\text{l}$ by bleeding air into the tunnel, but still bubble cavitation



Fig. 36 Photograph showing sheet cavitation (with some streaks) on NACA 16-012 hydrofoil for $\alpha = 3.09^\circ$ and $V_o = 20$ m/s.

remained absent. Final tests were made at $\alpha = 2.87^\circ (\pm 0.1^\circ)$ and an air content of $5.4 \text{ cm}^3/\text{l}$. After some experimenting, bubble cavitation was observed at low speeds.

For $\alpha = 4^\circ$, the appearance of cavitation is sheet cavitation (Figure 35c). A sequence of photographs taken at $V_o = 10$ m/s and at different cavitation numbers σ is presented in Figure 37. The cavitation number σ is

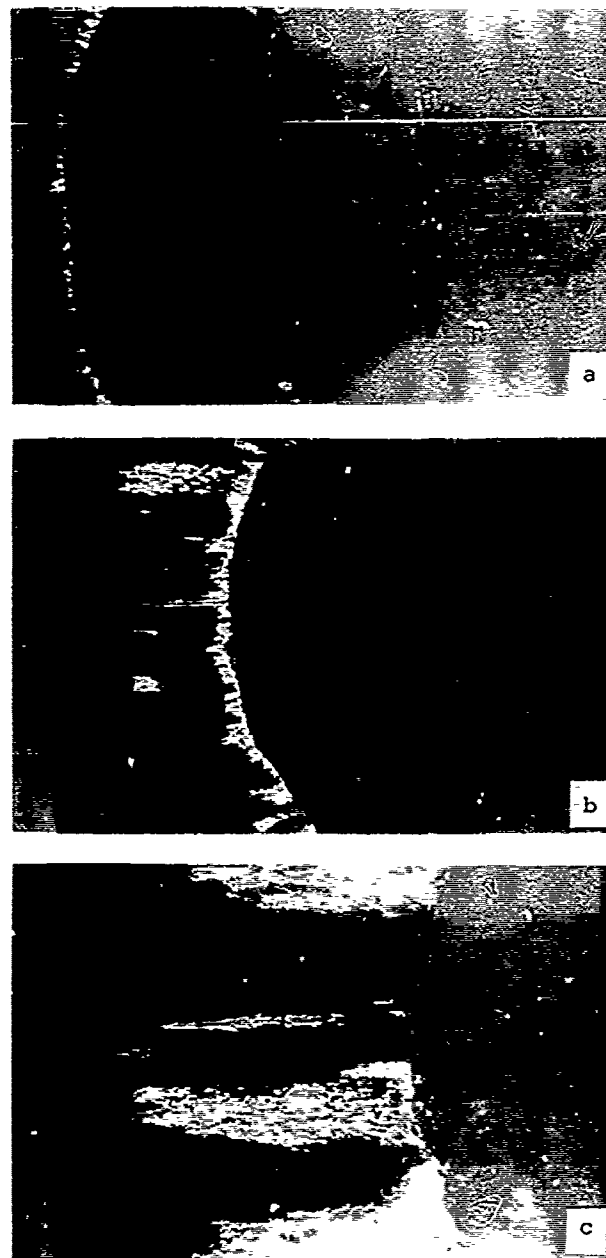


Fig. 37 Sequence of photographs showing development of sheet cavitation on NACA 16-012 hydrofoil for $\alpha = 4^\circ$, $V_o = 10$ m/s and σ -values of (a) 1.22, (b) 1.05 and (c) 0.98.

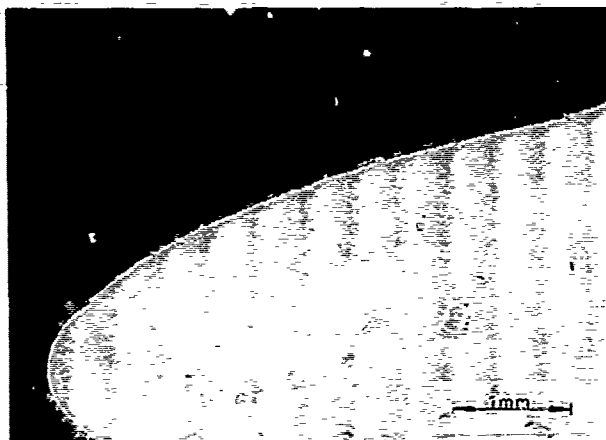


Fig. 38 Attached sheet cavity on nose of NACA 16-012 hydrofoil for $\alpha=5^\circ$, $V_0=4.9$ m/s and $c=1.77$.

defined as

$$c = \frac{P_0 - P_v}{\frac{1}{2} \rho V_0^2},$$

where P_0 and V_0 denote the undisturbed static pressure and flow velocity in the test section, P_v is the vapour pressure of the liquid and ρ its density.

Also for $\alpha = 5^\circ$, the type of cavitation is sheet cavitation (Figure 35d). A photograph taken from a hologram, showing the attachment of a sheet cavity to the hydrofoil nose at $V_0 = 4.9$ m/s and $c = 1.77$ is presented in Figure 38.

For $\alpha = 6^\circ$ at inception, cavitation appeared as a symmetrical band of small attached bubbles and sheets. When the pressure was lowered, an irregular sheet was created near the nose. Further downstream, the sheet transformed into cavitation with a cloudy appearance (Figure 35e).

For $\alpha = 7^\circ$ at inception, cavitation appeared as a symmetrical band of small attached transient bubbles near the nose. A detail of an attached cavity is shown in [9]. When the pressure was lowered, the cavitation obtained a cloudy appearance, but remained attached to the nose, occasionally showing areas with a transient sheet (Figure 35f).

For $\alpha = 10^\circ$, the cavities were no longer attached to the hydrofoil surface [9]. The type of cavitation observed is cloud cavitation (Figure 35g). At low speeds the clouds appeared to have a finer structure (consisting of many isolated bubbles) than at high speeds. This phenomenon is illustrated by the photographs presented in Figure 39, which were taken at (a) $V_0 = 5.1$ m/s and (b) $V_0 = 15.1$ m/s.

Also for $\alpha = 12^\circ$, the type of cavitation observed is cloud cavitation (Figure 35h). Holographic observations clearly show that the cavities are not attached to the hydrofoil surface but are located at some distance. Examples, taken at $V_0 = 4.9$ m/s

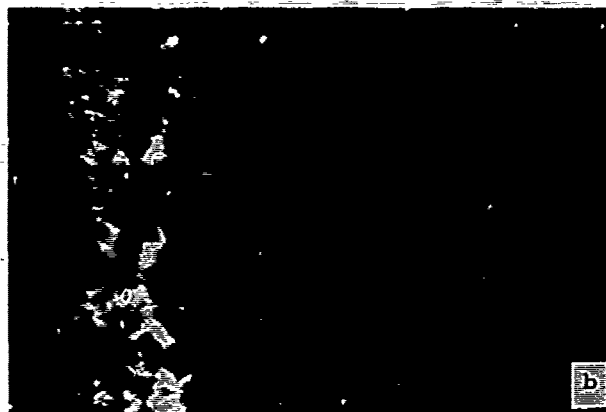


Fig. 39 Photographs showing cloud cavitation on NACA 16-012 hydrofoil for $\alpha=10^\circ$ and different speeds: (a) $V_0=5.1$ m/s ($c=3.07$) and (b) $V_0=15.1$ m/s ($c=3.41$).

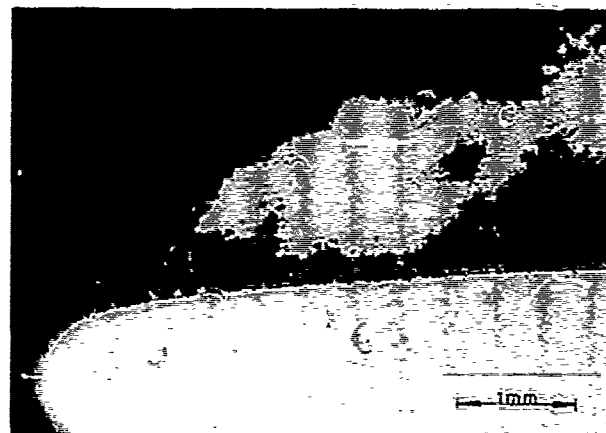


Fig. 40 Unattached cavities (cloud cavitation) near nose of NACA 16-012 hydrofoil for $\alpha=12^\circ$, $V_0=4.9$ m/s and $c=3.13$.



Fig. 41 Unattached cavities (cloud cavitation) near nose of NACA 16-012 hydrofoil for $\alpha=12^\circ$, $V_o=7.0$ m/s and $\sigma=3.21$.

and 7.0 m/s, are presented in Figures 40 and 41.

For $\alpha = 16^\circ$, the cavities are irregularly shaped and often have a threadlike appearance. Most of the cavities are located at some distance behind the leading edge. Examples, taken at $V_o = 10$ m/s, are presented in Figures 42 and 43. Similar patterns are reported by Kermeen and Parkin [14] behind sharp-edged disks, and by Keller [15] on a blunt axisymmetric body.

4.1.2 NACA 4412 hydrofoil

A photographic record of the cavitation appearance on the NACA 4412 hydrofoil for $\alpha = 0^\circ, 2^\circ, 4^\circ, 6^\circ, 8^\circ, 10^\circ, 12^\circ$ and 16° is presented in Figure 44. The photographs show moderately developed cavitation at $V_o = 10$ m/s.

For $\alpha = 0^\circ, 2^\circ$ and 4° , the appearance



Fig. 42 Photograph showing irregular, threadlike appearance of cavitation on NACA 16-012 hydrofoil for $\alpha=16^\circ$, $V_o = 10$ m/s and $\sigma=3.22$.

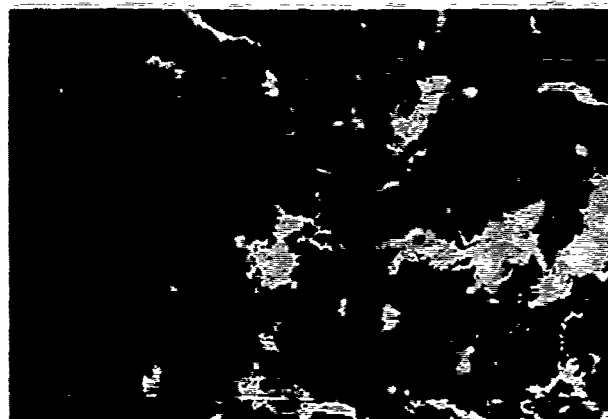


Fig. 43 Photograph showing irregular, threadlike appearance of cavitation on NACA 16-012 hydrofoil for $\alpha=16^\circ$, $V_o=10$ m/s and $\sigma=2.82$.

of cavitation is almost identical. At low speeds (till about 14 m/s) bubble cavitation is found (Figure 44a, b and c). At high speeds (above about 18 m/s) transient attached cavities are observed and, occasionally, travelling bubbles. The attached type of cavitation is named transient spot cavitation. At moderate speeds (around 16 m/s) both bubble and transient spot cavitation occur. Three examples of transient spot cavitation, taken at about 20 m/s, are presented in Figures 45, 46 and 47. The cavities are located at a large distance from the leading edge. They seem to originate from weak spots on the surface of the hydrofoil but, because of the transient character, these spots do not have fixed positions. Quite frequently, bubbles are observed with "tails". Examples are shown in Figure 44c and d. This phenomenon has been described before by Holli and Carroll [16]. Examples of holographic recordings showing bubble cavitation for $\alpha = 2^\circ$, are presented in Figures 48 and 49. In Figure 48, an attached and unattached bubble are observed for $V_o = 14.9$ m/s and $\sigma = 0.85$. The position of the attached bubble is at $x_c/c = 0.171$. Figure 49 shows an attached bubble for $V_o = 19.8$ m/s and $\sigma = 0.80$. The position of this bubble is at $x_c/c = 0.208$.

For $\alpha = 6^\circ$, the appearance of cavitation at low speeds (till about 14 m/s) is bubble cavitation (Figure 44d). At high speeds streak cavitation is observed.

The appearance of cavitation for $\alpha = 8^\circ$ and 10° is almost identical. The type of cavitation is essentially sheet cavitation. Occasionally, however, some bubbles were observed at low speeds (till about 10 m/s) for $\alpha = 8^\circ$. The sheet has a rather irregular appearance, as shown in Figure 44e and f. Apparently the sheet is very sensitive to small imperfections at the leading edge of the hydrofoil. A detail of the leading edge of the sheet cavity is presented in Figure 50. This photograph refers to $\alpha = 8^\circ$,

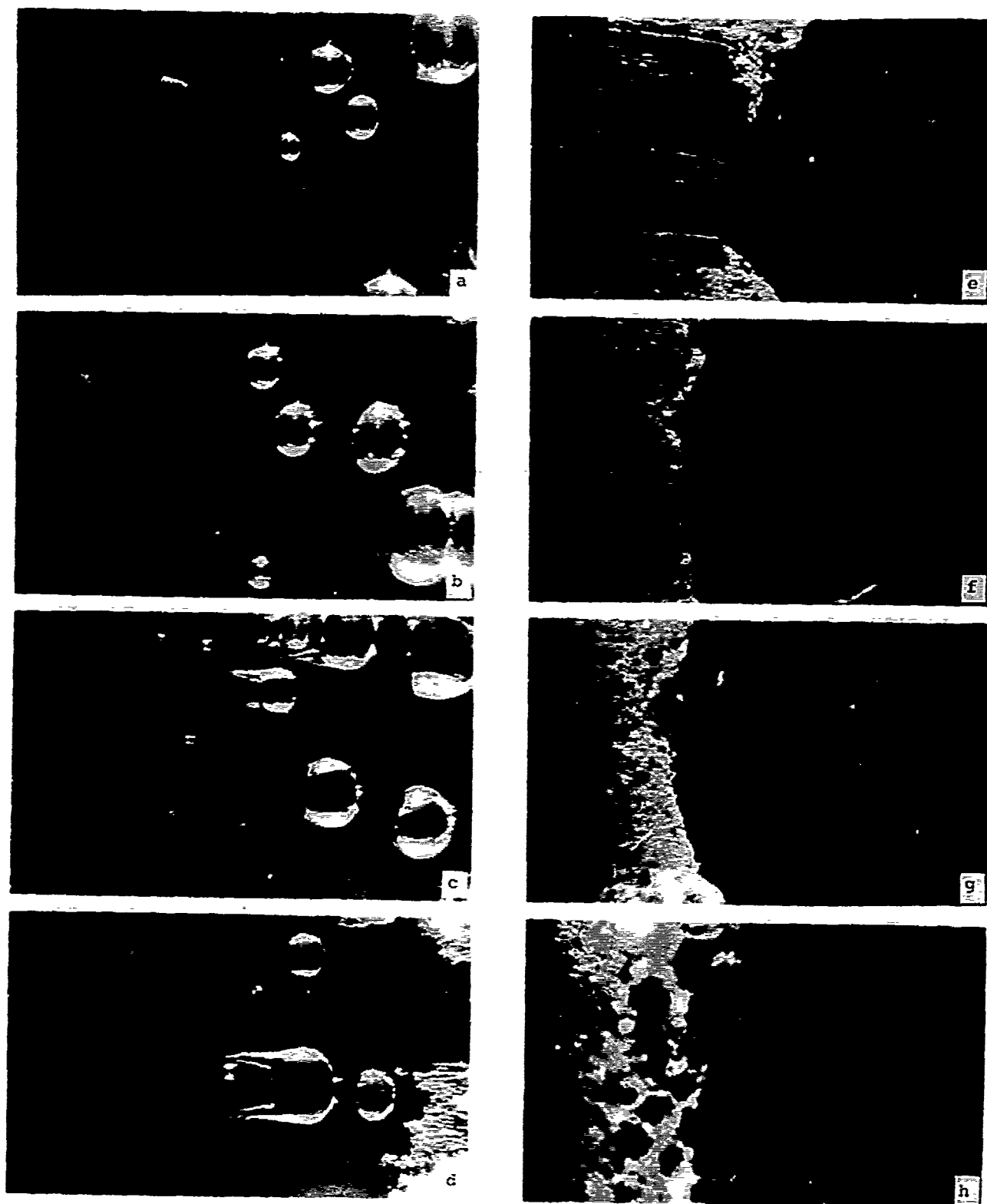


Fig. 44 Photographs showing appearance of cavitation on NACA 4412 hydrofoil at $V_0 = 10$ m/s and for angles of attack of (a) 0° , (b) 2° , (c) 4° , (d) 6° , (e) 8° , (f) 10° , (g) 12° and (h) 16° .

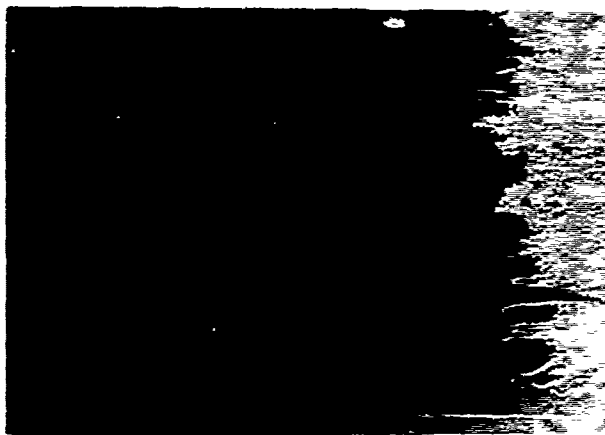


Fig. 45 Photograph showing transient spot cavitation on NACA 4412 hydrofoil for $\alpha=0^\circ$, $V_0=19.7$ m/s and $\sigma=0.60$.

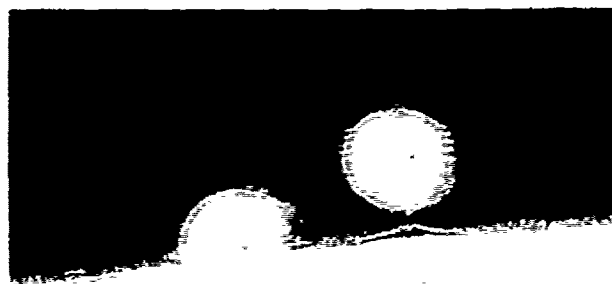


Fig. 48 Attached and unattached bubble on NACA 4412 hydrofoil for $\alpha=2^\circ$, $V_0=14.9$ m/s and $c=0.85$. $x_c/c=0.171$.

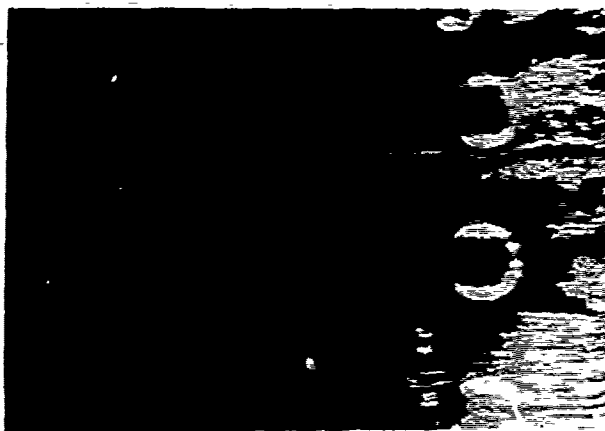


Fig. 46 Photograph showing transient spot (and bubble) cavitation on NACA 4412 hydrofoil for $\alpha=2^\circ$, $V_0=19.7$ m/s and $\sigma=0.55$.



Fig. 49 Attached bubble on NACA 4412 hydrofoil for $\alpha=2^\circ$, $V_0=19.8$ m/s and $\sigma=0.80$. $x_c/c=0.208$.

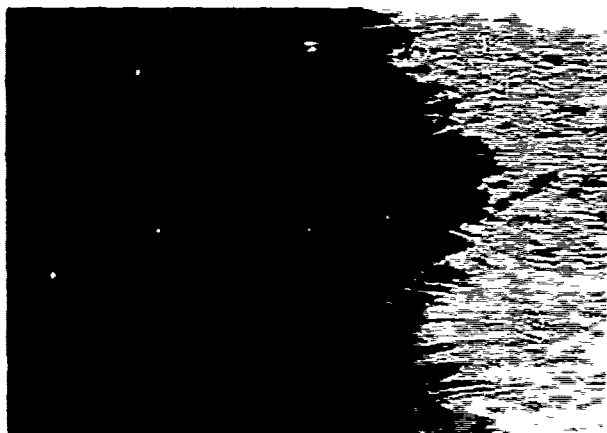


Fig. 47 Photograph showing transient spot cavitation on NACA 4412 hydrofoil for $\alpha=4^\circ$, $V_0=19.8$ m/s and $\sigma=1.06$.

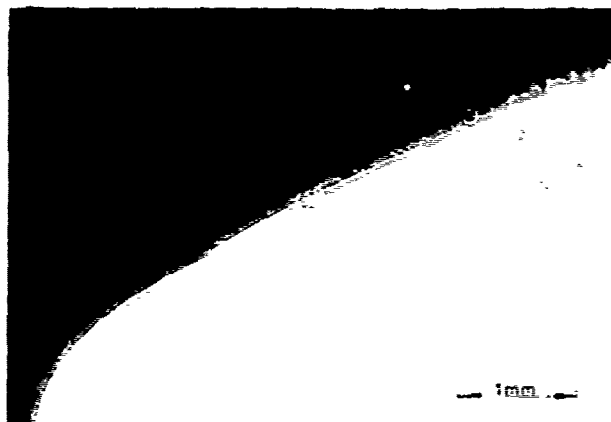


Fig. 50 Attached sheet cavity on nose of NACA 4412 hydrofoil for $\alpha=6^\circ$, $V_0=9.7$ m/s and $\sigma=2.06$. $x_c/c=0.0186$.



Fig. 51 Photograph showing partial sheet cavitation on NACA 4412 hydrofoil for $\alpha=12^\circ$, $V_o=5$ m/s and $\sigma=3.80$.

$V_o = 9.7$ m/s and $\sigma = 2.06$. The position of the leading edge of the sheet cavity is at $x_c/c = 0.0186$.

For $\alpha = 12^\circ$, the appearance of cavitation depends rather strongly upon the speed. At $V_o = 5$ m/s (Figure 51), the first part of the cavity is a sheet. At $V_o = 10$ m/s (Figure 44g), the length of the sheet is very small and the downstream part of the cavity has a cloudy appearance. Finally, at $V_o = 13.8$ m/s (Figure 52), the cavity is still attached to the nose, but most of the cavity has a cloudy appearance.

For $\alpha = 16^\circ$ at inception, a band of small attached bubbles is observed. A detail is shown in Figure 53. This photograph refers to $V_o = 7.1$ m/s and $\sigma = 5.34$. The position of the leading edge of the cavity is at $x_c/c = 0.0089$. When the pressure is lowered, the leading edge of the cavity remains attached to the hydrofoil nose, but further downstream the cavity has a cloudy appearance (Figure 44h).

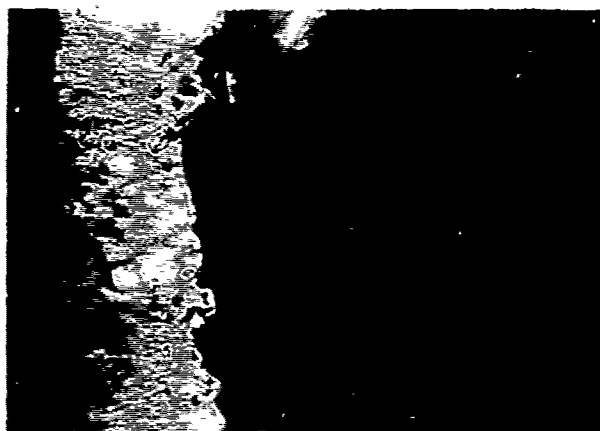


Fig. 52 Photograph showing cavitation with cloudy appearance on NACA 4412 hydrofoil for $\alpha=12^\circ$, $V_o=13.8$ m/s and $\sigma=4.10$.

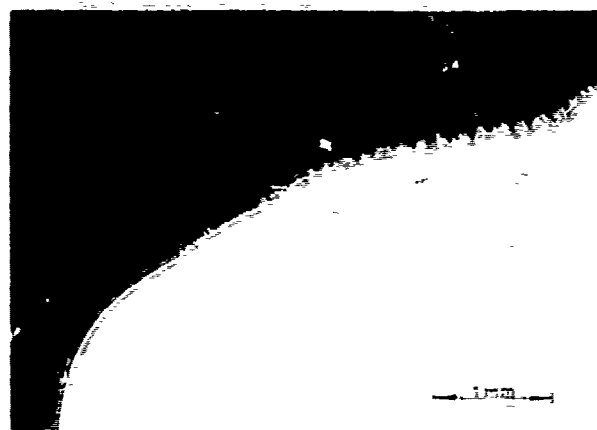


Fig. 53 Attached bubble (sheet) on nose of NACA 4412 hydrofoil for $\alpha=16^\circ$, $V_o=7.1$ m/s and $\sigma=5.34$. $x_c/c=0.0089$.

4.2 Cavitation Inception

To examine the beginning of cavitation, cavitation inception measurements were carried out for both hydrofoils. Cavitation inception is the limiting state between a non-cavitating flow and a cavity flow. This state can be attained in two different ways: starting from a non-cavitating condition and decreasing the pressure which leads to the incipient state of cavitation and yields the incipient cavitation number σ_i , and starting from a cavitating condition and increasing the pressure which leads to the desinent state of cavitation and yields the desinent cavitation number σ_d . The present study comprised both desinence and inception measurements. For each test velocity, desinence was measured prior to inception. The precise definition of inception is important in obtaining consistent results. Two aspects have to be considered in performing inception measurements on hydrofoils. First, the cavity may start on the leading edge in a small part along the span and spread out gradually when the pressure is lowered. Secondly, intermittent cavitation may occur, such as bubble or cloud cavitation. The problems associated with both aspects were solved by using the well-known 50% criterion of inception. The 50% may refer to the extent of cavitation along the span or to the time during which cavitation is present. The inception measurements were made under stroboscopic lighting.

When possible, inception data are compared with the pressure coefficient C_p , defined as

$$-C_p = \frac{P_o - P}{\frac{1}{2}\rho V_o^2},$$

where P denotes the static pressure on the hydrofoil. If the pressure coefficient is related to the minimum static pressure P_{min} on the hydrofoil, the minimum pressure

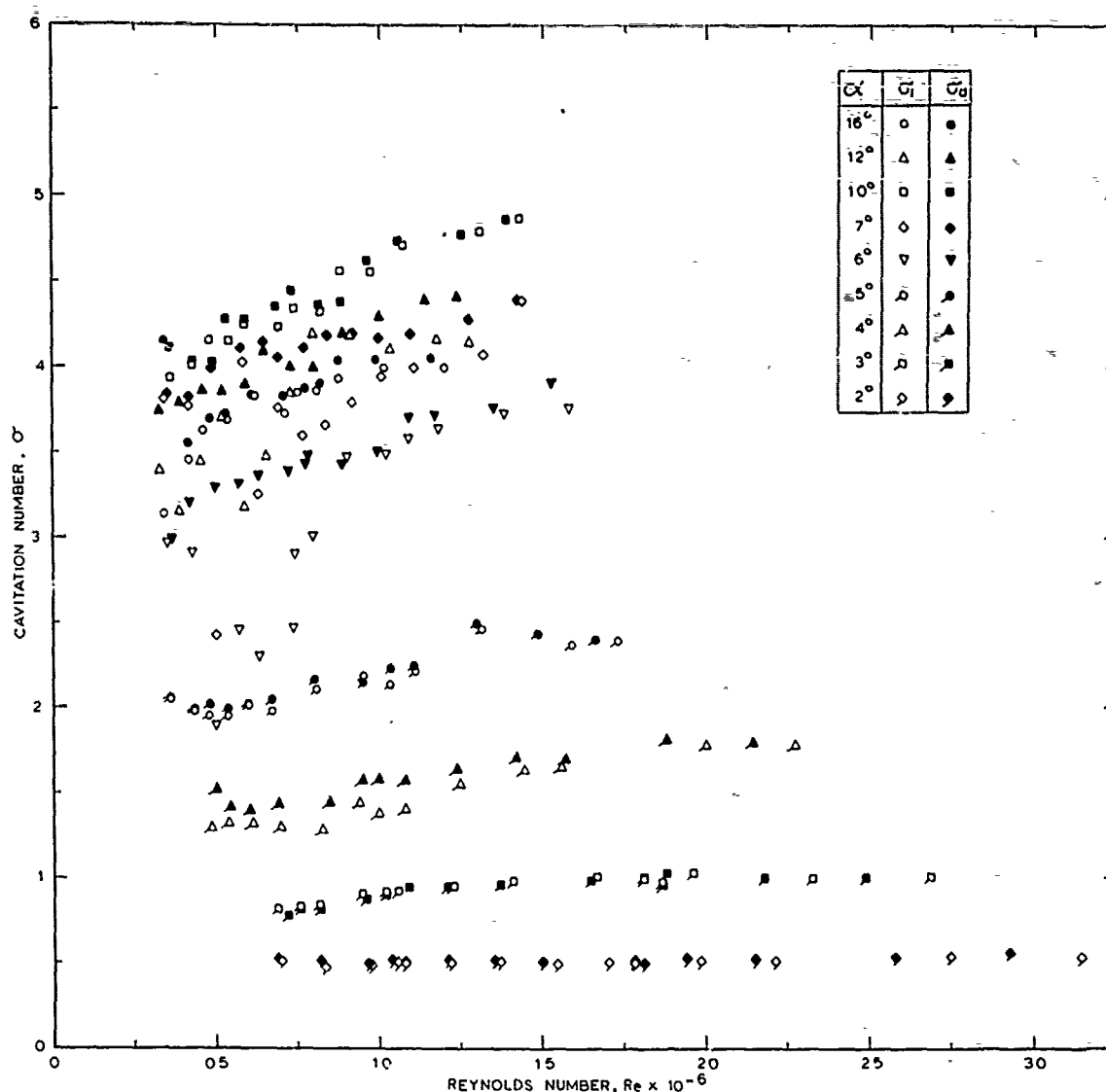


Fig. 54 Cavitation inception and desinence number versus Reynolds number for NACA 16-012 hydrofoil.

coefficient $C_{p_{min}}$ is given by

$$-C_{p_{min}} = \frac{p_o - p_{min}}{\frac{1}{2} \rho V_o^2}$$

The results of the cavitation inception measurements are plotted in Figures 54 and 55. In general, it is found that the σ_i and σ_d values are almost identical. Cavitation hysteresis effects [17] are observed only at low Reynolds numbers for the NACA 16-012 hydrofoil at $\alpha = 6^\circ$ and 7° .

The inception (or desinence) values for the NACA 16-012 hydrofoil increase gradually with an increase in α , but reach limiting values at $\alpha = 10^\circ$. In section 3.1,

it has been shown that for this angle laminar flow separation occurs near the leading edge without reattachment. Apparently, above this angle leading edge stall occurs and the lift coefficient and $-C_{p_{min}}$ decrease. This explains the lower inception values for $\alpha = 12^\circ$ and 16° .

For the NACA 4412 hydrofoil, a gradual increase in inception values is found with an increase in α up to the highest angle tested ($\alpha = 16^\circ$). In section 3.2, it has been shown that for this angle laminar flow separation occurs near the leading edge with reattachment. A direct comparison between the present inception values and those measured by Kermeen [11] is difficult to make because the present results are not

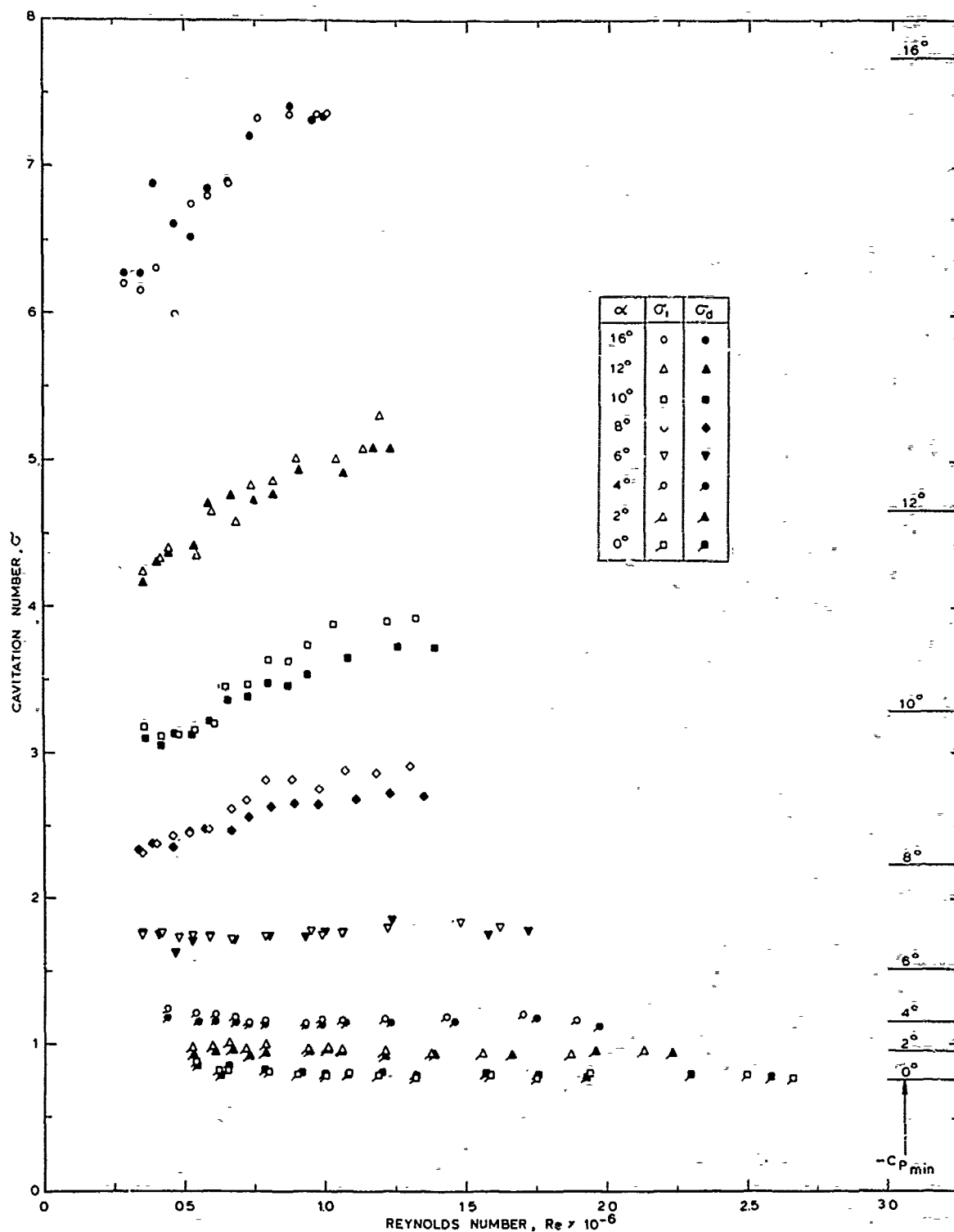


Fig. 55 Cavitation inception and desinence number versus Reynolds number for NACA 4412 hydrofoil. Also included are measured values of $-C_{p_{min}}$ according to Pinkerton [18], corrected for blockage.

corrected for blockage. The most important difference, however, is that Kermeen's data for $\alpha = 0^\circ, 2^\circ, 4^\circ$ and 6° show a Reynolds number dependency, whereas the present data for these angles are independent of Re. Kermeen [11] compared his inception data with accurate wind tunnel measurements of $-C_{p_{min}}$ made by Pinkerton [18] at $Re = 3 \times 10^6$, and found a reasonable to good agreement. In order to compare the present inception values with Pinkerton's values of $-C_{p_{min}}$, a correction method is used, which simply consists of multiplying the measured $-C_{p_{min}}$ values with a constant factor of 1.248. This factor represents the square of the ratio between the height of the test section and the height of the test section minus the hydrofoil thickness. These corrected $-C_{p_{min}}$ values are plotted in Figure 55. The $-C_{p_{min}}$ values for $\alpha = 6^\circ$ and 10° have not been measured and were obtained by interpolation. The agreement between measured inception values and corrected $-C_{p_{min}}$ values for $\alpha = 0^\circ, 2^\circ$ and 4° is excellent, but for larger angles the agreement is rather poor.

The inception values appear to be independent of the Reynolds number for all cases that bubble cavitation is found at low or moderate speeds (NACA 16-012 hydrofoil, $\alpha = 2^\circ$ and NACA 4412 hydrofoil, $\alpha = 0^\circ, 2^\circ, 4^\circ$ and 6°). Since the position of transition to turbulence of the laminar boundary layer is a function of Re, as shown in Figures 4, 19, 22 and 25, the pressure coefficient at transition, C_{p_T} , is also a function of Re, and thus it may be concluded that $\sigma_{1,d}$ does not correlate with C_{p_T} . Such a correlation has previously been reported by Arakeri and Acosta [1] on a 1.5 calibre ogive body. In our opinion, a correlation between $\sigma_{1,d}$ and $-C_{p_{min}}$ seems more appropriate, provided the water contains a sufficient number of nuclei.

5. DISCUSSION AND CONCLUSION

The appearance of cavitation on both hydrofoils at low to moderate speeds can be classified into four main types. The first type is bubble cavitation. It has been observed on the NACA 16-012 hydrofoil at $\alpha = 2^\circ$ and on the NACA 4412 hydrofoil at $\alpha = 0^\circ, 2^\circ, 4^\circ$ and 6° . In most of these cases the boundary layer behaviour was studied and a laminar boundary layer with, far downstream, transition to turbulence was found to occur. Bubble cavitation is the classical type of cavitation and has been extensively analysed by Knapp and Hollander [19] and Plesset [20]. It is merely dependent on the pressure distribution and nuclei content. At high speeds, streak cavitation or transient spot cavitation is observed. Streak cavitation is related with small surface irregularities or dirt particles on the leading edge of the hydrofoil. Transient spot cavitation is probably related with weak spots on the hydrofoil surface or in the turbulent boundary layer (bursts).

The second type observed is sheet cavitation. This type has been noticed on the NACA 16-012 hydrofoil at $\alpha = 3^\circ, 4^\circ$ and 5° and on the NACA 4412 hydrofoil at $\alpha = 8^\circ$ and 10° . It is closely related with the occurrence of laminar separation at the leading edge of the hydrofoil, with subsequent transition to turbulence and reattachment. The mechanism responsible for this relationship was clearly established by Arakeri and Acosta [1] and Arakeri [21]. Van der Meulen [3] compared the length of the separation bubble on a hemispherical nose with the length of the sheet cavity at equal Reynolds numbers and found corresponding values. The length of the sheet cavity on the hydrofoils, however, is much larger than the length of the separation bubble. In Figure 37, for instance, it is shown that the length of the smooth part of the cavity (the sheet) increases without bounds when σ is decreased. Whether this is due to a more favourable pressure distribution caused by the cavity itself or to other factors remains, as yet, unknown. The dominating role of the separation bubble in the cavitation inception process is clearly demonstrated by the flow and cavitation observations made with the NACA 16-012 hydrofoil at angles of attack around $\alpha = 3^\circ$. At a slightly smaller angle ($\alpha = 2.9^\circ$), a laminar boundary layer is found with normal transition to turbulence and the type of cavitation is bubble cavitation. At $\alpha = 3^\circ$, however, a separation bubble occurs and the type of cavitation observed is sheet (or streak) cavitation. This type of cavitation appeared to be dominant, since it could not be transformed into bubble cavitation by a large increase in dissolved or free air content.

The third type observed is bubble-band cavitation. This type was observed on the NACA 16-012 hydrofoil at $\alpha = 7^\circ$ and on the NACA 4412 hydrofoil at $\alpha = 16^\circ$. These cases refer to leading edge separation with subsequent transition to turbulence and, hardly present, reattachment. This is typically a transitional case between the separation bubble and the unattached free shear layer. When the cavity becomes slightly more developed, the downstream part of the cavity shows a cloudy appearance.

The fourth type observed is cloud cavitation. This type was observed on the NACA 16-012 hydrofoil at $\alpha = 10^\circ$ and 12° . The boundary layer observations for these angles showed the presence of an unattached free shear layer. Transition to turbulence is accompanied with the formation of vortices. These vortices appear in the bulk of the fluid flow, away from the hydrofoil surface. At inception, the vortices provide the locations for isolated cavities to be created. The continuous formation of vortices results in a formation of a large number of small cavities resembling a cloud.

A type of cavitation usually related with the flow around sharp edges and not with hydrofoils, is the type observed with the NACA 16-012 hydrofoil at $\alpha = 16^\circ$. The irregular cavities of threadlike appearance

in the flow downstream from the hydrofoil nose resemble the patterns observed behind disks [14] and blunt bodies [15].

In conclusion, it is stated that cavitation on hydrofoils at low to moderate speeds can be classified into four main types: bubble, sheet, bubble-band and cloud cavitation. Each type is uniquely related to a specific type of boundary layer flow behaviour. At high speeds, the bubble type of cavitation transforms into streak or transient spot cavitation, whereas the other types remain essentially unchanged.

REFERENCES

1. Arakeri, V.H. and Acosta, A.J., "Viscous Effects in the Inception of Cavitation on Axisymmetric Bodies", Journal of Fluids Engineering, Transactions ASME, Vol. 95, Dec. 1973, pp. 519-527.
2. Van der Meulen, J.H.J., "A Holographic Study of Cavitation on Axisymmetric Bodies and the Influence of Polymer Additives", Ph.D. Thesis, Enschede, 1976.
3. Van der Meulen, J.H.J., "A Holographic Study of the Influence of Boundary Layer and Surface Characteristics on Incipient and Developed Cavitation on Axisymmetric Bodies", Twelfth Symposium on Naval Hydrodynamics, Washington D.C., June 1978.
4. Gates, E.M., "The Influence of Freestream Turbulence Freestream Nuclei Populations and a Drag-Reducing Polymer on Cavitation Inception on Two Axisymmetric Bodies", California Institute of Technology Report No. 183-2, April 1977.
5. Gates, E.M. and Acosta, A.J., "Some Effects of Several Freestream Factors on Cavitation Inception on Axisymmetric Bodies", Twelfth Symposium on Naval Hydrodynamics, Washington D.C., June 1978.
6. Arakeri, V.H. and Acosta, A.J., "Viscous Effects in the Inception of Cavitation", International Symposium on Cavitation Inception, ASME Winter Annual Meeting, New York, Dec. 1979, pp. 1-9.
7. Casey, M.V., "The Inception of Attached Cavitation from Laminar Separation Bubbles on Hydrofoils", Conference on Cavitation, Edinburgh Scotland, Sept. 1974, pp. 9-16.
8. Blake, W.K., Wolpert, M.J. and Geib, F.E., "Cavitation Noise and Inception as Influenced by Boundary-Layer Development on a Hydrofoil", Journal of Fluid Mechanics, Vol. 80, Part 4, May 1977, pp. 617-640.
9. Van der Meulen, J.H.J., "Viscous Effects in the Appearance of Cavitation on a Hydrofoil", ASME 1978 Cavitation and Polyphase Flow Forum, Fort Collins, June 1978, pp. 7-9.
10. Van der Meulen, J.H.J., "Cavitation on Hemispherical Nosed Teflon Bodies", IUTAM Symposium, Leningrad, June 1971.
11. Kermeen, R.W., "Water Tunnel Tests of NACA 4412 and Walchner Profile 7 Hydrofoils in Noncavitating and Cavitating Flows", California Institute of Technology Report No. 47-5, Feb. 1956.
12. Van Renesse, R.L. and Van der Meulen, J.H.J., "In-Line Holography for Flow and Cavitation Visualization on Hydrofoils and for Nuclei Measurements", International Symposium on Flow Visualization, Bochum, Sept. 1980.
13. Gaster, M., "The Structure and Behaviour of Laminar Separation Bubbles", AGARD Conference Proceedings No. 4, Separated Flows, May 1966, pp. 813-854.
14. Kermeen, R.W. and Parkin, B.R., "Incipient Cavitation and Wake Flow Behind Sharp-Edged Disks", California Institute of Technology Report No. 85-4, August 1957.
15. Keller, A.P., "Cavitation Inception Measurement and Flow Visualisation on Axisymmetric Bodies at Two Different Free Stream Turbulence Levels and Test Procedures", International Symposium on Cavitation Inception, ASME Winter Annual Meeting, New York, Dec. 1979, pp. 63-74.
16. Holl, J.W. and Carroll, J.A., "Observations of the Various Types of Limited Cavitation on Axisymmetric Bodies", International Symposium on Cavitation Inception, ASME Winter Annual Meeting, New York, Dec. 1979, pp. 87-99.
17. Holl, J.W. and Treaster, A.L., "Cavitation Hysteresis", Journal of Basic Engineering, Transactions ASME, Vol. 88, March 1966, pp. 199-212.
18. Pinkerton, R.M., "Calculated and Measured Pressure Distributions over the Midspan Section of the N.A.C.A. 4412 Airfoil", NACA Report No. 563, 1936.
19. Knapp, R.T. and Hollander, A., "Laboratory Investigations of the Mechanism of Cavitation", Transactions ASME, Vol. 70, July 1948, pp. 419-435.
20. Plesset, M.S., "The Dynamics of Cavitation Bubbles", Journal of Applied Mechanics, Transactions ASME, Vol. 16, Sept. 1949, pp. 277-282.
21. Arakeri, V.H., "A Note on the Transition Observations on an Axisymmetric Body and Some Related Fluctuating Wall Pressure Measurements", Journal of Fluids Engineering, Transactions ASME, Vol. 97, March 1975, pp. 82-86.

Discussion

B.R. Parkin (Pennsylvania State Univ.)

The author has presented valuable new information on the relationship between boundary layer flows and cavitation forms on two hydrofoils. These data will provide us with most useful guidance for our own work in years to come.

In this discussion I wish to limit my questions to only one aspect of the experimental technique related to the author's ingenious use of slight taper of his foils in order to mitigate the laser-beam alignment problem associated with purely two dimensional experiments. The cavitation patterns shown in Figs.35 and elsewhere in the paper seem to suggest some departure from purely two-dimensional flow in these experiments. For the research carried out by the author this might not be a serious matter. However, in other applications of tapered foils departure from two dimensionality needs to be quantified. Can the author give us further information on this aspect of his experiments as far as noncavitating flow is concerned ?

H. Murai and A. Ihara (Tohoku Univ.)

We would like to comment about the inception and desinence of cavitation as well as the cavity length at the attack angles of 8° and 10° on NACA 4412 hydrofoil which appear in Fig.55 and section 5 of this paper.

According to the diagram, the incipient and disinent cavitation numbers show larger values than $-C_{pmin}$. This tendency is different from those in case of a hemispherical nosed body, on which σ_i and σ_d are smaller than $-C_{pmin}$ according to the reference [1] of this paper. It can be deemed that this was caused by a following reason. Since the effective attack angle is increased owing to the effect of flow shear near the wall, $-C_{pmin}$ in the neighborhood of corner is considered to be larger than that at the core region. And the boundary layer separation near the corner may take place at a smaller attack angle than that at the core region. According to our observation in the high speed motion pictures, which have been presented at the twelfth Symposium on Naval Hydrodynamics, the sheet cavitation of this kind has taken place at first in the neighborhood of the corner, and has propagated toward the spanwise direction, to cover throughout the span accompanied by a small decrease of static pressure. In the present case, as the aspect ratio of the hydrofoil is fairly small, the corner flow can affect considerably on the values of σ_i and σ_d as well as the cavity length compared with the length of separation bubble.

T.T. Huang (DTNSRDC)

As shown in Figs.36 and 37 the flow is not quite two-dimensional in your experiment. A two-dimensional flow condition will be much easier and in fact is of fundamental important for the future analyses of your valuable data. Is it possible to achieve a two-dimensional flow condition and to eliminate tunnel blockage in your experimental set-up ?

V.H. Arakeri (Indian Inst. of Science)

The author is to be congratulated for this excellent contribution. It is unfortunate that the tests were conducted with hydrofoil sections having aspect ratio less than one. This could lead to unknown strong three dimensional effects. It is also curious that the author has not compared his incipient cavitation index measurements with those of Kermeen (11) on the NACA 4412 hydrofoil. For example, at 16° angle of attack at a Reynolds number of about 5×10^5 the author finds σ_i value of close to 6.5. Whereas, Kermeen finds a value of 3.2. Is there any explanation for this fantastic difference ! In addition, Kermeen finds a Reynolds number dependence on his σ_i measurements at all the angles of attack. It should further be noted that a comparison of author, σ_i or σ_d values with $-C_{pmin}$ measurements of Pinkerton (18) may not be appropriate due to possible three dimensional effects in the authors tests with a low aspect ratio hydrofoil. Finally, it would be interesting to know what new flow regime has been found by the author on hydrofoil sections studied by him that is not possible or has not been found on axisymmetric bodies.

Author's Reply

J.H.J. van der Meulen (NSMB)

The author would like to thank the discussers for their valuable remarks. All discussers raise questions about the two-dimensionality of the flow in the experimental set-up applied. It is true that deviations from a two-dimensional flow occur due to the presence of a boundary layer on the side walls and the slightly tapered hydrofoils. However, the boundary layer flow was visualized in the central plane of symmetry for which the above influences are believed to be small. Cavitation inception measurements and observations of limited or moderately developed cavitation were related to the centre sec-

tions of the hydrofoils in order to minimize three-dimensional effects and to obtain direct comparisons with the boundary layer flow in the central plane. The author agrees with the comments by Prof. Murai and Dr. Ihara that cavitation inception on the NACA 4412 hydrofoil at $\alpha = 8^\circ$ and 10° takes place near the corners, but in the present experiments inception was related to the centre part of the hydrofoils. The finding in Figure 55 that the σ_i and σ_d values for $\alpha = 8^\circ$ and 10° are somewhat larger than the corresponding $-C_{pmin}$ values may be attributable to fluctuating pressures related with transition to turbulence of the separated free shear layer followed by reattachment. Referring to Dr. Huang's question about tunnel blockage, in the author's opinion there are two possible methods of reducing blockage effects for the present test section configuration. One method is to decrease the chord length, the other method is to investigate thinner hydrofoils. Both methods, however, have the disadvantage of increasing the experimental difficulties involved in visualizing the boundary layer flow.

Dr. Arakeri raises some interesting questions on the comparison between the present $\sigma_{i,d}$ measurements and those by Kermeen (11) for the NACA 4412 hydrofoil. For $\alpha = 16^\circ$, the present $\sigma_{i,d}$ values are still smaller than $-C_{pmin}$, and hysteresis effects do not occur. At a Reynolds number

of about 5×10^5 , Kermeen (11) found for σ_i a value of 3.2, but for σ_d a value of 11.7. Converted to the present test section, these values become 4.0 and 14.6 respectively. At a Reynolds number of about 7.5×10^5 , Kermeen found $\sigma_i = 5.6$ and $\sigma_d = 7.65$. Converted to the present test section, these values become 7.0 and 9.55 respectively. Hence, the "fantastic" differences mentioned by Dr. Arakeri are to be found within Kermeen's own measurements. Apparently they are due to nuclei effects associated with the presence of the resorber in the CIT high speed water tunnel. In the present experiments, no Reynolds number dependency is found for $\alpha = 0^\circ, 2^\circ, 4^\circ$ and 6° . In these cases a laminar boundary layer occurs followed by natural transition to turbulence. The fact that Kermeen (11) did find a Reynolds number dependency for these angles may have been caused by a lack of nuclei in the oncoming flow so that the pressure fluctuations related with transition became the predominant mechanism in the inception process.

In the author's opinion, flow regimes to be found on hydrofoil sections that have not (yet) been found on axisymmetric bodies are: (1) laminar separation for which the distance to the stagnation point is either small, moderate or large, whereas for axisymmetric bodies this distance is moderate, and (2) the unattached free shear layer leading to cloud cavitation.

The Influence of Hydrofoil Oscillation on Boundary Layer Transition and Cavitation Noise

Young T. Shen and Frank B. Peterson

David W. Taylor Naval Ship Research and Development Center
Bethesda, Maryland, U.S.A.

ABSTRACT

Significant effects of boundary layer characteristics on cavitation and the effect of unsteady cavitation on noise have been widely observed experimentally. In order to better understand these effects, an experiment with a two-dimensional hydrofoil, under sinusoidal pitching oscillation, was conducted in the 36-inch water tunnel at DTNSRDC. Three pin-hole-type pressure transducers were installed on the foil surface to measure pressure fluctuations and a hydrophone was used to measure the radiated cavitation noise. Two subjects are discussed in this paper: 1) relationship of boundary layer transition and pressure fluctuations with the hydrofoil in oscillation, and 2) noise generated by unsteady cavitation.

The magnitudes of pressure fluctuations in transition and turbulent regions are found to be independent of oscillation amplitude and frequency. However, the development of boundary layer and occurrence of transition are delayed with an increase in oscillation frequency. The influence of hydrofoil oscillation on cavitation inception is also discussed. With the occurrence of leading edge sheet cavitation, a significant effect of foil oscillation on cavitation noise is measured. At high reduced frequencies, extensive cloud cavitation is formed during the final phase of sheet cavity collapse and the noise level is significantly increased.

PREFACE

An earlier paper by the present authors at the 12th ONR symposium dealt with two subjects, the inception of cavitation on a two-dimensional foil and the physics of leading-edge sheet cavity stability and subsequent formation of cloud cavitation. The method developed to predict inception was based on Giesing's unsteady airfoil theory and assumed that viscous effects were of secondary importance. The present paper will explore the importance of the boundary layer development. In addition, as a continuation of the early study of cavitation instability, the importance of cloud cavitation in producing acoustic noise will be presented.

1. INTRODUCTION

Cavitation frequently is unavoidable on the lifting sur-

faces of hydrofoils and marine propellers. For many years, scientists and engineers have dealt with the problems of cavitation-induced noise, structural vibration and erosion associated with the operation of marine vehicles and hydraulic equipment. All three problems are related to the inception, growth, and collapse of vapor cavities.¹

Inception of cavitation in a fluid is the condition under which cavitation is first detected, either visually or acoustically. It had often been assumed that when making analytical predictions, cavitation inception occurs immediately after the static pressure on the body surface becomes equal to or less than the vapor pressure of the fluid. A research model, the International Towing Tank Conference (ITTC) headform, tested in different cavitation facilities demonstrates that cavitation inception on a given model can have many different physical forms and cavitation inception indices, depending on the environment and body surface condition.^{2,3} Departures of cavitation inception from the traditional rule are attributed to so-called "scale effects." The influence of boundary layer pressure fluctuations on cavitation inception is known to be one of the major sources of scale effect.^{2,4}

Rouse⁵ showed that the high pressure fluctuations generated in the turbulent shear layer of a free-jet can produce cavitation at static pressures which are higher than vapor pressure. Daily and Johnson⁶ showed that pressure fluctuations in the middle of a fully established turbulent boundary layer can initiate inception. Levkovskii and Chalov⁷ reported that turbulence in flow past a wing causes cavitation to inception earlier. Recent work by Arakeri and Acosta^{8,9} and Huang⁴ indicates that for supercritical Reynolds numbers for which bodies do not have laminar boundary layer separation, cavitation inception takes place in the region of transition from laminar to turbulent flow. For subcritical Reynolds numbers, cavitation inception is found to occur in the reattachment region following laminar boundary layer separation.

Significant boundary layer pressure fluctuations on body surfaces have been measured by Huang and Hannan¹⁰ and by Arakeri¹¹ in the reattachment region following laminar separation. In addition, Huang and Hannan reported that measured pressure fluctuations in a natural transition region are higher than fluctuations in a fully established turbulent boundary layer flow by a factor ranging from 2 to 3. Huang and Peterson¹² reported that a significant scale effect

on cavitation inception induced by boundary layer pressure fluctuations exists between full-scale and model propellers due to large differences in Reynolds numbers.

The properties of the wall fluctuating pressure field associated with the growth of turbulent spots in a transition boundary layer on a flat plate have been measured by DeMetz et al.,¹³ DeMetz and Casarella,¹⁴ and Gedney.¹⁵ Each reported that pressure fluctuations in the transition region are smaller than those in the fully developed turbulent region. This result is not in agreement with the measurements of Huang and Hannan.¹⁰

A basic question has been raised as to whether the boundary layer pressure fluctuations in a natural transition region can be greater than those in a fully established turbulent boundary layer region. The significance of this point is that if the pressure fluctuations at transition are greater than in the fully developed turbulent boundary layer, then one can expect cavitation to preferentially occur at the transition location. In view of the significance of this question in cavitation scaling, fluctuating pressure measurements for a two-dimensional hydrofoil are given in this paper.

When a hydrofoil operates in waves or a propeller operates behind a ship hull, the lifting surfaces are subjected to temporally and/or spatially varying velocity and pressure fields. The time varying pressure field can be expected to have a significant effect on the characteristics of cavitation inception, growth, and collapse. As a first approximation, the unsteady effect on cavitation has been studied with oscillating hydrofoils by Miyata et al.,¹⁶ Radhi,¹⁷ Bark and van Berlekom,¹⁸ Shen and Peterson,¹⁹ and van Houten.²⁰ The hydrofoil approach is especially attractive for simulating a propeller blade operating behind an inclined shaft with the effective angle of attack oscillating periodically during each cycle of rotation. Available data demonstrate that the cavitation-inception angle-of-attack at the leading edge is different from inception angles determined from quasi-steady analysis based on uniform flow experiments.

Shen and Peterson¹⁹ showed that the computed potential-flow pressure distributions are subject to a significant phase shift with respect to the foil oscillation angle, which in turn influences the occurrence of cavitation inception. As previously mentioned, significant physical effects of boundary layer characteristics on cavitation have been well documented. So far most transition and boundary layer pressure fluctuation studies have been limited to flat plates and headforms. In the first part of this paper the influence of oscillation on transition boundary-layer pressure fluctuations, and the possible effect of oscillation on cavitation inception for a two-dimensional hydrofoil, will be presented. As pointed out previously, cavitation frequently is unavoidable on the lifting surfaces of hydrofoils and marine propellers. In the second part of this paper the influence of oscillation on foil cavitation instability and noise will be presented.

2. EXPERIMENTAL APPARATUS AND TEST PROCEDURE

2.1 Foil and Instrumentation

A foil was machined from 17-4 PH stainless steel in the form of a rectangular wing of Joukowski section with the trailing edge modified to eliminate the cusp. The offsets are given by the following equation:

$$\begin{aligned} y/c &= 0.04077 \sin \theta - 0.02039 \sin (2\theta) & 0 \leq x/c \leq 0.7945 \\ \theta &= \cos^{-1} (1.888 x/c - 1) \\ y/c &= 0.08590 (1 - x/c) & 0.7945 \leq x/c \leq 1.0 \end{aligned} \quad (1)$$

To simulate prototype viscous effects at the leading edge as closely as possible, the model was designed with a chord

length c of 24.1 cm, a span of 77.5 cm and a relatively large leading-edge radius. The maximum thickness to chord ratio is 10.5 percent. The foil surface was hand finished within $0.38 \mu\text{m}$ rms surface smoothness.

Pressure transducers were installed at a distance of 7.96, 24.1 and 60.3 mm from the leading edge. These locations correspond to 3.3, 10, and 25 percent of chord length from the leading edge. Kulite semiconductor pressure gages of the diaphragm type (Model number LQM-10-250-305) were mounted within a Helmholtz chamber connected to the foil surface by a pinhole. This arrangement permitted measurement of unsteady surface pressures due to foil oscillation and high frequency pressure fluctuations inside the boundary layer over a pressure range of $\pm 207 \text{ KPa}$ ($\pm 30 \text{ PSI}$). In order to increase the spatial resolution in measuring the local pressure fluctuations inside the boundary layer, the diameter of the pinholes installed on the foil surface was kept at 0.31 mm (0.012 inches). This arrangement also reduces the danger of cavitation damage to the pressure transducers. Extreme care was taken to fill the Helmholtz-type chamber through the pinhole under vacuum with deaerated water to minimize the possible occurrence of an air bubble trapped inside the chamber. A flat pressure response was observed up to 2,000 Hz in dynamic calibration tests. The calibration procedure used here was developed by the National Bureau of Standards,²¹ modified to the extent that water, rather than silicone oil, was the fluid medium. Since it was very important to determine the relative phase difference between the foil angle and the pressure gage signals, all amplification and recording equipment was selected to minimize the introduction of unwanted phase shifts.

The cavitation noise was sensed by a flush mounted hydrophone 117 cm downstream from the foil axis, on the top of the water tunnel's close-jet test section. The hydrophone was uncalibrated, so all noise measurements are relative to an arbitrary level.

2.2 Test Section

The closed-jet test section of the 36-inch water tunnel was modified by the insertion of sidewall liners to provide two flat sides. On each end of the foil a disc was attached. This disc rotated in a sidewall recess; thus the foil could be rotated without gap cavitation occurring between the end of the foil and the sidewall of the tunnel. One sidewall assembly was fitted with clear plastic windows to permit side view photography.

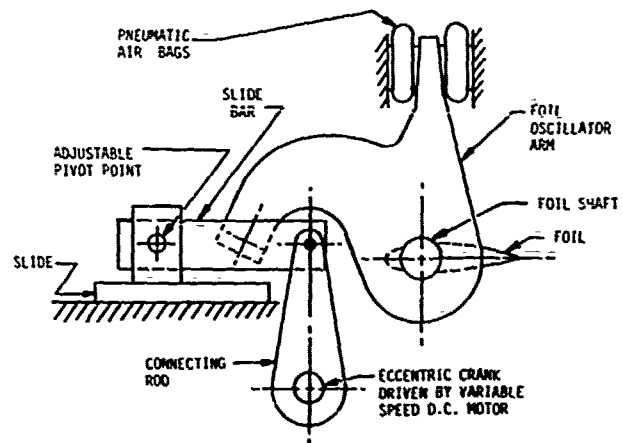


Figure 1 — Conceptual Design of Foil Oscillation Mechanism

The foil was oscillated in pitching motion around the quarter chord by a mechanism whose conceptual design is shown in Figure 1. With this type of design, the foil mean

angle (α_0) can be adjusted statically and the amplitude of foil oscillation (α_1) can be continuously adjusted between 0° to 4° while in operation. The oscillation frequencies cover the range between 4 Hz to 25 Hz. Air bags were installed to reduce the fluctuating torque requirements on the motor drive system.

2.3 Data Reduction

Due to installation of two sidewall liners in the test section, the tunnel speed was corrected according to the area-ratio rule. The tape-recorded time histories of foil angle and pressures were digitized by using a Hewlett Packard 2100 minicomputer and reduced by using algorithms implemented on the DTNSRDC CDC-6000 digital computer. The time histories were recorded on one inch magnetic tape at 15 inches per second (38 cm/s) using IRIG standard intermediate band frequency modulation techniques. During digitization, pressure fluctuation data were filtered using four-pole Butterworth bandpass filters that have a -3 dB signal attenuation at 80 and 2,000 Hz for boundary layer pressure fluctuations. The run lengths used in the data reduction were nominally 40 seconds. For the oscillating foil data, the computer output consisted of values of mean and standard deviations of pressure fluctuations.

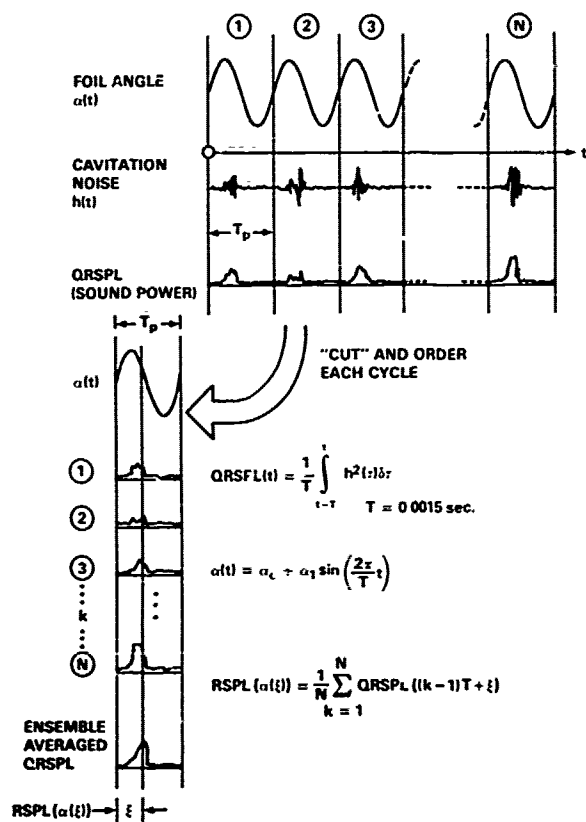


Figure 2 — Sequence of Ensemble Averaging

(From an unpublished report by R. Pierce, DTNSRDC)

The hydrophone signal was first bandpass filtered between 10 kHz and 40 kHz to minimize signal contamination from noncavitation related sources. This signal was then squared and passed through an averaging filter to obtain a "running average," i.e. quasi-stationary sound power levels,

p^2 as shown in Figure 2. This sound power level is also digitized along with the signals corresponding to the foil angle-of-attack and the mean foil angle. In order to obtain the average relative sound power, the digitized signal is averaged over the whole run. In order to determine the average waveform of the hydrophone signal during one cycle, a cycle is defined as being initiated and terminated when the increasing foil angle passes through its mean position. Each cycle is divided into $(1600/f)$ time increments, i.e. at a $f = 4$ Hz oscillation frequency, 400 time increments are used. The digitized hydrophone signal in each time increment is averaged over all of the cycles in a run. The averages in each of the increments then collectively represent the average waveform occurring for one cycle.

3. BOUNDARY LAYER PRESSURE FLUCTUATIONS ON A STATIONARY FOIL

Consider a steady uniform flow past a two-dimensional hydrofoil. Let the local pressure p on the foil surface be expressed in the following way:

$$p = p_p + \Delta p_t \quad (2)$$

where p_p is the mean pressure and Δp_t is the pressure associated with the boundary layer pressure fluctuations. Let C_p denote local pressure coefficient:

$$C_p = \frac{p - p_\infty}{\frac{1}{2} \rho V_\infty^2} \quad (3)$$

$$= C_{ps} + \Delta C_{pt}$$

where

$$C_{ps} = \frac{p_p - p_\infty}{\frac{1}{2} \rho V_\infty^2} \quad (4)$$

and

$$\Delta C_{pt} = \frac{\Delta p_t}{\frac{1}{2} \rho V_\infty^2} \quad (5)$$

here ρ , p_∞ , and V_∞ are fluid density, reference free-stream static pressure and reference free-stream velocity, respectively.

3.1 Laminar Boundary Layer Stability Calculations

Let $k = \frac{\omega c}{2V_\infty}$ denote the reduced frequency where ω is the circular frequency associated with foil oscillation. The limiting case $k = 0$ corresponds to a stationary condition. A uniform flow past a stationary foil at an angle-of-attack α of 3.25 degrees will be considered first. The computed steady potential flow pressure distribution for this foil angle is shown in Figure 3. The flow field to be measured by the pressure gages at 3.3, 10 and 25 percent chord length is seen to be in a strong adverse pressure gradient. This fact will be shown to have a significant effect on the magnitude of boundary layer pressure fluctuations. The prediction of laminar boundary layer separation is based on the criterion of zero shear stress. The Smith disturbance amplification method²² is used to correlate and predict flow transition.

Let A/A_0 denote the Smith cumulative spatial amplification ratio A to its amplitude A_0 at the point of neutral stability. Let Re_c denote the Reynolds number based on chord length. As a numerical example, the computed amplification ratio versus chordwise location x/c is given in Figure 4a at

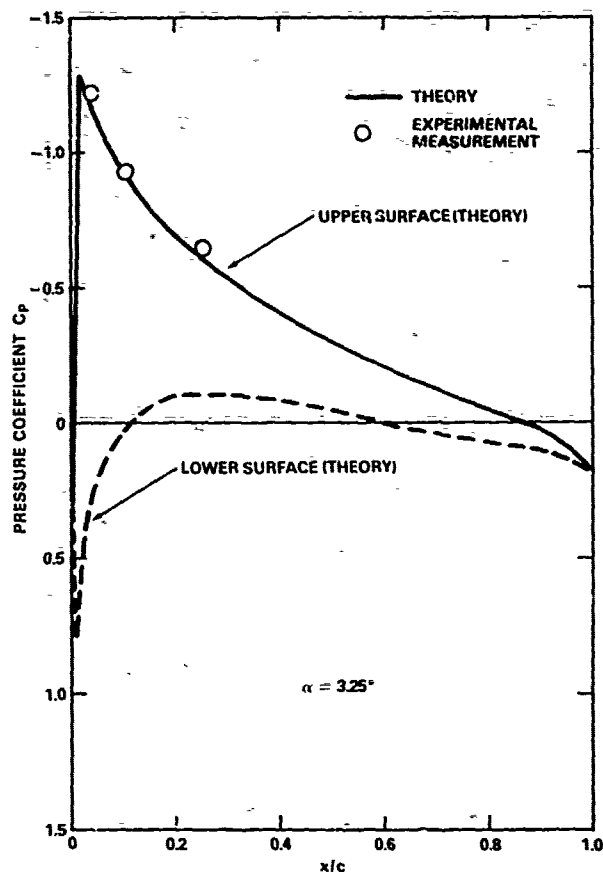


Figure 3 — Measured and Predicted Pressure Distributions

$R_{nc} = 1.6 \times 10^6$. The Smith cumulative spatial amplification ratio was computed for a range of nondimensional boundary layer disturbance frequencies $\bar{\Omega}$,

$$\bar{\Omega} = \frac{\Omega y}{V_{\infty}^2} \quad (6)$$

where Ω is the dimensional disturbance frequency. Figure 4a shows that disturbances will be significantly amplified in the frequency range of $\bar{\Omega} = 1.7 \times 10^{-4}$ to 3.2×10^{-4} which correspond to dimensional frequencies of 1,250 Hz to 2,350 Hz. Figure 4a also indicates that the frequency $\bar{\Omega} = 3.2 \times 10^{-4}$ has the largest amplification ratio up to $x/c = 0.11$. The free-stream velocity used in these computations is $V_{\infty} = 6.71$ m/s. The same method was used for stability calculations at other Reynolds numbers. The computed results are summarized in Figure 4b.

3.2 Experimental Results

The experiments with the foil at $\alpha = 3.25$ degrees were performed in the DTNSRDC 36-inch water tunnel. As seen in Figure 3, the measurements of static pressure coefficients are in good agreement with prediction. At speeds of 4.88, 6.71, 9.75, 13.11 and 14.94 meter/sec, the pressure responses measured at three foil locations are given in Figures 5a to 5e. The pressure gages located at 3.3, 10 and 25 percent chord lengths on the upper surface are denoted by P_3 , P_{10} and P_{25} , respectively. The purpose of steady runs was

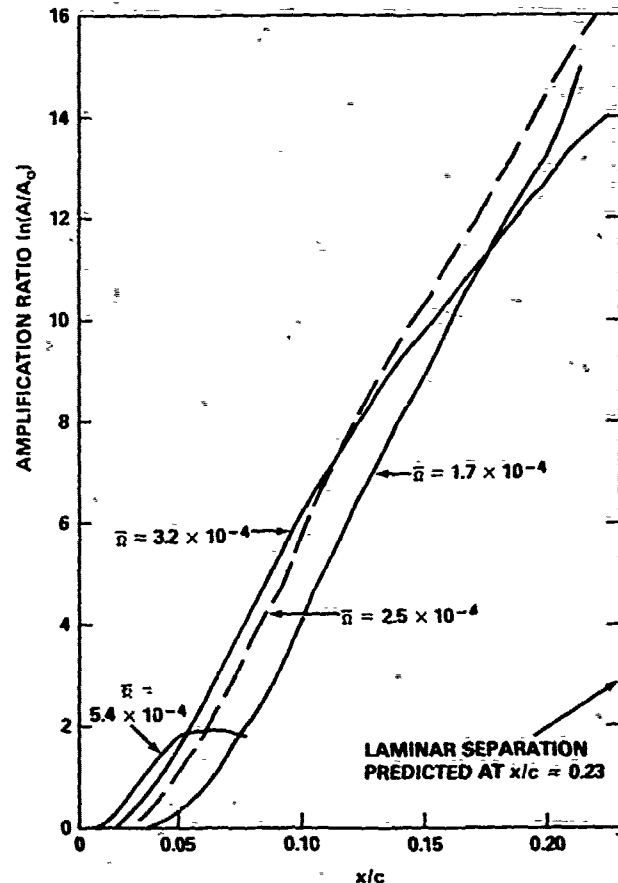


Figure 4a — Computed Amplification Ratios at Foil Angle $\alpha = 3.25$ deg and $R_{nc} = 1.6 \times 10^6$

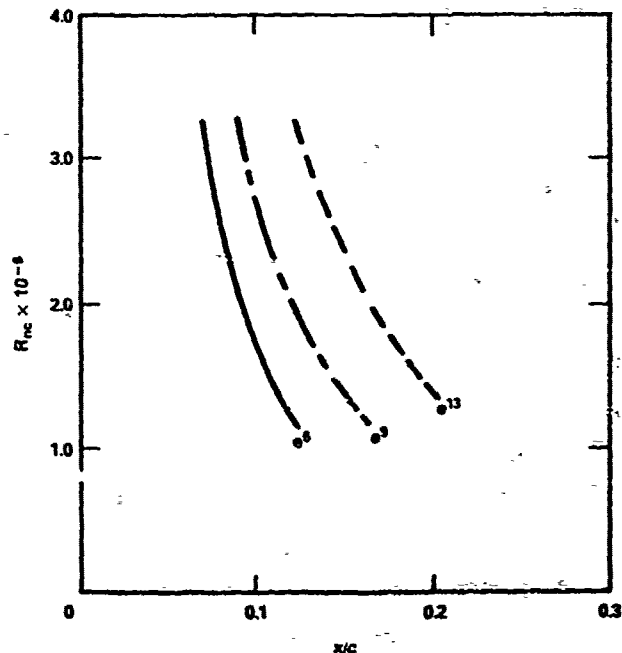


Figure 4b — Effect of Reynolds Numbers on Amplification Ratios at $\alpha = 3.25$ deg

to provide reference data to be used for comparison with dynamic runs. Consequently, the test runs given in Figures 5a to 5e were conducted with the oscillating mechanism in motion and the oscillating amplitude a_1 set to zero to incorporate the possible effect of noise and vibration on the measured phenomena.

RUN NO. 7001

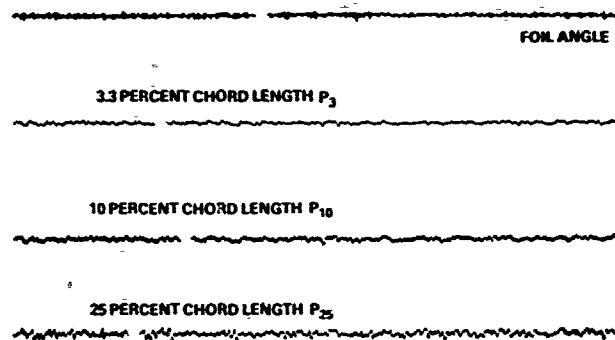


Figure 5a — Measured Pressure Fluctuations at $R_{nc} = 1.2 \times 10^6$ in a Steady Flow at $\alpha = 3.25$

RUN NO. 8028

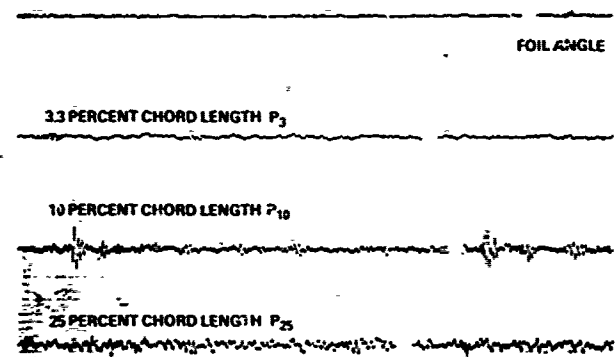


Figure 5b — Measured Pressure Fluctuations at $R_{nc} = 1.6 \times 10^6$ in a Steady Flow at $\alpha = 3.25$

RUN NO. 8046

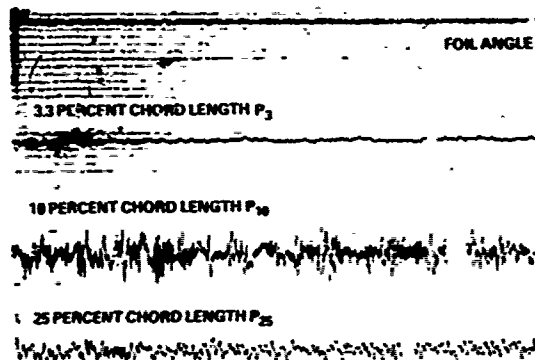


Figure 5c — Measured Pressure Fluctuations at $R_{nc} = 2.4 \times 10^6$ in a Steady Flow at $\alpha = 3.25$

RUN NO. 8044

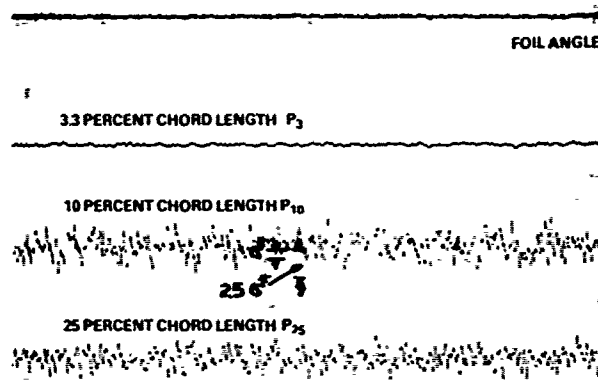


Figure 5d — Measured Pressure Fluctuations at $R_{nc} = 3.2 \times 10^6$ in a Steady Flow at $\alpha = 3.25$

RUN NO. 8056

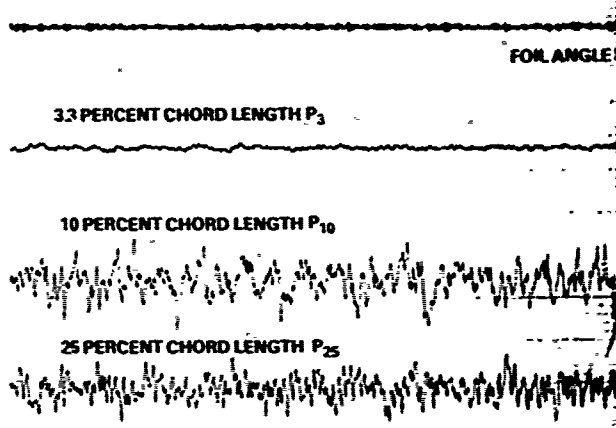


Figure 5e — Measured Pressure Fluctuations at $R_{nc} = 3.6 \times 10^6$ in a Steady Flow at $\alpha = 3.25$

The energy spectrum based on narrow band frequency analysis from 80 to 5040 Hz of Run 8028 at pressure gage P_{10} is given in Figure 6. The maximum fluctuating signal at P_{10} corresponds to 2650 Hz. This value is in close agreement with the computed frequency of the most unstable disturbances; see Figure 4a. The energy spectra of pressure responses based on narrow band frequency analysis were conducted for several test runs. Figure 6 shows a sharp peak at 4.7 kHz at pressure gage P_{10} . The same kind of sharp peak at 4.7 kHz was observed in all the runs analyzed. A similar phenomenon was observed at 5.0 kHz at pressure gage P_{25} . It is suspected that this may be resonance phenomenon associated with pinhole-type pressure gages. The pressure gages had been dynamically calibrated up to 2,000 Hz with flat response. Consequently, the data given in Figures 5a to 5e were bandpass filtered with 4 pole Butterworth filters from 80 to 2,000 Hz. Burton²³ has shown that the energy spectrum of a flow field in an adverse pressure gradient is compacted in a much narrower and lower frequency ranges than the energy spectrum associated with a flow field in a zero pressure gradient.

A comparison of pressure response measurements and stability calculations suggests that the boundary layer at P_{25} (25 percent chord length) for all the runs given in Figure 5a to 5e is fully turbulent. The measured root-mean-square (rms) pressure fluctuations normalized by the free-stream dynamic

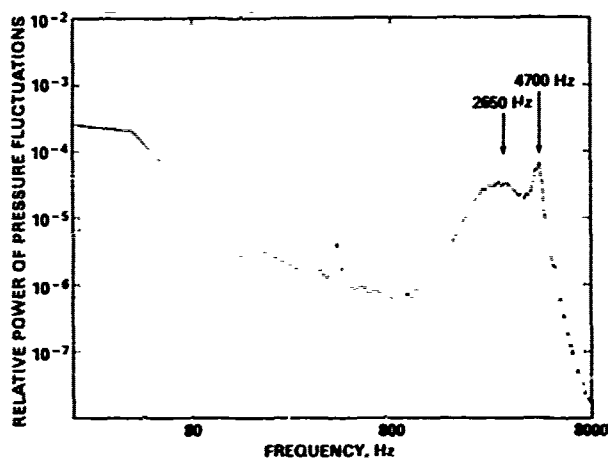


Figure 6 — Energy Spectrum of Run 8028 at $R_{Re} = 1.6 \times 10^6$

head are given in Table 1. The values of ΔC_{p4} range between 0.0065 to 0.011. Burton reported that the measured rms pressure fluctuation coefficient normalized by the free-stream dynamic head is measurably smaller in an adverse pressure gradient (around 0.0078) than in a favorable pressure gradient (around 0.010). Huang and Hannan¹⁰ measured 0.015 on an axisymmetric body. The present data were digitized through a bandpass filter from 80 to 2,000 Hz. The loss of high frequency range may influence the resolutions of pressure gage measurements and underestimate the magnitude of pressure fluctuations.

Run No.	$\frac{U}{U_\infty}$	$R_{Re} \times 10^{-6}$	ΔC_{p4} at P_{25}		ΔC_{p4} at P_{10}	
7081	4.88	1.2	0.0125	0.0113	0.0086	0.0082
8028	6.71	1.6	0.0097	0.0092	0.0117	0.0111
8040	9.75	2.4	0.0076	0.0074	0.0137	0.0136
8044	13.11	3.2	0.0065	0.0065	0.0095	0.0095
8066	14.98	3.6	0.0065	0.0065	0.0092	0.0092

*NOISE SIGNAL SUBTRACTED

TABLE 1 — ROOT-MEAN-SQUARE BOUNDARY LAYER PRESSURE FLUCTUATIONS AT 25 PERCENT CHORD (P_{25}) AND 10 PERCENT CHORD (P_{10})

Additionally, Table 1 shows that at a given location the measured pressure fluctuation coefficients decrease with an increase in speed. The same trend was also reported by Burton. Measurements by Ludwig and Tillman²⁴ showed that the shearing stress in a turbulent boundary layer decreased significantly with an increase in momentum thickness Reynolds number. Blake²⁵ reported that the shear stress rather than the free-stream dynamic head should be used to collapse the data. All these findings suggest that the boundary-layer pressure fluctuation coefficient to be used for model/full-scale cavitation scaling is not a universal constant, as used in Reference 12, but instead is a function of Reynolds number.

Stability calculations at $R_{Re} = 1.6 \times 10^6$ show that amplification ratios of e^4 , e^9 and e^{11} are reached at $x/c = 0.10$, 0.13 and 0.16, respectively. Laminar separation is

predicted to occur at $x/c = 0.23$. Theoretical computations suggest that natural transition from laminar to turbulent boundary layers is to be expected to occur upstream of the laminar separation point at this Reynolds number. Thus, natural transition precludes the possibility of laminar separation.

At a speed of 4.88 m/s, Figure 5a shows that the flow at 3.3 and 10 percent chord lengths are laminar. With an increase in speed to 6.71 m/s, corresponding to $R_{Re} = 1.6 \times 10^6$, a strong pressure fluctuating signal with intermittency is noticed at 10 percent chord; see Figure 5b. The bursting signal observed in Figure 5b is related to natural transition. It was found that the computed amplification ratio of e^6 correlated well with the measured location of natural transition for the present experimental setup at $R_{Re} = 1.6 \times 10^6$. For other Reynolds numbers the computed locations of the amplification ratios of e^6 were used to indicate the start of natural transition.

At a speed of 9.75 m/s, corresponding to $R_{Re} = 2.4 \times 10^6$, the stability calculations predict an amplification ratio of $e^{8.5}$ at P_{10} . Measured pressure responses suggest that the flow at 10 percent chord is in the final phase of transition with an intermittency factor close to unity; see Figure 5c. The rms pressure fluctuations normalized by the free-stream dynamic head, are given in Table 1. The measured rms pressure fluctuation at 10 percent chord in the transition region are seen to be greater than those measured at 25 percent chord in the turbulent region. This observation is based on data analysis with a bandpass filter of 80 to 2,000 Hz. In the few cases when the bandpass filter upper limit increased to 5,040 Hz, the same conclusion held.

The properties of the wall fluctuating pressure field associated with the growth of turbulent spots in a natural transition boundary layer on a flat plate have been measured by DeMetz et al.,¹³ DeMetz and Casarella,¹⁴ and Gednev.¹⁵ They all report that the pressure amplitudes in the wall pressure field of individual spots are approximately equal to those in the fully turbulent boundary layer region. As the intermittency factor γ increases, the power spectral densities increase systematically to a maximum value in the fully turbulent condition,¹³

$$p^2(\gamma) = \gamma p^2(\gamma), \quad (7)$$

These results suggest that the pressure fluctuations measured in a natural transition region are smaller than those in a turbulent region, which is not in agreement with the present measurements.

Pressure fluctuations in regions of natural flow transition on an axisymmetrical body were also measured by Huang and Hannan.¹⁰ Compared to the pressure fluctuations measured in a fully established turbulent region, the intensity of pressure fluctuations in the transition region is higher than in the turbulent region. The present results agree with the results of Huang and Hannan. These measurements and the present measurements were made in flows with adverse pressure gradients, whereas the linear relationship given in Equation (7) is derived from measurements on a flat plate with zero pressure gradient. It is suspected that the cause of differences in the two sets of data is differences in the pressure gradients. This difference is further amplified in the following series of tests. The pressure fluctuations at a speed of 13.11 m/s, corresponding to $R_{Re} = 3.2 \times 10^6$, are given in Figure 5d. This figure suggests that the flow is turbulent at 10 percent chord; this correlates with the stability calculations which indicated that the amplification ratio reached about e^9 to e^{10} at P_{10} . Figure 5d also suggests that the location of transition has moved ahead of P_{10} . The measured pressure coefficient at this speed is smaller than the one measured at a speed of 9.75 m/s. This fact seems to support the argument that the pressure fluctuation in a transition region is greater

than in a turbulent region with an adverse pressure gradient. A further increase in speed to 14.94 m/s reduces the pressure fluctuation further as shown in Figure 5e.

As a final remark, Figure 5d shows that the frequently-occurring large negative pressure fluctuations are approximately 2.5 times higher than their rms value in the transition region at P_{10} and 2.0 times higher than their rms value in the fully established turbulent region at P_{25} . These results are in close agreement with the Huang and Hannan measurements.¹⁰ Huang and Peterson¹² suggested that the frequently-occurring large negative pressure fluctuations in transition may be responsible for cavitation inception events.

4. BOUNDARY LAYER PRESSURE FLUCTUATIONS WITH FOIL IN OSCILLATION

4.1 The Oscillating Foil

The foil oscillates sinusoidally in pitching motion around the quarter chord point, measured from the foil leading edge. The instantaneous foil angle is denoted by:

$$\alpha = \alpha_0 + \alpha_1 \sin(\omega t) \quad (8)$$

where α_0 , α_1 , and ω are the mean foil angle, amplitude of foil oscillation and oscillation frequency, respectively. Let ϕ denote the phase angle between the pressure response and the instantaneous foil angle. At a given location on the foil, the time dependent local pressure and pressure coefficient are expressed by:

$$P(t) = P_s + |P_u| \sin(\omega t + \phi) + \Delta P_t$$

$$C_p(t) = C_{ps} + |\Delta C_{pu}| \sin(\omega t + \phi) + \Delta C_{pt}$$

where

$$C_{ps} = \frac{P_s - P_\infty}{\frac{1}{2} \rho V_\infty^2} \quad (9)$$

$$|\Delta C_{pu}| = \frac{|P_u|}{\frac{1}{2} \rho V_\infty^2}$$

$$\Delta C_{pt} = \frac{\Delta P_t}{\frac{1}{2} \rho V_\infty^2}$$

Here, C_{ps} , $|\Delta C_{pu}|$ and ΔC_{pt} respectively denote mean potential flow pressure coefficient, dynamic potential flow pressure coefficient, and the unsteady pressure coefficient associated with boundary layer pressure fluctuations. The objective of the work described here was to determine the influence of foil oscillation on transition and magnitudes of boundary layer pressure fluctuations.

4.2 Flow Description

For a typical propeller operating behind an inclined shaft, the lifting surface representing a propeller blade will encounter a periodic pressure field. The amplitude of pressure fluctuation depends on the ship speed and the angle of inclination. Angle-of-attack variations of 0.5 to 2.0 degrees at the 0.7 propeller radius are expected to represent a range of practical interest. The effect of unsteady angle-of-attack variations on lifting surface boundary-layer pressure fluctuations was investigated by pitching the previously-described two-dimensional hydrofoil sinusoidally.

A typical oscillograph plot of pressure responses with the foil in oscillation is shown in Figure 7. The data were bandpass filtered from 80 to 2,000 Hz. The low frequency

periodic part has been subtracted. To accommodate an oscillation cycle of the foil on a reasonably sized sheet, the trace was processed at 2 inches per second paper speed. (Figures 5a to 5e were processed at 10 inches per second paper speed.) The first line from the top gives the instantaneous foil angle. In this example, the frequency of foil oscillation is 4 Hz. The instantaneous foil angle is given by $\alpha = 3.25^\circ + 2.1^\circ \sin \omega t$. The speed is 9.75 m/s, corresponding to $Re_c = 2.4 \times 10^5$. Recall that in the steady run ($\alpha = 3.25^\circ$) at $Re_c = 2.4 \times 10^5$ (Figure 5b), the flow was in the final stage of transition at the 10 percent chord length. The low amplitude unsteady signal appearing at 3.3 percent chord length is due to mechanical noise caused by the oscillator motion and the electrical noise within the recording electronics.

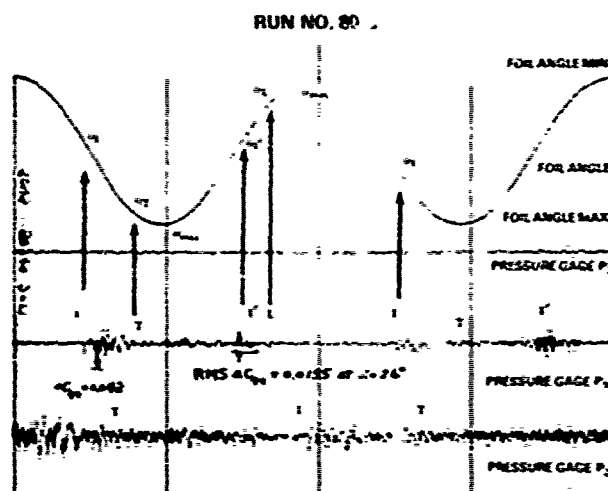


Figure 7 — Sample Oscillograph Record at $Re_c = 2.4 \times 10^5$, $f = 4$ Hz and $\alpha = 3.25 + 2.1 \sin \omega t$

In order to describe the observed change in transition location with foil angle, consider the pressure response at 25 percent chord length, P_{25} . Figure 7 suggests that the flow is turbulent and that the location of transition is ahead of P_{25} when the foil is at the maximum foil angle $\alpha = \alpha_{max}$. As the foil angle begins to decrease, the location of transition moves toward the trailing edge. At some intermediate foil angle $\alpha = \alpha_1$, the signals of pressure fluctuations are intensified and the transition is assumed to occur at P_{25} . After the foil reaches $\alpha = \alpha_{min}$, the foil angle begins to increase and the movement of transition is reversed toward the leading edge. Finally, the flow at P_{25} becomes fully turbulent again at $\alpha = \alpha_1$.

Next, consider the pressure response at 10 percent chord length, P_{10} . In this example, the minimum foil angle is $\alpha_{min} = 1.15^\circ$. Figure 7 suggests that the flow is laminar at P_{10} when the foil angle is at α_{min} . The location of transition is aft of the 10 percent chord length. As the foil angle begins to increase, transition moves forward with instability occurring at a certain foil angle, $\alpha = \alpha_1$. A further increase in the foil angle produces full turbulence at $\alpha = \alpha_1$. It should be remarked that the pressures at P_{10} must be multiplied by a factor of 1.15 to account for difference in gage sensitivities if a direct comparison of pressure fluctuations between P_{25} and P_{10} are to be made on the oscillograph plot. The flow remains turbulent when the foil angle reaches $\alpha = \alpha_{max}$. This is followed by a decrease in foil angle. At $\alpha = \alpha_1$, flow transition occurs again at P_{10} . A further decrease in foil angle produces laminar flow at $\alpha = \alpha_1$. The rms pressures at P_{10} derived from Figure 7 are given in Figure 8. Figure 8 shows that the rms value of ΔC_{pu} attains the maximum of 0.0155 at the foil

angle $\alpha = 2.6$ degrees. Figure 7 gives a measured large negative pressure fluctuations of $\Delta C_{pt} = 0.042$, which is approximately 2.7 times higher than the peak value (rms) shown in Figure 8. This result is in agreement with the previous stationary runs.

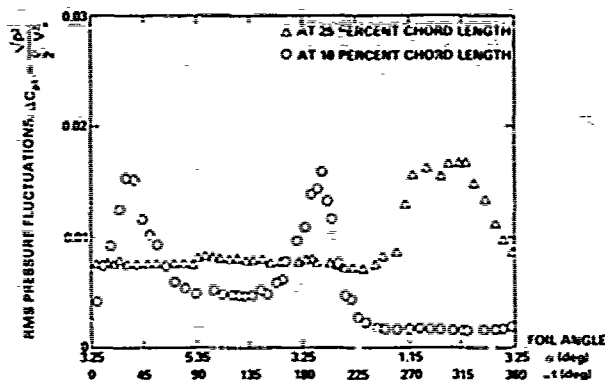


Figure 8 — Measured RMS Pressure Fluctuations on Run 8043 at $R_{Re} = 2.4 \times 10^6$ and $\alpha = 3.25 + 2.1 \sin \omega t$

4.3 Unsteady Effects

A series of dynamic runs was conducted to examine unsteady effects on boundary layer pressure fluctuations. A free-stream speed of $V_\infty = 9.75$ m/s was used for this series of experiments. The instantaneous foil angle α is given by $\alpha = 3.25 + a_1 \sin \omega t$. The oscillation amplitude a_1 covered the range from 0 to 2.1 degrees. The oscillation frequency, $f = \omega/2\pi$, covered the range from 4 to 15 Hz. Due to the increased background noise, the pressure fluctuation associated with the 25 Hz foil oscillation are not presented here.

Recall the case $a_1 = 0$, corresponding to Run 8040 as given in Figure 5c. The flow at P_2 (3.3 percent chord length) is seen to be laminar. The flow at P_{10} is seen to be in the final phase of transition. The flow at P_{25} is seen to be fully turbulent.

4.3.1 Pressure Fluctuations at 10 Percent Chord Length (P_{10})

The case with $a_1 = 0.5$ degrees is considered first. It is remarked that the flow at 3.3 percent chord is laminar throughout the whole series of runs. Because the pressure fluctuations in dynamic runs are non-stationary, the test data were digitized to obtain a rms value (see Figure 2). The corresponding rms pressure fluctuations at P_{10} are shown in Figure 9 for oscillation frequencies of 4, 5.5 and 15 Hz. The vertical axis gives rms pressure fluctuations normalized by the free-stream dynamic head. The horizontal axis gives the instantaneous foil angle α and the oscillation angle ωt . The magnitudes of the pressure fluctuations are seen to vary with the instantaneous foil angles. Figures 5c and 9 suggest that the location of transition is slightly aft of P_{10} at $\alpha = 3.25$ degrees. As the foil angles are increased, transition moves forward toward P_{10} . The measured rms pressure fluctuations at P_{10} are systematically intensified. As the foil angle approaches 3.60 degrees, the location of transition occurs at P_{10} and the magnitude of pressure fluctuations attains a maximum. A further increase in foil angle moves the transition ahead of P_{10} , and the magnitude of pressure fluctuations measured at P_{10} is reduced. After the foil angle reaches α_{max} the foil angle begins to decrease, transition moves downstream toward P_{10} and the intensity of pressure fluctuations

measured at P_{10} increases again. At a foil angle of about 3.25 degrees ($\omega t = 180$ degrees), the location of transition approximately coincides with P_{10} . A further decrease in foil angle moves the transition location toward the trailing edge and the pressure fluctuations measured at P_{10} begin to decrease. Transition is seen to pass through P_{10} twice in every cycle of oscillation. This results in the appearance of two peaks in pressure fluctuations. The whole sequence of variation in pressure fluctuations with instantaneous foil angle can be best illustrated with large oscillation amplitudes.

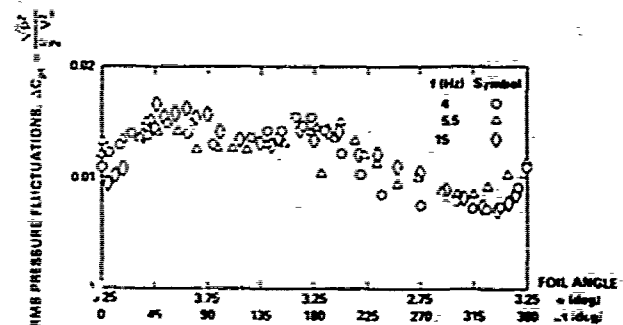


Figure 9 — Measured RMS Pressure Fluctuations at P_{10} with Oscillating Amplitude of 0.5 Degrees and $R_{Re} = 2.4 \times 10^6$

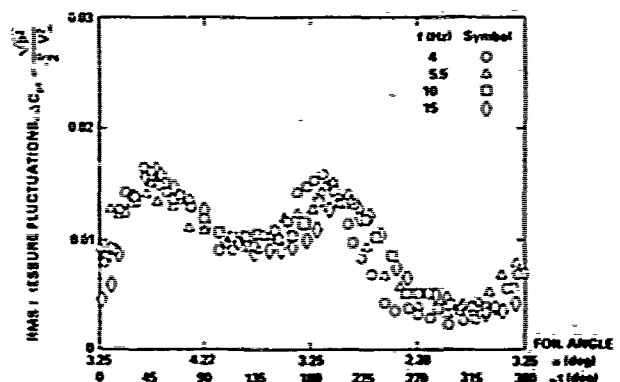


Figure 10 — Measured RMS Pressure Fluctuations at P_{10} with Oscillating Amplitude of 0.97 Degrees and $R_{Re} = 2.4 \times 10^6$

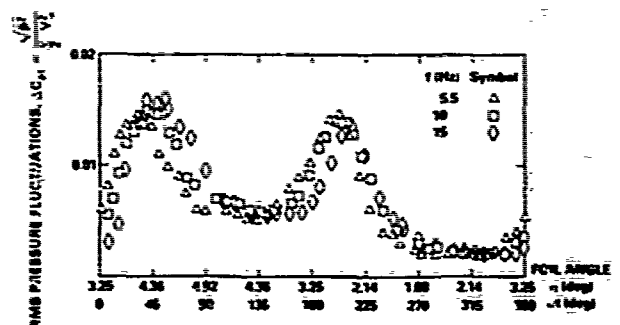


Figure 11 — Measured RMS Pressure Fluctuations at P_{10} with Oscillating Amplitude of 1.57 Degrees and $R_{Re} = 2.4 \times 10^6$

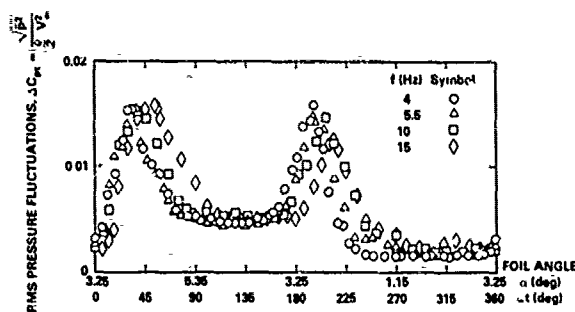


Figure 12 — Measured RMS Pressure Fluctuations at P_{10} with Oscillating Amplitude of 2.1 Degrees and $R_{nc} = 2.4 \times 10^6$

Figures 10, 11, and 12 give the rms pressure fluctuations measured at P_{10} for pitch oscillation amplitudes of 0.97, 1.57 and 2.10 degrees. The general patterns among these figures are similar. Based on this series of experiments, we can make the following observations concerning pressure fluctuations at the 10-percent chord location:

1. At the 10-percent point on the foil, there are two peaks of pressure fluctuations associated with advancing and receding transition locations during each cycle of oscillation. The magnitudes of the rms pressure amplitudes for both advancing and receding boundary layer transitions are the same at low values of oscillation frequency (4 and 5.5 Hz). However, at high values of oscillation frequency (10 and 15 Hz) the magnitude associated with advancing transition is generally greater than the magnitude of the receding transition.
2. The peak values of rms pressure fluctuations associated with advancing transition are seen to be independent of oscillation amplitudes and frequencies and they are almost the same with the values measured under steady conditions. These results provide a contrast between the boundary layer pressure fluctuations and unsteady potential flow pressure distributions. In the previous paper¹⁹ we showed that the magnitudes of dynamic pressure responses of the potential flow (first harmonic) depend linearly on the oscillation amplitudes and vary significantly with oscillation frequencies.
3. In the previous paper,¹⁹ we were able to successfully correlate all of the data on the phase relationship between the peak of dynamic pressure response in the time-varying mean flow and the instantaneous foil angle by use of the reduced frequency parameter K . However, in the present paper, due to the scattering of the data, we can only qualitatively state that the locations of boundary layer transition are delayed with an increase in reduced frequency.
4. Consider pressure fluctuations in the region between $90 < \omega t < 180$ degrees. It was stated previously that in this region, transition is located forward of P_{10} and that the magnitude of pressure fluctuations decreases systematically with increase of oscillation amplitude. Referring to Figure 12, for an oscillation amplitude $\alpha_1 = 2.10$ degrees, the fact that the pressure fluctuations remain at a constant value of $\Delta C_{pt} \approx 0.005$ for $90 < \omega t < 180$, indicates that the flow is fully turbulent in this region. This value ($\Delta C_{pt} \approx 0.005$) measured at P_{10} is smaller than the value ($\Delta C_{pt} \approx 0.008$) measured at P_{25} with turbulent flows at both locations. It is not clear

whether the magnitudes of adverse pressure gradients in these two locations control that difference.

5. Consider the flow characteristics in the region around $270 < \omega t < 360$ degrees. It was stated previously that the transition point is located far aft of P_{10} . With an increase in amplitude of oscillation the flow becomes laminar again at P_{10} as seen in Figures 11 and 12 where the ΔC_{pt} signal observed in the range $270 < \omega t < 360$ may be attributed to noise contamination.

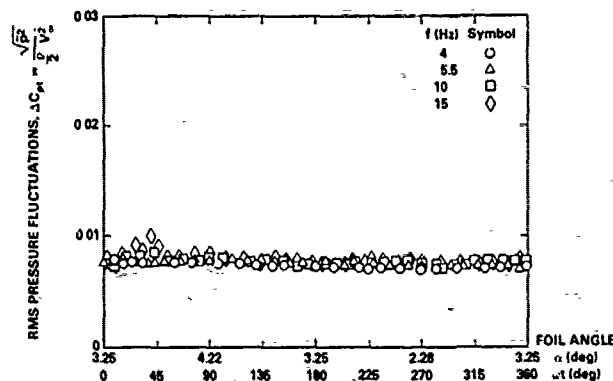


Figure 13 — Measured RMS Pressure Fluctuations at P_{25} with Oscillating Amplitude of 0.97 Degrees and $R_{nc} = 2.4 \times 10^6$

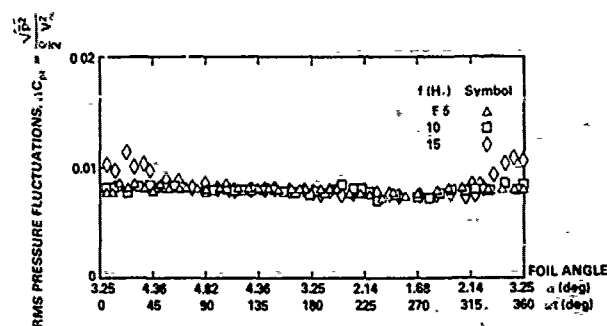


Figure 14 — Measured RMS Pressure Fluctuations at P_{25} with Oscillating Amplitude of 1.57 Degrees and $R_{nc} = 2.4 \times 10^6$

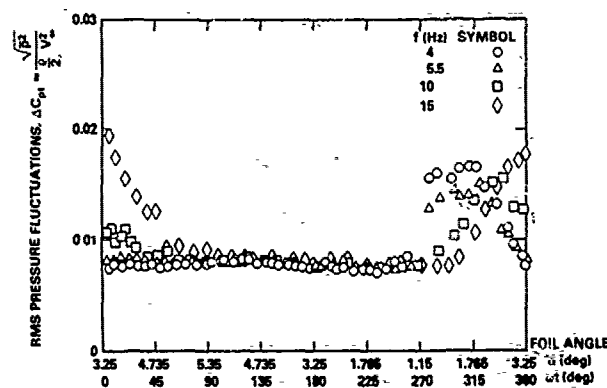


Figure 15 — Measured RMS Pressure Fluctuations at P_{25} with Oscillating Amplitude of 2.1 Degrees and $R_{nc} = 2.4 \times 10^6$

4.3.2 Pressure Fluctuations at 25 Percent Chord Length (P_{25})

Figures 13, 14, and 15 give rms pressure fluctuations at P_{25} for oscillating amplitudes of 0.97, 1.57, and 2.10 degrees, respectively. The flow at P_{25} is fully turbulent with $\alpha_1 = 0.5$ degree (not shown in the figures) throughout each cycle of oscillation. Based on this series of experiments, we can make the following observations:

1. The value of rms pressure fluctuations in a fully established turbulent flow ($\Delta C_{pt} = 0.0089$) is independent of oscillating amplitudes and frequencies. This value is almost identical to the value measured in the steady runs.
2. With an increase in oscillation amplitude, transition moves toward P_{25} in the region $270 < \omega t < 360$. The magnitudes of pressure fluctuations are consequently intensified at P_{25} as seen in Figure 15. Simultaneously, the flow becomes laminar at P_{10} (see Figure 12). Consistent with the observation at P_{10} , the occurrence of peak pressure fluctuations at P_{25} is delayed by increasing the oscillation frequency.
3. The influence of advancing and receding transition points on pressure fluctuations measured at P_{25} is seen to be compatible with the behavior at P_{10} .
4. As shown in Figures 11 to 15 boundary-layer transition in an oscillating foil is delayed by an increase in oscillation frequency. It is further noticed that the pressure fluctuations in a transition region ($\Delta C_{pt} = 0.016$) are greater than in a fully turbulent region ($\Delta C_{pt} = 0.0089$), by a factor of 2. This result is in agreement with the observations in steady runs.

4.4 Reynolds Number Effects

Consider a local Reynolds number R_{nc} based on chord length at the 0.7 propeller radius. Because the local Reynolds number associated with a model propeller may vary from one test facility to another, additional dynamic runs were conducted to examine the effect of Reynolds number on boundary layer pressure fluctuations. These additional runs were made at R_{nc} values of 1.2×10^6 , 1.6×10^6 and 3.6×10^6 . The earlier runs, already discussed, were made at the R_{nc} values of 2.4×10^6 .

4.4.1 Pressure Fluctuations at 10-Percent Chord Length (P_{10})

Figures 16 and 17 give the rms pressure fluctuations measured at P_{10} for $R_{nc} = 1.6 \times 10^6$ and 1.2×10^6 , respectively. The examples given in these two figures are for an oscillation amplitude of $\alpha_1 = 2.10^\circ$. Once again, two peaks in pressure fluctuations associated with advancing and receding transition locations are observed for each cycle of oscillation. The magnitudes of these two peaks are markedly different. Additionally, the rms magnitudes associated with advancing transition are significantly intensified at the lowest value of $R_{nc} = 1.2 \times 10^6$, reaching as high as 10 percent of the dynamic head. The ordinate in Figure 17 has been modified to accommodate the significant increase in magnitude.

The values of cumulative spatial amplification ratio and locations of laminar separation computed for steady flow are shown in Figure 18. It was previously shown in steady runs that the bursting signal associated with natural transition in the present test set-up is best correlated with an amplification ratio of e^6 . The chordwise locations for disturbances to achieve amplification ratios of e^6 are shown in Figure 18 for three values of Reynolds number. Within the range of foil angles tested, laminar boundary-layer stability computations indicate that natural transition will occur earlier

than laminar separation when $R_{nc} = 2.4 \times 10^6$. On the other hand, laminar separation will occur prior to natural transition at foil angles above 4.8 degrees at $R_{nc} = 1.6 \times 10^6$ and 4.2 degrees at $R_{nc} = 1.2 \times 10^6$.

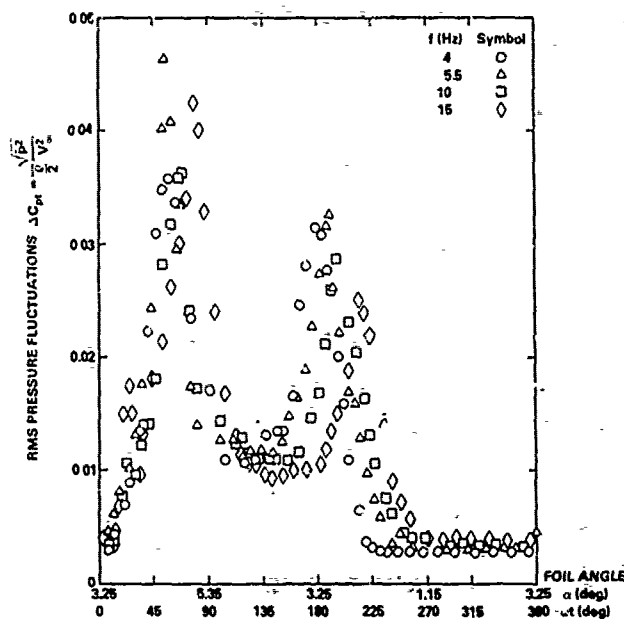


Figure 16 — Measured RMS Pressure Fluctuations at P_{10} with Oscillating Amplitude of 2.1 Degrees and $R_{nc} = 1.6 \times 10^6$

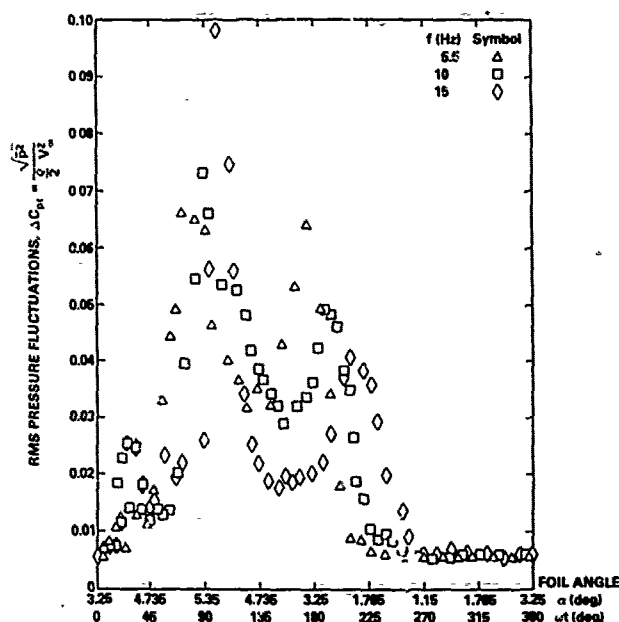


Figure 17 — Measured RMS Pressure Fluctuations at P_{10} with Oscillating Amplitude of 2.1 Degrees and $R_{nc} = 1.2 \times 10^6$

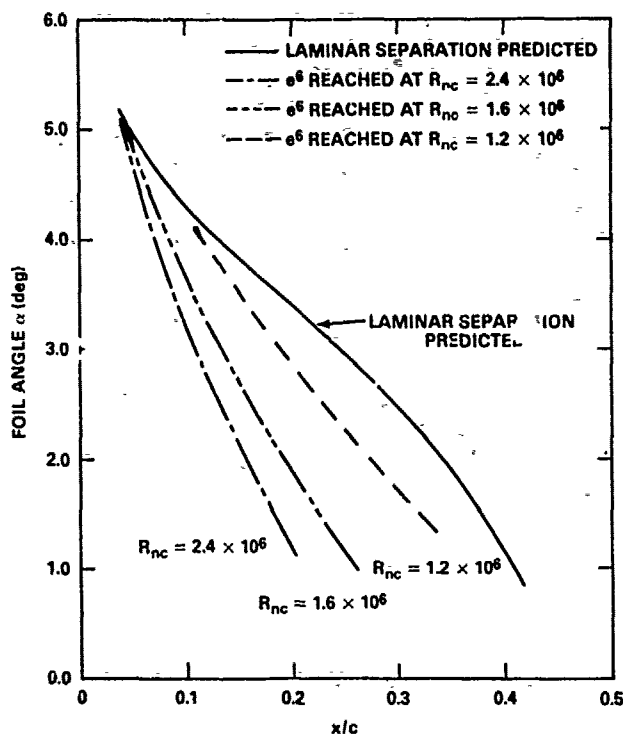


Figure 18 — Chordwise Location of Transition and Laminar Separation Versus α and R_{nc}

In comparison, Figure 12 shows the values of ΔC_{pt} at an oscillation amplitude of 2.1 degrees and $R_{nc} = 2.4 \times 10^6$. The maximum pressure fluctuations associated with advancing transition occur at about $\alpha = 4.5$ degrees for an oscillation frequency of 5.5 Hz. Figures 4 and 18 suggest that the maximum pressure fluctuations are related to a natural transition phenomenon. The rms pressure fluctuations due to advancing transition are $\Delta C_{pt} = 0.016$. On the other hand, at the lowest value of R_{nc} examined, $R_{nc} = 1.2 \times 10^6$, Figure 17 shows that the maximum pressure fluctuations occur at about 5.3 degrees at 5.5 Hz with rms pressure fluctuations reaching to $\Delta C_{pt} = 0.10$. Figure 18 suggests that this peak pressure is associated with laminar separation. The same discussion is applicable to Figure 16. The present result is in agreement with Huang and Hannan's finding that pressure fluctuations associated with laminar separation are much greater than for natural transition.

Figures 12, 16 and 17 show that the occurrence of advancing transition sets in earlier as Reynolds number increases. This trend is in agreement with the boundary layer stability calculations shown in Figure 4. To demonstrate this fact more clearly, the pressure fluctuations measured from three dynamic runs at $R_{nc} = 3.6 \times 10^6$, 2.4×10^6 and 1.2×10^6 are shown in Figure 19. The oscillation amplitude and frequency associated with this example are 0.97 degrees and 10 Hz, respectively. For $R_{nc} = 1.2 \times 10^6$, peak pressure fluctuations never reaches P_{10} . Consequently, only one major peak pressure associated with laminar separation is noticed in the whole cycle of oscillation. In Figure 19 the associated background noise was corrected in such a way that ΔC_{pt} became zero in the laminar flow region. Due to the phase shift associated with the potential flow pressure distributions and the foil angles, the process of becoming laminar flow is achieved at a foil angle greater than α_{min} .

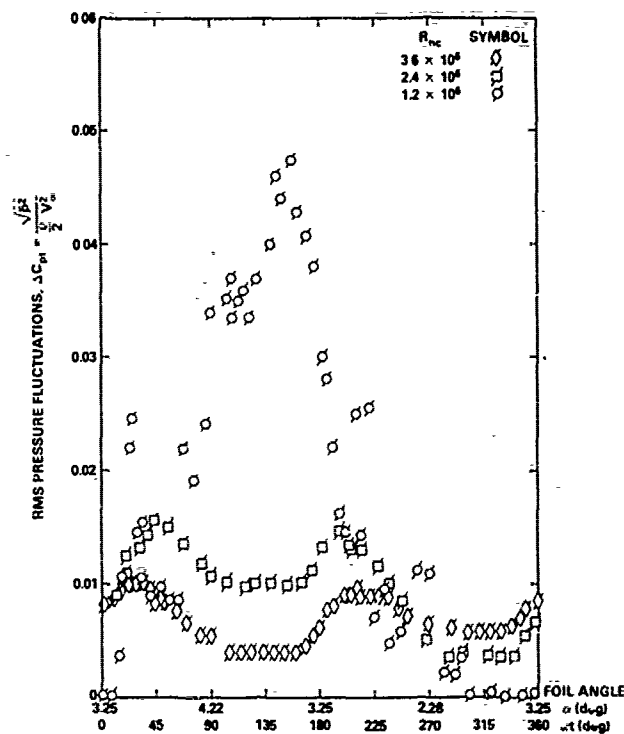


Figure 19 — Measured RMS Pressure Fluctuations at P_{10} with Three Reynolds Numbers and Oscillating Amplitude of 0.97 Degrees ($f = 10$ Hz)

4.4.2 Pressure Fluctuations at 25 Percent Chord Length (P_{25})

Figures 20 and 21 give rms pressure fluctuations measured at P_{25} for $R_{nc} = 1.6 \times 10^6$ and 1.2×10^6 , respectively. These two figures support the previous observation that ΔC_{pt} in a fully established turbulent region is independent of oscillation frequency. The same conclusion may be drawn from Figure 22. Additionally, the values of ΔC_{pt} are seen to increase with decreasing Reynolds numbers.

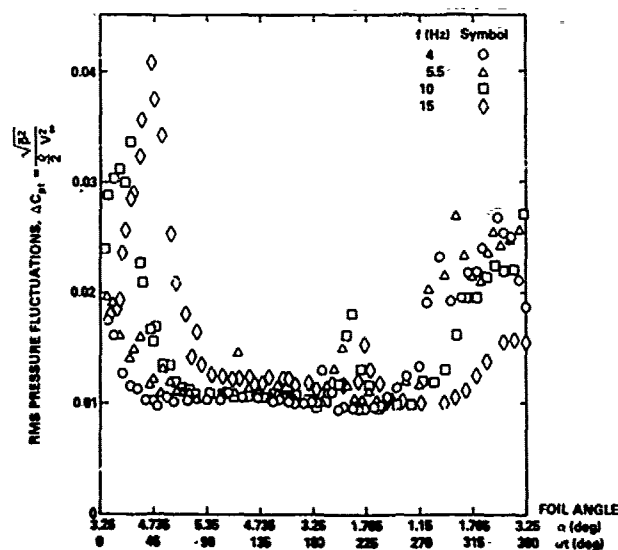


Figure 20 — Measured RMS Pressure Fluctuations at P_{25} with Oscillating Amplitude of 2.1 Degrees and $R_{nc} = 1.6 \times 10^6$

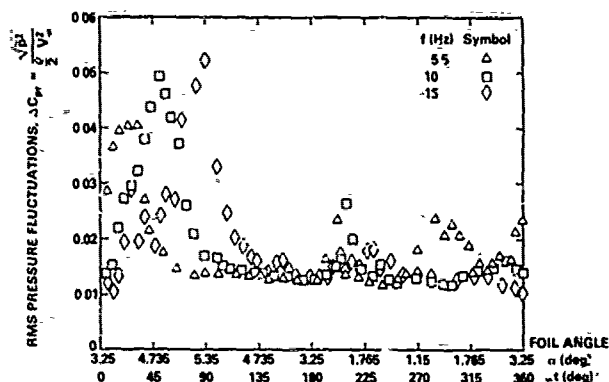


Figure 21 — Measured RMS Pressure Fluctuations at P_{25} with Oscillating Amplitude of 2.1 Degrees and $R_{nc} = 1.2 \times 10^6$

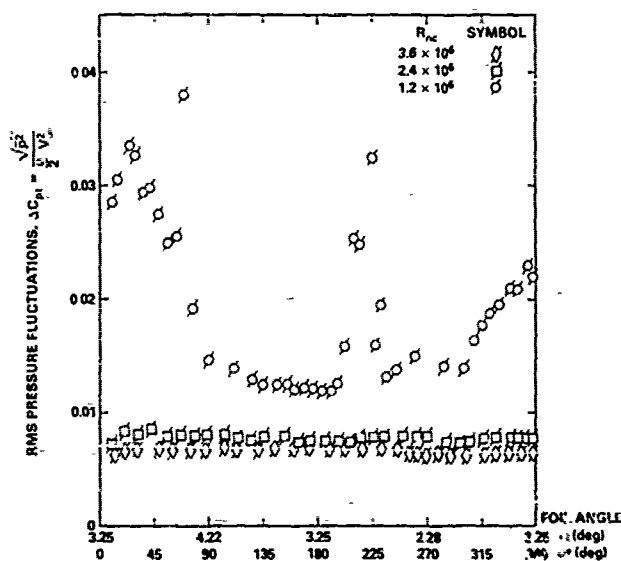


Figure 22 — Measured RMS Pressure Fluctuations at P_{25} with Three Reynolds Numbers and Oscillating Amplitude of 0.97 Degrees ($f = 10$ Hz)

5. INFLUENCE OF HYDROFOIL OSCILLATION ON CAVITATION INCEPTION

Let σ denote the vapor cavitation number:

$$\sigma = \frac{P_{\infty} - P_v}{\frac{1}{2} \rho V_{\infty}^2} \quad (10)$$

where P_v is the vapor pressure. If thermodynamic equilibrium prevails, then

$$\sigma = -C_{p_{min}} \quad (11)$$

at cavitation inception in pure fluids.² In practice significant deviation from this equation has been widely observed in the model cavitation tests. Arndt²⁶ stated that the so-called scale effects are due to deviations in two basic assumptions in-

herent in the cavitation scaling law; namely that the pressure scales with velocity squared and the critical pressure for inception is the vapor pressure. In practice, these two factors are interrelated, since the critical pressure is a function of the time scale of the pressure field. Consequently, depending on the cavitation resistance of the liquid, cavitation inception on the model may occur either (a) at the location of $C_{p_{min}}$, or (b) in the natural transition or laminar separation region of the model.¹²

5.1 Cavitation Inception at $C_{p_{min}}$

We will first consider the case when cavitation inception on the model occurs at the location of $C_{p_{min}}$. Since the magnitude of pressure fluctuations associated with a laminar flow is essentially zero, the present experiments show that the flow at 3.3 percent chord length is laminar for all of the dynamic runs so that $\Delta C_{pt} = 0$. Theoretical computations $\alpha = 3.25^\circ$ show that $C_{p_{min}}$ occurs around $x/c = 0.018$; see Figure 3. Thus, Equation (9) reduces to:

$$\begin{aligned} C_p(t) &= C_{ps} + C_{pu}(t) \\ &= C_{ps} + |\Delta C_{pu}| \sin(\omega t + \phi) \end{aligned} \quad \text{for } 0 \leq x/c \leq 0.033 \quad (12)$$

where $|\Delta C_{pu}|$ and ϕ are the amplitude and phase angle.

An earlier series of experiments conducted by Shen and Peterson¹⁹ reported measured values of the dynamic pressure coefficient $C_p(t)$. Fully wetted, time dependent, experimental pressure distributions were compared with results from Giesing's method²⁷ for calculating unsteady potential flow. Good correlation between the predictions and the experimental measurements was obtained for both dynamic pressure amplitude and phase angle within the range of reduced frequencies investigated ($K = 0.23$ to 2.30).

Let α_{is} and α_{iu} denote the steady and unsteady inception angles, respectively. Let $\xi(K)$ be the ratio of dynamic angular pressure gradient $(dC_p/d\alpha)_u$ versus static angular pressure gradient $(dC_p/d\alpha)_s$ at a given location on the foil, namely:

$$\xi(K) = \left(\frac{dC_p}{d\alpha} \right)_u / \left(\frac{dC_p}{d\alpha} \right)_s \quad (13)$$

Based on Equation (12), Shen and Peterson showed that the unsteady inception angle α_{iu} for a given reduced frequency K can be obtained from:

$$\begin{aligned} \alpha_{iu} &= \alpha_0 + (\alpha_{is} - \alpha_0) \frac{\cos \phi}{\xi} \\ &- \alpha_1 \sin \phi \sqrt{1 - \left(\frac{\alpha_{is} - \alpha_0}{\alpha_1 \xi} \right)^2} \quad (\alpha_1 \neq 0) \end{aligned} \quad (14)$$

The Shen and Peterson¹⁹ experimental results showed that cavitation inception always initiated around $x/c = 0.02$. This result is in good agreement with the assumption that cavitation inception occurs at the location of $C_{p_{min}}$. Due to a phase shift in the pressure distribution, a significant delay in inception of leading edge cavitation was observed with the foil in oscillation. It was concluded¹⁹ that the influence of hydrofoil oscillation on inception at $C_{p_{min}}$ of leading edge sheet cavitation can be reasonably predicted by Equation (14).

It is remarked that full-scale propellers are generally associated with high Reynolds numbers. The locations of boundary layer transition and $C_{p_{min}}$ may be coincided.¹² In this case, the pressure fluctuation term ΔC_p must be added in Equation (12).

5.2 Cavitation Inception at Transition

We now consider the second case, when cavitation inception occurs in the transition region of the model. Aside from the pressure field, cavitation also requires a time scale in order for nuclei to grow. Experiments on axisymmetrical bodies by Arakeri and Acosta,⁹ and Huang⁴ showed that cavitation inception can occur in the boundary layer transition region when the value of $(-C_{ps} - \Delta C_{pt})$ is smaller than $-C_{pmin}$. Huang and Peterson¹² in dealing with steady cavitation assumed that:

$$\sigma_M = -\tilde{C}_{ptr} - \Delta C_{pt}$$

where σ_M and \tilde{C}_{ptr} are model cavitation inception numbers and potential flow pressure coefficients, respectively. On the other hand cavitation inception at full scale was assumed to occur when $\sigma_F = -C_{pmin}$. The difference in these two assumptions is due to time scale associated with bubble growth and flow regime associated with boundary layer pressure fluctuations.

Consider a previously discussed dynamic run with an oscillation amplitude of 1.57 deg, frequency of 5.5 Hz and free-stream speed of 9.75 m/s, corresponding to $R_{nc} = 2.4 \times 10^6$ and $k = 0.432$. This is a typical value of K for a surface ship propeller if the chord length at 0.7 radius is used as the characteristic length. The computed unsteady potential flow pressure coefficients $C_{ps} + C_{pt}(t)$ are shown in Figure 23 for several values of ωt ; see Table 2. The computations are based on Giesing's non-linear unsteady potential flow theory.²⁷ Recall that $\alpha = 3.25 + 1.57 \sin \omega t$. For purposes of comparison, the dynamic and static pressure distributions are shown in Figure 24. This figure gives $\alpha = 4.0$ degrees at $\omega t = 30$ degrees. At the same foil-geometric angle, due to the phase lag, the magnitude of the dynamic pressures is noticeably smaller than the static pressures near the leading edge. This result supports the experimental finding¹⁹ that leading edge sheet cavitation is delayed with the foil in oscillation; see Equation (14). The same trend has also been reported for aerodynamic stall.²⁸

Figure 5c suggests that the flow is in the final stage of transition at 10 percent chord, P_{10} for $R_{nc} = 2.4 \times 10^6$. Figure 11 shows that the pressure fluctuations due to advancing transition attain a maximum value at P_{10} around $\omega t = 30$ degrees. The measured rms pressure fluctuations give $\Delta C_{pt} = 0.0145$. Figure 7 shows that the measured frequently-occurring large negative pressure fluctuations are approximately 2.7 times larger than the rms value in the transition region. If cavitation occurs at the natural transition point of the model, we have $\sigma_M = 0.98 + 0.04 = 1.02$. A much higher value of $\Delta C_{pt} = 0.25$ may be used if transition is caused by laminar separation. This value of σ_M is smaller than the value of $-C_{pmin}$. In the previous cavitation tests reported in Reference 19 with leading edge sheet cavitation, inception always occurred near the location of C_{pmin} . However, cavitation inception on axisymmetric bodies by Arakeri and Acosta, and Huang, did occur in the transition region where the quantity $(-C_{ptr} - \Delta C_{pt})$ is still smaller than $-C_{pmin}$.

Further studies required notably in three areas to determine: (1) why the magnitude of pressure fluctuation terms associated with natural transition and laminar separation are smaller in the present measurements than the values measured by Huang and Hannan¹⁰ with different instruments; (2) theoretically how the location of transition moves periodically with the foil in oscillation; and (3) the validity of the assumption used above that the location of transition measured at a steady mean foil angle is the critical location to trigger cavitation inception when the foil is in oscillation. This assumption requires further verification.

Two different types of cavitation inception phenomena have been considered in this study. One type is associated

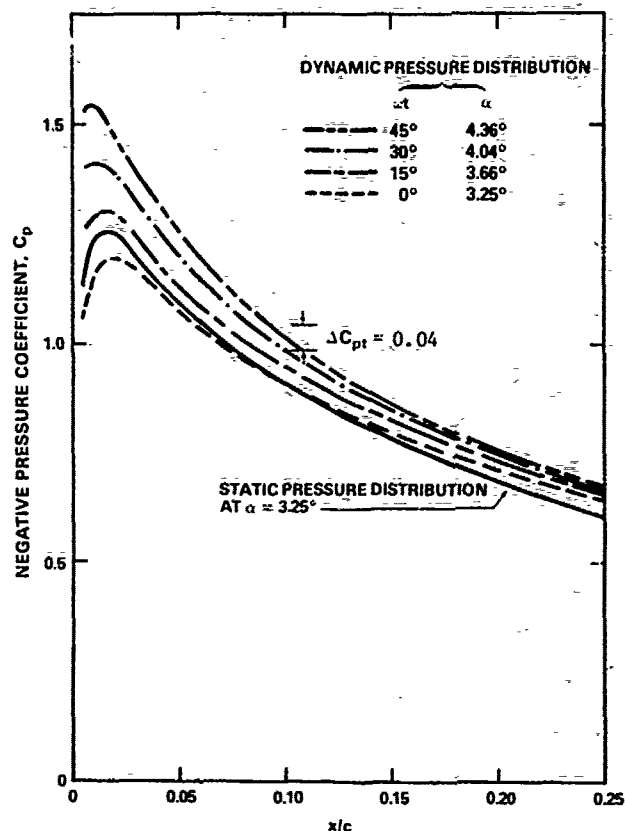


Figure 23 — Dynamic Pressure Distributions with $\alpha = 3.25 + 1.57 \sin \omega t$

x/c	α DEGREE	$\left(\frac{\partial C_p}{\partial t}\right)_x$	$\alpha = 0^\circ$	$C_{pt}(t)$	15°	30°	45°	60°
0.0073	-10.0	21.0	-0.100	0.050	0.197	0.330	0.441	
0.0017	-9.7	18.0	-0.083	0.046	0.171	0.285	0.379	
0.013	-9.1	15.3	-0.066	0.044	0.150	0.246	0.325	
0.026	-8.3	13.0	-0.051	0.042	0.132	0.213	0.280	
0.036	-7.5	11.3	-0.040	0.040	0.118	0.188	0.246	
0.058	-6.2	8.5	-0.021	0.040	0.098	0.149	0.190	
0.100	-2.6	5.2	-0.006	0.031	0.066	0.096	0.120	
0.250	20.7	2.7	0.226	0.043	0.067	0.067	0.073	

$$K = 0.432, V_\infty = 9.75 \text{ m/s}, f = 5.5 \text{ Hz}, \alpha = 3.25 + 1.57 \sin \omega t$$

$$C_{pt}(t) = \left(\frac{\partial C_p}{\partial t}\right)_x \sin \omega t + c_l$$

TABLE 2 — DYNAMIC PRESSURE COEFFICIENT $C_{pt}(t)$

with cavitation inception at the location of C_{pmin} . The other type is associated with cavitation inception in the transition region. Headform experiments by Arakeri and Acosta,⁹ and Huang⁴ were correlated with the second type of cavitation inception. On the other hand, the leading-edge sheet cavitation on a hydrofoil observed by the present authors corresponds to the first type of inception. It is possible that a cambered

hydrofoil with a smaller angle-of-attack, namely with a less severe suction pressure peak, could encounter cavitation inception at transition as observed by Kuiper²⁹ in his model propeller experiments.

Due to the existence of these two different types of cavitation inception, Huang and Peterson¹² computed a significant scale effect. They provided a method for correcting model/full-scale propeller cavitation scaling in a steady flow. The present work is intended to provide needed information to compute cavitation scaling corrections in unsteady flow. It is shown that a diagram of mean pressure coefficient, C_{ps} and low frequency dynamic pressure coefficient, $C_{pd}(t)$ versus chordwise location must be constructed first. Secondly, the location of boundary layer transition with the foil in oscillation must be determined either theoretically or experimentally. Thirdly, the magnitude of boundary layer pressure fluctuations associated with frequently occurring negative pressure is determined. The selection of this magnitude depends on the Reynolds number and amplitude of oscillation angles as shown in Figures 8 to 24.

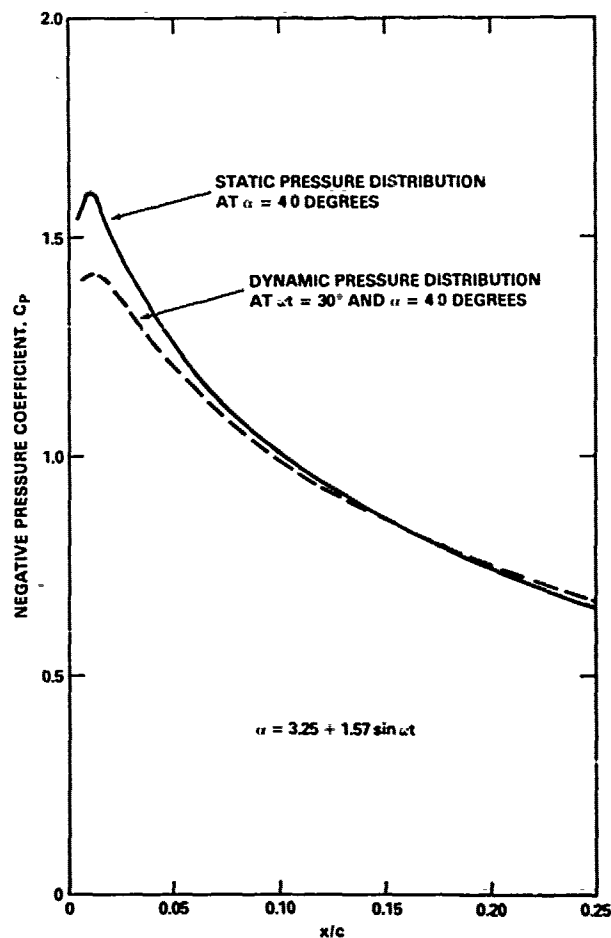


Figure 24 — Comparison of Dynamic and Static Pressure Distributions at $\alpha = 4.0$ Degrees

6. CAVITATION INSTABILITY AND NOISE

6.1 Foil Oscillation and Cloud Cavitation

Unsteady sheet cavitation has been recently reviewed by the 15th ITTC Cavitation Committee. The emphasis of this portion of the paper is on the salient features of sheet cavity instability. Tanibayashi³⁰ provided an insight into the subject with his description of cavitation on a propeller in both uniform and nonuniform flow. He concluded that the presence of sheet and bubble cavitation in nonuniform flow can be predicted by quasi-steady methods, but that the collapse process cannot be predicted. Unfortunately, the details of the collapse process are the controlling factor in erosion, noise, and induced structural vibration. When the sheet cavity produces "cloud" cavitation, erosion, noise and vibration are observed to significantly increase in magnitude. For example, Chiba and Hoshimo³¹ found that the induced hull pressure had superimposed upon it pressure impulses produced by the cloud cavitation formed from the breakup of the propeller sheet cavity. A physical description of cloud cavitation and its formation has been given as follows:¹⁹

1. A large portion of the sheet cavity becomes highly distorted and undergoes a significant increase of overall cavity height in the distorted region.
2. Once this distorted region begins to separate from the main part of the sheet cavity, the upstream portion of the sheet cavity develops a smooth surface and reduced thickness.
3. The separated portion of the sheet develops the appearance of a cloud and moves downstream and expands away from the foil surface. The trailing edge of the smooth-surfaced region then moves downstream, becomes unstable at its trailing edge, and quickly develops the characteristic appearance of the leading edge sheet cavity elsewhere along the span. Alternately, the trailing edge of the smooth portion of the sheet cavity moves upstream to the foil leading edge as the cavity collapses and disappears. Photographs depicting this process can be found in reference 19.

Ito,³² reporting one of the first detailed experiments on the subject, compared unsteady cavitation on propellers in a wake field with pitching three dimensional hydrofoils. He concluded that the reduced frequency for the blade element of a propeller in a wake field has an important influence on the formation of cloud cavitation. The implication of Ito's work is that the wake field and the propeller should be considered together to minimize the adverse effects due to the formation of cloud cavitation.

Later work by Miyata, et al.¹⁶ with oscillating two-dimensional hydrofoils instrumented with surface mounted pressure gages showed that unsteady wing theory was useful in explaining the relationship between the time-dependent pressure distribution and cavitation. They concluded that the cavity collapse process is strongly influenced by the unsteadiness of the pressure field and the reduced frequency associated with foil oscillation.

The present authors¹⁹ provided further details on the instability of sheet cavitation and the formation of cloud cavitation. Their experiments were done with an oscillating two dimensional hydrofoil over a Reynolds number range from 1.2×10^6 to 3.6×10^6 and reduced frequencies up to 2.3. The results indicated that the principal controlling parameters were reduced frequency, K , cavitation number, σ , and foil oscillation amplitude, α_1 . The maximum cavity length, l_m/c , is a function of these three parameters and cannot be predicted on the basis of $K = 0$ conditions. The role of reduced frequency can be demonstrated in the following example.

For constant α , it is possible to have marginal or no cloud cavitation at some finite K , even though it was present at the maximum unsteady angle when $K = 0$.

The importance of reduced frequency has also been shown by Matveyev and Gorshkoff.³³ They reported that for propellers in a uniform flow field, sheet cavitation was less noisy than bubble cavitation. However, when the propellers were in a nonuniform flow field, the sheet cavities become more unsteady and sheet cavitation then was noisier than bubble cavitation. As the work of Matveyev and Gorshkoff points out, it is of crucial importance that a similarity in cavitation time history exist between model and full scale. The noise scaling relations assume this similarity as a foundation and thus the importance of work such as reported by Bark and van Berlekom¹⁸ is reinforced.

Bark and van Berlekom tried to assess the cavitation noise produced by a propeller in nonuniform flow by studying the cavitation noise generated by a pitching hydrofoil. Based on a correlation of photos of cavity life cycles and their associated radiated noise, they concluded that good simulation of specific events is important and that these important events are not generally described by simple parameters (e.g. collapse time, T_c ; variation of cavity area with time, $A(t)$; and maximum cavity volume, V_{max}). One of the most important aspects of the process is the separation of the cavity (i.e. cloud cavitation formation) which must be correctly scaled. They found that cloud cavitation formation can occur at an early stage of the sheet cavity collapse. Furthermore, in agreement with the results of the present authors¹⁹ a combination of long (chordwise) cavity length and high reduced frequency causes extensive cloud cavitation. As can be concluded from the data presented in their paper, large noise transients were associated with the cloud cavitation.

6.2 Cloud Cavitation and Noise

The observed phenomena to be discussed in this paper can best be described by reference to examples shown in Figure 25. Table 3 summarizes all of the parameters associated with the tests reported here. To limit the scope of the test program, air content of the water was not varied. The air content was measured with 70 percent saturation in reference to atmospheric pressure at a water temperature of 22.2°C and tunnel pressure of 103.6 KPa. For a velocity of 16.4 m/s, $\alpha = 3.25 + 0.95 \sin \omega t$, $\sigma = 1.21$, a plot of relative sound power \bar{P}^2 versus K shows the existence of a "noise bucket." When $\alpha = 4.3^\circ$ and $K = 0$, extensive cloud cavitation is developing from the sheet cavity and the noise level is high. As the foil is oscillated, a leading edge sheet cavity experiences an inception, growth, and collapse cycle related to the impressed pressure distribution of the foil. At low reduced frequencies no cloud cavitation is produced, the sheet cavity collapses toward the foil leading edge, and there is a significant reduction in the noise relative to the condition of $\alpha = 4.3$ and $K = 0$. As the reduced frequency is increased further, a cloud cavity is produced during the collapse of the sheet cavity and the noise level again increases due to cloud cavitation collapses. This variation in \bar{P}^2 as a function of foil angle is shown in oscillograph records, Figure 26, for 2 foil oscillation periods and in Figure 27 as a mean noise variation based on the average of the cycles occurring in a 40 second period.

Figure 25 also presents data that demonstrate the strong dependence of \bar{P}^2 on the water velocity. For $\alpha = 4.3$, $K = 0$, and $\sigma = 1.13$, heavy cloud cavitation is present and the noise level increases by a nominal factor of 30 when the velocity is increased from 11.5 m/s to 16.4 m/s. Once foil oscillation starts the amount of cloud cavitation is significantly reduced and the velocity difference appears to have far less impact on the radiated noise. At large K when the cloud cavitation is produced upon sheet cavity desinence, the

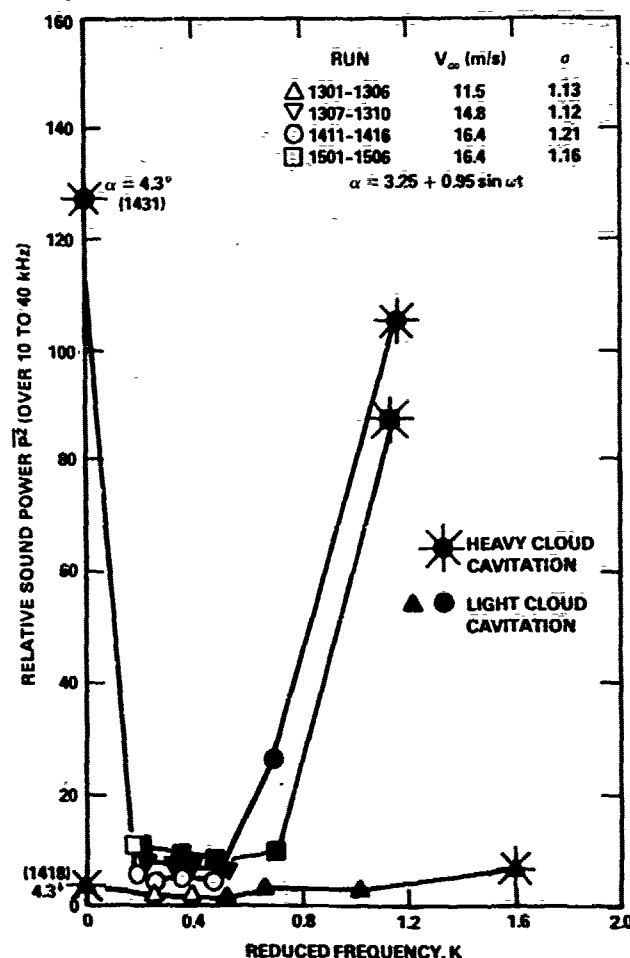


Figure 25 — Influence of V_∞ and Reduced Frequency on Relative Sound Power for $\alpha = 3.25 + 0.95 \sin \omega t$

strong influence of velocity is again apparent.

The influence of velocity on the radiated sound power is just as dramatic when the amplitude of oscillation is increased from 0.95 to 1.55 degrees, keeping σ constant, as shown in Figure 28. There it is seen that with the larger amplitude of oscillation cloud cavitation is present over the full range of reduced frequencies. Although the violence associated with the cloud cavitation at large reduced frequencies limited the ability to collect data, it is apparent that \bar{P}^2 has a strong dependence on K when the cloud cavitation is present. Reference to Figure 25 shows that this latter effect is not present when little or no cloud cavitation is present. The variation in \bar{P}^2 during the foil oscillation period is shown by oscillograph records in Figure 29 and as a mean variation based on the average of the cycles occurring in a 40 second period in Figure 30. Based on the limited data presented in Figures 25 to 30, it appears that for cloud cavitation originating from an unstable leading-edge sheet cavity $\bar{P}^2 \sim V_\infty^8$ when σ , K , α_0 , α_1 are constant.

The maximum cavity volume, area coverage, etc., of a leading edge sheet cavity have in the past been used as parameters associated with the magnitudes of the cavitation noise. Figure 31 presents the maximum length achieved by the leading edge sheet cavity as a function of the reduced frequency. From these data and the noise data of Figure 25, it is clear that the maximum cavity length has essentially no cor-

relation with P^2 . This basic conclusion was also deduced by Bark and Berlekorn.¹⁸ As has already been shown, the principal source of noise is the collapse of the cloud cavitation generated by the sheet cavity. As shown in Figure 32, for small reduced frequencies, the sheet cavity disappears after the radiated noise level has peaked. However, as the reduced frequency is increased and the formation of cloud cavitation is progressively delayed until it occurs at the sheet cavity desinent condition, the peak amplitude of the noise occurs after the sheet cavity has disappeared. In fact, for the reduced frequency of 1.65, maximum radiated noise does not occur until the foil reaches its minimum angle of attack. Before the cloud cavitation completely disappears, the inception of a new leading edge sheet cavity has occurred.

RUN NO.	V_∞ m/s	$R_{sc} \times 10^{-6}$	f Hz	K	α	"1 DEGREE
1301	11.49	2.8	4	0.264	1.13	0.95
1302	11.49	2.8	5.5	0.362	1.13	0.95
1303	11.49	2.8	7.5	0.494	1.13	0.95
1304	11.49	2.8	10	0.659	1.13	0.95
1305	11.49	2.8	15	0.983	1.13	0.95
1306	11.49	2.8	25	1.646	1.13	0.95
1307	14.78	3.6	4	0.205	1.12	1.00
1308	14.78	3.6	5.5	0.282	1.12	1.00
1309	14.78	3.6	7.5	0.384	1.12	1.00
1310	14.78	3.6	10	0.513	1.12	1.00
1401	11.49	2.8	4	0.264	1.13	1.55
1402	11.49	2.8	5.5	0.362	1.13	1.55
1403	11.49	2.8	7.5	0.494	1.13	1.55
1404	11.49	2.8	10	0.659	1.13	1.55
1405	11.49	2.8	15	0.983	1.13	1.55
1406	11.49	2.8	25	1.646	1.13	1.55
1407	14.78	3.6	4	0.205	1.14	1.55
1408	14.78	3.6	5.5	0.282	1.14	1.55
1409	14.78	3.6	7.5	0.384	1.14	1.55
1410	14.78	3.6	10	0.513	1.14	1.55
1411	16.42	4.0	4	0.185	1.21	0.95
1412	16.42	4.0	5.5	0.254	1.21	0.95
1413	16.42	4.0	7.5	0.346	1.21	0.95
1414	16.42	4.0	10	0.461	1.21	0.95
1415	16.42	4.0	15	0.691	1.21	0.95
1416	16.42	4.0	25	1.153	1.21	0.95
1418	11.49	2.8	0	0	1.12	4.25*
1431	16.42	4.0	0	0	1.21	4.30*
1501	16.42	4.0	4	0.185	1.15	0.95
1502	16.42	4.0	5.5	0.254	1.15	0.95
1503	16.42	4.0	7.5	0.347	1.15	0.95
1504	16.42	4.0	10	0.462	1.15	0.95
1506	16.42	4.0	15	0.684	1.15	0.95
1508	16.42	4.0	25	1.153	1.15	0.95
1509	16.42	4.0	0	0	0.93	3.25*
1509	16.42	4.0	0	0	0.93	3.05*
1510	16.42	4.0	4	0.185	0.93	0.32
1511	16.42	4.0	5.5	0.254	0.93	0.32
1512	16.42	4.0	7.5	0.346	0.93	0.32
1513	16.42	4.0	10	0.462	0.93	0.32
1514	16.42	4.0	15	0.684	0.93	0.32
1515	16.42	4.0	25	1.153	0.93	0.32

TABLE 3 - TEST RUN NUMBERS AND ASSOCIATED PARAMETERS

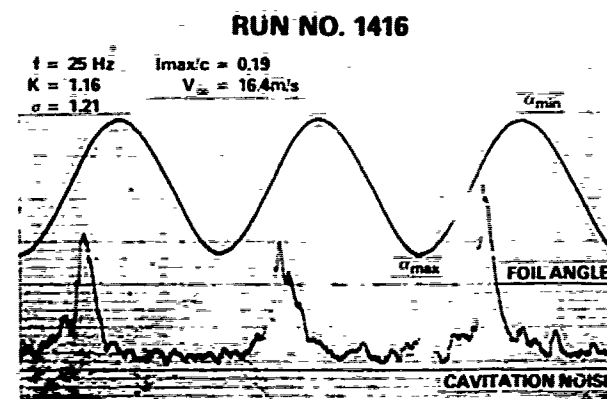
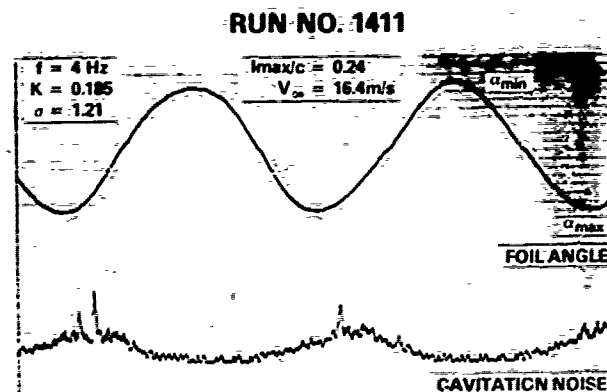


Figure 26 - Cavitation Noise Signals $\sqrt{P^2}$ and Foil Angles for Runs 1411 and 1416, $\alpha = 3.25 + 0.95 \sin \omega t$

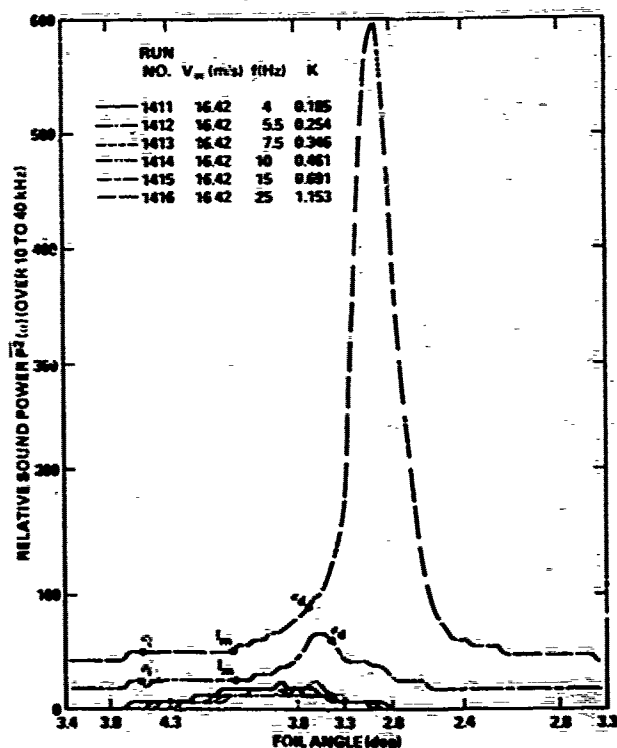


Figure 27 - Relative Sound Power $P^2(\alpha)$ as a Function of Foil Angle for Runs 1411 to 1416 with σ , l_m & α_d for Sheet Cavitation

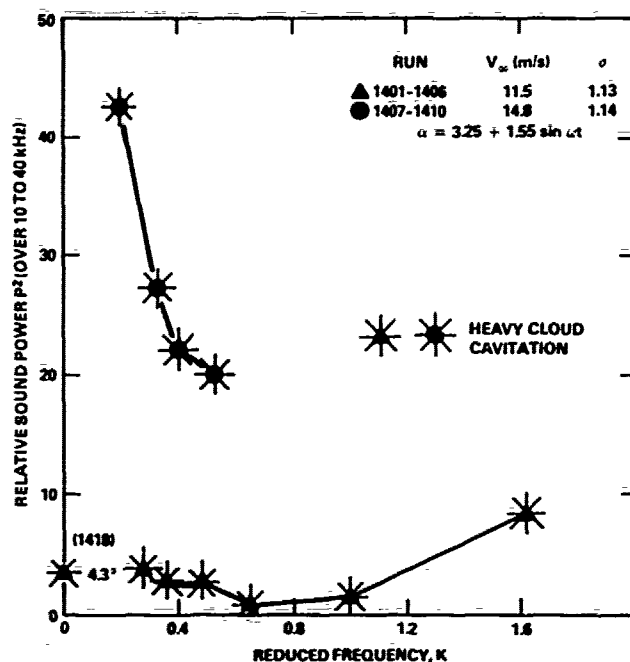


Figure 28 — Influence of V_∞ and Reduced Frequency on Relative Sound Power for $\alpha = 3.25 + 1.55 \sin \omega t$

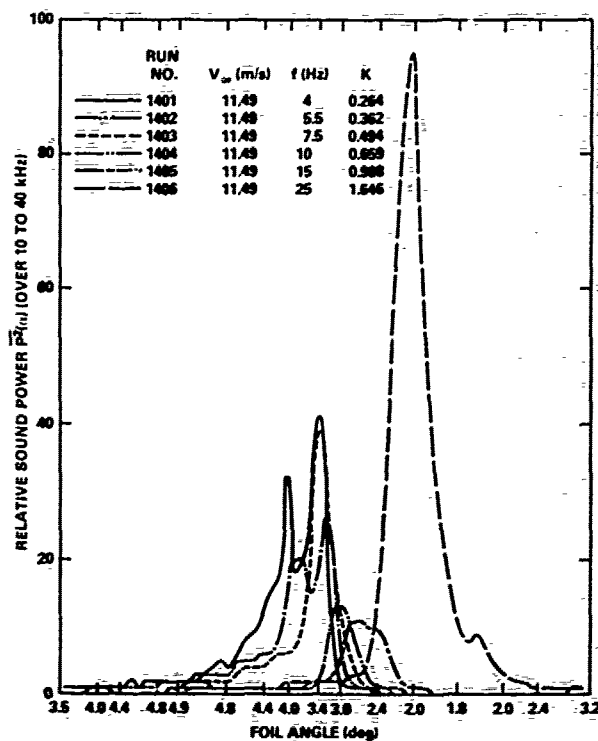


Figure 30 — Relative Sound Power $P_2(a)$ as a Function of Foil Angle for Runs 1401 to 1406

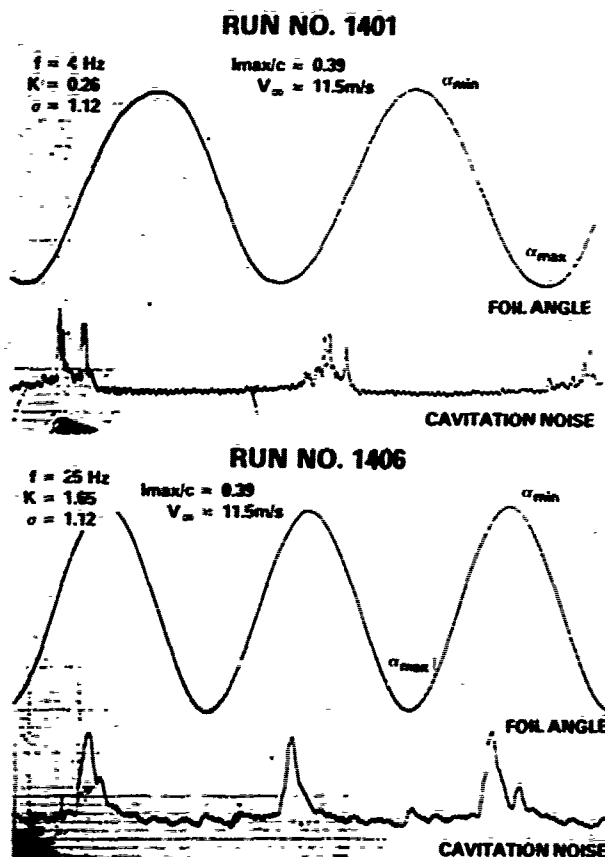


Figure 29 — Cavitation Noise Signals $\sqrt{P_2}$ and Foil Angles for Runs 1401 and 1406, $\alpha = 3.25 + 1.55 \sin \omega t$

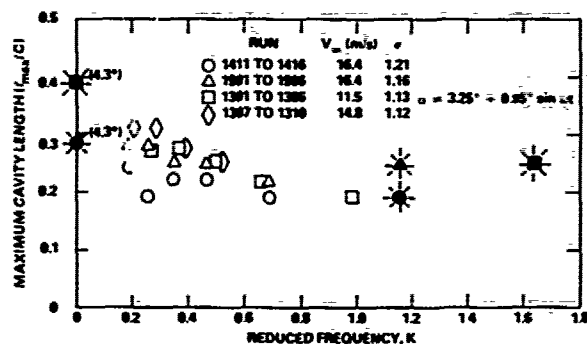


Figure 31 — Measured Maximum Cavity Length vs. Reduced Frequency

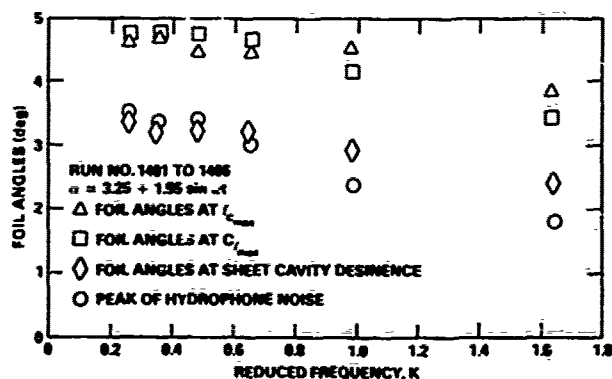


Figure 32 — Measured Foil Angles at Maximum Lift, Maximum Cavity Length, Noise Peak and Leading Edge Sheet Cavity Desirance for Runs 1401 to 1406

In many instances, partially cavitating hydrofoils are subjected to conditions that can be effectively simulated by small amplitude oscillation during which the leading edge sheet cavitation is continuously present. Based on results for the intermittent sheet cavity, it is known that sheet cavity stability, and hence propensity to produce cloud cavitation, is dependent on the reduced frequency. The noise level variation associated with this type of cavitation is found in Figure 33. As with intermittent sheet cavitation, the noise level is low when cloud cavitation is not present. Once cloud cavitation forms, then there is a dramatic increase in the mean sound power level and in the time variation of sound power level, as shown in Figures 33 and 34 respectively. It is apparent from these results that the desinent condition for the sheet cavity is not required for high radiated noise levels, but rather the existence of conditions that promote the formation of cloud cavitation.

If a leading edge sheet cavity is considered as similar to separated flow at a foil's leading edge, then some parallels can be drawn with the vast body of recently published data on dynamic stall. For example, the following conclusion from McAlister and Carr³⁴ closely parallels the description of cavity stability given by Shen and Peterson.¹⁹

"The free-shear layer that was created between the region of reversed flow and the inviscid stream was not stable. This instability resulted in a transformation of the free-shear layer into a multitude of discrete clockwise vortices, 'out of which emerged a dominant "shear-layer vortex".' McAlister and Carr go on to further describe the upstream movement of a thin layer of reversed flow along the foil surface. When this reversed flow reached the leading edge, "... a protuberance appeared over the first 6 percent of the surface in response to the sudden influx of fluid. This protuberance grew and eventually developed into the 'dynamic-stall vortex' that has been observed in high Reynolds number experiments." This dynamic stall vortex moves downstream and away from the airfoil surface just as cloud cavitation does on a cavitating hydrofoil. Furthermore, if the location of flow reversal is plotted against airfoil angle,³⁴ it is seen that foil oscillation (i.e. $K = 0.25$) will suppress the forward movement of the reversed flow region. This is again similar to the cavity stabilization at low reduced frequencies relative to the stationary hydrofoil.

These types of analogies must be used with great care. For example, one of the conclusions of Telonis and Koromilas³⁵ from their study of unsteady laminar separation is that separation is not affected by the amplitude of oscillation. The parallel with cavitating flows may break down here due to, among other reasons, the inertial considerations of growing cavities. Telonis and Koromilas also have concluded that for finite oscillation frequencies, the point of reverse flow is shifted downstream from the quasi-steady location.

7. CONCLUDING REMARKS

Depending on the cavitation resistance of the liquid, cavitation inception on a model may occur either (1) at the location of C_{pmin} , or (2) in the transition region of the model. In the present experiments for a hydrofoil with a large suction peak, leading edge sheet cavitation was observed to take place at C_{pmin} . In this case, the boundary layer was laminar at the location of C_{pmin} and an unsteady potential flow theory was shown to provide a good correlation between prediction and experimental measurements of cavitation inception.

For the case of cavitation occurring in a transition region, it is shown that a diagram of mean pressure coefficient and low frequency dynamic pressure coefficient versus chordwise location must be constructed first. Secondly, the location of boundary layer transition with the foil in oscillation must be determined either theoretically or experimentally. Thirdly, the magnitude of boundary layer pressure fluctua-

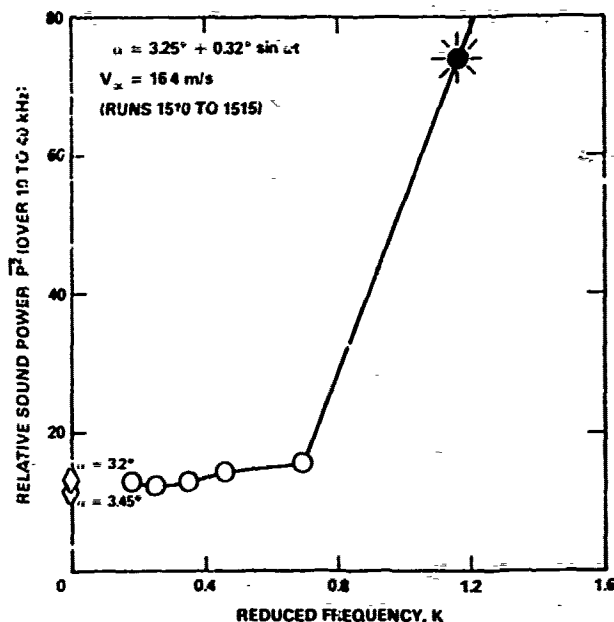


Figure 33 — Relative Sound Pressure \bar{P}_2 Over One Cycle for a Continuously Cavitating Hydrofoil

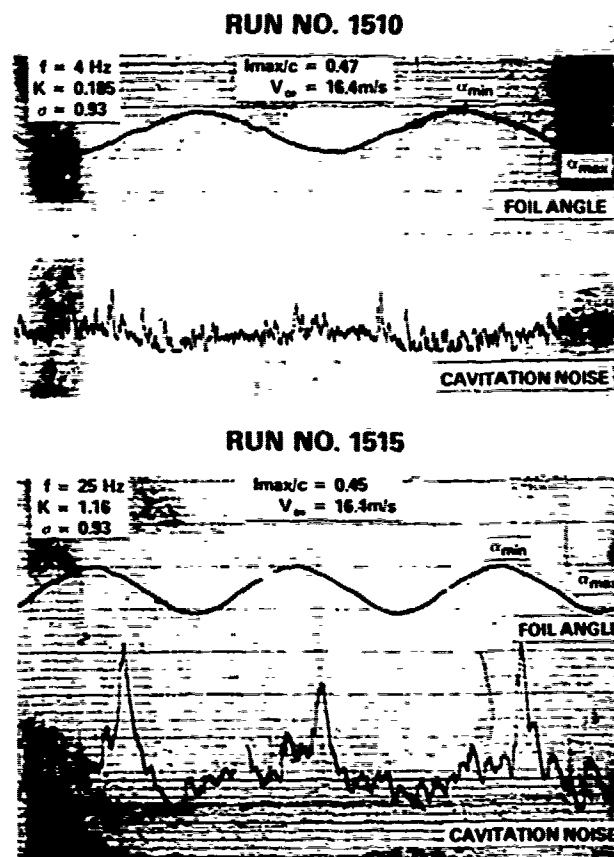


Figure 34 — Cavitation Noise Signals $\sqrt{P_2}$ and Foil Angles for Runs 1510 and 1515, $u = 3.25 + 0.32 \sin \omega t$

tions associated with frequently occurring negative pressure is determined. A general theory on boundary layer properties with a hydrofoil in oscillation is not yet available. The present work is intended to provide some needed information on this subject: the location of transition and the magnitudes of boundary layer pressure fluctuations. Experimental results show:

1. The movement of boundary layer transition can be detected by the measurement of pressure fluctuations on the foil surface.
2. The development of the foil's boundary layer is delayed with an increase in oscillation frequency.
3. The pressure peaks associated with advancing transition are independent of oscillation amplitude and frequency and are identical with the values measured in the transition regions on a stationary foil.
4. In a fully established turbulent region, the magnitudes of pressure fluctuations are independent of oscillation amplitude and frequency and identical with the values measured in the turbulent region on stationary foil.
5. The magnitude of pressure fluctuations measured on the present foil gives higher intensity in a natural transition region than in a fully established turbulent region.

With respect to cavitation noise the following conclusions were derived from water tunnel hydrophone measurements:

1. The stability of a leading edge sheet cavity determines the extent to which cloud cavitation is produced.
2. The formation of cloud cavitation during the life of a sheet cavity is suppressed at small reduced frequencies and correspondingly the noise level is low.
3. At high reduced frequencies, extensive cloud cavitation is formed during the final phase of sheet cavity collapse and the noise level is significantly increased. Thus P^2 plotted against K shows a "noise bucket." When the sheet cavity is continuous with time, a similar noise bucket is apparent.
4. When σ , K , α_0 , and α_1 are kept constant, the influence of velocity on P^2 is found to be very large if

cloud cavitation is present. From the limited data obtained from these experiments, the sound power associated with cloud cavitation appears to vary as:

$$P^2 \sim V^8$$

5. The amplitude of oscillation, α_1 , has an influence on the noise in that larger amplitudes promote cloud cavitation formation. However, the limited data available do not permit more detailed discussion of this point.
6. The cavitation noise generated by a stationary foil is not indicative of the noise produced when the foil is oscillated.
7. The reduced frequency parameter, K , does not include consideration of gross cavity dynamics. Thus it is not sufficient to predict the influence of free-stream velocity on the gross stability of the leading edge sheet cavity. This influence of velocity should be investigated further in order to establish the critical K at which the radiated noise increases at full scale speeds.

The subject of unsteady cavitation is a topic just in its embryonic state of understanding. Recent research confirms what has been empirically observed for many years, that is, reasonable simulation of erosion, noise and induced hull vibration requires a simulation of the flow field in which the hydrofoil or propeller operates. A propeller operated in uniform flow cannot simulate some of the critical details of the inception, growth and collapse process of leading edge sheet cavities.

ACKNOWLEDGMENTS

The authors would like to thank Mr. Robert Pierce for his assistance in the data processing. His development of new techniques allowed a much more quantitative evaluation than would otherwise have been possible. The assistance given by Mrs. Nancy Groves in linear stability calculations of laminar boundary layer is greatly appreciated.

The work reported herein was funded by the Naval Sea Systems Command, Code 035, under the General Hydrodynamic Research Program, Element 61153N, Task Area SR 0230101.

REFERENCES

1. Peterson, F.B. and R.E. Arndt, "Unsteady Cavitation," 19th American Towing Tank Conference, University of Michigan, Ann Arbor, July 1980
2. Acosta, A.J. and B.R. Parkin, "Report of the ATTC Cavitation Inception Committee," 19th American Towing Tank Conference, University of Michigan, Ann Arbor, July 1980
3. Acosta, A.J. and B.R. Parkin, "Cavitation Inception — A Selective Review," *Journal of Ship Research*, Vol. 19, No. 4, Dec. 1975, pp. 193-205
4. Huang, T.T., "Cavitation Inception Observations on Six Axisymmetric Headforms," paper presented at the ASME International Symposium on Cavitation Inception, New York, Dec. 2-7, 1979
5. Rouse, H., "Cavitation in the Mixing Zone of a Submerged Jet," *La Houille Blanche*, Jan.-Feb. 1973, pp. 9-19
6. Daily, J.W. and V.E. Johnson, "Turbulence and Boundary Layer Effects on Cavitation Inception from Gas Nuclei," *Trans. ASME*, Vol. 78, 1956, pp. 1695-1706
7. Levkovskii, Y.L. and A.V. Chalov, "Influence of Flow Turbulence on the Inception and Growth of Cavitation," *Sov. Phys. Acoust.* 24(2), March-April 1978 (English Translation)
8. Arakeri, V.H. and A.J. Acosta, "Viscous Effects in the Inception of Cavitation on Axisymmetric Bodies," *Trans. ASME, Journal of Fluids Engineering*, Vol. 95, Series 1, No. 4, Dec. 1973, pp. 519-527
9. Arakeri, V.H. and A.J. Acosta, "Cavitation Inception Observations on Axisymmetric Bodies at Supercritical Reynolds Numbers," *Trans. ASME, Journal of Fluid Engineering*, Vol. 97, Series 1, 1975, pp. 82-87
10. Huang, T.T. and D.E. Hanran, "Pressure Fluctuation in the Regions of Flow Transition," David W. Taylor Naval Ship Research and Development Center Report 4723, 1976
11. Arakeri, V.H., "A Note on the Transition Observations on an Axisymmetric Body and Some Related Fluctuating Wall Pressure Measurements," *Journal of Fluids Engineering, Trans. ASME*, Vol. 97, Series 1, No. 1, March 1975, pp. 82-86
12. Huang, T.T. and F.B. Peterson, "Influence of Viscous Effects on Model/Full Scale Cavitation Scaling," *Journal of Ship Research*, Vol. 20, Dec. 1976, pp. 215-223
13. DeMetz, F.C., Farabee, T.M. and M.J. Casarella, "Statistical Features of the Intermittent Surface Pressure Field in a Transition Boundary Layer," *Trans. ASME, Non-steady Fluid Dynamics*, Edited by D.E. Crow and J.A. Miller, 1978, pp. 33-39
14. DeMetz, F.C. and M.J. Casarella, "An Experimental Study of the Intermittent Properties of the Boundary Layer Pressure Field During Transition on a Flat Plate," *NSRDC, Report No. 4140*, Nov. 1973
15. Gedney, C.J., "Wall Pressure Fluctuations During Transition on a Flat Plate," M.I.T., Acoustic and Vibration Laboratory Report No. 84618-1, April 1979
16. Miyata, H. et al., "Pressure Characteristics and Cavitation on an Oscillating Hydrofoil," *Journal of the Society of Naval Architects of Japan*, Vol. 132, No. 10, 1972, pp. 107-115
17. Radhi, M.H., "Theoretische und Experimentelle Untersuchung über den Kavitationseinsatz an Schwingenden Tragflügelprofilen," PhD Thesis, Technische Universität Berlin, D83, 1975
18. Bark, G. and W. van Berlekom, "Experimental Investigations of Cavitation Noise," 12th Symposium on Naval Hydrodynamics, Washington, D.C., June 1978, pp. 470-493
19. Shen, Y.T. and F.B. Peterson, "Unsteady Cavitation on an Oscillating Hydrofoil," 12th Symposium on Naval Hydrodynamics, Washington, D.C., June 1978, pp. 362-384
20. Van Houten, R.J., "The Transient Cavitation on a Two-Dimensional Hydrofoil — Comparison of Theory and Experiment," M.I.T. Department of Ocean Engineering, OSF 87268, Aug. 1979
21. Hilten, J.S., et al., "A Simple Sinusoidal Hydraulic Pressure Calibration," National Bureau of Standards, Technical Note 720, 1972
22. Smith, A.M.O., "Transition, Pressure Gradient, and Stability Theory," *Proceeding of the Ninth International Congress of Applied Mechanics*, Brussels, Belgium, Vol. 4, 1957, pp. 234-243
23. Burton, T.E., "Wall Pressure Fluctuations at Smooth and Rough Surfaces Under Turbulent Boundary Layers With Favorable and Adverse Pressure Gradients," M.I.T. Acoustic and Vibration Laboratory, Report No. 70208-9
24. Ludwig, H. and W. Tillman, "Untersuchungen über die Wandschubspannung in Turbulenten Reibungsschichten," *Ing.-Arch* 17, 1949, pp. 288-299, (English translation) in: *NACA TM 1285*, 1950
25. Blake, W.K., "Turbulent Boundary-Layer Wall Pressure Fluctuations on Smooth and Rough Walls," *Journal of Fluid Mechanics*, Vol. 44, 1970, pp. 637-660
26. Arndt, R.E. and W.K. George, "Pressure Fields and Cavitation in Turbulent Shear Flows," 12th Symposium on Naval Hydrodynamics, Washington, D.C., June 1978, pp. 327-339
27. Giesing, J.P., "Two-Dimensional Potential Flow Theory for Multiple Bodies in Small-Amplitude Motion," *Douglass Aircraft Company, Report No. DAC-67028*, April 1968
28. McCroskey, W.J., "Some Current Research in Unsteady Fluid Dynamics — the 1976 Freeman Scholar Lecture," *Trans. ASME, Journal of Fluid Engineers*, Vol. 99, Series 1, March 1977, pp. 8-38
29. Kuiper, G., "Scale Effects on Propeller Cavitation Inception," 12th Symposium on Naval Hydrodynamics, Washington, D.C., June 1978
30. Tanabayashi, H., "Practical Approach to Unsteady Problems of Propellers," *Proc. Second Lips Propeller Symposium*, May 10-11, 1973, pp. 65-78

31. Chiba, N. and T. Hoshino, "Effect of Unsteady Cavity on Propeller Induced Hydrodynamic Pressure," Journal of the Society of Naval Architects of Japan, 139, 1976

32. Ito, T., "An Experimental Investigation into the Unsteady Cavitation of Marine Propellers," Proceedings of IAHR - Symposium on Cavitation and Hydraulic Machinery, Sendai, Japan, 1962

33. Marveyev, G.A. and A.S. Gorshkoff, "Cavitation Noise Modelling at Ship Hydrodynamic Laboratories," 12th Symposium on Naval Hydrodynamics, Washington, D.C., June 1978

34. McAlister, K.W. and L.W. Carr, "Water Tunnel Visualization of Dynamic Stall," Trans. ASME, Journal of Fluids Engineering, 101, September 1979, pp. 276-380

35. Telonis and Koromilas, "Flow Visualization of Transient and Oscillatory Separating Laminar Flow," Trans. ASME, Nonsteady Fluid Dynamics, Edited by D.E. Crow and J.A. Miller, 1978, pp. 21-32

Session III

HULL FORM 1

— WAVE MAKING PROBLEMS —

Chairman

**John V. Wehausen
University of California
Berkeley, California, U.S.A.**

Mathematical Notes on the Two-Dimensional Kelvin-Neumann Problem

Fritz Ursell
University of Manchester
Manchester, United Kingdom

ABSTRACT

A horizontal cylindrical body moves with constant velocity in the horizontal direction normal to its axis, near the free surface of a frictionless fluid under gravity. The calculation of the resulting fluid motion is an important problem of ship hydrodynamics. For a deeply submerged body the condition of constant pressure at the free surface can be linearized, but in some recent calculations the same linearized condition has been used also for partially immersed bodies. The resulting linear boundary-value problem for the velocity potential is the Kelvin-Neumann problem. In the present paper the two-dimensional Kelvin-Neumann problem is studied for the half-immersed circular cylinder. There are arguments which suggest that in the corners the velocity potential must be strongly singular but it is shown here that a unique velocity potential exists which has velocities bounded in the corners and at infinity. Similar results hold for other cross-sections intersecting the horizontal at right angles. It is hoped that the experience gained in this work may be of use in treating the full inviscid three-dimensional problem in the future.

1. INTRODUCTION

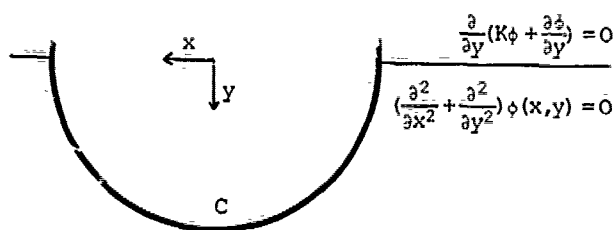
Consider a ship in steady uniform motion on the free surface of a fluid. It is well known that the ship is accompanied by a wave pattern which is steady relative to the ship; the calculation of this wave pattern and of the associated wave resistance is a central problem of ship hydrodynamics which however remains largely unsolved even although drastic simplifying assumptions have been made. Thus viscosity

is often neglected; then the fluid motion is irrotational and can be described by a velocity potential, the stress in the fluid is a pressure which can reasonably be assumed to be constant at the free surface, and the velocity normal to the ship's hull and the velocity normal to the free surface both vanish. Even this simplified problem cannot be solved. One difficulty is that the free surface is not prescribed but must be determined during the solution of the problem. Thus additional simplifying assumptions are usually made. Many calculations are concerned with thin-ship theory: the ship is assumed to be so thin that the fluid motion relative to the ship is nearly a uniform stream. A perturbation procedure can then be set up in terms of a small thickness-parameter. The first approximation is linear and can be treated mathematically, but its range of validity is not adequate for many applications, and various non-linear approximations have therefore been studied. For instance, in some work the full non-linear condition on the ship's hull has been used together with the linearized free-surface condition on the mean free surface. The resulting problem is the so-called Kelvin-Neumann problem with which the present work is concerned. This approximation can be justified when the translating body is deeply submerged, but in recent work it has also been used for bodies intersecting the free surface. It is well understood that the approximation is then inconsistent even for second-order thin-ship theory since only some of the second-order terms are retained while others are omitted. The corrections that are obtained are therefore of doubtful practical value but may perhaps turn out to be in the right direction. It is hoped also that the experience gained in this way may be of use

in treating the full inviscid problem in the future.

In the present work, however, we shall not be concerned with the practical applicability or logical consistency of the Kelvin-Neumann formulation for surface-piercing bodies but merely with certain mathematical aspects of the two-dimensional Kelvin-Neumann problem. The free surface of the fluid is then represented by a horizontal straight line, and the body is represented by a curve intersecting this line. It will also be supposed that the curve intersects the line at right angles. (According to the full theory, the corners would be stagnation points where the perturbation velocity is equal to the forward speed and where any perturbation scheme must fail, but we are ignoring this difficulty.) It has been suggested that any solution of the problem must have singularities in the corners. We shall see, however, that such singularities need not occur if at infinity the velocity potential is allowed to tend to infinity logarithmically with distance. The corresponding velocity components remain finite in the corners and at infinity.

2. STATEMENT OF THE MATHEMATICAL PROBLEM



A cylinder, with its generators horizontal, is moving along the free surface of the fluid with a constant velocity $-U$ which is horizontal and normal to the generators. Take coordinate axes moving with the cylinder, the x -axis horizontal and the y -axis vertical, y increasing with depth. We shall be concerned with motions which are steady relative to the cylinder. The velocity potential is then written in the form $Ux + \phi(x, y)$.

Since the density is assumed uniform we have

$$\left(\frac{\partial^2}{\partial x^2} + \frac{\partial^2}{\partial y^2}\right)\phi(x, y) = 0 \text{ in the fluid.} \quad (2.1)$$

Since there is no flow across the boundary C of the cylinder we have

$$\frac{\partial \phi}{\partial n} = -U \frac{\partial x}{\partial n} \text{ on } C \quad (2.2)$$

where $\partial/\partial n$ denotes differentiation normal to C .

Since there are no waves formed upstream of the cylinder we have

$$\frac{\partial \phi}{\partial x} \rightarrow 0 \text{ and } \frac{\partial \phi}{\partial y} \rightarrow 0 \text{ when } x \rightarrow -\infty. \quad (2.3)$$

As was stated in the introduction, the curve C is assumed to intersect the line

$y = 0$ at right angles. Near the corners, linearization cannot be justified. Let it nevertheless be applied along the whole of the free surface. Then the Kelvin-Neumann free-surface condition is

$$\frac{\partial}{\partial y} \left(K\phi + \frac{\partial \phi}{\partial y} \right) = 0 \text{ on } y = 0 \text{ outside } C, \quad (2.4)$$

where $K = g/U^2$. (See e.g. Wehausen and Laitone, 1960, eqn. 10.15.)

3. THE SOURCE POTENTIAL

In subsequent work we shall need the potential of a source at (ξ, η) . This will be denoted by $G(x, y; \xi, \eta)$; it also depends on K . It is known (Wehausen and Laitone, 1960, eqn. 13.44) that, except for an arbitrary additive constant,

$$\begin{aligned} G(x, y; \xi, \eta) = & \log[K\sqrt{(x-\xi)^2 + (y-\eta)^2}] + \log[K\sqrt{(x-\xi)^2 + (y+\eta)^2}] \\ & + 2 \int_0^\infty \frac{e^{-k(y+\eta)}}{k-K} \cos k(x-\xi) dk \\ & - 2\pi e^{-K(y+\eta)} \sin K(x-\xi) \end{aligned} \quad (3.1)$$

where the symbol \int indicates that the Cauchy Principal Value of the integral is to be taken. Let us write

$$\int_0^\infty \frac{e^{-kY}}{k-K} \cos kX dk = C(KX, KY).$$

Properties of this function are given in the appendix at the end of this paper. In particular,

$$C(K(x-\xi), K(y+\eta)) = \pi e^{-K(y+\eta)} \sin K(x-\xi) + O$$

when $x - \xi \rightarrow -\infty$,

and it follows that there are no wave terms in (3.1) when $x - \xi \rightarrow -\infty$. Thus $G(\quad)$ satisfies the radiation condition. Evidently $G(x, y; \xi, \eta)$ is not symmetric in (x, y) and (ξ, η) . It should be noted that the source potential is logarithmically infinite at infinity, and this suggests that the solution of the boundary-value problem (see §2 above) may have the same property. This will in fact be shown in §4 below. It is important to note that $G(\quad)$ is not an even function of $x - \xi$. It is also important to note that the surface singularity is replaced by a weaker singularity when $\eta \rightarrow 0$. The potential $G(x, y; \xi, 0)$ will be described as a weak surface singularity. Similarly $\partial G(x, y; \xi, 0)/\partial x$ (apparently a horizontal dipole) is a vortex. These results follow from the expansions in the appendix.

4. THE LEAST SINGULAR SOLUTION FOR THE HALF-IMMERSED SEMI-CIRCLE

Consider the potential $\phi(x, y) = \phi(r \sin \theta, r \cos \theta)$, given by the multipole expansion

$$\frac{\phi(x, y)}{Ua} = AP(Kx, Ky) + BQ(Kx, Ky)$$

$$+ \alpha_0 a \left(\frac{\cos \theta}{r} - K \log Kr \right) + \sum_{m=1}^{\infty} \alpha_m a^{2m+1} \left(\frac{\cos(2m+1)\theta}{r^{2m+1}} + \frac{K}{2m} \frac{\cos 2m\theta}{r^{2m}} \right) + \sum_{m=0}^{\infty} \beta_m a^{2m+1} \left(\frac{\sin(2m+1)\theta}{r^{2m+1}} + \frac{K}{2m+1} \frac{\sin(2m+1)\theta}{r^{2m+1}} \right), \quad (4.1)$$

where

$$P(Kx, Ky) = \left\{ \log Kr + \int_0^{\infty} e^{-ky} \cos kx \frac{dk}{K-K} \right\} + \left\{ -\pi e^{-Ky} \sin Kx \right\}, \\ = \{P_1(Kx, Ky)\} + \{P_2(Kx, Ky)\}, \text{ say,}$$

$$\text{and } Q(Kx, Ky) = \left\{ \int_0^{\infty} e^{-ky} \sin kx \frac{dk}{K-K} \right\} + \left\{ e^{-Ky} \cos Kx \right\}, \\ = \{Q_1(Kx, Ky)\} + \{Q_2(Kx, Ky)\}, \text{ say,}$$

where the Cauchy Principal Value is to be taken at $k = K$. (An arbitrary constant may be added to $\varphi(x, y)$.) It is readily verified that each term of the right-hand side of (4.1) satisfies Laplace's equation (2.1) and the free-surface condition (2.4) and the radiation condition (2.3). The boundary condition

$$\left\langle \frac{\partial \varphi}{\partial r} \right\rangle_{r=a} = -U \sin \theta, \quad -\frac{1}{2}\pi \leq \theta \leq \frac{1}{2}\pi, \quad (4.2)$$

on the semi-circle C is also satisfied if the coefficients A, B, α_m, β_m are chosen so that in the interval $-\frac{1}{2}\pi \leq \theta \leq \frac{1}{2}\pi$ the equations

$$A \left\langle a \frac{\partial}{\partial r} P_1 \right\rangle + B \left\langle a \frac{\partial}{\partial r} Q_2 \right\rangle - \alpha_0 (\cos \theta - Ka) - \sum_{m=1}^{\infty} (2m+1) \alpha_m \left\{ \cos(2m+1)\theta + \frac{Ka}{2m+1} \cos 2m\theta \right\} = 0 \quad (4.3)$$

and

$$A \left\langle a \frac{\partial}{\partial r} P_2 \right\rangle + B \left\langle a \frac{\partial}{\partial r} Q_1 \right\rangle + \sin \theta - \sum_{m=0}^{\infty} (2m+2) \beta_m \left\{ \sin(2m+2)\theta + \frac{Ka}{2m+2} \sin(2m+1)\theta \right\} = 0. \quad (4.4)$$

are satisfied. (Here and elsewhere brackets $\langle \rangle$ are used to indicate that r is put equal to a inside the brackets.) The equations (4.3) and (4.4) are series expansions resembling Fourier series. When A and B have been chosen arbitrarily, these equations can be shown to have unique solutions α_m, β_m ($m = 0, 1, 2, \dots$) except possibly at a discrete set of irregular values of Ka , and it can also be shown that $\alpha_m = O(1/m^2)$ and $\beta_m = O(1/m^2)$ by arguments used in the proof of Theorem 1 below. (The details are omitted.) The series for the two velocity components are thus seen to converge only slowly; at $\theta = \pm \frac{1}{2}\pi$ the horizontal velocity is in general discontinuous and the vertical velocity is logarithmically infinite.

We now obtain our principal result.

Theorem 1. The coefficients A and B in (4.1) can be chosen uniquely so that $\alpha_m = O(1/m^3)$ and $\beta_m = O(1/m^3)$. The corresponding solution (the least singular solution) has velocities which are continuous

and bounded in the corners. (Actually it will be seen that $\alpha_m = O(1/m^4)$ and $\beta_m = O(1/m^4)$.)

Proof of Theorem 1. If such a rapidly converging solution exists then we may put $\theta = \frac{1}{2}\pi$ in (4.3) and obtain

$$A \left\langle a \frac{\partial}{\partial r} P_1 \right\rangle_{\frac{1}{2}\pi} + B \left\langle a \frac{\partial}{\partial r} Q_2 \right\rangle_{\frac{1}{2}\pi} - Ka \sum_{m=0}^{\infty} \alpha_m \cos m\pi = 0. \quad (4.5)$$

On combining this with (4.3) we see that

$$A \left\langle a \frac{\partial}{\partial r} P_1 \right\rangle - \left\langle a \frac{\partial}{\partial r} P_1 \right\rangle_{\frac{1}{2}\pi} + B \left\langle a \frac{\partial}{\partial r} Q_2 \right\rangle - \left\langle a \frac{\partial}{\partial r} Q_2 \right\rangle_{\frac{1}{2}\pi} \\ = \sum_{m=0}^{\infty} (2m+1) \alpha_m \left\{ \cos(2m+1)\theta + \frac{Ka}{2m+1} (\cos 2m\theta - \cos m\pi) \right\}. \quad (4.6)$$

Similarly, on putting $\theta = \frac{1}{2}\pi$ in (4.4) we find that

$$A \left\langle a \frac{\partial}{\partial r} P_2 \right\rangle_{\frac{1}{2}\pi} + B \left\langle a \frac{\partial}{\partial r} Q_1 \right\rangle_{\frac{1}{2}\pi} - Ka \sum_{m=0}^{\infty} \beta_m \sin(m+\frac{1}{2})\pi = -1. \quad (4.7)$$

On combining this with (4.4) we see that

$$A \left\langle a \frac{\partial}{\partial r} P_2 \right\rangle - \sin \theta \left\langle a \frac{\partial}{\partial r} P_2 \right\rangle_{\frac{1}{2}\pi} + B \left\langle a \frac{\partial}{\partial r} Q_1 \right\rangle - \sin \theta \left\langle a \frac{\partial}{\partial r} Q_1 \right\rangle_{\frac{1}{2}\pi} \\ = \sum_{m=0}^{\infty} (2m+2) \beta_m \left\{ \sin(2m+2)\theta + \frac{Ka}{2m+2} (\sin(2m+1)\theta - \sin \theta \sin(m+\frac{1}{2})\pi) \right\} \quad (4.8)$$

We shall now verify that the solutions of (4.6) and (4.8) satisfy $\alpha_m = O(1/m^4)$ and $\beta_m = O(1/m^4)$, by transforming (4.6) and (4.8) into systems of simultaneous equations. Consider e.g. (4.8). Multiply in turn by the complete set $\sin(2l+2)\theta$ ($l = 0, 1, 2, \dots$) and integrate over $(-\frac{1}{2}\pi, \frac{1}{2}\pi)$. An infinite set of equations of the form

$$(2l+2) \beta_l + Ka \sum_{m=0}^{\infty} a_{lm} (2m+2) \beta_m = c_l, \quad l = 0, 1, 2, \dots, \quad (4.9)$$

is obtained where c_l is the Fourier coefficient of the left-hand side of (4.8) and where the coefficients a_{lm} can be found explicitly by elementary integrations. Write (4.9) in the form

$$(2l+2) \beta_l + Ka \sum_{m=0}^{\infty} \left(\frac{2l+2}{2m+2} \right)^2 a_{lm} (2m+2) \beta_m = (2l+2) c_l. \quad (4.10)$$

By integration by parts it can be shown that $c_l = O(1/l^3)$, thus $\sum (2l+2)^4 c_l^2$ is convergent; and it can also be shown that

$\sum \left(\frac{2l+2}{2m+2} \right)^2 a_{lm}^2$ is convergent. The theory of

the system (4.10) is therefore analogous to the theory of Fredholm integral equations of the second kind. It follows that (except possibly at a set of irregular values of Ka) there is a unique solution (β_l) such that

$\sum (2l+2)^5 \beta_l^2$ is convergent. To show that $\beta_l = O(1/l^4)$, note from (4.10) that

$$\left| (2\ell+2)^3 \beta_\ell - (2\ell+2)^2 c_\ell \right|^2 = (Ka)^2 \left| \sum_{m=0}^{\infty} \left(\frac{2\ell+2}{2m+2} \right)^2 a_{\ell m} (2m+2)^3 \beta_m \right|^2$$

$$\leq (Ka)^2 \left(\sum_{m=0}^{\infty} \left(\frac{2\ell+2}{2m+2} \right)^4 a_{\ell m}^2 \right) \left(\sum_{m=0}^{\infty} (2m+2)^6 \beta_m^2 \right),$$

by Cauchy's inequality,

$$\leq \text{const.} \sum_{m=0}^{\infty} \left(\frac{2\ell+2}{2m+2} \right)^4 a_{\ell m}^2.$$

It can be shown that $\sum_{m=0}^{\infty} \left(\frac{2\ell+2}{2m+2} \right)^4 a_{\ell m}^2 = O(1/\ell^2)$, and it follows that $\beta_\ell = O(1/\ell^4)$. Evidently, from (4.8), β_ℓ is of the form

$$\beta_\ell = A\beta_\ell(P_2) + B\beta_\ell(Q_1), \quad (4.11)$$

in an obvious notation, where $\beta_\ell(P_2)$ and $\beta_\ell(Q_1)$ are independent of A and B , and where $\beta_\ell(P_2) = O(1/\ell^4)$ and $\beta_\ell(Q_1) = O(1/\ell^4)$. Thus, from (4.7),

$$A \left\{ \left\langle a \frac{\partial}{\partial r} P_2 \right\rangle_{\frac{1}{2}\pi} - Ka \sum_{m=0}^{\infty} \beta_m(P_2) \sin(m+\frac{1}{2})\pi \right\} \quad (4.12)$$

$$+ B \left\{ \left\langle a \frac{\partial}{\partial r} Q_1 \right\rangle_{\frac{1}{2}\pi} - Ka \sum_{m=0}^{\infty} \beta_m(Q_1) \sin(m+\frac{1}{2})\pi \right\} = -1.$$

Similarly, from (4.6),

$$a_\ell = A\alpha_\ell(P_1) + B\alpha_\ell(Q_2), \quad (4.13)$$

where $\alpha_\ell(P_1) = O(1/\ell^4)$ and $\alpha_\ell(Q_2) = O(1/\ell^4)$, thus, from (4.5),

$$A \left\{ \left\langle a \frac{\partial}{\partial r} P_1 \right\rangle_{\frac{1}{2}\pi} - Ka \sum_{m=0}^{\infty} \alpha_m(P_1) \cos m\pi \right\} \quad (4.14)$$

$$+ B \left\{ \left\langle a \frac{\partial}{\partial r} Q_2 \right\rangle_{\frac{1}{2}\pi} - Ka \sum_{m=0}^{\infty} \alpha_m(Q_2) \cos m\pi \right\} = 0.$$

From (4.12) and (4.14) the values of A and B are uniquely determined except when the determinant of the system (4.12), (4.14) vanishes; hence α_ℓ and β_ℓ are determined from (4.13) and (4.11); hence $\phi(x, y)$ is determined from (4.1) except for an arbitrary additive constant. It is obvious that the potential $\phi(x, y)$ does indeed satisfy the boundary condition (4.2). It remains to be verified that the determinant of the system (4.12), (4.14) does not vanish identically; this can be done by considering the system for small Ka . Thus the procedure described above is effective except possibly at a discrete set of values of Ka and provides a construction for the least singular potential $\phi(x, y)$. It can be shown that for general values of Ka the logarithmic terms in (4.1) do not cancel, thus this potential is logarithmically infinite at infinity.

This concludes the proof of Theorem 1.

5. REPRESENTATION BY SOURCES

The method of multipoles, described in §4 above, is appropriate for the half-

immersed semi-circle; for other cross-sections it can be generalized by conformal mapping (see e.g. Ursell 1949 for the corresponding construction of wave-free potentials at zero mean speed). An alternative approach uses distributions of wave sources over the boundary curve C but additional terms are needed at the ends. Thus for the half-immersed semi-circle we find

Theorem 2. The least singular solution (obtained in Theorem 1 above) can be represented in the form

$$\phi(x, y) = U \int_{-\frac{1}{2}\pi}^{\frac{1}{2}\pi} u(\theta) G(x, y; a \sin \theta, a \cos \theta) d\theta \quad (5.1)$$

$$- \frac{U u(\frac{1}{2}\pi)}{K} G(x, y; a, 0) \quad (5.2)$$

$$- \frac{U u(-\frac{1}{2}\pi)}{K} G(x, y; -a, 0), \quad (5.3)$$

where the coefficients $u(\frac{1}{2}\pi)$ in (5.2) and $u(-\frac{1}{2}\pi)$ in (5.3) are the limits of the source-density function $u(\theta)$ when $\theta \rightarrow \pm\frac{1}{2}\pi$. A corresponding result holds for the least singular solution exterior to an arbitrary boundary curve C intersecting the horizontal at right angles.

To motivate the following proof let us recall the corresponding results in potential theory and in acoustics (Lamb 1932, §58 and §290). These are obtained from Green's theorem which states that the exterior solution $\phi(x, y)$ can be represented by sources of density $(2\pi)^{-1} \partial \phi / \partial n$ and normal dipoles of density $-(2\pi)^{-1} \phi$ distributed over C . Consider now the interior potential ϕ_{int} such that $\phi_{\text{int}} = \phi$ on C ; let the corresponding normal velocity on C be denoted by $\partial \phi_{\text{int}} / \partial n$. Then, by Green's theorem, sources of density $(2\pi)^{-1} \partial \phi_{\text{int}} / \partial n$ and normal dipoles of density $-(2\pi)^{-1} \phi_{\text{int}}$ generate a null field exterior to C . By subtraction it follows that the exterior solution $\phi(x, y)$ can be represented by a source distribution of density $(2\pi)^{-1} \partial (\phi - \phi_{\text{int}}) / \partial n$ over C .

Similar ideas will now be applied to the Kelvin-Neumann problem.

Proof of Theorem 2. (Not all the details will be given.) Apply Green's theorem to the least singular solution $\phi(x, y)$ and to the reversed source function $\bar{G}(x, y; \xi, \eta) = G(\xi, \eta; x, y)$ in the region bounded by the contour C , by a large semi-circle $S(R)$, and by the two segments of the x -axis between C and $S(R)$. (Note that ϕ and \bar{G} involve arbitrary additive constants.) It is assumed that (ξ, η) lies in this region. Then we find that

$$-2\pi \phi(\xi, \eta) = \int_C \left\{ \phi(x, y) \frac{\partial}{\partial n} \bar{G}(x, y; \xi, \eta) - \bar{G}(x, y; \xi, \eta) \frac{\partial}{\partial n} \phi(x, y) \right\} ds(x, y)$$

$$+ \int_{S(R)} \left\{ \right\} ds(x, y)$$

$$+ \int_a^R \left(\phi \frac{\partial \bar{G}}{\partial y} - \bar{G} \frac{\partial \phi}{\partial y} \right)_{y=0} dx + \int_{-R}^{-a} \left(\phi \frac{\partial \bar{G}}{\partial y} - \bar{G} \frac{\partial \phi}{\partial y} \right)_{y=0} dx.$$

$$\begin{aligned} \text{Also } & \int_a^R \left(\phi \frac{\partial \bar{G}}{\partial y} - \bar{G} \frac{\partial \phi}{\partial y} \right) dx \\ &= -\frac{1}{K} \int_a^R \left(\phi \frac{\partial^2 \bar{G}}{\partial y^2} - \bar{G} \frac{\partial^2 \phi}{\partial y^2} \right) dx \text{ from the free-surface condition} \\ &= \frac{1}{K} \int_a^R \left(\phi \frac{\partial^2 \bar{G}}{\partial x^2} - \bar{G} \frac{\partial^2 \phi}{\partial x^2} \right) dx \text{ from Laplace's equation,} \\ &= \frac{1}{K} \left[\phi \frac{\partial \bar{G}}{\partial x} - \bar{G} \frac{\partial \phi}{\partial x} \right]_{(a,0)}^{(R,0)} \end{aligned} \quad (5.4)$$

and similarly

$$\int_{-R}^{-a} \left(\phi \frac{\partial \bar{G}}{\partial y} - \bar{G} \frac{\partial \phi}{\partial y} \right) dx = \frac{1}{K} \left[\phi \frac{\partial \bar{G}}{\partial x} - \bar{G} \frac{\partial \phi}{\partial x} \right]_{(-R,0)}^{(-a,0)}$$

Thus

$$\begin{aligned} -2\pi\phi(\xi, \eta) &= \int_C \left\{ \phi \frac{\partial \bar{G}}{\partial n} - \bar{G} \frac{\partial \phi}{\partial n} \right\} ds + \frac{1}{K} \left[\phi \frac{\partial \bar{G}}{\partial x} - \bar{G} \frac{\partial \phi}{\partial x} \right]_{(a,0)}^{(-a,0)} \\ &+ \int_{S(R)} \left\{ \right\} ds - \frac{1}{K} \left[\phi \frac{\partial \bar{G}}{\partial x} - \bar{G} \frac{\partial \phi}{\partial x} \right]_{(R,0)}^{(-R,0)} \end{aligned} \quad (5.5)$$

let $\phi_{\text{int}}(x, y)$ denote the least singular interior potential satisfying $\phi_{\text{int}} = \phi$ on C . (The construction of this potential involves the superposition of regular wave potentials and resembles the construction of the least singular exterior potential. The details are omitted.) Apply Green's theorem to ϕ_{int} and to \bar{G} in the interior region bounded by C and by the x -axis. Then

$$\begin{aligned} 0 &= \int_C \left\{ \phi_{\text{int}} \frac{\partial \bar{G}}{\partial n} - \bar{G} \frac{\partial \phi_{\text{int}}}{\partial n} \right\} ds \\ &- \int_a^R \left(\phi_{\text{int}} \frac{\partial \bar{G}}{\partial y} - \bar{G} \frac{\partial \phi_{\text{int}}}{\partial y} \right) dx \\ &= \int_C \left\{ \right\} ds - \left[\phi_{\text{int}} \frac{\partial \bar{G}}{\partial x} - \bar{G} \frac{\partial \phi_{\text{int}}}{\partial x} \right]_{(a,0)}^{(-a,0)} \end{aligned} \quad (5.6)$$

as in (5.5) above. On subtracting (5.6) from (5.5) we find that

$$\begin{aligned} -2\pi\phi(\xi, \eta) &= - \int_C \frac{\partial}{\partial n} (\phi - \phi_{\text{int}}) \bar{G}(x, y; \xi, \eta) ds(x, y) \\ &+ \frac{1}{K} \left[\frac{\partial}{\partial x} (\phi - \phi_{\text{int}}) \bar{G} \right]_{(a,0)}^{(-a,0)} \end{aligned}$$

$$+ \int_{S(R)} \left\{ \right\} ds - \frac{1}{K} \left[\phi \frac{\partial \bar{G}}{\partial x} - \bar{G} \frac{\partial \phi}{\partial x} \right]_{(R,0)}^{(-R,0)} \quad (5.7)$$

Write

$$u(\theta) = \frac{2\pi}{U} \frac{\partial}{\partial n} (\phi - \phi_{\text{int}}), \quad (5.8)$$

where the normal gradients are to be evaluated at $(x, y) = (a \sin \theta, a \cos \theta)$; also note that $\bar{G}(x, y; \xi, \eta) = G(\xi, \eta; x, y)$. Then it is seen that (5.7) is equivalent to Theorem 2, except for the two terms arising from the large semi-circle. It can be shown that these contribute at most an additive constant. This concludes the proof of Theorem 2.

Note that for reasons of brevity we have omitted proofs that the least singular interior potential exists, and that the large semi-circle contributes at most a constant to the potential.

We can now see how the least singular potential can be constructed by means of an integral equation. Write

$$\begin{aligned} \phi(x, y) &= U \int_{-\frac{1}{2}\pi}^{\frac{1}{2}\pi} u(\theta) G(x, y; a \sin \theta, a \cos \theta) d\theta \\ &- UapG(x, y; a, 0) - UaqG(x, y; -a, 0), \end{aligned}$$

where the last two terms (apparently wave sources) are actually weak surface singularities. The function $u(\theta)$ and the constants p and q are to be determined. On applying the boundary condition (4.2) we find that

$$\begin{aligned} u(\alpha) &+ \int_{-\frac{1}{2}\pi}^{\frac{1}{2}\pi} u(\theta) \left\langle a \frac{\partial}{\partial r} G(r \sin \alpha, r \cos \alpha; a \sin \theta, a \cos \theta) \right\rangle d\theta \\ &= p \left\langle a \frac{\partial}{\partial r} G(r \sin \alpha, r \cos \alpha; a, 0) \right\rangle \\ &+ q \left\langle a \frac{\partial}{\partial r} G(r \sin \alpha, r \cos \alpha; -a, 0) \right\rangle \\ &- \sin \alpha. \end{aligned} \quad (5.9)$$

This is a Fredholm equation of the second kind, and (except possibly at a discrete set of irregular values of Ka) there is a unique solution which is evidently of the form

$$u(\theta) = pu_+(\theta) + qu_-(\theta) + u_0(\theta), \quad (5.10)$$

where the functions $u_+(\theta)$, $u_-(\theta)$, $u_0(\theta)$ are the solutions corresponding to the three known functions on the right-hand side of (5.9). From Theorem 2 we have $p = u(\frac{1}{2}\pi)/Ka$ and $q = u(-\frac{1}{2}\pi)/Ka$; thus, on putting $\theta = \frac{1}{2}\pi$ and $\theta = -\frac{1}{2}\pi$ in (5.10) we see that

$$Kap = pu_+(\frac{1}{2}\pi) + qu_-(\frac{1}{2}\pi) + u_0(\frac{1}{2}\pi),$$

$$\text{and } Kaq = pu_+(-\frac{1}{2}\pi) + qu_-(-\frac{1}{2}\pi) + u_0(-\frac{1}{2}\pi).$$

From these equations the two constants p and q can be found, and the source density is

then given uniquely by (5.10).

If p and q are instead given arbitrary values, then the solution (5.10) can be shown to have unbounded vertical velocities in the corners. This corresponds to the solution (4.1) above when A and B are given arbitrary values.

6. DISCUSSION

It has been shown that for the half-immersed semi-circle the Kelvin-Neumann problem has a two-parameter set of solutions if the singularities in the two corners are at most weak surface singularities. There is just one solution, the least singular solution, for which the velocity is bounded in both corners. It has been shown how this solution can be constructed, either by the method of multipoles or by a distribution of wave sources over the boundary. (The source density satisfies an integral equation (5.9) involving additional end-contributions.) There is however no obvious physical reason why the condition of boundedness should be imposed in the corners. In the physical problem the perturbation velocity is in fact not small in the corners, and the linearization is not valid there. It would thus be equally reasonable to look for solutions of the perturbation equations which have weak or strong singularities in the corners but there is then no obvious way of deciding what singularities would be appropriate.

In an earlier unpublished version (1978) of this work the representation (5.10) was used with $p = q = 0$, and it was shown that the vertical velocity in the corners is then unbounded. This choice is arbitrary, as was pointed out to me by Mr. Katsuo Suzuki, whose criticism led me to a more thorough study of the problem. Suzuki's own choice of p and q is based on additional physical conditions and does not lead to the least singular solution. Although there is no obvious physical reason why the least singular solution should be preferred in two dimensions there may well be physical reasons why a corresponding boundedness condition should be applied in three dimensions, and this is one of the motivations of the present study.

The perturbation potential $\phi(x, y)$ becomes logarithmically unbounded at infinity; the velocities due to the logarithmic terms tend to 0 at infinity. There appears to be no physical reason for excluding such a solution; it will be recalled that the total potential is linearly unbounded at infinity.

It is sometimes stated that the perturbation potential must have strong singularities in the corners; it has been seen in the present work that this conclusion is incorrect. The usual argument is based on (5.5) above which from the corner at $(a, 0)$ contributes terms

$$(2\pi K)^{-1} \phi(a, 0) \frac{\partial}{\partial \xi} G(\xi, \eta; a, 0) + (2\pi K)^{-1} \frac{\partial \phi}{\partial x}(a, 0) G(\xi, \eta; a, 0)$$

to the potential $\phi(\xi, \eta)$. Since $G(\xi, \eta; X, Y)$ represents a source at (X, Y) when $Y > 0$ this is often interpreted as the sum of a dipole term and a source term. This interpretation is in any case inconsistent since the dipole strength $\phi(a, 0)$ and the source strength $\partial \phi(a, 0)/\partial x$ would not be finite if there were strong singularities in the corners. Actually $G(\xi, \eta; a, 0)$ is a weak surface singularity, and $G(\xi, \eta; a, 0)/\partial \xi$ is a vortex as can be seen from the expansions in the appendix but even these weaker singularities are not present in the least singular solution. The correct interpretation can be inferred from the representation (5.1-5.3) of the least singular solution, which consists of a continuous distribution of sources together with a discrete weak surface singularity in each corner. Near each corner the end-effect of the source distribution is like a weak surface singularity and is cancelled by the corresponding discrete weak surface singularity term. Similarly near a corner the end-effect of the dipole distribution is like a vortex and is cancelled by the corresponding discrete vortex term.

7. ACKNOWLEDGEMENT

I am grateful to Mr. Katsuo Suzuki for his valuable comments on an earlier version of this paper.

APPENDIX. Power series expansions associated with the source potential.

We consider the functions

$$C(Kx, Ky) = \int_0^\infty e^{-ky} \cos kx \frac{dk}{k-K} \quad (A.1)$$

$$\text{and } S(Kx, Ky) = \int_0^\infty e^{-ky} \sin kx \frac{dk}{k-K} \quad (A.2)$$

where the Cauchy Principal Value is to be

taken at $k = K$. Write $F(\zeta) = \int_0^\infty e^{-k\zeta} \frac{dk}{k-K}$

where ζ has positive real part. Then

$$\begin{aligned} \int_0^\infty e^{-p\zeta} F(\zeta) d\zeta &= \int_0^\infty \frac{dk}{(k-K)} \frac{1}{(k+p)}, \text{ by changing} \\ &\quad \text{the order of integration,} \\ &= \frac{1}{p+K} \left[\log \left| \frac{k-K}{k+p} \right| \right]_{k=0}^{k=\infty} = \frac{1}{k+p} \log \frac{p}{k} \\ &= \sum_{m=0}^{\infty} \frac{(-K)^m}{p^{m+1}} \log \frac{p}{K}. \end{aligned} \quad (A.3)$$

Also, from Euler's definition of the gamma function,

$$\int_0^\infty e^{-p\zeta} \frac{(K\zeta)^v}{\Gamma(v+1)} d\zeta = \frac{K^v}{p^{v+1}}, \text{ whence by}$$

differentiation with respect to v ,

$$\int_0^\infty e^{-p\zeta} \left(\frac{\partial}{\partial v} \frac{(K\zeta)^v}{\Gamma(v+1)} \right) d\zeta = \frac{K^v}{p^{v+1}} \log \frac{K}{p}. \quad (A.4)$$

On comparing this with (A.3), we find that

$$F(\zeta) = \sum_{m=0}^{\infty} (-1)^{m+1} \left(\frac{\partial}{\partial \zeta} \frac{(K\zeta)^m}{\Gamma(m+1)} \right)_{\zeta=\infty} \\ = \sum_{m=0}^{\infty} (-1)^{m+1} \left\{ \frac{(K\zeta)^m \log K\zeta}{\Gamma(m+1)} - \frac{(K\zeta)^m}{(\Gamma(m+1))^2} \Gamma'(m+1) \right\}$$

whence

$$\int_0^{\infty} e^{-k\zeta} \frac{dk}{k-K} = - \sum_{m=0}^{\infty} (-1)^m \frac{(K\zeta)^m}{m!} \left(\log K - \frac{\Gamma'(m+1)}{\Gamma(m+1)} \right) \quad (A.5)$$

Now put $\zeta = y + ix = re^{i\theta}$, then

$$\int_0^{\infty} e^{-ky} (\cos kx - i \sin kx) \frac{dk}{k-K} \\ = \sum_{m=0}^{\infty} (-1)^{m+1} \frac{(Kr)^m}{m!} \left\{ \cos m\theta + i \sin m\theta \right\} \\ \left(\log Kr - \frac{\Gamma'(m+1)}{\Gamma(m+1)} + i\theta \right)$$

On taking real and imaginary parts we find that

$$C(Kx, Ky) = \int_0^{\infty} e^{-ky} \cos kx \frac{dk}{k-K} \\ = \sum_{m=0}^{\infty} (-1)^{m+1} \frac{(Kr)^m}{m!} \left\{ \cos m\theta \left(\log Kr - \frac{\Gamma'(m+1)}{\Gamma(m+1)} \right) - \theta \sin m\theta \right\}, \quad (A.6)$$

and that

$$S(Kx, Ky) = \int_0^{\infty} e^{-ky} \sin kx \frac{dk}{k-K} \\ = \sum_{m=0}^{\infty} (-1)^m \frac{(Kr)^m}{m!} \left\{ \sin m\theta \left(\log Kr - \frac{\Gamma'(m+1)}{\Gamma(m+1)} \right) + \theta \cos m\theta \right\}. \quad (A.7)$$

It is known that $\frac{\Gamma'(1)}{\Gamma(1)} = -\gamma$, and

$$\frac{\Gamma'(m+1)}{\Gamma(m+1)} = -\gamma + \frac{1}{1} + \frac{1}{2} + \dots + \frac{1}{m}, \text{ where}$$

$\gamma = 0.5772 \dots$ is Euler's constant.

To find the behaviour of $F(y+ix)$ when $x \rightarrow +\infty$, consider

$$F(\zeta) = \int_0^{\infty} e^{-k\zeta} \frac{dk}{k-K} \\ = \int_0^{\infty} e^{-k\zeta} \frac{dk}{k-K} - \pi i e^{-K\zeta},$$

by adding and subtracting the integral along a small indentation below $k = K$,

$$= \int_0^{\infty} \exp(-\frac{1}{2}i\pi) e^{-k\zeta} \frac{dk}{k-K} - \pi i e^{-K\zeta}, \quad (A.8)$$

where the indented path along the real k -axis has been deformed into the path $\arg k = -\frac{1}{2}\pi$, on which the integrand is bounded. The integral in (A.8) is easily seen to tend to 0 when $Kx \rightarrow +\infty$, and we thus find that

$$F(\zeta) = C(Kx, Ky) - iS(Kx, Ky) \\ \sim -\pi i e^{-K(y+ix)} = -\pi i e^{-Ky} (\cos Kx - i \sin Kx)$$

$$= -\pi i e^{-Ky} \sin Kx - \pi e^{-Ky} \cos Kx \text{ when } Kx \rightarrow +\infty$$

Since $C(\quad)$ is an even function of Kx and $S(\quad)$ is an odd function of Kx we infer that

$$C(Kx, Ky) \sim \pi e^{-Ky} \sin Kx \rightarrow 0 \text{ when } Kx \rightarrow -\infty, \quad (A.9)$$

$$\text{and } S(Kx, Ky) \sim \pi e^{-Ky} \cos Kx \rightarrow 0 \text{ when } Kx \rightarrow -\infty. \quad (A.10)$$

We also need the expansion for the horizontal dipole:

$$\frac{\partial C}{\partial x} = - \int_0^{\infty} k e^{-ky} \sin kx \frac{dk}{k-K} \\ = - \int_0^{\infty} e^{-ky} \sin kx dk - K \int_0^{\infty} e^{-ky} \sin kx \frac{dk}{k-K} \\ = - \frac{x}{x^2+y^2} - KS(Kx, Ky) \\ = - \frac{\sin \theta}{r} - KS(Kx, Ky); \quad (A.11)$$

and the well-known expansions

$$e^{-Ky} \cos Kx = \sum_{m=0}^{\infty} (-1)^m \frac{(Kr)^m}{m!} \cos m\theta \quad (A.12)$$

$$e^{-Ky} \sin Kx = \sum_{m=0}^{\infty} (-1)^{m+1} \frac{(Kr)^m}{m!} \sin m\theta \quad (A.13)$$

REFERENCES

1. Lamb, H., *Hydrodynamics*, 6th Ed. Cambridge University Press. 1932.
2. Ursell, F., On the rolling motion of cylinders in the surface of a fluid. *Quart. J. Mech. Appl. Math.*, 1949, 2, 335-353.
3. Wehausen, J.V. and Laitone, E.V., *Surface Waves*, *Handbuch der Physik*, Vol. 9, 1960, 446-778. Berlin: Springer.

Discussion

K. Suzuki (National Defense Academy)

The author has settled the problem of the uniqueness of the 2-D Kelvin-Neumann solution. The solution can be represented in various manners, for example, Green's representation, multipole expansion and so on. Furthermore, the solution can be determined arbitrarily, as shown by Bessho-Mizuno (Sci. Eng. Rep. Defense Academy 1-1, 1963) and Eggers (Disc. to Bessho, ISWR, 1976).

Prof. Ursell has made clear that the least singular solution can be determined uniquely if one assumes continuity and boundedness of the velocities at the corners. He has also indicated that there are infinitely many solutions according to the properties prescribed at the corners.

I had earlier calculated the 2-D Kelvin-Neumann solutions of the following form (1978, unpublished);

$$\phi(x, y) = U \int_{-\pi/2}^{\pi/2} v(\theta) G(x, y; a \sin \theta, a \cos \theta) d\theta$$

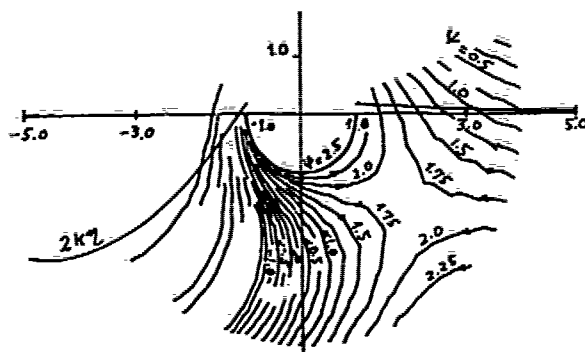
$$= U/K \{ \mu(\pi/2) G(x, y; a, 0) + \mu(-\pi/2) G(x, y; -a, 0) \}$$

$$+ U/KC_p [G(x, y; a, 0) - G(x, y; -a, 0)]. \quad (S-1)$$

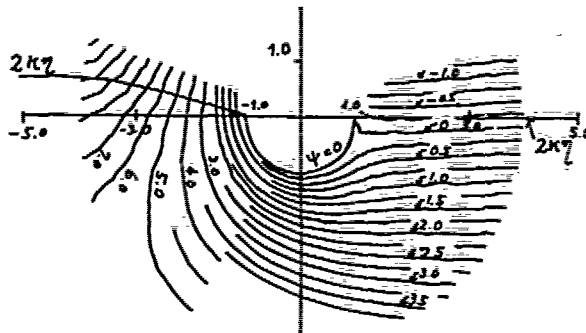
When $C_p = 0$, this representation gives the least singular solution. The streamlines are shown in Fig. S-1(a-d) for various singular solutions.

I have a question concerning the multipole expression (4.1), whether the logarithmic terms do not cancel? Once we assume that both the velocity potential and the flow are continuous (least singular) even in the corners, we had better replace the logarithmic singularity by a dipole singularity. This results from two reasons.

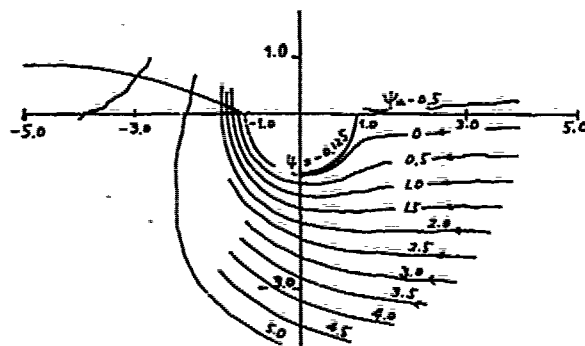
To show one of them we shall first deal with the linearized free-surface condition (Wehausen-Laitone, 1960, p471) as



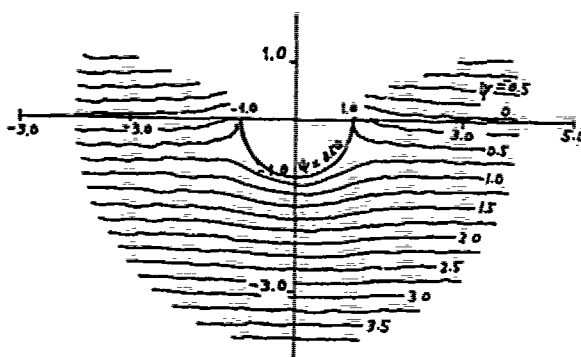
a) Least singular solution ($C_p=0$)



b) Zero-vertical flux flow ($C_p=2$)



c) Approximate flow for slightly sunken circle ($C_p=2.1$)



d) Wave-free flow ($C_p=1.568$)

Fig. S-1 Comparison of streamlines around a semi-submerged circle for various singular solutions ($Ka=0.4$)

$$K\psi + \phi_x = \text{const. for } y=0 \quad (S-2)$$

where ψ is a conjugate (stream) function for ϕ . We can put the constant in the right-hand side zero upstream from the body without losing validity, on the assumption that $\psi \rightarrow 0$ as $x \rightarrow -\infty$ (1) (see the number in Fig. S-2). As x tends to the forward corner point P_F along the line $y=0$, we take $\psi = -1/K$ ($\phi_x = -1$ = incident velocity) from the continuity of the velocity at the corner P_F (2). Since the stream function, $\bar{\psi} = y + \psi$, is constant on the body surface, we have $\bar{\psi} = -1/K$ there from the continuity of the stream function at the corner P_F (3). By using the continuity of the stream function and the velocity at the corner P_A , we can also derive the fact that $\phi_x = -1$, $\psi = -1/K$ at the corner P_A in the free surface $y=0$ (4). Finally we obtain the zero value for the constant in the right-hand side of eq. (S-2) downstream from the body (5).

Thus the linearized free-surface condition can be written in the following form:

$$\text{Re } L[f(z)] = 0 \text{ for } y=0, \text{ outside } C, \quad (S-3)$$

where $L = d/dz - iK$ (differential operator) and $f(z)$ is the perturbation complex potential. We introduce a new function, analytic for $|z| > 1$ (assume that the body is a semi-circle) as

$$g(z) = L[f(z)], \quad (S-4)$$

which satisfies the condition

$$\text{Re } g(z) = 0 \text{ for } y=0. \quad (S-5)$$

Such a function can be written as follows:

$$g(z) = i \sum_{m=1}^{\infty} a_m / z^m. \quad (S-6)$$

It should be noted that the function $g^*(z) = ia_1 \ln(z)$ does not satisfy the condition (S-5). Substitution of (S-6) into eq. (S-4) gives the function $f(z)$ as,

$$f(z) = 1/L[\zeta(z)] = \sum_{m=1}^{\infty} e^{iKz} \int z^{-iK\zeta} i \frac{a_m}{\zeta^m} d\zeta. \quad (S-7)$$

The above solution is rewritten as a combination of the two terms of wave doublets and the sequence of wave-free potentials as shown in the following:

$$f(z) = \sigma_1 W_m(z; 0) + \sigma_2 W_u(z; 0) + \sum_{n=1}^{\infty} \sigma_n h_n(z), \quad (S-8)$$

where

$$h_n(z) = 1/z^n (1 - i/Kz),$$

W_m, W_u are the wave doublets in the x - and y -directions respectively. If we use $g(z)$

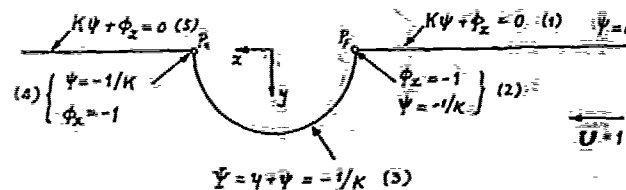


Fig. S-2

$g^*(z)$ instead of $g(z)$, we can show that the corresponding function $f(z)$ is written in the form of eq. (4.1). But such a solution can not satisfy eq. (S-3).

The next reason is that both the least singular solution (5.1-3) and a singular solution (S-1) do not become logarithmically unbounded at infinity. These solutions can be looked on as a point source potential at upstream infinity:

$$\phi(x, y) = 2U \left\{ \int_{-\pi/2}^{\pi/2} \mu(\theta) d\theta - \frac{1}{K} (\mu(\pi/2) + \mu(-\pi/2)) \right\} \times \log(KR), \quad (S-9)$$

where $R = \sqrt{(x^2 + y^2)}$. We can show that the strength of the point source is equal to the difference of the x -velocities at P_F and P_A , $\phi_{xP_A} - \phi_{xP_F}$, both of which are to be taken as the limiting values to P_A and P_F on the line $y=0$. This relation was shown for the 3-D Neumann-Kelvin solution by Tsutsumi (1976, unpublished) and is to be reviewed at continued Washington Workshop (Suzuki, 1980).

For the least singular solution the difference of the x -velocities vanishes because they both become -1 . As for the singular solution (S-1), we have $\phi_{xP_F} = \phi_{xP_A} = -1 + 1/2 C_p$. Accordingly, the strength of the point source in eq. (S-9) becomes zero. This tells us the above mentioned.

From the above two reasons, must we say that the logarithmic terms in eq. (4.1) cancel or that the multipole expansion for the least singular solution is to be expressed by eq. (S-8) instead of eq. (4.1)?

H. Isshiki (Hitachi S&E)

I believe that great progress has been made by Prof. Ursell from a theoretical view point, especially in its mathematical aspects.

I want to make some comments in the following. As the author says in his discussion in the paper concerning a rather popular misunderstanding that the perturbation potential must have strong singularities in the corners. This misunderstanding was also mine before I read this. I think this misunderstanding originates from two reasons.

As the author points out, one originates from the contribution from the corner (See Eqs. (5.2) & (5.3)), or the so-called

line-integral term in the three-dimensional problem. And the other may originate from a confusion with a stagnation point singularity in slender-body approximation.

The corner contribution is derived from a free-surface singularity distribution by processes such as shown by Eq. (5.4). Hence, in the original form, the potential is expressed by the sum of a singularity distribution on the cylinder surface and on the free surface. From this expression, we may have a feeling that the velocity at the corner may not be strongly singular. But this is nothing more than a feeling. We should pay enough attention to Prof. Ursell's finding that the source distribution on the cylinder surface given by Eq. (5.1) shows a weak singularity at each corner and this singularity cancels the similar singularity due to the corner contribution given by Eqs. (5.2) or (5.3).

Concerning the misunderstanding, if I'm not wrong, originating from a confusion with a stagnation point singularity in the slender-body approximation, my comment is as follows. In the case of a slender body, the potential makes a change of $O(1)$ in the neighbourhood of the stagnation point, and the size of the neighbourhood is $O(\epsilon)$. This may be the reason why the singularity appears there. On the contrary, in the present problem, the potential makes a change of $O(1)$ in the neighbourhood of each corner but the size is also $O(1)$. Therefore, the potential may be expressed without introducing a strong singularity at each corner, and this may be the reason why the least singular solution in the form of Eq. (4.1) is possible.

Finally, I would like to express again my surprise and admiration for the really great originality of this paper.

Author's Reply

F. Ursell (Univ. of Manchester)

In my paper I showed that there is a unique least singular solution which has finite velocities in the corners, and I suggested that the velocity potential would in general be logarithmically infinite at infinity. In his discussion Mr. Suzuki has given a convincing argument (based on the integral representation, equations (5.1 - 5.3),) to show that the potential is in fact bounded at infinity. I have now established the same conclusion for the potential in the alternative multipole form (4.1), using a simplified version of Suzuki's argument.

Let $\psi(x, y)$ denote the stream function conjugate to $\phi(x, y)$. On each segment of the free surface we have

$$\frac{\partial}{\partial y}(K\phi + \frac{\partial\psi}{\partial y}) = 0, \text{ i.e. } \frac{\partial}{\partial x}(K\psi + \frac{\partial\phi}{\partial x}) = 0,$$

i.e. $K\psi + \frac{\partial\psi}{\partial y} = 0$ on each segment of the free surface.

Thus for any point $(X, 0)$ on the positive X-axis outside C we have

$$K\psi(X, 0) + \frac{\partial\psi}{\partial y}(X, 0) = K\psi(a, 0) + \frac{\partial\psi}{\partial y}(a, 0),$$

and similarly

$$K\psi(-X, 0) + \frac{\partial\psi}{\partial y}(-X, 0) = K\psi(-a, 0) + \frac{\partial\psi}{\partial y}(-a, 0)$$

Since the total mass flux out of C vanishes we have $\psi(a, 0) = \psi(-a, 0)$, and from (2.2)

we have $\frac{\partial\psi}{\partial y}(a, 0) = \frac{\partial\psi}{\partial y}(-a, 0) = -U$.

It follows that

$$(K\psi + \frac{\partial\psi}{\partial y})(X, 0) = (K\psi + \frac{\partial\psi}{\partial y})(-X, 0). \quad (1)$$

Consider this equation when $X \rightarrow \infty$. From the expansion (4.1) we have

$$\frac{\phi(x, y)}{Ua} \sim -2\pi A e^{-Ky} \sin Kx + 2\pi B e^{-Ky} \cos Kx + (A - K\alpha_0) \log Kr,$$

when x is large and positive, and θ is near $\frac{1}{2}\pi$;

$$\frac{\phi(x, y)}{U} \sim (a - K\alpha_0) \log Kr,$$

when x is large and negative, and θ is near $-\frac{1}{2}\pi$.

It follows that the conjugate stream function $\psi(x, y)$ is given by

$$\frac{\psi(x, y)}{Ua} \sim 2\pi A e^{-Ky} \cos Kx + 2\pi B e^{-Ky} \sin Kx + (a - K\alpha_0)\theta,$$

when x is large and positive, and θ is near $\frac{1}{2}\pi$;

$$\frac{\psi(x, y)}{Ua} \sim (A - K\alpha_0)\theta,$$

when x is large and negative, and θ is near $-\frac{1}{2}\pi$.

Expressions for $\partial\psi/\partial y$ can be deduced by differentiation. On substituting in (1) above and noting that $\theta = \pm\frac{1}{2}\pi$ at $(\pm X, 0)$ we obtain $A - K\alpha_0 = 0$, i.e. the terms

$$AP(Kx, Ky) + \alpha_0 a \left(\frac{\cos \theta}{r} - K \log Kr \right)$$

combine to form a dipole singularity which is bounded at infinity. This is equivalent

to Suzuki's result. I wish once again to express my gratitude to Mr. Suzuki for his contributions to my work.

I also thank Dr. Isshiki for his valuable comments which help to elucidate the form of the least singular solution in the

corners. No physical argument had yet been given for preferring the least singular solution to other possible solutions, and other solutions may turn out to be physically more appropriate. This is a problem which requires further study.

Numerical Solution of Transient and Steady Free-Surface Flows about a Ship of General Hull Shape

Robert K.-C. Chan and Frank W.-K. Chan

JAYCOR

Del Mar, California, U.S.A.

ABSTRACT

This paper describes a finite-difference numerical technique for simulating transient and steady-state three-dimensional potential flow about a ship with blunt bow. The primary features of the method include the use of special coordinate transformations to allow rigorous application of hull surface and free surface boundary conditions, and application of Orlanski's numerical open boundary condition to prevent nonphysical wave reflections from boundaries of the computational region. The method has been applied to wave resistance of a tanker with and without protruded bow. It is found that the breaking of bow wave occurs at a higher Froude number for the protruded bow, thus reducing the wave drag considerably at higher Froude numbers.

NOMENCLATURE

A_1, A_2	Coefficients defined in Eq. (19)
B_1, B_2	Coefficients defined in Eq. (19)
C_1, C_2	Coefficients defined in Eq. (19)
C_w	Resistance coefficient defined in Eq. (31)
D_1, D_2	Coefficients defined in Eq. (14)
D/Dt	Particle derivative in the (x, y, z, t) system
F	An arbitrary scalar function
F_r	Froude number; $F_r = U/\sqrt{gL}$
f	A single-valued function which describes the hull surface [Eq. (6)] in the spherical polar coordinate system (r', θ', ϕ') .

f_0	A single-valued function which measures the distance of the hull surface from the ship's center plane in the rectangular cartesian system (x, y, z) .
G	An arbitrary scalar function
g	Gravitational acceleration
H	The distance between the origin of the coordinate system and the center of the semi-submerged sphere in Fig. 7.
I	Spatial coordinate along one of the mesh line directions (Fig. 6).
$IMAX$	Maximum value of the subscript i (Fig. 6).
J	Spatial coordinate along one of the mesh line directions (Fig. 6).
$JMAX$	Maximum value of the subscript j (Fig. 6).
K	Spatial coordinate along one of the mesh line directions (Fig. 6).
$KMAX$	Maximum value of the subscript k (Fig. 6).
L	Characteristic length of the problem
N	Time as measured at a given spatial point in the (i, j, k) system.
\hat{n}	Unit normal vector at the hull surface.
n_1, n_2, n_3	Components of \hat{n} in the (x, y, z) system

p	Fluid pressure	θ	One of the angular coordinates defined in Eq. (7)
R	Radius of a semi-submerged sphere.	θ'	One of the angular coordinates in Fig. 4.
R_w	Net horizontal force experienced by the ship.	π	3.14159
r	Radial coordinate defined in Eq. (7).	ρ	Fluid density
r'	Radial component of the spherical polar coordinate system shown in Fig. 4.	ϕ	Velocity potential
S	Area of wetted hull surface	ψ	One of the angular coordinates defined in Eq. (7).
T	Time as measured in the absolute inertial frame of reference.	ψ'	One of the angular coordinates defined in Fig. 4.
t	Time as measured in the moving coordinate system (x, y, z) , with the frame of reference fixed in the ship.	ω	Angular velocity of the ship: $\omega = \dot{\theta}_t$ [Eq. (3)].
U	The constant, final speed of the ship in its forward motion.	∇	Gradient
\bar{u}	Defined in Eq. (3)	∇^2	Laplacian operator
u_0	Defined in Eq. (3)	Superscript	
\bar{v}	Defined in Eq. (3)	n	Time level in numerical integration with respect to time.
v_0	Defined in Eq. (3)	Subscripts	
X, Y, Z	Rectangular cartesian coordinates in an inertial frame of reference.	i	Index for mesh points along the I-direction.
x, y, z	Rectangular cartesian coordinates in a frame of reference fixed in the ship.	j	Index for mesh points along the J-direction.
X_c, Y_c	Coordinates of the ship's center of rotation in the (X, Y, Z) system.	k	Index for mesh points along the K-direction.
a_{11}, a_{22}, a_{33}	Coefficients defined in Eq. (22)		
a_{12}, a_{13}, a_{23}	Coefficients defined in Eq. (22)		
a_1, a_2, a_3	Coefficients defined in Eq. (22)		
α	Angle between the forward direction of the ship and the X-axis (Fig. 1).		
$\gamma_1, \gamma_2, \gamma_3$	Coefficients defined in Eq. (22)		
Δt	Time increment in numerical integration.		
ζ	A scalar function defined in Eqs. (5) and (16).		
n	A single-valued function of r, ψ , and t , which is used to describe the position of the free surface [Eq. (16)].		

1. INTRODUCTION

The objective of this research is to develop a numerical solution procedure for simulating transient and steady flows about a surface ship of a fairly general hull configuration. Special emphasis is given to ships with a wide beam and a blunt bow. The assumption of potential flow is made in this study. However, the complete set of boundary conditions, including nonlinear terms, are applied at the correct locations. Our approach consists of numerically integrating a set of time-dependent, three-dimensional equations in a special, body-fitted computational mesh system. The method can be used to obtain both transient and steady-state solutions.

There are three major concerns when calculating three-dimensional flows about a ship by finite-difference techniques (and by many other numerical methods): 1. Wave reflections due to finite size of the computational region can render the solution totally meaningless. 2. The finite-difference schemes must meet some stability and accuracy requirements. 3. The computational mesh must conform to the boundaries (e.g., hull surface and free surfaces) of the

problem, so that boundary conditions can be applied rigorously. To utilize the limited computer storage efficiently, it is preferable to select a frame of reference fixed in the ship so that the mesh resolution is concentrated near the ship. In this reference frame, the ship appears to be stationary in a running stream. Computationally, this arrangement creates problems with boundary conditions at the "open-boundary," where the flow and waves are supposed to leave the computation region. Improper treatment of this type of boundary can result in nonphysical reflections. Fortunately, with the appearance of Orlandi's [1] excellent technique for numerically propagating waves out of a finite region, this difficulty is now removed. With implicit treatment of those terms that govern wave propagations, the finite-difference method given in this paper produces solutions that are stable all the way through the transient period to the steady state. As to the problems of geometry, a body-fitted coordinate system has been developed by deforming the spherical polar coordinate system in such a way that the new coordinate surfaces conform to the free surface and the hull.

In the sections that follow, a detailed description of the derivation of the coordinate system and related transformations of the governing equations are given. Some sample calculations of the flow about a semi-submerged sphere, and comparison between an HSVI tanker and a modified tanker with protruded bow are discussed.

2. FORMULATION OF THE PROBLEM

Potential flow is assumed in this study. As shown in Fig. 1, let (X, Y, Z, T) be the cartesian coordinates referred to an absolute inertial frame, and (x, y, z, t) be their counterparts with reference to a moving frame which is fixed in the ship. We assume further that the ship undergoes an arbitrary planar motion such that its mast (i.e., the vertical axis of the ship) always points vertically upward. The positive x -direction is the same as the longitudinal

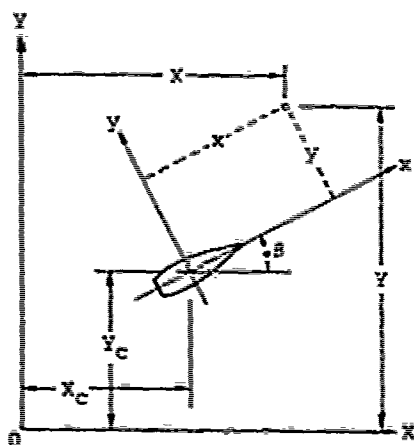


Fig. 1 Frames of Reference

axis of the ship, pointing to the front. Using formal coordinate transformation [2], we obtain the following governing equations for the velocity potential ϕ in the (x, y, z, t) system:

Laplace equation

$$\phi_{xx} + \phi_{yy} + \phi_{zz} = 0 \quad (1)$$

Bernoulli equation

$$\phi_t + \bar{u}\phi_x + \bar{v}\phi_y + \frac{1}{2}[(\phi_x)^2 + (\phi_y)^2 + (\phi_z)^2] + gz + \frac{p}{\rho} = 0 \quad (2)$$

where

$$\bar{u} = -u_0 + \omega y$$

$$\bar{v} = -v_0 - \omega x$$

$$u_0 = (X_c)_t \cos \beta + (Y_c)_t \sin \beta \quad (3)$$

$$v_0 = -(X_c)_t \sin \beta + (Y_c)_t \cos \beta$$

$$\omega = \dot{\beta}_t$$

In the equations above, subscripts x, y, z , and t denote partial differentiation, while (X_c, Y_c) are the coordinates of the instantaneous position of the ship's center of rotation in the (X, Y, Z, T) frame of reference. The forward motion of a ship is a special case in which $\omega = 0$, $\dot{\beta}_t = 0$, and $\beta = 0$ for convenience, $\bar{u} = -(X_c)_t$ and $\bar{v} = 0$. Note that X_c, Y_c , and β are generally functions of time; therefore, arbitrary planar motions of the ship can be prescribed.

Hull Surface Boundary Condition

$$\phi_x n_1 + \phi_y n_2 + \phi_z n_3 = -\bar{u} n_1 - \bar{v} n_2 \quad (4)$$

where (n_1, n_2, n_3) are the cartesian components of the unit normal vector \bar{n} at the hull surface, measured in the (x, y, z, t) system.

Kinematic Free Surface Condition

$$\frac{D\zeta}{DT} = 0 \quad (5)$$

where ζ is a scalar function defined in such a way that $\zeta = 0$ at the free surface for all times. $D\zeta/DT$ is the particle derivative of ζ in the inertial frame (X, Y, Z, T) . Explicit forms for Eq. (5) can not be given until the final body-fitted curvilinear coordinate system is selected. We will return to this equation later.

The primary goal of our effort is to develop a computational procedure utilizing a mesh system which conforms to the free surface and the surface of the body. Such a mesh system would allow rigorous application of the complete sets of free surface and hull surface boundary conditions at their exact positions. Reference 2 provides examples of calculations made in a body-fitted mesh system for ship hulls which can

be described by a single-valued function $y = f_0(x, z)$, where y is the distance of the hull surface measured from the ship's center plane (i.e., the x - z plane). The class of body shapes was therefore limited to those representable by $f_0(x, z)$, with a sharp-edged keel (Fig. 2).

To extend the method to hulls without the restriction of sharp-edged keel, a different choice of body-fitted coordinate system must be made. With applications to tankers and other wide-beam blunt-bow ships in mind, we choose a mesh which is obtained by deforming the usual spherical polar coordinate system (i.e., stretching) in the radial direction in such a way that the new coordinate surfaces conform to the free surface and the hull. At the time this work was started (1977), many researchers had explored the use of very general, body-fitted meshes to solve problems in computational fluid dynamics [3] with considerable success. This type of approach has been applied to two-dimensional, time-dependent problems with free surface and body interactions. For three-dimensional problems, however, this general approach is not practical because of its demand on computer time and storage. As the free surface moves, the new curvilinear mesh must be regenerated at each new time step and the coordinates (x, y, z) of each node point have to be stored. It would also be very expensive to solve the Laplace equation $\nabla^2 \phi = 0$ in such a system, unless all the coefficients of transformation are stored in the

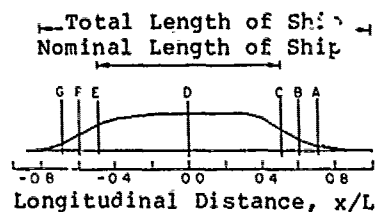
computer, which again consumes a large fraction of the precious storage.

Fortunately, for the ship wave problem under consideration, a general curvilinear mesh is not needed. The computation can be efficiently performed in a composite mesh system as shown in Fig. 3. The bulk of the flow field lies in the "lower region" which can be covered by a fixed mesh conforming to the body surface. In the "upper region," a more general, time-dependent mesh is used to conform to the hull surface, to the interface between the two regions, or to the moving free surface. The upper region is relatively small, the only requirement being that its lower boundary (i.e., the "interface") be placed low enough so that it is not crossed over by the free surface at any time. Since the more general mesh system is used only in the small upper region, the expensive part of the computation is minimized.

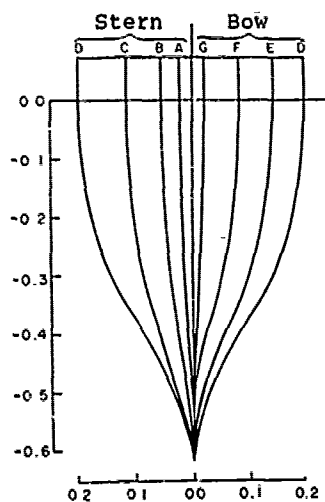
We now describe the coordinate transformations necessary to obtain the desired mesh system. Let (r', θ', ψ') be the spherical polar coordinates with origin at point 0 in Figs. 3 and 4. We use ψ' to designate the angle as shown in Fig. 4 to avoid confusion with the velocity potential ϕ . The origin is suitably located inside the body and placed at the same level as the interface between the upper and lower regions. For most hull shapes, the hull can be described by the single-valued function

$$r' = f(\theta', \psi') \quad (6)$$

To generate a body-fitted coordinate system (r, θ, ψ) , we make the following change of variables



(a) Top View



(b) Cross Sections

Fig. 2 Shiplike Body with Sharp Keel

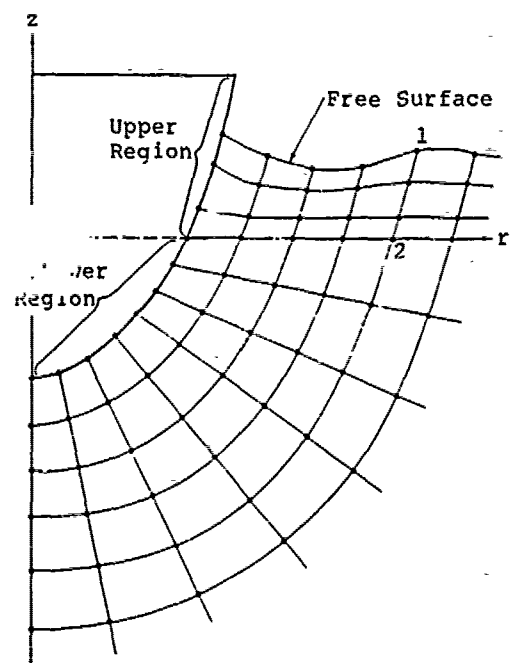


Fig. 3 Composite Mesh System

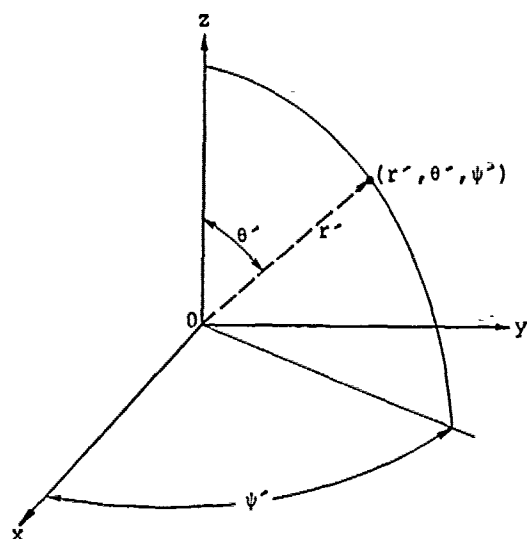


Fig. 4 Spherical Coordinate System

$$\begin{aligned} r &= r' - f(\theta', \psi') \\ \theta &= \theta' \\ \psi &= \psi' \end{aligned} \quad (7)$$

The surface $r = 0$ coincides with the hull surface, and the plane $\theta = \pi/2$ separates the upper region from the lower one. As shown in Fig. 3, the mesh points on and below the plane $\theta = \pi/2$ are fixed in space relative to the ship. The mesh points at the free surface, however, move with the free surface, and the region in between is divided into subregions with equal angular intervals, e.g., between points 1 and 2 in Fig. 3 (point 2 is fixed but point 1 is allowed to slide up and down along the mesh line $r = \text{constant}$). This arrangement allows effective resolution of the flow field near the intersection of the free surface and the hull.

Governing Equations in the (r, θ, ψ) Coordinate System

The relations between the cartesian coordinates (x, y, z) and the spherical polar coordinates (r', θ', ψ') are

$$\begin{aligned} x &= r' \sin \theta' \cos \psi' \\ y &= r' \sin \theta' \sin \psi' \\ z &= r' \cos \theta' \end{aligned} \quad (8)$$

For any scalar function G , defined in the space under consideration, we can write

$$\begin{aligned} G_x &= \sin \theta' \cos \psi' G_{r'} \\ &+ \frac{1}{r'} \cos \theta' \cos \psi' G_{\theta'} - \frac{1}{r'} \frac{\sin \psi'}{\sin \theta'} G_{\psi'} \\ G_y &= \sin \theta' \sin \psi' G_{r'} \\ &+ \frac{1}{r'} \cos \theta' \sin \psi' G_{\theta'} + \frac{1}{r'} \frac{\cos \psi'}{\sin \theta'} G_{\psi'} \\ G_z &= \cos \theta' G_{r'} - \frac{\sin \theta'}{r'} G_{\theta'} \end{aligned} \quad (9)$$

If F is another scalar function, we also have

$$\begin{aligned} \nabla G \cdot \nabla F &= G_{r'} F_{r'} + \frac{1}{(r')^2} G_{\theta'} F_{\theta'} \\ &+ \frac{1}{(r')^2 \sin^2 \theta'} G_{\psi'} F_{\psi'} \end{aligned} \quad (10)$$

By the transformation of Equations (7), we obtain

$$\begin{aligned} G_{r'} &= G_r \\ G_{\theta'} &= G_\theta - f_\theta G_r \\ G_{\psi'} &= G_\psi - f_\psi G_r \end{aligned} \quad (11)$$

Using Eqs. (8), (9), and (11), Eqs. (1) and (2) are transformed into

Laplace Equation

$$\begin{aligned} &\left\{ [(r+f)^2 + (f_\theta)^2] \sin^2 \theta + (f_\psi)^2 \right\} \phi_{rr} \\ &+ \sin^2 \theta \phi_{\theta\theta} + \phi_{\psi\psi} \\ &- 2f_\theta \sin^2 \theta \phi_{r\theta} - 2f_\psi \phi_{r\psi} + \sin \theta \cos \theta \phi_\theta \\ &+ \left\{ [2(r+f) - f_{\theta\theta}] \sin^2 \theta - f_\theta \sin \theta \cos \theta \right. \\ &\left. - f_{\psi\psi} \right\} \phi_r = 0 \end{aligned} \quad (12)$$

Bernoulli Equation

$$\begin{aligned} &\phi_t + (\tilde{u}A_1 + \tilde{v}A_2)\phi_r + (\tilde{u}B_1 + \tilde{v}B_2)\phi_\theta \\ &+ (\tilde{u}C_1 + \tilde{v}C_2)\phi_\psi + \frac{1}{2} \left\{ (\phi_r)^2 \right. \\ &+ \left[\frac{\phi_\theta - f_\theta \phi_r}{r+f} \right]^2 + \left[\frac{\phi_\psi - f_\psi \phi_r}{(r+f) \sin \theta} \right]^2 \Big\} \\ &+ g(r+f) \cos \theta + \frac{p}{\rho} = 0 \end{aligned} \quad (13)$$

Hull Surface Boundary Condition

The hull surface condition can now be derived. First, we observe that the function r , where $r = r' = f(\theta', \psi')$, has the value zero at the hull surface by definition, and that its gradient ∇r is normal to the hull surface. Therefore, $\nabla r / |\nabla r|$ is the unit vector whose components are (n_1, n_2, n_3) in the (x, y, z) system, as mentioned in connection with Eq. (4). Thus Eq. (4) can be written as

$$\nabla \phi \cdot \nabla r = -\bar{u}r_x - \bar{v}r_y \quad (14)$$

Using Eqs. (9), (10), (11), and applied at $r = 0$, Eq. (14) becomes

$$\left[1 + \left(\frac{f_\theta}{f} \right)^2 + \left(\frac{f_\psi}{f \sin \theta} \right)^2 \right] \phi_r - \frac{f_\theta}{f^2} \phi_\theta - \frac{f_\psi}{f^2 \sin^2 \theta} \phi_\psi + \bar{u}A_1 + \bar{v}A_2 = 0 \quad (15)$$

Kinematic Free Surface Condition

We define a scalar function

$$\zeta \equiv \theta - \eta(r, \psi, t) \quad (16)$$

The free surface corresponds to the surface $\zeta = 0$, or $\theta = \eta(r, \psi, t)$. Instead of the usual definition as vertical displacement of the free surface, η now is an angle, measured from the vertical axis of the (r, θ, ψ) coordinate system to the location of the free surface, along lines of constant r and ψ (Fig. 5). We can write Eq. (5) as

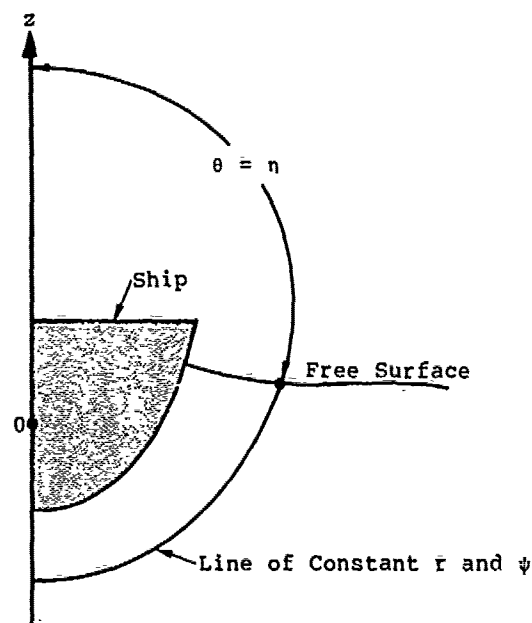


Fig. 5 Definition of η

$$\zeta_T + \zeta_X \zeta_X + \zeta_Y \zeta_Y + \zeta_Z \zeta_Z = 0$$

or

$$\zeta_T + \nabla \phi \cdot \nabla \zeta = 0 \quad (17)$$

From Eqs. (7), (10), (11), and

$$\zeta_T = \zeta_t + \bar{u}\zeta_x + \bar{v}\zeta_y$$

which relates time derivatives in the inertial system to those in the moving system, Eq. (17) becomes

$$\eta_t + D_1 \eta_r + D_2 \eta_\psi = \bar{u}B_1 + \bar{v}B_2 + \frac{(\phi_\theta - f_\theta \phi_r)}{(r+f)^2} \quad (18)$$

where

$$D_1 = \bar{u}A_1 + \bar{v}A_2 + \left[1 + \left(\frac{f_\theta}{r+f} \right)^2 + \left(\frac{f_\psi}{(r+f) \sin \theta} \right)^2 \right] \phi_r - \frac{f_\theta}{(r+f)^2} \phi_\theta - \frac{f_\psi}{(r+f)^2 \sin^2 \theta} \phi_\psi$$

$$D_2 = \bar{u}C_1 + \bar{v}C_2 + \frac{\phi_\psi - f_\psi \phi_r}{(r+f)^2 \sin^2 \theta}$$

In Eqs. (13) to (18), the following definitions are used:

$$A_1 = \sin \theta \cos \psi - \frac{f_\theta}{r+f} \cos \theta \cos \psi + \frac{f_\psi}{r+f} \left(\frac{\sin \psi}{\sin \theta} \right)$$

$$A_2 = \sin \theta \sin \psi - \frac{f_\theta}{r+f} \cos \theta \sin \psi - \frac{f_\psi}{r+f} \left(\frac{\cos \psi}{\sin \theta} \right)$$

$$B_1 = \frac{1}{r+f} \cos \theta \cos \psi$$

$$B_2 = \frac{1}{r+f} \cos \theta \sin \psi$$

$$C_1 = -\frac{1}{r+f} \left(\frac{\sin \psi}{\sin \theta} \right)$$

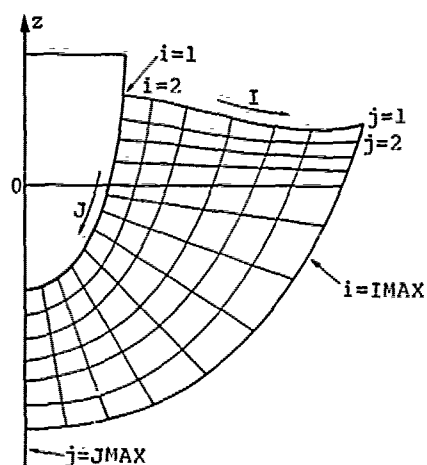
$$C_2 = \frac{1}{r+f} \left(\frac{\cos \psi}{\sin \theta} \right) \quad (19)$$

When the Bernoulli equation, Eq. (13), is applied at the free surface, we set $p = 0$ and all the terms are evaluated at $\theta = \eta$. Similarly, all the terms are evaluated at $\theta = \eta$ in Eq. (18). Note that $D_1 \equiv 0$ at the hull surface in view of Eq. (15) and the fact $r = 0$ at the hull.

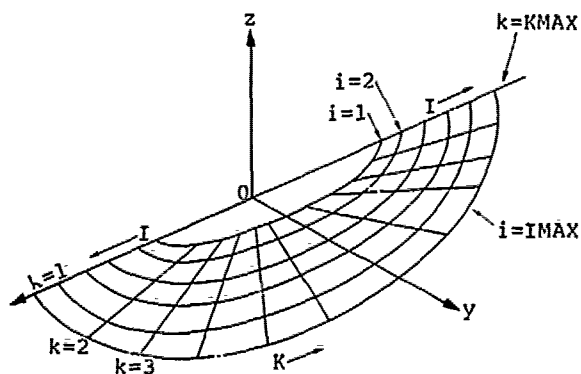
Equations (12), (13), and (15) are applicable to the lower region, since the (r, θ, ψ) coordinates are fixed with respect to the body and the mesh lines for the lower region are lines of constant r , θ , and ψ . For the upper region, however, one more transformation is needed to obtain equations appropriate to the mesh system moving with the free surface.

Governing Equations for Upper Region

Let (I, J, K) be the spatial coordinates along the three mesh line directions shown in Figs. 6(a) and 6(b). Also, let N be the time as measured at a given spatial point in the (I, J, K) system. These variables, i.e., I, J, K , and N , are all real, continuous numbers. In this system, we generally have



(a) Side View (I-J plane)



(b) Top View (I-K plane)

Fig. 6 Definition Sketch of the (I, J, K) System and Indexing of the Mesh Points

$$r = r(I, J, K, N) = r(I) \text{ only}$$

$$\theta = \theta(I, J, K, N) \quad (20)$$

$$\psi = \psi(I, J, K, N) = \psi(K) \text{ only}$$

$$t = t(N)$$

The derivatives of a scalar quantity G are related as follows:

$$G_r = (G_I - G_J \theta_I / \theta_J) / r_I$$

$$G_\theta = G_J / \theta_J$$

$$G_\psi = (G_K - G_J \theta_K / \theta_J) / \psi_K$$

$$G_t = (G_N - G_J \theta_N / \theta_J) / t_N \quad (21)$$

Due to the special construction of the mesh in the upper region, $\theta_{JJ} = 0$ there. Using Eqs. (21) in Eqs. (12), (13), (15), and (18), the governing equations for the upper region become

Laplace Equation

$$\begin{aligned} \alpha_{11} \phi_{II} + \alpha_{22} \phi_{JJ} + \alpha_{33} \phi_{KK} + \alpha_{12} \phi_{IJ} + \alpha_{13} \phi_{IK} \\ + \alpha_{23} \phi_{JK} + \alpha_1 \phi_I + \alpha_2 \phi_J + \alpha_3 \phi_K = 0 \end{aligned} \quad (22)$$

where

$$\alpha_{11} = (r_I)^{-2} \gamma_1$$

$$\begin{aligned} \alpha_{22} = (\theta_J)^{-2} [(r_I)^{-2} (\theta_I)^2 \gamma_1 + \sin^2 \theta \\ + (\psi_K)^{-2} (\theta_K)^2 + 2f_\theta \sin^2 \theta (r_I)^{-1} \theta_I \\ - 2f_\psi (r_I)^{-1} (\psi_K)^{-1} \theta_I \theta_K] \end{aligned}$$

$$\alpha_{33} = (\psi_K)^{-2}$$

$$\begin{aligned} \alpha_{12} = (r_I \theta_J)^{-1} [-2(r_I)^{-1} \theta_I \gamma_1 - 2f_\theta \sin^2 \theta \\ + 2f_\psi (\psi_K)^{-1} \theta_K] \end{aligned}$$

$$\alpha_{13} = -2(r_I \psi_K)^{-1} f_\psi$$

$$\alpha_{23} = (\theta_J \psi_K)^{-1} [-2(\psi_K)^{-1} \theta_K + 2(r_I)^{-1} \theta_I f_\psi]$$

$$\alpha_1 = (r_I)^{-1} \{ [(r_I)^{-1}]_I \gamma_1 + \gamma_2 \}$$

$$\begin{aligned}
\alpha_2 = & [\gamma_3(\gamma_3)_J - (r_I)^{-1}(\gamma_3)_I] \gamma_1 \\
& + \left\{ \frac{1}{2} (\psi_K)^{-2} [(\theta_J)^{-2} (\theta_K)^2]_J \right. \\
& - (\psi_K)^{-1} [(\psi_K \theta_J)^{-1} \theta_K]_K \left. \right\} \\
& - 2 f_\theta \sin^2 \theta (r_I)^{-1} [(\theta_J)^{-1}]_I \\
& - 2 f_\psi \left\{ \gamma_3 (\psi_K)^{-1} [(\theta_J)^{-1} \theta_K]_J \right. \\
& - (r_I \psi_K)^{-1} [(\theta_J)^{-1} \theta_K]_I \left. \right\} \\
& - \gamma_3 \gamma_2 + (\theta_J)^{-1} \sin \theta \cos \theta
\end{aligned}$$

$$\alpha_3 = \frac{1}{2} [(\psi_K)^{-2}]_K$$

$$\gamma_1 = \sin^2 \theta [(r + f)^2 + (f_\theta)^2] + (f_\psi)^2$$

$$\begin{aligned}
\gamma_2 = & \sin^2 \theta [2(r + f) - f_{\theta\theta}] \\
& - f_\theta \sin \theta \cos \theta - f_{\psi\psi}
\end{aligned}$$

$$\gamma_3 = (r_I \theta_J)^{-1} \theta_I$$

Hull Surface Boundary Condition

$$\begin{aligned}
& (r_I)^{-1} \left[1 + \left(\frac{f_\theta}{f} \right)^2 + \left(\frac{f_\psi}{f \sin \theta} \right)^2 \right] \phi_I \\
& + (\theta_J)^{-1} \left\{ (\psi_K)^{-1} \theta_K \left(\frac{f_\psi}{f^2 \sin^2 \theta} \right) - (r_I)^{-1} \theta_I \right. \\
& \times \left[1 + \left(\frac{f_\theta}{f} \right)^2 + \left(\frac{f_\psi}{f \sin \theta} \right)^2 \right] - \frac{f_\theta}{f^2} \left. \right\} \phi_J \\
& - (\psi_K)^{-1} \left(\frac{f_\psi}{f^2 \sin^2 \theta} \right) \phi_K + \bar{u}A_1 + \bar{v}A_2 = 0
\end{aligned} \tag{23}$$

Kinematic Free Surface Condition

$$\begin{aligned}
& (t_N)^{-1} \eta_N + D_1 (r_I)^{-1} \eta_I + D_2 (\psi_K)^{-1} \eta_K \\
& = \bar{u}B_1 + \bar{v}B_2 + \frac{\phi_\theta - f_\theta \phi_r}{(r + f)^2}
\end{aligned} \tag{24}$$

Bernoulli Equation

$$\begin{aligned}
& (t_N)^{-1} (\phi_N - \phi_J \theta_N / \theta_J) + (\bar{u}A_1 + \bar{v}A_2) \phi_r \\
& + (\bar{u}B_1 + \bar{v}B_2) \phi_\theta + (\bar{u}C_1 + \bar{v}C_2) \phi_\psi + \frac{1}{2} [(\phi_r)^2 \\
& + \left(\frac{\phi_\theta - f_\theta \phi_r}{r + f} \right)^2 + \left(\frac{\phi_\psi - f_\psi \phi_r}{(r + f) \sin \theta} \right)^2] \\
& + g(r + f) \cos \theta + \frac{p}{\rho} = 0
\end{aligned} \tag{25}$$

When used as the dynamic condition at the free surface, terms in this equation are to be evaluated at $\theta = \eta$.

In the equations above, i.e., Eqs. (22)-(25), coefficients A_1, A_2, B_1, B_2 , etc., are the same as given by Eqs. (19). In these coefficients and in Eqs. (24) and (25), spatial derivatives, such as ϕ_r, ϕ_θ , etc., are not expanded in terms of ϕ_I, ϕ_J , etc. Computationally, it is more efficient to compute ϕ_r, ϕ_θ , and ϕ_ψ by Eqs. (21) and temporarily store these values for use in both Eqs. (24) and (25). The same consideration applies to $f_\theta, f_\psi, f_{\theta\theta}$, and $f_{\psi\psi}$. The main purpose of deriving Eqs. (24) and (25) is to provide expressions for evaluating η_N and ϕ_N , the time rates of change of η and ϕ , respectively, at the moving free surface.

It should be pointed out here that all the equations (Laplace equation, hull surface condition, and the kinematic and dynamic free surface conditions) are employed in the upper region, while only the Laplace equation and the hull surface condition are used in the lower region. Furthermore, Eqs. (22) and (23) apply equally well to the lower region if we simply recognize that $\theta_N = \theta_I = \theta_K = 0$ in that region. Therefore, Eqs. (22)-(25) constitute the final set of equations for both regions. Hereafter, our discussion will be in the (I, J, K, N) system.

3. FINITE DIFFERENCE APPROXIMATIONS

The equations derived in the preceding section are to be solved by using finite-difference approximations. First, we must generate a computational mesh. Let (i, j, k, n) be the integer indices identifying the mesh points in the (I, J, K, N) directions, respectively. In the following discussions, as an example, $\phi_{i,j,k}^n$ represents the value of ϕ evaluated at the mesh point (i, j, k), and at the nth time level. Figures 6(a) and 6(b) show the relation of the indices (i, j, k).

Only constant mesh spacings are considered in this paper to simplify the discussion, although our computer program has been written for variable mesh spacings. Let $\Delta I = \Delta J = \Delta K = 1$ be the mesh spacings in the I, J, and K directions, respectively. Then we can write

$$(r_I)_i = (r_{i+1} - r_{i-1})/2$$

$$(\psi_K)_k = (\psi_{k+1} - \psi_{k-1})/2$$

$$(\theta_I)_{i,j,k} = (\theta_{i+1,j,k}^n - \theta_{i-1,j,k}^n)/2$$

$$(\theta_J)_{i,j,k} = (\theta_{i,j+1,k}^n - \theta_{i,j-1,k}^n)/2$$

$$(\theta_K)_{i,j,k} = (\theta_{i,j,k+1}^n - \theta_{i,j,k-1}^n)/2$$

$$(\phi_I)_{i,j,k} = (\phi_{i+1,j,k}^n - \phi_{i-1,j,k}^n)/2$$

$$(\phi_J)_{i,j,k} = (\phi_{i,j+1,k}^n - \phi_{i,j-1,k}^n)/2$$

$$(\phi_K)_{i,j,k} = (\phi_{i,j,k+1}^n - \phi_{i,j,k-1}^n)/2$$

$$(\phi_{II})_{i,j,k} = \phi_{i+1,j,k}^n - 2\phi_{i,j,k}^n + \phi_{i-1,j,k}^n$$

$$(\phi_{JJ})_{i,j,k} = \phi_{i,j+1,k}^n - 2\phi_{i,j,k}^n + \phi_{i,j-1,k}^n$$

$$(\phi_{KK})_{i,j,k} = \phi_{i,j,k+1}^n - 2\phi_{i,j,k}^n + \phi_{i,j,k-1}^n$$

$$(\phi_{IJ})_{i,j,k} = (\phi_{i+1,j+1,k}^n - \phi_{i-1,j+1,k}^n - \phi_{i+1,j-1,k}^n + \phi_{i-1,j-1,k}^n)/4$$

etc. (26)

Using these expressions in Eqs. (22) and (23) leads to a system of algebraic equations with ϕ as the only unknown. The finite-difference version of Eq. (22) applies to all interior points, i.e., $1 < i < \text{IMAX}$, $1 < j < \text{JMAX}$, $1 < k < \text{KMAX}$, while that of Eq. (23) applies to the hull surface, i.e., $i = 1$, $1 < j < \text{JMAX}$, $1 < k < \text{KMAX}$.

To apply the free surface conditions, Eqs. (24) and (25), we write

$$t_N = t^{n+1} - t^n = \Delta t \text{ (time step)}$$

$$\phi_N = \phi_{i,j,k}^{n+1} - \phi_{i,j,k}^n \quad (27)$$

$$\eta_N = \eta_{i,k}^{n+1} - \eta_{i,k}^n$$

Equation (24) can be expanded to read

$$\begin{aligned} & (t_N)^{-1} \eta_N + D_1(r_I)^{-1} \eta_I + D_2(\psi_K)^{-1} \eta_K \\ & = \bar{u}B_1 + \bar{v}B_2 - \frac{f_\theta(r_I)^{-1} \phi_I}{(r+f)^2} \\ & + (\theta_J)^{-1} \frac{1 + f_\theta \theta_I}{(r+f)^2} \phi_J \end{aligned} \quad (28)$$

Using Eqs. (27), Eq. (28) becomes

$$\begin{aligned} \eta_{i,k}^{n+1} = \eta_{i,k}^n + \Delta t & \left\{ -D_1(r_I)^{-1} \eta_I - D_2(\psi_K)^{-1} \eta_K \right. \\ & + \bar{u}B_1 + \bar{v}B_2 - \frac{f_\theta(r_I)^{-1} \phi_I}{(r+f)^2} \Big\}_{i,1,k}^n \\ & + \Delta t \left\{ (\theta_J)^{-1} \frac{1 + f_\theta \theta_I}{(r+f)^2} \right\}_{i,1,k}^n \\ & \cdot (\phi_{i,2,k}^{n+1} - \phi_{i,1,k}^{n+1}) \end{aligned} \quad (29)$$

In this equation, the term ϕ_J has been cast in implicit form, i.e., evaluated at the new time level $n+1$. Similarly, applying Eq. (25) at $\theta = \eta$ and finite differencing, we have

$$\begin{aligned} \phi_{i,1,k}^{n+1} = \phi_{i,1,k}^n + (\phi_J/\theta_J)_{i,1,k}^n (\eta_{i,k}^{n+1} - \eta_{i,k}^n) \\ - \Delta t \left\{ (\bar{u}A_1 + \bar{v}A_2) \phi_r + (\bar{u}B_1 + \bar{v}B_2) \phi_\theta \right. \\ + (\bar{u}C_1 + \bar{v}C_2) \phi_\psi \Big\}_{i,1,k}^n - \frac{\Delta t}{2} (\phi_r)^2 \\ + \left[\frac{\phi_\theta - f_\theta \phi_r}{r+f} \right]^2 + \left[\frac{\phi_\psi - f_\psi \phi_r}{(r+f) \sin \theta} \right]^2 \Big\}_{i,1,k}^n \\ - \Delta t g (r+f) \cos \eta_{i,k}^{n+1} \end{aligned} \quad (30)$$

In Eqs. (29) and (30), the subscript $j=1$ refers to a mesh point at the free surface. The last term in Eq. (30) is implicit. Thus, Eqs. (29) and (30) are to be solved simultaneously for the two unknowns $\phi_{i,1,k}^{n+1}$ and $\eta_{i,k}^{n+1}$. This implicit coupling is necessary to avoid restriction on the time step Δt by Courant condition based on the fastest wave component in the physical system. The treatment here is analogous to the implicit formulation for pressure in the ICE technique [4] to remove restriction on Δt by sonic speeds in calculating low speed compressible flows. When Eqs. (29) and (30) are applied at points lying on the water line (i.e., the intersection of free surface with the hull), the quantity ϕ_I appearing in these two equations must be computed by using Eq. (23), which can be rearranged to express ϕ_I in terms of ϕ_J and ϕ_K . This is done to insure that both the free surface conditions and the hull surface condition are satisfied.

4. OTHER BOUNDARY CONDITIONS AND INITIAL CONDITIONS

We have already discussed some of the boundary conditions. For example, Eq. (23) is to be satisfied by ϕ at the hull surface, and simultaneous solution of Eqs. (29) and (30) provides values of ϕ^{n+1} at free surface points. The only boundary condition remaining to be described is that occurring at the "outflow" boundary, where the flow field is truncated by the computational mesh [corresponding to $i = \text{IMAX}$ in Figs. 6(a) and (b)]. At these mesh points, proper outflow condition must be imposed so that waves can leave the region of interest with minimum amount of nonphysical reflections. This condition is crucial to successful computation of wave propagation in a limited domain. Details of the outflow condition can be found in References 1 and 2.

The initial conditions used in our study are quite simple. The ship is assumed to be at rest at $t = 0$, and then accelerated to a final constant velocity. In due time the flow field in the computation domain should reach a steady state. Thus, at $t = 0$, ϕ is zero everywhere, and η assumes the values for a flat free surface.

5. SOLUTION PROCEDURE

The evolution of the flow field is obtained by performing step-by-step numerical integration of the governing finite-difference equations with respect to time. The following is a description of the sequence of computations required to advance the flow field by one time step.

- Apply the outflow boundary condition to obtain new values of η and ϕ (i.e., η^{n+1} and ϕ^{n+1}) at mesh points on the outer boundary of the domain.
- Obtain η^{n+1} and ϕ^{n+1} at free-surface points by solving Eqs. (29) and (30) simultaneously.
- Obtain the internal distribution of ϕ by solving the finite-difference representation of Eq. (22), for both the upper and the lower region, using the method of successive relaxation. In solving this equation, various boundary conditions must be satisfied. For example, ϕ must be equal to the value of ϕ^{n+1} at the free surface, which was obtained in step b above; ϕ is equal to the value of ϕ^{n+1} for outflow points as computed in step a; at the hull surface, ϕ satisfies Eq. (23).

Because of the yet unknown quantity $\phi_{1,2,k}^{n+1}$ in Eq. (29), which is the value of ϕ at the first mesh point below the free surface, steps b and c must be iterated until a prescribed convergence criterion is met.

6. EXAMPLES AND DISCUSSIONS

The present method has been employed to compute the flow field and wave drag for several body shapes. For the purpose of

testing the various steps of the solution procedure and comparing with existing theories, the forward motion of a semi-submerged sphere was first simulated. As shown in Fig. 7, the origin of the (r, θ, ψ) system is located below the center of the sphere by a distance H . The "upper region" is thus bounded by the free surface and the plane containing the x -axis. The sphere is assumed to be at rest at the initial instant $t = 0$, and it is then accelerated to a constant, final velocity. This final velocity is maintained until the flow field in the computational domain reaches a steady state. During the early phase of the acceleration, when the free surface displacement is still very small, the force experienced by the sphere should be nearly equal to one half of that experienced by a sphere accelerating in an infinite expanse of fluid. Results of our calculations are in agreement with this limiting behavior.

The development of the surface wave pattern is shown in Figs. 8(a)-8(l), as a sequence of contour plots of the free surface displacement. In these plots the sphere is viewed from above and its motion is from left to right. Upward displacement is indicated by solid lines, while broken lines mean that the free surface is below the initially undisturbed water surface. In Fig. 8(a), the sphere has just started to accelerate. A surge of water appears at the bow and a depression forms at the rear. This pattern continues to grow until, at about $t = 3.4$, a new crest appears at the stern and the first bow wave begins to move away from the bow. At this time, a pair of troughs have developed along the sides. At $t = 4.6$, Fig. 8(h), the first bow wave has left the computational region completely, and a new bow wave just appears. This becomes more evident in Fig. 8(i). Figure 8(l) shows the free surface configuration when the steady state is finally reached. The Froude number for this case is $F_r = 0.15$, based on the final speed of the

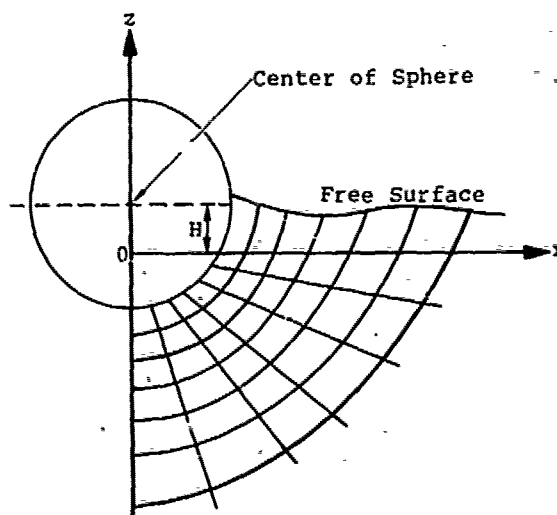
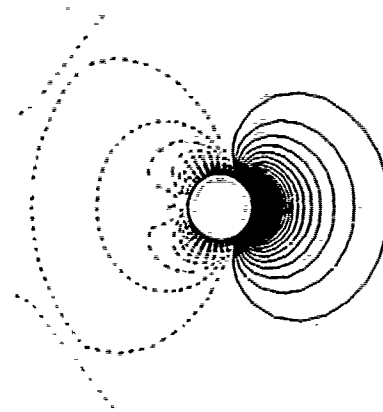


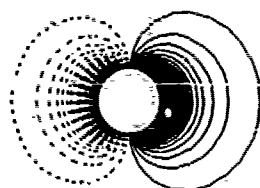
Fig. 7 Mesh Configuration for Semi-Submerged Sphere



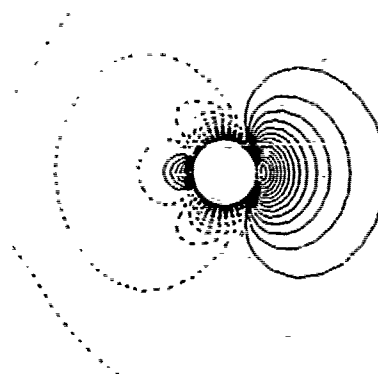
(a) $T = 0.3000$



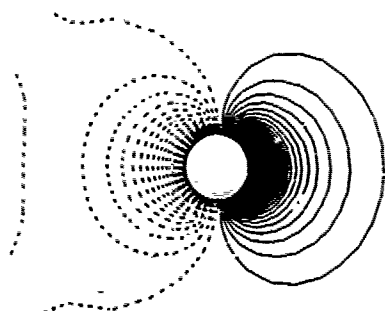
(d) $T = 3.1000$



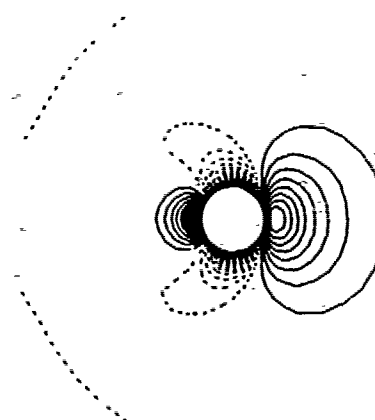
(b) $T = 1.3000$



(e) $T = 3.4000$

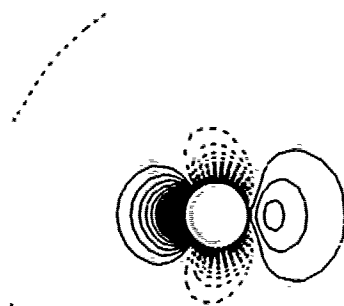


(c) $T = 2.3000$

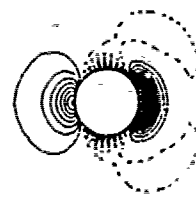


(f) $T = 3.6000$

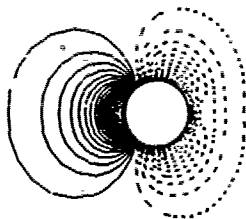
Fig. 8 Evaluation of Free Surface Displacement for the Forward Motion of a Semi-Submerged Sphere ($F_r = 0.15$)



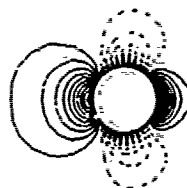
(g) $T = 3.9000$



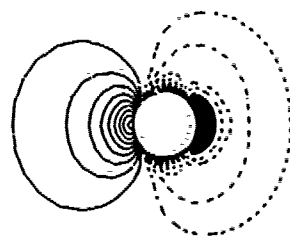
(j) $T = 5.9000$



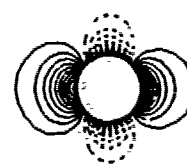
(h) $T = 4.6000$



(k) $T = 8.8000$



(i) $T = 5.5000$



(l) $T = 26.5000$

Fig. 8 (Continued)

sphere. U , its radius R , and the gravitational acceleration g . In all our discussions, lengths are normalized by L (characteristic length of the problem), velocities by \sqrt{gL} , and time by $\sqrt{L/g}$. In this case, $L = R$. Figures 9(a)-9(l) show a similar sequence of contour plots for the case $F_r = 0.10$. These close-up plots show more details of the wave pattern in the vicinity of the sphere than do Figs. 8(a)-8(l).

Wave drag can be calculated by integrating the pressure distribution over the wetted hull surface and taking the component opposite the direction of the ship's motion. The pressure at each mesh point lying on the hull surface can be easily computed by using the Bernoulli equation, Eq. (25). For $F_r = 0.10, 0.15$, and 0.20 , our computed wave drags are compared with the theory of Baba and Hara [5], in Fig. 10. Note that the characteristic length used in their Froude number is $L = 2R$. Thus, our $F_r = 0.2$ is equivalent to their $F_r = 0.2/\sqrt{2} = 0.141$. The resistance coefficient C_w is defined as

$$C_w = \frac{R_w}{\frac{1}{2} \rho U^2 (2R)^2} \quad (31)$$

where R_w is the net horizontal force experienced by the sphere.

As another test case, the flow about an HSVA tanker [6] and the associated wave drag were simulated. The hull geometry of an HSVA tanker is shown in Fig. 11. Again, the tanker is initially at rest, and then accelerated to a constant speed. The computation is terminated when the steady state is reached. The computed values of wave drag for several Froude numbers F_r are compared with experimental measurements in Fig. 12. The agreement is judged to be reasonably good. Steady states were obtained for $F_r < 0.15$. For $F_r = 0.16$, however, the flow field does not settle down to steady state. For $F_r > 0.17$ the bow wave steepens sharply and its amplitude grows rapidly. This behavior seems to be consistent with some experimental evidence that breaking of bow waves may occur at these values of Froude number.

An interesting application of the present method is to study the effect of change in hull geometry on the flow pattern and wave drag. The HSVA tanker in Fig. 11 is modified to add a protruded nose at the lower portion of the bow, as shown in Figs. 13 and 14. With the modified bow, we found the instability of the bow wave occurring at $0.18 < F_r < 0.19$, higher than that for the original HSVA tanker. Thus, the protruded bow seems to delay the threshold of wave breaking to a higher Froude number. The wave drag coefficients for this calculation are also shown in Fig. 12. Although the coefficient for the modified HSVA is greater than that for the original HSVA (at $F_r = 0.15$), it must be noted that for tankers most of the resistance comes from wave breaking, and therefore the delay on wave breaking can significantly contribute to

the reduction of the total wave drag. The sharp increase of wave resistance for $F_r > 0.15$ in the experimental data is in fact due to the formation of breaking waves. Thus, by comparing our computed value of C_w for the modified HSVA and the measured C_w , we can see that a 50% reduction of the wave drag is possible at $F_r = 0.17$, and even more at $F_r = 0.18$.

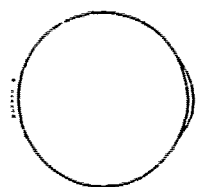
The development of free surface wave pattern near the hull of the modified HSVA tanker is shown in Figs. 15(a)-15(h). The motion of the ship is from left to right. The steady state is reached after $t > 3.70$, as in Figs. 15(g) and 15(h). The computational mesh on the center plane is shown in Fig. 16 for the HSVA and in Fig. 17 for the modified HSVA, with the bow of both pointing to the right. Close-up of the mesh near the bow for the HSVA is shown in Fig. 18(a). Velocity vectors associated with each mesh point are shown in Fig. 18(b) in an inertial frame of reference, while the same velocity field with frame of reference fixed in the ship is shown in Fig. 18(c). Similar plots are shown in Figs. 19(a)-19(c) for the stern region. Figures 20(a)-20(c) and Figs. 21(a)-21(c) show the same type of information for the modified HSVA tanker.

ACKNOWLEDGEMENT

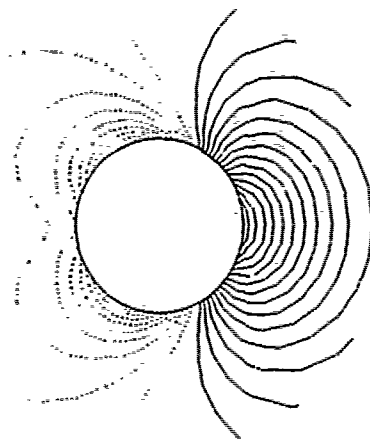
This work was sponsored by the Office of Naval Research under the Fluid Dynamics Program.

REFERENCES

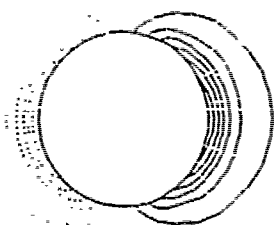
1. Orlanski, I., "A Simple Boundary Condition for Unbounded Hyperbolic Flows," *Journal of Computational Physics*, Vol. 21, 1976.
2. Chan, R. K.-C., "Finite Difference Simulation of the Planar Motion of a Ship," *Proceedings of the Second International Conference on Numerical Ship Hydrodynamics*, Berkeley, California, 1977, pp.39-52.
3. Thompson, J. F., Thames, F. C. and Mastin, C. W., "Automatic Numerical Generation of Body-Fitted Curvilinear Coordinate System for Field Containing Any Number of Arbitrary Two-Dimensional Bodies," *Journal of Computational Physics*, Vol. 15, 1974, pp. 299-319.
4. Harlow, F. H. and Amsden, A. A., "A Numerical Fluid Dynamics Calculation Method for All Flow Speeds," *Journal of Computational Physics*, Vol. 8, 1971, pp.197-213.
5. Baba, E. and Hara, M., "Numerical Evaluation of a Wave-Resistance Theory for Slow Ships," *Proceedings of the Second International Conference on Numerical Ship Hydrodynamics*, Berkeley, California, 1977, pp.17-29.
6. Collatz, G., "Mass-stabsuntersuchungen für ein Modell grosser Völligkeit," *Forschungszentrum des Deutschen Schiffbaus*, Hamburg, Bericht Nr. 28, 1972.



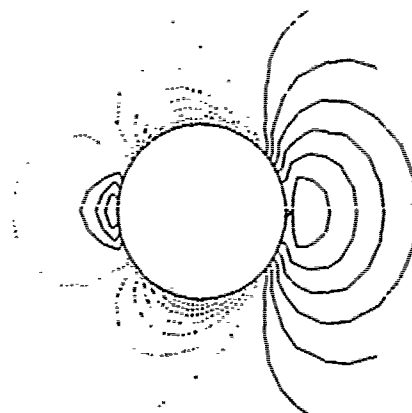
(a) $T = 0.2000$



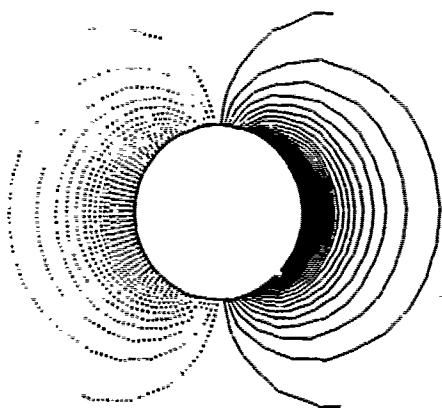
(d) $T = 3.1000$



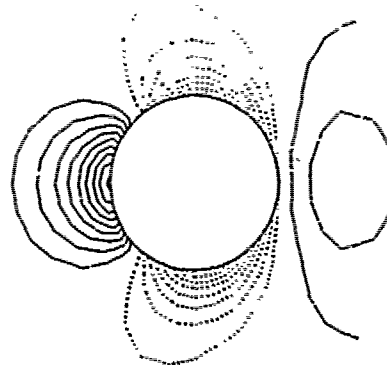
(b) $T = 0.5000$



(e) $T = 3.4000$

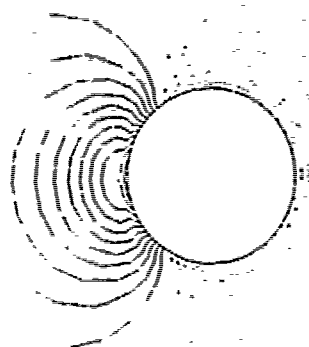


(c) $T = 1.3000$

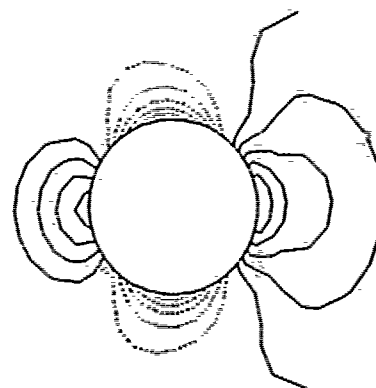


(f) $T = 3.7000$

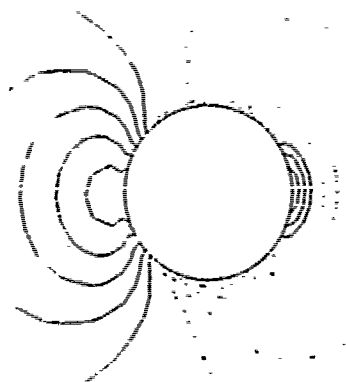
Fig. 9 Close-Up of Free Surface Displacement Contours for a Semi-Submerged Sphere ($F_r = 0.10$)



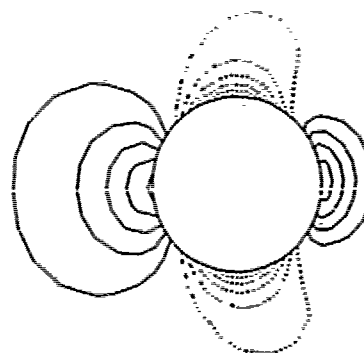
(g) $T = 4.4000$



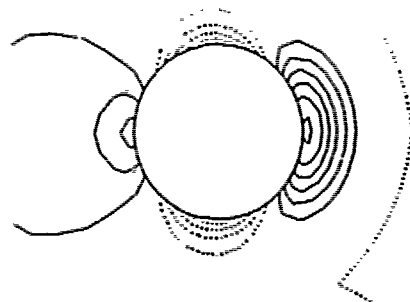
(j) $T = 7.2000$



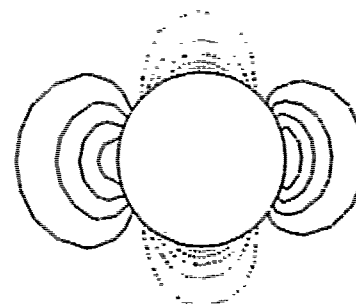
(h) $T = 5.1000$



(k) $T = 8.5000$



(i) $T = 5.7000$



(l) $T = 31.3000$

Fig. 9 (Continued)

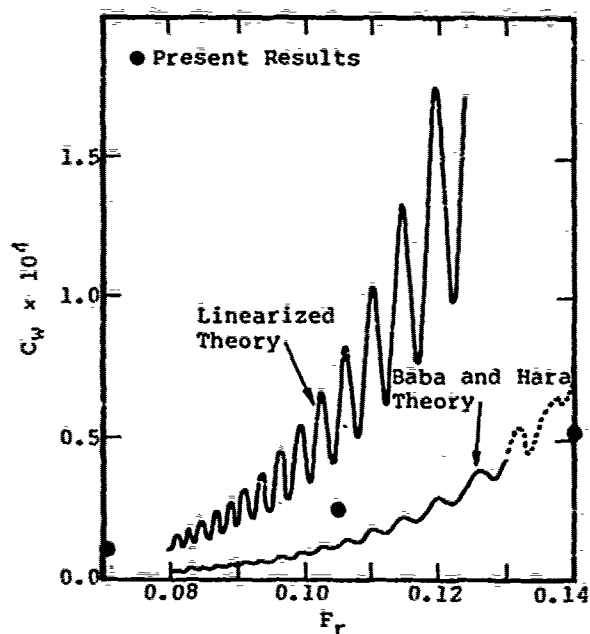


Fig. 10 Comparison of Wave Drag Coefficient C_w for a Semi-Submerged Sphere

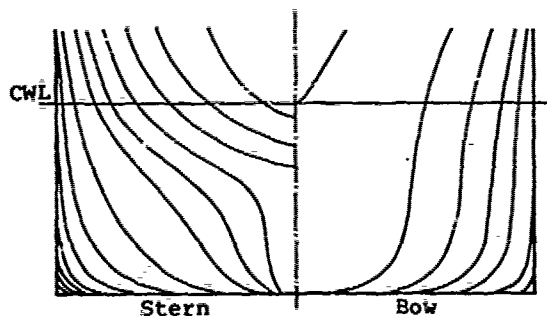


Fig. 11 Body Plan of HSVA Tanker (from Collatz [6])

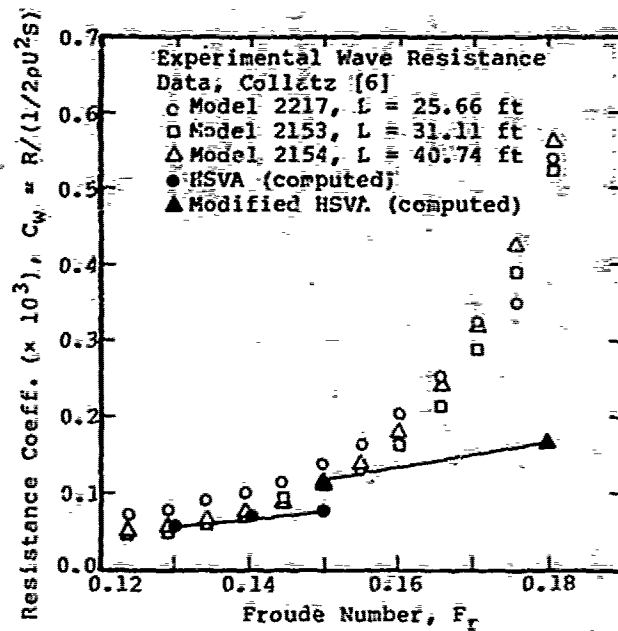


Fig. 12 Comparison of Wave Resistance Data for the HSVA Tanker

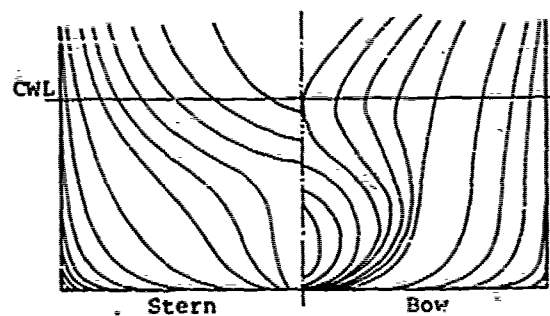


Fig. 13 Body Plan of Modified HSVA with Protruded Bow

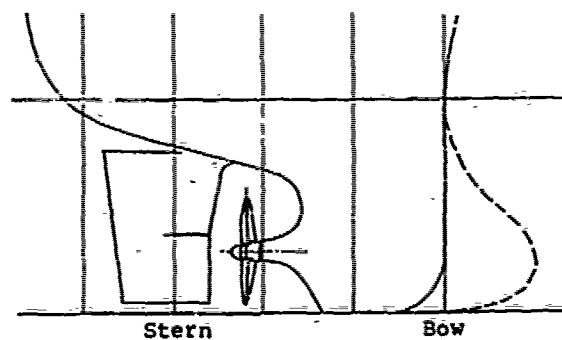
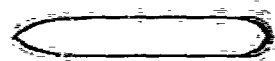


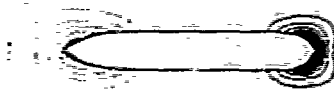
Fig. 14. Bow and Stern Profiles for the HSVA Tanker (from Collatz [6]). The protruded bow for the modified HSVA is indicated by the broken line.



(a) $T = 0.1200$



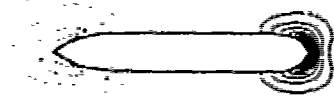
(e) $T = 0.7800$



(b) $T = 0.4000$



(f) $T = 1.6000$



(c) $T = 0.5000$



(g) $T = 3.7200$



(d) $T = 0.6400$



(h) $T = 8.4400$

Fig. 15 Contours of Free-Surface Displacement for the Modified HSVA Tanker

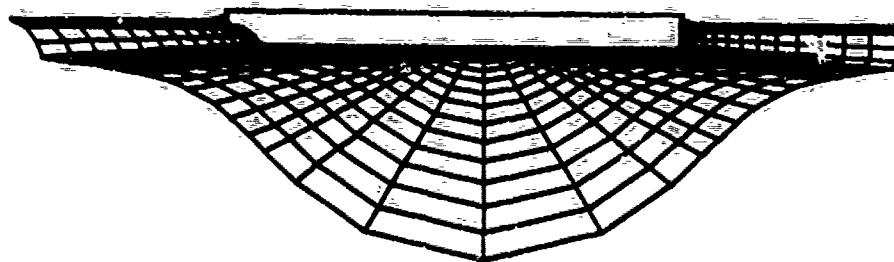


Fig. 16. Computational Mesh on the Center Plane of an HSVA Tanker

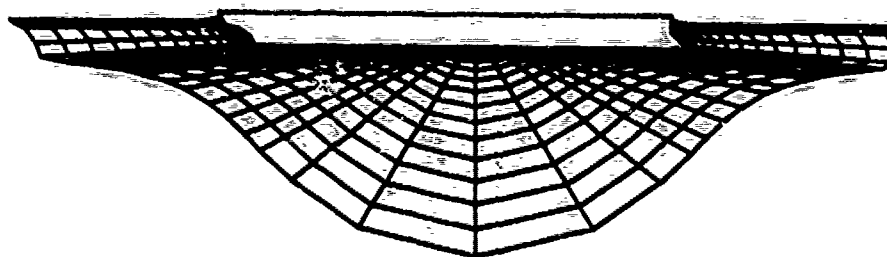
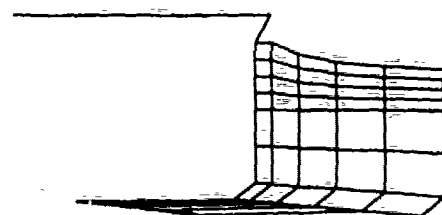
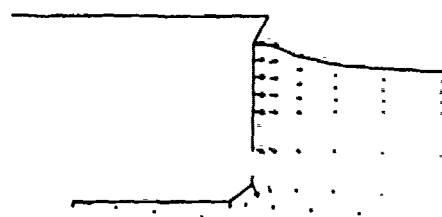


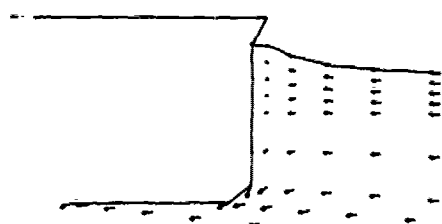
Fig. 17 Computational Mesh for the Modified HSVA Tanker



(a) Mesh

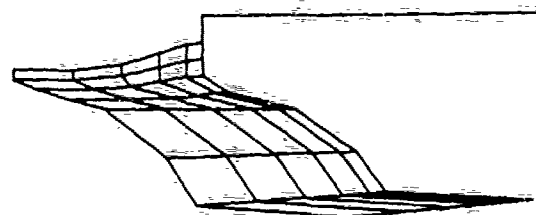


(b) Velocity Vectors in the (X,Y,Z,T) System

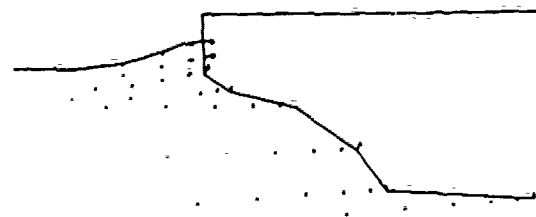


(c) Velocity Vectors in the (x,y,z,t) System

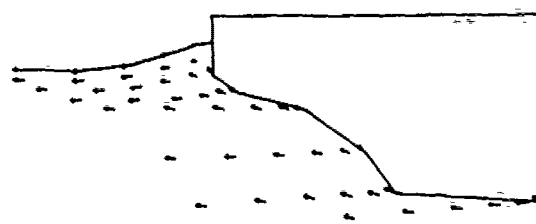
Fig. 18 Mesh and Velocity Vector Field Near the Bow of HSV A Tanker ($F_r = 0.15$)



(a) Mesh

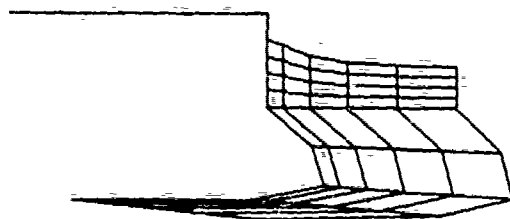


(b) Velocity Vectors in the (X,Y,Z,T) System

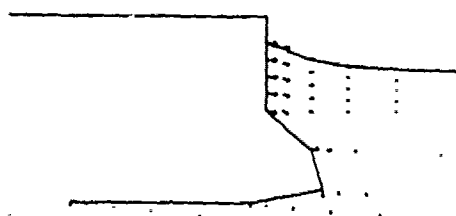


(c) Velocity Vectors in the (x,y,z,t) System

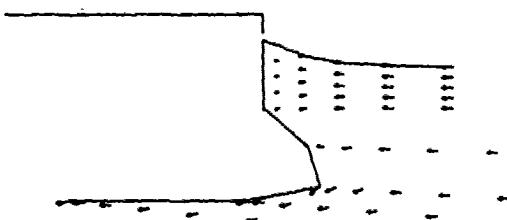
Fig. 19 Mesh and Velocity Field Near the Stern of HSV A Tanker ($F_r = 0.15$)



(a) Mesh

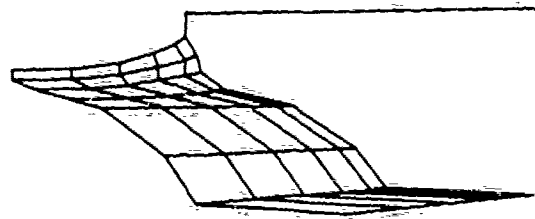


(b) Velocity Vectors in the (X,Y,Z,T) System

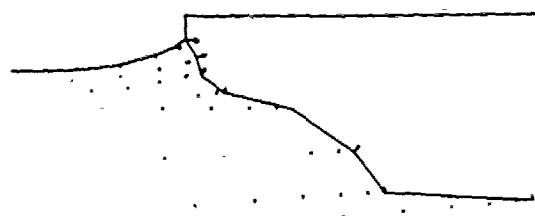


(c) Velocity Vectors in the (x,y,z,t) System

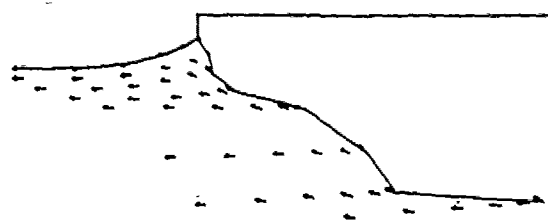
Fig. 20 Mesh and Velocity Field Near the Bow of Modified HSVA Tanker ($F_r = 0.15$)



(a) Mesh



(b) Velocity Vectors in the (X,Y,Z,T) System



(c) Velocity Vectors in the (x,y,z,t) System

Fig. 21 Mesh and Velocity Field Near the Stern of Modified HSVA Tanker ($F_r = 0.15$)

Discussion

H. Miyata (Univ. of Toky.o)

The authors' numerical method seems not to be effective for the estimation of the linear dispersive wave system but is effective for the estimation of local non-linear waves in the nearfield of ships, such as free-surface shock waves.

One of the authors developed a modified MAC method (SUMMAC) in 1970*. I think MAC method is preferable to the present method for the calculation of non-linear flows around the bow because it is a direct calculation of the Navier-Stokes equation.

The authors' opinion will be greatly appreciated.

* Journal of Computational Physics 6, 68-94 (1970)

K. Mori (Hiroshima Univ.)

The discussor appreciates the paper presented by Drs. Chan and Chan.

The method is quite general and promising. The generality brings forth, on the other hand, requirements of unrealistic computing time and huge memory storage. Then computations are forced to be carried out by use of coarse mesh sizes and domains of computation to be restricted insufficiently for our demands. According to the discussor's primitive experiences, the mesh size is crucial for the final results.

Fig. A1 shows the wave profiles due to a 2-D submerged point source compared with analytic solutions, where $K_0 f = 1.0$; K_0 : wave number, f : depth of submergence. The method is the Rankine-source method different from that of Drs. Chan and Chan. The mesh size of 0.25 may be the minimum in 3-D cases for usual computers. The results are not satisfying; the wave length is shorter and the amplitude is a little large (of course this depends on differencing schemes). The discussor recalls that the authors' last results were noted by Professor Newman for the same tendencies in wave length¹). Dr. Hess has also examined the errors through his pilot computations²). He proposes, in order to be free from such errors, the use of the higher approximations for free-surface figures and related quantities. The introduction of them improves the errors (+ in Fig. A1).

Though it is not clear how finite the mesh sizes of ΔI , ΔJ , $\Delta K=1$ are compared with the wave length, they are suspected to be rather coarse because the wave length of the present cases is very short. Be-

sides, to the discussor, the present results seem not to be free from the above errors; in spherical polar coordinates, the hull-surface panel sizes around bow and stern or free surface and the grid spacing near centerplane or free surface get unevenly coarse which are the most important domain in ship wave problems.

The discussor is of convince that it is primarily important the numerical scheme should be always checked for simple cases (the present computations for the sphere do not play that role). Only from the wave resistance results we can not evaluate the method properly.

REFERENCES

- 1) Newman, J.N., Discussions: Session I papers, "The proceedings of the Second International Conference on Numerical Ship Hydrodynamics", pp.53 (1977).
- 2) Hess, J.L., "Progress in the Calculation of Nonlinear Free-Surface Problems by Surface-Singularity Techniques", *ibid*, pp.278.

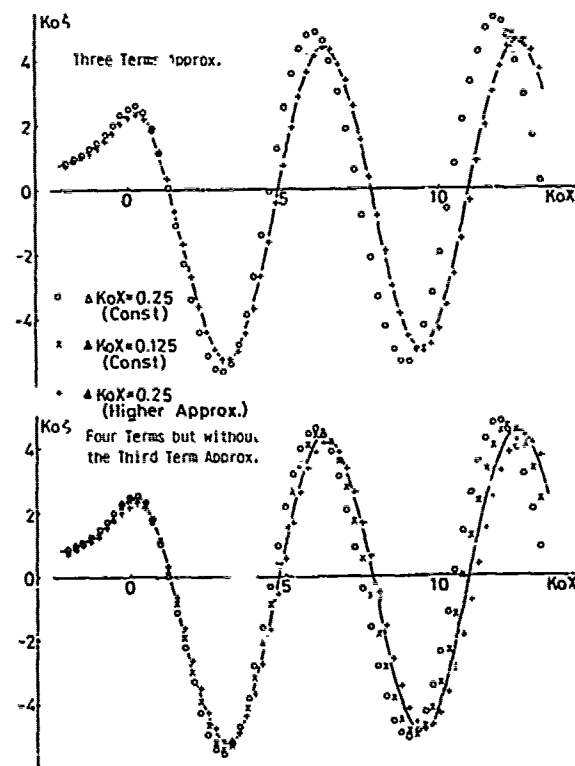


Fig. A1
Wave profiles of a 2-D submerged point source obtained by Rankine Source Method for different numerical schemes ($K_0 f = 1.0$, $\sigma_0 = 2\pi U/K_0$, σ_0 : source strength, U : uniform velocity)

Y Kayo (MHI)

I have enjoyed reading this paper and am impressed with the authors' effort to solve numerically the exact boundary-value problems within the framework of potential theory.

The authors found that the numerical simulation of the flow field around a full hull form did not settle down to the steady state at higher Froude numbers. The authors explained that the waves might break beyond these speeds when the bow wave steepened sharply and became unstable.

To get a better understanding of the wave-breaking phenomenon, the present discussor made an experimental study of a bow wave of a full ship model by a flow visualization technique. A 6^m model in length was used to observe the flow field around her bow in the Nagasaki Experimental Tank of Mitsubishi Heavy Industries.

Fig.1 is the photograph of the flow field observed at the central plane in front of the model. A vortical fluid

movement is seen just below the disturbed free surface where the wave breaks. This fluid region, which may be considered as turbulent flow, does not spread widely in depth. The thickness of this turbulent flow is nearly the same as the wave height itself.

From this observation the bow-wave breaking seems to resemble the phenomenon of the decelerated stagnation flow with separation as shown in Fig.2. It is known even in the case of free-surface flows that an upstream vortex is formed. The free surface is then considered to behave like a membrane as pointed out by Hori [1] in an experimental study around $Re \approx 10^4$. The very thin layer of the free surface moves with the body while the fluid below the layer does not move so fast. Therefore a thin layer such as a laminar boundary layer is developed beneath the free surface.

The present discussor considers that the shear flow at the free surface is the cause of the bow wave breaking of a full form. To clarify the mentioned instabili-

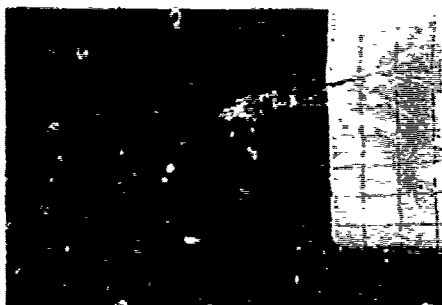


Fig. 1 Flow around the bow
 $V_m = 1.284 \text{ m/s}$ $Fn = 0.167$

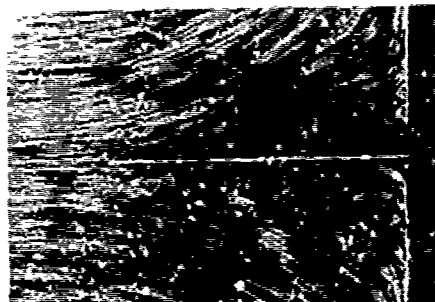


Fig. 2
Decelerated stagnation flow with separation (as photographed by Foettinger and printed in Ref.1)

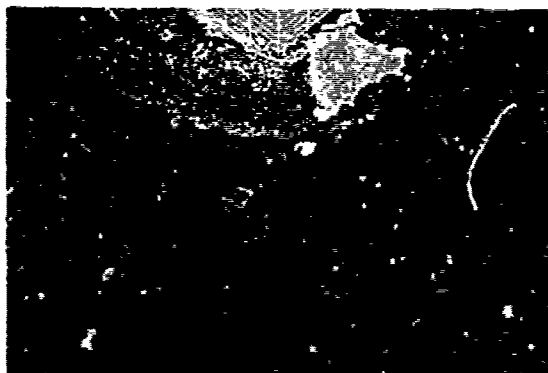


Fig. 3
Wave breaking around the bow
 $V_m = 1.284 \text{ m/s}$ $Fn = 0.167$

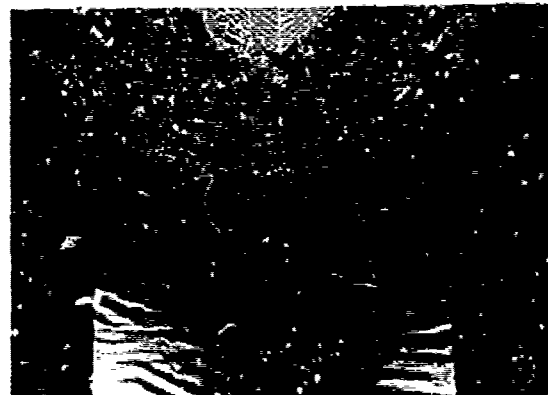


Fig. 4
Wave breaking around the bow with decelerated flow of a thin free-surface layer $V_m = 1.284 \text{ m/s}$ $Fn = 0.167$

ty of the free surface in the case of a flow of large Reynolds number, around $Re \approx 10^7$, the present discussor made some observations.

A sheet of vinyl film was made afloat and was towed with the same speed as the ship model in front of her to retard the flow of a thin free surface layer. When the sheet was present the wave breaking was developed more heavily and the area of breaking expanded widely. (Fig. 3 and 4)

It was also found that the bow-wave breaking could be controlled by a means usually used to prevent boundary-layer separation. Namely, when accelerating the thin surface layer by using a water spray or a blower, the wave breaking decreased considerably.

Judging from the above mentioned behavior of the bow-wave breaking, the present discussor thinks that it may be considered that the breaking of bow wave is due to flow separation at the free surface.

I would like to suggest that such flow characteristics of the free surface should be taken into account in the next stage of the development of numerical work.

REFERENCES

- 1) Schlichting, H., "Boundary Layer Theory", Sixth Edition, McGraw-Hill, New York, (1968)
- 2) Honji, H., "Observation of a Vortex in Front of a Half-Submerged Circular Cylinder", Journal of the Physical Society of Japan, Vol. 40, No. 5, (1976)

H. Maruo (Yokohama N. Univ.)

The authors have developed a purely numerical method to calculate the free-surface flow around a ship whose shape can be quite general. This paper is very interesting because the computation procedure is described in considerable detail. The method seems very versatile and is promising in the sense that the exact non-linear boundary-value problem can be handled directly. This is a kind of space-discretization method, and its shortcoming is the requirement of large computer capacity. On observing the computation results, I feel that the mesh division is not fine enough to obtain wave patterns which are comparable with measurement. I wish to hear the authors' opinion about the feasibility of this method by the use of existing large computers. There is another method of numerical computation of the free-surface flow, that is the method of boundary discretization. This method assumes source distribution over the free surface as well as hull surface. Starting from the initial rest, the solution is calculated in succession by a finite-difference method. Thus the mesh division is two-dimensional in contrast to the three-dimensional discretization of the present method. What is the authors' opinion about the relative merit

of the two methods ?

K. Nakatake (Kyushu Univ.)

I appreciate Drs. Chan and Chan for their pioneering work in this field.

I have two discussions.

In the Orlanski's boundary condition, what is the converged value of the phase velocity C at the final steady state ?

In their method, they must solve, for a huge number of unknowns. Most of them have no relation with wave motion directly. Is it possible to reduce them by using the solution of the double-body flow ?

Author's Reply

R.K.-C. Chan (JAYCOR)

Reply to Prof. Miyata

The present method is indeed designed for studying waves in the near field of ships. Both linear and nonlinear waves can be effectively computed if the mesh resolution is fine enough. As it stands now, of course, it cannot handle the formation of free surface shock waves, which involves rotation of fluid elements. The "upper region" of our model can be easily extended to use Navier-Stokes equation. The SUMMAC Method (Stanford-University-Modified-Marker-and-Cell Method) was developed by myself about 10 years ago. The problem with SUMMAC when applied to ship problem is that boundary conditions at the hull surface are difficult to apply for general hull geometry, because SUMMAC uses a fixed rectangular mesh. However, for simple geometries, such as a wedge-like prism with a truncated flat bottom, SUMMAC may be quite useful as a tool for nonpotential flow simulations.

Reply to Prof. Mori

Professor Mori is quite correct in pointing out the fact that the resolution of the computational mesh can affect the solution to a large extent. And, in fact, we have not used the kind of fine resolution which we'd like to use in the sample problems. In the sample calculations the mesh size was largely dictated by the small core memory of the CDC7600 system. We could have used the large core memory to increase resolution in our calculations. It is also quite true that generality of the method requires much higher cost of computation. A typical computation to reach steady state from the initial rest position costs about 100 US Dollars. (Which may not be too bad for our Japanese colleagues if the US dollar

keeps devaluating with respect to Yen) But seriously, our general approach is indeed much more expensive than other schemes that take advantage of the properties of potential flow. However, our model can be easily extended to include nonpotential flow features, such as the shear layer near the free surface as suggested by Dr. Kayo. For problems like that, I don't see how the Rankine source method would work. I think there simply isn't such thing as something for nothing. The objective of our work was to experiment with a fairly general numerical method, making use of fewer assumptions. Therefore, our present method must be considered as a research tool with which various hypotheses and mechanisms can be tested, but not as a tool for day-to-day calculation in ship design.

Reply to Dr. Kayo

From his experimental observations, Dr. Kayo offers an explanation for the bow wave breaking of a full form. He considers the shear flow at the free surface as the major cause for breaking. Since our present model assumes a potential flow, we are not able to compare our results with his observation. However, the "upper region" in our model can be generalized to simulate nonpotential, shear flows, which, together with more experimental work, may lead to a better understanding of the breaking mechanism and perhaps a more realistic mathematical model to handle the complicated interaction between the shear layer and the free surface.

Reply to Prof. Maruo

Professor Maruo has asked two questions. The first is about the feasibility of our method using existing large computers, and the second is the relative merit of our approach compared to the method of source distribution. To the first question, I would say that it is quite feasible to use our method with good spatial resolution in large computers, such as the CDC7600. As stated in my reply to Prof. Mori, our sample calculations reported in the paper were dictated by the size of the small core memory of the CDC7600. And the mesh used in these samples was rather coarse. By using the large core memory, we would be able to increase the resolution quite a bit. I should also point out that the dis-

crete distribution of velocity potential ϕ below the free surface is the major reason for requiring large amount of computer time and storage. Nowadays, there exist several very powerful methods for solving discretized elliptic equations which may be used to drastically reduce the computer time. In addition, the new vector processor in some computers can reduce the computer time even further. To the second question, I would agree that the method of boundary source distribution is superior to our method, if one is interested in steady-state potential flows only. But to include nonpotential-flow features, such as the free surface shock waves, it is not clear to me how the source distribution method can be extended, while our approach seems to have a reasonable chance of including additional physics which may not be representable by potential flow.

Reply to Prof. Nakatake

Professor Nakatake's first question refers to our outflow boundary condition which is described in an earlier paper by me and presented at the Second International Conference on Numerical Ship Hydrodynamics in Berkeley three years ago. As I recall, the value of C (the local wave velocity at the outflow boundary point) is never directly computed. The quantity C is used only in deriving the ultimate finite difference expression which gives a prediction for the flow variables at the boundary point as a function of the time step and the information inside the flow domain and backward in time. When steady state is reached, there is no more wave propagation through the boundary, and, therefore, the value of C (if computed) would approach zero. The second question is whether it's possible to perform calculations in a more limited flow domain, using the double-body flow as the base flow, and just focus on the perturbation. The answer is certainly yes. That, I think, would cut down the computer time and storage requirement considerably. In fact, by comparing the solutions produced by the more complete model and the double-body linearization, one can determine whether the simpler, double-body approach is sufficient for all practical purposes. I appreciate this suggestion from Professor Nakatake.

On the Time Dependent Potential and Its Application to Wave Problems

Hiroyuki Adachi and Shigeo Ohmatsu
Ship Research Institute
Tokyo, Japan

ABSTRACT

The 2-Dimensional time dependent potential, governed by the Laplace equation and satisfying the linearized free surface condition and the initial condition, has many applications to ship wave problems, especially to the problem of bodies making arbitrary motion starting from $t=0$.

The corresponding boundary value problem to the potential has some interesting features which are considered to be important from the point of the numerical analysis of the problem. We discuss this problem and propose the method of numerical treatment of the boundary value problem.

Three applications of the 2-D time dependent potential will be discussed. First the response of bodies to the given incident waves and the radiation wave problem of the motion of bodies are discussed. Secondly the so-called "high speed slender ship theory", that is a kind of "strip theory" with forward speed effect, is discussed. Thirdly the flow field around the bow near field in the steady ship motion problem is analysed by making use of the slender ship theory under the low speed assumption.

NOMENCLATURE

A	Constant in (56)
a	Half breadth of cylinder
B(y,z)	Normal velocity on hull
c(t), c(x)	Hull contour at t or x
C _{ij}	Restoring force or moment coefficient
De, Di	Exterior and interior regions
D(x,y)	Source distribution on free surface
E(x)	Memory effect function

E(x,y)	Source distribution on free surface
Fe, Fi	Free surface outside and inside of c
F _i (t)	External force in i th mode
F(x,y), F _j (x,y)	Source distribution on free surface
G(y,z,η,ζ,t-τ)	Green's function
G*(y,z,η,ζ,λ)	Green's function
G(x,y,z,ξ,η,ζ)	Green's function
g	Gravitational acceleration
H(t,g)	Kochin function in time domain
H*(λ,g)	Kochin function in frequency domain
H(k,ε)	Kochin function in steady wave making resistance
K, K _j	$= \lambda^2/g, \lambda_j^2/g$, Wave number
L _{ij} (t)	Memory effect coefficient function in (39)
m _{ij}	Mass or moment of inertia coefficient
\vec{n}	2-D normal directed into c
\hat{n}	3-D normal directed into S _B
n _i (Q)	i th component of generalized vector
P, \hat{P}	Field point in De and Di
Q	Point on hull
S _B	Ship hull surface
v(Q,t)	Normal velocity on hull
(x,y,z)	Cartesian coordinates
Y(x), Y*(λ)	Line source distribution and its Fourier transform
δ	Small parameter representing slowness
ε	Small parameter representing slenderness
(ξ,η,ζ)	Coordinates on hull
θ(x,y)	Free surface elevation
λ, λ _j	Frequency of motion, j th irregular frequency

μ_{ij}	Added mass or added moment of inertia
v	$=g/U^2$, wave number
ρ	Density of fluid
$\sigma(Q,t), \sigma^*(Q,\lambda)$	Source distribution and its Fourier transform
$\phi(P,t), \phi^*(P,\lambda)$	Velocity potential and its Fourier transform
$\psi(P,t)$	Temporal velocity potential
ω	Motion frequency

1. INTRODUCTION

In ship hydrodynamic problems, especially for motions of a floating body on the free surface, the full 3-D problem may be reduced to the 2-D problems. Notably if the ship were slender in some sense, the well known technique of the slender body theory will be applied to get the 2-D problem which is more easily analysed and calculated than the original 3-D problem. In many cases such simplified treatment gives us satisfactory results. For an extraordinary example, we can refer to the ship motion problem in regular sea waves by the strip theory. [1]

Now we confine ourselves to the potential flow problem of slender ships which make motions on the water surface either steadily or unsteadily. In the field near to the ship body, the slender ship theory suggests that the 3-D field equation, in the concerning case the 3-D Laplace equation for the disturbance potential, can be reduced to the 2-D field equation in the lateral (y,z) plane that is either the 2-D Laplace equation or the 2-D Helmholtz equation according to the mode of ship motion. The former equation appears in such problem as that for a ship running through the calm water making forced oscillations [2] or that for a ship running steadily on the calm water surface. [3] The latter equation appears when a ship with its motion fixed running through regular waves of relatively short wave length. [4] Therefore, we can consider the following degenerated field equations.

$$[L] \quad \phi_{xx} + \phi_{yy} + \phi_{zz} = 0$$

↓

$$[L]_{2D} \quad \phi_{yy} + \phi_{zz} = 0 \quad (1)$$

and

$$[L]_{2D} \quad \phi_{yy} + \phi_{zz} - k^2 \phi = 0 \quad (2)$$

The 3-D effect enters only indirectly into ϕ when the boundary condition does not include the 3-D effect. In ship motion problem [2] and [4] the free surface conditions take the following form,

$$[F] \quad K\phi - \phi_z = 0 \text{ on } z=0 \quad (3)$$

where $K=\omega^2/g$, and in the steady wave making problem, [3]

$$[F] \quad \phi_z = 0 \text{ on } z=0 \quad (4)$$

These conditions apparently lack the 3-D effect which may be represented by the differentiation with respect to x , so that the problem in the near field must be solved as the genuine 2-D boundary value problems. From the combination of the 2-D field equation and the free surface condition we can consider the three types of the basic 2-D boundary value problem which have been fully studied so far. They are composed of the combination of (1)-(2), (2)-(3) and (1)-(4) with suitable body boundary conditions and radiation conditions or matching conditions.

In the process of the development of the slender ship theory, another type of the basic boundary value problem has come out. When a slender ship runs with uniform speed, it is well recognized that some irregularity near to the bow appears in the slender ship theory. [5] To avoid this irregularity, the bow near field has been introduced. The bow near field concept for the steady motion problem leads to the free surface condition, [6]

$$[F] \quad \phi_{xx} + v\phi_z = 0 \text{ on } z=0 \quad (5)$$

where $v=g/U^2$. And when a ship is running with uniform speed making forced oscillations, the strip theory whose basic boundary problem is the combination (1)-(3) may become inadequate with increasing forward speed. It is believed that the forward speed effect has to be introduced in the free surface condition. For the attempt of the introduction of the forward speed effect in the free surface condition, the oscillation problem [7] leads to

$$[F] \quad \left\{ i\frac{\omega}{U} + \frac{\partial}{\partial x} \right\}^2 \phi + v\phi_z = 0 \text{ on } z=0 \quad (6)$$

The problem of combination (1)-(5) with the body boundary condition and the suitable causality condition gives us a new basic boundary value problem in ship hydrodynamics which is different from those mentioned previously. The combination (1)-(6) seems to be much more complicated than that of (1)-(5) however as will be shown in §3.2 the fundamental key problem can be reduced to the problem of the combination of (1)-(5).

The new basic boundary value problem which was first proposed by Ogilvie [6] for a simple wedge shaped bow, has other side of meaning. To understand this conceptually, let's change the space variable x into time variable t by $t=x/U$, getting

$$[F] \quad \phi_{tt} + g\phi_z = 0 \text{ on } z=0 \quad (7)$$

The combination (1)-(7) with the body boundary condition which may change with time and the initial condition defines a well established 2-D water wave problem. Since the free surface condition (7) depends on time, we call the basic boundary value problem with the initial condition the "time dependent boundary value problem", even if the condition (5) were adopted.

There may be many applications in the ship hydrodynamics whose basic problem coin-

cides with the time dependent boundary value problem. First of all the analysis of the motion of a floating body which makes arbitrary motion from time $t=0$ is a direct application of the problem. If the motion amplitude of the floating body is so small for the body boundary condition to be translated onto its equilibrium position, the time dependent boundary value problem becomes the most basic problem. It has applications in the 2-D ship motion problem in the time domain. [8], [9], [10] Secondly within the framework of the slender ship theory, the time dependent boundary value problem has possible application to the 3-D ship motion problem which will be reduced to the strip theory with forward speed correction. Thirdly the application to the steady wave making resistance theory can be expected.

This paper will deal with the above mentioned three applications of the time dependent boundary value problem. However, the general treatment for the problem has not been investigated so far, while the counterpart problem of the combination (1)-(3) has been fully studied both theoretically and numerically. Especially the integral equation approach in the (1)-(3) problem clarified the existence of the irregular frequency [11] and the methods of elimination of it from the solution. [12] Therefore we will mention in brief the analytical aspect of the time dependent boundary value problem when it is treated by the integral equation approach. Then the theoretical backgrounds for these applications of the problem will be discussed. As numerical example the 2-D ship motion in the time domain will be demonstrated with comparison to the experiment.

2. GENERAL PROPERTIES OF INTEGRAL EQUATION SOLUTION

The time dependent boundary value problem for an arbitrary 2-D body on the free surface is written as, (Fig. 1)

$$\left. \begin{aligned} [L] \quad & \phi_{yy}(y, z, t) + \phi_{zz} = 0 \quad \text{in De} \\ [F] \quad & \phi_{tt} + g\phi_z = 0 \quad \text{on Fe} \\ [H] \quad & \phi_N = -v(Q, t) \quad \text{on } c(t) \\ [I] \quad & \phi = \phi_t = 0 \quad t < 0 \end{aligned} \right\} \quad (8)$$

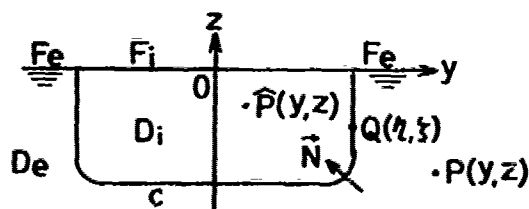


FIGURE 1. Geometry of the time dependent boundary value problem.

For simplicity the body shape $c(t)$ is assumed not to change with time. This may not lose the generality of the problem. Making use of the Green's theorem the potential is written as,

$$\int_0^t d\tau \int_c d\ell \left\{ \phi(Q, \tau) \frac{\partial}{\partial N_Q} G(P, Q, t-\tau) - \frac{\partial \phi}{\partial N_Q} G \right\} = \begin{cases} \phi(P, t) & P \text{ in De} \\ 0 & P \text{ in Di} \end{cases} \quad (9)$$

where G is the Green's function defined by, [13]

$$G(P, Q, t-\tau) = \frac{1}{2\pi} \delta(t-\tau) \ln \frac{r}{r'}, - \frac{g}{\pi} H(t-\tau) \int_0^\infty \frac{dk}{\sqrt{gk}} e^{k(z+\zeta)} \cos k(y-\eta) \sin \sqrt{gk}(t-\tau) \quad (10)$$

where $r = [(y-\eta)^2 + (z-\zeta)^2]^{1/2}$, $r' = [(y-\eta)^2 + (z+\zeta)^2]^{1/2}$ and $\delta(t)$ is the Dirac's delta function and $H(t)$ is the Heavieside's step function. $G(P, Q, t-\tau)$ is also the potential for a impulsive source at Q . Since ϕ_N is a given

quantity we can derive from (9) the integral equation for ϕ on c by letting P approach to Q from the outside of c . Then we have,

$$-\frac{1}{2} \phi(P, t) + \int_0^t d\tau \int_c d\ell \phi(Q, \tau) G_{NQ}(P, Q, t-\tau) = - \int_0^t d\tau \int_c d\ell v(Q, \tau) G \quad P \text{ on } c \quad (11)$$

The integral in the left hand side denotes the Cauchy principal value to be taken.

It is sometimes convenient to express the potential by the distribution of the singularities on the hull boundary c . In order to do so, let's introduce the interior potential $\psi(\hat{P}, t)$ which satisfies the condition (8) except [H] in the interior of c . From the Green's theorem, we have,

$$- \int_0^t d\tau \int_c d\ell \left\{ \psi G_{NQ} - \psi_{NQ} G \right\} = \begin{cases} \psi(\hat{P}, t) \\ 0 \end{cases} \quad \begin{matrix} \hat{P} \text{ in De} \\ \hat{P} \text{ in Di} \end{matrix} \quad (12)$$

We want to distribute only sources on c , then Dirichlet condition on c must be imposed on ψ , then,

$$[H] \quad \psi(Q, t) = \phi(Q, t) \quad Q \text{ on } c$$

Subtracting (12) from (9) and defining the temporal source distribution by

$$\sigma(Q, t) = \psi_N - \phi_N \quad Q \text{ on } c \quad (13)$$

we have the expression of potential by the source distribution,

$$\phi(P, t) = \int_0^t d\tau \int_c d\ell \sigma(Q, \tau) G(P, Q, t-\tau) \quad (14)$$

The integral equation for $\sigma(Q, t)$ can be derived by substituting (14) into [H] condition in (8).

$$-\frac{1}{2}\sigma(P, t) + \int_0^t d\tau \int_c d\lambda \sigma(Q, \tau) G_{Np}(P, Q, t-\tau) = -v(P, t) \quad P \text{ on } c. \quad (15)$$

By virtue of the properties of the Green's function, the integral equations have the memory effect which represents the effects before the time $t=\tau$. And the memory effect vanishes at $\tau=t$ by the factor of $\sin \sqrt{gk}(t-\tau)$. Then the integral equations at time $t=t$ can be in principle solved without fundamental difficulty.

When the body boundary $c(t)$ changes gradually with time, the expressions for potential and source are thought to be also valid. So we will use them for the case that the body shapes change with time.

In the time dependent boundary value problem, the irregular frequency appears when we solve the temporal source distribution by (15), while no such irregularity in solving the potential by (11). The irregular frequency phenomena were first noticed by Ohmatsu [14] when he tried to analyse the 2-D time dependent motion problem by (15). And the cause and the behavior of the irregular frequency in the time dependent problem have been clarified by Adachi and Ohmatsu. [15] We show one of examples of the irregular frequency effect in the temporal source in Fig. 2 for a circular cylinder making impulsive heave motion at $t=0$. Though the motion lasts for very short time interval, the temporal source oscillates forever with the definite frequency which turns out to be irregular frequency determined by the problem in the frequency domain that is the Fourier transform of the time dependent boundary value problem.

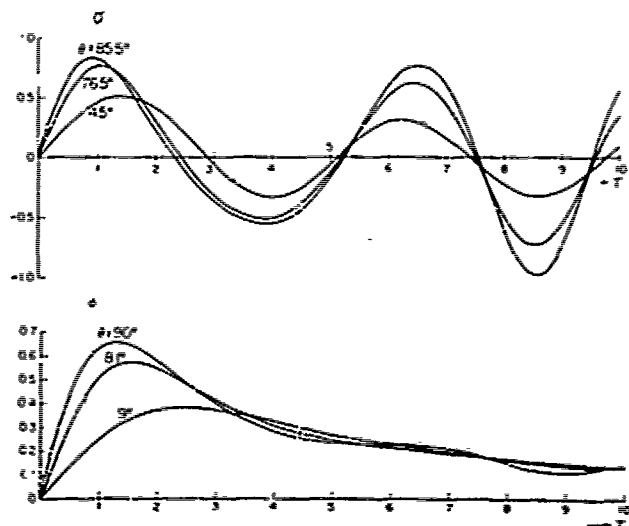


FIGURE 2. Temporal source and temporal potential of a circular cylinder making impulsive heave motion at $\tau=0$.

On the other hand, the potential on c decays with time showing the good agreement with the asymptotically estimated value at large t .

To understand the behavior of the irregular frequency, it is possibly better to think about the problem in the frequency domain. The Fourier transform of the time dependent boundary value problem gives the well established 2-D wave problem with the free surface condition (3). Let's define the Fourier transform and the inverse transform by

$$f^*(\lambda) = \int_{-\infty}^{\infty} dt e^{-i\lambda t} f(t), \quad f(t) = \frac{1}{2\pi} \int_{-\infty}^{\infty} d\lambda e^{i\lambda t} f^*(\lambda).$$

The problem (8) is transformed into

$$\left. \begin{aligned} [L] \quad & \phi^*_{yy} + \phi^*_{zz} = 0 \quad z < 0 \\ [F] \quad & K\phi^* - \phi^*_z = 0 \quad z = 0 \\ [H] \quad & \phi^*_N = -v^*(Q, \lambda) \quad \text{on } c \end{aligned} \right\} \quad (16)$$

where $v^*(Q, \lambda)$ is the Fourier transform of $v(Q, t)$. In the frequency domain the transformed potential and source distribution are solved by the transformation of (11), (15). In Fig. 3 we show the irregularity of source function and the numerical instability of potential in the frequency domain which have been calculated by the transformed integral equations. The singular behavior of the source with wave number K has been proved to be of type $1/(K-K_j)$ where K_j is j th irregular wave number. [16]

The Fourier transform of the source function in the frequency domain recovers the temporal source function, then the effect of the irregular frequency appears in general in the time domain as,

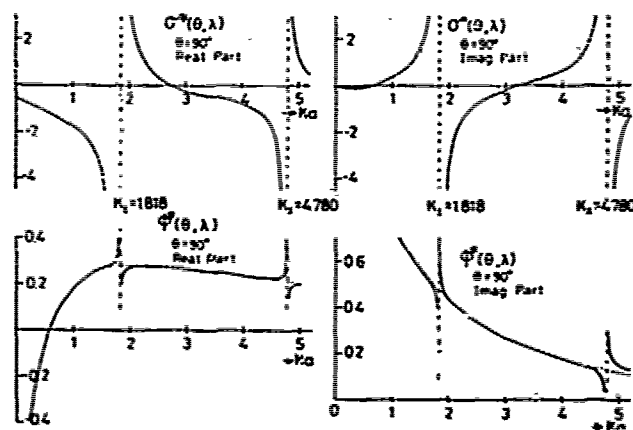


FIGURE 3. Source distribution function and potential on hull at the water line in the frequency domain for a circular cylinder in heave motion.

$$\int_{-\infty}^{\infty} d\lambda \frac{e^{i\lambda t}}{\lambda - \lambda_j} = \frac{1}{2i} e^{i\lambda_j t} \quad t > 0.$$

Therefore the effect of the irregular frequency in the time domain is presented by the factor $e^{i\lambda_j t}$ which does not blow up at λ_j . Thus we can solve the integral equation (15) without essential difficulty inherited from the integral equation in the frequency domain.

Although the temporal source distribution is affected by the irregular frequency, the potential expressed by the temporal source (14) will have no effect of the irregular frequency. This can be easily confirmed by applying the Green's theorem.

If we denote the part of the temporal source affected by the irregular frequency by, [15]

$$\Delta G(Q, t) \propto e^{i\lambda_j t} \frac{\partial \hat{\phi}_j^*}{\partial N}$$

where $\hat{\phi}_j^*$ is the j th eigen value interior potential in the frequency domain which is determined by the boundary value problem in the interior region D_i .

$$[L] \quad \hat{\phi}_{jyy}^* + \hat{\phi}_{jzz}^* = 0 \quad \text{in } D_i$$

$$[F] \quad K_j \hat{\phi}_j^* - \hat{\phi}_{jz}^* = 0 \quad \text{on } z=0$$

$$[H] \quad \hat{\phi}_j^* = 0 \quad \text{on } c.$$

This problem has eigen solutions with eigen value λ_j . What we need is the relation

$$\int_0^t d\tau \int_c d\lambda \Delta G(Q, \tau) G(P, Q, t-\tau) = 0 \quad (17)$$

Substituting the Green's function (10) into the above expression and integrating with respect to τ , we have

$$\begin{aligned} e^{i\lambda_j t} \left\{ \int_c d\lambda \frac{\partial \hat{\phi}_j^*}{\partial N} \ln \frac{r}{r_0} - 2 \int_c d\lambda \frac{\partial \hat{\phi}_j^*}{\partial N} \int_0^\infty dk \frac{e^{k(z+\zeta)}}{k - K_j} \cos k(y-n) \right\} \\ + 2 \int_c d\lambda \frac{\partial \hat{\phi}_j^*}{\partial N} \int_0^\infty \frac{dk}{\sqrt{k}} e^{k(z+\zeta)} \cos k(y-n) \cdot \\ \frac{\sqrt{k} \cos \sqrt{k} t + i \sqrt{K_j} \sin \sqrt{k} t}{k - K_j}. \quad (18) \end{aligned}$$

When t is large, the last term has the following asymptotic estimation

$$2\pi i e^{i\lambda_j t} e^{K_j(z+\zeta)} \cos K_j(y-n).$$

Therefore (18) becomes at large t as,

$$2\pi e^{i\lambda_j t} \int_c d\lambda \hat{\phi}_j^* G^*(P, Q, K_j)$$

where

$$G^*(P, Q, K_j) = \frac{1}{2\pi} \ln \frac{r}{r_0} - \frac{1}{\pi} \int_{0, L}^\infty dk \frac{e^{k(z+\zeta)}}{k - K_j} \cos k(y-n) \quad (19)$$

where the path of integration L indented above (below) the singularity $k=K_j$ according as $\lambda_j > 0$ ($\lambda_j < 0$). It is also noticed that G^* is the Fourier transform of the impulsive source potential (10). Now applying the Green's theorem to $\hat{\phi}_j^*$ and G^* in the interior region D_i together with boundaries F_i and c , and using the properties of the potential and the Green's function on the boundaries, we have,

$$\begin{aligned} \int_c d\lambda (\hat{\phi}_j^* G^* - \hat{\phi}_j^* G^*) &= \int_{F_i} d\lambda (\hat{\phi}_j^* G^* - \hat{\phi}_j^* G^*) = \\ (K_j - K_j) \int_{F_i} d\lambda \hat{\phi}_j^* G^* &= 0 \end{aligned}$$

Therefore the relation (17) can be proved at large t . It is probable this relation is valid for all positive t .

The above verification is also valid for the Kochin function in the time domain which is calculated from the temporal source function. To obtain the Kochin function, it may be better to use the Kochin function in the frequency domain which is given by,

$$\tilde{H}^*(\lambda, g) = 2i \int_c d\lambda \sigma^*(Q, \lambda) e^{k(\zeta+i\eta)} \operatorname{sgn} \lambda \quad (20)$$

The Kochin function in the time domain can be derived by taking the Fourier transform of (20), then we have,

$$\tilde{H}(t, g) = -\frac{g}{\pi} \int_0^t d\tau \int_c d\lambda \sigma(Q, \tau) \int_0^\infty \frac{dk}{\sqrt{k}} e^{k(\zeta+i\eta)} \sin \sqrt{k} (t-\tau). \quad (21)$$

If the body shape changes with time, it is difficult to establish the relations derived above. However, if the change in the shape is very gradual these relations will probably hold approximately. For a uniform cylinder the relation between temporal source and the potential has been shown in Fig. 2. When the body shape is a function of time, a numerical example is shown in Fig. 4. The body is an usual ship-like body with vertical side at the water surface. The source is apparently affected by the irregular frequency, while the potential on the hull seems not to be affected by it.

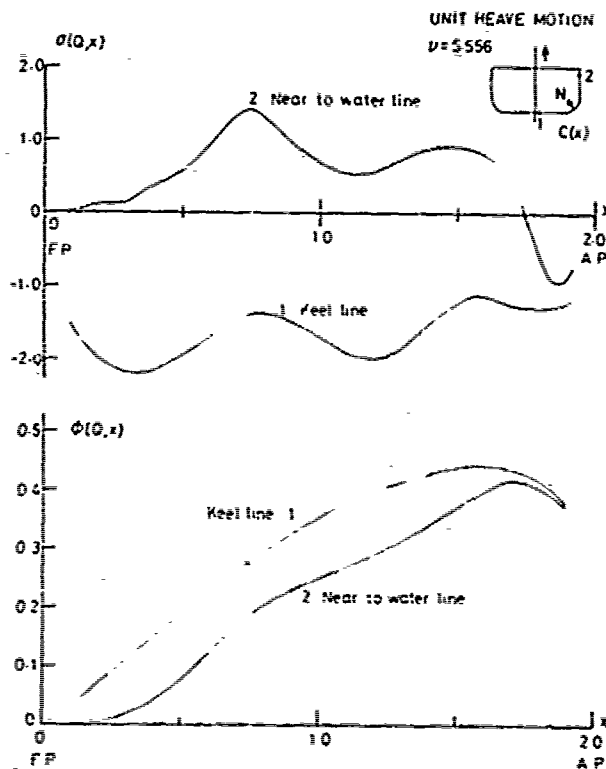


FIGURE 4. Temporal source and potential of a ship-like form.

3. APPLICATIONS OF TIME DEPENDENT PROBLEM

3.1 2-Dimensional Motion Problem in the Time Domain

The problem of the motion of a floating body in the time domain was seriously investigated by several researchers some ten years ago around 1960. [8], [9], [10]. Through their investigations, it became known that the equation of motion in the time domain takes the form of the integro-differential equation, while that in the frequency domain is given by the second order differential equation. And the relation of the equations of motion between the time domain and the frequency domain was also clarified. Shortly after the preceding works, Wehausen [17] derived the integral equation for the force coefficients which are required to calculate the equation of motion in time domain. Further he gave the relation analogous to the Haskind relation in the frequency domain [18], to obtain the exciting force without solving directly the diffraction problem.

However within the extent of authors' knowledge the equation of motion in the time domain has not been calculated, this seems mainly due to the complexity of the analytical and numerical aspects of the integral equations involved in the problem.

3.1.1 Equation of Motion in Time Domain

We will consider a 2-D floating body motion on the water surface. Suppose that the motion amplitude is so small that the

linearized free surface condition (7) holds and the body boundary condition can also be linearized and satisfied on its equilibrium position. Under these assumptions we can derive the equation of motion in the time domain.

Firstly we start from the Newton's equation of motion

$$\sum_{j=1}^3 m_{ij} \ddot{X}_j(t) = F_i(t) \quad i=1,2,3 \quad (22)$$

where $X_j(t)$ is the displacement or angle in j th mode motion, and m_{ij} denotes the matrix for either mass or moment of inertia of the body. The external force or moment $F_i(t)$ is assumed to be composed of three components,

$$F_i(t) = F_{Di}(t) + F_{Si}(t) + F_{Wi}(t) \quad (23)$$

where F_{Di} is hydrodynamic force, F_{Si} is hydrostatic restoring force and F_{Wi} is the exciting force of incident waves.

F_{Di} is due to the fluid disturbance caused by body motion. The mode of motion is classified as follows, $i=1$ sway, $i=2$ heave and $i=3$ roll. Let's define the potential $\phi_j(P, t)$ which describes the fluid disturbance caused by j th mode motion. Since the linearized pressure is $-\rho \partial \phi_j / \partial t$, F_{Di} is given by

$$F_{Di}(t) = \sum_{j=1}^3 F_{ij}(t) = -\rho \int_C \frac{\partial \phi_j}{\partial t}(Q, t) n_i(Q) \quad (24)$$

where F_{ij} denotes force component in i th mode due to j th mode motion, and $n_i(Q)$ denotes the generalized direction cosine which is defined as,

$$n_1 = N_1, \quad n_2 = N_2, \quad n_3 = YN_2 - ZN_1$$

The conditions which ϕ_j must satisfy are same as given in (8). In the problem concerned here, the body boundary condition is specified as

$$[H] \phi_{jN} = n_j(Q) \dot{X}_j(t) \quad Q \text{ on } c \quad (25)$$

The velocity potential ϕ_j can be treated by the method in §2, however $\dot{X}_j(t)$ has not been known yet at this stage. Therefore let's introduce one more time dependent velocity potential ψ_j which satisfies the following body boundary condition

$$[H] \psi_{jN} = n_j(Q) H(t) \quad Q \text{ on } c \quad (26)$$

Using this step response velocity potential, ϕ_j can be represented by superposing it.

$$\phi_j(P, t) = \int_0^t d\tau \dot{X}_j(\tau) \psi_j(P, t-\tau) \quad (27)$$

Substituting (27) into (25), we have

$$\dot{\phi}_{jN} = \int_0^t d\tau \ddot{X}_j(\tau) \phi_{jN}(Q, t-\tau) = n_j(Q) \dot{X}_j(t) \quad (28)$$

The hydrodynamic force $F_{ij}(t)$ is given by substituting (27) into (24),

$$F_{ij}(t) = -\rho \ddot{X}_j(t) \int_c d\ell \phi_{jt}(Q, 0) n_i(Q) - \rho \int_0^t d\tau \ddot{X}_j(\tau) \int_c d\ell \phi_{jt}(Q, t-\tau) n_i(Q) \quad (29)$$

Now let's define the following functions,

$$\mu_{ij} = \rho \int_c d\ell \phi_{jt}(Q, 0) n_i(Q) \quad (30)$$

and

$$L_{ij}(t) = \rho \int_c d\ell \phi_{jt}(Q, t) n_i(Q) \quad (31)$$

Therefore $F_{ij}(t)$ is written as

$$F_{ij}(t) = -\mu_{ij} \ddot{X}_j(t) - \int_0^t d\tau L_{ij}(t-\tau) \ddot{X}_j(\tau) \quad (32)$$

Next we will derive the expression for the exciting force. Let's suppose ϕ_I to be the given incident wave potential and ϕ_D to be the diffraction potential. The exciting force or moment is written in the same manner as (24), with using $\phi_I + \phi_D$ instead of ϕ_j then we have,

$$F_{Wi}(t) = -\rho \int_c d\ell \{ \phi_{It}(Q, t) + \phi_{Dt}(Q, t) \} n_i(Q) \quad (33)$$

The boundary conditions for ϕ_D are same as (8) except [H]. The body boundary condition is specified as,

$$[H] \quad \phi_{DN} = -\phi_{IN} \quad (34)$$

Then ϕ_D can be treated by the method in §2.

However in the boundary value problem in the frequency domain the exciting force can be usually expressed by the solution of the radiation problem by making use of the Haskind relation. [18] In the time domain similar relation will be derived. From the body boundary condition (34), we have,

$$\dot{\phi}_{DN}(Q, t) n_i(Q) = -\dot{\phi}_{IN}(Q, t) n_i(Q) \quad \text{on } c \quad (35)$$

Then by the analogy to the expression (27), we can formally obtain the following,

$$\dot{\phi}_D(Q, t) n_i(Q) = -\int_0^t d\tau \dot{\phi}_{IN\tau}(Q, \tau) \dot{\phi}_i(Q, t-\tau) \quad (36)$$

Therefore the exciting force or moment (33) can be written as,

$$F_{Wi}(t) = -\rho \int_c d\ell \dot{\phi}_{It}(Q, t) n_i(Q) + \rho \int_0^t d\tau \int_c d\ell \dot{\phi}_{IN\tau}(Q, \tau) \dot{\phi}_{it}(Q, t-\tau) \quad (37)$$

Finally since the relation of the hydrostatic restoring force or moment with the body geometry is well known, then we write it as,

$$F_{Si}(t) = -\sum_{j=1}^3 C_{ij} X_j(t) \quad (38)$$

Accordingly, substituting (32), (37) and (38) into (22) we obtain the representation of the equation of motion in the time domain.

$$\sum_{j=1}^3 \{ (m_{ij} + \mu_{ij}) \ddot{X}_j(t) + C_{ij} X_j(t) + \int_0^t d\tau L_{ij}(t-\tau) \ddot{X}_j(\tau) \} = F_{Wi}(t) \quad i=1,2,3 \quad (39)$$

Now it is clear that μ_{ij} has the nature of added mass and $L_{ij}(t)$ represents the memory effect coefficient. The expression (30) tells us that this added mass coefficient depends only on the body geometry, so that it was called the "legitimate added mass" by Cummins. [9]

Consequently, if the time dependent potential ϕ_j could be solved to get μ_{ij} and $L_{ij}(t)$, the equation of motion becomes to be able to be solved at least numerically. The time dependent boundary value problem for ϕ_j can be treated by the method in §2.

The above expression (39) for the motion in the time domain has the form of the integro-differential equation. However, since $L_{ij} \rightarrow 0$ as $t \rightarrow 0$, that is obvious from the body boundary condition (26), we can treat it as a differential equation and solve it numerically with marching step by step method.

In the latter chapter we will give some numerical examples of the present 2-D motion problem in the time domain with the comparison to the experiments.

3.2 High Speed Slender Ship Theory

The slender ship theory developed by Ogilvie and Tuck [2] provided the rational foundation for the strip theory of Korvin-Kroukovsky. [1] In their theory the key assumption is that the frequency of motion is high so that the wave length generated by the motion is compatible to the ship's lateral dimension. And in their theory the forward speed effect is considered not only for the body boundary condition but also for the free surface condition. The correction for the latter condition had never been treated adequately before their work.

The forward speed effect on the free surface condition in the framework of the strip theory was impressively demonstrated by Faltinsen. [19] He could show numerically that the improvement of the hydrodynamic coefficients has been actually accomplished by the inclusion of the correction term for the free surface condition which had been provided by Ogilvie and Tuck.

As for the forward speed correction for the strip theory, Chapman [7] proposed a newly-looked strip theory, by which he computed the force and moment of a oscillating flat plate in yaw and sway mode. The agreement between calculation and experiments is extraordinary good. Chapman's theory includes the forward speed effect which has been discarded in the most strip methods except Ogilvie and Tuck's. Both Faltinsen's calculation and Chapman's theory strongly suggest the importance of the forward speed effect in the ship motion theory, for which the 3-D calculation is still much more time-consuming even if not difficult in principle.

As indicated by Ogilvie [5], when formulating the ship motion problem in the bow near field where the distance from the bow is of order $O(\epsilon^{1/2})$, with ϵ being the small perturbation parameter, and the differentiation with respect to x changes the order by $O(\epsilon^{1/2})$ when operated on the physical quantity, it will be possible to obtain the same boundary condition on the free surface as Chapman's. That is, we have the same basic boundary value problem as that in §2 for the ship motion problem. We will analyze the bow near field problem to see how the forward speed effect can be treated and how the near field solution can match with the far field problem.

3.2.1. Problem for Uniform Cylinder

For simplicity a uniform cylinder will be considered which is placed in the uniform flow and oscillating in heave or pitch mode. Saito [20] also treated the same problem by the different method from the present one. Let's take the direction of x -axis in the same direction of the uniform flow U and the origin at the bow of the cylinder. The free surface is on $z=0$ and z -axis is taken upward vertically.

In the bow near field where $x=O(\epsilon^{1/2})$, $y=O(\epsilon)$ and $z=O(\epsilon)$, the problem for the disturbance potential $\psi(x,y,z)e^{i\omega t}$ is given as follows, to the leading order term, [21]

$$\left. \begin{aligned} [L] \quad \psi_{yy} + \psi_{zz} &= 0 \quad \text{in } z < 0 \\ [F] \quad (i\omega/U + \partial/\partial x)^2 \psi + v\psi_z &= 0 \quad \text{on } z=0 \\ [H] \quad \psi_N &= v(x)B(y,z) \quad \text{on } c \\ [I] \quad \psi_x &= \psi = 0 \quad \text{at } x < 0 \end{aligned} \right\} \quad (40)$$

where the body boundary condition is factorized into two parts, one is dependent on

only x and other one on Q on c . In order to analyze the above problem, it is useful to introduce an auxiliary potential $\phi(x,y,z)$ which is defined by,

$$\left. \begin{aligned} [L] \quad \phi_{yy} + \phi_{zz} &= 0 \quad \text{in } z < 0 \\ [F] \quad \phi_{xx} + v\phi_z &= 0 \quad \text{on } z=0 \\ [H] \quad \phi_N &= B(Q)H(x) \quad \text{on } c \\ [I] \quad \phi_x &= \phi = 0 \quad \text{at } x < 0 \end{aligned} \right\} \quad (41)$$

This auxiliary potential coincides with the time dependent boundary value problem discussed in §2.

In order to obtain the expression for the potential ψ , we will make use of the Fourier transform of the problem. The Fourier transform of (40) becomes,

$$\left. \begin{aligned} [F] \quad -(\lambda + \omega/U)^2 \psi^* + v\psi_z^* &= 0 \quad \text{on } z=0 \\ [H] \quad \psi_N^* &= v^*(\lambda)B(Q) \quad Q \text{ on } c \end{aligned} \right\} \quad (42)$$

and for the auxiliary potential, we have the conditions at the boundaries,

$$\left. \begin{aligned} [F] \quad -\lambda^2 \phi^* + v\phi_z^* &= 0 \quad \text{on } z=0 \\ [H] \quad \phi_N^* &= H^*(\lambda)B(Q) \quad Q \text{ on } c \end{aligned} \right\} \quad (43)$$

where $H^*(\lambda) = \pi\delta(\lambda) - i/\lambda$. The potential in the frequency domain can be written as, using the Green's function defined by (19);

$$\psi^*(\lambda, y, z) = \int_c d\lambda \hat{\gamma}^*(\lambda, Q) G^*(\lambda + \omega/U, P, Q) \quad (44)$$

and

$$\phi^*(\lambda, y, z) = \int_c d\lambda \sigma^*(\lambda, Q) G^*(\lambda, P, Q) \quad (45)$$

where $\hat{\gamma}^*$ and σ^* are source distribution functions in the frequency domain. The relation between ψ^* and ϕ^* is obtained immediately through comparing the boundary conditions.

$$\psi^*(\lambda, y, z) = i(\lambda + \omega/U)v^*(\lambda)\phi^*(\lambda + \omega/U, y, z). \quad (46)$$

The inverse transform of this relation gives

$$\psi(x, y, z) = \frac{i}{2\pi} \int_{-\infty}^{\infty} d\lambda e^{i\lambda x} (\lambda + \omega/U) v^*(\lambda) \cdot \phi^*(\lambda + \omega/U, y, z) \quad (47)$$

By making use of the Fourier transform and the Fourier convolution theorem, we finally have,

$$\psi(x, y, z) = -e^{-i\omega x/U} [v(0)\phi(x, y, z) +$$

$$+ \int_0^x d\xi \phi(x-\xi, y, z) \frac{\partial}{\partial \xi} \{v(\xi) e^{i\xi\omega/U}\} \quad (48)$$

This is the expression that Chapman first gave, and shows that if the time dependent potential has been solved the desired potential can be calculated by superposing it.

Now the near field problem is given without matching with the far field solution. That is, the problem (40) is self-consistent in some sense. However we will think about the far field solution to see whether it matches with the near field solution. For this purpose we first derive the outer expansion of the near field solution. Since the outer expansion of the 2-D potential in the frequency domain can be given by,

$$\phi^*(\lambda, y, z) \sim e^{(z-iy)\lambda^2/\nu} 2i \int_c d\lambda \sigma^*(\lambda, Q) \cdot e^{(\xi+in)\lambda^2/\nu} \operatorname{sgn} \lambda = e^{(z-iy)\lambda^2/\nu} \tilde{H}^*(\lambda, \nu) \quad (49)$$

where \tilde{H}^* is the Kochin function defined by (20). Substituting this into (47), we have

$$\psi(x, y, z) \sim \frac{i}{2\pi} \int_{-\infty}^{\infty} d\lambda e^{i\lambda x} (\lambda + \omega/U) v^*(\lambda) \cdot \tilde{H}^*(\lambda + \omega/U, \nu) e^{(z-iy)(\lambda + \omega/U)^2/\nu} \quad (50)$$

This is the outer expansion of the near field solution as $|y| \rightarrow 0(1)$.

3.2.2 Far Field Potential and Matching

It will be permissible in the far field to see the disturbance of the near field as a line source distribution on the body center line. Therefore for the far field potential $\psi(x, y, z)$ ($y=0(1)$), we have the conditions,

$$\left. \begin{array}{l} [L] \quad \psi_{xx} + \psi_{yy} + \psi_{zz} = \gamma(x) \quad z < 0 \\ [F] \quad (i\omega/U + \partial/\partial x)^2 \psi + \nu \psi_z = 0 \quad \text{on } z=0 \\ [R] \quad \text{Radiation condition} \end{array} \right\} \quad (51)$$

where $\gamma(x)$ is the source density function on the center line which represents the disturbance due to the motion of cylinder. The solution for (51) is given by, [2]

$$\psi(x, y, z) = -\frac{1}{4\pi} \int_{-\infty}^{\infty} d\lambda e^{i\lambda x} \gamma^*(k) \cdot \int_{-\infty}^{\infty} d\lambda \frac{e^{i\lambda y + z\sqrt{\lambda^2 + k^2}}}{\sqrt{\lambda^2 + k^2} - (\omega + Uk - \mu)/g}, \quad \mu > 0 \quad (52)$$

where $\gamma^*(k)$ is the Fourier transform of $\gamma(x)$. The inner expansion of the far field solution has been given in Ogilvie and Tuck [2]

as,

$$\psi(x, y, z) \sim \frac{i}{2\pi} \int_{-\infty}^{\infty} d\lambda e^{i\lambda x} \gamma^*(k) e^{(z-iy)(k+\omega/U)^2/\nu} \quad (53)$$

This should match with the outer expansion of the inner solution (50). Therefore we have the matching condition

$$\gamma^*(k) = (k + \omega/U) v^*(k) \tilde{H}^*(k + \omega/U, \nu) \quad (54)$$

And taking the Fourier transform, we finally have

$$\gamma(x) = ie^{-i\omega x/U} [v(0) \tilde{H}(x, \nu) + \int_0^x d\xi \tilde{H}(x-\xi, \nu) \frac{\partial}{\partial \xi} \{v(\xi) e^{i\xi\omega/U}\}] \quad (55)$$

From this the line source distribution is given by the convolution integral of the Kochin function in the time domain. It is very interesting that the inner expansion (53) matches with the near field solution whose free surface condition is different from that in the usual slender ship theory without the forward speed term.

3.2.3 Extension to Ship-like Body

For usual ship-like bodies which change its shape with x , the similar formulas as derived in the previous chapter seem to be held.

$$\psi(x, y, z) = -e^{-i\omega x/U} [A\phi(x, y, z) + \int_0^x d\xi E(\xi) \phi(x-\xi, y, z)] \quad (56)$$

This satisfies conditions posed on the potential except [H] condition. The constant A and the function $E(x)$ can be determined so as for the condition to be fulfilled. From the [H] condition we have

$$v(x) B(Q(x)) = -e^{-i\omega x/U} [A\phi_N(x, Q(x)) + \int_0^x d\xi E(\xi) \frac{\partial \phi}{\partial N}(x-\xi, Q(x))] \quad (57)$$

If we let $x \rightarrow 0$, A must be $-v(0)$. Thus (57) becomes the Volterra type integral equation for $E(x)$. This may be solved numerically without difficulty. For the source distribution we have the similar expression,

$$\gamma(x) = ie^{-i\omega x/U} [v(0) \tilde{H}(x, \nu) + \int_0^x d\xi E(\xi) \tilde{H}(x-\xi, \nu)] \quad (58)$$

The force and moment will be obtained by the linearized pressure distribution on hull or by the Kochin function in the far field.

3.3 Low Speed Slender Ship Theory

The time dependent boundary value problem had first introduced in the steady wave making resistance theory by Ogilvie [6] and the general problem of his was calculated by Daoud [22]. One of the purposes of the introduction of the time dependent boundary value problem is to mitigate the end effect inherent to the slender ship theory. However it is easily noticed from the time dependent boundary value problem the disturbance just ahead of the bow cannot exist because of the [I] condition. (see eq. (8).) This suggests the sudden change of flow at the bow. In actual at relatively low speed region there seems to be disturbance in front of the bow. To include the disturbance ahead of the bow in the slender ship theory, it may be effective to analyse the problem by the low speed wave making resistance theory [23]. In doing so, the use of the slender ship assumption will enable us to save the efforts in calculation of the higher order low speed theory which includes the diffraction effect of its own wave with hull. [24]

3.3.1 Formulation under Low Speed Assumption

The low speed formulation gives the following condition for the wavy velocity potential, [23]

$$\left. \begin{aligned} [L] \quad \nabla^2 \phi(x, y, z) &= 0 & \text{in } z < 0 \\ [F] \quad \left\{ (1 + \psi_x) \frac{\partial}{\partial x} + \psi_y \frac{\partial}{\partial y} \right\} \phi + v \phi_z &= D(x, y) & \text{on } z=0 \\ [H] \quad \phi_n &= 0 & \text{on } S_B \quad z < 0 \\ [R] \quad \text{Radiation condition} \end{aligned} \right\} \quad (59)$$

where ψ is the double body flow potential which satisfies the conditions,

$$\left. \begin{aligned} [L] \quad \nabla^2 \psi(x, y, z) &= 0 & \text{outside of the body} \\ [F] \quad \psi_z &= 0 & \text{on } z=0 \\ [H] \quad \psi_n &= -U \frac{\partial \zeta}{\partial n} & \text{on } S_B \\ [\infty] \quad \nabla \psi &\rightarrow 0 & \text{as } R \rightarrow \infty \end{aligned} \right\} \quad (60)$$

The potential gives the flow field when there is no free surface and is easily calculated when the hull geometry is given. The potential ϕ is the disturbance potential which is caused by the interaction between the flow field due to the double body potential and the free surface. $z=\theta(x, y)$ is the free surface displacement due to ψ ,

$$\theta(x, y) = -\frac{1}{v} \left(\psi_x + \frac{1}{2} (\nabla \psi)^2 \right)_{z=0} = O(\delta) = O(U^2).$$

$D(x, y)$ is a function over the free surface which is thought to represent the interaction between ψ and the free surface. This is one of main agents for disturbance to the wavy potential, and is defined by,

$$D(x, y) = -\frac{1}{2} \left(2\psi_{xx} + 2\frac{\partial}{\partial x} + \psi_x \frac{\partial}{\partial x} + \psi_y \frac{\partial}{\partial y} \right).$$

$$(\psi_x^2 + \psi_y^2) + (\psi_{xx} + \psi_{yy}) (2\psi_x + \psi_x^2 + \psi_y^2) \Big|_{z=0} \quad (61)$$

The perturbation parameter δ is proportional to $1/v=O(U^2)$ where U is thought to approach to zero asymptotically.

3.3.2 Bow Near Field in Slender Slow Ship

Let's take the slenderness parameter of the slender ship as ϵ . The classical slender body theory indicates the following orders for the potential in the bow near field where $x=O(\epsilon^{1/2})$, $y=O(\epsilon)$ and $z=O(\epsilon)$,

$$\psi = O(\epsilon^2), \quad \psi_x = O(\epsilon^{3/2}), \quad \psi_y, \quad \psi_z = O(\epsilon).$$

For the wavy potential when the differentiations with respect to space variables are operated, the order of magnitude is assumed to change as follows,

$$\frac{\partial}{\partial x} = O(\epsilon^{-1/2} \delta^{-1}), \quad \frac{\partial}{\partial y}, \quad \frac{\partial}{\partial z} = O(\epsilon^{-1} \delta^{-1}).$$

Then the condition (59) can be written as,

$$\left. \begin{aligned} [L] \quad \phi_{yy} + \phi_{zz} + \phi_{xx} &= 0 & z < 0 \\ [1] \quad [1] \quad [\epsilon] \\ [F] \quad \phi_{xx} + v \phi_z &= D(x, y) + E(x, y) & \text{on } z=0 \\ [\epsilon] \quad [\epsilon] \quad [\epsilon^{3/2}] \\ [H] \quad \phi_x h_x + \phi_y h_y - \phi_z &= 0 & \text{on } z=h(x, y) \end{aligned} \right\} \quad (62)$$

The similar free surface condition has been obtained by Newman [25] under the slightly different conditions. The order of the wavy potential is $O(\epsilon^2 \delta^2)$ from the condition [F] in (59) and $z=h(x, y)$ is the equation of ship surface and in the bow near field we can assume $h=O(\epsilon)$, $h_x=O(\epsilon)$ and $h_y=O(1)$. And D and $E(x, y)$ are defined in the bow near field as follows,

$$D(x, y) = -\left\{ \psi_{xx} + 2\psi_y \psi_{xy} + \psi_x \psi_{yy} + \frac{3}{2} \psi_y^2 \psi_{yy} \right\}_{z=0} \quad (63)$$

$[\epsilon] \quad [\epsilon^{3/2}] \quad [\epsilon^2]$

and

$$E(x, y) = -\left\{ 2\psi_y \phi_{xy} + \psi_y^2 \phi_{yy} \right\}_{z=0} \quad (64)$$

$[\epsilon^{3/2}] \quad [\epsilon^2]$

Immediately from (62) the first approximation is obtained as,

$$\left. \begin{aligned} [L] \quad \phi_{1yy} + \phi_{1zz} &= 0 & z < 0 \\ [F] \quad \phi_{1xx} + v \phi_{1z} &= D(x, y) & \text{on } z=0 \\ [H] \quad \phi_{1N} &= 0 & \text{on } z=h(x, y) \end{aligned} \right\} \quad (65)$$

This problem can be regarded as a 2-D water wave problem due to the time dependent pressure distribution on the free surface.

The second order potential is now given formally as,

$$\left. \begin{aligned} [L] \quad \phi_{2yy} + \phi_{2zz} &= 0 \quad z < 0 \\ [F] \quad \phi_{2xx} + v\phi_{2z} &= E \quad \text{on } z=0 \\ [H] \quad \phi_{2N} &= 0 \quad \text{on } z=h(x,y) \end{aligned} \right\} \quad (66)$$

We can decompose the potential ϕ_i into two parts,

$$\phi_i = \phi_i^P + \phi_i^D \quad i=1,2 \quad (67)$$

with conditions, respectively,

$$\left. \begin{aligned} [L] \quad \phi_{iyy}^P + \phi_{izz}^P &= 0 \quad z < 0 \\ [F] \quad \phi_{ixx}^P + v\phi_{iz}^P &= -F_i(x,y) \quad \text{on } z=0 \\ [\infty] \quad \phi_{ix}^P &\rightarrow 0 \quad \text{as } |x| \rightarrow \infty \end{aligned} \right\} \quad (68)$$

where $-F_i = D, E$ or $D+E$, and

$$\left. \begin{aligned} [L] \quad \phi_{iyy}^D + \phi_{izz}^D &= 0 \quad z < 0 \\ [F] \quad \phi_{ixx}^D + v\phi_{iz}^D &= 0 \quad \text{on } z=0 \\ [H] \quad \phi_{iN}^D &= -\phi_{iN}^P \quad \text{on } z=h(x,y) \\ [I] \quad \phi_{ix}^D &= \phi_{ix}^D \equiv 0 \quad x < 0 \end{aligned} \right\} \quad (69)$$

It is easily noticed that the pressure potential problem is a 2-D water wave problem due to the disturbance on the free surface. The time dependent pressure is given from the past to the future where it is zero because of the property of $D(x,y)$ function. The diffraction potential denotes the effect of the reflection of the wave due to the pressure potential on the hull. The initial condition for the diffraction potential comes out because at $x < 0$ there is no hull surface. This problem coincides with the time dependent boundary value problem considered in §2.

It is well known that the pressure potential can be given by the distribution of the impulsive sources on the free surface. Then we have for the pressure potential defined by (68),

$$\phi_i^P = \frac{1}{v} \int_{-\infty}^x \int_{-\infty}^{\infty} d\eta F_i(\xi, \eta) G(y, z, \eta, 0, x-\xi) \quad (70)$$

where G is the Green's function defined by (10) with substitution $t \rightarrow x$, $\tau \rightarrow \xi$ and $g \rightarrow v$. Therefore we can complete the near field problem. This has been done without matching with the far field solution. However, it is necessary to consider the far field

problem in order to derive the wave making resistance formula from the energy or momentum consideration in the far field.

3.3.3 Far Field Potential and Matching

In the far field the problem for the pressure potential and the diffraction potential will be given by the pressure distribution near to the ship hull that is a slender pressure distribution and a source distribution on the ship center line, respectively. Therefore we will have,

$$\phi_j^P = \frac{1}{v} \int_{-\infty}^{\infty} d\xi \int_{-\infty}^{\infty} d\eta F_j(\xi, \eta) \tilde{G}(x, y, z, \xi, \eta, 0) \quad (71)$$

and

$$\phi_j^D = \int_{-\infty}^{\infty} d\xi \gamma(\xi) \tilde{G}(x, y, z, \xi, 0, 0) \quad (72)$$

where $\gamma(\xi)$ is an unknown source distribution on the ship center line. And $\tilde{G}(x, y, z, \xi, \eta, \zeta)$ is the Green's function in the 3-D steady motion problem, [13]

$$\begin{aligned} \tilde{G}(x, y, z, \xi, \eta, \zeta) &= -\frac{1}{4\pi} \left(\frac{1}{R} - \frac{1}{R'} \right) + \frac{1}{\tau^2} \int_0^{\pi/2} d\theta \sec^2 \theta \cdot \\ &\text{P.V.} \int_0^{\infty} dk \frac{e^{k(z+\zeta)} \cos[k(x-\xi) \cos \theta] \cos[k(y-\eta) \sin \theta]}{k - v \sec^2 \theta} \\ &- \frac{v}{\pi} \int_0^{\pi/2} d\theta \sec^2 \theta e^{v \sec^2 \theta (z+\zeta)} \sin[v(x-\xi) \sec \theta] \cdot \\ &\quad \cos[v(y-\eta) \sin \theta \sec^2 \theta] \end{aligned} \quad (73)$$

where $R = [(x-\xi)^2 + (y-\eta)^2 + (z-\zeta)^2]^{1/2}$ and $R' = [(x-\xi)^2 + (y-\eta)^2 + (z+\zeta)^2]^{1/2}$.

The inner expansion of the far field potential into the bow near field can be derived by applying the technique by Baba [26] as follows,

$$\begin{aligned} \phi_j^P &\sim -\frac{1}{\pi} \int_{-\infty}^x d\xi \int_{-\infty}^{\infty} d\eta F_j(\xi, \eta) \int_0^{\infty} \frac{dk}{\sqrt{vk}} e^{kz} \cos k(y-\eta) \cdot \\ &\quad \sin \sqrt{vk}(x-\xi) \end{aligned} \quad (74)$$

and

$$\phi_j^D \sim -\frac{1}{\pi} \int_{-\infty}^x d\xi \gamma(\xi) \int_0^{\infty} \frac{dk}{\sqrt{vk}} e^{kz} \cos k y \sin \sqrt{vk}(x-\xi). \quad (75)$$

The inner expansion of the pressure potential is proved immediately to match with the near field solution (70). Let's think about the matching of the diffraction potential. Since the outer expansion of the near field potential will be derived as,

$$\phi_j^D = -\frac{v}{\pi} \int_0^x d\xi \int_0^\infty \frac{dk}{\sqrt{vk}} e^{k(z-iy)} \sin \sqrt{vk}(x-\xi) \cdot \int_0^x d\zeta \sigma(Q, \xi) e^{k\zeta} \cos k\eta \quad (76)$$

$$c(\xi)$$

where σ is the source distribution on hull c in the near field which can be determined by the integral equation (15). This outer expansion is derived by taking the Fourier transform of (49) which is the outer expansion of the potential in the frequency domain. This should match with (75), then the matching condition becomes,

$$\int_0^x d\xi \gamma(\xi) \sin \sqrt{vk}(x-\xi) = \operatorname{Re} \int_0^x d\xi \sin \sqrt{vk}(x-\xi) \cdot \int_0^x d\zeta \sigma(Q, \xi) e^{k(\zeta+i\eta)} \quad (77)$$

$$c(\xi)$$

Now multiplying $e^{-avk/4}/\sqrt{vk}$ to the both sides of (77) and integrating with respect to k in the interval $[0, \infty)$ where a is an arbitrary positive small constant, we have

$$\int_0^\infty \frac{dk}{\sqrt{vk}} e^{-avk/4} \sin \sqrt{vk} x = \frac{2\pi}{v} \delta(x)$$

Therefore the unknown source density function is now determined from (77) and the above relation. That is,

$$\gamma(x) = -\frac{1}{2} \tilde{H}(x, v) \quad (78)$$

where $\tilde{H}(x, v)$ is the Kochin function in the time domain (21).

Now the wave resistance formula can be written by the far field potentials as follows,

$$C_W = \frac{v^2}{4\pi} \int_{-\pi/2}^{\pi/2} d\theta |H(v \sec^2 \theta, \theta)| \sec^3 \theta \quad (79)$$

where $H(k, \theta)$ is the Kochin function defined in the far field by,

$$H(k, \theta) = \frac{1}{v} \int_{-\infty}^\infty d\xi \int_{-\infty}^\infty d\eta F(\xi, \eta) e^{ik(\xi \cos \theta + \eta \sin \theta)} + \int_{-\infty}^\infty d\xi \gamma(\xi) e^{ik\xi \cos \theta} \quad (80)$$

In the formula $F(x, y)$ and $\gamma(x)$ can be given by solving the time dependent boundary value problem (69) in the near field by the method in §2.

As shown in the analysis, the time dependent boundary value problem plays the essential role in the low speed slender wave making problem.

4. NUMERICAL ANALYSIS AND COMPARISON WITH EXPERIMENTS

4.1 Numerical Analysis

As an application of the 2-D time dependent boundary value problem, we will show some numerical examples of the 2-D motion problem in the time domain discussed in §3.1 and give some comparison with the results of experiment. [27]

It was shown that the time dependent velocity potential of §3.1 has to be solved in order to complete the equation of motion in the time domain (39). The potential ϕ_j in the j th motion can be solved making use of the integral equations (11) or (15) by imposing the specified body boundary condition (26). When we employ the equation (15) for the temporal source, the solution $\sigma_j(Q, t)$ will be affected by the irregular frequency. However if we substitute it into the equation (14) to get the potential, we will obtain the same solution as that calculated from (11) which has no influence of the irregular frequency. When the time t becomes large, it takes much computing time to solve the integral equations numerically. Then we will derive an asymptotic expression for the potential at large t .

The temporal source derived from (15) includes the effect of the irregular frequency. Then we will decompose it into two parts at large t . That is,

$$\sigma(Q, t) = \hat{\sigma}(Q, t) + \Delta\sigma(Q, t) \quad (81)$$

where $\hat{\sigma}(Q, t)$ is independent of the irregular frequency and will be possibly calculated by the method in [15] and $\Delta\sigma(Q, t)$ denotes the part which is affected by the irregular frequency. When the specific body boundary condition (26) is applied, (81) becomes

$$\sigma(Q, t) = \sigma^*(Q, 0) + \Delta\sigma(Q, t) \quad (82)$$

The velocity potential at large t can be obtained by substituting (82) into (14). By the relation verified in (17), we can say $\Delta\sigma$ does not affect the potential. Therefore the potential $\phi_j(P, t)$ can be written as,

$$\phi_j(P, t) = \int_0^t d\tau \int_c d\sigma^*(Q, 0) G(P, Q, t-\tau) \quad (83)$$

Substituting the Green's function (10) into the above, and integrating with respect to τ , we have

$$\phi_j(P, t) = \frac{1}{2\pi} \int_c d\sigma^*(Q, 0) \ln \frac{r}{r_0} - \frac{1}{\pi} \int_c d\sigma^*(Q, 0) \cdot \int_0^\infty \frac{dk}{k} e^{k(z+\zeta)} \cos k(y-\eta) (1 - \cos \sqrt{gkt}) \quad (84)$$

In the second term the integration with respect to k is written as, at large t ,

$$2\ln\frac{\sqrt{gt}}{2\sqrt{r}} + \gamma + \ln 4$$

where γ is the Euler's constant. From this we can deduce the following,

$$\dot{\phi}_j(P,t) \sim \frac{1}{\pi} \int_C d\lambda \sigma^*(Q,0) \left\{ \frac{1}{2} \ln \frac{r}{r} - 2\ln \frac{\sqrt{g}}{2\sqrt{r}} - \gamma - \ln 4 - 2\ln t \right\} \quad (85)$$

Then differentiating with respect t , we have,

$$\phi_{jt}(P,t) \sim -\frac{2}{\pi} \int_C d\lambda \sigma^*(Q,0) \cdot \frac{1}{t} \quad (86)$$

From the consideration of the flux through contour c , it is obvious that

$$\int_C d\lambda \sigma^*(Q,0) = \begin{cases} -2a & \text{for symmetric motion} \\ 0 & \text{for asymmetric motion} \end{cases} \quad (87)$$

where a is the half breadth of the cylinder. Consequently we have,

$$\phi_{jt}(P,t) \sim \begin{cases} \frac{4a}{\pi} \cdot \frac{1}{t} & \text{for } j=2 \\ 0 & \text{for } j=1,3 \end{cases} \quad (88)$$

and from (31),

$$L_{jj}(t) \sim \begin{cases} \frac{8\pi a^2}{\pi} \cdot \frac{1}{t} & \text{for } j=2 \\ 0 & \text{for } j=1,3 \end{cases} \quad (89)$$

These asymptotic expressions will be used in calculation at large t .

Though the equation of motion (39) has the form of the integro-differential equation, this can be treated as the differential equation because the memory effect term becomes 0 at $\tau=t$.

$$\sum_{j=1}^3 (m_{ij} + \mu_{ij}) \ddot{X}_j(t) + C_{ij} X_j(t) = - \int_0^t d\tau L_{ij}(t-\tau) \ddot{X}_j(\tau) + F_{wi}(t) \quad (90)$$

Then we will use the Runge-Kutta-Gill method to solve (90) with appropriate initial conditions. Now we consider the following initial conditions,

$X(0)$ =initial displacement $\dot{X}(0)=0$ for free damping motion in still water

$X(0)=\dot{X}(0)=0$ for motion in waves.

In the former case the exciting force $F_{wi}(t)=0$. The experiments will be considered for the motions with these initial conditions. And calculations also will be performed for the motions with these initial conditions.

4.2 Experiments

To examine the validity of the equation of motion in the time domain (39) and the Haskind relation in the time domain (37), following three experiments have been performed. Namely,

- free damping motion in still water,
- exciting force and moment acting on the restrained body in transient waves,
- free motion in transient waves.

These experiments were made at 2-Dimensional experimental tank ($L \times B \times d = 20m \times 1m \times 2m$) (Fig. 5), for two types cylinders: model A; half immersed circular cylinder, and model B; rectangular cylinder with rounded corner (Fig. 6). The motion displacements were measured by potentiometers attached to the guide connected with model, and forces were measured by the three forces components ballance. The transient waves were generated by one cycle of heave motion of a wedge installed at the midpoint of the tank.

In these experiments the coupled motions have not been treated for brevity. Experiments in sway and heave modes for model A and in sway, heave and roll modes for model B have been performed.

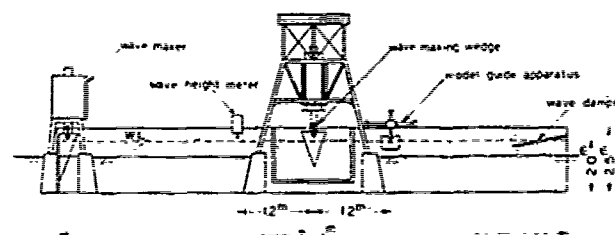


FIGURE 5. Arrangement of experimental apparatus.

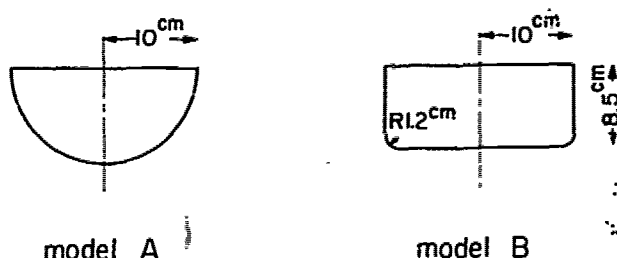


FIGURE 6. Model geometries.

4.3 Comparison Between Calculations and Experiments

In this paper we will show only the results in sway and heave modes for model A and roll for model B.

First the numerical results of ϕ_j , μ_{jj} and $L_{jj}(t)$ are shown in Figs. 7-9. Here τ denotes nondimensional time scale $t\sqrt{g/a}$, and the angle θ is measured from the negative z -axis, thus $\theta=90^\circ$ corresponds to the water line. In Fig. 8 we can see that the asymptotic formulas (88) and (89) are good approximations at large τ , then we use

these formulas for $\tau > 10$.

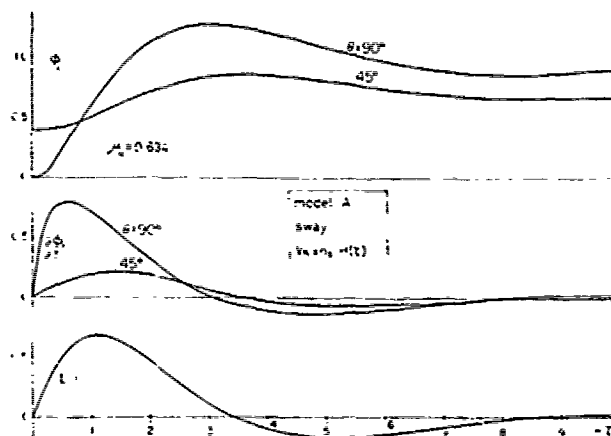


FIGURE 7. Step response potential and memory effect coefficient function in sway mode motion of Model A.

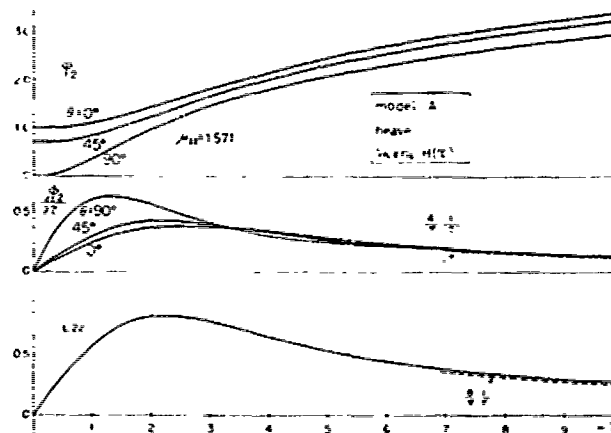


FIGURE 8. Step response potential and memory effect coefficient function in heave mode motion of Model A.

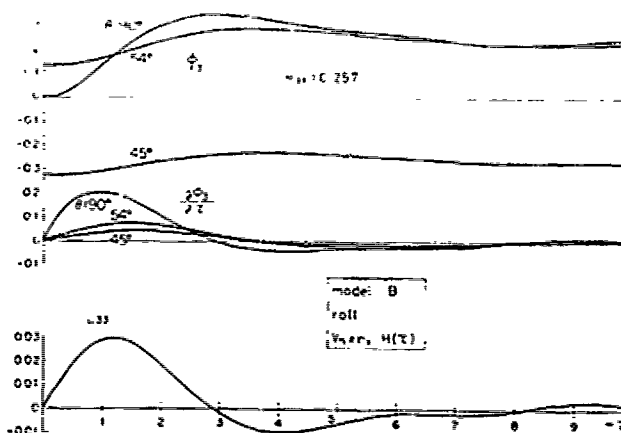


FIGURE 9. Step response potential and memory effect coefficient function in roll mode motion of Model B.

Figs.10,11 show the free damping motion in still water. In these figures full line shows calculated results and the points with small circles show measured values. For the case of free heave motion of a circular cylinder Ursell [28][29] has treated the same problem by different manner than that used here but both results agree very well, and they also agree with experimental results. However in the case of free roll motion of model B (Fig.11), the measured values show faster damping than the calculated. This may be due to the viscous effect.

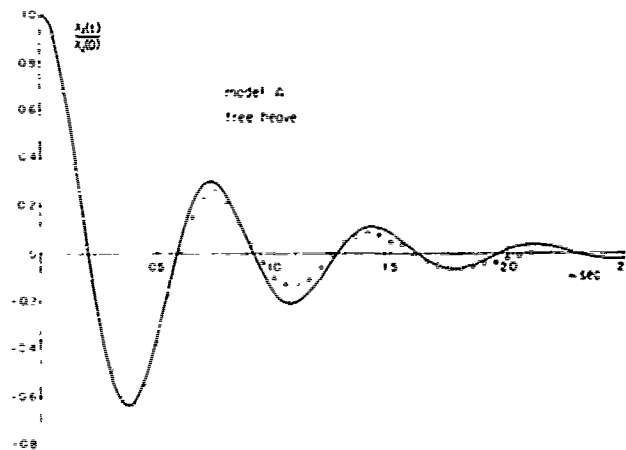


FIGURE 10. Free heave motion of Model A.

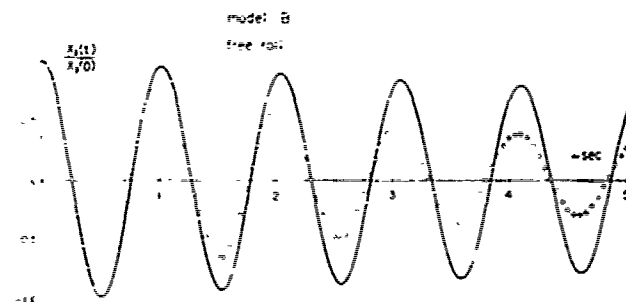


FIGURE 11. Free roll motion of Model B.

Figs.12-14 show the exciting force and moment exerted on the fixed models by the transient waves. As evident from these figures, the force and moment calculated by the Haskind relation in time domain (37) show good agreement with experimental results.

Finally, Figs.15-17 show the motion in transient waves. Through the experiment a) the utility of equation of motion in the time domain was made clear and by experiment b) the validity of the Haskind relation (right hand side of equation of motion) was proved, then as is expected the agreement between numerical and experimental results are fairly good in these figures too. (The discrepancy at initial stage of sway motion (Fig.15) is considered to be caused by the small friction of the guide apparatus.)

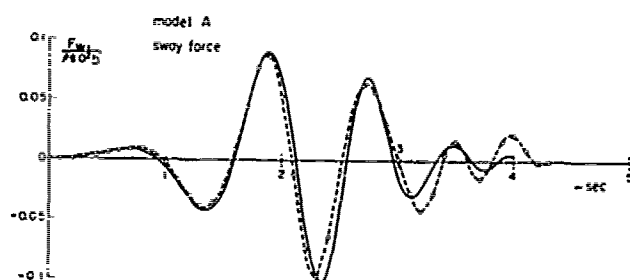


FIGURE 12. Sway force in transient wave on Model A.

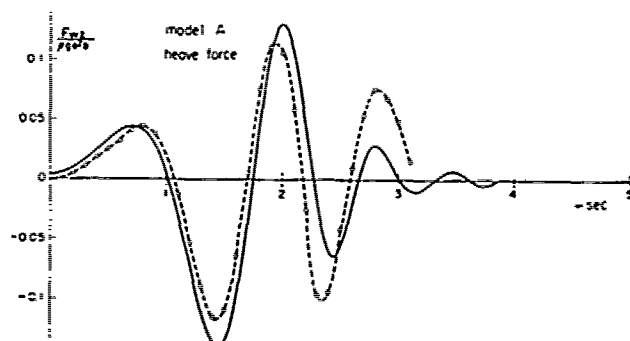


FIGURE 13. Heave force in transient wave on Model A.

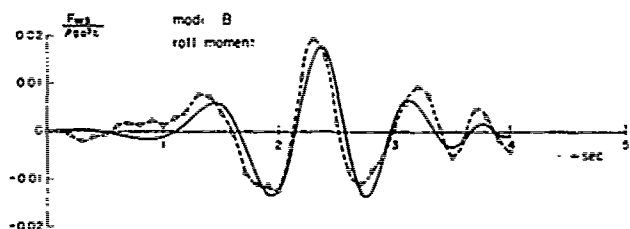


FIGURE 14. Roll moment in transient wave on Model B.

Consequently we can say as follows: if once we obtain the time dependent velocity potential $\phi_j(Q,t)$ for a body, we can solve the forces acting on that body and its motions in time base for any arbitrary incident waves.

5. CONCLUSION

Considering the attempts to apply the 2-D "time dependent boundary value problem" to the ship wave problem, the importance of the theoretical aspects as well as the numerical techniques has to be emphasized. For the cases analysed in this paper, the singular behavior of the integral equation solution of the temporal source function is the main object to be concerned about.

It is sometimes advantageous to calculate forces acting on a ship body from the radiated waves in the far field. To this purpose, the amplitude of the waves generated by a body should be known. We know that the Kochin function is connected with the wave amplitude and it is calculated

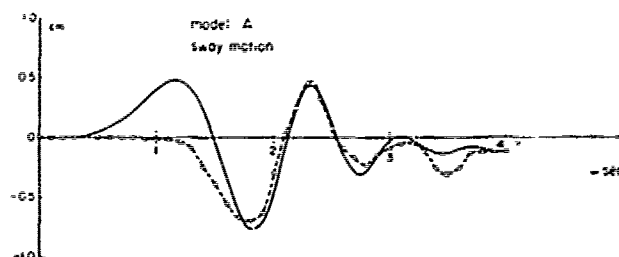


FIGURE 15. Sway motion in transient wave, Model A.

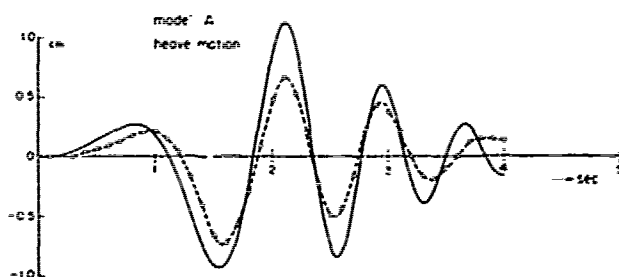


FIGURE 16. Heave motion in transient wave, Model A.

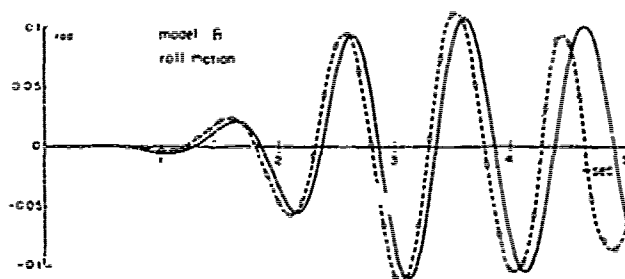


FIGURE 17. Roll motion in transient wave, Model B.

from the singularity distribution on the body surface. Therefore for the calculation of the forces of a ship, the temporal source distribution is the necessary quantity.

When solving the ship wave problem by making use of the time dependent boundary value problem, the property of the temporal source obtained from the integral equation approach have been clarified. The temporal sources are effectively utilized in the calculation of the potential at large t as seen in §4. And they are also used in the Kochin functions in the time domain.

The time dependent boundary value problem has been proved to be useful in the ship motion problem in the time domain, showing good agreement with the experiments. And the fact also has been shown that it could be used as the basic equation for the 2-D problems deduced from the 3-D ship motion problems under some assumptions. These 2-D problems with 3-D corrections may be most suitable ones when the original 3-D problems have some difficulties in the computation.

REFERENCES

1. Korvin-Kroukovsky, B. V., "Investigation of Ship Motions in Regular Waves", Transactions of the Society of Naval Architecture and Marine Engineering, Vol. 63, 1955, pp. 386-435.
2. Ogilvie, T. F. and Tuck, E. O., "A Rational Strip Theory for Ship Motion, Part 1", Report No. 013, Department of Naval Architecture and Marine Engineering, University of Michigan, Ann Arbor, 1969.
3. Tuck, E.O., "A Systematic Asymptotic Expansion Procedure for Slender Ships", Journal of Ship Research, Vol. 8, No. 1, 1964, pp. 15-23.
4. Ursell, F., "The Refraction of Head Seas by a Long Ship", Journal of Fluid Mechanics, Vol. 67, 1975, pp. 689-703.
5. Ogilvie, T. F., "Singular-Perturbation Problems in Ship Hydrodynamics", Advances in Applied Mechanics, Vol. 17, Academic Press, New York, 1977, pp. 91-188.
6. Ogilvie, T. F., "The Wave Generated by a Fine Ship Bow", Proceedings of the 9th Symposium on Naval Hydrodynamics, ACR-203, Office of Naval Research, Washington, D. C., 1972, pp. 1483-1525.
7. Chapman, R. B., "Numerical Solution for Hydrodynamic Forces on a Surface-Piercing Plate Oscillating in Yaw and Sway", Proceedings of the 1st International Symposium on Numerical Hydrodynamics, David W. Taylor Naval Ship Research and Development Center, Bethesda, MD, 1975, pp. 333-350.
8. Tick, L. J., "Differential Equation with Frequency-Dependent Coefficients", Journal of Ship Research, Vol. 3, No. 2, 1959, pp. 45-46.
9. Cummins, W. E., "The Impulse Response Function and Ship Motions", Schiffstechnik, Bd. 9, Heft 47, 1962, pp. 101-109.
10. Ogilvie, T. F., "Recent Progress Toward the Understanding and Prediction of Ship Motion", Proceedings of the 5th Symposium on Naval Hydrodynamics, ARC-112, Office of Naval Research, Bergen, Norway, 1964, pp. 3-80.
11. Frank, W., "Oscillation of Cylinders in or below the Free Surface of Deep Fluids", Report No. 2375, Naval Ship Research and Development Center, Bethesda, Maryland, 1967.
12. Ursell, F., "Short Surface Waves due to an Oscillating Immersed Body", Proceedings of the Royal Society, Ser. A, 1953, pp. 90-103.
13. Wehausen, J. V. and Laitone, E. V., "Surface Waves", Handbuch der Physik, Vol. 9, Springer-Verlag, Berlin and New York, 1960, pp. 446-778.
14. Ohmatsu, S., "On a wave Making Theory of Cylinders at the Early Stage of Oscillation", Journal of the Society of Naval Architects of Japan, Vol. 134, 1973, pp. 101-110. (Japanese)
15. Adachi, H. and Ohmatsu, S., "On the Influence of Irregular Frequencies in the Integral Equation Solutions of the Time-Dependent Free surface Problems", Journal of the Society of Naval Architects of Japan, Vol. 146, 1979, pp. 119-128.
16. Bessho, M. and Kyojuka, Y., "Inner problems of Water Wave in a Vessel", Transactions of the West-Japan Society of Naval Architects, No. 57, 1979, pp. 37-52. (Japanese)
17. Wehausen, J. V., "Initial-Value Problem for the Motion of a Body in an Undulating Sea", Report No. NA-65-4, University of California, Berkeley California, 1965.
18. Newman, J. N., "The Exciting Forces on Fixed Bodies in Waves", Journal of Ship Research, Vol. 5, No. 1, 1962, pp. 34-55.
19. Faltinsen, O. M., "A Numerical Investigation of the Ogilvie-Tuck formulas for Added Mass and Damping Coefficients", Journal of Ship Research, Vol. 18, No. 2, 1974, pp. 73-85.
20. Saito, K. and Takagi, M., "A Solution for the Oscillating Slender-Body with Forward-Speed", Journal of the Society of Naval Architects of Japan, Vol. 144, 1978, pp. 96-105.
21. Adachi, H., "Analysis of Ship Motion by Slender Body Theory Part 3", Report of Ship Research Institute, Vol. 17, No. 3, Mitaka, Tokyo, 1980. (Japanese)
22. Daoud, N., "Potential Flow Near to a Fine Ship's Bow", Report No. 177, Department of Naval Architecture and Marine Engineering, University of Michigan, Ann Arbor, 1975.
23. Baba, E. and Takekuma, K., "A Study on Free Surface Flow Around the Bow of Slowly Moving Full Forms", Journal of the Society of Naval Architects of Japan, Vol. 137, 1975, pp. 1-10.
24. Adachi, H., "Low speed Wave Making Theory by Slender Body Theory", Papers of Ship Research Institute, Mitaka, Tokyo, 1980.
25. Newman, J. N., "Linearized Wave Resistance Theory, Proceedings of International Seminar on Wave Resistance, Society of Naval Architects of Japan, 1976, pp. 31-43.
26. Baba, E., "Analysis of Bow Near Field of Flat Ships", Mitsubishi Technical Bulletin, No. 97, Mitsubishi Heavy Industries, Ltd., Japan, 1975.
27. Ohmatsu, S., "On the Initial Value Problem in the Theory of Oscillation of Floating Bodies", Doctoral Thesis Submitted to Kyushu University, Fukuoka, Japan, 1980, (Japanese).
28. Ursell, F., "The Decay of the Free Motion of a Floating Body", Journal of Fluid Mechanics, Vol. 19, 1964, pp. 305-319.
29. Maskell, S. J. and Ursell, F., "The Transient Motion of a Floating Body", Journal of Fluid Mechanics, Vol. 44, Part 2, 1970, pp. 303-313.

Discussion

F. Ursell (Univ. of Manchester)

More than 10 years ago I worked with Dr. Maskell on the transient motion of a half-immersed circular cylinder. (See Refs. 28 and 29). At that time it was not possible to solve the integro-differential equations numerically, but we found that the equations simplified considerably in the frequency-domain, where each frequency component satisfies the equations for a time-periodic motion. The transient motion was found by taking the inverse Fourier-transform. For example, it was found that the free heaving motion due to an initial impulse is proportional to the function

$$h_1(\tau) = \frac{1}{2\pi} \int_{-\infty}^{\infty} \frac{e^{-i\omega\tau} d\omega}{1 - \frac{1}{4}\omega^2 (1 + \Lambda(\omega))},$$

where $\Lambda(\omega)$ is the complex force coefficient for the cylinder heaving with angular frequency $\omega/(g/a)$. (Thus $\Lambda(\omega)$ describes the virtual mass and damping at this frequency). This integral would be an explicit solution, if the function $\Lambda(\omega)$ were known explicitly, but in fact the function $\Lambda(\omega)$ must be obtained from the solution of an infinite system of linear equations for every frequency $\omega/(g/a)$. Even when this has been done we found considerable difficulties; the integral was difficult to evaluate because the integrand is oscillatory (rapidly oscillatory for large τ) and decreases only slowly (like ω^{-2}) as $\omega \rightarrow \infty$. To obtain accurate results we found it necessary to increase the rate of convergence by deforming the integral in the complex ω -plane and using known analytical asymptotic results for $\Lambda(\omega)$. A large damped-harmonic contribution to $h_1(\tau)$ was found to come from the residues at the poles of the integrand, which could be evaluated very accurately. Analogous difficulties would be expected in the work of Adachi and Ohmatsu. We had no difficulties with irregular frequencies because we did not represent the potential by sources only.

Adachi and Ohmatsu have now been successful in a more direct approach. This is a very considerable achievement, and I trust that they will continue with this work. Nevertheless I would like to suggest to them that our earlier Fourier-transform approach may still have advantages and lead to considerable simplification. I hope that they will try it on their problems.

R.W. Yeung (MIT)

The authors are to be congratulated on a fine contribution that outlines the po-

tential applications of the solution of the two dimensional unsteady body-wave interaction problem. The authors have also given here a nice summary of their earlier work on irregular frequencies^{1,2}, a preprint of which I received too late last November to comment on before the JSNA meeting but I think it is not too late to add here that their work has shed much light on the difficulties associated with an integral-equation formulation based on source distribution.

It seems fair to say that the formulation described in §3.1 for the purely two-dimensional problems is reasonably well known. Although the authors are probably not aware of it, I have developed a related numerical capability for some time now. In 1977, Ito conducted some transient-motion experiments at the M.I.T. Towing Tank for a circular cylinder. His results were compared with the calculations of Maskell and Ursell²⁹. Not long after, I formulated an integral equation based on Green's theorem for this problem, but because of other applications in mind I allowed the rigid-body mechanics to be coupled with the fluid dynamics. The numerical results obtained were in excellent agreement with Ref. 29 and compares well also with Ito's data. Details of the treatment of the problem were presented in a SNAME H5 Panel Meeting in 1978 and will appear in Yeung (1980). Figure 1

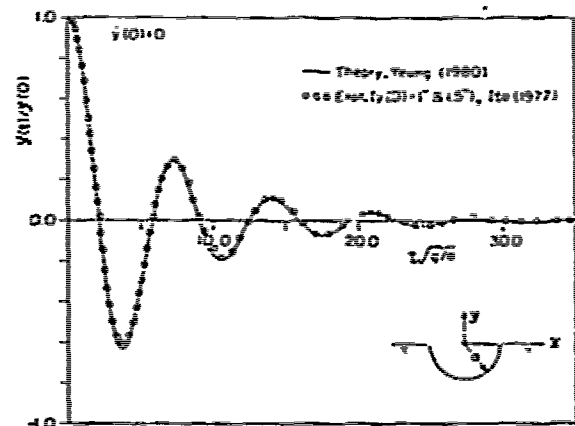


Fig. 1 Transient response of a floating circular cylinder (Yeung, 1980)

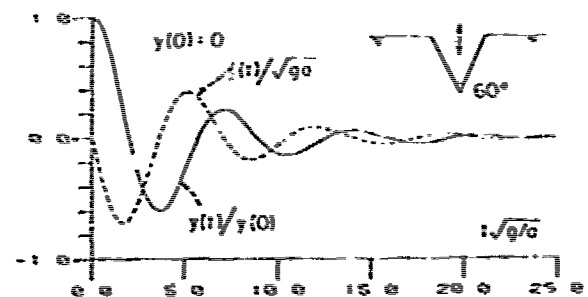


Fig. 2 Transient response of a 60°-angle wedge (Yeung, 1980)

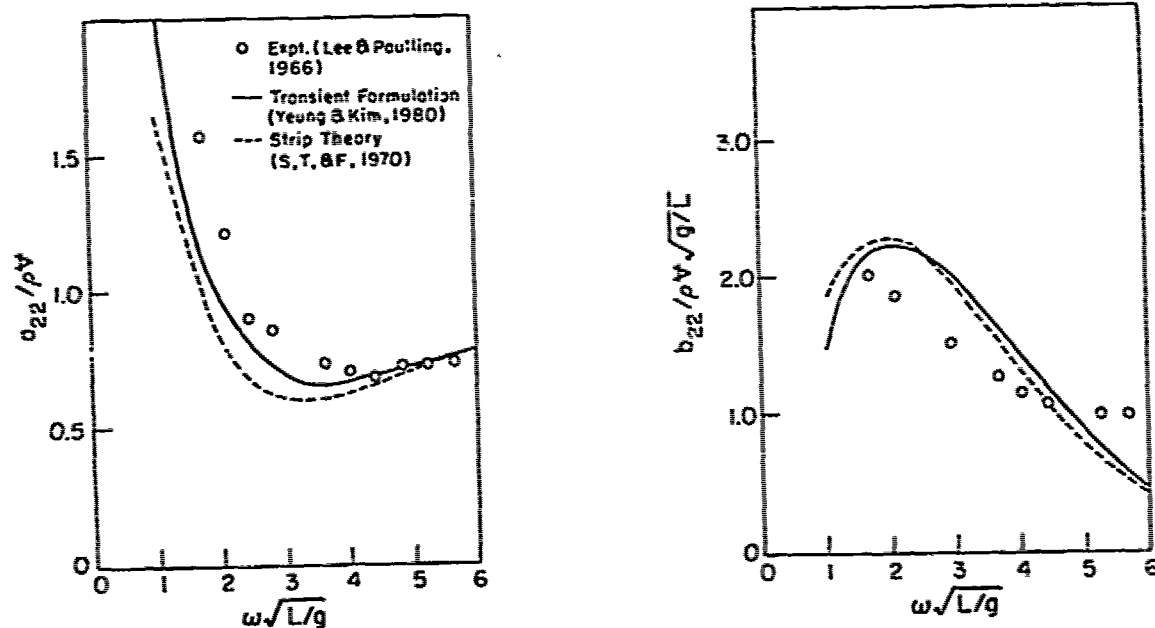


Fig. 3 Heave added mass a_{22} and damping b_{22} of a spheroid at Froude no. = 0.246 (Yeung & Kim, 1980)

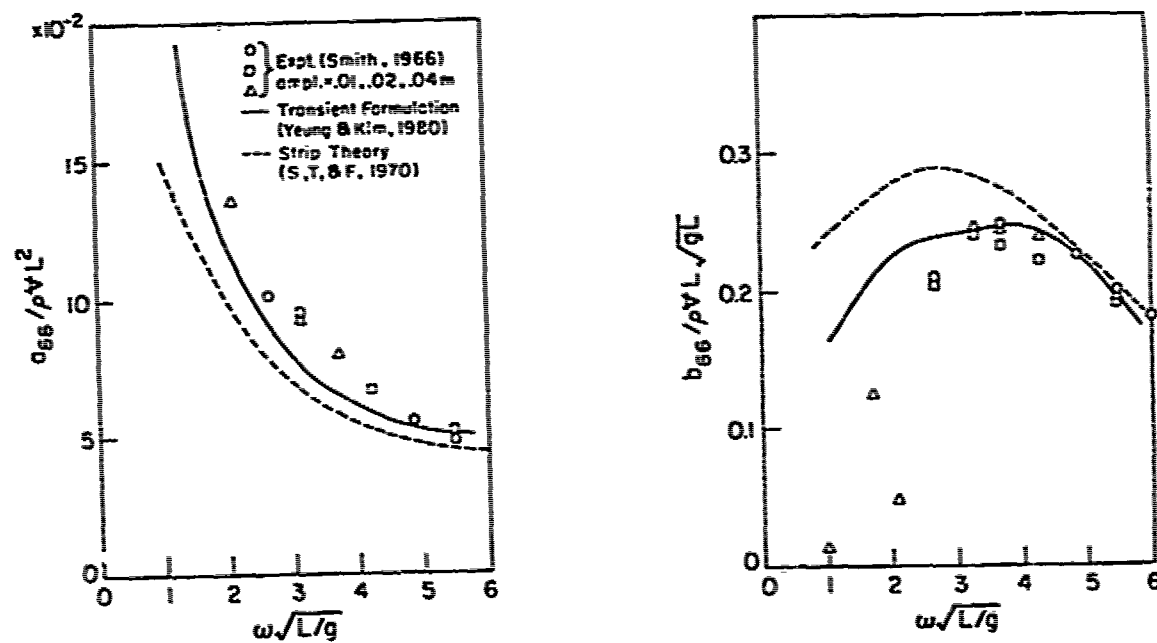


Fig. 4 Pitch added moment of inertia a_{66} and damping b_{66} of a Dutch destroyer at Froude no. = 0.15 (Yeung & Kim, 1980)

attached here shows the comparison between theory and experiment. Fig.2 shows similar calculations for a wedge-shaped body, whose damping characteristics is stronger than that of a circle. The authors' calculations in §4 are apparently wider in scope. However, it is not clear from the text of this paper what was used precisely to represent the transient incident wave potential. Some explanation will be desirable.

We have investigated the high-speed slender ship problem discussed in §3.2 by the authors. There are substantial difficulties when the body is no longer a simple uniform cylinder. As an example, the validity of equation (56) comes into question. Furthermore, the interpretation of (57), an integral equation proposed by the authors to determine $E(\xi)$ becomes obscure, since $E(x)$ would depend on where the point Q is on the body section. Based on a fixed frame of reference, we have developed a new but related approach. The mathematical structure of the near-field problem is similar to the authors. What seems most interesting is that our formulation yields a set of formula that are closely related to the traditional strip theory, but the hydrodynamic coefficients now include quasi three-dimensional effects. Fig.3 displays the heave added mass and damping of a spheroid, of length/beam ratio = 6, translating at a Froude number of 0.246. The experimental results b_{22} of Lee and Paulling (1966) were adjusted by a factor of $\sqrt{2}$ since their strip theory calculations were found to be off by this factor. The pitch added moment of inertia and damping for a Dutch destroyer is shown in Fig.4. Once again, similarly satisfactory agreement between theory and experiment can be noted. It is not obvious that these more mathematically involved theories yield substantially better predictions than ordinary strip theory, but preliminary results that we have obtained at this point seem to suggest that the cross-coupling terms can be better predicted. More specifics on this work will be available in Yeung and Kim (1980).

REFERENCES

- Ito, S., "Study of the Transient Heave Oscillation of a Floating Cylinder", M.S. Thesis, Dept. of Ocean Engineering, M.I.T. May (1977)
- Yeung, R.W., "On the Transient Response of Freely-Floating Cylinders", Manuscript to be submitted to J. of Engrg. Mathematics, Sept. (1980)
- Lee, C.M. and Paulling, J.R., "Measurements of Pressures on a Heaving Prolate Spheroid", University of California, Berkeley, Report No. NA-66-4, (1966)
- Smith, W.E., "Equation of Motion Coefficients for a Pitching and Heaving Destroyer Model", Laboratorium Voor Scheepsbouwkunde, Technische Hogeschool Delft, Report No.154, (1960)
- Yeung, R.W. and Kim, S.H., "A New Strip

Theory of Ship Motions", Manuscript in preparation, (1980)

C.M. Lee (MITSUBISHI)

The authors should be congratulated for their excellent work. By studying the numerical results shown in Figs.10 through 17, I could not help but asking the following questions.

1. From the results of Figs.10,13 and 16, I can conclude that the discrepancies shown in Fig.16 should be mainly due to the discrepancies in the wave excited heave force shown in Fig.13. However, from Figs. 15 and 12, one can conclude that it is not the wave excited sway force but the hydrodynamic force F_{p1} that should be causing the discrepancy in the early stage of motion. Could the authors think of any particular reasons for this seemingly contradictory results?

2. The authors reasoned that the discrepancy in the free-decaying motion shown in Fig.11 should be due to viscous effects. However, from Figs.14 and 17, one can observe that the roll motion in transient waves does not seem to be influenced by the viscous effects but rather by the wave-excited roll moment. This may imply that the roll motion is more influenced by F_{W3} than by F_{p3} . As far as I know, for the roll response in the frequency domain, particularly near the resonant frequency, the reverse is true. I would like to know if the authors experienced any noticeable differences in their computations for different modes of motions.

H. Maruo (Yokohama N. Univ.)

The authors appear to have followed Chapman's approach that the boundary-value problem is formulated in the time-space domain with respect to the absolute inertial frame. Though Chapman's analysis of the lateral oscillation of a flat plate shows considerable success, there are problems if one intends to apply the same technique to a displacement ship with forward speed. First of all, there is a contradiction between the elliptic-type boundary-value problem in the three-dimensional motion and the parabolic-type boundary-value problem employed in the present paper. As a consequence, the solution given here is not able to represent the elliptic nature of the three-dimensional solution. Such difficulty appears specifically in the fact that the inner solution is unable to match the inner expansion of the outer solution. Eq.(53) which the authors present as the inner expansion of the far-field potential is not correct except in the case of very high frequency. Correct expressions for the outer solution have been given by Newman,

Tuck (1964) and Maruo (1964, 1966). It is observed that the most important portion of the three-dimensional effect in the inner expansion is missed in the result of the present paper. This kind of difficulty appears in particular when one wishes to apply the same technique to the problem of the steady forward motion of a ship. The idea of bow near-field is not warranted because of the lack of logical rationality. The second point which I wish to discuss is that the authors employed the Fourier transform of the hull boundary condition as shown in eq. (42). However the validity of this treatment is rather doubtful because the hull boundary condition is satisfied on the contour c which becomes a function of x by itself. Most of the above is a repetition of my discussion to Saito's paper (Reference 20, 1978)

REFERENCES

- Newman, J.N., Tuck, E.O., "Current Progress in the Slender Body Theory for Ship Motions", Fifth Symposium on Naval Hydrodynamics, Bergen, Sept. (1964)
 Maruo, H., Discussion to the above paper (1964)
 Maruo, H., "An Application of the Slender Body Theory to the Ship Motion in Head Seas", Journal of the Society of Naval Arch. of Japan, Vol. 120, (1966) (in Japanese)

T.F. Ogilvie (Univ. of Michigan)

In this ambitious paper, the authors attempt to show the common nature of several important problems of ship hydrodynamics. They have helped to clarify several important points, but I question some of their conclusions. Also, I believe that more attention should be given to some restrictions on their approach.

If a source of constant strength moves along the free surface, the resulting wave-motion solution can be analyzed by the method of stationary phase. This results in the well-known separation into two parts: diverging waves and transverse waves. The stationary-phase expression is really valid only at large distance from the source. However, near the track, the diverging waves dominate, and they are predicted well by the stationary phase method even close to the source.

This diverging wave precisely matches the waves corresponding to the 2-D Green function given by the authors in (10). This fact leads to two observations: (i) The transverse waves are lost in the analysis in this paper. (ii) Near the source, the wave crests are parabolic in the horizontal plane, all of the parabolas in principle passing through the source point. Both of these observations lead to major consequences:

(i) Ignoring the transverse waves leads to a serious restriction. In Section

3.3 (low-speed problem), the wave number of the transverse waves near the track is $g/U^2 = \delta^1$. Thus the authors write symbolically that $\partial/\partial x = O(\epsilon^{1/2} \delta^1)$. If the term ϕ_{xx} is dropped from the Laplace equation, it means that $\epsilon \rightarrow 0$ while δ is held fixed. Physically, this means that ship beam and draft approach zero while $\lambda = 2\pi\delta$ is fixed. I question whether it is the authors' intention to develop a low-speed theory of this nature.

In time-dependent problems as well, some parts of the full 3-D wave system will be lost, introducing further restrictions.

(ii) In order to match a steady-motion bow solution to the far field, Daoud [22] found that the matching had to be carried out along parabolic curves passing through the bow. The usual kind of matching implied in Section 3.2 (in which $r = \sqrt{y^2 + z^2} \rightarrow \infty$ in the near field and $r \rightarrow 0$ in the far field) fails. This difficulty is masked in the paper by the use of Fourier transforms (in x), but it is a real difficulty that must be handled carefully.

Finally, I should comment on low-speed theories of the kind discussed in Section 3.3. In passing from (59) to (62), the authors lose a major low-speed effect, the distortion of wave-propagation rays by the nonuniform stream around the ship. Work in recent years at the University of Tokyo by Professor Inui and his associates indicates that this effect is not negligible. Indeed, Dagan showed in 1972 that even the free-surface condition, $[F]$, in (59) is not consistent: ψ should be augmented by a second-order non-wavy term.

Notwithstanding my lengthy and apparently negative comments here, I strongly commend the authors for trying to bring some order into this area of ship hydrodynamics, and I encourage them to continue their efforts.

Author's Reply

H. Adachi (SRI)

Prof. Ursell's suggestions are welcomed in many aspects. He raised the crucial points concerning the time dependent problem many years ago. In the time domain, when the time becomes large, the calculation begins to take a lot of time. At large time we have to include all the memory effect in the past. This is one of troublesome problems in the calculation of the time dependent potential. So the simplification for the problem is desired and the Fourier transform approach is deserved to be pursued with much attention. We would like to take labour with it in the near future.

We would like to appreciate Prof. Yeung for informing us the related works of the

transient motion problem. As for the incident waves used in the calculation in §4, waves are generated by the motion of a wedge shaped wave maker. The apex angle of the wedge is assumed to be small in order to utilize the thin body treatment. When the wedge moves up and down arbitrarily in time with velocity $V(t)$, the x-component of the velocity of the wedge is given by,

$$V_x(y, t) = V(t) \sin \theta \cos \theta \quad -d \leq y \leq 0$$

where d is the depth of the wedge. The motion of the wedge is assumed to be so small that the motion is described around its equilibrium position and is replaced by a time dependent source distribution on the center line at $x=0$, whose density is proportional to V_x . The incident wave potential can be written as follows.

$$\phi_I(x, y, t) = \frac{1}{\pi} \int_{-d}^0 d\eta V_x(\eta, t) \ln \frac{r}{r_0} - \frac{2g}{\pi} \int_0^t d\tau \int_{-d}^0 d\eta V_x(\eta, \tau)$$

$$\cdot \int_0^\infty dk \frac{1}{\sqrt{gk}} e^{k(y+\eta)} \cos kx \sin \sqrt{gk}(t-\tau)$$

The second point which the discussor raised is a pertinent one in the high speed slender ship problem. Indeed, there are some questions about the validity of the equation (57). However, the potential (56) satisfies the conditions (40) except [H], then if a ship is slender, the formula will be utilized at least as a leading order solution.

Since the potential (48) will coincide with the potential in the traditional strip theory as x/U becomes large. So the influence of the forward speed appears in the regime where x/U is small. The same is true for the hydrodynamic forces which will be calculated from the potential (48).

Dr. Lee raised very controversial questions about the experiments. The early stage of the motion of model A in sway mode apparently has discrepancy. We concluded this due to the defect in the experimental apparatus. However, the possibility of the hydrodynamic forces to that discrepancy may not be excluded. We can not say much about this point. As to the heaving motion result, looking carefully Fig. 13, the experiment becomes larger than the calculated at $\tau > 2.2$. However the wave excited motion in Fig. 16 is not larger than the calculated in the same region. Then the discrepancies in the motion are not necessarily attributed to the wave excited force F_{p1} .

As for the roll motion of model B, judging from the experimental result, we should conclude that F_{w3} is more dominant than F_{p3} as Dr. Lee said. Only the roll motion of model B shows the discrepancy in the free motion. Since we did not perform the forced motion tests, we can not say anything about other modes of motion.

Prof. Maruo questioned about the validity of the fundamental problem of ship motion in §3.2. In the analysis of this paper the key assumption is that the frequency of motion is high, so that the wave length generated by the motion is compatible to the ship's lateral dimension. Under this assumption and the additional slender bow near field assumption we can derive the fundamental boundary value problem in (40) for a ship running through waves with speed U . The inner problem (40) has a solution defined by (48). Its outer expansion (50) is valid for $x \rightarrow O(1)$ and $y \rightarrow O(1)$. Under the high frequency assumption, it is valid to derive the inner expansion (53) of the outer solution (52). And (53) can be shown to be valid an inner expansion into the bow near field. Thus the matching is correct. If we assume the motion frequency $O(1)$, the different treatment other than ours must be considered as Prof. Maruo suggested.

Prof. Ogilvie questioned very important points of the problem in the low speed slender body wave making problem. They are summarized as follows.

- 1) negligence of transverse waves
- 2) small parameters in the bow near field
- 3) validity of the matching
- 4) effect of local nonlinearity.

1) In this paper, the low speed slender body theory is adopted to treat the horizontal reflection of the ship generated waves on the ship hull in the bow near field. Horizontal reflection describes the wave reflection on the hull surface whose projection is parallel to ship center plane. So the divergence wave system may play role in the bow, while in the midship region the transverse wave may do the role in the interaction between waves and hull. However there must be discussion about the matching of the bow near field with the midship near field.

2) The assumption of the change of order in the differentiation in the bow near field may have some points of question. There, we have introduced two small parameters ϵ and δ . It is desirable to develop the dual parameter expansion in the bow near field. Such attempt is not successful in this paper, because ϵ and δ are treated as same thing in actual. Then $\partial/\partial x = O(\epsilon^{-1/2} \delta^{-1})$ is treated as $\partial/\partial x = O(\epsilon^{-3/2})$ and this is considered as the fundamental assumption. Therefore, $\lambda = 2\pi\delta$ becomes zero with the same order as ϵ . So the bow near field problem in this paper is for the one parameter expansion. However, such expansion leads to the interesting problem as given in §3.3.

3) The matching is correct in this paper. At first sight the outer expansion of the inner solution (49) seems to be the usual outer expansion as $r \rightarrow \infty$. This expansion is valid also as $x \rightarrow O(\epsilon^{1/2})$ becomes large like $x \rightarrow O(1)$. And the inner expansion (74) and (75) are valid along the parabolic line $x^2/y = \text{const.}$ as $\epsilon \rightarrow 0$.

4) The basic problem (62) with the inhomogeneous terms D and E in the free surface condition is a direct derivation from the full nonlinear problem under the low speed assumption. (62) can include all the nonlinear influences condensed in D and E terms. Then it can include the local nonlinear effect that is defined as the inter-

action between ship waves and the flow around the ship body. In this slender low speed problem, E function contains some of such interaction effect, though the slender ship assumption makes the problem very simplified one. So we do not entirely neglect the effect of the local nonlinearity in the analysis in §3.3.

Second-Order Theory of Oscillating Cylinders in a Regular Steep Wave

A. Papanikolaou and H. Nowacki
Technical University of Berlin, Berlin
Federal Republic of Germany

ABSTRACT

The nonlinear two-dimensional hydrodynamic problem of a cylinder with arbitrary cross-section shape performing finite amplitude oscillations in the free surface of a regular steep wave is treated on the basis of nonlinear system dynamics, potential and perturbation theory. A complete second order transfer model is developed from the assumptions of a second-order incident wave, a quadratic dynamic model of the system, and a second-order perturbation expansion of the hydrodynamic nonlinearities in potential flow.

The given nonlinear wave-body flow system is decomposed into six second-order subsystems to which a perturbation expansion in several small parameters is applied. This results in a set of linear boundary value subproblems of uniform type, which can be solved by close-fitting methods.

On this basis second-order expressions for the hydrodynamic pressures, forces, and moments are obtained and introduced in the equations of the body motions to obtain the motion response.

Numerical examples illustrate the solution procedure and several physical aspects of the second-order model.

NOMENCLATURE

Symbol	Description
a_w	wave amplitude
A	area of cylinder cross section
b	maximum half-beam
b_i	reference quantity for motion i , eq. (2)
B	waterline beam, Fig. 3

$\tilde{c}_{ik}^{(n)}$	generalized restoring force coefficient of order n for (i,k) , eq. (106)
$j_k^{f(1)}, j_{ik}^{f(2)}$	hydrodynamic force or moment amplitude of order n in direction j caused by problem k or by interaction between problems i and k , as applicable, eqs. (90) to (92), $n = 1$ or 2
$j^{F(n)}(t)$	hydrodynamic force or moment of order n in direction j , eq. (88), with ${}_2F^{(n)} \equiv H^{(n)}$, ${}_3F^{(n)} \equiv V^{(n)}$, ${}_4F^{(n)} \equiv M^{(n)}$
g	acceleration of gravity
$G^{(n)}(z, \tau)$	Green's function for order n , eq. (53)
h	water depth
$H^{(n)}$	horizontal hydrodynamic force of order n
i	imaginary unit (space), e.g. eq. (54)
\vec{i}	unit vector in positive x -direction
I_{44}	moment of inertia (roll), eq. (99)
j	imaginary unit (time), e.g. eq. (55)
\vec{j}	unit vector in positive y -direction
k	wave number, eq. (58)
\vec{k}	unit vector in positive roll axis direction
$1_{ik}^{(2)}$	free surface inhomog. for sec.-order problem (i,k) , (45), (49)

Symbol	Description		
$\hat{m}_{ik}^{(n)}$	generalized body mass coefficient of order n for (i,k), eq. (106)	α	angle between \vec{s} and pos. x-direction, Fig. 3
M	cylinder mass per unit length, eq. (99)	B	section area coefficient
$M^{(n)}$	hydrodynamic roll moment of order n	$\delta^{(n)}$	phase angle of order n, general, eq. (93)
$M_R^{(n)}$	moment of inertia of order n, eq. (100)	δ_w	incident wave phase angle, eq. (57), $\delta_w=0$ for regular sine-wave ($t=0$) in positive x-direction
\vec{n}	unit normal vector, positive outward, Fig. 3	ϵ_0	perturbation parameter for incident wave, eq. (2)
$j^{(n)}_{ik}$	directional cosine components of order n for direction j, eqs. (21) to (24)	ϵ_7	perturbation parameter for diffraction, eq. (2)
o-x-y	inertial right-handed Cartesian coordinate system, Fig. 3	ϵ_i	perturbation parameter for motion in direction i, eq. (2)
$\bar{o}-\bar{x}-\bar{y}$	body-fixed right-handed Cartesian coordinate system, Fig. 3	ϵ_k	perturbation parameter in general
$p^{(n)}(\bar{x}, \bar{y}, t)$	hydrodynamic pressure of order n	ζ	complex variable, source point, eq. (54)
$p_k^{(1)}(\bar{x}, \bar{y})$	hydrodynamic pressure amplitude of order n caused by problem k or by interaction of problems (i,k), as applicable, eqs. (67) to (79)	λ_w	incident wave length, eq. (58)
$p_{ik}^{(2)}(\bar{x}, \bar{y})$		$\chi^{(n)}_{ik}$	dimensionless hydrodynamic damping coefficient of order n, caused by (i,k), eq. (108)
\vec{r}	position vector in $\bar{o}-\bar{x}-\bar{y}$ -system, eq. (81)	$\chi^{(n)}_{ik}$	dimensionless hydrodynamic mass coefficient of order n, caused by (i,k), eq. (108)
$r_k^{(1)}, r_{ik}^{(2)}$	body boundary inhomogeneities for first (k) or second-order (i,k) problems, eqs. (30), (44), (47), (48)	ν	frequency parameter, eq. (58)
s	arc length on cylinder contour	ρ	fluid density
\vec{s}	unit tangent vector, Fig. 3	ρ_B	body mass density, eq. (99)
S(t)	wetted cylinder contour at time t, Fig. 3	$\phi(x, y, t)$	velocity potential, eq. (13)
S_0	wetted cylinder contour at time $t=0$, Fig. 3	$\phi_k^{(1)}(x, y)$	space potential functions of orders (1) or (2), eq. (13)
t	time	$\phi_{ik}^{(2)}(x, y)$	
T	draft, Fig. 3	$\psi_k^{(1)}(x, y)$	decomposed space potentials of orders (1) or (2), eqs. (16), (17)
\vec{V}	velocity vector of body motion	$\psi_{ik}^{(2)}(x, y)$	
V_n	normal component of body velocity, eq. (9)	ω	frequency of incident wave and of first-order motion response
$x_i(t)$	body motion in direction i, eq. (14), for sway ($i=2$), heave ($i=3$), and roll ($i=4$)	B{ }	body boundary differential operator, eq. (19)
$x_i^{(n)}, x_{ki}^{(n)}, x_{oi}^{(n)}$	body motion amplitudes of order n, eq. (14)	$\Delta\{ \}$	Laplace operator
\bar{y}_G	vertical coordinate of body center of gravity	$F(n^2 v)\{ \}$	free surface differential operator, eq. (18)
$X_R^{(n)}$	horizontal inertia force of order n, eq. (100)	$R(n^2 v)\{ \}$	radiation differential operator, eq. (20)
$Y(x, t)$	free surface elevation profile	$\nabla\{ \}$	Hamilton's nabla operator
$Y_R^{(n)}$	vertical inertia force of order n, eq. (100)		
z	complex variable, field point, eq. (54)		

Subscript Conventions:

The paper contains several multiply subscripted quantities in symbol expressions of the general form

$$m_j^{(n)} o_{ik}$$

where some or all of the subscripts may be present. These symbols denote:

- a) Superscript n in parentheses refers to the order n of the quantity in the per-

turbation expansion.

- b) Left subscript m denotes the dependence upon the motions of first ($m=1$) and second order ($m=2$) of the following quantities: potentials, eq. (17), associated disturbances, e.g. eqs. (44) to (49), pressures, eq. (65), and forces, eq. (87).
- c) Left subscript j ($j = 2, 3, 4$) is used with direction cosines, eqs. (21) to (24), or with forces, eqs. (90) to (92). It denotes the reference direction j . For the forces both subscripts m and j may occur, eq. (87).
- d) Right subscripts i, k ($i, k=0, 2, 3, 4, 7$) relate to the cause of the subscripted quantity. First-order quantities have a single subscript k , second-order quantities require at least two subscripts i, k ; second-order steady-state quantities carry the additional subscript o .

Other Conventions:

- Lengths are made dimensionless by b or $|a_w|$, angles by maximum wave slope or with respect to 1 radian, time by ω^{-1} , and mass per unit length by ρb^2 .

1. INTRODUCTION

The past decade has witnessed a rapid growth of interest in the nonlinear aspects of ship motions. It is well established that linear theory succeeds extremely well in predicting many important phenomena in ship motions within the accuracy required for design purposes; but it has also been recognized all along that the range of validity of the linear model is restricted by its fundamental assumptions of small wave heights and small motion amplitudes [1]. There has been growing experimental evidence in recent years, accompanied by basic theoretical results, suggesting that nonlinearities in waves and ship motions are also a matter of important practical consequence. This holds for the prediction of any large amplitude motion effects, particularly extreme values, and has received much attention in connection with large amplitude roll (capsizing), hydrodynamic impacts (slamming, section flare effects), wave-induced bending moments and other nonlinear phenomena.

The present paper addresses itself to one specific aspect of nonlinear ship motions, that is, the problem of an infinitely long cylinder oscillating in the free surface in sway, heave and roll in response to a regular incident beam wave of finite amplitude (on deep water or water of limited depth). This case is an important reference point for solving the much more general problem of ship motions in an irregular seaway, although a comprehensive nonlinear theory for the latter purpose remains to be developed.

The current two-dimensional hydrodynamic problem is approached by means of nonlinear system dynamics, perturbation theory and potential flow methods. This implies that several, but not all, of the nonlinearities present in the physical problem can be taken into account and that the results may be valid for moderate wave heights and moderate motion amplitudes, in other words, for nonlinearities of such degree that the second-order perturbation approximation will remain sufficiently realistic.

Specifically the approach will allow for nonlinearities in the

- Free surface boundary condition for incident and motion generated waves (by including second-order effects and satisfying this condition in the true free surface - in a perturbation sense),
- Body boundary condition (by satisfying it over the really wetted regime, approximating the shape of the latter by a Taylor expansion around the rest position of the body in the spirit of perturbation theory).

All derived responses such as pressures, forces, motions are also evaluated to the second order. However, nonlinearities of viscous origin (like separation at sharp corners) are disregarded, although subsequent, empirically based corrections of the system model remain feasible.

Much of the previous work on the subject of this paper has been devoted to the incident wave and forced oscillation subproblems. Numerous higher-order wave theories have been developed by Stokes [2], Levi-Civita, Sjelbreia and others. Papanikolaou has reviewed several of these theories, including a third order solution of his own, in [3]. For the present purpose a Stokes second-order wave will be sufficient to represent the incident wave flow.

In regard to the nonlinear forced motion problem Ogilvie [4] derived the second-order steady force on a submerged circular cylinder, which could be achieved without explicitly solving the second-order boundary value problem. This was done later by Parisi [5] for the circular cylinder heaving in the free surface and by C.M. Lee [6] for Lewis forms. Lee's solution to the second-order set of boundary value problems is based on multipole expansions and conformal mapping. Potash [7], working with close-fit techniques instead, extended the problem to sway, heave, and roll, including their coupling, and to arbitrary section shapes. Papanikolaou [8,9], on the basis of a similar approach, reexamined the foregoing results for the heaving cylinder and removed some inconsistencies in the analytical expressions and numerical results. Finally, Masumoto [10] developed an approach to the complete second-order oscillation problem using multipole expansions in analogy to C.M. Lee's treatment of the forced oscillation case.

Several approximate solutions to the second-order forced motion problem have been derived without solving the corresponding boundary value problem completely and rigo-

rously. C.H. Kim [11] dealt with forced heaving of triangular cylinders by an iteration which departed from a zero-frequency solution. Grim [12] derived approximate solutions based on low-frequency assumptions for large amplitudes of roll. Salvesen's approach in [13] to nonlinear heave (and pitch) is also based on low frequency approximations. Söding [14] used Green's theorem to derive the second-order force on an oscillating cylinder from first-order potentials of the problem. Yamashita [15] developed an approximate solution for "thin" oscillating cylinders with results up to the third order.

Several authors, e.g. [16-18], in contrast to the perturbation school of thought, have pursued direct time-domain solutions of the complete nonlinear problem, using initial value formulations and numerical integration schemes. These methods do not depend on linearizing assumptions and are attractive, in fact, sometimes perhaps the only available recourse, for dealing with very large motion amplitudes and waves. However, aside from some unresolved questions regarding the treatment of the radiation condition in the complete nonlinear case there are also some practical limitations: Computer time requirements tend to be heavy, and validation and generalization of results are difficult to perform for lack of frequency-dependent submodels.

Experimental results for several aspects of the nonlinear problem have been presented by Vugts [19], Tasai and Kotera-yama [20], Yamashita [15]. The agreement between individual test results and second-order theories is encouraging, although the available evidence is far from systematic and complete.

The research reported in this paper has the aim of defining a complete second-order model for a cylinder of arbitrary shape oscillating in the free surface in three degrees of freedom. This model combines a quadratic dynamic system model with a second-order hydrodynamic model. The incident beam wave is thus a second-order regular wave, that is, a "steep" wave in the sense of Stokes. The system model is subdivided into several separate, but interacting flow systems: Incident wave, forced motion, and diffraction are three primary subsystems familiar from linear theory. In second-order theory it is not sufficient to model these individual flows to the second order, but it is also necessary to account for the mutual second-order interactions in these flows. This requires introducing three further second-order subsystems.

A perturbation expansion in five small parameters is performed on the nonlinear system in order to recognize the "smallness parameters" characteristic of each subproblem. The expansion yields a corresponding set of 20 linear boundary value problems. The great majority of these can be regarded as radiation problems and represented by Fredholm integral equations of the second kind. This permits uniform numerical treat-

ment of all these subproblems by close-fitting methods. The standardized hydrodynamic coefficients obtained from the submodels are assembled into the complete transfer model via the equations of motion to solve for the motion response and other responses. The paper describes the solution procedure in detail. Some numerical examples are given to illustrate the physical properties of the transfer model and its components.

2. FORMULATION

2.1 Dynamic System Model

The nonlinear system of an incident wave and a body oscillating in response to this wave on the free surface of a fluid domain may be described by two sets of assumptions, called the dynamic system model and the hydrodynamic model. The former is related to the general dynamic behavior of the system in terms of its input and output, the latter consists of the hydrodynamic characteristics assumed for the flow system. The two models must, of course, be chosen in accordance with each other.

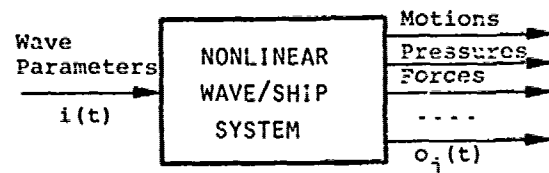


Fig. 1: Dynamic System Model

The dynamic system model of the nonlinear wave-ship system (Fig. 1) is characterized by the relation between its input signal $i(t)$ and its output signals $o_j(t)$, $j=1, \dots, J$. In the following we are interested in the steady-state behavior of the system, that is, in the time-periodic response of the ship to excitation by a regular steep wave. Initial transient phenomena of the response are disregarded. For this purpose we assume a nonlinear relationship between input and output of the form:

$$o_j(t) = \sum_{n=0}^N a_j^{(n)} \{i(t)\}^n, \quad (1)$$

and in particular a quadratic time response model ($N=2$). This model is introduced here (as in earlier work by Lee [21] and others) as an a priori working hypothesis, chiefly because it can be demonstrated to be compatible with the second-order hydrodynamic model to be developed by perturbation methods.

It is a particular property of this quadratic model that the response $o_j(t)$ to a monochromatic harmonic input signal $i(t)$ of frequency ω will contain harmonic terms of frequencies ω and 2ω , as well as a constant "d.c." shift term.

In view of the complexity of the total flow process it is now of practical advantage to decompose the system model into a set of separate, but interacting nonlinear flow subsystems, each individually better amenable to hydrodynamic analysis. This will be done much in analogy to the concepts of incident flow, forced motion and diffraction flow, familiar from linear theory.

At the same time it is convenient to introduce a system of several small dimensionless parameters ϵ_k suitable for defining characteristic "smallness ratios" in the perturbation expansions of the subproblems. We introduce:

$$\begin{aligned}\epsilon_0 &= \frac{2\pi}{\lambda_w} |a_w| = k |a_w| \\ \epsilon_7 &= |a_w| b^{-1} = \epsilon_0 (kb)^{-1} \\ \epsilon_i &= \frac{|x_i^{(1)}|}{b_i}, \quad i = 2, 3, 4\end{aligned}\quad (2)$$

with a_w = amplitude of regular beam wave (a_w in general complex)

λ_w = wave length

$k = \frac{2\pi}{\lambda_w}$ = wave number

$vb = \omega \frac{\lambda_w}{g}^{-1} b$ = dimensionless frequency parameter

and physically for a second-order wave on water depth h [3]:

$$\begin{aligned}kb &= (vb) \{c_0 (1 + \epsilon_0^2 c_1)\}^{-1} + O(\epsilon_0^3) \\ c_0 &= s/c, \quad c_1 = (8c^4 - 8c^2 + 9)/8s^4 \\ s &= \sinh(kh), \quad c = \cosh(kh)\end{aligned}$$

Further:

b = maximum half-beam of section

$i = 2, 3, 4$ for sway, heave, roll, respectively

$x_i^{(1)}$ = complex first-order amplitude in direction i

b_i = reference quantity for motion i

$b_2 = b_3 = b$ = maximum half-beam

$b_4 = 1 \text{ rad}$ = unit reference angle

The parameter ϵ_0 is a measure of wave steepness in the incident flow, ϵ_7 is characteristic of the magnitude of the diffraction flow, and the ϵ_i define the smallness

of the motion amplitudes in each degree of freedom. Thus we have available a set of physically relevant smallness parameters for the major subsystems of the flow model.

The use of five small parameters does not imply that they are meant to be independent of each other, but only that their physical interdependence need not be considered until after the subsystem flow problems are solved. In fact, ϵ_0 and ϵ_7 are both dependent on wave height, and $\epsilon_7(\epsilon_0)$ and ϵ_i are physically linked by body dimensions. However, at least two physically independent smallness assumptions can be made, for example, the traditional "small wave steepness" and "small motion amplitude" assumptions. To this extent our approach parallels Newman's in [22] who used three perturbation parameters in a thin ship oscillation problem to characterize the orders of beam-length ratio (thinness), wave steepness, and motion amplitudes.

The decomposition of the dynamic system model S into a set of second-order subsystem models jS , assuming for the time being that all ϵ_k are of equal order of magnitude, can now be expressed in terms of the characteristic small parameters present in each subsystem:

$$\begin{aligned}S(x, y; t; \epsilon_0, \epsilon_7, \epsilon_i) &= \\ &_1S(x, y; t; \epsilon_0) + _2S(x, y; t; \epsilon_7) + \\ &_3S(x, y; t; \epsilon_i) + _4S(x, y; t; \epsilon_i \epsilon_0) + \\ &_5S(x, y; t; \epsilon_i \epsilon_7) + _6S(x, y; t; \epsilon_0 \epsilon_7) + O(\epsilon_k^3)\end{aligned}\quad (3)$$

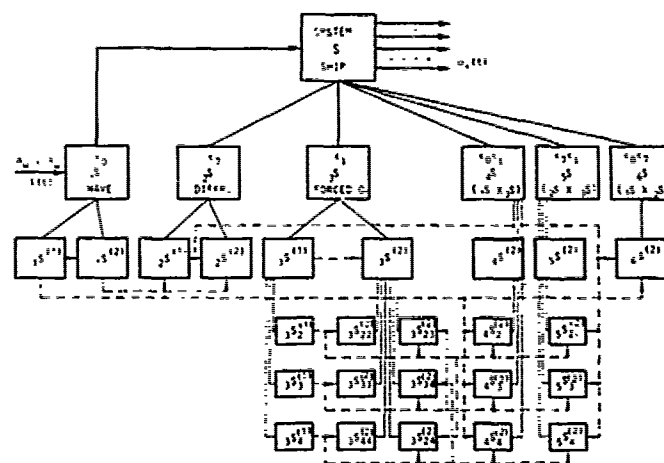


FIG. 2 : SECOND-ORDER DYNAMIC SYSTEM MODEL

Fig. 2 illustrates the mutual interactions of the six basic nonlinear subsystems:

- 1S: Nonlinear incident wave
- 2S: Nonlinear diffraction
- 3S: Nonlinear forced motion
- 4S: Nonlinear interaction of 1S and 3S
- 5S: Nonlinear interaction of 2S and 3S
- 6S: Nonlinear interaction of 1S and 2S

The second-order model of (3) differs from linear theory in two ways: The familiar basic flow systems 1S, 2S, 3S have to be extended to second-order level, and their second-order interactions have to be taken into account, which is done by the subsystem 4S, 5S, 6S. Each subsystem jS corresponds to a nonlinear boundary value problem of potential flow, which by perturbation methods can be reduced to classes of linear boundary value subproblems $jS^{(n)}$. Some of these classes are further subdivided into elements of types $jS^{(n)}$ and $jS^{(n)}$, that is, linear subproblems to be derived in detail from the hydrodynamic model. Fig. 2 shows the complete scheme of nonlinear flow subsystems jS and their subproblem classes and elements, connected by solid lines, whereas the dashed lines with arrows indicate how the nonlinear subsystems jS interact with each other via their linear boundary value subproblems.

2.2 Boundary Conditions

A cylinder of arbitrary cross section shape is oscillating in or just below the free liquid surface in response to a beam, regular, steep wave of amplitude a_w and frequency ω .

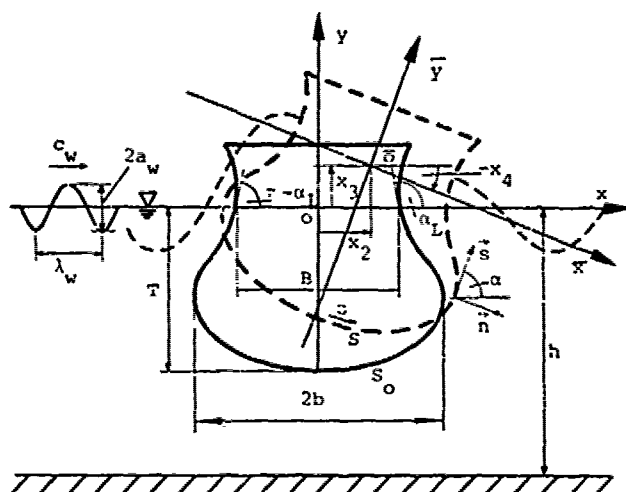


Fig. 3: Coordinate Systems

Two Cartesian coordinate systems are employed (Fig. 3): The right-handed system $o-x-y$ is fixed in space so that $o-x$ corresponds to the undisturbed fluid surface and y is positive upward; the right-handed system $\bar{o}-\bar{x}-\bar{y}$ is fixed in the moving body and coincides with $o-x-y$ when the body is in its equilibrium position. The displacements of sway, heave and roll are denoted by x_2 , x_3 and x_4 , respectively. Due to these motions a point (\bar{x}, \bar{y}) moving with the body has the following coordinates measured in the stationary system:

$$\begin{aligned} x &= x_2 + \bar{x} \cos x_4 - \bar{y} \sin x_4 \\ y &= x_3 + \bar{y} \cos x_4 + \bar{x} \sin x_4 \end{aligned} \quad (4)$$

The motion is assumed to have existed long enough for all transient effects to have decayed. Further, we assume inviscid, irrotational flow, which ensures the existence of a velocity potential $\phi(x, y, t)$ satisfying Laplace's equation for an incompressible fluid.

Combining the kinematic and dynamic boundary conditions on the free surface $y=Y(x, t)$, extending to infinity on both sides of the body, one obtains [8]:

$$\begin{aligned} \phi_{tt}(x, Y(x, t); t) + g \phi_Y &= \\ - 2(\phi_x \phi_{tx} + \phi_y \phi_{ty}) - \phi_x^2 \phi_{xx} - 2\phi_x \phi_y \phi_{xy} - \phi_y^2 \phi_{yy} \end{aligned} \quad (5)$$

If the fluid has a horizontal bottom at $y=-h$, then

$$\phi_Y(x, -h; t) = 0 \quad (6)$$

The kinematic body boundary condition implies that the normal velocity of the fluid $\dot{\phi}_n$ equals that of the body V_n (Fig. 3):

$$S(t): \dot{\phi}_n = (\vec{n} \cdot \vec{\nabla}) \phi(x, y; t) = V_n = \vec{n} \cdot \vec{v}(x, y; t) \quad (7)$$

$$\text{with } \vec{n} = \{\sin \alpha, -\cos \alpha\}, \vec{s} = \{\cos \alpha, \sin \alpha\} \quad (8)$$

$$\dot{\phi}_n = \sin \alpha \dot{\phi}_x - \cos \alpha \dot{\phi}_y \quad (9)$$

$$V_n = \sin \alpha \dot{x} - \cos \alpha \dot{y}$$

$$\begin{aligned} \dot{x} &= \partial x / \partial t = \dot{x}_2 - \dot{x}_4 (\bar{y} \cos x_4 + \bar{x} \sin x_4) \\ \dot{y} &= \partial y / \partial t = \dot{x}_3 + \dot{x}_4 (\bar{x} \cos x_4 - \bar{y} \sin x_4) \end{aligned} \quad (10)$$

$$\begin{aligned} \sin \alpha(t) &= \partial y / \partial s = \bar{y}' \cos x_4 + \bar{x}' \sin x_4 \\ \cos \alpha(t) &= \partial x / \partial s = \bar{x}' \cos x_4 - \bar{y}' \sin x_4 \end{aligned} \quad (11)$$

where the prime denotes the derivative with respect to arc length s , the dot indicates a time derivative, $\alpha(t)$ is the angle between unit tangent vector \vec{s} and the positive x -direction, and \vec{n} the unit normal vector which is positive outward.

At large distance from the body a suitable Sommerfeld radiation condition is imposed. Physically this corresponds to the fact that the incident wave and the motion generated by the ship are the only disturbances present. Mathematically this condition ensures uniqueness of the solution potentials.

In determining the potentials the motions of the body $x_i(t)$ will be assumed to be known. The normalized potentials and corresponding hydrodynamic forces determined on

this assumption will be substituted into the equations of motion later to derive the actual body motions in a given wave.

2.3 Perturbation Expansions

In order to reduce the nonlinear boundary value problem defined in the preceding section to a set of linear subproblems, we assume that the potential ϕ can be expanded into a power series in terms of five perturbation parameters ϵ_k ($k=0, 2, 3, 4, 7$) up to the second order in accordance with (3):

$$\phi(x, y; t; \epsilon_k) = \sum_k \epsilon_k \phi_k^{(1)}(x, y; t) + \sum_{i, k} \epsilon_i \epsilon_k \phi_{ik}^{(2)}(x, y; t) + O(\epsilon_k^3) \quad (12)$$

with $\phi^{(0)} \equiv 0$, $i, k = 0, 2, 3, 4, 7$

Questions concerning the convergence of the foregoing expansion, or particularly its uniform convergence, must be left open for the moment. Current calculation results suggest that the second-order potentials $\phi_{ik}^{(2)}$ are of equivalent order of magnitude to the first-order potentials $\phi_k^{(1)}$ so that the magnitude of the ϵ_i, ϵ_k will govern the convergence of the expansion. The series should converge for sufficiently small values of these parameters, but how this limits the physical range of validity of this second-order theory has yet to be found out. Special caution is in place for non-vertical section shapes in the waterline with regard to existence and uniqueness of solutions, although in our experience to date no serious practical difficulties have arisen yet.

According to the quadratic response model (1) a regular steep wave of frequency ω will produce physical output effects with frequencies ω and 2ω . Allowing for this fact in the separation of variables for the potentials in (12) by including terms of corresponding frequencies, expanding the potentials for small perturbations about the positions at rest, and treating the boundary conditions accordingly, one can show [8] that the relevant potential terms up to the second order are included in the simplified expression:

$$\phi(x, y; t; \epsilon_k) = \sum_k \epsilon_k \phi_k^{(1)}(x, y) e^{-j\omega t} + \sum_{i, k} \epsilon_i \epsilon_k \phi_{ik}^{(2)}(x, y) e^{-2j\omega t} + O(\epsilon_k^3) \quad (13)$$

This expression omits some trivial potentials as well as some time-independent second-order terms whose hydrodynamic effects are of fourth order.

By analogous reasoning one obtains expressions of equivalent form for the wave profile $y=Y(x, t)$ and for all physical quantities to be derived from the potential, that is, for example the pressures, forces and moment on the body. The unknown dis-

placements $x_i(t)$ may be correspondingly expanded into a perturbation series in terms of the small parameters ϵ_i , characterizing the magnitude of the motions in each direction i , eq. (2):

$$x_i(t) = \sum_{k=0}^2 \sum_{n=0}^2 \epsilon_i^n x_{ki}^{(n)} e^{-jk\omega t} \quad (14)$$

Neglecting trivial terms:

$$x_i(t) = \sum_{n=1}^2 x_i^{(n)} e^{-jn\omega t} + x_{oi}^{(2)} \quad (14a)$$

where we have introduced the abbreviated notation to be used from now on:

$$\epsilon_i^n x_{ki}^{(n)} \rightarrow x_i^{(n)}, \quad k \neq 0, \quad \epsilon_i^2 x_{oi}^{(2)} \rightarrow x_{oi}^{(2)} \quad (14b)$$

This change of notation is equivalent to saying that we will initially consider all hydrodynamic problems and their responses in a normalized way, namely for $\epsilon_i=1$. However, ϵ_i will be reintroduced later in solving the equations of motions and determining the actual response.

By substituting these perturbation expansions (13) and (14), and corresponding ones for the wave profile $y=Y(x, t)$ and its derivatives, into the Laplace equation and the boundary conditions formulated in section 2.2, it is possible [8] to reduce the given nonlinear time-dependent boundary value problem for $\phi(x, y, t)$ to a set of only space-dependent linear boundary value problems for $\phi^{(n)}(x, y)$. The nonlinear problem contains boundary conditions on free and moving boundaries, the linear subproblems involve only fixed boundaries, namely the undisturbed positions of the liquid and body surfaces. This is in the spirit of the perturbation method where the conditions at the true positions of these surfaces are approximated by Taylor series expansions about the positions at rest.

The linear boundary value problems resulting from this perturbation development are described in the following section. We restrict ourselves to the deep water case from here on. Details of the derivation and regarding the consequences of limited water depth can be found in [23].

2.4 Boundary Value Problems

In order to obtain a formulation for the boundary value problems for the potentials which is independent of the unknown motion amplitudes it is convenient to normalize the potentials in terms of the displacement, velocity and angular velocity components of the body or the exciting wave, where applicable. These components are for the first-order potentials, from (14) and the incident wave velocity:

$$\begin{aligned} v_i &= \dot{x}_i = \sum_{n=1}^2 v_i^{(n)} = \sum_{n=1}^2 v_i^{(n)} e^{-jn\omega t} \\ v_i^{(n)} &= -j n\omega x_i^{(n)}, \quad i = 2, 3, 4 \quad (15) \\ v_i^{(1)} &= -\omega k^{-1} \varepsilon_7 e^{j\delta_\omega}, \quad i = 0, 7 \end{aligned}$$

The phase angle δ_w measures the distance of the incident wave crest from the origin at time zero.

In terms of these velocity components the first order potentials may be expressed by introducing the normalized potentials $\tilde{\psi}_i^{(n)}$ as follows:

$$\epsilon_k \phi_k^{(1)} + \phi_k^{(1)} \quad , \quad \phi_k^{(1)}(x, y) = v_y \phi_k^{(1)} \quad , \quad (16)$$

for $k = 0, 2, 3, 4, 7$

The second-order potentials may be split up into two sets of normalized terms, those due to first-order displacements and velocities (left subscript equal to one), and those resulting from second-order velocities (left subscript two):

$$\begin{aligned} c_{ik} \phi_{ik}^{(2)} - \phi_{ik}^{(2)} &= 1 \phi_{ik}^{(2)} + 2 \phi_{ik}^{(2)} \\ 1 \phi_{ik}^{(2)} &= 0.5 \times v_i^{(1)} v_k^{(1)} \gamma_{ik}^{(2)}, \\ \text{for } i, k &= 0, 2, 3, 4, 7, \\ 2 \phi_{ii}^{(2)} &= v_i^{(2)} \gamma_{ii}^{(2)}, \\ \text{for } i &= 2, 3, 4, \end{aligned} \quad (17)$$

For the sake of brevity we introduce the following differential operators ([6], [8]):

Free-Surface Differential Operator

$$F(v) \equiv F(x, y) \equiv (F_v - vF), (x, y) \in S_F \quad (18)$$

Body-Surface Differential Operator

$$B[F(x,y)] = (\bar{y}'F_x - \bar{x}'F_y), \quad (x,y) \in S_0 \quad (19)$$

Radiation Condition Differential Operator

$$R(v)(F(x,y)) = \operatorname{Re}_j(F_x + jvF), (x,y) \in \left[\begin{smallmatrix} S_R \\ S_T \end{smallmatrix} \right] \quad (20)$$

The boundaries S_F , S_O , S_R and S_L are illustrated in Fig. 4.

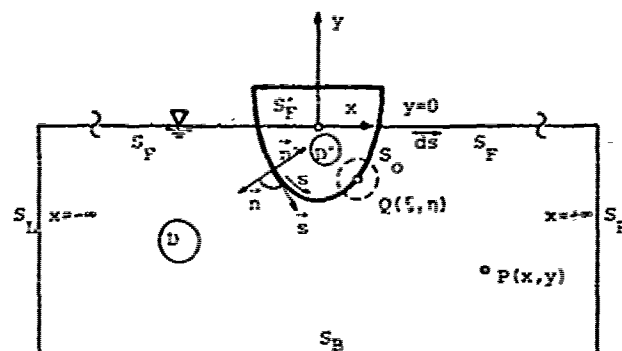


Fig. 4: Geometry of the Boundary-Value Problems

The time-dependent direction cosines of the unit normal vector \vec{n} , defined in (8), and (11), may be approximated by means of a perturbation expansion about the body position at rest and thus expressed in terms of body-fixed coordinates:

$$n_i = \sum_{n=0}^2 N_i^{(n)} e^{-jn\omega t} + N_{oi}^{(2)}, \quad i = 2, 3, 4 \quad (21)$$

With

$$\begin{aligned} N_i^{(0)} &= {}_i n^{(0)}, \quad N_i^{(1)} = x_4^{(1)} {}_i n^{(1)} \\ N_i^{(2)} &= (x_4^{(2)} {}_i n_{22}^{(2)} + 0.25 x_4^{(1)2} {}_i n_{21}^{(2)}), \\ N_i^{(3)} &= (x_4^{(3)} {}_i n_{22}^{(3)} + 0.25 |x_4^{(1)}|^2 {}_i n_{01}^{(3)}), \end{aligned} \quad (22)$$

$$i^n(0) = \begin{cases} \bar{y} & , i=2 \\ -\bar{x} & , i=3 \\ -(\bar{x}\bar{x} + \bar{v}\bar{v}) & , i=4 \end{cases} \quad i^n(1) = \begin{cases} \bar{x} & , i=2 \\ \bar{y} & , i=3 \\ 0 & , i=4 \end{cases} \quad (23)$$

$$i_{22}^{(2)} = i_{02}^{(2)} = i^{(1)}, \quad i_{21}^{(2)} = i_{01}^{(2)} \quad (24)$$

$$i_{21}^{(2)} = \begin{cases} -i^{(0)}, & i \neq 4 \\ 0, & i = 4 \end{cases}$$

A similar expansion is performed for the direction cosines of the unit tangent vector \hat{s} .

Collecting terms whose common factor is $c_i c_{n-i} e^{-jn\omega t}$ ($n=1, 2; i, k=0, 2, 3, 4, 7$), we obtain the following well-posed linear boundary value problems, generally of mixed form (third kind, Robin problem), for the unknown potential functions $\phi(n)$ [23]:

First-Order Boundary Value Problems

$$\Delta \phi_k^{(1)} = 0, (x, y) \in D \cup D'; \text{ for } k=0, \\ (x, y) \in D, \text{ for } k \neq 0 \quad (25)$$

$$F(v) \{ \phi_k^{(1)} \} = 0, (x, y) \in S_p \cup S_p', \text{ for } k=0 \\ (x, y) \in S_p', \text{ for } k \neq 0 \quad (26)$$

$$B \{ \phi_k^{(1)} \} = r_k^{(1)}, (x, y) \in S_0, k \neq 0 \quad (27)$$

$$\lim_{y \rightarrow -\infty} \phi_{ky}^{(1)} = 0, (x, y) \in S_B (y \rightarrow -\infty) \quad (28)$$

$$R(v) \{ \phi_k^{(1)} \} = 0, (x, y) \in S_L^R, k \neq 0 \quad (29)$$

with right-hand sides

$$r_k^{(1)} = r_k^{(0)}, k = 2, 3, 4 \\ r_7^{(1)} = -B \{ \phi_0^{(1)} \} \quad (30)$$

and symmetry conditions

$$\phi_k^{(1)}(-x, y) = (-1)^{k-1} \phi_k^{(1)}(x, y), \\ k = 2, 3, 4; k \neq 0, 7 \quad (31)$$

Second-Order Boundary Value Problems

1. Potentials caused by $v_k^{(2)}$, eq. (17), $k=2, 3, 4$:

$$\Delta \phi_{kk}^{(2)} = 0, (x, y) \in D \quad (32)$$

$$F(4v) \{ \phi_{kk}^{(2)} \} = 0, (x, y) \in S_F \quad (33)$$

$$B \{ \phi_{kk}^{(2)} \} = r_k^{(0)}, (x, y) \in S_0 \quad (34)$$

$$\lim_{y \rightarrow -\infty} \phi_{kky}^{(2)} = 0, (x, y) \in S_B (y \rightarrow -\infty) \quad (35)$$

$$R(4v) \{ \phi_{kk}^{(2)} \} = 0, (x, y) \in S_L^R \quad (36)$$

$$\phi_{kk}^{(2)}(-x, y) = (-1)^{k-1} \phi_{kk}^{(2)}(x, y) \\ k = 2, 3, 4 \quad (37)$$

2. Potentials caused by $x_i^{(1)} v_k^{(1)}$, $i, k=0, 2, 3, 4, 7$:

$$\Delta \phi_{ik}^{(2)} = 0, (x, y) \in D \quad (38)$$

$$F(4v) \{ \phi_{ik}^{(2)} \} = r_{ik}^{(2)}, (x, y) \in S_F \quad (39)$$

$$B \{ \phi_{ik}^{(2)} \} = r_{ik}^{(2)}, (x, y) \in S_0 \quad (40)$$

$$\lim_{y \rightarrow -\infty} \phi_{iky}^{(2)} = 0, (x, y) \in S_B (y \rightarrow -\infty) \quad (41)$$

$$R(4v) \{ \phi_{ik}^{(2)} \} = 0, (x, y) \in S_L^R \quad (42)$$

$$\phi_{ik}^{(2)}(-x, y) = (-1)^n \phi_{ik}^{(2)}(x, y) \quad (43)$$

with right-hand sides

a) $i = k = 2, 3, 4$

$$r_{kk}^{(2)} = \begin{cases} \phi_{2ys}^{(1)}, k=2 \\ \phi_{3xs}^{(1)}, k=3 \\ -(\phi_{4xs}^{(1)} + \phi_{4ys}^{(1)} + \phi_{4z}^{(1)}), k=4 \end{cases} \quad (44)$$

$$r_{kk}^{(2)} = v(2) \phi_{kx}^{(1)} + 3v(2) \phi_k^{(1)} + \phi_k^{(1)} \phi_{kxx}^{(1)} \quad (45)$$

$$n = k-1 \text{ in Eq. (43)} \quad (46)$$

b) $i \neq k$: Here it is convenient to evaluate jointly all coupling potentials $\phi_{ik}^{(2)}$ and $\phi_{ki}^{(2)}$. For this reason we let henceforth: $\phi_{ik}^{(2)} \leftarrow \phi_{ik}^{(2)} + \phi_{ki}^{(2)}$ with $i, k, i = 2, 3, 4, k = 0, 2, 3, 4, 7$. On this basis the right-hand sides become:

$$r_{ik}^{(2)} = \begin{cases} \phi_{3ys}^{(1)} - \phi_{2xs}^{(1)}, (i, k) = (2, 3) \\ -\phi_{2s}^{(1)} + \phi_{4ys}^{(1)} - \phi_{2xs}^{(1)} - \phi_{2ys}^{(1)}, \\ (i, k) = (2, 4) \\ -\phi_{3s}^{(1)} - \phi_{4xs}^{(1)} - \phi_{3xs}^{(1)} - \phi_{3ys}^{(1)}, \\ (i, k) = (3, 4) \end{cases} \quad (47)$$

$$r_{ik}^{(2)} = \begin{cases} \phi_{kys}^{(1)}, i=2 \\ -\phi_{kxs}^{(1)}, i=3 \\ -(\phi_{kxs}^{(1)} + \phi_{kys}^{(1)} + \phi_{ks}^{(1)}), i=4 \end{cases} k=0, 7 \quad (48)$$

$$r_{ik}^{(2)} = v(4) \phi_{ix}^{(1)} \phi_{kx}^{(1)} + 6 v(2) \phi_i^{(1)} \phi_k^{(1)} + \phi_i^{(1)} \phi_{kxx}^{(1)} + \phi_k^{(1)} \phi_{ixx}^{(1)} \quad (49)$$

$$n = i+k \text{ in Eq. (43), } k \neq 0. \quad (50)$$

The first and second order potentials for $k=0, 7$ (incident wave and diffraction problems) are in general nonsymmetric about the \bar{y} -axis. But the first order potentials can be split up into symmetric (k odd) and anti-symmetric (k even) parts. Then, for $k=0, 7$, the first-order problem must be solved twice for each k , modifying eq. (31) to apply to both the odd and the even case. This results in four complex first-order potentials $\phi_k^{(1)}$ ($k=0, 7$). Accordingly four second-order potential functions $\phi_{ik}^{(2)}$ ($k=0, 7$) are obtained, replacing eq. (50), in connection with (43), by relations for the odd and even cases.

It may be of interest to note in passing that previously published results for the forced oscillation case (Lee [6], Potash [7]) regarding the second-order free sur-

face inhomogeneous terms, corresponding to our eqs. (45) and (49) (both complex), are not consistent with each other nor with our results. However, there is full agreement with Lee's later (corrected) problem formulation [21]. For more details, see [8], [23].

3. PROBLEM SOLUTION

3.1 Boundary Value Problems Type

In the preceding section a set of linear boundary value problems was introduced by eqs. (25) to (31) for the first-order potentials $\phi^{(1)}$ and by eqs. (32) to (50) for the second-order potentials $\phi^{(2)}$. All potential functions are in general complex (with respect to time) according to eqs. (13) to (17). Referring back to Fig. 2 for orientation, one can now distinguish:

- First-order incident wave potential ($k=0$; $n=1$), solution known.
- First-order forced oscillation potentials ($k=2, 3, 4$; $n=1$), three unknown functions.
- First-order diffraction potential ($k=7$; $n=1$), symmetric and antisymmetric parts, two unknown potential functions.
- Second-order forced oscillation potentials ($i, k=2, 3, 4$; $i \leq k$; $n=2$), total of six unknown potential functions.
- Second-order incident wave and diffraction potentials ($k=0, 7$; $n=2$). On deep water these potentials are trivial and need not be considered.
- Second-order interaction potentials ($i=2, 3, 4$; $k=0, 7$; $n=2$), symmetric and antisymmetric parts, basically 12 unknown potential functions, but these may be reduced back to 6 numerical evaluations by combining the symmetric and antisymmetric parts, respectively, of the disturbances resulting from the first-order free wave and diffraction potentials.
- Second-order interaction potential between free wave and diffraction flow ($i, k=0, 7$; $n=2$), this vanishes trivially on deep water.

Aside from the incident wave problem, whose solution to the second order is well known, the boundary value problems for all of the potentials mentioned in the preceding are of the same type, whose general form is:

$$\begin{aligned} \Delta \phi^{(n)} &= 0, \quad (x, y) \in D \\ F(n^2 v) \{ \phi^{(n)} \} &= L^{(n)}, \quad (x, y) \in S_F \\ B(\phi^{(n)}) &= R^{(n)}, \quad (x, y) \in S, \\ \phi_y^{(n)} &= 0, \quad (x, y) \in S_B \quad (y \rightarrow -\infty) \\ R(n^2 v) \{ \phi^{(n)} \} &= 0, \quad (x, y) \in S_L \end{aligned} \quad (51)$$

The only essential difference between the first and the second order lies in the form of the free surface boundary condition: $L^{(1)}=0$ for the first, and $L^{(2)}=f(\phi^{(1)}) \neq 0$ for the second order.

Boundary value problems of type (51) may be addressed as "radiation problems" according to Sommerfeld, summarizing under this name all those problems which may be described by pulsating sources in a finite fluid domain.

The uniform format of the boundary value problem type describing the linear submodels of the nonlinear flow system has several practical advantages. Questions of existence and uniqueness of solutions may be discussed in a very general way once and for all. Above all, however, it is of immediate benefit that a single numerical solution approach may be applied to all subproblems under discussion.

3.2 Integral Equation Method

Green's third theorem of potential theory, applied to the $\phi^{(n)}$ -boundary value problem (51), yields the following inhomogeneous integral equation of Fredholm type of the second kind (Helmholtz integral equation), [8]:

$$\begin{aligned} -2\pi \phi^{(n)}(x, y) &+ \int_{S_0} \phi^{(n)}(\xi, \eta) \frac{\partial G^{(n)}(x, y; \xi, \eta)}{\partial n_Q} ds_Q \\ &= \int_{S_0} G^{(n)} R^{(n)}(\xi, \eta) ds_Q - \int_{S_F} G^{(n)}(x, y; \xi, \eta) L^{(n)}(\xi, \eta) d\xi d\eta \end{aligned} \quad (52)$$

In order to apply this formulation, suitable Green's functions must be available, i.e., functions which are solutions to a boundary value problem similar to (51), but with homogeneous boundary conditions [8].

On deep water the Green's function of n 'th order is, [8]:

$$\begin{aligned} G^{(n)}(z; \zeta) &= \text{Re}_j \{ \log(z - \zeta) - \log(z - \bar{\zeta}) + \\ &+ 2 \int_0^\infty \frac{e^{-ik(z - \bar{\zeta})}}{n^2 v - k} dk - j 2\pi e^{-in^2 v(z - \bar{\zeta})} \} \end{aligned} \quad (53)$$

with space complex variables for field point $P(z)$ and source point $Q(\zeta)$:

$$\begin{aligned} z &= x + jy \\ \zeta &= \xi + i\eta, \quad \bar{\zeta} = \xi - i\eta \end{aligned} \quad (54)$$

In the complex time domain the time-dependent Green's function of n 'th order is represented in accordance with eq. (13):

$$\phi^{(n)}(z; \zeta; t) = \operatorname{Re}_j \{ G^{(n)}(z; \zeta) e^{-jn\omega t} \} \quad (55)$$

The integral equation (52) represents actually a pair of coupled integral equations because the unknown functions $\phi^{(n)}$ are complex. A physical interpretation of this formulation is as follows: The potential $\phi^{(n)}(x, y)$ in a field point $P(x, y)$ is composed of contributions from a double layer potential of (unknown) intensity $\phi^{(n)}(\xi, \eta)$ produced by dipoles arranged along S_0 , from a single layer potential of known source intensity $-R^{(n)}(\xi, \eta)$ on S_0 , and in the event of second-order potentials a further single layer potential of known source intensity $L^{(2)}(\xi, 0)$ on S_p .

The Helmholtz integral equation formulation (52), which was apparently first introduced into ship motion theory by Potash [7], is analytically more general than Frank's well-known conventional source-sink method [24] by including boundary value problems of inhomogeneous mixed type. In addition, even when applied strictly to a Neumann problem, it has shown certain advantages numerically, especially for more complicated section shapes, and with regard to its sensitivity to the well-known irregular frequency phenomenon [8], [23], [25].

The discretization of the integral equation system (52) into an algebraic set of equations is conventional in the sense of close-fit methods and will not be discussed here. Details can be found in [8], [23]. In contrast to Frank's close-fit method the normal derivatives of Green's function in (52) are taken with respect to source point coordinates, which simplifies some integral expressions to be evaluated for the discrete panels [8].

Some particular analytical difficulties exist in evaluating the integral expressions in (52). One of these pertains to the line integral over S_p , which contains a singularity where S_p intersects with S_0 . This causes numerical difficulties in evaluating the potential and its derivatives in the vicinity of the singular point. Further the integration along S_p , which should be extended to infinity, must be truncated, so that some analytical criterion for the truncation limit is required. Our approach to these questions is discussed in section 3.3.3.

It is well-known [26] that integral equation formulations like (52), or as used by Frank, fail to provide finite, unique, physically meaningful solutions at or near certain "irregular" frequencies corresponding to eigenvalues of the adjoint interior potential boundary value problem. This phenomenon is known as "irregularity problem". In second-order theory this type of effect begins at much lower frequencies, the first second-order irregularity occurring at about one quarter the frequency of the corresponding first-order value. This suggests that

proper treatment of this effect is even more important than in linear theory.

Proposed cures to this problem may be analytical (Ursell [27], Ogilvie-Shin [28], Papanikolaou [8]), semi-analytical and -numerical (Paulling and Wood [29], Ohmatsu [30]), or purely numerical (Faltinsen [31], Papanikolaou [8, 23]). In the present context numerical methods, based on interpolation of regular frequency results, were preferred to others up to moderately high frequencies because they were convenient to use and gave reliable results, though not always without substantial expense of computer time [25]. But it must be mentioned that purely analytical methods for this purpose have not yet been extended to second-order situations with inhomogeneous free surface boundary conditions.

3.3 Solution Potentials

3.3.1 Incident Wave Problem

The derivation of second-order potentials for a regular, steep (Stokes) wave may be assumed to be known, e.g. [3]. It will be presented in a special, normalized form in the present context.

For water of infinite depth $\phi_0^{(2)}$ is trivial and need not be considered. For a second-order regular, steep wave propagating in the positive x -direction on deep water (beamwise), the first-order potential for the wave with amplitude a_w and wave length λ_w must satisfy eqs. (25), (26) and (28) and is of the form

$$\phi_0^{(1)} = (kb) \omega^{-1} e^{k(y+jx)} \quad (56)$$

This may be normalized according to (15), (16)

$$\phi_0^{(1)} = -g \omega^{-1} a_w e^{ky} e^{j(kx + \delta_w)} \quad (57)$$

where

$$(vb) = (kb) (1 - \epsilon_0^2) + O(\epsilon_0^4), \quad \epsilon_0 = k|a_w| \quad (58)$$

with the dimensionless frequency parameter

$$(vb) = \omega^2 g^{-1} b \quad (59)$$

Note that the wave corresponding to this potential is, in fact, exact to the third order although here nonlinear effects are visible only in the relation between wave frequency and wave length, eq. (58). The phase angle δ_w measures the position of the wave crest relative to the origin at time zero.

3.3.2 First-Order Radiation Problems

All remaining potential flow problems are radiation problems of the form (51), with $L_k^{(1)} = 0$ for the first order. These problems can all be solved by a uniform procedure: The integral equation formulation (52) is discretized by introducing N straight-line element panels of constant potential value on the body contour S_0 and, in the spirit of the close-fit method, setting up an algebraic system of equations based on the boundary conditions at the midpoints of the discrete panels. Details of the procedure and the system of influence coefficients and right-hand side terms in the algebraic equation system are given in [23].

The forced motion first-order potentials ($k=2, 3, 4$) are determined in a single calculation using symmetry or antisymmetry, whereas the diffraction problem ($k=7$) must be solved twice for the symmetrical and antisymmetrical parts of $r_{ik}^{(1)}$ in (30).

Once the potentials $\phi_k^{(1)}$ are known on S_0 , eq. (52) may be used again to calculate this potential at any desired point (x, y) in the fluid domain D . In particular the first-order potentials can be evaluated on the boundary S_F (free surface) which is required to obtain the inhomogeneous terms $r_{ik}^{(2)}$, eqs. (45) and (49), for the second-order problems.

3.3.3 Second-Order Radiation Problems

The general procedure in solving the second-order radiation problems is the same as for the first order, that is, eq. (52) is again discretized and applied to points on the body contour $(x, y) \in S_0$. In fact, the problems associated with second-order onset flows $v_k^{(2)}$ ($k=2, 3, 4$), eqs. (32) to (37), are completely analogous in form to the first-order problems and can be treated accordingly without difficulty.

However, the remaining second-order radiation problems, which are caused by first-order disturbances proportional to $x_{ik}^{(1)}$, $v_{ik}^{(1)}$ ($i, k=0, 2, 3, 4, 7$), do introduce some special questions regarding the evaluation of the right-hand sides, eqs. (44) to (49). These expressions involve first and second partial derivatives of the potential which are to be approximated numerically. The accuracy of these approximations must be examined carefully. In our computing experience for a variety of different section shapes it has been found advantageous to transform some of the second derivatives with respect to x and y , where required, to expressions with derivatives in the tangential direction s , eqs. (44) to (49). This has helped, in particular, to obtain stable results for $r_{ik}^{(2)}$ on S_0 .

Regarding the numerical evaluation of the term $r_{ik}^{(2)}$ on S_F some further problems arise. The improper integral over S_F in (52) involving this term in the integrand requires integration to infinity, but in practice integration must be truncated at a "sufficient" distance " x_∞ " from the body.

This problem is also familiar from time-domain and finite element formulations of the present problem [17], [32], [33], where in addition it is fundamentally difficult to meet the radiation condition at infinity. It can be shown by theory that due to the harmonic asymptotic behavior of $\phi_k^{(1)}$

$$\lim_{|x| \rightarrow \infty} r_{ik}^{(2)}(x) = 0 \quad (60)$$

Nevertheless an independent criterion must be used to measure the truncation error. In the present context the following indirect procedure was used: The first-order damping coefficient was first calculated from near field quantities (by pressure integration) and then compared to results derived from far field potentials (via radiated wave amplitudes), extending the range of integration on S_F step by step until sufficient agreement was reached asymptotically. This defined the truncation point x_∞ . In practice, x_∞ was found to depend on frequency (ω) and body shape.

A particular difficulty exists at the intersection between S_0 and S_F where $r_{ik}^{(2)}$ and $r_{ik}^{(1)}$ are singular. Assuming the singularity to be integrable, which cannot be taken for granted for any section shape, we treat this problem numerically by closely approaching, but still exempting the pole in the integrations. However, the fundamental analytical problem, particularly for non-vertical sections, remains unresolved despite John's valuable basic work [26].

3.4 Pressures, Forces, Moment

3.4.1 Pressures

The hydrodynamic pressure $P(x, y, t)$, measured relative to atmospheric pressure level, according to Bernoulli's equation is

$$P(x, y, t) = -\rho g y - \rho \phi_t(x, y, t) - \frac{1}{2} \rho |\nabla \phi|^2 \quad (61)$$

Using the abbreviations from eqs. (13) to (17)

$$\begin{aligned} \phi^{(1)} &= \sum_k \phi_k^{(1)}, \quad \phi^{(2)} = \sum_{i,k} \phi_{ik}^{(2)} \\ 2\phi^{(2)} &= \sum_{i,k} 2\phi_{ik}^{(2)}, \quad i = 2, 3, 4, k = 0, 2, 3, 4, 7 \end{aligned} \quad (62)$$

we obtain the hydrodynamic pressure on $S(t)$ up to the second order:

$$\begin{aligned} P(\bar{x}(s), \bar{y}(s); t) &= -\rho g \bar{y} - \{\rho g(x_3^{(1)} + \bar{x} x_4^{(1)}) - \\ &- j\rho\omega\phi^{(1)}(\bar{x}, \bar{y})\} e^{-j\omega t} - \{\rho g(x_3^{(2)} + \bar{x} x_4^{(2)}) - \\ &- 0.25\bar{y} x_4^{(1)2} - 2j\rho\omega(\phi_1^{(2)} + 2\phi_2^{(2)}) + 0.25\rho(\phi_n^{(1)2} + \phi_s^{(1)2}) - 0.5j\rho\omega(\bar{y} x_2^{(1)} - \bar{x} x_3^{(1)}) - \\ &- (\bar{x}\bar{x}' + \bar{y}\bar{y}')x_4^{(1)}\phi_n^{(1)} - 0.5j\rho\omega(\bar{x}'x_2^{(1)} + \bar{y}'x_3^{(1)} + \\ &- (\bar{x}\bar{y}' - \bar{y}\bar{x}')x_4^{(1)}\phi_s^{(1)})\} e^{-2j\omega t} - \{\rho g(x_{03}^{(2)} + \end{aligned}$$

$$\begin{aligned} & \bar{x} x_{o4}^{(2)} - 0.25 \bar{y} |x_4^{(1)}|^2 + 0.25 \rho (|\phi_n^{(1)}|^2 + \\ & |\phi_s^{(1)}|^2) + 0.5 j \rho \omega (\bar{y} x_2^{(1)} - \bar{x} x_3^{(1)} - (\bar{x} \bar{x}' + \bar{y} \bar{y}')) \\ & x_4^{(1)} \bar{\phi}_n^{(1)} + 0.5 j \rho \omega (\bar{x} x_2^{(1)} + \bar{y} x_3^{(1)} + (\bar{x} \bar{y}' - \bar{y} \bar{x}')) \\ & x_4^{(1)} \bar{\phi}_s^{(1)} \end{aligned} \quad (63)$$

These expressions were derived after expanding the potentials $\phi^{(1)}$ and $\phi^{(2)}$ into Taylor series about the equilibrium position of the body contour S_0 so that all potentials and their derivatives in (63) pertain to this position.

Eq. (63) represents a complete hydrodynamic transfer model for the pressures on the wetted body contour $S(t)$. This transfer model corresponds to the dynamic system model (3) and can be decomposed into terms of different orders (and frequencies) in analogy to (13):

$$\begin{aligned} p(\bar{x}, \bar{y}; t; \epsilon_k) &= p^{(0)}(\bar{y}) + \sum_k \epsilon_k p_k^{(1)}(\bar{x}, \bar{y}) e^{-j\omega t} \\ &+ \{ \sum_{i,k} \epsilon_i \epsilon_k p_{ik}^{(2)}(\bar{x}, \bar{y}) + \sum_i \epsilon_i^2 p_{ii}^{(2)} \} e^{-2j\omega t} \\ &+ \sum_{i,k} \epsilon_i \epsilon_k p_{oik}^{(2)}(\bar{x}, \bar{y}) + \sum_i \epsilon_i^2 p_{oii}^{(2)} \\ &i=2, 3, 4, k=0, 2, 3, 4, 7 \end{aligned} \quad (64)$$

where the left subscript is defined by the following convention:

$$\begin{aligned} 1p^{(2)} &= f_1(\phi^{(1)}; 1\phi^{(2)}; x_i^{(1)}) \\ 2p^{(2)} &= f_2(2\phi^{(2)}; x_{ki}^{(2)}) \end{aligned} \quad (65)$$

Comparing (64) with (63) yields the individual pressure terms $p^{(n)}$, dropping the factors $\epsilon_i^l, \epsilon_k^m e^{-jn\omega t}$:

1. Zeroth Order ($n=0, l=0, m=0$; hydrostatics)

$$p^{(0)} = -\rho g \bar{y} \quad (66)$$

2. First Order ($n=1, l=0, m=1$; $k=0, 2, 3, 4, 7$; hydrodynamics to the first order)

$$p_k^{(1)} = j \rho \omega \phi_k^{(1)} + \begin{cases} -\rho g x_3^{(1)}, & k=3 \\ -\rho g \bar{x} x_4^{(1)}, & k=4 \\ 0, & k \neq 3, 4 \end{cases} \quad (67)$$

3. Second Order ($n=2, l=1, m=1$; hydrodynamics to the second order)

a) $i=k=2, 3, 4$

$$\begin{aligned} 1p_{ii}^{(2)} &= 2j \rho \omega_1 \phi_{ii}^{(2)} - 0.25 \rho (\phi_{in}^{(1)2} + \phi_{is}^{(1)2}) + \\ &+ 0.5 j \rho \omega (i^n \phi_{in}^{(1)} + i^s \phi_{is}^{(1)}) x_i^{(1)} + \end{aligned}$$

$$+ \begin{cases} 0.25 \rho g \bar{y} x_4^{(1)2}, & i=4 \\ 0, & i \neq 4 \end{cases} \quad (68)$$

$$2p_{ii}^{(2)} = 2j \rho \omega_2 \phi_{ii}^{(2)} + \begin{cases} -\rho g x_3^{(2)}, & i=3 \\ -\rho g \bar{x} x_4^{(2)}, & i=4 \\ 0, & i \neq 3, 4 \end{cases} \quad (69)$$

b) $i, k=2, 3, 4; i < k$

$$\begin{aligned} 1p_{ik}^{(2)} &= 2j \rho \omega_1 \phi_{ik}^{(2)} - 0.5 \rho (\phi_{in}^{(1)} \phi_{kn}^{(1)} + \\ &\phi_{is}^{(1)} \phi_{ks}^{(1)}) + 0.5 j \rho \omega (i^n \phi_{kn}^{(1)} + i^s \phi_{ks}^{(1)}) x_i^{(1)} + \\ &+ (k^n \phi_{in}^{(1)} + k^s \phi_{is}^{(1)}) x_k^{(1)} \end{aligned} \quad (70)$$

c) $i=2, 3, 4; k=0, 7$

$$\begin{aligned} 1p_{ik}^{(2)} &= 2j \rho \omega_1 \phi_{ik}^{(2)} - 0.5 \rho (\phi_{in}^{(1)} \phi_{kn}^{(1)} + \\ &\phi_{is}^{(1)} \phi_{ks}^{(1)}) + 0.5 j \rho \omega (i^n \phi_{kn}^{(1)} + i^s \phi_{ks}^{(1)}) x_i^{(1)} \end{aligned} \quad (71)$$

d) $i, k=0, 7; i < k$

$$1p_{ik}^{(2)} = -0.5 \rho (\phi_{in}^{(1)} \phi_{kn}^{(1)} + \phi_{is}^{(1)} \phi_{ks}^{(1)}) \quad (72)$$

e) $i=k=0, 7$

$$1p_{kk}^{(2)} = -0.25 \rho (\phi_{kn}^{(1)2} + \phi_{ks}^{(1)2}) \quad (73)$$

4. Second Order ($n=0, l=1, m=1$; quasi-hydrostatics of second order)

a) $i=k=2, 3, 4$

$$\begin{aligned} 1p_{oii}^{(2)} &= -0.25 \rho (\phi_{in}^{(1)} \bar{\phi}_{in}^{(1)} + \phi_{is}^{(1)} \bar{\phi}_{is}^{(1)}) + \\ &- 0.5 j \rho \omega (i^n \phi_{in}^{(1)} + i^s \phi_{is}^{(1)}) x_i^{(1)} + \\ &+ \begin{cases} 0.25 \rho g \bar{y} x_4^{(1)2}, & i=4 \\ 0, & i \neq 4 \end{cases} \end{aligned} \quad (74)$$

$$2p_{oii}^{(2)} = \begin{cases} -\rho g x_3^{(2)}, & i=3 \\ -\rho g \bar{x} x_4^{(2)}, & i=4 \\ 0, & i \neq 3, 4 \end{cases} \quad (75)$$

b) $i, k=2, 3, 4; i < k$

$$\begin{aligned} 1p_{oik}^{(2)} &= -0.5 \rho (\phi_{in}^{(1)} \bar{\phi}_{kn}^{(1)} + \phi_{is}^{(1)} \bar{\phi}_{ks}^{(1)}) - \\ &- 0.5 j \rho \omega (i^n \phi_{kn}^{(1)} + i^s \phi_{ks}^{(1)}) x_i^{(1)} + \\ &+ (k^n \phi_{in}^{(1)} + k^s \phi_{is}^{(1)}) x_k^{(1)} \end{aligned} \quad (76)$$

c) $i=2, 3, 4; k=0, 7$

$$1P_{oik}^{(2)} = -0.5 \rho (\phi_{in}^{(1)} \bar{\phi}_{kn}^{(1)} + \phi_{is}^{(1)} \bar{\phi}_{ks}^{(1)}) - 0.5 j \rho \omega (\phi_{in}^{(0)} \bar{\phi}_{kn}^{(1)} + \phi_{is}^{(0)} \bar{\phi}_{ks}^{(1)}) x_i^{(1)} \quad (77)$$

d) $i, k=0, 7; i < k$

$$1P_{oik}^{(2)} = -0.5 \rho (\phi_{in}^{(1)} \bar{\phi}_{kn}^{(1)} + \phi_{is}^{(1)} \bar{\phi}_{ks}^{(1)}) \quad (78)$$

e) $i=k=0, 7$

$$1P_{okk}^{(2)} = -0.25 \rho (\phi_{kn}^{(1)} \bar{\phi}_{kn}^{(1)} + \phi_{ks}^{(1)} \bar{\phi}_{ks}^{(1)}) \quad (79)$$

In these expressions $i n^{(0)}$ and $i s^{(0)}$ denote the direction cosines of \vec{n} and \vec{s} at time $t=0$ with $i n^{(0)}$ from eq. (23) and

$$i s^{(0)} = \begin{cases} \bar{x}^-, i=2 \\ \bar{y}^-, i=3 \\ (\bar{x} \bar{y}^+ - \bar{y} \bar{x}^-), i=4 \end{cases} \quad (80)$$

3.4.2 Forces, Moment

Integration of the pressures P in (61) over the wetted body contour $S(t)$ leads to the hydrodynamic forces acting on the body and the moment about the origin O

$$\vec{F}(t) = - \int_{S(t)} P \vec{n} ds, \quad (81)$$

$$\vec{M}(t) = - \int_{S(t)} P (\vec{r} \times \vec{n}) ds, \quad \vec{r} = (x-x_2, y-x_3)$$

By means of Leibniz' integration rule the integration over $S(t)$ may be reduced to an integral over the wetted contour at rest, S_0 , and a few additional terms of second order [7], [23]:

$$I(S(t); \epsilon_k) = \int_{S_0} i(s; t; \epsilon_k) ds + I_R \quad (82)$$

$$I_R = R_+ i n_+^{(0)} - R_- i n_-^{(0)} \quad (83)$$

$$R_+ = -0.25 \rho g (x_3^{(1)} + \bar{x} x_4^{(1)} - j \omega g^{-1} \phi^{(1)})_{\pm}^2 - (\bar{y}^-)^{-1} e^{-2j\omega t} - 0.25 \rho g (x_3^{(1)} + \bar{x} x_4^{(1)} - j \omega g^{-1} \phi^{(1)})_{\pm}^2 (\bar{y}^-)^{-1} \quad (84)$$

where the subscripts denote

$$\begin{aligned} ()_+ &\equiv ()|_{(\bar{x}, \bar{y})=(0.5B, 0)} \\ ()_- &\equiv ()|_{(\bar{x}, \bar{y})=(-0.5B, 0)} \end{aligned} \quad (85)$$

The transfer model for the hydrodynamic forces and moment to the second order is derived by substituting the pressures (63) and normal vectors from (21) to (24) into (81). The resulting expression is of analogous form to (64):

$$j^F(t; \epsilon_k) = j^F(0) + \sum_k \epsilon_k j_k^{(1)} e^{-j\omega t} + \sum_{i,k} \epsilon_i \epsilon_k j_{ik}^{(2)} e^{-2j\omega t} + \sum_{i,k} \epsilon_i \epsilon_k j_{oik}^{(2)} \quad (86)$$

where, in accordance with (65):

$$\begin{aligned} j_{ii}^{(2)} &= j_1^{(2)} + j_2^{(2)} \\ j_{oii}^{(2)} &= j_1^{(2)} + j_2^{(2)} \end{aligned} \quad (87)$$

The left subscripts denote force and moment components, respectively:

$$j^{()} = \begin{cases} j=2, H \\ j=3, V \\ j=4, M \end{cases} \quad (88)$$

Collecting terms whose common factor is $\epsilon_i^l \epsilon_k^m e^{-jn\omega t}$ ($l, m, n=0, 1, 2; i=2, 3, 4; k=0, 2, 3, 4, 7$) the individual components are defined by the following expressions:

1. Hydrostatics ($n=0, l=0, m=0$)

$$j^F(0) = - \int_{S_0} P^{(0)} j^n(0) ds \quad (89)$$

2. First-Order Hydrodynamics ($n=1, l=0, m=1$)

$$j_{ik}^{(1)} = - \int_{S_0} P_k^{(1)} j^n(0) ds - \underbrace{\int_{S_0} P^{(0)} j^n(1) x_4^{(1)} ds}_{k=4} \quad (90)$$

3. Second-Order Hydrodynamics ($n=2, l=1, m=1$)

$$j_{ik}^{(2)} = - \int_{S_0} P_{ik}^{(2)} j^n(0) ds - \int_{S_0} P_{ii}^{(2)} j^n(0) ds - 0.5 \int_{S_0} P_k^{(1)} j^n(1) x_4^{(1)} ds - \int_{S_0} P^{(0)} (j_{22}^{(2)} x_4^{(2)} + \underbrace{j_{21}^{(2)} x_4^{(1)2}}_{i=k=4}) ds + j_R^{(2)} \quad (91)$$

4. Second-Order Quasi-Hydrostatics ($n=0, l=1, m=1$)

$$j_{oik}^{(2)} = - \int_{S_0} P_{oik}^{(2)} j^n(0) ds - \int_{S_0} P_{oii}^{(2)} j^n(0) ds$$

$$- 0.5 \int_{S_0} p_k^{(1)} j_n^{(1)} x_4^{(1)} ds - \int_{S_0} p^{(0)} (j_{n02}^{(2)} x_{04}^{(2)} + \underbrace{j_{n01}^{(2)} |x_4^{(1)}|^2}_{i=k=4}) ds + (92)$$

The expressions $f_R^{(2)}$ and $f_{OR}^{(2)}$ represent the contributions from the additional integrals (83) to (85) which approximate the effects of the actual wetted contour $S(t)$ deviating from S_0 .

The time-complex expressions for pressures $p^{(n)}$, eqs. (67) to (73), and forces $f^{(n)}$, eqs. (90), (91), can readily be converted to real notation for any quantity $a^{(n)}$, whose amplitude and phase are $A^{(n)}$, and $\delta_A^{(n)}$:

$$\begin{aligned} a^{(n)} &= A^{(n)} \sin(n\omega t + \delta_A^{(n)}) \\ A^{(n)} &= |a^{(n)}| = \{ \text{Re}_j^2 \{ a^{(n)} \} + \text{Im}_j^2 \{ a^{(n)} \} \}^{0.5} \\ \delta_A^{(n)} &= \arctg \{ \text{Re}_j \{ a^{(n)} \} / \text{Im}_j \{ a^{(n)} \} \} \end{aligned} \quad (93)$$

3.5 Body Motions

To determine the unknown motions $x_i(t)$, eq. (14), of the body in a given incident wave the equations of motion must be taken into consideration. These equations serve to determine, in a second-order sense, the actual motion amplitudes, hence the parameters ϵ_i ($i=2, 3, 4$), and further any other explicit hydrodynamic quantities of interest.

Force components relate to the inertial coordinate system $o-x-y$, the moment is taken with respect to the origin O of the coordinates fixed in the body. Equating hydrodynamic pressure forces (moments), subscript P , to inertia forces (moments), subscript R , in the equations of motion, we obtain:

$$\vec{F}_P = \vec{F}_R, \quad \vec{M}_P = \vec{M}_R \quad (94)$$

$$\vec{F}_P = - \int_{S(t)} p \vec{n} ds, \quad \vec{M}_P = - \int_{S(t)} p (\vec{r} \times \vec{n}) ds \quad (95)$$

$$\vec{F}_R = \int_A (g \vec{j} + \vec{\ddot{v}}) dm, \quad \vec{M}_R = \int_A \vec{r} \times (g \vec{j} + \vec{\ddot{v}}) dm \quad (96)$$

with \vec{F}_P , \vec{M}_P , \vec{r} from (81), \vec{v} from (10) and A = body cross sectional area.

The hydrodynamic pressure forces \vec{F}_P (\vec{M}_P) were derived in 3.4 except for the factors ϵ_i or $x_i^{(n)}$, respectively.

The inertia forces (moment) are defined L_R .

$$\vec{F}_R = x_R \vec{i} + y_R \vec{j}, \quad \vec{M}_R = k M_R \quad (97)$$

$$x_R = M \{ \ddot{x}_2 - \ddot{x}_4 \bar{y}_G \cos x_4 + \ddot{x}_4 \bar{y}_G \sin x_4 \}$$

$$y_R = M \{ g + \ddot{x}_3 - \ddot{x}_4 \bar{y}_G \sin x_4 - \ddot{x}_4 \bar{y}_G \cos x_4 \} \quad (98)$$

$$M_R = \ddot{x}_4 I_{44} - M \{ \ddot{x}_2 \bar{y}_G \cos x_4 + (g + \ddot{x}_3) \bar{y}_G \sin x_4 \}$$

with $x_i(t)$ from (14) and

$$\begin{aligned} M &= \rho_B A \\ I_{44} &= \int_A \int (x^2 + y^2) dm = k_4^2 M \\ \bar{y}_G &= M^{-1} \int_A y dm, \quad \bar{x}_G = 0 \end{aligned} \quad (99)$$

The expressions in (98) can be developed into a perturbation expansion to the second order with respect to ϵ_i , using $x_i(t)$ from (14) and a power series expansion of the trigonometric functions. The resulting expressions are of the form

$$\begin{aligned} x_R &= \sum_{n=1}^2 x_R^{(n)} e^{-jn\omega t} \\ y_R &= \sum_{n=0}^2 y_R^{(n)} e^{-jn\omega t} \\ M_R &= \sum_{n=1}^2 M_R^{(n)} e^{-jn\omega t} + M_{Ro}^{(2)} \end{aligned} \quad (100)$$

Substituting (100) and (86) to (88) into (94) and separating terms of different order (and frequency) the following sets of equations of motion are obtained for motion components of matching order (and frequency):

1. Hydrostatics ($n=0$)

$$\begin{aligned} H^{(0)} &= 0 \\ V^{(0)} &= y_R^{(0)} \\ M^{(0)} &= 0 \end{aligned} \quad (101)$$

2. Hydrodynamics of First Order ($n=1$)

$$\left. \begin{aligned} H^{(1)} &= \sum_{k=0}^7 H_k^{(1)} = x_R^{(1)} \\ V^{(1)} &= \sum_{k=0}^7 V_k^{(1)} = y_R^{(1)} \\ M^{(1)} &= \sum_{k=0}^7 M_k^{(1)} = M_R^{(1)} \end{aligned} \right\} \rightarrow x_i^{(1)}, \epsilon_i \quad (102)$$

3. Hydrodynamics of Second Order ($n=2$)

$$\left. \begin{aligned} H^{(2)} &= \sum_{i,k=0}^7 H_{ik}^{(2)} = x_R^{(2)} \\ V^{(2)} &= \sum_{i,k=0}^7 V_{ik}^{(2)} = y_R^{(2)} \\ M^{(2)} &= \sum_{i,k=0}^7 M_{ik}^{(2)} = M_R^{(2)} \end{aligned} \right\} \rightarrow x_i^{(2)} \quad (103)$$

4. Quasi-Hydrostatics of Second Order (n=2)

$$\left. \begin{aligned} H_o^{(2)} &= \sum_{i,k=0}^7 H_{oik}^{(2)} = 0 \\ V_o^{(2)} &= \sum_{i,k=0}^7 V_{oik}^{(2)} = 0 \\ M_o^{(2)} &= \sum_{i,k=0}^7 M_{oik}^{(2)} = M_{Ro}^{(2)} \end{aligned} \right\} \rightarrow x_{oi}^{(2)} \quad (104)$$

The first set of equations, (101), concerns hydrostatic effects due to zeroth order pressures, corresponding to the law of Archimedes. The set of eqs. (102) consists of the first-order differential equations for sway and roll (coupled), and for heave. The unknown parameters ϵ_i ($i=2, 3, 4$), defined in eq. (2), can be derived from the solution of (102). Eqs. (103), with ϵ_i substituted, comprise second-order equations of motion for coupled sway-roll and for heave, and are used to find second-order motion amplitudes $x_i^{(2)}$ (frequency 2ω). In (104), finally, time-independent second-order effects, called quasi-hydrostatic, are present and can be determined using the ϵ_i from the solution of (102). This yields the so-called drift components $x_{oi}^{(2)}$, where the sway drift $x_{o2}^{(2)}$ is equated to zero, by virtue of an assumed external force balancing the drift force.

The dynamic equations (102) and (103) can be written in dimensionless form as follows:

$$\sum_{k=2}^4 \tilde{x}_k^{(n)} \{-n^2(vb) \{ (\tilde{\nu}_{ik}^{(n)} + \tilde{m}_{ik}^{(n)}) + j \tilde{\lambda}_{ik}^{(n)} \} \tilde{d}_{ik}^{(n)} + \tilde{c}_{ik}^{(n)} \} = \tilde{E}_i^{(n)}, i=2, 3, 4 \quad (105)$$

with: $\bar{A} = A b^{-2}$, $\bar{I}_G = \bar{y} \bar{A}$, $\bar{I}_{44} = \bar{k}^2 \bar{A}$
 $\tilde{m}_{ik}^{(2)} = \tilde{m}_{ik}^{(1)} = \tilde{m}_{ik}$, $\tilde{c}_{ik}^{(2)} = \tilde{c}_{ik}^{(1)} = \tilde{c}_{ik}$, $\tilde{d}_{ik}^{(2)} = \tilde{d}_{ik}^{(1)} = \tilde{d}_{ik}$
 $\tilde{m}_{22} = \tilde{m}_{33} = 0.5 \bar{A}$, $\tilde{c}_{33} = 1$, $\tilde{d}_{ik} = (kb)^{0.5(k-i)}$
 $\tilde{m}_{24} = \tilde{m}_{42} = -0.5 \bar{I}_G$, $\tilde{c}_{44} = 0.5 \bar{GM} \bar{A}$, $\tilde{m}_{44} = 0.5 \bar{I}_{44}$
 else: $\tilde{m}_{ik} = 0$, $\tilde{c}_{ik} = 0$, $\tilde{d}_{ii} = 1$ (106)

The dimensionless hydrodynamic mass and damping in (105) are defined as

$$\tilde{\nu}_{ik}^{(n)} = \frac{\nu_{ik}^{(n)}}{2\rho d_i d_k}, \quad \tilde{\lambda}_{ik}^{(n)} = \frac{\lambda_{ik}^{(n)}}{2\rho d_i d_k n\omega}, \quad d_i = \begin{cases} b, i=2,3 \\ b^2, i=4 \end{cases} \quad (107)$$

$$\tilde{\nu}_{ik}^{(n)} + j \tilde{\lambda}_{ik}^{(n)} = -0.5 \int_{S_o} \tilde{\phi}_k^{(n)} \tilde{\phi}_i^{(0)} ds, \quad (108)$$

$$\tilde{\phi}_k^{(n)} = \begin{cases} \tilde{\phi}_k^{(1)}, & n=1 \\ \tilde{\phi}_{kk}^{(2)}, & n=2 \end{cases}$$

Exciting forces and moment are made dimensionless by

$$\tilde{E}_i^{(n)} = \frac{E_i^{(n)}}{2 \rho g b d_i \epsilon_7^n} \begin{cases} 1, i=2,3 \\ (kb)^{-1}, i=4, \epsilon_7 = \frac{|a_w|}{b} \end{cases} \quad (109)$$

$$\tilde{E}_i^{(1)} = \sum_{k=0,7}^4 \tilde{f}_k^{(1)} \quad (\text{from (86)}) \quad (110)$$

$$\tilde{E}_i^{(2)} = \sum_{i=2}^4 \sum_{k=0}^7 \tilde{f}_{ik}^{(2)} \quad (\text{from (86), (87)}) \quad (111)$$

The solutions to (105), which is of the form

$$\sum_{k=2}^4 \{ \tilde{a}_{ik}^{(n)} \} \tilde{x}_k^{(n)} = \tilde{E}_i^{(n)}$$

are obtained by matrix inversion

$$\tilde{x}_k^{(n)} = \sum_{i=2}^4 \{ \tilde{a}_{ik}^{(n)} \}^{-1} \tilde{E}_i^{(n)} \quad (112)$$

with

$$\tilde{x}_i^{(n)} = \begin{cases} x_i^{(n)} (|a_w| \epsilon_7^{n-1})^{-1}, & i=2,3 \\ x_i^{(n)} (k|a_w| \epsilon_7^{n-1})^{-1}, & i=4 \end{cases} \quad (113)$$

and

$$\epsilon_i = \begin{cases} \tilde{x}_i^{(1)} | \epsilon_7, & i=2,3 \\ \tilde{x}_i^{(1)} | \epsilon_0, & i=4 \end{cases} \quad (114)$$

The drift components (of second order) $x_{oi}^{(2)}$ result from the algebraic set of equations (104). The horizontal drift force is derived from $H_o^{(2)}$ ($x_{o2}^{(2)}$ remains indeterminate) and may be compared to Maruo's results [34] from a momentum theory. From (86) and (87):

$$\bar{H}_o^{(2)} = \frac{H_o^{(2)}}{2 \rho g b^2} = \sum_{i,k=0}^7 \epsilon_i \epsilon_k \bar{H}_{oik}^{(2)} \quad (115)$$

with

$$\bar{H}_o^{(2)} = \frac{H_o^{(2)}}{0.5 \rho g |a_w|^2} = 4 \bar{H}_o^{(2)} \epsilon_7^{-2}$$

The nondimensional vertical drift is

$$\bar{x}_{o3}^{(2)} = x_{o3}^{(2)} b^{-1} = \sum_{i=2}^4 \sum_{k=0}^7 \epsilon_i \epsilon_k \bar{V}_{oik}^{(2)} \quad (116)$$

with $\tilde{x}_{o3}^{(2)} = x_{o3}^{(2)} |a_w|^{-1} = \bar{x}_{o3}^{(2)} \epsilon_7^{-1}$

and, finally, the roll drift ("heel")

$$\tilde{x}_{o4}^{(2)} = x_{o4}^{(2)} (k|a_w|)^{-1} = \{ (k|a_w|)^{-1} \sum_{i=2}^4 \sum_{k=0}^7 \epsilon_i \epsilon_k \bar{M}_{oik}^{(2)} - 0.25(vb) \epsilon_7 \bar{I}_G \tilde{x}_3^{(1)} \tilde{x}_4^{(1)} \} \cdot \{ 0.5 \bar{GM} \bar{A} \}^{-1} \quad (117)$$

4. NUMERICAL RESULTS

A computer program [35] has been developed to numerically evaluate the boundary value problems described in the preceding sections and to calculate the physical quantities derived from the resulting integral equations. The results presented in the following were generally obtained with $N=25$ discrete panels on the body surface S_0 and about 50 discrete elements in the free surface S_f (second-order). The free surface disturbances for the second order on S_f were evaluated up to where the potentials reached an asymptotic limit, usually no more than 9 half-beams away from the body. The frequency range was $10^{-5} \leq (\nu b) \leq 2.5$ in steps of $\Delta(\nu b) = 0.05$.

The size of the program is 140 K words on a CYBER 175 computer. The program calculates in one pass all pertinent hydrodynamic quantities (potentials, pressures, forces, moments, and motions, where applicable) for any standard problem case of either first order ($k=0, 2, 3, 4, 7$) or second order ($i=2, 3, 4, k=0, 2, 3, 4, 7$). Compilation time is around 10 seconds per standard problem case. A complete evaluation up to the second order, comprising 13 standard problem cases after suitable rearrangements, takes about 1 minute of execution time per frequency.

The results presented in Figs. 5 to 36 (in back of the paper) with few exceptions pertain only to second-order quantities. They are based on first-order results, which cannot be included in the present paper. Nor does space permit a discussion of the "irregular frequency" phenomenon. Earlier publications by Papanikolaou [8], [23], [25] may be consulted for details on these issues, including numerous first-order results for different section shapes over a large frequency range [25].

Figs. 5 to 12 compare our numerical results for calm water forced heave motions up to the second order (problem $3S_{33}^{(2)}$ in Fig. 2 or eqs. (38) to (46) with $i=3, k=3$) to available experimental data from Yamashita [15] and Tasai-Koterayama [20]. This comparison is intended to demonstrate the physical relevance and numerical stability of these results. All forces are made dimensionless as indicated in the figures. The assumed heave amplitudes have been standardized to correspond to $\epsilon_3=1$ or $x_3^{(1)}=b$. Negative phase angles are always plotted with an increment of 360° .

Fig. 5 for the triangle of $B/T=0.8$ and $\epsilon_L = \pi/2$ (finite flare) demonstrates encouragingly good agreement between theory and experiment for the hydrodynamic force $\bar{V}_{33}^{(2)}$ and, with some allowance, for the phase angle $\delta_V^{(2)}$. The appreciable phase shift, which is more abrupt in the measurements, occurs at frequencies near where the force has a minimum, an observation made here for the triangle, although in the linear case similar effects are familiar from several other shapes. The calculated results for the steady-state second-order force $\bar{V}_{033}^{(2)}$ in Fig. 5

are not in agreement with Yamashita's measurements regarding the absolute level although both show a similar flat tendency; we are uncertain of his definition of this quantity.

In Fig. 6 a fine Lewis form for $B/T=0.8$ and $B=0.5$ (section coefficient) is investigated. Fig. 7 shows the ellipse for the same B/T . Hydrodynamic and steady state second-order forces show excellent agreement with measurements. The phase angles agree better for the ellipse; for the Lewis form the agreement improves for decreasing motion amplitudes, proportional to ϵ , as one must expect. In Fig. 8 for the ellipse at $B/T=1.4$ all results are in very good agreement.

Figs. 9 to 11 are related to wider sections ($B/T=2.0$) of different fullness. The triangle shows the strongest, the U-shape the weakest nonlinear effects. This appears reasonable because the nonlinearities should be responsive to how rapidly the section shape changes near the waterline. For the circle in Fig. 10 the overall agreement in all results with data from experiments appears extraordinary. The minor deviations that do exist increase with ϵ , but remain acceptable even at $\epsilon=0.6$.

The U-shape (Fig. 11) shows some, but not much greater scatter.

It is of interest to compare the steady-state forces in Figs. 9 to 12 in the limit of $(\nu b) \rightarrow 0$. The triangle with large positive flare in the waterline produces a net positive steady lift force, circle and U-shape have zero flare angles and a vanishing zero-frequency steady lift force, and the bulbous form with negative flare causes a small negative steady lift. At finite frequencies the steady-state vertical force may become positive or negative.

The results for the bulb (Fig. 12) should be viewed with caution due to the very large ϵ -values in the experiments. The magnitude of the nonlinear effects is rather small, the scatter in the measurements considerable, and comparisons with the theory for ϵ up to 1.917 are of questionable value.

In Figs. 13 to 16, for a Lewis form ($B/T=2.0, B=0.94$), further comparisons of forced motion results for pure sway, heave, and roll as well as coupled sway-roll motions (with reference to standardized parameters $\epsilon_1, \epsilon_k=1$) are presented relative to data from Potash's second-order theory [7]. (Similar comparisons with theories by other authors are also found in [3], [9], [23].)

Fig. 13 relates to the pure sway forced motion problem ($3S_{22}^{(2)}$ in Fig. 2). The agreement with Potash in the vertical forces, hydrodynamic and steady-state parts, is excellent. These can be calculated from first-order potentials exclusively. The second-order horizontal forces $\bar{H}_{22}^{(2)}$, which involve second-order potentials, differ appreciably from Potash. This seems due to a deviation in his second-order problem formulation [8] and the presence of irregular frequency effects in his results.

For heaving (problem $3S_{33}^{(2)}$ in Fig. 14 the hydrodynamic force $\bar{V}_{33}^{(2)}$ depends on

second-order potentials, but the agreement remains reasonable, in part because the heaving irregularities are milder. In rolling (Fig. 15, problem 3S₄₄⁽²⁾) the hydrodynamic nonlinear effects are relatively weak for this section shape. Fig. 16 illustrates the second-order effects in coupled forced sway and roll motions (problem 3S₄₄⁽²⁾) upon the vertical force component. This encompasses the second-order effects due to first-order disturbances resulting from coupled sway and roll motions. Comparisons with Potash's results are problematic because it is not clear whether he was dealing with the same flow subsystem. (He may have included the problems 3S₂₂⁽²⁾ and 3S₄₄⁽²⁾ simultaneously).

Figs. 17 to 19 present the steady-state forces and moments acting on a fixed body in a wave. These results stem from the steady-state part of problem 6S⁽²⁾. These investigations, and the ones that follow, were performed systematically for three section shapes, the triangle ($\beta=0.5$), the circle ($\beta=\pi/4$), and the rectangle ($\beta=1.0$). Forces, moments etc. are nondimensionalized with respect to wave amplitude $|a_w|$, as customary in the literature.

Fig. 17 concerns the horizontal steady-state force H_{007} ⁽²⁾. In the limit of $(vb) \rightarrow \infty$ our results for all section shapes approach unity in agreement with Maruo's [34] analytically derived result from momentum considerations. The quantity H_{007} ⁽²⁾, plotted in dashed lines, expresses the considerable contribution by the wetted part above water (rest integrals in eqs. (83), (84)) upon the total steady-state force. For $(vb) \rightarrow \infty$ this term tends to the limit of $2 \sin \alpha_L$ in agreement with [36]. The contribution made by the underwater part is smaller and negative, the sum of the two yields the net force.

The corresponding vertical steady-state forces (Fig. 18) are negative for circle and rectangle (sinkage force), and positive for the triangle (lift). The zero frequency limit of this force is zero for the wall-sided shapes ($\alpha_L = \pi/2$) and equal to 1 for the triangle ($\alpha_L = \pi/4$) $\rightarrow \cotg \alpha_L = \cotg \pi/4 = 1$.

The steady-state moments, Fig. 19, are negative, that is, heeling in the direction of the incident wave.

In order to determine the influence of the motions upon the hydrodynamic second-order contributions, it is necessary to solve the equations of motion to the first order (eq. (105), $n=1$) to start with. The results are required to solve for the small parameters ϵ_i ($i=2, 3, 4$) in terms of the initially assumed ϵ_7 (ϵ_0), which measures the relative size of the incident wave, using eq. (114). The first-order excitation forces for a circle in a sine wave ($\delta_w=0$) are shown in Fig. 20. Figs. 21 to 23 present the corresponding first-order motion amplitudes $x_i^{(1)}$ ($i=2, 3, 4$), where the results for sway and roll stem, of course, from their coupled equations of motion. Near resonance all amplitudes are considerable because hydrodynamic damping is small, above

all in roll, unless empirical corrections are made to allow for viscous damping. On the basis of the amplitude results we may now assign some bounds to the ϵ_i and limit the wave heights accordingly via ϵ_7 or we may assume some wave height, hence ϵ_7 , determine the corresponding values of ϵ_i , and avoid frequencies where ϵ_i exceeds a specified limit, especially near resonance.

In Figs. 24 to 28 some first results are presented describing the second-order forces and moments which result from the second-order interactions between motion potentials and the combined incident wave and diffraction potentials ($4S^{(2)}$ and $5S^{(2)}$ subproblems combined). These results take into account the small parameters $\epsilon_i = f(vb)$ of the motions, deduced from the linear response analysis (eqs. (105), (114)). The curves exhibit some more or less pronounced resonant peaks. These stem mainly from the behavior of the ϵ_i near resonance, modified in part according to the basic frequency dependence of the second-order hydrodynamic forces. The results presented here are still a function of the initially assumed parameter ϵ_7 .

By solving all standardized subproblems of the system and associating them with their pertinent small parameters ϵ_i, ϵ_k , it is possible to assemble all contributions of second-order for the body freely oscillating in the wave. The steady-state part of this summation corresponds to the so-called drifting forces. Fig. 29 compares horizontal drifting forces for three basic section shapes. The results are credible, except near resonance. Comparisons based on Maruo's familiar formulas [34] give similar answers. The asymptotic limit of this force for $(vb) \rightarrow \infty$ should be one, as in Fig. 17 for the fixed body, because the motion amplitudes go to zero at high frequencies.

Vertical drifting forces, eq. (116), are shown in Fig. 30, drifting moments, eq. (117), in Fig. 31. Rectangle and triangle have positive vertical drift (lift) for most frequencies. The drifting moments are negative, they tend to heel toward the wave. Masumoto's results [10] show similar tendencies.

It remains to solve the equations of motion of the second order, eq. (105), $n=2$. The excitation forces of second order are obtained from eq. (111) by summation of all second-order hydrodynamic terms, which are caused by the motions and velocities of first order. The vertical second-order excitation forces for a semi-circle are plotted in Fig. 32. According to eqs. (107), (108), $n=2$, the second-order hydrodynamic mass and damping coefficients for heaving have been made dimensionless with the displaced fluid mass of the semi-circle, as usual. The curves in Fig. 32 are obtained by contracting the frequency scale of the corresponding first-order curves, which are familiar, to one quarter so that the first-order results for $(vb)=4$ are shifted to $(vb)=1$.

The motion responses of the heaving circular cylinder to the first and second order are presented in Fig. 33. It is interesting

to note that two resonant peaks are present in the second-order heave amplitudes, one at the resonant frequency of the first-order system which tends to excite the second-order system, and one at the second-order system's own resonant frequency which lies at about one quarter of the first-order resonance. The second-order amplitudes are relatively small compared to the first-order values in this instance. This need not be so for other degrees of freedom.

To obtain an idea of the relative importance of second-order effects in forced heaving motions we may compare the curves in Fig. 34. They represent the ratio of second- to first-order force amplitudes for a heaving circular cylinder as a function of the amplitude parameter ϵ_3 . The agreement between calculated results and experimental data from Tasai and Koterayama [20] is very good. Only at higher frequencies and amplitudes (ϵ) do some differences develop. Viscous effects as a possible reason for part of these differences at higher frequencies are discussed in [20].

A comparable diagram for heave excitation forces, second- to first-order ratio, for a semi-circular cylinder oscillating in a wave is given in Fig. 35. This ratio depends directly on ϵ_7 , i.e., the relative size of the incident wave to the body dimensions. The nonlinear influence on this quantity has a peak at some intermediate frequency where larger motions are present due to resonance.

The time-dependence of the heaving motion of a circular cylinder in a "standard" wave ($\epsilon_7=1$), approximated to the first and second order, is shown in Fig. 36, together with the second-order steady-state term. The frequency (ω_b) of 0.25 corresponds to a peak in the second-order effects (Fig. 33). The nonlinear effects are not dramatic, but noticeable. Amplitudes are about 15% greater than in the linear analysis and a steady lift effect is present. The result confirms why for a shape like the circle linear theory has been so successful in practice whenever heaving motions and waves are reasonably small. That nonlinear effects upon vertical loads (and, of course, local pressures) can be much more substantial in certain frequency ranges will be appreciated from Figs. 34 and 35.

Although we have not yet examined motions in other degrees of freedom by the current method, we would also expect significant hydrodynamic nonlinearities in near-resonant roll, coupled with sway, in view of the associated large roll amplitudes.

5. CONCLUSIONS

By means of an approach based on nonlinear system dynamics and nonlinear hydrodynamic theory it has been possible to develop a complete second-order theoretical model for the motions and hydrodynamics of a cylindrical body of arbitrary cross section in a regular, second-order incident wave. A crucial first step is the decompo-

sition of the total second-order flow system into a set of nonlinear subsystems comprising the second-order equivalents of the familiar forced motion, incident wave, and diffraction flow systems, but also their mutual second-order interaction. Perturbation theory, using several small parameters, has then been applied systematically to derive a complete set of first- and second-order linear subsystems of the flow. These systems together form the basis for developing a second-order transfer model of the dynamic problem.

The equations of motion have been derived to the second order with all hydrodynamic couplings present. They include first-order terms of incident wave frequency ω , and second-order terms of frequency 2ω as well as a time-independent expression. All system responses are of the same basic form.

On the basis of this theoretical model a numerical solution method has been developed using an integral equation formulation for a Robin type problem and a close-fit discretization. The fact that all problems, with one trivial exception, were of the same boundary value type, that is, radiation problems, paved the way for a unified calculation procedure for all subproblems.

Numerical calculations were performed for a variety of section shapes over a wide frequency range. These calculations included some samples of each of the major subproblem types. No insurmountable, fundamental obstacles were found in the path of the numerical calculations.

In those relatively scarce cases (forced motions) where comparison with experimental results was possible the agreement in second-order effects was generally between good and excellent. For the heaving semi-circle, for which most experimental data are available, the agreement is outstanding, for sections with flare it is slightly worse.

The evaluation of drift forces as a second-order phenomenon is possible from subproblems of the system. The results obtained show good agreement with other theories.

The response of the system can be evaluated by assembling the results of all first- and second-order subproblems into the equations of motion with small parameter values assigned to each case on a physical basis. The overall transfer model is based on frequency domain techniques because the linear subproblems, of which the system consists, all have frequency domain transfer functions. This possibility evidently has significant practical advantages over time-domain solutions.

Investigations of the type reported are, of course, only a prelude to developing a systematic understanding of nonlinear ship motions in a nonlinear irregular seaway. We feel, however, that the remaining open questions, despite their great fundamental complexity, show a certain promise today of gradually being amenable to higher-order analysis via the frequency domain by

suitable extension of bi-spectral analysis and generalized three-dimensional flow analysis methods.

ACKNOWLEDGMENT

The work reported in this paper was supported by a grant of the Deutsche Forschungsgemeinschaft.

REFERENCES

1. St. Denis, M., "On the Spectral Technique for Describing the Seaway-Induced Motions of Ships - - A Review of Developments over the Past Two Decades and an Outline of Problems Now in Hand", SNAME T & R Symposium S-3 on Seakeeping 1953 - 1973, held at Webb Institute of Naval Architecture, Glen Cove, N.Y., June 1974.
2. Stokes, G.G., "On the Theory of Oscillatory Waves", Trans. Camb. Soc., vol. 8, 1849, pp. 441-455.
3. Papanikolaou, A., "On the Solution of the Nonlinear Problem of Waves of Finite Amplitude on Water of Limited Depth by the Method of Perturbation", in German, Schiffstechnik, vol. 23, 1976, pp. 63-84.
4. Ogilvie, T.F., "First- and Second-Order Forces on a Cylinder Submerged under a Free Surface", Journ. of Fluid Mech., vol. 16, 1963, pp. 451-472.
5. Parissis, G., "Second-Order Potentials and Forces for Oscillating Cylinders on a Free Surface", MIT-Rept. No. 66-10, Dept. of Ocean Engineering, 1966.
6. Lee, C.M., "The Second-Order Theory of Heaving Cylinders in a Free Surface", Journ. of Ship Res., vol. 12, 1968, pp. 313-327.
7. Potash, R.L., "Second-Order Theory of Oscillating Cylinders", Journ. of Ship Res., vol. 15, 1971, pp. 295-324.
8. Papanikolaou, A., "On the Nonlinear Problem of a Vertically Oscillating Cylinder of Arbitrary Shape", in German, Diss., Techn. Univ. of Berlin, D 83, 1977.
9. Papanikolaou, A., "Potential Theory of Second Order for Cylinders Oscillating Vertically", in German, Schiffstechnik, vol. 25, 1978, pp. 53-86.
10. Masumoto, A., "On the Nonlinear Hydrodynamic Forces for Oscillating Bodies in Regular Waves", in Japanese, Journ. of Kansai Soc. of Naval Arch., vol. 172, 1979, pp. 17-31.
11. Kim, C.H., "On the Influence of Non-linear Effects upon Hydrodynamic Forces in Forced Heaving Oscillations of Cylinders", in German, Schiffstechnik, vol. 14, 1967, pp. 79-91.
12. Grim, O., "Hydrodynamic Forces Caused by Roll Oscillations with Large Amplitude", in German, Schiffstechnik, vol. 24, 1977, pp. 143-160.
13. Salvesen, N., "Ship Motions in Large Waves", R. Timman Memorial, Delft, 1978.
14. Söding, H., "Second-Order Forces on Oscillating Cylinders in Waves", Schiffstechnik, vol. 23, 1976, pp. 205-209.
15. Yamashita, S., "Calculations of the Hydrodynamic Forces Acting upon Thin Cylinders Oscillating Vertically with Large Amplitude", in Japanese, Journ. Soc. Naval Arch. of Japan, vol. 141, June 1977, pp. 67-76.
16. Paulling, J.R., Wood, P.D., "Numerical Simulation of Large-Amplitude Ship Motions in Astern Seas", SNAME T & R Symposium S-3 on Seakeeping 1953-1973, held at Webb Inst. of Naval Arch., June 1974.
17. Faltinsen, O., "Numerical Solutions of Transient Nonlinear Free-Surface Motion outside or inside Moving Bodies", Proc. Sec. Intl. Conf. on Num. Ship Hydrodyn., Univ. of Calif., Berkeley, 1977, pp. 347-357.
18. Nichols, B.D., Hara, C.W., "Nonlinear Hydrodynamic Forces on Floating Bodies", Proc. Sec. Intl. Conf. on Num. Ship Hydrodyn. Univ. of Calif., Berkeley, 1977, pp. 382-394.
19. Vugts, J., "The Hydrodynamic Coefficients for Swaying, Heaving and Rolling Cylinders in a Free Surface", TH Delft Rept. No. 194, 1968.
20. Tasai, F., Koterayama, W., "Nonlinear Hydrodynamic Forces Acting on Cylinders Heaving on the Surface of a Fluid", Rept. No. 77, Res. Inst. of Appl. Mech., Kyushu Univ., 1976.
21. Lee, C.M., "Second-Order Theory for Nonsinusoidal Oscillations of a Cylinder in a Free Surface", Proc. of the 8th CNR Symp., Pasadena, Calif., 1970, pp. 905-950.
22. Newman, J.N., "A Linearized Theory for the Motion of a Thin Ship in Regular Waves", Journ. of Ship Res., vol. 5, June 1961, pp. 34-55.
23. Papanikolaou, A., "Calculation of Nonlinear Hydrodynamic Effects in Ship Motions by Means of Integral Equation Methods (Close-Fit)", in German, Rept. No. 79/1, Inst. f. Schiffstechnik, Techn. Univ. of Berlin, March 1979.

26. John, F., "On the Motion of Floating Bodies", parts I and II, Comm. Pure and Appl. Math., vol. 2, 1949, pp. 13-57, and vol. 3, 1950, pp. 45-101.

27. Sayer, P., Ursell, F., "Integral-Equation Methods for Calculating the Virtual Mass in Water of Finite Depth", Proc. Sec. Int. Conf. on Num. Ship Hydrodyn., Univ. of Calif., Berkeley, 1977, pp. 176-184.

28. Ogilvie, T.F., Shin, Y.S., "Integral Equation Solutions for Time-Dependent Free Surface Problems", Journ. Soc. Nav. Arch. Japan, 1978, pp. 43-53.

29. Paulling, T.R., "Stability and Ship Motion in a Seaway", Summary Rept. for U.S. Coast Guard, June 1970.

30. Ohmatsu, S., "On the Irregular Frequencies in the Theory of Oscillating Bodies in a Free Surface", Papers Ship Res. Inst., No. 48, Tokyo, 1975.

31. Faltinsen, O., "A Study of the Two-Dimensional Added-Mass and Damping Coefficients by the Frank Close-Fit Method", Norske Veritas Rept. No. 69-10-S, 1969.

32. Bai, K., Yeung, R., "Numerical Solutions to Free-Surface Flow Problems", Proc. 10th ONR Symp., Cambridge Mass., 1974, pp. 609-641.

33. Smith, D.A., "Finite Element Analysis of the Forced Oscillation of Ship Hull Forms", Nav. Postgr. Sch., Monterey, Calif., 1974.

34. Maruo, H., "The Drift of a Body Floating on Waves", Journ. of Ship Res., vol. 4, 1960, pp. 1-10.

35. Papanikolaou, A., "Computer Program NONLINEAR, Version June 1980", Techn. Univ. of Berlin, June 1980.

36. Kim, C.H., Dalzell, J.F., "Analytical Investigation of the Quadratic Frequency Response for Lateral Drifting Force and Moment", Rept. No. SIT-DL-79-9-2061, Stevens Inst. of Techn., Davidson Lab., May 1979.

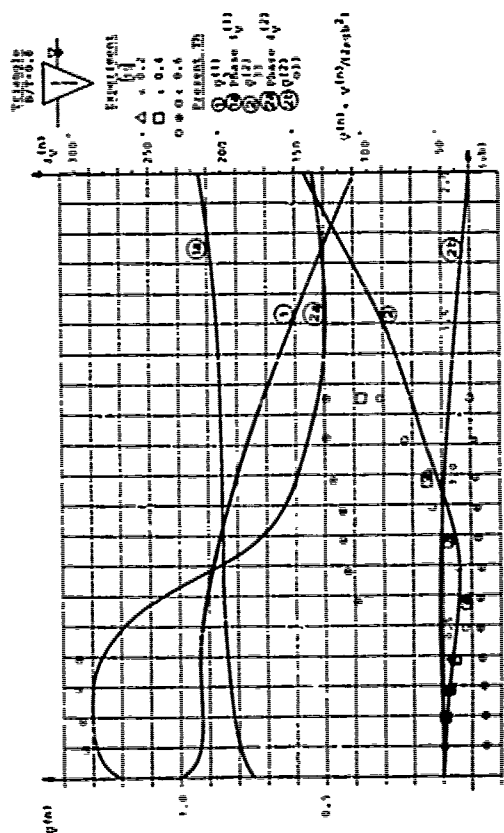


FIG. 5: FIRST- AND SECOND-ORDER FORCES FOR FORCED HEAVE MOTION

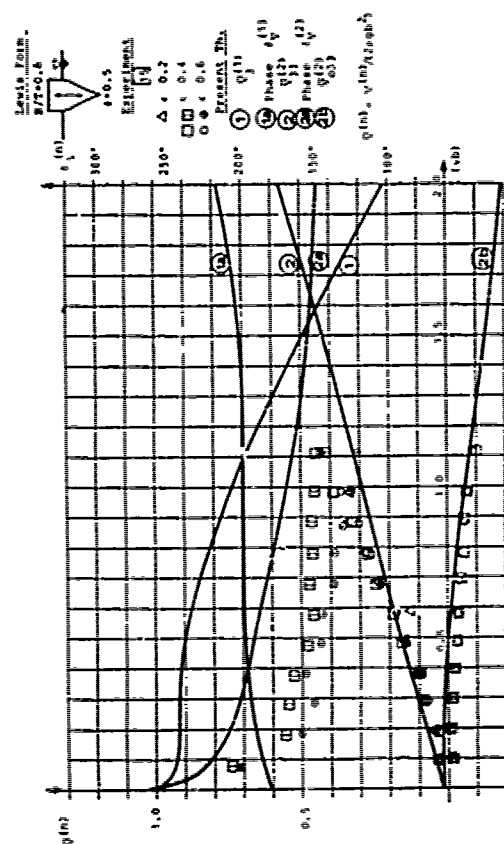


FIG. 6: FIRST- AND SECOND-ORDER FORCES FOR FORCED HEAVE MOTION

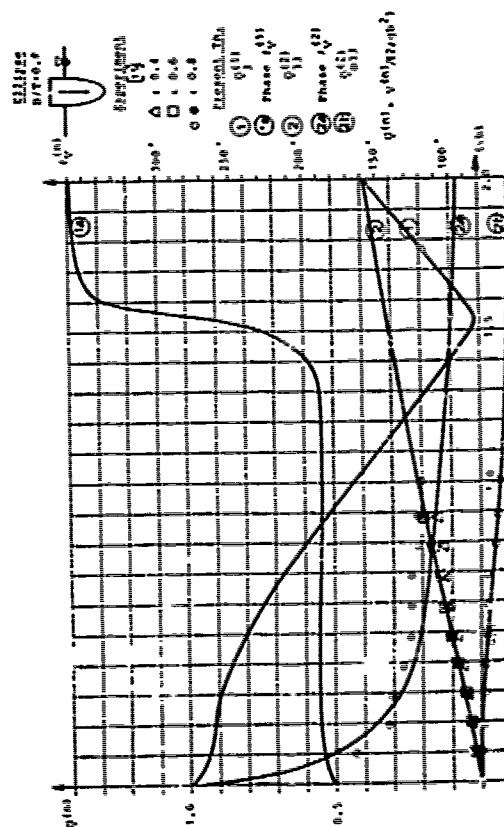


FIG. 7: FIRST- AND SECOND-ORDER FORCES FOR FORCED HEAVE MOTION

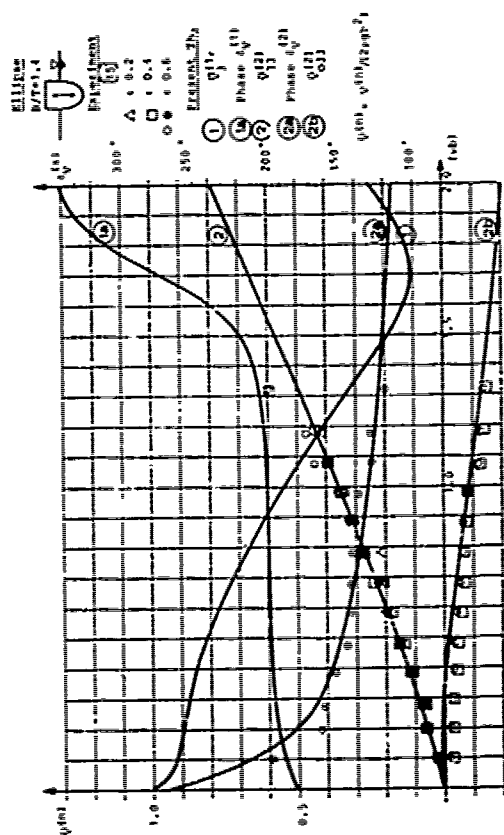


FIG. 8: FIRST- AND SECOND-ORDER FORCES FOR FORCED HEAVE MOTION

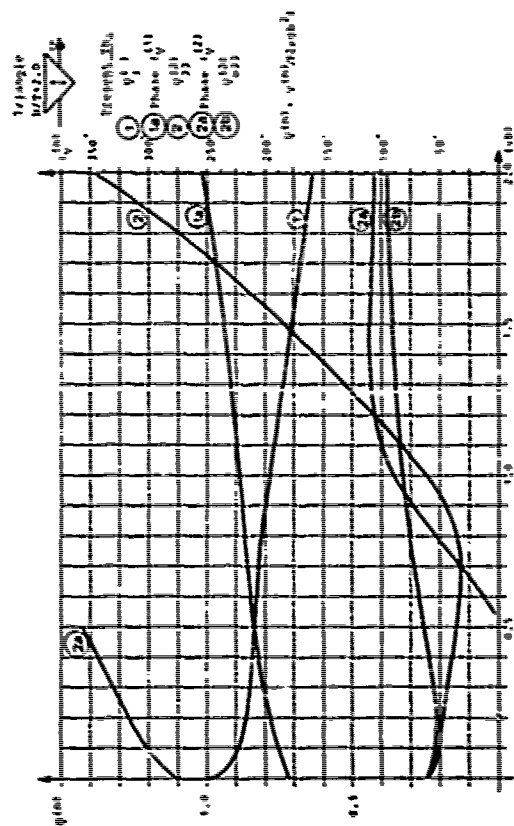


FIG. 9: FIRST- AND SECOND-ORDER FORCES FOR FORCED HEAVE MOTION

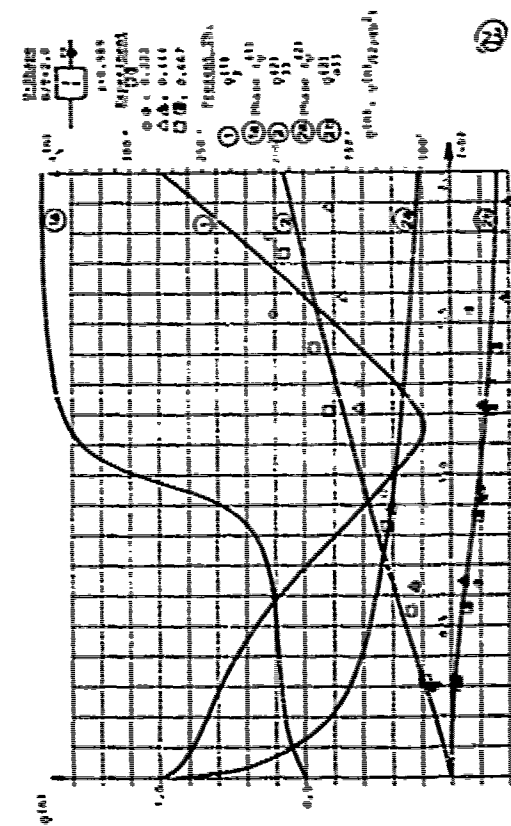


FIG. 11: FIRST- AND SECOND-ORDER FORCES FOR FORCED HEAVE MOTION

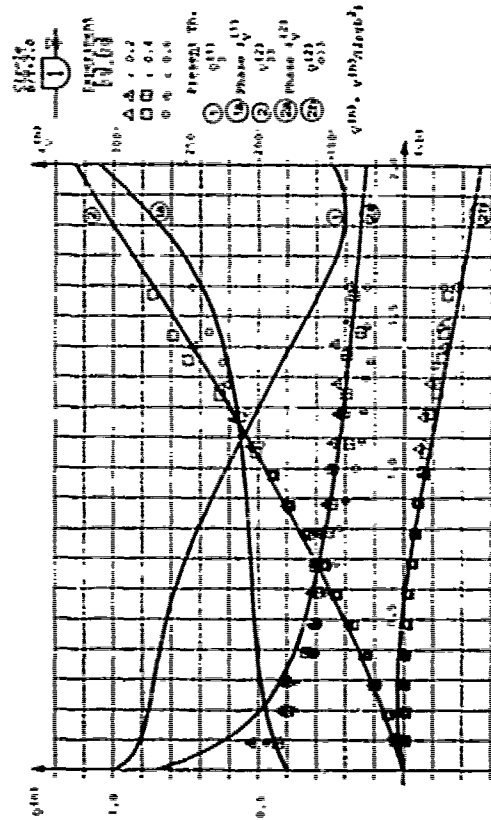


FIG. 10: FIRST- AND SECOND-ORDER FORCES FOR FORCED HEAVE MOTION

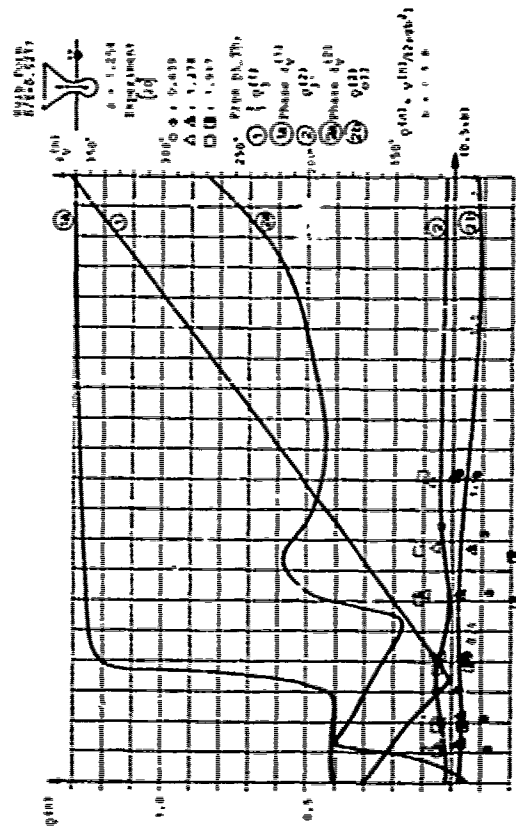


FIG. 12: FIRST- AND SECOND-ORDER FORCES FOR FORCED HEAVE MOTION

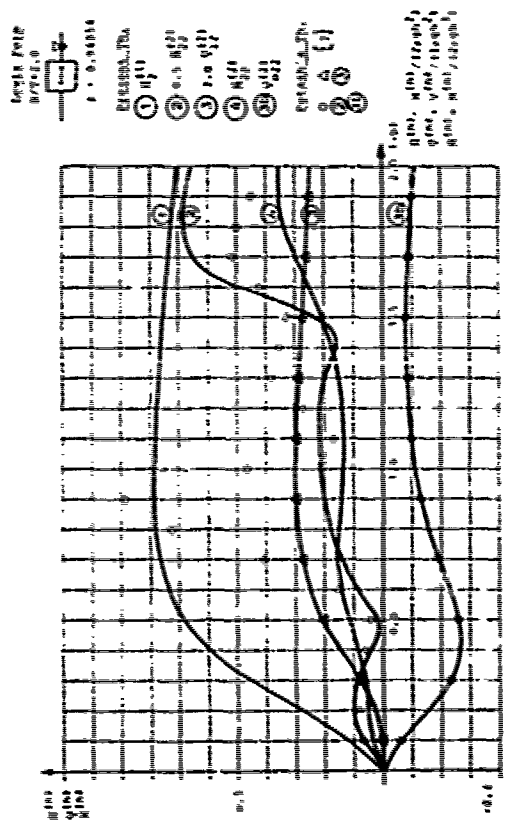


FIG. 13: FIRST- AND SECOND-ORDER FORCES AND MOMENT FOR FORCED BAR MOTION

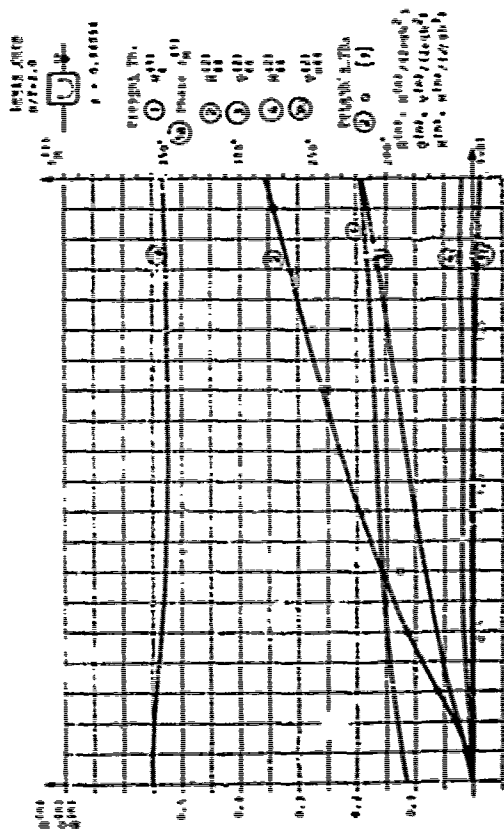


FIG. 15: FIRST- AND SECOND-ORDER FORCES AND MOMENT FOR FORCED ROLL MOTION

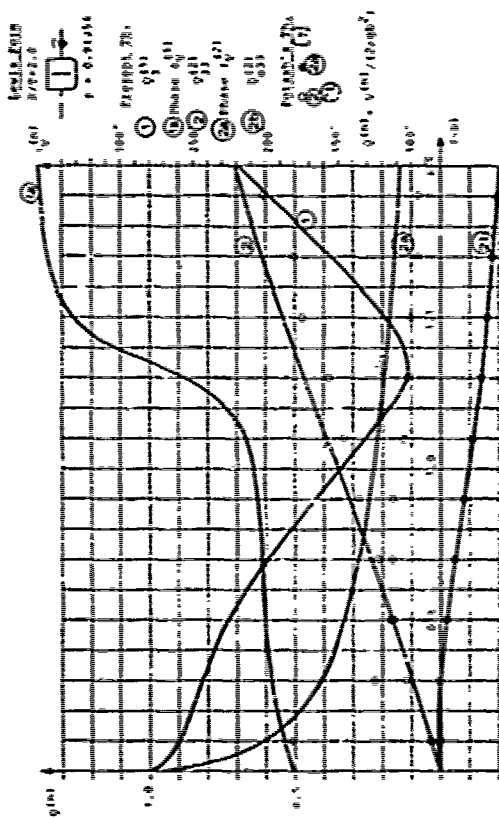


FIG. 16: FIRST AND SECOND-ORDER FORCES FOR FORCED HEAVE MOTION

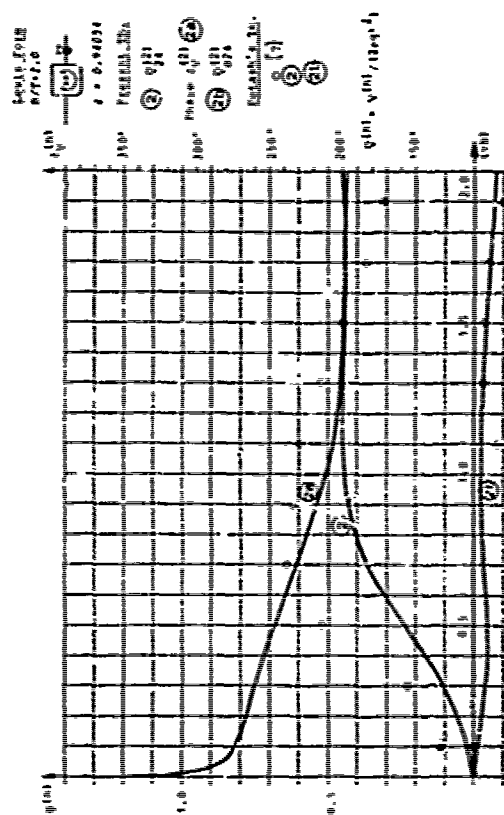


FIG. 18: SECOND-ORDER FORCES FOR COUPLED FORCED BAR AND ROLL MOTION

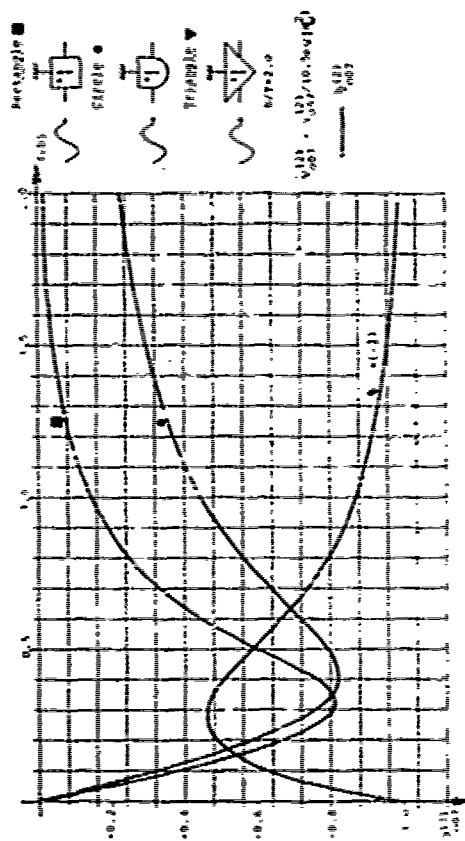


FIG. 16 SECOND-ORDER STEADY-STATE HORIZONTAL FORCE FOR RESTRAINED CYLINDERS IN WAVES

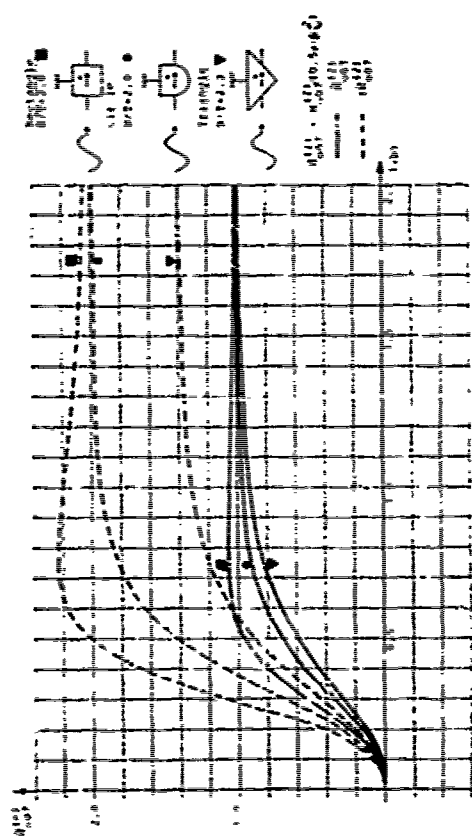


FIG. 17 SECOND-ORDER STEADY-STATE HORIZONTAL FORCE FOR RESTRAINED CYLINDERS IN WAVES

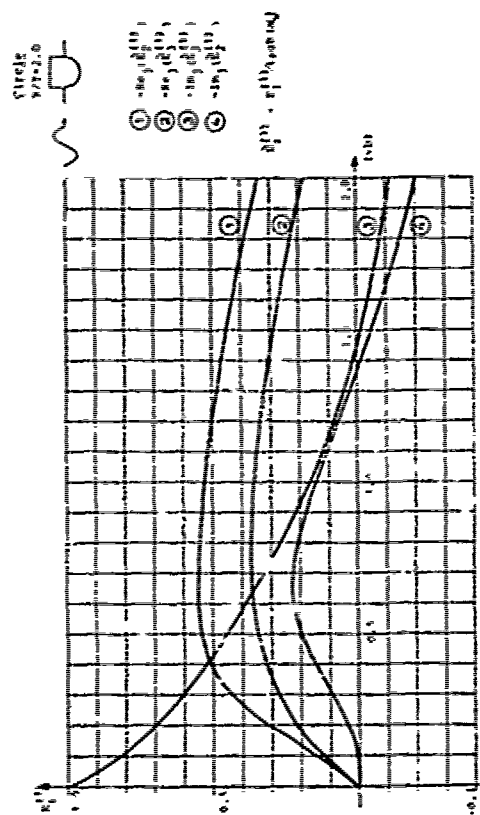


FIG. 20 FIRST-ORDER WAVE EXCITATION HORIZONTAL AND VERTICAL FORCES

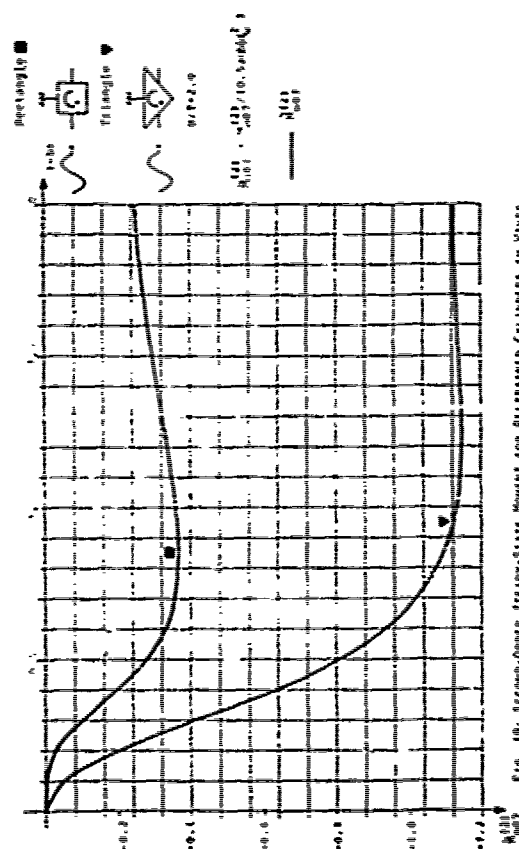


FIG. 19 SECOND-ORDER STEADY-STATE MOMENT FOR RESTRAINED CYLINDERS IN WAVES

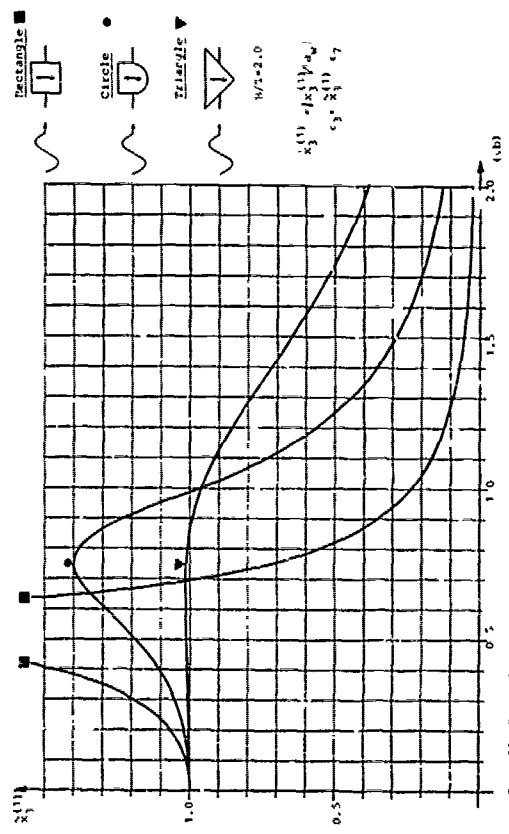


FIG. 21. FIRST-ORDER HEAVE MOTION AMPLITUDES FOR VARIOUS CYLINDERS

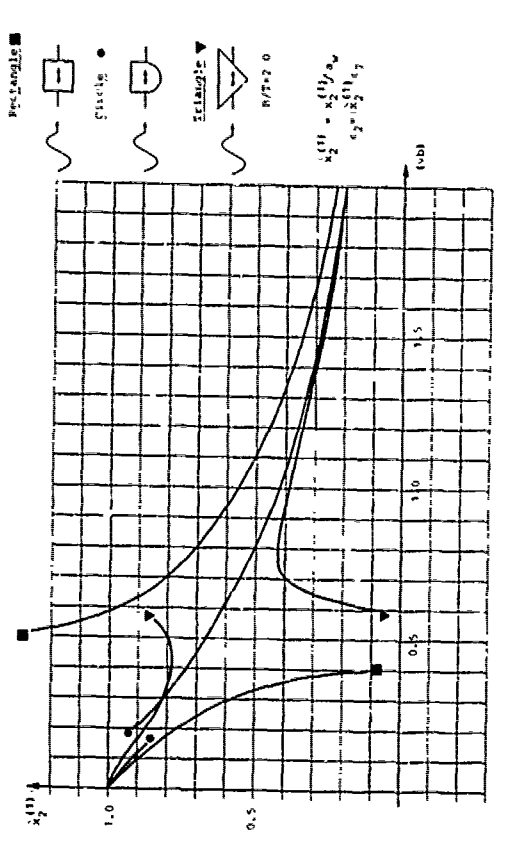


FIG. 22. FIRST-ORDER SWAY MOTION AMPLITUDES FOR VARIOUS CYLINDERS

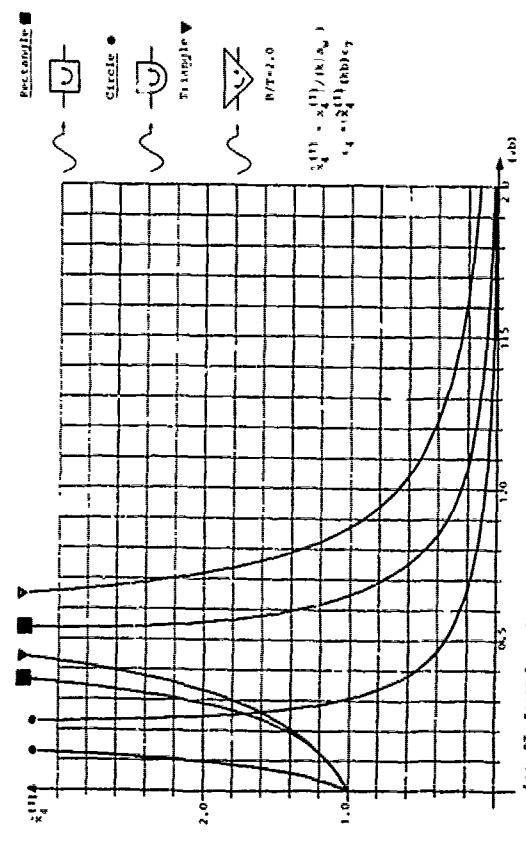


FIG. 23. FIRST-ORDER ROLL MOTION AMPLITUDES FOR VARIOUS CYLINDERS

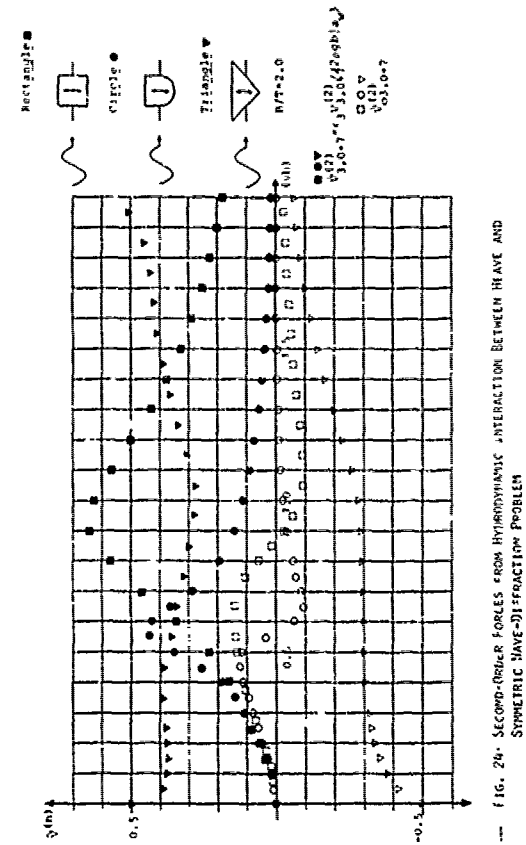


FIG. 24. SECOND-ORDER FORCES FROM HYDRODYNAMIC INTERACTION BETWEEN WAVE AND SYMMETRIC WAVE-OF-FRACTION PROBLEM

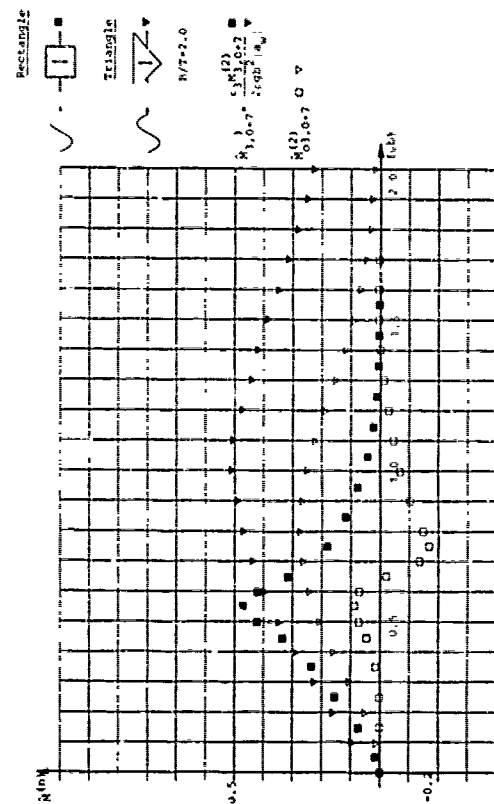


FIG. 25: SECOND-ORDER FORCES FROM HYDRODYNAMIC INTERACTION BETWEEN SWELL AND ANTISYMMETRIC WAVE-DIFFRACTION PROBLEM

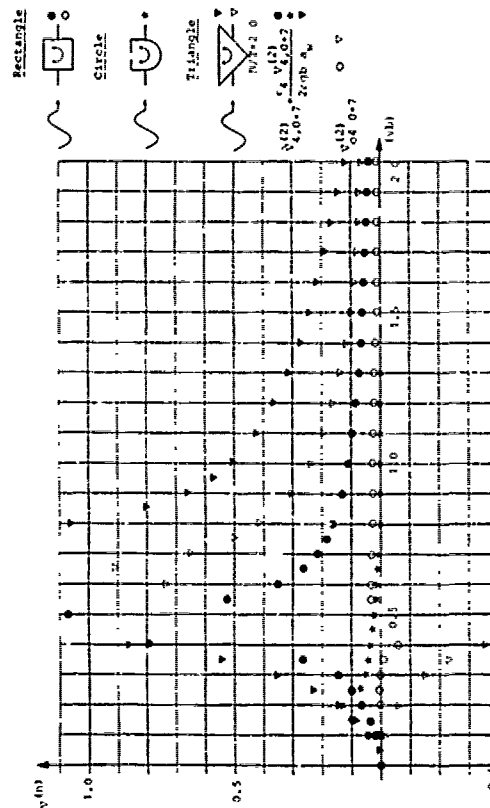


FIG. 26: SECOND-ORDER FORCES FROM HYDRODYNAMIC INTERACTION BETWEEN SWELL AND ANTISYMMETRIC WAVE-DIFFRACTION PROBLEM

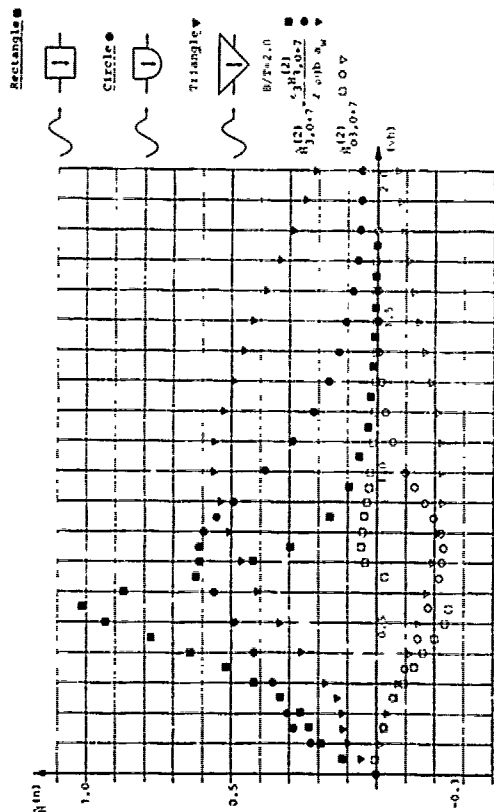


FIG. 27: SECOND-ORDER FORCES FROM HYDRODYNAMIC INTERACTION BETWEEN SWELL AND ANTISYMMETRIC WAVE-DIFFRACTION PROBLEM

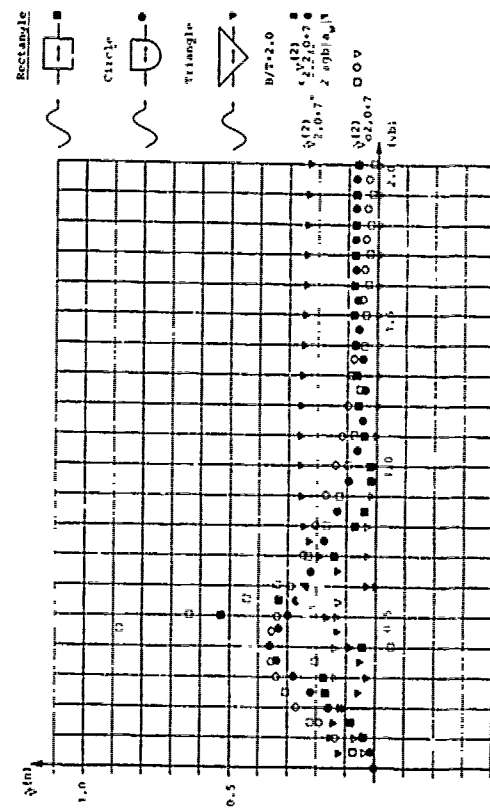


FIG. 28: SECOND-ORDER FORCES FROM HYDRODYNAMIC INTERACTION BETWEEN SWELL AND ANTISYMMETRIC WAVE-DIFFRACTION PROBLEM

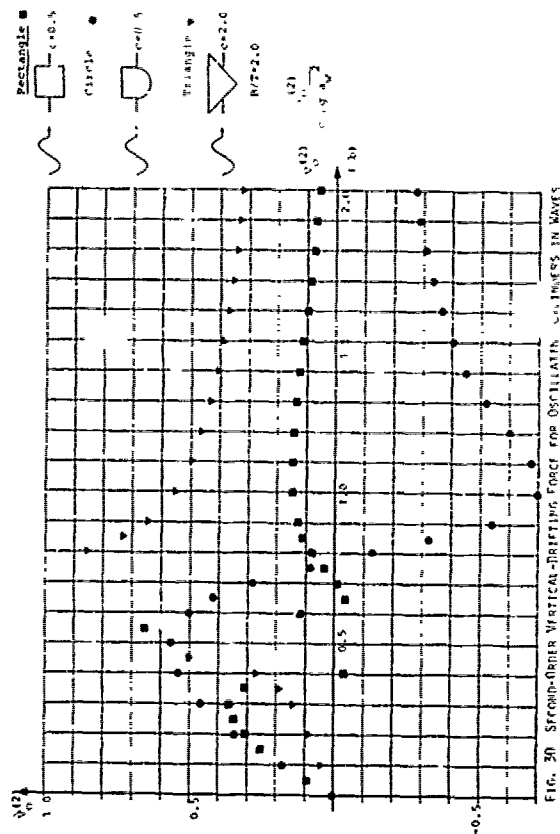


FIG. 27: SECOND-ORDER VERTICAL-DRIFTING FORCE FOR OSCILLATING CYLINDERS IN WAVES

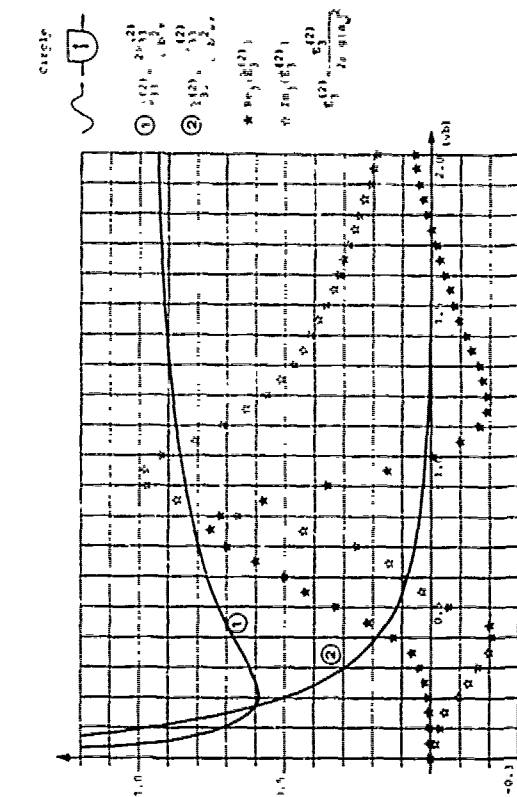


FIG. 32: SECOND-ORDER HYDRODYNAMIC COEFFICIENTS AND HEAVE EXCITATION FORCES

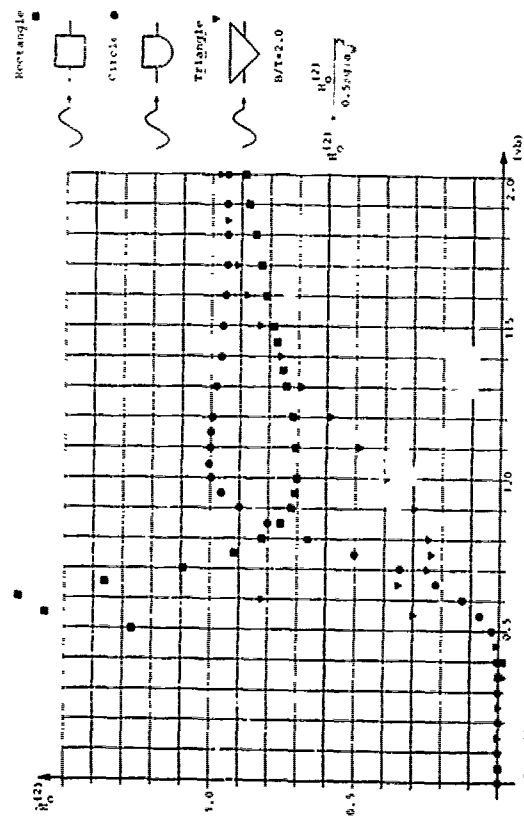


FIG. 31: SECOND-ORDER HEAVE-DRIFTING MOMENT FOR OSCILLATING CYLINDERS IN WAVES

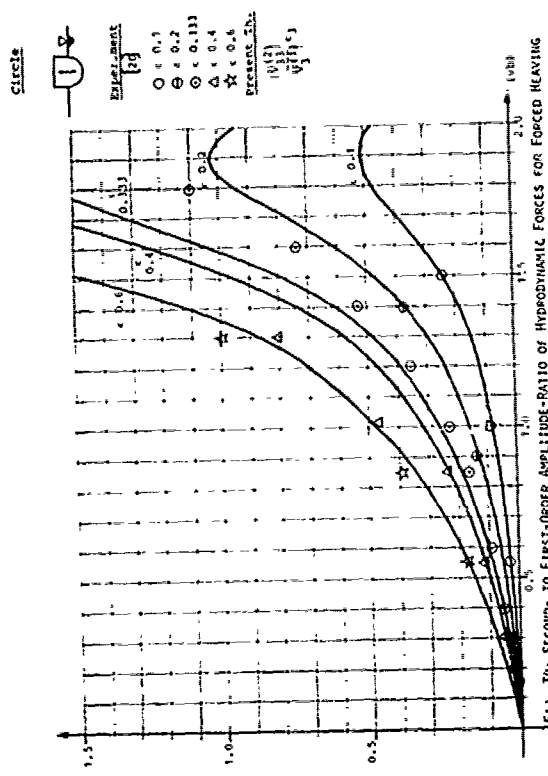


FIG. 34: SECOND- TO FIRST-ORDER AMPLITUDE-RATIO OF HYDRODYNAMIC FORCES FOR FORCED HEAVING

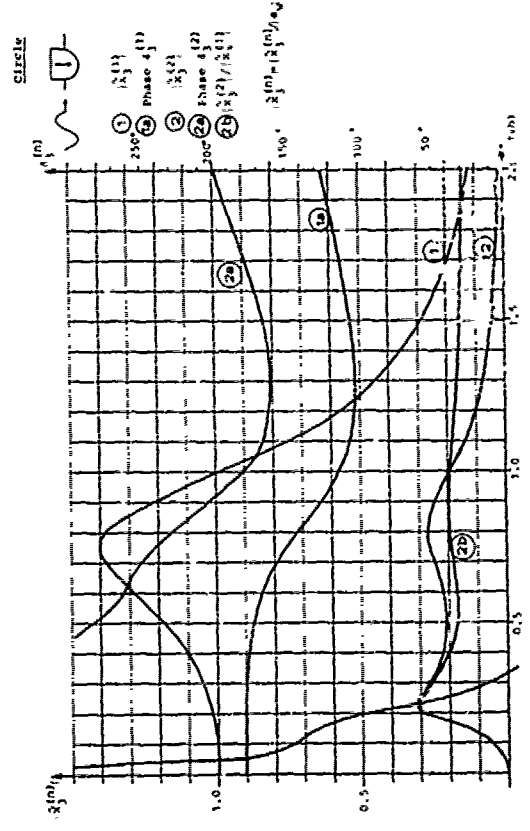


FIG. 33: FIRST- AND SECOND-ORDER HEAVE MOTION QUANTITY

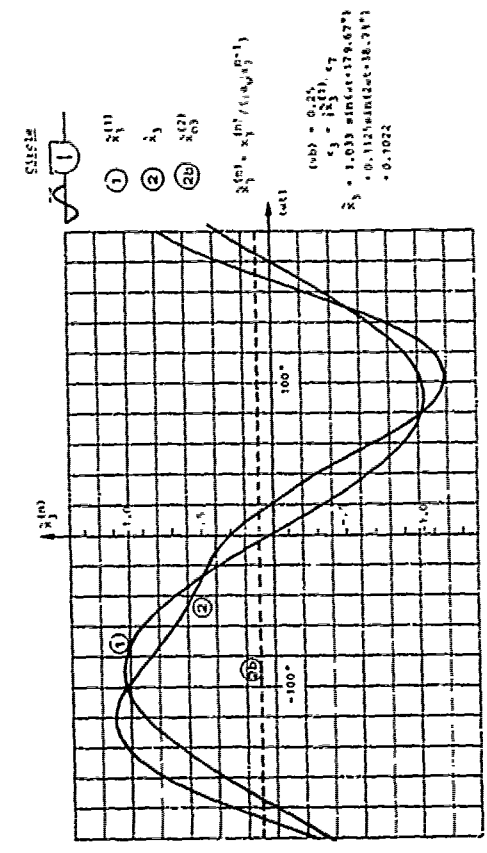


FIG. 35: FIRST- AND SECOND-ORDER HEAVE MOTION OF A CIRCULAR CYLINDER

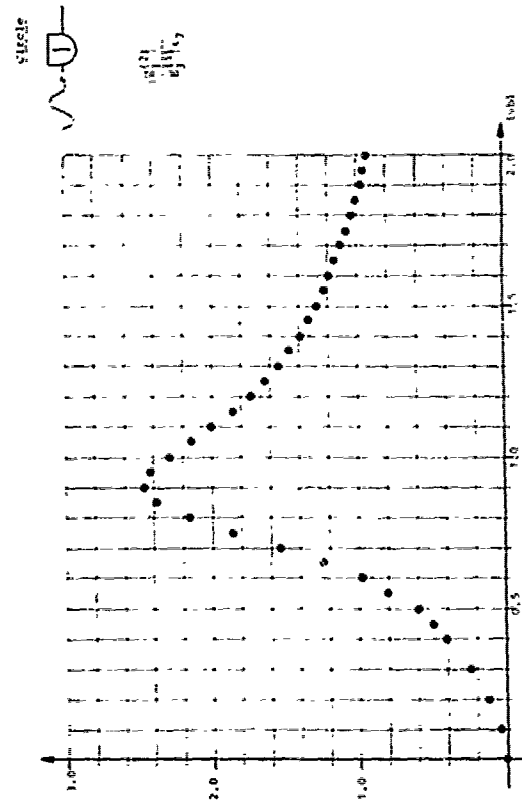


FIG. 36: SECOND- TO FIRST-ORDER AMPLITUDE-RATIO FOR THE HEAVE EXCITING FORCES

Discussion

F. Tasai and W. Koterayama (*Kyushu Univ.*)

The Writers would like to congratulate the Authors on this very interesting and valuable paper and would be most grateful if they be kind enough to comment on a few points.

1. Which boundary condition has the larger effect on the second-order force, the free-surface condition or the body-surface one?
2. The results of the forced heaving tests²⁰ indicate that the first-order forces and the amplitudes of progressive waves \bar{A}_3 depend on the amplitude parameter ϵ_3 . For example, \bar{A}_3 tends to decrease with an increase in ϵ_3 . Can these phenomena be explained with this theory?
3. In Fig. 17 and 29, the horizontal drifting forces $\bar{H}_x^{(2)}$ are greater than unity at a certain frequency. By Maruo's theory, the nondimensionalized drifting forces don't become larger than unity. Did you compare your calculated results with those by Maruo's theory?

H. Maruo (*Yokohama N. Univ.*)

In this paper, the authors have developed a general method of computing second-order hydrodynamic forces on a cylindrical body oscillating with three degrees of freedom on waves of large amplitude. The computation program seems to be very useful for the assessment of the lateral oscillation of a ship in beam seas where the motion amplitude is liable to be large so that the non-linearity in the motion is no longer negligible. One problem which I wish to point out is the fact that the theory upon which the computation method is based is a perturbation analysis in any case. The boundary-value problem is formulated on the body surface at its average position. It is suspected that the perturbation theory may present some difficulty in order to take account of the change of shape of the wetted portion with time which is liable to become large in the case of rolling. A question is, to what extent, is the perturbation analysis applicable at large motion amplitude?

C.M. Lee (*DTIC/SDC*)

The authors have completed the second-order solution for freely floating two-dimensional bodies subject to beam waves.

As a previous pursuer of the same kind of problem, I can fully appreciate the painstaking patience the authors must have required during the course of this work, particularly, in keeping the orders of magnitude consistent. I congratulate the authors for this excellent milestone work.

I have to confess that I did not have the patience to check every equation in this paper; however, with regard to the passage concerning the irregular frequencies, I have the following suggestion. This suggestion may only apply if the authors' statement* at the end of the Section 3.2 has been the main reason that they have not used the technique for removing the irregular frequencies described in [28] through [30].

If we let $f^{(n)}$ be the solution for the boundary-value problem given by Equation (51) except for the body-boundary condition, then let

$$h^{(n)} = z^{(n)} - f^{(n)}, \quad (x, y) \in D$$

such that

$$F(n^2\nu)\{h^{(n)}\} = 0, \quad (x, y) \in S_F$$

$$B\{h^{(n)}\} = R^{(n)} - \frac{2}{3n} f^{(n)}, \quad (x, y) \in S_0$$

and the rest of the boundary conditions remain the same as in Equation (51).

Since the new boundary-value problem for $h^{(n)}$ is identical with the first-order problem, one of the techniques in [28] - [30] should resolve the problem of indefinite solution at the irregular frequencies. I would think such an approach would save the computer time more significantly than the interpolation method used in this paper.

As to the solution for $f^{(n)}$, one can find the expression in Equations (21, 22) of "Surface Waves" by Wehausen and Laitone in which the expression should be for $-f^{(n)}$. When $L^{(n)}$ is nondecaying at $|x| \rightarrow \infty$ but behave as $e^{jn^2\nu x}$, the solution is given in my earlier work [21].

Author's Reply

A. Papanikolaou and H. Nowacki (*Tech Univ. Berlin*)

We would like to thank all discussers for their valuable comments.

Professors Tasai and Koterayama have

* Quote: But it must be mentioned that purely analytical methods for this purpose have not yet been extended to second-order situations with inhomogeneous free surface boundary conditions.

raised three interesting questions. In response to the first one, it is difficult to give a general answer because the relative importance of the body and free surface boundary conditions depends on section shape, frequency parameter, and upon which second-order subproblem is discussed. In many situations the body boundary condition and the free-surface condition must be regarded as being of equal importance.

Second, our perturbation expansion does not show any effect of the small parameter ϵ_3 on the linear heave damping coefficient \bar{A}_3 , which is consistent with the assumptions of linear theory. We appreciate, however, that a different situation may exist in analysing test results, where the subdivision of measured forces into contributions from different orders and frequencies does depend on the assumed orders in the evaluation model. For example, if a second-order evaluation model is assumed, but is not adequate to represent the measured effects, this may show up in a "false" dependence of \bar{A}_3 on ϵ_3 . However, such dependence may also have other reasons not accounted for in second-order potential theory, notably viscous effects.

Third, our drifting forces have been calculated from near-field potentials by integration of second-order pressures over the actually wetted body contour, whereas Maruo's theory [34] is based on far-field linear incident wave considerations. Our Fig.29 pertains to the horizontal drifting force on an unconstrained body, Fig.17 holds for a fixed body. In the former case the nondimensional drift force values for the rectangle far exceed unity in a certain frequency range, which is due to a resonant motion situation. As stated in the paper, the results near resonance must be viewed with caution because of the considerable magnitude of the small motion parameters. It also remains to be examined in which way Maruo's theory must be applied to this situation. For the fixed bodies investigated, only the rectangle has a nondimensional drifting force slightly greater than one. It must be noted that the reference quantity used for plotting the drifting forces is $0.5\rho g \cdot a_w^2$, corresponding to the kinetic energy of a linear wave of amplitude a_w . In reality the kinetic energy

of our second-order wave also includes second-order contributions, which must be taken into account in any direct comparisons with results derived from Maruo's theory. It may be noted that some experimental results also indicate the possibility of horizontal drifting forces exceeding unity.

Professor Maruo's remarks remind us of the basic limitations of the perturbation method. It lies in the nature of this method that the boundary conditions on any free or moving boundaries are met approximately by Taylor series expansions about their positions at rest. This is why we have stated in the paper that a second-order theory is apt to be valid for moderate motion amplitudes and moderate wave heights. When these limits are exceeded depends on section shape and frequency parameter. The present second-order extends these limits relative to linear theory by allowing for second-order hydrodynamic effects and, in particular, for the existing flare angle in the waterline.

We are grateful for Dr.Lee's comments based on his long experience with the present problem. His suggestion to transform the second-order subproblems to a homogeneous form equivalent to that of the first-order problems, in order to be able to rely on the well-known analytical methods for alleviating the irregularity problem is well conceived and should certainly be feasible. However, this would be at the expense of having to solve two boundary value problems instead of one for every second-order subproblem under discussion. In our experience, purely numerical schemes for the same purpose have worked very reliably for the first as well as for the second order. It may be added that we have also investigated analytical and semi-analytical methods for dealing with the irregularity problem [8], [23], which have worked quite adequately, too, although they only shift the irregularity to some other frequency, which may still lie in the range of interest, particularly for the second-order problem. Finally it is important to note that the severity of the irregularity phenomenon is much reduced by using the Helmholtz integral equation formulation with the potential as unknown function.

Characteristics of Nonlinear Waves in the Near-Field of Ships and Their Effects on Resistance

Hideaki Miyata
The University of Tokyo
Tokyo, Japan

ABSTRACT

The characteristics of nonlinear waves around ships are experimentally studied. These waves generate lines of discontinuity, and the abrupt velocity change across the wave front satisfies the shock relation. A kind of shock wave occurs around ships in translational motion in deep water in the same manner as it does in compressible fluid and shallow water flow. The characteristics can be analogically explained by the nonlinear shallow water theory, introducing equivalent shallow water depth. The existence of this nonlinear waves produces a deal of influence on the flow around ships and on ship resistance. The role of the nonlinear waves in the inviscid resistance component of ships and their effect on linear dispersive waves are discussed.

1. INTRODUCTION

Linear wave resistance theories based on the works of Kelvin, Michell and Havelock have contributed to the improvement of hull form design, and as a consequence, to energy saving for more than twenty years. However, there exist significant discrepancies between experimental facts and explanations by these theories or improved versions [2]. In case the discrepancies remain quantitative and one can obtain sound qualitative information from the linear theories the theories can continue to contribute to industrial purposes. In many cases, however, linear wave resistance theories turn out to be powerless neither quantitatively nor qualitatively depending on the hull particulars.

It is a popular opinion that the defect of wave resistance theories developed so far is originated from the linearization of the

problem and nonlinearity should be taken into account. The nonlinearity can be classified into two kinds. One is, so to speak, nonlinear effect on linear waves, in which governing equation is Laplace equation. The other is nonlinearity in characteristics of waves, which is governed by a nonlinear partial differential equation. Linear and nonlinear waves both have opportunity to occur. The former nonlinearity is treated in the framework of the linear wave theory, while the problem concerned with the latter nonlinearity is to treat nonlinear waves themselves. Most of the improved wave resistance theories recently developed take the former nonlinearity into account to some extent. For example, one of the most general method is one by Gadd[8] who has proposed a Rankine source method in which Laplace equation is solved under the nonlinear free surface condition. As is commonly recognized in high-speed aerodynamics and shallow water flow, the nonlinearity often plays a decisive role in the characteristics of waves and in fact nonlinear waves called shock waves occur. The appearance of nonlinear waves around ships in deep water was first pointed out by Baba[11], which have been called wave breaking. However, breaking of waves will not be the essence of nonlinear waves in the near-field of ships. The nonlinearity will consist in much more comprehensive characteristics of waves. Occurrence of shock waves will not be a marvel for ships in translational motion.

The author has experimentally clarified the nonlinearity of waves in the near-field and found out that a kind of shock wave occurs, which is named as free surface shock wave in 1977. Consequently, the basic nonlinearity must be examined in detail for the development of resistance theories for

In Fig. 1, a wave pattern picture of a full-scale passenger boat is shown, in which wave systems which are entirely different from Kelvin pattern are obvious. Following the discussion on the limitation of linear theories in chapter 3, the nonlinearity of the waves is clarified with a deal of experimental results with a simple model ship in chapter 4. The nonlinear waves have characteristics that allow us to call them "free surface shock waves". Therefore, as one imagines, the characteristics are very similar to nonlinear shallow water waves. In chapter 5, the analogy to nonlinear shallow water waves and application of the nonlinear shallow wave theory are discussed through experiments with wedge models. In chapter 6 and 7, effects of the nonlinear wave (free surface shock wave) on resistance components and on linear dispersive waves are discussed. The nonlinear waves directly render resistance to ships as momentum loss and, at the same time, they indirectly influence resistance by deformation of the dispersive waves. The nonlinear waves at the stern and a new practical method to reduce waves at the stern are described in

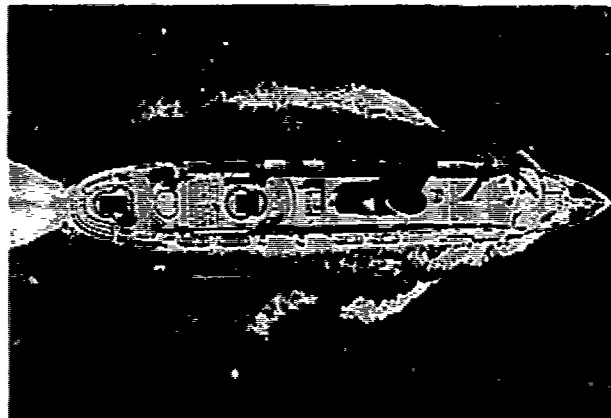


Table 1 Principal particulars of model ships

(m)	Lpp	B	d	L/B	E/d	Cb	remarks
WM1-C	2.400	.240	var.	10.00	var.	.67	parabolic water line, wall-sided, sharp-bow
WM1-B	2.400	.240	var.	10.00	var.	.68	D9, blunt-bow
WM2	2.400	.480	var.	5.00	var.	.67	D9, sharp-bow
WM4-A	1.200	.240	var.	5.00	var.	.67	D9, sharp-bow
M34	2.001	.308	.111	6.50	2.77	.39	fine ship
M40	2.000	.308	.105	6.50	2.94	.54	simplified modification of SR138
M41	2.000	.364	.105	5.50	3.47	.54	beam-length series ship
M42	2.000	.444	.105	4.50	4.25	.54	D9
M43	2.000	.364	.105	5.50	3.47	.54	simplified modification of M41
BULK1,2	2.000	.330	.073	6.06	4.52	.75	bulk carrier on ballast cond.
SR138(F)	2.500	.385	.135	6.49	2.85	.57	container carrier, full load cond.
SR138(T)	2.500	.385	.088	6.49	4.38		D9, trial condition
M6	2.000	.153	.142	13.07	1.08		Inuid
M7	2.000	.255	.177	7.84	1.44		Inuid
M8	2.000	.312	.204	6.47	1.53		Inuid

2. NOMENCLATURE

- | | |
|------------------|---|
| $A^*(\vartheta)$ | weighted amplitude function |
| B | beam length of ship |
| c | critical speed |
| C _w | wave resistance coefficient derived from towing test |
| C _{wp} | d ₀ derived from wave analysis |
| d | draft of ship |
| F _n | Froude number based on L |
| F _h | d ₀ based on \tilde{h}_1 |
| F _h | d ₀ based on \tilde{h}_1 |
| g | acceleration of gravity |
| h | shallow water depth |
| \tilde{h}_1 | equivalent shallow water depth |
| H | total head behind ship |
| H ₀ | d ₀ ahead of ship |
| L | length between perpendiculars |
| P | pressure |
| u | velocity in x-y plane |
| R _m | resistance measured as momentum loss |
| R _v | viscous resistance = $R_{f0}(1+k)$ |
| R _w | wave resistance derived from towing test |
| R _{wp} | d ₀ derived from wave analysis |
| u, v, w | disturbance velocity in x, y, z-direction, respectively; u includes uniform velocity in chapter 5 |
| U, V | velocity of uniform stream |
| x | axis parallel to ship centerline, aftward positive |
| y | axis parallel to ship beam |
| z | axis vertical, upward positive |
| α | entrance angle |
| β | shock angle |
| ζ | wave height |
| subscripts | |
| 1 | ahead of shock front |
| 2 | behind shock front |
| n | normal to shock front |
| t | tangential to shock front |

3.1 Wave Pattern Pictures of Model Ships

The legitimacy of theories must be guaranteed by real physical phenomena. The



Fig.2 Wave pattern picture of a simple model WM2 ($d = 6\text{cm}$, $Fn = 0.22$)



Fig.3 Wave pattern picture of M34 ($Fn = 0.333$)

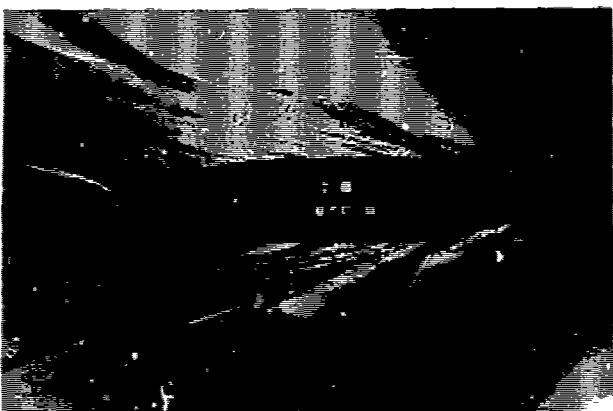


Fig.4 Wave pattern picture of M41 ($Fn = 0.267$)

development of the bulbous bow by Inui would not have been successful without the aid of experimental analyses. At the experimental tank of The University of Tokyo, measurement of wave height for two-dimensional wave contours and photographing wave pattern have been routine techniques of experiment for long years. The former presents quantitative information of wave height and the latter qualitative one. Wave pattern pictures by the latter technique have property to intensify the lines on which gradient of

wave height is steep rather than wave height itself.

Three examples are shown in Figs.2,3 and 4. The principal particulars of model ships are shown in Table 1. One can clearly notice that the wave systems in the neighborhood of the models are not similar to Kelvin pattern, or rather, they are similar to shock waves in compressible fluid. The lines of wave crest originated from the hull surface are usually convex and their angles to the center line of the ship varies depending on the hull particulars, advance velocity and so forth.

Wave pattern pictures at the University of Tokyo are present in references[1], [2], [3] and [5], which lead us to the same intuitive understanding of real wave making as mentioned above.

3.2 Discrepancies between Theory and Experiment

Discrepancies are outstanding between what wave resistance theories so far developed indicate and what experimental results show in the form of resistance force, wave height, disturbance velocity and so on. The discrepancies are both qualitative and quantitative, which have seldom been experienced in other fields of hydrodynamics. Some comparisons between calculated wave resistance, measured wave resistance by towing test and by wave analysis are shown in Figs.5, 6 and 7. Wave resistance is calculated by 'Michell's approximation in Fig.5 and by the low speed theory in Fig.7. General tendency of discrepancies are as follows.

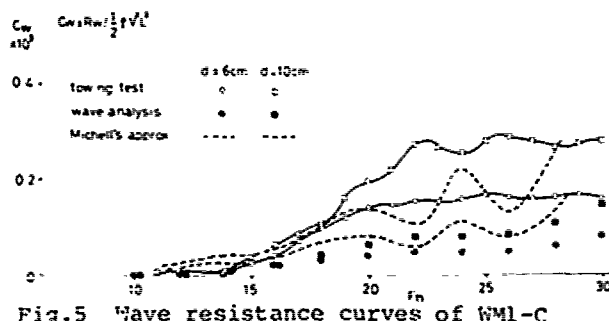


Fig.5 Wave resistance curves of WM1-C

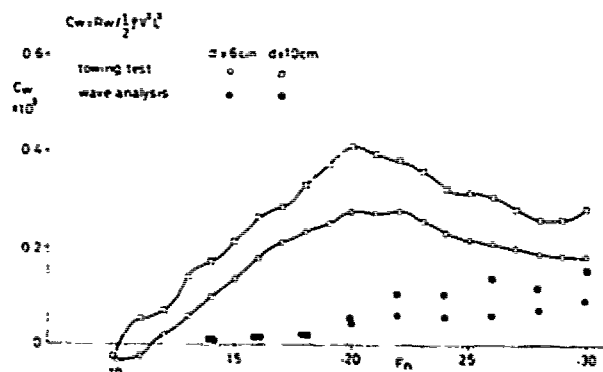


Fig.6 Wave resistance curves of WM1-B

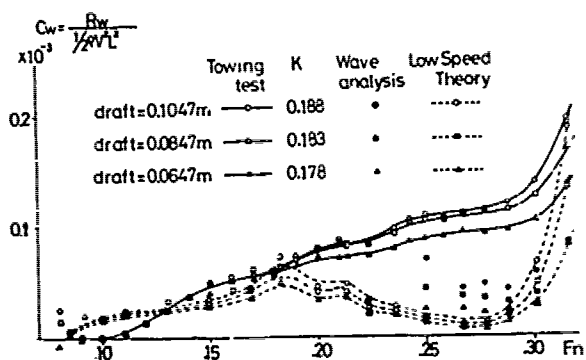


Fig. 7 Wave resistance curves of M43 varying draft

- 1) Calculated wave resistance curve shows conspicuous humps and hollows, while measured one shows only slight humps and hollows. This cannot be settled by the attempt to take viscous effect into account.
- 2) The wave pattern resistance (C_{wp}) is smaller than the wave resistance derived from towing test (C_w) without exception.
- 3) A hump or a hollow in C_w curve cannot always be observed in C_{wp} curve.
- 4) Discrepancy between C_w and C_{wp} is significant in the velocity range of $Fr < 0.35$.

Taking these results coolly, one will not be able to attribute the discrepancies to the minor defects that linear wave making theories have cherished. Or rather, they should be attributed to the new physical phenomena, which have been out of the scope of linear wave resistance theories for ships.

4. VERIFICATION OF THE EXISTENCE OF FREE SURFACE SHOCK WAVES

4.1 Distribution of Disturbance Velocity around a Simple Model

The characteristics of nonlinear waves have been clarified by measurement of disturbance velocity. The simple model WM2 has been selected for tested model whose second nonlinear wave is intense on the condition of $d=6\text{cm}$ and $Fr=0.22$ as is shown in Fig. 2. A five hole pitot tube whose diameter of the head is 6mm and a precise position setting equipment are utilized for this purpose. Contours of measured wave height in the vicinity of the crest of the second nonlinear wave are shown in Fig. 8, in which one can recognize the straight line of the wave front and the steep slope of the wave height along the line. Velocity measuring points are shown by circles in this figure. Velocities are measured on the two surfaces below the disturbed free surface by 10mm and 30mm for all points, and additional two surfaces below the disturbed free surface by 50mm and 70mm for selected points. Therefore, the measuring surfaces are curved ones.

The measured velocities are figured in three forms, i.e., disturbance velocity in

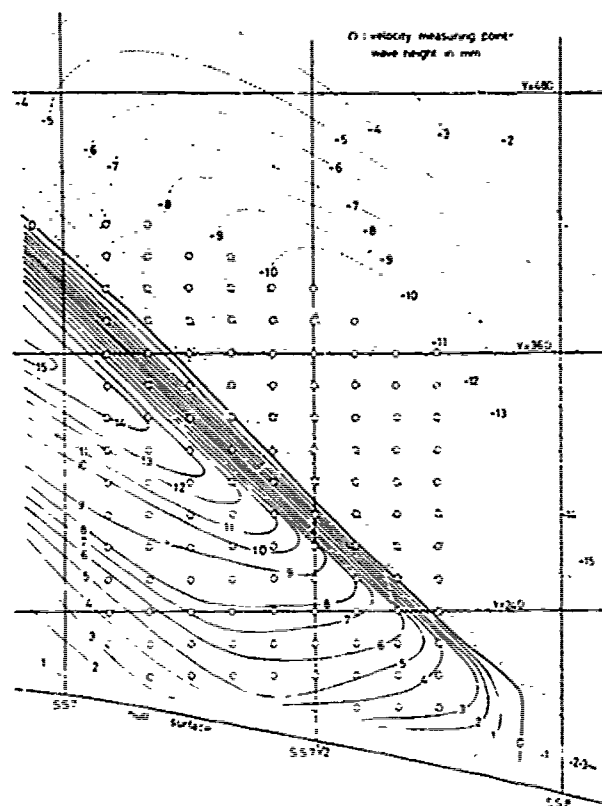


Fig. 8 Wave contours in the near-field of the second free surface shock wave and points for velocity measurement ($WM2$, $d=6\text{cm}$, $Fr=0.22$)

← 0.2U $Z = -1\text{cm}$

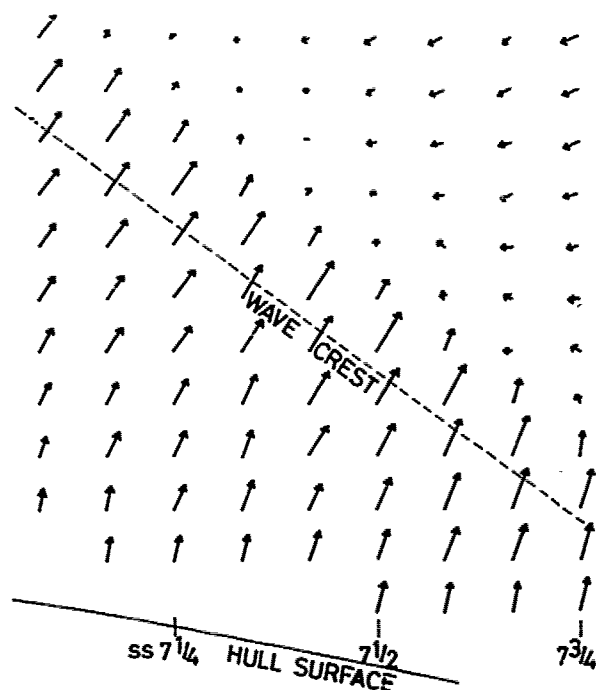


Fig. 9 Horizontal components of disturbance velocity (A)

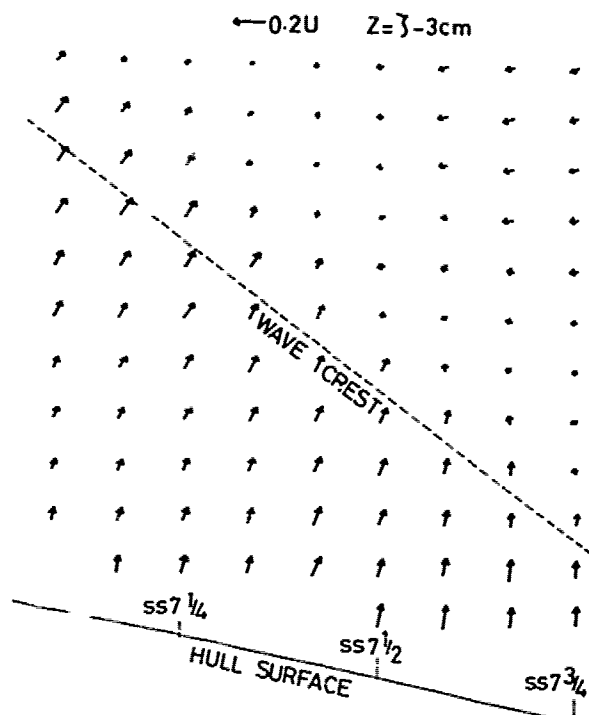


Fig.10 same as Fig.9 (B)

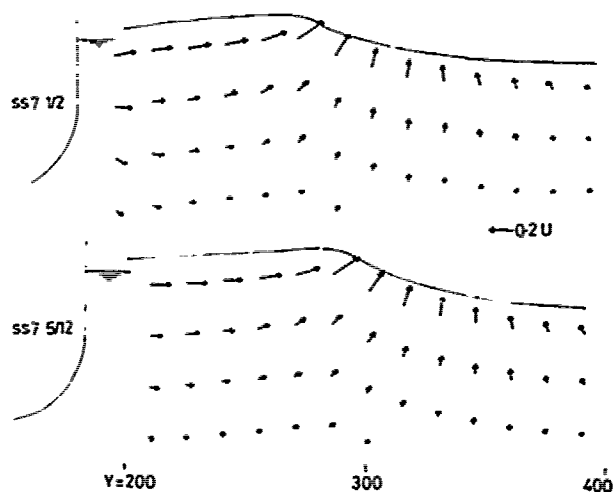


Fig.11 Components of disturbance velocity in y-z plane

X-Y and Y-Z planes and lateral distribution of disturbance velocity, as are shown in figures from Fig.9 to Fig.14. The characteristics of the second nonlinear wave, which is the representative of all the nonlinear waves in the neighborhood of ships, can be summarized as follows.

- 1) Change of velocity across the wave front is abrupt. The steepness of velocity change cannot be expressed by linear theories, on which some examples are shown in [2].
- 2) The abrupt change of velocity is so steep as to form a line of discontinuity.

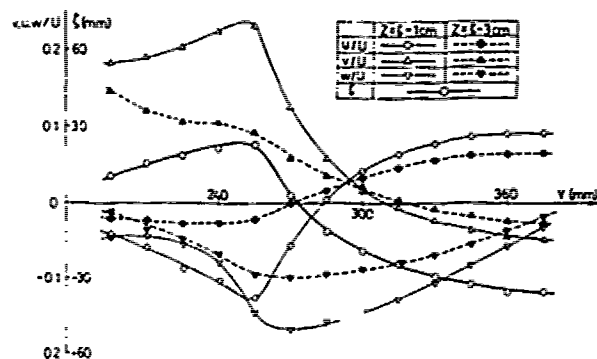


Fig.12 Lateral distribution of disturbance velocity at S.S. 7/12

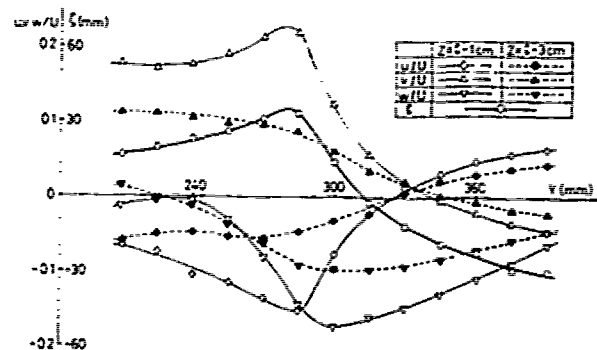


Fig.13 Lateral distribution of disturbance velocity S.S. 7 5/12 (A)

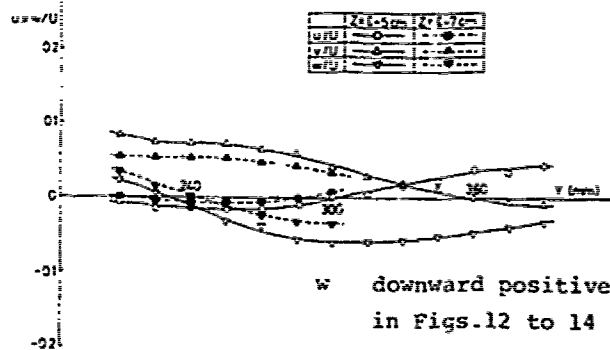


Fig.14 same as Fig.13 (B)

ity.

- 3) The disturbance velocity vectors behind wave front on the surface adjacent to free surface are normal to the wave front.
- 4) The steepness of velocity change is limited in the thin layer adjacent to free surface. On the planes $Z=5\text{cm}$ and $Z=7\text{cm}$, no abrupt change can be observed in velocity.

The nonlinearity of waves in the vicinity of ships is first noticed by Baba[11], and it has been considered as an effect of breaking waves. However, our successive works following his pioneering work indicate that the decisive property of the nonlinear wave is to generate a line of discontinuity.

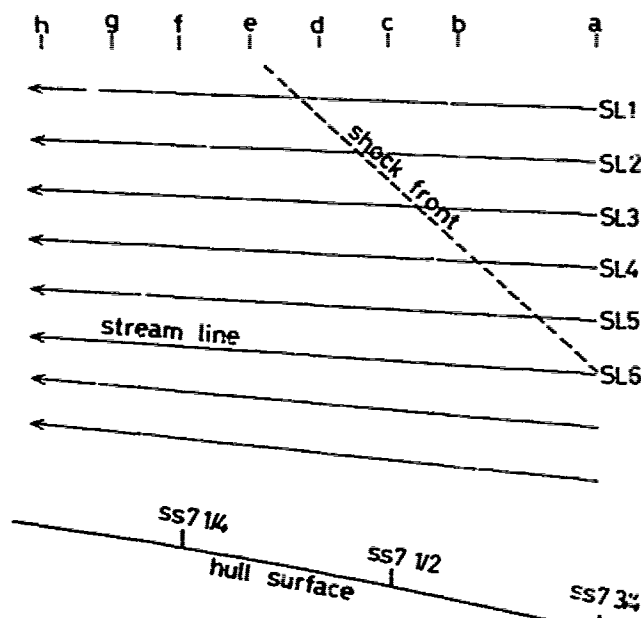


Fig.15 Stream lines of double model flow and points for velocity measurement

4.2 Shock Condition

The formation of wave system shown in wave pattern pictures and the existence of lines of discontinuity remind us of shock waves which are familiar in the flow of compressible fluid and the nonlinear shallow water flow. The main characteristics of shock waves in fluid are generation of discontinuity and satisfaction of shock relation expressed as follows,

$$q_{n2} = q_{n1} \quad (1)$$

$$q_{t2} = q_{t1} \frac{\tan(\beta - \alpha)}{\tan \beta} \quad (2)$$

This condition is examined with the measured velocity vectors of 'M2. The measured velocity vectors are traced along the stream lines of double model flow shown in Fig.15. Velocity vectors that include the uniform velocity at the x-coordinates from a to h in Fig.15 are shown in Fig.16 for each stream line. The origins of the vectors are concentrated on the wave front line. The lines normal to the wave front are drawn in dotted lines, and it can be concluded that the change of fluid velocity across the wave front satisfies the shock relation described above. Only the velocity component normal to wave front experiences abrupt change, while the tangential component is retained unchanged.

The nonlinear waves have pertinent characteristics to be classified into a kind of shock wave. This physical fact will be natural in a sense because nonlinearity often plays a decisive role. With the experimental results visualized in figures from Fig.1 to Fig.16, the author named this kind of nonlinear waves in the near-field

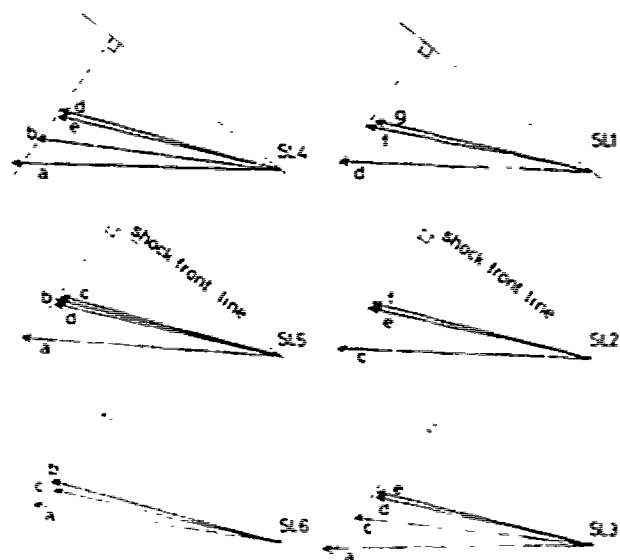


Fig.16 Change of velocity vector along double model stream lines including uniform velocity

of ships as "free surface shock wave" in 1977. In this paper the nonlinear waves are called as free surface shock waves and will sometimes be abbreviated as FSSW hereafter.

5. ANALOGY TO NONLINEAR SHALLOW WATER WAVES

5.1 Free Surface Shock Waves around Wedge Models

Occurrence of free surface shock waves have been experimentally investigated with wedge models to find out general laws that prescribe the characteristics of FSSW around bow [4].

Some examples of photographed formation of FSSW around bow are present in Fig.17. The shock angle, that is the angle of wave front to the centerline of the model, varies depending on the parameters, i.e., velocity of advance, draft and entrance angle. The change of shock angle is systematic as is shown in Fig.18 (left). This tendency is very analogous to that of shock waves in shallow water as is shown in Fig.18 (right) which is calculated by the theory for nonlinear shallow water waves [9], [13]. The shock angle decreases with the reduction of entrance angle, increase in velocity and decrease of draft or water depth. Measured wave profiles are present in Fig.19, which indicate that the wave height is increased with the increase of shock angle (forward advance of wave crest). This means that the increase of shock angle is accompanied with the intensification of the discontinuity, which is one of the properties of shock waves.

These physical facts guarantee the verification of the existence of FSSW described in the above chapter.



Fig.17 Wave formation around box of wedge

5.2 Equivalent Shallow Water Depth

The governing equation for linear dispersive waves is Laplace equation, that is,

$$\phi_{xx} + \phi_{yy} + \phi_{zz} = 0 \quad (3)$$

Linear dispersive waves have been explained by solving this equation under boundary conditions. In consequence, the solution is fundamentally linear. On the other hand, the governing equation for nonlinear shallow water waves and shock waves in compressible fluid is nonlinear partial differential equation, that is,

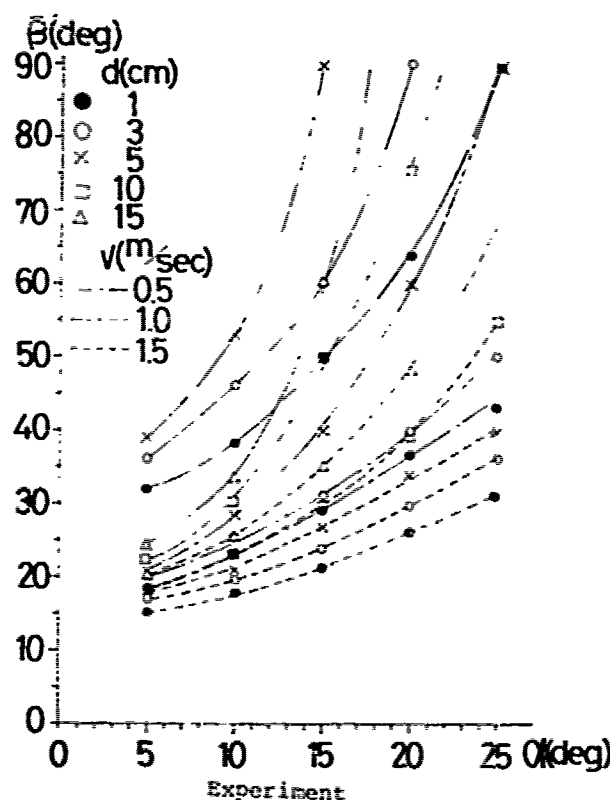
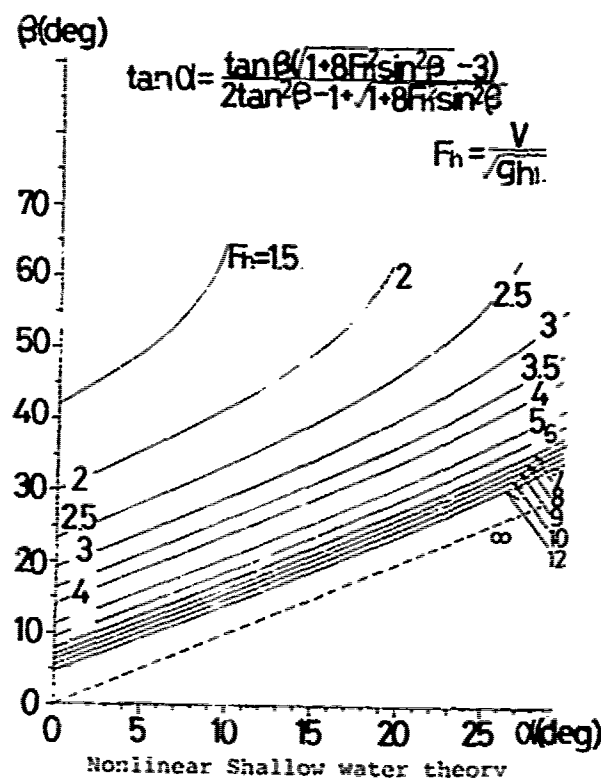


Fig.12 Relation between entrance angle and shock angle



$$(1 - \frac{u^2}{c^2}) \phi_{xx} - 2 \frac{uv}{c^2} \phi_{xy} + (1 - \frac{v^2}{c^2}) \phi_{yy} = 0 \quad (4)$$

Occurrence of FSSH will be explained by solving nonlinear differential equation as the governing equation.

The fundamental equations for steady fluid flow are the followings.

$$u_x + v_y + w_z = 0 \quad (5)$$

$$uu_x + vv_y + ww_z = -\frac{1}{\rho} p_x \quad (6)$$

$$uv_x + vv_y + ww_z = -\frac{1}{\rho} p_y \quad (7)$$

$$uw_x + vw_y + ww_z = -\frac{1}{\rho} p_z - g \quad (8)$$

Equations (6), (7) and (8) are nonlinear. Equation (4) is derived from the above four equations with some postulations, and it still remains nonlinear. The only nonlinear equation in the usual treatment of ship wave problem has been the exact free surface condition.

$$u^2 \phi_{xx} + v^2 \phi_{yy} + w^2 \phi_{zz} + 2(uv \phi_{xy} + vw \phi_{yz} + wu \phi_{zx}) = -g \quad (9)$$

This equation is derived from Euler's equations (6) (7) (8) and free surface condition as follows.

$$(6) \times u + (7) \times v + (8) \times w$$

$$\begin{aligned} &= u(u \phi_{xx} + v \phi_{xy} + w \phi_{xz}) \\ &+ v(u \phi_{yz} + v \phi_{yy} + w \phi_{yz}) \\ &+ w(u \phi_{zx} + v \phi_{zy} + w \phi_{zz}) \\ &= -\frac{1}{\rho} (u p_x + v p_y + w p_z) - g w \end{aligned} \quad (10)$$

The free surface condition is,

$$dP/dt = 0 \quad \text{on } z = \zeta \quad (11)$$

that is,

$$u p_x + v p_y + w p_z = 0 \quad (12)$$

(10) and (12) lead to equation (9), which implies that the nonlinearity of the free surface condition is, as a matter of course, originated from the Euler's equation and that linearization of the problem is not always permitted for water waves. Equations from (5) to (8) are the basis and the problem is essentially nonlinear. The occurrence of FSSH is not surprising.

Supposed approaches to the theoretical interpretation are to calculate equations (5) to (8) numerically or to develop simple governing equation with bold postulations, the latter of which was first attempted by Takekuma [12], though not satisfactory. In this chapter one of the latter approaches is pursued, which is encouraged by the analogous characteristics of FSSH to nonlinear shallow water waves.

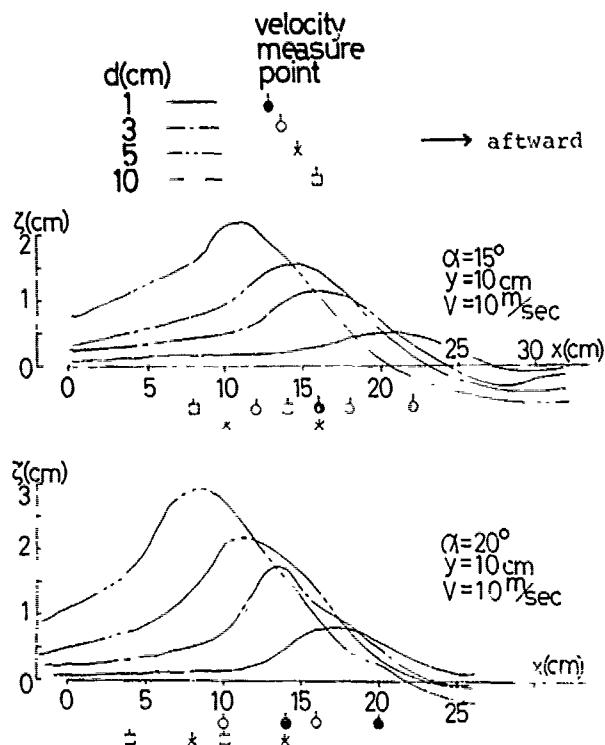


Fig.19 Longitudinal wave profile around wedge

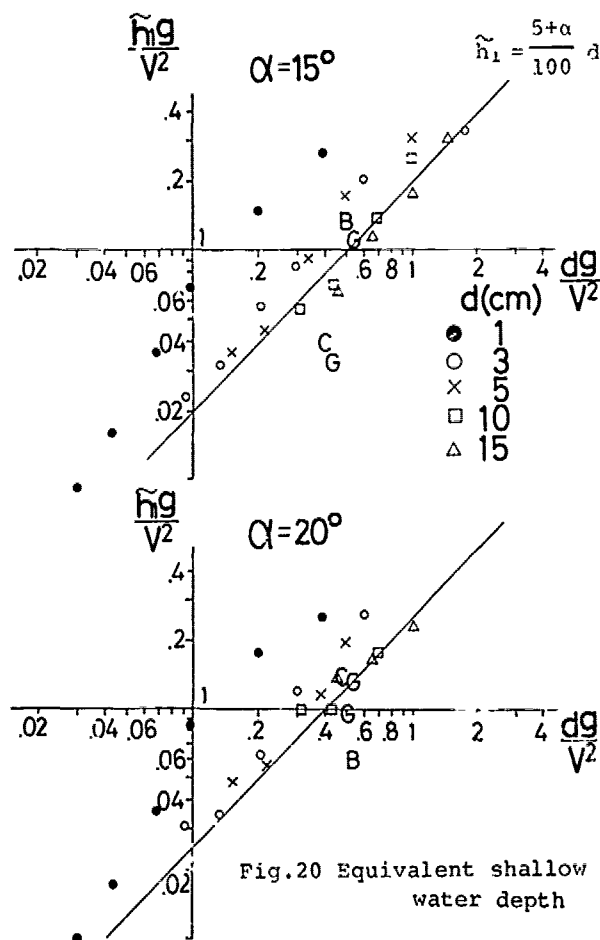


Fig.20 Equivalent shallow water depth

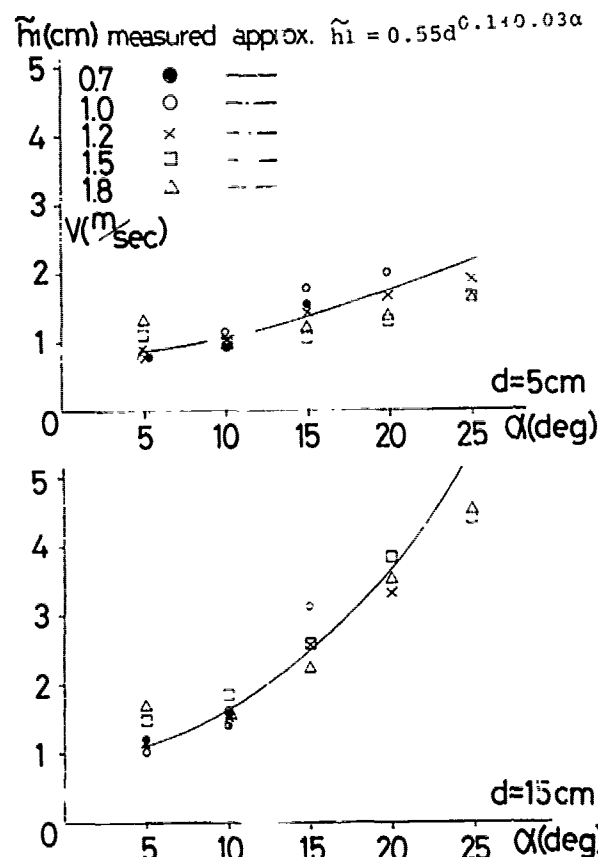


Fig.21 Relation between draft of model and equivalent shallow water depth

The change of the shock angle of FSSW is very similar to that of shock waves in shallow water as is shown in Fig.18. When one introduce the new concept of equivalent shallow water depth, the change of shock angle of FSSW can be explained by the formulation for shallow water shock waves. The critical speed for shallow water shock waves is $\sqrt{gh_1}$ and the shock angle is determined by entrance angle and Fh . For FSSWs the equivalent shallow water depth \tilde{h}_1 is determined so as to let Fig.18 (left) accord with Fig.18 (right). This is really a bold assumption; however, Fig.18 and Figs.9 to 14 support this assumption, in which resemblance between FSSWs and shallow water shock waves is evident. Fig.9 to Fig.14 indicate that the flow with discontinuity is limited in the thin layer adjacent to the free surface. The obtained equivalent shallow water depth approximately accords with the depth of the thin layer.

Calculated equivalent shallow water depth for wedge models are plotted in Fig.20 against draft in non-dimensional form. The relation between draft and equivalent shallow water depth is approximately linear except for extremely shallow-drafted conditions. This fact means that Froude's law of similitude is maintained and the occurrence of FSSWs is ruled by Froude number based on draft. The variation of the equivalent shallow

low water depth is visualized in another form in Fig.21. Equivalent shallow water depth is determined by draft and entrance angle; the absolute value of advance velocity has little to do with this [4].

5.3 Method of Characteristics

When equivalent shallow water depth \tilde{h}_1 is introduced, the problem turns into two-dimensional one and the governing equation is for irrotational motion,

$$(1 - \frac{\phi_x^2}{g\tilde{h}_1})\phi_{xx} - 2\phi_{xy} \frac{\phi_x \phi_y}{g\tilde{h}_1} + (1 - \frac{\phi_y^2}{g\tilde{h}_1})\phi_{yy} = 0 \quad (13)$$

This type of nonlinear equation has long been treated in the fields of high-speed aerodynamics [10], and there are some methods to solve it. In this section, an attempt to apply the method of characteristics is briefly discussed for the estimation of the curves of discontinuity, i.e., the pattern of the occurrence of FSSWs. Characteristic curves on physical plane and hodograph plane are in supercritical speed ($u^2 + v^2 > c^2$), respectively,

$$\frac{dy}{dx} = \frac{-\frac{uv}{c^2} \pm \sqrt{(u^2 + v^2)/c^2 - 1}}{1 - u^2/c^2} \quad (14)$$

$$\frac{dv}{du} = \frac{\frac{uv}{c^2} \pm \sqrt{(u^2 + v^2)/c^2 - 1}}{1 - v^2/c^2} \quad (15)$$

$$\text{where } c = \sqrt{g\tilde{h}_1}$$

On hodograph plane, shock polar can be drawn according to (15), and the obtained line of characteristics settle that on physical plane because they are represented by (14) and (15) are normal each other.

This method of characteristics is applied to an usual hull form whose hull form is assumed to be represented by the waterline. And besides, the water line is modified into succession of straight short lines for simplicity. An example for a fine hull form M34 is shown in Fig.22 at various velocity of advance. Although the calculated results do not quantitatively agree with the experimental curves, the qualitative agreement is good. These results imply that this method can be useful for hull form design, because qualitatively exact estimation of resistance can improve hull form by itself. The relation between shock angle and strength of discontinuity is rather simple as is shown in Fig.19. The reduction of shock angle will naturally lead to reduction of resistance due to FSSW.

The explanation described in this chapter is based upon irrotationality, which seems to be contradictory with the physical fact of the existence of discontinuity, because the flow with discontinuity is rotational. However, the rotational flow is simply a consequence of the occurrence of

Calculated	Measured	F_n	$L(m)$	$B(m)$	$d(m)$	L/B	C_s
---	---	25	2001	0.308	0.111	65	0.392
---	---	2887					
---	---	3333					
---	---	3780					

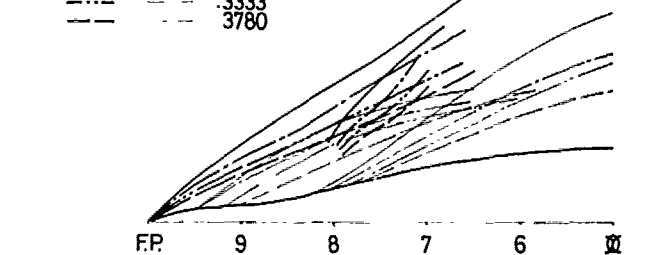


Fig.22 Shock front lines of M34 by the method of characteristics

FSSW. The interpretations in this chapter will hold true at the present stage of the cultivation of the new problem.

6. RESISTANCE COMPONENT DUE TO FREE SURFACE SHOCK WAVES

6.1 Momentum Loss Measured far behind Ships

Measurement of momentum loss far behind ships has been carried out for various ship models in 1978 and 1979 [2][5]. Two examples of contours of momentum loss are present in Fig.23 for WM2 at the draft of 200mm and 60mm. The area where momentum loss appears stretches widely in the vicinity of the free surface. This kind of momentum loss will be attributed to the velocity drop by FSSW through the relation described in equation (2). FSSW produce lines of discontinuity and, consequently momentum loss behind them. To the first order approximation the resistance due to FSSW is considered to be measured in this form instead of wave pattern resistance.

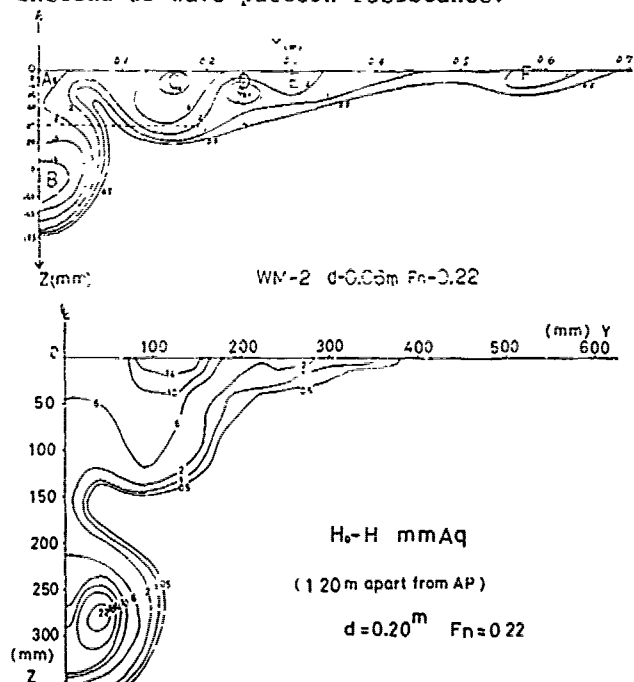


Fig.23 Contours of momentum loss of WM2

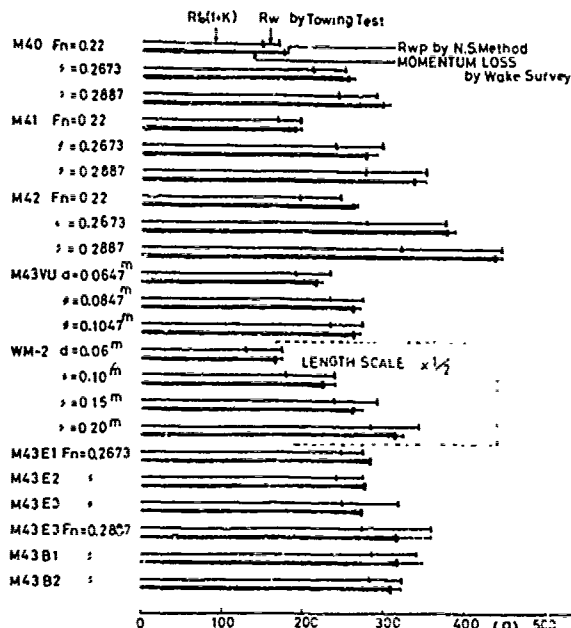


Fig. 24 Resistance components

6.2 Hull Particulars and Free Surface Shock Wave

The sum of viscous resistance and resistance due to FSSW can be approximately evaluated by the integration of the contours. Measurement of momentum loss is carried out on 11 model ships, and the result is summarized in Fig. 24. The towing force nearly agrees with the sum of momentum loss and wave pattern resistance, then,

$$R_w + R_v \approx R_m + R_{wp} \quad (16)$$

$$R_m - R_v \approx R_w - R_{wp} \quad (17)$$

Suppose that the momentum loss subtracted by the viscous resistance is the resistance due to FSSW, the difference between wave resistance and wave pattern resistance is the first approximation of the resistance due to FSSW. The amount of $R_m - R_v$ or $R_w - R_{wp}$ is commonly great in Fig. 24, though one has to take into account that the value of wave pattern resistance measured on models whose length is 2 or 2.4m is usually a little smaller than that on larger models.

Wave resistance obtained from towing test can be assumed to be composed of two components. They are linear wave resistance (R_{wp}) and resistance due to FSSW ($R_w - R_{wp}$). Strictly speaking, this separation of resistance is not exact because of complex interactions; for example, longitudinal wave recoupled for R_{wp} sometimes include steep wave height by FSSW. However, R_{wp} is considered to be the linear wave resistance which have already been experienced the effect of FSSWs in the near-field, and therefore, $R_w - R_{wp}$ is approximately the sum of resistance due to FSSWs

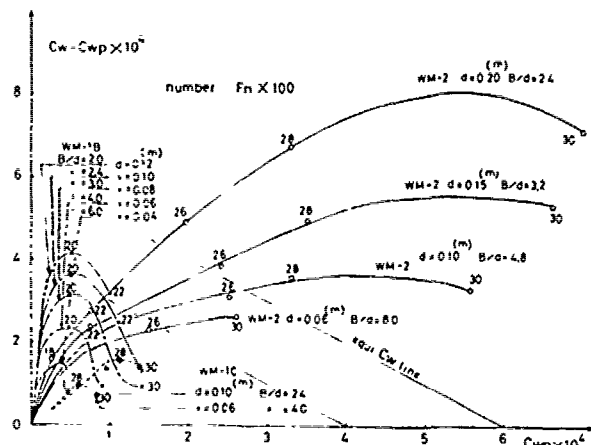


Fig. 25 Components of wave resistance (A)

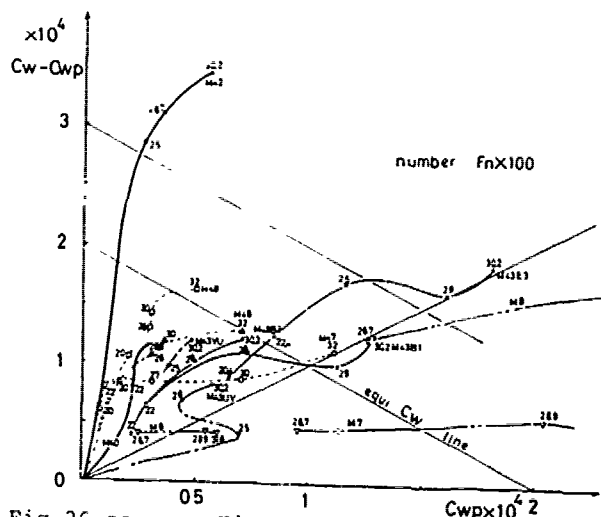


Fig. 26 same as Fig. 25 (B)

and resistance due to interactions between the two wave systems. This separation of resistance is very convenient for the recognition which component of wave resistance is significant among the inviscid resistance. Some examples are shown in Fig. 25 for simple wall-sided models and in Fig. 26 for practical ship models and inboards. $R_w - R_{wp}$ (nondimensionalized as $C_w - C_{wp}$ in the figures) plays a significant role in wave resistance of ships whose length-beam ratio is greater than 6.5. The effect of sectional area curve is visualized by the three dotted curves for three model ships whose particulars are same with M40 in Fig. 26. Length-beam ratio and beam-draft ratio, as one imagines, determines the trajectory at the first step. In most cases $R_w - R_{wp}$ tends to be small over a certain Froude number and has only single hump.

These figures can be the guidelines for hull form designers. Ships whose $C_w - C_{wp}$ is greater than C_{wp} must be designed with careful examination on the occurrence and strength of FSSWs. Generally speaking, practical hull forms whose L/B is less than 6.5 receive remarkable resistance by FSSW. Hull form design without consideration on FSSW will not be reliable for these ships.

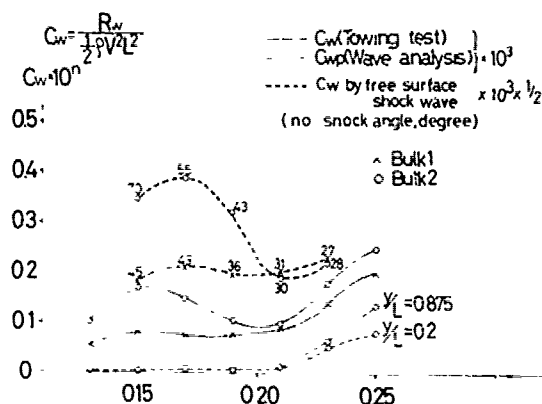


Fig. 27 Wave resistance curves of bulk carriers on ballast condition

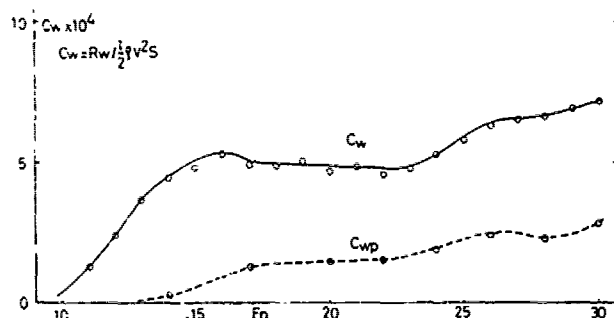


Fig. 28 Wave resistance curves of a container SR138X1 on trial conditions

6.3 Resistance Hump by Free Surface Shock Wave

Ship models on shallow drafted condition present a significant hump in C_w curve in low Froude number region. An example of two models of bulk carrier on ballast condition is shown in Fig. 27. A slight modification of the hull form at the bow give rise to great difference in the resistance humps around $Fn = 0.15$, while the measured wave pattern resistance do not have any difference; or rather, C_{wp} itself is negligible in the velocity range of $Fn < 0.20$. A case of a large container model on trial condition is shown in Fig. 28. C_{wp} is very small around $Fn = 0.15$ whereas C_w has a hump there.

These humps at low Froude number are commonly recognized for shallow-drafted ships, especially those with bulbous bow, and they make the definition of form factor very difficult. These humps could not have been reasonably explained. The wave pattern at the bow of the container model in Fig. 28 is shown in Fig. 29. Occurrence of FSSWs is obviously observed. The shock angle is maximum around $Fn = 0.13$ or 0.15 and it turns to be small with the increase of velocity. Greatness of shock angle means greatness of resistance due to FSSW as has already been described, which can qualitatively explain the hump at $Fn = 0.15$. The theory for shallow water shock waves which has been utilized in chapter 5 by introducing equivalent shallow water depth can roughly es-

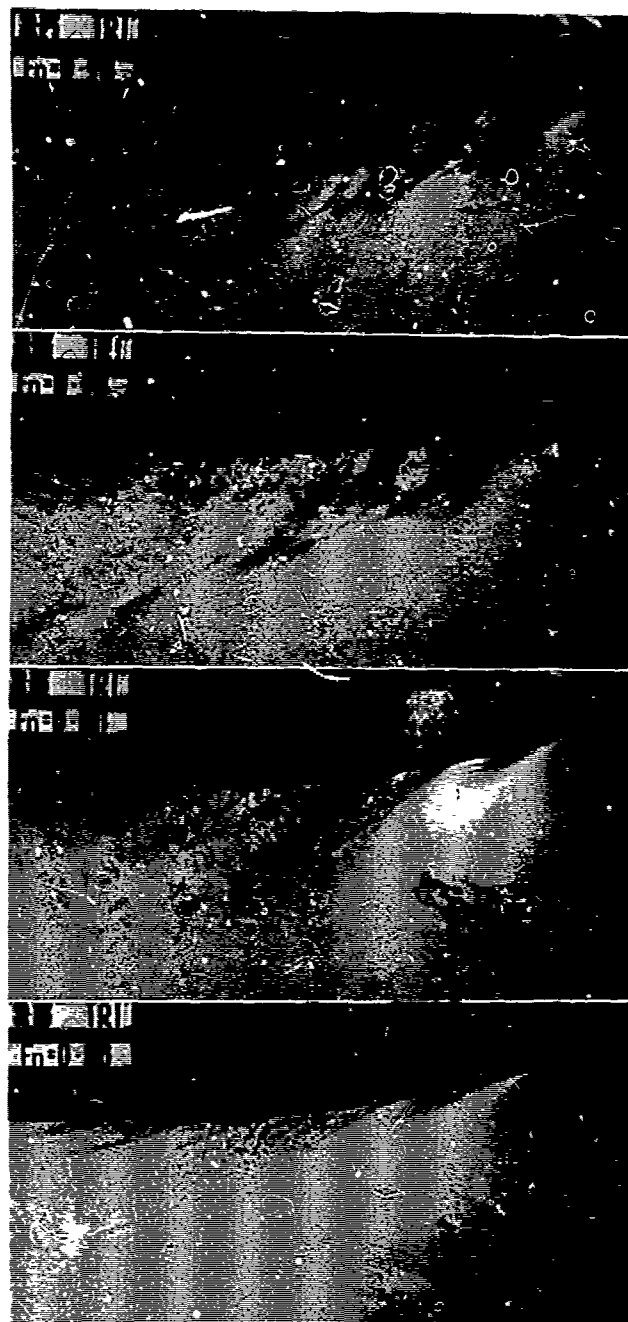


Fig. 29 Wave pattern pictures of SR138 on trial condition

timate the resistance due to FSSW. Calculated resistance due to the second free surface shock wave is shown by dotted curves for two bulk carriers in Fig. 27. The qualitative agreement of the theory with the experimental results is, again, excellent. One can conclude that the hump that is often observed in low Froude number is due to FSSW. With the decrease of draft the critical speed $\sqrt{gh_1}$ becomes small, which is shown in Fig. 21 as the dependence of h_1 on d or in Fig. 20 as relations between draft and equivalent shallow water depth, and, in con-

sequence, the hump in C_w curve where shock angle is great is shifted to the low speed range where C_{wp} is negligibly small, because a hump by FSSW is usually present around the critical speed. For shallow drafted low- and middle-speed ships, consideration on FSSW is decisively important.

7. EFFECT OF FREE SURFACE SHOCK WAVES ON LINEAR DISPERSIVE WAVES

7.1 Phase Shift

FSSWs coexist with linear dispersive waves around ships in translational motion. The problem of wave resistance comes to be complex, and it seems to be impossible to develop a comprehensive theory that explains the two wave systems simultaneously. There are two possible ways to be urgently pursued. The first is to evaluate the wave resistance due to linear dispersive wave system which has been influenced by the nonlinear flow caused by FSSWs in the near-field of ships. The second is to estimate the resistance due to FSSWs themselves. What is described in chapter 5 belongs to the latter way, and problems concerned with the former way are described in this chapter. In case both ways are successfully achieved, wave resistance can be estimated by summing the two results.

The phase of linear dispersive wave system is commonly shifted forward. An example on beam-length series ships is present in Fig.30. With the increase of beam-length the amount of forward phase shift becomes large. FSSWs, especially those at the bow, become intense with the enlargement of beam-length; the shock angle increases and discontinuity in wave height and disturbance velocity is strengthened. On sectional area series ship models whose particulars are the same with M40, the intensity of FSSWs at the bow and forward phase shift have intimate connection, though the result is abbreviated. FSSWs accompany lateral displacement velocity as is shown in Figs.9, 11, 12 and 13. It has an influence on the dispersive wave system to shift forward and sideways.

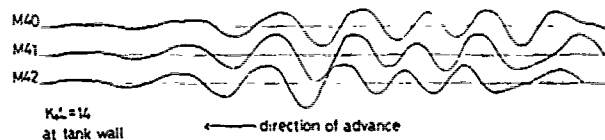


Fig.30 Comparison of longitudinal wave profile of beam-length series ships

7.2 Attenuation Effect

Longitudinal wave profiles of the wide-beamed fine ship M42 are shown in Fig.31 at various velocity of advance. One will notice that the rear parts of the wave records are extremely low, which implies attenuation of transverse waves. This attenuation cannot be understood as an effect of cancellation between the two linear wave systems generated

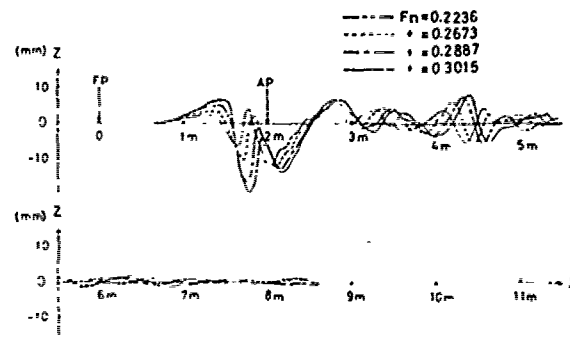


Fig.31 Longitudinal wave profiles of M42 ($\gamma/L = 0.2$)

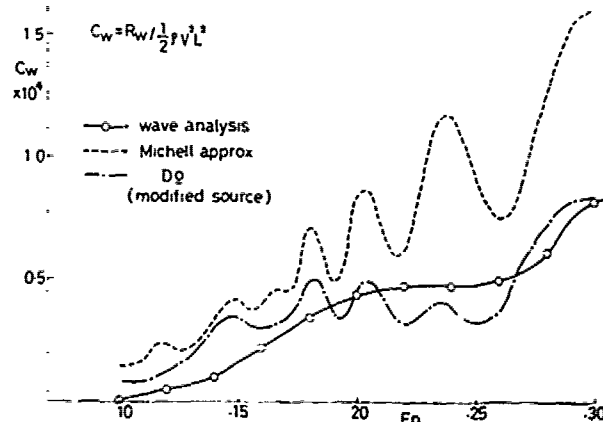


Fig.32 Wave pattern resistance curves of WML-C

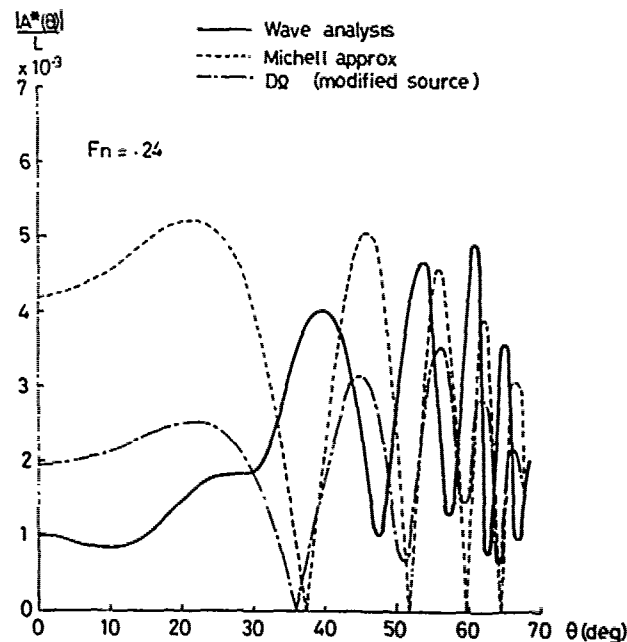


Fig.33 Comparison of wave spectra of WML-C

at the bow and the stern, because it does not depend on velocity of advance. This phenomena is also considered as an effect of the

existence of FSSW by the two reasons. They are that the attenuation becomes conspicuous in case FSSW is intense and that FSSW accompanies a kind of wide wake region as a result of the presence of discontinuity in velocity.

One of the great discrepancies between linear wave resistance theory and experiment consists in the humps and hollows in resistance curve. Linear theories show remarkable humps and hollows as an effect of cancellation and amplification of waves, whereas they can be scarcely observed in measured resistance curves in low and middle range of advance velocity except for very fine ship models. A typical example is shown in Fig.32. This qualitative discrepancy should have been very significant for the assessment of the validity of theories.

A simple calculation is carried out for WML to demonstrate that FSSW attenuate linear waves with the wake region behind the line of discontinuity. The wake region is represented by a rigid body whose depth is 20mm which stretches laterally along the line of discontinuity to a certain point and continues to infinity extending parallel to the centerline of the ship. Calculation is made by Michell's approximation for simplicity. The results are shown in Fig.32 for wave resistance curve and in Fig.33 for wave spectrum. Wave resistance by linear waves should accord with measured wave pattern resistance and this is approximately accomplished by this calculation. Fig.33 shows that the gap between theory and experiment is remarkable in the transverse wave system and that it is considerably remedied by taking the effect of FSSW into consideration.

8. FREE SURFACE SHOCK WAVES AT THE STERN

8.1 Occurrence of Free Surface Shock Waves at the Stern

It is naturally understood that FSSWs appear at any points in the near-field in various fashion. It is not limited in the bow-near-field. Especially FSSWs are clearly observed at the stern on high-speed fine ships. The passenger boat in Fig.1 generates intense FSSWs at the stern being accompanied with breaking of waves. Abrupt change in velocity and wave height have been measured and it has been verified that this kind of waves have the same characteristics as those of FSSWs at the bow [3]. Transverse wave profiles are shown in Fig.34 for a container ship model. A line of discontinuity can be recognized.

8.2 Development of Stern-End-Bulb

FSSWs at the stern look dominant in the wave pattern pictures of full-scale high-speed passenger boats, destroyers and container carriers. To reduce FSSWs at the stern and, simultaneously, linear waves from the stern, a new type of bulb is developed by the author and colleagues through extensive experimental

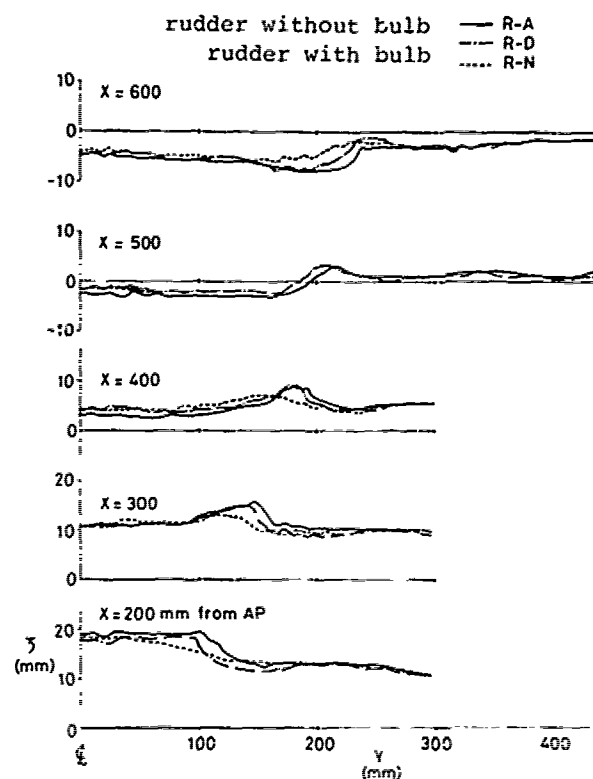


Fig.34 Transverse wave profile at the stern of SR138 on full condition

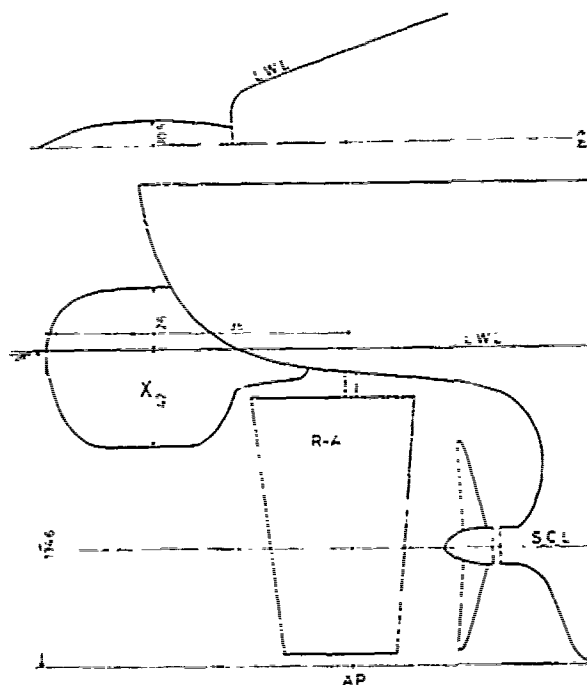


Fig.35 Configuration of stern-end-bulb for SR138

investigations [6], [7]. This bulb is named stern-end-bulb (abbreviated as SEB). This bulb is rather small in comparison with the bow-bulbs and equipped at the rear end of the waterline of ships. Stern-end-bulb is care-

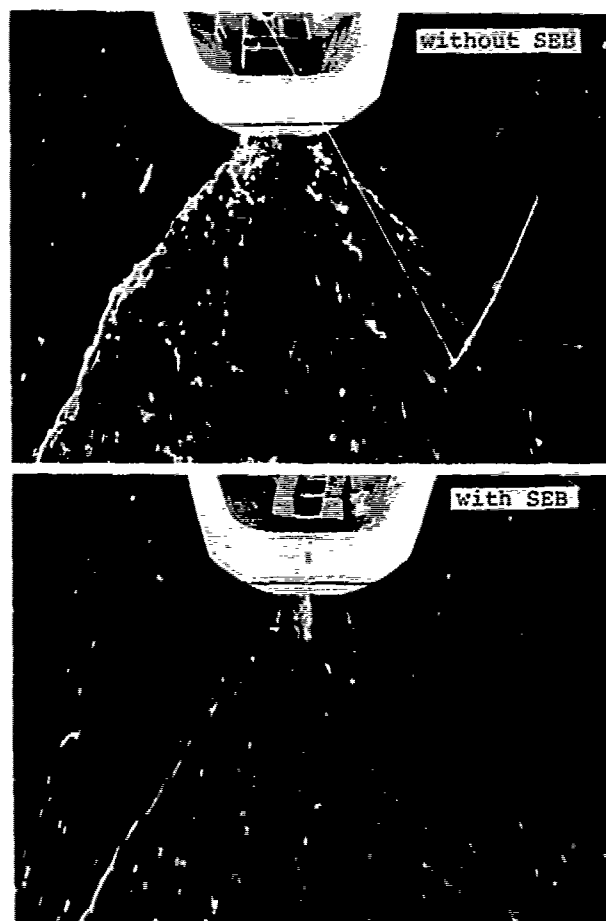


Fig.36 Comparison of stern wave pictures of SR138 and SR138X (10-m model)

fully designed so that it reduces wave resistance and minimizes increment of viscous resistance. One of the configurations of SEB for a container carrier is present in Fig.35.

The original form of SEB was a modified rudder called R-V which was a rudder with a bulb similar to SEB-X in Fig.35. SEB-X was connected to the hanging rudder R-A instead of the hull and the modified rudder is called R-N. The effect of R-V on waves is shown in Fig.34. The discontinuity in wave height is weakened by R-V, which means that it reduces FSSWs at the stern. The effect of SEB-X in Fig.35 is visualized in Fig.36. Wave resistance curves are shown in Fig.37 which are results of volume series experiments for the investigation on the optimum size of SEB. The decrease of C_w qualitatively accords with that of C_{wp} . However, the rate of decrease of C_w cannot be fully explained by that of C_{wp} . SEB reduced C_{wp} and $C_w - C_{wp}$ simultaneously, in other words, SEB is very effective for the reduction of both linear wave resistance and resistance due to FSSW at the stern. This interpretation is also true for bulbous bow. Bulbs generally contribute to reduction of two components of wave resistance [5]. Fig.27 shows an effect of bulbous bow of bulk carrier as an extreme case, in which the effect of the variation of the form

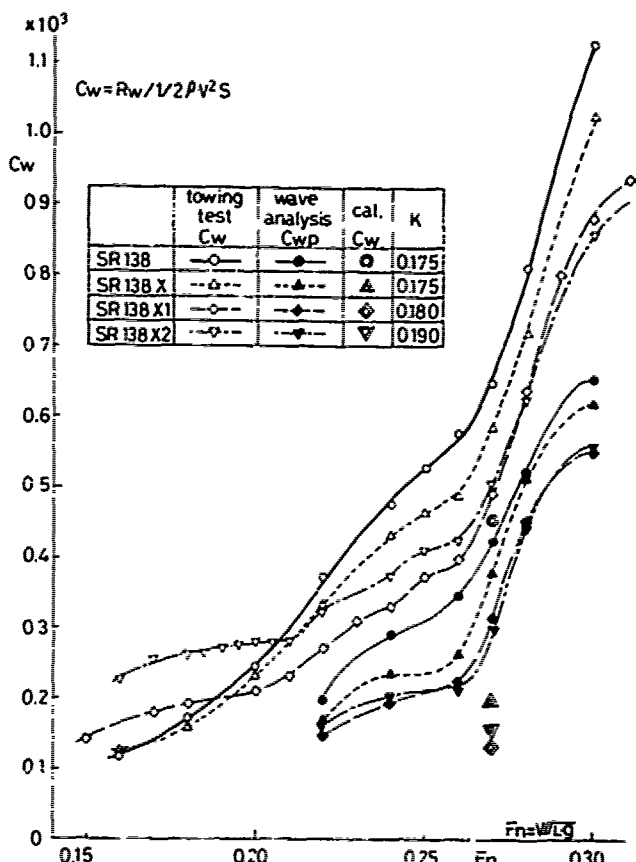


Fig.37 Resistance reduction by stern-end-bulb

of bulb on wave resistance can be recognized only in $C_w - C_{wp}$, i.e., resistance due to FSSW, in the low speed range.

The reduction of wave resistance by the stern-end-bulb (SEB) reaches up to 2.5 percent which leads to saving of propelling power of 6 percent for container carriers. The effectiveness of SEB have been verified on several high-speed ship models [7], and it is going to be put to practical use at Japanese shipyards.

9. NONLINEAR WAVES IN WIDE RANGE OF ADVANCE VELOCITY

9.1 Wave Pattern Picture

Examination of wave making properties in wide range of advance velocity will be useful for comprehensive understanding. Wave pattern pictures of two models are shown in Fig.38 and 39. The entrance angle of WM4-A is about 20 degree and the fore-end of the rudder is round, and therefore, FSSWs around the models are evidently observed. The free surface phenomena of a floating body in translational motion seems ultimately complex. Linear and nonlinear waves coexist and the nonlinear waves generate unsteady turbulent flow on the free surface.

9.2 Longitudinal Wave Profile

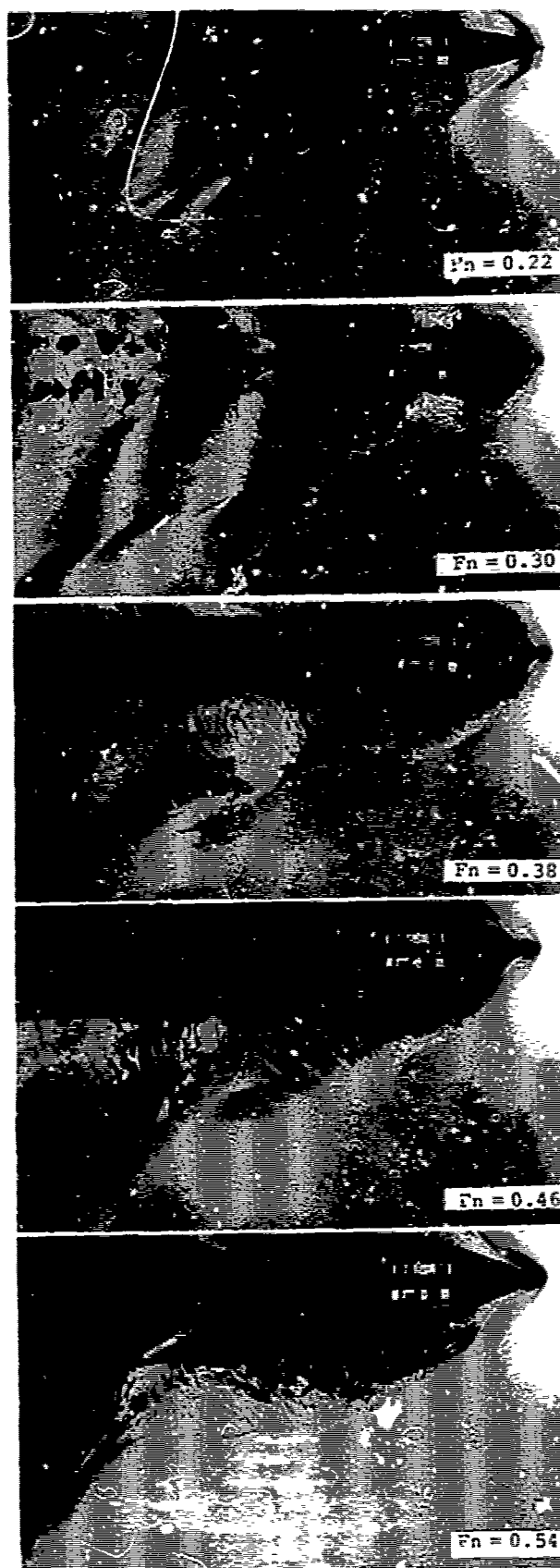


Fig.38 Wave pattern pictures of WM4-A

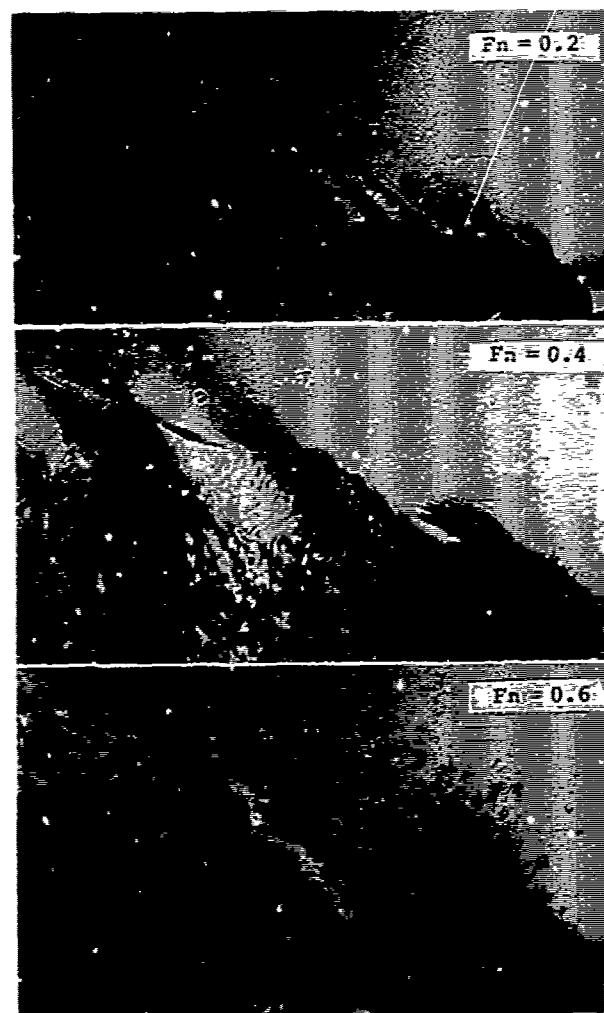


Fig.39 Wave pattern pictures of rudder model

A linear theory and experimental fact are compared in longitudinal wave profiles in Fig.40. The discrepancy between theory and experiment depends on Froude number. The calculated result by 'Michell's approximation accords fairly well in $Fn > 0.50$ except for the first wave crest (i.e. FSSW at the bow), while disagreement is remarkable in low Froude number region. This tendency coincides with the discrepancies in wave resistance curves, which is commonly recognized. The effect of FSSWs on linear waves is very significant in low and middle range of velocity, whereas it is not in high range of velocity. The discontinuity and its influence on free surface flow seem dominant in the pictures, however, the nonlinear flow is limited in the thin layer whose thickness is independent of advance velocity, while the wave length of the linear wave system is elongated and its motion scales up with the increase of velocity. In consequence, most part of wave height can be explained by a linear theory in the high Froude number region.

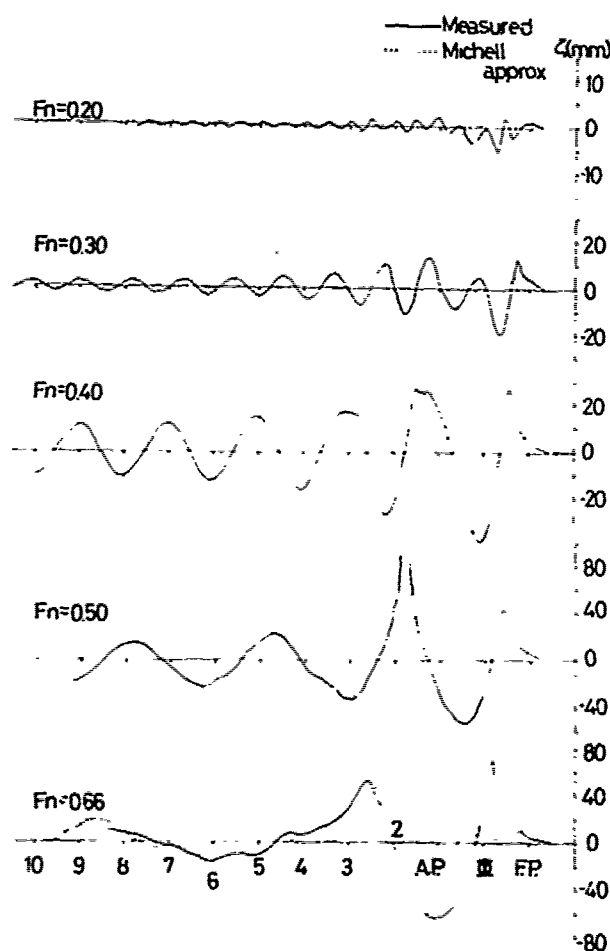


Fig.40 Longitudinal wave profile of WM4-A

ACKNOWLEDGEMENT

The author owes much gratitude to Professors T. Inui and H. Kajitani who dispensed generously advise and encouragement. This research has been supported by able technical staffs and graduate students at The Experimental Tank of The University of Tokyo. The author would express a lot of thanks to Mr. Y. Tsuchiya, Mr. M. Kanai, Mr. M. Takahashi, Mr. N. Kawamura, Mr. M. Tsuruoka and Mr. A. Suzuki.

REFERENCES

1. Inui, T., Kajitani, H., Miyata, H.: Experimental Investigations on the Wave Making in the Near-Field of Ships, J. of the Kansai Soc. of Naval Arch., Japan, Vol.173, (1979)
2. Inui, T., Kajitani, H., Miyata, H., Tsuruoka, M., Suzuki, A., Ushio, T.: Non-linear Properties of Wave Making Resistance of Wide-beam Ships, J. of the Soc. of Naval Arch. of Japan, Vol. 146, (1979)

3. Miyata, H., Inui, T., Kajitani, H.: Free Surface Shock Waves around Ships and Their Effects on Ship Resistance, J. of the Soc. of Naval Arch. of Japan, Vol 147, (1980)
4. Takahashi, M., Miyata, H., Kajitani, H., Kanai, M.: Characteristics of Free Surface Shock Waves around Wedge Models, to be presented to the autumn meeting of the Soc. of Naval Arch. of Japan, (1980)
5. Kawamura, N., Kajitani, H., Miyata, H., Tsuchiya, T.: Experimental Investigation on the Resistance Component Due to Free Surface Shock Waves on Series Ships, to be presented to the autumn meeting of the Kansai Soc. of Naval Arch., Japan, (1980)
6. Inui, T., Miyata, H.: On the Optimization of Overall Performance of Rudders (Second Report), J. of the Soc. of Naval Arch. of Japan, Vol. 145, (1979)
7. Miyata, H., Tsuchiya, Y., Inui, T., Kajitani, H.: Resistance Reduction by Stern-End-Bulb, to be presented to the autumn meeting of the Soc. of Naval Arch. of Japan, (1980)
8. Gadd, G.: Wave Theory Applied to Practical Hull Forms, Proc. of the International Seminar on Wave Resistance, Japan, (1976)
9. Preiswerk, F.: Anwendung Gasdynamischer Methoden auf Wasserströmung mit Freier Oberfläche, Mitt. Inst. Aerodynamik, Eidgen. Techn. Hochsch., Zürich, No.7, (1938)
10. Courant, R., Friedrichs, K.: Supersonic Flow and Shock Waves, Interscience Publications, (1948)
11. Baba, E.: A New Component of Viscous Resistance of Ships, J. of the Soc. of Naval Arch. of Japan, Vol.125, (1969)
12. Takekuma, K.: Study on the Non-Linear Free Surface Problem Around Bow, J. of the Soc. of Naval Arch. of Japan, Vol.132, (1972)
13. Wehausen, J. V., and Laitone, E. V.: Surface Waves, Handbuch der Physik, Vol.9, Springer-Verlag, Berlin, (1960)

Discussion

E. Baba (M:II)

I have enjoyed reading this paper and am impressed with the vast extent of the investigation of the free-surface phenomenon around ship models.

The author introduced a concept of equivalent shallow-water depth and tried to interpret the free-surface phenomenon observed around ship models by use of a two-dimensional partial differential equation (13).

In the derivation of this equation one should assume that change of velocity components u and v in the direction of water depth is small enough to be negligible.

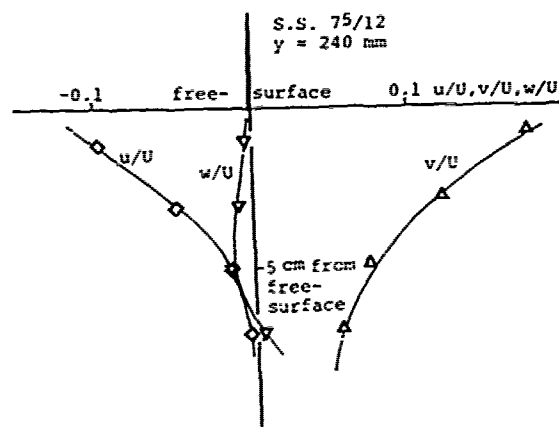


Fig. A Change of u/U and v/U in the direction of water depth at $y = 240$ mm

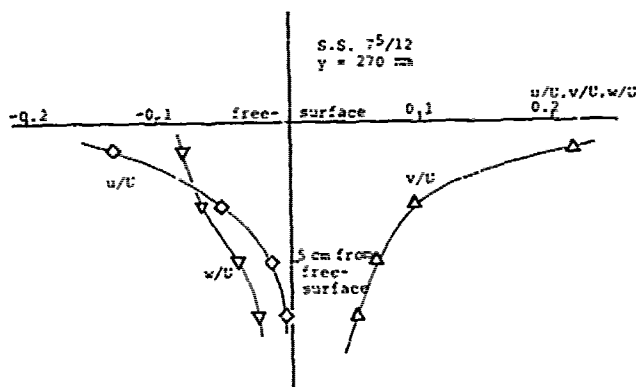


Fig. B Change of u/U and v/U in the direction of water depth at $y = 270$ mm

Figs. A and B are prepared from Fig. 13 and 14 of the author's paper. It is observed that the change of u/U and v/U in the direction of water depth is quite large in the vicinity of the free-surface. In 1972 Takekuma (Reference 12 of the present paper) already observed this phenomenon.

From these observations of the flow phenomenon near the free-surface, one wonders whether the partial differential equation such as (13) can be exploited as a governing equation for such flow phenomenon.

The author's view on this matter is very much appreciated.

H. Maruo (Yokohama N Univ.)

In this paper, the author has analysed the phenomenon of breaking of the free surface near the ship hull, assuming an analogy with the shock wave in compressible fluid or hydraulic jump in shallow water-flow. I cannot help regarding that this treatment is due to nothing but the author's misunderstanding of the true phenomena. The shock wave is an attribute of the motion in non-dispersive media, while the surface wave in deep water is a phenomenon in a dispersive media. Therefore no analogy exists between the shock wave and the surface wave around a ship hull, when the water is not restricted.

R.K.-C. Che (JAYCOR)

The various properties of free-surface shock waves (FSSW) as described by Professor Miyata are very interesting, especially in consideration of their impact on future directions of research of wave resistance. The analogy of FSSW to shallow water waves suggests strongly that conditions satisfied by shallow-water-wave theory must be present in the near field of the ship-wave system also. One fundamental feature of shallow-water waves is that the pressure distribution is essentially hydrostatic, i.e.,

$$p = \rho g(\eta - z), \quad (1)$$

where η is free-surface elevation and $z = 0$ defines the undisturbed water surface. Much insight would be gained if one could measure the pressure distribution in the free-surface layer and determine in which region and to what extent Eq. (1) is satisfied by the flow. One suggestion is to define the parameter ξ as

$$\xi = p - \rho g(\eta - z) \quad (2)$$

and plot the distribution of ξ on cross-sectional planes along the length of ship. If the flow field is not of the shallow-water type, ξ would be quite different from zero. For example, in two-dimensional deep-water waves,

$$\xi = p - \rho g(\eta - z) = \rho g a \cos(kx - ct) \frac{\cosh k(z+d)}{\cosh kd} - 1 \quad \dots (3)$$

which shows strong variation of ξ with depth, unless $kd \rightarrow 0$.

By plotting ξ , Professor Miyata may be able to actually measure the "equivalent shallow-water depth" h ; to further validate his theory. The instrumentation for measuring p and z simultaneously, however, may be quite involved. I would like Professor Miyata to think about this idea and comment on the feasibility of such measurements.

Y. Shimomura (Sumitomo Heavy Ind.)

The author describes the effectiveness of a stern-end bulb to reduce the free-surface shock waves (FSSWs) which have entirely different characteristics from those of linear dispersive waves.

The theoretical studies about attenuation of linear waves by a bulb have been studied by Prof. Inui and other researchers. However, I doubt that the interference of waves, which is the fundamental physics of reducing linear waves by a bulb, can directly lead us to a sound explanation of the effectiveness of a bulb in reducing the FSSWs. The theoretical background for a bulb's reducing the FSSWs is not clear in this paper. I would like to ask the author's views concerning the physical phenomena behind the fact that a bulb can attenuate not only linear waves but also the FSSWs.

And I also would like to receive some of the author's suggestions about the design of a bulb which would reduce the FSSWs.

Author's Reply

H. Miyata (Univ. of Tokyo)

To Dr. Baba

Nonlinearity plays a decisive role in the thin layer near the free surface and it does not in the deeper region. The motion of water is quite different between the two region. This will give rise to a steep change of velocity in the depthwise direction, because the water flow must be continuous.

The concept of equivalent shallow water depth was introduced mainly for the purpose of practical use. This concept can be helpful for the improvement of hull form as is exemplified with the method of characteristics. Notwithstanding the bold assumption, the application of nonlinear shallow water theory is successful to a certain degree.

Therefore, equation (3) is not a general governing equation but a simplified equation which can be utilized for practical purposes. The general governing equation will be Navier-Stokes equation, which can be numerically solved with boundary conditions. Further continuous efforts should be devoted.

To Prof. Maruo

I think the analogy is evident in the experimental results.

On the problem of introducing nonlinear shallow water theory, please see my response to Dr. Baba's discussion.

I hope that Professor Maruo will change his opinion by reading our succeeding papers.

To Dr. Chan

Thank you for your kind suggestion.

The characteristics of free surface shock waves in deep water are analogous to those of shallow water shock waves to a certain degree. However, there may be differences between the two non-dispersive nonlinear waves, which will be clarified by further detailed studies including Dr. R. Chan's proposal.

To Mr. Shimomura

Bulbs have two aspects of wave resistance reduction. Bulbs at the bow and stern-end reduce both linear wave resistance and resistance due to FSSWs. These facts are clarified in two papers in the reference ([5] and [7]). About half of the effect of SEB can be measured by usual method of wave analysis, and at the same time, the nonlinear wave system is reduced by SEB as is shown with pictures. Bow bulbs usually reduce shock angle and this leads to reduction of resistance due to FSSWs. Further detailed studies on the design method and its basis are now under way.

The design of SEB is now carried out making use of linear wave making theory based on the formulation of Neumann-Kelvin problem. However, the effectiveness of the application of this theory is limited. Towing tests are necessary. By the SEB, which was first imagined by Professor Inui and developed by the author and his colleagues, it is shown that theory is not almighty.

Flow Past Oscillating Bodies at Resonant Frequency

Gedeon Dagan and Touvia Miloh
Tel-Aviv University
Israel

ABSTRACT

This paper analyses the flow field about an oscillating body which moves with a constant velocity U near and parallel to a free surface.

Special attention is paid to frequencies of oscillation in the neighbourhood of the critical frequency $\omega_c = 0.25U/g$. It is well known that the classical linearized solution for this problem yields infinitely large wave amplitudes at resonant frequency. The singularity in the velocity potential, and hence also in wave amplitude, lift and drag at resonant conditions is found to be the inverse of the square root of $\delta\omega = \omega_c - \omega$ for two-dimensional flow and a somewhat weaker singularity of a logarithmic type in $\delta\omega$ for a three-dimensional flow.

It is demonstrated in the text how this resonance may be removed by considering a relatively simple non-linear case in which the oscillating flow-field is taken to be a small disturbance about the steady non-uniform flow field caused by the body. Even though the analysis presented is general, two representative cases are discussed in greater details: a concentrated two-dimensional vortex and a three-dimensional lifting surface. For both cases, a uniformly valid solution for the velocity potential, the amplitude and phase of the resulting free-waves in the neighbourhood of the resonant frequency is presented. Also computed are finite D.C. components of the drag and lift acting on the hydrofoil.

NOMENCLATURE

All variables are dimensionless with respect to U^2/g , U/g and ρ as length, time and density scales, respectively. U is the translatory velocity of singularities

system, g is acceleration of gravity and ρ is water density. FT and - stand as symbols of Fourier transform.

- $A^{(0)}, A^{(1)}$ - coefficients in the integral equation of the FT of the potential.
- $B^{(0)}$ - nominator in the decomposition of $\tilde{\psi}(q)$
- $c^{(0)}, c^{(1)}$ - nonhomogeneous terms in the free surface condition
- $C^{(0)}, C^{(1)}$ - FT of $c^{(0)}, c^{(1)}$
- D - drag
- h - depth beneath unperturbed free-surface
- i - imaginary unit
- k - variable in Fourier transform plane in two dimensions
- $k_c = 1/4$ - critical k value
- L - lift
- Lo, L_1 - free-surface differential operations
- M_ϕ, M_ψ - strength of doublet (steady and unsteady, respectively)
- p_ϕ, p_ψ - pressure terms
- P_ϕ - strength of pressure point
- t - time
- x - horizontal coordinate on the unperturbed free-surface in the direction of translatory motion.
- y - vertical coordinate positive upward
- z - horizontal coordinate normal to x
- α, β - variables in the Fourier space in three dimensions
- ϵ - common notation for $\Gamma_\phi, M_\phi, P_\phi$
- Γ_ϕ, Γ_ψ - circulation (steady and unsteady respectively)
- $\Gamma_\phi^T, \Gamma_\psi^T$ - total circulation for a lifting line
- ϕ - steady-state perturbation, potential

ϕ	- velocity potential (total)
ϕ_s, ϕ_r	- singular and regular potentials
λ, μ	- variables of Fourier transforms
μ	- artificial viscosity
η, η_0, η_1	- free-surface elevation
ψ	- unsteady potential
ψ_r, ψ_s	- regular and singular parts of unsteady potentials
$\psi_r^{(0)}, \psi_r^{(1)}$	- regular perturbation expansion terms of ψ_r
$\psi_{rg}^{(0)}, \psi_{rg}^{(1)}$	- generalized perturbation expansion terms of ψ_r
$\omega_c = 1/4$	- critical frequency
θ, ϑ	- polar coordinates in the Fourier transform space
$\delta\omega = \omega - \omega_c$	- frequency

1. INTRODUCTION

We consider here the motion of a singularities system in the presence of a free-surface. The motion is a superposition of a uniform translation parallel to the free-surface and an unsteady, oscillatory, component. The singularities system may represent a submerged body, e.g., a hydrofoil (which is the application which motivated the present work), a floating body or a travelling pressure patch.

In the frame of the inviscid theory the problem has been solved in the past in the first-order linear approximation for the unsteady potential and in the zero-order approximation for the steady flow component. The two-dimensional case has been investigated thoroughly in [1], [2], [3] and [4]. The three-dimensional problem has been treated at a lesser extent in [5], [6] and [7]. In both cases it has been found that a travelling singularity generates a system of four waves of different wave numbers. For dimensionless frequencies $\omega = 1/4$, three waves propagate downstream and one propagates upstream, whereas for $\omega < 1/4$ only two downstream waves are present. At the limit $\omega \rightarrow \omega_c$ resonance occurs and the amplitude of two of the free-waves tends to infinity. As a result the forces acting on the singularity system also become unbounded. This resonant effect is attributed to the inability of the wave energy to move away from the singularity and although it was hypothesized that accounting in theory for nonlinear effects may remove the resonance, no attempt has been made so far towards this aim.

Besides the intriguing theoretical problem, the resonant effects may be important in applications in which the body travels in sea waves. Depending on the relative velocity and on the angle of encounter, a wide range of frequency values is possible. In numerical simulations of body motions the resonant frequency is either discarded or it is ignored. Thus, in the review [8], the authors comment: "... $\omega = 1/4$ is a critical situation, for which the strip method does not apply. This does not prevent the numerical naval hydrodynamicists to apply it joyfully no matter what the result."

The aim of the present work is two-fold. First, the flow in the neighbourhood of the resonant frequency is examined in detail and the well-known result for 2D, namely that the amplitude tends to infinity like $(\omega_c - \omega)^{-1/2}$, is recovered. In the 3D case, it is found that the amplitude diverges like $\ln(\omega_c - \omega)$, result which to our best knowledge, was not derived previously.

The main part of the study deals, however, with removing the resonance by theoretical means for a limited but important class of flows. Namely, we consider the case in which the oscillatory motion is a small perturbation of the steady non-uniform flow generated by the singularity system. Thus, in the case of a hydrofoil the amplitude of the oscillations of the angle of attack is supposed to be small compared to the average, steady, angle of attack.

Our main result is that incorporating the first-order approximation of the steady flow component eliminates, after an appropriate uniformization procedure, the resonance effect for lifting surfaces. The amplitude of the otherwise resonant waves is finite at ω near ω_c and of order $\sqrt{\omega_c - \omega}$, instead of $(\omega_c - \omega)^{-1/2}$. Besides, the phase of the waves is changed by $(-\pi/2)$ as compared to that derived by the usual linearized solution and this has an important effect upon the time averaged drag and lift.

Our procedure does not remove the resonance for doublet type or pressure singularities and it seems that the second-order steady potential has to be taken into account in this case. Speculating that such a procedure, which becomes more involved, may succeed, the near resonant amplitude would become of order M_∞/M_∞^2 . Thus the cases of resonance of an oscillating ship or a travelling pressure patch are still open, but we hope the method outlined here is a promising starting point towards their solution too.

2. MATHEMATICAL STATEMENT OF THE PROBLEM

2.1 Definitions and exact equations

The flow is referred to a cartesian system which moves at the constant translatory horizontal velocity of the singularity system. The axes x, z lie in the horizontal plane of the unperturbed free-surface and y points upwards. All variables as defined in the Nomenclature, are made dimensionless with respect to U^2/g and U/g as length and time scales, respectively. The total velocity potential $\phi(x, y, z, t)$ is assumed to be of the form

$$\phi(x, y, z, t) = -x\phi(x, y, z) + \psi(x, y, z)e^{i\omega t} \quad (1)$$

where ϕ is the steady part associated with the uniform motion. The equations satisfied by ϕ are

$$\nabla^2 \phi = 0 \quad (\text{for } y \leq \eta(x, z, t)) \quad (2)$$

$$\phi_{,tt} + (\nabla\phi \cdot \nabla\phi)_{,t} + \frac{1}{2} \nabla\phi \cdot \nabla(\nabla\phi \cdot \nabla\phi) + \phi_{,y} + p_{,t} + \phi_{,x} p_{,x} + \phi_{,z} p_{,z} = 0 \quad (3)$$

$$\eta = -\phi_{,t} - \frac{1}{2} \nabla\phi \cdot \nabla\phi + \frac{1}{2} - p \quad (4)$$

supplemented by appropriate radiation conditions and by the equations for the singular parts of ϕ and ψ . Our aim is to derive approximative, linearized, solutions for $\psi(x,y,z)$ (1).

2.2 Linearized equations

An ordering is introduced by assuming that ϕ is a small perturbation of the uniform flow and ψ is small compared to ϕ . Furthermore, in the case of $p=0$, ϕ and ψ are written as follows

$$\phi = \phi_s + \phi_r; \quad \psi = \psi_s + \psi_r \quad (5)$$

where the singular parts ϕ_s and ψ_s are given and they obey the condition

$$\phi_s(x,0,z) = 0; \quad \psi_s(x,0,z) = 0 \quad (6)$$

ϕ_r and ψ_r are regular for $y < 0$ and satisfy the following well known equations, derived from (1)-(6)

$$\nabla^2 \phi_r = 0 \quad (\text{for } y < 0) \quad (7)$$

$$\phi_{r,xx} + \phi_{r,yy} = p_{\phi,x} - \phi_{s,y} \quad (\text{for } y=0) \quad (8)$$

$$\eta_\phi = \phi_{r,x} - p_\phi \quad (9)$$

with p_ϕ standing for a steady pressure on the free-surface and η_ϕ for the steady free-surface elevation. Generally either p_ϕ or ϕ_s is zero, but we shall keep both terms in (8) for the sake of brevity.

As for ϕ_r , the pertinent equations are

$$\nabla^2 \psi_r = 0 \quad (\text{for } y < 0) \quad (10)$$

$$L_0(\psi_r) + L_1(\psi_r) = c_0(x,z) + c_1(x,z) \quad (\text{for } y=0) \quad (11)$$

where the differential operators L_0 and L_1 are given by

$$L_0 = -\omega^2 - 2i\omega \frac{\partial}{\partial x} + \frac{\partial^2}{\partial x^2} + \frac{\partial}{\partial y} \quad (12)$$

$$L_1 = 2i\omega(\nabla\phi) \cdot \nabla - 2(\nabla\phi \cdot \nabla) \frac{\partial \phi}{\partial x} - 2(\nabla\phi \cdot \nabla) \frac{\partial \phi}{\partial y} + \eta_\phi \frac{\partial}{\partial y} \quad (13)$$

The nonhomogeneous term in (11) are

$$c_0(x,z) = -\psi_{s,y} - i\omega p_\phi + \eta_{\psi,x} \quad (14)$$

and a similar expression involving the given

functions ψ_s , ϕ and p_ϕ for $c_1(x,z)$. L_0 and c_0 are linear in ψ_r and zero-order in the steady flow. The equation $L_0(\psi_r) = c_0$ has constant coefficients and is the one adopted exclusively in previous works [1]-[8]. In contrast, L_1 and c_1 are linear in ϕ_r but with variable, first-order in ϕ , coefficients and is for the first time considered here.

The problem is now defined in mathematical terms: the solution for ψ_r satisfying (10) and (11) and appropriate radiation conditions is sought. The problem is recast in terms of Fourier transforms in the next section.

2.3 Integral equation for the FT (Fourier transform) of the potential

The Fourier transforms of ϕ_r and ψ_r are

$$\tilde{\phi}_r(\alpha, \beta, y) = \frac{1}{2\pi} \int_{-\infty}^{\infty} \int_{-\infty}^{\infty} \phi_r(x, 0, z) \exp[i(\alpha x + \beta z) + (\alpha^2 + \beta^2)^{1/2} y] dx dz \quad (15)$$

in 3D and

$$\tilde{\phi}_r(k, y) = \frac{1}{\sqrt{2\pi}} \int_{-\infty}^{\infty} \phi_r(x, 0) \exp[ikx + |k|y] dx \quad (16)$$

in the 2D case, with similar expressions for $\tilde{\psi}_r(\alpha, \beta, y)$ and $\tilde{\psi}_r(k, y)$, respectively.

Carrying out the FT of the steady flow equations (1)-(9) yields immediately the well known expressions

$$\tilde{\phi}_r(\alpha, \beta, 0) = \frac{\widetilde{\partial p_\phi / \partial x} - \widetilde{\partial \phi_s / \partial y}}{-\alpha^2 + (\alpha^2 + \beta^2)^{1/2} + i\mu\alpha} \quad (\text{for } y=0) \quad (17)$$

and

$$\tilde{\phi}_r(k, 0) = \frac{\widetilde{\partial p_\phi / \partial x} - \widetilde{\partial \phi_s / \partial y}}{-k^2 + |k| + i\mu k} \quad (\text{for } y=0) \quad (18)$$

in the 3D and 2D cases, respectively, with $\mu > 0$ an artificial viscosity coefficient which ensures that the poles in the FT plane are properly located to fulfill the radiation conditions.

The FT of (11) yields the integral equation for $\tilde{\psi}_r$ in the 3D case

$$\begin{aligned} A^{(0)}(\alpha, \beta; \omega) \tilde{\psi}_r(\alpha, \beta, 0) + \frac{1}{2\pi} \int_{-\infty}^{\infty} \int_{-\infty}^{\infty} A^{(1)}(\alpha, \beta, \lambda, \nu; \omega) \tilde{\psi}_r(\lambda, \nu, 0) d\lambda d\nu \\ = C^{(0)}(\alpha, \beta) + C^{(1)}(\alpha, \beta) \end{aligned} \quad (19)$$

From (12) and (13) we have

$$A^{(0)}(\alpha, \beta; \omega) = -\omega^2 - 2\omega\alpha - \alpha^2 + (\alpha^2 + \beta^2)^{\frac{1}{2}} \quad (20)$$

$$\begin{aligned} A^{(1)}(\alpha, \beta, \lambda, \nu; \omega) = & \{-i(\alpha - \lambda) \{ 2\lambda^2 + \nu^2 + 2\lambda\omega - \\ & - 2(\alpha - \lambda) [(\omega + \lambda) (\lambda^2 + \nu^2)^{\frac{1}{2}} - \lambda] - 2(\alpha - \lambda)^2 (\lambda^2 + \nu^2)^{\frac{1}{2}} + \\ & + 2i\nu(\beta - \nu) \} - 2i(\beta - \nu) (\omega\nu + \lambda\nu) \} \tilde{\phi}_r(\alpha - \lambda, \beta - \nu, 0) + \\ & + 2(\alpha - \lambda) (\lambda^2 + \nu^2)^{\frac{1}{2}} (\omega + \alpha) \tilde{p}_\phi(\alpha - \lambda, \beta - \nu) - \\ & - i(\alpha - \lambda) (\lambda^2 + \nu^2)^{\frac{1}{2}} A^{(0)}(\lambda, \nu) \tilde{\eta}_\phi(\alpha - \lambda, \beta - \nu) \end{aligned}$$

(for $y=0$) (21)

It is pointed out that the relationship $\partial\phi/\partial y = \alpha^2 \tilde{\phi}_r - i\alpha \tilde{p}_\phi$, based on (17), has been employed in (21). Furthermore, by (9) $\tilde{\eta}_\phi = -i\alpha \tilde{\phi}_r(\alpha, \beta, 0) - \tilde{p}_\phi(\alpha, \beta)$ so that $A^{(1)}$ (21) is expressed in terms of known steady-flow solutions. Finally, $C^{(0)}$ and $C^{(1)}$ stand for the FT of $c^{(0)}$ and $c^{(1)}$ in the r.h.s. of (19).

The corresponding integral equation for 2D flows is

$$\begin{aligned} A^{(0)}(k; \omega) \tilde{\psi}_r(k, 0) + \\ + \frac{1}{(2\pi)^{\frac{1}{2}}} \int_{-\infty}^{\infty} A^{(1)}(k, \lambda; \omega) \tilde{\psi}_r(\lambda, 0) d\lambda = \\ = C^{(0)}(k) + C^{(1)}(k) \end{aligned} \quad (22)$$

with

$$A^{(0)}(k; \omega) = -k^2 - 2k\omega - \omega^2 + |k| \quad (23)$$

$$\begin{aligned} A^{(1)}(k, \lambda; \omega) = & -2i(k - \lambda) \{ \lambda^2 + \lambda\omega - (k - \lambda) [(\omega + \\ & + \lambda) |\lambda| - \lambda] - (k - \lambda)^2 |\lambda| \} \tilde{\phi}_r(k - \lambda, 0) + \\ & + 2(k - \lambda) |\lambda| (\omega + \lambda) \tilde{p}_\phi(k - \lambda) - \\ & - i(k - \lambda) |\lambda| A^{(0)}(\lambda) \tilde{\eta}_\phi(k - \lambda) \end{aligned} \quad (24)$$

Eqs. (19) and (22) are Fredholm singular integral equations of the second kind for $\tilde{\psi}_r$. Once solved, ψ_r is obtained by inversion and the far-free waves are related to the poles of $\tilde{\psi}_r$. A general solution of (19) and (22) seems difficult to obtain. However, it will be shown in the sequel that the near resonance of the leading term of $\tilde{\psi}_r$ can be easily extracted from (19) and (22).

2.4 The zero-order solution and resonant conditions

The zero-order solution is obtained in (19) and (22) by retaining only the terms of order ψ_r and neglecting those of order $\phi\psi_r$.

Starting with the 3D flow, we have

$$\tilde{\psi}_r^{(0)}(\alpha, \beta, 0) = \frac{C^{(0)}(\alpha, \beta)}{A^{(0)}(\alpha, \beta; \omega)} \quad (25)$$

which is the approximation investigated in the past. $\tilde{\psi}_r^{(0)}$ is obtained by inversion as follows

$$\begin{aligned} \psi_r^{(0)}(x, y, z) = & \frac{1}{2\pi} \int_{-\infty}^{\infty} \int_{-\infty}^{\infty} \frac{C^{(0)}(\alpha, \beta)}{A^{(0)}(\alpha, \beta; \omega)} \exp[- \\ & - i(\alpha x + \beta z) + (\alpha^2 + \beta^2)^{\frac{1}{2}} y] d\alpha d\beta \end{aligned} \quad (26)$$

The zeros of $A^{(0)}$ are easily found by switching to polar coordinates in the FT plane ($\alpha = \rho \cos \theta$, $\beta = \rho \sin \theta$).

Thus, by (20)

$$A^{(0)}(\rho, \theta; \omega) = -\omega^2 - 2\omega\rho \cos \theta - \rho^2 \cos^2 \theta + \rho = 0 \quad (27)$$

has two real roots for any $\pi/2 > |\theta| > 0$ provided that $\omega \leq \omega_c$. For $\pi/2 > |\theta| > \pi/2$ we have

$$\rho_{3,4} = \frac{1 - 2\omega \cos \theta \pm (1 - 4\omega \cos \theta)^{\frac{1}{2}}}{2 \cos^2 \theta} \quad (28)$$

and an identical expression for $\rho_{1,2}$ in the case $-2 > |\theta| > 0$. However, it can be easily shown that the radiation conditions require different indentations on the inversion path in the FT plane, which is represented in Fig 1a.

When $\omega > \omega_c = 1/4$ the four real roots exist only for $|\theta| > \theta_c$, where $\theta_c = \cos^{-1}(1/4\omega)$, while for $\theta_c > |\theta| > 0$, $\rho_{1,2}$ become complex (for a detailed analysis see [5] and [7]). We can write now for $\psi_r^{(0)}$ (26), for any fixed x , by separating the polar contributions (semi-residues) at $\rho_{1,2}$ from the rest

$$\begin{aligned} \psi_r^{(0)} = & -i \int_{\theta_c}^{\pi/2} \frac{\rho_1 C^{(0)}(\rho_1, \theta) \cos(\rho_1 z \sin \theta) \exp(- \\ & - i\rho_1 x \cos \theta + \rho_1 y)}{(1 - 4\omega \cos \theta)^{\frac{1}{2}}} d\theta + \\ & - i \rho_2 x \cos \theta + \rho_2 y) + \rho_2 C^{(0)}(\rho_2, \theta) \cos(\rho_2 z \sin \theta) \exp(- \\ & - i\rho_2 x \cos \theta + \rho_2 y) d\theta + \\ & + \frac{1}{\pi} \int_0^{\pi} \int_0^{\infty} \frac{C^{(0)}(\rho, \theta) \cos(\rho z \sin \theta) \exp(-i\rho x \cos \theta + \\ & + \rho y)}{A^{(0)}(\rho, \theta; \omega)} \rho d\rho d\theta \end{aligned} \quad (29)$$

In (29) the symbol \int_{\pm} stands for an integral which is taken as a principal value at $\rho=\rho_1$ and $\rho=\rho_2$ solely. The far-free waves are obtained in (29) for $(x)\rightarrow\infty$ by extracting from the second term the polar contributions at ρ_3, ρ_4 , and the principal value contributions at ρ_1, ρ_2, ρ_3 , and ρ_4 . Then it is found that for $\omega<\omega_c$ the ρ_2 wave propagates upstream and the ρ_1, ρ_3, ρ_4 propagate downstream whereas for $\omega>\omega_c$ the surviving ρ_3, ρ_4 waves propagate downstream.

With

$$\delta\omega = \omega_c - \omega \quad (30)$$

we find that for $\delta\omega\rightarrow 0$ and $\theta_c=0$ the two poles ρ_1 and ρ_2 coalesce at $\rho=\rho_c=1/4$. At this limit the second term of (29) tends to a finite limit, whereas for the first we have

$$\psi_r^{(0)} \sim -\frac{1}{2} C^{(0)}(\rho_c, \theta_c) \cos(\rho_c z \sin \theta_c) \exp(-$$

$$-i\rho_c x + \rho_c y) \int_{\theta_c}^{\pi/2} \frac{d\theta}{(1-4\omega \cos \theta)^{1/2}} + O(1) \quad (31)$$

where $O(1)$ stands for finite terms under the limit $\delta\omega\rightarrow 0$. As for the integral in (31) we have

$$\int_0^{\pi/2} \frac{d\theta}{(1-4\omega \cos \theta)^{1/2}} \sim \sqrt{2} \int_0^{\pi/2} \frac{d\theta}{(\theta^2 + 8\delta\omega)^{1/2}} + O(1) = -\frac{1}{\sqrt{2}} \ln(\delta\omega) + O(1) \quad (32)$$

Hence, the singular term of ψ_r (31) can be rewritten as

$$\psi_r^{(0)} \sim \frac{\sqrt{2}iC^{(0)}}{4} (1/4, 0) \ln(\delta\omega) \exp(-ix/4 + y/4) \quad (33)$$

We have arrived at the conclusion that for any fixed x the potential $\psi_r^{(0)}$ tends to infinity like $\ln(\delta\omega)$ when ω approaches ω_c from below. For $|x|\rightarrow\infty$ the two free-waves associated with ρ_1 (downstream) and ρ_2 (upstream) become of infinite amplitude for $\theta=0$, i.e., for transverse waves.

In the case of 2D flows the results are very similar, though the algebra is simpler. Thus, from (23) we get for $\omega<\omega_c$ the four real zeroes

$$k_{1,2} = \frac{1-2\omega^{\pm}(1-4\omega)^{\pm}}{2}; k_{3,4} = \frac{-1-2\omega^{\pm}(1+4\omega)^{\pm}}{2} \quad (34)$$

which are depicted on the inversion path of Fig. 1b. Similarly to (29) we have after inversion

$$\begin{aligned} \psi_r^{(0)}(x, y) = & \frac{1}{(2\pi)^{1/2}} \int_{-\infty}^{\infty} \frac{C^{(0)}(k)}{A^{(0)}(k; \omega)} \exp(- \\ & -ikx + |k|y) dk = -\frac{1}{2} \left(\frac{\pi}{2}\right)^{1/2} (\delta\omega)^{-1/2} [C^{(0)}(k_1) \exp(- \\ & -ik_1 x + k_1 y) + C^{(0)}(k_2) \exp(-ik_2 x + k_2 y)] + \\ & + \frac{1}{(2\pi)^{1/2}} \int_{-\infty}^{\infty} \frac{C^{(0)}(k)}{A^{(0)}(k; \omega)} \exp(-ikx + |k|y) dk \quad (35) \end{aligned}$$

Hence, the singular term of $\psi_r^{(0)}$ diverges like $(\delta\omega)^{-1/2}$ for $\omega\rightarrow\omega_c$ from below and the same is true for the amplitude of the far-free waves associated with k_1 and k_2 .

The two-dimensional results have been derived explicitly in previous works ([1] - [4]), particularly in [2], which presents the solution of the transient problem in which the radiation conditions need not be imposed a-priori.

Returning to the integral equations (19) and (22) it is seen that no matter how small is the first-order term related to the nonuniform steady flow associated with ϕ , it may become the dominant one when $A^{(0)}\rightarrow 0$, i.e., at the poles of $\psi_r^{(0)}$. Its possible effect on removing the resonant conditions at the double zero of $A^{(0)}$ is examined separately, in the next sections, for 2D and 3D flows respectively.

3. REMOVAL OF RESONANCE FOR TWO-DIMENSIONAL FLOW PAST A LIFTING BODY

3.1. The regular perturbation expansion

An approximate solution of the integral equation (22) which is consistent with the ordering of Sect. 2.2 may be obtained by an asymptotic sequence for ψ_r as follows

$$\psi_r(k, y) = \psi_r^{(0)}(k, y) + \psi_r^{(1)}(k, y) + \dots \quad (36)$$

where $\psi_r^{(0)}$ is of zero-order in the steady flow potential (i.e. corresponds to an oscillating singularity in a uniform flow), and $\psi_r^{(1)}$ is of first-order in ϕ .

Substitution of (36) into (22) yields by collecting terms of same order

$$\psi_r^{(0)}(k, 0) = \frac{C^{(0)}(k)}{A^{(0)}(k; \omega)} \quad (37)$$

$$\begin{aligned} \psi_r^{(1)}(k, 0) = & \frac{C^{(1)}(k)}{A^{(0)}(k; \omega)} - \frac{1}{(2\pi)^{1/2} A^{(0)}(k; \omega)} \\ & \int_{-\infty}^{\infty} \frac{A^{(1)}(k, \lambda; \omega) C^{(0)}(\lambda)}{A^{(0)}(\lambda; \omega)} d\lambda \quad (38) \end{aligned}$$

The expressions (37), (38) are the first two terms of the Neumann series for the integral equation (22).

$\psi_r^{(1)}$ has been examined in detail in Sect. 2.4 and it was found that for $\delta\omega \rightarrow 0$ and $k_1, 2 \rightarrow k_c$, $\psi_r^{(1)} \sim (\delta\omega)^{-1/2}$. To examine the behavior of $\psi_r^{(1)}$ we substitute $A^{(0)}$ into the last term of (38) and carry out the decomposition of (35) to obtain

$$\begin{aligned} & \frac{1}{(2\pi)^{1/2}} \int_{-\infty}^{\infty} \frac{A^{(1)}(k, \lambda; \omega) C^{(0)}(\lambda)}{A^{(0)}(\lambda; \omega)} d\lambda = - \\ & - \frac{i}{2} \left(\frac{\pi}{2}\right)^{1/2} (\delta\omega)^{-1/2} \{ A^{(1)}(k, k_1; \omega) C^{(0)}(k_1) + \\ & + A^{(1)}(k, k_2; \omega) C^{(0)}(k_2) \} + \\ & + \frac{1}{(2\pi)^{1/2}} \int_{-\infty}^{\infty} \frac{A^{(1)}(k, \lambda; \omega) C^{(0)}(\lambda)}{A^{(0)}(\lambda; \omega)} d\lambda \end{aligned} \quad (39)$$

The last term in (39) remains finite when $\delta\omega \rightarrow 0$, whereas the first term is generally singular. Comparing now $\psi_r^{(1)}$ (38) and $\psi_r^{(0)}$ (37) and taking into account that $C^{(1)}(k)$ can be proved to be regular for $\delta\omega \rightarrow 0$, we obtain for the most singular term

$$\begin{aligned} \tilde{\psi}_r^{(1)}(k, 0) / \tilde{\psi}_r^{(0)}(k, 0) & \sim -i \left(\frac{\pi}{2}\right)^{1/2} (\delta\omega)^{-1/2} \\ & A^{(1)}(k, k_c; \omega_c) C^{(0)}(k_c) / C^{(0)}(k) \end{aligned} \quad (40)$$

Hence, for $\delta\omega = 0(1)$ the Neumann series (36) is uniform and $\tilde{\psi}_r^{(1)}$, and consequently $\psi_r^{(1)}$, is asymptotic to $\tilde{\psi}_r^{(0)}$ and $\psi_r^{(0)}$, respectively. If the perturbation potential of steady flow ϕ and consequently $A^{(1)}$ is characterized by a small parameter ε , it is seen from (40) that the Neumann series is not uniform for $\varepsilon/(\delta\omega)^{1/2} = 0(1)$ or $\delta\omega = 0(\varepsilon^2)$. In this neighbourhood of the critical frequency the first-order term becomes of the same order of magnitude as the zero-order term and $\psi_r^{(1)}$ is no more asymptotic to $\psi_r^{(0)}$.

As a matter of fact we are primarily interested in the convergence of (36) in the neighbourhood of $k = k_c$, i.e. after inverting $\tilde{\psi}_r^{(0)}$ and for the polar terms, associated with $k_1, 2$. Inspection of (40) shows that the convergence near k_c depends on the ratio $A^{(1)}(k_i, k_j; \omega_c - \delta\omega) / (\delta\omega)^{1/2}$

with $i, j = 1, 2$ which need not be singular for $\delta\omega \rightarrow 0$. The behavior of $A^{(1)}(k_i, k_j; \omega_c - \delta\omega) / (\delta\omega)^{1/2}$ is examined next.

3.2 Convergence of regular perturbation expansion.

At this point we have to examine $A^{(1)}$ (24) for different types of singularities which generate the steady flow component. Since $A^{(1)}$ is linear in $\tilde{\phi}_r$ it is enough to consider isolated singularities first. Three such types of singularities are contemplated: a pressure point of strength P_ϕ at the origin, a vortex of circulation Γ_ϕ at depth h beneath the unperturbed free-surface and a horizontal doublet of strength M_ϕ at $y = -h$ too. Hence, we can write

$$\begin{aligned} p_\phi(x) &= P_\phi \delta(x); \\ \phi_s &= -\frac{1}{2\pi} \operatorname{Re} \{ i \Gamma_\phi \ln[(x+iy-ih)(x+iy+ih)] \}; \\ \tau_s &= -\frac{1}{2\pi} \operatorname{Re} \left(\frac{M_\phi}{x+iy-ih} - \frac{M_\phi}{x+iy+ih} \right) \end{aligned} \quad (41)$$

respectively.

The evaluation of $\tilde{\phi}_r$ for ϕ_r satisfying (7) and (8) is a matter of routine computation of steady flows. The final results for all cases are as follows

$$\begin{aligned} \tilde{\phi}_r(k, 0) &= \frac{1}{|k| - k^2} \left\{ -\frac{ik}{(2\pi)^{1/2}} P_\phi; \right. \\ &- \frac{i}{(2\pi)^{1/2}} \frac{k}{|k|} e^{-|k|h} \Gamma_\phi; \\ &- \frac{ik}{(2\pi)^{1/2}} e^{-|k|h} M_\phi \} \end{aligned} \quad (42)$$

where the inversion path has to circumvent the poles $k = \pm 1$ from below to satisfy the radiation conditions. Substituting $\tilde{\phi}_r(k - \lambda, 0)$ in (24) and taking the limit $k = k_i; k_j$ ($i, j = 1, 2$) show that in the case of a vortex we have

$$\begin{aligned} A^{(1)}(k_i, k_j; \omega_c - \delta\omega) &= \\ &= \frac{1}{4(2\pi)^{1/2}} \Gamma_\phi + O(\omega\omega^{1/2}) \quad (i, j = 1, 2) \end{aligned} \quad (43)$$

where the relationships $k_1 = (1/4) + (\delta\omega)^{1/2} + \delta\omega$

$k_2 = (1/4) - (\delta\omega)^{1/2} + \delta\omega$, $\omega = (1/4) - \delta\omega$ (see 34) have been employed. In contrast, for a pressure point or a doublet the result in (24) is

$$A^{(1)}(k_i, k_j; \omega_c - \delta\omega) = - \frac{1}{4(2\pi)^{1/2}} (k_i - k_j) \{P_\phi; M_\phi\} + O(\delta\omega) \quad (i, j=1, 2) \quad (44)$$

Hence, the ratio $A^{(1)}(k_i, k_j; \omega_c - \delta\omega) / (\delta\omega)^{1/2}$ is of order P_ϕ or M_ϕ , while in the case of a vortex it is of order $\Gamma_c / (\delta\omega)^{1/2}$. This result remains the same in the case of a pressure patch or a distribution of vortices (to represent a lifting body) or doublets (to represent a closed body). Then P_ϕ represents the total pressure, M_ϕ the total doublet strength and Γ_c the circulation around the body.

We can summarize the important results of this section as follows: (i) in the cases of an oscillating pressure patch or a non-lifting closed body the Neumann series (36) is convergent near $\omega = \omega_c$, $k = k_c$. The amplitude of the far free-waves associated with the zero-order approximation $\tilde{\psi}_r^{(0)}$ is of order $C^{(0)}(k_c) / (\delta\omega)^{1/2}$ whereas $\tilde{\psi}_r^{(1)}$ yields amplitude of order $C^{(0)}(k_c) \epsilon / (\delta\omega)^{1/2}$ (ϵ stands for P_ϕ or M_ϕ). Hence, the first-order correction to the steady flow is weak and the resonant effect cannot be removed by incorporating it in the solution; (ii) in the case of a lifting body the perturbation series (36) is singular and the amplitude of the resonant far free-waves associated with $\tilde{\psi}_r^{(1)}$ is of order $C^{(0)}(k_c) \Gamma_c / (\delta\omega)$. Hence, for $\delta\omega = O(\Gamma_c^2)$ the first-order term becomes the dominant one in (22) and the solution of the integral equation (22) has to account for this term from the outset. A uniform approximative solution along this line is described in the sequel.

3.3 Derivation of zero-order uniform solution for a lifting body.

In the case of a lifting body the regular perturbation expansion of (22) is not uniform near resonance and a solution of the integral equation (22) by other means, is required. Although a complete solution may be obtained in principle, we choose here a simple procedure to derive a uniform zero-order approximation. We have shown previously that the non-uniformity of (22) stems from the polar contribution of $\tilde{\psi}_r$ near λ_{cr} , in the integral term which becomes large compared to the first term. Hence, we shall retain only this polar contribution in (22) rather than the entire expression of the integral term. Towards this aim we assume that $\tilde{\psi}_r$ can be expanded in a generalized asymptotic sequence of type.

$$\tilde{\psi}_r(k, y; \Gamma_\phi, \omega) = \tilde{\psi}_{rg}^{(0)}(k, y; \Gamma_\phi, \omega) +$$

$$+ \tilde{\psi}_{rg}^{(1)}(k, y; \Gamma_\phi, \omega) + \dots \quad (45)$$

such that for $\delta\omega = O(\Gamma_\phi^m)$, $m < 2$ $\tilde{\psi}_{rg}^{(0)}$, $\tilde{\psi}_{rg}^{(1)}$... are asymptotic to $\tilde{\psi}_r^{(0)}$, $\tilde{\psi}_r^{(1)}$ respectively. However, we require (45) to be an asymptotic sequence for $\delta\omega = O(\Gamma_\phi^m)$, $m \geq 2$ and $k \rightarrow k_{cr}$ as well. To facilitate the computations we try a representation of $\tilde{\psi}_{rg}^{(0)}$ as follows

$$\tilde{\psi}_{rg}^{(0)}(k, 0) = \frac{B^{(0)}(k; \Gamma_\phi)}{A^{(0)}(k; \omega)} \quad (46)$$

which is substituted in (22) to yield the integral equation for the amplitude function $B^{(0)}$

$$B^{(0)}(k; \Gamma_\phi) + \frac{1}{(2\pi)^{1/2}} \int_{-\infty}^{\infty} \frac{A^{(1)}(k, \lambda; \omega) B^{(0)}(\lambda; \Gamma_\phi)}{A^{(0)}(\lambda; \omega)} d\lambda = C^{(0)}(k) + C^{(1)}(k) \quad (47)$$

Assuming that $B^{(0)}$ is regular near $\lambda = k_c$, (47) is rewritten as follows by using the decomposition of (39)

$$B^{(0)}(k) - \frac{i}{2} \left(\frac{\pi}{2}\right)^{1/2} (\delta\omega)^{-1/2} [A^{(1)}(k, k_1; \omega) + B^{(0)}(k_1) + A^{(1)}(k, k_2; \omega) B^{(0)}(k_2)] = C^{(0)}(k) + C^{(1)}(k) - \frac{1}{(2\pi)^{1/2}} \int_{\Gamma} \frac{A^{(1)}(k, \lambda; \omega) B^{(0)}(\lambda; \Gamma_\phi)}{A^{(0)}(\lambda; \omega)} d\lambda \quad (48)$$

The last two terms in the r.h.s. of (48) are of order Γ_ϕ for $\delta\omega \rightarrow 0$. Hence, at the order of the leading terms we have for $B^{(0)}$ in the neighbourhood of k_c after taking $k_1 = k_2 = k_c$

$$B^{(0)}(k) - i \left(\frac{\pi}{2}\right)^{\frac{1}{2}} (\delta\omega)^{-\frac{1}{2}}.$$

$$A^{(1)}(k, k_c; \omega_c) B^{(0)}(k_c) = C^{(0)}(k) \quad (49)$$

All the remaining terms in (48) have to be collected in a first-order integral equation which is uniform for $\delta\omega \rightarrow 0$ and which would provide the next approximation $\tilde{\psi}_{rg}^{(1)}$. We limit, however, our calculations here to $B^{(0)}(k)$ solely. To determine $B^{(0)}(k_c)$ in (49) we take advantage of the fact that (49) is an identity in k and use it for $k=k_c$. Thus, with $A^{(1)}(k_c, k_c; \omega_c)$ given by (43) at the leading term, we immediately obtain from (49)

$$B^{(0)}(k_c) = \frac{C^{(0)}(k_c)}{1 + [i\Gamma_\phi/8(\delta\omega)^{\frac{1}{2}}]} \quad (50)$$

and by returning to (49)

$$B^{(0)}(k; \Gamma_\phi, \omega_c - \delta\omega) = C^{(0)}(k) + \frac{i(\pi/2)^{\frac{1}{2}} A^{(1)}(k, k_c; \omega_c) C^{(0)}(k_c)}{(\delta\omega)^{\frac{1}{2}} + (i\Gamma_\phi/8)} \quad (51)$$

This completes the calculation of $\tilde{\psi}_{rg}^{(0)}$ (46). It is seen that for $\delta\omega=0$ (Γ_ϕ^m), $m < \frac{1}{2}$ the last term of (51) is of order $\Gamma_\phi^{1-m/2}$ and $B^{(0)}(k)$ is indeed asymptotic to $C^{(0)}(k)$. For $\delta\omega \rightarrow 0$ and $k \rightarrow k_c$, however, (51) leads to

$$B^{(0)}(k) = -i \frac{8(\delta\omega)^{\frac{1}{2}} C^{(0)}(k)}{\Gamma_\phi} + O\left(\frac{\delta\omega}{\Gamma_\phi^{\frac{1}{2}}}\right) \quad (52)$$

At the leading term in $\delta\omega$, $B^{(0)}$ can be rewritten in the neighborhood of k_c as follows

$$B^{(0)}(k; \Gamma_\phi, \omega) = \frac{C^{(0)}(k)}{1 + [i\Gamma_\phi/8(\delta\omega)^{\frac{1}{2}}]} + O(\delta\omega) \quad (53)$$

Returning to the expression of $\tilde{\psi}_{rg}^{(0)}$ (46), and using (51), we obtain immediately the zero-order uniform solution by inverting (46) and retaining the contribution of the last term of (51) only for the poles $k_{1,2}$ (see 35)

$$\begin{aligned} \psi_{rg}^{(0)}(x, y; \Gamma_\phi, \omega) = & -\frac{i}{2} \left(\frac{\pi}{2}\right)^{\frac{1}{2}} \frac{1}{(\omega_c - \omega)^{\frac{1}{2}} + (i\Gamma_\phi/8)} \\ & [C^{(0)}(k_1) \exp(-ik_1 x + |k_1| y) + \\ & + C^{(0)}(k_2) \exp(-ik_2 x + |k_2| y) + \frac{1}{(2\pi)^{\frac{1}{2}}} \\ & \int_{-i}^{\infty} \frac{C^{(0)}(k)}{A^{(0)}(k; \omega)} \exp(-ikx + |k| y) dk \end{aligned} \quad (54)$$

Furthermore, the far free-waves are given by

$$\psi_{ry}^{(0)}(x, y; \Gamma_\phi, \omega) \sim -i \left(\frac{\pi}{2}\right)^{\frac{1}{2}} \frac{C^{(0)}(k_2)}{(\omega_c - \omega)^{\frac{1}{2}} + (i\Gamma_\phi/8)} \exp(-ik_2 x + k_2 y) \quad (x \rightarrow \infty) \quad (55)$$

$$\begin{aligned} \psi_{ry}^{(0)}(x, y; \Gamma_\phi, \omega) \sim & -i \left(\frac{\pi}{2}\right)^{\frac{1}{2}} \frac{C^{(0)}(k_1)}{(\omega_c - \omega)^{\frac{1}{2}} + (i\Gamma_\phi/8)} \\ & \exp(-ik_1 x + k_1 y) + \frac{i(2\pi)^{\frac{1}{2}} C^{(0)}(k_4)}{(1+4\omega)^{\frac{1}{2}}} \\ & \exp(-ik_4 x + |k_4| y) - \frac{i(2\pi)^{\frac{1}{2}} C^{(0)}(k_3)}{(1+4\omega)^{\frac{1}{2}}} \end{aligned}$$

$$\exp(-ik_3 x + |k_3| y) \quad (x \rightarrow -\infty) \quad (56)$$

where the contribution of the branch lines of (54) in the k plane vanishes for $|x| \rightarrow \infty$.

Summarizing the results of (54), (55) and (56), it is seen that in the case of a lifting surface the steady flow component has a profound influence on the flow solution near ω_c . Thus, while in the usual linearized solution the amplitude of the wave-like terms of wave number close to k_c tends to infinity like $C^{(0)}/(\omega_c - \omega)^{\frac{1}{2}}$, in the uniform solution (54) it remains finite and of order $C^{(0)}/\Gamma_\phi$. Hence, the smallness of the unsteady perturbation (represented by $C^{(0)}$) in comparison with that of the steady component, is a prerequisite for the validity of the

results. Furthermore, it is seen in (55), (56) that at the limit $\omega = \omega_c$ the phase of the far-free waves associated with $k_{1,2}$ is changed by $\pi/2$ as compared with that of the linearized solution (35).

The leading term of the polar contributions at $k = k_c$ is of order $C^{(0)}/\Gamma_\phi$, whereas at $k_{3,4}$ the order is $C^{(0)}$. Hence, the next order term $\psi_r^{(1)}$ is going to be of order $C^{(0)}$ near k_c and $C^{(0)}/\Gamma_\phi$ near $k_{3,4}$.

4. REMOVAL OF RESONANCE FOR A THREE-DIMENSIONAL FLOW PAST A LIFTING SURFACE

4.1 The Regular Perturbation Expansion

In order to obtain an approximate solution of the integral equation (19) for the three-dimensional potential function $\psi_r(\alpha, \beta, 0)$, we expand the latter in the following asymptotic sequence,

$$\tilde{\psi}_r(\alpha, \beta, y) = \tilde{\psi}_r^{(0)}(\alpha, \beta, y) + \tilde{\psi}_r^{(1)}(\alpha, \beta, y) + \dots \quad (57)$$

where, in a similar manner to the two-dimensional regular expansion (36), $\psi_r^{(0)}$ and $\psi_r^{(1)}$ denote the zero and the first order potential functions.

It thus follows from (19) and (57) that

$$\tilde{\psi}_r^{(0)}(\alpha, \beta, 0) = \frac{C^{(0)}(\alpha, \beta)}{A^{(0)}(\alpha, \beta; \omega)} \quad (58)$$

and

$$\begin{aligned} \tilde{\psi}_r^{(1)}(\alpha, \beta, 0) &= \frac{C^{(1)}(\alpha, \beta)}{A^{(0)}(\alpha, \beta; \omega)} - \\ &- \frac{1}{2\pi A^{(0)}(\alpha, \beta; \omega)} \\ &- \iint_{-\infty}^{\infty} \frac{A^{(1)}(\alpha, \beta, \lambda, \nu; \omega) C^{(0)}(\lambda, \nu)}{A^{(0)}(\lambda, \nu; \omega)} d\lambda d\nu \end{aligned} \quad (59)$$

The same procedure may be also used to obtain higher order terms in the regular expansion (57). By examining the ratio $\psi_r^{(1)}/\psi_r^{(0)}$, it may be shown by using the procedure by which (33) has been obtained, that

$$\tilde{\psi}_r^{(1)}(\alpha, \beta, 0)/\tilde{\psi}_r^{(0)}(\alpha, \beta, 0) = O(\ln(\delta\omega)) \quad (60)$$

where $\delta\omega = \omega_c - \omega$ as ω approaches ω_c from below. Denoting, as done in the analogous two-dimensional case, the small parameter which characterizes the steady-flow perturbation potential by ϵ , we conclude that for $\epsilon \ln(\delta\omega) = O(1)$ the Neumann series (57) is non-uniform. Hence in the domain of interest, namely in the neighbourhood of the critical frequency, $\delta\omega \rightarrow 0$, the Neumann regular expansion (57) is non-uniform. It

will be shown in the next section that near the critical point $A^{(1)}(\alpha, \beta, \lambda, \nu; \omega)$ is $O(\Gamma_\phi^T)$, where Γ_ϕ^T denotes the total circulation about the lifting surface corresponding to the steady potential ϕ . Hence, we obtain that the Neumann series will diverge for $\delta\omega = O(e^{-1/\Gamma_\phi^T})$ and for this region a uniform solution has to be sought.

4.2 The Zero-Order Uniform Solution for a Lifting Surface

We seek to obtain a uniform solution for a three-dimensional lifting planform surface which moves below and parallel to an otherwise undisturbed free-surface with constant angle of attack and forward speed. A small amplitude oscillatory motion is imposed on this steady motion, by varying periodically, for example, the angle of attack about the steady mean-value. A genuine feature of a three-dimensional lifting surface is the presence of a wake region even at steady state. The requirement that the pressure be continuous across the wake implies that only free vortices may exist in the wake, whereas, on the finite aspect foil both free and bound vortices must be present. If the flow is unsteady the presence of bound vortices in the wake must be also considered. The strength of the unsteady wake vortices vary harmonically in the downstream direction in contrast with the steady wake vortices which vary only in the spanwise direction.

In the case of a foil of large aspect ratio (usually larger than 4) which is typical for hydrofoils, one may use Prandtl lifting line theory in order to approximate the flow about the foil. Here the foil is represented by a system of vortices bound to the location of the span lines. Two trailing vortices are shedded at the trailing edge and they stream out in the wake in the direction of the undisturbed free-stream. For a simple foil the singularities are distributed over an open rectangular bounded by the span line $-s < z < s$ and lines stretching off from each foil tip parallel to the free-stream velocity.

The steady state potential ϕ may be recognized as the potential of a doublet distribution with axes in the negative y direction with strength equal to $\Gamma_\phi(z)/4\pi$ per unit wake area. Here $\Gamma_\phi(z)$ denotes the circulation about an arbitrary foil cross-section and the total circulation about the

$$\text{foil is } \Gamma_\phi^T = \int_{-s}^s \Gamma_\phi(z) dz.$$

We employ the Fourier transform of the regular part of the Havelock function of a unit source located at $(\xi, -h, \zeta)$

$$\tilde{\psi}_r = \frac{2 \exp[(y-h)(\alpha^2 + \beta^2)^{1/2}]}{\alpha^2 - (\alpha^2 + \beta^2)^{1/2} - i\alpha\beta} \exp(i\alpha\zeta + i\beta\zeta) \quad (61)$$

which is obtained from (17) by letting $p_\phi = 0$ and recalling the well-known transform,

$$\left. \left(\frac{\partial}{\partial y} \left(\frac{1}{R'} \right) \right) \right|_{y=0} = \exp(-h(\alpha^2 + \beta^2)^{\frac{1}{2}} + i\alpha\xi + i\beta\zeta).$$

$$R' = [(x-\xi)^2 + (y-h)^2 + (z-\zeta)^2]^{\frac{1}{2}} \quad (62)$$

Hence, the Fourier transform of the Havelock function of a single doublet of strength $\Gamma_\phi(\zeta)/4\pi$ located at $(\xi, -h, \zeta)$ and directed in the negative y direction is

$$\tilde{\phi}_r = -\frac{\Gamma_\phi(\zeta)}{2\pi} \cdot \frac{(\alpha^2 + \beta^2)^{\frac{1}{2}}}{\alpha^2 - (\alpha^2 + \beta^2)^{\frac{1}{2}} - i\alpha\mu} \exp[(y-h)(\alpha^2 + \beta^2)^{\frac{1}{2}} + i\alpha\xi + i\beta\zeta] \quad (63)$$

To obtain the regular part of the total steady potential ϕ_r , equation (63) is integrated over the region occupied by the foil and the wake, which yields

$$\tilde{\phi}_r(\alpha, \beta) = \int_{-S}^S \int_{-\infty}^0 \tilde{\phi}_r(\xi, \zeta) d\xi d\zeta = \frac{i}{\pi} \cdot \frac{(\alpha^2 + \beta^2)^{\frac{1}{2}} \exp[(y-h)(\alpha^2 + \beta^2)^{\frac{1}{2}}]}{\alpha(\alpha^2 - (\alpha^2 + \beta^2)^{\frac{1}{2}} - i\alpha\mu)} \int_0^S \Gamma_\phi(\zeta) \cos(\beta\zeta) d\zeta \quad (64)$$

In deriving (64) the Fourier transform of the Heaviside function, namely

$$\int_{-\infty}^0 \exp(+i\alpha\xi) d\xi = -i/\alpha \quad (65)$$

has been also used.

Substituting (64) in (21) and letting $p_\phi = 0$, yields for the resonant conditions,

$$A^{(1)}(\alpha_c, \beta_c, \lambda_c, \nu_c, \omega_c) = -\Gamma_\phi^T / (8\pi)$$

where $\alpha_c = \lambda_c = \omega_c = 1/4$ and $\beta_c = \nu_c = 0$. Thus $A^{(1)} = 0(\Gamma_\phi^T)$ and, as discussed in the previous section, the regular expansion (57) breaks

down for $\delta\omega = 0(e^{-1/\Gamma_\phi^T})$ while both $\psi^{(0)}$ and $\psi_r^{(1)}$ are singular at resonant frequency.

In order to obtain a uniform asymptotic solution which remains finite as $\delta\omega \rightarrow 0$, we postulate, like in the two-dimensional case (Eq. (45)), the following expression

$$\tilde{\psi}_{rg}^{(0)}(\alpha, \beta, 0; \Gamma_\phi^T, \omega) = \frac{B^{(0)}(\alpha, \beta; \Gamma_\phi^T)}{A^{(0)}(\alpha, \beta; \omega)} \quad (66)$$

where $\tilde{\psi}_{rg}^{(0)}$ denote the zeroth-order term in the generalized asymptotic sequence

$$\tilde{\psi}_{rg}(\alpha, \beta, y; \Gamma_\phi^T, \omega) = \tilde{\psi}_{rg}^{(0)}(\alpha, \beta, y; \Gamma_\phi^T, \omega) + \tilde{\psi}_{rg}^{(1)}(\alpha, \beta, y; \Gamma_\phi^T, \omega) + \dots \quad (67)$$

Substituting (66) into the integral equation (19) yields, in an analogous manner to (53), the following leading term in $\delta\omega$ expansion which is valid in the neighbourhood of the critical point,

$$B^{(0)}(\alpha, \beta; \Gamma_\phi^T) = \frac{C^{(0)}(\alpha, \beta)}{1 - i \frac{\sqrt{2}}{32\pi} \Gamma_\phi^T \ln \delta\omega} \quad (68)$$

It is thus found that for $\delta\omega = 0(e^{-1/\Gamma_\phi^T})$ $B^{(0)}$ is asymptotic to $C^{(0)}$, whereas for $\delta\omega \rightarrow 0$

$$B^{(0)}(\alpha_c, \beta_c; \Gamma_\phi^T) = i16\sqrt{2}\pi \frac{C^{(0)}(\alpha_c, \beta_c)}{\Gamma_\phi^T \ln \delta\omega} \quad (69)$$

Substituting (63), (14) and (20) into (66) yields after inversion similar to (54)

$$\begin{aligned} \psi_{rg}^{(0)}(x, y, z; \Gamma_\phi, \omega) = & -\frac{i}{1 - i \frac{(2)^{\frac{1}{2}}}{32\pi} \Gamma_\phi^T \ln \delta\omega} \\ & \int_{cr}^{\pi} \frac{d\theta}{(1 - 4\omega \cos \theta)^{\frac{1}{2}}} \{ \rho_1 C^{(0)}(\rho_1, \theta) \\ & \exp[\rho_1(y - ix \cos \theta)] \cos(\rho_1 z \sin \theta) \} + \\ & + \rho_2 C^{(0)}(\rho_2, \theta) \exp[\rho_2(y - ix \cos \theta)] \\ & \cos(\rho_2 z \sin \theta) \} + \frac{1}{\pi} \int_0^\pi d\theta \int_1^\infty \rho d\rho \frac{C^{(0)}(\rho, \theta)}{A^{(0)}(\rho, \theta)} \\ & \exp[\rho(y - ix \cos \theta)] \cos(\rho z \sin \theta) \end{aligned} \quad (70)$$

For $\delta\omega \rightarrow 0$ equation (70) yields to the leading order near ρ_c (see (32))

$$\begin{aligned} \psi_{rg}^{(0)} \approx & \frac{i \frac{(2)^{\frac{1}{2}}}{4} \ln \delta\omega}{1 - i \frac{(2)^{\frac{1}{2}}}{32\pi} \Gamma_\phi^T \ln \delta\omega} \\ & C^{(0)}(\rho_{cr}, 0) \exp\left[\frac{1}{4}(y - ix)\right] \end{aligned} \quad (71)$$

Hence, the singularity of $\psi^{(0)}$ at $\omega = \omega_c$ which is present in the regular asymptotic solution, is eliminated in the zero-order uniform solution where $\psi_{rg}^{(0)}$ is finite at the critical point and of order $C^{(0)}/\Gamma_\phi^T$. The next order term in the generalized expansion $\psi_{rg}^{(1)}$ is $O(C^{(0)})$ and hence it can be shown that the generalized asymptotic sequence (67) is uniformly convergent.

5. ILLUSTRATION OF RESULTS: LIFT AND DRAG OF AN OSCILLATING VORTEX LINE

The preceding developments permit one to calculate the velocity potential of flow past an oscillating hydrofoil. Towards this aim one has to determine first ψ_s , the singular potential for flow in an infinite domain supplemented by the appropriate image across the pressure-relief free-surface $y=0$, and then to calculate the FT of ψ_s, y for ($y=0$). This determines $C^{(0)}$ by Eq. (14), which has to be substituted in (54) and (70) in the two and three-dimensional cases, respectively. Then the lift, drag and power can be found by standard procedures.

To grasp the results we will limit the computations to the schematical case of a concentrated vortex (2D) and a lifting line (3D).

Starting with the two-dimensional case, a fixed vortex located at $x=0, y=-h$ and of steady circulation Γ_0 and oscillating circulation $\Gamma_0 \cos \omega t$ is considered first. For the sake of simplicity we consider sufficiently low frequencies to warrant neglect of the variation of the shed vorticity in the wake (it can be shown that this is the case for ω/ω_c and chord Froude number around 3 or larger). We have then

$$\psi_s(x, y) = \text{Re} \left\{ -\frac{i\Gamma_0}{2\pi} \ln(z^2 + h^2) \right\} \quad (72)$$

and by (14)

$$C^{(0)}(k) = -\frac{\partial \psi_s(x, 0)}{\partial y} = -\frac{i\Gamma_0}{(2\pi)^{1/2}} \frac{k}{|k|} e^{-|k|h} \quad (73)$$

Limiting the computations only to the DC terms, i.e., to the drag and lift averaged over a period $2\pi/\omega$, we generally have by using Blasius theorem

$$D_{DC} = \frac{1}{2} \Gamma_0 \text{Re} \frac{\partial \psi_r(0, -h)}{\partial y}; \quad L_{DC} = -\frac{1}{2} \Gamma_0 \text{Re} \frac{\partial \psi_r(0, -h)}{\partial x} \quad (74)$$

With $\psi_r = \psi^{(0)}$ (54) and after a few algebraic manipulations we arrive at the final expressions

$$D_{DC}/\Gamma_0^2 = -\frac{1}{8} \frac{(\omega_c - \omega)^{1/2}}{\omega_c - \omega + \Gamma_0^2/64} \cdot [k_1 \exp(-2k_1 h) + k_2 \exp(-2k_2 h)] + \frac{1}{4(1+4\omega)} [k_3 \exp(-2k_3 h) - k_4 \exp(-2|k_4|h)] \quad (75)$$

$$L_{DC}/\Gamma_0^2 = -\frac{1}{16} \frac{\Gamma_0^2}{\omega_c - \omega + \Gamma_0^2/64}$$

$$[k_1 \exp(-2k_1 h) + k_2 \exp(-2k_2 h)] + \frac{1}{4\pi} \left\{ \frac{1}{k_3 - k_4} [k_3 \exp(-2k_3 h) \text{Ei}(2k_3 h) - k_4 \exp(-2k_4 h) \text{Ei}(2k_4 h)] - \frac{1}{k_1 - k_2} [-k_1 \exp(-2k_1 h) \text{Ei}(2k_1 h) + k_2 \exp(-2k_2 h) \text{Ei}(2k_2 h)] \right\} \quad (76)$$

In (75), (76) k_1, k_2, k_3 and k_4 are functions of ω (34) and all terms related to k_1, k_2 have to be deleted for $\omega > \omega_c$. If $\Gamma_0 = 0$, (75) and (76) represent the results based on the usual linearized theory.

In the neighbourhood of ω_c the drag (75) reaches a maximum at $\omega_c - \omega = (\Gamma_0^2/8)^2$

$$|D_{DCMAX}/\Gamma_0^2| \approx \frac{1}{4} \frac{e^{-h/2}}{\Gamma_0^2} + 0.26 e^{-2.91h} \quad (77)$$

and then drops quickly to the value of the last term of (77).

The lift, which is negative, reaches its extremal value at $\omega = \omega_c - 0$ and the contribution of the leading term is then

$$L_{DCMAX}/\Gamma_0^2 \approx -\frac{2e^{-h/2}}{\Gamma_0^2} \quad (78)$$

At $\omega = \omega_c + 0$ L_{DC} jumps to the value of the usual linearized solution, i.e., the term related to k_3 and k_4 in (76).

To illustrate the results we have represented D_{DC} and L_{DC} as function of ω for $\Gamma_0 = 0.1$ and $h=0.1$ in Fig. 2.

The three-dimensional case to be considered next is that of a lifting line with time varying vorticity $\Gamma_\psi(z) \cos \omega t$ distributed along the span $|z| < s$. Again we assume that the frequency is low enough to warrant the neglect of shed vorticity variation in the wake. Thus, the case is similar to the steady one and in order to obtain $C^{(0)}(\rho, \theta)$ we recall the expression for ψ_s corresponding to a single doublet of strength $\Gamma_\psi(z)/4\pi$ directed in the negative y axis lying at $(\xi, -h, \zeta)$,

$$\psi_s(x, y, z, \xi, -h, \zeta) = \frac{\Gamma_\psi(\zeta)}{4\pi} \cdot \left\{ \frac{y+h}{[(x-\xi)^2 + (y+h)^2 + (z-\zeta)^2]^{3/2}} + \frac{y-h}{[(x-\xi)^2 + (y-h)^2 + (z-\zeta)^2]^{3/2}} \right\} \quad (79)$$

Hence by (14), (62) and (65) we obtain

$$C^{(0)}(\rho, \theta) = - \int_{-s}^s d\zeta \int_{-\infty}^0 d\xi \frac{\partial \tilde{\psi}(x, y, z, \xi, -h, \zeta)}{\partial y} \Big|_{y=0}$$

$$= - \frac{i}{\pi} \sec \theta e^{-\rho h} \int_0^s d\zeta \Gamma_{\psi}(\zeta) \cos(\rho \zeta \sin \theta) \quad (80)$$

Substituting (80) in (70) yields

$$\psi_{rg}^{(0)}(x, y, z, \Gamma_{\psi}^T; \omega) = -$$

$$- \frac{1}{\pi (1 - \frac{i\sqrt{2}}{32\pi} \Gamma_{\psi}^T \ln \delta \omega)}$$

$$\int_0^{\pi} \frac{d\theta}{\sqrt{1-4\omega \cos \theta}} \left[\frac{\rho_1}{\cos \theta} e^{\rho_1(y-h) - i x \rho_1 \cos \theta} \right.$$

$$\cos(\rho_1 z \sin \theta) \int_0^s d\zeta \Gamma_{\psi}(\zeta) \cos(\rho_1 \zeta \sin \theta) +$$

$$+ \frac{\rho_2}{\cos \theta} e^{\rho_2(y-h) - i x \rho_2 \cos \theta} \cos(\rho_2 z \sin \theta)$$

$$\left. \int_0^s d\zeta \Gamma_{\psi}(\zeta) \cos(\rho_2 \zeta \sin \theta) \right] - \frac{i}{\pi^2} \int_0^{\pi} d\theta \int_0^{\infty} d\rho \frac{\rho}{\cos \theta}$$

$$\frac{e^{(y-h) - i x \rho \cos \theta}}{\rho - (\omega + \rho \cos \theta)^2} \cos(\rho z \sin \theta) \int_0^s d\zeta \Gamma_{\psi}(\zeta)$$

$$\cos(\rho \zeta \sin \theta) \quad (81)$$

For the hydrofoil problem, in a similar manner to the two-dimensional vortex, we present only the DC terms of the lift and drag, namely

$$L_{DC} = - \frac{1}{2} \int_{-s}^s \Gamma_{\psi}(\zeta) \frac{\partial \psi_{rg}^{(0)}(0, -h, \zeta)}{\partial x} d\zeta \quad (32)$$

$$D_{DC} = \frac{1}{2} \int_{-s}^s \Gamma_{\psi}(\zeta) \frac{\partial \psi_{rg}^{(0)}(0, -h, \zeta)}{\partial y} d\zeta \quad (83)$$

where it is understood that only the real part of $\psi_{rg}^{(0)}$ need to be considered. Substitution of (81) yields

$$L_{DC} = - \frac{i}{\pi (1 - \frac{i\sqrt{2}}{32\pi} \Gamma_{\psi}^T \ln \delta \omega)}$$

$$\int_0^{\pi} \frac{d\theta}{\sqrt{1-4\omega \cos \theta}} \left[\rho_1^2 e^{-2\rho_1 h} \left(\int_0^s d\zeta \Gamma_{\psi}(\zeta) \right.$$

$$\cos(\rho_1 \zeta \sin \theta) \Big)^2 + \rho_2^2 e^{-2\rho_2 h}$$

$$\left. \left(\int_0^s d\zeta \Gamma_{\psi}(\zeta) \cos(\rho_2 \zeta \sin \theta) \right)^2 \right]$$

$$+ \frac{1}{\pi^2} \int_0^{\pi} d\theta \int_0^{\infty} d\rho \rho^2 \frac{e^{-2\rho h}}{\rho - (\omega + \rho \cos \theta)^2}$$

$$\left(\int_0^s d\zeta \Gamma_{\psi}(\zeta) \cos(\rho \zeta \sin \theta) \right)^2 \quad (84)$$

and

$$D_{DC} = - \frac{1}{\pi (1 - \frac{i\sqrt{2}}{32\pi} \Gamma_{\psi}^T \ln \delta \omega)} \int_0^{\pi} \frac{d\theta}{\sqrt{1-4\omega \cos \theta}}$$

$$\left[\rho_1^2 \sec \theta e^{-2\rho_1 h} \left(\int_0^s d\zeta \Gamma_{\psi}(\zeta) \cos(\rho_1 \zeta \sin \theta) \right)^2 \right.$$

$$+ \rho_2^2 \sec \theta e^{-2\rho_2 h} \left(\int_0^s d\zeta \Gamma_{\psi}(\zeta) \cos(\rho_2 \zeta \sin \theta) \right)^2$$

$$\left. - \frac{i}{\pi^2} \int_0^{\pi} d\theta \int_0^{\infty} d\rho \rho^2 \sec \theta \frac{e^{-2\rho h}}{\rho - (\omega + \rho \cos \theta)^2} \right.$$

$$\left. \left(\int_0^s d\zeta \Gamma_{\psi}(\zeta) \cos(\rho \zeta \sin \theta) \right)^2 \right] \quad (85)$$

In order to analyse the increment at leading order in the lift and drag due to the DC terms in the neighbourhood of the resonance frequency, it is permissible to set $\theta = \theta_c = 0$ and $\rho_1 = \rho_2 = \rho_c = 1/4$ in the single integrals (84) and (85) and to retain the term in $\ln \delta \omega$ to obtain by using (32)

$$L_{DC} \approx - \frac{e^{-h/2}}{2 + \left(\frac{32\pi}{\Gamma_{\psi}^T \ln \delta \omega} \right)^2} \cdot \frac{(\Gamma_{\psi}^T)^2}{\Gamma_{\psi}^T} \quad (86)$$

and

$$|D_{DC}| = \frac{16\sqrt{2}\pi e^{-h/2} (\ln\delta\omega)^{-1}}{2 + \left(\frac{32\pi}{\Gamma_{\psi}^T \ln\delta\omega}\right)^2} \left(\frac{\Gamma_{\psi}^T}{\Gamma_{\psi}^T}\right)^2$$

$$= -\frac{16\sqrt{2}\pi}{\Gamma_{\psi}^T \ln\delta\omega} L_{DC} \quad (87)$$

where

$$\Gamma_{\psi}^T = 2 \int_0^s \Gamma_{\psi}(\zeta) d\zeta$$

Again, the drag reaches its maximum very close to ω_c at $\omega - \omega_c = \exp(-16\pi/\sqrt{2}/\Gamma_{\psi}^T)$ and its value is, at leading term

$$|D_{DCMAX}/\Gamma_{\psi}^T| = \frac{e^{-h/2}}{4\Gamma_{\psi}^T} \quad (88)$$

whereas for the lift we have at $\omega = \omega_c - 0$

$$L_{DCMAX}/\Gamma_{\psi}^T = -\frac{e^{-h/2}}{\Gamma_{\psi}^T} \quad (89)$$

These results are also represented in Figs. 3(a) and 3(b), and are compared against the linearized solution only for the drag. The increment in the lift force given by the linearized theory is identical zero. Comparing the three-dimensional results for a lifting surface (Fig. (3)) with the two-dimensional equivalent (Fig. (2)), shows that the peak in the generalized solution for the lift and force as well as the singularity in the regular (linearized) solution is much more localized in the 3-D case and resemble the behaviour of a delta function. Hence most of the numerical solutions, which were performed for frequencies in the neighbourhood of ω_c , do not predict the occurrence of this concentrated singularity with the exception of [7].

6. SUMMARY, CONCLUSIONS AND RECOMMENDATIONS FOR FUTURE INVESTIGATIONS

The flow near resonant frequency past a singularities system has been examined for the case in which the time-dependent term is a small perturbation of the steady, non-uniform, flow term which in turn is a small disturbance of the uniform flow.

It has been found that in the case of a lifting surface the regular perturbation expansion, whose leading term is the usual linearized approximation for uniform flow, is not uniform near resonance and the steady flow term has to be retained in the zero-order approximation. A closer scrutiny of

(21) and (24) reveals that as a matter of fact only part of the steady flow terms has to be kept in (13) and the basic free-surface condition which renders a uniformly valid solution is

$$[-\omega^2 + 2i\omega(-1+u) \frac{\partial}{\partial x} + (1-2u) \frac{\partial^2}{\partial x^2} + \frac{\partial}{\partial y}] \psi_r = c_0(x, z) \quad (\text{for } y=0) \quad (90)$$

replacing (11) where $u = \partial z / \partial x$ is the horizontal component of the steady velocity on $y=0$. Eq. (90) may be in turn traced back to

$$[\frac{\partial^2}{\partial t^2} + 2(-1+u) \frac{\partial^2}{\partial x \partial t} + (-1+u)^2 \frac{\partial^2}{\partial x^2} + \frac{\partial}{\partial y}] (\psi_r e^{i\omega t}) = c_0(x, z) e^{i\omega t} \quad (91)$$

It is seen, therefore, that essentially it is the non-uniform horizontal current of velocity $-1+u$ which modulates the resonant waves. Further inspection of the results shows that at first-order only u_{s0} , the velocity induced by the vortex and its image across $y=0$ corresponding to zero Froude-number, is contributing at the leading term in (90). Thus, the far free-waves associated with the solution of (90) should be viewed as waves modulated by the uniform flow plus the current associated with the steady perturbation horizontal velocity u_{s0} . Finally, the solution by the Fourier Transform method developed in Sects. 3.3 and 4.2 indicates that the current is sufficiently strong to remove the resonance if $\lim_{k \rightarrow 0} u_{s0}(k) \neq 0$ in two dimensions or if $\lim_{\alpha \rightarrow 0} u_{s0}(\alpha, 0) \neq 0$ in three dimensions.

Hence, the current removes the resonant conditions if

$$\int_{-\infty}^{\infty} u_{s0}(x, 0) dx \neq 0 ; \quad \int_{-\infty}^{\infty} dx \int_{-\infty}^{\infty} dz u_{s0}(x, 0, z) \neq 0 \quad (92)$$

in two- and three- dimensions, respectively. Since a lifting surface, in contrast with a pressure patch or a non lifting body, leads to a constant value of the integrals in (92), it was possible to determine the finite amplitude of the free waves at $\omega = \omega_c$ in this case.

In other words, since the resonance in the usual linearized approximation is interpreted as the result of the inability of free-waves to propagate their energy away from the singularity because of the equality between the group velocity and the current velocity, it is seen that the removal of reso-

nance by a steady current satisfying (92) can be as well interpreted as the ability of such a current to let wave energy escape to infinity.

Another point of interest is the change of phase related to the non-uniform current, which results in a cancellation of the resonant drag and a substantial change of the time averaged lift in comparison with the linearized solution.

We pursue at present the removal of resonance for non-lifting bodies by incorporating higher order effects of the steady component. Another topic of theoretical interest is the nonlinear interaction of the time-depending terms and the solution of the initial value problem. We hope that these and related problems can be attacked along the lines of the present study.

REFERENCES

1. Haskind, M.D., "On the Motion with Waves of Heavy Fluids" (in Russian), *Prinkl. Mat. Mekh.*, Vol. XVIII, No.1, pp.15-26, 1954.
2. Debnath, L. and Rosenblat, S., "The Ultimate Approach to the Steady State in the Generation of Waves on a Running Stream", *Quarterly Journ. of Mech. and Appl. Math.*, Vol.22, Part.2, pp.221-233, 1969.
3. Kaplan, P., "The Waves Generated by the Forward Motion of Oscillating Pressure Distributions", *Proc. Fifth Midwestern Conf. on Fluid Mech.*, Ann Arbor Mich., pp.316-329, 1957.
4. Wu, Y.Y., "Water Waves Generated by the Translatory and Oscillatory Surface Disturbance", *Calif. Inst. of Tech., Engineering Div.*, Rep.85-3, 1957.
5. Becker, T., "Das Wellenbild einer unter der oberfläche eines stromes schwerer flüssigkeit pulsierender quelle", *ZAMM*, Vol. 38, pp. 391-399, 1978.
6. Taylor, A.B., and Vanden Driessche, P., "Small Amplitude Surface Waves due to a Moving Source", *Quarterly Journ. of Mech. and Appl. Math.*, Vol. 27, Part 3, pp. 317-345, 1974.
7. Doctors, L.J., "Hydrodynamic Power Radiated by a Heaving and Pitching Air-Cushion Vehicle", *Journal of Ship Res.*, Vol. 22, No. 2, pp. 67-79, 1978.
8. Euvrard, D., Jami, A., Morice, C., and Ousset, Y., "Calcul numérique des oscillations d'un navire engendrées par la houle", *Journal de Mécanique*, Vol. 16, No. 2, pp. 281-326, 1977.

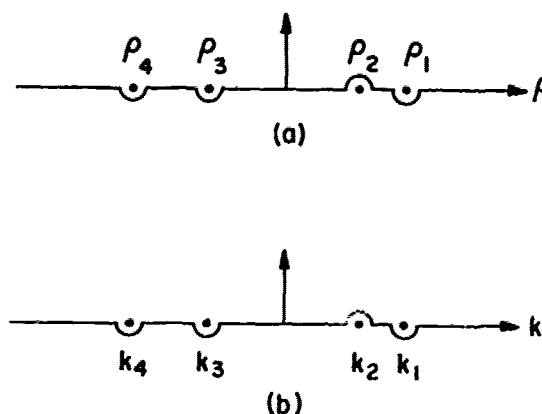


FIG. 1

INVERSION PATH IN THE FT PLANE (a) 3D FLOWS FOR $0 < \omega < \omega_c$ AND ANY θ OR FOR $\omega > \omega_c$, $\theta > \theta_c$. (b) 2D FLOWS FOR $\omega_c > \omega > 0$.

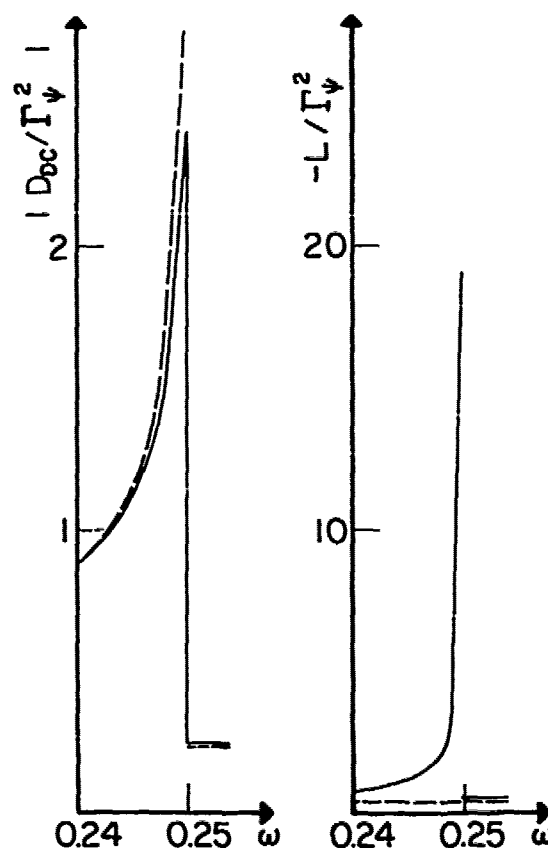


FIG. 2

VARIATION OF THE D.C TERMS OF DRAG AND LIFT ON A 2D POINT VORTEX IN THE NEIGHBORHOOD OF THE CRITICAL FREQUENCY FOR $h = 0.1$, $\Gamma_0 = 0.1$
 _____ GENERALIZED SOLUTION EQS. (75) AND (76)
 -----LINERIZED SOLUTION

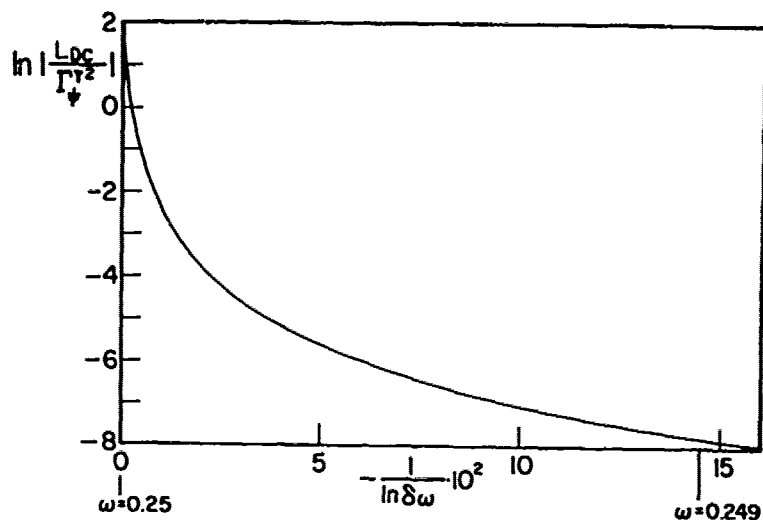


FIG. 3(a) VARIATION OF THE D.C INCREMENT COMPONENT OF THE LIFT EXPERIENCED BY A 3D LIFTING LINE IN THE NEIGHBORHOOD OF THE CRITICAL FREQUENCY. $h=0.1$, $\Gamma_{\phi}^T = 0.1$ (EQ.(86))

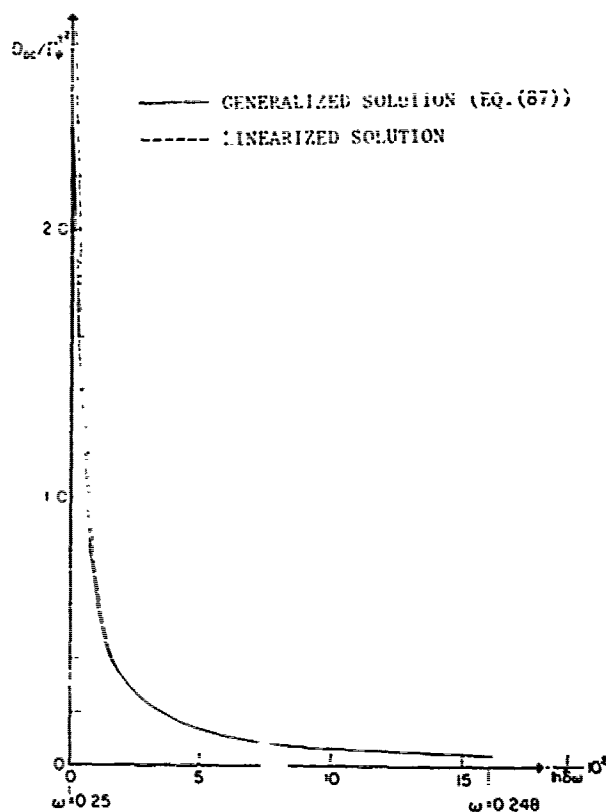


FIG. 3(b) VARIATION OF THE D.C INCREMENT COMPONENT OF THE DRAG EXPERIENCED BY A 3D LIFTING LINE IN THE NEIGHBORHOOD OF THE CRITICAL FREQUENCY FOR $h=0.1$, $\Gamma_{\phi}^T = 0.1$

Discussion

H. Maruo (Yokohama Univ)

The resonance phenomena associated with an oscillating body with forward speed under a free surface at critical frequency were first pointed out by Yamamoto (1946) in two- and three-dimensional cases of submerged bodies. Hanaoka (1951-1957) carried out extensive investigations in the case of thin ships in various modes of oscillations. He has attributed the divergence of the integral in the expression of hydrodynamic forces at the critical frequency $\tau = 1/4$ to a phenomenon analogous to one that occurs in the linearized theory of a thin wing in a compressible flow at Mach number one, and he considered this singularity to be removed in the actual phenomena on account of the non-linear effect which would possibly suppress the infinite heave of the free surface. These works are not quoted in this paper.

In the present paper, the authors have shown that the singularity is removed by the presence of the steady potential due to the forward motion. This result is very interesting because the effect of the steady potential to the periodical potential is not a genuine non-linear effect. It is usually accepted that the hydrodynamic damping force is determined by the asymptotic behavior of radiating waves at a great distance. The steady potential, on the other hand, decays rather rapidly except in the region inside the Kelvin angle. Since the outbreak of the singularity in the damping force is usually attributed to the singular behavior of the

radiating waves towards upstream side, I have a rather curious feeling about the fact that the steady potential gives such a drastic influence to the radiating waves. The asymptotic wave pattern was illustrated by several authors including Hanaoka. It would be instructive if the distortion of the radiating waves due to the presence of the steady potential were demonstrated.

Author's Reply

G. Dagan and T. Mikh (Tel-Aviv Univ)

We regret that we were not aware of the works of Yamamoto and Hanaoka when reviewing the linearized theory and we are thankful to Prof. Maruo for drawing our attention to them.

Herewith a few comments on Prof. Maruo's observations.

(i) We have shown that resonance is removed by the singular (local) term of the nonuniform steady potential. The latter is not confined into the downstream Kelvin angle, but influences equally the downstream and upstream flow regions.

(ii) Prof. Maruo quite rightly wonders about the drastic influence of the steady potential upon resonance. We would like to emphasize that only in the case of a lifting surface, with its long range influence expressed by Eq. (92) of our paper, the resonance is removed by the first-order correction of the steady flow.

Session IV

HULL FORM 2

— PROBLEMS IN WAVES —

Chairman
Seizo Motora
University of Tokyo
Tokyo, Japan

The Unified Theory of Ship Motions

J. Nicholas Newman and Paul Sclavounos

Massachusetts Institute of Technology

Cambridge, Massachusetts, U.S.A.

ABSTRACT

A linear theory is presented for the heave and pitch motions of a slender ship, moving with forward velocity in calm water. The velocity potential includes a particular solution similar to that of the high-frequency strip theory, plus a homogeneous component which accounts for interactions along the length in an analogous manner to the low-frequency "ordinary" slender-body theory. The resulting "unified" theory is valid more generally for all frequencies of practical importance.

Computations are presented for the added-mass and damping coefficients of a floating spheroid, a Series 60 hull, and a frigate. Comparisons with experimental data and with zero-speed exact theories confirm the utility of the unified theory.

This theory can be used to analyse the performance of elongated wave-energy absorbers. This application is illustrated for a hinged "Cockerell" raft.

1. INTRODUCTION

Conventional ship hulls are slender in the geometrical sense, with small beam and draft compared to their length. This is convenient from the standpoint of hydrodynamic analysis, since slender-body approximations simplify the governing equation and boundary conditions.

Geometrical slenderness is sufficient to justify the classical slender-body theory of incompressible aerodynamics, but in ship hydrodynamics the wavelength represents an

additional relevant length scale which must be considered in developing asymptotic theories of practical utility. This complication in slender-ship theory applies not only to unsteady motions in waves, but also to the analysis of steady-state wave resistance. The present paper is concerned only with the former problem, and is restricted to the solution of the radiation problem for forced heave and pitch motions in otherwise calm water. Work currently in progress by Sclavounos (1980) will extend this theory to the diffraction problem of incident waves, including the determination of the exciting forces and moments.

Substantial wave excitation in heave or pitch requires an incident wavelength greater than the ship length, typically by a factor of 1.5 or more. This implies a regime where, based on the beam and draft, a long-wavelength or low-frequency approximation is appropriate. Hydrostatic restoring forces and the Froude-Krylov exciting force are dominant, and the resulting theoretical description of ship motions is relatively simple. This is the leading-order result of "ordinary" slender-body theory.

For a ship proceeding with significant forward speed, the Doppler effect increases the frequency of encounter and shortens the radiated wavelength. Resonance occurs when this wavelength is comparable to the beam and draft, and therefore much less than the ship length. This is the applicable regime of strip theory, where three-dimensional interactions in the longitudinal direction are negligible.

The practical domain of ship motions in waves obviously embraces both of the above regimes, in the sense that the frequency of encounter may be low, especially for following seas, or high as in the case of a fast vessel in head seas. In the context of slender-body theory, it is desirable therefore to avoid restrictive assumptions concerning the wavelength or the frequency of encounter. That objective has led to the development of a "unified" slender body theory which embraces both long and short wavelengths in the sense defined above.

The theoretical framework for the unified theory of ship motions is developed in Newman (1978) and in more detail, for the special case of zero forward velocity, by Mays (1978). The latter work includes computations of the damping and added-mass coefficients for a floating spheroid, and the remarkable agreement of the latter with exact three-dimensional computations was an important motivation for extending the computations to ship-like forms, and to non-zero forward velocity. The present paper is intended to report on these efforts.

A brief review is given of the theoretical framework for the unified theory, in Section 2, and supplemented in Section 3 by the derivation of a simplified expression for the kernel function which governs longitudinal interactions along the ship's length. Numerical results for the added-mass and damping coefficients are presented in Section 4, to illustrate the practical utility of this theory in predictions of ship motions in waves. The unified theory also has been used to analyse the wave-energy absorption of elongated devices such as the Cockerell raft and Kaimei ship, and the results are described briefly in Section 5.

Before proceeding with the mathematical details of the unified theory, it may be useful to present a brief description which avoids so far as possible the use of mathematical arguments. The fundamental assumptions are that (1) the fluid motion is irrotational and incompressible, (2) the oscillatory motions of the ship and of the fluid are sufficiently small to linearize, and (3) the ship hull is geometrically slender.

For heave and pitch motions and, more generally, situations where the distribution of normal velocity on the hull surface is a slowly-varying function along the length, the flow is essentially two-dimensional in the near-field close to the hull. Changes in the x-direction are relatively small in this region, by comparison to changes in the transverse plane. Thus the flow in the near field is governed by the two-dimensional Laplace equation, and subject to the simplest linearized free-surface boundary condition which applies in two dimensions and is independent of forward velocity. These characteristics of

the *inner* problem, and its solution, are similar to strip theory.

The *outer* problem which applies far from the hull surface is fully three-dimensional, with gradients in the longitudinal direction comparable to those in the transverse plane. The three-dimensional Laplace equation governs the solution, subject to the complete linearized free-surface boundary condition (where the forward speed is a significant parameter) and the radiation condition of outgoing waves at infinity.

Neither the inner nor the outer problem is unique, as described above, since nothing has been stated about their respective asymptotic behavior far away in the inner problem, and close to the ship in the outer problem. Following the method of matched asymptotic expansions, this nonuniqueness is resolved by requiring the two solutions to be compatible in a suitably defined *overlap* region.

In the special case of ordinary slender-body theory, the frequency is asymptotically small in the inner solution, and the "rigid" free-surface condition applies. For vertical motions of the ship's section there is a net source strength, and thus the inner solution is logarithmically singular at "infinity", in the overlap domain. As in the classical slender-body theory of aerodynamics, this determines the effective source strength of the outer solution. Conversely, the inner limit of the outer solution determines a nontrivial additive "constant" in the inner solution, which is a function of the longitudinal coordinate.

By comparison, in the high-frequency domain of strip theory, waves are present in the inner problem via the free-surface condition. Their outgoing radiated behavior at "infinity" can be matched directly to the inner limit of an appropriate three-dimensional source distribution, along the ship's axis. The inner free-surface condition does not admit an additive constant, and hence the inner solution is not affected by the matching process, justifying the strip-theory solution itself.

Proceeding without restriction of the frequency requires that the inner free-surface condition is preserved, as in the high-frequency case. However, the corresponding strip-theory solution with outgoing waves at "infinity" is not sufficiently general to match with the outer solution. Therefore a homogeneous solution is included in the inner problem, with standing waves at "infinity"; the coefficient of this homogeneous solution is determined from an integral equation similar to that which determines the additive constant in ordinary slender-body theory.

In summary, the unified solution is an extension of the ordinary slender-body theory and strip theory which apply respectively in the low- and high-frequency limits. The inner solu-

tion is similar to, but more general than that of strip theory. The two-dimensional damping and added-mass coefficients are the fundamental parameters of this inner solution but, with forward velocity, the complete solution of the kinematic hull boundary condition requires additional parameters to be evaluated. The integral equation associated with the matching requirement is an additional complication, but its solution is a relatively minor chore by comparison to the numerical procedures required in the strip theory. Thus, while the concept of the unified theory is a nontrivial extension of strip theory, the computational effort required to utilize this more general approach is not substantially greater. The numerical results which follow more than justify this additional effort.

2. THEORETICAL DERIVATION

We consider a ship which moves in the positive x-direction, with constant forward velocity U , while performing small harmonic oscillations of frequency ω in heave and pitch. These and other oscillatory quantities are expressed in complex form, with the time factor $e^{i\omega t}$ understood throughout. Both U and ω are restricted to be >0 . The analysis in this Section is abbreviated from Newman (1978), where more details are provided.

The principal task is to solve for the complex velocity potentials ϕ_j , due to heave ($j=3$) and pitch ($j=5$) motions of unit amplitude. With the assumptions stated in the Introduction, these potentials are governed by the three-dimensional Laplace equation

$$\phi_{jxx} + \phi_{jyy} + \phi_{jzz} = 0 \quad (1)$$

and, in the frame of reference moving with the steady forward velocity of the ship, by the linearized free-surface boundary condition

$$-\omega^2 \phi_j - 2i\omega U \phi_{jx} + U^2 \phi_{jxx} + g \phi_{jz} = 0, \quad \text{on } z = 0. \quad (2)$$

Here $z = 0$ is the plane of the free surface and z is positive upwards. Far from the ship the potentials ϕ_j must satisfy a suitable radiation condition of outgoing waves and, for large depths, the condition of vanishing motion as $z \rightarrow -\infty$.

The potentials ϕ_j are distinguished by their respective boundary conditions on the wetted surface of the ship hull. With the instantaneous position of this surface replaced by its steady-state mean \bar{S} , the appropriate boundary conditions are

$$\phi_{3n} = i\omega n_3 + U m_3, \quad (3)$$

$$\phi_{5n} = -i\omega x n_3 - U x m_3 + U n_3. \quad (4)$$

Here the subscript n denotes normal differentiation, with the unit normal vector pointing out of the fluid domain, n_j is the component of this vector parallel to the x_j axis, and m_3 is an auxiliary function defined in terms of the steady-state perturbation potential $U\bar{\phi}$ by the relation*

$$m_3 = -n_2 \bar{\phi}_{yz} - n_3 \bar{\phi}_{zz}, \quad \text{on } \bar{S}. \quad (5)$$

Since $\bar{\phi}$ satisfies the rigid free-surface boundary condition in the inner region, m_3 is independent of U .

The boundary-value problem for ϕ_j can be restated separately in the inner region, where the transverse radius $r = (y^2 + z^2)^{1/2}$ is small compared to the ship's length, and in the outer region where r is large compared to the beam and draft. The radiation condition (and vanishing of the solution as $z \rightarrow -\infty$) are applicable only to the outer solution, and the boundary conditions (3) and (4) to the inner solution. The missing conditions in each case are replaced by the requirement of matching, in an overlap region where r is large compared to the beam and draft but small compared to the length.

Gradients in the x-direction are neglected in solving the inner problem. The governing equation is

$$\phi_{jyy} + \phi_{jzz} = 0, \quad (6)$$

subject to the free-surface boundary condition

$$-\omega^2 \phi_j + g \phi_{jz} = 0, \quad \text{on } z = 0 \quad (7)$$

Equations (6) and (7) are applicable to the two-dimensional strip theory of ship motions. In view of the boundary conditions (3) and (4), particular solutions of the inner problem can be expressed in the form

$$\phi_j^{(s)} = \epsilon_j + U \hat{\epsilon}_j, \quad (8)$$

where the latter potentials satisfy (6), (7), and, on the hull profile, in planes $x = \text{constant}$,

$$\phi_{3n} = i\omega n_3, \quad (9)$$

$$\hat{\phi}_{3n} = m_3, \quad (10)$$

$$\phi_5 = -x \phi_3, \quad (11)$$

$$\hat{\phi}_5 = -x \hat{\phi}_3 - (i/\omega) \phi_3. \quad (12)$$

*The subscripts $j=1,2,3$ correspond respectively to (x, y, z) .

The potentials in (8) also satisfy the extraneous two-dimensional radiation condition. Thus we add to (8) a homogeneous solution of (6), (7), and of the boundary condition on the hull. This homogeneous solution can be obtained simply in the form $(\phi_3 + \bar{\phi}_3)$ where the overbar denotes the conjugate of the complex potential ϕ_3 . This homogeneous solution behaves like a two-dimensional standing wave at large distance from the hull, and can be regarded physically as the superposition of two diffraction solutions with symmetric incident waves acting upon the fixed hull profile.

In summary, the general solution of the inner problem takes the form

$$\phi_j = \phi_j^{(s)} + C_j(x) (\phi_3 + \bar{\phi}_3) \quad (13)$$

where the interaction function $C_j(x)$ is an arbitrary "constant" in the inner solution to be determined from matching.

The outer solution follows by considering the complete Laplace equation (1) and free-surface condition (2), but ignoring the hull boundary conditions. Assuming symmetry about the plane $y=0$, an appropriate solution follows from a longitudinal distribution of sources along the ship's length,

$$\phi_j = \int_L q_j(\xi) G(x-\xi, y, z) d\xi. \quad (14)$$

Here $q_j(x)$ is the source strength, and G denotes the potential of a "translating-pulsating" source situated on the x -axis at the point $x = \xi$. This potential is expressed generally in the form of a double Fourier integral over the free surface. Of particular utility in our analysis is the Fourier transform of G , with respect to x , which can be expressed as

$$G^*(y, z; k) = \int_{-\infty}^{\infty} G(x, y, z) e^{ikx} dx \\ = -\frac{1}{4\pi} \int_{-\infty}^{\infty} du \frac{\exp[z(k^2 + u^2)^{1/2} + iyu]}{(k^2 + u^2)^{1/2} - \kappa}. \quad (15)$$

where

$$\kappa = (\omega + Uk)^2/g. \quad (16)$$

When $|k| < \kappa$, there are two symmetric real poles in (15), and the appropriate contour of integration is deformed in their vicinity such that $\text{Im}[u^2(\omega + Uk)] > 0$.

In order to match the inner approximation of (14) in the overlap region, an asymptotic approximation of (15) is required for small values of (ky, kz) . The desired result can be expressed in the

form

$$G^*(y, z; k) \approx G_{2D} - \frac{1}{2\pi} (1 + Kz) f^*(k), \quad (17)$$

where $G_{2D} \equiv G^*(y, z; 0)$ is the two-dimensional source potential, which satisfies (6) and (7), and

$$f^* = \ln(2K/|k|) + \pi i - \frac{\cos^{-1}(\kappa/|k|) - \pi}{(k^2/\kappa^2 - 1)^{1/2}}, \\ (k^2/\kappa^2 > 1), \quad (18)$$

$$f^* = \ln(2K/|k|) + \pi i - \frac{\cosh^{-1}(\kappa/|k|) + \pi i \text{sgn}(\omega + Uk)}{(1 - k^2/\kappa^2)^{1/2}}, \\ (k^2/\kappa^2 < 1), \quad (19)$$

where $K = \omega^2/g$.

It remains to match the inner and outer solutions (13) and (14). This may be carried out in the Fourier domain, using the convolution theorem to transform (14), and the appropriate matching condition takes the form

$$\phi_j^{(s)*} + [C_j(x) (\phi_3 + \bar{\phi}_3)]^* = q_j^* G^*. \quad (20)$$

Far from the hull in the inner domain, the two-dimensional potentials on the left side of (20) can be expressed in terms of the effective source strengths, in the form

$$\phi_j = \sigma_j G_{2D} \quad (21)$$

$$\hat{\phi}_j = \hat{\sigma}_j G_{2D} \quad (22)$$

Using (8), (17), and the fact that $\text{Im}(G_{2D}) = \frac{1}{2} e^{Kz} \cos Ky$, and equating separately the factors of G_{2D} in (20), it follows that

$$\sigma_j^* + U \hat{\sigma}_j^* + [C_j(\sigma_j + \bar{\sigma}_j)]^* = q_j^* \quad (23)$$

and

$$-i(C_j \bar{\sigma}_j)^* = -\frac{1}{2\pi} q_j^* f^*. \quad (24)$$

The error in the last equation is a factor $1 + O(K^2 r^2)$.

*Equation (16) corrects a sign error in equation (4.9), and in the denominators of (4.6) and (4.8) of Newman (1978).

The inverse Fourier transforms of the last equations provide the relations

$$\sigma_j + U\bar{\sigma}_j + C_j(\sigma_j + \bar{\sigma}_j) = q_j, \quad (25)$$

$$2\pi i C_j \bar{\sigma}_j = \int_L q_j(\xi) f(x-\xi) d\xi, \quad (26)$$

where

$$f(x) = \frac{1}{2\pi} \int_{-\infty}^{\infty} dk e^{-ikx} f^*(k). \quad (27)$$

After elimination of C_j from (25) and (26), the outer source strength is determined from the integral equation

$$q_j(x) - \frac{1}{2\pi i} (\sigma_j/\bar{\sigma}_j + 1) \int_L q_j(\xi) f(x-\xi) d\xi = \sigma_j(x) + U\bar{\sigma}_j(x). \quad (28)$$

Assuming a numerical solution for the two-dimensional potentials in (8), and the corresponding source-strengths $\sigma_j, \bar{\sigma}_j$, the integral equation (28) may be solved for the unknown outer source strength $q_j(x)$. The complete inner solution follows from (13) and (25), in the form

$$\phi_j = \phi_j^{(s)} + (2\pi i \bar{\sigma}_j)^{-1} (\sigma_j + \bar{\sigma}_j) \int_L q_j(\xi) f(x-\xi) d\xi. \quad (29)$$

The first term on the right side of (29) is the strip-theory potential (including the contribution from ϕ_j which usually is ignored). The remaining contribution to (29) represents the three-dimensional interaction between adjacent sections.

In the high-frequency domain the integral in (29) tends to zero, and the strip-theory solution remains. Conversely in the low-frequency regime the two-dimensional potentials in (29) simplify and the ordinary slender-body result is recovered as derived by Newman and Luck (1964). The unified potential (29) is valid more generally, for all wavenumbers between these two limiting regimes.

In the special case of zero forward velocity ($U=0$), the unified solution (29) reduces to a form closely related to the "interpolation solution" derived by Maruo (1970). Maruo's approach is rather different, but the only change in the final result is that the homogeneous solution ($\phi_j + \bar{\phi}_j$) is replaced by $(1+K_2)$, and the amplitude of the two-dimensional strip-theory potential is modified accordingly to satisfy the boundary condition on the body.

3. REDUCTION OF THE KERNEL

The kernel (27) in the integral equation (28) is defined by the inverse Fourier transform of the function f^* given by (18) and (19). This kernel can be interpreted as the value of the source potential on the x -axis, after subtraction of the two-dimensional oscillatory source potential G_{2D} . Singularities can be expected, especially at $x=0$, and a careful analysis is required.

The singular behavior at $x=0$ can be mitigated by considering the integral of $f(x)$, or the inverse transform of $f^*(-ik)$. If this modification is offset by multiplying the transformed source strength q_j^* by $(-ik)$, in (24), (29) is replaced by

$$\phi_j = \phi_j^{(s)} + (2\pi i \bar{\sigma}_j)^{-1} (\sigma_j + \bar{\sigma}_j) \int_L q_j'(\xi) F(x-\xi) d\xi. \quad (30)$$

Here q_j' denotes the derivative of the source-strength, and the new kernel is

$$F(x) = \frac{i}{2\pi} \int_{-\infty}^{\infty} f^*(k) e^{-ikx} Jk/k. \quad (31)$$

Since $f^*=0(k)$ as $k \rightarrow 0$, the integral (31) is convergent and $F(x)$ vanishes as $|x| \rightarrow \infty$. There is a logarithmic infinity in $f^*(k)$ as $|k| \rightarrow \infty$, and hence in $F(x)$ as $x \rightarrow 0$, but this singularity can be integrated in (30) without difficulty.

The integral in (31) can be simplified by considering the function

$$\Lambda(k) = \ln(2K/\kappa) - (1-k^2/\kappa^2)^{-1/2} \ln[\kappa/\kappa + (\kappa^2/k^2 - 1)^{1/2}], \quad (32)$$

where $\kappa(k)$ is defined by (16). $\Lambda(k)$ is analytic throughout the finite k -plane, except for a branch cut on the negative real axis. With appropriate values determined on each side of this branch cut, in the manner described by Slavounov (1980), it follows that

$$f^*(k) = \Lambda(k+i0) + \pi i \pm \pi i H(-k) + (|1-k^2/\kappa^2|)^{-1/2} g_2(k). \quad (33)$$

Here $H(-k)$ is the Heaviside unit function, equal to one for $k < 0$ and zero otherwise, and

$$g_+(k) = 2-i, \quad (-\infty < k < k_1), \quad (34a)$$

$$g_+(k) = 0, \quad (k_1 < k < k_2), \quad (34b)$$

$$g_+(k) = -2\pi i, \quad (k_2 < k < 0), \quad (34c)$$

$$g_-(k) = 0, \quad (-\infty < k < 0), \quad (34d)$$

$$g_+(k) = -\pi i, \quad (0 < k < k_3, \tau < 1/4), \quad (34e)$$

$$g_+(k) = \pi, \quad (k_3 < k < k_4, \tau < 1/4), \quad (34f)$$

$$g_+(k) = -\pi i, \quad (k_4 < k < \infty, \tau < 1/4), \quad (34g)$$

$$g_+(k) = -\pi i, \quad (0 < k < \infty, \tau > 1/4). \quad (34h)$$

The branch-points of the square-root function in (33) have been defined by

$$k_{1,2} = -(g/2U^2) [1+2\tau \pm (1+4\tau)^{1/2}], \quad (35)$$

$$k_{3,4} = (g/2U^2) [1-2\tau \mp (1-4\tau)^{1/2}], \quad (36)$$

and

$$\tau = \omega U/g. \quad (37)$$

Note that $k_{1,2}$ are real and negative, whereas $k_{3,4}$ are positive for $\tau < 1/4$, and complex-conjugate otherwise.

From Jordan's lemma

$$\int_{-\infty}^{\infty} \Lambda(k-i0) e^{-ikx} dk/k = 0, \quad (x \leq 0). \quad (38)$$

Hence, from (31) and (33),

$$F(x) = F_1(x) + F_2(x), \quad (x < 0), \quad (39a)$$

$$F(x) = F_2(x), \quad (x > 0), \quad (39b)$$

where

$$\begin{aligned} F_1(x) = & - \int_{-\infty}^{k_1} e^{-ikx} [1+(1-k^2/\kappa^2)^{-1/2}] dk/k \\ & - \int_{k_1}^{k_2} e^{-ikx} dk/k \\ & - \int_{k_2}^0 e^{-ikx} [1-(1-k^2/\kappa^2)^{-1/2}] dk/k, \end{aligned} \quad (40)$$

and

$$\begin{aligned} F_2(x) = & -\frac{1}{2} \left(\int_0^{k_3} + \int_{k_4}^{\infty} \right) e^{-ikx} [1-(1-k^2/\kappa^2)^{-1/2}] dk/k \\ & - \frac{1}{2} \int_{k_3}^{k_4} e^{-ikx} [1-i(1-k^2/\kappa^2)^{-1/2}] dk/k, \end{aligned} \quad (\tau < 1/4), \quad (41a)$$

$$F_2(x) = -\frac{1}{2} \int_0^{\infty} e^{-ikx} [1-(1-k^2/\kappa^2)^{-1/2}] dk/k, \quad (\tau > 1/4). \quad (41b)$$

The function F_1 is logarithmically infinite at $x=0$, but F_2 is regular at this point for $U>0$. From (39) it follows that the logarithmic singularity exists only on the downstream side of $x=0$.

The singularity in F_1 can be displayed explicitly by using properties of the sine and cosine integrals to express (40) in the alternative form

$$\begin{aligned} F_1(x) = & \left(\int_{-\infty}^{k_1} - \int_{k_2}^0 \right) e^{-ikx} [1-(1-k^2/\kappa^2)^{-1/2}] dk/k \\ & - \left(\int_{k_1}^0 + \int_{k_2}^0 \right) (1-e^{-ikx}) dk/k \\ & - 2[\ln(\omega|x|/U) + \gamma + \pi i/2]. \end{aligned} \quad (42)$$

Here $\gamma=0.577\dots$ is Euler's constant. The integrals in (41) and (42) are convergent for all values of x , if $U>0$, and can be evaluated by numerical quadratures.

Both limiting forms of the kernel, for zero forward velocity and for zero frequency, can be derived by letting $\tau \rightarrow 0$. The resulting integrals in (40) and (41a) are evaluated after replacing the branch-points (35) and (36) by their limiting values, $k_{1,4} \rightarrow \mp(g/U^2)$ and $k_{2,3} \rightarrow \mp K$, and approximating κ by $U^2 k^2/g$ or K , respectively. In this manner it can be shown that, for $\tau=0$,

$$F(x) = \pm \frac{1}{2} [\ln(2K|x|) + \gamma + \pi i]$$

$$\begin{aligned} & + \frac{\pi}{4} \int_0^{K|x|} [H_0(t) + Y_0(t) + 2i J_0(t)] dt \\ & - \frac{\pi}{4} [(2\bar{1}) Y_0(g|x|/U^2) - H_0(gx/U^2)], \\ & (x \geq 0). \end{aligned} \quad (43)$$

Here H_0 , Y_0 and J_0 are the Struve and Bessel functions of order zero.

The contribution from the last line in (43) vanishes for $U=0$, and the resulting kernel is equivalent to that derived by Ursell (1962). In this case, as in classical slender-body theory without a free surface, the logarithmic singularity is antisymmetrical.

For the steady-state case $\omega=0$, on the other hand, the integral in (43) vanishes and the result is consistent with that of Tuck (1963). As $x \rightarrow 0$, the resulting singularity from the first term on the right-hand side of (43) is cancelled by the Bessel function Y_0 and, as stated above for the more general unsteady case, there is no upstream logarithmic singularity. (The contribution from $\ln(K)$ in the first term is cancelled by a similar factor in the low-frequency limit of the two-dimensional source potential G_{2D} .)

The regular part of the kernel (27) as a function of x/L is shown in Figure 1 for a Froude number 0.2 and two values of τ , 0.2 and 0.7 less and greater than $1/4$ respectively.

4. ADDED-MASS AND DAMPING COEFFICIENTS

The principal application of the results above is to predict the hydrodynamic pressure force and moment, acting upon a heaving and pitching ship hull in response to its oscillations. With the usual decomposition, these forces and moments are expressed in terms of added-mass (a_{ij}) and damping (b_{ij}) coefficients, which are the factors of the acceleration and velocity, respectively, in a linear expression for the total force and moment. Here $i=3$, for the heave force, $i=5$ for the pitch moment, and $j=3,5$ respectively for the contribution due to each mode.

A total of eight coefficients must be considered, including cross-coupling between heave and pitch. These coefficients can be derived from the inner velocity potential (29) or (30), by means of Bernoulli's equation for the linearized pressure, and after using a theorem due to E. O. Tuck (Ogilvie and Tuck, 1969) the results can be summarized in the form

$$\begin{aligned} \omega^2 a_{ij} - i\omega b_{ij} &= -i\omega \rho \iint n_i \phi_j dS \\ &- \rho U \iint (i\omega n_i \hat{\phi}_j - m_i \phi_j) dS + \rho U^2 \iint m_i \hat{\phi}_j dS \\ &- \rho \iint C_j(x) (i\omega n_i - U m_i) (\phi_j + \bar{\phi}_j) dS. \end{aligned} \quad (44)$$

Here the surface integrals are over the submerged portion of the hull and, except for

$$m_5 = n_3 - x m_3, \quad (45)$$

the quantities in (44) are defined in Section 2.

The first integral in (44) is the zero-speed strip-theory contribution, or the integral along the length of the two-dimensional added-mass and damping coefficients. The second and third integrals in (44) represent linear and quadratic effects of the forward velocity which appear (to varying degrees) in the strip theories. (The quadratic terms are sometimes regarded as higher-order, and the potential ϕ is usually ignored.) Green's theorem can be used to show that the second integral in (44) vanishes when $i=j$.

The last integral in (44) represents the three-dimensional correction from the interaction function $C_j(x)$. As $\omega \rightarrow \infty$, the integral equation (29) can be used to show that $C_j \rightarrow 0$, and the "pure" strip theory is recovered. Except for this limiting case, however, three-dimensional effects are significant in (44).

The first computations of added mass and damping based on the unified theory were performed by Mays (1978) for a prolate spheroid, floating with its major axis in the plane of the free surface, and for zero forward velocity ($U=0$). From symmetry considerations there is no cross-coupling in this case. Comparisons with the ordinary slender-body theory, strip theory, and with "exact" three-dimensional numerical solutions are included by Mays for values of the beam-length ratio equal to $1/16$, $1/8$, and $1/4$. The results for $1/8$ are reproduced in Figure 2 and it is apparent that the added-mass and damping coefficients predicted by the unified slender-body theory are in virtually perfect agreement with the exact solutions of Kim (1964) and Yeung (Bai and Yeung, 1974). By comparison, the strip theory predictions are satisfactory only for relatively high frequencies ($KB \gg 1$), and the ordinary slender-body theory is useful only for $KL \ll 1$. For the beam-length ratio equal to $1/4$ Mays's computations show almost the same degree of agreement, and demonstrate the broad range of applicability of the unified theory for zero forward velocity.

Our first computations with nonzero forward velocity were performed for a floating spheroid of beam-length ratio 1/6, for comparison with the experiments of Lee and Paulling (1966). The results were generally in agreement, but the experimental scatter precludes a definitive judgement of the degree of improvement of the unified theory relative to strip theory.

Subsequent computations were performed for two realistic hull forms where experimental data is available. In each case we show the computations based on unified theory, and the strip theory results of Salvesen, Tuck and Faltinsen (1970).

The results for a Series 60 hull (block coefficient 0.7) are shown in Figures 3 and 4, and compared with the experimental data of Gerritsma and Beukelman (1964) and Gerritsma (1966). For zero forward velocity (Figure 3) the agreement between the unified theory and experiments is very good for a_{33} , b_{33} , and b_{55} . The remaining

coefficients show a departure of the experimental data at low frequencies. The cross-coupling coefficients are symmetric in this case, and only one pair are shown. For low and moderate frequencies the differences between the unified and strip theories are substantial, and the experiments generally support the unified theory. All eight coefficients are shown in Figure 4, for a Froude number of 0.2. In this case the differences between the two theories are reduced, suggesting in the strip theory that there is some cancellation between the approximations associated with forward velocity and three-dimensionality. The agreement between the unified theory and experiments is generally favorable, with the notable exception of the cross-coupling coefficients a_{35} , a_{53} , and b_{53} .

The coefficients a_{33} , a_{55} , b_{55} and a_{35} have also been computed for the Series 60 hull by Chang (1977), using a full three-dimensional theory but neglecting the contribution from the potential ϕ . For zero forward velocity Chang's results are indistinguishable from the unified theory. For the Froude number 0.2, the same is true of a_{33} and a_{55} , whereas Chang's comparison with experiments is better for a_{53} and worse for b_{55} .

Our final results are for the Friesland class frigate hull (block coefficient 0.554) where experimental data are given by Smith (1966). The comparisons in Figures 5 and 6 are for Froude numbers of 0.15 and 0.35, respectively. Once again there is a tendency in some coefficients for the experimental data to diverge from the unified theory at low frequencies, and the cross-coupling coefficient a_{35} shows poor comparison for all frequencies. The remaining results for the lower Froude number show good to excellent agreement between the unified theory and experiments. Similar conclusions apply for the higher Froude number, except that in this case the comparison for the coefficient b_{53} is unsatisfactory. In this case, unlike the

Series 60 hull, there is good agreement for the coefficient a_{53} .

These comparisons of the added-mass and damping coefficients can be summarized with the following conclusions. In the case of zero forward velocity excellent agreement exists between the unified theory, three-dimensional numerical solutions, and experimental data. With forward velocity included, there are no complete three-dimensional computations with which to compare, and the unified theory can be judged only on the basis of experiments. Good agreement exists in most cases, but the confirmation is not satisfactory for some of the cross-coupling coefficients. Relative to the strip-theory predictions with forward speed, the unified theory provides a noticeable improvement in the diagonal coefficients a_{33} , a_{55} , b_{33} and b_{55} .

Although the accuracy of the experimental data is not well established, one possible explanation for the remaining discrepancies is that the treatment of end effects in the unified theory requires some refinement. In this context we note that the steady-state disturbance potential $U\phi$ is approximated in the inner region in a stripwise manner by assuming no interaction between subsequent cross-sections. A wall boundary condition is satisfied on the free surface and conformal mapping is used for the evaluation of m_3 through expression (5). The two dimensional velocity potentials ϕ_3 satisfying a wave free-surface condition are then evaluated using a two dimensional numerical procedure due to Yeung (1975).

This procedure breaks down at the ship ends, introducing a significant overprediction of m_3 and consequently of ϕ_3 and ϕ_5 . This difficulty has been avoided by assuming a linear variation of m_3 within 5% of the ship length away from each end, and assuming $m_3=0$ at the ends. This problem could be overcome by evaluating m_3 from the full three-dimensional double-body steady disturbance potential.

The kernel of the integral equation defined in (41) and (42) was evaluated numerically using Simpson's integration formula, with appropriate truncation corrections based on asymptotic expansions of the integrand. The number of integration points is determined to ensure a relative error less than 10^{-5} .

The integral equation (28) is solved by iteration using the strip-theory source distribution as the first iteration. The solution obtained in this manner has been checked against an independent matrix-inversion solution.

The two-dimensional strip-theory calculations were performed on an IBM370. The kernel evaluation and the solution of the integral equation were performed on a PDP11-34 minicomputer. The computation times required are estimated as follows:

TABLE 1
COMPUTATION TIMES

	IBM370 (sec)	PDP11-34 (sec)
2D potentials (ϕ_3)	3	180
2D potentials ($\hat{\phi}_3$)	4	240
Kernel and integral equation ($U=0$)	0.16	10
($U>0$)	1	60
Total time required ($U=0$)	3.16	190
($U>0$)	8	480

These estimates suggest that for finite forward velocity the additional computational effort required by unified theory is of the order of 1/7 of the two-dimensional strip-theory calculations if the latter are complete. For zero forward velocity the corresponding ratio is 1/18.

5. ELONGATED WAVE-POWER DEVICES

The unified theory can be used to analyse the performance of elongated wave-power absorbers such as the Cockerell raft and Kaimei ship, in a similar manner to the results of Newman (1979) based on the ordinary slender-body theory. In this application the forward velocity is set equal to zero, with resulting simplification of the analysis.

Following Newman (1979), we consider the power absorbed by a slender body moored in the head-sea configuration and performing vertical oscillatory motions of appropriate amplitude and phase, along its length. The power absorbed by this motion can be represented as the product of the energy flux per unit width in the incident wave system, and an "absorption width" W . In ideal circumstances W is comparable to the wavelength or body length, and substantially larger than the projected width of the body.

The absorption width can be expressed in terms of the far-field radiated wave amplitude due to the body motions, or the Kochin function $H(\theta)$ which is proportional to the radiated wave amplitude in the direction θ relative to the x -axis. If the incident waves propagate in the $+x$ -direction, and if the body motions are controlled in an optimum manner to maximize the absorption width, this quantity

can be expressed in the form

$$W = \left(\frac{2\pi}{K} \right) \frac{|H(\pi)|^2}{\int_0^{2\pi} |H(\theta)|^2 d\theta} \quad (46)$$

In long wavelengths the optimum modal amplitudes of the body increase in proportion to the wavelength, and unrealistically large motions are required for (46) to be valid. To estimate the practical limit of the absorption width we define a parameter β as the product of the beam-length ratio (b/L) and the maximum allowed vertical displacement per unit wave amplitude. Assuming arbitrarily that the maximum displacement is twice the incident wave amplitude, and that the beam-length ratio is between 0.1 and 0.2, typical values for β are 0.2 and 0.4, respectively.

With the body motions limited in the above sense, the absorption width is given by

$$W = 2\beta |LH(\pi)/b| - \frac{1}{2\pi} \beta^2 K \int_0^{2\pi} |LH(\theta)/b|^2 d\theta \quad (47)$$

for small values of β , and by (46) when β is larger than the value where (47) attains its maximum. Alternatively, with β fixed, (46) holds for $K > K_0$ and (47) for $K < K_0$, where the transition wavenumber is defined by the condition that (46) and (47) are equal.

In ordinary slender-body theory, where $Kb \ll 1$, the Kochin function is given to leading order by

$$H(\theta) = -K \int_L f(\xi) b(\xi) e^{-ik\xi \cos \theta} d\xi. \quad (48)$$

Here $f(x)$ is the vertical displacement and $b(x)$ is the local beam at the waterplane. This approximation was used by Newman (1979) to calculate the absorption width of various modal shapes, with the symmetric and antisymmetric modes (with respect to x) treated separately and superposed to obtain the total absorption width. The curves in Figure 7 show the total absorption width for an articulated raft, consisting of three rigid segments connected by two symmetric hinges.*

In the unified theory, the Kochin function can be expressed in terms of the outer source strength $q(x)$, and (48) is replaced by

$$H(\theta) = -\frac{i\omega}{2g} \int_L q(\xi) e^{-ik\xi \cos \theta} d\xi, \quad (49)$$

*For this case, and also for the Legendre polynomial modes, the values of β given by Newman (1979) should be multiplied by a factor of 2.0. This error has been corrected in Figure 7.

with $q(x)$ determined from the integral equation (28). Computations have been performed on this basis, for an articulated raft with beam-length ratio 0.1 and beam-draft ratio 2.0. These new results are shown in Figure 7, and a comparison can be made with the absorption width based on the ordinary slender-body theory. This comparison reveals that the latter approximation overestimates the absorption width by a substantial amount, when the modal amplitudes are limited, but in the shorter wavelength regime where this limitation is not applicable, the ordinary slender-body theory is quite accurate. Similar conclusions have been reached by Haren (1980) based on a three-dimensional numerical solution in the case of a body with zero draft. It appears that the ordinary slender-body theory overpredicts the magnitude of the Kochin function, and hence the limited absorption width (47), but (46) is not sensitive to this error in view of its form.

In conclusion, the earlier results of Newman (1979) based on the use of ordinary slender-body theory overpredict the performance of an elongated wave-power device, particularly in the regime of wavelengths where the absorption width is a maximum. The unified theory can be used to provide a more precise estimate of the absorption width.

ACKNOWLEDGEMENTS

It is a pleasure to acknowledge the computational assistance of Professor R. W. Yeung, and the financial support provided by the Office of Naval Research, National Science Foundation, and the Naval Sea System Command's General Hydro-mechanics Research Program administered by the David W. Taylor Naval Ship Research and Development Center.

REFERENCES

1. Bai, K. J., and Yeung, R. W. (1974). Numerical solutions to free-surface flow problems. *Proc. Symp. Nav. Hydrodyn.*, 10th ACR-204, pp. 609-647. Off. Nav. Res., Washington, D.C.
2. Chang, M.-S. (1977). Computations of three-dimensional ship motions with forward speed. *Proc. Int. Conf. Numer. Ship Hydrodyn.*, 2nd, pp. 124-135. Univ. California, Berkeley.
3. Gerritsma, J. (1966). Distribution of Hydrodynamic forces along the length of a ship model in waves. Rep. No. 144. Shipbuilding Lab., Delft University of Technology, Delft.
4. Gerritsma, J., and Beukelman, W. (1964). The distribution of the hydrodynamic forces on a heaving and pitching ship model in still water. Publ. No. 22. Shipbuilding Lab., Delft University of Technology, Delft.
5. Haren, P. G. R. (1980). Wave energy: A hydrodynamic analysis of head sea absorbers. Ph.D. Thesis, Massachusetts Institute of Technology, Cambridge, Massachusetts.
6. Kim, W. D. (1966). On a free-floating ship in waves. *J. Ship Res.* 10, 182-191, 200.
7. Maruo, H. (1970). An improvement of the slender body theory for oscillating ships with zero forward speed. *Bull. Fac. Eng., Yokohama Natl. Univ.* 19, 45-56.
8. Mays, J. H. (1978). Wave radiation and diffraction by a floating slender body. Ph.D. Thesis, Massachusetts Institute of Technology, Cambridge, Massachusetts.
9. Newman, J. N. (1979). Absorption of wave energy by elongated bodies. *Appl. Ocean Research.* 1, 189-196.
10. Newman, J. N. (1978). The theory of ship motions. *Adv. Appl. Mech.* 18, 221-283.
11. Newman, J. N., and Tuck, E. O. (1964). Current progress in the slender-body theory of ship motions. *Proc. Symp. Nav. Hydrodyn.*, 5th ACR-112, pp. 129-167. Off. Nav. Res., Washington, D.C.
12. Ogilvie, T. F., and Tuck, E. O. (1969). A rational strip theory for ship motions. Part 1. Rep. No. 013. Dep. Nav. Archit. Mar. Eng., University of Michigan, Ann Arbor.
13. Lee, C. M., and Paulling, J. R. (1966). Measurements of pressures on a heaving prolate spheroid. Rep. No. NA-66-4. College of Engineering, University of California, Berkeley.
14. Salvesen, N., Tuck, E. O., and Faltinsen, O. (1970). Ship motions and sea loads. *Soc. Nav. Archit. Mar. Eng., Trans.* 78, 250-287.
15. Sclavounos, P. (1980). On the diffraction of free surface waves by an advancing slender body. Ph.D. Thesis, Massachusetts Institute of Technology, Cambridge, Massachusetts.
16. Smith, W. E. (1966). Computation of pitch and heave motions for arbitrary ship forms. Rep. No. 148. Shipbuilding Lab., Delft University of Technology, Delft.
17. Tuck, E. O. (1963). The motion of a slender ship or submarine. Ph.D. Thesis, University of Cambridge, Cambridge, England.

18. Ursell, F. (1962). Slender oscillating ships at zero forward speed. *J. Fluid Mech.* 14, 496-516.

19. Yeung, R. W. (1975). A hybrid integral-equation method for time-harmonic free-surface flow. *Proc. Int. Conf. Numer. Ship Hydrodyn., 1st*, pp. 518-607. Gaithersburg, Maryland.

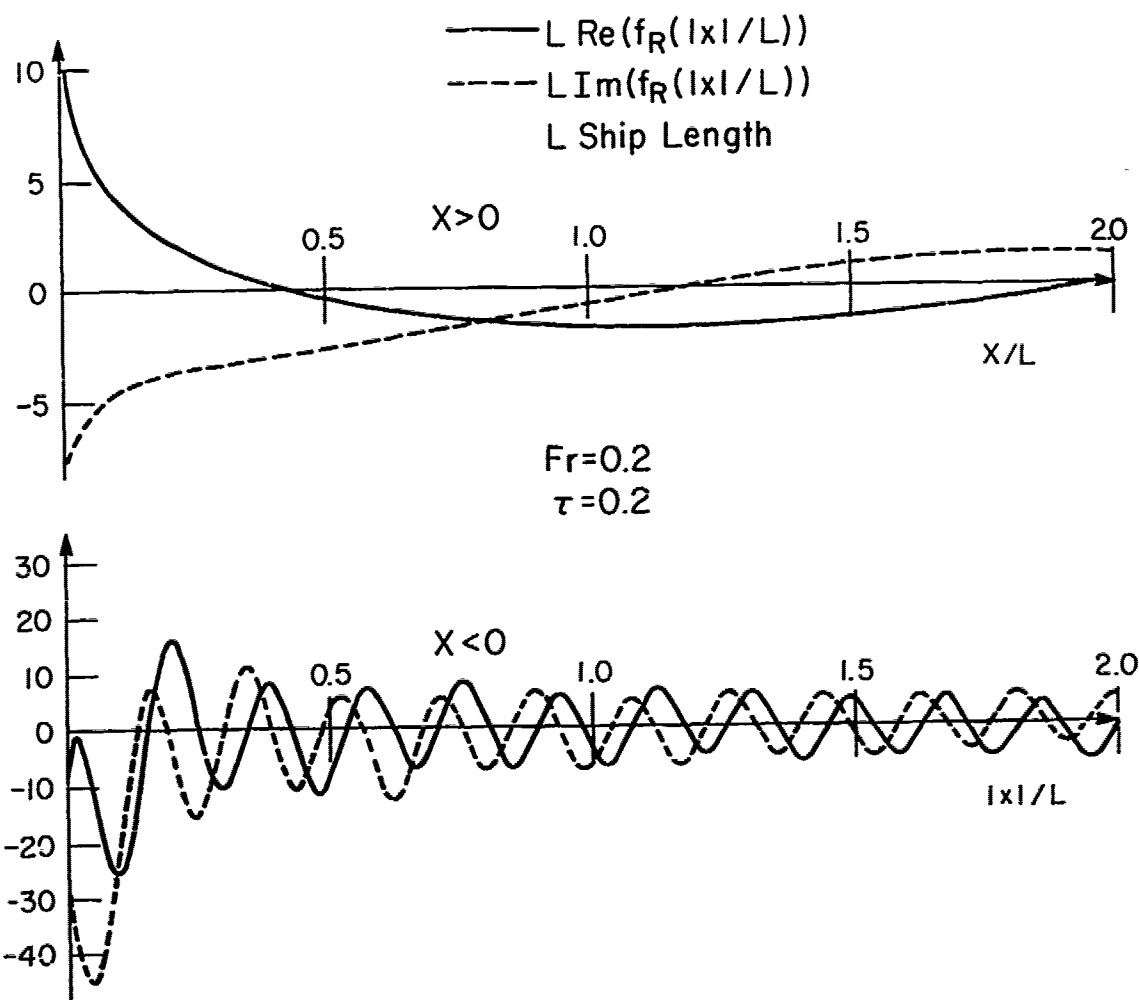


Figure 1a - Regular part (f_R) of the kernel (27) as a function of the longitudinal coordinate $|x|/L$ for $\tau = u/g$ equal to 0.2 and 0.7 (Figures 1a and 1b respectively). Waves are present upstream only for the first case, associated with the root k_3 in (36) and with the wavelength-to-ship-length ratio $2\pi/k_3 L \approx 3.3$. For $\tau = 0.7$ (Figure 1b) no waves exist upstream. Downstream of the disturbance the most obvious wave motion is associated with the largest root k_1 , and with the wavelength-to-ship-length ratio 0.19 ($\tau = 0.2$) and 0.12 ($\tau = 0.7$). Longer wavelengths also exist downstream, associated with the roots k_2 and k_4 for $\tau < \frac{1}{2}$ and with k_2 alone for $\tau > \frac{1}{2}$. Their superposition upon the shorter wave system is more apparent in Figure 1b.

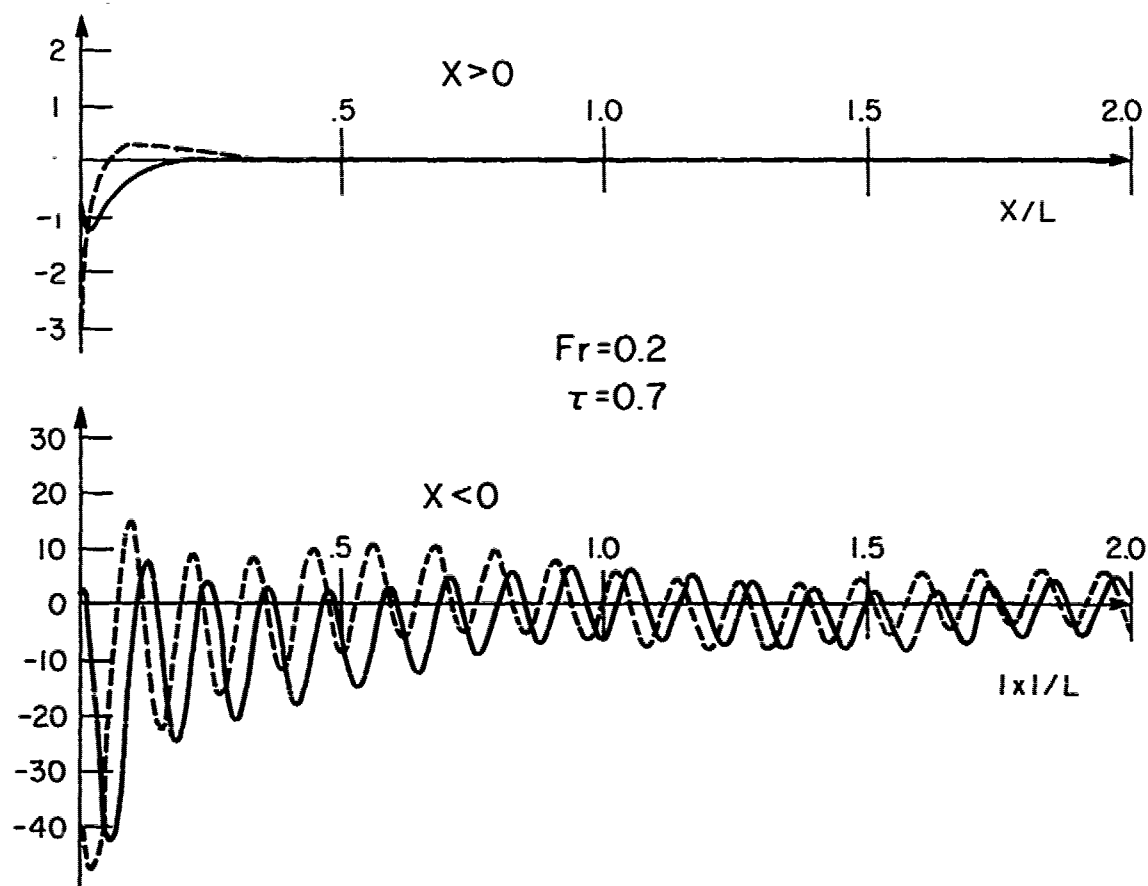


Figure 1b - see Figure 1a

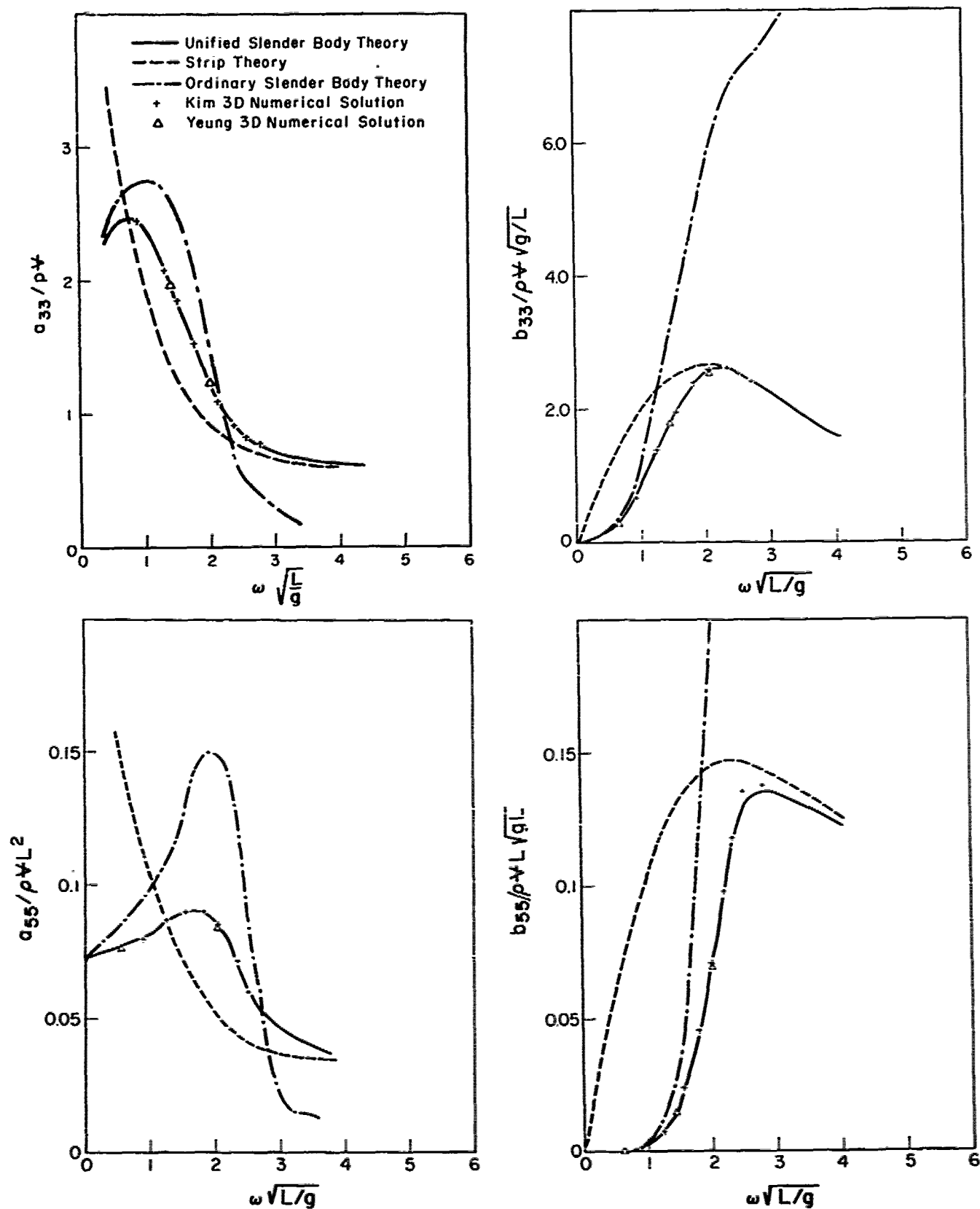


Figure 2 - Added-mass and damping coefficients of a prolate spheroid ($b/L = 1/8$) at $U=0$.

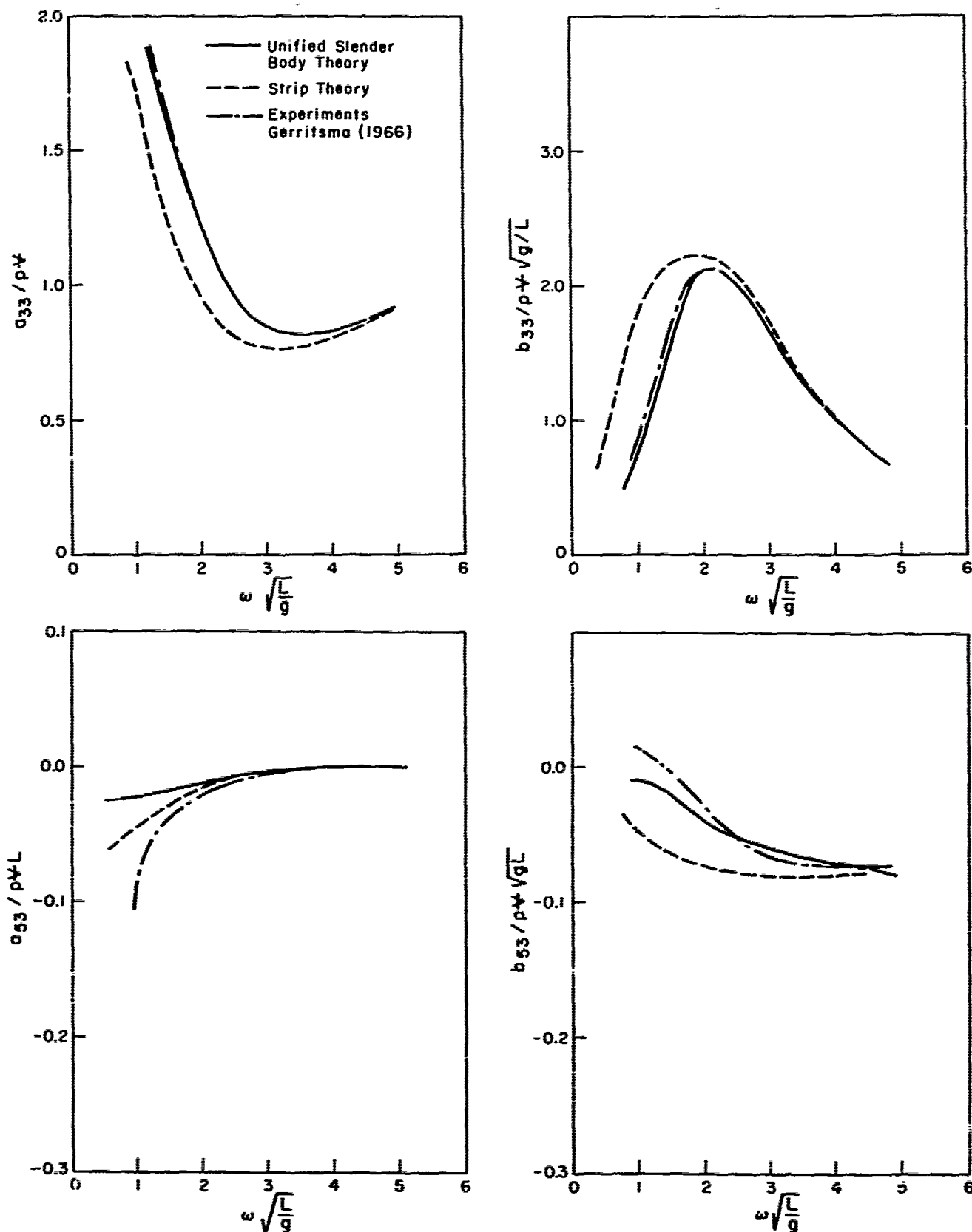


Figure 3 - Added-mass and damping coefficients of a Series 60 hull ($C_B = 0.7$) at $U=0$.

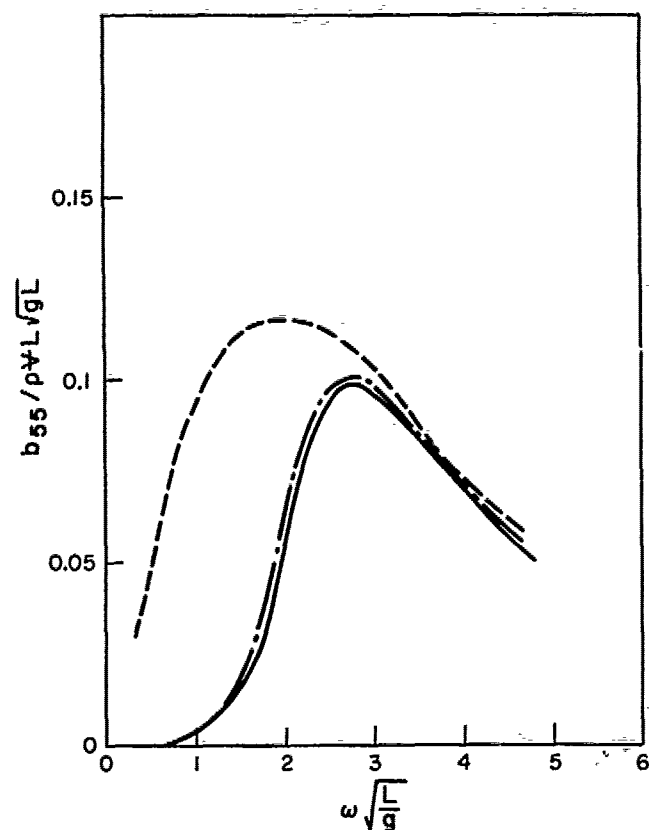
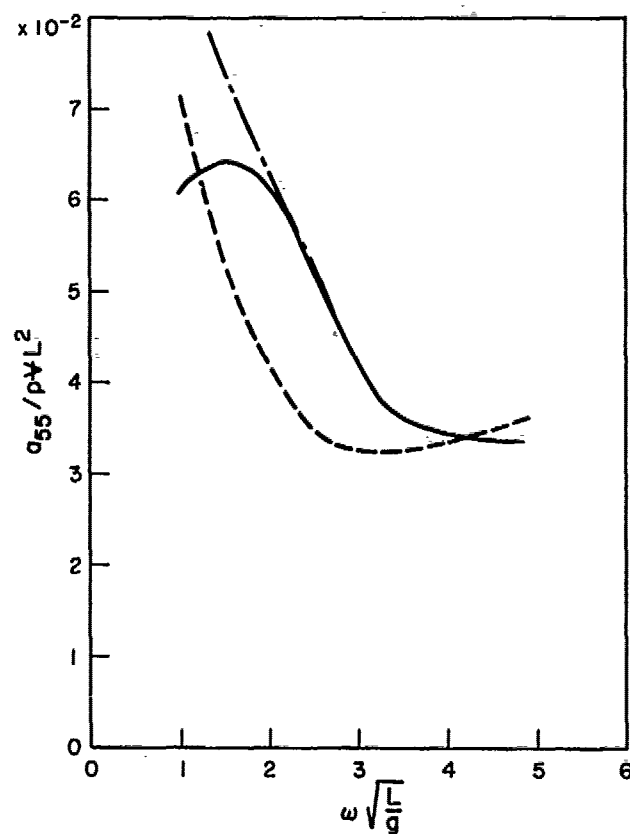


Figure 3 - continued

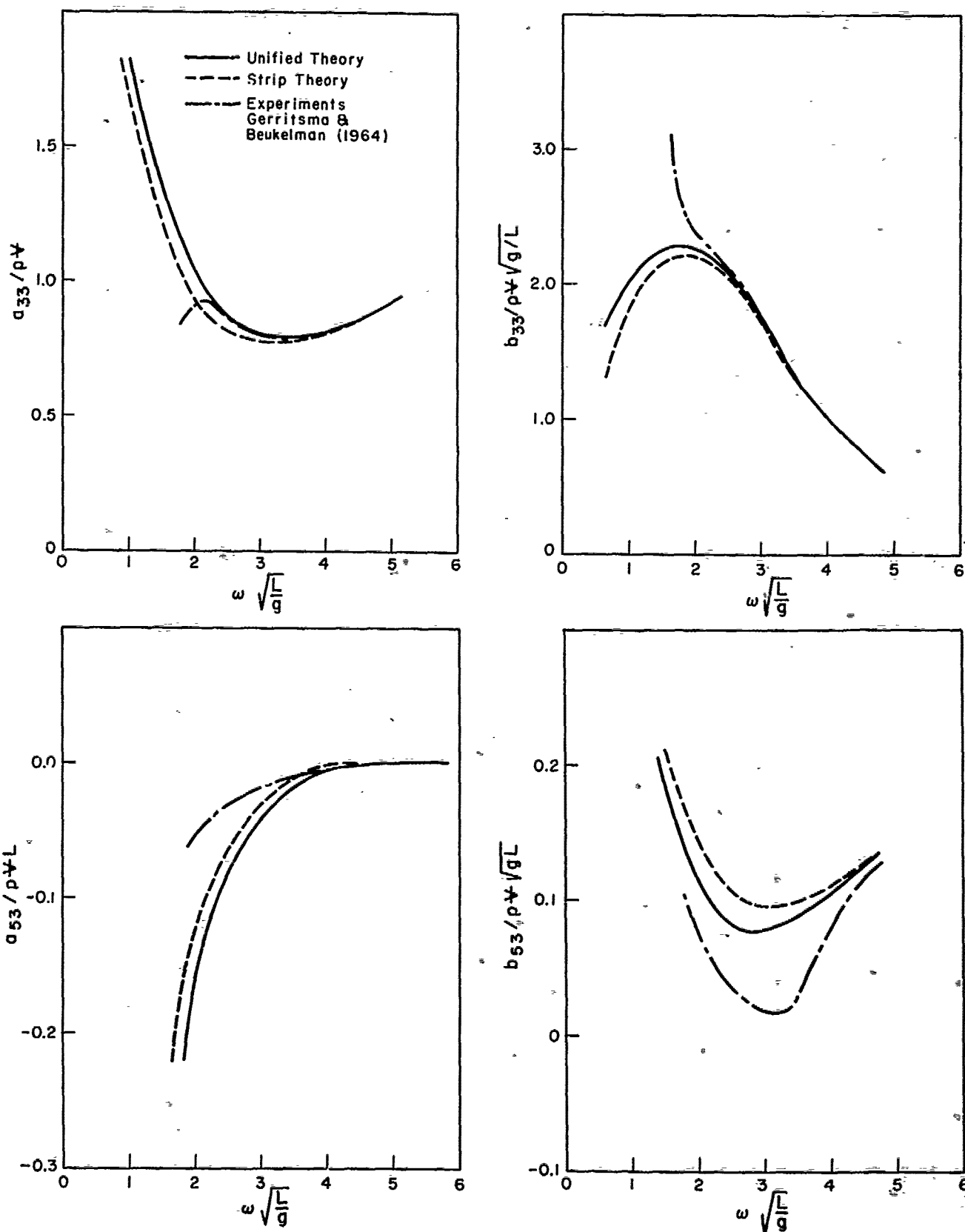


Figure 4 - Added-mass and damping coefficients of a Series 60 hull ($C_B = 0.7$) at $Fr = 0.2$.

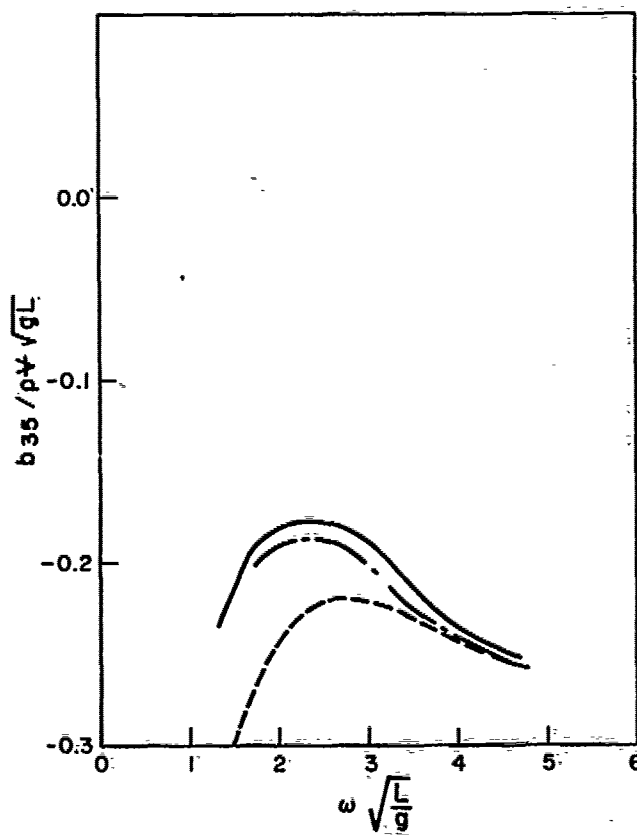
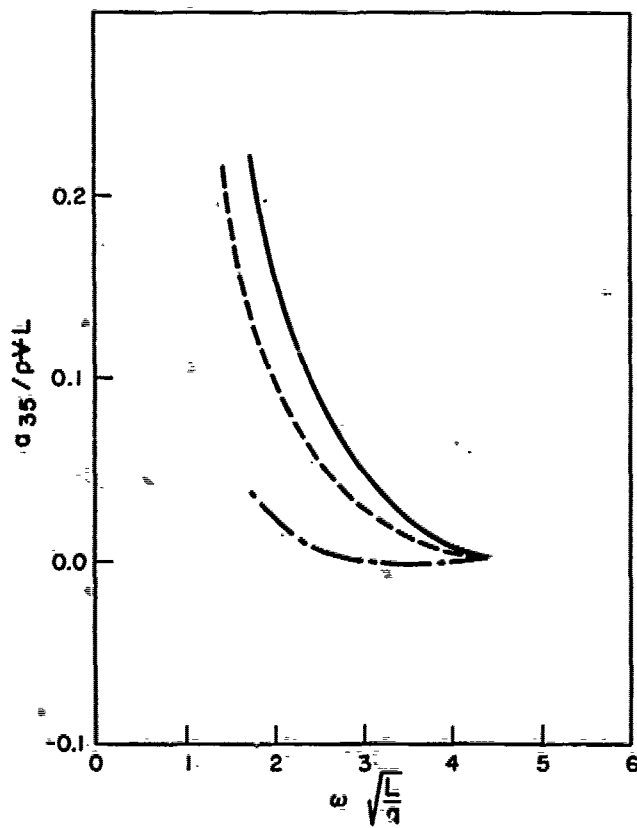
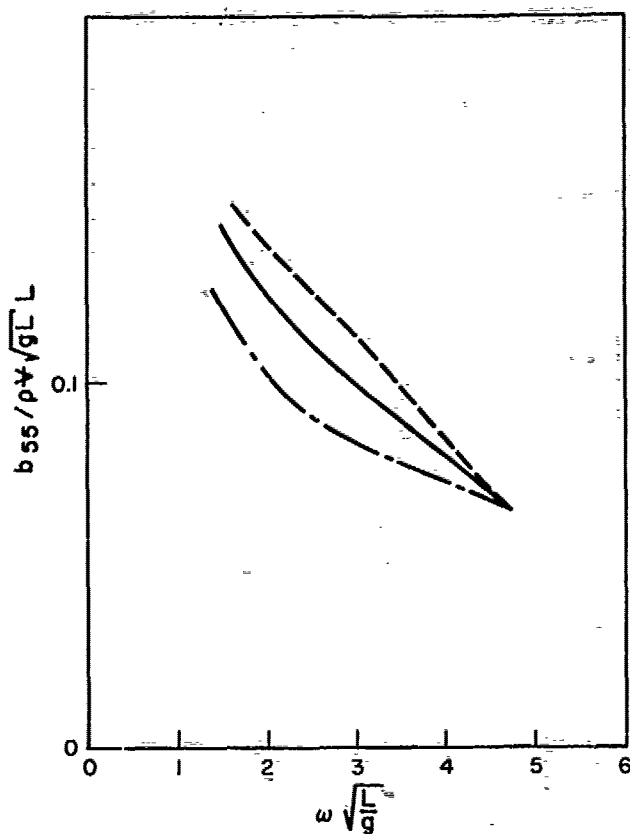
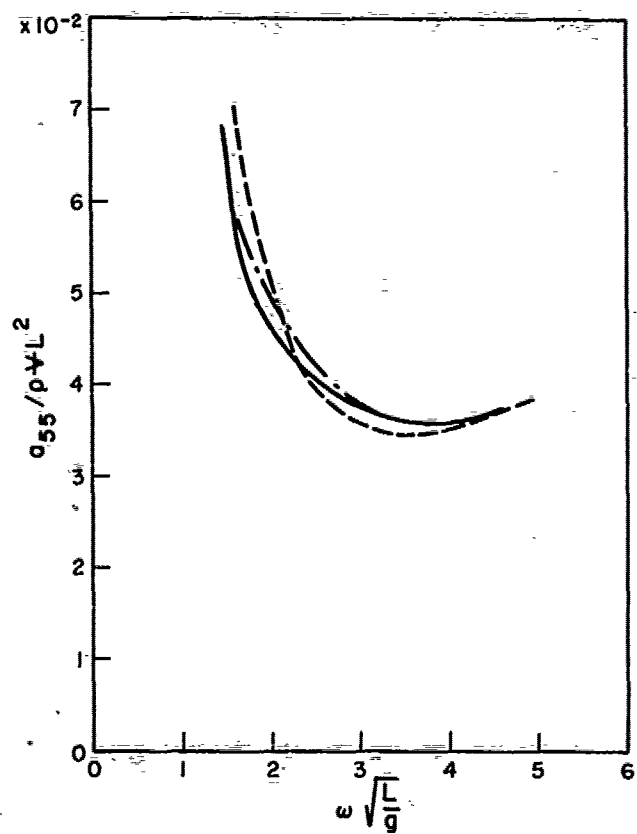


Figure 4 - continued

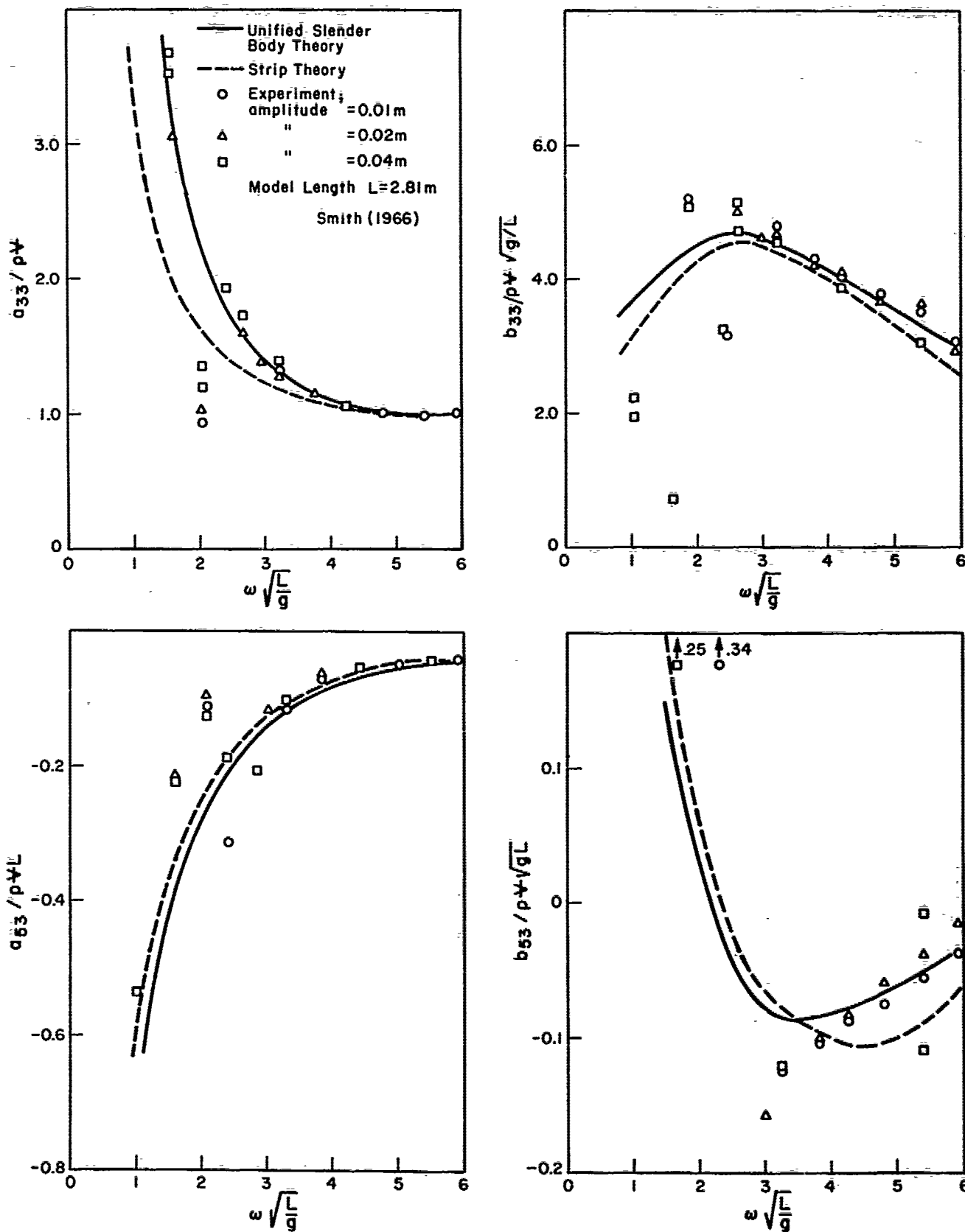


Figure 5 - Added-mass and damping coefficients of a frigate hull ($C_B = 0.55$) at $Fr=0.15$.

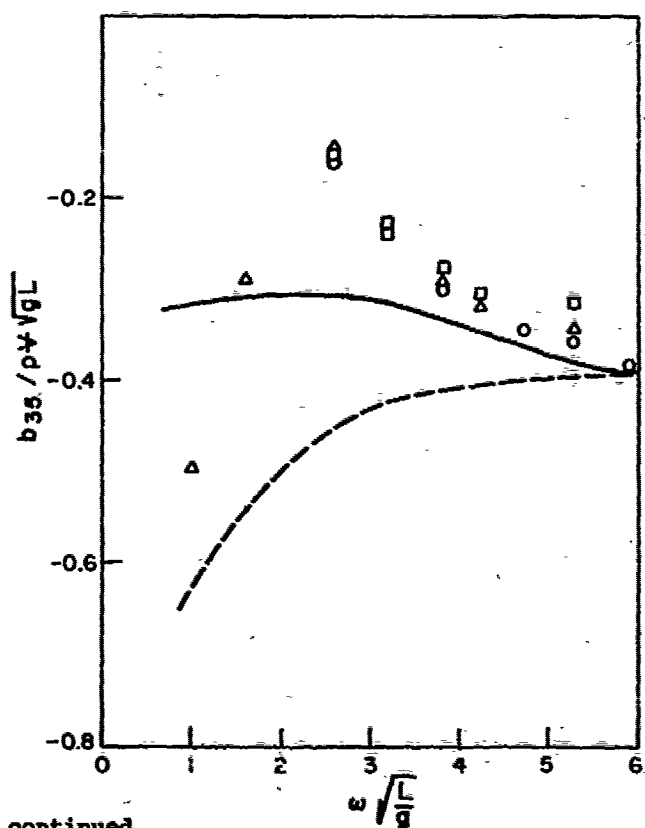
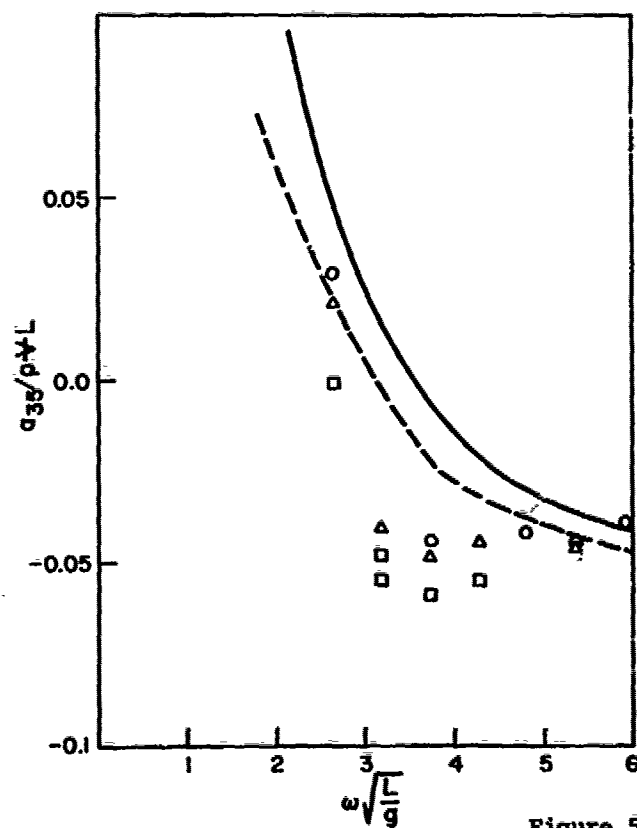
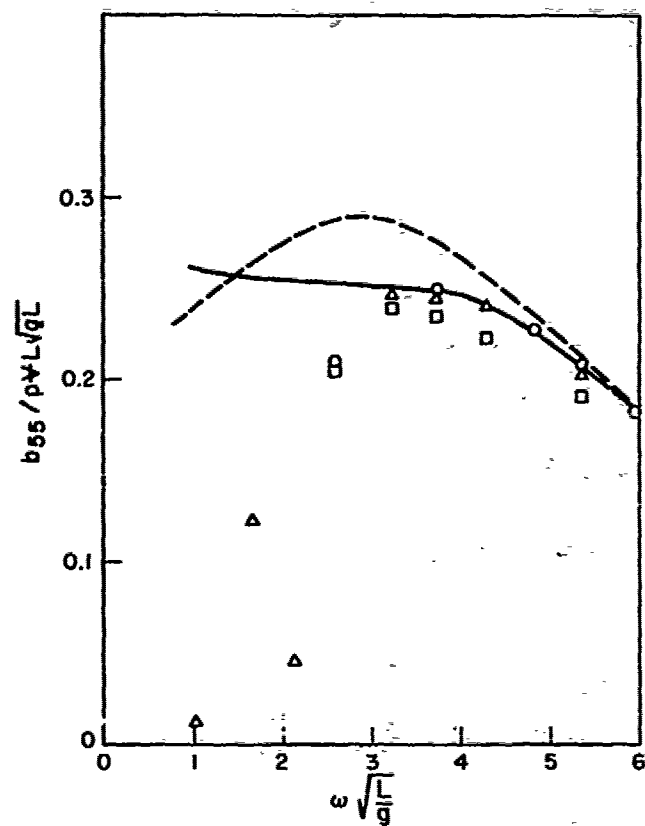
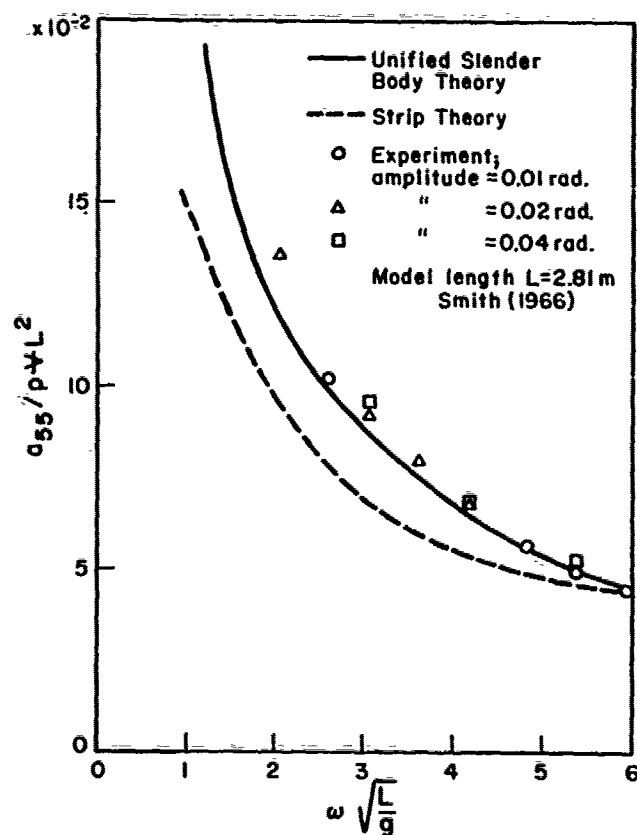


Figure 5 - continued

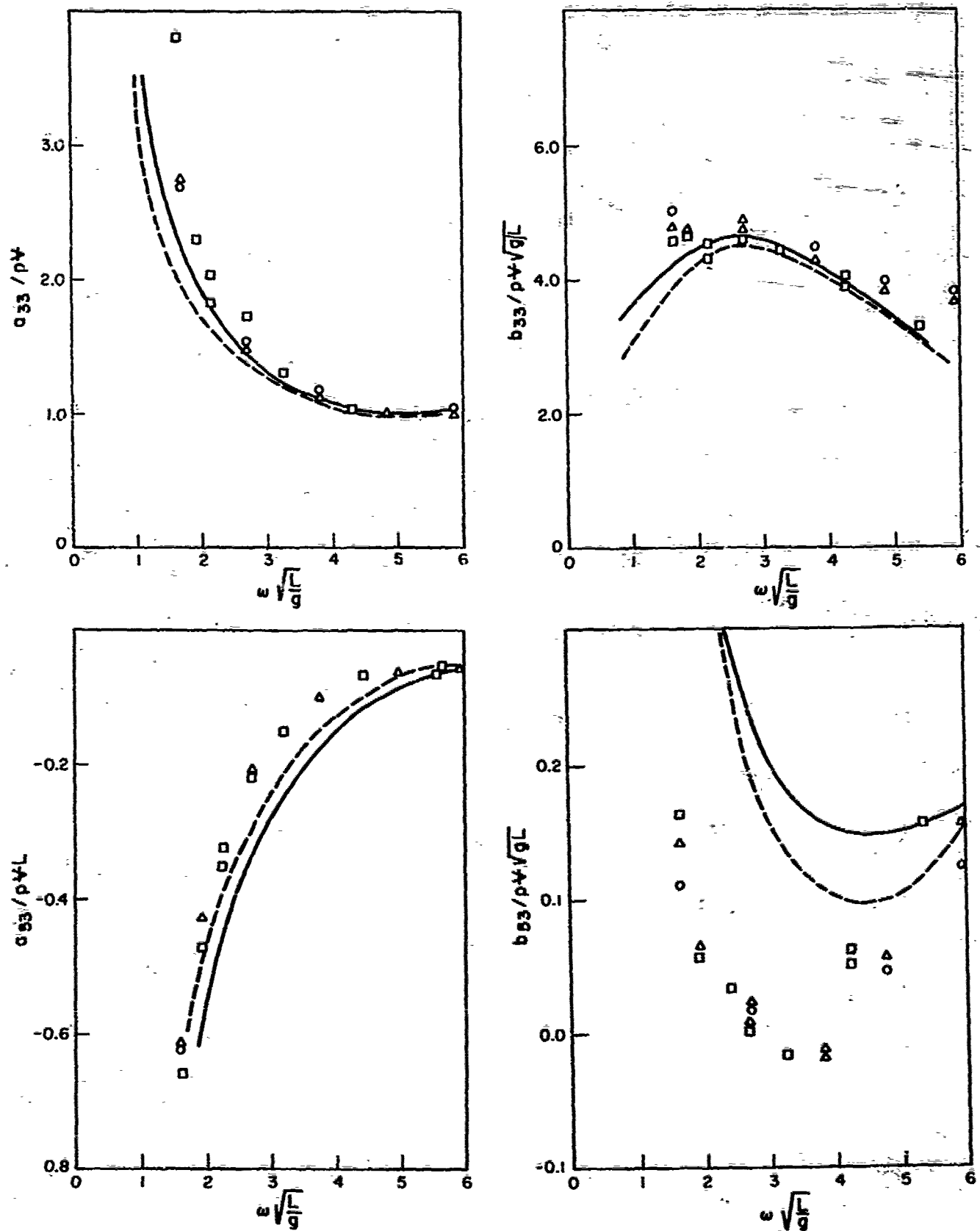


Figure 6 - Added-mass and damping coefficients of a frigate hull ($C_B = 0.55$) at $Fr=0.35$.

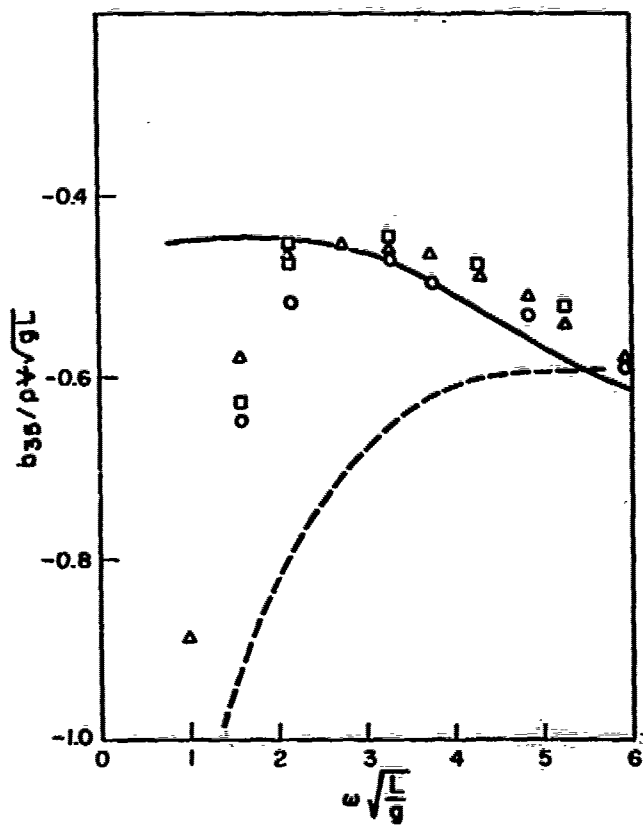
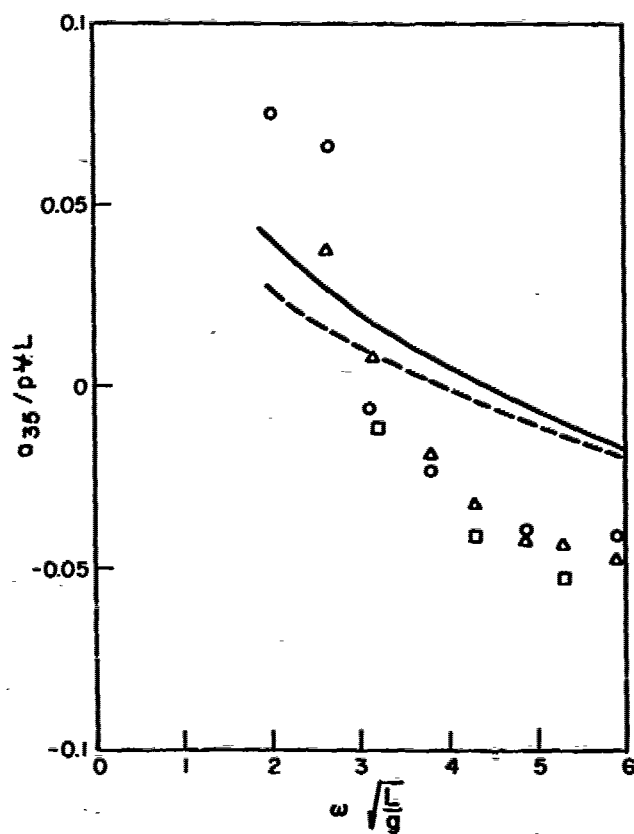
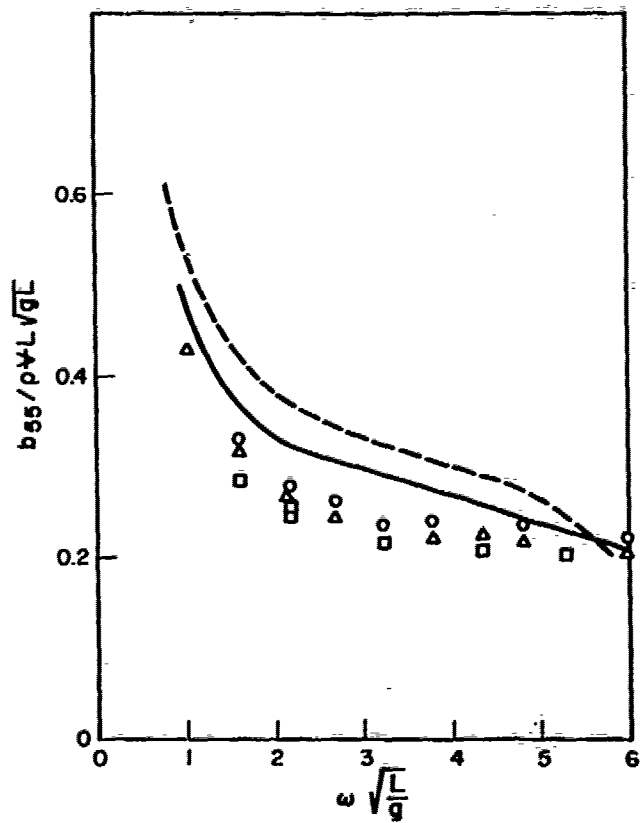
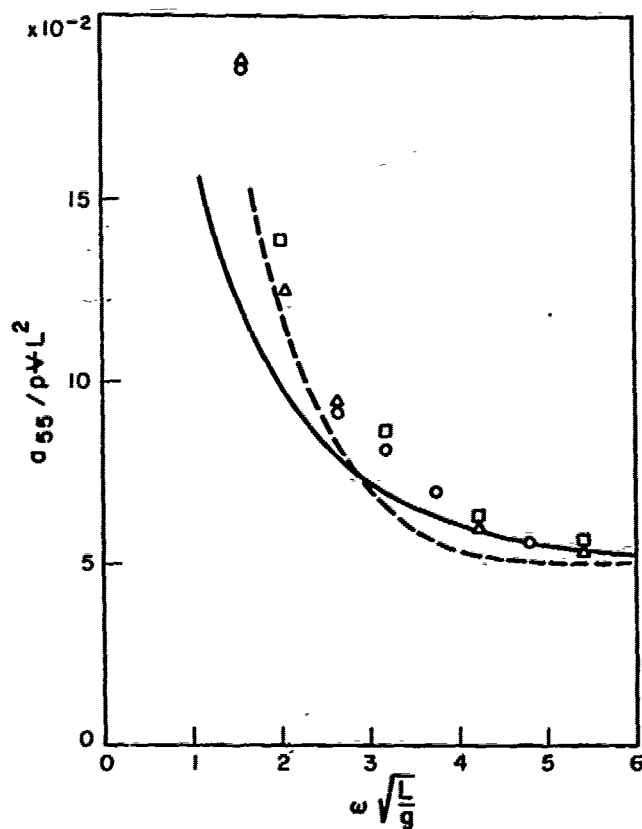


Figure 6 - continued

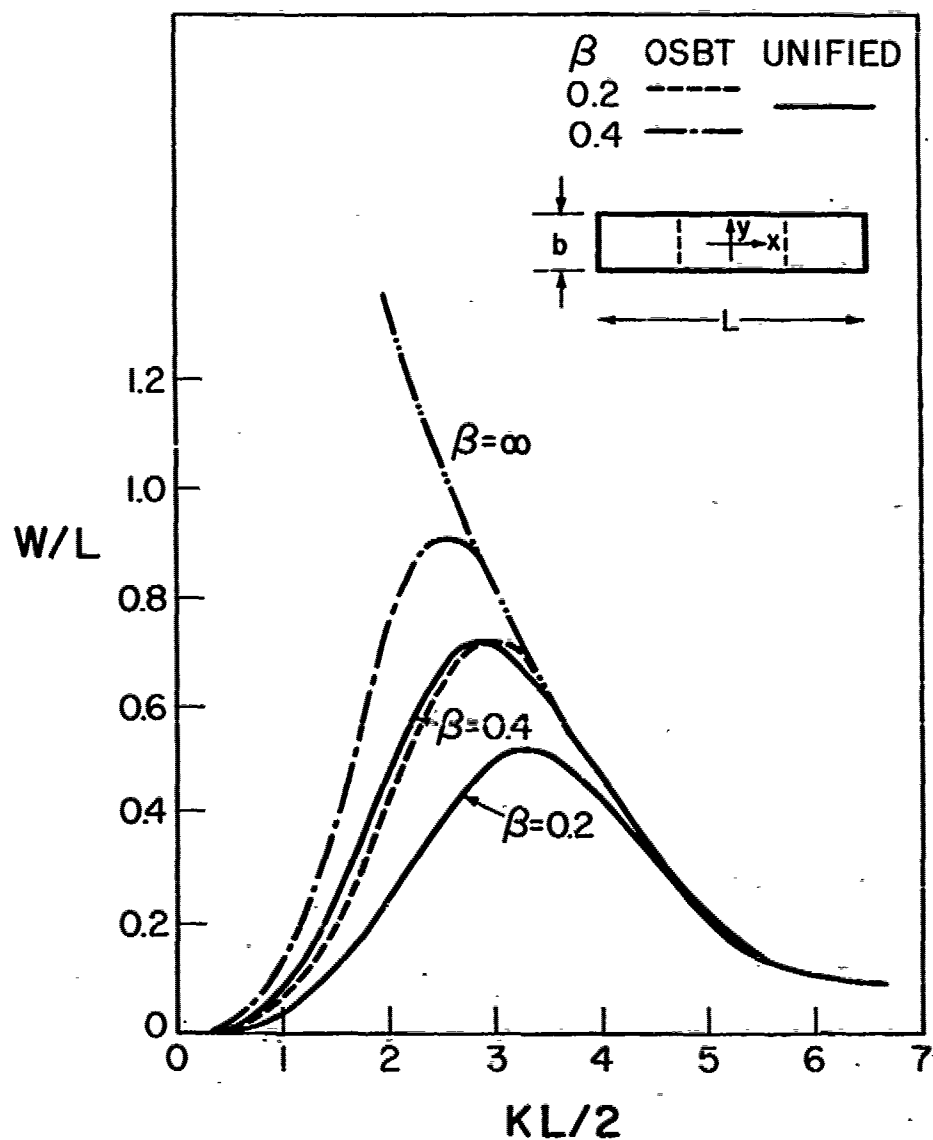


Figure 7 - Total absorption width, as a fraction of the body length, for an articulated raft with two symmetric hinges situated at the points $x = \pm L/5$. The curves for the ordinary slender-body theory (OSBT) are from Newman (1979), corrected as noted in the footnote, with superposition of the power obtained separately in the even and odd modes. The full lines are the values of the absorption width determined from the unified theory, for a beam-length ratio of 0.1, and a beam-draft ratio of 2.0. In all cases the body motions are of optimum phase. The maximum amplitude in each mode is equal to the product of $8L/b$ and the incident wave amplitude.

Discussion

H. Maruo (Yokohama N. Univ.)

In this paper, the theory is developed on the basis of the linearized free surface condition, eq. (2) or eq. (7). However it is known that this condition is not always valid in the near field. The validity of the linearized free surface condition is rather limited in the presence of the steady forward speed. A discussion of this situation was given in my paper of 1974. It is intrinsically hopeless to develop a consistent formulation of the slender body perturbation which is uniformly valid without restriction in the magnitude of frequency. The terminology 'Interpolation Theory' stands on the basis of this fact. It is consistent in both limit cases of low and high frequencies, but its logical foundation in view of the perturbation analysis has to be relaxed in the intermediate frequencies. The authors have pointed out that their unified theory replaces the factor $(1+Kz)$ in the interpolation solution by $\exp(Kz)$. However this replacement seems to be surplus. If K or ω^2/g is $O(1)$, $1+Kz$ is a rational representation of $\exp(Kz)$, while in the high frequency range of $K = O(\epsilon^{-1})$, the three-dimensional portion of the potential given by the last term of eq. (29) can be omitted because of the higher order. A considerable disadvantage may happen as a result of the above replacement, if one wishes to utilize the theory in routine computations of hydrodynamic coefficients of oscillating ships. In the case of the interpolation theory, one needs only the solution of the radiation problem of oscillating two-dimensional cylinders, which is generally used in the routine computation by the strip theory, while by the unified theory, on the other hand, a complete solution of the diffraction problem in beam seas is needed. This will result much complication in the practical application. The inclusion of the steady forward speed aggravates the difficulty in the development of a rational formulation. A possibility of the interpolation theory which is rational at both low and high frequencies appears in the assumption of low Froude number such as $Fn = O(\epsilon^{1/2})$. Formulations along this line have been developed by Matsunaga (1979).

REFERENCES

- 1) Maruo, H., Discussions of Relative Magnitude of Governing Parameters in the Problem of Slender Ships in Waves. Bulletin of the Faculty of Engineering, Yokohama National University, vol. 23, March 1974

2) Maruo, H., & Matsunaga, Y., An Analysis of the Radiation Problem in Uniform Flow by Means of the Slender Body Theory. 58th Meeting of Japan Towing Tank Committee, Seakeeping Session, May 1979. (in Japanese)

C.M. Lee (DTNSRDC)

It appears to me that one of the long overdue problems in ship motion theory is now resolved by the unified theory. I would like to congratulate the authors for introducing a theory which fills the gap between the ordinary slender body theory and the strip theory. Although the practical merits of this theory are yet to be assessed when the computed motion results are available to us, it is my opinion that the unified theory will contribute significantly to planting ship motion theory on a firmer mathematical ground.

I am anxiously looking forward to seeing the three-way comparisons of the motion results obtained by the unified theory, the strip theory and the model experiments. If one observes the comparisons shown in Figures 2 and 3, one would wonder whether the strip theory could ever produce meaningful motion predictions at all. However, the strip theory does, in fact, provide reliable results at the zero forward speed. Our investigation at DTNSRDC some years back revealed that a reliable prediction of motion of a ship in waves depends more on the balanced accuracies between the exciting terms and the reaction terms in the equations of motion than biased improvements on either side of the terms, i.e., a fairly visible improvement on the reaction terms while no improvement on the exciting terms could yield motion results worse than the case of no improvement on both terms at all. In this regard, we still have to wait to judge if the unified theory provides better prediction of motion results than the strip theory does.

The values of $\omega\sqrt{L/g}$ corresponding to $\tau=1/4$ at $F_r=0.15$, 0.2 and 0.35 are, respectively, 1.67, 1.25 and 0.71. The experimental results for $F_r=0.15$ in Figure 5 seem to show some scatterings at about $\omega\sqrt{L/g} = 1.67$. The scatterings of the experimental results at $\tau = 1/4$ could have been exaggerated due to the effects of the wave reflections by the tank walls. I tend to think that theoretical results at $\tau = 1/4$, may be singular but should be smooth elsewhere. I would like to know the authors' opinion on this subject.

It appears to me that the existence of m_z in Equation (3) is one of the main differences of the unified theory from the strip theory in the context that m_z introduces a part of the 3D-flow effects through the steady perturbation potential ϕ . The authors have already acknowledged the weakness of approximating ϕ by a strip fashion. I fully concur with the authors' suggestion

that δ should be evaluated with the full 3D double-body flow condition.

I am certain that the present paper will inspire many pursuers of ship hydrodynamic theories in the future.

M.S. Chang (DTNSRDC)

I have found this paper is very stimulating and its numerical results very interesting. We at DTNSRDC have calculated the motion coefficients for Friesland from a 3-D program after the receiving of the preprint of this paper. One of the interesting thing we found was that the 3-D results for $Fn = 0.15$ show significant oscillation at the frequencies near the resonance frequency $\omega = 1.66$ of $\tau = 1/4$. Although the oscillation may have been exaggerated due to the panel setup, it does, however, explain the apparent irregularity in the experimental data. In view of the smoothness of the result calculated by the present paper, I will like to ask the authors the following question. In what way (if any) were they able to suppress the effect of resonance effect at frequencies near $\tau = 1/4$? And do they think this could be related to the discrepancies between their results and the experimental data at the lower frequencies?

Also the steady potential is neglected in 3-D calculation, yet is partially included in the present paper. I will very much to know the significance of the steady potential contribution (if the authors have investigated), especially for the B_{ss} .

J.H. Hwang (Seoul N. Univ.)

The authors should be congratulated for their very fine contribution in the slender body theory applied to a complex ship hydrodynamics problem. Professor Newman has made many original contributions in our field. This time Professor Newman has presented a remarkable "Unified" slender body theory which is valid in all frequency range of practical interest.

Professor Newman has shown here that their new results based on this unified theory give better agreement with the experimental results than previous strip theory and ordinary slender body theory.

From our limited experience in water of finite depth, some change in the hydrodynamic coefficients seemed to be nearly insignificant in the final motion response. I would like to hear Professor Newman's opinion on how their present improvement would effect on the final motion?

A.Y. Odabasi (BSRA)

The authors present an extended slender body theory which, according to the assumptions used in the derivation, has a broader range of applicability. Although it is a welcome addition to the existing knowledge, to the present contributor's knowledge strip theory generally provides satisfactory heave and pitch prediction for the range of practical interest and the differences shown in Figures 3 to 6 could have been obtained by using alternative versions of the strip theory or alternative numerical evaluation schemes, which are known to produce little difference in the predicted responses. I would therefore like to know whether the authors also conducted bending moment calculations and compared them with experiments, since this is the area where the failures in the strip theory starts to show.

R.T. Schmitke (Defence Res. Est. Atlantic)

The authors are to be commended for providing an extension of strip theory which does not require substantially greater computational effort.

The paper presents comparisons of computed and measured added mass and damping, wherein the new theory generally agrees better with the experimental data than strip theory. This is encouraging. However, of far greater importance to the ship designer is how well theory predicts ship motions. For this, the paper offers no comparisons, in spite of its title, and I ask the authors to comment.

With regard to heave and pitch, the principal shortcoming of strip theory is over-prediction of peak response at high Froude number. This is especially true of pitch. Would the authors comment on whether this unified theory will provide an advance on strip theory in this regard?

Finally, I note that the paper makes no mention of dynamic lifting effects. These are known to be of fundamental importance in lateral motions, for example in roll damping and in manoeuvring. I strongly suspect that inclusion of dynamic lift effects in the heave-pitch equations will improve predictions. Would the authors care to comment on this comment?

Author's Reply

The authors would like to thank the discussers for their interesting comments.

In response to Prof. Maruo's discussion we would like to point out that unified theory extends the interpolation theory by including forward speed, based on a consistent perturbation scheme regarding the free surface and hull boundary conditions. The second point of Prof. Maruo, that unified theory replaces the factor $1 + kz$ of interpolation theory by e^{kz} is not correct. The factor $1 + kz$ is replaced by the homogeneous solution $\phi_j + \bar{\phi}_j$ which does not behave like e^{kz} in the inner region and on the ship hull. The approximation of $\phi_j + \bar{\phi}_j$ by $e^{kz}\cos(ky)$ or $1 + kz$ is only valid in the overlap region. The disadvantage that Prof. Maruo mentioned about the necessity of solving the 2-D diffraction problem is nonexistent since the homogeneous solution can be constructed by adding the strip theory potential to its complex conjugate.

Prof. Hwang, Dr. Lee, Mr. Schmitke and Dr. Odabasi raised a question on how well unified theory will predict the ship motion amplitude. A definite answer to this question will be possible only after the completion of our current work on the complementary diffraction problem. We may though speculate that if the agreement of the predicted and measured exciting forces is as good as that for the hydrodynamic coefficients, especially for zero speed, we can be quite optimistic that the final prediction of the ship motion amplitude will present an improvement over strip theory. This speculation is supported by Prof. Gerritsma's experimental validation of the linear decomposition of the radiation and diffraction problems in predicting the amplitude and phase of the ship motions.

Regarding the irregularity at $\tau = 1/4$ that Dr. Lee and Dr. Chang pointed out we must acknowledge that our numerical results for the hydrodynamic coefficients at $Fr = 0.15$ and at the critical frequency $\omega\sqrt{L/g} = 1.666$ seem to be smooth just because the numerical computations were performed at $\omega\sqrt{L/g} = 1, 2, \dots, 6$. Additional numerical computations are required within the nondimensional frequencies 1 and 2 to exhibit the presence of the logarithmic

singularity at $\tau = 1/4$. It is possible to prove that this is a weak singularity in the sense that its strength is proportional to Fr^2 . The weakness of the singularity has already been pointed out by Dagan and Miloh in their paper. Dr. Chang's numerical results present strong oscillations extending far beyond the critical frequency. It is the author's feeling that this may be associated with the number of panels used in the numerical scheme and not with the singularity at $\tau = 1/4$.

The numerical computations indicate that the interaction of the steady and oscillatory disturbance potentials gives a substantial contribution to the final values of the hydrodynamic coefficients and hence cannot be neglected. The interaction effects are especially pronounced at the ship ends where the slender body theory assumption fails. In response to Dr. Chang's question we notice that the pitch hydrodynamic coefficients are more sensitive to these effects. Dr. Lee correctly pointed out that one should evaluate the m_z term by using a three-dimensional procedure and it is our intention to pursue a further investigation in that direction.

In response to Dr. Odabasi's question, we will be able to present the total pressure force distribution over the ship hull after the study of the diffraction problem has been completed. We believe though that advantages of unified theory over strip theory will be more apparent in predicting bending moments than ship motion amplitudes.

Mr. Schmitke has noted the possible importance of dynamic lifting effects, in the context of pitch and heave motions, and we recall a similar suggestion made by G.I. Taylor more than twenty years ago. While it is difficult to estimate the importance of shed vorticity, either from a transom stern or from upstream points on the hull, it does seem to the authors that the situation for pitch and heave is significantly different from roll and lateral motions in maneuvering. In the latter cases inertial and hydrostatic forces are relatively small, and lifting effects from the "trailing edge" at the stern are clearly relevant. The role of shed vorticity is less obvious for vertical motions, but a definitive response to this question must await a more comprehensive analysis.

Diffraction Problems of a Slender Ship with a Blunt Bow Advancing in Head Seas

Shoichi Nakamura¹

Osaka University

Matao Takagi

Hitachi Shipbuilding & Engineering Co. Ltd.

Ryusuke Hosoda

University of Osaka Prefecture

Osaka, Japan

ABSTRACT

The diffraction problem of a slender-ship with blunt bow advancing in head seas is dealt with. In order to satisfy the longitudinal boundary condition, the vertical line singularities at bow and stern parts are introduced. For parallel part the slender-body theory is used. As examples of the application of the solution, the resistance increase in waves and the pressure acting on the hull of an ore-carrier are shown. The theoretical results explain some interesting characteristics in experiments.

NOMENCLATURE

B breadth of ship
L length of ship
T draft of ship
 C_B block coefficient
 \bar{T} mean draft of modified ship
 ϵ, β small parameter
U advance speed of ship
 $F_n = U/\sqrt{Lg}$ Froude number
 λ wave length of incident wave
 ζ_w wave height of incident wave
 ζ_a wave amplitude of incident wave
g acceleration of gravity

ω circular frequency of incident wave
 $K = \omega^2/g$, wave number of incident wave
 $\omega_e = \omega + KU$, circular frequency of encounter
 $\Omega = U\omega_e/g$, ratio of ship's speed to wave celerity
 $K_e = \omega_e^2/g$
 $K_0 = g/U^2$
 $\phi_w = \phi_w \exp[i(\omega_e t - Kx)]$, velocity potential of incident wave
 $\phi_1 = \phi_1 \exp(i\omega_e t)$, velocity potential due to bow part
 $\phi_2 = \phi_2 \exp[i(\omega_e t - Kx)]$, velocity potential due to parallel part
 $\phi_3 = \phi_3 \exp(i\omega_e t)$, velocity potential due to stern part
 $\sigma_1 \exp(i\omega_e t)$ strength of source per unit length at bow
 $\sigma_3 \exp(i\omega_e t)$ strength of source per unit length at stern
 $\sigma(x) \exp[i(\omega_e t - Kx)]$ strength of source per unit length in ship's parallel part
 σ^* inverse Fourier transform of σ
 $\sigma = \sigma_e + i\sigma_s$; σ_e, σ_s real
 σ_{ej}, σ_{sj} see eq. (64)
 G_2 two-dimensional wave source potential

$R = \sqrt{(x-x')^2 + (y-y')^2}$, horizontal distance between point (x, y) and point (x', y')

$R_1 = \sqrt{x^2 + y^2}$, see eq. (7)

$R_3 = \sqrt{(x-L+B)^2 + y^2}$, see eq. (8)

$R_1' = \sqrt{(x+B)^2 + y^2}$, see eq. (18)

$R_3' = \sqrt{(x-L)^2 + y^2}$, see eq. (19)

θ_1, θ_3 see Fig. 2

$\Phi_\sigma = \phi_\sigma \exp\{i(\omega_\sigma t - Kx)\}$ velocity potential due to $\sigma(x)$

f_{jn}, G_{jn} see eqs. (12) and (13)

Ψ_m wave free potential

$\phi_B = \phi_1 + \phi_3$

Ψ_R see eq. (31)

V_R see eq. (39)

V_m see eq. (40)

γ angle between r and n

n normal to hull surface

$r=r(\theta)$ equation of hull surface

$r_0 = r(0)$

$r_1 = r(\frac{\pi}{2})$

$\alpha(x)$ see eq. (41) or (50)

R_{AW} resistance increase in waves

H_1 Kochin function of σ_1

H_2 Kochin function of $\sigma(x)$

H_3 Kochin function of σ_3

P_e external pressure acting on hull

O-XYZ orthogonal coordinate system fixed to space (see Fig. 1)

o-xyz orthogonal coordinate system moving with ship advance speed (see Fig. 1)

δ factor of decrease of incident wave

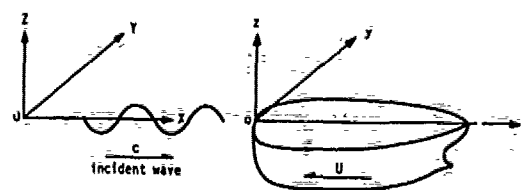


Fig. 1 Coordinate system

1. INTRODUCTION

The resistance increase of a ship advancing in waves is calculable by Maruo's formula^[1] when the distribution of the hydrodynamical singularity for the ship is known. The distributions of the singularity are given by many researchers. They are, however, obtained under the assumption of slender-ship. Therefore the theoretical predictions do not agree with the experimental values in case of full tankers and floating mine vessels with blunt bow.

Though several reasons are considered for the above mentioned disagreements, the main one is that the longitudinal boundary condition with respect to fluid velocity is not satisfied under the slender-ship assumption. Considering this fact, Fujii et al.^[2] studied the effect of bow upon the resistance increase. They replaced the bow part with a semi-circular cylinder and calculated its resistance increase by Havelock's formula.^[3] Higo et al.^[4] studied the case of a box-type floating vessel. They satisfied the longitudinal boundary condition using the strip method of longitudinal cut and introduced the resistance increase formula including the effect of blunt bow.

In the present investigation, we deal with the diffraction problems of a slender-ship with blunt bow and stern satisfying the longitudinal boundary condition by the vertical line singularities distributed at bow and stern parts.

The distribution of the singularities related with the vertical boundary condition is obtained following the method of Faltinsen^[5] or Maruo^[6] under the assumption of slender-ship.

To make sure, the orders of various quantities are written in the following.

- | | |
|---------------------------|---|
| (1) Ship breadth | $\beta = O(\epsilon)$ ($\epsilon \ll 1$). |
| (2) Wave length | $\lambda = O(\epsilon)$. |
| (3) Wave height | $\zeta_w = O(\epsilon \cdot \beta)$ ($\beta \ll 1$) |
| (4) Advance speed of ship | $U = O(\epsilon^{1/2})$ |

In the above, ship length $L = O(1)$.

2. DIFFRACTION POTENTIALS DUE TO BLUNT BOW AND STERN PARTS

In this section, we deal with the diffraction potential

which is not considered in the ordinary slender-ship theory but is necessary to satisfy the longitudinal boundary condition.

In order to treat the problem approximately, we modify a given ship's form into a wall-sided vessel which consists of semicircular cylinders in bow and stern parts and a parallel part as shown in Fig. 2. The radius a of the semicircular cylinder is given by $B/2$ and the draft T of the modified vessel is determined so as to coincide the displacement with the given one. Thus

$$\bar{T} = \frac{C_B \cdot L \cdot T}{L - B + \frac{\pi B}{4}} \quad (1)$$

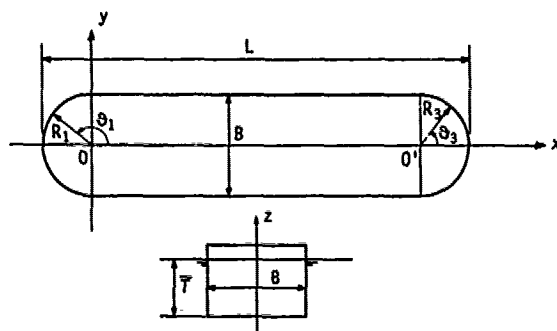


Fig. 2 Modified form of blunt ship

2.1 Zero-speed Problem

In order to satisfy the longitudinal boundary condition, we distribute sources on z axis and vertical axis through point O' corresponding fore and aft parts respectively as shown in Fig. 2.

Here we make several assumptions to determine the strength of the sources.

First we assume that Φ_1 and Φ_3 do not affect each other and Φ_1 is not affected by Φ_2 . Since incident wave decays through ship's parallel part, the velocity of the incident wave at stern part is decreased and we determine the factor of decrease δ by experimental data.

In the process of determination of source strength, we assume that the draft of the modified vessel is infinite. And if the source strength is once determined, then we assume that the singularities are distributed on $0 > z > -\bar{T}$ for the calculation of Φ_1 and Φ_3 .

We put the strength of the sources

$$\sigma_j = \sigma_{0j} e^{Kz} \quad (j=1, 3; \sigma_{0j} = \text{const.} \quad 0 > z > -\infty). \quad (2)$$

Because we assume infinite draft, the wave source potential G_2 by the source of unit strength placed at a point (x', y', z') is, as explained by Bessho^[7], given by

$$G_2 = 2\pi i K e^{K(z+z')} H_0^{(1)}(KR), \quad (3)$$

where $H_0^{(1)}$: the first kind of Hankel Function,

$$R = \sqrt{(x-x')^2 + (y-y')^2}. \quad (4)$$

Hence the diffraction potential due to σ_j is given by

$$\phi_j = \int_{-\infty}^0 \sigma_j G_2(x, y, z; x', y', z') \cdot dz'. \quad (5)$$

$$(j = 1, 3)$$

Substituting eqs. (2) and (3) into eq. (5) we get

$$\phi_j = i\pi e^{Kz} H_0^{(1)}(KR_j) \sigma_{0j} \quad (j = 1, 3), \quad (6)$$

where

$$R_1 = \sqrt{x^2 + y^2}, \quad (7)$$

$$R_3 = \sqrt{(x-L+B)^2 + y^2}. \quad (8)$$

Unknown constants σ_{0j} are determined so as to satisfy the average of the boundary condition

$$\frac{\partial \phi_j}{\partial n} = - \frac{\partial}{\partial n} \{ \phi_w \exp(-iKx) \} \quad (9)$$

on the bow and stern parts. In eq. (9) ϕ_w relates the potential of the incident wave and is put

$$\phi_w = \frac{g \zeta_a}{\omega} \exp(Kz). \quad (10)$$

Substituting eqs. (6) and (10) into eq. (9), we have

$$\sigma_{0j} i\pi e^{Kz} \frac{\partial}{\partial R_j} H_0^{(1)}(KR_j) = i\omega \zeta_a \times \exp(Kz - iKx) \cdot \cos \theta_j. \quad (11)$$

In order to satisfy eq. (11) on the average, we put

$$f_{jn} \equiv i\omega \zeta_a \exp(Kz_{jn} - iKx_{jn}) \cdot \cos \theta_{jn}, \quad (12)$$

$$G_{jn} \equiv i\pi \exp(Kz_{jn}) \frac{\partial}{\partial R_j} H_0^{(1)}(KR_j) \quad (13)$$

and define

$$J = \sum_{n=1}^N (f_{jn} - \sigma_{0j} \cdot G_{jn})^2, \quad (14)$$

where (x_{jn}, y_{jn}, z_{jn}) are the points on the bow ($j=1$) and stern ($j=3$) parts to satisfy the boundary condition. We can determine σ_{0j} so as to minimize J . From eq. (14) we get

$$\sigma_{0j} = \frac{\sum_{n=1}^N f_{jn} \cdot G_{jn}}{\sum_{n=1}^N G_{jn}^2}. \quad (15)$$

Substituting eqs. (12) and (13) into eq. (15), we get

$$\sigma_{0j} = \frac{\omega \zeta_a}{\pi K} \times \frac{\sum_{n=1}^N \exp(2Kz_{jn} - iKx_{jn}) \cdot \cos \theta_{jn} H_1^{(1)}(KR_{jn})}{\sum_{n=1}^N \exp(2Kz_{jn}) \{ H_1^{(1)}(KR_{jn}) \}^2}. \quad (16)$$

In eq. (16) σ_{0j} must be multiplied by δ considering the above mentioned assumption. And in the same way, if σ_{0j} is determined, considering the finite draft of the ship, ϕ_j becomes

$$\phi_j = \sigma_{0j} i \pi e^{Kz} (1 - e^{-2K\bar{T}}) H_1^{(1)}(KR_{jn}). \quad (17)$$

Essentially, the sources should be distributed on the surface of the ship. Hence for the far field problem the above mentioned centralization of the sources is reasonable but not for the inner field problem such as the calculation of effect of Φ_2 . In the latter case, we change the position of the centralization and assume

$$R_1 \longrightarrow R'_1 = \sqrt{(x+B)^2 + y^2} \quad \text{for } \phi_1, \quad (18)$$

$$R_3 \longrightarrow R'_3 = \sqrt{(x-L)^2 + y^2} \quad \text{for } \phi_3. \quad (19)$$

2.2 Forward-speed Problem

In this paper, since $\Omega = \omega_0 U/g = O(1)$ is assumed, there is a region before ship to which the wave does not propagate. Therefore, it seems that there are qualitative differences between the flow field of zero-speed problem and that of forward-speed problem. But, because we assume that the surfaces of the ship in bow and stern parts are blunt and $U = O(\epsilon^{1/2})$, the strength of the singularities in forward-speed problem may be determined by the same way in zero-speed problem.

Instead of eq. (6), we assume

$$\phi_j = i \pi e^{Kz} H_0^{(1)}(K_0 R_j) \sigma_{0j}, \quad (20)$$

then, through eq. (9) we get

$$\sigma_{0j} = \frac{\omega_{0j}^2}{\pi K_0} \times \frac{\sum_{n=1}^N \exp\{(K_0 + K)z_{jn} - iKx_{jn}\} \cos \theta_{jn} \cdot H_1^{(1)}(K_0 R_{jn})}{\sum_{n=1}^N \exp(2K_0 z_{jn}) \{H_1^{(1)}(K_0 R_{jn})\}^2} \quad (21)$$

and

$$\phi_j = \sigma_{0j} i \pi e^{Kz} (1 - e^{-2K_0 T}) H_0^{(1)}(K_0 R_j). \quad (22)$$

3. DIFFRACTION POTENTIAL DUE TO PARALLEL SLENDER PART

The disturbed velocity due to parallel part occurs from satisfying the boundary condition about the vertical velocity. Therefore it can be obtained by the use of the ordinary slender-ship theory, but the effect of the fore and aft blunt parts must be considered.

As slender-ship theory we use the method which was created by Faltinsen^[5] and improved by Maruo et al.^[6]

3.1 Zero-speed Problem

In order to obtain the far field's flow, we put a singularity distribution on the centerline of the ship. Then the velocity potential ϕ_0 becomes^[8]

$$\phi_0 = -\frac{1}{\pi} \int_{-\infty}^{\infty} \sigma^*(k) e^{ikx} \times \lim_{\mu \rightarrow 0} \int_{-\infty}^{\infty} \frac{\exp\{i\ell y + z\sqrt{(k-K)^2 + \ell^2}\}}{\sqrt{(k-K)^2 + \ell^2} - (K-i\mu)} d\ell dk, \quad (23)$$

where

$$\sigma^* = \int_{-\infty}^{\infty} \sigma(x) e^{-ikx} dx. \quad (24)$$

Under the assumption of the slender-ship, the near field expansion of eq. (23) becomes^[6]

$$\begin{aligned} \phi_0 = & -\sqrt{8\pi K} \exp(Kz - \frac{i\pi}{4}) \int_0^x \frac{\sigma(\xi)}{\sqrt{|x-\xi|}} d\xi \\ & -2\pi\sigma(x) \exp(Kz - \frac{i\pi}{2}) + 4\pi K|y|e^{Kz}\sigma(x) \\ & -4\sigma(x) \int_0^{\infty} \frac{ve^{-K|y|\sqrt{v^2+1}}}{(v^2+1)\sqrt{v^2+1}} \left\{ v \cos(Kvz) \right. \\ & \left. + \sin(Kvz) \right\} dv. \end{aligned} \quad (25)$$

If the diffraction potential due to parallel part Φ_2 is given by

$$\Phi_2 = \phi_2 \exp\{i(\omega t - Kx)\} \quad (26)$$

and ϕ_2 is slowly varying function with x , then Laplace equation becomes

$$\frac{\partial^2 \phi_2}{\partial r^2} + \frac{1}{r} \frac{\partial \phi_2}{\partial r} + \frac{1}{r^2} \frac{\partial^2 \phi_2}{\partial \theta^2} = K^2 \phi_2 \quad (27)$$

and the free-surface condition is

$$\frac{\partial \phi_2}{r \partial \theta} - K \phi_2 = 0 \quad \text{on } \theta = \pm \frac{\pi}{2}, \quad (28)$$

where

$$y = r \sin \theta, \quad z = -r \cos \theta. \quad (29)$$

The symmetrical wave-free potential, which satisfies eqs. (27) and (28) and is zero at infinity, is given by

$$\begin{aligned} \Psi_n = & K_{2n-2}(Kr) \cos\{(2n-2)\theta\} \\ & + 2K_{2n-1}(Kr) \cos\{(2n-1)\theta\} \\ & + K_{2n}(Kr) \cos(2n\theta), \end{aligned} \quad (30)$$

where K_n is the second kind of modified Bessel function.

Because we can represent the solution by the linear combinations of eqs. (25) and (30), putting

$$\begin{aligned} \Psi_R = & -4 \int_0^{\infty} \frac{ve^{-K|y|\sqrt{v^2+1}}}{(v^2+1)\sqrt{v^2+1}} \left\{ v \cos(Kvz) \right. \\ & \left. + \sin(Kvz) \right\} dv + 4\pi K|y|e^{Kz}, \end{aligned} \quad (31)$$

we write

$$\phi_2 = -\sqrt{8\pi K} \exp(Kz - \frac{i\pi}{4}) \int_0^x \frac{\sigma(\xi)}{\sqrt{|x-\xi|}} d\xi + \sigma(x) [\Psi_R + 2\pi i e^{Kz} + \sum_{m=1}^{\infty} p_m \Psi_m], \quad (32)$$

where p_m is to be determined.

On the other hand, the boundary condition on the ship surface is

$$\frac{\partial}{\partial n} \{ (\phi_2 + \phi_w) e^{-iKz} \} + \frac{\partial}{\partial n} (\phi_1 + \phi_3) = 0, \quad (33)$$

where n is normal to the ship surface.

But, assuming the slender-ship and following Maruo's process^[6], we obtain the equations for p_m and $\sigma(x)$ as follows:

$$\begin{aligned} & \sum_{m=1}^{\infty} p_m [\phi_{By1} \{ V_m(\theta) - V_m(0) e^{K(r_0 - r \cos \theta)} \} \\ & \times \cos(\theta + \gamma) - \{ (\phi_{Bz} - \phi_{Bz0}) e^{K(r_0 - r \cos \theta)} \} \\ & \times \cos(\theta + \gamma) + \phi_{By} \sin(\theta + \gamma) \} \times V_m(\frac{\pi}{2})] = \\ & \phi_{By1} \{ V_R(0) e^{K(r_0 - r \cos \theta)} \cos(\theta + \gamma) - V_R(\theta) \} \\ & + \{ (\phi_{Bz} - \phi_{Bz0}) e^{K(r_0 - r \cos \theta)} \} \\ & \cos(\theta + \gamma) + \phi_{By} \sin(\theta + \gamma) \} \times V_R(\frac{\pi}{2}), \end{aligned} \quad (34)$$

and

$$\begin{aligned} & \{ \alpha(x) - 2\pi i \} \sigma(x) = -\sqrt{8\pi K} e^{-\frac{i\pi}{4}} \\ & \times \int_0^x \frac{\sigma(\xi)}{\sqrt{|x-\xi|}} d\xi + \frac{g_{Bz}}{\omega} + \frac{\phi_{Bz0}}{K} e^{Kr_0 + iKx}, \end{aligned} \quad (35)$$

where

$$\begin{aligned} \phi_B &= i\pi e^{Kz} (1 - e^{-2KT}) \\ & \times \{ \sigma_{01} H_0^{(1)}(KR_1') + \sigma_{03} H_0^{(1)}(KR_3') \}, \end{aligned} \quad (36)$$

$$\phi_{By} = \frac{\partial \phi_B}{\partial y}, \quad \phi_{By1} = \frac{\partial \phi_B}{\partial y} \Big|_{r=r_1, \theta=\frac{\pi}{2}} \quad (37)$$

$$\phi_{Bz} = \frac{\partial \phi_B}{\partial z}, \quad \phi_{Bz0} = \frac{\partial \phi_B}{\partial z} \Big|_{r=r_0, \theta=0} \quad (38)$$

and $r = r(\theta)$ is the equation of the ship's hull. Furthermore, γ is the angle between r and n , and we put

$$\frac{V_R(\theta)}{r_0} = (\cos \gamma \frac{\partial}{\partial r} + \frac{\sin \gamma}{r} \frac{\partial}{\partial \theta}) \Psi_R, \quad (39)$$

$$\frac{V_m(\theta)}{r_0} = (\cos \gamma \frac{\partial}{\partial r} + \frac{\sin \gamma}{r} \frac{\partial}{\partial \theta}) \Psi_m, \quad (40)$$

$$\alpha(x) = \frac{e^{Kr}}{Kr_0} \{ V_R(0) + \sum_{m=1}^{\infty} p_m V_m(0) \}, \quad (41)$$

$$r_0 = r(0), \quad r_1 = r(\frac{\pi}{2}). \quad (42)$$

If p_m and $\sigma(x)$ are obtained by the method already mentioned, the velocity potential due to the parallel part is given by the following equation.

$$\begin{aligned} \phi_2 &= \sigma(x) \{ \Psi_R + \sum_{m=1}^{\infty} p_m \Psi_m - \alpha(x) e^{Kz} \} \\ &= \left(\frac{g_{Bz}}{\omega} + \frac{e^{Kr_0 + iKx}}{K} \phi_{Bz0} \right) e^{Kz} \end{aligned} \quad (43)$$

3.2 Forward-speed Problem

In the same way as in zero-speed problem, the far field solution of the slender-ship is obtained by the singularity distribution on the centerline of the ship and is given by

$$\begin{aligned} \phi_\sigma &= -\frac{1}{\pi} \int_{-\infty}^{\infty} \sigma^*(k) e^{ikx} \\ & \times \lim_{\mu \rightarrow 0} \int_{-\infty}^{\infty} \frac{\exp \{ i\ell y + z\sqrt{(k+K)^2 + \ell^2} \} d\ell dk}{\sqrt{(k-K)^2 + \ell^2} - \frac{1}{g} \{ \omega_e + U(k-K) - i\mu \}^2} \end{aligned} \quad (44)$$

The inner expansion of eq. (44) is given by Faltinsen^[5] as follows:

$$\begin{aligned} \phi_\sigma &= -\sqrt{\frac{8\pi K \omega}{\omega_e + KU}} \exp(Kz - \frac{i\pi}{4}) \\ & \times \int_0^x \frac{\sigma(\xi)}{\sqrt{|x-\xi|}} d\xi - e^{Kz} \frac{4\pi \sigma(x)}{\sqrt{2(2 + \frac{g}{\omega U})}} \\ & - 4\sigma(x) \left\{ \int_0^\infty \frac{v |v \cos(Kvz) + \sin(Kvz)|}{(v^2 + 1) \sqrt{v^2 + 1}} e^{-K|y|\sqrt{v^2 + 1}} dv \right. \\ & \left. - \pi K |y| \epsilon^{Kz} \right\} \end{aligned} \quad (45)$$

Eq. (45) is almost the same as Faltinsen's formula but has a little difference in the term with respect to advance speed. The third term does not appear in Faltinsen's formula, but the difference of the order of it from other term's is $O(\epsilon^{3/2})$ and so must be considered.

Now, because the equation of the near field solution in case of forward-speed problem is all the same as in zero-speed problem, ϕ_2 is given by the linear combinations of eqs. (45) and (30). Namely, putting

$$\begin{aligned} \Psi_R &= -4 \int_0^\infty \frac{v e^{-K|y|\sqrt{v^2 + 1}}}{(v^2 + 1) \sqrt{v^2 + 1}} \{ v \cos(Kvz) + \sin(Kvz) \} dv \\ & + 4\pi K |y| \epsilon^{Kz}, \end{aligned} \quad (46)$$

we have

$$\phi_2 = -\sqrt{\frac{8\pi K\omega}{\omega_e + KU}} \exp(Kz - i\frac{\pi}{4}) \times \int_0^x \frac{\sigma(\xi)}{\sqrt{|x-\xi|}} d\xi + \sigma(x) \left\{ \Psi_R - \frac{4\pi e^{Kz}}{\sqrt{2(2 + \frac{g}{\omega U})}} + \sum_{m=1}^{\infty} p_m \Psi_m \right\}. \quad (47)$$

The method of the determination of p_m and $\sigma(x)$ is all the same as in case of zero-speed problem, but the effect of the disturbed velocity due to the fore and aft parts is taken into consideration by the eqs. (21) and (22). The results are as follows:

The equation for p_m is

$$\sum_{m=1}^{\infty} p_m \left\{ V_m(0) e^{K(r_0 - r \cos \theta)} \cos(\theta + \gamma) - V_m(\theta) \right\} \phi_{By1} - V_m\left(\frac{\pi}{2}\right) \left\{ \phi_{Bz0} e^{K(r_0 - r \cos \theta)} \times \cos(\theta + \gamma) - \phi_{By} \sin(\theta + \gamma) \right\} = \left\{ V_R(\theta) - V_R(0) e^{K(r_0 - r \cos \theta)} \cos(\theta + \gamma) \right\} \phi_{By1} + V_R\left(\frac{\pi}{2}\right) \left\{ \phi_{Bz0} e^{K(r_0 - r \cos \theta)} \cos(\theta + \gamma) - \phi_{Bz} \cos(\theta + \gamma) - \phi_{By} \sin(\theta + \gamma) \right\}. \quad (48)$$

The integral equation for $\sigma(x)$ is

$$\alpha(x) \sigma(x) = -\sqrt{\frac{8\pi K\omega}{\omega_e + KU}} e^{-i\frac{\pi}{4}} \int_0^x \frac{\sigma(\xi)}{\sqrt{|x-\xi|}} d\xi + \frac{g_{\theta}^x}{\omega} + \phi_{Bz0} \frac{e^{Kx_0 + iKx}}{K}, \quad (49)$$

where

$$\alpha(x) = \frac{e^{Kx_0}}{K r_0} \left\{ V_R(0) + \sum_{m=1}^{\infty} p_m V_m(0) \right\} + \frac{4\pi}{\sqrt{2(2 + \frac{g}{\omega U})}}. \quad (50)$$

In eqs. (49) and (50)

$$\phi_B = i\pi e^{K_e z} (1 - e^{-2K_e \bar{r}}) \times \left\{ \sigma_{01} H_0^{(1)}(K_e R_1') + \sigma_{03} H_0^{(1)}(K_e R_3') \right\}, \quad (51)$$

and the other notations are the same as in zero-speed problem but eq. (46) must be used for Ψ_R .

Finally ϕ_2 in forward-speed problem is given by the

same form as eq. (43).

4. EXTERNAL PRESSURE AND RESISTANCE INCREASE

Before this paragraph, the method how to calculate the diffraction potentials of the slender-ship with blunt bow and stern is shown. In this paragraph, external pressure and resistance increase in head seas are treated as the application of it.

The total velocity potential Φ is given by

$$\Phi = \left\{ \phi_1 + \phi_3 + (\phi_2 + \phi_w) e^{-iKx} \right\} e^{i\omega_e t}. \quad (52)$$

Since the external pressure P_e is given by

$$P_e = -\rho \frac{\partial \Phi}{\partial t}, \quad (53)$$

the external pressure acting on the hull is obtained as follows:

$$|P_e| = |-\rho i \omega_e \left\{ \phi_1 + \phi_3 + (\phi_2 + \phi_w) e^{-iKx} \right\}|_{r=r(\theta)}. \quad (54)$$

If Kochin function is known, the resistance increase is given by Maruo's formula. That is

$$R_{Aw} = 4\pi\rho \left[-\int_{-\infty}^{-K'} + \int_{-K}^{\infty} \right] \frac{(m+K_0\Omega)^2 (m+K)}{\sqrt{(m+K_0\Omega)^4 - K_0^2 m^2}} \times |H(m)|^2 dm, \quad (\Omega \geq \frac{1}{2}) \quad (55)$$

where

$$K' = \frac{K_0}{2} (1 + 2\Omega + \sqrt{1+4\Omega}), \quad (56)$$

$$K_0 = g/U^2, \quad (57)$$

$$H(m) = \iint_{\Sigma} \nabla^2 \phi(x, 0, z) \times \exp(K_1 z + imx) ds, \quad (58)$$

$$K_1 = (m + K_0\Omega)^2 / K_0. \quad (59)$$

For the calculation of resistance increase, the singularities in bow and stern parts are assumed to be located at $x = 0$ and $x = L-B$ respectively. Hence Kochin function due to the singularity at bow part is

$$H_1 = \int_{-\bar{T}}^0 \sigma_{01} e^{K_e z} e^{K_1 z} dz = \frac{\sigma_{01}}{K_e + K_1} \left\{ 1 - \exp(-K_2 - K_1) \bar{T} \right\}. \quad (60)$$

In the same manner, Kochin function due to stern part is

$$H_3 = \int_{-1}^0 \sigma_{03} \exp\{(K_0 + K_1)z + i(L-B)m\} dz$$

$$= \frac{\sigma_{03}}{K_0 + K_1} \left\{ 1 - e^{-(K_0 + K_1)T} \right\} e^{i(L-B)m} \quad (61)$$

Kochin function due to parallel part is given by

$$H_2 = \int_{-a}^{L-a} \sigma(x) \cdot e^{imx} dx. \quad (62)$$

Because $\sigma(x)$ is zero at the fore and aft ends, we put

$$\sigma(x) = \sigma_c(x) + i\sigma_s(x)$$

$$= \sum_{j=1}^n \sigma_{cj} \sin \frac{j\pi(x+a)}{L}$$

$$+ i \sum_{j=1}^n \sigma_{sj} \sin \frac{j\pi(x+a)}{L}, \quad (63)$$

where

$$\left. \begin{aligned} \sigma_{cj} &= \frac{2}{L} \int_{-a}^{L-a} \sigma_c(x) \sin \frac{j\pi(x+a)}{L} dx, \\ \sigma_{sj} &= \frac{2}{L} \int_{-a}^{L-a} \sigma_s(x) \sin \frac{j\pi(x+a)}{L} dx. \end{aligned} \right\} \quad (64)$$

Substituting eq. (63) into eq. (62), we have

$$H_2 = \sum_{j=1}^n (\sigma_{cj} I_{cj} - \sigma_{sj} I_{sj})$$

$$+ i \sum_{j=1}^n (\sigma_{cj} I_{sj} + \sigma_{sj} I_{cj}), \quad (65)$$

where

$$I_{cj} = \int_{-a}^{L-a} \left\{ \sin \frac{j\pi(x+a)}{L} - \cos(mx) \right\} dx$$

$$= \frac{j\pi/L}{(j\pi/L)^2 - m^2} [\cos(ma) \{ 1 - (-1)^j \cos(mL) \}$$

$$- (-1)^j \sin(ma) \sin(mL)], \quad (66)$$

$$I_{sj} = \int_{-a}^{L-a} \sin \frac{j\pi(x+a)}{L} \sin(mx) dx$$

$$= \frac{-j\pi/L}{(j\pi/L)^2 - m^2} [(-1)^j \cos(ma) \sin(mL)$$

$$+ \sin(ma) \{ 1 - (-1)^j \cos(mL) \}]. \quad (67)$$

Substituting above Kochin functions into eq. (55), we have

$$R_{AW} = R_{AW1} + R_{AW2} + R_{AW3} + R_{AW13}$$

$$+ R_{AW23} + R_{AW12}, \quad (68)$$

where

$$R_{AW1} = 4\pi\rho \left[-\int_{-a}^{-K^*} + \int_{-K}^{\infty} \right] \frac{(m+K_0\Omega)^2 \cdot (m+K)}{\sqrt{(m+K_0\Omega)^2 - K_0^2 m^2}}$$

$$\times |H_1(m)|^2 dm, \quad (69)$$

$$R_{AW3} = 4\pi\rho \left[-\int_{-a}^{-K^*} + \int_{-K}^{\infty} \right] \frac{(m+K_0\Omega) \cdot (m+K)}{\sqrt{(m+K_0\Omega)^2 - K_0^2 m^2}}$$

$$\times |H_3(m)|^2 dm \quad (70)$$

and using Maruo's approximation^[9]

$$R_{AW2} = 8\pi^2 \rho K \int_{-a}^{\infty} |\sigma(x)|^2 dx. \quad (71)$$

Furthermore for the interference terms

$$R_{AW12} = 4\pi\rho K \left[-\int_{-a}^{-K^*} + \int_{-K}^{\infty} \right] \frac{(m+K_0\Omega)^2 \cdot (m+K)}{\sqrt{(m+K_0\Omega)^2 - K_0^2 m^2}}$$

$$\times (H_1 H_2^* + H_2 H_1^*) dm, \quad (72)$$

$$R_{AW13} = 4\pi\rho K \left[-\int_{-a}^{-K^*} + \int_{-K}^{\infty} \right] \frac{(m+K_0\Omega)^2 \cdot (m+K)}{\sqrt{(m+K_0\Omega)^2 - K_0^2 m^2}}$$

$$\times (H_1 H_3^* + H_3 H_1^*) dm, \quad (73)$$

$$R_{AW23} = 4\pi\rho K \left[-\int_{-a}^{-K^*} + \int_{-K}^{\infty} \right] \frac{(m+K_0\Omega)^2 \cdot (m+K)}{\sqrt{(m+K_0\Omega)^2 - K_0^2 m^2}}$$

$$\times (H_2 H_3^* + H_3 H_2^*) dm, \quad (74)$$

where H_1^* , H_2^* and H_3^* are complex conjugates of H_1 , H_2 and H_3 respectively.

In case of $\Omega < 1/4$, we must notice that eq. (55) takes the form

$$R_{AW} = 4\pi\rho K \left[-\int_{-a}^{-K^*} + \int_{-K}^{K^*} + \int_{K^*}^{\infty} \right]$$

$$\times \frac{(m+K_0\Omega)^2 \cdot (m+K)}{\sqrt{(m+K_0\Omega)^2 - K_0^2 m^2}} |H(m)|^2 dm, \quad (75)$$

where

$$\left. \begin{aligned} K'' \\ K''' \end{aligned} \right\} = \frac{K_0}{2} (1 - 2\Omega \mp \sqrt{1 - 4\Omega}). \quad (76)$$

5. NUMERICAL EXAPLES

Numerical calculations were carried out for full ore carrier "Kasagisan-Marui", which had been chosen as a subject of studies on the wave induced pressure acting on hull surface. The principal particulars of the ship are shown in Table 1.

The accurate expressions of the ship body are necessary for determining the longitudinal source distribution and the velocity potential around the parallel part. In this paper, however, Lewis form transformation was employed. The ship was divided into twenty transverse sections, and

Table 1 Main particulars

Length between perpendiculars	(Lpp)	247.00 m
Breadth moulded	(B)	40.60 m
Draft moulded	(T)	16.00 m
Length/Breadth ratio	(L/B)	6.0837
Breadth/Draft ratio	(B/T)	2.5375
Block coefficient	(CB)	0.8249
Midship coefficient	(CM)	0.9975
Center of gravity from midship	(LCB)	7.30 m fore

the beam, draft and sectional area of each section were used as parameters for the transformation.

There are two integral equations, (35) and (49), to be solved. Though both equations have the same singular kernel, it is shown that the integral equation of this type can be solved by means of numerical integration. In order to keep the accuracy of numerical integration, some devices were applied.

Eqs. (55) and (75) were numerically integrated by the method of Gauss. For the trigonometric series of Kochin function (65), ten terms were applied to the numerical calculation program.

The factor of the decrease of the incident wave was assumed to be 0.5 in case of $F_n=0$ and 0.6 in case of $F_n \neq 0$.^[10]

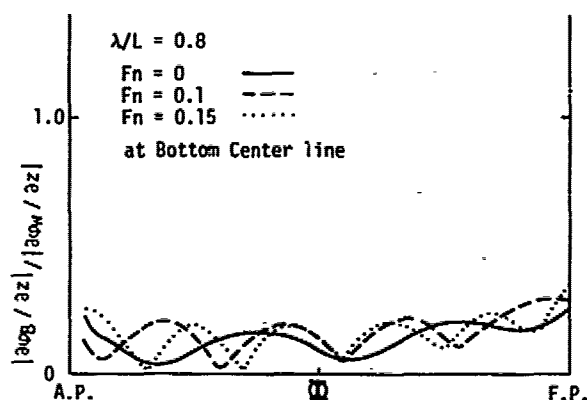


Fig. 3 Induced velocity due to bow and stern singularities ($\lambda/L = 0.8$, $F_n = 0, 0.1, 0.15$)

Numerical examples of the induced velocity of the diffracted waves due to the bow and stern singularities are shown in Fig. 3. In the figure the ratio of $\partial\phi_B/\partial z$ to $\partial\phi_W/\partial z$ along the bottom center line is shown.

Fig. 4 shows the longitudinal source distribution along the center line of the ship. It is obvious that there exists a significant fluctuation of the source intensity along the ship. Fluctuations are seen near the fore and aft end parts of the ship. This is considered to arise from that the sectional configuration varies rapidly in these parts. The

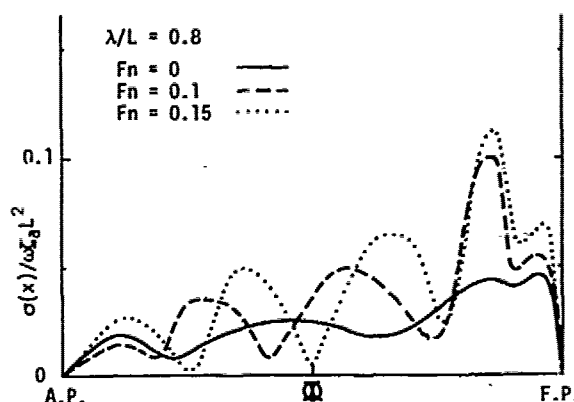


Fig. 4 Longitudinal source distribution along parallel part ($\lambda/L = 0.8$, $F_n = 0, 0.1, 0.15$)

fluctuation in the parallel part is supposed to be due to the singularities at bow and stern parts and does not appear in the solutions of strip theory or slender-body theory.

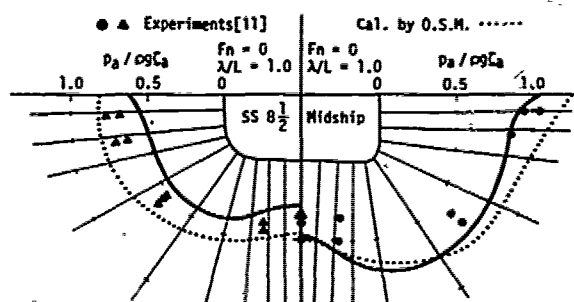


Fig. 5 Transverse distribution of hydrodynamic pressure acting on hull surface ($\lambda/L = 1.0$, $F_n = 0$)

The transverse distributions of the hydrodynamic pressure acting on the hull surface are shown in Fig. 5 for the cases of $\lambda/L=1.0$, $F_n=0$ and $\lambda/L=1.0$, $F_n=0$. The values of the pressure are plotted on the normals of the hull. In the figure, the numerical results by means of ordinary strip method and the measured results^[11] are shown too. It is obvious that the results of the present calculation agree very well with the measured results. They also agree with those of the strip method in case of $F_n=0$. But, in case of $F_n=0.15$, the strip method gives a little bigger value.

The longitudinal distributions of the hydrodynamic pressure are shown in Fig. 6 and 7. Fig. 6 shows the cases of $\lambda/L=0.8$; $F_n=0, 0.1, 0.15$ and the values of the pressure on the centerline of the bottom. The measured values in case of $\lambda/L=0.75$; $F_n=0.015$ ^[12] are also plotted. Fig. 7 shows the case of $\lambda/L=1.0$; $F_n=0.15$ and the values of the pressure on the bottom centerline ($\theta=0^\circ$), bilge ($\theta=50^\circ$) and side ($\theta=80^\circ$) respectively. The measured values in the same conditions^[13] as in the calculation are plotted in this figure. As is obvious from the figures, the agreement between the calculation

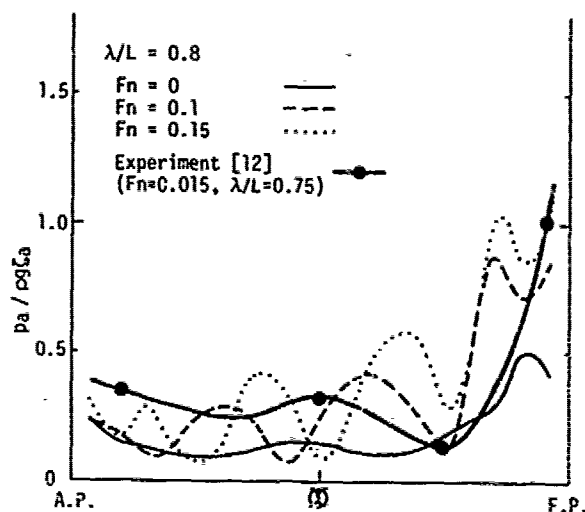


Fig. 6 Longitudinal distribution of hydrodynamic pressure acting on hull surface ($\lambda/L = 0.8$, $F_n = 0, 0.1, 0.15$)

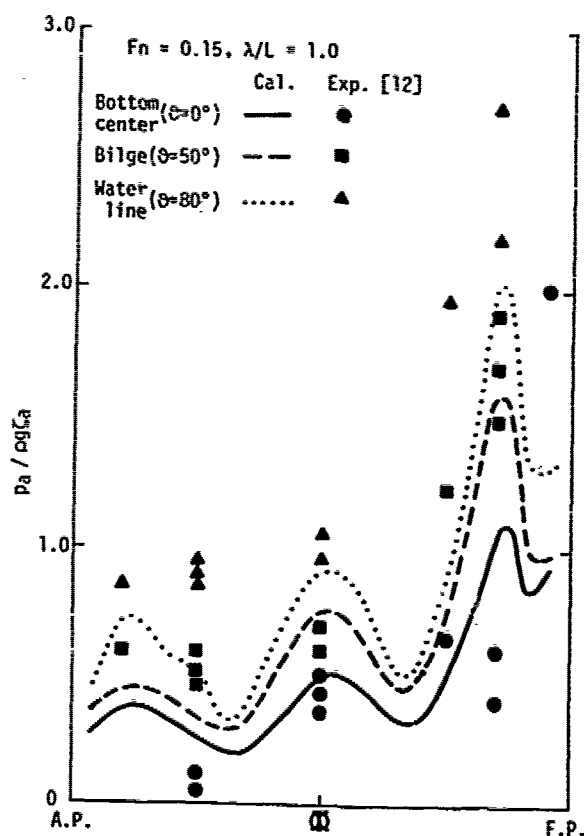


Fig. 7 Longitudinal distribution of hydrodynamic pressure acting on hull surface ($\lambda/L = 1.0$, $F_n = 0.15$)

and the experiment is generally good and the theoretical calculation shows the fluctuation. This tendency of fluctuation is seen obviously in the measured values in Fig. 6 and is supposed to be due to the effect of the singularities at bow and stern parts.

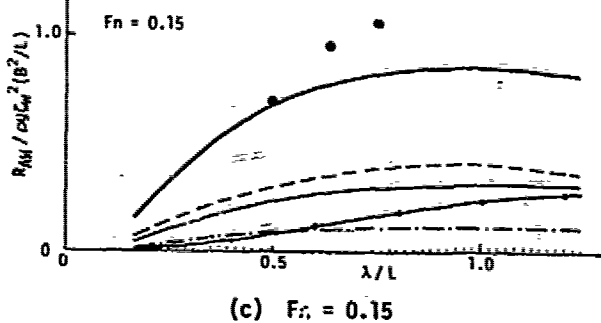
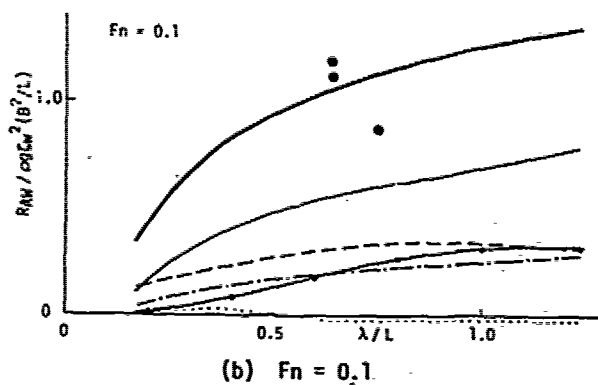
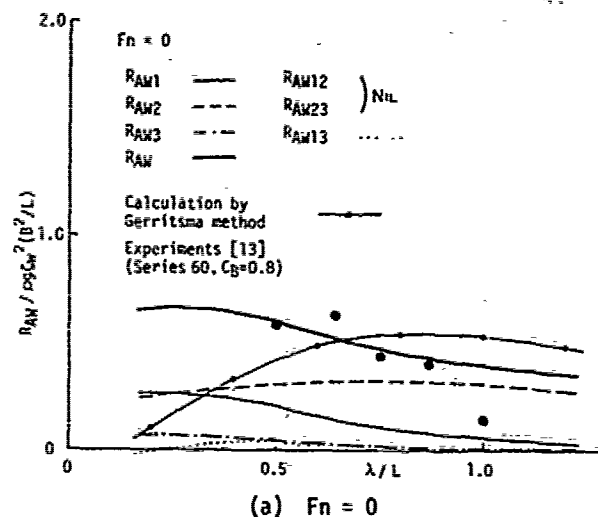


Fig. 8 Added resistance due to diffraction in regular head waves ($F_n = 0, 0.1, 0.15$)

The calculated results of the added resistance due to diffraction in regular head waves are shown in Fig.8.

Since there is no experimental result directly compared with the present calculation, the results for Series 60, $C_B=0.8$ ship form^[13] are plotted in the figure. The calculated results by Gerritsma's method^[14] are also shown. For the present calculation, the components of the added resistance are shown. But the interference terms are so small that R_{AW12} and R_{AW23} are neglected. The figures show that the present method explains the qualitative characteristics of added resistance in short wave region, where full ships generally have large added resistance.

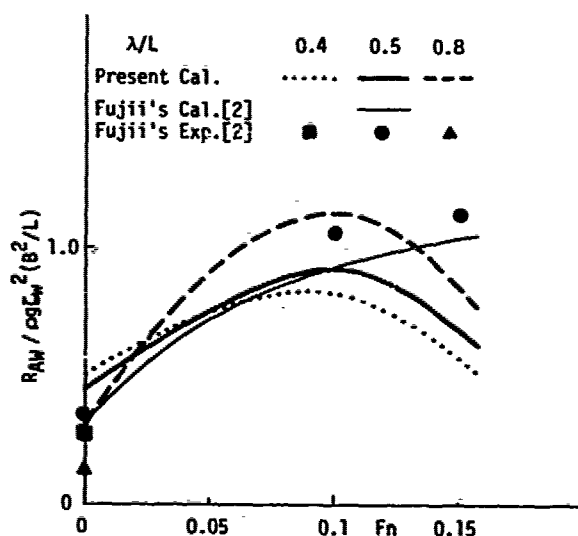


Fig. 9 Effect of advance speed on added resistance in regular head waves

Fig.9 shows the effect of advance speed upon added resistance in short wave region. In the figure, Fujii's curve and his experimental data^[2] are also shown. Though Fujii's curve shows that the added resistance increases with speed, the present curve has a maximum point beyond which the curve has the tendency of decrease. But, roughly speaking, the agreement of the both curves is good.

6. CONCLUDING REMARKS

The authors show an analytical method which approximately solves the diffraction problem of a slender ship with blunt bow advancing in head seas.

In order to satisfy the longitudinal boundary condition at blunt parts, vertical line singularities are introduced. These cause fluctuation of hydrodynamic pressure and large added resistance in short wave region. Some numerical examples seem to explain the characteristics of external pressure and added resistance.

But, since the determination of vertical line singularities is very rough, the quantitative agreement between calculation and experiment is not so good. This is especially true in case of forward-speed problem. Further investigation would be necessary.

ACKNOWLEDGEMENTS

The authors deeply appreciate the valuable discussions by Professor J.V. Wehausen. Thanks are also due to Dr. S. Naito for his kind help in this study. For the numerical calculation, ACOS600 of Computer Center, University of Osaka Prefecture was used.

REFERENCES

1. Maruo, H., "Resistance in Waves", The Society of Naval Architects of Japan 60th Anniversary Series, Vol.8, Chap.5, 1963, pp.67-97.
2. Fujii, H. and Takahashi, T., "Experimental Study on the Resistance Increase of a Large Full Ship in Regular Oblique Waves", *Journal of the Society of Naval Architects of Japan*, Vol.140, Dec. 1976, pp.132-137.
3. Havelock, T.H., "The Pressure of Water Waves upon a Fixed Obstacle", *Proc. Roy. Soc. Series A* No.963, Vol.175, July 1940, pp.409-421.
4. Higo, Y., Nakamura, S. and Takagi, M., "A Study on the Resistance Increase of a Towed Pontoon Among the Waves", *Journal of the Kansai Society of Naval Architects, Japan*, No.174, Sept. 1979, pp.45-56.
5. Faltinsen, O., "Wave Forces on a Restrained Ship in Head-Sea Waves", 9th Symposium on Naval Hydrodynamics, Paris, Aug. 1972, pp.1763-1840.
6. Maruo, H. and Sasaki, N., "On the Wave Pressure Acting on the Surface of an Elongated Body Fixed in Head Seas", *Journal of the Society of Naval Architects of Japan*, Vol.136, Dec. 1974, pp.107-114.
7. Bessho, M., "On the Wave Pressure Acting on a Fixed Cylindrical Body", *Journal of the Society of Naval Architects of Japan*, Vol.101, Aug. 1957, pp.1-10.
8. Ogilvie, T.F. and Tuck, E.O., "A Rational Strip Theory of Ship Motions: Part 1", Department of Naval Architecture and Marine Engineering, College of Engineering, The University of Michigan, Ann Arbor, Michigan, Report No. 013, March 1969.
9. Maruo, H. and Ishii, T., "Calculation of Added Resistance in Head Sea Waves by Means of a Simplified Formula", *Journal of the Society of Naval Architects of Japan*, Vol.140, Dec. 1976, pp.136-141.
10. Naito, S., "Disturbance of incident wave,, 1975, Private communication.
11. Report of Ship Research Association of Japan, SR131, Report No.163, 1972.
12. Report of Ship Research Association of Japan, SR131, Report No.176, 1973.

13. Shintani, A., "Influence of Ship Form Particulars on Resistance Increase in Regular Waves", Journal of the Kansai Society of Naval Architects, Japan, No.139, March 1971, pp.35-42.

14. Gerritsma, J. and Beukelman, W., "Analysis of the Resistance Increase in Waves of a Fast Cargo Ship", International Shipbuilding Progress, Vol.19, No.217, Sept. 1972, pp.285-293.

Discussion

T. Takahashi (MHI)

It has been considered that a consistent treatment is necessary for the estimation of the added resistance of large full ships in short wavelength region. Now, the authors show us an useful theoretical method as well as interesting calculation results.

I appreciate this paper very much. Would you please let me ask some questions?

(1) If we want to evaluate the effect of different bow shape on added resistance in short wavelength, is it possible by authors' method using the plane distribution of vertical singularity?

(2) According to the calculation results shown in Fig.8, added resistance decreases as advance speed increases where $\lambda/L = 0.2$. This tendency seems to be reverse to our experimental results for full ship models in short wavelength. I suppose that energy dissipation due to reflected waves on bow surface per unit time increases when a ship is running, compared with the case of zero speed, owing to increase of encounter waves. How can be explained from the theory that added resistance due to diffraction waves on bow of running ship is smaller than the zero speed case?

I am much obliged to you if a plain explanation is given.

Y. Himeno (Univ. of Osaka Prefecture)

(1) You mentioned that in Fig.4 the fluctuation of the source distribution in the midship region is due to the bow and stern singularities, and that it does not appear in the solution of strip method. If you have the results of strip method, would you show us the comparison of the singularity distribution between your method and the strip method?

(2) In Fig.8(b), how does your result behave when the wave length becomes very large?

Author's Reply

R. Hosoda (Univ. of Osaka Prefecture)

Mr. Takahashi asked the applicability of the present method to more general case.

The authors think that basically it is possible to apply the present method to more general and complicated problems, by replacing the vertical line singularities with a surface or plane distribution of singularity. But, some difficulties are expected in satisfying the body boundary conditions at the ship bow and stern. It may be especially true when the ship has a big bulbous bow. There will be much more difficulties in evaluating the diffraction effects from bow and stern on the fluid motions in the middle parallel body domain. Also, a lot of computer time will be necessary for the numerical calculation.

As for his second question, in case of, zero-forward speed, the authors agree with his comments that the energy dissipation will increase with the frequency of encounter. When the ship has a speed of advance, however, it should be noticed that there exists a region in front of the ship bow where are no waves reflected from ship bow. In such a case, the rise of the advance-speed does not necessarily mean the increase of energy dissipation.

However, the similar method as that in zero-speed problem was used for the determination of bow and stern singularities. And, as we can easily understand from Eq. (21), the strength of vertical singularities at bow and stern parts decreases while the frequency of encounter increases. This is another reason why the rise of the frequency of encounter or the advance speed gives the small value of the added resistance.

But, as is mentioned in the concluding remarks, the procedure employed here is simplified one, therefore the authors think that the results may not necessarily explain the real phenomena.

Professor Himeno asked that how is the difference between the longitudinal source distribution obtained by means of the present method and of the strip theory. Fig.A-1 replies to his question. In the figure, solid line indicates the result by the slender-body theory, namely the strip theory. It is obtained by the same way as Maruo and Sasaki's method. As is mentioned in the paper, hump and hollow near the fore and aft ends are due to the rapid change of the sectional shape of the ship. At the middle parallel body part, the curve by strip theory does not have any hump or hollow.

He also questioned the behavior of the added resistance when the incident wave becomes very long. According to the calculated results presented here, the added resistance due to diffraction seems to increase with the incident wave length. This increase is considered to come from that in determining the source strength of forward speed problem, we used the same method as that in zero-speed problem. In the fundamental assumptions, we assumed that the incident wave length is small compared with the ship length, namely $\Omega (= \omega U/g) \geq 1/4$. Therefore, nothing should be mentioned about the added resistance in the range

of $Q < 1/4$, i.e. in the range of very long incident waves. But, the diffraction effect generally decreases with increase

of the incident wave-length. Consequently, the added resistance due to diffraction may decrease and tend to zero.

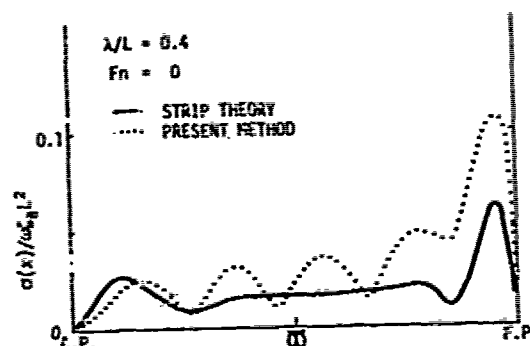


Fig. A-1

Added Resistance in Waves in the Light of Unsteady Wave Pattern Analysis

Makoto Ohkusu

Research Institute for Applied Mechanics

Kyushu University

Fukuoka, Japan

ABSTRACT

The measurement and the analysis of the unsteady waves generated by a ship model running with a constant forward velocity into regular head waves are proposed for deriving the spectrum of those waves and for getting directly the added resistance by the computation of the energy flux of the measured waves far away from the model without relying upon the resistance test in waves.

We need to measure the distribution, along a line parallel to the running course of a ship model, of the amplitude and the phase of the wave motions sinusoidal in time for carrying out the wave analysis proposed. It is not so easy as in the measurement of the stationary wave pattern to get those informations on the unsteady waves with the way usually used for measuring the wave elevations in a water tank. A special wave measuring system is also proposed with which we can measure the distribution of the amplitude and the phase of the wave elevations without difficulty.

The unsteady waves around a ship model running in waves are supposed to be a superposition of the radiation waves induced by its oscillation in incident waves and the diffraction waves made by the scattering of the incident waves on its hull surface when it is running in waves with its oscillations suppressed. The radiation waves of a tanker model forced to undergo prescribed heaving motion and pitching motion are measured by means of the proposed measuring system and analyzed to decompose them into the Kochin functions. The Kochin functions thus obtained of the radiation waves compared with the theoretical prediction given by Ogilvie-Tuck slender body theory support that the slender body theory can predict well the far-field radiation wave pattern in minute

details even for a full hull form. On the other hand the diffraction waves of a ship model in regular head waves are found to be not so well predicted in details by a slender body theory, for example, given by Adachi, even though they are qualitatively in good agreement with the theoretical predictions.

The Kochin function of the unsteady waves generated when a ship model is progressing into regular waves can be also theoretically computed as a summation of those of the radiation waves and the diffraction waves. They are again not in so good agreement with the Kochin function derived experimentally with the wave analysis, though the radiation wave component of them are supposed to be predicted well as concluded above by the theory. Some theories seem to give the correct value of the added resistance. This results shows, however, that sometimes they may not predict the wave field around a ship as a cause of the added resistance. The more accurate prediction of the diffraction waves and of their interaction with the radiation waves should be studied further. The added resistance of the model evaluated using the measured Kochin function is well correlated to the value measured in the resistance test. This fact is understood to reveal that the added resistance is completely a wave resistance under little direct influence of water viscosity and accordingly we can compute it correctly with the energy flux of the wave field far away from ships.

NOMENCLATURE

F_n	=Froude number
g	=gravitational acceleration
$H_{1,2}$	=Kochin functions of elementary waves
k	=wave number (ω^2/g)

$k_{1,2}$	=wave numbers of elementary waves
L	=ship length
AR	=added resistance of ship
V	=forward velocity of ship
θ	=angle of propagation of elementary wave
ζ	=total wave elevation
ζ_0	=stationary wave elevation
ζ_c, ζ_s	=amplitude of sinusoidal wave motion
ζ_a	=incident wave amplitude
ω	=wave frequency of encounter in rad/sec
Ω	= $\omega V/g$

1. INTRODUCTION

When a ship is running in waves, it generates the unsteady waves around it as well as the steady ones. The unsteady waves are caused by both the diffraction and the motions in the incident waves. The energy carried away by those unsteady waves leads to the increase of the resistance of the ship — the added resistance in waves.

There have been a number of significant contributions made to predict theoretically the added resistance of ship in waves and to verify experimentally the theoretical predictions. In most of those contributions the added resistance forces theoretically computed are compared with those obtained in resistance tests in waves. The unsteady waves generated by a ship moving in even regular waves have a complex structure and are, as mentioned above, a composite of the diffraction waves of the incident waves and the radiation waves made by its oscillatory motions of various modes. On the other hand, the added resistance itself is determined merely by the total flux of those waves and does not reflect such a complicated structure of the wave field as a result of the integrated effect. Accordingly the experiments of measuring simply the added resistance of ship models are not sufficient for examining the details of the theories of the added resistance because we can not tell they are really valid unless they can predict the detailed structure of the wave fields around the models as well as the resulting added resistance. Those experiments can not explicitly clarify how much the added resistance is influenced by the diffraction waves, even though we have some evidences supporting indirectly that the diffraction waves dominate the added resistance of full hull forms in shorter waves. We can not also get information about the effect of water viscosity on the added resistance with the measured added resistance alone.

For the objectives of making up with such insufficiencies of the experiments on the added resistance and of understanding the structure of the unsteady wave field as the cause of the added resistance, the measurement of the unsteady wave patterns around a ship model running into regular head waves are proposed in this report and the "spectrum" of the wave pattern is derived from them. The unsteady waves generated away from a ship model are supposed to be

decomposed into long-crested waves — hereafter called as elementary waves — traveling into all the directions from it except a region of direction dependent on its forward velocity and the frequency of its encounter with regular incident waves. The distribution of the amplitudes and the phase of those long-crested waves with respect to the direction of their propagation — the "spectrum" — is derived from the measured wave records and used to study the minute structure of the unsteady wave field generated by the model running in regular head waves as well as the resulting added resistance. The comparison of the theoretical and the experimental spectrum will be more strict test of the theories for predicting the added resistance because with it we can examine how accurate they are in predicting the "components" of the added resistance integral. This technique of experiments will resolve most of the ambiguities about the added resistance. The structure of the measured diffraction waves obtained for a ship model towed with a constant forward velocity in incident waves with its oscillatory motions suppressed is compared with that of the waves generated by the model running with the same velocity and in the same incident waves but with no restriction on its motions to evaluate the relative importance of the diffraction waves in the added resistance. The integration of the "spectrum" of the measured unsteady waves generated by a ship model moving in regular waves gives directly the added resistance of the model, which is not regarded to include the resistance due to the water viscosity. If we compare it with the added resistance value provided in the measurement of the fluid force on the model, we can get an idea of the effect of the viscosity on the added resistance.

In this report the added resistance of a full ship hull form is investigated examining the radiation waves, the diffraction waves and the combination of them generated when it moves into regular incident waves by means of the analysis of those waves measured in the model test. With the results of this analysis we check a slender body theory's validity in predicting the radiation wave field, the diffraction wave field and the total unsteady wave field around the hull form moving in waves respectively as well as the resulting added resistance. Moreover the importance of the diffraction waves in the added resistance of a full hull form is clarified with respect to the far-field waves.

The values of added resistance directly derived from the measured wave pattern are also compared with those obtained in the resistance test.

2. ANALYSIS OF UNSTEADY WAVE PATTERN AROUND A SHIP

Let us suppose a ship model running in regular waves with a constant forward velocity V . The reference frame $O-x y z$ is assumed to move with the average position of

the model. The x-y plane is taken as shown in Fig. 1 to coincide with the calm water free surface and the z axis vertically upward. Excluding the incident regular waves, the wave elevation at a point in the moving reference frame of the model is generally expressed by

$$\begin{aligned} \zeta(x, y, t) = & \zeta_0(x, y) \\ & + \zeta_c(x, y) \cos(\omega t + \varepsilon) \\ & + \zeta_s(x, y) \sin(\omega t + \varepsilon) \end{aligned} \quad (1)$$

where the first term on the right hand side denotes the stationary wave elevation which might be identical with the one generated at the same location when the model is towed in otherwise calm water with the velocity V . Both the second and the third terms are the unsteady waves caused by the diffraction of the incident waves on the model hull surface and its oscillatory motions induced in the incident waves. In the moving reference frame of the model the incident waves arrive with the frequency of encounter ω and the elevation of them is $\zeta_a \cos(\omega t + \varepsilon)$ at the location of the model's midship. If $\zeta(x, y, t)$ is the radiation wave generated when the incident waves are suppressed and the model is forced to undergo prescribed oscillatory motion of a mode, $\zeta_a \cos(\omega t + \varepsilon)$ denotes the prescribed oscillatory motion.

The wave elevation $\zeta(x, y, t)$ might contain other components than the terms appearing in the right hand side of the equation (1), for example, the wave elevations oscillatory in time like $\cos(n\omega t)$ ($n=1, 2, \dots$). They are, however, supposed to be so small as to be ignored and even if they were not, their effects could be removed from the measured data through the processing described later to get the correct measurements of the second and the third terms in the equation (1).

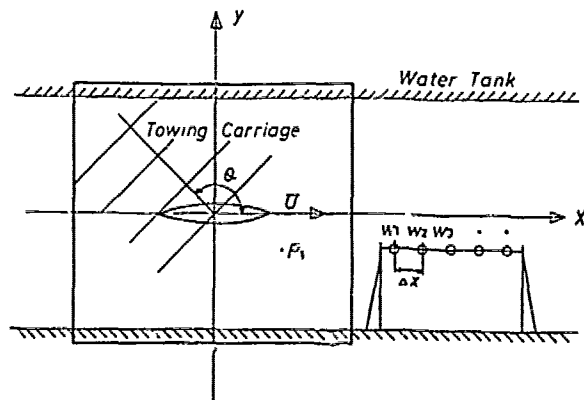


Fig.1 Coordinate system

The unsteady part of the wave elevation of the equation (1) is generally, at the location away from the model, expressed in the form

$$\begin{aligned} \zeta_c(x, y) - i\zeta_s(x, y) = & \frac{2\omega}{g} \left[\int_{-\pi/2}^{0} - \int_{\pi/2}^{0+\pi/2} \right] (1 + k_1/k \cdot \Omega \cos \theta) \\ & \times H_1(\theta) k_1 \\ & \times \frac{\exp[-ik_1 x \cos \theta - ik_1 y \sin \theta]}{\sqrt{1 - 4\Omega \cos \theta}} d\theta \\ & + \frac{2\omega}{g} \left[\int_{0-\pi/2}^{0+\pi/2} \right] (1 + k_2/k \cdot \Omega \cos \theta) H_2(\theta) k_2 \\ & \times \frac{\exp[-ik_2 x \cos \theta - ik_2 y \sin \theta]}{\sqrt{1 - 4\Omega \cos \theta}} d\theta \\ & + O\left(\frac{1}{\sqrt{x^2 + y^2}}\right) \end{aligned} \quad (2)$$

where

$$k_{1,2} = \frac{g}{V^2} \frac{1 - 2\Omega \cos \theta \pm \sqrt{1 - 4\Omega \cos \theta}}{2 \cos^2 \theta}$$

and $k = \omega^2/g$, $\Omega = V\omega/g$ and $\theta = \tan^{-1}(y/x)$.

The expression (2) shows that the unsteady wave pattern around a ship model is composed of the component waves, hereafter called as elementary waves, progressing in various directions of the angles θ with the x axis. For each θ , we have generally two elementary waves with different wave numbers k_i ($i=1, 2$) and different complex amplitudes proportional to the Kochin functions $H_i(\theta)$ ($i=1, 2$).

The knowledge of the Kochin functions $H_i(\theta)$ of the unsteady wave pattern around a ship model provides us the added resistance in waves or the damping forces of the model's motions in the form of integrals of them. The added resistance ΔR in regular head waves is given (Ref.1) by

$$\begin{aligned} \Delta R = & 4\pi\rho \left[\int_{\alpha_0}^{\pi/2} - \int_{\pi/2}^{\pi} \right] \\ & \times \frac{|H_1(\theta)|^2 k_1 (k_1 \cos \theta + k)}{\sqrt{1 - 4\Omega \cos \theta}} d\theta + \end{aligned}$$

$$+ 4\pi\rho \int_{\alpha_0}^{\pi} \frac{|H_2(\theta)|^2 k_2 (k_2 \cos \theta + K)}{\sqrt{1 - 4\Omega \cos \theta}} d\theta \quad (3)$$

where $\alpha_0 = \cos^{-1}(K/\Omega)$.

The purpose of the analysis of the unsteady wave pattern proposed in this report is to derive those Kochin functions from the wave elevation records measured for a ship model running in regular waves. If we can measure ζ_c and ζ_s on the line of $y = \text{constant}$, say, the distributions of them on the line parallel to the running course of the model, the Fourier transforms of them with respect to x give the Kochin functions of the unsteady wave pattern which depend on the model hull form and the forward velocity as well as the amplitude, the length and the angle of incidence of the incident waves. Assuming the wave pattern is port-and-starboard symmetrical, this is the case with a ship model moving in head seas, the Kochin functions of the unsteady wave pattern around the model are given (Ref.2) by

$$\begin{aligned} H_1(\theta) = & \frac{g}{2\omega} \int_{-\infty}^{\infty} [\zeta_c(x; y) - i\zeta_s(x, y)] \\ & \times e^{ik_1 x \cos \theta} dx \\ & \times \frac{1}{2\pi} \sin \theta \cdot \text{sgn}[\cos \theta] \\ & \times \frac{\exp[ik_1 y \sin \theta \cdot \text{sgn}(\cos \theta)]}{(1 + k_1/K \cdot \Omega \cos \theta)} \end{aligned} \quad (4)$$

$$\begin{aligned} H_2(\theta) = & \frac{g}{2\omega} \int_{-\infty}^{\infty} [\zeta_c(x, y) - i\zeta_s(x, y)] \\ & \times e^{ik_2 x \cos \theta} dx \\ & \times \frac{1}{2\pi} \sin \theta \frac{\exp(ik_2 y \sin \theta)}{(1 + k_2/K \cdot \Omega \cos \theta)} \end{aligned} \quad (5)$$

If we put a single wave probe at a location in the moving reference frame, say, at a point fixed to the towing carriage, to measure ζ_c and ζ_s , a record of the motions of the free surface provided with this wave probe will give those terms at only one location. It is practically impossible to get the full distribution of them along a line of $y = \text{constant}$ by such a single wave probe. A special system described in the next section is needed to realize the measurement of ζ_c and ζ_s distributions along the line. In addition the wave elevation data can not be collected further than some distance behind a ship model, since the wave pattern is contaminated by the tank wall reflections far in the rear of the model.

If we can not get the wave data behind $x = -X$, where X is sufficiently large positive

number, then the integrals over $-\infty < x < -X$ of the Fourier transform (4) and (5) are evaluated by introducing a technique analogous to that used by Newman (Ref.3) in the analysis of the stationary wave pattern around a ship model running in calm waters. Assuming x is much larger than y in the asymptotic expression of the unsteady wave pattern (Ref.4, 5), the wave elevation on the line $y = \text{constant}$ takes the form

$$\zeta_c - i\zeta_s \sim A_1 \frac{e^{i\bar{k}_1 x}}{\sqrt{|x|}} + A_2 \frac{e^{i\bar{k}_2 x}}{\sqrt{|x|}} \quad (6)$$

where $A_i (i=1, 2)$ are complex constants and

$$\bar{k}_{1,2} = g/v^2 (1 + 2\Omega + \sqrt{1 + 4\Omega})/2$$

Substituting the expression (6), with A_i determined such that the curve (6) gives the best fitting of the measured unsteady wave elevation in the vicinity of $x = -X$, for $\zeta_c - i\zeta_s$ from $-X$ to the negative infinity in the integrals (4) and (5), we can evaluate them after $-X$ in the form of Fresnel integrals.

There is not such a problem in the integration ahead of a ship model, because we are concerned here with only the case $\Omega > \frac{1}{4}$ and accordingly waves do not exist, except the incident waves, far ahead of the model. When Ω is smaller than 0.25, waves propagate forward from the model and their reflections on the tank wall will disturb the wave pattern at almost all the surface of water. So the idea of the analysis of the unsteady wave pattern generated by a ship model in incident waves can not apply to this case.

It is evident that the accuracy of the Kochin functions derived with the formulae (4) and (5) from the measured unsteady waves is dependent on the y coordinate of a line along which the waves are measured. But some results of the wave analysis done with different values of y show that the values of H_2 , at least, are not so much influenced by the magnitude of y if it is larger than one thirds of the model length (Ref.2).

3. MEASUREMENT OF UNSTEADY WAVE PATTERN

The unsteady wave elevation around a ship model moving in regular waves is expressed by the equation (1) as already described. In it both $\zeta_c(x, y)$ and $\zeta_s(x, y)$ are just what we need to measure along a line of $y = \text{constant}$. One possible way for measuring them might be as follows. Measurement, continued during a run of the model, of wave elevation with a probe P_1 installed on the towing carriage as shown Fig. 1 provides us with a time history of the sinusoidal motion of water surface at a point in the coordinate system moving forward with the model. That is, it gives $\zeta(x, y, t)$ in the left hand side of equation (1) for a fixed value of x and y , the coordinate corresponding to the wave probe location.

From the time history thus obtained we can get ζ_0 on the right hand side of equation (1) as the averaged bias of it from zero level and, ζ_c and ζ_s as the cosine and the sine components of the sinusoidal variation of it in time. This measurement has an advantage that it makes it possible for us to acquire reliable data on three terms on the right hand side of the equation (1) with other noise components completely removed. Measurement continued during one run of the model gives, however, no more than the values of them at only one location in the reference frame moving with the carriage. Accordingly if we want to know them at so many locations along a line of y -constant enough to carry out the Fourier integral of them on the right hand sides of the equations (4) and (5), we have to repeat the experiments many times with different locations of the wave probe, or a tremendously large number of wave probes have to be set. This way of measurement is, of course, unpractical in spite of its advantage in providing reliable data.

A measuring system was derived for realizing the wave measurement mentioned above with only one wave probe placed at a location in the water tank but with repeated experiments for the same frequency and the same forward speed of the model. This measurement which was successfully used for the measurement of the radiation waves, is as follows. If the model is forced to undergo a prescribed oscillation $\cos(\omega t + \epsilon_i)$ with the time t counted from a moment when the model's midship passed the spot of the wave probe set in the water tank, then the record of the wave motions there (no incident waves exist for the radiation wave test) takes the form

$$\begin{aligned} \zeta_i(-vt, y, t) = & \zeta_0(-vt, y) \\ & + \zeta_c(-vt, y) \cos(\omega t + \epsilon_i) \\ & + \zeta_s(-vt, y) \sin(\omega t + \epsilon_i) \end{aligned} \quad (7)$$

Repeated runs of the model at the same frequency of the oscillatory motion and the same forward velocity of the model will provide as many wave records with different ϵ_i as the number of the repeated measurements, since it is impossible to adjust ϵ_i to be identical for all the runs. This fact is rather convenient for us. For a fixed y and t , the unknowns ζ_0 , ζ_c and ζ_s in the equation (7) are determined with several different ϵ_i and also with several different data on the left hand side. Thus we can get the amplitude and the phase of the sinusoidal wave motions for every t , in other words, for every $x = -vt$ along the line with the coordinate y , with a finite number of repeated measurements by one wave probe. However this system can apply neither to the diffraction waves nor to the waves generated by a freely floating ship model in incident waves. It is because we can never repeat to generate completely the same regular in-

cident waves in the water tank and all the wave records obtained by the repeated experiments are not regarded to be those in the same incident waves but with different phases of the encounter.

A raw system, effective even for the measurements of the diffraction waves, described below was devised as a substitute for those two systems.

We set several number of wave probes W_1, W_2, \dots and W_N in the water tank as shown in Fig. 1 with an equal spacing x and on the line of y -constant along which we need to obtain ζ_c and ζ_s . When a ship model runs in the regular head waves, each wave probe will record wave motion at its location which, of course, includes that due to the incident wave. The expression, given by the equation (1), of the wave elevation at a point in the reference frame attached to the moving average position of the ship model gives us the expression for the wave record $\zeta_J(y, t)$ taken at probe W_J ($J=1, 2, \dots, N$). That is

$$\begin{aligned} \zeta_J(y, t) = & \zeta_0(-vt, y) \\ & + \zeta_c(-vt, y) \\ & \times \cos[\omega t + \epsilon + (J-1) \cdot \Delta x / V \cdot \omega] \\ & + \zeta_s(-vt, y) \\ & \times \sin[\omega t + \epsilon + (J-1) \cdot \Delta x / V \cdot \omega] \\ & + \text{the incident wave} \end{aligned} \quad (8)$$

where the time t is measured from the instant when the model's midship passes the position of the probe W_J and ϵ is the phase of the encounter of the incident waves with the midship at the instant when it passes the position of the probe W_1 . If we can exclude the incident waves from the right hand side of the equation (8) and if we replace $-vt$ with x in every record, then $\zeta_J(y, t)$, even though really they are the records at different spots, are equivalent to the wave elevations which might be measured at a spot (x, y) in the reference frame moving with the model but at different time instants $t - (J-1) \Delta x / V \cdot \omega$. So we can determine $\zeta_0(x, y)$, $\zeta_c(x, y)$ and $\zeta_s(x, y)$ from those N records at every x along the line parallel to the course of the model.

The way of excluding the effect of the incident waves from the record obtained by W_J is as follows.

When the running model locates some distance behind the probe W_J , the wave record at this probe does not contain yet the disturbance by the model but the incident waves (the unsteady wave measurement is possible and done only for $\Omega > 0.25$). This record taken during several periods of the incident waves before the model comes close to the probe is

expressed in a Fourier series with respect to t . Assuming this Fourier series expression to give the estimates of the incident wave motions at the probe W_j even when the model proceeds and the record there includes the disturbances by the model's diffraction and radiation, we can subtract it from ζ_j . The remainder gives the unsteady wave motions with the incident wave motions not included.

In order to confirm the accuracy of such extrapolated incident waves, we measured the motions of regular waves generated in our tank without putting any ship model disturbing them and compared them with the estimates of the identical regular waves extrapolated by the procedure described earlier on the assumption that we could not measure the wave motions after an assumed moment. The results shows that the regular waves in our tank seem to gradually change their shape. Their amplitude, for instance, decreases or increases by a few millimeters in about 10 seconds. Then the extrapolated waves may have probably the error of several percents. But this rather large error has the same frequency as a fundamental one, that is, the wave length of the error is just the length of the incident waves. The elementary wave among the unsteady wave disturbances by a ship model which is influenced the most by this error is the one with the wave number k_2 which propagates right backward from the model and it hardly has the effect on the added resistance.

4. THEORETICAL PREDICTION OF UNSTEADY WAVE AROUND A SHIP MOVING IN WAVES

The time-dependent waves in the far-field of a ship advancing into incident waves are regarded as a superposition of the radiation waves and the diffraction waves. The former are the time-dependent waves caused around the ship made to advance with steady forward velocity in otherwise calm water and forced to undergo just the same oscillatory motions as induced in the incident waves. The latter are the scattering of the incident waves on ship running with its oscillatory motions suppressed. If we linearize our time-dependent problems, there is no loss of generality in so dividing the wave field around the ship between the radiation and the diffraction waves.

In order to evaluate theoretically the Kochin functions of the radiation and the diffraction waves and compare them with those obtained in the analysis of the measured waves around a ship model in regular head waves, we adopt Ogilvie-Tuck's theory (Ref.6) and Adachi's theory (Ref.7) respectively. Knowing the amplitudes and the phases of the ship's oscillatory motions resulting from the wave exciting forces, we can evaluate the actual waves around the ship as a linear superposition of both the waves predicted by those two theories.

Following the Ogilvie-Tuck's slender body theory based upon the assumption of the motions of high frequency, the radiation waves of a ship making an oscillatory motion

of heaving mode or pitching mode with frequency ω are given in the far-field by the pulsating sources distributed on the longitudinal axis, coinciding with the x -axis of the reference frame employed here. The source strength $\sigma(x)e^{i\omega t}$ is expressed by

$$\sigma(x) = \frac{g}{4\pi\omega} \delta \bar{A} e^{i\epsilon(x)} \quad (9)$$

where $\bar{A}(x)$ and $\epsilon(x)$ are the amplitude and the phase of the out going wave motions determined by solving the 2-dimensional problem of forced unit-amplitude heaving motion of each transverse section at x . We have already had quite a few techniques (Ref.8, 9) for computing them of any arbitrary shape section. δ denotes the heaving amplitude of each transverse section and is not independent of x when we are concerned with the pitching motion of the ship.

The Kochin functions of the radiation waves induced by the heaving or the pitching mode of oscillations is expressed using the source strength determined by the equation (9), in the form

$$\begin{aligned} H_j(\theta) &= \int_{-L/2}^{L/2} \sigma(x) \exp[ik_j x \cos \theta] dx \\ &= \frac{g}{4\pi\omega} \int_{-L/2}^{L/2} \delta \bar{A}(x) e^{i\epsilon(x)} \\ &\quad \times \exp[ik_j x \cos \theta] dx \end{aligned} \quad (10)$$

Adachi showed a solution of the diffraction problem for a ship running into head waves which was obtained with the method of matched asymptotic expansions. He assumed both the slow forward velocity and the short incident waves, and gave the solution almost identical with Maruo's solution (Ref.10) at zero forward velocity. He also claims that his solution is valid even for much larger . Anyhow we are concerned with the far-field velocity potential of the diffraction waves. The Adachi's theory gives it as follows.

Regular head waves of unit amplitude defined with respect to the reference frame moving with a ship are

$$\exp i(\omega t + \bar{k}_2 x)$$

Then the diffraction waves are expressed by the waves of the singularity distribution

$$\sigma(x) \exp i(\omega t + \bar{k}_2 x)$$

on the x -axis just as for the radiation waves. This singularity strength is the solution of an integral equation

$$\begin{aligned} & \sqrt{\frac{\bar{k}_2}{2\pi(1+2\Omega)}} e^{-i\pi/4} \int_x^{L/2} \frac{\sigma(\xi)}{\sqrt{x-\xi}} d\xi \\ & + \left(\frac{1}{2\sqrt{2}} - \frac{1}{4\pi E} \right) \sigma(x) \\ & - \frac{ig}{4\pi\omega_0} = 0 \end{aligned} \quad (11)$$

where

$$E = \int_c \bar{k}_2 \gamma(s) \exp[i\bar{k}_2 z(s)] ds \quad (12)$$

$\gamma(s')$ is the distribution of Helmholtz wave source on the contour c of each transverse section at x . It is determined as the solution of a 2-dimensional boundary value problem for Helmholtz equation by solving numerically the equation

$$\begin{aligned} & \pi \bar{k}_2 \gamma(s) - \int_c \bar{k}_2 \gamma(s) \frac{\partial G}{\partial N} ds \\ & = \frac{\partial}{\partial N} \exp[i\bar{k}_2 z(s)] \end{aligned} \quad (13)$$

where G is Green's function satisfying Helmholtz equation, the linearized free surface condition and a radiation condition. N denotes outward normal, $z(s)$ the z -coordinate of a point and s the distance measured on the contour.

Substituting the source density thus obtained into the equation (10) gives the Kochin functions of the diffraction waves.

5. RESULTS OF WAVE ANALYSIS

Measurements and analysis of waves were done for a tanker model ($L=2.0m$, B (breadth) $=0.312m$, T (draft) $=0.119m$, $C_B=0.817$ and $C_M=0.996$). Those experiments were carried out in the large tank of Research Institute of Applied Mechanics, Kyushu University (80mL x 8mB x 3.5mD).

Eight wave probes were set on the line parallel to the tank wall and at a distance 50cm from the model center line. Spacings between the neighbouring probes were selected according to the period of the model's oscillatory motions and the forward speed such that we could get the best $\Delta x/V \cdot \omega$ for carrying out the first step of analysis to derive ζ_c and ζ_s from the wave records at all the probes.

In the first we measured the radiation waves induced by the forced heaving and pitching motions of the model for various oscillating periods and forward speeds, Fig. 2 is one example of the Kochin function $H_2(\theta)$ obtained analyzing those radiation

waves with the procedure proposed in the section 2. The wavenumbers $kL=11.7$ and 17.42 (L is the model length) are those of the forced heaving oscillation. They correspond to the encounter frequency when the model is assumed to run at a forward speed $Fn=0.15$ in the head waves of $\lambda/L=1.0$ and 0.75 respectively where λ is the length of the incident waves. This example shows that the Ogilvie-Tuck's slender body theory can surprisingly well predict the Kochin function $H_2(\theta)$ even for a not-slender hull form such as a tanker hull form. $H_1(\theta)$ is not so well predicted, although it is done so qualitatively. $H_1(\theta)$ is, however, very small compared with $H_2(\theta)$ and hardly has importance from the practical point of view. Hereafter the results for $H_1(\theta)$ are not illustrated in this report. Since we could get the results of the same good correlation for a more slender hull form (Ref.2) when forced to make heaving and pitching motions, we may conclude that the practically predominant part of the radiation waves for those modes of motions can be predicted by the slender body theory.

The good agreement shown in Fig. 2 seems to reveal another fact that the accuracy of both the measurement and the analysis of the radiation waves is fairly high. Considering the very small amplitude of elementary waves propagating toward the direction of around $\theta=180^\circ$ and the large wave length, measured parallel to the x -axis, around $\theta=90^\circ$ (the data ζ_c and ζ_s can be collected over three model length, backward from F.P. of the model and they have to be estimated after that as described in the section 2), the accuracy is so good and we are convinced that the analysis is correctly done for almost all the directions of the elementary waves.

As evident from both the theoretical and the experimental $H_2(\theta)$ shown in Fig. 2, it has a big peak around $\theta=90^\circ$ and is very small in the vicinity of $\theta=180^\circ$. Moreover the integrand of added resistance integral is much weighted for θ close to or smaller than 90° . It means that even the simpler 2-D theory can predict well the added resistance if λ/L is comparatively large and the radiation waves are dominant in the added resistance.

The results of the diffraction wave analysis are shown in Figs.3 and 4. The steepness of regular incident waves used in the experiments is about $1/50$. They show also good agreements between the measured Kochin functions and the theoretical ones computed using the singularity distributions given by the Adachi theory especially when the length of the incident waves are not so short. Considering the model hull form is not slender, this agreement is again surprising. We can conclude from those results that we can predict fairly well the diffraction wave fields around a ship by the slender body theory when we want to predict the added resistance in waves with taking into account the diffraction waves. However the tendency is found in those figures that the agreement is the worse when the incident waves are shorter and the forward speed is

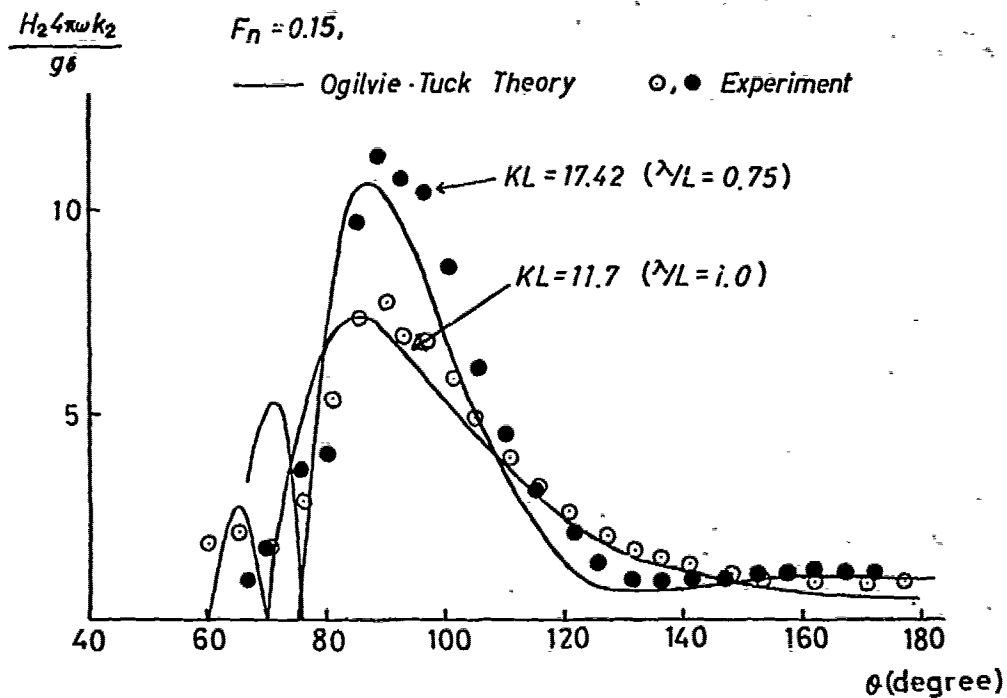


Fig.2 Kochin function of radiation waves

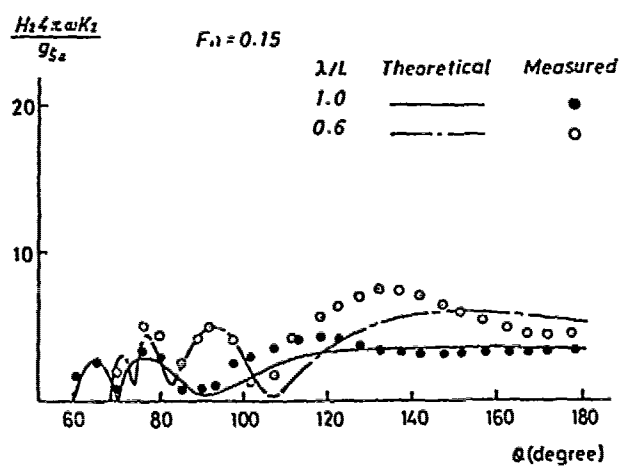


Fig.3 Kochin function of diffraction waves

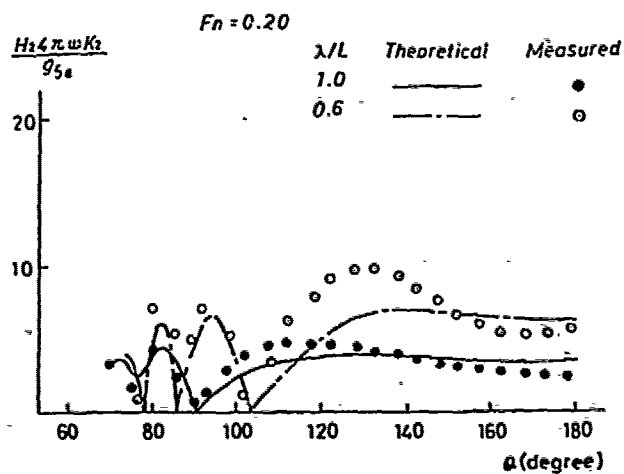


Fig.4 Kochin function of diffraction waves

faster. Since the theory used here is based upon the assumption of very low forward speed, such a disagreement does not seem to be strange. The disagreements found for shorter incident waves are remarkable around $\theta=120^\circ\sim 140^\circ$ and their extent is the larger for the shorter incident waves (the peak around $\theta=130^\circ$ is much higher in the results not illustrated here for much shorter incident waves). The length of elementary waves propagating to the direction of $\theta=130^\circ$, if measured not along the direction of propagating but parallel to the x-axis, is about one and half times as large as that of the incident waves. Such long waves are not found in the error of the extrapolated incident waves which are to be removed from the measured wave records as described in the section 3. Consequently it may be true the

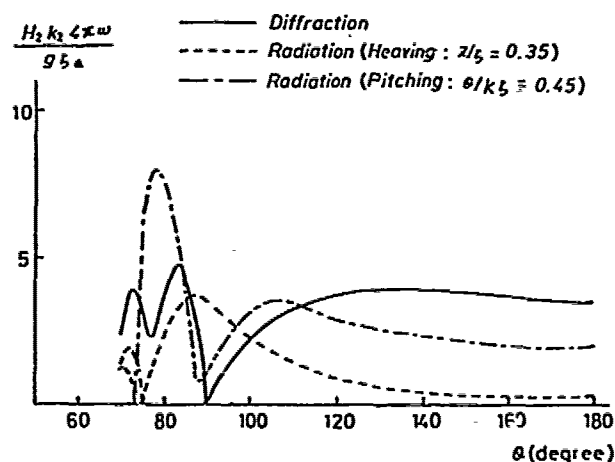


Fig.5 Kochin function of each wave component
($F_n=0.20$, $\lambda/L=1.0$)

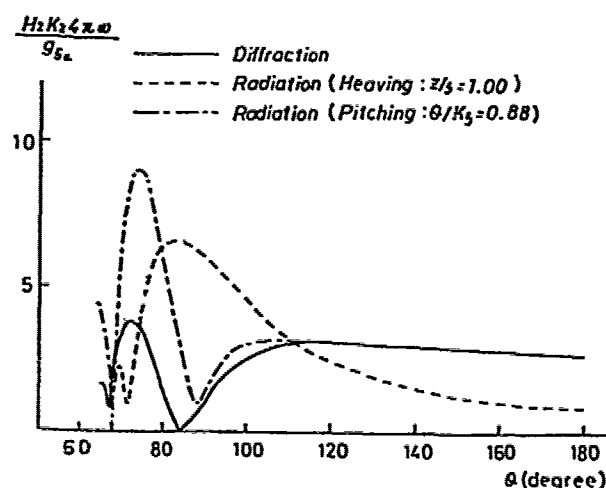


Fig.6 Kochin function of each wave component
($F_n=0.20$, $\lambda/L=1.25$)

diffraction waves of a full hull form are not so completely for short incident waves as the radiation waves by the present slender body theory. The disagreement is thought to be attributed to the bluntness of the bow of the hull form and the better theory should be able to explain it.

Fig. 5 and 6 are the comparisons of the theoretical Kochin functions of the radiation and the diffraction waves of the model. We multiplied the theoretical Kochin functions of the heaving and pitching motions of unit amplitude by the amplitudes of those motions measured in the experiments. The diffraction waves are dominant in the elementary waves propagating backward but the elementary waves propagating there are not so important in the added resistance integral. From these figures we may understand the relative importance of the diffraction and the radiation waves in the total wave field around the model.

Finally the results are described of the wave analysis when the model runs with a constant forward speed in incident head waves without any restrictions on its motions. In Figs. 7 and 8 are shown the records of unsteady waves along the line of $y=50\text{cm}$. The distance along the line is measured from F.P. to backward on a unit of the model length L . We must be careful that they are not real records of wave motions taken with a wave probe, but the distributions of ζ_c and ζ_s along the line which are obtained through the processing of wave records taken with all the wave probes — eight probes — set in the tank as explained in the section 3.

The vertical coordinate shows ζ_c and ζ_s divided by the amplitude of the incident waves A . Fig. 7 is the results for $F_n=0.2$, $\lambda/L=0.6$ and Fig. 8 for $F_n=0.2$, $\lambda/L=1.0$. The data until $3L$ to $3.5L$ from F.P. of the model do not include the tank wall reflection and can be used as the integrands of the integrals (4) and (5). At and behind this distance they were found to be almost completely fitted with the expression (6) given in the section 2.

In Figs. 9 to 11 the spectrums of elementary waves are illustrated of the measured unsteady wave field around the model running in head waves. Those spectrums are defined in the form

$$\left(\frac{H_2 K_2 4 \pi \omega}{g \zeta_a} \right)^2 \frac{(\cos \theta + \bar{k}_2 / k_2)}{\sqrt{1 - 4 \Omega \cos \theta}} \quad (14)$$

and therefore integrating them from α_0 to π gives almost the added resistance of the model since the contribution of $H_1(\theta)$ is very small.

The theoretical spectrums shown in those figures were computed using the diffraction waves and the radiation waves predicted by Ogilvie-Tuck theory and Adachi theory respectively as well as the amplitudes and the phases of the oscillatory motions obtained experimentally. The spectrum of the added resistance is predicted fairly well with the

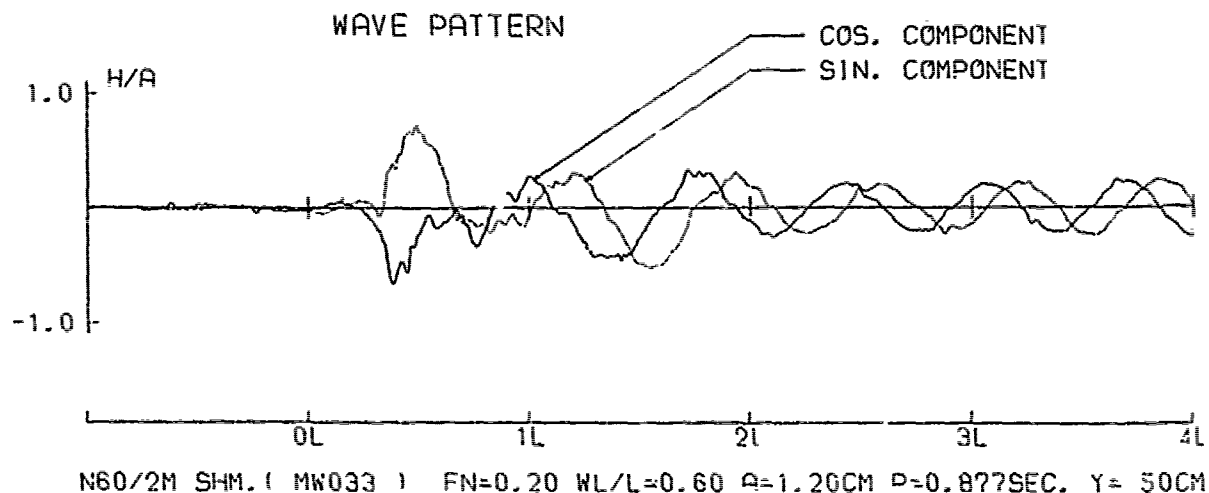


Fig.7 Wave record

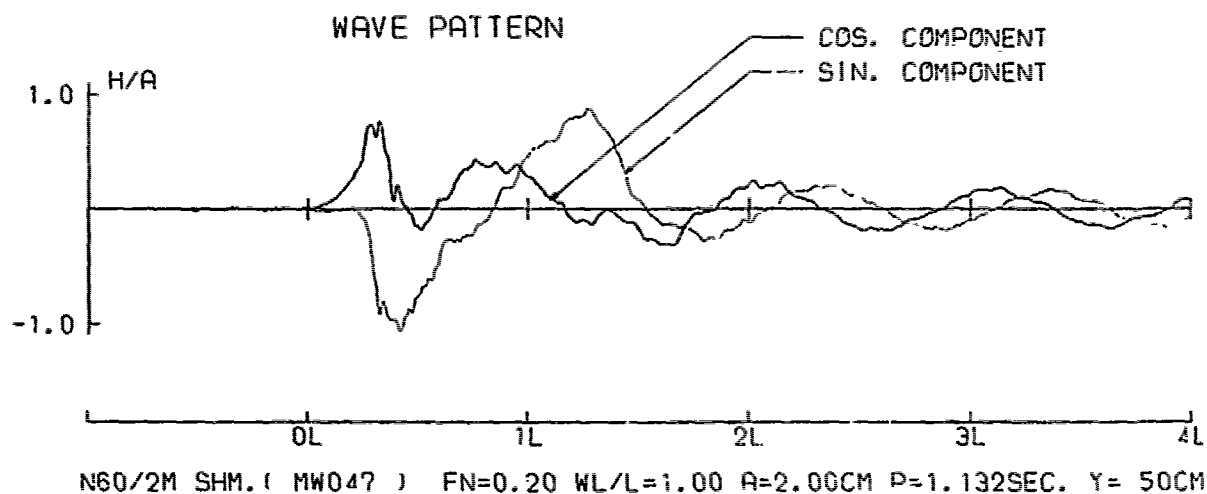


Fig.8 Wave record

slender body theories as the superposition of the radiation and the diffraction waves even for such short incident waves as $\lambda/L=0.6$, since the diffraction waves propagating to the direction of $\theta=130^\circ$, where the discrepancy is found, does not have so much the weight in the spectrum of the form(14) and consequently the difference with such a magnitude as found for $\lambda/L=0.6$ does not have so much influence on the spectrum of the added resistance. We may conclude that we can predict with the rational basis even the spectrum of the added resistance as well as the resulting added resistance of a blunt bow hull form, taking into account rationally the effect of the diffraction waves, unless the incident waves length λ/L is smaller than 0.6. For much shorter incident

waves, the discrepancy between the theoretical predictions and the reality in the diffraction waves is much more and the present theory is not enough to predict accurately the added resistance, let alone the spectrum of it.

Integrating the measured spectrums illustrated in Figs. 9 to 11, if a small contribution from $H_1(\theta)$ components added, gives the added resistance derived from the measured wave field. They are compared with those obtained in the resistance tests in waves in Fig. 12. The added resistances measured with those two methods are correlated with each other, but the ones derived directly from the wave pattern are a little smaller than the ones measured in the resistance tests. This difference is interpreted

to be originated from the errors in the resistance tests or the effect of water viscosity or the errors in the numerical integration of the measured spectrum especially around small θ where we have to analyze the wave pattern with much more fine mesh of θ . To get some conclusion on those problems, we need further investigations. Here we are satisfied with concluding that we can derive the added resistance from the wave pattern.

The theoretical added resistances shown in Fig. 12 are obtained by integrating the theoretically predicted spectrums illustrated in Figs. 9 to 11. It is remarkable that both the added resistances at $\lambda/L=0.6$ obtained by the wave analysis and by the theory are smaller than the one in the re-

sistance tests. It means there is the possibility that the comparatively large added resistance measured in the resistance tests of a blunt bow hull form for short waves is not attributed to only the diffraction waves.

6. CONCLUDING REMARKS

For the objective of studying added resistance of a ship, measurement and analysis of the unsteady wave pattern formed around the ship running and moving in regular head waves were proposed and carried out for a tanker hull form.

It can be concluded from the results that the slender body theory developed on the assumption of short waves predicts sur-

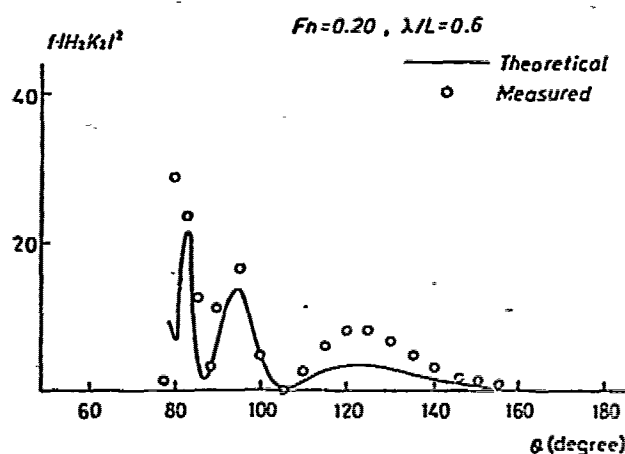


Fig.9 Spectrum of wave pattern in the far-field

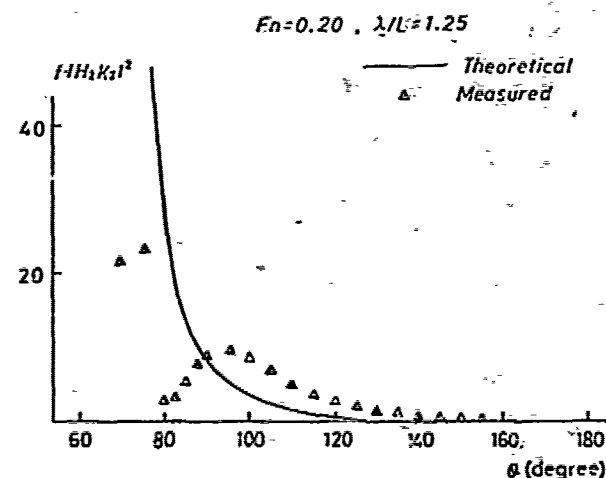


Fig.11 Spectrum of wave pattern in the far-field

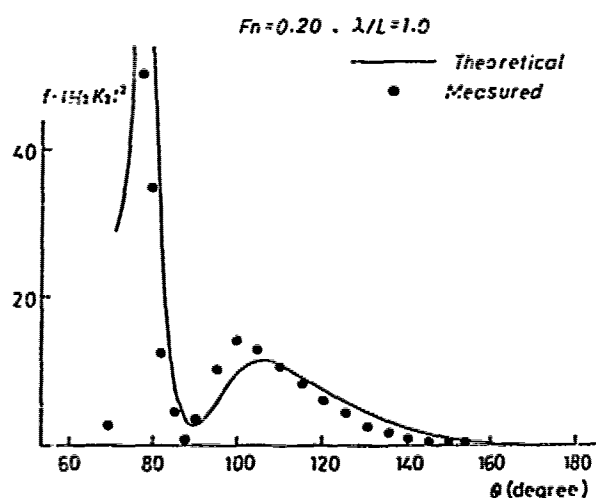


Fig.10 Spectrum of wave pattern in the far-field

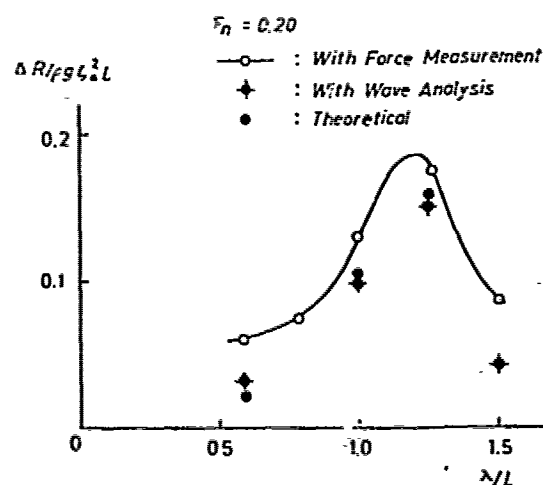


Fig.12 Added resistance coefficient

prisingly well the detailed structure of the radiation waves generated in the far field by the motion of heaving and pitching modes even if hull form is not slender. The prediction of the diffraction waves in the far field is accurate except for very short incident waves and for faster forward velocity. It means that we can get the precise added resistance of a full hull form except for very short incident waves with the diffraction waves taken into account rationally with making use of the slender body theory.

The total wave field of the ship freely floating in waves is supposed to be a superposition of the radiation and the diffraction waves. The theoretical prediction based on the assumption of such a linear superposition does give so good results as expected of the spectrum of the total wave field apart from the troublesome diffraction waves for much shorter incident waves. The added resistance computed from the total flux of the theoretical wave field is in good agreement with that derived from the spectrum of the measured wave field. The agreement reveals that the added resistance as a wave pattern resistance is predicted well theoretically.

Investigation should be done further on the difference between the added resistance derived from the wave pattern and the one from the resistance test.

ACKNOWLEDGEMENT

The author acknowledges his appreciation to Professor F. Tasai, Research Institute for Applied Mechanics, Kyushu University for his encouragement and support in the course of this study. His thanks also go to Mr. M. Yasunaga for his cooperation in carrying out experiments and his efforts in developing the data processing systems. Further he is grateful to Mr. H. Adachi, Ship Research Institute, for tendering a part of the computing program.

REFERENCES

1. Maruo, H., "Resistance in Waves", 60th Anniversary series of JSNAME, Vol.8, 1963, pp.67-100.
2. Ohkusu, M., "Analysis of Waves Generated by a Ship Oscillating and Running on a Calm Water with Forward Velocity", J.S.N.A.Japan, Vol.142, 1977, pp.36-44.
3. Newman, J. N., "The Determination of wave resistance from Wave Measurements along a Parallel Cut", International Seminar on Theoretical Wave Resistance, Ann Arbor, Michigan, 1963, pp. 353-376.
4. Hanaoka, T., "On the Velocity Potential in Michell's System and the Configuration of the Waveridges due to a Moving Ship (Non-Uniform Theory of Wave Resistance-4)", J.S.N.A.Japan, Vol.93, 1953, pp.1-10.
5. Newman, J.N., "The Damping and Wave Resistance of a Pitching and Heaving Ship", Journal of Ship Research, Vol.3, No.1. 1959, pp.1-19.
6. Ogilvie, T. F. and Tuck, E. O., "A Rational Strip Theory of Ship Motions, Part I", Report No.013, Dept. of Naval Architecture and Marine Engineering, the University of Michigan, 1969.
7. Adachi, H., "On the Calculation of Wave Exciting Forces on Ship Translating in Head Sea Waves", J.S.N.A.Japan, Vol.143, 1978, pp.34-40.
8. Tasai, F., "On the Damping Force and Added Mass of Ships Heaving and Pitching", Report of Research Institute for Applied Mechanics, Kyushu University, Vol.26, 1959, pp.131-152.
9. Maeda, H., "Wave Excitation Forces on Two Dimensional Ships of Arbitrary Sections", J.S.N.A.Japan, Vol.126, 1969, pp.55-83.
10. Maruo, H. and Sasaki, N., "On the Wave Pressure Acting on the Surface of an Elongated Body Fixed in Head Seas", J.S.N.A. Japan, Vol.136, 1974, pp.107-114.

Discussion

T. Takahashi and E. Baba (MHI)

At first, we would like to pay our respect to the author who developed a new field of "unsteady wave pattern analysis". As very interesting results are shown in this paper, we expect further fruits of this new method.

Our discussion is related to the discrepancies of added resistance between wave analysis results and resistance test ones, shown in Fig.12.

Author interprets that difference is originated from the errors in the resistance tests or the effect of water viscosity or the errors in the numerical integration of the measured spectrum especially around small θ . Furthermore, author suggests the existence of other factor not attributed to only diffraction wave in short wave length.

As for the errors in the resistance test, it will be settled by making use of a large size ship model. And, as for the error of wave analysis, the accuracy can be evaluated by generating numerically theoretical unsteady wave patterns and analysing them through the same process as in measured data, and checking the results how coincide with the original Kochin function of the generated wave pattern.

When a full ship with $C_b = 0.817$ as tested by the author runs at relatively high speed $F_n = 0.2$, it can be supposed that wave breaking will occur near the blunt bow and incident waves superposed on it also will break. So, we supposed that there

will be other factor not contained in wave pattern at far field, as suggested by the author, and it will give smaller added resistance compared with the one obtained from resistance test.

We would like to ask the author, in the case of not full ship as shown in the reference 2, whether same degree of differences were found or not between wave analysis results and resistance test results.

Author's Reply

M. Ohkusu (Kyushu Univ.)

I appreciate your valuable discussions and instructive suggestions.

As for the way to confirm the accuracy of the wave analysis I completely agree with you. However, the good agreement between the theoretical predictions and the results of the analysis for the Kochin function might be interpreted to show the reliability of the wave analysis.

I believe the wave breaking is possible near the blunt bow. Our knowledge on the detail structures of the unsteady waves around ships oscillating and running in waves is too limited to draw any definite conclusion on this possibility. So I think we should continue to study those unsteady waves along the line I proposed here.

To my regret I do not have data on the added resistance derived from the wave pattern analysis of not full ship.

Rolling and Steering Performance of High Speed Ships

— Simulation Studies of Yaw-Roll-Rudder Coupled Instability —

Haruzo Eda

Davidson Laboratory, Stevens Institute of Technology
Hoboken, New Jersey, U.S.A.

ABSTRACT

Equations of yaw, sway, roll and rudder motions are formulated to represent realistic maneuvering behavior of high-speed ships such as container ships. Important coupling terms between yaw, sway, roll and rudder were included on the basis of recent captive model test results of a high-speed ship. Roll-induced yaw-moment can be explained by the concept of hull-form-camberline, which is equivalent to that of the wing section.

A series of computer runs was made by using the equations of yaw, sway, roll and rudder motions. Results indicate substantial coupling effects between yaw, roll, and rudder, which introduce changes in maneuvering characteristics and reduce course stability in high-speed operation. These effects together with relatively small GM (which is typical for certain high-speed ships) produce large rolling motions in a seaway as frequently observed in actual operations. Results of digital simulations and captive model tests clearly indicate the major contributing factors to such excessive rolling motions at sea.

INTRODUCTION

When a ship is proceeding at a high-speed in a seaway, serious rolling motions are frequently observed in actual ship operations and in model testing in waves [1],[2]. Anomalous behavior of rolling and steering was clearly evident, for example, in full-scale tests of a high-speed container ship during cross-Atlantic and cross-Pacific operations [1].

Most of the high-speed container ships and naval ships have the following hull form characteristics which have major impacts on ship performance, in particular, maneuvering and rolling behavior:

- (1) High speeds with large L/B ratio and relatively small GM.
- (2) Fore-and-aft asymmetry (e.g., with a low bulb at the bow, see Figure 1 [3]).

(3) Relatively large rudder.

These particular characteristics introduce the possibility of fairly significant yaw-sway-roll-rudder coupling effects during high-speed operations.

The major objective of this study is to examine the coupled motions of yaw, sway, roll and rudder for high-speed ships (e.g., hull forms similar to destroyers) through digital simulation studies.

Due to the lack of available hydrodynamic data, no extensive digital simulation effort has previously been made in the area of maneuvering performance with inclusion of roll motion effect which should have an important impact during high-speed operations. Recently, high-speed ships were extensively tested in the rotating-arm facility with inclusion of roll motion effect. Test results clearly indicated fairly significant couplings between yaw-sway-roll-rudder motions.

One of the most important coupling terms, i.e., the roll-induced yaw-moment, can be explained by the concept of hull-form-camberline as described in the paper.

Accordingly, a mathematical model was formulated on the basis of these experimental results combined with analytical estimations, for a 500-ft-long hull form which is similar to that of high-speed container ships or naval ships.

A series of computer runs were made by using equations of yaw, sway, roll and rudder motions on a digital computer.

Results indicated substantial coupling effects between yaw, sway, roll and rudder, which introduce changes in maneuvering and rolling behavior. For example, coupling terms introduce destabilizing effects on course stability and increase turning performance at high speeds. This tendency agrees with actual observations made during ship trials and free-running model tests of a high-speed container ship.

These coupling effects together with relatively small GM and autopilot feedback produce large rolling motions in operations in seaways. Effects of

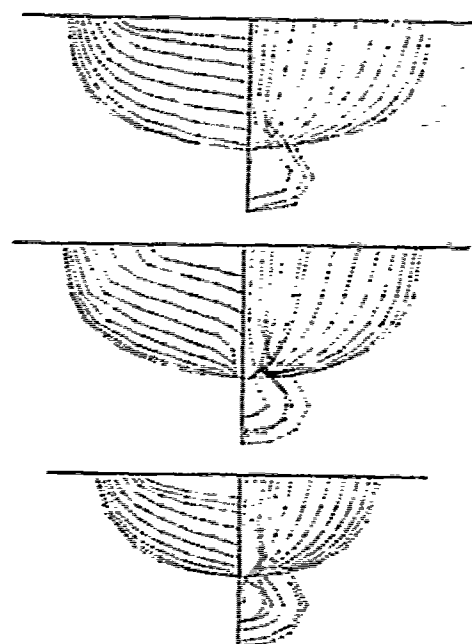


FIG.1. Body Plans of Representative High Speed Ship

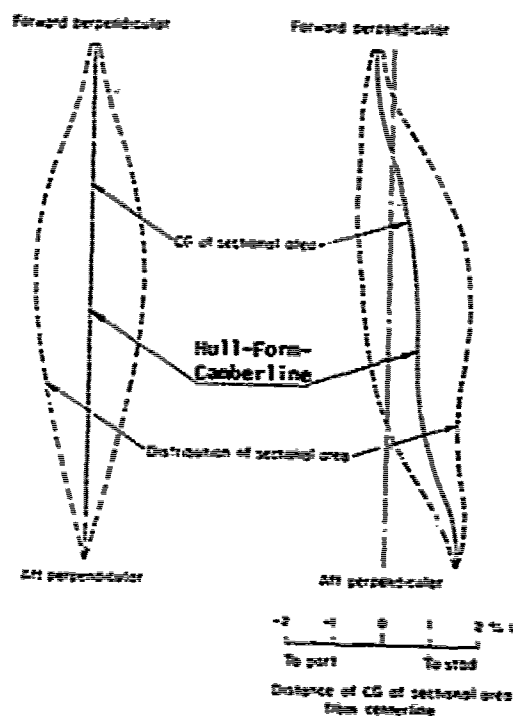
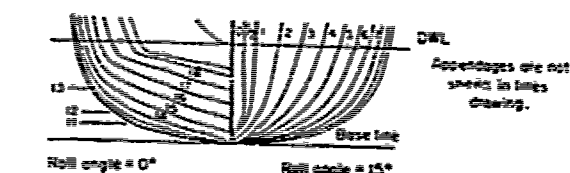


FIG.2. Longitudinal Asymmetry Due to Roll (Destroyer) [Hull-Form-Camberline]

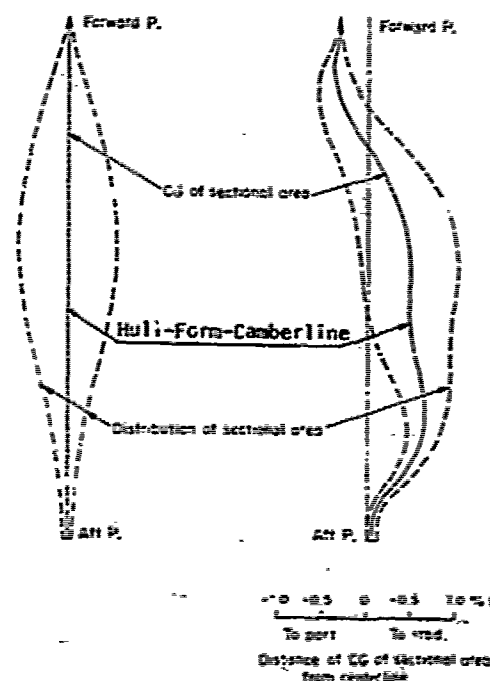
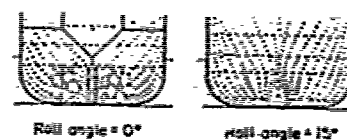


FIG.3. Longitudinal Asymmetry Due to Roll (High Speed Container Ship). [Hull-Form-Camberline]

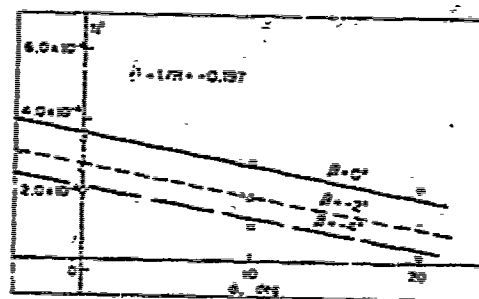


FIG.4. Yaw Moment Coefficient Due to Roll Angle

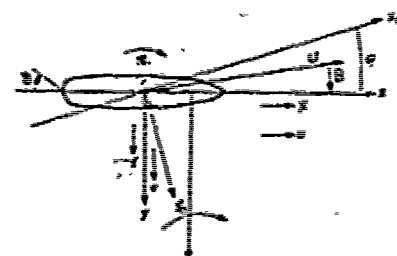


Fig.5. Orientation of Coordinate Axes Fixed in Ship

yaw-sway-roll-rudder coupling on the possibility of yaw-roll instability were clearly demonstrated in simulation results. Such a possibility of roll-coupled yaw instability was observed during autopiloted-model tests of a high-speed ship under oblique-sea conditions.

HULL CONFIGURATIONS

A high-speed hull form to be considered in this study includes the following characteristics as shown in the table below:

- (1) High length-beam ratio and relatively small GM for high-speed operation.
- (2) Fore-and-aft asymmetry, which is more pronounced for high-speed ships with bow bulb.
- (3) Relatively large rudder.

Length, L_{pp} , ft	500.0
Beam at WL, B, ft	60.0
Draft, H, ft	17.0
Rudder Area Ratio, A_r/L_H	1/40
Block Coefficient, C_b	0.56

The above-mentioned hull-form characteristics introduce fairly substantial hydrodynamic coupling effects between yaw-sway-roll-rudder motions.

Figure 2 shows two curves which indicate the distance of CG of the local sectional area from the longitudinal centerline at roll angle $\varphi = 0$ and 15 degrees. The curves can be considered to be hull-form-camberline, which is equivalent to camberline of the wing section.

Figure 3 shows the other example of the hull-form-camberline shown in the top of the figure.

When roll angle is not zero, the camberline is not a straight line, as shown in these figures introducing hydrodynamic yaw moment and side force. This trend is more pronounced because of the fore-and-aft asymmetry of hull form, in particular, during high-speed operation.

Figure 4 shows, for example, captive model test results of yaw-roll coupling effect, indicating hydrodynamic yaw moment to port introduced by roll angle to starboard. Similar yaw-roll coupling was evident in captive model test results obtained by L. Motter and also M. Hamamoto [7].

BASIC EQUATIONS FOR YAW-SWAY-ROLL-RUDDER MOTIONS

On the basis of captive model test results together with analytical estimations, an effort was made to formulate the equations of yaw-sway-roll-rudder motions to represent realistic maneuvering and rolling behavior of a high-speed ship.

Figure 5 shows the coordinate system used to define ship motions with major symbols which follow the nomenclature used in previous papers. Longitudinal and transverse horizontal axes of the ship are represented by the x- and y-axes with origin fixed at the center of gravity. By reference to these body axes, the equations of motion of a ship in the horizontal plane can be written in the form:

$$\begin{aligned} I_z \ddot{\psi} &= N & (\text{Yaw}) \\ I_x \ddot{\varphi} &= K & (\text{Roll}) \\ m(\dot{v} + ur) &= Y & (\text{Sway}) \\ m(\dot{u} - vr) &= X & (\text{Surge}) \end{aligned} \quad (1)$$

where N, K, Y, and X represent total hydrodynamic terms generated by ship motions, rudder and propeller.

Hydrodynamic forces are expressed in terms of dimensionless quantities, N' , K' , Y' , and X' based on non-dimensionalizing parameters ρ (water density), U (resultant ship velocity relative to the water), and A, i.e.,

$$N' = \frac{N}{\frac{\rho}{2} U^2 A L}, \quad Y' = \frac{Y}{\frac{\rho}{2} U^2 A}, \quad \text{etc.} \quad (2)$$

Hydrodynamic coefficients vary with position, attitude, rudder angle, propeller revolution, and velocity of the ship; for example, in the case of hydrodynamic yaw moment coefficient,

$$N' = N'(v', r, \delta, y_0', \dot{v}', \dot{r}', n', u, \varphi, \dot{\varphi}', \ddot{\varphi}') \quad (3)$$

where

$$v' = \frac{V}{U}, \quad r' = r \frac{L}{U}, \quad y_0' = \frac{y_0}{L}, \quad n' = \frac{n}{\omega}, \quad u' = \frac{u}{U}, \quad \text{etc.}$$

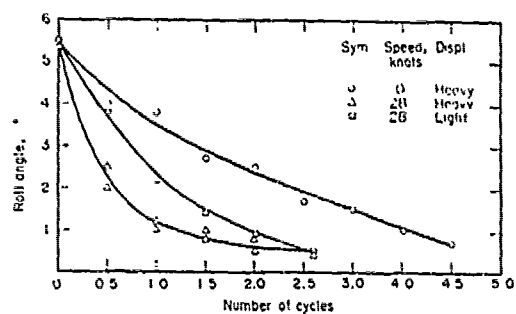
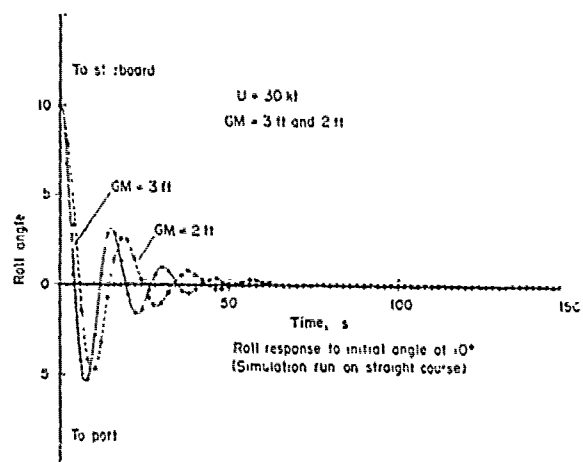
Finally, the following polynomials were obtained for predictions of ship dynamic motions:

$$\begin{aligned} N' &= a_1 + a_2 v' + a_3 r' + a_4 \delta + a_5 y_0' + a_6 v'^2 + a_7 v' r' + a_8 v'^3 \\ &\quad + a_9 r'^3 + a_{10} \delta^3 + a_{11} y_0'^3 + a_{12} \dot{v}' + a_{13} \dot{r}' + a_{14} \ddot{\varphi}' + a_{15} \ddot{\varphi}'^2 + a_{16} \ddot{\varphi}'^3 \\ Y' &= b_1 + b_2 v' + b_3 r' + b_4 \delta + b_5 y_0' + b_6 v'^2 + b_7 v' r' + b_8 v'^3 \\ &\quad + b_9 r'^3 + b_{10} \delta^3 + b_{11} y_0'^3 + b_{12} \dot{v}' + b_{13} \dot{r}' + b_{14} \ddot{\varphi}' + b_{15} \ddot{\varphi}'^2 + b_{16} \ddot{\varphi}'^3 \\ X' &= c_1 + c_2 v' + c_3 v'^2 + c_4 \delta^2 + c_5 \dot{u}' + X_p' \\ K' &= d_1 + d_2 v' + d_3 r' + d_4 \delta + d_5 \varphi + d_6 \dot{\varphi}' + d_7 \dot{\varphi}'^2 + d_8 \ddot{\varphi}' + d_9 \ddot{\varphi}'^2 \end{aligned} \quad (4)$$

ROLL-YAW COUPLED INSTABILITY

Figure 6 shows roll extinction curves obtained in simulation runs on a straight course at 30 knots having GM values of 3 feet and 2 feet. This particular result was obtained in the roll equation uncoupled from yaw and sway equations. The roll response shown in the figure can be considered to be realistic on the basis of comparison with results obtained from model tests of a similar high-speed ship shown in the same figure.

When roll extinction curves were obtained in simulation runs in equations of roll-yaw-sway coupled motions, an important change in rolling and yawing behavior was taken place. Roll-yaw coupled instability was clearly indicated in test runs. Figure 7 shows time history of roll and yaw motions starting on a straight course at 30 knots with an initial roll angle of 10 degrees. The roll extinction curve is approximately the same as that shown in the



Roll response to initial roll angle
(6.29 ft model tests)

FIG.6. Rolling Characteristics

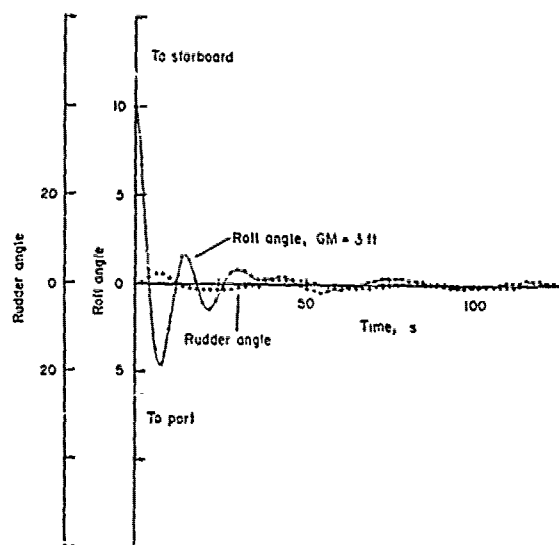
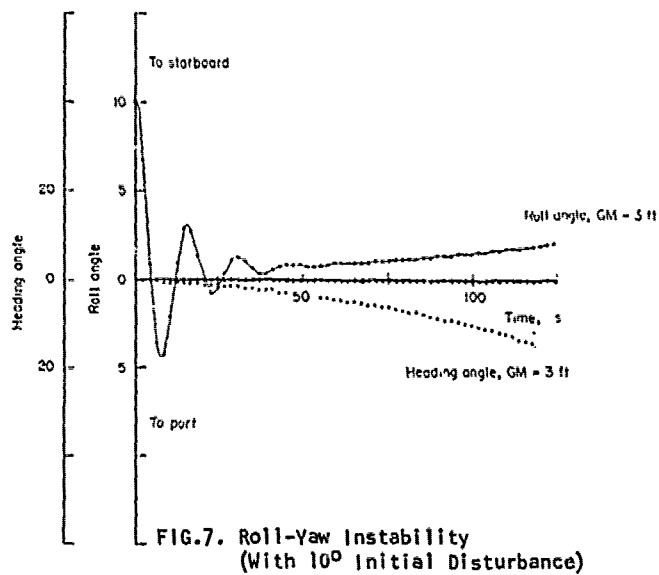


FIG.8. Roll Extinction Curve (With Autopilot)

previous figure at the initial portion of the run. However, subsequent roll and yaw motions are divergent, indicating roll-yaw coupled instability. When an autopilot is adequately included in these yaw-sway-roll coupled motions, stability characteristics of the ship system are improved as shown in Figure 8 where the above-mentioned roll-yaw instability is eliminated.

PREDICTIONS OF RESPONSE TO TURNING AND Z-MANEUVERS

Figures 9 and 10 show response to 20° - 20° Z-maneuver having GM of 3.0 and 25.0 feet. The approach speed is 30 knots in the tests. A comparison of heading angle response is shown in Figure 9 which clearly indicates a greater overshoot angle with GM at 3.0 feet relative to that with GM of 25.0 feet. It is clearly evident in this figure that course stability characteristics are deteriorated with reduction in GM. This significant effect of GM on ship response during Z-maneuver was fairly well confirmed by free-running model tests and actual ship trials in the case of a high-speed container ship.

Figure 10 shows a substantial difference in rolling behavior with GM of 3 and 25 feet. It should be noted in this figure that the largest roll angle is generated for the case of GM of 3.0 feet when the rudder angle is shifted to the other direction. This clearly indicates that the rudder angle has a counteracting effect to outward heel angle during steady turning.

Figures 11 and 12 show computer-plotted turning and rolling characteristics in deep water. The major parameter changes in computer runs were as follows:

1. Rudder angle = 35°
2. GM = 2.0', 3.0', 25.0'

Roll angle during enter-a-turn is shown, for example, in Figure 12, which confirms very well previous full-scale observations.

Figures 11 and 12 clearly show the effect of GM on turning and rolling characteristics. Substantial changes in maneuvering characteristics (i.e., reduction in course-keeping and increase in turning performance) are clearly evident in these figures with a decrease in GM.

Recently, Hirano reported similar changes in turning trajectory due to roll motion for a car-carrier [1].

YAW-SWAY-ROLL-RUDDER COUPLED MOTIONS WITH AUTOPILOT

Roll-yaw coupled instability was clearly indicated in yaw-sway-roll coupled motions in the previous test runs. In actual ship operations, the rudder is actively used, introducing important effects on yaw-sway-roll motions.

Let us consider the ship dynamic behavior under the following conditions:

When a ship is proceeding on a straight course, a certain external disturbance (e.g., the roll moment due to beam wind) is given stepwise to the ship. When the ship is rolled to starboard, for example, due to beam wind from the port, an asymmetry is formed in the underwater portion of the hull as shown in the previous figure (i.e., Figure 2). As a result, hydrodynamic yaw moment is

generated to deviate the ship heading to the port. Subsequently, the rudder is activated by the autopilot to the starboard to correct heading angle deviation. This starboard rudder angle produces the roll angle further to the starboard. Under this condition, the possibility of instability exists in the ship systems.

Accordingly, simulations were carried out under the following conditions:

The 500-ft-long ship was proceeding on a straight course at an approach speed of 30 knots. A stepwise roll moment (e.g., due to beam wind from the port) was given to the ship. The magnitude of the moment is equivalent to a statically generated roll angle of 5 degrees. The subsequent dynamic response of the ship was computed with inclusion of the autopilot system, which can be represented as:

$$\delta_d = a(\psi - \psi_d) + b'\dot{\psi}$$

where

δ_d = desired rudder angle

ψ_d = desired heading angle

a = yaw gain

b' = yaw-rate gain

Figures 13 and 14 show oscillatory motions for the case where GM = 2 feet, yaw gain = 3, and yaw-rate gain = 0. Instability of the ship systems is clearly evident in the figures.

When GM is increased to 3 feet, the stability characteristics are improved as shown in Figures 15 and 16.

When the autopilot is refined with addition of yaw-rate gain of 0.5, further improvement in the stability characteristics is shown in Figures 17 and 18. It should be noted here that the autopilot refinement substantially improved the rolling behavior as shown in these figures.

The results mentioned in the above clearly indicate the possibility of instability due to a stepwise disturbance. During actual operations in seaways, continuous disturbances are given to the ship due to wind and waves. Accordingly, even marginal yaw-roll-rudder instability can introduce serious rolling problems in seaways. Such difficulties have frequently been indicated in full-scale observations and model tests [1],[2]. Figure 19 shows, for example, the possibility of yaw instability obtained by J.F. Dalzell during model tests of a high-speed ship in waves [2].

CONCLUDING REMARKS

The purpose of this study was to develop mathematical equations of yaw, sway, roll and rudder to represent realistic maneuvering behavior of high-speed naval ships, and subsequently to examine yawing and rolling motions during high-speed operations through a series of simulation runs.

Based on recent captive-model test results of a high-speed ship configuration, important coupling effects between yaw, sway, roll and rudder motions were included in the mathematical model. Certain terms such as yaw moment due to roll angle were not adequately considered in previous studies in the area of maneuvering and seakeeping. It was

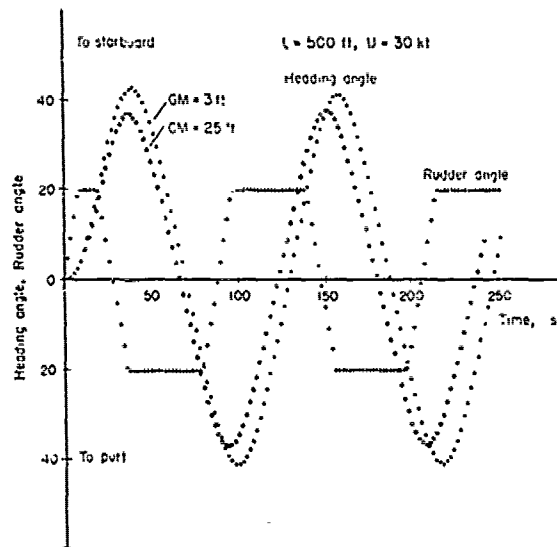


FIG. 9. Z-Maneuver Response

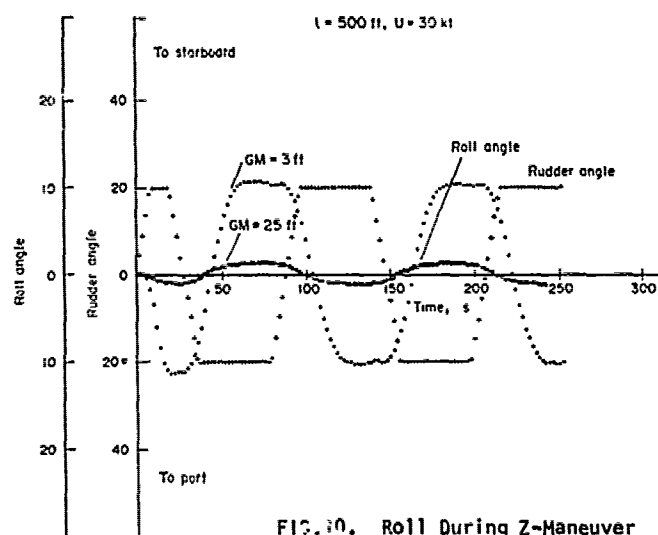


FIG. 10. Roll During Z-Maneuver

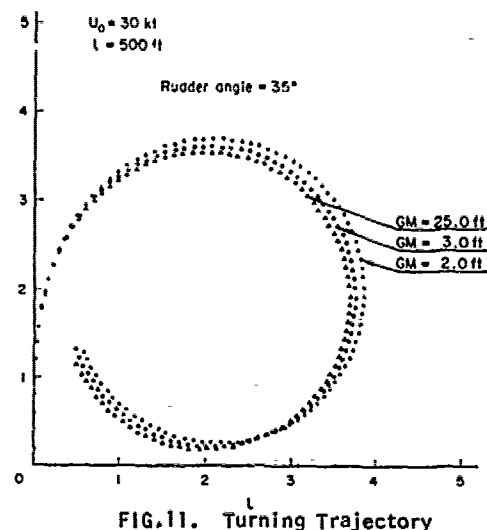


FIG. 11. Turning Trajectory

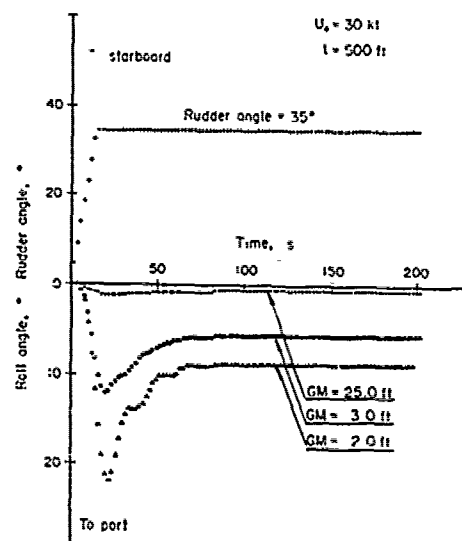
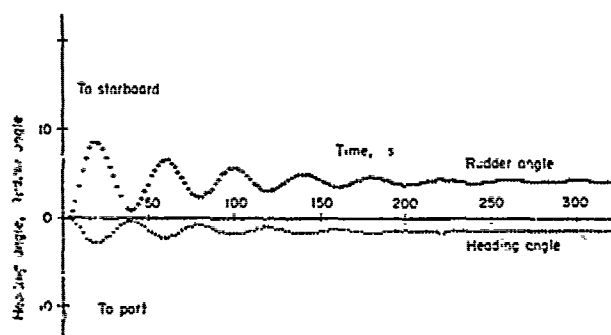
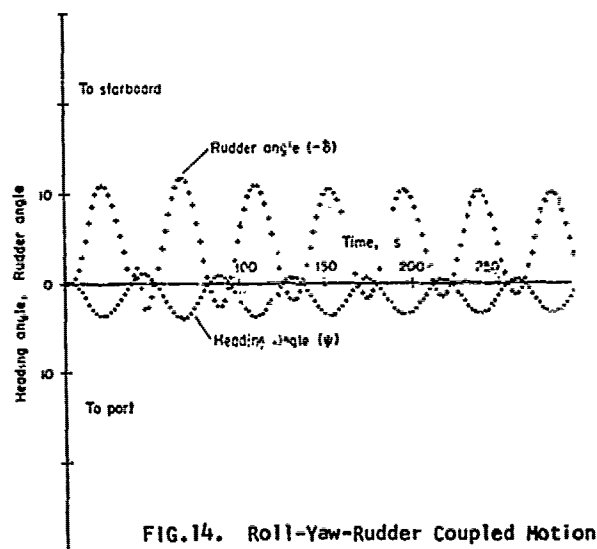
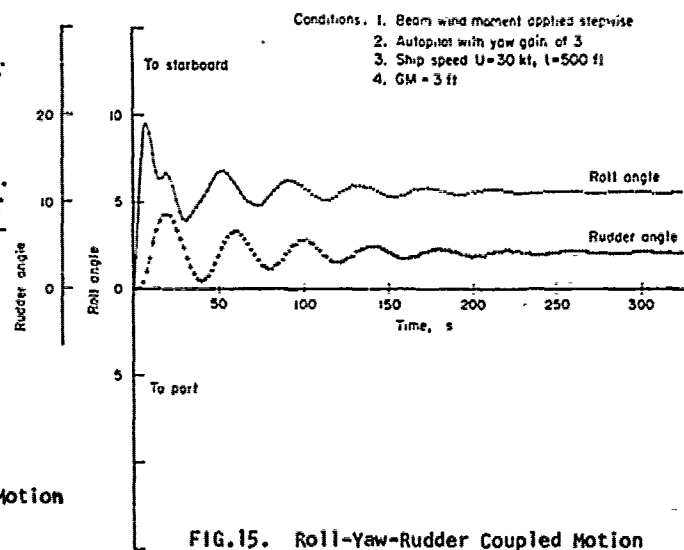
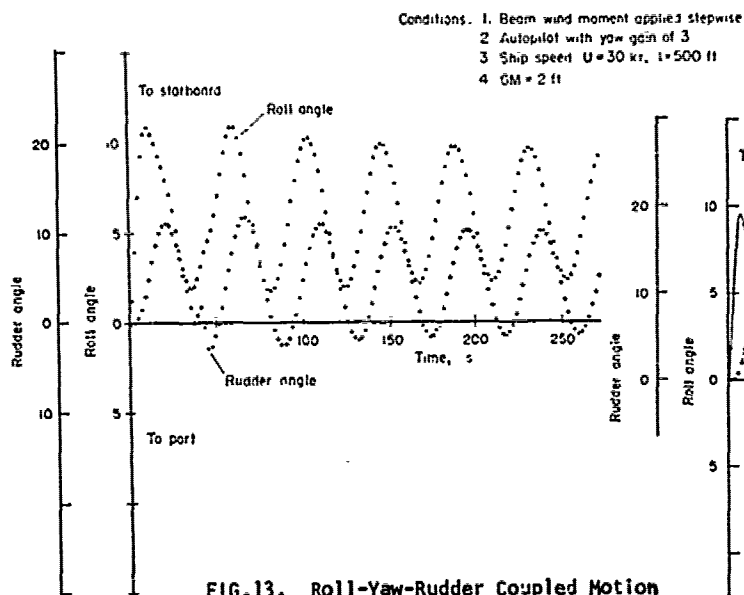
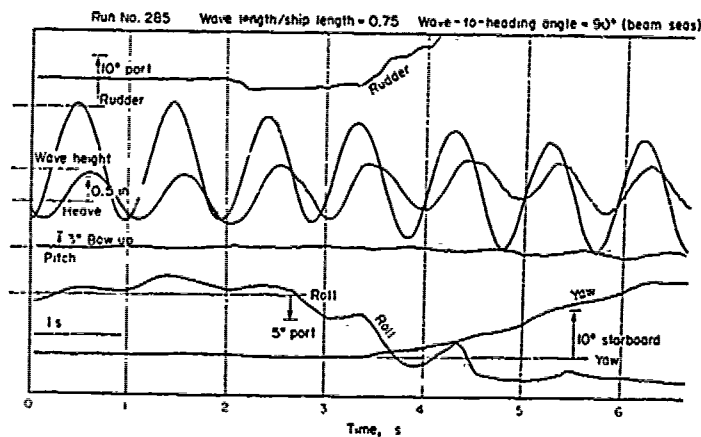
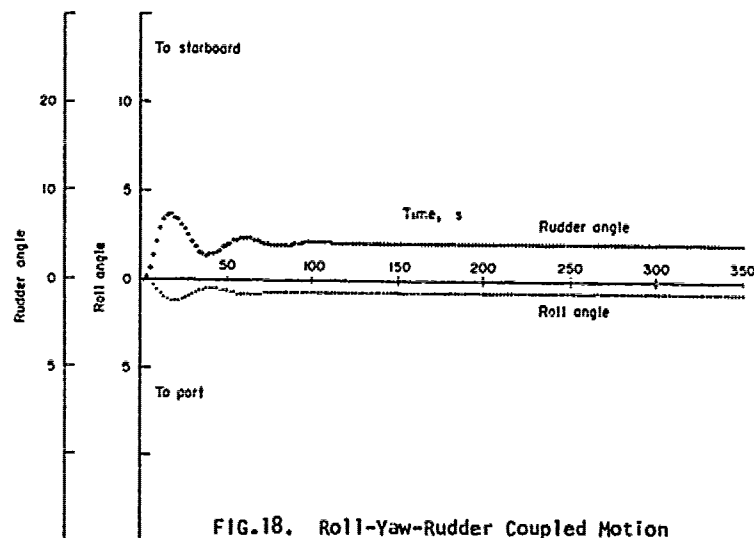
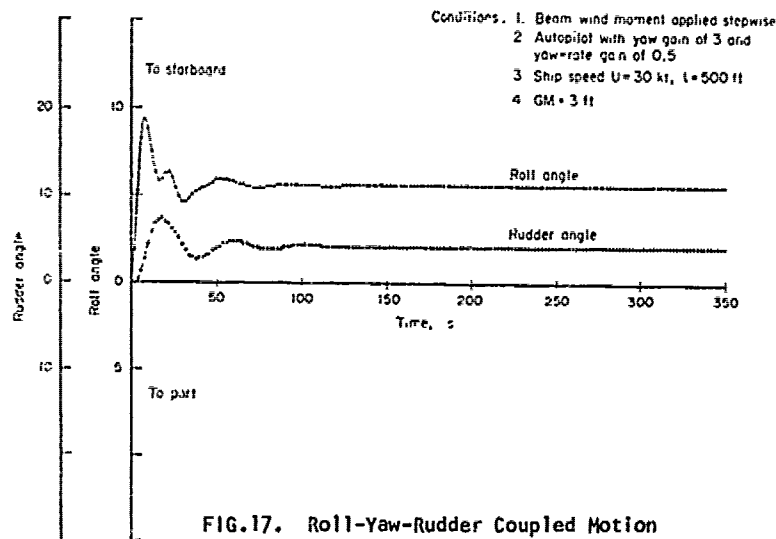


FIG. 12. Roll Angle Due to Turning





found in this study that these terms have important impact on maneuvering and rolling behavior, introducing the possibilities of instability and serious rolling problems during high-speed operations in seaways.

The major findings obtained in this study are summarized as follows:

- (1) Roll angle introduces asymmetry of underwater portion of hull form relative to the longitudinal centerline, which generates yaw moment due to roll (i.e., $N_{\phi\phi}$).
- (2) This roll-introduced yaw-moment can be explained by the hull-form-camberline, which is equivalent to that of the wing section. When roll angle is not zero, the camberline is not a straight line and introduces yaw-moment and side force, in particular, at a high speed.
- (3) The roll-introduced yaw-moment generates a tendency to turn to one side when the ship is heeled (e.g., to turn to port when the ship is heeled to starboard). This moment contributes to possible inherent yaw instability along with autopilot feedback and other coupling terms such as K_Y and K_{δ} (i.e., roll-moment due to sideslip and rudder angle, respectively).
- (4) When GM is relatively small (which is the case for most high-speed ships), the above mentioned coupling terms can introduce severe rolling motions in a seaway. This was clearly indicated in substantial rolling motions during turning and Z-maneuvers.
- (5) The possibility of yaw-roll instability exists for the ship system with autopilot during high-speed operations with small GM.
- (6) Refinement of the autopilot characteristics has important effects on yawing and rolling behavior of the ship.
- (7) Serious rolling problems frequently observed during high-speed operation in waves can be due partly to inherent yaw-roll instability (or marginal stability).

It should be stated here that a possibility of the above-mentioned roll-rudder coupled yaw instability is only pronounced during high-speed operations with a small GM.

ACKNOWLEDGMENTS

The author wishes to acknowledge the Office of Naval Research and the U.S. Maritime Administration for the research program that made the preparation of this paper possible.

The author also wishes to thank Mr. J. F. Dalzell and Dr. A. Strumpf for their valuable discussions during various stages of this study.

REFERENCES

1. Taggart, R., "Anomalous Behavior of Merchant Ship Steering Systems," Marine Technology, Vol.7, No.2, 1970.
2. Dalzell, J.F. and Chiocco, M.J., "Wave Loads in Model of a Container Ship Running at Oblique Heading in Regular Waves," Technical Report SSC-239, prepared for the Ship Structural Committee, 1973.
3. Baitis, A.E., Meyers, W.G., and Applebee, T.R., "A Non-Aviation Data Base for Naval Ships," NSRDC-SPD-738-01, 1976.
4. Eda, H., "Directional Stability and Control of Ships in Restricted Channels," TSNAME, Vol.87, 1971.
5. Eda, H. and Crane, C.L., Jr., "Steering Characteristics of Ships in Calm Water and Waves," TSNAME, Vol.74, 1965.
6. Eda, H., "Steering Control of Ships in Waves," Davidson Laboratory Report 1205, June 1967. (Presented at the International Theoretical and Applied Mechanics Symposium in London, April 1972.)
7. Hamamoto, M., "Hydrodynamic Derivatives for Directional Stability of Ships in Following Seas," J. of N.A. of Japan, Vol.133, 1973.
8. Eda, Haruzo, "Low-Speed Controllability of Ships in Winds," J. of Ship Research, Vol.12, No.3, 1968.
9. Eda, H., "Course Stability, Turning Performance and Connect on Force of Barge Systems in Coastal Seaways," TSNAME, Vol.80, 1972.
10. Eda, H., "Ship Maneuvering Safety Studies," TSNAME, Vol.87, 1979.
11. Hirano, M., "On the Calculation Method of Ship Maneuvering Motion at Initial Design Stage," J. of S.N. of Japan, Vol.147, 1980.

NOMENCLATURE

- A reference area ($A = L^2$)
- a, b yaw and yaw-rate gain constants
- B ship beam
- F_r Froude number (U/\sqrt{gL})
- I_z moment of inertia referred to z-axis
- K hydrodynamic roll moment
- L, m ship length and ship mass
- N hydrodynamic yaw moment
- n propeller revolutions per second
- r yaw rate
- t_r time constant of rudder in control system
- U ship speed ($U = \sqrt{u^2 + v^2}$)
- u component of ship speed along x-axis
- v component of ship speed along y-axis
- X hydrodynamic force in x-axis direction
- X_p propeller force along x-axis
- Y hydrodynamic force along y-axis
- δ rudder angle
- ϕ roll angle
- ψ heading angle of ship

Discussion

N. Toki (MHI)

It is my pleasure to have a chance to discuss this interesting topic. My discussion consists of two parts. At first, I would like to mention our experience similar to the one pointed out by the author.

In Nagasaki Experimental Tank, we have noticed roll-instability of a semidisplacement type high speed boat, during its resistance and self-propulsion test in calm water. To be more in detail, sway-yaw restricted model with small GM value unexpectedly heeled without any additional heel moment, when its advance speed was higher than a certain value. And, for further continuation of the experiments, we had to lower the center of gravity of the model. We tried to find out the paper which dealt with the instability phenomena of high speed crafts, and found several ones 1), 2) 3). For example, Suhrbier²⁾ reported that a free running model with small GM and high advance speed suddenly heeled and began turning without any steering actions. He called this phenomenon "Broaching". Another information given by these papers is that attaching a pair of spray strips on the fore hull is sometimes effective to improve the stability of rolling. However, we could find out no paper which dealt with this phenomenon as sway-roll-yaw coupled motion.

Referring to these papers, we measured heel moment, sway force and yaw moment acting on the model, varying heel angle and advance speed. The same series of measurement were carried out in both cases; model with spray strips and without them, to investigate the effect of spray strips. Thus, we obtained the values of hydrodynamic coefficient of roll moment and roll-yaw, roll-sway coupling coefficients. Making use of these coefficients and estimating the others, we composed the linear equation of manoeuvring motion and made an attempt to simulate sway-roll-yaw coupled motion.

Two examples of the results are presented in Figs.1 and 2. Their principal items are shown below.

Dimension of ship :
Length of water line = 51.5m
Breadth = 7.2m, Draft = 1.8m
Displacement = 274.5ton, GM = 0.53m
Advance speed = 44 knots
Initial heel angle = 2°
Initial heading angle = 0°
Rudders are fixed at 0°

Fig.1 shows simulated time histories of

roll and heading angle in the case of without spray strips, and Fig.2 shows the same in the case of with spray strips. From comparison of these two results, it is found that attaching spray strips can be an effective countermeasure to stabilize sway-roll-yaw coupled motion.

In connection with our experience, I would like to ask two questions about the author's paper.

1. The latter part of the computer run shown in the Fig.7 reminds me of time histories obtained from pull-out manoeuvre tests of an unstable ship. So, I presume this ship has an unstable loop with certain height in the rate-of-turn versus helm angle characteristics as a part of the roll-yaw coupling effect. In this case the $r' - \delta$ curves in both cases, with and without the consideration of roll-yaw coupling, might show the effect more clearly.

If the author could kindly present $r' - \delta$ curves or time history of yaw-rate in Fig.7, I would appreciate it very much.

2. As to Figs.13 - 16, my impressions are as follows. Generally speaking, sway-roll-yaw-rudder system with an autopilot has two free oscillation modes. In the one mode, rolling would play the main part, and it would have shorter period and larger damping, as shown in Fig.8. In the other mode, sway-yaw-rudder system would play the main part, and it would have longer period and smaller damping. Because the oscillations shown in Figs.13 - 16 have longer period than that in Fig.8 and converge very slowly, they must be the latter free oscillation. Therefore, in these computer runs, rolling caused by stepwise disturbance activates yawing, at first. After the first stage, however, sway-yaw-rudder system plays the main part and begins free oscillation. And, as the reaction rolling is activated again. In this case, I can easily guess that adding the damping effect by way of positive yaw-rate gain in the autopilot improves the convergence of free oscillation.

May I understand your result in this way?

REFERENCES

- 1) Ferguson, A.M. and Conn, J.F.C. : The Effect of Forward Motion on the Transverse Stability of a Displacement Vessel Trans, IEES, Vol.113, 1970
- 2) Suhrbier, K.R. : An Experimental Investigation on the Roll Stability of a Semi-Displacement Craft at Forward Speed RINA Symp. on Small Fast Warships and Security Vessels, 1978
- 3) Marwood, W.J. and Bailey, D. : Transverse Stability of Round-Bottomed High-Speed Craft Underway NPL, Ship Rep. 98. 1968

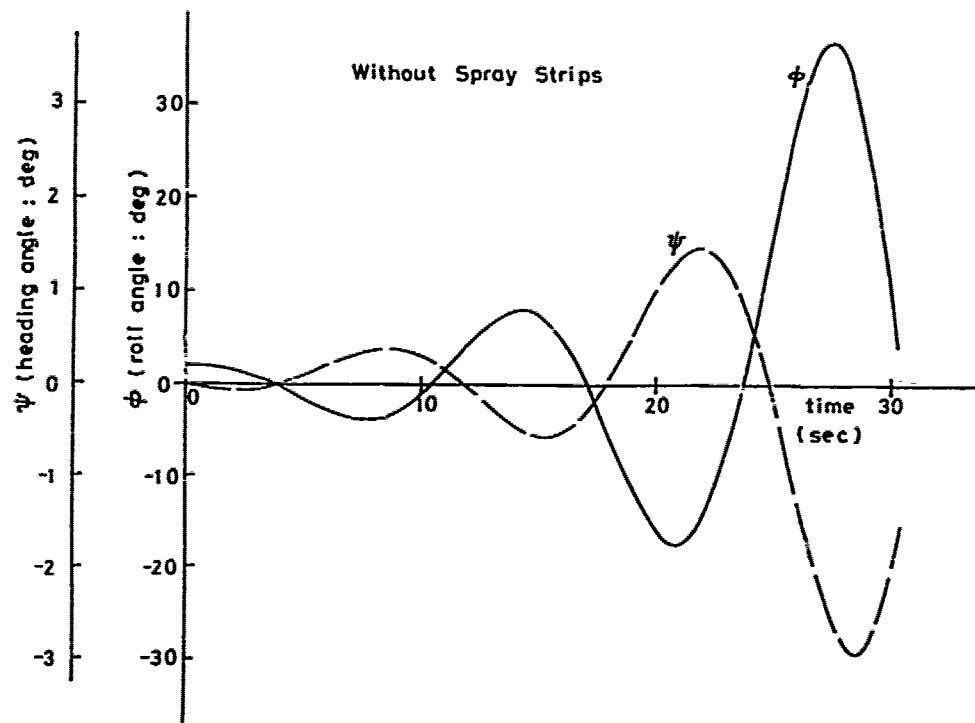


Fig. 1 Simulation result in the case of high speed craft without spray strips

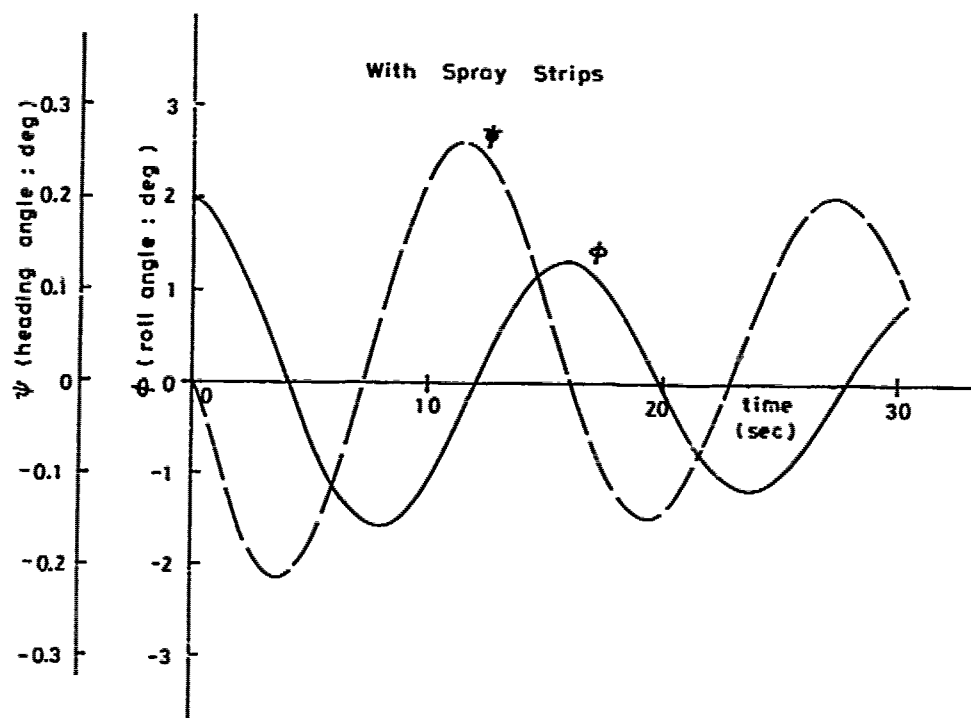


Fig. 2 Simulation result in the case of high speed craft with spray strips

I appreciate this author who has presented an interesting paper relating to both seakeeping and maneuverability of ship. The rudder movement of auto-pilot system should be included to estimate lateral motions as rolling, yawing and swaying motions in oblique waves. Today we can estimate these responses having the same period as the encounter wave period by using the strip theory inclusive the rudder effects (Takaishi 1976). The yawing motion has a natural frequency when the auto-pilot system is used. The coupled oscillations between roll-yaw-rudder illustrated in Figs. 13 and 14 show this natural frequency which is lower than that of rolling motion. This motion could not be estimated by the strip theory.

Since this coupled motion will become significant for the transverse stability of such a high-speed vessel running in quartering or following seas where the encounter frequency of waves could approach to the natural period of yaw, the phenomena pointed out by this author should be attracted attention not only by the ship operator but

also by the ship hydrodynamicists. This yawing moment due to heeling of ship will become large on the ship having large asymmetry of fore and aft body. Mori (1979) has shown the effect of heel angle upon the course stability of a high-speed container ship with the quadruple propellers having an remarkably asymmetric ship body between fore and aft, i.e. the fore body having an extraordinary large bulbous bow with a fine water plane configuration and the aft body having rather flat and wide stern shape. The result shows that the turning radius to starboard due to heeling angle of 6.7 degrees to port is equivalent to that due to about 2 degrees rudder angle to the starboard, as is shown in Fig. A-1. The seakeeping tests of this model have been carried out at Ship Research Institute. The re-examination of the test results from the viewpoint proposed by the author would be interesting.

REFERENCES

- 1) Takaishi, Y. and Saruta, T., J. of Kansai SNA, No. 161, (1976), pp. 25-32
- 2) Mori, N. and Mori, M., Report of SRI, Vol. 16, No. 2, (1979), pp. 1-12

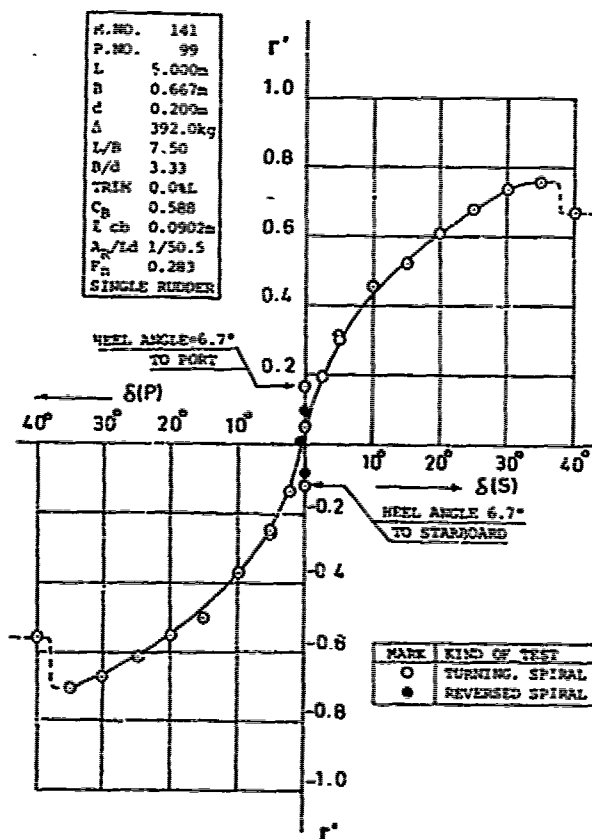


Fig. A-1 $r'-\delta$ Curve, Single rudder
 $F_R=0.283$

Author's Reply

H. Eda (Stevens Inst. Tech.)

The author was encouraged to learn that Mr. Toki of Mitsubishi Towing Tank had similar experience with roll-coupled yaw instability for a semidisplacement-type high speed boat, although there exists a substantial difference in configurations between a displacement-type ship and a high-speed boat. His simulation results clearly indicate typical roll and yaw coupled instability, which is introduced by a small initial roll angle. It should be noted here that this instability of the high-speed boat was due to roll-yaw coupling effect without feedback control of rudder. On the other hand, yaw instability of a high-speed ship mentioned in the paper was introduced by a combination of yaw-sway-roll coupling effects along with feedback controlled rudder.

His first question is whether the ship is dynamically stable or not on course, with and without consideration of roll-yaw coupling effect. It is clearly evident, for example, in the overshoot obtained in Z-maneuvers. (Accordingly, it is unnecessary to go out for spiral maneuvers to obtain $r'-\delta$ curves.) A large overshoot shown in a simulation run with an actual

GM value (i.e., 20° overshoot in 20°-20° Z-maneuver with GM of 3 ft) indicates that the ship is inherently unstable. With a hypothetically large GM of 25 ft, the magnitude of overshoot is reduced, indicating the improved course stability characteristics.

The author fully agrees with Mr. Toki's interpretation of the results shown in Figure 13 through 16, which illustrate the improvement of inherent yaw instability by adding damping effect. Whereas the refined auto-pilot is effective to improve overall yaw and roll stability characteristics, the author believes that the best solution under this condition is application of an anti-rolling fin stabilizer together with a refined auto-pilot, which should introduce an excellent overall system performance with less rolling, less steering, and less increased resistance.

The author wishes to acknowledge the useful comments given by Dr. Takaishi, who has been actively engaged in seakeeping

studies of high-speed container ships. As he points out, oscillations due to roll-yaw-rudder coupling cannot be adequately treated by currently available stripwise theories. Accordingly roll-yaw-rudder coupled instability problems mentioned in the paper should be examined from the viewpoint of both seakeeping and maneuvering with inclusion of feedback controlled rudder, where yaw moment due to hull-form-camberline plays an important role. The author is encouraged once again to learn that similar effects of heel angle on turning and course-keeping characteristics were observed in recent free-running model tests of a multi-propeller high-speed ship, at The Ship Research Institute, which has a significant fore-and-aft asymmetry with relatively small GM. The author is looking forward to reviewing these model test results from the viewpoint of roll-yaw-rudder coupling effects.

Finally, the author wishes to thank the discussers of his paper for their valuable contributions and references.

Session V

HULL FORM 3

— PROBLEMS IN DESIGN —

Chairman

Odo Krappinger

Hamburg Ship Model Basin

Hamburg, Federal Republic of Germany

Vertical Impact of a Disk on Compressible Fluid Surface

Chiu-Si Chen

China Ship Scientific Research Center

Wusih, Jiangsu, China

ABSTRACT

The problem of the vertical impact of a disc on the surface of a compressible fluid has been dealt with in this paper. On the basis of linearized assumption, the equation fulfilled by disturbance velocity potential of fluid has been reduced to a wave equation. The wave equation has been solved with the aid of spheroidal wave functions. The hydrodynamic pressure, force and pressure impulse, force impulse, and their changes with time have been given analytically. The dependence of impact force on the mass and radius of disc, and on the content of gas bubbles contained in the liquid have been given as well.

NOMENCLATURE

c_0 = speed of sound in undisturbed water
 c = speed of sound in water-gas mixture
 ϵ = constant, equation (11), $\epsilon = c/r_0$, is the time-decay coefficient
 ϵ_0, ϵ_1 = coefficient of impact force in formulas (40) and (40')
 $D(\epsilon)$ = function defined by equation (43), or (44)
 $d_{2n+1}^{(1)}(-\epsilon)$ = expansion coefficients, eqs. (27) and (28)
 F = impact force acting on disc
 F_i = impulse of impact force
 m = mass of disc, or $m = \rho_0/\rho$, the ratio of density of liquid to that of gas in the mixture
 M_0 = Mach number
 n = outward normal to the disc plane
 P = impact pressure acting on disc, or the pressure in the fluid
 p_0 = atmospheric pressure on free surface
 p_i = pressure impulse, or instantaneous impulsive pressure
 $R_{2n+1}^{(1)}, R_{2n+1}^{(2)}, R_{2n+1}^{(3)}$ = radial spheroidal wave functions of order zero

and degree $2n+1$ of the first, second, and third kind respectively

r_0 = radius of disc

(r, θ, z) = cylindrical co-ordinates

(η, θ, ω) = nondimensional cylindrical coordinates $\eta = r/r_0, \omega = z/r_0$

S_{2n+1} = angle spheroidal wave functions of the first kind of order zero and degree $2n+1$

t = time

t_0 = nondimensional time $t_0 = \epsilon_0/r_0$

v = velocity of disc

V_l, V_g = volume of liquid and gas in the mixture of liquid and gas respectively

v_0 = velocity of disc at first instant of impact

δ = mass number

(η, θ, ω) = spheroidal co-ordinates, fig. 2

μ = ratio of the mass of the gas to the mass of the liquid in the mixture of water and gas

ρ = mean density of the mixture of water and gas

ρ_0 = density of undisturbed water

ρ_g = density of air in the mixture of water and air

ρ_l = density of liquid in the mixture of water and air

1. INTRODUCTION

The problem treated here is related to water entry of flat-or blunt-nosed underwater weapons (e.g. aerial torpedo, project depth charges, antisubmarine missile). It may be also related to water impact of air launched sonars or other sensor equipment. The impact of disc on water surface is a reasonable approximation to the initial stages of impact of a flat-nosed cylinder and flat-or blunt-nosed body of revolution on water surface.

It may be noted that ship slamming, seaplane landing, and splash landing of space

capsules usually have water contact configurations approximated by a disc better than by a 2-dimensional plane.

In all cases where the impact velocity of flat or blunt-nosed bodies is not exceptionally small—and indeed, it is generally never very small, it is necessary to take the fluid compressibility into account, otherwise, unrealistically large calculated values of impact force and body acceleration may be obtained. However, to take the fluid compressibility into account, means to add complexity to an already complicated problem of unsteady flow with free surface. So far, most water entry problems were treated without taking fluid compressibility into consideration, Egorov [1] studied the 2-dimensional problem of vertical compressible impact. He is the first author to take the change of velocity of the falling plate into account, and approached the solution of a wave equation by the method of separation of variables. However, there seem to be some mistakes in his calculation which influenced the correctness of his conclusions. Ogilvie [2] studied the compressibility effects on ship slamming, and gave very interesting results for the case of 2-dimensional flat plate. Popuchkov [3] studied the axisymmetrical problem of the impact of a rigid disc on a compressible fluid and solved it for the time interval $0 \leq t \leq r/a$.

Popuchkov's impact force depends on the velocity of disc during impacting; the latter, however, is left undetermined in his solution. The work presented here by the author was essentially completed in 1964, consequently he did not enjoy the privilege of referring to Dr. Ogilvie's and Popuchkov's papers, except that due to Egorov. In order to simplify the problem and to study the effects of body mass, body dimensions and degree of compressibility on the transient process of water impact, it is necessary to work with simple forms. The author therefore attempts to treat the basic problem of vertical impact of a disc on a compressible fluid surface. The phenomena of air being trapped between the falling plate and the water surface was studied early by some investigators. The author did not take this into account however in his work in 1964, therefore, the problem treated in the paper is equivalent to that of a disc initially floating on the water surface, and then suddenly pushed down with an initial velocity u_0 . It is interesting to note that many authors discovered by experiment the escaping of air into water in the form of bubbles.

2. FORMULATION OF PROBLEM

Let a rigid disc of radius r_0 , mass m , impact vertically on the water surface. By vertical impact, is meant: The velocity of the disc points vertically downwards, the plane of the disc is always horizontal, and water initially at rest completely fills the lower half-space. The initial velocity of the disc is u_0 . Obviously the velocity of

disc will attenuate with time. We shall see later that the rate of this attenuation depends on the fluid density, the acoustic velocity in fluid, the disc radius and the disc mass.

At the initial stage, the motions are of an impulse nature. As compared with inertial force, the gravity force may be neglected. Because of the impulse nature of the fluid motion, the effect of fluid viscosity on flow is of no significance in most part of flow field except where the velocity gradient is large. Thus, the fluid may be regarded as nonviscous and the motion of fluid set up by the body is consequently irrotational.

For a liquid containing small gas bubbles, it is natural that its compressibility should be greater than that of the "solid" liquid, the amount of increase of compressibility may be characterized by the decrease in sound speed in the fluid. As a matter of fact, water immediately beneath the free surface owing to its disturbance by wave motion and the motions of the ship, always contain more or less small amounts of gas bubbles.

We assume that the initial velocity of impact of the disc is not very small, but that it is smaller than the sound velocity in the undisturbed fluid. In practice, this is only too true. Therefore, the subject may be treated under linearized considerations.

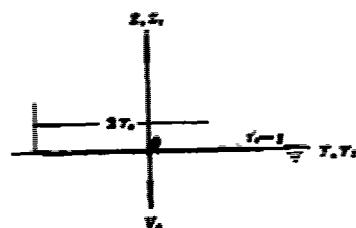


Fig.1 Sketch of the problem and cylindrical coordinate system

Let a cylindrical coordinate system (r, θ, z) be fixed with respect to the undisturbed fluid, its origin being in the plane of the undisturbed free surface with z -axis pointing vertically upwards (Fig.1). The linearized velocity potential may be expressed in this coordinate system as a wave equation

$$\frac{\partial^2 \phi}{\partial r^2} + \frac{1}{r} \frac{\partial \phi}{\partial r} + \frac{\partial^2 \phi}{\partial z^2} = -\frac{1}{a^2} \frac{\partial^2 \phi}{\partial t^2} \quad (1)$$

where a is the sound speed in undisturbed fluid. Or, by introducing non-dimensional variables r^*, z^*, t^* , eq.(1) becomes

$$\frac{\partial^2 \phi}{\partial r^{*2}} + \frac{1}{r^*} \frac{\partial \phi}{\partial r^*} + \frac{\partial^2 \phi}{\partial z^{*2}} = \frac{\partial^2 \phi}{\partial t^{*2}} \quad (2)$$

There is a relationship between the instantaneous impulsive pressure (i.e. pressure impulse) p and the velocity potential

$$p = -\rho_0 \varphi \quad (3)$$

On the free surface, pressure is finite and constant, i.e. $p=0$, and the boundary condition on the free surface is thus

$$r_1 > 1, z_1 = 0, \varphi = 0 \quad (4)$$

On the body surface $f(r, \theta, z) = 0$ the normal velocity of the fluid must be equal to that of body itself. It is difficult to exactly satisfy this boundary condition since the motion of body is unknown for the moment. However, making use of the property of the impacting process, i.e. the velocity change is finite, while the displacement is infinitesimal, the boundary condition on the body surface may be considered to be satisfied on plane $z_1 = 0$. Hence, the boundary condition on the body surface may be written as

$$r_1 < 1, z_1 = -0, \frac{1}{r_0} \frac{\partial \varphi}{\partial z_1} = v \quad (5)$$

Since the velocity is actually vertically downwards, the values of v and v_0 are considered as negative in the following calculations.

In addition to above conditions, there is the boundary condition at infinity to be satisfied.

The boundary condition on free surface, permits analytical continuation of the potential function across the free surface into the entire upper half-space. Let

$$\varphi(r_1, \theta, -z_1, t_1) = -\varphi(r_1, \theta, z_1, t_1) \quad (6)$$

then we have

$$\begin{aligned} \frac{\partial \varphi(r_1, -z_1, t_1)}{\partial r_1} &= -\frac{\partial \varphi(r_1, z_1, t_1)}{\partial r_1} \\ \frac{\partial \varphi(r_1, -z_1, t_1)}{\partial z_1} &= \frac{\partial \varphi(r_1, z_1, t_1)}{\partial z_1} \end{aligned}$$

It is easily seen that if P and P' are points of symmetry with respect to the free surface and lying, respectively, on the disc surface Σ and its mirror image Σ' , then

$$\left(\frac{\partial \varphi}{\partial n}\right)_P = -\left(\frac{\partial \varphi}{\partial n}\right)_{P'} \quad (7)$$

Therefore, the determination of the velocity potential in a region Ω , which is exterior to the surface $\Sigma + \Sigma'$, is a Neumann problem. The normal derivative $\frac{\partial \varphi}{\partial n}$ on Σ is given by boundary condition (5), while that on Σ' is defined by relation (7). Here Σ is the lower wall of the disc, and n is the exterior normal of the body surface.

According to (7), condition (5) may be rewritten as

$$r_1 < 1, z_1 = \pm 0: \frac{1}{r_0} \frac{\partial \varphi}{\partial z_1} = v \quad (8)$$

Besides these boundary conditions, potential function must also satisfy the initial conditions:

$$\left. \begin{aligned} r_1 = 0, r_1 > 1, z_1 = 0: \varphi = 0, \frac{\partial \varphi}{\partial z_1} = 0 \\ r_1 = 0, r_1 < 1, z_1 = \pm 0: \frac{1}{r_0} \frac{\partial \varphi}{\partial z_1} = v, \end{aligned} \right\} \quad (9)$$

Therefore, the problem is reduced to one of finding a solution for wave equation (2) under conditions (8) and (9).

When φ is known, the hydrodynamic pressure is found by

$$p - p_0 = -\rho_0 \frac{\partial \varphi}{\partial t_1} \quad (10)$$

Integrating $p - p_0$ over the entire surface of the disc, we obtain the total hydrodynamic force.

3. SOLVING THE WAVE EQUATION FOR φ

Considering the impulsive property of the motion, we look for a solution of φ in the form of an exponential time-decaying function. We set

$$\varphi(r_1, z_1, t_1) = \psi(r_1, z_1) e^{-ct_1}, \psi(r_1, -z_1) = -\psi(r_1, z_1) \quad (11)$$

where c is a constant to be decided.

Substituting (11) into (2), one obtains a Helmholtz's equation:

$$\frac{\partial^2 \psi}{\partial r_1^2} + \frac{1}{r_1} \frac{\partial \psi}{\partial r_1} + \frac{\partial^2 \psi}{\partial z_1^2} - c^2 \psi = 0 \quad (12)$$

Conditions (4) and (8) become respectively

$$r_1 > 1, z_1 = 0: \psi = 0 \quad (13)$$

$$r_1 < 1, z_1 = \pm 0: \frac{\partial \psi}{\partial z_1} = r_0 v_0 \quad (14)$$

Apparently, conditions (13) and (14) are also consistent with the initial conditions.

ψ must also satisfy the condition of Helmholtz's equation at infinity [4]:

$$R_1 = \sqrt{r_1^2 + z_1^2} \rightarrow \infty, \psi = 0 \quad (15)$$

Taking into account the geometric property of disc, I shall next adopt an oblate spheroidal coordinate system (η, ξ, θ) which is related to the cylindrical coordinate system by the transformation (Fig.2)

$$r_1 + iz_1 = \cosh(\mu + i\nu), \theta = \theta \quad (16)$$

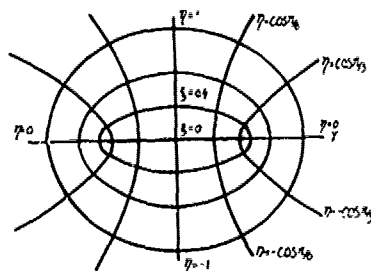


Fig.2 The oblate spheroidal coordinate system

where $\eta = \cos \alpha$, $\xi = \sinh \mu$. Hence

$$\begin{aligned} r_1 &= \sqrt{(1+\xi^2)(1-\eta^2)}, \quad -1 \leq \eta \leq 1, \quad 0 \leq \xi < \infty \\ z_1 &= \eta \xi, \end{aligned} \quad (17)$$

In the oblate spheroidal coordinate system (Fig.2) the surface $\xi = \text{const.} > 0$ is a flattened ellipsoid of revolution with its major axis $2(\xi^2+1)^{1/2}$ and minor axis 2ξ . The degenerate surface $\xi=0$ is a circular disk of radius $r_0=1$ lying in the plane $z_1=0$, with its center at the origin. This is exactly the disc discussed in the present paper. The surface $|\eta| = \text{const.} < 1$ is a hyperboloid of revolution of one sheet with an asymptotic cone whose generating line passes through the origin and is inclined at the angle $\alpha = \arccos \eta$ to the Z-axis. The degenerate surface $\eta=1$ and $\eta=-1$ is the positive half Z-axis and the negative half Z-axis respectively. Plane $\eta=0$ corresponds to that part of plane $Z_1=0$ exterior to the disk which is exactly the free surface.

When the focal length is finite (in the present case, it is equal to unity), surface $\xi = \text{const.}$ approaches to a spherical surface as ξ approaches to infinity. Thus

$$\xi \rightarrow R_1 \rightarrow \infty, \quad \eta = \cos \alpha \quad (18)$$

where R_1 and α is the radial coordinate and the colatitude coordinate respectively in spherical coordinates.

According to (18), the condition at infinity may be written as

$$\xi \rightarrow \infty, \quad \psi = 0 \quad (19)$$

In the new coordinate system, boundary conditions (13) and (14) become, respectively

$$\eta = 0: \quad \psi = 0 \quad (20)$$

$$\text{and } \xi = 0: \quad \frac{\partial \psi}{\partial \xi} = r_0 \eta v_0. \quad (21)$$

The initial conditions will automatically be satisfied if condition (20) and (21) are satisfied.

In the oblate spheroidal coordinates η, ξ, θ noting that the Lamé's coefficients are

$$h_\eta = \sqrt{\xi^2 + \eta^2}, \quad h_\xi = \sqrt{\frac{\xi^2 + \eta^2}{1 + \xi^2}} \quad (22)$$

and making use of the expression for Laplace operator ∇^2 in orthogonal curvilinear coordinates, equation (12) becomes

$$\left[\frac{\partial}{\partial \eta} (1 - \eta^2) \frac{\partial}{\partial \eta} + \frac{\partial}{\partial \xi} (\xi^2 + 1) \frac{\partial}{\partial \xi} - c^2 (\eta^2 + \xi^2) \right] \psi = 0 \quad (23)$$

Finally, the problem is reduced to that of solving eq.(23) under conditions (19) - (21).

4. SOLUTION OF HELMHOLTZ EQUATION FOR ψ

By the usual procedure of separation of variables, eq.(23) may be solved in the form of Lamé's products [5]

$$\psi = S_\eta(-c, \eta) R_\xi(-c, -i\xi)$$

Substituting the above expression into eq.(23), we have

$$\left\{ -\frac{d}{d\eta} \left[(1 - \eta^2) \frac{d}{d\eta} \right] + \lambda_n - c^2 \eta^2 \right\} S_\eta(-c, \eta) = 0 \quad (24)$$

$$\left\{ \frac{d}{d\xi} \left[(\xi^2 + 1) \frac{d}{d\xi} \right] - \lambda_n - c^2 \xi^2 \right\} R_\xi(-c, -i\xi) = 0 \quad (25)$$

where λ_n s are the separation constants.

Solutions $S_\eta(-c, \eta)$ and $R_\xi(-c, -i\xi)$ may be found for different values of parameter c^2 . In order to satisfy all the boundary conditions under discussion, I construct the solution in the form of a function series

$$\psi = r_0 v_0 \sum_{n=0}^{\infty} A_{n+1} S_{n+1}(-c, \eta) R_{n+1}^{(2)}(-c, -i\xi) \quad (26)$$

where A_{n+1} are the expansion coefficients to be decided by boundary conditions. $S_{n+1}(-c, \eta)$ are the angle spheroidal wave functions of the first kind, which satisfy the ordinary differential equation (24). $R_{n+1}^{(2)}(-c, -i\xi)$ are the radial spheroidal wave functions of the third kind, which satisfy the ordinary differential equation (25). $R_{n+1}^{(2)}(-c, -i\xi)$ are related to radial functions of the first kind and of the second kind by the following relationship:

$$R_{n+1}^{(2)}(-c, -i\xi) = R_{n+1}^{(1)}(-c, -i\xi) + i R_{n+1}^{(3)}(-c, -i\xi)$$

For the present purpose, we may expand $S_{n+1}(-c, \eta)$ into a series of zero order functions and expand $R_{n+1}^{(2)}(-c, -i\xi)$ in series of modified spherical Hankel functions of the first kind:

$$S_{n+1}(-c, \eta) = \sum_{l=0}^{\infty} d_{l,n+1}^{(0)}(-c) P_{l,n+1}(\eta) \quad (27)$$

$$R_{n+1}^{(2)}(-c, -i\xi) = \frac{1}{\sum_{l=0}^{\infty} d_{l,n+1}^{(0)}(-c)} \sum_{l=0}^{\infty} d_{l,n+1}^{(2)}(-c) h_{l,n+1}^{(2)}(ic\xi) \quad (28)$$

In the above two expressions, $d_{l,n+1}^{(2)}$ are the expansion coefficients.

Since $P_{2n+1}(\eta)$ are odd functions, $S_{2n+1}(-c, \eta)$ ($\eta=0, 1, 2, \dots$) are also odd functions of η which satisfy the free surface condition described above.

From the properties of the spheroidal wave functions, one can derive the following asymptotic expression

$$\lim_{\xi \rightarrow \infty} R_{2n+1}^{(2)}(-c, -i\xi) = \lim_{\xi \rightarrow \infty} \frac{1}{ic\xi} \exp\{i[ic\xi - (n+1)\pi]\} = 0 \quad (29)$$

which means that solution (26) satisfies the condition at infinity (19).

A_{2n+1} are determined by the boundary condition

$$\left(\frac{\partial \psi}{\partial \xi}\right)_{\xi=0} = r_0 v_0 \sum_{n=0}^{\infty} A_{2n+1} S_{2n+1}(-c, \eta) R_{2n+1}^{(2)}(-c, -i0) = r_0 \eta v_0 \quad (30)$$

where

$$R_{2n+1}^{(2)}(-c, -i0) = \left[\frac{d}{d\xi} R_{2n+1}^{(2)}(-c, -i\xi) \right]_{\xi=0}$$

Utilizing the orthogonality of S_n , we obtain

$$\begin{aligned} A_{2n+1} &= \frac{\int_{-1}^1 S_{2n+1}(-c, \eta) \eta d\eta}{2R_{2n+1}^{(2)}(-c, -i0) \sum_{r=0}^{\infty} \frac{[d_{2r+1}^{2n+1}(-c)]^2}{4r+3}} \\ &= \frac{d_{2n+1}^{2n+1}(-c)}{3R_{2n+1}^{(2)}(-c, -i0) \sum_{r=0}^{\infty} \frac{[d_{2r+1}^{2n+1}(-c)]^2}{4r+3}} \quad (31) \end{aligned}$$

Substituting (31) into (26), and then substituting the resulting expression of ψ into (11), we finally obtain

$$\begin{aligned} \varphi(r_1, z_1, t_1) &= \frac{r_0 v_0}{3} \sum_{n=0}^{\infty} \frac{d_{2n+1}^{2n+1}(-c)}{R_{2n+1}^{(2)}(-c, -i0) \sum_{r=0}^{\infty} \frac{[d_{2r+1}^{2n+1}(-c)]^2}{4r+3}} \\ &\quad \cdot S_{2n+1}(-c, \eta) R_{2n+1}^{(2)}(-c, -i\xi) e^{-\alpha_1 t_1} \quad (32) \end{aligned}$$

which is the velocity potential required.

5. CALCULATION OF HYDRODYNAMIC FORCE

From eq. (10), the hydrodynamic pressure is

$$\begin{aligned} p - p_0 &= -\rho_0 \frac{a_0}{r_0} \frac{\partial \psi}{\partial t_1} \\ &= \rho_0 a_0 v_0 c \sum_{n=0}^{\infty} \frac{d_{2n+1}^{2n+1}(-c)}{3R_{2n+1}^{(2)}(-c, -i0) \sum_{r=0}^{\infty} \frac{[d_{2r+1}^{2n+1}(-c)]^2}{4r+3}} \\ &\quad \cdot S_{2n+1}(-c, \eta) R_{2n+1}^{(2)}(-c, -i\xi) e^{-\alpha_1 t_1} \quad (33) \end{aligned}$$

and the resultant hydrodynamic force acting on the bottom plane of the disk is

$$\begin{aligned} F_1 &= \rho_0 a_0 r_0 \int_0^{2\pi} d\theta \int_0^1 \left(\frac{\partial \psi}{\partial t_1}\right)_{t_1=0} r_1 dr_1 + \pi r_0^2 p_0 \\ &= -2\pi \rho_0 a_0 r_0 \int_{-1}^1 \left(\frac{\partial \psi}{\partial t_1}\right)_{t_1=0} \eta d\eta + \pi r_0^2 p_0 \quad (34) \end{aligned}$$

The resultant hydrodynamic force acting on the top plane of the disk is

$$\begin{aligned} F_2 &= -\rho_0 a_0 r_0 \int_0^{2\pi} d\theta \int_0^1 \left(\frac{\partial \psi}{\partial t_1}\right)_{t_1=0} r_1 dr_1 - \pi r_0^2 p_0 \\ &= 2\pi \rho_0 a_0 r_0 \int_{-1}^1 \left(\frac{\partial \psi}{\partial t_1}\right)_{t_1=0} \eta d\eta - \pi r_0^2 p_0 \quad (35) \end{aligned}$$

Hence, the total hydrodynamic force acting on both sides of the disk is

$$F^* = F_1 + F_2 = -2\pi \rho_0 a_0 r_0 \int_{-1}^1 \left(\frac{\partial \psi}{\partial t_1}\right)_{t_1=0} \eta d\eta \quad (36)$$

Note that $\left(\frac{\partial \psi}{\partial t_1}\right)_{t_1=0}$ is antisymmetric with respect to η in the vicinity of plane $z_1=0$, and that the last integrand is an even function of η .

F^* is the impact force acting upon the disk assuming the fluid to be unbounded. In our case, the impact force exerted upon the disk by the fluid is

$$\begin{aligned} F &= F^*/2 = -\pi \rho_0 a_0 r_0^2 D(c) \frac{d}{dt_1} (v_0 e^{-\alpha_1 t_1}) \\ &= \pi r_0^2 \rho_0 a_0 v_0 D(c) e^{-\alpha_1 t_1} \quad (37) \end{aligned}$$

or

$$F = -\pi r_0^2 \rho_0 v_0^2 \frac{D(c)c}{M_0} e^{-\alpha_1 t_1} \quad (38)$$

where

$$\begin{aligned} D(c) &= \sum_{n=0}^{\infty} \frac{d_{2n+1}^{2n+1}(-c) R_{2n+1}^{(2)}(-c, -ic)}{3R_{2n+1}^{(2)}(-c, -i0) \sum_{r=0}^{\infty} \frac{[d_{2r+1}^{2n+1}(-c)]^2}{4r+3}} \int_{-1}^1 S_{2n+1}(-c, \eta) \eta d\eta \\ &= \frac{2}{9} \sum_{n=0}^{\infty} \frac{[d_{2n+1}^{2n+1}(-c)]^2 R_{2n+1}^{(2)}(-c, -i0)}{R_{2n+1}^{(2)}(-c, -i0) \sum_{r=0}^{\infty} \frac{[d_{2r+1}^{2n+1}(-c)]^2}{4r+3}} \quad (39) \end{aligned}$$

and $M_0 = |v_0|/a_0$ is the impact Mach number.

Eq. (37) or (38) yields the coefficient of impact force

$$c_p = \frac{F}{\pi r_0^2 \rho_0 a_0 |v_0|} = -D(c) c e^{-\alpha_1 t_1} \quad (40)$$

or

$$c_p = \frac{F}{\pi r_0^2 \cdot \frac{1}{2} \rho_0 v_0^2} = -\frac{2D(c)c}{M_0} e^{-\alpha_1 t_1} \quad (40')$$

From eqs. (37) - (40), it is seen that in order to determine the impact force or its coefficient, one must calculate c and $D(c)$ first.

6. CALCULATION OF $D(c)$

$$R_{2n+1}^{(3)}(-c, -i0) = R_{2n+1}^{(1)}(-c, -i0) + iR_{2n+1}^{(2)}(-c, -i0)$$

$$= \frac{3i^{2n+1} \sum_{r=0}^{\infty} d_{2r+1}^{2n+1}(-c)}{c^3 d_1^{2n+1}(-c)} \quad (41)^*$$

*Incidentally, it is found that eqs. (4,6,14), (4,6,15b), (4,6,16b) in reference [5] is not correct, the correct expressions deduced by the author is:

$$R_{2n+1}^{(1)}(-ic, i0) = \frac{i^{n-m-1} 2^n n! c^{m+1} d_1^{m+1}(-ic)}{(2m+3) \sum_{r=0}^{\infty} d_r^{2m}(-ic) \frac{(2m+r)!}{r!}}, \quad n-m = \text{odd}$$

$$R_{2n+1}^{(2)}(-ic, i0) = \frac{i^{n-m+1} (2m+3) \sum_{r=1}^{\infty} d_r^{2m}(-ic) \frac{(2m+r)!}{r!}}{2^n n! c^{m+1} d_1^{m+1}(-ic)}, \quad n-m = \text{odd}$$

$$R_{2n+1}^{(3)}(-ic, i0) = \frac{i^{n-m-2} (2m-3)(2m-1)n! c^{m-2}}{2^{2m-m+1} (2m)! d_{2m+1}^{2m}(-ic) \sum_{r=1}^{\infty} d_r^{2m}(-ic) \frac{(2m+r)!}{r!}} \times \left[\frac{(n+m+1)!}{\left(\frac{n-m-1}{2}\right)! \left(\frac{n+m+1}{2}\right)!} \right]^2, \quad n-m = \text{odd}$$

$$R_{2n+1}^{(3)}(-c, -i0) = -i^{2n+1} \left\{ \frac{c d_1^{2n+1}(-c)}{3 \sum_{r=0}^{\infty} d_{2r+1}^{2n+1}(-c)} + \frac{3\pi}{2^{2n+3} c^3 d_1^{2n+1}(-c) \sum_{r=0}^{\infty} d_{2r+1}^{2n+1}(-c)} \left[\frac{(2n+2)!}{n!(n+1)!} \right] \right\} \quad (42)$$

Substituting (41) and (42) into (39), one gets

$$D(c) = -\frac{2}{3} \sum_{n=0}^{\infty} \frac{d_1^{2n+1}(-c) \sum_{r=0}^{\infty} d_{2r+1}^{2n+1}(-c)}{\left\{ \frac{c^3 d_1^{2n+1}(-c)}{3 \sum_{r=0}^{\infty} d_{2r+1}^{2n+1}(-c)} + \frac{3\pi}{2^{2n+3} c^3 d_1^{2n+1}(-c) \sum_{r=0}^{\infty} d_{2r+1}^{2n+1}(-c)} \left[\frac{(2n+2)!}{n!(n+1)!} \right]^2 \right\} \sum_{r=0}^{\infty} \frac{[d_{2r+1}^{2n+1}(-c)]^2}{4r+3}} \quad (43)$$

or

$$D(c) = -\frac{2}{3} \sum_{n=0}^{\infty} \frac{\left(\sum_{r=0}^{\infty} d_{2r+1}^{2n+1}(-c) \right)^2}{\left\{ \frac{c^3}{3} + \frac{3\pi}{2^{2n+3} [d_1^{2n+1}(-c)]^2} \left[\frac{(2n+2)!}{n!(n+1)!} \right]^2 \right\} \sum_{r=0}^{\infty} \frac{[d_{2r+1}^{2n+1}(-c)]^2}{4r+3}} \quad (44)$$

Hence one can see that the calculation of $D(c)$ is reduced to one of calculating $d_{2r+1}^{2n+1}(-c)$. The values of d_{2r+1}^{2n+1} and the method used to calculate it for certain range of values of c have been given in textbooks on spheroidal wave functions, but the range of c given is not large enough for our needs. Accordingly basing on theory of spheroidal wave functions, I have recalculated values of $d_{2r+1}^{2n+1}(-c)$ for a much larger range of c . Using these values of d_{2r+1}^{2n+1} the function $D(c)$ was calculated and shown in Fig.3.

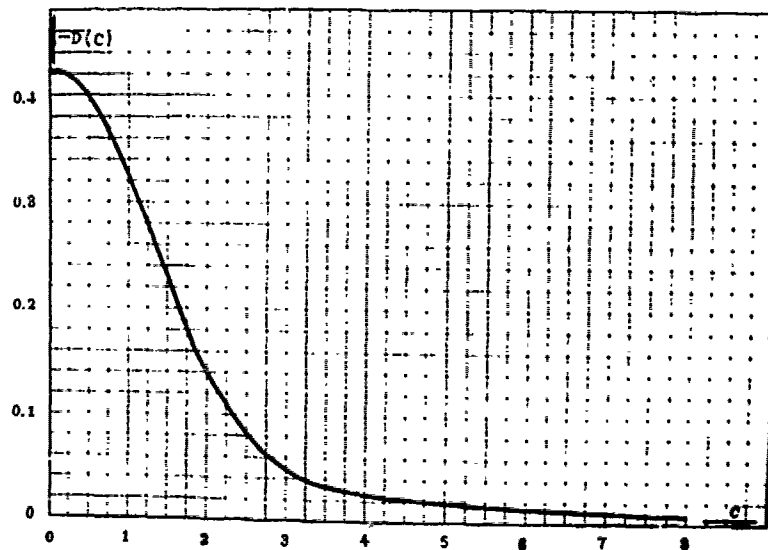


Fig.3 The function of $D(c)$

7. CALCULATION OF C AND THE VELOCITY OF DISC

It is seen from eqs. (38) and (43), that in order to calculate the impact force, we must know the values of c for the particular problem. To this end, we must first turn our attention to solving the equation of motion of the body during the impacting process. Neglecting the forces of gravity on disc, the equation of motion may be written as

$$m \frac{dv}{dt} = F \quad (45)$$

where F is given in eqs. (37) or (38). Noting the initial condition $t=0, v=v_0$, we get for the solution of eq. (45)

$$v = v_0 \left[1 + \frac{3}{4} \pi \delta D(c) (1 - e^{-\alpha_1}) \right] \quad (46)$$

where $\delta = \frac{1}{3} \rho_0 r_0^2 / m$, and $\frac{1}{3} \rho_0 r_0^2$ is half of the added mass of the disc of radius r_0 moving with a velocity normal to its plane in an infinite mass of incompressible liquid.

At the initial moment of impact of a rigid disc on a compressible liquid surface, a compression layer is formed in the liquid. In the compression layer the pressure is very high. The impact pressure thus propagates outwards in the form of compression waves with velocity of sound in liquid. At great distances away from the disc, the compression wave behaves as a spherical one, while the pressure amplitudes attenuates rapidly. At the end of the impact, the impact pressure attenuates down to zero, and the pressure in the liquid will be the same

as that in an ordinary field of flow past the disc.

The duration of the impact process is very short, because the compressibility of water is very small. If the liquid were absolutely incompressible then the impact process will conclude instantaneously. Assuming that an incompressible flow is built up after impact, the velocity of disc is, according to the law of conservation of momentum, $V_0 / (1 + \delta)$.

Substituting this into (46), we get

$$D(c) = -\frac{4}{3\pi} \frac{1}{1+\delta} \quad (47)$$

and

$$v = \frac{v_0}{1+\delta} (1 + \delta e^{-\alpha_1}) \quad (48)$$

Knowing the value of $D(c)$ from δ , we may read the values of c from Fig. 3.

8. PRESSURE DISTRIBUTION

From eq. (34), hydrodynamic pressure exerted on the bottom plane of the disc is

$$p = \rho_0 a_0 v_0 c \sum_{n=0}^{\infty} \frac{d_{2n+1}^{2n+1}(-c) R_{2n+1}^{(2n+1)}(-c, -i0)}{3 R_{2n+1}^{(2n+1)}(-c, -i0) \sum_{r=0}^{\infty} \frac{[d_{2r+1}^{2r+1}(-c)]^2}{4r+3}} S_{2n+1}(-c, \eta) e^{-\alpha_1} \quad (49)$$

$$0 \geq \eta = -\sqrt{1-r_0^2} \geq -1$$

Substituting (27), (41), (42) into above expression, we obtain

$$p = -\rho_0 a_0 v_0 c \sum_{n=0}^{\infty} \frac{\left[\sum_{r=0}^{\infty} d_{2r+1}^{2r+1}(-c) \right] \sum_{r=0}^{\infty} d_{2r+1}^{2r+1}(-c) P_{2n+1}(-\sqrt{1-r_0^2}) e^{-\alpha_1}}{d_{2n+1}^{2n+1}(-c) \left\{ \frac{c^2}{3} + \frac{3\pi}{2^{2n+1} [d_{2n+1}^{2n+1}(-c)]^2} \left[\frac{(2n+2)!}{n!(n+1)!} \right]^2 \right\} \sum_{r=0}^{\infty} \frac{[d_{2r+1}^{2r+1}(-c)]^2}{4r+3}} \quad (50)$$

The expression (50) may be rewritten as

$$p = \rho_0 a_0 v_0 \sum_{n=0}^{\infty} \frac{\left[\sum_{r=0}^{\infty} d_{2r+1}^{2r+1}(-c) \right]^2 \sum_{r=0}^{\infty} d_{2r+1}^{2r+1}(-c) P_{2n+1}(-\sqrt{1-r_0^2}) \frac{d}{dt_1} (e^{-\alpha_1 t_1})}{d_{2n+1}^{2n+1}(-c) \left\{ \frac{c^2}{3} + \frac{3\pi}{2^{2n+1} [d_{2n+1}^{2n+1}(-c)]^2} \left[\frac{(2n+2)!}{n!(n+1)!} \right]^2 \right\} \sum_{r=0}^{\infty} \frac{[d_{2r+1}^{2r+1}(-c)]^2}{4r+3}}$$

From this, it can be seen that, only when c approaches to zero, or when the impact is done with constant velocity, is the amplitude of impact pressure acting at the centre of disc equal to $\rho_0 a_0 v_0$.

It is relatively easy to calculate the distribution of pressure according to above expression. The factor

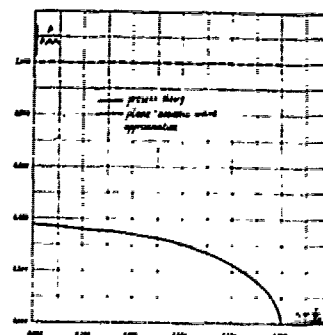
$$\frac{\left[\sum_{r=0}^{\infty} d_{2r+1}^{2r+1}(-c) \right]^2}{\left\{ \frac{c^2}{3} + \frac{3\pi}{2^{2n+1} [d_{2n+1}^{2n+1}(-c)]^2} \left[\frac{(2n+2)!}{n!(n+1)!} \right]^2 \right\} \sum_{r=0}^{\infty} \frac{[d_{2r+1}^{2r+1}(-c)]^2}{4r+3}}$$

has already been calculated in the calculation of $D(c)$. It is sufficient now only to calculate the factor

$$\frac{\sum_{r=0}^{\infty} d_{2r+1}^{2n+1}(-c) P_{2r+1}(-\sqrt{1-r_0^2})}{d_{2n+1}^{2n+1}(-c)}$$

and multiply

it by the preceding factor correspondingly. As an example, I assume that $c=2.2$ and calculate the distribution of the pressure at the time $t=0$. The results are shown in Fig.4. In the same figure is shown the pressure distribution as calculated by the plane acoustical wave approximation which is suggested by some authors, e.g. Von Karman [6].



$c=2.2$

Fig.4 Pressure distribution

9. CALCULATION OF IMPULSE

In structural design, it is important to know the magnitude of the impulse. From eq.(50), the pressure impulse from $t=0$ to $t=\tau$ is given by

$$\begin{aligned} p_i(\tau) &= \int_0^{\tau} p(t_1) \cdot \frac{r_0}{a_0} dt_1 \\ &= -\rho_0 v_0 r_0 \sum_{n=0}^{\infty} \frac{\left[\sum_{r=0}^{\infty} d_{2r+1}^{2n+1}(-c) \right]^2 \sum_{r=0}^{\infty} d_{2r+1}^{2n+1}(-c) P_{2r+1}(-\sqrt{1-r_0^2}) (1-c \frac{a_0}{r_0} \tau)}{d_{2n+1}^{2n+1}(-c) \left\{ \frac{c^2}{3} + \frac{3\pi}{2^{n+1} [d_{2n+1}^{2n+1}(-c)]^2} \left[\frac{(2n+2)!}{n!(n+1)!} \right]^2 \right\} \sum_{r=0}^{\infty} \frac{[d_{2r+1}^{2n+1}(-c)]^2}{4r+3}} \\ &= p(0) \frac{r_0}{a_0 c} (1 - e^{-c^2 \tau}), \quad \tau_1 = \frac{a_0 \tau}{r_0} \end{aligned} \quad (51)$$

where $p(0) = p(t)|_{t=0}$.

From eq.(37), the impulse of impact force, from $t=0$ to $t=\tau$ is given by

$$\begin{aligned} F_i(\tau) &= \int_0^{\tau} F(t) dt = -\pi r_0^2 \rho_0 v_0 D(c) (1 - e^{-c^2 \tau}) \\ &= F(0) \frac{r_0}{a_0 c} (1 - e^{-c^2 \tau}), \quad \tau_1 = \frac{a_0 \tau}{r_0} \end{aligned} \quad (52)$$

where $F(0) = F(t)|_{t=0}$.

For incompressible liquid, a_0 approaches to infinity but the value of c is finite. It is determined from r_0 , the radius of the disc; m , the mass of the disc; and ρ_0 , the density of undisturbed fluid. It is seen from eqs.(37), (50), (51), and (52), that, for incompressible fluid the impact pressure and impact force are indefinite, but their impulse is finite. In other words, the impact pressure and force approach to infinity during the initial moment of impact; however, the infinite values only last for an infinitesimal time, and they are integrable.

10. EFFECT OF PHYSICAL PARAMETERS ON IMPACT PROCESS

By the formulation of the problem presented in this paper, hydrodynamic impact force is related to following physical parameters: m and r_0 , the mass and the radius of the disc; v_0 , the initial velocity of impacting body; t , the time; ρ_0 and a_0 , the density and the speed of sound in the undisturbed fluid, i.e.

$$F = F(m, r_0, v_0, t, \rho_0, a_0) \quad (53)$$

After the similarity theory and the method of dimensional analysis, the seven physical quantities in eq.(53) can be composed into four independent dimensionless combinations, i.e. the four criteria of similarity:

Mach number $M_s = v_s/a_s$
 Mass number $\delta = \frac{4}{3} r_0^2 \rho_s / m$
 Time number $\tau = a_s t / r_s$
 Impact force coefficient $c_F = F / \pi r_0^2 \rho_s a_s v_s$
 Thus, eq. (53) may be simplified into

$$c_F = f(M_s, \tau, \delta) \quad (54)$$

So far, we have determined the function $c_F = f(M_s, \tau, \delta)$ and the effect of each parameter on the impact force and impact process which is given by the particular form of the function f . In what follows we shall lay special stress on the effects of sound speed and the density of the liquid.

From eq. (37) the impact force is proportional to the density ρ of the fluid and to the velocity of sound in the undisturbed fluid. By virtue of the disturbance by wind, waves, and the motions of ship or other entering bodies, as well as by virtue of any trapped-air being forced into water, the water immediately beneath the free surface always contain some gas bubbles. Actually it is a mixture of water and air. This will lead to a large reduction of impact force. In order to calculate the amount of reduction of the impact force, one must calculate the average density of, and the velocity of sound in, the mixture.

Mallock [7] considered the velocity of transmission of compression waves in a mixed fluid (such as a liquid containing gas bubbles) the same as it would be in a homogeneous fluid of equal average density and equal mean modulus of elasticity. Let $\bar{\rho}$ and \bar{E} be the mean density and mean modulus of elasticity of the mixture, and let volume, density, and modulus of elasticity of the liquid and gas be respectively denoted by V_l, ρ_l, E_l , and V_g, ρ_g, E_g .

Since the velocity of transmission of compression wave equals $\sqrt{\frac{E}{\rho}}$, and

$dV_l/V_l = dp/E_l$, $dV_g/V_g = dp/E_g$, where dp is the variation in stress, then if $V_l = lV_g$, $\rho_l = m\rho_g$, $E_l = nE_g$, one has in terms of E_g :

$$E = E_g \frac{l+1}{n+1} \quad (55)$$

$$\rho = \rho_g \frac{ml+1}{m(n+1)} \quad (56)$$

$$\sqrt{\frac{E}{\rho}} = \sqrt{\frac{E_g m}{\rho_g}} (l+1) / \sqrt{(l+n)(ml+1)} \quad (57)$$

$$\rho \sqrt{\frac{E}{\rho}} / \rho_l \sqrt{\frac{E_l}{\rho_l}} = (ml+1) / \sqrt{(l+n)(ml+1)} \quad (58)$$

Eq. (58) is the expression of the ratio of the impact force on the water containing gas bubbles to that on "solid" water.

Campbell [8] assumed that the liquid is incompressible and the gas perfect. He also assumed that the gas obeys Boyle's law, which implies that the liquid is able to act as a constant-temperature heat reservoir for the gas. Then he gave an expression for calculating the speed of sound in the mixture

$$a = \sqrt{\frac{p}{\rho \left[1 - \frac{\rho}{(1+\mu)\rho_l} \right]}} \quad (59)$$

where, p is the pressure of the mixture, μ the ratio of the mass of the gas to the mass of the liquid in the mixture. μ is related to ρ_l , ρ , and the mean density $\bar{\rho}$ in the following way

$$\frac{1+\mu}{\bar{\rho}} = \frac{\mu}{\rho_g} + \frac{1}{\rho_l} \quad (60)$$

Expression (59) derived by Campbell differs only slightly from eq. (57) given by Mallock.

It can be expected, that the assumptions underlying expression (59), namely, that the gas in bubbles obeys Boyle's law and that the mixture behaves like an equivalent homogeneous medium, are valid only for small bubbles and for low wave frequencies. Similar limitations are tacitly made also in deriving expression (57).

From eqs. (58) and (60), we get

$$\sqrt{\frac{E}{\rho}} \cdot \rho / \sqrt{\frac{E_l}{\rho_l}} \cdot \rho_l = \sqrt{\frac{1+\mu}{1+m\mu}} \quad (61)$$

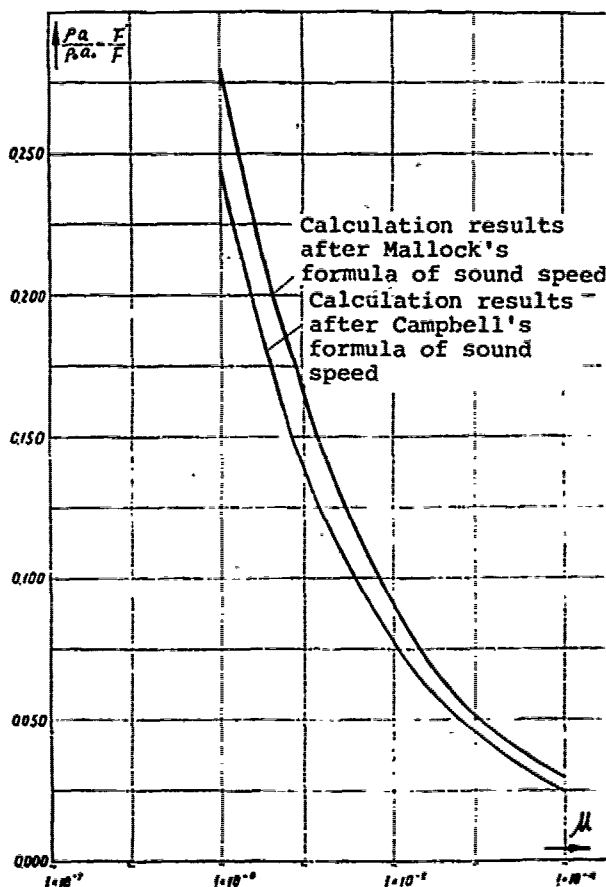


Fig. 5 Ratio of the impact force on water containing gas bubbles to that on water containing no gas bubbles ("solid" water)

Then using Campbell's assumption and eq.(59), and noting that the undisturbed density and the velocity of sound in the undisturbed fluid are used in eq.(37) with $\rho_1 = \rho_0$, and $p = p_0$, I get an alternative expression for the ratio of impact force on water-gas mixture to that on "solid" water

$$\frac{\rho_0 c_0}{\rho_0 c_0} = \sqrt{\frac{p_0 \rho}{1 - \frac{\rho}{(1+\mu)\rho_0}}} / \rho_0 c_0 = \sqrt{\frac{p_0(1+\mu)}{m\mu\rho_0}} / c_0 \quad (62)$$

Using eqs.(61) and (62), different ratios of impact force were calculated for different values of μ . In the calculation, we assumed roughly $m=800$, $n=14800$, $p_0=10^4$ Kg.M², $\rho_0=102$ Kg.M⁻³.sec⁻² and $c_0=1450$ M.sec⁻¹. The computed results are plotted in Fig.5. It may be seen that with water containing gas bubbles, the reduction of impact force is large. For example, with $\mu=0.0001$, the impact force is reduced to as much as 1/41 of the "solid" water value. Correspondingly, the velocity of sound in water containing gas bubbles is reduced to 1/38 of its value in the "solid" water case and the mean density of mixture is 95% of the original. Therefore, it is important to know the content of gas bubbles in the water immediately beneath the free surface.

REFERENCES

[1] И.Т.Егоров, "Удар о Сжимаемую Жидкость", Прикладная Математика и Механика, Том 20, Вып.1, Стр.67-72, 1956.

[I.T.Egorov, "Udar o Szhimaemuuiu Zhidkost", (Impact on a Compressible Fluid), Prikladnaya Matematika i Mekhnika, (Applied Mathematics and Mechanics) Vol.20, No.1,

1956 (Translated in NACA TM1413), Feb., 1958)].

[2] T.Francis Ogilvie, "Compressibility Effects in Ship Slamming", Schiffstechnik, Band 10, Heft 53, S.147-154, Sep., 1963.

[3] В.Б.Поручков, "Удар Диска по Поверхности Идеальной Сжимаемой Жидкости", Прикладная Математика и механика, Том 28, Вып.4, Стр.797-800, 1964.

[V.B.Popuchkov, "Udar Diska po Poverkhnosti Idealnoi Szhimaemoi Zhidkosti", (Impact of a Disc on Ideal Compressible Fluid Surface), Prikladnaya Matematika i Mekhnika (Applied Mathematics and Mechanics) Vol.28, No.4, pp.797-800, 1964].

[4] А.Н.Тихонов, А.А.Самарский, "Уравнения Математической Физики", Г.7, §2, Государственное Издательство Техничко-Теоретический Литературы, Москва, 1953.

[A.N.Tikhonov, A.A.Samarskii, "Uravneniya Matematicheskii Fiziki", (Equations of Mathematical Physics), C.7, §2, Gosudarstvennoe Isdatel'stvo Techniko-teoreticheskoi Literatury, Moscow, 1953].

[5] C.Flammer: "Spheroidal Wave Functions", C.2-4, Stanford University Press, California, 1957.

[6] T.Von Karman, F.L.Wattendorf: "The Impact on Seaplane Floats During Landing", NACA TN no.321, 1929.

See also "Collected Works of Theodore Von Karman" Vol.2, pp.309-313, London, Butterworths Scientific Publication, 1956.

[7] A.Mallock, "The Damping of Sound by Frothy Liquids", Proceedings of the Royal Society, Series A. Vol.84, No.572, pp.534-545, Dec, 1910.

[8] I.J.Campbell & A.S.Pitcher, "Shock Waves in a Liquid Containing Gas Bubbles" Proceedings of the Royal Society, Series A, Vol.243, No.1235, pp.534-545, 1957.

Discussion

J.L. Baldwin (Naval Surface Weapons Center)

I wish to compliment Mr. Chen for his interesting and important paper. The White Oak Laboratory of NSWC has an ongoing program investigating fluid entry phenomenon. Based on our experience, I wish to make the following comments.

(1) Water entry applications occur over a wide speed range from less than 10M/sec to more than 2000M/sec.

(2) Compressibility effects are important when the forebody wetting time is short, ie, $t \sim r_0/a_0$.

(3) Our method of predicting fluid entry forces does not include compressibility effects but still gives good engineering design results.

(4) The experimental solution to the problem of the vertical entry of a disk will require greater care.

I wish to ask Mr. Chen to comment on the effects on his results caused by, missile elasticity, slightly curved water surface and small errors in geometry (such as disk surface not exactly parallel to the water's surface).

T.F. Ogilvie (Univ. of Michigan)

This is a remarkable paper to have been prepared (essentially) more than 15 years ago. Today it is still a substantial contribution to our knowledge of this subject.

I have two questions for the author :

(1) The assumed form of the solution of the wave equation, as stated in (11), is equivalent to what would be obtained by using the method of separation of variables with physical arguments being used to eliminate some possible forms of solution. However, it appears that all exponentially decaying solutions should be admitted, which then suggests that the final solution would have been expressed as a Laplace transform. However, the author retains only a simple exponentially decaying solution. Did he consider the possibility of superposing all possible exponential solutions ? If so, was there some evidence (unstated in the paper) for keeping just a simple exponential solution ?

(2) In view of work in the last 15 years on the effects of the air gap between the impacting body and the water surface, would the author care to comment on the relative importance of compressibility and air-gap effects ?

Author's Reply

C.-S. Shen (China SSRC)

I have read many of Dr. Baldwin's papers, I am delighted to his opinion on my paper.

Missile elasticity, slightly curved water surface and small errors in geometry, in my opinion, will affect the process of impact. Elasticity induces high frequency component of impact force, however, the interval of time in which elasticity makes its effect felt is very short, so it will not generally affect the water-entry ballistics. Deformation of water surface may influence the impacting force in two ways; (1) When the wave length is relatively long compared with the dimension of the body head, the effect is a change in the entry angle; (2) When the wave length is very small (ripples), then it will reduce the contacting areas between body and fluid, which will generally reduce the impact loading. Errors in geometry, I think, will affect the impacting process in some way similar to the last mentioned case.

The encouragement of Prof. Ogilvie is very much appreciated and I thank Prof. Ogilvie for his discussion on my paper. As to the question I could only make a short reply here, as there isn't much time to consider between my late arrival yesterday afternoon and this morning session.

(1) I agree with Prof. Ogilvie in that superposition of exponential decaying solution could be adopted, or in other words, the solution may be solved as a Laplace transform. However, there is some difficulty in solving it this way straight through — the velocity of the body is unknown in the process and hence also the impact force is unknown.

(2) Dr. Fujita first proposed to investigate into the effect of air trapped in 1954. Works of last 15 years by many authors have confirmed the existence of an air layer between the impacting body and the water surface during the initial stage of impact (e.g. Sheng-Lun Chuang, 1966, 1967; J.H.G. Verhagen, 1967; G. Lewison and W.M. McLean, 1968). Before the air has escaped, the air compressibility and its buffering action is important; water compressibility is of secondary importance. However, after the air has escaped, especially for a flat- or blunt-nosed body impacting water at high speed, the body would move on and eventually impact on the surface of a liquid containing many minute air bubbles at its vicinity. During this stage, I consider water compressibility as very important.

Seakeeping and Resistance Trade-Offs in Frigate Hull Form Design

R. T. Schmitke

Hydrodynamics Section

Defence Research Establishment Atlantic

Dartmouth, Nova Scotia

D. C. Murdey

Marine Dynamics and Ship Laboratory

National Research Council

Ottawa, Ontario

Canada

ABSTRACT

The seakeeping and resistance trade-offs arising in frigate hull form design are addressed. The sources of model test data on frigate seakeeping and resistance are reviewed. A methodical series of model tests on frigate-type hull forms is described, and results are presented showing the effect of hull form parameters on resistance and seakeeping. An analytical parametric study of frigate seakeeping is described. In presenting the results of this study, emphasis is placed on slamming; key seakeeping parameters are identified and design priorities recommended. Design of a frigate hull form is discussed, and model test results are presented for this hull. It is concluded that important improvements in the seakeeping qualities of frigates may be achieved by the selection of appropriate hull design parameters.

NOTATION

B	beam
C_B	block coefficient
C_P	prismatic coefficient
C_W	waterplane area coefficient
C_V	displacement coefficient
F_n	Froude number
H_W	significant wave height
L	ship length

LCB	longitudinal position of the centre of buoyancy
LCF	longitudinal position of the centre of flotation
\bar{M}	length/displacement ratio, $L/\nabla^{1/3}$
R	total resistance
T	draft
T_W	energy-averaged wave period
V	speed
g	gravitational constant
h	ship operating time in hours
k	sectional form factor for impact pressure calculation
Δ	displacement in tons
V	displaced volume
δ	deadrise angle
ρ	density of water
σ_{RM}	root mean square relative motion
σ_{RV}	root mean square relative velocity
ω	wave frequency

1. INTRODUCTION

Warship designers have always been interested in achieving high speeds, and the

evolution of warship hulls reflects this interest. The approach until recently has been to design the hull to achieve the minimum resistance at top speed in calm water with a check on the cruising speed performance to ensure that endurance requirements could be met. Reference to earlier designs was frequently made to determine initial hull form parameters, such reference being almost always on a basis of minimum top speed resistance. The estimated shaft horsepower requirements for this calm water top speed were frequently used to design a "tailor made" steam propulsion system. In the absence of an understanding of the performance of ships in waves and without suitable techniques to analyse the effects of waves on the ship, a small, fairly arbitrary margin of shaft power was added to provide some capability to maintain speed in waves.

Research developments of the past twenty years have, fortunately, improved this situation considerably. Experimental and theoretical techniques for the prediction of ship motions in waves have been developed and validated. Considerable effort has also been devoted to establishing operationally significant measures of ship performance in waves. As a result of this maturing of seakeeping technology, a more rational approach is now being taken toward the achievement of high speeds at sea by introducing the assessment of performance in waves into the ship design process.

During the same period, model tests have provided much fundamental data on resistance, especially through the testing of methodical series. Series data of this type enable systematic investigation of the effect of hull form parameters on resistance. Hence, given present methods for seakeeping analysis, the capability is provided for trade-off studies of seakeeping and resistance in frigate hull form design, as discussed in this paper.

The Frigate Seakeeping Problem

It is useful at this point to present an overview of the seakeeping problem from the standpoint of the frigate designer. The term "seakeeping" is used herein to describe the motions and related phenomena experienced by a ship in response to rough seas. The sea acts on the ship to produce adverse phenomena which may be grouped under three major headings: motions, slamming and green water. (There are, of course, other seakeeping phenomena of generally lesser significance, such as involuntary speed loss, reduced stability and broaching, which this paper does not consider.) The primary seakeeping phenomena adversely influence the crew, the hull structure and the ship's various systems, as will now be discussed.

The crew of a modern warship must often perform demanding and highly skilled tasks at sea, either operationally or in a maintenance role. The effects of ship motions are to degrade performance and to

cause excessive fatigue and motion sickness. Certain tasks may become dangerous or even impossible to accomplish, making work restrictions necessary. Injuries may occur, and even loss overboard.

In heavy seas, the hull may suffer damage from bottom and flare slamming. In deed, it is the concern of frigate captains that slamming damage may occur which primarily motivates decisions to reduce speed in adverse sea conditions. Other structural problems are damage to superstructure from green water, whipping, and fatigue.

Performance degradation of equipment can take many forms, for example: reduced accuracy of weapons, reduced detection capability of sensors, and loss of propulsive efficiency. With increasing ship motions, the probability of breakdowns also increases, as well as the susceptibility to damage from inertial loads and green water. The ship can also suffer equipment loss, of which an example is loss of a towed body.

The operation of helicopters from frigates and destroyers deserves special mention. The helicopter is an extremely potent weapon system and provides these small to medium sized warships with a high capability in terms of both scope and flexibility of tasks. The detrimental effects of the seaway are: slowdown in operations, landing and take-off restrictions, restricted on-deck movement, reduced capability to refuel and rearm, and, at worst, damage.

The foregoing discussion has identified many ways in which the seaway adversely affects frigate operations and has shown the importance of including seakeeping considerations in frigate design. The question naturally arises, then, as to what aspects of seakeeping should govern the selection of frigate hull form parameters. For frigates, the most important motions are pitch, heave, vertical accelerations, and roll. Schmitke has shown that the influence of hull form on rolling is of secondary importance. This leaves vertical plane motions, slamming and green water as the factors which should influence frigate hull form design. Of the vertical plane motions, vertical accelerations are usually of primary concern.

A further important simplification may also be made. Ship response in a seaway depends strongly on the heading of the ship relative to the waves. For a typical frigate, it may be shown² that bow vertical accelerations, slamming and deck wetness reach their most severe levels in head seas. Moreover, Reference 2 also shows that in head seas, values computed for unidirectional and short-crested areas are very similar. Hence, one may consider only unidirectional head seas when seeking to optimize frigate hull forms for seakeeping.

Seakeeping and Resistance Trade-Offs

Although the discussion to this point has emphasized seakeeping, this does not lessen the importance of resistance. Indeed, given present and projected fuel costs, the

motivation to design fuel-efficient ships is probably greater now than ever before. Hence, a fundamental goal in frigate hull form design is to achieve superior seakeeping without compromising resistance. As will be shown in the following, in only a few instances are resistance and seakeeping requirements in conflict, and compromises consequently necessary. It will also be shown that existing analytical tools and model test data together provide the capability to make these trade-offs quantitatively.

2. REVIEW OF SOURCES OF INFORMATION

2.1 Resistance in Calm Water

The traditional sources of data for predicting ship resistance in calm water are the published results of model tests of methodical series forms. Many such series have been tested, References 3 to 8 for example, and they differ from one another in the type of parent form used, the parameter variations explored and the speed range over which the tests were carried out. The use of methodical series data is a subject covered in detail in standard texts such as Reference 9. In this section, those series of relevance to frigate design will be discussed briefly.

The best known series, The Taylor Series³, covers speeds up to $F_n = 0.6$, where F_n is Froude number. The forms have round sterns, fine ends and full midship sections which are inappropriate to ships operating at speeds in excess of about $F_n = 0.35$. The series is thus of limited application to frigates since, although economical cruising speed is of importance, it is not the main criterion for the selection of the hull form for such ships.

Most present day frigates have a design speed between F_n 's of 0.35 and 0.5 (the hump speed). The HSVA "C" series⁴ is appropriate to this speed range. The parent form has a transom stern and the main parameters varied are length-displacement ratio (M) , beam/draft ratio B/T and prismatic coefficient C_p . Also included in the series are models which give the effect of changing the transom width and of fitting a bulbous bow.

When speed is increased beyond the hump speed but not so fast that dynamic lift is of any importance, the traditional solution to the design problem is to use slender forms. The DTNSRDC Series 64⁵ and the Davidson series of models of high speed ships⁶ typify this approach. Both investigate the effects of variations in (M) and B/T with C_p held constant. The data from these series are useful in the design of large vessels but the narrow beams and the associated lack of stability make these forms impractical for modern small warships.

For speeds extending into the semi-

planing regime, valuable data are contained in the NPL High Speed Round Bilge Displacement Hull Series⁷ and the SSPA High Speed Displacement Vessel Series⁸. In the NPL series (M) , B/T , length/beam ratio L/B and the position of the longitudinal centre of buoyancy LCB are varied, while in the SSPA series only the effects of varying (M) and B/T are explored.

As an alternative to methodical series, attempts have been made to use regression techniques to identify trends in resistance with changes of hull form parameters from results of model tests with unrelated forms. Careful statistical analysis of such data can yield insight into the importance of individual hull form parameters and establish trends of resistance with hull form geometry. However, such methods have not yet been generally made available to naval architects for the prediction of ship resistance and will not be considered further in this paper.

2.2 Seakeeping

Data and information on seakeeping are less readily available than for performance in calm water. Unlike performance in calm water where even model tests carried out over fifty years ago are relevant, much published seakeeping data are insufficiently comprehensive to be used with modern prediction techniques. It is now generally recognized that predictions of performance in irregular waves based on response curves measured on a model or calculated by theory, provide a satisfactory basis for comparing different hull forms. Unfortunately, much of the published data from experiments with models from methodical series are for tests carried out in only a limited number of regular waves, insufficient to enable response curves to be adequately defined. Furthermore, the parameters which have usually been varied in methodical series, like (M) , B/T and C_p may not be those which are of most

importance for seakeeping. Series developed primarily for investigations of calm water performance may be of limited value for seakeeping studies.

Several models from HSVA "C" series were tested in regular waves over a speed range corresponding to $F_n = 0.2$ to 0.6. The wave height was maintained constant at $1/40$ of the model length, and the wave lengths set in turn to 0.75, 1.0, 1.25, 1.5 and 2.0 times the model length. Measurements made included pitch, heave, vertical acceleration and relative bow motion. These data are presented in Reference 4 as plottings of the corresponding non-dimensional quantities against F_n for each wave length tested. The diagrams are very difficult to interpret, and it is to be noted that Reference 4 does not draw any conclusions concerning the relative merits of seakeeping performance of the designs tested. Attempts to derive response curves from the measured data have not been successful, primarily because so

few wave-lengths were used in the test program.

One reason for preferring to compare predictions of performance in irregular waves rather than data measured in regular waves is that of flexibility. The predictions may be calculated for a wide range of sea states and ship sizes. This aspect was exploited in the analysis of the SSPA series⁹ to give comparisons of three designs with different B/T in a non-dimensional form relating the motion response to the length of the ship and the average period and significant wave height of the irregular waves. It was concluded that the influence of B/T on the performance in waves was less than that of the longitudinal distribution of weight along the hull.

In some cases, Reference 6 for example, a choice has been made to carry out the experiments in irregular waves. In interpreting the results of such tests the model must always be considered to represent a particular full-scale situation and the data produced cannot be generalized to ship sizes or wave conditions other than those tested. It is concluded in Reference 6 that for the Davidson series models in the sea states tested, increasing M at constant displacement and increasing B/T both tend to improve seakeeping qualities. However, the data in Reference 6 do not enable quantitative trends to be deduced for other types or sizes of ships, and are thus not applicable to frigates.

Reference 10 contains results of series of tests in both regular and irregular waves with 16 models derived from the form of a large twin screw ship to give a wide variation of block coefficient C_B , waterplane area coefficient C_W , LCB and longitudinal centre of flotation LCF. The data measured in irregular waves were in this case used to justify the use, for making comparisons, of predictions of performance in irregular waves based on responses measured in regular waves. As with the SSPA data discussed above, the seakeeping predictions are presented in a way which enables their convenient determination for any practical combinations of ship lengths, average wave period and significant wave height. This series is of particular value in that the forms tested cover wide variations in section shape and the results show the tendency for increases in waterplane area coefficient to improve seakeeping performance. The specific data given in Reference 10 are, however, not applicable directly to frigate designs.

The statistical approach, the analysis of trends from data from random models, has been more successful in the case of seakeeping than resistance. An analysis of data for single screw merchant ships, Reference 11, relates pitch and heave to the principal particulars of hull form and weight distribution. An independent check, Reference 12, of the simple equations contained in Reference 11, concludes that for such ships,

the results are at least as good as sophisticated strip theory predictions. Unfortunately, similar statistical analyses for frigates have not yet been published.

One of the reasons for so little model data being published for methodical series in waves is the cost and time required to carry out such tests, compared with resistance tests. A methodical set of theoretical calculations is a much cheaper alternative which, subject to the usual assumptions concerning the theoretical approach to the solution of seakeeping problems, should give results of much value. Such a set of theoretical calculations has been carried out for Series 60 designs, Reference 13, but, of course, yet again, the results are not applicable to frigates.

Much model and theoretical work continues to be carried out to explore the effects on seakeeping of variations in the hull form of specific designs. However, there is a need, particularly for frigate-like hulls, for sources of quantitative data on performance which may be used in the earlier stages of the design process before the hull lines have been fully defined. The methodical series experiments and the results of the systematic theoretical calculations which are described in Sections 3 and 4, respectively, were carried out in order to satisfy this requirement.

3. THE NRC SERIES

3.1 Description of the Series

As shown in Section 2, there is comparatively little published information on the seakeeping and resistance of high speed displacement ships. Systematic seakeeping data are especially scarce. For these reasons, the Hull Form Series for Fast Surface Ships was initiated at the Marine Dynamics and Ship Laboratory of the National Research Council of Canada (NRC), to both complement and extend existing published data. In planning the NRC series, particular emphasis was placed on seakeeping, and the choice of parent form and variations was largely governed by this requirement.

A review of published work and results from a preliminary parametric study, similar to that described in Section 4, had indicated that, for seakeeping, the characteristics of the waterplane were of great importance. The waterplane area coefficient was, therefore, selected to be a basic parameter for the series.

A second fundamental requirement to influence the design of the series was that parameters varied would be restricted to those which were likely to be known or easily estimated at the earliest stages of design. In addition to waterplane area coefficient, parameters such as length, beam, draft and displacement only would be considered. For seakeeping, M and B/T are appropriate combinations of these parameters, since they may be related to the added mass and damping characteristics of the hull form. How-

ever, when predicting ship performance, length itself is of great importance. It is necessary to be able to distinguish between the changes in Δ achieved by changing length on one hand and by changing displacement at constant length on the other. For these reasons, it was felt desirable to include variations in fullness explicitly by changing block coefficient C_B within the series. In any systematic series, important parameters should be included but once. Following the inclusion of block coefficient, it becomes necessary to replace Δ (which implicitly includes block coefficient) with a slenderness parameter L^2/BT to relate the beam and draft to the length of the hull.

To carry out a series of seakeeping model tests is expensive and time-consuming. To ensure that the trends in performance with hull form parameters investigated would be defined beyond any reasonable doubt, the variations in the selected parameters tested must be as large as possible. In the NRC series, this was accomplished within the limits of practical (if not always desirable) hull forms.

A final consideration in the design of the series was that a maximum of useful results should be obtainable before all the testing was complete. To some large extent, the series was developed in response to requests from designers for information on resistance and seakeeping of high speed displacement hull forms. These requirements guided not only the experiment design and choice of parameters but also the priority in testing the models.

The experiment design finally adopted is shown in Table 1. This is essentially a factorial design, with two levels of each of the four design parameters included, except for beam draft ratio which is tested at three levels. The beam draft ratios 3.28 and 4.2 cover the frigate range, the additional high value of 5.2 being included to extend the series to include fast patrol vessels, where extra stability is required. The range of L^2/BT , which corresponds effectively to a Δ range of 6.8 to 7.9, was selected after an inspection of the principal particulars and nominal speeds of many warships. The values of C_B and C_W were selected to include several practical design alternatives.

The series will enable trends in performance with variations in one parameter to be determined for different values of the remaining three. It will be possible to establish, for example, how the effect of increasing C_W depends upon the value of B/T , L^2/BT and C_B .

The parent form for the series is design 6, (Table 1, Fig. 1). This form is very close to that of an existing frigate design with known satisfactory seakeeping performance. In contrast to many series parent forms, it is not in the center of the parameter ranges but at one limit.

TABLE 1: HULL FORM SERIES FOR FAST SURFACE SHIPS EXPERIMENT DESIGN

L^2/BT	C_B	0.48		0.52	
		C_W	B/T	C_W	B/T
150	5.2	1	7	13	19
	4.2	2	8	14	20
	3.28	3	9	15	11
238	5.2	4	10	16	22
	4.2	5	11	17	23
	3.28	6*	12	18	24

* Basic Form

□ Designs considered in this paper

Three new hull forms, designs 12, 18 and 24, were developed from the parent form, and the remaining designs obtained simply by scaling beam and draft from the four basic forms. Design 12 differs from design 6 in that it has a new waterplane corresponding to the larger C_W . In the new waterplane

curve, the width of the transom is increased to 0.748 compared with 0.438 for the parent form. The sectional area curves for designs 6 and 12 are identical. Designs 18 and 24 each have the same sectional area curve (different from that of designs 6 and 12) and have waterplane curves the same as for designs 6 and 12, respectively. Designs 6, 12, 18 and 24 have identical midship sections. In all cases, LCE and LCF are the same. The method used to derive sections corresponding to the various combinations of sectional area and waterplane curves followed closely the scheme described in Reference 10.

Bodyplans for the four designs are shown in Fig. 1. From these figures it can be seen that the series includes two normal hull forms, an extreme 'V' form with a knuckle, and an extreme 'U' form.

At the present time ten models out of the twenty-four of Table 1 have been fully tested and the results analysed. These are shown blocked out in Table 1. All four designs with parameters closest to those of existing frigates (designs 6, 12, 18 and 24) have been tested, together with the designs with $C_B = 0.52$ and $B/T = 3.28$ and 4.2. The model size selected was 11.125 ft. on the waterline. All the models are the same length.

The models were made in two halves split amidships and, since the midship sections were identical for the four models with the same beam and draft, it was possible to create new forms by combining the bow of one design with the stern of another.

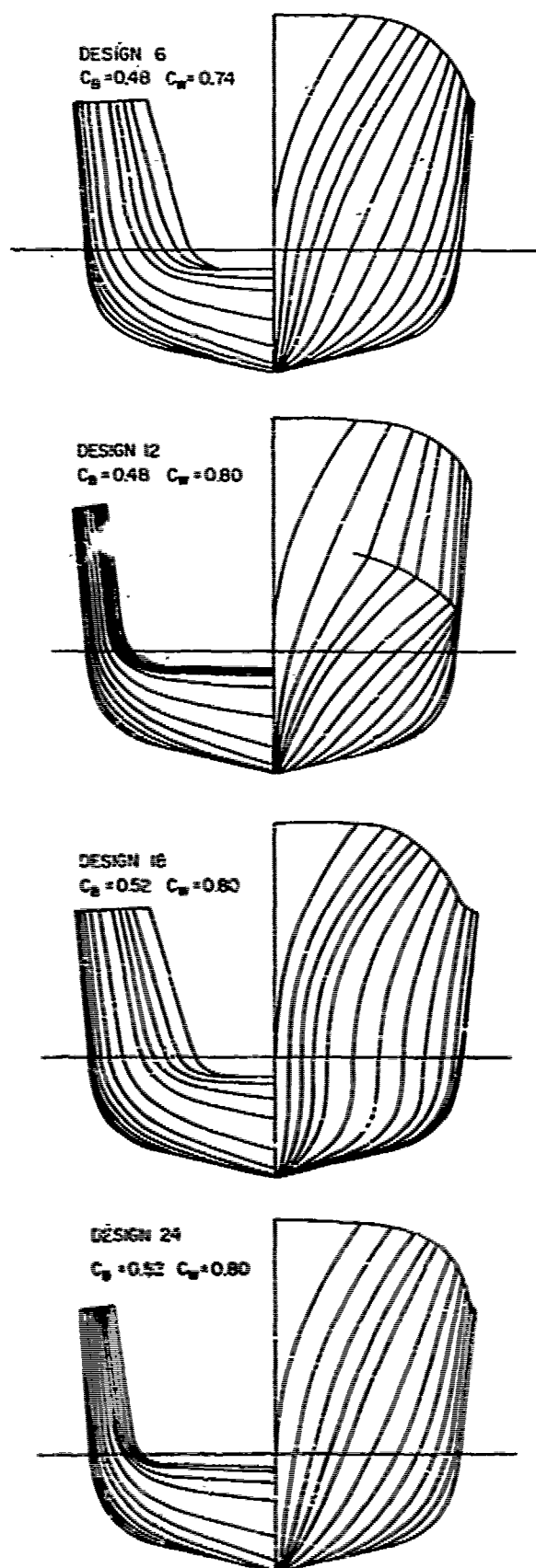


Fig. 1 Body Plans

This was done for designs 6, 12, 18 and 24, and the resulting twelve additional designs enable the effect of changes in LCB and LCF to be determined. The designations of combined designs are of the form Bow Design/Stern Design. For example, design 12/6 has the bow of design 12 and the stern of design 6.

3.2 Resistance Trends

Calm water naked resistance experiments have been carried out for twenty-two models, including the ten models given initial priority, as shown in Table 1, and the additional twelve bow/stern combinations described above.

For the purpose of presenting resistance data in this paper, predictions have been made from the model test data of the resistance of 3500 ton ships. The predicted resistance has been expressed as the resistance displacement coefficient,

$$C_R = R / (.5 \rho V^2 V^{1/3})$$

where R is total resistance, ρ is water density, V is speed, and V is displaced volume. The ITTC 1957 skin friction line without any correlation allowance has been used in calculating frictional resistance.

Although it is, of course, possible to compare plottings of resistance curves for various designs, the series lends itself to an alternate presentation which makes trends particularly easy to identify: by plotting differences in C_R against speed for a pair of designs which differ in only one major parameter. For example, the effect of increasing C_B from 0.48 to 0.52 may be obtained from four pairs of designs: (6, 18), (12, 24), (6/12, 18/24) and (12/6, 24/18). For all eight designs, $L^2/BT = 238$, $B/T = 3.28$, and LCB is constant. The remaining primary hull coefficients are shown below.

Designs	C_W	LCF
18-6	0.74	-5.61
24-12	0.80	-5.61
18/24-6/12	0.77	-4.24
24/18-12/6	0.77	-7.05

The differences in C_R between each pair of models are plotted against speed in Fig. 2. The notation 18-6 means that the differences in C_R between designs 18 and 6 have been obtained as follows:

$$\text{Change in } C_R = C_R(18) - C_R(6)$$

Similar groupings may be identified to show the effect of varying L^2/BT , B/T and C_W . However, in the interests of brevity, a figure is presented herein only for C_W .

Fig. 3, as the effects of L^2/BT and B/T are well known: increasing L^2/BT reduces re-

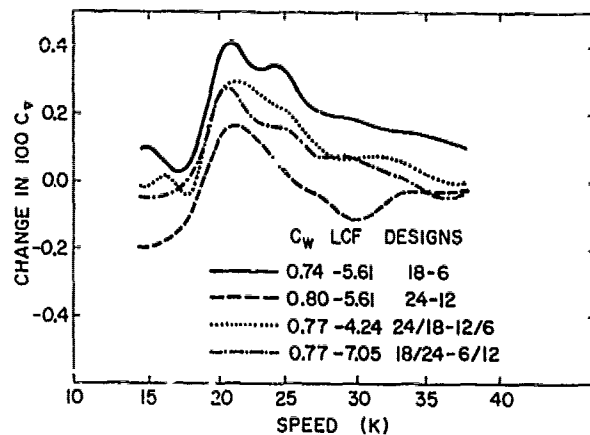


Fig. 2 Effect on Resistance of Increasing C_B

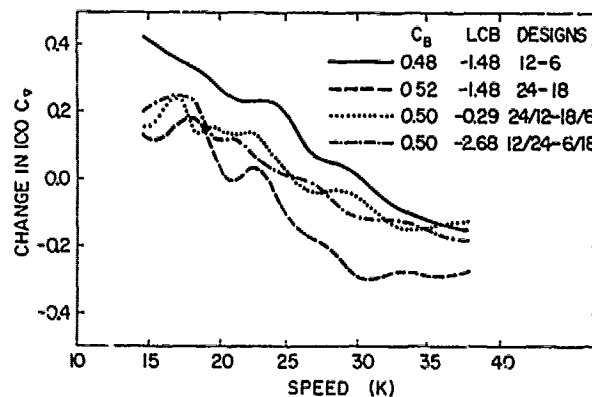


Fig. 3 Effect on Resistance of Increasing C_W

sistance at high speed, while increasing B/T increases resistance slightly over the whole speed range.

A notable feature of both Fig. 2 and 3 is that, in each figure, all four pairs of designs show the same trends. Increasing C_B generally increases resistance, especially between 20 and 25 kt. Increasing C_W increases resistance at low speed, but at high speed the reverse is true.

The group of 16 designs made by combining bows and sterns of design 6, 12, 18 and 24 enable study of the effects of increasing bow U-ness and varying transom width. For example, the change from bow 12 to bow 6, Fig. 4, is a change from extreme V to normal sections. Analogously, the change from stern 12 to stern 6, Fig. 5, is a change from wide to narrow transom.

Increasing the U-ness of the bow, Fig. 4, reduces resistance over the entire speed range. Making the stern wider and flatter, Fig. 5, increases resistance at low speed and reduces resistance at high speed. As in Fig. 2 and 3, data from different pairs of designs are very consistent.

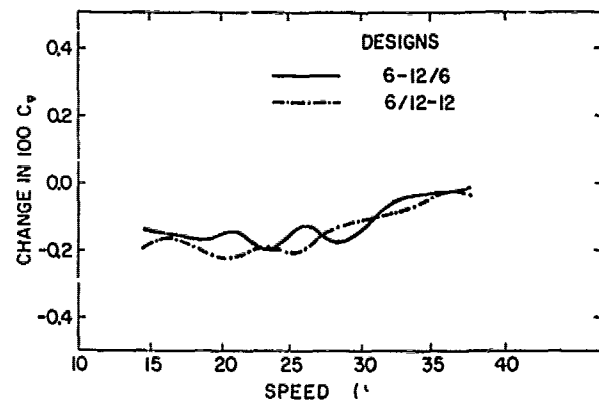


Fig. 4 Effect on Resistance of Increasing Bow U-ness - $C_B = 0.48$

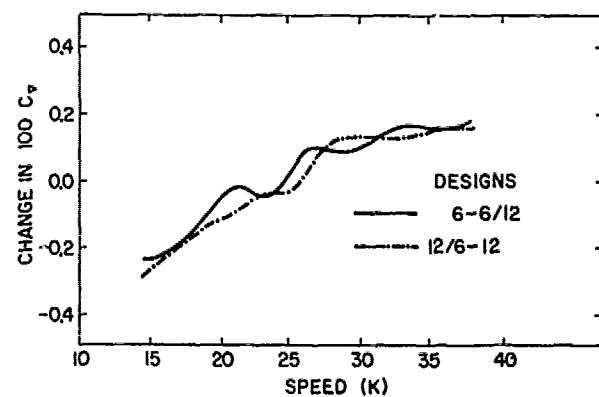


Fig. 5 Effect on Resistance of Decreasing Transom Width - $C_B = 0.48$

3.3 Seakeeping Tests

Experiments were carried out with the model self-propelled with no external tow force in regular head waves. The wave height was maintained at a value nominally 1/50th of the wave length, and the wave length was varied in about 20 steps from one-half to three times the waterline length of the model. The experiments were repeated at each of four speeds corresponding to $F_n = 0.2, 0.3, 0.4$ and 0.5 . Measurements relevant to this paper were pitch and heave amplitudes and phases. The measured data were expressed in standard non-dimensional form and smooth lines drawn through them.

As discussed in Section 2.2, comparisons between different designs are best made on the basis of predictions of motions in irregular seas. Hence, predictions of pitch, heave, relative bow motion (RBM) and vertical acceleration at .25L have been made for ships of 3500 tons in irregular head seas, using the measured response

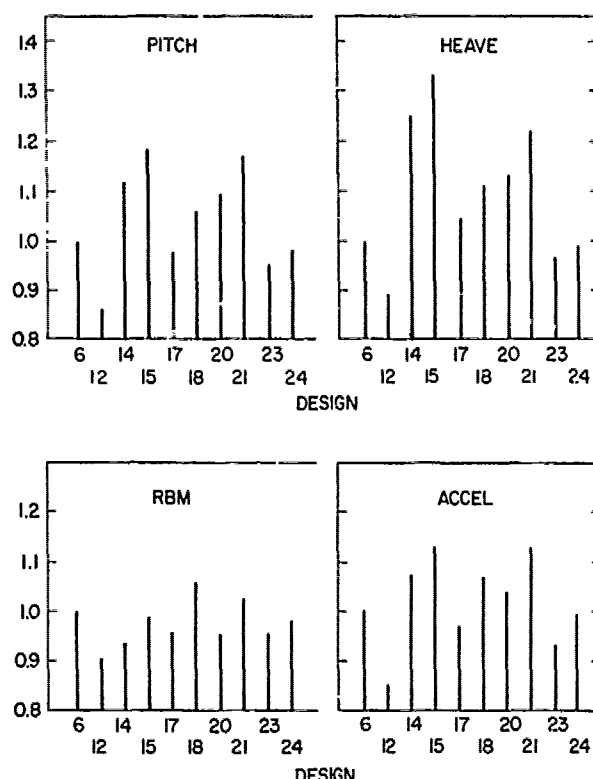


Fig. 6 Ship Motion Comparisons, $\Delta = 3500$ Tons

curves and the quadratic regression spectrum of Reference 14. In this section, results are discussed for a significant wave height of 12 ft, averaged over a wave period range of 7.28 to 10.92 sec and over a speed range of 15 to 30 knots. (For the rationale underlying this choice of wave height and period, see Section 4.3). To facilitate comparisons, the data have been made non-dimensional by dividing by the appropriate motion value for design 6 (basic form).

The results are presented in Fig. 6. The bar graph form of presentation enables a rapid visual comparison of the seakeeping merits of different designs. The superiority of design 12 is evident. For all four ship motions plotted, it has the lowest values. Moreover, its motions are significantly lower than the basic form. It is also interesting to note that pitch, heave and acceleration are substantially affected by the variations in hull form parameters (especially heave), while relative bow motion is affected to a lesser degree.

Again, it is convenient to study seakeeping trends by comparing ship motions for pairs of designs which differ in only one major hull form parameter. Fig. 7 to 10 show the variations in pitch, heave, relative bow motion and acceleration with variations in L^2/BT , B/T , C_B and C_W . In these figures, each straight line corresponds to

a pair of models in which one major hull form parameter is varied while the other three are held constant at the values given in the legend.

The data show, in general, a remarkable consistency between the trends identified from different pairs of models. Pitch, heave and acceleration are reduced by increasing L^2/BT , B/T and C_W . Increasing C_B results in an increase in these motions. Relative bow motion is reduced by increasing B/T and increased by increasing C_B . For three pairs of designs, L^2/BT has very little effect on relative bow motion, but at low C_W and B/T relative bow motion increases with increasing L^2/BT . For designs with high L^2/BT and low B/T , increasing C_W reduces relative bow motion, but the remaining C_W variations have small effect of relative bow motion.

The comparisons described above are for ships of 3500 tons displacement, and, since block coefficient and L^2/BT vary, cover a range of ship length from 329 to 394 feet on the waterline. Since the effect of changing length is in itself of importance for seakeeping performance, it is useful to establish whether the trends attributed above to C_B and L^2/BT may not be more closely associated with the corresponding changes of length. For a constant displacement of 3500 tons, the increase in C_B from 0.48 to 0.52 requires a reduction in length from 394 feet to 383 feet on the waterline, while the increase in L^2/BT from 150 to 238 is associated with an increase in length from 329 to 383 feet. Calculations have been made for ships of constant length, 383 feet, at the same speeds and sea conditions used for the comparisons between the 3500 ton ships. The effects of variations in L^2/BT and C_B have been re-evaluated on this basis.

The small change in length associated with the change in C_B has little effect on the trends, but, as shown in Fig. 11, this is not the case for L^2/BT . Pitch, for example, now increases slightly as L^2/BT is increased. In the case of acceleration, a trend of acceleration to decrease as L^2/BT increases at constant displacement is reversed at constant length. Changes to the trends of heave and relative motion are much smaller. It is concluded that the beneficial effects of increasing L^2/BT at constant displacement are mainly due to the corresponding increase in ship length.

The effect on seakeeping of variations of parameters included in the series may be summarized as follows:

- (1) Increasing ship length reduces ship motions and accelerations.
- (2) Increasing B/T also reduces motions and accelerations.
- (3) Increasing C_W generally improves seakeeping performance.

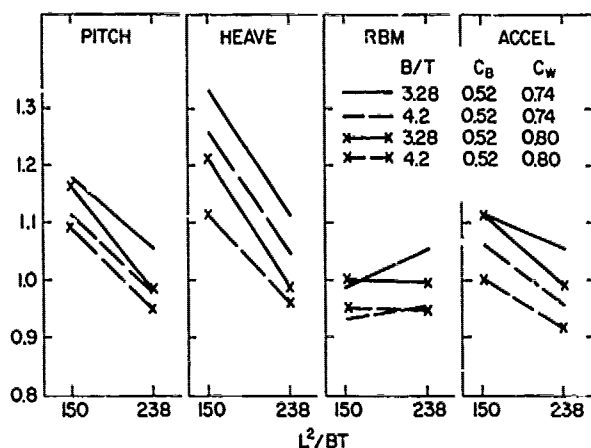


Fig. 7 Effect of L^2/BT on Seakeeping, $\Delta = 3500$ Tons

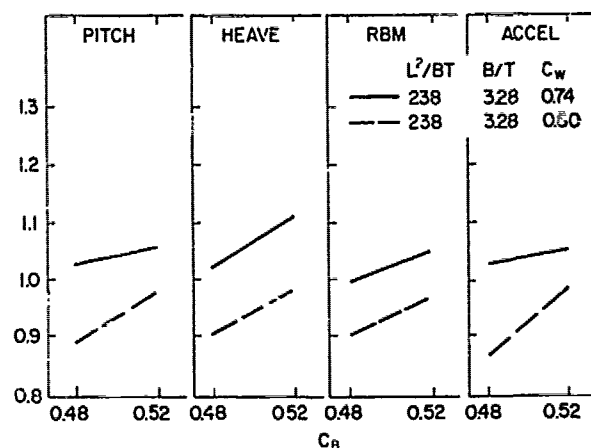


Fig. 9 Effect of C_B on Seakeeping, $\Delta = 3500$ Tons

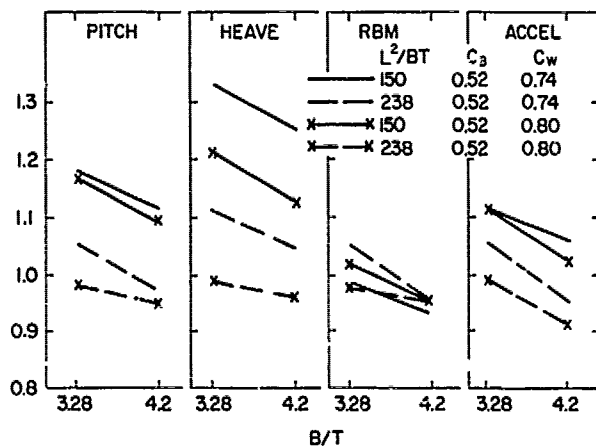


Fig. 8 Effect of B/T on Seakeeping, $\Delta = 3500$ Tons

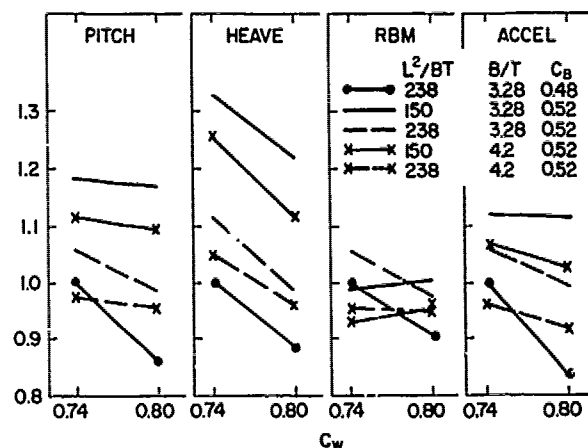


Fig. 10 Effect of C_W on Seakeeping, $\Delta = 3500$ Tons

- (4) Increasing C_B tends to increase ship motions.
- (5) Increasing L^2/BT at constant displacement has a beneficial effect due to the associated increase in length.
- (6) Increase in beam and draft at constant length have a small detrimental effect.

It must be emphasized that these conclusions apply only to frigates or similar vessels with principal particulars within the ranges included in the series. It should be noted, moreover, that in the process of deriving the variations in C_B and C_W from the basic hull form, undefined geometric factors have been changed, and these changes probably influence the results to some extent.

3.4 Model Tests for Design Alternatives

In the ship design process, many factors besides hydrodynamics govern the selection of the principal particulars of the hull. Considerations of payload, mission,

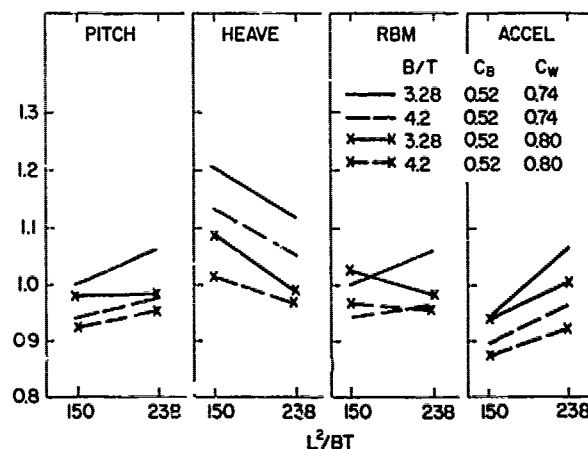


Fig. 11 Effect of L^2/BT on Seakeeping, $L = 383$ Ft

stability and financial aspects all play their part, particularly in fixing displacement, length, beam and draft. Of the four parameters considered in the NRC series, the ship designer probably has greatest freedom to select C_W on the basis of hydrodynamics.

From the calm water point of view, a low C_W associated with a narrow transom would seem to be best for speeds up to about 20 knots, while, for high speeds, a wide transom and high C_W should be better. For seakeeping, increasing C_W tends to reduce motions over the whole speed range.

As the results from the resistance and seakeeping tests of the series were being analyzed, a requirement arose for a ship design which would combine economical cruising speed performance with best possible seakeeping qualities. The results of the series seemed, at first, to suggest that these two requirements are mutually exclusive. A possible way out of this dilemma would be to try to combine an aft body with a narrow transom and low waterplane area with a forebody with large waterplane area. Companion analytical studies had suggested that this approach would be successful.

Since design 12 had shown exceptional performance in waves, it was of interest to test how this might degrade if the bow of this design were coupled to the stern of design 6, which had good performance in calm water at lower speeds. The inverse question of how performance of design 6 in calm water might degrade when the bow was changed to that of design 12 is also relevant.

The three designs under consideration (6, 12 and 12/6) had already been tested in calm water and, as shown in Fig. 5, the effects of changing from the wide stern of design 12 to the narrow stern of design 6 was beneficial up to a speed of about 20 knots. On the other hand, the calm water performance of design 6 was compromised somewhat by the change in bow as shown in Fig. 4.

Seakeeping tests were performed on model 12/6, and the results analyzed in the same way as for the main designs in the series. The results are shown in Fig. 12 which shows that the reduction of C_W in the aft body alone caused only a small seakeeping penalty.

It is concluded that bow form is of major importance for seakeeping and that the stern may be optimized for performance in calm water with little effect on seakeeping.

4. PARAMETRIC STUDY OF FRIGATE SEAKEEPING AND RESISTANCE

Approximately 2 1/2 years after work started on the NRC model series, the Canadian Department of National Defence began a comprehensive frigate design study. In order to provide hydrodynamic data for hull design, a parametric study was conducted of the influence of hull form parameters on

frigate seakeeping and resistance. This study will now be described.

Predictions of resistance for the study were made on the basis of the HSVA "C" series (Section 3). However, since the study took place before seakeeping data were available from the NRC series, the seakeeping performance predictions were made using a ship motion computer program¹⁵. This was not felt to be a serious restriction since for the particular case of ship motions in head seas, the limitations of such computer programs are reasonably well understood and, within these limitations, these programs predict ship motions with engineering accuracy.

Particular confidence can be placed in the results of studies made using ship motion computer programs if the data are interpreted in a comparative manner. Murdey¹⁶ has shown that for frigate-size ships, theory predicts the effect of major changes in hull form or proportions on motions in head seas to within 5% of the motions of the initial design. This means that if, for example, a certain design change is shown by model tests to increase pitch by 15%, theory may be expected to predict a change between 10% and 20%.

An important advantage of using ship motion computer programs in parametric studies is that seakeeping performance of new designs can be compared to existing ships for which model test data are not available.

4.1 Study Plan

The parametric study involved making predictions for a number of different designs, all derived from the same parent ship. The following leading particulars were selected for the parent ship:

Δ	3300 tons
L	380 ft
B	43.8 ft
T	13.4 ft
(M)	7.80
B/T	3.28
C_B	0.52
C_W	0.80

The above values for B/T, C_B and C_W are the same as for design 24 of the NRC model series, while (M) is slightly higher. As with the model series, variations in four parameters were investigated: (M), B/T, C_B and C_W . In all cases but C_W , increments below and above the parent value were taken. Displacement was held constant at 3300 tons - a typical frigate value. The cases included in the study are shown in Table 2.

The range of parameters in Table 2 is generally within the envelope of the NRC model series. In fact, ships, 0, 1, 2, 4, 6, 7 and 8 were based on hulls drawn for that series, with linear dimensions adjusted

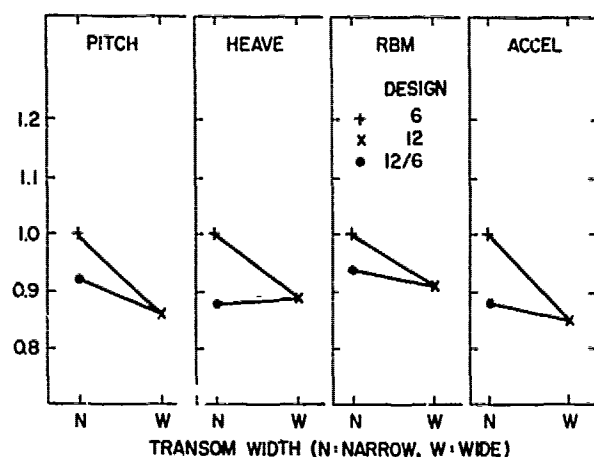


Fig. 12 Effect of Transom Width on Seakeeping, $\Delta = 3500$ Tons

as required. New hulls were generated for ships 3, 5 and 9, using a computer program for warship hull lines generation. It is important to emphasize that the study included no unrealistic hulls and that all parameters were within practical limits.

4.2 Resistance

Residuary resistance was estimated on the basis of both the NRC series and the HSVA "C" series, using the computer programs described in References 17 and 18. Reference 17 ("C" series) was used for the variations in M , B/T and C_B , while Reference 18 (NRC series) was used for the C_W variation. Frictional resistance was calculated using the ITTC 1957 skin friction line. To facilitate comparisons, all resistance data were non-dimensionalized by dividing by the value computed for the parent ship at the corresponding speed.

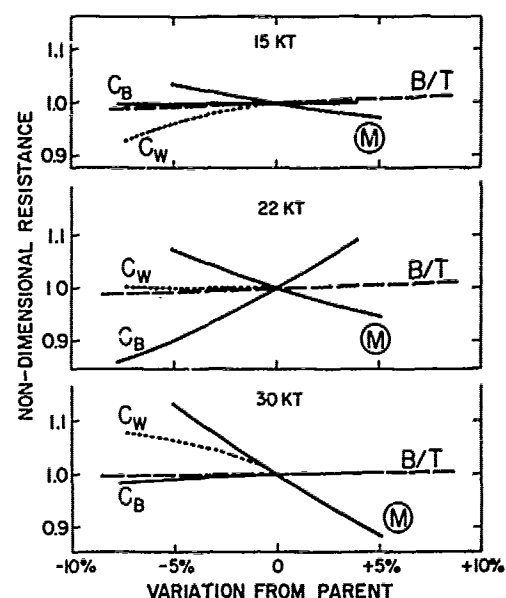


Fig. 13 Effect of Hull Form Parameters on Resistance

Results are plotted in Fig. 13 for ship speeds of 15 and 22 knots, which represent typical frigate patrol speeds, and 30 knots, representing top speed. The ordinate is non-dimensional resistance, computed as described above, while the abscissa is the percentage variation in each hull form parameter from its parent value; for example, the M variation is 5.1% below and above the parent value of 7.80.

Fig. 13 shows that if efficiency at top speed (30 knots) is a paramount consideration, the hull should be more slender (higher M). At 22 knots, C_B is the dominant parameter; reducing C_B to .48 from .52 reduces power requirements at 22 knots by 14%. At 15 knots, only C_W has a sig-

TABLE 2: LEADING PARTICULARS OF PARAMETRIC STUDY VARIANTS

CASE	PARAMETRIC VARIATION	M	C_B	B/T	C_W	L (ft)	B (ft)	T (ft)
0	Parent	7.80	.52	3.28	.80	380.0	43.79	13.35
1	$-\delta M$	7.40	.52	3.28	.80	360.4	44.96	13.71
2	$+\delta M$	8.20	.52	3.28	.80	399.4	42.71	13.02
3	$-\delta C_B$	7.80	.50	3.28	.80	380.0	44.65	13.61
4	$-2\delta C_B$	7.80	.48	3.28	.80	380.0	45.57	13.89
5	$+\delta C_R$	7.80	.54	3.28	.80	380.0	42.97	13.10
6	$-\delta B/T$	7.80	.52	3.00	.80	380.0	41.88	13.96
7	$+\delta B/T$	7.80	.52	3.56	.80	380.0	45.62	12.81
8	$-2\delta C_W$	7.80	.52	3.28	.74	380.0	43.79	13.35
9	$-\delta C_W$	7.80	.52	3.28	.77	380.0	43.79	13.35

nificant effect on resistance; here, the beneficial effect of a narrow transom is readily apparent. However, at 30 knots high C_W (wide transom) is advantageous. At all three speeds, resistance increases slightly with increasing B/T, but the effect is very small.

4.3 Seakeeping

Measures of Seakeeping

As discussed in the Introduction, the seakeeping factors which should have primary influence on frigate hull form design are vertical accelerations, deck wetness and slamming. Consequently, the measures of seakeeping chosen for comparative purposes in the parametric study were:

- (1) root mean square vertical accelerations at .25L (approximate location of forward end of the bridge);
- (2) root mean square relative bow motions (RBM) at the forward perpendicular (for two ships with the same freeboard, the ship with greater RBM will have a wetter deck);
- (3) most probable maximum impact pressure at .2L.

Peak impact pressures were actually calculated at four stations along the forebody (from .1L to .25L), but for the purpose of making comparisons .2L is chosen because in rough seas this is typically the forebody location of maximum slamming pressure. Because of the primary importance of slamming as a seakeeping measure, some details on the impact pressure calculations are given in Appendix A.

For each ship, predictions of short-term statistics in unidirectional head seas were made from the computed response functions using the quadratic regression spectrum of Gospodnetic and Miles¹⁴ to define the seaway. Motions were computed for five significant wave heights: 8, 12, 16, 20 and 24 feet. Wave period was varied with wave height according to the following formula:

$$T_W = 7.73 + .114 H_W$$

where T_W is energy-averaged wave period in seconds and H_W is significant wave height in feet.

Particular consideration was given to the significant wave height of 12 feet, since this is the upper limit of sea state 5, which often figures prominently in operational specifications. For $H_W = 12$, motions were computed for 5 wave periods: $.8T_W$, $.9T_W$, T_W , $1.1T_W$, $1.2T_W$, where $T_W = 9.1$; these motions were then averaged to give the presentative motions for 12 feet significant wave height.

Motions were computed for the speed range 8 - 26 knots. Emphasis was placed on 15 and 22 knots, as these represent speeds at which frigates may spend a great deal of

their operational time.

Basis of Comparison

Computed results for two warships of frigate/destroyer size and with proven satisfactory performance at sea were used to provide the datum for comparative purposes. Leading particulars of these ships are:

Ship designation	F	D
Δ (tons)	2700	4600
L (ft)	356	398
B (ft)	42	50
(M)	7.80	7.31
B/T	3.2	3.2
C_B	0.48	0.52
C_W	0.75	0.77

Seakeeping data were non-dimensionalized using the appropriate values computed for Ship F at 22 knots in seas of 12 feet significant wave height.

Seakeeping Comparisons

Fig. 14 presents computed data comparing the seakeeping performance of the ships considered in the study. Fig. 14 applies to seas of 12 feet significant wave height, with the data averaged over the speed range 18 - 26 knots. The ordinates are vertical acceleration at the bridge, relative bow motion, and impact pressure at .2L. The abscissa is the percentage variation in each parameter from its parent value, as in Fig. 13. It should be noted that considerably more data were generated and analyzed during the study than are presented herein. Since these additional data show the same trends as Fig. 14, they have been omitted in the interests of brevity.

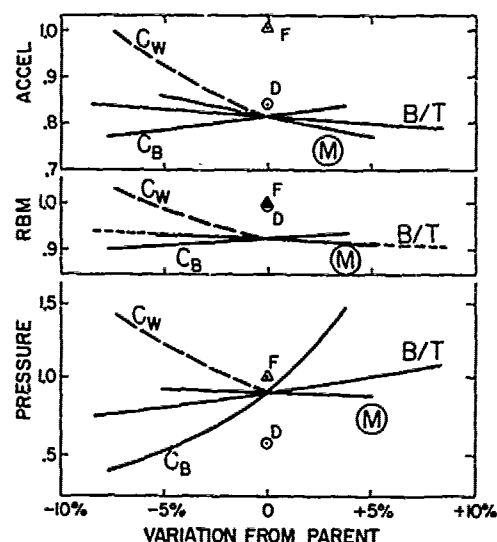


Fig. 14 Motions and Impact Pressures in 12 Ft. Seas, Averaged over 18 - 26 Kt

The seakeeping measures most strongly affected by variations in hull form parameters are impact pressures and vertical accelerations, especially the former. Relative bow motions are affected very little by the parametric variations. However, for almost all the parametric study variants, RBM are lower than for ships F and D.

The benefit of low C_B is clearly demonstrated, as well as the penalties of low C_W . The combination of low C_B and high C_W clearly shows to advantage, with both impact pressures and vertical accelerations significantly lower than ship F. The reduction in slamming pressure achieved by reducing C_B is due mostly to the attendant increase in deadrise angles on the forebody. Although variations in the hull parameters have little effect on relative bow motions, Fig. 14 shows that, even with the same freeboard as ship F, ships with high C_W will have drier decks.

Within practical limits, B/T has little effect. However slamming pressures are alleviated somewhat by reducing B/T to 3.0. Increasing M to 8.2 (lengthening the hull to 400 ft) has some benefit in reducing vertical accelerations, but affects the other seakeeping measures very slightly. Hence, from a seakeeping point of view, there is little justification to lengthen the hull beyond the parent ship value of 380 ft.

Several further remarks on the choice of C_W are in order. During the course of the study, the question arose as to the relative importance of C_{WF} and C_{WA} , the forward and after waterplane coefficients, respectively. This problem was studied analytically, and it was shown that for good seakeeping, C_{WF} should be high while C_{WA} is of lesser importance. Subsequent model tests (see Section 3.4) confirmed this finding.

4.4 Over-All Assessment

On the basis of the parametric study, the following observations are made regarding the influence of hull form parameters on frigate seakeeping and resistance. It is emphasized that these apply strictly to ships of the frigate type.

- (1) Frigates with superior seakeeping qualities to existing classes can be designed without compromising power requirements.
- (2) C_W is a key seakeeping parameter. More specifically, a high value of C_{WF} is required to achieve superior seakeeping. C_{WA} should be determined by powering and arrangement requirements.
- (3) A low value of C_B is very beneficial for seakeeping. Low C_B also reduces power requirements at intermediate speeds.

- (4) Best seakeeping is obtained with a hull combining high C_{WF} with low C_B . Such a hull has bow sections which are very fine (V-form) near the keel and a full waterplane.
- (5) Although increases in length will always improve seakeeping, equivalent percentage changes in C_W and C_B have far greater effect. The choice of M should therefore be dictated primarily by powering and arrangement considerations.
- (6) B/T has the least effect of all the parameters considered on both seakeeping and powering. Thus, B/T should be chosen primarily on the basis of stability. Remember, however, that slamming qualities will deteriorate somewhat with increases in B/T.

4.5 Recommended Hull Form

A primary objective of the parametric study was to develop a hull form which would achieve superior seakeeping qualities without compromising resistance. This hull form may be viewed as the hydrodynamicist's recommendation to the frigate designer. The process of deriving this hull form will now be described.

The performance of this frigate, henceforth called ship X, will then be compared to three warships of frigate/destroyer size all of which enjoy above average reputations for seakeeping. Two of these are the ships F and D, previously introduced, while the third, called ship FRN, has the following leading particulars:

Δ	2880 tons
L	360 ft
B	41 ft

Choice of the hull form parameters for ship X was based on the results of the foregoing parametric study. Seakeeping considerations favour high C_W and low C_B , practical upper and lower limits are $C_W = .8$ and $C_B = .48$. Taking B/T = 3.0 alleviates slamming pressures somewhat, while lengthening the hull within reasonable limits is of little overall seakeeping benefit. Fortunately, as seen in Section 4.2, powering considerations also favour $C_B = .48$ and B/T = 3.0, although not as strongly as seakeeping. C_W requirements are contradictory, with low C_W beneficial at 15 knots and high C_W beneficial at 30 knots.

It was assumed that a length of 380 feet met powering and arrangement requirements and that the seakeeping and top speed resistance benefits of high C_W outweighed the resistance penalty in the vicinity of 15 knots. Hence, the leading particulars of ship X were chosen as follows:

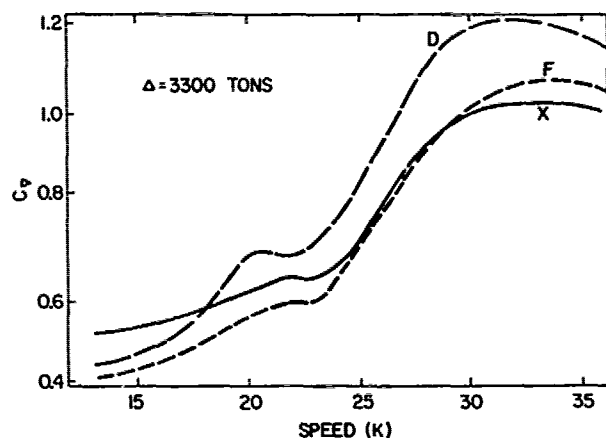


Fig. 15 Example Hull vs. Existing Ships - Resistance

Δ	3300 tons
L	380 ft
B	43.6
T	14.5
\bar{M}	7.80
B/T	3.0
C_B	0.48
C_W	0.80

The lines for ship X were developed from ship 4 of Table 2 (design 12 of the NRC Hull Form Series) by linear adjustments in beam and draft.

Fig. 15 presents resistance predictions for ships F, D and X. (A curve for ship FRN is not shown because it is virtually coincident with the curve for ship F.) These predictions have been made from the NRC series using the computer program of Reference 18. To make the resistance comparisons strictly on the basis of hull form, all predictions have been made for a displacement of 3300 tons, with the principal dimensions of ships F and D scaled accordingly. Because the emphasis is on comparison, the data are plotted relative to the C_V of ship X at 30 knots.

Fig. 15 shows that hull form X is generally superior to D, especially at high speed. This is primarily a consequence of the differences in \bar{M} (7.31 and 7.80 for ships D and X, respectively). F is slightly better than X at patrol speeds, but slightly inferior at high speed. This is a direct consequence of the choice of high C_W , and associated wide transom, for ship X. As noted in Section 3.4, this patrol speed resistance penalty may be reduced by narrowing the transom, without incurring an appreciable seakeeping penalty.

Fig. 16 and 17 present computed accelerations and impact pressures for ships X, F, D and FRN at speeds of 15 and 22 knots. As in Fig. 14, the plotted data are non-dimensionalized using computed results for ship F at 22 knots in 12 ft seas.

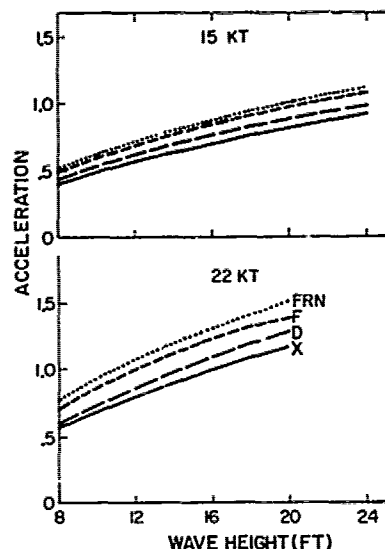


Fig. 16 Example Hull vs. Existing Ships, Accelerations

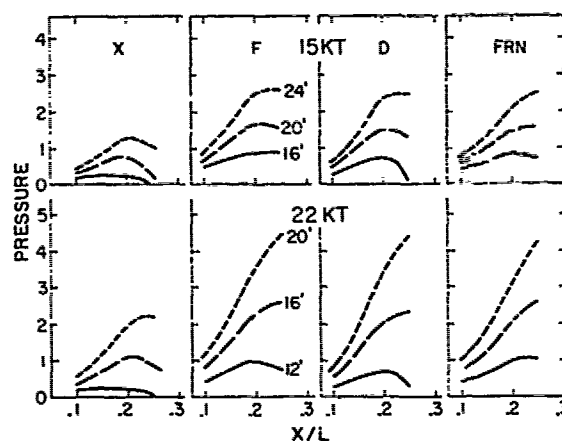


Fig. 17 Example Hull vs. Existing Ships, Impact Pressures

In Fig. 16, vertical accelerations at .25L are plotted against significant wave height. It is seen that a noteworthy reduction in accelerations has been achieved in ship X. For example, at 22 knots in 12 ft seas, accelerations are 20% higher for ship F than for ship X.

Fig. 17 compares impact pressures over the forward quarter of the hull length. At 15 knots data are presented for seas of significant height 16 - 24 ft, while at 22 knots results are plotted for 12 - 20 ft. The superiority of ship X with regard to slamming is clearly evident. As a general rule, in seas of a given wave height, ship X experiences roughly the same impact pressures on the forebody as the other ships experience in seas 4 ft lower. For example, at 22 knots the $H_W = 16$ impact pressure curve for ship X is roughly similar to the $H_W = 12$ curves for the other three ships.

Since slamming has been consistently identified by frigate operators as the predominant speed-limiting factor in rough seas, this improvement in slamming characteristics is of special significance.

It is concluded that in ship X, superior seakeeping qualities to existing frigate classes are achieved without unduly compromising resistance.

5. DESIGN APPLICATION

5.1 Development of a Frigate Hull Form

The parametric study described in Section 4 was undertaken in order to provide hydrodynamic guidance for a frigate design study. The process of developing a hull form for this design study will now be described. In particular, it will be shown how practical design considerations force changes from the hull form (such as that of ship X) derived primarily on the basis of seakeeping and resistance.

At the beginning of this project, the following information was available:

- (1) results of the parametric study;
- (2) resistance data for twenty-two models of the NRC series;
- (3) preliminary seakeeping data for several key models of the NRC series.

As the work progressed, further model seakeeping data became available and influenced the design process. In general, these data provided experimental verification of the trends identified in the parametric study.

The choice of leading particulars and hull form coefficients was governed by the following principles:

- (1) Choose length and beam on the basis of arrangement and powering considerations.
- (2) Choose B/T primarily to satisfy stability requirements.
- (3) Keep C_B low for both low resistance and good seakeeping.
- (4) Keep C_{WF} high for best seakeeping.
- (5) Keep bow sections very fine near the keel.
- (6) Choose C_{WA} to meet arrangement and powering requirements.

Given these ground rules plus the data available from the model tests and the parametric study, the following hull form coefficients were chosen to start body plan development:

$$\begin{aligned} B/T &= 3.28 \\ C_B &= 0.48 \\ C_{WF} &\text{ as for series design 12} \end{aligned}$$

Initially, two stern variants were considered:

- low C_{WA} (narrow transom) as for design 6
- high C_{WA} (wide transom) as for design 12.

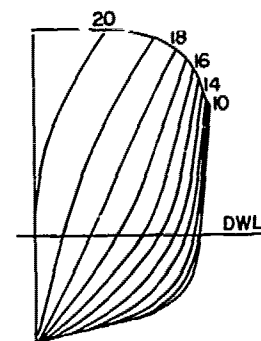


Fig. 18 Bow Sections - First Iteration

Design of the bow sections used the bow of design 12 as the starting point, Fig. 1. It was considered that this bow had two structurally undesirable features: concave sections near the stem and a knuckle too near the design waterline. These were eliminated, resulting in the forebody plan of Fig. 18. Subsequent development of bow sections in the design process was based on Fig. 18.

As the design study progressed, operational requirements became better defined and necessitated substantial increases in principal dimensions to accommodate changed payload and fuel. In particular, upper deck area requirements drove length and beam to approximately 400 and 48 ft, respectively while internal volume requirements pushed C_B to roughly 0.50 and displacement to 4300 tons. Arrangement requirements also governed the final choice of stern configuration: a wide transom was selected because it was felt that the advantages with regard to equipment fitting offset the patrol speed resistance penalty.

Throughout the manipulations of hull form which accompanied evolution of the design, those characteristics of Fig. 18 with primary influence on seakeeping were preserved. In particular, careful attention was paid to deadrise angles, bow fineness and C_{WF} . At each stage in the development, seakeeping assessments were made to ensure that performance levels were maintained.

The leading particulars for the final hull form of the design study are listed below.

Δ	4300 tons
L	404 ft
B	48.5 ft
T	15.3 ft
Φ	7.61
B/T	3.18
C_B	0.50
C_W	0.79

5.2 Evaluation of the Final Design

The design developed in the previous

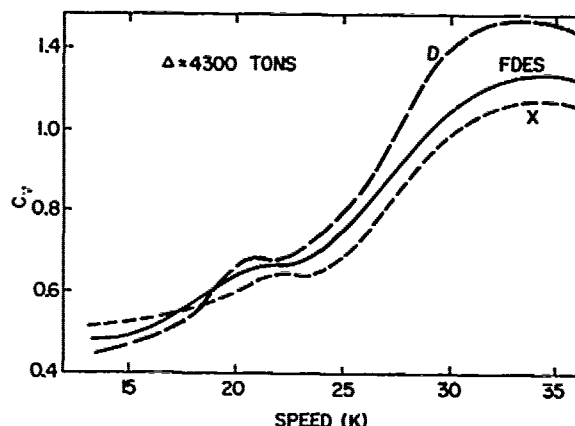


Fig. 19 Ships FDES, X and D - Resistance

section was evaluated in two ways. First, it was compared with designs X and D (introduced in Section 4 above) using data interpolated from the NRC series for resistance and theoretical predictions for seakeeping; second, a model was made and tested, and the results compared with two designs from the NRC series.

Comparison with X and D

The resistance of the final design, henceforth called ship FDES, was estimated from the NRC series in the same way as for design X, the example used in Section 4.5. Fig. 19 compares the estimated resistance for FDES with the estimated resistance of design X and ship D, both scaled to 4300 tons displacement. The ordinate is scaled relative to the C_D of ship X at 30 knots.

FDES is not as good as design X, although generally better than D. The difference between FDES and X may be attributed to the lower M of FDES, 7.6 compared with 7.8 for design X, and the increased C_B , 0.50 compared with 0.48.

Following the example given in the previous section, the seakeeping performance was assessed by comparing predictions of acceleration at $0.25L$ and impact pressures over the forward quarter of the hull length for speeds 15 and 22 knots. In making the seakeeping comparisons, the displacements of design X and ship D have been maintained at their original values (3300 and 4600 tons respectively). This enables seakeeping comparison of the final design with the ships of the parametric study. As in Section 4, seakeeping data are non-dimensionalized using values computed for Ship F at 22 knots in seas of 12 ft significant wave height.

Fig. 20 shows that FDES is expected to have virtually identical vertical accelerations to design X. The computed impact pressures, Fig. 21, show a significant improvement over ship D for the whole range of speeds and wave heights investigated. Thus, despite the influence of operational

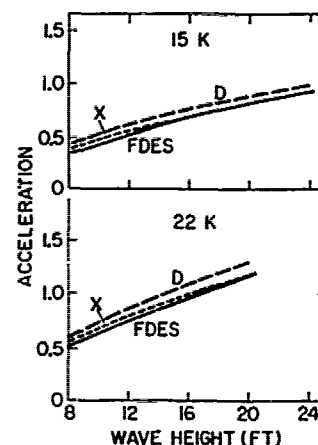


Fig. 20 Ships FDES, X and D - Accelerations

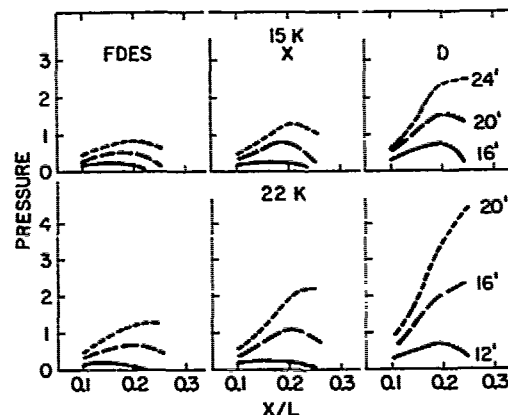


Fig. 21 Ships FDES X and D - Impact Pressures

requirements on the final design, the choice of deadrise angles and waterplane characteristics in the forebody have still resulted in a hull form which may be expected to have superior overall seakeeping performance.

Model Test Results

A 1:25 scale model, $L = 16.177$ ft, was made to the final lines. Resistance and seakeeping experiments were carried out with the model, designated 316, at NR' using identical techniques to those used for the hull form series, (Section 3).

The results of the resistance tests are shown in Fig. 22, in comparison with data for designs 6 and 12 from the series. Design 6 is used for comparative purposes because it is the parent form, while design 12 is chosen because it is the best seakeeping form tested to date. The comparisons are made on the basis of a displacement of 4300 tons, and the data are scaled relative to the C_D of the design 6 at 30 knots. As for the other comparisons of resistance in this paper, ship predictions have been made for the naked hulls using the 1957 ITTC line with no additional correlation allowance.

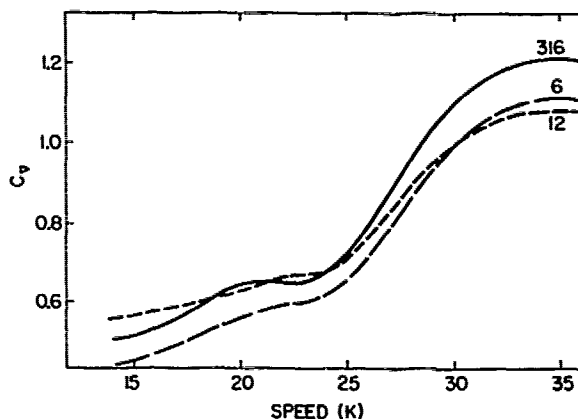


Fig. 22 Models 316, 6 and 12 - Resistance

Up to about 24 knots, the results for Model 316 fall roughly where they were expected, close to design 12. Design 6 has a lower resistance over the whole speed range under consideration due to its higher M , lower C_B and narrow transom. On the other hand, design 12, with the extreme 'v' bow and wide transom has generally higher resistance than Model 316, except at speeds over 24 knots, where the wide transom adds to the beneficial effects of higher M and lower C_B .

Fig. 23 and 24 present comparisons of accelerations and impact pressures between Model 316 and designs 6 and 12. The predictions are for 4300 tons displacement and in each case are based on model test results. Since the model test program did not include the measurement of impact pressure, these data were calculated from the measured motions using the method outlined in Appendix A. The data are non-dimensionalized using values predicted for design 6 at 22 knots in seas of 12 ft significant wave height.

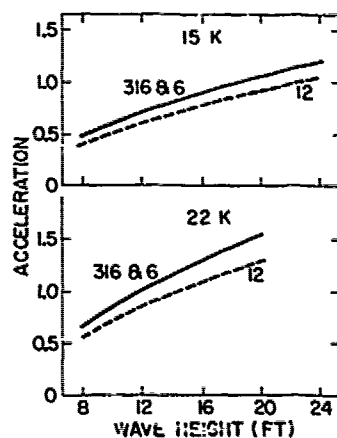


Fig. 23 Models 316, 6 and 12 - Accelerations

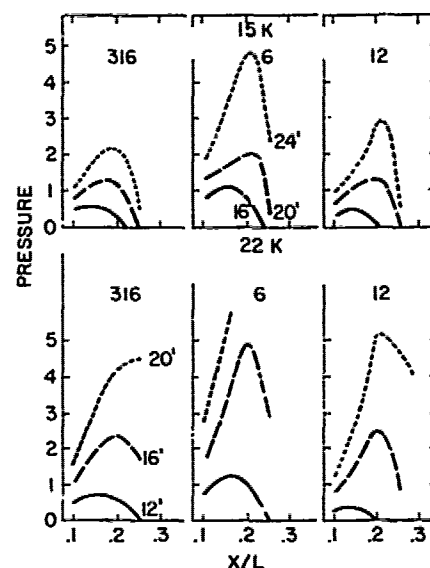


Fig. 24 Models 316, 6 and 12 - Impact Pressures

The accelerations for Model 316 are a little disappointing, being almost identical to design 6 and not approaching the superior performance of design 12. In this case the shorter length of Model 316 (404 ft compared to 421 ft for designs 6 and 12) and the increased C_B (from 0.48 to 0.50) are primarily responsible. A comparison of the same three designs for the same length (differing displacements) puts 316 between 6 and 12.

As had been expected from the analytical comparison, Fig. 21 above, the impact pressures are much more encouraging. Fig. 24 indicates that despite the slightly higher motions, the performance of 316 in this critical area is generally slightly better than design 12 and substantially superior to design 6.

6. CONCLUSIONS

- (1) Important improvements in the seakeeping qualities of frigates may be achieved by the selection of appropriate hull design parameters.
- (2) The development of a hull form with superior seakeeping may require a compromise with resistance characteristics in calm water. For seakeeping, the design of the forebody is more critical than the aft-body and major changes in aft-body may be made to improve calm water performance with little effect on seakeeping.
- (3) The NRC Hull Form Series for Fast Surface Ships provides a valuable data base for making seakeeping and resistance trade-offs in frigate hull form design.
- (4) A method of hull design combining analytical studies, analysis of the results of methodical series for both

seakeeping and resistance, and interpretation of test results with models of specific designs enables evaluation of designs to be made more quickly and with more confidence than by use of any of these approaches alone.

REFERENCES

1. Schmitke, R.T., "The Influence of Displacement, Hull Form, Appendages, Metacentric Height and Stabilization on Frigate Rolling in Irregular Seas", SNAME Ship Technical and Research Symposium, June 1980.
2. Whitten, B.T. and Schmitke, R.T., "SHIPMO - A FORTRAN Program for Prediction of Ship Motions in Waves", DREA Technical Memorandum in review.
3. Gertler, N., "A Re-analysis of the Original Test Data for Taylor Standard Series", DTMB Report No. 806, 1952.
4. Grim, O. and Kracht, A., "Widerstand, Propulsion, Bewegung und Beanspruchung Schneller Verdrängungsfahrzeuge in Glattem, Wasser und in Regelmässigem Seegang", Institute für Schiffbau der Universität Hamburg, Bericht NR.167, July 1966.
5. Yeh, H.Y.H., "Series 64 Resistance Experiments on High Speed Displacement Forms", Marine Technology, Vol. II, No. 3, 1965.
6. VanMater, P.R., Zubal, R.B. and Bays, P.N., "Hydrodynamics of High Speed Ships", Davidson Laboratory Report No. 876, 1961.
7. Bailey, D., "The NPL High Speed Round Bilge Displacement Hull Series", Royal Institution of Naval Architects, Marine Technology Memorandum No. 4, 1976.
8. Lindgren, A. and Williams, A., "Systematic Tests with Small Fast Displacement Vessels Including a Study of the Influence of Spray Strips", SSPA Report No. 65, 1969.
9. Comstock, J.(Ed), Principles of Naval Architecture, published by the Society of Naval Architects and Marine Engineers, 1967.
10. Moor, D.I., "Effects on Performance in Still Water and Waves of Some Geometric Changes to the Form of a Large Twin-Screw Ship", Trans. SNAME, Vol. 78, 1970.
11. Moor, D.I. and Murdey, D.C., "Motions and Propulsion of Single Screw Models in Head Seas", Trans. RINA, Vol. 1010, 1968.
12. Bowden, B.S. and Neville, E.J., "Pitch and Heave in Irregular Head Seas. A Comparison of Experimental and Theoretical Value for 50 Hull Forms", NPL Ship Division Report TM401, 1974.
13. Loukakis, T.A. and Chrysosostomidis, C, "Seakeeping Standard Series for Cruiser Stern Ships", Trans. SNAME 1975.
14. Gospodnetic, D. and Miles, M., "Some Aspects of the Average Shape of Wave Spectra at Station 'India' (59° 19'W)", International Symposium on the Dynamics of Marine Vehicles and Structures in Waves, London, April 1974.
15. MacKay, M. and Schmitke, R.T., "PHHS - A FORTRAN Program for Ship Pitch, Heave and Seakeeping Prediction", DREA Technical Memorandum 78/B, April 1978.
16. Murdey, D.C., "Seakeeping of the NRC Hull Form Series: A Comparison Between Experiment and Theory", 19th American Towing Tank Conference, Ann Arbor, Michigan, July 1980.
17. Drummond, T.G., "A Program for the Comparative Estimation of Displacement Ship Resistance and Power", DREA Working Paper with Limited Circulation, September 1976.
18. Schmitke, R.T., "A Computer Program for Fast Surface Ship Resistance and Power Estimation". DREA Technical Memorandum 78/E, August 1978.
19. Ochi, M.K. and Motter, L.E., "Prediction of Slamming Characteristics and Hull Responses for Ship Design", Trans. SNAME, Vol. 81, 1973.
20. Schmitke, R.T., "Improved Slamming Predictions for the PHHS Computer Program", DREA Technical Memorandum 79/A, February 1979.
21. Conolly, J.E., "Standards of Good Seakeeping for Destroyers and Frigates in Head Seas", International Symposium on the Dynamics of Marine Vehicles and Structures in Waves, London, April 1974.
22. Chuang, S.L., "Slamming Tests of Three-Dimensional Models in Calm Water and Waves", NSRDC Report 4095, September 1973.

APPENDIX A

IMPACT PRESSURE CALCULATION

The calculation of impact pressures is based on the statistical formulation of Ochi and Motter¹⁹. The probable maximum slamming pressure at a given hull section in h hours of ship operation time is given by²⁰

$$P_h = \rho k \sigma_{RV}^2 \ln \{ 3600 h \sigma_{RV} / (2\pi \sigma_{RM}) \exp(-.5T^2/c_{RM}^2) \}$$

where σ_{RM} and σ_{RV} are rms relative motion and velocity, respectively, T is draft and k is the form factor. k is evaluated using the method proposed by Conolly²¹: the hull section is regarded as a truncated wedge with deadrise angle β , as defined in Fig. 25, and k is calculated using experimental data on slamming of wedge-shaped bodies²². Specifically, the following empirical expression¹⁵ is used in this paper:

$$k = 1 + [1 - \exp(-5\beta)] (.5\pi \cot \beta)^2$$

Equivalent deadrise angles for a typical V-bow frigate are shown in Fig. 25. Note that for the results presented in this paper, $h = 1$.

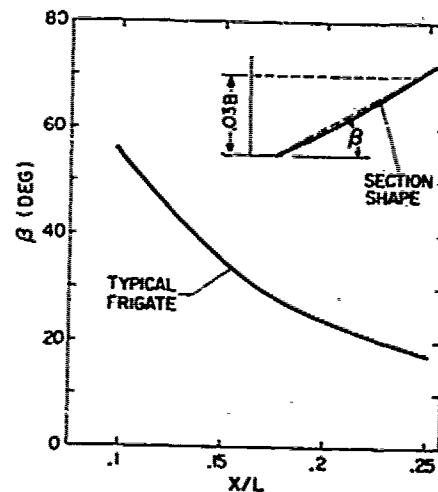


Fig. 25 Equivalent Deadrise Angles

Discussion

N.K. Bales (DTNSRDC)

Mr. Schmitke and Mr. Murdey describe a frigate hull design process which effectively utilizes state-of-the-art technologies in the areas of seakeeping and calm-water resistance. My own work attempting to relate hull geometry to seakeeping and thence to synthesize seakeeping optimum hull geometries^{1,2}, though exclusively analytical, is predicated upon broadly similar reasoning; and leads to similar results. There are, however, significant differences. I consider a larger set of potentially limiting responses, and take them to be equally important. My rationale for restricting the trend identification process to long-crested, head seas is very different; and requires subsequent validation in short-crested seas and at oblique relative headings. I take the viewpoint that good seakeeping should accrue as a result of qualitatively similar hull configurations for all classes of displacement monohulls, and base much of my work for destroyer-type hulls on earlier results for dry cargo ship hulls. Finally, I relate seakeeping to a different set of hull parameters.

The last difference cited appears most important for a formal discussion. In concluding their description of the NRC Series, Mr. Schmitke and Mr. Murdey observe that, in the course of standard series hull form changes, parameters other than those explicitly varied are also modified; and that these incidental modifications may influence the results obtained. This is, in fact, probably the greatest danger associated with standard series techniques. If the incidentally-modified parameters happen to be those which govern the output of the series, direct interpolations can lead to erroneous design decisions.

For a hull of given size, analytical procedures indicate that vertical-plane seakeeping responses are essentially governed by the distributions of beam, draft, and sectional fullness over the length of the hull. The conventional, naval architectural parameters which I think provide a minimal description of these distributions are the waterplane coefficients forward and aft of amidships, C_{WF} and C_{WA} ; the draft-to-length ratio, T/L ; the ratio of the distance between the forward perpendicular and the cut-up point to length, c/L ; and the vertical prismatic coefficients forward and aft of amidships, C_{VPF} and C_{VPA} . In my work on destroyer-type hulls, construed to include frigates, these parameters are related to seakeeping as

$$\begin{aligned}\hat{R} = & 8.442 + 45.104 C_{WF} + 10.078 C_{WA} \\ & - 378.465 (T/L) + 1.273 (c/L) \\ & - 23.501 C_{VPF} - 15.875 C_{VPA}\end{aligned}$$

where \hat{R} is an estimator of seakeeping rank which varies from the order of 1.0 for hulls with very poor seakeeping qualities to the order of 10.0 for hulls with excellent seakeeping qualities.

An indication of the validity of the estimator can be obtained using the results of the NRC Series. From Figure 1, it appears that the applicable form coefficients are approximately as follows:

Design	C_{WF}	C_{WA}	C_{VPF}	C_{VPA}
6	0.62	0.86	0.72	0.58
12	0.68	0.92	0.66	0.54
18	0.62	0.86	0.78	0.62
24	0.68	0.92	0.72	0.58

As I understand the design of the series, these coefficients should be fixed for the associated columns in Table 1. Further, c/L appears, again from Figure 1 and the series description, to be fixed at about 0.6 for all of the designs. Finally, a value of T/L for each design can be computed from L^2/BT and B/T as used to define the series. With these definitions, seakeeping rank can be estimated for any design in the series. For instance, it equals 6.1 for the "parent" Design 6.

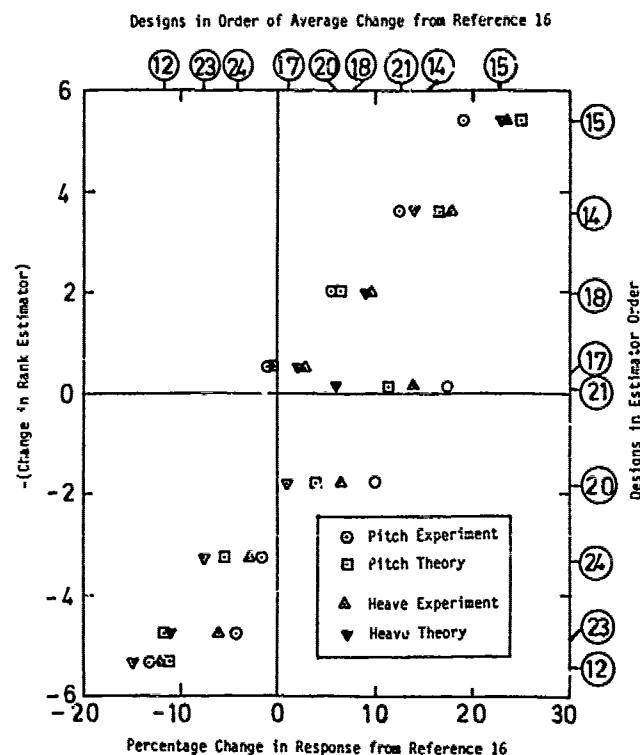
In Reference 16, Mr. Murdey gives percentage changes with respect to the parent in pitch and heave both as measured and as computed for a critical combination of operating conditions. The following figure exhibits the correlation between the differences reported in Reference 16 and those computed from the estimator given above. It is as would be expected for a valid but primitive and rather generalized estimator applied to particular conditions. There is considerable scatter at midrange, but the response extremes are indicated with reasonable accuracy.

The NRC Series has overall waterplane coefficient as a defining parameter. Overall block coefficient is also used, and the discussion implies that this parameter is considered an adequate measure of sectional fullness. Draft and length are used in defining the series but are always explicitly related to beam. The authors comment on the relevance of forebody versus afterbody parameters, but never make them explicit and do not make a distinction between them in defining the series. I would suggest that they make the forebody/afterbody distribution of form coefficients an integral element of the series definition, and that they consider the possibility of using the parameters in the estimator cited above.

The following table recasts Table 1 using the parameters of the estimator to order the series designs. The numbers given parenthetically after each design number are the average of the percentage changes in pitch and heave from Reference 16 and minus the estimated rank difference

for that design with respect to the parent design. In this form, the averages of the hull-to-hull differences in pitch and heave show moderate coherency. The estimator results indicate that the poorest seakeeping hulls in the series (lower right in the table) have been tested, but that those with the best seakeeping (upper left in the table) have not. With respect to the designs estimated to have extreme seakeeping qualities, it should, however, be pointed out that both $T/L = 0.028$ and $T/L = 0.045$ are outside the strict range of the rank estimation equation. It will obviously be of considerable relevance to determine whether or not Designs 12 and 7, 24 and 19, et al., have similar seakeeping characteristics.

Quite aside from the foregoing differences of opinion as to the hydrodynamic basis of good seakeeping, one must inquire as to the success of the final product. In the case of Design FDES, it appears that Mr. Schmitke and Mr. Murdey have negotiated the treacherous waters of design tradeoffs with minimal compromise of their hydrodynamic principles. The level of detail provided regarding the design is inadequate for a rigorous assessment, but from the description provided, my perception is that Design FDES probably has an estimated seakeeping rank on the order of ten. Such being the case, it will be, ton-for-ton, among the best seakeeping hulls afloat. I wish that I could say that I had done as well with my own efforts to support the hull design process.



Correlation between NRC series results and rank estimator

The NRC series ordered by estimator parameters

$\frac{L^2}{BT}$	$\frac{B}{T}$	$\frac{T}{L}$	C_B	0.48	0.52	0.48	0.52
			C_H	0.80	0.80	0.74	0.74
			C_{WF}/C_{WA}	0.68/0.92	0.68/0.92	0.62/0.86	0.62/0.86
			C_{VPF}/C_{VPA}	0.66/0.54	0.72/0.58	0.72/0.58	0.78/0.62
238	5.20	0.028		10 (*, -8.4)	22 (*, -6.3)	4 (*, -3.0)	16 (*, -1.0)
	4.20	0.032		11 (*, -6.9)	23 (-8.1, -4.8)	5 (*, -1.5)	17 (+0.8, +0.5)
	3.28	0.036		12 (-11.9, -5.4)	24 (-4.3, -3.3)	6 (0, 0)	18 (+7.6, +2.0)
150	5.20	0.036		7 (*, -5.4)	19 (*, -3.3)	1 (*, 0.0)	13 (*, +2.0)
	4.20	0.040		8 (*, -3.8)	20 (+5.4, -1.8)	2 (*, +1.5)	14 (+15.2, +3.6)
	3.28	0.045		9 (*, -2.0)	21 (+12.4, -0.1)	3 (*, +3.4)	15 (+22.7, +5.4)

* Value Not Available

The subject treated in this paper is one of the eventual goals of naval ship designers and opens a new challenging avenue for ship hydrodynamicists.

With a short duration of my experience in the parametric studies for the seakeeping hull designs for conventional catamarans, I can fully appreciate the extent of endeavors involved in studies such as those presented here. Contrary to ones investment of a great deal of time and effort, a subject like this would always induce differing opinions from the people who are also engaged in similar work. One of the major arguing points would be how one should define the seakeeping qualities and predict these qualities. For example, should the severity of slamming be represented by a point pressure or the integrated pressures over a certain unit area of the hull? Or, even a question such as "Is the peak intensity of the slamming pressure during unit time of operation more important than the frequency of occurrence of the slamming with the lesser intensity in the peak pressure?" could be argued on. Again, even for the slamming alone, the criterion can depend upon whether the local impact or the broad impact causing the hull girder vibration should be our major concern.

As described briefly above, unless we narrow down the criteria involved in seakeeping to a manageable level (may be an impossible task), the trade-offs between the seakeeping and resistance could remain a formidable task to accomplish. However, a paper such as this seems to me very encouraging since it provides not only valuable guidelines for the future investigations in similar nature of works but also amplifies the necessity for changing the traditional design concept of "the resistance first and the seakeeping later."

I would like to congratulate the authors for the pioneering and inspiring work they have accomplished.

E.V. Lewis (Consultant)

This paper is significant, not only for providing useful guidance for the design of frigates with good seakeeping performance, but for developing a systematic way to show graphically the effect of important hull parameters on performance. The paper stresses the importance of length as a seakeeping parameter and gives particular attention to the problem of isolating it from other parameters. The authors favor the slenderness parameter L^2/BT as a basis for plotting, since it does not involve C_B . This parameter has merits, and in Fig.7 trends of length are easily shown. But since both Δ and C_B are held constant, the figure could just as well have been plotted against M . Furthermore,

Fig.9, which purports to show the effect of C_B alone must involve a change in length, along with other dimensions, as well, to hold Δ constant. (Fig.14 makes use of M instead of L^2/BT .)

This writer long ago recommended the use of $L/V^{1/3}$ as a parameter*, since in design one is concerned mainly with ships of different lengths to meet the same requirements, and hence to have the same (approx.) displacement. Another consideration in that earlier work, not considered in this paper, was the influence of natural periods of pitch and heave on performance. It was shown* that the generally favorable effect of length, as reported here, is the result of the influence of length on pitching period — provided the ship is in the subcritical range of operation.

The paper also stresses the favorable effect of increasing C_W on motions. Again — as pointed out in my earlier work*—this advantage (greater damping) can be related to its favorable effect on natural periods. Hence, it would be of interest to make a supplementary study of the natural periods of all models tested. If for any reason it is difficult to determine these values experimentally, then they can be established by plotting motion amplitudes vs. speed with constant wave length (and height) and noting the encounter frequency corresponding to the peak response.

The theoretical parametric study, showing results for irregular seas, is interesting in that it leads to similar conclusions as the model tests. But again no consideration is given to the effect of natural frequencies, and it would be of interest to plot the sea spectrum and the RAO's on a frequency base for a number of cases as a means of clarifying and explaining the trends shown, for example, in Fig.14.

The summary under "Over-All Assessment" (p.467) seems to be an excellent guide for frigate designers. Exception might be taken only to the statement under (5) that the choice of M "should be dictated primarily by powering and arrangement considerations", since it follows an admission that "increases in length will always improve seakeeping". The only obvious reason for caution — from the seakeeping viewpoint — in increasing length seems to be to avoid reducing draft to the point that bow emergence and slamming become serious. Fig.14 shows an increase in bow pressures with increase in B/T , and hence reduction in draft, but not with reduction in M . **

* E.V.Lewis, "Ship Speeds in Irregular Seas" Trans. SNAME, (1955)

**Hamlin and Compton, "Evaluating the Seakeeping Performance of Destroyer-type Ships in the North Atlantic", Marine Technology, Jan. (1970)

In conclusion, this is a valuable paper that deserves a great deal of careful study. It may well be that the results have greater generality than the authors suggest.

B. Johnson (US Naval Academy)

May I add my congratulations to the authors on their very excellent paper. Such efforts are very important to ship designers who are faced with maintaining mission effectiveness (good seakeeping qualities) while attempting to improve fuel efficiency, especially at cruising speeds.

The section which reviews the sources of information is a good "state-of-the-art" summary. What the overall assessment section points out, however, is that some of the most important parameters such as C_{WF} and C_{WA} are frequently not tabulated in comparative seakeeping studies, including this one. K. Bales of DTNSRDC has suggested that C_{yPF} and C_{yPA} are also significant for good seakeeping performance along with the after cut up ratio C/L . I would like to request that the authors supply an additional table which lists these important parameters for each hull form.

G. Bellone (Cantieri Navali Riuniti)

As we had available Dr. Schmitke's seakeeping calculation program, particularly fit for slender, high speed vessels, and frigates are our company's main production, we have carried out a systematic analysis similar to the one which has been described by the author. Here I want to show some of the results we obtained, most of which are in good agreement with those obtained by Dr. Schmitke. We checked the parameters indicated in Table 1, together with the range of their variation. The study has been divided into 2 phases, of which only the first (regarding C_{WL} , C_B , $L/\Delta^{1/3}$) has been so far completed. In Tables 2, 3 and 4 indications about the basic form hull, which has generated all the others, the sea state representation employed in the computation, and the criteria which have allowed the formulation of an "effectiveness index" for the different examined solutions, are reported.

For the different sea states, the above said criteria, have led to the quantification of a "maximum sustainable speed" which has been considered as the index representative of the good seakeeping behaviour of the different hulls checked. In Table 5 these speeds are shown for sea state 6 (for sea state 5 similar trends have been observed, while for lower sea states no limitations to maximum speed were found).

As regards the conclusions that can be drawn from this study, only two points

differ from the observations made by the author:

(a) Vertical accelerations at bow seem to us strongly affect the seakeeping behaviour of a ship and create the necessity of a speed reduction before the probability of slamming gets its upper limit.

(b) The variations of parameters C_B and $L/\Delta^{1/3}$, according to our computations, have nearly the same effect on seakeeping. (The author, on the contrary says that equivalent percentage change in C_B has far greater effect).

Therefore the questions are the following:

(1) Is it possible that these differences are due to the fact that we have chosen the probability of slamming at bow as a restrictive criterion, instead of the intensity of the slamming impact pressure?

(2) We would extend our parametric study to the longitudinal distribution of weights on board (pitch gyration radius K_{yy}), but the author, in this and previous papers states that the influence of this parameter is negligible. Could he explain more in detail what led him to this conviction? To my opinion, based only on an impression, it should be a rather important element.

Author's Reply

R.T. Schmitke (DREA) and D.C. Murdey (NRC)

We thank Mr. Bales for his discussion, which is based on his own extensive work on this subject.

We agree with him that it would be desirable to include more parameters in the series. However, we have already included four parameters, plus bow and stern interchanges, and this makes a total of ninety-six models. To include more parameters, although desirable, is quite impractical.

We would like to add that before embarking on the series, we performed a comprehensive analytical study of seakeeping to provide guidance for experiment design. In this study, we investigated approximately twelve hull form parameters, of which the most important turned out to be L^2/BT , B/T and C_{WF} . C_B (or C_P) was found to be of secondary seakeeping importance, but was included in the series from resistance considerations.

Mr. Bales mentions the possibility that direct interpolation of the series data may be misleading. In this context, we are happy to report that for model 316, the series interpolation agrees very well indeed with the model test data, for both resistance and seakeeping. We had intended originally to include these comparisons in the paper, but space was insufficient.

We agree that C_{WF} and C_{yPF} are impor-

tant seakeeping parameters. In fact, we have specifically said so for C_{WF} . As regards C_{VPP} , our statement that "best seakeeping is obtained with a hull combining high C_{WF} with low C_B " amounts to much the same thing as "keep C_{VPP} low". This is roughly the same message as one obtains from Mr. Bales's work.

With regard to Mr. Bales's table, we are happy to say that testing of the models with $B/T=5.2$ is in hand. However, we do not have the same expectations as Mr. Bales with regard to the seakeeping performance of these models. While the trend of increasing B/T is to reduce motions and accelerations, it is to increase slamming pressure. In our view, the latter will outweigh the former. However, time will tell.

Finally, we reiterate our gratitude to Mr. Bales for his comments and note that although our path is somewhat different from his in arriving at a final hull form, we achieve very similar results.

We thank Dr. Lee for his kind words. As he points out, the selection of seakeeping criteria is not a simple task and, for particular applications, may result in a rather more extensive set than we have used in the paper. However, we emphasize that in frigate hull form design, the designer should, at a minimum, address slamming, deck wetness and vertical accelerations.

Slamming may be treated in several ways, but it is our firm opinion that slamming severity must be included. In the paper, we have used most probable maximum slamming pressure, but on other occasions we have used slamming force. The latter is probably more satisfying intuitively. However, it is our experience in frigate studies that either criterion will push the ship designer in the same direction, that is to V-bows with full waterplanes forward.

We agree with Prof. Lewis that in Fig. 7 L^2/BT may be replaced by (M) . However, similar data will be available for a different value of C_B , and in analysing the series as a whole L^2/BT is preferred.

As mentioned in the paper, the change of C_B shown in Fig. 9 does involve a change of length from 394 to 383 ft. This change was shown to have little effect on the motions nor on the derived trends with C_B .

The importance of natural periods of pitch and heave is recognised. However, in this paper the authors did not take them into account directly, since they are difficult to estimate at the early design stages. It is believed that changes in the parameters selected imply changes in the natural periods. Furthermore, natural periods are greatly affected by weight distribution, which is not, within practical limits, dependent on hull form.

The effects of varying the wave period in relation to the RAO's have been studied, and the trends of performance found to be similar over relevant ranges of ship length and wave period. For this reason simple averages over wave period were used in the analysis.

The conclusion that length should be selected primarily in the basis of calm water performance objectives rather than seakeeping was made directly from the analyses described in the paper, as shown for example, in Figures 13 and 14. We agree with Prof. Lewis that major increases in (M) will, at constant displacement, lead to shallow draft for which bow emergence may offset the benefit of smaller motions, but this does not occur for the changes of length considered in this paper.

Prof. Johnson asks for more data defining the hull forms. This paper is intended to give an outline of a particular approach to providing design data on seakeeping, and the data relevant to this approach are given. Other approaches will require different data, C_{VPP} and C_{VP} used by Mr. Bales being but two examples, and it was not possible in this paper to give all the possibly useful numerical data. However the body plans, Fig. 1, are given, and these may be used to derive other coefficients, as has been done by Mr. Bales in his contribution.

We thank Mr. Bellone for presenting results of related studies which he and his colleagues have recently performed. With regard to his query regarding seakeeping criteria, it is our opinion that his slamming criterion is not sufficiently stringent whereas the opposite is true of his vertical acceleration criterion. For example, in frigate studies we have found the following criteria to work reasonably well:

significant vertical acceleration at
 $0.2L = 0.4g$

most probable maximum slamming pressure
 $= 40\text{psi}$

most probable maximum slamming force
 $= 0.15\Delta$

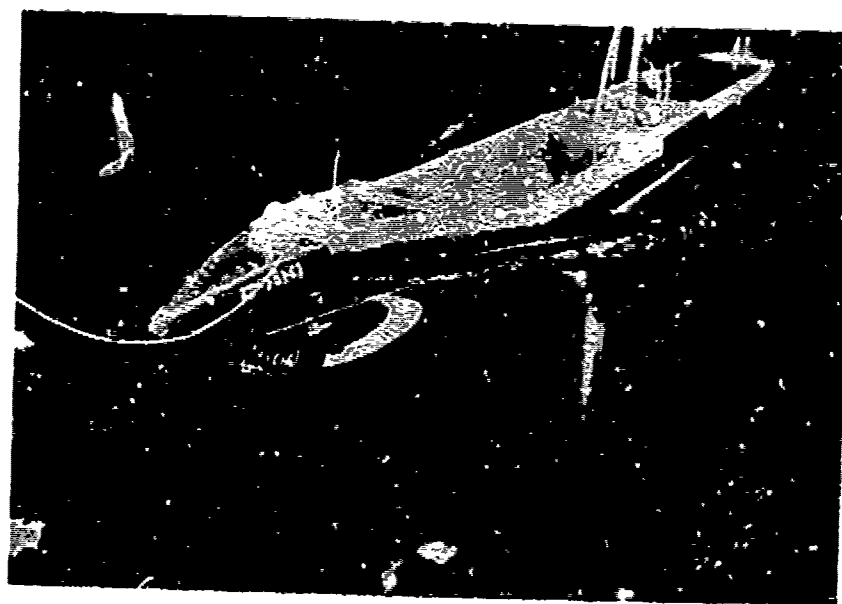
The latter two are evaluated for a period of one hour.

As to his query regarding pitch radius of gyration, we did not include it in our studies first because it is not a hull form parameter and second because the ship designer has little control over it. We do not mean to imply that its influence on ship motions is negligible, and we would certainly favour further work on this topic.

Optimizing the Seakeeping Performance of Destroyer-Type Hulls

Nathan K. Bales

*David W. Taylor Naval Ship Research and Development Center
Bethesda, Maryland U.S.A.*



The Seakeeping Optimum Hull in Waves:
A Perfect Fit

ABSTRACT

A model which relates ship hull geometry to an index of seakeeping merit is developed. This model is quantified for destroyer-type hulls of specified displacement in long-crested, head seas. The quantified model is validated by using it to define a destroyer-type hull with exceptional seakeeping qualities. Necessary conditions are demonstrated for generalizing the model to other displacements and headings; and for applying it under circumstances involving specific, mission-related criteria. Hypothesizing the existence of sufficient conditions where necessary conditions were demonstrated, the model is rewritten in a manner suitable for use in optimizing seakeeping performance under rather arbitrary constraints on hull geometry. It is shown that the optimization can be accomplished using non-linear programming techniques, and that appreciable improvements in seakeeping performance can be realized even when highly restrictive constraints are imposed. The limitations associated with the results obtained are discussed. It is concluded that these results provide a viable basis for early-design synthesis of destroyer-type hulls with superior seakeeping performance.

NOMENCLATURE

A	Local sectional area
A_{WA}	Waterplane area aft of amidships
A_{WF}	Waterplane area forward of amidships
A_X	Maximum of A
a_i	Constant
B	Beam amidships
b	Local beam
C_{VPA}	Vertical prismatic coefficient aft of amidships
C_{VPF}	Vertical prismatic coefficient forward of amidships
C_{WA}	Waterplane coefficient aft of amidships
C_{WF}	Waterplane coefficient forward of amidships
$(C_s)_3$	Slamming constant at Station 3
c	Distance from Station 0 to cut-up point
F_n	Froude number
L	Ship length between perpendiculars
m	Meter(s)
$(N_s)_3$	Number of slams per hour at Station 3
$(P_s)_3$	Probability of bottom slamming at Station 3

R	Seakeeping rank
\hat{R}	Estimated value of R
$(r_{1/3})_0$	Significant single amplitude of vertical-plane ship-to-wave relative motion at Station 0
$(r_{1/3})_{20}$	Significant single amplitude of vertical-plane ship-to-wave relative motion at Station 20
s	Second(s)
$(s_{1/3})_{20}$	Significant single amplitude of absolute vertical motion at Station 20
$(\dot{s}_{1/3})_{15}$	Significant single amplitude of absolute vertical velocity at Station 15
$(\ddot{s}_{1/3})_0$	Significant single amplitude of absolute vertical acceleration at Station 0
T	Draft amidships
$(T_w)_0$	Modal wave period
t	Metric ton(s) or local draft
V	Ship speed
x_i	Underwater hull form parameter
$z_{1/3}$	Significant single amplitude of heave
$\ddot{z}_{1/3}$	Significant single amplitude of heave acceleration
Δ	Ship displacement
$(\zeta_w)_{1/3}$	Significant wave height
$\theta_{1/3}$	Significant single amplitude pitch
μ	Linear ratio
ρ	Density of salt water
σ	Standard deviation
V_A	Displaced volume aft of amidships
V_F	Displaced volume forward of amidships

1. INTRODUCTION

Seakeeping came of age as a discipline of applied hydrodynamics in the mid-1950's with the emergence of strip theory and linear superposition. Subsequent advances and refinements led to the development of technologies which are useful in the later stages of the ship design process. These technologies are now being introduced into the earlier stages of ship design and into ship operations. There is, however, one critical need in the early stages of ship design which cannot be directly addressed by our mature technologies. That need is for a means of synthesizing hull geometries leading to superior seakeeping qualities.

The need for a synthesis technology is widely recognized. Papers attempting to develop relationships between hull geometry and seakeeping, the fundamental prob-

lem associated with development of such a technology, have been appearing in the literature for two decades. These, however, have had little or no impact on the design process.

Within the past few years, there has been a flurry of activity attempting to develop surface combatant hull forms with superior seakeeping qualities. For these ships, increasingly sophisticated weapons systems are demanding more stable platforms at the same time that economic pressures are demanding smaller ships. Thus, the payoff associated with good seakeeping is very high for surface combatants.

The author has been sporadically involved with work in the area under discussion since the mid-1960's. His early efforts failed in the sense of having little or no impact on the ship design process. In the 1977-78 time frame, he enjoyed partial success with two efforts involving particular surface combatant designs. During this same time frame, he undertook a more generalized effort to relate seakeeping to the hull characteristics of destroyer-type ships.

The latter effort was, in view of the historical difficulty of the problem, remarkably successful. Accordingly, the results thereof were used to develop a synthesis technology which is now being applied to the design of United States Navy ships. The development of the model relating hull form to seakeeping and of the associated synthesis technology are described hereinafter.

2. DEVELOPMENT OF A MODEL RELATING SEAKEEPING TO HULL FORM

The fundamental premise of the modeling effort was that a meaningful, comparative index of overall seakeeping performance could be defined and thence quantitatively related to a small number of conventional hull form parameters. It was further assumed that both the index and the relationship could be adequately quantified using analytically-based results for long-crested, head seas. The implications of this assumption are that rolling motion can be adequately controlled by subsequent appendage design, and that coupling effects from the lateral modes at oblique relative headings and/or in short-crested seas will not significantly alter trends identified under the relatively simple conditions evaluated. Finally, it was assumed that only the characteristics of the underwater hull had to be considered. The implications of this assumption are that deck wetness can be limited to an acceptable level by subsequent design of the above-water b_w , and that above-water hull effects will not distort trends identified on the basis of underwater hull geometry. These hypotheses were formulated on the basis of past experience, relevant literature, and unabashed intuition.

The approach which evolved included five basic steps. First was development

of a general model. The next two steps were to quantify the seakeeping index used for the model and its general-form coefficients. The quantified model then had to be validated. Finally, the model had to be generalized, i.e., it had to be shown that some of the specific assumptions made to develop and quantify the model were not necessarily required. Each step is described in the sections which follow.

2.1 The General Model

To begin, let us postulate the existence of a comparative measure of seakeeping performance in head waves: say R for seakeeping "rank". Further postulate the existence of a small set of underwater hull form parameters, say x_i , $i = 1, 2, \dots, n$, which effectively govern R for a homogeneous class of hull geometries. Then our immediate objective is to define R , the x_i 's, and the functional relationship between them, i.e., to write

$$R = f(x_1, x_2, \dots, x_n) \quad (1)$$

in explicit terms.

For R we need a robust, criteria-free index which is not dependent on specific details such as ship subsystems or the planned area of operation. On the other hand, the selected index must ultimately be valid for a wide range of specific criteria and dependencies. This dilemma drives us to adopt an equal distribution of ignorance approach to defining R .

We must compute a set of vertical plane ship responses which is comprehensive in the sense that it includes all such responses upon which criteria are likely to be based. These computations must be performed for comprehensive ranges of ship speed and of sea condition. The response statistics resulting from the computations must then be normalized and averaged. For the averaging process, all responses, ship speeds, and sea conditions are taken to be equally important. It is the absence of any weighting or prioritizing in the final average which gives rise to the "equal distribution of ignorance" descriptor.

The basically philosophical definition of seakeeping rank just given is considered adequate for development of the general model. Specific definitions are dependent upon the ship class considered. Such a definition will be supplied for destroyer-type hulls when quantification of the model is discussed.

It is now in order to focus on selection of the underwater hull form parameters, x_i in the notation of (1), to be used for the model. To make these selections, the author relied heavily on his earlier work with analytically-defined seakeeping standard series. This work is exemplified by his 1970 paper with Cummins^{1*}.

* A complete listing of references is given on page 503

The Bales and Cummins series is based on the fact that a viable approximation to the vertical plane responses of a ship among waves can be obtained using a Lewis section representation of the hull. This concept is equally applicable to the problem at hand. Though a detailed mathematical representation of the variation of the Lewis section parameters over ship length, such as used in Reference 1, seemed too complex for the present application, it appeared possible that a carefully selected set of hull form parameters might effectively define the waterlines, underwater profiles, and sectional fullness characteristics of a homogeneous class of ships.

Another insight gleaned from the standard series work was that it is very desirable to treat forebody and afterbody characteristics separately as the former have a greater impact on vertical plane responses than do the latter. The waterplane coefficient forward of amidships was found to be especially prominent. Increases in this parameter invariably improved seakeeping, and the magnitudes of the response changes which it caused exceeded those associated with any of the other coefficients considered.

Finally, the standard series provided some insight into the comparative seakeeping characteristics of hulls with and without transoms. It was found that hulls without transoms generally exhibited seakeeping characteristics superior to nominally equivalent hulls with transoms. These differences were found to be attributable to the typical differences between the afterbody, underwater profiles of the two types of ships rather than to the transom itself.

Parameters for the model were selected on the basis of the foregoing comments and of such other knowledge of the influence of hull form on seakeeping as the author could bring to bear. Appendix A provides an abbreviated rationale for each selection. Here, the selected parameters will be identified and briefly commented upon.

A total of six parameters were selected for the model. They are:

1. Waterplane coefficient forward of amidships, C_{WF} ;
2. Waterplane coefficient aft of amidships, C_{WA} ;
3. Draft-to-length ratio, T/L , where T is draft and L is ship length;
4. Cut-up ratio, c/L , where c is the distance from the forward perpendicular to the cut-up point;
5. Vertical prismatic coefficient forward of amidships, C_{VPF} ; and
6. Vertical prismatic coefficient aft of amidships, C_{VPA} .

Seakeeping was projected to improve with

increasing C_{WF} , C_{WA} , c/L and C_{VPA} ; and with decreasing T/L and C_{VPF} . The projection for improvement with increasing C_{WF} was considered the strongest in the set. That for improvement with increasing C_{VPA} was weakest.

With the foregoing, (1) can be written

$$R = f(C_{WF}, C_{WA}, T/L, c/L, C_{VPF}, C_{VPA}) \quad (2)$$

and it remains only to define the nature of the functional relationship to be used.

In defining this relationship, the author again relied heavily on his earlier seakeeping standard series work. A ruled surface function was used for interpolations over the standard series data base. Such a function consists of the algebraic sum of a constant, a linear term in each independent variable, and all of the linear, interaction terms which can be formed from the set of independent variables under consideration. Thus, a ruled surface equation for the six-parameter model now under consideration would have 64 terms. This was considered to be too complex a function for the present effort.

A feature of the ruled surface function is that it reduces to a simple, linear equation when only one of its parameters is varied. In the course of the series work, this led to an exploration of using only the constant and the single-variable terms from the ruled surface equation to approximate the results of the latter when more than one parameter was changed. The exploration indicated that the linear approximation was correct in a qualitative sense whenever appreciable changes in the dependent variable were involved. The qualitative results, though erroneous, appeared to provide an adequate bases for tradeoff decisions. In view of this, it was decided to employ a simple, linear model, i.e., to write (2) as

$$R = a_0 + a_1(C_{WF}) + a_2(C_{WA}) + a_3(T/L) + a_4(c/L) + a_5(C_{VPF}) + a_6(C_{VPA}) \quad (3)$$

where a_i , $i = 0, 1, 2, \dots, 6$, are constants to be determined.

2.2 Quantification

Equation (3) was quantified using a data base consisting of the geometric characteristics and seakeeping responses of an ad hoc selection of destroyer-type hull designs. A "destroyer-type hull" is taken to be a rather fine, naval hull intended for high-speed operation and a warfare mission such as antisubmarine or anti-aircraft warfare. Classes of ships which satisfy this definition are frigates, destroyers, and light cruisers.

In the preceding material, the idea of a "homogeneous" class of hulls was

invoked on several occasions. The functional similarity of frigates, destroyers, and light cruisers has led to their constituting a rather homogeneous set in terms of hull form. However, their sizes vary widely. This required that ship size be normalized in some manner before the data base needed to quantify the general model relating hull geometry to seakeeping was developed.

It was decided to normalize on the basis of displacement. There were three reasons for selecting displacement in preference to length as the normalizing factor. First, the author's past results indicate that displacement is, for realistic ship forms, better correlated with seakeeping performance than is ship length. Second, displacement is a more fundamental metric of ship cost than is ship length. Third, and strongly tied to the second reason, is that most early-design decisions as to ship size are made in terms of displacement.

Twenty destroyer-type hulls were chosen for the data base. Care was taken to include hulls representative of a wide scope of design practice. Care was also taken to avoid inclusion of pathological hulls judged to be unbuildable or unlikely to be built.

Each hull selected was normalized to a displacement, 4300t, considered to be typical of the class under consideration. The normalization was performed by multiplying the linear dimensions of each hull by the cube root of the ratio of 4300t to its as-designed displacement. Table 1 characterizes the 20 displacement-normalized hulls. Both the parameters included in the model relating hull form to seakeeping and the overall dimensions of the hulls are included in this tabulation. The symbol B represents beam amidships. All other notation in Table 1 is as previously introduced.

Based on the general definition of seakeeping rank (R) given previously, it was decided (see Appendix B for rationale) to compute eight seakeeping responses for each of the data-base hulls. The responses selected were pitch, heave, ship-to-wave relative motion at Stations 0 and 20*, bottom slamming at Station 3, absolute vertical acceleration at Station 0, heave acceleration, and absolute vertical motion at Station 20. In two particulars, this set of responses fails to support the general definition of R. Heave was included, not because it is a criterion response, but because it seemed inadvisable to omit half of the modal motions relevant to the problem. Absolute vertical velocity, a criterion response for helicopter landings, was omitted. The omitted response will be utilized subsequently in the context of generalizing the model.

Again based on the general definition of R, it was decided to compute these

* Stations are numbered from 0 at the forward perpendicular to 20 at the after perpendicular.

responses in Bretschneider wave spectra with modal periods, $(T_w)_0$, from 6 to 14s in two-second increments and for Froude number, F_n , from 0.05 in increments of 0.10 to 0.45. Characterizing the wave spectra on the basis of modal wave period alone is viable because we are assuming linearity. The Froude numbers selected yield speeds covering a 5 to 30 knot range for each hull in the data base. Appendix B provides additional comments on the selection of operating conditions.

The computations were performed using an upgraded version of the linear strip theory computer program developed by Frank and Salvesen². A 20-station, close-fit representation was used for each hull. The radius of gyration in pitch was taken equal to 0.25 L for all of the hulls.

These computations produced 200 response statistics (5 modal wave periods x 5 Froude numbers x 8 responses) for each of the 20, data-base hulls. Unweighted averaging over modal period and Froude number, as advocated in the general definition of R, reduced this data set to the 20 x 8 matrix exhibited in Table 2. In this table, $(\zeta_w)_{1/3}$ represents significant wave height, and is used to normalize all of the simple, linear responses. These responses are in terms of significant single amplitudes (subscript 1/3), and are further subscripted, when required, by the applicable Station number. General notation used is θ for pitch, z for heave, r for relative motion, and s for absolute motion.

The response statistic designated $(C_s)_3$ in Table 2 is related to the probability of occurrence of bottom slamming at Station 3, say $(P_s)_3$, by

$$(P_s)_3 = \exp\{-2(C_s)_3 / [(\zeta_w)_{1/3}]^2\} \quad (4)$$

It may then be described as a slamming incidence parameter. Appendix B defines $(C_s)_3$ using threshold relative velocity as defined by Ochi³. Let it be noted that $(P_s)_3$ is inversely proportional to $(C_s)_3$. Hence, in contrast to the other responses considered, a large value of $(C_s)_3$ is "good" while a small value is "bad".

A few interesting facts can be gleaned from inspection of Table 2. Hull 06 is evidently a good one: it minimizes pitch, heave, both accelerations, and relative motion at Station 0. Hull 05 exhibits the best slamming characteristics. As to the Station 20 responses, Hull 10 is best in absolute motion while Hull 04 is best in relative motion. It is also worthwhile to observe that the total variability in the Station 20 responses is relatively small. These vary by only 5 percent over the 20-ship data base while the other responses considered vary by 8 to 28 percent.

Prior to response averaging, each Table 2 datum had to be nondimensionalized.

To accomplish this, all of the $(C_g)_3$ values in Table 2 were divided by the largest value thereof; and the other average responses were divided by their respective minima. Thus, the "best" hull in terms of each response considered was assigned a 1.0 for that response while the other hulls were assigned proportionately lower values. These nondimensionalized values were then averaged over the eight responses for each ship.

It can be noted that these average responses are implicitly weighted by the attainable range of variability of the

individual responses. It was felt that this implicit weighting was compatible with the general definition of R. An averaging procedure assigning strictly equal weights to all of the responses considered might have allowed those with little potential for improvement to drive us in the direction of little overall improvement.

The average responses derived by the procedure just described and discussed satisfy the general definition of R. However, it was decided to perform one additional operation to formally define the index. This was normalization of the overall averages to a scale from 1.0 to 10.0 with the hull having the best (highest) average assigned the 10.0 and that having the worst average being assigned the 1.0. There were two motivations for this final step. First, use of the normalized scale admits quick judgments as to the relative seakeeping qualities of a given hull. Second, the resultant increases in the numerical magnitudes of the hull-to-hull differences involved were thought to be of

Table 1 Characteristics of the Displacement-Normalized (4300t) Hulls

Hull	L, m	B, m	T, m	C_{WP}	C_{WA}	T/L	c/L	C_{TPP}	C_{TPA}
01	124.3	13.01	4.48	0.694	0.917	0.0367	0.850	0.747	0.644
02	135.8	14.26	4.28	0.634	0.884	0.0315	0.850	0.740	0.613
03	128.2	14.94	4.20	0.583	0.899	0.0328	0.850	0.803	0.638
04	127.2	14.21	4.75	0.603	0.864	0.0374	0.800	0.807	0.573
05	122.0	12.68	4.95	0.698	0.911	0.0406	0.850	0.770	0.611
06	134.4	13.80	4.26	0.687	0.872	0.0317	0.850	0.737	0.636
07	118.7	13.53	4.88	0.641	0.921	0.0411	0.800	0.729	0.656
08	124.8	14.88	4.05	0.674	0.834	0.0320	0.800	0.773	0.690
09	129.4	14.98	4.50	0.584	0.832	0.0348	0.850	0.732	0.616
10	130.2	13.89	4.62	0.648	0.922	0.0355	0.800	0.724	0.580
11	129.5	14.29	4.56	0.611	0.912	0.0352	0.850	0.752	0.587
12	126.0	14.76	4.62	0.614	0.886	0.0366	0.700	0.719	0.603
13	126.7	13.12	5.14	0.574	0.902	0.0406	0.650	0.794	0.587
14	132.2	14.52	4.80	0.615	0.848	0.0363	0.650	0.720	0.551
15	134.0	13.66	4.26	0.687	0.876	0.0318	0.850	0.752	0.636
16	123.6	14.57	4.79	0.637	0.848	0.0388	0.700	0.749	0.584
17	131.2	14.29	4.59	0.633	0.841	0.0350	0.800	0.677	0.590
18	117.8	14.27	4.68	0.635	0.892	0.0397	0.800	0.745	0.636
19	131.6	13.63	4.88	0.656	0.893	0.0370	0.600	0.791	0.577
20	124.4	14.53	4.66	0.592	0.881	0.0371	0.850	0.727	0.635

Table 2 Average Response Statistics for the Data Base Hulls

Hull	$\frac{\sigma_{1/3}}{(\frac{\sigma_{1/3}}{f})_{1/3}}$ deg/m	$\frac{\sigma_{1/3}}{(\frac{\sigma_{1/3}}{f})_{1/3}}$ m/s	$\frac{(\sigma_{1/3})_0}{(\frac{\sigma_{1/3}}{f})_{1/3}}$ m/s	$\frac{(\sigma_{1/3})_0}{(\frac{\sigma_{1/3}}{f})_{1/3}}$ m/s	$(C_g)_3$ m ²	$\frac{\sigma_{1/3}}{(\frac{\sigma_{1/3}}{f})_{1/3}}$ m/s	$\frac{(\sigma_{1/3})_{20}}{(\frac{\sigma_{1/3}}{f})_{1/3}}$ m/s	$\frac{(\sigma_{1/3})_{20}}{(\frac{\sigma_{1/3}}{f})_{1/3}}$ m/s
01	0.538	0.241	0.917	0.811	156	0.231	0.521	0.443
02	0.480	0.234	0.921	0.787	113	0.229	0.498	0.446
03	0.545	0.268	0.993	0.884	99	0.274	0.510	0.431
04	0.540	0.314	0.994	0.850	122	0.323	0.507	0.418
05	0.566	0.264	0.937	0.846	178	0.262	0.541	0.457
06	0.470	0.226	0.888	0.747	128	0.218	0.494	0.458
07	0.598	0.237	0.966	0.911	132	0.255	0.538	0.433
08	0.516	0.245	0.909	0.778	113	0.234	0.517	0.454
09	0.536	0.257	0.948	0.868	171	0.255	0.521	0.452
10	0.501	0.239	0.925	0.786	141	0.233	0.491	0.435
11	0.530	0.243	0.974	0.858	119	0.265	0.506	0.435
12	0.546	0.261	0.964	0.750	103	0.259	0.514	0.436
13	0.588	0.309	1.051	0.955	123	0.326	0.538	0.426
14	0.501	0.236	0.948	0.829	140	0.254	0.512	0.440
15	0.474	0.231	0.893	0.756	124	0.226	0.496	0.458
16	0.563	0.275	0.966	0.764	156	0.272	0.537	0.454
17	0.497	0.237	0.912	0.778	143	0.225	0.508	0.455
18	0.597	0.269	0.966	0.878	136	0.262	0.536	0.431
19	0.548	0.294	1.029	0.925	117	0.308	0.518	0.428
20	0.543	0.256	0.881	0.897	117	0.255	0.535	0.452

Table 3 Seakeeping Ranks of the Data Base Hulls

Hull	R	C_{WP}	C_{WA}	T/L	c/L	C_{TPP}	C_{TPA}
06	10.00	0.687	0.872	0.0317	0.950	0.737	0.636
15	9.22	0.687	0.876	0.0318	0.850	0.752	0.636
17	8.99	0.653	0.841	0.0350	0.800	0.677	0.593
10	8.99	0.648	0.922	0.0355	0.800	0.724	0.580
01	8.44	0.694	0.917	0.0367	0.859	0.747	0.644
02	7.93	0.634	0.884	0.0315	0.850	0.740	0.613
08	6.92	0.674	0.834	0.0320	0.800	0.773	0.690
05	6.70	0.698	0.911	0.0406	0.850	0.770	0.611
14	6.53	0.615	0.848	0.0363	0.650	0.720	0.551
11	5.08	0.611	0.912	0.0352	0.850	0.752	0.587
16	4.91	0.637	0.848	0.0388	0.700	0.749	0.584
09	4.58	0.584	0.832	0.0348	0.850	0.732	0.616
07	4.58	0.641	0.921	0.0411	0.800	0.729	0.656
12	4.41	0.614	0.886	0.0366	0.700	0.719	0.603
18	4.30	0.635	0.892	0.0397	0.800	0.745	0.636
20	3.96	0.592	0.881	0.0371	0.850	0.727	0.635
03	3.46	0.583	0.899	0.0328	0.850	0.803	0.638
04	2.73	0.603	0.864	0.0374	0.600	0.807	0.573
19	2.45	0.565	0.893	0.0370	0.600	0.791	0.577
13	1.00	0.574	0.902	0.0406	0.650	0.794	0.587

Table 4 Coefficients and Characteristics of the Parameters in the Seakeeping Rank Equation

Parameter	Equation (3) Constant	Min.	Parameter Max.	Characteristic Range	Potential Change
a_0	+8.422	—	—	—	—
C_{WP}	$a_1 = +45.104$	0.565	0.695	0.133	5.999
C_{WA}	$a_2 = +10.078$	0.834	0.922	0.088	0.887
T/L	$a_3 = -378.445$	0.0315	0.0411	0.0096	3.633
c/L	$a_4 = +1.273$	0.690	0.850	0.250	0.318
C_{TPP}	$a_5 = -23.501$	0.677	0.807	0.130	3.5
C_{TPA}	$a_6 = -15.875$	0.551	0.690	0.139	2.20

potential value for that portion of the quantification effort yet to be undertaken.

Application of the procedure just defined to the data base hulls produced the R-value data presented in Table 3. This table shows the data base hulls in order of rank from best ($R = 10.00$) to worst ($R = 1.00$). The table includes the hull form parameters in terms of which R has been modeled. Gross tendencies toward increasing rank with increasing C_{WF} and with decreasing C_{VPF} are discernible, but it is evident that no one of the parameters considered provides a reliable indication of the behavior of the index.

To complete the quantification effort, a multivariate, linear regression analysis was performed using the Table 3 data with R as the dependent variable and the six hull form parameters as the independent variables. The regression analysis provided estimates of the constants a_i , $i = 0, 1, \dots, 6$, in (3). Table 4 presents the estimated values. It also defines (from Table 3) the parameter ranges to which the estimates are strictly applicable. Finally, Table 4 gives the potential change in seakeeping rank associated with each parameter. These data are obtained by multiplying the estimated constant for a parameter by its range.

2.3 Validation

Initially, it should be noted that the constants estimated by the quantification process are in broad agreement with the projections made in the course of developing the general model. The exceptions are

the effects of C_{VPA} and c/L . The former parameter has an effect opposite to that anticipated while the latter has a smaller relative effect than anticipated. Both reversals are probably attributable to the difficulties associated with defining after-body geometry which are discussed in Appendix A.

A simple validity check can be made by comparing predicted and directly computed R-values for the data base hulls. Figure 1 presents the results of this exercise. The symbol R is used (and will be used hereinafter) for the predicted values to distinguish them from those directly computed. Figure 1 includes lines defining a two standard deviation (σ) bound about the predicted value. The magnitude of σ is 0.508, and the largest single deviation is 1.073.

It was felt that the most relevant validation effort which could be undertaken was to use the R predictor to define a hull which had parameters within the data base ranges thereof but better seakeeping characteristics than any hull in the data base. The form coefficients for such a hull can be obtained by inspection of Table 4. One simply assigns each parameter the data base extreme which will tend to maximize \hat{R} . The transition from this point to a hull sufficiently well-defined to admit strip theory computations is rather tedious. Dimensional quantities must be introduced; and these, too, must be kept within their data base ranges. Finally, a "ship-like" configuration satisfying all of the imposed restraints must be developed. Appendix C describes the process in detail. Here the characteristics of the resultant hull will be presented and briefly discussed.

The hypothetically optimum hull defined by the work described in Appendix C will be identified as Hull 21. It is 135.8 m in length, has a beam of 14.72 m and a draft of 4.28 m. Its displacement is 4302t. Its coefficients, as associated with the model developed here, are as follows:

$$C_{WF} = 0.690, C_{WA} = 0.915, T/L = 0.0315, \\ c/L = 0.850, C_{VPF} = 0.689 \text{ and } C_{VPA} = 0.552.$$

The Hull 21 characteristics involving volumes and areas are slightly different from their ideal values, e.g., C_{WF} is 0.008 less than the data base maximum. All of these differences are such that the coefficients of Hull 21 fall inside the data base ranges.

Seakeeping computations were performed for Hull 21. These computations were identical to those performed for the data base hulls except that a Lewis section representation was used for Hull 21. Such a representation was the best which could be derived at the level of hull definition available, and was thought to be adequate for the purpose at hand.

The results of the Hull 21 seakeeping computations were used to recompute the

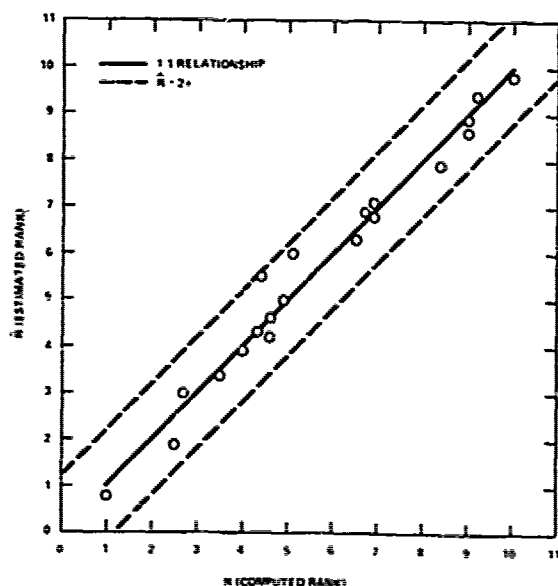


Fig. 1 Estimated versus Directly-Computed Ranks for the Data Base Hulls

seakeeping rank index, R , under the assumption that this hull was a member of the data base set. It was found that, had Hull 21 been a member of the data base, it would have attained the maximum rank of 10.0. Hull 06, which received the 10.0 rank in the actual data base, would have been second-ranked at $R = 7.2$. Hence, the R predictor has been used to define a hull that is within the geometric scope of the data base hulls but has seakeeping qualities superior to all of these hulls.

The foregoing conclusion equates "seakeeping qualities" with the rank index, R . The equal distribution of ignorance approach taken to defining R is, accordingly, implicit to it. We must, for credibility if not for validity, inquire as to the degree to which the local seakeeping qualities of Hull 21 are inferior as a result of this. Figures 2 through 9 were developed for the inquiry.

Each of the eight cited figures treats one of the seakeeping responses considered here. The response being evaluated is plotted as a function of modal wave period for each of the five Froude numbers evaluated. Five curves are shown on each plot. These illustrate the local seakeeping qualities of Hull 21 and of the data base hulls which are best (Hull 06) and worst (Hull 13) in the sense defined by R . They also define the data base envelope, i.e., the highest

and lowest local responses of any hull in the data base. When no envelope is explicitly shown, the implication is that it is defined by either Hull 06 or Hull 13.

Insights which can be gained from inspection of Figures 2 through 9 are discussed in the following paragraphs. Minor trend reversals in waves of six-second modal period are neglected in the discussion. These reversals involve relatively small response magnitudes, and are at least as much attributable to numerical procedures, e.g., spectral closure, as to realistic differences between the hulls involved.

Excepting the slamming incidence parameter (Figure 6) and relative motion at the stern (Figure 9), the results shown by the figures under discussion are remarkably consistent. Hull 06 typically defines the best envelope or is very close to it. Hull 13 is only slightly less consistent in approximating the worst envelope than is Hull 06 in approximating the best envelope. Hull 21 is generally equal or superior to Hull 06. In some instances when Hull 06 does not define the data base best envelope, Hull 21 is superior to the hull which

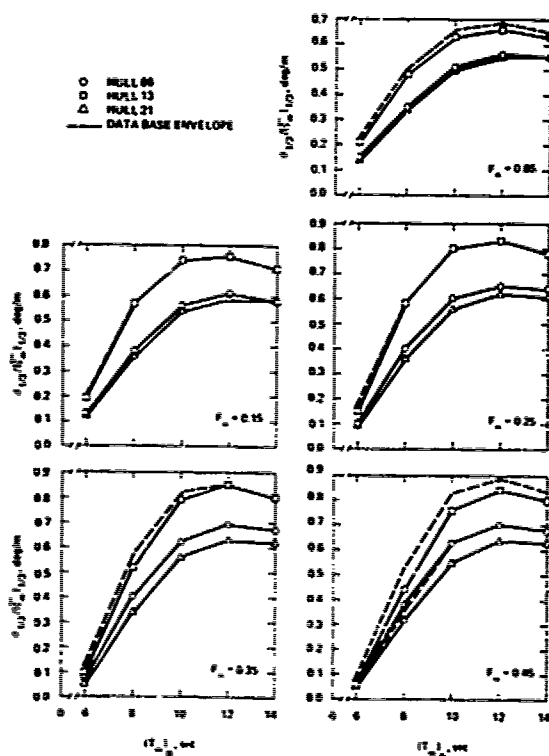


Fig. 2 Pitch Comparisons between Hull 06, Hull 13, Hull 21, and the Data Base Envelope

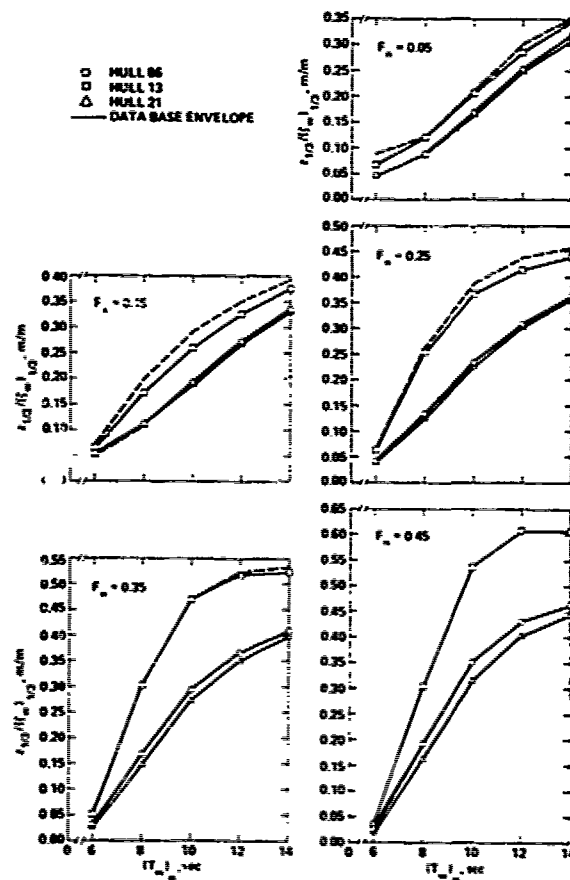


Fig. 3 Heave Comparisons between Hull 06, Hull 13, Hull 21, and the Data Base Envelope

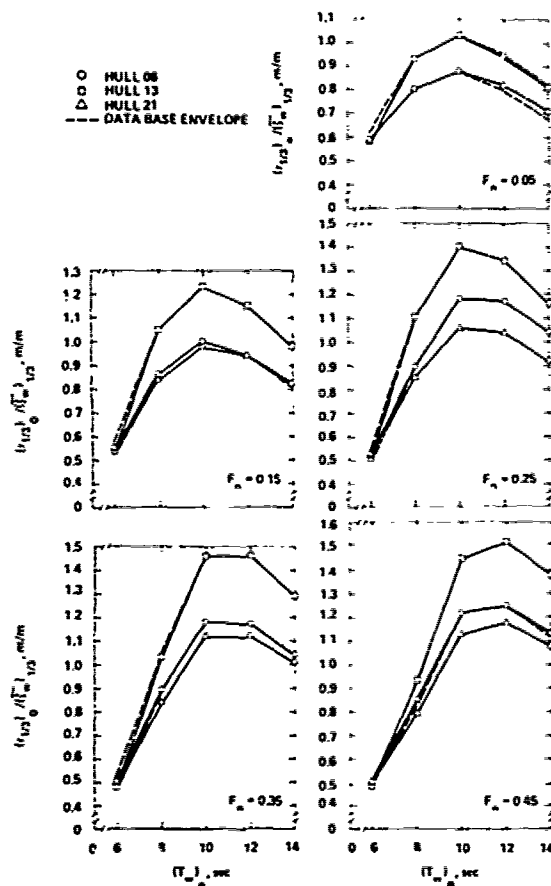


Fig. 4 Station 0 Relative Motion Comparisons between Hull 06, Hull 13, Hull 21, and the Data Base Envelope

defined it.

It was noted earlier that the Station 20 responses considered had relatively small ranges, and that the response averaging procedure employed was biased against responses with relatively little potential for improvement. One of the exceptions cited in the foregoing paragraph, relative motion at the stern, appears to reflect these circumstances. Such being the case, the favorable results found for absolute motion at the same location must be considered fortuitous. However, the behavior of relative motion at Station 20 with variations in modal period and Froude number can be seen to be different from that of the other responses considered. This may account for the anomaly.

In any case, Figure 9 indicates that a reversal of the overall trends found occurs in the case of relative motion at Station 20. The roles of the best and worst data base hulls in an overall sense are reversed. Hull 21 is intermediate in most cases, but exhibits superiority in long waves at the highest Froude number considered.

It is pointed out in the appendix on parameter selection for the general model (Appendix A) that the author's preconcep-

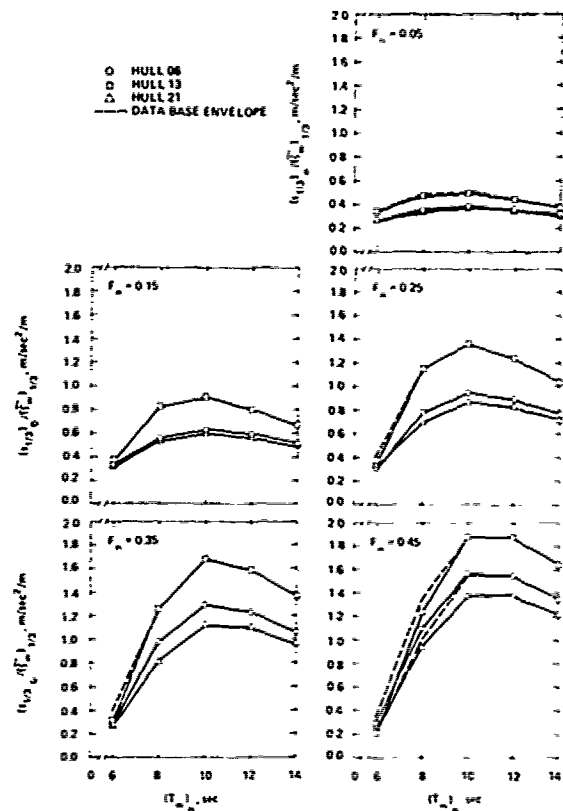


Fig. 5 Station 0 Absolute Acceleration Comparisons between Hull 06, Hull 13, Hull 21, and the Data Base Envelope

tion to the effect that a decrease in draft-to-length ratio should improve sea-keeping contradicted common sense arguments regarding the effect of draft on bottom slamming. Quantification of the model supported the author's contention. However, the Figure 6 plots of the slamming incidence parameter (which was the second response accepted from the initial discussion of local response comparisons) indicate that the common sense argument has merit in the limit as encounter frequency increases. When this frequency is high, most notably at combinations of low $(T_w)_0$ and high F_n , absolute ship motions are very small; and relative motion (in the kinematic sense, at least) is approximately equal to wave elevation. Then the incidence of bottom slamming comes close to exhibiting a reciprocal correlation with draft.

Recalling that the incidence of slamming is inversely proportional to $(C_s)_3$, Figure 6 is seen to reflect the situation just described. In 6s waves, Hull 13 with $T = 5.14$ m is usually better than either Hull 06 ($T = 4.26$ m) or Hull 21 ($T = 4.28$ m). A 2s increase in modal period reverses the situation. As modal period continues to increase, Hull 13 converges to the data base worst envelope. Then Hull 06 is intermediate, and Hull 21 converges to the

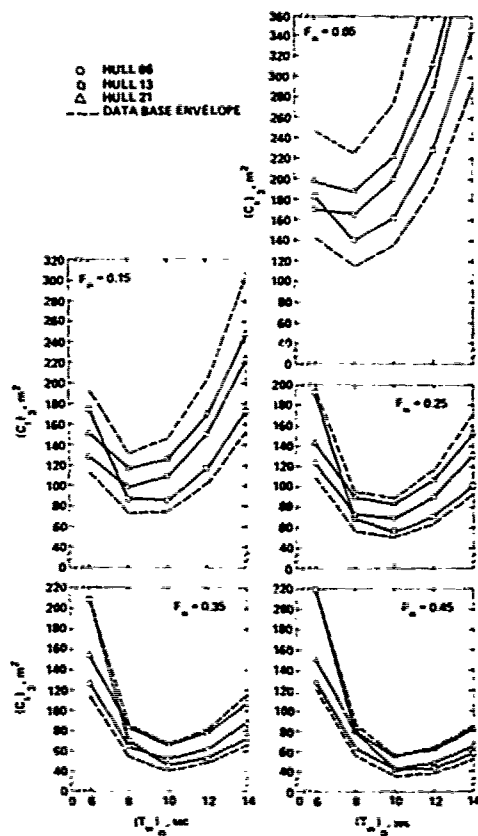


Fig. 6 Station 3 Slamming Incidence Parameter Comparisons between Hull 06, Hull 13, Hull 21, and the Data Base Envelope

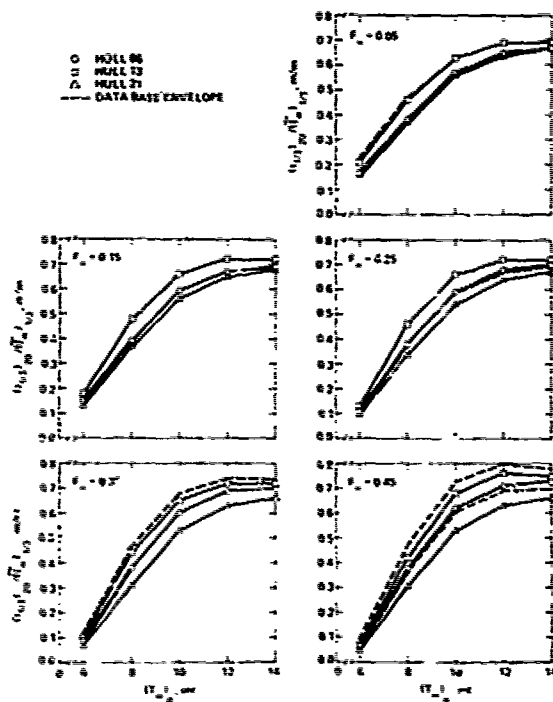


Fig. 8 Station 20 Absolute Motion Comparisons between Hull 06, Hull 13, Hull 21, and the Data Base Envelope

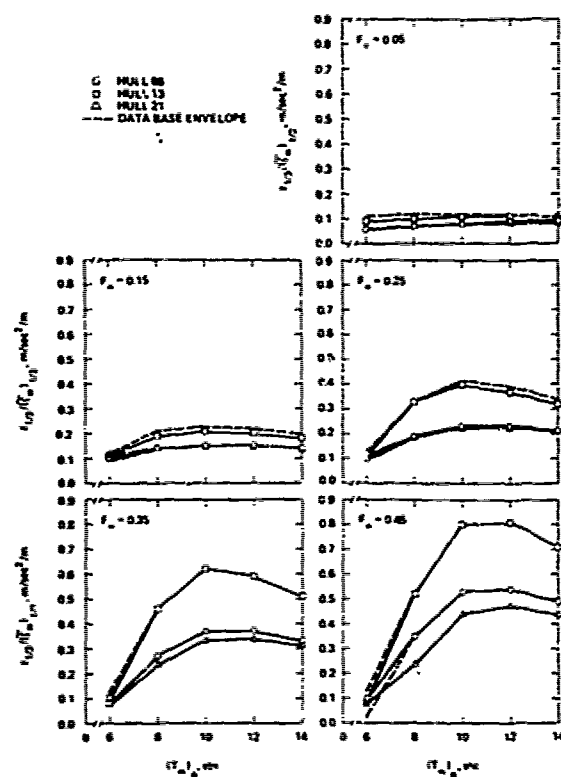


Fig. 7 Heave Acceleration Comparisons between Hull 06, Hull 13, Hull 21, and the Data Base Envelope

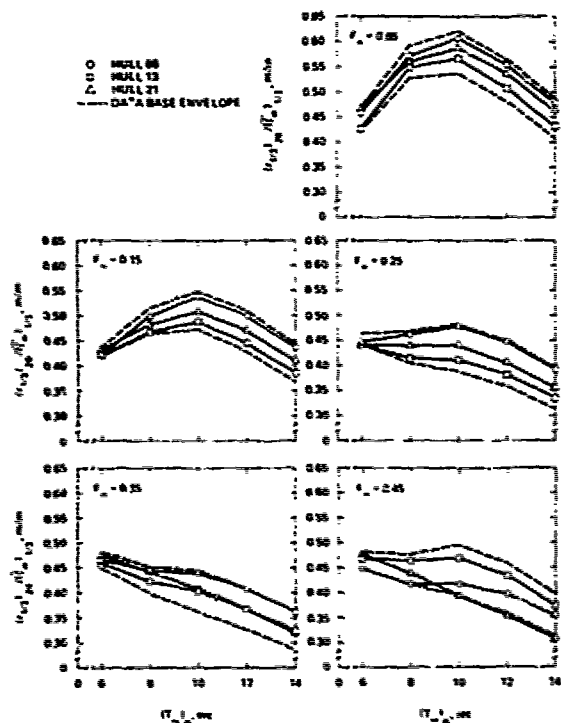


Fig. 9 Station 20 Relative Motion Comparisons between Hull 06, Hull 13, Hull 21, and the Data Base Envelope

data base best envelope.

Since the magnitudes of $(C_s)_3$ at the 6s modal period are relatively high (implying a lower incidence of the phenomenon), the reversal which occurs in that condition is not considered too deleterious. The low-draft ships which are good in an overall sense have good slamming incidence characteristics under those conditions in which slamming is most likely to limit operability. One other matter seems worth pointing out in the present context. Slamming is treated here purely from the viewpoint of its incidence, but the fine forebody sections implied by the low value of C_{VPF} applicable to Hull 21 can be expected to minimize the deleterious effects of the phenomenon when it does occur.

Overall, it is thought that the local comparisons presented in Figures 2 through 9 provide strong support for both the equal distribution of ignorance approach to defining R and the excellence of Hull 21. The only definitive reversal found is that of relative motion at Station 20, and it is minor in the sense that the attainable variation in this response is small. Perhaps the most exciting feature of Hull 21 is that its superiority is greatest when conditions are worst, i.e., at the higher Froude numbers in seas which maximize the responses of hulls in its size range.

2.4 Generalization

The assumptions made in the course of deriving the general model relating hull form to seakeeping and of quantifying it for destroyer-type hulls are so restrictive as to make the results obtained useless in any practical sense. These results apply only to selected seakeeping responses of 4300t, destroyer-type hulls operating in long-crested head seas. Lifting the hull type restriction was beyond the scope of the investigation being described. The possibility of relaxing the restrictions as to response, displacement, and/or relative heading was explored at the level of necessary conditions.

Initially, Hull 21 was scaled (by the cube root of the displacement ratio as described in context of developing the displacement-normalized data base) to the size of an existing small frigate and to the size of an existing light cruiser. The seakeeping responses of the existing hulls and their Hull 21 equivalents were then computed using the same procedures as for the data base. Absolute vertical velocity at the after quarter point, noted previously to be a criterion response omitted from the data base computations, was determined. The responses of the two pairs of hulls were then compared.

Subsequently, the general approach of scaling Hull 21 to the sizes of two existent hulls was applied for 'round-the-clock' relative headings in both long and short-crested seas. This effort was extended to

assessment of the capabilities of the hulls considered to support antisubmarine warfare by conducting helicopter operations. The performance assessment used specific criteria magnitudes, and required consideration of a number of responses not considered in the data base computations. Hence, this effort encompasses the initial generalizations. In addition, it tests the ability of the results which have been derived to yield a hull which exhibits superior seakeeping in a specialized situation. It will be recalled that it was the need for a seakeeping index that was very generalized yet applicable to specialized circumstances which motivated the adoption of the equal distribution of ignorance approach to defining the seakeeping rank, R, used here.

The results of the initial generalization effort continue to be of academic interest because they were obtained without any complicating changes in the computational frame of reference used for the earlier elements of the investigation. Hence, these results will be briefly reviewed. The subsequent generalization to 'round-the-clock' relative headings will then be described in some detail.

The initial generalization effort indicated that the displacement-scaled versions of Hull 21 were superior to their existing counterparts except in relative motion at the stern (for which response the differences involved were small) and in slamming incidence at combinations of high F_n and low $(T)_0$ for which the incidence of the phenomenon was relatively small. Further, the magnitude of the differences involved appeared to reflect R differences between the hulls which were computed assuming that the predictor could be applied independent of displacement. Absolute vertical velocity was found to exhibit typical trends with $(T)_0$ and F_n and in hull-to-hull comparisons.

Prior to attempting the generalization to 'round-the-clock' relative headings, a detailed design of Hull 21 was developed. The procedure followed is described in Appendix D. Here it should be noted that attention was given to minimizing resistance, that the author's procedure for computing minimum freeboard requirements⁴ was applied, and that bilge seals were sized in accord with the principles set forth by Cox and Lloyd⁵. Further, the responses of the detailed design were computed by the same procedures employed previously to verify that its seakeeping characteristics had not been seriously altered by the detailed design effort.

Figure 10 presents the body plan which resulted from the detailed design. In this figure and hereafter, this design is referred to as Hull 21D to distinguish it from the Lewis section version considered up to now. Hull 21D has the same overall dimensions as Hull 21, but it differs slightly from the latter in displacement and some coefficients. Specifically, it displaces 4343t, and has $C_{WF} = 0.698$,

$C_{WA} = 0.922$, $C_{VPF} = 0.678$ and $C_{VPA} = 0.560$. The coefficients remain within their respective, data-base ranges.

Two existing hulls, both designed to support helicopter operations, were selected for comparison with Hull 21D as scaled to their respective displacements. The smaller of the two hulls selected is 124.4 x 13.8 x 4.52 m, and displaces 3595t. It will be designated Hull A. The larger, designated Hull B, is 161.2 x 16.8 x 5.94 m, and displaces 7948t.

Hull 21D as scaled to the displacement of Hull A will be identified as Hull 21D/A. Its dimensions are 127.5 x 13.8 x 4.02 m. By corresponding identification, Hull 21D/B is 166.1 x 18.0 x 5.25 m. The displacement-scaled versions of Hull 21D are, then, generally longer and shallower than the existing hulls. Breadth comparisons vary. This parameter is the same for Hull 21D/A as for Hull A, but significantly greater for Hull 21D/B than for Hull B.

Six-degree-of-freedom motion computations for the two pairs of hulls just described were performed using the United States Navy's Standard Ship Motion Prediction Computer Program, SMP-79. This program is based on the linear strip theory of Salvesen, Tuck and Faltinsen⁶ with improvements in roll prediction based on Schmitke⁷ and on the Cox and Lloyd paper (Ref. 5) previously cited in the context of bilge keel sizing. Appendix E describes the computations performed in detail. Here it should be noted that speed polar diagrams, as introduced by Covich and Comstock⁸, were used to assess performance.

As mentioned previously, the performance of the hulls under consideration was assessed in terms of their ability to carry out helicopter operations. These operations were divided into three categories: launch, recovery, and support. The "support" opera-

tion consists of on-deck handling of the helicopter and its equipment. The categorization is required because each of the three operations involves different criteria variables and/or magnitudes. Further, in order to obtain an operationally relevant assessment, criteria for avoiding hull damage and for personnel limitations were superimposed upon the criteria for each category of helicopter operation.

Complete results of the performance assessment are presented in Figures 11 through 16. Each of these figures presents an Operability Index (OI) as a function of modal wave period for a specified helicopter operation (and, implicitly, for the hull and personnel) and a specific significant wave height. The OI's are defined such that they equal 1.0 in a seaway so benign that the operation under consideration can be carried out at any relative heading and at any speed up to design speed (taken to be 30 knots for all of the hulls evaluated). For more severe seaways, the OI is fractional: and when the seaway becomes sufficiently severe to make the operation untenable, the OI is zero. For instance, an OI of 0.40 indicates that, in the seaway to which it applies, the ship under consideration can perform the operation being evaluated in 40 percent of the possible combinations of 0 to 360 degrees in relative heading and 0 to 30 knots in ship speed.

Larger OI's are considered to be indicative of superior seakeeping because they imply that the "window" in which the operation considered can be performed will be easier to locate initially and thence offer more flexibility in the speeds and headings at which the operation can be conducted. In this context, Figures 13 through 16 indicate that the displacement-scaled versions of Hull 21D are invariably superior to their existing counterparts. It can also be observed that, in the cases for which four-way comparisons are possible, the performance of the 3595t Hull 21D/A typically equals or exceeds that of the 7948t Hull B. This finding raises serious questions as to the validity of the prevalent conception to the effect that the gross size of a hull is the primary determinant of its seakeeping characteristics.

Quantitative comparisons of competing hulls can be made either in terms of OI ratios or OI differences. Ratio comparisons are logical from the hydrodynamics perspective, but difference comparisons seem more meaningful from the viewpoint of ship operations as they are absolute measures of gain or loss in window size. Ratio comparisons for the A-hulls in 4.0 m waves indicate that the superiority of Hull 21D/A over Hull A ranges from 50 percent to a factor of eight. Factors of two to three are common. Difference comparisons for the same data show Hull 21D/A to be superior to Hull A by 12 to 51 percent. Differences between 20 and 30 percent are prevalent.

The remainder of the comparative data (for the B-hulls and for the A-hulls in

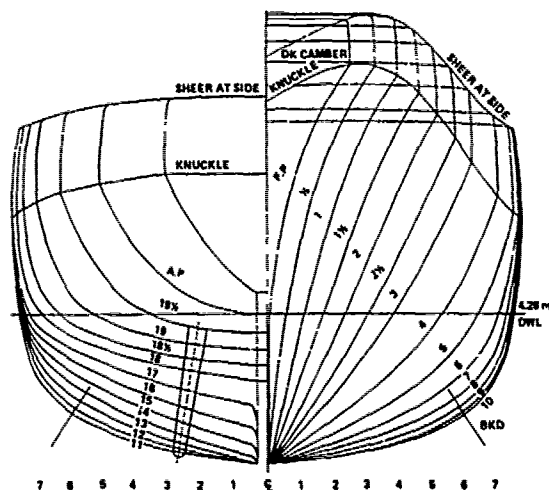


Fig. 10 Hull 21D Body Plan

6.0 m waves) cannot be rationally quantified because it contains OI's of zero. In retrospect, a 5.0 m wave height would have been a better choice to evaluate the B-hulls than the 6.0 m actually chosen. In any case, the superiority of Hull 21D/B over Hull B is evident in a qualitative sense from Fig. 14, 15 and 16.

The foregoing results are held to demonstrate necessary conditions for several generalizations of the results which have been obtained here. The direct generalizations are with respect to hull displacement, seakeeping response and relative heading. In addition, the results show that a hull design based on the very generalized seakeeping rank estimator developed here can exhibit superior seakeeping performance even in a highly specialized operational scenario involving particular criteria. Finally, it is worthy of note that the superiority of the Hull 21D variants over their existing counterparts is well in excess of the incremental improvements so frequently associated with ship hydrodynamics.

3. OPTIMIZATION

The definition of Hull 21 (Appendix C) was a very simple exercise in optimization. All hull parameters in and associated with the seakeeping rank estimator R were

assigned the data base extreme values that would tend to maximize it. Simple algebra led to a unique solution. In a realistic ship design environment, it must be expected that some parameters will be fixed and others tightly constrained. Then the R equation will be overspecified. There will not necessarily be a unique solution, and obtaining any viable solution will require more elaborate mathematics.

Though the hull form constraints explicitly imposed to define Hull 21 were lax, there were highly restrictive conditions implicit to the process. These were the limitations associated with the definition of seakeeping rank, i.e., selected seakeeping responses of 4300t, destroyer-type hulls in long-crested, head seas. The immediately preceding section demonstrated necessary conditions for relaxation of all but the destroyer type hull limitation. It also showed necessary conditions for the practical value of seakeeping rank in the context of a highly-specialized operational scenario. To develop a utilitarian optimization technique, we must go beyond the mathematics of overspecified systems of equations. We must make a bold assumption to the effect that all of the generalizations for which necessary conditions have been shown are, in fact, universally applicable. In other words, we must assume sufficient conditions where only necessary conditions have been demonstrated.

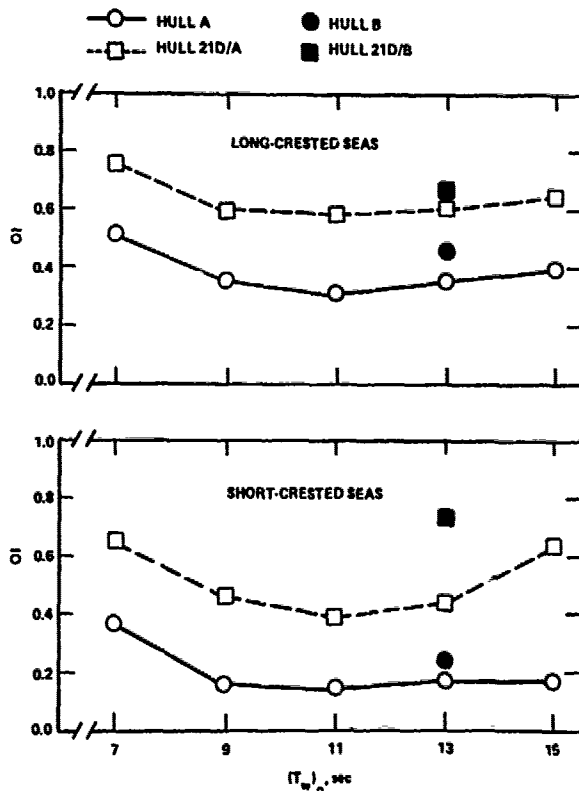


Fig. 11 Operability Index Comparisons for Helicopter Launch in 4.0m Waves

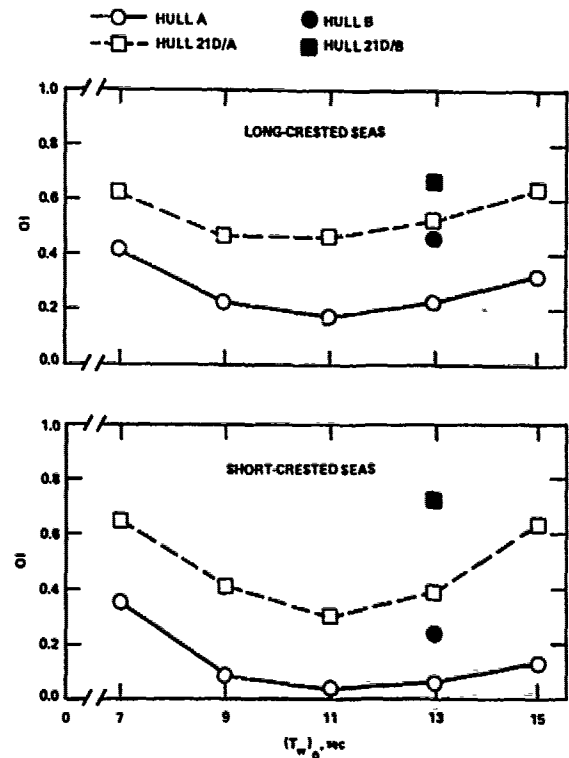


Fig. 12 Operability Index Comparisons for Helicopter Recovery in 4.0m Waves

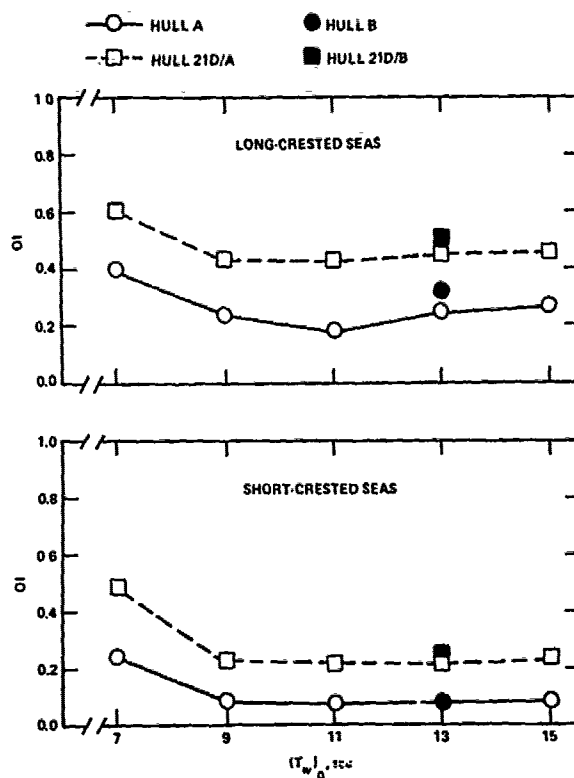


Fig. 13 Operability Index Comparisons for Helicopter Support in 4.0m Waves

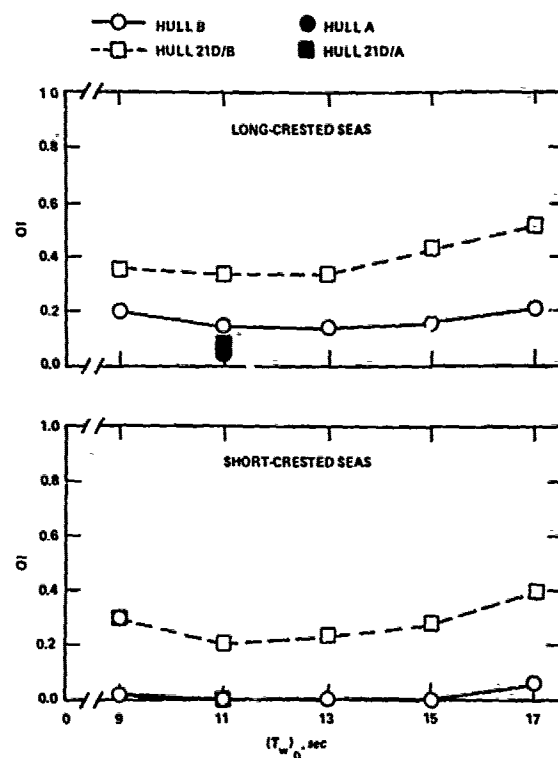


Fig. 15 Operability Index Comparisons for Helicopter Recovery in 6.0m Waves

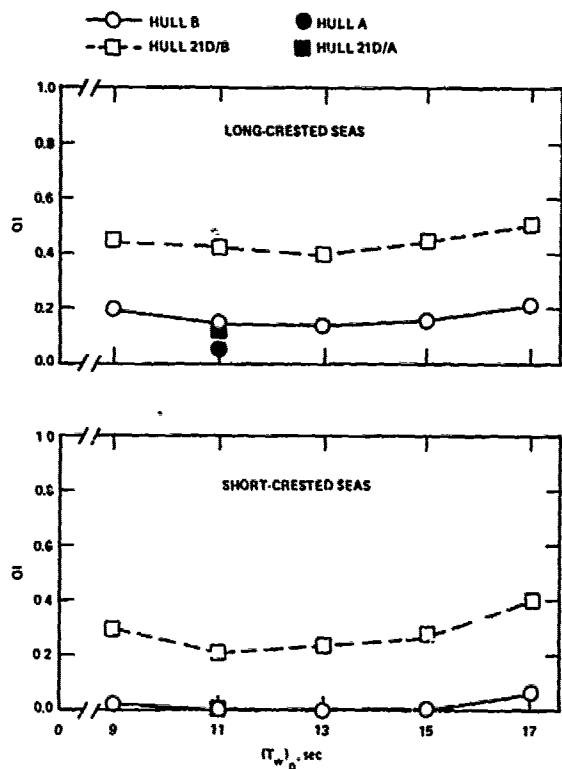


Fig. 14 Operability Index Comparisons for Helicopter Launch in 6.0m Waves

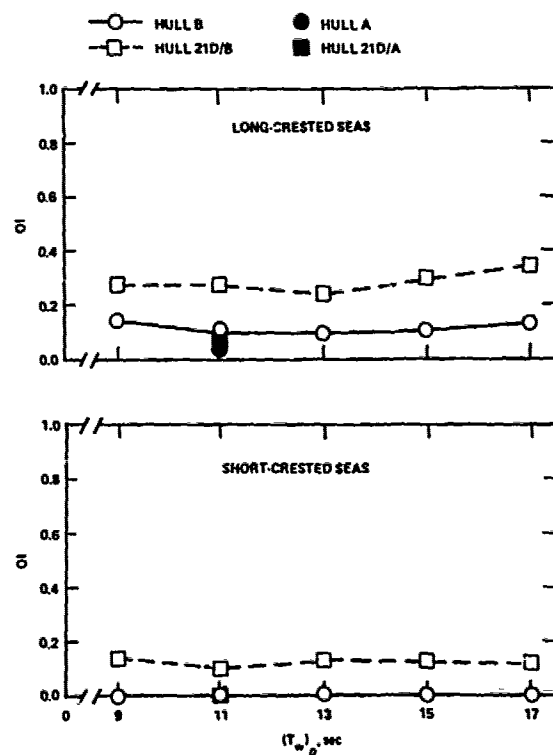


Fig. 16 Operability Index Comparisons for Helicopter Support in 6.0m Waves

Even given this assumption, a philosophical dilemma remains. Having shown necessary and assumed sufficient conditions for the "practical value" of seakeeping rank in a specialized situation does not imply that we can obtain a true optimum for any particular ship mission. The formal optimization is strictly in terms of the rank estimator. The assumption only implies that optimization of \hat{R} will yield a hull which is "good" in a particular scenario. Hull 21D is optimized in terms of \hat{R} . In terms of ability to support helicopter operations, we only know that it is good.

With the above commentary in mind, it is in order to proceed with the details of optimization. The immediately following section outlines an appropriate methodology. Then this methodology is exercised to demonstrate its capabilities in a variety of problems.

3.1 Methodology

The optimization methodology must be based upon the estimator, \hat{R} , of seakeeping rank. From (3) and Table 4, this estimator can be written as

$$\begin{aligned}\hat{R} = & 8.422 + 45.104 C_{WF} + 10.078 C_{WA} \\ & - 378.465 (T/L) + 1.273 (c/L) \\ & - 23.501 C_{VPF} - 15.875 C_{VPA}\end{aligned}\quad (5)$$

where the parameter ranges are as specified in Table 4. In this form, the estimator is not fully responsive to the restrictions likely to be imposed by the ship design process or to the ultimate requirement that hull lines be derived from it. A more suitable form can be obtained by expanding the coefficients of (5) into their constituent, dimensional measures of hull geometry. Then the estimator is

$$\begin{aligned}\hat{R} = & 8.422 + 45.104 (2 A_{WF}/LB) + 10.078 \\ & (2 A_{WA}/LB) - 378.465 (T/L) + 1.273 (c/L) \\ & - 23.501 (\nabla_F/A_{WF} T) - 15.875 \\ & (\nabla_A/A_{WA} T)\end{aligned}\quad (6)$$

where A_{WF} and A_{WA} are waterplane areas forward and aft of amidships, respectively; and ∇_F and ∇_A are displaced volumes forward and aft of amidships, respectively.

The assumption of generality with respect to displacement can be used to write a constraint on (6) as

$$\Delta = \rho (\nabla_F + \nabla_A) \quad (7)$$

where Δ is displacement and ρ is the density of salt water in t/m^3 . It should be noted that this constraint uses the assumption to fix displacement at a specified value for a particular optimization problem. This is thought to be compatible with the fact that a displacement normalized data base was used to quantify (6) and with the manner in which sufficient conditions for generality in displacement were demonstrated.

Using Δ as specified in (7) and the dimensions of the 4300t data base hulls from Table 1, the limits of the overall hull dimensions in (6) can be defined. Letting

$$\mu = \left(\frac{\nabla}{4300}\right)^{1/3} \quad (8)$$

these are

$$117.8 \leq \frac{L}{\mu} \leq 135.3 \text{ m}$$

$$12.68 \leq \frac{B}{\mu} \leq 14.98 \text{ m}$$

and

$$4.05 \leq \frac{T}{\mu} \leq 5.14 \text{ m} \quad (9)$$

These displacement-generalized, dimensional ranges and the coefficient ranges in Table 4 combine to define the parameter space in which optimization can be performed without extrapolation.

The optimization so bounded consists of maximizing \hat{R} as defined by (6) given Δ as related to (6) by (7) and subject to any consistent combination of the following constraints:

$$L_1 \leq L \leq L_2 \text{ or } L = L_0$$

$$B_1 \leq B \leq B_2 \text{ or } B = B_0$$

$$T_1 \leq T \leq T_2 \text{ or } T = T_0$$

$$c_1 \leq c \leq c_2 \text{ or } c = c_0$$

$$(A_{WF})_1 \leq A_{WF} \leq (A_{WF})_2 \text{ or } A_{WF} = (A_{WF})_0$$

$$(A_{WA})_1 \leq A_{WA} \leq (A_{WA})_2 \text{ or } A_{WA} = (A_{WA})_0$$

$$(\nabla_F)_1 \leq \nabla_F \leq (\nabla_F)_2 \text{ or } \nabla_F = (\nabla_F)_0$$

$$(\nabla_A)_1 \leq \nabla_A \leq (\nabla_A)_2 \text{ or } \nabla_A = (\nabla_A)_0$$

$$(C_{WF})_1 \leq C_{WF} \leq (C_{WF})_2 \text{ or } C_{WF} = (C_{WF})_0$$

$$(C_{WA})_1 \leq C_{WA} \leq (C_{WA})_2 \text{ or } C_{WA} = (C_{WA})_0$$

$$(T/L)_1 \leq T/L \leq (T/L)_2 \text{ or } T/L = (T/L)_0$$

$$(c/L)_1 \leq c/L \leq (c/L)_2 \text{ or } c/L = (c/L)_0$$

$$(C_{VPF})_1 \leq C_{VPF} \leq (C_{VPF})_2 \text{ or } C_{VPF} = (C_{VPF})_0$$

and

$$(C_{VPA})_1 \leq C_{VPA} \leq (C_{VPA})_2 \text{ or } C_{VPA} = (C_{VPA})_0 \quad (10)$$

where a parameter magnitude subscripted 2 exceeds that subscripted 1 and the subscript 0 indicates a specified value. When a parameter is not explicitly constrained by (10), it is implicitly constrained by the Table 4 coefficient ranges or by the hull dimension ranges in (9). Direct constraint of the parameters c , A_{WF} ,

A_{WA} , ∇_F and ∇_A appears unlikely to be required, but including them adds flexibility and is useful for subsequent definition of the optimum hull.

The optimization problem just outlined is amenable to solution by nonlinear programming techniques. Basically, (6) is taken as an object function with (7) acting as an equality constraint thereon. The nondimensionalized estimator (5) functions as a variable transformation link between (7) and related constraints from (10). Then the parameters in (6) (and, effectively, (5)) which maximize \hat{R} under the specified constraints can be determined by a nonlinear programming algorithm. The Augmented Lagrangian method described by Pierre and Lowe³ has been found to work well for the problem under discussion. Even given an intentionally poor initial estimate of the optimum parameters, acceptable convergence occurs in less than 10s of CDC 6700 central processing unit time.

3.2 Examples

The most intriguing question to be explored "by example" is whether or not the optimization methodology just outlined can lead to appreciable seakeeping improvements in a heavily constrained case. The first example presented here addresses that question, and is carried through a limited verification. Subsequent examples are treated only in the strict context of optimization.

For the initial example, we will consider a redesign of Hull A as used for the generalization effort described earlier. It will be recalled that this hull has dimensions of 124.4 x 13.8 x 4.52 m and displaces 3595t. The Hull A coefficients relevant to the seakeeping rank model are $C_{WF} = 0.615$, $C_{WA} = 0.848$, $T/L = 0.0363$, $c/L = 0.650$, $C_{VPF} = 0.720$, and $C_{VPA} = 0.551$. Hence, from (5), its estimated seakeeping rank is $\hat{R} = 6.2$.

The redesign will take the dimensions and displacement of Hull A to be fixed. Its coefficients will be allowed to vary over limited ranges encompassing their original values. Specifically, Δ in (7) is set equal to 3595t and (10) is written as follows:

$$\begin{aligned} L &= 124.4 \text{ m}, B = 13.8 \text{ m}, T = 4.52 \text{ m}, \\ 0.58 &\leq C_{WF} \leq 0.68, 0.85 \leq C_{WA} \\ &\leq 0.90, T/L = 0.0363, 0.60 \leq c/L \\ &\leq 0.80, 0.68 \leq C_{VPF} \leq 0.80, 0.55 \\ &\leq C_{VPA} \leq 0.65. \end{aligned}$$

Under these constraints, the nonlinear programming solution for the unspecified parameters was found to be as follows:

$C_{WF} = 0.651$, $C_{WA} = 0.850$, $c/L = 0.800$, $C_{VPF} = 0.680$, and $C_{VPA} = 0.550$. It can be noted that the last three parameters attained the "best" values within their specified ranges in the sense of maximizing \hat{R} in (5). On the other hand, C_{WA} was driven to its worst value, and C_{WF} was assigned an improved value intermediate to its range.

The redesigned version of Hull A, say Hull AX, has $R = 8.9$. This represents an improvement of over 40 percent in R , and is certainly encouraging for an optimization limited to hull form changes. To explore its dimensional significance, a Lewis section model of Hull AX was developed in the same manner as done earlier for Hull 21 (see Appendix C). The head sea, seakeeping responses of Hull A and of Hull AX were then computed using the same procedures applied previously to construct the data base; and the responses of the two hulls were compared.

Excepting minor reversals at low modal period and relative motion at the stern, Hull AX was increasingly superior to Hull A as ship speed increased. In the case of relative motion at the stern, Hull A was slightly superior to Hull AX at low-to-moderate speeds, but the comparison reversed

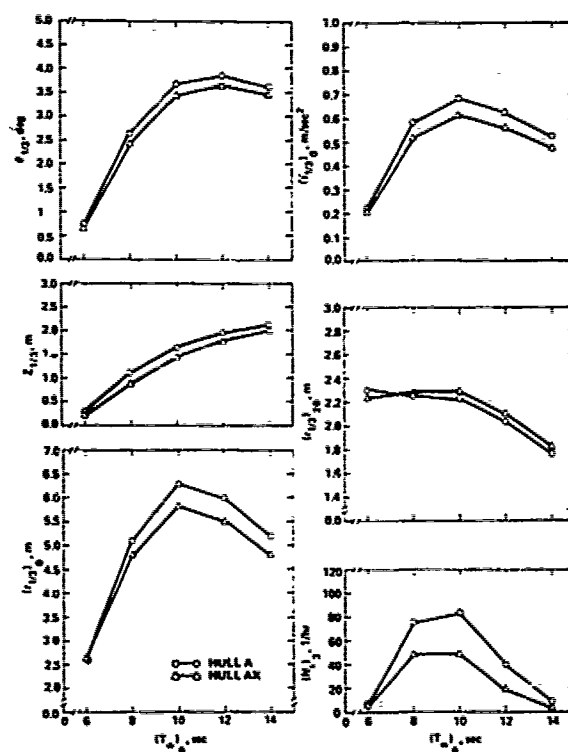


Fig. 17 Representative Comparisons between Hull A and Hull AX at 20 Knots in Waves of 5.0m Significant Height

at high speed. The degree of difference between the two hulls was, of course, less than found in earlier comparisons between Hull 21 and others. Figure 17 illustrates this. Here (N_s)₃ is the number of slams per hour at Station 3, and all other nota-

tion is as previously introduced. It can be observed that reversals in slamming do not occur at low modal periods. The failure of this tendency to appear as it did in earlier comparisons based on Hull 21 is attributable to the fact that the drafts of

Table 5 Optimization of a Small Frigate Hull

Parameter	Constraint	Solution
Δ , t	2500	2500.
L, m	110 to 115	115.
B, m	11 to 13	11.6
T, m	3.5 to 4.0	3.50
c, m	---	71.5
A_{WF} , m ²	---	435.1
A_{WA} , m ²	---	635.9
V_F , m ³	---	989.9
V_A , m ³	---	1446.8
C_{WF}	0.55 to 0.65	0.650
C_{WA}	0.88 to 0.95	0.950
T/L	---	0.0304
c/L	0.60 to 0.65	0.622
C_{VFF}	0.65 to 0.75	0.650
C_{VFA}	0.65 to 0.69	0.650
\bar{R}	---	11.0

Table 7 Optimization of a 6177t Destroyer Hull

Parameter	Constraint	Solution
Δ , t	6177	6177
L, m	132	132
B, m	16.48	16.48
T, m	5.191	5.191
c, m	---	92.4
A_{WF} , m ²	---	739.6
A_{WA} , m ²	---	1033.3
V_F , m ³	---	2687.5
V_A , m ³	---	3331.0
C_{WF}	0.57 to 0.68	0.680
C_{WA}	0.90 to 0.95	0.950
T/L	---	0.0393
c/L	0.60 to 0.70	0.700
C_{VFF}	0.70 to 0.80	0.700
C_{VFA}	0.60 to 0.70	0.621
\bar{R}	---	8.4

Table 6 Optimization of a 6119t Destroyer Hull

Parameter	Constraint	Solution
Δ , t	6119	6119
L, m	132	132.
B, m	17.40	17.40
T, m	5.120	5.120
c, m	---	92.4
A_{WF} , m ²	---	780.3
A_{WA} , m ²	---	1033.0
V_F , m ³	---	2794.3
V_A , m ³	---	3169.6
C_{WF}	0.57 to 0.68	0.679
C_{WA}	0.90 to 0.95	0.900
T/L	---	0.0380
c/L	0.60 to 0.70	0.700
C_{VFF}	0.70 to 0.80	0.700
C_{VFA}	0.60 to 0.70	0.600
\bar{R}	---	8.4

Table 8 Optimization of a Cruiser Hull

Parameter	Constraint	Solution
Δ , t	10000	10000
L, m	156 to 160	160.
B, m	17 to 19	19.0
T, m	6.0 to 6.5	6.40
c, m	---	101.4
A_{WF} , m ²	---	896.8
A_{WA} , m ²	---	1307.2
V_F , m ³	---	4306.4
V_A , m ³	---	5440.2
C_{WF}	0.57 to 0.59	0.590
C_{WA}	0.84 to 0.86	0.860
T/L	---	0.0400
c/L	0.60 to 0.65	0.634
C_{VFF}	0.75 to 0.80	0.750
C_{VFA}	0.65 to 0.69	0.650
\bar{R}	---	1.4

Hull A and Hull AX are identical.

Generally, then, the comparisons between Hull A and Hull AX are very much as expected given the validity of the various assumptions and procedures used to define the latter hull. Further, the comparison indicates that appreciable seakeeping improvements can be realized in the presence of rather severe constraints. This is considered to be a vital result in the context of practical applications.

The second example to be presented concerns optimization of a small (2500t) frigate. Both the principal dimensions and the coefficients are allowed moderate variability, but the afterbody parameters are constrained in such a manner as to admit a full transom/appendage skeg configuration. Table 5 presents the details of the example. Inspection of this table indicates that best values (again in the sense of maximizing R) were attained for all coefficients except c/L . The estimated seakeeping rank reflects the liberal constraints by attaining a value of 11.0. (Values of R exceeding its nominal maximum value of 10.0 are not uncommon in lightly constrained problems. Hull 21D, constrained only by the data base ranges, has $R = 13.5$.)

The third and fourth examples both concern optimization of a destroyer displacing about 6100t. Both examples admit modest coefficient variability, but fix principal dimensions. Coefficient ranges for the two examples are identical, but the principal dimensions and displacement differ slightly. The results, presented in Table 6 and 7, indicate that the optimization process is sensitive to the perturbation in hull dimensions. In the first case (Table 6, $\Delta = 6119t$), C_{WA} is compromised. In the

second case (Table 7, $\Delta = 6177t$), C_{UPA} is compromised. In spite of these differences, R is the same (8.4) for the two examples.

The fifth, and final, example presented concerns a 10,000t cruiser. Both principal dimensions and coefficients are allowed to vary, but the ranges are selected to be poor ones from the perspective of seakeeping. Table 8 summarizes this example. The evident moral of the ultimate result, $R = 1.4$, is that external constraints can obviate the value of optimization. One must be cognizant of seakeeping from the beginning of the design process in order to avoid imposition of constraints which preclude good seakeeping.

4. DISCUSSION

The modeling described here is fundamentally intuitive. Quantification and generalization of the model are empirical. Complete reliance is placed upon analytical predictions. Major assumptions are required to apply the results obtained to realistic optimization problems.

Intuition and empiricism stand in lieu of causal knowledge. Such knowledge of seakeeping exists only from hull geometry to motions. The reverse path is nonunique;

and therefore, more difficult to follow. However, it is the path which must be taken to provide a causal basis for optimization. If a solution to the reverse problem existed, we could specify motion requirements and synthesize the hull geometries which satisfied them in a fully-rational manner. Lacking such a solution, we are driven to employ intuition and empiricism.

There is no reason to believe that hydrodynamic theory respects the traditional, naval architecture coefficients. However, those employed here were rationalized from consideration of Lewis section-based, strip theory representations of hull geometry. That tenuous link may provide rudimentary insights into the causal nature of the synthesis problem.

Linear strip theory is, of itself, marked by a number of intuitive and/or empirical features. Yet, it has become the standard by which more rational ship motion theories are validated. For destroyer-type hulls, at least those without large bow domes, linear strip theory seems very capable of predicting hull-to-hull trends which are of sufficient magnitude to be of practical importance.

Linear superposition works unbelievably well. Even in conditions for which our senses tell us nonlinearities must exist, it produces useful statistics. There are, of course, limits; but they appear to lie primarily in the realm of seaway survivability rather than that of operability and habitability which is of concern here.

Two detailed reservations about the analytical procedures employed must, however, be expressed. One concerns relative motion. The other concerns the seakeeping characteristics of Hull 21D.

Except in synthesizing the above-water bow design for Hull 21D, relative motion has been treated as though it was a purely kinematic response, i.e., it has been defined to be the vector sum of absolute ship motion and incident wave elevation. The absolute accuracy of these kinematic predictions is significantly lower than for the principal, modal motions or for truly-kinematic responses such as acceleration. However, stringently-limited experimental data indicates that the nonkinematic components of relative motion are not extremely sensitive to local geometry within a homogeneous class of hulls. An assumption to this effect is implicit to the viability of the relative motion trends established here.

The author is not altogether comfortable with such an assumption, but can offer nothing better at the current state-of-the-art. More satisfactory methods for both computing and measuring relative motion are, however, emerging. As these methodologies are validated, their application to identification of trends with hull geometry should be a high-priority research area.

It would seem that the range of applicability of a fully rational theory could be rationally bounded. When empiricism is involved, as has been noted to be the case

with the linear strip theory used here, one is forced to question the unusual result. The computed seakeeping characteristics of Hull 21D constitute an "unusual result" in that they imply improvements over existing hulls which can be interpreted as factors rather than percentage points. Accordingly, an experimental verification of the computed seakeeping responses of Hull 21D is in order.

A physical model of Hull 21D has been constructed, and an experiment was performed with it while this document was being prepared: see the Frontispiece. Preliminary results from the experiment indicate that Hull 21D performs as well in water as on paper. Local correlations between theory and experiment differ slightly from those typical of more-conventional, destroyer-type hulls; but the overall level of correlation appears to be comparable. The complete results of the experiment will be the subject of a future publication.

Bounding the implications of the assumptions made in order to treat realistic optimization problems will require much experience with applications, further work of the type pursued here, and/or the introduction of second-generation optimization technologies. In the interim, it should be evident that what has been developed is not a methodology for the casual practitioner to apply by rote. Rather, it is a tool for the studied professional who can reject an analytically-correct result which is wrong quite as easily as accepting one which is right.

5. CONCLUSION

Given appropriate attention to the limitations just discussed, the results presented here provide a viable basis for early-design synthesis of destroyer-type hulls with superior seakeeping performance.

APPENDIX A SELECTION OF PARAMETERS FOR THE GENERAL MODEL

This appendix outlines the rationale which led to selection of parameters for the general model relating hull form to seakeeping. In accord with the philosophy set forth in the text, the discussion treats three, basic sets of descriptors: those of the waterline, of the underwater profile, and of sectional fullness. Further, the descriptors are treated separately for the forebody and for the afterbody.

With respect to the waterline, the prominence of waterplane coefficient forward of amidships has already been remarked upon. The fullness of the afterbody waterplane is also relevant. Though its effect is neither as dramatic nor as consistent as that of its forward counterpart, an overall tendency for increases in after waterplane coefficient to improve seakeeping is anticipated. The influence of beam appears to be

very minor within ship class limits. Transom width was dismissed in the text. Hence, the waterline will be described by two parameters: waterplane coefficient forward of amidships, C_{WF} ; and waterplane coefficient aft of amidships, C_{WA} .

Draft to length ratio provides an overall bound on a ship's underwater profile, and appears to be a significant parameter from the perspective of seakeeping. Contrary to "common-sense" arguments regarding the effect of draft on bottom slamming, reductions in this parameter appear to improve overall seakeeping in head seas. Bottom slamming per se may be reduced or stabilized by reductions in relative motion attendant to reductions in draft-to-length ratio.

The discussion of the seakeeping characteristics of ships with and without transoms which is presented in the text implies that special consideration must be given to the underwater profile characteristics of the afterbody. This can be done in terms of the location of the cut-up point, i.e., the longitudinal location at which draft begins decreasing to accommodate propulsion gear. Taking L to be ship length between perpendiculars and c to be the distance from the forward perpendicular to the cut-up point, we can characterize the location of the cut-up point by c/L . This parameter will be referred to as the "cut-up ratio." The cut-up ratio is typically smaller for ships with transoms than for ships without transoms. Hence, it is anticipated that seakeeping will improve as the cut-up ratio increases.

Other underwater profile parameters which might be considered include trim, forefoot and stem characteristics, and transom depth. These, however, are thought to be of secondary importance. Hence, underwater profile will be characterized by two parameters: draft-to-length ratio, T/L , where T is draft amidships; and cut-up ratio, c/L .

The vertical prismatic coefficient appears to be the naval architecture coefficient best correlated with our normal perception of sectional fullness. For the forebody, it is, in fact, an excellent measure of this quality; and appears to have a rather consistent effect on seakeeping in head waves. Fine forebody sections, as represented by a small vertical prismatic coefficient forward of amidships, lead to good seakeeping in terms of both motions and minimal bottom slamming loads.

Aft of amidships, the utility of the vertical prismatic coefficient is less well-defined. Two, related factors cloud the issue. These are the cut-up ratio and skeg type. As a convention, the author interprets integral, displacement skegs as part of the hull for purposes of computing hydrostatic and hull form characteristics. Appendage skegs are neglected for these same computations. Thus, for transom stern ships in particular, integral displacement

skegs produce larger cut-up ratios than do appendage skegs. Further, an integral displacement skeg will lead to a much smaller sectional area coefficient, i.e., a "finer" section, than will an appendage skeg for an otherwise identical section.

The afterbody, vertical prismatic coefficient integrates out much of this detail, and cannot be said to provide a rigorous indicator of sectional fullness for classes of ships which may have either appendage or integral displacement skegs. However, it is accepted here as the best available, simplistic measure of sectional character aft of amidships. For classes of ships with conventional sterns, full after sections have been found to offer some advantage in seakeeping. It is, therefore, hypothesized that increasing vertical prismatic coefficient aft of amidships may improve seakeeping in the more general case of concern here.

The parameters selected to represent sectional fullness are, then, the vertical prismatic coefficient forward of amidships, C_{VPF} , and vertical prismatic coefficient aft of amidships, C_{VPA} .

APPENDIX B SELECTION OF RESPONSES AND OPERATING CONDITIONS FOR THE DATA BASE COMPUTATIONS

Responses and operating conditions must be selected in light of the general definition of the seakeeping rank index, R , which is given in the text. Briefly, this definition requires that the vertical plane responses upon which performance criteria are likely to be based be considered; and that a comprehensive range of operating conditions be evaluated. Operating conditions are interpreted to include both the seaway and ship speed.

Destroyer-type hulls are subject to performance criteria associated with personnel, subsystems and the hull per se. Subsystems prominent in this context are sensors (sonar and radar), helicopters, guns, and missile launchers. The vertical-plane seakeeping responses upon which such criteria may be based include pitch, kinematic responses (absolute and relative motions, velocities, and accelerations) at specific points, and discrete events such as slamming and deck wetness. The effort here is to select as small a representative set as possible.

Pitch criteria are used both for personnel and for helicopter operations. Hence, pitch should be considered. Heave, the other modal motion of concern in the head-wave case, appears to have no criterion related use. However, in view of its fundamental role in determining the various responses of direct concern it seems that heave should be included.

Kinematic responses are involved in all the major criteria areas. Applicable locations are often a function of subsystem arrangements, and can only be approximated

here. Absolute motion will be considered at the stern where it influences towed array work. Relative motion will be considered both at the bow and at the stern. At the bow, this response influences deck wetness and slamming; and controls the emergence of hull-mounted sonar domes. At the stern, this response can, like absolute motion at the same location, influence towed array work. In addition, it controls propeller emergence. Absolute velocity is used to establish criteria for helicopter landing and for weapon firing. It should be considered at a representative location in way of the after quarter point. Acceleration criteria are applicable to personnel and to a variety of subsystems. Forebody locations are critical, and it will be assumed that an adequate representation can be obtained by considering this response at the longitudinal center of buoyancy location (heave acceleration) and at the forward perpendicular.

Four discrete events upon which criteria can be based were mentioned in the context of kinematic responses. These were deck wetness, slamming, dome emergence, and propeller emergence. Since freeboard is not considered in this investigation, direct evaluation of relative motion at the bow is the best approach available for incorporating consideration of deck wetness. For the other cited events, draft is analogous to freeboard in deck wetness; so more elaborate options are available. Since, as noted in Appendix A, the author's preconception as to the effect of draft-to-length ratio on seakeeping performance contradicts common-sense arguments as to the effect of draft on slamming, adopting a more elaborate option for this event appears worthwhile.

A suitable option can be derived from the state-of-the-art relationship for probability of occurrence of bottom slamming if we define a slamming incidence parameter, C_s , as

$$C_s = \left[\frac{T}{r_{1/3}/(\xi_w)_{1/3}} \right]^2 + \left[\frac{\dot{\xi}_t}{\dot{\xi}_{t_c}/(\xi_w)_{1/3}} \right]^2 \quad (B1)$$

Here T is draft, $r_{1/3}$ and $\dot{\xi}_{1/3}$ are the significant single amplitudes of relative motion and relative velocity, respectively, $(\xi_w)_{1/3}$ is significant wave height, and $\dot{\xi}_{t_c}$ is threshold relative velocity as defined by Ochi¹. The formulation must be referenced to a particular location. Again following Ochi, Station 3 will be used here.

Equation (4) of the text provides the relationship between C_s as defined above the probability of occurrence of bottom slamming.

As to operating conditions, a speed range from 5 to 30 knots is thought to provide good coverage. Destroyer-type hulls typically have design speeds on the order of 30 knots, and 5 knots can be taken as a threshold of controllability. Destroyer-

type hulls of the size under consideration here are expected to experience maximum responses in waves of 9 to 12s modal period. Available wave statistics for the North Atlantic, an operational area typically specified for such hulls, indicate that the bulk of the seaways which occur there have characteristic periods in the range from 6 to 14s. Hence, the latter wave period range provides adequate coverage both in terms of the natural environment and the characteristics of the hulls being investigated.

APPENDIX C DEFINITION OF HULL 21

The objective here is to define a hull which maximizes estimated seakeeping rank, \hat{R} , as defined in the text, within the parametric limits of the data base hulls. It follows from inspection of Table 4 that this hull (designated Hull 21) should have the following characteristics:

$$C_{WF} = \frac{2 A_{WF}}{BL} = 0.698$$

$$C_{WA} = \frac{2 A_{WA}}{BL} = 0.922$$

$$T/L = 0.0315$$

$$c/L = 0.850$$

$$C_{VPF} = \frac{V_F}{A_{WF} T} = 0.667$$

and

$$C_{VPA} = \frac{V_A}{A_{WA} T} = 0.551 \quad (C1)$$

where A_{WA} and A_{WF} are, respectively, the waterplane areas forward and aft of amidships; V_F and V_A are, respectively, displaced volumes forward and aft of amidships; and all other notation is as previously defined. In addition to the foregoing, we must add the fixed displacement relationship

$$\rho(V_F + V_A) = 4300 \quad (C2)$$

where ρ is the density of salt water in t/m^3 . Data base limits for the hull dimensions intrinsic to (C1) can be read from Table 1. They are:

$$117.8 \leq L \leq 135.8 \text{ m}$$

$$12.68 \leq B \leq 14.98 \text{ m}$$

and

$$4.05 \leq T \leq 5.14 \text{ m}$$

Equations (C1) and (C2) constitute a set of seven equations in eight unknowns.

The unknowns are $L, B, T, c, A_{WF}, A_{WA}, V_F$, and V_A . By assigning a value to any one of those unknowns, the seven equations can be solved simultaneously for the remaining unknowns. As we are dealing with a constant Froude number data base, an advantage in absolute ship speed accrues with increasing ship length. It is, accordingly, logical to assign ship length its maximum, data base value, i.e., $L = 135.8 \text{ m}$.*

With $L = 135.8 \text{ m}$, (C1) and (C2) yield the following values for the remaining seven unknowns: $T = 4.28 \text{ m}$, $c = 115.43 \text{ m}$, $B = 14.72 \text{ m}$, $A_{WF} = 697.64 \text{ m}^2$,

$$A_{WA} = 921.53 \text{ m}^2, V_F = 2021.45 \text{ m}^3 \text{ and}$$

$$V_A = 2173.23 \text{ m}^3. \text{ This is all the information which the } \hat{R} \text{ predictor can provide.}$$

It remains to distribute local beams, drafts, and sectional areas within the $135.8 \times 14.72 \times 4.28 \text{ m}$ prism in such a manner that the derived area and volume conditions are satisfied.

An iterative procedure was employed to distribute local hull characteristics. Initial distributions of beam, draft and sectional area coefficient were postulated. The three were multiplied to obtain sectional area; and integrations over length were performed to determine waterplane areas and displaced volume. The results of the integrations were compared to the desired values, and the initial distributions were modified as deemed necessary to reduce the discrepancies found. On the fourth such iteration, the distributions shown in Figure C1 were obtained; and judged to be adequate.

In Figure C1, b is local beam, t is local draft, A is local sectional area, and A_x is the maximum value of A . Hence, A/bt is sectional area coefficient. Obtaining the desired coefficients seemed to lead to a counter stern configuration with an integral, displacement skeg as sketched in the t/T plot included in Figure C1. The coefficients corresponding to the distribution of local characteristics shown by the figure are reported in the text.

APPENDIX D DETAILED DESIGN OF HULL 21

The preceding appendix provides only a crude definition of Hull 21. Here, this definition is taken as a starting point to derive complete lines, including those of the above-water hull, and appendage details. For underwater hull design, the guidelines adopted were to preserve the characteristics defined by the preceding appendix as well as possible while minimizing penalties in

* It can, in fact, be shown that, in order to obtain all of the desired coefficients while maintaining B and T within their data base ranges, L must exceed 134.4 m .

resistance. Freeboard requirements computed in accord with the procedure^{*} which the author developed for that purpose were used to aid in development of the above-water hull. Bilge keels were sized using the procedure outlined by Cox and Lloyd⁵. Rudders size was selected largely on the basis of precedent established by past designs with acceptable maneuvering characteristics.

Freeboard specification was undertaken first as these data were needed to fair-out the underwater hull lines. Required freeboards for Stations 0 through 6 were computed using the same Lewis section representation of Hull 21 which was employed for the verification work described in the text. The requirements so determined were unusually high for a hull of the length under consideration. This was foreseeable.

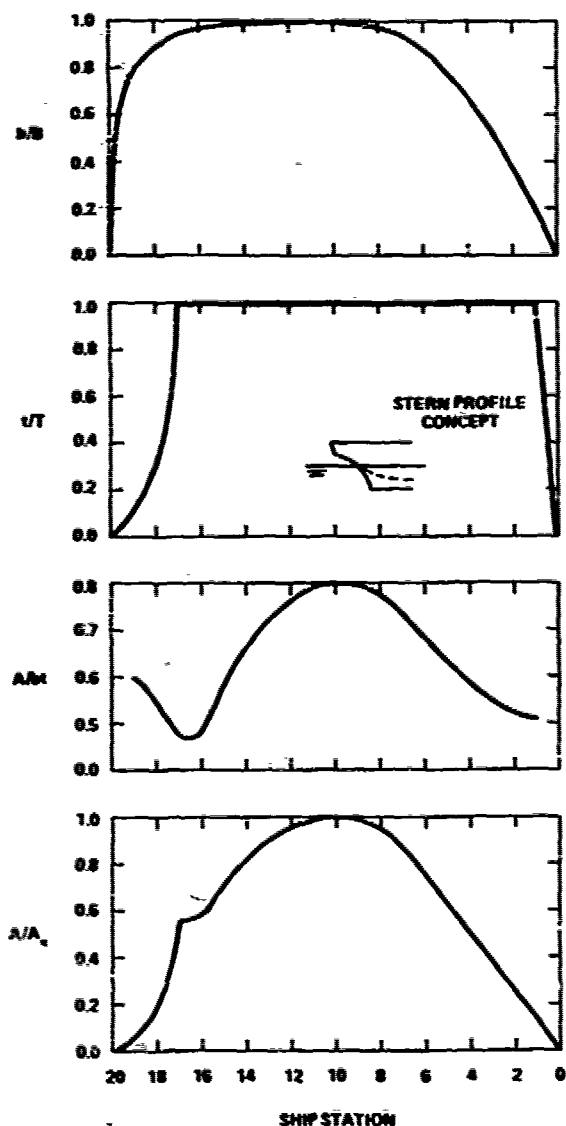


Fig. C1 Local Characteristics of Hull 21

Good underwater hull characteristics from the perspective of seakeeping require high freeboards to "balance" the ship.

Subsequent to publication of Reference 4, the author initiated development of a procedure for optimizing freeboard under circumstances such as the one just described for Hull 21.* The technology necessary for the optimization procedure was not fully developed at the time the work under discussion was performed. However, enough preliminary results had been obtained to suggest that the required freeboards could be slightly reduced without incurring serious degradation due to deck wetness. In view of these circumstances, it was decided to risk a simple, speed weighting of the computed freeboard requirements. The weighting emphasized speeds in the 15 to 25 knot range. Figure D1 compares the resultant freeboard requirements to a sheer line representative of present-day design practice.

Maximization of required freeboard at a location aft of the stem, as seen in Figure D1, is a typical result of the methodology employed. It occurs because the nonkinematic components of relative motion are considered. For Hull 21D, it was decided to use a sheer line which followed this trend, i.e., to maximize freeboard near Station 1 rather than at the stem. Justifying such a reflexive sheer line in traditional Naval Architecture terms would be difficult. However, it was thought that this type of sheer line would reduce the blockage effect of the hull on some shipboard sensors; and that the combination of hydrodynamic and combat capability rationales provided sufficient justification to explore the reflexive sheer line.

It was also decided to flare the above-water hull sections up to a full-length knuckle. There were several reasons for

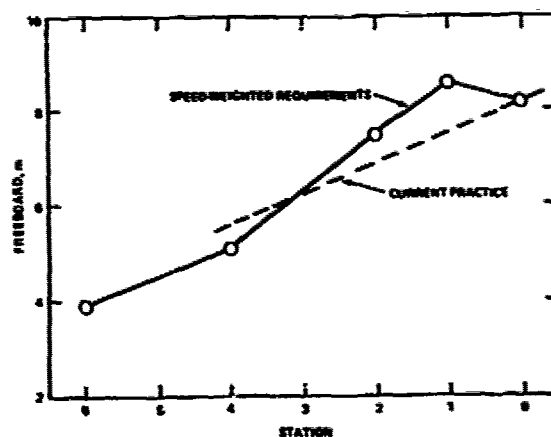


Fig. D1 Required and Design Practice Freeboards for Hull 21

* This procedure will be the subject of a future publication.

this. From the hydrodynamic viewpoint, the author felt that such sections might lead to "favorable" nonlinearities, i.e., to reductions in response per unit wave height with increasing wave height. Flared sections are also attractive from the perspective of stability. In addition, it appeared that the stern sections, if not flared, would require a rather hard radius just below the waterline. Finally, a flare and knuckle bow configuration was thought to be desirable in the context of minimizing deck wetness associated with bow wave profile overtopping at high speeds.

Preliminary sketches indicated that it was probably possible to obtain the desired afterbody parameters using a transom stern configuration. However, the lines required to obtain such a configuration seemed rather forced. It was, thus, decided to use the counter stern/integral, displacement skeg configuration to which it was felt that the original definition of Hull 21 had been leading.

In addition to producing more natural lines, choosing the counter stern opened some intriguing possibilities in the context of resistance. It seemed possible that change of level at the stern might cause transom immersion at high speeds. This, it was rationalized, could reduce high-speed resistance due to both the transom effect and the reduction in Froude number occasioned by the accompanying increase in waterline length. Lacking a priori knowledge of the trim and sinkage characteristics at the hull, these possibilities could not be pursued in detail. However, it was decided to draw-in a distinct "appendage transom" to expedite future explorations.

Detailed lines were developed under the foregoing constraints. The waterline was laid down first, and it was determined that a 9 degree entrance angle could be held without a notable shoulder. For an assumed design speed of 30 knots, it appeared that the prismatic coefficient should be on the order of 0.6, so this constraint was added to those already in place to derive an A/A_X distribution. This distribution produced a prismatic of 0.613 and thence amidship section coefficient of 0.807. The stem was given a generous rake (very limited experimental data indicates that high rake angles may be beneficial as regards deck wetness), and this led to cutting away the forefoot back to Station 1. The centerline profile of the afterbody, constrained by cut-up location and the requirement for an appendage transom, was carefully drawn to ensure good buttock flow.

The body plan and the seakeeping-related hull coefficients which resulted from the effort just described are presented in the text. Here it remains to describe appendage design. As noted earlier, rudder design was based largely on precedent while bilge keels were sized analytically. Propulsion appendages were not considered.

A twin rudder arrangement was selected because its intrinsic redundancy was thought to be desirable for a combatant ship. The rudder design was developed only to the extent of profile and location. Each rudder has a profile area of 10.9 m², and is located as shown in Figure 10 of the text.

A 55-degree bilge keel diagonal was selected as it seemed to provide the best "fit" to the sectional characteristics of the hull. Six bilge keel sizes, all constrained not to ground in a 5-degree heel condition, were investigated. The six were defined by the possible combinations of bilge keel length to ship length ratios of 0.27 and 0.33 and of bilge keel span to ship length ratios of 0.0037, 0.0073 and 0.0110. The shorter bilge keels of intermediate span appeared to offer a reasonable compromise between roll reduction and wetted surface penalty, and were, accordingly, selected. They were placed between Stations 7.3 and 12.7 along the 55-degree diagonal.

To ensure that detailing the design had not had a major effect on seakeeping, a close-fit representation of the detailed design was put through the same computations used for the data base hulls; and the results were compared to those obtained previously for the Lewis section representation. The only appreciable differences found between the seakeeping responses of the two hulls were in the slamming incidence parameter (C_s)₃. Detailing had increased slamming incidence at low F_n , but decreased it at high F_n . The differences involved were about 10 percent at each extreme. The other responses were generally within two percent. This level of agreement was considered satisfactory.

APPENDIX E PERFORMANCE ASSESSMENT

For the basic, six-degree-of-freedom motion computations, all four hulls were assigned pitch and yaw gyradii of 0.25 L and roll gyradii of 0.36 B. The vertical center of gravity location for each displacement-scaled version of Hull 21D was specified such that its metacentric height would equal that of the existing hull to which it was to be compared. The computations were performed for relative headings from zero degrees (head waves) to 180 degrees (following waves) in 15-degree increments, and for ship speeds from zero to 30 knots in 5-knot increments.

Bretschneider wave spectra were used to represent random sea conditions. Short-crestedness was modeled by a +90 degree, cosine-squared spreading function. Different spectral parameters were specified for the two pairs of hulls in view of their size difference. Table E1 presents the selected parameters. It can be noted that both pairs are evaluated in two seaways to admit direct comparisons of all four hulls.

The results of the random wave com-

putations were used to assess the ability of the hulls considered to conduct helicopter operations. These operations were divided into three categories: launch, recovery, and support. The "support" operation consists of on-deck handling of the helicopter and its equipment. The categorization is required because each of the three operations involves different criteria variables and/or magnitudes. Further, in order to obtain an operationally meaningful assessment, criteria for avoiding hull damage and for personnel limitations must be superimposed upon the criteria set for each category of helicopter operation. Table E2 summarizes the criteria imposed.

Speed polar diagrams, as introduced by Covich and Comstock⁸, were used to assess performance. These diagrams, as exemplified by Figure E1, present criterion contours in a coordinate system of ship speed versus relative heading for a particular ship in a specified seaway. Figure E1 applies to Hull A in a short-crested seaway of 4.0 m significant height and 9.0 s modal period. The criterion contours shown are those associated with the helicopter landing operation (and, implicitly, with the hull

and personnel) which are exceeded at some point within the speed polar plane for the particular seaway considered.

Each criterion contour shown has tic marks indicating the direction in which that criterion is exceeded. The portion

Table E1 Random Wave Parameters for Relative Heading Generalization

$(T_w)_0, s$	$(\zeta_w)_{1/3}, m$	
	4.0	6.0
7.0	A-Pair	None
9.0	A-Pair	B-Pair
11.0	A-Pair	Both Pairs
13.0	Both Pairs	B-Pair
15.0	A-Pair	B-Pair
17.0	None	B-Pair

Table E2 Criteria Imposed for Performance Assessment

Criterion Response	Location	Criteria Levels for		
		Launch	Recovery	Support
Pitch	About CC	3.0 deg		
Roll		5.0 deg		3.5 deg
Deck Wetness	Station 0	30 occurrences per hour		
Bottom Slamming	Station 3	10 occurrences per hour		
Vertical Acceleration	Bridge	0.4 g		
Lateral Acceleration		0.2 g		
Vertical Velocity	Helicopter Touchdown Point	None	2.0 m/s	None

Notes: (1) Criteria Levels for continuous responses are given as significant single amplitudes.
(2) Bridge and Touchdown Point locations for the Hull 21D variants were taken to be at the same stations and levels as for the existing hulls.

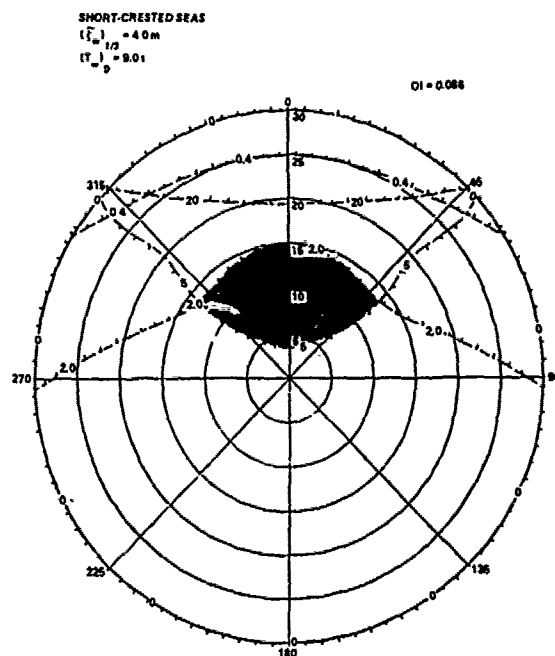


Fig. E1 Speed Polar Performance Assessment of Helicopter Landing for Hull A

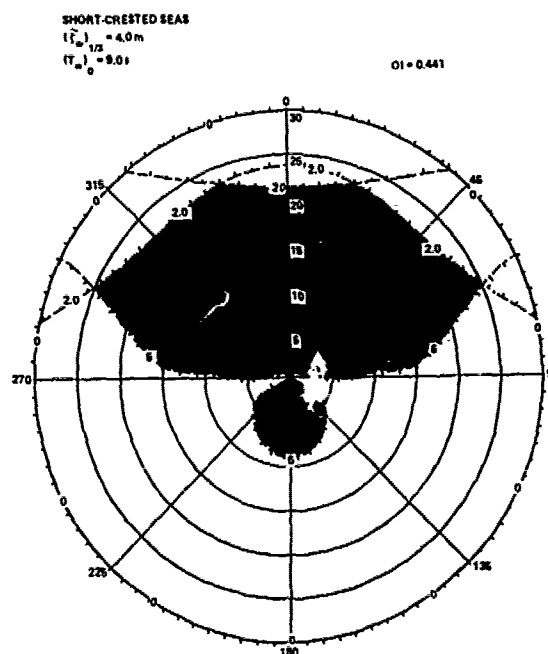


Fig. E2 Speed Polar Performance Assessment of Helicopter Landing for Hull 21D/A

of the speed polar plane in which none of the criteria are exceeded is the "window" in which the operation under consideration can be performed. The window in which Hull A can support helicopter landing operations in a 4 m/9 s, short-crested seaway is shaded in Figure E1.

In a sufficiently benign seaway, Hull A could support helicopter operations anywhere within the 360 deg x 30 knot speed polar plane defined by Figure E1. Hence, the ratio of the polar area of the window to that of the plane can be taken to define an Operability Index (OI) for the case under consideration. Figure E1 indicates an OI of 0.086 for the case which it depicts. Thus, Hull A can support helicopter landing operations in less than 9 percent of the speed polar plane given a 4 m/9 s, short-crested seaway.

Figure E2 presents the analogous speed polar diagram for Hull 21D/A. The window is again shaded. The OI of 0.411 indicates that this hull can support helicopter landing operations in over 40 percent of the speed polar plane for 4 m/9 s short-crested seaways. This represents an improvement, as compared to Hull A, of nearly a factor of five if the two are compared by OI ratio or of 35 percent if they are compared by OI difference.

Complete OI comparisons are presented and discussed in the text.

REFERENCES

1. Bales, N.K. and W.E. Cummins, "The Influence of Hull Form on Seakeeping," Trans., Society of Naval Architects and Marine Engineers, Vol. 78 (1970).
2. Frank, W. and N. Salvesen, "The Frank Close-Fit Ship Motion Computer Program," Naval Ship Research and Development Center Report 3289 (June 1970).
3. Ochi, M.K., "Extreme Behavior of a Ship in Rough Seas," Trans., Society of Naval Architects and Marine Engineers, Vol. 72 (1964).
4. Bales, N.K., "Minimum Freeboard Requirements for Dry Foredecks: A Design Procedure," Proc., Fourth Ship Technology and Research (STAR) Symposium (1979).
5. Cox, G.G. and A.R. Lloyd, "Hydrodynamic Design Basis for Navy Ship Roll Motion Stabilization," Trans., Society of Naval Architects and Marine Engineers, Vol. 85 (1977).
6. Salvesen, N., E.O. Tuck and O. Faltinsen, "Ship Motions and Sea Loads," Trans., Society of Naval Architects and Marine Engineers, Vol. 78 (1970).
7. Schmitke, R.T., "Ship Sway, Roll and Yaw Motions in Oblique Seas," Trans., Society of Naval Architects and Marine Engineers, Vol. 86 (1978).
8. Covich, P. and E.N. Comstock, "Assessment of Carrier Hull Form Performance," American Society of Naval Engineers Aircraft Carrier Technical Symposium (1976).
9. Pierre, D.A. and M.J. Lowe, Mathematical Programming via Augmented Lagrangians: An Introduction with Computer Programs, Addison-Wesley Pub. Co. (1975).

Discussion

B. Johnson (U.S. Naval Academy)

I congratulate the author for a very interesting paper. The contrast between this paper and that of Schmitke and Murday in the same session is both striking and complimentary. However, to compare the results of these two approaches several important parameters are not tabulated. Since Bales did not use C_p and C_m in his analytical model for "R", we can't calculate the block coefficient for comparison with the Schmitke and Murday trends. I again request that all significant coefficients be included in hull form comparison tables.

The Hull 21D Body Plan is unusual, especially above the designer's water line. It is ashame that we don't yet possess any analytical methods of optimizing flare angles in the above water hull form. On the other hand, ship designers who depend on intuition and towint tank operators may appreciate that their jobs are still secure.

R.T. Schmitke (DREA) and D.C. Murday (NRC)

This morning's session provides an opportunity rarely given to researchers working in closely related fields. First, we present our paper, Mr. Bales comments upon it, and we reply. Then he presents his (rather unexpected) paper, we make comment, and he gives his rebuttal. The problem is, from our point of view, that he gets the last word.

We are struck, first of all, by the fact that beam does not appear in the rank equation (2). We might expect, for example, a term involving B/T. We ask the author's comments.

A major difference between our approach and the author's is the treatment of slamming. We include slamming severity, whereas the author does not. Neglect of slamming severity may, in the absence of constraints on beam and draft, lead to unrealistically high beam/draft ratios.

Another major difference is the fact that we assign greater importance to slamming than to other measures of seakeeping performance. This is a direct reflection of operational experience.

Notwithstanding the above, the author's approach has much to recommend itself. As we have noted in our reply to Mr. Bales's discussion of our paper, the results he obtains are much the same as ours. The similarity in forebodies between our Fig.18

and his Fig.10 is readily apparent. We look forward to publication of his model test results.

Author's Reply

N.K. Bales (DTNSRDC)

Certainally Mr. Johnson's request that "all significant coefficients be included" is a reasonable one. Who, though, will bell the cat? At least I can point-out that block can be computed from the coefficients which I employ as $CB = C_W CVP$ where $C_W = (C_{WF} + C_{WA})/2$ and $CVP = (C_{VPF} + C_{VPA})/2$.

With respect to Mr. Johnson's comments on above-water flare, I can note that there is an on-going project in this area at DTNSRDC. Progress is being made toward providing both analytical and experimental methods to assess this characteristic in terms of its influence on flare slamming, deck wetness, and the relationship between these two phenomena. Mr. H.D. Jones and I presented the initial results of the project at the 19th American Towing Tank Conference.

I do not believe that Mr. Schmitke and Mr. Murday need be too concerned over this being the last word!

The rank estimation equation is intended to model the distributions of beam, draft, and sectional fullness over ship length in terms of a minimum set of Naval Architectural parameters. Maximum beam appears to me to contribute very little to such a model. Therefore, it is not included.

The largest beam-draft ratio which the optimization procedure admits without extrapolation, see equation (9), is 3.7. Further, beam and draft can be independently constrained via equation (10). Accordingly, the optimization procedure will lead to unrealistically high beam-draft ratios only if the user forces it to do so. Nonetheless, I do appreciate the importance of slamming severity. If the imposed constraints lead to unusually high beam-draft ratios or full sections, the user will be well advised to evaluate the implications thereof with respect to slamming severity.

My perception is that slamming should limit the mobility of a well-designed frigate in head seas. However, it is to be hoped that our frigates will fight more than they run; and weapons system limits may then over-ride mobility limits. It is for this reason that I have chosen to consider a fairly large set of potentially-limiting responses and weight them equally.

Prediction of Resistance and Propulsion of a Ship in a Seaway

Odd M. Faltinsen

Norwegian Institute of Technology, Trondheim-NTH

Knut J. Minsaas

Norwegian Hydrodynamic Laboratories, Trondheim

Nicolas Liapis

Norwegian Hydrodynamic Laboratories, Trondheim

Svein O. Skjördal

Kaldnes Mek. Verksted, Tønsberg

Norway

ABSTRACT

A procedure for calculating added resistance, transverse drift force and mean yaw moment on a ship in regular waves of any wave direction is presented. An asymptotic formula for small wave lengths has also been derived. The influence of wave induced motions on the wake, open water propeller characteristics, thrust deduction and relative rotative efficiency is discussed. The reason to false values for the propulsion factors are pointed out. Determination of RPM and HP in irregular waves is discussed.

NOMENCLATURE

R_{AW}	added resistance due to waves
R_T	total resistance
T	thrust of the propeller
Q	torque at the propeller
Q_m	torque at the engine
n	number of revolutions
V_a	speed of advance
U	Ship's speed
t	thrust deduction factor (also used as time variable)
w	wake fraction. Used both as effective wake and radial wake distribution
η_m	mechanical efficiency of the shaft bearings
η_R	relative rotative efficiency
η_P	propeller efficiency
η_H	hull efficiency
η_O	propulsive efficiency
C	water-line curve

K_T	thrust coefficient
K_Q	torque coefficient
D	diameter of propeller
R	radius of propeller
J_A	advance coefficient of the propeller
L	ship length between perpendiculars
B	ship beam midships
C_b	block coefficient
F_n	Froude number
α	wave direction ($\alpha=0$ is head sea)
η_j	displacements ($j=1,2,\dots,6$ refer to surge, sway, heave, roll, pitch and yaw respectively, see Fig. 1)
ζ_a	incident wave amplitude
g	acceleration c: gravity
ω_0	circular wave frequency
ω_e	circular frequency of encounter
k	wave number
λ	wave length
x,y,z	coordinate system as defined in Fig. 1
\bar{x},\bar{y},\bar{z}	coordinate system fixed to the ship and coinciding with the x,y,z -system when the ship is not oscillating
n,s	local coordinate system (see Fig. 4)
i	complex unit
β	thrust diminuation factor (see equations (73) and (74))
$\bar{\beta}$	average β -value over one wave period (see equation (76))
S_B	average wetted surface of the body

h	distance between water surface and propeller shaft center
δ_0	boundary layer thickness
δ_2	momentum thickness
v_{\max}, v_0	see equation (68)
θ	see Fig. 4
n_1	Generalized normal directions (see equations (12) and (13). Positive normal direction into the fluid
M	Mass of the ship
$\phi^{(1)}$	see equation (19)

1. INTRODUCTION

Estimation of ship speed, machinery power and propeller revolutions is traditionally based on still water performance. But ocean-going vessels often meet sea conditions where the seaway influences the ship resistance and propulsive coefficients; and in the case of extreme ship motions, the ship master may reduce the ship speed due to green water on deck, slamming, propeller racing or excessive accelerations.

The increase of fuel cost has increased the importance of the prediction of ship speed and power in a seaway. It is necessary to ensure that the ship will not only be economical on a ship trial in calm water but also on a voyage in wind and waves. This is some of the background why we started our study.

We have focused our attention on problems connected with involuntary speed reduction and how to find the increase in power required to maintain ship speed in a seaway. We have in particular studied the added resistance and propulsive factors of a ship in regular waves. The change of propulsive factors due to waves is of greatest importance when there is significant wave energy at frequencies in the vicinity of the natural pitch and heave frequencies of the ship. This will normally correspond to severe sea conditions. Further, the change in propulsive factors due to waves is most pronounced when the ship is in ballast condition. The added resistance on ships may also be of importance for moderate sea conditions, in particular for ships with blunt bow-forms.

At the end of the paper, we have discussed how the results from regular waves can be applied to irregular waves. Hopefully our results may later on be useful tools in designing economical hull forms and propulsion systems, or for instance in determining how the trim of a ship can be used to determine an economical ship speed in a seaway.

2. BASIC FORMULATION

If we want to determine the speed, shaft horse power or propeller revolutions of a ship in regular waves, we may average forces and moments over one wave period and set up the following two basic equations

$$Q_m \eta_m = Q / \eta_R \quad (1)$$

$$R_T / (1-t) = T \quad (2)$$

where Q is the torque delivered by the machinery, η_m is the mechanical efficiency between the machinery and the propeller shaft, Q is the hydrodynamic torque on the propeller in open water, η_R is the relative rotative efficiency, R_T is the resistance of the ship without propeller, T is the propeller thrust in open water and t is the thrust deduction. The propeller thrust and torque is dependent on the particulars of the propeller, propeller revolution n and the speed of advance

$$V_a = U(1-w) \quad (3)$$

where w is the effective wake and U is the forward velocity of the ship. The propeller characteristics will also depend on the immersion and the wave induced motions of the propeller shaft. This will be discussed later on.

We will in the following text first introduce a new theory for the added resistance of a ship in waves and then discuss how the waves affect the wake, the propeller characteristics, the relative rotative efficiency and the thrust deduction. Finally we will discuss how we may determine RPM, HP and ship speed in a seaway.

3. ADDED RESISTANCE

Theoretical methods for added resistance of a ship in regular waves are either derived by directly integrating pressure over the wetted ship surface or by using the equations for conservation of momentum and/or energy in the fluid. The procedures are derived by a perturbation scheme where the linear wave induced motions and loads are a first order approximation to the problem. The added resistance is then found as the mean longitudinal second order force. This implies that the theoretical added resistance is proportional to the square of the wave amplitude. This is a valid approximation for moderate wave steepnesses. But when the waves are breaking or close to breaking, one may question the procedures.

Maruo (1) has used the equations for conservation of energy and momentum to derive a theoretical method for added resistance. His procedure is valid for any wave length and wave heading. The disadvantage with the method is that it is difficult to apply from a practical point of view. The accuracy of the method is dependent on how well the linear problem is solved. The far more simpler method by Gerritsma and Beukelman (2) is easier to apply. Gerritsma and Beukelman (2) derived their formula by energy considerations, but the rational basis for their method is not quite clear.

Maruo and Ishii (3) have simplified the original formula by Maruo (1) considerably by using a high frequency assumption consistent with strip theory. The formula resembles Gerritsma and Beukelman's formula,

but the importance of the differences has not been clearly pointed out. Takagi, Hosoda and Higo (4) have derived the same formula as Maruo and Ishii (3). They also use the equations of momentum and energy in the fluid, but used other control surfaces than Maruo.

Added resistance in oblique sea has been studied by Hosoda (5) by applying Maruo's method. He concluded that the contribution of lateral motions to added resistance is relatively small. According to this conclusion, the added resistance in oblique waves can easily be calculated on the basis of the extension of prediction method for head sea waves (Fujii, H. and Takahashi, T. (6)). In a similar way, Gerritsma and Journée (7) generalized Gerritsma and Beukelman's method to oblique sea.

Another way to derive a formula for added resistance is to directly integrate pressure forces over the wetted surface of the ship (Boese (8)). It should be noted that Boese has neglected the quadratic velocity term in Bernoulli's equation and one term arising from using pressure on the instantaneous position of the wetted surface of the ship instead of using pressure on the average position of the ship. These terms are of importance and will be included in this paper. Both procedures are quite simple to apply in practice. The advantage of a method based on directly integrating pressure forces compared to a method using the equations for conservation of momentum and/or energy in the fluid, is that it is easier to understand the physical reason for added resistance. Boese derived his formula only for head sea waves, while our procedure is valid for any wave direction and includes the effect of the lateral motions. We also calculate transverse drift force and yaw moment. Further, we do not base the calculation of the diffraction potential of the first order problem on the relative motion hypothesis.

All the formulas above are based on some kind of slenderness assumption, which makes them questionable to apply for blunt ship forms. This has some practical consequences. Fujii and Takahashi (9) have pointed out the importance of added resistance on blunt ship forms in the small wave length case for speed predictions in moderate sea conditions. They propose to divide the added resistance into two parts. One part is added resistance due to ship motions and another part is added resistance due to wave reflection at the bow (or stern if following sea). The added resistance due to ship motions may be calculated by the conventional methods while Fujii and Takahashi have derived a quasi-rational method for resistance increase due to the reflection at the bow. Their formula gives a correct asymptotic behaviour for low wave lengths and zero Froude numbers as long as the ship surface is vertical at the water line. But the effect of finite draught and forward speed is only included in an approximate way. It may be noted that the forward speed

effect may be quite important (see Fujii and Takahashi (9)).

We will in this paper present a new asymptotic theory for small wave lengths which takes into account the forward speed effect. From a rational point of view, one can argue against dividing the added resistance into two parts in the way that Fujii and Takahashi (9) did. Generally speaking, the reflection of the waves and the ship motions may interact in a more complicated way on the added resistance. But their procedure makes some sense for certain wave lengths regions, i.e. for small wave lengths where the effect of ship motions may be disregarded and in vicinity of pitch and heave resonance where the relative motion between the ship and the waves are important. But it should be noted that it is possible to derive one expression valid for all wave lengths if for instance the first order motions and loads are calculated by a three-dimensional sink source technique.

The calculation of mean added resistance in irregular sea is straightforward if the wave spectrum and the added resistance in regular waves is known. But it should be pointed out that the added resistance will not have a constant value in irregular sea. It will be slowly varying approximately as the envelope of the wave elevation.

We will in the following text discuss how we calculate the linear wave induced motions and loads on a ship. This is a necessary building brick in the theory of added resistance. We will then present a method for added resistance based on directly integrating the pressure over the wetted body surface. At the same time, we will show how other mean force or moment components in waves can be evaluated. As an example, we will study transverse drift force and drift yaw moment. Afterwards we will derive asymptotic formulas for added resistance, transverse drift force and yaw moment in the low wave length case. Finally, we will present numerical results and comparisons with other methods and experiments.

3.1 Linear wave induced motions and loads

Let us study a ship advancing at constant mean forward speed with arbitrary heading in regular sinusoidal waves. We assume that the first order motions are linear and harmonic. Let (x, y, z) be a righthanded coordinate system fixed with respect to the mean position of the ship with z vertically upwards through the centre of gravity of the ship, x in the aft direction and the origin in the plane of the undisturbed free surface. Let the translatory displacements in the x, y and z directions with respect to the origin be η_1, η_2 and η_3 respectively, so that η_1 is the surge, η_2 is the sway and η_3 is the heave displacement. Furthermore, let the angular displacement of the rotational motion about the x, y and z -axis be η_4, η_5 and η_6 respectively, so that η_4 is the roll, η_5 is the pitch and η_6 is the yaw angle. The coordinate system

and the translatory and angular displacements are shown in Fig. 1. We will also operate with a coordinate system (x, y, z) that is fixed in the ship and coincide with the (z, y, z) coordinate system when the ship is not oscillating.

We will use the Salvesen, Tuck and Faltinsen theory (10) to find the wave induced motion. This method does not determine the pressure distribution because it is based on a generalized Haskind relation when evaluating the wave exciting forces and moments. When we later shall derive a procedure for calculating added resistance, we will need expressions for the linear pressure distribution on the hull. It is also necessary to know the pressure distribution at the mean free surface if we want to find the relative motion and velocity along the ship. This is of interest in evaluating voluntary speed reduction due to slamming and green water on deck. We will therefore present two different ways of calculating the linear pressure distribution on the ship hull. The differences in the method are in the calculation of the diffraction potential. We will write the total velocity potential as

$$\phi = Ux + \phi_S(x, y, z) + \phi_T(x, y, z) e^{-i\omega_e t} \quad (4)^*$$

where $Ux + \phi_S(x, y, z)$ is the steady contribution which determines the wave resistance. We will assume that ϕ_S has no influence on the linear wave induced motions of the ship (Salvesen, Tuck and Faltinsen (10)). The time dependent pressure will be divided into three parts

$$\phi_T(x, y, z) e^{-i\omega_e t} = \phi_I + \phi_F + \phi_D \quad (5)$$

where i is the complex unit, ω_e the frequency of encounter and t is the time variable. Further, ϕ_I is the incident wave potential, ϕ_F is the velocity potential due to forced motions in six degrees of freedom and ϕ_D is the diffraction potential of the restrained ship. We will write the incident wave potential as

$$\phi_I = \frac{ig\tau_a}{\omega_o} e^{kz + ikx\cos\alpha + ikysin\alpha - i\omega_e t} \quad (6)$$

where g is the acceleration of gravity, τ_a is the wave amplitude, k is the wave number, α is the heading angle, $\omega_o = \sqrt{kg}$ is the wave frequency which is related to the frequency of encounter ω_e by

$$\omega_e = \omega_o + kU\cos\alpha \quad (7)$$

According to Salvesen, Tuck and Faltinsen, we may write the forced motion potential as

* It is understood that real part is to be taken in all expressions involving $e^{-i\omega_e t}$.

$$\begin{aligned} \phi_F = & \phi_2 n_2 + \phi_3 n_3 + \phi_4 n_4 \\ & + (-x + \frac{U}{i\omega_e}) \phi_3 n_5 + (x - \frac{U}{i\omega_e}) \phi_2 n_6 \end{aligned} \quad (8)$$

where ϕ_i satisfies the following boundary value problem

$$\frac{\partial^2 \phi_i}{\partial y^2} + \frac{\partial^2 \phi_i}{\partial z^2} = 0 \quad \text{in the fluid} \quad (9)$$

$$-\omega_e^2 \phi_i + g \frac{\partial \phi_i}{\partial z} = 0 \quad \text{on } z=0 \quad (10)$$

$$\frac{\partial \phi_i}{\partial n} = -i\omega_e n_i \quad \text{on the average wetted surface } S_B \text{ of the ship} \quad (11)$$

$$\text{Here } n_i \text{ is determined by} \quad (12)$$

$$n = (n_1, n_2, n_3) \quad (13)$$

where \vec{n} is the normal vector to the body surface (positive into the fluid) and $r = x\vec{i} + y\vec{j} + z\vec{k}$. Further, ϕ_i satisfies a radiation condition of two-dimensional outgoing waves. The ϕ_i -problems can be solved by the Frank Closefit method.

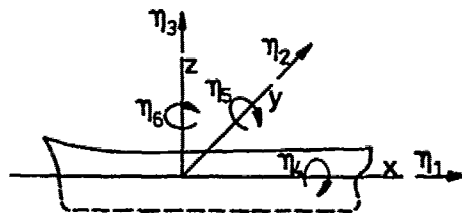


Fig. 1 Coordinate system

The diffraction problem may be difficult to solve, in particular in the low wave length range. We will apply two different methods. One method is what we will call a "relative motion method". A second method is due to Skj rdal and Faltinsen (11) and is only applicable in head sea. This method takes into account that the waves are modified as they propagate along the ship.

The "relative motion method" implies that the wave length is large compared to the cross-dimensions of the ship, that the ship is slender and that three-dimensional effects can be neglected. The diffraction potential can then be found as a solution of the two-dimensional Laplace equation (9), the classical free surface condition (10), a radiation condition of outgoing two-dimensional waves. The body boundary condition can be written as

$$\frac{\partial \phi_D}{\partial n} = -n_2 \bar{u}_y - n_3 \bar{u}_z \quad \text{on } S_B$$

where

$$\bar{u}_y = \frac{kz + ikx\cos\alpha - i\omega_e t}{\omega_o \tau_a \sin\alpha} e$$

and

$$\bar{u}_z = -i\omega_0 r_a e^{kz_m + ikx \cos \alpha - i\omega_e t}$$

Here z_m is an average vertical cross-sectional coordinate, which may be chosen as $-T/2$, where T is the local draught. We may now write the total time dependent velocity potential as

$$\begin{aligned} \phi_T e^{-i\omega_e t} = & \phi_1 + \phi_2 \left(\eta_2 - \frac{1}{\omega_e} \bar{u}_y \right) \\ & + \phi_3 \left(\eta_3 - \frac{1}{\omega_e} \bar{u}_z \right) \\ & + \phi_4 \eta_4 + \left(-x + \frac{U}{i\omega_e} \right) \phi_3 \eta_5 \\ & + \left(x - \frac{U}{i\omega_e} \right) \phi_2 \eta_6 \end{aligned} \quad (14)$$

The dynamic first order pressure at a fixed submerged point can be written as

$$p = -\rho \left(\frac{\partial \phi}{\partial t} + U \frac{\partial \phi}{\partial x} \right) \phi_T e^{-i\omega_e t} \quad (15)$$

and the dynamic wave elevation ζ can be written as

$$\zeta = \frac{p}{\rho g} \Big|_{z=0} \quad (16)$$

We will now show how we may find added resistance by directly integrating pressure over the hull surface.

3.2 Added resistance by pressure integration method

We start out with the complete Bernoulli equation

$$p = -\rho g z - \rho \frac{\partial \phi}{\partial t} - \frac{\rho}{2} V^2 + p_0 + \frac{\rho}{2} U^2 \quad (17)$$

where V is the fluid velocity and p_0 is atmospheric pressure. If we neglect the influence of the stationary perturbation potential ϕ_s (see equation 4), we may write

$$\begin{aligned} p = & -\rho g z - \rho \frac{\partial \phi}{\partial t} - \rho U \frac{\partial \phi}{\partial x} - \frac{\rho}{2} \left\{ \left(\frac{\partial \phi}{\partial x} \right)^2 + \left(\frac{\partial \phi}{\partial y} \right)^2 \right. \\ & \left. + \left(\frac{\partial \phi}{\partial z} \right)^2 \right\} + p_0 \end{aligned} \quad (18)$$

Here ϕ is due to the incident waves and its interaction with the ship. Let us proceed by a perturbation scheme, i.e. we write

$$\phi \sim \phi^{(1)} + \phi^{(2)} + \dots \quad (19)$$

where $\phi^{(1)}$ is the linear first order potential discussed in the last chapter, and $\phi^{(2)}$ is a second order approximation which is proportional to the square of the wave amplitude.

Let us now make a Taylor expansion of the pressure about the mean position of the ship. The pressure p_s on the ship correct to second order in wave amplitude may then be written as

$$\begin{aligned} p_s = & -\rho g z - \rho \left(\frac{\partial \phi}{\partial t} + U \frac{\partial \phi}{\partial x} \right)_m \\ & - \rho \left(\frac{\partial \phi}{\partial t} + U \frac{\partial \phi}{\partial x} \right)_m \\ & - \rho (\eta_2 + x\eta_6 - z\eta_4) \frac{\partial}{\partial y} \left(\frac{\partial \phi}{\partial t} + U \frac{\partial \phi}{\partial x} \right)_m \quad (20) \\ & - \rho (\eta_3 - x\eta_5 + y\eta_4) \frac{\partial}{\partial z} \left(\frac{\partial \phi}{\partial t} + U \frac{\partial \phi}{\partial x} \right)_m \\ & - \frac{\rho}{2} \left(\left(\frac{\partial \phi}{\partial x} \right)^2 + \left(\frac{\partial \phi}{\partial y} \right)^2 + \left(\frac{\partial \phi}{\partial z} \right)^2 \right)_m + p_0 \end{aligned}$$

Here m indicates that the variables should be evaluated on the average position of the wetted ship hull. We will now study separately the contribution to added resistance from each pressure term in equation (20).

The contribution from the $-\rho g z$ -term can be split up into one part which comes from pressure forces over the exact position of the body surface below $z=0$ (i.e. the surface area S_0 in Fig. 2), and in another part from integrating over the wetted area above $z=0$. It is possible to show by Gauss' theorem that the pressure forces over S_0 due to the $-\rho g z$ -term result in a vertical force. We may therefore write the contribution to the added resistance from the $-\rho g z$ -term as

$$\overline{F_1^{HS}} = \rho g \int_{S_0} \zeta z n_1 dz ds = \int_{S_0} \frac{\rho g}{c^2} \zeta n_1 ds \quad (21)$$

The bar over the expressions indicates time-averaged values. Further, ζ is the wave elevation calculated by linear theory and c is the water-line curve.

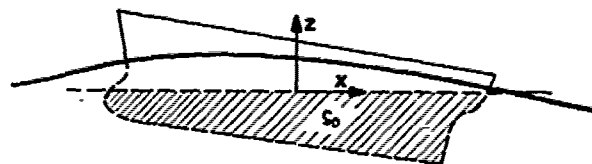


Figure 2 Ship surface

The contribution from the linear pressure term $-\rho \left(\frac{\partial \phi}{\partial t} + U \frac{\partial \phi}{\partial x} \right)_m$ cannot be neglected. The reason is that we in linear theory integrate over an average wetted surface and an average direction. In a second order theory, we have to make corrections for the integration over the correct wetted area of the ship hull and for the correct instantaneous force direction.

The correction for the integration of pressure forces over the correct wetted area of the ship hull gave a mean longitudinal force

$$\overline{F_1^{CA}} = - \int_{S_0} \rho g \zeta (\zeta - (\eta_3 - x\eta_5 + y\eta_4)) n_1 ds \quad (22)$$

where equation (16) has been used.

When we integrate $-\rho \left(\frac{\partial \phi}{\partial t} + U \frac{\partial \phi}{\partial x} \right)_m$ over the rest of the wetted area of the ship, we have to be careful with what coordinate system we use. Since we must integrate over the instantaneous position of the wetted area of the ship, we should start out with the coordinate system $(\bar{z}, \bar{y}, \bar{x})$ fixed to the ship. In a first order theory, it does not really matter if we had used the (x, y, z) coordinate system instead of the $\bar{x}, \bar{y}, \bar{z}$ -system. But in a second order problem, we have to be careful. The \bar{z} -component $F_{\bar{z}}$ of the force on the average wetted surface due to the pressure term $-\rho \left(\frac{\partial \phi}{\partial t} + U \frac{\partial \phi}{\partial x} \right)_m$ is the same as the vertical hydrodynamic force used in the linear theory. By using the equation of the first order motions, we may therefore write

$$F_{\bar{z}} = M \frac{d^2 \eta_3}{dt^2} + C_{33} \eta_3 + C_{35} \eta_5 \quad (23)$$

where M is the mass of the ship. C_{33} and C_{35} are hydrostatic restoring coefficients which may be written

$$C_{33} = \rho g \int_L b d\xi = \rho g A_{WP}$$

$$C_{35} = -\rho g \int_L \xi b d\xi = -\rho g M_{WP}$$

Here b is the sectional beam of the ship and the integration is over the length of the ship. A_{WP} and M_{WP} are the area and the moment of the waterplane.

By decomposing expression (23) along the x -axis (see Fig. 3), we find the following mean longitudinal force contribution

$$\bar{F}_{CDz} = (-\omega_e^2 M + C_{33}) \eta_3 \eta_5 + C_{35} \eta_5^2 \quad (24)$$

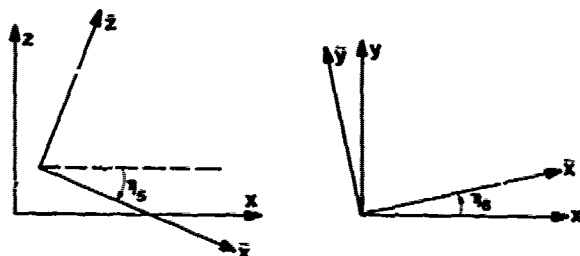


Figure 3 Coordinate system

In a similar way we can decompose the \bar{y} -component of the force on the average wetted surface due to the pressure term

$-\rho \left(\frac{\partial \phi}{\partial t} + U \frac{\partial \phi}{\partial x} \right)_m$ along the x -axis. We will find the following mean longitudinal force

$$\bar{F}_{CD\bar{y}} = \omega_e^2 M (\eta_2 - z_G \eta_4) \eta_6 \quad (25)$$

Here z_G is the z -coordinate of the centre of gravity of the ship.

The contribution to the mean force from the pressure term $-\rho \left(\frac{\partial \phi}{\partial t} + U \frac{\partial \phi}{\partial x} \right)_m$ can be

shown to be zero (Faltinsen and Løken (12)).

The contribution from the rest of the pressure terms in equation (20) is straightforward and will be presented later. But first we will rewrite the expression for the longitudinal force in a more convenient way by introducing the relative wave amplitude along the ship in the expressions.

We then use the theorem

$$\iiint_{Vol} \nabla \phi d\tau = \oint_S \nabla \phi \cdot \bar{n} ds$$

where S is the surface enclosing the volume Vol . Further, the normal vector \bar{n} is positive out of the volume. We may then show that

$$\begin{aligned} & -\frac{\rho g}{2} \int_C \{ (\eta_3 - x \eta_5 + y \eta_4) (\eta_3 - x \eta_5 + y \eta_4) \} n_1 ds \\ & = C_{33} \eta_3 \eta_5 + C_{35} \eta_5^2 \end{aligned}$$

By using this relation in equation (24), we may write the added resistance as

$$\begin{aligned} \bar{F}_1 = & \int_C \left\{ -\frac{\rho g}{2} \zeta_r^2 \right\} n_1 ds \\ & - \omega_e^2 M \eta_3 \eta_5 + \omega_e^2 M (\eta_2 - z_G \eta_4) \eta_6 \\ & + \rho \int_{S_B} \left\{ (\eta_2 + x \eta_6 - z \eta_4) \frac{\partial}{\partial y} \left(\frac{\partial \phi}{\partial t} + U \frac{\partial \phi}{\partial x} \right) \right\}_m \\ & + (\eta_3 - x \eta_5 + y \eta_4) \frac{\partial}{\partial z} \left(\frac{\partial \phi}{\partial t} + U \frac{\partial \phi}{\partial x} \right) \Big|_m \\ & + \frac{1}{2} \left(\left(\frac{\partial \phi}{\partial x} \right)^2 + \left(\frac{\partial \phi}{\partial y} \right)^2 + \left(\frac{\partial \phi}{\partial z} \right)^2 \right) n_1 ds \end{aligned} \quad (26)$$

where

$$\zeta_r = \zeta - (\eta_3 - x \eta_5 + y \eta_4) \quad (27)$$

is the relative wave amplitude along the ship, and c is the water line curve.

Boese (8) has derived a formula for added resistance which resembles equation (26). First of all, it should be noted that his formula neglected the influence of sway, roll, yaw and any flow which is antisymmetric with respect to the x - z -plane. That means in reality that Boese's formula should be applied for head and following sea. But even if we limited ourselves to head or following sea, Boese's formula would be missing the integral over S_B in equation (26).

The procedure described above may be generalized to calculate other mean force and moment components. For instance, we may write the transverse average force (i.e. force components in the y -direction) F_2 and the average yaw moment \bar{F}_6 about the z -axis as

$$\begin{aligned} \bar{F}_i = & \int_C \left\{ -\frac{\rho g}{2} \zeta_r^2 \right\} n_i ds \\ & + \rho \int_{S_B} \left\{ (\eta_2 + x \eta_6 - z \eta_4) \frac{\partial}{\partial y} \left(\frac{\partial \phi}{\partial t} + U \frac{\partial \phi}{\partial x} \right) \right\}_m \\ & + (\eta_3 - x \eta_5 + y \eta_4) \frac{\partial}{\partial z} \left(\frac{\partial \phi}{\partial t} + U \frac{\partial \phi}{\partial x} \right) \Big|_m + \end{aligned} \quad (28)$$

$$+\frac{1}{2}\left(\left(\frac{\partial\phi}{\partial x}\right)^2+\left(\frac{\partial\phi}{\partial y}\right)^2+\left(\frac{\partial\phi}{\partial z}\right)^2\right)n_1ds$$

$$+K_i$$

where

$$K_2=\omega_e^2 M \eta_3 \eta_4 - \omega_e^2 M (\eta_1 - z_G \eta_5) \eta_6 \quad (29)$$

and

$$K_6 = -(-I_{44} \omega_e^2 \eta_4 + \rho g V (z_B - z_G) \eta_4 + M z_G \omega_e^2 \eta_2$$

$$+ \omega_e^2 I_{46} \eta_6; \eta_5 \quad (30)$$

$$+ (-\omega_e^2 I_{55} \eta_5 + \rho g V (z_B - z_G) \eta_5) \eta_4$$

Here I_{44} and I_{55} are moments of inertia in roll and pitch, I_{46} is the product of inertia between roll and yaw, and z_B is the z-coordinate of the centre of buoyancy.

Similar procedures for mean forces and moments as described above have been used in the zero-speed case by Pinkster (13) and Faltinsen and Løken (12). The latter considered only two-dimensional bodies.

3.3 Asymptotic low wave length case

We will now derive formulas for added resistance, transverse drift force and mean yaw moment in the asymptotic low wave length case.

Consider a ship in incident regular waves. We assume the ship has vertical sides at the waterplane, and that the wave length is small compared to the draught of the ship. Due to the small wave length assumptions the wave excitation forces will be small. If resonance oscillations are not excited, it implies that the influence of the wave induced motions of the ship can be neglected. Due to the small wave length assumption and the rapid exponential decay of the waves down in the fluid, it is only the part of the ship close to the waterplane that will affect the flow field. This implies that we may replace the ship by a stationary, vertical, infinitely long cylinder with cross-section equal to the waterplane area of the ship.

We will neglect all viscous effects, and base the procedure on potential theory. In the analysis, we neglect diffraction effects from sharp corners of a structure, and assume that the change in the waterplane area is small over a wave length.

We will write the incident potential as

$$\phi_I = \frac{g \tau_a}{\omega_0} e^{k_0 z} e^{ik_0 x \cos \alpha + ik_0 y \sin \alpha - i \omega_e t} \quad (31)$$

where g is the acceleration of gravity, τ_a the amplitude of the incident waves, ω_0 the circular frequency of the waves, k_0 the wave number, α the wave propagation direction with respect to the x-axis (see Fig. 4), t is the time variable and ω_e is the circular frequency of encounter.

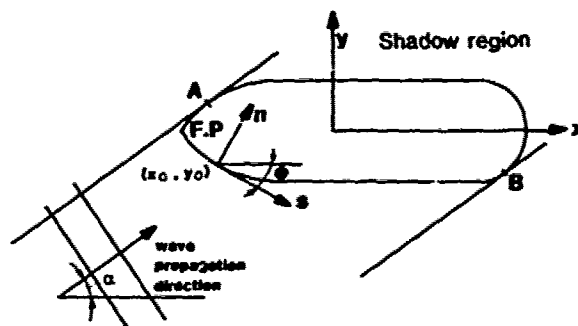


Figure 4: Coordinate system in the low wave length case

We will introduce local coordinate systems (n, s) along the water plane area curve, where n is orthogonal to the waterplane area curve and s tangential to the waterplane area curve (see Fig. 4). Further, (x_0, y_0) are the x, y -coordinates of the origin of the local coordinate system. We may then write the incident wave potential as

$$\phi_I = \frac{g \tau_a}{\omega_0} e^{k_0 z} e^{ik_0 n \sin(\theta + \alpha) + ik_0 s \cos(\theta + \alpha)}$$

$$e^{ik_0 x_0 \cos \alpha + ik_0 y_0 \sin \alpha - i \omega_e t} \quad (32)$$

where θ is defined in the figure. Note that n is opposite to the definition of the normal vector \vec{n} in the chapters above.

When the incident waves hit the structure, they will be diffracted. If we use the wave length as a scaling factor and stretch the n, s and z -coordinates with this factor, it becomes evident that the diffraction problem in the low wave length case is equivalent to studying incident waves on an infinitely long vertical plane wall (see Fig. 5). Parallel to the wall there is a horizontal steady velocity of magnitude V , which is a function of x_0 and y_0 . We will limit ourselves to the low speed case. It should be recognized that the steady flow can only be horizontal in the low-speed case. It is evident that the incident waves cannot reach certain domains. This will be shadow regions, i.e. no time dependent flow at all.

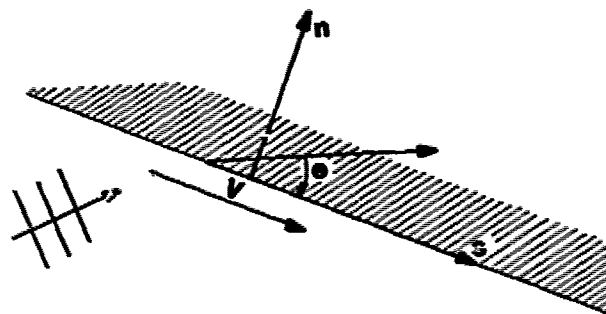


Figure 5: Two-dimensional flow situation

The total velocity potential in the non-shadow region will be written as

$$\phi = Vs + \phi_I + \phi_D \quad (33)$$

where ϕ_D is the unknown diffraction potential which satisfies the following body boundary condition

$$\frac{\partial \phi_D}{\partial n} = -i\omega_0 \zeta_a \sin(\theta + \alpha) e^{k_0 z + ik_0 s \cos(\theta + \alpha)} - e^{ik_0 x_0 \cos \alpha + ik_0 y_0 \sin \alpha - i\omega_0 t} \quad (34)$$

We recognize that the body boundary condition varies as

$$e^{ik_0 s \cos(\theta + \alpha)}$$

This implies we may write

$$\phi_D = \phi e^{ik_0 s \cos(\theta + \alpha) - i\omega_0 t} \quad (35)$$

By introducing equation (35) into the three-dimensional Laplace equation, we find that ϕ satisfies the Helmholtz equation

$$\frac{\partial^2 \phi}{\partial n^2} + \frac{\partial^2 \phi}{\partial z^2} - k_0^2 \cos^2(\theta + \alpha) \phi = 0 \quad (36)$$

The linearized free surface condition can be written as

$$\left(\frac{\partial}{\partial r} + v \frac{\partial}{\partial s}\right)^2 \phi_D + g \frac{\partial \phi_D}{\partial z} = 0 \quad \text{on } z=0 \quad (37)$$

which implies that

$$\{-i\omega_0 + V k_0 \cos(\theta + \alpha)\}^2 \phi + g \frac{\partial \phi}{\partial z} = 0 \quad \text{on } z=0 \quad (38)$$

In addition, ϕ_D has to satisfy a radiation condition, i.e. it cannot represent incident waves far from the body.

It will be evident later that it is not necessary for us to know the detailed behaviour of ϕ_D close to the body. Many wave lengths from the wall we may write the outgoing wave part as

$$A e^{k_1 z - ik_2 n + ik_0 s \cos(\theta + \alpha) - i\omega_0 t} \quad (39)$$

where k_2 have to be positive if it should represent outgoing waves. From equation (38), we find that

$$k_1 = \frac{(\omega_0 - V k_0 \cos(\theta + \alpha))^2}{g} \quad (40)$$

From equation (36), we find that

$$k_2 = \sqrt{k_1^2 - k_0^2 \cos^2(\theta + \alpha)} \quad (41)$$

It is necessary to require that

$$|k_1| > |k_0 \cos(\theta + \alpha)|$$

to have an outgoing wave solution. This is normally the case. If not, we must require that

$$k_2 = i|k_2|$$

so that the diffraction potential is exponentially decaying when $n \rightarrow \infty$.

We will now find A in equation (39) in the case of $k_2 > 0$. This will be done by first considering a fictitious problem and apply Green's second identity.

The fictitious problem we study is incident waves on the same wall as described in Fig. 5. We write the incident fictitious wave potential

$$\phi_I = e^{k_1 z} e^{ik_2 n - ik_0 s \cos(\theta + \alpha) - i\omega_0 t} \quad (42)$$

where ϕ_I satisfies

$$-k_1 \phi_I + \frac{\partial \phi_I}{\partial z} = 0 \quad \text{on } z=0 \quad (43)$$

i.e. the same free surface condition as ϕ_D . It is easy to find that the total velocity potential has to be

$$\phi_A = \phi_I + \phi_D = 2e^{k_1 z} \cos(k_2 n) e^{ik_0 s \cos(\theta + \alpha) - i\omega_0 t} \quad (44)$$

We will now study the following generalized force on the wall

$$F = \int_{-a}^0 (\phi_I + \phi_D) e^{k_0 z} dz \quad (45)$$

which can be easily calculated by equation (44).

We will now rewrite (45) by Green's second identity. We introduce the normalized velocity potential ϕ_2 defined by

$$\phi_D = -i\omega_0 \zeta_a \sin(\theta + \alpha) e^{ik_0 s \cos(\theta + \alpha)} - e^{ik_0 x_0 \cos \alpha + ik_0 y_0 \sin \alpha - i\omega_0 t} \quad (46)$$

(see equation (34)). It is easy to see that ϕ_2 satisfies the same Helmholtz equation as ϕ .

Further, ϕ_2 has to satisfy the same free-surface condition as ϕ_D and when $n \rightarrow \infty$

$$\phi_2 = \frac{A e^{k_1 z - ik_2 n}}{-i\omega_0 \sin(\theta + \alpha) \zeta_a} e^{-ik_0 x_0 \cos \alpha - ik_0 y_0 \sin \alpha} \quad (47)$$

(if $\sin(\theta + \alpha) = 0$) (see equation (39) and (46)).

By using the boundary condition for ϕ_2 , we may write equation (45) as

$$F = \int_{-a}^0 (\phi_I + \phi_D) \frac{\partial \phi_2}{\partial n} dz \quad (48)$$

We will now apply Green's second identity with the potentials $\phi_I + \phi_D$ and ϕ_2 , and to a domain enclosed by the wall, the free surface, a vertical control surface far away from the wall and a horizontal control surface far down in the fluid. By using that

$(\psi_1 + \psi_D)$ and ψ_2 satisfies the same Helmholtz equation, the same free surface condition together with the body condition for $(\psi_1 + \psi_D)$, we find that (48) may be rewritten

$$F = \frac{Ae^{-ik_0 x_0 \cos \theta - ik_0 y_0 \sin \theta}}{\omega_0 \sin(\theta + \alpha) \zeta_a} e^{ik_0 x_0 \cos \theta - i\omega_e t} \frac{k_2}{k_1} \quad (49)$$

By using that F also can be directly calculated, we find that

$$A = \frac{2k_1}{k_1 + k_0} \frac{\omega_0 \sin(\theta + \alpha) \zeta_a}{k_2} e^{ik_0 x_0 \cos \alpha + ik_0 y_0 \sin \alpha} \quad (50)$$

We have now determined the form of the velocity potential many wave lengths from the wall. We may write

$$\begin{aligned} \psi &= \psi + V_s \\ &= \frac{g \zeta_a}{\omega_c} e^{k_0 z} \cos(k_0 x_0 \cos(\theta + \alpha) + k_0 y_0 \sin(\theta + \alpha) + \alpha_0 - \omega_e t) \\ &+ \frac{g \zeta_a}{\omega_c} e^{k_1 z} \cos(k_0 x_0 \cos(\theta + \alpha) - k_2 y_0 \sin(\theta + \alpha) + \alpha_0 - \omega_e t) \quad (51) \end{aligned}$$

+Vs

where

$$\alpha_0 = k_0 x_0 \cos \alpha + k_0 y_0 \sin \alpha \quad (52)$$

and

$$B = \frac{2k_1}{k_1 + k_0} \frac{k_0}{k_2} \sin(\theta + \alpha) \quad (53)$$

We are now going to find average force pr. unit length on the wall in Fig. 5. This expression will be the important tool to find added resistance, transverse drift and mean yaw moment on the ship in the asymptotic low wave length case.

By using the equation for conservation of momentum in the fluid, we may write the normal average force per unit length on the wall as

$$\bar{F}_n = \int_{n=-\infty}^{\zeta_a} [p + \rho v_n^2] dz \quad (54)$$

where ζ_a is the wave amplitude at $n=-\infty$ and the integrand has to be evaluated at $n=-\infty$

By using the equation for conservation of energy, we find that

$$\int_{-\infty}^{\zeta_a} \frac{\partial \psi}{\partial t} \frac{\partial \psi}{\partial n} dz = 0 \quad (55)$$

By using equation (51) in equation (55), we find that

$$\begin{aligned} &\sin(k_0 x_0 \cos(\theta + \alpha) - k_2 y_0 \sin(\theta + \alpha) + \alpha_0 - \omega_e t) \\ &\cdot \sin(k_0 x_0 \cos(\theta + \alpha) + k_0 y_0 \sin(\theta + \alpha) + \alpha_0 - \omega_e t) \end{aligned}$$

$$= \frac{(k_0 + k_1)}{B(k_2 - k_0 \sin(\theta + \alpha))} \frac{1}{4} (\sin(\theta + \alpha) - B^2 \frac{k_2}{k_1}) \quad (56)$$

if $k_2 \neq k_0 \sin(\theta + \alpha)$

By using Bernoulli's equation, we may write (54) correct to second order in wave amplitude as

$$\bar{F}_n = \frac{1}{2} \rho g \zeta_a^2 - \frac{\rho}{2} \int_{-\infty}^{\zeta_a} \left\{ \left(\frac{\partial \psi}{\partial s} \right)^2 + \left(\frac{\partial \psi}{\partial z} \right)^2 - \left(\frac{\partial \psi}{\partial n} \right)^2 \right\} dz \quad (57)$$

where

$$\zeta_a = -\frac{1}{g} \left(\frac{\partial \psi}{\partial t} + V \frac{\partial \psi}{\partial s} \right) \Big|_{z=0}$$

By using equation (56), we will now find that equation (57) can be written as

$$\begin{aligned} \bar{F}_n &= \frac{1}{2} \rho g \zeta_a^2 \left\{ \left[\frac{k_1}{k_0} - \frac{1}{2} \cos^2(\theta + \alpha) \right] \right. \\ &\quad \left. + \frac{k_2}{k_0} \sin^2(\theta + \alpha) \right\} \quad (58) \end{aligned}$$

where k_1 and k_2 are given by equation (40) and (41). Generally speaking, it will be complicated to find the steady fluid velocity V in equation (40). We will therefore propose to set

$$V = U \cos \theta \quad (59)$$

This is consistent with slender body theory. It gives also the right answer for $\theta = \pi/2$, i.e. for extreme blunt ships. In case of small U -values and by using equation (59), we will find by Taylor expansion that

$$\bar{F}_n = \frac{1}{2} \rho g \zeta_a^2 \left\{ \sin^2(\theta + \alpha) + \frac{2\omega_0 U}{g} (1 - \cos \theta \cos(\theta + \alpha)) \right\} \quad (60)$$

When \bar{F}_n is found, we may write the mean drift force components and yaw moment correct to second order in wave amplitude as

$$\bar{F}_i = \int_L \bar{F}_n n_i dl \quad (61)$$

where i is 1, 2 or 6 and \bar{F}_1 is the added resistance, \bar{F}_2 is the transverse drift force and \bar{F}_6 is the drift yaw moment with respect to the z -axis, and

$$\begin{aligned} n_1 &= \sin \theta \\ n_2 &= \cos \theta \\ n_3 &= x_0 \cos \theta - y_0 \sin \theta \end{aligned}$$

The integration in (61) is along the non-shadow part L of the waterplane curve (see Fig. 4).

We should note that equation (58) is different from Fujii and Takahashi's asymptotic formula for head sea. The differences can be most easily established by using the approximate formula (60) for small U -values. According to Fujii and Takahashi's formula, the forward speed term in the brackets of equation (60) should be twice as large. It should be noted that the forward speed dependence in both formulas are significant.

Fujii and Takahashi compared their formula with experimental results for $\lambda/L=0.5$. The agreement was good. But it should be kept in mind that they only considered one wave length, which may be too high according to the short wave length assumption inherent in the theory. If we study their experimental results for $\lambda/L=0.3$, it seems to indicate less forward speed effect than their formula predict. But a more extensive experimental program is necessary to judge the validity of the different formulas.

Fujii and Takahashi have proposed a practical way to combine the asymptotic formula and the conventional formulas for added resistance. They propose to multiply the asymptotic formula with a quasianalytical formula containing the draught-dependence of the ship and add this expression to the conventional formulas.

3.4 Comparison between theoretical and experimental values for added resistance

The "direct pressure integration" method has been used to calculate added resistance on Series 60, $C_b=0.6, 0.7, 0.8$ and the container hull from S-175, which was used for the comparative hull motion calculation by the member organization of ITTC (14).

The calculated values for the Series 60, $C_b=0.6, 0.7$ and 0.8 are presented in Figs. 7, 8 and 6 together with experimental and theoretical results presented by Ström-Tejsen, Yeh and Moran (15). Ström-Tejsen et al. used Gerritsma and Beukelman's formula together with motion calculations by the Salvesen, Tuck and Faltinsen method. We may note the poor agreement between Ström-Tejsen et al.'s theoretical calculations and experimental results for the fine ship forms. It was pointed out in a discussion by Gerritsma and Beukelman that it was possible to achieve far better agreement between Gerritsma and Beukelman's method and the experimental results if their own computer program for motion calculations was used. From the figures, we note the good agreement between our theoretical calculations of added resistance and the experimental results. We should note the small difference in the results by using either the relative motion hypothesis or by using Skjærdal and Faltinsen's (11) procedure to calculate the diffraction potential. We have also plotted in theoretical values by our asymptotic theory. We note that the theoretical values are significant smaller than the experimental values for $C_b=0.6$ and 0.7 , while there is tendency to agreement between the asymptotic theory and experimental values for $C_b=0.8$. But the great scatter in experimental values indicates great difficulties in performing model tests.

Theoretical and experimental results for for the ITTC ship S-175 are presented in Figs. 9 - 16. We have compared the theoretical results by the "direct integration method" with the theoretical and experimental results presented by Gerritsma and

Journée (7). The results are for different Froude numbers, wave headings and wave lengths. Generally speaking, both theoretical methods agree quite good with the experimental results. But there are significant differences in the results by the two theories. Further, it is not known how reliable the experimental results are in oblique sea. Some of the experimental results for small wave lengths are peculiar.

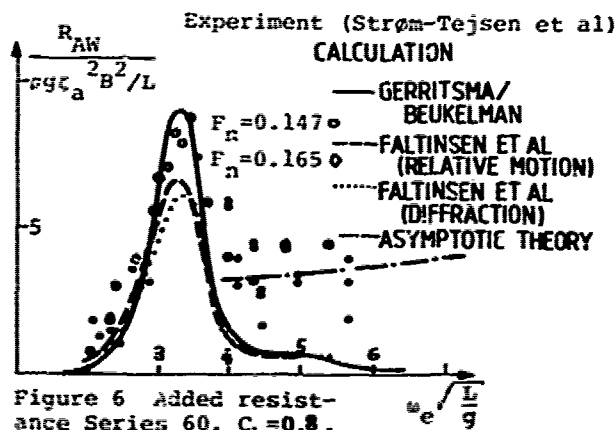


Figure 6 Added resistance Series 60, $C_b=0.8$.

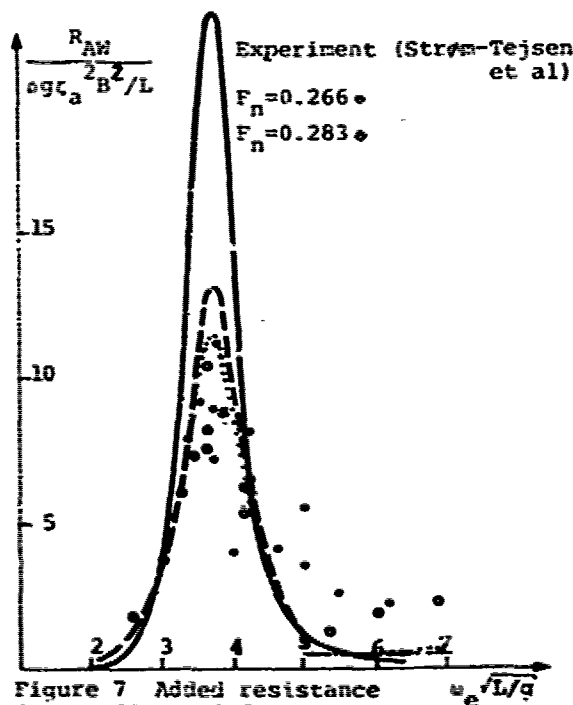


Figure 7 Added resistance Series 60, $C_b=0.6$.

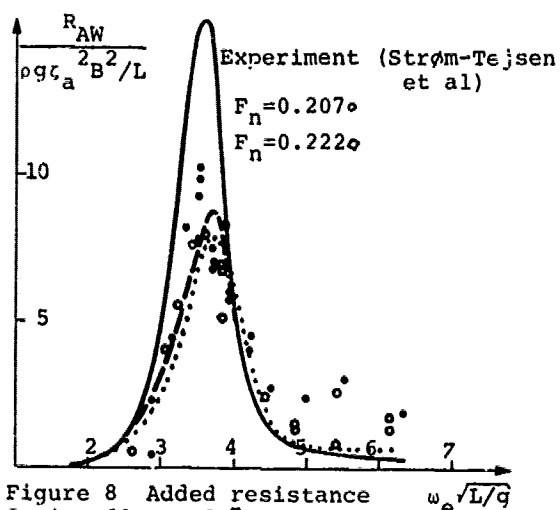


Figure 8 Added resistance Series 60, $C_b=0.7$.

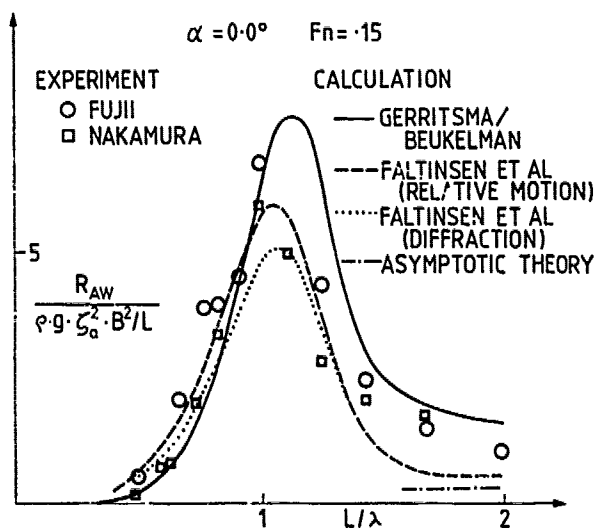


Figure 9 Added resistance S-175 $\alpha=0^\circ$

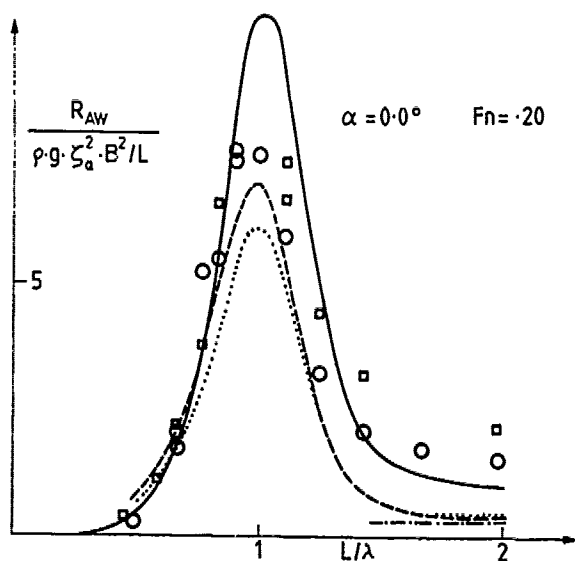


Figure 10 Added resistance S-175, $\alpha=0$

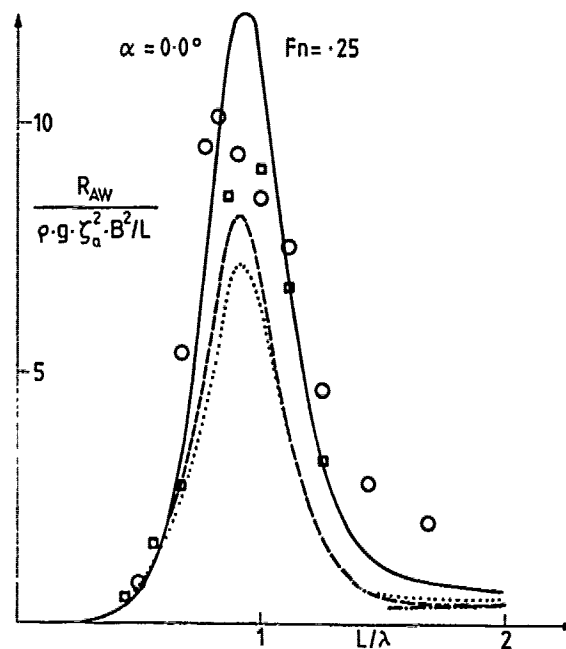


Figure 11 Added resistance S-175, $\alpha=0$

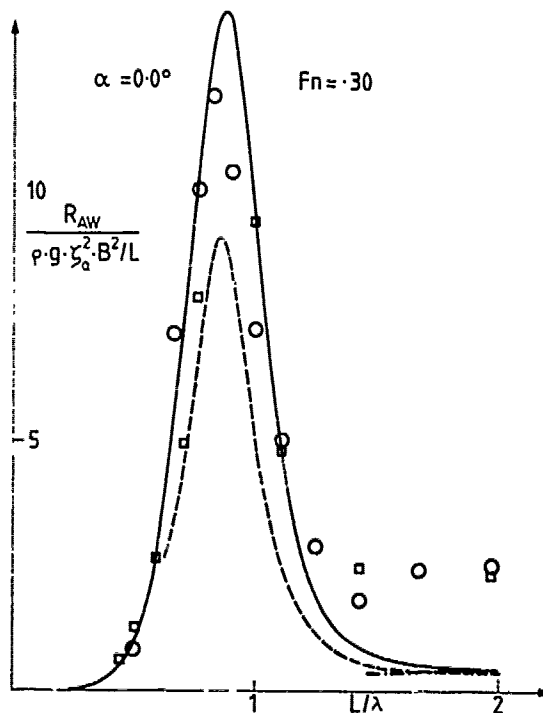


Figure 12 Added resistance S-175 $\alpha=0$

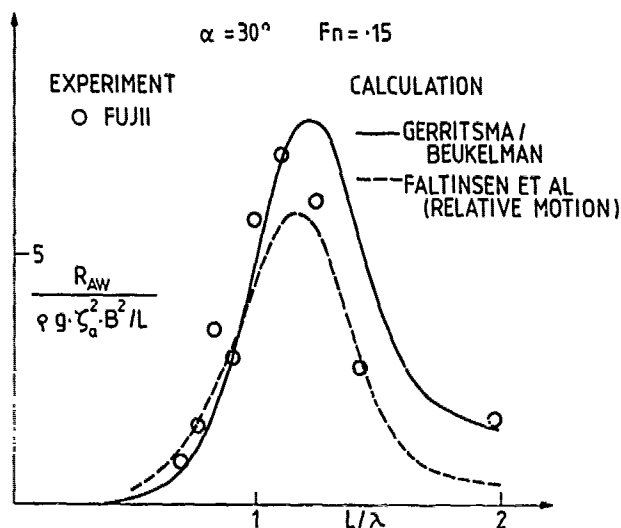


Figure 13 Added resistance S-175 $\alpha=30^\circ$

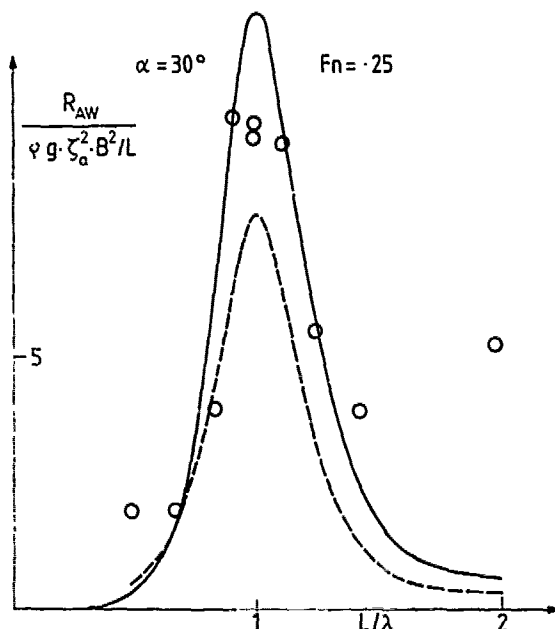


Figure 14 Added resistance S-175 $\alpha=30^\circ$

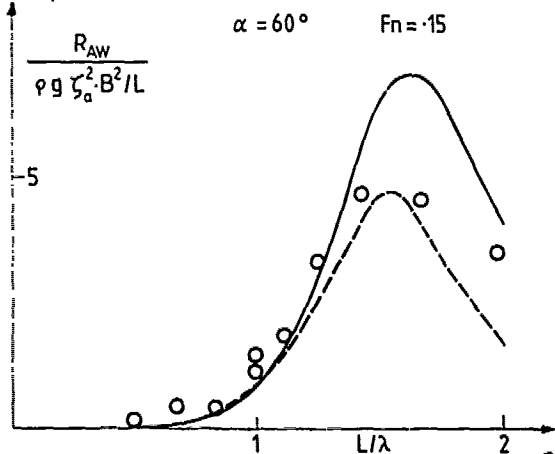


Figure 15 Added resistance S-175 $\alpha=60^\circ$

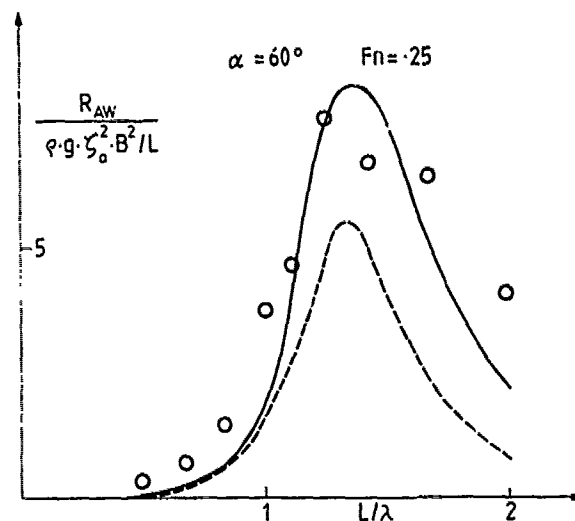


Figure 16 Added resistance S-175 $\alpha=60^\circ$

4.0 CHANGE OF PROPULSION FACTORS DUE TO WAVES

4.1 Change of the wake due to waves

Measurements by Nakamura and Naito (16) and Moor and Murdey (17) have shown that the wave induced motions of the ship increase the wake velocities. When the ship model was oscillating in regular waves, Nakamura and Naito showed that the change in wake velocities increased with wave height and that the change in wake was most pronounced around the natural period of pitch. They also performed forced oscillation tests in pitch and showed that the wake velocities increased with pitch angle and frequency. Their experiments indicated that the pitch motion of the ship was a major reason to the increase in wake velocities. This can be qualitatively understood by examining the influence of the wave induced motions on the mean pressure along the ship. The change in mean pressure at a fixed point in the fluid due to oscillatory fluid motion can be written as

$$\Delta \bar{p} = -\frac{\rho}{2} \left[\left(\frac{\partial \phi^{(1)}}{\partial x} \right)^2 + \left(\frac{\partial \phi^{(1)}}{\partial y} \right)^2 + \left(\frac{\partial \phi^{(1)}}{\partial z} \right)^2 \right] \quad (62)$$

(see equation 20). This pressure causes a change in the mean flow along the hull and therefore also in the wake velocities. If a flat plate of large extent is used as a rough model of the bottom of the ship and the plate is pitching harmonically, a rough approximation of equation (62) below the bottom of the ship can be written as

$$\Delta \bar{p} \sim -\frac{\rho}{4} \omega^2 |\eta_5|^2 x^2 \quad (63)$$

This indicates that the pitching motion of the ship will cause a drop in mean pressure from the middle of the ship towards the stern. This change in pressure gradient will cause the flow to be sucked more towards the

stern of the ship and thereby increase the flow velocities to the propeller.

A consequence of the increased flow velocities is that the boundary layer thickness is reduced. Another consequence is that the shear forces on the ship is changed, and that the separation point is delayed. This causes a change in the resistance of the ship, which may be interpreted as a wave-viscous interaction force. This is not included in our theoretical procedure. The importance of this interaction force is unknown.

If we use the same simple model to study the influence of forced harmonic heave motion, we will find that

$$\Delta \bar{p} \sim -\frac{\rho}{4} \omega_e^2 |\eta_3|^2 \quad (64)$$

Since the associated pressure gradient is zero, we do not anticipate that the heave motion will influence the wake velocities significantly. It is more difficult to tell in simple terms about the influence of the incident and diffracted waves on the wake velocities. But we may use equation (62) together with velocities obtained from linear strip theory calculations to estimate more accurately the change in the mean pressure when the ship is oscillating in regular waves. This includes the effect of the heaving and pitching motion as well as the incident and diffracted waves. Fig. 17 shows one example from such calculations for a Series 60 ship with $C_b = 0.6$ in regular head sea waves. The wave length is $\lambda/L = 0.913$ and the Froude number is 0.2. This is close to the resonance condition of the ship in pitch. The results in Fig. 17 have been obtained by using equation (62) at the mean position of the ship. For each cross-section of the ship we have averaged the mean pressure. This averaged mean pressure is denoted $\Delta \bar{p}$ in the figure. We see that this pressure-distribution is of a similar nature as one would expect from equation (63). If we make similar calculations away from the resonance in pitch we will find a less pronounced decrease in the pressure towards the stern of the ship. The discussion above is a theoretical indication that the pitch motion of the ship is a major reason to the increase in wake velocities for a ship oscillating in regular waves.

In order to quantitatively evaluate the effect of the pressure distribution (62) on the boundary layer and the wake, we have adopted a rough theoretical model. We would certainly like to stress that our model has shortcomings. In the boundary layer calculations we have assumed that the boundary layer is thin, which is highly questionable at the stern of the ship. It is difficult to know how the boundary layer is following the ship in the oscillatory motion, but it is intuitively felt that the ship should not move out of its own boundary layer. We will use the following procedure. We calculate first the boundary layer as if the ship was in its mean oscillatory position. But note that we in those calculations will take into account the effect of the oscillatory motion

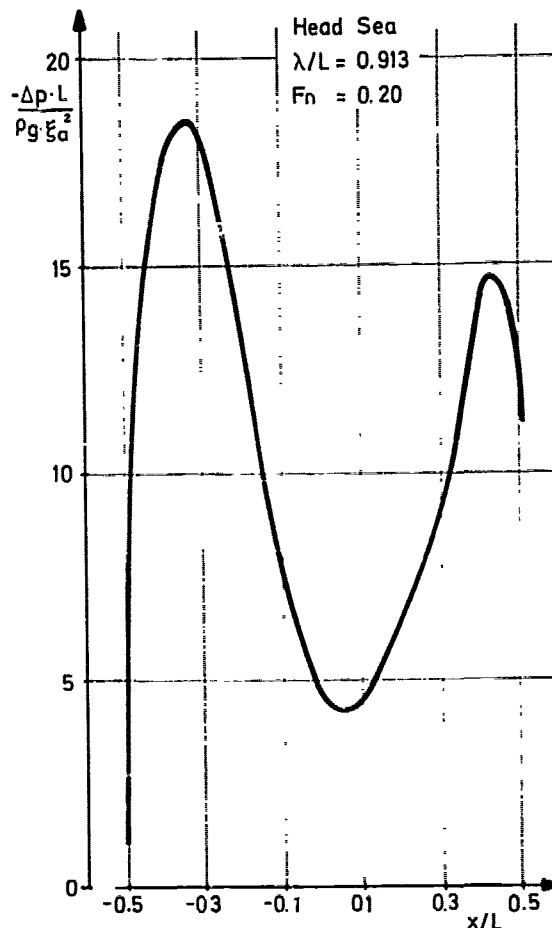


Figure 17 Average mean pressure due to wave induced motions

of the ship on the mean pressure distribution around the ship. After we have calculated the steady boundary layer due to both the still water pressure distribution and the oscillatory fluid motion, we assume that this boundary layer is attached to the oscillating ship. We have used a two-dimensional model for the boundary layer calculations and assumed that the boundary layer thickness is only a function of the longitudinal coordinate of the ship. Physically we should interpret this boundary layer as an averaged boundary layer for each cross-section. The pressure gradient that we apply is obtained from averaging the pressure over each cross-section. Associated with this average pressure distribution $p(x)$, there is a fluid velocity $V(x)$ outside the boundary layer. According to Bernoulli's equation, we may write

$$V(x) = \sqrt{1 - \frac{p(x)}{\frac{1}{2}\rho U^2}} U \quad (65)$$

where U is the free stream velocity. The boundary layer was calculated applying the equations

$$\theta(x) = v^{-4}(x) \cdot 0.0106 \int_{-L/2}^x v^4(\zeta) d\zeta \quad (66)$$

and

$$\delta_2 = \theta(x) / \left(\frac{v(x)\theta(x)}{v} \right)^{0.1666} \quad (67)$$

where δ_2 is the momentum thickness (see Thwaites (18)) and L is the length between perpendiculars of the ship. We have assumed that the flow is turbulent from the bow of the ship.

We have applied equations (66) and (67) on a pressure distribution similar to that measured on a Series 60 model ($C_b=0.6$) in still water at $F_n=0.2$. The average pressure distribution $p(x)$ that we applied is presented in Table 1.

Table 1

x/L	-0.45	-0.35	-0.25	-0.15	-0.05
$\frac{p(x)}{\frac{\rho}{2}U^2}$	0.2	-0.1	-0.2	-0.22	-0.2
	0.05	0.15	0.25	0.35	0.45
	-0.19	-0.18	-0.17	-0.1	0.15

When the boundary layer thickness obtained by using equations (66) and (67) was compared to values calculated by Webster and Huang (19) by a more accurate procedure, we found a quite satisfactory agreement. The momentum thickness at $x/L=0.45$ which is close to the stern, was found to be $\delta_2/L=0.00442$. If we added the pressure distribution presented in Fig. 17, we found that $\delta_2/L=0.00403$ for $\zeta_a/L=0.01$ and $\delta_2/L=0.00332$ for $\zeta_a/L=0.02$ at $x/L=0.45$. This confirms the expected decrease in the boundary layer thickness due to the wave induced motions of the ship.

When the boundary layer along the hull has been calculated, we may evaluate the wake behind the body. We assume that the velocity in the wake behind a two-dimensional body or a body of revolution can be written as

$$v\left(\frac{n}{\delta_0}\right) = v_0 - v_{\max} \left(1 - \left(\frac{n}{\delta_0}\right)^m\right)^2 \quad (68)$$

where n is a coordinate defined below. In the case of a body of revolution, n is equal to the radial distance from the rotational symmetry axis. In the case of a vertical plane coinciding with the centre plane of the ship n will be equal to the y -coordinate defined in Figure 1. In the case of the ship the wake distribution will be a mixture of these two cases, and we will define n as the radial distance from the propeller shaft centre. Further, δ_0 in equation (68) is the boundary layer thickness, v_0 is the velocity at $n=\delta_0$, $v_0 - v_{\max}$ is the velocity at $n=0$, and m is an empirical constant which we have set equal to 1.5. In a practical case, v_{\max} and v_0 have to be experimentally determined.

If the boundary layer is changed, $\frac{v_{\max}}{v_0}$ will change. We have

$$\left(\frac{v_{\max}}{v_0}\right)' \delta_0' = \left(\frac{v_{\max}}{v_0}\right) \delta_0 \quad (69)$$

(see for instance Tanaka (20)). Here the apostrophe indicates the changed values. This implies that with

$$\left(1 - w\left(\frac{n}{\delta_0}\right)\right) = 1 - \frac{v_{\max}}{v_0} \left(1 - \left(\frac{n}{\delta_0}\right)^m\right)^2 \quad (70)$$

in still water, we may write the wake in waves as

$$\left(1 - w\left(\frac{n}{\delta_0}\right)\right) = 1 - \frac{v_{\max}}{v_0} \frac{\delta_2'}{\delta_2} \left(1 - \left(\frac{n}{\delta_0}\right)^m\right)^2 \quad (71)$$

where w is the radial wake fraction. We have assumed that $\delta_2'/\delta_2 = \delta_0'/\delta_0$ in equation (71). We are now going to use this procedure to compare with the experimental results by Nakamura and Naito (16) (see Fig. 18).

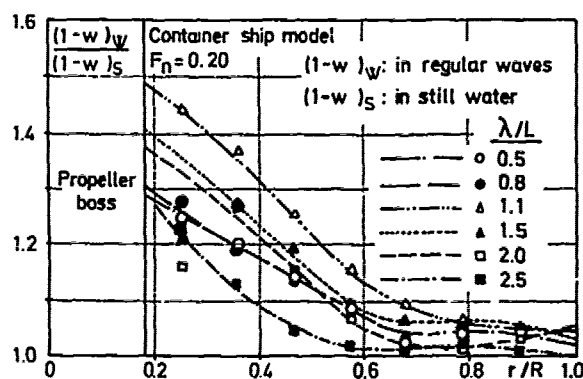


Figure 18 Nakamura and Naito's experimental wake results

They measured the radial wake distribution in the propeller plane when the propeller was not there, and the ship was oscillating in waves. As stated earlier in the text, our results are for the same condition. According to Nakamura and Naito's still water results, we find that $\frac{v_{\max}}{v_0}=0.8$. Further, they got the results in regular waves for $\zeta_a/L=0.01$. We have earlier calculated δ_2'/δ_2 for $\zeta_a/L=0.01$ and 0.02 . We have found $\delta_2'/\delta_2=0.91$ and 0.75 respectively. If we use $\delta_2'/\delta_2=0.75$ in our calculations, we will find the following wake distribution by equation (70) and (71) (see Table 2)

Table 2

$\frac{n}{\delta_0}$	0.1	0.2	0.3	0.4	0.5
$\frac{(1-w)_w}{(1-w)_s}$	1.835	1.644	1.51	1.401	1.314
	0.65	1.0			
	1.19	1.0			

If we instead use $\delta_2'/\delta_2=0.9$, we will find that (see Table 3)

Table 3

$\frac{n}{\delta_0}$	0.1	0.2	0.3	0.4	0.5
$\frac{(1-w)_w}{(1-w)_s}$	1.33	1.225	1.200	1.161	1.13
	0.65	0.9			
	1.091	1.0			

In Nakamura and Naito's experiments it seems like $\delta_0 \sim 2-3R$. The values in table 2-3 are of the same order of magnitude as the experimental values by Nakamura and Naito (16) and show a similar radial distribution as their results. As an extra control we also found that the volumetric mean wake is of the same order of magnitude as Nakamura and Naito's results. We therefore believe that we have clarified important physical reasons to the change of the wake due to wave induced motions of the ship.

4.2 Change of the open water propeller characteristics due to the waves

Analysis of propulsion factors based on resistance and propulsion tests in waves is traditionally done by fitting data into open water propeller diagram derived from tests with the propeller deeply immersed. But it is well known that the open water propeller diagram is a function of submergence, in particular when $h/R < 1.5$, where h is the distance between the water surface and the propeller shaft center. When the propeller is oscillating in waves, it may very well periodically be in instantaneous positions where $h/R < 1.5$. This is particularly true when the ship is in ballast condition. This implies that it may be physically wrong to use deeply submerged open water diagram in the analysis of a propeller in waves. This may lead to wrong conclusions about effective wake, relative rotative efficiency and propeller efficiency. In order to develop a more physical open water propeller diagram when the propeller is oscillating in waves, we have adopted a simple theoretical model. Since the wave induced motion occur with a significant lower frequency than the propeller revolution, we have used a quasi-dynamic approach. At each instantaneous position of the propeller shaft centre relative to the water surface we are using the propeller characteristics that would be valid if the propeller was not heaving and pitching in waves. We will therefore discuss how the open water propeller diagram is a function of propeller submergence.

The propeller sets up a steady wave motion when it is working close to the free surface. This will lead to a reduction in the propeller thrust. This reduction is a function of the propeller loading and the Froude number V/\sqrt{gh} as originally showed by Dickmann (21). Later on Nakatake (22) and Nowacki and Sharma (23) made similar calculations. We have in our example presented below used Nakatake's results.

Corrections due to wave effects are of particular importance when $1 < h/R < 1.5$. But when $h/R < 1$, the thrust must be corrected due to ventilation and the emergence of the propeller. The ratio of the immersed disc area A_1 of the propeller to the disc area A_0 of the propeller is

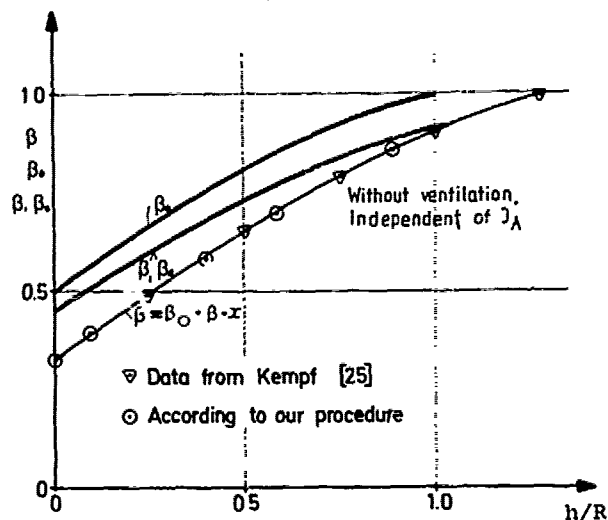
$$\beta_0 = \frac{A_1}{A_0} = 1 - \frac{\theta}{2\pi} + \frac{h}{\pi R} \sqrt{1 + \left(\frac{h}{R}\right)^2} \quad (72)$$

where

$$\epsilon = 2 \arccos \frac{h}{R}$$

We have assumed that the thrust is proportional to A_1 .

Another effect we have to take into account is what we call the Wagner-effect. When a propeller blade splashes into the water, there will be a sudden increase in lift. Wagner (24) studied a related problem for the two-dimensional foil, and found that the sudden increase amounted to 50% of the value for the fully developed lift. The so-called Wagner function gives the ratio between the instantaneous lift and the fully developed lift as a function of chordlengths travelled after the sudden change. One procedure would be to use blade element theory and study the distance each blade element travel compared to the chord length after the sudden change, and then apply the Wagner function. In our calculation, we have followed a simpler procedure by examining an "equivalent" section of the propeller. The results are presented in Fig. 19, where x is the ratio between the real thrust of the propeller and the fully developed thrust of the immersed propeller disc and β_1 is due to the steady wave motion created by the propeller.

Figure 19 β -diagram for a propeller

We may now write

$$K_T = \beta K_{T_0} \quad (73)$$

where K_{T_0} and K_T are the thrust coefficients for the deeply immersed propeller and for the propeller at immersion h/R . The thrust diminution factor β without the effect of ventil-

ation can be written as

$$\beta = \beta_0 \cdot \beta_1 \cdot x \quad (74)$$

where β_0 is defined in equation (72), β_1 is due to the steady wave motion created by the propeller and x is due to the Wagner effect. A comparison between the procedure described above and experimental results by Kempf (25) is presented in Fig. 19. The agreement is certainly too good. Note that we have not taken into account neither partly nor full ventilation, which is of particular importance for smaller $J_A = V_a / nD$ -numbers, than we have considered in the example. The effect of ventilation is illustrated in Fig. 20, where the efficiency of a propeller is given for both the partly and fully developed range as a function of immersion and loading.

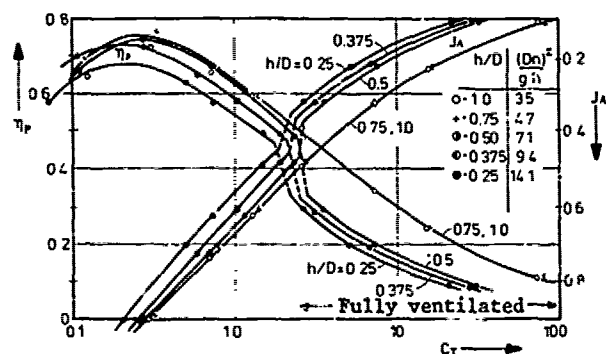


Figure 20 Change in propeller efficiency due to propeller loading, immersion and ventilation (from Gutsche (26)).

If the propeller thrust is changed with immersion, there is also a change in the torque coefficient K_Q . But due to the drag force on the propeller, the change in K_Q is not the same as the change in K_T . Model tests by Kempf (25) and Gutsche (26) indicate that

$$K_Q = \beta^m K_{Q0} \quad (75)$$

where m is a constant between 0.8 and 0.85, and K_{Q0} is the propeller torque coefficient for the deeply immersed propeller.

The final part of our procedure is to average β and β^m over one wave cycle. It is then necessary to know either from model tests or theoretical calculations the relative vertical motion between the propeller shaft centre and the water surface. We may now write the open water diagrams for the propeller operating behind a ship oscillating in regular waves as

$$K_T = \bar{\beta} K_{T0} \quad (76)$$

$$K_Q = \bar{\beta}^m K_{Q0} \quad (77)$$

where the bar indicates average values of β and β^m over one wave period.

From the discussion above, we may anticipate that the change in open water propeller characteristics due to waves is most pronounced in the vicinity of the natural periods in heave and pitch and for a ship in ballast condition.

4.3 False changes in propulsive coefficients due to waves

We have in the last chapter pointed out that it is not physically correct to use the open water diagram for the deeply immersed propeller if the propeller is heaving and pitching and operating close to the free surface. If we use wrong open water diagram it may lead to false changes in the propulsive coefficients. This is explained below.

Denoting in accordance with Fig. 21 the propulsion factors when an open water diagram corrected for immersion is used in the analysis by:

w^* , t^* , η_R^* , η_P^* , η_H^* , η_Q^* , K_T^* , K_Q^* and the corresponding values with a noncorrected open water diagram by:

w , t , η_R , η_P , η_H , η_Q , K_T , K_Q , J_A we must have $\eta_P \cdot \eta_R \cdot \eta_H = \eta_P^* \cdot \eta_R^* \cdot \eta_H^*$. If thrust identity is used in the analysis ($K_T = K_T^*$) and the torque coefficient in the behind condition is K_Q^* we get approximately

$$\eta_P^* = \frac{J_A - \left(\frac{K_T}{\beta} - K_T \right) \left(\frac{dK_{T0}}{dJ_A} \right)^{-1}}{2\pi} \quad (78)$$

and

$$\eta_R^* = \frac{\frac{K_T}{\beta^m} \left[\frac{dK_{Q0}}{dJ_A} \left(\frac{K_T}{\beta} - K_T \right) \left(\frac{dK_{Q0}}{dJ_A} \right)^{-1} + \eta_R \cdot K_Q^* \right]}{K_Q^*} \quad (79)$$

where $\frac{dK_{T0}}{dJ_A}$ and $\frac{dK_{Q0}}{dJ_A}$ are the slopes of the diagram for the deeply immersed propeller at the advance coefficient J_A . For the wake we find that

$$\frac{1-w}{1-w^*} = \frac{J_A}{J_A - \left(\frac{K_T}{\beta} - K_T \right) \left(\frac{dK_{T0}}{dJ_A} \right)^{-1}} \quad (80)$$

Further, if $t = t^*$

$$\frac{1-w}{1-w^*} = \frac{\eta_H^*}{\eta_H}$$

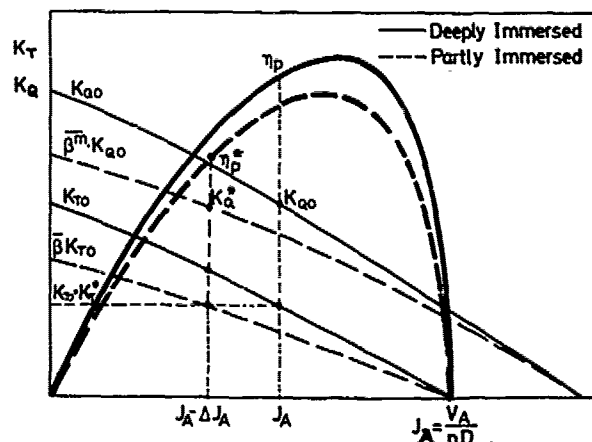


Figure 21 Open water diagram for partly and deeply immersed propeller

Equations (78) - (80) have been used in the example presented in Fig. 22. The results are given as functions of β . The open water propeller diagram that was used, was a typical propeller diagram for a merchant ship.

In the example: $J_A = 0.4$ $\frac{dK_Q}{dJ_A} = 0.0474$
 $\eta_H = 1.0$
 $K_T = 0.227$ $\frac{dK_T}{dJ_A} = 0.428$
 $K_Q = 0.029$
 $\eta_R = 1.079$

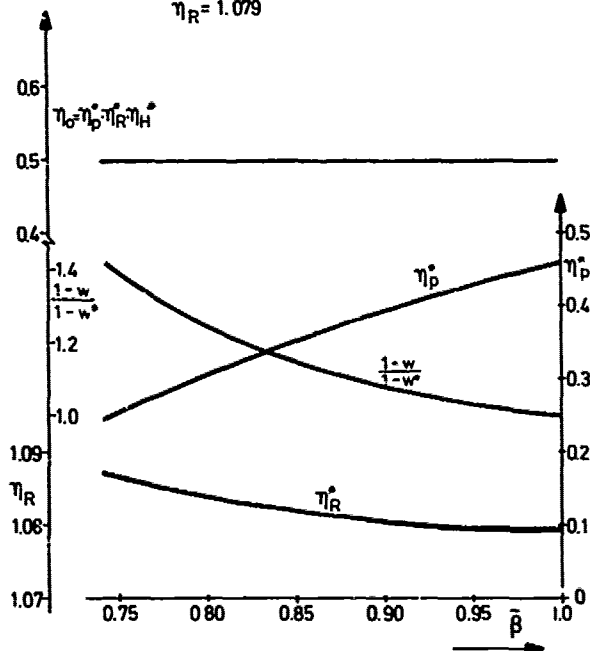


Figure 22 False changes in propulsion factors.

The results that one will get if one uses the open water diagram for deeply submerged propeller, corresponds to $\beta=1$. But for a propeller operating close to the free surface, β may differ substantially from 1. From the figure, we note that the propulsive factors are quite sensitive to β .

Obviously we may in principle use any open water diagram in the analysis but we will end up with false values for w , η_P , η_H and η_R if we are not using a diagram corresponding to the correct β -value. With false values, we mean that the result will not reflect the physical realities.

4.4 Changes of η_R due to waves

Moor and Murdey (17) and later Nakamura and Naito (16) showed that η_R sometimes changed in severe wave conditions compared to still water. Both increasing and decreasing values were reported. This change in η_R can to some extent be explained as false changes due to use of an open water diagram for deeply submerged propeller. But there may be real changes in η_R due to changes in the wake field and the propeller loading. This has been showed theoretically by Yama-

zaki (27) and experimentally by Johnsson (28).

Yamazaki calculated the changes in η_R due to the radial distribution of the mean load and the influence of the different harmonics of the unsteady components of the wake. The latter being the most important factor. The calculations and the experiments showed that η_R for a given wake distribution will increase with decreasing K_T .

Nakamura and Naito (16) measured the wake behind the model in waves and found that the radial wake distribution was more homogeneous in waves than in still water. If also v_{max}/v_0 (see equation (62)) is reduced due to the decrease in boundary layer thickness, this may result in a reduced η_R -value.

It is impossible to draw general conclusions about the influence of waves on η_R from the experimental data we have at the moment. The reason is presence of false effects. But it should be reasonable to use the still water value also in severe conditions if the propeller characteristics is corrected for immersion.

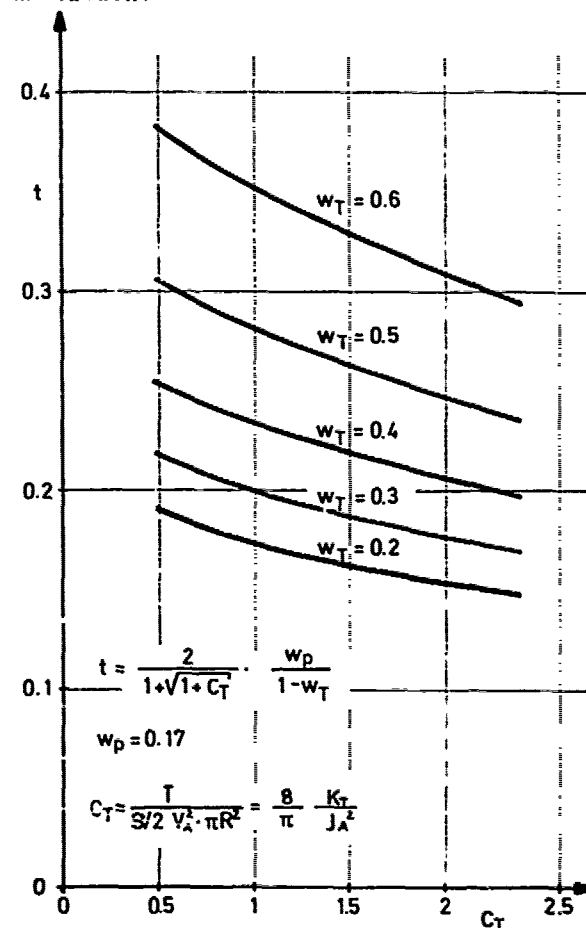


Figure 23 Change in thrust deduction due to propeller loading

4.5 Changes of thrust deduction due to waves

Moor and Murdey (17) observed that the thrust deduction decreased with increasing wave height and reached a minimum around the

natural period in pitch. Nakamura and Naito (16) made similar observations. Neglecting the wave induced wake and assuming a uniform source distribution over the propeller disc Nowacki and Sharma (23) came to the following simplified expression for the potential thrust deduction fraction in still water

$$t = \frac{2}{1 + \sqrt{1 + C_T}} \frac{w_p}{1 - w} \quad (81)$$

(see Fig. 23) where $C_T = T_p / (\frac{1}{2} \rho V_a^2 \pi R^2)$, T_p = Propeller thrust, w = effective wake, w_p = potential wake. R = propeller radius and V_a defined in equation (3). Equation (81) could probably be applied in waves. If we do that and use information about propeller loading in waves compared to still water, we will find a decrease int of the same order as measured in model tests. Overload tests in still water gave similar results to those in Fig. 23 (Bindel (29)). This indicates that overload tests in still water can give information about thrustdeduction in waves.

One consequence of the dependence of t on the loading is that there will be no linearity between thrust and resistance increase. This can be seen for instance by examining equation (2) and by using the results above.

5. DETERMINATION OF RPM AND HP IN A SEAWAY

We have in the text above discussed how the propulsive coefficients and added resistance change in regular waves. We may then use equations (1) and (2) to find RPM and HP in regular waves.

If the forward speed of the ship is given, we may use equation (2) to find propeller revolution and then use equation (1) to find the horsepower in regular waves. We have done that in a case near the natural period in pitch. The propulsion factors are then influenced by the wave induced motions. As anticipated we found that the added ship power in regular waves did not vary as the square of the wave amplitude, which is the functional dependence of the added resistance. This complicates the prediction of added power in irregular sea.

We will here propose a new method to handle the irregular sea case when the propulsion factors are dependent on the waves. This effect is most pronounced when there is significant wave energy for frequencies in the vicinity of the natural frequencies in heave and pitch, and for a ship in ballast condition. We assume that the effect of wind can be added as a constant resistance force. The method resembles a procedure used in calculating slowdrift oscillations of a ship in irregular waves (Hsu and Blenkarn (30)) and is based on a narrow banded wave spectrum. The procedure implies that we create a time-trace realization of the irregular waves and locate the zero-upcrossing wave elevation time instants. We then approximate the wave between each zero-upcrossing time instants by a regular wave of wave amplitude ζ_a and wave period T . For that particular regular wave we estimate the added resistance and

the propulsion factors. When that has been done, we solve equations (1) and (2) and find RPM and HP. By repeating this procedure we will find a slowly varying time trace of RPM and HP. We may also find a slowly varying time trace of the ship speed if we assume that the machinery characteristics are given. Traditionally one has been interested in average values for ship speed and/or power in a seaway. This is easy to obtain from the procedure above, but one may question why one should not consider the extreme values of added power.

If the propulsion factors in waves are the same as in still water, for instance in moderate sea conditions, it is easy to generalize equations (1) and (2) to irregular waves by introducing mean added resistance in irregular waves in the left hand side of equation (2). This has been done by Journée (31). We may note that this procedure do not find the slowly varying time trace of RPM, HP and/or ship speed. It only provides us with mean values.

The procedure described above may be avoided if we carry out propulsion tests of a model with propeller in waves. An obvious disadvantage with the direct procedure is that it leads to extensive and expensive model testing in order to cover many sea states. One should also be careful with the model testing procedure. Tests are usually carried out at model self-propulsion point. This may lead to erroneous answer. In a calculation that we carried out, we found that increases in power and RPM measured on a model working in a seaway at the model self-propulsion point will in severe conditions be much larger than if the model was working at the self-propulsion of the ship. This indicates that one should run the model at ship propulsion point.

6. CONCLUSIONS

1. A procedure for calculating added resistance, transverse drift force and mean yaw moment on a ship in regular waves of any wave direction is derived. An asymptotic formula for small wave lengths have also been derived. The agreement between theoretical and experimental results is generally good. It is pointed out that model tests in the low wave length range for blunt ships are needed.

2. In severe conditions there will be a negative wake induced by the motions of the ship. This change in wake may be roughly estimated or determined experimentally.

3. Analysis of propulsion tests in waves based on a propeller diagram not corrected for immersion effects will give "false" w , η_R and η_P values and results, that do not reflect the physical realities if the model has been tested in severe wave conditions.

4. Prediction of RPM and HP of a ship in irregular sea, in particular when the ship is close to resonance condition in heave and pitch and/or in ballast condition, is not straightforward. A procedure to handle the

problem is proposed.

ACKNOWLEDGEMENT

The theories for added resistance have been derived by O. Faltinsen. K. Minsaas and O. Faltinsen have cooperated on the chapter about "Change of propulsion factors due to waves". K. Minsaas is the originator to most of the ideas presented about propulsion factors in waves. S. O. Skjördal has derived the computer programs on added resistance. N. Liapis has derived the computer program for diffraction of waves in head sea. O. Ørritsland and Y. Robertsen have participated in the computer calculations.

REFERENCES

1. Maruo, H., "Resistance in Waves, Researches on Seakeeping Qualities of Ships in Japan", The Soc. of Naval Arch. of Japan, 60th Anniversary Series, Vol. 8, Chap. 5 (1963).
2. Gerritsma, J. and Beukelman, W., "Analysis of the Resistance Increase in Waves of a Fast Cargo Ship", Appendix 5 of Report Seakeeping Committee, Proc. 13th I.T.T.C. Vol. 2 (1972) p.902; I.S.P., Vol. 19, No. 217 (Sept. 1972) p.285.
3. Maruo, H. and Ishii, T., "Calculation of Added Resistance in Head Sea Waves by Means of a Simplified Formula (in Japanese); Journal of the Society of Naval Architects of Japan, Vol. 140, 1976.
4. Takagi, M., Hosoda, R. and Higo, Y., "An Investigation into Gerritsma's formula of the Resistance Increase by Energetics", (in Japanese), J. of the Kansai SNA, Japan, No. 170, Sept. 1978, pp. 59.
5. Hosoda, R., "The added Resistance of Ships in Regular Waves", Journ. of Soc. of Naval Arch. of Japan, Vol. 133 (June 1973), p. 7.
6. Fujii, H. and Takahashi, T., "Experimental Study on the Resistance Increase of a Ship in Regular Oblique Waves", Proc. 14th ITTC, Vol. 4. (1975), p.351.
7. Gerritsma, J. and Journée, J.M.J., Proc. 15th ITTC, Part 2 1978. p.70.
8. Boese, P., "Eine einfache Methode zur Berechnung der Widerstandserhöhung eines Schiffes im Seegang". Ifs-Bericht nr. 258, Febr. 1970.
9. Fujii, H. and Takahashi, T., "Experimental Study on the Resistance Increase of a Ship in Regular oblique Waves", Proc. 14th ITTC, Vol. 4 (1975), p.351.
10. Salvesen, N., Tuck, E.O. and Faltinsen, O., "Ship Motions and Sea Loads", Trans SNAME, Vol. 78, 1970.
11. Skjördal, S.O. and Faltinsen, O., "A linear theory of springing", Journal of Ship Research, June 1980.
12. Faltinsen, O. and Løken, A.E., "Slow Drift Oscillations of a Ship in Irregular Waves", Applied Ocean Research, 1, 1979.
13. Pinkster, J.A., "Mean and Low Frequency Wave Drifting on Floating Structures", Ocean Engineering, 1979.
14. Report of Seakeeping Committee, Proc. 15th ITTC, 1978.
15. Strøm-Tejsten, J., Yeh, H.Y.H. and Moran, D.D., "Added resistance in waves", Trans. SNAME, 1973.
16. Nakamura, S. and Naito, S., "Propulsive Performance of a Container Ship in Waves", The Society of Naval Architects of Japan, Naval Architecture and Ocean Engineering Vol. 15, 1977.
17. Moor, D.J. and Murdey, D.E., "Motions and Propulsion of Single Screw Models in head Seas, Part II". TINA. Vol. 112, 1970.
18. Thwaites, B., "Incompressible Aerodynamics", Oxford at the Clarendon Press, 1960.
19. Webster, W.C. and Huang, T.T., "Study of the Boundary Layer on Ship Forms" Journal of Ship Research, Sept. 1970.
20. Tanaka, J., "Scale Effects on Wake Distribution and Viscous Pressure Resistance of Ships", The Society of Naval Architects of Japan, Naval Architecture and Ocean Engineering, Vol. 17, 1979.
21. Dickmann, E., "Wechselwirkung zwischen Propeller und Schiff unter besonderer Berücksichtigung des Welleneinflusses" Jahrbuch STG. 40, 1939.
22. Nakatake, K., "Free Surface Effect or Propeller Thrust". International Seminar On Wave Resistance, 1976, Japan.
23. Nowacki, H. and Sharma, S.D., "Free Surface Effects in Hull Propeller Interaction". Proceedings of 9th ONR, Paris 1972.
24. Wagner, H., "Über die Entstehung des dynamischen Auftriebes vom Tragflügel". Z.f.a.M.M., Vol. 5. Heft 1. Feb. 1925, s.17-35.
25. Kempf, G., "Immersion of Propeller". T.NEC, Vol. 50, 1933-1934.
26. Gutsche, F., "Einfluss der Flutung auf Schub und Wirkungsgrad von Schiffspropellern". 45. Mitteilung der Schiffbau-Versuchsanstalt, Berlin 1967.
27. Yamazaki, R., "On the Theory of Screw Propellers in Non-uniform Flows". Memoirs of the Faculty of Engineering, Kyushu University, Vol. XXV, No. 2-1966.
28. Johnsson, C.A., "On Theoretical Predictions of Characteristics and Cavitation Properties of Propellers". Publications of the Swedish State Shipbuilding Experimental Tank, Nr. 64. Göteborg 1968.
29. Bindel, S., "The Effect of Loading on Wake and Thrust Deduction". Tenth International Towing Tank Conference, Teddington 1963.
30. Hsu, F.H. and Blenkarn, K.A., "Analysis of peak mooring forces caused by slow vessel drift oscillations in random seas", Offshore Technol. Conf., Houston, paper 1159.
31. Journée, J.M.J., "Prediction of speed and behaviour of a ship in a seaway", Technische Hogeschool Delft, Afdeling der Scheepsbouw- en scheepvaartkunde, Laboratorium voor scheepshydronechanica, Rapport no. 427, March 1976.

Discussion

Y. Himeno (Univ. of Osaka Prefecture)

My question is concerning the wake decrease in waves. The authors method consists of 2 points: The first is to introduce an additional time-mean pressure field due to oscillating fluid motion. The other is to apply it to a steady boundary layer equation. However, it is still unclear to me whether the 2nd point is reasonable or not. Furthermore, a simple heaving motion and incoming wave itself do not make large contribution to the decrease of the stern wake in your method.

I'd like to propose another approach to this problem. Let us assume the flow velocity outside the boundary layer consists of 2 parts: one is the steady flow, the other is a small-order harmoniously oscillating flow, which is progressing along the main flow direction. We can substitute these velocities into an unsteady (time-dependent) boundary layer equation, and expand it up to the 2nd order terms.

Then the steady-flow solution will come out from the zero-th order term and the 2nd order term, too. The 2nd-order steady-flow term is proportional to the square of the amplitude of the oscillating velocity outside the boundary layer, and this will increase the flow velocity inside the boundary layer.

This method has already been developed by some workers in the case of 2-d. laminar flow. So I think this can be easily applied to the case of turbulent boundary layer. I'd like to hear your opinion on this point.

H. Maruo (Yokohama N Univ)

In this paper, the authors develop a computation method of the added resistance and lateral drift force in waves, by means of direct integration of the hydrodynamic pressure on the hull surface. The average forces which are independent of time are computed so far usually by formulae derived by energy and momentum analysis on a control surface at a great distance from the ship. The latter method has an advantage that we need only the asymptotic behavior of radiating and diffracted waves at a great distance where the fluid motion is expressed by simple equations. If we wish to calculate the pressure on the hull surface, we necessitate a full equation for the fluid motion near the ship, which is so complicated that its exact formulation is far to reach. Approximation is indispensable resulting lack of accuracy and reliability. One of great disadvantages is that the steady drift force is a quantity of second order. One has to take up all terms of second order without omission. This is a tremendous task if we

intend a correct estimation of the second order pressure in the near field, because not only the quadratic term in the pressure equation must be evaluated, but the effect of the deviation of the hull surface from its average position to the second order terms should be taken into account. By the momentum analysis on the control surface fixed in space at a great distance, on the other hand, is relieved of this difficulty and the second order terms can be collected quite easily. I wonder if the authors would point out a definite merit of the method of direct integration of pressure with all its above mentioned disadvantages.

H. Fujii (MHI)

At first, we would like to show our respect to the very rigorous investigation presented by authors on a procedure for calculating added resistance of a ship in a seaway. We appreciate this interesting paper very much.

Authors dealt with the added resistance of a ship consistently by theoretical calculation taking account of added resistance due to wave reflection at blunt bow and derived the asymptotic formula for the low wave length case. In this case, the effect of ship speed on added resistance due to wave reflection may be quite important as pointed out by the authors. They stated the forward speed term in the brackets of equation (60) should be twice as large in comparing with our approximate formula. However, putting $\alpha = 0$ in equation (60),

$$\bar{F}_n \sim \frac{1}{2} \rho g \zeta_A^2 \sin^2 \theta \left(1 + \frac{2\omega_0 U}{g} \right)$$

while our approximation is, using the same notation to the above equation,

$$\bar{F}_n \sim \frac{1}{2} \rho g \zeta_A^2 \sin^2 \theta (1 + \alpha_2) \alpha_1$$

where

α_1 : correction factor for wave length and finite draft

α_2 : correction factor for forward speed $\alpha_2 = 5\sqrt{F_n}$, based on experimental results (Ref.1)).

This is the similar expression to the authors' one.

In Nagasaki Experimental Tank, we have already carried out experiments on the added resistance of ship in low wave length for several kinds of ship models. Therefore, we compared our experimental data with the calculated values by use of equation (60) for two fine ship models and four full ship models. Results are shown in Fig.1 to Fig.6. It seems that equation (60) gives good estimation for full ship models including the effect of forward speed and is very attractive formula from practical point of view.

PASSENGER SHIP MODEL $L_{pp}=6.0^m$ $C_b=0.52$

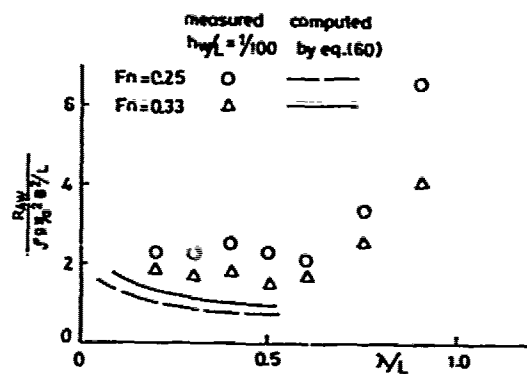


Fig. 1

CARGO SHIP MODEL $L_{pp}=42^m$ $C_b=0.61$

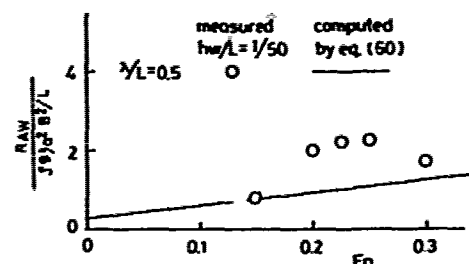


Fig. 2

TANKER MODEL $L_{pp}=42^m$ $C_b=0.79$

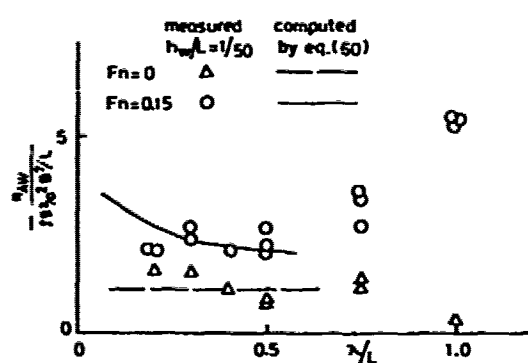


Fig. 3

SERIES 60 $C_b=0.8$ MODEL $L_{pp}=42^m$

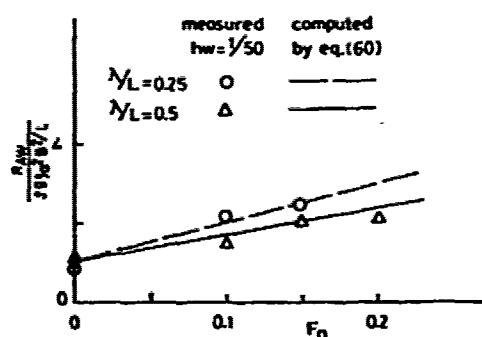


Fig. 4

TANKER MODEL $L_{pp}=42^m$ $C_b=0.84$

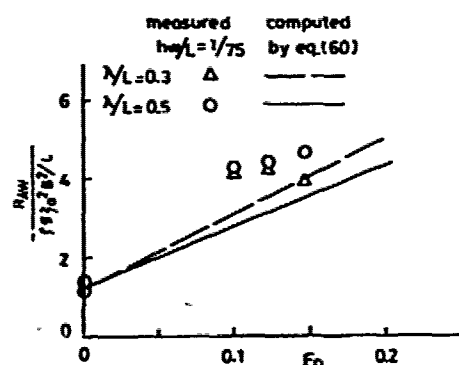


Fig. 5

TANKER MODEL $L_{pp}=30^m$ $C_b=0.85$

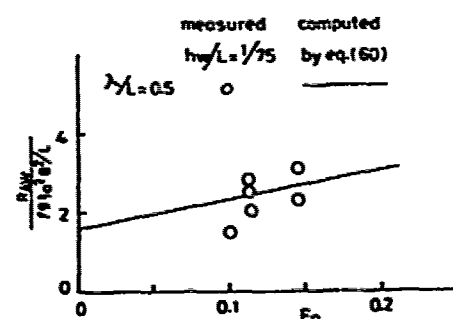


Fig. 6

Comparison of added resistance in low wave length

computed values : by the authors' asymptotic formula
measured values : obtained in Nagasaki Exp. Tank

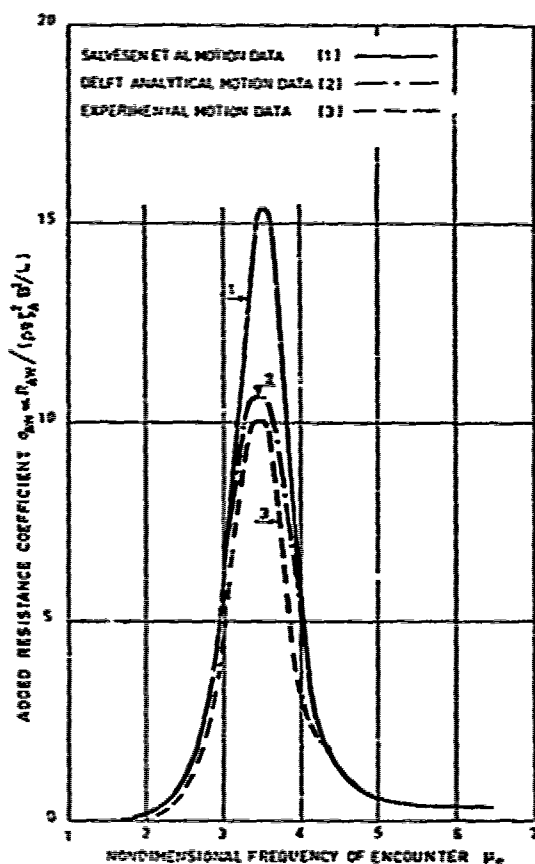
For added resistance of fine ship model in high Froude number, $Fn = 0.25 - 0.35$, however, there are found considerable large difference between the computed values and the measured one. This tendency is the same for our approximation. It might be necessary to review the assumptions in the derivation of asymptotic formula for fine ship. In respect to this fact, we consider, further investigation would be necessary.

REFERENCE

- 1) H. Fujii and T. Takahashi, "Experimental Study on the Resistance Increase of a Large Full Ship in Regular Oblique Waves", Journal of the Society of Naval Architects of Japan. Vol. 137, (1975)

J. Gerritsma and W. Beukelman (T. Univ. Delft)

The author's give an interesting comparison of the calculated added resistance and the corresponding experimental values in a few cases. The method as described in their presentation gives satisfactory results for three Sixty Series models but for the ITTC S-175 ship there is some tendency to underestimate the added resistance.



Series 60 hull form; $C_B = 0.70, Fn = 0.20$

In this respect the influence of an accurate determination of the vertical ship motions should be emphasized, because the added resistance is to a fair degree proportional to the squared motion amplitudes. The influence of motion amplitudes on the magnitude of added resistance is clearly demonstrated in the accompanying figure where the added resistance according to the Gerritsma-Beukelman method has been calculated by using three different motion amplitude response functions. Curve no. 1. has been obtained by using the motion prediction by the Salvesen et al. method. Curve 2 gives the results when the Delft motion calculation is used. Finally curve 3 is the result of added resistance calculation when experimental motion amplitudes are used.

The calculations have been carried out for a Series Sixty $C_B = 0.70$ shipform at $Fn = 0.20$.

These last two results correlate very well with the data given in Figure 8 of the present paper.

In view of this result and the comparison of the calculated and experimental values in the Figures 9 to 16, it would be of interest to compare the predicted and measured motion amplitudes in the considered cases. Such data would be extremely interesting for a more detailed analysis of the differences between calculation and experiment.

M. Takagi (Hitachi S&E)

In the prediction of the added resistance of a full ship advancing among the waves, the disagreement between theory and experiment in the region of short wavelength is a problem to be solved.

Prof. Faltinsen presented a new asymptotic theory of the added resistance with a fine method but under a somewhat bold assumption. I would like to discuss about this point.

Prof. Faltinsen gives eq. (37) as the free surface condition of the diffraction waves, which includes the effect of the local steady flow. It is correct in the near field of the ship but not in the far field. Nevertheless, the far field solution is used in order to obtain the normal average force acting on the wall.

For the sake of brevity, let us take the case of $\alpha = 0$ and $\theta = \frac{\pi}{2}$, which corresponds to the case where a two-dimensional full body is advancing among the waves.

In such a case, if we assume the usual linearized free surface condition instead of eq. (37), we have three reflection waves and one transmission wave with reference to a coordinate-system fixed to the earth. And the added resistance of the body is owing to the three reflection waves. When the parameter $U_{\infty}/g > 1/4$, however, the two reflection waves of the three disappear. The rest of the three, which is seen behind

the body, is generally so small that the added resistance is imagined to become small with the increase of U or u_e . This tendency contradicts with that of eq. (60).

Anyway, we need to study about the behaviour of the waves in a field of non-uniform steady flow in order to clarify the above question.

As for the experimental data, I quite agree with the authors on the point that more extensive and more careful experiments are necessary. Because the measurements of the added resistance are feared to include various errors such as mechanical friction of measurement system, effect of slow-drift and so on.

D.C. Murdey (NRC)

This comprehensive paper draws together the results of research published over the past ten years and goes on to add significantly to the state of art in the subject.

On the prediction of added resistance the authors' approach certainly leads to improved agreement with the results from model tests although, as stated in the paper, there are problems at high frequencies. The effects of short waves are of particular importance in predicting ship speed on trial where, although motions are usually negligible, wave diffraction effects can be significant. Generally the authors' asymptotic theory underpredicts the measured resistance increase. It is difficult to understand why it should agree well in just one case, the series 60 block coefficient 0.8 model. Although it is agreed that model tests are difficult to perform in such short waves (especially if the waves are of constant slope when both R_{AW} and ϵ_a will be small and their ratio subject to large scatter) the trends shown in Figures 6 to 12 are common, both in response curves of resistance and thrust increase.

Coming to the subject of propulsive coefficients in waves, when Ref.17 to the present paper was published it was pointed out that the variations in propulsion factors demonstrated in that reference were due, not only to variations of propeller loading but also to then undefined effects of changes in flow as the model passed through the waves. The breakdown of these effects into those due to the oscillating propeller near the free surface, changes in mean flow along the hull and propeller loading is logical and goes a long way to explaining the observations in a qualitative sense. However, the paper does not include an overall check of the authors' hypotheses. Have the authors made any comparisons between predictions of measured responses of propeller revolutions, torque and thrust increase from measured resistance increase? A satisfactory outcome of such a comparison would simplify

model testing considerably since it would imply that, given suitably sophisticated prediction procedures based on the theory presented in the paper, it would be sufficient to carry out only resistance tests in waves.

At the present time most self-propulsion tests in waves are carried out in models self-propulsion point. The experiments described in Ref.17 were carried out specifically to determine the effects of changes of self-propulsion point on the increases in rpm torque, thrust and power. The results of those experiments show that, while power increase is overestimated by tests at model self-propulsion point (which is in agreement with the authors' conclusion) the increases in rps (together with those of torque and thrust) are, contrary to the authors' deduction, underestimated. These effects were considered to be due in part to non-linearities of the rps (etc.) with resistance in waves.

One of the reasons for selecting model of self-propulsion point for tests in waves is to provide a maximum amount of comparable data from which design trends may be obtained. An analytical method is then required to correct such data to any particular ship size and sea condition. Could the authors' comment on how their approach may be used to derive such corrections?

H. Nowacki (T.U. Berlin)

This paper takes an interesting fresh look at the complex and practically very significant topic of the propulsive performance of ships in a seaway. This subject does not seem to have received sufficient systematic attention in the past. I would like to address a few comments chiefly to some aspects of propulsion and hull-propeller interaction in a regular seaway.

In order to develop a systematic approach to this problem it appears useful to me to discuss the physical phenomena in terms of the same concepts and categories that are familiar from the theories of seakeeping, propulsion, and hull-propeller interaction, allowing for all mutual dependencies among these basic effects. This suggests that one should examine the mutual relation between seakeeping effects, that is flows induced by the incident wave, forced ship motions and diffraction, and those due to propulsion and hull-propeller interaction, subdivided into potential, viscous and wave-induced flow effects. The interaction of these elements causes further flows, much in analogy to the way that propeller action modifies the nominal into the effective wake. A complete description of the flow situation should, in principle, account for longitudinal, radial, and circumferential wake components and for all pertinent degrees of freedom in ship motions.

It appears to me that the authors have recognized most, if not necessarily all, of

the aforementioned effects. I appreciate that they did not aim at a complete analysis of this multifaceted problem, but wanted to concentrate on what they felt to be the dominant effects. Nevertheless it would be helpful if they could summarize in a few words which effects in the foregoing check list they have taken into consideration and which ones remain to be examined further.

I would now like to turn to a few more detailed questions. First, most of the interaction analysis is quasi-steady. This appears plausible for some of the slowly varying, relatively stable flow situations; but how such instabilities as separation at the stern are affected by ship motions and the seaway is another matter. Do the authors have any evidence on this? E.g. equation (81) for the thrust deduction neglects viscous effects and hence cannot be expected to reflect any changes in the separation pattern that may be caused by the seaway.

Second, it is interesting to note that some of the influences of the seaway upon the propulsion factors are favorable, while others are adverse. E.g., a decreasing thrust deduction looks attractive provided that the associated wake changes do not offset this advantage. The nagging question is what may be the net effect of the seaway on all factors of propulsive efficiency combined? Would the authors venture to express an opinion on this?

In closing I would like to comment that in my view this paper has contributed several useful and original thoughts to this complex topic, which, I hope, will stimulate much needed further research in this important area.

Author's Reply

O.M. Fjølhusen (Norwegian Inst. of Tech.)

Reply to Prof. Himeno

Professor Himeno proposes a different method than ours in order to explain the effect of the ship motions, incident and diffracted waves on the wake. In our method there will be an effect of all ship motions, the incident and diffracted waves. But it is right that we anticipate that the pitching motion has a dominant effect. We have not included the effect that Professor Himeno has suggested because we believe it is not a dominant effect. But we may be wrong, and it would be interesting to see the results of his approach. But if his approach is used in connection with strip theory calculations of the ship motion problem, he will find a small influence of pitch motion. The reason is that it seems that he bases his boundary layer calculations on tangential veloci-

ties. The small influence of pitch motion contradicts experimental evidence that pitch motion has a significant influence on the wake distribution.

Reply to Prof. Maruo

We do not mean that the "direct pressure integration method" is any superior method to Maruo's method which is based on the equation for conservation of momentum in the fluid. But it is an alternative method which is equally correct to second order in wave amplitude, and which has the advantage that one more directly sees the physical reasons to added resistance. Further it is necessary with knowledge about the second order mean pressure distribution when one wants to estimate the influence of the ship motions, incident and diffracted waves on the wake distribution.

Professor Maruo gives the impression that our method is a difficult method to apply. But we think he has misunderstood. Our method uses the first order velocity potential on the ship in a simple manner, and includes all necessary terms correctly to second order in wave amplitude. Maruo's comment implies that the first order velocity potential is difficult and nearly impossible to calculate on the ship. But this is what we do anyway when we calculate with good results linear ship motions, bending moments, shear forces and pressure distribution along the ship. So we cannot see why we should not also use the first order velocity potential on the ship when we calculate the added resistance.

Reply to Dr. Fujii et al

It is interesting to see the favorable comparison between the discussers experiments and our proposed formula for added resistance on blunt ship forms in the low wave length case. However in the case of fine ship forms and high Froude numbers the agreement between experiments and theory is not satisfactory. But we would like to stress that the theory is not supposed to be valid in the high Froude number case. In reality we assume a low speed solution of the steady forward motion problem. Further there is a possible effect of bow flare and sharp ship ends that we have neglected.

Reply to Prof. Gerritsma et al

We thank the discussers for their interesting comment on how very sensitive the added resistance can be on predicted heave and pitch motion. We therefore agree that it would have been interesting to compare the predicted and measured motion amplitudes in the considered cases.

Reply to Dr. Takagi

We think that Dr. Takagi has misunder-

stood our use of "far-field" when we derive the formula for added resistance in the low wave length case. We are using "far-field" as a distance of many wave lengths from the body. But in our case the wave length is understood to be very small compared to the draft of the ship. That means that our "far-field" in this case is in the "near-field" in the conventional slender body sense. We therefore do not think that his comments about the use of equation (37) is appropriate.

Reply to Dr. Murdey

The differences in RPM increases between the Moor-Murdey results and our calculations may be reasonable if the propellers have been well immersed during the tests. In such cases also the calculations will give the smallest values at the self propulsion point of the model.

In order to obtain full scale results at any sea condition with our approach we need information about the immersion of the propeller for a specific number of speeds and wave lengths. This information must either be obtained from model tests in waves or from calculations. Through a comparison between propulsion test results and calculated performance of the model we will then have the basis for estimation of the full scale performance. We doubt that our approach even with the most advanced refinements will exclude model testing.

A reply to his comments on the added resistance for fine ship forms is similar

to our reply to Dr. Fujii and Mr. Takahashi.

Reply to Prof. Nowacki

It has been our attempt to explain physically some of the most important effects upon propulsive coefficients caused by waves and wave induced motions.

The most important effect seems to be changes in mean wake and changes in propeller characteristics. The remaining effects seem to be of minor importance. A complete solution of the problem is extremely complicated and would for example require a complete boundary layer calculation with motion induced velocities included. The change in wake distribution due to waves and wave induced motions will mainly have an influence on the relative rotative efficiency but we do not think that it will significantly influence on the effective mean wake.

Due to the motions of the ship we get an acceleration of the flow in front of the propeller and may therefore expect a reduction in separation. It is reasonable to assume that this will have a beneficial effect on the thrust deduction but we are not at the time being able to give a clear answer to that point.

According to our opinion the most important thing at the moment must be to concentrate the efforts in refining the propeller model by taking cavitation and ventilation into consideration.

The Seakeeping Characteristics of a Small Waterplane Area, Twin-Hull (SWATH) Ship

James A. Fein, Margaret D. Ochi and Kathryn K. McCreight

David W. Taylor Naval Ship Research and Development Center

Bethesda, Maryland, U.S.A

ABSTRACT

This paper addresses the motions of a Small Waterplane Area, Twin-Hull (SWATH) ship in a seaway. The current status of full scale trials, model experience and prediction capability is presented and the hydrodynamic factors contributing to the generally low motions of SWATH ships are identified. Correlation between transfer functions from modified strip theory predictions and full scale results for SSP KAIMALINO, a SWATH ship, is given along with response spectra from full scale trials including the effect of automatic motion control. Comparisons of model and full scale motions in Sea States 4 and 5 are shown. Predictions of natural periods are given as a function of speed and are compared to trial results. The design philosophy for SWATH natural periods is described and prediction of severest motions to be expected in an encountered seaway is made by a statistical estimation technique. The overall good motions and habitability characteristics to be expected of the SWATH type of ship are shown for a range of speeds and headings to the sea.

1. INTRODUCTION

The analysis of the seakeeping performance of any ship design depends on good theoretical predictions validated by model experiments and full scale trials. For a new type of ship the dependence on experimental data is vital to build confidence in the analytical tools and to gain insight into the hydrodynamic phenomena unique to that ship type. In this paper a full scale trial of a prototype is used to gain confidence in an analytical method that is then applied to the design problems of extreme value prediction and natural periods estimation.

This paper has two primary objectives. One is to present the seaworthiness trial data on SSP KAIMALINO to the ship hydrodynamics community with an interpretation of the ship's motion behavior. The other is to demonstrate how trials, model experiments and theoretical predictions enhance the development of seakeeping design considerations for SWATH ships.

2. THE SWATH CONCEPT

The SWATH ship presents a unique challenge to naval architects and hydrodynamicists, since its seakeeping characteristics can be dictated by the designer to a far greater extent than for conventional monohulls. SWATH ships can offer excellent motions and sustained speed capability in a seaway. The SWATH concept was derived from conventional catamarans and ocean oil-drilling platforms. It combines the speed and large deck area of the conventional catamaran with the seakindliness and platform stability of the drilling rig. A SWATH ship consists of two streamlined submerged hulls that are torpedo-like in shape connected to an above water structural box by one or two thin struts on each side. Propellers located behind each hull provide the propulsive force. Control surfaces on the submerged lower hull enhance stability and can be activated to control trim and further reduce motions when the ship is underway.

A typical SWATH design would have only 20 percent of the waterplane area of a conventional monohull. The reduced waterplane area and redistribution of buoyant volume into submerged hulls reduce the excitation forces of the seaway and increase the natural periods of motion of the craft. The relatively infrequent occurrence of storm waves with long periods makes it possible for ships with equally long natural periods to avoid synchronous response in the most commonly occurring seaways. This decoupling of the ship from wave excitation forces is the fundamental idea behind the SWATH concept. The reduced waterplane area also allows the SWATH ship to be more responsive to the forces generated by control surfaces than a conventional ship.

Other parameters which strongly influence seakeeping are longitudinal metacentric height (GM_L), transverse metacentric height (GM_T), separation of longitudinal center of buoyancy and center of flotation (LCB-LCF), strut configuration and size, and area and position of the control surfaces. The influence of these parameters as reflected by the natural periods of a SWATH ship will be discussed later.

The U.S. Navy's development of the SWATH concept began in 1969 with the design of SSP KAIMALINO by T.

G. Long of the Naval Ocean Systems Center (NOSC) in California and the MODCAT program at the David Taylor Naval Ship Research and Development Center (DTNSRDC). MODCAT was renamed SWATH (Small Waterplane Area Twin Hull) in 1972 to differentiate the concept from conventional catamarans. Over the last ten years progress has been made in the prediction of drag, stability, maneuvering, motions, and loads for SWATH ship designs. A summary of this work is contained in Lamb and Fein (Ref. 1). In particular two-dimensional strip theory has been applied to SWATH ship motions prediction by Lee and Curphey (Ref. 2). A computer program applying this theory has shown good correlation with model tests for motions, wave excitation forces and oscillation coefficients. The predictions can be made for regular or irregular waves. This technique is rather time-consuming so simplified techniques for estimating the potential flow added mass and damping for two-dimensional SWATH sections have been developed by Dalzell (Ref. 3) and Lee (Ref. 4). These programs can be used to screen a wide range of potential designs in a short time.

SSP KAIMALINO was the first experimental prototype for SWATH ships. The goal of the U.S. Navy's SWATH program is larger prototypes that can demonstrate the advantages of SWATH ships in relation to Naval missions. The Mitsui Semi-Submerged Catamaran (SSC) /Mesa-80 (Ref. 5) is a recent addition to the family of SWATH prototypes. Its attributes will greatly advance the development of SWATH technology.

3. SEMI-SUBMERGED PLATFORM (SSP) KAIMALINO

3.1 Description

Semi-Submerged Platform (SSP) KAIMALINO is the first SWATH ship built in the United States. Designed by T. G. Long (Ref. 6), it was intended as a workboat for the Naval Ocean Systems Center (NOSC) Hawaii Laboratory. It has proven valuable both as a workboat and as a platform for demonstrating the seakeeping advantages of the SWATH concept. Constructed in 1973 by the Curtis Bay Coast Guard Shipyard in Baltimore, Maryland, the ship was modified at Dillingham Shipyard in Hawaii by the addition of displacement increasing buoyancy blisters in 1975. The current displacement is 220 tonnes.

The particulars of SSP KAIMALINO are presented in Table 1. Original design values and values for the most recent seakeeping trials are given. The addition of the blisters is responsible for most of the changes. As sketched in Figure 1, the ship consists of two cylindrical lower hulls connected to the upper box by two struts per hull. Buoyancy blisters are located on the inboard side of each hull, extending with constant thickness from approximately 7 to 16 meters aft of the nose and terminating at 21 meters aft of the nose. Tapered all movable control fins (called canards) are located inboard just aft of the noses. A constant chord flapped hydrofoil spans the space between the hulls aft of amidships. Rudders are mounted in the propeller slipstream behind each hull. The forward struts increase in chord and thickness from a point just below the waterline to the connection to the box, the aft struts also increase in thickness as the box is approached. Both starboard struts are outfitted with spray rails above the waterline that help in deflecting sheets of water that might climb the struts in waves. The above water box is flat bottomed except for slanted, shaped sections on the forward end. These sections tend to cushion slams in head seas.

SSP KAIMALINO has naturally good motion characteristics in many sea conditions. An automatic

Table 1 Characteristics of the SSP KAIMALINO

	Original Design	As Tested 1976 and 1979
Length, Underwater, m	24.8	24.8
Length, Overall, m	26.9	26.9
Displacement, MTSW	192.2	220.0
Draft, m	4.6	4.8
Beam, Maximum Submerged, m	15.1	15.1
KG, Height of Center of Gravity above Baseline, m	4.7	4.6
Diameter of Lower Hulls, m	1.98	1.36
KB, Height of CB above Baseline	1.75	1.65
GM _L , m	4.42	3.84
GM _T , m	2.01	1.01
Waterplane Area, m ²	23.0	23.0
Longitudinal Distance CG Forward of Aft Perpendicular, m	12.9	13.4
Longitudinal Distance CF Forward of Aft Perpendicular, m	13.5	13.5
Pitch Radius of Gyration, m	7.1	7.0
Roll Radius of Gyration, m	4.8	5.5
Aft Foil, Projected Area, m ²	25.1	25.1
Forward Canards, Total Area, m ²	7.1	7.1

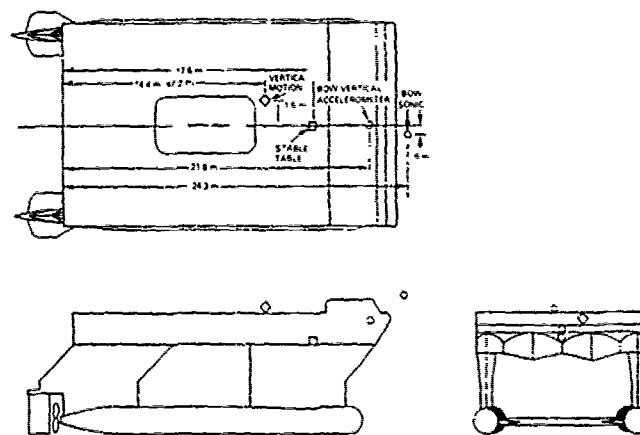


Fig. 1 Sketch of SSP KAIMALINO Showing Instrument Locations

motion control system designed to reduce motions in all sea conditions was designed and documented by Higdon (Ref. 7). The system uses the forward canards and the stern foil flaps to minimize pitch and roll motions. Heave is not minimized but it can be controlled so as to minimize relative motion with respect to the wave in order to reduce water contacts in low encounter frequency situations such as following seas. This control mode relies on pressure (height) sensors located in the underwater hulls in conjunction with minimized inertial pitch and roll. Heading control is maintained by the rudders keyed to a yaw rate gyroscope. The ship has 153 kilowatts (200 horsepower) available for fin and rudder actuation, which scales up to values that are unacceptable for larger SWATH designs. However, more efficient actuators could provide acceptable control deflection

rates for less power on larger ships as shown by Higdon (Ref. 8).

SSP KAIMALINO is outfitted with two 1660 kilowatt (2230 horsepower) aircraft type gas turbine engines in the upper box that drive controllable pitch propellers through a chain drive system. SSP KAIMALINO reached 25 knots in 1974 before the blisters were added. Current torque limitations on drive train components reduce the top speed to about 18 knots.

SSP KAIMALINO does not represent current design philosophy for SWATH ships; for example, the full span stern foil is larger than either stability or control requires. The small overall size of SSP KAIMALINO makes her motion in high sea states worse than larger SWATH ships. In addition, her waterplane area and metacentric heights result in natural motion periods at low speeds that are not optimum for larger SWATH ship designs. These differences are discussed in detail in Lamb and Fein (Ref. 1) within the context of current SWATH design practice. Nevertheless SSP KAIMALINO does demonstrate the advantages of the SWATH concept. It also provides a means for relating full scale performance to theoretical and experimental model work, thus verifying the design tools that apply to any SWATH ship.

3.2 Model Experiments

Model experiments were conducted at DTNSRDC on a 1/7.8 scale model of SSP KAIMALINO in 1971 as the design was being finalized. The objective of the experiments was to evaluate the design and identify problem areas. The 3.35 meter (11 foot) long model built at DTNSRDC was outfitted for drag, propulsion, stability, seakeeping, and structural measurements. Experiments were conducted on Carriage 2 (DTNSRDC's Deep Water Straightline Basin) and in the seakeeping tank of the Maneuvering and Seakeeping Facility (MASK). For the seakeeping experiments the model was self-propelled and tethered by power cables and safety lines to the towing carriage. Pitch and roll angles were measured by gyroscopes. Relative bow motion was obtained from an ultrasonic transducer mounted on the bow. An accelerometer placed at the forwardmost point of the model measured bow vertical acceleration. Heading was maintained by servo-controlled rudders that reacted to sway and yaw rate feedback. Powering was controlled from the carriage and varied to keep slack in the cables and safety lines regardless of the wave induced surge. The aft foil and canards were fixed at angles required to give level trim and design sinkage in calm water at the speed under study. The irregular waves were provided by pneumatic wavemakers driven by magnetic tape. The waves approximated Pierson-Moskowitz sea spectra for Sea States 4 and 5. All headings were investigated over a range of speeds from 4.2 to 21 knots full scale. The bow acceleration was highest in head seas while pitch motion was largest in following seas. No significant slamming was noted at any heading. These early results did not give a complete picture of seakeeping of SSP KAIMALINO but they did show that there were no major problems. Large motions in stern quartering and following seas were of some concern though they were associated with long periods. The conclusions of these experiments were generally verified by subsequent full scale trials.

A second series of model experiments was conducted in 1973 as construction of the ship was ending. The objective was to investigate synchronous conditions where the encounter period in waves corresponded to the ship's natural periods. A 1.5 meter long radio-controlled model designed by NOSC was utilized. This model allowed for more time at speed in the MASK facility and could be run

without power from the towing carriage. The model was instrumented to measure impact pressures, pitch, roll, relative bow motion, and bow vertical acceleration. The experiments consisted of the determination of calm water natural periods at zero speed, evaluation of regular wave responses and investigations in a seaway representing a full scale modal period of 9.5 seconds and significant wave height of 4 meters.

The natural periods at zero speed were 8.49 seconds for pitch, 8.06 seconds for heave and 15.7 seconds for roll in full scale terms. The regular wave work emphasized encounter frequencies that might excite synchronous motions. Largest motions were found in following seas when ship speed was close to the wave speed. In that case a large bow down static trim occurred due to the action of the wave on the full span aft foil. This condition, which could lead to the upper structure bow being buried in the wave and the propeller broaching, was later observed in full scale trials.

In the irregular wave experiments significant slamming was experienced in head Sea State 6 at speeds above 10 knots full scale. It should be noted that all these model experiments were conducted with controls fixed. Severe motions and impacts at speed could be expected to be alleviated by the use of automatic control.

3.3 Full Scale Trials

SSP KAIMALINO has undergone extensive trials beginning in 1974. The first series of trials was conducted (as were the model experiments) on the original configuration. These were completed in 1975 and included investigations of powering, structural loads, control response, maneuvering, and seakeeping. The trial conditions were later repeated after SSP KAIMALINO was outfitted with buoyancy blisters. In addition, control system evaluation trials, helicopter landing trials, and comparison trials with two Coast Guard ships have been conducted. The powering results are documented by Stenson (Ref. 9) and Woo and Mauck (Ref. 10). The maneuvering results are summarized in Lamb and Fein (Ref. 1). Figure 2 is a photograph of SSP KAIMALINO undergoing trials.

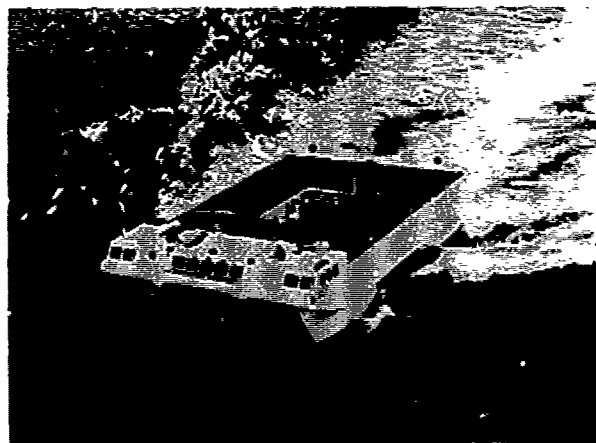


Fig. 2 SSP KAIMALINO Undergoing Trials

The first series of seakeeping trials in 1975 was conducted in the Kaiwi Channel between the islands of Oahu and Molokai (See Figure 3). Measurements were made of the ship's rigid body motions (pitch, roll, relative bow motion), accelerations (surge, sway, heave, bow

vertical and port vertical), rates (yaw, pitch, and roll), and impact pressures at 20 locations. The seaway was measured by a free floating buoy that was deployed by the chase boat. The buoy contained a double integrating accelerometer and telemetered the wave height signal back to the ship. The buoy tended to drift and at times was far enough from the operating area to make the relevancy of some of the wave measurements questionable. Significant wave height was about 1.75 meters.

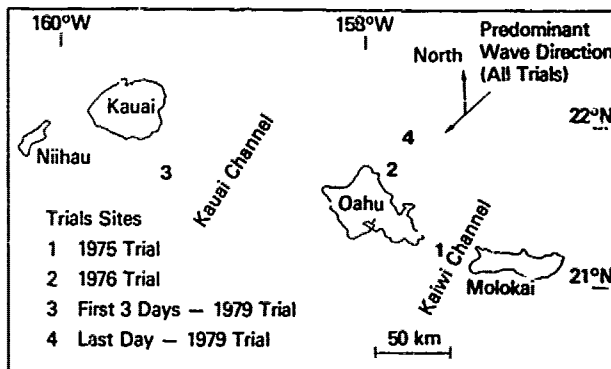


Fig. 3 Hawaiian Islands Trials Locations

Trials were conducted at nominal speeds of 16.5, 12.5 and 9.5 knots. Average speeds, significant wave heights, and trial conditions are listed in Table 2. The control system was not employed for these trials so canards and the stern foil were fixed at deflections designated for mean trim at the given speed. The trials procedure consisted of adjusting the ship to level trim at zero speed and recording displacement. Before each run the ship was set on course at the desired heading to the waves as determined by a deck observer. As with any full scale trial, there was some doubt about the directionality of the seaway although the direction of primary energy was carefully observed. At least 30 minutes of data were taken for each trial condition. No changes in propulsion or control deflection were permitted during the data collection period. Few impacts were noted. The only case where deck wetness occurred was in following seas when the wave speed approached the ship speed and a large amplitude but gentle bow "plow-in" occurred. Propeller broaching occurred in similar conditions in quatering seas. As reported by Kallio (Ref. 11), the data were inadequate for power spectral analysis; however, significant values of the motions and accelerations were obtained at all headings.

In November of 1976 low speed trials were conducted by DTNSRDC on SSP KAIMALINO to obtain bending moments in beam seas. In conjunction with that effort, the motions, bow vertical acceleration, and seaway were measured at all headings at the nominal speed of 5 knots. These results provided information about SSP KAIMALINO motions in a high Sea State 5 at low speed. The ship had been modified prior to these experiments by the addition of buoyancy blisters on the inboard lower hulls. The ship was operating on only one propeller during these trials. Pitch and roll were measured at the stable table (located about 6 meters forward of the CG on the centerline) while bow motion was determined from an ultrasonic height sensor located 1.0 meter forward of the bow on the ship centerline. Bow vertical acceleration was measured as in the earlier trials in the pilot house. Wave spectra were again obtained from a free floating buoy and in these trials the buoy was deployed from the ship and was very near the trial location near Oahu Island.

Table 2 Seakeeping Trial Conditions

Title	Date	Location	Sea State	Significant Wave Ht m	Number of Conditions	Speeds kt.	Control Evaluated
Seakeeping Evaluation	7/28/75	KAIWI STRAIT	4	1.8	6	9.8, 12.8	No
	7/31/75	KAIWI STRAIT	4	1.7	10	9.8, 17	No
Structural Evaluation	11/26/78	North-East of Oahu	5	3.6	6	5	No
Control Evaluation	1/21/79	South-East of Kauai	5	2.9	10	15.5	Yes
	1/23/79	South East of Kauai	4	2.5	4	0, 10	Yes
	1/25/79	South-East of Kauai	4	2.0	18	3.5, 10, 15.5	Yes
	1/31/79	North-East of Oahu	5	3.2	19	7, 10, 15.5	Yes*

* One blister missing, data not reported herein.

Significant wave height is given in Table 2. The trials were conducted without the use of the control system, as the speed was too low for sufficient control effectiveness. Spectra from these trials will be discussed in Section 5.

The most recent seakeeping trials were conducted in January of 1979 in order to extend the range of seakeeping results, to obtain data that could be used to generate transfer functions, and to quantify the effect of automatic control on the motions of SSP KAIMALINO. These trials were conducted off Kauai and Oahu as noted in Figure 3. Measurements were made of rigid body motions, accelerations and the seaway. Impact pressures and strains were recorded but not analyzed since there were few impacts. The transducer locations in this trial are shown in Figure 1. Waves were again measured by a free floating buoy in close proximity to the trial area. When not in the water the buoy was attached to the deck and thereby provided a vertical displacement measurement near the longitudinal center of gravity (CG) that was almost equivalent to heave.

In preparation for each particular run, the ship was steadied on course at approximately the desired speed. The speed varied slightly due to wind and wave conditions. The ship course was set to maintain a heading which was constant relative to the predominant seaway as determined by observations. Once the heading and speed were set, manual control settings were made or the control system was turned on, and then the data collection portion of a run began. Collection time was governed by the need for sufficient encounters at the given speed and heading and varied from 20 to 50 minutes. No changes in manual control surface deflection or propulsion settings were made during the runs. Results from these trials will be discussed in forthcoming sections.

In addition, SSP KAIMALINO participated in a three ship comparative trial that was conducted in May of 1978. It is documented by Woolver and Peters (Ref. 12). SSP KAIMALINO was run alongside a 100 tonne patrol craft 30 meters long, and a 3000 tonne Coast Guard Cutter. The trials were conducted in Sea State 3. Emphasis was on human factors and comparative relationships rather than on absolute data. The results demonstrate that SSP KAIMALINO has superior motions to a ship of 10 times greater displacement in the same Sea State 3.

4. MOTIONS RESULTS FOR SSP KAIMALINO

The results of seakeeping experiments are describable in several ways. One is in the form of the ratio of significant responses to significant wave height. A significant value is the average of the one-third highest values and may be obtained from a time history of the motions or wave excursions. Another method of analysis is the power spectral density distribution which relates the energy of the motion or wave to the frequency. SSP KAIMALINO full scale trials spectral data are presented in the next section. A third method of analysis used in Section 6.3 involves the transfer functions. The transfer functions provide the unit response of a motion to a unit wave height throughout the frequency range.

The ratios of significant responses to significant wave height are presented in Figures 4 to 13 for the model and full scale ship. The data were obtained in Sea States 4 and 5. The wave spectra for the model experiments were different from those in the full scale trials. The effect of control at high speed is also included for pitch and roll in Figures 10 through 13.

Figures 4 through 7 show the effect of speed on free body motions without any form of control in head seas. The results show linearity throughout the wave height range examined. Correlation between model and full scale is good for pitch throughout the speed range. The model results were obtained from the 1971 and 1973 experiments. From a maximum at zero speed, pitch decreases to a minimum at 10 knots, then peaks at about 14 knots. Between 10 and 14 knots the wave drag hump occurs. At 10 knots the ship is "climbing" its self-generated bow wave and thus it is heavily damped in pitch. At 14 knots the ship-generated wave is behind the ship and may act in a destabilizing manner. Trial conditions after the addition of the buoyancy blisters are indicated by solid points. The data with buoyancy blisters show good agreement with the earlier data which indicates that the blisters, which are centered at the longitudinal CG, have little effect on pitch motion.

Figure 5 presents roll in head seas. The model experiments which were conducted in a unidirectional head sea show minimal roll motion while the full scale trial results show significant roll. This may be attributed to the fact that wave components are present in the real environment from other than the direction of the predominant energy. The vertical acceleration in Figure 6 remains relatively constant with speed, slightly increasing at the higher speeds. The ratio of significant relative bow motion to significant wave height in Figure 7 shows almost no speed effect. Except for a single point near 16 knots, the model data agree quite well with the full scale results.

Figures 8 and 9 show speed dependence of the pitch and roll motions in beam seas. Pitch in beam seas at speeds below 5 knots is slightly higher for the full scale trials than for the model results. The difference is probably due to uncertainties in heading and wave direction, but even so the model data do show the presence of pitch in beam seas. The pitch is probably due to the fore and aft asymmetry of the ship. The large aft foil excites pitch as the ship responds to the beam waves, and since there is no area forward to cancel this effect a net pitch motion ensues. The model roll motions agree quite well with the full scale over the speed range in Figure 9. Again the blisters seem to have little effect on significant roll. The peak in pitch and roll at about 14 knots is again present in beam seas. Roll follows the same trend with speed as pitch, decreasing to about 10 knots and then showing an increase in the wave drag hump regime.

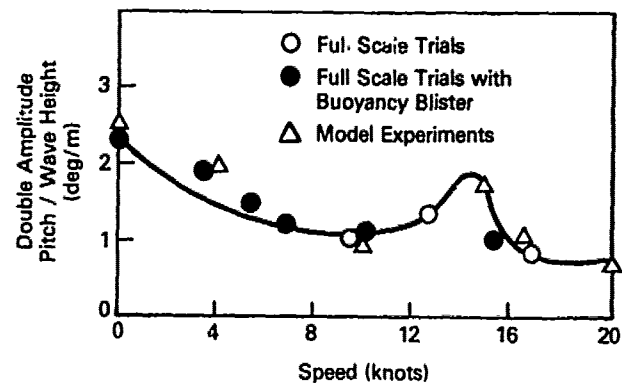


Fig. 4 Pitch Motion for SSP KAIMALINO in Head Seas

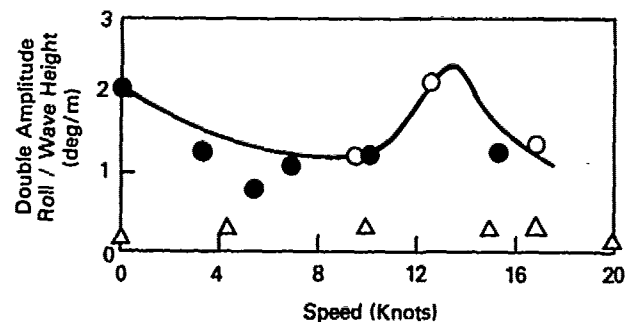


Fig. 5 Roll Motion for SSP KAIMALINO in Head Seas

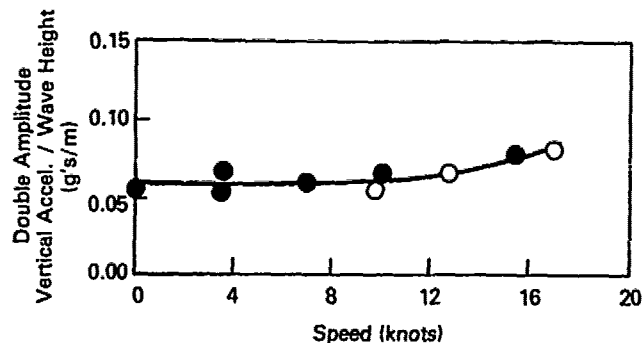


Fig. 6 Vertical Acceleration for SSP KAIMALINO in Head Seas

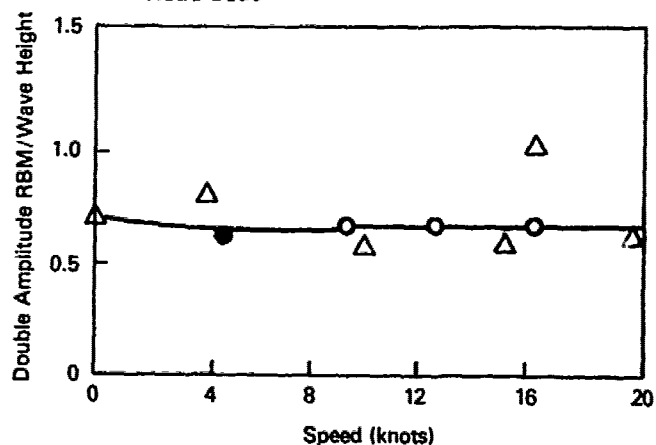


Fig. 7 Relative Bow Motion for SSP KAIMALINO in Head Seas

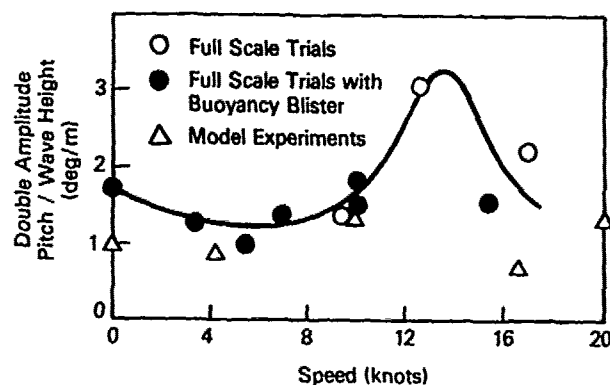


Fig. 8 Pitch Motion for SSP KAIMALINO in Beam Seas

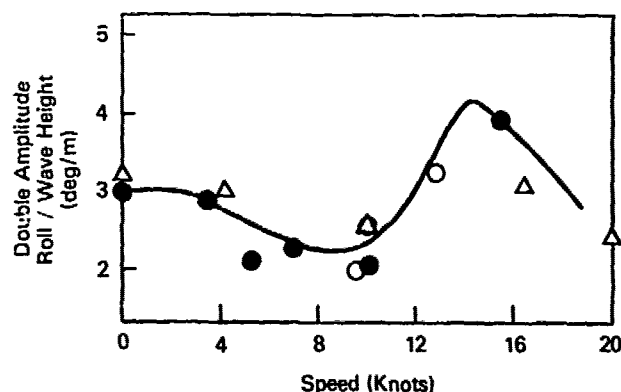


Fig. 9 Roll Motion for SSP KAIMALINO in Beam Seas

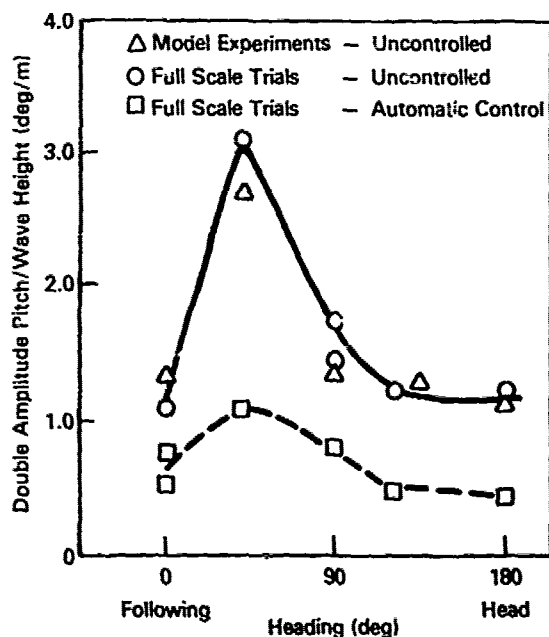


Fig. 10 Pitch Motion for SSP KAIMALINO at 10 Knots

The effects of automatic motion control are clearly demonstrated in Figures 10 through 13 where the data is plotted as a function of heading. The full scale data were obtained during the control system evaluation, trials of 1979. The model data in Figures 10 and 11 are from experiments in Sea States 5 and 6 (without blisters). There are no model data with active control. Agreement between model and full scale pitch motion is excellent at all headings for 10 knots. Roll magnitude is low for the models in head and following seas because of the purely unidirectional environment in the towing tank but agrees with trials quite well at the other headings. The effect of motion control at 10 knots is significant. Maximum pitch motion which occurs in quartering seas is reduced to about one-third its uncontrolled value. Roll is reduced by approximately one-half at all headings. The control evaluation trials results show a large reduction in significant values of motions at 10 and 15.5 knots and some reduction at 7 knots. At lower speeds the control surface effectiveness is not sufficient to affect the motions.

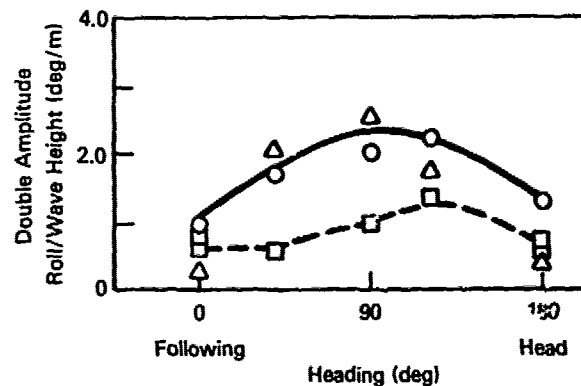


Fig. 11 Roll Motion for SSP KAIMALINO at 10 Knots

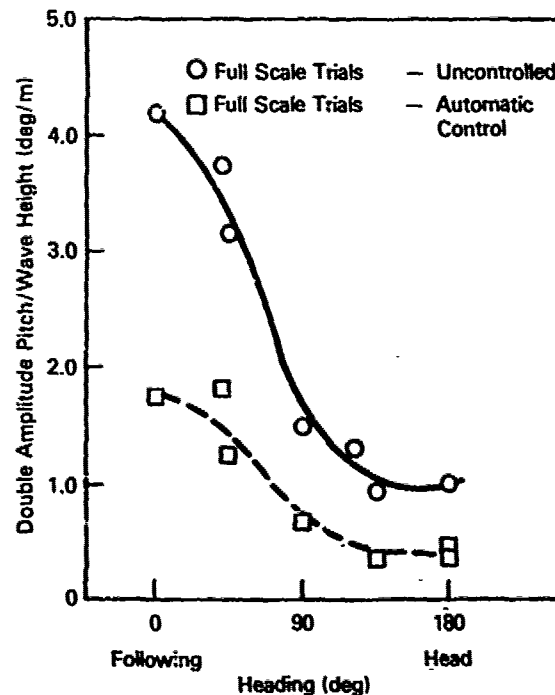


Fig. 12 Pitch Motion for SSP KAIMALINO at 15.5 Knots

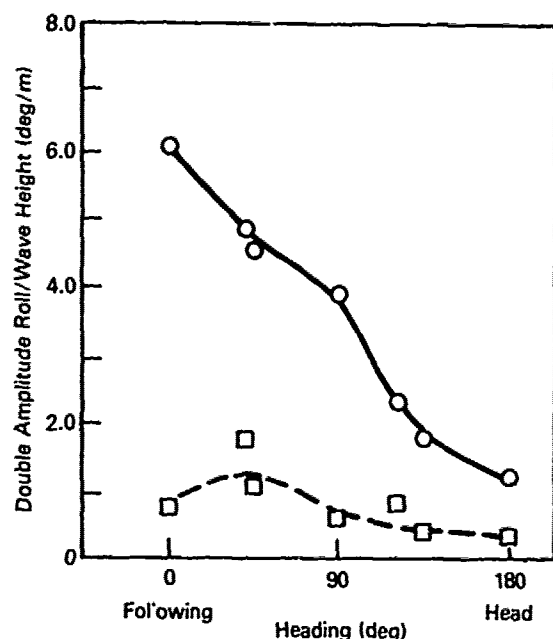


Fig. 13 Roll Motion for SSP KAIMALINO at 15.5 Knots

At 15.5 knots (Figures 12 and 13) roll and pitch are both maximum in following seas. The control system reduces significant roll motion by 90 percent at this speed in following seas and by about 70 percent at other headings. Pitch is reduced by over 50 percent at all headings. These significant values demonstrate the effectiveness of motion control. Significant values are important in establishing seakeeping criteria for designs since motion limits for weapon systems or aircraft operations are generally expressed in terms of significant responses.

5. DISCUSSION OF FULL SCALE TRIAL SPECTRA

Power spectral densities as functions of encounter frequency were obtained by Fourier analysis of the motions data and are presented for three speeds in Figures 14, 15 and 16. The response spectra in combination with the wave spectra of encounter provide a good insight into the sources of the motions. The 5 knot speed data were obtained in 1976 and the 10 and 15.5 knot speeds are from the control evaluation trials of 1979. For the two higher speeds, spectra with and without automatic motion control are given. Relative bow motion (RBM) was measured in 1976 but not in 1979. Vertical motion near the CG was obtained for most conditions in 1979 and is presented in place of RBM for the higher speeds. Wave spectra are presented in Figures 17, 18 and 19 for each trial day for which motion spectra were obtained. The modal period of the wave spectra is indicated on each motion spectrum by the symbol T_0 to show the location of the maximum wave energy in the encounter frequency domain.

The results for a 5 knot speed from the 1976 trials in a high Sea State 5 appear in Figure 14. For each heading RBM, pitch and roll are presented. The RBM depends on pitch, heave and the encountered wave at the bow. At high frequencies and low speed SSP KAIMALINO tends to platform the waves. That is, the ship tends not to experience motion as it encounters the waves. Since the RBM spectrum reaches a maximum in the high frequency region where pitch and roll are small, this indicates that the relative motion may be due primarily to heave and the

motion of the shorter waves. At lower frequencies contouring occurs as the ship follows the wave. This leads to lower RBM energy at those frequencies even though significant pitch and roll energy may be present. In all cases the RBM peak energy occurs at frequencies higher than the wave modal frequency (indicated by T_0 on the figures). The RBM is largest in head and bow seas and shows double or secondary peaks at these headings.

The pitch spectra at 5 knots are all single peaked and the peaks tend to occur at $\omega_e = 0.65$ rad/sec, which is close to the estimated natural frequency in pitch at this speed. For head and bow seas the peak corresponds to the peak of the encountered wave spectra indicating considerable excitation near the natural frequency for these headings. Pitch response is minimum in beam seas as expected.

The roll spectra are not as uniform as the pitch spectra and tend to be somewhat broader. The primary peak in the roll response occurs at the peak in the wave spectra at all headings with the exception of head seas. A secondary peak is evident at 0.8 rad/sec in quartering seas. The head sea roll spectrum is flat with small peaks above and below the wave modal frequency.

The spectra for 10 knots are contained in Figure 15. The spectra are presented for vertical motion near the CG, pitch, and r.l.l. The data were obtained during the control evaluation trials on January 25, 1979, in a Sea State 4. The results are presented with and without utilization of automatic control. The controlled cases are indicated by the dashed lines. The control system on SSP KAIMALINO is intended to minimize pitch and roll but not vertical motion. The vertical motion component due to pitch and/or roll is reduced in some cases, but heave is small in all conditions, even without control. The vertical motion peak corresponds to the wave modal period in all cases except head seas. A secondary peak at lower frequency in head and bow seas corresponds to a peak in the roll spectrum.

The pitch spectra at 10 knots show maximum energy in quartering seas. Wave modal periods correspond to pitch energy peaks in beam, quartering and following seas. In head seas the pitch response is very flat, with a small response over a wide range of frequencies. In bow seas there is a secondary peak at the modal frequency of the waves at about 0.85 rad/sec while the primary peak is at 0.72 rad/sec. In all conditions the control system greatly decreases the pitch response. For example, in following seas the controls are least effective but still reduce the peak value by over 50 percent. At low frequencies in quartering and following seas the controlled response exceeds the uncontrolled response. These long period motions are attributable to the control system's feedback loop response.

The roll spectra at 10 knots for SSP KAIMALINO show maximum response in beam seas with almost as great a response in quartering and bow seas. Control is effective in reducing roll motions in all sea headings. In all cases the main roll peak is associated with the wave modal period and there is a secondary peak at a lower frequency that can be attributed to the natural period in roll. The low frequency peak is in the frequency range where measurements are doubtful which leads to difficulties in fixing its magnitude. A third peak at a higher frequency than the wave peak is noted for bow and quartering seas. This is due to a significant component of wave energy at those frequencies of encounter.

It is also of interest to point out that in beam seas at 10 knots the wave modal period was approximately the same as the natural periods of heave and pitch, causing substantial response in these modes. The natural period in roll of the ship at this speed is about 21 seconds or

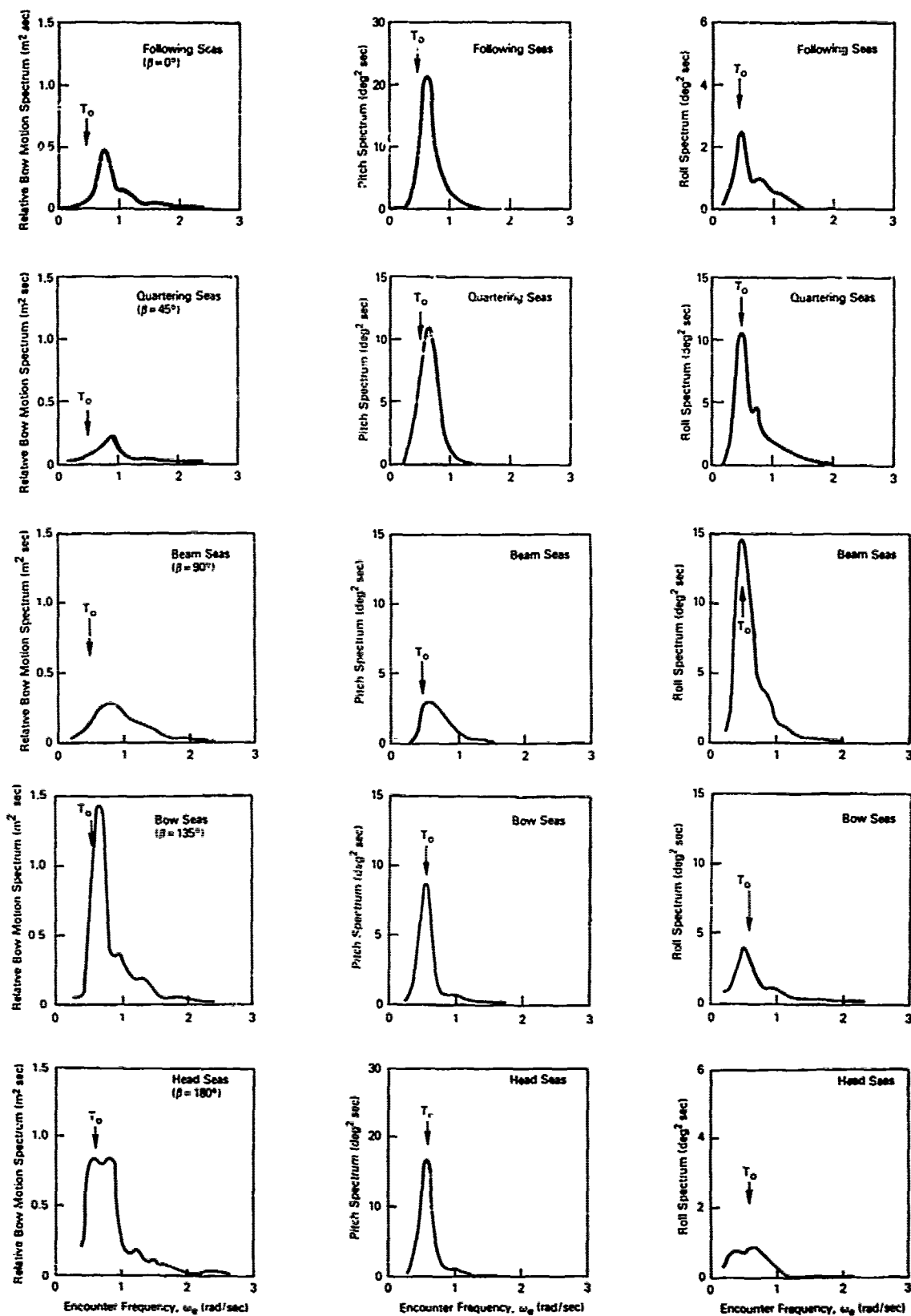


Fig. 14 Motion Spectra for SSP KAIMALINO at 5 Knots

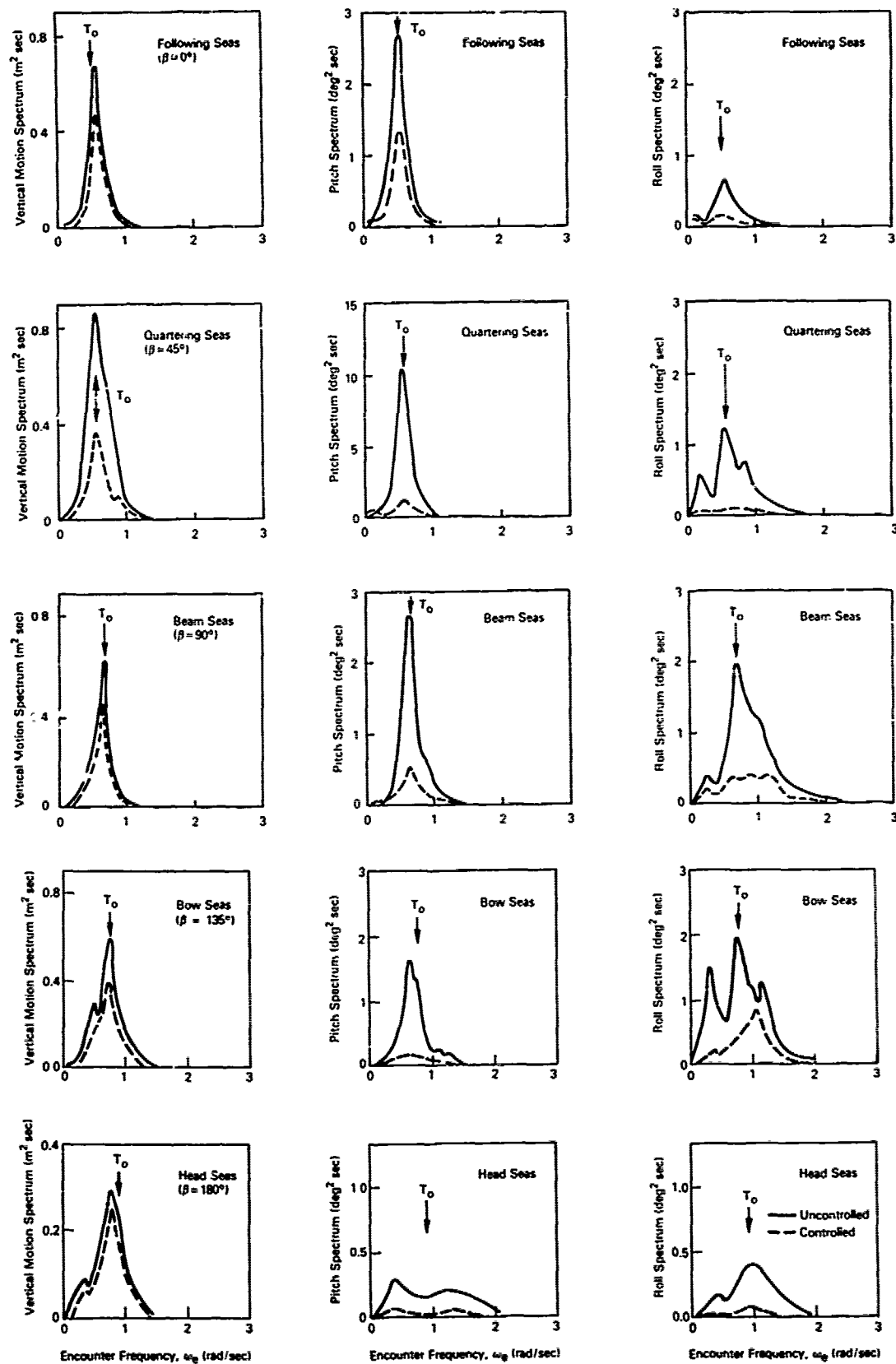


Fig. 15 Motion Spectra for SSP KAIMALINO at 10 Knots

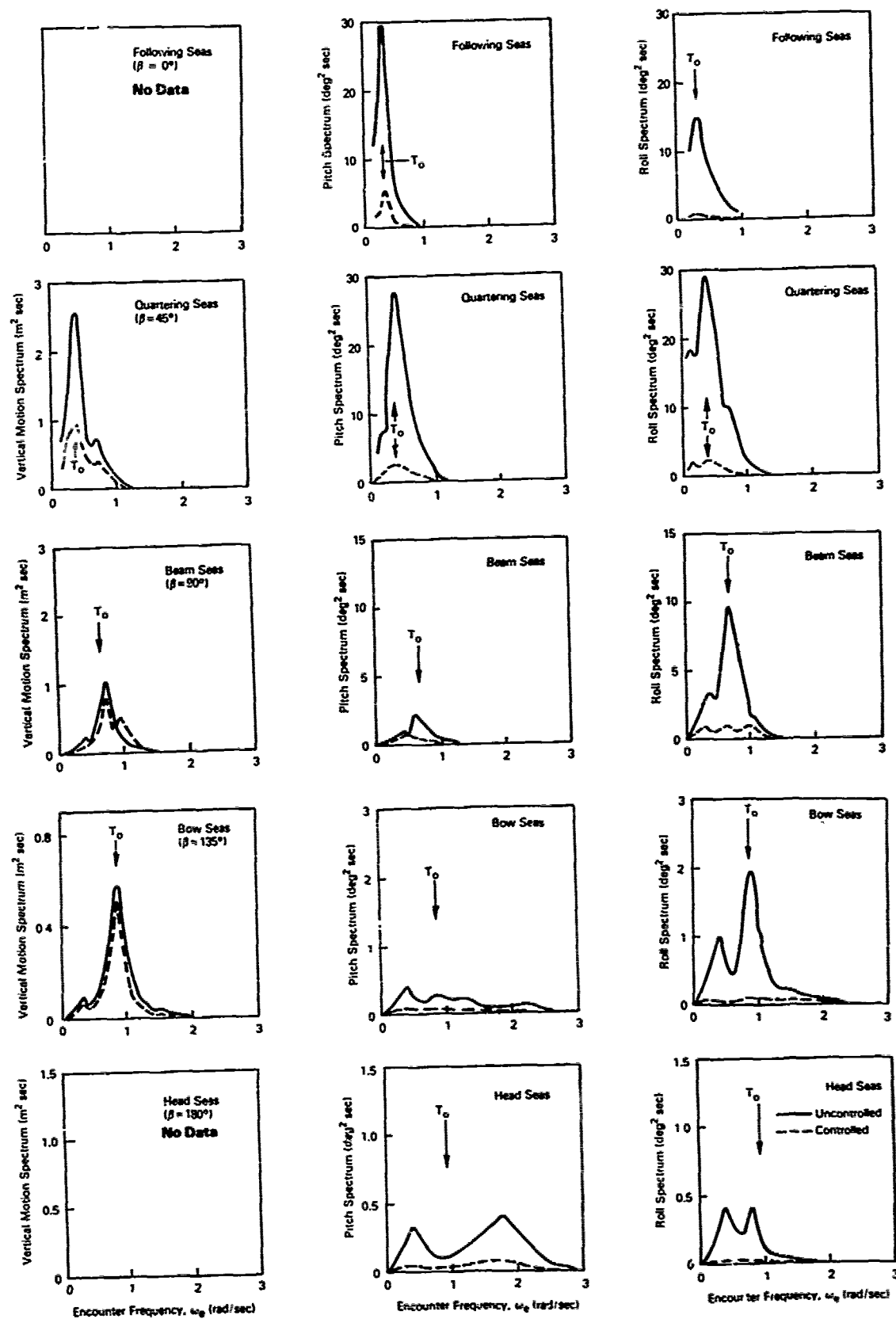


Fig. 16 Motion Spectra for SSP KAIMALINO at 15.5 Knots

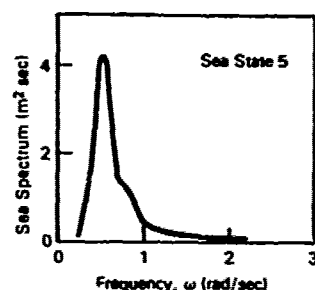


Fig. 17 Wave Spectrum for 5 Knot Motion Spectra

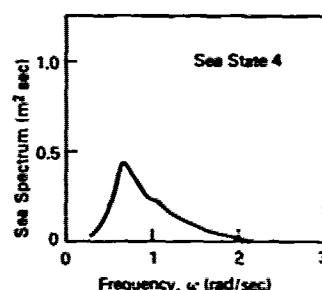


Fig. 18 Wave Spectrum for 10 Knot Motion Spectra

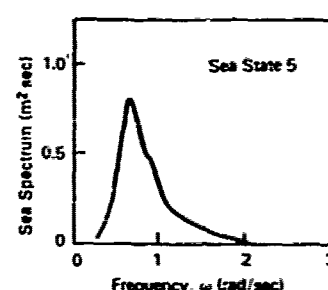


Fig. 19 Wave Spectrum for 15.5 Knot Motion Spectra

approximately twice its pitch period. Although little wave energy exists at the roll natural frequency, some small roll motion does appear. However the prime response in roll occurs within the same frequency regime as pitch which has large excitation at its natural frequency. This behavior is exhibited in bow and quartering seas as well. Thus, at least for this speed, there appears to be significant coupling between the three modes (pitch, heave and roll) of motion.

The response spectra at 15.5 knots obtained in a Sea State 5 (on January 21, 1979) during the control evaluation trial are given in Figure 16. Response of vertical motion near the CG, pitch and roll are included, though vertical motion was not available for the head and following sea cases. Among the cases available, vertical motion response is greatest in quartering seas. Control of pitch and roll has little effect on the vertical motion except in quartering seas. In all cases the primary peaks for vertical motion correspond to the frequency of maximum wave energy. A secondary peak in quartering seas at $\omega_e = 0.72$ rad/sec may result from the fact that there is significant wave energy near the heave and pitch natural periods.

Pitch response is more than an order of magnitude larger in following and quartering seas than in head, bow or beam seas. Pitch response is primarily wave induced in beam, quartering and following seas, and in following seas the encountered wave spectrum has considerable energy near the natural pitch period at the 15.5 knot speed. The large responses in quartering and following seas occur at low frequencies where the waves travel at speeds close to the ship speed. The large stern control foil in the SSP can induce large motions under such conditions. In bow seas pitch response is flat over a broad range with the most energy at $\omega_e = 0.4$ rad/sec. The head sea pitch response spectrum is distinctive in that there is little response at the wave modal period but instead peak values of response occur at encounter frequencies of 0.4 and 1.8 rad/sec. The high frequency peak is in a region where there is little pitch response for any other heading. Active control significantly decreases the pitch response for all headings.

Roll spectra at 15.5 knots exhibit wave modal period induced rolling for all sea headings. Also there is a secondary peak in head, bow and beam seas at a lower frequency of encounter which is approximately 0.35 rad/sec, close to the estimated roll natural frequency. In following seas this same frequency is close to the modal period of the encountered waves, resulting in an amount of roll response greater than the roll response in beam seas and only slightly less than the roll in quartering seas. Control of roll motion is very effective at all headings as controlled responses are almost insignificant compared to the uncontrolled cases. In particular, the severe rolling in following seas is virtually eliminated by the control system.

Figures 17, 18 and 19 give the wave spectra in the wave frequency domain for each of the three days on which the data in the response spectra were obtained. There is very little wave energy below $\omega_e = 0.3$ rad/sec which causes difficulties in defining low frequency effects in the motion spectra. Each wave spectrum is single peaked though there are some indications of secondary humps. The significant wave heights for these spectra are given in Table 2.

Overall, the seakeeping trials of SSP KAIMALINO demonstrated that the ship could operate over its full speed range in wave conditions up to a high Sea State 5. Excessive slamming was not encountered at any heading either with or without automatic motion control. Slamming at 15.5 knots in a head Sea State 5 was virtually eliminated by trimming the ship bow up two degrees. The ship's tendency to heave (following the waves) helped in moderating the impacts. At no time did the ship slow down due to sea conditions even though the average magnitude of the one-tenth highest waves (double amplitude) was more than twice the clearance height of 1.8 meters. During the Sea State 5 trials on January 21, 1979, the average of the one-tenth highest waves was 3.65 meters which is 15 percent of the length of the ship. On that day SSP KAIMALINO operated for over 10 hours at speeds around 15.5 knots at a variety of headings with no degradation of crew or ship performance.

6. COMPARISON WITH THEORETICAL MOTION PREDICTION

6.1 SWATH Ship Prediction Methodology

Confidence in the ability of theory to predict trends and general magnitudes of motion is particularly important for the SWATH ship designer since the SWATH concept lacks the extensive experience in design available to the monohull designer. While model experiments are required before a design is finalized, theoretical predictions must be used to analyze the motion of potential configurations at an early stage of design.

The development of the theory used at DTNSRDC to describe the motions of SWATH ships is presented by Lee and Curphey (Ref. 2). Strip theory provides the basis for this development. That is, it is assumed that the flow at one transverse two-dimensional section of the ship is independent of the flow at another section. This approach has been used successfully to predict the motions of conventional displacement ships; however, SWATH ships differ from conventional displacement ships in significant ways, creating a more complex problem. For example, the interaction effects resulting from the closeness of the two hulls must be described. The relatively small waterplane area of SWATH ships implies a small heave

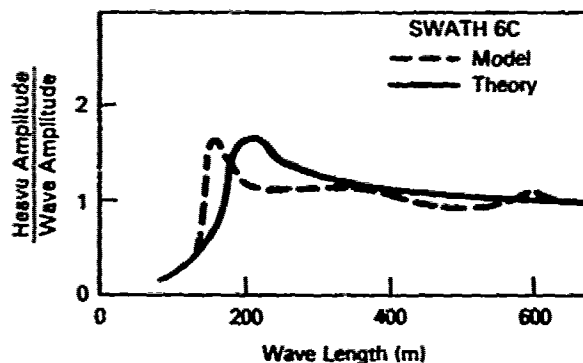


Fig. 20 Heave Transfer Function for SWATH 6C at Zero Speed in Beam Seas

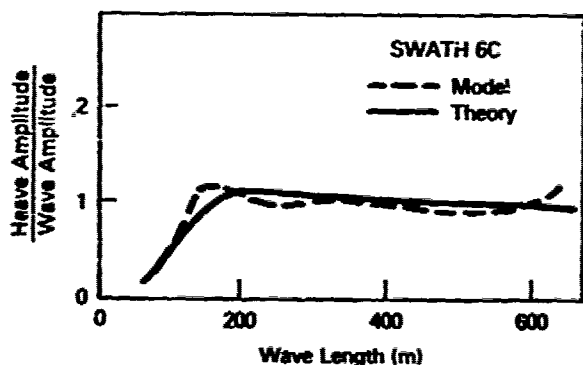


Fig. 21 Heave Transfer Function for SWATH 6C at 20 Knots in Beam Seas

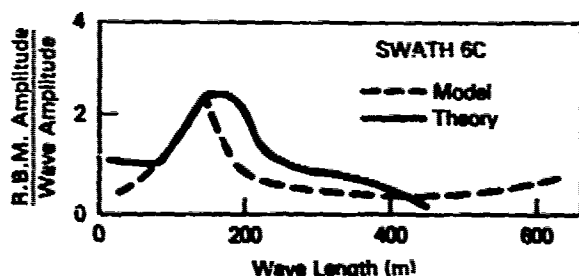


Fig. 22 Relative Bow Motion Transfer Function for SWATH 6C at Zero Speed in Beam Seas

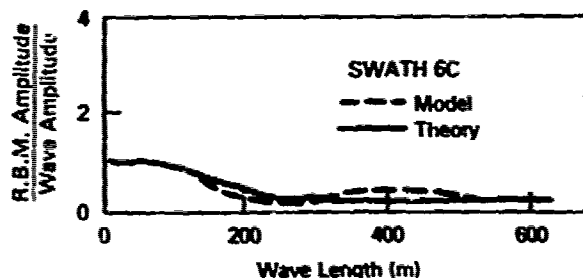


Fig. 23 Relative Bow Motion Transfer Function for SWATH 6C at 20 Knots in Beam Seas

restoring force. Consequently, viscous damping effects which may be ignored in modelling the vertical plane motions of conventional displacement ships become relatively important for SWATH ships. The effect of forward speed on the wave train is not modelled for either SWATH or conventional ships. For the SWATH ship the wake created by a strut will affect the flow at sections aft of it. It can be expected that this effect will be greater for ships with two struts per hull than for ships with one long strut and that slender struts will generate less wake than thicker ones.

Correlation of theory with model experiments has shown generally good agreement for a range of speeds and headings. A series of experiments for the SWATH 6 series was carried out by Kallio (Ref. 13). These were models for a 2900 tonne, 73 meter design with various GM's. The configurations, denoted A, B, and C, had the same lower hulls but different strut configurations. The 6A and the 6B are single strut configurations whereas the 6C is a twin strut configuration. Correlation between theory and model experiments is generally good; however, certain problems emerge. Zero speed predictions are somewhat inconsistent in quality. This is probably due to problems in the general modelling of the nonlinear viscous damping. At higher speed, behavior is well described but for some conditions some discrepancies in magnitude exist. Comparisons of Kallio's model experiments and predictions for the 6C configurations are presented in Figures 20 to 23 for zero and 20 knots in beam seas. Heave and relative bow motion response per unit wave amplitude are given as a function of wave length. At zero speed the peak value of heave is well predicted though it is predicted to occur at a slightly greater wave length than found in the measurements. The discrepancy in heave also seems to be reflected in the relative bow motion predictions. The correlation for 20 knots is very good as shown in Figures 20 and 22.

6.2 Excitation Force Comparisons for SSP KAIMALINO

The good correlation with model scale transfer functions for SWATH 6C implies that predictions for SSP KAIMALINO, also a twin strut design, should be reasonable. Unfortunately, there are no model scale transfer functions available for SSP KAIMALINO with which to make theoretical comparisons. However, model scale results do exist for the wave exciting heave force and pitch moment. Since they are an important element in motion prediction, they give some indication of the relevancy of the motion predictions for SSP KAIMALINO. The forces and moments on the model in head seas were obtained as part of an experimental program documented by Fein and Stahl (Ref. 14). The model did not have blisters, whereas the predictions include the effect of blisters. The blisters were shown to have small effect on the head sea motion in Figures 4 and 5; even though motions are the same, exciting forces are not necessarily the same.

The nondimensional heave force ($F_{30}(\omega)$) and phase (ϕ_3) with respect to the wave are given in terms of nondimensional encounter frequency. The nondimensionalization for encounter frequency is:

$$\omega_e = \omega_e \sqrt{L/g} \quad (1)$$

where

ω_e is the encounter frequency in rad/sec,
 L is nominal length in meters and
 g is gravitational constant in m/sec².

Nondimensional heave force is given by:

$$F_{30}(e) = \frac{\bar{F}_{30} L}{mgh} \quad (2)$$

where

\bar{F}_{30} is the measured force amplitude in newtons,
 m is mass of the ship in kilograms and
 h is wave height in meters.

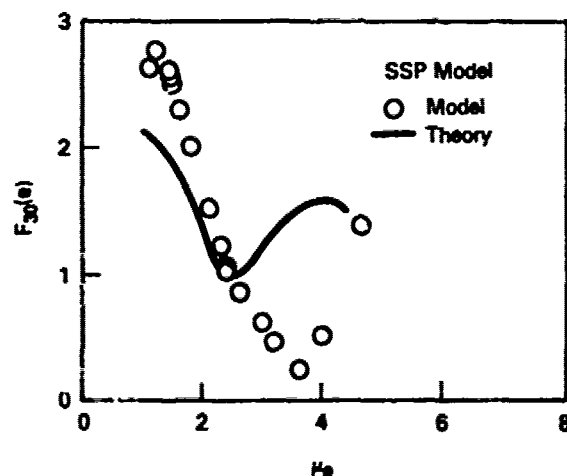


Fig. 24 Heave Exciting Force in Head Seas at 7 Knots

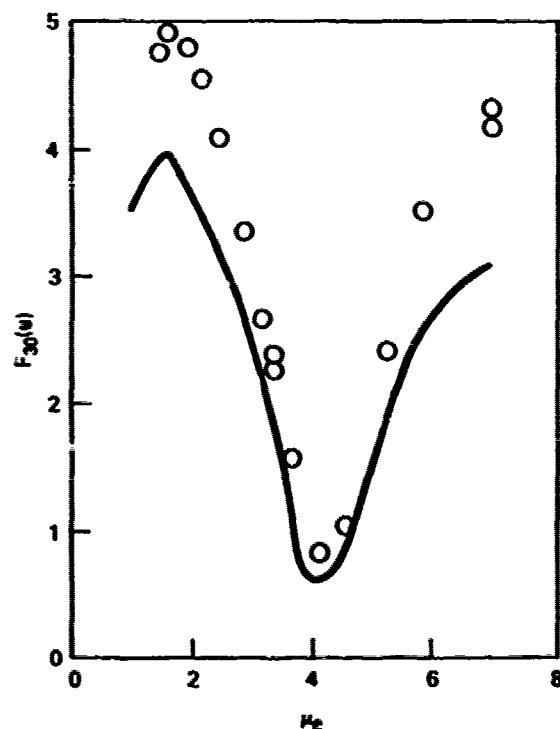


Fig. 25 Heave Exciting Force in Head Seas at 15.5 Knots

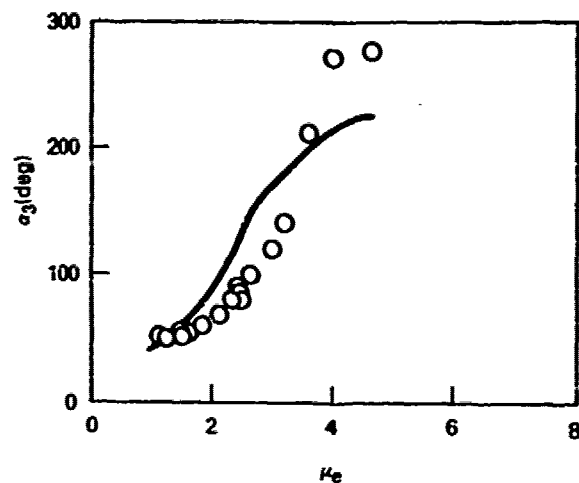


Fig. 26 Heave Force Phase Angle in Head Seas at 7 Knots

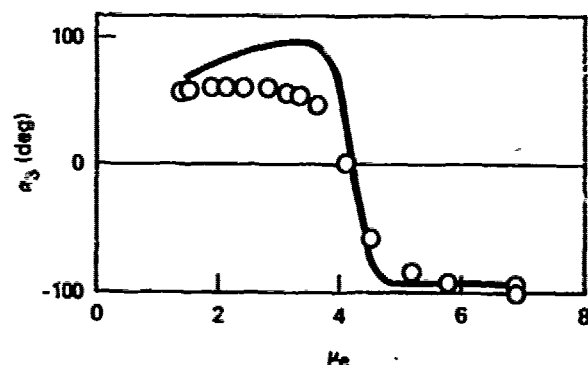


Fig. 27 Heave Force Phase Angle in Head Seas at 15.5 Knots

The results for wave excitation force and phase at 7 and 15.5 knots are given in Figures 24 to 27. These results are typical of the correlation at other speeds. Agreement between theory and model results for heave exciting force were quite good at all speeds. Magnitude and position of the peaks are well predicted in Figure 25 for the high speed. For the 7 knot speed, Figure 24 shows good agreement up to $\mu_e = 2.6$, which is equivalent to an encounter frequency of 1.7 rad/sec for the ship. This covers the range of frequencies found in most sea spectra. Phases agree closely for both speeds over the entire frequency range.

6.3 Transfer Function Comparisons for SSP KAIMALINO

Although model scale transfer functions are not available for SSP KAIMALINO, transfer functions can, in principle, be extracted from the full scale trial data, although this is not an ideal approach because of problems associated with wave measurements and determination of directionality aspects of the seaway.

Prediction of the motions for SSP KAIMALINO is more difficult than for ships in the SWATH 6 series. The 6C results indicate that the presence of two struts per hull does not in itself create problems in predicting SWATH responses. However, a dominant feature of SSP KAIMALINO is its large aft mounted hydrofoil. The stern foils used on the SWATH 6 series do not span the

separation between hulls and are much smaller in area relative to the ship size. Observations during full scale SSP KAIMALINO trials indicate that ventilation can occur as the height of the free surface over the foil varies at some speeds, resulting in reduction of the effectiveness of the foil. This is not modelled currently in the SWATH prediction programs.

With these reservations, predictions for heave and pitch for SSP KAIMALINO travelling in beam seas are presented in Figures 28 to 34. Full scale results were available for this heading at 7, 10 and 15.5 knots for uncontrolled heave (vertical motion corrected to the CG) and pitch motion. Heave is presented in nondimensional form and pitch in degrees per meter. Both motions are presented as a function of the wave frequency. Predictions are shown with solid lines, full scale results with dashed lines. The degree of correlation for heave is not as good as for the SWATH 6C. The heave predictions for SSP KAIMALINO are heavily damped whereas the full scale results are not. This predicted characteristic is probably due to the modelling of the effect of the aft foil. The lift curve slope values were estimated by theory and confirmed by model results. Degradation in lift due to changes in the free surface conditions are not included in the theory. For 10 knots two sets of results for nominally the same trial conditions are given in Figure 29. The trials were conducted on the same day but separated by a number of hours. The results differ somewhat in magnitude, although they exhibit the same trends. The major differences occur over the frequency range where there was little wave energy, illustrating the difficulties in obtaining transfer functions from full scale trial data.

The correlation for pitch motion of SSP KAIMALINO is better than for heave motion. The correlation for zero and 7 knots is quite good, though again the agreement between theory and trials at 10 knots is not. For this speed a large free surface deformation was observed during the trials. The 10 knot results in Figure 33 show

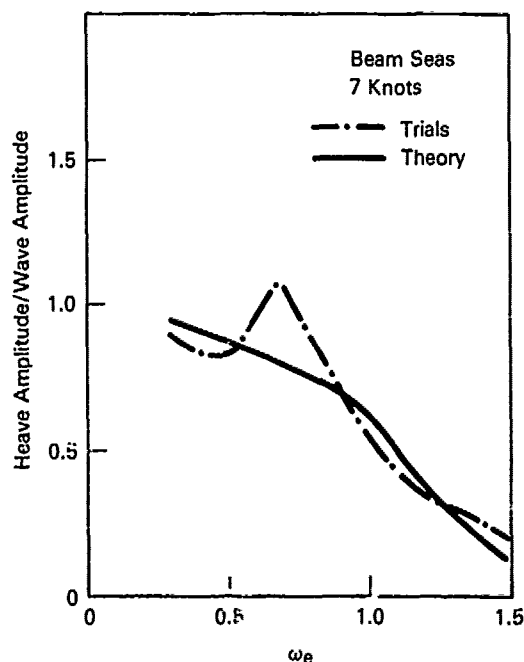


Fig. 28 Heave Transfer Function for SSP KAIMALINO at 7 Knots

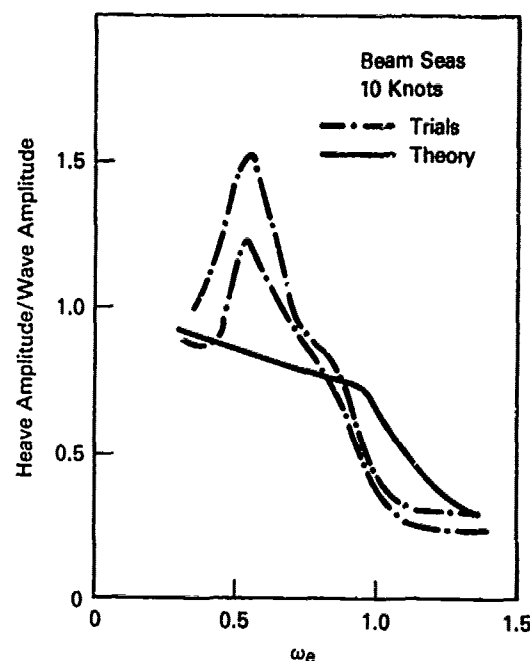


Fig. 29 Heave Transfer Function for SSP KAIMALINO at 10 Knots

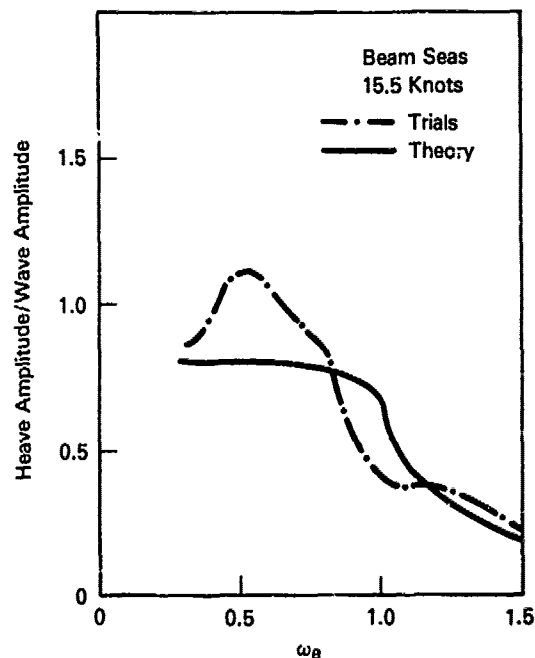


Fig. 30 Heave Transfer Function for SSP KAIMALINO at 15.5 Knots

differences between the two experimental conditions as large as the differences between the theory and one of the trial results. The 15.5 knot correlation is better than at 10 knots.

The overall accuracy of the SWATH ship motions program has been established using model experiments. Its applicability to SSP KAIMALINO motion prediction can be inferred from the reasonable correlation in the cases given.

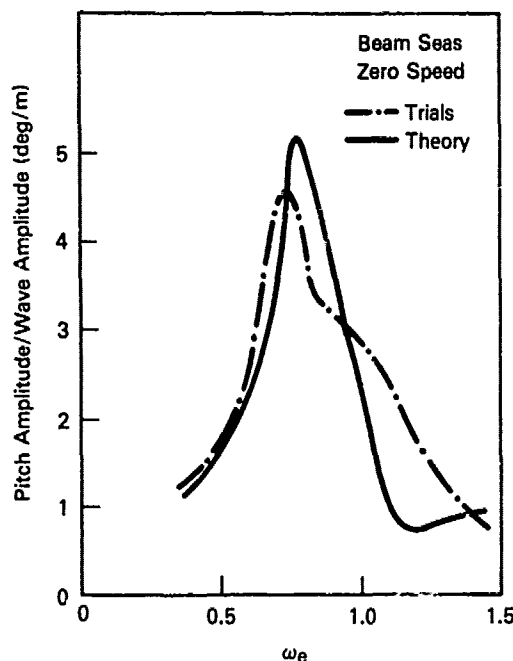


Fig. 31 Pitch Transfer Function for SSP KAIMALINO at Zero Speed

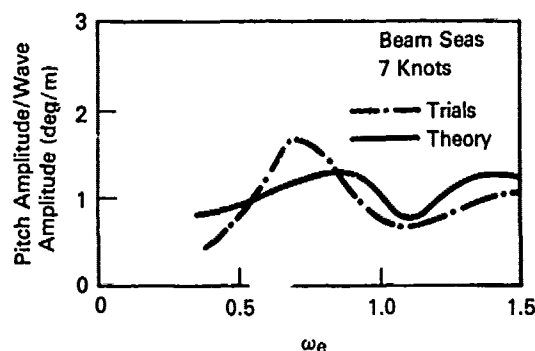


Fig. 32 Pitch Transfer Function for SSP KAIMALINO at 7 Knots

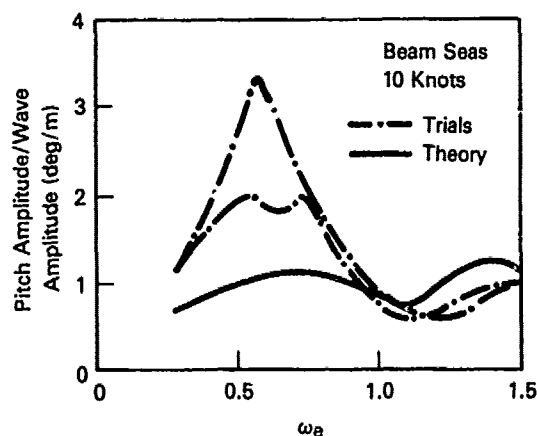


Fig. 33 Pitch Transfer Function for SSP KAIMALINO at 10 Knots

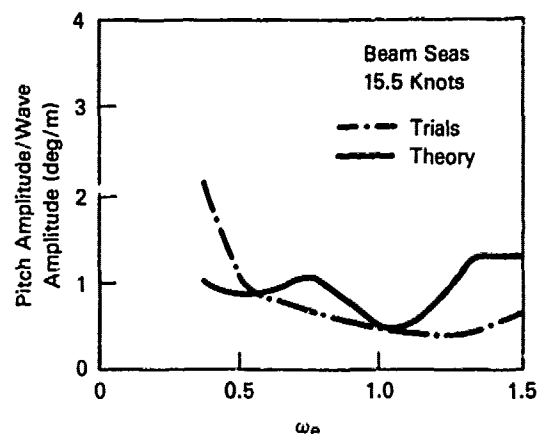


Fig. 34 Pitch Transfer Function for SSP KAIMALINO at 15.5 Knots

7. DESIGN CONSIDERATIONS

7.1 Natural Period Results

Knowledge of the natural periods of motion in heave, pitch and roll are vital to analyzing the seakeeping behavior of all ships, especially SWATH ships. The designer of a SWATH ship desires to avoid synchronous motion conditions under normal operations. As noted earlier the periods are highly dependent on parameters that vary widely in a SWATH design. The standard relationships for natural periods as given in Comstock (Ref. 15) are:

$$T_z = 2\pi \left[\frac{\Delta (1 + C_z)}{g \rho A_w} \right]^{1/2} \quad (3)$$

pitch period,

$$T_\theta = 2\pi \left[\frac{K_\theta^2 (1 + C_\theta)}{g \overline{GM}_L} \right]^{1/2} \quad (4)$$

and roll period,

$$T_\phi = 2\pi \left[\frac{K_\phi^2 + d^2 C_\phi}{g \overline{GM}_T} \right]^{1/2} \quad (5)$$

where

- A_w is the waterplane area in m^2 ,
- Δ is the ship displacement weight in kilograms,
- g is the gravitational constant in m/sec^2 ,
- ρ is the density of water in kg/m^3 ,
- C_z is the added mass coefficient,
- C_θ is the added pitch moment of inertia coefficient,
- C_ϕ is the added roll moment of inertia coefficient,
- K_θ is the pitch radius of gyration in meters,
- K_ϕ is the roll radius of gyration in meters and
- d is half the hull centerline separation in meters.

As these equations indicate, several factors affect the natural periods. The added mass and moment coefficients are a function of lower hull geometry. The waterplane area and metacentric heights are a function of the geometry near the waterline. The radii of gyration are dependent on the ship's mass distribution.

Equations 3, 4 and 5 ignore coupling between modes and damping but do provide an estimate of natural periods. Assuming simple geometrical added mass and moment values for SSP KAIMALINO of $C_z = C_\theta = C_\phi = 0.9$ as an approximation following Numata (Ref. 16) and

using the data in Table I for the as-tested ship gives: $T_z = 8.6$ seconds, $T_\phi = 9.7$ seconds, and $T_\theta = 15.8$ seconds. The periods also were calculated using Equations 3, 4 and 5 in which C_z , C_θ , and C_ϕ , the added mass and added inertia coefficients, were obtained from strip theory. C_θ increases with speed while C_z and C_ϕ are independent of speed. These values are plotted in Figures 35, 36 and 37 along with the natural periods obtained from the 1976 trials and the 1979 control evaluation trials. The ship had buoyancy blisters for these trials. The trial natural periods are the periods associated with the peaks of the transfer functions. Analysis of data for some conditions resulted in different natural periods. These have been included in the figures to demonstrate the accuracy with which natural periods may be obtained by this technique. Natural periods obtained in 1973 by applying impulses to a scale model of the original design at zero speed also are included.

Heave natural periods as determined from the trial data (Figure 35) are fairly constant with speed as theory predicts. The slight variations between theory and trials may be due to changes in the waterline at various speeds which are not accounted for in the theory. Pitch natural period (Figure 36) tends to increase with speed. The period based on added inertia from strip theory shows this speed effect reasonably well. The roll period in Figure 37 is predicted by theory to be 18.5 seconds, irrespective of speed. The trial results for roll are sparse since at these long periods there was very little wave energy and generally unreliable data. The trial data that are available agree fairly well with the theory. The model test result is lower than the trial value. The model represented the original design configuration, and does not fully represent the ship as tested. The estimated roll period is low. In this case the value of C_ϕ is based on the assumption that rolling is equivalent to the heaving of one hull up while the other moves down.

There are certain static errors inherent in comparing natural periods from trials with predicted values. One is uncertainty about the exact fuel and ballast load during the trial. Though the ship was ballasted to the same condition every day, fuel use and weight shifting can occur. This effect on metacentric height and moments of inertia cannot be estimated. Also viscous damping has a strong influence on pitch natural period underway. A better method for obtaining natural periods is to apply a force impulse to the ship while underway, which unfortunately has not been done to SSP KAIMALINO since the addition of the blisters.

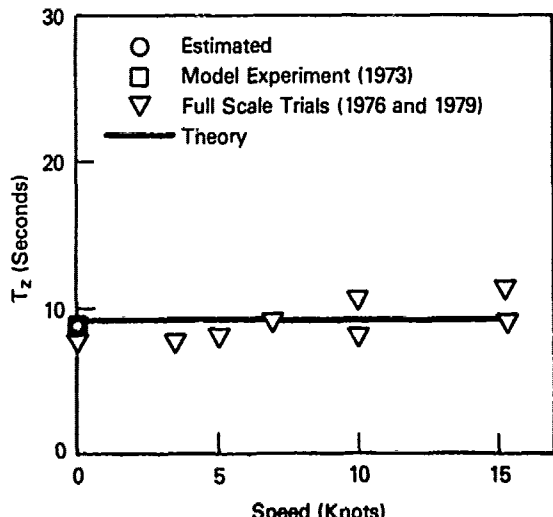


Fig. 35 Heave Natural Period for SSP KAIMALINO

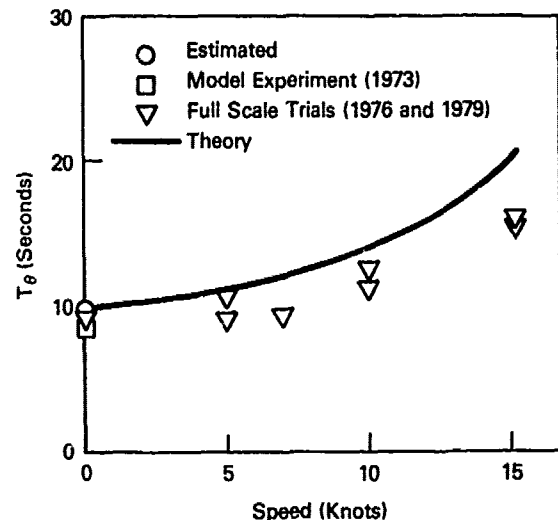


Fig. 36 Pitch Natural Period for SSP KAIMALINO

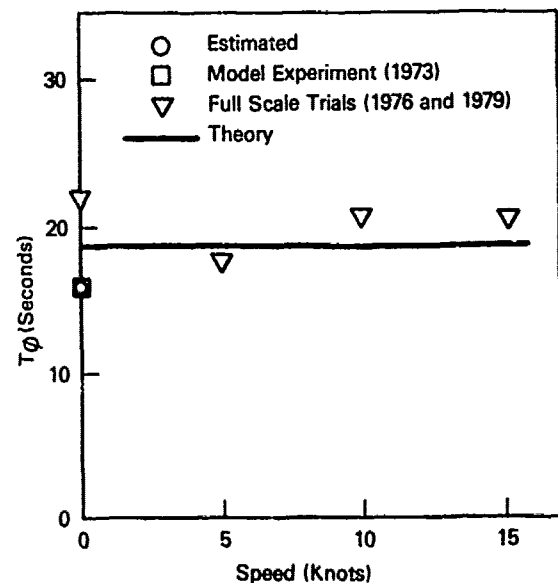


Fig. 37 Roll Natural Period for SSP KAIMALINO

7.2 Natural Periods and Design

The advantage of the long natural periods attainable by SWATH ship designs is that resonant conditions leading to large motions and degraded operability will not occur for most wave conditions. The designer desires platforming conditions to minimize pitch and heave motion in head seas. If the natural periods in pitch and heave are about 20 percent greater than the encountered modal period of the seaway this supercritical behavior can be accomplished.

If natural periods are sufficiently long the extreme motions associated with resonance will not lead to severe velocities or accelerations since encounter periods would be low. This was found to be true in the case of SSP KAIMALINO when operating in following seas at 15.5 knots without control. Pitch motions of 20 degrees crest-to-trough were recorded but operability was not adversely affected as long as the propeller remained submerged and the bow was not impacting. Simple automatic or even manual control could easily prevent

such extremes of motion. Similar thinking applies to beam sea rolling. A very long roll period assures that resonant conditions will not occur in beam seas under almost all conditions. Resonant conditions that might occur in following seas at moderate speeds can be controlled by automatic motion reduction. Thus the trend in SWATH ship design is to take advantage of long natural periods for good inherent seakeeping in most sea conditions while relying on automatic control and other means to decrease motions when resonant conditions are reached in following seas at moderate speeds.

The SWATH ship designer must also be aware of the interrelationships among the various natural periods. Pitch and roll periods should be separated so that uncomfortable "corkscrewing" motions will not occur in quartering seas as in the case of SSP KAIMALIMO at 15.5 knots when T_{θ} (16 seconds) and T_{ϕ} (21 seconds) were both excited at the same time. The change in periods with speed underlines the importance of having a good motion prediction technique that can be used in the early stages of design. Roll and heave periods and pitch and heave periods should also be separated if possible. The interrelationships among the natural periods is particularly important at low speeds where control fins are not effective in modifying motions. The choice of natural periods may be dictated by low speed behavior, particularly if the ship's mission requires a long duration at low speeds.

The natural periods are closely related to three other design issues: the amount of waterplane area, the bridging structure clearance height and the metacentric heights. The heave natural period can be increased by decreasing waterplane area. Such a decrease also will decrease the heave exciting force in waves, and probably decrease resistance as well. It must be remembered however that as the waterplane area is decreased, the restoring force also is decreased. This can result in the situation that, should resonance occur at these longer periods, the motions can be rather large even though the exciting force is small as shown in Pien and Lee (Ref. 17). The final selection of waterplane area must reflect a balance between the above requirements. Other issues that will come into the decision are structural and arrangements considerations.

Longitudinal metacentric height is a function of the distribution of the waterplane area. Increasing GM_L decreases the pitch natural period but provides a "stiffer" ship in terms of pitch restoring force for surviving in extreme seas. Increased clearance height tends to decrease both metacentric heights while imposing a severe structural weight penalty. Platforming (not responding in) all waves would require a high clearance. This is the approach taken by designers of column stabilized platforms. Changing from platforming to contouring as seaways get higher with longer associated periods is the desirable approach for SWATH ships. This puts an upper limit on the desired natural periods. Automatic control and bow up trim are further considerations that may influence the final clearance design of a SWATH ship.

Overall seakeeping is both a constraint and an opportunity to the designer as hydrostatics, structures, arrangements, powering and other factors are balanced to obtain a good design. The dependence of seakeeping on metacentric heights, moments of inertia and clearance points out that the usual weight growth of ships can be a serious problem for a SWATH hull. Thus, until experience is gained in design and construction, the SWATH ship will require larger margins than conventional hulls. Nevertheless the SWATH concept offers the opportunity to design a hull with low motions and therefore enhances

its capability for naval operations such as aircraft landing and takeoff, weapons firing, and towing sonar.

7.3 PREDICTION OF EXTREME MOTIONS

In previous sections the motions of SSP KAIMALINO have been presented as obtained in seas of a specified severity characterized by the specific wave spectra given in Figures 17, 18, and 19. The shape of wave spectra, however, can vary considerably (even though the significant heights are the same) depending on duration and fetch of wind, stage of growth and decay of a storm, or the existence of swell. Thus, during her lifetime, a SWATH ship may encounter a vast variety of wave situations. For design consideration, therefore, it is important to examine the effect of wave severity as well as wave spectral formulations on the magnitude of responses of SWATH ships. For this, computations of the probable extreme values of heave and pitch of SSP KAIMALINO in a seaway have been carried out in three different mathematical spectra following the method for short term response prediction presented in Reference 18. The probable extreme value is the largest value likely to occur in a specified ship operation time, here taken as the duration of the sea condition. The Bretschneider, Pierson-Moskowitz and the Ochi six-parameter spectral formulations were used in the computations, and these were applied to the transfer functions obtained from an analysis of SSP KAIMALINO data obtained in beam seas at a speed of 10 knots.

Computations using the Bretschneider and the Ochi six-parameter representations were made for a family of wave spectra from which the upper and lower bounds of responses with confidence coefficient of 0.95 were determined as well as those responses most likely to occur; that is, the responses in the most probable wave spectrum for a given sea severity. These responses were then compared with those computed using measured spectra at Station India in the North Atlantic (Weather Station 1) in order to determine how well the bounds cover the variation of responses in the measured spectra. The results are shown in Figures 38 and 39 for pitch and in Figures 40 and 41 for heave for wave heights up to 4.9 meters. Included also in the figures are the responses in the Pierson-Moskowitz spectrum. Wave heights greater than 4.9 meters (Sea State 6) were not investigated since craft linearity has not been verified in seas of severity greater than this.

The scatter of the responses computed in the measured Station India spectra shown by the crosses indicates that the probable extreme values of both pitch and heave amplitude vary considerably for a given significant wave height. The Pierson-Moskowitz spectrum underpredicts the motions in the lower wave heights while it tends to predict values somewhat high in the higher significant wave heights. It is also apparent from the figures that, in general, for both pitch and heave motions, the upper and lower bounds of the values computed using the six-parameter spectral formulation better encompass the data from the measured spectra in the North Atlantic than do those obtained using the Bretschneider formulation. While the former appears to cover the range of magnitudes computed using the measured spectra reasonably well, the latter tends to overpredict the lower bounds and underpredict the upper bounds of both modes of motion. The six-parameter spectral formulation can better describe the shape of spectra (e.g., double peaks) than the Bretschneider formulation. This allows for a better description of some seaways, and probably accounts for the good correlation between the responses

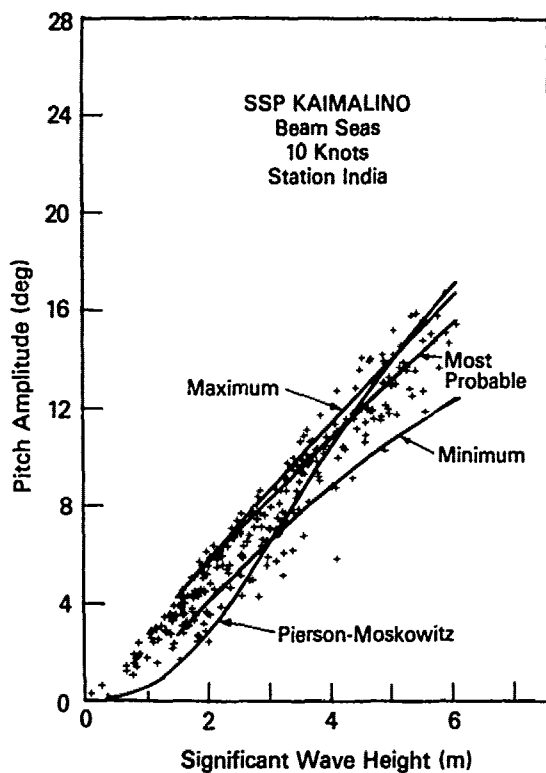


Fig. 38 Probable Extreme Pitch Amplitudes for Measured Spectra at Station India, Pierson-Moskowitz and Bounds of Bretschneider Spectra

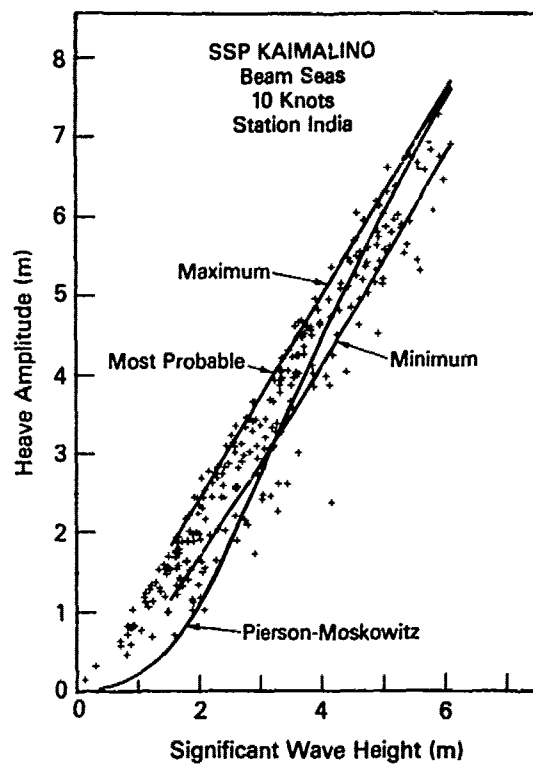


Fig. 40 Probable Extreme Heave Amplitudes for Measured Spectra at Station India, Pierson-Moskowitz and Bounds of Bretschneider Spectra

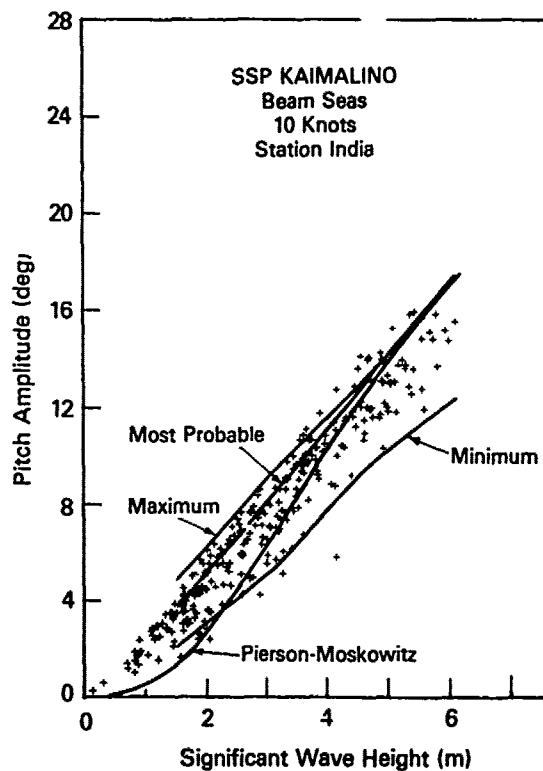


Fig. 39 Probable Extreme Pitch Amplitudes for Measured Spectra at Station India and Bounds of Ochi 6-Parameter Spectra

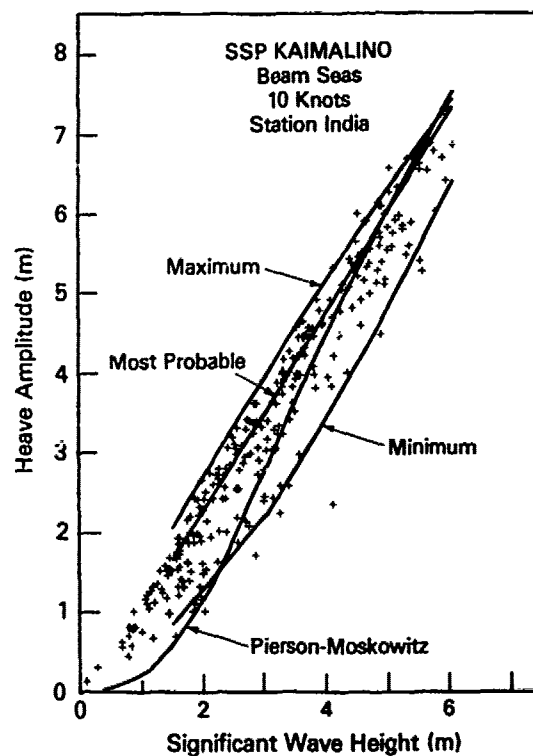


Fig. 41 Probable Extreme Heave Amplitude for Measured Spectra at Station India and Bounds of Ochi 6-Parameter Spectra

based on the six-parameter formulation and the Station India data.

While the most probable extreme value of a motion in a specified seaway is that which is most likely to occur, the probability that the extreme value will exceed the most probable value is quite large (theoretically 63 percent). Hence, it is highly desirable to predict the extreme value for which the probability of being exceeded is a preassigned small value β . Ochi (Reference 18) developed a formula for predicting this extreme value which he calls the "design extreme value," and it is expressed as follows:

$$\hat{Y}_N(\beta) = \sqrt{2 \ln \left(\frac{(60)^2 t}{2 \pi (\beta/k)} \sqrt{\frac{m_2}{m_0}} \right)} \sqrt{m_0} \quad (6)$$

where

- t is the observation time in hours,
- m_0 is the area under the response spectrum,
- m_2 is the second moment of the response spectrum,
- β is the risk parameter and
- k is the number of encounters with a specified sea in a ship's lifetime.

The risk factor, β , can be assigned at the designer's discretion but is given a value of 0.01 if it is desired to design for 99 percent assurance that this (single) amplitude will not be exceeded. The number of encounters with a specified sea, k , involves the ship operation time at the specified speed in the sea considered and the maximum duration of the sea.

As noted previously, an important consideration in the design of SWATH ships is the sizing of the bridging structure clearance height, since it must reflect a balance between requirements to limit weight and to assure adequate transverse metacentric height, and the requirement for sufficient clearance to minimize water contact and slamming on the bridging structure.

Therefore, it may be of interest to examine how the extreme relative bow motion that may be experienced by SSP KAIMALINO without any form of control relates to its clearance height of 1.83 meters. Computations using Equation 6 were therefore carried out for a head Sea State 5 (significant wave height of 3.05 meters) at a speed of 7 knots using the Bretschneider formulation for a range of modal periods appropriate for the specified wave height. The risk factor β was taken as 0.01 and the lifetime exposure, k , or the number of encounters with the specified sea, heading, and speed was assumed to be approximately ten. The calculations were made for the centerline of the cross structure at the forwardmost location of the flat bottom just before the start of the curved bow. The results are presented in Figure 42 where they are shown as a function of operation time. It is seen that the extreme value increases significantly during the first several hours and thereafter increases very slowly throughout the 44 hour period which is the estimated duration of a sea of the specified severity. The figure also shows that the extreme relative bow motion of the ship will exceed the cross structure clearance height within four hours operation time if no motion control is used. However, its performance during the remainder of the storm (about 40 hours in this case) should not degrade much after the initial time period.

Although water contact can be expected it does not necessarily imply a slam. Indeed, experience aboard SSP KAIMALINO during the seakeeping trials did show that while there was a fair amount of water contact with the bridging structure in head Sea State 5, these contacts tended at the lower speeds to be gentle wave slaps that

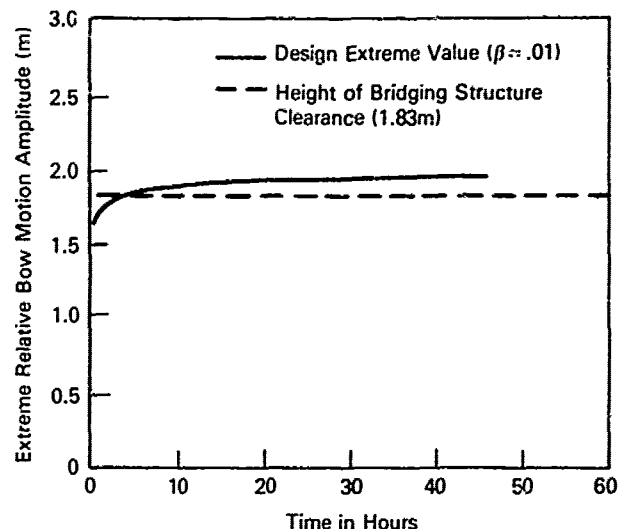


Fig. 42 Extreme Values of Relative Bow Motion of SSP KAIMALINO in Head Sea State 5 at 7 Knots

did not impart an arresting motion to the ship. Though some variability may exist between the assumptions made here regarding SSP KAIMALINO operations and the actual operational experience over her lifetime, this analysis does demonstrate the importance of the relationship between clearance height and relative bow motion.

8. CONCLUDING REMARKS

The results of the full scale trials of SSP KAIMALINO demonstrate the good motions characteristics of SWATH ships and the benefits of automatic motion control. The agreement between the significant values of motions from model and full scale results is reassuring for the application of future model scale results. The theoretical predictions agree with the twin-strut SWATH 6C model data. For SSP KAIMALINO the agreement between theory and model exciting forces is reasonable, while the transfer functions derived from the trials data have an inherent uncertainty that makes firm conclusions difficult. The motion results for SSP KAIMALINO illustrate the importance of separation of natural periods and the influence of these periods on the motion response. The extreme value predictions offer a means of applying experiments and theory to design and operational problems.

The SWATH ship offers great potential for achieving good seakeeping. To the designer this means increased operability and mission effectiveness. The small waterplane area alters the seakeeping characteristics and allows for a relatively small control force to make large changes in the motion responses. The SWATH concept lacks the long design history of monohulls; however, the tools required for predicting motions, natural periods, and extreme values are well developed. Through these prediction techniques, the effects on seakeeping of natural periods, metacentric heights, waterplane area, and other parameters are becoming understood.

REFERENCES

1. Lamb, G. R. and Fein, J. A., "The Developing Technology for SWATH Ships", presented at AIAA/SNAME Advanced Marine Vehicles Conference, Baltimore, Md, Oct. 1979.
2. Lee, C. M. and R. M. Curphey, "Prediction of Motion, Stability and Wave Loads of Small-Waterplane-Area, Twin-Hull Ships", Trans. Soc. Naval Architects and Marine Engineers, Vol. 85, 1977, pp. 94-130.
3. Dalzell, J. F., "A Simplified Evaluation Method for Vertical Plane, Zero Speed, Seakeeping Characteristics of SWATH Vessels", DL-78-1970, July 1978, Stevens Institute of Technology, Hoboken, N.J.
4. Lee, C. M., "Approximate Evaluation of Added Mass and Damping Coefficients of Two Dimensional SWATH Sections", 78/084, Oct. 1978, David W. Taylor Naval Ship R&D Center, Bethesda, Md.
5. Oshima, M., H. Narita and Y. Kunitake, "Experiences With 12 Meter Long Semi-Submerged Catamaran (SSC) "Marine Ace" and Building of SSC Ferry for 446 Passengers", AIAA/SNAME Advanced Marine Vehicles Conference Paper 79-2019, Baltimore, Md, Oct. 1979.
6. Long, T. G., Hightower, J. D. and Strickland, A. T., "Design and Development of the 190-Ton Stable Semi-Submerged Platform (SSP)", TP 397, July 1974, Naval Ocean Systems Center, San Diego, Ca.
7. Higdon, D. T., "Active Motion Reduction in SSP KAIMALINO in a Seaway", AIAA/SNAME Advanced Marine Vehicles Conference Paper 78-740, San Diego, Ca., April 1978.
8. Higdon, D. T., "Active Motion Reduction for a 3000 Ton SWATH Ship Underway in Regular Head and Following Waves", 80-05-01, May 1980, Seaco Inc., Kailua, Hawaii.
9. Stenson, R. J., "Full-Scale Powering Trials of the Stable Semisubmerged Platform, SSP KAIMALINO", SPD 650-01, April 1976, David W. Taylor Naval Ship R&D Center, Bethesda, Md.
10. Woo, E.L. and Mauck, J.L., "Standardization Trials of the Stable Semi-Submerged Platform, SSP KAIMALINO, with a Modified Buoyancy Configuration", 80/049, April 1980, David W. Taylor Naval Ship R&D Center, Bethesda, Md.
11. Kallio, J.A., "Seakeeping Trials of the Stable Semi-Submerged Platform (SSP KAIMALINO)", SPD-650-03, April 1976, David W. Taylor Naval Ship R&D Center, Bethesda, Md.
12. Woolaver, D. and Peters, J.B., "Comparative Ship Performance Sea Trials for the U.S. Coast Guard Cutters Mellon and Cape Corwin and the U.S. Navy SWATH Ship KAIMALINO", 80/037, March 1980, David W. Taylor Naval Ship R&D Center, Bethesda, Md.
13. Kallio, J., "Seaworthiness Characteristics of a 2900-Ton SWATH", SPD-620-03 Sept. 1976, David W. Taylor Naval Ship R&D Center, Bethesda, Md.
14. Fein, J.A. and Stahl, R., "Head and Following Wave Exciting Force Experiments on Two SWATH Configurations", SPD 0928-01, June 1980, David W. Taylor Naval Ship R&D Center, Bethesda, Md.
15. Comstock, J.P. (ed.), Principles of Naval Architecture, Society of Naval Architects and Marine Engineers, 1977, pp. 659-670.
16. Numata, E., "Predicting Hydrodynamic Behavior of Small Waterplane Area, Twin Hull Ships", Presented to the New York Section of Society of Naval Architects and Marine Engineers, May 1980.
17. Pien, P.C. and Lee, C.M., "Motion and Resistance of a Low Waterplane Area Catamaran", Presented at the 9th Symposium on Naval Hydromechanics, Paris, France, 1972.
18. Ochi, M.K., "Wave Statistics for the Design of Ships and Ocean Structures", Trans. Soc. Naval Architects and Marine Engineers, Vol. 86, 1978, pp. 47-76.

Discussion

C. Kennell (Naval Sea System Command)

The introduction of a new ship concept is a high risk venture due to the high cost of today's ocean vessels and the vulnerability of man and his machines to nature's forces. These anxieties can be reduced significantly by demonstrating that the behavior of a new vehicle can be accurately predicted prior to committing large sums of money to construction. This paper demonstrates such a capability for some of the most important aspects of SWATH ship seakeeping. The correlation of the authors' analytical predictions with test results from the three meter model and the 25 meter model is most reassuring. Documenting the wave spectra "used" for the large model tests lends a sense of completeness to the paper.

A curious feature of the motions data in figures 4, 5, 8, and 9 is the noticeable scarcity of data for speeds from 10 to 16 knots. This part of the curve is particularly interesting since both pitch and roll responses show peaks for these speeds. The authors discuss the role of the ship's bow wave in dampening pitch below 10 knots. Perhaps at higher speeds the ship is balanced on its bow wave and is not sufficiently stable to allow data collection. Elaboration on this point would be appreciated.

A related aspect that is puzzling is the apparent lack of influence of the buoyancy blisters on motions. The location of these hull appendages representing about 15 percent of the displacement should lead to cancellation of hull and strut generated waves, including the bow wave. As a result, the vessel with blisters should be less sensitive to sinkage and trim effects. However, motions at 10 knots are the same with and without the blisters indicating the same heavy pitch damping due to the bow wave. The scarcity of data above 10 knots limits further speculation. Perhaps the authors can provide some additional insight into this matter.

Heave responses for the SSP Kaimalino are conspicuous by their absence. The reasons for not collecting such data are of interest.

The reasons for selecting beam seas for extreme motions predictions rather than the more conventional head seas would be appreciated.

This fine paper is clearly a product of the R&D community. However, by assembling such a comprehensive treatment of SWATH motions predictions, the authors will find that the importance of their work extends well beyond the technical community. Demonstration of technical capabilities in this discipline as well as many others may well convince decision makers to accept the

residual risks inherent in producing functional SWATH ships such as the MESA 80 built by Mitsui Engineering & Shipbuilding and the Dutch DUPLUS. I would like to thank the authors for taking this important step in that direction.

N. Toki (MHI)

In DTNSRDC, very sophisticated researches have been performed on SWATH ships, and today, the authors added another valuable report. At first, I would like to express my highest regard to your vast studies on the seakeeping characteristics of SWATH ships.

In Nagasaki Experimental Tank, we have studied this type of ships referring to the papers of DTNSRDC, and performed several tank tests both in calm water and in waves. On the basis of our experience, I would like to ask the authors' opinion on the following points.

1. In the present paper, the authors mentioned "Largest motions were found in following seas when ship speed was close to the wave speed." Reading the same comment in the earlier paper of DTNSRDC, we have been thinking over the cause of this phenomenon. The authors considered that large motions were activated mostly by a full span aft foil of SSP KAIMALINO. From our study, however, contribution to these large motions should be shared by several factors: such as, fore-aft asymmetry of the hull represented in the value of LCB-LCF, Munk's unstable moment which reduces the stability of pitching, and of course, the arrangement of foils.

Let me explain more in detail. We have been using the following formula to estimate the motion amplitudes of SWATH in the specified condition, i.e. $\omega_e = 0$ in following waves, neglecting all of the terms expressing the dynamic effect.

$$\begin{bmatrix} R_{3,3} & R_{3,5} \\ R_{5,3} & R_{5,5} \end{bmatrix} \begin{bmatrix} z \\ \theta \end{bmatrix} = \begin{bmatrix} F_3 \\ F_5 \end{bmatrix}$$

where

$R_{3,3}$, $R_{3,5}$, $R_{5,3}$, and $R_{5,5}$: elements of restoring coefficient matrix

z , θ : complex amplitudes of heave and pitch

F_3 , F_5 : complex amplitudes of wave exciting heave force and pitch moment

$$R_{3,3} = \rho g A_w$$

$$R_{3,5} = \rho g A_w (LCB-LCF) + \rho U^2 \sum_{i=1}^N A_i(f) C_{Lai}$$

$$R_{5,3} = \rho g A_w (LCB-LCF)$$

$$R_{5,5} = \rho g \nabla GM_L - \rho U^2 C_z \nabla - \rho U^2 \sum_{i=1}^N l_i A_i(f) C_{Lai}$$

$$F_3 = a_1 \rho g A_w A - j B_1 \rho \omega_e U A \sum_{i=1}^N A_i(\xi) C_{Lai}$$

$$F_5 = j\alpha_2 \rho g \nabla GM_L kA + \beta_2 \rho \omega_0 UA \sum_{i=1}^N l_i A_i(f) C_{Lai}$$

$A_i(f)$: projected area of i-th foil to horizontal plane

l_i : x-coordinate of quarter-chord point of i-th foil

C_{Lai} : lift curve slope per radian of i-th foil

$\alpha_1, \alpha_2, \beta_1, \beta_2$: correction factors

The other nomenclature is same as the authors' one.

Making use of published data of SWATH 6-A given in Ref. (2), I would like to explain the causes of large motions in following waves. The value of (LCB-LCF) is assumed to be 3 m. The amplitudes of heave and pitch were calculated in the case of $\omega_e = 0$ where $\lambda/L = 1.0$, $\beta = 0^\circ$, and $U = 20$ knots. In this condition, $\alpha_1, \alpha_2, \beta_1$, and β_2 are assumed to be 0.1, 0.3, 0.1, and 0 respectively, based on our experience. Calculations were made for the various hull configurations as follows. The results of calculation are shown in the table.

- 1) Original SWATH 6-A
- 2) SWATH 6-A with foils, each projected area of which is twice as large as the original one.
- 3) SWATH 6-A with foils, each projected area of which is three times as large as the original one.
- 4) Same SWATH 6-A as 3), but assumed LCB-LCF = 0.
- 5) Same SWATH 6-A as 3), but the effect of Munk's unstable moment is not considered.

	z_A/A	$LC_A/2A$
Original SWATH 6-A measured at DTNSRDC	0.6	2.0
P R E S E N T F O R M U L A		
1) Original SWATH 6-A	0.89	3.47
2) Foil area : twice	1.46	3.52
3) Foil area : three times	2.09	3.67
4) Foil area : three times LCB-LCF = 0	0.94	1.74
5) Foil area : three times without Munk's moment	0.77	1.25

From this calculation, it is understood that following three factors, too large foils, fore-aft asymmetry of the hull, and Munk's unstable moment, equal contributed to invite large motions in the case of $\omega_e = 0$.

2. According to our experience, in the region where Froude number nearly equals 0.35, rather high transverse wave is generated by bow in the part from midship to square station 3 inside of two hulls, and make the bridging structure clearance small.

ler. We were afraid that in waves severe slamming might occur on the bottom of bridging structure, and performed a series of tank experiments. As the result we found there is rather high possibility of slamming, if the SWATH keeps its advance speed at the specified value for a long time.

On the other hand, we hope there might be no fear of slamming in the practical operation, because we know that keeping its advance speed at that particular value is very difficult and advance speed deviates easily. Hence, we have not arrived at a conclusion.

For SSP KAIMALINO, Froude number nearly equals 0.35 when its advance speed is 10 knots. If I could ask the authors for any further explanation to the point in relation with the sea trial of SSP KAIMALINO at 10 knots, it would be appreciated very much.

3. During the tank test of our SWATH model in regular waves, I have noticed several times the phenomenon which seems to be the so-called "unstable rolling".¹⁾ The phenomenon occurred in the cases where encounter period nearly equals the natural period of heave-pitch coupled motion, and the natural period of rolling is twice as long as the period. In this case, incident wave activates rolling motion of its natural period together with resonant heave-pitch coupled motion. This phenomenon is resonance of rolling motion with 2-nd order hydrodynamic force generated by large amplitude vertical motion.

In the authors' paper, there are some expressions suggesting the existence of "unstable rolling". Therefore, I presume that SSP KAIMALINO also have had the experience similar to the one appeared in our model test. Any comments by the authors on this phenomenon would be most instructive for us in both theoretical and practical viewpoints.

REFERENCE

- 1) Paulling, J.R. and Rosenberg, R.M.: On Unstable Ship Motions Resulting from Nonlinear Coupling, Journal of Ship Research, Vol.3, No.1 June 1959

H. Maruo (Yokohama N. Univ.)

I appreciate the authors' presentation of full scale performances because existing data for this kind of hull configuration are rather seldom.

I would like to make a brief comment about the hull shape of Kaimalino shown in Fig.1. I don't think the hull configuration is not optimized from the point of view of wave resistance theory. According to my earlier study, effective cancellation of waves generated by the lower hulls and those of surface piercing structure cannot be realized by this configuration.

We are thinking of initiating a methodical model series for SWATH ships, aimed primarily at the 2000 - 10000 ton size range. We are thinking in terms of roughly 10 models. The series would address both resistance and seakeeping. Would the authors offer some guidance regarding experiment design ?

Author's Reply

J.A. Fein, M.D. Ochi and K.K. McCreight (DTNSRDC)

The authors wish to thank Mr.Kennel, Mr.Toki, Mr.Schmitke and Professor Maruo for their very valuable discussions. It was of special interest to learn about the Mitsubishi SWATH research from Mr.Toki.

Both Mr.Kennel and Mr.Toki have inquired about the motions data above 10 knots. From just over 10KTS to 13KTS the ship is overtaking its bow wave and thus constant speeds in that range are difficult to maintain. The ship generated bow wave does reduce the clearance height of the SSP in the aft portion of the ship in this speed range as Mr.Toki has pointed out. This is a phenomenon that must be considered in the operation of the ship, however, since sustained operation in this transition speed range is difficult to maintain increased slamming frequency in this condition is not expected to pose a problem in practice. The scarcity of data above 13KTS is unfortunately due to a lack of sufficient operating time with the instrumented ship as well as speed limitation of the ship.

The lack of influence of the blisters on the pitch motions we attribute to their location near midships on the inboard side of the lower hulls. The blisters attached to the ship during the trials were smaller than those now installed and were not designed to cancel ship generated waves. Thus we agree with Professor Maruo's comment regarding hull optimization. The SSP does not reflect current design philosophy in the United States but it does provide a vehicle for assessing some of the merits of the SWATH concept. We are currently involved in an effort to increase SSP displacement in which we are giving consideration to certain parametric changes for improved performance from both the seakeeping and wave making resistance point of view.

The pure heave motion of the SSP was not measured directly since the longitudinal

center of gravity is located in the open ship well area. The vertical motion data and vertical acceleration data from transducers located close to the LCG presented in Figures 6, 15 and 16 provide an indication of heave behavior. We agree with Mr.Kennel that heave motion is an important parameter in the correlation with SWATH predictions.

The use of beam sea conditions for extreme motion predictions reflects our belief, based on other SWATH model data, that unlike conventional monohull ships, beam sea heading appears to be better for survivability for SWATH than head-into-the-wave conditions.

We agree with Mr.Toki that the fore-aft hull asymmetry and Munk's unstable moment can lead to large motions along with the large foil near $\omega_g = 0$. However, model tests and analytical results addressing other similar hull shapes suggest smaller motions in following seas than experienced by SSP KAIMALINO. Further, a comparison of motions computed by our colleague, Dr.Lee, at the Center at $\omega_g \approx 0$, assuming only the presence of static terms, with model results shows that the static assumption may not be completely adequate for describing the motions in this region. Therefore we are not sure that an evaluation of the contribution of the various factors to the motions in this condition can be adequately made from such an approach.

Regarding the cause of the unstable rolling motion we agree that the Mathieu type of coupled instability could exist under certain conditions. We have not observed this behavior in our model tests so far. However, we have observed some roll motion instability in waves whose period was one-half the roll period. Roll motion would become large with rolling occurring at its natural frequency. Thus was observed on our SWATH 6B model. Pitch and heave, however, were not large and the encounter frequency was not synchronous with the pitch-heave coupled motions. Similar results were observed during model tests at the Davidson Laboratory of SIT. Dr.Lee of DTNSRDC has carried out an analytical study which suggests that waves having a natural frequency twice the natural frequency in roll can cause a roll instability due to the presence of nonlinear behavior occurring in the restoring force. However, we are very interested to learn that Mr.Toki has also observed unstable behavior of a dynamic origin and feel that future investigations are warranted in this area.

Finally, on response to Mr.Schmitke we wish to encourage his country's efforts. Areas where series experiments are needed include fin size and location, rudder configuration, and upper hull bow design. In addition, the distribution and amount of waterplane area, which influences natural periods, metacentric heights, and LCB-LCF differences, could serve as a framework for the parametric variations.

Hull Form Design of the Semi-Submerged Catamaran Vessel

Yuzo Kusaka, Hiroshi Nakamura and Yoshikuni Kunitake
Mitsui Engineering & Shipbuilding Co., Ltd
Japan

ABSTRACT

The hull form design procedure of the SSC (Semi-Submerged Catamaran) is discussed from the viewpoint of minimizing wave resistance. The effects of hull configuration of the SSC on wave resistance are briefly presented using the results of series model tests of hull elements. A mathematical model for wave resistance based on the thin ship theory has been developed, in which Michell's source distribution is used to represent the strut's geometry and the equivalent line doublet distribution to the lowerhull is introduced. The correction factors included in the mathematical model are derived from comparison of the theoretical results with the measured data. The design procedure to obtain an SSC hull form with minimum wave resistance are described, and examples of the optimized hull form are presented. Design and sea trial results of the first commercial SSC 'MESA 80' are presented.

NOMENCLATURE

L	Length of lowerhull
f	Submergence of lowerhull
D	Diameter of lowerhull
S	Wetted surface area
V	Displacement volume of ship
U	Velocity of fluid
F_n	Froude number
g	Gravitational acceleration constant
K_0	Wave number
θ	Direction of wave propagation
R _w	Wave resistance

R _r	Residual resistance
S(θ)	Amplitude function of sine wave
C(θ)	Amplitude function of cosine wave
ρ	Fluid density
m	Density of source distribution
μ	Density of line doublet distribution
M	Density of normal doublet distribution
V	Ship speed

1. INTRODUCTION

Many attempts to develop a new type of marine vehicle have been made to break the various performance limitations imposed by the conventional monohull and the conventional catamaran. The Semi-Submerged Catamaran (SSC), which the U.S. Navy calls SWATH, is one of such high performance advanced vehicles, and has two lowerhulls which account for a major part of the displacement below the water level, and this submerged part and the deck structure are connected with streamlined struts.

As well as the extensive researches on this type of vessel carried out by the U.S. Navy [1],[2],[3],[4],[5], Mitsui Engineering & Shipbuilding Co., Ltd. to which the authors belong, has done a lot of developmental work on the SSC since 1970 [6].

Encouraged by the satisfactory performance achieved by the experimental SSC 'MARINE ACE' (Photo 1) built in 1977 which is 12 meters long, the first commercial SSC prototype 'MESA 80' (Photo 2) was built in 1979 as a passenger ship carrying 446 persons. The extensive sea trials of the 'MESA 80' in 1980 proved the high performance of the SSC and the great potential for

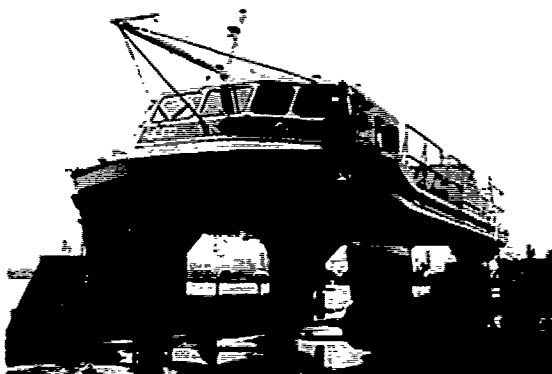


Photo. 1 'MARINE ACE'

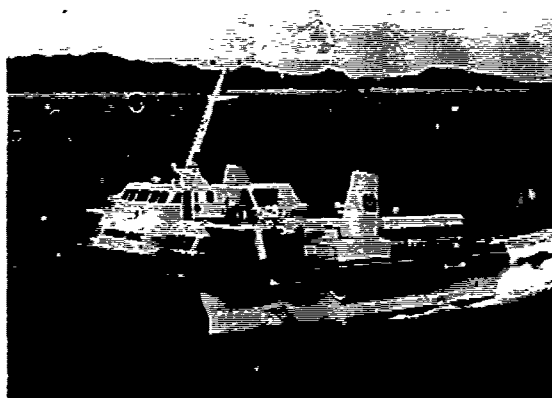


Photo. 2 'MESA 80'

its application in the field of marine transportation and ocean development.

In order to expand the SSC's application and to enhance the operational economy of the SSC much more, possible reduction of required power in calm water will be required in addition to the high performance in waves on motion and speed which has been already proved by many full scale test results. As the wetted surface area of the SSC is almost twice as much as the monohull, which results in some penalty from frictional resistance, great attention in the hull form design of the SSC must be paid to reducing wave resistance as well as to attaining high propulsive efficiency.

Due to the complicated combinations of hull elements of the SSC, there is more degree of freedom in hull form design than in that of a monohull. Therefore it is of prime importance to understand the fundamental wave resistance characteristics of the hull elements. Typical experimental results, varying the lowerhull proportion and its submergence etc., are presented in chapter 2 of this paper.

In designing the hull form of the SSC taking into account the various design limitations as well as the basic design requirements, design synthesis technology is re-

quired so as to attain a well-balanced SSC design. As part of such useful design technology, the authors have developed a mathematical model for wave resistance which shows a good agreement with the model test results. This mathematical model is presented in chapter 3. Also in chapter 4, a hull form design procedure for minimizing wave resistance is presented.

Design and sea trial test results of the 'MESA 80' are briefly presented in chapter 5.

2. FUNDAMENTAL WAVE RESISTANCE CHARACTERISTICS OF HULL ELEMENTS

In the initial design stage of the SSC, prior to deciding hull dimensions, the preliminary design work for selecting basic hull configurations, hull material, propulsion system and machinery arrangement, etc. shall be made from the viewpoints of hull weight and cost so as to keep the overall performance of the design within the specified requirements of the performance such as capacity or payload, speed and motion.

However, due to not only lack of accumulated design data for the SSC, but also the sensitivity of the hull elements such as lowerhull, strut and fins on the SSC's performance, the hull form design of the SSC seems to become more difficult than that of a conventional ship. Under these circumstances, understanding of the hydrodynamic characteristics of hull elements is necessary to obtain a well-balanced SSC design.

As is well known, the SSC has about twice the wetted surface area of a conventional monohull of equal displacement, which results in some penalty in the total resistance. Accordingly, design considerations must be mainly taken care of realizing the SSC hull form with minimum wave resistance.

(1) Lowerhull

Series model tests of the lowerhull to investigate the characteristics of wave resistance were carried out at Mitsui Akishima Laboratory, changing the submergence to diameter ratio f/D and the length to diameter ratio L/D of the lowerhull. Models were manufactured so as to have the same sectional area curve and displacement, and each model had a symmetrical shape lengthwise and the parallel part was 60 percent of the total length. The wave resistance of the lowerhull was obtained by subtracting the total resistance measured in the fully submerged condition where the wave resistance is very close to zero from the total resistance measured at a given submergence.

Figure 1 shows typical results of the wave resistance of the lowerhulls with different f/D . As seen from this figure, the wave resistance coefficients of the lowerhull remarkably change by Froude number. As the f/D of the lowerhull decreases, the coefficient increases over the whole speed range, specially at hump speed. In Figure 2, the wave resistance coefficient denoted by displacement are presented for different

length to diameter ratios of the lower-hull. The effect of L/D of the lowerhull on wave resistance is quite different between higher speeds over Froude Number 0.4 and the speed range below that Froude number. In the case of a high speed SSC, therefore, it will be desirable to have a larger L/D of the lower-hull than about 12.

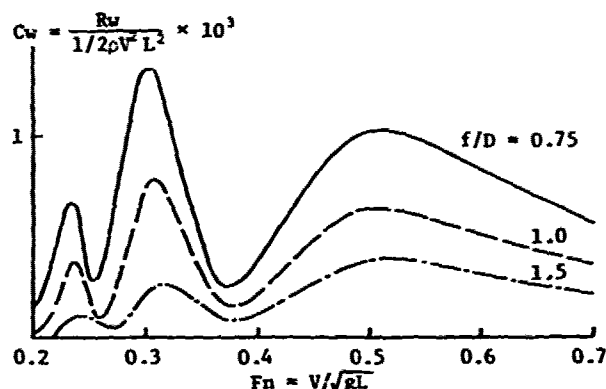


Fig. 1 Wave Resistance of Lowerhull (Effect of Lowerhull Submergence)

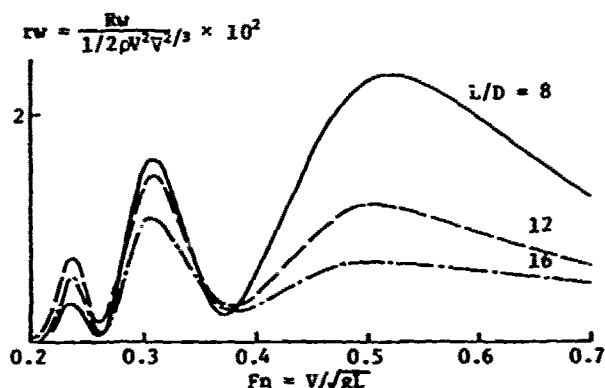


Fig. 2 Wave Resistance of Lowerhull (Effect of Length to Diameter Ratio)

(2) Strut

In order to investigate the fundamental characteristics of the strut on wave resistance, some strut models were tested in the towing tank of Akishima Laboratory. Figure 3 shows the residual resistance of struts with different thickness to length ratios t/L . Also in Figure 4, the effects of strut immersion are shown. As seen in these figures, it can be found that the strut with smaller t/L and smaller immersion will be more favourable in the speed range over Froude number 0.4. However, the magnitude of the wave resistance caused by the strut is much smaller than that of the lowerhull in the case of 'MESA 80'.

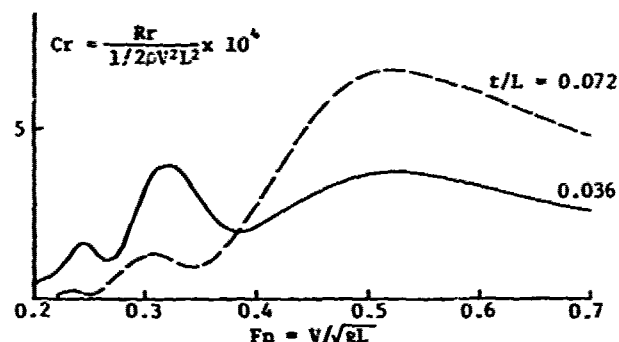


Fig. 3 Residual Resistance of Struts with Different t/L

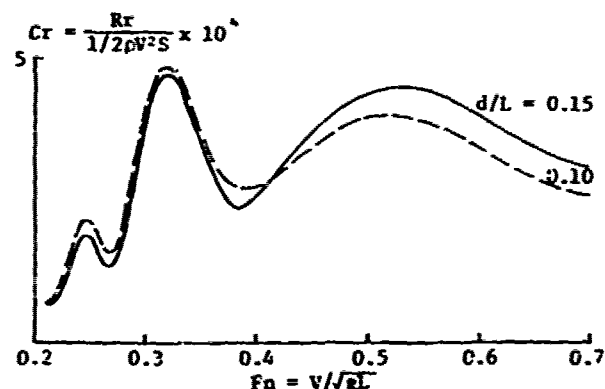


Fig. 4 Residual Resistance of Struts with Different Depth ($t/L=0.036$)

(3) Twin Hull

As well as the wave resistance characteristics of both lowerhull and strut, it is necessary to investigate the interaction effect of a twin hulled SSC for the hull form design. Figure 5 shows the estimated breakdown of the wave resistance of the 'MESA 80', of which the design is presented in chapter 5. The Froude number at the design speed is about 0.7.

It can be found from this figure that the wave resistance of the lowerhulls is the largest among other components, and that of the struts is the smallest at the design Froude number. While, the magnitude of the wave resistance caused by the strut-lowerhull interaction is almost the same as that of the lowerhulls, the resistance caused by the port-stbd. interference is small at the design speed. Since there is hardly any possibility of utilizing the interaction effect well for the SSC designed at a high Froude number, it becomes more essential for such an SSC to make both lowerhull and strut as slender as possible to reduce wave resistance.

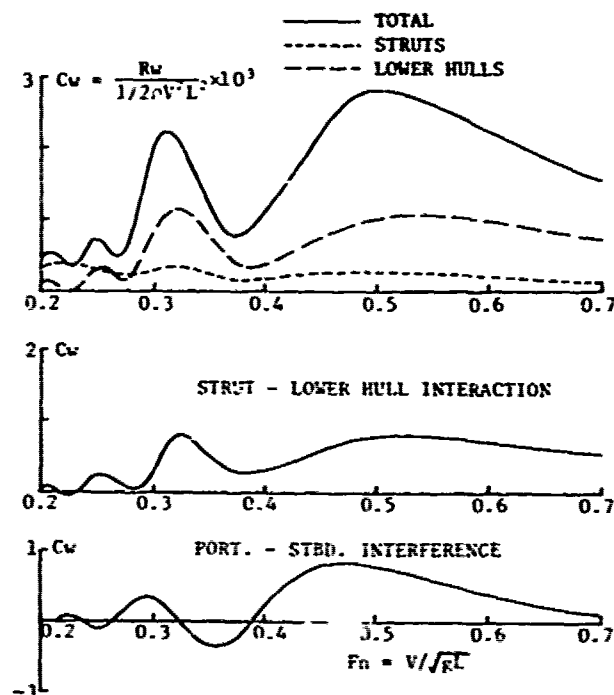


Fig. 5. Components of the Calculated Wave Resistance of 'MESA 80'

3. MATHEMATICAL MODEL FOR WAVE RESISTANCE

3.1 Theory

A lot of sophisticated theories of wave resistance have recently been developed for conventional ships. However, considering that the SSC consists of a pair of demihulls with much smaller beam-length ratio than that of a conventional ship, the classical thin ship theory is still effective for estimating the wave resistance of a ship with a slender hull form like the SSC [7], [8], [9].

The mathematical model for wave resistance described in this paper is based on the thin ship theory applying Michell's source distribution for struts and the line doublet distribution for lowerhulls. A coordinate system (ζ, x, y, z) moving with the ship is set up on the demihull, in which the x axis is positive to the direction of motion. Both struts and lowerhulls are assumed to be symmetric about their centerplane $y = 0$.

3.1.1 Strut

Considering that the strut has a wall-sided hull surface, the hull geometry of the strut is described by

$$y = \pm f(x) \quad (1)$$

The source distribution $m(x)$ equivalent to this hull form is obtained by Eq. (2) from thin ship approximation,

$$m(x) = -2U \frac{\partial f(x)}{\partial x} \quad (2)$$

Then the wave resistance coefficient $C_w = R_w / (1/2 \rho U^2 L^2)$ is given by

$$C_w = 2\pi \int_0^{\pi/2} \{S_s^2(\theta) + C_s^2(\theta)\} \cos^3 \theta d\theta \quad (3)$$

where

$$S_s(\theta) = \frac{K_s}{2\pi} \int_{-\infty}^{\infty} m(x) dx \int_{-\infty}^{\infty} dz \sec^3 \theta \exp(K_s z \sec^2 \theta) \times \sin(K_s x \sec \theta) \quad (4)$$

$$C_s(\theta) = \frac{K_s}{2\pi} \int_{-\infty}^{\infty} m(x) dx \int_{-\infty}^{\infty} dz \sec^3 \theta \exp(K_s z \sec^2 \theta) \times \cos(K_s x \sec \theta)$$

3.1.2 Lowerhull

Assuming that the lowerhull is a fully submerged revolutional body, the equivalent line doublet distribution representing the lowerhull is described as follows by using the sectional area curve of lowerhull $A(x)$.

$$v(x) = UA(x) \quad (5)$$

These line doublets are placed on the centerline of lowerhull. And the wave resistance coefficient is

$$C_{LD} = 2\pi \int_0^{\pi/2} \{S_D^2(\theta) + C_D^2(\theta)\} \cos^3 \theta d\theta \quad (6)$$

where

$$S_D(\theta) = \frac{K_D}{2\pi} \int_{-\infty}^{\infty} v(x) dx \sec^3 \theta \exp(K_D z \sec^2 \theta) \times \cos(K_D x \sec \theta) \quad (7)$$

$$C_D(\theta) = -\frac{K_D}{2\pi} \int_{-\infty}^{\infty} v(x) dx \sec^3 \theta \exp(K_D z \sec^2 \theta) \times \sin(K_D x \sec \theta)$$

3.1.3 Twin Hull

The wave resistance of a twin hull ship can be obtained by Eqs. (4) and (7). Taking the distance of hull separation as $2b$, the total wave resistance coefficient is described by

$$C_{wT} = 2\pi \int_0^{\pi/2} \{S_T^2(\theta) + C_T^2(\theta)\} \cos^3 \theta d\theta \quad (8)$$

where

$$S_T(\theta) = 2S_s(\theta) \cos \omega + 2S_D(\theta) \cos \omega$$

$$C_T(\theta) = 2C_s(\theta) \cos \omega - 2C_D(\theta) \cos \omega \quad (9)$$

$$\omega = K_s b \sec^2 \theta \sin \theta$$

Eq. (8) can be written in another form,

$$\begin{aligned} C_{wT} = 2\pi \int_0^{\pi/2} 2(1 + \cos 2\omega) \{ & [S_s^2(\theta) + C_s^2(\theta)] \\ & + [S_D^2(\theta) + C_D^2(\theta)] \\ & + 2[S_s(\theta)S_D(\theta) - C_s(\theta)C_D(\theta)] \} d\theta \\ = & C_w(\text{struts}) + C_w(\text{lowerhulls}) \\ & + C_w(\text{interaction}) \end{aligned} \quad (10)$$

Where, the factor $2(1+\cos 2\omega)$ indicates the interference effect of the twin hull.

3.1.4 Camber Effect

The theory mentioned above is based on the assumption that the flow around the demihull is symmetric. However, for the twin hulled SSC, it may be easily found that the demihull will actually be placed in a curved flow due to the deformation of the flow by the presence of another demihull.

In order to reflect this phenomena in the theory, it must be considered that the symmetric demihull has an apparent camber corresponding to the effect of the curved flow. This effective camber can be expressed theoretically by the normal doublet distribution on the centerplane of each demihull.

A strut with geometric camber is introduced to investigate the camber effect on wave resistance. Amplitude functions of the wave generated by the thickness of the strut are given by Eq. (4). And, denoting the equivalent doublet distribution to the camber as $M(x)$, the amplitude functions by camber are

$$\begin{aligned} S_c(\theta) &= \frac{K_0}{2\pi} \int M(x) dx / dz \sec^5 \theta \sin \theta \\ &\quad \times \exp(K_0 z \sec^2 \theta) \cos(K_0 x \sec \theta), \\ C_c(\theta) &= -\frac{K_0}{2\pi} \int M(x) dx / dz \sec^5 \theta \sin \theta \\ &\quad \times \exp(K_0 z \sec^2 \theta) \sin(K_0 x \sec \theta). \end{aligned} \quad (11)$$

Then the wave resistance coefficient of the strut is given by

$$C_{ws} = \pi \int_{-\pi/2}^{\pi/2} \{ [S_s(\theta) + S_c(\theta)]^2 + [C_s(\theta) + C_c(\theta)]^2 \} \times \cos^3 \theta d\theta. \quad (12)$$

Where, $S_s(\theta)$ and $C_s(\theta)$ are the even function of θ , on the other hand $S_c(\theta)$ and $C_c(\theta)$ become the odd function due to the term $\sin \theta$ in the Eq. (11). Therefore, the wave resistance can be described by

$$\begin{aligned} C_{ws} &= 2\pi \int_0^{\pi/2} \{ [S_s^2(\theta) + C_s^2(\theta)] + [S_c^2(\theta) + C_c^2(\theta)] \} \\ &\quad \times \cos^3 \theta d\theta \\ &= C_w(\text{thickness}) + C_w(\text{camber}). \end{aligned} \quad (13)$$

Eq. (13) indicates that the thickness and the camber of the strut contribute independently to the wave resistance.

For the struts placed in parallel, the wave resistance coefficient is given by

$$\begin{aligned} C_w &= 2\pi \int_0^{\pi/2} \{ 2(1+\cos 2\omega) [S_s^2(\theta) + C_s^2(\theta)] \\ &\quad + 2(1-\cos 2\omega) [S_c^2(\theta) + C_c^2(\theta)] \\ &\quad - 4\sin 2\omega [S_s(\theta)C_s(\theta) + C_c(\theta)S_c(\theta)] \} \\ &\quad \times \cos^3 \theta d\theta \\ &= C_w(\text{thickness}) + C_w(\text{camber}) \\ &\quad + C_w(\text{interaction}). \end{aligned} \quad (14)$$

However, it is troublesome work to evaluate the density of doublet distribution equivalent to the effective camber. Also, the camber effect appears more influentially in the magnitude of diverging waves than in transverse waves due to the term $\sin \theta$ in Eq. (11). Therefore, as regards the wave resistance, this camber effect is not very significant as compared with the effect of thickness because the diverging waves contribute much less effectively to the wave resistance than the transverse waves. For these reasons there is no consideration of the camber effect in the mathematical model.

Nevertheless, it can be easily expected that the properly selected geometric camber of the strut may cancel the camber effect, which diminishes the last two terms in Eq. (14). As one approach to obtain the optimum geometric camber, Pien [10] proposes the rational scheme to deform each demihull along the streamline generated by the opposite demihull.

3.2 Validation Study

Theoretical calculations were made for a typical SSC in order to confirm the validity of the mathematical model. In this calculation, singularity distributions as shown in Eq. (2) and (5) are expressed in a form of the polynomial function. The coefficients of the function are decided by the least square method from input data of the strut offset and the sectional area curve of lowerhull. Amplitude functions of Eq. (4) and (7) are analytically calculated for each elementary wave angle θ , then the wave resistance is obtained by Eq. (8).

Figure 6 shows the comparison between the calculated and the measured wave resistance coefficient of an SSC. The calculated results, on the whole, seem to show the possible use of the thin ship theory to estimate the wave resistance of an SSC. However, as seen in the figure, the difference in phase and magnitude will not be desirable for ship designers. This may cause a serious problem in required power estimation.

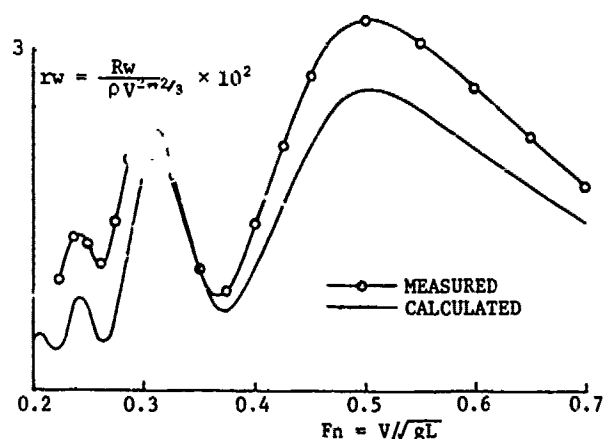


Fig. 6 Comparison of Wave Resistance of an SSC between the Measured and the Calculated

As described in chapter 2, the wave resistance by the lowerhull has a fairly large portion of the total wave resistance. Therefore it becomes of prime importance to carefully compare the calculated wave resistance of the lowerhull with the measured one, in order to obtain good agreement between them.

Figure 7 shows example results of lowerhull series tests presented in chapter 2, associated with its theoretical results, and there is still a little disagreement both in phase and magnitude between the measured and the calculated values.

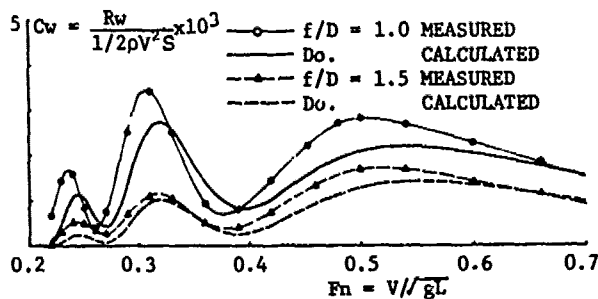


Fig. 7 Comparison of Wave Resistance of Lowerhull between the Measured and the Calculated without Correction

As regards these problems on wave resistance, Inui [11] has found several correction factors for the displacement ship due to precise observation of the wave pattern and analytical investigations. These factors are corresponding to the so-called sheltering effect and the viscous effect. From the data obtained, the authors have found that the phase difference could be expressed in the following form in case of the SSC.

$$K_0 L(\text{measured}) = K_0 L(\text{calculated}) - \Delta K_0 L$$

$$\Delta K_0 L = F(K_0 L, f/D) \quad (15)$$

where

$$\Delta K_0 L : \text{phase difference}$$

$$K_0 L : 1/Fn^2$$

$$F : \text{linear combination}$$

Also, the authors found that, instead of the geometric centroid of the lowerhull, the equivalent centroid for wave making effect should be adopted into calculation and the submergence of the lowerhull had to be reduced by the factor α which is the function of f/D to get more precise value in magnitude. The equivalent submergence \bar{f} is expressed by

$$\bar{f} = \alpha f, \quad (16)$$

where

f : geometric submergence

Results calculated by using these correction factors are shown in Figure 8. The good agreement between the calculated and the measured wave resistance suggests that this method brings a better prediction of the wave resistance of the SSC and by which an optimized hull form will be developed.

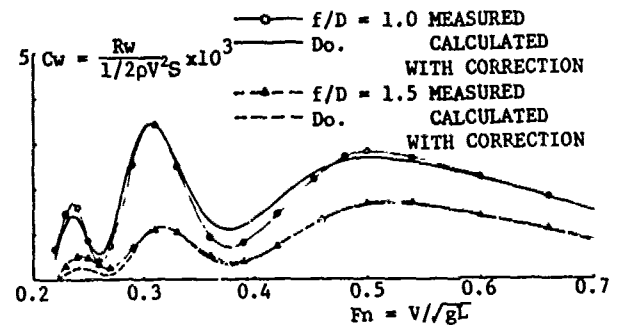


Fig. 8 Comparison of Wave Resistance of Lowerhull between the Measured and the Calculated with Correction

4. HULL FORM OPTIMIZATION STUDY

The theoretical design procedure to obtain the hull form with minimum wave resistance has been achieved by many hydrodynamicists for the conventional ships, but the effort is very limited for the SSC hull form [12], [13].

This paper presents the design procedure to obtain the optimum hull form of the SSC generated from combinations of a source distribution on the centerplace of strut and a line doublet distribution of the centerline of lowerhull, using the thin ship theory.

4.1 Singularity System and Restrained Condition

Singularities composed of the sources $m(x)$ and the line doublets $\mu(x)$ are expressed by the polynomial function as follows,

$$m(x) = \sum_{i=1}^N a_i x^{i-1}, \quad (17)$$

$$\mu(x) = \sum_{i=1}^M b_i x^{i-1}. \quad (18)$$

As the singularity distributions described in Eq. (17) and (18) represent the 'single strut per hull' configuration without having any parallel part of the hull, other singularity distributions are also introduced for the different hull configurations such as the 'tandem struts per hull' configuration.

Restrain conditions for the principal particulars and hull geometries can be expressed in the following forms.

(1) Displacement:

$$V_s = \sum_{i=1}^N a_i \int x^i dx dz \quad \text{for strut,} \quad (19)$$

$$V_D = \sum_{i=1}^M b_i \int x^{i-1} dx \quad \text{for lowerhull.}$$

(2) Midshipsection area:

$$A_s = \sum_{i=1}^N a_i \int x^{i-1} dx dz \quad \text{for strut,} \quad (20)$$

$$A_D = \sum_{i=1}^M b_i x^{i-1}_{(\text{midship})} \quad \text{for lowerhull.}$$

(3) Waterplane area:

$$A_W = \sum_{i=1}^N a_i \int x^i dx \quad \text{for strut.} \quad (21)$$

Other constraints can be written in the same way.

4.2 Optimization Scheme

Then the wave resistance can be written as follows from the equations (4), (7), (17) and (18).

$$C_W = \sum_{i=1}^N \sum_{j=1}^N a_i a_j I_{ij} + 2 \sum_{i=1}^N \sum_{j=1}^M a_i b_j II_{ij} + \sum_{i=1}^M \sum_{j=1}^M b_i b_j III_{ij} \quad (22)$$

where

$$I_{ij} = 2\pi \int_0^{\pi} \{S_i(\theta) S_j(\theta) + C_i(\theta) C_j(\theta)\} \cos^3 \theta \times (1 + \cos 2\omega) d\theta,$$

$$S_i(\theta) = \frac{K_0}{2\pi} \int x^{i-1} dx \int dz \sec^3 \theta \exp(K_0 z \sec^2 \theta) \times \sin(K_0 x \sec \theta),$$

$$C_i(\theta) = \frac{K_0}{2\pi} \int x^{i-1} dx \int dz \sec^3 \theta \exp(K_0 z \sec^2 \theta) \times \cos(K_0 x \sec \theta). \quad (23)$$

and II_{ij} , III_{ij} are given by the same way. Then the optimization functional ψ is written by,

$$\psi = \sum_{i=1}^N \sum_{j=1}^N a_i a_j I_{ij} + 2 \sum_{i=1}^N \sum_{j=1}^M a_i b_j II_{ij} + \sum_{i=1}^M \sum_{j=1}^M b_i b_j III_{ij} + \sum_{k=1}^K \lambda_k \left(\sum_{i=1}^N P_{ik} a_i - r_k \right) + \sum_{l=1}^L \lambda_{l+K} \left(\sum_{j=1}^M Q_{jl} b_j - r_{l+K} \right), \quad (24)$$

where

λ : Lagrange multipliers,
 r : restrain conditions such as V_s , V_D and P_{ik} , Q_{jl} are given by Eq. (19), (20), (21).

From the following variational principle

$$\frac{\partial \psi}{\partial a_i} = 0, \quad \frac{\partial \psi}{\partial b_j} = 0, \quad (25)$$

the Lagrange optimization equation can be expressed in the form,

$$A X = B, \quad (26)$$

where A is the symmetric matrix,

$$A = \begin{vmatrix} 2I_{NN} & 2II_{NM} & P_{NK} & 0 \\ 2II_{MN} & 2III_{MM} & 0 & Q_{ML} \\ P_{KN} & 0 & 0 & 0 \\ 0 & Q_{LM} & 0 & 0 \end{vmatrix}, \quad (27)$$

and B is the column matrix defining the restrain conditions,

$$B = (0, \dots, 0, V_s, A_s, A_w, \dots, V_D, A_D, \dots) \quad (28)$$

The solution of the simultaneous equation (26) gives the optimum coefficients of singularity distributions.

4.3 Numerical Examples

The computer program for the hull form optimization of the SSC was developed by the authors based on the abovementioned theory. This optimization program is available for the various hull combinations as well as for the hull element.

Numerical examples are illustrated graphically. Figure 9 shows the optimized sectional area curves of the lowerhull with $f/L = 0.08$ and the equal displacement for different midshipsection area A_0 at $F_n = 0.32$.

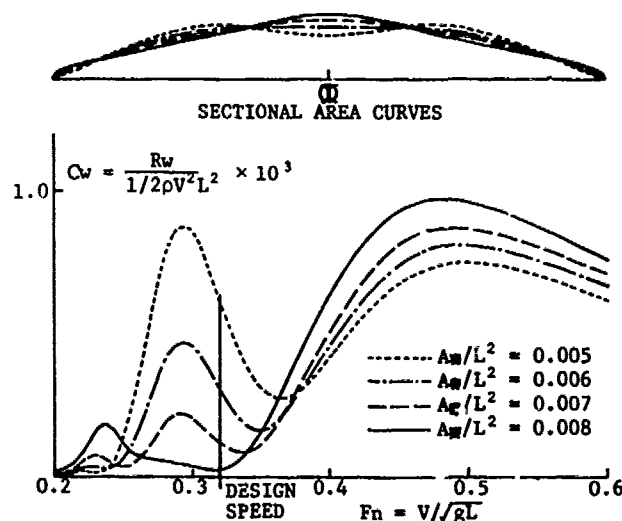


Fig. 9 Optimized Lowerhull for Different A_0/L^2

It can be seen from the calculated wave resistance shown in this figure that the case of $A_m/L^2 = 0.008$ gives the minimum wave resistance and the optimum prismatic coefficient.

Figure 10 shows the optimized hull form of the lowerhull with $f/L = 0.1$ for different Froude number under the combination of the given strut as shown in the figure. With the increase of design speed, the end shape of the lowerhull tends to have larger bluntness and the midship section area of the lowerhull becomes smaller. The wave resistance coefficients for these optimized configurations are shown in Figure 11.

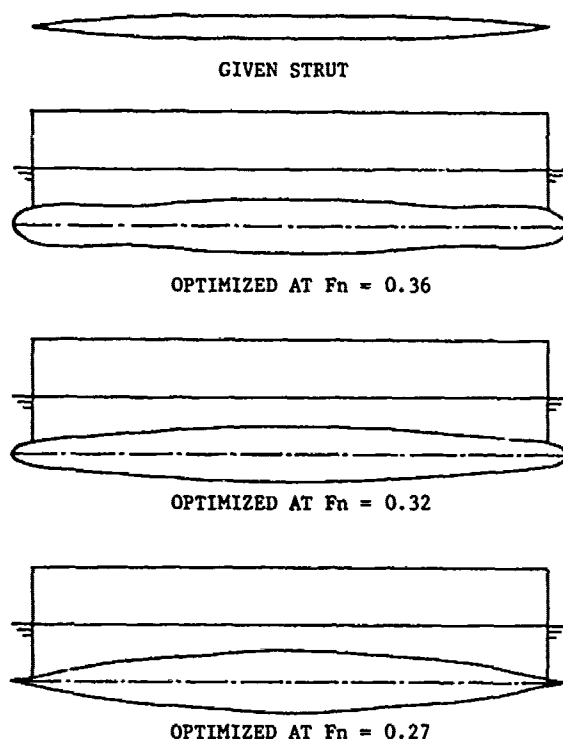


Fig. 10 Optimized Lowerhull with Given Strut for Different Froude Number

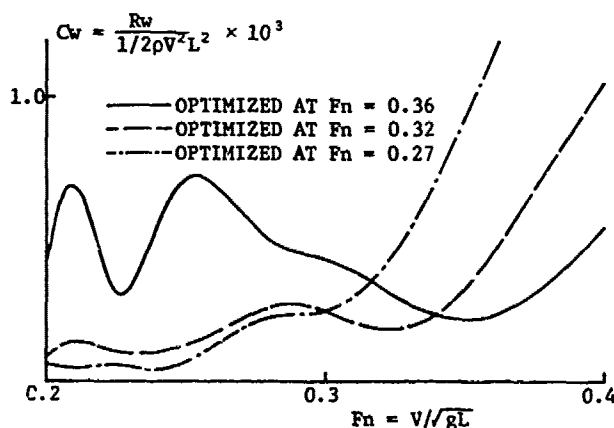


Fig. 11 Wave Resistance of Optimized Lowerhull (Shown in Fig. 10)

Sometimes, an optimized but unpractical hull form of the lowerhull is obtained at the higher Froude number than 0.4. In such a case, necessary restrain conditions for obtaining the practical hull form must be introduced into the calculation. Also, in designing the practical hull form, the aft-body shape of the lowerhull shall be modified from a viewpoint of the propulsive performance.

5. DESIGN AND SEA TRIAL RESULTS OF THE 'MESA 80'

5.1 Design

The first commercial prototype SSC 'MESA 80' being capable of carrying 446 passengers was designed at her service speed of 23 knots and required to be stably serviceable even in rough seas with the significant wave height up to 3.5 meters. Under the basic design requirement briefly mentioned above, a lot of preliminary designs were compared in the early design stage, changing hull configuration, hull material and propulsion system, etc. to attain the reasonable SSC design.

Then, the anti-corrosive aluminum alloy was chosen as hull material so as to reduce the structural weight. Although a gas turbine was considered as the prime mover, the diesel engine with light weight was selected because of its cheaper operating and maintenance cost in spite of its heavier weight and larger size than that of a gas turbine.

Since the main engines were located on the second deck, the newly developed power transmission system of so-called Z-drive type was adopted, which has higher transmission efficiency and reliability than the other transmission systems considered. As regards the hull configuration, the 'single strut per hull' was considered to be more favourable than the 'tandem struts per hull' from the viewpoints of space availability, stability and speed.

Table 1 Principal Particulars of 'MESA 80'

Length overall	about 35.9 m
Length b.p.	31.50 m
Breadth (mid.), Max.	17.10 m
Depth (mld.)	5.845 m
Design draft (mld.)	3.15 m
Maximum design draft (mld.)	3.65 m
Passenger capacity (all seated)	446 persons
Crew complement	7 persons
Maximum speed at design draft	27.1 knots
Main engine: Fuji-S.E.M.T. marine-diesel	
Max. continuous output:	
4,050 PS/1,475 rpm	2 sets

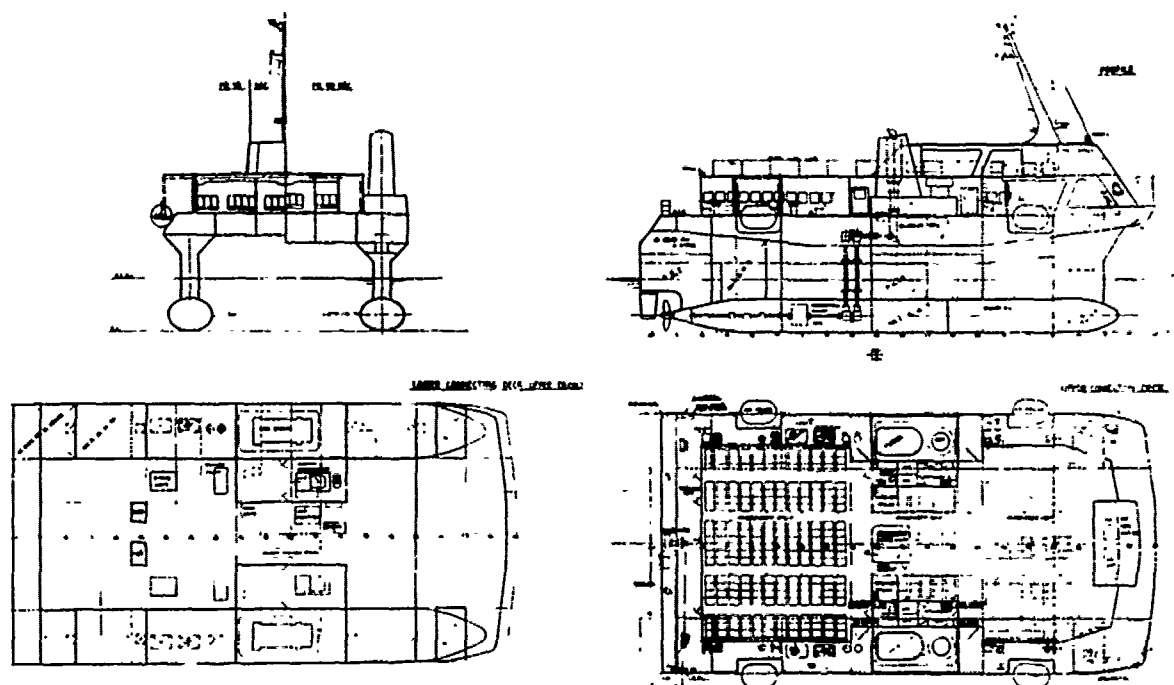


Fig. 12 General Arrangement Plan of
'MESA 80'

After the candidate design with its displacement of about 370 tons was selected, detailed parametric studies on hull dimensions were carried out, and the final design was decided. Principal particulars and the general arrangement plan of the 'MESA 80' are shown in Table 1 and Figure 12 respectively.

In deciding the hull dimensions of the 'MESA 80', a lot of design trade-off studies were made. As a result, the proportion of the lowerhull and its submergence were finally set L/D_e of 12.1 and f/D_e of 0.99 for the maximum design draft, where D_e means the equivalent diameter of the lowerhull. The lowerhull with large L/D ratio was not adopted because of its weight increase, although only a little gain in resistance was obtained as compared with the lowerhull adopted in the 'MESA 80'. Selection of the submergence of the lowerhull was restricted by the maximum draft of 3.8 meters, desirably 3.65 meters. Also the elliptical cross section of the lowerhull was considered to be more favourable than the circular cross section because of the greater f/D , easiness for the reduction gear arrangement and the larger damping force of motion.

The amount of the waterplane area and the distance between demihulls were decided mainly from the motion performance and the requirements on stability. These dimensions were selected so as to have enough large natural period of motion except heaving to avoid motion resonance for the design wave with its period of about 6 seconds.

The designed natural periods of motion of the 'MESA 80' are shown in Table 2. Despite of a short natural period of the heaving motion, the acceptably small amplitude even in the resonant waves was confirmed in the model tests because of increasing the motion damping forces by fins and the lowerhull with elliptical cross sections.

Table 2 Natural Periods of Motion of 'MESA 80' at Maximum Design Draft

	Heave	Pitch	Roll
T(sec)	6.2	9.5	10.9

5.2 Typical Results of Sea Trial Tests

From September 1979, the extensive sea trials of the 'MESA 80' were conducted to confirm the full scale performance and to evaluate the theoretical and/or model predictions. Especially, the propulsion tests and the seakeeping tests which evidently reflect the effort of the hull form design, were extensively carried out several times at the different sea conditions. During these test period, the highest significant wave measured by the wave-rider buoy was 2.6 meters

and also the wave height of about 3 meters in significant value was visually observed in another test.

The speed tests in the calm sea condition were conducted by use of the mile-post in Tokyo Bay, changing ship's draft, trim and engine load. The maximum speed attained at the design draft was 27.1 knots. This result showed the good agreement with the predicted speed from the model propulsion tests. While, the speed in waves was measured on the maximum design draft by using the electro-magnetic type log. Figure 13 shows the measured speeds at service power for different sea conditions. Also in the figure, the measured speed are compared with the speed in the calm sea condition in a form of the ratio. It can be found from this figure that the speed loss of the 'MESA 80' even in high Sea State 4 is only less than 2 percents, which is much smaller than predicted.

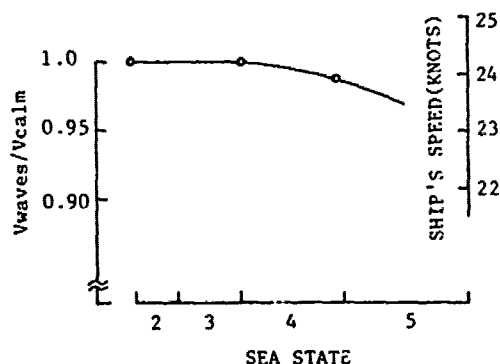


Fig. 13 Speed in Waves of 'MESA 80'

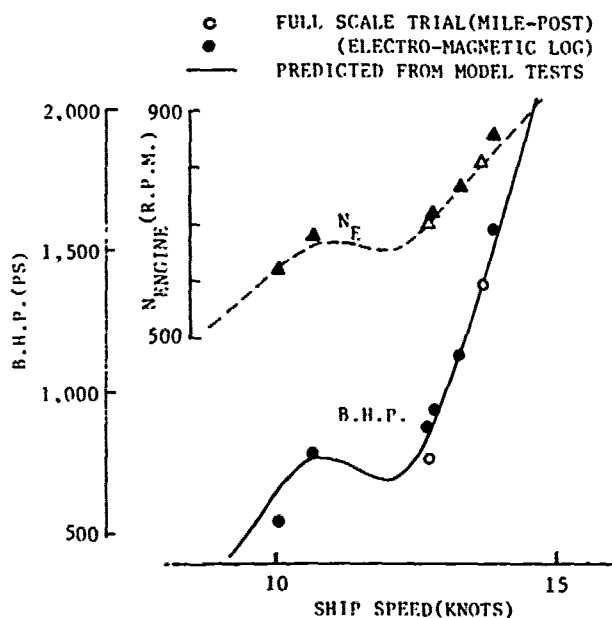


Fig. 14 Speed-Power Relation of 'MESA 80' in Low Speed Region

It was predicted in advance from the model test results that the large secondary hump of the wave resistance coefficient of the 'MESA 80' as seen in Figure 5, would cause the unstableness in the speed-power relation. Therefore, the speed measurements in the low speed region from 10 knots to 13 knots were carefully carried out. The results of these tests are shown in Figure 14 associated with the predicted curve from the model tests. Although it is a minor problem in the case of the 'MESA 80' because of her sufficient engine power to get over such unstable speed region, careful attention must be paid for the hull form design of the SSC with design Froude number up to 0.4.

The seakeeping tests were also carried out extensively, changing the ship's speed and the ship's heading to the wave. Typical results of the measurements in the sea of 2.4 meters' significant wave height are shown in Figure 15. The automatically controlled fins were used in the tests. Figure 15 shows the pitching response (single significant amplitude) for different heading angles. As can be seen in the figure, pitching angle is less than 1 degree for all headings.

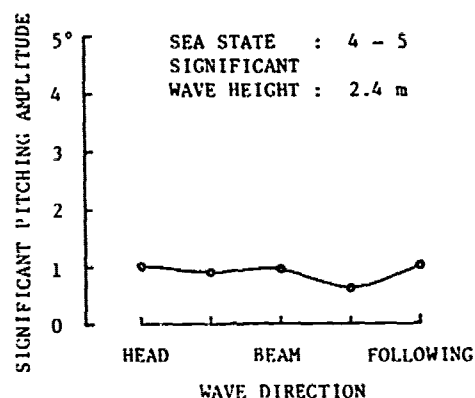


Fig. 15 Pitching Amplitude of 'MESA 80'

The sea trial results of the 'MESA 80' briefly presented above have shown fairly good agreement with the predicted results from the theoretical calculation and the model tests. Also, the data obtained by these full scale tests gave a lot of useful information towards establishing the technology for future SSCs.

6. CONCLUDING REMARKS

Owing to the efforts on SWATH by the U.S. Navy as well as our developmental work on the SSC, recognition of the SSC is now gradually spreading in the field of marine transportation and ocean development.

Although it was the most essential outcome to confirm her various advantageous performance in actual seas at the developmental stage of the SSC, the design technologies for the hull form optimization is nowadays being required.

In the paper presented here, a theoretical approach for minimizing the wave resistance of the SSC has been made based on the thin ship theory with some correction factors, and it has been found that the mathematical model newly developed was practically quite useful in designing the optimum hull form of the SSC.

Finally in order to expand SSC applications, it will be necessary to establish the design synthesis technology to obtain a highly economical SSC.

ACKNOWLEDGMENT

The authors wish to note that this paper is based on the efforts of many persons concerned with the SSC project at Mitsui Engineering and Shipbuilding Company.

The authors are deeply grateful to Dr. T. Tomita, Mr. M. Oshima and Dr. H. Narita who are promoting the SSC project at Mitsui for their encouragement in carrying out the R & D work for the SSC.

REFERENCES

1. Lang, T.G., Hightower, J.D., Strickland, A.T., "Design and Development of the 190-Ton Stable Semisubmerged Platform (SSP)" Transactions of the ASME, ASME Winter Annual Meeting, Paper No. 73-WA/Oct. 2, Detroit, Mich., November 1973.
2. Hightower, J.D., Seiple, R.L., "Operational Experiences with the SWATH Ship SSP KAIMALINO", AIAA/SNAME Advanced Marine Vehicles Conference, San Diego, CA, Paper No. 78-741, April 1978.
3. Hawkins, S., Sarchin, T., "The Small Waterplane-Area Twin Hull (SWATH) Program --- A Status Report", AIAA/SNAME Advanced Marine Vehicles Conference, San Diego, CA, Paper No. 74-324, February 1974.
4. Lamb, G.R., Fein, J.A., "The Developing Technology for SWATH Ships" AIAA/SNAME Advanced Marine Vehicles Conference, Baltimore, Maryland, Paper No. 79-2003, October 1979.
5. Lamb, G.R., "The SWATH Concept: Designing Superior Operability into a Surface Displacement Ship", DTNSRDE Report No. 4570, December 1975.
6. Oshima, M., Narita, H., Kunitake, Y., "Experiences with 12 Meter Long Semi-Submerged Catamaran (SSC) 'MARINE ACE' and Building of SSC Ferry for 446 Passengers", AIAA/SNAME Advanced Marine Vehicles Conference, Baltimore, Maryland, Paper No. 79-2019, October 1979.
7. Chapman, R.B., "Hydrodynamic Drag of semisubmerged Ships", Trans. ASME, J. Basic Eng. Vol. 94, 1972.
8. Lin, W.C., "The Force and Moment on a Twin-Hull Ship in Steady Potential Flow", Tenth Symposium on Naval Hydrodynamics 1974.
9. Beasho, M., "On the Wave Resistance Theory of a Submerged Body", JSNA JAPAN Vol. 99, 1956.
10. Pien, P.C., "Catamaran Hull-Form

Design", Int. Seminar on Wave Resistance, 1976.

11. Inui, T., Iwata, T. and Sen, P., "On the Humps and Hollows of the Wave-making Resistance of Ships", JSNA JAPAN, Vol. 97, 1955.

12. Lee, A.Y.C., "Source Generated Ships of Minimum theoretical Wave Resistance", RINA Vol. 111, 1969.

13. Maruo, H., "Theory and Application of Semi-Submerged Ships of Minimum Wave Resistance", Japan Shipbuilding & Marine Engineering, Vol. 4, 1969.

Discussion

C. Kennell (Naval Sea System Command)

The Semi-Submerged Catamaran is a promising displacement ship concept that allows the naval architect new freedom to design more efficient ships to challenge the worlds oceans. Mitsui Engineering and Shipbuilding has been advancing our understanding of this new technology in a most impressive manner. This paper marks yet another significant achievement in this difficult effort. I would like to congratulate the authors on their interesting and thought provoking paper. There are a few questions I would like to ask the authors to better appreciate their fine work.

The curves for lower hull wave drag in Figure 1 were derived by subtracting the total resistance at deep submergence from the resistance at shallow submergence. I would like to know how deep the deep submergence was and how the effects of model supports were treated.

Figure 4 presents strut residual resistance curves for two submergence depths (10% & 15% of strut length). My design experience has convinced me that submergence depths of about 5% of strut length are best. In addition, Mitsui's MESA 80 has a submergence depth under 5%. I would like to hear the authors' opinions on the effect of these much smaller submergence depths. Also, I would like to know how strut end effects were treated. Figure 6 shows excellent correlation between measured residual resistance and calculated wavemaking resistance for a SSC. Comparisons I made in 1973 with model test data for several hull forms showed similar agreement in curve shape, but, the difference between theory and experiment varied for the different cases. I finally concluded that a correlation factor

$$\Delta C_R = \frac{\Delta R_R}{\frac{1}{2} \rho V^2 S} = 0.0005$$

was a good value to add to wavemaking resistance for design estimates. This seems to be roughly in agreement with the authors' data. I would like to know if the authors have made such comparisons for other configurations (particularly tandem strut forms). If so, is the correlation similar?

My approach to hull form optimization is to treat the problem as a total ship design rather than a resistance optimization problem. As a result, realistic limitations imposed by machinery arrangement, intact and damaged stability, structural design, and access requirements must be observed. Nevertheless, my conclusions appear to be in complete agreement

with those of the authors' as shown in Figures 9 & 10. For Froude Number greater than 0.4, the most important consideration in wave resistance is "thinness" (ie low hull diameter and low strut thickness). At lower speeds, "slenderness" is most important (ie low hull prismatic coefficient

$$C_P = V_H / \pi \frac{D_{MAX}^2}{4} L_H$$

low waterplane area coefficient

$$C_{WP} = W.P. \text{ Area} / t_{MAX} \cdot L$$

This later conclusion should not surprise devoted readers of old naval architecture books which refer to the wave drag hump at $F_n = 0.3$ as the "prismatic hump". I would like to ask the authors if they have done similar optimization studies for tandem strut forms?

While the quality of SSC technology being developed by Mitsui is evident from this paper, the true value of Mitsui's effort can best be appreciated by observing their ship MESA 80. I am extremely grateful to Mitsui for allowing me to inspect MESA 80 while underway last week. This high speed ship is indeed impressive. Although the waves on Tokyo Bay were small during my voyage, data I have seen and movies showing MESA 80 traveling at high speeds in a state 5 seaway show that the Semi-Submerged Catamaran concept works in a most impressive manner. Mitsui Engineering and Shipbuilding and the authors are to be congratulated for their significant achievements.

C.M. Lee (DTNSRDC)

The authors presented a procedure how to optimize the hull form for semi-submerged catamarans based on wave resistance reduction. As is well known, the semi-submerged twin-hull concept has evolved mainly due to its advantages on seakeeping qualities. Thus, any optimum-hull design for SSC should pay an equal attention, at least, to the seakeeping performance.

It appears that MESA 80 is a fairly successful design in the viewpoint of both resistance and seakeeping performance. I would like to know how the seakeeping aspects of that ship was reflected in the hull design procedure.

At DTNSRDC, an optimum hull design methodology based on both resistance and seakeeping has been sought, and I would say, a certain degree of success has been achieved. As a part of this effort, a simplified prediction of motion in waves has been developed by using approximate means of obtaining the added mass, damping, and wave excited coefficients. The computation time for motion has been significantly reduced, which allows a more effective iterations necessary in the hull

design.

I would like to end my discussion with a sincere congratulation to the authors for their valuable and successful work.

H. Tanaka (SRI)

I congratulate the authors on their fine works and have great respect for many efforts in the long time. My simple asking is concerned with the principle of linearity in a resultant wave. The authors prediction method of the wave resistance, essentially depends on the linear combination of waves due to hull elements. Unlike conventional ship hull forms, complicated hull forms in a semi-submerged catamaran (ssc) seems to be difficult to realize the linearity in the synthesis of the ship waves. I can imagine that the linearity is spoiled by characteristics of a submerged body with shallow submergence which generates a couple of vortices as a trailing vortex of a wing. Furthermore, concerning high speed catamarans, the interaction of ship waves between both demi-hulls are left unsolved.

Studying their paper, I hardly confirm about realization of the linearity because none of wave patterns or wave spectra were shown in this paper. For the optimization of special hull forms such as ssc's, checking on realization of the linearity plays important role at the beginning of studies. I would like to have their experiences or opinions on this problem.

H. Maruo (Yokohama N Univ)

Extensive investigations into semi-submerged hulls have been carried out by Ishii and a synthetical report of the investigation was submitted to Osaka University as a thesis in 1967. Several results of this study have been published partly in other publications from time to time. The research involves a thorough examination of the condition of optimal hull configuration, and feasibility study of the semi-submerged hulls including catamarans in the practical operation from the point of view of design practice. The principle of the interference between waves generated by the underwater main hull and those by the surface piercing strut is fully exploited to minimize the wave resistance, and model tests have proved successfully the validity of the theoretical assessment. From the theoretical point of view, the optimization of the semi-submerged hull form can be attained only by taking advantage of the above principle, and the method described in the present paper can never realize the true optimization. The investigation includes also a study of the effect of mutual interference between each demihull of a catamaran and the optimal condition on the spacing between demihulls

is fully examined.

On comparing with the above mentioned investigations, the result described in the present paper seems to be far less extensive and less complete. Nevertheless the present authors have not given any reference to the above achievements. I wish to ask if the authors do not have any knowledge about the above investigations at all, or have ignored them intentionally by some other reasons.

C.C. Hsueh (Huazhong Inst of Tech)

I'm glad to hear the theoretical approach for minimizing the wave resistance of the SSC, because I am investigating a method of minimizing the wave resistance with the shipform as follows (Ref.1)).

A new shipform of flat bow and cochleachannelled stern is described whose excellent performance is compared with those of conventional shipforms and the fundamental principles are tentatively explained. The effect of the bow and stern on ship performance and some abnormal phenomena observed during the investigation are discussed.

Comparative tests on the ship models show that when $K_R = 2.8 \sim 3.7$, the resistance of the new ship is decreased by 25 ~ 40%, the wave height from the bow is decreased by 60%, propulsive efficiency is increased by 35 ~ 45% and horsepower of the engine can be saved in the amount of 35 ~ 45%.

The first full-scale ship's trial trip has also been discussed.

The facts that the design of the conventional ship is finalized and that this type of ship is still being built make it appropriate to be chosen as a typical shipform for comparison.

Let me summarize as follows:

(1) In spite of the fact that the cochleachannels have given the new ship added resistance and the wetted surface is also rather large, this shipform still has fairly low total resistance for medium and high speed ships because it can considerably reduce residual resistance.

(2) The new ship has relatively large wake fraction, small thrust deduction fraction, and reduce energy loss of the rotating race, thus possessing better than average propulsive coefficient.

(3) The new ship is a promising inland river new shipform because it has good wave-dissipating capacity, appreciable increase in speed, evident improvement on stability, manoeuvrability and anti-flooding.

(4) Such questions as the resistance, propulsion factors and slamming of new ship are to be studied further.

REFERENCES

- 1) Hsueh, Chung-Chuan et al., "An In-

Author's Reply

Y. Kunitake (Mitsui E&S)

The authors are extremely grateful for valuable discussions on the paper which describes a hull form design method of the SSC and the design procedure of the MESA 80 as well as her trial results.

Unlike a conventional monohull ship, the SSC has so complicated hull form that the change of a design parameter of the SSC influences on various ship performance much more sensitively than the conventional ships. Therefore, careful design synthesis has to be conducted for hull form optimization from the view point of the total ship design on which Mr. Kennell mentioned in his discussion.

Also, the remarks of Dr. Lee on seakeeping performance in the SSC design work are quite agreeable with the authors. The authors should say that great attention for seakeeping of the MESA 80 as well as for wave resistance was paid in selecting the sectional shape of the lowerhull, amount of the waterplane area and distance between demihulls, etc.

The authors are very pleased to answer Mr. Kennell's questions which make the author's paper more precise and understandable. As to his question on Figures 1 & 4 of the paper, the authors should say that the submergence depth of lowerhull in fully submerged condition was four times of diameter of the lowerhull, and the difference of resistance between the model supports with different depth was eliminated by using the calculated frictional resis-

tance of each model support. In the resistance tests of struts, no special consideration was paid for strut end effects.

Regarding Mr. Kennell's contribution on the optimal depth of strut, the authors should say that the submergence depth of strut at design draft condition has to be decided so as to minimize the total resistance, and the strut depth should be minimized in the high Froude number region where the wave resistance of lowerhull may be fairly small as compared with the total resistance.

Since researches on the SSC's hull form by the authors have been carried out mostly for the 'single strut per hull' configuration, the authors have not yet enough informations for hull form optimization of the 'tandem strut per hull' configuration. However, the authors would like to agree with Mr. Kennell's suggestion on the hull form parameters which strongly influence to wave resistance reduction.

As Dr. Tanaka points out in his discussion, it seems to be very important to consider precisely the actual hydrodynamic phenomena of waves generated by hull elements of SSC into the mathematical model for better prediction of wave resistance. It is observed in the model tank tests of the SSC that the waves inside the both demihulls show complicated behavior which suggests the presence of the non-linearity. Although the measured wave resistance shows a fairly good agreement with the calculated value by the mathematical model presented here, which is based on the assumption of the linear combination of the waves, the authors will intend to refine further our mathematical model so that the actual phenomena can be more exactly described.

In reply to Prof. Maruo, the authors should say that the interference effects of the hull element on the wave resistance are fully included in the optimization described in the paper, and Dr. Ishii's work will be kept in mind for future work on this problem.

Prof. C.C. Hsueh's contribution is also welcomed.

Theoretical and Experimental Investigations of Non-Equilibrium Jet of Air Cushion Vehicles

Tao Ma, Wei-Lin Zhou and Xiong Gu
Shanghai Ship Design and Research Institute
Shanghai, China

ABSTRACT

Mathematical models of two types of cushion configuration, i.e. wall jet and plenum chamber, are established for bag-finger skirt system under equilibrium, overfed and underfed operating conditions. The wall jet theory is based on turbulent jet theory and boundary layer theory for the part of wall jet, and on momentum equation for the part of jet curtain, similar relationships are set up for plenum chamber theory according to Bernoulli's equations, thus yielding general theoretical expressions for bag-finger skirt systems. Agreement between theory and test results is verified through non-equilibrium jet test performed in a skirt test rig. The present theoretical formulae are applicable to the determination of general hovering parameters and the prediction of such motion characteristics as stability and seakeeping quality.

NOMENCLATURE

- X, Y. — wall jet coordinates. X is along-side the wall and Y is perpendicular to the wall.
 X_0 — distance from jet core to jet exit.
 δ — boundary layer thickness.
 δ^m — momentum loss thickness.
 b — jet mixing layer thickness.
 b_1 — coordinate of escape flow boundary streamline.
 ξ, η — non-dimensional boundary streamline coordinate in boundary layer and jet mixing layer respectively.
 Φ, Ψ — integral functions defined by equations (15) (17).

- t — jet thickness.
 l — finger length.
 h — hover height
 θ — finger inclination.
 ν — motion viscous coefficient.
 ρ — air density.
 τ — wall tangential stress.
 P — pressure.
 Q — flow rate.
 M — jet momentum.
 N — hovering power.
 T — non-equilibrium flow coefficient
 m_h, m_p, m_θ — derivatives of non-equilibrium cushion flow versus hover height, cushion pressure and finger inclination respectively
 C_e — cushion flow escape coefficient.

Foot Notations

- m — maximum value
 j — nozzle value
 $t.c$ — under pressure, respectively representing bag and cushion pressure
 e — escape value
 ea — escape into the atmosphere
 c — under Q , representing underfed or overfed flow out of or into cushion

1. INTRODUCTION

In the field of basic theoretical research of air cushion principle, there have appeared various mathematical models since 1960's on the basis of large amount of experimental and theoretical investigations, of which thin jet theory [1] and exponential theory [2] for peripheral skirt, wall jet

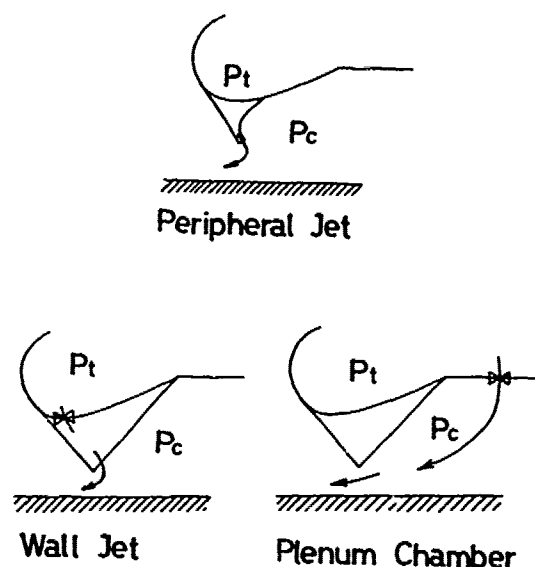


Fig. 1 Three Types of Basic Cushion Configurations

theory [3] and plenum chamber theory [4] for bag-finger skirt are comparatively practical. By using these theories, one can calculate flow rate, pressure head, lift power and select fans for hovering condition. These theories, however, are only applicable to equilibrium jets.

But actually, for a three dimensional air cushion vehicle, equilibrium jet flow pattern may not be maintained because of the following facts: non-uniformity of bag pressure in different sections due to unsymmetrical arrangement of fans and ducting, differences of hover-height in different sections due to inclination of craft, changes of pressure distribution of cushion outside due to forward motion of craft, differences of skirt configurations in different sections, and heave, pitch, roll motion of craft. This will result in overfed flow, where part of the flow enters into the cushion, as well as underfed flow, where part of cushion air escapes from underneath the jet curtain into the atmosphere, thus causing cross flow in the cushion.

To investigate motion characteristics of air cushion vehicles, some literature extend momentum law to analyse the three different flow patterns (overfed, equilibrium and underfed) without considering viscous effects, and this gives results in which the flow at equilibrium point is

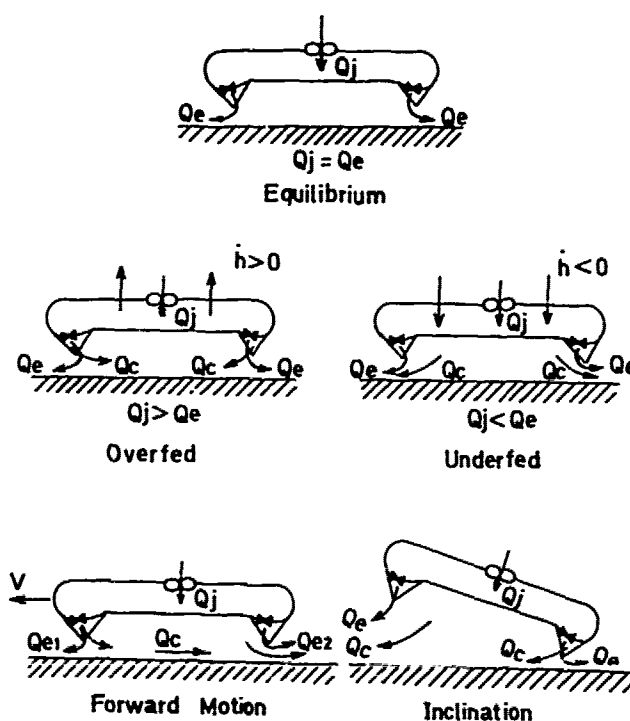


Fig. 2. Practical Examples of Non-equilibrium Cushion Flow

discontinuous. Matsuo [6] used viscous turbulent jet theory to replace the above theories and overcame this defect. This theory is, however, only applicable to peripheral jet skirt. West [3] applied experimental results of two dimensional turbulent wall jet velocity distribution for the calculation of the momentum along wall, and established equilibrium jet equation for single wall skirt.

According to the authors knowledge, the research of non-equilibrium flow pattern of bag-finger skirt is so far largely based on plenum chamber theory. But in fact, the flow pattern of wall jet is very different from that of plenum chamber, it will exert a different influence on the behavior of ACV's motion. Especially when we are investigating stability on calm water, the steady flow and hence steady pressure distribution of wall jet and plenum chamber in the cushion will be totally different from each other. However, literature dealing with non-equilibrium wall jet appears to be still lacking.

This paper discusses theoretical flow patterns of two types of cushion configuration, i.e. wall jet and plenum chamber, of bag-finger skirt operating under most

general conditions. The theory has been verified by quasi-static simulation tests performed in a skirt test facility, whereby air is blown into or out of the cushion.

2. NON-EQUILIBRIUM JET THEORY OF AIR CUSHION

2.1 Wall Jet Theory

This theory consists of two parts, turbulent wall jet and cushion jet curtain. Basic assumptions are as follows:

1) Bag holes, after introducing a loss coefficient, is idealized as a wall nozzle with good contraction.

2) Bag pressure is homogeneous and cushion pressure is uniform within the whole cushion area.

3) The jet near the wall has a boundary layer velocity distribution and that near the cushion side has a free jet velocity distribution.

4) Jet curtain will tend to curve under the action of pressure difference between the two sides of jet, and will eventually contact surface and separate. Viscous effect is approximately negligible as hover height is generally small.

5) To simplify calculation, simple momentum equation are applied for cushion jet curtain.

2.1.1 Turbulent Wall Jet

The flow pattern of turbulent wall jet is shown in fig.3.

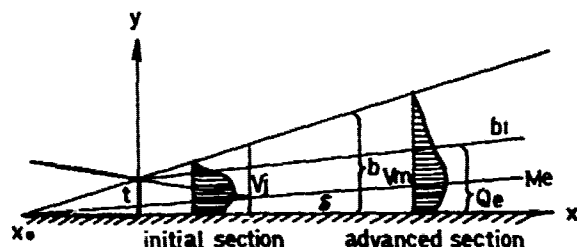


Fig.3. Turbulent Wall Jet Flow Pattern

Wall jet is quite similar to free jet. It is a mixing process of jet ejecting tangentially along wall with ambient static medium.

It is comprised of three sections, i.e. initial, gradual and advanced sections. In the initial section there is a core of uniform velocity V_j . The flow near the wall is in boundary layer, while the flow on the cushion side is a mixing layer of jets. In the advanced section, which is far from the jet nozzle, there exists only wall boundary layer ($y < \delta$) and mixing layer of jet ($\delta < y < b$). At the point $y = \delta$, the flow possesses its maximum velocity V_m , and decelerates down-

stream. The core velocity of the gradual section is equal to the velocity of nozzle outlet. But because gradual section is relatively short, so it can be included in the advanced section.

The velocity distribution within the mixing layer of jet is considered to obey free jet law [7], that is:

$$\frac{V}{V_m} = \left[1 - \left(\frac{y - \delta}{b - \delta} \right)^{1.5} \right]^2 \quad (1)$$

diffusion angle $\approx 16^\circ$

$$b = \tan 16^\circ (X + X_0) = 0.287(X + 3.48t) \quad (2)$$

The velocity distribution exponential of boundary layer is different from the $1/7$ value of usual flat turbulent boundary layer due to the influence of mixing layer of jet. Its value is approximated to be $1/10$ according to test results and [7] i.e.

$$\frac{V}{V_m} = \left(\frac{y}{\delta} \right)^{1/10} \quad (3)$$

According to [8] the corresponding expression for $1/10$ velocity distribution is as follows,

$$\frac{V}{V^*} = 11.5 \left(\frac{y V^*}{\nu} \right)^{1/10} \quad (4)$$

Where $V^* = \sqrt{\frac{\tau}{\rho}}$, tangential stress velocity

$$\tau = 0.01175 \rho V^2 \left(\frac{V}{y V^*} \right)^{11} \quad (5)$$

At the interface of boundary layer and mixing layer of jet, $y = \delta$, $V = V_m$, then

$$\tau_\delta = 0.01175 \rho V_m^2 \left(\frac{V}{\delta V_m} \right)^{11} \quad (6)$$

From boundary layer momentum integral equation

$$\rho \frac{d}{dx} \int_0^\delta V^2 dy - \rho V_m \frac{d}{dx} \int_0^\delta V dy = -\tau_\delta \quad (7)$$

the thickness of boundary layer is obtained,

$$\delta = 0.237 \left(\frac{\nu}{V_m X} \right)^{2/13} X \quad (8)$$

In usual full scale case,

$$Re = \frac{V_m l}{\nu} \approx 10^5$$

so the above equation can be rewritten as

$$\delta = 0.0402 (X + 3.48t) \quad (9)$$

Friction

$$R_f = \int_0^x \tau_\delta dx = \rho V_m^2 \delta^{**}$$

Thickness of momentum loss

$$\delta^{**} = \frac{n}{(n+1)(n+2)} \delta \quad (10)$$

Where n is the inversion of the power of velocity distribution, i.e. $n=10$, therefore

$$R_f = 0.018 \rho V_m^2 \left(\frac{y}{V_m X} \right)^{\frac{2}{13}} X \quad (11)$$

Substitute full scale R_e Number into the above, then

$$R_f = 0.00306 \rho V_m^2 (X + 3.48t) \quad (12)$$

Referring to fig.1, take the whole velocity field from nozzle outlet to X station as control surface, and apply momentum theory in X direction,

$$\begin{aligned} \rho V_j^2 t &= \rho V_m^2 \delta \int_0^1 \left(\frac{y}{\delta} \right)^{\frac{1}{5}} d \left(\frac{y}{\delta} \right) \\ &+ \rho V_m^2 (b-\delta) \int_0^1 \left[1 - \left(\frac{y-\delta}{b-\delta} \right)^{1.5} \right]^4 d \left(\frac{y-\delta}{b-\delta} \right) \\ &+ 0.00306 \rho V_m^2 (X + 3.48t) \quad (13) \end{aligned}$$

From the above, the maximum downstream velocity distribution is obtained,

$$\frac{V_m}{V_j} = \sqrt{\frac{8.72}{3.48 + x/t}} \quad (14)$$

From $V_m = V_j$ the length of the initial section is found to be

$$X = 5.23t$$

The maximum downstream velocity decrease is calculated by using the above equation and is shown in fig.4.

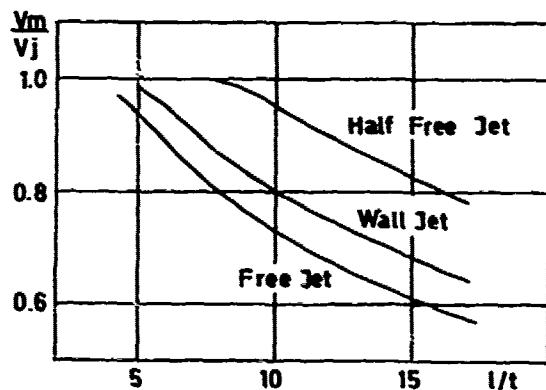


Fig.4. Maximum Sectional Velocity Downstream Distribution

In order to analyse non-equilibrium jet (i.e. overfed and underfed), let

$$\Gamma = \frac{Q_e}{Q_j} \quad \begin{array}{ll} < 1 & \text{overfed} \\ = 1 & \text{equilibrium} \\ > 1 & \text{underfed} \end{array}$$

If the boundary streamline of escape flow is within the mixing layer of jet i.e.

$$\delta < b_1 < b \quad \text{then}$$

$$Q_e = V_m \delta \int_0^{\xi_1} \xi^{\frac{1}{5}} d\xi + V_m (b-\delta) \int_0^{\eta_1} (1-\eta^{1.5})^2 d\eta \quad (15)$$

Where $\xi = \frac{y}{\delta}$, $\eta = \frac{y-\delta}{b-\delta}$ non-dimensional coordinate, $\eta_1 = \frac{b_1-\delta}{b-\delta}$ non-dimensional coordinate of escape boundary streamline.

Let

$$\Phi(\eta_1) = \int_0^{\eta_1} (1-\eta^{1.5})^2 d\eta$$

If boundary streamline of escape flow is within the boundary layer when hover height is small, $b_1 < \delta$, then

$$Q_e = V_m \delta \int_0^{\xi_1} \xi^{\frac{1}{5}} d\xi \quad (16)$$

Where $\xi_1 = \frac{b_1}{\delta}$, non-dimensional coordinate of escape boundary streamline.

When $\delta < b_1 < b$, the ratio of escape momentum

$$\frac{M_e}{M_j} = \left(\frac{V_m}{V_j} \right)^2 \left\{ \frac{\delta}{t} \int_0^{\xi_1} \xi^{\frac{1}{5}} d\xi + \frac{b-\delta}{t} \int_0^{\eta_1} (1-\eta^{1.5})^2 d\eta \right\} \quad (17)$$

Let

$$\Psi(\eta_1) = \int_0^{\eta_1} (1-\eta^{1.5})^2 d\eta$$

If $0 < b_1 < \delta$ the ratio of escape momentum will then be

$$\frac{M_e}{M_j} = \left(\frac{V_m}{V_j} \right)^2 \frac{\delta}{t} \int_0^{\xi_1} \xi^{\frac{1}{5}} d\xi \quad (18)$$

If $\frac{L}{t}$, $\frac{Q_e}{Q_j}$ is given, Φ or ξ_1 can be obtained from equations (15), (16), and escape boundary η_1 from the integral equation $\Phi(\eta_1)$. Then according to η_1 or ξ_1 , escape momentum ratio M_e/M_j can eventually be obtained from equations (17), (18). Shown in fig.5 are the

curves of $\frac{M_e}{M_j} \sim \frac{Q_e}{Q_j}$ for different $\frac{l}{t}$ values, and in fig.6 the curves of $\frac{M_e}{M_j} \sim \frac{l}{t}$ for different $\frac{Q_e}{Q_j}$ values.

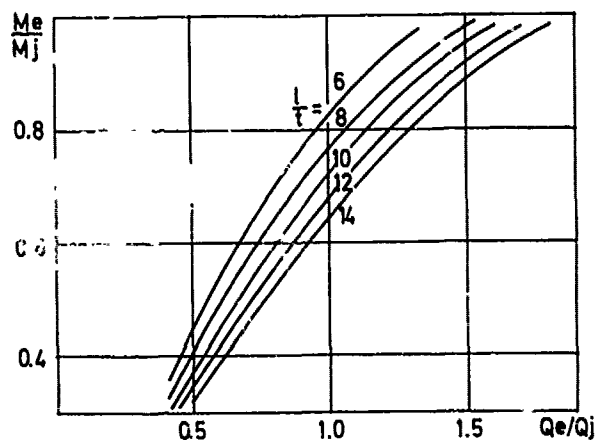


Fig.5. Variation of Escape Momentum with Overfed or Underfed Flow

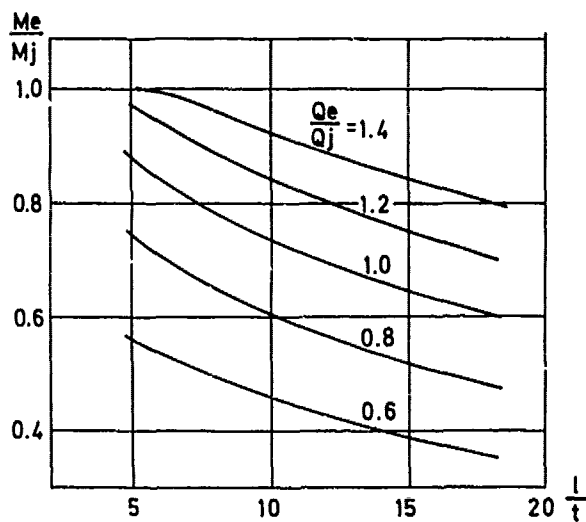


Fig.6. Variation of Escape Momentum with Finger Length

In general equilibrium conditions, $6 < \frac{l}{t} < 12$, $\frac{M_e}{M_j}$ is approximated to be

$$\frac{M_e}{M_j} \approx e^{-0.0316 \frac{l}{t}} \quad (19)$$

The function $\frac{M_e}{M_j} = f\left(\frac{Q_e}{Q_j}, \frac{l}{t}\right)$, may be approximately expressed by the following equation through regression analysis:

$$\begin{aligned} \frac{M_e}{M_j} = & -0.0575 + 1.4835 \left(\frac{Q_e}{Q_j}\right) - 0.06082 \left(\frac{l}{t}\right) \left(\frac{Q_e}{Q_j}\right) \\ & - 0.4048 \left(\frac{Q_e}{Q_j}\right)^2 + 0.02445 \left(\frac{l}{t}\right) \left(\frac{Q_e}{Q_j}\right)^2 \\ & + 0.001178 \left(\frac{l}{t}\right)^2 \left(\frac{Q_e}{Q_j}\right) - 0.000486 \left(\frac{l}{t}\right)^2 \left(\frac{Q_e}{Q_j}\right)^2 \end{aligned} \quad (20)$$

2.1.2 Jet Curtain of Cushion

The flow pattern of cushion jet curtain is shown in fig.7.

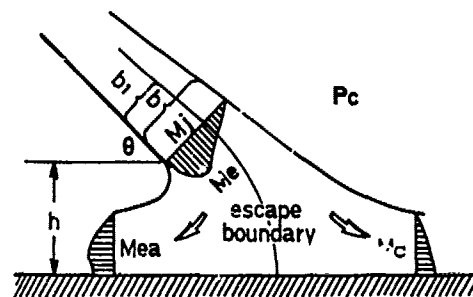


Fig.7. Curved Jet Curtain Flow Pattern

From Bernoulli's equation through bag holes

$$P_t = P_c + \frac{1}{2} \rho V_j^2 \quad (21)$$

and with contraction coefficient of bag holes area assumed to be 0.64, the nozzle momentum may be obtained

$$M_j = 1.28 (P_t - P_c) t \quad (22)$$

Taking the flow field around the jet curtain as a control face, as shown in fig. 7, and applying momentum theory in horizontal direction,

$$P_c h = M_j \cos \theta + M_{ea} - (M_j - M_e) \quad (23)$$

we can obtain cushion pressure and flow rate:

$$\frac{P_c}{P_t} = \frac{1}{\frac{h}{1.28t} / (\cos \theta - 1 + \frac{M_e + M_{ea}}{M_j}) + 1} \quad (24)$$

$$\frac{Q_j}{h \sqrt{\frac{2}{\rho} P_c}} = \sqrt{\frac{0.32}{\frac{h}{t} (\cos \theta - 1 + \frac{M_e + M_{ea}}{M_j})}} \quad (25)$$

The escape momentum changes from M_e , which is alongside the wall, to M_{ea} , which is out of the cushion, and generally speaking, $M_{ea} \approx M_e$. When hover height is small, escape streamtube will not be diffusing but contracting. In such case, the escape velocity will increase, and thus escape momentum out of cushion will be larger than that alongside the wall. But if hover height is large, the escape momentum out of cushion will be smaller than that alongside the wall due to the fact that the escape streamtube has the property of viscous diffusing and its turbulent mixing effect is the same as free turbulent jet.

If $\frac{l}{t}$, $\frac{Q_e}{Q_j}$ are given, by calculating ϕ from equation (15), and corresponding η , from the integral of $\phi(\eta)$, the escape width at the end of finger may be obtained from equations (2) and (8):

$$\frac{b_l}{t} = (0.247\eta + 0.04) \left(\frac{l}{t} + 3.48 \right) \quad (26)$$

The value of $\frac{b_l}{t}$ only varies with $\frac{Q_e}{Q_j}$ for general $\frac{l}{t}$ conditions.

When

$$\frac{Q_e}{Q_j} = 1, \quad \frac{b_l}{t} = 1.3$$

At a certain point where h is slightly greater than b_l , jet does not contract nor diffuse, therefore $M_{ea} = M_e$. But if h is less or greater than b_l , jet will either contract or diffuse, thus $M_{ea} > M_e$ or $M_{ea} < M_e$.

Escape flow Q_e will not change when

momentum changes from M_e to M_{ea} , but velocity varies because of diffusion or contraction while $M_{ea} = \rho Q_e V_{ea}$, so $\frac{M_{ea}}{M_j} = \frac{V_{ea}}{V_j}$. From equation (13), it may be seen that the variation of velocity is inversely proportional to the square root of the length of diffuse section or of hover height when hover height is large, while in the contracted escape flow tube the velocity varies inversely with hover height when hover height is small.

At present, most bag-finger skirt have low bag pressure and small hover height, therefore jets are generally in contracted state. But because of the three dimensional effect of the escape area at triangular region of finger end for the smaller hover height, jet will tend to turn upwards along the outer side of finger, thus resulting in additional momentum loss.

On the basis of test results, the following approximation is adopted

$$\frac{M_{ea}}{M_j} = \frac{M_e}{M_j} \cdot K \sqrt{\frac{t}{h}} \quad (27)$$

It has been found that in the usual range of $\frac{l}{t}$, $\frac{Q_e}{Q_j}$, i.e.

$$\frac{l}{t} = 6 \sim 10, \quad \frac{Q_e}{Q_j} = 0.5 \sim 1.5$$

theoretical calculations and experimental results coincide with each other very well, if K is taken to be of the value of 1.3

(corresponding to the value of $\frac{b_l}{t}$ when $\frac{Q_e}{Q_j} = 1$).

Substitute equation (27) into (24), (25), we have

$$\frac{P_c}{P_t} = \frac{1}{\frac{h}{1.28t} / [\cos \theta - 1 + \frac{M_e}{M_j} (1 + 1.3 \sqrt{\frac{t}{h}})] + 1} \quad (28)$$

$$\frac{Q_j}{h \sqrt{\frac{2}{\rho} P_c}} = \sqrt{\frac{0.32}{\frac{h}{t} [\cos \theta - 1 + \frac{M_e}{M_j} (1 + 1.3 \sqrt{\frac{t}{h}})]}} \quad (29)$$

The calculated results corresponding to various $\frac{l}{t}$, $\frac{Q_e}{Q_j}$ are shown respectively in figs. 8, 9, 10, 11.

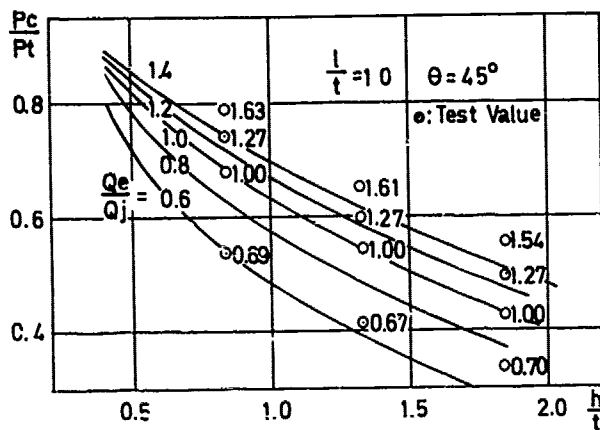


Fig. 8. Non-equilibrium Cushion Pressure of Wall Jet

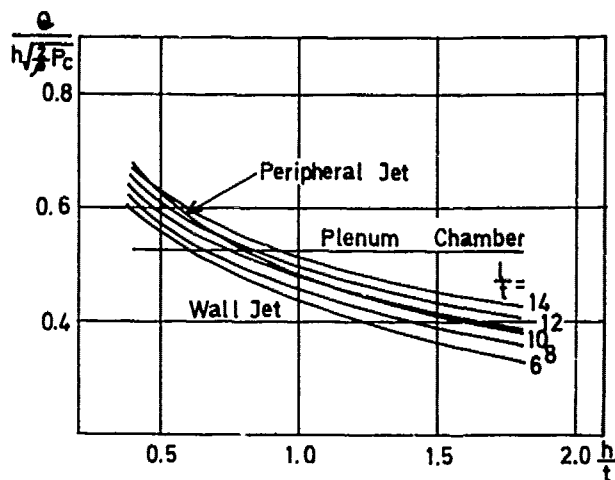


Fig. 11. Escape Flow for Three Types of Cushion

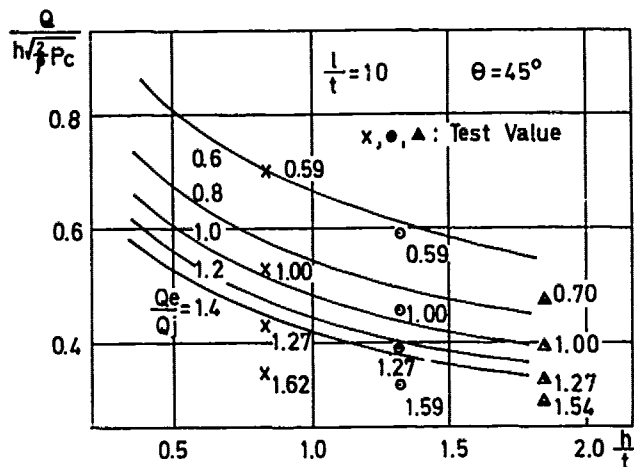


Fig. 9. Non-equilibrium Escape Flow of Wall Jet

Besides, the curves of lift power may also be calculated,

$$N_j = P_t \times Q_j$$

By nondimensionalizing it, we have the following

$$\bar{N}_j = \frac{P_t}{P_c} \cdot \frac{Q_j}{h \sqrt{\frac{2}{\rho}} P_c}$$

Shown in figure 12 are the results.

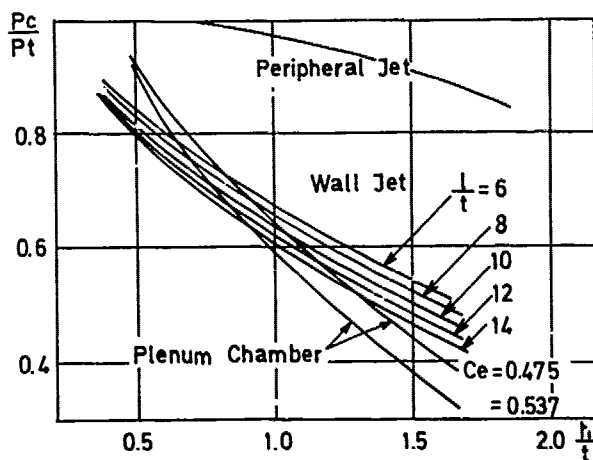


Fig. 10. Pressure for Three Types of Cushion

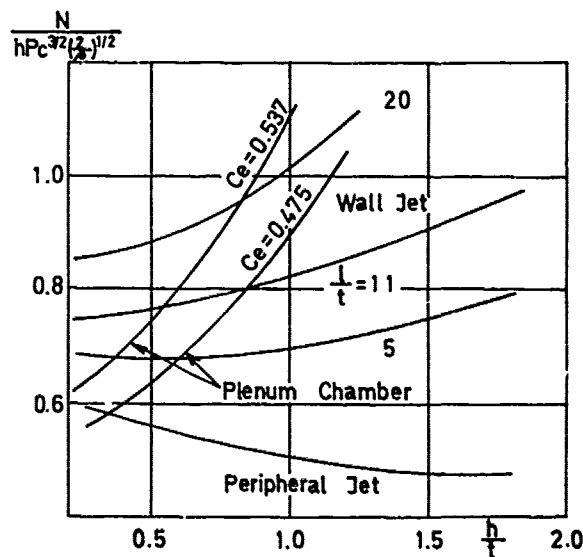


Fig. 12. Lift Power for Three Types of Cushion

2.1.3 Linear Perturbation Equation of Non-Equilibrium Jet

In dealing with motion performance of hovercraft, one has to consider the variation of flow and pressure in the cushion. According to equation(29)

$$\frac{Q_c}{Q_j} = f\left(\frac{h}{t}, \frac{p_c}{p_t}, \theta\right) \quad \left(\frac{Q_c}{Q_j} = 1 - T\right)$$

After performing linear small perturbation expansion of the above, we obtain

$$\Delta\left(\frac{Q_c}{Q_j}\right) = m_h \Delta\left(\frac{h}{t}\right) + m_p \Delta\left(\frac{p_c}{p_t}\right) + m_\theta \Delta\theta \quad (30)$$

$$\text{where } m_h = - \frac{\frac{1}{1.28(p_t/p_c - 1)} + 0.65 \frac{M_e}{M_j} \left(\frac{h}{t}\right)^{-\frac{3}{2}}}{\frac{\partial(M_e/M_j)}{\partial T} \left[1 + 1.3 \left(\frac{h}{t}\right)^{-\frac{1}{2}}\right]}$$

$$m_p = - \frac{\frac{1}{1.28} \frac{h}{t} \cdot \frac{1}{(1 - p_c/p_t)^2}}{\frac{\partial(M_e/M_j)}{\partial T} \left[1 + 1.3 \left(\frac{h}{t}\right)^{-\frac{1}{2}}\right]}$$

$$m_\theta = - \frac{\sin \theta}{\frac{\partial(M_e/M_j)}{\partial T} \left[1 + 1.3 \left(\frac{h}{t}\right)^{-\frac{1}{2}}\right]}$$

$\frac{\partial(M_e/M_j)}{\partial T}$ is obtained from fig.5 or equation (20).

The calculated results are shown in figs.13, 14 and 15. In order to analyse stability, m_h/m_p curves, which are shown in fig.16, are also calculated.

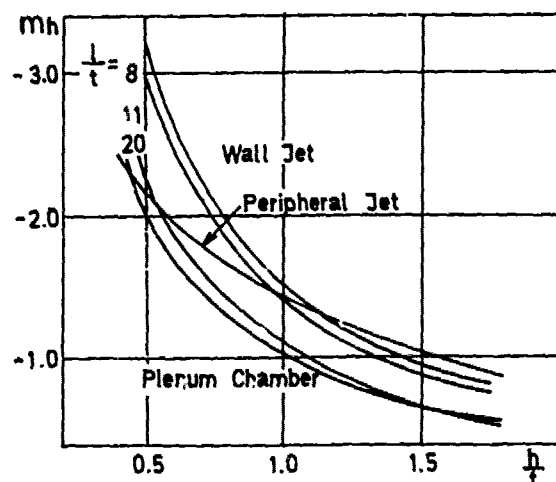


Fig.13. Derivatives of Non-equilibrium Cushion Flow Versus Hover Height

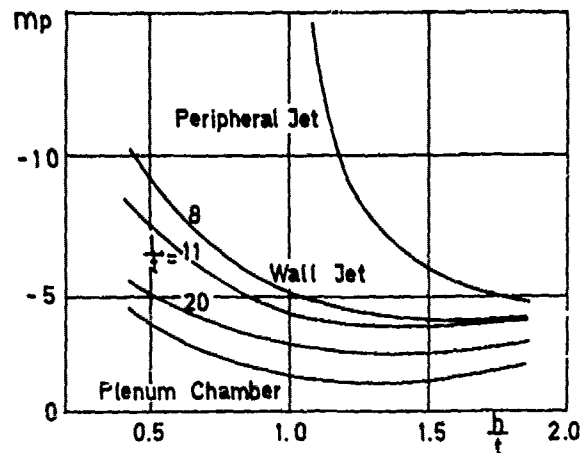


Fig.14. Derivatives of Non-equilibrium Cushion Flow Versus Pressure

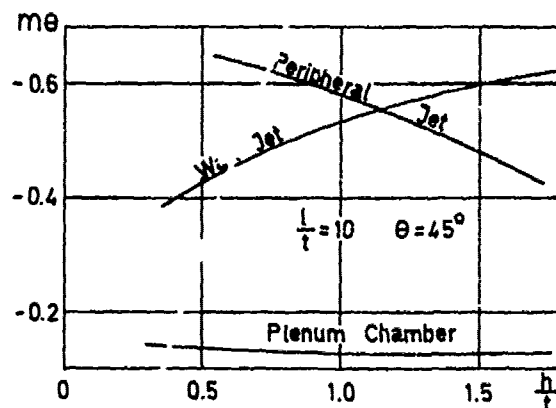


Fig.15. Derivatives of Non-equilibrium Cushion Flow Versus Finger Inclination

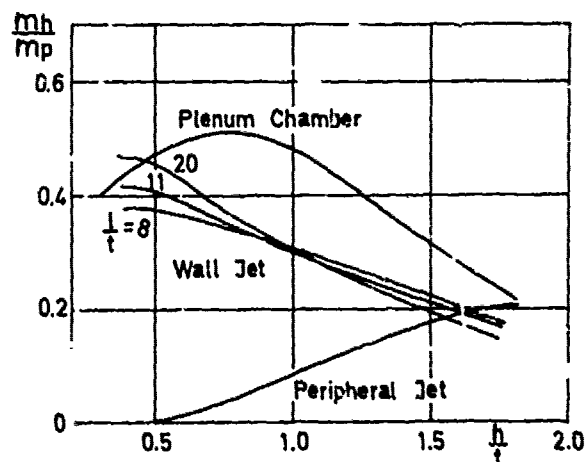


Fig.16. Cushion Static Stability Derivatives

2.2 Plenum Chamber Theory

For plenum chamber with separate ducting and cushion, such as when bag escape holes are near the inside of cushion and hence the discharging air can not be formed into wall jet, and the momentum from ducting outlet is totally lost in the cushion, the escape flow is expressed as:

$$Q_e = C_e h \sqrt{\frac{2}{\rho} P_c} \quad (31)$$

Escape coefficient C_e only depends on inclination of fingers. According to (4),

$$C_e = 0.5 + 0.4 \times 10^{-3} \theta + 0.109 \times 10^{-4} \theta^2 - 0.494 \times 10^{-7} \theta^3 + 0.345 \times 10^{-9} \theta^4 \quad (32)$$

For the usual design value

$$\theta = 45^\circ, C_e = 0.537.$$

The Bernoulli's equation from bag to cushion will be

$$P_t = P_c + \frac{1}{2} \rho \left(\frac{Q_j}{0.64t} \right)^2 \quad (33)$$

where 0.64 is the contraction coefficient of bag holes. t is equivalent jet width.

$$\text{Thus } \frac{P_c}{P_t} = \frac{1}{1 + \left(0.839 \frac{h}{t} \cdot \frac{1}{T} \right)^2} \quad (34)$$

$$\text{Where } T = \frac{Q_e}{Q_j}$$

It's curves are shown in fig.17.

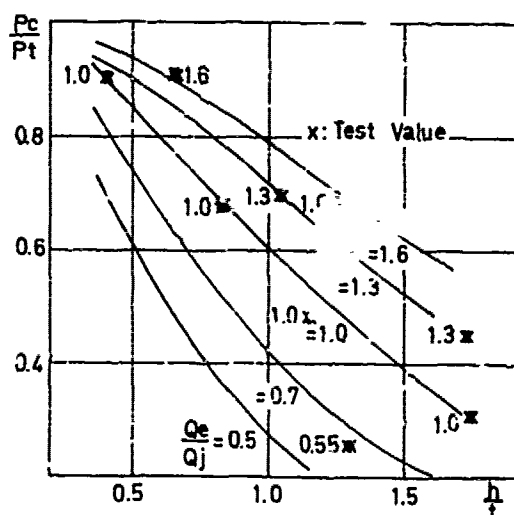


Fig.17. Non-equilibrium Cushion Pressure of Plenum Chamber

The three derivatives of m_h , m_p , m_θ for plenum chamber may be calculated by means of equation (24).

$$m_h = -0.84 \sqrt{\frac{P_c/P_t}{1 - P_c/P_t}}$$

$$m_p = -0.42 \frac{h}{t} \sqrt{\frac{1 - P_c/P_t}{P_c/P_t}} \cdot \frac{1}{(1 - P_c/P_t)^2}$$

$$m_\theta = -1.56 \frac{h}{t} \sqrt{\frac{P_c/P_t}{1 - P_c/P_t}} \cdot \frac{\partial C_e}{\partial \theta} \quad (35)$$

$\frac{\partial C_e}{\partial \theta}$ is obtained from equation (32).

Their curves are respectively shown in figs.13, 14, 15 and 16.

3. COMPARISON OF THEORETICAL PREDICTIONS WITH EXPERIMENTAL RESULTS

3.1 Verification of Theoretical Predictions by Experiments

During the process of theoretical analysis, extensive experimental investigations by using a two-dimensional skirt test box were made for the verification of the above theories.

The width of the test facility is two meters. It's floor can be elevated or lowered. Shown in fig.18 is its schematic view.

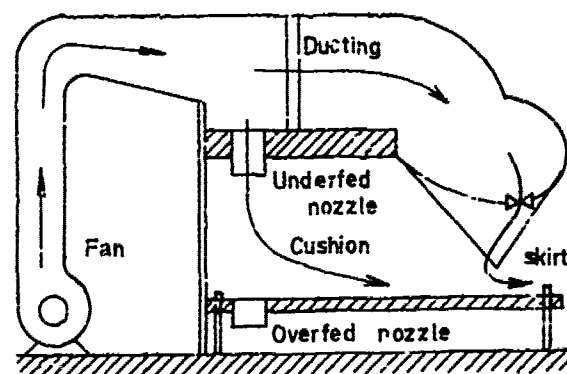


Fig.18. Skirt Test Box

In order to simulate overfed and underfed flow, four nozzles were separately attached to the top and bottom plates of plenum chamber. The range of variation of Q_e/Q_j was from 0.4 to 1.7.

For the bag-finger skirt tested, the ratio of finger height to skirt height was $\frac{1}{2}$, $l/t = 10$.

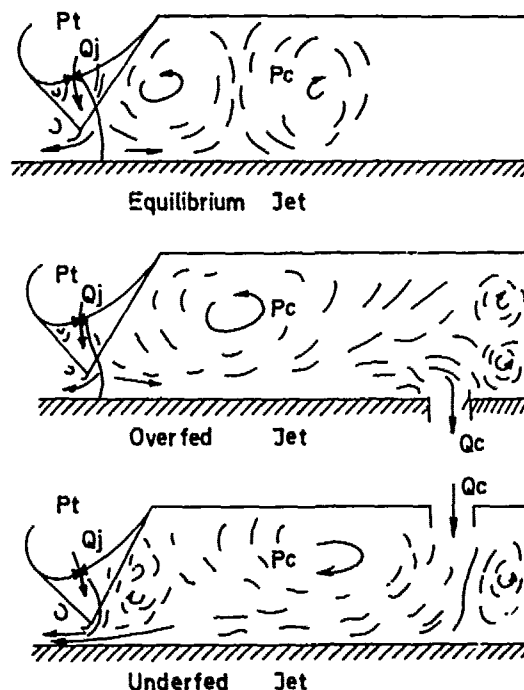


Fig.19. Visualized Flow Patterns of Wall Jet in Skirt Box

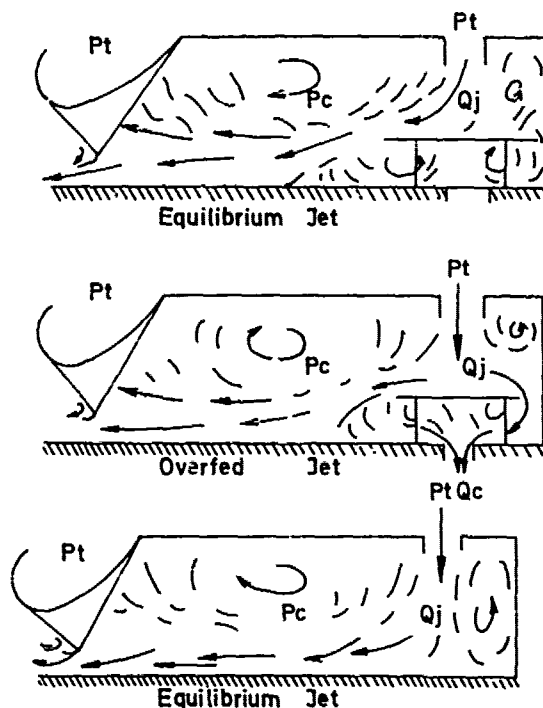


Fig.20. Visualized Flow Patterns of Plenum Chamber in Skirt Box

The flow patterns in the cushion are visualized through the use of silk threads while performing the three state tests of equilibrium, overfed and underfed jet. The visualized flow patterns are shown in fig.19.

During the process of plenum chamber tests, all bag holes were enveloped. Non-equilibrium jet tests were carried out by making use of the nozzles on the top and bottom plates of the plenum chamber. Shown in fig.20 are the visualized flow patterns in cushion for plenum chamber.

3.2 Agreement between Theory and Test Results

As shown in figs.8 and 9, there is quite a good agreement between theory and test results for the non-equilibrium cushion pressure and flow characteristics of wall jet. In the region where overfed is severe and hover height is small, the test pressure values are slightly smaller than the prediction. While in the region where there are much underfed and small hover height, the test flow values are also smaller than the prediction. It is possibly because that the value of K in equation (27) does not vary with overfed or underfed flow. It would be considered to be more appropriate if we had adopted the value of K proportional to escape width b_1 , but it will have the equations (28)(29) become much more complex.

As for plenum chamber, agreement between the test results and theory is also relatively good when the opening area on the top of the chamber was $4 \times \phi 170$, because the obstruction existing in the cushion caused jet to lose all its momentum. But when the area was $2 \times \phi 170$, since the obstruction had been cleared away, so the jet retained its partial momentum until it escaped into the air and thus had a higher cushion pressure. In that case escape coefficient C_e becomes 0.475 from 0.54. The agreement between theory and test results is also very good for non-equilibrium plenum.

4. ANALYSIS OF CUSHION CHARACTERISTICS

4.1 Hovering Performance

From fig.10 it may be seen that, out of the cushion pressure curves of the three cushion systems, i.e. wall jet (for various l/t), plenum chamber (two different types) and peripheral jet, for the same h/t peripheral jet will yield higher cushion pressure. Wall jet gives the similar performance as plenum chamber with the only exception that cushion pressure of plenum chamber drops more quickly with the increase of hover height. Wall jet momentum loss increases with l/t and hence the cushion pressure decreases. Plenum chamber can yield a higher cushion pressure when the jets have not yet lost all its momentum at the region of escape. For the design operating point which is about $\frac{h}{t} = 0.6 \sim 1.2$, $\frac{l}{t} = 6 \sim 12$ for most hovercrafts, both wall jet and plenum chamber

are very much alike, only the pressure curve of plenum chamber is more steep.

Three types of escape coefficient curves are shown in fig.11, of which that of wall jet and peripheral jet are very close. Their escape coefficient decreases with the increase of hover height. For wall jet, the escape coefficient increases slightly with the

increase of $\frac{h}{t}$. The escape coefficient of plenum chamber keeps constant, being 0.475 when the momentum has not totally lost and 0.54 when the momentum is totally lost. Cushion flow requirement is very close for three systems at normal design operating point.

From the curves of non-dimensional lift power shown in fig.12, it is found that peripheral jet has a smallest power requirement, while the power required by both wall jet and plenum chamber at normal design

operating point of $\frac{h}{t}, \frac{1}{t}$ has a little difference. The power requirement of plenum chamber increases most quickly when hover height increases, while that of wall jet increases quickly when $\frac{1}{t}$ increases.

4.2 Motion Performance

The main parameters determining motion performance of hovercraft are the three derivatives m_h, m_p, m_θ derived from the small perturbation of non-equilibrium jet. Generally speaking, jet angle variation due to craft motion is not large and m_θ is also small, therefore, the effect of jet angle may be negligible. According to theoretical analysis, cushion stability is proportional to m_h/m_p , which is just the steepness of the characteristic curves of cushion pressure, and cushion damping is proportional to $1/m_p$.

It may be seen from fig.13 that plenum chamber pressure curve is the steepest and the peripheral jet curve is the flatest. From fig.15 it may be seen that the stability of plenum chamber is the largest because

its m_h/m_p is the maximum, while that of peripheral jet is the smallest because its m_h/m_p is the minimum. Both the variation

of $\frac{1}{t}$ for wall jet and the fact whether the momentum of plenum chamber is totally lost have very slight effect on stability. Within the range of very small hover height, cushion stability increases with hover height, and reaches the maximum value at about $\frac{h}{t} \approx 0.5$ for wall jet, $\frac{h}{t} \approx 0.5 \sim 1.0$ for plenum chamber, and at larger value of $\frac{h}{t}$

for peripheral jet (not shown in the figure), and will then immediately decrease after passing these points. These points are shown in fig.10 as the point of inflexion of the curves.

It may be seen from fig.14 that plenum chamber has a smallest derivative m_p but a maximum damping, while peripheral jet has a maximum m_p but a smallest damping, and wall jet has a intermediate value. The damping for peripheral jet increases rapidly with

the increase of hover height. The damping for plenum chamber and wall jet also

increases when $\frac{h}{t} < 1.0$, but will stop increasing if hover height is still larger. With the increase of $\frac{1}{t}$ the damping for wall jet increases and gradually approaches that of plenum chamber.

ACKNOWLEDGEMENT

The authors wish to acknowledge their thanks to Mr. Guo Zhi-xue, Mr. Zhu Bing-shuan, Mr. Zhou Ling-hua and Mr. Zhu Huei-chiang, of China Ship Research Centre for their technical assistance during the experimental investigations. Thanks are also due to Mr. Yuan Shui-shan, Deputy Chief Naval Architect of Shanghai Ship Design and Research Institute, and Mr. Chang Hin-hua, who have helped with the manuscript and given the authors valuable suggestions.

REFERENCES

1. Chaplin, H.R.: Theory of the Annular Nozzle in Proximity to the Ground, David Taylor Model Basin Report 1373, July 1957.
2. Standton Jones R.: Some Design Problems of Hovercraft, IAS Paper No.61-65, 1961.
3. A.A. West: On the Performance of the Hovercraft Single-Wall Skirt, Aeronautical Quarterly, November 1967.
4. G.H. Elsley and A.J. Devereux: Hovercraft Design and Construction.
5. H. Maeda: Longitudinal Stability Characteristics of Peripheral Jet Type of GEM, Journal of the Society of Aeronautical and Aerospace of Japan, N.172 vol.16, 1968.
6. Hideo Matsuo: A Study of the Peripheral Jet of ACVs, Journal of the Society of Naval Architects of Japan, Vol.127, 1970.
7. Wu Chao-yun: The Turbulent Single Wall Jet of Non-Equivalent Temperature Ejecting into Static Medium, West North Industrial University of China, 1965.
8. Schlichting: Boundary Layer Theory.
9. The Experimental Research of Two Dimensional Hovering Performance of Bag-Finger Skirt, Shanghai Ship Design and Research Institute of China, 1974.
10. The Experimental Research of Dimension Effect and Heave Stability of Bag-Finger Skirt in Hovering, Shanghai Ship Design and Research Institute of China, 1975.
11. Rinichi Murao et al.: A Study of the Two-Dimensional Peripheral Jet Curtain, Journal of the Society of Aeronautical and Aerospace of Japan, 1970

Discussion

F. Murao (Aoyama Gakuin Univ.)

I should be interested to know in what problem of non-equilibrium cushion flow might this simulation model be used most effectively.

I should like to pose some questions and comments.

First, is the experimental coefficient K of the equation (27) found from the direct measurements of jet momentum M_{ea} and M_e , or is it found indirectly as it does not conflict with the results shown in Fig.8?

The flow model of free jet curtain was given in my paper¹⁾ presented in Japan National Congress for Applied Mechanics 1969. Using this flow model one can predict the velocity distribution after the impingement of jet. Although this is for free jet curtain, same concept should be easily used to the wall jet, so that the introducing of experimental coeff. K would be not necessary.

Second, are the experiments planned to simulate the flow model proposed here, or to simulate the actual configuration of bag and skirts? The actual bag and finger skirts are, of course, not two-dimensional but three-dimensional. Furthermore, the jet holes are located as a free jet issued from the hole attaches to the wall. How is the difference considered in this topics?

REFERENCES

- 1) Murao R. et al: A Study of the Two-Dimensional Peripheral Jet Curtain, Proc. 19th Japan National Congress for Applied Mechanics, 1969

D.D. Moran (DTNSRDC)

The authors are to be congratulated on the excellent technical work presented in their paper on "Theoretical and Experimental Investigations of Non-Equilibrium Jet of Air Cushion Vehicles." I was particularly impressed with the advanced analysis of escape flow velocity distributions. The excellent agreement the authors have obtained between predicted discharges and the experimental measurements is unrefutable evidence of the quality of their analytic modeling. I believe the authors are in an excellent position to comment upon a difficult problem which has faced the dynamic performance assessment community. Analytic models of air cushion vehicle dynamic response require a determination of the location of the exact free surface boundary

and the location of the equi-flow line passing under the lip of the skirt. This second flow line marks the division between air which discharges directly from the skirt ducting or boundary cell and the air which discharges from the cushion. Knowledge of the relative discharge between these two sources is vital to the practical determination of the pitch/heave/roll dynamics of an air cushion vehicle in waves.

It is a pleasure to have an opportunity to comment upon the fine research being performed on air cushion vehicles in the Peoples' Republic of China and I look forward to following their continued successes in this field.

H. Matsuo (Kumamoto Univ.)

I would like to compliment the authors for their interesting work in an area that is difficult and challenging. The discussions of the wall jet scheme are particularly useful.

(1) The difference between M_{ea} and M_e (Fig.7) would be due to the existence of the viscous force and the stream-wise pressure gradient. It would seem that the same situation might occur in the flow directing towards the cushion, and M_c is not necessarily equal to $M_j - M_e$. Could the authors comment on the assumption of $M_c = M_j - M_e$?

(2) P_c in eq.(31) is not identical with P_c in eq.(33). In fact, P_c in eq.(33) is the local static pressure around the nozzle exit, and not the cushion pressure. According to my opinion (see Ref.1) below), eq.(33) and (34) shall be replaced by

$$Q_c = Q_j - Q_e,$$

$$P_t \div P_c.$$

REFERENCES

- 1) Hideo Matsuo et al., "Effects of Fan, Ducting and Power Plant Characteristics on the Cushion Stability of Air Cushion Vehicles". Journal of Aircraft (to be published).

Author's Reply

T. Ma (Shanghai Ship Design and Res. Inst.)

The authors are grateful to Prof.

Murao for his remarks and the answers are as follows :

The purpose of this paper is to offer a practical means for the design of hovering performance and the calculation of motion behaviour of ACV with bag-finger skirt. The actual flow model of bag-finger skirt may be very complex, as Prof. Murao said, not two-dimensional but three-dimensional. But because the distance of bag holes from finger walls is very short as compared with finger length, the three-dimensional effect can be neglected. In order to simplify the theory, we would rather adopt the approximation of Mea on the basis of test results, as shown in formula (27), than calculate it theoretically. In this meaning it may also be said that the theory belongs to a semi-experimental method.

According to the constructive proposition of Prof. Murao, the momentum Mea can be derived from the following equations:

$$\begin{cases} V(y)dy = V(z)dz \\ P_c + \frac{1}{2} \rho V^2(y) = \frac{1}{2} \rho V^2(z) \end{cases} \quad (D-1)$$

Substitute formulas (1), (3) and (26) into (D-1), the jet width escaped into the air

$$z(b_1) = \int_0^1 \frac{1}{\sqrt{1 + \frac{P_c}{\frac{\rho}{2} V^2(y)}}} dy \quad (D-2)$$

$$\text{thus } Mea = \int_0^{z(b_1)} \rho Q_e V(z) dz \quad (D-3)$$

By the same means the momentum M_c can also be derived. This is an elaborate model of curved cushion jet curtain without considering viscous diffusion, but it follows that the evident expression (28) and (29) can not be gotten, and the difficulty in analysis of linear perturbation expansion will be brought about.

The authors are sincerely grateful to Dr. Moran, we fully agree with his comments that the viscous diffusion and the location of the escape flow line or the ratio of overfed or underfed flow to total flow have an important effect on the practical determination of the stability and the dynamic response of air cushion vehicles. Equation (30) is the fundamental formula, which has been applied for the calculation of the static and dynamic characteristics of hovercraft with bag-finger skirt. Thanks to Dr. Moran for his encouragement of our research work.

The authors would like to thank Prof. Matsuo for his comments and the answers are as follows:

The momentum towards cushion M_c , theoretically, should be equal to $M_j - M_e$, if neglecting the lost due to the impact on the ground. And the effect of viscous diffusion could not change the total momentum towards cushion M_c .

Regarding the second point, P_t refers to the pressure of bag or ducting, which could not equal to the cushion pressure except that the cushion is totally sealed. We take no account of the unsymmetry of cushion pressure, so equation (31) should be consistent with equation (33).

Session VI

VISCOUS FLOW 1
— BOUNDARY LAYER —

Chairman

Hajime Maruo

Yokohama National University

Yokohama, Japan

Calculation of Viscous-Inviscid Interaction in the Flow Past a Ship Afterbody

Martin Hoekstra and Hoyte C. Raven
Netherlands Ship Model Basin
Wageningen, The Netherlands

ABSTRACT

This paper describes an attempt to improve the prediction of the flow near the stern of a ship by taking into account the interaction between the boundary layer and the external, inviscid flow. An iterative coupling procedure is used, based on the surface transpiration method. Five iterations have been made with strong underrelaxation in the first iterations. Although the results give in general an improvement of the flow prediction, the iteration procedure diverges close to the stern due to a non-local reaction of the boundary layer on a change in the potential flow. This suggests that the use of a simultaneous solution technique for the viscous and inviscid regions may be the only practical way to deal with the interaction in the flow past a ship afterbody.

NOMENCLATURE

h_1, h_2	metric coefficients of x, y, z coordinate system
i	iteration index
L	ship length
\bar{n}	unit normal vector
u, v, w	components of \bar{v} in x, y, z direction respectively
\bar{v}	velocity vector
v_S	ship speed
v_x	$= (v_x)_S - \delta(\partial v_p / \partial y)$
X	Cartesian coordinate in longitudinal direction ($X=0$ at the bow, positive at the stern)
x, y, z	curvilinear, body-fitted coordinates
α	underrelaxation factor
δ	boundary-layer thickness
δ_1	displacement thickness of streamwise velocity profile
Δ	indicates a change between two

successive iterations.

Subscripts:

p	refers to potential flow
b	refers to boundary-layer flow
H	refers to the hull surface
S	refers to the outer edge of the viscous-flow region.

1. INTRODUCTION

Boundary-layer computation techniques are now being widely applied to the flow past a ship. Successful predictions have been made of the flow over a large part of the hull, but boundary-layer calculations usually fail to give sufficient accuracy in the prediction of the stern flow. This failure is due partly to the inadequacy of the thin shear layer approximations and partly to neglect of the interaction between the boundary layer and the external inviscid flow. A remedy of the failure is to be found in avoiding one or both of these simplifications.

The implications of abandoning the thin shear layer approximations are considerable:

- (i) we can no longer use the shell-geometry concept, i.e. the assumption that geometrical coefficients in the equations to be solved are independent of y , the coordinate normal to the hull. Instead a complicated, probably non-orthogonal, curvilinear coordinate system has to be adopted and at every mesh point of the computational grid the geometrical coefficients must be determined.
- (ii) we have to solve an extra equation, viz. the y -momentum equation and the total set of equations becomes of elliptic nature which implies a considerable complication of the

solution technique and requires an increase of storage capacity.

- (iii) we have to reconsider the turbulence modelling in view of the role played by extra rates of strain.

The interaction between the boundary layer and the external inviscid flow (or, in short, viscous-inviscid interaction) can be incorporated in various ways. One way is the simultaneous computation of both viscous and inviscid flow. Flow fields in which extensive separation occurs seem to demand such an approach but in many other cases the simpler method of the alternate computation of boundary layer and inviscid flow suffices and is more attractive from a viewpoint of computational economy. The simplest forms of this iterative technique are straightforward because available computer codes need only be applied consecutively.

In view of the relative simplicity of taking into account the viscous-inviscid interaction by an iterative procedure it seems natural to investigate first to what extent the stern flow calculation can be improved by such an interaction procedure alone.

In the literature some practical information on the effect of viscous-inviscid interaction is available. The subject has recently attracted many researchers in the aeronautical field (see Refs 1 and 2 for reviews). Various iterative schemes have been applied but most of the work is related to two-dimensional or infinite-swept-wing flows. Also for bodies of revolution studies on viscous-inviscid interaction have been made (e.g. Refs 3, 4). But cases in which the external flow is not only displaced outwards by the boundary layer but also sideways, as can happen in general three-dimensional flows, have received comparatively little attention.

For ship-like forms only three papers are known to the authors to deal with viscous-inviscid interaction. Hatano and Hotta (Ref. 5) applied a rudimentary form of Lighthill's equivalent-source method to an Inuid-model; the strength of the added sources was taken constant in girthwise direction. Larsson (Ref. 6) made a similar exercise for a sailing yacht. Finally Nagamatsu (Ref. 7) presented results of calculations with and without viscous-inviscid interaction for two ship hulls. Unfortunately the information about the calculation method and the comments on the results were very brief indeed. In all three papers only one iteration was made.

We concluded that the existing literature provides insufficient information about the relative importance of viscous-inviscid interaction in 3-D flows and the applicability of an iterative procedure to calculate it. In this paper, therefore, a case-study of viscous-inviscid interaction is reported, supplying more information on the subject, specifically with regard to ships.

2. THE VISCOUS-INVISCID INTERACTION PROCEDURE

The Navier-Stokes equations for viscous, incompressible flow are generally accepted to give an adequate description of the complete flow field around a ship. But as yet these equations are intractable when applied to the ship-flow problem. Simplifications have therefore been introduced such as time-averaging, adoption of a turbulence model and the assumption of the spreading of the vorticity, generated at the hull surface, being confined to a layer of relatively small thickness. The latter assumption has led to the division of the flow field into two regions each with its own mathematical description of the flow, viz. the boundary layer + wake (BLW in Fig. 1) and the external potential flow (domain P in Fig. 1).

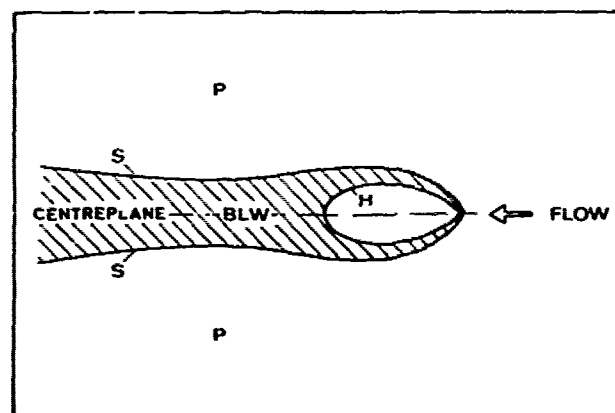


Fig. 1. Schematic flow field representation.

In the conventional computational approach, which relies on the application of matched asymptotic expansions, the flow field in the outer region is calculated in absence of BLW under the condition of zero normal velocity at the hull surface. The resulting tangential velocity at the hull surface is used as an outer-edge boundary condition in the subsequent boundary-layer calculation. Thus, although the boundary-layer development depends on the external flow, the reverse is not true: there is no interaction between the two flow regions.

We might improve the flow prediction by coupling the inner and the outer flow in an exact sense, i.e. by trying to find solutions in the inner and the outer region such that all velocity components are continuous at the common boundary S (Fig. 1). This coupling can be accomplished by the iterative calculation of the inner and outer flow fields which are now mutually dependent through their boundary conditions. Starting point is the calculation of the potential flow in P with boundary condition

$\bar{v}_b \cdot \bar{n}$ at S for the normal velocity, where \bar{v}_b is an initial guess of the velocity field in BLW. In absence of a free surface the solution (the velocity field \bar{v}_p) can be represented by a source distribution on S. Next the boundary layer is calculated with $\bar{n} \times (\bar{v}_p \times \bar{n})$ as a boundary condition for the tangential velocity at S. The results will provide a new value for $\bar{v}_b \cdot \bar{n}$ at S and the calculations are repeated until $\bar{v}_p = \bar{v}_b$ at S. The changes in the flow due to this coupling process are denoted as viscous-inviscid interaction.

There arises a problem, however. The surface S, the outer boundary of BLW, is changing in the course of the iteration process. So, the potential-flow calculation requires at each iteration step the determination of a large matrix of influence coefficients, which leads to a prohibitive increase of computation time.

One can avoid this problem in two ways. The surface S can be chosen well outside the boundary layer as a fixed surface, such that there is no chance of the boundary layer growing beyond S. The other possibility is to translate the boundary condition $\bar{v}_b \cdot \bar{n}$ at S to an equivalent boundary condition at the hull surface H.

In this paper we apply the second possibility; the first is hard to use in conjunction with the shell-geometry concept of boundary-layer theory. The transfer of the boundary condition to the hull surface proceeds as follows. We assume a fictitious potential flow in BLW. Applying thin shear layer approximations to the condition of irrotationality for this flow leads to

$$\frac{\partial u}{\partial y} = \frac{\partial w}{\partial y} = 0 \quad (1)$$

where we have used in the notation the body-fitted boundary-layer coordinates x, y, z . In the same coordinate system mass conservation yields

$$\frac{\partial v}{\partial y} = -\frac{1}{h_1 h_3} \left(\frac{\partial h_3 u}{\partial x} + \frac{\partial h_1 w}{\partial z} \right) \quad (2)$$

which is independent of y in view of (1). Therefore

$$\begin{aligned} (\bar{v}_b \cdot \bar{n})_S - (\bar{v}_p \cdot \bar{n})_H &= (v_b)_S - (v_p)_H = \\ &= \int_0^{\delta} \frac{\partial v}{\partial y} dy \end{aligned} \quad (3)$$

is easily integrated to yield

$$\begin{aligned} (v_p)_H &= (v_b)_S - \delta \left(\frac{\partial v}{\partial y} \right)_H = \\ &= (v_b)_S + \delta \left(\frac{1}{h_1 h_3} \left(\frac{\partial h_3 u}{\partial x} + \frac{\partial h_1 w}{\partial z} \right) \right)_H \end{aligned} \quad (4)$$

in which δ is the boundary-layer thickness.

What we have obtained now is a procedure in which we calculate alternately

- (i) the potential flow in P+BLW with a boundary condition on the hull surface H according to (4)
- (ii) the boundary layer in BLW with a boundary condition at S obtained from the velocities at the hull surface calculated in step (i), using (1).

We have applied this procedure to one of the three Ro-Ro vessels for which comparative boundary-layer calculations have been made earlier (Ref. 8). Before the results of this application will be presented in Section 4, a brief account is given of the calculation methods for the viscous and inviscid flows and their coupling in Section 3. We finish this section with the following comments:

—The adopted iterative procedure corresponds with Lighthill's equivalent source method (Ref. 9). The only difference is that Lighthill suggested a direct formula for the source strength which neglects the influence of the sources upon each other, whereas we start from a normal-velocity boundary condition and solve the Neumann problem for the velocity potential properly.

—Perturbation theory also gives a solution of the above kind when a first-order boundary-layer calculation is combined with a second-order potential flow (Ref. 10). Only one iteration is involved since perturbation theory provides equations and matching conditions to give a pertinent solution of the problem; it does not aim at an exact coupling of the two flows. We shall comment on its use later in section 4.

—According to available literature (e.g. Ref. 1, 2, 3, 11) the interactive procedure must preferably be underrelaxed to improve the convergence or to avoid divergence. So, instead of using (4) we should use

$$(v_p)^{i+1}_H = (v_p)^i_H + \alpha (dv)^i \quad (5)$$

in which i is the iteration index, α is the underrelaxation factor and dv is given by

$$(dv)^i = (v_b)^i_S - \left(\delta \frac{\partial v}{\partial y} \right)^i_H - (v_p)^i_H \quad (6)$$

A commonly used value for α is ca. 0.65. With $\alpha=1.0$ we obtain (4) again.

—The transfer of the boundary condition at S to the hull surface H applies to that part of S formed by the edge of the boundary layer. However, the part of S related to the edge of the wake transfers to the centreplane. The potential flow representation in viscous-inviscid interaction computations requires then in general also sources at the centreplane in the wake of the ship. In this paper these sources are neglected; the determination of their strengths would require a continuation of the boundary-layer calculation into the wake, which we were not able to perform.

—Of course a viscous-inviscid interactive procedure is not restricted to the use of a first-order boundary-layer method for the region BLW. A more sophisticated method might be used as well, provided that (1) and (4) are modified accordingly.

3. DESCRIPTION OF CALCULATION MODULES

From the preceding section the calculation procedure appeared to consist of an iterative application of calculation methods for potential flow and boundary-layer flow respectively. In this section a brief description will be given of the main features of these two calculation modules as well as of the module which couples them.

3.1. Potential Flow

The potential flow calculations in this paper have been made with the Hess & Smith source-panel method (Ref. 12). Since the method is well-known and well-documented it suffices here to say that it is based on a flow representation by a discretised source distribution on the hull surface. The strength of the sources is found from the boundary condition for the normal velocity at the hull surface.

In the present calculations use has been made of three symmetry planes. The centreplane is a genuine symmetry plane and so is the undisturbed free surface in the double-model approach. The midship section plane ($X/L=0.5$) on the other hand is not a true symmetry plane. It was nevertheless used as such* because

-we are interested here in the stern flow only

-a symmetry plane doubles the effective number of source elements and thus allows a more detailed body representation at the same computation time.

-the approximate representation of the forebody by the afterbody does not significantly affect the accuracy of the flow prediction at the stern.

In the present application about 800 source panels were used for one half of the afterbody, giving about 6400 panels for the complete double model.

3.2. Boundary-Layer Flow

In the boundary-layer computation method the first-order, 3-D boundary-layer equations are solved in a body-fitted, orthogonal coordinate system. The method of solution belongs to the class of differential methods. Two finite-difference schemes are employed, viz. the Crank-Nicolson scheme and the Krause "zig-zag" scheme. Both are implicit and unconditionally stable in y-direction. In x and z-direction they are explicit and where necessary the step-size in x-direction is reduced to meet the Courant-Friedrichs-Lewy condition. The turbulent shear stresses are calculated

*Incidentally it is noticed that the $X/L=0.5$ plane is a symmetry plane in geometrical sense (positioning of source panels) only. It is an anti-symmetry plane for the source strengths: a source at the afterbody is complemented by a sink at the forebody and vice versa.

in accordance with the isotropic-eddy-viscosity hypothesis. The eddy viscosity is determined with a two-equation turbulence model ($k-k_l$, Ng-Spalding, Ref. 13). For more information the reader is referred to Refs 8 and 14.

The computation domain for the present boundary-layer calculations covered the region $0.55 < x < 0.95$. Within that domain we marched about 100 steps in x-direction, while the number of mesh points in y and z-direction was 40 and 28 respectively.

3.3. Coupling Module

A third module is required to link the two flow calculations and to control the iteration process. In this module the relevant output of the boundary-layer program is recast into a form suitable for input to the potential-flow program. The x-steps in the boundary-layer calculations were chosen such as to conform with a column of centroids of source panels (which is approximately a line $x=\text{constant}$), so one-dimensional interpolation sufficed to transfer the normal-velocity data from boundary-layer grid points to centroids of source panels. We used linear interpolation. The new value of $(v_p)_H$ at the j^{th} source element was determined by substituting for the variables in (5) and (6) their local values. For those source panels located outside the domain of the boundary-layer calculations $(v_p)_H$ was guessed: over some distance downstream of the domain it was found by extrapolation of the data calculated within the domain and at the hull surface above the propeller $(v_p)_H$ was put zero.

The outer-edge boundary condition for the boundary-layer calculation was obtained with two-dimensional spline interpolation in the output of the potential-flow program.

4. RESULTS AND DISCUSSION

The results to be presented were obtained for a Reynolds number based on ship length and advance speed of $Rn=1.07 \times 10^7$. We started with the data obtained in Ref. 8 with the conventional approach: a potential flow calculation with $v_n=0$ at the hull surface and the subsequent boundary-layer calculation. Where the latter broke down a guess had to be made of the normal velocity.

Our initial choice of the value of the underrelaxation factor α , taken equal in the whole computation domain, was $\alpha=0.5$ in the first iteration, rather low because of the complex nature of the flow. In Fig. 2 the distribution of $(V_p)_S - \delta(\partial v_p / \partial y)$ (which we shall denote as v_{Σ} henceforth) obtained in the first iteration is compared with the original values at a station near $X/L=0.8$. What was originally a maximum has become a minimum now and two new peaks appear, of which one is higher than the original peak. Apparently the underrelaxation factor is still too great.

We recall: perturbation theory indicates that the result of the first

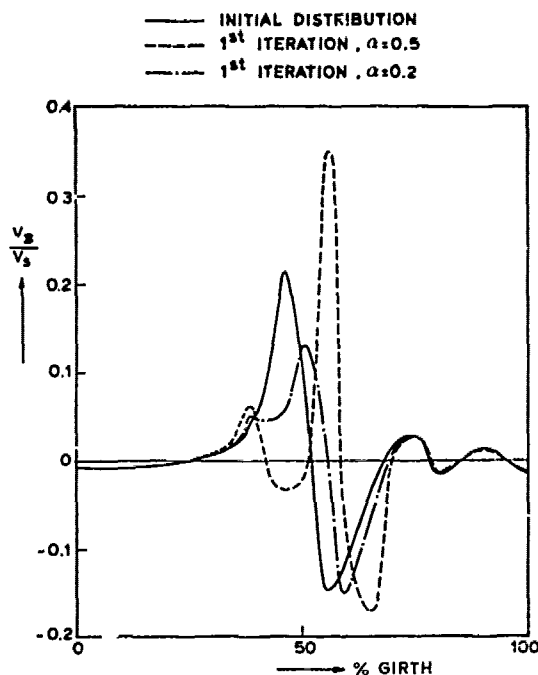


Fig. 2. Influence of relaxation factor on normal velocity distribution, $X/L=0.80$

iteration with $\alpha=1.0$ (!) should yield an improved solution. It is evidently inappropriate when it is applied to a case where δ is not really small as on the present ship. Considering our results, it is surprising that Nagamatsu (Ref. 7), who applied this single-iteration process without underrelaxation with apparent success to two ships, did not experience anomalies. A detailed comparison of his calculation method with ours and of the ways in which the two methods were applied is needed to reveal the reason for that.

The results obtained with $\alpha=0.5$ were rejected and we proceeded with a lower value for α and an additional reduction of the peaks:

$$(v_p)_H^{i+1} = (v_p)_H^i + 0.2(dv)^i(1-2|dv|^i) \quad (7)$$

where dv is again given by (6). We made five iterations, increasing α to 0.4 in the fourth iteration and using in the last iteration values for α which varied over the computation domain ($0.4 < \alpha < 0.8$) to obtain as far as possible a converged state.

In the forward part of the calculation domain ($0.55 < X/L < 0.75$), where the interaction is weak, full convergence was obtained without trouble. As a matter of fact it could have been obtained with fewer iterations than five. Fig. 3 gives some results at $X/L=0.74$. The v_{*} distribution is primarily changed in the region where it shows a typical maximum-minimum pattern. The extremes are reduced to about half their original value and the maximum of the displacement thickness δ_1 has slightly decreased.

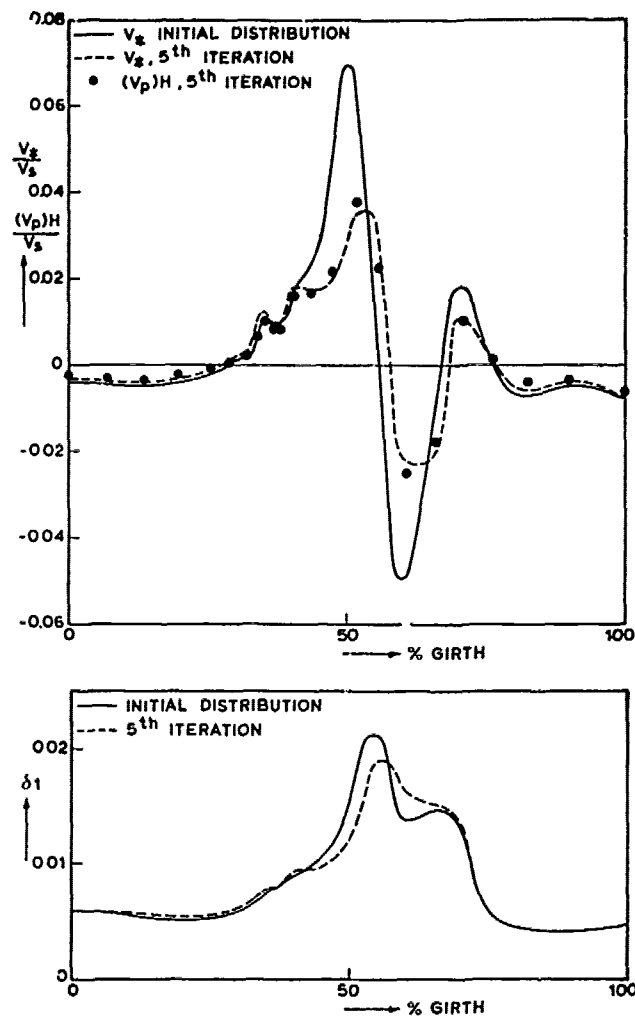


Fig. 3. Distributions of normal velocity and displacement thickness, $X/L=0.74$.

Further aft, around $X/L=0.8$, some discrepancies between $(v_p)_H$ and v_{*} remained after the fifth iteration. These discrepancies could not be removed: the resolution obtained with the girthwise source panel distribution and the finite-difference grid was insufficient. Results at $X/L=0.8$ are given in Fig. 4. We notice the shift of the δ_1 -maximum.

Still closer to the stern the iteration process diverged; especially the minimum value of v_{*} decreased more rapidly than the associated $(v_p)_H$. We shall return to this divergence in a while, but first some additional results will be presented. Fig. 5 shows the potential flow streamlines on the hull surface without interaction and the corresponding lines with interaction (determined by disregarding the normal velocity at the hull surface which causes that the hull surface is not a stream surface actually).

The results of a paint-flow test, visualizing the limiting streamlines, are the only data available for an experimental verification of the calculated results. A comparison of the measured and calculated

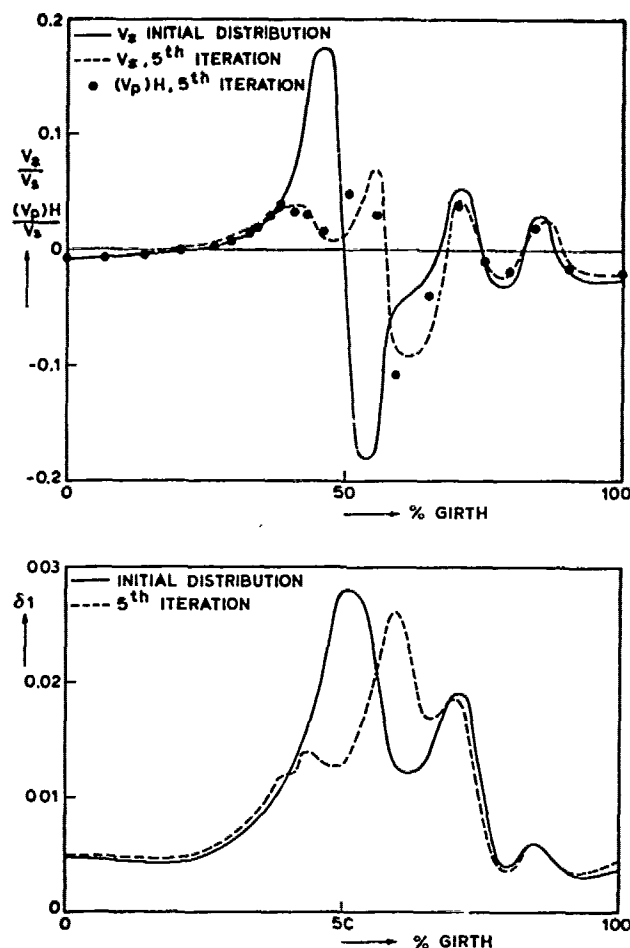


Fig. 4. Distributions of normal velocity and displacement thickness, $X/L=0.8$.

direction of the limiting streamlines is made in Fig. 6. The figure gives computed results with and without viscous-inviscid interaction. The shift in the position of maximum crossflow convergence, corresponding with the earlier-mentioned shift of the δ_1 -maximum and calculated as an effect of viscous-inviscid interaction, leads to a better correspondence between measurements and calculations up to $X/L \approx 0.85$. Further aft the correlation remains poor. In this region the iteration process diverged and it is appropriate to consider this divergence more closely now.

The iteration process diverges when

$$|(\Delta v)^{i+1}| > |(\Delta v)^i| \quad (8)$$

Suppose for convenience that both $(\Delta v)^{i+1}$ and $(\Delta v)^i$ are positive (when $(\Delta v)^{i+1}$ and $(\Delta v)^i$ are both negative the analysis proceeds analogously; opposite signs of $(\Delta v)^{i+1}$ and $(\Delta v)^i$ can be avoided by a suitable choice of the value of α). By substitution of (6) in (8) we obtain

$$\Delta v_{\star} > \Delta(v_p)_H \quad (9)$$

where Δ indicates the change between two successive iterations: $\Delta(\) = (\)^{i+1} - (\)^i$. The velocity v_{\star} is a complicated, non-linear function of the $(v_p)_H$ distribution. But following Brune et al. (Ref. 15) we may linearise this functional relation if $|\Delta(v_p)_H|$ is sufficiently small and after discretising to centroids of source panels may write Δv_{\star} at the j th source element as

$$(\Delta v_{\star})_j = - \sum_{k=1}^N P_{jk} \{ \Delta(v_p)_H \}_k \quad (10)$$

where N is the number of source elements and P_{jk} is the matrix of influence coefficients

$$P_{jk} = \frac{d(v_{\star})_j}{d\{(v_p)_H\}_k}$$

Substitution of (10) in (9) yields that divergence occurs when

$$(1 + P_{jj}) \{ \Delta(v_p)_H \}_j < - \sum_{k=1, k \neq j}^N P_{jk} \{ \Delta(v_p)_H \}_k \quad (11)$$

The minus sign in (10) has been introduced to make $P_{jj} > 0$ in normal circumstances. This can be illustrated with e.g. the well-known fact that the flow in the inner part of the boundary layer reacts on a lateral pressure gradient with much stronger streamline curvature than the external flow. A positive $\{ \Delta(v_p)_H \}_j$ results in a change of the pressure gradients that decreases the streamline convergence of the potential flow; the expected stronger decrease of the streamline convergence in the boundary layer gives a negative $(\Delta v_{\star})_j$, so $P_{jj} > 0$.

A "local" reaction of the boundary layer on a change in the potential flow can be identified with the case that the condition

$$P_{jj} > \sum_{k=1, k \neq j}^N |P_{jk}| \quad (12)$$

is satisfied, i.e. the change of $(v_{\star})_j$ is largely determined by $\Delta(v_p)_H$ at the same position j . Comparing (11) and (12), we see that with such a local reaction divergence is unlikely (although not strictly excluded). Usually $(v_{\star})_j$ and $\{ \Delta(v_p)_H \}_j$ will be of opposite sign, and the difference Δv is quickly reduced. It is this behaviour that is implicitly assumed in the iteration procedure.

When, on the other hand, $\Delta(v_{\star})_j$ is mainly determined by $\Delta(v_p)_H$ at a different position k (large value of $|P_{jk}|$, and a small or even negative P_{jj}), there is a large risk of divergence. Such a non-local reaction can occur when the flow experiences a lateral pressure gradient: as a result of the stronger streamline curvature in the inner part of the boundary layer, the location where the inner-flow streamlines come nearer to each other (j) can then differ from the corresponding location for the outer flow (k). This means a significant

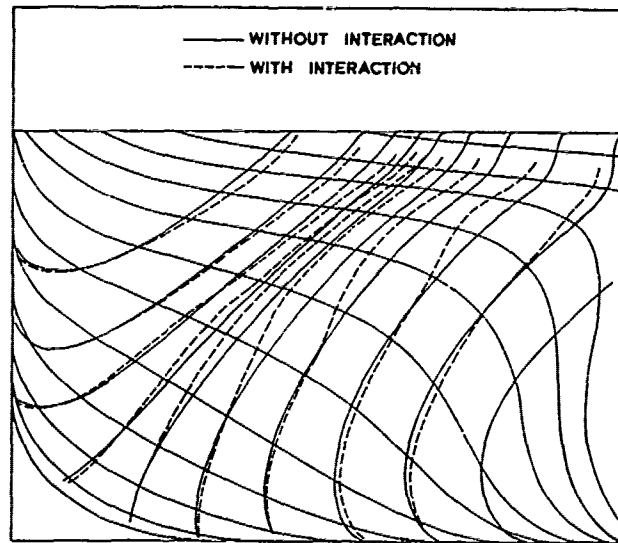


Fig. 5. Potential flow

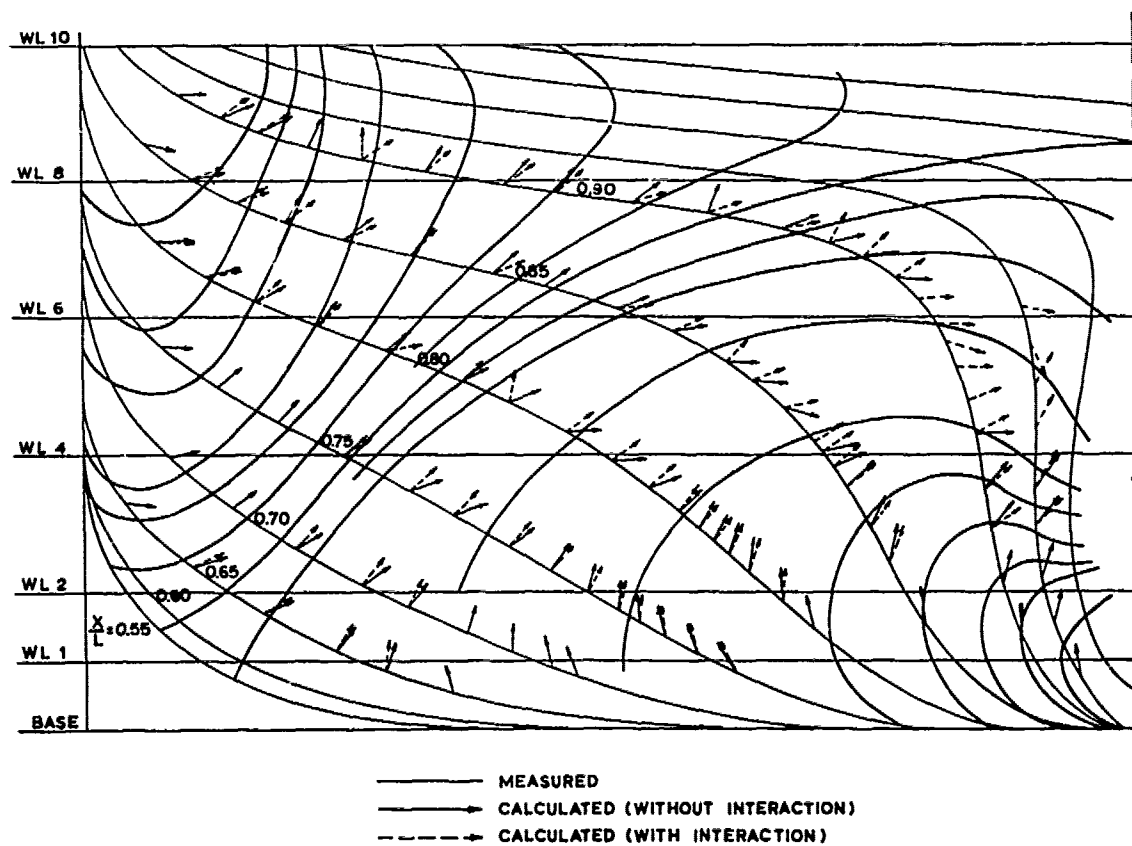


Fig. 6. Wall shear stress directions

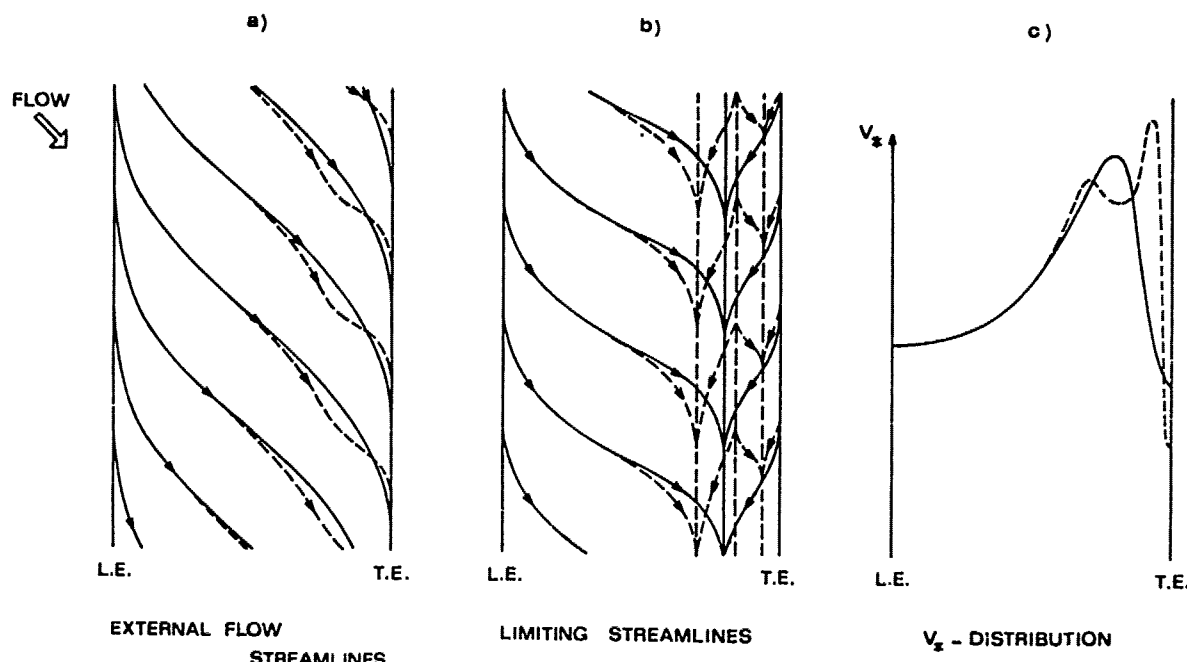


Fig. 7. Flow on a infinite swept cylinder.

positive value of P_{jk} , and opposite signs of $\{\Delta(v_p)_H\}_j$ and $\{\Delta(v_p)_H\}_k$ (as occurring e.g. in the maximum-minimum pattern, Fig. 4) can make the iteration procedure divergent.

One can get some appreciation for what happens by considering the application of the present iterative surface transpiration method to the flow past an infinite swept cylinder (Fig. 7). The original external flow streamlines are schematically drawn by solid lines in Fig. 7a. The limiting streamline pattern indicated by solid lines in Fig. 7b is conceivable as being associated with them. The corresponding v_z -distribution will then resemble that in Fig. 7c (again solid lines): where the inner flow converges*, the boundary layer gives a strong ejection ($(v_p)_s$ large) while the potential flow only slightly converges ($\delta(\partial v_p / \partial y)$ small); where the potential flow converges (at the trailing edge) the inner flow diverges. In the next iteration sinks will be placed at the trailing edge and sources where $v_z > 0$. The changes due to these additional sources and sinks are indicated by the dotted lines in Fig. 7. The potential flow streamlines show a wiggle (compare Fig. 5) and as a result the pattern of limiting streamlines is likely to show some more envelopes. Important now is that the sinks placed at the trailing edge have not succeeded to

bring about a convergence of the inner flow at the trailing edge itself. Instead, the inner flow converges at a position slightly upstream where a new peak of v_z appears. As a result of this the condition (11) may be satisfied and the iteration process diverges.

The question whether this behaviour is necessarily associated with vortex-layer separation, as in the above example, or more generally with the occurrence of strong cross-flow variations cannot be answered before a definition of the start of this type of separation is given. But the possible relation with vortex-layer separation recalls the fact that the boundary-layer equations show singular behaviour at a separation line (Ref. 16, 17). One could speculate that the divergence of the iteration scheme is due to this singular behaviour. To overcome the divergence problem, two possibilities might then be suggested. Either an inverse boundary-layer method (e.g. based on the prescription of the displacement thickness instead of the outer edge velocity) could be adopted, or we could abandon the thin shear layer approximations and solve the y -momentum equation. In both cases the singularity is avoided; the latter method has the additional advantage of being more accurate in flows like the present one: the large values of the normal velocity as calculated make the assumption (1) dubious and, as a consequence the coupling at S inaccurate, such that a solution based on the thin shear layer approximations will represent the interaction effect only qualitatively.

*Streamline convergence /divergence has to be clearly distinguished from convergence/divergence of the iteration process.

However, in our opinion it is not a singularity (which is a result of the boundary-layer approximation) that causes the divergence, but the physical phenomenon that we have called a "non-local reaction". This phenomenon seems to be a characteristic of thick three-dimensional boundary layers, irrespective of their mathematical description. In the case of the infinite swept cylinder, avoiding the singularity in one of the ways mentioned would prevent possible pathological behaviour resulting from that singularity but would not be a guarantee for convergence of the iteration process.

This implies that improvement of the iterative approach can only be obtained by a better iteration control. What we did is applying a strictly local iteration process in which the new value of $(v_p)_H$ is determined by local values of $(v_p)_S$, $\delta(\partial v_p / \partial y)$ and $(v_p)_H$ of the previous iteration. One might think of an iteration process in which $(v_p)_H$ is made dependent on the results in a region surrounding the point of application. We did not attempt such an approach: even if it will be made successful for the present test case, it is hard to imagine that such a process can be fully self-controlled, which reduces its practical value.

Thus, we come to the conclusion that probably the only practical way to deal with viscous-inviscid interaction in a case as the present one is, to abandon the thin shear layer approximation and to solve the viscous and inviscid flow problems simultaneously, instead of alternately. Though simpler and more economical methods like the one applied in the present study may be successful in certain cases, they remain liable to break down, and their applicability to the flow past a ship afterbody will be limited.

5. CONCLUSIONS

In an attempt to improve the prediction of the flow near the stern of a ship at $Rn=1.07 \times 10^7$, an iterative viscous-inviscid interaction procedure has been applied. A calculation method based on first-order boundary-layer theory was used for the viscous flow and a surface singularity method for the inviscid flow. Although the application has been restricted to one hull form, we believe that the conclusions drawn from the present study and summarised below have a wider validity and apply to a lot of merchant-ship hull forms.

This work showed that

1. A viscous-inviscid interaction procedure based on a single iteration without underrelaxation does not give meaningful results for ships at $Rn \times 10^7$.
2. Where the viscous-inviscid interaction procedure can be made to converge, the results show an improvement of the flow prediction.
3. Divergence of the iteration process can, however, occur near the stern due to a non-local reaction of the boundary layer

on a change in the potential flow. It is likely, that any iterative procedure ignoring this non-local reaction will diverge close to the stern, irrespective of the fact whether it is based on the thin shear layer approximations or not.

4. The divergence might be prevented by application of a non-local iteration procedure, but this will be difficult to prescribe. After all, the simultaneous calculation of the viscous and inviscid flow may be the only reliable means to handle the viscous-inviscid interaction problem for ships. Such an approach implies the abandoning of the thin-shear-layer approximations.

ACKNOWLEDGEMENT

This work was sponsored in part by the Netherlands Maritime Institute (Project CTEC 101-79).

REFERENCES

1. Rom, J., "Flows with Strong Interaction Between the Viscous and Inviscid Regions", Proceedings of the International Symposium on Modern Developments in Fluid Dynamics, SIAM, 1977, pp. 285-304.
2. Kordulla, W., "Calculation of Three-Dimensional Transonic Flows", VKI Lecture Series on Computational Fluid Dynamics, 1980.
3. Nakayama, A., Patel, V.C. and Landweber, L., "Flow Interaction Near the Tail of a Body of Revolution", Journal of Fluids Engineering, ASME, Sept. 1976, pp. 531-549.
4. Landweber, L., "Viscid and Inviscid Flows and Their Interactions", Fifth David Taylor Lecture, May 1978.
5. Hatano, S. and Hotta, T., "A Second Order Calculation of Three-dimensional Turbulent Boundary Layer", Naval Architecture and Ocean Engineering, Vol. 15, 1977.
6. Larsson, L., "Theoretical Performance Predictions for the 5.5 m Yacht Antiope", 6th HISWA Symposium on Yacht Architecture, Amsterdam, Sept. 1979.
7. Nagamatsu, T., "Ship Boundary Layer Calculations by a Higher Order Theory", Contribution to SSPA-ITTC Workshop on Ship Boundary Layers, Göteborg, June 1980.
8. Raven, H.C., "Calculation of the Boundary-Layer Flow around Three Ship Afterbodies", Int. Shipbuilding Progress, Vol. 27-305, Jan. 1980.
9. Lighthill, M.J., "On Displacement Thickness", Journal of Fluid Mechanics, Vol. 4-4, 1958.
10. Van Dyke, M., "Higher Approximations in Boundary-layer Theory", Journal of Fluid Mechanics, Vol. 14, 1962.
11. Lemmerman, L.A. and Sonnad, V.R., "Three-Dimensional Viscous-Inviscid Coupling Using Surface Transpiration", Journal of Aircraft, Vol. 16-6, June 1979.
12. Hess, J.L. and Smith, A.M.O., "Calculation of Non-Lifting Potential Flow about Arbitrary Three-Dimensional Bodies", Report No. E.S. 40622, Douglas Aircraft Division, Long Beach, California, March 1962.

13. Ng, K.H. and Spalding, D.B., "Turbulence Model for Boundary Layers near Walls", Physics of Fluids, Vol. 15-1, Jan. 1972.
14. Hoekstra, M., "Boundary-Layer Flow past a Bulbous Ship Bow at Vanishing Froude Number", Symposium on Ship Viscous Resistance, Göteborg, 1978.
15. Brune, G.W., Rubbert, P.E. and Nark, T.C., "A New Approach to Inviscid Flow/Boundary Layer Matching", AIAA paper No. 74-601, 7th Fluid and Plasma Dynamics Conference, Palo Alto, California, June 1974.
16. Williams, J.C., "Incompressible Boundary-Layer Separation", Annual Review of Fluid Dynamics, 1977.
17. Bradshaw, P., "Singularities in Unsteady Boundary Layers", AIAA Journal, Vol. 17-7, July 1979.

Discussion

T. Nagamatsu (MHI)

The authors applied the iterative procedure with underrelaxation method to the calculation of the interaction between the boundary layer and the external inviscid flow, and obtained an improvement of the flow prediction. I would like to express my appreciation to the authors for their presentation of this valuable paper.

The authors pointed out that a detailed comparison between the calculation method of the authors and that of the present discussor is needed in order to make clear the reason why the present discussor's calculations without underrelaxation did not result in anomalies.

I would like to express my view on this matter as follows. In my calculations, the velocity potential including the viscous-inviscid interaction was obtained by solving the Neumann problem under the boundary condition with normal velocity V_* . The initial distributions of the normal velocity V_* for a cargo ship model [Ref.1)] is shown in Fig.A as an example.

It is observed that V_* at $\theta = -60^\circ$ and $\theta = -70^\circ$ varies incredibly near the stern. I thought this is doubtful as physical phenomenon and is due to the unreliable results of the boundary layer calculation near the stern where the numerical breakdown occurs.

V_* values near the stern were, therefore, obtained by the extrapolation method using V_* far the stern. The distribution of the extrapolated values of V_* is also shown in Fig.A.

This intuitive procedure seems to have a similar function as your underrelaxation procedure.

Only one iteration was made in my calculation. In this calculation I inferred that the first iteration represents major part of viscous-inviscid interaction. However, I have not examined yet the validity of my conjecture.

It would be grateful if you could show us the results of the first iteration in Fig.3.

REFERENCES

- 1) Nagamatsu, T., "Calculation of Viscous Pressure Resistance of Ships Based on a Higher Order Boundary Layer Theory", Journal of the Society of Naval Architects of Japan, Vol.147 (1980)

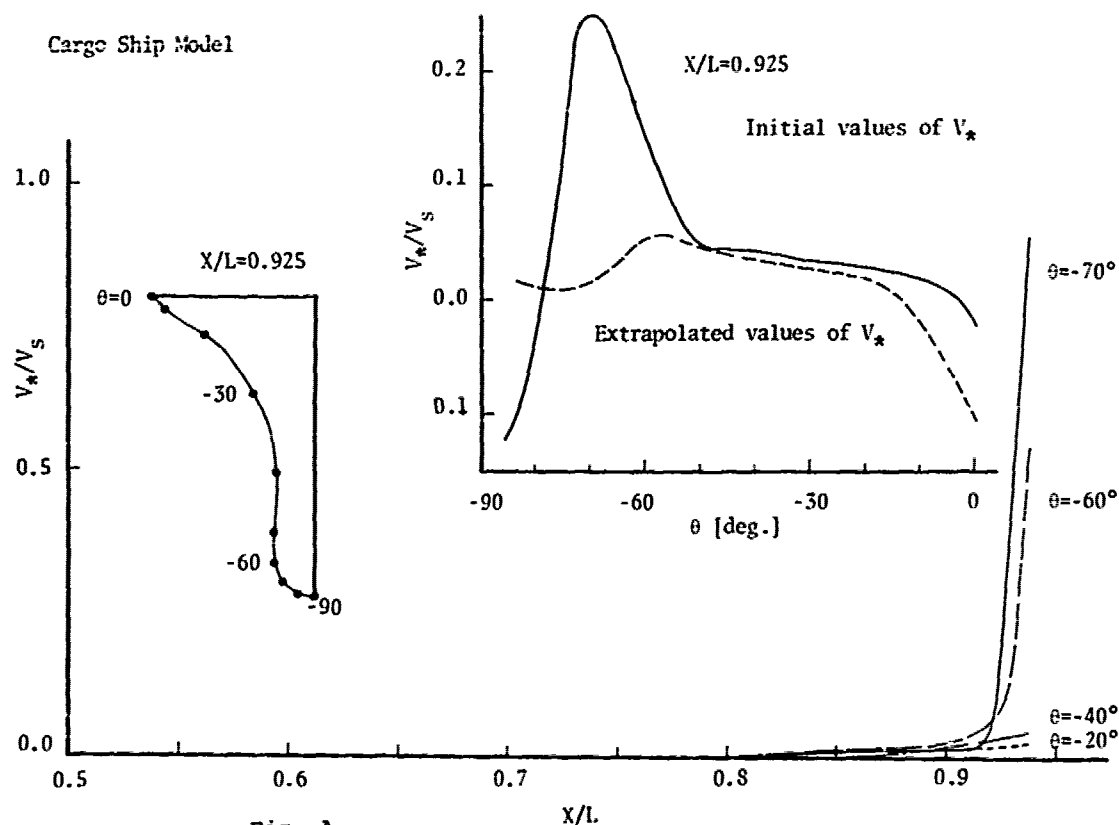


Fig. A

G.E. Gadd (NMI)

The attempt made by the authors to solve the boundary layer equations allowing for the interaction with the external flow is praiseworthy, even though the results obtained so far are disappointing. There are only real signs of improvement upstream of station 0.75. Downstream of this, instabilities in the solution become evident, particularly in the region where the potential flow streamlines converge.

I attempted a very crude assessment of the interaction effect in Ref.1), making some allowance for the fact that where a ridge of locally thickening boundary layer develops, as along a region of streamline convergence, the external flow will tend to flow down the sides of this ridge, modifying the assumed streamline convergence. To incorporate this effect I had to set up an iteration scheme in which the terms in the boundary layer equations involving crosswise velocity derivatives were multiplied by a factor which was initially small but was gradually increased to unity as the iteration proceeded. Would such an idea be useful to the present authors, perhaps in terms of the derivatives parallel to the framelines?

Ref. 1), Gadd, G E, "A simple calculation method for assessing the quality of the viscous flow near a ship's stern" Paper presented at International Symposium on Ship Viscous Resistance, SSPA, Göteborg, Sweden, 1978

V.C. Patel (Univ of Iowa)

I would like to relate two recent experiences we have had at Iowa which have a bearing on the subject of this paper. First, we have continued to develop a method for the solution of the flow over the tail of a body of revolution using a viscous-inviscid matching technique. The convergence of the iterative procedure has been found to depend very critically on the treatment of the viscous flow very near to the tail and in the near wake due to the high sensitivity of this flow to small changes in the pressure field. In view of this, I would like to ask the authors whether the neglect of the wake in their analysis may be responsible for the lack of convergence.

Secondly, we have made measurements in the boundary layer on a body of revolution at 15° incidence (to be published in J. Fluid Mech) which contain many of the features observed on ship sterns, e.g. rapid thickening of the boundary layer in the transverse direction, large and reversing crossflow and vortex formation. The measured surface pressure distributions were compared with potential flow. The substantial differences between these indicate a global ("non-local") influence of the

viscous-inviscid interaction, similar to that observed by the authors, in spite of the fact there was no reversal of the primary flow. I would therefore recommend that future experiments include a detail pressure survey. This would serve two purposes: first, the measured pressure field can be used to assess the accuracy of the viscous-flow calculation methods independently of the interaction with the external flow, and second, enable the evaluation of the procedures used to allow for the influence of the viscous flow on the outer inviscid flow. In short, it is desirable to have a complete set of data to guide the development of viable analytical models.

P. Bradshaw (Imperial College of Sci and Tech)

The authors are to be congratulated on their contribution to a difficult problem. Their identification of "non-local reaction" of the shear layer to a change in potential flow as the main cause of difficulty seems likely to be close to the truth. However lifting airfoils are an example of even stronger non-local reaction and there it is possible to obtain solutions even at incidences fairly close to the stall. The problem with the rapidly-thickening ship boundary layer is probably that the use of the boundary layer equations prevents the propagation of upstream influence within the shear layer so that - to put it crudely - external-flow pressure changes take the shear layer by surprise. Oddly enough, upstream (x-wise) influence is permitted if the y-momentum equation is properly solved. As we have shown (Ref.1)) the iterative solution of the resulting elliptic system of shear layer equations can be combined with the viscous-inviscid matching iteration so that programming complications and increases in run times are not severe: also $p(y)$, being a smoothly-varying function, can be stored from iteration to iteration as the coefficients of a low-order polynomial at each x, z . Furthermore, the geometrical coefficients (metrics) should be included whenever the boundary layer becomes thick whether the y-component momentum equations is being solved or not.

I hope that these comments will encourage the authors to look again at the normal-component momentum equation!

REFERENCES

- 1) Mahgoub, H.E.H. and Bradshaw, P. "Calculation of Turbulent-Inviscid Flow Interactions with Large Normal Pressure Gradients" AIAA.J. 17, 1025 (1979)

A.Y. Odabaşı (BSRA)

The authors presented a very well

written paper which summarises their research at N.S.M.B. on the computation of flow around the aft-ends of ships. Since we had similar research activities at B.S.R.A. for the last six years the remarks I shall make will be of a complementary nature to the views expressed in the paper and I shall also attempt to suggest some explanation and remedies for the problems reported by the authors.

The authors start by stating the limitations imposed on a thin shear layer approximation. If one follows the strict perturbation approximation (ϵ -theoretical approach!) their criticisms are certainly valid. However, the real test for any theoretical approach is their ability to predict the real flow situation and if some of the higher order terms (not all of them) in the transport and closure equations are large enough it is advantageous to retain these terms. In our experience the use of such a pragmatic approach is preferable to the perturbation since the development of a more systematic approach will require the accumulation of detailed experimental data. One such approach is the fairly-thin shear layer approach of Bradshaw 1). The use of this approach for 90° bend 2) and for the flow around the aft-ends of ships 3) demonstrated reasonable success in predicting flow features.

The next point raised by the authors is the compatibility of a matching surface with a shell-geometric coordinate system. They state that they preferred to use a varying boundary layer edge surface at each iteration to be compatible with the shell-geometry concept of boundary layer theory. However, a strict analysis conducted by Wesseling 4) indicates that the only real constraint is the requirement that one of the coordinate lines should be aligned with the body normal due to the semi-invariant nature of the boundary layer equations. Furthermore, it is known in practice small misalignments with the body normal (up to $\sim 30^\circ$) do not produce any significant inaccuracy. Use of polar cylindrical coordinates for laminar and turbulent flow computation around non-axisymmetric bodies are examples of such applications, cf. Ref. 5), 6). Therefore, if the authors would choose an appropriate fixed matching surface some of the difficulties they have encountered might have been avoided.

The authors report a divergence mechanism in their interaction scheme which they call the "non-local reaction", and they interpret it as a physical phenomenon and propose the abandoning of the thin-shear-layer approximation. Although I can agree with their conclusion on the non-local behaviour of interaction it is hard to accept their proposal since it can easily be avoided by a suitable choice of the numerical calculation scheme. Since this is one of the most important conclusions of the paper I shall try to expand

the subject somewhat further to bring the non-local behaviour into a proper context as done in Ref. 7).

In a viscous-inviscid interaction (within the limits of thin-shear-layer theory) one matches the solutions determined in two different regions governed by different equations. Within the boundary layers these equations are parabolic (or hyperbolic depending on the turbulence model) and outside the boundary layer they are elliptic. Therefore, any change in the boundary conditions of the elliptic problem, even when they are local, will influence solution in a neighbourhood of the location of change (theoretically within the entire domain). Furthermore, since the solution of the elliptic problem determines the boundary conditions of the parabolic problem these non-local changes will also produce a non-local change in the boundary layer calculation and alter the solution within the domain of influence of the boundary region where the changes take place. One should therefore expect numerical instabilities if a local procedure is employed to account for the interaction unless the boundary surface is planar and parallel to the main-stream direction.

When an improved shear layer model is used the problem becomes slightly more complicated because now the shear layer equations too become elliptic, cf. Refs. 2), 6). The use of partially-parabolic (or hyperbolic) solution techniques where the normal momentum equation is solved out-of-core and the results are carried upstream at every iteration, can resolve difficulty provided that the newly calculated pressure values are used during the next iterative sweep (Jacobi iteration) instead of the same iteration sweep (Gauss-Seidel iteration).

The authors relate the divergence in their interaction scheme to the presence of either a vortex-layer separation or the occurrence of strong cross-flow variations. Since the Krause integration method, employed by the authors, is unconditionally stable and has successfully been applied for flows with cross-flow reversal, cf. Dwyer et. al. 8), the physical justification of this explanation is highly unlikely. In the light of the previous discussions it is quite possible that the authors fell into one of the unfortunate traps of numerical fluid dynamics.

REFERENCES

- 1) Bradshaw, P. "The Understanding and Prediction of Turbulent Flow", Aeronautical J., Vol. 76, p. 739 (1972)
- 2) Mahgoub, H.E.H. and Bradshaw, P. "Calculation of Turbulent Inviscid Flow Interactions with Large Normal Pressure Gradients", AIAA Journal, Vol. 17, p. 1025 (1979)
- 3) Odabaşı, A.Y. and Şaylan, Ö. "GEMAK-A Method for Calculating the Flow around Aft-End of Ships", 13th Symposium on Naval Hydrodynamics, Tokyo, p. 747 (1980)

4) Wesseling, P. "The Calculation of Incompressible Three-Dimensional Turbulent Boundary Layers, Part 1, Formulation of a System of Equations", National Aerospace Laboratory NLR, The Netherlands, Report AT-69-01

5) Blottner, F.G. and Ellis, M. "Three-Dimensional, Incompressible Boundary Layer on Blunt Bodies, Part 1, Analysis and Results", Sandia Laboratories, Albuquerque, Report SLA-73-0366 (1973)

6) Abdelmeguid, A.M., Markatos, N.C.G., Muraoka, K. and Spalding, D.B., "A Comparison between the Parabolic and Partially Parabolic Solution Procedures for Three-Dimensional Turbulent Flows around Ships' Hulls", Appl. Math. Modelling, Vol. 3, P. 249 (1979)

7) Odabasi, A.Y., "Boundary Layer-Inviscid Flow Matching in Thickening Boundary Layers", BSRA Report WG/PHIVE 42 (1978)

8) Dwyer, D.L., Lewis, C.H. and Gogineni, P.R., "Three-Dimensional Incompressible Boundary Layers on Blunt Bodies Including Effects of Turbulence, Surface Curvature and Heat and Mass Transfer, Part 1, Analysis and Results", Virginia Polytechnic Institute and State University, Report VPI & SU Aero-063 (1977)

Author's Reply

M. Hoekstra and H.C. Raven (NSMB)

We are glad to learn from Mr. Nagamatsu that he did not apply an iteration scheme with $\alpha = 1.0$, actually. His introduction of an intuitive approach is a confirmation of the first conclusion of our paper.

We cannot show results of the first iteration without underrelaxation because we never tried to obtain such results, anticipating them to be inappropriate anyway.

Dr. Gadd suggests to reduce the influence of crosswise derivatives to avoid the divergence of the iteration process. Indeed the crosswise derivatives have a dominant influence and a complete or almost complete deletion of such terms would prevent trouble. However, we expect that on letting these terms gradually appear again the divergence of the iteration process will be an accompanying feature. Nevertheless the suggestion is worth a try. Prof. Patel asks whether the neglect of singularities in the wake may be responsible for the lack of convergence. We simply do not know how important the effect of the wake is in calculations like the present ones (3-D flow). But the difficulties appear already at $X/L = 0.8$ and seem to be governed by transverse gradients. The wake singularities are not particularly close to the trouble region and are expected to have a stronger influence on longitudinal than on transverse

gradients.

We agree with the further comments by Prof. Patel.

Both Prof. Bradshaw and Dr. Odabasi have a different conception of a "non-local reaction" than we have. They associate it with influences carried upstream via the pressure field while we think that the problem involves more than that. Below we shall try to clarify our ideas.

In both Bradshaw's method and ours the pressure field is fixed within one iteration. In our method upstream influences are transmitted only via the external flow (and are equal along a normal to the hull surface) whereas in Bradshaw's method this transfer can take place via the external flow as well as within the shear layer. Bradshaw's arguments thus imply that the possibility of upstream influences within the boundary layer is the essential feature necessary to prevent divergence. If we put a singularity (say a sink) at a point (x_0, z_0) , the external flow will, in our terminology, react locally on it, i.e. the sink will bring about a convergence of the potential flow which is strongest at (x_0, z_0) and weaker in its surroundings. Also the boundary layer reacts on the sink but not necessarily in a similar way; when there is a strong crossflow the maximum convergence of the streamlines within the boundary layer (and thus a high $(v_b)_s$) may occur at another position (x_1, z_1) . The introduction of a thick-boundary-layer method may change the position (x_1, z_1) but there is no reason to suppose that it will let (x_1, z_1) coincide with (x_0, z_0) . In the usual iteration process one attempts to reduce $(v_b)_s - (v_p)_s$ at (x_1, z_1) by adding a source or a sink at (x_1, z_1) - not at (x_0, z_0) ! It appears that not the boundary-layer equations but this iterative method is based on an inadmissible simplification for such cases. We think that this phenomenon simply does not occur in 2-D flows; it is a typical feature of 3-D flows. Inclusion of the y-momentum equation in the set of governing equations will undoubtedly change the values of the required blowing velocities but in our opinion it does not necessarily prevent the phenomenon that the boundary layer flow converges maximally at another position than that of the singularity causing the convergence. We conjecture that even Bradshaw's method would fail in the present case, unless the outer boundary of the computation domain is chosen so far from the body that actually a simultaneous calculation of viscous and inviscid flow is made.

To the further comments by Dr. Odabasi we reply as follows.

Our statements in the introduction on abandoning the thin-shear-layer approximations have no direct bearing on any perturbation approximation. Even a "pragmatic" method that tries to compute a thick-boundary-layer flow will satisfy the three characteristics listed in our paper. Indeed, the example of a pragmatic approach cited by Dr. Odabasi, viz. the Mahgoub/Bradshaw

method, does not use shell geometry, does solve an extra momentum equation and does pay attention to extra rates of strain.

Contrary to what Dr. Odabaşı seems to have read in our paper we do not at all prefer to use a varying boundary-layer edge surface in the iteration process. In the present application on a ship with locally a strong concave curvature the outer edge surface is not uniquely determined when using the shell-geometry concept. We therefore had to transfer the outer edge data to the hull surface. But of course a matching at a non-varying outer boundary, provided that it is well-defined, is to be preferred.

Finally, from the fact that the numeri-

cal integration scheme used is stable, Dr. Odabaşı concludes that the physical explanation given in our paper is unlikely. This argument is not altogether clear to us. Moreover, we must correct Dr. Odabaşı: the Krause scheme is conditionally stable for reverse crossflow. We satisfied the appropriate condition by adaptation of the step size in longitudinal direction. We agree therefore that the divergence of the iteration process is not caused by a numerical instability due to the use of an inappropriate difference scheme. But we never said so in the paper.

We thank all the discussers for their interest in our work.

Calculation of Thick Boundary Layer and Wake of Ships by a Partially Parabolic Method

Kenji Muraoka

Research Institute

Ishikawajima-Harima Heavy Ind. Co. Ltd

Yokohama, Japan

ABSTRACT

A method is described for calculating thick boundary layer and wake of ships on the assumption of Spalding's partially parabolic flow concept and K- ϵ model of turbulence. The governing equations are solved by differential method. Numerical results of turbulent properties, velocity distribution and viscous pressure are shown with experiments for an axisymmetric body and a liner ship model. The turbulent properties around the axisymmetric body can be predicted well. So the K- ϵ model of turbulence is considered to be more useful tool than any other 0- and 1-equation model of turbulence in considering the turbulent properties in the viscous flow. The calculated wake distributions for a liner ship model are qualitatively coincident with experiment. Especially the bilge vortex is seemed to occur. Through these numerical examples the present method is confirmed to be appropriate for the calculation of thick boundary layer and wake of ships.

NOMENCLATURE

Alphabet Symbols

d	; draft of ship
f	; distribution profile of K
g	; distribution profile of ϵ
i, j	; subscripts in Cartesian coordinates
l	; length scale of turbulence
l_m	; mixing length
r_{max}	; maximum radius of axisymmetric body

r_o	; radius of outer boundary
r_s	; radius of ship hull
u, v, w	; velocity components
u_i, u_j	; velocity components of Cartesian coordinates
S	; distance from the leading edge
x_i, x_j	; Cartesian coordinates
x, r, θ	; cylindrical polar coordinates
B	; beam of ship
C_0, C_1, C_2	; proportionality constants
C_B	; block coefficient
C_p	; pressure coefficient $(P - P_o) / \frac{1}{2} \rho v^2$
C_{pa}	; prismatic coefficient of aft body
F, G	; distorted terms in coordinate transformation
G_e, G'_e, G''_e	; production terms in K- and ϵ -equation
$J_{K,j}, J_{\epsilon,j}$; viscous terms of K- and ϵ -equation
K	; turbulent kinetic energy
L	; length of ship
P, P_o	; static pressures
Pr_K, Pr_ϵ	; Prandtl/Schmidt number
Re	; Reynolds Number
S_s	; source terms
V	; uniform flow velocity

Greek Symbols

δ	; boundary layer thickness
ϵ	; K's dissipation rate
γ	; denote $\gamma_0 - \gamma_s$
$\mu_t, \mu_l, \mu_{eff}, \nu$; viscosities
ξ, η, ζ	; distorted cylindrical polar coordinates
ρ	; density
σ	; stress
ϕ	; variable in fluid
ψ	; denote $\pi/2$
μ, μ_k, μ_ϵ	; correspond to viscosities

1. INTRODUCTION

In solving the viscous flow around ships, there are two problems, what kind of approximation for Navier-Stokes equation should be adopted and what kind of turbulent model should be applied. Larsson (1974), Himeno-Tanaka (1976), Okuno (1976) and others chose the thin boundary layer approximation and skin friction formula instead of turbulent model, and solved the flow around ship by integral method. Cebeci et al. (1975) and Raven (1980) did it by differential method. Hoekstra (1980) also solved the flow around the bow in detail by using the thin boundary layer approximation. Although these methods gave good results for the calculation of the flow around the main part of ship hull, it was pointed that the thin boundary layer approximation was not adequate for the flow around the ship stern because in the stern region the boundary layer became thick in comparison with the local radius of curvature of the hull surface.

For the thick boundary layer around ship stern, Nagamatsu (1980) solved the higher order boundary layer equations by using integral method. Soejima (1980) also did it by differential method. These numerical results showed a better agreement with experiment than the numerical results of thin boundary layer approximation. Thick boundary layer approximation is, however, seemed to be insufficient for the calculation of the bilge vortex and the wake behind the stern region.

For the calculation of the flow around and behind ship stern, Hatano et al. (1977) presented a method to utilize vorticity diffusion equation. Mori-Doi (1978) presented the method based on the concept of the matched asymptotic expansion method. On the other hand, Spalding (1975) proposed the partially parabolic flow concept and suggested to apply this

concept with K- ϵ model of turbulence for the flow around the ship stern.

The partially parabolic flow concept is characterized by:

- (1) there exists a predominant direction of flow,
- (2) the diffusion of momentum in that direction is negligible, and
- (3) the pressure is main transmitter of downstream effects.

The Spalding's method is considered to have the following merits:

- (1) 3-dimensional pressure variation can be estimated,
- (2) the recirculating cross flow can be treated, and
- (3) the turbulent properties in the flow can be evaluated.

However, as the method is categorized into the differential method with 2-equation model of turbulence and permits the pressure variation in 3-dimensional direction, the numerical techniques are highly complicated and are taken much more costs. Spalding's method was, for the first time, applied to the internal flow problem by Pratap (1975). Abdelmeguid et al. (1978) tried to apply this method for the flow around a tanker model, but accuracy of calculation was not enough. Muraoka (1979, 1980) refined the numerical techniques of this method through examining the effect of grid numbers and improving the inlet conditions for K and ϵ . But for the calculating the flow around and behind ship stern, the Spalding's method is still on the way of improving and developing its capability.

This paper is concerned of describing the present stage of Spalding's method clearly and searching its possibility. In section 2, the fundamental equations of the partially parabolic flow concept and the K- ϵ model of turbulence are derived. And the boundary conditions and the solution procedure are mentioned. Section 3 deals with the numerical examples. The calculation method is applied to the flow around axisymmetric body and liner ship model, and the validity of the method is examined. At last, the concluding remarks are written in section 4.

2. THEORETICAL BASIS

2.1 Basic Equations

The governing equations for turbulent viscous flow are described in tensor notation as follows:
Continuity Equation:

$$\frac{\partial}{\partial x_j} (\rho u_j) = 0 \quad (1)$$

Momentum Equations:

$$\frac{\partial}{\partial x_j} (\rho u_i u_j) = -\frac{\partial P}{\partial x_i} - \frac{\partial}{\partial x_j} (\sigma_{ij}) , \quad (2)$$

where $u_i, u_j (i, j=1, 2, 3)$ are velocity components in Cartesian coordinates $x_i, x_j (i, j=1, 2, 3)$; P and ρ are the pressure and density, respectively; $\sigma_{ij} (i, j=1, 2, 3)$ are the stresses in the fluid and defined by

$$\sigma_{ij} = -\mu_{eff} \left(\frac{\partial u_j}{\partial x_i} + \frac{\partial u_i}{\partial x_j} \right) , \quad (3)$$

In equation (3), μ_{eff} is effective viscosity and defined by

$$\mu_{eff} = \mu_l + \mu_t = \mu_l + C_0 \cdot \rho \cdot K^2 / \epsilon , \quad (4)$$

where μ_l and μ_t are the laminar and turbulent viscosity, respectively; C_0 is a proportionality constant; K is the turbulent kinetic energy and ϵ is its dissipation rate. The equation for K and ϵ are given as follows:

$$\frac{\partial}{\partial x_j} (\rho K u_j) = -\frac{\partial}{\partial x_j} (J_{K,j}) + G_e'' - \rho \epsilon , \quad (5)$$

$$\begin{aligned} \frac{\partial}{\partial x_j} (\rho \epsilon u_j) = & -\frac{\partial}{\partial x_j} (J_{\epsilon,j}) + C_1 G_e'' \epsilon / K \\ & + C_2 \rho \epsilon^2 / K , \end{aligned} \quad (6)$$

where

$$J_{K,j} = -\left(\frac{\mu_{eff}}{Pr_K}\right) \frac{\partial K}{\partial x_j} , \quad J_{\epsilon,j} = -\left(\frac{\mu_{eff}}{Pr_\epsilon}\right) \frac{\partial \epsilon}{\partial x_j} ,$$

$$G_e'' = \mu_t \left(\frac{\partial u_j}{\partial x_i} + \frac{\partial u_i}{\partial x_j} \right) \frac{\partial u_i}{\partial x_j} .$$

In these equations, Pr_K and Pr_ϵ are Prandtl/Schmidt Numbers; C_1 and C_2 are proportionality constants. The values of C_0, C_1, C_2, Pr_K and Pr_ϵ are shown in Table 1 (Launder and Spalding 1972).

Table 1. Proportionality Constants

C_0	0.09
C_1	1.44
C_2	1.92
Pr_K	1.00
Pr_ϵ	1.23

Here, according to the Spalding's method, we assume that the flow is partially parabolic as follows:

$$(i) \quad \sigma_{i1} \approx 0 , \quad J_{K,1} \approx 0 , \quad J_{\epsilon,1} \approx 0 ,$$

$$\partial/\partial x_1 \approx 0 \quad \text{in } G_e'' .$$

(ii) terms involving $\partial u_2/\partial x_1$ and $\partial u_3/\partial x_1$ are neglected in the viscous terms of the x_1 -momentum equation, where subscripts 1 denotes the main flow direction.

Then, the equations (1) through (6) become:

$$\frac{\partial}{\partial x_1} (\rho u_1) + \frac{\partial}{\partial x_2} (\rho u_2) + \frac{\partial}{\partial x_3} (\rho u_3) = 0 , \quad (7)$$

$$\left. \begin{aligned} & \frac{\partial}{\partial x_1} (\rho u_1 u_1) + \frac{\partial}{\partial x_2} (\rho u_1 u_2) + \frac{\partial}{\partial x_3} (\rho u_1 u_3) \\ & = -\frac{\partial P}{\partial x_1} - \frac{\partial}{\partial x_2} (\sigma_{12}) - \frac{\partial}{\partial x_3} (\sigma_{13}) , \\ & \frac{\partial}{\partial x_1} (\rho u_2 u_1) + \frac{\partial}{\partial x_2} (\rho u_2 u_2) + \frac{\partial}{\partial x_3} (\rho u_2 u_3) \\ & = -\frac{\partial P}{\partial x_2} - \frac{\partial}{\partial x_2} (\sigma_{22}) - \frac{\partial}{\partial x_3} (\sigma_{23}) , \\ & \frac{\partial}{\partial x_1} (\rho u_3 u_1) + \frac{\partial}{\partial x_2} (\rho u_3 u_2) + \frac{\partial}{\partial x_3} (\rho u_3 u_3) \\ & = -\frac{\partial P}{\partial x_3} - \frac{\partial}{\partial x_2} (\sigma_{32}) - \frac{\partial}{\partial x_3} (\sigma_{33}) , \end{aligned} \right\} \quad (8)$$

where

$$\sigma_{12} = -\mu_{eff} \left(\frac{\partial u_1}{\partial x_2} \right) , \quad \sigma_{13} = -\mu_{eff} \left(\frac{\partial u_1}{\partial x_3} \right) ,$$

$$\sigma_{22} = -\mu_{eff} \left(\frac{\partial u_2}{\partial x_2} + \frac{\partial u_2}{\partial x_2} \right) , \quad \sigma_{23} = -\mu_{eff} \left(\frac{\partial u_3}{\partial x_2} + \frac{\partial u_2}{\partial x_3} \right) ,$$

$$\sigma_{32} = -\mu_{eff} \left(\frac{\partial u_2}{\partial x_3} + \frac{\partial u_3}{\partial x_2} \right) , \quad \sigma_{33} = -\mu_{eff} \left(\frac{\partial u_3}{\partial x_3} + \frac{\partial u_3}{\partial x_3} \right) .$$

$$\begin{aligned} & \frac{\partial}{\partial x_1} (\rho K u_1) + \frac{\partial}{\partial x_2} (\rho K u_2) + \frac{\partial}{\partial x_3} (\rho K u_3) \\ & = \frac{\partial}{\partial x_2} \left(\frac{\mu_{eff}}{Pr_K} \frac{\partial K}{\partial x_2} \right) + \frac{\partial}{\partial x_3} \left(\frac{\mu_{eff}}{Pr_K} \frac{\partial K}{\partial x_3} \right) + G_e' - \rho \epsilon , \end{aligned} \quad (9)$$

$$\begin{aligned} & \frac{\partial}{\partial x_1} (\rho \epsilon u_1) + \frac{\partial}{\partial x_2} (\rho \epsilon u_2) + \frac{\partial}{\partial x_3} (\rho \epsilon u_3) \\ & = \frac{\partial}{\partial x_2} \left(\frac{\mu_{eff}}{Pr_\epsilon} \frac{\partial \epsilon}{\partial x_2} \right) + \frac{\partial}{\partial x_3} \left(\frac{\mu_{eff}}{Pr_\epsilon} \frac{\partial \epsilon}{\partial x_3} \right) \end{aligned}$$

$$+C_1 G_e' \varepsilon / K - C_2 \rho \varepsilon^2 / K, \quad (10)$$

where

$$G_e' = \mu_t \left[2 \left\{ \left(\frac{\partial u_2}{\partial x_2} \right)^2 + \left(\frac{\partial u_3}{\partial x_3} \right)^2 \right\} + \left(\frac{\partial u_2}{\partial x_3} + \frac{\partial u_3}{\partial x_2} \right)^2 + \left(\frac{\partial u_4}{\partial x_2} \right)^2 + \left(\frac{\partial u_4}{\partial x_3} \right)^2 \right]$$

2.2 Equations for Ship

We assume that the ship moves straight with constant speed V . It is taken a cylindrical polar coordinate system (x, r, θ) fixed to the ship, where x axis is positive towards the stern. $\theta=0$ coincides with the undisturbed water plane and $\theta=\pi/2$ coincides with the center vertical plane as indicated in Fig. 1. The flow around ship is assumed to be symmetric with respect to the center plane and the ship wave on the free surface to be negligible.

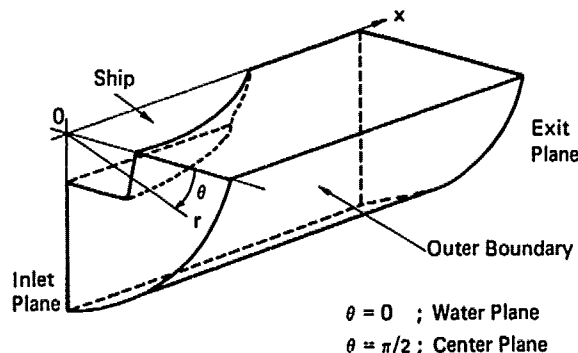


Fig. 1 Coordinate system

The Cartesian coordinate system (x_1, x_2, x_3) in the previous section is transformed into the cylindrical polar coordinate system (x, r, θ) by the following equations:

$$\begin{aligned} x &= x_1, \\ r &= \sqrt{x_2^2 + x_3^2}, \\ \theta &= \tan^{-1} \left(\frac{x_3}{x_2} \right) \end{aligned} \quad (11)$$

Furthermore, the cylindrical polar coordinate system (x, r, θ) is transformed into the distorted cylindrical polar coordinate system (ξ, η, ζ) by the following equations:

$$\xi = x, \quad \left. \begin{aligned} \eta &= r - r_s \\ \zeta &= \theta / \pi/2 \end{aligned} \right\} \quad (12)$$

where $r=r_s(x, \theta)$ and $r=r_o(x, \theta)$ denote the radius of ship hull and the outer boundary, respectively.

Then, the following transformations are derived:

$$\begin{aligned} \frac{\partial}{\partial x} &= \frac{\partial}{\partial \xi} - \frac{F}{\lambda} \frac{\partial}{\partial \eta} \\ \frac{\partial}{\partial r} &= \frac{1}{\lambda} \frac{\partial}{\partial \eta} \\ \frac{\partial}{\partial \theta} &= \frac{1}{\psi} \frac{\partial}{\partial \zeta} - \frac{r G}{\lambda} \frac{\partial}{\partial \eta} \end{aligned} \quad (13)$$

where

$$\begin{aligned} F &= \left\{ \frac{\partial r_s}{\partial x} + \eta \frac{\partial (r_o - r_s)}{\partial x} \right\}, \\ G &= \frac{1}{r} \left\{ \frac{\partial r_s}{\partial \theta} + \eta \frac{\partial (r_o - r_s)}{\partial \theta} \right\}, \\ \lambda &\equiv r_o - r_s, \quad \psi = \pi/2. \end{aligned}$$

By using transformations (11), (12) and (13), the basic equations (7) through (10) are summarized in the following form:

$$\begin{aligned} \rho \left[\frac{1}{r\lambda} \frac{\partial}{\partial \xi} (r\lambda u \phi) + \frac{1}{r\lambda} \frac{\partial}{\partial \eta} \{ r(v - uF - wG) \phi \} \right. \\ \left. + \frac{1}{r\lambda\psi} \frac{\partial}{\partial \zeta} (\lambda w \phi) \right] \\ = \frac{1}{r\lambda} \frac{\partial}{\partial \eta} \left\{ \frac{\rho \phi}{\lambda} r(1 + G^2) \frac{\partial \phi}{\partial \eta} \right\} \\ + \frac{1}{r\lambda\psi} \frac{\partial}{\partial \zeta} \left(\frac{\rho \phi}{r\psi} \lambda \frac{\partial \phi}{\partial \zeta} \right) + S \phi, \quad (14) \end{aligned}$$

where, u, v, w are the velocity components in the x, r, θ -directions; $\phi, \Gamma_\phi, S_\phi$ denote flow variables, viscosity and additional sources or sinks of the corresponding property which is being transported. For continuity equation:

$$\phi = 1, \quad \Gamma_\phi = S_\phi = 0.$$

For u -momentum equation:

$$\begin{aligned} \phi = u, \quad \Gamma_\phi = \mu_{eff}, \\ S_\phi = -\frac{\partial P}{\partial \xi} + \frac{F}{\lambda} \frac{\partial P}{\partial \eta} - G \left\{ \frac{1}{r\psi} \frac{\partial}{\partial \zeta} \left(\frac{\mu_{eff} \partial u}{\lambda} \right) \right\} \end{aligned}$$

$$+ \frac{1}{\lambda} \frac{\partial}{\partial \eta} \left(\frac{\mu_{eff}}{r\psi} \frac{\partial u}{\partial \xi} \right) \left\} - \frac{\mu_{eff}}{r\psi} \frac{\partial u}{\partial \xi} \frac{1}{r\lambda\psi} \frac{\partial \lambda}{\partial \xi} \right. \\ \left. - \left(\frac{\mu_{eff}}{\lambda} \frac{\partial u}{\partial \eta} \right) \left(\frac{\xi^2}{r} + \frac{1}{r\psi} \frac{\partial \xi}{\partial \xi} + \frac{\xi}{\lambda} \frac{\partial \xi}{\partial \eta} \right) \right\}.$$

For v-momentum equation:

$$\phi = v, \quad \Gamma_\phi = \mu_{eff}, \\ S_\phi = -\frac{1}{\lambda} \frac{\partial P}{\partial \eta} + \frac{\rho w^2}{r} - \frac{2\mu_{eff} v}{r^2} + \frac{1}{\lambda} \frac{\partial}{\partial \eta} \left(\frac{\mu_{eff}}{\lambda} \frac{\partial v}{\partial \eta} \right) \\ + \frac{1}{r\psi} \frac{\partial}{\partial \xi} \left(\frac{\mu_{eff}}{\lambda} \frac{\partial w}{\partial \eta} \right) + \frac{\mu_{eff}}{r\lambda} \frac{\partial v}{\partial \eta} - \frac{2\mu_{eff}}{r^2\psi} \frac{\partial w}{\partial \xi} \\ - \frac{1}{r^2\psi} \frac{\partial}{\partial \xi} (\mu_{eff} w) - \xi \left\{ \frac{1}{r\psi} \frac{\partial}{\partial \xi} \left(\frac{\mu_{eff}}{\lambda} \frac{\partial v}{\partial \eta} \right) \right. \\ \left. + \frac{1}{\lambda} \frac{\partial}{\partial \eta} \left(\frac{\mu_{eff}}{r\psi} \frac{\partial v}{\partial \xi} \right) + \frac{1}{\lambda} \frac{\partial}{\partial \eta} \left(\frac{\mu_{eff}}{\lambda} \frac{\partial w}{\partial \eta} \right) \right\} \\ - \frac{\mu_{eff}}{\lambda} \frac{\partial v}{\partial \eta} \frac{\xi^2}{r} - \frac{\mu_{eff}}{\lambda} \frac{\partial v}{\partial \eta} \left(\frac{1}{r\psi} \frac{\partial \xi}{\partial \xi} + \frac{\xi}{\lambda} \frac{\partial \xi}{\partial \eta} \right) \\ + \frac{2\mu_{eff}}{r} \frac{\xi}{\lambda} \frac{\partial w}{\partial \eta} - \frac{\mu_{eff}}{r\psi} \frac{\partial v}{\partial \xi} \frac{1}{r\lambda\psi} \frac{\partial \lambda}{\partial \xi} \\ + \frac{\xi}{r\lambda} \frac{\partial}{\partial \eta} (\mu_{eff} w)$$

For w-momentum equation:

$$\phi = w, \quad \Gamma_\phi = \mu_{eff}, \\ S_\phi = -\frac{1}{r\psi} \frac{\partial P}{\partial \xi} + \frac{\xi}{\lambda} \frac{\partial P}{\partial \eta} - \frac{\rho v w}{r} - \frac{\mu_{eff} w}{r^2} \\ + \frac{1}{r\psi} \frac{\partial}{\partial \xi} \left(\frac{\mu_{eff}}{r\psi} \frac{\partial w}{\partial \xi} \right) + \frac{1}{\lambda} \frac{\partial}{\partial \eta} \left(\frac{\mu_{eff}}{r\psi} \frac{\partial v}{\partial \xi} \right) \\ + \frac{2}{r^2\psi} \frac{\partial}{\partial \xi} (\mu_{eff} v) - \frac{1}{r\lambda} \frac{\partial}{\partial \eta} (\mu_{eff} w) \\ + \frac{2\mu_{eff}}{r^2\psi} \frac{\partial v}{\partial \xi} + \frac{\mu_{eff}}{r\lambda} \frac{\partial w}{\partial \eta} + \xi^2 \left\{ \frac{1}{\lambda} \frac{\partial}{\partial \eta} \left(\frac{\mu_{eff}}{\lambda} \frac{\partial w}{\partial \eta} \right) \right. \\ \left. - \xi \left\{ \frac{2}{r\psi} \frac{\partial}{\partial \xi} \left(\frac{\mu_{eff}}{\lambda} \frac{\partial w}{\partial \eta} \right) + \frac{2}{\lambda} \frac{\partial}{\partial \eta} \left(\frac{\mu_{eff}}{r\psi} \frac{\partial w}{\partial \xi} \right) \right. \right. \\ \left. \left. + \frac{1}{\lambda} \frac{\partial}{\partial \eta} \left(\frac{\mu_{eff}}{\lambda} \frac{\partial v}{\partial \eta} \right) \right\} + \frac{\mu_{eff}}{\lambda} \frac{\partial w}{\partial \eta} \left(-\frac{2}{r\psi} \frac{\partial \xi}{\partial \xi} \right. \right. \\ \left. \left. - \frac{\xi^2}{r} \right) - \left(\frac{\mu_{eff}}{\lambda} \frac{\partial v}{\partial \eta} \right) \left(\frac{1}{\lambda} \frac{\partial \xi}{\partial \eta} + \frac{2\xi}{r} \right) \right. \\ \left. - \frac{2\xi}{r\lambda} \frac{\partial}{\partial \eta} (\mu_{eff} v) - \frac{\mu_{eff}}{r\psi} \frac{\partial w}{\partial \xi} \frac{1}{r\lambda\psi} \frac{\partial \lambda}{\partial \xi} \right\}.$$

For K-equation:

$$\phi = K, \quad \Gamma_\phi = \frac{\mu_{eff}}{P_{r,K}} = \Gamma_K, \\ S_\phi = \xi e - \rho \varepsilon - \xi \left\{ \frac{1}{\lambda} \frac{\partial}{\partial \eta} \left(\frac{\Gamma_K}{r\psi} \frac{\partial K}{\partial \xi} \right) \right. \\ \left. + \frac{1}{r\psi} \frac{\partial}{\partial \xi} \left(\frac{\Gamma_K}{\lambda} \frac{\partial K}{\partial \eta} \right) \right\} - \frac{1}{r\lambda\psi} \frac{\partial \lambda}{\partial \xi} \frac{\Gamma_K}{r\psi} \frac{\partial K}{\partial \xi} \\ - \left(\frac{1}{r\psi} \frac{\partial \xi}{\partial \xi} + \frac{\xi}{\lambda} \frac{\partial \xi}{\partial \eta} \right) \frac{\Gamma_K}{\lambda} \frac{\partial K}{\partial \eta} \\ - \frac{\xi^2}{r} \frac{\Gamma_K}{\lambda} \frac{\partial K}{\partial \eta}$$

For ε-equation:

$$\phi = \varepsilon, \quad \Gamma_\phi = \frac{\mu_{eff}}{P_{r,\varepsilon}} = \Gamma_\varepsilon, \\ S_\phi = C_1 \xi e \frac{\varepsilon}{K} - C_2 \rho \frac{\varepsilon^2}{K} - \xi \left\{ \frac{1}{\lambda} \frac{\partial}{\partial \eta} \left(\frac{\Gamma_\varepsilon}{r\psi} \frac{\partial \varepsilon}{\partial \xi} \right) \right. \\ \left. + \frac{1}{r\psi} \frac{\partial}{\partial \xi} \left(\frac{\Gamma_\varepsilon}{\lambda} \frac{\partial \varepsilon}{\partial \eta} \right) \right\} - \frac{1}{r\lambda\psi} \frac{\partial \lambda}{\partial \xi} \frac{\Gamma_\varepsilon}{r\psi} \frac{\partial \varepsilon}{\partial \xi} \\ - \left(\frac{1}{r\psi} \frac{\partial \xi}{\partial \xi} + \frac{\xi}{\lambda} \frac{\partial \xi}{\partial \eta} \right) \frac{\Gamma_\varepsilon}{\lambda} \frac{\partial \varepsilon}{\partial \eta} \\ - \frac{\xi^2}{r} \frac{\Gamma_\varepsilon}{\lambda} \frac{\partial \varepsilon}{\partial \eta}$$

where

$$\xi e = \mu_t \left[2 \left\{ \left(\frac{1}{\lambda} \frac{\partial v}{\partial \eta} \right)^2 + \left(\frac{1}{r\psi} \frac{\partial w}{\partial \xi} - \frac{\xi}{\lambda} \frac{\partial v}{\partial \eta} + \frac{v}{r} \right)^2 \right\} \right. \\ \left. + \left(\frac{1}{r} \frac{\partial w}{\partial \eta} - \frac{w}{r} + \frac{1}{r\psi} \frac{\partial v}{\partial \xi} - \frac{\xi}{\lambda} \frac{\partial v}{\partial \eta} \right)^2 \right. \\ \left. + \left(\frac{1}{r\psi} \frac{\partial v}{\partial \xi} - \frac{\xi}{\lambda} \frac{\partial v}{\partial \eta} \right)^2 + \left(\frac{1}{\lambda} \frac{\partial v}{\partial \eta} \right)^2 \right].$$

2.3 Boundary Conditions

The flow field in interest is surrounded by six boundaries; hull surface ($r=r_s$), outer boundary ($r=r_o$), water plane ($\theta=0$), center vertical plane ($\theta=\pi/2$), inlet plane and exit plane (see Fig. 1). In solving the governing equations (14), it is necessary to determine the boundary conditions.

The problem is where we should fix the location of outer boundary, inlet plane and exit plane. The outer boundary may be desirable to be placed far from the ship hull, where the flow is uniform. In the present method, the location of the outer boundary is determined empiri-

cally. That is not so far from the hull but the solution of inviscid flow is available there (Muraoka 1979). The inlet plane may be located near the stern region if the upstream flow can be predicted by an appropriate theory. In the present method, midship section is chosen as the inlet plane and the boundary conditions for velocities, pressure and turbulent properties are given from the results of flat plate for simplicity. At the exit plane, pressure is necessitated to be given. So the exit plane is desirable to be taken at the plane where the pressure of the potential flow is available.

The conditions at the boundaries are defined as follows:

(1) Hull Surface

$$U = V = W = K = \epsilon = 0, \text{ at } r = r_s,$$

and near the surface the 'wall function method' (Patankar and Spalding 1972) is applied to account the damping effect of the wall on turbulence.

(2) Outer Boundary

The flow velocities and the pressure at the outer boundary are obtained from the calculation of the potential flow around the ship, and

$$\frac{\partial K}{\partial r} = \frac{\partial \epsilon}{\partial r} = 0, \text{ at } r = r_0.$$

(3) Water Plane and Center Plane

$$W = 0,$$

$$\frac{\partial u}{\partial \theta} = \frac{\partial v}{\partial \theta} = \frac{\partial K}{\partial \theta} = \frac{\partial \epsilon}{\partial \theta} = 0, \text{ at } \theta = 0, \pi/2.$$

(4) Inlet Plane

It is assumed that the boundary layer is uniform along the girth of the hull and the boundary layer thickness is calculated by Schlichting's formula for flat plate:

$$\delta = 0.37 s \left(\frac{V \cdot s}{\nu} \right)^{-1/2},$$

where V is uniform velocity; ν is kinematic viscosity; s is the distance from leading edge. The velocity components u , v and w are as follows:

$$u = \begin{cases} V \cdot \left\{ \frac{(r-r_s)}{\delta} \right\}^{1/2} & \text{at } r-r_s \leq \delta, \\ V & \text{at } r-r_s > \delta, \end{cases}$$

$$U = W = 0$$

As the turbulent properties seem to be confined within the boundary layer, these are treated separately within and outside of the boundary layer.

The turbulent properties K and ϵ are assumed as follows:

$$K = \begin{cases} f(r-r_s) \cdot V^2 & \text{at } r-r_s \leq \delta, \\ \approx 0 & \text{at } r-r_s > \delta, \end{cases}$$

where $f(r-r_s)$ is determined from the experimental data of Klebanoff for flat plate (for example, Rotta 1972). The mixing length ℓ_m is determined using the value $g(r-r_s)$ which Bradshaw et al. (1967) have given for thin boundary layer.

$$\ell_m = \begin{cases} g(r-r_s) & \text{at } r-r_s \leq 1.2\delta, \\ g(1.2\delta) & \text{at } r-r_s > 1.2\delta. \end{cases}$$

The value of ϵ is determined from the mixing length as follows:

$$\epsilon = C_0^{3/4} \cdot K^{3/2} / \ell_m.$$

(5) Exit Plane

The pressure P is obtained from the calculation of the potential flow.

2.4 Calculation Procedure

First of all, the flow field in interest is divided into many small subdivision by the intersecting grid lines which are parallel to ξ -, η - and ζ -direction. Next, the finite difference equations are derived by integrating the governing equation (14) over the each small subdivision (Muraoka 1979). The unknowns in the finite difference equations are three velocities u , v and w , the pressure P , the turbulent properties K and ϵ . The pressure is stored as three dimensional array and the other variables are stored as two dimensional arrays at every r - θ plane. Then, the finite difference equations are solved as following steps:

- At the start of the calculation, the pressure in the flow field is guessed from the potential flow solution. The pressure is improved as the calculation proceeds.
- The momentum equations for 3 velocities are solved separately at r - θ plane.
- As the velocities solved at step (b) do not satisfy the continuity equation, the velocities and the pressure are corrected to satisfy the continuity equation by using iterative procedure.
- After obtaining three velocities and pressure at step (c), the equations for K and ϵ are solved so as to pro-

vide K - ϵ distributions appropriate to next downstream plane.

- (e) Then, the same manner from step (b) to (d) are repeated at all the downstream plane in the flow field. Reaching the exit plane, one marching is completed.
- (f) The marchings from inlet plane to exit plane are repeated several times, and the pressure in three dimensional array is improved at every marching.
- (g) Finally, the calculation is terminated when the pressure of the flow field in current marching do not alter comparing the pressure in previous marching.

3. NUMERICAL RESULTS

Calculations are performed for two models by using the method in the previous section. The first one is an axisymmetric body which is named Afterbody 1 by Huang et al. (1978). The second one is a liner ship model which is named Model B (Muraoka 1979).

Comparing the flow properties between calculation and experiment for the axisymmetric body, the basic possibility of the present calculation method is examined. The validity of the method to the complicated flow around actual ship is tested by calculating the flow around the liner ship model.

3.1 Calculation for Axisymmetric Body

The principle particulars of the axisymmetric body are shown in Table 2 and the afterbody configuration is shown in Fig. 2.

Table 2. Principle Particulars of axisymmetric body

L (m)	3.066
r_{max} (m)	0.1397
Re	6.60×10^6

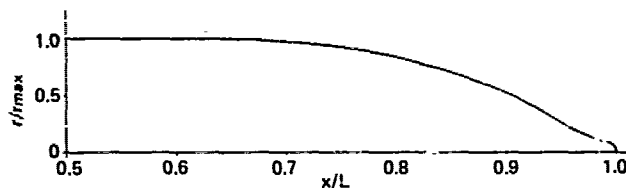


Fig. 2 Aftbody configuration of axisymmetric body

The numerical calculation of the flow around the body is carried out in the following way. The location of outer boundary in the present calculation is assumed to place at the constant distance from the hull,

$$r_0 = r_s + r_{max}$$

where r_{max} is the maximum radius of the body. The inlet plane is located at $0.5L$ from the leading edge and the exit plane is at $0.18L$ behind the body. The grid nodes at r - θ plane are 12×12 whose configuration is shown in Fig. 3(a). The grid lines along x -direction are 35 whose interval is every $0.02L$. The grid configuration of x - r plane in stern region is shown in Fig. 3(b).

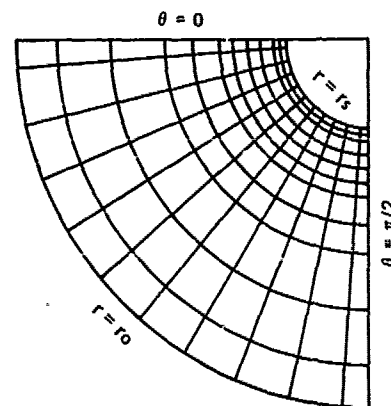


Fig. 3(a) Grid configuration of r - θ plane for axisymmetric body

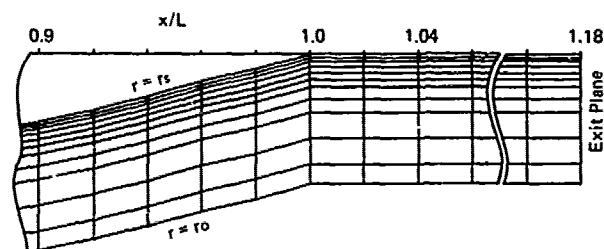


Fig. 3(b) Grid configuration of x - r plane for axisymmetric body

The inlet conditions are shown in Fig. 4 where the circles indicate the values at grid nodes. The comparison of calculated and measured velocity components, u/V and $-v/V$ are shown in Fig. 5 and Fig. 6, respectively. In Fig. 6, the calculated result of $-v/V$ at $x/L=1.057$ is nearly equal to zero and is slightly different from the experiment. The calculated velocity component by the present method have the same high accuracy as the numerical results of boundary layer theories of Huang et al. (1978) and Soejima (1980). In Fig. 7, the pressure variations in the flow field in interest are shown comparing with the measured ones and the numerical results of potential flow. The viscous effect on pressure is appeared only near the vicinity of hull surface around the stern region and the calculated results agree with the ex-

periment except at $x/L=1.057$.

Fig. 8 shows the comparison of turbulent properties. The measured K is determined by the finition $\frac{1}{2}(u'^2 + v'^2 + w'^2)$ where u' , v' and w' means the velocity fluctuation in x -, r - and θ -directions.

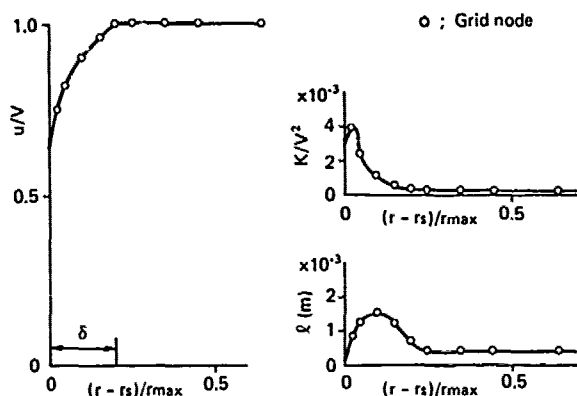


Fig. 4 Boundary conditions at inlet plane $x/L=0.5$ for axisymmetric body

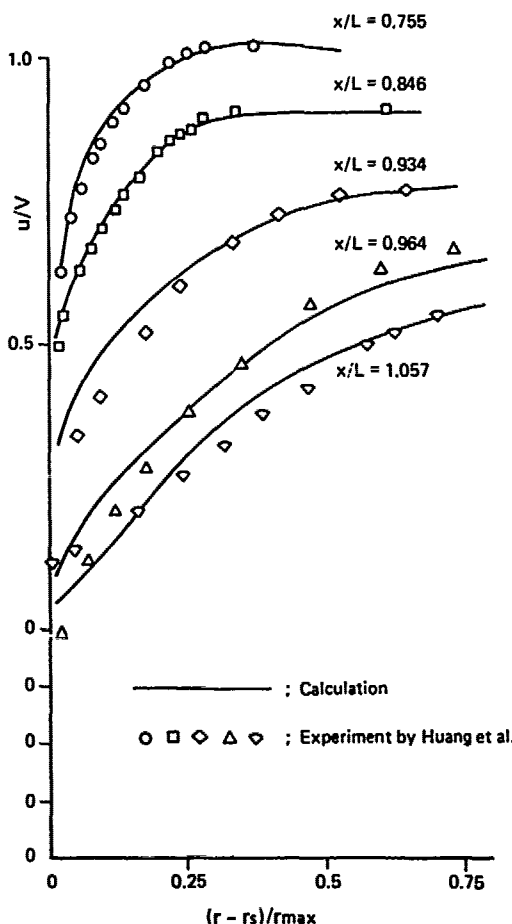


Fig. 5 Comparison of velocity component u/V for axisymmetric body

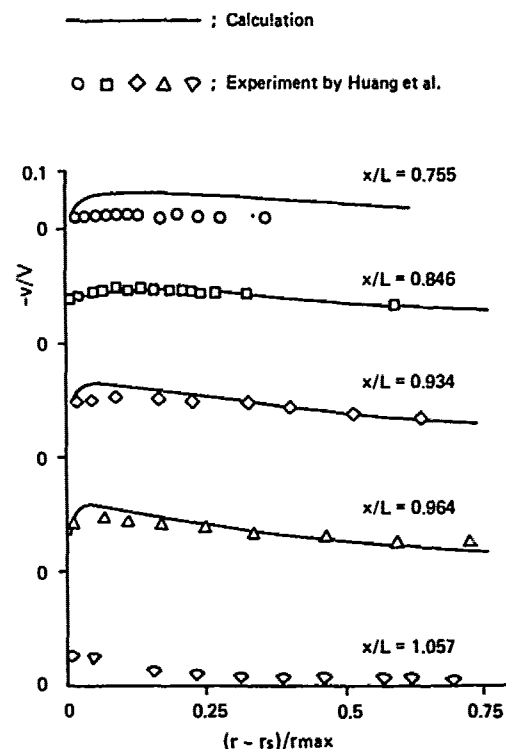


Fig. 6 Comparison of velocity component $-v/V$ for axisymmetric body

The measured l is determined by $\nu_t / K^{1/2}$ while the calculated l is determined by $C_\mu K^{1/2} / \epsilon$. The coincidences of turbulent properties between calculation and experiment are fairly good, although the accuracy of calculation becomes worse as x/L increase. The comparison of turbulent kinematic viscosity ν_t are shown in Fig. 9. In this figure, the values of U_s , S_τ^* and Δ_r are all derived from the experiment of Huang et al. The numerical results of Huang et al's method are coincident with one line by nondimensionalizing because of 0-equation model of turbulence, but the experimental values are not coincident with one line and diminish towards the stern. On the other hand, the numerical results of the present method present fair agreement with the experiment at each section. From the above examination, it can be said that in evaluating the turbulent properties like K , l and ν_t around the axisymmetric body, the $K-\epsilon$ model of turbulence is effective.

3.2 Calculation for Liner Ship Model

In the previous section, the validity of the present method for axisymmetric body was confirmed by comparing the calculation of velocity profile, pressure distribution and turbulent properties with experiment. Here, the present method is tested to the liner ship model B (Muraoka 1979).

The principle particulars of the model is shown in Table 3 and the body plan,

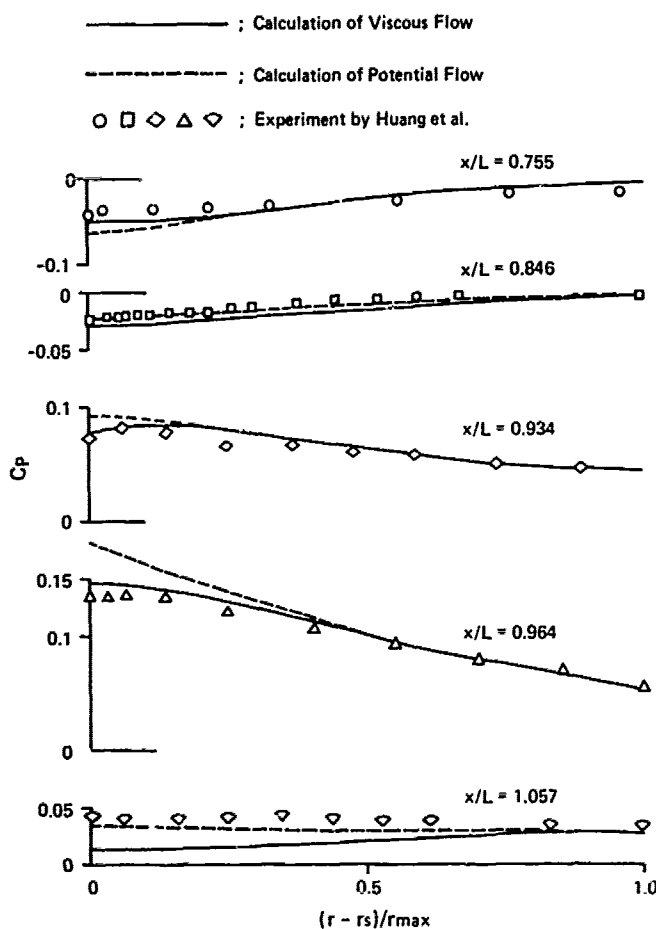


Fig. 7 Comparison of pressure variations in the flow around axisymmetric body

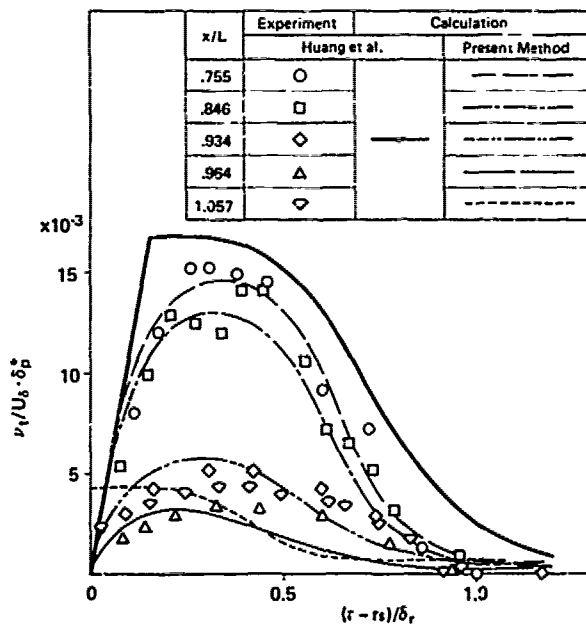


Fig. 9 Comparison of turbulent viscosity for axisymmetric body

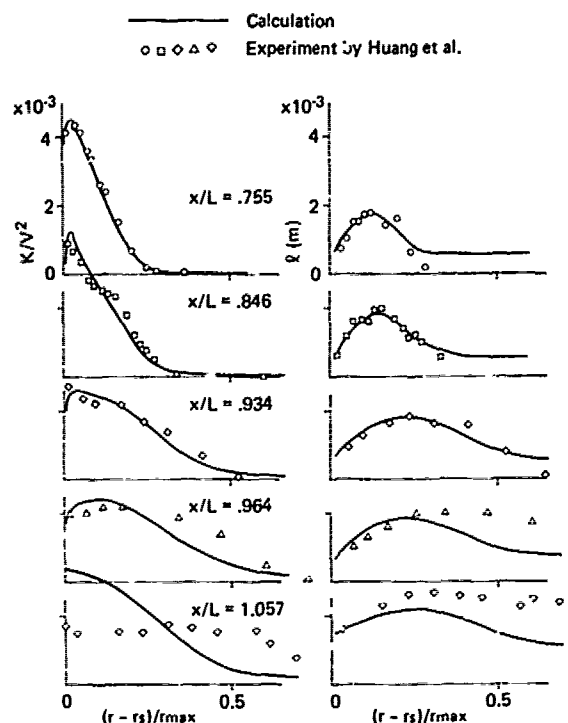


Fig. 8 Comparison of turbulent properties for axisymmetric body

Table 3. Principle particulars of liner ship model

L (m)	6.00
B (m)	0.9231
d (m)	0.3231
C _B	0.5720
C _{PA}	0.6248
Re	1.03 × 10 ⁷

stern and stem profiles are shown in Fig. 10. The outer boundary in the present calculation is placed at the cylindrical shape of constant radius $r_0/8/2 = 1.78$. The inlet plane is located at St. 5 and the exit plane is located at 0.1L behind ship. The grid nodes at $r-\theta$ plane are 12×12 whose configuration is shown in Fig. 11(a). The grid lines along x -direction are 31 whose interval is every 0.02L. The grid configurations of center vertical plane and water plane in stern region are shown in Fig. 11(b) and Fig. 11(c), respectively. The stern profile used in calculation is different from the actual ship model as shown in Fig. 11(b).

The calculated wake distributions around stern region from St. 1 3/5 to St.

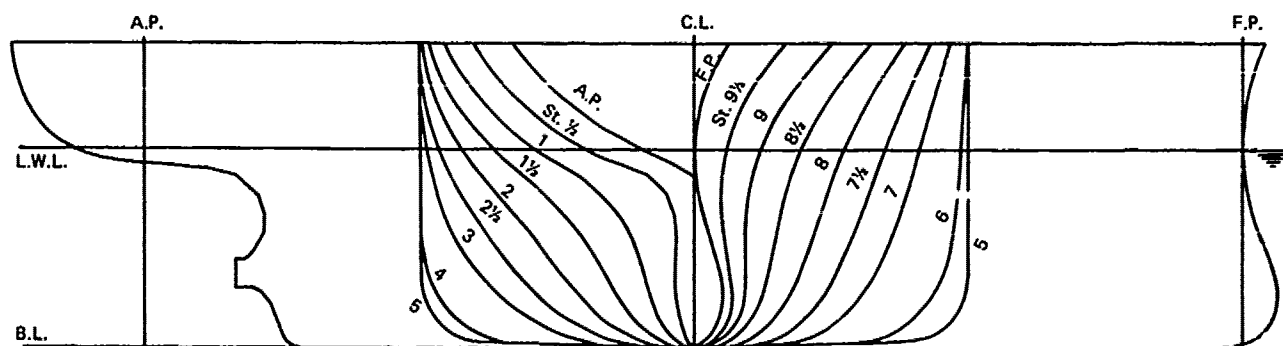


Fig. 10 Body plan, stem and stern profiles of liner ship model

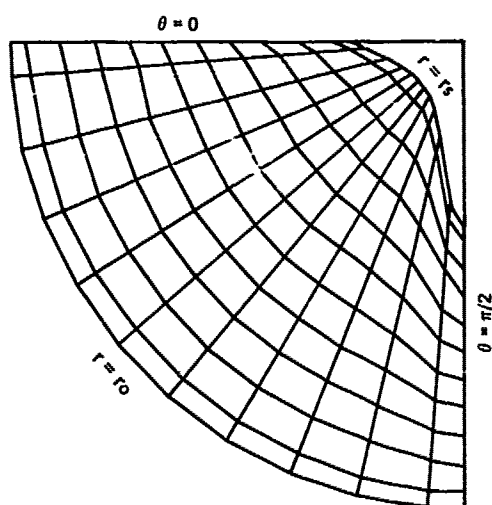


Fig. 11(a) Grid configuration of r - θ plane for liner ship model at St. $3/5$

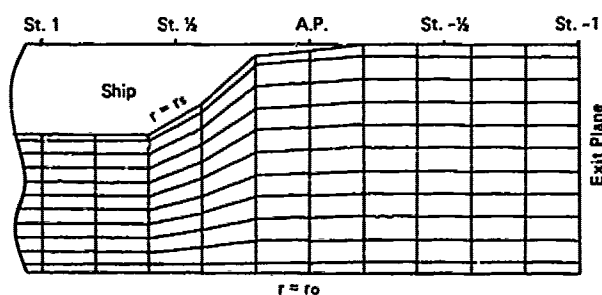


Fig. 11(b) Grid configuration of center vertical plane in stern region for liner ship model

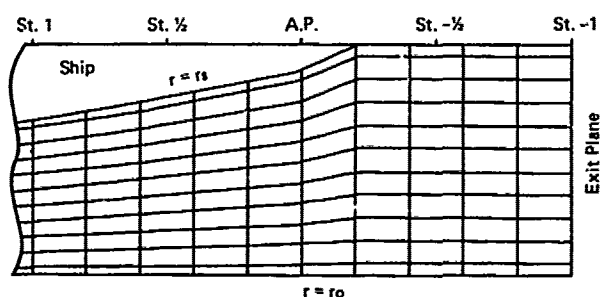


Fig. 11(c) Grid configuration of water plane for liner ship model

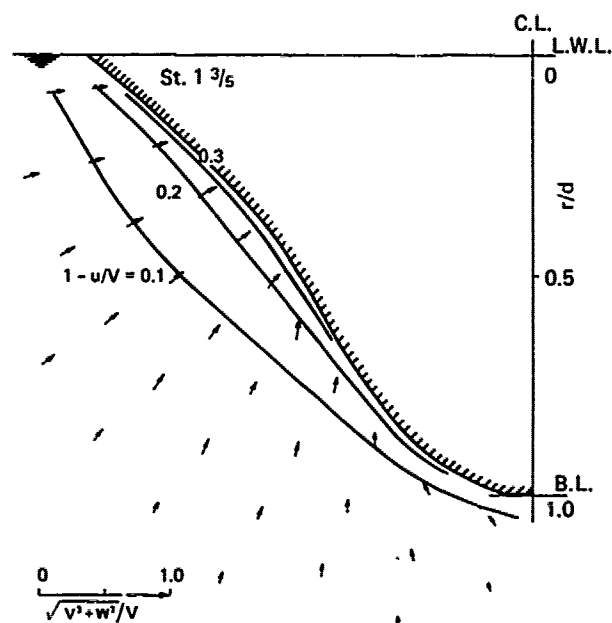


Fig. 12(a) Calculated wake distribution for liner ship model at St. $1 \frac{3}{5}$ and $Re = 1.03 \times 10^7$

-2/5 are shown in Fig. 12(a) through Fig. 12(e). The recirculating flow is seemed to occur around the bilge at St. 3/5, and to develop towards ship stern. In Fig. 12(e) at St. -2/5, the ring shape of equi-velocity contour is observed near the cross point of center line and base line. In

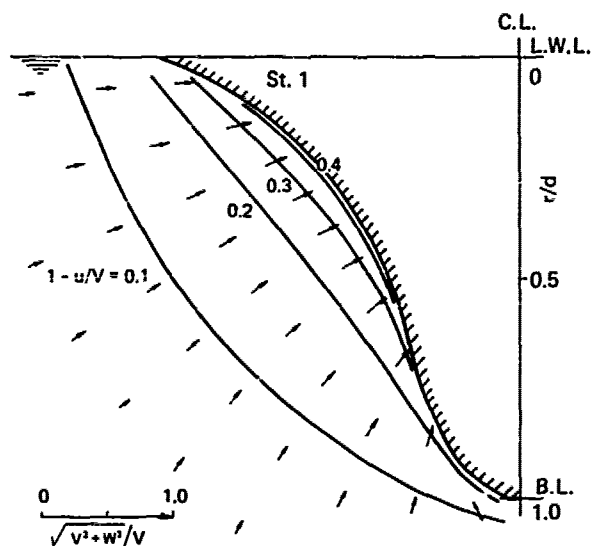


Fig. 12(b) Calculated wake distribution for liner ship model at St. 1 and $Re = 1.03 \times 10^7$

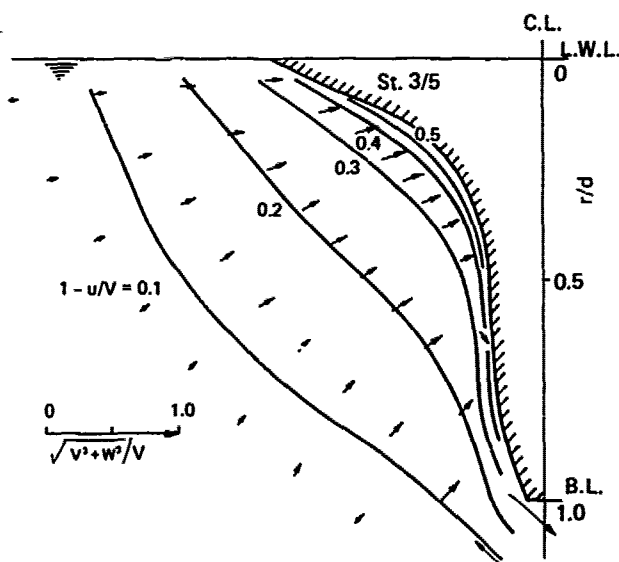


Fig. 12(c) Calculated wake distribution for liner ship model at St. 3/5 and $Re = 1.03 \times 10^7$

Fig. 13, the measured wake distributions at St. 1/5 is shown. Although the calculated radial velocity near center line is larger than the measured one, the calculated wake

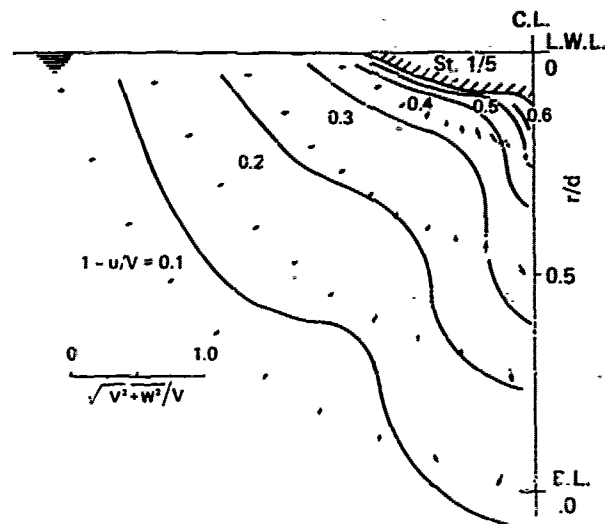


Fig. 12(d) Calculated wake distribution for liner ship model at St. 1/5 and $Re = 1.03 \times 10^7$

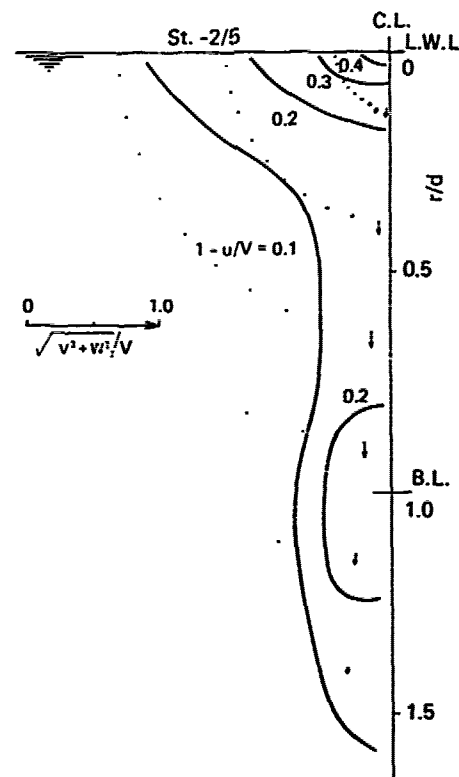


Fig. 12(e) Calculated wake distribution for liner ship model at St. -2/5 and $Re = 1.03 \times 10^7$

distributions are seemed to show qualitatively the tendency of the flow behind ship stern. Fig. 14 shows the calculated viscous pressure distribution on the hull surface from St. 5 to St. 1/2 along five diagonal lines comparing with the pressure of the potential flow and the experiment (Namimatsu 1976: this ship is named M7). The calculated viscous pressure from water plane to $\theta=45^\circ$'s diagonal line are closer to the measured one than the pressure of the potential flow. On $\theta=67.5^\circ$'s diagonal line, the calculated viscous pressure is different from the measured one.

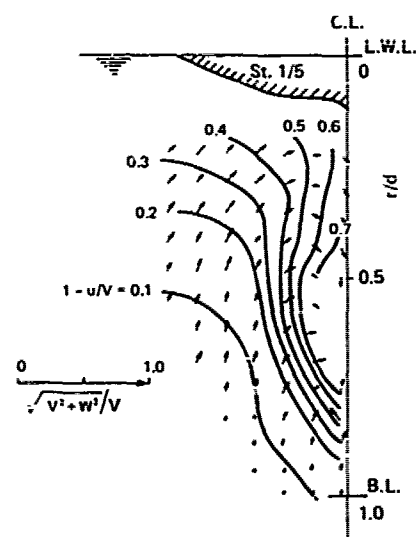


Fig. 13 Measured wake distribution for liner ship model at St. 1/5 and $Re = 1.03 \times 10^7$

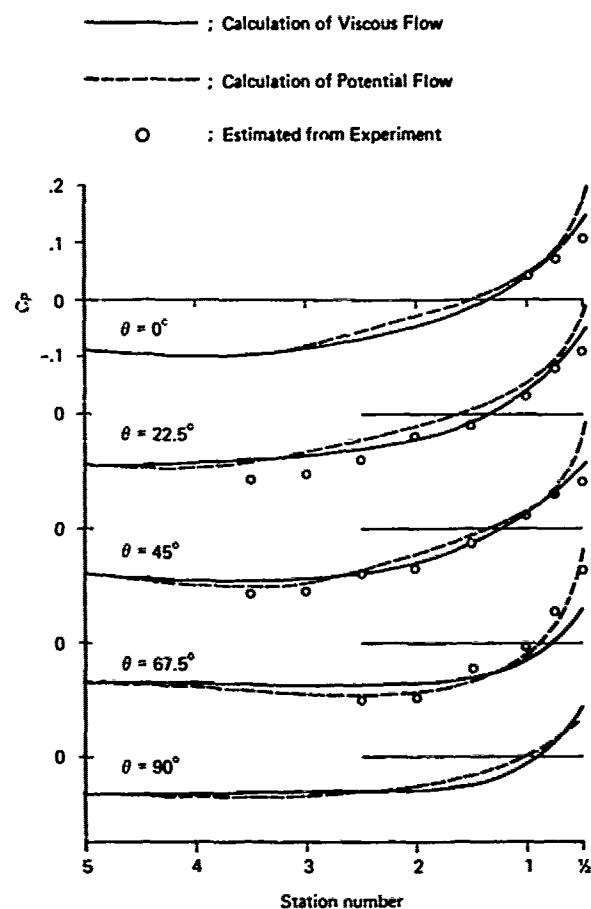


Fig. 14 Comparison of pressure distribution on hull surface of liner ship model at $Re = 1.03 \times 10^7$

Table 4 Resistance Components of Liner Ship Model at $Re = 1.03 \times 10^7$

Resistance Component	Calculation (kg)	Experiment (kg)	Remarks
Viscous Pressure Resistance (R_{vp})	1.46	0.87	Cal.; From surface integral of $P-P_0$ on the surface of afterbody Exp.; Pressure resistance minus wave pattern resistance
Frictional Resistance (R_f)	4.17	4.29	Cal.; From Cumpsty & Head method for forebody and from present method for afterbody Exp.; Total resistance minus pressure resistance
Viscous Resistance ($R_{vp}+R_f$)	5.63	5.16	
Do. (R_v)	5.65	5.03	From the law of momentum by using wake distribution at $0.3L$ behind ship.

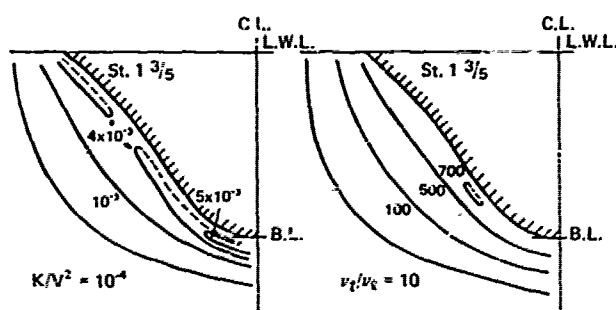


Fig. 15(a) Calculated distributions of K/V^2 and ν_t/ν_l for liner ship model at St. $1 \frac{3}{5}$ and $Re = 1.03 \times 10^7$

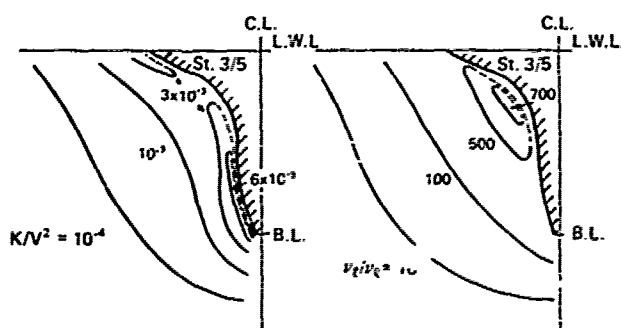


Fig. 15(b) Calculated distributions of K/V^2 and ν_t/ν_l for liner ship model at St. $3/5$ and $Re = 1.03 \times 10^7$

Table 4 shows the viscous resistance and viscous pressure resistance derived from the calculation of the same ship under the similar condition to the present calculation (Muraoka 1979). The calculated viscous resistance R_v is reasonably coincident with the sum of calculated viscous pressure resistance R_{vp} and calculated frictional resistance R_f , and the numerical results show roughly coincident with the experiment.

In Fig. 15(a) through Fig. 15(c), the calculated distributions of K/V^2 and ν_t/ν_l are shown where ν_l denotes the laminar viscosity. The turbulent kinetic energy K at St. $3/5$ in Fig. 15(b) is very intensive at the bilge part. The turbulent properties are high only within the boundary layer and the wake.

From the above calculation, it is confirmed that the wake distribution around and behind ship can be predicted reasonably with the viscous pressure and turbulent properties. However, in order to make the present method more practical, the following items are required:

- (1) To utilize the differential method of

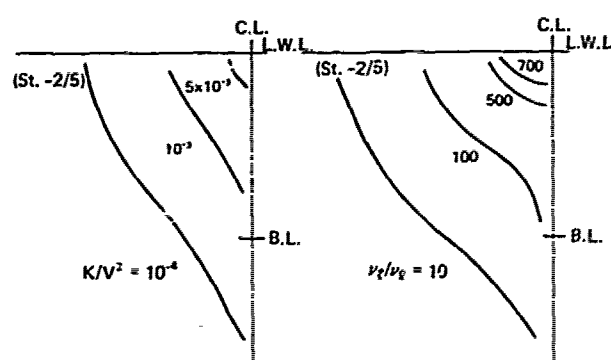


Fig. 15(c) Calculated distributions of K/V^2 and ν_t/ν_l for liner ship model at St. $-2/5$ and $Re = 1.03 \times 10^7$

thin boundary layer theory in order to improve the inlet conditions.

- (2) To refine the calculation techniques in respect of economy.
- (3) To make refinement of grid configuration in order to obtain stable convergence.
- (4) To test other coordinate system in order to perform item (3).

4. CONCLUDING REMARKS

On the assumption of partially parabolic flow and $K-\epsilon$ model of turbulence, the calculations are performed for an axisymmetric body and a liner ship model. The following results are derived:

- (1) The turbulent properties around the axisymmetric body can be predicted well.
- (2) The calculated wake distributions for a liner ship model are qualitatively coincident with the phenomena. Especially the bilge vortex is seemed to occur.
- (3) The evaluations of the pressure, turbulent properties and resistance components for ship are possible.

Thus, the present method is made clear to be appropriate for the calculation of thick boundary layer and wake of ships through the numerical examples. Further refinement of the present method is necessitated in order to improve the accuracy of calculation for practical use.

ACKNOWLEDGMENT

Before closing this paper, the author expresses his grateful thank to Prof. R. Yamazaki of Kyushu University for his advice and encouragement. The author would like to express his gratitude to Dr. R. Tasaki and Mr. M. Namimatsu of Ishikawajima-Harima Heavy Ind. Co. Ltd. (IHI) for their encouragement. The author also expresses his heartfelt thank to Dr. T. Tsutsumi of IHI for his stimulating discussion and suggestion. Thanks are extended to Mr. Y. Shirosé of IHI for his cooperative works.

REFERENCE

- (1) Abdelmequid, A. M., Markatos, N. C., Spalding, D. B. and Muraoka, K., "A Method of Predicting Three-Dimensional Turbulent Flows around Ships' Hulls", International Symposium on Ship Viscous Resistance, SSPA, (1978)
- (2) Bradshaw, P., Ferris, D. H. and Atwell, N. P., "Calculation of Boundary Layer Development Using the Turbulent Energy Equation", Journal of Fluid Mechanics, No. 28, (1967)
- (3) Cebeci, T., Kaups, K. and Moser, A., "A General Method for Calculating Three-Dimensional Incompressible and Turbulent Boundary Layers. Three-Dimensional Flows in Curvilinear Orthogonal Coordinates", Douglas Aircraft Co., Report MDC J6867, (1975)
- (4) Hatano, S., Mori, K. and Suzuki, T., "Calculation of Velocity Distributions in Ship Wake", Journal of the Society of Naval Architects of Japan, Vol. 141, (1977)
- (5) Himeno, Y. and Tanaka, I., "An Exact Integral Method for Solving Three-Dimensional Turbulent Boundary Layer Equation around Ship Hulls", Journal of Kansai Society of Naval Architects, Vol. 159, (1976)
- (6) Hoekstra, M., "Boundary Layer Flow past a Boulbous Ship-Bow at Vanishing Froude Number", International Symposium on Ship Viscous Resistance, SSPA, (1978)
- (7) Huang, T. T., Santelli, N. and Belt, G., "Stern Boundary Layer Flow on Axisymmetric Bodies", 12th Symposium on Naval Hydrodynamics, (1978)
- (8) Larsson, L., "Boundary Layer on Ships, Part 4", SSPA Report No. 47, (1974)
- (9) Launder, B. F. and Spalding, D. B., "Mathematical Models of Turbulence", Academic Press, (1972)
- (10) Mori, K. and Doi, Y., "Approximate Prediction of Flow Field around Ship Stern by Asymptotic Expansion Method", Journal of the Society of Naval Architects, Vol. 144, (1978)
- (11) Muraoka, K., "Calculation of Viscous Flow around Ship Stern", Transactions of the West-Japan Society of Naval Architects, No. 58, (1979)
- (12) Muraoka, K., "Examination of a 2-Equation Model of Turbulence for Calculating the Viscous Flow around Ships", Journal of the Society of Naval Architects of Japan, Vol. 147, (1980)
- (13) Nagamatsu, T., "Calculation of Viscous Pressure Resistance of Ships Based on a Higher Order Boundary Layer Theory", Journal of the Society of Naval Architects of Japan, Vol. 147, (1980)
- (14) Namimatsu, M., "A Measuring Method of Hull Pressure and Its Application", Journal of the Society of Naval Architects of Japan, Vol. 139, (1976)
- (15) Okuno, T., "Distribution of Wall Shear Stress and Cross Flow in Three-Dimensional Boundary Layer on Ship Hull", Journal of the Society of Naval Architects of Japan, Vol. 139, (1976)
- (16) Patankar, S. V. and Spalding, D. B., "A Calculation Procedure for Heat, Mass and Momentum Transfer in Three-Dimensional Parabolic Flows", Journal of Heat and Mass Transfer, 15, (1972)
- (17) Pratap, V. S., "Flow and Heat Transfer in Curved Ducts", Imperial College Report HTS/75/25, (1975)
- (18) Raven, H. C., "Calculation of the Boundary Layer Flow around Three Ship Afterbodies", International Shipbuilding Progress, Vol. 27 (No. 305), (1980)
- (19) Rotta, von J. C., "Turbulence Stromungen", B. G. Teuber, (1972)
- (20) Soejima, S., "Calculation of Thick Boundary Layers around Ship Stern", Trans. of the West-Japan Society of Naval Architects, No. 60, (1980)
- (21) Spalding, D. B., "Calculation Procedure of 3-D Parabolic and Partially-Parabolic Flows" Imperial College Report HTS/75/5, (1975)

Discussion

K. Mori (Hiroshima Univ.)

T.T. Huang (DTNSRDC)

Could the author give the specific iterative procedure used in statement (c) of 2.4 Calculation Procedure? Why the computed mixing length parameter $l(m)$ shown in Figure 8 does not approach zero when the value of r becomes greater than the value of $(\delta + r_s)$?

G.E. Gadd (NMI)

Although there are encouraging qualitative similarities between the theoretical predictions and the measurements, it is clear as the author admits that further refinement of the calculation method is needed. When fig.12d is compared with fig. 13 the most obvious deficiencies of the theory are seen to be:

- (1) insufficient prediction of the vortex effect
- (2) failure to predict the high shear region, with closely spaced velocity contours, outside a region of stagnant flow.

Obviously the grid configuration shown in fig.11a is far from ideal for the flow near the stern. Does the author think that this may be a contributory factor to the defects of the prediction? Also, is it possible that the turbulent shear stress model may become inadequate in such a situation?

M. Hoekstra (NSMB)

Just two questions and one comment.

(1) How did you handle the kink in the coordinate lines at the tail of the body of revolution?

(2) Did you experience in this work or in any other study with the $K - \epsilon$ model any trouble with the length-scale equation (ϵ -equation) at the outer boundary of the computation domain?

I think that the author's conclusion about the adequacy of the $K - \epsilon$ model for the flow past axisymmetric bodies is premature. The present application is on a body with high length-diameter ratio so that longitudinal curvature effects are weak. I suspect that the predictions for fuller bodies would have been worse because the $K - \epsilon$ model does not include properly the effects of longitudinal streamline curvature on turbulence.

(1) Through the calculation of the axisymmetric body, the author concluded that the validity of the present method is confirmed. But, in case of 2-D flows, the partially parabolic approximation reduces to the boundary layer approximation with higher orders. So the discussor does not think that the partially parabolic approximation is checked by the present calculation for the axisymmetric body.

(2) The partially parabolic approximation neglects the diffusion in the main flow direction and keeps that in the girth direction. The discussor still can convince neither that the latter is more important than the former in cases of ship-like bodies nor that such a complicated approximation is necessary even for upstream region like S.S.13/5 or i. The results of the axisymmetric body which show good agreements with experiments for $x < 0.964$ but not so much for $x = 1.057$ may support the above; for the upstream region the boundary layer approximation works quite well and for the wake region the neglect of the diffusion in the main flow direction is crucial. Have you any data how far improvements are reached by the revival of the girth direction diffusion terms?

(3) The method to estimate the viscous resistance by the hull surface pressure integration is always of possible error in case of ship-like blunt bodies. Therefore the discussor appreciates that obtained by the momentum law still more. For the latter method, good predictions of velocity and pressure profiles are necessary in the wake, a little behind ships. How much the velocity and the pressure profiles at 0.3L behind ship agree with experiments? Although the estimated value of R_x in Table 4 shows rather good agreement with experiment, as far as the results of S.S.1/5 are concerned, on the contrary to the author's comment, the discussor never suppose that Fig.12(d) (calculated results) agrees with Fig.13 (measured) even qualitatively.

Author's Reply

K. Muraoka (NMI)

I would like to express gratitude for Dr. Huang's valuable discussion and appreciation for providing the detailed experimental data of axisymmetric body in the previous symposium which all quoted in my manuscript.

At first calculation of momentum equations at one $r-\theta$ plane, the coefficients of the finite difference equations are calculated based on the solved velocities and pressure at upstream plane. The solved velocities of first time at current plane do not satisfy the continuity equation, so the velocities are corrected so as to satisfy the continuity equation through the pressure correction. Next, at current plane the momentum equations are solved using the first solution of velocities and pressure as new coefficients of finite difference equations. These procedures are repeated several times. And when the error of continuity equation comes practically zero, the iterations at current plane are terminated.

Next, at the inlet plane, we give the small value of mixing length at the outside of boundary layer. When we take nearly zero value of mixing length at this region, the calculation has not converged well. This causes the small value left at the outside of boundary layer.

Thank you for Dr. Gadd's discussion. I think that the grid configurations may be one of the main factors to improve the results of prediction. Although the large number of grid nodes brings the large computer storage, expensive costs and difficulty of convergence, I would like to test grid refinement in order to make use of this method for practical purpose.

Next, the present turbulent model is based on the assumption of homogeneous turbulence and gradient diffusion hypothesis. In case of axisymmetric body, the present turbulent model is examined to be effective. From this, it is applied to the flow around ship stern. As there is no data of measured turbulent behaviour around ship stern region, the present model is not examined and I think, it is necessary to examine the validity of $K-\epsilon$ model of turbulence around ship stern through comparing with the measurement of turbulent behaviour.

Thank you very much for Mr. Hoekstra's valuable discussion and interesting comment.

In the calculation of axisymmetric body, the grid line along x -direction is placed at the tail end of the body, therefore the calculations around body and behind body are separated. In case of stag-

gered control volume in obtaining the finite difference equations, the tail end of the body is shifted half distance of grid length.

Next, about the calculation of $K-\epsilon$ model of turbulence. When we used the improper inlet value of length scale model at the outer region, too high or too small, the calculation has not converged well or the unreasonable result has been obtained.

I would like to express gratitude for Prof. Mori's valuable discussion.

To the first discussion

In the present calculation of axisymmetric body, it is assumed that the flow is 3-dimensional partially parabolic flow. The calculated results show 2-dimensionality because that the angular velocity is zero and the other properties have not changed in the angular direction. Judging from this, I think that the present method works well. And also the $K-\epsilon$ model of turbulence is examined to be very effective for calculating the turbulent properties around axisymmetric body.

To the second discussion

At the upstream region, the partially parabolic flow concept may not be necessary because that the flow of that region can be solved simply. About the stern region, as the flow of liner ship contains the bilge vortex and the pressure varies in the flow, the partially parabolic approximation is adopted in the present calculation. From the calculated results of realizing the recirculating cross flow and the ring shape of velocity contour behind ship, the partially parabolic flow concept is reasonable to calculate the flow around stern region.

To the third discussion

In the table of resistance component, one of the interesting things is that the viscous resistance which is derived from the law of momentum is coincident with the sum of viscous pressure resistance and frictional resistance which is derived from surface integral. This shows the consistency of calculation. The other is that the calculated components show same order to the measured one in case of qualitative coincidence. And the present method provides a way to evaluate the resistance components.

However, it is necessary to improve the refinement of calculation techniques for practical purpose.

Influence of Wall Curvature on Boundary Layer Development on Ship Hulls

Jürgen Kux
Institut für Schiffbau der
Universität Hamburg, Hamburg
Federal Republic of Germany

ABSTRACT

The geometry of the ship hull determines the development of the flow around the ship. Different ways of treating the influence of curvature are reviewed and basic general formulations of differential geometric character are presented. Formulations based on the geometry of curves (stream lines or coordinate lines) and based on the geometry of surfaces are given.

NOMENCLATURE

a^r_n base vector on surface
 a_{rs} surface metrics
 a determinant of a_{rs}
 b_{rs} tensor of the second fundamental form of the surface
 b^r binormal vector on curve
 g^r_n base vector in normal coordinate system tangential to surface
 h^r principal normal on curve
 H mean curvature
 K Gaussian curvature
 ℓ metric on curve
 n^r normal unit vector on surface
 n^r base vector normal to surface
 p pressure
 τ arbitrary coordinate along curve
 s arc length along curve

s^r, s^u tangential unit vector on curve
 s^v shifter
 \bar{t} coordinate along tangential coordinate normal to s coordinate line
 t^r, t^u tangential unit vector normal to s^r and n^r
 $v^r(v^u)$ velocity vector in space (or on the surface)
 v magnitude of v^r
 \bar{x}^r vector in Cartesian system defines surface
 \bar{x}^r vector in Cartesian system defines curve
 $\{\bar{x}^r\}$ Christoffel symbol
 δ^r_s Kronecker symbol
 ϵ^{rsu} totally antisymmetric tensor
 ϵ_{rst} " " "
 α^r vector curvature of curve
 κ_1, κ_2 principal curvatures
 $\kappa_{gs}(\kappa_{gt})$ geodesic curvature of s -line (t -line)
 $\kappa_{ns}(\kappa_{nt})$ normal curvature of s -line (t -line)
 σ_{11} stress tensor
 τ_s torsion
 τ_g geodesic torsion
 φ angle between h^r and n^r (between b^r and t^r)

INTRODUCTION

General Remarks

Flow fields are vector fields which we try to visualize using different aids. They are generally three-dimensional and we visualize them using the concept of field lines or by drawing arrows in discrete points or by isolines all of them generally presented in planes, planes that are mere two-dimensional cuts through the complex three-dimensional field.

The vector lines, streamlines or vorticity lines, are curves in three-dimensional space with curvature and torsion. Though we know that our physical space is not curved, at least if we treat domains of the order of magnitude we are usually confronted with, we see that the flow field shows a certain curvature as a whole. This curvature is ruled by the laws of flow dynamics and the boundary conditions imposed.

Boundary conditions are imposed by the physical boundaries of the domain. These will be surfaces, two-dimensional spaces with a certain geometry which is reflected by the flow field. Specially the curvature of the bounding surface induces effects showing up in the vector fields of flow. These effects lead to corresponding terms in the equations.

The mathematics we use only allows for a one-dimensional approach for the description of reality: We construct sets of one-dimensional entities to describe what happens in two or three dimensions. We proceed along lines, coordinate lines, stream lines, etc. It is therefore of paramount importance to distinguish what is inherent to the field, domain or boundary we describe and what has been artificially introduced by us by the construction of the mentioned lines. This applies particularly to the notion of curvature.

On a plane surface we may introduce polar coordinates and those coordinate lines being circles show a varying degree of curvature while the plane is flat. The straightness of a meridian on a sphere does not bear information on the curvature of the spherical surface. We know from differential geometry the difference between geodesic curvature and surface curvature.

On applying this to flow field calculations, specially boundary layer calculations, we see, that in order to investigate curvature influence of bounding surfaces the additional effect of the curvature of the coordinate lines must be eliminated.

It is also evident that any geometrical characterization of bounding surfaces and of flow lines or sheets or layers should be given in terms independent of the

system of coordinates. The same applies to flow field parameters, for instance integral boundary layer parameters, as long as they are scalars. Comparison between results of calculation methods which do not make use of identical coordinates and geometrical characterization is only possible in terms of such invariant magnitudes.

Many methods developed in the last years for boundary layer calculation in ship hydrodynamics have proceeded along similar lines. The influence of wall curvature was generally neglected and one reason for this may be the formulation of the basic equations from which the authors start. It is the aim of this essay to recapitulate forms of formulation where the surface curvature appears explicitly in the equations.

GEOMETRY

Geometrical Description of Bounding Wall Surfaces

The fixed boundaries of the domain of interest will generally be given as an array of discrete points in space. For the purpose of calculations these points will be given as sets of coordinates \bar{x}^i referring to an over all coordinate system which will be assumed to be a cartesian system. Magnitudes referred to this system will be labeled with capital latin indices running from 1 to 3, corresponding to the three dimensions of space. The surface is a two-dimensional subspace and the set of points is thus a two-dimensional array. This determines a system of coordinate lines on the surface and each point is characterized in this system by two coordinates x^* , $x^* = 1, 2$. These surface coordinates will be characterized by greek indices which may take values 1 and 2. There is a one to one correspondence between the $\{x^*\}$ and the $\{\alpha\}$, even if there is no analytical function representing the connection. With a representation of the surface by bicubic splines we may cast this correspondence into functional form

$$\bar{x}^i = \bar{x}^i(x^*, x^*) \quad (1)$$

Coordinate systems on the surface are often chosen conforming the flow field. In a first order boundary layer calculation this may be the field of outer flow obtained as potential flow. To obtain the potential flow the surface had to be represented in a suitable manner, what means that the construction of flow oriented coordinates comes out to be the second coordinate system to be constructed. This construction has to be repeated for every flow case to be investigated. Thinking of a ship hull, another trim angle will require another coordinate system based on an outer flow field calculation for that angle. So there

are reasons not to use so called streamline coordinates but a system fixed to the surface independent of the flow situation.

The surface coordinates will generally be nonorthogonal and curvilinear and base vectors are defined as

$$a_{\alpha}^i = \bar{x}^i_{,\alpha} = \frac{\partial \bar{x}^i}{\partial x^{\alpha}} \quad (2)$$

They are called the covariant base and are functions of the coordinates again their direction in space changing with position on the surface. The shorthand notation for the partial derivatives $_{,\alpha} = \partial/\partial x^{\alpha}$ will be used. With this base a metric is defined, determined by the tensor $a_{\alpha\beta}$ of the first fundamental form of the surface

$$a_{\alpha\beta} = a_{\alpha}^i a_{\beta}^i = \left(\sum_i \frac{\partial \bar{x}^i}{\partial x^{\alpha}} \frac{\partial \bar{x}^i}{\partial x^{\beta}} \right) \quad (3)$$

$\alpha, \beta = 1, 2$

a covariant tensor. The Einstein summation convention will also be used throughout: The appearance of two identical indices in one term shall imply a summation over their value range.

Through

$$a_{\alpha}^i a_i^{\beta} = \delta_{\alpha}^{\beta} \quad (4)$$

another set of base vectors is defined, the contravariant base. Accordingly these define the contravariant metric tensor

$$a^{\alpha\beta} = a^{\alpha i} a_i^{\beta} \quad (5)$$

In nonorthogonal coordinates one has to distinguish between the covariant components v_{α} (index in the lower position) referring to the base a_{α}^i

$$v^i = v_{\alpha} a^{\alpha i} \quad (6)$$

of a given vector and the contravariant components v^{α} (index in the upper position) referring to the base a_{α}^i

$$v^i = v^{\alpha} a_{\alpha}^i \quad (7)$$

of the same vector. The two forms of metric tensor give the connection between them

$$v^{\alpha} = a^{\alpha\beta} v_{\beta}, \quad v_{\alpha} = a_{\alpha\beta} v^{\beta} \quad (8)$$

i.e. the metric tensor may be used to rise or lower indices.

Since the surface is two-dimensional in three-dimensional space there is only one dimension left for a normal space to the surface.

We define the normal through

$$n^i = \frac{1}{2} \epsilon^{ijk} \epsilon_{kj} a_{\alpha}^i a_{\beta}^j \quad (9)$$

as base vector for this dimension. Here

$$\epsilon^{ijk} = \begin{cases} 1 & \text{if } i, j, k = \begin{Bmatrix} 1, 2, 3 \\ 3, 1, 2 \\ 2, 3, 1 \end{Bmatrix} \\ -1 & \text{if } i, j, k = \begin{Bmatrix} 2, 1, 3 \\ 3, 2, 1 \\ 1, 3, 2 \end{Bmatrix} \\ 0 & \text{otherwise} \end{cases} \quad (10)$$

$$\epsilon_{kj} = \sqrt{a} \begin{pmatrix} 0 & 1 \\ -1 & 0 \end{pmatrix} \quad (11)$$

with

$$a = a_{11} a_{22} - a_{12} a_{21} = \det(a_{\alpha\beta}) \quad (12)$$

A rule for obtaining derivatives in curvilinear coordinates must be given. An infinitesimal displacement leads to a two-fold change in vectors. They eventually vary as functions in relation to the

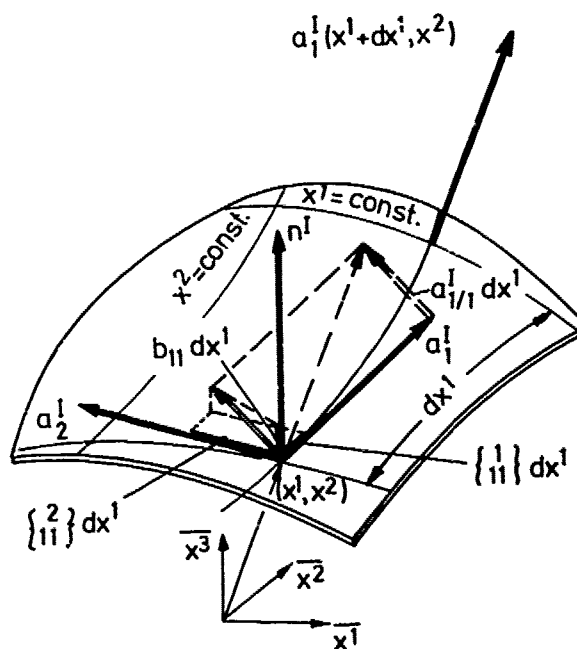


Fig. 1 Base vectors and their derivatives on the surface

local base vectors and in addition these base vectors may have suffered a change in direction in space. This change may be visualized as a difference vector (obtained as difference between the original and the displaced base vector as shown in Fig. 1). This difference vector is decomposed (as shown) into its projections onto the base vectors a_1^i, a_2^i and onto the normal n^i . In order to compensate for the variation of the base, the covariant differentiation for a vector is defined by

$$v^i{}_{;\mu} = v^i{}_{,\mu} + \{ \begin{smallmatrix} i \\ \mu \nu \end{smallmatrix} \} v^\nu = v^i{}_{,\mu} + [\begin{smallmatrix} \mu \nu \\ \lambda \end{smallmatrix}] a^\lambda{}_\mu v^\nu \quad (13)$$

(We will use ${}_{;\mu}$ for the covariant differentiation in the surface coordinate system, as ${}_{,\mu}$ was used for $\partial/\partial x^\mu$, the ordinary differentiation.) The components $b_{\mu\lambda}$ will be zero if the surface is a plane. So the $b_{\mu\lambda}$ emerge as a convenient measure of curvature. The $b_{\mu\lambda}$ are the components of the tensor of the second fundamental form of the surface. It is evident that this tensor depends on the coordinate system on the surface.

By a transformation to principal axes the eigenvalues (characteristic values, proper values) κ_1 and κ_2 of $b_{\mu\lambda}$ may be found. These eigenvalues are termed the principal curvatures and the corresponding eigenvectors (characteristic vectors) determine the directions of the principal curvatures and are orthogonal to each other.

A measure for the curvature not depending on the specific surface coordinate system is desirable. The tensor $b_{\mu\lambda}$ has two invariants

$$H = b_1^1 + b_2^2 = \text{tr}(b_{\mu\lambda}) \quad (14)$$

and $K = b_1^1 b_2^2 - b_2^1 b_1^2 = \det(b_{\mu\lambda}^*)$

($b_{\mu\lambda}^*$ is obtained from $b_{\mu\lambda}$ by rising one index $b_{\mu\lambda}^* = a^{\nu\mu} b_{\nu\lambda}$).

These invariants are appropriate to quantify curvature. A picture of the isolines of H and K on the surface projected onto a suitable plane will give a rather complete picture of the curvature distribution. Fig. 3 shows such isolines for the bulbous bow region of a ship hull.

Boundary layers develop under the pressure field of the outer flow, a field we may represent by isolines of pressure on the hull surface. At the same time the boundary layer suffers the influence of the curvature which we may visualize in an invariant manner by such charts of isolines for the fields of H and K .

The facts about the differential geometry of surfaces reviewed here are well known and this formalism is also found in textbooks on fluid dynamics (Ref.1). This formalism has found broad application in sciences where curvature is important like elasticity theory, shell theory, general relativity, etc.

Generally in papers on boundary layer calculation the coordinate systems were chosen to be orthogonal. The equations are formulated neither in terms of covariant nor in terms of contravariant components of the velocity vector but generally the so called physical or natural components are chosen because they have the physical dimensions as one expects them to be. The matter of physical components has been reviewed by Truesdell (Ref.2). In his paper rules are given to relate the physical components of vectors to their covariant and contravariant components. $g_{\mu\lambda}$, being the metrics of the coordinate system, it is shown that

$$\frac{v_\mu}{\sqrt{g_{\mu\mu}}} = v^\mu \sqrt{g_{\mu\mu}}$$

are the appropriate choices in our notation. In orthogonal coordinates it has become usual to write

$$L_\mu = \sqrt{g_{\mu\mu}}$$

With the rules given how to obtain physical components of vectors, tensors, Christoffel symbols, etc. the equations may be translated. Most papers on boundary layer calculations start from equations written in physical components but for a general treatment of the equations the covariant or contravariant form is more manageable. It should be remarked that there are different possible ways to define physical components (Ref.3).

In order to be able to formulate differential equations in the wall oriented coordinate system a_1^i, a_2^i and n^i (one may take the system a_1^i, a_2^i and n^i as well) we need expressions for $a^{\mu\nu}$ and $n^{\mu\nu}$, as related to this base. These derivatives are tensors and the appropriate tensor base is:

$$\begin{pmatrix} a_1^i a_1^j & a_1^i a_2^j & a_1^i n^j \\ a_2^i a_1^j & a_2^i a_2^j & a_2^i n^j \\ n^i a_1^j & n^i a_2^j & n^i n^j \end{pmatrix} \quad (15)$$

The components of $a^{\mu\nu}$ and $n^{\mu\nu}$ relative to this base are

$$(a^{\mu\nu}) = \begin{pmatrix} \{ \begin{smallmatrix} 1 \\ \mu \end{smallmatrix} \} & \{ \begin{smallmatrix} 2 \\ \mu \end{smallmatrix} \} & 0 \\ \{ \begin{smallmatrix} 1 \\ \nu \end{smallmatrix} \} & \{ \begin{smallmatrix} 2 \\ \nu \end{smallmatrix} \} & 0 \\ b_{\mu 1} & b_{\mu 2} & 0 \end{pmatrix} \quad (16)$$

$\alpha = 1, 2$

$$(n^i_{,j}) = \begin{pmatrix} -b^1_1 & -b^1_2 & 0 \\ -b^2_1 & -b^2_2 & 0 \\ 0 & 0 & 0 \end{pmatrix} \quad (16)$$

Equivalently

$$\begin{aligned} a^i_{,j} &= \{a^i_{,\mu}\} a^{\mu}_j + n^i b_{\mu j} a^{\mu}_j \\ n^i_{,j} &= -b^i_{\mu} a^{\mu}_j a^{\mu}_j \end{aligned} \quad (17)$$

In the matrix $(a^i_{,j})$ the last column contains zeros just because we are dealing with a single surface. It is of course possible to construct a so called system of normal coordinates where the base vectors g^i_1 and g^i_2 are defined by

$$g^i_1 = s^i_1 a^i_1 \quad (18)$$

and the s^i_2 are shifters (Ref.4)

$$s^i_2 = \delta^i_2 - x^j b^i_j \quad (19)$$

while n^i is kept as third base vector g^i_3 . The g^i_3 thus span coordinate surfaces parallel to the given surface. In the matrix $(n^i_{,j})$ the last elements of the two first rows are zero because we have straight lines as coordinate lines in normal direction. This principle may well be abandoned in favor of coordinate lines that bend, a possibility that could become important to be used in concave regions of the wall surface in order to avoid the intersection of the straight normals.

The Geometry of a Single Curve

Again a curve shall be given in the over all Cartesian coordinate system by

$$\tilde{x}^I = \tilde{x}^I(\tau) \quad , \quad I=1, 2, 3 \quad (20)$$

τ being a parameter, our coordinate on the curve. Since the curve is a one-dimensional space we have only one base vector, the tangential vector s^I . It is obtained by differentiation

$$s^I \sim \tilde{x}^I_{,\tau}$$

The curve may be embedded in a two-dimensional space (a surface) or in three-dimensional space. In the first case only one base vector is needed in addition to span the normal space to the curve which now also has merely one dimension. In the second case the normal space will have two dimensions (planes perpendicular to the curve) and two base vectors are needed to

span it.

The parameter τ along the curve may or may not be the arc length s along the curve. We have

$$ds^2 = \tilde{x}^I_{,\tau} \tilde{x}_{I,\tau} d\tau^2 \quad (21)$$

and we may identify

$$\ell_s^2 = \tilde{x}^I_{,\tau} \tilde{x}_{I,\tau} \quad (22)$$

with the metrics on the curve (now a 1 times 1 matrix) corresponding to a_{ij} on the surface. As base vector on the curve the unit tangential vector (Fig. 2)

$$s^I = \frac{\tilde{x}^I_{,\tau}}{\ell_s} = \tilde{x}^I_{,s} \quad (23)$$

is chosen. The vector s^I being a unit vector implies

$$s^I s_{I,s} = s^I \frac{ds^I}{ds} = 0$$

what means that the direction of $s_{I,s} ds/ds$ is at right angles to s^I . This direction is taken for the first of the two base vectors needed to span the normal space and we define this base vector called the principal normal h^I by

$$h^I = \frac{1}{\kappa_s} \frac{ds^I}{ds} = \frac{s^I_{,s}}{\kappa_s} \quad (24)$$

or with the coordinate τ

$$h^I = \frac{1}{\kappa} \frac{ds^I}{d\tau} = \frac{1}{\kappa} \frac{ds^I}{ds} \frac{ds}{d\tau} = \frac{\ell_s}{\kappa} \frac{ds^I}{d\tau}$$

$\kappa_s = \kappa/\ell_s$ is termed the curvature. s^I and h^I determine the so called osculating plane (Fig. 2). As second base vector for the normal space a unit vector at right angles to s^I and h^I is chosen. It is termed b^I , the binormal.

Again the variations of the base vectors ds^I/ds , dh^I/ds and db^I/ds are considered when proceeding along the curve to a point in the infinitesimal neighbourhood of the starting point. Projecting the variation ds^I/ds onto s^I would give us the Christoffel symbol. We have seen that this is equal to zero s^I being a unit vector. Projection of the variations onto h^I and b^I will proportionate magnitudes which are the equivalents to b_{ij} on the surface. The result are the well known Serret-Frenet formulae

$$\begin{aligned} s^I_{,s} &= s^I_{,s} s^I = \kappa_s h^I \\ h^I_{,s} &= h^I_{,s} s^I = -\kappa_s s^I + \tau_s b^I \\ b^I_{,s} &= b^I_{,s} s^I = -\tau_s h^I \end{aligned} \quad (25)$$

$$\begin{aligned}\tau_g &= \varepsilon_{ijk} s^i n^j n^k_{,i} \\ &= \varepsilon_{ijk} s^i t^j t^k_{,i}\end{aligned}\quad (30)$$

$$\kappa_g = \varepsilon_{ijk} t^i \kappa^j_{,k}$$

with the vector curvatures

$$\begin{aligned}\kappa^i_s &= s^j_{,i} = \alpha^j_s s^i_{,j} + \kappa^j s^i b_{j\sigma} s^\sigma \\ \kappa^i_t &= t^j_{,i} = \alpha^j_t t^i_{,j} + \kappa^j t^i b_{j\sigma} t^\sigma\end{aligned}\quad (31)$$

are readily shown to lead to the expressions given.

By scalar multiplication with s^j equations for the rate of variation of s^i , t^i and κ^i due to a translation along the curve are found

$$\begin{aligned}s^i_{,i} &= \kappa_{gs} t^i + \kappa_{ns} \kappa^i \\ t^i_{,i} &= -\kappa_{gs} s^i + \tau_g \kappa^i \\ \kappa^i_{,i} &= -\kappa_{ns} s^i - \tau_g t^i\end{aligned}\quad (32)$$

These are the Burali-Forti formulae, the equivalent to the Frenet-Serret formulae.

A connection between the magnitudes κ_s and τ_s of the s^i, h^i, b^i representation and the magnitudes κ_{gs} , κ_{ns} and τ_g of the s^i, t^i, κ^i representation is desirable. Denoting by φ the angle between h^i and κ^i (or between b^i and t^i) (see Fig. 2) this connection is given by

$$\begin{aligned}\kappa_s^2 &= \kappa_{ns}^2 + \kappa_{gs}^2 & \kappa_{ns} &= \kappa_s \sin \varphi \\ \tau_s &= \tau_g + \frac{\kappa_{gs} \kappa_{ns} - \kappa_{ns} \kappa_{gs}}{\kappa_{gs}^2 + \kappa_{ns}^2} & \kappa_{gs} &= \kappa_s \cos \varphi \\ \varphi &= \arctan \frac{\kappa_{ns}}{\kappa_{gs}} & \tau_g &= \tau_s - \varphi_{,s}\end{aligned}\quad (33)$$

BASIC FLOW EQUATIONS

General Remarks

With the geometrical relations so far reviewed the basic equations of fluid flow may be formulated or relating to a normal coordinate system on the wall surface ($a^i, a^i_{,2}, \kappa^i$) or as intrinsic equations along stream lines. In the latter case there are two base systems which might be chosen, one (s^i, h^i, b^i) really intrinsic to the streamline, the other one (s^i, t^i, κ^i) being oriented in relation to the wall surface. A formulation is possible such that one may discriminate between terms accounting merely for the geodesic curvature of the curves and terms accounting for the curvature of the wall surface as well in the ($a^i, a^i_{,2}, \kappa^i$) as in the (s^i, t^i, κ^i) representation.

Evidently nothing is gained concerning turbulence whatever representation is chosen and the problem of modeling the Reynolds stresses assuming appropriate relations in order to obtain a closure of the system of equations remains open. Nevertheless, some features clearly appear. If the concept of eddy viscosity is generally applied a proportionality to $v^i_{,j}$ is postulated v^i being the mean velocity vector. In general coordinates in the expression for $v^i_{,j}$ terms regarding the geodesic curvature of the coordinate lines appear. To assume the turbulent stresses to depend on them will not be very meaningful. A dependence on the lateral spreading and the geodesic curvature of streamlines clearly may be of importance. If a closure is achieved by additional transport equations then a certain influence of curvature has been taken into account through curvature terms that might appear in this additional equations. On the other side expressions for the eddy viscosity have been applied where curvature effects are taken into account (Ref.7, Ref.8). Depending on the model chosen for closure the influence of curvature enters at different levels. A clear statement about the influence of curvature may not be made as long as there are no computations made with the same method, using the same turbulence model or closure assumptions on various test cases with different geometrical characteristics. Even then a different performance of the turbulence model might obscure any results since generally experimental data on turbulence is not available against which to check the model assumptions.

In the following the complete form of the equations will not be written down. The terms originating from the second derivatives lead to lengthy expressions. We choose to write σ_{ns} for the stresses in order to differentiate against the τ used for the geometrical magnitude torsion and will include both the viscous and the turbulent stress in the σ .

The buoyancy-curvature analogy forwarded by Prandtl (Ref.9) has been reviewed elsewhere (Ref.10) and compared to experimental evidence (e.g. Ref.11). It will not be pursued in the frame of this paper.

The Flow Equations in Wall Oriented Coordinates

With a coordinate system on the wall surface which may be curvilinear nonorthogonal a three-dimensional coordinate system may be constructed by taking straight lines along the direction normal to the surface as third family of coordinate lines. A base vector g^{α} (equation 18) at a certain distance from the wall surface will not be parallel to the corresponding a^{α} on the surface. The metrics in such coordinates will thus be strongly dependent on $b_{\alpha\beta}$, the surface curvature. This dependence is usually neglected and

$$g^{\alpha} g^{\beta} = g^{\alpha\beta} = \delta^{\alpha\beta} \quad (34)$$

is assumed. In the equations given at continuation we will consider the interesting domain adjacent to the wall to have an extension normal to the wall small as compared to wall curvature radius so as to ensure the validity of the assumption (34) (boundary layer). For thick boundary layers this will no longer be valid and the equations will become more complex (Ref.12). For the case of orthogonal coordinates the equations are well known (Ref.13, Ref.14). For the special case of curvature lines (lines in direction of the principal curvatures) as coordinate lines on the surface (Ref.15) there is a certain simplification. Since derivatives of base vectors and metrics are needed it becomes evident that not only the magnitude of wall curvature but also the magnitude of its variation will appear in the equations. Little attention has been given to this effect though it has been pointed out from time to time (Ref.12, Ref.16).

With $\{v^{\alpha}, v^3\}$ as velocity vector we have:

$$S_{;t} + (S v^{\alpha})_{;\alpha} = 0 \quad (\text{continuity})$$

$$S(v^{\alpha}_{;t} + v^{\alpha}_{;\beta} v^{\beta} - b^{\alpha}_{\gamma} v^{\gamma} v^3 + v^{\alpha}_{;3} v^3) = -\tau^{\alpha}_{;t} + \tau^{\alpha}_{;\beta} v^{\beta} + \sigma^{\alpha}_{\gamma\nu} v^{\gamma} - b^{\alpha}_{\gamma} \sigma^{\gamma}_{\nu} \quad (35)$$

$$\alpha = 1, 2$$

$$S(v^3_{;t} + v^3_{;\beta} v^{\beta} + b_{\gamma\mu} v^{\gamma} v^{\mu} + v^3_{;3} v^3) = -\tau^3_{;t} + \sigma^3_{;\beta} v^{\beta} + \sigma^3_{\gamma\beta} v^{\gamma} \quad (\text{momentum})$$

Using the short hand notation for the covariant differentiation all the terms with the Christoffel symbols have been absorbed into the derivatives, only the dependence on the surface curvature appearing explicitly. So in detail

$$\begin{aligned} v^{\alpha} v^{\alpha}_{;\beta} &= v^{\alpha}_{;\beta} v^{\alpha} + \{\overset{\alpha}{\beta}\}_{\gamma}^{\alpha} v^{\gamma} v^{\alpha} \\ &= v^{\alpha}_{;\beta} v^{\alpha} + a_{\gamma}^{\alpha} a^{\gamma}_{;\beta} v^{\gamma} v^{\alpha} \end{aligned} \quad (36)$$

leading to the terms for the geodesic curvature of the coordinate lines which in the case of orthogonal coordinates are usually labeled $K_{\alpha\beta}$.

Thinking of boundary layers $\sigma^{\alpha\alpha}$ will be the predominant component of the stress tensor and the last term in the first equation will become noticeable. The curvature term on the left hand side of the second equation has often been used to derive pressure variation through the boundary layer.

The Flow Equations in Intrinsic Streamline Coordinates

With $v^s = v g^s$ the basic equations for the velocity field may be constructed in intrinsic coordinates, that is in the system uniquely attached to the S -curve which now is a streamline. This representation is restricted in its practical applicability by the fact that we have no direct relation available to show the influence of the geometry of a bounding surface.

The component matrices $(S^s_{;t})$, $(h^s_{;t})$ and $(b^s_{;t})$ (related to the base given in equation 26) contain elements $(\kappa_s$ and $\tau_s)$ describing the curvature and the torsion of a streamline (they appear as the coefficients in the Serret-Frenet formulae) as well as elements describing the normal and the shear deformation of the curve (6 additional magnitudes). The description of the lateral divergence of the streamlines is given by the sum of the diagonal elements of $(S^s_{;t})$, $(h^s_{;t})$ and $(b^s_{;t})$.

In cases where the curvature and torsion are predominant the formulae otherwise crowded with coefficients become simple. As an example we give the expression for the vector $\sigma^s_{;t}$, the divergence of the stress tensor σ^{st} :

$$(\sigma^s_{;t}) = \begin{pmatrix} \sigma_{st;1} - \sigma_{st} \kappa_s \\ \sigma_{st;2} + \sigma_{st} \kappa_s - \sigma_{st} \tau_s \\ \sigma_{st;3} - \sigma_{st} \tau_s \end{pmatrix} = \begin{pmatrix} \partial/\partial s & -\kappa_s & 0 \\ \kappa_s & \partial/\partial s & -\tau_s \\ 0 & \tau_s & \partial/\partial s \end{pmatrix} \begin{pmatrix} \sigma_{st} \\ \sigma_{st} \\ \sigma_{st} \end{pmatrix} \quad (37)$$

The Flow Equation in Wall Oriented Stream-line Coordinates

With the expressions for the derivatives of the base vectors s^x , t^x and n^x in this system (equation 27) the flow equations may be formulated in components relating to this orthogonal system:

$$\begin{aligned} v_{,1s} - v \kappa_{gt} &= 0 && \text{(continuity)} \\ \rho v v_{,1s} &= -\rho_{,1s} + \sigma_{s1s} + \sigma_{st1t} + \sigma_{ns1n} \\ &+ (\kappa_{nt} - 2\kappa_{ns})\sigma_{ns} - 2\kappa_{gt}\sigma_{st} - \tau_g\sigma_{tn} + \kappa_{gt}(\sigma_{tt} - \sigma_{nn}) \\ \rho v^2 \kappa_{gt} &= -\rho_{,1t} + \sigma_{s1t} + \sigma_{tt1t} + \sigma_{tn1n} \\ &- \tau_g\sigma_{ns} - 2\kappa_{gt}\sigma_{st} + (2\kappa_{nt} - \kappa_{ns})\sigma_{tn} + \kappa_{gt}(\sigma_{tt} - \sigma_{nn}) \\ \rho v^2 \kappa_{ns} &= -\rho_{,1n} + \sigma_{s1n} + \sigma_{tn1t} + \sigma_{nn1n} \\ &- \kappa_{gt}\sigma_{ns} - \kappa_{gt}\sigma_{tn} + 2\tau_g\sigma_{st} - \kappa_{nt}(\sigma_{nn} - \sigma_{tt}) \end{aligned} \quad (38)$$

(momentum)

Expressions for the vorticity vector, vorticity diffusion equation and all those well known basic equations may be formulated. They will not be given here.

Neglecting all the components of the stresses but σ_{ns} and their derivatives and assuming derivatives in the direction tangential to the wall to be small we would obtain as simplified equations of motion:

$$\begin{aligned} \rho v v_{,1s} &= -\rho_{,1s} + \sigma_{s1n} + (\kappa_{nt} - 2\kappa_{ns})\sigma_{ns} \\ \rho v^2 \kappa_{gt} &= -\rho_{,1t} - \tau_g\sigma_{ns} \\ \rho v^2 \kappa_{ns} &= -\rho_{,1n} - \kappa_{gt}\sigma_{ns} \end{aligned} \quad (39)$$

APPLICATION TO BOUNDARY LAYER FLOW ON SHIP HULLS

Experimental Data

One of the main problems for the thorough testing of prediction methods and calculation procedures is the lack of data from experiments. In order to investigate the influence of curvature on three-dimensional boundary layer flow detailed experimental surveys of such flows must become available. The points in space where the values are taken should be so closely spaced that the flow line pattern in three dimensions may be constructed. The spacing should also allow for a numerical determination of derivatives. Only then a detailed comparison with the intrinsic equations along stream-

lines will become feasible.

Efforts were made to obtain data of the required completeness (Ref.17) at the Institut für Schiffbau, Hamburg University. These measurements were made with pressure probes and therefore no information on the turbulence and on the turbulent stresses was obtained. Only with the availability of information on the turbulence parameters a critical evaluation of the different models of turbulence will be possible. But with the knowledge of the field of the main velocity and the curvature terms derived from wall curvature an agreement or disagreement with the intrinsic equations should be found within the frame of measurement errors and applying one or the other model for the stress terms.

An evaluation of the vorticity distribution as derived from these measurements is under way. Vorticity fields have been obtained previously for the wake region (Ref.18). From the vorticity distribution in the boundary layer region conclusions may be drawn as to the influence of the curvature on the vorticity field and on vortex structures in the flow.

Methods of Calculation

There is a large number of methods available now for the calculation of the boundary layer flow around ship hulls, differential methods as well as integral methods. Different additional equations are applied (entrainment, moment of momentum, etc.) and different empirical relations as models for turbulence dependent quantities. Due to this diverse approaches a dependence on the wall curvature can be expected to be detected only if there is agreement between results of the methods independent of the approach chosen. In the 1980 SSPA-ITTC Workshop on Ship Boundary Layers (Ref.19) comparative calculations on two test cases were performed by 16 different methods competing. The scatter of the results was disappointing and there are even indications that a dependence on step length or mesh width used in the numerical calculations is still present in some methods.

On the other side the power of the prediction methods has long been demonstrated. An example is the integral method by Himeno and Tanaka (Ref.20) which was shown to be able to reproduce certain features of the wake when extended far downstream (Ref.21, discussion). Integral calculation methods where the normal curvature of the wall is taken into account have been presented in the last years. Two fine examples are the method by Himeno and Okuno (Ref.22) and by Nagamatsu (Ref.23) where the boundary layer thickness is considered in a second computation step by an additional normal outflow velocity as proposed by Lighthill (Ref.24).

The large differences in turbulence distribution due to different models have been shown by Raven (Ref.24) in a differential method (presented by Hoekstra and Raven at the SSPA-ITTC Workshop on Ship Boundary Layers, Ref.19).

The state of the art being this there is some doubt about the detectability of curvature effects in such calculations. It was decided that no additional new calculation method should be developed but that calculations would have to be performed with available and well proven methods, some of which had been put kindly at our disposition, by introducing into them step by step curvature dependent features and conserving the computing philosophy of the method unchanged as far as possible. An interchange of turbulence models will also be considered.

First step in such an investigation would be the computation of metrics, Christoffel symbols, curvature magnitudes, etc. This was performed for a series of digitized ship hull forms including the test cases of the SSPA-ITTC Workshop on Ship Boundary Layers at Göteborg and some of the test cases of the Workshop on Ship Wave Resistance Computations at DTNSRDC, Bethesda, 1979. Fig. 3 shows schematically a part of the results for another hull. The ship is the "Sydney Express" and the isolines of the mean and the Gaussian curvature have originally been plotted by computer as projections to the midship plane. These quantities



— $H = \text{const.}$
 --- $K = \text{const.}$

Fig. 3 Isolines of mean (H) and Gaussian (K) curvature on the bow region of a ship hull

are well suited to give a surface curvature characterization since they are invariants, independent of the coordinate system chosen on the surface. Extreme care is needed to deduce smooth curvature information since it is obtained from the second derivatives. Good spline approximations have to be constructed first. Here still some improvements are desirable. This geometrical in-

formation is stored in the computer. The well documented test case of the mentioned workshop in Göteborg (Ref.19, Ref.17) is the first object being studied. Results are not yet available. Since hot wire investigations will also be performed these will enhance considerably the information about this complex flow and provide means to check the reliability of turbulence model assumptions.

CONCLUDING REMARKS

Experimental results are disclosing the full complexity of the flow around a ship hull. We are used to treat the flow in the spirit of classical boundary layer theory. We will possibly have to learn that the simple division into boundary layer and outer potential flow will not work with the regions of high vorticity (and also detached vortices) extending so far out.

This should not prevent the application of calculation methods available with all the care that is needed regarding numerics, step size and the geodesic curvature of coordinate lines used. The influence of wall curvature may then be tracked using the appropriate formulation as far as uncertainties due to the empirical treatment of turbulence can be overcome. It was the aim of this paper to review the matter of curvature and the pertinent relations. Considerable computation work will have to be done in order to show the influence of curvature by comparing different test cases using different turbulence models.

REFERENCES

1. Aris, R., "Vectors, Tensors and the Basic Equations of Fluid Mechanics", Prentice Hall, Inc., Englewood Cliffs, N.J., 1962.
2. Truesdell, C., "The Physical Components of Vectors and Tensors", *Zeitschrift für Angewandte Mathematik und Mechanik*, Vol. 33, 1953, pp. 345-356.
3. Williams, G., Hector, D.L., "A Note on Physical Components", *Zeitschrift für Angewandte Mathematik und Mechanik*, 49, 1969, pp. 665-670.
4. Ericksen, I.L., "Tensor Fields" in *Encyclopedia of Physics*, Flügge, S. editor, Vol. III/1, Springer-Verlag, 1960, pp. 94-858.
5. Marris, A.W., "Vector Fields of Solenoidal Vector-Line Rotation", *Arch. Rat. Mech. Anal.*, 27, 1967, pp. 195-232.
6. Marris, A.W. and Passman, S.L., "Vector fields and flow on developable surfaces", *Arch. Rat. Mech. Anal.*, 32, 1969, pp. 29-86.
7. Huang, T.T., Santelli, N., Belt, G., "Stern Boundary-Layer Flow on Axisymmetric Bodies", proceedings of the Twelfth Symposium on Naval Hydrodynamics, Washington, pp. 127-157.

8. Soejima, S., Yamazaki, R., Nakatake, H., "Calculation of Thick Three-Dimensional Turbulent Boundary Layers on Ship Stern", presented at the SSPA-ITTC Workshop on Ship Boundary Layers, Ref.19.
9. Prandtl, L., "Essentials of Fluid Dynamics" ("Führer durch die Strömungslehre"), London, Blackie, 1952.
10. Bradshaw, P., "Effects of Streamline Curvature on Turbulent Flow", AGARDograph No. 169, 1973.
11. So, M.C. and Mellor, G.L., "Experiment on Convex Curvature Effects in Turbulent Boundary Layers", Journal of Fluid Mechanics, Vol. 60, 1973, pp. 43-62.
12. Kux, J., "Über dreidimensionale Grenzschichten an gekrümmten Wänden", Institut für Schiffbau der Universität Hamburg, Bericht Nr. 273, 1971.
13. Nash, J.F. and Patel, V.C., "Three-Dimensional Turbulent Boundary Layers", SBC Technical Books 1972, Scientific and Business Consultants, Inc., Atlanta.
14. Mori, K., "An Assessment of Theoretical Methods", Memoirs of the Faculty of Engineering, Hiroshima University, Vol. 7, 1980, pp. 31-47.
15. Landweber, L., "Characteristics of Boundary Layers", proceedings of the 8th Symposium on Naval Hydrodynamics, Pasadena, 1970, pp. 449-472.
16. Betz, A., "Verlauf der Strömungsgeschwindigkeit in der Nähe einer Wand bei un stetiger Änderung der Krümmung", Luftfahrtforschung, 19, 1942, pp. 129-131.
17. Kux, J. and Wieghardt, K., "Three-dimensional Measurements Near the Stern of a Double Model of a Ship", proceedings of the 5th Federal Republic Germany - U.S. Air Force Data Exchange Agreement Meeting on Viscous and Interacting Flow Field Effects, Annapolis, 1980, to appear.
18. Hatano, S., Mori, K., Fukushima, M., Yamazaki, R. and Suzuki, T., "Calculation of Velocity Distribution in Ship Wake", Journal of the Society of Naval Architects of Japan, Vol. 138 (1975) and Vol. 141 (1977).
19. Proceedings of the SSPA-ITTC Workshop on Ship Boundary Layers, Larsson, L., editor, Göteborg, 1980, to appear.
20. Himeno, Y. and Tanaka, J., "An Integral Method for Predicting the Behaviors of Three-Dimensional Turbulent Boundary Layers on Ship Hull Surfaces", Technology Reports of the Osaka University, Vol. 23, No. 1146, 1973, pp. 617-647.
21. Kux, J., "Three-Dimensional Turbulent Boundary Layers", proceedings of the Tenth Symposium on Naval Hydrodynamics, Cambridge, Massachusetts, 1974, pp. 685-703.
22. Himeno, Y. and Okuno, T., "Study on Cross Flow in Ship Boundary Layer", proceedings of the International Symposium on Ship Viscous Resistance, Göteborg, 1978, Larsson, L., editor.
23. Nagasatsu, T., "Calculation of Viscous Pressure Resistance of Ships Based on a Higher Order Boundary Layer Theory", Journal of the Society of Naval Architects of Japan, Vol. 147, 1980, pp. 21-35, and
- "Comparison between Calculated and Measured Results of Turbulent Boundary Layers around Ship Models", Mitsubishi Technical Bulletin No. 133, 1979.
24. Raven, H.C., "Calculation of the Boundary Layer Flow around Three Ship Afterbodies", International Shipbuilding Progress, 27, 1980, p. 10.

Discussion

A.Y. Odabaşı (SSR)

Dr. Kux, in his paper, presents us the basic concepts of the differential geometry from which he develops alternative forms for the boundary layer equations and proposes a way to assess the relative influence of curvature on the flow development. Since, we at BSRA spent a considerable amount of time and effort on the same subjects, I would like to bring some relevant points to the author's attention and also to shed some light into a point which is related to the use of invariant, covariant and contravariant transformations in relation to the transformation of physical quantities, cf. 1).

In many practical problems it is often necessary to employ a coordinate system which suits the problem. The difficulty associated with the coordinate transformation is in expressing the equations describing the system behaviour. Provided that the coordinate transformation is admissible 2) that is the transformation equations

$$y_i = y_i(x_1, \dots, x_n) \quad (1)$$

$$(i = 1, 2, \dots, n)$$

are continuous together with their first partial derivatives and the Jacobian determinant $J = |\partial y_i / \partial x_j|$ does not vanish at any point in the region of interest, one may speak of three types of transformations: (1) transformation by invariance, (2) transformation by covariance, and (3) transformation by contravariance.

When the quantity of interest is a scalar field quantity, such as kinematical viscosity or any other scalar field function, its value remains unchanged although its expression may differ. For example temperature of in field point in x_i coordinate system may be $T(x_1, \dots, x_n)$ and after the coordinate transformation it becomes

$$T(x_1(y_1, \dots, y_n), x_2(y_1, \dots, y_n), \dots, x_n(y_1, \dots, y_n)) = G(y_1, \dots, y_n) \quad (2)$$

but its numerical value at a point P does not change. We can regard the scalar function $F(P)$ as being defined by the totality of components $T(x_i)$, $G(y_i)$, etc., each of which is related to one another by the substitution law typified by formula (2). This substitution transformation is called "transformation by invariance".

Instead of dealing with a function $f(x_1, x_2, \dots, x_n)$ of a scalar $F(P)$ one may be interested in its gradient which is

formed from a set of n partial derivatives

$$\frac{\partial f}{\partial x_1}, \dots, \frac{\partial f}{\partial x_n} \text{ or } \{f_{x_i}\}. \quad (3)$$

The question is then what does the set $\{f_{x_i}\}$ become when the coordinates x_i are subjected to a transformation

$$x_i = x_i(y_1, \dots, y_n), (i = 1, \dots, n). \quad (4)$$

The answer depends what the corresponding functions in the Y -frame is to mean in any given situation. For example, one may insert in each function $f_{x_i}(x_1, \dots, x_n)$ the values of x 's from (4). This will yield a set of functions $g_i(y_1, \dots, y_n)$. If, however, one has in mind the notion of a gradient of $f(P)$, the corresponding functions are not $g_i(y_1, \dots, y_n)$ but the set of n partial derivatives

$$\frac{\partial f}{\partial y_1}, \frac{\partial f}{\partial y_2}, \dots, \frac{\partial f}{\partial y_n}$$

which are computed by the rule for differentiation of composite functions

$$\frac{\partial f}{\partial y_i} = \frac{\partial f}{\partial x_j} \frac{\partial x_j}{\partial y_i} \quad (i, j = 1, 2, \dots, n) \quad (5)$$

here and onwards the summation is understood over the repeated indices.

We can think of $\{\partial f / \partial x_i\}$, $\{\partial f / \partial y_i\}$, etc., as representing the same entity in different reference frames. If we have a set of n functions $A_i(x)$, \dots , $A_n(x)$ associated with the X -coordinate system and if the corresponding functions $B_i(y)$, \dots , $B_n(y)$ in the Y -coordinate system is calculated by means of the "covariant law"

$$B_i(y) = \frac{\partial x_j}{\partial y_i} A_j(x) \quad (i, j = 1, 2, \dots, n) \quad (6)$$

the sets $\{A_i(x)\}$ and $\{B_i(y)\}$ represent the components of covariant vectors in the X - and Y -coordinate systems, respectively, and this form of transformation is called "transformation by covariance".

Finally, we may think of two points $P_1(x_1, \dots, x_n)$ and $P_2(x_1 + dx_1, \dots, x_n + dx_n)$ and consider a set of n differentials

$$dx_1, dx_2, \dots, dx_n.$$

These differences are components of a displacement vector in the X -coordinate system and the same displacement vector when referred to the Y -coordinate system has its components

$$dy_1, dy_2, \dots, dy_n$$

which, by virtue of the transformation (1), are related to dx_i 's by

$$dy_i = \frac{\partial y_i}{\partial x_j} dx_j \quad (i, j = 1, 2, \dots, n). \quad (7)$$

If we have a set of quantities $A_1(x), \dots, A_n(x)$ in the X-coordinate system and determine the corresponding functions $B_1(y), \dots, B_n(y)$ in the Y-coordinate system by means of the "contravariant law"

$$B_i(y) = \frac{\partial y_i}{\partial x_j} A_j(x) \quad (i, j = 1, 2, \dots, n) \quad (8)$$

the sets $\{A_i(x)\}$ and $\{B_i(y)\}$ become the components of contravariant vectors in the X- and Y-coordinate systems, respectively, and the transformation of this kind is known as the "transformation by contravariance".

The next point is related to the equivalence of otherwise of curvature or streamline related wall coordinate. Wesseling 3) in a study on the nature of the TSL equations proved that these equations are semi-invariant with respect to a coordinate transformation and if one of the coordinates coincides with the body surface they become invariant and consequently different coordinate systems with normal being a coordinate should reflect the influence of curvature equally well. As to the eddy viscosity formulae, Mellor and Herring 4) proposed an alternative definition which is invariant under a Galilean transformation.

The final point I would like to take up is relative merit attached to the extra strain rate effects of curvatures, Ref. [10]. If one scans the recent literature in the field of complex boundary layers, one would notice that representatives of all three different turbulence modeling have, in one way or another, employed extra strain rate corrections to obtain a better correlation with data, cf. Cebeci 5), Rastogi and Rodi 6), Wilcox and Chambers 7), and Bradshaw [10]. In fact, recently Hunt and Joubert 8) showed that a third order study of the experimental data on a duct flow indicated the correctness of Bradshaw's engineering approximation method. Since we do not want to rediscover the things that have been well-accustomed in the field of aeronautics we should pay more serious attention to this subject.

REFERENCES

- 1) Odabaşı, A.Y. and Fulthorpe, C.F.

"AFACAN- A Geometry Package for the Ship Boundary Layer Calculations", BSRA Report WG/PHIVE 41. (1979)

2) Sokolnikoff, I.S. "Tensor Analysis Theory and Applications to Geometry and Mechanics of Continua", J. Wiley and Sons, Inc., Second Edition, (1964)

3) Wesseling, P. "The Calculation of Incompressible Three Dimensional Turbulent Boundary Layers. Part 1. Formulation of a System of Equations", National Aerospace Laboratory NLR, The Netherlands, Report AT-69 -U1, (1969)

4) Mellor, G.L. and Herring, H.J. "Simple Eddy Viscosity Relations for Three-Dimensional Turbulent Boundary Layers", AIAA Journal, Vol. 15, p. 886 (1977)

5) Cebeci, T. "Wall Curvature and Transition Effects in Turbulent Boundary Layers", AIAA Journal, Vol. 9, p. 1868, (1971)

6) Rastogi, A.K. and Rodi, W. "Calculation of General Three-Dimensional Turbulent Boundary Layers", AIAA Journal, Vol. 16, p. 151 (1978)

7) Wilcox, D.C. and Chambers, T.L. "Streamline Curvature Effects on Turbulent Boundary Layers", AIAA paper 76-353, (1976)

8) Hunt, I.A. and Joubert, P.N. "Effects of Small Streamline Curvature on Turbulent Duct Flow", J. Fluid Mech., Vol. 91, p. 633 (1979)

Author's Reply

J. Kux (FS)

I thank Dr. Odabaşı for his discussion. He gives an extensive contribution regarding the transformation of physical quantities. I appreciate his comment on the work done in the field of aeronautics because in fact there are possibilities that results obtained in that field might be overlooked by ship-hydrodynamicists. Nevertheless I had knowledge of most of the additional references Dr. Odabaşı cites. It is my opinion that the approach I have chosen in my paper is somewhat different.

Prediction of Viscous Flow around a Fully Submerged Appended Body

Nicholas-Christos G. Markatos

CHAM Limited, Wimbledon, London

Colin Brian Wills

Admiralty Marine Technology Establishment

Haslar

United Kingdom

ABSTRACT

This paper describes the first stages in the development and application of a finite-difference calculation procedure employing a two-equation turbulence model (k, ϵ), to the prediction of the flow around an appended, submerged body.

Initial studies were conducted to predict the steady flow field over and behind an appendage protruding through a plane boundary layer. The procedures developed to calculate both the two- and three-dimensional wake fields are presented. For the two-dimensional case the method employed is partially-parabolic and thus takes account of lateral pressure variation but cannot predict flow separation and recirculation. The three-dimensional flow field is also non-parabolic; however, by using the two-dimensional partially-parabolic solution it is possible to decouple the pressure in the momentum equations and thus render the solution parabolic. This considerably simplifies the computation procedure compared with that of a three-dimensional partially-parabolic solution. Comparison between calculated velocities and measured data demonstrate that the technique has the potential to warrant extension to consideration of the flow around an appended body.

The application of the partially-parabolic calculation procedure to an unappended axisymmetric body is described and comparison again made between predicted and measured parameters. The calculated axial variation of skin friction and boundary layer thickness are shown to be in close agreement with experimental values but the static pressure gradient and total velocity are both over predicted in the tail region. The implications of the above

comparison on the application of the prediction method to submerged bodies is discussed and proposals made for further work.

NOMENCLATURE

C_1, C_2, C_D	constants of the (k, ϵ) turbulence model.
F_j	body force in the j -momentum equation.
$J_{\phi, i}$	flux of ϕ along the i -th direction.
k	kinetic energy of turbulence.
ℓ	dissipation length scale.
ℓ_{wake}	mixing length in wake flow.
L_m	mixing length.
p	static pressure.
\bar{p}	space averaged pressure over a cross section.
q_p	total velocity at point P.
r, θ, z	cylindrical polar coordinates.
r_s	hydrofoil radius.
r_N	radius of the outer boundary of calculation domain.
s	distance along a streamline.
s^ϕ	source/sink term for variable ϕ .
U_i	velocity component in direction i .
u, v, w	circumferential, radial and axial velocity components in a cylindrical polar coordinate system.
u, v	streamwise and lateral velocity components in a ψ - x coordinate system.

x axial coordinate.
 x_T axial coordinate of trailing edge.
 $y(\psi, x)$ the lateral coordinate of point (ψ, x) .

Greek Symbols

α angle made by streamlines with the x -axis.
 ϵ dissipation rate of turbulence energy.
 η, ζ, ξ curvilinear coordinates.
 θ_1, θ_2 characteristic distances used in mixing length calculations.
 $\theta_{3,0}^{\text{wake}}$
 κ Von-Karman constant.
 λ universal constant in mixing length calculation.
 μ viscosity.
 μ_{eff} effective viscosity.
 ρ density.
 σ_{ij} stress tensor.
 $\sigma_{\text{eff}, \phi}$ effective Prandtl number for variable ϕ .
 τ shear stress.
 ϕ a general fluid variable.
 ψ stream function.

1. INTRODUCTION

For many classes of marine vessel the propeller operates in a thick boundary layer at the aft end of the hull and thereby achieves an improved propulsive performance. The variation in velocity over the propeller disc, due to the wake from the hull and appendages, can however, give rise to the generation of unsteady forces on the propeller and unsteady pressures on the hull. Both of these phenomena can lead to excessive vibration of the ship's structure and equipment. In order to design the propeller and to estimate the unsteady forces and pressures generated by the propeller, it is thus essential to have a detailed knowledge of the full-scale flow conditions at the propeller. This is normally estimated from measurements made on a model and modified to take account of the difference in Reynolds number, and hence boundary layer characteristics, between the model and full-scale. Since the model data is often obtained from unpowered tests, further allowance has to be made for the flow acceleration induced by the propeller.

An approximate method for determining the above corrections to model flow measurements, based on the boundary layer prediction method of Myring (1) was presented by Moore and Wills (2) at the 12th Symposium on Naval Hydrodynamics. The procedure adopted was to replace the appended hull by an equivalent body of

revolution and then to carry out powered and unpowered boundary layer predictions to determine mean circumferential velocities for model and full-scale Reynolds numbers. These results were then used to derive the corrections for changes in Reynolds number and propeller induction and these applied to the model data. Agreement with model and full-scale data was limited and further experimental data is being obtained to refine the method.

While the above approach has been found to give results of reasonable engineering accuracy it cannot be regarded as entirely satisfactory. Thus, studies have been initiated to investigate the potential of the method described in (3,4,5,6) for the calculation of the boundary layer on an unsymmetric appended body. This work has been carried out by CHAM Limited, under a contract from AMTE and is the subject of this paper. The ability to estimate accurately the appended boundary layer over a ship's hull would also enable theoretical prediction of many of the parameters currently obtained by means of expensive and time consuming model testing. Although it is likely that the requirement for model experiments will always remain, many of the investigations conducted to optimise hull and appendage design could be carried out theoretically, and the model testing restricted to the final configuration.

In pursuing the above objective it was decided to consider initially a fully submerged body and to break the work down into distinct stages, so that different aspects of the mathematical modelling could be introduced separately viz,

1. Prediction of the two-dimensional turbulent flow over and behind an isolated hydrofoil.
2. Prediction of the three-dimensional turbulent flow behind a hydrofoil mounted normal to a plane surface and protruding through the boundary layer on the plane surface.
3. Prediction of the flow field around an axisymmetric body.
4. Amplification of the mathematical model to permit departures from axial symmetry of the hull.
5. Amplification of 4. to include appendages.
6. Inclusion of a propeller at the stern of an axisymmetric body.

In the following sections of the paper, the mathematical model developed during Stages 1 to 4 will be described and some of the results obtained for Stages 1 to 3 presented and compared with experimental data.

2. CONSTRUCTION OF THE COMPUTATIONAL MODELS

2.1 Two-Dimensional Turbulent Flow Over and Behind an Isolated Hydrofoil

2.1.1 Theoretical formulation. The basic geometrical model for which two-dimensional calculations were made was a standard NACA 0017 section hydrofoil. The flow over and behind this section was computed by using the partially-parabolic method of Pratap and Spalding (5), full account being taken of the solution domain curvature and variation of domain area. Two basic assumptions are made in the partially-parabolic method; firstly it is presumed that recirculation is absent from the main flow direction, and secondly, that the diffusion fluxes and stresses may be neglected in this direction. In contrast to conventional boundary layer methods, however, full account is taken of the lateral pressure variations which may occur in the flows under consideration, due to high flow curvature, and which can significantly influence the upstream flow conditions. It is this feature which, in the situations considered herein, renders the flow partially-parabolic. The significance of the partially-parabolic analysis is that, compared with fully-elliptic flows, the computation can proceed with greatly reduced computer storage because only the pressure field, which is treated as fully-elliptic, needs to be stored two-dimensionally.

The coordinate system employed in the calculations comprised one set of coordinate lines which were perpendicular to the chord of the hydrofoil, the latter being conveniently chosen as the x-axis, so that the coordinate lines become x-constant lines. The second set were the streamlines of the flow itself i.e. $\psi = \text{constant}$ lines (Figure 1).

The following variables were calculated at each point P of the solution domain:

- u, the streamwise velocity;
- v, the lateral velocity;
- p, the static pressure of the fluid;
- y, the lateral coordinate of P(ψ, x).

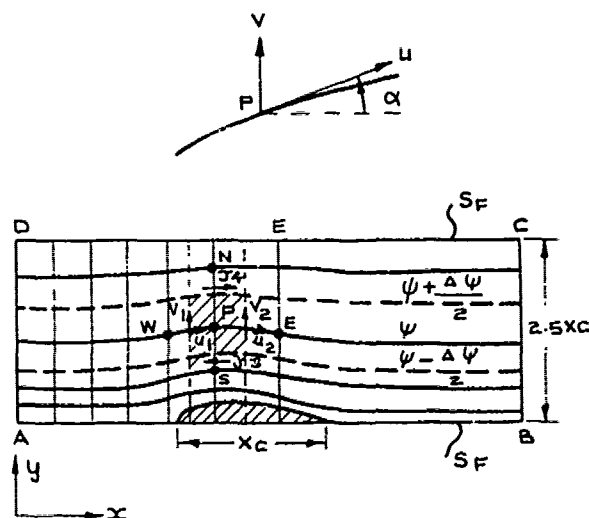


Fig 1 Coordinate System and Grid Convention

The flow around the foil is governed by the following equations:

Continuity

$$\frac{\partial}{\partial x} (\rho u \cos \alpha) \Big|_y + \frac{\partial}{\partial y} (\rho v \sin \alpha) \Big|_x = 0, \quad (1)$$

$$\text{where, } \sin \alpha \equiv \frac{v}{u}. \quad (2)$$

v-momentum

$$\rho u \frac{\partial v}{\partial s} \Big|_\psi = - \frac{\partial p}{\partial y} \Big|_x. \quad (3)$$

u-momentum

$$\rho u \frac{\partial u}{\partial s} \Big|_\psi = - \frac{\partial p}{\partial s} \Big|_\psi + \frac{1}{\rho u} \frac{\partial \tau}{\partial y} \Big|_x, \quad (4)$$

where s denotes distance along a streamline, and α is the angle made by the streamline at P with the x-axis.

The derivation of these equations from the basic equations of inviscid dynamics for steady-plane flow is immediate upon observing that they are simply alternative forms of the Eulerian equations with a different choice of dependent variables and the addition of the viscous term. For turbulent flow τ must be regarded as encompassing both the action of viscosity and the effect of turbulent exchange, i.e. the Reynolds stress.

To calculate y in the (Ψ, x) system, the following relation is used:

$$\left. \frac{\partial y}{\partial \Psi} \right|_x = \frac{1}{\rho u \cos \alpha} \quad (5)$$

The introduction of Ψ as an independent variable with the coordinate function $y(\Psi, x)$ of the streamlines as a dependent variable leads to certain interesting relations. The introduction of Ψ satisfies the equation of continuity, identically. However, in the Ψ - x system there must exist some relation which expresses the kinematic compatibility of the above transformation and which is necessary for the complete solution of the differential equations.

From the definition of α ,

$$\left. \frac{\partial y(\Psi, x)}{\partial x} \right|_{\Psi} = \tan \alpha \quad (6)$$

Equations (5) and (6) are compatible if and only if,

$$\frac{\partial^2 y}{\partial \Psi \partial x} = \frac{\partial^2 y}{\partial x \partial \Psi} \quad (7)$$

which leads to the following kinematic compatibility equation, which plays the role of the equation of continuity:

$$\left. \frac{\partial}{\partial \Psi} (\tan \alpha) \right|_x = \frac{\partial}{\partial x} \left(\frac{1}{\rho u \cos \alpha} \right) \Big|_{\Psi} \quad (8)$$

Eliminating y entirely from the system and using $ds \cos \alpha \equiv dx$, it is concluded that the dependent variables u , v , α and p satisfy the following system of equations.

u-momentum

$$\rho u \left. \frac{\partial u}{\partial x} \right|_{\Psi} \cos \alpha = - \left. \frac{\partial p}{\partial x} \right|_{\Psi} \cos \alpha + \left. \frac{\partial \tau}{\partial \Psi} \right|_x \cos \alpha \quad (9)$$

v-momentum

$$\rho u \cos \alpha \left. \frac{\partial v}{\partial x} \right|_{\Psi} = - \left. \frac{\partial p}{\partial \Psi} \right|_x \rho u \cos \alpha \quad (10)$$

Kinematic compatibility

$$\left. \frac{\partial}{\partial x} \left(\frac{1}{\rho u \cos \alpha} \right) \right|_{\Psi} = \left. \frac{\partial}{\partial \Psi} (\tan \alpha) \right|_x \quad (11)$$

In the turbulent flows under consideration, it is assumed that the shear stress obeys a law similar to that in laminar flows, with an enhanced coefficient. Thus,

$$\tau = \mu_{\text{eff}} \frac{\partial u}{\partial y} \quad (12)$$

where the effective viscosity (μ_{eff}) is assumed to be governed by Prandtl's mixing length model.

For the calculation of the mixing length, the solution domain was divided into three regions, the first upstream of the foil, the second over the foil and the third in the wake region. The effective viscosity is related to the mixing length (L_m) by:

$$\mu_{\text{eff}} \equiv \rho L_m^2 \left| \frac{\partial u}{\partial y} \right| \quad (13)$$

The mixing length is calculated in these three regions in terms of the following quantities.

λ - a 'universal constant' $\equiv 0.12$;

κ - Von Karman constant $\equiv 0.4$;

$\theta_1 \equiv 0.0175 \times \text{chord}$;

$\theta_2 \equiv$ distance between the boundary streamline ψ_1 corresponding to the blade surface, and ψ_2 which has the property:

$$\left(\frac{\psi_2 - \psi_1}{\psi_E - \psi_1} \right) = 0.005 \quad (14)$$

i.e. the mass flow $\psi_2 - \psi_1$ is 1% of the total mass flow through the solution domain.

$$\theta_3 \equiv \frac{\lambda}{\kappa} \cdot \theta_2 \quad (15)$$

$$\theta_{\text{wake}} \equiv \theta_{\text{wake}}^{\text{wake}} / 0.18 \quad (16)$$

where

$$\theta_{\text{wake}}^{\text{wake}} \equiv 0.105 \cdot (x - x_T) \left(1 - \frac{u^{\text{wake}}}{u_{\text{in}}^{\text{wake}}} \right) \quad (17)$$

(for $x \geq x_T$)

and $u_{\text{wake}}^{\text{wake}}$ is the wake 'centre-line' velocity at x_{wake} .

Then in the region ahead of the foil,

$$L_m \equiv \lambda \theta_1 \quad (18)$$

In the region over the foil.

$$L_m \equiv \lambda \theta, \quad v_n > \theta_1 \quad (19)$$

$$\equiv \langle y_n \rangle, \quad y_n < \theta_3 \quad (20)$$

$$\equiv \langle \theta_3 \rangle + \lambda \theta_1 (1 - u), \quad \theta_3 \leq y_n \leq \theta_1 \quad (21)$$

where

$$\mu \equiv \left(\frac{\theta_1 - y_n}{\theta_1 - \theta_3} \right) \quad (22)$$

In the wake,

$$L_m \equiv \ell_{\text{wake}} \quad (x \geq x_T; y_n \leq \theta_{\text{wake}}) \quad (23)$$

$$L_m \equiv \ell_{\text{wake}} \mu' + \lambda \theta_1 (1 - \mu') \quad (24)$$

$$\theta_{\text{wake}} \leq y_n \leq y_E$$

where

$$\mu' \equiv \left(\frac{y_E - y_n}{y_E - \theta_{\text{wake}}} \right) \quad (25)$$

and y_n is the perpendicular distance from point P at which L_m is being calculated to the I-boundary. The relationships for ℓ_{wake} and θ_{wake} are given by Schlichting (7). All the other formulae used above are adapted from Launder and Spalding (4) for the present problem.

The boundary conditions and fluid properties for the calculations were defined as given below.

Inlet conditions: Inlet stagnation pressure, streamwise velocity, and flow angle were specified at one chord distance ahead of the foil, i.e. $u(u^2/2 + p/\rho)$ and $\alpha(=0)$.

Outlet conditions: A uniform pressure distribution was specified at three chord lengths aft of the foil, i.e. $\frac{\partial p}{\partial y}|_{\text{outlet}} = 0$.

The pressure level at the outlet was not specified, but was an outcome of the computation.

Hydrofoil surface: The surface inclinations with respect to x were specified. The foil surface was assumed impermeable and no-slip conditions were applied, e.g. $u \equiv v \equiv 0$. The effects of wall turbulence are taken into account by wall functions to be discussed later.

Free surfaces: The boundaries marked S_F in Figure 1 were assumed to be symmetry planes and therefore $v \equiv 0$ (i.e. $\alpha \equiv 0$) and $\frac{\partial u}{\partial y} = 0$. The distance of this boundary from the foil was selected, after preliminary computations, so that the zero gradient condition was a realistic one, i.e. at 2.5 times chord.

Fluid properties: The fluid was assumed incompressible and the laminar viscosity and density taken to be values appropriate to fresh water at a constant temperature.

2.1.2 Solution Procedure. In the finite-difference formulation of the problem, a "staggered-grid" practice was

adopted, whereby the velocity components and pressure were stored in the "staggered" positions on the finite-difference grid, shown in Figure 1. Upwind differences of momentum fluxes were used in the momentum equations, and diffusion through the vertical faces of the control volume was neglected.

The space-marching, partially-parabolic algorithm of Pratap and Spalding (5) was used to solve the above finite-difference equations with the specified boundary conditions. In this scheme, the finite-difference equations are solved at one axial station at a time, starting with the inlet. The solution 'marches' downstream from inlet to outlet. The marches are repeated until convergence is obtained.

2.2 Three-Dimensional Turbulent Flow Over and Behind a Hydrofoil

2.2.1 Theoretical formulation. The basic geometrical model for which three-dimensional calculations were made was again a standard NACA 0017 section. The inability of the procedure described in Section 2.1 above, to be extended to three dimensions, lead to the development of a general three-dimensional model. This model has been included in a computer program which can be used directly in either two- or three-dimensional, and in either parabolic or partially-parabolic modes.

Since the cross-section of the hydrofoil, and of a ship's hull, varies with axial position, a cartesian or cylindrical coordinate system for the governing equations is not suitable. It is more convenient to construct a curvilinear system which has one axis normal to the axis of the body, and the other two axes orthogonal to the first, but not necessarily to each other. This system can be applied to ship forms where the frames are not generally orthogonal to the streamlines.

The elements of the system (η, ζ, ξ) are defined in terms of orthogonal, cylindrical polar coordinates (r, θ, z), and in accordance with Figure 2.

Thus:

$$\eta = \frac{r - r_S}{r_N - r_S}; \quad \xi = \frac{\theta - \theta_W}{\theta_E - \theta_W}; \quad \zeta = z \quad (26)$$

where r_S is the hull radius, r_N is the radius of the outer boundary, and $(r_N - r_S)$, $(\theta_E - \theta_W)$ are the radial and angular width of the domain of interest, respectively.

The above definitions make possible the use of coordinates that vary between 0 and 1 only. In this respect the ζ - η grid at each station has as boundaries those of the flow domain, thus avoiding waste of computer storage.

The dependent variables for the problems considered are:-

- w, v, u : the axial, radial and circumferential velocity com-

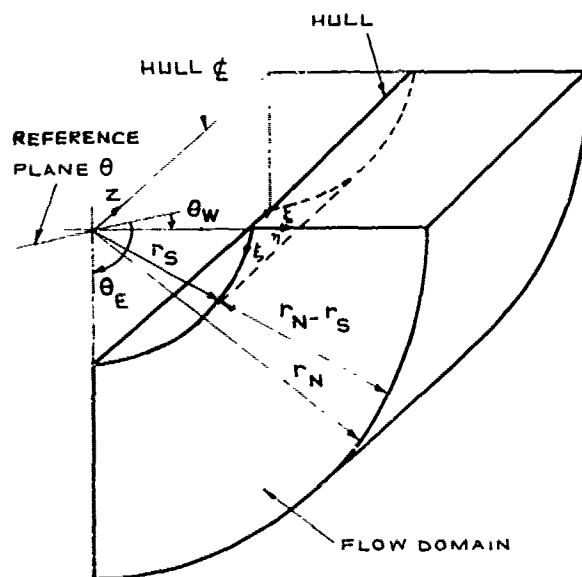


Fig. 2 Coordinate System for a Ship Hull

- p : the static pressure;
- k, ϵ : the turbulence kinetic energy and its dissipation rate, respectively.

The partial differential equations, which govern steady, three-dimensional motion of fluids can be expressed in tensor notation as follows:

Continuity

$$\frac{\partial}{\partial x_i} (\rho U_i) = 0. \quad (27)$$

Transport of fluid property ϕ

$$\frac{\partial}{\partial x_i} (\rho U_i \phi) = S^\phi - \frac{\partial J_{\phi,i}}{\partial x_i} \quad (28)$$

where U_i is the velocity component in direction x_i , ϕ may represent a velocity component, kinetic energy of turbulence or its dissipation rate, S^ϕ is the source/sink term for variable ϕ , and $J_{\phi,i}$ is the flux of ϕ along the i -th direction. For the transport of the velocity component U_j , for example, equation (28) takes the form of the j -momentum equation:

$$\frac{\partial}{\partial x_i} (\rho U_i U_j) = F_j - \frac{\partial p}{\partial x_j} - \frac{\partial \sigma_{ij}}{\partial x_i} \quad (29)$$

F_j being a body force acting on the fluid, and σ_{ij} the stress tensor.

In turbulent flows it is assumed that the shear stress and other fluxes obey laws similar to those in laminar flows, with enhanced coefficients, thus the following exchange laws are formed:

$$\sigma_{ij} = -\nu_{\text{eff}} \left(\frac{\partial U_i}{\partial x_j} + \frac{\partial U_j}{\partial x_i} \right), \quad (30)$$

$$J_{\phi,i} = - \left(\frac{\nu_{\text{eff}}}{\sigma_{\text{eff},\phi}} \right) \frac{\partial \phi}{\partial x_i}, \quad (31)$$

where $\sigma_{\text{eff},\phi}$ is the effective Prandtl number for variable ϕ .

If the flow is laminar the effective viscosity, ν_{eff} becomes the laminar viscosity, ν_ℓ . For turbulent flows ν_{eff} is calculated in accordance with the k - ϵ model of turbulence (Launder & Spalding, {4}) as:

$$\nu_{\text{eff}} = \nu_\ell + \nu_t = \nu_\ell + C_D k^2 / \epsilon, \quad (32)$$

where C_D is a proportionality constant, and k and ϵ are determined by solving separate partial differential equations for their transport.

The governing equations relative to the above coordinate system are given by Abdelmeguid, Markatos and Spalding {6} and hence are not repeated herein. The turbulence model contains five empirical constants {4} which for the problem described here are assigned the values given in Table 1.

C_1	C_2	C_D	$\sigma_{\text{eff},k}$	$\sigma_{\text{eff},\epsilon}$
1.44	1.92	0.09	1.0	1.23

Table 1 Constants of the Turbulence Model

The length scale of turbulence, in this model is given by:

$$l = C_D k^{3/2} / \epsilon \quad (33)$$

This turbulence model is valid only for fully-turbulent flows. Close to solid walls there are regions where the local turbulent Reynolds number ($\rho k^{1/2} l / \mu$) is small, and the viscous effects predominate over, or are of equal importance with turbulent effects. The rigorous incorporation of the effects of the vicinity of a wall to turbulence proves expensive in computer time. Thus "wall functions" {3} were employed as outlined in {6} such that the numerical solution was forced to behave in a prescribed manner in the immediate vicinity of the wall.

Although the above theoretical model is presented in its partially-parabolic mode, the predictions made during this

investigation were obtained by using the method in its fully parabolic mode, but with an important novelty which is described below. The reasons behind this are economy of calculation and the desire to utilise the results already obtained for the two-dimensional case.

For fully parabolic procedure, the pressure in the z-momentum equation is different from the pressure in the two other momentum equations. This is a deliberate inconsistency introduced into the treatment of pressure and its purpose is to decouple the pressure gradients. By this means, marching integration can be employed and two-dimensional computer storage used for all variables (3). Often the pressure in the z-momentum equation, (\bar{p}), is taken as the space averaged pressure over a cross section, and the gradient $\partial \bar{p} / \partial z$ is assumed to be known (or calculated) before calculation of the lateral gradients $\partial p / \partial \eta$, and $\partial p / \partial \xi$. This practice is implicit in two-dimensional boundary layer theories also.

In the case considered here, the presence of the hydrofoil in the flow field will cause non-parabolic effects. These are taken into account by employing the two-dimensional pressure field calculated by the partially-parabolic procedure of Section 2.1 in calculating the axial pressure gradient (and only the axial pressure gradient) for each marching station. This decouples the pressure in the momentum equations and renders the latter parabolic.

The boundary conditions for this stage of the investigations were selected to represent the hydrofoil mounted normal to the floor of the Circulating Water Channel as described in Section 3.

Inlet conditions: At the inlet to the solution domain (a distance of 0.8 chord from the airfoil leading edge) plug profiles were assigned to all variables, except the longitudinal velocity w , for which experimental profiles in the absence of the foil were used. The u and v components were set to zero.

Two values for the mean level of inlet turbulence were used, namely, 5 and 10% of the mean inlet velocity. The dissipation rate of turbulence at inlet was specified according to a prescribed length scale distribution, and was given by:

$$\varepsilon = f k^{3/2} \quad (34)$$

where

$$f = 1/(0.07H) \quad (35)$$

and H was the total width of the domain.

The nature of the boundary layer formed around the foil and along the floor at the flow channel, implied that the flow was expected to be 3-D in the vicinity of the corner formed between the foil and the floor. Far from the fin or the floor, the flow was expected to become two-dimensional.

Thus, the region of interest was that close to the corner (Figure 3).

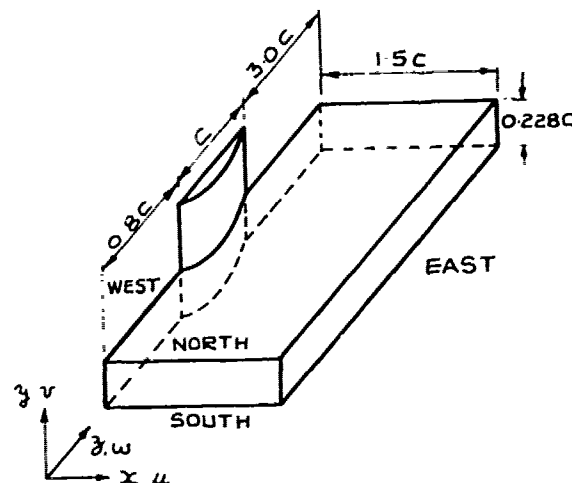


Fig 3 Three-Dimensional Flow Domain

The boundaries of this domain are the free boundaries (North and East), the solid boundaries (West, along the aerofoil and South), and the axis of symmetry (West, before the leading edge and after the trailing edge of the foil). The conditions at these boundaries are given below:

South boundary: $u=v=w=0$. The values of k , ε were obtained from the "wall functions".

West boundary: For the foil solid boundary, the no-slip conditions and "wall functions" were employed. For the symmetry plane zero-gradient conditions were assigned.

North boundary: Far from the floor, the flow is 2-D, therefore the results from Section 2.1 were used as boundary conditions, e.g.

$$w = w_{2D}, \quad u = u_{2D}, \quad p = p_{2D} \quad (36)$$

$$\text{and } \frac{\partial k}{\partial \eta} = \frac{\partial \varepsilon}{\partial \eta} = 0. \quad (37)$$

Because of entrainment at this boundary, the v -velocity was calculated by satisfying the local continuity at each calculation station. This velocity was used only in the continuity equation, whilst the momentum equations assumed zero North boundary v -velocity.

East boundary: Far from the aerofoil the flow becomes 2-D, so that normal gradients of the variables were taken as zero across the boundary except for pressure which was assigned its known value at the North East corner of the domain.

It should be noted that both the North and East boundaries are physically the

same, i.e. free, yet they are treated differently. At the North boundary inflow and outflow is allowed, whereas the East boundary is considered as a symmetry plane. Thus, the latter is consistent with the boundary conditions used in the two-dimensional calculations.

As already discussed the pressure gradient calculated for the two-dimensional case was used as the pressure gradient in the downstream (z) direction. In the direction normal to the floor (y) the pressure was assumed to be uniform and equal to the pressure at the North boundary.

2.2.2 Solution procedure. The grid layout used was a "staggered" grid system as before.

Integration of the partial differential equation governing the transport of each variable yields an algebraic equation for each grid location, representing the discretized form of the balance of the variable, over the control volume corresponding to that location. A special treatment is applied to the momentum equations, developed in (3). This yields a Poisson equation for the "pressure correction" which is used to update the velocity and pressure fields. Upwind differencing is used and the difference equations are solved in turn for each variable by the application of the tri-diagonal matrix algorithm.

More details on the solution method may be found in the above reference. The innovation to the method introduced here is that iteration is provided at each axial station of the marching integration, in order to improve the convergence and the accuracy of the results.

2.3 Prediction of the Turbulent Flow Field Around An Axisymmetric Body

2.3.1 Theoretical formulation. The basic geometrical model for which two-dimensional calculations were obtained during this stage of the work was the body considered by Patel et al (8). The flow over and behind this was computed using the partially-parabolic procedure described in Section 2.2 in its two-dimensional mode.

The coordinate system and the governing differential equations are the same as described in Section 2.2 but omitting the third dimension, ξ . The dependent variables considered are also the same except for the disappearance of the u-velocity component. It should be noted that for the predictions obtained during this stage, no parabolic assumption is made concerning pressure. The two-dimensional pressure distribution is the outcome of the computational procedure which now operates in its partially-parabolic mode.

The boundary conditions for these calculations were as given below:

Wall conditions: At the body surface, the velocities were zero from the no-slip

condition. Close to the surface a modified wall function accounting for axial pressure gradient was employed. This function is given by:

$$\frac{q_p}{(\tau/\rho)^{1/2}} = \frac{1}{\kappa} \ln \left[\frac{E y_p (\tau/\rho)^{1/2}}{u_{\tau}} F \right] \quad (38)$$

where q_p and y_p are the total velocity at the near-wall point P and its distance from the wall, and F is the modification factor given by:

$$F = (1 + \frac{1}{2} \frac{y_p}{\tau} \frac{dp}{dz})^{1/2} \quad (39)$$

The point P must be located in the fully turbulent region, i.e.

$$y^+ = \frac{\tau y_p}{u_{\tau}} > 11.5 \quad (40)$$

The turbulence kinetic energy at the near wall point was fixed at a value proportional to τ/c , and the dissipation rate of turbulence at that point calculated from a linear length scale distribution.

Symmetry-plane conditions: Downstream of the stern, the boundary which was previously the Patel body becomes a symmetry-plane.

Free-boundary conditions: At the free-boundary of the calculation domain, the axial velocity, w, and the static pressure p were given the values obtained from a potential flow solution along that particular surface. The mass flow rate across the boundary was computed from local continuity during the calculations.

Inlet conditions: Calculations were performed starting either at half the body length from the nose or at 15% of the length upstream of the nose. At the half-body plane the radial velocity was assumed to be zero and the boundary layer parameters taken from predictions by the method of Myring (1). The velocity profile was scaled linearly from the edge of the boundary layer to the free boundary. The turbulence kinetic energy k was taken to be uniform and equal to a percentage of the free stream velocity squared. For the dissipation rate, ϵ , the Escudier formula, (9), was used to calculate the distribution of length scale l .

When the calculations started ahead of the body, uniform values of $v=0$ and $w=12.192\text{m/s}$ were used at inlet. Other conditions remained the same as given above.

Exit boundary conditions: Because of the partially-parabolic nature of the solution procedure an additional boundary condition was needed for the pressure, at the exit boundary of the calculation domain (i.e. 1/3 of body length downstream of the stern). It was assumed that the exit pressure was uniform, at the value given by the potential flow solution.

Initial guess for pressure: The pressures prevailing at the free-boundary were taken as the initial guess to the pressure field.

2.3.2 Solution Procedure. There are two basic differences between the solution procedure used and that described in Section 2.2.3. Firstly, it requires several sweeps of marching integration, from the upstream to the downstream end of the calculation domain, thus, it is an iterative procedure. Secondly, full account is taken of the effects of pressure, on axial velocity. This allows pressure effects to be transmitted in both upstream and downstream directions.

More details on the sequence of calculation steps may be found in [6].

3. COMPARISON BETWEEN THEORETICAL PREDICTIONS AND EXPERIMENTAL RESULTS

In the computations which are discussed below finite-difference grids were used which ensured that the results were grid independent. For the two-dimensional flow over the hydrofoil, the grid possessed 36 points in the longitudinal direction and 16 in the lateral direction. For the three-dimensional flow a grid of 12 nodes in each of the lateral directions and 40 in the longitudinal direction was adequate. For the half Patel body, a grid of 20 nodes radially and 30 nodes axially was used. In the case of the full Patel body the number of nodes were 17 and 37 respectively. The grid spacing for all cases was non-uniform, the grid lines being more closely spaced near the wall and in the nose and tail region of the body. These grids were determined after calculations had been carried out with different grid densities. From these studies, it was concluded that grids finer than those above led only to marginal changes in the results but to considerably increased cost.

Convergence was monitored by observing changes from sweep to sweep for flow variables at particular locations, and by computing mass continuity errors. In general, convergence was fast and monotonic. After about 50 sweeps, variables were changing by less than 1% and the maximum integral mass imbalance at any plane was less than 0.01% of the inlet mass flow rate.

3.1 Two and Three Dimensional Wake Behind a Hydrofoil

Prior to commencing the theoretical studies described in this paper, an experimental investigation had been carried out at ANTE(H) into the wake generated behind a hydrofoil protruding through the boundary layer developed on a plane surface. These experiments were carried out in the Circulating Water Channel (CWC) at Haslar and consisted of velocity surveys at a position 2/3 chord aft of the trailing edge of a

NACA 0017 section foil. The height of the foil was such that the outer sections were well clear of the surface boundary layer and the flow could be regarded as two-dimensional. Measurements were taken at Reynolds numbers of 2.0×10^6 and 0.5×10^6 , based on the foil chord of 450mm and in the latter case an adverse pressure gradient was generated by inclining the plane surface 2.5 degrees to the flow direction.

The non-dimensional boundary layer profiles, on the plane surface at the position of the fin leading edge but in the absence of the foil, are given in Figure 4. The longitudinal variation of static pressure coefficient with the inclined surface, again in the absence of the foil is shown in Figure 5. This pressure variation has been non-dimensionalised using the velocity outside the boundary layer at the position of the foil leading edge.

The procedure described in Section 2.1 has been used to predict the two-dimensional wake behind a NACA 0017 section foil and a flat plate in uniform flow. The variation of the wake centre-line velocity with downstream distance is given in Figure 6, for the NACA 0017 foil and in Figure 7 for the flat plate. Also given for the foil are values from the CWC experiment, and from an empirical curve based on the correlations of Spence [10] and Lieblein and Roudebush [11]. For the flat plate the experimental results of Chevray and Kovaszny [12] have been included in Figure 7.

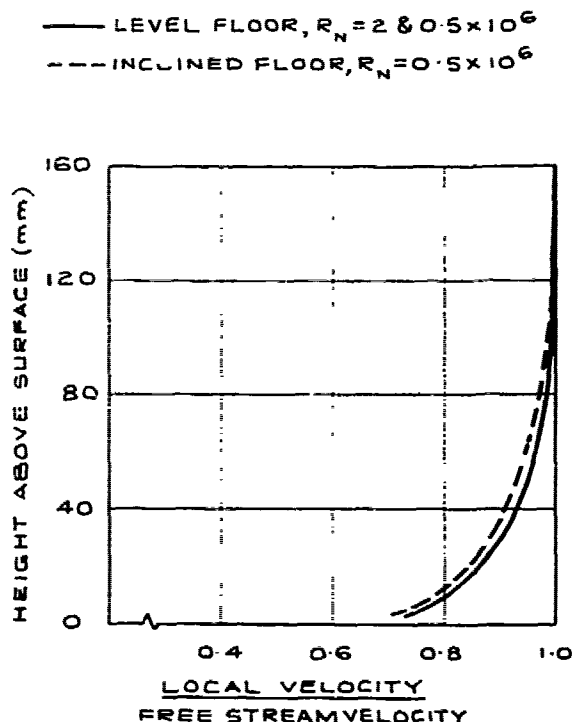


Fig 4 Boundary Layer Profile at Foil Leading Edge

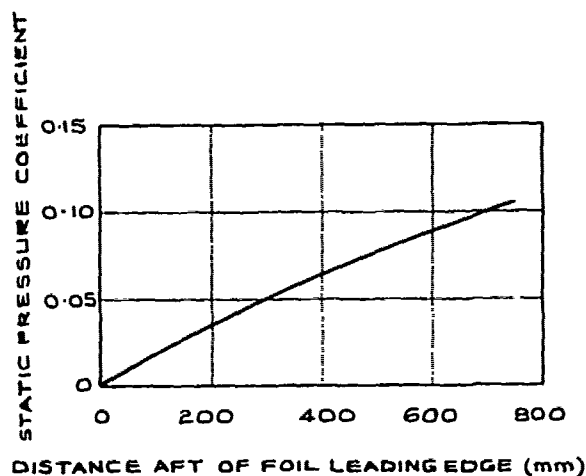


Fig 5 Variation of Static Pressure in the Circulating Water Channel

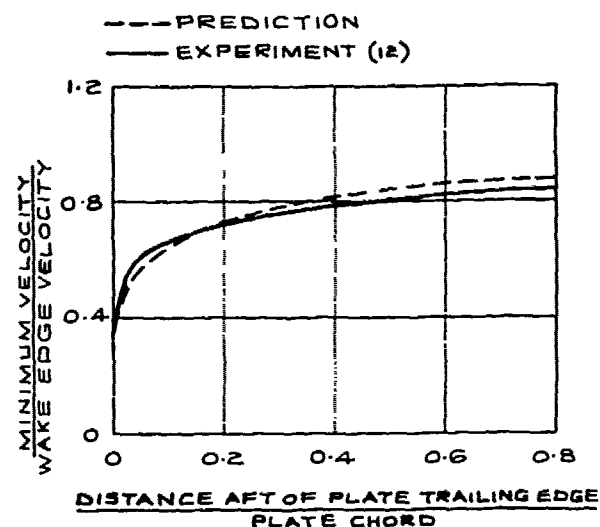


Fig 7 Variation of Wake Centreline Velocity Behind a Flat Plate

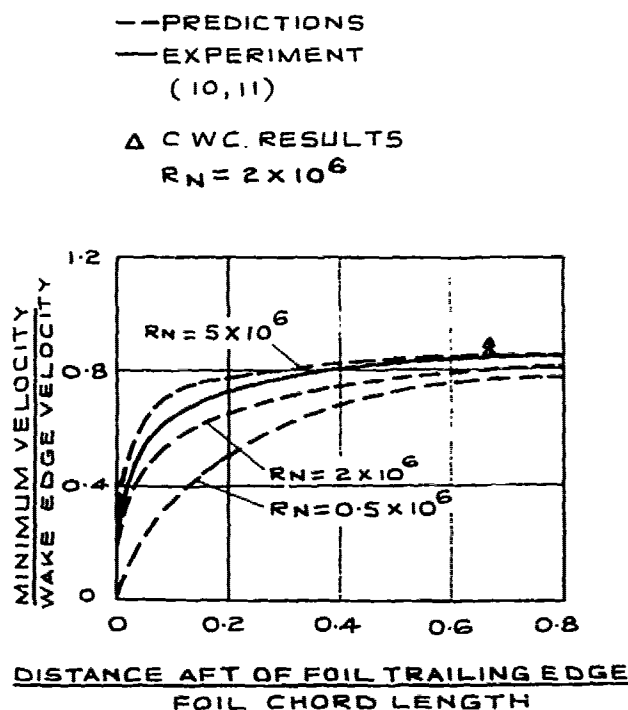


Fig 6 Variation of Wake Centreline Velocity Behind a Hydrofoil

It can be seen from Figure 6 that the effect of varying Reynolds number is most significant close to the trailing edge of the foil and that reducing the Reynolds number produces a slower recovery of the wake centreline velocity. This is the result of less turbulence in the wake at lower Reynolds numbers and hence less rapid mixing of the flow in the near wake region. At a position about one chord aft of the foil trailing edge however, the effect of Reynolds number is very much reduced.

The empirical curve for aerofoil sections given in Figure 6 was based on data from tests run at Reynolds numbers from 0.5×10^6 to 5×10^6 and conducted on foils of varying section shape, thickness and incidence. It can be seen from this Figure that the predictions for the NACA 0017 foil at high Reynolds number are in good agreement with the empirical curve; however, the predicted variation with Reynolds number is considerably higher than that of the data used for the two correlations. In particular, the lowest Reynolds number prediction shows a much slower wake recovery than the experimental data; however, this Reynolds number is well below the full-scale value for major ship appendages. Comparison between the predicted centre-line velocity at a position $2/3$ chord aft of the trailing edge and the CWC results show the predictions to be 9% low. Generalisation from these results is difficult; however, it appears that the predictions give a somewhat slower wake recovery than shown in the experimental data.

The prediction of the wake behind the thin flat plate is a less severe test of the finite-difference grid employed in the theoretical model than the finite thickness

foil case. This is reflected in the very good agreement between the experimental results and the predictions for the flat plate given in Figure 7.

Comparison between the results for the hydrofoil and the flat plate suggest that the less satisfactory predictions in the former case may be associated with the specification of the finite-difference grid.

The above results were found to be insensitive to the variation of inlet turbulence produced by a 70% increase in the inlet mixing length and to the change in the wake mixing length law resulting from a doubling of δ_2 (Section 2.2.1).

The three-dimensional solution described in Section 2.2 was used to predict the axial velocity profiles behind the NACA 0017 foil under the conditions of the tests in the Circulating Water Channel. The results of these predictions are given in Figures 8 to 11 together with the experimental data.

The influence of Reynolds number on the predictions is shown in Figure 8 from which it can be seen that near the channel floor the highest Reynolds number leads to the highest velocities. This is consistent with the thinning of the boundary layer on the channel floor as the Reynolds number increases. Clearly as the distance from the floor increases this effect

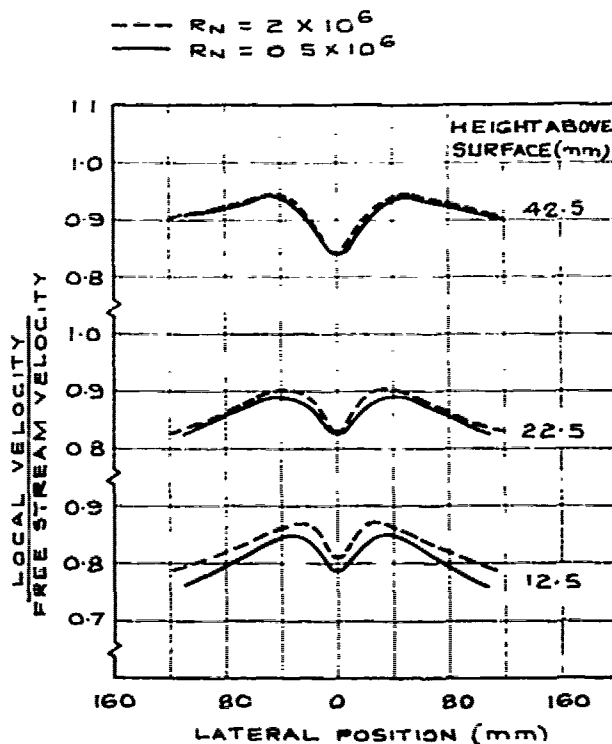


Fig 8 Effect of Reynolds Number on Predicted Velocity Profiles (Level Floor)

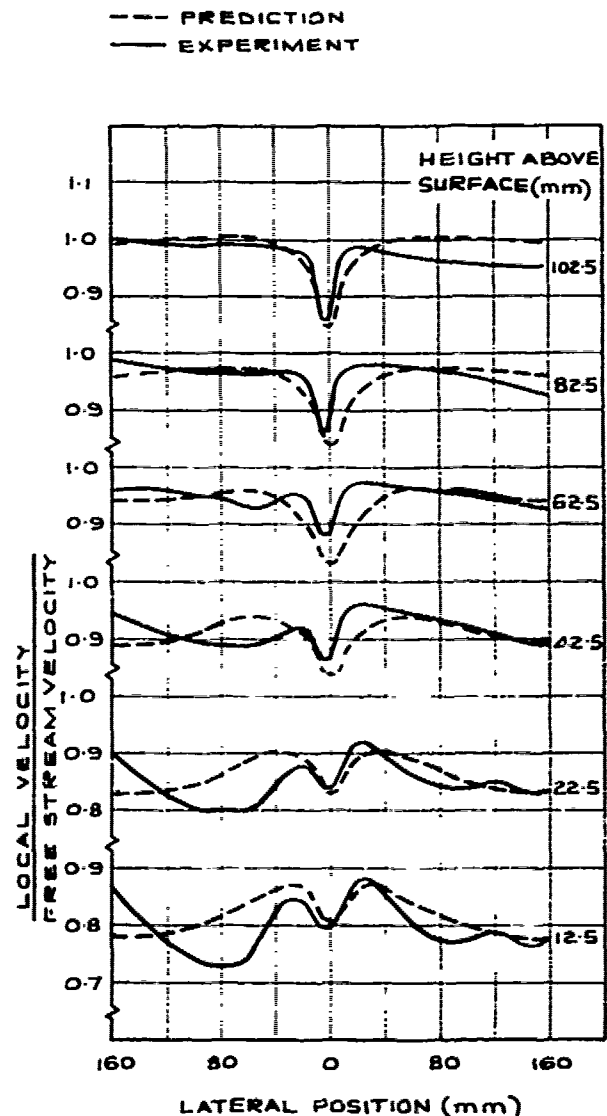


Fig 9 Velocity Profiles Behind a Hydrofoil ($Re=2 \times 10^6$, Level Floor)

becomes less significant so that by about 40mm from the floor the results are virtually independent of Reynolds number. This distance compares with a channel wall boundary layer thickness of the order of 100mm (Figure 4).

Direct comparison between the predicted and measured velocity profiles (Figures 9, 10 and 11) is hindered by the non-symmetry of the latter; however, the agreement between the two is generally good. For all three cases, two Reynolds numbers with zero pressure gradient, and one adverse pressure gradient condition, the predictions appear to be most accurate near the channel floor. This is

particularly encouraging because this is the region where there are significant three-dimensional effects. As the distance from the floor increases and the flow becomes more two-dimensional the wake defect is generally over predicted, as was the case for the purely two-dimensional predictions. This is especially true for the adverse pressure gradient case, however, the test flow conditions were rather unstable in this situation and the measured data is thus not as reliable as that for the zero pressure gradient condition. The predicted velocity profiles near the channel floor clearly demonstrate the change in flow conditions which occur in the presence of the adverse pressure gradient caused by the inclination of the channel floor. In the latter case the variation in velocity is considerably reduced.

The influence of inlet turbulence on the above solutions was investigated using values of $\frac{\sqrt{k}}{W_\infty}$ of 0.05 and 0.10. As in the two dimensional case this variation was found to have little significant effect upon the predicted velocities.

The results discussed above were considered to have demonstrated that the technique employed represented a sound framework for the prediction of the three-dimensional flow behind a hydrofoil.

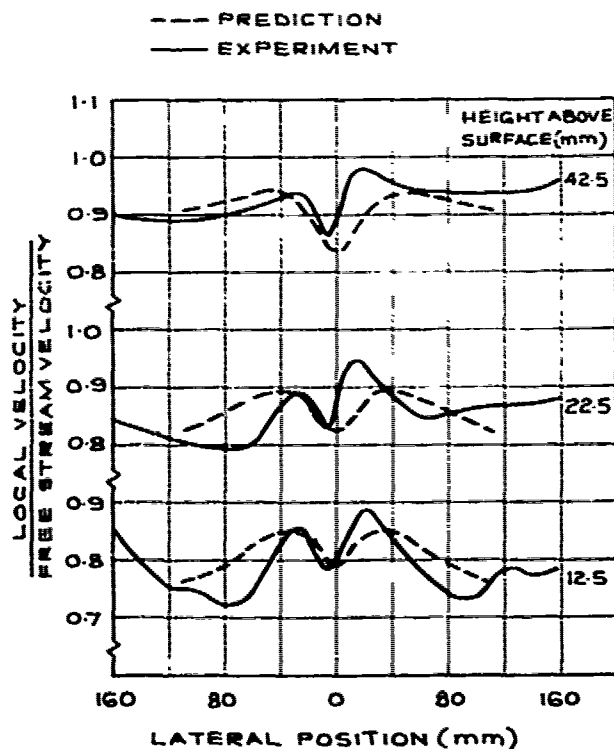


Fig 10 Velocity Profiles Behind a Hydrofoil ($Re=0.5 \times 10^6$, Level Floor)

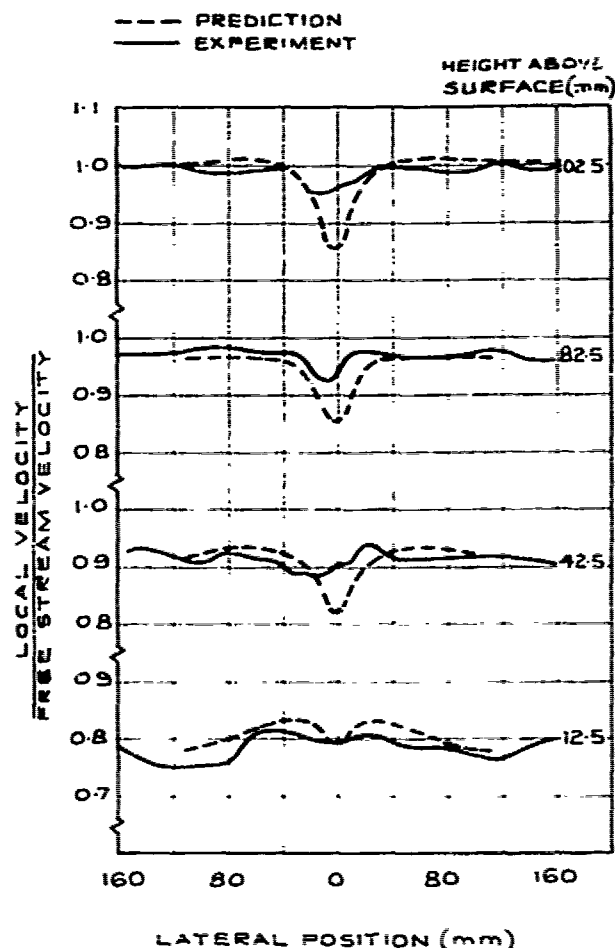


Fig 11 Velocity Profiles Behind a Hydrofoil ($Re=0.5 \times 10^6$, Inclined Floor)

3.2 Flow Over the Tail Region of an Axisymmetric Body

The correlation between the predictions and measurements described in Section 3.1 were regarded as sufficient to warrant extension of the prediction method to an axisymmetric body. The most extensive set of experimental data available for this case was considered to be that of Patel et al (8) and hence predictions have been made for comparison with the data given therein. The method of solution described in Section 2.3 was used to predict the flow parameters over the tail region of this body. The free boundary conditions were determined from a potential flow solution for the complete body. The inlet boundary conditions were determined either at the body mid-length from predictions of the boundary layer parameters given by the method of Myring (1) or at a position 15% of the body length ahead of the body from the conditions of uniform inflow.

Initially studies were carried out using the half body inlet conditions to determine the sensitivity of the solution to the position of the free boundary, to the form of the finite-difference grid and to the inlet turbulence level, and the results used to select these parameters. Predictions were then carried out for the stern half of the Patel body and the results are compared with the experimental data in Figures 12 to 17

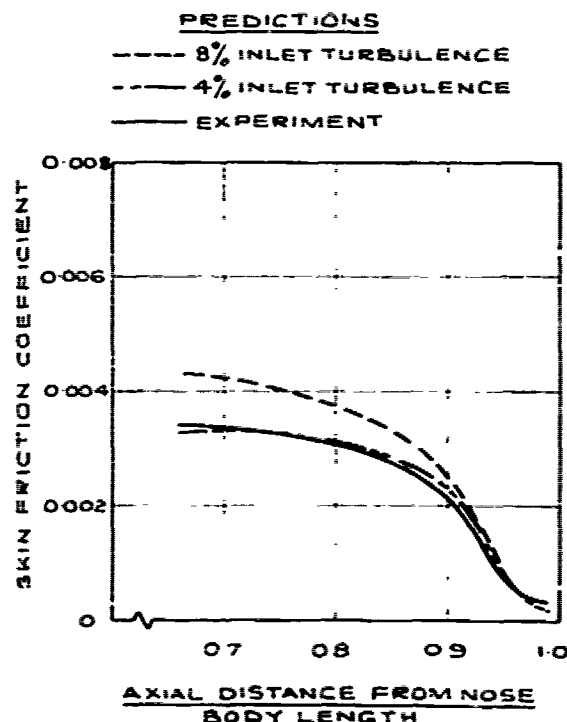


Fig 12 Axial Variation of Skin Friction Coefficient

The predicted axial variation of the skin friction coefficient is given in Figure 12 for two inlet turbulence levels, since this was the only parameter found to be significantly dependent upon inlet turbulence level within the range of

$\frac{\sqrt{k}}{u} = 0.04$ to 0.15 . It can be seen that the lower level of turbulence leads to predicted values of skin friction coefficient which are very close to the measured values.

The variation of turbulence kinetic energy (\sqrt{k}/u_δ , where u_δ is the velocity at the edge of the boundary layer) in the direction perpendicular to the body at 96% of body length from the nose is given in Figure 13 for 8% and 15% inlet turbulence.

It is apparent that the predicted turbulence level at this axial location is independent of inlet turbulence specification. Furthermore, the predictions are in fair agreement with Patel's measurements (8) over the boundary layer thickness

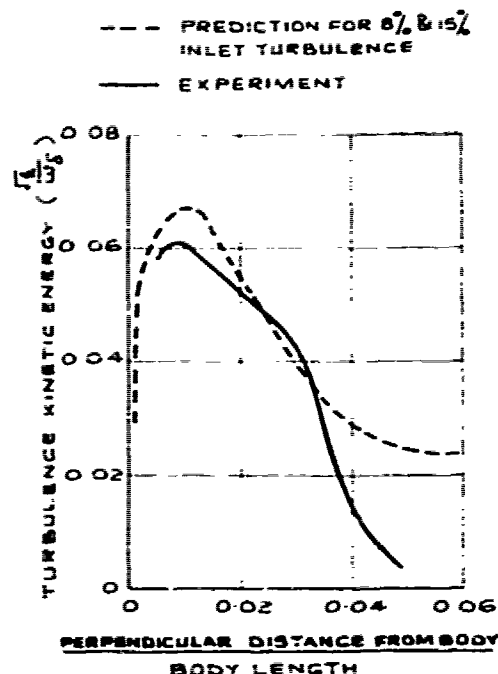


Fig 13 Variation of Turbulence Kinetic Energy at 96% of Body Length From Nose

but indicate a residual of 2% turbulence up to the outer boundary. This is a consequence of the inlet plane assumption that the flow is fully turbulent all the way from the body to the outer boundary. This evidently is not a reasonable assumption since the outer boundary is located far from the boundary layer edge, and the experiments indicate that the turbulent region is confined within the boundary layer. Therefore, in future work the turbulence quantities should be treated differently inside and outside the boundary layer at the inlet plane.

The axial variation of the boundary layer thickness is given in Figure 14 from which it is clear that there is very close agreement between the predicted and experimental values.

The axial variation of the static pressure coefficients at the wall and at the edge of the boundary layer are given in Figure 15. The experimental coefficients used a tunnel wall pressure as reference which was lower than the free stream static pressure, thus the total head coefficient outside the boundary layer was approximately 1.06 instead of the ideal value of 1.0. The predicted pressure coefficients have therefore been increased by 0.06 so that they are consistent with the experimental data. A similar correction was made by Dyne (13) and was approved by Patel. It is evident from Figure 15 that the static pressure gradient is under-predicted between approximately 80% and 90% of the body length but considerably over predicted for the last 10% of the body length.

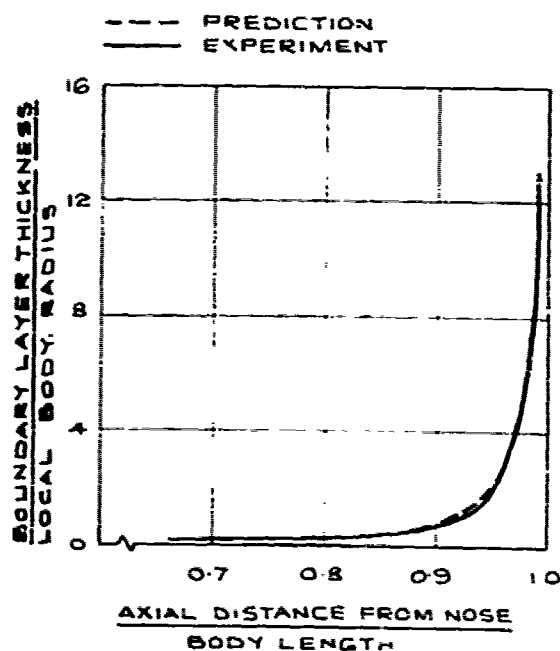


Fig 14 Axial Variation of Boundary Layer Thickness

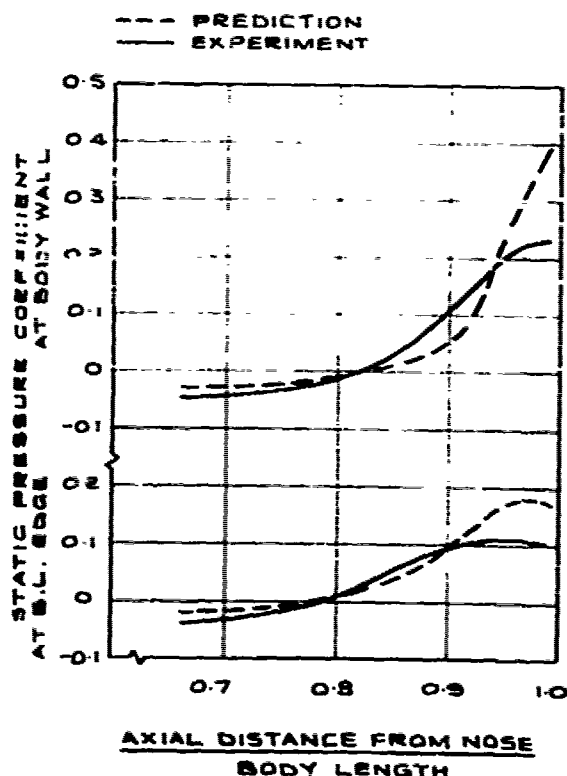


Fig 15 Axial Variation of Static Pressure Coefficients

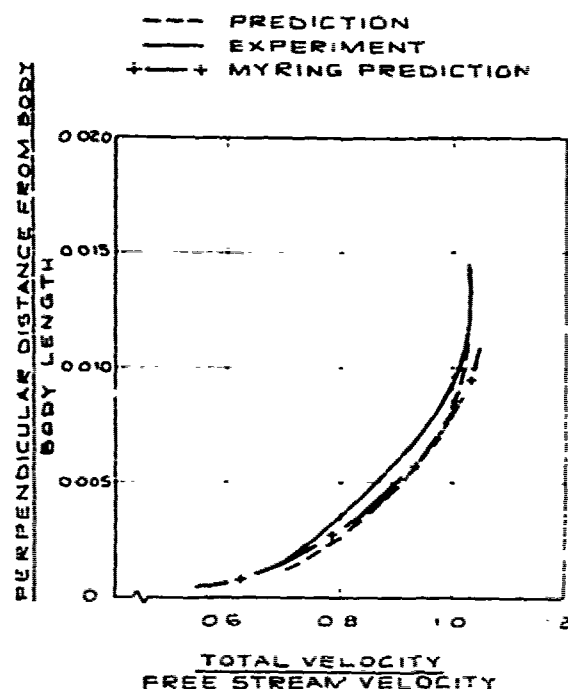


Fig 16 Total Velocity Profile at 66.2% of Body Length From Nose

The total velocity profiles for axial locations 66.2% and 99% of the body length from the fore-end are given in Figures 16 and 17. Also shown for the most forward location is the velocity predicted by the Myring calculation which was used to determine the inlet boundary conditions at the 50% body length position. From these results it can be seen that the velocity profiles are over-predicted, the error becoming larger with distance along the body so that at 99% of body length errors up to approximately 55% occur. At the forward position the maximum error can be seen to be only about 6%. From comparison between this prediction and the Myring estimate it is considered that this error is probably due to a similar order of over-prediction present in the data used to specify the inlet conditions. Thus, to some degree the over-prediction of the total velocity is the result of incorrect inlet conditions; however, this clearly would not account for the large errors near the tail of the body.

The results of predictions of the total velocity profiles at 50% and 96% of the body length and the axial variation of skin friction coefficient and wall pressure coefficient for the full Patel body are given in Figures 18 to 21.

It is apparent from Figures 18 and 19 that the velocity profiles are further over-predicted compared with the half body calculation. This is possibly the result of the mechanism which leads to the over-prediction operating over a larger range in the full-body case. The skin

friction coefficient (Figure 20) can be seen to be higher than for the half body calculations at all stations and hence further from the experimental data. The wall static pressure (Figure 21) shows a steeper pressure gradient at the stern for the full-body case although this difference is not large.

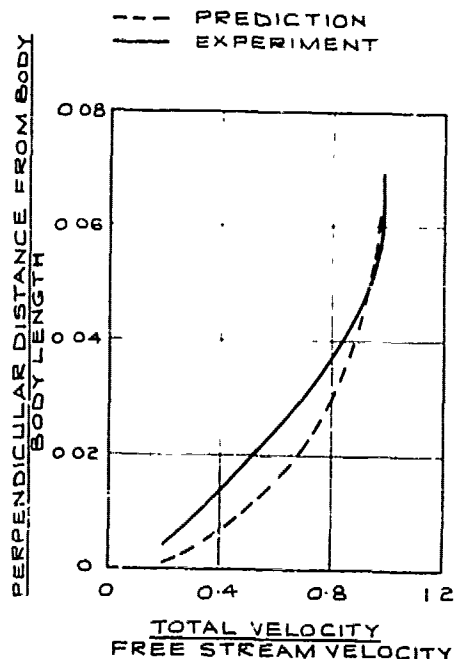


Fig 17 Total Velocity Profiles at 99% of Body Length From Nose

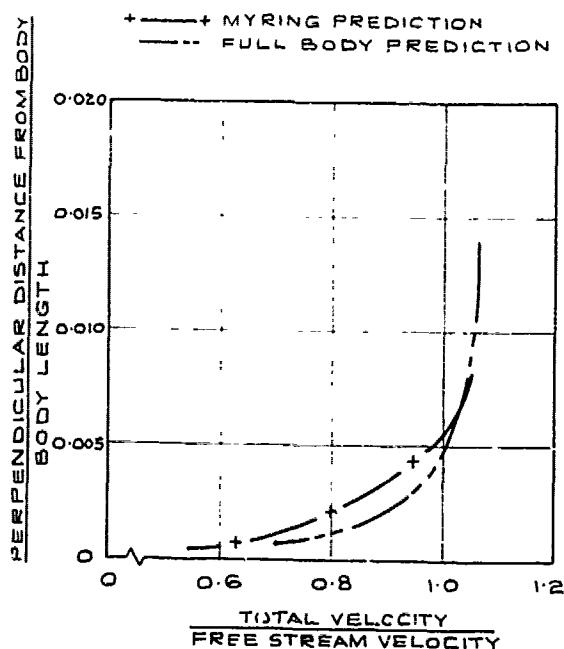


Fig 18 Total Velocity Profiles at 50% of Body Length From Nose

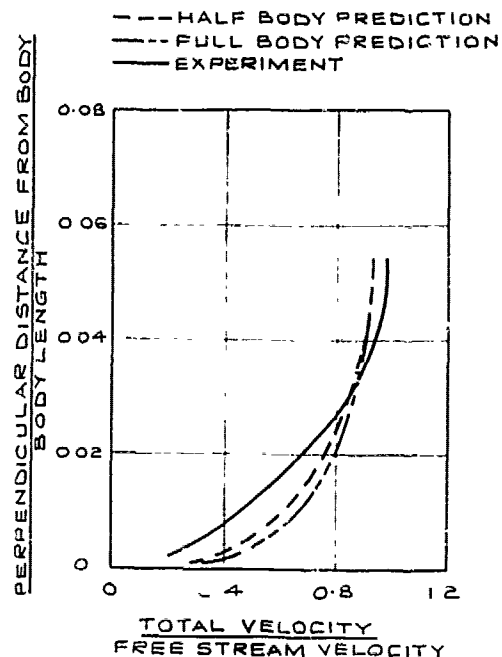


Fig 19 Total Velocity Profiles at 96% of Body Length From Nose

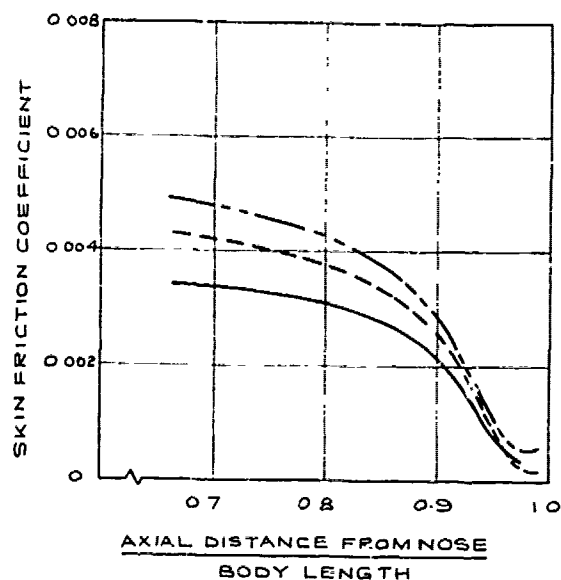
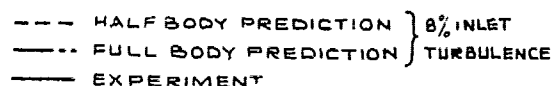


Fig 20 Axial Variation of Skin Friction Coefficient

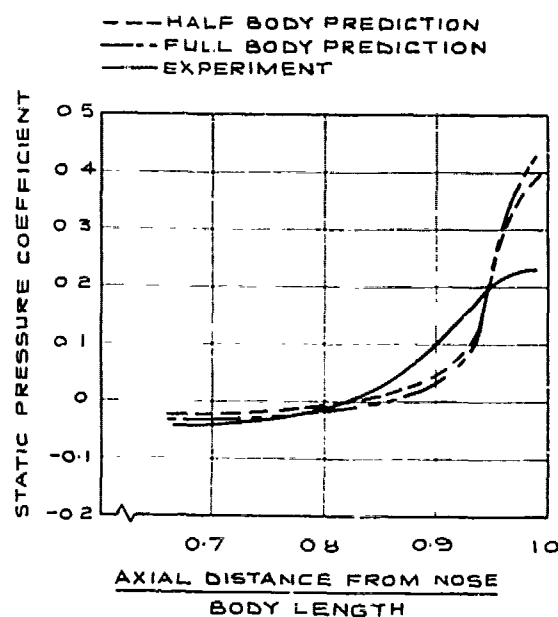


Fig 21 Axial Variation of Wall Static Pressure Coefficient

It was concluded by Patel et al {8} that in the tail region of a body of revolution, there is interaction between the turbulent rotational flow within the boundary layer and the potential flow outside, so that neither can be calculated independently of the other. Since the potential solution for the body alone was used to specify the pressure at the free boundary in the above calculations this may be a significant factor in the poor prediction of total velocity and pressure.

The above results have demonstrated the capability and limitations of the $k-\epsilon$ prediction technique when initially applied to an axisymmetric body. It is encouraging to see that the computed results indicate the correct trends, and that only a few minutes are required to produce solutions for different input parameters. It is disappointing, however, to see that better agreement could not be secured between predicted and experimental data.

The space here is too limited, and the information presented too little, for a rigorous analysis of the causes of disagreement. The study has highlighted, however, the following problem areas. Firstly, there is the difficulty of formulating the finite-difference equations, with due allowance for non-uniformities of cell shapes, so that the proper relations between pressures and velocities are precisely preserved. This was apparent in the calculations performed which sometimes exhibited stagnation-pressure distributions which were inaccurate. This effect is particularly significant at the planes of the nose and tail of the body, because of

the turning of the flow; it was precisely at these planes where the maximum inaccuracies occurred.

A possible way to eliminate this source of inaccuracy is to solve for a velocity component which follows the grid-lines, instead of the axial velocity, which was used in the previous analysis. The advantage is that this velocity is simply driven by the pressure gradient term between its upstream and downstream grid points.

The most serious limitation to the potential of the described method, is the need to prescribe boundary conditions at the free-boundary. This is done at present by utilising the potential flow solution. This itself is a source of further uncertainty, and leads to the need for a different potential flow solution for each new location of the outer boundary and each new body.

Removal of this limitation is the subject of current work, together with the use of a velocity component which follows the grid lines. The basic concept is that the solution domain is extended to very far from the body in all directions, and an additional equation is introduced, namely, that for the velocity potential. The latter will be solved over the whole calculation domain, the rest of the equations being solved only over the narrow viscous region around the body. The boundary between the viscous and inviscid regions will be determined by successive applications of the potential and viscous solution procedures.

Current work also includes extension of the above methods to consideration of the flow around appended bodies.

4. CONCLUSIONS

Methods have been derived using a two-equation turbulence model ($k-\epsilon$), to predict the two- and three-dimensional wake behind a hydrofoil and demonstrated to have the potential to warrant extension to consideration of flow prediction around an appended body.

Comparison between predicted values of the wake centre-line velocity behind an isolated hydrofoil section and experimental data shows that the prediction method gives a somewhat slower wake recovery than occurs in practice. This discrepancy is largest at low Reynolds numbers and close to the foil trailing edge. For a NACA 0017 foil, at a Reynolds number of 2×10^6 , the predicted wake centre-line velocity at a position $2/3$ chord aft of the trailing edge was found to be 9% below the experimental value.

Comparison between predicted values of the wake centre-line velocity behind an isolated flat plate and experimental data shows that in this case the method gives a very good prediction of the wake recovery.

Good agreement has been obtained between predicted and measured velocity profiles at a position $2/3$ chord aft of the

trailing edge of a hydrofoil protruding through a plane boundary layer. The predictions are found to be most accurate close to the plane boundary where the three-dimensional effects are most significant. The effect of an adverse pressure gradient on the flow in this region is also well predicted.

Initial application of the $k-\epsilon$ prediction technique to an unappended axisymmetric body has shown promising agreement with experimental data. The predicted axial variation of skin friction and boundary layer are close to measured values. The static pressure gradient and total velocity are, however, both considerably overpredicted in the tail region.

The use of a potential flow solution to prescribe the free boundary conditions and the definition of the finite-difference equations at the body nose and tail are major factors influencing the accuracy of flow predictions around submerged bodies. Further work is in progress in these two areas in order to improve the accuracy of the prediction technique.

REFERENCES

1. Myring D F: "The Profile Drag of Bodies of Revolution in Subsonic Axisymmetric Flow". RAE TR 72234 (unpublished).
2. Moore A W and Wills C B: "Theoretical Computation and Model and Full-Scale Correlation of Flow at the Stern of a Submerged Body". Proc. of 12th Symposium of Naval Hydrodynamics, Washington, USA, 1978.
3. Patankar S V and Spalding D Brian: "A Calculation Procedure for Heat, Mass and Momentum Transfer in Three-Dimensional Parabolic Flows". Int. Journal Heat and Mass Transfer, Vol 15, 1787-1806, 1972.
4. Launder B E and Spalding D Brian: "The Numerical Computation of Turbulent Flows". Computer Methods in Applied Mechanics and Engineering, Vol 3, 1975, p 269.
5. Pratap V S and Spalding D Brian: "Numerical Computations of the Flow in Curved Ducts". The Aeronautical Quarterly, Vol XXVI, 1975.
6. Abdelmeguid A M, Markatos N C G and Spalding D Brian: "A Method for Predicting Three-Dimensional, Turbulent Flows Around Ships' Hulls". International Symposium on Viscous Resistance SSPA, Goteborg, Sweden, 1978.
7. Schlichting H: "Boundary Layer Theory". McGraw-Hill Book Co, Inc, 1960.
8. Patel V C, Nakayama A and Damian R: "An Experimental Study of the Thick Turbulent Boundary Layer Near the Tail of a Body of Revolution". Iowa Institute of Hydraulic Research, Report No. 142, 1973.
9. Escudier M P: "The Distribution of Mixing Length in Turbulent Flows Near Walls". Imperial College, Heat Transfer Section, London, Report TWF/TN/1, 1966.
10. Spence D A: "Growth of the Turbulent Wake Close Behind an Aerofoil at Incidence". Aero. Res. Council, CP No.125, 1953.
11. Lieblein S and Roudebush W H: "Low Speed Wake Characteristics of Two-Dimensional Cascade and Isolated Airfoil Sections". NACA TN 3771, 1956.
12. Chevray R and Kovasznay S G: "Turbulent Measurements in the Wake of a Thin Flat Plate. AIAA Journal, Vol 7, No.8, 1969.
13. Dyne G: "A Streamline Curvature Method for Calculating the Viscous Flow Around Bodies of Revolution". International Symposium on Viscous Resistance, SSPA, Goteborg, Sweden, 1978.

Discussion

G.E. Gadd (NMI)

Fig. XII.34 of Thwaites' book "Incompressible Aerodynamics" shows that a circular cylinder protruding through a boundary layer on a plate produces a horseshoe vortex trailing downstream with counter rotating vortices outboard of it. This vortex system causes spanwise variations of the boundary layer thickness on the plate rather like those shown in figs. 9 and 10, so presumably the hydrofoil must give rise to a similar pattern of vortices. Are these evident in the numerical solution?

M. Hoekstra (NSMB)

The present users of the partially-parabolic method are on the right track now, I think, in studying carefully the performance of the method in comparatively simple external flows. I like to encourage the authors to continue this work.

What astonished me is that the authors apply their method, which is essentially inadequate for separating flows, to the case of a hydrofoil on a flat plate which is known to give separation at the root of the hydrofoil. What kind of results were obtained in this root region? Can the authors comment?

According to eq. 40 the authors match their solution to a wall law at $y_+ \geq 11.5$. How is the actual boundary value of y_+ chosen and is there any influence of the choice on the results?

L. Larsson (SSPA)

The methods developed by Prof. Spalding and his group have been very successful for internal flows. However in external applications several new problems appear. It therefore seems like a good idea to apply the methods to fairly simple cases before turning to the complicated flow around a ship's stern.

My first question concerns the 2-D case: Rather than matching the viscous calculation to an external potential flow at the edge of the BL an artificial boundary condition has been introduced 2.5 chords from the foil. Judging from Fig.9 this distance corresponds approximately to 100 times the BL thickness at the trailing edge. I doubt that an efficient use can be made of a viscous flow program in this way. How many grid points were there in the BL? You use 16 altogether in the lateral direc-

tion.

The 3-D flow configuration consisting of an obstacle protruding from a flat surface has been used frequently as a test case for 3-D BL methods. The interest has however mostly been directed towards the region in front of, or beside the obstacle. In this paper the flow behind the obstacle is compared. As is well known this region is highly vortical, containing strong longitudinal vortices. Accurate predictions could therefore hardly be expected if the pressure is not allowed to vary in both lateral directions.

W.-D. Xu (Harbin Shipbuilding Eng. Inst)

For calculation of turbulent boundary layer, the empirical formulas used may be examined first. For example, in order to solve the energy-integral equation, we may first find out the velocity distribution and thickness of different regions as shown in my paper titled "Velocity Distribution and Energy Equation of Flat Plate Turbulent Boundary Layer". After analysing twenty-one $u^+ \sim y^+$ curves converted from experimental data of Klebanoff & Diehl, I obtained the following results by Method of Least Squares. The velocity distribution of inner region (I.R.) is well known as the logarithmic law: $u^+ = 5.75 \log y^+ + B$. But I found that B is no longer a constant, it is a function of R_0 : $B = 2.086 \log R_0 - 3.225$, i.e. when $R_0 = 10^4$,

$$u^+ = 5.75 \log y^+ + 5.12 \text{ (for I.R.)}. \quad (1)$$

For more easily integrating the energy equation, I found that velocity distribution of outer region (O.R.) can also be expressed by the above logarithmic law but with a different slope:

$u^+ = 10.4 \log y^+ - D$. The term D is also a function of R_0 :
 $D = 1.973 \log R_0 + 0.879$, i.e. when $R_0 = 10^4$,

$$u^+ = 10.4 \log y^+ - 8.78 \text{ (for O.R.)} \quad (2)$$

Of course, for laminar sublayer (L.S.): $u^+ = y^+$. From the intersecting points of these three expressions, the thickness of different regions can be determined

$$y_e^+ = (\sqrt{R_0} + 341)/40 \text{ (for L.S.)} \quad (3)$$

$$y_1^+ = 0.837 \log R_0 - 0.372 \text{ (for I.R.)} \quad (4)$$

when $R_0 = 10^4$, $y_e^+ = 11.03$, $y_1/\delta = 0.257$.

Then the friction term of the energy equation can be calculated for each region, finally I obtained the following $R_x \sim R_0$ relation

$$R_x = \frac{63 R_0^{11/8}}{(\log R_0 + 0.211)^{0.94}} \quad (5)$$

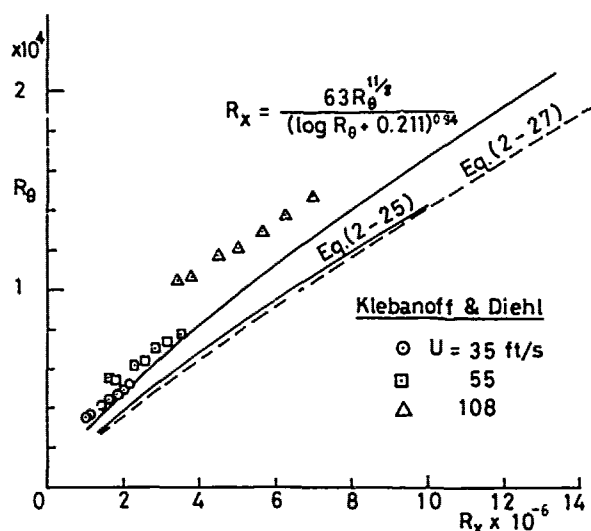
It agrees better with the experiment of Klebanoff & Diehl than other formulas often used as shown in the Fig.* (one of them is deduced from 1/7 law).

* Eq. (2-25) is deduced from the 1/7 law

$$R_x = 63.771 R_0^{5/4}$$

Eq. (2-27) is as follows

$$R_x = 143.11 R_0^{7/6}$$



Author's Reply

N.C. Markatos (CHAM Ltd)

Reply to Dr. Gadd

Vortices are not evident in the solution, because, in the reported calculations, the pressure field was derived by considering an isolated hydrofoil (see text); and that two-dimensional field was applied uniformly all the way down to the plate. The procedure, used is not, therefore, a full "partially parabolic" one. The latter would have failed near the plate, in the presence of vortices.

We did not use such a procedure because a full analysis was intended at this stage. If we were to carry out a complete analysis we would have used the elliptic version of the code (reported in the slide panels of my presentation). Therefore, the absence of vortices in the numerical solution is a consequence of the way we chose to treat the problem. It is interesting, however,

that the current predictions in the wake are in fair agreement with the experiments, indicating that the effects of vortices may be localised and not very significant in the wake of the hydrofoil considered.

Reply to Mr. Hoekstra

I thank Mr. Hoekstra for his encouragement. I would like to point out that our method is adequate for separating flows, and the code includes all three options, namely parabolic, "partially-parabolic" and elliptic. Indeed, it was the last version that was reported in the slide panels of my presentation. Simply, we did not attempt to predict the separation adequately, and attention was not focused at the root region of the hydrofoil, but only in the wake. The apparent fair agreement of the predictions with experiments in the wake tends to indicate that effects of vortices may not be very significant in the wake region of the hydrofoil considered.

Concerning the second question, the first grid line next to a solid surface is set at such a distance from the surface, y , so that the calculated y^+ at the first grid line is in the range $30 < y^+ < 120$, over which it is reasonable to assume that the log law prevails. An initial guess and subsequent adjustment may be necessary. Within the above limits the results were virtually uninfluenced by the precise value of y^+ . A few runs with varying distances of the first grid line from the wall are therefore in general sufficient to ensure results independent of y^+ .

Reply to Dr. Larsson

Concerning the first question, the figure 9 mentioned refers to the three-dimensional case, for which the North Boundary was located at only 0.228x chord from the floor. For the 2-D case the outer boundary was indeed set at 2.5x chords from the foil, but this is only 15-20 times the B.L thickness, if I recall correctly. The general policy is to locate the outer boundary far enough from the viscous region, so that known boundary conditions can be applied, and then to investigate the sensitivity of the results to the grid both inside and outside the viscous region. It is because we performed the second stage and demonstrated grid independency that we used such a grid distribution. The grid points in the B.L were 10, at the trailing edge.

Despite the above considerations, I do realise that this is not an efficient use of a viscous flow program. This realisation is among several reasons that led to the development of our new approach which was explained in my presentation. This approach consists of using two calculation schemes for the irrotational external

flow and the rotational flow close to and in the wake of the body, full account being taken of interactions.

The answer to the second statement is the same as for Dr. Gadd's question. We did not intend, and have not predicted the presence of vortices.

Reply to Prof. Wei-de Xu

I thank Professor Wei-de Xu for supplying me with his interesting modifications to the log law. We will study them thoroughly for future inclusion in our wall functions.

Effective Wake : Theory and Experiment

Thomas T. Huang and Nancy C. Groves

David W. Taylor Naval Ship Research and Development Center

Bethesda, Maryland, U.S.A.

ABSTRACT

An improved theoretical method is presented for computing the effective wake of propulsors operating in thick stern boundary layers on axisymmetric bodies. The hydrodynamic interaction between the nominal velocities upstream of the propulsor and at the propulsor location is assumed to be inviscid in nature and the total energy is assumed to be conserved along a given streamline with and without the propulsor in operation. Theoretical predictions using the method are compared with experimental data obtained in the United States and Japan for five different propulsor/axisymmetric body configurations. For all five cases examined, the computed total velocity profiles immediately upstream of the propulsor (with the propulsor in operation) are in good agreement with the measured values. In addition, the volume-mean values of effective velocity profiles computed from the measured nominal velocity profiles are in good agreement with the measured values of the Taylor wake fraction ($1-w_T$) for all five nominal wake distributions over a wide range of propulsor thrust loading coefficients.

1. INTRODUCTION

The velocity profile at the location of the propulsion device in the absence of a propulsor is called the nominal velocity profile. The effective inflow velocity distribution experienced by the propulsor depends on the mutual interaction of the propulsor (loading distribution and geometric characteristics) and the stern boundary layer. It can be significantly different from the nominal velocity distribution. In the design of a wake-adapted propulsor, the radial distribution of effective inflow velocity is often estimated by ratioing the measured nominal circumferential-mean axial profile up or down by a constant factor. The factor is sometimes taken to be $(1-w_T)/(1-w_N)$, where w_T is the Taylor wake fraction and w_N is the measured volume-mean nominal wake. Naval architects derive the Taylor wake fraction from propeller open water curves on the basis of thrust identity between propeller powering experiments in open water and behind the ship model.

The constant-factor empirical approach for obtaining effective inflow distribution is not based on a rational hydro-

dynamic theory. Until recently, detailed velocity surveys in the presence of an operating propulsor were not available, and the actual distribution of effective velocity into a propulsor had not been examined fully. Providing the correct distribution of effective inflow for wake-adapted propulsor design is essential to meeting the ever increasing demand for improving propulsion performance and energy conservation. In order for a propulsor to produce a required thrust to power a ship with minimum power and minimum cavitation at a prescribed propulsor rotational speed, the effective velocity distribution used in the propulsor design must be very accurate.

In 1976, a Laser Doppler Velocimeter (LDV) was successfully used by Huang et al.¹ to measure velocity profiles very close to the propulsor. The measured velocity profiles, stern pressure distributions, and stern shear stress distributions with and without an operating propulsor provided the necessary clues to the proper understanding of the interaction between a propulsor and stern boundary layer on axisymmetric bodies. The influence of propulsors on axisymmetric stern boundary layers was found to be contained within a limited region extending two propulsor diameters upstream of the propulsor. The propulsor/stern boundary layer interaction was found to be inviscid in nature. The inviscid approximation computer program developed by Huang et al.¹ predicted very well the measured total velocities in front of the operating propulsor. Subsequent detailed measurements of the velocity profiles with and without a propulsor operating in two axisymmetric wakes were made by Nagamatsu and Tokunaga.² An inviscid approximation again predicted well the measured total velocities in front of the operating propulsor.

Schetz and Favini^{3,4} have formulated a numerical procedure based on the full Navier-Stokes equations to compute the flow near body/propulsor configurations. The computed axial velocities at two propulsor diameters downstream of the propulsor compared satisfactorily with the measured results. This numerical procedure has not been applied to the computation of effective wake in design of wake-adapted propulsors.

The influence of a stern-mounted propulsor on the flow field past bodies of revolution and a flat plate was measured by Hucho,^{5,6,7} although no attempt was made to ac-

tually calculate the effective wake distribution. Other investigations related to this subject were made by Wertbrecht,⁸ Hickling,⁹ Tsakonas and Jacobs,¹⁰ and Wald.¹¹ Methods to estimate effective wake were proposed by Raestad,¹² Nagamatsu and Sasajima,¹³ and Titoff and Odesnov.¹⁴ The only known previous effort to theoretically address this problem is due to D.M. Nelson* who developed a computer program for calculating the effective wake from the measured nominal wake and static pressure distribution across the boundary layer.

In the present paper, an improved method for computing effective wake distribution from the measured nominal wake distribution is derived. Serious effort has been made in this work to compare the theoretical velocity predictions with velocity distributions measured by an LDV or a five-hole pitot probe immediately upstream of an operating propulsor. For all five cases examined, the computed total velocities upstream of the operating propulsors are in good agreement with the measured values.

The computed volume-mean effective wake distributions are shown to compare favorably with the measured Taylor wake fractions derived from self-propulsion experiments of five different nominal wakes. A considerable amount of experimental data and relevant computational results are tabulated to permit the independent assessment of the present method by other investigators.

2. THEORY

2.1 Propulsor/Stern Boundary Layer Interaction

The experimental data given in References 1 and 2 allow one to conclude that the influence of propulsors on upstream stern boundary layers is detectable only within two propulsor diameters upstream of the propulsor. Upstream of the propulsor, the mean circumferential velocity, v_θ , is identically equal to zero on an axisymmetric body both with and without the propulsor in operation. The following assumptions are made to derive a theoretical approximation of the hydrodynamic interaction between a propulsor and a thick stern boundary layer upstream of the propulsor: (a) the flow is axisymmetric and the fluid is incompressible; (b) the interaction of propulsor and nominal velocity profile is considered to be inviscid in nature; thus, propulsor-induced viscous losses and turbulent Reynolds stresses are neglected; (c) the conventional boundary-layer assumption, $\partial v_r / \partial x \ll \partial u_x / \partial r$ is assumed to be valid for the nominal boundary layer in the absence of a propulsor; and (d) upstream of the propulsor, no energy is added to the fluid by the propulsor, and the propulsor-induced velocity field upstream of the propulsor is irrotational. The theoretical formulation of propulsor/stern boundary layer interaction subject to the above assumptions has already been given by Huang et al.,¹ and will only be briefly outlined here.

The vector equation of steady motion for an inviscid fluid is given by (see, for example, Reference 15)

$$\vec{V} \times \vec{\omega} = \frac{1}{\rho} \text{grad } H, \quad (1)$$

where \vec{V} is the fluid velocity, $\vec{\omega} = \nabla \times \vec{V}$ is the vorticity vector, and $H = p + \frac{1}{2}\rho(\vec{V} \cdot \vec{V})$ is the total head, with ρ mass density and p pressure. For cylindrical polar coordinates (r, θ, x) with $\vec{V} = (v_r, v_\theta = 0, u_x)$, the radial component of Equation (1) may be written¹ as

$$u_x \left(\frac{\partial u_x}{\partial r} - \frac{\partial v_r}{\partial x} \right) = \frac{1}{\rho} \frac{\partial H}{\partial \psi} \frac{d\psi}{dr} = \frac{ru_x}{\rho} \frac{\partial H}{\partial \psi}, \quad (2)$$

*Private communication, unpublished

where ψ is the stream function for an incompressible axisymmetric flow defined by

$$u_x = \frac{1}{r} \frac{\partial \psi}{\partial r},$$

$$v_r = -\frac{1}{r} \frac{\partial \psi}{\partial x}.$$

Since the flow velocities are increased due to the action of the propulsor, stream surfaces are shifted closer to the body surface. As shown in Figure 1, a typical stream surface moves inward from r to r_p while the resultant velocity is higher than the nominal velocity. The resultant velocity u_{pr} , as would be measured in front of the propulsor, will be called the total velocity.

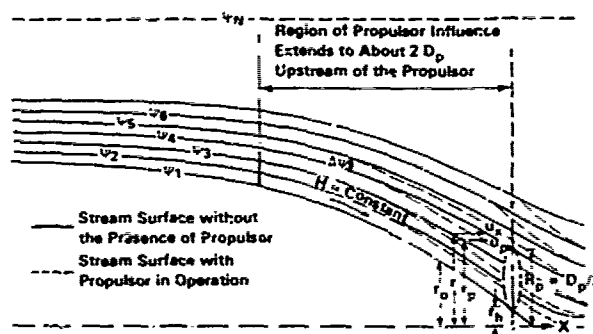


Figure 1 — Definition Sketch for Propulsor Stern Boundary Layer Interaction

Since no energy is added to the upstream fluid by the propulsor and since we assume no change of viscous losses due to propulsor induction effects, the total pressure head within a given stream annulus upstream of the propulsor remains constant with the propulsor (denoted by a subscript p) and without the propulsor in operation; thus, upstream of the propulsor

$$\frac{1}{\rho} \frac{\partial H}{\partial \psi} = \frac{1}{\rho} \left(\frac{\partial H}{\partial \psi} \right)_p$$

or from Equation (2)

$$-\frac{\omega_\theta}{r} = \frac{1}{r} \left(\frac{\partial u_x(r)}{\partial r} - \frac{\partial v_r(r)}{\partial x} \right) = \frac{1}{r_p} \left[\frac{\partial u_{pr}(r_p)}{\partial r_p} - \frac{\partial (v_r(r_p) + v_{pr}(r_p))}{\partial x} \right], \quad (3)$$

where ω_θ is the θ -component of the vorticity vector. The value of ω_θ/r must therefore be conserved along the stream annulus with and without an operating propulsor. The radial velocity with the propulsor in operation is assumed equal to $v_r + v_{pr}$, where v_r is the radial velocity without propulsor and v_{pr} is the circumferential-average propulsor-induced radial velocity. Since the propulsor-induced velocity field is assumed to be irrotational, we require

$$(\vec{\nabla} \times \vec{V}_{pr})_\theta = \frac{\partial v_{pr}}{\partial x} - \frac{\partial u_{pr}}{\partial r_p} = 0,$$

where \vec{V}_{pr} is the resultant propulsor-induced velocity, and u_{pr} is the circumferential-average propulsor-induced axial velocity. Substitution into Equation (3) yields a simple relationship for the location of the new stream surface r_p .

$$\frac{1}{r} \frac{\partial u_x}{\partial r} = \frac{1}{r_p} \left(\frac{\partial u_p}{\partial r_p} - \frac{\partial u_a}{\partial r_p} \right) - \left[\frac{1}{r_p} \frac{\partial v_r(r_p)}{\partial x} - \frac{1}{r} \frac{\partial v_r(r)}{\partial x} \right] \quad (4)$$

The normal boundary-layer approximation $\partial v_r / \partial x \ll \partial u_x / \partial r$ is now assumed to be valid for the nominal velocity profiles. In order to check this assumption, the radial nominal velocity profiles were measured by a TSI, Inc. Model 1241 "X" - wire at two axial planes, one immediately upstream ($x/D_p = -0.227$) of the propulsor and one on the propulsor plane. The values of $\partial v_r / \partial x$ determined from velocity measurements on Afterbodies 1 and 2 of Reference 16 were found to be less than $0.05 \partial u_x / \partial r$. The radial velocity v_r was found to vary very slowly across the boundary layer.¹⁶ Therefore, we may assume that $v_r(r) \approx v_r(r_p)$. Furthermore, the value of $(r-r_p)/r_p$ represents the percentage change in radial location of a given streamline with and without the propulsor operating; its value is found to be less than 0.2 for most of the cases considered. Thus, the order of magnitude of the last term in Equation (4) can be estimated as

$$\frac{1}{r_p} \frac{\partial v_r(r_p)}{\partial x} - \frac{1}{r} \frac{\partial v_r(r)}{\partial x} \approx \frac{\partial v_r(r)}{\partial x} \frac{r-r_p}{rr_p} < 0.01$$

$$\frac{1}{r} \frac{\partial u_x}{\partial r}$$

and, therefore, will be neglected in the following analysis. Equation (4) then reduces to

$$\frac{1}{r} \frac{\partial u_x}{\partial r} = \frac{1}{r_p} \left(\frac{\partial u_p}{\partial r_p} - \frac{\partial u_a}{\partial r_p} \right) \quad (5)$$

Within a given stream annulus the massflow is constant with or without a propulsor operating. Thus, at a given axial location x , we may write,

$$d\psi = ru_x dr = r_p u_p dr_p \quad (6)$$

Inserting this expression into Equation (5) yields

$$u_x du_x = u_p d(u_p - u_a) \quad (7)$$

Equations (6) and (7) are the governing equations for the propulsor and stern boundary-layer interaction. The nominal velocity $u_x(r)$, and the circumferential-average propulsor-induced axial velocity, $u_a(r_p)$, can be used to obtain the new location of the stream surface r_p with total velocity u_p . In Equation (6), the values of r and r_p are equal on the body surface. Far outside of the boundary layer, the flow is uniform without any vorticity. Then we have $du_x = 0$ as $r \rightarrow \infty$ in Equation (6), which implies $d(u_p - u_a) = 0$, and $u_p - u_a = \text{constant} = V$ (ship speed), or $u_p = V + u_a$, since u_a is zero and u_p has to be equal to V as $r \rightarrow \infty$.

Similarly, for an open propulsor in uniform flow, $du_x = 0$ in equation (7), and we have $u_p = V + u_a$. The total velocity u_p for an open propulsor in uniform flow is the sum of the uniform ship speed V and the propulsor-induced velocity u_a without any interaction.

If the nominal velocity field is irrotational, the left-hand side of Equation (3) must be zero; thus, the right-hand side of Equation (3) becomes

$$\frac{\partial u_r(r_p)}{\partial r_p} - \frac{\partial v_r(r_p)}{\partial x} - \frac{\partial v_{pr}(r_p)}{\partial x} = 0.$$

Using the ir. otationality condition applies to the nominal velocity as well as propulsor-induced velocity fields, e.g.

$$\frac{\partial v_{pr}(r_p)}{\partial x} = \frac{\partial u_a(r_p)}{\partial r_p} \quad \text{and} \quad \frac{\partial v_r(r_p)}{\partial x} = \frac{\partial u_x(r_p)}{\partial r_p}.$$

The above equation becomes

$$\frac{\partial}{\partial r_p} [u_p(r_p) - u_x(r_p) - u_a(r_p)] = 0,$$

or

$$u_p(r_p) = u_x(r_p) + u_a(r_p).$$

Thus, the total velocity u_p for a propulsor operating in an irrotational nominal velocity field is the sum of the corresponding nominal velocity and the propulsor-induced velocity without any additional interaction.

2.2 Effective Velocities

In current propulsor design and performance prediction practice, only the measured model nominal velocity profile is available. The full-scale nominal velocity profile can then be estimated as the sum the measured model nominal velocity profile plus an appropriate Reynolds-number correction. The nominal velocity profile for either the model or the full-scale propulsor is assumed to be available at the outset. The present theory can be applied to obtain the effective velocity distribution using the nominal velocity profile as input.

If the effective velocity is defined to be the total velocity with the propulsor in operation minus the propulsor-induced axial velocity, $u_e(r) = u_p(r_p) - u_a$, then Equation (7) becomes

$$u_x du_x = (u_e + u_a) du_e \quad (8)$$

At large radial distances from the propulsor axis ($r \rightarrow \infty$), the value of the propulsor-induced velocity becomes zero and, hence, the effective velocity is equal to the nominal velocity as $r \rightarrow \infty$. The finite-difference form of Equation (8) can be written as

$$[u_{x_{i+1}} + u_{x_i}][u_{x_{i+1}} - u_{x_i}] = [u_{e_{i+1}} + u_{e_i} + u_{a_i} + u_{a_i}][u_{e_{i+1}} - u_{e_i}],$$

or

$$u_{e_i} = \sqrt{\left(u_{e_{i+1}} + \frac{u_{x_{i+1}} + u_{x_i}}{2}\right)^2 + (u_{x_i}^2 - u_{x_{i+1}}^2)} - \frac{u_{x_{i+1}} + u_{x_i}}{2} \quad (9)$$

In practice, the nominal velocities are known from the innermost radius of the propulsor to a radial position (e.g., $r \geq 3.0 R_p$) large enough for the propulsor-induced axial velocity u_a to be zero. The value of the effective velocity at that point is equal to the nominal velocity. This condition can be used to solve the effective velocity in Equation (9) step by step from this initial radial position inward towards the body surface. The nominal velocity at the hub of the propulsor is usually taken to be the linearly extrapolated value of the measured nominal velocities near the body surface rather than zero in order to avoid an unnecessarily large number of computational grid points near the body surface.

Since the induced velocity u_a is not known initially, the present theory can be applied in an iterative procedure to propulsor design of performance prediction. The circumferential-average propulsor-induced axial velocity u_a will be assumed to

be the same within the same stream annulus with and without the propulsor in operation in every iteration.

In conventional propulsor design, when the nominal wake distribution is given and either the propulsor thrust at a given speed or the delivered shaft power is given, the following procedure may be followed:

(a) First, estimate the thrust loading coefficient C_{TS} of the propulsor and then estimate the propulsor-induced axial velocity by using the actuator disk approximation,¹⁷ i.e.,

$$\frac{r}{R_p} \quad 0.2 \quad 0.3 \quad 0.4 \quad 0.5 \quad 0.6 \quad 0.7 \quad 0.8 \quad 0.9 \quad 1.0$$

$$\frac{u_a}{VC_{TS}} \quad 0.147 \quad 0.206 \quad 0.254 \quad 0.290 \quad 0.311 \quad 0.315 \quad 0.293 \quad 0.233 \quad 0$$

An initial estimate of effective velocities can then be obtained by solving Equation (9).

(b) The conventional propulsor lifting-line computational method^{18,19,20} may be used to design a propulsor to operate in the estimated effective velocity profile u_e with a prescribed nondimensional circulation distribution G which produces the required thrust. An improved solution estimate of the circumferential-average propulsor-induced axial velocity, u_a , can be computed from the output of the lifting line computer program¹⁹ by a simple integration,²¹

$$\frac{u_a}{V} = -\frac{K}{2} \int_{\tilde{r}_h}^1 \frac{dG(\tilde{r})}{d\tilde{r}} \frac{d\tilde{r}}{\tilde{r} \tan \beta(\tilde{r})} \quad (10)$$

where $G = \Gamma/2\pi R_p V$, $\tan \beta_i = (u_e + \tilde{u}_a)/(\Omega \tilde{r} R_p - \tilde{u}_a)$, K is the number of blades, Ω is the propulsor angular velocity, $\tilde{r} = r/R_p$, \tilde{r}_h is the dimensionless hub radius, and \tilde{u}_a and \tilde{u}_t are the axial and tangential propulsor induced velocities at lifting line, respectively.

(c) A new effective velocity profile can be obtained by using the new lifting-line solution of u_a in Equation (9).

(d) Steps (b) and (c) are repeated until the values of G and u_e converge to within some specified tolerance. Two iterations have been found to be sufficient for preliminary design.

(e) If a final lifting surface design^{20,22,23} is required, the final solution of circumferential-average propulsor-induced axial velocity, u_a , at the propeller plane can be calculated by using a field-point velocity program²⁰ which includes lifting surface corrections and thickness distributions. The final effective velocity profile is obtained by using the final lifting-surface solution of u_a in Equation (9).

For calculation of the performance of a propulsor of given geometry and rpm, a computational method²⁴ is available to predict G and $\tan \beta_i$ for estimated values of u_e . A new effective velocity profile can be calculated using the new induced velocity u_a computed from the field-point velocity program.²⁰

2.3 Total Velocities Upstream of Propulsor

The total velocities at the propulsor plane are rather difficult to measure. Therefore, in order to evaluate the present theory a comparison of total velocity u_p between theory and experiment must be made immediately upstream of the propulsor. The total velocity is $u_p = u_a + u_e$ where u_e is solved by Equation (9) and the value of the propulsor-induced velocity u_a must be calculated at the position where the total velocities are measured. The new radial position for u_p can be obtained from Equation (6). The nominal velocity u_x can be approximated very accurately over a small increment of radius dr as a linear function of r . Although the velocity at the wall is zero, the velocity profile in the present approxima-

tion will be extrapolated linearly toward the wall, resulting in a nonzero velocity at the wall. Since u_x and u_p can be approximated locally by a linear function of r and r_p , the mass flux within the stream tube annulus given by $dr = r_{i+1} - r_i$ and $dr_p = r_{pi+1} - r_{pi}$ can be integrated from Equation (6) as

$$\psi_{i+1} - \psi_i = \Delta\psi_i = \int_{r_i}^{r_{i+1}} r u_x dr = \int_{r_{pi}}^{r_{pi+1}} r_p u_p dr_p$$

with $u(r) = u_i + [(r - r_i)/(r_{i+1} - r_i)](u_{i+1} - u_i)$ and $r_i \leq r \leq r_{i+1}$

to obtain the finite difference form of Equation (6) as

$$\begin{aligned} (r_{i+1}^2 - r_i^2) \left[(2u_{x,i+1} + u_{xi}) - (u_{x,i+1} - u_{xi}) \frac{r_i}{r_{i+1} + r_i} \right] \\ = (r_{pi+1}^2 - r_{pi}^2) \left[(2u_{p,i+1} + u_{pi}) - (u_{p,i+1} - u_{pi}) \frac{r_{pi}}{r_{pi+1} + r_{pi}} \right] \end{aligned} \quad (11)$$

At the body surface $r_i = r_{pi}$. This condition can be used to solve for r_{pi+1} step by step from the body surface outward, e.g.

$$r_{pi+1} = \frac{-C + \sqrt{C^2 - 4BD}}{2B} \quad (12)$$

where $B = 2u_{p,i+1} + u_{pi}$

$$C = -r_{pi}(u_{p,i+1} - u_{pi})$$

$$D = -r_{pi}^2(u_{p,i+1} - 2u_{pi}) - F$$

$$F = (r_{i+1}^2 - r_i^2)(2u_{x,i+1} + u_{xi}) - r_i(u_{x,i+1} - u_{xi})(r_{i+1} - r_i)$$

Both the effective velocity u_e and the new radial position r_{pi+1} for the total velocity $u_{p,i+1} = u_{e,i+1} + u_{a,i+1}$ are the simple solutions of the quadratic Equations (9 and 12). The effective velocity is solved (independent of r_p) inward from a large radial position where the propulsor-induced velocity is zero. Once the values of u_e are obtained, the new radial position r_{pi+1} can be solved from the body surface outward. These two solutions are decoupled without any need for employing an iterative numerical procedure. These solutions can readily be incorporated in most propulsor design practices.

3. EXPERIMENT

3.1 Two Propulsors in Five Nominal Wakes

The experimental data used to evaluate the present theory are derived from two propulsors operating in five different nominal wakes. The geometrical characteristics of the propulsor used at DTNSRDC, denoted Propulsor T, are given in Reference 1 and those of the propulsor used at Nagasaki Experimental Tank by Nagamatsu and Tokunaga, denoted Propulsor J, are given in Reference 2.

Three axisymmetric bodies, designated as Models 1, C, and D, were used to generate thick stern boundary layers for Propulsor T. The offsets of the three models are given in Tables 1 through 3. The propulsor was located at $x/L = 0.983$, where x is the axial distance from the nose and L is the total body length. The ratio of the propulsor radius to the maximum hull radius, R_p/r_{max} , is 0.545 for Model 1 and 0.484 for Models C and D. The maximum radius of the model (r_{max}) is 13.97 cm for Model 1 and 31.18 cm for Models C and D. The three models were constructed of molded fiberglass; specified profile tolerances were held to less than ± 0.4 mm, all

imperfections were removed, meridians were faired, and the fiberglass was polished to a 0.64-micron rms surface finish.

One axisymmetric body was constructed by Nagamatsu and Tokunaga² for their investigation. The total length of the body was 3.085 m and the maximum radius was 10.66 cm. The propulsor was located at 2.57 propeller diameters downstream of the after perpendicular. A wire mesh was wrapped around the aft portion of the parallel middle body. The nominal wakes without and with the wire mesh will be designated as wakes A and B, respectively. The value of R_p/r_{max} was 0.610.

The measured distributions of the nominal axial velocities at the propulsor plane for the five wakes are shown in Figure 2. There is considerable variation in the nominal velocity distributions among the five wakes selected for the present investigation.

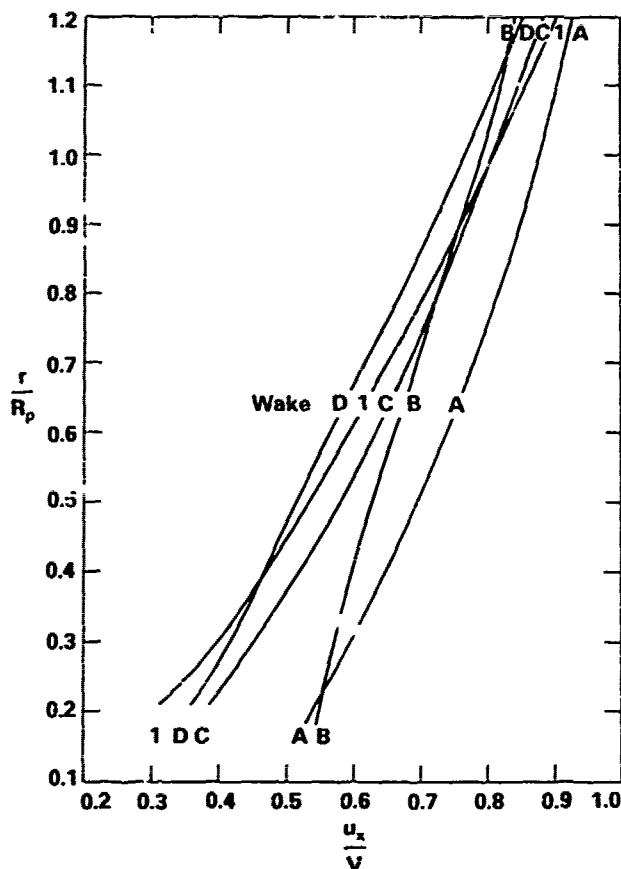


Figure 2 — Measured Nominal Axial Velocity Profiles of the Five Nominal Wakes

3.2 Experimental Technique

The experimental investigation of Models 1, C, and D was conducted in the DTNSRDC anechoic wind tunnel. The wind tunnel has a 2.438- by 2.438-m test section with a maximum air speed of 61 m/s. The model was supported by two streamlined struts separated by roughly one-third of the model length. The upstream strut had a 15-cm chord and the downstream strut had a 3-cm chord. The disturbances generated by the supporting struts were within the region below the horizontal centerplane. All the measurements of the nominal and the total velocities were made in the vertical centerplane along the upper meridian and there was little extraneous effect from the supporting struts. Each stern of the model protruded from the closed-jet working section of the wind tunnel

into the anechoic chamber (6.4 x 6.4 x 6.4 m) located upstream of the diffuser. Propulsor T was driven by a 9-kW high-speed motor mounted inside the stern of the model. The rotational speed of the propulsor shaft was measured by a magnetic pickup.

Time-average nominal velocities at the propulsor plane and at a plane immediately upstream of the propulsor plane in the absence of the propulsor were measured by a Laser Doppler Velocimeter (LDV) and checked by a TSI, Inc. Model 1241 "X" wire monitored by a two-channel TSI Model 1050-1 hot-wire anemometer¹⁵. The axial velocity profiles inside the stern boundary layer measured by the LDV and by the hot-wire anemometer were found to agree within two percent of the free-stream velocity. The total velocities immediately upstream of the propulsor were measured by the LDV with the propulsor in operation. Some of the data have already been reported in Reference 1. Most data presented in this investigation were measured after the publication of Reference 1 although the same LDV measurement techniques were used. The overall accuracy of the measured axial velocities by the LDV is about two percent of the free-stream velocity.

In the investigation of Nagamatsu and Tokunaga,² the model was also supported by two struts and propulsor J was mounted on and driven by the dynamometer used for open-water propulsion testing. The experiments were conducted in a towing tank. The propulsor plane was located at 5.13 R_p downstream of the after perpendicular of the model; the model centerline depth of submergence was 4.6 R_p , where R_p is the radius of the propulsor. A five-hole pitot probe of NPL type was used to measure the axial and the radial velocities with and without the propulsor in operation. The overall accuracy of this type of pitot probe for measuring velocity is about three percent of the free-stream velocity. Standard self-propulsion and open-water experiments were conducted to determine the Taylor wake fraction.

Standard self-propulsion experiments were also conducted in the DTNSRDC model basin using a large model; the centerline depth of submergence was 17 R_p to avoid the effect of the free surface. The towing strut had a 20-cm chord and was located at 40-percent of body length downstream from the nose. The conditions of the self-propulsion experiments for the two propulsors operating in the five nominal wakes are tabulated in Table 4, to be discussed below.

4. RESULTS AND DISCUSSIONS

4.1 Effective Wake

The two propulsors used in the self-propulsion experiments (Table 4) were stock propulsors and were not operated at their design conditions. A propulsor performance prediction computer program²⁴ was used to compute the values of non-dimensional circulation G and hydrodynamic pitch angle $\tan\beta$ for the estimated values of u_e . The final values of $\tan\beta$ were scaled up or down by the ratio of the measured value of K_T to the computed value of K_T . The values of G and modified $\tan\beta$ were then used to compute the propulsor-induced velocities by a field-point velocity computer program²⁰ with a lifting-surface option. The new values of u_e were then used to compute a second estimate of the effective velocity u_e by using Equation (9). Three iterations were sufficient for the computed values of u_e to converge to within 0.2 percent accuracy. Table 4 shows the computed values of K_Q , η_D , the volume-mean effective and nominal velocities, $(u_e)_0$ and $(u_e)_p$, and the effective velocity at the 0.7 propulsor radius. The notation used in Table 4 is as follows:

$$G = \frac{\Gamma}{2\pi R_p V} = \text{non-dimensional circulation}$$

$$C_{TS} = \frac{T}{\frac{\rho}{2} V^2 \pi R_p^2} = \text{thrust loading coefficient based on ship speed}$$

$$K_T = \frac{T}{\rho n^2 D^4} = \text{thrust coefficient}$$

$$K_Q = \frac{Q}{\rho n^2 D^5} = \text{torque coefficient}$$

$$\eta_D = (1-t) \frac{J_v K_T}{2\pi K_Q} = \text{propulsive efficiency}$$

$$J_v = \frac{V}{nD} = \text{ship-speed advance coefficient}$$

V = ship speed

F = circulation

T = Thrust

Q = Torque

t = Thrust deduction fraction

ρ = mass density of the fluid

n = Rate of revolution

$D = 2R_p$ = Propulsor diameter

$$[u_e]_V / V = \frac{\int_{r_h}^{R_p} 2\pi r \frac{u_e}{V} dr}{\pi(R_p^2 - r_h^2)} = \text{Volume-mean effective velocity ratio}$$

$$[u_n]_V / V = \frac{\int_{r_h}^{R_p} 2\pi r \frac{u_n}{V} dr}{\pi(R_p^2 - r_h^2)} = \text{Volume-mean nominal velocity ratio}$$

and r_h = Hub radius of the propulsor

The experimentally determined value of the Taylor wake fraction w_T is also shown in Table 4. It is important to note that the measured values ($1-w_T$) agree to within ± 0.03 with the computed values of the volume-mean effective velocity ratio, $[u_e]_V / V$, and effective velocity ratio at 0.7 propulsor radius, $[u_e]_{0.7} / V$, for all twelve propulsion conditions. The overall accuracy of the propulsion experiments is about $\pm 2\%$. There is no reason that the value of ($1-w_T$) should be exactly equal to $[u_e]_V / V$. However, the general agreement between the measured values of ($1-w_T$) and the computed values of $[u_e]_V / V$ for a wide variety of nominal wakes and propulsion loading conditions does provide an indirect confirmation of the present theory.

Typical values of the computed effective and total velocities at the plane of the propulsor are shown in Figure 3 and listed in Table 5. The final computed values of G , $\tan\beta$, and u_e are listed in Table 6 for the conditions used in this investigation. This information is sufficient for other investigators to perform independent calculations.

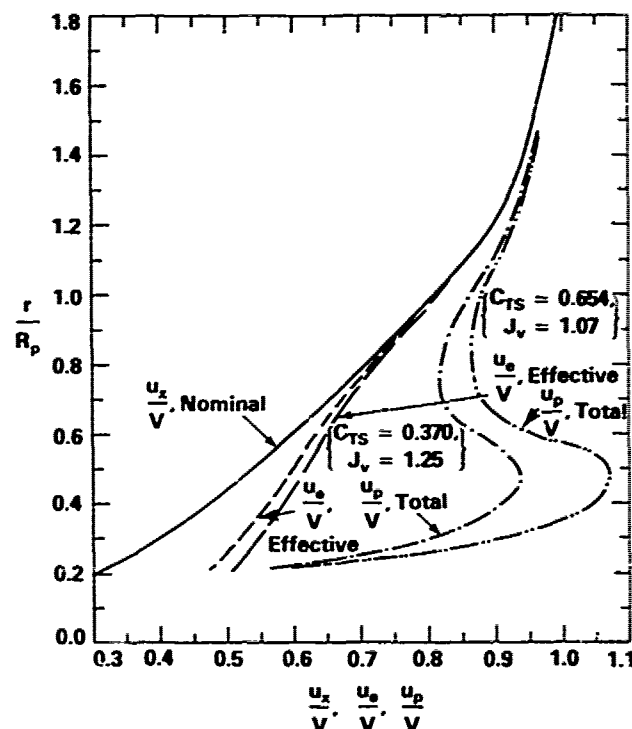


Figure 3 — Typical Total and Effective Axial Velocity Profiles Computed from the Measured Nominal Axial Velocity Profiles at the Location of Propulsor T in Wake 1

4.2 Total Velocities Upstream of Propulsor

With the final computed values of G , $\tan\beta$, and u_e , the field-point velocity computer program²⁰ with the lifting-surface option was used to compute the induced velocity u_a upstream of the propulsor. The total velocity u_p and the radial position r_p were then computed using Equations (9) and (11). The detailed results of the computation and the measured data are tabulated in Table 7. The comparisons between the measured total velocity profiles and the computed total velocity profiles are shown in Figures 4 through 9. The agreement between the measured and computed values of u_p is excellent for all cases. Thus, it may be concluded that the present inviscid approximation provides a good representation of the complex hydrodynamic interaction between the propulsor and the wake and can be used with confidence to calculate the effective velocity profile for a propulsor in an axisymmetric wake. The ratio of the measured total and nominal velocities shown in Figures 4 through 9 is found to be largest near the propulsor hub and to decrease toward the propulsor tip. Hence, the computed ratio of effective and nominal velocities is largest at the propulsor hub and decreases to about 1.0 at the propulsor tip, which is quite different from methods which assume that the effective wake profile is a constant multiple of the nominal wake profile.

5. CONCLUSION

In this paper, we have summarized recent experimental and theoretical investigations of the effective wake for the axisymmetric propulsor/stern boundary layer interaction problem. A comprehensive set of experimental data in tabulated form is presented for two propulsors operating in five quite different nominal wakes. The data are compared with calculations based on an inviscid propulsor/stern boundary layer interaction theory and provide valuable insights into the

manner in which the propulsor interacts with a thick stern boundary layer.

The numerical procedures for computing the effective wake and the total velocity upstream of the propulsor have been simplified to the solution of two quadratic algebraic equations. The procedure can readily be incorporated into any propulsor design and performance prediction practice.

It is shown that for twelve self-propulsion conditions covering a wide range of propulsion thrust loading coefficients, the computed volume-mean effective wakes agree well with the measured Taylor wake fractions based on thrust identity. The present inviscid propulsor/stern boundary-layer interaction theory predicts very well the measured total velocity profile immediately upstream of the operating propulsor. The computed ratio of the effective and nominal velocities is largest near the propulsor hub and decreases to about 1.0 at the propulsor tip. This is contrary to some older methods which assume that the effective wake profile is a constant multiple of the nominal wake profile.

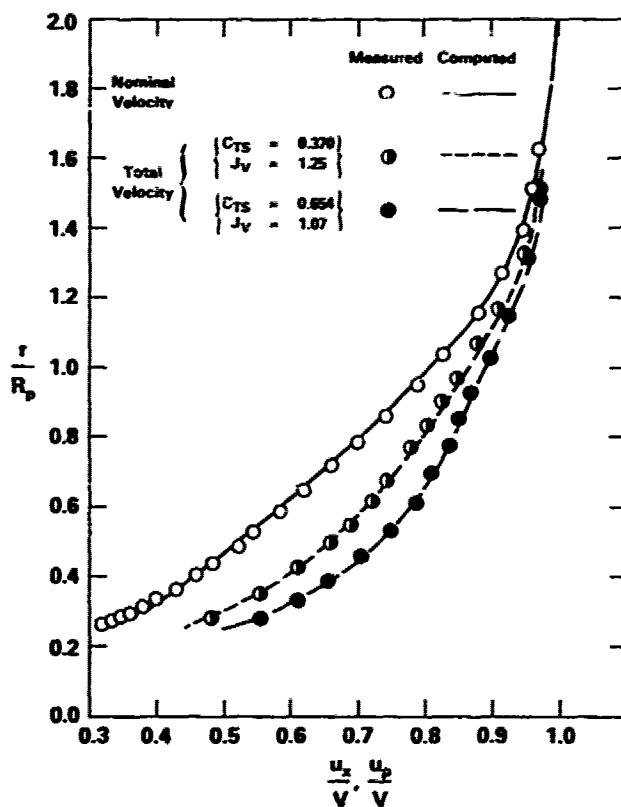


Figure 4 -- Measured and Computed Axial Velocity Profiles Immediately Upstream of Propulsor ($x/D_p = -0.227$) With and Without Propulsor T Operated in Wake 1

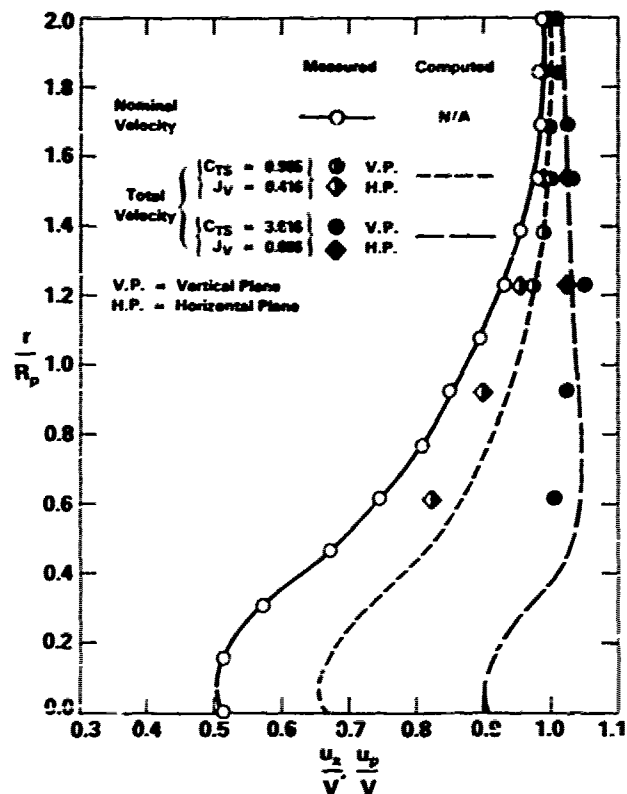


Figure 5 -- Measured and Computed Axial Velocity Profiles Immediately Upstream of Propulsor ($x/D_p = -0.336$) With and Without Propulsor J Operated in Wake A

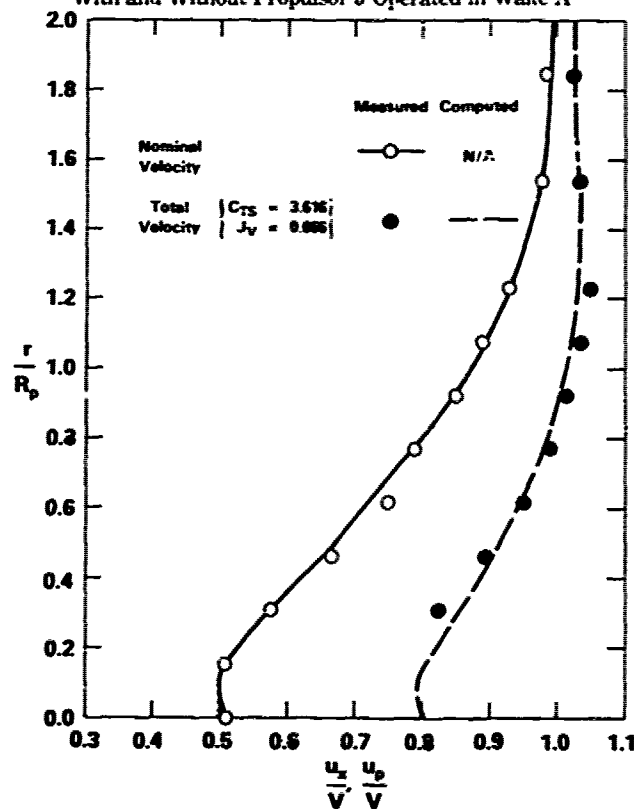
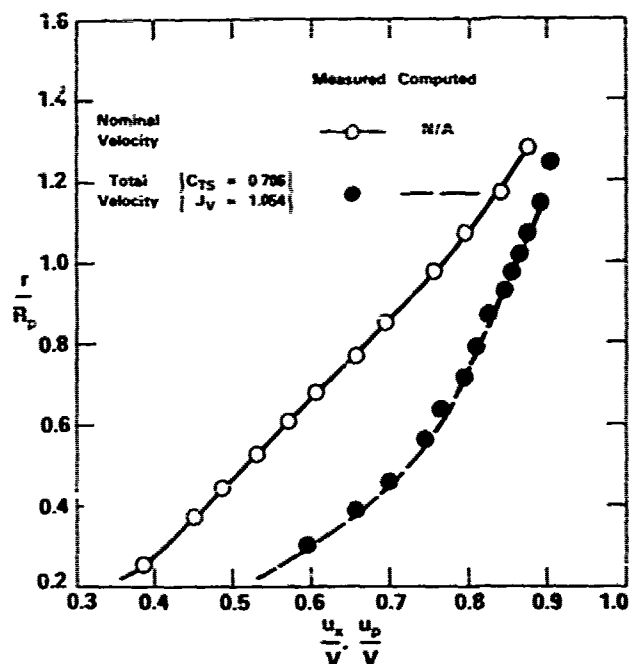
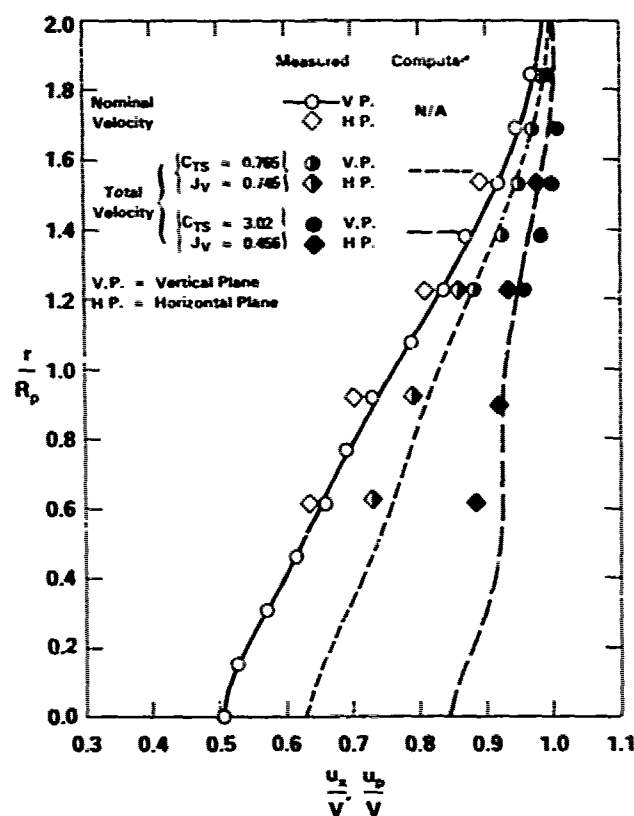
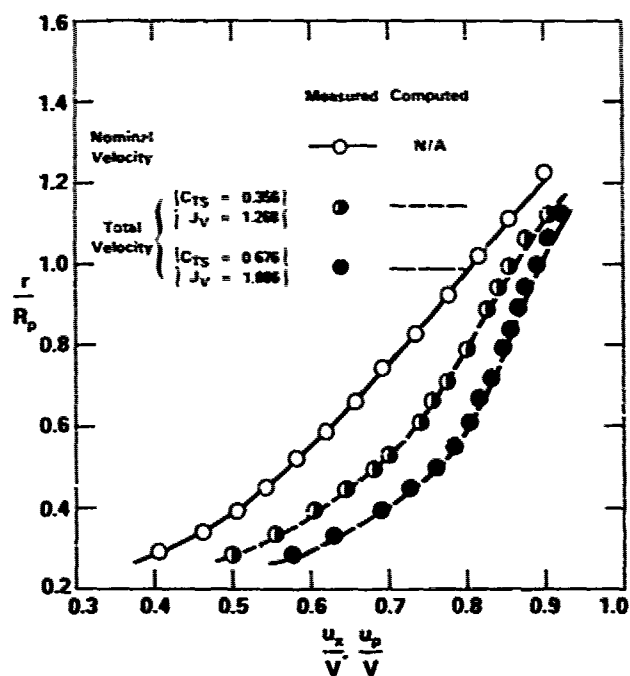


Figure 6 -- Measured and Computed Axial Velocity Profiles Upstream of Propulsor ($x/D_p = -0.489$) With and Without Propulsor J Operated in Wake A



**Figure 7 — Measured and Computed Axial Velocity Profiles
Immediately Upstream of Propulsor ($x/D_p = -0.227$)
With and Without Propulsor J Operated in Wake B**

**Figure 9 — Measured and Computed Axial Velocity Profiles
Immediately Upstream of Propulsor ($x/D_p = -0.239$)
With and Without Propulsor T Operated in Wake D**

TABLE 1 – OFFSETS FOR MODEL 1[illegible]

*L = Total Hull Length
**B = Maximum Hull Breadth

TABLE 2 - OFFSETS FOR MODEL C

X/L	Y/L	Y/R	X/L	Y/L	Y/R	X/L	Y/L	Y/R
0.00000	0.00000	0.00000	0.05143	0.3264	35804	0.25171	0.4475	50000
0.00002	0.00257	0.0642	0.05563	0.3306	36339	0.25531	0.4475	50000
0.00006	0.01115	0.1284	0.05984	0.3348	36875	0.25892	0.4475	50000
0.00014	0.01772	0.1924	0.06404	0.3390	37411	0.26252	0.4475	50000
0.00026	0.02279	0.2563	0.06825	0.3432	37947	0.26613	0.4475	50000
0.00040	0.02706	0.3201	0.07246	0.3474	38483	0.26973	0.4475	50000
0.00057	0.03133	0.3839	0.07667	0.3516	39019	0.27333	0.4475	50000
0.00078	0.03400	0.4467	0.08088	0.3558	39555	0.27693	0.4475	50000
0.00104	0.03556	0.5095	0.08509	0.3600	40091	0.28053	0.4475	50000
0.00128	0.03512	0.5719	0.08930	0.3642	40627	0.28413	0.4475	50000
0.00157	0.03267	0.6338	0.09351	0.3684	41163	0.28773	0.4475	50000
0.00189	0.02822	0.6953	0.09772	0.3726	41699	0.29133	0.4475	50000
0.00223	0.02077	0.7562	0.10193	0.3768	42235	0.29493	0.4475	50000
0.00251	0.01731	0.8165	0.10614	0.3810	42771	0.29853	0.4475	50000
0.00300	0.01284	0.8752	0.11035	0.3852	43307	0.30213	0.4475	50000
0.00342	0.00837	0.9351	0.11456	0.3894	43843	0.30573	0.4475	50000
0.00385	0.00409	0.9934	0.11877	0.3936	44379	0.30933	0.4475	50000
0.00432	0.00110	1.0508	0.12298	0.3978	44915	0.31293	0.4475	50000
0.00474	0.00041	1.1075	0.12719	0.4020	45451	0.31653	0.4475	50000
0.00529	0.00000	1.1632	0.13140	0.4062	45987	0.32013	0.4475	50000
0.00580	0.00040	1.2181	0.13561	0.4104	46523	0.32373	0.4475	50000
0.00632	0.00138	1.2719	0.13982	0.4146	47059	0.32733	0.4475	50000
0.00685	0.00190	1.3248	0.14403	0.4188	47595	0.33093	0.4475	50000
0.00741	0.00232	1.3767	0.14824	0.4230	48131	0.33453	0.4475	50000
0.00797	0.00277	1.4274	0.15245	0.4272	48667	0.33813	0.4475	50000
0.00853	0.00322	1.4770	0.15666	0.4314	49203	0.34173	0.4475	50000
0.00910	0.00365	1.5255	0.16087	0.4356	49739	0.34533	0.4475	50000
0.00967	0.00408	1.5727	0.16508	0.4398	50275	0.34893	0.4475	50000
0.01025	0.00449	1.6187	0.16929	0.4440	50811	0.35253	0.4475	50000
0.01082	0.00491	1.6635	0.17350	0.4482	51347	0.35613	0.4475	50000
0.01139	0.00528	1.7073	0.17771	0.4524	51883	0.35973	0.4475	50000
0.01197	0.00560	1.7495	0.18192	0.4566	52419	0.36333	0.4475	50000
0.01254	0.00583	1.7909	0.18613	0.4608	52955	0.36693	0.4475	50000
0.01312	0.00609	1.8314	0.19034	0.4650	53491	0.37053	0.4475	50000
0.01369	0.00635	1.8710	0.19455	0.4692	54027	0.37413	0.4475	50000
0.01427	0.00659	1.9098	0.19876	0.4734	54563	0.37773	0.4475	50000
0.01484	0.00678	1.9478	0.20297	0.4776	55099	0.38133	0.4475	50000
0.01542	0.00693	1.9844	0.20718	0.4818	55635	0.38493	0.4475	50000
0.01600	0.00705	2.0196	0.21139	0.4860	56171	0.38853	0.4475	50000
0.01658	0.00714	2.0536	0.21560	0.4902	56707	0.39213	0.4475	50000
0.01716	0.00720	2.0864	0.21981	0.4944	57243	0.39573	0.4475	50000
0.01774	0.00723	2.1184	0.22402	0.4986	57779	0.39933	0.4475	50000
0.01832	0.00723	2.1494	0.22823	0.5028	58315	0.40293	0.4475	50000
0.01890	0.00720	2.1794	0.23244	0.5070	58851	0.40653	0.4475	50000
0.01948	0.00714	2.2084	0.23665	0.5112	59387	0.41013	0.4475	50000
0.02006	0.00705	2.2364	0.24086	0.5154	59923	0.41373	0.4475	50000
0.02064	0.00693	2.2634	0.24507	0.5196	60459	0.41733	0.4475	50000
0.02122	0.00678	2.2894	0.24928	0.5238	60995	0.42093	0.4475	50000
0.02180	0.00660	2.3144	0.25349	0.5280	61531	0.42453	0.4475	50000
0.02238	0.00639	2.3384	0.25770	0.5322	62067	0.42813	0.4475	50000
0.02296	0.00614	2.3614	0.26191	0.5364	62603	0.43173	0.4475	50000
0.02354	0.00585	2.3834	0.26612	0.5406	63139	0.43533	0.4475	50000
0.02412	0.00551	2.4044	0.27033	0.5448	63675	0.43893	0.4475	50000
0.02470	0.00512	2.4244	0.27454	0.5490	64211	0.44253	0.4475	50000
0.02528	0.00469	2.4434	0.27875	0.5532	64747	0.44613	0.4475	50000
0.02586	0.00421	2.4614	0.28296	0.5574	65283	0.44973	0.4475	50000
0.02644	0.00369	2.4784	0.28717	0.5616	65819	0.45333	0.4475	50000
0.02702	0.00312	2.4944	0.29138	0.5658	66355	0.45693	0.4475	50000
0.02760	0.00250	2.5094	0.29559	0.5699	66891	0.46053	0.4475	50000
0.02818	0.00183	2.5234	0.29980	0.5741	67427	0.46413	0.4475	50000
0.02876	0.00111	2.5364	0.30401	0.5783	67963	0.46773	0.4475	50000
0.02934	0.00034	2.5484	0.30822	0.5825	68499	0.47133	0.4475	50000
0.02992	0.00000	2.5594	0.31243	0.5867	69035	0.47493	0.4475	50000
0.03050	0.00000	2.5694	0.31664	0.5909	69571	0.47853	0.4475	50000
0.03108	0.00000	2.5784	0.32085	0.5951	70107	0.48213	0.4475	50000
0.03166	0.00000	2.5864	0.32506	0.5993	70643	0.48573	0.4475	50000
0.03224	0.00000	2.5934	0.32927	0.6035	71179	0.48933	0.4475	50000
0.03282	0.00000	2.6004	0.33348	0.6077	71715	0.49293	0.4475	50000
0.03340	0.00000	2.6064	0.33769	0.6119	72251	0.49653	0.4475	50000
0.03398	0.00000	2.6114	0.34190	0.6161	72787	0.50013	0.4475	50000
0.03456	0.00000	2.6164	0.34611	0.6203	73323	0.50373	0.4475	50000
0.03514	0.00000	2.6204	0.35032	0.6245	73859	0.50733	0.4475	50000
0.03572	0.00000	2.6244	0.35453	0.6287	74395	0.51093	0.4475	50000
0.03630	0.00000	2.6284	0.35874	0.6329	74931	0.51453	0.4475	50000
0.03688	0.00000	2.6324	0.36295	0.6371	75467	0.51813	0.4475	50000
0.03746	0.00000	2.6364	0.36716	0.6413	76003	0.52173	0.4475	50000
0.03804	0.00000	2.6404	0.37137	0.6455	76539	0.52533	0.4475	50000
0.03862	0.00000	2.6444	0.37558	0.6497	77075	0.52893	0.4475	50000
0.03920	0.00000	2.6484	0.37979	0.6539	77611	0.53253	0.4475	50000
0.03978	0.00000	2.6524	0.38400	0.6581	78147	0.53613	0.4475	50000
0.04036	0.00000	2.6564	0.38821	0.6623	78683	0.53973	0.4475	50000
0.04094	0.00000	2.6604	0.39242	0.6665	79219	0.54333	0.4475	50000
0.04152	0.00000	2.6644	0.39663	0.6707	79755	0.54693	0.4475	50000
0.04210	0.00000	2.6684	0.40084	0.6749	80291	0.55053	0.4475	50000
0.04268	0.00000	2.6724	0.40505	0.6791	80827	0.55413	0.4475	50000
0.04326	0.00000	2.6764	0.40926	0.6833	81363	0.55773	0.4475	50000
0.04384	0.00000	2.6804	0.41347	0.6875	81899	0.56133	0.4475	50000
0.04442	0.00000	2.6844	0.41768	0.6917	82435	0.56493	0.4475	50000
0.04500	0.00000	2.6884	0.42189	0.6959	82971	0.56853	0.4475	50000
0.04558	0.00000	2.6924	0.42610	0.7001	83507	0.57213	0.4475	50000
0.04616	0.00000	2.6964	0.43031	0.7043	84043	0.57573	0.4475	50000
0.04674	0.00000	2.7004	0.43452	0.7085	84579	0.57933	0.4475	50000
0.04732	0.00000	2.7044	0.43873	0.7127	85115	0.58293	0.4475	50000
0.04790	0.00000	2.7084	0.44294	0.7169	85651	0.58653	0.4475	50000
0.04848	0.00000	2.7124	0.44715	0.7211	86187	0.59013	0.4475	50000
0.04906	0.00000	2.7164	0.45136	0.7253	86723	0.59373	0.4475	50000
0.04964	0.00000	2.7204	0.45557	0.7295	87259	0.59733	0.4475	50000
0.05022	0.00000	2.7244	0.45978	0.7337	87795	0.60093	0.4475	50000
0.05080	0.00000	2.7284	0.46399	0.7379	88331	0.60453	0.4475	50000
0.05138	0.00000	2.7324	0.46820	0.7421	88867	0.60813	0.4475	50000
0.05196	0.00000	2.7364	0.47241	0.7463	89403	0.61173	0.4475	50000
0.05254	0.00000	2.7404	0.47662	0.7505	89939	0.61533	0.4475	50000
0.05312	0.00000	2.7444	0.48083	0.7547	90475	0.61893	0.4475	50000
0.05370	0.00000	2.7484	0.48504	0.7589	91011	0.62253	0.4475	50000
0.05428	0.00000	2.7524	0.48925	0.7631	91547	0.62613	0.4475	50000
0.05486	0.00000	2.7564	0.49346	0.7673	92083	0.62973	0.4475	50000
0.05544	0.00000	2.7604	0.49767	0.7715	92619	0.63333	0.4475	50000
0.05602	0.00000	2.7644	0.50188	0.7757	93155	0.63693	0.4475	50000
0.05660	0.00000	2.7684	0.50609	0.7799	93691	0.64053	0.4475	50000
0.05718	0.00000	2.7724	0.51030	0.7841	94227	0.64413	0.4475	50000
0.05776	0.00000	2.7764	0.51451	0.7883	94763	0.64773	0.4475	50000
0.05834	0.00000	2.7804	0.51872	0.7925	95299	0.65133	0.4475	50000
0.05892	0.00000	2.7844	0.52293	0.7967	95835	0.65493	0.4475	50000
0.05950	0.00000	2.7884	0.52714	0.8009	96371	0.65853	0.4475	50000
0.06008	0.00000	2.7924	0.53135	0.8051	96907	0.66213	0.4475	50000
0.06066	0.00000	2.7964	0.53556	0.8093				

TABLE 5 - TOTAL AND EFFECTIVE AXIAL VELOCITY PROFILES COMPUTED FROM NOMINAL AND PROPULSOR INDUCED AXIAL VELOCITIES AT THE LOCATION OF PROPU' SOR

(a) PROPULSOR T IN WAKE 1, $C_{TS} = 0.370$, $J_V = 1.25$

INPUT				OUTPUT			
NOMINAL		INDUCED		TOTAL		EFFECTIVE	
$\frac{r}{R_p}$	$\frac{u_z}{V}$	$\frac{u_z}{V}$	$\frac{v_{\theta}}{V}$	$\frac{r}{R_p}$	$\frac{u_z}{V}$	$\frac{r}{R_p}$	$\frac{u_z}{V}$
0.211	0.313	0.088	0.082	0.211	0.564	0.211	0.476
0.250	0.354	0.152	0.093	0.233	0.650	0.250	0.498
0.300	0.396	0.214	0.083	0.263	0.735	0.300	0.521
0.350	0.434	0.254	0.067	0.295	0.796	0.350	0.542
0.400	0.470	0.288	0.053	0.328	0.849	0.400	0.561
0.450	0.502	0.315	0.031	0.362	0.894	0.450	0.579
0.500	0.530	0.323	0.008	0.398	0.918	0.500	0.595
0.550	0.560	0.320	-0.013	0.435	0.933	0.550	0.613
0.600	0.590	0.303	-0.038	0.474	0.934	0.600	0.631
0.650	0.620	0.268	-0.063	0.515	0.915	0.650	0.651
0.700	0.650	0.205	-0.084	0.560	0.877	0.700	0.672
0.750	0.680	0.143	-0.108	0.608	0.844	0.750	0.695
0.800	0.710	0.099	-0.121	0.659	0.819	0.800	0.720
0.850	0.738	0.073	-0.111	0.712	0.818	0.850	0.745
0.900	0.762	0.054	-0.101	0.766	0.821	0.900	0.767
0.950	0.786	0.039	-0.093	0.821	0.829	0.950	0.790
1.000	0.810	0.030	-0.084	0.878	0.843	1.000	0.813
1.050	0.834	0.023	-0.074	0.931	0.859	1.050	0.836
1.100	0.856	0.017	-0.066	0.985	0.874	1.100	0.900
1.200	0.900	0.010	-0.052	1.094	0.910	1.200	0.925
1.300	0.925	0.006	-0.042	1.202	0.931	1.500	0.960
1.500	0.960	0.003	-0.300	1.415	0.963		
2.000	1.000						

(b) PROPULSOR T IN WAKE 1, $C_{TS} = 0.654$, $J_V = 1.07$

0.211	0.313	0.090	0.119	0.211	0.597	0.211	0.507
0.250	0.354	0.161	0.129	0.232	0.690	0.250	0.529
0.300	0.396	0.245	0.126	0.260	0.795	0.300	0.550
0.350	0.434	0.322	0.107	0.289	0.891	0.350	0.569
0.400	0.470	0.368	0.091	0.320	0.954	0.400	0.586
0.450	0.502	0.408	0.056	0.351	1.010	0.450	0.602
0.500	0.530	0.427	0.029	0.383	1.043	0.500	0.616
0.550	0.560	0.427	-0.001	0.417	1.059	0.550	0.632
0.600	0.590	0.425	-0.040	0.453	1.073	0.600	0.648
0.650	0.620	0.396	-0.082	0.491	1.061	0.650	0.665
0.700	0.650	0.321	-0.129	0.531	1.004	0.700	0.683
0.750	0.680	0.232	-0.164	0.576	0.936	0.750	0.704
0.800	0.710	0.162	-0.180	0.625	0.889	0.800	0.727
0.850	0.738	0.126	-0.174	0.677	0.876	0.850	0.750
0.900	0.762	0.095	-0.166	0.731	0.865	0.900	0.770
0.950	0.786	0.072	-0.155	0.786	0.864	0.950	0.792
1.000	0.810	0.055	-0.140	0.841	0.869	1.000	0.814
1.050	0.834	0.037	-0.123	0.896	0.874	1.050	0.837
1.100	0.856	0.027	-0.109	0.952	0.865	1.100	0.858
1.200	0.900	0.015	-0.086	1.064	0.916	1.200	0.901
1.300	0.925	0.009	-0.070	1.174	0.934	1.300	0.925
1.500	0.960	0.005	-0.048	1.391	0.965	1.500	0.960
2.000	1.000		-0.024				

TABLE 6 — COMPUTED RESULTS OF PROPULSOR/WAKE INTERACTION

(a) PROPULSOR T IN WAKE 1

WAKE 1									
$\frac{r}{R_p}$	$\frac{u_x}{V}$	$C_{TS} = 0.370, J_V = 1.25$				$C_{TS} = 0.654, J_V = 1.07$			
		$\frac{u_a}{V}$	$\frac{u_b}{V}$	$\tan \beta_i$	G	$\frac{u_a}{V}$	$\frac{u_b}{V}$	$\tan \beta_i$	G
0.211	0.313	0.088	0.476	0.910	0.0000	0.090	0.507	0.847	0.0000
0.25	0.354	0.152	0.498	0.794	0.0029	0.161	0.529	0.706	0.0038
0.30	0.396	0.214	0.521	0.797	0.0060	0.245	0.550	0.733	0.0078
0.40	0.470	0.288	0.561	0.748	0.0118	0.368	0.586	0.719	0.0158
0.50	0.530	0.323	0.595	0.670	0.0160	0.427	0.616	0.657	0.0222
0.60	0.590	0.303	0.631	0.591	0.0179	0.425	0.648	0.584	0.0257
0.70	0.650	0.205	0.672	0.518	0.0172	0.321	0.683	0.511	0.0258
0.80	0.710	0.099	0.720	0.452	0.0140	0.162	0.727	0.443	0.0224
0.90	0.762	0.054	0.767	0.390	0.0086	0.095	0.770	0.377	0.0153
0.95	0.786	0.039	0.790	0.361	0.0053	0.072	0.792	0.345	0.0103
1.00	0.810	0.030	0.813	0.334	0.0000	0.055	0.814	0.316	0.0000
1.05	0.834	0.023	0.836	—	0.0000	0.037	0.837	—	0.0000
1.10	0.856	0.017	0.857	—	0.0000	0.027	0.858	—	0.0000
1.20	0.900	0.010	0.900	—	0.0000	0.015	0.900	—	0.0000

(b) PROPULSOR J IN WAKE A

WAKE A									
$\frac{r}{R_p}$	$\frac{u_x}{V}$	$C_{TS} = 0.965, J_V = 0.666$				$C_{TS} = 3.62, J_V = 0.416$			
		$\frac{u_a}{V}$	$\frac{u_b}{V}$	$\tan \beta_i$	G	$\frac{u_a}{V}$	$\frac{u_b}{V}$	$\tan \beta_i$	G
0.182	0.528	0.000	0.669	1.114	0.0000	0.291	0.739	1.135	0.0000
0.250	0.565	0.363	0.690	0.906	0.0153	0.751	0.755	0.894	0.0346
0.300	0.593	0.434	0.705	0.772	0.0206	0.892	0.765	0.753	0.0464
0.400	0.644	0.484	0.732	0.591	0.0260	1.026	0.783	0.567	0.0584
0.500	0.690	0.480	0.757	0.481	0.0284	1.051	0.800	0.459	0.0647
0.600	0.735	0.455	0.783	0.406	0.0291	1.030	0.817	0.383	0.0671
0.700	0.777	0.422	0.809	0.349	0.0280	0.982	0.834	0.325	0.0660
0.800	0.816	0.362	0.834	0.305	0.0254	0.883	0.852	0.277	0.0607
0.900	0.848	0.256	0.857	0.269	0.0199	0.690	0.868	0.237	0.0488
0.950	0.863	0.193	0.869	0.253	0.0147	0.525	0.961	0.224	0.0374
1.000	0.876	0.105	0.880	0.236	0.0000	0.270	0.885	0.209	0.0000
1.050	0.889	0.000	0.000	—	0.0000	0.000	0.000	—	0.0000
1.100	0.900	0.000	0.000	—	0.0000	0.000	0.000	—	0.0000
1.200	0.924	0.000	0.000	—	0.0000	0.000	0.000	—	0.0000

TABLE 6 — COMPUTED RESULTS OF PROPULSOR/WAKE INTERACTION

(c) PROPULSOR J IN WAKE B

WAKE B									
$\frac{r}{R_p}$	$\frac{u_x}{V}$	$C_{TS} = 0.765, J_V = 0.745$				$C_{TS} = 3.02, J_V = 0.456$			
		$\frac{u_a}{V}$	$\frac{u_o}{V}$	$\tan \beta_i$	G	$\frac{u_a}{V}$	$\frac{u_o}{V}$	$\tan \beta_i$	G
0.182	0.544	0.000	0.639	1.148	0.0000	0.050	0.693	1.144	0.0000
0.250	0.555	0.335	0.646	0.924	0.0133	0.668	0.699	0.891	0.0311
0.300	0.567	0.386	0.652	0.786	0.0181	0.813	0.703	0.750	0.0417
0.400	0.598	0.436	0.669	0.602	0.0233	0.933	0.715	0.567	0.0530
0.500	0.630	0.434	0.687	0.487	0.0257	0.957	0.727	0.455	0.0586
0.600	0.663	0.422	0.706	0.413	0.0265	0.944	0.739	0.384	0.0614
0.700	0.694	0.377	0.725	0.350	0.0253	0.905	0.752	0.325	0.0607
0.800	0.727	0.319	0.746	0.305	0.0227	0.814	0.766	0.277	0.0561
0.900	0.760	0.227	0.770	0.267	0.0173	0.586	0.783	0.239	0.0452
0.950	0.776	0.163	0.783	0.252	0.0128	0.427	0.792	0.223	0.0343
1.000	0.792	0.090	0.797	0.239	0.0000	0.252	0.803	0.117	0.0200
1.050	0.806	0.000	0.000	—	0.0000	0.000	0.000	—	0.0000
1.100	0.820	0.000	0.000	—	0.0000	0.000	0.000	—	0.0000
1.200	0.842	0.000	0.000	—	0.0000	0.000	0.000	—	0.0000

(d) PROPULSOR T IN WAKE C

WAKE C													
$\frac{r}{R_p}$	$\frac{u_x}{V}$	$C_{TS} = 0.356, J_V = 1.268$				$C_{TS} = 0.498, J_V = 1.157$				$C_{TS} = 0.676, J_V = 1.066$			
		$\frac{u_a}{V}$	$\frac{u_o}{V}$	$\tan \beta_i$	G	$\frac{u_a}{V}$	$\frac{u_o}{V}$	$\tan \beta_i$	G	$\frac{u_a}{V}$	$\frac{u_o}{V}$	$\tan \beta_i$	G
0.211	0.387	0.080	0.512	0.945	0.0000	0.078	0.526	0.947	0.0000	0.106	0.542	0.913	0.0000
0.250	0.417	0.142	0.531	0.844	0.0023	0.147	0.545	0.787	0.0028	0.170	0.559	0.755	0.0035
0.300	0.454	0.202	0.554	0.834	0.0051	0.225	0.566	0.780	0.0059	0.251	0.580	0.747	0.0071
0.400	0.520	0.279	0.593	0.776	0.0107	0.321	0.604	0.747	0.0127	0.367	0.615	0.732	0.0152
0.500	0.579	0.315	0.629	0.696	0.0150	0.378	0.637	0.680	0.0182	0.445	0.646	0.674	0.0220
0.600	0.631	0.292	0.662	0.614	0.0172	0.346	0.668	0.603	0.0213	0.410	0.675	0.601	0.0261
0.700	0.677	0.204	0.694	0.535	0.0169	0.244	0.698	0.526	0.0214	0.302	0.704	0.524	0.0266
0.800	0.720	0.095	0.729	0.463	0.0140	0.123	0.732	0.453	0.0184	0.161	0.736	0.451	0.0235
0.900	0.763	0.056	0.768	0.398	0.0089	0.077	0.770	0.387	0.0123	0.132	0.772	0.381	0.0164
0.950	0.785	0.042	0.789	0.368	0.0055	0.057	0.790	0.356	0.0081	0.078	0.791	0.350	0.0112
1.000	0.806	0.031	0.809	0.340	0.0000	0.043	0.809	0.327	0.0000	0.058	0.810	0.319	0.0000
1.050	0.826	0.000	0.000	—	0.0000	0.000	0.000	—	0.0000	0.000	0.000	—	0.0000
1.100	0.845	0.000	0.000	—	0.0000	0.000	0.000	—	0.0000	0.000	0.000	—	0.0000
1.200	0.880	0.000	0.000	—	0.0000	0.000	0.000	—	0.0000	0.000	0.000	—	0.0000

TABLE 6 - COMPUTED RESULTS OF PROPULSOR/WAKE INTERACTION

(e) PROPULSOR T IN WAKE D

WAKE D													
$\frac{r}{R_p}$	$\frac{u_x}{V}$	$C_{TS} = 0.360, J_V = 1.290$				$C_{TS} = 0.500, J_V = 1.174$				$C_{TS} = 0.706, J_V = 1.054$			
		$\frac{u_a}{V}$	$\frac{u_b}{V}$	$\tan \beta_i$	G	$\frac{u_a}{V}$	$\frac{u_b}{V}$	$\tan \beta_i$	G	$\frac{u_a}{V}$	$\frac{u_b}{V}$	$\tan \beta_i$	G
0.211	0.360	0.071	0.484	0.957	0.0000	0.078	0.501	0.904	0.0000	0.074	0.515	0.843	0.0000
0.250	0.388	0.122	0.501	0.794	0.0822	0.143	0.517	0.748	0.0027	0.155	0.532	0.696	0.0035
0.300	0.420	0.196	0.521	0.790	0.0050	0.217	0.536	0.741	0.0058	0.244	0.549	0.688	0.0070
0.400	0.488	0.279	0.548	0.743	0.0189	0.320	0.562	0.717	0.0128	0.374	0.574	0.691	0.0154
0.500	0.516	0.330	0.575	0.670	0.0155	0.387	0.587	0.656	0.0185	0.462	0.597	0.642	0.0226
0.600	0.567	0.293	0.606	0.593	0.0178	0.355	0.615	0.584	0.0217	0.431	0.623	0.576	0.0269
0.700	0.628	0.205	0.642	0.520	0.0175	0.257	0.649	0.512	0.0219	0.323	0.654	0.505	0.0276
0.800	0.672	0.097	0.683	0.452	0.0145	0.129	0.688	0.443	0.0188	0.173	0.691	0.435	0.0243
0.900	0.722	0.060	0.728	0.389	0.0082	0.082	0.731	0.378	0.0126	0.112	0.732	0.367	0.0170
0.950	0.745	0.046	0.749	0.380	0.0057	0.062	0.752	0.348	0.0083	0.088	0.752	0.336	0.0115
1.000	0.767	0.034	0.770	0.331	0.0080	0.047	0.771	0.318	0.0080	0.064	0.772	0.305	0.0080
1.050	0.790	0.000	0.000	-	0.0000	0.000	0.000	-	0.0000	0.000	0.000	-	0.0000
1.100	0.811	0.000	0.000	-	0.0000	0.000	0.000	-	0.0000	0.000	0.000	-	0.0000
1.200	0.849	0.000	0.000	-	0.0000	0.000	0.000	-	0.0000	0.000	0.000	-	0.0000

TABLE 7 - MEASURED AND COMPUTED VELOCITY PROFILES IMMEDIATELY UPSTREAM OF PROPULSOR WITH AND WITHOUT AN OPERATING PROPULSOR

(a) AT $X/D_p = -0.227$, PROPULSOR T IN WAKE 1, $C_{TS} = 0.370$, $J_V = 1.25$

MEASURED NOMINAL VELOCITY*			INPUT				PROPELLER TOTAL VELOCITY			
			$\frac{r}{R_p}$	$\frac{u_x}{V}$	COMPUTED		COMPUTED		MEASURED	
					$\frac{u_a}{V}$	$\frac{v_{\theta}}{V}$	$\frac{r_p}{R_p}$	$\frac{u_p}{V}$	$\frac{r_p}{R_p}$	$\frac{u_p}{V}$
0.262	0.318	-0.033	0.250	0.324	0.0388	0.0091	0.2500	0.4411	0.288	0.488
0.274	0.334	-0.039	0.300	0.377	0.0435	0.0130	0.2887	0.4859	0.350	0.554
0.284	0.345	-0.041	0.350	0.420	0.0519	0.0150	0.3300	0.5281	0.424	0.613
0.294	0.360	-0.042	0.400	0.458	0.0619	0.0122	0.3727	0.5685	0.499	0.659
0.314	0.381	-0.046	0.450	0.490	0.0698	0.0058	0.4163	0.6023	0.574	0.698
0.334	0.400	-0.047	0.500	0.522	0.0757	-0.0017	0.4606	0.6344	0.634	0.722
0.364	0.422	-0.055	0.550	0.551	0.0793	-0.0108	0.5056	0.6620	0.699	0.745
0.405	0.459	-0.055	0.600	0.583	0.0888	-0.0201	0.5512	0.6903	0.769	0.780
0.435	0.483	-0.049	0.650	0.614	0.0787	-0.0288	0.5976	0.7146	0.836	0.805
0.487	0.524	-0.049	0.700	0.644	0.0740	-0.0356	0.6447	0.7360	0.900	0.825
0.528	0.545	-0.045	0.750	0.675	0.0683	-0.0412	0.6926	0.7576	0.983	0.849
0.588	0.585	-0.045	0.800	0.704	0.0619	-0.0456	0.7412	0.7773	1.065	0.880
0.649	0.620	-0.044	0.850	0.732	0.0552	-0.0478	0.7903	0.7962	1.165	0.912
0.720	0.661	-0.040	0.900	0.758	0.0486	-0.0487	0.8400	0.8136	1.322	0.950
0.782	0.701	-0.036	0.950	0.783	0.0420	-0.0485	0.8901	0.8305	1.518	0.973
0.860	0.742	-0.033	1.000	0.807	0.0362	-0.0472	0.9406	0.8474		
0.954	0.790	-0.035	1.050	0.830	0.0308	-0.0455	0.9914	0.8640		
1.036	0.827	-0.033	1.100	0.852	0.0263	-0.0433	1.0423	0.8807		
1.157	0.880	-0.030	1.200	0.896	0.0192	-0.0385	1.1446	0.9184		
1.270	0.915	-0.028	1.300	0.925	0.0141	-0.0339	1.2472	0.9398		
1.391	0.947	-0.029	1.500	0.960	0.0083	-0.0258	1.4521	0.9685		
1.514	0.960	-0.025	2.000	1.000	0.0026	-0.0154				
1.625	0.970	-0.020								

(b) AT $X/D_p = -0.227$, PROPULSOR T IN WAKE 1, $C_{TS} = 0.654$, $J_V = 1.07$

0.262	0.318	-0.033	0.250	0.324	0.0652	0.0195	0.2500	0.5025	0.288	0.554
0.274	0.334	-0.039	0.300	0.377	0.0748	0.0230	0.2844	0.5475	0.334	0.611
0.284	0.345	-0.041	0.350	0.420	0.0889	0.0231	0.3219	0.5917	0.391	0.656
0.294	0.360	-0.042	0.400	0.458	0.1027	0.0178	0.3613	0.6327	0.460	0.706
0.314	0.381	-0.046	0.450	0.490	0.1143	0.0079	0.4019	0.6677	0.529	0.751
0.334	0.400	-0.047	0.500	0.522	0.1228	-0.0049	0.4435	0.6999	0.612	0.787
0.364	0.428	-0.055	0.550	0.551	0.1282	-0.0187	0.4860	0.7271	0.695	0.810
0.405	0.459	-0.055	0.600	0.583	0.1290	-0.0326	0.5294	0.7524	0.772	0.837
0.435	0.483	-0.049	0.650	0.614	0.1260	-0.0465	0.5738	0.7737	0.851	0.853
0.487	0.524	-0.049	0.700	0.644	0.1191	-0.0574	0.6193	0.7909	0.923	0.870
0.528	0.545	-0.045	0.750	0.675	0.1107	-0.0664	0.6659	0.8081	1.025	0.898
0.588	0.585	-0.045	0.800	0.704	0.1010	-0.0734	0.7134	0.8229	1.145	0.924
0.649	0.620	-0.044	0.850	0.732	0.0903	-0.0772	0.7618	0.8364	1.310	0.955
0.720	0.661	-0.040	0.900	0.758	0.0795	-0.0788	0.8110	0.8486	1.481	0.973
0.782	0.701	-0.036	0.950	0.783	0.0689	-0.0789	0.8609	0.8606		
0.860	0.742	-0.033	1.000	0.807	0.0588	-0.0773	0.9113	0.8725		
0.954	0.790	-0.035	1.050	0.830	0.0505	-0.0746	0.9623	0.8856		
1.036	0.827	-0.033	1.100	0.852	0.0430	-0.0711	1.0136	0.8988		
1.157	0.880	-0.030	1.200	0.896	0.0311	-0.0631	1.1168	0.9290		
1.270	0.915	-0.028	1.300	0.925	0.0227	-0.0552	1.2206	0.9487		
1.391	0.947	-0.029	1.500	0.960	0.0131	-0.0421	1.4279	0.9735		
1.514	0.960	-0.025	2.000	1.000	0.0043	-0.0253				
1.625	0.970	-0.020								

* (), MEASURED ALONG HORIZONTAL PLANE
OTHERWISE, MEASURED ALONG VERTICAL PLANE

TABLE 7 - MEASURED AND COMPUTED VELOCITY PROFILES IMMEDIATELY UPSTREAM OF PROPULSOR WITH AND WITHOUT AN OPERATING PROPULSOR (Continued)

(c) AT $X/D_p = -0.336$, PROPULSOR J IN WAKE A, $C_{TS} = 0.965$, $J_V = 0.666$

MEASURED NOMINAL VELOCITY		INPUT				PROPELLER TOTAL VELOCITY				
		$\frac{r}{R_p}$	$\frac{u_x}{V}$	COMPUTED		COMPUTED		MEASURED		
				$\frac{u_x}{V}$	$\frac{v_{\theta}}{V}$	$\frac{r_p}{R_p}$	$\frac{u_p}{V}$	$\frac{r_p}{R_p}$	$\frac{u_p}{V}$	$\frac{v_{\theta}}{V}$
0.0000	0.514	0.00	0.515	0.0941	0.0000	0.0000	0.6653			
0.1537	0.513	0.05	0.501	0.0941	-0.0018	0.0438	0.6546			
0.3074	0.573	0.10	0.503	0.0941	-0.0041	0.0876	0.6561			
0.4610	0.672	0.15	0.514	0.0941	-0.0065	0.1315	0.6646			
0.6147	0.745	0.20	0.526	0.0941	-0.0090	0.1758	0.6739	0.6147	(0.821)	(-0.029)
0.7684	0.810	0.25	0.548	0.0941	-0.0106	0.2205	0.6912			
0.9221	0.850	0.30	0.570	0.0941	-0.0145	0.2656	0.7088	0.9221	(0.900)	(-0.059)
1.0758	0.895	0.35	0.597	0.0940	-0.0176	0.3113	0.7306			
1.2294	0.931	0.40	0.631	0.0938	-0.0207	0.3576	0.7584	1.2294	0.973 (0.952)	-0.044 (-0.056)
1.3831	0.956	0.45	0.666	0.0930	-0.0242	0.4044	0.7870	1.3831	0.988	-0.039
1.5368	0.982	0.50	0.692	0.0918	-0.0275	0.4516	0.8079	1.5368	0.999 (0.995)	-0.032 (-0.043)
1.6905	0.986	0.55	0.720	0.0902	-0.0315	0.4992	0.8304	1.6905	0.997	-0.026
1.8442	0.984	0.60	0.741	0.0880	-0.0349	0.5471	0.8465	1.8442	0.987	-0.017
1.9978	0.989	0.65	0.762	0.0854	-0.0380	0.5952	0.8624	1.9978	0.994	-0.017
2.1515	0.982	0.70	0.782	0.0825	-0.0409	0.6436	0.8773	2.1515	0.992	-0.013
2.3052	0.985	0.75	0.802	0.0791	-0.0440	0.6922	0.8918	2.3052	0.995	-0.011
		0.80	0.820	0.0756	-0.0462	0.7410	0.9045			
		0.85	0.834	0.0708	-0.0481	0.7901	0.9125			
		0.90	0.846	0.0664	-0.0496	0.8393	0.9191			
		0.95	0.860	0.0618	-0.0508	0.8888	0.9274			
		1.00	0.874	0.0569	-0.0510	0.9385	0.9355			
		1.10	0.898	0.0484	-0.0509	1.0881	0.9496			
		1.20	0.924	0.0403	-0.0490	1.1383	0.9659			
		1.30	0.943	0.0332	-0.0465	1.2393	0.9774			
		1.50	0.969	0.0224	-0.0395	1.4421	0.9918			
		1.70	0.982	0.0154	-0.0331	1.6454	0.9976			
		2.00	0.990	0.0129	-0.0262	1.9500	1.0030			

(d) AT $X/D_p = -0.336$, PROPULSOR J IN WAKE A, $C_{TS} = 3.62$, $J_V = 0.417$

0.0000	0.514	0.00	0.515	0.272	0.000	0.0000	0.9088			
0.1537	0.513	0.05	0.501	0.272	-0.004	0.0374	0.9010			
0.3074	0.573	0.10	0.503	0.272	-0.012	0.0747	0.9021			
0.4610	0.672	0.15	0.514	0.272	-0.019	0.1123	0.9003			
0.6147	0.745	0.20	0.526	0.271	-0.028	0.1503	0.9141	0.6147	(1.011)	(-0.096)
0.7684	0.810	0.25	0.548	0.270	-0.036	0.1890	0.9260			
0.9221	0.850	0.30	0.570	0.269	-0.045	0.2285	0.9382	0.9221	(1.025)	(-0.136)
1.0758	0.895	0.35	0.597	0.268	-0.054	0.2689	0.9538			
1.2294	0.931	0.40	0.631	0.267	-0.062	0.3101	0.9745	1.2294	1.051 (1.024)	-0.116 (-0.130)
1.3831	0.956	0.45	0.666	0.263	-0.072	0.3524	0.9935	1.3831	1.043	0.104
1.5368	0.982	0.50	0.692	0.259	-0.082	0.3955	1.0072	1.5368	1.032 (1.026)	-0.090 (-0.102)
1.6905	0.986	0.55	0.720	0.254	-0.092	0.4393	1.0217	1.6905	1.026	-0.077
1.8442	0.984	0.60	0.741	0.247	-0.101	0.4837	1.0296	1.8442	1.013	-0.062
1.9978	0.989	0.65	0.762	0.239	-0.111	0.5286	1.0369	1.9978	1.009	-0.054
2.1515	0.982	0.70	0.782	0.229	-0.118	0.5741	1.0417	2.1515	1.001	-0.045
2.3052	0.985	0.75	0.802	0.218	-0.126	0.6201	1.0459	2.3052	1.007	-0.041
		0.80	0.823	0.206	-0.132	0.6668	1.0479			
		0.85	0.834	0.194	-0.137	0.7140	1.0469			
		0.90	0.846	0.182	-0.141	0.7616	1.0446			
		0.95	0.860	0.170	-0.143	0.8097	1.0440			
		1.00	0.874	0.156	-0.144	0.8583	1.0416			
		1.10	0.898	0.132	-0.143	0.9569	1.0381			
		1.20	0.924	0.109	-0.137	1.0572	1.0369			
		1.30	0.943	0.0890	-0.139	1.1589	1.0350			
		1.50	0.969	0.0600	-0.111	1.3644	1.0301			
		1.70	0.982	0.0415	-0.090	1.5715	1.0240			
		2.00	0.990	0.0325	-0.070	1.8813	1.0227			

TABLE 7 - MEASURED AND COMPUTED VELOCITY PROFILES IMMEDIATELY UPSTREAM OF PROPULSOR WITH AND WITHOUT AN OPERATING PROPULSOR (Continued)

(e) AT $X/D_p = -0.485$, PROPULSOR J IN WAKE A, $C_{TS} = 3.62$, $J_V = 0.416$

MEASURED NOMINAL VELOCITY		INPUT				PROPELLER TOTAL VELOCITY				
		$\frac{r}{R_p}$	$\frac{u_z}{V}$	COMPUTED		COMPUTED		MEASURED		
$\frac{r}{R_p}$	$\frac{u_z}{V}$			$\frac{u_z}{V}$	$\frac{v_{\theta}}{V}$	$\frac{r_p}{R_p}$	$\frac{u_p}{V}$	$\frac{r_p}{R_p}$	$\frac{u_p}{V}$	$\frac{v_{\theta}}{V}$
0.0000	0.511	0.00	0.511	0.1930	0.0000	0.0000	0.0010			
0.1537	0.509	0.05	0.502	0.1927	-0.0050	0.0398	0.7950			
0.3074	0.577	0.10	0.500	0.1920	-0.0117	0.0795	0.7930	0.3074	0.825	-0.004
0.4610	0.665	0.15	0.500	0.1912	-0.0173	0.1194	0.7973	0.4610	0.895	-0.030
0.6147	0.777	0.20	0.526	0.1899	-0.0228	0.1590	0.8076	0.6147	0.952	-0.056
0.7684	0.789	0.25	0.540	0.1894	-0.0271	0.2009	0.8216	0.7684	0.909	-0.072
0.9221	0.851	0.30	0.571	0.1863	-0.0330	0.2428	0.8340	0.9221	1.014	-0.077
1.0750	0.891	0.35	0.596	0.1844	-0.0390	0.2855	0.8495	1.0750	1.037	-0.080
1.2294	0.930	0.40	0.621	0.1820	-0.0439	0.3288	0.8548	1.2294	1.051	-0.077
1.5368	0.978	0.45	0.646	0.1798	-0.0493	0.3728	0.8608	1.5368	1.036	-0.061
1.8442	0.984	0.50	0.670	0.1750	-0.0546	0.4174	0.8938	1.8442	1.027	-0.048
2.1515	0.907	0.55	0.690	0.1710	-0.0590	0.4625	0.9049	2.1515	1.017	-0.037
		0.60	0.713	0.1655	-0.0640	0.5081	0.9171			
		0.65	0.734	0.1600	-0.0685	0.5542	0.9289			
		0.70	0.755	0.1557	-0.0715	0.6008	0.9405			
		0.75	0.778	0.1500	-0.0758	0.6478	0.9534			
		0.80	0.801	0.1440	-0.0785	0.6953	0.9663			
		0.85	0.820	0.1372	-0.0819	0.7432	0.9754			
		0.90	0.840	0.1308	-0.0841	0.7914	0.9859			
		0.95	0.857	0.1240	-0.0858	0.8400	0.9937			
		1.00	0.872	0.1171	-0.0870	0.8889	0.9998			
		1.10	0.901	0.1040	-0.0879	0.9876	1.0122			
		1.20	0.925	0.0922	-0.0868	1.0871	1.0220			
		1.30	0.943	0.0803	-0.0853	1.1873	1.0265			
		1.50	0.975	0.6605	-0.0783	1.3894	1.0365			
		1.70	0.985	0.0455	-0.0697	1.5929	1.0389			
		2.00	0.993	0.0342	-0.0590	1.8985	1.0273			

(f) AT $X/D_p = -0.336$, PROPULSOR J IN WAKE B, $C_{TS} = 0.765$, $J_V = 0.745$

0.0000	0.506	0.00	0.506	0.0030	0.0000	0.0020	0.5316			
0.1537	0.527	0.05	0.508	0.0033	-0.0021	0.0442	0.6335			
0.3074	0.571	0.10	0.516	0.0037	-0.0039	0.0896	0.5483			
0.4610	0.615	0.15	0.530	0.0040	-0.0062	0.1347	0.6513			
0.6147	0.650 (0.637)	0.20	0.541	0.0041	-0.0081	0.1801	0.7210	0.6147	(0.730)	(-0.021)
0.7684	0.692	0.25	0.556	0.0042	-0.0109	0.2257	0.6731			
0.9221	0.730 (0.704)	0.30	0.568	0.0042	-0.0135	0.2715	0.6834	0.9221	(0.790)	(-0.054)
1.0750	0.790	0.35	0.584	0.0041	-0.0161	0.3176	0.6966			
1.2294	0.838 (0.810)	0.40	0.597	0.0039	-0.0185	0.3639	0.7074	1.2294	0.802 (0.861)	-0.034 (-0.052)
1.3831	0.872	0.45	0.610	0.0029	-0.0216	0.4104	0.7174	1.3831	0.924	-0.037
1.5368	0.918 (0.893)	0.50	0.624	0.0019	-0.0245	0.4571	0.7283	1.5368	0.947 (0.943)	-0.027 (-0.051)
1.6905	0.947	0.55	0.637	0.0020	-0.0275	0.5041	0.7384	1.6905	0.969	-0.022
1.8442	0.969	0.60	0.650	0.0023	-0.0308	0.5513	0.7472	1.8442	0.982	-0.015
1.9978	0.972	0.65	0.664	0.0022	-0.0339	0.5988	0.7573	1.9978	0.983	-0.011
2.1515	0.968	0.70	0.676	0.0030	-0.0369	0.6465	0.7654	2.1515	0.986	-0.009
2.3052	0.980	0.75	0.689	0.0066	-0.0392	0.6944	0.7738	2.3052	0.986	-0.005
		0.80	0.709	0.0669	-0.0412	0.7427	0.7835			
		0.85	0.717	0.0631	-0.0431	0.7912	0.7914			
		0.90	0.732	0.0580	-0.0445	0.8400	0.8000			
		0.95	0.747	0.0545	-0.0454	0.8892	0.8103			
		1.00	0.762	0.0505	-0.0460	0.9385	0.8201			
		1.10	0.795	0.0426	-0.0455	1.0380	0.8431			
		1.20	0.826	0.0348	-0.0439	1.1383	0.8648			
		1.30	0.854	0.0288	-0.0413	1.2392	0.8856			
		1.50	0.907	0.0190	-0.0358	1.4421	0.9281			
		1.70	0.951	0.0132	-0.0291	1.6455	0.9647			
		2.00	0.983	0.0102	-0.0217	1.9505	0.9933			

TABLE 7 - MEASURED AND COMPUTED VELOCITY PROFILES IMMEDIATELY UPSTREAM OF PROPULSOR WITH AND WITHOUT AN OPERATING PROPULSOR (Continued)

(g) AT $X/D_p = -0.336$, PROPULSOR J IN WAKE B, $C_{TS} = 3.02$, $J_V = 0.456$

MEASURED NOMINAL VELOCITY		INPUT				PROPELLER TOTAL VELOCITY				
$\frac{r}{R_p}$	$\frac{u_x}{V}$	$\frac{r}{R_p}$	$\frac{u_x}{V}$	COMPUTED		COMPUTED		MEASURED		
				$\frac{u_o}{V}$	$\frac{v_w}{V}$	$\frac{r_p}{R_p}$	$\frac{u_p}{V}$	$\frac{r_p}{R_p}$	$\frac{u_p}{V}$	$\frac{v_w}{V}$
0.0000	0.506	0.00	0.506	0.243	0.000	0.0000	0.8450			
0.1537	0.527	0.05	0.508	0.244	-0.005	0.0307	0.8400			
0.3074	0.571	0.10	0.516	0.245	-0.012	0.0775	0.8530			
0.4610	0.615	0.15	0.530	0.246	-0.018	0.1167	0.8634			
0.6147	0.650 (0.637)	0.20	0.541	0.246	-0.025	0.1564	0.8781	0.6147	(0.884)	(-0.003)
0.7684	0.692	0.25	0.556	0.246	-0.032	0.1964	0.8796			
0.9221	0.730 (0.704)	0.30	0.568	0.245	-0.040	0.2368	0.8862	0.9221	(0.896)	(-0.122)
1.0758	0.790	0.35	0.584	0.244	-0.048	0.2776	0.8955			
1.2294	0.830 (0.810)	0.40	0.597	0.242	-0.056	0.3189	0.9021	1.2294	0.959 (0.934)	-0.105 (-0.127)
1.3831	0.872	0.45	0.610	0.239	-0.064	0.3607	0.9077	1.3831	0.903	-0.093
1.5368	0.910 (0.893)	0.50	0.624	0.237	-0.074	0.4028	0.9152	1.5368	1.000 (0.978)	-0.084 (-0.102)
1.6905	0.947	0.55	0.637	0.232	-0.083	0.4453	0.9132	1.6905	1.000	-0.069
1.8442	0.969	0.60	0.650	0.225	-0.093	0.4884	0.9213	1.8442	0.994	-0.052
1.9978	0.972	0.65	0.664	0.216	-0.101	0.5321	0.9222	1.9978	0.901	-0.047
2.1515	0.958	0.70	0.676	0.209	-0.108	0.5763	0.9239	2.1515	0.908	-0.044
2.3052	0.900	0.75	0.689	0.200	-0.115	0.6210	0.9245	2.3052	0.991	-0.038
		0.80	0.704	0.188	-0.121	0.6664	0.9238			
		0.85	0.717	0.178	-0.125	0.7124	0.9238			
		0.90	0.732	0.167	-0.129	0.7590	0.9246			
		0.95	0.747	0.154	-0.132	0.8063	0.9236			
		1.00	0.762	0.142	-0.133	0.8543	0.9239			
		1.10	0.785	0.119	-0.131	0.9520	0.9286			
		1.20	0.826	0.099	-0.125	1.0518	0.9356			
		1.30	0.854	0.092	-0.118	1.1532	0.9436			
		1.50	0.907	0.054	-0.100	1.3590	0.9645			
		1.70	0.951	0.038	-0.083	1.5670	0.9903			
		2.00	0.983	0.028	-0.064	1.8783	1.0112			

(h) AT $X/D_p = -0.239$, PROPULSOR T IN WAKE C, $C_{TS} = 0.356$, $J_V = 1.268$

0.291	0.411	0.260	0.375	0.0368	0.0070	0.260	0.472	0.285	0.590	
0.341	0.462	0.300	0.423	0.0405	0.0109	0.293	0.514	0.332	0.555	
0.392	0.506	0.350	0.473	0.0473	0.0120	0.336	0.563	0.391	0.604	
0.447	0.542	0.400	0.510	0.0560	0.0104	0.380	0.600	0.446	0.646	
0.520	0.582	0.450	0.543	0.0628	0.0058	0.425	0.637	0.495	0.681	
0.597	0.620	0.500	0.572	0.0691	-0.0023	0.470	0.669	0.530	0.701	
0.660	0.650	0.550	0.600	0.0720	-0.0107	0.516	0.695	0.610	0.742	
0.741	0.692	0.600	0.628	0.0724	-0.0182	0.562	0.720	0.667	0.756	
0.826	0.735	0.650	0.652	0.0700	-0.0240	0.609	0.740	0.716	0.776	
0.920	0.777	0.700	0.675	0.0675	-0.0315	0.656	0.757	0.795	0.803	
1.018	0.815	0.750	0.698	0.0628	-0.0363	0.704	0.773	0.836	0.812	
1.105	0.853	0.800	0.722	0.0578	-0.0399	0.753	0.789	0.889	0.828	
1.226	0.895	0.850	0.745	0.0510	-0.0423	0.801	0.805	0.942	0.841	
		0.900	0.767	0.0457	-0.0438	0.851	0.819	0.997	0.855	
		0.950	0.788	0.0403	-0.0440	0.901	0.833	1.065	0.877	
		1.000	0.809	0.0352	-0.0432	0.951	0.848	1.125	0.905	
		1.050	0.831	0.0303	-0.0419	1.001	0.864			
		1.100	0.852	0.0261	-0.0401	1.051	0.880			
		1.200	0.900	0.0193	-0.0361	1.153	0.920			

TABLE 7 - MEASURED AND COMPUTED VELOCITY PROFILES IMMEDIATELY UPSTREAM OF PROPULSOR WITH AND WITHOUT AN OPERATING PROPULSOR (Continued)

(i) AT $X/D_p = -0.239$, PROPULSOR T IN WAKE C, $C_{TS} = 0.676$, $J_V = 1.066$

MEASURED NOMINAL VELOCITY		INPUT				PROPELLER TOTAL VELOCITY			
		$\frac{r}{R_p}$	$\frac{u_x}{V}$	COMPUTED		COMPUTED		MEASURED	
				$\frac{u_x}{V}$	$\frac{v_{\theta}}{V}$	$\frac{r_p}{R_p}$	$\frac{u_p}{V}$	$\frac{r_p}{R_p}$	$\frac{u_p}{V}$
0.291	0.411	0.260	0.375	0.0728	0.0163	0.260	0.542	0.285	0.576
0.341	0.462	0.300	0.423	0.0812	0.0179	0.285	0.585	0.332	0.631
0.392	0.506	0.350	0.473	0.0920	0.0176	0.328	0.632	0.391	0.689
0.447	0.542	0.400	0.510	0.1047	0.0108	0.368	0.673	0.446	0.726
0.520	0.582	0.450	0.543	0.1148	0.0017	0.410	0.708	0.495	0.761
0.587	0.620	0.500	0.572	0.1217	-0.0103	0.452	0.737	0.538	0.777
0.660	0.658	0.550	0.600	0.1243	-0.0230	0.496	0.762	0.610	0.803
0.741	0.692	0.600	0.628	0.1240	-0.0351	0.540	0.794	0.667	0.816
0.826	0.735	0.650	0.652	0.1218	-0.0464	0.585	0.801	0.716	0.831
0.920	0.777	0.700	0.675	0.1147	-0.0562	0.630	0.813	0.795	0.846
1.018	0.815	0.750	0.698	0.1076	-0.0640	0.677	0.825	0.836	0.854
1.105	0.853	0.800	0.722	0.0985	-0.0698	0.724	0.825	0.889	0.866
1.226	0.899	0.850	0.745	0.0890	-0.0737	0.772	0.847	0.942	0.874
		0.900	0.767	0.0781	-0.0758	0.821	0.856	0.997	0.890
		0.950	0.788	0.0689	-0.0759	0.870	0.865	1.065	0.905
		1.000	0.809	0.0600	-0.0754	0.920	0.876	1.125	0.920
		1.050	0.831	0.0522	-0.0727	0.971	0.867		
		1.100	0.852	0.0448	-0.0698	1.022	0.901		
		1.200	0.900	0.0330	-0.0627	1.124	0.935		

(j) AT $X/D_p = -0.239$, PROPULSOR T IN WAKE D, $C_{TS} = 0.706$, $J_V = 1.054$

0.255	0.387	0.220	0.366	0.0711	0.0170	0.220	0.539	0.384	0.596
0.370	0.452	0.250	0.386	0.0757	0.0205	0.241	0.549	0.391	0.657
0.444	0.487	0.300	0.414	0.0878	0.0210	0.279	0.581	0.462	0.699
0.525	0.530	0.350	0.441	0.0100	0.0197	0.321	0.524	0.565	0.744
0.607	0.572	0.400	0.467	0.1129	0.0123	0.363	0.647	0.636	0.766
0.680	0.606	0.450	0.492	0.1232	0.0019	0.404	0.675	0.715	0.795
0.769	0.657	0.500	0.516	0.1310	-0.0108	0.445	0.701	0.794	0.811
0.852	0.694	0.550	0.542	0.1346	-0.0241	0.486	0.723	0.871	0.826
0.978	0.756	0.600	0.567	0.1341	-0.0370	0.529	0.742	0.930	0.846
1.071	0.795	0.650	0.592	0.1306	-0.0501	0.573	0.758	0.975	0.855
1.170	0.842	0.700	0.618	0.1238	-0.0608	0.618	0.772	1.020	0.865
1.283	0.875	0.750	0.644	0.1156	-0.0690	0.664	0.784	1.071	0.875
		0.800	0.670	0.1061	-0.0753	0.711	0.797	1.145	0.892
		0.850	0.696	0.0957	-0.0792	0.759	0.808	1.244	0.905
		0.900	0.721	0.0842	-0.0820	0.807	0.819		
		0.950	0.745	0.0856	-0.0821	0.856	0.831		
		1.000	0.768	0.0643	-0.0808	0.906	0.841		
		1.050	0.790	0.0558	-0.0784	0.957	0.852		
		1.100	0.810	0.0479	-0.0752	1.008	0.863		
		1.200	0.850	0.0351	-0.0675	1.111	0.888		

ACKNOWLEDGMENTS

The investigation reported herein was funded under the David W. Taylor Naval Ship R&D Center's Independent Research Program, Task Area ZR 0230101, Element No. 61152N. The authors would like to thank their co-workers, Messrs. N. Santelli and G. Belt for velocity measurements, Messrs. R.P. Cross, L.B. Crook, and W.G. Day Jr. for self-propulsion experiments, Mr. D.H. Fuhs and Dr. B. Cox for practical applications of the present theory, and Mr. J.H. McCarthy and Dr. William B. Morgan for their continuous support and technical guidance. The authors wish to express their gratitude to Mr. T. Nagamatsu and Mr. K. Tokunaga of Nagasaki Experimental Tank, Japan, for providing detailed information of their experiments and data.

REFERENCES

1. Huang, T.T., H.T. Wang, N. Santelli, and N.C. Groves, "Propeller/Stern Boundary Layer Interaction on Axisymmetric Bodies: Theory and Experiment," David W. Taylor Naval Ship Research and Development Center Report 76-0113 (Dec 1976).
2. Nagamatsu, T. and K. Tokunaga, "Prediction of Effective Wake Distribution for a Body of Revolution," Journal of Society of Naval Architects of Japan, Vol. 143, pp. 93-100 (June 1978).
3. Schetz, J.A. and S. Favin, "Numerical Solution for the Near Wake of a Body with Propeller," Journal of Hydro-nautics, Vol. 11, No. 4, pp. 136-141 (Oct 1977).
4. Schetz, J.A. and S. Favin, "Numerical Solution of a Body-Propeller Combination Flow Including Swirl and Comparisons with Data," Journal of Hydro-nautics, Vol. 13, No. 2, pp. 46-51 (April 1979).
5. Hucho, W.H., "Über den Einfluss einer Heck-schraube auf die Druckverteilung und die Grenzschicht eines Rotationskörpers - Teil II: Untersuchungen bei höheren Schubbelastungsgraden," Institut Für Strömungsmechanik der Technischen Hochschule Braunschweig, Bericht 64/45 (1965).
6. Hucho, W.H., "Über den Zusammenhang zwischen Normalsog, Reibungssog und dem Nachstrom bei der Strömung um Rotationskörper," Schiff und Hafen, Heft 10, pp. 689-693 (1968).
7. Hucho, W.H., "Untersuchungen über den Einfluss einer Heckschraube auf die Druckverteilung und die Grenz-schicht Schiffsähnlicher Körper," Ingenieur-Archiv Vol. XXX-VII, pp. 288-303 (1969).
8. Wertbrecht, H.M., "Vom Sog, ein Versuch Seiner Berechnung," Jahrbuch Schiffbautechnische Gesellschaft, Vol. 42, pp. 147-204 (1941).
9. Hickling, R., "Propellers in the Wake of an Ax-isymmetric Body," Transactions of the Royal Institute of Naval Architects, Vol. 99, pp. 601-617 (1957).
10. Tsakonas, S. and Jacobs, W.R., "Potential and Viscous Parts of the Thrust Deduction and Wake Fraction for an Ellipsoid of Revolution," Journal of Ship Research, Vol. 4, No. 2, pp. 1-16 (1960).
11. Wald, Q., "Performance of a Propeller in a Wake and the Interaction of Propeller and Hull," Journal of Ship Research, Vol. 9, No. 1, pp. 1-8 (1965).
12. Raestad, A.E., "Estimation of Marine Propeller's Induced Effects on the Hull Wake-Scale Effect on the Hull Wake Field," Det norske Veritas Report No. 72-3-M, Chapter 1 (1972).
13. Nagamatsu, T. and T. Sasajima, "Effect of Pro-peller Suction on Wake," Journal of the Society of Naval Ar-chitects of Japan, Vol. 137, pp. 58-63 (1975).
14. Titoff, I.A. and Otlesnov, Yu. P., "Some Aspects of Propeller-Hull Interaction," Swedish-Soviet Propeller Sym-posium, Moscow (1975).
15. Thwaites, B., *Incompressible Aerodynamics*, Chapter XI. Oxford University Press (1960).
16. Huang, T.T., N. Santelli, and G. Belt, "Stern Boundary-Layer Flow on Axisymmetric Bodies," Twelfth Symposium on Naval Hydrodynamics 5-9 June 1978, Printed by National Academy of Sciences, Wash., D.C., pp. 127-157 (1979).
17. Hough, G.R. and D.E. Ordway, "The Generalized Actuator Disk," Developments in Theoretical and Applied Mechanics, Vol. 11, Pergamon Press, New York, pp. 317-336, Table 1 (1965).
18. Morgan, W.B. and J.W. Wrench, "Some Computa-tional Aspects of Propeller Design," Methods in Computa-tional Physics, Vol. 4, Academic Press, New York, pp. 301-331 (1965).
19. Caster, E.B., J.A. Diskin, and T.A. LaFone, "A Lifting Line Computer Program For Preliminary Design of Propellers," DTNSRDC Ship Performance Department Report No. SPD-595-01 (Nov 1975).
20. Kerwin, J.E. and L. Leopold, "A Design Theory for Subcavitating Theory," Transactions of the Society of Naval Architects and Marine Engineers, Vol. 72, pp. 294-335 (1964).
21. Huang, T.T. and B.D. Cox, "Interaction of After-body Boundary Layer and Propeller," paper presented at Symposium on Hydrodynamics of Ship and Offshore Propul-sion Systems, Sponsored by Det Norske Veritas, Hovix out-side Oslo, (March 20-25, 1977).
22. Cheng, H.M., "Hydrodynamic Aspects of Pro-peller Design Based on Lifting Surface Theory. Parts 1 and 2," DTMB Report 1802 and 1803 (1964-1965).
23. Kerwin, J.E., "Computer Techniques for Propeller Blade Section," International Shipbuilding Progresses, Vol. 20, No. 227, pp. 227-251 (July 1973).
24. Cummings, D.E., "Numerical Prediction of Pro-peller Characteristics," Journal of Ship Research, Vol. 17, Part 3, pp. 12-18 (1973).

Discussion

G Dyne (SSPA)

May I first congratulate the authors on another fine and well documented paper on the important subject: propeller-wake interaction.

My comments are concentrated to the following two sentences in Section 2.2 of the paper:

"In principle the nominal velocities are known from the innermost radius of the propulsor to a radial position... large enough for the propulsor induced velocities u_A to be zero. The value of the effective velocity at this point is equal to the nominal velocity."

I agree with this wording only if it means that the effective wake at this radius is the same as the corresponding nominal wake at a larger radius, the difference in radius being caused by the contraction of the flow field. Some results presented in the paper indicate, however, that the authors have not used this assumption.

The nominal wake, l , is transformed into the effective wake by the action of the propeller as illustrated in Fig. 1 when $C_{TS} = 0.654$. As seen there are two effects: a decrease in local wake along each stream annulus and a shift in streamline position caused by the contraction. The first of these effects is most pronounced close to the hub, the second one being more important at the outer radii. Due to the contraction the effective wake at the propeller tips, calculated by a method developed at SSPA, is lower than the nominal wake at the same radius but almost the same as the nominal wake at the corresponding stream annulus which has a larger radius. A similar result was given by Dr. Huang in [21]. In the present paper, however, there is almost no difference between the effective and nominal wake figures at the propeller tips. Since the contraction is significant in the example given, this must mean that the effective wake is larger than the nominal wake at the corresponding stream annulus at the propeller tips but lower at the inner radii. Since I cannot understand why it can be so, I would like to have the authors' explanation.

It is true that the procedure used in the paper gives a better agreement between the volumetric mean effective wake and the Taylor wake, but in my opinion the reason for these discrepancies is instead that no regard is paid to the displacement or potential wake. The authors have shown that the existence of a displacement wake has very little influence upon the effective wake. When doing so they have, however, ignored the fact that the propeller due to

the limited axial extension of the displacement wake is working in an accelerating flow which may influence the propeller induced velocities. If these velocities are decreased by the flow acceleration the Taylor wake will be too high and if no regard is paid to this effect the calculated effective mean wake will be too low. A detailed study of the influence of the displacement wake on the effective wake is at present going on at SSPA.

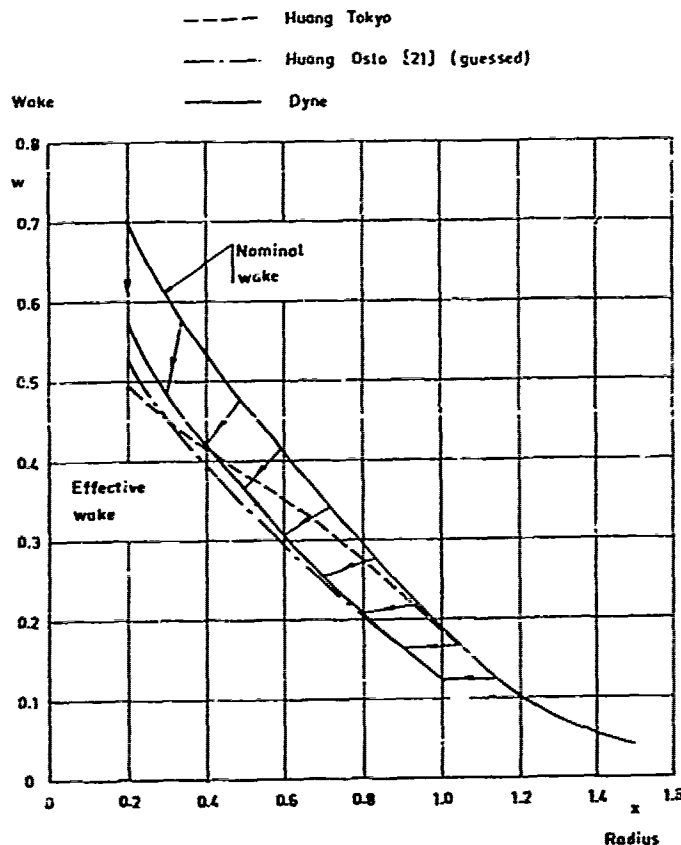


Fig. 1 Different effective wake assumptions

Wake l : $C_{TS} = 0.654$

T. Nagamatsu (MHI)

Recently, great interest is focussed on the effective wake distribution which should be used to design a wake-adapted propeller and to estimate the propeller vibratory forces precisely. The authors should be commended for their efforts in this important field of ship hydrodynamics.

In the present paper, the authors presented an improved method for predicting the effective wake flow and examined the

applicability of the method by comparing the predicted results with the experimental ones.

Mr. Tokunaga and I also made a study on the prediction of the effective wake flow for an axisymmetric wake. The volume-mean effective velocity ratios predicted by our method for wake A and B agree well with those by the authors' method. We are encouraged by this result.

In our prediction method we did not take into account the effect of propeller action on the behavior of the boundary layer in front of the propeller. This is the same to the authors' method.

In order to avoid this effect, therefore, our experiments were made under the condition that the propeller was arranged at the position far downstream of the body. The prediction method was examined to compare with the experiment.

On the other hand, the propeller was located at stern of the body in the authors' experiments. The predicted results, however, agree well with the experimental ones.

It would be grateful if you could show us your view on the influence of propeller on the development of viscous boundary layer near the stern.

W. van Gent (NSMB)

I highly appreciate this paper in which a nice correlation between theory and experiment is shown for the very important propeller-wake interaction problem. It seems that the correlation close to the propeller is better than further upstream if you compare Figs. 5, 6 with the other Figs. A reason can be that the theoretical models for the propeller and for the wake are not consistently developed. This can be seen as follows:

(1) The authors start with the exact solution of the equation of motion $\omega_e/r =$ conserved along the streamannulus without swirl.

(2) The total flow is composed of nominal flow + propulsor induction + interaction, which means axially, that total = $u_x + u_a + (u_e - u_x)$ and also radially : total = $v_r + v_{pr} + v_{interaction}$.

(3) The authors give satisfactory reasons for their assumption to neglect the nominal part v_r and their assumption that the propulsor induced part v_{pr} belongs to an irrotational field. However, they disregard without notice the radial part of the interaction field. This assumption is only valid far downstream where all radial velocities vanish, but there the exact solution, see item 1, is no longer valid as behind the propeller the flow has swirl. This means in fact that the authors' assumption only is valid when the equation of motion is linearized, but this has to be done in a consistent way.

(4) At the Netherlands Ship Model

Basin we derived the linearized set of equations for the present case and it turns out that the interaction velocity field is very similar to the propulsor induced velocity field for lightly and moderately loaded propellers. Numerical results come very close to those of the authors.

(5) A conclusion from the linearized model is that the radial velocity of the interaction is symmetric with respect to the propeller plane. Then the implied assumption of the authors, viz $\partial v_r / \partial x = 0$, is also valid there. This may explain why the results shown by the authors have good agreement between theory and experiment close to the propeller but not further upstream.

(6) Finally I like to emphasize that, in the study of propeller-wake interaction, it is important to use uniformly valid assumptions for the propeller induced flow and for the wake flow.

I. Tanaka (Osaka Univ)

I think the authors show a very interesting idea in Eqs. (6) and (7) and they are very much congratulated.

I would like to ask the authors about one thing on the assumptions made. They assumed no change of viscous losses due to propulsor induction effects, i.e., the total pressure head within a given stream annulus upstream of the propulsor remains constant with and without the propulsor. In one sense this seems to be a good, obvious approximation. But, in another sense, I would like to know how good it is. Apparently the authors' method seems to be applicable to the cases including thick boundary layer ones. In such cases, however, the deviation of streamlines with and without the propulsor may be appreciable. Change in thicknesses of boundary layers for these two cases is also large. Therefore the nature of viscous loss due to Reynolds stress etc. might be considerably different between the two cases with and without propulsors. So, it is very nice thing to have either experimental evidence by measuring pressure distribution or theoretical consideration of the magnitude of the error. If the authors show them to us, I am extremely happy.

M. Abe (Mitsui S&E)

It would be much appreciated that the authors have carried out the very fine calculations and experiments in detail. Especially I have much interests in the velocity measurements in front of a propulsor.

In practical point of view to obtain the effective wake at a ship stern, the velocity measurement in a propeller operat-

ing should be required in my opinion, because the nominal wake calculated and/or measured can not be fairly correlated with the effective wake in special cases of hulls with wider beam and smaller draft, namely, RO/RO, LNG and car carriers etc..

The emphasis should be made that the nominal wake shown in the figure could not give good informations concerning cavitation, vibration as well as the performance of propeller itself. In this respect, I keenly desire to calculate and measure the effective wake directly and I hope that the authors would measure the effective wake with the mentioned ship hull both in model and in full scale.

Author's Reply

T T. Huang (OTNSRDC)

The authors wish to thank their international colleagues of propeller/wake interaction research for submitting many valuable discussions.

In response to Dr. Dyne's question regarding the definition of effective velocity, we have used the following definition in this paper

$$u_e(r) = u_p(r_p) - u_a,$$

where the total energy is conserved for the nominal flow at point r and for the total flow with the propeller in operation at point r_p , e.g.,

$$\frac{1}{2} \rho u_x^2(r) + p_o(r) = \frac{1}{2} \rho u_p^2(r_p) + p_p(r_p).$$

The net change of momentum in the two flows

$$\text{is } [\rho u_p^2(r_p) + p_p(r_p)] dr_p - [\rho u_x^2(r) + p_o(r)] dr$$

However, the effective velocity is not defined by

$$u_e(r_p) = u_p(r_p) - u_a,$$

because the total energy of the nominal flow at point r_p is less than that of the total flow with the propeller in operation at the same point r_p . Therefore, an additional energy of

$$[\frac{1}{2} \rho u_x^2(r) + p_o(r) - \frac{1}{2} \rho u_x^2(r_p) - p_o(r_p)]$$

must be added to the nominal flow at r_p by

the propeller and an additional force of

$$[\rho u_x^2(r) + p_o(r)] dr - [\rho u_x^2(r_p) + p_o(r_p)] dr_p$$

must be expended by the propeller to cause the necessary contraction of nominal flow from r to r_p . It is important to note that the definition of the effective velocity used not only gives a better agreement between the computed volumetric mean effective wake and the measured Taylor wake, but is also derived from the theoretical basis of conserving energy between the total flow with the propeller in operation and the nominal flow without the propeller.

On Mr. Nagamatsu's question of the influence of the propeller on the development of the viscous boundary layer near the stern, the influence of the propeller was found to be limited to only two propeller diameters upstream of the propeller. Additionally the inviscid interaction of the flow by the propeller was found experimentally¹ to be dominant in this region. The change in the nominal boundary-layer development in this region can be represented by the new boundary-layer thickness parameter δ_p which can be estimated to be

$$\frac{\delta_p}{R_p} \approx 4 \times 0.37 \left(\frac{VL}{V} \frac{2D}{L} \right)^{-\frac{1}{5}} \approx$$

$$\begin{cases} 0.092 & \text{for } R_L = 10^7 * \frac{2D}{L} = \frac{1}{10}, \\ 0.037 & \text{for } R_L = 10^8 * \frac{2D}{L} = \frac{1}{10}. \end{cases}$$

Hence, the influence of the propeller on the development of the viscous boundary layer near the stern is limited to the inner-most radii of the flow and is of secondary importance. Furthermore, the inviscid effect of the propeller is found to vary with the propeller radius. This variation, which is properly modeled by the present theory, is not easily modeled by the normal boundary layer computation method without allowing for pressure variations across the thick boundary layer.

The authors are very pleased to learn from Dr. van Gent that the radial velocity of the propeller/wake interaction is symmetric with respect to the propeller plane. Therefore, the author's unstated assumption that the interaction of the radial velocity is small and can be neglected, is valid at the propeller plane. Dr. van Gent questions the validity of this assumption further upstream from the propeller. The propeller-induced radial velocity decreases very rapidly with distance from the propeller, and the radial velocity interaction can reasonably be neglected. The authors agree to use uniformly valid assumptions for the propeller/wake interaction whenever possible. It remains a challenge for us to achieve this common goal.

The authors appreciate the concern of

Professor Tanaka regarding the equality of the total energy without the propellers,

$$H_0(r) = \frac{1}{2} \rho u_x^2(r) + p_0(r) \text{ and with the pro-}$$

$$\text{peller, } H_p(r_p) = \frac{1}{2} \rho u_p^2(r_p) + p_p(r_p). \text{ Our}$$

preliminary measurements at $x = -0.5 R$ of Afterbody 1 indicated that the values P_{of} $H_p(r_p) - H_0(r) / H_0(r)$ are less than 2%, which are about the overall accuracy of the measurements of H .

Mr. Abe clearly shows us the difference between the nominal wake and effective wake for practical ships. However, the propeller induced velocities must be subtracted from the velocities measured in front of a propeller to obtain a correct effective velocity distribution. The present axisymmetric theory has not been examined fully for the possible applications to the ship hulls you mentioned. We will share our experience with you whenever we have reached a sound conclusion.

Experiments on the Reduction of Bilge Vortex Formation by Discharging Air into Boundary Layer

Valter Kostilainen
Helsinki University of Technology
Finland

ABSTRACT

A system for reduction of bilge vortex formation is studied experimentally. In this system comparatively small amounts of air are discharged into the boundary layer. Air bubbles turn the direction of the surface flow in stern and reduce the streamline convergence and separation near the bilge. Systematic model tests with a full tanker form were carried out in order to determine the effect of air discharging on the wake pattern, resistance and propulsion. Five different air discharge hole configurations are studied. Results of the tests indicate favourable changes in wake pattern with small and medium air flow rate in the case of two air discharge hole configurations. In general high local wake values are decreased and the widths of wake peaks are larger than in the original distribution without air.

NOMENCLATURE

K_T = propeller thrust coefficient
 K_Q = propeller torque coefficient
 L = length of ship
 l = length of air discharge hole region
 n = propeller revolutions per second
 p_G = air pressure
 R_m = model resistance
 R = propeller radius
 U_L = water speed
 \dot{V}_G = air flow rate

V_m = model speed
 V_x = axial velocity in propeller plane
 V_{zv} = velocity vector on propeller disc plane
 w_L = local wake factor
 w = mean wake factor
 η_D = propulsion efficiency
 μ = dynamic viscosity
 ν = kinematic viscosity
 ρ_L = water density
 ψ = angle co-ordinate in propeller plane

1. INTRODUCTION

Although the phenomenon of propeller excited vibration has been experienced from the very early stages of machinery driven ships, it is during the last twenty years that the problem has grown to form one of the most important design considerations.

Non-uniformity of the flow into the propeller especially in cavitating conditions is one of the main causes of propeller excited vibrations. U-frames with a modified hull are commonly used in the sterns of full ships. This gives gently sloping wake peak in the upper part of the propeller disc. If the stern form below the propeller shaft is made gently sloping also in the lower part of the disc a good wake distribution is attained. However, there exist more or less pronounced bilge vortices. If these vortices become too strong, they may cause trouble in the form of vibratory forces and cavitation and increase the resistance of the hull.

The theoretical calculation methods of turbulent three-dimensional boundary layers have advanced significantly. There are still, however, great difficulties in obtaining the flow pattern on a ship stern theoretically, especially when separation is present. Separation is an unsteady phenomenon and even small changes in conditions can have an effect on the separation. At the present time therefore, the quality of velocity distribution in the stern is studied at the design stage by wake surveys with a model and results are scaled to ship scale with known methods. If the new hull design indicates an unfavourable wake distribution, the afterbody shape is modified until an acceptable wake distribution is obtained. In a number of cases where an inhomogeneous wake field caused serious vibration problems, the situation was improved by fitting afterbody fins or tunnels. These modifications have nearly always been carried out after the ship was in service and vibration troubles had been found. If the fins are fitted above the propeller they in general equalize the flow field in the upper part of the disc but they do not reduce the development of bilge vortices.

As yet no efficient methods have been developed to reduce the formation of bilge vortices and full ship forms are continuously used. The present paper introduces a method for the reduction of bilge vortices. The main idea is to turn the downward component of the cross flow by air bubbles and in this way to control vortex sheet separation.

2. THE FLOW NEAR THE STERN OF FULL SHIPS

Recent theoretical and experimental research on viscous flow of ship-like forms has helped us to understand and explain the flow near the stern of full ship forms. The nature of the flow in the boundary layer has been studied and one important finding is the existence of a heavy cross flow in the stern region. The surface streamlines of normal full ship forms in stern ahead propeller generally turn down and converge in the upper part of the bilge. This convergence of streamlines may result in a vortex sheet separation as was described by van Berlekom [1].

This pair of bilge vortices rotates the water so that decelerated water particles near the ship hull move out and water with higher axial velocity from the outer parts of the boundary layer takes their place. Thus strong bilge vortices will also be seen in axial wake velocity distribution in the form of a pair of additional wake peaks in model scale in the outer part of the propeller disc.

The downward component of the surface flow ahead of the propeller is the primary cause of the bilge vortices. Some attempts have been made to fit horizontal fins ahead of the propeller approximately

at the height of the propeller shaft in order to prevent this vortex formation. These fins prevent the downward cross flow and according to model tests vortex formation is reduced. The additional resistance of these fins is considerable and they are not applied in general. Possibly the bilge vortex formation can be prevented in the future by shaping the stern form on the basis of an exact theoretical solution of the problem. Within the current 'state of the art' it is not possible.

3. THE REDUCTION OF BILGE VORTEX FORMATION BY DISCHARGE OF AIR

If air is discharged through the shell into the water, it will disintegrate into bubbles, which under the action of gravity rise along the ship hull. Rising air bubbles increase the upward momentum of the surrounding water near the ship hull. If air amounts are large, this phenomenon can be used to pump water between the shell and ice and reduce the resistance of ships in severe ice conditions [2] or even for the propulsion of vessels [3].

If air amounts are small, the effect of air bubbles is limited inside the boundary layer. If water in the boundary layer previously had a horizontal or downward direction, the upward velocity due to the action of air bubbles will turn the direction of the flow near the ship hull.

In normal full ship forms, surface velocity ahead of propeller is inclined downward. The convergence of streamlines and bilge vortex separation result. If small amounts of air are discharged into the water, the direction of the surface flow will be changed. This method has been experimentally studied in the Ship Hydrodynamics Laboratory of Helsinki University of Technology. Preliminary results were reported in [4]. The outcome of systematic tests is reported in this paper.

4. TEST CONDITIONS AND MEASURING TECHNIQUE

Model tests were made in the 130 m x 11 m x 5.5 m towing tank of Helsinki University of Technology. The model used in the experiments was a 1:37.5 scale model of a 115 000 tdw tanker.

Ship and model particulars are presented in Table 1 and afterbody sections in Fig. 1.

After preliminary tests, three basic air discharge hole configurations I, II and III were used, each having the same longitudinal location of holes but different heights. Later two modification IIIA and IIIB of hole configuration III were tested. All tested air discharge hole configurations are presented in Fig. 2.

Air was supplied from a small compressor through a pressure balancing tank to the holes. Before testing, the amount of air blown out from each hole was visually checked by means of an underwater tv-camera and individual hoses were

throttled with clamps until the out-flowing air was equally distributed. All tests were run with a model speed of 1.4 m/s corresponding to 8.57 m/s full scale. Air flow rate was varied during tests from 0 to 0.001 m³/s. Air flow was measured with a turbine-type flow-meter and air pressure and temperature were measured with electronic transducers.

Wake surveys were made with the five-hole pitot tube device of the laboratory presented in [5]. All measured signals were electronically registered and handled with the on-line computer located in the carriage.

For flow visualisation tests tufts were fixed on the surface of the after part of the model. Observations were made with underwater photography and video tape recorder.

MODEL M-10
STERN SECTIONS

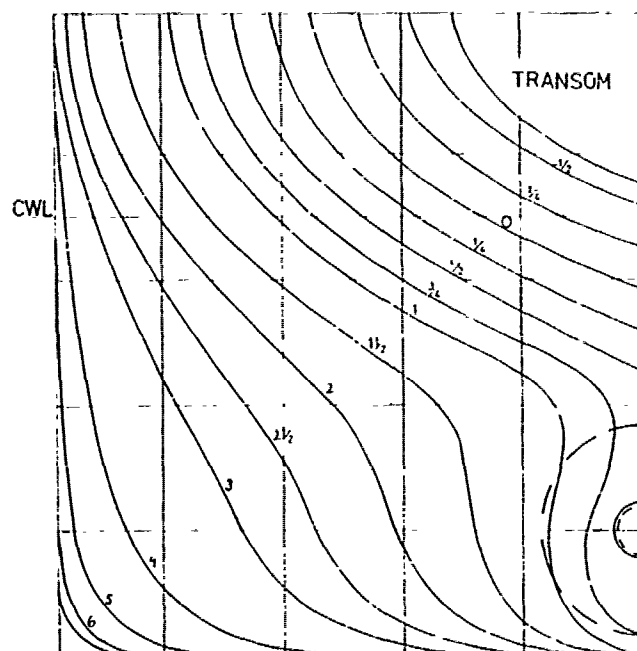


Fig. 1 Afterbody Sections of Tested Tanker Form

TABLE 1 Principal Particulars of Ship and Model

	SHIP	MODEL
BLOCK COEFFICIENT	.838	.838
LENGTH L_{pp}	258 m	6.98 m
BREADTH	39 m	1.04 m
DRAUGHT	14 m	.373 m
PROPELLER DIAMETER	6.70 m	.179 m
PITCH	CPP	FIXED, .705
BLADE AREA	0.53	0.53
RATIO		

TABLE 2 Test Programme

HOLE CONFIGURATION	I	II	III	IIIA	IIIB
RESISTANCE TESTS	X	X	X		
PROPULSION TESTS	X	X			
WAKE SURVEYS	X	X	X	X	X
FLOW VISUALISATION TESTS	X	X			

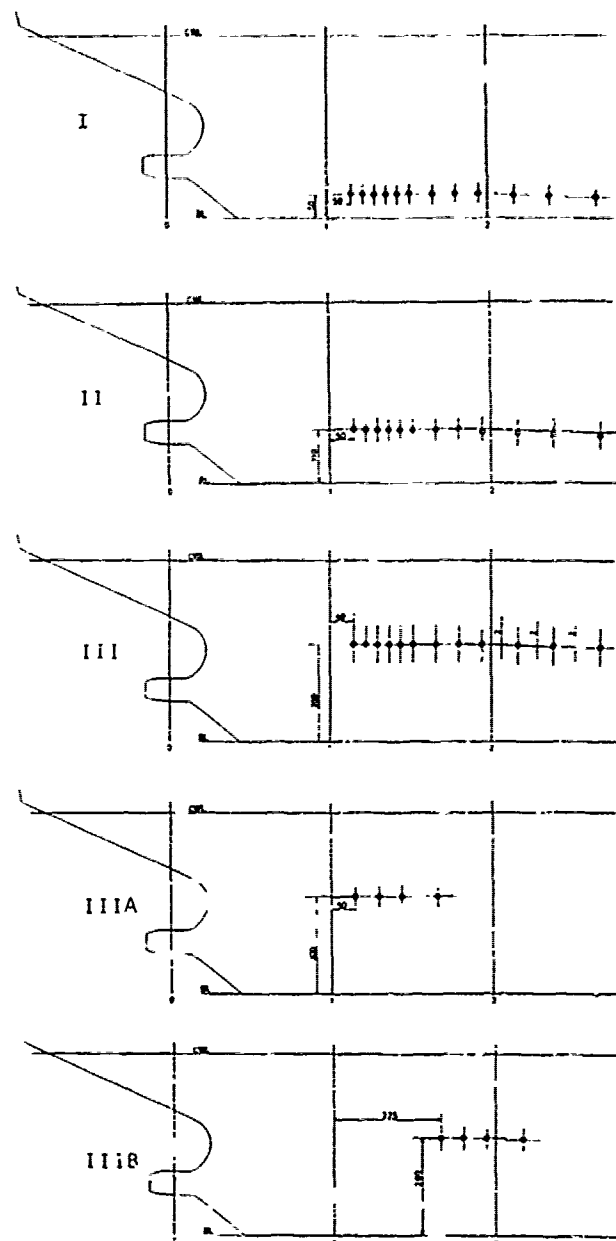


Fig. 2 Tested Configurations of the Air Discharge Holes in the Stern of the Model

5. RESULTS

5.1 Resistance

Results of the resistance tests are presented in Table 3 for air discharge hole configurations I and II. In both configurations the resistance was decreased at smaller air flow rates more than the possible thrust of the waterflow momentum increase due to air bubbles. This additional resistance decrease is apparently the result of decreased eddy-making resistance. At a higher air flow rate the decrease of effective power approaches the power of compressed air.

TABLE 3 Results of Resistance Tests

SPEED V_m m/s	AIR FLOW RATE \dot{V}_G m^3/s	AIR PRESS- URE p_G Pa	MODEL RESIS- TANCE R_m N	AIR DIS- CHARGE HOLE CON- FIGURATION
1.40	0	0	43.1	I
1.40	.00031	3012	41.8	
1.40	.00054	3023	41.8	
1.40	.00102	3052	41.0	
1.40	0	0	43.0	II
1.40	.00034	2513	41.8	
1.40	.00052	2552	41.8	
1.40	.00099	2557	41.5	

5.2 Propulsion

Propulsion tests were run with four propeller loadings. Two of the loadings were chosen on both sides of ship self propulsion point and the other two on both sides of model self propulsion point and the exact values of both model and ship self propulsion point were attained by interpolation. The verification of model self propulsion point was considered necessary because of unsteadiness of the separation. The measured quantities behaved, however, similarly both in model and ship self propulsion point. Results of propulsion tests on ship self propulsion point are illustrated in Fig. 3 for air discharge hole configurations I and II.

From the results of air discharge hole configuration I it can be seen that when the air flow rate is increased from .0003 to .0005 m^3/s , revolutions are suddenly increased and torque and thrust coefficients are decreased. The reason for this is apparently that air is drawn into the propeller disc and the density of fluid accelerated by the propeller is decreased. Changes in propulsion efficiency are however small even with large air flow rates. This ventilation of the propeller and the two-phase flow in general between the hull and the propeller can, according to Huse

[6], reduce cavitation noise and propeller-induced pressure fluctuations. In the results of air discharge hole configuration II, where air holes are on the upper level, a similar sudden change of quantities can not be noticed.

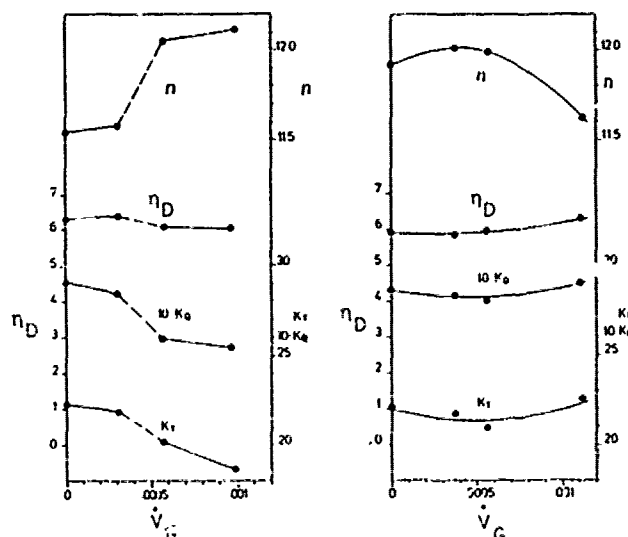


Fig. 3 Results of Self Propulsion Tests, Ship Self Propulsion Point. Air Discharge Hole Configuration I on the Left, II on the Right.

5.3 Wake Surveys

Axial velocity distribution in propeller disc without air discharge is given in Fig. 4. Corresponding velocity distributions of all air discharge hole configurations with air flow rate .0003, .0005 and .001 m^3/s are presented in Fig. 5, 6, 7, 8 and 9.

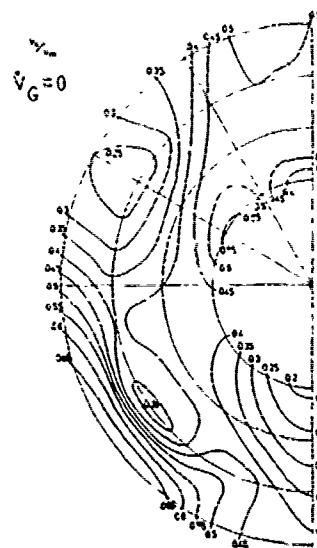


Fig. 4 Axial Velocity Distribution without Air Discharge

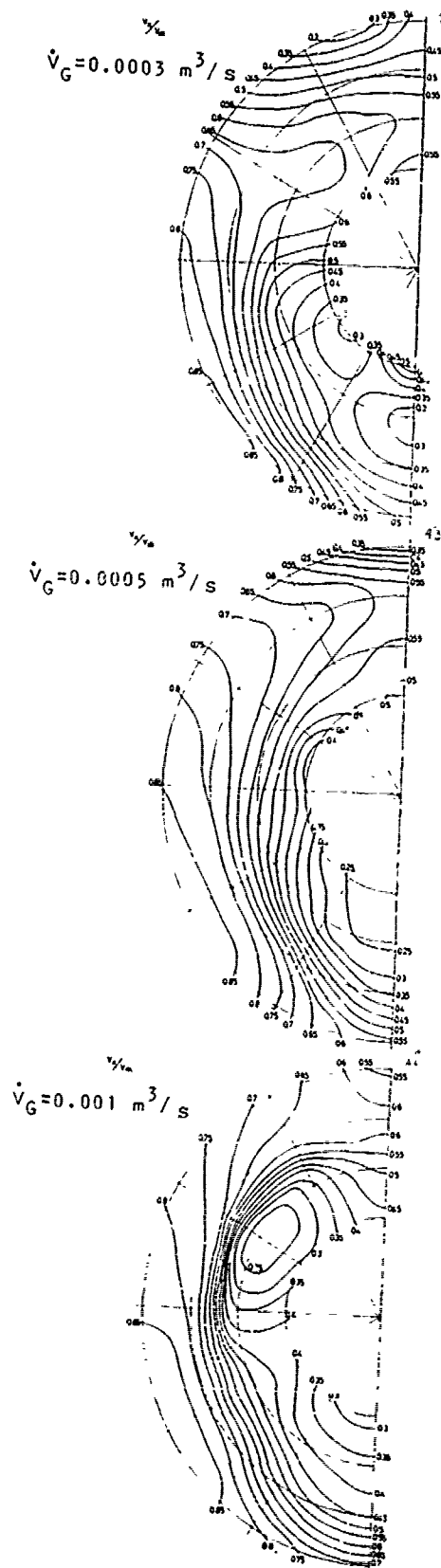


Fig. 5 Axial Velocity Distributions, Air Discharge Hole Configuration I

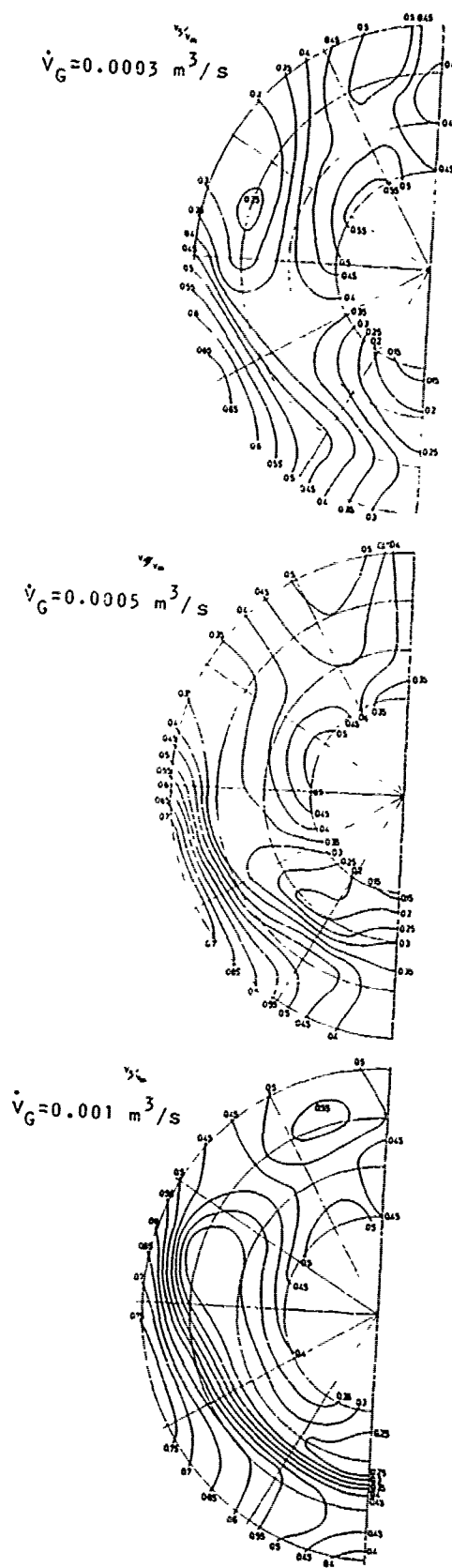


Fig. 6 Axial Velocity Distributions, Air Discharge Hole Configuration II

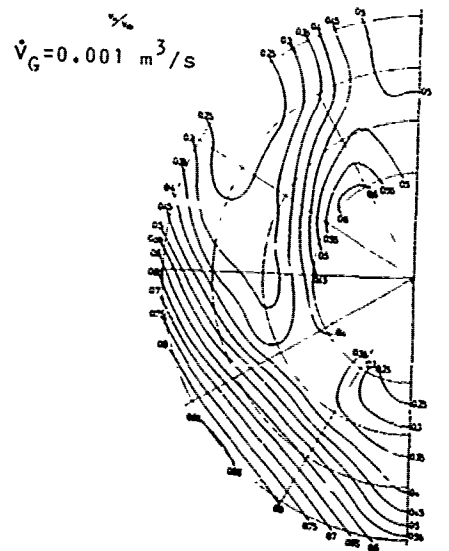
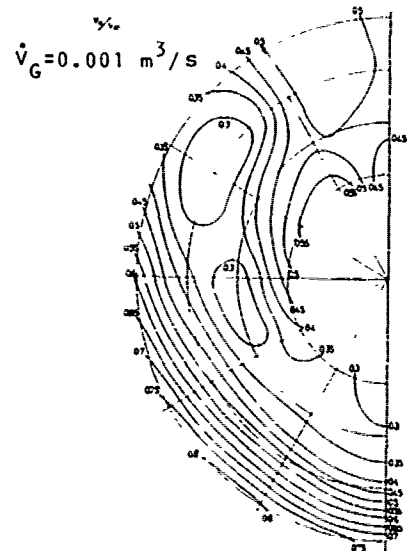
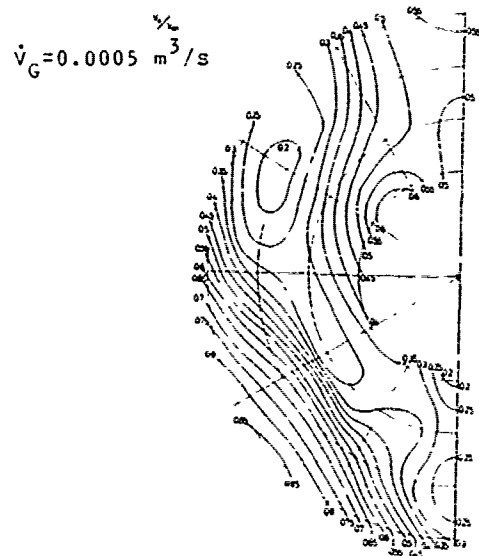
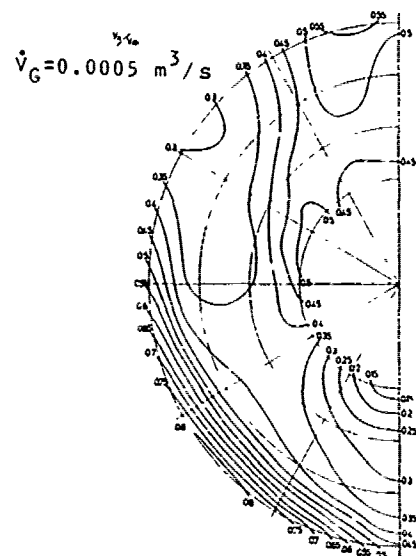
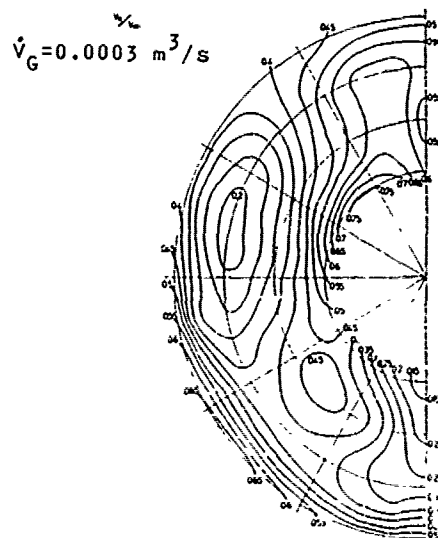
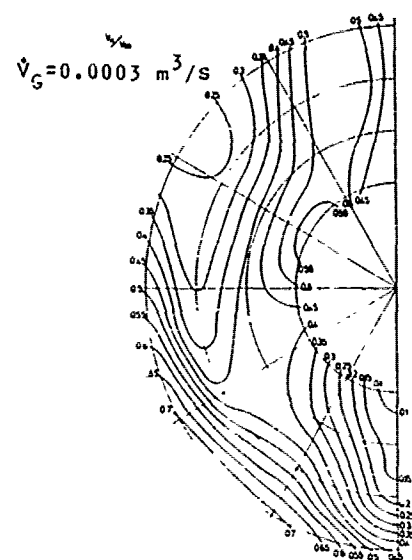


Fig. 7 Axial Velocity Distributions, Air Discharge Hole Configuration III

Fig. 8 Axial Velocity Distributions, Air Discharge Hole Configuration IIIA

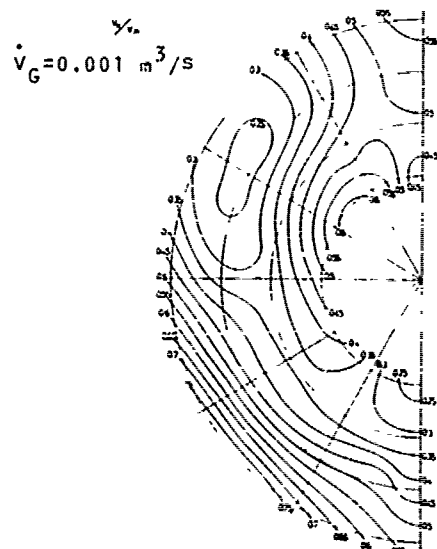
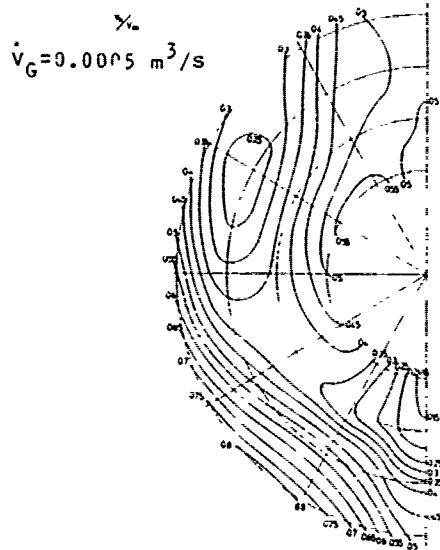
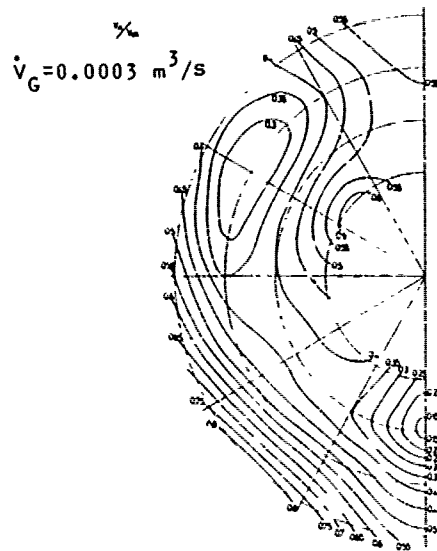


Fig. 9 Axial Velocity Distributions. Air Discharge Hole Configuration IIIB

In these diagrams the distribution of dimensionless axial velocity $\frac{v_x}{v_m}$ is given.

Local wake w_L can be obtained from $w_L = 1 - \frac{v_x}{v_m}$

v_x = axial inflow velocity

v_m = model speed.

Vector diagrams on propeller disc are presented in Fig. 10 for model without air discharge and in Figures 11, 12, 13, 14 and 15 for model with air discharge of all hole configurations. In these diagrams the speed v_{zy} is given.

By comparison of Figures 4...9 and 10...15 at the same time it can be seen that the effect of air discharge is consistent. The best results are obtained with the air discharge hole configuration I. Then even with small air flow rate 0.0003 m^3/s the wake peak due to bilge vortices is reduced and bilge vortices are smaller and have moved near to the centerplane of the ship. The situation is still better with air flow rate 0.0005 m^3/s . Then the bilge vortices disappear. However if air flow rate is increased to 0.001 m^3/s , the situation is changed and a new wake peak is formed near to the centerplane.

Discharging of air from the holes of configuration II does not have such an evident effect on velocity distribution. Only with large air flow rate 0.001 m^3/s is wake distribution improved a little and bilge vortices removed near to the centerplane.

Results obtained with air discharge hole configuration III show no improvement with small and medium air flow rates. With large air flow rates wake distribution becomes worse.

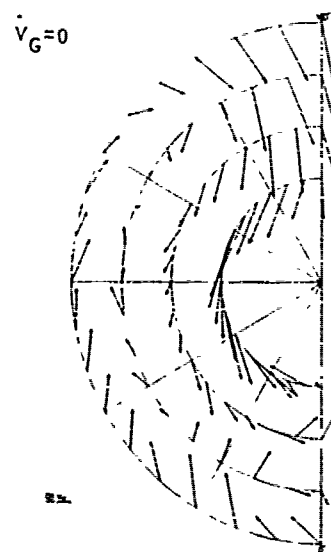


Fig. 10 Velocity Vectors V_{zy} on Propeller Disc, No Air Discharge

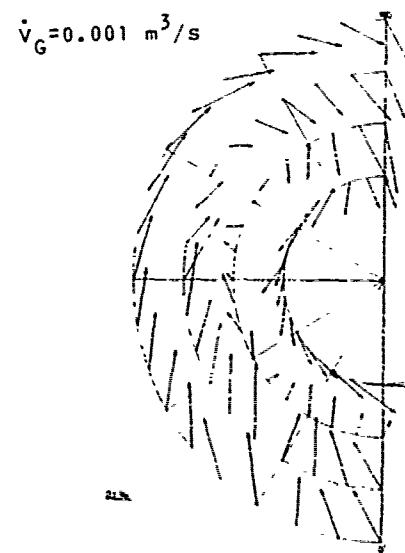
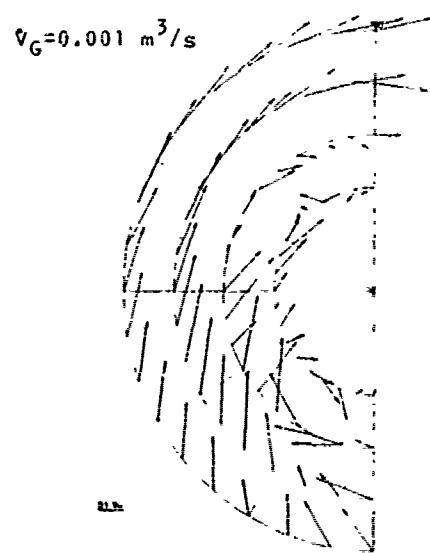
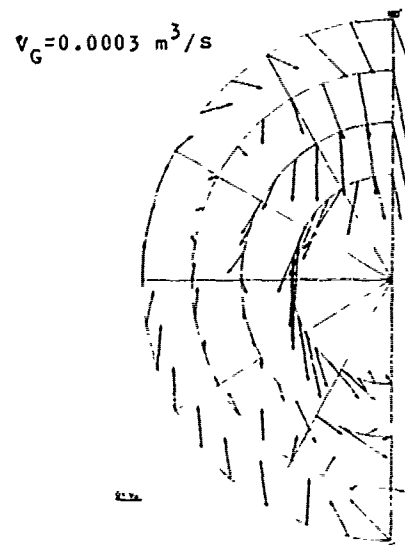
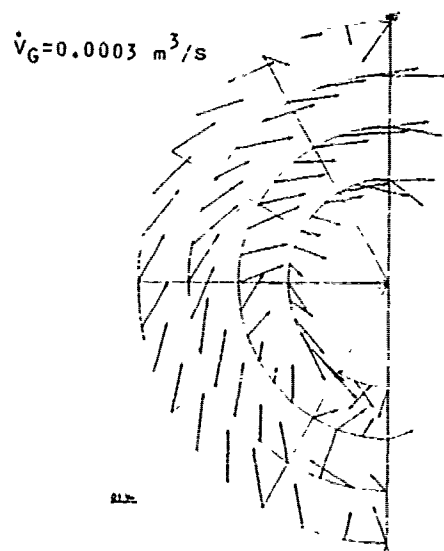
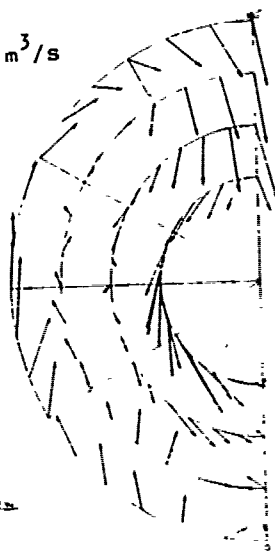


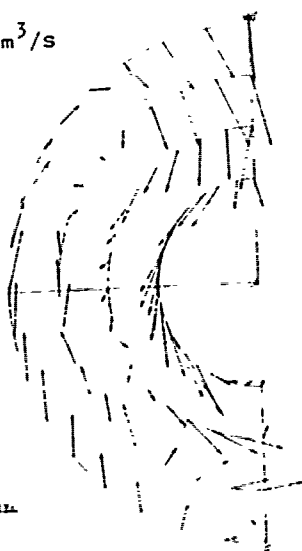
Fig.11 Velocity Vectors on Propeller Disc,
Air Discharge Hole Configuration I

Fig.12 Velocity Vectors on Propeller Disc,
Air Discharge Hole Configuration II

$$\dot{V}_G = 0.0003 \text{ m}^3/\text{s}$$



$$\dot{V}_G = 0.0005 \text{ m}^3/\text{s}$$



$$\dot{V}_G = 0.001 \text{ m}^3/\text{s}$$

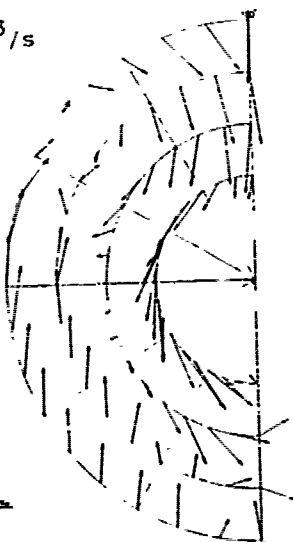
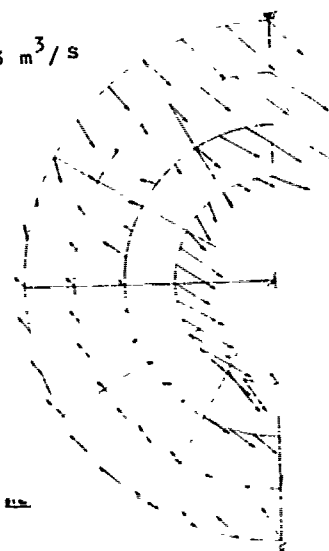
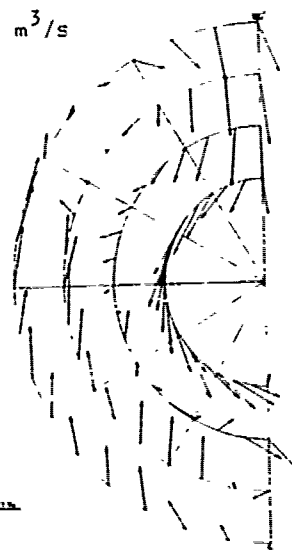


Fig.13 Velocity Vectors on Propeller Disc,
Air Discharge Hole Configuration III

$$\dot{V}_G = 0.0003 \text{ m}^3/\text{s}$$



$$\dot{V}_G = 0.0005 \text{ m}^3/\text{s}$$



$$\dot{V}_G = 0.001 \text{ m}^3/\text{s}$$

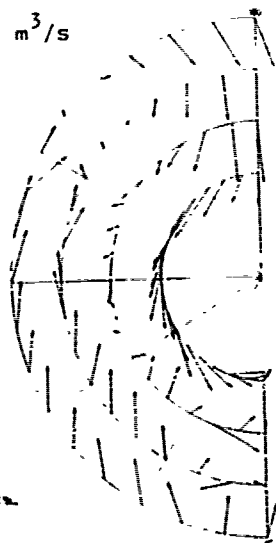


Fig.14 Velocity Vectors on Propeller Disc,
Air Discharge Hole Configuration IIIA

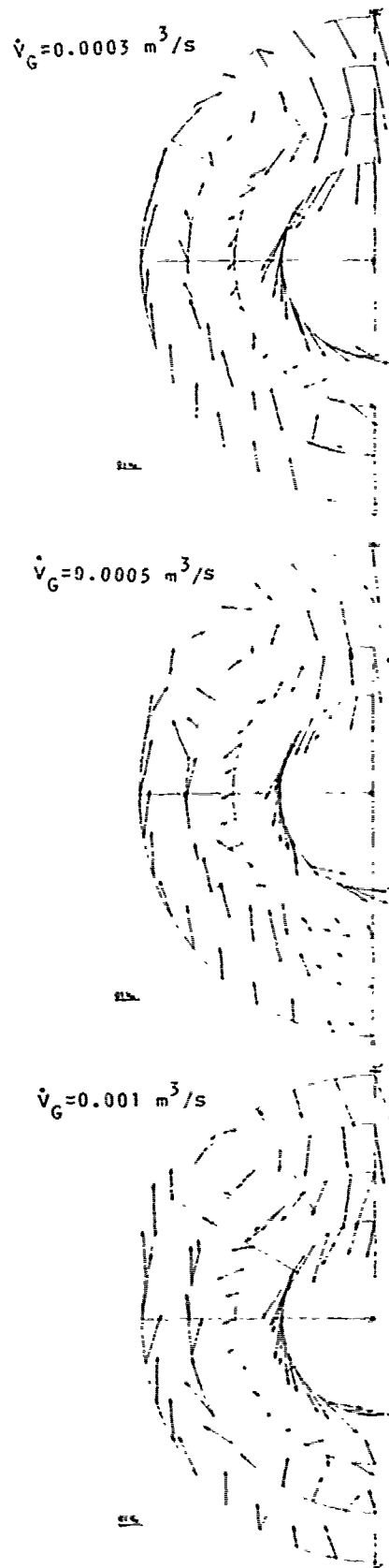


Fig. 15 Velocity Vectors on Propeller Disc, Air Discharge Hole Configuration IIIB

The two modifications IIIA and IIIB of air discharge hole configuration III results in even worse wake distributions. Vortex formation is pronounced apparently due to disturbance of concentrated air discharge.

Mean wake values were calculated by integration of axial velocity distributions. Results are presented in Fig.

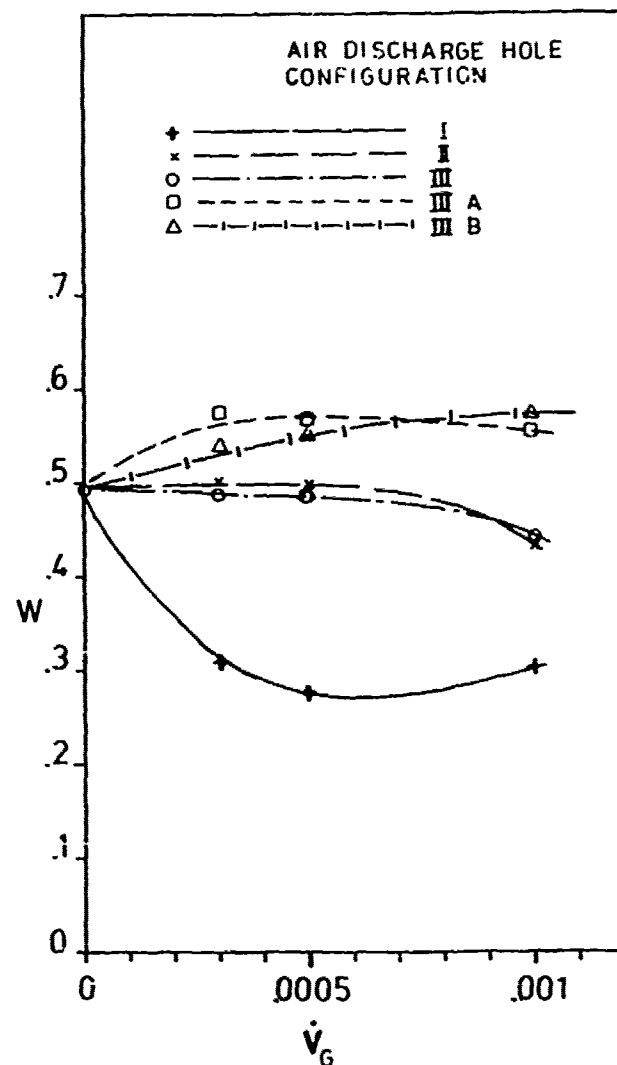


Fig. 16 Mean Wake Values w as a Function of Air Flow Rate

This figure confirms the general picture given by the axial velocity distribution diagrams and V_{zy} -vector diagrams.

Mean wake values of air hole configuration I are clearly at a lower level than mean wake without air discharge. This is a result of reduced vortex formation and separation. With air discharge hole configurations II and III the changes in wake distributions were small and also the mean wake remains practically unchanged.

When air was discharged from the hole configurations IIIA and IIIB the vortex formation was increased and this can also be seen from the increased mean wake values of Fig. 16.

For evaluation of changes in flow-conditions at propeller sections the circumferential axial velocity variations of the air discharge hole configurations I, II and III are presented together with the corresponding velocity variation of the model without air discharge in Fig. 17, 18, 19 and 20. Here again configuration I gives the best results. Very small

$\frac{V_x}{V_{in}}$ -values at 0.4 and 0.8R are increased with air flow rates 0.0003 and 0.0005 m³/s and in general wake curves are gently sloping. The widths of wake peaks are much larger than in the original distribution without air.

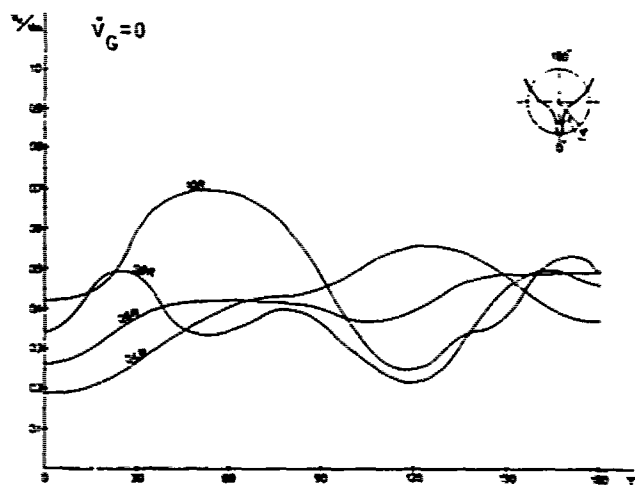


Fig. 17 Circumferential Axial Velocity Variation, without Air

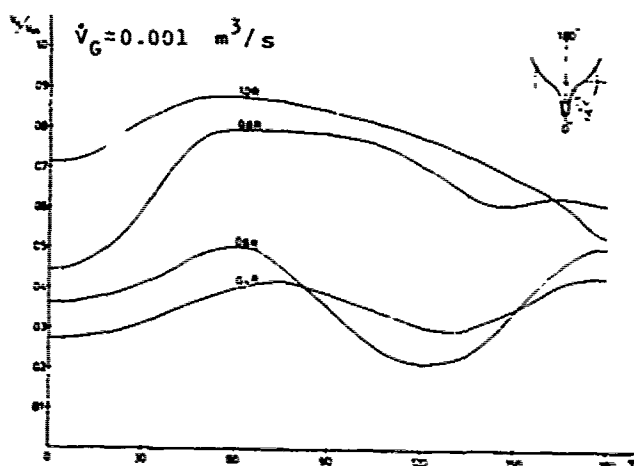
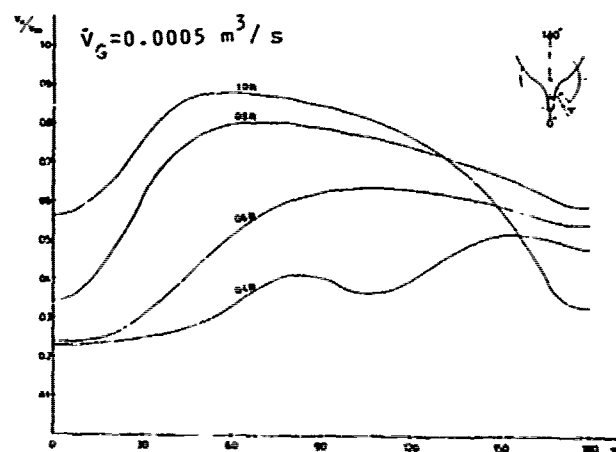
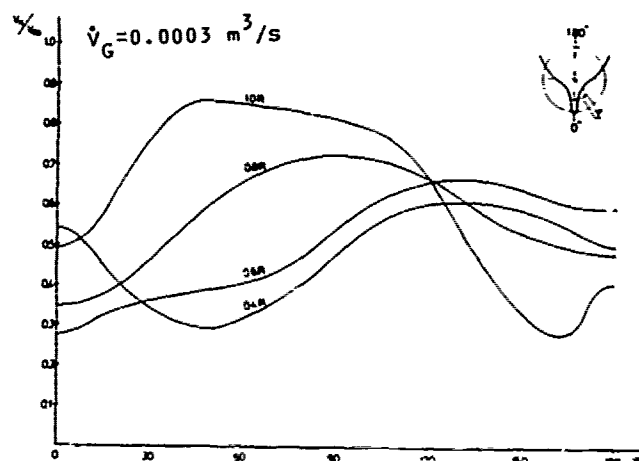


Fig. 18 Circumferential Axial Velocity Variation. Air Discharge Hole Configuration I

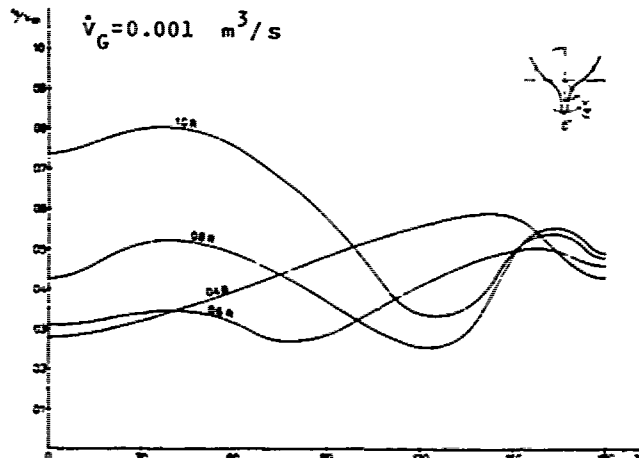
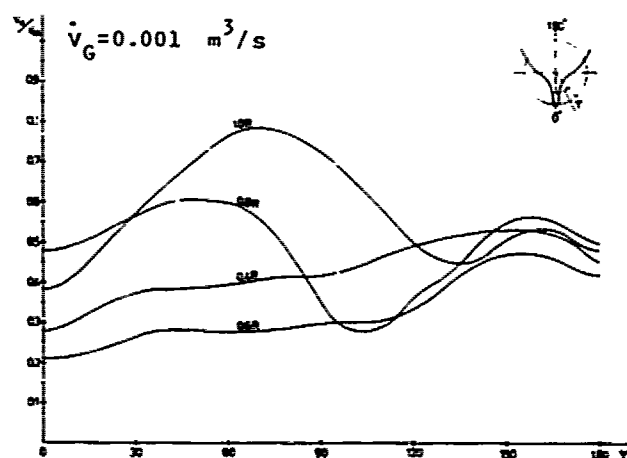
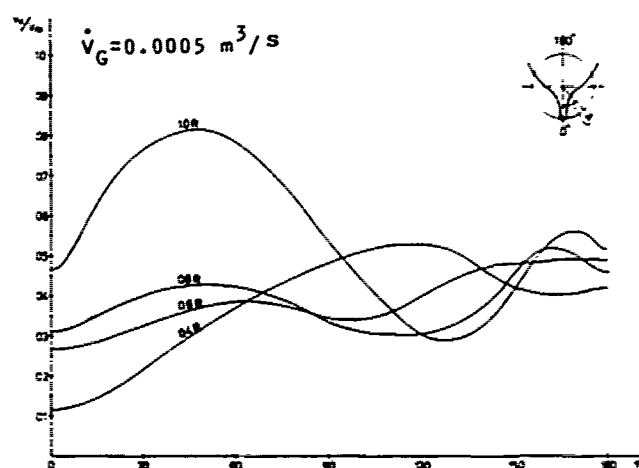
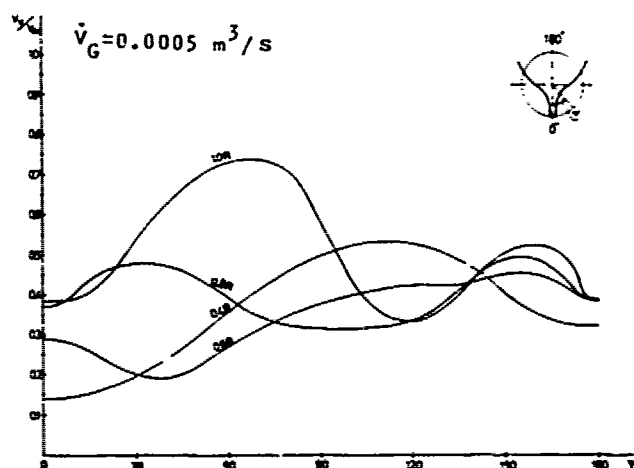
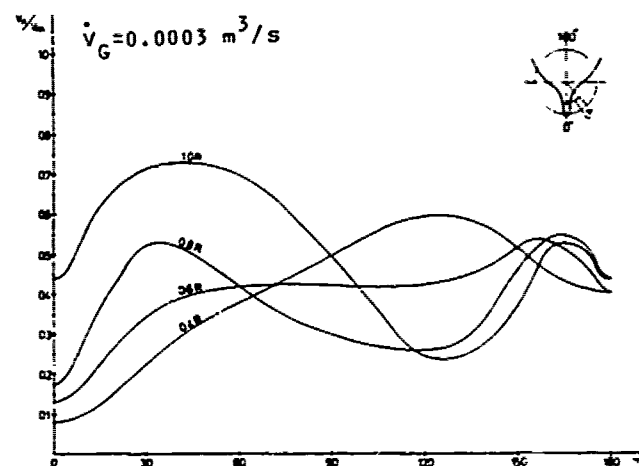
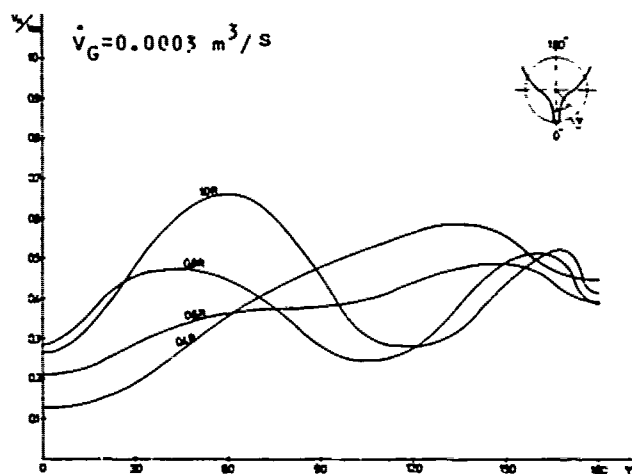


Fig. 19 Circumferential Axial Velocity Variation. Air Discharge Hole Configuration II

Fig. 20 Circumferential Axial Velocity Variation. Air Discharge Hole Configuration III

6. DISCUSSION

The present results appear to confirm the suggestion made in Section 1 that the bilge vortex formation can be reduced by discharge of air into the boundary layer.

Such an effect can only be attained by discharge of small amounts of air down on the level of the upper turn of the bilge, as in air discharge hole configuration I. Then bilge vortex formation decreased and even completely disappeared and in general very

large local wake values are decreased and circumferential wake curves became gently sloping. This is an obvious improvement considering the vibratory forces of unsteady cavitation. However, if air flow rate is too large vortex formation may even increase.

These results seem promising. However, some reservations have to be made. At medium and large air flow rates air is drawn into the propeller and revolutions are increased. This does not affect propeller efficiency but it must be taken into consideration in propeller design. The functioning of the system in ship scale in general requires further consideration. The boundary layer is then relatively thinner. It can be shown that volumetric water flow through a certain cross section in boundary layer is proportional to $l^{\frac{3}{4}}$ power of length scale if model speed is scaled according to Froude. If the required air flow rate is proportional to this water flow rate in the boundary layer, it should also be proportional to the $l^{\frac{3}{4}}$ power of length scale. In the two-phase applications mentioned in Section 3, where air flow rates are very large, they are in general considered to be proportional to the $2^{\frac{1}{2}}$ power of length scale.

On the other hand due to the fact that the maximum rising speed of air bubbles is proportional to the square root of the radius of the corresponding spherical bubble, there is a limit in changing the momentum of basic water flow. All this requires further consideration before possible full scale applications.

Most of the present results are based on the measurements made with a 5-hole pitot tube. The accuracy of this instrument in general has been questioned by Harvald and Hee [7]. The author agrees that differences in local wake values at the same point may differ by 0.25 or even more for repeated tests. This is quite natural when such an unsteady phenomenon as separation is present. If there are areas of separated flow in the propeller disc, fully automated computer methods for plotting isowakes directly from the measured local wake values should not be used. Measured local values for instance at the same radius should first be faired manually. Separated areas could then be traced. The author recommends the marking of traced separated areas on the velocity distribution diagrams for instance by diagonal lines. This would increase the usefulness of these diagrams in subsequent stages of the design.

7. CONCLUSIONS

The present report describes an experimental verification for a system of reducing the formation of bilge vortices. In this system comparatively small amounts

of air are discharged into the boundary layer. Systematic model tests with a full tanker form were carried out using five air discharge hole configurations. If air discharge holes are on the level of the upper turn of the bilge and extend from about 0.05 L to at least 0.15 L measured from the after perpendicular, then air bubbles turn the direction of surface flow in stern and reduce the streamline convergence and separation near the bilge. With small and medium air flow rates favourable changes in wake pattern can be discovered.

The resistance tests indicate that the discharging of air reduced the resistance and this reduction arises from the reduction of eddy-making resistance. Propulsion efficiency remains practically unchanged when air is discharged in the system. Revolutions are increased with large air flow rates.

Although the results of model tests are encouraging, they are based on model tests with speed scaled according to Froude's law. Therefore scale effects require careful consideration. Also, special features of two-phase flow in this mode of bubble formation require additional studies.

8. ACKNOWLEDGEMENTS

This study was carried out in the Ship Hydrodynamics Laboratory of Helsinki University of Technology. The author would like to express his thanks to Mr. Matti Lietepohja for performing the tests and to all those who contributed to this study.

REFERENCES

1. van Berlekom, W.B., "Separation on Ship-Like Bodies", International Symposium on Ship Viscous Resistance, Gothenburg 1978.
2. Juurmaa, K., "WABS, a Method for Improving the Icebreaking Performance of Ships", Symposium on Ice, Ships and Winter Navigation, Oulu University 1977.
3. Kostilainen, V., "Two-Phase Air-Water Propulsion System Based on the Gravity Effects", International Shipbuilding Progress, Vol. 15, No. 169, 1968.
4. Kostilainen, V., "Reduction of the Development of Bilge Vortices by Discharge of Air into the Boundary Layer", International Shipbuilding Progress, Vol. 27, No. 305, 1980.
5. Kostilainen, V., "Testing Facilities and Instrumentation at the Ship Hydrodynamics Laboratory of the Helsinki University of Technology, 14th International Towing Tank Conference, Ottawa, 1975.
6. Huse, E., "Reduction of Propeller-Induced Pressure Fluctuations by an Air Layer at the Hull", Norwegian Maritime Research, Vol. 1978.
7. Harvald, Sv. Aa. and Hee, J.M., "Wake Distributions", International Symposium on Future Tasks and Problems of Model Basins, Berlin 1978.

Discussion

S. Tamiya (Univ. of Tsukuba)

(1) Professor Kostilainen shows us very interesting idea of air bubble utilization for improving wake distribution. It is a kind of air lift pump as the author noticed, where the excited water flow (mainly wake following air bubble) near hull surface acts as a motivational medium. For getting better understanding and development of the experimental results it will be necessary to make clear the process of bubble formation as well as motion of air bubble in shear flow attached to rigid wall. The discussor should like to expect Professor Kostilainen would complete this work by giving such a kind of informations in future.

(2) The rate of work done by air bubbles is measured by the product of volume rate of air flow and rising velocity. In case of actual ship rising velocity must be small because of relatively small bubble size, so that increased volume rate will be necessary to obtain equivalent motivation. On the other hand the thinner boundary layer may require somewhat reduced volume rate. May I have any opinion of the author in this respect?

(3) May I have the diameter of the air hole as well as the reason why it was decided?

A.Y. Odabaşı (BSRA)

Professor Kostilainen presented us a very interesting and well written paper in which he also drew our attention to a number of points in relation to a possible full scale application. Since the paper is self-contained my contribution will be confined to the clarification of certain points raised by the author in the light of the experience gained in B.S.R.A.

The first point worth mentioning is the effectiveness and cost of flow improvement devices. As mentioned in the paper the use of fins almost always brings a penalty of added resistance. The important problem here is the ability to predict the occurrence of severe flow retardation in an early design stage so that a remedy can be found. If the hull form cannot be changed due to other design constraints the use of flow deflectors (similar to vortex generators) appears to be the most feasible approach since the added resistance penalty is only marginal. During the development of the PHIVE (Propeller Hull Interaction Vibration Excitation) project such flow deflectors have been designed and fitted to two ships; a fast

cargo ship and a fishing boat, with success.

The next point is the similarity or otherwise between the vortex layer separation and the bilge vortex separation. Figure A1 illustrates the vortex layer separation as proposed by Maskell 1). As can be seen there, vortex layer separation requires the existence of an attachment line to the body where very strong cross flow also exists. Further studies in the field of aeronautics also indicates this phenomenon exists for flows at high Mach number and high incidence, cf. Hahn, et. al 2). A closer examination of bilge vortex formation does not indicate the presence of an attachment line as suggested by van Berlekom [1]. In fact it rather resembles a tip vortex formation. Wind tunnel experiments conducted at NMI did not indicate a persistent streamline coalescence. The presence of the velocity profiles as shown in Figure A2 seem to appear as a result of a different phenomenon which was named as "shear separation" and it will be discussed in another paper to this Symposium, Odabaşı and Şaylan 3).

My final contribution is related to the possibility of calculating the effect of air injection. As the author points out the main contribution of air injection is an additional momentum due to the buoyancy of air bubbles. This, however, should not be taken as a straightforward upward momentum addition since the air injection will create an oblique strain on the established flow. The amount of strain and its direction will obviously depend on the amount, speed and orientation of the air injectors. If one can estimate the added momentum and its direction, changes that will happen in the downstream direction can be calculated approximately, by using the extra strain rate corrections in the turbulent flow calculations, cf. Bradshaw 4), together with the modification of the continuity equation and the body surface boundary condition to account for the transpiration. Calculations performed by Higuchi and Rubesin 5) indicate that prediction of velocity profiles and shear stresses under similarly strained conditions are quite reasonable. The validity of this explanation is fairly easy to check since if the most important effect is the extra strain rates, the use of local surface rotation or local surface heating (or cooling) should produce similar results.

REFERENCES

- 1) Maskell, E.C. "Flow Separation in Three Dimensions", *RAE Report*, AERO 2565 (1955)
- 2) Hahn, M., Rubbert, P.E. and Mahal, A.S. "Evaluation of Separation Criteria and their Application to Separated Flow Analysis", *AFDL-TR-72-145* (1973)
- 3) Odabaşı, A.Y. and Şaylan, Ö. "GEMAK - A Method for Calculating the Flow around Aft-Ends of Ships", *13th Symposium on Naval*

Hydrodynamics, Tokyo, p.747 (1980)

4) Bradshaw, P. "Effects of Streamline Curvature on Turbulent Flow" AGARDograph 169 (1973)

5) Higuchi, H. and Rubesin, M.W. "Behaviour of a Turbulent Boundary Layer to Sudden Transverse Strain", AIAA Journal, Vol.17, p.931 (1979)

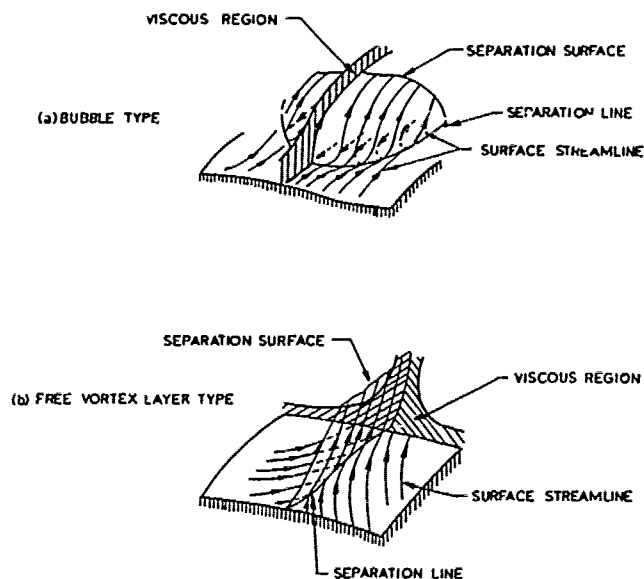


Fig. A1 Maskell's Three-Dimensional Separation Concepts

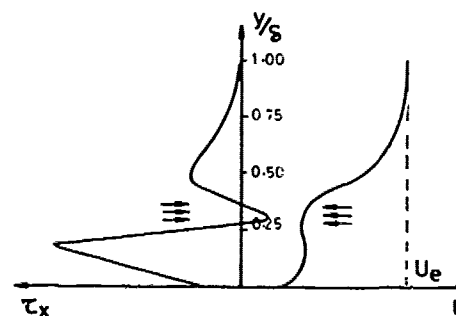
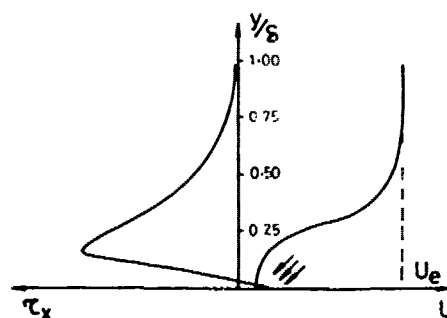
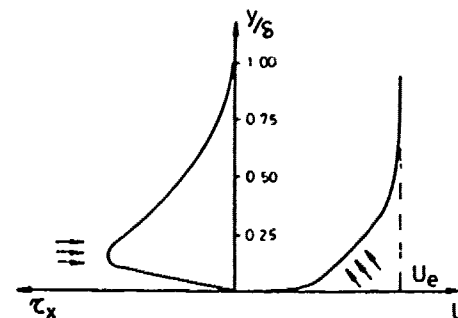
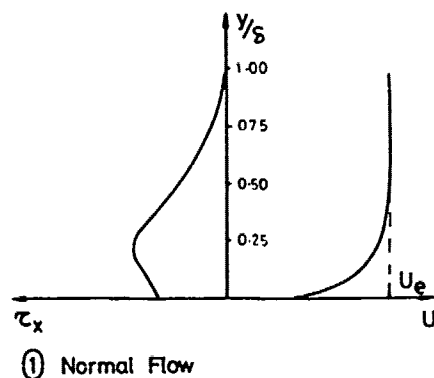


Fig. A2 Kink Formation in Streamwise Velocity Component

E. Huse (Norwegian Hydrodynamic Lab).

First of all, Professor Kostilainen is to be congratulated on his bringing new and refreshing ideas into our field of ship technology. I have three brief comments/questions:

(1) What is the additional power or fuel consumption of the air compressors compared to the gain in resistance and propulsive efficiency?

(2) I think that extreme bilge vortices of this type described in the paper should preferably be avoided at the design stage by applying more V-shaped sections in the afterbody. This will also reduce resistance, and the effect of the higher wake peak at the top of the propeller disc can be counteracted by other means, for instance a highly skewed propeller.

(3) As a last comment I think it is worth mentioning that the air injection suggested by Prof. Kostilainen could have an additional beneficial effect in reducing cavitation erosion on the propeller blades by ventilating the cavities.

Author's Reply

V. Kostilainen (Helsinki Univ. of Tech.)

I am grateful to Prof. Tamiya for his expert comments and question.

I agree with Prof. Tamiya in that, that more basic research should be done on two phase flow in these conditions.

To my opinion, the second notice of Prof. Tamiya is also right. There is a contradiction in the scale effect, on the rising velocity of the air bubbles on the other side and on the thickness of the boundary layer on another side. I am not able to give you any quantitative information on this problem.

The diameter of air holes was 7mm. But this diameter has practically no effects on bubble formation in these rates of air flow. If air flow rate is very low, then the form and size of air holes have certain effect on bubble formation.

I thank Dr. Odabaşı for his discussion. Dr. Odabaşı brings to our knowledge important new information. It happens less frequently that vortex generators are fitted in full scale ships with success.

Further Dr. Odabaşı told us about a new form of separation called shear separation. I consider this to be an interesting finding and we may hear more about it tomorrow, when Dr. Odabaşı and Şaylan will present their paper.

Finally Dr. Odabaşı considers the calculation of the effect of air injection to be fairly easy. This is easy if the mediums of basic flow and injected flow are the same. We have found it difficult to determine the change of momentum if air is discharged into the water. We have tried to do it experimentally with poor success. This is because in this regime of two-phase flow, the bubble formation is a very irregular phenomenon and because part of the potential energy of air bubbles goes to the vortex generation.

I thank Prof. Huse for his question and kind comments. In reply to his first question I can say that we notice a gain in overall efficiency of this system in resistance tests only, with the best hole configuration and small and medium air flow rates. Then the power of compressed air to be produced for the system was much less than the decrease in effective power of the model. As I say in my paper, reason to this is apparently decreased vortex formation. In propulsion tests no changes in required propulsion power were noticed.

I fully agree with Prof. Huse in that that the best way to reduce the bilge vortex is to design the form of the ship in such a way that no vortex formation exists. Unfortunately at the present state of the knowledge it is not always possible.

I thank Prof. Huse of the additional information given in his last comment.

Session VII

VISCOUS FLOW 2

— INTERACTIONS AND SCALE EFFECT —

Chairman

**R.E.D. Bishop
University College London
London, United Kingdom**

Viscous Effect on Waves of Thin Ship

Takeshi Kinoshita
Institute of Industrial Science
The University of Tokyo
Tokyo Japan

ABSTRACT

By means of a linearized theory for ship waves in a viscous fluid under assumptions of the Oseen's equations and an equivalent laminar wake, it is confirmed that a wave pattern and a wave making resistance at high Reynolds numbers are determined by a potential component of the flow field, that the effect of a rotational component is negligible and that viscous effects on a wave pattern and a wave making resistance are due to modification of potential flow by a boundary layer and a viscous wake. A boundary layer and a viscous wake of a surface-piercing 2-dimensional thin strut are measured carefully, as well as wave patterns. It is discovered that turbulence occurs beside and behind a ship near the free surface, and that it originates another sort of viscous wake. The measured boundary layer at deep points which is not affected by free surface is compared with calculations using rather simple methods of turbulent boundary layer theories which do not consider the "thick boundary layer" and trailing edge effects. The measured viscous wake at deep points is compared with calculated results of Squire & Young's method. Making use of the measured displacement thickness, the wave patterns and the wave making resistances are calculated and compared with measured values. A qualitative but plausible agreement is obtained.

NOMENCLATURE

B	breadth
b	half breadth
d	draught
\mathbf{E}	rate-of-strain tensor
\mathbf{F}	surface force acting on the hull
F_n	Froude number
f	hull shape
\mathbf{G}	velocity induced by a potential source
g	gravity acceleration
\mathbf{i}	unit vector of x direction
k_0	half of Reynolds number
k_{0e}	half of effective Reynolds number
L	length
l	half length
$m_i, i=0\sim 3$	density of singularity distribution
$\mathbf{n}=(n_1, n_2, n_3)$	unit normal (positive out of ship)
\mathbf{P}	pressure vector induced by Oseenlets

p	pressure
p^*	$= p + \gamma_0 z$
p_+	pressure of inside flow
\mathbf{q}	velocity
\mathbf{q}'	perturbation velocity
$\bar{\mathbf{q}}$	perturbation velocity of reverse Oseen flow
R_e	Reynolds number
R_{ne}	effective Reynolds number
S	wetted hull surface
$\mathbf{T}=(t_1, t_2, t_3)$	velocity tensor induced by Oseenlets
U	uniform stream velocity
V	full fluid domain
γ_0	$= g / U^2$
δ	boundary layer thickness
δ^*	displacement thickness of a boundary layer or a wake
$\delta(\xi)$	Dirac's delta
ω	thinness parameter of a ship
ζ	free surface elevation
θ	momentum thickness of a boundary layer or a wake
μ	fluid viscosity
ν	fluid kinematic viscosity
ν_T	eddy viscosity
ρ	fluid density

1. INTRODUCTION

An interference between free surface waves and actions of water viscosity has been investigated for a long time associating with an improvement of scaling procedures from model resistances to ship resistances and an explanation of discrepancy between measurements and theoretical wave resistances. Existing investigations were reviewed by Maruo [1]. He concluded that no complete theory for the wave resistance in a viscous fluid had been established so far. Any existing theories have arbitrariness about a flow model so that they can explain the interference only qualitatively but quantitatively. In this paper it is attempted that the arbitrariness about a flow model is removed under these basic assumptions which are a linearity of the fluid motion by a thin ship and a representation of a turbulent boundary layer and wake by an "equivalent" laminar flow. Another assumption is that a ship wave damps only by molecular viscosity not by turbulence.

Though the linearity of the fluid motion is assumed, the

linearized equation of motion of viscous fluid, i.e. the Oseen equation does not hold near the surface of the body at high Reynolds number. This linearization is justified at a far field where a problem loses boundary condition on the surface of the body. The problem should be matched with a near field problem. The near field problem is about a turbulent boundary layer including a thick boundary layer near a stern, its separation on occasions and a near wake. Theoretical investigations of this important but difficult problem have just been started about not only 3-d but also 2-d and axisymmetric body [2]. The greater part of this problem is left for future researches. Objective of this paper is limited to a quantitative estimation of a viscous effect on a wave pattern and a wave pattern resistance of a thin ship under above assumptions. For this purpose a far field is matched with experiments of a near field quantity, which is distribution of displacement thickness of the turbulent boundary layer and wake, since it is shown by a new representation of a thin ship in a viscous fluid that a far field should be matched with the displacement thickness.

This paper consists of three parts.

- 1) Representation of a thin ship in a viscous fluid
- 2) Measurements of a viscous fluid flow and stern wave patterns
- 3) Calculations of a viscous effect on a wave pattern and a wave pattern resistance of a thin ship

This paper also includes descriptions about turbulence which is found occurring beside a ship, spreading behind on the free surface and originating another sort of viscous wake.

2. REPRESENTATION OF A THIN SHIP IN A VISCOUS FLUID

The fluid flow around the ship is turbulent, because its Reynolds number is sufficient large. Reynolds equations including Reynolds' stress which is a pretended stress are the equations of motion for turbulent flow. This equation have not been able to be calculated without any assumptions yet. The most universal assumptions about Reynolds' stress have been pursued by a lot of researches about a turbulent flow.

In order to make it possible to analyze the problem of the interference between waves and wake of a ship, adopted assumptions in this paper are that the Reynolds' stress is expressed using coefficient of eddy viscosity and further that the eddy viscosity is constant everywhere, which are so primitive and rough that this is not an exact situation. Validity of these assumptions will be considered later.

From above assumptions the fluid flow can be considered to be an equivalent laminar flow. Equations of motion are the Navier-Stokes equations for a steady incompressible viscous flow. If we normalize the length by a half length of the ship l , the velocity by a uniform stream velocity U and the pressure by twice of the stagnation pressure ρU^2 ,

Momentum equation:

$$(\underline{q} \cdot \text{grad}) \underline{q} + \text{grad } p^* = \frac{1}{R_e} \Delta \underline{q}; \quad (1)$$

Continuity equation:

$$\text{div } \underline{q} = 0; \quad (2)$$

where

ρ = density of fluid = constant,

μ = viscosity = constant,

ν = kinematic viscosity = $\frac{\mu}{\rho}$ = constant,

$\gamma_0 = gl/U^2$,

$R_e = Ul/\nu$,

p = pressure,

$p^* = p + \gamma_0 z$,

\underline{q} = velocity: $\underline{q} = u\mathbf{i} + v\mathbf{j} + w\mathbf{k}$,

in Cartesian coordinates.

Boundary condition at infinity is

$$\underline{q} = \underline{i}, \quad p + \gamma_0 z = 0. \quad (3)$$

Hull surface condition is no-slip condition, as

$$\underline{q} = 0. \quad (4)$$

And boundary conditions on a free surface are a stress free condition and a kinematic condition.

We introduce another main assumption which is that the ship is so thin like Michell's model that its disturbance is sufficient small compared with a uniform stream. This assumption yields a set of linearized conditions. But a hull surface condition (4) cannot be applied for the linearized problem, because a perturbation velocity near the ship is comparable with a uniform stream by an action of water viscosity, whether the ship is very thin or not. Now let us use an integral representation of the Navier-Stokes equations.

For a perturbation velocity $\underline{q}' = \underline{q} - \underline{i}$, equation (1) may be written as

$$\frac{\partial}{\partial x} \underline{q}' = -(\underline{q}' \cdot \text{grad}) \underline{q}' - \text{grad } p^* + \frac{1}{R_e} \Delta \underline{q}', \quad (5a)$$

or

$$\frac{\partial}{\partial x} \underline{q}' = \underline{q}' \times \text{rot } \underline{q}' - \text{grad} (p^* + \frac{1}{2} |\underline{q}'|^2) + \frac{1}{R_e} \Delta \underline{q}'. \quad (5a')$$

The quadratic term of \underline{q}' cannot be neglected near the ship as mentioned above. If we consider the relation

$$\frac{\partial}{\partial x} \underline{q}' = \underline{F} \delta(\xi) \delta(\eta) \delta(\zeta) - \text{grad } p^* + \frac{1}{R_e} \Delta \underline{q}', \quad (6a)$$

$$\text{div } \underline{q}' = 0, \quad (6b)$$

which is the linearized equation of motion for steady flow with a point force of strength \underline{F} , where $\delta(\xi)$ being the Dirac's delta, we can understand that equations (5) and (2) mean Oseen flow with volume force distribution of strength $-(\underline{q}' \cdot \text{grad}) \underline{q}'$ or $\underline{q}' \times \text{rot } \underline{q}'$. So the velocity is written by an induced velocity of Oseenlets.

$$\underline{q}' = \int_S \underline{F} \underline{F} \, ds - \int_V \underline{F} (\underline{q}' \cdot \text{grad}) \underline{q}' \, d\tau \quad (7a)$$

$$= \int_S \underline{F} \underline{F} \, ds + \int_V \underline{F} (\underline{q}' \times \text{rot } \underline{q}') \, d\tau. \quad (7a')$$

And

$$p^* = \int_S \underline{P} \underline{F} \, ds - \int_V \underline{P} (\underline{q}' \cdot \text{grad}) \underline{q}' \, d\tau. \quad (7b)$$

$$p^* + \frac{1}{2} |\underline{q}'|^2 = \int_S \underline{P} \underline{F} \, ds + \int_V \underline{P} (\underline{q}' \times \text{rot } \underline{q}') \, d\tau. \quad (7b')$$

From (7a') and (7b'),

$$p^* + \frac{1}{2} |\underline{q}'|^2 = \int_S [\underline{P} + (t_{ij})] \underline{F} \, ds + \int_V [\underline{P} + (t_{ij})] (\underline{q}' \times \text{rot } \underline{q}') \, d\tau + \frac{1}{2}. \quad (7b'')$$

Here \underline{F} and \underline{P} are a velocity tensor and pressure vector induced by Oseenlets, respectively, and \underline{F} is a surface force acting on the hull. S is the hull surface and V is a full fluid domain (see Appendix A).

When R_e tends to infinity, $\underline{P} + (t_{ij})$ tends to zero exponentially except $\theta = 0$, where θ is an angle from x -axis. So the equation (7b'') may be written as

$$p^* + \frac{1}{2} |\underline{q}'|^2 = \frac{1}{2}, \quad R_e \rightarrow \infty. \quad (8)$$

This is the same form as the Bernoulli's theorem for potential flow.

If \underline{T} is replaced by a velocity tensor of Havelock Oseenlets [1], [3] which satisfy both the linearized free surface condition and the infinity condition, equations (7) are representations of fluid flow field about a ship.

The equations (7) are very interesting since they are representations of the Navier-Stokes equations by Oseenlets which are singular solutions of the linearized equations (the Oseen's equations). They are similar integral representations to Green theorem of a potential flow. Of course the equations (7) are non-linear since the last term contains quadratic terms of \underline{q} . But note that the integral domain V is restricted extremely near the body surface S , if Re is very large, because the integrand is almost zero except near S^+ .

Considering an order of magnitude of the volume distribution of Oseenlets $-(\underline{q}, \text{grad})\underline{q} \equiv (\sigma_1, \sigma_2, \sigma_3)$,

$$\begin{aligned} -\sigma_1 &= u' u_x' + v' u_y' + w' u_z' = O(1) \\ -\sigma_2 &= u' v_x' + v' v_y' + w' v_z' = O(\delta \text{ or } \epsilon), \\ -\sigma_3 &= u' w_x' + v' w_y' + w' w_z' = O(\delta \text{ or } \epsilon), \end{aligned} \quad (9)$$

where δ is a thickness of a boundary layer or a half breadth of a wake and ϵ is a thinness parameter of a ship, the strength of a lifting Oseenlet is negligible compared with the strength of a dragging Oseenlet.

Integrating the volume distribution of dragging Oseenlet,

$$\begin{aligned} \int_{-1}^x dx \int_{-d}^y dy \int_{-d}^z dz (-\sigma_1) &= \int_{-1}^x dy \int_{-d}^z dz u'^2 + \text{exponentially small} \\ &= \int_{-d}^0 (\delta^* - \theta) dz + O(\delta \cdot \epsilon), \end{aligned} \quad (10)$$

where δ^* and θ are a displacement thickness and momentum thickness of the boundary layer or the wake, respectively.

Equations (7) show that the motion of viscous fluid flow can be represented by center plane distributions of Oseen singularities in a sense of singular perturbation theory, if both ϵ and δ are sufficient small. Hence a far field solution is written as follows,

$$\underline{q}' = \int_{-1}^1 d\xi \int_{-d}^0 d\zeta (m_0 \underline{G} + m_1 \underline{t}_1 + m_2 \underline{t}_2 + m_3 \underline{t}_3), \quad (11)$$

where \underline{G} is an induced velocity of a potential source and $\underline{T} = (\underline{t}_1, \underline{t}_2, \underline{t}_3)$.

Note that a potential source is one of Oseen singularities which satisfy Oseen's equation and which cannot be constructed with multi-poles of Oseenlets. Let's determine m_0, m_1, m_2 , and m_3 , from equations (7) and other conditions.

From (A-5), (A-6), we have

$$I \equiv \int_S \underline{T} \cdot \underline{F} ds = \int_S (-P \underline{T} \cdot \underline{n} + \frac{1}{Re} \underline{T} \cdot \underline{E} \cdot \underline{n}) ds, \quad (12)$$

where $\underline{E} = (e_{ij})$ is a rate-of-strain tensor. Let the hull be described by $y = \pm f(x, z) = O(\epsilon)$. Considered the order of magnitudes of e_{ij} as done in (9) and these relations

$$\begin{aligned} n_1 &= -\frac{\partial f}{\partial \xi} + O(\epsilon^2), \quad n_2 = \pm 1 + O(\epsilon^2), \\ n_3 &= -\frac{\partial f}{\partial \zeta} + O(\epsilon^2). \end{aligned} \quad (13)$$

† It is possible to calculate the equations iteratively. A convergent solution had been got for a case of laminar wake of a flat plate at high Reynold's number [8] (see Appendix B).

equation (12) is

$$\begin{aligned} I &= 2 \int_{-1}^1 d\xi \int_{-d}^0 d\zeta [p^{(0)} (1_1 \frac{\partial f}{\partial \xi} - \frac{\partial 1_2}{\partial \eta} + 1_3 \frac{\partial f}{\partial \zeta}) \\ &\quad + \frac{1}{Re} 1_1 \frac{\partial u}{\partial y}]_{\eta=0} + O(\epsilon^2 \text{ or } \epsilon \delta \text{ or } \delta^2), \end{aligned} \quad (14)$$

where

$$p = p^{(0)} + O(\epsilon \text{ or } \delta). \quad (15)$$

Integrating by part and substituting these relations,

$$p^{(0)} = p_c \quad (\text{since (A-11)}), \quad (16)$$

and

$$\frac{\partial 1_1}{\partial \xi} + \frac{\partial 1_2}{\partial \eta} + \frac{\partial 1_3}{\partial \zeta} = 0, \quad (17)$$

we have

$$I = 2 p_c \int_{-1}^1 f 1_3|_{\eta=0} d\xi + \frac{2}{Re} \int_{-1}^1 \int_{-d}^0 \frac{\partial u}{\partial y} 1_1|_{\eta=0} d\xi d\zeta. \quad (18)$$

of which first term vanishes both in a case of submerged and surface piercing ship, because in the latter case we should take $p_c = 0$.

From equation (1) a non-dimensional frictional stress of the hull is expressed as follows,

$$\tau_0 \equiv \frac{1}{Re} \left(\frac{\partial u}{\partial y} \right)_{y=f} = \frac{\partial \theta}{\partial \xi} + O(\delta \cdot \epsilon). \quad (19)$$

From (10), (18) and (19), we have

$$m_1 = 2 \frac{\partial \delta^*}{\partial \xi}, \quad m_2 = 0, \quad m_3 = 0. \quad (20)$$

And it seems as if $m_0 = 0$. But note that a near field problem loses a hull surface boundary condition for v , because v is higher order compared with u in the near field. So we cannot determine m_0 from (7). We can use a conservation law of mass. From the hull surface condition (A-10), flow flux from the hull is

$$\int_S (-\underline{q}' \cdot \underline{n}) ds = 2 \int_{-1}^1 \int_{-d}^0 \frac{\partial f}{\partial \xi} d\xi d\zeta + \text{higher order}, \quad (21)$$

hence we have the relation,

$$m_0 = 2 \frac{\partial f}{\partial \xi}. \quad (22)$$

Now the lowest order term of a far field solution is found to be

$$\underline{q}' = \int_{-1}^1 \int_{-d}^0 \left[2 \frac{\partial f}{\partial \xi} \underline{G} + 2 \frac{\partial \delta^*}{\partial \xi} \underline{t}_1 \right] d\xi d\zeta. \quad (23)$$

Equation (23) is similar to the intuitive models of Havelock [4], Wigley [5], and so on [6], [7], since a main part of a dragging Oseenlet is a potential source when Re is very large, as described later. But it is different from them about two points. One of them is that the second term of (23) is divergent free unlike Betz sources and another is that (23) contains a viscous damping effect of wave propagation. Special attention should be paid to the facts that equation (23) is derived by consistent manner and that it includes a viscous wake unlike potential flow models.

A surface elevation or a wave pattern of the distribution of Havelock Oseenlets is given by

$$\begin{aligned} \zeta &= \frac{1}{4\pi^2} \int_{-\pi}^{\pi} d\theta \int_0^{\infty} k dk \\ &\quad \times \frac{F(k, \theta) e^{ik(x \cos \theta + y \sin \theta)}}{k (\cos \theta - ik/k_0)^2 - \gamma_0 + (k/k_0)^2 / k^2 + 2ik_0 k \cos \theta}, \end{aligned} \quad (24)$$

$$\begin{aligned} F(k, \theta) &= -2 \int \{ (m_0 + m_1) (i \cos \theta + \frac{k}{k_0}) e^{kz} \\ &\quad + \frac{m_1}{k_{oe}} \sqrt{k^2 + 2ik_{oe} k \cos \theta} e^{\sqrt{k^2 - 2ik_{oe} k \cos \theta} z} \}. \end{aligned} \quad (25)$$

where $k_0 = R_e/2$ and $k_{oe} = U/2\nu_T = R_{ne}/2$. (26)

Here ν_T is an eddy viscosity in a representative boundary layer and wake, which we look on as different from a molecular viscosity. The wave is assumed to be damped only by a molecular viscosity not by turbulence. This assumption may or may not be justified by future works.

When both k_0 and k_{oe} are sufficient large, a free wave of (24) is

$$\zeta^{(0)} = \zeta^p + \zeta^r. \quad (27)$$

$$\zeta^p = 4\gamma_0 \int_{-\pi/2+\omega}^{\pi/2} [F^p \cos(\gamma_0 \bar{p} \sec^2 \theta + \phi) + Q^p \sin(\gamma_0 \bar{p} \sec^2 \theta + \phi)] e^{-\lambda \bar{p} \sec^2 \theta} d\theta + O(R_e^{-3/2}). \quad (28)$$

$$\zeta^r = 4\gamma_0 \int_{-\pi/2+\omega}^{\pi/2} [P^r \cos(\gamma_0 \bar{p} \sec^2 \theta + \frac{3}{4}\pi) + Q^r \sin(\gamma_0 \bar{p} \sec^2 \theta + \frac{3}{4}\pi)] e^{-\lambda \bar{p} \sec^2 \theta} \sqrt{2} \gamma_0 \lambda_r \sec^4 \theta d\theta + O(R_e^{-1}). \quad (29)$$

$$P^p = \frac{R_e}{-lm} \iint (m_0 + m_1) e^{(\gamma_0 \sec^2 \theta + i\lambda)(Z' - ix' \cos \theta)} dx' dz', \quad (30)$$

$$Q^r = \frac{R_e}{-lm} \iint m_1 e^{k_{oe} \lambda_r (1-i)Z' - i\gamma_0 x' \sec \theta} dx' dz'. \quad (31)$$

where $\bar{p} = x \cos \theta + y \sin \theta$.

$$\begin{aligned} \omega &= \tan^{-1} [y/(x-x')] \\ \lambda &= \frac{4\gamma_0^2}{R_e} \sec^5 \theta \\ \lambda_r &= \sqrt{\frac{\gamma_0 \sec \theta}{R_{ne}}} \\ \sin \phi &= \frac{10\gamma_0}{R_e} \sec^3 \theta. \end{aligned} \quad (32)$$

From (27) ~ (32), it is understood that effects of the water viscosity on a free wave of a thin ship consist of three effects, namely

- a viscous damping effect of wave propagation, which is given by λ and of which phase lag is ϕ ,
- an effect of rotational flow of a wake, which is given by ζ^r ,
- an effect of deformation of a potential flow due to the boundary layer and wake, which is given by m_1 in equation (30).

The first effect is negligible except both for a case of very big x , y or γ_0 and a case of nearby $\theta = \pi/2$, because λ and ϕ are of $O(R_e^{-1})$, of which R_e is about $10^8 \sim 10^9$ for ships and about $10^5 \sim 10^6$ even for model ships. The second effect ζ^r is of $O(R_{ne}^{-1} \cdot m_1)$, because P^r and Q^r are of $O(R_{ne}^{-1/2} \cdot m_1)$, so that it depends upon how large the effective Reynolds number R_{ne} is. Let us presume R_{ne} from diffusing pattern of a ship wake. A thin strut is taken as an example, of which particulars will be given in the next section. The wakes of a center plane distribution of 2-d Oseenlets given by (20), are calculated and compared with measured velocity profiles. The used δ^* in (20) and the measured velocity profiles are given by measurements of the next section. The calculated and measured velocity profiles at s.s.-1/2 and at s.s.-4 are shown in Fig. 1 and Fig. 2, respectively. They show that Reynolds number of relative agreement depends upon the positions. It means that the assumption of constant eddy viscosity is not valid concerning velocity profiles. But the assumption is valid about viscous effects on ship waves, because it is concluded that the second effect ζ^r is negligible since it is understood that $R_{ne} = 2000 \sim 10000$.

Since both first and second effects are negligible, waves of a thin ship in a viscous fluid are the same as waves of a source distribution $m_0 + m_1$ in an ideal fluid. In order to investigate the third effect, we need a distribution of $m_1(x)$, so that $\delta^*(x)$. Theoretical investigations of a thick boundary layer near a stern, its separation, and a near wake have just been started about not

only 3-d but also 2-d and axisymmetric body. They have not been established yet. In this paper $\delta^*(x)$ is given by experiments which described in the next section.

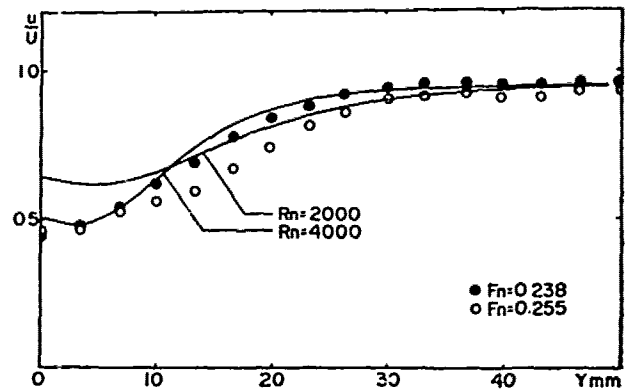


Fig. 1 Velocity profile of wake at s.s. -1/2

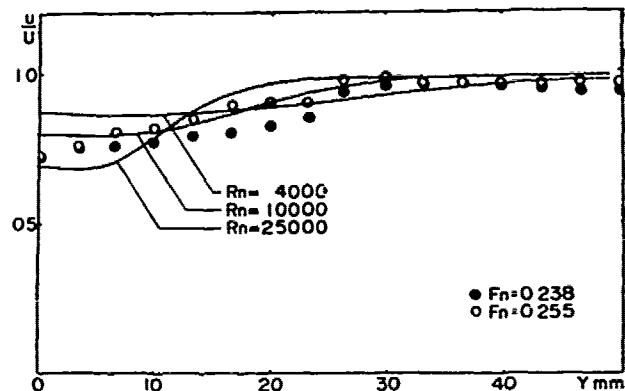


Fig. 2 Velocity profile of wake at s.s. -4

3. MEASUREMENTS OF A VISCOUS FLUID FLOW AND STERN WAVE PATTERNS

In order to know the distribution of the displacement thickness $\delta^*(x)$, velocity profiles of the boundary layer and wake are measured in a towing tank, as well as stern wave patterns which are compared with calculations described in the next section. The model used for measurements is wall-sided thin strut called WM3, which is 1.2m long, 0.12m wide and 0.60m deep. The water line f is parabolic as

$$f = \epsilon(1-x^2), \quad \epsilon = B/L = 0.1. \quad (33)$$

The reason why we choose deep draught wall-sided model is that it is possible to investigate effects of a free surface on the boundary layer and wake. Velocity profiles are measured by a traverser with a hot film. Out put velocities are considered as x-axis velocities, because cross flow components are negligible small since the model is thin and wall-sided. Speeds of advance of the model are chosen as Froude numbers of hump and hollow of a wave making resistance curve, namely $Fn = 0.283$ and 0.255 . Corresponding Reynolds number is $0.564 \times 10^6 \sim 0.388 \times 10^6$. Measured velocity profiles at 283mm below the undisturbed free surface ($z/d = -0.472$, d = draught of the model) are shown in Fig. 3, where both effects of a bottom of the model and a free surface

are negligible. We can see velocity profiles of a turbulent boundary layer transform into velocity profiles of a wake. Velocity profiles near the free surface are also measured. They include a wave wake due to an orbital motion of waves as well as a viscous wake. The viscous wake taken off the wave wake from the total wake at 20mm below the undisturbed free surface ($z/d = -0.03$) is found to be different from Fig. 3 and to be spread and stronger than Fig. 3, though it seems to be uniform in direction of depth since the model is wall-sided. At this time the wave wake u^w is estimated by

$$u^w = -\xi \gamma_0 e^{\gamma_0 z}, \quad (34)$$

where ξ is a surface elevation which is measured. An error of (34) is negligible, since the wave wake is very small.

So that measurements of wake distribution at s.s.-1 are carried out. Results of $Fn = 0.238$ and $Fn = 0.255$ are shown in Fig. 4 and Fig. 5, respectively. Both results show that the wake is spread and strong near a free surface, though the extent is different each other. We could not find wave breaking phenomena anywhere. It suggests an existence of an interaction of a viscous wake and a free surface of which an outcome is the added wake near a free surface.

Surface elevations are measured by the traverser with an untouched type wave gauge. Results are shown in Fig. 6 with wake distributions at $z/d = -0.472$. In hatched area, turbulent disturbances are found on the free surface, which starts from the side wall of the model of about s.s.7.5, streams along the wall and spreads into a diverging wave of the stern. The viscous wake without effects of the free surface distributes in much narrower region. The free surface elevations measured by continuously, slowly moving traverser are shown in Fig. 7 and Fig. 8, which display the turbulent disturbance clearly. In Fig. 9 both the free surface fluctuations and velocity profiles at s.s.-1/2 and s.s.-1 are shown, where full lines are velocity profiles at $z = -20\text{mm}$ and dotted lines are velocity profiles at $z = -283\text{mm}$. Differences of them correspond to the fluctuations very well.

From the above experimental results, it may be sufficient to understand that the difference of the viscous wake in direction of depth is caused by the turbulent disturbance of the free surface. Namely it originates another sort of viscous wake.

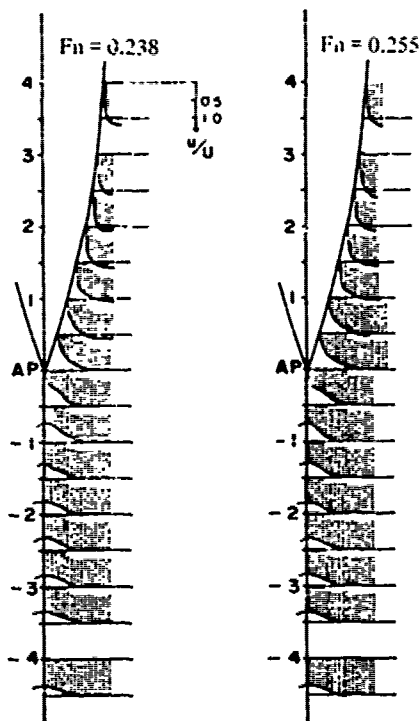


Fig. 3 Velocity profiles of wake of stern flow

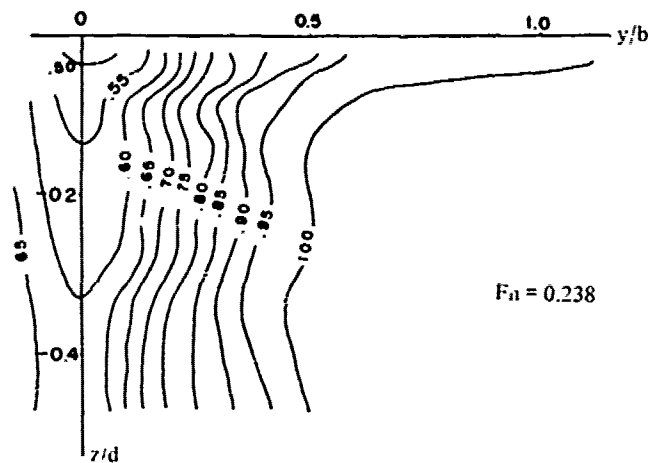


Fig. 4 Wake distribution at s.s.-1 ($Fn = 0.238$)

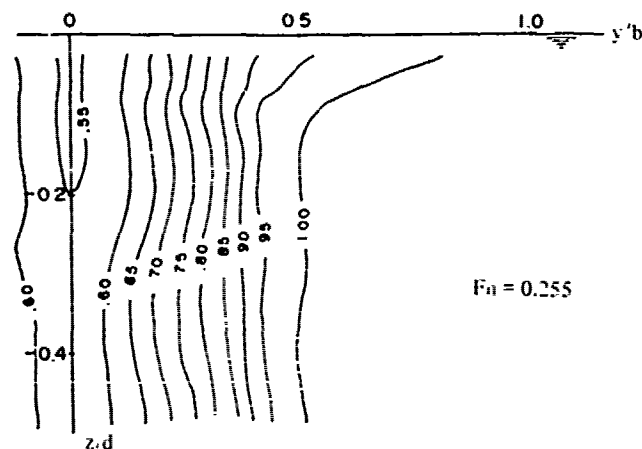


Fig. 5 Wake distribution at s.s.-1 ($Fn = 0.255$)

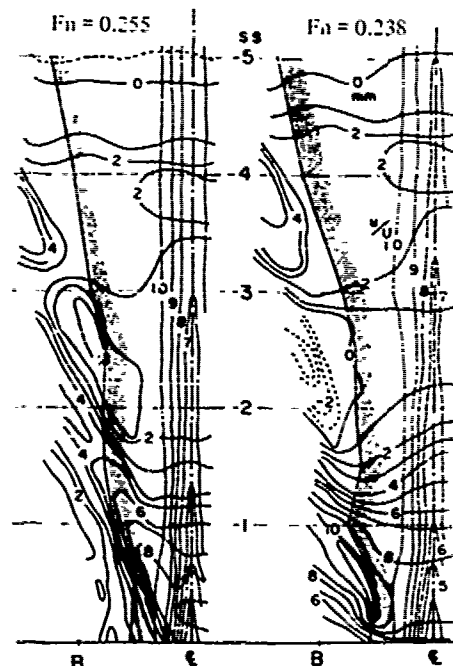


Fig. 6 Wave patterns and wake distributions

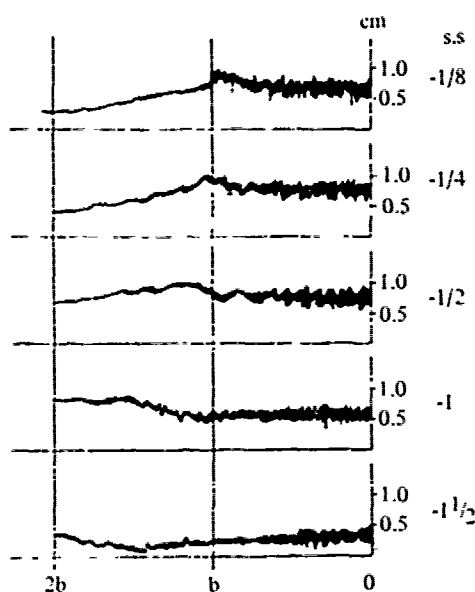


Fig. 7 Free surface elevations with fluctuation behind stern ($F_n = 0.238$)

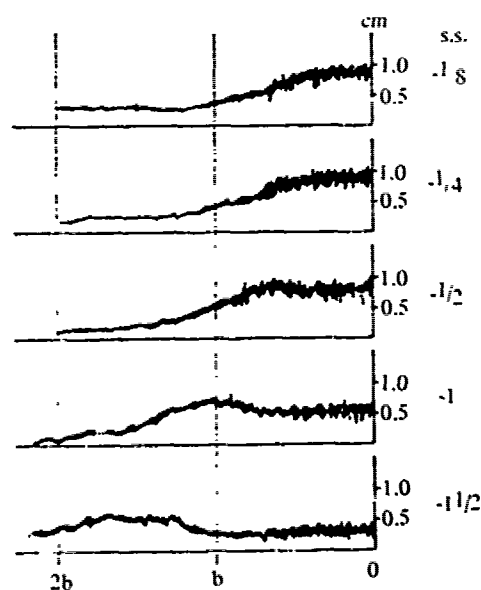


Fig. 8 Free surface elevations with fluctuation behind stern ($F_n = 0.255$)

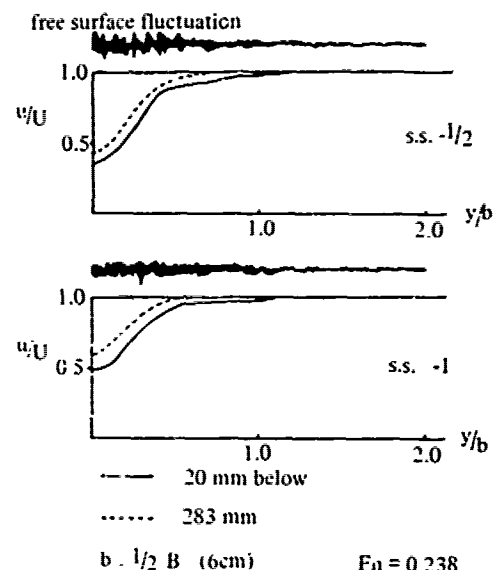


Fig. 9 Free surface fluctuation and velocity distributions

The displacement thickness δ^* and the momentum thickness θ obtained from the measured velocity profiles are shown in Fig. 10 and Fig. 11, compared with calculations by rather simple methods of turbulent boundary layer theory, though "thick boundary layer theory including effects of trailing edge" should be applied for the viscous fluid motion near a stern substantially, where the boundary layer is not thin and the displacement thickness rapidly changes, as mentioned in the previous section. One of the reasons why the more precise method is not applied in this paper is that any methods have not been established yet, and another is that it is thought to be significant to confirm the problem. In Fig. 10, δ^* and θ are calculated by means of Truckenbrodt's method [9] as an example of approximated integral method. In Fig. 11, they are calculated by means of Tanaka-Himeno's method [10] as an example of integral method. Both in Fig. 10 and Fig. 11, a fine dotted line and a dotted line mean calculations of δ^* and θ , respectively, of which pressure distribution is modified by the measured displacement thickness of the boundary layer and wake, and which are considered to include a part of higher order effects. They show that calculated δ^* and θ using the modified pressure distribution are quite different from original δ^* and θ at the stern, and that they give a qualitative agreement with experiments both in a case of Truckenbrodt's method and Tanaka-Himeno's method. Especially in the latter case, the state of δ^* near the stern is very similar to the experiments. However, these simple calculations of a turbulent boundary layer are not sufficient to predict $d\delta^*/dx$ which plays important role for the wave making, as described later.

One of the reasons of disagreements of the calculations with the experiments near s.s.4, where these should agree with each other because the boundary layer is thin enough, is the error of the estimation of boundary layer edge speeds when δ^* and θ are obtained from the measured velocity profiles. Delicate care is necessary to measure the edge speeds and to analyze them, though they include an essential difficulty.

The measured displacement thickness δ^* and the measured momentum thickness θ after the stern are shown in Fig. 12 compared with calculations by Squire-Young's method [11], of which initial values are the results of the calculations by Truckenbrodt's method at the stern. A fine dotted line and a dotted line are calculations of δ^* and θ , respectively, of which pressure distribution is modified by the measured displacement thickness. Fig. 12 shows a fairly good agreement of experiments and calculations, because Squire-Young's method is empirical method.

A Froude number of all calculations in Fig. 10, Fig. 11 and Fig. 12 is $F_n = 0.238$. Calculations at $F_n = 0.255$ is almost same as calculations at $F_n = 0.238$.

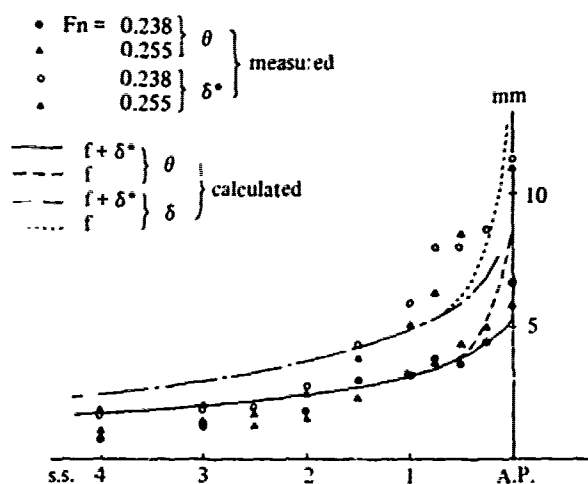


Fig. 10 Calculated δ^* and θ by means of Truckenbrodt's method compared with experiments

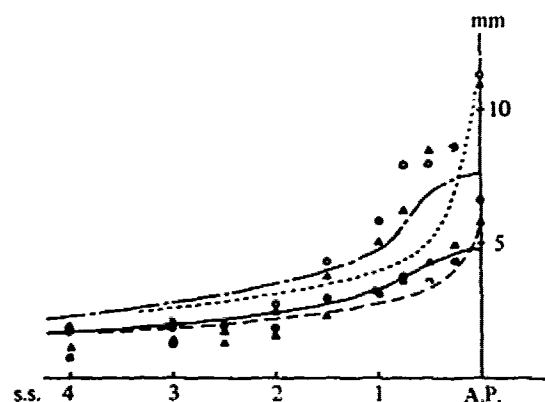


Fig. 11 Calculated δ^* and θ by means of Tanaka-Himeno's method compared with experiments

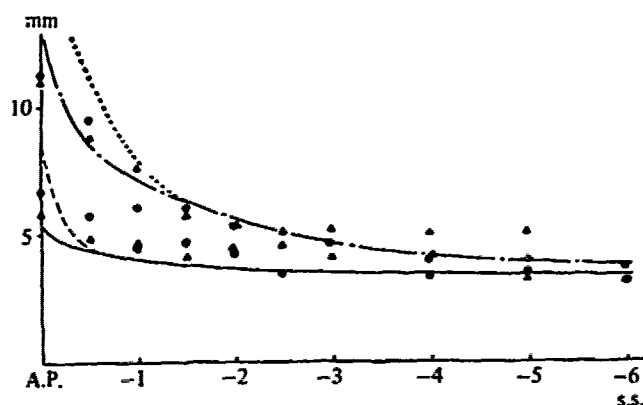


Fig. 12 Calculated δ^* and θ by means of Squire-Young's method compared with experiments

4. CALCULATIONS OF A VISCOUS EFFECT ON A WAVE PATTERN AND A WAVE PATTERN RESISTANCE OF A THIN SHIP

It is described in §2 that waves of a thin ship in a viscous fluid are the same as waves of a source distribution $m_0 + m_1$ in an ideal fluid. In this section let us calculate the wave patterns and wave pattern resistances by means of (28) and (30) with $\lambda=0$ and $\phi=0$, using δ^* measured in §3. Though the final formula of the calculations is the same as Okabe and Jinnaka's [6] and Lavrentiev's [7], the used displacement thickness distributions are different, namely, their displacement thickness distributions were not the real state of affairs but the displacement thickness distribution of following calculations are measured ones.

In order to investigate the effect of the displacement thickness, wave patterns of following source distributions are calculated.

- (I) A source distribution without a viscous effect which is Michell's approximation,

$$m = m_0 = 2 \frac{\partial f}{\partial x},$$

since $m_1 = 0$

- (II) A source distribution with the effect of displacement thickness which is uniform in direction of depth,

$$m = m_0 + m_1 = 2 \frac{\partial}{\partial x} (f + \delta^*),$$

where δ^* is represented by δ^* measured at $z/d = -0.472$. The source distribution is shown in Fig. 13. It is significantly different from the distribution of (I) near the stern.

- (III) A source distribution with the effect of displacement thickness which is varied near the free surface by the interaction and which is approximated as step function like as,

$$m = m_0 + m_1' = m_0 + C m_1,$$

where

$$C = 1.7 \dots 0 \leq z/d < 0.03,$$

$$C = 1.3 \dots 0.03 \leq z/d < 0.06,$$

$$C = 1.0 \dots 0.06 \leq z/d < 1.0.$$

The modeled wake section is shown in Fig. 14, which is determined from experiments as Fig. 4 and Fig. 5.

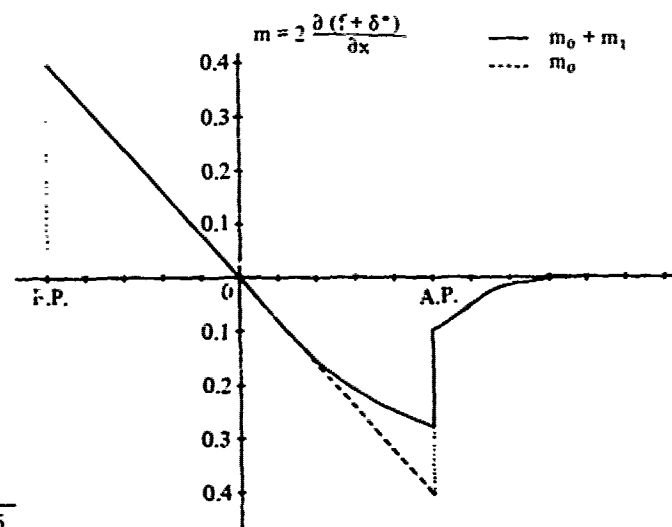


Fig. 13 Source distribution

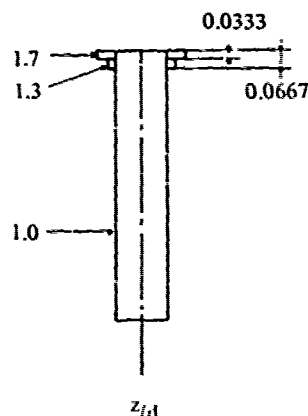


Fig. 14 Model of wake section

Calculations of wave patterns and wave making resistance which are defined in a case of an ideal fluid, whereas its definition in a case of a viscous fluid is not necessarily rigorous [1], are carried out for the three cases. Calculated wave profiles are compared with experiments in Fig. 15 and Fig. 16 at $Fn = 0.238$ and $Fn = 0.255$, respectively. At a center line of the ship (the experiments from F.P. to A.P. are made at the side of the ship), they are found remarkably that the case (I) shows an extraordinary hump at vicinity of the stern and that it is kept down in both the case (II) and (III) like as measured values. Gaps of phases of the stern waves between the calculations and the experiments of the case (II) and (III), however, are larger than the case (I). At $10/3$ times half beam b besides the center line, the wave height of the case (II) or (III) is similar to the measured values than the case (I), but the tendency is not the same about its phase.

An example of wave energy spectra is shown in Fig. 17, of which $Fn = 0.304$. Experiments are made by longitudinal cut method with a probe beside 4m from the center line. Ikehata et al.'s experiments [12] are also plotted, which was made by the same method with a probe beside 1.8m from the center line with the same model. Fig. 17 and other comparisons show that the case (II) are allowed to come near the experiments from the case (I) concerning their magnitudes, but their phases are not, and that these tendencies are emphasized in the case (III).

Wave making resistances are compared with both wave pattern resistances obtained by wave analyses and residual resistances from towing tests in Fig. 18. Significant differences between the wave pattern resistances and the residual resistances are recognized like as other many cases. Though one of the reasons of these differences is considered to be the interaction of a viscous wake and a free surface described in §3, further researches have not been carried out. Fig. 18 shows that the case (II) are smaller than the case (I), that the hump and hollow of the wave making resistance curve are moderated, and that these tendencies are emphasized in the case (III). The case (II) and (III) agree well with the residual resistances.

Last of all, stern wave patterns are shown in Fig. 19 and Fig. 20 at $Fn = 0.238$ and $Fn = 0.255$, respectively. They show that the measured wave height is much smaller than the case (I), that a crest angle of the stern wave is larger than the case (I), and that its start point is before the case (I). The wave height and the crest angle of the case (II) are allowed to come near the experiments. The wave height of the case (III) is smaller than the case (II) and the wave pattern lacks clearness extremely.

The following conclusions are derived from the above comparisons.

- (1) The effect of the displacement thickness of the boundary layer and wake on waves of the thin ship is severe and allows the wave height of stern waves, wave energy spectra and wave making resistances to come near the experiments.

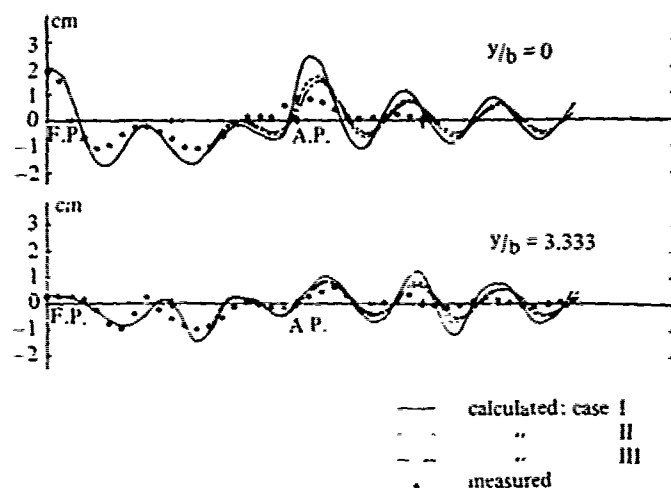


Fig. 15 Wave profiles ($Fn = 0.238$)

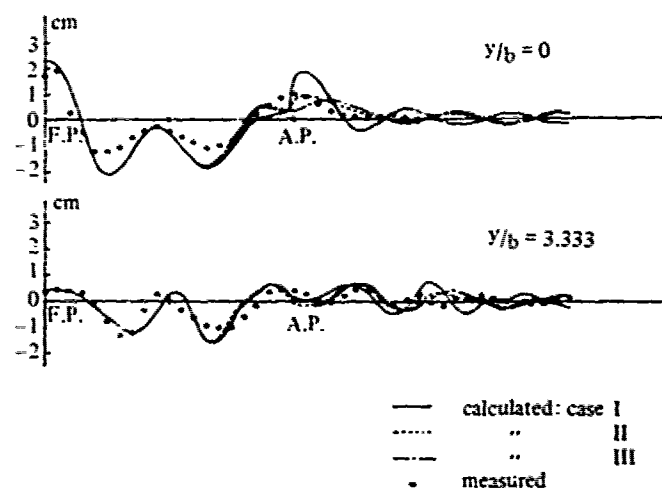


Fig. 16 Wave profiles ($Fn = 0.255$)

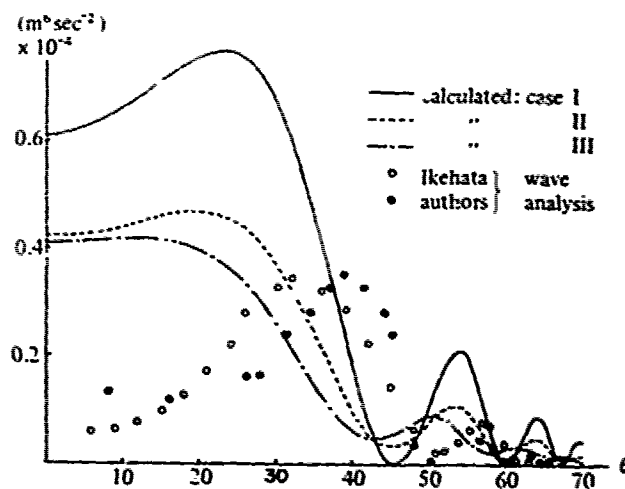


Fig. 17 Energy spectrum

- (2) Especially, the hump and hollow of the wave making resistance curve are moderated and the curve agrees well with the residual resistances in a case of WM3.
- (3) But paying attention to the discrepancy of the wave patterns and a shift of wave energy spectra of the calculations to low values of θ , it is evident that it is not sufficient to explain the discrepancy by the viscous effect, between measurements and calculations by potential theories in a case of WM3. It may be concluded that WM3 of which $B/L = 0.1$ is not so thin that a thin ship theory can be applied.

The difference between the waves of the case (II) and the case (III) is interesting as an example of an interference between a free surface and a wake, since the wake near the free surface is originated by the phenomena at the free surface.

5. CONCLUSION

The results of this paper are summarized as follows

- i) Using a first order representation of a thin ship in a viscous fluid, they are shown that both a viscous damping effect of wave propagation and an effect of rotational flow of a wake are negligible and that the most important viscous effect on a wave pattern is a deformation of a potential flow due to the boundary layer and wake, which is represented by the displacement thickness
- ii) In order to know the distribution of the displacement thickness, velocity profiles are measured, as well as stern wave patterns which are to be compared with calculations. The experiments show that
 - a) the viscous wake is not uniform in direction of depth but spread and strong near a free surface, even though the model is a wall-sided thin strut.
 - b) turbulent disturbances exist on the free surface corresponding to the viscous wake near the free surface, so that they are understood to cause the wake.

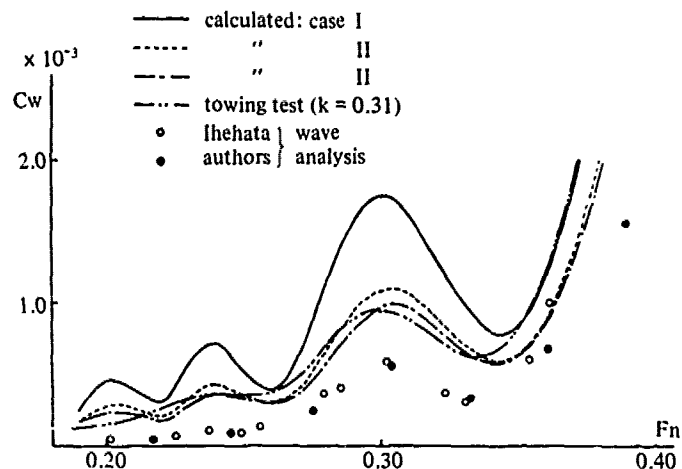


Fig. 18 Wave making resistance coefficients

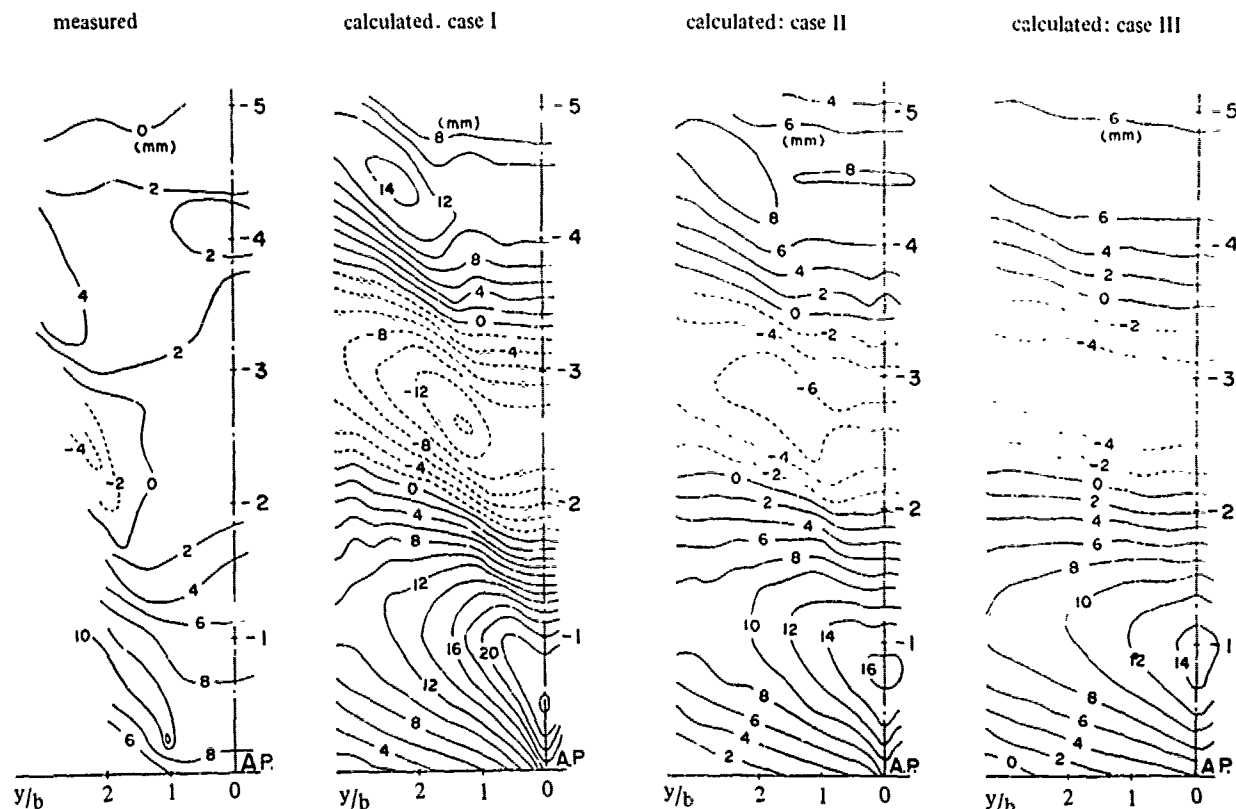


Fig. 19 Wave patterns ($F_n = 0.238$)

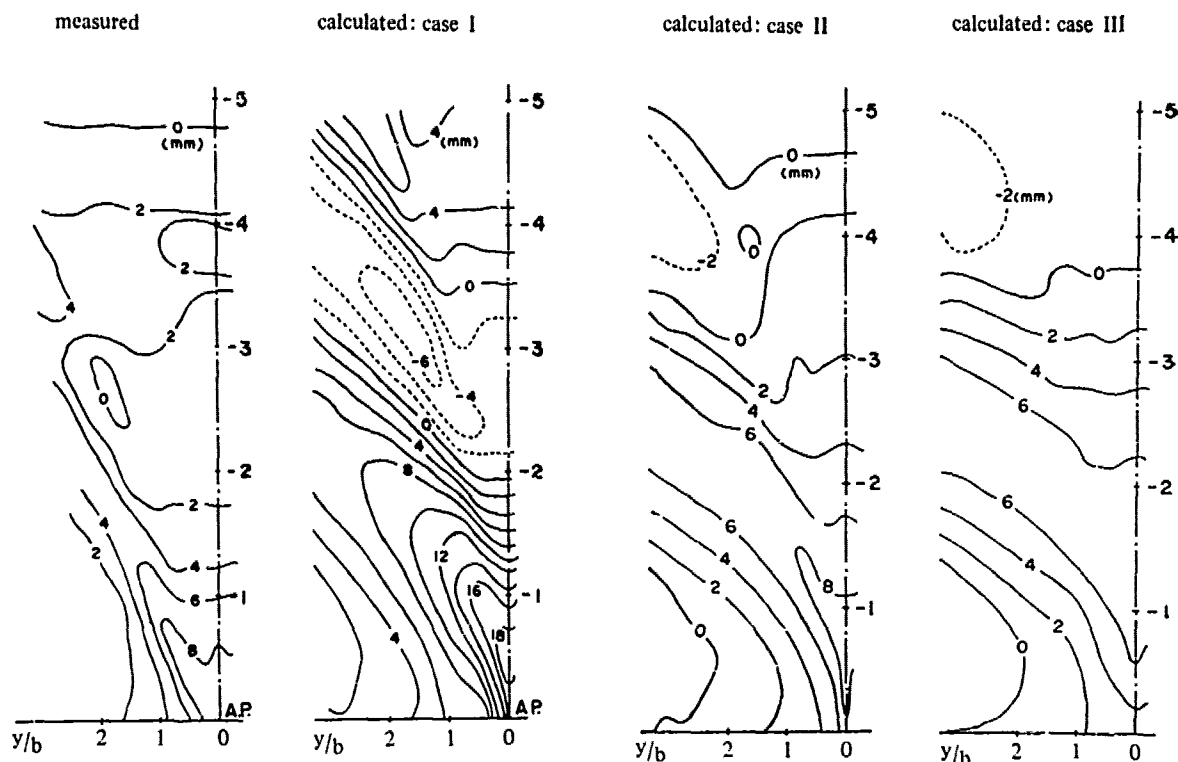


Fig. 20 Wave pattern ($F_n = 0.255$)

- c) the displacement thickness and the momentum thickness of the boundary layer and wake without the free surface effect can be roughly estimated by rather simple methods like Truckenbrodt's, Tanaka-Himeno's and Squire-Young's, but their accuracy is not enough.
- ii) Using the measured displacement thickness, calculations of wave patterns and wave pattern resistances are carried out. They show that
 - a) the effect of the displacement thickness on waves of the thin ship is severe and allows the wave height of stern waves, wave energy spectra and wave making resistances to come near the experiments,
 - b) but paying attention to the discrepancy of wave patterns or the phases of wave energy spectra, it is evident that it is not sufficient to explain the discrepancy by the viscous effect, between measurements and calculations by potential theories in a case of WM3, so that WM3 of which $B/L=0.1$ is not so thin that a thin ship theory can be applied.

ACKNOWLEDGEMENT

The author wishes to express his deep gratitude to Prof. H. Maruo of Yokohama National University for his advice and encouragement. Thanks are also extended to Prof. K. Mori of Hiroshima University for providing his valuable program to calculate wave patterns. The author sincerely expresses his appreciation to Mr. M. Nitoh and Mr. T. Matano who carried out the experiments and calculations as a part of their graduation thesis.

REFERENCES

- 1) Maruo, H., "Ship Waves and Wave Resistance in a Viscous Fluid," *I.S.W.R.*, (1976).
- 2) Mori, K., "An Assessment of Theoretical Methods for Determining Near Wake Flow and Some Applications to Ship-Wake Prediction," *Memoirs of the Faculty of Engineering Hiroshima University*, Vol. 8, (1980).
- 3) Wilson, M.B., "A Michell Oseen Flow Theory for Thin Ships," Thesis, Calif. Inst. Tech., (1971).
- 4) Havelock, T.H., "Ship Waves: the Relative Efficiency of Bow and Stern," *Proc. Roy. Soc. (A)* 149, (1935).
- 5) Wigley, W.C.S., "Effects of Viscosity on the Wave-making of Ships," *Trans. Inst. Eng. & Ships*, Scotland, 81, (1973).
- 6) Okabe, J. & Jinnaka, T., "On the Waves of Ships," *Report of Research Inst. for Fluid Engineering, Kyushu Univ.*, 71, (1950).
- 7) Lavrentiev, V.W., "The Influence of the Boundary layer on the Wave Resistance of a Ship," *Akad. Nauk URSS*, 80-6, (1951).
- 8) Konoshita, T. & Isoi, S., "An Iterative Method Based on Oseen Flow which is Applied to a Laminar Boundary Layer on a Flat Plate and a Laminar Wake of It," prepared.
- 9) Schlichting, H., *Boundary Layer Theory*, 7th ed., McGraw Hill.
- 10) Tanaka, I. & Himeno, Y., "Methods for Predicting Two-dimensional Turbulent Boundary Layers Using Eddy Viscosity Hypothesis," *J. of the Kansai Society of Naval Architects*, Japan, Vol. 146, (1974).
- 11) Squire, H.B. & Young, A.D., "The Calculation of Profile Drag of Aerofoils," *ARCR & M.* No. 1838, (1938).
- 12) Ikehata, M. & Nozawa, K., "Determination of Wave-Making Resistance of a Ship by the Method of Wave Analysis, II," *J. Soc. Nav. Arch. Jap.*, Vol. 124, (1968).

Appendix A

The equations (7) are derived mathematically as follows. Let's consider \tilde{q}' which satisfies an adjoint differential equation of a linearized equation of motion that is reverse Oseen flow, as

$$-\frac{\partial}{\partial x} \tilde{q} = -\text{grad } p^* + \frac{1}{R_e} \Delta \tilde{q}. \quad (\text{A-1})$$

And introduce an reciprocal integral,

$$E(\tilde{q}', \tilde{q}) = \frac{1}{R_e} \int_{i,j=1}^3 e_{ij} \tilde{e}_{ij} d\tau. \quad (\text{A-2})$$

where

$$e_{ij} = \frac{\partial u_i}{\partial x_j} + \frac{\partial u_j}{\partial x_i}. \quad (\text{A-3})$$

Integrating (A-2) by part and substituting (5) and (2) to (A-2), we have

$$E = - \int_V \tilde{q} \cdot [(i + q') \cdot \text{grad}] \tilde{q} d\tau + \int_S \tilde{q} \cdot \tilde{F} ds, \quad (\text{A-4})$$

where

$$\tilde{F} = \underline{S} \cdot \underline{n}; \quad \underline{n} \text{ is a unit normal positive out of a ship,} \quad (\text{A-5})$$

$$\underline{S} = (-p\delta_{ij} + \mu e_{ij}). \quad (\text{A-6})$$

From (A-2), (A-1) and (2), we have

$$E = \int_V (q' \cdot \text{grad}) \cdot \tilde{q} d\tau + \int_S \tilde{q} \cdot \tilde{F} ds. \quad (\text{A-7})$$

And from (A-4) and (A-7),

$$\begin{aligned} & \int_S (\tilde{q} \cdot \tilde{F} - q' \cdot \tilde{F} - q' \cdot \tilde{q} n_i) ds \\ &= \int_V \tilde{q} \cdot (q' \cdot \text{grad}) \cdot \tilde{q} d\tau \\ &= \frac{1}{2} \int_S |q'|^2 \tilde{q} \cdot \underline{n} ds - \int_V \tilde{q} \cdot (q' \times \text{rot } q') d\tau. \end{aligned} \quad (\text{A-8})$$

We may take Oseenlets as \tilde{q}' , since they satisfy (A-1) with respect to (ξ, η, ζ) which is a location of them. Considering their singularity, we have

$$\begin{aligned} q' &= \int_S (\underline{T} \cdot \underline{F} - q' \cdot \tilde{F} - \underline{T} \cdot q' n_i - \frac{1}{2} |q'|^2 \underline{T} \cdot \underline{n}) ds \\ &+ \int_V \underline{T} \cdot (q' \times \text{rot } q') d\tau, \end{aligned} \quad (\text{A-9})$$

for (x, y, z) in V . For (x, y, z) out of V , the left hand side of (A-9) equals zero. We assume that both inside and outside flow of V satisfy the boundary condition (4), namely

$$q' = -1. \quad (\text{A-10})$$

Since the inside flow is apparently uniform, \tilde{F} of inside flow is

$$\tilde{F} = -p_c \underline{1}, \quad (\text{A-11})$$

where p_c is a pressure of inside uniform flow. Taking the inside flow away from outside flow (A-9), we have the equations(7).

Appendix B

The equations (7) were computed iteratively in both cases of a laminar boundary layer on a semi-infinite flat plate aligned parallel to a uniform stream and a laminar wake of a flat plate aligned parallel to a uniform stream by the present author and other [8]. The fluid domain and the flat plate are divided into many subdivisions. The integrals are evaluated numerically. The Reynolds number is chosen as large enough that the Blasius' solution can be regarded as an exact solution of the former case. The concrete number is 4×10^4 . For such a high Reynolds number, any purely numerical methods can not be applied, and asymptotic expansion methods is helpful. On a point of view of an application to various flows, this iterative method which is combined analytical method with numerical method is hopeful. Another merit of this method is that it is suitable to know stream-lines and velocity profiles. Before computing fluid fields around complicated shapes of body, it is necessary to compute the fluid flows about simple cases and to compare them with other known results. This was the reason why they chose the former case.

The computed velocity profiles of the former case are shown in Fig. A-1, where $x^* = 0$ is taken at the leading edge of the flat plate. It is shown that they tend to the Blasius' solution from Oseen's approximation which is the first step solution of this iteration.

For the latter case, the computed converged velocity profiles are shown in Fig. A-2, where $x^* = 0$ is taken at the trailing edge. An overshoot can be seen in the outer part near the trailing edge. In Fig. A-3 the computed velocity profiles near a center-line are compared with the lowest deck solution of the triple-deck theory by Jobe & Burggraf [1974], which is one of the most reliable solutions of this problem at present, though it is not fully satisfactory, because a drag have not been obtain with correction of $O(R_e^{-1})$, which is not so small compared with the solution of $O(R_e^{-7/8})$. These results approximately coincide with each other near the center-line. It means the results of this iterative computation converge to reasonable solution, though they include some errors of discrete computations and others.

The obtained drag coefficient C_D , to which leading edge effects which are safely estimated by Imai's formula [1957], since R_e is sufficient large, is added, is as follows,

$$C_D = \frac{1.328}{\sqrt{40000}} + 0.00016 + \frac{2.526}{40000}. \quad (\text{B-1})$$

If we express C_D in a form as

$$C_D = 1.328 R_e^{-1/2} + d R_e^{-7/8}, \quad (\text{B-2})$$

The coefficient d becomes 2.32 from (B-1), which is comparable with 2.694, 2.661 and 2.651 ± 0.003 , which are given by Jobe & Burggraf, by Melnik & Chow [1975] and by Veldman & van de Vooren [1974], respectively. They say the subsequent terms to (B-2) must either have much small coefficient than the first two, or tend to cancel one another.

The coefficient d determined by the numerical solution with $Re = 10^4$ by Dennis & Dunwoody [1966], which is the largest Reynolds number of all except the present authors', is 2.59. It may become small when R_e is very large. But nothing of accuracy can be concluded only by these data.

References

- Dennis, S.C.R., & Dunwoody, J., "The steady flow of a viscous fluid past a flat plate," *J. Fluid Mech.* 24, 577-595, (1966).
- Imai, I., "Second approximation to the laminar boundary-layer flow over a flat plate," *J. Aeronaut. Sci.* 24, 155-156, (1957).
- Jobe, C.E., & Burggraf, O.R., "The numerical solution of the asymptotic equations of trailing edge flow," *Proc. Roy. Soc. Ser. A* 340, 91-111, (1974).
- Melnik, R.E., & Chow, R., "Asymptotic theory of two-dimensional trailing edge flows. Aerodynamic Analyses Requir-

ing Advanced Computers," NASA SP No. 347, (1975).
 Veldman, A.E.P., & Van de Vooren, A.I., "Drag of a finite flat
 plate," Proc. 4th Internat. Conf. Numer. Methods Fluid
 Dyn., Boulder, Colo., Lecture Notes in Physics 35, 423-
 430, (1974).

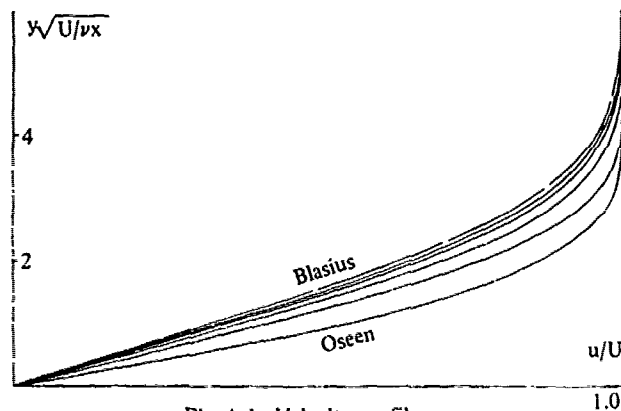


Fig. A-1 Velocity profile

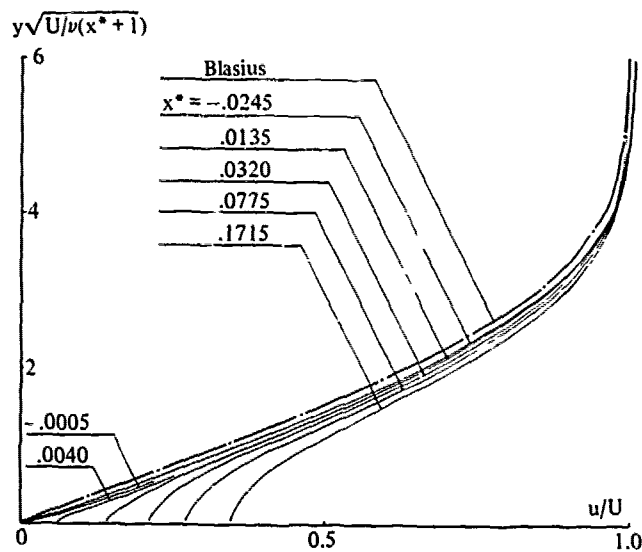


Fig. A-2 Velocity profile

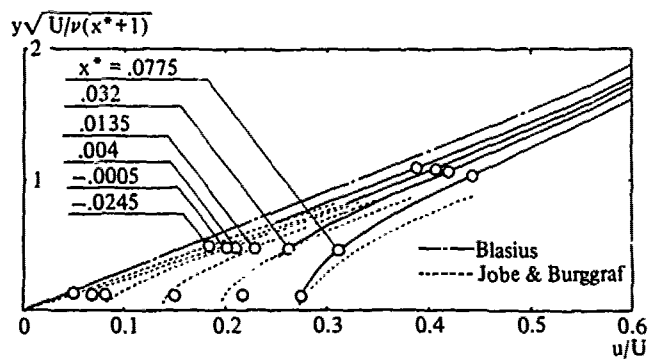


Fig. A-3 Velocity profile

Discussion

Y. Himeno (Univ. of Osaka Prefecture)

When we calculate pressure distribution on the ship hull by using displacement surface, a problem may arise at the end of the stern. The displacement thickness may usually have a knuckle there, so that the potential flow velocity becomes zero, or otherwise infinity. I'd like to see the pressure distribution near the stern which is calculated by the author and is used as an input of boundary layer calculation.

L. Landweber (Univ. of Iowa)

The author's solution for the wave-making of a thin body with a wake generated by Oseenlets is an impressive mathematical achievement. Since the result is considerably more complicated than that for inviscid flow, applications of this model to the nonlinear wave problem would probably become discouragingly complicated. It is suggested that this model be applied to wake calculations alone, but that simpler models, in which the wake is replaced by an equivalent irrotational flow, be used to calculate viscous effect on wavemaking. These have the advantage that the wave-making Green function for irrotational flow can be used, so that inclusion of viscous effect does not complicate the calculations.

The simpler model suggested above is justified by the experimental results of Gadd, and of Landweber & Swain, that the wake of a flat plate does not generate waves; and the result, by T. Huang et al, that the pressure distribution of the equivalent irrotational flow is in very good agreement with the measured values. Some additional comments on results with this simple model will be made in the discussion of the next paper, by Chang and Larsson.

H. Isshiki (Hitachi S & E)

I would like to express my sincere thanks for your contribution to Prof. Kinoshita, and it is very nice for me to have a chance to make some comments on your paper.

I think that the viscosity effect may not be so great in a problem like yours. But I think that it is not only important but also interesting to clarify the viscous effect on the wave making resistance from a theoretical point of view. Further, your experience on this paper will be helpful in future.

Now, in order to stimulate your knowl-

edge, I would like to draw your interest to Prof. Lighthill's paper on jet noise, because the so-called Lighthill equation seems to be useful to obtain a far field solution of water waves due to turbulent or Reynolds stresses.

For example, the first term on the righthand side of Eq.(5a) in your paper is considered to be a volume distribution of force. But I prefer to consider this term as a volume distribution of stress. I explain this in the following.

From the equation of motion and the equation of continuity, an equation for the hydrodynamic pressure p is obtained as

$$\frac{\partial^2 \bar{p}}{\partial x_i^2} = U \frac{\partial \bar{m}}{\partial x_1} + \frac{\partial \bar{f}_i}{\partial x_1} + \frac{\partial^2 \rho u_i' u_j'}{\partial x_i \partial x_j} \quad (1)$$

where

x_i ($i = 1, 2, 3$): Cartesian coordinates
 U : velocity of the uniform flow
 u_i' : perturbation velocity
 ρ : density of fluid
 m : volume discharge
 f_i : external force applied to water

and "bar" means to take the mean of the corresponding quantity. When the Reynolds stress $\rho u_i' u_j'$ is considered to be given, Eq.(1) may correspond to the Lighthill equation in aeroacoustics. In your case, the velocity of sound is assumed to be infinity because of incompressibility assumption.

From this equation, we can see how each term on the righthand side contributes to the hydrodynamic pressure p . From mathematical point of view, their contributions are clearly different each other. Therefore, I prefer to call the last term as the stress term.

Prof. Lighthill explained based on his equation that the sound power of jet noise is proportional to the eighth power of the exit velocity of jet and that a jet noise shows very characteristic directionality.

I would be very happy if you could make me clear about the following items in future:

- (1) Is there any applicability of Eq.(1) in my discussion to your problem?
- (2) Is similar results obtained by using Eq.(1)?

Author's Reply

T. Kinoshita (Univ. of Tokyo)

I would like to express my gratitude to very kind discussions, suggestions and comments of Profs. Himeno, Landweber and

Dr. Isshiki.

For Prof. Himeno's discussion ; The pressure is rapidly changed at the end of the stern, as you say. This fact is very important for near field problem. An example of calculations including this effect is shown in Appendix B, which is a case of laminar flow. When the author calculated the boundary layer and wake by simple methods, he skipped the narrow ditch.

For Prof. Landweber's comment and suggestions ; I agree with you. For the latter half of your discussion, I think the theoretical results in section 2 of this paper confirm the justification of the simpler model you suggest in case of a thin ship.

For Dr. Isshiki's comment ; Lighthill's equation in aeroacoustics is very impressive for me. I think the similar result will be got by the way that you suggest.

Numerical Viscous and Wave Resistance Calculations Including Interaction

Lars Larsson

Swedish Maritime Research Centre (SSPA)

Goteborg, Sweden

Ming-Shun Chang

David W Taylor Naval Ship Research and Development Center

Bethesda, Maryland, U S A

ABSTRACT

Predictions are presented for the flow field, as well as for the resistance components of a mathematical hull form at several Froude numbers. To obtain the viscous flow near the stern a new boundary layer-wake method including higher order effects is developed and applied interactively with the potential flow calculations for the double model case. The resulting displacement thickness is used for computing the wave resistance reduction at non-zero Froude numbers employing a numerical source panel method. Comparisons are made with results from thin ship theory using two different wake shapes.

NOMENCLATURE

A	Area
B	Ship breadth
C_E	Entrainment coefficient
C_F	Skin friction coefficient (total)
C_f	Skin friction coefficient (local) in x-direction
C_p	Pressure coefficient
C_V	Viscous resistance coefficient
C_{VP}	Viscous pressure resistance coefficient
C_w	Wave resistance coefficient
C_{w0}	Wave resistance coefficient for bare hull
$C_{w\delta}$	Wave resistance coefficient for displacement body
C_{wF}	Free surface resistance

E	Entrainment rate
F_n	Froude number V_S/\sqrt{gL}
g	Acceleration of gravity
H_1	Head's shape factor for the velocity profile
H_{12}	Shape factor for the velocity profile
h_1, h_2, h_3	Metrics
I_{px}, I_{pz}	Pressure integrals defined by (7a) and (7c)
I_{Kx}, I_{Kz}	Curvature integrals defined by (7b) and (7d)
$I_{K1x}, I_{K3x}, I_{K1z}, I_{K3z}$	Curvature integrals defined by (13)
K_1, K_3	Constants of proportionality for y-variation of h_1 and h_3
K_{12}, K_{32}	Normal curvatures of surfaces $y=\text{const}$ along lines $z=\text{const}$ and $x=\text{const}$ resp
K_{120}, K_{320}	As above, but for $y = 0$
K_{13}, K_{31}	Geodesic curvatures of lines $z=\text{const}$ and $x=\text{const}$ on surfaces $y=\text{const}$
K_{130}, K_{310}	As above, but for $y = 0$
L	Ship length
N_x, N_y, N_z	Direction cosines of the normal to the surface
p	Static pressure
p_0	Static pressure on the surface
p_e	Static pressure at the edge of the boundary layer
R	Radius of curvature of the surface

R_n	Reynolds number $V_S \cdot L/\nu$
R_w	Wave resistance
U, V, W	Mean velocity components
u', v', w'	Fluctuating velocity components
U_e, V_e, W_e	Mean velocity components at the edge of the boundary layer
V_N	Transpiration velocity
V_S	Ship speed
X, Y, Z	Global coordinate system. (X downstream, Z upwards)
x, y, z	Local coordinate system. (x along U_e , y normal)
β_0	Wall cross-flow angle
ΔC_p	Pressure change across the boundary layer, eq (17a)
ΔC_{pK}	Contribution to the pressure change by the normal curvature of the surface, eq (17d)
ΔC_{pv}	Contribution to the pressure change by the first acceleration term in the y-momentum equation, eq (17b).
ΔC_{pv2}	Contribution to the pressure change from the second acceleration term in the y-momentum equation, eq (17c)
ΔC_w	Change in wave resistance due to viscous effects
δ	Boundary layer thickness
δ^*	Defined by equation (8)
$\bar{\delta}$	Generalized boundary layer thickness, eq (10)
δ_1, δ_2	Displacement thickness, eq (4)
δ_1^*, δ_2^*	Defined by equation (4)
$\bar{\delta}_1, \bar{\delta}_2$	Generalized displacement thickness, eq (10)
θ_{11}, θ_{12}	Momentum thicknesses, eq (4)
θ_{21}, θ_{22}	
$\theta_{11}^*, \theta_{12}^*$	Defined by equation (4)
$\theta_{21}^*, \theta_{22}^*$	
$\bar{\theta}_{11}, \bar{\theta}_{12}$	Generalized momentum thicknesses, eq (10)
$\bar{\theta}_{21}, \bar{\theta}_{22}$	
ν	Kinematic viscosity
ρ	Density
τ_{xy}, τ_{zy}	Wall shear stress in x and z directions resp.

1. INTRODUCTION

Already some 35 years ago interactive viscous-inviscid calculations for 2-D wings were carried out by Preston [1]. Since then a large number of methods for both types of flow have been developed and, by matching calculations of the two kinds using the displacement thickness concept (see Lighthill [2]), good results might be ex-

pected

To be able to obtain the displacement thickness close to the stern it could, however, be necessary to include higher order effects in the boundary layer calculations. For axisymmetric cases such effects were taken into account in the methods by Dyne [3], Nakayama [4] and Huang [5], developed in the mid-seventies. Even more recent are the attempts to produce higher order 3-D methods. Spalding's group [6], [7] developed a very ambitious finite difference procedure taking into account the normal pressure variation as well as the crosswise momentum diffusion. Another interesting approach was presented by Mori in 1978 [8] considering separation. The potentials of these methods have not yet been fully exploited.

The most recent attempts to the problem were reported at the SSPA-ITTC Workshop on Ship Boundary Layers. Soejima et al [9] presented a finite difference method including the normal pressure variation and other effects of the curvature of the surface, and Nagamatsu [10] gave results from an integral method having similar features. In Section 2 of this paper a new integral method is developed. It takes the essential higher order effects into account and the results, which are given in Section 3, show a marked improvement as compared to the first order ones.

In Section 3 the double model potential flow is used, but this restriction is released in Section 4, where the previously computed displacement thickness is employed for estimating the magnitude of the wave resistance reduction due to viscous effects. This has since long been a controversial issue and there have been two essentially different ways of handling the wake. Laurentieff [11], Wigley [12] and Milgram [13] assumed the wake to be parallel aft of the stern, which resulted in a very low wave drag reduction. To get more realistic results, Wigley closed the displacement body in a cusp at some distance behind the body. This had been tried earlier by Havelock [14] and resulted in very substantial reductions. Maruo [15] varied the wake shape more systematically considering the wake width variation aft of the stern. More reasonable results were then obtained. In all investigations mentioned, the thin ship theory was used for the potential flow, while no calculations were carried out for the viscous wake, which was just chosen arbitrarily.

Himeno [16] and Kang [17] were the first to compute the wake using extended boundary layer theory, and recently Mori [18], [19] used his asymptotic expansion method, mentioned above, for computing the wake velocities, which were introduced in the low speed theory of Baba [20] to check the influence of viscosity on the wave drag. Mori's work seems to be the first one, where a modern method for 3-D viscous flows has been combined with a wave resistance method applicable to ships of normal fullness. These are the features also of the present work.

2. METHODS USED

Three different potential flow methods have been used: Hess & Smith's for the double model case and Chang's source panel method together with thin ship theory for the non-zero Froude numbers. The first and last are so well known that no presentation seems necessary. Relevant references are [21] and [22] respectively. Chang's method has also been presented elsewhere, see [23] and [24], so it is described only very briefly in paragraph 2.1.

The boundary layer and wake calculations have been carried out using Larsson's method [25], which has been extended to take into account higher order effects close to the stern. Appropriate modifications for computing the wake have also been introduced. A very brief account of the basic method is given in 2.2, while in 2.3 and 2.4 the new improvements are described more in detail.

2.1 Chang's Method [23] and [24]

In its most general form Chang's method computes ship motions in a seaway, taking into account the effect of forward speed. The computer program employed in the present investigation is however specialized for the case with no oscillatory motions.

The problem in question is to solve the Laplace equation for the potential, satisfying boundary conditions on the surface of the hull (zero normal velocity) on the free surface (constant pressure) and at infinity (no disturbance except in a wedge behind the hull). There is no method available today for solving this problem exactly, but an approximation, the so called Neumann-Kelvin problem, is easier to attack. In this simplification the free surface boundary condition is linearized and applied at the undisturbed level of the water. Covering the submerged part of the body with Kelvin wave-making sources, this condition as well as the condition at infinity are automatically satisfied. The body boundary condition yields an integral equation for the source strength and from the corresponding solution the potential can be computed anywhere.

In Chang's method the Neumann-Kelvin problem is solved by discretization of the integral equation. The surface of the hull is approximated by a large number of panels, each one having a constant source strength. Since the sum of the contributions from all panels plus the undisturbed velocity shall yield zero normal velocity at the centre of each panel a set of linear equations in the source strength may be formulated. The solution yields the potential at any point by integration over the panels. Velocities may then be obtained by differentiation using either finite differencing or spline techniques.

2.2 Larsson's Basic Method [25]

Larsson's method for 3-D turbulent boundary layers is of the integral type, making use of a co-ordinate system based on streamlines traced from the potential flow results. Solutions are obtained along each individual streamline by Runge Kutta integration of the governing equations, keeping derivatives across the streamlines constant in each step. By iteration the derivatives are updated using spline functions along the equi-potential lines.

Head's entrainment equation [27] is used as auxiliary relation and several formulae due to Michel et al are employed for connecting the integral thickness and for computing the skin friction.

2.3 A Method for Computing the Thick Boundary Layer Close to the Stern

The derivation of the governing equations for the higher order method is described in a condensed form in the following. More details are given in [26].

2.3.1 Governing Equations

The governing equations are (see NOMENCLATURE)

$$\frac{U}{h_1} \frac{\partial U}{\partial x} + V \frac{\partial U}{\partial y} + \frac{W}{h_3} \frac{\partial U}{\partial z} + K_{12}UV + (K_{13}U - K_{31}W)W + \frac{1}{h_1} \frac{\partial (p/\rho)}{\partial x} - \frac{1}{h_1 h_3} \frac{\partial}{\partial y} (h_1 h_3 \tau_{xy}/\rho) = 0 \quad (1a)$$

$$\frac{U}{h_1} \frac{\partial V}{\partial x} + V \frac{\partial V}{\partial y} + \frac{W}{h_3} \frac{\partial V}{\partial z} - K_{12}U^2 - K_{32}W^2 + \frac{\partial (p/\rho)}{\partial y} = 0 \quad (1b)$$

$$\frac{U}{h_1} \frac{\partial W}{\partial x} + V \frac{\partial W}{\partial y} + \frac{W}{h_3} \frac{\partial W}{\partial z} + (K_{23}W - K_{13}U)U + K_{32}VW + \frac{1}{h_1} \frac{\partial}{\partial z} (p/\rho) - \frac{1}{h_1 h_3} \frac{\partial}{\partial y} (h_1 h_3 \tau_{zy}/\rho) = 0 \quad (1c)$$

and

$$\frac{1}{h_1} \frac{\partial U}{\partial x} + \frac{\partial V}{\partial y} + \frac{1}{h_3} \frac{\partial W}{\partial z} + K_{12}U + (K_{12} + K_{32})V + K_{13}W = 0 \quad (2)$$

As to the mean flow, equations 1a, c and 2 are identical to the set of second order equations derived by Nash & Patel [37]. Terms of order δ/R and larger have been retained. In 1b Nash & Patel drop the first three terms as being of too high order. This does not seem justified in the present case since it would imply that the pressure variation across the boundary layer should be determined by the normal curvatures of the surfaces, $y = \text{const}$ (K_{12} resp K_{32}), i.e. essentially the curvatures of the hull surface, while in reality the streamline curvature close to the stern may be of the opposite

sign.

In Nash & Patel's derivation the Reynolds stresses are assumed to be of the order δ/R . This coupling of stresses to the boundary layer thickness seems however doubtful and at least for axisymmetric cases [4] the magnitude of the stress terms does not generally increase when approaching the stern. To shed some light on this, an experimental investigation is under way at SSPA, but meanwhile only the stresses of first order theory are retained. Apart from the inclusion of $v^{1/2}$ in the pressure term of (1b) in Soejima's et al [9] equations they are then identical to the present ones.

2.3.2 Metrics

Since the normal curvatures of the surface are now considered, the metrics h_1 and h_3 become functions of y . In the present approximation a linear dependence is assumed

$$h_1 = h_{10}(x, z)(1 + K_1 y); \quad h_3 = h_{30}(x, z)(1 + K_3 y) \quad (3)$$

K_1 and K_3 are taken as the normal curvatures of the surface

$$K_1 = K_{120} \quad K_3 = K_{320}$$

h_2 is still assumed identically equal to unity, and this has already been introduced in the equations above.

2.3.3 Momentum Integral Equations

The derivation of the two momentum integral equations in the x and z directions follows in principle the one for the corresponding first order equations. After integrating the equations in the y -direction it is convenient to introduce the following integral quantities

$$\begin{aligned} \delta_1 &= \int_0^\delta \left(1 - \frac{U}{U_e}\right) dy & \delta_2 &= \int_0^\delta -\frac{W}{U_e} dy \\ \theta_{11} &= \int_0^\delta \left(1 - \frac{U}{U_e}\right) \frac{U}{U_e} dy & \theta_{12} &= \int_0^\delta \left(1 - \frac{U}{U_e}\right) \frac{W}{U_e} dy \\ \theta_{21} &= \int_0^\delta -\frac{UW}{U_e^2} dy & \theta_{22} &= \int_0^\delta -\frac{W^2}{U_e^2} dy \\ \delta_1^* &= \int_0^\delta y \left(1 - \frac{U}{U_e}\right) dy & \delta_2^* &= \int_0^\delta -y \frac{W}{U_e} dy \\ \theta_{11}^* &= \int_0^\delta y \left(1 - \frac{U}{U_e}\right) \frac{U}{U_e} dy & \theta_{12}^* &= \int_0^\delta y \left(1 - \frac{U}{U_e}\right) \frac{W}{U_e} dy \\ \theta_{21}^* &= \int_0^\delta -y \frac{UW}{U_e^2} dy & \theta_{22}^* &= \int_0^\delta -y \frac{W^2}{U_e^2} dy \end{aligned} \quad (4)$$

The first six are known from first order theory while the latter six are new. The factor y in the kernel appears when introducing the expressions (3) in the equations. If the metrics are assumed independent of y all the starred quantities vanish. This assumption is made by Nagamatsu [10].

Two relations follow directly from the definitions

$$\theta_{12} = \theta_{21} - \delta_2$$

$$\theta_{12}^* = \theta_{21}^* - \delta_2^* \quad (5)$$

Using (4) the momentum integral equations may be written

$$\begin{aligned} \frac{1}{h_{10}} \frac{\partial \theta_{11}}{\partial x} + (2\theta_{11} + \delta_1) \frac{1}{U_e h_{10}} \frac{\partial U_e}{\partial x} + \frac{1}{h_{30}} \frac{\partial \theta_{12}}{\partial z} + \\ + (\theta_{12} + \theta_{21}) \left(\frac{1}{U_e h_{30}} \frac{\partial U_e}{\partial z} + K_{330} \right) + K_{310} (\theta_{11} - \theta_{22}) + \\ + K_1 \left[(\theta_{12}^* + \theta_{21}^*) \left(\frac{1}{U_e h_{30}} \frac{\partial U_e}{\partial z} + K_{330} \right) + \frac{1}{h_{30}} \frac{\partial \delta_{12}^*}{\partial z} \right] + \\ + (\theta_{12}^* + \theta_{21}^*) \frac{1}{h_{30}} \frac{\partial K_1}{\partial z} + \\ + K_3 \left[(\theta_{12}^* + \theta_{21}^*) \frac{1}{U_e h_{10}} \frac{\partial U_e}{\partial x} + K_{310} (\theta_{11}^* - \theta_{22}^*) + \frac{1}{h_{10}} \frac{\partial \theta_{11}^*}{\partial x} \right] + \\ + (\theta_{11}^* - \theta_{22}^*) \frac{1}{h_{10}} \frac{\partial K_3}{\partial x} = \frac{C_f}{2} + I_{px} + I_{Kx} \end{aligned} \quad (6a)$$

$$\begin{aligned} \frac{1}{h_{10}} \frac{\partial \theta_{21}}{\partial x} + 2\theta_{21} \left(\frac{1}{U_e h_{10}} \frac{\partial U_e}{\partial x} + K_{310} \right) + \frac{1}{h_{30}} \frac{\partial \theta_{22}}{\partial z} + \\ + \theta_{22} \left(\frac{2}{U_e h_{30}} \frac{\partial U_e}{\partial z} + K_{330} \right) - K_{330} (\theta_{11} + \delta_1) + \\ + K_1 \left[\frac{1}{h_{30}} \frac{\partial \theta_{22}^*}{\partial z} + \theta_{22}^* \left(\frac{2}{U_e h_{30}} \frac{\partial U_e}{\partial z} + K_{330} \right) - K_{330} (\theta_{11}^* + \delta_1^*) \right] + \\ + \frac{1}{h_{30}} \frac{\partial K_1}{\partial z} (\theta_{22}^* - \theta_{11}^* - \delta_1^*) + \\ + K_3 \left[\frac{1}{h_{10}} \frac{\partial \theta_{21}^*}{\partial x} + 2\theta_{21}^* \left(\frac{1}{U_e h_{10}} \frac{\partial U_e}{\partial x} + K_{310} \right) \right] + \\ + \frac{1}{h_{10}} \frac{\partial K_3}{\partial x} 2\theta_{21}^* = \frac{C_f}{2} \tan \beta_0 + I_{pz} + I_{Kz} \end{aligned} \quad (6b)$$

The "I" quantities on the right hand side member are integrals, which appear due to the inclusion of, on the one hand, pressure gradients through the layer (I_{px} , I_{pz}) and, on the other, normal curvatures of the surface (I_{Kx} , I_{Kz}). They are defined as

$$I_{px} = \frac{1}{h_{10} h_{30} U_e^2} \int_0^\delta h_3 \frac{\partial}{\partial x} \left(\frac{p - p_e}{\rho} - \frac{v_e^2}{2} \right) dy \quad (7a)$$

$$I_{Kx} = \frac{1}{h_{10} h_{30} U_e^2} \int_0^\delta h_1 h_3 K_{12} UV dy \quad (7b)$$

$$I_{pz} = \frac{1}{h_{10}h_{30}U_e^2} \int_0^{\delta} h_1 \left(\frac{\partial}{\partial z} (p/\rho) - U_e^2 h_3 K_{13} \right) dy \quad (7c)$$

$$I_{Kz} = \frac{1}{h_{10}h_{30}U_e^2} \int_0^{\delta} h_1 h_3 K_{12} V W dy \quad (7d)$$

The pressure integrals are not symmetric with respect to x and z since, in the streamline co-ordinate system used, $W_e = 0$.

2.3.4 The Entrainment Equation

As auxiliary relation the entrainment equation is used. Defining δ^* by

$$\delta^* = \frac{\delta^2}{2} \quad (8)$$

the equation may be written

$$U_e K_{130} \left[(\delta - \delta_1) + K_3 (\delta^* - \delta_1^*) \right] +$$

$$+ \frac{1}{h_{10}} \frac{\partial}{\partial x} U_e \left[(\delta - \delta_1) + K_3 (\delta^* - \delta_1^*) \right] -$$

$$- U_e K_{130} \left[\delta_2 + K_1 \delta_2^* \right] - \frac{1}{h_{30}} \frac{\partial}{\partial z} U_e \left[\delta_2 + K_1 \delta_2^* \right] =$$

$$= (1 + K_1 \delta) (1 + K_3 \delta) E \quad (9)$$

where E is the entrainment coefficient, for which Head's relations may be used.

2.3.5 Transformation of the Equations to a More Convenient Form

The general idea is to try to make the equations (6) and (9) as similar as possible to the first order ones, so that existing computer programs can be used, without much modification. To achieve this six new quantities are introduced.

$$\bar{\theta}_{11} = \theta_{11} + K_3 \theta_{11}^*$$

$$\bar{\theta}_{12} = \theta_{12} + K_1 \theta_{12}^*$$

$$\bar{\theta}_{21} = \theta_{21} + K_3 \theta_{21}^*$$

$$\bar{\theta}_{22} = \theta_{22} + K_1 \theta_{22}^*$$

$$\bar{\delta - \delta_1} = \delta - \delta_1 + K_3 (\delta^* - \delta_1^*)$$

$$\bar{\delta_2} = \delta_2 + K_1 \delta_2^* \quad (10)$$

The equations (6) and (9) may now be written

$$\frac{1}{h_p} \frac{\partial \bar{\theta}_{11}}{\partial x} + (2\theta_{11} + \delta_1) \frac{1}{U_e h_{10}} \frac{\partial U_e}{\partial x} + \frac{1}{h_{30}} \frac{\partial \bar{\theta}_{12}}{\partial z} +$$

$$+ (\theta_{12} + \theta_{21}) \left(\frac{1}{U_e h_{30}} \frac{\partial U_e}{\partial z} + K_{130} \right) + K_{310} (\theta_{11} - \theta_{22}) =$$

$$= \frac{C_f}{2} + I_{px} + I_{K1x} + I_{K3x} \quad (11a)$$

$$\frac{1}{h_{10}} \frac{\partial \bar{\theta}_{21}}{\partial x} + 2\theta_{21} \left(\frac{1}{U_e h_{10}} \frac{\partial U_e}{\partial x} + K_{310} \right) +$$

$$+ \frac{1}{h_{30}} \frac{\partial \bar{\theta}_{22}}{\partial z} + \theta_{22} \left(\frac{2}{U_e h_{30}} \frac{\partial U_e}{\partial z} + K_{130} \right) -$$

$$- K_{130} (\theta_{11} + \delta_1 - \theta_{22}) = \frac{C_f}{2} \tan \beta_0 + I_{pz} + I_{K1z} + I_{K3z} \quad (11b)$$

$$\frac{1}{h_{10}} \frac{\partial}{\partial x} \left[U_e (\bar{\delta - \delta_1}) \right] + U_e K_{130} (\bar{\delta - \delta_1}) -$$

$$- \frac{1}{h_{30}} \frac{\partial}{\partial z} (U_e \bar{\delta_2}) - U_e K_{130} \bar{\delta_2} = (1 + K_1 \delta) (1 + K_3 \delta) E \quad (12)$$

where

$$I_{K1x} = I_{Kx} -$$

$$- K_1 \left[(\theta_{12}^* + \theta_{21}^*) \left(\frac{1}{U_e h_{30}} \frac{\partial U_e}{\partial z} + K_{130} \right) \right] -$$

$$- \theta_{21}^* \frac{1}{h_{30}} \frac{\partial K_1}{\partial z}$$

$$I_{K1x} =$$

$$= -K_3 \left[(2\theta_{11}^* + \delta_1^*) \frac{1}{U_e h_{10}} \frac{\partial U_e}{\partial x} + K_{310} (\theta_{11}^* - \theta_{22}^*) \right] -$$

$$- \theta_{22}^* \frac{1}{h_{10}} \frac{\partial K_3}{\partial x}$$

$$I_{K1z} =$$

$$= -K_1 \left[\theta_{22}^* \left(\frac{2}{U_e h_{30}} \frac{\partial U_e}{\partial z} + K_{130} \right) - K_{130} (\theta_{11}^* + \theta_{22}^*) \right] -$$

$$- (\theta_{11}^* + \delta_1^* + \theta_{22}^*) \frac{1}{h_3} \frac{\partial K_1}{\partial z}$$

$$I_{K3z} = I_{Kz} - K_3 \left[2\theta_{21}^* \left(\frac{1}{U_e h_{10}} \frac{\partial U_e}{\partial x} + K_{310} \right) \right] -$$

$$- \frac{1}{h_{30}} \frac{\partial K_3}{\partial x} \theta_{21}^* \quad (13)$$

The equations (11) and (12) differ from the corresponding first order ones in three respects: the pressure and curvature integrals (13) on the right hand side, the bars over certain quantities and the terms proportional to $[(1/U_e h_{30}) \partial U_e / \partial z + K_{130}]$. The latter sum is zero in first order theory, provided streamline co-ordinates are used.

Now it turns out to be possible to use ordinary first order computer programs without too many alterations. Apart from the inclusion of the sum just mentioned, the following new relations are needed.

1. Relations to compute initial values of $\bar{\theta}_{11}$, $\bar{\theta}_{21}$ and $\bar{\delta}-\delta_1$, given θ_{11} , θ_{21} and H_{12}
2. Relations to compute the 'I' integrals
3. Relations to compute the "barred" quantities in the crosswise derivatives knowing $\bar{\theta}_{11}$, $\bar{\theta}_{21}$ and H_{12}
4. Relations to compute $\bar{\theta}_{11}$, $\bar{\theta}_{21}$ and H_{12} from $\bar{\theta}_{11}$, $\bar{\theta}_{21}$ and $\bar{\delta}-\delta_1$

Having introduced this new information the original computer program may be used. The governing equations will yield the "barred" quantities as solutions but, using relations 1 and 4 above, the input and output will be the ordinary integral quantities. As a matter of fact the changes to the program reduces to less than 100 Fortran statements.

2.3.6 Velocity and Pressure Variations across the Layer

In order to compute the necessary relations listed above some information is needed on the distributions of velocities and static pressure across the boundary layer.

For the tangential velocity components the well-known power-law-Mager assumptions are made

$$\frac{U}{U_e} = \left(\frac{y}{\delta}\right)^{\frac{1}{n}} = \left(\frac{y}{\delta}\right)^{\frac{H_{12}-1}{2}} \quad (14a)$$

$$\frac{W}{U_e} = \left(\frac{y}{\delta}\right)^{\frac{H_{12}-1}{2}} \left(1 - \frac{y}{\delta}\right)^2 \tan \delta_0 \quad (14b)$$

while for the normal velocity a linear variation is assumed

$$\frac{V}{U_e} = \frac{y}{\delta} \quad (14c)$$

The pressure variation is obtained by the integrating equation (1b). If this is done, employing equations (14), a quite complicated expression appears. It may however be simplified considerably making an order of magnitude analysis of the different terms. In the relations given below the following assumptions are made

$$x, z, U, h_1, h_2 = O(1)$$

$$y, V, W, K_1\delta, K_2\delta = O(\delta/R) \quad (15)$$

Only terms of order $O(1)$ and $O(\delta/R)$ will be retained.

The condition $W = O(\delta/R)$ is recognized as the small cross-flow assumption. This is not a necessary condition for the theory and it has not been applied when deriving the governing equations (11) and (12). However, in the computations to be presented in this paper the small cross-flow assumption has been employed, and since the necessary relations are consider-

ably simpler in this case, the general expressions will not be given here.

Integrating equation (1b) considering (14) and (15) there is obtained

$$\Delta C_p = \Delta C_{pv} \left[1 - (y/\delta)^{1/n+2} \right] + \Delta C_{pv2} \left[1 - (y/\delta)^2 \right] - \Delta C_{pk} \left[1 - (y/\delta)^{2/n+1} \right]$$

$$\text{where } n = \frac{H_{12}-1}{2} \quad (16)$$

$$\Delta C_p = \frac{P-P_e}{\frac{1}{2}\rho U_e^2} \quad (17a)$$

$$\Delta C_{pv} = \frac{4\delta^2}{(H_{12}+3)U_e} \frac{1}{h_1} \frac{\partial}{\partial x} \left(\frac{V_e}{\delta} \right) \quad (17b)$$

$$\Delta C_{pv2} = \left(\frac{V_e}{U_e} \right)^2 \quad (17c)$$

$$\Delta C_{pk} = \frac{2K_1\delta}{H_{12}} \quad (17d)$$

C_{pv} , C_{pv2} and C_{pk} are the contributions from the first second and fourth term respectively in equation (1b). The first two are of order $O((\delta/R)^2)$ while the third one is of order $O(\delta/R)$.

2.3.7 The Necessary New Relations

Since the governing equations (1) include terms of order $O(\delta/R)$ the integrated equations (6) are of order $O((\delta/R)^2)$. This is the order of magnitude considered in most relations below. However, as mentioned above, the pressure integrals are evaluated to higher accuracy.

Introducing the velocity profiles (14) in the definitions of the integral thicknesses (4) and (10) the initial value of the "barred" quantities may be obtained from $\bar{\theta}_{11}$, $\bar{\theta}_{21}$ and H_{12} .

$$\bar{\theta}_{11} = \theta_{11} (1 + K_1 A(H_{12}) \theta_{11}) \quad (18a)$$

$$\bar{\theta}_{21} = \theta_{21} \quad (18b)$$

$$\bar{\delta}-\delta_1 = \delta-\delta_1 + \frac{K_2 \theta_{11}^2}{2} [B^2(H_{12}) - A(H_{12})H_{12}+1] \quad (18c)$$

where $A(H_{12})$ and $B(H_{12})$ are functions of H_{12} .

$$A(H_{12}) = \frac{H_{12}^2(H_{12}+1)}{(H_{12}-1)(H_{12}+3)} \quad (19a)$$

$$B(H_{12}) = \frac{H_{12}^2(H_{12}+1)}{H_{12}-1} \quad (19b)$$

A procedure for computing $\delta-\delta_1$ from θ_{11} and H_{12} is already available in the first order theory.

The curvature integrals I_{K1x} , I_{K3x} , I_{K1z} and I_{K3z} defined in (13) may be

evaluated, using the velocity profiles (14) in the definitions (4) of the "starred" quantities.

$$I_{K1x} = \frac{2K_1 V_e \theta_{11}}{U_e} \frac{B(H_{12})}{H_{12}+3} \quad (20a)$$

$$I_{K3x} = -K_1 \theta_{11}^2 A(H_{12}) \left[\frac{H_{12}+5}{2U_e h_{10}} \frac{\partial U_e}{\partial x} + K_{110} \right] \quad (20b)$$

$$I_{K1z} = 0.5 K_1 K_{110} \theta_{11}^2 A(H_{12}) (H_{12}+3) \quad (20c)$$

$$I_{K3z} = 0 \quad (20d)$$

The pressure integrals I_{px} and I_{pz} (7a, c) can be obtained by introducing the pressure given by equations (16) and (17)

$$I_{px} = \frac{1}{2U_e^2} \left[\frac{H_{12}+3}{H_{12}+5} \frac{\partial}{\partial x} (U_e^2 \delta \Delta C_{pv}) - \frac{1}{3} \frac{\partial}{\partial x} (U_e^2 \delta \Delta C_{pv2}) - \left(\frac{H_{12}}{H_{12}+1} + \frac{K_1 \delta H_{12}}{H_{12}+2} \right) \frac{\partial}{\partial x} (U_e^2 \delta \Delta C_{pk}) \right] \quad (21a)$$

$$I_{pz} = \frac{1}{2U_e^2} \left[\frac{H_{12}+3}{H_{12}+5} \frac{\partial}{\partial z} (U_e^2 \delta \Delta C_{pv}) + \frac{2}{3} \frac{\partial}{\partial z} (U_e^2 \delta \Delta C_{pv2}) - \left(\frac{H_{12}}{H_{12}+1} + \frac{K_1 \delta H_{12}}{H_{12}+2} \right) \frac{\partial}{\partial z} (U_e^2 \delta \Delta C_{pk}) \right] + \frac{1}{2} \frac{\partial}{\partial z} (h_1 \delta^2) - \frac{1}{4} \delta \frac{\partial}{\partial z} (K_1^2 \delta^2) \quad (21b)$$

To second order the "barred" quantities in the cross-wise derivatives are

$$\bar{\theta}_{12} = \theta_{12} \quad (22a)$$

$$\bar{\theta}_{22} = \theta_{22} \quad (22b)$$

$$\bar{\delta}_2 = \delta_2 \left[1 + \frac{K_1 \theta_{11} B(H_{12}) (H_{12}+1)}{H_{12}+7} \right] \quad (22c)$$

while the last relations required are obtained by inverting equations (18)

$$\theta_{11} = \frac{\sqrt{1+4K_1 A(H_{12}) \bar{\theta}_{11}} - 1}{2K_1 A(H_{12})} \quad (K_1 \neq 0) \quad (23a)$$

$$\theta_{11} = \bar{\theta}_{11} \quad (K_1 = 0) \quad (23b)$$

$$\theta_{21} = \bar{\theta}_{21} \quad (23c)$$

$$\delta - \delta_1 = \bar{\delta} - \delta_1 - 0.5 K_1 \theta_{11}^2 [B^2(H_{12}) - (H_{12}+1)A(H_{12})] \quad (22d)$$

2.4 A Method for Computing the Wake

The basic difference between the boundary layer and the wake is the inner boundary condition. In the boundary layer the stresses between the surface and the flow retard

the velocity to zero on the surface, while in the wake no such retarding stresses exist. The velocity at the center of the wake therefore increases from zero at the trailing edge to the undisturbed velocity at infinity. Apart from the difference in boundary condition the wake should behave like a boundary layer, so the same computer program can be used with some modifications. The most obvious change is to put the skin friction identically equal to zero which is easily done. The relevance of other empirical relations in the program is however more difficult to establish.

Since the inner velocity does not drop to zero, it seems to be necessary to exchange the assumption for the longitudinal velocity profile. In the program all profile assumptions (which are never written out explicitly) are based on similarity solutions by Michel et al, using their differential boundary layer method. The longitudinal and cross-wise profiles are tied together so exchanging one means that the other one cannot be used.

In the present approach an approximation of Coles' wake function is employed for the longitudinal velocity profile, while Mager's assumption is used for the cross-flow.

$$\frac{U}{U_e} = 1 - \lambda \cos^2 \left(\frac{\pi}{2} \frac{y}{\delta} \right) \quad (24a)$$

$$\frac{W}{U_e} = \left(1 - \frac{y}{\delta} \right)^2 \frac{U}{U_e} \tan \delta_w \quad (24b)$$

Introducing these expressions in the definitions of the basic integral parameters the following relations appear

$$\delta_1 = \delta A_1 \lambda \quad (25a)$$

$$\theta_{11} = \delta (A_1 \lambda - A_2 \lambda^2) \quad (25b)$$

$$\delta_2 = -\delta \tan \delta_w (A_3 - A_4 \lambda) \quad (25c)$$

$$\theta_{12} = \delta \tan \delta_w (A_5 \lambda - A_6 \lambda^2) \quad (25d)$$

$$\theta_{22} = -\delta \tan^2 \delta_w (A_6 - A_7 \lambda + A_8 \lambda^2) \quad (25e)$$

$$\theta_{21} = \delta_2 + \theta_{12} \quad (25f)$$

By definition $H_{12} = \delta_1 / \theta_{12}$, which yields

$$H_{12} = \frac{A_1}{A_1 - A_2 \lambda} \quad \text{or} \quad (26a)$$

$$\lambda = \frac{A_1}{A_2} \frac{H_{12} - 1}{H_{12}} \quad (26b)$$

The constants A_1, \dots, A_8 attain the following numerical values

$$A_1 = 0.5$$

$$A_2 = 0.375$$

$$A_3 = 0.333$$

$$A_4 = 0.468$$

$$A_5 = 0.233$$

$$A_6 = 0.200$$

$$A_7 = 0.359$$

$$A_8 = 0.165$$

Since the centerplane is used as the inner boundary of the wake the normal curvatures are identically zero, so the "starred" quantities and the curvature integrals will disappear. Parts of the pressure integrals I_{px} and I_{pz} are however still left.

An important quantity for the entrainment equation is the shape factor $H_1 = (\delta - \delta_1)/\theta_{11}$. Using (25a, b) and (26b) this can be related to H_{12} as

$$H_1 = \frac{H_{12} \left(\frac{A_2}{A_1} - 1 \right) + 1}{H_{12} - 1} \quad (27)$$

Equation (27) is compared with Head's [27] relation

$$H_1 = 1.535(H_{12} - 0.7)^{-2.715} + 3.3 \quad (28)$$

in Fig 1, where the results from three different experimental investigations are also plotted. Chevray & Kovaznay [28] measured the wake behind a flat plate, Kang [17] investigated the flow behind a thin ship model and Himeno et al [16] studied the wake of a Series 60, $C_B = 0.70$ model*. Although the points are scattered, it seems obvious that the relation (27) represents a better average than (28), except perhaps for the largest H_{12} 's (close to the stern).

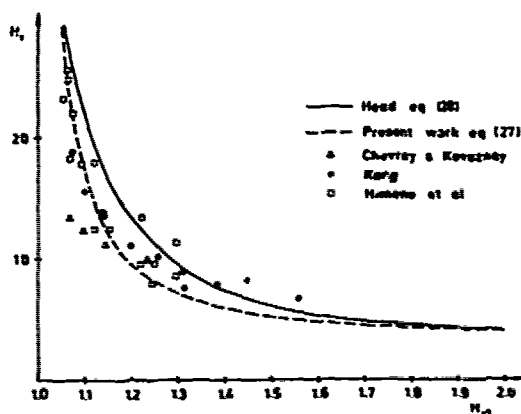


Fig 1 Different relations between H_{12} and H_1

* Unfortunately this work is not fully documented in English.

According to Head's theory [27] the entrainment rate may be related to H_1 via the relation

$$C_E = \frac{E}{U_e} = 0.0306(H_1 - 3.0)^{-0.553} \quad (29)$$

This is compared in Fig 2 with experiments and with a relation due to Kang [17]

$$C_E = 0.11299 - 0.048275 \ln H_1 + 0.0051395 (\ln H_1)^2 \quad (30)$$

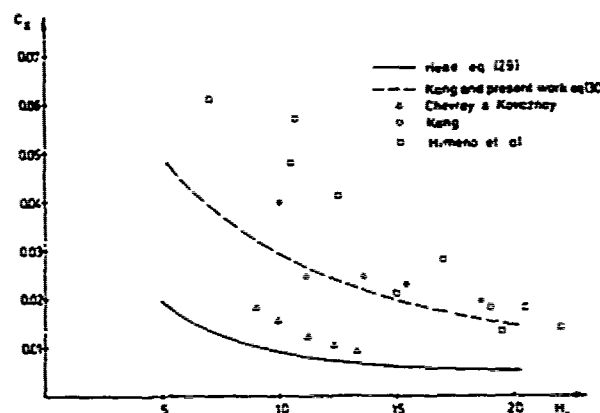


Fig 2 Different relations for the entrainment rate

Two conclusions may be drawn from this Figure: the scatter is large and Head's relation yields too low C_E 's in the wake. Due to lack of better information Kang's relation (30) is chosen here.

In Fig 3 results from the present method** are shown together with Kang's measurements in the wake of his thin model. Changing from (28) to (27) abruptly at the stern causes a sudden drop in H_{12} . In reality, this change takes place over a certain distance behind the hull. No general relations are at hand for computing this development but as a first approximation it might be related to the momentum thickness at the stern. Judging from Fig 3, the predictions seem to merge with the experiments at about $x = 1.15$ which corresponds to a distance about 60 times the stern momentum thickness. A similar result is obtained when predicting the wake of Chevray & Kovaznay. Therefore in the present calculations the relation (28) gradually turns into (27) according to the formula (for $0 \leq X-L \leq 60\delta_s$)

** Without higher order effects. The model is very thin ($L/b = 37.7$)

$$H_1 = f(H_{12}) = f_{(28)}(H_{12}) + \frac{X-L}{600} [f_{(27)}(H_1) - f_{(28)}(H_1)] \quad (31)$$

As appears from Fig 3, this relation produces a reasonable development of H_{12} close to the stern.

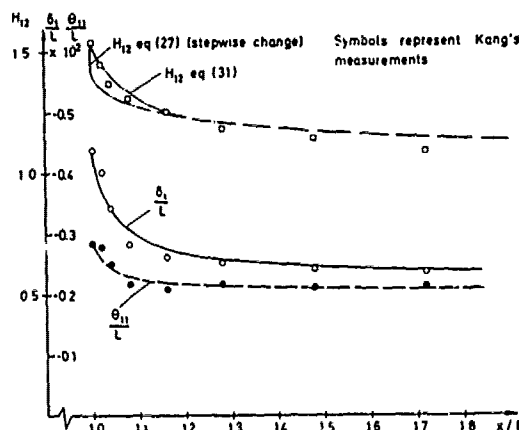


Fig 3 Test of the wake method. Kang's friction plane model

3. VISCOUS RESISTANCE (DOUBLE MODEL) CALCULATIONS

The test case common to both types of calculations is a mathematical form, usually referred to as the Wigley model. Its equation is

$$Y = \pm 0.1(1 - X^2)(1 - 64Z^2) \\ -1.0 \leq X \leq 1.0; -0.125 \leq Z \leq 0.125 \quad (32)$$

A body plan is shown in Fig 4. As appears from the equation the side view is rectangular.

The reason for choosing this hull is that boundary layer measurements have been carried out in the presence of a free surface. Hogben[29] measured 2-D velocity profiles at a number of stations along a 20 ft (6.1 m) model in a towing tank and Hatano et al [30] and Mori [31] recorded the 3-D velocity vector using five hole tubes on the afterbody and in the near wake of a 3 m model in their tank. Pressure measurements for the double model case are available from Relf [32]. A considerable number of resistance tests and wave analyses seems to have been carried out for this hull (see for instance [33]).

Unfortunately the boundary layer data is somewhat incomplete. In Hogben's case no information is given on the cross-flow within the boundary layer and no wake data is reported. Hatano et al measured the velocity at a large number of stations but in the lower regions of the hull few points were located within the boundary

layer, making it difficult to compute H_{12} accurately. As to the pressure measurements there seems to be an unusually large scatter and there are probably some blockage effects. Nevertheless the advantage of having data for a hull at different Froude numbers was considered so important that it would outweigh the disadvantages.

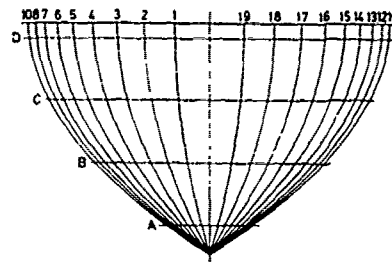


Fig 4 Test case for viscous and wave resistance calculations. Wigley hull.

3.1 The Calculations Carried Out

Four sets of calculations have been carried out. The potential flow was first computed for the bare hull and the boundary layer was calculated using the original theory. This is the ordinary first order approach.

To obtain a better pressure distribution close to the stern, off-body points were then used to compute the pressure somewhat outside the hull. The points were located at the intersection between the normals to the panels in the region $0.8 \leq 2X/L \leq 1.0$ and a cylindrical surface of constant cross-section equal to the hull section at $2X/L = 0.8$. This location would correspond fairly well with the displacement surface. Velocities obtained at the off-body points were resolved in components along and normal to the surface and the latter were used to trace streamlines, etc, and for carrying out the boundary layer calculation. Also in this case the first order boundary layer method was used.

The higher order calculations started with a potential flow solution for off-body points located in a similar way as above, but on a cylindrical surface having the shape of the mid-ship section. This should correspond to the boundary layer edge. In the region $0.8 \leq 2X/L \leq 1.0$ new streamlines were traced on the hull using the off-body velocities. The curvature $K_{1,0}$ then had to be computed independently (in first order theory it is obtained from the pressure distribution) and the boundary

layer could be calculated using the method described in Section 2.3. Initial values were taken from the first order solution at $2X/L = 0.8$ and the I_K and I_D integrals were computed in advance, taking $H_{1,2}$ as 1.4 and the boundary layer thickness as the distance between the off-body points and the corresponding null point on the hull. See Fig 5. Normal curvatures $K_{1,20}$ and $K_{3,20}$ had of course to be computed first. In this approach the computations were extended into the wake, using the method described in Section 2.4.

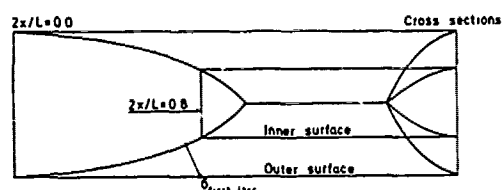


Fig 5 Location of off-body points. (Schematic)

The fourth calculation was carried out in an attempt to take the interaction into account. Therefore a set of transpiration velocities for simulating the boundary layer effect on the potential flow was computed from the displacement thickness distribution obtained in the first iteration (using the higher order method). The potential flow was then recalculated taking the transpiration velocities as the body boundary condition, and the off-body solution for the outer surface was used in connection with the higher order method, as described above, to obtain a new boundary layer solution. As it turned out that this corresponded very well to the one from the first iteration the iterations were terminated.

Drag estimates were finally made in two ways, by integrating the pressure and frictional forces along the hull, and by computing the momentum loss in the far wake.

It should be emphasized that the small cross-flow approximation has been employed throughout.

3.2 Computed Pressures

The pressure distributions along the load water-line for the different calculations are shown in Fig 6. Measurements are also given, although they were carried out at a different Reynolds number and, in

general, seem very scattered. A small blockage correction (0.01 at the ends of the model) has been applied to the measured points.

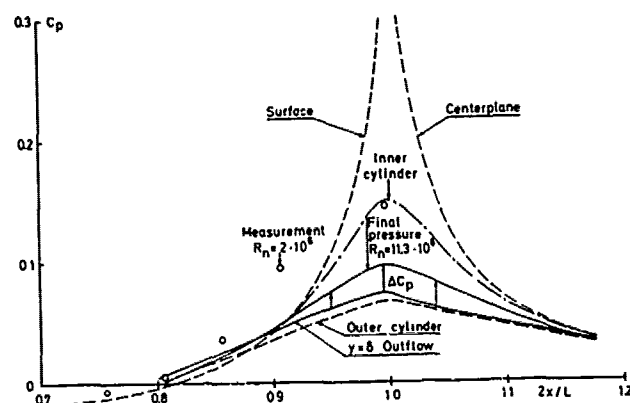


Fig 6 Different pressure computations at $Z = 0$ in the stern region

The ordinary first order pressure on the hull and in the wake is of course too high near the stern. However, using the off-body points at the inner cylinder (from $2X/L = 0.8$) results in a much more reasonable development. At the outer cylinder the pressure distribution is smoothed and the gradient is much smaller than the one measured on the surface. Therefore this pressure can only be used in conjunction with the computed pressure variation across the boundary layer.

The transpiration velocity used in the fourth calculation is computed according to Lighthill [2]. In principle his derivation could be extended to take into account higher order effects in a manner similar to the one of Section 2, but this was not considered necessary, since the effect of the transpiration velocity is in itself of higher order.

Lighthill's expression may be written in the following form

$$V_N = \delta_1 U_e \left(K_{1,10} + \frac{1}{U_e h_0} \frac{\partial U_e}{\partial x} \right) + U_e \frac{\partial \delta}{\partial h_0} \frac{1}{x} + U_e \frac{\partial \delta}{\partial h_0} \frac{1}{y} \quad (33)$$

In accordance with the small cross-flow approximation, the last term has been dropped in the present calculations.

The pressure computed in the second iteration at the edge of the boundary layer, considering the transpiration, is not very different from the one on the outer surface in the first iteration. It is still very smooth as appears from Fig 6. The pressure on the hull surface is obtained by adding the change across the boundary layer, and this improves the situation, as can be seen from Fig 6. It seems however as though the increase is too small, if comparisons are

made with the measurements.

In Fig 7 the vertical pressure distribution at $2X/L = 1.0$ is shown. Similar conclusions as from Fig 6 may be drawn, although the "final" pressure seems in this case to correspond better to the measurements. The deviation is most pronounced close to the water-line, where the boundary layer is thickest. In this region the computed pressure increase across the layer is too small to account for the difference between the computations at the edge and the measurements on the surface.

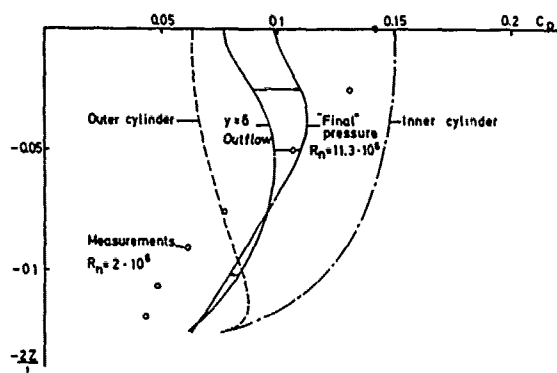


Fig 7 Different pressure computations at $2X/L = 1.0$

The reasons for the deviations at the water-line may be investigated by checking the derivation of equation (16). There are essentially three assumptions made: 1) The cross-flow is so small that the third and fifth terms of (1b) can be dropped, 2) The longitudinal velocity is assumed to depend on a power law, where the exponent is determined from $H_{1,2}$, and 3) The normal velocity varies linearly between zero at the wall and the potential flow V_p at the edge.

The first one of the assumptions can not influence the results at the water-line where the cross flow is zero, and it is easily shown that the components of ΔC_p are quite insensitive to the shape of the longitudinal velocity profile (provided the shape is reasonable, i.e. $H_{1,2}$ is between 1 and 2). The assumption of a linear variation of the normal velocity thus seems to be the critical one, although ΔC_{pv2} as well as ΔC_{pk} are independent of this, ΔC_{pv} is on the other hand very dependant on the distribution of V , and as a numerical experiment V was assumed to be constant through the layer. This resulted in a six-fold increase in ΔC_{pv} at $2X/L = 1.0$, $Z = 0$. There are several ways of improving the V -assumption, which will be considered in the further improvement of the method.

In Fig 8 the distribution of the components of ΔC_p along the water-line is given. In the region $0.8 \leq 2X/L \leq 1.0$ the curvature of the surface is convex, which

means that if the flow had followed surfaces of $y = \text{const.}$ the pressure would have decreased towards the hull, i.e. ΔC_{pk} is negative. ΔC_{pv} and ΔC_{pv2} are however positive, tending to increase the pressure. This is due to the fact that the flow is concave relative to the surfaces $y = \text{const.}$ For $2X/L \leq 0.9$ the concavity is not large enough to counteract the convexity of the $y = \text{const.}$ surfaces so there the pressure on the hull is lower than at the edge of the boundary layer. The opposite is true for $2X/L \geq 0.9$. It is quite obvious that dropping the terms ΔC_{pv} and ΔC_{pv2} (according to a strict second order theory) would have led to quite erroneous results.

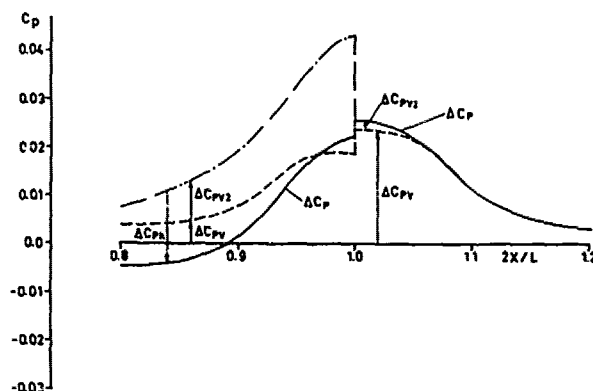


Fig 8 Contributions to the pressure difference across the boundary layer. $Z = 0$

It should be mentioned that the curvature of the surface $y=0$ exhibits a stepwise change at $2X/L=1.0$ where it drops from a finite value to zero. This is a weakness of the co-ordinate system used. In fact, there is a region close to the stern, where the system is non-unique. Normals from the hull will intersect normals from the centerplane. This region is in the present case very short, only 0.75% of the ship length, and its problems have not been considered in this work. The calculations are carried out on the hull all the way to $2X/L = 1.0$, thereafter restarting in the wake. In this way the undeterminacy of the co-ordinate system is avoided, although the true solution will probably not be obtained close to the surface at the after end.

The final pressure plot is shown in Fig 9. It represents the variation of the three components of ΔC_p across the boundary layer at $2X/L = 1.0$, $2Z/L = 0.0$. The variation is computed using equation (16). Unfortunately no measurements are available for comparison.

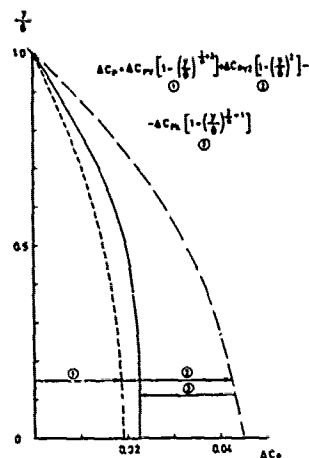


Fig 9 Contributions to the pressure variation across the boundary layer
 $2X/L = 1.0, Z = 0$

3.3 Boundary Layer - Wake Solution

In Fig 10 the calculated momentum thickness along four water-lines (A-D in Fig 4) is compared with Hogben's measurements at $R = 7.4 \times 10^6$. The Froude number in the tests was only 0.156 so the effect of the waves may be considered negligible.

The calculations were started at $2X/L = -0.7$ using the measured quantities as initial data. First order solutions could be obtained up to the stern, but aft of $2X/L = 0.8$ several other computations were also tried, as explained above. The curves given in Fig 10 aft of $2X/L = 0.8$ correspond to the final solution in the second iteration.

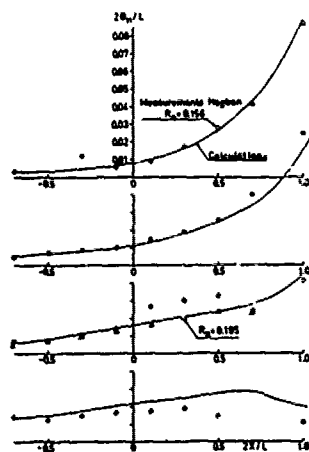


Fig 10 Calculated momentum thickness along water-lines A-D

As appears from Fig 10 the solution is quite good except for the aft half of the lowest line. The discrepancy in this region is due to the sharp keel, close to which the boundary layer equations are not valid. The apparent discrepancy for $0 < 2X/L \leq 0.5$,

line B, is most likely due to measurement errors, since the results from other Froude numbers exhibit a much closer correspondence with calculations. As an example the measurements along line B are given for the next higher F_n , which is 0.195.

In Fig 11 the results of some of the calculations of Section 3.1 are shown for the uppermost line (D) in the region $0.8 \leq 2X/L \leq 1.2$. Comparisons are made with Hogben's [29] measurements (only one point) and with the data given by Mori [31]. Unfortunately, both the Reynolds and the Froude numbers are different in the latter case (3.2×10^6 and 0.200 respectively) so the comparisons should be made with some care.

The ordinary first order calculation based on the pressure on the surface yields, as expected, a too large momentum thickness at the stern. Making use of the pressure from the inner cylinder (starting at $2X/L = 0.8$) results in a more reasonable development of the momentum thickness. It seems however clear that the best solutions are obtained by the higher order approach, and the difference between the first and second iteration is quite small, indicating that a converged solution has been obtained. In the figure only the results from the second iteration are shown in the wake.

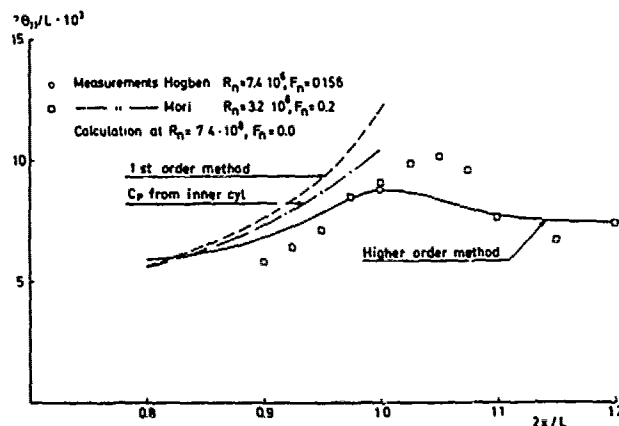


Fig 11 Different predictions of the momentum thickness along line D close to the stern

Further down on the hull the differences between the various solutions become smaller as can be seen from Fig 12, showing the vertical distribution of the momentum thickness at $2X/L = 1.0$. There are two effects of the problems at the keel. The computed thickness does not drop to zero at $2Z/L = -0.125$ as it should, according to the measurements, and in the region $2Z/L = -0.07 - -0.09$ there is an unwanted kink in the computations. As appears from Fig 13 the region close to the keel is extremely divergent, which means that it will be covered very badly by streamlines, which are evenly distributed around

$2X/L = 0.0$. Therefore two extra lines have been started at $2X/L = 0.8$ and initial data has been obtained by interpolation between the keel streamline (which is fixed) and the ones further up. This yields initial values which are somewhat too high, since the divergence further forward has not been fully accounted for. It is, on the other hand, impossible to trace the two new streamlines all the way, since they will get very close to the keel-line at the mid-ship, yielding unreasonably high values of the momentum thickness. (In reality the boundary layer may be distributed around the keel while in the boundary layer calculations it is forced to stay in the region above the normal at $2Z/L = -0.125$, see Fig 14,) The problems cannot be avoided using boundary layer theory unless the edge is rounded. However, other coordinate systems might be more suitable than the present one in the lower region of the hull.

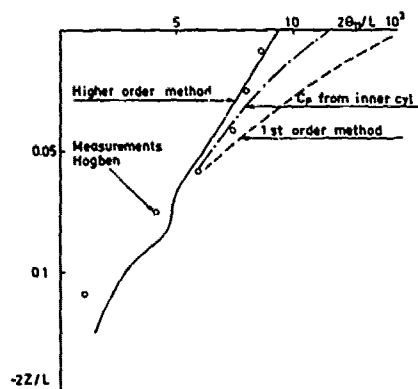


Fig 12 Different predictions of the momentum thickness at $2X/L = 1.0$

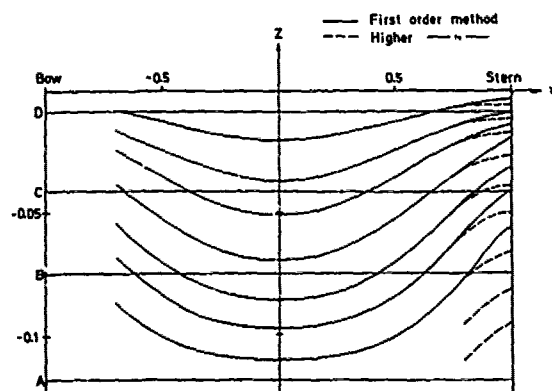


Fig 13 Computed streamlines. (Horizontal scale 1/10 of vertical scale)

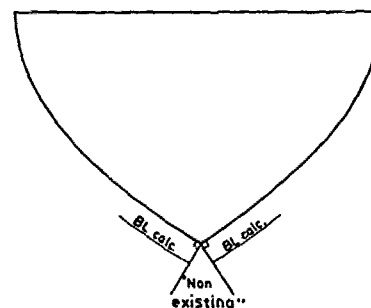


Fig. 14 Difficulties at the sharp keel line

In Fig 15 an attempt is made to compare measured and calculated cross-flow angles at $2X/L = 1.0$. Since Hogben did not measure cross-flow the only available data is Mori's. Unfortunately the innermost point of his measured profiles is at $2y/L = 0.01$ which corresponds to $y/\delta = 0.10-0.15$. Extrapolations to $y/\delta = 0.0$ have therefore been made. Also in this case the angles computed by the higher order method are superior to the ones obtained by the first order method based on the pressure on the surface. If the potential flow solution from the inner cylinder is used the first order solution is not too bad.

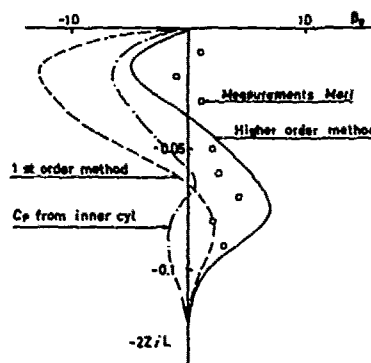


Fig 15 Different predictions of the wall cross-flow angle at $2X/L = 1.0$

The most important quantity with reference to the resistance is the momentum thickness. By considering its distribution depthwise, the total momentum loss may be computed, and the drag can be obtained from the momentum theorem. To avoid the influence of pressure forces, the momentum loss is conveniently computed "far" behind the

body. How far behind the integration is to be carried out may be seen from Fig 16, where the momentum thickness distribution is shown for three sections of the wake. Obviously the change between $2X/L = 2.0$ and $2X/L = 10.0$ is negligible, indicating that the integration can be made fairly close to the body.

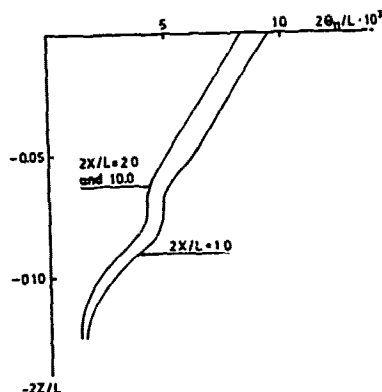


Fig 16 Predicted momentum thickness at different sections of the wake

It might also be of interest to look at the change in displacement thickness (here taken as δ_1) with the distance from the hull. As appears from Fig 17 δ_1 adjusts itself more slowly to its final value (which is equal to θ_{11}).

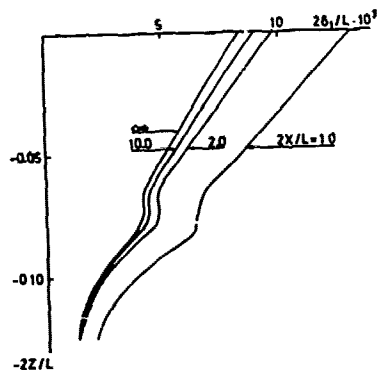


Fig 17 Predicted displacement thickness at different sections of the wake

The change in displacement thickness is related to the transpiration velocity according to equation (33). This velocity is achieved by adding extra sources to the panels of the hull. In Fig 18 the distribution of such sources along the lines B and D is shown. Up to the stern the sources are positive, thereafter dropping to negative in the near wake. The combined effect of all

sources in the wake is to reduce the displacement area (see Fig 17) from its value at $2X/L = 1.0$ to its value at infinity.

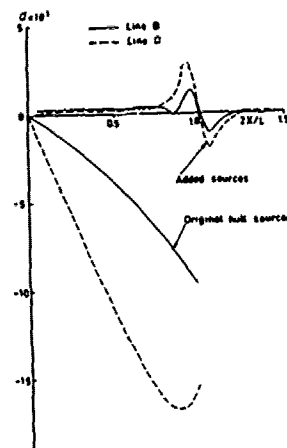


Fig 18 Source distribution along two water lines

3.4 The Viscous Resistance

The skin friction resistance was computed by adding the contributions from all hull panels

$$C_F = \sum_i C_{fi} \times \sqrt{1 - N_{xi}^2} \times A_i / \sum_i A_i \quad (34)$$

where C_{fi} was obtained by interpolation among the streamlines. In the formula the deviation of the flow direction from the horizontal is neglected since it will reduce the C_F by less than 1 %.

A problem was encountered at the bow where neither experimental nor calculated results exist. It was assumed that the boundary layer was tripped at $2X/L = -0.9$, so laminar C_f 's were used in front of this station, while turbulent C_f 's were extrapolated forward to $2X/L = -0.9$ from $2X/L = -0.7$, where the computations started. For $R_n = 7.4 \times 10^6$ the skin friction coefficient computed in this way was 3.00×10^{-3} .

To obtain the pressure drag a similar summation was carried out

$$C_{VP} = \sum_i C_{pi} \times N_{xi} \times A_i / \sum_i A_i \quad (35)$$

C_{pi} in this expression was taken from the off body points at $y = \delta_1$ including the transpiration velocities. Using the computed C_p 's on the hull from the higher order theory might have been more interesting, but this solution was, as mentioned above, only obtained for $0.8 \leq 2X/L \leq 1.0$.

In the bow region, where very high C_p 's might be expected, the original panelling (288 panels) of the hull was not considered accurate enough. Therefore a very fine mesh was used close to the stem. For $-1.0 \leq 2X/L \leq -0.9$ the corresponding pressure on the hull was employed in (35). This is

motivated by the fact that δ_1 should be very small in this region of laminar flow. For $-0.9 \leq 2X/L \leq -0.7$ δ_1 was obtained by extrapolation of the results obtained further aft.

The viscous pressure coefficient, computed by (35) is only 0.82×10^{-4} , or 2.6 % of C_F . According to Relf [32] C_{VF} should be around 2 % of C_F , so this is in good agreement with the computations. The accuracy of Relf's estimate is however questionable since it was based on an integration of the very scattered measured pressures.

For comparison the total viscous drag was computed from an integration of the momentum loss at $2X/L = 10.0$. This yielded $C_V = 3.82 \times 10^{-3}$.

According to Relf, the total viscous resistance at $R_n = 7.4 \times 10^{-3}$ should be 3.26×10^{-3} . Adding the computed frictional and pressure drags yields 3.08×10^{-3} which seems good enough considering the fact that the tripping assumption might be in error. It is however obvious that the momentum loss in the wake is too large. The reasons for this are being investigated.

4. WAVE RESISTANCE CALCULATIONS

In this section the effect of the boundary layer-wake on the wave resistance is investigated. To this end, the computed displacement thickness is added to the hull and wake (centerplane) and the reduction in wave resistance as compared with the one for the bare hull is sought. Chang's source panel method is employed in these calculations. However, as explained in the introduction, a common way of investigating the viscous effect on the wave resistance in the past has been to add a wake of constant thickness to the hull, thereafter computing the resistance using thin ship theory. This approach is therefore tested first, and, as a possible improvement, the thin ship theory is also employed in connection with the actually computed wake. Comparisons are made between the three different results.

The displacement thickness to use in these calculations might of course be obtained by using the actual pressure distribution for each speed (i.e. each F_n and R_n) but this would be quite time-consuming. Fortunately, in an earlier work [34] the present authors have shown that the boundary layer computation based on the double model pressure is quite reasonable also for non-zero F_n 's. In fact, due to difficulties in matching the upper streamlines to the waves, the non-zero F_n computations might even be inferior to the double model ones. Therefore, in the present work, the displacement thickness employed is the one obtained in the calculations of the previous section. As is seen from Fig 6, the Reynolds number for obtaining the displacement thickness was 11.3×10^6 , corresponding to a Froude number of 0.276, the

lowest one considered in the wave resistance calculations. The Reynolds number variation in the speed range may be considered small enough to be neglected.

4.1 Calculations Based on Thin Ship Theory

The wave resistance of a thin-ship is expressed as

$$R_w = 16\pi\rho K_0^2 \int_0^{\pi/2} (P^2 + Q^2) \sec^3\theta d\theta$$

with

$$K_0 = g/V_S^2$$

and

$$P = \iint_A -\frac{V_S}{2\pi} \frac{\partial Y}{\partial X} \cos(K_0 X \sec\theta) \times \\ \times e^{K_0 Z \sec^2\theta} dA$$

For flows without any viscous effects, the surface integral is taken over the center plane of the hull, but in the case of a hull modified according to the boundary layer displacement thickness concept, the surface integral might extend into the wake aft of the stern. This is the case for shape B in Fig 19, which corresponds to the wake computed in Section 3. The integration is here extended to $2X/L = 2.0$. Wake A has a constant thickness which means that no sources exist in the wake, so the integration can be stopped at $2X/L = 1.0$. In both cases the hull sources are modified to account for δ_1 .

The following discussion will be focused on the reduction, due to viscous effects, of the wave resistance coefficient, $\Delta C_w = C_{w0} - C_{w\delta}$, and the percentage reduction, $\Delta C_w/C_{w0}$. Here C_{w0} is the wave resistance of the original hull, and $C_{w\delta}$ is the wave resistance of the displaced hull. The calculated reductions in values of wave resistance coefficient for wakes A and B are given at five different Froude numbers in Table 1 and shown in Fig 20. As one may note, in the case of wake A, where the wake opens immediately after the stern, the reduction of the wave resistance is 7 per cent at $F_n = 0.276$ and 10 per cent at $F_n = 0.313$. With further increases of the Froude number, the reduction of the wave resistance becomes smaller, (e.g., the reduction is 4 per cent at $F_n = 0.45$). In the case of wake B, a significantly larger reduction of the wave resistance occurs. The reductions in the wave resistance coefficients are approximately 0.20×10^{-3} at all Froude numbers except those near 0.313. There the transverse wave length is a little longer than half the ship's length. The reduction in wave resistance for wake B is between 17 per cent at $F_n = 0.276$ and 6 per cent at $F_n = 0.45$. A comparison of the results for wake shapes A and B provides an estimate of the importance of the wake shape aft of the stern when computing viscous flow effects on a ship's wave resistance. The effect of the wake shape is evidently very significant.

Table 1 Reduction of wave resistance for Wigley hull

METHOD	$F_n = 0.276$		$F_n = 0.313$		$F_n = 0.350$		$F_n = 0.405$		$F_n = 0.450$	
	$\Delta C_w \times 10^3$	$\Delta C_w / C_{w0} (\%)$	$\Delta C_w \times 10^3$	$\Delta C_w / C_{w0} (\%)$	$\Delta C_w \times 10^3$	$\Delta C_w / C_{w0} (\%)$	$\Delta C_w \times 10^3$	$\Delta C_w / C_{w0} (\%)$	$\Delta C_w \times 10^3$	$\Delta C_w / C_{w0} (\%)$
Chang's method										
Wake B	.24	19	.40	21	.18	13	.45	14	.43	12
Thin ship										
Wake B	.23	17	.23	12	.16	13	.24	8	.24	6
Thin ship										
Wake A	.09	7	.20	10	.09	7	.12	4	.17	4

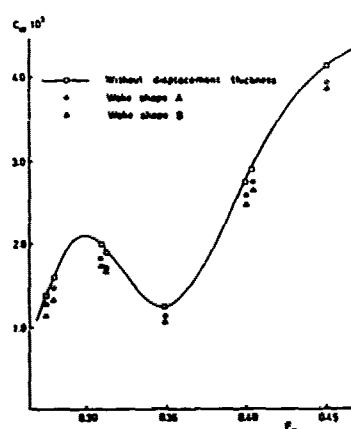


Fig 20. Wave resistance computed by thin ship theory

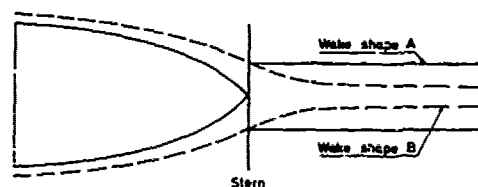


Fig 19. Wakes used in thin ship theory (schematic)

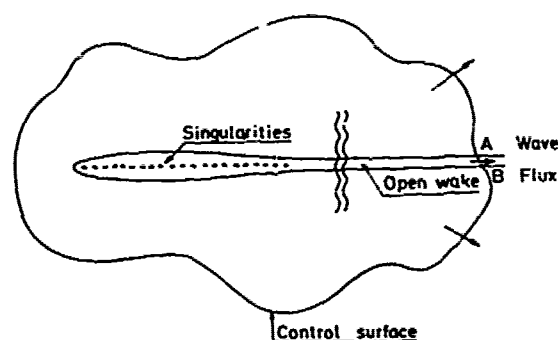


Fig 22. The control surface around the displacement body

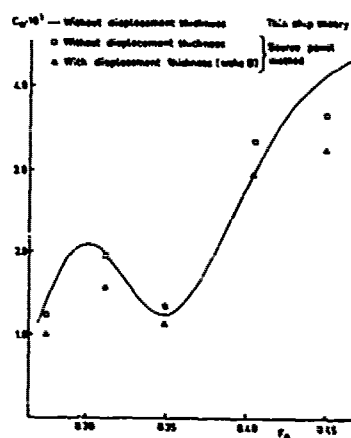


Fig 21. Wave resistance computed by Chang's source panel method

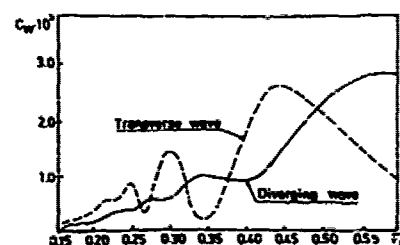


Fig 23. Components of the wave resistance. Wigley hull.

Table 2 Reduction of wave drag for axisymmetric body

METHOD	$F_n = 0.40$		$F_n = 0.45$		$F_n = 0.50$		$F_n = 0.55$		Form drag
	$\Delta C_w \times 10^3$	$\Delta C_w / C_{w_0} (\%)$	$\Delta C_w \times 10^3$	$\Delta C_w / C_{w_0} (\%)$	$\Delta C_w \times 10^3$	$\Delta C_w / C_{w_0} (\%)$	$\Delta C_w \times 10^3$	$\Delta C_w / C_{w_0} (\%)$	$C_{VP} \times 10^3$
Chang's method $R_n = 6.6 \times 10^6$.13	11	.20	9	.20	7	.12	5	.22
Slender body $R_n = 6.6 \times 10^6$.15	14	.28	12	.28	9	.22	8	.22

4.2 Calculations Using Chang's Method

In Chang's source panel method the pressure is computed at the control points of each panel. The total pressure resistance can therefore be obtained using a relation equivalent to (35). If the computation is carried out at non-zero Froude numbers, the pressure resistance contains two components, C_{yp} as defined in section 3, and C_{wf} , the free surface drag. The latter component is equivalent to the wave drag of thin ship theory.

For non-viscous flows the computation of $C_{yp} + C_{wf}$ is straightforward and can be carried out knowing the hull geometry. If viscosity is considered, assumptions have to be made about the pressure field. In the present calculation an assumption essentially equivalent to the one used in paragraph 3.4 has been used for computing the pressure on the hull. It is simply assumed that C_p at a point $(x, y, z) = (x, y, z) + \delta \cdot N$. This approach has been experimentally verified by Huang et al [35] for several axisymmetric bodies.

From the source panel method the pressure drag was calculated for both the original Wigley hull and the new displacement surface hull at five different Froude numbers. The free-surface drag, C_{wf} , was obtained from the pressure drag computed at a given Froude number minus the corresponding pressure drag at zero Froude number, C_{yp} . The latter, calculated for wake B, is 0.12×10^{-3} , i.e. 4.0% of C_F . This should be compared with the C_{yp} of 2.7% computed in Section 3.4, using a different potential flow method and a slightly different assumption for the displacement effect.

Fig 21 shows the wave resistance computed by thin ship theory and the free-surface drag computed by the source panel method with and without the boundary layer displacement effect (see Table 1). Table 1 shows that the computed free-surface drag with the inclusion of the boundary layer displacement thickness is significantly decreased at all five Froude numbers studied, with reductions falling between 12 to 20 per cent. For wake B the wave resistance calculated from thin ship theory indicates smaller reductions than the free-surface drag computed by the source panel method.

As a matter of fact they differ almost by a factor of two, except at $F_n = 0.276$ and 0.35.

The question may be raised as to why the wave resistance predicted by the thin ship theory differs significantly from the free-surface drag. Wigley [12] questioned the applicability of thin ship theory to an open body, such as the displacement body in the present calculations, and suggested that thin ship theory could overestimate the wave resistance. The present free-surface drag calculation seems to agree with Wigley's remark. In Wigley's study of the boundary layer effect on wave resistance, he closed the wake aft of the stern in order to obtain a more realistic solution. In the case of an open body, there does not exist a closed control surface which does not cut through the body, as shown in Fig 22. Thus, the wave resistance, obtained from integrating the wave energy propagating out of the entire control surface, should be overestimated by the amount of wave energy propagating through the wake cross-sectional area AB shown in Fig 22. During the course of the present work, it was found that the discrepancy between the thin ship theory prediction of wave resistance and the free-surface drag was correlated with the wave resistance contributed by the transverse wave system. Fig 23, taken from Lunde [22] shows the components of wave resistance contributed by the divergent and the transverse waves for the Wigley hull. One may see that at $F_n = .276$ and .35, the transverse waves are relatively small and the discrepancies between the predictions of thin ship theory and the free-surface drag are also small. At $F_n = 0.313, 0.405$ and 0.45 , the transverse waves are large and the discrepancies are large. This could mean that thin ship theory, when applied to an open displacement body, does not properly account for the transverse wave system. A correction which considers the contribution of the transverse wave energy propagating through the open wake may improve the validity of thin ship theory, with consideration of the displacement body concept.

The present wave drag reductions may be compared with corresponding results obtained by Chang & Huang [36] for a submerged

axisymmetric body. In that case, one might expect the effect of the open body on thin ship theory to be reduced because the open wake is submerged below the surface. The calculations were performed using slender body theory and the source panel method for the body submerged at one hull diameter below the surface. A better agreement between the two methods was obtained in this case, as appears from Table 2, but curiously enough the reductions of slender body theory were larger than the ones for the panel method.

5. CONCLUSIONS

- o A new theory has been developed for computing thick boundary layers. Significant improvements have been obtained in the prediction accuracy of the boundary layer close to the stern of the hull investigated. Further improvements of the method, particularly with respect to the pressure variation across the boundary layer should, however, be considered.
- o Using first order theory in combination with the pressure computed slightly outside the hull results in better agreement with measurements as compared with the ordinary first order approach. The results are, however, not as good as for the higher order method.
- o The viscid-inviscid interaction is fairly weak in the case tested and the changes between the boundary layer calculations of the first and second iteration are quite small.
- o Adding the skin friction and pressure drags computed by the higher order method results in a viscous resistance in good correspondence with measurements. Integrating the momentum loss in the far wake, computed by a higher order wake method, seems to result in too high viscous drags.
- o The importance of correctly modelling the wake when computing the wave drag in a viscous fluid has been demonstrated using thin ship theory.
- o The wave drag reduction due to the boundary layer displacement effect is smaller for the thin ship theory than for the source panel method. A reason for this might be the wave flux through the open wake in case of the thin ship theory. This explanation is supported by results from axisymmetric calculation for a submerged body.

6. ACKNOWLEDGEMENTS

The present work was initiated in 1979, when L. Larsson was visiting scientist at DTNSRDC. He is much indebted to the managements of DTNSRDC and SSPA for the possibi-

lity to stay and work at the Center for about six months. Particular thanks are extended to Mr J.H. McCarthy who organized the visit, took an active part in the planning of the project and encouraged the authors through many interesting discussions.

Thanks are also due to several other members of the DTNSRDC and SSPA staffs, particularly Miss E. Samuelsson, SSPA, for great help in coding and running computer programs.

The authors further want to express their gratitude to Prof. K. Mori, Hiroshima University for providing the original data of his wake experiments for the Wigley hull.

The work was funded by the U.S. General Hydrodynamics Research Program, Element 61153N, Task Area SR-023-01-01, The Swedish Board for Technical Development, Cnr 78-6038, and the Naval Material Department of the Defence Material Administration of Sweden.

REFERENCES

1. Preston, J. H., "The Effect of the Boundary Layer and Wake in the Flow Past a Symmetrical Aerofoil at Zero Incidence, Part I", Aeronautical Research Council, Reports and Memoranda, No 2107, London, 1945.
2. Lighthill, M. J., "On Displacement Thickness", Journal of Fluid Mechanics, Vol. 4, 1958, p 383.
3. Dyne, G., "A Streamline Curvature Method for Calculating the Viscous Flow Around Bodies of Revolution", International Symposium on Ship Viscous Resistance, SSPA, 1978.
4. Nakayama, A., Patel, V. C. and Landweber, L., "Flow Interaction near the Tail of a Body of Revolution. Part 2: Iterative Solution for Flow Within and Exterior to Boundary Layer and Wake", Journal of Fluids Engineering, Trans. ASME Serie I, Vol. 98, No 3, pp 538-549, September 1976.
5. Huang, T. T. and Cox, B. D., "Interaction of Afterbody Boundary Layer and Propeller". DnV Symposium on Hydrodynamics of Ship and Offshore Propulsion Systems, Høvik, Oslo, March 26-25, 1977, Paper 4/2. Session 1.
6. Abdelmeguid, A. M., Markatos, N. C. G., Spalding, D. B. and Muraoka, K., "A Method of Predicting Three-Dimensional Turbulent Flows around Ships' Hulls", International Symposium on Ship Viscous Resistance, SSPA, 1978.
7. Muraoka, K. and Shirose, Y., "Calculation of SSPA 720 and HSVA Tanker", SSPA-ITTC Workshop on Ship Boundary Layers, G3teborg, June, 1980.

8. Mori, K. and Doi, Y., "Approximate Prediction of Flow Field around Ship Stern by Asymptotic Expansion Method", Journal of the Society of Naval Architects of Japan, Vol. 144, Dec. 1978.
9. Soejima, S., Yamazaki, R. and Nakatake, K., "Calculation of Thick Three-Dimensional Turbulent Boundary Layers on Ship Stern", SSPA-ITTC Workshop on Ship Boundary Layers, Göteborg, June, 1980.
10. Nagamatsu, T., "Ship Boundary Layer Calculations by Higher Order Theory", SSPA-ITTC Workshop on Ship Boundary Layers, Göteborg, June, 1980.
11. Laurentieff, V. M., "The Influence of the Boundary Layer on the Wave Resistance of a Ship", DTMB Translation No 245 by Ralph Cooper, 1952.
12. Wigley, C., "Effects of Viscosity on Wave Resistance", International Seminar on Theoretical Wave Resistance, Ann Arbor, 1963, Vol. III.
13. Milgram, J. H., "The Effect of a Wake on the Wave Resistance of a Ship", Journal of Ship Research, Vol. 13, No 1, 1969.
14. Havelock, T. H., "Calculations Illustrating the Effect of Boundary Layer on Wave Resistance", The Collected Papers of Sir Thomas Havelock on Hydrodynamics (C. Wigley editor). Office of Naval Research, Department of the Navy, ONR/ACR-103.
15. Maruo, H., "Ship Waves and Wave Resistance in a Viscous Fluid", International Seminar on Wave Resistance Tokyo-Osaka, 1976.
16. Himeno, Y., "Displacement Effect of Three-Dimensional Turbulent Boundary Layer and Wake of Ship", International Seminar on Wave Resistance, Tokyo-Osaka, 1976.
17. Kang, S.-H., "Viscous Effects on the Wave Resistance of a Ship", Phd Thesis, Iowa University, 1978.
18. Mori, K., "Prediction of Viscous Effects on Wave Resistance of Ship in Framework of Low Speed Theory", Mem. of the Faculty of Eng. of Hiroshima University, Vol. 7, No 1, 1979.
19. Mori, K., "Calculation of Ship Wave Resistance Including the Effects of Boundary Layer and Wake", DTNSRDC-ITTC Workshop on Ship Wave Resistance, Washington D.C., Nov., 1979.
20. Baba, E., "Wave Resistance of Ships in Low Speed", Mitsubishi Tech. Bul. No 109, 1976.
21. Hess, J. L. and Smith, A. M. O., "Calculation of Potential Flow about Arbitrary Bodies", Progress in Aeronautical Sciences, Vol. 8, Oxford, 1967.
22. Lunde, J. K., "The Linearized Theory of Wave Resistance and Its Application to Ship-Shaped Bodies in Motion on the Surface of a Deep, Previously Undisturbed Fluid", Skipsmodelltanken, Norges Tekniske Høgskole, Trondheim, Skipsmodelltanken, Meddelelse nr 23, March 1953.
23. Chang, M.-S., "Computations of Three-Dimensional Ship Motions with Forward Speed", Second International Conference on Numerical Ship Hydrodynamics, Berkeley, 1977.
24. Chang, M.-S., "Wave Resistance Predictions Using a Singularity Method", DTNSRDC-ITTC Workshop on Ship Wave Resistance, Washington D.C., Nov. 1979.
25. Larsson, L., "A Calculation Method for Three-Dimensional Turbulent Boundary Layers on Ship-Like Bodies", First International Conference on Numerical Ship Hydrodynamics, Washington D.C., 1975.
26. Larsson, L. and Löfdahl, L., "A Method for Calculating Thick Three-Dimensional Turbulent Boundary Layers. Part I. Equations and General Principles", SSPA Report No 2360-1, 1979.
27. Head, M. R., "Entrainment in the Turbulent Boundary Layer", Aeron. Res. Council, R & M 3152, 1958.
28. Chevray, R., "Turbulence Measurements in the Wake of a Thin Flat Plate", AIAA Journal, Vol. 7, No 8, 1969.
29. Hogben, N., "Record of a Boundary Layer Exploration on a Mathematical Ship Model", National Physical Laboratory, Ship Division, Ship Rep. 52, 1964.
30. Hatano, S., Mori, K., Fukushima, M., Yamazaki, R. and Suzuki, T., "Calculation of Velocity Distribution in Ship Wake", Journal of the Society of Naval Architects of Japan, Vol. 138, Dec. 1975.
31. Mori, K., Personal communication
32. Relf, E. F., "Wind Tunnel Measurements on a Double or 'Reflex' Model of Mathematical Form", Trans. RINA, Vol. 107, p 482, 1965.
33. Shearer, J. R., Cross, J. J., "The Experimental Determination of the Components of Ship Resistance for a Mathematical Model", Trans. RINA, Vol. 107, 1965.
34. Larsson, L. and Chang, M.-S., "Numerical Viscous and Wave Resistance Calculations Including Interaction. Part I: The Boundary Layer Wake Prediction", SSPA Report 2361-1, 1979.
35. Huang, T. T., Santelli, N. and Belt, G., "Stern Boundary Layer Flow on Axisymmetric Bodies", 12th Symposium on Naval Hydrodynamics, Washington D.C., 1978.
36. Chang, M.-S. and Huang, T.T., "Calculation of the Boundary Layer Displacement Effect on a Submerged Axisymmetric Body", Unpublished work at DTNSRDC, 1980.
37. Nash, J.F. and Patel, V.C., "Three Dimensional Turbulent Boundary Layers", SBC Technical Books, Atlanta, 1972

Discussion

T. Okuno (Univ. of Osaka Prefecture)

I have two simple questions.

(1) For the normal velocity, a linear variation was assumed in your paper. Using the power law for the streamwise velocity profile, I think it is better to assume a power form for the normal velocity considering the continuity equation.

(2) The surface curvature is very important factor in this calculation. What method did you use for the numerical calculation?

K. Mori (Fukuoka Univ.)

The discussor can not agree with the use of Eqs(24-a,b) for the near wake flow profiles. They are just for far wake flows.

In Fig. A1, velocity profiles expressed by Eq(24-a) are compared with those measured in case of the 3m Wigley model. The curves are determined as follows; first the boundary layer thickness δ and the outer velocity U_e are determined and then λ is determined for the errors to be minimum by curve fitting method. So they are most fitted ones in their family.

As suspected, though the profile of $x = 1.4$, a little downstream, is rather well reproduced, those of $x = 1.025$ and 1.1 are not; the tendencies of curves are quite opposite to the measured profiles around the centerlines where the wall effects seem still existing.

L. Landweber (Univ. of Iowa)

A comparison of the results of Drs. Chang and Larsson with the residuary resistance of Shearer & Cross, corrected for sinkage and trim, shows that the viscous correction has improved the agreement at all Froude numbers except $F = 0.35$, as is shown in the following table:

WAVE-RESISTANCE COEFFICIENTS

F =	0.266	0.313	0.350	0.402	0.452
S. & C.	0.92	1.70	1.55	2.43	3.16
Inviscid	1.12	1.93	1.58	2.93	3.64
with Viscosity	0.88	1.53	1.46	2.48	3.21

Our experience with a similar study on the very thin Weinblum, Kendrick, Todd form (PhD thesis of S.-H. Kang, Ref. 17 of paper) suggests that continuation of work on the Wigley form, to obtain a consistent

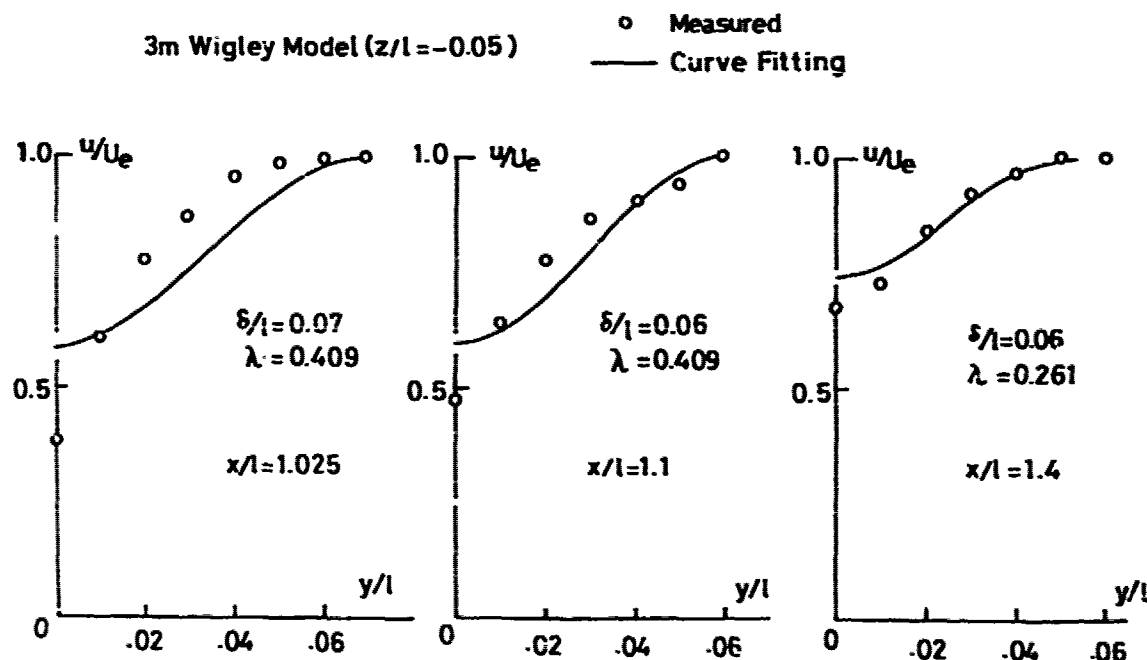


Fig. A1

second-order solution, may be rewarding. With the W.-K.-T. form, the first-order solution, including a first-order correction for the boundary layer and wake, was also in good agreement with the residuary. Inclusion of some second-order corrections worsened the agreement, but the best agreement was obtained when all the boundary conditions and the effects of viscosity were satisfied to second order.

A. Y. Odabasi (SSRA)

The authors presented us an original and valuable paper on the viscous-inviscid flow interaction and direct resistance calculations. I would like to raise a few questions both to improve my own understanding on the method and to offer some possible improvements.

The authors state that they employed the solution of the Neumann-Kelvin problem as the inviscid outer flow. From our experience at B.S.R.A. we know that the predictions obtained by this approach become particularly unreliable towards the stern, if no ad hoc correction is made. This, at least in the first iteration, may produce unacceptable integral boundary layer parameters at the region of aft-end. I would suggest that the use of the solution of the Neumann problem at the first iteration may increase the speed of convergence.

The next point I would like to take up is the normal momentum transfer equation (1b). Although the equation used by the authors is correct according to the order of magnitude analysis carried out by them, it does not comply with the measured behaviour in thickening boundary layers as it does not contain the Reynolds stress gradient terms, as suggested by Bradshaw¹ and extended by Odabasi². A more appropriate equation would be

$$\frac{U}{h_1} \frac{\partial V}{\partial x} + V \frac{\partial V}{\partial y} + \frac{K}{h_1} \frac{\partial V}{\partial z} - K_1 U^2 - K_2 W^2$$

$$= - \frac{\partial}{\partial x} \left(\frac{p}{\rho} + \langle v^2 \rangle \right) - \frac{1}{h_1} \frac{\partial}{\partial x_1} \langle uv \rangle - \frac{1}{h_1} \frac{\partial}{\partial z} \langle vw \rangle$$

The authors rightly point out to the effect of variation of the metric coefficients across the boundary layer and draw attention to the fact that the sign of streamline curvatures may change along the normal. Such a change, however, will not immediately imply a change in the velocity profiles since their essential influence will appear through the action of the extra strain rates which, in turn, carries the effects of the upstream flow history. In this respect it should also be mentioned that in order to account for the extra strain rate effects Head's en-

trainment function needs to be modified, cf. Bradshaw¹.

The method proposed by the authors for the computation of the wake also deserves some attention. Since the measurements made on aerofoil and axially symmetric body wake indicate that the shear vector needs not vanish in the symmetry plane, as one would expect in a mixing layer, their assumption on vanishing skin friction is suspect. In our computations we adopted Bradshaw's interactive hypothesis³ which (although may need some further modification) has been proved to work for aerofoil and axially symmetric body wakes. According to this approach there exists a region, called inner-wake region, which displays somewhat different behaviour (i.e. overlapping boundary layers) than the ordinary boundary layers.

In employing the displacement surface concept, the authors discard the terms related to δ_1 in equation (33). Although, as a result of the small cross-flow assumption δ_1 may be small, it does not necessarily imply that $\partial \delta_1 / \partial x$ and, in particular, $\partial \delta_1 / \partial z$ should be small. Our calculations showed that the contribution from $\partial \delta_1 / \partial z$ is comparable with the other terms, especially in the regions where the sign of lateral curvature changes.

The final question I would like to ask is related to the cost of computation. Since the main advantage of using an integral method is its computational ease, and hence the lower computation cost, with the additions and improvements made by the authors, one needs to ask whether this same advantage remains in favour of an integral method.

I will be very pleased to know the response of the author to the points raised in this discussion.

REFERENCES

- 1) Bradshaw, P. "Higher-Order Viscous-Inviscid Matching", Dept. of Aeronautics, Imp. College of Science and Technology, I.C.Aero.Tech.Note 78-103, (1978)
- 2) Odabasi, A.Y. "Boundary Layer-Inviscid Flow Matching in Thickening Boundary Layers", B.S.R.A. Report WG/PHIVE 42, (1978)
- 3) Bradshaw, P. "Effects of Streamline Curvature on Turbulent Flow", NATO Advisory Group for Aerospace Research & Development, AGARD-AG-169, (1973)
- 4) Bradshaw, P. "Prediction of the Turbulent Near-Wake of a Symmetrical Aerofoil", *AIAA Journal* Vol. 8, p.1507, (1970)

Author's Reply

L. Larsson (SSRA)

Reply to Mr. Okuno

(1) We agree that it would be more accurate to consider the continuity equation instead of assuming a linear variation of the normal velocity. Although this will considerably complicate some expressions, we have been considering this as a possible improvement.

(2) The surface curvature along and normal to the streamlines is calculated using standard formulae from differential geometry. Second order derivatives of the surface function are then needed as are the derivative of the streamline slope. Since this is a mathematical hull form the former may be obtained analytically, while the latter is obtained by means of cubic splines. The computation is greatly simplified by the smoothness of the hull and we know from experience that much more care is needed for real ships where measured offsets are used for defining the hull.

Reply to Prof. Mori

The authors are grateful to Prof. Mori for presenting this interesting comparison of his measurements and the wake assumption for the longitudinal velocity. By the time the wake method was designed we did not have access to these measurements. Obviously the assumption is not very accurate close to the stern. However, it is not for sure that this will have a large influence on the wake development. As a matter of fact, Gadd in his paper to the International Symposium on Ship Viscous Resistance in 1978 concluded that the difference between the present wake assumption and the power-law is so small when they are used for obtaining relations between integral thicknesses that it might not be worthwhile taking the extra effort of introducing these new relations. Prof. Mori's results seem to fall somewhere in between, so the difference between the measured and assumed profiles might not be crucial. It would however be pointed out that for the relation $H_1 = H_1(H_{1,2})$ we have used a continuous change from one assumption to the other, see Eq.(31).

Reply to Prof. Landweber

Prof. Landweber's comparisons between the measured and computed wave resistance coefficients are extremely interesting. The only reason why such a comparison was not made in the paper was that we did not

have access to measurements in the absence of sinkage and trim. Now Prof. Landweber has corrected the Shearer and Cross measurements for these effects and the comparison with our calculations seems very promising.

In the oral discussion Prof. Landweber expressed some doubts on the magnitude of the computed pressure drag at zero F_n . We have computed this in two ways (cf sections 3.4 and 4.2) yielding 2.7% resp. 4.0% of C_F . According to Relf's wind tunnel measurements this drag should be around 7% (according to the experimenter) but this figure might be questioned since the pressure measurements are scattered. However, the total drag was only about 5% higher than the Schoenherr line or we think our prediction should be reasonable.

Reply to Dr. Odabasi

We have the same experience as Dr. Odabasi as to the use of the Neumann-Kelvin solution for the first boundary layer iteration. In the calculation presented in the paper, the Neumann solution has therefore been used for this purpose, introducing the (linearized) free surface condition only in the second iteration.

Dr. Odabasi's suggestions as to the stress gradient terms in the normal momentum equations, the modification of the entrainment function to account for the extra strain rates and the wake symmetry condition are much appreciated. We will carefully study the references cited, for possible improvements in our method.

In our opinion the term $\partial \delta_2 / \partial z$ can be safely neglected in this case. This appears from Fig.15, where the gradient of the measured δ_2 is quite small. It is not surprising, though, that Dr. Odabasi has found large transverse gradients of δ_2 in his calculations. A common feature of boundary layer methods applied to ship sterns seems to be that they exaggerate crosswise fluctuations. This appears for instance from the results of the SSPA-ITTC Ship Boundary Layer Workshop.

The computations using the integral method presented are still considerably cheaper than the ones using a differential method. However since the cost of the potential flow solutions (the Neumann-Kelvin's solution in particular) is so great the relative difference in total cost may not be too significant. If detailed knowledge of the flow field around the stern is expected a differential method might therefore be preferred.

Calculation of Near Wake Flow and Resistance of Elliptic-Waterplane Ships

Kazuhiro Mori
Hiroshima University
Hiroshima, Japan

ABSTRACT

The present paper is concerned with theoretical predictions of near wake flow of elliptic-waterplane ships and estimations of their resistance. Computed results are compared with corresponding experimental results.

Viscous flow predictions around sterns are carried out 2-dimensionally by the matching methods; the related separated flow field is divided into five subregions and different approximations are adopted for each subregion. Satisfactory results are obtained in the velocity and pressure distributions compared with those measured.

The viscous resistance and the wave resistance are estimated by use of the predicted viscous flows. The former is estimated by direct integrations of momentum loss behind ships. The latter is estimated in the framework of the low speed theory; the viscous flow field is taken into account by entraining the predicted viscous flows on the low speed theory.

The viscous resistance is well reproduced while the wave resistance shows still discrepancies between the towing test results but significant viscous effects on it, however, are detected.

NOMENCLATURE

L, ℓ	ship model length and half length
b	ship model half breadth
S_0	length along waterline of model
ρ	fluid density
ν	kinematic viscosity coefficient
ν_e	eddy viscosity coefficient
g	gravity acceleration
U	ship speed
F_n	Froude number ($=U/\sqrt{gL}$)
R_n	Reynolds number ($=UL/\nu$)
x, y, z	Cartesian coordinate
x_1, x_2, x_3	curvilinear orthogonal coordinate
p	pressure

u, v, w	double model velocity components in x, y, z directions
q_1, q_2, q_3	mean velocity components in x_1, x_2, x_3 directions
q_1', q_2', q_3'	fluctuating velocity components in x_1, x_2, x_3 directions
$\omega_1, \omega_2, \omega_3$	vorticity components in x_1, x_2, x_3 directions
R	total resistance
R_v	viscous resistance
R_w	wave resistance
R_f	frictional resistance
K	form factor for Schoenherr's friction line
τ_0	skin friction
θ_1	momentum thickness
H_1	shape factor

1. INTRODUCTION

Theoretical predictions of flow field around ship stern including the affects of separation is one of the most important problems in the naval hydrodynamics. It will serve not only for the determination of the wake contour on propeller disk but for theoretical estimations of ship resistance.

During a past decade theoretical researches in the viscous flow problems are mainly concerned on boundary layer flows. Developments in boundary layer computations are quite remarkable. The workshop on ship boundary layer computations, which was held at SSPA recently, shows us the present state vividly.

Though there still remain important problems such as handling of bilge keels or concave framelines, contributions done through boundary layer computations should not be underestimated. This is because the boundary layer is the very region to which all kinds of viscous problems are related; theoretical developments in the boundary layer flow will provide robust tools for theoretical studies in viscous flows.

However, the application of the boundary layer approximation to the ship wake predictions should be claimed for the beyond use of its approximation. The method for the prediction

of wake must be free from the separation; it must afford the backward effects also. The boundary layer assumption is, strictly speaking, not valid any more for such flows. Even though significant separations are not occurring, the outer flow gets to have ambiguous meanings to the inner flow when the boundary layer thickness is not thin. It is true some iterative calculations may contrive these unfavorable situations, but it must still be founded on the first iteration solution which has been almost diverging.

Though remarkable successes in the boundary layer approximation leave us much reluctances in its application to the near wake predictions, we should bravely provide some alternative ways instead.

Several attempts have been made to predict the ship wake by different methods apart from the boundary layer approximation (e.g., Hatano et al [1], Mori et al [2], Muraoka [3] etc.), but we have not yet succeeded satisfactorily. We are still under the birth-pangs.

In the present paper the velocity predictions are attempted first by the matching method [2]; we confine ourselves to the 2D flows around the elliptical waterplane ships in order to be free from numerical errors as possible.

Precise predictions of near wake flows provide not only a way to estimate the viscous resistance but a way to discuss the viscous effects on the wave resistance.

Recent remarkable developments in the wave resistance theory have unveiled relative significances of what have been overlooked or neglected because deviations from measured resistance were large. One of them may be the neglect of viscosity; the interaction between the boundary-layer-wake and the wave.

The neglect of the viscosity has been sometimes a refuge of insufficiencies of the potential wave resistance theory. So the introductions of viscosity have been often carried out to compensate the discrepancies between the inviscid theory and experiments. It is rather important, however, to make clear how far the neglect of viscosity is responsible for the discrepancies than making up them. For this sake the prediction of the viscous flow should be the same order in approximations as those used in the potential theory. But it was so unhappy that the boundary layer and wake flows have been approximated irreverently to the real flows when they were dealt with by potential-born researchers (e.g., Havelock [4], Maruo et al [5]); they were determined in some cases only to make up gaps. On the contrary, most of boundary-layer-born researchers calculated the wave resistance by the Michell approximation while they estimate the displacement thickness exactly from the boundary layer calculation (e.g., Himeno [6]). Of course their works are milestones in the related problem.

It should be stressed again that the present author does intend neither to make up the gaps nor to point out the seriousness of the neglect of viscosity, but to predict the wave resistance including viscous effects consistently as possible.

Secondly in the present paper, the viscous resistance together with the wave resistance including the viscous effects are predicted from the above viewpoint. The former is determined by applying the momentum theory directly to the yielded velocity profiles; the latter is estimated by entraining the yielded viscous flow field on the double-hull linearized free surface condition.

The present paper is reporting recent computational results according to author's previous works [2] [7] together with experimental results. Some of the main streams of computations may be repeated here compactly but precise descriptions

are left for the references

2. PREDICTION OF NEAR WAKE FLOW FIELD

Navier-Stokes equations are the governing equations for flows around ship stern. It is not an exaggeration to say that what kinds of approximations of them are adopted is the all for the present problem.

Now we divide the flow field into five subregions as shown in Fig. 1 to find out the most suitable approximations for each subregion. By such a subdivision, no universal approximations valid for the whole flow field are necessary. The subdivision is carried out after the observation of real flow, Fig. 2 shows the free surface flow of EM-200, one of the models used here, which makes us recognize the subdivision.

The subregion A is the potential flow region, B is the region where the boundary layer approximation is thoroughly valid, C is the region into which the vorticity generated in the upstream boundary layer is shed; D is where complicated retarding flows are existing, sometimes recirculating flows; E is the sublayer like the viscous sublayer where the nonslip condition is required. The border line (or surface) is tentatively called dividing streamline (DSL).

Following approximations are made for each subregion. A-region : inviscid potential flow; Euler equations are used. B-region : boundary layer approximation, boundary layer equations are used.

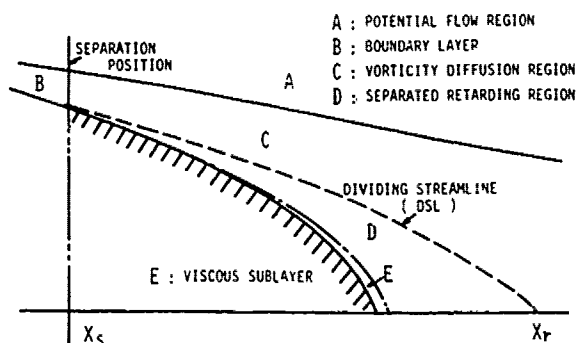


Fig. 1 Subdivision of Separated Near Wake Flow Field

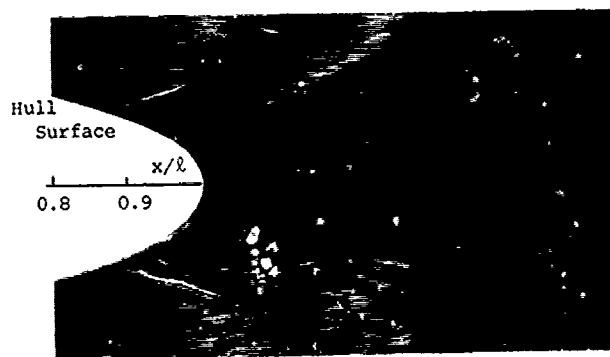


Fig. 2 Free-Surface Flow around Stern of EM-200
($F_n = 0.157$, $R_n = 1.295 \times 10^6$)

C-region : constant eddy viscosity approximation; the vorticity equations are used.

D-region : original Reynolds equations are used.

E-region : turbulent intensity is assumed negligibly small.

The original Reynolds equations and the vorticity equations are written in Appendix. The coordinate systems are shown in Fig. 3; O-xyz is a Cartesian coordinate whose origin is at the midship and on the still waterplane. The ship is fixed and the uniform flow is oncoming to x-direction with velocity U. Broadly speaking, x_1 coincides with the main flow direction and x_3 is the normal direction to the hull surface.

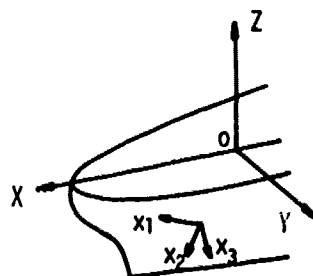


Fig. 3 Coordinate Systems

The approximation of the constant eddy viscosity for C-region may be open to discussions. But because the region to which this approximation is applied is restricted, we can be optimistic in its employment. The reason why the vorticity equations are used for C-region is that the pressure term which is somewhat delicate in handling due to interactions disappears from the momentum equations by operating rotation to them. Of course boundary conditions for the vorticity are required which are not so clear as that of velocity.

If we define small parameter ϵ by

$$\epsilon = R_n^{-1/6}, \quad (1)$$

ϵ can be enough small when Reynolds number is large. Eventually each term of the power series of ϵ yields significant differences each other.

Now we expand velocity, vorticity and pressure in power series of ϵ whose assumed leading orders for C-, D- and E-regions are shown in Table 1. The related variables are expanded starting

Table 1 Leading Orders for C-, D- and E-regions

	q_1	q_2	q_3	ω_1	ω_2	ω_3	p	$\partial/\partial x_3$
C-region	1	ϵ	ϵ^2	ϵ^{-1}	ϵ^{-2}	ϵ^{-1}		ϵ^{-2}
D-region	ϵ	ϵ	ϵ^3				ϵ	ϵ^{-3}
E-region	ϵ	ϵ	ϵ^4				ϵ^2	ϵ^{-4}

from the above orders, e.g., the velocity components of C-region are expanded as follows,

$$\begin{aligned} q_1/U &= \tilde{u}_0 + \epsilon \tilde{u}_1 + \epsilon^2 \tilde{u}_2 + \dots, \\ q_2/U &= \epsilon \tilde{v}_1 + \epsilon^2 \tilde{v}_2 + \dots, \\ q_3/U &= \epsilon^2 \tilde{w}_1 + \epsilon^3 \tilde{w}_2 + \dots \end{aligned} \quad (2)$$

It is assumed that changes in orders by differentiations with respect to x_1 and x_2 are $O(1/\epsilon)$ and orders of K_{ij} are all $O(1)$.

Convergences of such expansions may be examined together with the order assumptions. But no one can say at this stage that they are assured or not. It is important, however, that assumptions should be kept consistent throughout the problem and yielded equations can potentially afford to govern the related flows.

Substitutions of the power series expansions of velocity, vorticity and pressure into the Reynolds equations or the vorticity equations, Eqs. (A-1-A-10) shown in Appendix, yield the following equations as the leading order terms.

C-region :

$$\frac{\partial}{\partial x_2}(\omega_2 q_1) + \frac{\partial}{\partial x_3}(\omega_3 q_1) = 0, \quad (3)$$

$$\nu \frac{\partial^2 \omega_2}{\partial x_3^2} - \frac{\partial}{\partial x_1}(\omega_2 q_1) = 0, \quad (4)$$

$$\nu \frac{\partial^2 \omega_3}{\partial x_3^2} - \frac{\partial}{\partial x_1}(\omega_3 q_1) = 0. \quad (5)$$

D-region :

$$q_1 \frac{\partial q_1}{\partial x_1} + q_2 \frac{\partial q_1}{\partial x_2} + q_3 \frac{\partial q_1}{\partial x_3} = -\frac{1}{\rho} \frac{\partial p}{\partial x_1} \quad (6)$$

$$+ \epsilon_1 \left(\frac{\partial^2 q_1}{\partial x_1^2} + \frac{\partial^2 q_1}{\partial x_2^2} - \frac{1}{h_1 h_3} \frac{\partial^2 q_3}{\partial x_1 \partial x_3} \right) + \epsilon_2 \frac{\partial^2 q_1}{\partial x_3^2},$$

$$q_1 \frac{\partial q_2}{\partial x_1} + q_2 \frac{\partial q_2}{\partial x_2} + q_3 \frac{\partial q_2}{\partial x_3} = -\frac{1}{\rho} \frac{\partial p}{\partial x_2} \quad (7)$$

$$+ \epsilon_1 \left(\frac{\partial^2 q_2}{\partial x_1^2} + \frac{\partial^2 q_2}{\partial x_2^2} - \frac{1}{h_2 h_3} \frac{\partial^2 q_3}{\partial x_2 \partial x_3} \right) + \epsilon_2 \frac{\partial^2 q_2}{\partial x_3^2},$$

$$\frac{\partial p}{\partial x_3} = 0. \quad (8)$$

E-region :

$$\begin{aligned} q_1 \frac{\partial q_1}{\partial x_1} + q_2 \frac{\partial q_1}{\partial x_2} + q_3 \frac{\partial q_1}{\partial x_3} \\ = -\frac{1}{\rho} \frac{\partial p}{\partial x_1} + \nu \frac{\partial^2 q_1}{\partial x_3^2}, \end{aligned} \quad (9)$$

$$q_1 \frac{\partial q_1}{\partial x_1} + q_2 \frac{\partial q_2}{\partial x_2} + q_3 \frac{\partial q_3}{\partial x_3} = -\frac{1}{\rho} \frac{\partial p}{\partial x_2} + \nu \frac{\partial^2 q_2}{\partial x_3^2}, \quad (10)$$

$$\frac{\partial p}{\partial x_3} = 0. \quad (11)$$

The continuity equation is

$$\frac{\partial q_1}{\partial x_1} + \frac{\partial q_2}{\partial x_2} + \frac{\partial q_3}{\partial x_3} = 0. \quad (12)$$

The governing equations for C-region, Eqs. (4-5), are the diffusion equations where q_1 is the convective velocity and ν_e is the diffusion constant. Therefore they can be solved in the marching scheme. Then the velocity induced by vorticities, (u_v , v_v , w_v), can be given by virtue of Biot-Savart's law:

$$u_v = -\frac{1}{4\pi} \iiint_V \left\{ \frac{(y-y')\omega_z' - (z-z')\omega_y'}{r_0^3} + \frac{(y-y')\omega_z' + (z+z')\omega_y'}{r_1^3} \right\} dx' dy' dz',$$

$$v_v = -\frac{1}{4\pi} \iiint_V \left\{ \frac{(z-z')\omega_x' - (x-x')\omega_z'}{r_0^3} - \frac{(z+z')\omega_x' + (x-x')\omega_z'}{r_1^3} \right\} dx' dy' dz', \quad (13)$$

$$w_v = -\frac{1}{4\pi} \iiint_V \left\{ \frac{(x-x')\omega_y' - (y-y')\omega_x'}{r_0^3} - \frac{(x-x')\omega_y' - (y-y')\omega_x'}{r_1^3} \right\} dx' dy' dz',$$

where ω_x' , ω_y' and ω_z' are the vorticity components at (x' , y' , z'), and

$$\begin{aligned} r_0^2 &= (x-x')^2 + (y-y')^2 + (z-z')^2 \\ r_1^2 &= (x-x')^2 + (y-y')^2 + (z+z')^2, \end{aligned} \quad (14)$$

and V is the non-zero vorticity regions; B-, C-, D- and E-regions.

The velocity components, (u_v , v_v , w_v), given by Eq. (13) correspond to the viscous components in wake fraction. The final velocity in C-region is given by the additions of potential components;

$$\begin{aligned} u &= u_v + u_0 + u_1, \\ v &= v_v + v_0 + v_1, \\ w &= w_v + w_0 + w_1. \end{aligned} \quad (15)$$

The second terms of Eq. (15) are those obtained by inviscid calculations, which correspond to the potential wake. The last terms of Eq. (15) come from the image vorticity to the hull surface. They can be represented equivalently by additive hull surface sources; they represent viscid-inviscid interactions, in other words, the displacement effects. They are given as follows;

$$\begin{aligned} u_1 &= \frac{1}{4\pi} \iint_{S_H} \sigma_1 \left(\frac{x-x'}{r_0^3} + \frac{x-x'}{r_1^3} \right) dS, \\ v_1 &= \frac{1}{4\pi} \iint_{S_H} \sigma_1 \left(\frac{y-y'}{r_0^3} + \frac{y-y'}{r_1^3} \right) dS, \\ w_1 &= \frac{1}{4\pi} \iint_{S_H} \sigma_1 \left(\frac{z-z'}{r_0^3} + \frac{z+z'}{r_1^3} \right) dS, \end{aligned} \quad (16)$$

where S_H is the hull surface and σ_1 is the additive source distribution. σ_1 is determined to satisfy the following equation.

$$\begin{aligned} \frac{1}{2} \sigma_1 + \frac{1}{4\pi} \iint_{S_H} \sigma_1 \frac{\partial}{\partial n} \left(\frac{1}{r_0} + \frac{1}{r_1} \right) dS \\ + (u_v n_0 + v_v m_0 + w_v n_0) = 0 \end{aligned} \quad (17)$$

n is the outward normal on hull whose direction cosines are (k_e , m_0 , n_0).

The governing equations for D-region, Eqs. (6-7) are elliptic type and they may govern recirculating flows. Then the problem gets a boundary value problem; they are solved under the boundary conditions prescribed on the hull surface, DSL and axis. In the reduction of Eqs. (6-8), the turbulent terms are expressed by the eddy viscosity of a vectorial constant whose components are κ_1 and κ_2 .

The governing equations for E-region, Eqs. (9-11), are exactly the boundary layer equations; D-region flow plays the role of the outer flow.

The B-region solutions are obtained by the usual boundary layer calculations while the potential flow can be supplied by the well-familiar method.

The matching conditions between each subregion are derived in the original paper [2], but in the numerical calculations exact satisfactions of them are almost impossible and we confine ourselves here only to impose the condition that the velocity and the pressure are continuous (not always their gradients) throughout the region.

The assumption of DSL may leave some arbitrariness, but this is inevitable in the present scheme. Iterative computations may remove it; the assumption of DSL can be understood as a first iteration.

All predictions in the present section are without free surface; under the double-hull condition.

3. ESTIMATION OF RESISTANCE

If the velocity components are represented by the sum of the double-hull velocity (u, v, w) and the gradient of the wavy potential ϕ , then, by use of the momentum theorem, the total resistance of ship is given as follows [7];

$$R = R_v + R_w + R_{vw} \quad (18)$$

$$R_v = \rho g \int_{-\infty}^{\infty} dy \int_{-\infty}^0 (H_0 - H) dz + \frac{\rho}{2} \int_{-\infty}^{\infty} dy \int_{-\infty}^0 \left\{ -(U-u)^2 + v^2 + w^2 \right\} dz, \quad (19)$$

$$R_w = \frac{\rho}{2} \int_{-\infty}^{\infty} dy \int_{-\infty}^0 \left\{ -\left(\frac{\partial \phi}{\partial x}\right)^2 + \left(\frac{\partial \phi}{\partial y}\right)^2 + \left(\frac{\partial \phi}{\partial z}\right)^2 \right\} dz + \frac{\rho}{2} g \int_{-\infty}^{\infty} \zeta^2 dy, \quad (20)$$

$$R_{vw} = \rho \int_{-\infty}^{\infty} dy \int_{-\infty}^0 \left\{ (U-u) \frac{\partial \phi}{\partial x} + v \frac{\partial \phi}{\partial y} + w \frac{\partial \phi}{\partial z} \right\} dz, \quad (21)$$

where ζ is the free surface elevation; H_0 and H are total heads given by

$$\rho g H_0 = P_0 + \frac{1}{2} \rho U^2, \quad (22)$$

$$\rho g H = P + \frac{1}{2} \rho (u^2 + v^2 + w^2).$$

The integrations are carried out on the control surfaces properly chosen.

R_v and R_w give the viscous resistance and wave resistance respectively, while R_{vw} is their interaction component. The integrations of Eqs. (19–20) can be rather easily carried out as described later. On the contrary, that of Eq. (21) is a little complicated. For this reason the interaction component will be not included in the present calculation.

Alternatively, representing the total resistance by the sum of the frictional force and the normal force, it is sometimes estimated by the hull surface integrations;

$$R_f = \iint_{S_H} \tau_{0x} dS, \quad (23)$$

$$R_p = - \iint_{S_H} P \ell_n dS, \quad (24)$$

where τ_{0x} is the x-component of the skin friction τ_0 . R_f gives

the frictional resistance while R_p the pressure resistance.

In the expression of Eqs. (23–24) interaction component is included implicitly in τ_{0x} and P . So they seem more convenient for full estimations of resistance. But, contrary to the easiness of the integration of Eq. (23), the integration of Eq. (24) often yields significant errors in the final results in case of ship-like bodies where ℓ_0 is not small; even slight error in the pressure prediction may cause significant errors. In the present paper only the frictional resistance is estimated by Eq. (23).

All the quantities necessary for the estimation of the viscous resistance by Eq. (19) are provided by the calculations of section 2 except the pressure.

The pressure in C-region can be determined by invoking the y-direction Navier-Stokes equation with a constant eddy viscosity;

$$u \frac{\partial v}{\partial x} + v \frac{\partial v}{\partial y} + w \frac{\partial v}{\partial z} = -\frac{1}{\rho} \frac{\partial p}{\partial y} + \nu_e \left(\frac{\partial^2 v}{\partial x^2} + \frac{\partial^2 v}{\partial y^2} + \frac{\partial^2 v}{\partial z^2} \right). \quad (25)$$

With the neglecting of the first and the second terms in bracket of rhs of Eq. (25), which are safely approved, it can be transformed as follows;

$$u \omega_z - w \omega_x + \frac{1}{2} \frac{\partial}{\partial y} (u^2 + v^2 + w^2) = -\frac{1}{\rho} \frac{\partial p}{\partial y} + \nu_e \frac{\partial^2 v}{\partial y^2}, \quad (26)$$

where ω_x and ω_z are the vorticity components in x- and z-directions respectively; they are given by

$$\omega_x = \frac{\partial w}{\partial y} - \frac{\partial v}{\partial z}, \quad (27)$$

$$\omega_z = \frac{\partial v}{\partial x} - \frac{\partial u}{\partial y}.$$

The integration of Eq. (26) with respect to y yields the explicit expression for the pressure;

$$P = P_0 + \frac{1}{2} \rho U^2 - \frac{1}{2} \rho (u^2 + v^2 + w^2) + \rho \int_y^{y_0} (u \omega_z - w \omega_x) dy - \nu_e \frac{\partial v}{\partial y}, \quad (28)$$

where p_0 is the static pressure at far upstream. In Eq. (28), y_0 is a point just outside of the wake where the total head is equal to that at far upstream; the relation of

$$\frac{1}{2} \rho U^2 + P_0 = P + \frac{1}{2} \rho (u^2 + v^2 + w^2) \Big|_{Y=Y_0} \quad (29)$$

can be assumed.

Eq. (28) tells us that the static pressure, eventually the total head also, reduces owing to two sources; one is due to the vorticity shedding which corresponds to the third term of rhd of Eq. (28) and the other is due to the viscosity, the fourth term.

The expression of the pressure by Eq. (28) is of a convenient form when the present method of the near wake flow prediction is employed, because the vorticity distributions in wakes are being supplied during the computing scheme.

Next, let's consider the wave resistance component given by Eq. (20).

When the Reynolds number is enough large head losses due to viscosity may occur exclusively in the two regions: in the free surface boundary layer and in the hull boundary layer and its accompanied wake. Eventually only flows in these two regions may yield some viscous effects on the wave resistance. However, according to the conclusion of the previous work [7], the neglect of the free surface boundary layer effects is allowed within the approximations made in the inviscid wave resistance theory on which we are going to entrain. Therefore it is enough only for the head loss in the hull boundary layer and its accompanied wake to be taken into account in the wave resistance estimation.

If the low speed assumption is appreciated [8], the double-hull linearized free surface condition is given by

$$\frac{1}{g} \left[u(x, y, 0) \frac{\partial}{\partial x} + v(x, y, 0) \frac{\partial}{\partial y} \right]^2 \phi(x, y, z) + \frac{\partial}{\partial z} \phi(x, y, z) = D(x, y), \quad (30)$$

where

$$D(x, y) = -\frac{1}{g} \left\{ u^2 \frac{\partial u}{\partial x} + u v \left(\frac{\partial u}{\partial y} + \frac{\partial v}{\partial x} \right) + v^2 \frac{\partial v}{\partial y} \right\} - \frac{\partial w}{\partial z} \left\{ \frac{1}{2g} (U^2 - u^2 - v^2) - (H_0 - H) \right\}. \quad (31)$$

u , v and w , appearing in rhs of Eq. (31), are the double hull velocity components and the gradients of $H_0 - H$ at $z=0$ are given by

$$\frac{\partial}{\partial x} (H_0 - H) = -v \omega_z,$$

$$\frac{\partial}{\partial y} (H_0 - H) = u \omega_z. \quad (32)$$

Then the quantities of rhs of Eq. (30) are all provided by the calculations of section 2.

Under the free surface condition of Eq. (30), the wavy potential can be determined and Eq. (20), which is giving the wave resistance, can be written in another form [8];

$$R_w = \pi \rho U^2 \int_0^{\pi/2} |A^*(\theta)|^2 d\theta, \quad (33)$$

where

$$A^*(\theta) = -\frac{g}{\pi U^3} \sec^{3/2} \theta \times \iint_{-\infty}^{\infty} D(\xi, \eta) e^{i \frac{g}{U^3} \sec^2 \theta (\xi \cos \theta + \eta \sin \theta)} d\xi d\eta. \quad (34)$$

The expressions of Eqs. (33-34) are formally the same as those of the inviscid case except $D(x, y)$ contains the head loss term. But the velocity components (u, v, w) are viscous and the pressure field differs from that of inviscid case.

4. NUMERICAL COMPUTATIONS AND EXPERIMENTS

4.1 Used Models

Three EM-series models which have elliptic-waterplanes are given by

$$\frac{x^2}{a^2} + \frac{y^2}{b^2} = 1 \quad (35)$$

and have vertical hull sides are used for the present studies. Their rough view is shown in Fig. 4. The ratios of major and minor axes are varying from 0.125 to 0.30; 0.125, 0.20 and 0.30 for EM-125, EM-200 and EM-300 respectively. The length and the draft are 2.00 m and 0.50 m respectively for all the models.

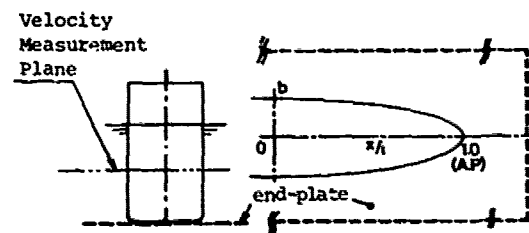


Fig. 4 Rough Sketch of Used Models

It is expected by such a choice of models that flows may be simple but with some separations and the affections of separation may change serially between each model.

All the near wake computations are carried out 2-dimensionally, while the corresponding experiments are carried out with end-plates beneath the model bottoms, as shown in Fig. 4, by which full 2-D flows may be realized.

The wave resistance computations are carried out 3-dimensionally. This is because the formation of section 3 are not applicable to 2-D flows [7] and also because the 2-D resistance tests by towing tank are not easy.

4.2 Near Wake Flow

The numerical computations for near wake flow are started by the potential calculation. In the present case, the potential velocity components u_0 and v_0 are given analytically by

$$u_0/U = \frac{\xi+b}{2c^2h^2} \{ \xi (\cosh 2\xi - \cos 2\eta) - \sinh 2\xi \}, \quad (36)$$

$$v_0/U = -\frac{\xi+b}{2c^2h^2} b \sin 2\eta,$$

where

$$\begin{aligned} x &= c \cosh \xi \cos \eta, \\ y &= c \sinh \xi \sin \eta, \\ h^2 &= \cosh^2 \xi - \cos^2 \eta, \\ c^2 &= \xi^2 - b^2. \end{aligned} \quad (37)$$

Next, the boundary layer calculation is carried out. The higher approximations are not necessary because it is ceased

before the boundary layer thickness gets thick. The integral momentum equations are

$$\frac{\partial \theta_1}{h_1 \partial x_1} = -(H+2) \frac{\theta_1}{U_0} \frac{\partial U_0}{h_1 \partial x_1} + \frac{\tau_0}{\rho U_0^2}, \quad (38)$$

$$\begin{aligned} \frac{\partial H}{h_1 \partial x_1} &= \frac{H(H-1)}{\theta_1} \frac{\tau_0}{\rho U_0^2} - \frac{H(H+1)(H-1)}{U_0} \frac{\partial U_0}{h_1 \partial x_1} \\ &\quad - \frac{(H-1)^2}{2\theta_1} E, \end{aligned} \quad (39)$$

where

$$h_1 = \frac{(\xi^2 - c^2 \cos^2 \eta)^{1/2}}{\sin \eta}, \quad (40)$$

$$\frac{1}{U_0} \frac{\partial U_0}{h_1 \partial x_1} = -\frac{b^2}{\xi^3} \frac{1}{\tanh \eta} (\xi^2 - c^2 \cos^2 \eta)^{-3/2},$$

and U_0 is the resultant velocity at the boundary layer edge; E is the entrainment. Ludwig-Tillmann's formula and Head's function are used for the skin friction and the entrainment respectively. Computations are made for Reynolds numbers of 1.68×10^6 for EM-125 and EM-300, and of 1.295×10^6 for EM-200.

The results are shown in Fig. 5. For all the cases, the calculations diverged around $x/l = 0.95$ where the skin frictions have still non-zero values. (Referring to the free surface flow of EM-200, shown in Fig. 2, the separations are suspected before $x/l = 0.9$.) The momentum thickness and the shape factor do not differ between models, but the skin frictions do, which will show the form effects on the frictional resistance.

The results of the boundary layer calculation supply the initial vorticity distributions for the C-region calculation. They

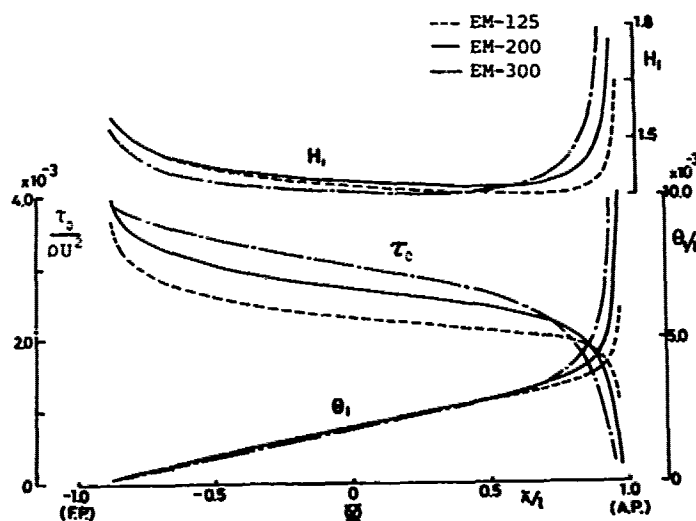


Fig. 5 Results of Boundary Layer Computations

also provide the separation positions necessary for the initial assumption of DSL.

DSL is determined by a tangent at the separation position. In the present calculation, it is determined for three models as shown in Fig. 6; the positions of departures of DSL are at $x/L = 0.85, 0.80$ and 0.75 for EM-125, EM-200 and EM-300 respectively. These positions seem to be a little upstream when the results of boundary layer calculation or the free surface flow, shown in Figs. 2 and 5, are referred to. But it is of safe side to assume the separation position upstream because the governing equations for D-region, Eqs. (6-8), can govern the boundary layer flow too.

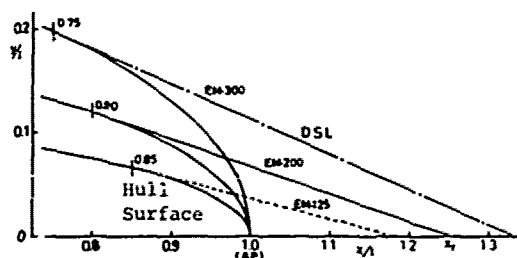


Fig. 6 Assumed Dividing Streamlines (DSL)

Assumed DSL is chosen for $x_3 = 0$ surface. Then the vorticity diffusion equation in x_1 direction, Eq. (4), can be transformed in a finite difference form as follows:

$$A_j \omega_2(i+1, j-1) + B_j \omega_2(i+1, j) + C_j \omega_2(i+1, j+1) = D_j, \quad j \geq 1 \quad (41)$$

where $\omega_2(i, j)$ etc. denote values at $x_1 = x_{1i}$, $x_3 = x_{3j}$ and

$$\begin{aligned} A_j &= \frac{v_e}{\Delta \zeta_1' (\Delta \zeta_1' + \Delta \zeta_2')} \\ B_j &= -\frac{v_e}{\Delta \zeta_1' \Delta \zeta_2'} - \frac{q_1(i+1, j)}{\Delta \xi_1} \\ C_j &= \frac{v_e}{\Delta \zeta_2' (\Delta \zeta_1' + \Delta \zeta_2')} \\ D_j &= -B_j \omega_2(i, j-1) + \left(\frac{v_e}{\Delta \zeta_1 \Delta \zeta_2} - \frac{q_1(i, j)}{\Delta \xi_1} \right) \omega_2(i, j) - C_j \omega_2(i, j-1) \end{aligned} \quad (42)$$

$\Delta \xi_1$ etc. are short line segments as shown in Fig. 7.

Eq. (41) is a tridiagonal linear equation which can be solved if $\omega_2(i, 0)$ and $q_1(i, j)$ are provided. $\omega_2(i, 0)$ is the value of vorticity at $x_3 = 0$, namely, on DSL and it is zero after

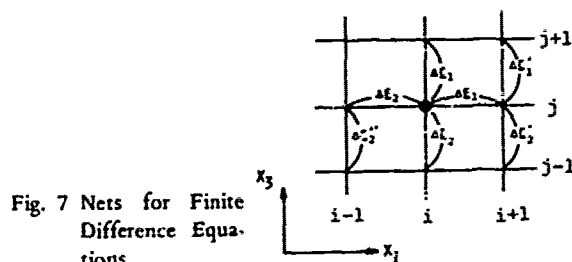


Fig. 7 Nets for Finite Difference Equations

the reattaching point x_1 , where DSL intersect x_1 -axis for the sake of symmetry. So $\omega_2(i, 0)$ is given a priority by a linear function which gets equal to zero at $x = x_1$. $q_1(i, j)$ is supplied approximately, by the use of the solution at the previous step, by

$$q_1(i, j) = U - \sum_{j'=j}^N \omega_2(i-1, j') \Delta \zeta_2'' \quad (43)$$

N means the position where vorticity is almost zero. Of course v_e should be also supplied: here it is assumed to be equal to 50 times of the molecular viscosity.

Invoking Eq. (13), viscous velocity components are determined by integration of yielded vorticity distributions. In the integration of Eq. (13) the vorticity distribution in B-region is also included which is determined by Eq. (A-11); by use of the boundary layer calculation results. The interaction components due to the image vorticities, u_1, v_1 , given by Eq. (16), are added to it together with the potential components, given by Eq. (36).

Then the velocity field of C-region has been fully determined. But at the present stage it has been determined independently on the D-region flow. This is of quite the same situation as the ordinary boundary layer calculation where the potential flow is calculated with neglect of the boundary layer flow at first. The D-region contribution will be taken into account after the D-region calculation.

Finally, the D-region calculation is carried out. Eq. (6) is transformed into a finite difference form:

$$\begin{aligned} & q_1(i, j) \frac{q_1(i+1, j) - q_1(i-1, j)}{\Delta \xi_{12}} \\ & + q_1(i, j) \frac{q_1(i, j+1) - q_1(i, j-1)}{\Delta \zeta_{12}} = -\frac{1}{\rho} \frac{\partial P}{\partial x_1} \\ & + \kappa_1 \left(\frac{2q_1(i+1, j)}{\Delta \xi_1 \Delta \xi_{12}} - \frac{2q_1(i, j)}{\Delta \xi_1 \Delta \xi_2} + \frac{q_1(i-1, j)}{\Delta \xi_2 \Delta \xi_{12}} \right) \\ & - \frac{q_1(i+1, j-1) - q_1(i+1, j+1) - q_1(i-1, j+1) + q_1(i-1, j-1)}{\Delta \xi_{12} \Delta \zeta_{12}} \\ & + 2\kappa_2 \left(\frac{q_1(i, j+1)}{\Delta \zeta_1 \Delta \zeta_{12}} - \frac{q_1(i, j)}{\Delta \zeta_1 \Delta \zeta_2} + \frac{q_1(i, j-1)}{\Delta \zeta_2 \Delta \zeta_{12}} \right) \end{aligned} \quad (44)$$

where $\Delta \xi_{12}$ etc. are the sum of $\Delta \xi_1$ and $\Delta \xi_2$. The velocity com-

ponents q_1 and q_3 in D-region can be obtained by solving Eq. (44) together with the continuity equation, Eq. (12). The required boundary conditions are

$$q_1 = q_{1c} , \quad q_3 = q_{3c} \quad \text{on DSL}, \quad (45)$$

$$q_3 = 0 , \quad \frac{\partial q_1}{\partial x_3} = 0 , \quad \text{on } y=0,$$

$$\frac{\partial}{\partial x_3} \left(\frac{\partial q_1}{\partial x_3} \right) = 0 , \quad q_3 = 0 \quad \text{on Hull},$$

where q_{1c} , q_{3c} are C-region velocities. The pressure gradient appearing in Eq. (44) is known, because the pressure is constant in x_3 direction in D-region (Eq. (8)), they are supplied by the C-region results on DSL. They are given by

$$\frac{1}{\rho} \frac{\partial P}{\partial x_1} = v_e \frac{\partial}{\partial x_3} \left(\frac{\partial q_1}{\partial x_3} \right) - q_1 \frac{\partial q_1}{\partial x_1} - q_3 \frac{\partial q_1}{\partial x_3} \quad \text{on DSL}, \quad (46)$$

where q_1 , q_3 are already known in the C-region calculation.

For the constants κ_1/l^2 , κ_2/UL , appearing in Eq. (44), 0.2 and 0.001 are used after some numerical trials.

Now the flow for all the region* have been determined. The results at the present stage may be called the first iteration solution because the existence of D-region is not taken into account for the outer flow (so this stage may correspond to the ordinary boundary layer approximation).

The second iteration is carried out by including D-region also in the non-zero vorticity region in Eq. (13). The vorticity distribution in D-region can be determined by Eq. (A-11). The addition of its induced velocity (this may be called D-region

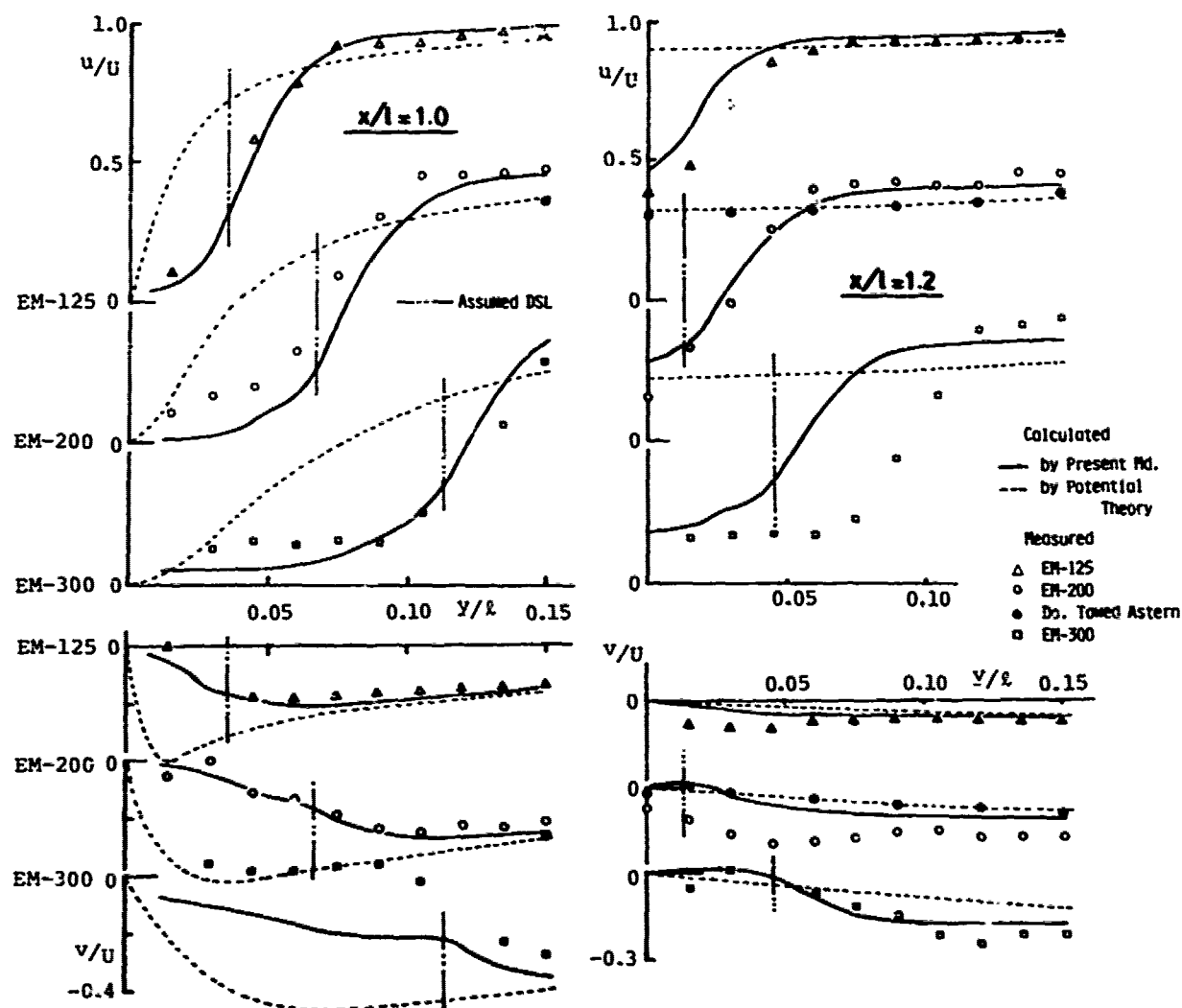


Fig. 8 Comparisons of Velocity Distributions ($x/l = 1.0, 1.2$)

contribution) gives the final results for the C-region flow. Then the D-region calculation and interaction calculation are carried out again for the new boundary conditions on DSL which gives the final velocity field.

In the present scheme the E-region flow is neglected. In this connection the first boundary condition on hull in Eq. (45) has come; in E-region q_1 is assumed to be linear in x_3 direction.

The final results of velocity distributions at $x/l = 1.0$ and 1.2 are shown in Fig. 8 together with those measured. The Reynolds numbers are 1.68×10^6 for EM-125 and EM-300, 1.295×10^6 for EM-200 respectively.

The measurements are carried out at the half of draft by 5-hole pitot tube with its axis coincident with main flow direction. By such a method we can not be sure of the possibility of measurements for recirculating flows. So results of the D-region flow, where recirculating or retarding flows are suspected, may be just for references. It is confirmed that 2-D flows are really realized by the equipment of end-plates.

As a whole the computed results show good agreements with measured except in case of EM-300. According to flow observations significant fluctuations of wake flow are observed in case of EM-300, which may suggest limitations of the present method where quasi-steady flows are assumed. In case of EM-200, velocity measurements are carried out by towing ship astern. It is very interesting that the potential velocities are providing good agreements with those measured in such a way.

Fig. 9 is one of the examples which shows the components of the C-region flow. The interaction term, u_1, v_1 is not so small while the D-region contribution is small.

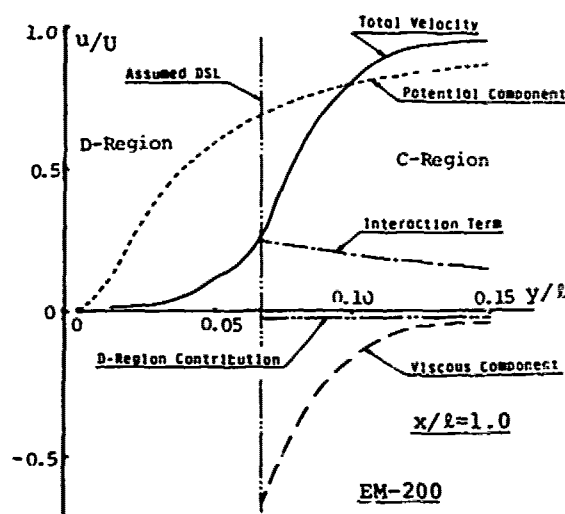


Fig. 9 Decomposition of Velocity at $x/l = 1.0$ (EM-200)

Fig. 10 is the additive source distributions which induce the interaction components. They do not increase monotonously like displacement thickness but they get maximum around the separation positions and once decrease, then increase again. The present results seem reasonable because boundary layer developments get significantly less by separations.

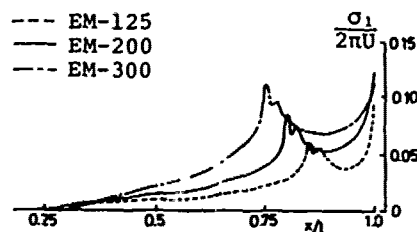


Fig. 10 Hull Surface Source Distributions Representing Interaction Component

Fig. 11 shows the vorticity distributions at $x/l = 1.1, 1.2$ and 1.3 . There measured results are also shown in case of EM-200 which are obtained by differentiations of measured velocity. Some of calculated results are not continuous on DSL due to the dissatisfaction of the continuity in velocity gradients on DSL which is not required in the present computations.

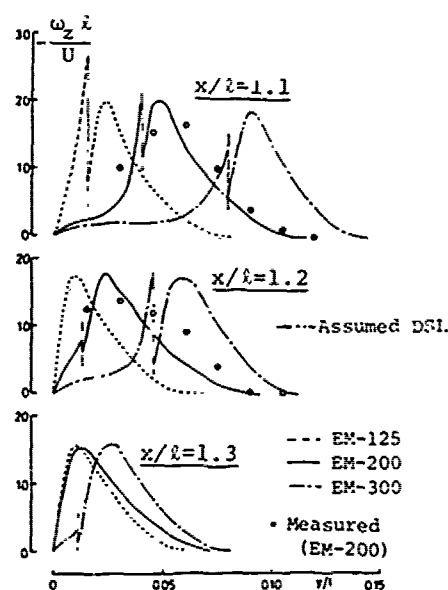


Fig. 11 Vorticity Distributions ($x/l = 1.1, 1.2, 1.3$)

Comparisons between models show just dislocation of the peaks but not significantly in magnitudes. The dislocation means the wake of EM-300 is wider than others and eventually the head loss too. The measured distributions are more mild than calculated; the peak is less and the wake width is wider. This means the diffusion is more intensive in real flows. This discrepancy seems to be removed by choosing a larger diffusion constant than 50ν , but the value of the diffusion constant does not affect so much. For the improvements some of neglected terms should be revived, which is left for future works.

Any way we can safely conclude that the present results are applicable to the resistance estimations with required accuracy.

4.3 Viscous Resistance

Before the calculation of viscous resistance, pressure distributions, which are necessary for it, are determined; by Eq.

(28) for the C-region and by Eq. (8) for the D-region.

In Fig. 12 calculated results are compared with measured in case of EM-200. The pressure is measured by a static pressure tube which is of 1.2 mm diameter with two 0.4 mm ϕ holes on diametrically opposite sides. (The accuracy of the measure

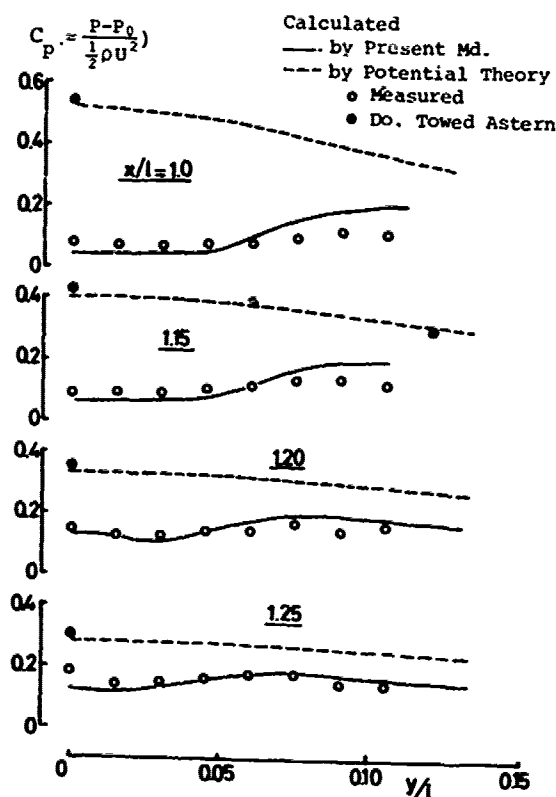


Fig. 12 Pressure Distributions in Wake of EM-200 ($x/l = 1.0, 1.15, 1.2, 1.25$)

ments is checked by measuring the pressure field by towing a model astern; they show good agreements with potential calculations as shown in Fig. 12.) Though discrepancies still exist in the outer parts of wake, they are rather well reproduced. In the calculation, ν_e is assumed 10^4 times of the molecular viscosity which differs much from that used in the diffusion calculation. This may be open to discussions, but the present author is of opinion that ν_e can not be always related to a single constant but it may depend on the related physical variables, e.g., pressure, vorticity and so on.

The viscous resistance calculation can be carried out now by invoking the previous results. In the present calculation, the integrations in Eq. (19) are carried out on more than a single control surface and averaged; two or three control surfaces are chosen around $x/l = 1.2$ in calculations. Experiments are carried out at far downstream; $x/l = 1.9$ for EM-125 and EM-200, $x/l = 2.8$ for EM-300 respectively.

The measured total head losses are shown in Fig. 13

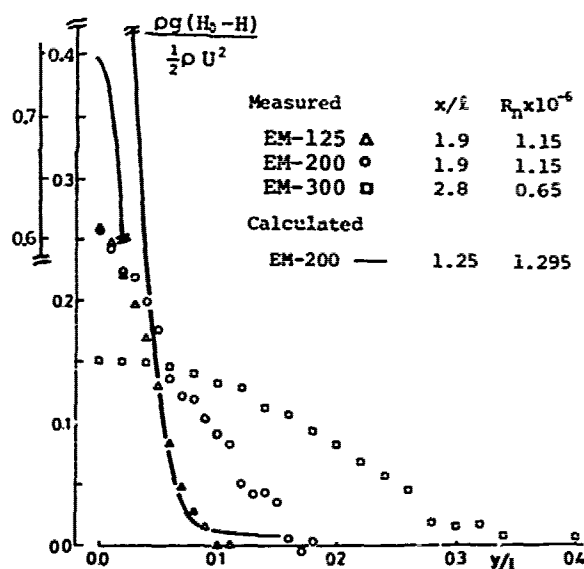


Fig. 13 Total Head Losses

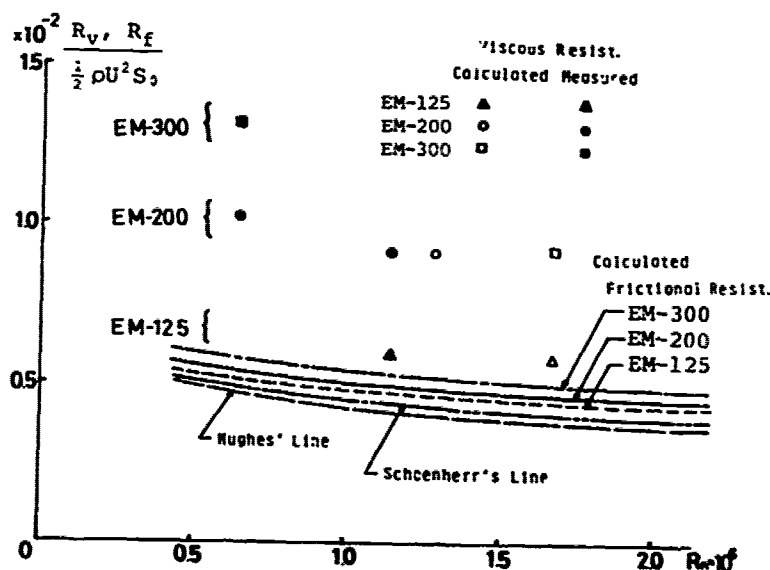


Fig. 14 Comparison of Viscous Resistance

together with the calculated result of EM-200. Their integrations provide the viscous resistance, the first term of Eq. (19). Because the calculation is carried out just behind the stern, the head loss is keenly concentrated (the coordinate should be changed from the right to the left when y approaches to zero). Measurements are carried out by a pitot tube with end-plates.

Fig. 14 shows comparisons of the viscous resistance. Calculated results agree well with measured except EM-300 which is unnaturally smaller than measured (this may be due to the same reason as mentioned in 4.2). In Fig. 14 the frictional resistance curves are also shown which are obtained by Eq. (23) where skin frictions of the boundary layer calculation are used. Subtractions give the viscous pressure resistance indirectly.

As far as the present results are appreciated, it is safely concluded that the viscous resistance can be proportional to the frictional resistance. Of course, this may be limited to the case where significant free surface effects are not existing.

4.4 Wave Resistance

In the present case, because $\partial w / \partial z$ at $z = 0$ vanishes for all the used models, the second term of Eq. (31) disappears. Calculated velocity distributions are substituted into Eq. (31). For the velocity distributions far behind in wakes, namely, $x \geq 1.20, 1.25$ and 1.35 for EM-125, EM-200 and EM-300 respectively, similar profiles are assumed; the maximum velocity defect at $y = 0$, $U - u(x, 0)$, is assumed to be proportional to $x^{-2/3}$ while the breadth of wake spreads to proportionally to $x^{1/3}$.

In Fig. 15, the calculated wave resistance is compared with experiments in the total resistance form after adding it to the viscous resistance curves. This is because some difficulties are found in determination of the form factor K (experiments are carried out 3-dimensionally and the viscous resistance is differing from the results of the previous section).

The results of viscid calculations are less in magnitude

than those of inviscid but no significant shifts in the hump-hollow phases are still observed. But, as far as low speed ranges are concerned (we should remind here the wave resistance theory on which we have entrained is based on the low speed assumption), the present results are well reproducing relatively to the inviscid cases. So it may be safely concluded that the neglect of viscosity is partially responsible for the discrepancies between the inviscidly calculated results and experiments.

The above conclusion can be supported from another point of views. The total resistance curves show us that the hump-hollow phases are shifting to lower speed side in the order of EM-300, EM-200 and EM-125. This means the effective length of ships, the length between the bow and the stern wave origins, gets shorter in this order, in other words, the stern wave origins move forward in this order. And if experimental results are plotted against Froude numbers based on the effective length, the phase shift will disappear. It is easily guessed, as shown in Fig. 2, the stern waves are generated around the separation positions. So phase shifts, which are giving fatal discrepancies between inviscid calculations and experiments, are related to the separation, in other words, related to the viscosity.

Apart from the present discussions, it is interesting the resistance curve of EM-300 is significantly different from others: the wave resistance does not increase so much against the speed (we have found there difficulties to determine the form factor). In case of EM-300 more intensive interactions between wave and wake may be existing than those taken into account in the present paper (free surface effects on wake flow or separation are not taken into account here). More precise experimental studies may be necessary.

In Fig. 16, typical example of amplitude function is shown comparing with inviscid and viscid results (EM-200, $F_n = 0.17$). There significant reductions in amplitude of transverse wave components are observed which mainly contribute to the reduction of wave resistance. But no significant phase shifts are observed.

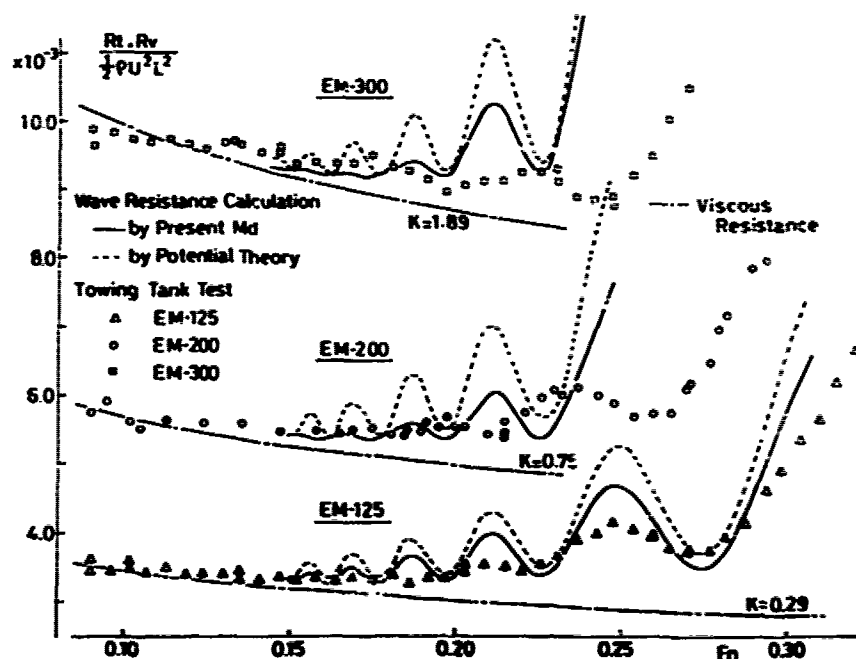


Fig. 15 Comparisons of Wave Resistance

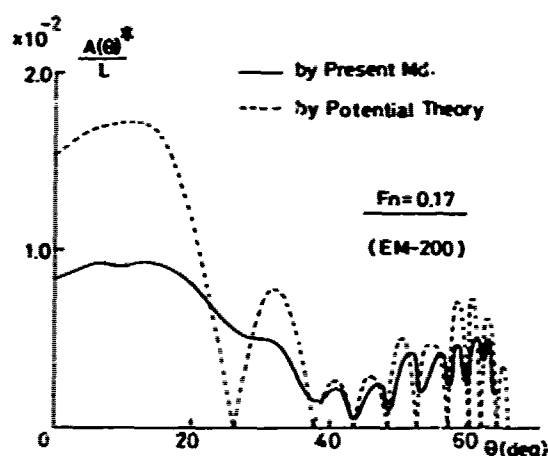


Fig. 16 Amplitude Function of EM-200 ($F_n = 0.17$).

5. CONCLUDING REMARKS

Following remarks can be mentioned as conclusions.

- 1) The present method for predictions of near wake flow is employable at least for the 2-D flows: not only the velocity but the pressure distributions are well reproduced.
- 2) The viscous resistance is estimated together with the frictional resistance. As to the 2-D flows, the viscous resistance is proportional to the frictional resistance.
- 3) The wave resistance is estimated including viscous effects. Though the evaluation of viscosity does not compensate all of the insufficiencies of the potential theory, viscous effects are appreciable.

In the present method the vorticity plays an important role which can relate the boundary layer flow to the near wake flow. In view of this character, the situations do not much differ between the 2-D and the 3-D flows and the applications of the present method to the ship wake predictions are possibly expected.

Through the present studies, the necessity of following further experiments can be pointed out: velocity measurements in recirculating or retarding flow regions by non-pressure type probes and turbulent flow measurements which serve for reasonable determinations of constants related to Reynolds stress.

Finally, one point should be mentioned for the future works not taken in the present studies: it is the effects of the free surface on the viscous flow or separation which may be also appreciable in case of blunt bodies.

ACKNOWLEDGEMENTS

The present studies are partially undertaken as students projects at Hiroshima University. All graduate students related to the present project are appreciated: especially Mr. Doi, Mr. Ohguma and Mr. Nishimoto are appreciated for their cooperations.

Cordial appreciations should be extended to Prof. Hatano

of Hiroshima University for his discussions and encouragements through the present work.

All the numerical computations are carried out by HITAC 8700 of Hiroshima University Computer Center.

REFERENCES

1. Hatano, S., Mori, K., Fukushima, M., and Yamazaki, R., "Calculation of Velocity Distributions in Ship Wake", *Journal of The Society of Naval Architects of Japan*, Vol. 139, Dec. 1975, pp. 55-63.
2. Mori, K. and Doi, Y., "Approximate Prediction of Flow Field around Ship Stern by Asymptotic Expansion Method", *Journal of The Society of Naval Architects of Japan*, Vol. 144, Dec. 1978, pp. 11-20.
3. Muraoka, K., "Calculation of Viscous Flow around Ship Stern", *Transactions of The West-Japan Society of Naval Architects*, Vol. 58, Aug. 1979, pp. 235-253.
4. Havelock, T. H., "Ship Waves: The Relative Efficiency of Bow and Stern", *The Collected Papers of Sir T. Havelock on Hydrodynamics*, ONR, 1963, pp. 398-407.
5. Maruo, H. and Muramatsu, J., "Ship Waves and Wave-Resistance in a Viscous Fluid", *Journal of The Society of Naval Architects of Japan*, Vol. 134, Dec. 1975, pp. 15-29.
6. Himeno, Y., "Displacement Effect of Three-Dimensional Turbulent Boundary Layer and Wake of Ship", *Proceedings of International Seminar on Wave Resistance*, Feb. 1976, pp. 299-303.
7. Mori, K., "Prediction of Viscous Effects on Wave Resistance of Ship in Framework of Low Speed Wave Resistance Theory", *Memoris of The Faculty of Engineering Hiroshima University*, Vol. 7, No. 1, Jan. 1979, pp. 9-19.
8. Baba, E. and Takekuma, K., "A Study on Free Surface Flow around Bow of Slowly Moving Full Forms", *Journal of The Society of Naval Architects of Japan*, Vol. 137, June 1975, pp. 1-10.

APPENDIX REYNOLDS EQUATIONS AND VORTICITY EQUATION

The full expression of Reynolds equations in the curvilinear orthogonal coordinate are as follows [9]:

$$\begin{aligned}
 & q_1 \frac{\partial q_1}{\partial x_1} + q_2 \frac{\partial q_1}{\partial x_2} + q_3 \frac{\partial q_1}{\partial x_3} \\
 & \quad + (K_{12}q_1 - K_{22}q_2)q_2 + (K_{13}q_1 - K_{33}q_3)q_3 \\
 & = - \frac{\partial}{\partial x_1} \left(\frac{\rho}{\sigma} \right) - \frac{\partial q_1^2}{\partial x_1} - \frac{\partial}{\partial x_2} q_1' q_2' - \frac{\partial}{\partial x_3} q_1' q_3' \\
 & \quad - (2K_{12} + K_{22})q_1' q_2' - (2K_{13} + K_{33})q_1' q_3' - (K_{22} + K_{33})q_2'^2 \\
 & \quad + K_{22}q_2'^2 + K_{33}q_3'^2 + \left[\rho^2 q_1 - 2K_{21} \frac{\partial q_2}{\partial x_2} + 2K_{31} \frac{\partial q_3}{\partial x_3} \right. \\
 & \quad \left. - 2K_{23} \frac{\partial q_3}{\partial x_3} + 2K_{33} \frac{\partial q_3}{\partial x_1} + \alpha_{11}q_1 + \alpha_{22}q_2 + \alpha_{33}q_3 \right].
 \end{aligned}
 \tag{A.1}$$

$$\begin{aligned}
& q_1 \frac{\partial q_2}{h_1 \partial x_1} + q_2 \frac{\partial q_1}{h_2 \partial x_2} + q_3 \frac{\partial q_2}{h_3 \partial x_3} \\
& + (K_{21}q_2 - K_{12}q_1)q_1 + (K_{22}q_2 - K_{22}q_3)q_1 \\
& = -\frac{\partial}{h_2 \partial x_2} \left(\frac{p}{\rho} \right) - \frac{\partial}{h_1 \partial x_1} q_1' q_2' - \frac{\partial q_2'^2}{h_2 \partial x_2} - \frac{\partial}{h_3 \partial x_3} q_2' q_3' \\
& - (2K_{21} + K_{31})q_1' q_2' - (2K_{22} + K_{13})q_2' q_3' + K_{12}q_1'^2 - (K_{22} \\
& + K_{12})q_2'^2 + K_{22}q_3'^2 + \nu \left[\nabla^2 q_2 - 2K_{22} \frac{\partial q_2}{h_3 \partial x_3} + 2K_{22} \frac{\partial q_3}{h_2 \partial x_2} \right. \\
& \left. - 2K_{12} \frac{\partial q_1}{h_1 \partial x_1} + 2K_{21} \frac{\partial q_1}{h_2 \partial x_2} + \alpha_{11}q_1 + \alpha_{22}q_2 + \alpha_{33}q_3 \right].
\end{aligned}
\tag{A-2}$$

$$\begin{aligned}
& q_1 \frac{\partial q_3}{h_1 \partial x_1} + q_2 \frac{\partial q_3}{h_2 \partial x_2} + q_3 \frac{\partial q_1}{h_3 \partial x_3} \\
& + (K_{31}q_3 - K_{13}q_1)q_1 + (K_{32}q_3 - K_{23}q_2)q_2 \\
& = -\frac{\partial}{h_3 \partial x_3} \left(\frac{p}{\rho} \right) - \frac{\partial}{h_1 \partial x_1} q_1' q_3' - \frac{\partial}{h_2 \partial x_2} q_2' q_3' - \frac{\partial q_3'^2}{h_3 \partial x_3} \\
& - (2K_{31} + K_{11})q_1' q_3' - (2K_{32} + K_{22})q_2' q_3' + K_{13}q_1'^2 + K_{23}q_2'^2 \\
& - (K_{33} + K_{23})q_3'^2 + \nu \left[\nabla^2 q_3 - 2K_{13} \frac{\partial q_1}{h_1 \partial x_1} + 2K_{31} \frac{\partial q_1}{h_3 \partial x_3} \right. \\
& \left. - 2K_{23} \frac{\partial q_2}{h_2 \partial x_2} + 2K_{32} \frac{\partial q_2}{h_3 \partial x_3} + \alpha_{11}q_1 + \alpha_{22}q_2 + \alpha_{33}q_3 \right].
\end{aligned}
\tag{A-3}$$

where

$$\begin{aligned}
K_{ij} &= \frac{1}{h_i h_j} \frac{\partial h_i}{\partial x_j} \quad (i, j = 1, 2, 3) \\
h_i^2 &= \left(\frac{\partial x}{\partial x_i} \right)^2 + \left(\frac{\partial y}{\partial x_i} \right)^2 + \left(\frac{\partial z}{\partial x_i} \right)^2 \quad (i = 1, 2, 3)
\end{aligned}
\tag{A-4}$$

and

$$\begin{aligned}
\alpha_{11} &= -(K_{21}^2 + K_{12}^2 + K_{13}^2 + K_{31}^2) \\
\alpha_{22} &= \frac{\partial K_{12}}{h_1 \partial x_1} - \frac{\partial K_{21}}{h_2 \partial x_2} - K_{22}(K_{11} + K_{21}) + K_{21}K_{12} \\
\alpha_{33} &= \frac{\partial K_{13}}{h_1 \partial x_1} - \frac{\partial K_{31}}{h_3 \partial x_3} - K_{22}(K_{11} + K_{21}) + K_{21}K_{13} \\
\alpha_{21} &= \frac{\partial K_{21}}{h_2 \partial x_2} - \frac{\partial K_{12}}{h_1 \partial x_1} - K_{11}(K_{22} + K_{32}) + K_{22}K_{31}
\end{aligned}
\tag{A-5}$$

$$\alpha_{22} = -(K_{21}^2 + K_{22}^2 + K_{23}^2 + K_{12}^2),$$

$$\alpha_{23} = \frac{\partial K_{23}}{h_2 \partial x_2} - \frac{\partial K_{32}}{h_3 \partial x_3} - K_{13}(K_{12} + K_{22}) + K_{12}K_{23},$$

$$\alpha_{31} = \frac{\partial K_{31}}{h_3 \partial x_3} - \frac{\partial K_{13}}{h_1 \partial x_1} - K_{21}(K_{23} + K_{13}) + K_{23}K_{31},$$

$$\alpha_{32} = \frac{\partial K_{32}}{h_3 \partial x_3} - \frac{\partial K_{23}}{h_2 \partial x_2} - K_{12}(K_{23} + K_{13}) + K_{13}K_{22},$$

$$\alpha_{33} = -(K_{13}^2 + K_{31}^2 + K_{23}^2 + K_{32}^2).$$

The operator ∇^2 is

$$\begin{aligned}
\nabla^2 &= \frac{\partial^2}{h_1^2 \partial x_1^2} + \frac{\partial^2}{h_2^2 \partial x_2^2} + \frac{\partial^2}{h_3^2 \partial x_3^2} + (-K_{11} + K_{21} + K_{31}) \frac{\partial}{h_1 \partial x_1} \\
&+ (K_{12} - K_{22} + K_{32}) \frac{\partial}{h_2 \partial x_2} + (K_{13} + K_{23} - K_{33}) \frac{\partial}{h_3 \partial x_3}.
\end{aligned}
\tag{A-6}$$

The continuity equation is

$$\begin{aligned}
& \frac{\partial q_1}{h_1 \partial x_1} + \frac{\partial q_2}{h_2 \partial x_2} + \frac{\partial q_3}{h_3 \partial x_3} + (K_{21} + K_{31})q_1 \\
& + (K_{22} + K_{12})q_2 + (K_{13} + K_{23})q_3 = 0.
\end{aligned}
\tag{A-7}$$

If the constant eddy viscosity approximation is appreciated, we get the following vorticity diffusion equations after operating the rotation to Eqs. (A-1) - (A-3):

$$\begin{aligned}
& \left(K_{22} + \frac{\partial}{h_2 \partial x_2} \right) (\omega_1 q_3 - \omega_3 q_1) - \left(K_{22} + \frac{\partial}{h_2 \partial x_2} \right) (\omega_2 q_1 - \omega_1 q_2) \\
& = \nu \left\{ \nabla^2 \omega_1 - 2K_{22} \frac{\partial \omega_1}{h_2 \partial x_2} + 2K_{12} \frac{\partial \omega_2}{h_1 \partial x_1} - 2K_{13} \frac{\partial \omega_3}{h_3 \partial x_3} \right. \\
& \left. + 2K_{13} \frac{\partial \omega_3}{h_1 \partial x_1} + \alpha_{11}\omega_1 + \alpha_{12}\omega_2 + \alpha_{13}\omega_3 \right\},
\end{aligned}
\tag{A-8}$$

$$\begin{aligned}
& \left(K_{13} + \frac{\partial}{h_3 \partial x_3} \right) (\omega_2 q_1 - \omega_1 q_2) - \left(K_{13} + \frac{\partial}{h_3 \partial x_3} \right) (\omega_3 q_2 - \omega_2 q_3) \\
& = \nu \left\{ \nabla^2 \omega_2 - 2K_{22} \frac{\partial \omega_2}{h_2 \partial x_2} + 2K_{23} \frac{\partial \omega_3}{h_3 \partial x_3} - 2K_{12} \frac{\partial \omega_1}{h_1 \partial x_1} \right. \\
& \left. + 2K_{12} \frac{\partial \omega_1}{h_2 \partial x_2} + \alpha_{21}\omega_1 + \alpha_{22}\omega_2 + \alpha_{23}\omega_3 \right\}.
\end{aligned}
\tag{A-9}$$

$$\begin{aligned}
& \left(K_{12} + \frac{\partial}{h_2 \partial x_2} \right) (\omega_3 q_2 - \omega_2 q_3) - \left(K_{21} + \frac{\partial}{h_1 \partial x_1} \right) (\omega_1 q_3 - \omega_3 q_1) \\
& = \nu \left\{ \rho^2 \omega_3 - 2K_{13} \frac{\partial \omega_1}{h_1 \partial x_1} + 2K_{31} \frac{\partial \omega_1}{h_3 \partial x_3} - 2K_{23} \frac{\partial \omega_2}{h_2 \partial x_2} \right. \\
& \quad \left. + 2K_{32} \frac{\partial \omega_2}{h_3 \partial x_3} + \alpha_{31} \omega_1 + \alpha_{32} \omega_2 + \alpha_{33} \omega_3 \right\}, \quad (A-10)
\end{aligned}$$

where

$$\begin{aligned}
\omega_1 &= \frac{1}{h_2 h_3} \left(\frac{\partial}{\partial x_2} (h_3 q_3) - \frac{\partial}{\partial x_3} (h_2 q_2) \right), \\
\omega_2 &= \frac{1}{h_3 h_1} \left(\frac{\partial}{\partial x_3} (h_1 q_1) - \frac{\partial}{\partial x_1} (h_3 q_3) \right), \quad (A-11) \\
\omega_3 &= \frac{1}{h_1 h_2} \left(\frac{\partial}{\partial x_1} (h_2 q_2) - \frac{\partial}{\partial x_2} (h_1 q_1) \right).
\end{aligned}$$

REFERENCE

9. Nash, J. H. and Patel, V. C., "Three-Dimensional Turbulent Boundary Layers", SBC Technical Books, 1972, Scientific and Business Consultants, Inc., Atlanta.

Discussion

V.C. Patel (Univ of Iowa)

Professor Mori's model of the flow over the stern, as depicted in Fig.1, appears to be valid for a two-dimensional bluff body where a region of reverse flow can usually be identified. Figure 2 for EM-200 and similar pictures for MS-02 (whose aft section also had elliptic framelines, see Hatano, Mori and Hotta : 12th Sym. Naval Hydrodynamics) indicate that slender, nearly two-dimensional forms also lead to pockets of reversed flow. However, such flow reversals are usually not observed on the highly three-dimensional sterns of real ships except perhaps at the free surface. Instead, one observes reversal of the cross-flow within a thickening boundary layer and the formation of a longitudinal vortex. Would the author comment on the possibilities of extension of the proposed model and solution procedures to such cases ?

N Kato (Tokai Univ)

I appreciate the author's paper which contributes to the theoretical analysis of near wake including separated vortices. I have three questions ;

(1) Although the author derived the three governing equations from the Navier-Stokes equations by the use of small parameter ϵ defined in the equation (1), the author made an additional assumption of the location of the dividing streamline which is ought to be solved essentially in a closed procedure. I would like to have the author's comment on this problem.

(2) The author expressed that the disagreement of the calculated results about the velocity distributions of the near wake flow and the viscous resistance of EM-300 model with measured is due to an unsteady wake flow of the model which is not taken into account in the proposed method by the author. But I think the disagreement is also due to the assumed location of the dividing streamline which is influential on the solution. May I have a comment of the author ?

(3) I would like to ask if the author has any idea to develop the proposed method to analyse three dimensional separated flows including longitudinal bilge vortices as observed in the wakes of full ships.

S.H. Kang (KRIS)

I deeply appreciate the research of near-wake and resistance calculations by Prof. Mori. Congratulations ! Here I would like to make two suggestions and one question.

It seems to be quite valuable to develop the calculation technique of the vorticity diffusion region further by using experimental data of simple cases, without D region before the theory is extended to more complicate or three dimensional cases for practical purposes. Vorticity diffusion method might be promising to handle the thick boundary layer and near-wake in such cases. Velocity fields around the thin body ¹ have been measured in the wind-tunnel by Kang ².

When we estimate the wave-making resistance, both viscous effects and wave potential effects are important of the same order even in the low-speed range ³. Therefore corrections for the body boundary condition violated by the wave-potential near the bow will be good for the estimation of wave resistances.

The author decomposes the total velocity into three components ; pure potential, viscous, and interaction term. The last one is obtained by distributing additional sources on the body-surface to satisfy the zero-normal velocity. It is still not clear whether we should keep the non-slip condition/ or zero-normal velocity on the surface. If we consider non-slip condition to be more reasonable, I'd like to remind the author a vorticity theorem suggested by Landweber ⁴ as follows.

Consider a steady mean flow of an incompressible fluid about a body at rest in an unbounded fluid, with mean vorticity present in the boundary layer and wake, BLW, bounded internally by the body surface S and externally by the surface T ; see Fig. The boundary conditions to be satisfied are the non-slip condition on the external side of S and the irrotationality of the flow exterior to T. Then the disturbance flow exterior to S can be generated by the vorticity in BLW only.

Therefore viscous components by Eq. (13) in the paper already include the others implicitly except the incident uniform flow, if correct vorticities are obtained. We can find the summation of viscous component and D-region contribution make very amount of the velocity defect of the total velocity profile in Fig.9. Vorticity distributions have already taken account of displacement effects of the boundary layer and wake.



Figure

REFERENCES

- 1) Weinblum, G. et al, "Investigation of Wave Effects Produced by a Thin-Body-TMB Model 4215," DTMB Report 840, (1952)
- 2) Kang, S.H. "Viscous Effects on the Wave Resistance of a Thin Ship" Ph.D. Thesis, The Univ. of Iowa, July, (1978)
- 3) Kang, S.H. "Second-Order Wave Resistance Calculation of Thin-Ship" Vol. 16, No. 3, JSNA Korea, Sept. (1979)
- 4) Landweber, L. "On Irrotational Flows Equivalent to the Boundary Layer and Wake" DTNSRDC-78/111, Nov. (1978)

Author's Reply

K. Mori (Hiroshima Univ)

Thank you Prof. Patel for your discussions. Prof. Patel's understanding is true for the cases of real ships.

In my scheme, the longitudinal vorticity component ω_1 is assumed to be of higher order by ϵ than that of the girth direction component ω_2 . So eventually the diffusion of ω_1 is neglected. But if we make another assumption that the order of ω_1 is the same as other components, we may be possible to predict the ship stern flow. In that case near the separation position, the boundary layer equation should be solved appreciating even reverse cross-flows; unless, the revival of ω_1 is meaningless.

Of course, significant interactions between the longitudinal vortex and the outer flow can not be presented by the present scheme generally.

Thank you Dr. Kato.

(1) It is true that the dividing streamline is ought to be solved in a closed procedure. The author supposes that the velocity field obtained by using the assumed dividing streamline corresponds to that of the first iteration. For the second iteration it can be determined from the velocity field of the previous iteration. Such a procedure to assume the direction of the vorticity shedding is very common in the airfoil theory.

(2) The author has attempted velocity prediction for another dividing streamline. But, unfortunately, no significant improvements can be obtained.

(3) The answer to Professor Patel may be referred.

Thank you Dr. Kang for your valuable suggestions.

(1) Your suggestion to carry out for simple cases without D-region flow is quite important to check the validity of the present method. It has been already carried out in case of a flat plate in our paper of 1978. See Fig. A1. The second iteration is also carried out there.

(2) Unfortunately I have not yet read Dr. Kang's paper. But it may be true that the introduction of the exact hull surface condition including the free-surface effects may bring forth improvements to some extent. The author, however, is convinced that neglect of the free surface effects may be within the order of our approximations (see, ref. 7 in my text). Aparting from the viscous flow problem, neglect of the free surface effects in the hull surface condition does not matter so significantly (see the results of the Washington workshop results).

(3) It may be true that the vorticity distributed in BWL is enough to produce the velocity defect, if and only if the vorticity distribution has been obtained to satisfy the hull surface condition. In my present scheme, the vorticity distribution is solved without hull surface condition at the first stage. Unless it may get very difficult to solve the diffusion equation; one of the possible way is to solve by the time-step method. The mirror image of vorticity is determined, at the second stage, in order to satisfy the hull surface condition. So, hopefully, the final results may be the same.

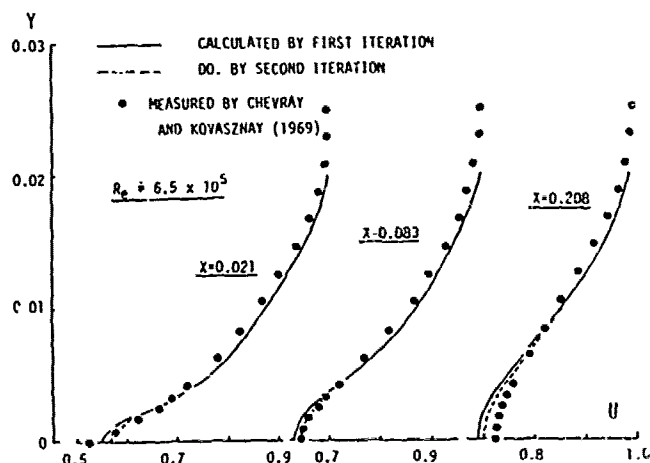


Fig. A1 Comparison of Velocity Profiles in Near Wake Flow of a Flat Plate. (x is non-dimensional length divided by the plate length, which is 240 cm. Its origin is at the trailing edge.)

GEMAK—A Method for Calculating the Flow around Aft-End of Ships

A. Yücel Odabaşı

*The British Ship Research Association
Wallsend, United Kingdom*

Öner Şaylan

The Technical University of Istanbul, Turkey

ABSTRACT

This paper summarises a method developed for the calculation of the flow development around the aft-end of ships at the British Ship Research Association (BSRA) within the context of the Propeller-Hull Interactive Vibration Excitation (PHIVE) Project.

The method consists of four parts. The first part is the computation of the potential flow with surface singularity distribution. The second part calculates the development of the boundary layer by means of a relatively simple integral method which provides approximate information on the outer edge of the boundary layer as well as the numerical values for integral flow parameters, such as displacement thicknesses, momentum thicknesses, etc. The third part modifies the potential flow calculations due to the displacement effect of the boundary layer and wake and provides velocity and pressure values at the edge of the boundary layer. The fourth part calculates the boundary layer development at the aft-end by using a modified version of Bradshaw's turbulent energy method.

The program developed for the implementation of this method is used to calculate the boundary layer development of a ship model and the results are compared with experimental data. Some conclusions are drawn and areas for further progress are proffered.

1. INTRODUCTION

The need to predict the flow around ship afterbodies, in particular ship wakes arises from the fact that in order to avoid unsteady cavitation and consequential high levels of vibration and noise,

propeller and hull designers need to know the velocity distribution in the propeller plane to distinguish between acceptable and unacceptable wake flows and where necessary to alter the hull geometry to improve the flow. Studies at BSRA during the recent PEV (Propeller Excited Vibration) Project indicated the importance of the knowledge on the flow around afterbodies of a ship, as far as the cavitation induced vibratory excitation is concerned, cf. Odabaşı and Fitzsimmons (Ref. 1). Additionally, it has been known for some time that the existence of an early separation and heavy vortex shedding increases the total resistance of ships whereas light vortex shedding can contribute towards the improvement of the wake. Knowledge on the flow around the aft-end of ships, therefore, can also provide useful information for reducing the total resistance of a given parent form.

To reduce the vibration excitation due to propeller-hull interaction and to prepare guidelines for aft-end design of ships it is considered necessary to be able to predict the flow around the aft-end and work towards this end has been an important part of the PHIVE (Propeller-Hull Interaction: Vibration Excitation) project. The work reported summarises the method developed in BSRA to calculate aft-end flow and near wake of ships, including the effect of propeller-hull interaction. Since the aim of the PHIVE Project was to produce methods and procedures to be used by the industry rather than a purely theoretical research, development of the BSRA method has been based on three principles:

- (1) making best use of the existing capabilities such as methods and computer programs,
- (2) making the method, and hence the program suite GEMAK, an economically viable proposition by adopting programs which require less computational cost, and
- (3) making sure that the final output correlates well with the experimental data and that the predictions made by the method can provide reasonable estimates for ship wakes.

To fulfil the first requirement an extensive review study has been conducted to assess the feasibility of alternative methods calculating the flow fields around ship hulls and the general outline of the BSRA method has emerged. The second requirement necessitated some numerical experimentation in order to optimise the numerical computation schemes, and the last requirement gave us the opportunity to re-examine the various schemes employed in the method (in the light of the detailed boundary layer and near wake measurements conducted by NMI) and reformulate some of them by making a term-by-term order of magnitude analysis rather than a hypothetical order of magnitude analysis. The final outcome became a hybrid method as illustrated in Fig. 1 which will be discussed in more detail later.

The method has been tested against a number of model test results for which the boundary layer results are available, and to illustrate its application a comparison of computed results and experimental data for the Hoffmann's tanker form (Ref. 2) and for NMI test forms are presented together with some discussion.

The final part of the paper discusses the merits and the shortcomings of the method developed with some comments on the scope for possible further improvements.

2. PROBLEM FORMULATION AND METHOD OF SOLUTION

Following the initial review study it became evident that a number of choices had to be made for the solution of a number of sub-problems. The first question was on the type of flow around aft-end of ships. Since a large amount of extra strain rates are present in the flow it was necessary to decide whether the flow should be considered as a thickening shear layer or a distortion layer. This choice is crucial because to use an ideal vortical flow approximation would be more appropriate if the flow was considered as a distortion layer. From a study of a limited amount of data we concluded that the role of the Reynolds stresses in the aft-end flow was still important, and hence it should be treated as a complex turbulent shear layer.

The next task was to devise a methodology and a computational scheme suitable for the calculation of a complex shear

layer, which requires sequential computation. Since, in our experience, integral methods produce sufficiently accurate result for the initial 75 per cent of the ship where the flow is a simple shear layer with the exception of the flow around the bow, we concentrated only on the aft-end flow. In the light of the experience of other researchers, cf. Landweber (Ref. 4), Larsson (Ref. 5), Himeno and Tanaka (Ref. 6), it was understood that, at present, integral methods could not produce the desired result and hence a differential method had to be used. It was also clear that almost all of the available differential methods were suitable mainly for simple shear layers and hence some additional modifications would be necessary independent of the choice being made on the method. As will be discussed later, analysis led to the belief that the Bradshaw's turbulent energy method (Ref. 7) was the best choice for this particular flow. The next consideration was the determination of initial and boundary conditions for the boundary layer calculation. The initial conditions were obtained from Gadd's integral method (Ref. 8) by employing it for the forward part of the hull. To obtain the boundary conditions at the edge of the shear layer a reasonable estimate (not necessarily very accurate) of the boundary layer development at the aft-end was required in order to account for the boundary layer displacement effect. Gadd's method (Ref. 8) was again used to determine both the displacement and the boundary layer thicknesses from which the velocities on the matching surface (which encloses the boundary layer) were obtained.

There were still further problems regarding the choice of the potential flow calculation method, inclusion of the extra strain rates and normal pressure gradient, the choice of the coordinate system and the numerical scheme for the shear layer calculations which is discussed below. However, the scheme of calculation, as shown in Fig. 1 emerged at this state of the investigation.

3. CALCULATION OF POTENTIAL FLOW

As is well known flow around a body, moving with a constant velocity on the otherwise undisturbed free surface of a liquid, can only be computed by adopting certain assumptions. Although the basic assumptions allow us to formulate the problem within the framework of the classical potential theory, the existence of a free surface and the representation of the body surface create additional problems, which necessitates some further simplifications.

For the solution of the irrotational flow about a ship form, a number of potential-flow methods have been developed. In reality however all of them are restricted due to the complexity of the two

major boundary conditions, namely the body surface and the free surface conditions, which can be treated in their linearised form. As is well known, from theoretical wave resistance studies even for the time consuming second order theory, the agreement with experimental results is not particularly good. Therefore in recent years methods satisfying the exact body surface condition have received much more attention. Following the first success of Hess and Smith (Refs. 9, 10), the methods of Surface Source Distribution, (SSD) have been applied to various problems.

The original approach by Hess and Smith does not include the free surface effect and hence gives the solution of Neumann problem for a given form and its image, (i.e. Double model in an infinite fluid). In order to improve the accuracy of the results obtained from the Neumann problem, Brard (Ref. 11), and many others studied the Neumann-Kelvin problem which again takes the exact body surface condition into account and includes the effect of free surface in its linearised form. In an attempt to include the non-linear free surface effects, Gadd (Ref. 12) introduced the idea of additional source distribution in the region surrounding the double model in the undisturbed free surface plane; recently he has improved his method by extending the free surface panels to cover a larger portion of the disturbed free surface region and by adding a new distribution of Kelvin sources along the axis of the hull at one third of the draft, (Ref. 13). Critical evaluation of existing methods can be found in the review studies of Wehausen (Ref. 14), Timman (Ref. 15), Chapman (Ref. 16) and many others. A number of sophisticated SSD methods are available, but even with current computers, the computation of the flow around a three-dimensional body requires a large amount of computer time and also careful thought for the rational discretisation of the body surface; that is, to avoid unrealistic results and numerical instabilities, the size, shape and the number of surface source facets have to be carefully selected beforehand.

In the early stages of the PHIVE project extensive work was carried out at BSRA to find the optimum solution of various discretisation problems and to reduce the computer costs for the potential flow calculations of a given three-dimensional body. In this work classical Neumann and Neumann-Kelvin problems have been solved.

In most of the SSD methods, the body surface is replaced by quadrilateral elements or facets. One of the major drawbacks of this approximation is that the planes formed by all four corners of each element do not necessarily match the real body surface hence, either a discontinuity will occur on the source surface or the centroids of each element (so called control points) will form a different body shape than the original one. This statement

becomes particularly significant at highly curved regions such as the aft-ends of ships. To avoid such errors it is possible (1) to increase the number of elements and hence to reduce the element sizes or (2) to employ curved surface elements with variable source density as is investigated by Hess (Ref. 17, 18 and 19), or (3) to use only triangular surface elements, cf. Webster (Ref. 20), Şaylan (Ref. 21). As is expected any increase in the number of surface elements will increase the computer costs dramatically. The second alternative, the use of higher-order surface elements, has also its own drawbacks. Hess was the first to show that the effect of surface curvature and the effect of the variation of singularity distribution are of the same order of magnitude. Therefore inclusion of only one of them is inconsistent and also does not improve the accuracy of the results sufficiently. Use of the consistent higher-order formulation, such as paraboloidal-panel linear-source or cubic-panel quadratic-source, is generally not feasible because of the complication of problem formulation and because of the much increased computer time requirements. The last alternative, to increase the accuracy, that is to represent the real body surface more correctly by the use of the triangular surface elements, has been investigated by BSRA. Although the control points of triangular elements are closer to the real body surface and all three corners of an element will lie on the same plane, it is found that if the characteristic length of an element is larger than 2.5 times the distance between adjacent control points numerical computations become unstable. This limit is generally exceeded when only triangular elements are considered and some undesirable waviness appears in the final results. Figure 2 illustrates this type of waviness for a simple axisymmetric Huang form, cf Huang, et al. (Ref. 22). Another drawback of the triangular discretisation is that the control points generally do not lie in the same vertical plane which makes additional interpolation routines necessary to calculate the desired properties at given vertical positions.

Having considered these arguments it has been decided that body surface should be discretised by using quadrilateral flat elements (each having approximately the same size and area) and triangular elements should be used only where necessary. As an obvious result of this choice higher computational costs become almost unavoidable. In other words, for better representation of body surfaces and for better results, the total number of elements should be kept as high as possible, or else, to fulfil the requirements explained in the first section, a different approach has to be found. During the PHIVE project, following the choice of element shapes, a new discretisation technique has been developed and a pronounced saving on computer costs was obtained with no appreciable decrease in

accuracy. For ships or ship-like bodies discretisation is made by using an expanded surface and in the data generation stage of the potential flow programs (Double model and N-K programs) special emphasis has been attached to the fore- and aft-ends and to the regions where the curvatures change suddenly. It is considered that the user should have the opportunity of using his engineering judgement in the preparation of the surface elements. Although the data generation takes longer compared to the standard process, the flexibility introduced in this way is worth the extra effort. In addition to the shell expansion type discretisation, separated modules are formed for the bottom part and the side walls and triangular elements are also used to provide a better approximation to the hull geometry. Figures 3 and 4 give an idea about the accuracy of the results obtained from double-model program. As can be seen from these figures, for the Hoffmann tanker form, it is possible to achieve a reasonable pressure distribution with fewer number of elements.

As the main purpose of the study is to provide information on the flow around the aft-ends of ships, possibilities of using a simplified representation of the forebody have also been considered to reduce the number of surface elements. This idea becomes more meaningful if the variation of pressure and streamlines along the parallel middle body is considered. Having investigated the effect of forebody it has been found that, to compute the aft end flow, the front 25-40% of the ship can be neglected or at least fewer elements of larger size can be used to represent the forebody. Figures 5 and 6 illustrate this feature for a Huang body and for Hoffman's tanker form. As an overall comparison of BSRA's discretisation method, the streamlines around the same tanker form have been calculated for a total 74 surface elements and are plotted in Figure 7 against Hoffmann's calculated streamlines for 414 elements, (Ref. 2).

In the literature there is a large number of published information for the double body problem but, in the case of the (N-K) problem, both theoretical and experimental results are rather scarce. In employing the (N-K) approach the biggest difficulty is the relatively large computer time required. The reason leading to the development and implementation of the (N-K) program is that the results of the double body approach are only valid for very low Froude numbers and inclusion of the linearised free surface condition is expected to provide a larger range of applicability. On the other hand the computer time required for the numerical integration of the free surface related terms increases considerably, i.e. for a ICL 1904-S computer the elapsed time is found to be nearly 2½ hours for a ship form presented by 60 surface elements. From the limited studies conducted at BSRA the

following findings can be expressed:

- (1) Following the procedure explained in Ref. (21), the results obtained from the (N-K) program agree well with the results of the double model program for very low Froude number ($Fr = 0.01$). This is illustrated in Figure 8 and gives the confidence for the use of the (N-K) program.
- (2) If the free surface effect is considered the non-dimensional pressure distribution changes from that obtained for the double body, cf. Figure 9. In this Figure the experimental results of Huang and von Kerczek (Ref. 23) and the theoretical results reported by Adey, et al (Ref. 24, 25) are also included for comparison.
- (3) In the propeller plane the effect of a linearised free surface appears to be important. For the Huang body No.1, the differences in axial velocities are found to be very small, however in tangential and radial velocity components there is a significant effect, cf. Figures 10 and 11. These results confirm the belief that all three components of the velocities in the propeller plane should be measured in order to make meaningful comparisons.

As is shown in Figure 1, within the PHIVE project, potential flow calculations have been used only to provide the necessary information for the three-dimensional boundary layer calculations and, as is explained in Section 2, for the same reason a multi-stepped procedure has been designed including Gadd's integral method and the program unit for the boundary layer displacement effect, (blow-out program). The linearised free surface effect has been excluded from the final program package in order to keep computer requirements within reasonable limits, but the experiences gained from the (N-K) program and surface discretisation technique have been widely used through the whole hull flow suite.

4. CALCULATION OF BOUNDARY CONDITIONS ON MATCHING SURFACE

The potential flow solution gives the velocity and pressure distribution around a three-dimensional body, together with the characteristics related to body geometry, i.e. coordinates of the control points, areas, components of the unit normal vectors etc. In the BSRA program suite GEMAK, this information was used both for computing the boundary layer development by Gadd's program and for determining the displacement effect by the blow-out program.

Gadd's Integral Method:

To compute the boundary layer development by an integral method, Gadd has solved the streamwise and transverse momentum integral equations together with an entrainment condition at the edge of the boundary layer, cf. (Ref. 8). The formulation of

these equations has been made by considering a locally rectilinear but non-orthogonal axis system that is, at each control point, x' is taken in the direction of the potential flow, y' normal to the hull surface and z' parallel to the transverse line of the control points. Since the integral methods predict only the integrated properties at points on the body surface, the boundary layer integral quantities are defined as:

$$\delta_1 = \int_0^\delta \frac{u_1' - u'}{U} dy' \quad \text{(streamwise displacement thickness)}$$

$$\delta_2 = \int_0^\delta \frac{w_1' - w'}{U} dy'$$

$$\theta_{11} = \int_0^\delta \frac{u'(u_1' - u')}{U^2} dy' \quad \text{(streamwise momentum thickness)}$$

$$\theta_{22} = \int_0^\delta \frac{w'(w_1' - w')}{U^2} dy'$$

$$\theta_{12} = \int_0^\delta \frac{w'(u_1' - u')}{U^2} dy'$$

$$\theta_{21} = \int_0^\delta \frac{u'(w_1' - w')}{U^2} dy'$$

where u' and w' are the velocities in the x' and z' directions, U is the external velocity and u_1' , w_1' are the velocities at the edge of the boundary layer ($y' = \delta$). The number of these unknowns are reduced by the choice of velocity profiles. In the streamwise direction velocity profiles are assumed to belong to the Coles profiles cf. (Refs. 26, 27), whereas in the transverse direction Mager's form has been chosen (Ref. 28). The local skin friction coefficient in the streamwise direction (C_f) is determined as a function of the shape parameter H and the momentum thickness Reynolds number $R_{\theta_{11}}$, ($R_{\theta_{11}} = U \cdot \theta_{11} / \nu$),

and the Ludwig-Tillmann relation (Ref. 29) has been used for the initial estimate of C_f . Finally, Gadd has proposed a new formulation for the entrainment coefficient C_E :

$$C_E = 0.011 \cdot H (1 + \tanh(5H-7)) - \frac{\theta_{11}}{H-1} \cdot \frac{dH}{dx}$$

In order to compare the results with experiments, the integral quantities have been transformed into the streamwise and perpen-

dicular axis system, for this transformation the angle between the transverse and the perpendicular (normal to the potential flow direction at each control point) directions is assumed to be small. It has been shown that, for ship hulls, the results obtained from this method agree well with the experimental results specially for the regions where the boundary layer is thin and the body curvatures are not high. Near the ship sterns however the method generally overestimates the boundary layer development. To avoid such unrealistic results Gadd assumed that the velocity potential for the flow outside the boundary layer can be approximated as:

$$\phi = U \cdot x - \cos kze^{-ky}$$

and the displacement effect of the boundary layer can be modelled roughly by altering the w components of velocity by

$$\left\{ -\frac{U \cdot G}{\pi} \cdot \frac{\partial}{\partial z} \left(\frac{\partial \delta_1}{\partial x} \right) \right\},$$

where G is the length of the surface from waterline to keel. However, during the PHIVE project a different approach has been adopted for the calculation of displacement effect.

Blow-out Method:

It is known that a boundary layer displaces inviscid flow outward from the body creating effectively a semi-infinite pseudo-body (Fig. 12). When the boundary layer is thin this displacement effect is small and its influence on the boundary layer calculations is negligible. For thicker boundary layers, however, this statement is not true and the displacement effect manifests its influence on the boundary layer calculations in two ways. Firstly the streamwise and the spanwise pressure gradients differs from those calculated from the potential flow around the naked hull due to the differences between the geometries of the hull and the pseudo-body. Secondly, the assumption that pressure is constant along the normal within the boundary layer (i.e. the normal pressure gradient is equal to zero) is no longer valid.

As is well known, one of the assumptions employed within all the boundary layer theories is that the flow outside the boundary layer is equivalent to the irrotational flow of an ideal fluid. This assumption immediately suggests that if the flow around the pseudo-body is solved as an external Neumann problem then determination of the improved external boundary conditions for the boundary layer calculations becomes a routine task.

The first person known to apply this idea is Stüper (Ref. 30) who made an attempt to calculate the lift of a Joukowski aerofoil. He was able to estimate the distribution of the displacement thickness

over the wing. He then replaced the wing by a new boundary displaced out from the wing and calculated the potential flow about the new shape. Preston (Refs. 31, 32) provided a more rigorous derivation of the equivalent flow for two-dimensional flows. Moore (Refs. 33, 34) generalized the idea to three-dimensional flows in general orthogonal coordinates. Lighthill (Ref. 35) proposed four alternative methods for the boundary layer displacement effect for both two and three-dimensional flow problems. The blow-out method (or equivalent source method in Lighthill's terminology) received a wide acceptance in the field of aeronautics and has been used extensively, cf. Giesing and Smith (Ref. 36), Jacob (Ref. 37), Rubbert and Saaris (Ref. 38). Recently Landweber (Ref. 39) critically reviewed the methods proposed by Preston and Lighthill and proposed a centreline singularity distribution.

The method adopted by BSRA follows mainly the approach proposed by Lighthill (Ref. 35) and, due to the coordinate transformation, only minor modifications have been made.

In order to improve one's physical appreciation of the blow-out method, one can consider two-dimensional flow problem for a (s-n) coordinate system, where s is measured along the body contour from the front stagnation point and n is measured along the normal; for this the difference between the external stream velocity and the velocity component within the boundary layer ($U-u$), represents the reduction in flow velocity due to the presence of the boundary layer. From the continuity equation there must be a constant volume flow per unit span between the surface and any streamline just outside the boundary layer. There is however a flow reduction due to the above-mentioned velocity defect which is expressible as:

$$\int_0^{\infty} (U - u) \, dn.$$

The constant volume flow is obtained if the flow reduction inside the layer is compensated by an outward displacement of the body contour by an amount δ_1 which is given as:

$$\delta_1 = \frac{1}{U} \int_0^{\infty} (U - u) \, dn.$$

where δ_1 is the displacement thickness of the boundary layer.

Determination of the strengths of the equivalent sources on the body surface is made either by using an equivalent body and solving a new Neumann problem or by using Gauss' flux theorem. In the first approach the physical body is replaced with a pseudo-body by adding the displace-

ment thickness to the body and the ideal flow is computed around this new geometry. To implement the second approach, let us consider the mass transfer at two sections in the boundary layer (see Fig. 12). At the first section the potential flow outside the boundary layer will be moving with a velocity U_1 and the mass flux per unit span will be $U_1 \cdot \delta_1$. At the second station the flux can be written as:

$$U_1 \cdot \delta_1 + \frac{\partial}{\partial s} (U_1 \cdot \delta_1) \cdot \Delta s.$$

The difference between the two stations will be

$$\left\{ \frac{\partial}{\partial s} (U_1 \cdot \delta_1) \right\} \cdot \Delta s.$$

This difference in flux can be supplied by blowing from the surface with a velocity v_w , such that:

$$v_w = \frac{\partial}{\partial s} (U \cdot \delta_1)$$

This blow-out velocity is then used to modify the boundary condition on the body

surface, (i.e. $\frac{\partial \phi}{\partial n} = v_n + v_w$). As the influence coefficient matrix for the potential flow was already calculated to determine the initial flow, determination of the total source strengths amounts to the solution of a system of linear equations with a new right hand side.

In three-dimensional flows this procedure requires some modifications due to the existence of cross flow within the boundary layer. Following the notation used by Gadd (Ref. 8) one can consider a locally orthogonal rectilinear axis system, centred at the control point of a surface element, with axes x in the stream direction and y normal to the element plane and z in the crossflow direction, then the streamwise and perpendicular displacement thicknesses can be defined as:

$$\delta_1 = \frac{1}{U} \int_0^{\delta} (u_1 - u) \, dy$$

$$\delta_2 = \frac{1}{U} \int_0^{\delta} (w_1 - w) \, dy$$

where u_1 and w_1 are velocity components at the edge of the boundary layer and U is the total external velocity ($w_1 = 0$ and $u_1 = U$).

The equation of continuity takes the form:

$$\frac{\partial v}{\partial y} = - \left[\frac{\partial u}{\partial x} + \frac{\partial w}{\partial z} \right]$$

Integrating this equation across the boundary layer:

$$v = - \int_0^h \left(\frac{\partial u}{\partial x} + \frac{\partial w}{\partial z} \right) dy$$

$$v = \int_0^h \left[\frac{\partial}{\partial x} (u_1 - u) + \frac{\partial}{\partial z} (w_1 - w) \right] dy - \int_0^h \left(\frac{\partial u_1}{\partial x} + \frac{\partial w_1}{\partial z} \right) dy$$

where, for $h > \delta$, the upper limit of the integrals can be replaced by ∞ , cf. Lighthill (Ref. 35), and hence:

$$v = \int_c^\infty \frac{\partial}{\partial x} (U \cdot \delta_1) dy + \int_0^\infty \frac{\partial}{\partial z} (U \cdot \delta_2) dy - y \frac{\partial U}{\partial x}$$

In this equation the last term alone comes from the normal potential flow calculations. Therefore the first two terms will give the additional blow-out flux due to the boundary layer, as if there were an additional source distribution on the ship surface. The strength of this imaginary distribution can be expressed as:

$$m_w = \frac{\partial}{\partial x} (U \cdot \delta_1) + \frac{\partial}{\partial z} (U \cdot \delta_2).$$

In the blow-out program, streamwise and perpendicular displacement thicknesses have been taken from Gadd's calculations and for the numerical solution of the last equation, use has been made of an adopted numeric derivation routine based on a least square scheme.

As is already mentioned for the two-dimensional case, solution of the problem is trivial since the influence coefficient matrix is available from the initial potential flow calculation.

As the boundary layer extends beyond the body to form the wake the blow-out scheme is not confined to the body surface, it has to be continued sufficiently far downstream. Experience gained in potential flow computations shows that this distance should be of the order of five times the boundary layer thickness at the aft-end of the ship. However, in practice the displacement thickness of wake is hardly ever computed. This poses a serious problem in the inclusion of wake effect on the boundary values at the edge of the boundary layer. Normally the displacement thicknesses are expected to decrease in the near wake as the momentum thickness remains approximately constant. When there is no information on the wake flow, it may be a reasonable approximation to use the displacement thicknesses at the aftmost position of the hull as the displacement thicknesses of the computation region in the wake.

The resulting source strengths have been used to evaluate the velocity distribution at the edge of the boundary layer (matching surface) to provide the improved

boundary values for the final stage of the boundary layer calculations. For Hoffmann's tanker form, the effect of blow-out on the source strength distribution can be seen in Fig. 13.

5. TURBULENCE MODEL

As is well-known, due to the present speed and storage capacity of computers one is not able to solve the N-S (Navier-Stokes) equations and some form of approximation has to be made. A convenient method of approximation is the "turbulent shear flow" approximation where the principal quantities of the N-S equations are assumed to consist of a mean and a fluctuating part and the governing equations are obtained by applying time averaging, cf. Townsend (Ref. 41). Further simplification results in what is known to be "the boundary layer" or more correctly "the thin shear layer" (TSL) approximation. As the name implies TSL approximation assume some form of thinness for the shear layer thickness (δ) compared to the principal radii of curvature (R) of the streamlines. However the restriction can be relaxed in the "fairly thin shear layer" (PTSL) approximation where $\partial \delta / \partial x_1$ is assumed to be small, x_1 being the main stream direction, cf. Bradshaw (Ref. 42).

The equations obtained with these approximations are incomplete and the difference between various differential methods appears in the choice of the closure equations which are introduced to model the transport of Reynolds stresses. In our assessment we considered three differential methods; the zero equation model, cf. Cebeci et.al. (Refs. 43, 44), the one equation model, cf. Bradshaw (Refs. 7 & 45), and the two equation model, cf. Rastogi and Rodi (Ref. 46) and Abdelmeguid et.al. (Ref. 47). The merits and shortcomings of these methods were compared on their physical and mathematical basis, and on their evolutions, i.e. the type of data used in the determination of empirical constants or function. The conclusion was that, accepting the fact that none of the methods was universal, the Cebeci's method was easiest to modify but such a modification would require a large amount of ship boundary layer data which was not available, and Bradshaw's method was both physically and mathematically more correct than the others for the aft-end flow.

Within the TSL approximation the governing equation and the Reynolds stress transport equations for the selected turbulence model are:

Momentum transfer equations for $i=1$ and 3

$$U_j \frac{\partial U_i}{\partial x_j} = \frac{\partial}{\partial x_i} \left[-\delta_{ij} \frac{P}{\rho} + \tau_{ij} \right] \quad (1)$$

Momentum transfer equation for $i=2$

$$\frac{\partial}{\partial x_2} \left(\frac{P}{\rho} + \langle u_2^2 \rangle \right) = 0 \quad (2)$$

Continuity equation

$$\frac{\partial U_j}{\partial x_j} = 0 \quad (3)$$

Reynolds stresses transfer equations for $i=1, 3$

$$\begin{aligned} \frac{U_j}{2a_1} \frac{\partial \tau_i}{\partial x_j} &= |\tau| \frac{\partial U_i}{\partial x_2} - \left(\frac{|\tau|}{\rho} \right)^{\frac{1}{2}} \frac{\tau_i}{L} \\ &- \frac{\partial}{\partial x_2} \left[G \left(|\tau_{\max}| / \rho \right)^{\frac{1}{2}} \tau_i \right] \end{aligned} \quad (4)$$

where x_1, x_2, x_3 are, respectively, the coordinates in streamwise, normal, and girthwise directions*, U_j and u_j ($j=1,2,3$) are, respectively, the mean and the fluctuating velocity components, P and p are, respectively, the mean and the fluctuating dynamic pressures, τ_i ($i=1,3$) are the Reynolds stress, ρ is the density of fluid, $|\tau|$ is the magnitude of the total shear vector and τ_{\max} is the maximum value of τ outside the viscous sublayer.

This formulation contains three empirical quantities; a_1 ($\frac{1}{2} |\tau| / q^2$) the stress-energy ratio where q^2 is the turbulent kinetic energy, L the dissipation length scale, and G the entrainment function. As a result of a comparative study of experimental data, Bradshaw (Ref. 48) showed that the motion within the boundary layers consist of an "active" universal component scaling with $(\tau/\rho)^{\frac{1}{2}}$ and x_2 , which produces the shear stress, and an "inactive" component imposed by the eddies and pressure fluctuations in the outer part of the boundary layer, which does not produce shear stresses and can be regarded as a quasi-steady oscillation of the inner layer flow. Measurements indicated at that time that a suitable value of a_1 was 0.15. Later experiments, however, indicate that a_1 takes smaller values near the wall and near the outer edge of the boundary layer and remains almost constant between $0.2 x_2/\delta$ and $0.8 x_2/\delta$, the value of the constant being between 0.135 and 0.18 depending on the flow configuration. Computations at BSRA, however, indicated that the effect of change of a_1 on the overall turbulence structure is only marginal. This is due to the fact that the flow in the viscous sub-layer is governed by the law of the

wall, and furthermore the contribution from the outer edge of the boundary layer to the generation of shear stress is quite small. The law of the wall used in BSRA's method is due to van den Berg (Ref. 49) and his results are modified for the extra strain rates as proposed by Bradshaw and Maroney (Ref. 50).

The dissipation length scale parameter L is defined by the relationship

$L = (\tau/\rho)^{\frac{3}{2}}/\epsilon$ where ϵ denotes the viscous dissipation. This parameter is a measure of the scale of eddies which contains most of the kinetic energy and which are responsible for the transport of momentum. At high Reynolds numbers the rate of energy dissipation is equal to the rate at which energy is transferred to progressively smaller eddies, and this rate is determined by the structure of energy containing eddies. Therefore, the dissipation rate is not a function of viscosity. In the original method (Ref. 49) Bradshaw proposed a universal distribution function $L = L(x_2/\delta)$ for the variation of dissipation length scale across the boundary layer, and in the later version of the method (Ref. 45) a transport equation is used to determine L . Calculations carried out at BSRA indicated that this is the most important quantity, as far as the velocity and the shear profiles are concerned, and in agreement with Bradshaw (Ref. 42), the existence of extra strain rate, i.e. streamline curvature, divergence, swirl, etc., can produce significant changes in the dissipation length scale. Although it has been argued that the change in L due to extra strain rates is caused by a reduction in the production of turbulent kinetic energy rather than with an increase in dissipation, cf. Ref. (41) p.74, since L expresses a ratio as $(\tau/\rho)^{\frac{3}{2}}/\epsilon = a_1^{\frac{3}{2}} \langle u_2^2 \rangle^{\frac{3}{2}}/\epsilon$, this argument does not alter the final outcome.

Finally, Bradshaw's empirical function G which is also known as the entrainment function represents the diffusion of turbulence and again is related to energy spectra of turbulence. This function is used to model the effects of pressure redistribution and transport of turbulent kinetic energy in the normal direction and is defined by:

$$\frac{\langle u_2^2 q^2 \rangle}{2} + \frac{\langle u_2^2 p \rangle}{\rho} = G \frac{\tau}{\rho} \left(\frac{\tau_{\max}}{\rho} \right)^{\frac{1}{2}}$$

This definition is consistent with the structural similarity assumption, cf. Townsend (Ref. 41) p.121-129, and it also corresponds to the observations that the energy transfer depends mostly on flow in eddies large enough to span most of the boundary layer, taking the form either of convection of smaller eddies or transfer of energy from one part of the large eddy to another. As a result of the observed effects of extra strain rates one would

* Equations are written in Cartesian tensor notation and conversion to any system or coordinates can be done by the relationship $x_i = g_{ij} \xi_j$ where g_{ij} is the metric tensor and ξ_j ($j=1,2,3$) are the new coordinates.

expect that the entrainment function too should be modified since it is known that negative extra strain rates increase entrainment whereas positive extra strain rates reduce the same. During the PHIVE project such modifications have been implemented in BSRA. The changes due to these modifications, however, were less spectacular than the effect of the changes in the dissipation length parameter.

Improved Turbulence Model

The description of and the improvements on the method given so far is valid for TSL approximation and to make it suitable for the aft-end flow calculation further changes were necessary. These were the incorporation of extra terms from the FSTL approximation, normal pressure gradient, effects of extra strain rates, and the choice of a convenient coordinate system. The first modification is fairly straightforward and mainly involves some curvature terms and turbulence production terms. In their inclusion into the governing equations the order of magnitudes of each term were also checked against the boundary layer measurements made by NMI.

Incorporation of normal pressure gradient was more troublesome because of the numerical problems. Within the TSL approximation pressure is rendered constant across the boundary layer. Although this assumption holds approximately for a large majority of the boundary layers of practical interest it becomes unsatisfactory when the boundary layer becomes thicker especially in regions of high curvature. The use of the blow-out scheme and the pseudo-body concept certainly help towards the improvement of the solution but only by improving the boundary conditions at the outer edge of the boundary layer. The assumption that, on the normal, pressure is constant still remains. Accepting the fact that the full N-S equations cannot be solved, there were three alternatives:

- (1) Use of higher order boundary layer approximation.
- (2) Refinement of TSL approximation based on experimental evidence.
- (3) Empirical modelling of the normal pressure gradient.

The first alternative is certainly the scientifically consistent approach. However, from an examination of the second order governing equation it is seen that due to both the additional terms and the elliptic nature of the equations computations become prohibitively expensive. Furthermore, the only additional terms in the normal momentum equation are curvature related terms and the terms related to the normal velocity and the Reynolds stress gradients do not appear, which are known to be important from the analyses of experimental data. To pursue this alternative any further was therefore not considered worthwhile.

The second alternative is due to Bradshaw (Ref. 52). He proposes that the guiding principle in a pragmatic approach is to inspect the terms which are present in the N-S equations but are neglected in the boundary layer equations and devise approximations for these that are inconvenient to retain in exact form. Worthwhile improvements in the boundary layer equations can be made if a degenerate form of the normal component momentum equation is included to predict $P(x_2)$ reflecting the missing upstream influence. Inclusion of this equation into the governing equations still makes the system elliptic, necessitating an iterative calculation scheme. However, the computation load may be reduced by solving the normal component equation separately, as done by Pratap and Spalding (Ref. 53) and Mahgoub and Bradshaw (Ref. 54). Although this alternative looked very promising considerations of the computation cost has meant that it has had to be kept for possible further development.

The last alternative is the use of empirical normal pressure profiles which, considering the empirical information used in both the integral and differential methods, is justifiable provided they are based on experimental evidence. Inspection of experimental data indicates that pressure variation in the normal direction is mostly regular, cf. Patel and Lee (Ref. 55), and a quadratic expression may be sufficient to approximate this variation. Given both the physical appeal and the relative success in its use, the centrifugal approximation was chosen for the BSRA approach and correlation with experimental data was achieved by introducing a new velocity scale.

Although the early theoretical and experimental work on the effect of extra strain rates go as far back as 1929, cf. Prantl (Ref. 56), Wattendorf (Ref. 57), concerted efforts in this direction appeared only after 1960. It is common practice that when the flow around a curved object is studied analytically a body oriented curvilinear coordinate system is employed. Adoption of such a coordinate system produces some extra terms in the boundary layer equations which are related to the curvature of the coordinate lines. If one carries out an order of magnitude analysis in laminar and turbulent boundary layers by using δ/R , R being the radius of streamline curvature, the extra terms that appear are of order δ/R times the largest existing terms, cf. Nash and Patel (Ref. 58). Although this result seems to be confirmed by experiment for laminar boundary layers, experiments on turbulent boundary layers indicate that the change in the Reynolds stresses due to the extra strain rates is roughly ten times the prediction obtained from a straightforward order of magnitude analysis. In the light of this experimental evidence it is imperative that special emphasis should be placed on the inclusion of the effects of the extra

strain rates in the calculation of the boundary layer development around the aft-end of ships.

In 1969 Bradshaw (Ref. 59) proposed an engineering calculation method by using an analogy between buoyancy and curvature effects. Although the present state of knowledge on the subject is far from complete, experiments carried out by Meroney and Bradshaw (Ref. 51), Patel and Lee (Ref. 56), So and Mellor (Ref. 60), Castro and Bradshaw (Ref. 61), Cebeci (Ref. 62) and Hunt and Joubert (Ref. 63) indicate that Bradshaw's method produces reasonably accurate results. In fact recent experiments by Smits, Young and Bradshaw (Ref. 64), and Smits, Eaton and Bradshaw (Ref. 65) demonstrated that the method also works for curvature impulses and for three dimensional curvatures. An excellent review on the subject is available by Bradshaw (Ref. 52).

The essence of the method is to modify the dissipation length scale by

$$\frac{L}{L_{eff}} = 1 + (\alpha e)_{eff}$$

where L_{eff} is the effective dissipation length scale, e is the extra strain rates obtained by using stress Richardson number, α is the empirical magnification constant, and $(\alpha e)_{eff}$ is given by

$$X_1 \frac{d}{dx_1} (\alpha e)_{eff} = \alpha_0 e - (\alpha e)_{eff}$$

where $X_1 = 10^5$ and this relationship allows for the effect of memory to be taken into account. The effect of extra strain rates for moderate curvatures on streamwise velocity component and Reynolds stress is illustrated in Fig. 14.

6. COORDINATE SYSTEM AND NUMERICAL SOLUTION

At the beginning of this research we were made aware of the difficulties on the choice of the appropriate coordinate system by the conclusions of the previous investigators, cf. Mangler and Murray (Ref. 66). Therefore, a considerable amount of effort was spent for the design of a method for the automatic generation of a suitable coordinate system and a program suite, called "AFACAN", was developed to achieve this end where the mapping method of Tuck and Von Kerczek (Ref. 67) was used to determine approximate streamlines.

As one gained more experience in turbulent flow computations it was realised that provided; (1) one of the coordinates is nearly aligned with the normal (see Wesseling (Ref. 68) for the need to have this condition), and (3) the marching direction, i.e. x_1 -axis, does not make an angle more than thirty degrees with the flow-direction, any coordinate system is equally acceptable. Furthermore, if the concept of matching surface is adopted

restrictions on the coordinate system could further be relaxed. This last point was also important in relation to the numerical computation.

In the numerical computation side, the problem was not only the choice of an integration method, but also the choice of the integration region. After a review study the conclusion was reached that implicit methods, in spite of their unconditional stability, were not suitable for BSRA's purpose due to the demand for inversion of fairly large matrices to determine the flow quantities which was too costly in BSRA's ICL 1904S computer. Amongst the available explicit methods we tested an extended version of Lister's method of characteristics (Ref. 69) and Lindhout's version of Co. t-Isaacson-Rees scheme (Ref. 70). After some testing we decided on the former method due to its flexibility. Stability of numerical integration was ensured by using a modified Courant-Friedrick's-Lewy stability criteria, cf. Raetz (Ref. 71).

The complete program suite GEMAK has been designed to consist of component programs which are interlinked as shown in Fig. 1. Discretised hull geometry and ship forward speed are used to run the potential flow program which also drives Gadd's integral boundary layer method program. As the computation of the free surface contribution (Neumann-Kelvin problem) is quite time consuming and costly, the double-body (Neumann problem) computer program is being used at present. The output of this stage contains integral boundary layer parameters as well as velocity profiles. Displacement thicknesses obtained in this way are used to re-evaluate velocity and pressure distribution at the edge of the matching surface which is determined by a special smoothing of the edge surface of calculated boundary layer. This task is achieved by the explained blow-out scheme. The output of this stage together with the discretised-hull geometry provides the necessary information for the running of Bradshaw's turbulent energy method program. The output of this program produces the velocity and shear profiles, and the internal parameters along the boundary layer and near wake for a given ship form and speed.

Since the computational domain for the turbulent flow calculations is now decided beforehand by the choice of the matching surface numerical integration of the governing equations has to be made in a somewhat different fashion especially since it was desirable to avoid a complete iterative scheme as used by Abdelmeguid et.al. (Ref. 72) and Mahgoub and Bradshaw (Ref. 54). The use of smoothed boundary layer edge surface in place of a semi-arbitrary matching surface helps towards the achievement of this purpose but in itself it is not sufficient. Therefore, a procedure called "stitching" has been developed by the authors. In this procedure calculation starts from the matching

surface towards the wall, after wall boundary condition is satisfied the computation is carried out from wall to the matching surface. If the velocities agree then the computation goes to the next step otherwise the velocities and Reynolds stress are updated by using an under-relaxation scheme and the boundary conditions at the matching surface is updated and the computation restarts from the matching surface as before and the procedure is repeated until convergence is achieved.

7. NOMINAL AND EFFECTIVE WAKE CALCULATION

7.1 Nominal Wake

Most of the present boundary layer calculation methods attempts to solve for the near wake either by using a fictitious flat plate at the centre plane or terminating the boundary layer calculation from this point onwards. In the first type of calculation, velocities near the centre plane are underestimated as a result of the wall boundary conditions and exclusion of mixing. In the latter case, the assumption of the mixing layer does not strictly hold because in the near wake some of the boundary layer flow behaviour is still observed as a result of the memory effect of the flow. To find a satisfactory solution to the problem two alternatives were investigated:

- (1) the use of Bradshaw's interaction hypothesis (Ref. 73), and
- (2) derivation of new boundary conditions for the wake centre plane.

Efforts were spent in both directions, but because of its success in airfoil and axisymmetric flow applications cf. Worel and Torda (Ref. 74), Huffman and Ng (Ref. 75), Andreopoulos (Ref. 76), the former approach has been adopted.

According to the interaction hypothesis, the near-wake consists of three regions (see Fig. 15); the inner wake region is the place where the mixing takes place. The second region is the extension of the wall layer of the boundary layer which now matches to the edge conditions of the inner wake layer, and the last region is the continuation of the wake region of the boundary and it is the least influenced part by moving from the boundary layer to wake. Since most of the structure of the near wake is similar to the boundary layer with the exception of the inner wake layer, interaction hypothesis suggest that it can be treated like an overlapping boundary layer, and overlapping takes place in the inner wake region.

So far as numerical computation is concerned the change to be made to the boundary layer calculation scheme is minimal and the change from boundary layer to near wake is identified by using a logical control statement.

Propeller-Hull Interaction and Effective Wake Calculation

From the practical point of view the determination of effective wake distribution was of a paramount importance both for the propeller design calculations and for providing the necessary input in the computation of the cavitation induced hull surface forces. Our preliminary studies revealed that most of the relevant analytical work was based on the studies of Dickmann (Refs. 77-78) and the recent research efforts were mainly aimed at deriving an empirical or a semi-empirical correction method for the derivation of effective wake from the measured nominal wake by using available data, cf. Sasajima and Tanaka (Ref. 79), Hoekstra (Ref. 80). The work carried out at DTNSRDC by Huang and his co-workers (Ref. 81) on axisymmetric bodies was not in line with the writers' method of approach, because he used an inviscid flow model (vorticity included), hence assumed that the flow at the aft-end of ships is a distortion layer rather than a complex turbulent shear layer. Since there was no clear indication on the method to be adopted, the writers after a careful examination of available data, decided to employ an improved version of Dickmann's conception without resorting to the separation of the flow into potential, viscous, and wave making components.

Since the BSRA approach consists of two steps the effect of the propeller operation on the flow development has been taken into account in each step. In the first step the effect of propeller is assumed to be potential in origin and hence the source strengths in the potential flow programs are modified to account for the propeller induced normal velocities. This modified potential flow is then used to drive the integral calculation method for the estimation of boundary layer and displacement thicknesses. Due to the change in the external potential field the newly calculated boundary layer differs from the nominal flow boundary layer, and consequently the region of integration for the detailed boundary layer calculation also changes. The next step is the modification of the boundary conditions on the matching surface. This modification takes place because (1) the new matching surface location and the new source strengths are different from the nominal flow case, and (2) on the matching surface propeller induced velocities are linearly added to the velocities induced by the pseudo-body (hull plus displacement thickness).

Following the re-determination of the computational region and the boundary conditions, the turbulent flow and near wake calculations remains the same as in the nominal flow calculation since the form of the governing equations for the field does not change with the presence of the

propeller-hull interaction. A flow chart illustrating the sequence of operations in the computation of effective wake is illustrated in Fig. 16.

8. RESULTS AND DISCUSSION

During the development of the hull flow studies three different types of application have been considered. They are: (1) application for program control purposes, (2) application for validation against the experimental data, and (3) application with the systematic changes in the design variables to provide guidance for the design and modification of aft-end forms of ships. In the following part of this section results of these applications are given.

Application for Program Control

Since the computers obey only the commands issued in the program as specified by the programmer various routines employed in the program suite GEMAK for the purposes of numerical integration, differentiation, smoothing, interpolation etc., have to be checked against numerical instability, artificial viscosity arising from numerical differentiation, and the usual execution errors such as overflow, negative argument in logarithm etc. Grave consequences of neglecting this vital check in numerical fluid dynamics is best illustrated by Roache (Ref. 82) and Holt (Ref. 83).

Application for Program Validation

The aim of this stage was to establish the credibility of each individual program separately and the program suite GEMAK as a whole. Apart from the intermediate data handling program there were three main programs involved in the suite and at the first instance each program has been tested separately. Since the comparison of the potential flow calculation program with experimental data and with the published results of other investigators have already been discussed before they will not be repeated here. These tests, however, indicated that the potential flow computation schemes were quite satisfactory at the hull discretisation scheme devised within the project was efficient. Another important result of these numerical tests was that so far as the aft-end flow calculations are concerned, depending on the hull shape, between 25 and 40 percent of the forward part of the ship can be excluded from the potential flow computation without incurring any significant error in the calculated velocity field.

The integral boundary layer calculation method program was already tested for a number of hull forms by Gadd (Ref. 8) and his results indicated that it was at least as good as any other available integral method. The BSRA testing on this program was essentially confined to assess

the sensitivity of the method to the variation of initial conditions and of the built-in empirical correction factors. These tests indicated that the sensitivity to the variation of the initial conditions was very high, indicating that the integral parameters employed to start the computations must be chosen very carefully. Variation of the pressure rise reduction factor (an empirical factor to avoid the formation of a stagnation point at the aft-end) and the blow-out scheme showed that this parameter had a controlling influence on the development of flow around the stern and in order to obtain a reasonable agreement with the experimental data it was necessary to change this parameter for differing hull forms. The method, generally, gave good agreement with experimental data for the forward 80 to 85 percent of ships and for extreme V-shape hull forms this distance reached up to 90 percent of the ship length. For the last 10 to 20 percent of the ship, the method generally over-estimated the boundary layer development. This, however, was a useful feature so far as the BSRA computation scheme is concerned since it was assumed that the matching surface obtained from the application of Gadd's method (Ref. 8) would enclose the real boundary layer.

As explained within the text the blow-out scheme was achieved by a modified use of the boundary layer program and the only tests to be carried out on this part was the comparison of panel source strengths with and without the blow-out scheme to make sure that when the boundary layer is quite thin the values obtained are close.

Verification of the program BRADSHAW was the most time consuming and important part of the total program verification process since the outcome of this stage would decide the success or otherwise of the program suite GEMAK. During the program development stage the initial version of the program was tested against the published experimental data on wings giving quite satisfactory results. The next verification stage was to compare the fully developed program results with the wind tunnel data for scaled ship models. The published data on a full form ($C_D = .85$) tanker model has been chosen for this purpose. The data on the Hoffmann tanker form (Ref. 2) was limited to mean velocities and static pressures on a number of points on five stations along the ship's length and only the last station ($x/L_{WL} = 0.916$, $x/L_{BP} = 0.942$) was of interest for the BSRA computation scheme. Hull geometry around this station and the measurement points used for comparison are presented in Fig. 17 and a comparison of measured and calculated streamwise and crosswise velocity profiles for the measurement points 184 and 185 are presented in Fig. 18. As can be seen from these figures the agreement for the streamwise velocity component is very good and for the crossflow components is fair.

It should be mentioned that for the point 185 an integral method would provide the same level of agreement since it is a smooth flow location. As the flow becomes more complicated with severe velocity gradient near the hull the advantages of using a differential method such as the one used by BSRA becomes apparent. Since the most severe measured flow condition for the Hoffmann tanker form occurs at the measurement point 183 this point was chosen to test the BSRA method against both the experimental data and Gadd's integral method (Ref. 8) and the result is shown in Fig. 19. Here the strong flow retardation near the hull surface is quite well predicted by the BSRA method whereas the integral method, due to the limitation in its assumption, predicts still a fairly smooth flow condition. Although the amount of flow retardation around $y/\delta = 0.25$ seems to be over-estimated by the BSRA method there is also a considerable amount of scatter in the data in the same location when different measuring arrangements were employed.

The intention for the comparison of measured and calculated wake was not realised because of a flow peculiarity first indicated by the program BRADSHAW. During the test runs the program indicated negative wall shear stresses in some of the calculation lines which in the usual turbulence understanding indicates separation and consequent flow reversal. However, shear stresses away from the wall were all positive. To ensure the continuation of the flow computation as far downstream as possible an artificial scheme called "bubble capturing" has been developed with which hull boundary is artificially displaced to the first point on the normal with a positive shear stress, resulting in some form of boundary layer shrinking. With the application of this technique the following computational steps indicated that the wall shear stress became positive again further downstream but within the boundary layer there was a region starting on the hull surface and moving away from the hull in further downstream direction, effectively forming a pocket. The unusual side of this phenomenon was that the mean flow did not change its direction but attained values as small as 9 percent of the forward speed within a distance of 10 to 20 percent of the boundary layer thickness. Eventually, when the negative shear away from the wall was large enough to invalidate the hyperbolic flow calculation assumption, computations on that calculation line had to be stopped.

A check on the experimental data from NMS indicated that our results were quite in agreement with the data and the start of negative shear predictions was accurate within 2 percent of the ship length. Evolution of this phenomenon (which we called "shear separation") is schematically illustrated in Fig. 20.

This result is particularly important for it is probably one of the crucial reasons in the formation of severe wake gradients. Obviously it is quite possible that for the full scale Reynolds number such a phenomenon may disappear. If, however, computations indicate the presence of shear separation it is advisable to alter the hull form.

Application for Design Guidance

At the beginning of the project it was believed that such guidance would be obtained by a systematic calculation scheme with varying hull forms. However, as the understanding in BSRA on the turbulent flow development increased a great deal of useful information relevant to the aft-end design have been gathered either by the study of the existing data and the critical examination of the governing equations employed in the calculation method, or by making small changes in the flow parameters for the same hull form.

The main contribution of the developed analytical aft end flow calculation scheme is to identify the trouble region and to provide insight on the consequences of possible hull form alterations. In this respect, it may be useful to re-identify the differences between the differential method used by BSRA and the integral methods. By the use of the differential methods detailed information on almost all the important flow quantities are calculated by taking into account local variation of the hull form with its consequences on the flow including those arising due to the extra strain rates as well as the continuity of the fluid flow. Therefore, if a hull form appears to be likely to have severe velocity gradients with low velocities at the top of the propeller disc either from the result of the model tests or from the hull flow and wake calculations the method explained here can be used both to trace the origin of the undesirable flow, i.e. where it starts, and to indicate the necessary changes in the aft-end geometry. To have a better appreciation on the effect of form changes on the flow development around the aft-end of ships it will be useful to indicate the effects of external boundary conditions and extra strain rates, i.e. curvatures, on the turbulent flow structure.

(1) Change in the velocity without any change in the pressure gradient. If the velocities at the edge of the boundary layer are uniformly increased or decreased the change in the total flow structure is only marginal, since this will mainly change the velocities at the outer edge of the boundary layer. As a rough indication the change in the streamwise velocity components due to a small change in the external velocity changes velocities in the normal direction as $e^{k(1 - y/\delta)}$ where $k = -11.5$.

(2) Change in the pressure gradient.

A change in the streamwise pressure gradient produces two main effects on the turbulent flow. They are: (1) a change on the wall shear stress and the velocity profiles in the wall region ($y/\delta = 0.0-0.20$) and (2) a change in the maximum shear stress. The effect of the first change is quite apparent since the all important very low velocity values and steep velocity gradients are formed in this region. The second change on the other hand determines the amount of energy loss and hence the change in ship resistance, because a change in the streamwise pressure gradient determines the magnitude of the maximum shear stress value in the outer layer of the boundary layer ($y/\delta = 0.25-1.00$) which in turn determines the diffusion of turbulence and the length scale of turbulent eddies, and hence the amount of energy lost in this region. It is for this reason that sometimes optimal hull forms from the naked hull resistance point of view (such as V-forms) are not so desirable when a more uniform wake distribution is required. This effect however is generally coupled with the curvature effects.

(3) Change in streamline curvatures.

As mentioned in section 5 and Appendix 5, extra strain rates resulting mainly from the streamline curvatures play a significant role on the structure of the turbulent flow. Since as a rough approximation flow streamlines on the hull can be represented by equal curvature lines, the amount of extra strain rate can be directly related to the variation of the hull form geometry. It is known that positive curvature (i.e. convex) produces positive extra strain rate and negative curvature (i.e. concave) produces negative extra strain rate and as a rough guide the extra strain rates changes the velocities near the hull surface as

$$U^* = U/[1 + \{n/(n+1)\}e]$$

where U and U^* are, respectively, the streamwise velocity components without and with the streamline curvature effects, e is the effective extra strain rate and n is the power law exponent for the velocity profile near the hull surface, and it takes values between 5 and 7 for concave surfaces and between 2 and 5 for convex surfaces.

In the outer part of the boundary layer their main effect is seen on the eddy length scale and positive curvatures tends to reduce the boundary layer thickness and hence reduce the loss of energy giving rise to steeper velocity gradients near the hull whereas negative curvatures increase the loss of energy and hence the resistance. Figure 34 is given as a rough guide to compare the velocity defect profiles for convex and concave hull surfaces.

The method reported here can be used both to identify the trouble area and the amount of pressure gradient and extra strain rates to be compensated. Figure 21 schematically illustrates the determination of the region of flow improvement which can be determined by the program suite GEMAK. The information on the incoming and outgoing characteristics and on the local pressure gradients and extra strain rates are contained in the output of the BSRA method.

9. CONCLUDING REMARKS

This paper summarises the work conducted at BSRA on the development of an analytical calculation method for the determination of flow around the aft-ends of ships within the context of the PHIVE Project. As explained within text the method consists of a number of steps as shown in Fig. 1, and in every step the best available techniques are used to produce a reliable and cost-effective computer program suite. Based on the experience gained so far the following tentative conclusion may be drawn:

- (1) To the knowledge of the authors this is the first hybrid method developed for the hull flow calculation; in this method the flow up to 80-85 per cent of the hull is calculated with the Gadd's integral method (Ref. 8) and a version of Bradshaws turbulent energy method (Refs. 7 and 25) is employed to determine the flow around last 15 to 20 percent of the ship. The method takes the displacement effect of boundary layer and the effects of normal pressure gradient and of extra strain rates arising from the streamline curvature into account. The "stitching" process to satisfy both the hull surface boundary condition and the matching surface (obtained from a preliminary iteration with Gadd's method (Ref. 8)) boundary condition and the "bubble capturing" technique to calculate the flow after the shear separation are some of the procedures developed by BSRA which has extended the current capability and understanding on the turbulent flow computation.
- (2) Comparison of results with the experimental data for the Hoffmann tanker form (Ref. 2) showed very encouraging agreement even for the severest flow conditions as demonstrated in Fig. 19.
- (3) A mechanism giving rise to severe flow retardation and high velocity gradient has been identified as shear separation in which the shear stress reverses without a mean flow reversal. Although this was first discovered during the development of the program suite GEMAK, the wind tunnel data of NMI has confirmed this finding.

- (4) As a result of the studies conducted to provide guidelines for the aft-end design, information on the role of various parameters in the development of aft-end flow has been gathered and presented, together with the role the BSRA method can play in the identification of the trouble area.
- (5) From the results obtained it appears that a fully computerised scheme to modify the aft-end of a parent form to produce a more desirable wake may be designed by an extended use of the program suite GEMAK.
- (6) The methodology employed in the development of the program BRADSHAW can further be utilised to devise a more rational scheme to account for the scale effects during the scaling of the model wake for cavitation testing.

ACKNOWLEDGEMENT

The authors express their thanks to the Council of the British Ship Research Association for permission to publish this paper, to The Ship and Marine Technology Requirements Board as the major financial sponsor of the work, and to British Shipbuilders, The General Council of British Shipping, Lloyd's Register of Shipping and Stone Manganese Marine who provided financial support as the industry sponsors. Thanks are also due to Professor P. Bradshaw of Imperial College for his help and valuable suggestions, to Dr. G.E. Gadd and Dr. M.E. Davies of NMI for their stimulating discussions, and to Professor T. Cebeci of California State University, Professor V.C. Patel of Iowa University, Dr. B. van den Berg of the National Aerospace Laboratory NLR, Professor W.C. Reynolds of Stanford University and Dr. F.G. Blottner of Sandia Laboratories for supplying invaluable information and advice.

REFERENCES

1. Odabaşı, A.Y. and F. Zsimmons, P.A. Alternative Methods for Wake Quality Assessment. International Shipbuilding Progress, Vol. 25, no. 282, (1978), p.34.
2. Untersuchung der 3-dimensionalen turbulenten Grenzschicht an einem Schiffsdoppelmodell im Windkanal. Institut für Schiffbau der Universität Hamburg, Bericht Nr. 343, (1976).
3. Bradshaw, P. (with an Appendix by V.C. Patel). The Strategy of Calculation Methods for Complex Turbulent Flows. Imperial College of Science and Technology, I.C. Aero Report 73-05, (1973).
4. Landweber, L. Characteristics of Ship Boundary Layers. 8th Symp. on Naval Hydrodynamics, Pasadena, California, (1968).
5. Larsson, L. Boundary Layers of Ships, Parts I, II, III and IV. SSPA General Reports, Nos. 44, 45, 46 and 47, (1974).
6. Himeno, Y., and Tanaka, I. An Integral Method for Predicting Behaviour of Three-Dimensional Turbulent Boundary Layers on Ships Hull Surfaces. Technology Reports of the Osaka University, Vol. 23, No. 1146, (1973).
7. Bradshaw, P. Calculation of Three-Dimensional Turbulent Boundary Layers. J. Fluid Mech., Vol. 46, p.417, (1971).
8. Gadd, G.E. A Simple Calculation Method for Assessing the Quality of the Viscous Flow near a Ship's Stern. Int. Symp. on Ship Viscous Resistance, SSPA, Goteborg, (1978).
9. Hess, J.L. and Smith, A.M.O. Calculation of Non-Lifting Potential Flow about Arbitrary Bodies. Douglas Aircraft Co., Report No: E.S. 40622, (1962).
10. Hess, J.L. and Smith, A.M.O. Calculation of Potential Flow About Arbitrary Bodies. Progress in Aeronautical Sciences, Vol.8, (1966).
11. Prard, R. The Representation of a Given Ship Form by Singularity Distributions when the Boundary Condition on the Free Surface is Linearised. Journal of Ship Research, Vol.16, March, (1972).
12. Gadd, G.E. A Method of Computing the Flow and Surface Wave Pattern Around Full Forms. Trans. RINA, Vol.118, p.207, (1976).
13. Gadd, G.E. Contribution to Workshop on Ship Wave Resistance Computations. Workshop on Ship Wave Resistance Computations, DTNSRDC, Bethesda, Maryland, (1979).
14. Wehausen, J.V. The Wave Resistance for Ships. Advances in Applied Mechanics, Vol.13, p.93, (1973).
15. Timman, R. Numerical Methods in Ship Hydrodynamics. First Int. Conf. on Num. Ship Hydrodynamics, p.1 (1975).
16. Chapman, R.B. Survey of Numerical Solutions for Ship Free-Surface Problems by Surface-Singularity Techniques. Second Int. Conf. on Num. Ship Hydrodynamics, p.5 (1977).
17. Hess, J.L. Higher Order Numerical Solution of the Integral Equation for the Two-Dimensional Neumann Problem. Computer Methods in Applied Mechanics and Engineering, Vol.2, No.1, p.1, (1972).
18. Hess, J.L. The Use of Higher-Order Surface Singularity Distributions to Obtain Improved Potential Flow Solutions for Two-Dimensional Lifting Airfoils. Computer Methods in Applied Mechanics and Engineering, Vol.5, No.1, (1975).
19. Hess, J.L. Status of a Higher-Order Panel Method for Non-Lifting Three-Dimensional Potential Flow. Douglas Aircraft Co., Report No.: NACS-76118-30, August, (1977).
20. Webster, W.C. The Flow About Arbitrary, Three-Dimensional Smooth Bodies. Journal of Ship Research, Vol.19, No.4, p.206, (1975).

21. Şaylan, Ö. Theoretical Wave-Resistance of a Ship with Bulbous Bow. Istanbul Technical Uni., Faculty of Shipbuilding and Nav. Arch., (1977). (In Turkish).
22. Huang, T.T. and Santelli, N. and Belt, G. Stern Boundary Layer Flow on Axisymmetric Bodies. 12th Symposium on Naval Hydrodynamics, Washington D.C., (1978).
23. Huang, T.T. and von Kerczek, C.H. Shear Stress and Pressure Distribution on a Surface Ship Model: Theory and Experiment. 9th Symposium on Naval Hydrodynamics, Paris, (1972).
24. Adey, B.H. and Harvey, P.J. An Analysis of Ship Resistance. Dept. Mech. Eng., Uni. of Washington, Report UWME-BHA-75-01, March, (1975).
25. Adey, B.H. and Fung, K.L. An Investigation of the Fluid Flow About Ships. U.S. Dept. Comm., Nat. Techn. Inf. Service, PB-261084, August, (1976).
26. Coles, D.E. The Law of the Wake in turbulent Boundary Layer. Journal of Fluid Mechanics. Vol. 1, Part 2, p.191, (1956).
27. Coles, D.E., and Hirst, E.A. Proceedings: Computation of Turbulent Boundary Layers - 1968. (Editors), AFOSR-IFP. Stanford Conference, Vol. II, (1968).
28. Mager, A. Generalization of Boundary-Layer Momentum-Integral Equations to Three-Dimensional Flows Including those of Rotating System. NACA Report 1067, (1952).
29. Ludwig, H., and Tillmann, W. Untersuchungen über die Wandschubspannung in turbulenten Reibungsschichten. Ingenieur Archiv, Vol. 17, p.288 (1949), English Translation as NACA TM 1285, (1950).
30. Stüper, G. Auftriebsverminderung eines Flügels durch seinem Widerstand. Zeitschrift für Flugtechnik und Motorluftschiffahrt, Vol. 33, 439, (1933).
31. Preston, J.H. The Approximate Calculation of the Lift of Symmetrical Aerofoils taking Account of the Boundary Layer, with Application to Control Problems. A.R.C. Reports and Memoranda No. 1996, (1943).
32. Preston, J.H. The Effect of the Boundary Layer and Wake on the Flow Past a Symmetrical Aerofoil at Zero Incidence. A.R.C. Reports and Memoranda No. 2107, (1945).
33. Moore, F.K. Three-Dimensional Boundary-Layer Flow. Journal of the Aeronautical Sciences, Vol. 20, No. 8, p.525; (1953).
34. Moore, F.K. Displacement Effect of a Three-Dimensional Boundary-Layer. NACA Report 1124, (1953).
35. Lighthill, M.J. On Displacement Thickness. Journal of Fluid Mechanics, Vol. 4, Part 4, p.383, (1958).
36. Giesing, J.P., and Smith A.M.O. Potential Flow about Two-Dimensional Hydrofoils. Journal of Fluid Mechanics, Vol. 28, p.113, (1967).
37. Jacob, K. Computation of Separated Incompressible Flow Around Airfoil and Determination of Maximum Lift. AVA Report, 67A62, (1967).
38. Rubbert, P.E., and Saaris, G.R. Review and Evaluation of a Three-Dimensional Lifting Potential Flow Analysis Methods for Arbitrary Configurations. AIAA Paper, 72-188 (1972).
39. Landweber, L. On Irrotational Flows Equivalent to the Boundary Layer and Wake - The Fifth David W. Taylor Lectures. David W. Taylor NSRDC, Report DTNSRDC-78/111, (1978).
40. Myring, D.F. An Integral Prediction Method for Three-Dimensional Turbulent Boundary Layers in Incompressible Flow. Royal Aircraft Establishment, Technical Report 70147, (1970).
41. Townsend, A.A. The Structure of Turbulent Shear Flow. Cambridge Univ. Press, Cambridge, 2nd Ed., (1976).
42. Bradshaw, P. The Understanding and Prediction of Turbulent Flow. Aeronautical J., Vol. 76, No. 739, p.403, (1972).
43. Cebeci, T., Kaups, K., and Ramsey, J. Calculation of Three-Dimensional Boundary Layers on Ship Hulls. Proc. 1st Int. Conf. on Numerical Ship Hydrodynamics, Bethesda, Maryland, p.409, (1975).
44. Cebeci, T., Chang, K.C., and Kaups, K. A General Method for Calculating Three-Dimensional Laminar and Turbulent Boundary Layers on Ship Hulls. Proc. 12th Symp. on Naval Hydrodynamics, Maryland, p.188, (1978).
45. Bradshaw, P., and Unsworth, K. Computation of Complex Turbulent Flows, in Review-Viscous Flow. Lockheed Report L77EROO44, (1976).
46. Rastogi, A.K., and Rodi, W. Calculation of General Three-Dimensional Turbulent Boundary Layers. AIAA Journal, Vol. 16, p.151, (1978).
47. Abdelmeguid, A.M., Markatos, N.C.G., and Spalding, D.B. A Method of Predicting Three-Dimensional Turbulent Flows Around Ships' Hulls. Int. Symp. on Ship Viscous Resistance, SSPA, Goteborg, (1978).
48. Bradshaw, P. The Turbulence Structure of Equilibrium Boundary Layers. J. Fluid Mech., Vol. 29, p.625, (1967).
49. Van Den Berg, B. Investigations of Three-Dimensional Incompressible Turbulent Boundary Layers. National Aerospace Laboratory NLR, The Netherlands, Report NLR TR 76001 U, (1976).
50. Maroney, R.N., and Bradshaw, P. Turbulent Boundary Layer Growth over a Longitudinally Curved Surface. AIAA Journal, Vol. 13, p.1448, (1977).
51. Bradshaw, P. Effects of Streamline Curvature on Turbulent Flow. AGARDograph 169, (1973).
52. Bradshaw, P. Higher-Order Viscous-Inviscid Matching. Imperial College of Science and Technology, I.C. Aero. Tech. Note 78-103, (1978).

53. Pratap, V.S., and Spalding, D.B. Numerical Computation of the Flow in Curved Ducts. Aero-Quart., Vol. 26, p.219, (1975).
54. Mahgoub, H.E.H., and Bradshaw, P. Calculation of Turbulent-Inviscid Flow Interactions with Large Normal Pressure Gradients. AIAA Journal, Vol. 17, p.1025, (1979).
55. Patel, V.C., and Lee, Y.T. Thick Axisymmetric Boundary Layers and Wakes: Experiment and Theory. Int. Symp. on Ship Viscous Resistance, SSPA Goteborg, (1978).
56. Prandtl, L. Effect of Stabilising Forces on Turbulence. NACA Tech. Mem. No. 625, (1931), (German original appeared in 1929).
57. Wattendorf, F.L. A Study of the Effect of Curvature on Fully Developed Turbulent Flow. Proc. of Royal Soc., Series A, Vol. 148, p.565, (1935).
58. Nash, J.F., and Patel, V.C. Three Dimensional Turbulent Boundary Layers. SBC Technical Books, Atlanta, (1972).
59. Bradshaw, P. The Analogy Between Streamline Curvature and Buoyancy in Turbulent Shear Flow. J.Fluid Mech., Vol. 36, p.177 (1969).
60. So, R.M.C., and Mellor, G.L. An Experimental Investigation of Turbulent Boundary Layers Along Curved Surfaces. NASA-CR-1940, (1972).
61. Castro, I.P., and Bradshaw, P. The Turbulence Structure of a Highly Curved Mixing Layer. J. Fluid Mech., Vol. 73, p.265, (1976).
62. Cebeci, T. Wall Curvature and Transition Effects in Turbulent Boundary Layers. AIAA Journal, Vol. 9, p.1868, (1971).
63. Hunt, I.A., and Joubert, P.N. Effects of Small Streamline Curvature on Turbulent Duct Flow. J.Fluid Mech., Vol. 91, p.633, (1979).
64. Smits, A.J., Young, S.T.B., and Bradshaw, P. The Effect of Short Regions of High Surface Curvature on Turbulent Boundary Layers. J.Fluid Mech., Vol. 94, p.209, (1979).
65. Smits, A.J., Eaton, J.A., and Bradshaw, P. The Response of a Turbulent Boundary Layer to Lateral Divergence. J.Fluid Mech., Vol. 94, p.243, (1979).
66. Mangler, K.W., and Murray, J.C. Systems of Coordinates Suitable for the Numerical Calculation of Three-Dimensional Flow Fields. Royal Aircraft Establishment, RAE TR 73034 (1973).
67. Tuck, E.O., and Von Kerczek, C. Streamline and Pressure Distribution on Arbitrary Ship Hulls at Zero Froude Number. J. Ship Research, Vol. 12, p.231, (1968).
68. Wesseling, P. The Calculation of Incompressible Three-Dimensional Turbulent Boundary Layers. Part 1. Formulation of a System of Equations. National Aerospace Laboratory NL, The Netherlands, Report AT-69-01, (1979).
69. Lister, M. The Numerical Solution of Hyperbolic Partial Differential Equation by the Method of Characteristics, in Mathematical Methods for Digital Computers. ed. by A. Ralston and H.S. Wilf, Wiley, p.165, (1960).
70. Lindhout, J.P.F. An Algol Program for the Calculation of Incompressible Three-Dimensional Turbulent Boundary Layers. National Aerospace Laboratory NLR, The Netherlands, NLR TR 74159U, (1975).
71. Raetz, G.S. A Method of Calculating Three-Dimensional Laminar Boundary Layers of Steady Compressible Flow. Aeronautical Research Council, A.R.C. 23634, (1962).
72. Abdeleguid, A.M., Markatos, N.C., Muraoka, K., and Spalding, D.B. A Comparison between the Parabolic and Partially Parabolic Solution Procedures for Three-Dimensional Turbulent Flows Around Ships' Hulls. Appl. Math. Modelling, Vol. 3, p.249, (1979).
73. Bradshaw, P. Prediction of the Turbulent Near-Wake of a Symmetrical Aerofoil. AIAA Journal, Vol. 8, p.1507, (1970).
74. Morel, T., and Torda, T.P. Calculation of Free Turbulent Mixing by the Interaction Approach. AIAA Journal, Vol. 12, p.533, (1974).
75. Huffman, G.D., and Ng, B.S.H. Modelling of an Axisymmetric Turbulent Near Wake Using the Interaction Hypothesis. AIAA Journal, Vol. 16, p.193, (1978).
76. Andreopoulos, J. Symmetrical and Asymmetrical Turbulent Near Wakes. Imperial College of Science and Technology, London, Ph.D. Thesis, (1978).
77. Dickmann, J. Schiffskörpersog, Wellenwiderstand eines Propellers und Wechselwirkung mit Schiffswellen. Ing. Arch., Vol. 9, p.452, (1938).
78. Dickmann, J. Wechselwirkung zwischen Propeller und Schiff unter besonderer Berücksichtigung des Welleneinflusses. Jahrbuch der STG, Vol. 40, p.234, (1939).
79. Sasajima, H., and Tanaka, I. On the Estimation of Wake of Ships. Proc. 11th ITTC, Tokyo, (1966).
80. Hoekstra, M. Prediction of Full Scale Wake Characteristics based on Model Wake Survey. Symp. on High Powered Propulsion of Ships, Wageningen, (1974).
81. Huang, I.T., and Cox, B.D. Interaction of Afterbody Boundary Layer and Propeller. Symp. on Hydrodynamics of Ship and Offshore Propulsion Systems, Paper 4/2, Oslo, (1977).
82. Roache, P.J. Computational Fluid Dynamics. Hermosa Publishers, Albuquerque, Revised Printing (1976).
83. Holt, M. Numerical Methods in Fluid Dynamics. Springer Verlag, New York (1970).

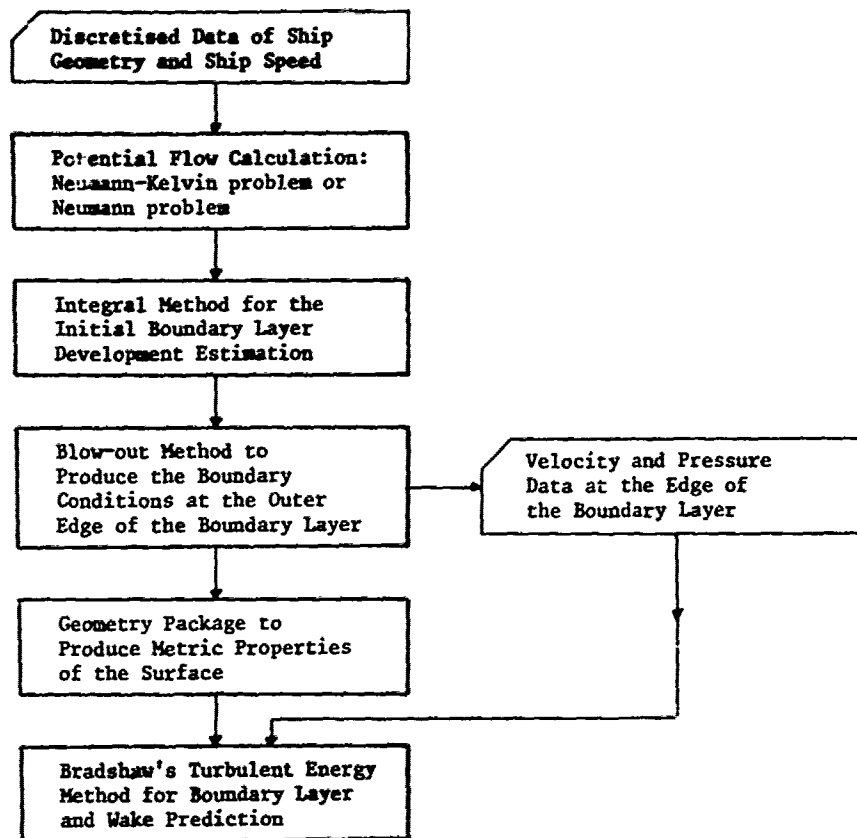


Fig. 1 Flow Chart of the BSRA Computer Program Suite for the Calculation of Boundary Layer Development on Ships

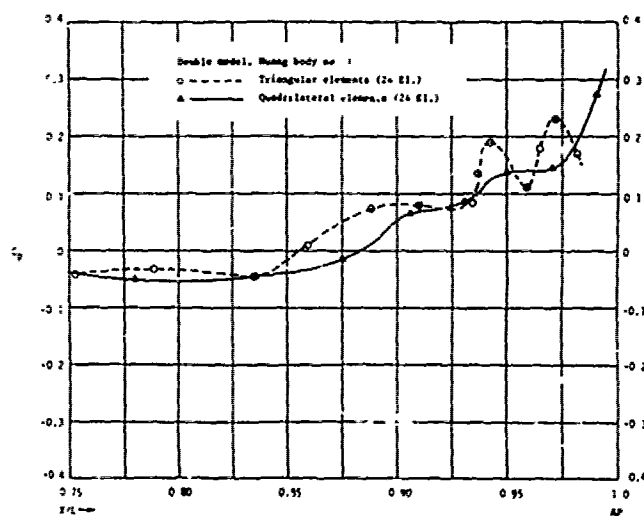


Fig. 2 Comparison between Triangular and Quadrilateral Elements

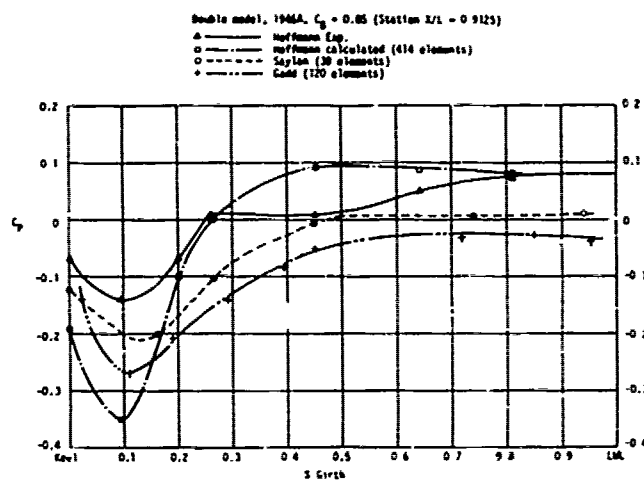


Fig. 3 Comparison of Different Methods

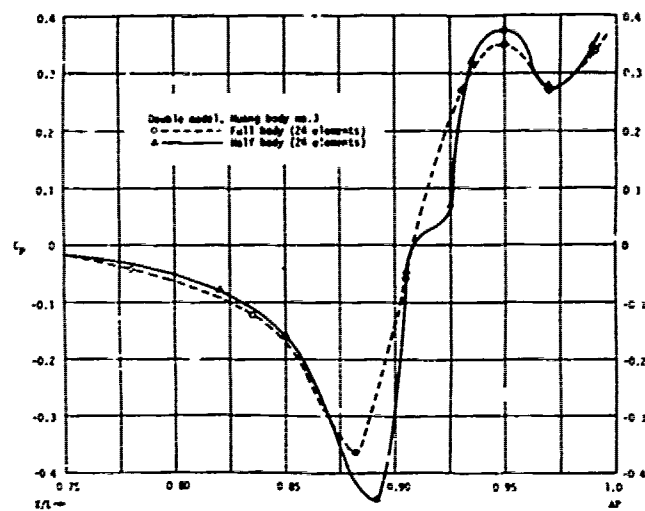


Fig. 5 Effect of Forebody

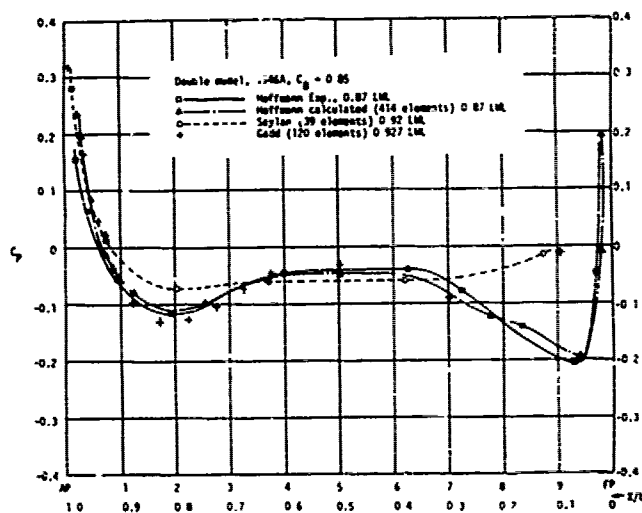


Fig. 4 Comparison of Different Methods

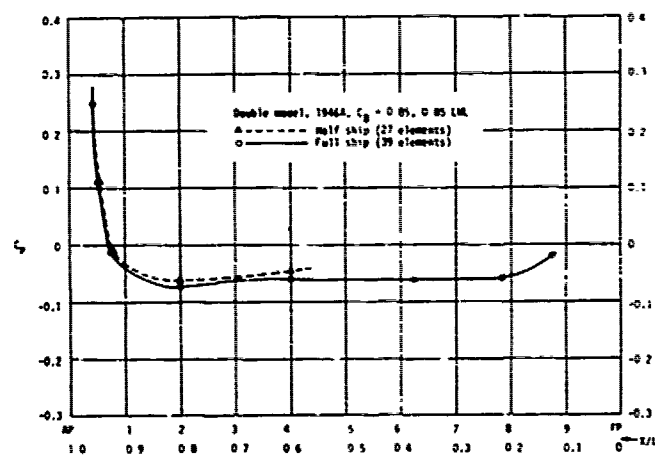


Fig. 6 Effect of Forebody

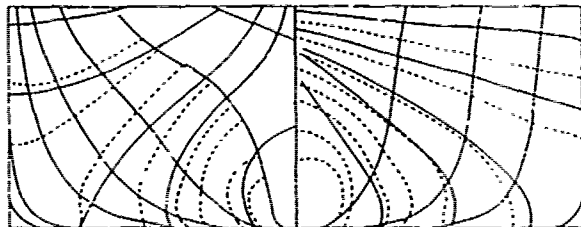


Fig. 7 Comparisons of Streamlines for Hoffmann's Tanker Form
 ----- BSRA Results for 74 Elements
 _____ Hoffmann Results for 414 Elements

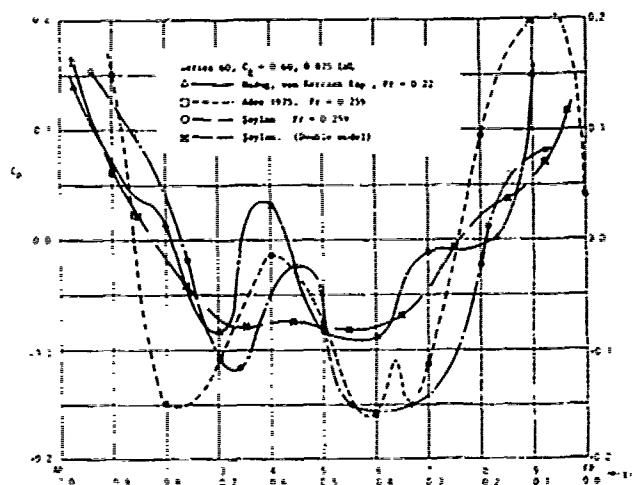


Fig. 9 Comparison of Different Results (with Free Surface)

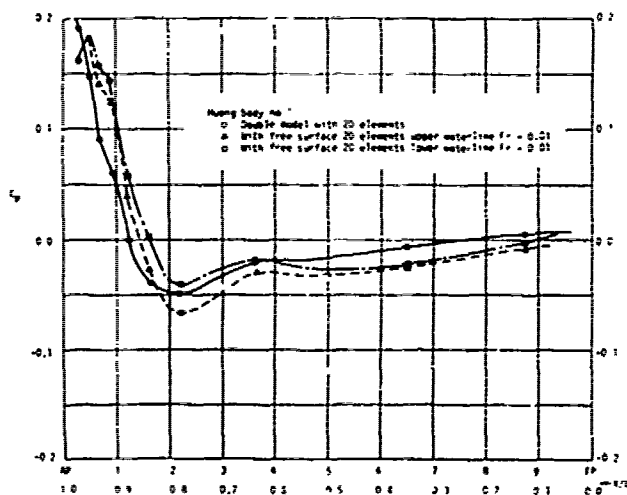


Fig. 8 Free Surface Effect for Low Froude Number

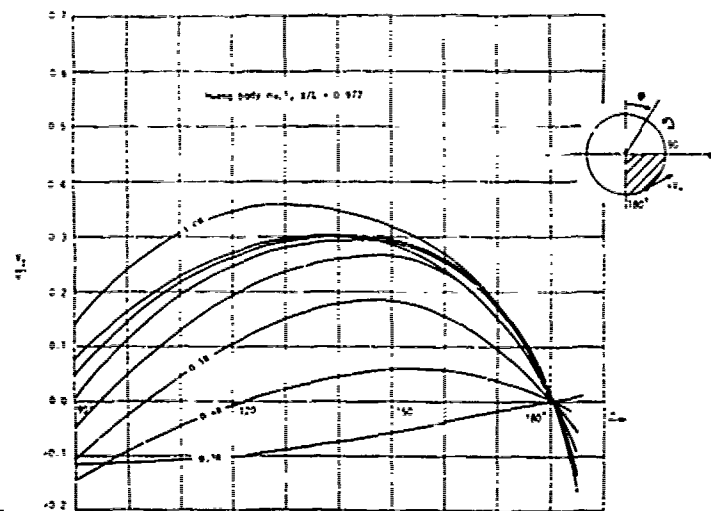


Fig. 10 Tang. Velocities on Propeller Plane (Free Surface Effect)

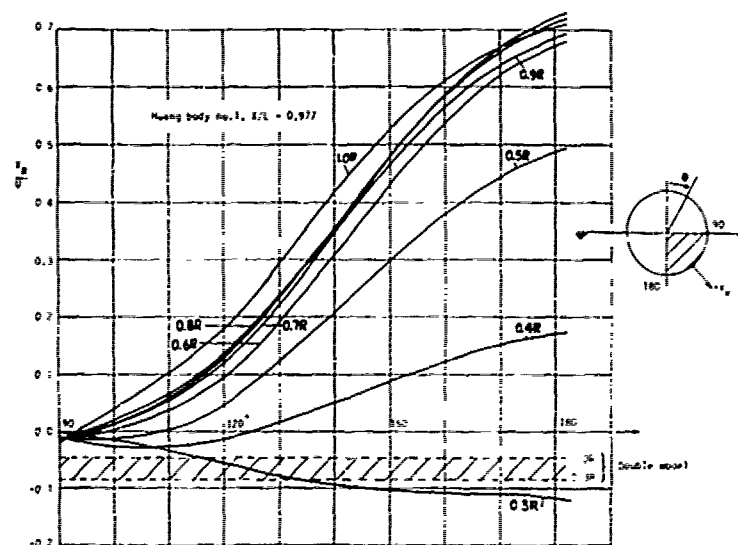


Fig. 11 Radial Velocities on Propeller Plane (Free Surface Effect)

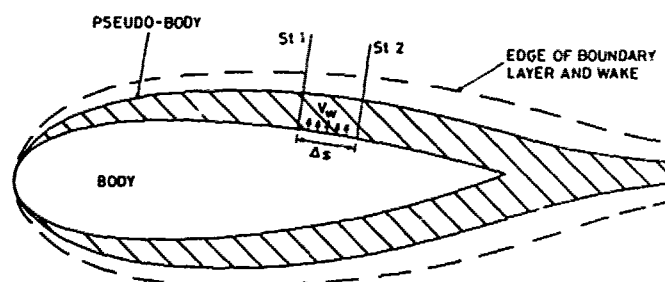


Fig. 12 Schematic Representation of the Body, Boundary Layer, Wake and Pseudo-Body

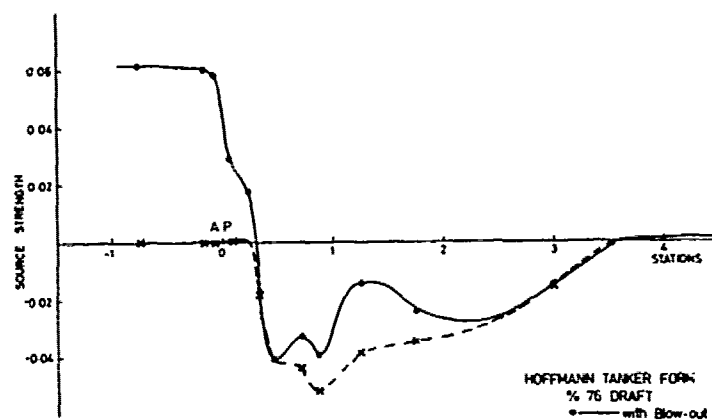


Fig. 13 Effect of Blow-Out

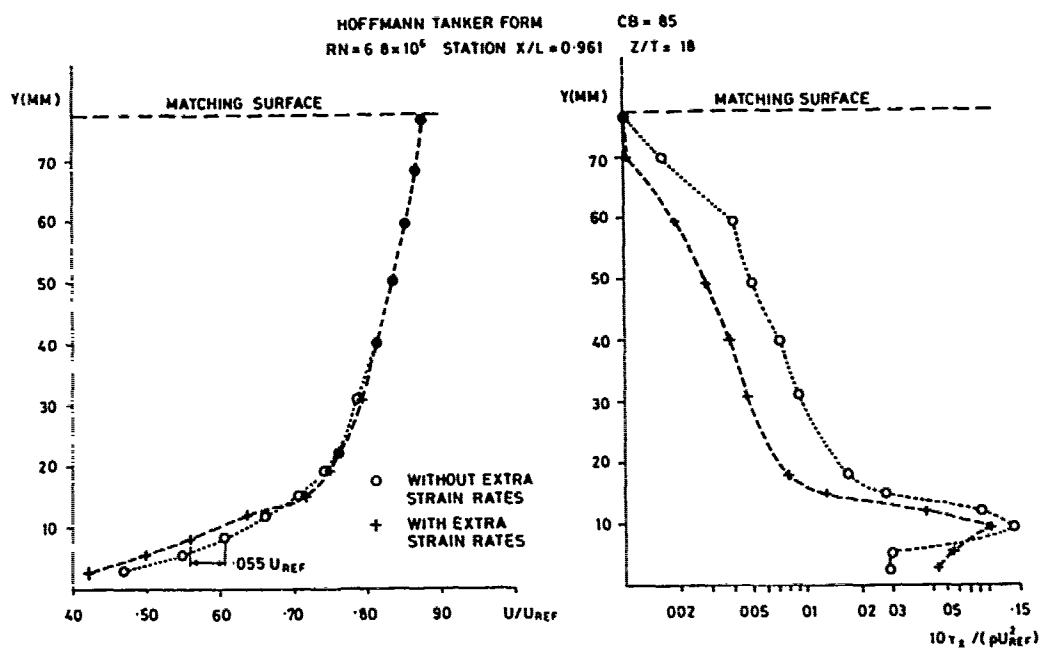


Fig. 14 Effect of Extra Strain Rates on Flow Properties

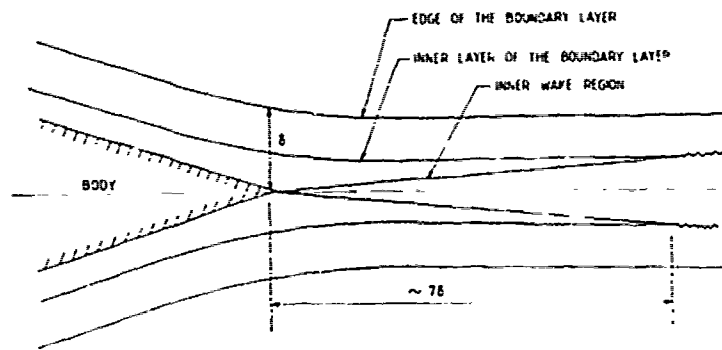


Fig. 15 Schematical behaviour of Near Wake

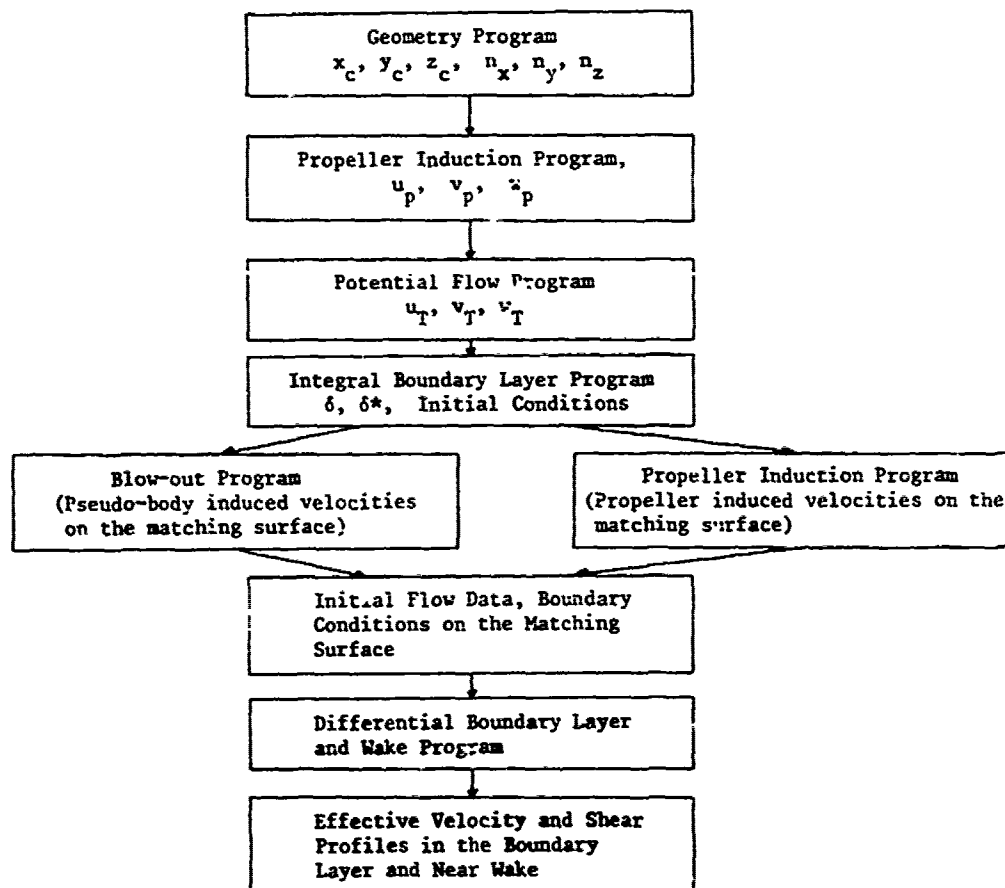


Fig. 16 Computation Scheme for the Determination of Effective Flow Field

HOFFMANN TANKER FORM $Re = 6.8 \times 10^4$
 $CB = 85$

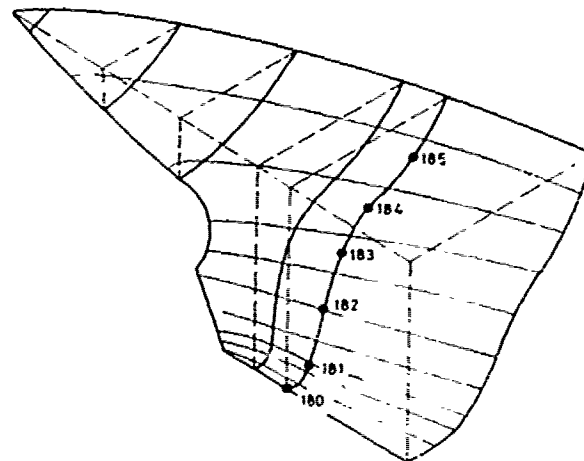


Fig. 17 Location of Comparison Points

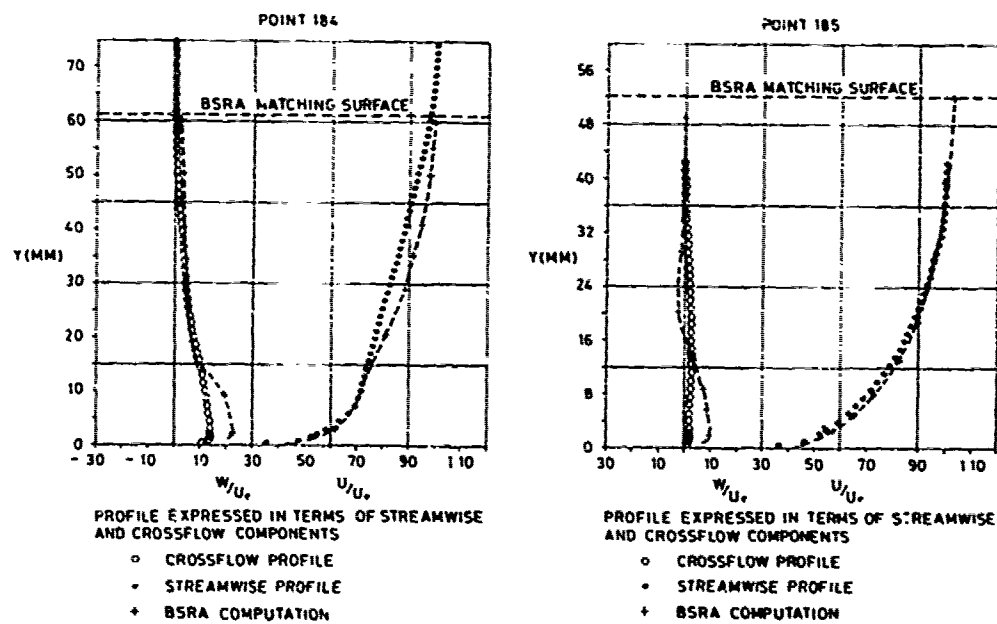
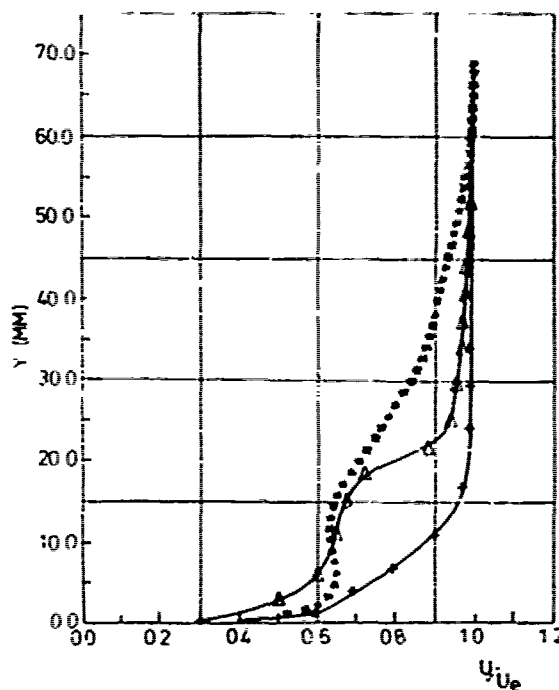
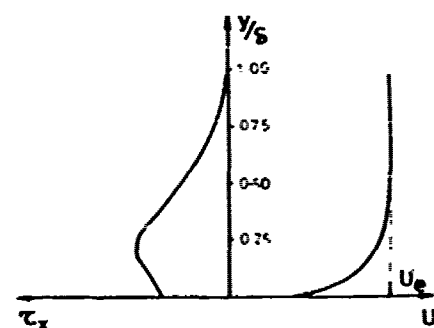


Fig. 18 Comparison of Measured and Calculated Velocity Profiles
for Hoffmann Tanker Form $X/L = .916$

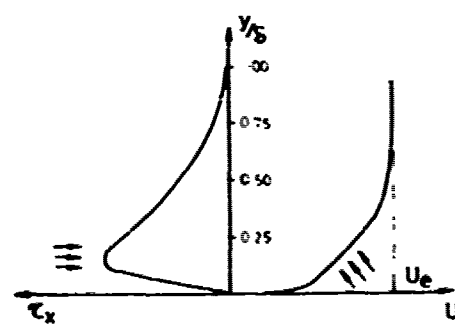


..... EXPERIMENT
 —+— CALCULATION RESULTS
 WITH GADD'S METHOD
 —△— CALCULATION RESULTS
 WITH BSRA METHOD

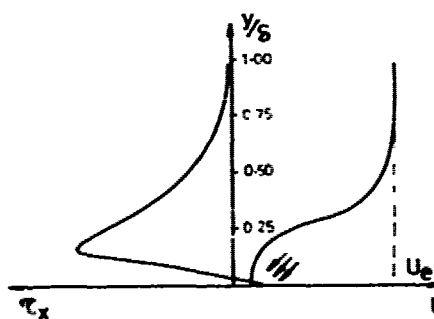
Fig. 19 Comparison of BSRA Method with Experimental Data with Gadd's Method



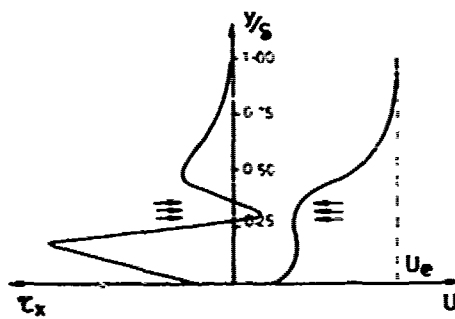
① Normal Flow



② Start of shear separation



③ Development of severe retardation



④ Formation of a kink in the velocity profile

Fig. 20 The Phenomenon of Shear Separation

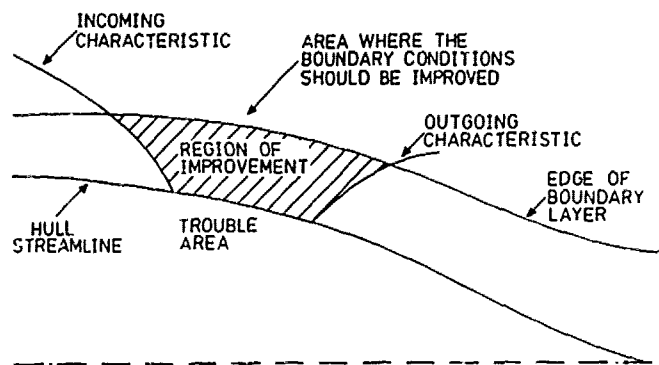


Fig. 21 Determination of Region of Improvement

Discussion

V.C. Patel (Univ. of Iowa)

The authors have described the many problems encountered in the calculation of stern flows. I have a number of comments and questions. For convenience, these are divided into three parts.

1. Inviscid Flow

The differences among the results of the various inviscid-flow calculations and experimental data (Figs. 3, 4, 7, 9) are quite substantial since the boundary layer responds to the GRADIENTS of pressure and the CURVATURES of the streamlines. An accurate description of the hull and coordinate geometry, and the pressure gradients, is therefore a prerequisite for reliable boundary-layer calculations. In view of the marked sensitivity of the integral method to its own initial conditions, would the authors comment on (a) the sensitivity of the method to uncertainties in the pressure gradients implied by the differences in the pressure distributions, and (b) the influence of the initial conditions resulting from Gadd's method on the subsequent stern-flow calculations using the differential method?

2. Viscous-Flow Calculations

It is not evident from the paper whether the authors use the TSL or the FTSL equations in the differential method for the flow over the stern. The treatment of the static-pressure variation is also not clear. It is my understanding that the TSL equations are used with the inviscid-flow pressure distribution in the first boundary layer calculation and then the centrifugal approximation is used for the pressure variation in a second solution of the TSL equations. Is this correct? Would the authors comment on the possibilities of obtaining a converged solution after further iterations, especially in view of the results of Hoekstra and Raven (Paper VI-1)?

With regard to the turbulence model of Bradshaw, it should be noted that the modification of L for the extra rates of strain was proposed for small extra rates of strain and that hitherto it has been used only in 2D and axisymmetric boundary layers. Did the authors include extra strain rates arising from the longitudinal and transverse surface curvatures and how large were these corrections in the flow over the stern?

Finally, the interactive hypothesis for the calculation of the near wake, to my knowledge, has been applied thus far to 2D wakes. What additional assumptions were required to extend it to the highly 3D wake and how were the necessary boundary conditions determined?

3. Result

Fig. 18 (point 184) appears to indicate that the match boundary is located too close to the hull. The comparison in Fig. 19, for the "most severe" point 183, is, in my view, incomplete insofar as the corresponding crossflow profile is not shown. I believe it would also be useful to make a comparison between the inviscid pressure distribution on the hull and that obtained after allowing for the boundary layer growth. Additionally, since the boundary layer continues to grow beyond $X/L = 0.916$ on Hoffmann's tanker model, and the ultimate goal is to predict the velocity field in the wake at the propeller plane, it would have been interesting to present the results beyond this station. This would have offered an opportunity to make a comparison between the predictions of this method and the data being collected by Kux and Wieghardt at several stations on the stern and in the near wake of this model.

The term "shear separation" (Fig. 20) is a new one. It is known that kinky velocity profiles of the type shown in Fig. 19 and sketched in Fig. 20 occur in regions of crossflow reversal and are associated with "free-vortex" (Maskell) or "open" (Wang) separation leading to the formation of a longitudinal vortex. $\tau_{wx} < 0$ is not a sufficient indication of a catastrophic flow phenomenon since its value depends upon the local coordinate orientation. A complete picture can be constructed only by examining both components of the velocity and shear-stress vectors. I would therefore advise some caution in the interpretation of these results.

Finally, the authors refer to boundary layer and near wake data collected at NMI. Are these available in the open literature? If so, I would appreciate their explicit mention.

M. Hoekstra (NSMB)

The scope of this paper is so wide that many essential features of the authors' method remain obscure. I hope that some points can be clarified in the reply to the following questions.

1. (Chapter 4) In the discussion of the blow-out method the problem of how to take into account the influence of the wake is addressed. The conclusion is that, when there is no information on the wake flow, it is reasonable to use the displacement thicknesses at the aftmost position of the hull for the computation region in the wake. Thus I would expect a rather weak source strength in the wake. However, considering Fig. 13 of the paper, the authors found a very high and apparently constant source strength in the wake in the interactive calculation. Can the authors explain this?

Actually the displacement thickness

will gradually decrease in the wake so that the presence of sinks in the wake seems to be more likely.

2. In chapter 5 Bradshaw's suggestion is followed for modifying the dissipation length scale in the turbulence model for extra rates of strain. What kind of extra strain rates did you take into account? Did you simply add their separate effects?

3. (Chapter 6) I do not fully understand what kind of coordinate system is used. Is it a non-orthogonal system while assuming it to be orthogonal in the finite-difference equations? What was the grid spacing? Did you check whether your solution is grid independent? Are the metric coefficients and curvatures in your equations dependent on the coordinate normal to the hull? If so, how did you determine them?

4. In chapter 8 the authors state that their computer code had to be checked against numerical stability, artificial viscosity, etc. I would agree with that but can you tell how you checked against artificial viscosity?

5. Many of the features of what the authors identify as shear separation are not new to me. We experienced them in many boundary-layer calculations and in my opinion they are directly related to vortex-layer separation. If the authors have a different opinion can they explain? What puzzles me is Fig. 20³. Can the authors explain how they can find a negative wall shear stress without finding main-flow reversal?

Usually calculation methods break down very soon after appearance of the phenomena shown in Fig. 20⁴. The "bubble capturing" technique seems to me a questionable remedy to the problem.

L. Larsson (SSPA)

The authors have developed an interesting hybrid technique for ship flow calculations. A simple integral boundary layer method is used to provide initial and boundary data for a differential method. The potential flow and integral boundary layer solutions are described fairly completely and I have only one question on this:

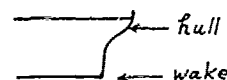
1. It is stated that Gadd's method is very sensitive to the initial conditions. How are these chosen?

The most interesting part is the stern boundary layer calculations, but the paper is very vague in its description of these, so I have a number of questions:

2. Which coordinate system is used? It is stated that the mapping method of Tuck & V. Kerczek is used to determine approximate streamlines. This must surely be an error since the Tuck & V. Kerczek method is based on slender body theory while in this case the exact solution is already available.

Maybe the authors employ a system where the $X_2 = \text{const}$ lines are defined by constant polar angle in the mapped plane? It has been used by V. Kerczek and several others.

3. Is the coordinate system based on the TSL approximation or on the metrics functions of X_2 ?
4. It is stated that X_2 is (at least nearly) orthogonal to the surface. How do you handle the coordinate system when passing from the stern of a blunt hull into the wake?
5. Which extra terms are included in the FTSL equations compared with the TSL equations? Do you account for cross-wise (X_3) momentum diffusion?
6. Do the equations contain all Reynolds stresses? In that case how are the normal stresses ($\overline{u_1^2}$, $\overline{u_2^2}$, $\overline{u_3^2}$) and the extra shear stress ($\overline{u_1 u_2}$) determined?
7. In the stern region of most ship models the normals intersect close to the boundary layer edge. Do you still think it is reasonable to express empirical turbulence functions as L and G as functions of X_2 ? Isn't it necessary to introduce transport equations?
8. You refer to measurements at NMI, from which you judge the magnitude of the terms of the governing equations. Since these measurements must contain very detailed turbulence data it could be very interesting to see them published. No such results are available today in the literature. On the second page of your paper, you refer to results presented in the paper for the NMI form. They seem to have been dropped. Will they be included in the proceedings?
9. What is the exact meaning of the "centrifugal approximation" to the pressure. Which radius of curvature do you use? The hull normal curvature cannot be used close to the stern since it is of the opposite sign as compared with the curvature of the streamline.
10. You use the v.d. Bug wall law on the hull but how do you handle the inner boundary condition in the wake? Only minor changes should be made to the program, according to §7.1.
11. The blow-out sources in Fig. 13 can hardly be correct. Even as far aft as 10% of L_{pp} aft of A.P. you have very strong positive sources. Stronger in fact than the original hull sources. In the wake region you would expect negative sources. Can you explain this?
12. How do you carry the numerical solution past the point of the hull where you have a wake in the lower region and a hull in the upper area.



13. Has the viscid-inviscid computation converged after only two iterations? (c.f. Martin Hoekstra's paper)
14. Will the appendices be included in the Proceedings? These questions are certainly not meant to reduce the value of this contribution, but it would be of great interest to others who are working in the same field to know the method better. It is a great pity that BSRA did not participate in the Boundary Layer Workshop last June, where most experts were present.

Author's Reply

A.Y. Odabasi (BSRA)

We would like to express our gratitude to the discussers for their interest in our paper. Since the organising committee has requested that the replies should be made available by the end of this symposium, replies to some of the questions will not be complete as some of the relevant data, graphs, and details are not readily available. Questions raised by different contributors seem to converge on certain areas and in order to avoid repeating we shall attempt to reply them following the sequence adopted in the paper.

1. Initial Calculations (Potential Flow-Integral Method-Blow Out)

Professor Patel raises the question of sensitivity of the method to uncertainties in the pressure gradient. This question needs to be stated in three stages; (i) Sensitivity of the integral method, and (ii) sensitivity of the differential method on second loop. To remedy the high sensitivity in the integral method Gadd [8] developed a procedure which was presented and discussed previously. From our experience these modifications bring the pressure gradient to an acceptable level of accuracy. In the differential method the potential flow pressure gradient is determined on the matching surface which is much less sensitive to small errors on the determination of the displacement thickness since the matching surface is further away from the hull surface where the sources are distributed. In our application to-date we did not encounter any serious problem.

We found the questions raised by Dr. Larsson and Mr. Hoekstra on the strength and the sign of the sources in the near wake region somewhat amusing. If the contributors would notice the location given

they will realise that this is the place where the boundary layer as near wake gets thicker and reaches to this value from the zero thickness value in the initial iteration. The values demonstrated in Figure 13 are therefore what one would expect. The essential nature of the wake singularities will be of a source character since they produce thickness which is not there in the first iteration although depending on transverse variation of the displacement thickness they may sometimes take negative values (i.e. sinks).

Professor Patel indicates that for Figure 18 the matching surface remains within the boundary layer. As an experienced experimenter, I am sure he is well aware that in 3-D boundary layers the edge of boundary layer is not quite determinate. If one examines the values of Reynolds stresses corresponding to our matching surface location it will be found that they have diminishingly small values. In the developed program suite there is a special precaution for that kind of possibilities and if (τ/u^2) takes larger values than 10^{-5} the matching surface is redetermined. In a number of applications this possibility did not arise and since Hoffmann [2] did not provide Reynolds stress measurements we did not take the situation in Figure 18 seriously.

Dr. Larsson asks the initial conditions used for the Gadd's method. They are modified flat plate formulae for the integral boundary layer quantities. The differential method is much less sensitive to the variation of initial conditions (provided they are sensible enough) and the effect of small variations vanishes within a few boundary layer thickness downstream.

2. Coordinate System

The questions related to the coordinate system are quite numerous and they are raised by Dr. Larsson and Mr. Hoekstra. We think they missed the real message in our remarks on the choice of a coordinate system. During the development of the PHIVE project we developed four different curvilinear coordinate system and employed every one of them in the computations which led us to the conclusions expressed in the paper. Although all of these coordinate systems are available as options for the calculations reported here we employed a method which employs Tuck & van Kerczek mapping method as its basis. The remarks by Dr. Larsson on the validity of this approach are quite inappropriate and I would suggest him to examine the results of Jinnaka Ref.1) who uses only three parameters to describe the section and excludes the free-surface contribution. The computational ease of this approach, in the light of the remarks made on the choice of the coordinate system, make it more attractive compared to streamline tracing methods.

Determination of metric coefficients for both orthogonal and nonorthogonal systems do not present any difficulty except the accuracy in numerical derivation. In

this respect we developed and tested a number of approaches including Bicubic splines. Finally on a generalisation the Lanczos method developed by us was utilised since it demonstrated the highest degree of accuracy and reliability, including the initial and final regions of computation.

The coordinate system is so chosen that the metrics are allowed to vary linearly along the normal coordinates and the variation is allowed between 0.26 and δ . For the region $0 < x < 0.26$ metrics are taken as constant. This procedure complies with our turbulence conception since for $x_2 < 0.26$ there is wall and buffer layers. In the light of this explanation the question raised by Dr. Larsson on the transition of coordinates from hull to wake regions is also provided.

Finally, Dr. Larsson raises the question of intersecting normals around the aft-end. This, at least for likely ship forms, is a two dimensional visualisation of a three dimensional occurrence. If one thought in 3-D it can be seen that such a possibility is highly unlikely. The coordinate systems developed within the PHIVE project however do not suffer from this problem even it occurs because firstly they are based on the geometries of (hull + 0.26) and (hull + δ) surfaces. Furthermore linear variation of metrics allows for a parabolic normal coordinate direction.

3. Turbulence Model and Numerical Computation

Almost all of the contributors ask for further details on the equations of motions and complain on the lack of details. If however one remembers the present size of the paper which is already above the page restriction imposed by the Organising Committee, inclusion of further details would make the printing prohibitive. Since the detailed equations and the reasoning on their choice will be presented in Stanford-1982 Conference we shall refrain ourselves from filling a few extra pages. We shall be content with stating that the equations used are FTSL equations, where all the Reynolds stress terms are employed, except τ_2 . No transport equations are used for $\langle u \rangle$, $\langle u^2 \rangle$, $\langle u_1 \rangle$ and they are determined in a manner similar to the one used by Townsend in the rapid distortion approach (i.e. by relating to $|\tau|$). Although τ_2 can take fairly large values its gradients are fairly small and hence neglect of its contribution does not create any inaccuracy. Crosswise momentum diffusion is obviously taken into account.

Extra strain rates are included in two different ways. The effect of streamline curvature is accounted as

$$e = (|\tau_1| e_1 + |\tau_2| e_2) / |\tau|$$

where e_1 and e_2 are streamwise and cross-flow extra strain rates by streamline curvatures. The effects of $\partial u_2 / \partial x_1$ and $\partial u_1 / \partial x_2$ are considered separately and added

into shear transport equations but are not included in the length scale correction. The magnitude of e_{eff} is compared with the mean shear

$$E = (|\tau_1| \partial u_1 / \partial x_2 + |\tau_2| \partial u_2 / \partial x_1) / |\tau|$$

at every step and if exceed 0.5E an error message is printed and the calculation are re-adjusted.

Since we have already replied the question raised on intersecting normals, Dr. Larsson's question on the choice of functions L and G becomes irrelevant. His suggestion on the use of transport equations is answered within the text since the later version of Bradshaw's turbulent energy method [45] contains a length scale transport equation and diffusion is certainly not a transportable quantity.

Dr. Larsson indicates the possible change in sign of curvatures between the hull and outer streamlines and raises the question on the choices of radius in the centrifugal approximation. In this approximation

$$\frac{dp}{dx_2} = k\rho \frac{\bar{u}^2}{R}$$

where \bar{u} is $(\int_0^\delta (u_1^2 + u_2^2) \frac{1}{2} dx_2) / (u_{ref} \delta)$, R is the local value of $(|\tau_1| R_1 + |\tau_2| R_2) / |\tau|$ which is assumed to vary along the normal and k is an empirical constant determined from the experimental data. As a result, the problem raised by Dr. Larsson does not arise.

Mr. Hoekstra raises questions on the numerical scheme employed. In principle there is neither any difference nor any extra difficulty in the determination of bi-characteristics and integration along them whether an orthogonal or non-orthogonal coordinate system is used, and we would have hoped that Mr. Hoekstra would give us that much credit to distinguish between an orthogonal and non-orthogonal system. Checks on the accuracy of finite difference schemes are performed by solving somewhat simpler equation with known analytic solutions. Further information and methods may be found in the excellent book of Roache [82].

4. Determination of Wake

Extension of interactive hypothesis to 3-D is carried out in a straightforward manner as we are only interested in the near wake. Therefore, the body is extended in the direction of tangent at the aftmost station and the interaction is then used as in 2-D or axisymmetric case. The only difference appears in the interpolation procedure and hence no additional assumption is required other than a change in the dissipation length scale equation. We hope this brief explanations answer Professor Patel's question.

Dr. Larsson's question on the extensions to near wake gives the impression that he is not acquainted with the inter-

active hypothesis. Since the explanation of the basics of this concept will be quite lengthy we would like to refer Dr. Larsson to Refs. [73 to 76].

5. Shear Separation and Convergence

Both Professor Patel and Mr. Hoekstra raises doubts about shear separation and ask whether it is a vortex layer separation. As indicated by one as in the discussion of Professor Kostilainen's paper, shear and free vortex layer separation are distinct things for a number of reasons which can be summarised as follows :

1) Vortex layer separation requires the presence of a strong cross-flow velocity component and can only initiate at the region of streamline coalescence, whereas none of these conditions are necessary for the presence of shear separation.

2) Examination of hull streamlines and suggested visualisation indicate that the free vortex layer separation should take place around the bilges whereas shear separation can exist along the whole girth of the ship.

In the light of our experience the suggestion on the existence of a vortex layer separation is ill-founded and, apart from the visual similarity appearing in the wake contours, there is no justification since the vortices can be formed with cross-flow reversal without the presence of a vortex separation. Our further thought on the subject is available in Ref. 2).

The questions related to the convergence iterations need to have two-fold answer. As presented in the discussion of the paper by Hoekstra and Raven (by Odabaşı) we believe that the instability mentioned in this paper appears as a result of the handling of the numerical integration rather than a physical instability. Additionally, we do not iterate for the boundary conditions on the matching since what we do is a modified application of the matching surface concept as used by Mahgoub and Bradshaw [54] where they choose their matching surface more arbitrarily. The only mean-

ingful iterations are the stitching (i.e. simultaneous satisfaction of both the wall and the matching surface boundary conditions) and inclusion of normal momentum equation to improve the estimation of the pressure which is being implemented since the preparation of this paper.

Finally, Mr. Hoekstra asks how the velocity and the shear vectors can be in opposing directions and questions the validity of our bubble capturing technique. Shear separation appears as a form of weak singularity which propagates in the direction of the downstream bi-characteristic. Therefore, procedures of integration through weak singularities like upwind differencing can be modified and used as we did in our approach.

6. Additional Information

As mentioned before, since the replies have to be handed to the Organizing Committee by 10th October, 1980 the cross-flow velocity and shear profiles and the calculated wake details cannot be included within the replies as they are back at U.K. We shall however try to make them available in the earliest possible opportunity.

Since this project was financed by Industrial Sponsors mentioned in our acknowledgement list further dissemination of information, including NMI wind tunnel data, will be subject to their approval. We however hope that more information will be published in the open literature in the near future.

REFERENCES

- 1) Jinnaka, T. "On the Streamlines around a Ship's Hull", Selected Papers from J.Soc. of Naval Arch. of Japan, Vol.3, p.40 (1969-Japanese original published in 1965).
- 2) Odabaşı, A.Y. "A Contribution to the Calculation of Flow around the Aft-Ends of Ships", to appear in Int. Shipbuilding Progress, (1980), also available as BSRA Report NADH/24 (1980).

An Investigation of Certain Scale Effects in Maneuvering Tests with Ship Models

Peter Oltmann, Som D. Sharma and Karsten Wolff
 Institut für Schiffbau der
 Universität Hamburg, Hamburg
 Federal Republic of Germany

ABSTRACT

Maneuvering tests, like all hydrodynamic tests with ship models, are necessarily subject to certain scale effects owing primarily to the enormous discrepancy between the Reynolds numbers of the model and the full-scale. The crucial element in maneuvering tests is the rudder which is susceptible to rather perplexing scale effects of multiple origin. Sometimes, the Reynolds number of the model rudder may be too low to sustain fully turbulent flow. More importantly, the inflow to the rudder is always dynamically dissimilar between model and full-scale due to dissimilar hull wake and propeller race. The novel Computerized Planar Motion Carriage (CPMC) installed at the Hamburg Ship Model Basin (HSVA) in 1975 and first introduced to the international naval hydrodynamic community at the Eleventh ONR Symposium on Naval Hydrodynamics at London in 1976 has afforded an opportunity to study this effect closely on the ITTC standard model of a MARINER type ship. The test program included a unique series of zigzag maneuvers in which the model was unconstrained in all six degrees of freedom and yet subject to a controlled towing force in the longitudinal direction. As a result of this investigation the authors hope to have shed new light on the traditionally controversial issue of whether it is more expedient to operate the model propeller at the self-propulsion point of the full-scale or at the self-propulsion point of the model itself.

NOMENCLATURE

Abbreviations

CPMC Computerized planar motion carriage

HSVA *Hamburgische Schiffbau-Versuchsanstalt*
 (Hamburg Ship Model Basin)
 IfS *Institut für Schiffbau*, Hamburg
 ITTC International Towing Tank Conference
 MSPP Model self-propulsion point
 SSPP Ship self-propulsion point
 SFB 98 *Sonderforschungsbereich "Schiffstechnik"*
 (Special research pool for ship technology at Hamburg and Hanover)

Symbols

A_R Total rudder area
 A_{RP} Rudder area swept by propeller race
 B Beam
 c Effective flow velocity past rudder
 D Diameter of propeller
 d Distance between propeller disk and quarter mean chord of rudder
 F_D Towing force on self-propelled model
 F_n Froude number
 G Center of gravity
 g Acceleration due to gravity
 I_{zz} Moment of inertia about the z -axis
 K_T Propeller thrust coeff. $\approx T/\rho n^2 D^4$
 k Correction factor, see Eq. (3)
 L Length between perpendiculars
 m Mass
 n Rate of revolutions of propeller
 N Hydrodynamic moment about z -axis
 O Coordinate origin fixed in the body usually amidships in the waterplane
 p Arbitrary hydrodynamic coefficient in sensitivity analysis
 r Rate of turn about z -axis (yaw rate)
 S_p^x Sensitivity factor (x versus p)
 T Thrust of propeller
 T Period of zigzag maneuver (Fig. 3)
 t Time

U	Resultant velocity of 0 in the horizontal plane
U_A	Axial velocity induced by propeller
$U_{A\infty}$	Asymptotic value of U_A as $x \rightarrow -\infty$
U_0	Steady value of U in approach phase
u, v	Components of U along x and y axes
V_A	Speed of advance of propeller
w	Taylor wake fraction
X, Y	Hydrodynamic forces along x, y axes
x	Arbitrary output variable used for sensitivity analysis
x, y, z	Coordinate axes fixed in the body
x_G, y_G, z_G	Coordinates of center of gravity
x_0, y_0, z_0	Coordinates of 0 in an earth-fixed system (see Fig. 2)
α_0	Overshoot angle in zigzag maneuver
β	Drift angle
δ	Rudder angle
δ_0	Neutral rudder angle ($r = 0$)
δ_m	Max. value of δ in zigzag maneuver
θ	Pitch angle
ρ	Mass density of water
τ	Characteristic times of zigzag maneuver (see Fig. 3)
τ_a	Time to attain switching value ψ_s
τ_b	Time to brake (check) yaw rate r
τ_c	Time for counterturn
τ_r	Reach time (see Fig. 3)
ϕ	Roll angle
ψ	Heading angle
ψ_s	Switching value of ψ in zigzag man.
ω	Circular (radian) frequency

Notes

As far as possible, ITTC standard symbols have been used. A prime (') denotes that the quantity has been non-dimensionalized using as fundamental units $\rho L^3/2$ for mass, L for length and L/U for time. A hat (^) is used to denote some specific value of a motion variable, usually the amplitude in a harmonic oscillation. As usual, superscript bar (¯) and dot (·) denote time average and time derivative respectively.

Dimensional numerical values in the paper refer to the 1 : 25 scale model rather than to the full-size ship, unless explicitly otherwise indicated.

The fundamental and derived units of measurement (as well as their abbreviations) used in the paper conform to the SI system.

1. INTRODUCTION

Four years ago [1] the Authors had introduced to this audience a novel Computerized Planar Motion Carriage (CPMC), then recently installed at the Hamburg Ship Model Basin (HSVA). Besides a description of this new facility, that paper also contained some preliminary results of basic maneuvering tests with a 1 : 25 scale model of a MARINER

type ship. It was subsequently confirmed that the CPMC model testing technique is capable of identifying the maneuvering behavior of an ordinary ship with almost arbitrary precision at the *model scale*. This validation rests upon the unique capability of the CPMC to perform on the same ship model in the same model tank both force measurements in a captive state (Mode A = towing) and trajectory measurements in a free-running state (Mode B = tracking). The corresponding results for the MARINER model are fully documented elsewhere [2] and will be only summarized here for the sake of ready reference.

However, it was also found that a substantial discrepancy exists between our results at the model scale and the famous full-scale measurements of Morse and Price [3]. In search of a satisfactory explanation we were contemplating *inter alia* an investigation of possible scale effects. The call for papers issued by the United States Office of Naval Research, listing "Scale effects of viscous flow about hulls and wave-wake interactions with and without maneuvering motions" as a subject of special interest for this Symposium, therefore hit upon fertile ground and inspired us to conduct a special series of tests with the MARINER model, specifically designed to assess the effect of propeller race on maneuverability, taking advantage of the perfect tracking capability of the CPMC. In this singular experiment the ship model performed zigzag maneuvers in the tank without physical constraint in any of its six degrees of freedom but for a controlled external towing force in the longitudinal direction required to balance the propeller overload or underload. This paper is devoted to the presentation and discussion of the results of this experiment in the general context of scale effects in maneuvering tests, with special focus on rudder phenomena.

2. MATHEMATICAL MODEL AND ITS IDENTIFICATION

Our basic mathematical model for simulating arbitrary rudder maneuvers is a purely formal generalization of the model originally proposed by Abkowitz [4] and now in common use. The rather lengthy equations of motion are documented in Appendix A using standard ITTC nomenclature as explained above in conjunction with Figs. 2 and 3. Let us demonstrate the power of such formal models using the MARINER type ship as an example. Evidently, any and all of the unknown force coefficients occurring in Appendix A can be identified directly by means of a suitable sequence of experiments, given a facility capable of continuous force measurements while imposing arbitrarily prescribed surge, sway and yaw motions on a ship model with preset rudder angle and propeller rate of revolutions. The CPMC is such a facility. Omitting unimportant technical details, which may be found elsewhere [1,2], we reproduce here in Table 1 a set of 88 force coefficients determined from captive tests for the MARINER model at a preset propeller rate of revolutions corresponding to the self-

propulsion point of the 1:25 scale model at an approach speed of 1.543 m/s corresponding to 15 knots full-scale. These coefficients were evaluated by a sequential linear regression analysis on the entire set of force records until a reasonable fit was achieved within the bounds of experimental scatter.

Given this set of coefficients, one may now simulate any arbitrary rudder maneuver (at constant propeller revolutions) by prescribing the desired sequence or strategy of rudder commands as the input and computing the model response by numerically integrating the equations of motion. The entire scheme can be stringently verified and validated by comparison with multi-component trajectory records obtained by letting the CPMC (in Mode B) track the free-running model during any rudder maneuver executable in the tank. Just this kind of comparison is shown in Figs. 4 to 7 for four quantitatively different zigzag maneuvers of the MARINER model. It is needless to say that fair agreement prevails throughout between computer simulation and direct trajectory measurement.

We note parenthetically that this agreement may also be construed as indirect evidence for the general adequacy of the subset of coefficients represented in Table 1 and hence of the superfluity of including time history effects in simulating rudder maneuvers. Incidentally, a systematic study of the relative importance of each of the previous 88 coefficients for the simulation of various maneuvers was conducted in Reference [5]. A typical rank order based on suitably defined sensitivity factors is reproduced in Table 6. Obviously, many of the force coefficients can be dropped without significant loss of accuracy in the trajectory simulation of ordinary maneuvers.

The above procedure may be called *direct* system identification and validation. An alternative approach, which we prefer to call *indirect* system identification, was worked out by one of the Authors and documented in Reference [6]. In this method no captive model tests are required in principle. Instead, the unknown coefficients of the equations of motion are determined by an iterative curve fitting procedure applied to the recorded trajectories of a suitable set of *source* maneuvers executed by the free-running ship (model). For this purpose it is expedient to rewrite the original equations of motion in the form of decoupled acceleration equations as explained in Appendix B. The success of this scheme is enhanced by the availability of accurate, high resolution trajectory data produced by the CPMC. The predictive power of the coefficients thus derived depends on how well the source maneuvers cover the desired performance envelope of the ship. It may be verified and validated by comparing computer simulations of independent *test* maneuvers with actual trajectory records.

As an illustration of this technique we present in Table 3 a set of 41 force coefficients derived from a set of four source

maneuvers chosen to cover uniformly almost the entire practical range of motion variables u, v, r and the control variable δ as displayed in Fig. 8. It may be noted in passing that our algorithm for indirect system identification automatically determines the unknown coefficients sequentially in the rank order of their significance through multiple linear regression analysis controlled by error and truncation criteria judiciously devised by the user. The extreme curve fitting effectiveness of the above set of coefficients is verified by the fact that computer simulations of *source* maneuver trajectories are almost indistinguishable from the original records, as seen for instance in Fig. 9. Their predictive power is exhibited by the almost equally good match between the computer simulation and direct trajectory measurements of independent *test* maneuvers, as seen for example in Fig. 10. In short, for many practical applications the relatively economic indirect system identification by trajectory analysis might well substitute the considerably more elaborate direct system identification by force analysis.

3. SPECIFIC STUDY OF RUDDER EFFECTIVENESS

3.1. Motivation

We have just shown the feasibility of identifying and validating the general mathematical model of Appendix A by means of suitable CPMC tests and hence of simulating all ruder maneuvers with almost arbitrary precision in the *model tank*. However, as will be seen shortly, an appreciable discrepancy, persists between model tank and full-scale performance, at least for the MARINER type ship. One might be tempted to blame it on experimental error due to nonideal test conditions in the full-scale trials [3]. But in search of a more satisfactory explanation we decided to examine the possibility of systematic scale effects, especially on the rudder which is naturally the crucial element in ship maneuvering.

3.2. Literature Scan

There exists, of course, a appreciable amount of literature on rudder scale effects. Not surprisingly, it is marked with considerable confusion and contradictory claims. Conventional Froude scaling properly takes care of the primary inertial and wavemaking effects in ship hydrodynamics. The so-called "scale effects" are residual secondary effects resulting mainly from the inevitable inequality of Reynolds, Weber and Thoma numbers—representing dynamic dissimilarity of fluid friction, aeration and cavitation respectively—between model and full-scale. These phenomena have usually minor and often mutually compensatory effects on maneuvering performance, so that the sum total of all scale effects is fortunately small in quantity, but annoyingly unpredictable in quality. For instance, it is not possible to say with generality whether the turning capabil-

ity (or any other maneuvering characteristic for that matter) of the full-scale should be (slightly) higher or lower than that of the Froude model as a consequence of scale effects, which makes it difficult to devise empirical "correlation factors" otherwise so popular in tankery. As early as 1959 Suarez and Strumpf [7] concluded from a systematic survey of 11 widely different ship types that the ratio of the turning capability (as expressed by the reciprocal of the tactical diameter) of (five-foot) models to that of the prototypes varied from 0.7 to 1.2 approximately.

In his concise but competent survey of scale effects in ship maneuvering and control Mandel [8] calls attention to the need of distinguishing between direct scale effects on the rudder as such and indirect, i.e. hull and propeller induced, scale effects on the rudder. The former comprise reduced maximum foil lift coefficient and stall angle (due to lower Reynolds number, especially if turbulent flow cannot be sustained), reduced aeration on a surface piercing rudder (due to relatively higher surface tension) and reduced cavitation (due to relatively higher ambient pressure) on the model rudder as compared to full-scale. The latter comprise relatively lower inflow velocity (and hence lower forces) due to stronger hull boundary layer and wake, but relatively higher inflow velocity (and hence higher forces) due to stronger propeller loading and race on the model rudder compared to full-scale. This important distinction between intrinsic and extrinsic scale effects on the rudder has also been noted by various other authors.

As regards the scale effect on different maneuvering characteristics, Thieme [9] argued on theoretical grounds that the effect on course keeping and checking capability should be only half as strong as the effect on turning capability. On the other hand Kawano [10] and others have ascertained by experiment that scale effects are most marked in course keeping and almost negligible in hard turns. Surely such apparent contradictions can be resolved by scrutinizing the details of the case. But it is obvious that rudder scale effects arise as small differences of mutually compensatory phenomena and that on reasonably sized ship models (i.e. not less than 5 m long) the dominant effect is due to the hull and propeller induced components of the flow velocity past the rudder, see for instance [11].

3.3. Propeller Overload and Underload Tests

One of the traditional controversies in tankery rages over the question whether maneuvering experiments ought to be conducted with the model propeller operating at the actual model self-propulsion point (MSPP) or the corresponding ship self-propulsion point (SSPP). Whereas the champions of Planar Motion Mechanisms, e.g. [12,13,14], usually advocate SSPP which can be realized easily in captive model tests, the operators of Maneuvering Basins for free-running models

make a virtue out of necessity by claiming that contradictory scale effects balance each other more evenly at MSPP! Fortunately we do not have to take sides in this delicate issue as we happen to possess a facility which can conduct not only captive tests but also free-running maneuvers with the model propeller operating at any desired rate of revolutions. Thanks to the imperceptibly small tracking lag of the CPMC in x_0 , y_0 and ψ directions in Mode B, a controlled towing assistance or resistance can be applied to the freely maneuvering model in the body-fixed longitudinal direction (x) in order to compensate for the propeller underload or overload respectively. Previous attempts to conduct such experiments with the aid of deck-mounted air screws, e.g. [15], must be discarded as cumbersome and inaccurate.

In order to determine directly the dependence of maneuvering performance on propeller loading (via rudder effectiveness) for the MARINER type ship we performed systematic sets of at least five parametrically different zigzag maneuvers ($\psi_s/\delta_m = 30^\circ/10^\circ$, $20^\circ/10^\circ$, $10^\circ/10^\circ$, $10^\circ/10^\circ$ and $20^\circ/20^\circ$) at each of eight distinct propeller rates of revolution ranging from 5.30 Hz to 6.65 Hz. Note that the MSPP of the 1:25 scale model lies at 6.09 Hz, whereas the SSPP extrapolated according to the Schoenherr friction line for an ideal smooth hull lies at 5.51 Hz for the model corresponding to 66.1 RPM for the full-scale. The towing force F_D required to compensate for the model propeller overload or underload is given in Table 2. For practical purposes the maneuvering performance is perhaps best expressed by certain characteristic parameters of the 20°/20° standard zigzag maneuver as defined schematically in Fig. 3. The experimentally ascertained variation of nine such characteristic parameters with propeller loading is plotted in Fig. 11. As qualitatively expected, the ship response to helm improves with increasing propeller loading, as indicated by decreasing times to attain switching value of heading angle τ_a , to check yaw rate τ_b , to return to initial heading τ_c , as well as reach time τ_r and period T . The turning capability as expressed by the maximum negative yaw rate $\dot{\psi}_{min}$ in the first half-swing also increases with propeller overload. The overshoot angles α_{01} and α_{02} are not appreciably affected, while the "transfer" y_{omax} as measured by the maximum distance normal to the original path in the first half-swing decreases with propeller overload! For the sake of completeness, the numerical values of these nine characteristic zigzag output parameters are assembled in Table 4 for the 32 major runs comprising all combinations of the four zigzag input parameter pairs (ψ_s/δ_m) with the eight distinct propeller loadings (F_D or n).

Undoubtedly, the effect of propeller loading on maneuvering performance arises predominantly from altered rudder effectiveness in the propeller race and not so much from forces acting directly on the propeller blades. (Note, however, that the compensatory wake effect which would occur if the

propeller overload were required only to overcome an increased friction or the hull surface, was not simulated in our experiments.) To facilitate a hydrodynamic explanation of this phenomenon it is useful to estimate the effective flow velocity past the rudder c as proposed for instance by Norrbin [16] and further refined by Thulin [17] as follows:

$$c^2 = \frac{1}{A_R} \{ A_{RP} (V_A + U_A)^2 + (A_R - A_{RP}) V_A^2 \} \quad (1)$$

$$U_A = k \{ -V_A + \sqrt{V_A^2 + \frac{8}{\pi} K_T n^2 D^2} \} \quad (2)$$

$$k = U_A / U_{A\infty} \quad (3)$$

$$V_A = (1 - w) U_0 \quad (4)$$

with the Symbols defined previously. Using the known mean wake fraction for the model $w_M = 0.25$, reading the thrust coefficient K_T as a function of the advance coefficient $J = V_A / n D$ from the openwater propeller chart, and taking the reduction factor k as a tabulated function of nondimensional distance $2d/D$ from the propeller, the effective flow velocity past the rudder c was calculated for each test condition, see Table 2. Corresponding values for the full-scale were also estimated by first extrapolating the wake fraction according to the ITTC 1978 standard recommendation:

$$w_S = (t + 0.04) + (w_M - t - 0.04) C_{FS} / C_{FM} \quad (5)$$

Calculating the coefficients of friction C_F according to the ITTC 1957 line and substituting 0.12 for the thrust deduction fraction t yielded a numerical value of $w_S = 0.20$, which led to the right half of Table 2.

Of course, captive model tests were also conducted at different propeller loadings. In particular, two comprehensive test series in CPMC Mode A were performed to completely identify the mathematical model of Appendix A at $n = 6.09$ Hz (MSPP) and $n = 5.51$ Hz (SSPP). The MSPP coefficients (Table 1) were discussed earlier in the context of our basic techniques of system identification and validation. The SSPP coefficients (Table 5) will be discussed in the next section in the context of correlation between model and full-scale. Suffice it to say at this point that significant differences between the two sets were found mainly in the rudder angle coefficients and that the rudder angle dependent forces seem to vary approximately in proportion to c^2 , that is the square of the estimated effective flow velocity past the rudder, see Table 2. This makes sense in terms of airfoil theory and suggests a simple computational procedure for simulating the effects of varying hull wake and propeller race in general, and scale effects in particular.

In passing we note that a more radical variation of propeller loadings was investigated for the captive MARINER model by Laudan [19] including separate multi-component force measurements on the hull, propeller and rudder, and even covering cavitation effects [18] within the framework of a related project of the SFB 98, but space limitations prohibit a detailed discussion and incorporation of his results into this paper.

4. CORRELATION WITH THE FULL-SIZE SHIP

We are now ready to compare minutely our model tank results versus the full-scale trials documented in Reference [3]. Let us first examine, following conventional practice, how the computer simulations based on SSPP coefficients (Table 5) compare with the full-scale spiral maneuver (Fig. 12a) and $20^\circ/20^\circ$ standard zigzag maneuver (Fig. 13). Note parenthetically that our zigzag simulation duplicates not the $20^\circ/20^\circ$ rudder strategy, but the actual full-scale trial record of rudder angle as a function of time; the former tends to be self-correcting and hence provides a less stringent test of the simulation accuracy! Although the correlation is not bad, clearly there are significant discrepancies between model and full scale. Firstly, the full-size ship exhibits a far more pronounced port/starboard asymmetry in the turning characteristic ($r - \delta$ curve) than the model. This was also observed by Chislett and Strøm-Tejsen [20], who attributed it conjecturally to a possible asymmetrical fouling of the full-scale hull! Secondly, if we compare the average of the port and starboard rates of turn at moderate rudder angles, the full-size ship appears to possess about 15% greater turning capability than our model. Thirdly, the neutral rudder angles of the model and full-scale seem to have opposite signs; curiously, the same (minor) discrepancy was ascertained in the earlier simulations reported from Lyngby [20] but eliminated without comment in the revised simulations based on a new series of tests [13]. This latter Reference also contains a thorough analysis of the possible causes of the anomalous behavior of the full-size ship, the most plausible of which is that the full-scale trials were conducted at disproportionately high propeller loadings either by mistake or by necessity owing to increased hull resistance. Note that in Ref. [3] the 15 knots approach speed maneuvers are recorded to have been started with an initial propeller rate of about 76 RPM whereas the tank prediction for a smooth hull is only about 66 RPM.

Next, let us compare directly the free-running model zigzag maneuver ($20^\circ/20^\circ$) with the corresponding full-scale maneuver (Fig. 15), and a computer simulation of the spiral maneuver based on MSPP coefficients (Table 1) with the full-scale data (Fig. 12b). Obviously, the model response to rudder is significantly slower than full scale (Fig. 15). The spiral maneuver correlation (Fig. 12b) is somewhat better than with SSPP

(Fig. 12a), which is not surprising in view of the suspected overload of the full-scale propeller. However, a considerable discrepancy still persists.

In a further attempt to reconcile model with full scale, the following corrections were applied to the SSPP coefficients of Table 5. Firstly, additional tests were conducted to identify the true propeller-induced port/starboard asymmetry, which arises partly from forces acting directly on the propeller blades (side force and thrust eccentricity resulting from wake nonuniformity) and partly from forces induced by the propeller on the hull and the rudder. Depending upon the delicate balance of these forces, the first three of which generate a yawing moment to starboard and the last to port, a single screw ship might turn out to be starboard prone or port prone [21,22]. Without going into the details of this question, which is worth a paper by itself, let us simply note that we discovered what amounted to a yaw alignment error of 0.1° in our model set-up, leading to corrected values $Y'_0 = +2.58 \times 10^{-5}$, $N'_0 = -1.07 \times 10^{-5}$, which made the model slightly port prone in conformity with the full-size ship. Secondly, we estimated by means of Eq. (1-4) that at the recorded propeller rate of 76 RPM the ship would have had an effective rudder inflow velocity squared corresponding to $c^2 = 2.456 \text{ m}^2/\text{s}^2$ in the model versus only $1.942 \text{ m}^2/\text{s}^2$ at the nominal SSPP, see Table 2. In order to simulate this effect we multiplied all rudder angle coefficients in Table 5 by the factor $2.456/1.942 = 1.265$. Thirdly, in order to simulate the possible influence of the sonar dome fitted to the full-size ship but not to the model, we estimated the effect on the drift angle coefficients and obtained the modified values:

$$Y'_v = -1224.4 \times 10^{-5} \quad N'_v = -370.8 \times 10^{-5} \quad (6)$$

When these three corrections were applied to the SSPP coefficient set of Table 5, the simulated spiral maneuver (Fig. 12c) and zigzag maneuver (Fig. 14) naturally showed improved correlation with the full-scale data. The second continuous $r - \delta$ curve plotted in Fig. 12c was obtained with only the first two corrections applied. It shows that the sonar dome simulation also contributed a slight increase in turning capability, but the major effect was that due to propeller loading.

It is apparent from Table 2 that at $n = 6.47 \text{ Hz}$ the free-running model has almost exactly the c^2 -value estimated for the full-size ship at 76 RPM. Hence, as a final exercise, the spiral maneuver was simulated also with the indirectly identified coefficient set of Table 3, cf. Section 2, now with and without correction for the 0.1° model alignment error mentioned above, and compared again with the same full-scale data, see Fig. 12d. Moreover, the corresponding $20^\circ/20^\circ$ zigzag maneuvers were compared directly in Fig. 16. The correlation is still imperfect, but significantly better than in

any of the alternative attempts.

5. CONCLUSIONS

Four years ago, we have concluded our introductory CPMC paper [1] with the thought: "The task ahead is to find a judicious combination of Modes A and B for identifying a general mathematical model for simulating arbitrary ship maneuvers on the basis of a few runs with a physical model under the CPMC". At that time we had not exactly envisioned that the "judicious combination of Modes A and B" would literally turn out to be free-running model maneuvers executed with controlled towing assistance or resistance. This "mixed" Mode has been rendered feasible by the unique capacity of the CPMC to follow a freely maneuvering model so closely in the tracking mode that uninitiated observers almost invariably mistake it for the towing mode. Our study of the MARINER model indicates that the easiest way of beating scale effects in maneuvering tests in the model tank is by choosing a propeller rate of revolutions which best generates the corresponding estimated rudder inflow velocity of the full-scale. This rate need neither coincide with the model self-propulsion point nor with the ship self-propulsion point.

However, despite all reasonable corrections for the known differences between model and full-scale, there persists a small residual discrepancy between the turning capability of the full-size MARINER type ship and the model tank predictions, which cannot simply be discarded as random experimental scatter. Apart from the possibility of a systematic measurement error in the full-scale trials [3], the multifarious problem of "scale effects" will continue to claim the attention of tankery for a long time to come.

ACKNOWLEDGMENTS

This study was carried out with the steady financial support of the German Research Association (*Deutsche Forschungsgemeinschaft*) provided through the Special Research Pool for Ship Technology (SFB 98) at Hamburg and Hanover. The unflagging cooperation of Bernhard Zimmermann (IfS) and Jan Fischer (HSVA) in conducting the experiments as well as the patient assistance of Ingeborg Jurschek in the technical preparation of the paper are gratefully acknowledged.

REFERENCES

1. Grim, O., Oltmann, P., Sharma, S.D. and Wolff, K., "CPMC - A Novel Facility for Planar Motion Testing of Ship Models", Proceedings of the 11th Symposium on Naval Hydrodynamics, University College, London, 1976, pp. 115-131.
2. Oltmann, P. and Wolff, K., "Vergleichende Untersuchung über das Manövrierverhalten des MARINER-Standardschiffes", Bericht Nr. 385, Sep. 1979, Institut für Schiffbau, Hamburg.
3. Morse, R.V. and Price, D., "Maneuvering Characteristics of the Mariner Type Ship (USS Compass Island) in Calm Seas", Publ. No. GJ-2232-1019, Dec. 1961, Sperry Gyroscope Co., Syosset, N.Y..
4. Abkowitz, M.A., "Lectures on Ship Hydrodynamics - Steering and Manoeuvrability", Report No. Hy-5, May 1964, Hydro- and Aerodynamics Laboratory, Lyngby, Denmark.
5. Oltmann, P., "Parameterstudie zu den Bewegungsgleichungen für horizontale Schiffsbewegungen", Schrift Nr. 2307, Oct. 1978, Institut für Schiffbau, Hamburg.
6. Oltmann, P., "Bestimmung der Manöviereigenschaften aus den Bahnkurven freimanövrierender Schiffsmodelle", Bericht Nr. 364, Feb. 1978, Institut für Schiffbau, Hamburg.
7. Suarez, A. and Strumpf, A., "Experimental Methods for Prototype Trajectory Prediction with some Data Correlations", Note No. 548, Aug. 1959, Davidson Laboratory, Hoboken, N.J..
8. Mandel, P., "Ship Maneuvering and Control" in *Principles of Naval Architecture* ed. J. P. Comstock, SNAME, New York, 1967, pp. 463-606.
9. Thieme, H., "Zur Formgebung von Rudern", *Jahrbuch der Schiffbautechnischen Gesellschaft*, 56. Bd., 1962, pp. 381-422.
10. Kawano, K., Murata, Y., Matsuoka, F. and Yasui, S., "Some Model Experiments and Ship Correlation in Respect to Manoeuvrability", *Selected Papers from the Journal of The Society of Naval Architects of Japan*, Vol. 3, 1969, pp. 125-135. (Originally in *Zosen Kiokai*, Vol. 113, June 1963).
11. Yumuro, A., "Influences of Propeller and Rudder on Maneuvering Stability Derivatives", *Naval Architecture and Ocean Engineering*, Vol. 16, 1978, pp. 1-14 (Originally in *Zosen Kiokai*, Vol. 141, June 1977).
12. Strøm-Tejse, J. and Chislett, M.S., "A Model Testing Technique and Method of Analysis for the Prediction of Steering and Manoeuvring Qualities of Surface Vessels", Proceedings of the 6th Symposium on Naval Hydrodynamics, Washington, D.C., 1966, pp. 317-381.
13. Smitt, L.W. and Chislett, M.S., "Large Amplitude PMM Tests and Manoeuvring Predictions for a MARINER Class Vessel", Proceedings of the 10th Symposium on Naval Hydrodynamics, Massachusetts Institute of Technology, Cambridge, Ma., 1974, pp. 131-151.
14. Goodman, A., Gertler, M. and Kohl, R., "Experimental Techniques and Methods of Analysis Used at Hydronautics for Surface-Ship Maneuvering Predictions", Proceedings of the 11th Symposium on Naval Hydrodynamics, University College, London, 1976, pp. 55-113.
15. Bindel, S., "MARINER Class Vessel - Influence of the Testing Procedure on Manoeuvrability Characteristics", Proceedings of the 11th IITC, Tokyo, 1966, p. 558.
16. Norrbin, N.H., "Theory and Observations on the Use of a Mathematical Model for Ship Maneuvering in Deep and Confined Waters", Proceedings of the 8th Symposium on Naval Hydrodynamics, Pasadena, California, 1970, pp. 807-904.
17. Thulin, S.A.R., "Discussion to Smitt/Chislett (1974), Ref. 13", Proceedings of the 10th Symposium on Naval Hydrodynamics, Massachusetts Institute of Technology, Cambridge Ma., 1974, pp. 153-156.
18. Laudan, J., "Einfluß der Kavitation auf die Propellerkräfte und -momente beim geradlinigen Stoppmanöver", Bericht F8/76, Oct. 1976, Hamburg Ship Model Basin (HSVA), Hamburg.
19. Laudan, J., "Zweiquadrantenmessungen bei Schräganströmung hinter einem Schiffsmodell", Bericht Nr. 1508, Dec. 1977, Hamburg Ship Model Basin (HSVA), Hamburg.
20. Chislett, M.S. and Strøm-Tejse, J., "Planar Motion Mechanism Tests and Full-Scale Steering and Manoeuvring Predictions for a MARINER Class Vessel", Hydro- and Aerodynamics Laboratory, Lyngby, Report No. Hy-6, Apr. 1965.
21. Saunders, H.E., "Hydrodynamics in Ship Design", Vol. I, SNAME, New York, 1957.
22. Shiba, H., "Model Experiments about the Maneuverability and Turning of Ships", Proceedings of the First Symposium on Ship Maneuverability, David Taylor Model Basin Report 1461, Oct. 1960, Washington, D.C., pp. 49-126.

APPENDIX A

The equations of motion for maneuvering in the horizontal plane may be written in the following form:

$$m(\ddot{u} - v\dot{r} - r^2\dot{x}_G) = X$$

$$m(\dot{v} + ur + \dot{r}x_G) = Y$$

$$I_{zz}\ddot{r} + m(ur + \dot{v})x_G = N$$

The hydrodynamic forces X , Y and moment N occurring above were identified by means of captive model tests using the following general expression in each case:

$$\begin{aligned} F = & F(u, v, r, \dot{u}, \dot{v}, \dot{r}, \delta) \\ = & F_0 u^2 \\ & + F_u u \Delta u + F_{uu} \Delta u^2 + F_{uuu} \Delta u^3 / u \\ & + F_u^* \dot{u} + F_{uu}^* \dot{u} \Delta u / u + F_{uuu}^* \dot{u} \Delta u^2 / u^2 \\ & + F_v uv + F_{vv} v^2 + F_{vvv} v^3 / u + F_{vvvv} v^4 / u^2 + F_{vvvvv} v^5 / u^3 \\ & + F_v |v| + F_v^* \dot{v} + F_{vv}^* \dot{v} v / u + F_{vvv}^* \dot{v} v^2 / u^2 \\ & + F_r ur + F_{rr} r^2 + F_{rrr} r^3 / u + F_{rrrr} r^4 / u^2 + F_{rrrrr} r^5 / u^3 \\ & + F_r |r| + F_r^* \dot{r} + F_{rr}^* \dot{r} r / u + F_{rrr}^* \dot{r} r^2 / u^2 \\ & + F_\delta u^2 \delta + F_{\delta\delta} u^2 \delta^2 + F_{\delta\delta\delta} u^2 \delta^3 + F_{\delta\delta\delta\delta} u^2 \delta^4 + F_{\delta\delta\delta\delta\delta} u^2 \delta^5 \\ & + F_\delta |\delta| + F_{vu} v \Delta u + F_{vuu} v \Delta u^2 / u + F_{vvu} v^2 \Delta u / u + F_{vvvu} v^3 \Delta u / u^2 + F_{v|v|u} v |v| \Delta u / u \\ & + F_{ru} r \Delta u + F_{ruu} r \Delta u^2 / u + F_{rru} r^2 \Delta u / u + F_{rrru} r^3 \Delta u / u^2 + F_{r|r|u} r |r| \Delta u / u \\ & + F_{\delta u} u \delta \Delta u + F_{\delta uu} \delta \Delta u^2 + F_{\delta\delta u} u \delta^2 \Delta u + F_{\delta\delta\delta u} u \delta^3 \Delta u + F_{\delta|\delta|u} u \delta |\delta| \Delta u \\ & + F_{vr} vr + F_{vrr} vr^2 / u + F_{vrrr} vr^3 / u^2 + F_{vvrr} v^2 r / u + F_{vvrrr} v^2 r^2 / u^2 \\ & + F_{vvrrr} v^3 r / u^2 + F_{v|r|} v |r| + F_{v|r|u} v |r| u \\ & + F_{v\delta} uv \delta + F_{v\delta\delta} uv \delta^2 + F_{vv\delta} v^2 \delta + F_{v|v|\delta} v |v| \delta + F_{v|\delta|} v |\delta| \\ & + F_{r\delta} ur \delta + F_{r\delta\delta} ur \delta^2 + F_{rr\delta} r^2 \delta + F_{r|r|\delta} r |r| \delta + F_{r|\delta|} r |\delta| \\ & + F_{vru} vr \Delta u / u + F_{v\delta u} v \delta \Delta u + F_{r\delta u} r \delta \Delta u + F_{vr\delta} vr \delta \end{aligned}$$

The symbol Δu denotes forward speed change ($u - U_0$); the subscript u stands for Δu .

APPENDIX B

The equations of motion used for indirect system identification by trajectory analysis (as well as for subsequent maneuver simulation):

$$\begin{aligned}\ddot{u} = & A_1 u \Delta u + A_2 \Delta u^2 + A_3 \Delta u^3 / u \\ & + A_4 v^2 + A_5 r^2 + A_6 u^2 \delta^2 + A_7 v r + A_8 u v \delta + A_9 u r \delta \\ & + A_{10} v^2 \Delta u / u + A_{11} r^2 \Delta u / u + A_{12} u \delta^2 \Delta u + A_{13} u v + A_{14} v \Delta u + A_{15} v \Delta u^2 / u \\ & + A_{16} u r + A_{17} r \Delta u + A_{18} r \Delta u^2 / u + A_{19} v r \Delta u / u + A_{20} v \delta \Delta u + A_{21} r \delta \Delta u \\ & + A_{22} v^2 \delta + A_{23} r^2 \delta + A_{24} u^2 \delta + A_{25} u \delta \Delta u + A_{26} \delta \Delta u^2 \\ & + A_{27} v^2 r / u + A_{28} v r^2 / u + A_{29} u v \delta^2 + A_{30} u r \delta^2 + A_{31} v^3 / u + A_{32} r^3 / u \\ & + A_{33} u^2 \delta^3 + A_{34} u^2 \delta^4\end{aligned}$$

$$\begin{aligned}\ddot{v} = & B_1 u^2 + B_2 u \Delta u \\ & + B_3 u v + B_4 v^2 + B_5 v^3 / u + B_6 v r^2 / u + B_7 u v \delta^2 + B_8 v \Delta u \\ & + B_9 v \Delta u^2 / u + B_{10} u r + B_{11} r^2 + B_{12} r^3 / u + B_{13} v^2 r / u + B_{14} u r \delta^2 \\ & + B_{15} r \Delta u + B_{16} r \Delta u^2 / u + B_{17} u^2 \delta + B_{18} u^2 \delta^2 + B_{19} u^2 \delta^3 + B_{20} v^2 \delta \\ & + B_{21} r^2 \delta + B_{22} u \delta \Delta u + B_{23} \delta \Delta u^2 + B_{24} v r \delta + B_{25} u v \delta + B_{26} v \delta \Delta u \\ & + B_{27} u r \delta + B_{28} r \delta \Delta u + B_{29} v r + B_{30} v r \Delta u / u + B_{31} v |v| + B_{32} r |r| \\ & + B_{33} v |r| + B_{34} r |v| + B_{35} v^5 / u^3 + B_{36} r^5 / u^3 + B_{37} u^2 \delta^4 + B_{38} u^2 \delta^5 \\ & + B_{39} u \delta^2 \Delta u + B_{40} u \delta^3 \Delta u + B_{41} u \delta |v| + B_{42} u \delta |r|\end{aligned}$$

$$\begin{aligned}\ddot{r} = & C_1 u^2 + C_2 u \Delta u \\ & + C_3 u v + C_4 v^2 + C_5 v^3 / u + C_6 v r^2 / u + C_7 u v \delta^2 + C_8 v \Delta u \\ & + C_9 v \Delta u^2 / u + C_{10} u r + C_{11} r^2 + C_{12} r^3 / u + C_{13} v^2 r / u + C_{14} u r \delta^2 \\ & + C_{15} r \Delta u + C_{16} r \Delta u^2 / u + C_{17} u^2 \delta + C_{18} u^2 \delta^2 + C_{19} u^2 \delta^3 + C_{20} v^2 \delta \\ & + C_{21} r^2 \delta + C_{22} u \delta \Delta u + C_{23} \delta \Delta u^2 + C_{24} v r \delta + C_{25} u v \delta + C_{26} v \delta \Delta u \\ & + C_{27} u r \delta + C_{28} r \delta \Delta u + C_{29} v r + C_{30} v r \Delta u / u + C_{31} v |v| + C_{32} r |r| \\ & + C_{33} v |r| + C_{34} r |v| + C_{35} v^5 / u^3 + C_{36} r^5 / u^3 + C_{37} u^2 \delta^4 + C_{38} u^2 \delta^5 \\ & + C_{39} u \delta^2 \Delta u + C_{40} u \delta^3 \Delta u + C_{41} u \delta |v| + C_{42} u \delta |r|\end{aligned}$$

The above equations are obtained by solving the general equations of motion (Appendix A) explicitly for \ddot{u} , \ddot{v} and \ddot{r} . However, not all the terms resulting from the general expressions for F have been retained, but only a significant subset based on judicious choice and experience.

The "acceleration" coefficients occurring here are related to the "force" coefficients of Appendix A by simple transformations such as

$$A_1 = X_u / (m - X_u^*)$$

$$B_1 = \{ (I_{zz} - N_r^*) Y_o - (m x_G - Y_r^*) N_o \} / \{ (m - Y_v^*) (I_{zz} - N_r^*) - (m x_G - N_v^*) (m x_G - Y_r^*) \}$$

$$C_1 = \{ (m - Y_v^*) N_o - (m x_G - N_v^*) Y_o \} / \{ (m - Y_v^*) (I_{zz} - N_r^*) - (m x_G - N_v^*) (m x_G - Y_r^*) \}$$

Table 1

Hydrodynamic coefficients of the MARINER model at a propeller rate of revolutions corresponding to the selfpropulsion point of the model ($n = 6.09$ Hz)

X - Equation		Y - Equation		N - Equation	
Sub-script	Non-dim. value	Sub-script	Non-dim. value	Sub-script	Non-dim. value
\dot{u}	-21.44	\dot{v}	-748.87	\dot{v}	7.82
		$\dot{v}vv$	-4107.03	$\dot{v}vv$	84.94
		\dot{r}	-14.37	\dot{r}	-44.43
		$\dot{r}rr$	-130.36	$\dot{r}rr$	21.09
u	-276.08	o	-2.03	o	0.81
uu	0.0	ou	-20.81	ou	6.48
uuu	-221.03				
v	-22.04	v	-1159.27	v	-346.67
vv	-465.77	vv	0.0	vv	0.0
		vvv	-9504.01	vvv	0.0
		$v v $	0.0	$v v $	168.73
vu	205.26	vu	-106.76	vu	0.0
vuv	0.0	vuv	-361.44	vuv	0.0
$vuvu$	-2276.50	$vuvu$	0.0	$vuvu$	-3549.49
r	27.97	r	352.90	r	-208.33
rr	-43.27	rr	0.0	rr	0.0
rrr	-19.16	rrr	74.41	rrr	-113.40
		$r r $	178.96	$r r $	-48.50
ru	-38.89	ru	-140.57	ru	-13.57
rru	-36.21	rru	0.0	rru	15.21
$rrru$	0.0	$rrru$	180.62	$rrru$	0.0
δ	5.42	δ	264.04	δ	-128.24
$\delta\delta$	-142.04	$\delta\delta$	67.54	$\delta\delta$	-23.61
$\delta\delta\delta$	0.0	$\delta\delta\delta$	-686.89	$\delta\delta\delta$	340.12
$\delta\delta\delta\delta$	95.76	$\delta\delta\delta\delta$	-131.77	$\delta\delta\delta\delta$	44.11
		$\delta\delta\delta\delta\delta$	410.57	$\delta\delta\delta\delta\delta$	-201.45
		$\delta \delta $	198.43	$\delta \delta $	-100.08
δu	0.0	δu	-371.12	δu	199.79
δuu	229.64	δuu	0.0	δuu	40.86
$\delta\delta u$	194.44	$\delta\delta u$	-54.44	$\delta\delta u$	36.19
$\delta\delta\delta u$	140.81	$\delta\delta\delta u$	587.17	$\delta\delta\delta u$	-273.73
vr	230.49	vr	0.0	vr	0.0
		vvr	813.15	vvr	0.0
		vrr	-2214.32	vrr	387.05
		$v r $	-618.32	$v r $	0.0
$ v r$	-67.49	$ v r$	644.35	$ v r$	-719.96
$v\delta$	101.37	$v\delta$	55.91	$v\delta$	-29.61
		$v\delta\delta$	149.01	$v\delta\delta$	0.0
$v \delta $	-15.83	$v \delta $	0.0	$v \delta $	34.99
		$ v \delta$	206.58	$ v \delta$	-106.64
$r\delta$	-48.51	$r\delta$	0.0	$r\delta$	0.0
		$r\delta\delta$	0.0	$r\delta\delta$	130.04
		$r \delta $	-103.10	$r \delta $	-38.13
		$ r \delta$	84.55	$ r \delta$	-47.13

All values have to be multiplied by 10^{-5} !

All numerical values are given above in a uniform fixed-point format for the convenience of any reader who might wish to duplicate our experiments or computations, but it is in no way implied that the numbers are statistically significant up to the last digit! The same applies to the subsequent tables.

Table 2

Calculated effective rudder advance velocity c as a function of propeller rate of revolutions n and wake fraction w

Measured model wake fraction $w_M = 0.25$						Extrapolated full-scale wake fraction $w_S = 0.20$				
F_D N	n Hz	J 1	K_T 1	c^2 m^2/s^2	c m/s	n Hz	J 1	K_T 1	c^2 m^2/s^2	c m/s
13.73	5.30	0.815	0.141	1.835	1.355	5.30	0.869	0.115	1.929	1.389
11.77	5.42	0.797	0.151	1.894	1.376	5.42	0.850	0.122	1.973	1.405
8.34	5.51	0.784	0.159	1.942	1.394	5.51	0.836	0.129	2.014	1.419
3.92	5.88	0.734	0.184	2.131	1.460	5.88	0.783	0.158	2.206	1.485
0.0	6.09	0.709	0.197	2.247	1.499	6.09	0.756	0.171	2.314	1.521
-3.92	6.32	0.683	0.210	2.380	1.543	6.32	0.729	0.186	2.448	1.565
-7.85	6.47	0.667	0.217	2.465	1.570	6.47	0.712	0.194	2.533	1.592
-11.77	6.65	0.649	0.226	2.576	1.605	6.65	0.693	0.205	2.649	1.628

Table 3

Hydrodynamic coefficients of the MARINER model obtained by indirect system identification at a propeller rate of revolutions of $n = 6.47$ Hz together with a towing force of $F_D = -7.85$ N

\dot{u} - Equation				\dot{v} - Equation				\dot{r} - Equation			
Term	Coef.	Value	Unit	Term	Coef.	Value	Unit	Term	Coef.	Value	Unit
$u\Delta u$	A_1	-0.0580	1/m	u^2	B_1	-0.0011	1/m	u^2	C_1	0.0007	1/m ²
Δu^2	A_2	-0.0516	1/m	uv	B_2	-0.1057	1/m	uv	C_3	-0.0789	1/m ²
$\Delta u^3/u$	A_3	-0.1583	1/m	v^2	B_4	-0.0282	1/m	vr^2/u	C_6	20.9040	1
v^2	A_4	-0.7505	1/m	$uv\delta^2$	B_7	0.0983	1/m	ur	C_{10}	-0.2607	1/m
r^2	A_5	-0.6390	m	ur	B_{10}	-0.2998	1	r^2	C_{11}	-0.4819	1
$u^2\delta^2$	A_6	-0.0232	1/m	r^2	B_{11}	0.9198	m	$u^2\delta$	C_{17}	-0.0342	1/m ²
$u\delta^2\Delta u$	A_{12}	0.0379	1/m	r^3/u	B_{12}	39.1629	m ²	$u^2\delta^3$	C_{19}	0.0233	1/m ²
uv	A_{13}	-0.0309	1/m	$u^2\delta$	B_{17}	0.0296	1/m	$v^2\delta$	C_{20}	-0.5620	1/m ²
$v^2\delta$	A_{22}	0.2838	1/m	$u^2\delta^2$	B_{18}	0.0040	1/m	$u\delta\Delta u$	C_{22}	0.0344	1/m ²
v^2r/u	A_{27}	-10.7699	1	$u^2\delta^3$	B_{19}	-0.0225	1/m	$v\delta\Delta u$	C_{26}	-0.4142	1/m ²
vr^2/u	A_{28}	-20.3132	m	$r^2\delta$	B_{21}	0.4441	m	$r\delta\Delta u$	C_{28}	-0.9780	1/m
				$u\delta\Delta u$	B_{22}	-0.0423	1/m	$vr\Delta u/u$	C_{30}	-0.3966	1/m
				$uv\delta$	B_{25}	-0.0359	1/m	$v v $	C_{31}	0.5587	1/m ²
				$v v $	B_{31}	-0.6348	1/m	$r r $	C_{32}	0.3643	1
								v^5/u^3	C_{35}	-48.4074	1/m ²
								$u\delta^2\Delta u$	C_{39}	-0.0416	1/m ²

Table 4

Selected characteristics of a series of zig-zag maneuvers conducted at systematically varied propeller loadings

Maneuver	F_D N	τ_a s	τ_b s	τ_c s	τ_r s	α_{01} deg	α_{02} deg	$\dot{\psi}_{\min}$ deg/s	y_{\max} m	T s
20°/20° Zig-zag	13.73	8.45	5.05	11.40	24.90	10.44	10.58	-3.60	9.73	44.90
	11.77	8.20	4.90	11.65	24.75	10.91	10.44	-3.60	9.86	44.30
	8.34	8.00	4.90	11.05	23.95	10.37	10.62	-3.62	9.67	44.25
	3.92	7.95	4.85	10.90	23.70	10.94	10.62	-3.78	9.46	42.90
	0.0	7.65	4.60	10.55	22.80	10.51	10.84	-3.80	9.01	41.95
	-3.92	7.45	4.65	10.25	22.35	10.80	11.34	-3.92	9.18	41.65
	-7.85	7.20	4.55	9.90	21.65	11.09	11.23	-3.95	8.96	40.55
	-11.77	7.15	4.40	9.85	21.40	10.80	11.40	-4.03	8.71	40.20
30°/10° Zig-zag	13.73	4.85	5.40	7.75	18.00	13.82	14.11	-4.16	5.48	32.35
	11.77	4.95	5.30	7.85	18.10	14.04	14.65	-4.25	5.54	32.45
	8.34	5.00	5.25	7.60	17.85	13.76	14.73	-4.30	5.32	32.35
	3.92	4.80	5.20	7.55	17.55	14.36	15.05	-4.51	5.50	31.05
	0.0	4.80	5.10	7.15	17.05	14.18	15.44	-4.60	5.22	30.70
	-3.92	4.50	5.35	6.95	16.80	15.01	15.80	-4.71	5.47	30.25
	-7.85	4.35	5.20	6.75	16.30	14.65	15.95	-4.83	5.25	29.80
	-11.77	4.65	5.10	6.90	16.65	15.05	16.02	-4.93	5.18	29.50
20°/10° Zig-zag	13.73	5.40	4.75	8.40	18.55	9.86	9.97	-3.51	4.89	32.65
	11.77	5.35	4.75	8.25	18.35	10.04	10.08	-3.58	4.92	32.15
	8.34	5.35	4.70	8.00	18.05	9.81	10.51	-3.55	4.73	32.40
	3.92	5.20	4.75	7.95	17.90	10.26	10.80	-3.65	4.88	32.05
	0.0	5.05	4.55	7.60	17.20	9.99	10.78	-3.80	4.57	30.90
	-3.92	4.60	4.65	7.30	16.55	10.40	10.58	-3.88	4.74	30.35
	-7.85	4.40	4.45	6.95	15.80	10.04	10.87	-3.86	4.55	29.45
	-11.77	4.85	4.40	7.00	16.25	9.94	11.22	-3.99	4.34	29.10
10°/10° Zig-zag	13.73	6.85	6.00	11.40	24.25	6.84	6.19	-2.46	5.91	40.75
	11.77	6.45	5.65	11.00	23.10	6.44	6.26	-2.46	5.72	40.20
	8.34	6.50	5.00	11.20	22.70	6.12	6.70	-2.62	5.42	39.60
	3.92	6.45	5.15	11.00	22.60	6.77	6.05	-2.51	5.57	38.40
	0.0	6.60	4.75	10.60	21.95	6.26	5.98	-2.55	5.04	36.95
	-3.92	5.50	5.50	9.95	21.00	6.95	5.98	-2.56	5.62	36.60
	-7.85	5.60	4.90	9.50	20.00	6.70	5.76	-2.62	5.18	35.75
	-11.77	6.15	4.45	10.05	20.65	6.26	6.30	-2.69	5.00	35.80

Table 5

Hydrodynamic coefficients of the MARINER model at a propeller rate of revolutions corresponding to an ideal extrapolated selfpropulsion point of the full-size ship ($n = 5.51$ Hz)

X - Equation		Y - Equation		N - Equation	
Sub-script	Non-dim. value	Sub-script	Non-dim. value	Sub-script	Non-dim. value
\dot{u}	-24.08	\dot{v}	-776.72	\dot{v}	5.66
		$\dot{v}v$	-3791.23	$\dot{v}v$	0.0
		\dot{r}	-11.17	\dot{r}	-40.96
		$\dot{r}r$	-137.29	$\dot{r}r$	14.81
u	-222.92	o	2.10	o	2.56
uu	0.0	ou	-16.70	ou	1.90
uuu	-168.21				
v	0.0	v	-1151.61	v	-355.52
vv	-417.88	vv	0.0	vv	0.0
		vvv	-9063.77	vvv	0.0
		$v v $	0.0	$v v $	234.03
vu	0.0	vu	0.0	vu	0.0
vuu	0.0	vuu	0.0	vuu	0.0
$vuvu$	0.0	$vuvu$	0.0	$vuvu$	0.0
r	22.16	r	352.63	r	-201.96
rr	-42.28	rr	0.0	rr	0.0
rrr	-15.90	rrr	100.79	rrr	-112.52
		$r r $	158.80	$r r $	-51.17
ru	0.0	ru	0.0	ru	0.0
rru	0.0	rru	0.0	rru	0.0
$rrru$	0.0	$rrru$	0.0	$rrru$	0.0
δ	10.38	δ	234.67	δ	-116.16
$\delta\delta$	-127.10	$\delta\delta$	4.85	$\delta\delta$	-1.00
$\delta\delta\delta$	0.0	$\delta\delta\delta$	-563.97	$\delta\delta\delta$	299.80
$\delta\delta\delta\delta$	69.05	$\delta\delta\delta\delta$	0.0	$\delta\delta\delta\delta$	0.0
		$\delta\delta\delta\delta\delta$	352.93	$\delta\delta\delta\delta\delta$	-189.43
		$\delta \delta $	164.91	$\delta \delta $	-86.26
δu	0.0	δu	-357.76	δu	158.60
δuu	0.0	δuu	0.0	δuu	0.0
$\delta\delta u$	228.68	$\delta\delta u$	-65.74	$\delta\delta u$	61.84
$\delta\delta\delta u$	0.0	$\delta\delta\delta u$	549.33	$\delta\delta\delta u$	-19.54
vr	230.49	vr	0.0	vr	0.0
		vvr	813.15	vvr	0.0
		vrr	-2214.32	vrr	387.05
$ v r$	-67.49	$v r $	-618.32	$v r $	0.0
$v\delta$	90.93	$ v r$	644.33	$ v r$	-719.96
		$v\delta$	50.15	$v\delta$	-26.56
		$v\delta\delta$	133.66	$v\delta\delta$	0.0
$v \delta $	-14.20	$v \delta $	0.0	$v \delta $	31.39
		$ v \delta$	185.30	$ v \delta$	-95.66
$r\delta$	-43.51	$r\delta$	0.0	$r\delta$	0.0
		$r\delta\delta$	0.0	$r\delta\delta$	116.65
		$r \delta $	-92.48	$r \delta $	-34.20
		$ r \delta$	75.84	$ r \delta$	-42.28

All values have to be multiplied by 10^{-5} !

Table 6 Relative sensitivity of yaw rate r to variation of individual coefficients, based on simulated turning circles with maximum rudder angle of $\delta = -30^\circ$

Rank order	Non-dim. coeff.	Sensit. factor S_p^r	Rank order	Non-dim. coeff.	Sensit. factor S_p^r	Rank order	Non-dim. coeff.	Sensit. factor S_p^r
1	N_r	-0.5436	31	$X_{\delta uu}$	-0.0221	60	$X_{ v r}$	-0.0079
2	N_δ	0.4616	32	$N_{\delta\delta\delta\delta}$	0.0220	61	X_v	0.0071
3	N_v	0.3403	33	X_{vv}	-0.0216	62	X_δ	-0.0063
4	$N_{\delta\delta\delta}$	-0.3167	34	N_{vvvu}	-0.0207	63	$Y_{\delta\delta\delta\delta}$	-0.0056
5	$N_{r v }$	-0.2589	35	$X_{r\delta}$	0.0205	64	N_o	0.0054
6	X_u	0.2150	36	X_{vu}	0.0198	65	X_{vvvu}	-0.0044
7	$N_{\delta u}$	0.2016	37	$Y_{r v }$	0.0196	66	N_{rru}	-0.0039
8	$N_{\delta \delta }$	0.1846	38	$N_{\delta\delta u}$	-0.0194	67	Y_{ou}	0.0035
9	Y_v	0.1091	39	$Y_{v r }$	0.0188	68	$Y_{v\delta\delta}$	-0.0033
10	$X_{\delta\delta}$	-0.0889	40	$N_{v \delta }$	-0.0175	69	X_{rru}	0.0031
11	$N_{r\delta\delta}$	0.0646	41	Y_{vvv}	0.0171	70	$X_{v \delta }$	0.0027
12	$N_{\delta\delta\delta u}$	-0.0771	42	$X_{v\delta}$	0.0170	71	Y_{vu}	-0.0025
13	Y_δ	-0.0753	43	$X_{\delta\delta\delta\delta}$	0.0160	72	$Y_{\delta\delta u}$	0.0025
14	Y_r	0.0744	44	$N_{v\delta}$	-0.0148	73	$Y_{v\delta}$	0.0024
15	$N_{\delta r }$	0.0588	45	$Y_{\delta\delta\delta u}$	0.0143	74	X_{rrr}	-0.0020
16	$Y_{\delta\delta\delta}$	0.0571	46	$X_{\delta\delta\delta u}$	0.0134	75	Y_{rrr}	0.0020
17	$N_{\delta v }$	0.0536	47	$Y_{r r }$	0.0134	76	Y_{rrru}	-0.0014
18	$N_{\delta\delta\delta\delta\delta}$	0.0528	48	X_{uuu}	0.0131	77	Y_{vvu}	0.0013
19	N_{vrr}	-0.0496	49	X_{rr}	-0.0127	78	Y_o	-0.0011
20	$N_{r \delta }$	-0.0484	50	N_{ou}	-0.0127	79	Y_{vvvr}	-0.0005
21	$N_{r r }$	-0.0430	51	$N_{\delta uu}$	-0.0123	80	X_u^*	0.0
22	$N_{\delta\delta}$	-0.0428	52	$Y_{r \delta }$	-0.0110	81	Y_v^*	0.0
23	N_{rrr}	-0.0367	53	$Y_{\delta\delta}$	0.0105	82	Y_{vvv}^*	0.0
24	$X_{\delta\delta u}$	-0.0339	54	N_{ru}	0.0096	83	N_r^*	0.0
25	$Y_{\delta u}$	-0.0310	55	X_{ru}	0.0093	84	Y_{rrr}^*	0.0
26	$Y_{\delta \delta }$	-0.0303	56	$Y_{\delta\delta\delta\delta\delta}$	-0.0091	85	Y_r^*	0.0
27	X_{vr}	-0.0270	57	$Y_{\delta r }$	-0.0090	86	N_v^*	0.0
28	Y_{vrr}	0.0245	58	$Y_{\delta v }$	-0.0087	87	N_{rrr}^*	0.0
29	$N_{v v }$	-0.0232	59	Y_{ru}	0.0086	88	N_{vvv}^*	0.0
30	X_r	0.0225						

Note: The relative sensitivity of any response variable x (here yaw rate r) to any parameter p (here the 88 coefficients listed above) is defined as the relative change in the value of the response variable (at a suitably chosen instant) resulting from a given change of the parameter value, that is

$$S_p^x = \frac{x_2 - x_1}{x} / \frac{p_2 - p_1}{p_1}$$

where x is an appropriate reference value of the response variable x , see Reference [5].

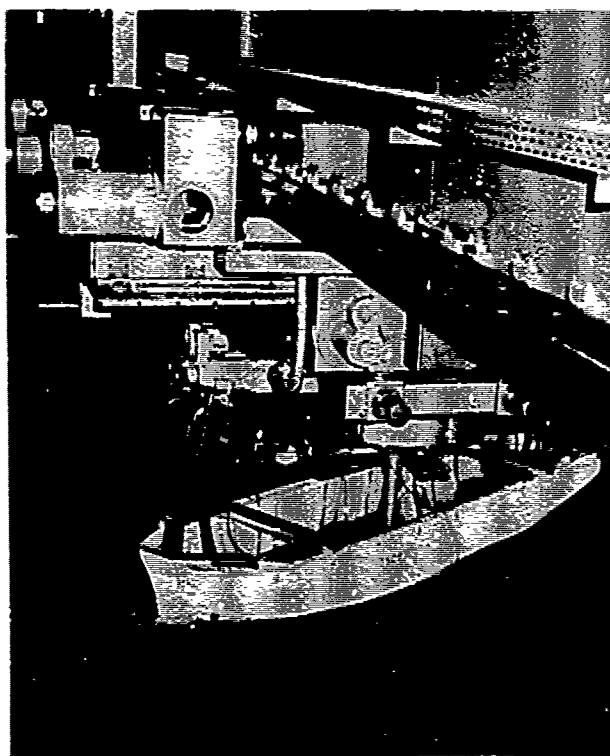


Fig. 1
CPMC following a freely maneuvering tug-boat

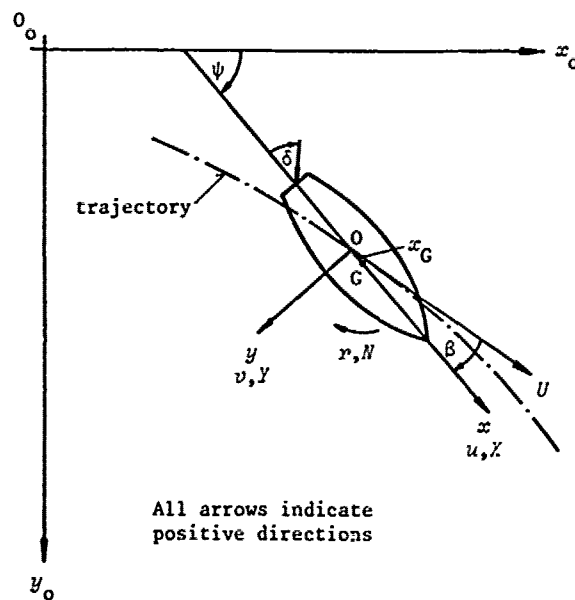


Fig. 2 Coordinate system

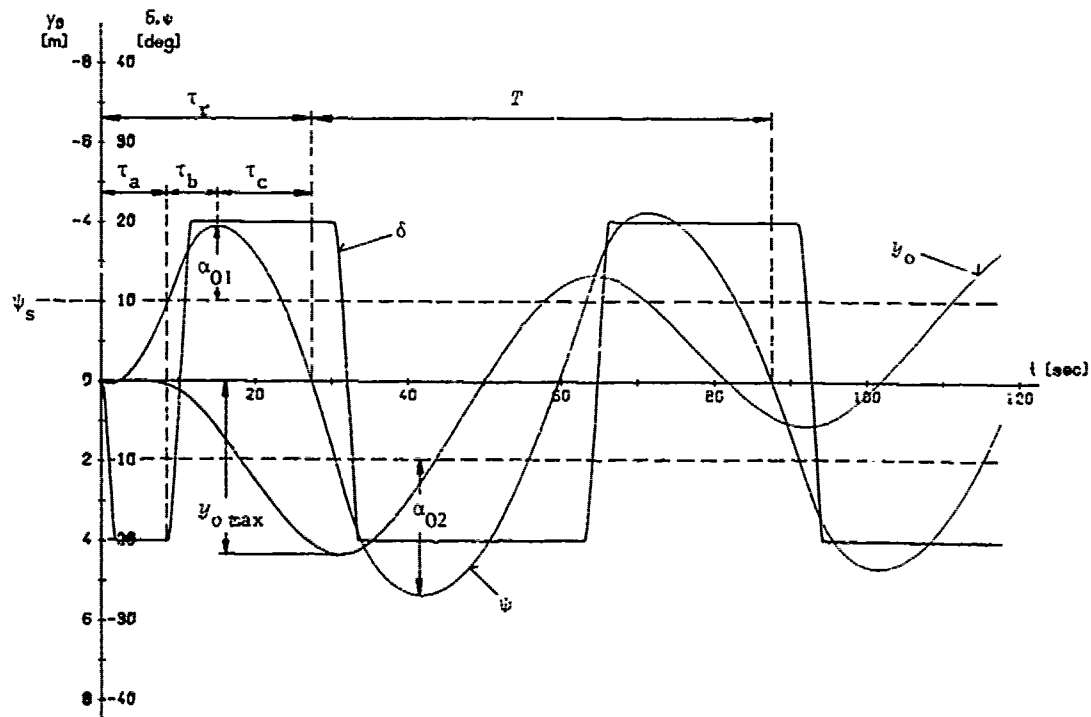


Fig. 3 Definition of characteristic parameters of zigzag maneuvers

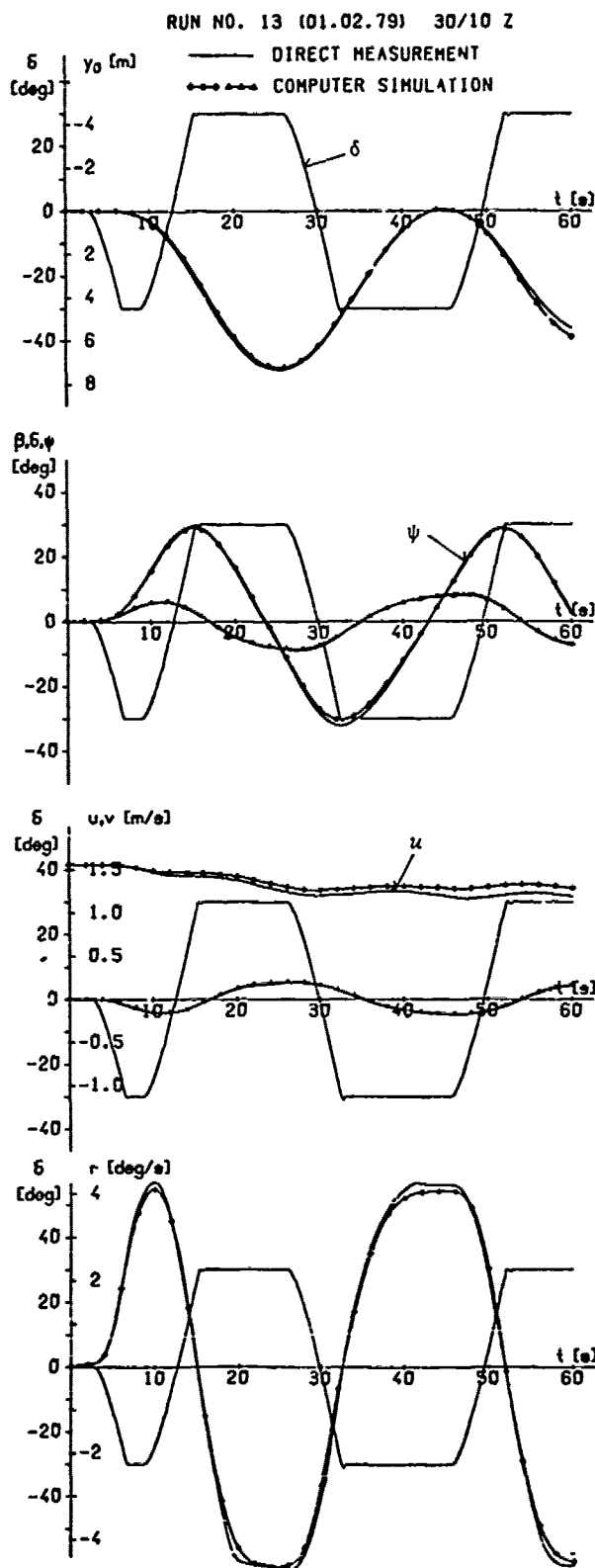


Fig. 4 30°/10° zigzag maneuver (model)
Direct measurement versus computer
simulation based on Table 1

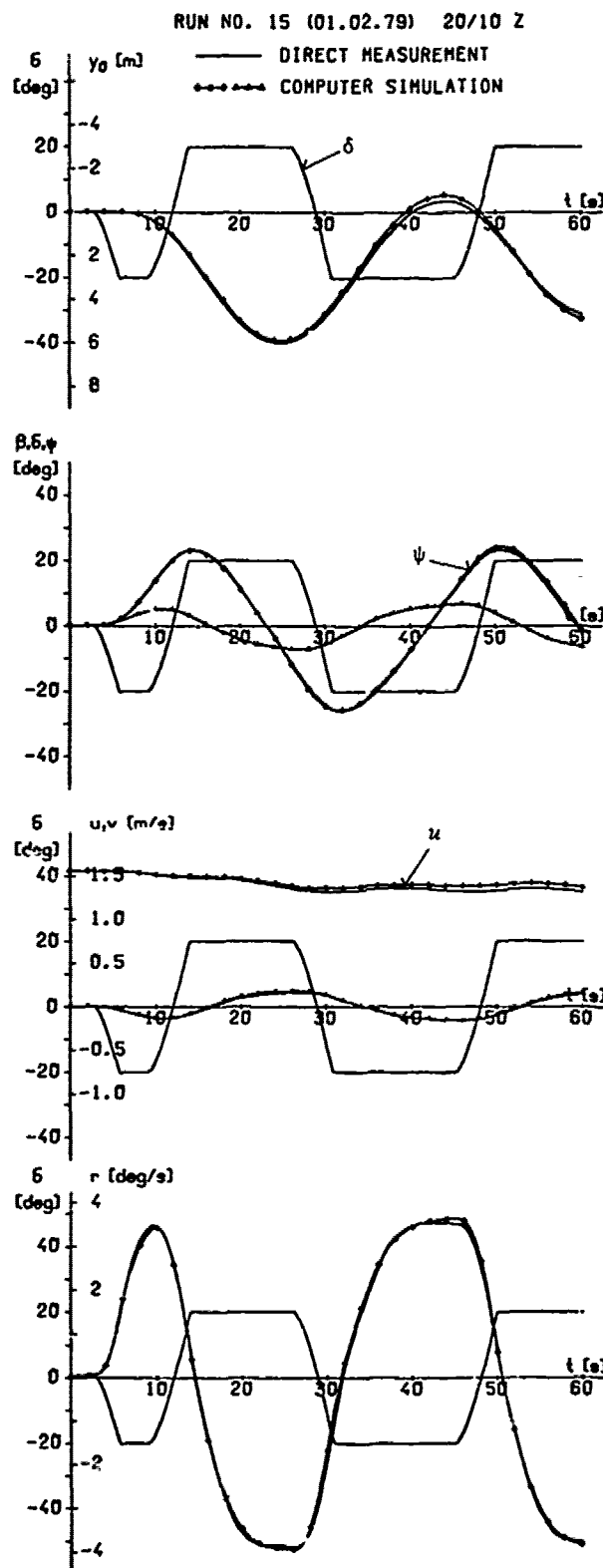


Fig. 5 20°/10° zigzag maneuver (model)
Direct measurement versus computer
simulation based on Table 1

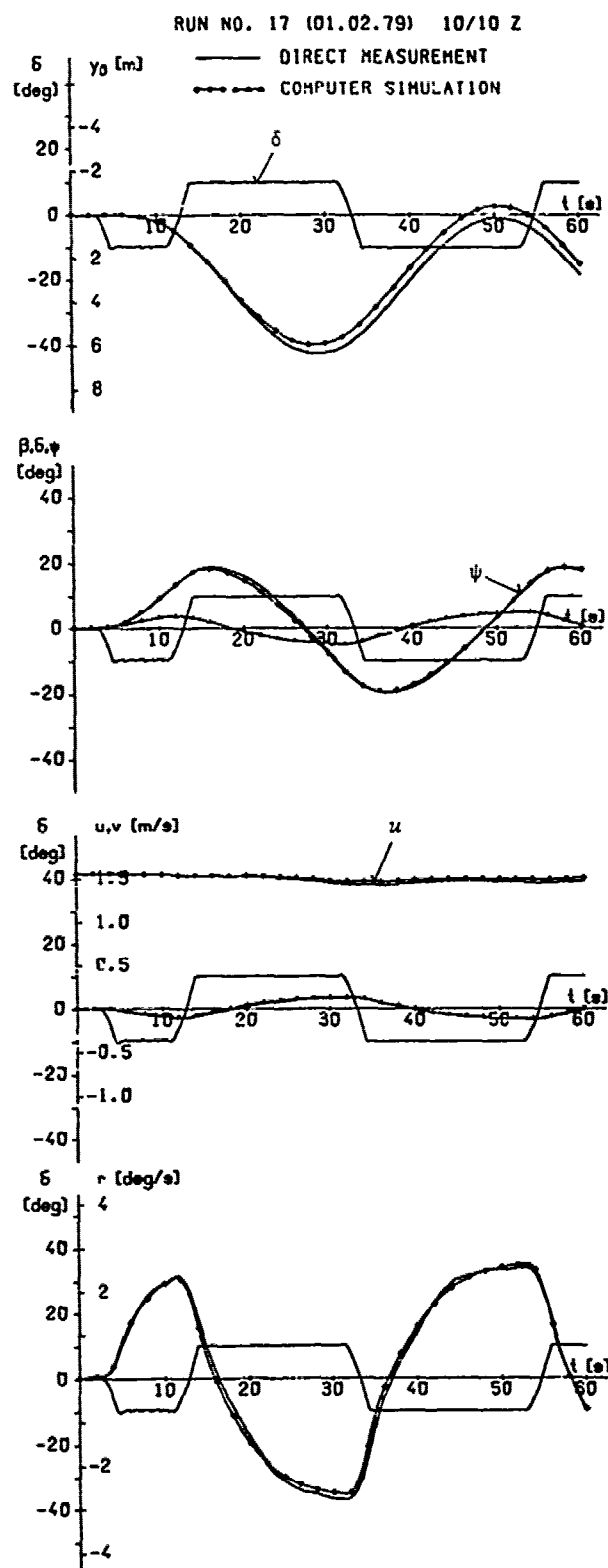


Fig. 6 $10^\circ/10^\circ$ zigzag maneuver (model)
Direct measurement versus computer
simulation based on Table 1

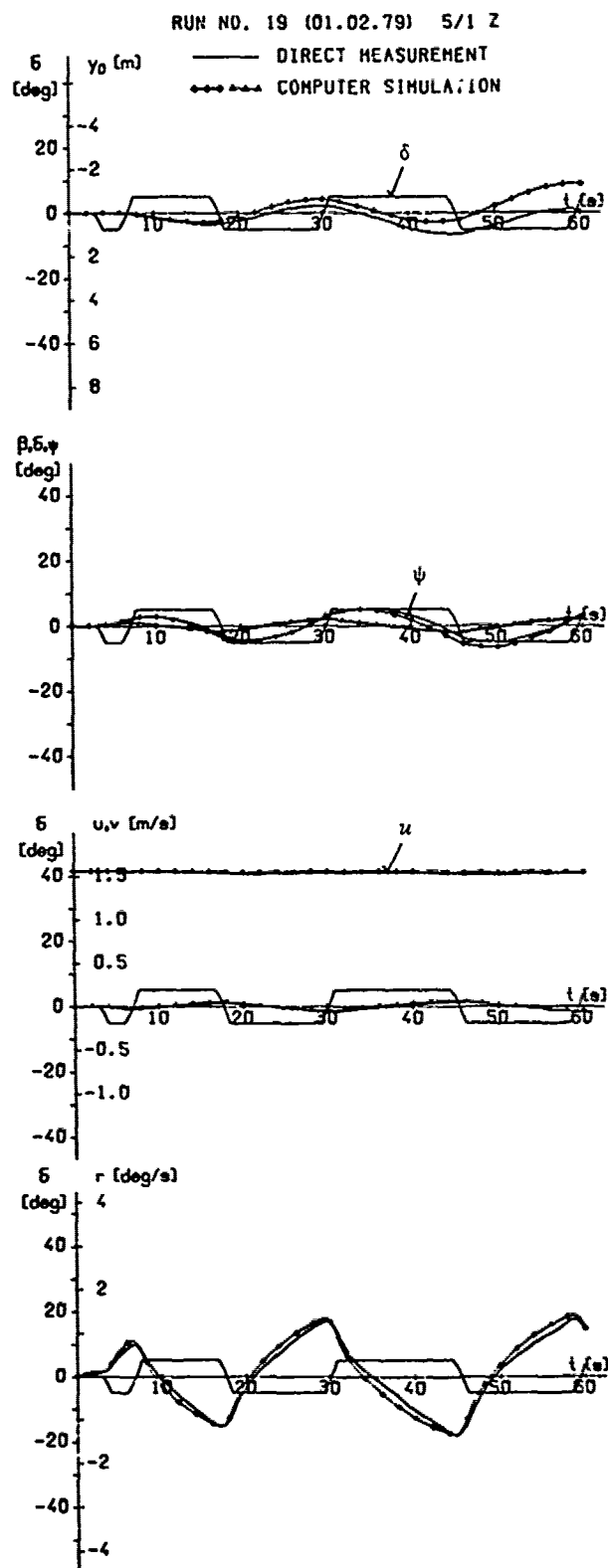


Fig. 7 $5^\circ/1^\circ$ zigzag maneuver (model)
Direct measurement versus computer
simulation based on Table 1

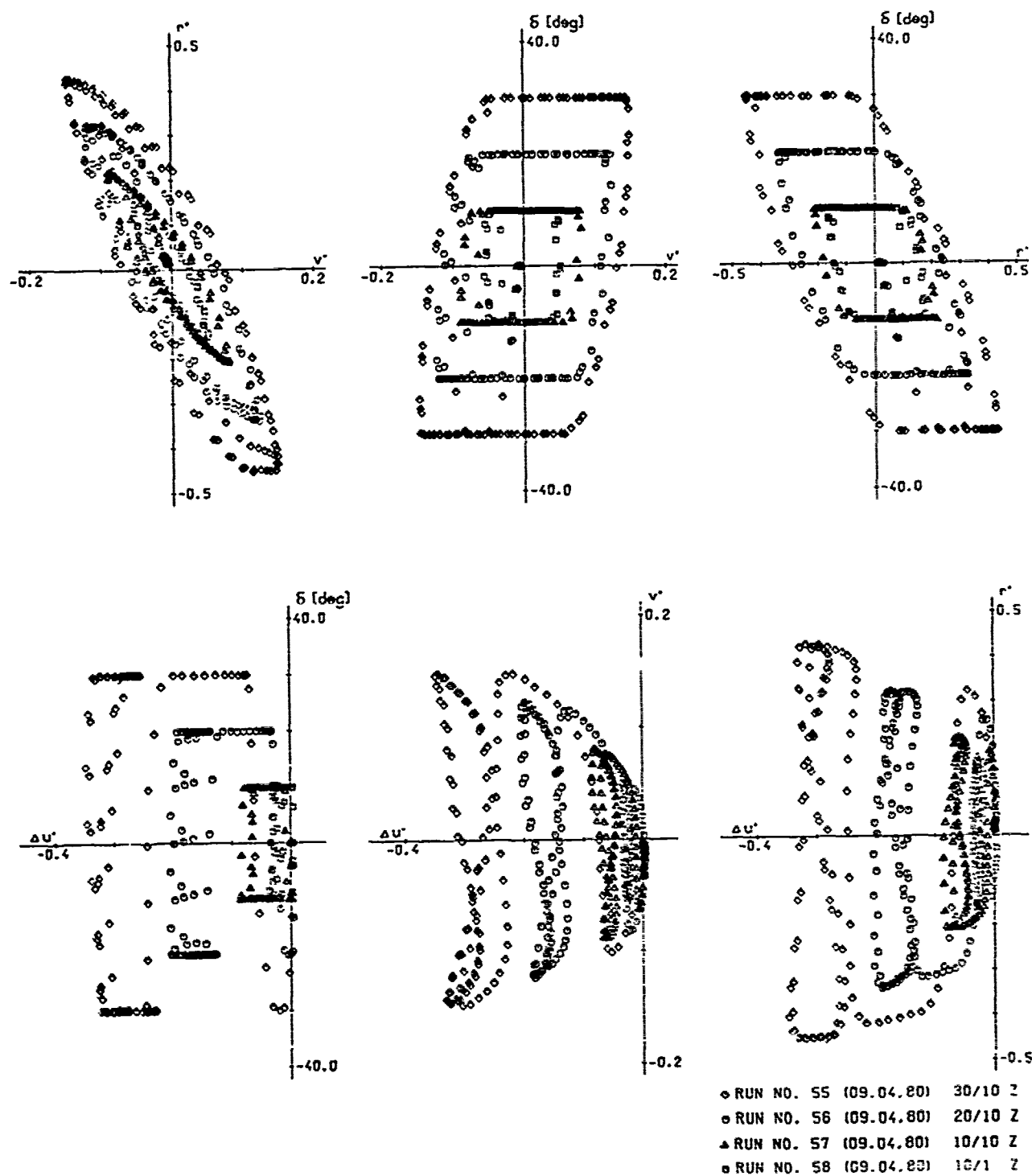


Fig. 8 Range of variables occurring in the maneuver trajectories used for indirect system identification leading to Table 3

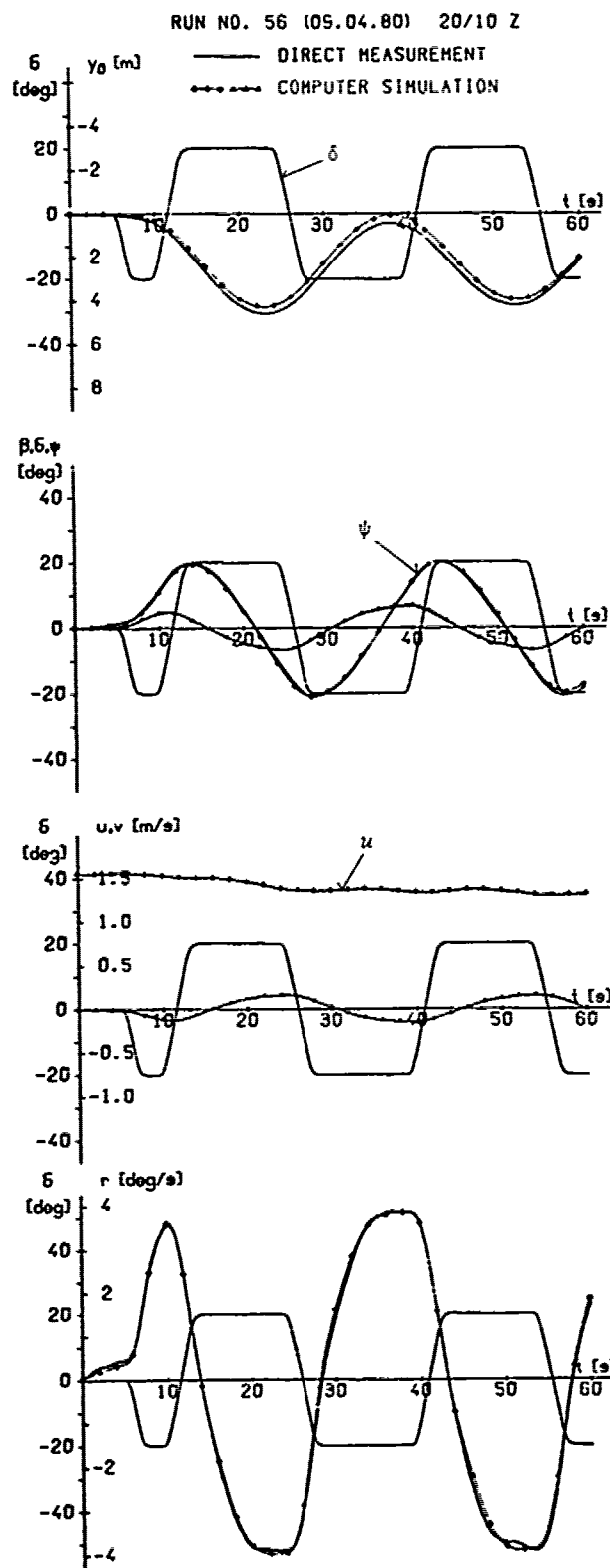


Fig. 9
20°/10° zigzag source maneuver (model)
Direct measurement versus computer
simulation based on Table 3

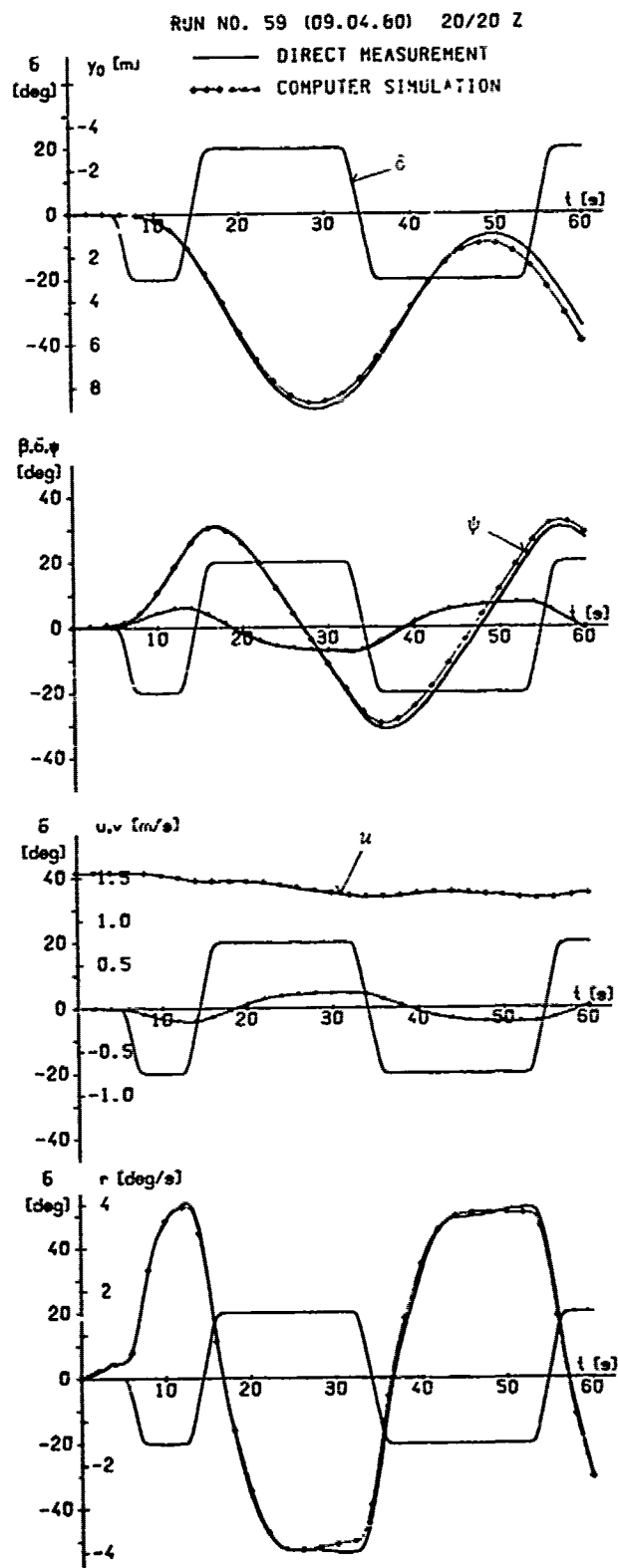


Fig. 10
20°/20° zigzag test maneuver (model)
Direct measurement versus computer
simulation based on Table 3

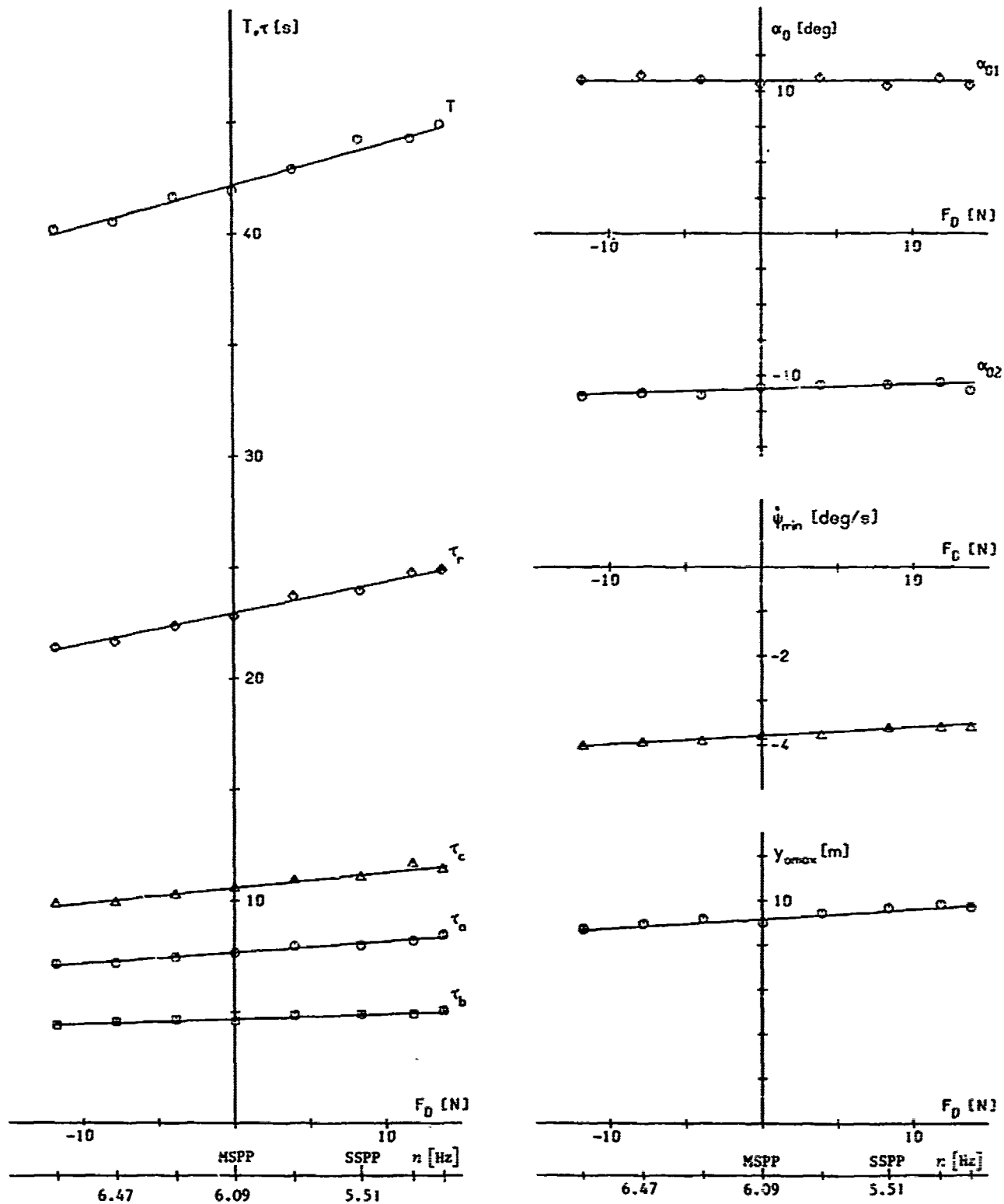
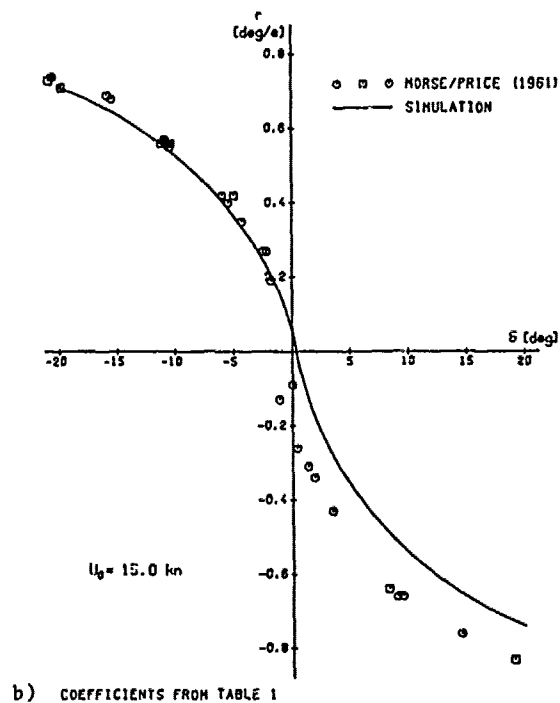
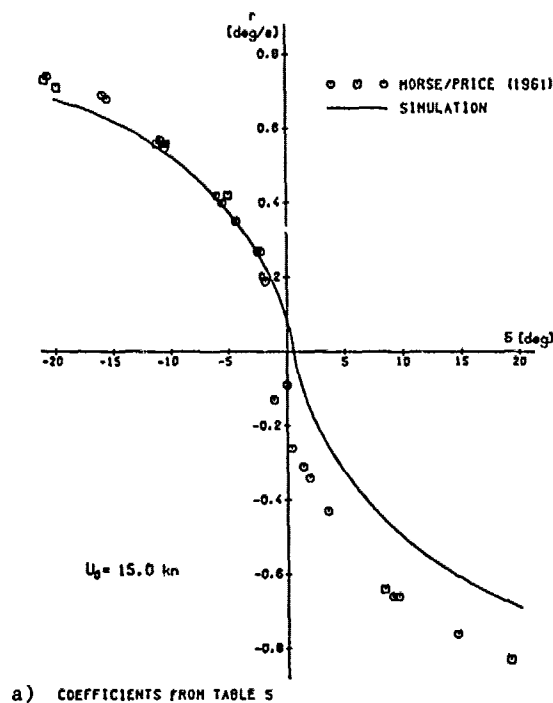
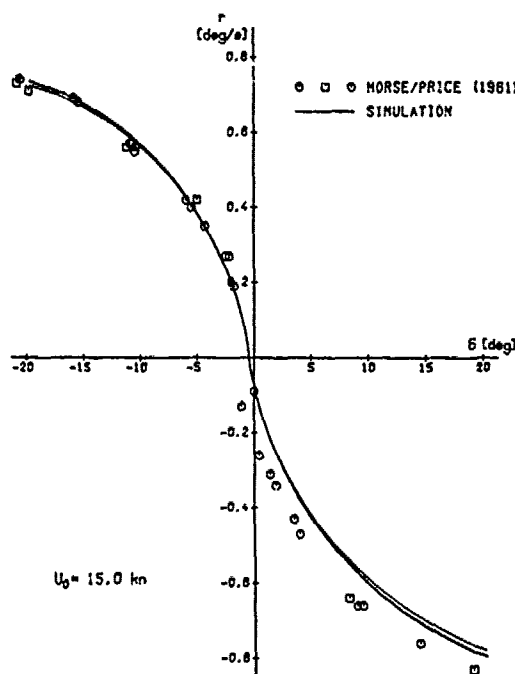


Fig. 11 Characteristic parameters of 20°/20° zigzag maneuver as functions of applied towing force F_D (model)

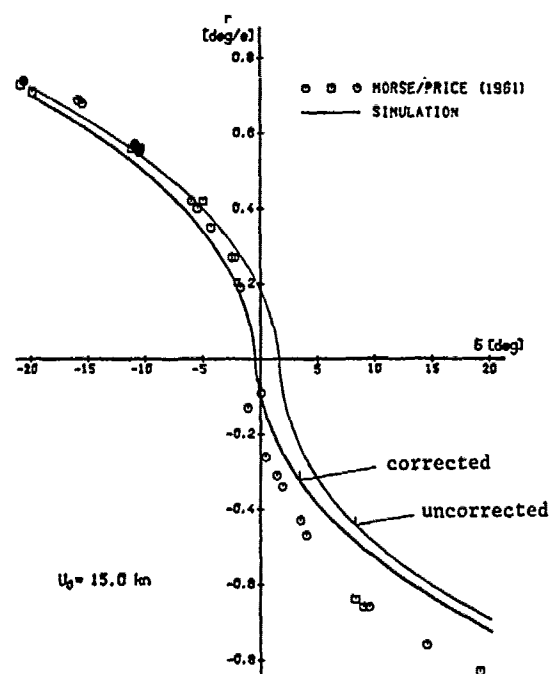


a) COEFFICIENTS FROM TABLE 5

b) COEFFICIENTS FROM TABLE 1



c) COEFFICIENTS FROM TABLE 5 (CORRECTED)



d) COEFFICIENTS FROM TABLE 3

Fig. 12 Spiral maneuver - Full-scale measurements versus computer simulations based on alternative sets of coefficients

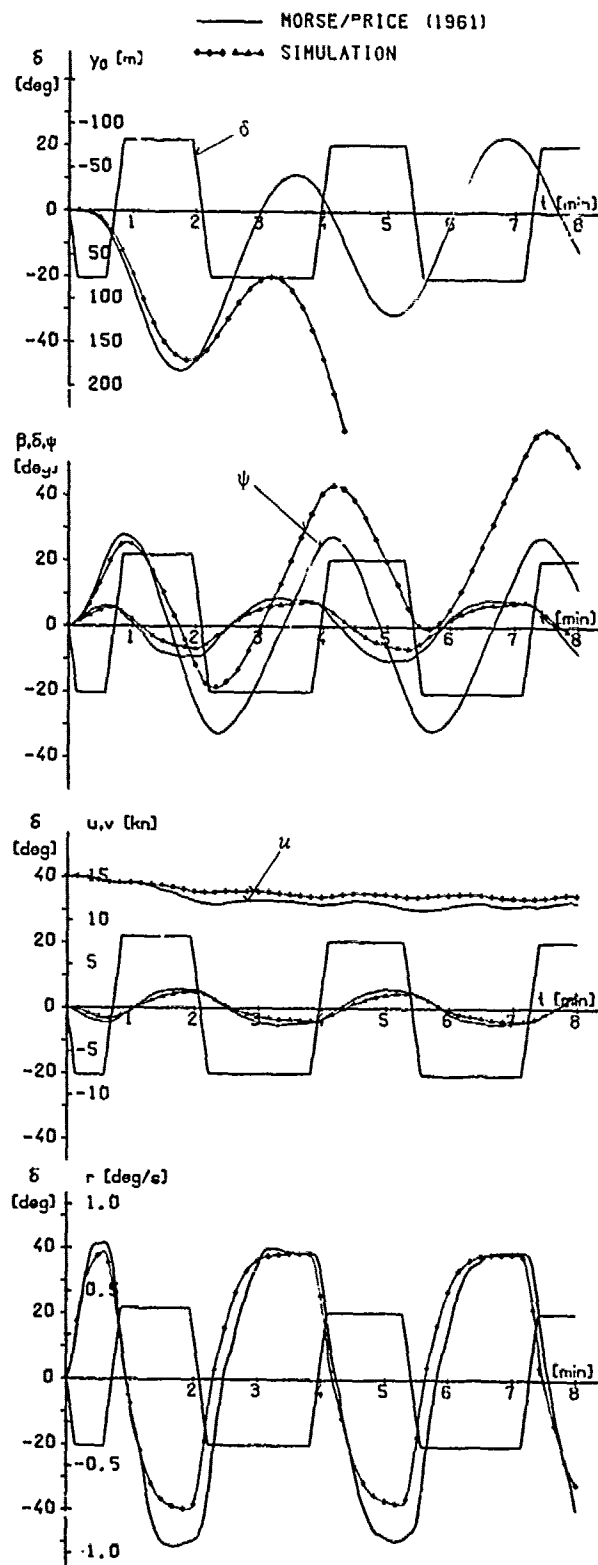


Fig. 13
20°/20° zigzag maneuver
Full-scale measurement versus computer
simulation based on Table 5 (uncorrected)

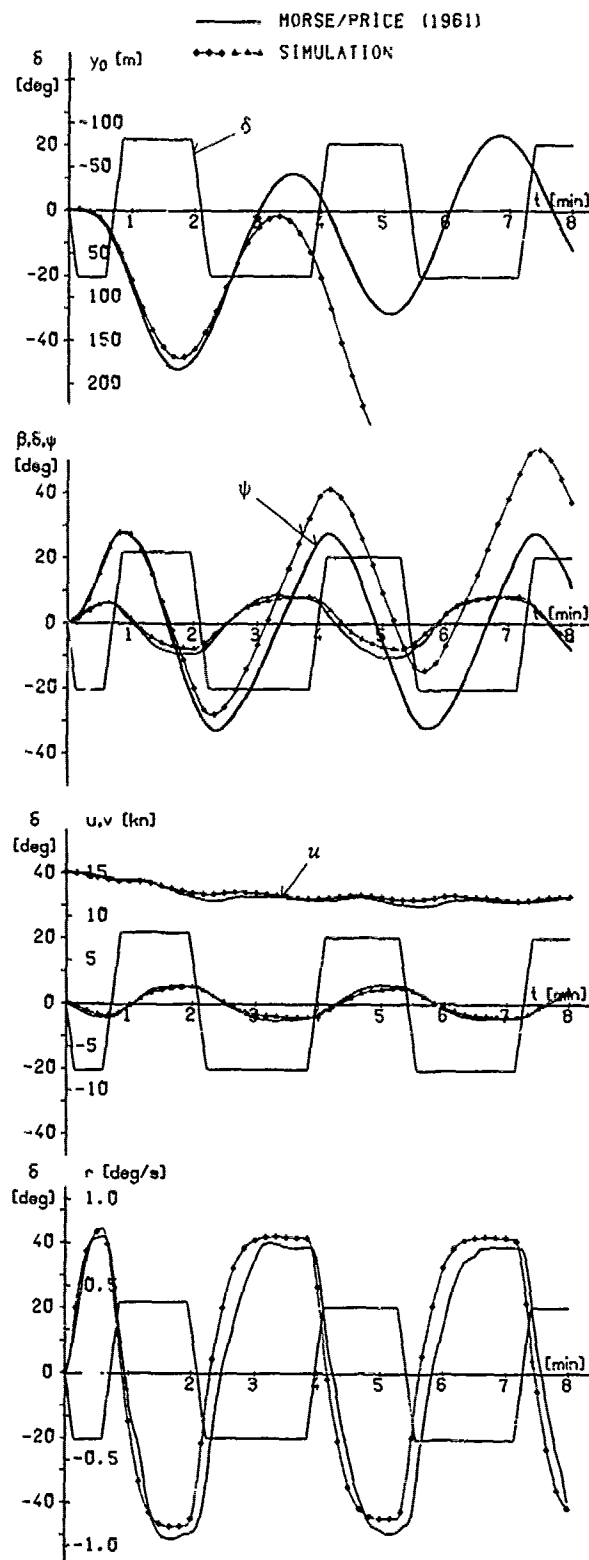


Fig. 14
20°/20° zigzag maneuver
Full-scale measurement versus computer
simulation based on Table 5 (corrected)

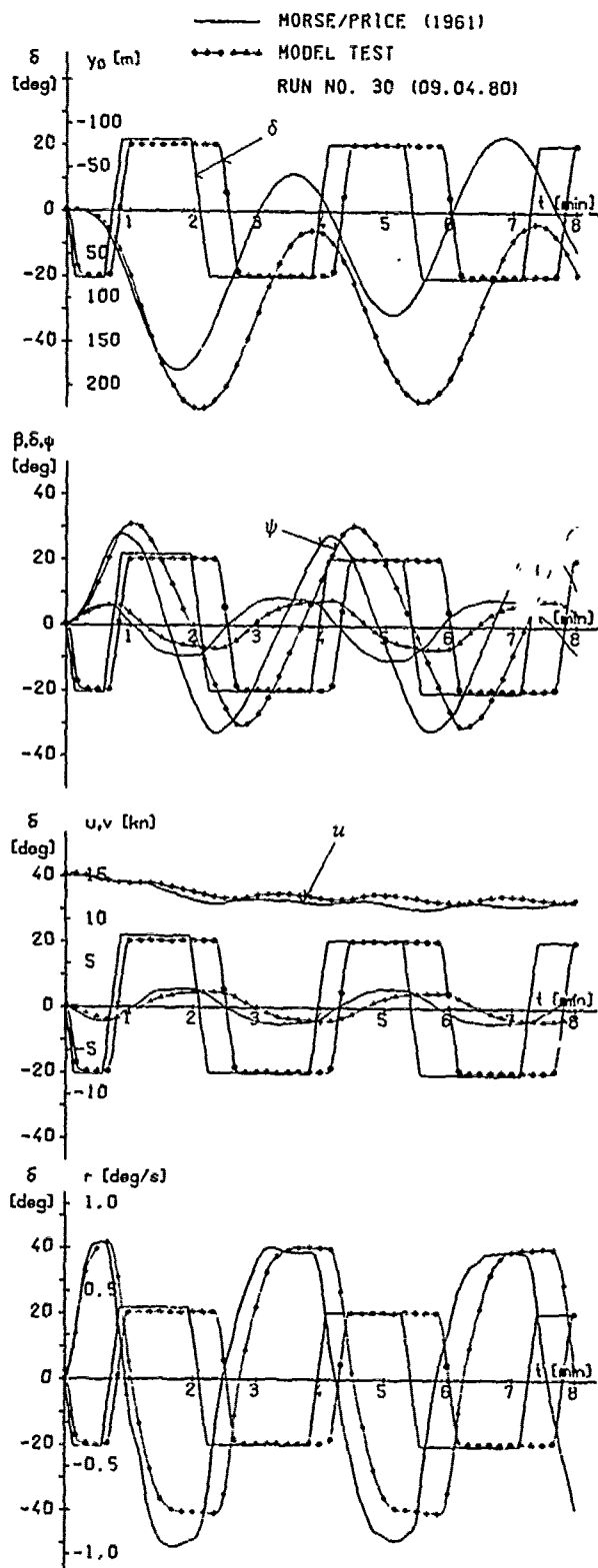


Fig. 15 20°/20° zigzag maneuver
Full-scale measurement versus model
measurement conducted at model self-
propulsion point ($n = 6.09$ Hz)

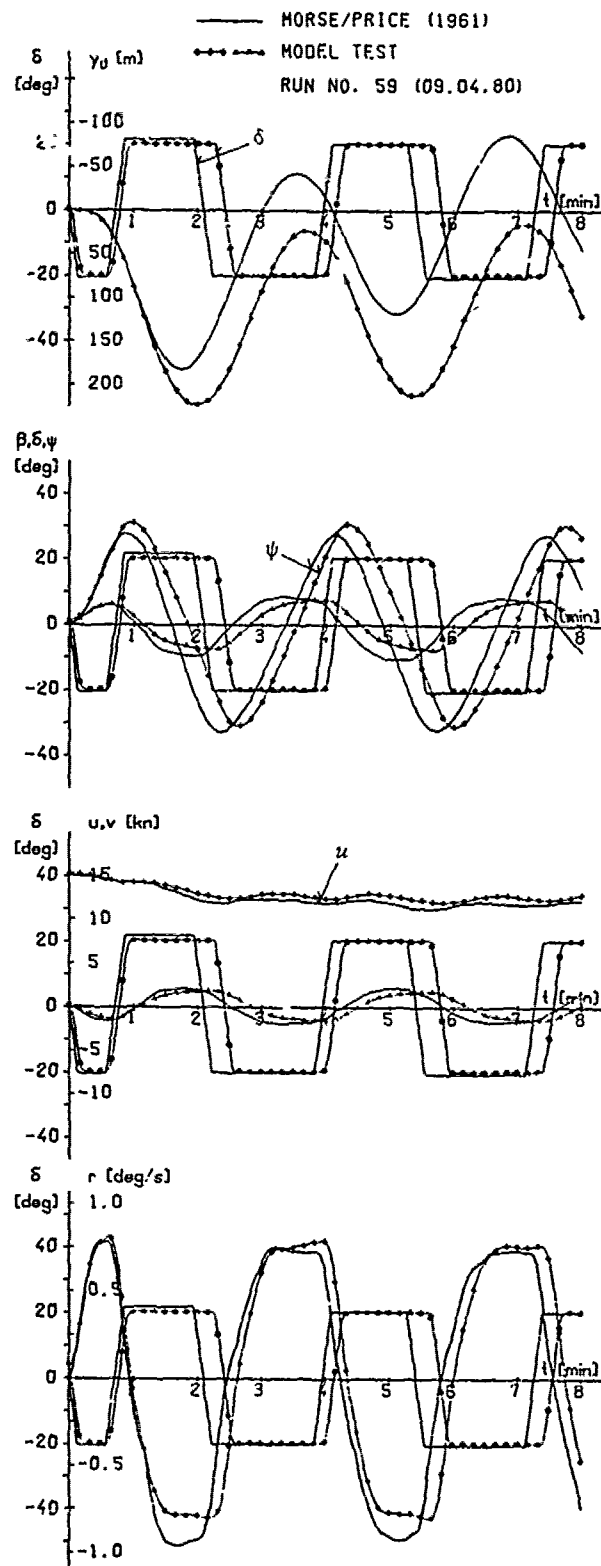


Fig. 16 20°/20° zigzag maneuver
Full-scale measurement versus model
measurement conducted with an applied
towing force $F_D = -7.85$ N ($n = 6.47$ Hz)

On the Nature of Scale Effect in Manoeuvring Tests with Full-Bodied Ship Models

Evgeny Nikolaev and Marina Lebedeva
Krylov Shipbuilding Research Institute
Leningrad, U S S R.

ABSTRACT

The paper covers the results of scale effect investigations on the basis of free-running tanker models. It also deals with the results of captive model tests carried out on the rotating arm in the Krylov Institute basin presented as a function of hydrodynamic characteristics of drift angle, radius of rotation, speed and rudder angle. The analysis of the data obtained leads to the conclusion that the scale effect occurs as a crisis of the flow around the model's hull. It is caused by the trajectory curvature inherent in the manoeuvring ship. To create a stable turbulent boundary layer separation it is suggested to use models with sand-roughened surface. The paper provides data on free-running and rotating-arm sand-roughened model tests.

NOMENCLATURE

L	- length of ship
B	- beam of ship
T	- draught of ship
W	- displacement
C _B	- block coefficient
D _B	- propeller diameter
A _R	- rudder area
V _R	- speed of ship
α _R	- rudder angle
α _D	- drift angle
R	- radius of gyration
$\bar{R} = \frac{R}{L}$	- dimensionless radius of gyration
ω	- dimensionless angular velocity
Y _R	- lateral force on the rudder
Y _S	- dimensionless lateral force on the rudder

\bar{Y}	- dimensionless lateral force on the hull
\bar{N}	- dimensionless yawing moment on the hull
$Rn = \frac{VL}{\nu}$	- Reynolds number
$Fn = \frac{V}{\sqrt{gL}}$	- Froude number
ρ	- mass density
ν	- coefficient of kinematic viscosity

1. INTRODUCTION

In the last decade scientists have been studying the scale effect in full-bodied ship model manoeuvring tests (Refs. 1 through 5). This effect is observed as a considerable discrepancy in turning test data for small and large free-running models. As a rule, ship steering and manoeuvring data based on small model tests are more optimistic than those obtained with large models.

It is essential to predict correctly manoeuvrability characteristics of full-bodied ships, since they are conducive to safety of such ships at sea. It appears important to study the causes of the scale effect and methods of reducing its influence on the ship's manoeuvrability.

The above-mentioned papers review manoeuvrability test data for ship models of various sizes as well as for full-scale ships and provide conclusive evidence of the scale effect at different rudder angles. The following assumptions of the causes of the scale effect have been put forward:

- (1) differences in the flow around models of different sizes and full-scale ships make the forces applied to the hull and the rudder a function of the model's size;

- (2) relatively greater forces on the rudder behind the propeller of smaller models (compared to those normally obtained by the scaling law) resulting from relatively higher velocities induced by their propellers account for excessive course stability of small models.

The published studies deal with some methods of reducing the scale effect, namely, the use of various fins on models to obtain at the stern a flow similar to that of a full-scale ship and, mainly, the use of large models up to 30 m in length.

Evidence of the scale effect was also obtained during model tests in the Krylov Institute basin when comparison was made between the turning test data for 2 m and 5-7 m long models. In a number of cases the comparison revealed a substantial discrepancy in values of dimensionless angular velocity at small rudder angles.

The point of this paper is to study causes of the scale effect which is made evident by full-bodied model tests carried out to estimate the steering capability of full-scale ships. So the emphasis is made on the specificity of the turning test data at small rudder angles in the so-called hysteresis loop.

2. TEST OBJECTS AND PROCEDURES

The objects of the investigations were tanker models whose hull lines are shown in Fig. 1, and schematic models with stern shapes that differ from those shown in Fig. 1 by a greater volume of the deadwood as shown in Fig. 2. To obtain turning curves, i.e. the relationship between dimensionless angular velocity at a steady ship circulation and the rudder angle, the authors of this paper tested self-propelled models in the Krylov Institute basin. The geometry of these models corresponded to the following characteristics of the ship:

length	- L - 170 m
beam	- B - 25.3 m
draught	- T - 9.5 m
displacement	- W - 31,000 ton
block coefficient	- C _B - 0.75
propeller diameter	- D _B - 6 m
rudder area	- A _R - 24.5 m ²

Steady circulation parameters were estimated by recording the model's trajectory in the "spiral" test and by recording the value of the rudder angle in the "reversed spiral" test. In the former case throughout the experiment the propeller speed was maintained constant assuring a set speed of the model on the straight course. In the "reversed spiral" tests, as well as in all captive model tests of the hull-propeller-rudder complex, the speed in circulation varied with the radius. The value of the speed was defined by the empirical formula:

$$V = V_0 \frac{\bar{R}}{\bar{R} + 1.9} \quad (1)$$

where V_0 is the speed on the straight course.

The above procedure was applied for testing four geosim tanker models 2, 4, 6 and 8 m long (Fig. 1). The test data are shown in Fig. 3, and it may be seen that the test points corresponding to 4, 6 and 8 m models lie on the same curve with the width of the hysteresis loop about 10°, while the curve with the hysteresis loop less than 5° wide corresponds to the model 2 m long. The data obtained prove that in this case as the length of the model is increased from 2 m to 4 m there occurs a considerable change in the turning curve, whereas with a further increase of the length up to 8 m no noticeable changes in the curve are observed. Such an "abrupt" change in the turning curve with a gradual increase in the length of the models had been described earlier (Ref. 1).

Further studies of the scale effect were made with tanker models having their stern shapes modified as shown in Fig. 2, with the view to obtain a turning curve with a wider hysteresis loop. It was assumed that a larger difference between test data for small and large models would help find the causes of the scale effect. The assumption has been found to be true, as seen from the results (shown in Fig. 4) of tests with 2 and 6 m long models made in accordance with Fig. 2. Here the hysteresis loop of the small model is about 10°, and that of the large model exceeds 20°.

Searching for causes of the scale effect the authors undertook model tests on the rotating arm in the circular basin of the Krylov Institute which provided data on the forces applied to the rudder and the hull of small and large models towed on circular trajectories.

3. DYNAMOMETRIC TEST DATA AND HYPOTHESIS OF THE CAUSE OF THE SCALE EFFECT

Tr: geosim models 2 and 6 m long with schematic hull lines (Fig. 2) were tested in the circular basin. The models were equipped with a propulsion device which assured a smooth change in the propeller speed, as well as with two dynamometers for measuring forces and moments applied to the hull and the rudder. The test program included measurements of the full lateral force and its moment applied to the hull of the self-propelled model with the propeller operating in the steady circulation mode and recording of the lateral force on the rudder and the lateral force and its moment on the naked hull of the model. As for the signs of the forces, the positive sign was given to the lateral force directed to the center of circulation and to the moment turning the model

to the center of circulation. The moment was measured with respect to the center of the model. All the measured values were converted to dimensionless form by being divided by the values of dynamic pressure, length and draught of the model according to the following formulas:

$$\bar{Y} = \frac{Y}{0.5\rho V^2 l T} \quad (2)$$

$$\bar{N} = \frac{N}{0.5\rho V^2 L^2 T} \quad (3)$$

The data obtained from measurements of the lateral force on the rudders of the small and large self-propelled models are shown in Fig. 5 and present the lateral force versus the rudder angle and the relative turning radius. The drift angle and the propeller speed correspond to the values of these parameters at a steady turning. Fig. 5 shows that the scale effect develops at rudder angles exceeding 10° . In the range of rudder angles $-10^\circ < \delta < +10^\circ$ embracing the zone of the hysteresis loop the values of the forces on the rudders of the two models are practically identical (in dimensionless form). In this case it was possible to rule out the force on the rudders as a cause of the scale effect in the zone of the hysteresis loop.

The results of measurements on the naked model hulls are shown in Figs. 6 and 7 and present the full lateral force and its moment versus the drift angle and the relative radius of trajectory curvature. The full lateral force on the naked hull is the algebraic sum of hydrodynamic and centrifugal forces affecting the towed model. Here of specific interest is the run of curvatures obtained for the small model. The lateral force on the hull is generally assumed to change monotonically as R increases and to approach asymptotically the meaning corresponding to $R = \infty$. In the figures shown here such pattern of curvature is observed only with the large model. The curvatures obtained from the results of the small model tests are characterized by extrema which suggest occurrence of an unsteady breakdown of the flow around the model's hull.

The study of the influence of the Reynolds number on hydrodynamic performance of the naked hull was carried out on the above-mentioned geosim tanker models. R_n ranged from 10^6 to 10^7 . The Froude number was kept constant at 0.217. The test data are given in Figs. 8 and 9. The diagrams make it clear that the shape of the curvatures obtained corresponds to the relationships typical of the unsteady boundary layer separation (Refs. 6, 7). Of the two groups of curvatures those of the lateral force exhibit the greater influence of the Reynolds number. Turning leads to some differences in these relationships as compared to those obtained in translational movement tests. Because of turning,

crisis phenomena are observed even at zero drift angle, whereas in translational movement the crisis appears only at drift angles larger than 40° . In addition, as the drift angle increases turning shifts the location of the extrema of the relationships $Y(R_n)$ towards lower values of (R_n) , while in translational movement the location of these extrema does not practically depend on the drift angle.

The test data on the lateral force and the moment applied to the hull of self-propelled models with an operating propeller are shown in Figs. 10 and 11. The rudder angle is zero. The variables are the radius of the trajectory curvature and the drift angle. Here again there is evidence of the validity of lateral force relationships obtained for the small model. The pattern of these curvatures which resemble the ones noted in the description of the naked hull test data makes it possible to affirm that the unsteady breakdown of the flow around the hull of a small model takes rise even with the propeller in operation.

A study of the hydrodynamic characteristics obtained for self-propelled models and their hull has outlined the region where the breakdown of the flow occurs. The experimental data given in this paper provide sufficient evidence showing that the region is located somewhere near the midstation section rather than at the stern counter as has been assumed so far. This can be proved by the fact that crisis phenomena are revealed mainly in lateral force relationships and have virtually no effect on curvatures of the hydrodynamic moment.

Thus the analysis of the data obtained in these tests proves the unsteady breakdown of the flow around the hull of a model to be the cause of the scale effect.

4. TEST DATA FOR SAND-ROUGHENED SURFACE MODELS

The authors of the paper have made an attempt at stabilizing the breakdown of the flow near the hull of a model through artificial turbulization of the flow. Use was made of a turbulization method convenient for model tests with variable drift angles. This method had been developed by members of the Krylov Institute for wind tunnel model tests (Ref. 7) and consists in applying an artificial roughened layer to the surface of the model.

After the surface of the small model was given a sand-roughened layer with an average size of grain of about 1.5 mm the model was tested again according to the procedure described above. The resulting test data are shown in Figs. 4, 9, 10 together with the data for smooth hull models. A comparison of the two sets of data indicates that the characteristics of the small model with the sand-roughened surface are substantially different from those for the same model before application of the sand-roughened layer and that they are virtually

identical with the characteristics of the large smooth model. This holds true both for the turning curve and the hydrodynamic performance of the hull of the self-propelled model and the naked hull. The value of the lateral force on the rudder at small angles practically did not change (Fig. 5).

This flow turbulization method was checked on other models, in particular, on the basic tanker model (Fig. 1). The test data for 2 m sand-roughened surface tanker model are shown in Figs. 3, 6, 7 and demonstrate a perfect agreement with those for large smooth models.

The sand-roughened small model was also used in an additional experiment aimed at substantiating the assumption that the zone of the boundary layer breakdown affecting the manoeuvrability performance lies in the region of the bilge along the parallel middlebody. With this end in view the zone along the port side of the model was cleaned of sand and made smooth again. The turning curve obtained for such a model is shown in Fig. 12. The dotted lines are the turning curves of smooth models. It is obvious that the curves for the starboard and port side turnings differ considerably. In the port side turning test when the zone external to the center of circulation was smooth the turning curve for the sand-roughened surface model practically coincided with that for the small smooth model. During the starboard turning tests when the bilge of the external side was roughened the curve for the small model with the sand-roughened surface was identical to that for the large smooth model. The data obtained in the additional experiment make it possible to assert that the zone of breakdown of the unsteady flow lies in the region of the bilge of the side external to the center of circulation.

5. CONCLUSIONS

- (1) The cause of the scale effect in turning model tests of full-bodied ships is a change in the hydrodynamic force on the hull of the model which takes rise as the size of the model is varied. The change has a crisis nature characteristic of unsteady breakdown of the flow.
- (2) Of decisive importance for the occurrence of the unsteady breakdown of the flow during manoeuvrability tests is the circulation of the model.
- (3) The zone of the flow breakdown lies in the region of the bilge of the side external to the center of circulation.
- (4) Use of models with sand-roughened surface is an effective method of stabilizing the flow breakdown around the model. It helps prevent the scale effect when small models are used to estimate the manoeuvrability of full-bodied ships.

REFERENCES

1. Okamoto, H., Tamai, H., and Oniki, H., "Correlation Studies of Manoeuvrability of Full Ships", Proceedings of the 13th ITTC, 1972, pp.227-233.
2. Okamoto, H., Tamai, H., and Oniki, H., "Some Experimental Studies of Manoeuvrability of Ships", Proceedings of the 14th ITTC, 1975, pp.591-605.
3. Nomoto, K., and Fujii, H., "Studies of Model-Ship Correlation in Manoeuvrability by Use of Large Size Free-Running Models", Proceedings of the 14th ITTC, 1975, pp.375-378.
4. Tagano, H., and Asai, Sh., "On the Unusual Phenomena in Manoeuvring Motions of a Full Ship Model", Mitsubishi Technical Bulletin, No. 116, 1976.
5. Sato, S., and Nakamura, I., "Some Conspect for UICC with Small I/B Ratio", Selected papers from the Journal of Society of Naval Architects of Japan, Vol.12, 1974.
6. Treshchevsky, V. N., Volkov, L. D., and Korotkin, A. I., "Aerodynamic Experiment in Shipbuilding", Sudostroenie, Leningrad, 1976, pp.89-102 (in Russian).
7. Treshchevsky, V. N., and Korotkin, A. I., "Some Characteristics of the Flow around Ships at Different Drift Angles in Shallow Water", Proceedings of the 11th Symposium on Naval Hydrodynamics, 1976, pp.693-703.
8. Nikolaev, E. P., and Lebedeva, M.P., "On the Scale Effect in Ship Model Manoeuvring Tests", 16th ITTC Newsletter, No.1, Oct. 1979.

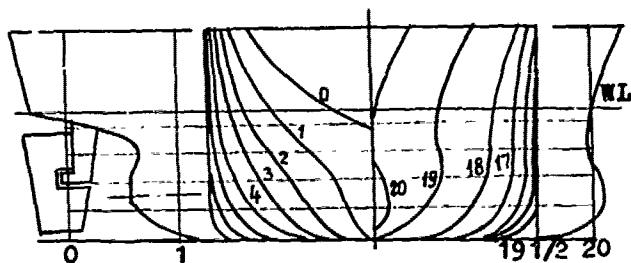


Fig. 1 - Hull Lines of Tanker

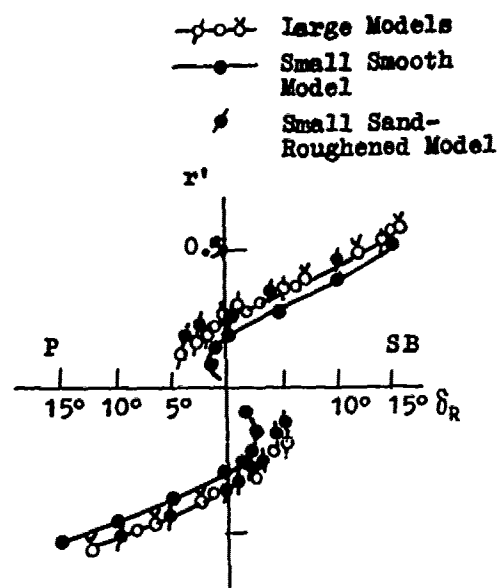


Fig. 3 - Comparison of Turning Curves of Geosim Tanker Models

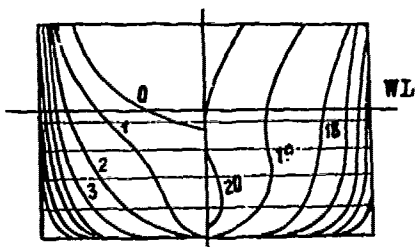


Fig. 2 - Hull Lines of Model with an Increased Width of Deadwood

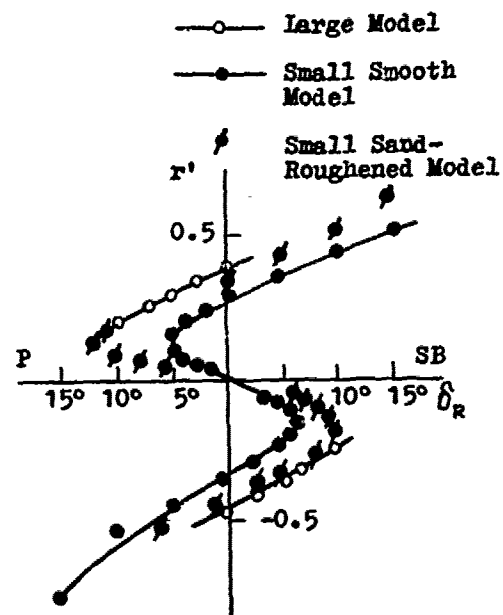


Fig. 4 - Comparison of Turning Curves of Models with an Increased Width of Deadwood

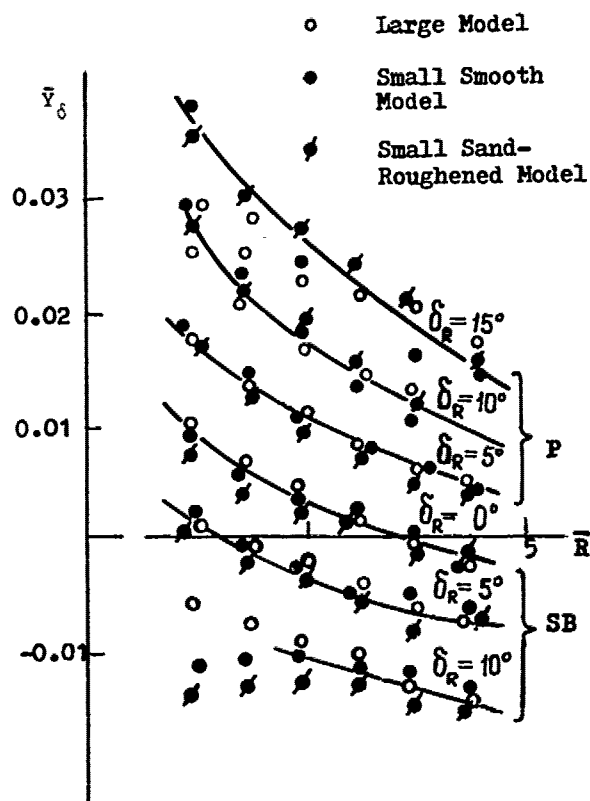


Fig. 5 - Comparison of lateral forces on models' rudders (Starboard Circulation)

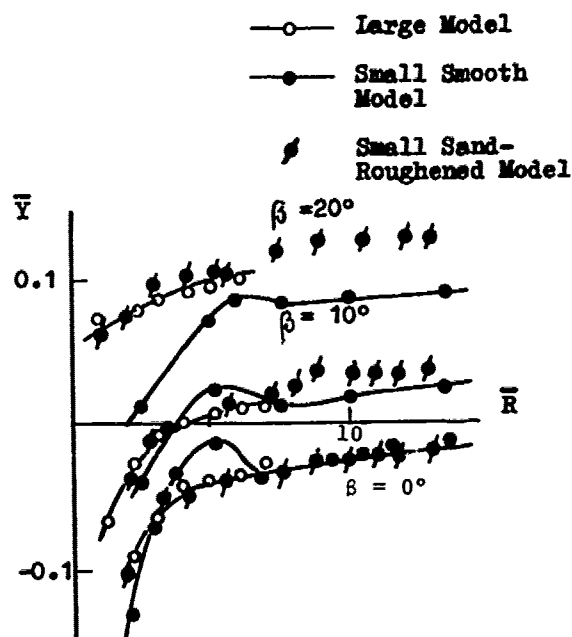


Fig. 6 - Full lateral force on model's naked hull

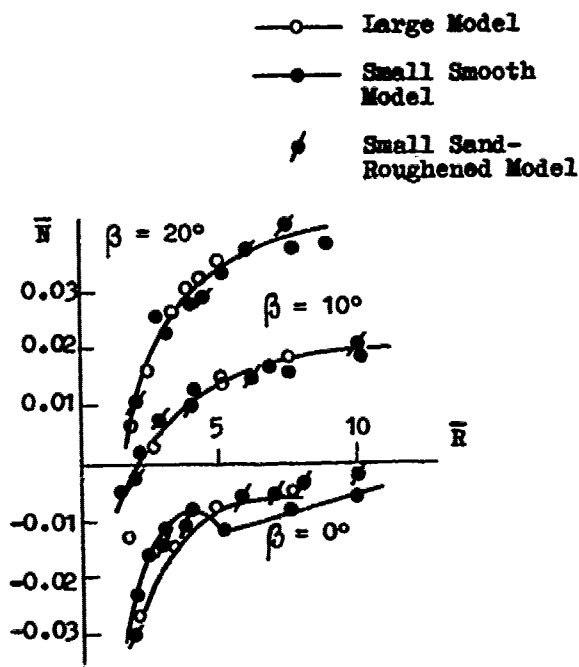


Fig. 7 - Moment on model's naked hull

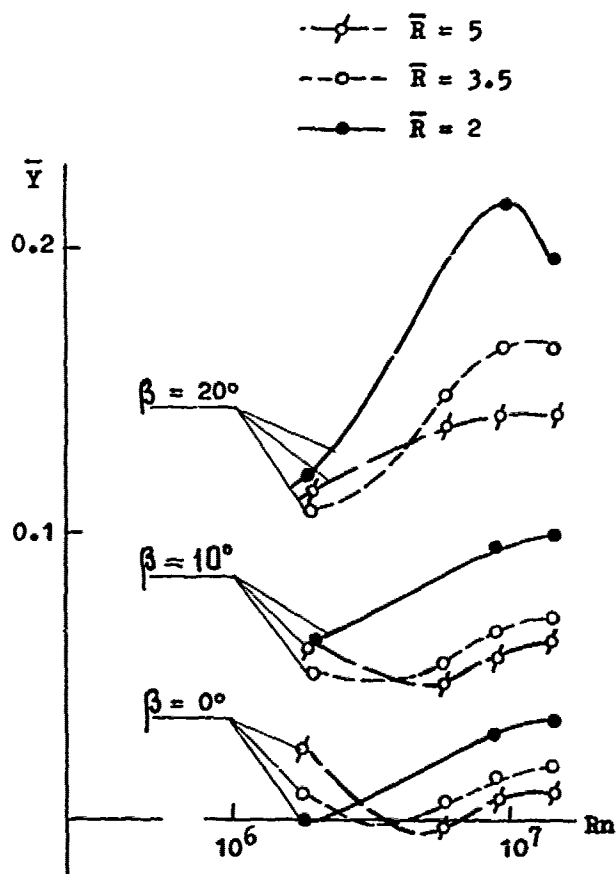


Fig. 8 - Influence of R_n on Hydrodynamic Force on Model's Naked Hull

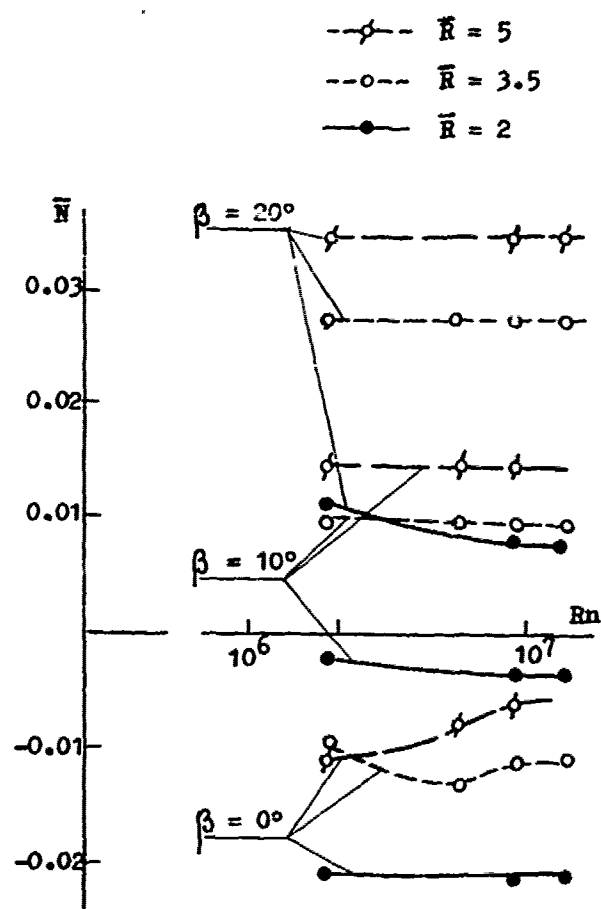


Fig. 9 - Influence of R_n on Hydrodynamic Moment on Model's Naked Hull

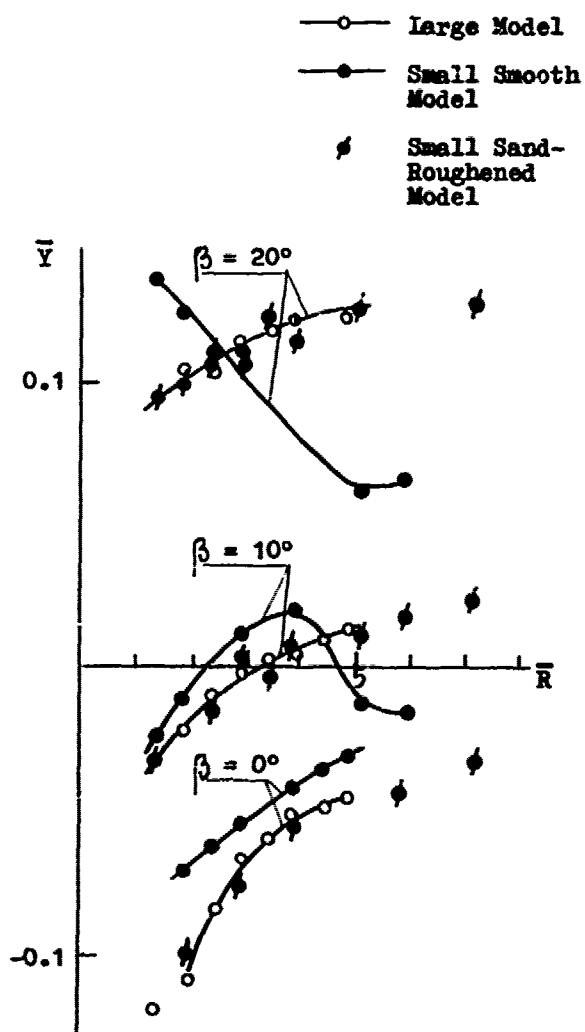


Fig. 10 - Full Lateral Force on Self-Propelled Model's Hull (Starboard Circulation)

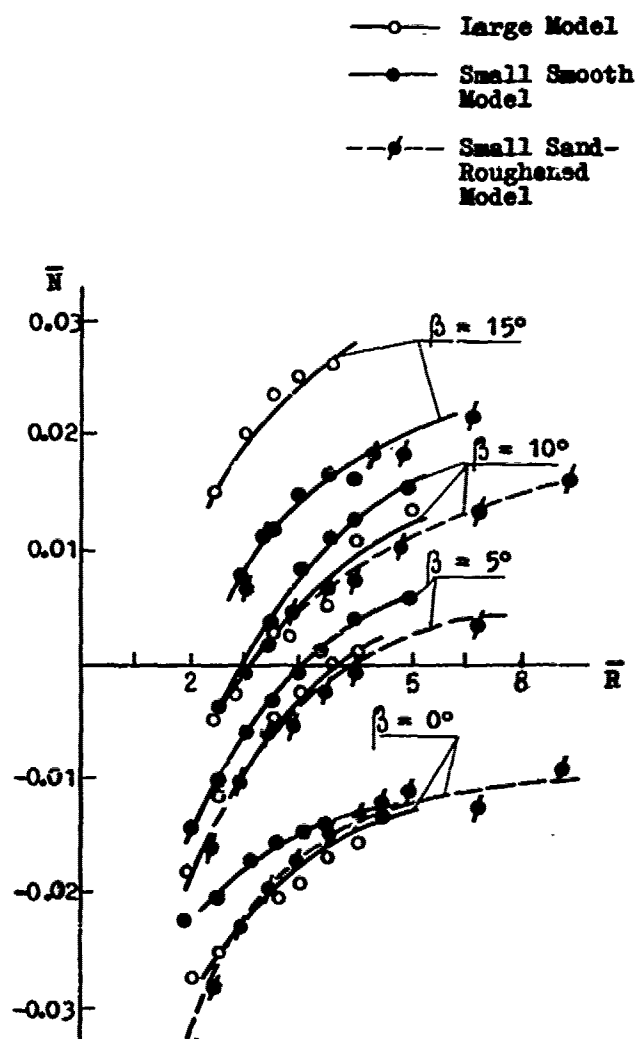


Fig. 11 - Moment on Self-Propelled Model's Hull (Starboard Circulation)

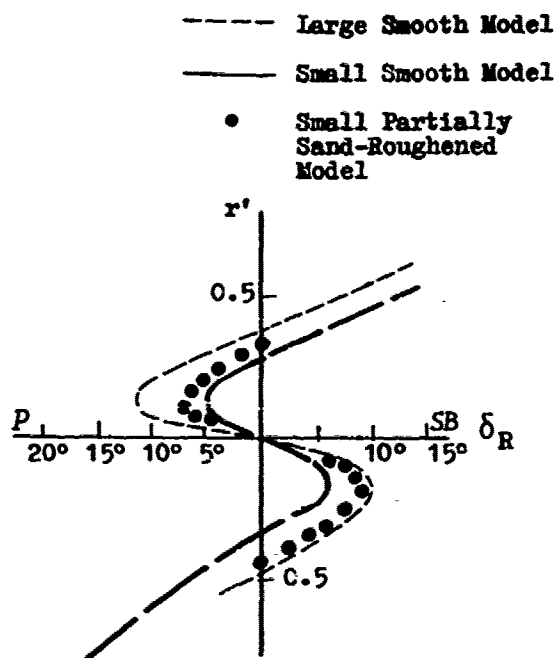


Fig. 12 - Turning Curve of Partially Sand-Roughened Model

Discussion

M. Fujino (Univ of Tokyo)

The authors should be congratulated for presenting the very interesting results of experiments the purpose of which is to enable one to predict the manoeuvring characteristics of a full-scale ship from the results of test with a small model. Out of many illustrations, I am interested in figures 6, 7, 10, and 11 which show the hydrodynamic force and moment on the naked and the self-propelled models. The hydrodynamic lateral force, for example, on the self-propelled model is considered as the algebraic sum of three dominant components; the hydrodynamic lateral force on the naked hull, the lateral force on the rudder behind the main hull and the propeller, and the hydrodynamic lateral force on the main hull induced by the presence of rudder. Needless to say, most part of the hydrodynamic lateral force on the self-propelled model is the hydrodynamic force on the naked hull as clearly understood by comparing the lateral force of the large model shown in Fig. 6 with that shown in Fig. 10.

On the contrary, comparing the lateral force on the small smooth model shown in Fig. 6 with that shown in Fig. 10, it is found that the hydrodynamic lateral force on the small smooth model remarkably differs from each other qualitatively as well as quantitatively according to whether the model is naked or self-propelled. What is the cause of this great discrepancy? Moreover, I wish to know how the presence of the rudder and the propeller affects the flow pattern, especially the breakdown phenomenon of the flow, around the main hull because the model of 2 m in length is one of the standard model sizes of our sea-keeping and manoeuvring basin of University of Tokyo.

K. Nomoto (Osaka Univ)

I would like to congratulate the authors for their most interesting finding on manoeuvrability scale effect.

At the same time there are many data indicating that the different rudder effectiveness between models and actual ships is a substantial source of manoeuvrability scale effect. For single-screw ships, model rudder is normally more effective than ship's because of stronger propeller slip stream. This effect is sometimes cancelled by heavy wake of full-bodied models, however.

In this connexion I would like to ask a question. Do the authors consider their roughened model technique useful also for fine hull forms, for example, destroyers and container ships?

H. Tamai (Akashi Ship Model Basin)

By using sand-roughened surface models, the authors have shown the favorable results as for the scale effect. I would like to congratulate the authors for their interesting work.

In the present case, the average grain size for surface-roughening was described to be abt. 1.5mm, I would like to know how to determine the grain size.

The sand-roughened surface would increase the propeller slip ratio in a free running model and result in the relatively larger rudder force in comparing with that of large smooth models. That may cause some unfavorable effect on the stability index (T) derived from the dynamic model test like the zig-zag test. From this view point, I suppose that the area for sand-roughening should be limited only to the necessary zone.

In manoeuvrability tests by models of blunt hull form, abnormally stable characteristics are sometimes obtained. Previously, Prof. Nomoto confirmed, by flow survey, the unusual flow like separation of boundary layer at the stern of the outside of turning circle and explained that this unusual flow pattern is the cause of the abnormally stable characteristics (11th ITTC). The unsteady flow, described as the cause of the scale effect, in the present paper and the flow survey result by Prof. Nomoto seem to have a common feature except for their occurrence zone. I feel deep interest in using the sand-roughened surface for blunt hull form model which clearly has the abnormally stable characteristics in case of smooth surface.

Author's Reply

E. Nikolaev (KSRI)

1. I thank very much Professor M. Fujino for his very interesting and valuable discussions. He has raised two questions.

The hydrodynamic lateral forces on the self propelled small smooth model differ indeed quantitatively and qualitatively. It might be explained by the fact that unsteady breakdown of the flow occurs in both cases. Presence of a working propeller and rudder changes the flow pattern, which is reflected in Figs. 6 and 10, but does not change the principal feature of the flow, namely unsteady character of the breakdown. Taking this in view we made an attempt to stabilize the breakdown of the flow of self-propelled small model by means of sand-

roughness. The result was rather sufficient as it might be seen from Figs. 6 and 10. There is satisfactory agreement between the characteristics of large smooth model and small sand-roughened model in both cases: for bare and self-propelled hulls.

2. Now I have the pleasure to express my gratitude to Mr. H. Tamai for his very interesting discussions concerning the important questions of principal character that he has raised.

Sand-roughened surface really might influence an exaggerated rudder force. To check this we carried out force measurements on the models' rudders. We find that this influence is insufficient in the rudder helm range of $\pm 10^\circ$, i.e. in the range embracing the hysteresis loop. Some exaggerating of the rudder force on the sand-roughened model was found at larger rudder angles. This might lead to some error in estimation of the tactical diameter and may cause an unfavourable effect on the zig-zag test results too, if the rudder angles are too large. It seems to me that such a test is hardly appropriate for the purposes of evaluating of stability characteristics due to strong non-linearities inherent to a full-bodied model.

The proposal to test partially sand-roughened models seems to be attractive if one takes into account results shown in Fig. 11. It's a pity we can't define the necessary and sufficient zone.

I value very highly the results obtained by Japanese Colleagues in the field of manoeuvrability scale effect. Especially interesting results were reported by Prof. K. Nomoto. Phenomenon observed by Prof. K. Nomoto and the one described in the present paper are not similar in one more respect besides the place of breakdown zone. From my viewpoint in the case described by Prof. K. Nomoto, there was a stable break-

down of the boundary layer that generated a strong flow behind the model which improved her course stability. Here we deal with unstable breakdown of the flow on the hull of a small model. Stabilization of the breakdown by means of sand-roughness makes small blunt models more unstable. This is similar to large models with respect to dynamic stability characteristics. If I was right in suggestion that, in case of abnormally stable characteristics, the breakdown of the flow on the blunt model was stable, then I would hardly expect any positive result due to sand-roughening such a model.

And one more question concerning the grain size measurement. We used for this purpose a micrometer.

I am very pleased by the fact that Professor K. Nomoto, one of the first investigators of the manoeuvrability scale effect, has paid attention to our paper. He has raised the important question if the sand-roughened model method is applicable for slim-bodied models. In my opinion this method might be effective in cases of unsteady breakdown of the boundary layer which behaviour strongly depends on the size of the model in a manner characteristic to crossflow breakdown around a blunt body. That occurs when we deal with full-bodied models. I am not very optimistic regarding the extrapolating of the method to fine hull forms.

Finally I would like to thank once again Prof. M. Fujino, Mr. H. Tamai and Prof. K. Nomoto for their discussions and to express my gratitude to the Japanese Colleagues who have carried out so many original and important investigations in the field of manoeuvrability scale effect and who provoked in a way the presented paper.

Session VIII

WAVE ENERGY

Chairman

T. Francis Ogilvie

Department of Naval Architecture and Marine Engineering

University of Michigan

Ann Arbor, Michigan, U.S.A.

Wave Power, The Primary Interface

Brian M. Count

Marchwood Engineering Laboratories

UK Central Electricity Generating Board

Edward R. Jefferys

University College, London

United Kingdom

ABSTRACT

Analysis of Wave Energy devices based entirely upon linear hydrodynamic theory demonstrates that all shapes are potentially equivalent in their ability to absorb energy from water waves. Therefore, the main feature with which one concept may be separated from another will be their engineering characteristics that determine the feasibility of obtaining high capture efficiencies.

In this paper a survey of the hydrodynamic properties of various device types is given and experimental evidence is produced to confirm the validity of linearised theory.

NOMENCLATURE

- A Incident Wave Amplitude
- B Hydrostatic Spring Matrix
- C General form of Power Take-off Control Matrix
- D Damping Matrix
- F₀ Wave Exciting Force
- I_M (M x M) Unit Matrix
- K Wave Number
- M(ω) Added Mass Matrix
- N(ω) Added Damping Matrix
- P⁺, P⁻ Upstream and Downstream radiation Potential Amplitudes
- P_w Incident Wave Power per unit width of frontage
- X Vector of displacements
- g Gravitational acceleration
- λ Wavelength
- ρ Density of Water
- ω Angular Frequency

1. INTRODUCTION

The concept of harnessing Ocean Wave power has captured the imagination of

inventors for many years and there are numerous suggestions for wave power devices, which are claimed to convert wave energy to some other form - mechanical, hydraulic or pneumatic - economically. More serious studies have recently been undertaken in the United Kingdom, Norway, Japan, Sweden and the U.S.A. to determine the technical and economic feasibility of exploiting this energy resource.

In the United Kingdom the studies have been disappointing in their predictions for the likely cost of a feasible system although possible improvements are recognised. However, a single device has not been identified upon which research effort can be concentrated in spite of a general desire to select one. The choice of a preferred system involves many different objectives with consideration of all aspects of the problem from the waves themselves to the energy consumer. In order to select a favoured, rational design a thorough understanding of the interaction of waves and devices will be required since this determines the design of the remainder of the system. Therefore, in this paper the problems and nature of this primary interface will be examined based entirely upon linear wave theory which may at first sight appear restricting but will be shown to describe many interesting characteristics that have been experimentally confirmed.

Historically, studies on the primary interface to the waves were based on two dimensional theory and supporting experimental work confined to narrow wave flumes. In both cases devices of infinite width are being simulated and this has led to a large number of devices that are designed to align themselves perpendicular to the prevailing wave direction. These types of devices are commonly known as terminators. The

early experimental work was particularly important since the extremely high conversion efficiencies measured were previously not thought likely and the analytical calculations subsequently correlated well with these tests, demonstrating the validity of linearised hydrodynamic theory.

Only recently has there been an increased interest in three dimensional behaviour of devices. This has been simulated by three new concepts being studied separately in Britain, Norway and Japan. The Japanese, Kaimei,⁽¹⁾ a ship shaped device has been tested at full scale. The Point Absorber of Budal and Falnes⁽²⁾ has attracted a great deal of attention particularly by its ability to absorb energy extremely effectively in a linear array and in Britain an invention by Professor French⁽³⁾ is being investigated. The latter is a long thin beam with bags mounted on it which enclose pressurised air. In common with Kaimei, its alignment is at right angles to the wave fronts and these devices are generically known as attenuators.

In this paper both two and three dimensional hydrodynamic theory will be used to investigate the performance of various wave power devices. Particular emphasis is given to the theory of optimal control which determines the upper limit on performance. In considering the primary interface, the first stage of power conversion cannot be neglected and a section is devoted to developing a time domain model of hydrodynamics which is used to solve a novel, nonlinear, control system proposed by Budal and Falnes.

2. OPTIMAL CONTROL

Consider any wave power device, or array of devices, with N independent degrees of freedom which can be described by the equation of motion

$$I\ddot{x} + B\dot{x} = f^w(t) + f^{ext}(t) \quad (1)$$

where I is the inertia matrix of the system, B the linearised hydrostatic spring, $f^w(t)$ is a vector of wave induced forces, $f^{ext}(t)$ are externally applied forces and x is a vector of displacements. In general the wave forces are expressed as

$$f^w(t) = f_o(t) - M(\omega)\ddot{x} - N(\omega)\dot{x}$$

where $f_o(t)$ is the wave induced force on a stationary device and $M(\omega)$ and $N(\omega)$ are the added mass and damping matrices respectively whose elements are frequency dependent. Strictly this representation is only valid for steady harmonic oscillations at angular frequency ω but since the hydrodynamic equations have been linearised, then for optimal power extraction the motion must be harmonic and therefore this restriction is not limiting.

Rearranging equation (1) and considering the case of harmonic oscillations where

$$x(t) = X(\omega)e^{i\omega t},$$

and

$$f_o(t) = F_o(\omega)e^{i\omega t}$$

gives an equation

$$GX = F_o + f^{ext}(t)$$

where

$$i\omega G = B - \omega^2[I + M(\omega)] + i\omega N(\omega)$$

Suppose that it is possible to control the motion through the external forces in M modes of motion ($M \leq N$) such that

$$f^{ext}(t) = -RCR^T X$$

where R is an $(N \times M)$ matrix whose columns are unit vectors in the direction of the modes of motion that are under control. The displacements are then given by

$$X = [G + RCR^T]^{-1} F_o$$

and the absorbed power is

$$\frac{1}{2} \omega^2 \text{Re} [\bar{X}^T RCR^T X]$$

where the overbar denotes the complex conjugate and T the matrix transpose.

Substituting for X , gives the power as

$$\frac{1}{4} \omega^2 F_o^T \left[[\bar{G} + R\bar{C}R^T]^{-1} \right]^T R(C + \bar{C})R^T [G + RCR^T]^{-1} F_o$$

and maximising this expression with respect to the elements of the matrix C gives a condition.

$$RI_M R^T = R(C + \bar{C})R^T (G + RCR^T)^{-1} RI_M R^T$$

where I_M is an $(M \times M)$ unit matrix.

To solve this equation for C , it is convenient to partition the $(N \times N)$ matrices so that in matrix notation we have

$$\begin{bmatrix} 0 & 0 \\ 0 & I_M \end{bmatrix} = \begin{bmatrix} 0 & 0 \\ 0 & C + \bar{C} \end{bmatrix} \begin{bmatrix} \alpha & \beta \\ \gamma & \delta \end{bmatrix} \begin{bmatrix} 0 & 0 \\ 0 & I_M \end{bmatrix}$$

where α , β , γ and δ are the partition elements of $(G + RCR^T)^{-1}$. This gives a relation

$$I_M = (C + \bar{C}) \delta$$

and it can be shown that

$$\delta^{-1} = [R^T G^{-1} R]^{-1} + C$$

giving the optimum controller as

$$C = [R^T G^{-1} R]^{-1} - \delta^{-1}$$

It should be noted that this result assumes that δ^{-1} exists and in some cases this is not true.

The most important feature of this analysis is that the efficiency of wave energy absorption is crucially affected by the form of the external forces and in many cases there is a unique characteristic which achieves optimum conditions. Therefore in any analysis of the primary interface it is important to consider both the

wave/device interaction together with the characteristics of the first stage of power conversion whose function is primarily to provide the correct 'resistance' to the waves to enable effective absorption.

If power is extracted from all degrees of freedom, then $M=N'$, and

$$C = \bar{G},$$

to give

$$\dot{X} = \frac{1}{2} [N(\omega)]^{-1} F_0$$

and the absorbed power is

$$\frac{1}{8} \bar{F}_0^T [N(\omega)]^{-1} F_0 \quad (2)$$

since the added damping matrix is symmetric. The results of this section are generally applicable to both two and three dimensional theory.

3. TWO DIMENSIONAL THEORY

3.1 Maximum Efficiencies

Considering in the first instance the simple case where $N=M=1$, the maximum wave power that can be absorbed is given by equation (2) where all the terms are now scalars. Some simple identities can be derived in two dimensions (Newman(4)) in terms of the upstream and downstream radiation potential amplitudes, P^+ and P^- , derived by considering unit forced oscillations of the device in otherwise calm fluid. Newman has shown that

$$N(\omega) = \frac{1}{2} \rho \omega \left[|P^+|^2 + |P^-|^2 \right] \quad (3)$$

and

$$F_0(\omega) = \rho g A P^+ \quad (4)$$

where A is the amplitude of the incident wave. Therefore normalising the absorbed power per unit width to the corresponding incident wave power, P_w , where

$$P_w = \frac{1}{4\omega} \rho g A^2$$

gives a maximum efficiency of

$$\frac{|P^+|^2}{|P^+|^2 + |P^-|^2}$$

This has been derived by a number of authors (e.g. Evans(5)) and demonstrates that the ability to generate waves in a single preferred direction is advantageous for high efficiency.

Moreover, if N is greater than unity equations (3) and (4) can be generalised as

$$[N(\omega)]_{mn} = \frac{1}{2} \rho \omega \left[\bar{P}_m^+ (P_n^+)^T + \bar{P}_m^- (P_n^-)^T \right]$$

for $m, n = 1, 2, \dots, N$, and

$$F_0^m = \rho g A P_m^+$$

where now the added damping is a matrix and the potential amplitudes constitute a vector corresponding to forced oscillations

in each separate mode of motion. Using expression (2) for the maximum absorption, gives an efficiency of 100% for $N=M=2$, provided that

$$P_1^- P_2^+ + P_1^+ P_2^-$$

This latter condition ensures that both modes are not entirely symmetric ($P_m^+ = P_m^-$) or asymmetric ($P_m^+ = -P_m^-$).

If this analysis is extended any further to cases involving more than two modes of motion which are all controlled, then the expression for the maximum absorption given by equation (2) is invalid since the added damping matrix is singular. This can be observed from the general form given above which is a sum of two rank one dyadic forms and therefore the rank of the matrix can be no greater than 2. Such a result is not surprising since control in two modes has been shown to enable 100% efficiency and it is not possible to do any better!

From the above analysis it can be deduced that for any device, described by two dimensional theory, 100% capture efficiency can be obtained through control in two modes of motion only. Even in the case where $N>M$, the optimal controller given in Section 2 will ensure 100% efficiency provided $M=2$. This result has been confirmed experimentally by Evans(3) who tested an immersed cylinder controlled in both translational modes of motion (heave and sway) to ensure perfect wave absorption.

3.2 Non-Optimum Operation

The optimal controller derived in Section 2 necessarily incorporates a substantial reactive component whereas most experimental work has concentrated on simple resistive loads. Referring to equation (1), the case of

$$f^{\text{ext}}(t) = -D\dot{X},$$

gives a harmonic solution whose amplitude can be determined from equation (1). The absorbed power in this case can be calculated as

$$\frac{1}{2} \text{Re} \left[\omega^2 \bar{X}^T D X \right]$$

and to evaluate this it is necessary to determine the hydrodynamic added mass and damping matrices and the exciting forces by solving the fluid dynamic equations. This is achieved in two dimensions by approximating the device cross section as a polygon and placing a point source of waves at the centre of each line element. These are given strengths which are chosen to satisfy the prescribed boundary conditions on the body surface.

Calculations for the Salter Duck(6) operating in a single degree of freedom (roll motions only) agreed very well with experiment and in Figures 1(a) and (b) results are shown for the performance and translational forces that were monitored during these tests.

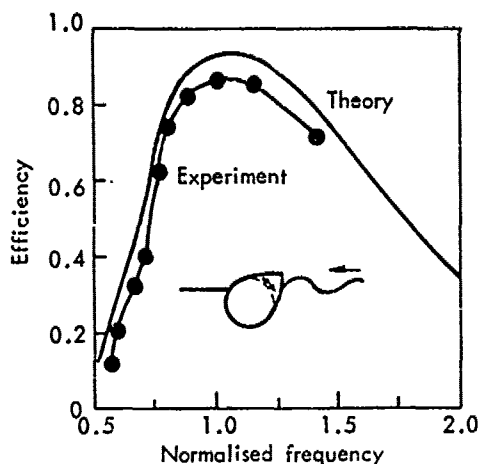


Figure 1(a). The Performance of a Salter Duck - Theory and Experiment.

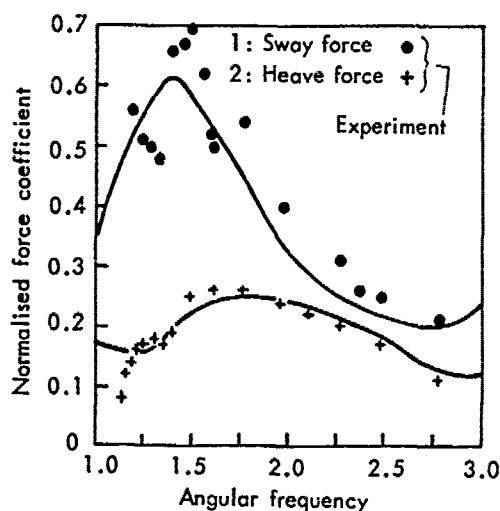


Figure 1(b). Vertical and Horizontal forces measured on a Salter Duck.

Further results in two dimensions were more satisfying since the analytical work preceded the experimental results. The two devices considered are very similar, the first being the Cockerell Raft which was originally conceived as a large number of hinged floats that articulate in response to the waves. The engineering problems associated with each hinge created difficulties and theory demonstrated that a single hinged system with a fixed rear float would be as effective as, say, a duck and this was subsequently confirmed experimentally. (see Figure 2).

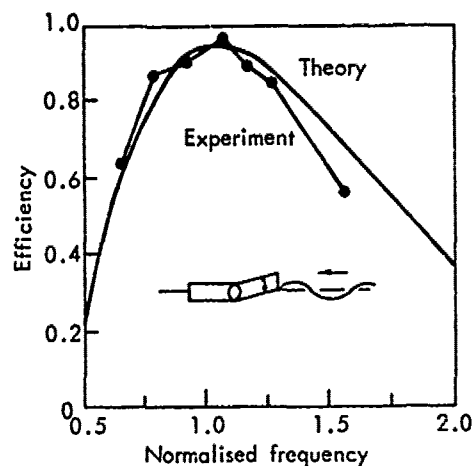


Figure 2. The Performance of a Raft Pair - Theory and Experiment.

The second device has been conceived through the desire to utilise air as a transfer medium between the wave and the mechanical power extraction system. A device that is simply a shallow draught section with an enclosed water column in its front section has been shown to work efficiently and results are given in Figure 3.

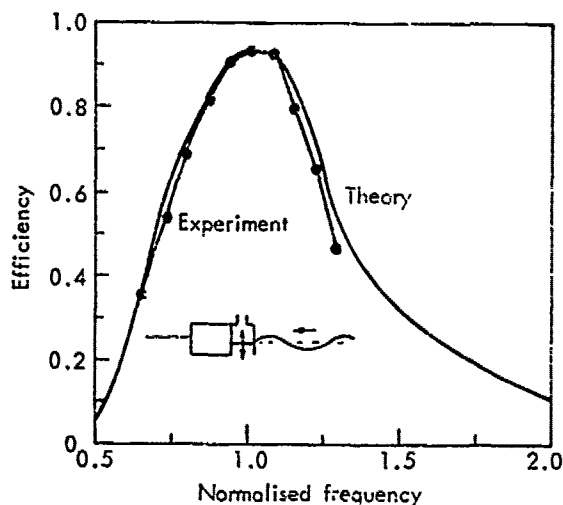


Figure 3. The Performance of an Oscillating Water Column - Theory and Experiment.

It is important to note that all of these devices are designed to operate in a single mode of motion and therefore are effective unidirectional wave generators

when driven in reverse. They have also been designed to ensure that the frequency of peak efficiency coincides with the prevailing wave frequency.

3.3 Practical Problems

A major problem with these devices has been to restrict the translational (heave and surge) motions in a floating system since calculations demonstrate that if no restraint is applied to these modes then in plane waves the performance is significantly reduced. Salter, however, has suggested that such devices should be mounted on a long common element, called a spine, which will be stabilised by virtue of the phase cancellation of the wave forces along its length due to the directional spread of ocean waves. Moreover, it is suggested that if by either a wise choice of material, or controlled joints along this spine and the appropriate translational spring stiffnesses achieved it is possible to improve upon the performance of the device operating in a single degree of freedom. It would appear that all floating terminators operating in a single degree of freedom therefore require a spine of some form in order that a compact structure can be efficient.

Evans, on the other hand, whilst still using a device that is a good wave generator, has produced a simpler structure which needs control in two modes of motion. Therefore, there appears to be an interchange between civil and mechanical engineering complexity and it is not clear which route is preferable. In both cases the ability to simulate reactive power take-off has the effect of reducing the size of the structure although the mechanical achievement of such control may well be extremely difficult.

4. THREE DIMENSIONAL THEORY

4.1.1 Single Absorbers

In three dimensions there is again a simple relation between the added damping coefficients and the wave exciting forces such that

$$[N(\omega)]_{mn} = \frac{1}{8\lambda P_w} \int_0^{2\pi} F_o^m(\theta) [\bar{F}_o^n(\theta)]^T d\theta$$

where the $F_o^m(\theta)$ is the force on a fixed body due to a wave incident from an angle of θ and

$$P_w = \frac{1}{4\omega} \rho g^2 A^2,$$

which is the incident power per metre of wave frontage. In the particular case of a single body the maximum energy for operation in a single mode of motion can therefore be derived as

$$P_w |F_o(\theta)|^2 / \int_0^{2\pi} |F_o(\theta)|^2 d\theta$$

Now the exciting force, $F_o(\theta)$ is directly proportional to the radiated wave in a direction θ created by a forced oscillation and this expression clearly demonstrates that high energy capture is obtained if the device radiates in a narrow band of angles but at the expense of being extremely directional. Normalising the above expression to P_w , gives a capture width for the device and in the case of a radially symmetric device vertically oscillating, $F_o(\theta)$ is independent of angle this reduces to $\lambda/2\pi$. If horizontal (sway) oscillations are considered $F_o(\theta)$ varies as $\cos\theta$ and the capture width is doubled to λ/π .

If, further, a combination of vertical and horizontal oscillations are considered ($N' = 2$) then the cross coupling terms vanish in the added damping matrix since the integral of $\cos\theta$ is zero. Letting $F_o^1(\theta) = \alpha$ and $F_o^2(\theta) = \beta \cos\theta$ then $N(\omega)$ is given by the matrix

$$\frac{1}{8\lambda P_w} \begin{bmatrix} 2\pi \alpha \bar{\alpha} & 0 \\ 0 & \pi \beta \bar{\beta} \end{bmatrix},$$

and the maximum capture width is

$$\frac{\lambda}{2\pi} (1 + 2 \cos^2\theta)$$

Combining the orthogonal horizontal mode to the sway would make this expression independent of angle and give a value $3\lambda/2\pi$. It is interesting to note that in three dimensions the added damping matrix is not singular for $N > 2$ as could have been deduced from the representation as an integral of rank one dyadic forms which can have arbitrarily high rank.

4.1.2 Arrays of Devices

Perhaps the most interesting use of the three dimensional analysis is to examine arrays of devices which has previously been considered by Evans⁽⁷⁾ (1980). He has analysed configurations of axially symmetric devices that are each constrained to vertical (heave) oscillations and assumed that the devices were small in relation to both the incident wavelength and their spacing so that the form of the exciting force, $F_o^m(\theta)$, was not influenced by the presence of the other structures. He therefore assumed that

$$F_o^m(\theta) = F_e^{ikl_m} \cos(\theta - \alpha_m)$$

where l_m is the distance of the m th device from the origin and α_m is the angle the line l_m makes with the positive x axis. The latter term merely represents a phase change due to the position of device m .

In this case the added damping matrix reduces to a particularly simple form

$$R_{mn} = J_0(KR_{mn}) \bar{F} \bar{F} / 4\lambda P_w$$

where R_{mn} is the distance between the m th and n th devices and J_0 is the zero order

Bessel function. Therefore the capture width may be expressed as,

$$\frac{\lambda}{2\pi} \bar{L}^T J^{-1} L,$$

where J^{-1} is the inverse of the matrix $J_0(KR_{mn})$ and L is a vector whose components are

$$L_m = e^{ikl_m \cos(\theta - \alpha_m)}$$

Now for N devices, their summed capture width working in isolation is $N\lambda/2\pi$ and a q -factor can be defined as the change in performance due to the presence of other devices and is given by

$$q(\theta) = \frac{1}{N} \bar{L}^T J^{-1} L$$

It may appear remarkable at first sight that any interaction factor exists since it has been assumed that the exciting force, and hence the radiated waves are not changed by the presence of the other devices but apparently the energy capture is influenced. The explanation for the q -factor lies in the fact that much of the structure of the hydrodynamics has been incorporated, particularly in formulating the added damping coefficients which estimate the forces induced by moving a device, both on itself and the other bodies. In this analysis it is assumed that the forces induced on body n , by motion of body m , are due to the radiated wave of device m and the diffraction of this wave by all other devices is neglected. The q -factor therefore arises since there is an induced force coupling the devices together and depending on the magnitude and phase of these forces energy capture can be advantageously or adversely affected.

4.2 Numerical Calculations

Evans' assumptions can be tested using numerical calculations to determine the added damping coefficients. The technique used to solve the hydrodynamic equations is to partition the device into plane facets and position a point source of waves at each facet centroid. Results for the added damping coefficients are given for a pair of devices which are cylinders with hemispherical bases. In Figure 4(a), the ratio of the diagonal damping coefficient to that of a single body is plotted for various values of the spacing d , normalised by the wavenumber $K = 2\pi/\lambda$. Evans assumes a constant value of unity whereas it is apparent that the wave diffracted from the other device causes this value to oscillate about unity. These calculations are carried out for device of normalised radius 0.47 and changes of up to 10% in the added damping coefficient can be observed for spacings less than 5 diameters. For larger spacings the wave scattering becomes less significant

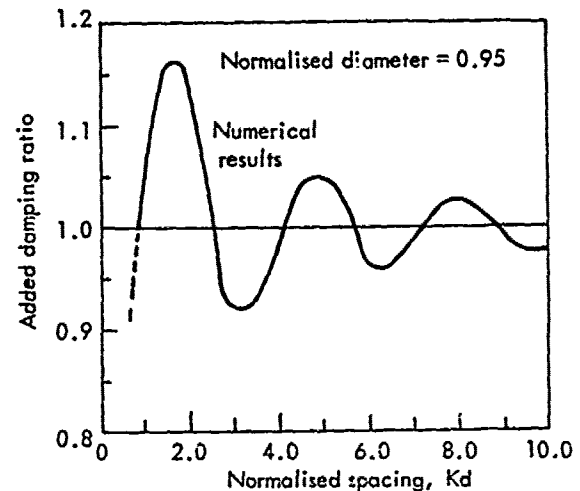


Figure 4(a). The Diagonal element of the Added Damping Matrix for a Pair of Point Absorbers.

When considering the coupling coefficients where the force on body n is evaluated due to a forced movement of the m th device with all others held stationary then the diffracted wave field of the n th body will be of the same magnitude as the radiated field at this position. Therefore the simple form of $J_0(Kd)$ will not represent the cross coupling terms and a comparison with the numerical calculations is shown in Figure 4(b) for a device pair.

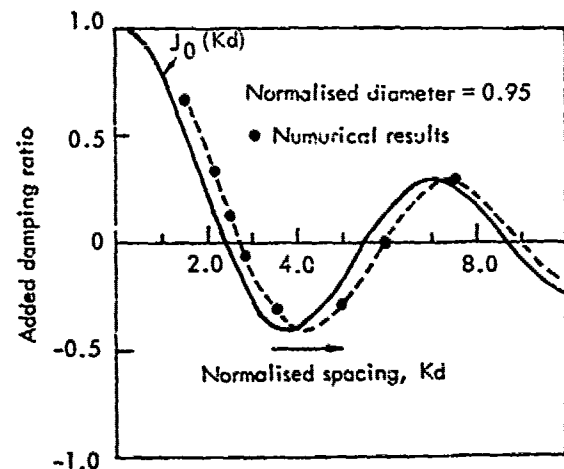


Figure 4(b). The Cross-coupling term of the Added Damping Matrix for a Pair of Point Absorbers.

Associated with these modifications are changes in the exciting forces which adjust appropriately to maintain the integral relation between them and the added damping matrix elements.

In Figure 5 the q -factors evaluated from the simplifying assumptions made by Evans are compared with numerical calculations for a line of two and three equally spaced absorbers which demonstrate a remarkable degree of agreement. Further calculations on an array of ten equally spaced devices which take account of first order diffraction from other devices gives a q -factor of 2.31 compared to the value of Evans of 2.37 for a normalised spacing of 4.99.

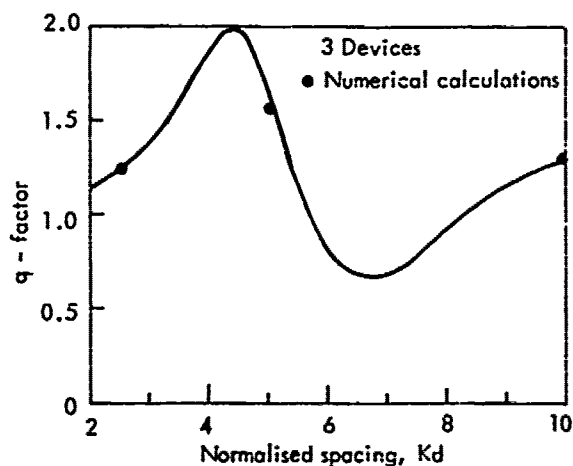
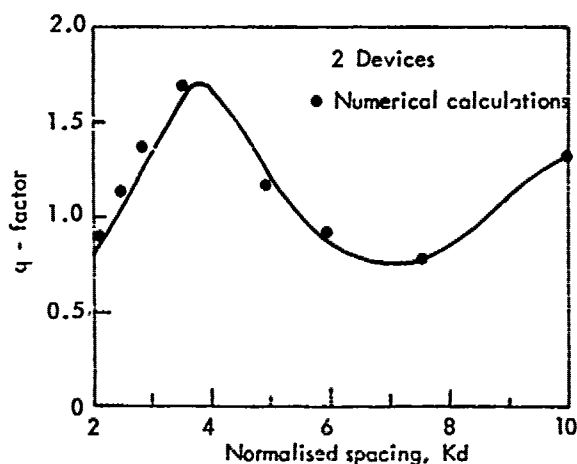


Figure 5. A Comparison between Evans approximate Theory and Numerical Calculations for array of 2 and 3 absorbers.

Numerical calculations have also been carried out for array configurations where each device has a simple resistive damping load rather than the optimal controller. Experiments were conducted to model this

situation in a wave tank at Edinburgh University that is 30m wide. Array configurations of point absorbers were tested in regular wave conditions and measured powers were normalised to the power absorbed by the isolated devices, albeit with non-optimal control. The results are shown for two and ten devices in Figures 6 for a range of angles of incidence indicating an excellent agreement with theory and demonstrating a marked advantage in absorption when devices are correctly placed in an array.

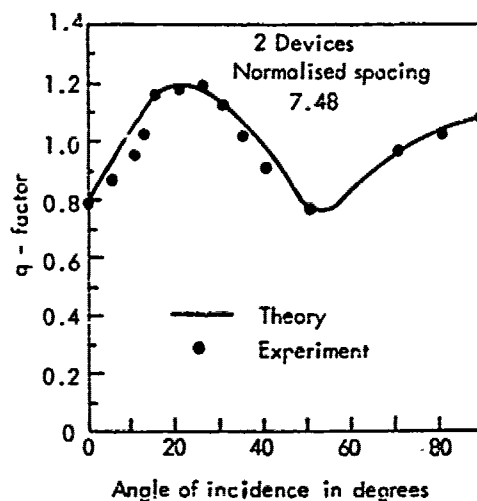


Figure 6(a). A Comparison between Theory and Experiment for a pair of Point Absorbers.

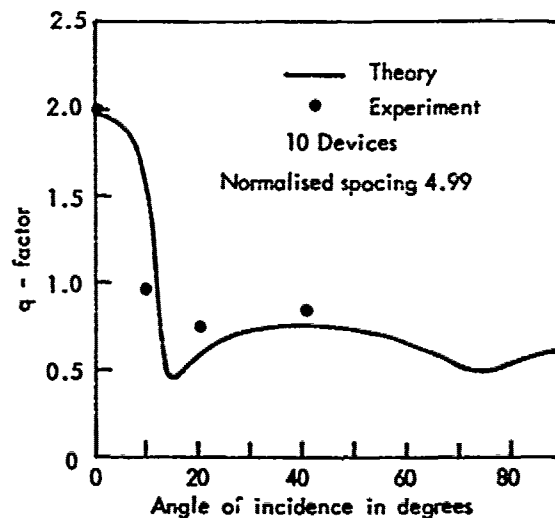


Figure 6(b). A Comparison between Theory and Experiment for an array of ten Point Absorbers.

4.3 Some Indication of Attenuator Performance

The analysis of arrays of point absorbers can be carried out for various angles of wave incidence; in particular results for a wave approaching along the line of the array can be considered to model attenuator behaviour. In the simple approach of Evans, which has been demonstrated as a reasonable model, there is essentially no difference between waves approaching at an angle of θ or $\pi - \theta$. If the devices in the array are therefore labelled from 1 to N then

$$|X_m| = |X_{N-m+1}| \quad m = 1, 2 \dots N,$$

and the rear element should absorb as much power as the front under optimal conditions. Therefore the term 'attenuator' is inaccurate in this particular case. It should be noted, however, that when diffraction terms are taken into account and non-optimum control is applied the above relationship is not true although the particular case of attenuation is not desirable for effective absorption.

Results for the maximum q-factors, using the Evans formula are given in Figure 7 for both the terminator mode ($\theta = 0$) and the attenuator one ($\theta = \pi/2$) using two and ten devices.

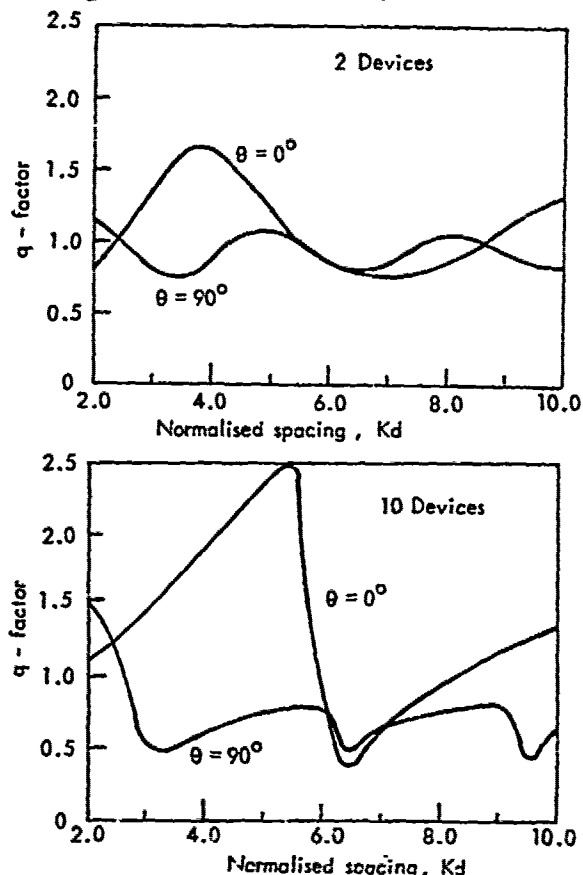


Figure 7. The Performance of Point Absorber arrays in the Terminator and Attenuator mode.

These show that the very high q-factors are best achieved with terminator configurations and in the attenuator mode there is a decreasing incentive to use an increasing number of absorbers. It would appear, therefore, that a small number of active elements are desirable for an attenuator and these configurations should themselves form a linear array to permit effective absorption.

Perhaps it should be emphasised that as the size of an array increases, whether it is of point absorbers or attenuators, the configuration tends towards two dimensional behaviour simulated by a single device placed in a narrow wave tank. This models an infinite array but unfortunately can only test the effect of normally incident waves. It is interesting to note that in this particular case two modes of motion only are needed for complete wave energy absorption and the results of Section 3 are applicable, with only minor modification. Therefore, the concepts of the Kaimei device and the Lancaster Bag which are intended to form a linear array should perhaps be modified to incorporate only two active elements, with more emphasis on control.

5. SOME ASPECTS OF CONTROL

Throughout this paper the effectiveness of wave energy absorption has been analysed under optimal conditions and with simple linear resistive loading. The first point to note is that realistic methods of primary power conversion will invariably be nonlinear and not have the instantaneous response that has been assumed in the previous analysis. This may well lead to slightly different optimal control strategies which not only account for the wave/body interaction but all of the system components that are necessary to enable the production of useful energy.

Secondly, the approach to optimal control has always been linear which to practically achieve would involve the storage and release of large amounts of energy involving many mechanical operations. This is likely to be difficult, and with the associated losses of mechanical components there may be no overall gain in energy capture. However, the theory of optimal power take-off is useful since it highlights the importance of control. Without active control devices tend to be large and rather inefficient leading to uneconomic designs.

The Norwegians, Budal and Falnes, have recognised this and have developed a nonlinear control system which arrests the motion of the device in order to advantageously phase its motion relative to the wave. The effect of this is to store and release energy at prescribed times and allows a small device to work extremely effectively in the prevailing wave conditions. Moreover, this method is mechanically simple, involving a single valve operation, twice per wave cycle, which

is likely to have relatively small losses associated with it.

The analysis of realistic system components, and a nonlinear control strategy will require a time domain model of the hydrodynamics instead of the more familiar frequency domain representation that has been used throughout this paper.

5.1 Time Domain Model

In Section 2.1 the wave induced forces were separated into two components, diffraction forces due to a wave incident on a stationary structure, and radiation forces due to the movement of the device. Since the diffraction forces for monochromatic waves can be expressed as

$$F_0(\omega) = R(\omega) A(\omega)$$

then a simple superposition gives a time domain representation as

$$\int_0^{\infty} R(\omega) A(\omega) e^{i\omega t} d\omega = f_0(t)$$

where $A(\omega)$ are the amplitudes (complex) of the incident wave spectrum and $R(\omega)$ is a vector of exciting forces in unit amplitude waves.

The radiation force can be described as

$$-M(\omega) \ddot{x} - N(\omega) \dot{x} = [-i\omega M(\omega) - N(\omega)] \dot{x}(\omega) e^{i\omega t},$$

for harmonic forced oscillations and this is represented by a convolution in the time domain as,

$$-\int_0^t H(t-\tau) \dot{x}(\tau) d\tau - M(\infty) \ddot{x}(t),$$

where

$$H(t) = \frac{1}{2\pi} \int_0^{\infty} [-i\omega M(\omega) - M(\infty)] + N(\omega) e^{i\omega t} d\omega.$$

The value of added mass of infinite frequency, $M(\infty)$, has been subtracted out to make $H(t)$ converge since its effect would make the system impulsive at $t = 0$ if retained and represents a constant additional mass of the system due to the fluid. The expression for $H(t)$ can be simplified by using the Kramers - Kronig relations(8) reducing to

$$H(t) = \frac{2}{\pi} \int_0^{\infty} N(\omega) \cos \omega t d\omega.$$

Therefore the equation of motion (1), can be written generally as,

$$[I + M(\infty)] \ddot{x} + B\dot{x} + \int_0^t H(t-\tau) \dot{x}(\tau) d\tau = f_0(t) + f^{\text{ext}}(t)$$

This equation can be integrated numerically given the necessary hydrodynamic parameters. The phase control system of Budal and Falnes has been modelled using this representation where

$$f^{\text{ext}}(t) = -D\dot{x},$$

and if the magnitude of the velocity is smaller than some prescribed value, ϵ ,

$$|\dot{x}(t)| < \epsilon$$

then the device remains stationary for a prescribed time Δt . Solutions for an isolated point absorber are given in Figure 8 where the incident wave frequency is one half of the natural frequency and a comparison between the optimal controller, the phase control and the simple resistive loading is given. These results demonstrate the value of using intelligence in the primary conversion system.

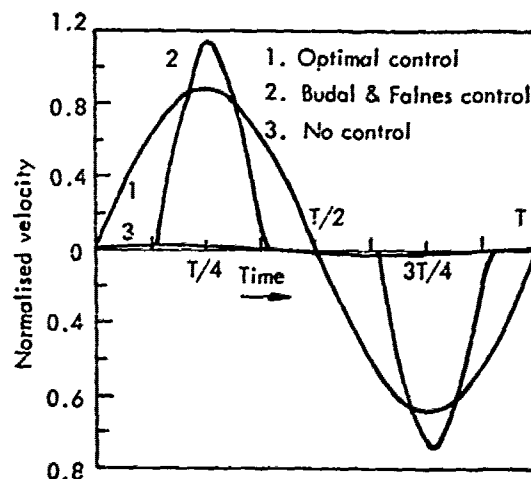


Figure 8. A Comparison between optimal control and that adopted by Budal and Falnes for the same value of damping constant. Note the enormous gains available from control over the response with pure resistance alone which is barely visible.

The whole aspect of system analysis requires more detailed investigation to account for the inter-relation between all the elements of a wave power system. One of us (Jefferys)(9) has been particularly concerned with this aspect and has produced an approximate model of hydrodynamics that replaces the convolution integral in the time domain representation as a finite order linear system of differential equations. The numerical solution of this is quicker and the powerful techniques of modern optimal control may be used with this representation.

6. CONCLUSIONS

The results presented in this paper do not give a unified picture of the primary interface of any wave power system but hopefully give a first indication of its characteristics. Perhaps the most important aspects are firstly that the

experimental evidence correlates extremely well with linear hydrodynamic theory which can now be used with confidence when examining device behaviour in modest wave conditions. Naturally in extreme waves, or with large motion amplitudes of the structure the linearity breaks down and whilst these conditions are important to the designer, efficiency is not a major concern!

Secondly, the importance of providing a controlled load by the first conversion stage has been emphasised since this forms the direct link between the wave/device interaction and the wave power system. The conflict between large structures with simple mechanical conversion systems and more complex conversion coupled with smaller devices is an important area that requires further study which could offer reduced costs.

Thirdly, the analysis in this paper tends to suggest that any individual device should only ever attempt to absorb wave energy through two modes of motion and all device concepts are identical in their potential efficiency. Naturally this is only a very tentative conclusion and the three dimensional analysis, in particular, is based upon some simple results. However, the problem of assessing the characteristics of the primary interface of a wave power system has opened up many new and interesting aspects of hydrodynamic theory which will hopefully be found useful in other fields of research.

7. ACKNOWLEDGMENTS

This paper is published by kind permission of the Central Electricity Generating Board describing work undertaken at Marchwood Engineering Laboratories. The authors would also like to thank Mr. S. Salter and the Department of Energy for use of the excellent experimental facilities from which many of the results were obtained.

8. REFERENCES

1. Masuda, Y. and Miyazaki T. (1978) 'Wave Power Electric Generation Study in Japan', Proc. Int. Symposium on Wave and Tidal Energy, B.H.R.A. Fluid Engineering, Cranfield, Bedford, England, Vol. 1 Paper No. B6.
2. Budal, K. and Falnes J. (1978) 'Wave Power Conversion by Point Absorbers', Norwegian Maritime Research, Vol.6 No.4 pp.2 - 11.
3. Chaplin, R.V. and French M.J. (1980) 'Aspects of the French Flexible Bag Device', Proc. of I.M.A. Conference on Power from Sea Waves, Edinburgh 1979, to be published by Academic Press.
4. Newman, J.N. (1962) 'The Exciting Forces on Fixed Bodies in Waves', J. Ship Res. 6, pp. 10 - 17.

5. Evans, D.V. et al (1979), 'Submerged Cylinder Wave-Energy Device - Theory and Experiment', Applied Ocean Research 1, No.1, pp. 3 - 12.

6. Salter, S. (1974), 'Wave Power', Nature 249 pp. 720 - 724.

7. Evans, D.V. (1980) 'Some Analytic Results for Two and Three Dimensional Wave-Energy Absorbers', Proc. of I.M.A. Conference on Power from Sea Waves, Edinburgh 1979, to be published by Academic Press.

8. Kotik, J. and Mangalus, V. (1962) 'On the Kramers-Kronig Relations for Ship Motions', Int. Shipbuilding Progress, 9, No.97.

9. Jefferys, E.R. (1979) 'The Modelling and Optimisation of a Wave Energy Converter', Ph.D. Thesis, Cambridge.

Discussion

J.N. Newman (MIT)

Mr. Count has discussed a variety of two- and three-dimensional devices for absorbing wave energy.

I particularly welcome his discussion and advocacy of optimal control, and figure 8 suggests the extent to which this can be achieved with relatively simple phase controls. It might be noted that the approach of Budal and Falnes is nonlinear, and therefore introduces higher harmonic radiative losses, but simple estimates indicate that these are minor for a relatively deep device such as a heaving spar buoy.

The discussion of "Attenuator" performance in section 4.3 leads to a conclusion that only two active elements are necessary for efficient operation. I believe that this conclusion is based on two dimensional considerations which may not hold, even for a transverse array, in a realistic directional spectrum. There are fundamental differences between the two- and three-dimensional optimum designs, and in the latter case increasing the degrees of freedom leads to increased bandwidth. This is illustrated by comparison of the predictions shown in figure 7 of our own paper to this symposium, and more recent estimates which I have performed for an idealized "KAIMEI" with six active elements. In the latter case there are twice as many degrees of freedom, and the bandwidth is practically doubled as a result. One also should warn against replacing, say, a long four-degree-of-freedom device by two shorter two-degree of freedom devices, since the loss of "ANTENNA" effect may exceed a factor of two. For example, the peak performance shown in our figure 7 at about $KL/2 = 3$ is typically reduced to less than 50% of its peak value at $KL/2 = 1.5$.

C.C. Mei (MIT)

The author's inference on attenuators in §4.3 and in the conclusions is based on the weak-interaction approximation for wide spacing between point absorbers. In most attenuators so far proposed, the total length is about one wavelength or so. For the same numbers of, equally spaced absorbers, say 10, does the author think that a long column with one wavelength spacing between adjacent absorbers behaves the same as a short column with (0.1) wavelength spacing?

G. Kai (JAMSTEC)

Your paper says in Fig.7 that 2 Devices for attenuator are the best configuration than others.

Do you think this result can be applied in practical applications?

M.J. French (Univ of Lancaster)

While this paper is a very useful collection of important results in the hydrodynamics of wave energy some of the conclusions it arrives at are plainly unsound.

The authors suggest that the Lancaster wave energy device might be improved by incorporating only two active elements, with more emphasis on control. The first part of this suggestion is rather like suggesting that old warships would have done better with two guns per ship, because they could be brought to bear better. The second part ignores the fact that we have used since 1974 a 'Latched' system which works very like the one proposed later by Budal and Falnes. Our choice of a manifolded 'Constant Pressure' system in which air is collected from a range of bags was originally made because it possesses this advantage.

With regard to the relative merits of attenuators and terminators, the authors conclude that high absorbed powers per device are best achieved with the latter. But, by analogy with sailing warships, the spacing of devices will be small in any practical design, at or beyond the leeward end of Figure 7, where it would seem attenuators have higher q 's than terminators. But there are other advantages to attenuators - for example, for a given section, an attenuator has active collector surface on both sides instead of one, a very substantial virtue.

The fact remains that relative to its size, the Lancaster device extracts much more power than any of its rivals (although per unit area of active collecting surface it is not particularly outstanding).

Author's Reply

B.M. Count (UK Central Electricity Generating Board)

I would be appropriate to take all the discussions together since they all refer to the speculation concerning attenuators where I propose that two active elements per device may be sufficient for effective wave energy absorption. Professor Newman points out that the con-

clusion is based upon the results of two dimensional theory which can be used to model an infinite array of wave power devices which are excited by head seas and therefore all of the devices move in phase. This, of course, will not be the case in a fully three dimensional environment where waves are incident from many directions and the array comprises of a finite number of bodies.

Professor Newman gives some interesting results for an attenuator device, using unified field theory, demonstrating that a device with six modes of motion has a broader bandwidth than a two mode of motion system in addition to having a higher peak performance. This is not surprising since it is obvious that the more modes of motion there are available to tune, the better the overall performance of the system by virtue of the "antenna" effect.

Whilst I accept the comments of Professor Newman and Mei as casting uncertainty on my conclusions I would, however, wish to make the following point. The results derived from the unified theory are for a single attenuator in three dimensions with six elements. My speculation, however, refers to the optimum arrangement of a large number of absorbers and the work on p 'nt

absorbers suggests that the "antenna" effect of spacing them strategically along the wave front is superior to the attenuator configuration for head seas in terms of total energy absorption. The extrapolation to the two degree of freedom attenuator is based upon this result and two dimensional theory and needs further study to investigate its validity.

With regard to the question from Mr. Kai, I believe that the configurations suggested could be practical option although their performance expectations must be confirmed.

Professor French's views demonstrate his absolute belief in the Flexible Bag Device. His arguments concerning the two degree of freedom system may have some substance as shown more explicitly by Professor Newman. However, his claim that a simple constant pressure manifold to a good approximation to optimum control is simply not true and a more sophisticated algorithm is required to achieve a latched phase control. Finally, his claim that the Lancaster Device extracts much more power, relative to its size, than any other wave power device is a speculative claim and it would be interesting to know from what theoretical or experimental work this claim is based.

Extraction of Energy from Wind and Ocean Current

Theodore Y. Wu
California Institute of Technology
Pasadena, California, U S A

ABSTRACT

Basic fluid dynamic principle is applied to develop a mechanical device involving lifting surfaces in unsteady motion by which energy can be extracted from a prevailing stream such as wind, current in the ocean, and tidal and river currents. The fundamental case considered here is based on pitch-and-heave motion of a single airfoil-shaped blade mounted on a vertical axis and moving in a uniform stream, for which motion the hydrodynamic force and moment acting on the blade and the energy relationship are evaluated on unsteady wing theory. The operation is optimized to give the highest possible efficiency under the isoperimetric condition of fixed specific loading (in proportion to the reactive drag the blade must withstand); this optimum motion corresponds to the least possible loss of flow energy while a required amount of stream power is being extracted. The present simple case is explored with prospects for further generalization to systems of multiple-blade configurations.

1. INTRODUCTION

This paper attempts to explore the developmental potential of a fluid mechanical device involving lifting surfaces in pitch-and-heave type of unsteady motion by which energy can be extracted from prevailing wind, from current in the ocean, and from tidal and river currents. Unlike the horizontal-axis, low-solidity (high-angular-velocity) type of wind turbines and the vertical-axis Darrieus turbine, the blade movement of this new type 'stream-power generator' is undulatory and primarily transverse to the main stream and hence should enhance its application to water streams, as compared with the other types, on account of its associated gain in safety to marine lives and to its own blade.

The fundamental case studied here is based on pitch-and-heave motion of a single airfoil-

shaped blade mounted on a vertical axis, and operated in such a manner as to extract, under a chosen isoperimetric condition, the greatest possible amount of energy from the incident primary stream, which is assumed uniform. Clearly, this mode of blade movement is quite similar to the undulatory motion of the lunate tail found in carangiform fish propulsion and to the flapping wing motion of birds in flight. A chief intent of this work is to make a unified comparative study of the two modes, namely the 'self-propulsion mode' and the 'power-extraction mode' from the viewpoint that they belong to the same family of solutions. For the self-propulsion mode, a two-dimensional linear theory has been pursued, as a first approximation, by Lighthill (1970 [6]) and Wu (1971 [7]) in their study of the carangiform motion of aquatic animals with lunate tails. An important concept in these studies was that high values of the hydromechanical efficiency of lunate-tail movements can be achieved with an optimum combination of the amplitude ratio of, and phase difference between the modes of pitch and heave, a goal of improving speed and performance that is beyond reach by either mode in operation alone. On energy consideration, the mean power required, \bar{P} , for maintaining a specified motion has been shown to always exceed the work by the mean thrust, \bar{T} , at the rate of forward speed of swimming, and between the two the rate of loss of mean energy (convected away in the trailing sheet of cross-stream elements of vorticity) makes up the difference. The optimum motion was evaluated by Wu (1971 [7]) using calculus of optimization to give the required forward thrust (for overcoming the fluid viscous resistance) with the least possible power input (hence the least energy loss). This line of analysis is readily extended to evaluate the optimum power-extraction mode, as will be discussed here.

The distinction between the self-propulsion mode and the power-extraction mode is $\bar{P} > \bar{T}U > 0$ for the former and $0 > \bar{P} > \bar{T}U$ for the latter, where U is the free stream velocity relative to

the wing. The optimum motion is found to depend on two dimensionless parameters: the reduced frequency $\sigma (= \omega l/U)$, where ω is the angular frequency of wing oscillation, l the semi-chord length and the specific-loading factor, $\bar{C}_{T,0}$ (a coefficient form of \bar{T} rated at unit amplitude of heaving). Detailed investigation of the characteristics of the optimum motion and pertinent physical quantities in terms of these two parameters are carried out, with the aim 1. to examine feasibility of the high fluid mechanical efficiency predicted by the optimum solution, and 2. to explore the range of a high rated power output (based on available incident flux of wind energy) to see if the limit imposed by Betz (1926 [1]) can be approached. These two factors are essential to a successful development of this type of stream-power generator (especially for industrial applications) and require further study.

The present rather simplified case is chosen to elucidate as much as possible the basic principles involved and to provide useful results as a guide to more complicated situations, with prospects for further generalization to systems of multiple-blade configurations. Many important physical effects, such as those of flow shear, unsteadiness and turbulence that can arise in practice, are not considered here. However, from the previous studies of Wu (1972 [8]), Wu and Chwang (1975 [9]) on the effects of stream waviness for the self-propulsion mode, it may be expected that extra energy associated with a wavy stream can also be extracted (in addition to the mean-flow energy) with suitable modification of the present solution.

2. AN OSCILLATING RIGID-WING STREAM-POWER GENERATOR

We consider here the fundamental case of a rigid, symmetric, airfoil-shaped blade performing a simple-harmonic pitch-and-heave movement in a prevailing stream (of an incompressible fluid) which is assumed to be otherwise steady, with a uniform velocity U along the x -axis. The lateral displacement of the wing, $y = h(x, t)$ in time t , may be written in the basic linear-parametric form

$$h(x, t) = \left[\frac{1}{2} \xi_0 + (\xi_1 + i\xi_2)x \right] e^{i\omega t} \quad (|x| < 1), \quad (1)$$

with real ξ_0, ξ_1, ξ_2 as parameters. Here the half-chord length, l , is normalized to be unity. In the three-dimensional parametric space $\xi = (\xi_0, \xi_1, \xi_2)$, (1) represents a heaving (taken as of the reference phase) of the blade with amplitude $\xi_0/2$ and pitching about the midchord point with amplitude $\alpha = (\xi_1^2 + \xi_2^2)^{1/2}$, at a phase angle $\alpha_p = \tan^{-1} \xi_2/\xi_1$ with respect to heaving. This parametric form is convenient, because of its linearity, for evaluating the optimum motion by which a maximum flow energy can be extracted from the prevailing stream for specified streamwise loading on the wing.

For certain purposes, such as when lift and moment of the wing and their separate contributions to power output are evaluated in connection with engineering design and for our later discussion on stability and control of the optimum motion, it is desirable not to limit the axis of pitch to the mid-chord point as prescribed by (1), but to refer both pitch and heave to an arbitrary axis, say $x = b$,

$y = 0$, so that, alternatively,

$$h(x, t) = [h_0 + \alpha e^{i(\alpha_p - \alpha_h)(x-b)}] e^{i(\omega t + \alpha_h)}, \quad (2)$$

where

$$h_0 = \left[\left(\frac{1}{2} \xi_0 + b\xi_1 \right)^2 + (b\xi_2)^2 \right]^{1/2},$$

$$\alpha_h = \tan^{-1} [b\xi_2 / (\frac{1}{2} \xi_0 + b\xi_1)], \quad (3)$$

$$\alpha = (\xi_1^2 + \xi_2^2)^{1/2}, \quad \alpha_p = \tan^{-1} (\xi_2/\xi_1).$$

Clearly, the heaving phase angle α_h in (2) is by itself irrelevant since it can be eliminated by a shift of the time origin. If b is further taken as a free parameter, then the three original parameters, $(\xi_0, \xi_1, \xi_2) \equiv \xi$, and the three new ones,

$(h_0, \alpha, \alpha_p - \alpha_h) \equiv \eta$, are related by (3), or symbolically $\eta = \eta(\xi; b)$, which has a unique inverse, $\xi = \xi(\eta; b)$ say, provided that $\xi_0 \neq 0$, in which case the two representations are equivalent to each other. As a point of further clarification, we remark that if the solution to the irrotational flow problem is obtained in terms of ξ for the wing motion prescribed by (1), it can readily be converted to an expression in η with a free choice of b , and vice versa. The choice of b is not the only free one that keeps (1) and (2) equivalent. In fact, one may take $\alpha_p \equiv \alpha_p - \alpha_h$ as arbitrary

$(-\pi < \alpha_p < \pi)$ and regard (h_0, α, b) as three independent parameters, which are uniquely related to (ξ_0, ξ_1, ξ_2) . In particular, for $\alpha_p = -\pi/2$, we have Lighthill's (1970 [6]) representation

$$h(x, t) = [h_0 - i\alpha(x - b)] e^{i\omega t}. \quad (4)$$

Finally, we may also take h_0 as the third choice for a free parameter, leaving (α, α_p, b) uniquely related to (ξ_0, ξ_1, ξ_2) . However, since these new parametric sets are nonlinear in their expressions for h , it is simpler to work with the basic form (1) in our variational calculation of the optimum motion.

For the required momentum and energy calculations, the basic fluid mechanical theory based on two-dimensional small-disturbance assumptions is known (Lighthill 1970 [6]; Wu 1971 [7]); we recapitulate the results to facilitate our subsequent discussion. In terms of the basic form (1) of wing motion, the instantaneous lift L and moment M about the mid-chord point (positive in the nose-up sense) are

$$L/\pi\rho U l = -[(b_0 + b_1) \odot + \frac{1}{2} i\sigma b_0], \quad (5)$$

$$M/\pi\rho U l^2 = -\frac{1}{2} [(b_0 + b_1) \odot - (1 + \frac{1}{4} i\sigma) b_1], \quad (6)$$

$$b_0 = U \{ i\sigma \xi_0 + 2(\xi_1 + i\xi_2) \} e^{i\omega t}, \quad (7a)$$

$$b_1 = U i\sigma (\xi_1 + i\xi_2) e^{i\omega t}, \quad \odot(\sigma) = F + iG, \quad (7b)$$

where ρ is the fluid density, $\sigma = \omega l/U$ is the frequency based on half-chord length l ($l = 1$ by normalization), and F, G denote the real and

imaginary components of the Theodorsen function σ . Here and in the sequel, the real part of a complex representation is meant for physical interpretation, as denoted by a square bracket.

In generality (not limited to linear approximations of the kinematics), energy consideration of propulsion or energy extraction processes involving flows of an inviscid fluid seeks a relationship between the thrust, T , of a wing (T taken positive, or negative, when directed into, or along, the main stream), the power, P , required for maintaining the motion (P taken positive, or negative, when it is supplied, or absorbed, by an external agency), and the rate of imparting kinetic energy, hence lost, to the fluid, E . They satisfy the simple relation

$$P = TU + E, \quad (8)$$

which physically means that mechanical power is required just to balance the rate of working by the thrust and the rate of energy loss. In the present case with the simple geometry of an oscillating rigid wing, the thrust is given by

$$T = [L][\partial h / \partial x] + S, \quad (9a)$$

$$S = \frac{1}{2} \pi \rho [a_0]^2, \quad a_0 = b_1 - (b_0 + b_1) \sigma(\sigma), \quad (9b)$$

in which S represents the leading-edge suction. The power required is equal to the rate of working against the lift and moment, which is

$$P = [-L][h_t(0, t)] + [M][h_{xt}], \quad (10)$$

where the subscripts x, t denote partial differentiation. Finally, the rate of energy loss, E , can be calculated from the net work performed by the surface pressure at the rate of local flow velocity; this result together with (9) and (10) is found to satisfy the first energy principle (8). The mean values of thrust \bar{T} , power \bar{P} , and energy loss \bar{E} (averaged over a time period) will be given in the same coefficient form as used by Wu (1971 [7]) for propulsion studies, $(C_P, C_E, C_T) = (\bar{P}, \bar{E}, \bar{T}U) / \frac{1}{4} \pi \rho U^3 l$, with the result:

$$C_P = C_T + C_E \quad (11)$$

$$C_P = \sigma(\xi, \bar{P} \xi), \quad C_E = B(\sigma)(\xi, \bar{Q} \xi), \quad (12)$$

where $\xi = (\xi_0, \xi_1, \xi_2)$ is regarded as a vector, (ξ, ξ) denotes the inner product of ξ and ξ , $B(\sigma) = F - (F^2 + G^2)$, and \bar{P} and \bar{Q} are 3x3 symmetric matrices with elements

$$P_{11} = \sigma F, \quad P_{12} = G + \frac{1}{2} \sigma, \quad P_{13} = F - \sigma G, \quad (13)$$

$$P_{22} = P_{33} = \sigma(1-F) - 2G, \quad P_{23} = 0;$$

$$Q_{11} = Q_{12} = \sigma^2, \quad Q_{13} = 2\sigma, \quad (14)$$

$$Q_{22} = Q_{33} = 4 + \sigma^2, \quad Q_{23} = 0.$$

The above C_E is a non-negative quadratic form,

as can be seen from the properties that $B(\sigma) \geq 0$ for all σ and that the three eigenvalues of \bar{Q} , namely, 0, $(\sigma^2 + 4)$, $(2\sigma^2 + 4)$, are non-negative. Therefore, for the case of uniform main stream, $C_T < C_P$.

Clearly, the criterion of propulsion is $C_T > 0$, so that a sufficient thrust is produced to overcome the viscous resistance of a real fluid, and the criterion of stream-power extraction is $C_P < 0$, which means a net power being extracted from the prevailing stream at the cost of available kinetic energy of the fluid. It is also clear that when $C_P < 0$, $C_T < C_P < 0$ but numerically $|C_T| > |C_P|$, implying that while energy is being extracted from the main stream, the wing just withstand a mean drag, $D = -\bar{T} > 0$, which is reactive instead of resistive in nature, and, by (8) and the property $E \geq 0$, cannot be less than $|\bar{P}|/U$ for given power extraction, $-\bar{P} > 0$. When $\bar{P} < 0$, a fluid mechanical efficiency of extracting flow energy can be defined as

$$\eta = \bar{P}/\bar{T}U = C_P/C_T \quad (\text{for } C_T < C_P < 0). \quad (15)$$

So this η gives a measure of the power extracted, $-\bar{P}$, as a fraction of the rate of working, DU , against the reactive drag; the latter may be regarded as the power required to create the main stream by moving the wing through the fluid originally at rest. (Note that for the propulsion mode, $0 < C_T < C_P$, the definition adopted for the efficiency is $\eta = C_T/C_P$.)

From another point of view to provide a scale of the power that can be extracted from the incident flux of available energy in a prevailing stream, we will also introduce a 'rated power-output-ratio', similar to that first introduced by Betz (1926 [1]), as

$$\eta_B = -\bar{P}/P_{av} = -\bar{P}/\frac{1}{2} \rho U^3 \xi_0 = -\frac{\pi}{2} \left(\frac{l}{\xi_0}\right) C_P, \quad (16)$$

in which P_{av} is the total power available in the incoming stream, equal to the incident flux of kinetic energy across an area swept by the wing of unit segmental length in heaving. For the present pitch-and-heave type of stream-power generator, this power ratio is related to the mechanical efficiency by

$$\eta_B = -\eta \frac{\pi}{2} \left(\frac{l}{\xi_0}\right) C_T, \quad (C_T < 0) \quad (17)$$

where C_T is a quadratic function of (ξ_0, ξ_1, ξ_2) given by (11) and (12).

Based on a momentum theorem for an actuator disc operating at an ideal condition, Betz (1926 [1]) showed that the maximum power that can be extracted from the available wind energy flux by the actuator disc is $P_{max} = -(16/27) P_{av}$, and so in general

$$\eta_B \leq (\eta_B)_{max} = -\bar{P}_{max}/P_{av} = 16/27 = 0.593. \quad (18)$$

Subsequent theoretical efforts (e.g. Glauert 1935 [3]; Hütter 1977 [4]) have shown that the Betz limit can be somewhat increased by making more accurate corrections to the original simplifying assumptions. On the other hand, there have been

various practical attempts trying to surpass this theoretical limit with resort to the so-called 'wind-concentrator' concepts such as by employing the front-nozzle-type, diffuser-type, rotor-tip-vane and other kinds of augmentation (for a review, see de Vries 1979 [2]). Nevertheless, this classical limit has served well as a useful guide to assessing performance of windmills and their more recent variations, most of which can achieve no better than half of this theoretical maximum of Betz's. As for the present oscillating wing type of device, it is of interest to analyze the optimum condition under which high values of both the fluid mechanical efficiency and the rated power-ratio can be achieved.

3. THE OPTIMUM PITCH-AND-HEAVE MOTION

The optimum-motion problem for the power-extraction mode is to find the optimum set of $\xi = (\xi_0, \xi_1, \xi_2)$ which will minimize C_E under the isoperimetric condition of a fixed, negative thrust coefficient,

$$C_T = C_{T,0} < 0, \quad (19)$$

the reduced frequency σ being regarded as a fixed parameter.

This problem as formulated above has been solved by Wu (1971 [7]) for the propulsion mode with $C_{T,0}$ assuming positive, instead of negative values as required here; the solution, however, is just as applicable to the present case. Lighthill (1970 [6]) also discussed the important features of the optimum motion of lunate-tail propulsion by examining the effects of changes in value of the parameters appearing in (4) and their derived ones with a view on enhancing the hydromechanical efficiency. Here, the reason of choosing to specify negative values of C_T , rather than negative values of C_P (which would be sufficient to discuss power extraction), is to keep the same basis for discussion and comparison (with the propulsion mode) and to have a complete scope of covering C_T , especially the range of $C_T < 0$ and $C_P > 0$ which may be of side interest. If desired, the two bases of constant C_T and constant C_P can be mutually converted by some cross interpolation. We therefore proceed on the premise of (19) by summarizing the analysis for the power-extraction mode.

First, the singular nature of the problem as noted earlier (ascribable to the property that the matrix Q in (12) has a zero eigenvalue, see Wu (1971 [7])) is removed by the transformation

$$\xi_0 = (4 + \sigma^2)\zeta_0, \quad \xi_1 = \zeta_1 - \sigma^2\zeta_0, \quad \xi_2 = \zeta_2 - 2\sigma\zeta_0, \quad (20)$$

which reduces the order of the quadratic form C_E by one, giving

$$C_E = B(\sigma) Q_{22}(\zeta_1^2 + \zeta_2^2), \quad (21)$$

$$C_P = \sigma \{ P_{22}(\zeta_1^2 + \zeta_2^2) + 2\zeta_0(A_1\zeta_1 + A_2\zeta_2) \}, \quad (22)$$

$$A_1 = P_{12}Q_{22} - Q_{12}P_{22}, \quad (23)$$

$$A_2 = P_{13}Q_{33} - Q_{13}P_{33}.$$

By extremizing the function $C_E^* \equiv C_E - \lambda^1 C_P$, λ^1 being a Lagrange multiplier, in the largest common subspace (ζ_1, ζ_2) of C_E and C_P , we obtain

$$\zeta_1 = \lambda A_1 \zeta_0, \quad \zeta_2 = \lambda A_2 \zeta_0, \quad (24)$$

where λ is a new multiplier. Upon using condition (19), λ is found to have two roots

$$\left. \begin{matrix} \lambda_1 \\ \lambda_2 \end{matrix} \right\} = \frac{\sigma}{T_{22}} \{-1 \pm (1 + \Lambda)^{1/2}\}, \quad (25)$$

where

$$\begin{aligned} T_{22} &= \sigma P_{22} - BQ_{22}, \\ \Lambda &= \bar{C}_{T,0} T_{22}(\sigma^2 + 4)/(\sigma A)^2, \\ \bar{C}_{T,0} &= C_{T,0}(\ell/\xi_0)^2, \quad A^2 = A_1^2 + A_2^2. \end{aligned} \quad (26)$$

These roots depend on two parameters: the reduced frequency σ and the 'specific-loading factor' (rated at unit amplitude of heaving), $\bar{C}_{T,0} (< 0)$. Negative values of $\bar{C}_{T,0}$ provide a measure of the reactive drag loading on the wing.

From the known property of $T_{22}(\sigma) \geq 0$ according as $\sigma \geq \sigma_* \approx 1.781$, we see that for fixed $\bar{C}_{T,0} < 0$, $\Lambda(\sigma, \bar{C}_{T,0})$ decreases monotonically from $+\infty$ as σ increases from 0, reaching 0 at $\sigma = \sigma_*$ and when $\bar{C}_{T,0} < -9/16$, $\Lambda < -1$ for $\sigma > \sigma_*(\bar{C}_{T,0})$, where $\Lambda(\sigma_*, \bar{C}_{T,0}) = -1$. Thus, there exist two real optimum solutions for $0 \leq \sigma \leq \sigma_*$; the upper cut-off frequency σ_* is generally very large, if exists, for nearly all cases of practical interest ($0 > \bar{C}_{T,0} > -1$ say). Within this frequency range, the optimum motion is given by (20), (24) and (25), and it has two branches. In the first of the two, $\lambda = \lambda_1$, which is always negative and numerically smaller than λ_2 , and corresponds to the highest efficiency attainable under condition (19),

$$\eta_{\max} = \frac{C_P}{C_T} = (1 - \frac{C_E}{C_P})^{-1} = \frac{\sigma(P_{22}\lambda_1 + 2)}{T_{22}\lambda_1 + 2\sigma} \quad (0 < \sigma < \sigma_*) \quad (27)$$

The other branch, with $\lambda = \lambda_2$, gives the lowest efficiency (with λ_1 in (27) replaced by λ_2).

The numerical results of these two extreme η 's are shown in Fig. 1 for several negative values of $\bar{C}_{T,0}$. In contrast to the propulsion mode ($\bar{C}_{T,0} > 0$, in which case the optimum motion has a low-frequency cut-off), the optimum motion of the power-extraction mode ($C_P < 0$) exists for all frequencies up to a high-frequency cut-off (all too high to appear in the figure), though the maximum efficiency decreases appreciably with increasing magnitude of $\bar{C}_{T,0}$. The lowest efficiencies are seen to be all negative, which signifies the need of an externally supplied power ($C_P > 0$) while still withstanding a reactive drag. It remains to be seen if this particular mode of motion might be utilized in nature, such as by a bird flapping its wing forward to retard itself quickly for landing on a tree branch or by a fish rowing its pectoral fins broadwise to stream to stall. In the sequel only the maximum efficiency branch of the optimum motion will be discussed.

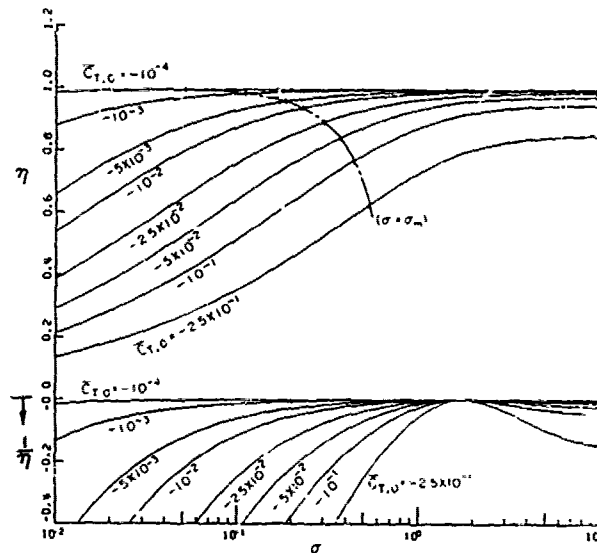


Fig. 1 Maximum and minimum efficiencies of a flow-driven oscillating wing (stream-power generator) that extracts flow energy while withstanding a reactive drag (given in coefficient form, $-\bar{C}_{T,o}$). The lower branch shows the inverse of minimum efficiency.

As found by Lighthill (1970 [6]) and Wu (1971 [7]) for the propulsion mode, the suction force acting on a well-streamlined leading edge of a well-feathered oscillating wing, unlike in the steady-state case, is no longer always a second-order small quantity associated with small incidence angles alone, but can vary with frequency to reach great values. Such drastic changes in forces have been contended to suggest a likely occurrence of flow separation from the leading edge, causing a wide departure from the all-attached flow assumed here. For the power-extraction mode, the ratio of the mean suction coefficient C_S (which is the mean suction force nondimensionalized on the same basis as C_T) to the reactive-drag coefficient, $|\bar{C}_T|$, is shown in Fig. 2 for the optimum motion of the maximum efficiency. Quite similar to the results of the propulsion mode, this ratio, for a fixed $\bar{C}_{T,o} < 0$, is relatively small only near its minimum at $\sigma = \sigma_m(\bar{C}_{T,o})$ and grows very rapidly, as $|\sigma - \sigma_m|$ increases. The greater the specific loading factor $|\bar{C}_{T,o}|$, the higher the values of both of the minimum of the ratio $C_S/|\bar{C}_T|$ and its corresponding σ_m . This latter behavior of the leading-edge suction might turn out to impose an upper limit to the loading factor $|\bar{C}_{T,o}|$ and in turn to the rated-power ratio, η_B , as will be discussed later. This is a point of significance and requires further investigation.

To give a complete description of the kinematics, the magnitude ratio of pitch-to-heave, $Z_p = 2\alpha/\xi_0$, and their phase difference $\alpha_p = \tan^{-1}(\xi_2/\xi_1)$, are shown in Figures 3 and 4 for the optimum motion (of the maximum efficiency branch) as a basic case of reference, in which the axis of pitch is taken at the mid-chord point. For each fixed $\bar{C}_{T,o}$, Z_p has a minimum at a frequency somewhat lower than $\sigma = \sigma_m$, a line drawn in to signify the local minimum leading-edge suction;

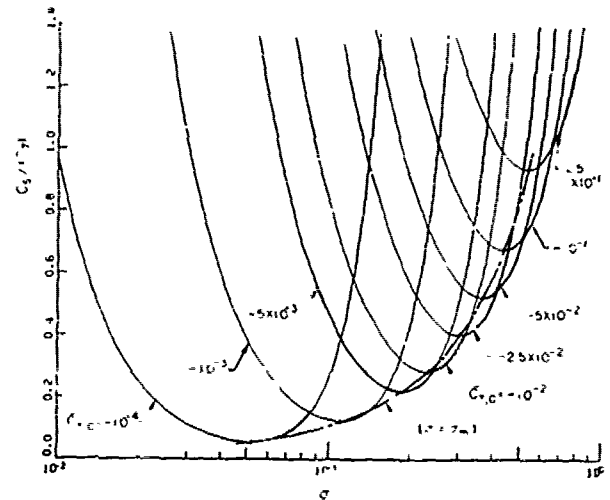


Fig. 2 The ratio of the leading-edge suction coefficient C_S to the reactive drag coefficient $|C_{T,o}|$, ($C_{T,c} < 0$).

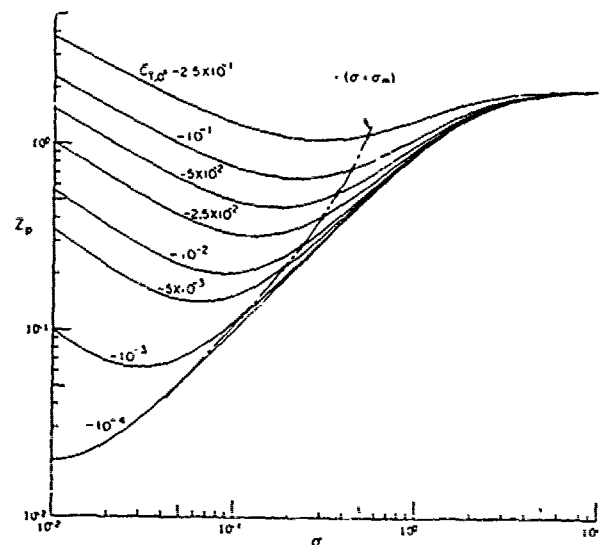


Fig. 3 The pitching-to-heaving amplitude ratio $Z_p(\sigma, \bar{C}_{T,o})$ with reference to the mid-chord point as the axis of pitch. The $\sigma = \sigma_m$ line signifies the local minimum leading-edge suction.

and along this line Z_p increases rather rapidly as $|\bar{C}_{T,o}|$ becomes greater in a magnitude. From Fig. 4 we see that for power extraction, the optimum pitching is at a nearly constant phase lag of 90° behind heaving for $\sigma < 0.2$ and from there starts to lag more behind at higher frequencies. It is of interest to note that in a favorable range of operation (a narrow belt centered at the $\sigma = \sigma_m$ line), α_p has nearly the same value in both the power-extraction and self-propulsion modes. In contrast, we observe that for equal and opposite values of $\bar{C}_{T,o}$, Z_p is invariably greater in the power-extraction

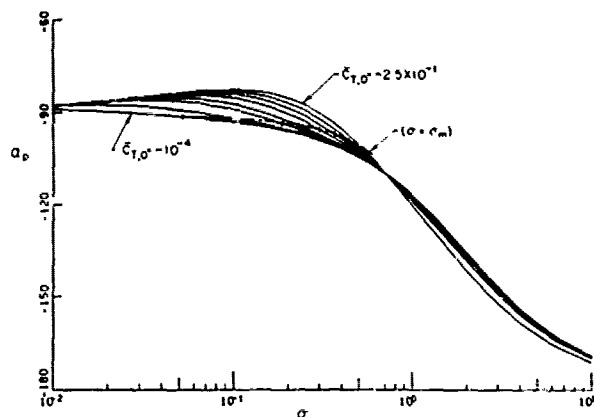


Fig. 4 The phase angle $\alpha_p(\sigma, \bar{C}_{T,0})$ of pitching (about the mid-chord point) with reference to heaving; negative values of α_p signify phase lag.

than in the self-propulsion mode (for the latter case, see Wu 1971 [7], Fig. 6).

The last point is conspicuously exhibited by the 'proportional-feathering parameter', $\theta = U\alpha/\omega h$, where α and h are, respectively, the amplitude of pitch and heave defined in Lighthill's form (4), or to put in the present notation,

$$\theta = \frac{U\alpha}{\omega h_0} \approx -\frac{2}{\sigma} (\xi_1^2 + \xi_2^2) / \xi_0 \xi_2 = -\frac{1}{\sigma} Z_p \csc \alpha_p. \quad (28)$$

By comparison between θ of the optimum power-extraction mode, as shown in Fig. 5 and the corresponding result for the propulsion mode (see Wu

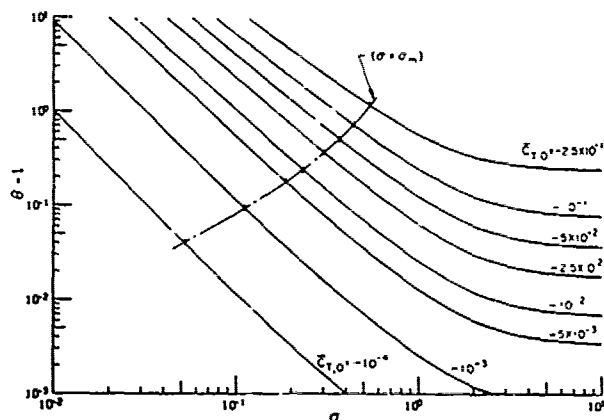


Fig. 5 Variation of the feathering parameter θ with the reduced frequency σ and loading factor $\bar{C}_{T,0}$.

1971 [7], Fig. 8), we see the important distinction that the optimum motion is characterized by sub-feathering ($\theta < 1$) in the latter case ($\bar{C}_{T,0} > 0$) and by superfeathering ($\theta > 1$) in the former ($\bar{C}_{T,0} < 0$). The optimum feathering is nearly perfect ($|\theta - 1| \ll 1$) for vanishingly light loading ($|\bar{C}_{T,0}| \rightarrow 0$), but

progressively departs from the state of perfect feathering ($\theta = 1$) as the specific-loading increases in magnitude. Although the basic characteristics of sub- and super-feathering of these different modes can be explained qualitatively even by a quasi-steady flow type of argument, the precise dependence of θ on loading and frequency σ_m seems crucial.

4. OPTIMUM LOCATION OF THE AXIS OF PITCH

As has been explained above, the optimum motion expressed in the basic form (with pitching about the mid-chord point) can be represented equivalently by (2), with the axis of pitch referred to an arbitrary point ($x = b$, $y = 0$), without altering the original optimum performance, such as its capacity of power absorption and its efficiency. Changes in position of the axis of pitch do not change the lift, but will generally alter the moment and the rate of working by the lift and moment. It is these changes that makes the choice of the axis of pitch a point of primary interest.

From the standpoint of engineering design, the problem of finding an optimum axis of pitch must include two main factors for consideration: (i) the resulting moment is required to be self-stabilizing so that sudden increases of wing incidence in a gusty stream will be restored to design condition rather than being further amplified, and (ii) the manner in which the optimum pitching is controlled depend on whether the moment of force is passive (flow-driven) or active (exerted by an external agency). We now proceed to discuss these two aspects with special reference to the optimum motion.

For simplicity of application, we choose the axis of pitch at a fixed point $x = b$, $y = 0$. Clearly, the moment about this new axis is related to the lift and the original moment (M , about $x = 0$, $y = 0$) by

$$M_b = M + bL. \quad (29)$$

If we require that the mean square (averaged over a time period) of M_b be minimum (with respect to b) at $b = b^*$, we immediately find that

$$M^* = M + b^* L, \quad b^* = -\overline{ML}/\overline{L^2}, \quad (30)$$

where \overline{ML} and $\overline{L^2}$ denote the time averages of ML and L^2 , and M^* is the minimum of the root-mean-square of M_b . In Fig. 6 the numerical values of b^* (based on unit half-chord length) are shown for the optimum motion (of the maximum efficiency branch). For the various values of $\bar{C}_{T,0}$, b^* approaches asymptotically the 1/4-chord point ($b^* = -0.5$) as the low-frequency limit and the 3/8-chord point ($b^* = -0.25$) as the high-frequency limit; between these two limits the $\sigma = \sigma_m$ line (minimum leading-edge suction) marks a gradual transition over the range of σ_m covered. It is a point of significance that the b^* -axis lies just behind the 1/4-chord point on a lightly loaded wing and moves only slightly backwards ($< 10\%$ of the chord length) with increasing loading — it is significant because the b^* -axis may be regarded as a good approximation of the effective center of pressure evaluated on the minimum root-mean-square basis. On this argument we may conclude that it

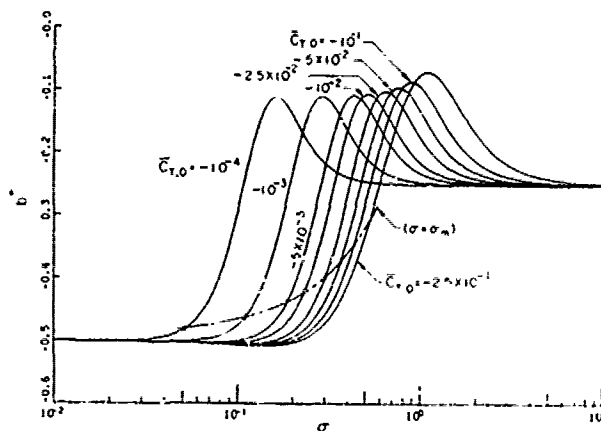


Fig. 6 The optimum location of the axis of pitch, $x = b^*$, $y = 0$, about which the moment of force of the optimum motion has its mean-square value minimum.

is advantageous in practice to choose the axis of pitch at the 1/4-chord point for the optimum power-extraction motion (or at some point between $b = -1/2$ and b^* for moderate to high loadings, but the difference in performance due to such more refined relocation of b is small).

The kinematics of the optimum motion expressed here in the new form with $b = b^*$ is given by (2), which is now characterized by two new parameters, the pitch-to-heave amplitude ratio, $Z_p^* = \alpha/h_0^* = Z_p(\xi_0/2h_0^*)$, and the phase difference between pitch and heave, $\alpha_p^* = \alpha_p - \alpha_h^*$, in which both h_0^* and α_h^* are given by (3), now incorporated with the optimum values of ξ_0, ξ_1, ξ_2 and with $b = b^*$. As can be seen from Figures 7 and 8, the

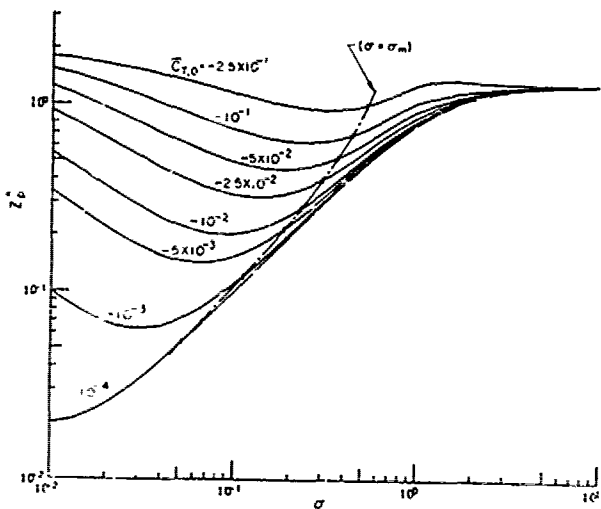


Fig. 7 The pitch-to-heave amplitude ratio, Z_p^* , when pitching is about the b^* -axis.

difference between Z_p^* and Z_p is very small along the $\sigma = \sigma_m$ line. At the same time, the phase difference between heave and pitch about the new b^* -axis is found to vary from 90° to 120° along the $\sigma = \sigma_m$ line, as shown in Fig. 8, a variation which is somewhat more appreciable than in the

original case of $b = 0$ (see Fig. 4).

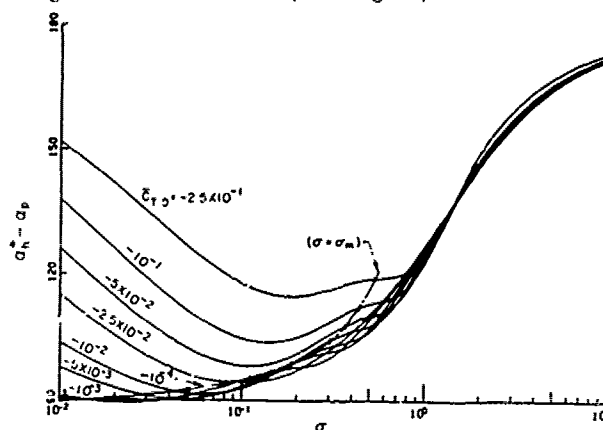


Fig. 8 The phase lag of pitching (about the b^* -axis) behind the phase of heaving.

With the axis of pitch changed from $b = 0$ to $b = b^*$ or $b = -1/2$, the accompanying changes of the moment are shown in Fig. 9 for the optimum motion at three values of the loading factor $C_{T,0}$ and at their corresponding frequencies of σ_m . The force and the moments are represented by their specific-coefficients defined as

$$\bar{C}_L = \frac{1}{2} / \left(\frac{1}{4} \pi \rho U^2 l \xi_0 \right), \quad (31a)$$

$$(\bar{C}_{M_0}, \bar{C}_M^*, \bar{C}_{M 1/4}) = \frac{(M, M + b^* l L, M - \frac{1}{2} l L) / (\frac{\pi}{4} \rho U^2 l^2 \xi_0)}{(31b)}$$

These coefficients are referred to a unit amplitude of heaving of the mid-chord point as a common basis. Several interesting features are noted from this quantitative comparison. First, for $b = b^*$, \bar{C}_M^* attains the smallest possible amplitude of all the moment coefficients (with respect to changes in b) and a nearly constant phase difference of 90° from that of \bar{C}_L , whereas the phase difference between \bar{C}_L and \bar{C}_{M_0} is appreciably smaller (from 60° down to 45°). Further, the difference between \bar{C}_M^* and $\bar{C}_{M 1/4}$ is seen to be very small at light loadings, and they become more differentiated only at higher values of $C_{T,0}$. This small difference makes the 1/4-chord point a desirable choice as the design axis of pitch since it satisfies the dynamic stability criterion at all levels of drag loading.

To exhibit the overall behavior of the lift and moment that result from the optimum motion at arbitrary frequencies, the root-mean-square values of \bar{C}_L and \bar{C}_M^* are shown versus σ in Figures 10 and 11. This result indicates that \bar{C}_L decreases whereas \bar{C}_M^* increases as the reduced frequency σ is increased across σ_m , which infers that the component of power delivered by the lift decreases whereas that by the moment increases as σ is increased in the neighborhood of σ_m .

This naturally leads into the second question concerning whether the moment is passive or

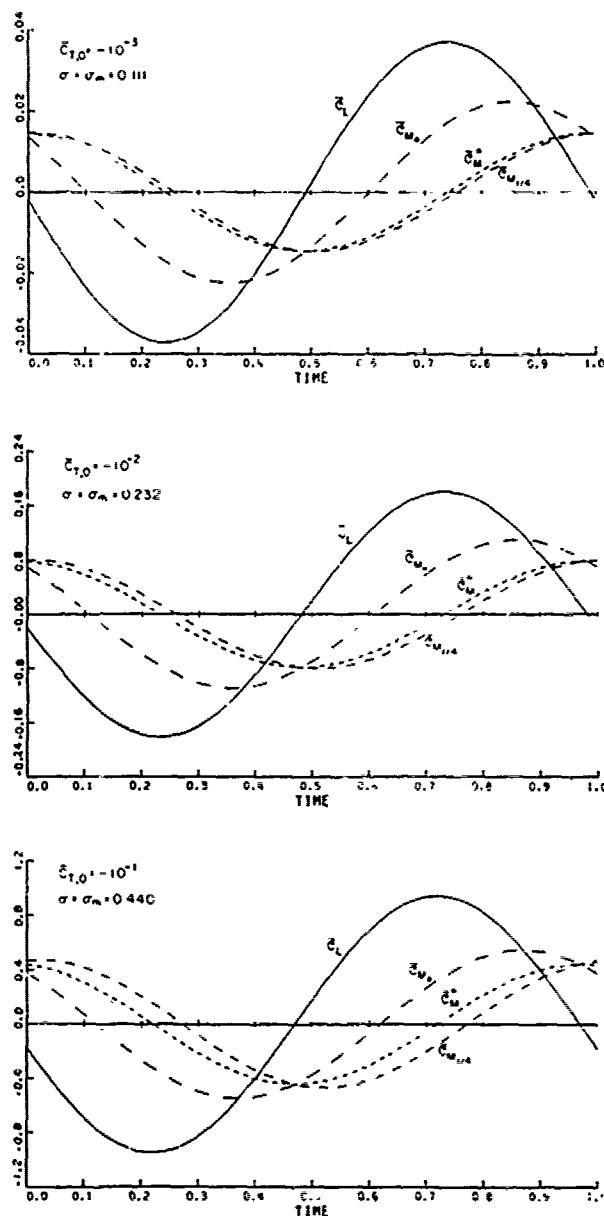


Fig. 9 The specific-moment-coefficients of the optimum motion at $\sigma = \sigma_m(\bar{c}_{T,0})$: $\bar{c}_{M,0}$ (about the mid-chord point), $\bar{c}_{M,b}$ (about the b^* -axis), and $\bar{c}_{M,1/4}$ (about the 1/4-chord point) are shown with \bar{c}_L over a time period.

or active. To find the answer, we decompose the total power required (taken positive) or absorbed (negative) into two components contributed separately by the lift and moment according to

$$P = P_L + P_M \quad (32a)$$

$$P_L = -[L][h_t(b, t)] \quad , \quad P_M = [M_b][h_{xt}] \quad , \quad (32b)$$

where M_b is given by (29), or to put in the specific-

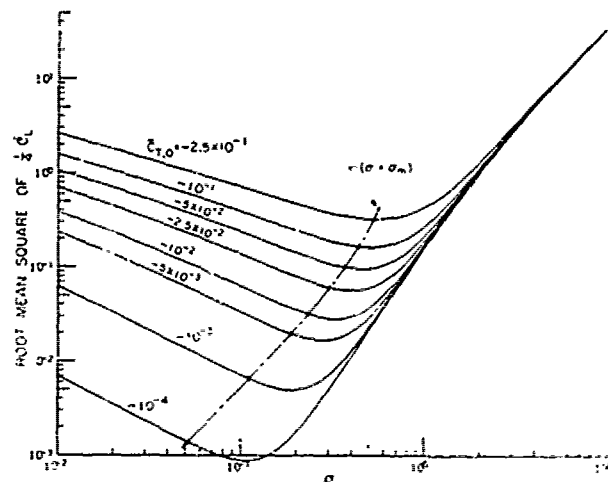


Fig. 10 Variation of the root-mean-square of the specific-lift-coefficient versus the reduced frequency σ .

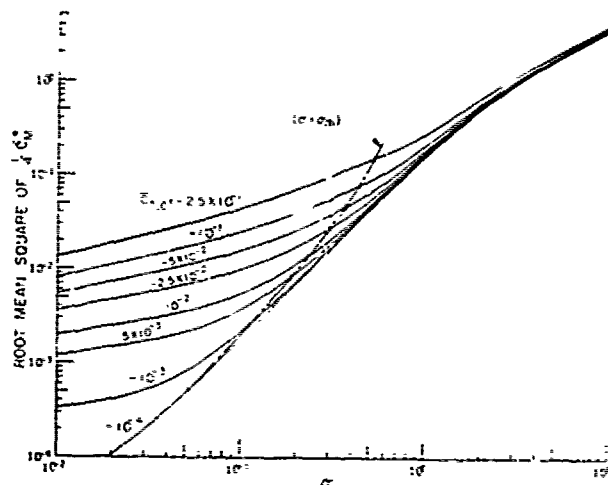


Fig. 11 Variation of the root-mean-square of the specific-moment-coefficient \bar{c}_M (about the b^* -axis) versus the reduced frequency σ .

coefficient form,

$$\bar{c}_P = \bar{c}_{PL} + \bar{c}_{PM} \quad (33a)$$

$$(\bar{c}_P, \bar{c}_{PL}, \bar{c}_{PM}) = (P, P_L, P_M) /$$

$$\left(\frac{1}{4} \pi \rho U^3 l^2 \xi_0^2 \right) \quad (33b)$$

The time mean value of \bar{c}_P , denoted by \bar{c}_P , is related to the mean power coefficient defined prior to (11) by

$$C_P = \xi_0^2 \bar{c}_P \quad , \quad \bar{c}_P = \frac{1}{\tau} \int_0^\tau \bar{c}_P(t) dt \quad , \quad (34)$$

τ being the time period ($= 2\pi/\omega$).

In Fig. 12, the numerical results of \bar{C}_{PL} , \bar{C}_{PM} and \bar{C}_P are shown for $b = b^0$ and $\sigma = \sigma_m$ corresponding to three values of $\bar{C}_{T,o}$. We note that the power components \bar{C}_{PL} and \bar{C}_{PM} are almost in phase, while the amplitude ratio of $|\bar{C}_{PM}|/|\bar{C}_P|$ increases with increasing loading (equal to 0.05, 0.11, 0.24 at $\bar{C}_{T,o} = 10^{-3}, 10^{-2}, 10^{-1}$, respectively). More significantly, with $b = b^0$, \bar{C}_{PM} is virtually all positive, implying that the

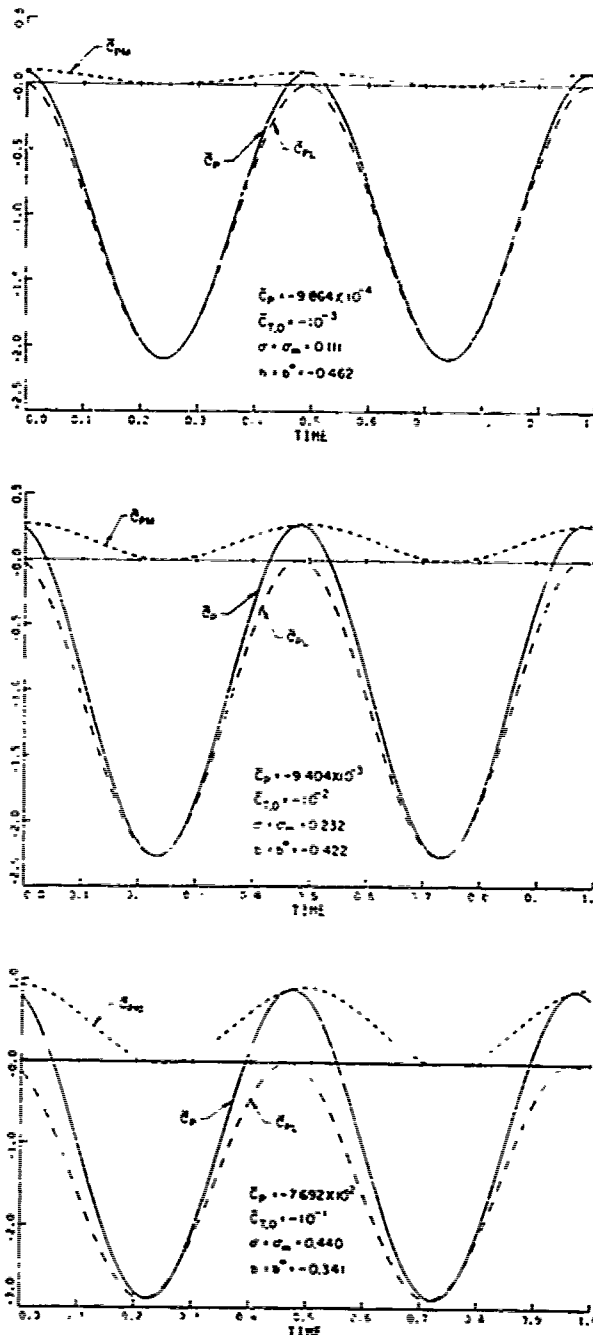


Fig. 12 $\bar{C}_P = \bar{C}_{PL} + \bar{C}_{PM}$; contribution to the instantaneous specific-power-coefficient from the lift and moment (about the b^0 -axis) over a cycle of the optimum motion - with the scale referred to $|\bar{C}_P|$.

corresponding moment is never passive (not flow driven) because external power is required to provide the given rate of working against the fluid dynamic moment of force. We can therefore conclude that the pitching of the optimum motion is stable when the axis of pitch is taken at $b = b^0$. This situation is scarcely changed when pitching is shifted to the 1/4-chord point but is somewhat weakened when pitching is kept at the mid-chord point (results not shown). In practical application, the power required for maintaining pitching, \bar{C}_{PM} , can be supplied by diverting a part of the power absorbed by the oscillating lift, \bar{C}_{PL} , to offset \bar{C}_{PM} , and this is at no expense to the total power output as previously determined.

5. THE RATED POWER OUTPUT

Our ultimate interest is of course to ascertain a theoretical upper limit to the amount of power that can be extracted from the available stream energy. To investigate this important limitation we first rewrite the relation (17) for the optimum motion with $\sigma = \sigma_m(\bar{C}_{T,o})$, and notin: $C_{T,o} = \xi_o^2 \bar{C}_{T,o}$, so that

$$\eta_B = -\frac{\pi}{2} \eta(\sigma_m(\bar{C}_{T,o}), \bar{C}_{T,o}) (\xi_o/l) \bar{C}_{T,o} \quad (\bar{C}_{T,o} < 0). \quad (35)$$

Since $\eta(\sigma_m, \bar{C}_{T,o})$ is seen (from Fig. 1) to be a slowly varying function of $\bar{C}_{T,o}$, true at least for $\bar{C}_{T,o}$ not too large, and since $\bar{C}_{T,o}$ is by definition independent of ξ_o for the optimum motion, it follows that the rated-power-output ratio, η_B , is linearly proportional to ξ_o/l . This seems to imply that η_B could be increased by taking greater and greater values of ξ_o/l . However, the present linear theory is not sufficient to determine if there exists an upper limit to ξ_o/l beyond which the optimum motion becomes infeasible.

On the other hand, if we adopt a momentum theorem, similar to that used by Betz (1926 [1]), with the simplifying assumption that the surface, of area $\xi_o \times 1$, swept by the heaving wing of unit span may be regarded as an actuated disc across which a uniform pressure jump can be sustained, then, as can readily be shown, the mean reactive drag, $-\bar{T}$, cannot exceed $(1/2)\rho U^2 \xi_o$. Putting this upper limit in the coefficient form, we have

$$0 < -\bar{T}/(\frac{1}{2}\rho U^2 \xi_o) = -\frac{\pi}{2} (\xi_o/l) \bar{C}_{T,o} < 1. \quad (36)$$

Under this condition, it appears possible for η_B to approach the hydromechanical efficiency η . However, the validity of the inequality (36) seems open to question in view of its over-simplified assumptions used.

As an example to give a plausible estimate of the upper limit to η_B , we provide the following table with entries derived from Fig. 1, 2 and equation (35) together with the values of ξ_o/l assumed in line with (36).

$\bar{C}_{T,o}$	σ_m	$C_S/ C_T $	η	ξ_o/l	η_B
-0.05	0.37	0.53	0.84	7.6	0.5
-0.1	0.44	0.68	0.77	5	0.6

In this connection we may remark that in the experimental study by Lang and Daybell (1963 [5]) on the tail fluke movement of a cruising porpoise, values of ξ_0/l as high as 8.3 were observed, and they were used by Wu (1971 [7]) for evaluating the propulsive efficiency.

In the present discussion on power extraction, the effects of viscosity and nonlinearity, and those other factors that may play a significant role in causing leading-edge separation under high loadings, and possibly imposing an ultimate limitation to η_B , have not been pursued. The importance of these effects cannot be assessed in full without further study.

ACKNOWLEDGMENT

I wish to acknowledge with deep appreciation the benefit I have derived from the sessions of valuable discussions with Dr. George T. Yates and his expert assistance in making available the numerical results for this study.

This work was partially sponsored by the Office of Naval Research, under Contract N00014-76-C-0157, NR062-230, and by the National Science Foundation, under Grant NSF CME-77-21236 A01. It is gratifying that the basic studies carried out earlier under these supports have inspired potentially useful applications.

REFERENCES

1. Betz, A. 1926 Windenergie und ihre Ausnutzung durch Windmühlen. (Vandenhoeck und Ruprecht, Göttingen.)
2. deVrie, O. 1979 Fluid Dynamic Aspects of Wind Energy Conversion. AGARDograph No. 243, Publ. AGARD.
3. Glauert, H. 1935 Airplane Propellers. In Aerodynamic Theory IV, ed. W.F. Durand, 170-360. Berlin:Springer.
4. Hütter, U. 1977 Optimum Wind-Energy Conversion Systems. Ann. Rev. Fluid Mech. 9, 399-419.
5. Lang, T. G. & Daybell, D. A. 1963 Porpoise Performance Tests in a Sea-water Tank. NAYWEPS Rep. 8060, NOTS TP 3063. Naval Ordnance Test Station, China Lake, California.
6. Lighthill, M. J. 1970 Aquatic Animal Propulsion of High Hydromechanical Efficiency. J. Fluid Mech. 44, 265-301.
7. Wu, T. Y. 1971 Hydromechanics of Swimming Propulsion. Part 2. Some Optimum Shape Problems. J. Fluid Mech. 46, 521-544.
8. Wu, T. Y. 1972 Extraction of Flow Energy by a Wing Oscillating in Waves. J. Ship Res. 14, No. 1, 66-78.
9. Wu, T. Y. & Chwang, A. T. 1975 Extraction of Flow Energy by Fish and Birds in a Wavy Stream. In "Swimming and Flying in Nature" Vol. II, 687-702, Eds. T. Y. Wu, C. J. Brokaw & C. Brennen. Plenum Press, New York/London.

NOMENCLATURE

- a_o, b_n - complex coefficients
- b^* - variable pitching axis, $x=b, y=0$
- b^* - value of b rendering the mean square of the moment M_b minimum
- A - $A^2 = A_1^2 + A_2^2$
- A_1, A_2 - functions of σ defined by (23)
- $B(\sigma)$ - $F - (F^2 + G^2)$
- C_E, C_P, C_T - mean-value coefficients of energy loss, power, and thrust, respectively
- $\bar{C}_L, \bar{C}_{M_o}, \bar{C}_M^*, \bar{C}_{M1/4}$ - specific lift and moment coefficients, defined in (31)
- $\bar{C}_P, \bar{C}_{FL}, \bar{C}_{PM}$ - instantaneous specific power coefficients, defined in (33)
- \bar{C}_P - mean specific-power coefficient
- C_S - $\bar{S}/(\frac{1}{2}\pi\rho U^2 l)$, mean leading-edge-suction coefficient
- $\bar{C}_{T,o}$ - $C_{T,o}/\xi_0^2$, specific-loading factor
- E - energy imparted to fluid; \bar{E} , its mean
- $F(\sigma), G(\sigma)$ - real, imaginary part of $\omega(\sigma)$
- $h(x, t)$ - wing displacement, in y -direction
- h_o - heaving amplitude of the b -axis of pitch
- h_o^* - value of h_o when $b = b^*$
- l - half-chord length of wing ($l = 1$)
- L - lift
- M - moment of force about mid-chord point
- $M_b = M - bL$ - moment about $x = b, y = 0$
- M_b - least root-mean-square of M_b
- \bar{P} - power required for maintaining wing motion; \bar{P} , its mean
- P_L, P_M - power required associated with L, M
- P_{av} - power available in incident flux of flow energy
- P, Q - two 3×3 matrices with elements P_{ij}, Q_{ij} defined in (13)
- S - leading-edge suction force
- T - thrust force, \bar{T} its mean value
- t - the time variable
- U - free stream velocity
- (x, y) - a rectangular coordinate system
- $Z_p = 2\alpha/\xi_0$ - pitch-to-heave magnitude ratio, pitching about mid-chord point
- $Z_p^* = \alpha/h_o^*$ - value of Z_p with $b = h_o^*$
- α - angular amplitude of pitching
- α_h, α_p - phase angle of heaving, pitching
- ξ_0, ξ_1, ξ_2 - parameters of wing motion
- $\zeta_0, \zeta_1, \zeta_2$ - parameters defined by (20)
- $\gamma = \bar{P}/\bar{T}U$ - fluid mechanical efficiency
- $\eta_B = -\bar{P}/P_{av}$ - rated power-output ratio
- $\xi = U\alpha/\omega h_o$ - proportional feathering parameter
- $\omega(\sigma) = F + iG$ - the Theodorsen function
- $\lambda, \lambda_1, \lambda_2$ - Lagrange multipliers
- Λ - real coefficient, defined in (26)
- ρ - fluid density
- $\sigma = \omega l/U$ - reduced frequency
- $\sigma_m = (\bar{C}_{T,o})$ - value of σ for minimum leading-edge suction at given $\bar{C}_{T,o}$
- ω - circular frequency of wing oscillation

Discussion

W. van Gent (NSMB)

The author is studying the power extraction from flow by one lifting surface. This is meant to be a starter for multiple blade systems. Does not he think that the wellknown cycloidal propeller with many blades (vertical-axis propeller) is a much closer approach to this problem? I think in the present environment of ONR the knowledge of this type of propulsion is also readily available in the turbine-mode. Is the author willing to comment on this?

J.N. Newman (MIT)

Professor Wu has treated us to a brilliant exposition, describing the absorption of energy from a steady moving fluid by an oscillatory lifting surface. The converse problem arises in the field of wave energy, where a Wells turbine is used to extract energy from an oscillatory air stream. Idealizing the latter problem, we may envisage the steady horizontal translation of an uncambered lifting surface, through a fluid with vertical oscillatory velocity. The resultant oscillatory inflow angle generates a mean positive thrust on the lifting surface, with resulting power output. Professor Wu's comments on this converse problem would be most enlightening.

Author's Reply

T.Y. Wu (CIT)

I very much appreciate Dr. van Gent's comments regarding possible variations of the pitch-and-heave mode that I have just discussed with an intent to have it serve as a basic case study. As briefly mentioned in the paper, our research is continuing to explore other alternative modes of operation, including rocking blades, multiple oscillating blades and vertical-axis rotating-propeller-like stream power generators. The last mode is being investigated by my student Jean-Luc Cornet with primary objectives to analyze the optimum motion for stream power extraction and to evaluate the stability and control of the

motion. With special reference to these aspects and the previous work by Edwin C. James (Ref.1), new operational parameters arise in our investigation of the power extraction mode and appear to require further study. In the present state of the art, I feel that our knowledge is still insufficient for us to draw an overall judgement on the superiority of any one operational mode with respect to such major factors as the hydromechanical efficiency, cost effectiveness, and safeguard (which we wish to emphasize for operations in water streams) of both marine lives and generator blades.

In regard to Professor Sparenberg's theory of actuator-disc optimum propulsion, I think that practical applications of his basic theory to power generating operations certainly seem to be feasible, but would require further effort in design and engineering development.

Professor Newman's question brings up a valuable extension of the present scope to consider the performance of a Wells turbine operating in an oscillatory unidirectional stream. My first reaction to this problem is that the hydromechanical efficiency of the "Wells-type turbine" can be considerably improved by giving the turbine blades an additional degree of freedom in pitching (which it now lacks) and by having the pitch motion optimized with respect to the oscillatory stream. I am greatly indebted to Professor Newman for bringing this interesting problem to our attention and wish to offer my optimism, to those interested, that one can obtain the solution to the optimum motion for this case by following the approach of this preliminary study and an earlier paper by myself (Ref.[8], cited in text) which deals with the optimum extraction of flow energy from a wavy stream for the purpose of propulsion.

Finally, I think it is important that our Session Chairman, Professor Ogilvie, raises the question on the value of studying the optimum motion, for this immediately brings together the hydromechanical problem with the economic aspects of a new industrial development whose success must depend on its prospect in winning competition over existing sources of commercial power. Further, it is also essential that we should tap energy from natural resources with the least perturbation of our natural environment, lest we may face, in time, some undesirable, unforeseen, but inevitable consequences to inefficient handling of natural resources to such an extent that results in unbeneficial changes in the climate, land conservation and the courses of ocean streams.

REFERENCE

- 1) James, E.C. "1970 A Small Perturbation Theory for Cycloidal Propellers", Ph.D.Thesis, California Institute of Technology, Pasadena, California

Characteristics of New Wave-Energy Conversion Devices

Masatoshi Bessho

National Defense Academy, Yokosuka

Osamu Yamamoto, Norihisa Kodan and Mikio Uematsu

Tsu Research Laboratories of Nippon Kokan K.K., Tsu

Japan

ABSTRACT

A theory is given herein for the absorption of wave energy by means of a symmetrical body with wave energy conversion systems oscillating in a sinusoidal wave. Conditions for achieving a complete wave energy absorption were derived from the expressions for complete wave absorption. Moreover, as a practical application of the theory, two new wave energy absorbing devices were proposed and theoretical calculations and model tests were carried out on the wave and wave energy absorption of regular and irregular waves. Results of the experiments agreed well with the theoretical calculations. Moreover the results of the model tests verified a complete wave energy absorption.

NOMENCLATURE

A_R	= amplitude of reflected wave
A_T	= amplitude of transmitted wave
B	= breadth of floating body
C_R	= reflection coefficient
C_T	= transmission coefficient
C_{ij}	= coefficient of Eq. (12)
C_g	= group velocity
C_2, C_3	= hydrostatic restoring coefficient
D, D_1, D_3	= determinant of Eq. (12)
E_i	= wave exciting force in i -th direction
F_{ij}, f_{ij}	= hydrodynamic force in i -th direction caused by j -th mode's oscillation, Eq. (10)
g	= gravitational acceleration
GM	= metacentric height above C.G.
$H_i^*(K)$	= Kochin function of i -th mode's oscillation
I	= mass moment of inertia of the body

i	= unit of imaginary
K	= wave number = $2\pi/\lambda$
M	= mass of the body
n	= normal vector
R_i	= reaction force in i -th direction
P_e, P_r	= absorbed power in regular wave
P_i	= power of incident regular wave
P_i'	= absorbed power in irregular wave
P_i'	= power of incident irregular wave
p	= pressure on the surface of the body
$S(\omega)$	= incident wave energy spectrum
S_{ij}	= restoring coefficient of energy absorbing system
L	= girth length of the body
t	= time
W	= electric power absorbed by generator
X_i	= amplitude of i -th mode oscillation
∇	= displaced volume
Δl	= distance between two wave height meters (Fig. 4)
S_{ij}	= mass or mass moment of inertia of energy conversion system
C_a	= amplitude of incident wave
C_i	= displacement of i -th mode oscillation
η	= surface elevation
η_e	= efficiency of wave power absorption = $1 - C_T^2 - C_R^2$
η_c	= efficiency of wave power conversion
μ_{ij}	= damping coefficient of energy conversion system
R	= radius of gyration in rolling oscillation
λ	= wave length
ρ	= mass density of fluid
ω	= circular frequency

1. INTRODUCTION

Recently many studies have been made concerning the utilization of wave energy. The Wave-Activated Generator is one practical application of wave energy. Masuda[1]

invented this device in 1965 and Ryokuseisha put it into practical use. McCormick [2], [3] developed theoretical analysis of the pneumatic wave-energy conversion bouy system and the results of his analysis agreed with the experiment results of Masuda. Contrary to these studies, Isaacs [4] invented a wave powered pump which converts wave energy into water pressure that accumulates in an accumulator tank and which activates a hydraulic turbogenerator when the water pressure is released from the tank.

Independent of these practical applications of wave energy, Milgram [5] investigated the problem of absorbing two-dimensional water waves in a channel by means of a moving terminator at the end of the channel. Though the object of his study was to devise and develop a self-actuating wave-absorbing system, his idea, to generate a radiation wave that is exactly opposite to the reflected wave, could be easily extended to the problem of achieving wave energy absorption through the use of an oscillating body with wave energy conversion systems. As just such an extension of Milgram's idea, Bessho developed a theory for achieving wave and wave energy absorption by means of a symmetrical body with wave energy conversion systems oscillating on a free surface and his theory was read at the second subcommittee of Japan Towing Tank Committee in 1973.

In 1976, Evans [6] carried out a theoretical study on predicting the absorption of wave energy by means of a damped, oscillating, and partly or completely submerged body. He derived expressions on the efficiency of power absorption for the case where the body is a two-dimensional cylinder oscillating in either a single mode or in a certain combination of two modes and when the body is a heaving half-immersed sphere. In 1978, Count [7] applied Evans' theory to a two-dimensional asymmetrical wave power device and made a comparison between the calculated and measured efficiencies of a Salter duck. Recently Srokosz and Evans [8] investigated the problem of two arbitrary cylinders oscillating independently and capable of absorbing energy in a single mode from a given incident wave.

Contrary to these studies on the two-dimensional problem of wave energy absorption, the recent theoretical studies were directed on the efficiency of three dimensional wave energy absorption. Budal and Falnes [9] began a study on a resonant point absorber and defined power absorption length in 1975. Budal [10] also theoretically analyzed a wave power absorbing system that consists of a number of rigid, interspaced, oscillating bodies in 1977. Using slender-body approximation, Newman [11] provided a rough analysis of the maximum rate of wave energy absorption by a flexible or hinged raft.

The present paper is intended to outline Bessho's theory and to show the

results of theoretical and experimental studies conducted on the two new wave energy conversion devices which were developed as a part of results of Bessho's theory.

On the contrary to other theories, his theory was developed by using the condition for complete wave absorption, which is substantially similar to the condition for achieving 100% wave energy absorption. Following to his theory, it is shown in §2 that the complete wave and wave energy absorption can be attained in the case when the floating body with energy conversion systems oscillates in its natural period and the damping coefficients of the energy conversion systems are the same as the one of the wave diffraction.

One of the two new wave energy conversion devices is moored at dolphins in shallow waters (abbreviate as "Dolphin Type") and the other is moored by chain in the deep sea (abbreviate as "Chain Type"). In the case of the "Dolphin Type", a half-immersed symmetrical body oscillates in only two modes, heaving and rolling, and the swaying motion is constrained so that 100% wave energy absorption may be attained. In the latter case, since the floating symmetrical body oscillates in three modes, complete wave energy absorption is not yet completed. The results of the theoretical and experimental studies made on these two devices are described in §3 and §4. Wave absorption achieved by the "Dolphin Type" in the case of irregular waves is discussed in §5. The experimental data is also given

2. THEORY OF WAVE-ENERGY ABSORPTION

2.1. Formulation

Two-dimensional motions are considered and cartesian co-ordinates (x, y) are chosen as shown in Fig. 1. It is assumed that the fluid motion is inviscid and incompressible, and that the resulting oscillatory motions are linear and harmonic.

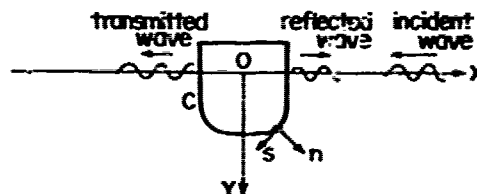


Fig. 1 Co-ordinate system

When a body oscillates in a incident wave of unit amplitude, the amplitudes of the reflected and transmitted wave far from the body can be expressed as:

$$A_R = iK \sum_{j=1}^N X_j H_j^*(\kappa) \quad (1)$$

$$A_T = 1 + iK \sum_{j=1}^N X_j H_j^*(\kappa) \quad (2)$$

where κ = wave number = $2\pi/\lambda$

X_j = amplitude of j -th mode oscillation

$$X_4 = 1/K$$

$H_j^{\pm}(K)$ = Kochin function of j -th mode oscillation

Here $j = 1, 2, 3$ refer to sway, heave, roll, respectively, and $j = 4$ refers to diffraction of incident wave by the fixed body. When the body is fixed in a incident wave, the expressions for the reflected and transmitted wave (1) and (2) become:

$$A_R = \frac{1}{2} H_4^+(K) \quad (3)$$

$$A_T = 1 - \frac{1}{2} H_4^-(K) \quad (4)$$

These waves may be called as the scattered waves and can be considered as the sum of the symmetrical and asymmetrical waves progressing to far away from the body. On the other hand, if the floating body has a symmetrical sectional form, the heaving motion generates a symmetrical radiation wave and the swaying or rolling motion generates an asymmetrical radiation wave.

Using the characteristics of the Kochin functions for a symmetrical body (See Appendix I, (A.14) - (A.17)), the symmetrical and asymmetrical components of the scattered wave can be expressed as following.

$$A_R + A_T = \frac{H_4^+}{H_4^-} + 2 \frac{1}{K} K X_4 H_4^+ \quad (5)$$

$$A_R - A_T = \frac{H_4^-}{H_4^+} + 2 \frac{1}{K} K \{X_1 H_1^+ + X_2 H_2^+\} \quad (6)$$

As above mentioned, the conditions for the complete wave absorption are:

$$A_R + A_T = 0 \quad (7)$$

$$A_R - A_T = 0 \quad (8)$$

If we can realize such motions that satisfy the equations (7) and (8) by adding suitable wave-energy conversion systems, the symmetrical and asymmetrical radiation waves cancel out each components of the scattered wave respectively due to interference. In other words, the incident wave is completely absorbed and consequently wave energy absorption can be completely attained.

2.2. Equations of Motion

Under the assumptions that the responses are linear and harmonic and that the sectional form of the floating body is symmetry, the equations of motion can be written as:

$$\begin{aligned} M \ddot{\zeta}_1 &= F_1 + F_{13} + E_1 + R_1 \\ M \ddot{\zeta}_2 &= F_2 - C_2 \zeta_2 + E_2 + R_2 \\ I \ddot{\zeta}_3 &= F_3 + F_{33} - C_3 \zeta_3 + E_3 + R_3 \end{aligned} \quad (9)$$

where ζ_i is a displacement of i -th mode's motion. F_{ij} is hydrodynamic force in i -th direction caused by j -th mode of motion, C_i is restoring coefficient, E_i is wave exciting force in i -th direction, and R_i is reaction force in i -th direction acting on the floating body from the energy absorbing system. ζ_i , F_{ij} , and E_i can be written as follows:

$$\begin{aligned} \zeta_i &= X_i e^{i\omega t} \\ F_{ij} &= S \omega^2 X_j \int_{ij} e^{i\omega t} \\ &= S \omega^2 X_j (\int_{ijc} + \int_{ijs}) e^{i\omega t} \\ E_i &= -S g H_i^+(K) \end{aligned} \quad (10)$$

It is assumed that the wave energy absorbing system operates independently with respect to the symmetrical and asymmetrical mode of motion, the reaction forces R_i can be expressed as following:

$$\begin{aligned} R_1 &= S g \{ (K S_{11} - S_{11} - i K \mu_{11}) \zeta_1 + (K S_{12} - S_{12} - i K \mu_{12}) \zeta_2 \} \\ R_2 &= S g (K S_{22} - S_{22} - i K \mu_{22}) \zeta_2 \end{aligned} \quad (11)$$

Substituting the expressions (10) and (11) into the equations (9), and abbreviating the term $e^{i\omega t}$, the equations of motion become:

$$\begin{aligned} C_{11} X_1 + C_{13} X_3 &= H_1^+(K)/K \\ C_{22} X_2 &= H_2^+(K)/K \\ C_{31} X_1 + C_{33} X_3 &= H_3^+(K)/K \end{aligned} \quad (12)$$

where

$$\begin{aligned} C_{11} &= \nabla + \int_{11c} + \delta_{11} - S_1/K - i \{ \mu_{11} + |H_1^+(K)|^2 \} \\ C_{13} &= \int_{13c} + \delta_{13} - S_{13}/K - i \{ \mu_{13} + \overline{H_1^+(K)} H_3^+(K) \} \\ C_{22} &= \nabla + \int_{22c} + \delta_{22} - (S_{22} + B)/K - i \{ \mu_{22} + |H_2^+(K)|^2 \} \\ C_{31} &= \int_{31c} + \delta_{31} - S_{31}/K - i \{ \mu_{31} + \overline{H_3^+(K)} H_1^+(K) \} \\ C_{33} &= \nabla K^2 + \int_{33c} + \delta_{33} - (S_{33} + B)/K - i \{ \mu_{33} + |H_3^+(K)|^2 \} \end{aligned} \quad (13)$$

The solutions of equations (12) can be easily obtained and written as:

$$\begin{aligned} K X_1 &= D_1/D \\ K X_2 &= H_2^+(K)/C_{22} \\ K X_3 &= D_3/D \end{aligned} \quad (14)$$

where

$$\begin{aligned} D &= \begin{vmatrix} C_{11} & C_{13} \\ C_{31} & C_{33} \end{vmatrix} \\ D_1 &= \begin{vmatrix} H_1^+(K) & C_{13} \\ H_3^+(K) & C_{33} \end{vmatrix} \\ D_3 &= \begin{vmatrix} C_{11} & H_1^+(K) \\ C_{31} & H_3^+(K) \end{vmatrix} \end{aligned} \quad (15)$$

2.3. Wave Absorption

At first, by substituting the solutions of the equations of motion into (7), the condition that should be satisfied for absorbing the symmetrical component of the scattered wave is obtained as follows:

$$C_{22} = -iZ |H_2^*(K)|^2 \quad (16)$$

or

$$\left. \begin{aligned} \nabla^2 + f_{22} + \delta_{22} - (S_{22} + B)/K &= 0 \\ \mu_{22} &= |H_2^*(K)|^2 \end{aligned} \right\} \quad (17)$$

It is known by (17) that if we have the system resonates with the incident wave in heaving motion and the magnitude of the damping coefficient of the energy conversion system is equalized with that of wave making heave damping of the body, $(A_R + A_T)$ becomes to zero.

On the other hand, the absorbed wave power in the aforementioned condition becomes:

$$P_e = \frac{1}{2} \rho \omega^3 \mu_{22} |X_2|^2 = \frac{S_2^2}{2} = \frac{P_i}{2} \quad (18)$$

where P_i represents the incident wave power

Expression (18) shows that half of the incident wave power is absorbed by the system.

Secondly, let us investigate the condition that satisfies the equation (8). By substituting the expression (14) into (8), the condition that should be satisfied for absorbing the asymmetrical component of the scattered wave is obtained as:

$$\frac{D_1 H_1^*(K) + D_2 H_2^*(K)}{D} = \frac{i H_1^*(K)}{2 H_1^*(K)} \quad (19)$$

It should be noted here that both rolling and swaying motions as known by (6) are not always necessarily employed. If the swaying motion is restricted, Eq. (19) can be simply rewritten as:

$$C_{23} = -iZ |H_2^*(K)|^2 \quad (20)$$

or

$$\left. \begin{aligned} \nabla^2 + f_{23} + \delta_{23} - (S_{23} + \nabla \bar{G})/K &= 0 \\ \mu_{23} &= |H_2^*(K)|^2 \end{aligned} \right\} \quad (21)$$

In the same way as the symmetrical part of scattered wave, it is known by (21) that if we have the system resonates with the incident wave in the rolling motion and the magnitude of the damping coefficient of energy conversion system is equalized with that of wave making roll damping of the body, $(A_R - A_T)$ becomes to zero.

In this case, the absorbed wave power becomes:

$$P_e = \frac{1}{2} \rho \omega^3 \mu_{23} |X_2|^2 = \frac{S_2^2}{2} = \frac{P_i}{2} \quad (22)$$

Therefore, if we choose the parameters of wave-energy conversion system so

as to satisfy (17) and (21) simultaneously, both the transmitted wave and reflected wave are diminished to zero and the incident wave power is perfectly absorbed by this wave-energy conversion system.

To verify these theoretical results, two kind of wave-energy absorbing systems were made, and the tank test was carried out. One of these is a system using two modes of motion (heaving and rolling) and swaying motion is restricted by dolphins. The other is a system that freed all modes of motion and moored by chain. The former is described in the following section and the latter in §4.

3. WAVE ENERGY CONVERSION: DEVICE MOORED AT A DOLPHIN

3.1. Model Experiments

(1) Model Characteristics

The principal dimensions and characteristics of the model are shown in Table 1.

Table 1 Characteristics of model

item	
Length	2.960 m
Width	1.000 m
Draft	0.300 m
Displacement	444.12 Kg
Center of buoyancy ($\bar{K}B$)	0.1957 m
Center of gravity ($\bar{K}G$)	0.300 m
Metacenter height ($\bar{G}M$)	0.451 m
Water plane area	2.960 m ²
Radius of gyration	0.332 m
Natural period of heaving motion	1.35 sec
Natural period of rolling motion	1.35 sec

This 1:10 scale model has a Lewis Form section, as shown in Fig. 2.

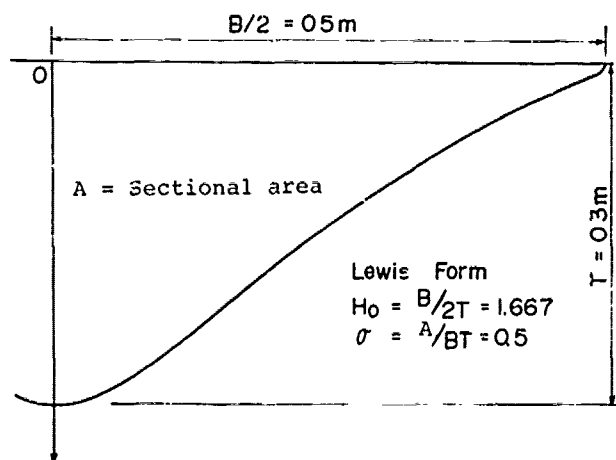


Fig. 2 Section of model

(2) Experimental Apparatus

The experiments were conducted in 50m (length) x 3m (width) x 1.5m (water depth) wave basin. The basin was equipped with a piston type wave maker which could generate regular and irregular waves. The maximum wave height is 0.5m and the range of wave period is from 0.5 to 4.0 sec.

The model was set at the center of the basin and was connected to a beam, which had been built over the basin instead of the dolphin by three connecting rods with hinges to permit free oscillation. The arrangement is shown in Fig. 3.

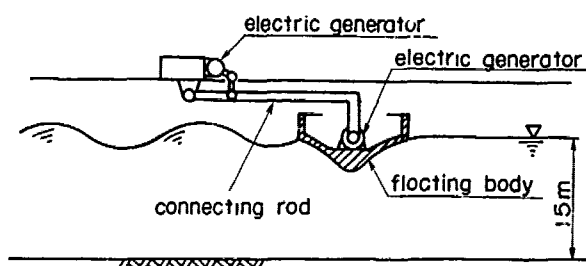


Fig. 3 Experiment apparatus

In this arrangement, the relative motions of the floating body and connecting rods and of the connecting rods and beam (dolphin) drove the electric generators which were located at both ends of the center rod.

In the external circuits of the generators, the variable electric resistors were connected so that the damping factors of the wave energy conversion devices may be adjusted to the wave generation damping factors.

And then one-way clutches and gears were set up at the each electric generators so that the electric generators could

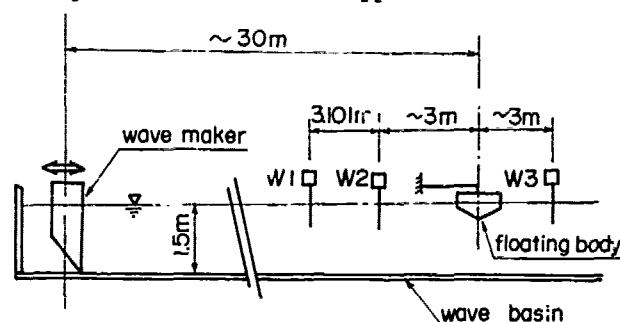
revolve in one direction despite the alternative motion of connecting rod. The gears multiplied the rotation 300 times for heaving motion and 200 times for rolling motion. Since it had been estimated that, in this experiment, the maximum incident wave power would be about 160 watts (wave length 3.0m and wave height 0.2m), two 80 watt direct current generators were selected for heaving motion and rolling motion respectively.

(3) Measurement

The following items were measured:

-Wave height

Incident wave height and reflected wave height were measured by means of capacitance type wave height meters W1 and W2 which had been arranged as shown in Fig. 4. Transmitted wave height was measured by W3 (see Fig. 4). The method used to calculate the incident wave height and reflected wave height is described in Appendix-II.



(W1, W2, W3 ; wave height meter)

Fig. 4 Measuring of wave height

-Motions of the floating body

The motions of the floating body were measured by means of a displacement meter which was composed of potentiometers, with 6-degrees of freedom. The measuring system is shown in Fig. 5. The measuring arm was attached just at the center of gravity of the floating body.

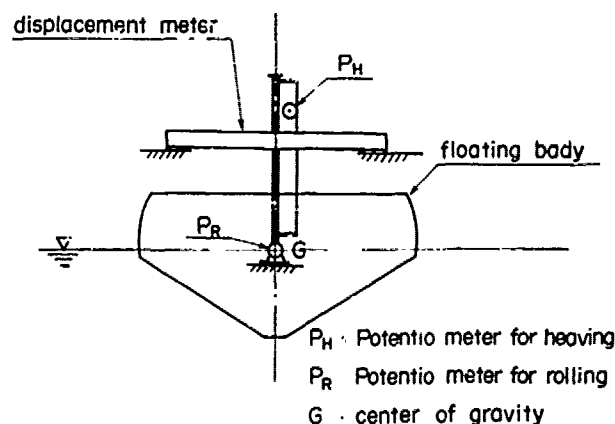


Fig. 5 Measuring of motions

-Generated electric power

The voltages which were generated by the heaving device and rolling device were measured by means of volt meters (see Fig. 6).

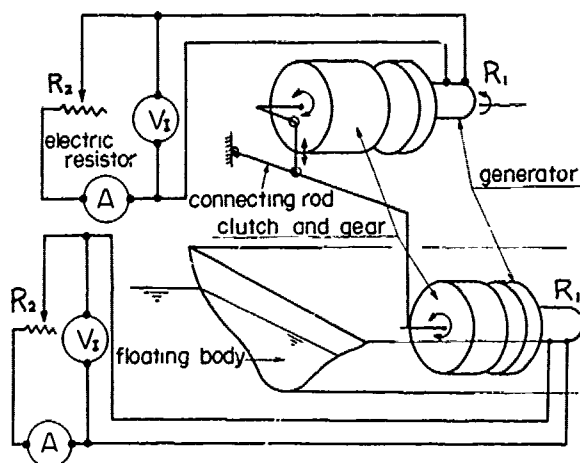


Fig. 6 Damping devices

The circuit current was calculated by dividing the voltage (V_1) by the resistance of the external circuit (R_2). Then the electric power was calculated as the product of the circuit current and the square of the total resistance which is the sum of the external and internal resistance (R_1 , see Fig. 6).

The measured values were then recorded on an analogue data-recorder and analyzed with the aid of a electric computer.

(4) Wave Conditions

The incident waves were regular ones. The range of wave heights was from 0.1 to 0.2m and the wave period from 0.9 to 2.82 sec.

3.2. Results of the Experiment

(1) Motions of the Floating Body

Figs. 7 and 8 show the heaving motion and rolling motion of the floating body.

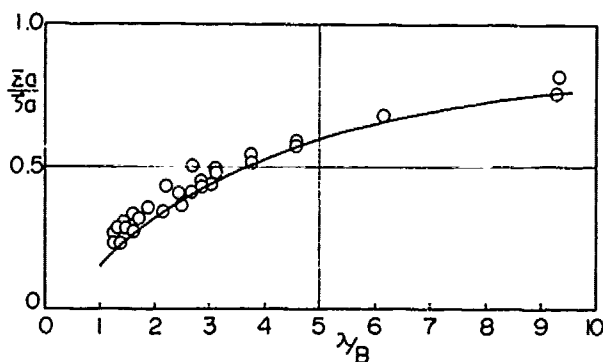


Fig. 7 Heaving motion

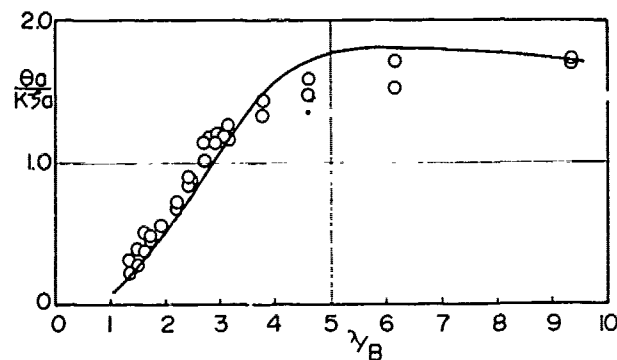


Fig. 8 Rolling motion

The small circles in the figures represent the experimental data, and the full lines represent the theoretical values. These values are divided by the incident wave amplitude (λ_a) or wave slope ($K\lambda_a$). The abscissa represents the ratio of the wave length (λ) to the width of the floating body (B).

It is recognized that the experimental data agree well with the theoretical results.

(2) Characteristics of Wave Transmission and Wave Reflection

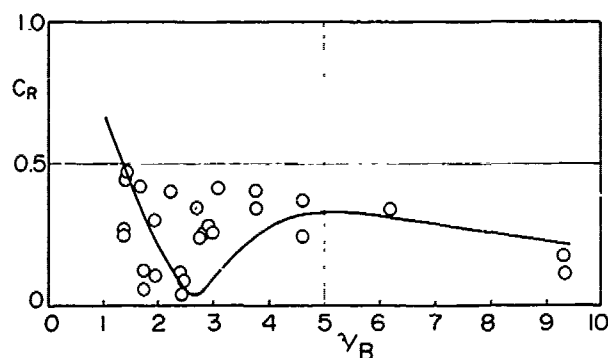


Fig. 9 Wave reflection coefficient

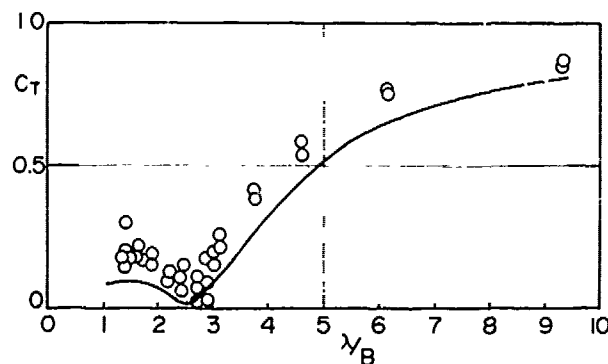


Fig. 10 Wave transmission coefficient

Figs. 9 and 10 show the reflection coefficient (C_R) and the transmission coefficient (C_T). C_R means the ratio of the reflected wave height to the incident wave height, and C_T , the ratio of the transmitted wave height to the incident wave height. (The method used to calculation C_R and C_T is described in Appendix-II.)

In these figures, C_R , together with C_T , has the minimum value (nearly equal to zero), when $\lambda/B=2.5$; that is, when wave length reached 2.5 times as long as the width of the floating body, the incident wave energy is almost completely absorbed. Hence, a calm sea appears behind the floating body.

When the incident wave length is less than 4.7m ($\lambda/B \leq 4.7$), the transmitted wave height is reduced to below 50%.

(3) Efficiency of Wave Power Absorption

The efficiency of wave power absorption is shown in Figs. 11 and 12.

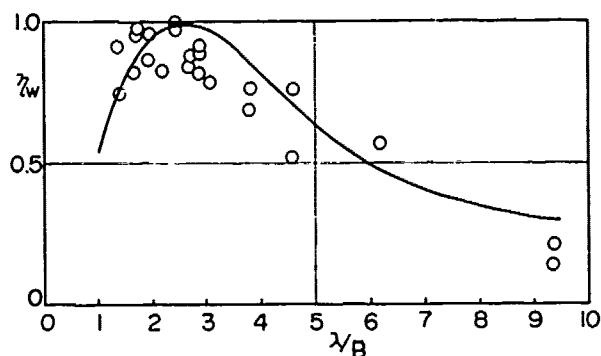


Fig. 11 Efficiency of wave power absorption

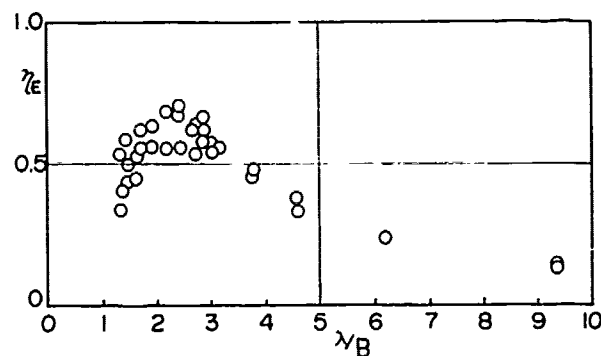


Fig. 12 Efficiency of wave energy conversion

In these figures, wave energy absorption efficiency, η_w is defined by equation (28).

$$\eta_w = 1 - C_T^2 - C_R^2 \quad (28)$$

Whereas, energy conversion efficiency is expressed by equations (29) and (30).

$$\eta_E = W / P_w \quad (29)$$

$$\begin{cases} W = \frac{1}{T_0} \int_0^{T_0} (R_1 + R_2) (V_z(t))^2 / R_1^2 dt \\ P_w = \frac{1}{2} \rho g^2 J_a^2 C_g L \end{cases} \quad (30)$$

where, W means the electric power converted by the electric generator, P_w means the incident wave power and L means the length of the floating body.

In regards to wave absorption efficiency η_w , it is evident that the wave energy is completely absorbed by the device when the reflected wave and the transmitted wave are diminished simultaneously ($\lambda/B = 2.5$, see Figs. 9 and 10). On the other hand, the experiment results of energy conversion efficiency η_E were short of the theoretical values by 20~30% (see Fig. 12). This loss may be composed of mechanical loss (mainly in the gears and clutches) and of scattering waves of higher order.

To confirm this point, free oscillation tests of the wave energy absorption device were carried out, in which the electric resistors had been removed so that the generated power was not consumed, and about 20~30% absorption of wave energy was verified.

4. WAVE ENERGY CONVERSION DEVICE MOORED BY CHAINS

4.1. Model Experiments

(1) Model Characteristics

The principal dimensions and characteristics of this model are given in Table 2. This model has a Lewis-Form section, as shown in Fig. 13.

Table 2 Characteristics of model

Item	
Length	2.900 m
Width at water plane	1.000 m
Draft	0.500 m
Displacement	870.0 Kg
Metacenter height (\overline{GM})	0.200 m
Center of gravity (\overline{KG})	0.418 m
Radius of gyration	0.350 m
Natural period of heaving motion	1.56 sec
Natural period of rolling motion	1.85 sec

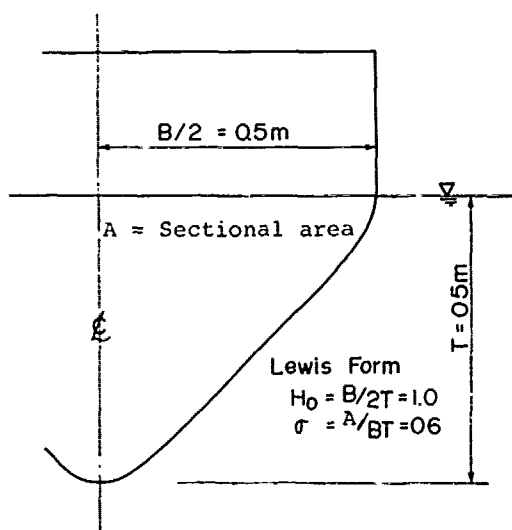


Fig. 13 Section of model.

(2) Experiment Apparatus and Measured Items

Experiments concerning the "Chain Type" device were conducted in the same basin that had been used to test "Dolphin Type" device.

The arrangement of experiment apparatus is shown in Fig. 14.

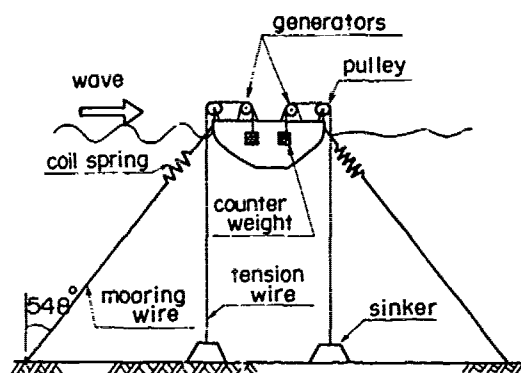


Fig. 14 Experiment apparatus

The floating body was moored by 4 sets of stainless steel wire and coil spring, instead of by chains. The angle between the mooring wire and vertical line was 55° . The spring constant of the coils was about 1.0 kg/cm .

The damping devices were, as shown in Fig. 14, composed of electric generators, pulleys, sinkers, tension wires and counter weights. One end of the tension wire was connected to the sea bed (this is, to the sinker), and the other end was led into the hull of the floating body via

pulleys and a damping device, and was attached to the counter weight (30 kg).

The gears, clutches and electric generators were similar to those used in the "Dolphin Type" device tests.

In order to control the damping factors 70Ω electric resistors were connected to the electric generators in series. The electric circuits were also similar to those used in the "Dolphin Type" device tests.

The measured items were wave heights, motions of the floating body (heaving, rolling and swaying motion) and generated voltage, and these were measured by systems similar to those used in "Dolphin Type" device tests.

(3) Wave Conditions

The experiments were performed in regular waves. The wave height was constant, 0.1m , and the wave length varied from 1.3m to 9.3m .

4.2. Results of the Experiments

(1) Motions of the Floating Body

Figs. 15, 16 and 17 show the heaving, rolling and swaying motions of the floating body.

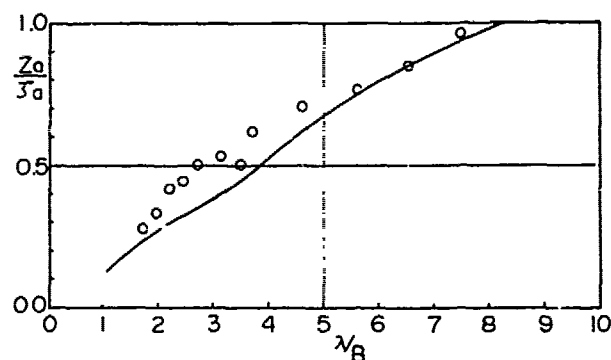


Fig. 15 Heaving motion

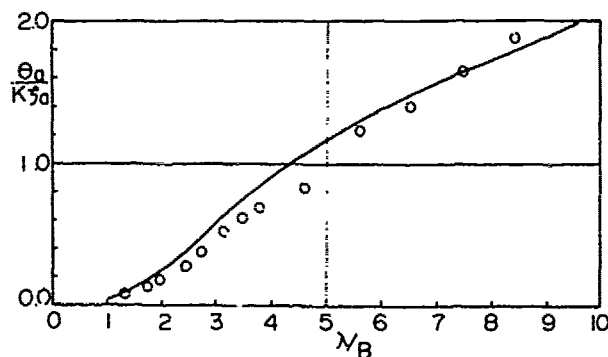


Fig. 16 Rolling motion

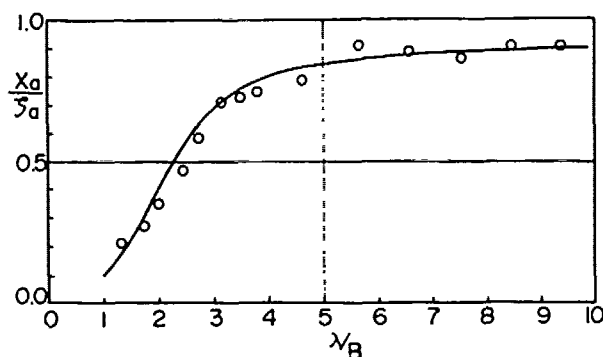


Fig. 17 Swaying motion

In the figures, the small circles represent the results of the experiment and the full lines the theoretical values, which were divided by the incident wave amplitude (λ_a) or wave slope ($K\lambda_a$).

Close agreement between the results of the experiment and the theoretical values was observed.

(2) Characteristics of Wave Transmission and Wave Reflection

Figs. 18 and 19 give the wave reflection coefficient C_R and the wave transmission coefficient C_T . C_T is about 0.5 for those waves with 3.8m wave length ($\lambda/B = 3.8$).

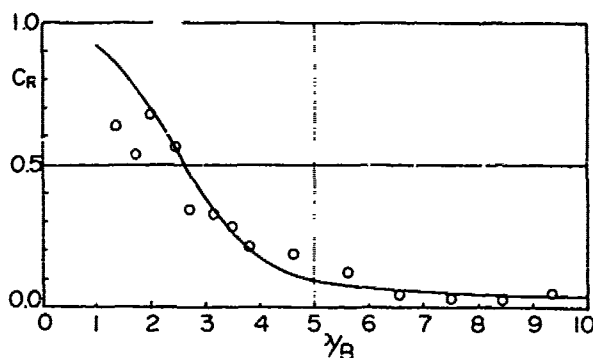


Fig. 18 Wave reflection coefficient

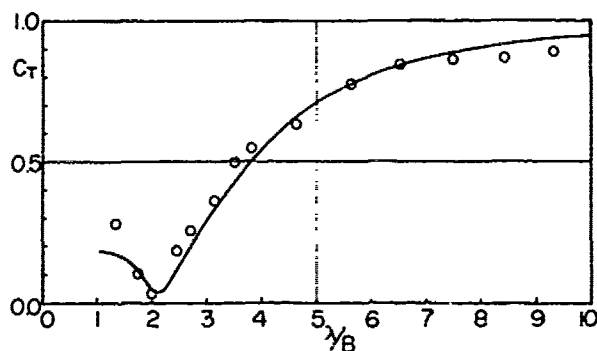


Fig. 19 Wave transmission coefficient

As for C_R and C_T , the results of the experiment agreed well with the theoretical values, and it was thus confirmed that the theory was reasonable.

(3) Efficiency of Wave Power Absorption

Wave energy absorption efficiency η_w and energy conversion efficiency η_E (defined by equations (28) and (29), respectively) are shown in Figs. 20 and 21.

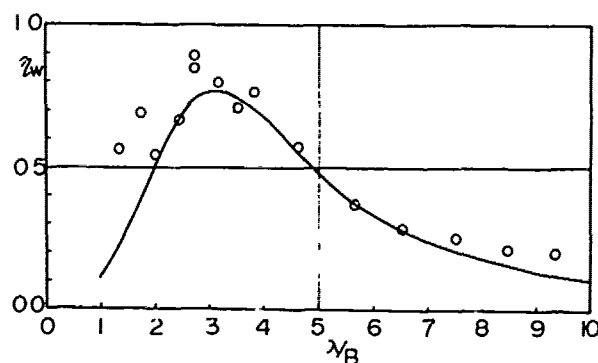


Fig. 20 Efficiency of wave power absorption

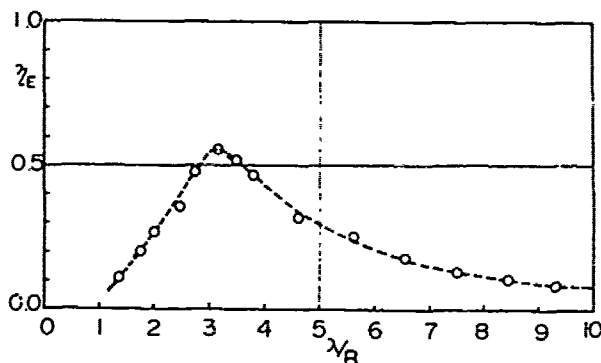


Fig. 21 Efficiency of wave energy conversion

η_w has the maximum value for $\lambda/B=3.0$, the theoretical value being 76% and experiment value 80%. The theoretical results and the experiment results agreed well. (Scattering of η_w when $\lambda/B=3$ were caused by errors made in the calculation of the reflected wave heights.)

η_E , as shown in Fig. 21, also has a maximum value for $\lambda/B=3.0$; however, the value is about 55%. It is believed that the difference between η_w and η_E was due to the mechanical loss in the gears.

Compared with that of the "Dolphin Type" device, η_w of the "Chain Type" device is somewhat inferior. The reason may be considered as that the swaying motion of the floating body for the "Chain Type" device is not controlled to absorb wave energy, though the swaying motion of the "Dolphin Type" device is restrained. Therefore, the reflecting energy caused by the non-controlled swaying motion makes absorption efficiency low.

5. WAVE POWER ABSORPTION OF IRREGULAR WAVES

It is common to adopt the linear superposition theorem for predicting some phenomena that occur in irregular waves; for example, ship motions in a random sea-way. In this section we shall consider the applicability of this theorem for predicting wave power absorption of irregular waves in the two-dimensional case.

The power absorbed by a wave energy conversion device in irregular waves can be represented as the difference between incident wave power and the total power of reflected and transmitted waves. If we adopt the linear superposition theorem to predict reflected and transmitted waves, then we can denote incident wave power P_i , reflected wave power P_R and transmitted wave power P_T as the following:

$$\begin{aligned} P_i &= \frac{1}{2} \rho g^2 \int_0^\infty \frac{S(\omega)}{\omega} d\omega \\ P_R &= \frac{1}{2} \rho g^2 \int_0^\infty \frac{C_R^2(\omega) S(\omega)}{\omega} d\omega \\ P_T &= \frac{1}{2} \rho g^2 \int_0^\infty \frac{C_T^2(\omega) S(\omega)}{\omega} d\omega \end{aligned} \quad (21)$$

where $S(\omega)$ is an energy spectrum of an incident wave. Absorbed power P_A is described in the following:

$$\begin{aligned} P_A &= P_i - (P_R + P_T) \\ &= \frac{1}{2} \rho g^2 \int_0^\infty \frac{\{1 - C_R^2(\omega) - C_T^2(\omega)\} S(\omega)}{\omega} d\omega \end{aligned} \quad (32)$$

Consequently, efficiency of wave power absorption is

$$\begin{aligned} \eta_w &= \frac{P_A}{P_i} \\ &= \frac{\int_0^\infty \{1 - C_R^2(\omega) - C_T^2(\omega)\} S(\omega) d\omega}{\int_0^\infty S(\omega) d\omega} \end{aligned} \quad (33)$$

If reflected coefficient $C_R(\omega)$ and transmission coefficient $C_T(\omega)$ in regular waves are known, absorbed power P_A and efficiency of wave power absorption η_w can be easily calculated by using equation (32) and (33).

In these equations energy spectrums of reflected and transmitted waves are expressed by the product of the incident wave energy spectrum and the square of the reflection or transmission coefficient in regular waves respectively. In order to verify these relations, we conducted an experiment using a model of the "Dolphin Type" at the wave basin.

Characteristics of the model, experiment apparatus and measuring systems are described in §3. A typical example of an incident wave energy spectrum, reflected wave energy spectrum and transmitted wave energy spectrum measured during the model test is shown in Fig. 22 and Fig. 23.

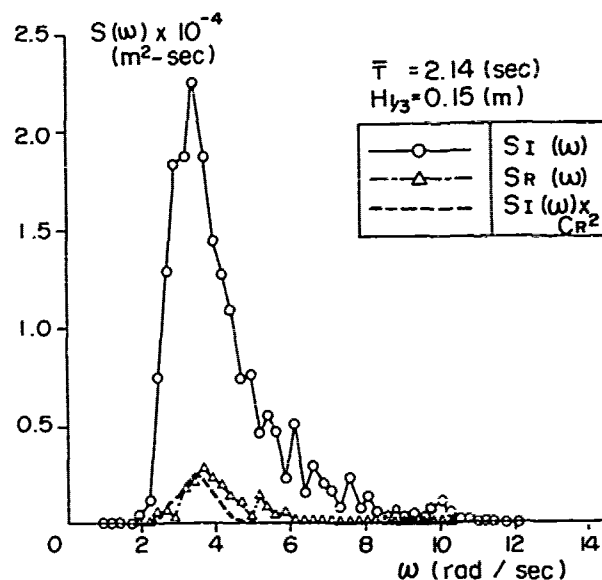


Fig. 22 Energy spectrums of incident wave and reflected wave

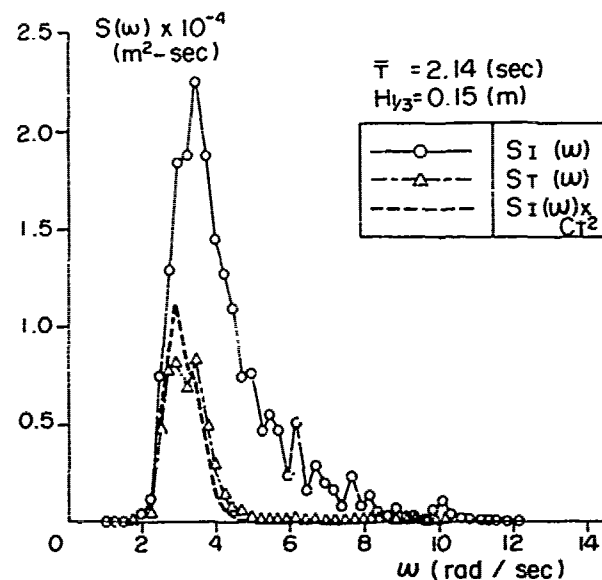


Fig. 23 Energy spectrums of incident wave and transmitted wave

The full lines in these figure represent the results of the model experiment and the broken lines represent the results of calculation in which theoretical values were used for the reflection and transmission coefficients and experimental values for the incident wave energy spectrum. These figures show that the results of calculation agree well with the experimental results on the reflection and transmission coefficients in irregular waves. From this result, we may conclude that equation (31) is useful for predicting the reflected and transmitted wave powers in

irregular waves. Therefore we can reasonably predict absorbed power and efficiency of wave power absorption by using equation (32) and (33).

6. CONCLUSION

A theory for predicting wave energy absorption by using a two-dimensional, half-immersed, symmetrical body with wave energy conversion systems is outlined in §2. The theory was developed by the use of the condition for achieving complete wave absorption and led to the conclusion, that the complete wave absorption can be attained if the natural frequencies of the symmetrical and asymmetrical oscillation modes are tuned to the desired frequency and the damping coefficients of the wave energy conversion systems are the same as the wave generation damping coefficients for the symmetrical and asymmetrical oscillation modes. Furthermore it was showed that, if the above conditions are satisfied, a complete wave energy absorption can be also attained and each half of an incident wave power is absorbed by each energy conversion systems for the symmetrical or asymmetrical oscillation modes.

Applying the conclusions of the theory, we proposed two new wave energy conversion devices and carried out theoretical calculations and model experiments. The theoretical and experimental studies concerning motion and wave absorption showed good agreement with each other. The results of model experiments conducted on the "Dolphin Type" were especially good as they verified a complete wave energy absorption which had been predicted by the theoretical calculations.

On the other hand it was difficult to attain a complete wave energy absorption in the case of the "Chain Type". Because the floating body oscillates in three degrees of freedom, two asymmetrical radiation waves are generated by the swaying and rolling motions and, although the natural period of rolling can be easily attuned to a given period, it is very difficult to attune the natural period of swaying in the same manner because the restoring forces of the mooring lines are too small. For these reason, in the present study we could not attain complete wave energy absorption. Thus, the maximum efficiency of wave energy absorption for this type device was only 80% both in the model experiment and in theoretical calculations.

In §5, the prediction of wave energy absorption in irregular waves was considered and it was confirmed that the linear superposition theorem is useful for this purpose. We also showed that the energy spectrums of reflected and transmitted waves can be predicted as the product of the incident wave energy spectrum and the square of the reflection or the transmission coefficient respectively.

ACKNOWLEDGEMENT

We wish to acknowledge kind advices that we received from Professor S. Motora and his constant encouragement.

REFERENCES

1. Masuda, Y., "Wave Activated Generator", International Colloquium on the Exposition of the Oceans, Bordeaux, France, March 1971.
2. McCormick, M.E., "Analysis of Wave-Energy Conversion Bouy", Journal of Hydronautics, Vol. 8, No.3, July 1974, pp.77-82.
3. McCormick, M.E., "A Parametric Study of a Wave-Energy Conversion Bouy", Proceedings of Offshore Technology Conference, Paper No. OTC2125, May 1974, pp.959-966.
4. Isaacs, J.D., Castel, D. and Wick, G. L., "Utilization of the Energy in Ocean Waves", Ocean Engineering, Vol. 3, 1976, pp. 175-187.
5. Milgram, J.H., "Active Water-Wave Absorbers", Journal of Fluid Mechanics, Vol. 43, Part 4, 1970, pp.845-859.
6. Evans, D.V., "A Theory for Wave-Power Absorption by Oscillating Bodies", Journal of Fluid Mechanics, Vol. 77, Part 1, 1976, pp. 1-25.
7. Count, B.M., "On the Dynamics of Wave-Power Devices", Proceedings of Royal Society of London, Vol. 363, Series A, 1978, pp.559-579.
8. Srokosz, M.A. and Evans, D.V., "A Theory for Wave Power Absorption by Two Independently Oscillating Bodies", Journal of Fluid Mechanics, Vol. 90, Part 2, 1979, pp. 337-362.
9. Budal, K. and Falnes, J., "A Resonant Point Absorber of Ocean Wave Power", Nature, Vol. 256, 1975, pp.478-479.
10. Budal, K., "Theory for Absorption of Wave Power by a System of Interacting Bodies", Journal of Ship Research, Vol. 21, No.4, Dec. 1977, pp.248-253.
11. Newman, J.N., "Absorption of Wave Energy by Elongated Bodies", Applied Ocean Research, Vol. 1, No.4, 1979, pp.189-196.
12. Kotik, J., "Damping and Inertia Coefficients for a Rolling or Swaying Vertical strip", Journal of Ship Research, Vol. 7, No.2, Oct. 1963, pp.19-23.
13. Wu, T.Y., "Extraction of Flow Energy by a Wing Oscillating in Waves", Journal of Ship Research, Vol. 16, No.1, Mar. 1972, pp. 66-78.
14. Bessho, M., "On the Theory of Rolling Motion of Ships among Waves", Scientific and Engineering Reports of the Defense Academy, Vol. 3, No.1, May 1965.
15. Bessho, M., "On the Theory of Rolling Motion of Ships among Waves", Scientific and Engineering Reports of the Defense Academy, Vol. 3, No.3, Jan. 1966.

16. Goda, Y., Suzuki, Y., Kishinami, Y., Kikuchi, O., "Estimation of Incident and Reflected Waves in Random Wave Experiments", Technical Note of the Port and Harbour Research Institute, No.248, 1976.

APPENDIX I

We denote the velocity potential $\Phi(x, y, t)$ as:

$$\Phi(x, y, t) = \operatorname{Re} \{ \varphi(x, y) e^{i\omega t} \} \quad (\text{A.1})$$

where (x, y) satisfied the following linearized free surface condition.

$$K\varphi(x, 0) + \frac{\partial}{\partial y} \varphi(x, 0) = 0 \quad (\text{A.2})$$

where K = wave number = $2\pi/\lambda$ while the surface elevation is expressed by using as:

$$H(x, t) = \operatorname{Re} \{ \eta(x) e^{i\omega t} \} \quad (\text{A.3})$$

where
$$\eta(x) = \frac{\omega}{ig} \varphi(x, 0) \quad (\text{A.4})$$

The incident wave and the diffraction wave velocity potentials are written as:

$$\varphi_i(x, y) = i \frac{g}{\omega} \phi_i(x, y) \quad (\text{A.5})$$

where $i = 0$: incident wave
 $i = 4$: diffraction wave

and
$$\phi_0(x, y) = e^{-ky + ikx} \quad (\text{A.6})$$

On the other hand, the radiation wave velocity potential is written as:

$$\varphi_i(x, y) = i \omega X_i \phi_i(x, y) \quad (\text{A.7})$$

where $i = 1$: swaying
 $= 2$: heaving
 $= 3$: rolling
and X_i : amplitude of i -th mode oscillation

Assuming that the motions are linear and harmonic, the total velocity potential $\varphi(x, y)$ can be written as:

$$\varphi(x, y) = i \omega \sum_{i=0}^4 X_i \phi_i(x, y) \quad (\text{A.8})$$

where $X_0 = X_4 = 1/K$

Here the Kochin function $H_i^+(K)$ can be introduced as:

$$H_i^+(K) = \int_c \left(\frac{\partial \phi_i}{\partial n} - \phi_i \frac{\partial}{\partial n} \right) e^{-ky + ikx} d\delta \quad (\text{A.9})$$

Hence, the progressing wave at $x \gg 1$ is expressed asymptotically as:

$$\phi_i(x, y) \rightarrow i H_i^+(K) e^{-ky + ikx} \quad (\text{A.10})$$

Let us divide the velocity potential into real part with subscript c , and imaginary part with subscript s , and is

described as:

$$\phi = \phi_c + i \phi_s \quad (\text{A.11})$$

The corresponding Kochin functions are written as:

$$H_{c,s}^+(K) = \int_c \left(\frac{\partial \phi_{c,s}}{\partial n} - \phi_{c,s} \frac{\partial}{\partial n} \right) e^{-ky + ikx} d\delta \quad (\text{A.12})$$

and
$$H_i^+(K) = H_{ic}^+(K) + i H_{is}^+(K) \quad (\text{A.13})$$

If the floating body has a symmetrical sectional form, the following relations are obtained.

$$H_1^+(K) = -H_1^-(K) \text{ (swaying)} \quad (\text{A.14})$$

$$H_2^+(K) = H_2^-(K) \text{ (heaving)} \quad (\text{A.15})$$

$$H_3^+(K) = -H_3^-(K) \text{ (rolling)} \quad (\text{A.16})$$

Furthermore, the Kochin function corresponding to the diffraction wave is described by that of radiation wave as:

$$H_4^+(K) = \frac{H_{2s}^+(K)}{H_2^+(K)} \pm \frac{H_{1s}^+(K)}{H_1^+(K)} \quad (\text{A.17})$$

where $H_i^+(K)$ means the conjugate of $H_i^+(K)$

Substituting (A.10), (A.8) into expression (A.4), the progressing waves propagate to outward are described at $|x| \rightarrow \infty$ as:

$$\eta^+(x) = i K \sum_{i=1}^4 X_i H_i^+(K) e^{i\omega t + ikx} \quad (\text{A.18})$$

From expression (A.18), the amplitude of the wave propagates in the $+x$ direction (reflected wave) is

$$A_R = i K \sum_{i=1}^4 X_i H_i^+(K) \quad (\text{A.19})$$

Similarly that of the transmitted wave, including the incident wave, is

$$A_T = 1 + i K \sum_{i=1}^4 X_i H_i^-(K) \quad (\text{A.20})$$

APPENDIX II

This appendix describes the calculation method of reflected wave height [16].

Generally, using the Fourier Analysis, time domain data $J(t)$ expands in a series of wave components with circular frequency ω_n (rad/sec).

The wave amplitude J_a , of which wave frequency is ω_0 (rad/sec), can be described by the following equations:

$$J_a = \sqrt{A^2 + B^2} \quad (\text{A.21})$$

$$A = \frac{1}{t_0} \int_0^{t_0} J(t) \cos \omega_0 t dt \quad (\text{A.22})$$

$$B = \frac{1}{t_0} \int_0^{t_0} J(t) \sin \omega_0 t dt \quad (\text{A.23})$$

where t_0 is the time duration of $J(t)$.

When the Fourier coefficients A and B are known, $J_{\omega_0}(t)$, wave component having circular frequency ω_0 , can be expressed as the following equation:

$$J_{\omega_0}(t) = A \cos \omega_0 t + B \sin \omega_0 t \quad (A.24)$$

It should be noted that if the Fourier coefficients of the wave data measured by means of one set of height meters located in front of the floating body (see Fig. 4), incident wave amplitude J_{a1} and reflected wave amplitude J_{aR} are calculated by using the following equations:

$$J_{a1} = \frac{1}{2|SIN k a L|} \left[(A_1 - A_1 \cos k a L - B_1 \sin k a L)^2 + (B_1 + A_1 \sin k a L - B_1 \cos k a L)^2 \right]^{1/2} \quad (A.25)$$

$$J_{aR} = \frac{1}{2|SIN k a L|} \left[(A_2 - A_1 \cos k a L + B_1 \sin k a L)^2 + (B_2 - A_1 \sin k a L - B_1 \cos k a L)^2 \right]^{1/2} \quad (A.26)$$

where A_1 and B_1 are the Fourier coefficients derived from the measured value of wave height meter W1, and A_2 and B_2 are the Fourier coefficients of W2, respectively.

Wave reflection coefficient C_R can be described as follow:

$$C_R = J_{aR} / J_{a1} \quad (A.27)$$

Discussion

K. Ikegami (MHI)

At first, I would like to show my respect to the first study on practical application of Prof. Bessho's theory on complete wave energy absorption.

I would like to ask some questions about the model test of "Chain type" device.

(1) The characteristics of model used in the "Chain type" device test is different from the ones in "Dolphin type" device test. It seems to me that it is more advantageous to use the same model in both tests in order to compare the characteristics of two types of devices. How did the authors decide the characteristics of model?

(2) Natural periods of heaving motion and rolling motion are not equal in "Chain type" device test. In order to attain a complete wave energy absorption, however, it is necessary to equalize both the natural periods of heaving and rolling motions as in "Dolphin type" device test. And it seems to me that the natural period of rolling motion can be easily attuned to a given period. Why did not the authors equalize both the natural periods of heaving and rolling motions?

(3) The rolling amplitude of floating body is shown in Fig.16. I can understand that the tendency of rolling amplitude to wave length shows the characteristics of motion influenced by larger damping. However, it seems to me that the values are very large in longer wave length range. May I understand that this is caused by coupling effect of rolling and swaying motions? If we could ask the authors for further explanation of the characteristics of the motion of the floating body in rather detail, especially the rolling motion, it would be highly informative, and appreciated very much.

(4) In the case of "Chain type" device test, swaying motion of floating body was not controlled. To the extent of my understanding, the condition for a complete wave energy absorption is to make both the symmetrical motion and either one of the asymmetrical motions resonant at the same frequency, and to give sufficient damping to each motions. Let me call your attention to a well-known formula, for further explanation.

$$\eta_{\text{rad,ASY}} = (X_1 + l_w X_3) H_1^+(k)$$

where

l_w : Sway-roll coupling lever for damping

This formula shows that asymmetric wave is

generated in far field by the transverse motion of the point which lies at the depth l_w below the water plane. It should be noted that rotational motion around the point is waveless motion at the specified frequency. Therefore, we can pay attention only to the transverse motion of that point. I think it is important to design a control system for the purpose to control the transverse motion of that point composed of swaying and rolling motions.

From this viewpoint, I think, changing the direction of tension wire might result in higher efficiency of wave energy absorption. Have the authors made such experiments or calculations? If I could hear the authors' opinion on these points, I would appreciate it very much.

Author's Reply

M. Bessho (National Defense Academy)

We thank Mr. Ikegami for his remarks on the model test of "the Chain type". At first, we decided the configuration as shown in Fig.14 on the standpoint of practical use and carried out parametric study with varying H_0 and σ of Lewis Form. Then we chose the sectional form of Fig.13 because it showed better efficiency than others.

In the case of Fig.14, as the tension wires are installed vertically, some coefficients of (13) become :

$$\begin{aligned} u_{11} &= u_{13} = u_{31} = 0 \\ c_{13} &= c_{31} = 0 \end{aligned} \quad (R.1)$$

Substituting eq. (R.1) into eq. (19), we obtain following equation.

$$C_{33R} = \frac{C_{11R} \{C_{13R}^2 - (H_1^+ \bar{H}_1^+ l_w)^2\} + 2C_{13R} H_1^+ \bar{H}_1^+ l_w^2}{C_{11R} + (H_1^+ \bar{H}_1^+)^2} \quad (R.2)$$

where $C_{ijR} = R_e \{C_{ij}\}$

The right hand of eq.(R.2) is not equal to zero in general. Therefore the natural period of rolling motion should differ from that of heaving motion for complete absorption of the asymmetrical scattered wave. But in our model test, eq.(R.2) could not be satisfied completely.

On the third question, it was shown by Prof. Tasai that nondimensional rolling response becomes to slightly less than unity in long wave range if additional restoring forces are attached. This fact must be also true in the case of "the Chain type". Unfortunately we did not calculate the response function in the long wave range. Thus we can not say how high the response function growth or where it begins to reduce.

On the last question, we suppose that there may be such a case as Mr. Ikegami pointed out. In the case where both swaying and rolling motions exist, the condition for complete absorption of the asymmetrical scattered wave is expressed by

eq.(19) or rewritten as :

$$(C_{11} + i2H_1^+ H_1^+) (C_{33} + i2H_3^+ H_3^+) - (C_{13} + i2H_1^+ H_3^+ l_w) (C_{31} + i2H_3^+ H_1^+ l_w) = 0 \quad (R.3)$$

If we adopt some restrictions on the coefficients of (13), that is :

$$u_{11} = u, u_{13} = u_{31} = l_w, u_{33} = l_w^2$$

$$C_{13} R = C_{31} R \quad (R.4)$$

We can find more simple relations than eq.(R.3) but we have not yet tested such a case.

Theoretical and Experimental Study on Wave Power Absorption

Hisaaki Maeda

*Institute of Industrial Science
The University of Tokyo Tokyo*

Hirohisa Tanaka

Yokohama National University, Yokohama

Takeshi Kinoshita

*Institute of Industrial Science
The University of Tokyo Tokyo*

Japan

ABSTRACT

In this paper, we show theoretical analyses and syntheses for floating-type wave power absorbers by comparing theoretical characteristics with experimental ones of the prototype which consists of Salters Duck and hydraulic power conversion mechanisms. Theoretical analyses are based on the time-reversed velocity potential proposed by Bersho, and the motions of six-rigid-body degrees of freedom in finite water depth are discussed.

We investigate theories and experiments with regard to hydrodynamic forces, absorbed wave power, load reaction forces which act on the two-dimensional or three-dimensional slender bodies with asymmetric sections oscillating in regular or irregular waves, and discuss about the effects of oblique waves, coupled motions and hydraulic load characteristics on the wave power absorption efficiencies.

From the test results, we confirm the following conclusions: the linear theory is applicable to the prediction of the performances of the absorber, the Salters Duck absorbs efficiently both regular and irregular wave power, and the hydraulic power conversion mechanism is successful in converting wave energy to mechanical energy due to its easy control and storage of energy.

Nomenclature

a	incident wave amplitude
B_0	floating body width
c_{ij}	hydrostatic restoring force coefficient
\underline{c}	restoring force coefficient matrix
D_0	draft of floating body
D	shallow water parameter
d_i	damping coefficient of load of the hydraulic system
\underline{d}	damping coefficient matrix of load
δ_{ij}	Kronecker's delta
E_0	wave excitation
\underline{E}	column vector of wave excitation
dE_i/dt	time averaged energy per unit time

η	wave power absorption efficiency (2-D), wave power absorption coefficient or 1.0n-dimensional absorption width ratio (3-D)
F_{ij}	radiation force
f_{ij}	standardized radiation force
f_{ij}	sectional standardized radiation force
\underline{F}	column vector of hydrodynamic force
F_D	drift force
$\bar{F}_{L,i}$	normalized load force (torque)
g	gravity acceleration
g_{ij}	linear restoring force coefficient of mooring system
\underline{g}	linear restoring force coefficient matrix of mooring system
Γ_{ii}	wetted hull surface
h	water depth
$H_i(\beta)$	radiation Kochin function
$H_d(\beta, \theta)$	diffraction Kochin function
H	wave height
H_w	visual wave height or significant wave height
$H_{\eta w}(\omega)$	response function of absorbed wave power
$H_{(i)w}(\omega)$	response function of j-th mode motion
$H_{Dw}(\omega)$	response function of drift force
K	wave number
k_i	restoring force coefficient of hydraulic system
\underline{k}	restoring force coefficient matrix of hydraulic system
l_i	amplitude of i-th mode motion
\underline{l}	column vector of amplitude of motion
l_p	laminar tube length
\bar{l}	distance between the origin and rolling axis
m_{ij}	generalized added mass
M_i	generalized mass
\underline{M}	generalized mass matrix
\underline{m}	generalized added mass matrix

2.1 Hydrodynamic forces

The radiation force component F_{ij} is written as

$$F_{ij} = \rho \omega^2 l_{ij} f_{ij} \quad (1)$$

where f_{ij} is a force component in direction i due to a unit velocity of the body in the direction j and l_{ij} is a complex amplitude of i -th mode motion. Here ρ is density of fluid and ω is a circular frequency. l_{ij} is given by

$$f_{ij} = \iint_{\Gamma_H} \phi_j \frac{\partial \phi_i}{\partial n} ds = f_{ji}^* \quad (2)$$

where ϕ_j is a radiation potential due to a unit velocity of the body in the direction j . The suffix denotes the direction of six rigid-body degrees of freedom, namely, surge, sway, heave, roll, pitch and yaw for $j = 1 \sim 6$, respectively. The term "force" is used here in a generalized sense, to include the moment.

The added mass m_{ij} and the wave damping coefficient N_{ij} are given by

$$m_{ij} = \rho (f_{ij} + f_{ji}^*)/2 \quad (3)$$

$$N_{ij} = -\rho \omega (f_{ij} - f_{ji}^*)/2i \quad (4)$$

respectively. A superscript $*$ indicates a complex conjugate. From the Hask relations, the wave excitation is

$$L_j = \rho g a D H_j(\beta + \pi) \quad (5)$$

Here g is a gravity acceleration, a is an amplitude of an incident wave, D is a shallow water parameter defined by

$$D = \tanh Kh + Kh \operatorname{sech}^2 Kh \quad (6)$$

and $H_j(\beta + \pi)$ is a radiation Kochin function defined by

$$H_j(\beta + \pi) = \frac{1}{D} \iint_{\Gamma_H} \phi_j(\beta) \frac{\partial \phi_j}{\partial n} ds \quad (7)$$

where $\phi_j(\beta)$ is a scattering potential defined by

$$\phi_j(\beta) = \phi_0(\beta) + \phi_d(\beta)$$

Here $\phi_0(\beta)$ is an incident wave potential defined by

$$\phi_0(\beta) = \frac{\cosh K(z+h)}{\cosh Kh} \exp[-iK(x \cos \beta + y \sin \beta)] \quad (8)$$

and $\phi_d(\beta)$ is a diffraction potential due to the body, where $K = 2\pi/\lambda$ is a wave number, λ is a wave length and $i = \sqrt{-1}$. The dispersion relation is

$$\omega^2 = Kg \tanh Kh \quad (9)$$

and a group velocity V_g is

$$V_g = \frac{K}{2\omega} D \quad (10)$$

A diffraction Kochin function is defined by

$$H_d(\beta, \theta) = \frac{1}{D} \iint_{\Gamma_H} \phi_d(\beta) \frac{\partial \phi_d(\theta + \pi)}{\partial n} ds \quad (11)$$

where the arguments β and θ denotes a Kochin function of direction θ due to an incident wave of direction β . The double integral should be replaced by a single integral in 2-D problems in (2), (7) and (11).

It is known that some useful relations exist between N_{ij} , $H_j(\beta)$ and $H_d(\beta, \theta)$. A time-reversed velocity potential is help-

ful to derive the relations as shown firstly by Bessho [2]. A time-reversed motion corresponding to the time-reversed velocity potential is, for example, a motion of reversed rotating movies. The time-reversed velocity potential is a complex conjugate of the original velocity potential. And it is also expressed in another form, by taking account of a uniqueness of a solution of the boundary-value problem. Namely the time-reversed velocity potential of a radiation (or a scattering) potential is a sum of the original radiation potential (or a scattering potential due to a reverse incident wave) and a scattering potential due to the time-reversed velocity potential. Let us derive this relation in case of 2-D radiation problems as an example.

An asymptotic behaviour of the radiation potential is

$$\phi_j \sim -iH_j(\pm \frac{\pi}{2}) \phi_0(\pm \frac{\pi}{2}) \cdot y \rightarrow \pm \infty \quad (12)$$

where arguments $\pm \pi/2$ correspond to $y \rightarrow \pm \infty$. And the complex conjugate ϕ_j^* is

$$\phi_j^* \sim iH_j^*(\pm \frac{\pi}{2}) \phi_0^*(\pm \frac{\pi}{2}) \cdot y \rightarrow \pm \infty \quad (13)$$

which denotes incoming waves at infinity, considering the time-dependent factor $\exp(i\omega t)$. Now introduce a supplementary potential ϕ_j^* which has out-going progressive waves at infinity,

$$\phi_j^* = \phi_j^* - i[H_j^*(\frac{\pi}{2}) \phi_0^*(-\frac{\pi}{2}) + H_j^*(-\frac{\pi}{2}) \phi_0^*(\frac{\pi}{2})] \quad \text{in } \Omega \quad (14)$$

where Ω is a fluid domain. Using the hull surface boundary condition of a scattering problem and considering that $\partial \phi_j / \partial n$ is a real function on the hull, the boundary condition of the supplementary potential ϕ_j^* is written as

$$\frac{\partial \phi_j^*}{\partial n} = \frac{\partial \phi_j}{\partial n} + i[H_j^*(\frac{\pi}{2}) \frac{\partial \phi_0^*}{\partial n}(-\frac{\pi}{2}) + H_j^*(-\frac{\pi}{2}) \frac{\partial \phi_0^*}{\partial n}(\frac{\pi}{2})] \quad \text{on } \Gamma_H$$

where Γ_H is the wetted hull surface.

From a uniqueness of the boundary-value problem with the radiation condition, ϕ_j^* defined by (14) is equal to

$$\phi_j^* = \phi_j + i[H_j^*(\frac{\pi}{2}) \phi_0^*(-\frac{\pi}{2}) + H_j^*(-\frac{\pi}{2}) \phi_0^*(\frac{\pi}{2})] \quad (15)$$

in the full fluid domain Ω , not only on the hull surface Γ_H . So that another form of the representation of the time-reversed potential ϕ_j^* is derived for a case of 2-D radiation problems. In the same manner, the following results are derived for cases of 2-D scattering problems and 3-D problems as well as 2-D radiation problems.

$$\phi_j^* = \phi_j + i[H_j^*(\frac{\pi}{2}) \phi_0^*(-\frac{\pi}{2}) + H_j^*(-\frac{\pi}{2}) \phi_0^*(\frac{\pi}{2})] \quad \text{in } \Omega \quad (16a)$$

$$\phi_j^* = \phi_j + \frac{iK}{2\pi} \int_0^{2\pi} \phi_d(\theta + \pi) H_d^*(\beta, \theta) d\theta \quad \text{in } \Omega \quad (16b)$$

$$\phi_j^* = \phi_j + i[H_d^*(\beta, \frac{\pi}{2}) \phi_0^*(-\frac{\pi}{2}) + H_d^*(\beta, -\frac{\pi}{2}) \phi_0^*(\frac{\pi}{2})] \quad \text{in } \Omega \quad (17a)$$

$$\phi_j^* = \phi_j + \frac{iK}{2\pi} \int_0^{2\pi} \phi_d(\theta + \pi) H_d^*(\beta, \theta) d\theta \quad \text{in } \Omega \quad (17b)$$

Here and hereafter a and b after a number of the equations denote

2-D case and 3-D case, respectively. The equations (16) and (17) were derived firstly by Bessho [2] for a case of an infinite depth of water. These relations are also held in case of a finite depth, if an incident wave and Kochin functions are defined by (8), and (7) and (11), respectively.

Substitution of (2) and (16) into (4) yields

$$N_{ij} = \begin{cases} \frac{\rho\omega D}{2} [H_1^* (\frac{\pi}{2}) H_j (\frac{\pi}{2}) + H_1^* (-\frac{\pi}{2}) H_j (-\frac{\pi}{2})] , \\ \frac{\rho\omega KD}{4\pi} \int_{-\pi}^{\pi} H_j (\theta) H_1^* (\theta) d\theta , \end{cases} \quad (18a)$$

$$(18b)$$

The right-hand side of (18) denotes the energy dissipation [2], [14].

Relations between Kochin functions are also derived from (16) and (17). Considering the conditions of original potentials and their time-reversed potentials at infinity like as (12) and (13), (16) and (17) yield

$$H_j^* (\beta) = H_j (\beta + \pi)$$

$$= \begin{cases} i [H_j^* (\beta + \pi) H_d (\beta, \beta + \pi) + H_j^* (\beta) H_d (\beta + \pi, \beta + \pi)] , \end{cases} \quad (19a)$$

$$= \begin{cases} \frac{iK}{2\pi} \int_{-\pi}^{\pi} H_d (\theta + \pi, \beta + \pi) H_j^* (\theta) d\theta , \end{cases} \quad (19b)$$

$$H_d^* (\beta, \theta) = H_d (\beta + \pi, \theta + \pi)$$

$$= \begin{cases} i [H_d^* (\beta, \theta + \pi) H_d (\theta, \theta + \pi) \\ + H_d^* (\beta, \theta) H_d (\theta + \pi, \theta + \pi)] , \end{cases} \quad (20a)$$

$$= \begin{cases} \frac{iK}{2\pi} \int_{-\pi}^{\pi} H_d (\alpha + \pi, \theta + \pi) H_d^* (\beta, \alpha) d\alpha . \end{cases} \quad (20b)$$

Here β and θ are either of $\pm\pi/2$ in (19) cases [2], [14].

From above relations and Green's theorem, some relations between reflected waves and transmitted waves as well as relations between reflected and transmitted waves and radiation Kochin functions are derived, which are helpful to check the accuracy of numerical calculations of 2-D hydrodynamic forces [8].

Let ξ_r^+ and ξ_r^- be a complex amplitude of reflected and transmitted waves of a fixed body, respectively, corresponding to the incident wave $\phi_0 (\mp\pi/2)$ of a unit amplitude. They are written as

$$\xi_r^+ = -iH_d (\mp\frac{\pi}{2}, \pm\frac{\pi}{2}) , \quad (21a)$$

$$\xi_r^- = 1 - iH_d (\mp\frac{\pi}{2}, \mp\frac{\pi}{2}) .$$

And from Green's theorem, we have

$$\xi_r^+ = \xi_r^+ \equiv \xi_r^- . \quad (22)$$

From (21) and (22), (20a) yields

$$\begin{cases} |\xi_r^+|^2 + |\xi_r^-|^2 = 1 , \\ \xi_r^- \xi_r^{+*} + \xi_r^+ \xi_r^{-*} = 0 . \end{cases} \quad (23)$$

$$|\xi_r^+| = |\xi_r^-| , \quad (24)$$

$$\arg (\xi_r^+) + \arg (\xi_r^-) = (2n+1)\pi + 2\arg (\xi_r^+) ,$$

$$n = 0, \pm 1, \pm 2, \dots , \quad (25)$$

and (19a) yields

$$H_j^* (\pm\frac{\pi}{2}) \xi_r^+ + H_j^* (\mp\frac{\pi}{2}) \xi_r^- = H_j (\pm\frac{\pi}{2}) , \quad j = 2, 3, 4 . \quad (26)$$

The linear equation (26) can be solved for ξ_r^+ , ξ_r^- and $\xi_r^+ = \xi_r^- = \xi_r$. From the uniqueness of the solutions, the modes of motion j are not independent each other. There are two linear independent modes. We can arbitrarily choose any two modes out of three modes of sway, heave and roll in case of an asymmetric shape of body about $y=0$. But note that roll and sway are linear dependent modes each other in case of a symmetric shape of body.

2-2 Equations of motion

A linear theory of the prediction of the motion of the floating body of wave power absorption is following. Without generality we can define an incident wave $\phi_0 (\pi/2)$ which progresses to positive y -axis. Let M , d , k , g , c , m , N and E be a mass of a floating body, a damping and a restoring force coefficient of an energy absorbing device which is a hydraulic system in this case, a linear restoring force coefficient of a mooring system, a hydrostatic restoring force coefficient, an added mass and a wave damping coefficient due to radiation and a wave excitation, respectively. The term "mass" in a generalized sense includes the moment of inertia, and similarly the term "force" includes the moment.

The equations of motion are

$$\begin{aligned} \sum_{j=1}^6 [(M_i \delta_{ij} + m_{ij}) \ddot{\xi}_j + (N_{ij} + d_i \delta_{ij}) \dot{\xi}_j \\ + (c_{ij} + k_i \delta_{ij} + g_{ij}) \xi_j] = E_i e^{i\omega t} , \\ i = 1, 2, 3, \dots, 6 , \end{aligned} \quad (27)$$

where

$$\delta_{ij} = \begin{cases} 1 & (i=j) , \\ 0 & (i \neq j) . \end{cases} \quad (28)$$

$$\xi_j = \xi_j e^{i\omega t} . \quad (29)$$

(27) are rewritten in a matrix forms,

$$\underline{A} \ddot{\underline{\xi}} + \underline{B} \dot{\underline{\xi}} + \underline{C} \underline{\xi} = \underline{E} e^{i\omega t} , \quad (30)$$

where $\underline{\xi}$ and \underline{E} are column vectors as follows.

$$\underline{\xi} = [\xi_j] = [1_j] e^{i\omega t} = \underline{1} e^{i\omega t} , \quad j = 1, 2, \dots, 6 , \quad (31)$$

$$\underline{E} = [E_j] , \quad j = 1, 2, 3, \dots, 6 , \quad (32)$$

and \underline{A} , \underline{B} and \underline{C} are square matrices, which correspond to coefficients of (27) of an acceleration, a velocity and a displacement, respectively. They are decomposed as follows.

$$\begin{aligned} \underline{A} &= \underline{M} + \underline{m} , \\ \underline{B} &= \underline{N} + \underline{d} , \\ \underline{C} &= \underline{c} + \underline{k} + \underline{g} . \end{aligned} \quad (33)$$

where the square matrices of mass \underline{M} , damping coefficient of a load \underline{d} and its restoring force coefficient \underline{k} are all diagonal, and those of added mass \underline{m} , wave damping coefficient \underline{N} , hydrostatic restoring force coefficient \underline{c} and linear restoring force coefficient of a mooring system \underline{g} are symmetric.

From (30) and (29), the response in regular waves is

$$\underline{1} = [\underline{C} - \omega^2 \underline{A} + i\omega \underline{B}]^{-1} \underline{E}, \quad (34)$$

where $[\]^{-1}$ denotes an inverse matrix. From (30) and (33), the hydrodynamic force defined by a sum of radiation forces and a wave excitation is represented in two forms, as

$$\begin{aligned} \underline{F} &= \underline{E} e^{i\omega t} - \underline{m} \underline{\ddot{x}} - \underline{N} \underline{\dot{x}} \\ &= \underline{M} \underline{\ddot{x}} + \underline{d} \underline{\dot{x}} + (\underline{c} + \underline{k} + \underline{g}) \underline{x}. \end{aligned} \quad (35)$$

2.3 Absorbed wave power and power characteristics

An absorbed wave energy is the work done by the hydrodynamic forces acting on the floating body. The time-averaged absorbed wave energy per unit time dE/dt is:

$$\frac{dE}{dt} = \frac{1}{T} \int_0^T \left[\int_{\Gamma_H} P \frac{\partial \Psi}{\partial n} ds \right] dt, \quad (36)$$

where the fluid pressure P and the velocity potential Ψ include the time-dependent factor, as follows

$$P = \text{Re} \left[-i\rho\omega \left(\sum_{j=1}^6 \Phi_j + \Phi_s \right) e^{i\omega t} \right], \quad (37)$$

$$\Psi = \text{Re} \left[\left(\sum_{j=1}^6 \Phi_j + \Phi_s \right) e^{i\omega t} \right], \quad (38)$$

here

$$\Phi_j = i\omega l_j \phi_j, \quad (39)$$

$$\Phi_s = \frac{iga}{\omega} \phi_s. \quad (40)$$

And we can derive the following relation,

$$\int_{\Gamma_H} P \frac{\partial \Psi}{\partial n} ds = \text{Re} \left[\underline{F}^T \underline{1} \right] \text{Re} \left[\underline{\dot{x}} \right], \quad (41)$$

where the superscript T denotes a transposed matrix.

Substituting (41) and (35) to (36), we have representations of dE/dt in two different forms, which are corresponding to the two forms of the hydrodynamic force column vector \underline{F} of (35). From the upper form of (35), which is a representation of the force from a point of view of a fluid, (36) yields

$$\begin{aligned} \frac{dE}{dt} &= \frac{i\omega}{4} \left[\underline{E}^* \underline{1} - \underline{E} \underline{1}^* - \frac{\omega^2}{2} \underline{1}^T \underline{N} \underline{1} \right] \\ &= -\frac{\omega}{2} \text{Im} \left[\sum_{j=1}^6 l_j \underline{E}_j^* \left(\frac{\pi}{2} \right) \right] - \frac{\omega^2}{2} \sum_{i=1}^6 \sum_{j=1}^6 l_i l_j^* N_{ij}, \end{aligned} \quad (42)$$

which was derived by Newman [14] and Mei & Newman [12]. From the lower form of (35), which is a representation of the force from a point of view of a body, (36) yields

$$\begin{aligned} \frac{dE}{dt} &= \frac{\omega^2}{2} \underline{1}^T \underline{d} \underline{1} \\ &= \frac{\omega^2}{2} \sum_{j=1}^6 d_{jj} l_j^*, \end{aligned} \quad (43)$$

which is an extension of the representation derived by Evans [4] to a case of 6 modes of motion.

(43) is more convenient than (42) from a point of view of optimization of a wave energy absorption system, since (43) includes the characteristics of the load of an energy absorbing

device explicitly. Both (42) and (43) are available in 3-D cases as well as in 2-D cases.

The optimal characteristics of the load, which are the damping coefficient d_j and the restoring force coefficient k_j , can be determined by the following conditions,

$$\frac{\partial}{\partial k_j} \left[\frac{dE}{dt} \right] = 0, \quad \frac{\partial}{\partial d_j} \left[\frac{dE}{dt} \right] = 0, \quad (44)$$

when a geometry of a floating body, a mooring system and a wave frequency ω are given.

If there are no coupling terms among each mode in the equations of motion, dE/dt is maximized when

$$d_j = N_{jj}, \quad (45)$$

$$k_j = \omega^2 (M_j + m_{jj}) - (c_{jj} + g_{jj}), \quad (46)$$

namely the damping coefficient is equal to the wave damping coefficient and the restoring force coefficient is chosen for its motion to be resonant [1], [4]. At this time, the amplitude of the motion is

$$l_j = \begin{cases} -\frac{iga}{\omega^2} \frac{H_j(-\frac{\pi}{2})}{|H_j(\frac{\pi}{2})|^2 + |H_j(-\frac{\pi}{2})|^2}, & (47a) \\ -\frac{i2\pi ga}{\omega^2 k} \frac{H_j(-\frac{\pi}{2})}{\int_{-\pi}^{\pi} |H_j(\beta)|^2 d\beta} & (47b) \end{cases}$$

And the maximized absorbed wave power is

$$\max \frac{dE}{dt} = \begin{cases} \frac{1}{2} \rho g a^2 V_k \sum_j \frac{|H_j(-\frac{\pi}{2})|^2}{|H_j(\frac{\pi}{2})|^2 + |H_j(-\frac{\pi}{2})|^2} & (48a) \\ \frac{1}{2} \rho g a^2 V_k \frac{2\pi}{k} \sum_j \frac{|H_j(-\frac{\pi}{2})|^2}{\int_{-\pi}^{\pi} |H_j(\beta)|^2 d\beta} & (48b) \end{cases}$$

where j denotes the independent modes. A number of the independent modes in 2-D cases is 2 at the most.

For general coupling motions, d_j and k_j which are given by the conditions (44) are different from (45) and (46), respectively. The conditions (44) give simultaneous higher order algebraic equations.

The time-averaged energy per unit time of an incident wave per unit length of the wave crest is $\rho g a^2 V_k / 2$. Now the wave energy absorption efficiency / coefficient (in 3-D cases) η is defined by

$$\eta = \begin{cases} \frac{dE/dt}{\frac{1}{2} \rho g a^2 V_k} & (49a) \end{cases}$$

$$\eta = \begin{cases} \frac{dE/dt}{\frac{1}{2} \rho g a^2 V_k B_0} & (49b) \end{cases}$$

where B_0 is the width of the floating body. The wave energy absorption coefficient is "the absorption width" non-dimensionalized by B_0 , which is able to be called "absorption width ratio".

It is convenient to express the dynamic characteristics of the hydraulic system as an energy absorbing device in terms of

the power characteristics, namely the relation between the load force (or torque), which corresponds to the pressure in the hydraulic cylinder, and the velocity (or angular velocity), which corresponds to the flow flux. Let \bar{F}_{Lj} and \bar{V}_{Lj} be the component of load force (or torque) with the same phase as the velocity (or angular velocity) normalized by a wave excitation and the velocity (or angular velocity) normalized by the velocity at the so-called natural frequency ω_0 of a j -mode motion, respectively. They are given by

$$\bar{F}_{Lj} = d_j \omega |l_j| / |E_j|, \quad (50)$$

$$\bar{V}_{Lj} = \frac{\omega |l_j|}{\omega_0 |l_j| \omega_0}, \quad (51)$$

where

$$\omega_0 = \sqrt{(k_j + c_{jj} + g_{jj}) / (M_j + m_{jj})}.$$

2-4 Characteristics of a floating breakwater and its drift force

The high efficiency of energy extraction means good characteristics as a floating breakwater. Not only 2-D devices but also 3-D devices with proper arrays can be used as a floating breakwater. An infinite array at regular intervals is one of the examples, since both its reflected and transmitted waves are sums of finite number of 2-D plane waves.

Firstly consider 2-D problem. Let the transmitted and reflected waves be ξ_T^- and ξ_R^- , respectively, corresponding to the incident wave ϕ_0 ($\pi/2$) of a unit amplitude. ξ_T^- (or ξ_R^-) is a sum of the transmitted (or reflected) waves ξ_T^- (or ξ_R^-) of a fixed body and the radiation waves, those are,

$$\xi_T^- = -\frac{i\omega^2}{g} \sum_j l_j H_j(\frac{\pi}{2}) + \xi_T^-, \quad (52)$$

$$\xi_R^- = -i \frac{\omega^2}{g} \sum_j l_j H_j(-\frac{\pi}{2}) + \xi_R^-, \quad (53)$$

where l_j is an amplitude of the motion of the body due to ϕ_0 ($\pi/2$), which is given by (34)

The drift force is

$$F_D / (\frac{1}{2} \rho g a^2 V_k \frac{2K}{\omega}) = \frac{1}{2} [2 - \xi_T^- - \xi_T^{*-} - (|\xi_T^-|^2 + |\xi_R^-|^2)] \quad (54)$$

Since

$$\eta = \frac{d\bar{F}}{d\bar{V}} / (\frac{1}{2} \rho g a^2 V_k) = 1 - (|\xi_T^-|^2 + |\xi_R^-|^2), \quad (55)$$

(54) yields

$$F_D / (\frac{1}{2} \rho g a^2 V_k \frac{2K}{\omega}) = |\xi_R^-|^2 + \frac{1}{2} \eta. \quad (56)$$

The drift force in 3-D cases is

$$\begin{aligned} F_D / (\frac{1}{2} \rho g a^2 V_k \frac{2K}{\omega} B_0) &= -\frac{\omega^2 B_0}{2g} \sin \beta \sum_{j=1}^7 [l_j H_j(\beta) + l_j^* H_j^*(\beta)] / B_0^2 \\ &\quad - \frac{KB_0}{4} (\frac{\omega^2 B_0}{g})^2 \int_{-\pi}^{\pi} |\sum_{j=1}^7 l_j H_j(\theta)|^2 \sin \theta d\theta / B_0^4, \quad (57) \end{aligned}$$

where $l_j = \frac{g}{\omega^2}$ and $H_j(\theta) = H_d(\beta, \theta)$.

Since

$$\begin{aligned} \eta &= \frac{d\bar{F}}{d\bar{V}} / (\frac{1}{2} \rho g a^2 V_k B_0) \\ &= -\frac{\omega^2 B_0}{g} \sum_{j=1}^7 [l_j H_j(\beta) + l_j^* H_j^*(\beta)] / B_0^2 \\ &\quad - \frac{KB_0}{2\pi} (\frac{\omega^2 B_0}{g})^2 \int_{-\pi}^{\pi} |\sum_{j=1}^7 l_j H_j(\theta)|^2 d\theta / B_0^4, \quad (58) \end{aligned}$$

then

$$\begin{aligned} F_D / (\frac{1}{2} \rho g a^2 V_k \frac{2K}{\omega} B_0) &= \frac{KB_0}{4\pi} (\frac{\omega^2 B_0}{g})^2 \int_{-\pi}^{\pi} |\sum_{j=1}^7 l_j H_j(\theta)|^2 (\sin \beta - \sin \theta) d\theta / B_0^4 \\ &\quad + \frac{1}{2} \eta \sin \beta. \quad (59) \end{aligned}$$

2-5 3-D effect

For calculations of 3-D hydrodynamic forces, the interpolation solution of Maruo et al [9] is expanded to an asymmetric shape of body about $y=0$ [7]. According to the solution, hydrodynamic force f_{ij} defined by (2) is

$$f_{ij} = \int_{-B_0/2}^{B_0/2} U_j(x) h_{ij}'(x) dx, \quad (60)$$

in a deep sea. Here

$$\begin{aligned} U_j(x) &= 1, & j' &= j & \text{for } j=2\sim 4 \\ U_j(x) &= (-1)^{j'} x, & j' &= 8-j & \text{for } j=5, 6, \end{aligned} \quad (61)$$

and

$$h_{ij}'(x) = h_{ij}'^{(2D)} + h_{ij}'^{(3D)}, \quad (62)$$

$$h_{ij}'^{(2D)} = f_{i'j'}^{(2D)} U_{i'}(x) - f_{3j'}^{(2D)} W_{i'}(x), \quad (63)$$

where $f_{i'j'}$ is a sectional hydrodynamic force and

$$\begin{aligned} i' &= i & \text{for } i=2\sim 4, \\ i' &= 8-i & \text{for } i=5, 6. \end{aligned} \quad (64)$$

and

$$h_{ij}'^{(3D)} = W_{i'}(x) [-S_{j'}(x) + B_{j'}(x)/K], \quad (65)$$

$$\begin{aligned} S_2(x) &= 0, S_3(x) = S, \text{ which is a sectional area,} \\ S_4(x) &= \iint_{\Gamma_H} y dy dz, \text{ which is a moment of} \\ &\text{sectional area, } B_2(x) = 0, B_3(x) = y_1 - y_2', \\ &\text{which is width of water line, } B_4(x) = (y_1^2 - y_2'^2)/2. \end{aligned} \quad (66)$$

Here $W_{i'}(x)$ is defined by

$$\begin{aligned} W_{i'}(x) &= \frac{K}{2} a_0(x) [N(K|B_0/2+x|) + N(K|B_0/2-x|)] \\ &\quad + \frac{K^2}{2} \int_{-B_0/2}^{B_0/2} [a_0(x') - a_0(x)] N'(K|x-x'|) dx', \quad (67) \end{aligned}$$

where

$$\begin{aligned} N(u) &= -\pi i - \ln 2u + \frac{\pi}{2} \int_0^u [H_0(u') + Y_0(u') \\ &\quad + 2iJ_0(u')] du', \quad (68) \end{aligned}$$

$$N'(u) = -\frac{K}{u} + \frac{\pi}{2} [H_0(u) + Y_0(u) + 2iJ_0(u)],$$

and H_0 is a Struve function, Y_0 and J_0 are Bessel functions and γ is a Euler's constant. The a_0 in (67) is a solution of the following integral equation,

$$2\pi a_0 = [H_1(\frac{\pi}{2}) + H_1(-\frac{\pi}{2})] U_1(x) - [H_3(\frac{\pi}{2}) + H_3(-\frac{\pi}{2})] W_1(x). \quad (69)$$

By making use of $W_1(x)$, we have a Kochin function $H_1(\beta)$ in 3-D cases as

$$H_1(\beta) = -\int_{-H_0/2}^{H_0/2} (\gamma_1 + \gamma_2 \sin \beta) e^{ikx \cos \beta} dx, \quad (70)$$

where

$$\begin{aligned} \gamma_1 &= \frac{1}{2} [H_1(\frac{\pi}{2}) + H_1(-\frac{\pi}{2})] U_1(x) \\ &\quad - \frac{1}{2} [H_3(\frac{\pi}{2}) + H_3(-\frac{\pi}{2})] W_1(x), \\ \gamma_2 &= \frac{1}{2} [H_1(\frac{\pi}{2}) - H_1(-\frac{\pi}{2})] U_1(x) \\ &\quad - \frac{1}{2} [H_3(\frac{\pi}{2}) - H_3(-\frac{\pi}{2})] W_1(x). \end{aligned} \quad (71)$$

By the use of $H_1(\beta)$, we have a wave damping coefficient N_{11} as

$$N_{11} = \frac{\rho \omega K}{4\pi} \int_{-\pi}^{\pi} H_1(\theta) H_1^*(\theta) d\theta, \quad (72)$$

from (18b).

Note that the approximate hydrodynamic force f_{11} given by (60) is not necessarily symmetric and that a wave damping coefficient N_{11} given by (60) and (4) is not necessarily equal to N_{11} given by (72), because this approximation is inconsistent. But the discrepancy among reciprocal relations is proved to be negligible numerically.

2-6 Absorbed wave power in irregular waves

The time-averaged wave energy per unit time \overline{dE}/dt of regular waves with wave height $H=2a$ and period T in a deep sea is written as

$$\begin{aligned} \left(\frac{dE}{dt}\right)_{reg} &= \frac{1}{2} \rho g a^2 V_k \\ &= \frac{\rho}{32\pi} g^2 H^2 T \end{aligned} \quad (73)$$

The time-averaged wave energy per unit time per unit length of long crested irregular waves \overline{dE}/dt is

$$\left(\frac{dE}{dt}\right)_{irr} = \frac{\rho g^2}{8\pi} \int_0^\infty \frac{2\pi}{\omega} 2S'(\omega) d\omega, \quad (74)$$

where $S'(\omega)$ is a sea spectrum. ISSC Spectrum $S'(\omega)$ based on the Pierson-Moskowitz sea spectrum with visual wave height H_w and visual wave period T_w is

$$S'(\omega) = \frac{0.11}{2\pi} H_w^2 T_w (T_w \omega / 2\pi)^{-5} \exp [-0.44 (T_w \omega / 2\pi)^{-4}], \quad (75)$$

and JONSWAP spectrum, as

$$\begin{aligned} S'_j(\omega) &= \frac{0.072}{2\pi} H_w^2 T_w^{\alpha} (T_w \omega / 2\pi)^{-5} \exp [-0.44 (T_w \omega / 2\pi)^{-4}] \\ &\quad \times 3.3 \exp \left[-\frac{1}{2\sigma^2} (1.296 T_w \omega / 2\pi - 1)^2 \right], \end{aligned} \quad (76)$$

where

$$\sigma = \begin{cases} 0.07 & \text{for } \omega \leq 4.85 T_w^{-1}, \\ 0.09 & \text{for } \omega > 4.85 T_w^{-1}. \end{cases} \quad (77)$$

Substitution of (75) or (76) into (74) yields

$$\left(\frac{dE}{dt}\right)_{irr} = \begin{cases} 0.54 H_w^2 T_w \text{ kw/m (ISSC)}, \\ 0.57 H_w^2 T_w \text{ kw/m (JONSWAP)}, \end{cases} \quad (78)$$

respectively.

From the joint probability density function $p(H_w, T_w)$ at an area where wave absorbers are set, the expected time-averaged wave energy per unit time per unit length is derived as

$$E\left[\left(\frac{dE}{dt}\right)_{irr}\right] = \int_0^\infty \int_0^\infty \left(\frac{dE}{dt}\right)_{irr} p(H_w, T_w) dH_w dT_w, \quad (79)$$

A response spectrum of the time-averaged absorbed wave energy per unit time in irregular waves is

$$2S_{\eta}(\omega) d\omega = H_{\eta w}(\omega) 2S'(\omega) d\omega, \quad (80)$$

where $H_{\eta w}$ is a response function of the time averaged absorbed wave energy per unit time, which is expressed as

$$H_{\eta w}(\omega) = \left(\frac{dE}{dt}\right) / a^2, \quad (81)$$

and given by (42) or (43) corresponding to an incident wave of unit amplitude.

A variance \bar{P} of the time-averaged absorbed wave energy per unit time in irregular waves is

$$\bar{P} = \int_0^\infty 2S_{\eta}(\omega) d\omega \quad (82)$$

The wave energy absorption efficiency coefficient (in 3-D cases) η_{irr} is defined by

$$\eta_{irr} = \bar{P} / \left[\left(\frac{dE}{dt}\right)_{irr} B_0\right], \quad (83)$$

where B_0 is a unit in 2-D cases. The expected time-averaged wave energy per unit time at an area where absorbers are set is

$$E[\bar{P}] = \int_0^\infty \int_0^\infty \bar{P} p(H_w, T_w) dH_w dT_w, \quad (84)$$

which is comparable with (79).

By the use of a response function $H_{\eta(w)}(\omega)$ of an amplitude of motions which is given by (34) corresponding to an incident wave of a unit amplitude, we have a response spectrum $S_{\eta(w)}(\omega)$ of the motion in irregular waves, as follows

$$2S_{\eta(w)}(\omega) d\omega = |H_{\eta(w)}(\omega)|^2 2S'(\omega) d\omega. \quad (85)$$

And using a response function $H_{D(w)}(\omega)$ of a drift force F_D which is given by (56) or (59) divided by a^2 in the same way as in (81), we have a response spectrum $S_D(\omega)$ of a drift force in irregular waves, as follows

$$2S_D(\omega) d\omega = |H_{D(w)}(\omega)|^2 2S'(\omega) d\omega. \quad (86)$$

3. EXPERIMENTS

In order to clarify the applicability of the linear theories to the prediction of the performance of the wave power absorber, we investigated experimentally the characteristics of absorbed wave power, wave excitation, and motion of the body in regular or irregular waves, and characteristics of radiation waves generated by the forced oscillation test in calm water. Their characteristics are tested in the two-dimensional model basin with $20 \times 1.8 \times 1$ m (length \times width \times depth) or in the sea-keeping basin with $50 \times 30 \times 2.5$ m, both of which belong to University of Tokyo.

Water depth effect on Salters Duck is so small that the experiments are carried out only in deep water [13].

3-1 Shape of the model (Salters Duck)

Principal particulars of the model are shown in Fig. 2. Its radius of the submerged circular cylinder is $R_0 = 15.9$ cm, horizontal distance between rolling axis and the edge of the water plane is 30 cm, and width of the body is 163 cm. The slenderness ratio is 1/3.55. The sectional shape and the draft of the model were decided by the results of theoretical calculations in order to absorb wave power efficiently in our model basin (See Appendix A). The moment of inertia of the model about rolling axis with hydraulic power conversion mechanism is $0.494 \text{ kg}\cdot\text{m}\cdot\text{sec}^2$, and the one without the hydraulic power conversion mechanism is $0.346 \text{ kg}\cdot\text{m}\cdot\text{sec}^2$. Restoring force coefficients in roll mode and heave mode are $13.9 \text{ kg}\cdot\text{m}/\text{rad}$ and $489 \text{ kg}/\text{m}$, respectively. The vertical distance between the rolling axis and the origin is $l = 15.9$ cm.

The body is supported at both ends of the body through rotational bearings by the frame which permits the heave and sway motions (Fig. 4). The weights of the model in heave and sway direction are 176 kg and 199 kg, respectively.

3-2 Forced oscillation test

The model oscillates sinusoidally in roll mode by an oil-hydraulic servomechanism in calm water in the 2-D model basin. The reaction roll moment is measured by the block gauge with capacity of 100 kg, which is used for the measurement of wave excitation force, too. Radiation hydrodynamic force is decomposed to predicted added moment of inertia and wave damping by analyzing the relation between magnitude and phase of this force.

3-3 Wave power absorption system

Wave power is converted to hydraulic power by hydrostatic power conversion mechanism which consists of a hydraulic cylinder, a flow rectifying valve and laminar tubes for loads. This mechanism is compact and has the advantage of easy control and storage of energy (Fig. 4).

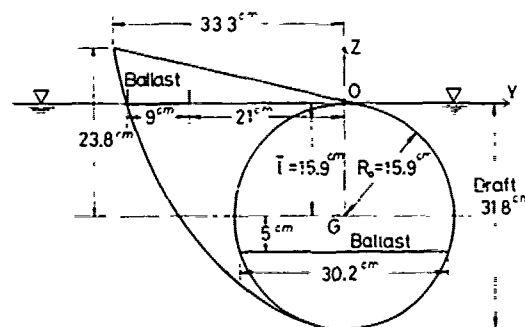


Fig. 2 Section of Salter Duck

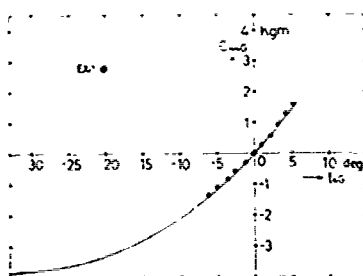


Fig. 3 Hydrostatic restoring force coefficient

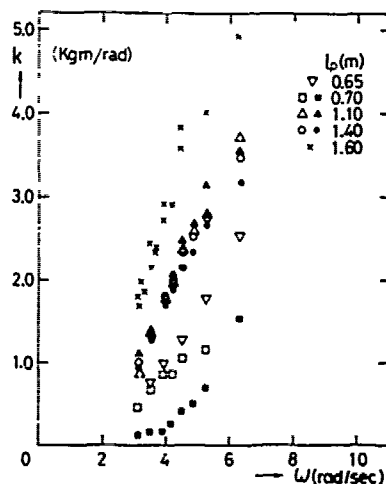
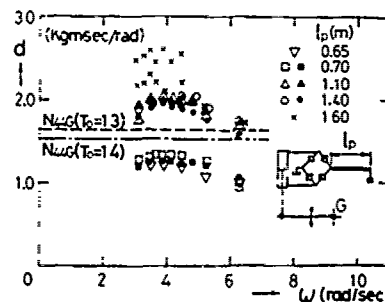


Fig. 4 Schematic drawing of wave power absorber.

1. Floating body
2. Torque measuring gauge
3. Hydraulic cylinder
4. Hydraulic rectifying valve
5. Laminar tube
6. Spring for sway

We test first the reaction-torque characteristics of this mechanism, because it has effects on both the motion and the absorbed wave power efficiency of the floating body. Especially it is important to clarify the effect of the suction capability of cylinder and of the volumetric efficiency of the rectifying valve on the reaction torque characteristics. The reaction torque is measured by the strain-gauge with capacity of $6.0 \text{ kg}\cdot\text{m}$ fixed on the cantilever which supports the cylinder and the body.

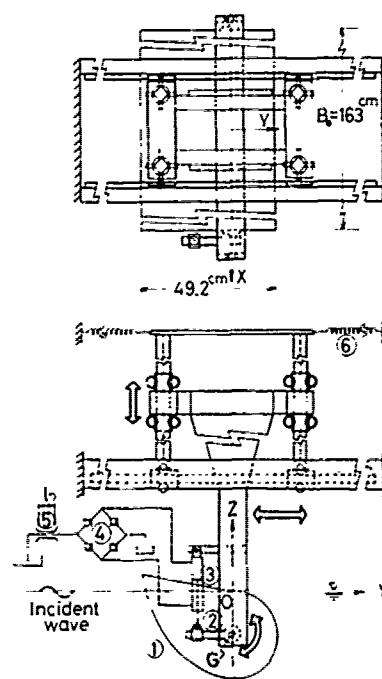


Fig. 4 Schematic drawing of wave power absorber.

1. Floating body
2. Torque measuring gauge
3. Hydraulic cylinder
4. Hydraulic rectifying valve
5. Laminar tube
6. Spring for sway

Reaction torque characteristics are examined by forced oscillation test of the hydraulic cylinder, and analyzed by Fourier analysis. We get the test results that the mechanism has not only damping characteristics but also spring one due to cavitation or aeration of fluid in the cylinder chamber. The both characteristics are shown in Fig. 5. In these figures, d and k represent the load damping coefficient and restoring force coefficient of the hydraulic power conversion mechanism.

The power conversion mechanism consists of a hydraulic cylinder of 20 mm in diameter and 150 mm in stroke, a flow-rectifying valve with 3/8 inch ports, and laminar tubes of 0.65 to 1.6 m long and 1.55 mm in diameter of which pressure and flow characteristics are in linear relation. Working fluid is turbine oil with kinematic viscosity of 0.2 cm²/sec at 30°C.

3-4 Experimental condition

Test results of 2-D model experimented in the model basin is called "2-D Experiment" in this paper, and those of 3-D model in the sea-keeping basin is called "3-D Experiment". The motion of the model is tested first without hydraulic power conversion mechanism with the incident wave of height of $H_w = 2, 4$ and 6 cm and period of 1 to 2 seconds, and secondly tested with hydraulic system with the wave of height of 4 and 6 cm. The length of laminar tubes for hydraulic load is selected to $l_p = 0.65, 0.7, 1.1, 1.4$ and 1.6 m long. Effect of oblique wave is tested at the encounter angles of incident wave $\beta = 65^\circ$ and 90° .

The motions of the body are classified into four categories. One is 1 mode (roll) which denotes only roll motion, the second is 2 mode (roll-sway) which denotes the roll-sway coupled motion, similarly the third is 2 mode (roll-heave) and the fourth is 3 mode (roll-sway-heave) denotes the roll-sway-heave coupled motion. For the sway-mode motion, the body is supported by additional springs. The spring constant is $g_{22} = 41.7$ kg/m which makes the drift displacement be one tenth of the supposed water depth (200 m) in regular waves of seven times of significant wave height of operating condition when the drift force coefficient is assumed to be 1. In case of 2 mode (roll-heave), mechanical friction of heave mode which is estimated to be 1.3 kg is added.

In the forced oscillation test, the model oscillates in 1 mode (roll) of amplitude $|H_{4G}| = 3^\circ$ in the 2-D model basin. In this experiments, when the model rolls, water runs up the slope from the lee wave side. The effect of water running up the slope is examined by using two types of bodies, one with wall-sided hull surface and the other with inclined surface.

Wave excitations of 2-D and 3-D experiments are measured in regular waves with height $H_w = 2, 4$ and 6 cm and period $T_w = 1$ to 2 sec.

Length of laminar tube is $l_p = 0.7, 1.1$ and 1.4 m. 3-D experiments in irregular waves of JONSWAP with significant wave height $H_w = 5.16$ cm and peak periods of $T_p = 1.2, 1.4, 1.6$ and 1.8 seconds are carried out. Duration time of irregular waves are about three minutes. The scale ratio of JONSWAP is settled to be 1/30.98.

Wave power is absorbed only in roll mode.

4. THE RESULTS OF CALCULATION AND EXPERIMENT

The theoretical calculations of hydrodynamic forces are determined by the source distribution method making use of stream functions. The evaluation of the accuracy of the calculation depends on three different methods which use the Haskind relation of (18a), the reciprocal theorem of hydrodynamic forces of (2) and the relations between reflected and transmitted waves of (22, 24, 25). The number of segments on the wetted hull surface is 90 ~ 100. The hydrodynamic force f_{44G} etc. of rolling mode about the rolling axis G is determined by the following equations.

$$\begin{aligned} f_{44G} &= f_{44} + \bar{l}^2 f_{22} - 2\bar{l} f_{42} \\ f_{24G} &= f_{24} - \bar{l} f_{22} \end{aligned} \quad (87)$$

$$f_{34G} = f_{34} - \bar{l} f_{32}$$

where, \bar{l} is the vertical distance between the origin and the rolling axis G . The Kochin function about G is as follows.

$$H_{4G}(\pm \frac{\pi}{2}) = H_4(\pm \frac{\pi}{2}) - \bar{l} \cdot H_2(\pm \frac{\pi}{2}) \quad (88)$$

Equations (87) and (88) are available to 3-D case. But in this case 3-D modification should be applied to hydrodynamic forces. Because the section of the floating body is uniform and its slenderness ratio is 1 : 3.55, there are two kinds of problem left with regard to the application of the slender ship theory. One is that the assumption of the end of the slender body is not satisfied and the other is the slenderness ratio. The precise discussion should be necessary, but it is left in future. The end effect is treated in the following manner. The second term of the (69) is neglected as the approximate solution in case of $K \rightarrow 0$ and $K \rightarrow \infty$. The remainder is substituted into (67), then

$$\begin{aligned} W_1(x) &= \frac{K}{2} U_1(x) - \frac{H_1(\frac{\pi}{2}) + H_1(-\frac{\pi}{2})}{2\pi} \\ &\times [N(K|B_0 - 2 + x|) + N(K|B_0 - 2 - x|)] \end{aligned} \quad (89)$$

The relation between Kochin functions and radiation wave amplitude ratio \bar{A}_j in 2-D problem is as follows.

$$\xi_j \cdot l_j = iKH_j(\pm \frac{\pi}{2}), j = 2, 3 \quad (90)$$

$$\bar{A}_j = \xi_j$$

$$\xi_j \cdot l_j R_0 = -\frac{1}{R_0} H_j(\pm \frac{\pi}{2}),$$

$$j = 4, 4G \quad (91)$$

Fourier analysis is used for the analysis of the experimental data in regular waves. The in-phase and out-of-phase components of first to fourth order are analysed from data of five to ten periods. FFT (Fast Fourier Transform) is used to analyze the data in irregular waves. The number of samples is 2048 and the sampling time is 0.07 sec. Q window is applied.

The results of the experiment and numerical calculation are classified and listed under the following items, hydrodynamic force, motion, absorbed energy and power characteristics, characteristics of a floating breakwater and drift force, results in oblique waves, and results in irregular waves.

4-1 Hydrodynamic forces

Fig. 6 shows the added moment of inertia about the rolling axis G tested by forced oscillation of the body in 2-D model basin. Experiments of both wall-sided and inclined hull surface are carried out. In the figure, results of numerical calculation are shown in case of both 2-D and 3-D.

Fig. 7 shows the tests results and calculation results of hydrodynamic damping coefficient. In the figure, not only damping measured by torque gauge but also damping calculated by measured radiation waves are shown.

Fig. 8 shows the test results and calculated results of wave excitation. In the figure, experiments of exciting moment about a rolling axis G and of amplitude ratios of radiation waves are shown with the expression of Kochin function.

4-2 Motions

Fig. 9 shows the roll amplitudes of 1 mode (roll) in case of wave power absorbed and not absorbed. Magnitude of hydraulic load is adjusted by the length of laminar tubes [Fig. 5]. In this experiments, the natural period of the body is adjusted to be about $T_0 = 1.3$ sec. The length of laminar tube l_p is $l_p = 1.4$ m.

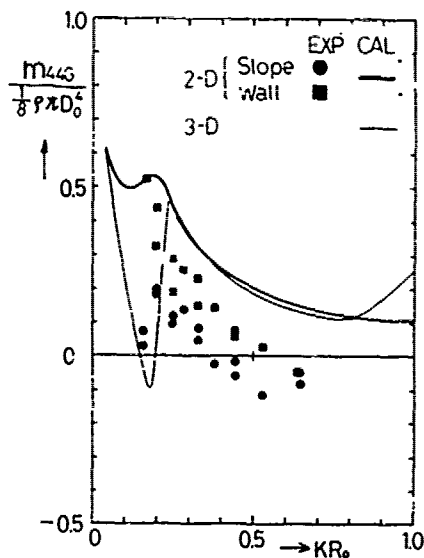


Fig. 6 Added moment of inertia

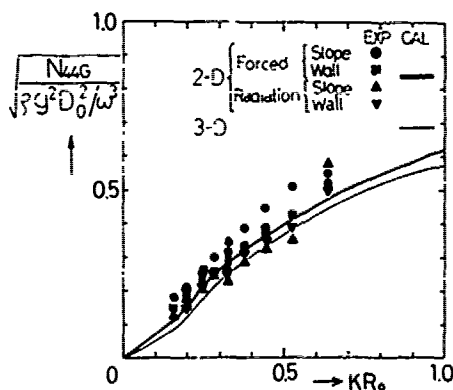


Fig. 7 Hydrodynamic damping coefficient

The coupled motions of roll-heave and roll-sway are shown in Fig. 10 and 11, respectively. Each of them shows the rocking amplitude characteristics in which heave or sway motion of the body is allowed. In the calculation of Fig. 9, 10 and 11, the added moment of inertia is estimated by the experiment.

4-3 Absorbed wave power

Fig. 12 shows the wave power absorption efficiency or ratio of 2-D or 3-D experiments of 1 mode (roll). Natural period is tuned to be about $T_0 = 1.3$ sec and length of laminar tubes for hydraulic load is adjusted to $l_p = 0.7, 1.1$ and 1.4 m. The added moment of inertia is estimated by the theory with regard to the results of the calculation of CAL*, and by the experiment m_{44G} (exp.) with regard to CAL.

Fig. 13 shows the comparison of efficiencies affected by allowance of coupled motions. Wave power is absorbed in roll mode of 2-D experiment with natural period about $T_0 = 1.1$ sec., of 3-D experiment with about $T_0 = 1.3$ sec and hydraulic load of $l_p = 1.4$ m tube length. In the calculation, the added moment of inertia is estimated by the experiment m_{44G} (exp.).

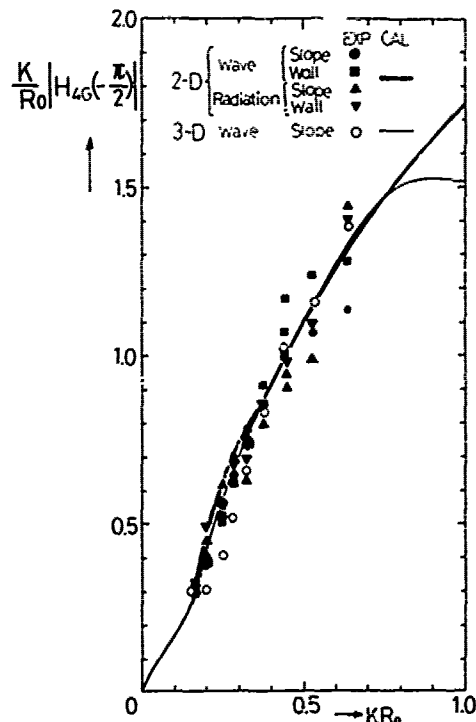


Fig. 8 Wave exciting moment

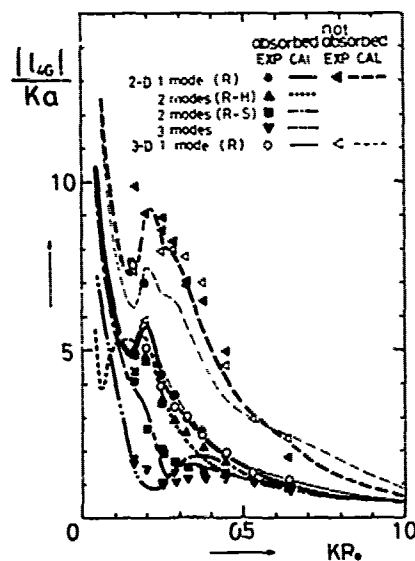


Fig. 9 Roll amplitude

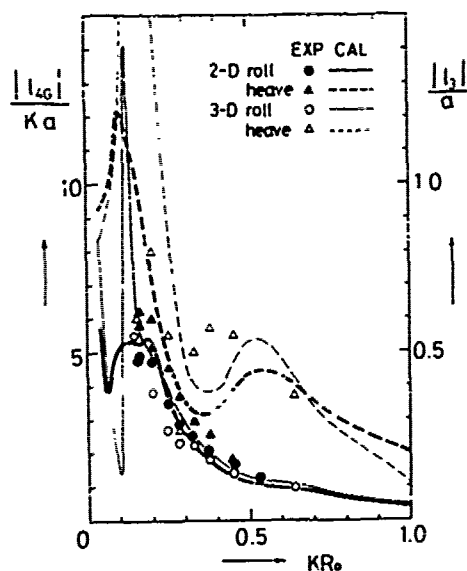


Fig. 10 Amplitudes of coupled motion (roll-heave)

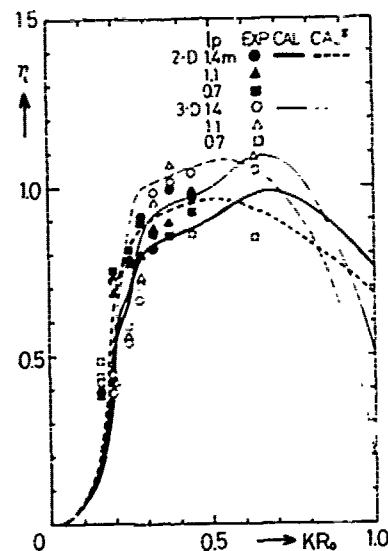


Fig. 12 Absorption width ratio (pure roll)

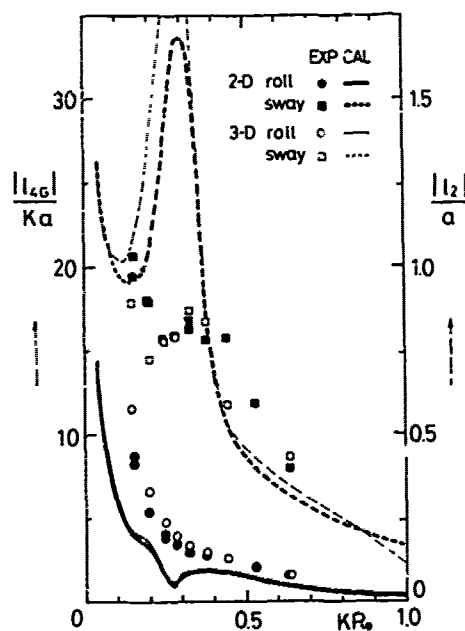


Fig. 11 Amplitudes of coupled motion (roll-sway)

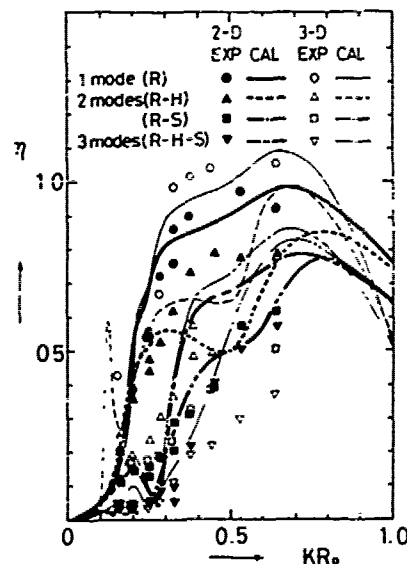


Fig. 13 Absorption width ratio (coupled motion)

Fig. 14 shows the power characteristics of relation between torque and angular velocity of 2-D experiment, moment of inertia of which is adjusted to be $M_{4G} = 0.494 \text{ kg} \cdot \text{m} \cdot \text{sec}^2$. The body oscillates in one roll mode in sinusoidal wave trains, and the magnitude of hydraulic load is adjusted by the length of laminar tubes. In the figure, the solid lines and broken lines show the calculated power characteristics and efficiencies, respectively.

Fig. 15 shows the characteristics of wave power absorbing torque and velocity of 3-D experiment with moment of inertia of $M_{4G} = 0.494 \text{ kg} \cdot \text{m} \cdot \text{sec}^2$.

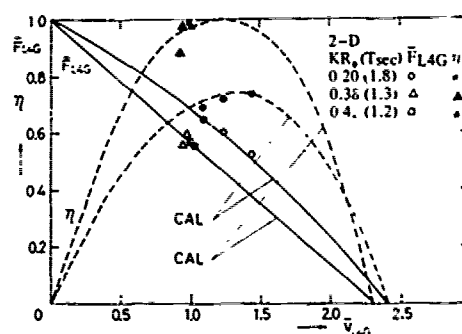


Fig. 14 Power characteristics (2-D)

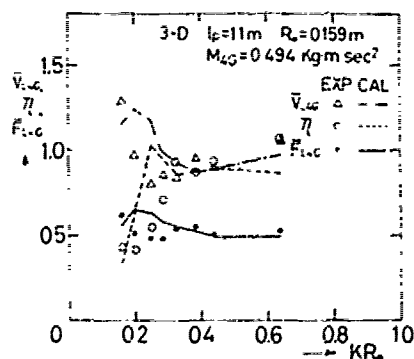


Fig. 15 Power characteristics (3-D)

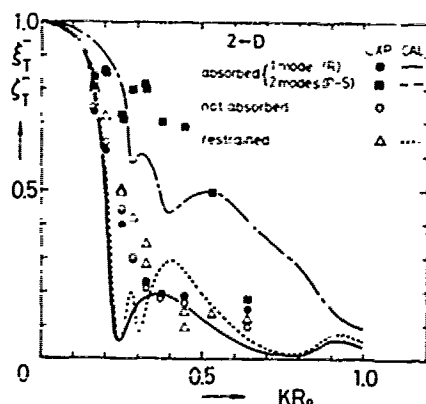


Fig. 16 Transmission coefficient (load damping effect)

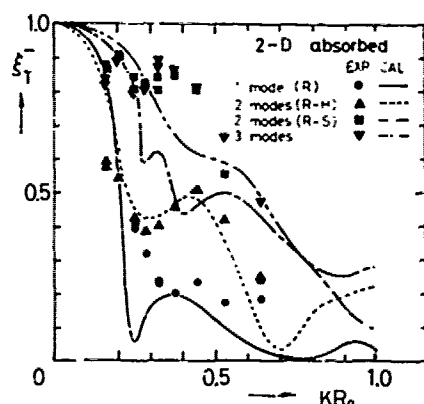


Fig. 17 Transmission coefficient (coupled motion effect)

4-4 Characteristics of a floating breakwater and drift force

Experimental results of transmitted waves in 2-D case are plotted in Fig. 16. There are three experimental conditions described as follows: in case of free oscillation in waves without absorbing energy, with absorbing energy and restrained condition in waves. The corresponding numerical results are shown in the same figure. The result of the calculation of not-absorbed case in Fig. 16 coincides with that of absorbed 1 mode (roll) case. The coupled motion effect on transmission coefficient is shown in Fig. 17.

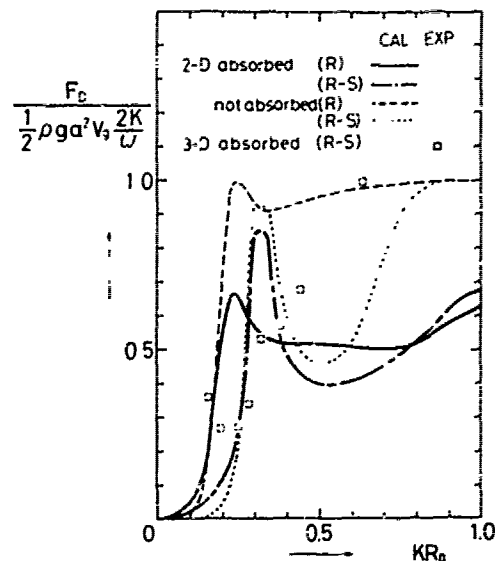


Fig. 18 Drift force

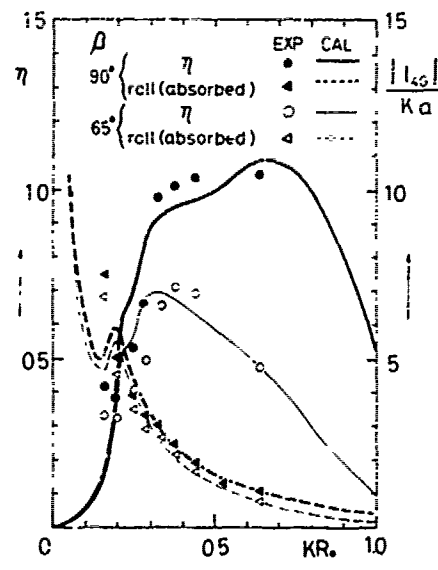


Fig. 19 Absorption width ratio (oblique waves)

The experimental results of drift force of 2 mode (roll-sway) cases are plotted in Fig. 18. The conditions are as follows: with absorbing energy in 3-D cases, the length of laminar tube is $l_p = 1.4$ m and designed natural period is $T_0 = 1.3$ sec. In the calculation of Fig. 16, 17 and 18, the added moment of inertia is estimated by the experiment m_{44G} (exp.).

4-5 Results in Oblique waves

3-D experiments are carried out in the sea-keeping basin of 30 m x 50 m and by the use of the model with the slenderness ratio of 1.63 m x 0.46 m. The encounter angles of incident waves are $\beta = 90^\circ$ (beam sea) and 65° . The length of laminar tube is $l_p = 1.4$ m and the designed roll natural period is $T_0 = 1.3$ sec. The experimental and numerical results of absorbed energy and motion are shown in Fig. 19. The added moment of inertia in the calculation is estimated by the experiment m_{44G} (exp.).

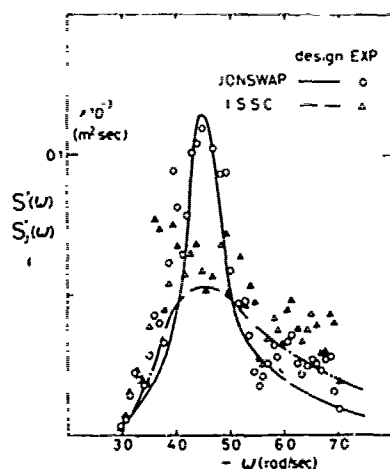


Fig. 20 Wave spectra (JONSWAP & ISSC)

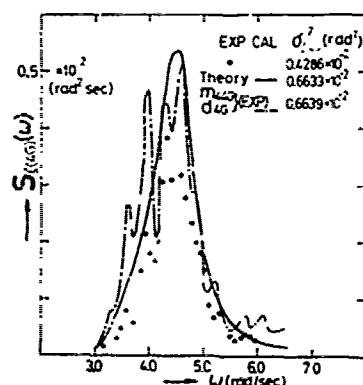


Fig. 21 Roll spectrum (JONSWAP)

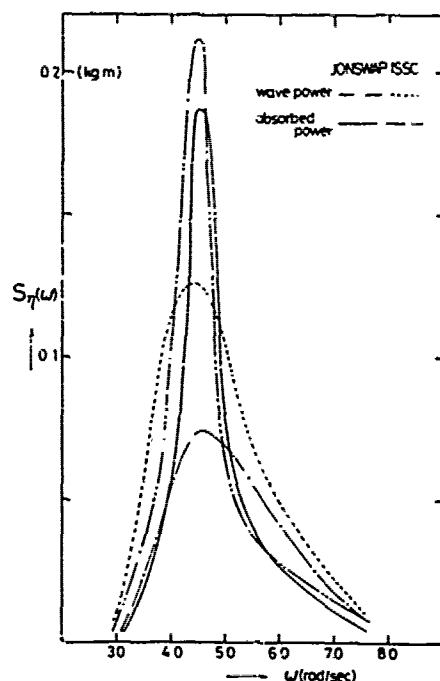


Fig. 22 Absorbed wave power spectra (JONSWAP & ISSC)

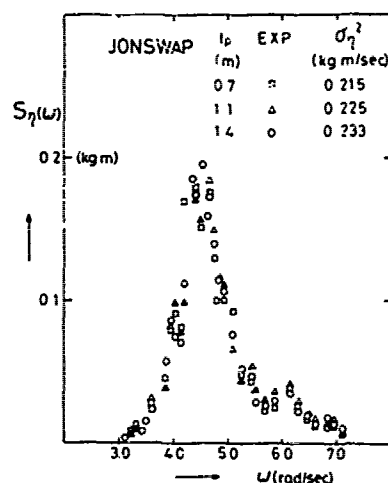


Fig. 23 Absorbed wave power (load damping effect)

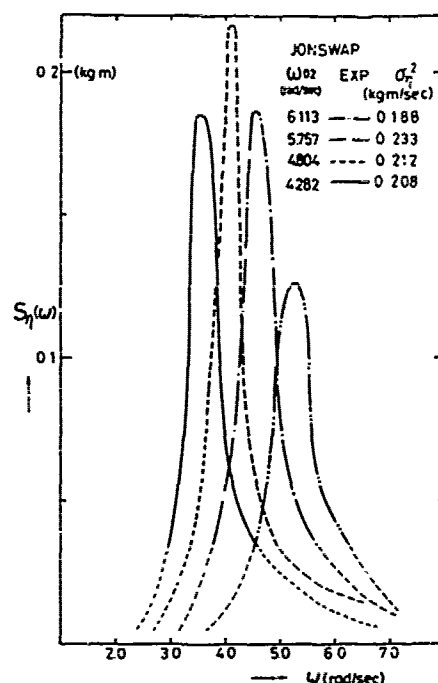


Fig. 24 Absorbed wave power spectra (effect of mean wave period)

4-6 Results in irregular waves

Experiments in irregular waves are carried out in case of only 3-D. The spectra of the irregular waves of JONSWAP and ISSC are shown in Fig. 20. The peak period of ISSC is $T_p=1.4$ sec and those of JONSWAP are $T_p=1.2, 1.4, 1.6$ and 1.8 sec. The designed waves and the corresponding measured results are shown in the figure. The results of experiments and two kinds of calculations of the roll spectrum of 1 mode (roll) are shown in Fig. 21. These calculations are theoretical one in which design wave spectrum, design damping coefficient of hydraulic load and theoretical response function with m_{44G} (exp.) are used, and the one is which the experimental results of wave spectrum, added moment of inertia and damping coefficient of hydraulic load are used. The peak period of JONSWAP is $T_p=1.4$ sec and the length of laminar tube is $l_p=1.4$ m.

The spectra of absorbed wave power are shown in Fig. 22, 23, 24 and 25.

The analytical methods of absorbed wave power from the time series of the experimental data in irregular waves are described as follows. We assume that the column vector of load forces \underline{T} can be expressed linearly like

$$\underline{T} = \underline{d}\dot{\underline{\xi}} + \underline{k}\underline{\xi} \quad (92)$$

as compared with (35). The virtual absorbed wave power is written

$$\begin{aligned} \frac{dE'}{dt} &= \text{Re} [\underline{T}^T] \text{Re} [\dot{\underline{\xi}}] \\ &= \sum_j [d_j \dot{\xi}_{jc} + k_j \xi_{jc} \dot{\xi}_{jc}] \end{aligned} \quad (93)$$

where

$$\xi_j = \xi_{jc} + i\xi_{js}, \quad \dot{\xi}_j = \dot{\xi}_{jc} + i\dot{\xi}_{js} \quad (94)$$

Then,

$$\begin{aligned} \lim_{T \rightarrow \infty} \frac{1}{2T} \int_{-T}^T \frac{dE'(t)}{dt} dt &= \sum_j [d_j \langle \dot{\xi}_{jc}(t) \xi_{jc}(t) \rangle \\ &\quad + k_j \langle \xi_{jc}(t) \dot{\xi}_{jc}(t) \rangle] \\ &= \sum_j d_j R_{\dot{\xi}_{jc}}(0) \\ &= \sum_j d_j \int_{-\infty}^{\infty} \omega^2 S_{\xi_{jc}}(\omega) d\omega \\ &= \lim_{T \rightarrow \infty} \frac{1}{2T} \int_{-T}^T \frac{dE(t)}{dt} dt \end{aligned} \quad (95)$$

Now,

$$\begin{aligned} R_{\underline{T}\underline{\xi}}(\tau) &= \lim_{T \rightarrow \infty} \frac{1}{2T} \int_{-T}^T \text{Re} [\underline{T}^T(t)] \text{Re} [\underline{\xi}(t+\tau)] dt \\ &= \sum_j [d_j \langle \dot{\xi}_{jc}(t) \xi_{jc}(t+\tau) \rangle \\ &\quad + k_j \langle \xi_{jc}(t) \dot{\xi}_{jc}(t+\tau) \rangle] \\ &= \sum_j d_j R_{\dot{\xi}_{jc}}(\tau) = -\sum_j d_j \ddot{R}_{\xi_{jc}}(\tau) \end{aligned} \quad (96)$$

Therefore the cross-spectrum of $\text{Re} [\underline{T}]$ and $\text{Re} [\underline{\xi}]$ which corresponds to (96) is

$$S_{\underline{T}\underline{\xi}}(\omega) = \sum_j d_j S_{\dot{\xi}_{jc}}(\omega) = \sum_j d_j \omega^2 S_{\xi_{jc}}(\omega) \quad (97)$$

So far we assume the Ergodic and stationary hypothesis of $\text{Re} [\underline{T}]$ and $\text{Re} [\underline{\xi}]$.

As comparing (97) with (95) the spectrum of absorbed wave power $S_\eta(\omega)$ is defined rationally in the following manner,

$$S_\eta(\omega) = S_{\underline{T}\underline{\xi}}(\omega) = \omega S_{\underline{T}\underline{\xi}}(\omega) \quad (98)$$

As is similar to (82), the total power \bar{P} (the variance of $S_\eta(\omega)$) which is absorbed by a wave absorbing device is described as

$$\begin{aligned} \bar{P} &= \int_0^\infty 2S_\eta(\omega) d\omega = 2 \int_0^\infty S_{\underline{T}\underline{\xi}}(\omega) d\omega \\ &= \sum_j R_{\dot{\xi}_{jc}}(0) = \sum_j \ddot{R}_{\xi_{jc}}(0) \end{aligned} \quad (99)$$

Fig. 22 shows the comparison of JONSWAP with ISSC with regard to spectra of wave power of incident waves and absorbed wave powers. The length of laminar tube is $l_p = 1.4$ m. The effect of hydraulic load on absorbed wave power spectra is shown in Fig. 23. The peak period of JONSWAP is $T_p = 1.4$ sec, and the length of laminar tube varies from $l_p = 0.7, 1.1$ to 1.4 m. Fig. 24 shows the effect of the mean wave period of wave

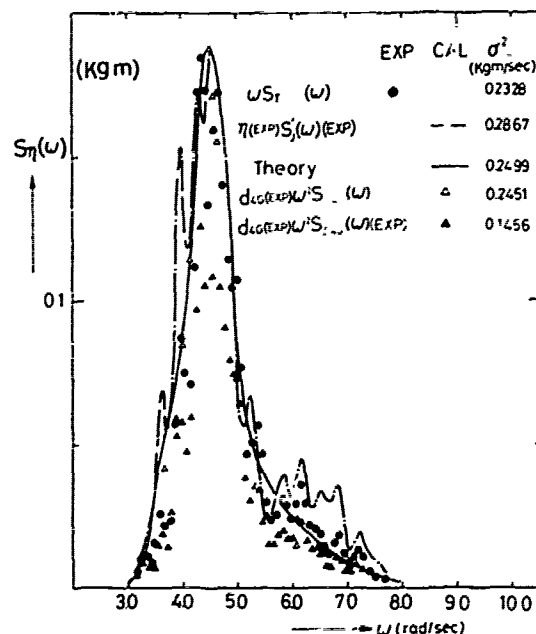


Fig. 25 Absorbed wave power spectrum (EXP & CAL)

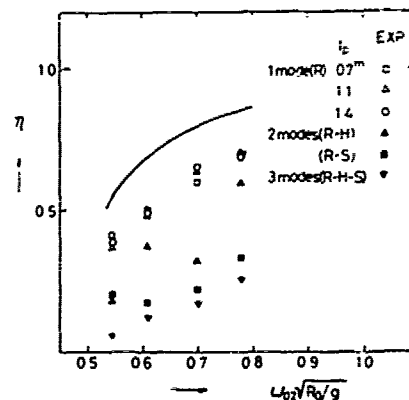


Fig. 26 Variance of absorbed wave power spectrum (JONSWAP)

spectrum which has the constant significant wave height. The peak period of the corresponding JONSWAP varies from $T_p = 1.2, 1.4, 1.6$ to 1.8 sec, and the length of laminar tube is $l_p = 1.4$ m. The comparison of theoretical calculation with experimental results is shown in Fig. 25. There are three kinds of calculations, these are, the theoretical calculation according to (80) in which only the added moment of inertia is estimated by the experiment m_{44G} (exp.), the one in which the experimental results of $H_{\eta\eta}(\omega)$ of (80) in regular waves and measured wave spectrum are used, and the one in which the experimental results are applied to the damping coefficient of (97) and roll spectrum. The peak period of JONSWAP is $T_p = 1.4$ sec and the length of laminar tube is $l_p = 1.4$ m.

The absorbed wave power coefficient (or absorption width ratio) in irregular waves which is analyzed by (99) and (83) is shown in Fig. 26[3]. The solid line corresponds to the results of calculation of $l_p = 1.4$ m in which the design wave spectrum and the added moment of inertia m_{44G} (exp.) are used.

5. DISCUSSION

We first investigate the application of linear theory which is based on (27). Hydrodynamic forces on the asymmetric floating body is handled first. With regard to hydrodynamic forces of roll mode, the linear theory is applicable to damping coefficient and wave excitation. Radiation wave amplitude ratio can be also estimated by the linear theory. On the contrary, the non-linear effect occurs on added moment of inertia of Salter Duck (the circular cylinder part of which is fully submerged and the linear theory does not work for added moment of inertia of roll mode).

Next hydrostatic restoring force is handled. Because the floating body is asymmetric, the restoring force is not only non-linear, but also asymmetric (Fig. 3). Because of this fact, it seems that non-linear effect may occur on large rolling motions. But from the results of motion (Fig. 9), absorbed wave power (Fig. 12) and responses in irregular waves (Fig. 25), the linear theory is considered to be effective in case of not so big roll angles. The linear theory is applicable, because the incident wave amplitude in operating condition is small and roll amplitude is relatively small in case of absorbing wave power. The non-linear effect presents fractional harmonic oscillation when the Salter Duck does not absorb wave power and it oscillates in large roll amplitude. The steady heave force is produced in case of 2 mode (roll-heave) motion and the sinkage is observed as a non-linear phenomenon.

Besides roll motion and absorbed wave power of asymmetric floating body such as Salters Duck, its coupled motions effect (Fig. 9, 13), transmission coefficients (Fig. 16, 17), drift force (Fig. 18), and absorbed wave power in irregular waves (Fig. 25), can be predicted by the use of linear equations of motion if the coefficients, especially the added moment of inertia of the equations of motion are estimated correctly.

Second we investigate the linearity of load of the hydraulic system. The experiment proved that there existed non-linear components of load damping and also of spring term. But as long as Fig. 9, 12, 25 show, these non linear components do not have effects on motion and absorbed wave power. Essentially appropriate radius of a hydraulic cylinder and appropriate working oil should be selected so as to exclude the spring term in a hydraulic system.

Considerations will be done in the order of the items in chapter 4 as follows.

5-1 Hydrodynamic forces on an asymmetric floating body

The accuracy of numerical calculations on Salter Duck of singularity distribution method using stream function is getting worse as the draft is increased. Especially in case of the circular cylinder be fully submerged at lee wave side the accuracy gets worst. While 50 segments are enough for the draft be as deep as that of the radius of the circular cylinder, however, in case of fully submerged circular cylinder, 100 segments are required. The body boundary condition at the corner of free surface and hull surface is assumed to be wall sided. The condition of "wall sided" is necessary in order to get the linear unique solution, because the corner of free and hull surface is generally singular. But as the corner has a slope in fact, it is easy to imagine that non-linear effect may occur. This local non-linearity is considered to have a strong effect on added moment of inertia. Fig. 6 shows this fact. In the forced oscillation test the following phenomenon was observed, that is the waves ran up the slope from the side of fully submerged circular cylinder the so called lee wave side. The negative added moment of inertia occurred at this stage. The negative added moment of inertia also happens when a fully submerged rectangular cylinder gets close to water surface. This fact tells us that the negative added moment of inertia is caused by the behavior of water between hull surface and water surface. The additional experiment in which the boundary condition at the corner of hull surface and water surface was changed to be wall sided was carried out and the results were different from those of the former tests. But the latter experimental results did not agree with the linear

theory prediction either. That is to say, by making use of the linear theory we could not predict the added moment of inertia of a floating body, the rear side of which is fully submerged just under the water surface.

On the other hand the prediction of the damping coefficient based on linear theory is in good agreement with the corresponding experiment. This fact tells that almost all of the components of damping force is wave damping force. The Haskind relation holds among the experimental results of wave excitation, damping coefficient and radiation wave amplitude (Fig. 7, 8). Though the forced oscillation tests are carried out only for roll mode, the same conclusion seems to be derived for sway and heave modes. That is, in case of a floating body the rear part of which is fully submerged, good predictions of damping force, wave excitations and radiation wave amplitudes may be obtained, while it is hard to predict generalized added mass by the use of linear theory. When the draft is getting closer to the radius of the rear circular cylinder part, that is, the section from becomes shiplike, good prediction of even generalized added masses are considered to be obtained.

The above mentioned conclusions are derived from the results of experiments which are carried out within $\pm 3^\circ$ of the roll amplitude of forced oscillation tests. Those conclusions could not be applied when roll amplitude becomes as large as the tip of the Salters Duck gets under water surface, because the large non-linear effect seems to occur. But the above mentioned conclusion can be applied to the response prediction of Salters Duck under operating condition. The non-linear effects under survival condition are not considered here though it is necessary to investigate them in order to design a practical device.

5-2 Motion characteristics

The roll motion can be predicted by a linear theory under operating sea condition so long as the experimental result of the added moment of inertia m_{22c} (exp) is used. The big difference between roll motion prediction methods of usual ships and Salters Duck is that the wave damping is enough as the component of hydrodynamic damping forces in case of Salters Duck. And another is that asymmetric floating body such as Salters Duck may not get the maximum value at the resonant frequency because of the dependency of hydrodynamic forces such as added moment of inertia (Fig. 9), though roll motion of usual ships generally gets the maximum amplitude at the resonant frequency. It has been already mentioned that non linear effect is strong on the added moment of inertia because of the steep slope at the intersection of water surface and the hull surface of the Salters Duck which is used in this paper. The same kind of non linear effect is observed when it oscillates freely in calm water; that is, it is difficult to measure the natural period by making use of data of only three or four rolls, because the damping is very large and the period changes not slightly at each roll.

When the wave power is not absorbed, the roll double amplitude becomes large, that is, about 35° . Then three kinds of non-linear phenomena are observed. One is that fractional harmonic oscillation is observed within the range of the period $T_w = 1.2 \sim 1.4$ sec. Next is that the mean position of roll oscillation is not the same as the equilibrium position in calm water. And the difference is at most 5° . The other is that heave oscillation of 2-mode (roll-heave) motion is asymmetric with regard to the equilibrium position in calm water. And the non-equilibrium quantity, that is sinkage, is as large as the heave amplitude. Those three kinds of non-linear phenomena are caused by non-linear hydrostatic restoring force.

5-3 Absorbed power and the power characteristics of hydraulic system

2-D experimental results in Fig. 12 shows that the absorbed wave power efficiency of Salters Duck with a hydraulic system is excellent. Salter [15] already proved by experiment that the

absorbed wave power characteristics of Salters Duck was fine, and Takaka [10] carried out the experiment of Salters Duck in which a load of a hydraulic system was used. But this is the first experiment of Salters Duck in which the characteristics of a hydraulic system is investigated in detail.

Though the load of a hydraulic system contains non-linear terms and its damping and spring components are functions of frequency, the results of numerical calculation by linear theory are in good agreement with those of 2-D experiments in regular waves. The optimum load in the experiment was designed according to (45) and (46). In Fig. 14, 2-D system absorbs wave power in high efficiency, when the hydraulic load damping force is adjusted to half of wave excitation force at resonance. The design conditions for the optimum load are predicted to be the length of laminar tube $l_p = 1.4$ m and the natural period $T_0 = 1.3$ sec. ($KR_0 = 0.38$). It seems in fact that the optimum value of the length of laminar tube is between $l_p = 1.4$ m and 1.1 m. The accuracy of the experiments of absorbed wave power depends mainly on the accuracy of wave measurement. While roll angle is in proportion to wave height, absorbed wave power coefficient is in proportion to square of wave height. Therefore it is difficult for the accuracy of absorbed wave power to get better than of roll motion. In any case it is possible to design Salters Duck with a hydraulic system which has excellent efficiency when the characteristics of load of a hydraulic system are given.

The spring characteristics shown in Fig. 5 of the mechanism will be derived both from the separation of fluid column in the cylinder chamber or in the pipeline at cylinder suction interval, and from the elastic deformation of aerated or cavitated bubbles at cylinder discharge interval. The apparent spring constant acted on the cylinder increases as discharged pressure of the fluid is higher and cylinder suction speed is larger. The linear prediction of power characteristics is fairly good in case of 2-D (Fig. 14). That of 3-D case is not so bad.

5-4 Characteristics of a floating breakwater and its drift force

The characteristics of a floating breakwater of Salters Duck are described as follows. Transmitted waves are almost disappeared in case of a floating body restrained in waves, and in case of 1 mode (roll) motion with absorbing wave power and also without absorbing wave power. The performance of the floating breakwater is reduced in the order of 2 mode (roll-heave), 2 mode (roll-sway) and 3 mode (roll-heave-sway) motion.

Drift force increases as the draft increases in case of restrained floating body. When wave power is fully absorbed, the drift force coefficient decreases to about 0.5 in case of 2-D and 1 mode (roll) motion. Therefore absorbing wave power rather becomes an advantage from the stand point of a mooring system. There is no difference noticed between drift forces of restrained Salters Duck in waves and of freely rolling one in case of 2-D 1 mode (roll) motion (Fig. 16). The coupled motion effect of roll-sway on the drift force is remarkable in 2-D case (Fig. 18).

5-5 3-D effect

While 2-D floating body can absorb incident wave power of a width of a floating body at most, absorbed wave power of a 3-D floating body may be greater than that of 2-D, because the absorbed wave power is affected by incident waves the width of which is larger than the width of a floating body. The slenderness ratio of the model used in this paper is 1.355. Theoretical calculation is based on Kuwashita's method [7] which is described in section 2-5. 3-D effect on radiation and diffraction hydrodynamic forces occurs at low frequency range (Fig. 6, A-3). As mentioned in section 2-5, there are two calculation methods of wave damping coefficients N_{ij} . Around zero of frequency, numerical calculation of wave damping by making use of pressure integration does not tend to zero, but that by making use of Kochin function tends to zero (Fig. A-3). Therefore the Kochin function method looks better for the prediction of 3-D effect

on wave damping. So that it is used in this paper.

In case of a present model with adopted natural frequencies, the 3-D effect on roll is quite little in experimented wave frequency region, as calculations predict (Fig. 9). The real 3-D effect on absorbed wave power is not so apparent as the calculations predict (Fig. 12). But the prediction of the effect of oblique waves is not bad (Fig. 19). Oblique wave effect on absorbed wave power is obvious, while roll motion is not influenced very much by that effect (Fig. 19). But there is some problem left with regard to the accuracy of prediction of absorbed wave power. The end effect and slenderness ratio have to be investigated in future.

5-6 Characteristics in irregular waves

Though the agreement of roll between theory and experiment is fairly good in regular waves, Fig. 21 shows that numerical results are a little bit larger than experimental ones. The reason seems to be based on non-linearity of hydrodynamic and hydrostatic forces.

Fig. 22 shows the difference between absorbed wave power spectra of JONSWAP and ISSC wave spectra. The mean wave period and significant wave height of each wave spectra are the same as one another. According to (78), the total wave power of JONSWAP spectrum is larger than that of ISSC spectrum. The absorbed wave power of JONSWAP is larger than that of ISSC.

Fig. 23 shows the effect of the load of the hydraulic system. The length of laminar tube varies from $l_p = 0.7$ m, 1.1 m to 1.4 m. There is no significant difference among $l_p = 0.7$ m, 1.1 m and 1.4 m with regard to absorbed wave power spectra, but the variance of $l_p = 1.4$ m is largest among them. The load damping coefficient which corresponds to $l_p = 1.4$ m is close to the wave damping coefficient of the natural period $T_0 = 1.3$ sec. (Fig. 5).

Fig. 24 shows the effect of measured mean period of the irregular waves JONSWAP. The absorbed wave power is getting larger as the corresponding peak period T_p is closer to the natural period $T_0 = 1.3$ sec. of a floating body. The total wave power is increasing in the order of $\omega_{0.2} = 6.1, 5.8, 4.8$ and 4.3 rad/sec, because the significant wave height is constant in (78). But the absorbed wave power coefficient defined by (83) may be optimum around $T_p = 1.3$ sec. (Fig. 26). When we consider both Fig. 23, 24 and Fig. 26, it seems that the optimum conditions in which the absorbed wave power obtains the maximum are as follows: the natural period of roll of the wave power absorbing device coincides with the corresponding peak period of the irregular waves, and the load of the hydraulic system is made to be as same as the wave damping at the corresponding peak period.

Fig. 25 shows the comparison of theoretical results with experimental ones. The prediction method of total absorbed wave power by linear theory still works well.

5-7 Coupled motion effect

In case of absorbing wave power, the roll amplitude in regular waves is getting smaller in the order of 1 mode (roll), 2 mode (roll-heave), (roll-sway) and 3 mode (roll-sway-heave) motion (Fig. 9). And absorbed wave power is also decreasing in the same order (Fig. 13). Fig. 26 shows that the same conclusion holds even in irregular waves.

6. CONCLUSIONS

With regard to hydrodynamic forces which act on Salters Duck, we conclude that damping forces of roll mode and roll exciting moment can be predicted by linear theory so long as the amplitude of roll motion and incident waves are small. If the rear side of submerged circular cylinder of the Salters Duck is fully submerged, it is difficult to predict added moment of inertia of roll mode.

With regard to roll motion, we conclude that when wave power is absorbed, roll motion which is relatively small can be predicted by the linear theory by making use of the experimental result of the added moment of inertia $m_{44G}(\text{exp})$.

With regard to absorbed wave power, we conclude that in case of 2-D and 3-D problem linear prediction method works well. And the 3-D effect on a floating body which has the slenderness ratio 1:3.55 is not remarkable. The oblique wave effect is obvious. The coupled motion effect makes the wave power absorbing characteristics worse in the order of heave, sway and heave-sway. There is an example in which loads of a hydraulic system include spring constant. The linearity holds for the damping coefficient and spring constant of the load of a hydraulic system. But it is hoped that the hydraulic system with small spring constant will be produced by taking account of the shape of a cylinder and check valve.

The drift force on Salters Duck is smaller when wave power is absorbed than when wave power is not absorbed.

The following conclusions are derived from 3-D experiment in irregular waves. The linearity holds on the load of the hydraulic system in the operating condition. The wave power absorption characteristics of Salters Duck in irregular waves looks good, because the spectrum of irregular waves is relatively narrow band as compared with the frequency band width at which 3-D wave power absorption coefficient performs very well. The optimum conditions to obtain the maximum absorbed wave power by 1 mode (roll) motion in irregular waves seems to be equivalent to those in regular waves which depends on (45) and (46).

ACKNOWLEDGEMENT

The authors would like to acknowledge the deep understanding and warmest encouragement of Professor S. Motora and Professor T. Ishihara, the university of Tokyo. They also wish to thank Messrs. S. Eguchi, F. Suzuki and K. Saijo of the Institute of Industrial Science, the University of Tokyo. Mr. R. Iwase Yokosuka Technical High School, Messrs. S. Kato and Y. Imai, the graduate students of the University of Tokyo, and H. Maeno, the graduate student of Yokohama National University for their excellent cooperation and assistance in the experiment and in the preparation of this paper. Mrs. M. Narisawa in typing the manuscript is also greatly acknowledged.

This work has been supported in part by the Grant-in-Aid for Scientific Research of the Ministry of Education, Science and Culture of Japan. The numerical calculations have been done by the aid of the Computer Center of the University of Tokyo.

REFERENCES

1. Bessho, M., "Feasibility study of a floating type wave absorber", 34th Japan Towing Tank Committee, (Japan Patent No. S. 48-65398), 1973.
2. Bessho, M., "On time-reversed velocity potentials in the theory of water waves", *Journal of Society of Naval Architects of Kansai*, 159, 1975.
3. Carmichael, A.D., "An experimental study and engineering evaluation of the Salter cam wave energy converter", Sea Grant College Program M.I.T., Report No. MITSG 78-22, 1978.
4. Evans, D.V., "A theory for wave power absorption by oscillating bodies", 11th Symp. on Ship-Hydrodynamics, 1976.
5. Glendenning, I., "Energy from waves", *Oceanology International* 78, 1978.
6. Kan, M., "Wave energy absorbing effect of asymmetric floating bodies", *Lecture of Ship Research Institute*, 32, 1978.
7. Kinoshita, T., "Hydrodynamic forces and moments acting on a floating slender body with zero forward speed", *Seisan-Kenkyu*, 31-9, Univ. of Tokyo, 1979.
8. Maeda, H., Tanaka, H. and Iwase, R., "On absorbing energy from ocean waves (1st report)", *J. of Society of Naval Architects of Japan*, 146, 1979.
9. Maruo, H. and Tokura, J., "Prediction of hydrodynamic forces and moments acting on ships in heaving and pitching oscillations by means of an improvement of slender ship theory", *J. of Society of Naval Architects of Japan*, 143, 1978.
10. Masuda, Y., "Wave Power", *Ocean Age*, May, 1977.
11. Mei, C.C., "Power Extraction from Water Waves", *J. of Ship Research*, Vol.20, No.2, June, 1976.
12. Mei, C.C., and Newman, J.N., "Wave-power extraction by floating bodies", *First Symp. on Wave Energy Utilization*, Gothenburg, Sweden, 1979.
13. Mynett, A.E., Serman, D.D. and Mei, C.C., "Characteristics of Salter's cam for extracting energy from ocean waves", *Ocean Research*, Vol.1, No.1, 1978.
14. Newman, J.N., "The Interaction of Stationary Vessels with Regular Waves", 11th Symp. on Ship-Hydrodynamics, 1976.
15. Salter, S.H., "Wave Power", *Nature*, Vol.249, June 21, 1974.
16. Tanaka, H. and Saito, M., "Wave power absorption characteristics of a rocking body (1st report. Fundamental characteristics)", *Bulletin of 56th annual meeting of Japan Society of Mechanical Engineering*, 1978.

APPENDICES

Appendix A Materials to design a floating body.

A-1. The shape of the body should have characteristics of a large radiation Kochin function on one side and small one on the other side as shown in (48). The amplitude of motion in a designed condition can be made the smaller, if the body has the larger radiation Kochin function, as shown in (47).

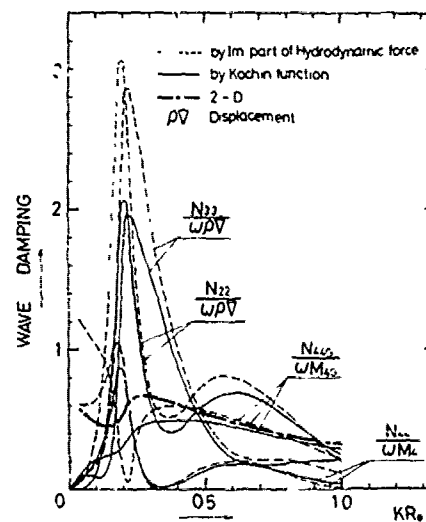
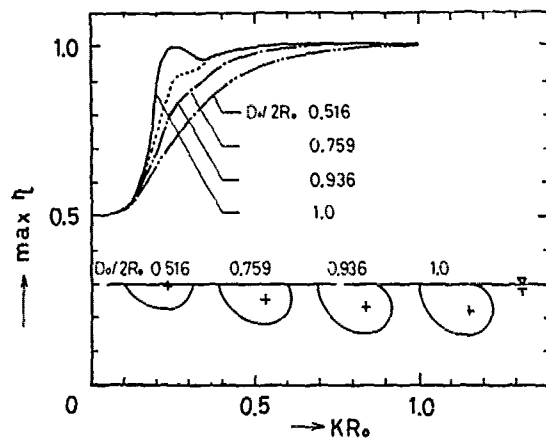
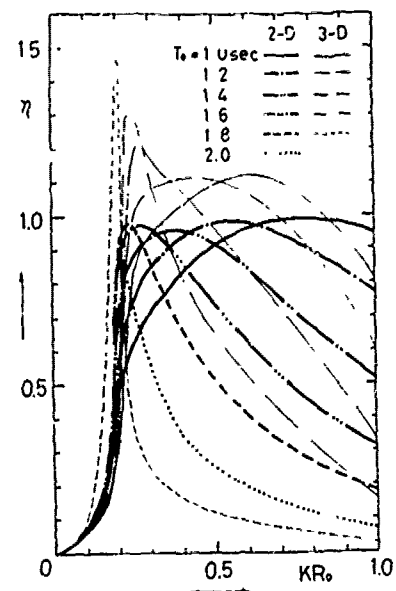
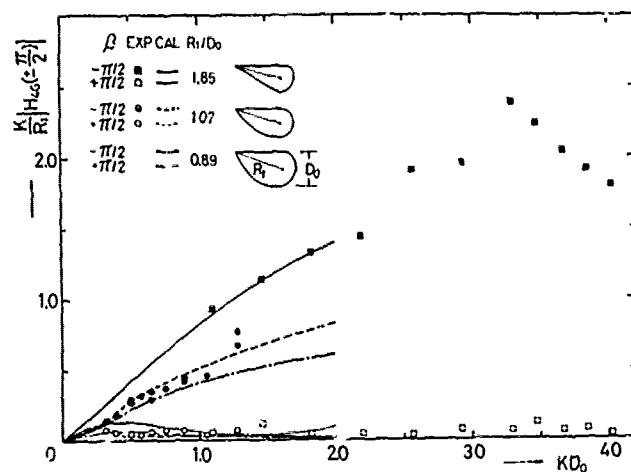
Radiation Kochin functions non-dimensionalized by the bill length R_1 , which is defined by the distance between rolling axis and tip of the cross section, vs. wave number which is non-dimensionalized by a draft D_0 of the body are shown in Fig. A-1 for three Salters Ducks with different bill length draft ratios $R_1/D_0 = 1.85, 1.07$ and 0.89 [6]. For the former two Ducks, they are compared with experiments.

Maximized absorbed power efficiencies defined by (48) are shown in Fig. A-2 for the Duck with $R_1/D_0 = 0.89$ with a parameter of draft and twice of radius ratio $D_0/2R_0 = 0.156, 0.759, 0.936$ and 1.0 . The Maximized absorbed power efficiency curve of the Duck with $R_1/D_0 = 1.07$ and $D_0/2R_0 = 1.0$ coincides with the curve of the Duck with $R_1/D_0 = 0.89$ and $D_0/2R_0 = 1.0$. Fig. A-2 shows the fully submerged Duck is the best for high efficiency.

A-2. Natural frequency of the body should be determined so that the band width of high efficiency is wide. The absorbed wave power efficiencies with constant load dampings, which are equal to wave damping of the natural frequencies, are shown in Fig. A-3 with a parameter of natural periods $T_0 = 1.0, 1.2, 1.4, 1.6, 1.8$ and 2.0 . The 3-D effect is also shown in Fig. A-3. The 3-D effect is apparent at small wave numbers.

Appendix B 3-D effect on N_{ij} .

Wave damping coefficients N_{ij} are given by (60) and by (72) independently in 3-D cases. Both calculated results by (60) and by (72) are shown in Fig. A-4. They do not coincide with each other. On the other hand, the approximate 3-D hydrodynamic forces f_{ij} given by (60) are proved to be symmetric practically by numerical calculations.



Discussion

S H Saiter (*Univ of Edinburgh*)

The authors have presented an excellent combination of theoretical and experimental methods and it is interesting to compare their results with those of the group in Edinburgh which have up to now been mainly experimental.

The shape of our ducks has been changed in a few respects. We have added a bulge to the back section so that recovery from capsize is assisted in extreme seas. The most critical parameters are the water line length, the hub depth, the position of the centre of gravity and the moment of inertia in roll. The shape of the forward curve is uncritical except where it breaks the surface. This should be designed to increase the linearity of the hydrostatic restoring force in roll (Fig 3 of the author's paper). These shape changes allow a convenient space for our power conversion mechanism and a cheaper civil engineering design.

The full scale duck backbones have to allow some flexure and so there have to be gaps between ducks. At present we expect to use a 24 metre wide duck and a 30 metre spacing. We find that the 6 metre gap does not lose any power but does reduce the mooring force by a factor of two. This now is only 25 tonnes per duck and seems to be almost independent of wave amplitude or spectrum period.

While we share the author's preference for oil hydraulics at full scale all our model apparatus uses electronic controls for the power take-off and for mounting control. This gives us very convenient measurements and adjustments and allows us to change the phase of the power take off forces and use a variety of non-linear techniques. We can measure the power generated by heave and sway movements and find that sway can provide some useful output. It also turns out that compliance of the mounting can be very valuable. We can double the efficiency at the long end of the spectrum by letting the rear of the model act like an Evans cylinder.

None of our work so far has been in oblique waves and so it is interesting to see section 4.5 and fig 19. But we hope that it will eventually prove possible to avoid any loss of efficiency in oblique seas provided that the duck width is small in comparison to the wavelength and that an array of ducks is used. The argument runs as follows:- A bank of narrow wavemakers with the right drive signals can create any directional sea, even one including waves moving at 90° to the line of wavemakers. Wavemakers and wave absorbers are interchangeable if time is reversed so that the

array of ducks should be able to 'unmake' the sea.

Finally may I make a plea for a change in the way results are plotted. Nearly all theoretical work uses frequency as the horizontal axis. The commercially relevant parts of the spectrum are mainly between $KR_0 = 0.2$ and 0.3 . There is very little energy in the sea at $KR_0 = 0.8$. Plotting against a frequency axis clamps the useful parts and expands the unwanted region. This may mask an economically valuable result. Fig 12 illustrates the point well. A better understanding is given if period or wavelength are used. But it may be that the best results will come if we use a period axis with intervals proportional to the useful energy in that period at a particular wave field.

An independent assessment of the cost of electricity generated by ducks suggests that it is now cheaper than that from new oil-fired plant. But before wide scale production can begin a further reduction of two must be achieved. The combination of theoretical and experimental work such as that of the authors with sound production engineering of equal standard will make this possible.

Author's Reply

H. Maeda (*Univ of Tokyo*)

The authors thank Mr. Salter for his valuable comments. The authors are interested in countermeasures in extreme conditions which are accepted by Mr. Salter's group in Edinburgh. Countermeasures in extreme conditions are necessary for practical design. Extreme value prediction of wave load in random seas is very important. This kind of prediction is well investigated in the case of ordinary ships which have weak non-linearity or in the case of large scale of offshore structures the hydrodynamic forces of which is almost independent of frequency. But in the case of Salter's Duck the hydrodynamic force of which is strongly dependent of frequency and which has strong non-linear effect on hydrodynamic forces, restoring forces and mooring forces, the prediction method of extreme value has not been investigated well. Because the purpose of this paper is to investigate the characteristics of absorbing wave energy in operating conditions, safety problems in extreme conditions are not referred to.

Mr. Salter pointed out that appropriate gaps do not lose any power because of 3-D effect but do reduce the mooring force. The authors have had the same experience on

multi shiplike breakwater.

There are two kinds of standpoint with regard to energy convertor such as hydraulics or apparatus with electronic control. One is the standpoint of a model in a model basin and another is that of full scale. From the point of view of full scale, the authors prefer to hydraulics because of their easy control and storage of energy. But from the standpoint of a model basin we share Mr. Salter's preference for apparatus with electronic controls.

Most of the horizontal axis of figures

in this paper is used as non-dimensional frequency KR_0 . The authors merely follow the conventional way of ship hydrodynamics. As mentioned by Mr. Salter, effective wave frequency may be limited within $KR_0 = 0.2 \sim 0.5$. The authors agree with Mr. Salter's proposal in which wanted region is expanded. $\sqrt{KR_0}$ may be also useful expression (see Fig. 26). But hydrodynamic forces in whole frequency range is required theoretically with regard to response in irregular waves. One needs at least a frequency range in which energy convertor responds.

Rafts for Absorbing Wave Power

Pierre Haren and Chiang C. Mei
Massachusetts Institute of Technology
Cambridge, U S A

ABSTRACT

Slender articulated rafts floating on the water surface can be used to extract energy from incident sea waves. For a single train of rafts in head seas, we assume that a power converter is attached to each hinge which connects two rafts, and seek the converter impedances for optimum absorption. In particular, it is found that the converter should have sufficient inertia or negative effective spring stiffness. The effects of the width and the number of rafts and the angle of incidence are also studied. Wave forces are calculated.

NOMENCLATURE

A incident wave amplitude
 $A(\theta)$ angular variation of total radiated waves
 B width of raft
 L total length of raft train
 R_n vertical force exerted by raft $n - 1$ on raft n through hinge n , positive if upward. The bow and the stern are unconstrained hence $R_1 = R_{N+1} = 0$
 F_n^D vertical hydrodynamic force on raft n due to diffraction
 M_n^D hydrodynamic moment about mid-

section of raft n due to diffraction

$F_n^{(m)}$ vertical hydrodynamic force on raft n due to mode m .

$M_n^{(m)}$ hydrodynamic moment about mid-section of raft n due to mode m .

L_n length of raft n

M_n mass of raft $n = \rho D L_n$

I_n moment of inertia of raft n about the mid-section = $\frac{1}{12} \rho D B L_n^3$ for homogeneous raft

K wave number

P dynamic pressure

T physical time

XYZ physical coordinates, Z is positive upward, origin on the mean free surface

xyz dimensionless coordinate

L_a absorption length

ϕ^S potential of scattered waves

ϕ^I potential of incident wave

ϕ^R potential of radiated waves

θ_n pitch angle of raft n , positive if

counter-clock-wise

$\phi^{(m)}$ radiation potential due to mode m .

λ wave length

ω frequency

$\bar{\alpha}_n$ damping rate of converter n at hinge

n

\bar{C}_n stiffness of converter n at hinge n

η free surface displacement

1. INTRODUCTION

In a penetrating paper, Newman [1] analyzed an elongated floating body which extracts energy from head seas. By adroit use of the indentities in the linearized diffraction theory, and slender body approximation, he predicted the optimum efficiency for a wide range of frequencies when the rafts are allowed to have a variety of smooth and piece-wise linear modes of motion. Other questions of engineering interest such as the power converter characteristics needed to achieve the optimum, the wave forces on the body, and the effect of non-slenderness were not investigated. In order to understand better the mechanics of power absorption and to obtain more specific guidelines for future design, we shall study in this paper these questions for a train of articulated rafts of small draft, also in the context of linearized theory.

To model the power converter mathematically, our attention will be focussed on the most straightforward design that each hinge has a power converter which extracts power from the relative rotation between two adjacent rafts. In Newman's analysis, the motion of the articulated rafts is decomposed into a set of orthogonal modes. This suggests that a power converter may be also designed for each of these modes which may involve the motion of more than two rafts.

To calculate all hydrodynamic quantities, a method of integral equation is used.

The basic design of the power absorbing rafts is independently to G. Hagen [4] and C. Hall [5]

2. OUTLINE OF THEORY

We consider a train of N rectangular rafts of equal width B and total length L . The draft D of all the rafts will be assumed to be negligibly small for diffraction analysis, although some value is clearly necessary for buoyancy. Let the x -axis be the longitudinal axis of the rafts and, for the most part of this paper, also the direction of the incident wave with the potential

$$\phi^I = \frac{-igA}{\omega} e^{iKX} e^{KZ} \quad (2.1)$$

The time factor $e^{-i\omega T}$ is implied but omitted.

Let ϕ^S and ϕ^R denote respectively the scattering potential due to the presence of the fixed train and the radiation potential due to the induced motion of the floating train. The total potential can clearly be expressed as

$$\phi = \phi^I + \phi^S + \phi^R \quad (2.2)$$

Let us introduce A_m as the amplitude of the vertical displacement of joint m with $m = 1$ at the bow and $m = N+1$ at the stern. By linearity we may write

$$\phi = \phi^I + \phi^S + \sum_{m=1}^{N+1} A_m \phi^{(m)} \quad (2.3)$$

where $\phi^{(m)}$ corresponds to the radiation potential of mode m which is induced by the vertical oscillation of joint m at unit amplitude, with all other joints remaining on the x - y plane. Clearly, for a prescribed geometry, the hydrodynamic boundary value

problems for ϕ^S and $\phi^{(m)}$ are similar and may in principle be solved by a number of numerical methods. The integral equation method sketched below is similar to Kim [6] and is described more fully in [2]. It is designed specifically for zero draft.

We only outline the essential ingredients of our method for the diffraction problem. Define the Green's function G by the Laplace equation, the radiation condition, and the following condition on the free surface

$$\frac{i\omega g}{\omega} \left(\frac{\omega^2}{g} G - \frac{\partial G}{\partial Z} \right) = \delta(X - X_0) \delta(Y - Y_0) \quad \text{on } Z = 0 \quad (2.4)$$

Thus the Green function is the potential due to a point pressure on the free surface. The scattering potential is then

$$\phi^S(X, Y, Z) = \iint_B \left[\frac{i\omega g}{\omega} \left(\frac{\omega^2}{g} \phi^S(X_0, Y_0, 0) + \frac{\partial \phi^S}{\partial Z}(X_0, Y_0, 0) \right) \right] G(X, Y, Z; X_0, Y_0, 0) dX_0 dY_0 \quad (2.5)$$

where ϕ^I represent the incident waves. The no-flux condition on the body B is already satisfied. The explicit form for G is, in dimensionless form:

$$G = g(\vec{x}, \vec{x}_0) / \frac{\rho g}{3} \quad (2.6)$$

$$g(x, y, z; x_0, y_0, 0) = -\frac{1}{2\pi r} + \frac{e^z}{4} [\quad (2.7)$$

$$\mathbb{H}_0(\rho) + Y_0(\rho) - 2iJ_0(\rho)]$$

$$+ \frac{e^z}{2} \int_z^0 \frac{e^{-\tau} d\tau}{\sqrt{\tau^2 + \rho^2}}$$

$$\text{where } (x, y, z) = \frac{\omega}{g}(x, y, z)$$

$$\rho^2 = (x - x_0)^2 + (y - y_0)^2,$$

$$r^2 = \rho^2 + z^2$$

and \mathbb{H}_0 is the Struve function.

Letting $z = 0$ in (2.5) an equation for ϕ on B is obtained, which can be solved numerically [2].

After the potentials are found the dynamic pressure under the raft n follows from the Bernoulli equation

$$P_n = i\rho\omega\phi - \rho g\eta = i\rho\omega \left(\phi - \frac{g}{2} \frac{\partial\phi}{\partial z} \right) \quad (2.8)$$

$$z = 0$$

where η is the vertical displacement of the raft. The diffraction (exciting) pressure is

$$P_n^D = i\rho\omega (\phi^S + \phi^I), \quad z = 0 \quad (2.9)$$

while the radiation (restoring) pressure is

$$P_n^{(m)} = i\rho\omega \left(\phi^{(m)} - \frac{g}{2} \frac{\partial\phi^{(m)}}{\partial z} \right) \quad (2.10)$$

The dynamic equations for raft n may now be derived. Referring to the list of notations at the beginning of this paper we point out that the pitch angle of raft n is related to the vertical displacements of the ends A_n and A_{n+1} by

$$\theta_n = (A_{n+1} - A_n) / L_n \quad (2.11)$$

A power converter attached to each hinge n produces a resisting moment

$$(\bar{C}_n - i\omega\bar{\alpha}_n) (A_n - \theta_{n-1}) \quad (2.12)$$

$$n=2, \dots, N$$

Thus the converter is characterized by a

damping rate $\bar{\alpha}_n$ and a torsional spring constant \bar{C}_n ; $\bar{C}_n - i\omega\bar{\alpha}_n$ may be called the hinge impedance. Instead of a spring, we can of course use an inertia; \bar{C}_n should then be replaced by $-\omega^2 i_n$.

The dynamic equations for raft n are

$$\frac{-\omega^2 M_n}{2} (A_n + A_{n+1}) = \sum_{m=1}^{N+1} A_m F_n^{(m)} + F_n^D \quad (2.13)$$

$$+ R_n - R_{n+1}$$

where the superscript D denotes "diffraction problem" ($= S+I$), and

$$-\omega^2 I_n \theta_n = \sum_{m=1}^{N+1} A_m M_n^{(m)} + M_n^D - \frac{1}{2} L_n$$

$$(R_n + R_{n+1})$$

$$- (\bar{C}_n - i\omega\bar{\alpha}_n) (\theta_n - \theta_{n-1}) + (\bar{C}_{n+1} - i\omega\bar{\alpha}_{n+1}) (\theta_{n+1} - \theta_n) \quad (2.14)$$

with

$$\bar{\alpha}_1 = \bar{C}_1 = \bar{\alpha}_{N+1} = \bar{C}_{N+1} = R_1 = R_{N+1} = 0 \quad (2.15)$$

where θ_n and A_n are related by (2.11)

When $\bar{C}_n - i\omega\bar{\alpha}_n$ is given for $n = 2, \dots, N$, there are $2N$ equations (2.13) and (2.14) for equal number of unknowns A_n : $n = 1, \dots, N+1$; and R_n : $n = 2, \dots, N$. Their solution completes the entire dynamic problem.

The absorbed energy from all hinges may now be calculated

$$\bar{E} = \frac{\omega}{2\pi} \int_c^{2\pi/\omega} dT \sum_{n=2}^N \bar{\alpha}_n \{ \text{Re} [-i\omega(\theta_n - \theta_{n-1}) e^{-i\omega T}]^2 \} \quad (2.16)$$

Following Newman we define the absorption width L_a by

$$\frac{L_a}{\lambda} = \frac{\bar{E}}{K} \cdot K / 2\pi (\frac{1}{2} \rho g A^2 C_g) \quad (2.17)$$

The next step is to maximize L_a/Λ . We proceed by first prescribing a set of values for $K = 2\pi/\Lambda$, B , L , N and L_n . For each set the hinge impedances are optimized by a relaxed gradient method familiar in non-linear optimization and described in Simmons [7]. The computer program is fully recorded in [2]. The rate of convergence for this optimization scheme is found to be quite variable but all optimum values L_a/Λ are checked by using two starting values; the results are usually within 0.5% of each other.

The entire analysis was executed in terms of the following dimensionless variables

$$(x, y, z) = K(X, Y, Z)$$

$$(b, \ell) = K(B, L)$$

$$\phi = -\frac{igA}{\omega} \psi \quad \text{for } \phi = \phi^I \text{ or } \phi^S$$

$$\phi^{(m)} = -\frac{ig}{\omega} \psi^{(m)}$$

$$P = \rho g A p \quad A_n = A a_n$$

$$\bar{\alpha}_n = \frac{\rho g}{\omega K^4} \alpha_n \quad \bar{C}_n = C_n \frac{\rho g}{K^4}$$

We now present and discuss the numerical results.

3. EFFECTS OF NUMBER OF RAFTS ON L_a/Λ

In this section we fix the ratios $L/\Lambda = 1$ and $B/L = 0.1$. For computing the buoyancy we take $KD = 0.1$ or $D/B = 0.016$.

3.1 Two-Raft Train

When only two rafts are joined by one hinge, the optimal hinge impedance and efficiency are listed in Table I. L_a/Λ is

rather low, and does not vary significantly as the hinge position is changed. It is a curious fact that the optimum impedance is the same (i.e. same converter) although L_a/Λ changes when the direction of the

incident wave is reversed. More important, the optimal spring constant is always negative, suggesting that the converter should have inertia instead of a spring. The

latter possibility has been demonstrated by Salter in his "duck".

TABLE I Optimum hinge impedances for Two-raft trains with $L=\Lambda$ and $B/L=0.1$. $KD = 0.1$, ($D/B = 0.16$). $L=L_1+L_2$

$\frac{L_1}{L}$	$\frac{L_2}{L}$	L_a/Λ	α_2	C_2
.21	.79	.360	.025	-.127
.26	.74	.356	.045	-.189
.32	.68	.349	.068	-.249
.37	.63	.341	.091	-.299
.42	.58	.331	.109	-.335
.47	.53	.320	.119	-.353
.53	.47	.308	.118	-.353
.58	.42	.295	.109	-.334
.63	.37	.282	.091	-.299
.68	.32	.267	.069	-.249
.74	.26	.256	.045	-.189
.79	.21	.245	.025	-.127

3.2 Three-Raft Train

The optimal trains for a variety of hinge positions are given in Table II. A number of symmetric and asymmetric trains are included. Note that L_a/Λ is insensitive to L_n hence to the position of the hinges;

this result was already found by Newman [1]. It is significant that not only the spring constants must be negative at both hinges, but also the damping coefficient of the down-wave hinge ($m=3$) must be negative. Thus to achieve optimum, energy must be fed to the down-wave hinge in order to maximize the total absorption. It must be remarked that allowing negative α_3 can lead to negative

absorption width when the incident wave frequency is different from the design value i.e., the rafts are detuned.

TABLE II Optimum impedances for variable L_1, L_2, L_3 Three-raft trains with $L = 1$ and $B/L = 0.1$, $KD = 0.1$ ($D/B = 0.16$). $L = L_1+L_2+L_3$.

$\frac{L_1}{L}$	$\frac{L_2}{L}$	$\frac{L_3}{L}$	L_a/Λ	α_2	α_3	C_2	C_3
.21	.58	.21	.621	.036	-.053	-.111	-.092
.26	.48	.26	.714	.063	-.048	-.104	-.116
.32	.36	.32	.728	.074	-.058	-.095	-.118
.37	.26	.37	.737	.078	-.063	-.065	-.101
.42	.18	.42	.708	.089	-.070	-.014	-.081
.21	.21	.58	.724	.025	-.081	-.042	-.057
.21	.26	.53	.723	.022	-.083	-.053	-.067
.21	.32	.47	.724	.023	-.096	-.064	-.084
.21	.37	.42	.725	.028	-.102	-.070	-.113
.26	.21	.53	.729	.048	-.097	-.052	-.073
.26	.26	.48	.735	.040	-.084	-.066	-.085
.26	.32	.42	.732	.044	-.098	-.078	-.106
.26	.37	.37	.728	.052	-.088	-.091	-.123
.26	.42	.32	.723	.059	-.069	-.096	-.131
.32	.21	.47	.737	.060	-.084	-.055	-.079
.32	.26	.42	.701	.054	-.099	-.102	-.051
.32	.32	.36	.733	.067	-.070	-.082	-.115
.32	.42	.26	.721	.086	-.046	-.115	-.108
.36	.21	.42	.739	.060	-.061	-.053	-.076
.42	.21	.36	.731	.095	-.064	-.036	-.093

We now study the sensitivity of L_a/Λ to changes in α_n and C_n . In particular the effect of not allowing α_n and C_n to be negative will be examined. Consider two trains T1 and T2 which have different hinge locations as shown in Table III. When no restriction is set on the signs of α_n and C_n the optimum L_a/Λ is around 0.73. When α_2 and α_3 are both positive, the new optimum L_a/Λ is reduced by more than half. Finally when all α_n and C_n with $n = 2, 3$ are kept positive, the maximum efficiency is further halved.

TABLE III Optimal impedances and efficiencies under constraint for three-raft trains. $L = \Lambda$ and $B/L = 0.1$ KB = 0.1 D/B = 0.16

The train with length ratios

(0.37, 0.26, 0.37) will be called (T1).
(0.32, 0.36, 0.32)

$\frac{L_1}{L}$	$\frac{L_2}{L}$	$\frac{L_3}{L}$	L_a/Λ	α_2	α_3	C_2	C_3
-----------------	-----------------	-----------------	---------------	------------	------------	-------	-------

Unrestrained Optimization

0.32	0.36	0.32	.728	.074	-.058	-.095	-.118
0.37	0.26	0.37	.737	.078	-.063	-.065	-.101

Restrained Optimization $\alpha_i > 0$,

0.32	0.36	0.32	.337	.089	11.49	-0.30	-0.21
0.37	0.26	0.37	.346	.069	12.06	-0.25	-0.21

Restrained Optimization , $C_i \geq 0$

0.32	0.36	0.32	.170	.386	.586	0.00	0.00
0.37	0.26	0.37	.180	.267	.347	0.00	0.00

It is interesting to note that in the last case of non-negative C_i , the optimal α_i can only be positive and the optimal C_i is zero. Comparing the three alternatives above, it seems necessary to design for negative C_i for good efficiency.

For better physical understanding of these optimum impedances we turn to a general formula derived by Newman [1]. Let the far-field of the total radiated

$$\phi^S + \phi^R = \frac{-iqA}{\omega} \cdot e^{KZ} \mathcal{A}(\theta) \sqrt{\frac{2}{\pi KR}} e^{i(KR - \pi/4)} e^{KZ} \quad (3.1)$$

then

$$L_a/\Lambda = \frac{1}{\pi} \left[-\frac{2}{\pi} \int_0^{2\pi} |\mathcal{A}(\theta)|^2 d\theta - 2 \operatorname{Re} \mathcal{A}(0) \right] \quad (3.2)$$

Thus to maximize L_a/Λ one must strive for $\mathcal{A}(0)$ being negative, real and large, and the integral in (3.2) small. Thus the total radiation must be focussed in the forward direction. We recall from [1] that for one degree of freedom, a good wave absorber must be a good radiator in the backward direction. When there are two or more degrees of freedom, the amplitudes of all the modes must be so orchestrated so that the total $\mathcal{A}(0)$ is large. Intuitively the effect of positive α_2 but negative α_3 is precisely to achieve

large $\mathcal{A}(0)$. In Figure 1, $|\mathcal{A}(\theta)|^2$ is plotted for train T2 under various restrained optimizations. (Curve B with $C_i \geq 0$) gives

small $|\mathcal{A}(\theta)|^2$ in both forward and backward directions. But Curve D without any constraint on the sign of α_i and C_i is strongly

focussed in the forward direction. Compared

with $\mathcal{A}^S(\theta)$ for the scattered wave, it is clear that $\mathcal{A}(\theta)$ is predominated by the

radiated wave $\mathcal{A}^R(\theta)$, giving further evidence that the train must have ample motion to radiate sufficiently large waves toward $\theta = 0$.

3.3 Four-Raft Train

Table IV gives the results for seven trains with the same total length and width. The optimum efficiency is somewhat improved over the three-raft trains, but the gain is probably not large enough to justify the added cost of the third hinge. Note again that all C_i 's are negative and the downwave

hinge must have negative damping $\alpha_4 < 0$.

4 EFFECT OF RAFT-WIDTH

So far all results presented are for a very slender rafts T1 and T2 with $B/L = 0.1$. Now a slender raft is expected to have a large displacement at optimum which may cause difficulties in structural design, not to mention the loss of relevance of the linearized theory. Newman's choice is to impose a limit of the vertical displacement, possibly by changing the hinge impedance away from optimum. An alternative is to use

wider rafts. Table V shows the optimum results of trains with the same length distributions as T1 and T2, to be called classes I and II respectively, but with different widths. The dimensionless displacement of the unrestrained bow* $|a_1|$, i.e.

the ratio amplifying the incident amplitude A, is also listed along with the optimum impedances. It may be seen that for $B/L = 0.1$, $|a_1| = 4.75$ which is probably too large

for structural safety and is expected to be still larger for longer waves. Increasing the width not only reduces the displacement, but also increases the efficiency. Figure 2 plots L_a/λ vs B/L for class I trains.

Note that the curve has a horizontal tangent at $B/L = 0$ showing that L_a/λ increases very

little for increasing but small B/L . Clearly economical considerations accounting for structural strength and converter design must enter for choosing the proper width.

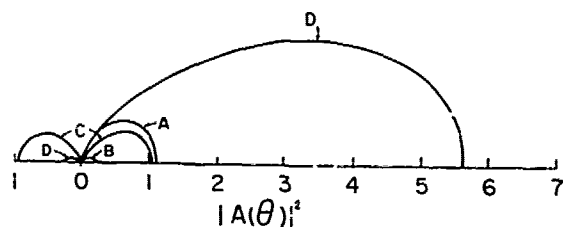


Fig. 1: Angular variation of total radiation intensity $|A(\theta)|^2$, $A = A^S + A^R$

- A: Scattering only
- B: Optimum under $C_i \geq 0$
- C: Optimum under $\alpha_i \geq 0$
- D: Unconstrained optimum

* This end has the largest displacement among all joints.

TABLE IV Optimum impedances for four-raft trains
 $L = \lambda$ and $B/\lambda = 0.1$, $L = L_1 + L_2 + L_3 + L_4$

L_1/λ	L_2/λ	L_3/λ	L_4/λ	L_a/λ	α_2	α_3	α_4	C_2	C_3	C_4
.21	.21	.21	.37	.742	.100	.131	-.094	-.073	-.105	-.100
.26	.21	.21	.32	.752	.110	.114	-.075	-.053	-.139	-.092
.32	.21	.21	.26	.755	.115	.101	-.059	-.043	-.154	-.082
.37	.21	.21	.21	.741	.116	.125	-.033	-.067	-.176	-.066
.21	.26	.21	.32	.758	.072	.097	-.069	-.058	-.118	-.081
.22	.26	.26	.26	.760	.063	.065	-.075	-.019	-.154	-.076
.21	.37	.21	.21	.766	.048	.076	-.054	-.052	-.149	-.049

TABLE V Optimum impedances and efficiencies for Three-raft

LENGTH CLASS I: $L_1 = 0.37 L$, $L_2 = 0.26 L$, $L_3 = 0.37 L$

B/L	$ a_1 $	L_a/λ	α_2	α_3	C_2	C_3
0.1	4.75	.737	.078	-.063	-.065	-.101
0.2	3.23	.750	.137	-.104	-.101	-.172
0.3	2.65	.780	.190	-.132	-.120	-.243
0.4	2.40	.825	.241	-.160	-.138	-.314
0.5	2.24	.883	.298	-.191	-.153	-.389
0.6	2.12	.952	.358	-.224	-.164	-.470
0.7	2.05	1.03	.423	-.261	-.173	-.555
0.8	2.01	1.12	.491	-.302	-.183	-.642
0.9	1.97	1.20	.559	-.343	-.194	-.729
1.0	2.04	1.30	.628	-.384	-.203	-.819

LENGTH CLASS II: $L_1 = 0.32 L$, $L_2 = 0.36 L$, $L_3 = 0.32 L$

B/L	L_a/λ	α_2	α_3	C_2	C_3
0.1	.728	.074	-.058	-.095	-.118
0.2	.739	.140	-.091	-.137	-.209
0.3	.768	.199	-.118	-.174	-.290
0.4	.813	.261	-.141	-.201	-.376
0.5	.871	.327	-.166	-.225	-.467
0.6	.941	.395	-.192	-.245	-.562
0.7	1.02	.468	-.224	-.269	-.659
0.8	1.11	.543	-.259	-.292	-.760
0.9	1.19	.621	-.295	-.314	-.865
1.0	1.29	.697	-.331	-.336	-.969

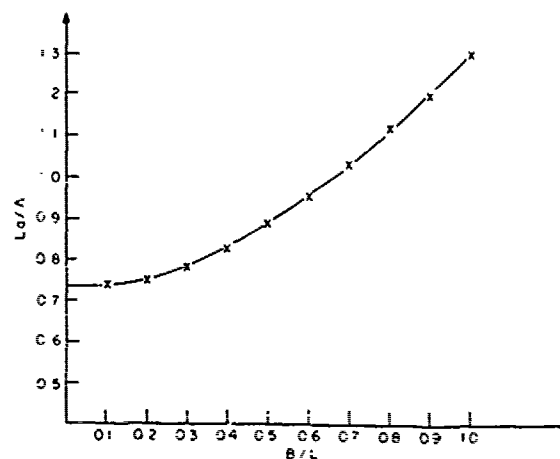


Fig. 2: Optimal efficiency for three-raft trains of Class I with different widths.

5. EFFECTS OF CHANGING WAVELENGTH ON L_a/λ

In this section two widths are considered $B/L = 0.1$ and $B/L = 0.3$; the draft is still $D/L = 0.016$. The raft lengths are of class I. The optimum data for $B/L=0.3$ are given in Table VI. The optimum L_a/λ for

$B/L = 0.1$ and 0.3 are also plotted as curves C and A in Figure 3.

TABLE VI Optimum results for variable L/λ .
 $B/L = 0.3$ $D/L = 0.016$, for two trains of different length ratios.

TRAIN T3: $L_1 = 0.37L$, $L_2 = 0.26L$, $L_3 = 0.37L$

L/λ	L_a/λ	L_a/L	$ a_1 $	a_2	a_3	C_2	C_4
0.3	0.414	1.38	54.54	$2.15 \cdot 10^{-4}$	-.089	-.013	-.200
0.4	0.415	1.04	19.47	$2.86 \cdot 10^{-3}$	-.088	-.040	-.170
0.5	0.487	0.97	10.39	.039	-.085	-.070	-.067
0.6	0.730	1.22	7.97	.052	-.051	-.049	-.050
0.7	0.785	1.12	5.57	.076	-.070	-.070	-.080
0.8	0.819	1.02	4.89	.064	-.062	-.096	-.094
0.9	0.803	0.89	3.23	.115	-.094	-.111	-.160
1.0	0.780	0.78	2.65	.190	-.133	-.120	-.243
1.1	0.752	0.68	2.32	.281	-.164	-.110	-.345
1.2	0.718	0.60	2.11	.400	-.193	-.007	-.469
1.3	0.675	0.52	1.94	0.560	-.220	0.000	-0.61
1.5	0.565	0.38	1.61	1.080	-0.31	0.380	-0.92
1.7	0.438	0.26	1.32	2.160	-0.82	1.000	-1.07
2.0	0.292	0.15	1.19	6.680	-5.33	3.070	-1.14
2.3	0.238	0.10	0.68	16.51	-21.34	12.21	-13.85

TRAIN T4: $L_1 = 0.32L$, $L_2 = 0.36L$, $L_3 = 0.32L$

L/λ	L_a/λ	L_a/L	a_2	a_3	C_2	C_4
0.3	0.414	1.38	$1.03 \cdot 10^{-4}$	-.089	-.010	-.200
0.4	0.415	1.04	$1.33 \cdot 10^{-3}$	-.088	-.030	-.170
0.5	0.488	0.98	.020	-.075	-.063	-.069
0.6	0.768	1.28	.035	-.042	-.061	-.052
0.7	0.787	1.12	.051	-.064	-.101	-.078
0.8	0.817	1.02	.066	-.056	-.112	-.129
0.9	0.794	0.88	.120	-.087	-.147	-.199
1.0	0.768	0.77	.200	-.118	-.174	-.290
1.1	0.737	0.67	.306	-.141	-.181	-.404
1.2	0.701	0.58	.452	-.154	-.155	-.537
1.3	0.658	0.51	0.65	-.160	-0.09	-0.68
1.5	0.552	0.37	1.280	-0.24	0.190	-0.92
1.7	0.438	0.26	2.530	-0.75	0.730	-0.94
2.0	0.323	0.16	7.070	-5.75	2.950	-1.19
2.3	0.294	0.13	15.47	-17.2	11.22	-17.3

First we note that for very long waves the displacement is very large, in qualitative agreement with Newman. For comparison we calculated the optimum efficiency L_a/λ .

for $B/L \approx 0$ according to Newman's theory as shown by dashed lines. When $L/\lambda > 1$ our

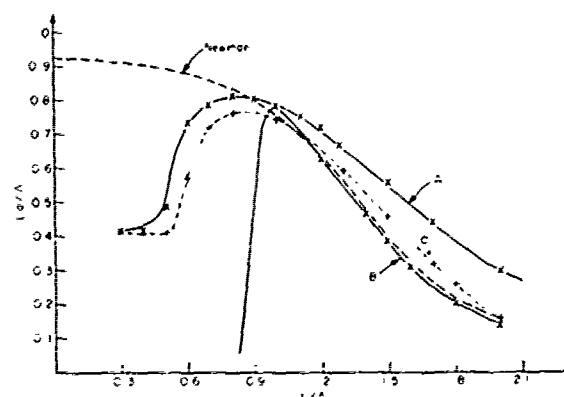


Fig. 3: Efficiency curves.

A: $B/L = 0.3$ Optimum at all frequencies

B: $B/L = 0.3$ Optimum for $L = \lambda/2$

C: $B/L = 0.1$ Optimum at all frequencies

optimum for $B/L = 0.1$ agrees well with his and is somewhat higher for $B/L = 0.3$ due to the greater raft width. However, for longer waves convergence towards Newman's optimum was too slow; the values of L_a/λ reported here are only half of Newman's.

Upon closer examination of our calculations it is found that the discrepancy is associated with the fact that only the even mode is fully excited but not the odd mode; the modes being those defined in Ref. [1]. Since Newman already showed that both even and odd modes give comparable efficiency, the nearly 50% reduction of L_a/λ , therefore, corroborates with the weak excitation of the odd mode. Haren [2] has calculated for $L = \lambda/2$ that Newman's theory predicts the optimal amplitudes of the even and odd modes to be 8 and 30 respectively, while our computation only gives 8.45 and 3.33 respectively. For small KL it can also be inferred from [1] that the optimum displacements of the two modes are in the ratio of

$$\frac{\lambda_e}{\lambda_o} \sim \frac{5KL}{24} \frac{a}{(2+a)(1+a^2)}, \quad 0 < a < 1 \quad (5.1)$$

which is very small where aL is the length of the middle raft ($a = 0.26$ for T1). The vastly larger λ_e implies that the odd mode is much more sharply tuned than the even mode, and demands much higher numerical accuracy in the present optimization program. In another example for a train in a channel, the two modes have comparable and moderate amplitudes and the present optimization program gives the same result as Newman [1]. While a more efficient optimization technique can in principle bring further agreement with Newman, the present experience suggests that

the same difficulty must also exist in designing a control system which would optimize both even and odd modes. In any case, the extraordinarily large amplitudes for long waves should be avoided.

Finally we show in Curve B the efficiency when the dimensional \bar{a}_1 and \bar{C}_1 take the optimal values only at $L = \Lambda$. The sharpness of the peak means that the system is rather highly tuned, and an inertial converter with electronic control to optimize according to incident seas is highly desirable.

From preceding discussions it is clear that proper design of power converters whose impedances are automatically adjustable with respect to hinge location and incident wave characteristics is essential to good efficiency. Using the same converter of fixed impedance at all hinges is unwise. This point appears not to have been appreciated by many inventors with the notable exceptions of Salter for beam-sea absorbers and Budal and Falnes for point absorbers.

6. WAVE FORCES

In Figure 4 we plot the vertical forces and the moment on the up-wave hinge ($m = 2$) corresponding to Table VI (hence the values for $L/\Lambda < 1$ are imperfectly optimal). The force and moment on the down-wave hinge are similar and are not presented here. In addition the second order drift force can be calculated from the far field amplitude according to the theory of Maruo [8]

$$\begin{aligned} \langle F \rangle = & \frac{-\rho g A^2}{2K} \left\{ \frac{1}{\pi} \int_0^{2\pi} \cos \theta \left| \dot{\eta}(\theta) \right|^2 d\theta \right. \\ & \left. + 2 \operatorname{Re} \dot{\eta}^*(0) \right\} \end{aligned} \quad (6.1)$$

and is shown as curve C. Note that all forces become large for long waves implying in practice that the system should be detuned to sacrifice the theoretical optimum.

7. MODIFICATION FOR OBLIQUE INCIDENCE

The incident wave is now given by

$$\begin{aligned} e^{ik(x \cos \beta + y \sin \beta)} \\ = e^{ikx \cos \beta} [\cos(y \sin \beta) \\ + \sin(y \sin \beta)] \end{aligned} \quad (7.1)$$

The first term above gives rise to a pressure distribution which is even in y , while the second term is odd in y . The odd pressure distribution affects roll only. However, because of the zero draft, roll is completely uncoupled with the other modes of motion symmetrical in y . Thus we need only replace

$$e^{ikx} \text{ by } e^{ikx \cos \beta} \cos(y \sin \beta)$$

in all hydrodynamical calculations. The

optimal L_a/Λ for $L = \Lambda$ is shown in Figure 5 as a function of β . The curve is reasonably flat for small β . For example for $\beta = 15^\circ$ the reduction from head sea incidence is 10% while for $\beta = 25^\circ$ the reduction is 20%. Since it is typical that 95% of the energy is within $\beta \leq 25^\circ$ the reduction of efficiency due to oblique sea is not serious.

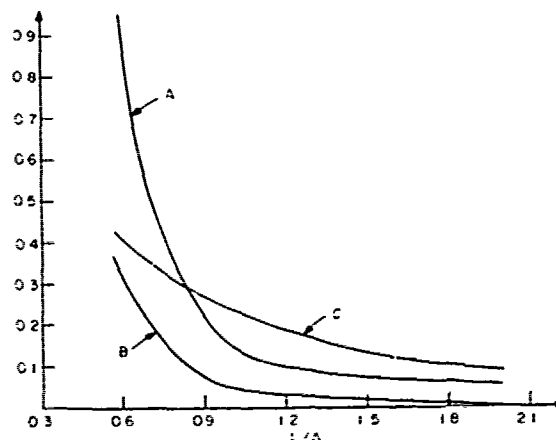


Fig. 4: Wave forces on three-raft train T3

A: Normalized vertical force at hinge

$$2: 10|R_2|/\rho g A L^2$$

B: Normalized moment at hinge 2:

$$10|M_2|/\rho g A L^3$$

C: Normalized drift force: $\langle F \rangle / \rho g A^2 L$. Results for $L/\Lambda < 1$ are imperfectly optimized.

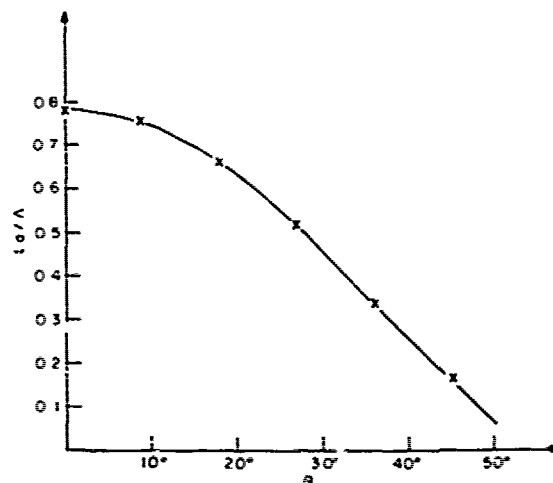


Fig. 5: Variation of efficiency with incidence angle β , for train T3 with $L = \Lambda$. a_1 and C_1 are optimal for $\beta = 0$.

8. CONCLUDING REMARKS

For Hagen-Cockerell rafts the following criteria for maximum efficiency may be summarized.

- (1) The power converters must be controlled to vary with the incident sea.
- (2) The converters must have proper inertia or negative spring.
- (3) The forward converter may require energy input to focus energy forward. Thus for best overall absorption, the forward hinge must lose energy.
- (4) Increasing raft width can increase the absorption width and reduce the raft displacement.
- (5) Loss of optimum efficiency in oblique seas is not serious.

ACKNOWLEDGEMENT

We have benefited from extensive discussions with Professor J.N. Newman on the entire subject.

The authors acknowledge the support of Department of Energy (contract DE-AC-02-79 ET21062) Office of Naval Research (Task NONR-062-521) and French Ministere de L'Environnement et du Cadre de Vie.

REFERENCES

1. Newman, J. N. (1979), "Absorption of Wave Energy by Elongated Bodies," Applied Ocean Research, Vol. 1, pp. 189-196.
2. Haren, P. (1980), "Wave Energy A Hydrodynamic Analysis of Head-Sea Absorbers," Ph.D. Thesis Civil Engineering, M.I.T.
3. Haren, P. and Mei, C. C. (1980), "Head Sea Diffraction by a Slender Raft With Application to Wave Power Absorption," (to be published).
4. Hagen, G. (Patent), "Wave-Driven Generator," U.S. Patent 4,077,213
5. Wooley, M. and Platts, J. (1975), "Energy on the Crest of a Wave," New Scientist May 75, pp. 241-243.
6. Kim, W. D. (1963), "On the Forced Oscillations of Shallow-Draft Ships," Journal of Ship Research, Vol. 7, pp. 7-18.
7. Simmons, D. M. (1975), "Nonlinear Programming for Operations Research," Prentice-Hall, Englewood Cliffs, N. J.
8. Maruo, H. (1960), "The Drift of a Body Floating on Waves," Journal of Ship Research 4.1.

FURTHER NOTE

In our paper numerical evidences are given that for maximum absorption the rafts must be moved to radiate waves which are sharply focused in the forward direction (c.f. Figure 1 Haren and Mei), and this is

achieved by absorbing energy from hinge 2 while releasing energy from hinge 3. We now have the theoretical proof that forward focusing is a general criterion for optimal absorption.

The incident wave

$$\eta^I = A e^{ikx} = A \sum_{n=0}^{\infty} \epsilon_n(i)^n J_n(kr) \cos n\theta \quad (1)$$

behaves in the far field as:

$$\eta^I = \frac{A}{2} \sqrt{\frac{2}{\pi kr}} \sum_{n=0}^{\infty} \epsilon_n(i)^n \cos n\theta \left[\exp(ikr - \frac{i\pi}{4} - \frac{in\pi}{2}) + \exp(-ikr + \frac{i\pi}{4} + \frac{in\pi}{2}) \right] \quad (2)$$

In the brackets, the first term is the diverging part while the second term the converging part of mode n . To maximize power absorption one must try to radiate waves in order to cancel, in combination with the scattered waves, as many diverging parts in the incident wave as possible. The converging parts of these modes then contribute to the absorbed power. For a slender raft in head seas the scattered waves are negligible. Ideally, to cancel all the outgoing modes of the incident waves, the radiated waves by the body motion should have the following far field amplitude

$$B(\theta) = \frac{A}{2} \sum_{n=0}^{\infty} \epsilon_n(i)^n e^{-in\pi/2} \cos n\theta = \frac{A}{2} \delta(\theta) \quad (3)$$

where $\delta(\theta)$ is the Dirac δ -function. If this could be achieved the absorption width would be infinite. Of course this cannot be achieved in practice since the raft length and the motion amplitude must both be limited. In any case the above result implies that a good slender head-sea absorber must strive for maximum focusing in the forward direction.

The preceding argument can also be used to provide an alternative proof of Newman's (1976) conclusion for an axially symmetric body with a vertical axis. If the body is allowed to heave only, the radiated wave is isotropic and can at most cancel out the outgoing part of the isotropic mode J_0 in the incident wave. It may be shown that the energy absorbed from the converging part of J_0 gives $L_a = 1/k$. Similarly if the body is allowed to sway only, the radiated wave can only cancel out the outgoing part of $J_1 \cos \theta$; the converging part gives $L_a = 2/k$.

Discussion

H. Tanaka (Yokohama N. Univ.)

It will be respected to clarify the mechanism of wave power absorption of rafts. I want to ask the following points and to make some proposals.

(1) It will be necessary to take a mooring condition into consideration in Eq. (2.13) and (2.14), please show the supporting of rafts in the calculated results of Table 1 to 3.

(2) For designing power conversion mechanism, it is convenient to have an information on the load factor defined by the ratio of damping force of load versus wave exciting force. Please show an example shown in Table 1.

load factor = viscous frictional torque / wave exciting moment

$$= \alpha_2 \omega^* (\theta_2 - \theta_1) / M_1^D$$

at $L_1/L = 0.21$ and 0.47 , where (*) means optimal condition.

(3) It will be better to define the hinge impedance not by $(\bar{c}_n - i\omega\alpha_n)$ but by

$(\bar{a}_n - \bar{c}_n / i\omega)$ because of the correspondence to mechanical impedance.

(4) The problem of negative spring c_n will

be solved by the addition of inertia load i_n for optimal load.

Author's Reply

P. Haren (MIT)

We thank Prof. Tanaka for his remarks and suggestions.

Question (1) relates to the mooring condition. Because our trains have zero draft there is no first order mooring condition (no first order horizontal force). We assume a slack mooring to prevent second order drift. Otherwise our body is freely floating.

Question (4) deals with our "negative spring" assertions. The exact "generalized" spring is $(\bar{c}_n - i_n \omega^2)$ and indeed negative values can be obtained by choosing $\bar{c}_n = 0$ and $i_n > 0$. The variations of $(\bar{c}_n - i_n \omega^2)$ with ω are very different if $\bar{c}_n < 0$ and $i_n = 0$ or if $\bar{c}_n = 0$ and $i_n > 0$. It appears that a fixed \bar{c}_n leads to a broader bandwidth than a fixed i_n .

All this only corresponds to a phase shift between the resisting moment and the displacement which could eventually be dealt with by a "smart" electronically controlled hinge.

The Sea Trials and Discussions on the Wave Power Generator Ship "KAIMEI"

Yoshio Masuda, Gentaro Kai, Takeaki Miyazaki

Japan Marine Science and

Technology Center (JAMSTEC), Yokosuka

Yoshiyuki Inoue

Yokohama National University, Yokohama

Japan

1. INTRODUCTION

Very large amounts of energy are stored in the Oceans of the world in the form of waves.

In principle, this energy could replace a significant part of that currently being provided through exhaustible fuels.

However, the potential of wave power generation's only practical application in the world today is in a navigation light buoy. Thus, the utilization of wave energy is still limited to a small scale.

The Japan Marine Science and Technology Center (JAMSTEC) has been carrying out a five-year development research project on a large output wave power generator since 1976.

Since the objective of the research is the conversion of wave energy into electricity, a wave power generator, "Kaimei," was constructed in order to perform two series of open-sea trials during 1978 - 1980.

From these tests, much of the results obtained through experiments using model vessels have been proven on the actual seas.

Among the various findings, generator No.9 has recorded a maximum output of about 291KW, exceeding all expectation.

2. PRINCIPLE OF THE SYSTEM

Various applicable methods for the conversion of wave power into electrical power have been proposed by experts throughout the world. However, JAMSTEC has been concentrating its efforts on the research of a wave power generator employing air turbines. In this type of generator, a bottomless box is floated on the surface of the sea, and an entering and

exiting flow of air is actuated by the upward and downward movement of the water in the box. An air turbine and generator unit are installed on the box and utilize these air currents to generate electricity.

After various types of model tests, the steelmade 80-m long, 12-m wide "Kaimei" was constructed as shown in Figure 1. The hull of the Kaimei consists of four buoyancy rooms and a number of air pump rooms where wave energy is converted into air flow.

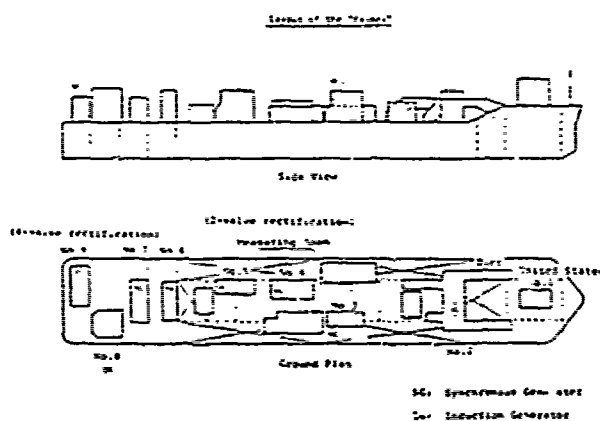


Fig. 1 Kaimei 1979 The Second Trials

3. OPEN-SEA TRIALS

The open-sea trials of the Kaimei were performed twice. The first series were carried out during the winter of 1978-79, since wave activity at the test site in the Japan Sea is at its peak during this period. During the trials, the Kaimei

carried three Japanese made generators.

Following the trials, the Kaimei was returned to harbour to allow refitting with a new group of generators, seven of Japanese design and manufacture and one from the U.K. With the exception of the non-arrival of the generator from the USA, the work was completed on schedule and in time to allow the Kaimei to be returned to the test site for the second open-sea trials during the winter of 1979-80.

The second sea trial was a joint research project involving five countries as an International Energy Agency undertaking.

The participants are as follows.

Canada -The National Research Council of Canada

Ireland-The Government of Ireland

Japan -The Japan Marine Science and Technology Center

U.K. -The Secretary of State of Energy

USA -The Department of Energy

3.1 The Test Site

The test site was situated 3km off Yura (N: $38^{\circ}44'$, E: $139^{\circ}39'$) on the West coast of Japan as shown in Figure 2. Wave activity at the test site in the Japan Sea is at its peak during the winter.

The Kaimei was moored heading to WNW since the maximum winds are predominantly out of between W and NW.

The fetch is open to the W for about 1000km and to the NW for about 700km.

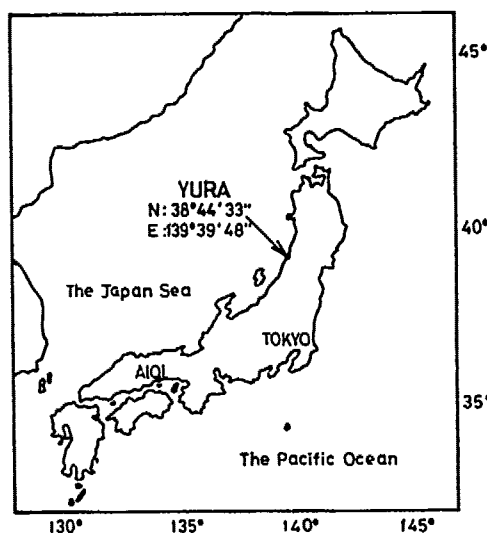


Fig. 2 Test Site

3.2 Construction of the Kaimei

In conformity with the average wave period of 6 - 7 sec. in the Japan Sea, the

length of the Kaimei was designed to be 80 m. Estimating maximum wave height at 12m, the strength of each section of the hull was calculated based on this assumption. For the first open-sea trials, the displacement of the Kaimei including the three generator units was found to be 599 tons, and GM was 7.25M. Through forced pitch and roll tests made under calm water conditions, the natural period of rolling was found to be $T = 5.2\text{sec}$.

For the second open-sea trials, displacement including the eight generator units was 723.6 tons, GM was 4.49M, and the natural period of rolling was $T = 6.3\text{sec}$. Since the natural period of rolling was so close to the wave period, there were apprehensions of resonance. However, after confirming safety through studies, 52.4 tons of concrete ballast was placed at the bottom of the ship for trim adjustment. This increased the displacement to 776 tons under normal conditions, and 821.2 tons during the open-sea experiments with the weight of the mooring chains -- 45.2 tons -- added (the weight of generator unit No.1 was not included).

3.3 Design of Mooring

The primary concern in conducting the open-sea trials was related to the mooring.

The Kaimei was moored at four points at the bow and one point at the stern with a buoy in the middle of the chain. As a result, a slack mooring method using heavy chains was confirmed to be the safest. The two main lines are 95mm super grade 4 chain chains and the other three lines are 76mm grade 3 chains.

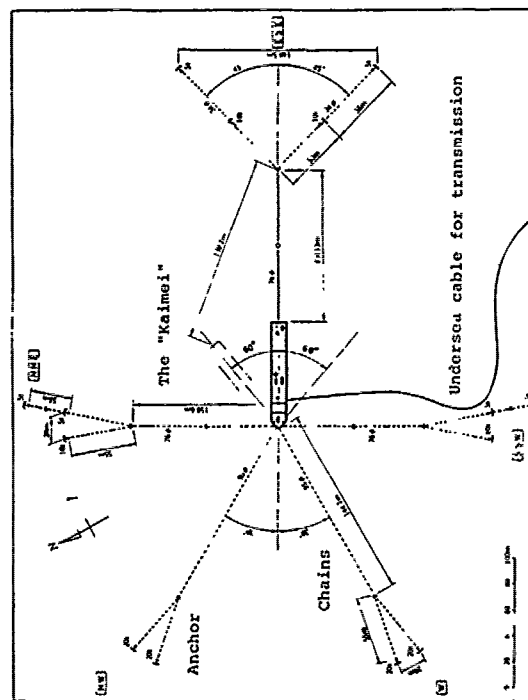


Fig. 3 Outline of Mooring System

Fig.3 illustrates the mooring arrangement. This system was applied to restrict the range of movement due to the use of transmission cables. Although the direction of the bow changed in accordance with the direction of the wind and waves, actual observations showed that its movement was within a 120° range, almost the same figure as had been projected.

The method of mooring calculations was the same as in reference [1]. Design considerations included waves with 1/3 significant wave height of 8m and period of 10 seconds, wind velocity of 100kt, and currents of 3kt. The wind and waves are out of the head of the Kaimei, and a maximum tension of 87 tons was expected on the main mooring lines.

3.4 Generator Units

The alternating air flow generated in the air pump rooms is made to flow in the same direction through the air turbine by the flap valves in the valve box as illustrated in Figures 4 and 5. The difference in air pressure inside and outside the valve box causes the flap valves to open and to close. FRP material which is light and strong is generally used for the valve board. Figure 5 illustrates a 2-valve system in which two air pump rooms are used in pair: one reacting to the upward movement of the waves, and the other, to the downward. Figure 6 shows a 4-valve system whose air pump room reacts to both periods of the waves.

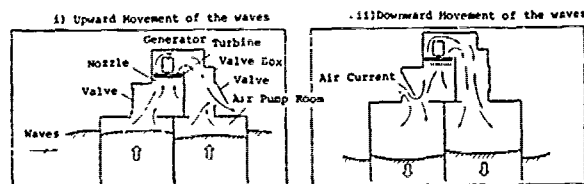


Fig. 4 2-valve System

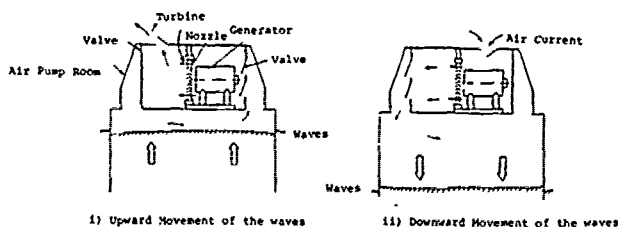


Fig. 5 4-valve System

According to comparative studies made in the water tank tests, it was found that with long-period waves a 4-valve system obtained an output almost twice that of a 2-valve system. Tests are being carried out with a 4-valve system plus a damper tank system as shown in Figure 6. In this case, the air output from the four air

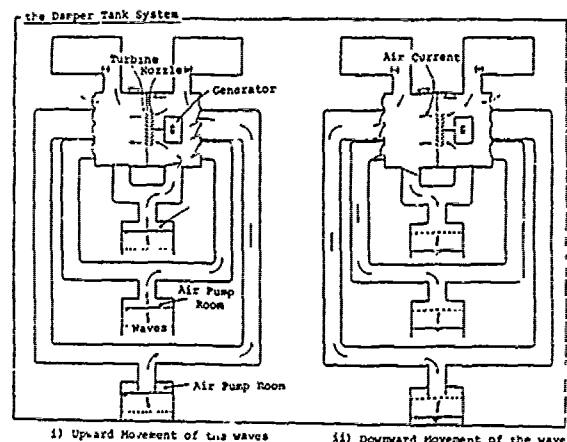


Fig. 6 Damper Tank System

pump rooms are collected to turn one turbine. However, in order to reduce the fluctuation of air pressure as much as possible, one large damper tank is employed for each of the plus and minus sides. This system was applied to unit No.2. While there is an advantage in that the number of turbines and generators are reduced in accordance with the number of air pump rooms, there is also a disadvantage in that the number of valves must be increased to 120 thus requiring the use of a large valve box.

For damper tanks, the buoyancy rooms on the left and right sides of the Kaimei are utilized. Although the tanks in both the plus and minus side have a capacity of approximately 400m³ each, as a result of computer simulation, it was desirable to double the capacity.

An air turbine with a diameter of 1.4m installed aboard the Kaimei is shown in Figure 7. All seven of the Japanese-made units employ the same type of air turbine. As a result of the model tests, impulse turbines with round frontal blades were developed taking into consideration the fluctuations of air flow. Anti-corrosion aluminum alloy (hydronalium) was used for the turbines in order to prevent corrosion by sea water. The turbines were inspected after the first open-sea trials, but no abnormality was observed.

A generator is directly connected to the turbine and made to rotate at the same speed. The six Japanese-made generators, excluding the one employing the damper tank system, are synchronous types and produce 125KW of electrical power at 840rpm. Since the rotation speed of the turbines changes accordance with the fluctuations of the air flow, generated output also changes. The generated electrical power is dissipated in a resistor aboard the Kaimei, and measurements of the electrical current and voltage are observed and recorded.

The generator employing a damper tank system differs in that it is designed to transmit electricity to electrical power systems on land. As a result, it requires the use of an induction generator which

facilitates hook-up to the land power system.

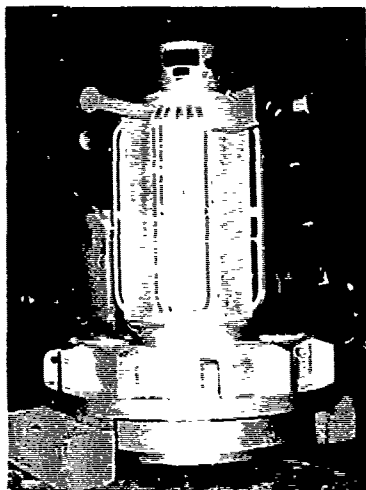


Fig. 7 Turbine and Generator

Japan employed 2 and 4-valve systems, and the U.K., a 4-valve system. Table 1 illustrates the specifications of the generating units of each country participating in the test on the Kaimei.

Table 1 Turbines and Generators on the Kaimei

Country	Japan			U. K.
Item	2-valve	4-valve	4-valve (air-dumper method)	4-valve
Turbine type	Impulse	Impulse	Impulse	50% reaction
Turbine outer diameter	1400 mm	1400 mm	1400 mm	990 mm
Material of turbine	Hydronalium	Hydronalium	Hydronalium	Aluminum-copper alloy
Generator type	Alternating-current synchronous generator (vertical)	Alternating-current synchronous generator (horizontal)	Squirrel-cage induction generator (horizontal)	Alternating-current synchronous generator
Rated output voltage	125KW, 200V	125KW, 200V	125KW, 200V	125KW, 200V
Unit number	Nos 3, 5 and 6	Nos 4, 7 and 9	No 2	No. 8
Number of generators	3	3	1	1

There are also turbines which utilize alternating air flow to rotate in one direction without the use of valve mechanisms.

A non-valve special turbine, called the Wells turbine, was tested on the Kaimei from April 1980.

3.5 Theoretical Analysis

Theoretical analysis was made to clarify essential phenomena of the ship-type model Kaimei, especially the influ-

ence of the air pump room, decrement of wave height, motion of the model, and distribution of air pressure and air output.

The method of theoretical analysis was the same as in reference [2] and was compared with the tank test results. It was clear that air output changed depending on the position of the air pump room. Figure 8 shows that the results of theoretical analysis agree well to the experimental results. By using this theory, the total air output power of the 80 meter Kaimei was found to be 4,000 KW. If efficiency of air output to electrical output was 50%, 2,000 KW of total electrical output would be expected. This value represents the first stage estimate at the beginning of the Kaimei study.

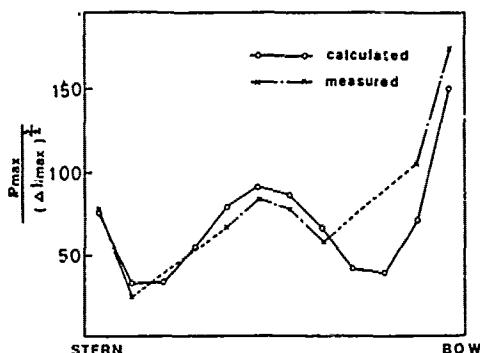


Fig. 8 Variation of Output

3.6 Measurement System

Since the Kaimei was designed for unmanned power generation tests in rough seas, an automated measurement system using reliable apparatus was adopted.

The measurement items can generally be classified as: weather, waves, hull movements, mooring forces, relative wave heights in and out of the air pump room, air pressure in the air pump room, differential pressure of the turbines, revolutions of the turbines, electrical current, voltage, and electrical power. The 82 data items were simultaneously transmitted through a wireless telemeter to the shore station where they were monitored and recorded. Although the major measurement items were under continuous observation, the other items, as a rule, were monitored for 20 minutes (actual time 19 minutes) for every three hours. The monitored data were input into computers at a sampling interval of 0.5 seconds, recorded in magnetic tape, and preserved.

In addition, a control function for transferring the generated electricity to the main land network was also incorporated into the telemeter system.

4. TEST RESULTS

4.1 Waves

Four types of wave height meters

(wave rider, ship-borne wave height meter, ultrasonic wave height meter, and buoy-type wave height meter) were employed in the open-sea tests. The measured data obtained by the wave rider and the ultrasonic wave height meter were very close. Satisfactory results were also obtained from the other wave height meters.

All wave data were analyzed as follows: max, mean and significant wave heights and wave periods were lead by the zero crossing method, spectral density, wave periods defined by wave spectrum and others. Figure 9 shows wave spectrum in storm sea. Figure 10 shows wave power recorded during the first and second open-sea trials.

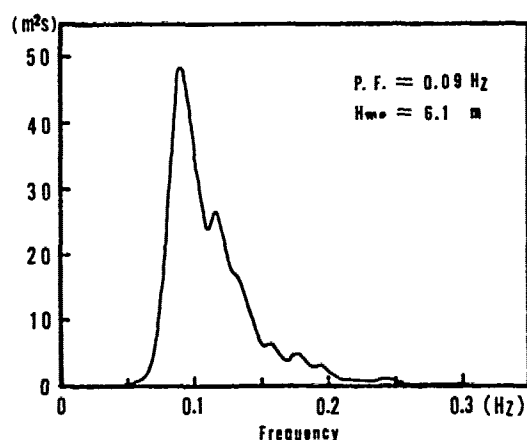


Fig. 9 Wave Spectrum

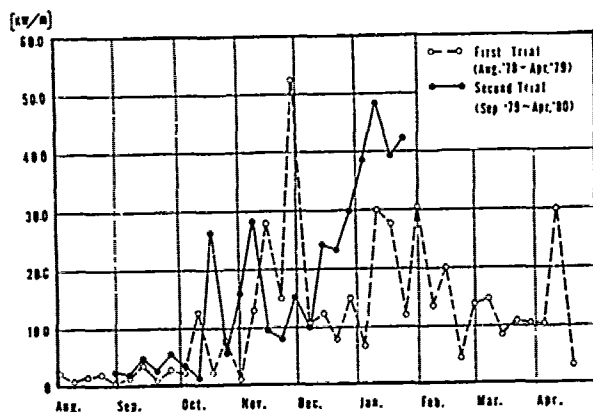


Fig. 10 Wave Power Record

Wave power, P , can be obtained by the following equation:

$$P = \frac{\rho g^2 \tilde{H}_{1/3}^2}{64 \pi} T_p \quad (1)$$

where $\tilde{H}_{1/3}$ is the significant wave height and T_p is peak period of wave spectral density.

In Figure 10, the waves recorded during the first open-sea trial are indicated by the dotted line; that of the second open-sea trial, up until July, is indicated by the solid line. In general, wave power in the winter is higher than

that in summer. Moreover, wave power recorded during the winter of the second open-sea trial was considerably higher than that in the first.

Figure 11 shows the scatter diagram of the second trial. Every point was taken from an analysis of 19 minutes every 3 hours. Wave distribution was mainly 4 - 10 seconds in period and 1 - 4 in wave height.

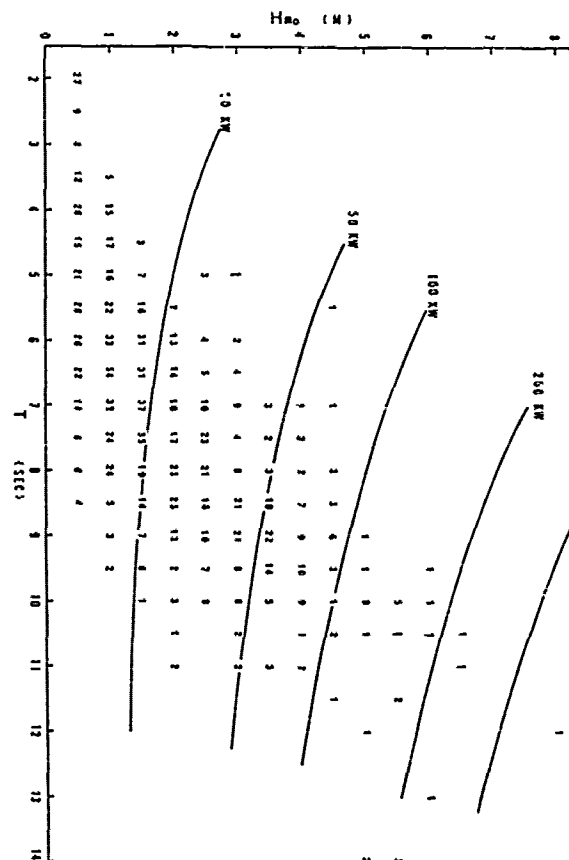


Fig. 11 Scatter Diagram of the Second Trial

Figure 12 shows comparison of $H_{1/3}$ as the 1/3 significant wave height computed by the zero-up crossing method with H_{m0} as computed from the variance spectra density. H_{m0} can be obtained by the equation (2):

$$H_{m0} = 4.004 \sqrt{m_0} \quad (2)$$

$$m_n = \int_0^\infty f^n S(f) df \quad (3)$$

where m_n is the n -th moment of frequency spectrum defined by Eq. (3)

From Fig. 12, the relation of $H_{m0} = 1.05 H_{1/3}$ can be obtained. Then, it is considered that the constant number, 4.004 of Eq. (2) for H_{m0} , requires to be corrected to 3.81. It has been reported that the number 3.81 is applicable to the area of large waves.

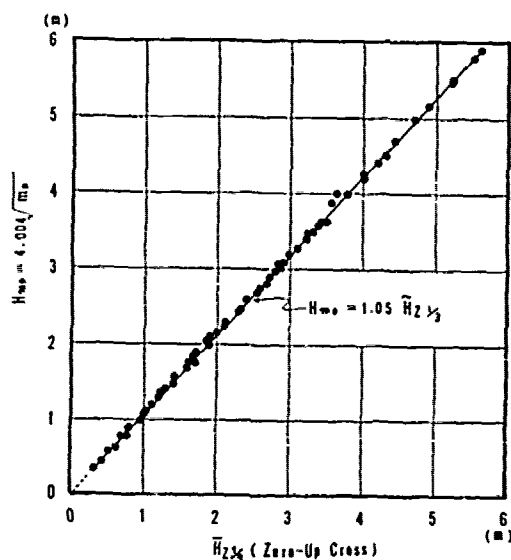


Fig. 12 Comparison of H_{m0} and $\tilde{H}_{1/2}$

In the sea of Japan, this relationship was established from calm seas to storm seas.

According to the statistical theory, the mean zero crossing wave period can be estimated from the frequency spectrum as:

$$\tilde{T}_p \approx (m_0/m_2)^{1/2} \equiv T_{m02} \quad \text{..... (4)}$$

As the mean wave period actually observed in the wave record usually shows some deviation from the value of Eq.(4) due to wave nonlinearity and other reasons, the symbol of T_{m02} is employed to denote the value calculated by Eq.(4). Another mean wave period is defined by:

$$T_{m01} = m_0/m_1 \quad \text{..... (5)}$$

The mean wave periods T_{m01} and T_{m02} are calculated using the formulas by Mitsuyasu(1970) and Ferdinande et al. (1975) as in the following:

$$T_m = 0.7718 T_p ;$$

$$T_m = 0.7104 T_p$$

Actual wave measurements and spectral analyses at the test site showed the difference of the theoretical values.

Fig. 13 and Fig. 14 show comparison of spectral moments with spectral peak. From these figures, T_{m01} , T_{m02} in terms of T_p will be $T_{m01} = 0.69T_p$, $T_{m02} = 0.62T_p$. These values will show little differences against the theoretical values.

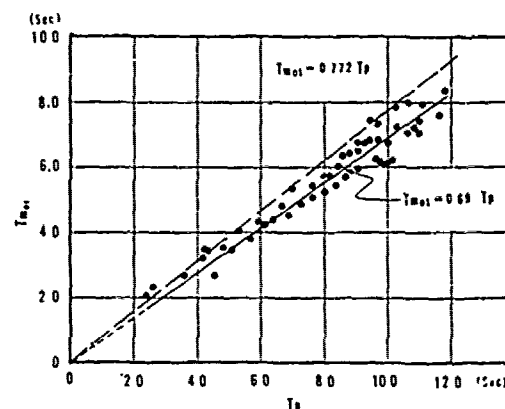


Fig. 13 Comparison of Spectral Moment T_{m01} to T_p

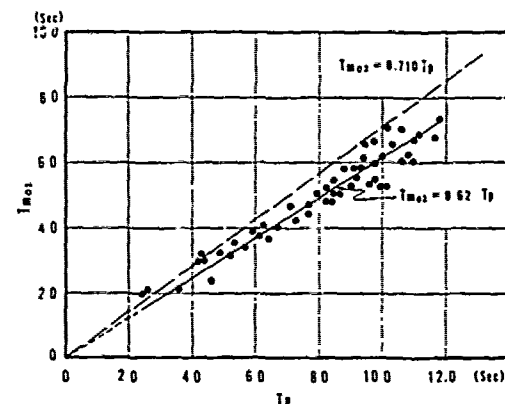


Fig. 14 Comparison of T_{m02} to T_p

4.2 Tension of Mooring Line

The mooring tension was measured by a Strain stall tension meter in the first trials of 1978, and maximum tension was found to be only 50 tons.

Since the Kaimei in the second trials was approximately 200 tons heavier than in the first, the surface area subjected to wind pressure was larger. Consequently, an increase in the mooring force was expected.

The maximum mooring tension recorded during the second trial was 84.4 tons on the NW line, recorded on October 19. Figure 15 shows the data of mooring tension.

On that day, wind direction was 283° , average velocity was 32.4kt, H_s was 5.9m, and H_{max} was 9.1m. Fortunately, this recorded tension value was very close to the estimated 87 ton value. The fluctuations of tension include long period fluctuations of 104 seconds and short period fluctuations of 7.7 seconds. The 7.7 second short period coincides with the pitching period of the Kaimei, while the motion of the 1.4 second long period is considered as the low frequency drift of the Kaimei.

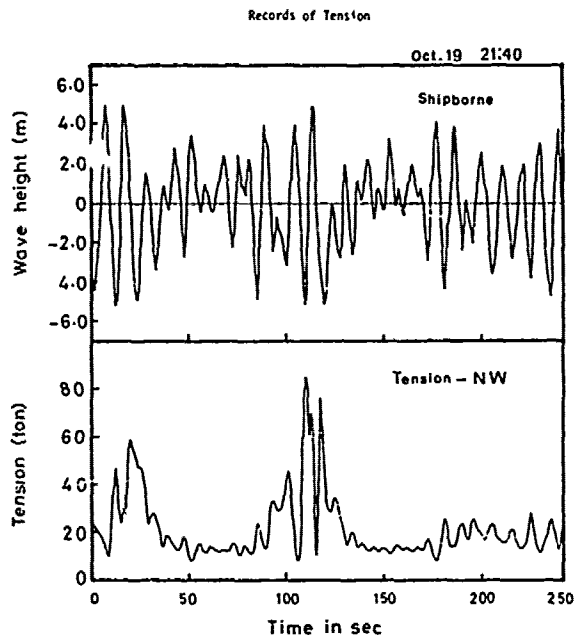


Fig. 15 Record of Wave and Tension(NW)

4.3 Transmission Cable

The electrical power generated by the No.2 induction generator is transmitted to land through a transmission cable laid on the sea bottom. The installation of such a cable to a floating structure is difficult, especially to a floating vessel as the Kaimei which can move freely within a limited range. With the cooperation of an electrical manufacturing company, we have produced a special FRP armored cable which is effective against kinking. The cable between the sea bottom and Kaimei, installed with the combination of weights and buoys shown in Figure 16, gave good results during the first open-sea trials. Consequently, the same method was applied for the second trials. A widely used iron armored cable was employed as the undersea cable.

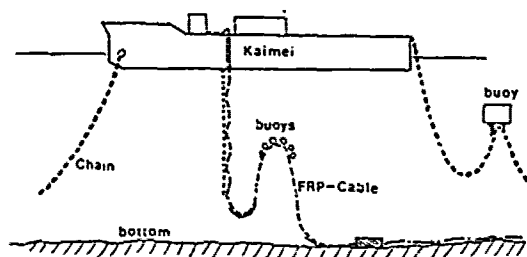


Fig. 16 Installation of Cable

4.4 Relative Wave Height

Since the Kaimei is a floating struc-

ture, it makes pitching, rolling, and heaving movements in conjunction with the elevation of the waves.

These movements influence relative wave height in the air pump rooms.

During the second open-sea trials, relative wave height gauges measured the height of the waves which exert actual influence on the air pump rooms. Two meters each was installed on both sides of the bow, the midship, and the stern.

The measured data are shown in Figure 17. Relative wave height ratios are derived by dividing relative wave heights by significant wave heights at the location of a wave rider.

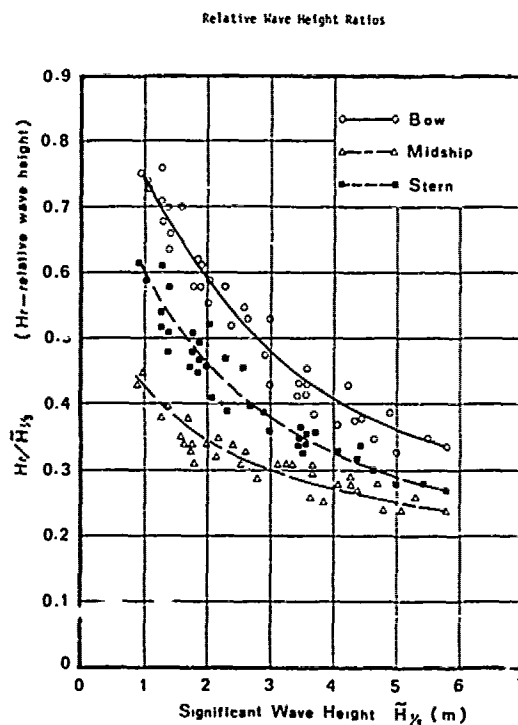


Fig. 17 Relative Wave Height by H_s

When wave height, H_s , increases, wave period and length also increase. As a consequence, the Kaimei begins to pitch, and the relative wave heights at the bow and stern become as low as 50% - 40% below that of the wave height outside. Particularly at midship, wave height is about 3/10 of the wave height outside. Such unexpectedly low relative wave height is a negative factor for increased generated output of the Kaimei. Thus, some improvement must be done to raise relative wave height.

4.5 Generated Output

The major objectives of the experiment were to learn the Kaimei's generated output characteristics and areas for improvement. In this section, the following subjects will be discussed: improvement of

generating output through use of a 4-valve system; output and efficiency of the No.9 generator; test on the electricity network linkage using the No.2 generator; and comparisons between actual output of the generators and results of the water-tank tests.

4.5.1 Improvement of generated output employing the 4-valve system

The 2-valve system operates with a single cycle of the air flow, whereas the 4-valve system operates with alternating air flows. Because it was desirable to reduce the number of valves in designing a valve box for the Kaimei, three 2-valve systems, with only half the number of valves as the 4-valve system, were tested in the first trials.

The results of the water-tank test indicated that the generated output of a 4-valve system, as compared with the 2-valve system, could be increased two-fold with long wave lengths. Based on the above results, in the second trials three 4-valve systems were tested for comparison.

Comparison between the generating outputs of the 2-valve and 4-valve systems is shown in Figure 18. At the start, there was almost no difference between the systems. Later, with an increase in the period, the output of the 4-valve system became twice that of the 2-valve system.

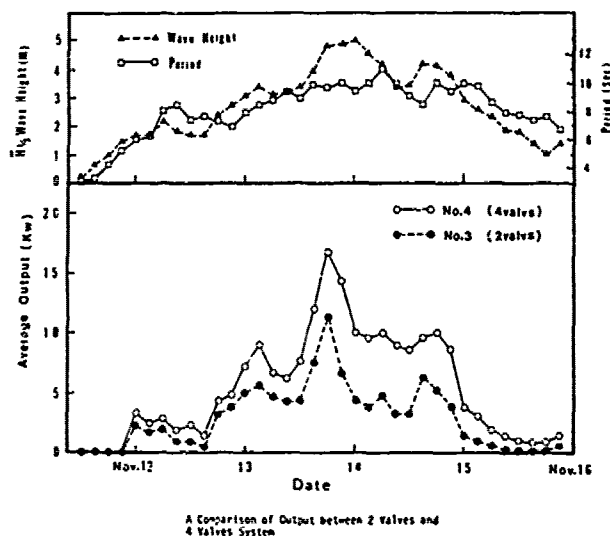


Fig. 18 A Comparison of Output between 2 Valves and 4 Valves System

4.5.2 Output and efficiency of No.9 generator

The generated outputs were highest at the bow and stern of the Kaimei. Since the U.S. unit was not installed at the bow, the No.9 unit installed at the stern generated maximum output. Figure 19 shows the output of the No.9 generator recorded under the large waves of October 19. The waves were recorded at $H_{1/2} = 5.9m$, $H_{max} = 9.8m$,

and $T_{mean} = 6.3$ secs, and maximum and average output were 290 KW and 50 KW respectively.

The generating efficiency of the No.9 unit can be calculated by obtaining the air output from air pressure, P , the inside wave height, H_{in} , of the air chamber, and the generated electricity from electric current and voltage. The resulting efficiency of impulse turbine (No.9), as shown in Figure 20, was 45% - 75%. Efficiency, of course, increased along with air pressure.

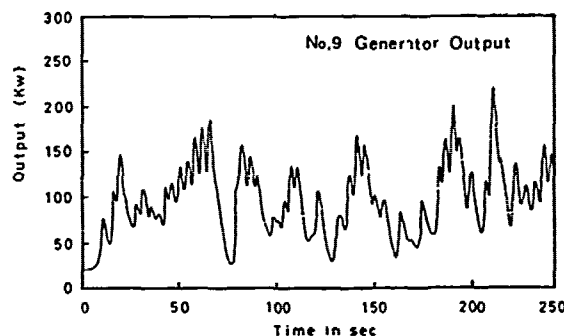


Fig. 19 Generating Conditions of the No.9, 4-Valve Synchronous Generator

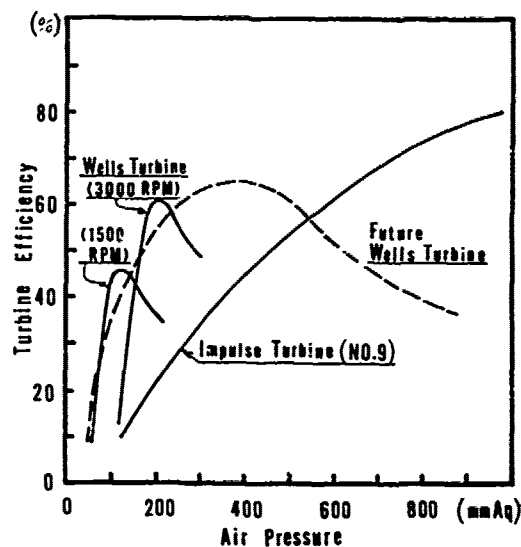


Fig. 20 Turbine Efficiency of Impulse and Wells

4.5.3 Power transmission test (No.2 generator)

The highlight of the second trials was the power transmission test.

This was an epoch-making event, unprecedented in the world. Electricity generated from the No.2 induction generator was transmitted to the electricity system on land through cables.

The experiment on the No.2 generator also included a test on the stabilization of air output employing an air damper tank.

The test of the induction generator linkage to the land system was conducted in December, January, and the middle of April. At first, there were technical problems which included rush currency upon the input of the induction generator, voltage fluctuation of the main power system due to the nature of waves, and self-excitation in case of disconnection. Consequently, the linkage tests were conducted very carefully under joint research with the Tohoku Electric Power Co., Inc. Every test results were below the permissible limit, and thus the tests were completed successfully without any problems.

Results of the long-term continuous transmission test conducted from January 14 to 31 are shown in Table 2. Comparisons are made with results taken from the No.9 unit (synchronous generator) at different significant wave heights.

Table 2 Generated Outputs of the No.2 and No.9 Units in the Latter Half of January

Wave Height (1/3 significant) (m)		0.5	1	2	3	4	5	6
No. 2 Induction Generator	Maximum Output (KW)	20	35	66	9.5	125	150	No data, due to the action of the breaker
	Average Output (KW)	3	5.4	10.4	14.7	20	25	
No. 9 Synchronous Generator	Maximum Output (KW)	5	20	60	110	160	220	300
	Average Output (KW)	0.5	2	7.5	17.5	28	35	50

In order to avoid any influence of voltage fluctuation on the general power system caused by excessively large waves, maximum voltage for the test was limited to 178KW. In fact, when output exceeded 150KW, the breaker would react, and the safety valves in the valve box would open and halt generation. This may have been attributable to a discrepancy in data sampling. During the period of experiment which lasted for half a month, there were seven occasions when generation was stopped automatically because generating output exceeded the limit. The rated output of the induction generator is 125KW.

Its air turbine is the same as other Japanese-made synchronous generators, with a diameter of 1.4m.

Voltage of the generator was 200V, and rotation speed was set at 600RPM in accordance with the 50-cycle main power system. Output, increased to 6000V, was transmitted to the land power system.

4.6 Differences in the Generated Output at Different Locations of the Kaimei

The first open-sea trials recorded the

same generated output for the units installed at the bow and stern of the Kaimei, and one-half of the output value for the one installed at midship. Comparison of the output of the generators during the second trials were made in terms of average output. Figure 21 shows the changes in output of each generator by significant wave heights.

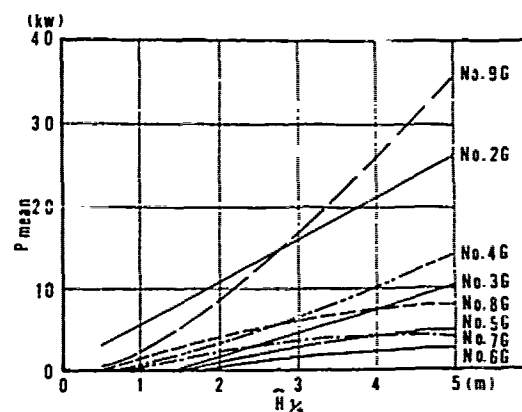


Fig. 21 Average Output for each Generator by Wave Height

4.7 Mean-maximum Generating Output Rates

The biggest problem in improvement of wave power generation is fluctuation of generated output. The cycle of fluctuation runs from 30 secs to 100 secs. Moreover, the ratio of average output over maximum output is about 1/6 - 1/7.

The 4-valve system observed a smaller fluctuation margin than the 2-valve system. The mean-maximum output ratio of 1/6 - 1/7 can be understood as follows:

$$\text{mean}/\text{maximum} = (0.72)^2 / (1.8)^2 = 1/6,$$

where $0.72 \bar{H}_{1/3}$ is average energy wave height, and $1.8 \bar{H}_{1/3}$ is maximum wave height.

During the second trials, the only experiment conducted on normalization of generated output was on the air damper tank method. However the normalization problem is a vital field of study as it may determine whether wave power generation can be utilized commercially.

5. CONCLUSION

The two series of open-sea trials on the wave power generator Kaimei were performed in safety.

a) From actual wave measurements and spectral analyses at the test sites, mean wave periods of T_{m21} , T_{m22} were found to be $0.69T_p$ and $0.62T_p$ respectively.

b) The maximum mooring tension recorded during the second trials was 84.4 tons agreeing to the theoretical results.

- c) The occurrence of power cable kinking between the floating vessel and the sea bottom could be avoided by using an FRP armored cable.
- d) The output of the 4-valve system was twice that of the 2-valve system with long wave periods.
- e) Leakage tests on the No.2 induction generator were completed successfully and without any problem.

ACKNOWLEDGEMENT

The second open sea trial was an International Energy Agency project supported by Japan, UK, USA, Canada and Ireland. The authors are grateful for the permission of the IEA Executive Committee to publish its paper which consists solely of their own interpretations of the data and views which are not necessarily shared by the other participants.

We would like to extend our greatest appreciation to the members of JAMSTEC, and to the researchers both in Japan and abroad for the cooperation and valuable advice which have made the experiments and studies with the Kaimei possible.

REFERENCES

1. Inoue, Y. "The Design Criteria for the Mooring Systems of Offshore Structures", Journal of the Society of Naval Architects of Japan, Vol. 145, June 1979.
2. Miyazaki, T. and Masuda, Y. "Research and Development of Wave Power Generation System", Oceanology International '78, Brighton 1978, pp.45 - 49.
3. Hiramoto, A. "The Theoretical Analysis of an Air Turbine Generation System", Symposium on Wave and Tidal Energy, BHRA Fluid Engineering, Vol. 1, 1978, pp.73 - 84.
4. Masuda, Y. and Miyazaki, T. "Wave Power Electric Generation Study in Japan", Symposium on Wave and Tidal Energy, BHRA Fluid Engineering, Vol. 1, 1978, pp.85 - 92.
5. Masuda, Y. "Experimental Full Scale Result of Wave Power Machine Kaimei in 1978", Symposium on Wave Energy Utilization, Chalmers University of Technology, Sweden, November, 1979, pp.349 - 363.
6. Miyazaki, T. and Masuda, Y. "Tests on the Wave Power Generator Kaimei", Offshore Technology Conference 1980, OTC 3689, pp.101 - 111.

TECHNICAL REFERENCE

In order to evaluate characteristics related to the Kaimei, much of the data were analyzed; and in order to make improvements, several basic tank tests and turbine tests were carried out.

The main results are as follows.

- a) Relative wave height must be increased in order to increase air output, NEL's idea of a side opening with a bottom plate will be one of the promising ideas. The length and depth of the Kaimei, etc., must be reconsidered from this point of view.

- b) Side opening with bottom plate (Figure 22)

This idea was proposed by NEL, U.K. A model Kaimei with a bottom plate showed an increased air pressure ratio of about 1.6 - 2 times of that without a bottom plate. Therefore, a 2.5 - 4 fold increase in air output can be expected through this method.

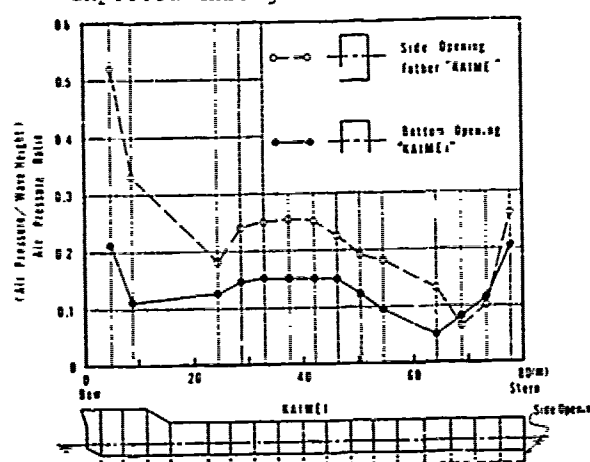


Fig. 22 Comparison of Air Pressure Ratio of a Kaimei Model with and without bottom plate

- c) Turbine nozzle ratio (turbine nozzle area/air pump room area)

A 1/230 nozzle throttle ratio was adopted for Kaimei's turbine, but the tank test with the 8m model indicated that a 1/75 nozzle throttle ratio was best and would increase power 1.8 times greater than that with a 1/230 nozzle throttle ratio.

- d) Wells turbine test result

A non-valve wells turbine of 0.6m diameter with 4 wings operated on the Kaimei. Its energy conversion efficiency was found to be relatively high (more than 60%) with very small waves, and its features of high speed rotation and simple construction may greatly decrease the cost of turbine and generator units. Figure 20 shows a comparison of turbine efficiency between the wells turbine and the impulse turbine. The impulse turbine shows low efficiency with low air pressure and high efficiency with high air pressure. The wells turbine, however, showed high efficiency with low air pressure and low efficiency with high air pressure. This different characteristic may give a safety factor to the wells turbine in very high seas.

e) Damper tank model test

The damper tank method represents one way of smoothing wave power.

It was tested using the 8 m model and the entire buoyancy room as the damper tank.

Smoothing effect was observed. A main feature of this method entailed decreasing the nozzle throttle ratio. A ratio of 1/400 gave maximum output, therefore turbine diameter will be relatively small with Damper tank method.

f) Output normalization methods

Output normalization methods, and its water tank testing must be researched.

Since the damper tank is not sufficient for output normalization of 1 - 2 minute variations, use of a fly wheel, etc. must be researched.

Discussion

B.M. Count (UK Central Electricity Generating Board)

I would like to congratulate Mr. Masuda on establishing the feasibility of wave power with the construction of KAIMEI. I would just like to add that in the UK we are very interested in using air turbines for wave energy absorption. We have analyzed and tested the Well's Turbine which requires no valves to operate in a cyclic flow.

Our tests confirm our theory that efficiencies of about 70% can be obtained

in steady air flow and welcome the activities of JAMSTEC in this area.

Author's Reply

Y. Masuda (JAMSTEC)

Our test result of the Wells turbine is shown in Fig. 20.

Efficiency was more than 60%, it agrees to UK's theoretical analysis. Non valve turbine is very useful for improvement of KAIMEI, but further study including hydrodynamic is necessary to develop this turbine.

LIST OF PARTICIPANTS

BRASIL

Nishimoto, Kazuo, Univ. of São Paulo

BULGARIA

Khadjimihalev, P., Bulgarian Ship Hydrodynamics

CANADA

Miles, M.D., National Res. Council

Murdey, David C., National Res. Council

Schmitke, R.T., Defence Res. Est. Atlantic

CHINA

Chen, Chiu-Si, China Ship Sci. Res. Ctr.

Fang, Wen-Chun, China Ship Sci. Res. Ctr.

Gu, Mao-Xiang, China Ship Sci. Res. Ctr.

Hsueh, Chung-Chuan, Huazhong Inst. of Tech.

Jiang, Ci-Ping, Shanghai Jiao Tong Univ.

Liu, Da-Kai, East China College of Hydraulic Eng.

Ma, Tao, Shanghai Ship Design and Res. Inst.

Xu, Wei-De, Harbin Shipbuilding Eng. Inst.

DENMARK

Munk, Torben, Danish Ship Res. Lab.

EGYPT

Edvis, Bakri, Egyptian Shipbuilding & Repair Co., Ltd.

FINLAND

Kostilainen, Valter, Helsinki Univ. of Tech.

FRANCE

Aucher, Max, Ingr. Bassin d'Essais des Carenes

Balquet, Bassin d'Essais des Carenes

Cordonnier, J.P.V., Ecole National Supérieure de Mécanique

Dern, Jean-Claude, Bassin d'Essais des Carenes

Lecoffre, Yves, NEYRTEC

Le Goff, Jean Pierre, Direction des Recherches, Etudes et Techniques

Rowe, Alain Robert, Inst. de Mécanique de Grenoble

FEDERAL REPUBLIC OF GERMANY

Albrecht, Klaus, Fraunhofer-Institut für Hydroakustik

Blume, Peter, Hamburgische Schiffbau-Versuchsanstalt

Feischer, Klaus Peter, Versuchsanstalt für Wasserbau und Schiffbau

Krappinger, Odo, Hamburgische Schiffbau-Versuchsanstalt

Kux, Jürgen H., Institut für Schiffbau

Laudan, Jochen, Hamburgische Schiffbau-Versuchsanstalt

Merbt, Horst, Fraunhofer-Institut für Hydroakustik

Müller-Graf, Burkhard, Versuchsanstalt für Wasserbau und Schiffbau

Nowacki, Horst, Tech. Univ. Berlin

Oltmann, Peter, Institut für Schiffbau

Papanikolaou, Apostolos, Tech. Univ. Berlin

Remmers, Bernd, Kempf & Remmers

Schmiechen, Michael, Versuchsanstalt für Wasserbau und Schiffbau

Weitendorf, Ernst-August, Hamburgische Schiffbau-Versuchsanstalt

Wolff, Karsten, Institut für Schiffbau

ISRAEL

Dagan, Gedeon, Tel-Aviv Univ.

Miloh, Touvia, Tel-Aviv Univ.

ITALY

Bellone Guglielmo, Cantieri Navali Riuniti
Podenzana-Bonvino, Carlo, CE. TE. NA. S.p.A. Genova

JAPAN

Abe, Mitsuhiro, Mitsui E & S Co.
Adachi, Hiroyuki Ship Research Inst.
Aizawa, Koji, Niigata Eng. Co.
Ando, Noritaka, Shipbuilding Res. Ass. of Japan
Arai, Makoto, Ishikawajima-Harima Heavy Ind.
Arakawa, Chuichi, Univ. of Tokyo
Ashidate, Isao, Nippon Kokan K.K.
Azuma, Tetsuro, Osaka Shipbuilding Co.
Bessho, Masatoshi, National Defense Academy
Chiba, Noritane, Mitsubishi Heavy Ind.
Fujii, Hitoshi, Mitsubishi Heavy Ind.
Fujimoto, Ryosuke, Nippon Kokan K.K.
Fujimura, Hiroshi, Mitsubishi Heavy Ind.
Fujino, Masataka, Univ. of Tokyo
Fujino, Ryosuke, Ishikawajima-Harima Heavy Ind.
Fukuda, Jun-ichi, Kyushu Univ.
Fuwa, Takeshi, Ship Research Inst.
Hamano, Kazuo, Mitsui E & S Co.
Hasegawa, Kazuhiko, Hiroshima Univ.
Hatano, Shuji, Hiroshima Univ.
Hayashi, Nobuyuki, Niigata Eng. Co.
Himeno, Yoji, Univ. of Osaka Prefecture
Hirano, Masayoshi, Mitsui E & S Co.
Hirano, Susumu, Univ. of Osaka Prefecture
Hirayama, Tsugukiyo, Yokohama National Univ.
Hoshino, Tetsuji, Mitsubishi Heavy Ind.
Hosoda, Ryusuke, Univ. of Osaka Prefecture
Hotta, Takio, Hiroshima Univ.

Ikebuchi, T. Kawasaki Heavy Ind.
Ikeda, Yoshiho, Univ. of Osaka Prefecture
Ikegami, Kunihiko, Mitsubishi Heavy Ind.
Ikehata, Mitsuhsa, Yokohama National Univ.
Imazu, Hayama, Tokyo Univ. of Mercantile Marine
Inoue, Shosuke, Kyushu Univ.
Inoue, Yoshiyuki, Yokohama National Univ.
Inui, Takao, Univ. of Tokyo
Isshiki, Hiroshi, Hitachi S & E Co.
Ito, M., Kobe Steel Co.
Iwata, Tatsuzo, Mitsui E & S Co.
Jinnaka, Tatsuo, Nagasaki Inst. of Applied Science
Jingu, Norio, Nippon Kokan K.K.
Jingu, Norio, Nippon Koban K.K.
Kadoi, Hiroyuki, Ship Research Inst.
Kagemoto, Hiroshi, Ship Research Inst.
Kai, G., Japan Marine Sci. & Tech. Ctr.
Kaiho, Toshimitsu, Japan Defense Agency
Kaizu, Genji, Nakashima Propeller Co.
Kajitani, Hisashi, Univ. of Tokyo
Kan, Makoto, Ship Research Inst.
Kano, Masayoshi, Hitachi S & E Co.
Karasuno, Keiichi, Kobe Univ. of Mercantile Marine
Kasahara, Yoshikazu, Nippon Kokan K.K.
Kashiwadani, Tatsuo, Japan Defense Agency
Kato, Hiroharu, Univ. of Tokyo
Kato, Naomi, Tokai Univ.
Kawaguchi, Noboru, Mitsubishi Heavy Ind.
Kawashima, Toshihiko, National Research Inst. of Fishery's Eng.
Kayo, Yoshio, Mitsubishi Heavy Ind.
Kijima, Katsuro, Kyushu Univ.
Kinoshita, Masao, Hitachi S & E Co.
Kinoshita, Takeshi, Univ. of Tokyo
Kishi, Yasutaro, Mitsui E & S Co.
Kishimoto, Masahiro, Nippon Kokan K.K.
Kishimoto, Osamu, Mitsui E & S Co.
Kitazawa, Takamune, Hitachi S & E Co.

Kobayashi, Masanori, Mitsui E & S Co.
 Kodama, Yoshiaki, Ship Research Inst.
 Kodan, Norihisa, Nippon Kokan K.K.
 Koga, Shigeichi, Shipbuilding Res. Ass. of Japan
 Kojima, Ryoichi, Hitachi S & E Co.
 Komatsu, Masahiko, Japan Defense Agency
 Koyama, Koichi, Ship Research Inst.
 Koyama, Takeo, Univ. of Tokyo
 Kudo, Kimaki, Hiroshima Univ.
 Kunitake, Yoshikuni, Mitsui E & S Co.
 Kuroi, Masaaki, Hitachi S & E Co.
 Kusaka, Mikio, Osaka Shipbuilding Co.
 Kusaka, Yuzo, Mitsui E & S Co.
 Kyozuka Yusaku, National Defense Academy
 Maeda, Hisaaki, Univ. of Tokyo
 Makizono, Masataka, Yamashita Shin Nihon Steamship Co.
 Maruo, Hajime, Yokohama National Univ.
 Masumoto, Akira, Akashi Ship Model Basin
 Masuda, Koichi, Nihon Univ.
 Masuda, Yoshio, Japan Marine Sci. & Tech. Ctr.
 Masuyama, Yutaka, Kanazawa Inst. of Tech.
 Matsui, Masahiro, Hitachi S & E Co.
 Matsumoto, Norihiro, Nippon Kokan K.K.
 Matsumura, Kiyoshige, Osaka Univ.
 Matsuoka, Tsuyoshi, Japan Defense Agency
 Minematsu, Hiroshi, Ishikawajima-Harima Heavy Ind.
 Miyata, Hideaki, Univ. of Tokyo
 Miyazaki, T., Japan Marine Sci. & Tech. Ctr.
 Miyazawa, Masaru, Mitsubishi Heavy Ind.
 Mizoguchi, Sumitoshi, Ishikawajima-Harima Heavy Ind.
 Mizuno, Toshiaki, National Defense Academy
 Mokunaka, Masaru, Hitachi S & E Co.
 Mori, Kazuhiro, Hiroshima Univ.
 Mori, Masahiko, Ishikawajima-Harima Heavy Ind.
 Moriyama, Fumio, Ship Research Inst.
 Matora, Seizo, Univ. of Tokyo
 Murahashi, Tatsuya, Hitachi S & E Co.

Murakami, Mitsunori, Hitachi S & E Co.
 Murakami, T., Japan Defense Agency
 Murao Rin-ichi, Aoyama Gakuin Univ.
 Muraoka, Kenji, Ishikawajima-Harima Heavy Ind.
 Nagamatsu, Nobuo, Kawasaki Heavy Ind.
 Nagamatsu, Shuichi, Sumitomo Heavy Ind.
 Nagamatsu, Tetsuo, Mitsubishi Heavy Ind.
 Naito, Shigeru, Osaka Univ.
 Nakamura, Shirochi, Osaka Univ.
 Nakashima, Minoru, Nakashima Propeller Co.
 Nakatake, Kuniharu, Kyushu Univ.
 Nakato, Michio, Hiroshima Univ.
 Nakazaki, Masatoshi, Osaka Shipbuilding Co.
 Narita, Hitoshi, Mitsui E & S Co.
 Narita, Shuumei, Nippon Kokan K.K.
 Nomoto, Kensaku, Osaka Univ.
 Nonaka, Koji, Ship Research Inst.
 Nozawa, Kazuo, Kawasaki Heavy Ind.
 Numata, T., Mitsui Ocean Dev. Eng.
 Obotaka, Jun, Sumitomo Heavy Ind.
 Ogawa, Akihiro, Ship Research Inst.
 Ogino, Shigeyuki, Sanoyasu Dockyard Co.
 Ogiwara, Seikoo, Ishikawajima-Harima Heavy Ind.
 Ogura, Michihito, West Japan Fluid Eng. Lab. Co.
 Ohkusu, Makoto, Kyushu Univ.
 Ohtagaki, Yoshio, Ishikawajima-Harima Heavy Ind.
 Ohtsu, K., Tokyo Univ. of Mercantile Marine
 Okamoto, Hiroshi, Kawasaki Heavy Ind.
 Okamura, Naoaki, Ishikawajima-Harima Heavy Ind.
 Okai, Akio, Mitsubishi Heavy Ind.
 Oku, M., Kobe Steel Co.
 Okuno, Taketoshi, Univ. of Osaka Prefecture
 Onogi, Hiroshi, Nippon Kokan K.K.
 Orito, Hironobu, Mitsui O.S.K. Line
 Oshima, Masanao, Mitsui E & S Co.
 Saito, Kimio, Osaka Univ.
 Saito, Yasuo, Akashi Ship Model Basin

Sakai, Sakae, Yamashita Shin Nihon Steamship Co.
 Sasaki, Noriyuki, Sumitomo Heavy Ind.
 Sato, Kazunori, Shipbuilding Res. Ctr. of Japan
 Sato, Ryuichi, Ishikawajima-Harima Heavy Ind.
 Seo, Akio, Nippon Kokan K.K.
 Seto, Hideyuki, Mitsubishi Heavy Ind.
 Shimomura, Yoshihiro, Sumitomo Heavy Ind.
 Shimoyama, K., Kawasaki Heavy Ind.
 Shintani, Atsushi, Japan Defense Agency
 Shirakami H., Hitachi S & E Co.
 Shiraki, Akira, Nippon Kokan K.K.
 Shiroye, Yasushi, Ishikawajima-Harima Heavy Ind.
 Shoji, Kuniaki, Tokyo Univ. of Mercantile Marine
 Sudoh, Masanobu, Nippon Kokan K.K.
 Sugai, Kazuo, Ship Research Inst.
 Sugano, Hiroshi, Nakashima Propeller Co.
 Sugimura, Yasushi, Mitsui E & S Co.
 Sujaku, Ken, Niigata Eng. Co.
 Suzuki, Katsuo, National Defense Academy
 Tagori, Tetsuo, Univ. of Tokyo
 Takada, Kazumi, Sumitomo Heavy Ind.
 Takagi, Matao, Hitachi S & E Co.
 Takahashi, Hajime, Ship Research Inst.
 Takahashi, Takeshi, Mitsubishi Heavy Ind.
 Takahashi, Yoji, Ishikawajima-Harima Heavy Ind.
 Takaishi, Yoshifumi, Ship Research Inst.
 Takahei, Tetsuo, Akashi Ship Model Basin
 Takaki, Mikio, Kyushu Univ.
 Takekawa, Masao, Sumitomo Heavy Ind.
 Takeshi, Haruya, Ship Research Inst.
 Takezawa, Seiji, Yokohama National Univ.
 Tamai, Hiromasa, Akashi Ship Model Basin
 Tamashima, Masahiro, West Japan Fluid Eng. Lab. Co.
 Tamiya, Shin, Univ of Tsukuba
 Tamura, Kinya, Mitsubishi Heavy Ind.
 Tanaka, Akira, Kawasaki Heavy Ind.

Tanaka, H., Japan Defense Agency
 Tanaka, Hiraoku, Ship Research Inst.
 Tanaka, Hirohisa, Yokohama National Univ.
 Tanaka, Ichiro, Osaka Univ.
 Tanaka, Kunio, Ishikawajima-Harima Heavy Ind.
 Tanaka, Minoru, Ishikawajima-Harima Heavy Ind.
 Tasaki, Ryo, Ishikawajima-Harima Heavy Ind.
 Terao, Yutaka, Tokai Univ.
 Toki, Naoji, Mitsubishi Heavy Ind.
 Torige, Keizo, Nippon Kokan K.K.
 Tominaga, Hiroyuki, Sasebo Heavy Ind.
 Tomita, Tetsujiro, Mitsui E & S Co.
 Tsuda Tatsuo, Akashi Ship Model Basin
 Tsukada, Osamu, Nippon Kokan K.K.
 Tsukamoto, Osamu, Mitsubishi Heavy Ind.
 Tsutsumi, Takayuki, Ishikawajima-Harima Heavy Ind.
 Ueda, Takayasu, Ship Research Inst.
 Uematsu, Mikio, Nippon Kokan K.K.
 Ukon, Yoshitaka, Ship Research Inst.
 Watanabe Akira, Yamashita Shin Nihon Steamship Co.
 Watanabe, Iwao, Ship Research Inst.
 Watanabe, Takanori, Mitsubishi Heavy Ind.
 Yamaguchi, Masahiro, Ship Research Inst.
 Yamaguchi, Masayuki, Nippon Kokan K.K.
 Yamamoto, Osamu, Nippon Kokan K.K.
 Yamamoto, Shigeru, Akashi Ship Model Basin
 Yamano, Tadao, Kawasaki Heavy Ind.
 Yamanouchi, Yasufumi, Mitsui E & S Co.
 Yamasaki, S., Kobe Steel Co.
 Yamashita, Masao, Japan Defense Agency
 Yamashita, Seiya, Ishikawajima-Harima Heavy Ind.
 Yamazaki, Ryusuke, Kyushu Univ.
 Yazaki, Atsuo, Oil Spill Prevention Inst.
 Yokoo, Koichi, Shipbuilding Res. Ctr. of Japan
 Yoshida, Yasushi, Japan Defense Agency
 Yoshino, Nobuharu, Mitsui E & S Co.

Yuasa, Hajime, Mitsui E & S Co.

Yuguchi, T., Hitachi S & E Co.

Yumuro, Akinori, Ishikawajima-Harima Heavy Ind.

KOREA

Hong, Sung-Wan, Inha Univ.

Hwang, J. H., Seoul National Univ.

Kim, Bong Geon, Hyundai Heavy Ind.

Kim, Hun Chol, Korea Res. Inst. of Ships

Kim, Jae Shin, Hyundai Heavy Ind.

Lee, Byung Ha, Hyundai Heavy Ind.

Lee, Chang-Sup, Korea Res. Inst. of Ships

THE NETHERLANDS

Hoekstra, M., Netherlands Ship Model Basin

Muntjewerf, J.J., Netherlands Ship Model Basin

Oosterveld, M.W.C., Netherlands Ship Model Basin

van der Meulen, J.H.J., Netherlands Ship Model Basin

van Gent, W., Netherlands Ship Model Basin

van Oortmerssen, G. Netherlands Ship Model Basin

van Sluys, M.F., Netherlands Ship Model Basin

NORWAY

Faltinsen, Odd M., Norwegian Inst. of Tech.

Gisvold, Kaare M., Norwegian Hydrodynamic Lab.

Huse, Erling, Norwegian Hydrodynamic Lab.

Minsaas, Kunt J., The Ship Res. Inst. of Norway

Persson, Bror, Det norske Veritas

Tørum, Alf, Norwegian Hydrodynamic Lab.

Walderhaug, Harald, Norwegian Inst. of Tech.

SPAIN

Gomez, G. Perez, Astilleros Españoles S.A.

SWEDEN

D. Gilbert, Swedish Maritime Res. Ctr.

Larsson, Lars, Swedish Maritime Res. Ctr.

Rutgersson, Olle, Swedish Maritime Res. Ctr.

Wahl, Gösta, Swedish Maritime Res. Ctr.

UNITED KINGDOM

Bishop, R.E.D., Univ. College London

Bowden, Brian, National Maritime Inst.

Count, Brian Morrison, Central Electricity Generating Board

Davies, Melvyn E., National Maritime Inst.

Knight, Gerald, British Hovercraft Corp.

Odabasi, Yücel, The British Ship Res. Ass.

Rowe, Stephen J., National Maritime Inst.

Stevens, Martin John, British Hovercraft Corp.

Suhrbier, K.R., Vosper Thornycroft (UK), Ltd.

Ursell, Fritz Joseph, Univ. of Manchester

U.S.A.

Bai, Kwang June, DTNSRDC

Baldwin, John L., U.S. Navy

Bales, Nathan K, DTNSRDC

Bhattacharyya, R., U.S. Naval Academy

Billet, Michael L., Pennsylvania State Univ.

Carrier, George F., Harvard Univ.

Chan, Robert K.C., JAYCOR

Chang, Ming-Shun, DTNSRDC

Coder, David W., DTNSRDC

Cooper, Ralph D., Office of Naval Research

Eda, Haruzo, Stevens Inst. of Tech.

Fein, James A., DTNSRDC

Furuya, Okitsugu, Tetra Tech, Inc.

Haren, Pierre, Massachusetts Inst. of Tech.

Hsu, C.C., Hydronautics, Inc.

Huang, Thomas T., DTNSRDC

Hunt, Lee M., National Research Council

Johnson, Bruce, U.S. Naval Academy

Keane, Robert, Naval Sea Systems Command

Kennell, Colen, Naval Sea Systems Command

Landweber, Louis, Univ. of Iowa

Lee, Choung Mook, DTNSRDC

Lin, Wen C., DTNSRDC

Mac Lane, Saunders, National Academy of Sciences

McCarthy, Justin H., DTNSRDC

Magnuson, Allen H., V.P.I. & S.U.

Marcus, Rudolph J., Office of Naval Research

Mei, Chiang C. Massachusetts Inst. of Tech.

Monacella, Vincent, DTNSRDC

Morgan, Wm B., DTNSRDC

Naghdi, Paul M., Univ. of California

Newman, J. Nicholas, Massachusetts Inst. of Tech.

Noblesse, Francis, Massachusetts Inst. of Tech.

Ochi, Margaret D., DTNSRDC

Ogilvie, T. Francis, Univ. of Michigan

Parkin, Blaine R., Pennsylvania State Univ.

Patel, Virendra C., Univ. of Iowa

Peterson, F.B., DTNSRDC

Pool, James C.T., Office of Naval Research

Powell, Alan, DTNSRDC

Sclavounos, Paul, Massachusetts Inst. of Tech.

Sedgwick, Dean L., U.S. Naval S&T Group, Far East

Shen, Young T., DTNSRDC

St. Denis, M., Univ. of Hawaii

Takashima, Gary T., U.S. Naval S&T Group, Far East

Tulin, Marshall P., Hydronautics, Inc.

van Eseltine, Richard T., DTNSRDC

Wehausen, John, Univ. of California

Wu, Theodore Y., California Inst. of Tech.

Yim, Bohyun, DTNSRDC

U.S.S.R

Kuznetsov, Y.I., Krylov Shipbuilding Res. Inst.

Nikolaev, Evgeny, Krylov Shipbuilding Res. Inst.

YUGOSLAVIA

Vucinic, Alice, Univ. of Rijeka

PREVIOUS BOOKS IN THE NAVAL HYDRODYNAMICS SERIES

"First Symposium on Naval Hydrodynamics."
National Academy of Science-National Research
Council, Publication 515, 1957. Washington,
D. C.; PB133732.

"Second Symposium on Naval Hydrodynamics:
Hydrodynamic Noise and Cavity Flow," Office
of Naval Research, Department of the Navy,
ACR-38, 1958; PB157668.

"Third Symposium on Naval Hydrodynamics:
High Performance Ships," Office of Naval
Research, Department of the Navy, ACR-65,
1960; AD430729.

"Fourth Symposium on Naval Hydrodynamics:
Propulsion and Hydroelasticity," Office of
Naval Research, Department of the Navy,
ACR-92, 1962; AD447732.

"The Collected Papers of Sir Thomas Havelock on
Hydrodynamics," Office of Naval Research,
Department of the Navy, ACR-103, 1963;
AD623589.

"Fifth Symposium on Naval Hydrodynamics: Ship
Motions and Drag Reduction," Office of Naval
Research, Department of the Navy, ACR-112,
1964; AD640539.

"Sixth Symposium on Naval Hydrodynamics:
Physics of Fluids, Maneuverability and Ocean
Platforms, Ocean Waves, and Ship-Generated
Waves and Wave Resistance," Office of Naval
Research, Department of the Navy, ACR-136,
1966; AD676079.

"Seventh Symposium on Naval Hydrodynamics:
Unsteady Propeller Forces, Fundamental
Hydrodynamics, Unconventional Propulsion,"
Office of Naval Research, Department of the
Navy, DR-148, 1968; AD721180.

"Eighth Symposium on Naval Hydrodynamics:
Hydrodynamics in the Ocean Environment,"
Office of Naval Research, Department of the
Navy, ACR-179, 1970; AD748721.

"Ninth Symposium on Naval Hydrodynamics:
Unconventional Ships, Ocean Engineering,
Frontier Problems," Office of Naval Research,
Department of the Navy, ACR-203, 1972; Two
Volumes; Vol. 1, ADA010505; Vol. 2,
ADA010506.

"Tenth Symposium on Naval Hydrodynamics:
Hydrodynamics for Safety, Fundamental
Hydrodynamics," Office of Naval Research,
Department of the Navy, ACR-204, 1974;
ADA022379.

"Eleventh Symposium on Naval Hydrodynamics:
Unsteady Hydrodynamics of Marine Vehicles,"
Office of Naval Research, Department of the
Navy. Also available from Mechanical
Engineering Publications Limited, London and
New York.

"Twelfth Symposium on Naval Hydrodynamics:
Boundary Layer Stability and Transition, Ship
Boundary Layers and Propeller Hull In-
teraction, Cavitation, Geophysical Fluid
Dynamics," Office of Naval Research,
Department of the Navy. Also available from
Office of Publications National Academy of
Sciences, 2101 Constitution Avenue, N.W.
Washington, D.C. 20418.

NOTE: The above books are available on
microfilm and microfiche from the
National Technical Information Service,
U.S. Department of Commerce,
Springfield, Virginia 22151. Some early
issues are also available in paper copies.
The catalog numbers, as of the date of
this issue, are shown for each book.